Proceedings Book

XVII

CLCA 2016

Latin American Conference on Automatic Control

Medellín - Colombia

Editors

Gómez A,
Henao S,
Quintero O. L.
Universidad EAFIT

ISBN: 978-958-8483-37-5

October 13th-15th, 2016

IFAC INTERNATIONAL FEDERATION OF AUTOMATIC CONTROL

AMCA

AADECA Asociación Argentina de Control Automático

ACCA

REPCA RED PERUANA DE CONTROL Y AUTOMATIZACIÓN

UNAM

Pontificia Universidad JAVERIANA Colombia

UNIVERSIDAD EAFIT Vigilada Mineducación

Universidad de los Andes Colombia

RIELAC revista de ingeniería electrónica, automática y comunicaciones

UNIVERSIDAD DE ANTIOQUIA 1803

DACI

UNIVERSIDAD NACIONAL DE COLOMBIA

Sciences School of Universidad EAFIT | Departament of Mathematics Universidad EAFIT | Mathematical Modeling Research Group - Universidad EAFIT

CONFERENCE PROCEEDINGS

Editors
Alejandro Gómez, Sarah Henao, and O. Lucia Quintero
ISBN: 978-958-8483-37-5

Conference proceedings of the
XVII LATIN AMERICAN CONFERENCE IN AUTOMATIC CONTROL
Universidad EAFIT
School of Sciences
2016

Preface / Acknowledgments

On behalf of the School of Sciences of Universidad EAFIT, we would like to thank all those who made the XVII Latin American Conference on Automatic Control and this proceedings book possible.

Of course as a conference, the objectives to share technical discussions and experiences, allowed many students to learn how to construct a real society of Control Engineers. Nothing is perfect but we are completely sure that this conference will lead us to improve and enhance our skills for research. Academic friction is essential to grow but we need to look ahead and work on the top research areas to build a new era of Automatic Control, without forget the basics.

The successful completion of a project like this requires the help and cooperation of many people. First of all, we would like express our sincere thanks the authors that contributed to the conference and submitted their papers. They trusted us and received our comments and improved their work. The papers submitted from all around Latin America and Europe were the core of the project and the level of their work has raised the level of the School of Sciences and the university. We greatly appreciate the authors for giving us the opportunity in putting together this book and joined the conference. The work of each one of the authors was crucial in creating this book and in the success of the conference.

It was a great pleasure to work along side with our colleagues from different countries. We would also like to express our appreciation to the reviewers that participated in this project. Their dedication to the execution of the conference is truly noticed. Each paper had three reviewers in the submission/acceptation process and after the conference a new review from the chair team. I feel to acknowledge a deep sense of gratitude to our colleagues because of their support and hard work during the evaluations post conference and the conference courses (pre -during -post) in which the students had the possibility to learn from real experts about several applied and theoretical topics.

The successful execution of the conference is also due to the hard work and availability of the chair committee who has been irreplaceable. The chairmen who participated in this project had the responsibility of choosing the top papers of this conference in which we sent to the RIELAC Journal.

Furthermore, we would like to share our gratitude for Juan Fernando Duque Cardona from the CEC (Centro de Educación Continua) for his undeniable patience. This project would not have been possible without the cooperation of Alejandro Gómez Montoya, Luz Elena Giraldo, Lina Marcela Duque and Sarah Henao Gallego on their commitment on the project “XVII Latin American Conference on Automatic Control”.

As student use this book to learn about how to progressively contribute in several fields from the theoretical and practical point of view, both simulation and experimental works will illustrate the capabilities of the people who work in our countries improving the knowledge by teaching the basic steps to the new generation of Control Engineers.

Lucía

CONTENTS

Chairs

Antonio Morán. Dr.
Profesor Titular
Pontificia Universidad Católica del Perú
Perú

Danilo Chávez, Dr.
Profesor Agregado
Jefe del Laboratorio de Robótica y Sistemas Inteligentes
Departamento de Automatización y Control Industrial
Facultad de Ingeniería Eléctrica y Electrónica
Escuela Politécnica Nacional
Ecuador

Carlos Mario Vélez. Dr.
Profesor Titular
Jefe Departamento Ciencias Matemáticas
Escuela de Ciencias
Universidad EAFIT
Colombia

Carlos Ocampo. Dr.
Profesor Asociado
Senior Research Fellow
Technical University of Catalunya
Automatic Control Department (ESAII)
Deputy Director of the Institut de Robótica i Informática Industrial
CSIC-UPC
España

Gerardo Espinosa Pérez, Dr.
Profesor de Carrera Titular B
Departamento de Ingeniería de Control y Robótica
Facultad de Ingeniería
Universidad Autónoma de Mexico
México

Gustavo Scaglia. Dr.
Investigador Adjunto CONICET
Instituto de Ingeniería Química
Facultad de Ingeniería
Universidad Nacional de San Juan
Argentina

Iván García Triana. Dr.
Investigador
Department of Applied Mathematics
EWI, TU Delft
The Netherlands

Universidad de Los Andes
Venezuela

Santiago Rivadeneira. Dr.
Profesor
Facultad de Minas
Sede Medellín
Universidad Nacional de Colombia
Colombia

ISBN: 978-958-8483-37-5

International Reviewers

Adriana Natacha Amicarelli	INAUT - Argentina
Andrea Angel Zea	EMGESA - Colombia
Antonio Morán	PUCP - Perú
Carlos Alberto Cadavid Moreno	UNIVERSIDAD EAFIT - Colombia
Carlos Andrés Sánchez López	CELSIA - Colombia
Ceso de la Cruz Casaño	Universidad Continental – Perú
César A Uribe	University of Illinois at Urbana-Champaign
Daniel Sierra-Sosa	UNIVERSIDAD EAFIT – Colombia
David Ortiz	UNIVERSIDAD EAFIT – Colombia
Emanuel Serrano	IIQ- UNSJ – Argentina
Fabian Leonardo Jaramillo Palacios	Universidad de Cuenca – Ecuador
Flavio Roberti	INAUT – Argentina
Gustavo Pérez	PUCP – Perú
Héctor Antonio Botero Castro	UNAL – Colombia
Jan. H. van Schuppen	TUDelft – The Netherlands
Javier Sotomayor M	PUCP – Perú
Jesús Antonio Hernandez Riveros	UNAL – Colombia
Juan Fernando García Tirado	ITM – Colombia
Juan Carlos Rivera	UNIVERSIDAD EAFIT – Colombia
Juan Diego Sánchez Torres	ITESO – México
Juan Guillermo Paniagua Castrillón	ITM – Colombia
Juan Marcos Toibero	INAUT – Argentina
Manuel Betancur Betancur	UPB – Colombia
Maria Gulnara Baldoquín de la Peña	UNIVERSIDAD EAFIT – Colombia
Mario Fernández-Fernández	Universidad de Talca – Chile
Natalia Martina López	GATEME – UNSJ- Argentina
Pablo Santiago Rivadeneira	UNAL – Colombia
Ricardo Carelli	INAUT – Argentina

CHAPTER 1

ARTIFICIAL INTELLIGENCE

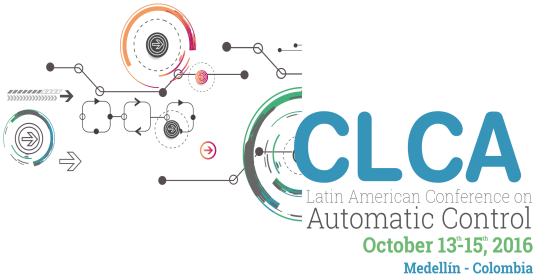

Automatic Face Recognition in Thermal Images Using Deep Convolutional Neural Networks ⋆

Rubén D. Fonnegra * **Andrés Felipe Cardona-Escobar** *
Andrés Felipe Pérez-Zapata * **Gloria Mercedes Díaz** *

* *Grupo de Investigación Automática, Electrónica y Ciencias Computacionales*
Instituto Tecnológico Metropolitano, Medellín, Colombia
(e-mail: rubenfonnegra@itm.edu.co,
andrescardona134713@correo.itm.edu.co,
andresperez75267@correo.itm.edu.co, gloriadiaz@itm.edu.co).

Abstract: Recently, the use of infrared images has shown be a feasible technique for addressing problems as illumination dependency and facial expressions in face recognition applications. Due the recent approaches that use deep learning methodologies for image analysis, which have had remarkable performances, a deep learning strategy for facial recognition in thermographic images is proposed. A convolutional neural network is designed and evaluated for recognizing different people in an experimental home-made database. The use of convolutional networks avoids to implement preprocessing and feature extraction algorithms, which is one of the important parts in image classification. Results show significant improvements compared to others works reported in the literature, which demonstrates robustness and effectiveness of the proposed approach.

Keywords: Face recognition, Thermal images, Deep learning, Convolutional neural networks

1. INTRODUCTION

Face recognition remains an active and challenging area in the computer vision field. Although, several approaches have been proposed, problems such as illumination requirements for image acquisition are unsolved yet. Infrared imagery (IR) have shown promising results in this area, due its invariance to changes in the illumination condition, which allows to acquire approachable images even in the absence of visible light (Ghiass et al., 2014).

Face recognition based on infrared images are commonly classified in four categories (Ghiass et al., 2014; Arya et al., 2015): holistic appearance based, feature based, multi-spectral based, and multi-modal fusion based approaches. The first one were the earliest attempts to use IR for recognition purposes. These methods use all infrared face information in the recognition task; eigenfaces approaches fall into this category. Feature based approaches represent images as a feature vector, which can be obtained applying general feature extraction techniques, such as wavelets coefficients, local descriptors, among others; or context-dependent features such as vascular network patterns or blood perfusion measurements. On the other hand, multi-spectral and multi-modal approaches take advantages of the possibility of use information from different spectra or other image modalities for improving recognition capabilities.

⋆ This work was supported by the Instituto Tecnológico Metropolitano from Medellín, Colombia trough Research Group in Automática, Electrónica y Ciencias Computacionales.

The majority of the proposed approaches are characterized by a complex processing pipeline that involves, preprocessing, feature extraction and selection, and recognition learning techniques, which results in a large number of parameters that must be tuned. Recently, Deep learning has emerged as the best strategy for solving several traditional machine learning problems (LeCun et al., 2015). So, because a biometric system must be able to provide enough roughness, we considered using convolutional artificial neural networks (CNN) approaches as face recognition algorithm. The use of CNN provides the alternative of discard every preprocessing or feature extraction algorithm due the net capacity of recognizing characteristics of images by the use of convolutional transformations in their layers. Although the results show that the extracted features of previous works found in the state-of-the-art are highly relevant; our methodology based on CNN significantly improves performance without the need of a preprocessing or feature extraction stages. This advantage allows to cover all recognition structures in one same procedure.

This paper is organized as follows: section 2 introduces the theoretical concepts for the implementation of the proposed CNN; section 3 describes details of database acquisition process (section 3.1) and presents the architecture of the proposed neural network (section 3.2). Section 4 presents the experimental evaluation and results obtained when different image scales are used as input to the CNN; and finally, conclusions and future work are discussed in section 5.

2. BACKGROUND

Deep learning is the concept that involves a set of machine learning approaches that use complex architectures of non-linear transformations to representing relevant information in non-structured data with high levels of abstraction (Schmidhuber, 2015). These approaches appear a few years ago due to the development of new processors with the capacity of executing different processes using parallel programming strategies. From the proposed Deep learning approaches, convolutional neural networks have recently been widely adopted due that it is easier to train and generalized much better than other architectures. In this paper, a convolutional neural network is proposed to solve the problem of identification of people in thermal images (Hassairi et al., 2015).

2.1 Convolutional Neural Networks (CNN)

CNN is a feed-forward neural network with a particular architecture that allows to process an entire image without preprocessing requirements. It consists of a set of convolutional and subsampling layers followed by fully connected layers. Each convolutional layer accepts a feature map (in this case an image) and transforms it to another feature map (another image) through a differentiable function (i.e., kernels). Neurons in the same feature map share the same kernel, which allows to go deeper between every convolution for the transformation of the images Gong et al. (2015). Because CNNs can learn from raw data automating the process of feature extraction (Ji et al., 2013), these are known as *end-to-end* methods i.e., they can compute feature maps using spatial information of pictures. The CNN algorithms have demonstrated high performance in pattern recognition tasks over the past few years, especially in computer vision where CNNs outperform conventional classifiers, for instance at the ImageNet Classification challenge, CNNs have been used by the better proposals in the last years (Krizhevsky et al., 2012), (Simonyan and Zisserman, 2014) (Szegedy et al., 2015).

2.2 Rectified linear Units (ReLU)

Rectified Linear Units (ReLU) is an activation function, which is the most commonly deployed activation function for the outputs of the CNN neurons. This function was developed as an alternative to classical way of to determine the output of a neuron x in a net, it is given by Equation 1.

$$F(x) = tanh(x) = (1 - e^{-x})^{-1} \tag{1}$$

According to Glorot et al. (2011), the main advantage of ReLU activation is that non-linear units are not saturated compared to other non-linear activation functions (such as Logistic or Tanh units). This characteristic implies expensive processing, doing that networks with saturated neurons be slower than those using ReLU function. Although ReLU is not symmetric, this property can be achieved by combining two units Glorot et al. (2011), and sometimes this function is replaced with a smooth version named *softplus*.

In a general form, the output of a neuron with ReLU activation function can be computed by Equation 2.

$$ReLU(x_i) = max(0, x_i) \tag{2}$$

2.3 Softmax

Softmax function is an activation function, which is a generalization of a logistic function that maps a K-dimensional vector $\mathbf{Z}$ of real values to a K-dimensional vector $\sigma(\mathbf{Z})$ of real values in the range 0, 1. This function allows to handle multiclass in the output layer; it is computed one unique output when there are several units in the output layer. Due that Softmax function mapping is now considered as scores with unnormalized log probabilities for each class, the cost function correction named Cross entropy loss can be defined by Equation 3.

$$L_i = -Log(\frac{e^{f_{y_i}}}{\sum_J^{j=1} e^{f_j}}) \tag{3}$$

with f_j being the $j-th$ element of class vector scores f.

Likewise, the Softmax activation function is defined by equation 4.

$$softmax(\mathbf{z}) = \frac{e^{zj}}{\sum_K^{k=1} e^{zk}} \quad forj = 1, ..., K. \tag{4}$$

with z being an arbitrary vector with real values to be scaled into a zero-to-one values.

2.4 Dropout Regularization

Dropout regularization is used for preventing co-adaption among units. This novel technique detailed in (Srivastava et al., 2014) avoids overfitting by dropping out units randomly in hidden layers during training. for doing so, outputs of units with a probability of 0.5 in hidden layers are set to zero during the forward pass, as it is explained in Krizhevsky et al. (2012). The "Dropped out" neurons not participate in backpropagation. So, every algorithm execution changes the net architecture, but neurons also share its weights. This characteristic reduces co-adaptations of the net since every neuron does not depend on other neurons in the net. Therefore, the main goal of dropout is to add stochastically noise in the activation states of certain hidden units (Srivastava et al., 2014).

2.5 Adaptive Moment Estimation (Adam Optimizer)

Adam is a stochastic optimization algorithm introduced in Kingma and Ba (2014), which employs first order gradients as updating mechanism, it uses exponential moving averages denoted by m_t and squared gradients v_t. Parameters updating is performed defining an objective function $f(\theta)$, which is tuned by evaluating random subsets known as mini batches.

3. MATERIALS AND METHODS

3.1 The thermal Image Database

An image database was acquired using a FLIR A655SC thermographic camera, configured to a 6.3 Hz sampling frequency. A group of 21 people with ages between 22 and

45 years was involved. For each persona thermographic video with approximately 80 images of 640×480 pixels was recorded. During recording, each person was instructed to rotate his/her head in four directions (up, down, right and left). Resulting videos were converted to gray-scale, with pixel values distribution remaining those of infrared radiation for each frame. From each video, a set of images were manually selected, for doing so it was considered that heads were completely forward or slightly tilted. In this sense; the database was composed of 588 images, i.e., 21 people and 28 images per person.

Discarding the implementation of any preprocessing algorithm (this means that every input for the network corresponds to every pixel of the input image to be classified for the network), the use of original sized images represented a high computational cost to training stages. So, images were conveniently scaled using a typical bicubic interpolation. Preserving spectral relationship, We evaluate three different scales, i.e. 320×240, 160×120 and 80×60 pixels. Although this down-scaling could means losing information; the loss is not considerable enough to prevent the net to recognize all people. In Fig. 1 could be observed some examples of the subsets of images involved in this study.

Fig. 1. Example images from the home-made database. Two subjects with different pose are showed.

3.2 Neural Network Architecture

With the purpose of developing a biometric system capable of identifying every person according to the experimental database described in subsection 3.1; a convolutional neural network was implemented. The main goal of using CNN was to reach that without to apply any preprocessing technique. The Architecture of the proposed net is illustrated in Figure 2. It consists of 6 convolutional layers followed by 2 densely-connected layers that were randomly weighted. Convolving layers implemented kernels using the RelU function activation for image transformations. Every convolutional layer was connected to the immediately next convolutional layer so that there were no connections between nonconsecutive layers. The last convolving layer was connected to two densely-connected layers, which were composed of 200 and 100 output neurons, respectively. Last of them uses Softmax and dropout functions for handling multiple classes in the output layer and avoiding overfitting.

The number of input layers was varied according to the number of pixels in the input images. So, input layers with 76800, 19200 and 4800 neurons were evaluated (for 320×240, 160×120 and 80×60 pixels, respectively). This means that each neuron in the first layer possesses information of each pixel in the image. Size image variations also modify the size of the image in the last convolutional layer but did not change operations in others layer sizes because these do not depend on the size of the input vector.

4. EXPERIMENTAL RESULTS

4.1 People recognition using CNN

Implementation of the convolutional neural network was performed using TensorFlow framework Abadi et al. (2015); proposed approach was evaluated using a 10-fold cross validation strategy . For picking the training samples, it was considered to keep a stratified probability function by selecting the 10% of data per class for validation test. Along with the 10-fold cross validation, the data were randomly permuted before of evaluating the model. This also guaranteed that each experiment had different input data for training and validation stages; and demonstrates independence of them for learning task.

Figure 3 shows the average accuracy in the validation stage for different image size evaluated (320×240, 160×120 and 80×60), when number of iterations was varied between 10 and 100. In the three cases, perfect recognition i.e., a 100% of accuracy is obtained before of 30 iterations, although it is faster for larger images (around of 10 iterations), which was expected because this kind of image preserves more information than the small one.

4.2 Processing optimization with GPU

Due that the high computational cost of training a CNN, We considered the use of parallelization process in the network, using graphical processing units (GPU). For doing it, training and validation stages were implemented using NVIDIA series Quadro K4000 GPU along with CUDA Toolkit 7.5 libraries and computational cost was compared with them obtained when it was performed on a Workstation with CPU Intel® Xeon® E5 - 2687 (32 cores) and 32GB RAM inside. Tables 1 and 2 show the time consuming in the GPU and CPU configurations. Interation time refers to processing time (in seconds) for each execution cycle of the algorithm; training time is the time (in seconds) taken for training the overall net, when accuracy of 100% is accomplished; Validation time is the cost of classifying a subject after training process and memory consumption corresponds to RAM memory required to execute the training of the network.

Table 1. Processing times for GPU Implementation

Size	Iteration Time (s)	Training Time (s)	Validation Time (s)	Memory consumption (MB)
320x240	8.6211	283.927	0.210511	2440
160x120	2.29826	47.9025	0.0594253	2360
80x60	0.615124	24.1448	0.017618	2298

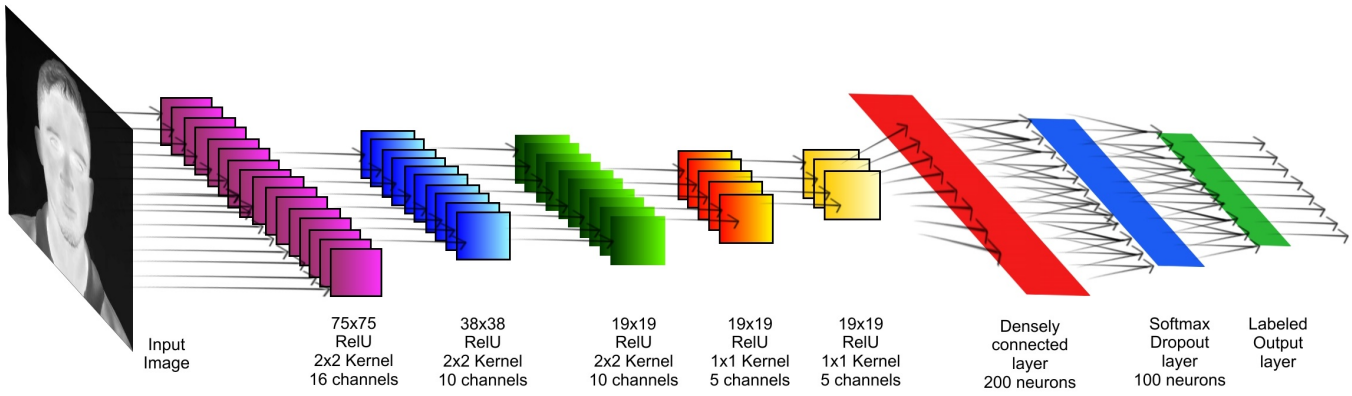

Fig. 2. Architecture of the implemented convolutional neural network.

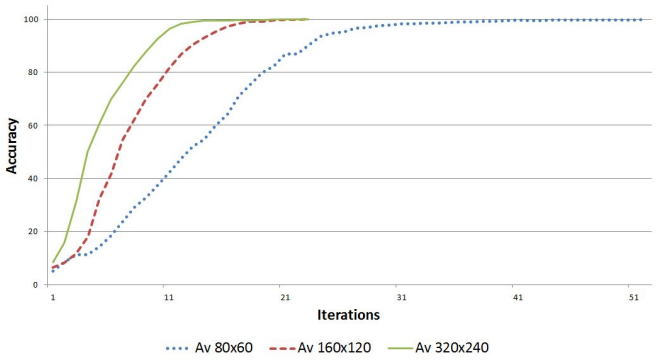

Fig. 3. Accuracy in the validation stage for input images with 320 × 240 (Green, continued line), 160 × 120 (red,discontinued line) and 80 × 60 (blue, dot line) pixels, when number of iterations in the training stage is varied

Table 2. Processing times for CPU Implementation

Size	Iteration Time (s)	Training Time (s)	Validation Time (s)	Memory consumption (MB)
320x240	31.7805	810.902	0.460278	1762
160x120	7.95153	130.649	0.139201	1103
80x60	1.9524	107.607	0.0426403	501

GPU parallelization allows to reduce the training and validation processes in 2 to 4 times respect to CPU implementation but It requires more RAM memory capacities.

5. CONCLUSIONS

In this work a biometric system for facial recognition using thermographic images was presented. Involving deep learning approaches introduced through a convolutional neural network frame, the proposed approach was able to identify each person in a home-made image database without previous face segmentation, image preprocessing or feature extraction and selection stages. The proposed framework demonstrated high performances in the training and validation tests even when the input image were scaled to a quarter of the original one. Those results are comparable to other works reported in the state of the art; obtaining notable accuracy during training and validation experiments.

Computational times are considerably reduced when the proposed neural network is implemented on GPU, although RAM memory requirements are also incremented. This results make the proposed approach a promissory alternative for real biometric applications, which could to take advantage of illumination invariance of thermographic images and the recognition performance of deep neural networks.

In the future, we plan to perform an evaluation with a higher number of subjects and to combine information from another spectrum such as near infrared or visual spectra.

REFERENCES

Abadi, M., Agarwal, A., Barham, P., Brevdo, E., Chen, Z., Citro, C., Corrado, G.S., Davis, A., Dean, J., Devin, M., Ghemawat, S., Goodfellow, I., Harp, A., Irving, G., Isard, M., Jia, Y., Jozefowicz, R., Kaiser, L., Kudlur, M., Levenberg, J., Mané, D., Monga, R., Moore, S., Murray, D., Olah, C., Schuster, M., Shlens, J., Steiner, B., Sutskever, I., Talwar, K., Tucker, P., Vanhoucke, V., Vasudevan, V., Viégas, F., Vinyals, O., Warden, P., Wattenberg, M., Wicke, M., Yu, Y., and Zheng, X. (2015). TensorFlow: Large-scale machine learning on heterogeneous systems. URL `http://tensorflow.org/`. Software available from tensorflow.org.

Arya, S., Pratap, N., and Bhatia, K. (2015). Future of face recognition: A review. *Procedia Computer Science*, 58, 578–585.

Ghiass, R.S., Arandjelović, O., Bendada, A., and Maldague, X. (2014). Infrared face recognition: A comprehensive review of methodologies and databases. *Pattern Recognition*, 47(9), 2807–2824.

Glorot, X., Bordes, A., and Bengio, Y. (2011). Deep sparse rectifier neural networks. In *International Conference on Artificial Intelligence and Statistics*, 315–323.

Gong, T., Fan, T., Guo, J., and Cai, Z. (2015). Gpu-based parallel optimization and embedded system application of immune convolutional neural network. In *2015 International Workshop on Artificial Immune Systems (AIS)*, 1–8. doi:10.1109/AISW.2015.7469248.

Hassairi, S., Ejbali, R., and Zaied, M. (2015). Supervised image classification using deep convolutional wavelets network. In *Tools with Artificial Intelligence (ICTAI),*

2015 IEEE 27th International Conference on, 265–271. doi:10.1109/ICTAI.2015.49.

Ji, S., Xu, W., Yang, M., and Yu, K. (2013). 3d convolutional neural networks for human action recognition. *Pattern Analysis and Machine Intelligence, IEEE Transactions on*, 35(1), 221–231.

Kingma, D. and Ba, J. (2014). Adam: A method for stochastic optimization. *arXiv preprint arXiv:1412.6980*.

Krizhevsky, A., Sutskever, I., and Hinton, G.E. (2012). Imagenet classification with deep convolutional neural networks. In *Advances in neural information processing systems*, 1097–1105.

LeCun, Y., Bengio, Y., and Hinton, G. (2015). Deep learning. *Nature*, 521(7553), 436–444.

Schmidhuber, J. (2015). Deep learning in neural networks: An overview. *Neural Networks*, 61, 85–117.

Simonyan, K. and Zisserman, A. (2014). Very deep convolutional networks for large-scale image recognition. *arXiv preprint arXiv:1409.1556*.

Srivastava, N., Hinton, G., Krizhevsky, A., Sutskever, I., and Salakhutdinov, R. (2014). Dropout: A simple way to prevent neural networks from overfitting. *The Journal of Machine Learning Research*, 15(1), 1929–1958.

Szegedy, C., Liu, W., Jia, Y., Sermanet, P., Reed, S., Anguelov, D., Erhan, D., Vanhoucke, V., and Rabinovich, A. (2015). Going deeper with convolutions. In *Proceedings of the IEEE Conference on Computer Vision and Pattern Recognition*, 1–9.

Classification of emotions by Artificial Neural Networks: a comparative study

Fernando J. Muñoz*, Emanuel B. Tello*, Daniel Patiño, Flavio Roberti**, Elisa Pérez*, Natalia M. López***

**Universidad Nacional de San Juan. Facultad de Ingeniería. Gabinete de Tecnología Médica - San Juan, Argentina.*

***Universidad Nacional de San Juan. Facultad de Ingeniería. Instituto de Automática - San Juan, Argentina.*

Abstract: Every emotion evidences a biological sign while predisposes the body to a different kind of response. In Human-Computer interaction area, the voice recognition techniques are widely used in text engines. In this context, the automatic emotion recognition of the speech aims at identifying the emotional or physical condition of a human being from his voice. Both emotional and physical states of a speaker are included in so-called paralinguistic aspects. In this work we used a speech database containing 7 different emotions in which 4 emotions were selected and 12 features were extracted. Emotions were classified by different types of neural networks in order to compare the efficiency of them to discriminate different moods.

Keywords: Classifiers, Speech recognition, Neural-Network Models, Emotions, Audio Features.

1. INTRODUCTION

Emotions govern almost all modes of human communication: facial expressions, gesture, posture, voice tone, words, breathing, body temperature, etc. Human perception of emotions is about 55 % from facial expressions, and 38 % from 7% speech from text (Busso et al., 2004). Although the emotional state does not alter the linguistic content, this is an important human communication factor as it provides feedback information for the development of applications in a wide spectrum, such as assistive technologies, psychiatric diagnosis and lie detection (Nasr and Ouf, 2012).

Emotion recognition methods require the extraction of certain characteristics of speech (Espinosa and Reyes García, 2010). Some are based on acoustic features such as Mel Frequency Cepstrum Coefficients (MFCC) and the Fundamental Frequency to detect emotional signs. Others use prosodic features in speech to achieve higher classification accuracy.

Many researches focus on the classification using artificial neural networks (ANN) (Pérez-Gaspar et al., 2015). In this work different topologies of ANN based on naive Bayes (NB), Support Vector Machines (SVM), Multi-layer Perceptron (MLP) and Radial Basis Function (RBF) classifiers were designed in order to compare and classify a set of audio signals from Berlin database, which show opposite emotional states. A total of 12 features were taken from the audio signals. The performance of the classifiers was evaluated through 2 stages. In the first stage, three emotions (happiness, sadness, and neutral) were selected. In the second stage, a fourth emotion (fear) was added. The ANNs were adjusted to achieve optimal classification. Finally the comparison between the different hit rates obtained by the classifiers was established in order to evidence the performance of classifiers and the capacity of description of the features set used.

2. MATERIALS AND METHODS

2.1 Database

The Berlin database was used, containing about 500 speech audio files performed by 10 different actors, expressing different emotions: happiness, anger, sadness, fear, boredom and disgust, as well as a neutral expression (serene). There are a total of ten different phrases. Four emotions of the database were selected: happiness, sadness, fear and neutral. The choice was based on the regionalization proposed in Russell circumplex model (Figure 1) in which each selected emotion characterizes one quadrant model (Russell, 1980).

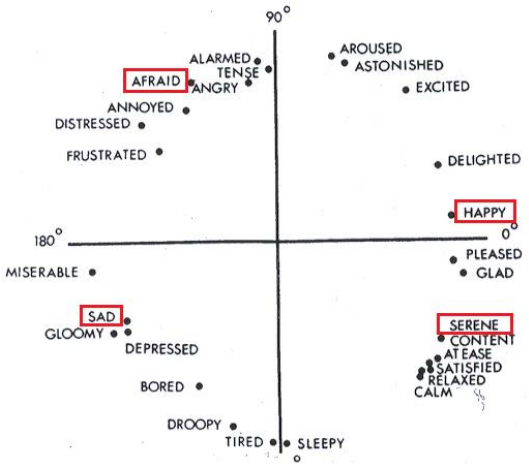

Fig 1. Russell Circumplex model (Russell, 1980)

2.2 Feature Extraction

A total of 12 Features of the audio signals were extracted and divided into 3 groups: prosodic, temporary and frequency features. The number of selected parameters is based on recent literature of emotions and audio signal processing (Bustamante et al., 2015).

The statistical and temporal parameters were mean (ME), variance (VAR), standard deviation (SD), zero crossings (ZC) and kurtosis (K). Prosody has a very important paralinguistic role that complements the linguistic message and reflects the emotional state of the speaker (Espinosa, 2010). Prosodic parameters were based on the energy (E) related to the intensity of the audio signal, the duration of pauses and phonemes (D) and the fundamental frequency (pitch). In frequency domain the extraction of formant, frequency cepstral coefficients in Mel scale (MFCC) and power spectral density (PSD) was performed.

2.3 ANN structures

This work was made in two stages in order to analyze and track changes in the performance of classifiers when a new emotion is introduced. As pre-processing of the audio signal, an initial re-sampling to 16 KHz was performed. The signal was normalized and limited in a frequency band by a recursive Chebyshev type 1 band pass filter, with a lower cut-off frequency at 20 Hz and upper cut-off frequency at 6800 Hz.

A voice detector was applied to the filtered signal in order to extract the voice segments and eliminate silences. Finally it was carried out a windowing of the signal, setting the limit at 20 ms. with 50% overlap.

The structures for the four models of ANN selected were established. 105 samples for the first stage and 140 for the second stage were taken from database as training set (35 samples of each emotion: happiness, sadness, neutral and fear). The input data, corresponding to the 12 selected features, were previously normalized. Modelling of different ANNs was performed in MATLAB®.

2.3.1 Multi-Layer Perceptron

In the first stage, a MLP network was configured with 12 input nodes, 2 hidden layers and three output nodes. Activation functions employed were established empirically, defining hyperbolic functions for the hidden layers and logistic functions for the output layer. The Levenberg-Marquardt was implemented as learning rule. For each emotion only one output is in high state (Y=1), while the others remain in the low state (Y=0). In the second stage, was added a new output node in order to identify the emotion "fear", then was applied the same process mentioned before. The Figure 2 shows the topologies used for these architectures.

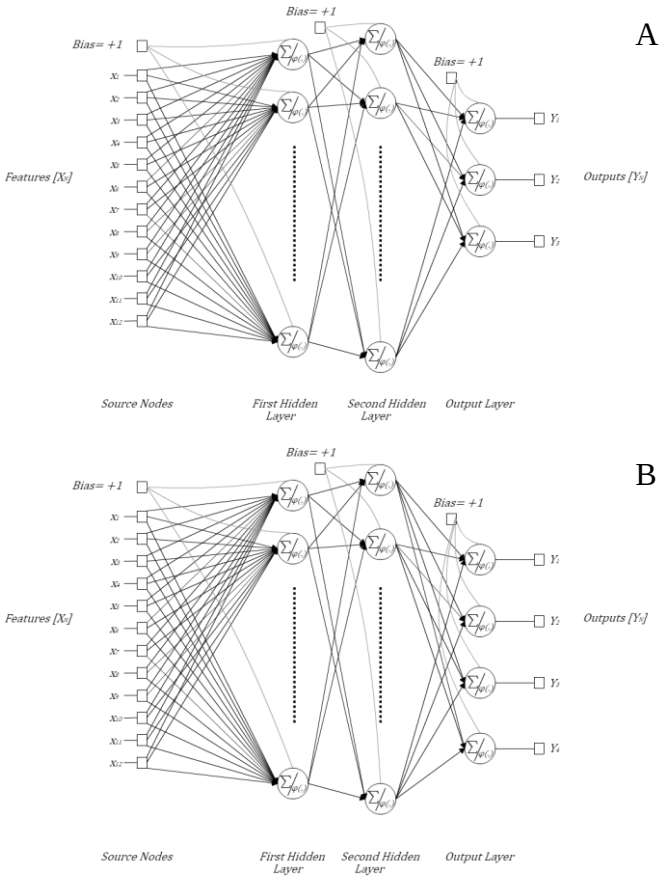

Fig 2. MLP structures for three (A) and four (B) emotions.

2.3.2 Radial Basis Function

The RBF network was designed with 12 input nodes and one output neuron (Figure 3). It can be considered as a special MLP network of three layers. Neurons in the hidden layer containing Gaussian transfer functions whose outputs are inversely proportional to the distance from the centre of the neuron. The activation function for the output node presents a linear behaviour.

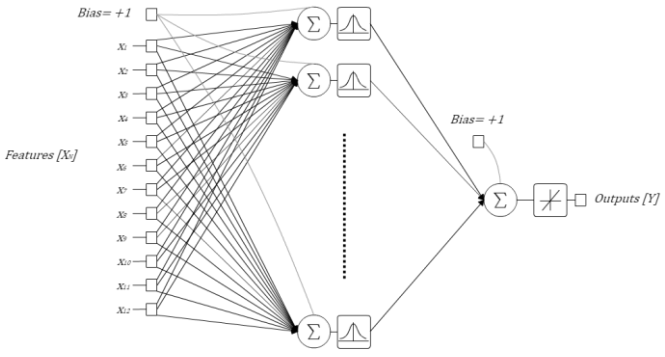

Fig 3. RBF structure.

2.3.3 Support Vector Machines

SVM is a type of supervised learning machine that belongs to the category of linear classifiers, since they induce linear separators or hyperplanes, either in the original space of input

examples, if they are separable or quasi-separable, or in a transformed space (feature space), if the examples are not linearly separable in the original space. In these cases, the search for the hyperplane will be done implicitly using kernel functions (Chavan and Gohokar, 2012).

In this work, a total of three SVM classifiers (Figure 4) were designed based on combinations of the emotions selected: Happiness/Sadness; Happiness/Neutral; Sadness/Neutral. After training, different kernels of inner product were used (Linear, Quadratic, Polynomial, Radial Basis Function and Multilayer Perceptron) to analyse which of them provided a better performance in data classification. Then, three new classifiers were designed to include the emotion "Fear": Happiness/Fear; Neutral/Fear; Sadness/Fear.

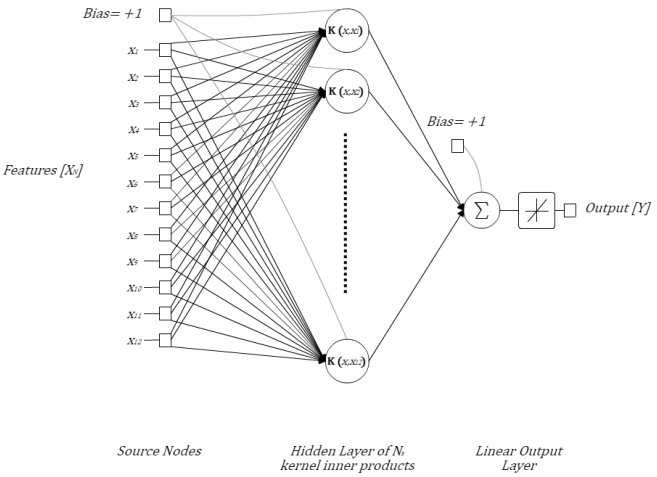

Fig 4. SVM structure.

2.3.4 Naive Bayes

The NB network was configured as a typical Naive Bayes classifier (Figure 5) with three possible classes, corresponding to the emotions selected for the first stage. Uniform probabilities were supposed and the algorithm assumes that predictors (inputs) are conditionally independent given the class (Castillo Reyes et al., 2014; Vinay et al., 2013).

For the second stage, a new class was added. The NB network was then configured with four possible classes: Happiness, Neutral, Sadness and Fear.

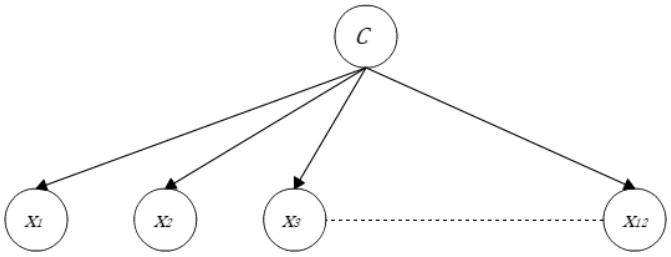

Fig 5. NB classifier.

2.4 Simulation

In the first simulation stage of ANNs a total of 45 known samples of audio were used as test set, picked from Berlin database, 15 for each emotion (happiness, sadness and neutral). The 12 features of the samples were extracted, normalized and introduced in the different topologies. The estimated outputs were compared with the expected values. The percentages of successes and overall performance for emotions classified in different network models are shown in Table 1.

In the second stage, 35 samples were added to the training set, corresponding with the "fear" emotion and 15 samples were used for simulation. The estimated outputs were compared with the expected values. The percentage of hits and overall performance are shown in Table 2.

Table 1. Hit rate and overall performance, with three emotions.

ANN	Happiness	Sadness	Neutral	Overall Performance
MLP	73.33%	66.67%	66.67%	68.89%
RBF	46.67%	80%	33.33%	53.33%
SVM-L	73.33%	86.66%	93.33%	84.44%
SVM-Q	46.67%	66.67%	53.33%	55.56%
SVM-P	73.33%	60%	40%	57.77%
SVM-RBF	80%	93.33%	46.67%	73.33%
SVM-MLP	73.33%	66.67%	60%	66.67%
NB	86.67%	93.33%	80%	86.67%

Table 2. Hit rate and overall performance, with four emotions

ANN	Happiness	Sadness	Neutral	Fear	Overall Performance
MLP	53.33%	60%	80%	46.67%	40%
RBF	33.33%	73.33%	53.33%	33.33%	48.33%
SVM-L	73.33%	86.67%	66.67%	46.67%	68.33%
SVM-Q	20%	66.67%	46.67%	40%	43.33%
SVM-P	53.33%	60%	20%	46.67%	44.99%
SVM-RBF	66.67%	93.33%	33.33%	46.67%	59.99%
SVM-MLP	60%	66.67%	46.67%	33.33%	51.66%
NB	86.67%	86.67%	66.67%	40%	70%

3. RESULTS

The values obtained in Tables 1 and 2 are the result of the optimization of the training process for the designed configurations, based on the analysis and the number of features used as inputs to the ANNs.

In the recognition with three emotions, the SVM-L, SVM-RBF and NB structures showed the best overall performances (over 70 %), with variability in their hits rates according to the emotion considered.

Figure 6 shows the detection rate of classifiers for each emotion. It is observed that the mean values for "happiness" and "sadness" are close to 75%, and the dispersion of classifiers in the recognition of emotion "sadness" is the smallest of the three cases. In the case of the "neutral" emotion, it is evident that the mean value is less than 60% and the dispersion of the hit rate is greater than 50%.

This evidences the relation between the descriptors used as inputs with the performance of the ANNs designed. Temporal and prosodic features, as the zero crossings and the duration of speech segments, are useful in distinguishing the emotion

"sadness" from the others, because usually a speaker in high state of excitation / valence tends to speak quickly with fewer and shorter breaks, while a depressed speaker talks slowly, introducing longer pauses.

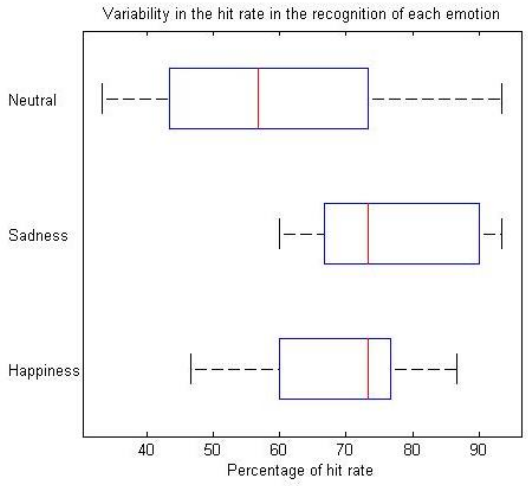

Fig 6. Hit rate variability with three emotions

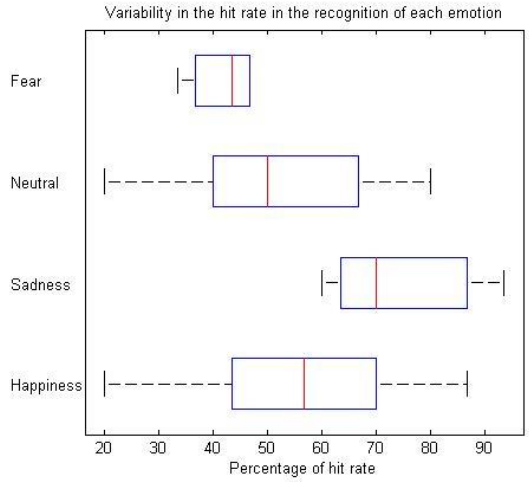

Fig 7. Hit rate variability with four emotions

When a fourth emotion is added (Figure 7), the emotion "sadness" keeps its hit percentage in relation to "happiness", "fear" and "neutral". Table 2 shows that the overall performance for these emotions is about 50%, obtaining in the best cases a percentage of 75%.

Some pairs of emotions are usually confused. This is the case of "happiness" and "fear". The same trend appears between "happiness" and "neutral". Speech associated with "fear" and "happiness" has a longer utterance duration, shorter breaks, higher pitch and energy values with wider ranges. Therefore, these emotions are difficult to be classified.

Although the overall performance decrease when "fear" is incorporated, the classifiers SVM-L, SVM-RBF and NB (that showed the best performances in the first stage) are still higher compared to others, with percentages around 60%. The emotion "sadness" remains as the most recognizable, with a success rate above 70%.

4. CONCLUSIONS

In this paper we have evaluated the performance of several classifiers in distinguishing four emotional states under two stages.

In the analysis with three emotions, for the classifiers NB and SVM-L the overall performances are of 86.67% and 84.44% respectively. With four emotions, the best classifiers remain NB (70%) and SVM-L (68.33%) whose hit rates for "happiness" and "sadness" are above 60 %. Considering the capacity of the classifiers to discriminate between different emotions, it is evident that "sadness" proves to be the most distinguishable, regard to the others. This may indicate the need to incorporate new features of the processed audio signals, or even combine the best classifiers in order to achieve better performances.

This work shows that the performance of classifiers is given by the number and capacity of description of the input features. Although the selected emotional states are located in visually separable regions, according to the Russell model, certain features of the audio signals have similar values, making it difficult to recognize them by ANNs. An increase in the number of descriptors and a deeper understanding analysis of the relations between them and the proposed emotions might be necessary in future works.

REFERENCES

Busso, C., Deng, Z., Yildirim, S., Bulut, M., Lee, C., Kazemzadeh, A., et al. (2004). Analysis of Emotion Recognition Using Facial Expressions, Speech and Multimodal Information. International Commission on Mathematical Instruction, pp. 205-211.

Bustamante P., López N., Perez E., Quinteros L. (2015). Recognition and regionalization of emotions in the arousal-valence plane. Engineering in Medicine and Biology Society (EMBC), 37th Annual International Conference of the IEEE. Milan -Italia.

Castillo Reyes G. et al. (2014). Técnica de clasificación bayesiana para identificar posible plagio en información textual. Cuba cienc informat [online]. 2014, vol.8, n.4, pp. 130-144. ISSN 2227-1899.

Chavan, V.M., Gohokar, V.V. (2012) Speech emotion recognition by using SVM-classifier. International Journal of Engineering and Advanced Technology (IJEAT) 1(5), 11-15

Espinosa H., Reyes García C. (2010). Reconocimiento de Emociones a Partir de Voz Basado en un Modelo Emocional Continuo. Reporte Técnico No. CCC-10-005

Vinay , Shilpi Gupta, Anu Mehra. (2013). Vocal Emotion Recognition using Naïve Bayes Classifier. Proc. of Int. Conf. on Advances in Computer Science, AETACS, 2013

Nasr, M., Ouf, S. (2012). A Proposed Smart E-Learning System Using Cloud Computing Services. PAAS, IAAS and Web 3.0, Helwan University, Helwan, Egypt; iJET, Volume 7, Issue 3, http://dx.doi.org/10.3991/ijet.v7i3.2066

Pérez-Gaspar L., Caballero-Morales S., Trujillo-Romero F. (2015). Integración de optimización evolutiva para el reconocimiento de emociones en voz. Research in Computer Science, Vol.93, pp. 9-21

Russell J. (1980) A Circumplex Model of Affect. Journal of Personality and Social Psychology – Vol.39, Nº6, 1161-1178

Song, M., You, M., Li, N., Chen, C. (2008) A robust multimodal approach for emotion recognition. Neurocomputing 71, 1913-1920.

Detection and Diagnosis of Breast Tumors using Deep Convolutional Neural Networks

J. D. Gallego-Posada. * **D. A. Montoya-Zapata.** ** **O. L. Quintero-Montoya.** ***

* *Research Group on Mathematical Modeling, Universidad EAFIT, Medellín, Colombia (e-mail: jgalle29@eafit.edu.co)*
** *Research Group on Mathematical Modeling, Universidad EAFIT, Medellín, Colombia (e-mail: dmonto39@eafit.edu.co)*
*** *Research Group on Mathematical Modeling, Universidad EAFIT, Medellín, Colombia (e-mail: oquinte1@eafit.edu.co).*

Abstract: We present an application of Deep Convolutional Neural Networks (CNN) for the detection and diagnosis of breast tumors. The images used in this study have been extracted from the mini-MIAS database of mammograms. The proposed system has been implemented in three stages: (a) crop, rotation and resize of the original mammogram; (b) feature extraction using a pretrained CNN model (AlexNet and VGG); (c) training of a Support Vector Machine (SVM) at the classification task using the previously extracted features. In this research, the goal of the system is to distinguish between three classes of patients: those with benign, malign or without tumor. Experiments show that feature extraction using pretrained models provides satisfactory results, achieving a 64.52% test accuracy. It is worth noting the impact of the data augmentation process and the balance of the number of examples per class on the performance of the system.

Keywords: Breast tumor, classification, convolutional neural network, mammogram, support vector machine

1. INTRODUCTION

Breast cancer is the most common cancer in women and is commonly thought to be a disease of the developed world but nearly 50% of breast cancer cases and 58% of deaths occur in less developed countries. It is estimated that around the world over 508.000 women died in 2011 due to this condition. According to the World Health Organization (2016), detection of breast cancer in its early stages dramatically increases the chances of establishing a successful treatment plan.

As part of the current efforts to control this condition, the development of computer-aided diagnosis systems which can assist medical personnel with the early detection of tumors pose a crucial alternative. In such systems a high reliability in the accuracy of the classifier is a top priority.

In the study by Suckling et al. (1994), the diagnosis was performed employing a SVM trained with features extracted using AlexNet and VGG pretrained models fed with preprocessed mammograms. Our data source is the database of the Mammographic Image Analysis Society (MIAS).

The paper is structured as follows: in Section 2 we provide a review of the application of Deep Learning techniques to the image classification problem. Section 3 presents an outline of previous studies of breast cancer detection and classification using Deep Learning and Artificial Intelligence-based approaches. In Section 4, the employed methodologies are described. Next, in Section 5 the specifications of the implemented system are presented. Finally, Section 6 contains the main conclusions of this work and some possibilities for future improvements on this research.

2. RELATED WORK

The study of computer-aided breast cancer diagnosis has been addressed from several perspectives. The aim of this section is to briefly illustrate the state of the art in this field using artificial intelligence and additionally using strictly Deep Learning-related techniques.

2.1 Analysis of Breast Cancer using Artificial Intelligence Techniques

Alolfe et al. (2009) used a SVM and linear discriminant analysis to distinguish between benign and malign tumors on the MIAS database. Using this approach, they classified 90% and 87.5% of benign and malignant images correctly, respectively. A region of interest (ROI) of 32×32 pixels was selected from the images and 224 features were extracted. These features were divided into five groups: wavelet, first order statistics, second order statistics, shape and fractal dimension data. Finally, 13 features were selected with the forward stepwise linear regression method.

Wang et al. (2014) used the mammographies from 482 patients to compare the accuracies from an extreme learning machine (ELM) and a SVM to classify between images with and without tumors. In the preprocessing stage a median filter was used to reduce the noise and the wavelet

transformation of local modulus maxima in conjunction with the region growing algorithm were used as edge segmentation method. Finally, five textural features and five morphological features were extracted from the resulting image and these were used at the classification task. The ELM classifier exhibited better performance than the SVM classifier.

Dheeba et al. (2014) obtained an accuracy of 93.67% classifying between normal and abnormal tissues with an optimized neural network using Particle Swarm Optimization. The experiment was carried out with their private database of mammograms and the classification was done with the Laws Texture Energy Measures extracted from a ROI of dimension 15×15 pixels.

Peng et al. (2016) obtained an accuracy of 96% using an artificial neural network to classify the mammograms from MIAS database. They defined three different categories to carry out the experiment: normal, with presence of a benign tumor and with presence of a malign tumor. A median filter and the seeded region growing algorithm were used to remove the noise of the original images. Then, they extracted 16 features related to the texture properties of the images and five of them were selected. The feature selection algorithm, which is based on the rough-set theory, was developed by the authors.

Mahersia et al. (2016) achieved recognition rates of 97.08% and 95.42% on the MIAS database using a neural network with a Bayesian back-propagation algorithm and an ANFIS system as classifiers, respectively. The breasts were classified into two categories: normal and cancerous. The mammograms from this database were first enhanced, removing the noise and details that may interfere with the recognition of the tumors. Then a generalized Gaussian density model for wavelet coefficients was used as feature extractor.

2.2 Analysis of Breast Cancer using Deep Learning

Ertosun and Rubin (2015) used three different architectures of CNNs to locate masses in mammography images. They selected 2420 images from the DDSM dataset and divided these images into training, validation and test sets, containing 80%, 10% and 10% of the images, respectively. They also used cropping, translation, rotation, flipping and scaling techniques to get an augmented training set, in order to improve the generalization ability of the system. The experiment was divided into two stages: the first consisted in the classification of a mammography as containing or not masses and the second in the localization of masses in the images.

Arevalo et al. (2015) obtained 86% of area under the Receiver Operating Characteristic (ROC) curve by classifying mammography mass lesions using a CNN as feature extractor and a SVM as classifier. The data to carry out the experiment was the BCDR-F03 dataset, which is part of the BCDR database. This data was composed by 736 images, 426 containing benign mass lesions and the rest containing malignant lesions. The data augmentation was achieved by flipping and rotating the images. In addition, the mammography images were normalized by the use of global and contrast normalization. The CNN was trained using both dropout and max-norm regularization techniques.

Jiao et al. (2016) obtained an accuracy of 96.7% classifying the breast masses between benign and malign from the DDSM database using a CNN as feature extractor and a SVM as classifier. The images were previously normalized and whitened. On the other hand, the CNN was trained with a subset of ImageNet, dataset produced by Russakovsky et al. (2015), and the features to perform the classification were extracted from two different layers of the CNN.

Abdel-Zaher and Eldeib (2016) developed a classifier using the weights of a previously trained deep belief network as the initial parameters for a neural network with Liebenberg Marquardt learning function. This model was tested on the Wisconsin Breast Cancer Dataset, obtaining an accuracy of 99.68%.

3. DEEP LEARNING FOR IMAGE CLASSIFICATION

This section is based on the works from Guo et al. (2015) and LeCun et al. (2015).

Around 2006, the results obtained by a group of researchers working together in parallel projects in the Canadian Institute for Advanced Research renovated the interest of the community for the deep neural networks. The main four works Bengio et al. (2006); Hinton (2005); Hinton et al. (2006); Marc'Aurelio Ranzato et al. (2006), introduced unsupervised learning procedures to pure supervised learning procedures. The objective of each layer in the neural network was to learn the inputs of the previous layer, as stated by LeCun et al. (2015). This approach performed well in comparison with the existent artificial intelligence techniques in tasks such as recognizing handwritten digits, specially when the amount of labeled data was limited, as mentioned by Sermanet et al. (2013).

Since the rise of Deep Learning, the CNN model outperformed the fully connected neural networks in tasks related to natural image classification. However, this approach was not seriously used at classification problems until 2012. During six years in which CNNs were laid aside, the methods based on the *Bag of Visual Words* model, that were the state of the art techniques for image classification, were improved by Lazebnik et al. (2006) with the incorporation of spatial geometry, through the use of spatial pyramids.

The turning point for image classification was 2012. In this year, AlexNet, a CNN with five convolutional layers and three fully connected layers developed by Krizhevsky et al. (2012), outperformed the existing methodologies and won the ImageNet Large Scale Visual Recognition Challenge (ILSVRC) in 2012, almost halving the error rate of the model in second place from Russakovsky et al. (2015). According to LeCun et al. (2015), this success reflected the new developments in graphic hardware and algorithms: the increased chip processing abilities (GPU units), the use of Rectified Linear Unit (ReLU) as neural activation functions, a novel regularization technique developed by Srivastava et al. (2014) and the advances in algorithms for data augmentation.

Since the success of AlexNet in 2012, several improvements of this model have been performed. Zeiler and Fergus (2014) established a technique to analyze the responses of intermediate layers, what enabled them to implement Clarifai, winning the ILSVRC.

In 2014, deeper architectures were finally used. VGG from Simonyan and Zisserman (2015) and GoogLeNet from Szegedy et al. (2015) networks obtained the second and first place in ILSVRC, respectively. The VGG network from had 13-16 convolutional layers, while GoogLeNet had 21 convolutional layers.

He et al. (2015b) proposed a model that surpassed for the first time human-level performance on the ImageNet 2012 test dataset, with a network with the same architecture of VGG. In addition, He et al. (2015a) also established a new framework to train deeper networks called the residual learning. They developed ResNet, a 152-layers network and won ILSVRC.

For Guo et al. (2015), researchers are focusing in three main aspects to further improve the performance of Deep Learning models: (a) the implementation of larger networks: ResNet, GoogLeNet and VGG models have shown that the networks with a larger number of layers outperform the simpler ones; (b) the use of multiple networks, where every network can execute all the process independently, so the responses of all the networks are combined in order to obtain the final result; and (c) the introduction of external information from other resources and the use of shallow structures. In this aspect, one of the most important developments is *Regions with CNN Features* method by Girshick et al. (2014), in which the features extracted from a CNN feed a SVM.

Other research projects have focused their efforts on getting a further understanding of what deep neural networks learn, addressing the problem from both a theoretical and a empirical perspective. For instance, Li et al. (2016) have recently studied convergent learning, aiming to analyze cases in which different neural networks learn similar representations. In this work, they propose a method for quantifying the similarity between deep neural networks and showed that there exist basic features which are learned by multiple networks with the same architectures but different random initialization.

4. THEORETICAL BACKGROUND

4.1 Convolutional Neural Networks

CNNs are a type of biologically-inspired feed-forward networks characterized by a sparse local connectivity and weight sharing among its neurons. A CNN can also be seen as a sequence of convolutional and subsampling layers in which the input is a set of $H \times W \times D$ images, where H is the height, W is the width and D is the number of channels which, in the case of RGB images corresponds to $D = 3$.

Following Ng et al. (2010), a typical convolutional layer (volume) is formed by K filters (kernels) of size $F \times F \times D$, where $F \leqslant H$ and $F \leqslant W$. These filters are usually randomly initialized and are the parameters to be tuned in the training process. Since the size of the filter is generally strictly smaller than the dimensions of the image, this leads to a local connectivity structure among the neurons. Each of this convolutional volumes has an additional hyper-parameter, S, which corresponds with the stride that the filter is going to slide spatially in the image.

Let's denote a particular training example as $X_{H\times W\times D}$ and a convolution filter $W_{F\times F\times D}$. As it is familiar from the usual Multi-Layer Perceptron, it is customary to add a bias term b to each of the linear combinations formed. Finally, a (commonly non-linear) activation function, for example ReLU, is applied to the convolution between the input image and the kernels, which yields an activation map A of the dimensions $1 + \frac{N-F}{S} \times 1 + \frac{N-F}{S} \times 1$:

$$A = f(X \circledast W + b)$$

where $\circledast$ represents the *valid* convolution between the operands and f is the activation function.

Appending the activation maps found by applying K diferent kernels to the input example, an activation volume of dimensions $1+\frac{N-F}{S}\times 1+\frac{N-F}{S}\times K$ is obtained. Note that depending on the dimensions of the image, the filter and the size of the stride, the resulting activation volume may reduce its spatial dimensions very quickly. An alternative to control this situation in advance is the use of *padding* techniques to the original image.

Finally, in order to perform dimensionality reduction directly on the data, pooling layers are applied to an activation volume or even the input image itself. These layers subsample its inputs, typically with mean or max pooling, over contiguous regions of size $P \times P$.

Figure 1 shows an example of a typical architecture for a CNN in which two convolutional and two pooling layers are applied to the original image. In this case, the extracted features obtained as are fed into a fully connected layer to perform the classification task. Note that it is possible to change the classifier set up at the end of the network with, for example, a SVM or a softmax classifier.

4.2 Back-propagation Algorithm

The summary presented in this section is heavily based on the Unsupervised Feature Learning and Deep Learning Tutorial from Ng et al. (2010). For simplicity, we will illustrate the algorithm assuming that we have a CNN with the input layer followed by a convolutional volume, a pooling layer and finally a fully connected layer.

Let's denote by $\delta^{(l+1)}$ the error term in the $(l+1)$-th layer in the network with labeled training data (x, y), parameters (W, b) and cost function $J(W, b; x, y)$. If the l-th layer is densely connected to the former, the error for this layer can be computed by:

$$\delta^{(l)} = \left((W^{(l)})^t \delta^{(l+1)}\right) \bullet f'(z^{(l)})$$

where $\bullet$ represents element-wise multiplication and f is the activation function.

The gradients are:

$$\nabla_{W^{(l)}} J(W, b; x, y) = \delta^{(l+1)}(a^{(l)})^t$$
$$\nabla_{b^{(l)}} J(W, b; x, y) = \delta^{(l+1)}$$

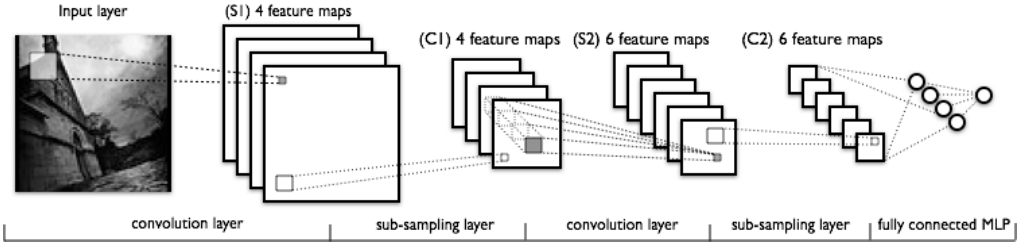

Fig. 1. Example of a CNN architecture. Taken from: LISA Lab (2016).

If the l-th layer is a convolutional and subsampling layer, then the error is propagated through as:

$$\delta_k^{(l)} = upsample\left((W_k^{(l)})^t \delta_k^{(l+1)}\right) \bullet f'(z_k^{(l)})$$

where k indexes the filter number and the *upsample* function propagates the error through the pooling layer by calculating the error related to each input unit.

Finally, the gradient for each filter map can be found by:

$$\nabla_{W_k^{(l)}} J(W, b; x, y) = \sum_{i=1}^{m} (a_i^{(l)}) \circledast rot90(\delta_k^{(l+1)}, 2)$$

$$\nabla_{b_k^{(l)}} J(W, b; x, y) = \sum_{a,b} \left(\delta_k^{(l+1)}\right)_{a,b}$$

where $a^{(l)}$ is the input to the l-th layer and $rot90(A, k)$ rotates the input array A counterclockwise by $k * 90$ degrees.

4.3 Linear Support Vector Machines

Suppose we are given a training data set of size n examples of the form:

$$\{(X_1, y_1), (X_1, y_1), ..., (X_n, y_n)\}$$

where each y_i is either 1 or -1 and each X_i is a p-dimensional vector. Thus, assuming that the data is linearly separable, we want to find the hyperplane that separates the group of $\{X_i\}$ for which $y_i = 1$ from those for which $y_i = -1$ so that the distance between the hyperplane and the nearest point from either group is maximized. For that reason, it is also called a *maximum-margin classifier*. This can be formally expressed as:

$$\min_{w \neq 0, b} \frac{1}{2} ||w||^2$$

$$\text{s.t.} \quad y_i(w^t X_i + b) \geqslant 1 \qquad (i = 1, 2, ..., n)$$

. Recall that $\frac{b}{||w||}$ represents the separation of the hyperplane from the origin along the normal vector w when the hyperplane is expressed as $wX - b = 0$.

4.4 Confusion Matrix

Consider a classification problem with only two classes: positive (P) and negative (N). For every training example, there are only four possible outcomes. If the training example is positive and the prediction is positive, we call it a *true positive*; and if the prediction is negative, it is called a *false negative*. On the other hand, if the training example is negative and it is classified as negative, it is called a *true negative*; otherwise, it is a *false positive*. Table 1 displays an example of a confusion matrix for a two-class problem.

Table 1. Confusion Matrix

		Predicted Class	
		P	**N**
Actual Class	**P**	True Positives	False Negatives
	N	False Positives	True Negatives

Fawcett (2006) defines a confusion matrix as a tool that allows to visualize the performance of a classifier in a supervised learning problem. By means of this matrix it is possible to asses whether the system is commonly confusing pairs of classes. In the aforementioned problem, the confusion matrix summarizes the four possible outcomes from the classifier.

5. MAMMOGRAMS CLASSIFICATION

5.1 Data

The mammograms used for the commitment of this work were retrieved from the database of the MIAS, collected by Suckling et al. (1994), which is known as mini-MIAS since the images of the original MIAS database has been reduced to 200 micron pixel edge and the dimension of the mammograms has been fixed to 1024 × 1024 pixels. This database contains 322 mammograms and the intensity of every pixel is between 0 and 255. This database also includes information about the class and the severity of abnormalities that may be present in the mammograms, as well as the coordinates of the center of these abnormalities.

It must be mentioned that we only used the mammogram images and the required information to divide the mammograms into three categories: patients with benign, malign or without tumor.

5.2 Data Preprocessing

Mammogram Cropping Mammograms contain black zones in the borders which may difficult the classification task. For this reason, we designed an algorithm to eliminate these black zones based on the sum of the pixels over the column. The algorithm finds the first column, say C_l, on the left of the mammogram in which the sum of the pixels exceeds a given threshold P. Now, from this point, the algorithm finds the first column, C_r, in which the sum of the pixels is not greater than P. Then, the new image is the one enclosed between C_l and C_r. This algorithm was applied to every mammogram of the 322 retrieved from the aforementioned database, taking $P = 500$. An example of

the images obtained at this stage is illustrated in Figure 2, in which Figure 2a is an original mammogram of the mini-MIAS database and Figure 2b is the resultant image after the application of the cropping algorithm.

Data Augmentation Due to the lack of mammograms corresponding to malign tumors (51 out of 322), it was necessary to perform a data augmentation operation in order to get a balanced dataset with at least 600 mammograms. For this purpose, after the cropping procedure, every resultant mammogram was rotated $-90°$, $90°$ and $180°$. The label assigned to the three artificially generated mammograms corresponded with the label of the original image.

5.3 Feature Extraction

As mentioned in Sections II and III, CNNs are being widely used to carry out image classification tasks because of their outstanding performance in comparison with other classification techniques. For this reason, they have become an emerging alternative in the computer-aided diagnosis field.

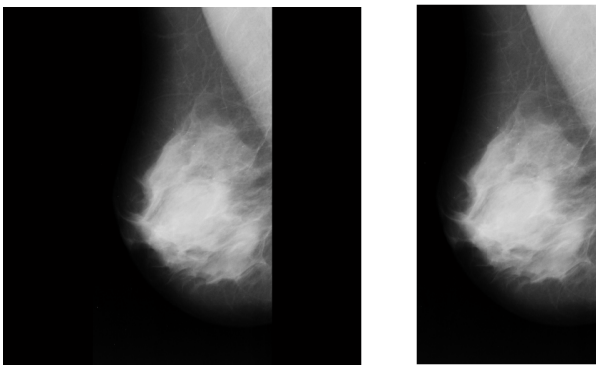

(a) Original. (b) Cropped.

Fig. 2. Mammograms obtained after the cropping stage.

In this work, two different experiments were carried out using a CNN previously trained on the ImageNet database as feature extractor. In the first experiment, the CNN used was AlexNet from Krizhevsky et al. (2012) while in the second experiment the CNN used was VGG-F from Chatfield et al. (2014). The features selected to perform the classification of mammograms were the activations of the last convolutional layer of the CNN. Then, in both cases, 4096 features have been extracted for each image.

In order to feed both pretrained CNNs with the cropped images, it was necessary to convert every mammogram into a three channel image by repeating the single channel three times. Then, the resulting image was resized depending on the input dimension of the CNN (227×227 pixels for AlexNet and 224×224 pixels for VGG-F). Finally, the average image (which is included with the tuned parameters of the pretrained models used) was subtracted from the resized image.

5.4 Classification

The goal of the system was to distinguish between three classes: patients with benign, malign or without tumor. Therefore, based on the works from Alolfe et al. (2009); Arevalo et al. (2015); Jiao et al. (2016), we decided to adopt a SVM as our classifier.

In order to evaluate our methodology, 120 and 80 mammograms of each category were selected from the augmented dataset to define the training and test stages of the SVM, respectively. Hence, our training set was composed by 360 mammograms and our testing set by 240 mammograms.

To carry out the training of the SVM, each of the 360 mammograms selected was given as the input for the CNN and the features obtained at this step became the inputs for the SVM. Then, using the Statistics and Machine Learning Toolbox from MATLAB, the SVM was trained.

The classification accuracy of the trained SVM was evaluated with the 240 mammograms belonging to the test set, following the same process described above for the extraction of the features for every mammogram.

5.5 Results

In Table 2 the confusion matrix obtained using AlexNet as feature extractor without augmenting the dataset is shown. This experiment was carried out with a training set of 30 mammograms per category and a test set of 20 per category. This confusion matrix is based on the response of the system on the test set and this low accuracy rate of only 35%, which corresponds to 21 well classified mammograms of the 60 that conformed the test set, is an evidence of the necessity of performing a data augmentation operation.

Table 2. Confusion matrix for MIAS test set predictions and feature extraction using AlexNet.

		Target			
		Benign	**Malign**	**Normal**	**Total**
Output	**Benign**	**36.53**	48.12	15.35	**36.53**
	Malign	27.39	**56.12**	16.49	**56.12**
	Normal	31.34	56.29	**12.36**	**12.36**
	Total	**38.35**	**34.96**	**27.97**	**35.01**

In Tables 3 and 4 the confusion matrices corresponding to the response of the system when AlexNet and VGG-F CNNs are used as feature extractors in conjunction with a SVM as classifier are exhibited. Table 3 shows the accuracy of the system on the test set after performing the data augmentation when the CNN used is AlexNet.

Table 3. Confusion matrix for Augmented MIAS test set predictions and feature extraction using AlexNet.

		Target			
		Benign	**Malign**	**Normal**	**Total**
Output	**Benign**	**61.79**	20.33	17.87	**61.79**
	Malign	18.79	**61.75**	19.46	**61.75**
	Normal	22.88	20.67	**56.46**	**56.46**
	Total	**59.73**	**60.10**	**60.20**	**60.01**

On the other side, Table 4 shows the response of the system when VGG-F is the feature extractor. It can be noted that the performance of the system has dramatically increased after artificially augmenting the dataset: from 35% to 60.01% and 64.52% using AlexNet and VGG-F, respectively.

Table 4. Confusion matrix for Augmented MIAS test set predictions and feature extraction using VGG.

		Target			
		Benign	**Malign**	**Normal**	**Total**
Output	**Benign**	**63.63**	18.45	17.92	**63.63**
	Malign	17.86	**64.37**	17.77	**64.37**
	Normal	16.91	17.54	**65.55**	**65.55**
	Total	**64.66**	**64.14**	**64.75**	**64.52**

6. CONCLUSIONS

Based on the results obtained in this work, the Deep Learning approach, particularly using pretrained CNNs as feature extractors, is a promising methodology when addressing the problem of diagnosing breast cancer with mammogram images. Since in this context the reliability of the system is highly relevant, it is desirable to increase the achieved 64.52% test accuracy. This outcome could be improved via fine-tuning of the final layers or training the whole network parameters. Additionally, it is worth noting the impact of the data augmentation process and the balance of the number of examples per class on the performance of the system.

The implemented system has three main advantages: (a) the mammograms are classified directly as with benign or malign tumor and without tumor, (b) it is not necessary to define a specific area in which the tumor is located and (c) apart from the mammogram, additional information must not be provided.

Future research could be focused on the evaluation of the following techniques:

- To extract features from multiple layers of the CNN instead of only using the activations obtained from the last convolutional layer.
- To use different pretrained CNNs as feature extractors, such as GoogLeNet from Szegedy et al. (2015) or ResNet from He et al. (2015a).
- To include a feature selection phase in which the best extracted features from a CNN could be selected to perform the classification of the mammograms.
- To test other classifier structures: neural networks, fuzzy inference systems or clustering techniques.

REFERENCES

Abdel-Zaher, A.M. and Eldeib, A.M. (2016). Breast cancer classification using deep belief networks. *Expert Systems with Applications*, 46, 139 – 144. doi: http://dx.doi.org/10.1016/j.eswa.2015.10.015.

Alolfe, M.A., Mohamed, W.A., Youssef, A.B.M., Mohamed, A.S., and Kadah, Y.M. (2009). Computer aided diagnosis in digital mammography using combined support vector machine and linear discriminant analysis classification. In *2009 16th IEEE International Conference on Image Processing (ICIP)*, 2609–2612. doi: 10.1109/ICIP.2009.5413992.

Arevalo, J., González, F.A., Ramos-Pollán, R., Oliveira, J.L., and Lopez, M.A.G. (2015). Convolutional neural networks for mammography mass lesion classification. In *2015 37th Annual International Conference of the IEEE Engineering in Medicine and Biology Society (EMBC)*, 797–800. doi:10.1109/EMBC.2015.7318482.

Bengio, Y., Lamblin, P., Popovici, D., and Larochelle, H. (2006). Greedy Layer-Wise Training of Deep Networks. *Advances in neural information processing systems*, 19(1), 153. doi:citeulike-article-id:4640046.

Chatfield, K., Simonyan, K., Vedaldi, A., and Zisserman, A. (2014). Return of the devil in the details: Delving deep into convolutional nets. In *British Machine Vision Conference*.

Dheeba, J., Singh, N.A., and Selvi, S.T. (2014). Computer-aided detection of breast cancer on mammograms: A swarm intelligence optimized wavelet neural network approach . *Journal of Biomedical Informatics*, 49, 45 – 52. doi:http://dx.doi.org/10.1016/j.jbi.2014.01.010.

Ertosun, M.G. and Rubin, D.L. (2015). Probabilistic visual search for masses within mammography images using deep learning. In *Bioinformatics and Biomedicine (BIBM), 2015 IEEE International Conference on*, 1310–1315. doi:10.1109/BIBM.2015.7359868.

Fawcett, T. (2006). An introduction to ROC analysis . *Pattern Recognition Letters*, 27(8), 861 – 874. ROC Analysis in Pattern Recognition .

Girshick, R., Donahue, J., Darrell, T., and Malik, J. (2014). Rich feature hierarchies for accurate object detection and semantic segmentation. In *Proceedings of the IEEE Computer Society Conference on Computer Vision and Pattern Recognition*, 580–587. doi: 10.1109/CVPR.2014.81.

Guo, Y., Liu, Y., Oerlemans, A., Lao, S., Wu, S., and Lew, M.S. (2015). Deep learning for visual understanding: A review. *Neurocomputing*. doi: 10.1016/j.neucom.2015.09.116.

He, K., Zhang, X., Ren, S., and Sun, J. (2015a). Deep residual learning for image recognition. *arXiv preprint arXiv:1512.03385*.

He, K., Zhang, X., Ren, S., and Sun, J. (2015b). Delving Deep into Rectifiers: Surpassing Human-Level Performance on ImageNet Classification. *Proceedings of the ICCV*, 1–11. doi:10.1109/ICCV.2015.123.

Hinton, G.E. (2005). What kind of graphical model is the brain? In *International Joint Conference on Artificial Intelligence*, volume 5, 1765–1775.

Hinton, G.E., Osindero, S., and Teh, Y.W. (2006). A fast learning algorithm for deep belief nets. *Neural computation*, 18(7), 1527–54. doi:10.1162/neco.2006.18.7.1527.

Jiao, Z., Gao, X., Wang, Y., and Li, J. (2016). A deep feature based framework for breast masses classification. *Neurocomputing*, 197, 221 – 231. doi: http://dx.doi.org/10.1016/j.neucom.2016.02.060.

Krizhevsky, A., Sutskever, I., and Hinton, G.E. (2012). ImageNet Classification with Deep Convolutional Neural Networks. *Advances In Neural Information Processing Systems*, 1–9. doi: http://dx.doi.org/10.1016/j.protcy.2014.09.007.

Lazebnik, S., Schmid, C., and Ponce, J. (2006). Beyond bags of features: Spatial pyramid matching for recognizing natural scene categories. In *Proceedings of the IEEE Computer Society Conference on Computer Vision and Pattern Recognition*, volume 2, 2169–2178. doi:10.1109/CVPR.2006.68.

LeCun, Y., Bengio, Y., and Hinton, G. (2015). Deep learning. *Nature*, 521(7553), 436–444. doi: 10.1038/nature14539.

Li, Y., Yosinski, J., Clune, J., Lipson, H., and Hopcroft, J. (2016). Convergent Learning: Do different neural networks learn the same representations? In *ICLR*, 1–21.

LISA Lab (2016). *My LeNet*. Retrieved 2016-5-26.

Mahersia, H., Boulehmi, H., and Hamrouni, K. (2016). Development of intelligent systems based on Bayesian regularization network and neuro-fuzzy models for mass detection in mammograms: A comparative analysis . *Computer Methods and Programs in Biomedicine*, 126, 46 – 62. doi:http://dx.doi.org/10.1016/j.cmpb.2015.10.017.

Marc'Aurelio Ranzato, C.P., Chopra, S., and LeCun, Y. (2006). Efficient learning of sparse representations with an energy-based model. In *Advances in Neural Information Processing Systems*, volume 19, 1137–1144.

Ng, A., Ngiam, J., Foo, C.Y., Mai, Y., and Suen, C. (2010). UFLDL tutorial. *http://ufldl.stanford.edu/wiki/index.php/UFLDL_Tutorial*.

Peng, W., Mayorga, R., and Hussein, E. (2016). An automated confirmatory system for analysis of mammograms. *Computer Methods and Programs in Biomedicine*, 125, 134 – 144. doi: http://dx.doi.org/10.1016/j.cmpb.2015.09.019.

Russakovsky, O., Deng, J., Su, H., Krause, J., Satheesh, S., Ma, S., Huang, Z., Karpathy, A., Khosla, A., Bernstein, M., Berg, A.C., and Fei-Fei, L. (2015). ImageNet Large Scale Visual Recognition Challenge. *International Journal of Computer Vision (IJCV)*, 115(3), 211–252. doi:10.1007/s11263-015-0816-y.

Sermanet, P., Kavukcuoglu, K., Chintala, S., and LeCun, Y. (2013). Pedestrian detection with unsupervised multi-stage feature learning. In *Proceedings of the IEEE Conference on Computer Vision and Pattern Recognition*, 3626–3633.

Simonyan, K. and Zisserman, A. (2015). Very Deep Convolutional Networks for Large-Scale Image Recognition. *Proceedings of the ICLR*, 1–14. doi: 10.1016/j.infsof.2008.09.005.

Srivastava, N., Hinton, G., Krizhevsky, A., Sutskever, I., and Salakhutdinov, R. (2014). Dropout: A simple way to prevent neural networks from overfitting. *The Journal of Machine Learning Research*, 15(1), 1929–1958.

Suckling, J., Parker, J., Dance, D., Astley, S., Hutt, I., Boggis, C., Ricketts, I., Stamatakis, E., Cerneaz, N., Kok, S., et al. (1994). The mammographic image analysis society digital mammogram database. In *Exerpta Medica. International Congress Series*, volume 1069, 375–378.

Szegedy, C., Liu, W., Jia, Y., Sermanet, P., Reed, S., Anguelov, D., Erhan, D., Vanhoucke, V., and Rabinovich, A. (2015). Going deeper with convolutions. In *Proceedings of the IEEE Conference on Computer Vision and Pattern Recognition*, 1–9.

Wang, Z., Yu, G., Kang, Y., Zhao, Y., and Qu, Q. (2014). Breast tumor detection in digital mammography based on extreme learning machine. *Neurocomputing*, 128, 175 – 184. doi: http://dx.doi.org/10.1016/j.neucom.2013.05.053.

World Health Organization (2016). Breast cancer: prevention and control. URL `http://www.who.int/cancer/detection/breastcancer/en/`. [Accessed: 19- May- 2016].

Zeiler, M.D. and Fergus, R. (2014). Visualizing and understanding convolutional networks. In *Proceedings of the ECCV International Workshop on Statistical Learning in Computer Vision*, 818–833. Springer.

Dynamic clustering for process supervision ⋆

Nathalie A. Barbosa *,** **Louise Travé-Massuyès** ** **Victor H. Grisales** ***

* *Universidad Nacional de Colombia, Department of Electrical and Electronics Engineering, Bogotá, Colombia (e-mail: nabarbosa@unal.edu.co)*
** *LAAS-CNRS, Université de Toulouse, CNRS, UPS, Toulouse, France. (e-mail: {nabarbos,louise}@laas.fr)*
*** *Universidad Nacional de Colombia, Department of Mechanical and Mechatronics Engineering, Bogotá, Colombia (e-mail: vhgrisalesp@unal.edu.co)*

Abstract: In the context of data-driven monitoring, evolving environments challenge researchers with non-stationary data flows where the concepts (or states) being tracked can change over time. This issue is common in real industrial environments that suffer wear over time, implying for instance that the "normal" state undergoes drift. This requires monitoring algorithms suited to represent the evolution of the system behavior and in real industrial environments, also suited to represent time dependent features. This paper proposes a unified clustering approach to monitoring evolving environments using a two-stages distance-based and density-based algorithm. In this approach the system measurements trends, found on the fly, are characterized and then used as input to the clustering algorithm that provides as output clusters representing the system current state. Due to a forgetting process, clusters may emerge, drift, merge, split or disappear, hence following the evolution of the system. The dynamic clustering algorithm shows good outlier rejection capability when tested on an industrial benchmark suffering faults with varying magnitude.

Keywords: Dynamic clustering, Fault Detection, Supervision, Evolving environments

1. INTRODUCTION

Technological advances of past decades have resulted in systems highly adaptive to a constantly changing environment. In addition, they have changed the way enterprises get information about the state of their systems. Huge amounts of data, arising from various sources, are generally collected and they are available for further analysis. These two facts have promoted the success of machine learning approaches for diagnostics tasks, although they must face new challenges, in particular building efficient classification algorithms that adapt the targeted model – or classifier – to the evolution of the system and that scale to big data.

Many researchers have used pattern recognition, neural networks and clustering techniques for fault diagnosis (Maurya et al., 2010; Hedjazi et al., 2010; Eduardo Mendel et al., 2011). To carry out diagnosis using a pattern recognition method, there are two principal stages: training (or learning) and recognition. One known disadvantage of classic data-driven techniques is that they often address only anticipated fault conditions (Vachtsevanos et al., 2007), missing new or unknown data of which it was not aware of during training. Other disadvantage is that training examples usually follow static distributions that remain unchanged over time. If the performance of the algorithm decreases below a given threshold it should be re-learned, but it does not adapt dynamically (its structure and sometimes even its parameters).

The classification techniques can establish a model of the system functional states by extracting knowledge from various attributes. This knowledge is related to a particular behavior, without being represented by a set of analytic relations. The modifications of these characteristics enable the detection of abnormal operations (Isaza et al., 2009).

In the context when new objects submitted to the classifier during the recognition stage do not imply novelty detection nor a change of the classifier the classification is called *static classification* ((Joentgen et al., 1999)). If the classifier changes in time (dynamically), following the system, the classification task becomes a *dynamic classification problem*.

Dynamism in the classifier is achieved when not only the parameters but the classifier structure changes according to input data in an automatic way. Abrupt changes in the data can be captured by cluster creation or elimination. Smooth changes are usually reflected as cluster drifts and less frequently as cluster merging and splitting.

Among the techniques that have been used for dynamic classification, we can mention: evolving clustering ((Angelov, 2011)), Self-Adaptive feed-forward neural network (SAFN) ((Li et al., 2011)), LAMDA (Learning Algorithm for Multivariate Data Analysis) ((Kempowsky et al., 2006)), Growing Gaussian Mixture Models (2G2M) ((Bouchachia and Vanaret, 2011)), CluStream (Aggarwal et al., 2003), ClusTree (Kranen et al., 2011) and DenStream (Cao et al., 2006). Some of these alternatives

⋆ This work was supported in part by the Colombian administrative department of science, technology and innovation COLCIENCIAS, the Universidad Nacional de Colombia and the Laboratory for Analysis and Architecture of Systems LAAS-CNRS

are really complex and hence not suited to handle online large amounts of process data, such as data arriving in a stream. Their requirements in terms of memory and processor power are too high. Two-stages clustering (online/offline) has emerged as an alternative to deal with large amounts of data arriving at fast rates. Examples of this approach can be found in (Aggarwal et al., 2003; Kranen et al., 2011; Cao et al., 2006).

Qualitative trends (QT) is a user friendly representation of features that have been successfully applied in the fields of process monitoring and fault diagnosis (Dash et al., 2004; Maurya et al., 2007, 2010; Gamero et al., 2014). This non model-based technique exploits historical data of a process to characterize its behavior using a qualitative language. This representation reduces the complexity of system states by allowing only a finite set of descriptors (Gamero et al., 2014). Polynomial fit-based methods have been used to extract time-series trends owing to its shorter computational time and higher robustness to noise. The main advantages of the QT representation are its interpretability, the complexity reduction and the robustness in presence of noise. On the contrary, one main drawback is the lack of differentiation of episodes following the same qualitative trend, i.e. the concept of magnitude is completely lost.

In (Barbosa et al., 2015) we proposed a monitoring algorithm which couples a dynamic clustering method with an on-line trend extraction algorithm that works incrementally on the incoming data. The algorithm was used to achieve on-line diagnosis on the continuous stirred tank heater (CSTH) model developed by (Thornhill et al., 2008). In this paper we improve our previous work by: (1) introducing a global and local density analyses that improves the system tracking specially in presence of novel unknown behavior. (2) Introducing a variable representation that allows quick detection by an operator. (3) Proposing several functions to represent the forgetting process. This **Dy**namic **Cl**ustering algorithm for tracking **E**volving **E**nvironments is called ***DyClee***. We especially want to address the outlier rejection and the evolution characterization capabilities of our algorithm both in a local and global sense.

This paper is organized as follows: Section 2 introduces our algorithm including the dual global and local density analysis. Section 3 presents ***DyClee*** forgetting process including the new proposed functions. Section 4 presents outlier detection and its application to detect unknown system behaviors. Section 5 shows some capabilities of our algorithm in toy examples and Section 6 shows the same capabilities in the CSTH benchmark. Finally the conclusions are presented in section 7

2. DYNAMIC CLUSTERING ALGORITHM

This paper uses the distance- and density-based clustering approach introduced in (Barbosa et al., 2015) improved to be able to detect local and global outliers and to follow different evolution dynamics. The algorithm description is shown in figure 1.

System data is considered to arrive in stream. Data streams take the form of time series providing the values of the signals measured on a given process at each sampled time. In order to extract trend information, this work proposes to process each time series x_i into *episodes*, to generate an abstraction of the original signal into a simpler *qualitative-like*, yet quantitative, representation.

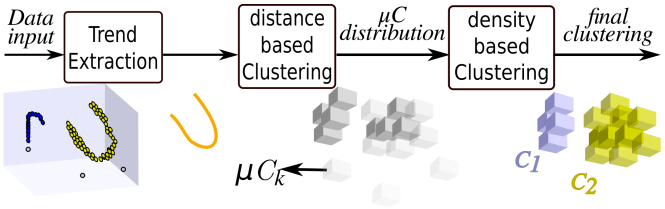

Fig. 1. Principle of ***DyClee***

Episodes are defined by three elements: a trend context TC, a set of auxiliary variables AV and a time interval T_i leading to (1):

$$e(x_i) = \{TC, AV, T_i\} \tag{1}$$

As introduced before, to find the trend context polynomial fit can be used. Instead of using an entirely qualitative representation using an alphabet of primitives like Maurya et al. (2007) or Gamero et al. (2014), we use the polynomial coefficients as trend context.

When data arrives, the preprocessing stage performs a polynomial fit in order to find the underlying trend. If the polynomial representation is considered as good, i.e. the polynomial fitting error is lesser than the signal noise variance, the polynomial coefficients are used as TC and the polynomial start and end time-stamps define T_i.

The distance-based clustering stage creates μ-clusters that are summarized representations of the data set made by using some statistical and temporal information. Formally, a μ-cluster is a hyper box representing a group of data points **close in all dimensions** and whose information is summarized in the tuple:

$$\mu C_k = (n_k, LS_k, SS_k, t_{lk}, t_{sk}, D_k, Class_k) \tag{2}$$

where n_k is the number of objects in the μ-cluster k, $LS_k \in \Re^d$ is the vector containing the linear sum of each feature over the n_k objects, $SS_k \in \Re^d$ is the square sum of feature over the n_k objects, t_{lk} is the time when the last object was assigned to that μ-cluster, t_{sk} is the time when the μ-cluster was created, D_k is the μ-cluster density and $Class_k$ is the μ-cluster label if known. In order to maintain an up-to-date structure allowing to track system evolution, μ-clusters are weighted with a forgetting function.

The density-based stage analyses the distribution of those μ-clusters whose density is considered as medium or high and creates the final clusters by a density based approach, that is, dense μ-clusters that are close enough (connected) are said to belong to the same cluster. A μ-cluster is qualified as one of three options: dense μ-cluster ($D\mu$C), semi-dense μ-cluster ($S\mu$C) or low density (outlier) $O\mu$-cluster ($O\mu$C).

In our previous work the dense character of a μ-cluster was found using a user specified parameter named α. Specifically, being K the total number of μ-clusters, $D\mu$Cs are the μ-clusters with $D_j \geq \alpha\ avg\,(D_1 \cdots D_K)$, $S\mu$C are the μ-clusters with $D_j \geq \frac{\alpha}{2} avg\,(D_1 \cdots D_K)$, and $O\mu$C are the μ-clusters with densities lower than that. The problem with this approach is that it demands user knowledge about the density distribution of the clusters and it does not guarantee cluster homogeneity.

In this paper we implements two different automatic approaches to establish the dense character of the μ-clusters, named global-density approach and local-density approach. The former approach allows to detect clusters with similar

densities while the later allows the detection of clusters with varied densities. ***DyClee*** global- and local-density approaches are further explained in the following subsections. These approaches are the first contribution of this paper.

2.1 Global-density analysis

In the global-density approach density is considered as a μ-cluster characteristic regarding all the μ-clusters. In this sense, two measures are considered as representative of the μ-clusters in a global sense, the average of μ-cluster's density and the median. These measures will work as thresholds for establishing the dense character of a μ-cluster. The intuition behind the selection of these measures is that the median and average densities of an heterogeneous group are significantly different, although, if the group is uniformly dense, these two quantities are equal.

Formally, a μ-cluster μC_z is said to be dense at time t if its density is greater than or equal to both global measures, i.e. the median and the average. On the contrary if its density is bigger or equal to one of the two measures and lower than the other the μ-cluster is said to be semi-dense. Finally if the μ-cluster μC_k have a density bellow both thresholds it is said to be an OμC. These conditions are represented in inequalities 3 to 5, where D_i is the density of the μ-cluster i and K is the total number of μ-clusters.

$$D\mu C \Leftrightarrow D_z \geq median\left(D_1 \cdots D_K\right) \wedge D_z \geq avg\left(D_1 \cdots D_K\right) \quad (3)$$

$$S\mu C \Leftrightarrow D_z \geq median\left(D_1 \cdots D_K\right) \vee D_z \geq avg\left(D_1 \cdots D_K\right) \quad (4)$$

$$O\mu C \Leftrightarrow D_z < median\left(D_1 \cdots D_K\right) \wedge D_z < avg\left(D_1 \cdots D_K\right) \quad (5)$$

As stated before, in order to find the final clusters, the dense character of the μ-clusters and its connections are analyzed. A set of connected μ-clusters is said to be a *group*. Groups of μ-clusters are analyzed recursively in order to find the clusters within. A cluster is created if every inside μ-cluster of the group is a $D\mu$C and every border μ-cluster is either a $D\mu$C or an $S\mu$C.

2.2 Local-density analysis

Density-based clustering algorithms as those from (Ester et al., 1996), proposing the DBSCAN algorithm, and (Barbosa et al., 2015), in which we proposed an initial version of ***DyClee***, group data samples according to density. Nevertheless, in these implementations, the concept of 'dense' is related to a global value ($MinPts$ in the case of (Ester et al., 1996) and α in the case of (Barbosa et al., 2015)). The problem of taking a global value to identify a point as dense appears when clusters with varied densities are present in the same data set as can be seen in Figure 2, where density is represented as μ-cluster opacity. In this case, density-based algorithms using a global approach may misclassify low density clusters as noise.

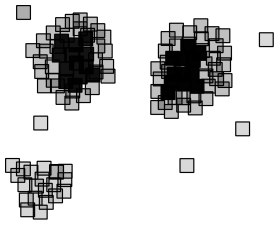

Fig. 2. μ-cluster groups of varied densities in 2D

Unlike the previously named approaches, ***DyClee*** analyses the dense character of each μ-cluster regarding the density of the other μ-clusters in the same group. This approach allows what is called multi-density clustering (Mitra et al., 2003).

As in the global approach the average and the median are chosen as thresholds, but they are applied recursively in the μ-clusters groups. In other words, for each group G_k, the μ-clusters having their density higher than or equal to the average density of the group ($avg(D_{G_k})$) and higher than or equal to the median density of the group ($median(D_{G_k})$) are considered as dense. μ-clusters having a density higher than or equal to only one of those measures (either average or median) are considered as $S\mu$Cs and those with density below both measures are considered as $O\mu$Cs. Summarizing:

$$D\mu C \Leftrightarrow D_z \geq median\left(D_{G_k}\right) \wedge D_z \geq avg\left(D_{G_k}\right), \quad (6)$$

$$S\mu C \Leftrightarrow D_z \geq median\left(D_{G_k}\right) \vee D_z \geq avg\left(D_{G_k}\right), \quad (7)$$

$$O\mu C \Leftrightarrow D_z < median\left(D_{G_k}\right) \wedge D_z < avg\left(D_{G_k}\right). \quad (8)$$

The μ-clusters group shown in Figure 2 is analyzed in this manner: First, the groups of μ-clusters are found and then, for each group, a cluster is formed with the denser connected μ-clusters as shown at the left of Figure 3. Once formed, the rest of the group is analyzed looking for the denser μ-clusters (with respect to the remaining elements of the group). If no dense region is found the next group in analyzed following the same method until all groups are analyzed. The final classification is shown at the right of Figure 3. The group or groups with the lower density are taken as outliers. It is worth noting that global-density approaches are unable to detect the green cluster since the densities of the μ-clusters in that group are low, with respect to the others clusters.

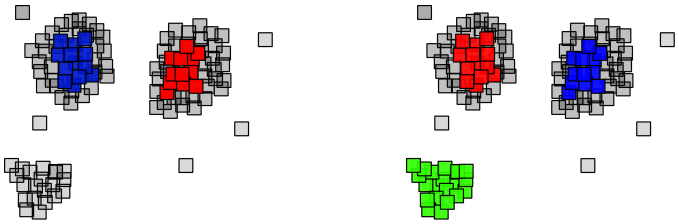

Fig. 3. Global-(left) and local-(right) density analysis results

3. TRACKING SYSTEM EVOLUTION

DyClee implements a forgetting process in order to cope with cluster evolution. Specifically, μ-clusters are weighted with a decay function dependent on the current time t and the last assignation time t_{lk}. This function $f\left(t, t_{lk}\right)$ emulates a forgetting process. When a new d-dimensional object $E_x = \left[x^1, \ldots, x^d\right]^T$ is assigned to a μ-cluster μC_k at t, the cluster last assignation time is updated to $t_{lk} = t$. The other attributes of the feature vector are updated as follows:

$$n_k^{(t)} = n_k^{(t-1)} f\left(t, t_{lk}\right) + 1 \quad \forall k \quad (9)$$

$$LS_{k,i}^{(t)} = LS_{k,i}^{(t-1)} f\left(t, t_{lk}\right) + x_i \quad \forall i, i = 1, \ldots, d. \quad (10)$$

$$SS_{k,i}^{(t)} = SS_{k,i}^{(t-1)} f\left(t, t_{lk}\right) + x_i^2 \quad \forall i, i = 1, \ldots, d. \quad (11)$$

Numerous machine learning methods have implemented some kind of forgetting function (also called decay function) to be able to detect or track concepts that drift or shift over time. As

introduced before in this work we propose several functions that may be used in the representation of the forgetting process.

The simplest forgetting function corresponds to a linear decay as given in equation (12). The function slope m could be inversely proportional to the time it takes to the function to go from one to zero, $m = 1/t_{w=0}$. This function with $t_{w=0} = 6000$ is plotted in blue in Figure 4. A linear decay has been used above all in biological and physical systems.

$$f(t, t_{lk}) = \begin{cases} 1 - m(t - t_{lk}) & t - t_{lk} \leq t_{w=0} \\ 0 & t - t_{lk} > t_{w=0} \end{cases} \quad (12)$$

If a non-forgetting time range is appended to a linear decay, we get a trapezoidal decay profile. This type of function is used as profile in electronic applications. The trapezoidal decay function is given in equation (13) where t_a represents the no forgetting time, and $t_{w=0}$ the time when the function reaches zero. This function is represented in red in Figure 4.

$$f(t, t_{lk}) = \begin{cases} 1 & t - t_{lk} \leq t_a \\ \dfrac{m - t}{m - t_a} & t_a \leq t - t_{lk} \leq t_{w=0} \\ 0 & t - t_{lk} > t_{w=0} \end{cases} \quad (13)$$

Statistical processes use overall an exponential decay function. This function is shown in equation (14), where λ_d is a positive rate known as exponential decay constant. The function is plotted in magenta in Figure 4. This type of functions is the most widely used to model decay since it has applications in all fields of science. A generalization of exponential decay is shown in equation (15). It is the decay function used by (Aggarwal et al., 2003) and (Kranen et al., 2011) and a graphical representation can be found in green in Figure 4. The change in the base from e to any value β gives interesting properties. For example, if β is chosen to be $\beta = 2\psi$, then the time at which half of the data is forgotten, is $\frac{1}{\psi\lambda_d}$. This function is known as the half life function and is widely used in biological processes.

$$f(t, t_{lk}) = e^{-\lambda_d(t - t_{lk})} \quad (14)$$

$$f(t, t_{lk}) = \beta^{-\lambda_d(t - t_{lk})} \quad (15)$$

Figure 4 shows the shape for the named functions in the case where $t_{w=0} = 6000$, $t_a = 2000$. For simplicity in the figure t_{lk} is set to zero. As previously mentioned, ***DyClee*** implements all the functions shown in equations (12) to (15), allowing proper adaptation to all kind of process evolutions. In ***DyClee*** the forgetting process impacts clusters density. As explained in the previous section, each t_{global} period the density of all μ-clusters is recalculated. Density change implies μ-cluster type change, its decrease makes $D\mu$-clusters become $S\mu$-clusters and $S\mu$-clusters become $O\mu$-clusters, and vice-versa.

4. OUTLIER DETECTION AND NOVELTY DETECTION

Outlier detection has been a widely investigated problem in several disciplines, including statistics, data mining and machine learning and several approaches have been proposed to deal with the outliers rejection problem ((Hawkins, 1980),(Markou and Singh, 2003),(Zimek et al., 2012)). Outlier detection methods can be classified according to several characteristics: the use of training (pre-labeled) data, the assumption of a standard statistical distribution, the type of data set, dimension of detected outliers, type of detected outliers (global/local), among

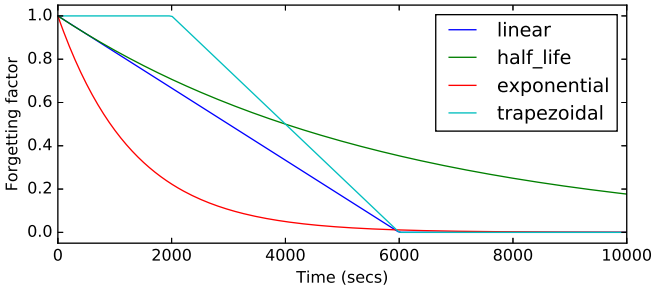

Fig. 4. Decay functions used to emulate data forgetting

others. Most of classification monitoring techniques focus on reject the abnormal observations derived from noised data.

In general, outliers indicate noise, damage or errors. Nevertheless, outliers can also be an indication of the occurrence of unknown events or unexpected patterns resulting from system evolution or reconfiguration.

Most commonly used outlier detection approaches are those classified as distribution-based, distance-based (Knorr et al., 2000), density-based (Breunig et al., 2000) or angle-based (Kriegel et al., 2008). If the probability density function (or functions) is (are) known and alleged to follow a normal distribution, the simplest approach to outlier detection is to compute the probability of a sample to belong to a class (or classes), and then use a threshold to establish its outlier character. This approach is equivalent to finding the distance of the sample to class means and threshold on the basis of how many standard deviations away the sample is (Markou and Singh, 2003).

Unfortunately, in most real world applications the data distribution is not known *a priori*, as a result, non-parametric methods are generally preferred. Non parametric approaches like distance-based, density-based or angle-based make no assumption about the statistic properties of the data which makes them more flexible than parametric methods. In this paper we use the clustering distance and density framework to detect abnormal data which may or may not represent the evolution of a known state or the emergence of a novel behavior.

Since no formal unique definition of outlier exists, the notion of outlier may greatly differ from one outlier detection technique to another. In this work, the outlierness or not of a sample is related to the outlierness of the μ-cluster that contains its information. Explicitly, for ***DyClee***, an *outlier sample* is defined as: *A sample contained in an* $O\mu C$ and an $O\mu C$ is defined as *a representation of samples that, due to their position and density, do not correspond to any of the identified clusters nor represents relevant novel behavior.*

The distance and density analysis that ***DyClee*** performs allows it to detect both, global and local multivariate outliers, the former in all configurations and the latter when multi-density clustering is used. The outlier character of a sample is binary, that is, a sample can only be considered as outlier or not outlier. Nevertheless, the outlierness of a μ-cluster may be associated with its density which provides a score about how much outlier a μ-cluster is. In other words, the set of all $O\mu$-clusters can exhibit different densities although their densities remain close to each other, that is, in the same relative level with respect to the clusters densities ($S\mu$-clusters and $D\mu$-clusters).

If global density is used, ***DyClee*** detects only global outliers. As said in the previous section, in general, a μ-cluster is considered

as outlier if its density is lower than the median and the average of all clusters densities, as shown in equation 5. If local-density analysis is used, the equation 8 shows that an μ-cluster is considered as outlier iff its density is lower than the group median density and the group average density, being its group the set of all the μ-clusters connected (directly or indirectly) to it.

Using the local-density analysis allow low density populations (as faults) to be represented as well as high density populations (as is usually the case of normal behavior). In addition, the local-density analysis allows the detection of novelty behavior in its early stages when only a few objects giving evidence of this evolution are present. While it is deemed desirable to detect clusters of multiple densities, it is also important to maintain the ability to reject outliers. ***DyClee***'s solution to outlier rejection is based on the exclusion of the μ-clusters found to have low density in each analyzed group.

5. TESTING IN TOY EXAMPLES

This section will illustrate how ***DyClee*** can be used to achieve some important features in supervision. The first test aims to show the capability of tracking the system through different operation points, even if these points are relatively close to each other. To this end, we select the R15 dataset from (Veenman et al., 2002). This dataset of 600 points is generated by 15 similar 2D Gaussian distributions. ***DyClee*** deals with high overlapped data distributions from its conception. Figure 5 shows ***DyClee*** clustering results compared to those achieved in (Veenman et al., 2002). The 15 classes are correctly recognized.

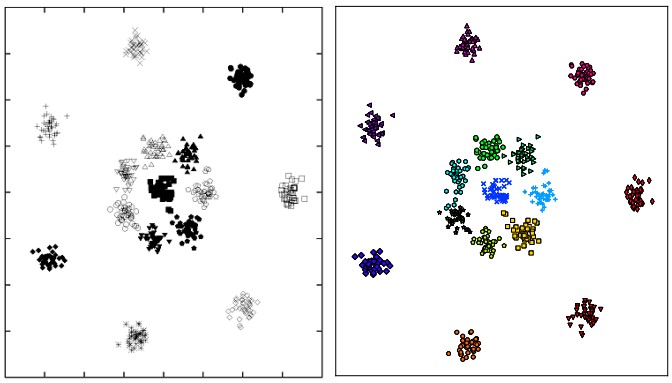

Fig. 5. Veenman Maximum Variance Cluster Algorithm (left) and ***DyClee*** clustering results (right)for R15 test set.

An academic industrial example suffering from this situation is the Tennessee Eastman Process. In this benchmark, two different products are produced from four reactants and the mass ratios between them vary from one operation mode to another.

As a second test we explore the ability of our algorithm to cluster multi-density distributions. As stated before, the ability to detect distributions evidencing different amount of samples or concentrations is a desirable feature in supervision since it can improves the detection and characterization of unknown behaviors. Multi-density situation are very common in industrial environments, where the measures coming from the process in normal operation mode(s) are wide more abundant that those coming from start-up or maintenance routines. Even more,

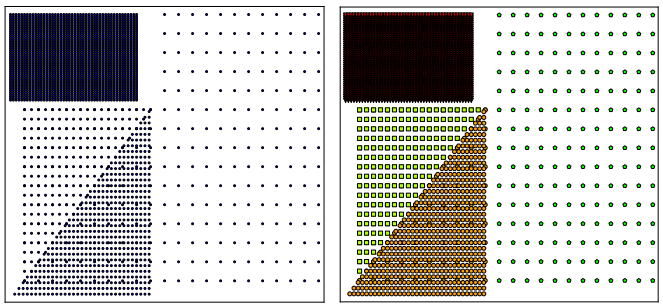

Fig. 6. At left, Clusters of varied density. At right ***DyClee*** clustering results

since faulty states are uncommon samples from those states will be also rare.

The toy example chose to test this feature is the multi-density set used in (Fahim et al., 2010). In this set four different clusters exhibit densities varying in a wide range. Two of these classes present also overlapping. The clustering results of our algorithm are shown in Figure 6. We can see that the four classes are correctly recognized.

Another highly desired feature comes from the fact that, in most of the real world applications, non-stationarity is typical and data is expected to evolve over time. In this example our algorithm is confronted with slowly time changing distributions, or as is usually called in the online learning scenario, concept drift (Gama et al., 2014).

These drifts can come, for example, from physical wear of some mechanical parts, by the sensitivity loss of some sensors or by the addition of a new source of noise. In order to shown ***DyClee*** performance over this issue, a synthetic set was created. Three clearly differentiated distributions are used to form three clusters. Two of this groups drift in time until shift positions as can be seen in Figure 7. Synthetic data are generated changing the center of the distribution each 100 samples.

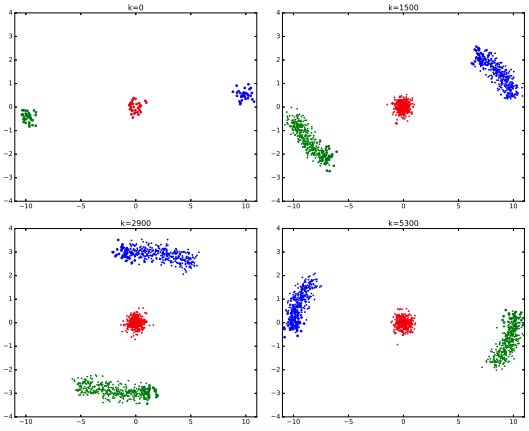

Fig. 7. Concept Drift toy example

Dynamic data cause several clusterers to fail in finding clusters distribution change since they cannot cope with evolution, losing hence, the tracking over the system state. Snapshots showing the distribution of μ-clusters in several time instants are depicted in Figure 8. It can be seen how clusters evolution is followed thanks to the drift of some of the existent μ-clusters and to the creation of new μ-clusters. Growth in the amount of clusters can be seen between snapshots one and two, and again

between snapshots two and three. $O\mu$-clusters are represented as gray boxes. This dynamic tracking is possible thanks to the implementation of the forgetting process that increase the clusterer reactivity to data changes.

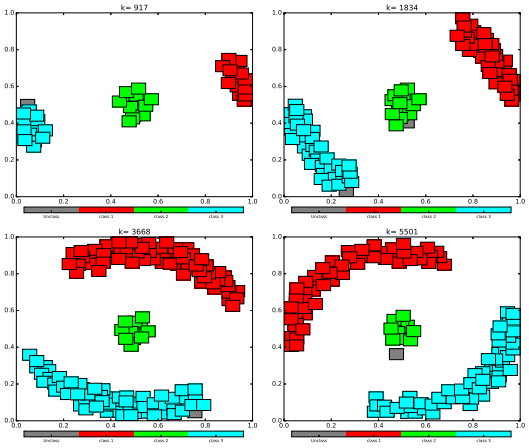

Fig. 8. μ-clusters following system evolution

In the next section these features help in the diagnosis of the CSTH benchmark introduced in (Thornhill et al., 2008).

6. DIAGNOSIS CASE STUDY: THE CSTH

The CSTH is a benchmark of a stirred tank in which hot (50°) and cold (24°) water are mixed and further heated using steam; the final mix is then drained using a long pipe. The configuration of this benchmark, developed by (Thornhill et al., 2008), is shown in Figure 9. It is assumed that the tank is well mixed so the temperature of the outflow is the same as that in the tank. Process inputs are set-points for the cold water, hot water and steam valves. Process outputs are hot and cold water flow, tank level and temperature. Process inputs and outputs represent electronic signals in the range $4-20mA$. The benchmark is tested in closed-loop. PID controllers are used to guide the plant as suggested in (Thornhill et al., 2008).

Thornhill *et al.* also suggests two operation points depending in whether or not the hot water flow is used. The suggested set-points for the operation points $OP1$ and $OP2$ are shown in table 1. Simulink models, with and without disturbances, are available at (Thornhill, web resource) website. The provided disturbances are real data sequences experimentally measured from the pilot plant at the University of Alberta.

We adapted this benchmark in order to implement dynamic events as evolving leaks or pipe clogging. The first simulated

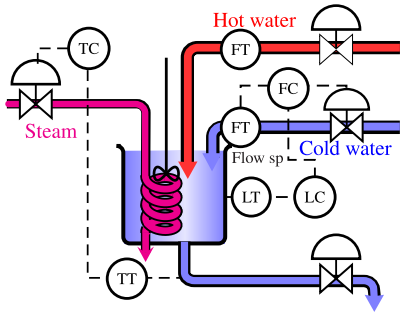

Fig. 9. Diagram of the continuous stirred tank heater

Variable	OP 1	OP 2
$Level$	12.00	12.00
$CW flow$	11.89	7.330
$CW valve$	12.96	7.704
$Temperature$	10.50	10.50
$Steam valve$	12.57	6.053
$HW valve$	0	5.500

Table 1. Suggested operational points for the CSTH in mA

scenario is that of a pipe clogging. The second scenario implements several faults occurring alone or in pairs. Among the considered faults, tank leakage and valve stuck are found.

6.1 Scenario 1:Tracking state drift

One common problem in industrial applications is that states might drift when the physical parts of the system are exposed to wearing processes. In the case of the CSTH we simulate the evolution of $OP1$ when residues accumulate in the border of the output pipe causing a drop in the maximal output flow. The process measurements for this scenario can be seen as continuous lines in Figure 10. This figure also shows that our clustering algorithm is capable of following this evolution. The polynomial fit is also show in the figure, represented as dashed lines.

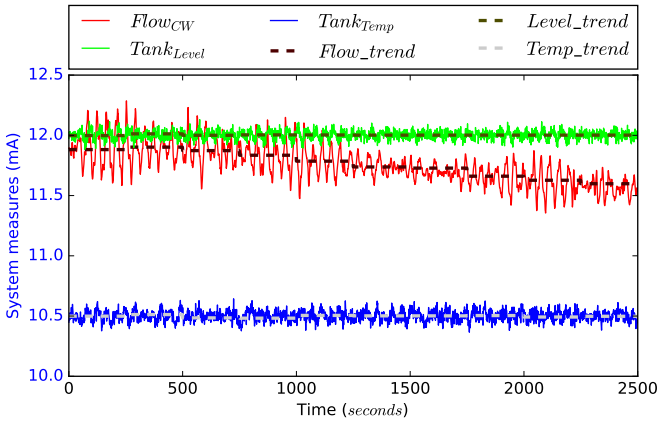

Fig. 10. ***DyClee*** TC and process measurements for scenario 1

As was said before following the system evolution at seen its measures can be a difficult task and even impossible when dozens of signals are analyzed at the same time. We propose to use a radar-like graphic representation to follow variables evolution. For the simulated scenario the graphics for $t = 250$ and $t = 2500$ are shown in Figure 11. The drift in the $Flow_{CW}$ variable are depicted as the filled area between the original characterized point and the current point.

6.2 Scenario 2: Tracking of multiple fault scenarios

Several faults between evolving leaks and stuck valves were simulated in this scenario. The total simulation time of this scenario is equivalent to a timespan of a month (2.419.200 $seconds$) in which the plant works the half of the time in $OP1$ and the other half in $OP2$ (operational points described in table 1). The faulty events included in this scenario are detailed in table 2. CSTH output signals are shown as background in Figure 12. At the beginning of the simulation the CSTH was working in $OP1$. Simple fault events and multiple faults events

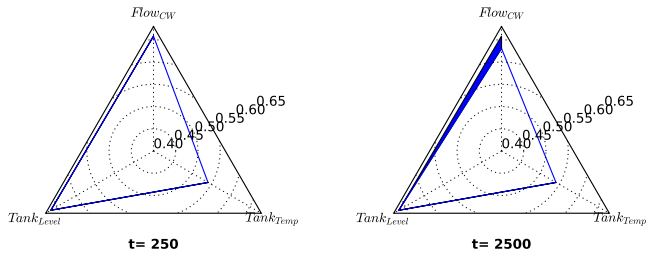

Fig. 11. ***DyClee*** clustering results for scenario 1.

t	Event	t	Event
0	Start at $OP1$	9.0	e-leak starts.
1.5	e-leak starts.	9.6	e-leak fixed
2.4	e-leak fixed	12.0	Changed to $OP2$
3.5	e-leak starts.	15.0	S_{valve} stuck 10%
3.8	2^{nd} e-leak starts.	15.6	Valve repaired
4.5	Leaks fixed	18.0	e-leak starts.
5.5	S_{valve} stuck 0%	18.4	Leak fixed
5.8	Valve repaired	20.0	HW_{valve} stuck 40%
6.5	HW_{valve} stuck 10%	20.6	Valve repaired
7.0	Valve repaired	24.2	End

Table 2. Scenario 2: Multiple fault simulation over a month timespan. (Simulation time in $sec \times 10^5$)

were simulated. ***DyClee*** Clustering results are shown in Figure 12.

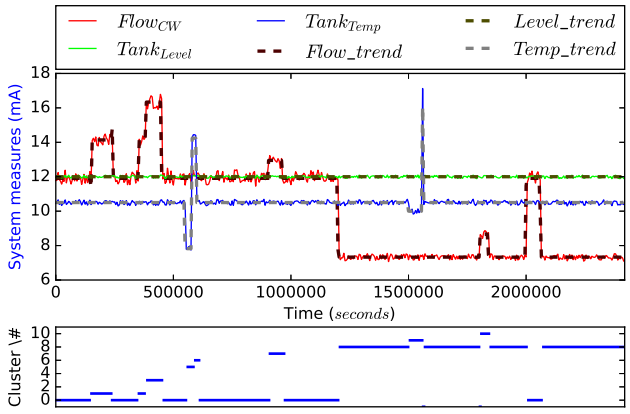

Fig. 12. ***DyClee*** clustering results and process measurements for scenario 2

Since ***DyClee*** works under a non-supervised learning paradigm, only the system measures are necessary as input for the algorithm. Unlike most of the tracking algorithms that can only track known behaviors, ***DyClee*** start of not behavior at all and built his knowledge when new behaviors are recognized. This can be seen in Figure 12 where ***DyClee*** can successfully track online the process and its evolution. Ten different behaviors are recognized. The label associated to these clusters is related to their order of apparition, and zero represents the non-representative behavior caused by extremely noised samples or by transition states.

In order to illustrate ***DyClee*** structural evolution a snapshot of the μ-clusters distribution in t between 405000 and 900000 seconds is presented in Figure 13. For this experiment the sampling time were $T_s = 0.5s$. The algorithm start window size

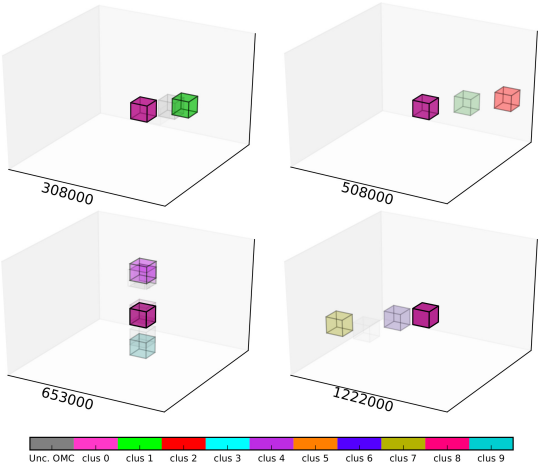

Fig. 13. Dynamic Clustering of the CSTH for scenario 2. t between 308000 and 1222000 seconds

was established as $win_{length} = 5000$ samples (2500 seconds), the minimum size as 1000 samples and the maximum as 10000 samples. The forgetting process were activated and the 'linear' forgetting function were selected with $\beta = 150000$, that is, thirty times the normal window size.

Clusters are represented in compact way in the radar plot shown in Figure 14. This figure shows the cold water flow as the key feature to detect the system evolution in most of states. Nevertheless, the tank temperature change is what characterize the cluster 5, corresponding to the stream valve fault.

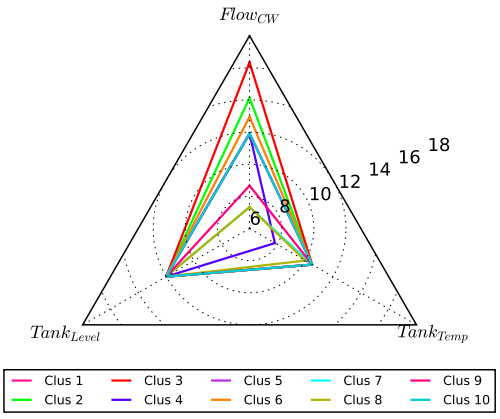

Fig. 14. Radar clusters' representation for scenario 2

7. CONCLUSIONS

In this paper, we propose a multi-density improvement to dynamic clustering that follows system evolution by adapting its forgetting process. This work illustrates with practical examples, how data-based clustering under non supervised learning paradigm can help in process supervision. The proposed algorithm is used to monitor industrial processes and has proved to be capable to detect different types of faults including those with time varying dynamics on the selected benchmark. The algorithm shows good performance in presence of disturbances and the results follow the evolution of the system. Tests have shown performance improvement when local-density analyses are used together with the fast distance-based clustering.

From a technical point of view, it would be interesting to compare the proposed algorithm with systems of different nature and include categorical features, which may consolidate the proposed methodology.

REFERENCES

Aggarwal, C.C., Han, J., Wang, J., and Yu, P.S. (2003). A framework for clustering evolving data streams. In *Proceedings of the 29th international conference on Very large data bases-Volume 29*, 81–92. VLDB Endowment.

Angelov, P. (2011). Fuzzily connected multimodel systems evolving autonomously from data streams. *Systems, Man, and Cybernetics, Part B: Cybernetics, IEEE Transactions on*, 41(4), 898–910.

Barbosa, N., Massuyes, L.T., and Grisales, V.H. (2015). A data-based dynamic classification technique: A two-stage density approach. In *SAFEPROCESS 2015, Proceedings of the 9th IFAC Symposium on Fault Detection, Supervision and Safety for Technical Processes*, 1224–1231. IFAC.

Bouchachia, A. and Vanaret, C. (2011). Incremental learning based on growing gaussian mixture models. In *Machine Learning and Applications and Workshops (ICMLA), 2011 10th International Conference on*, volume 2, 47–52. IEEE, Elsevier.

Breunig, M.M., Kriegel, H.P., Ng, R.T., and Sander, J. (2000). Lof: Identifying density-based local outliers. *SIGMOD Rec.*, 29(2), 93–104.

Cao, F., Ester, M., Qian, W., and Zhou, A. (2006). Density-based clustering over an evolving data stream with noise. In *SDM*, 326–337.

Dash, S., Maurya, M.R., Venkatasubramanian, V., and Rengaswamy, R. (2004). A novel interval-halving framework for automated identification of process trends. *AIChE journal*, 50(1), 149–162.

Eduardo Mendel, F.M.V., Rauber, T.W., and Batista, R.J. (2011). Condition monitoring based on kernel classifier ensembles. In *9th IEEE International Conference on Industrial Informatics (INDIN)*, 81 –85. doi:10.1109/INDIN.2011.6034841.

Ester, M., Kriegel, H.P., Sander, J., and Xu, X. (1996). A density-based algorithm for discovering clusters in large spatial databdata with noise. In *KDD*, 226–231.

Fahim, A., Salem, A.E., Torkey, F., Ramadan, M., Saake, G., et al. (2010). Scalable varied density clustering algorithm for large datasets. *Journal of Software Engineering and Applications*, 3(06), 593.

Gama, J., Žliobaitė, I., Bifet, A., Pechenizkiy, M., and Bouchachia, A. (2014). A survey on concept drift adaptation. *ACM Computing Surveys (CSUR)*, 46(4), 44.

Gamero, F.I., Melndez, J., and Colomer, J. (2014). Process diagnosis based on qualitative trend similarities using a sequence matching algorithm. *Journal of Process Control*, 24(9), 1412 – 1424.

Hawkins, D.M. (1980). *Identification of outliers*, volume 11. Springer.

Hedjazi, L., Kempowsky-Hamon, T., Despnes, L., Le Lann, M.V., Elgue, S., and Aguilar-Martin, J. (2010). Sensor placement and fault detection using an efficient fuzzy feature selection approach. In *Decision and Control (CDC), 2010 49th IEEE Conference on*, 6827 –6832.

Isaza, C.V., Orantes, A., Kempowsky-Hamon, T., and Lann, M.V.L. (2009). Contribution of fuzzy classification for the diagnosis of complex systems. In *Fault Detection, Supervision and Safety of Technical Processes*, 1132–1137.

Joentgen, A., Mikenina, L., Weber, R., and Zimmermann, H. (1999). Dynamic fuzzy data analysis based on similarity between functions. *Fuzzy Sets and Systems*, 105(1), 81–90.

Kempowsky, T., Subias, A., and Aguilar-Martin, J. (2006). Process situation assessment: From a fuzzy partition to a finite state machine. *Engineering Applications of Artificial Intelligence*, 19(5), 461–477.

Knorr, E.M., Ng, R.T., and Tucakov, V. (2000). Distance-based outliers: algorithms and applications. *The VLDB Journal – The International Journal on Very Large Data Bases*, 8(3-4), 237–253.

Kranen, P., Assent, I., Baldauf, C., and Seidl, T. (2011). The ClusTree: indexing micro-clusters for any stream mining. *Knoledge and information systems*, 29(2), 249–272.

Kriegel, H.P., Shubert, M., and Zimek, A. (2008). Angle-based outlier detection in high-dimensional data. In *Proceedings of the 14th ACM SIGKDD International Conference on Knowledge Discovery and Data Mining*, KDD '08, 444–452. ACM, New York, NY, USA.

Li, K., Yao, F., and Liu, R. (2011). An online clustering algorithm. In *Fuzzy Systems and Knowledge Discovery (FSKD), 2011 Eighth International Conference on*, volume 2, 1104–1108. IEEE.

Markou, M. and Singh, S. (2003). Novelty detection: a review–part 1: statistical approaches and part 2: neural network based approaches. *Signal processing*, 83(12), 2481–2497.

Maurya, M.R., Paritosh, P.K., Rengaswamy, R., and Venkatasubramanian, V. (2010). A framework for on-line trend extraction and fault diagnosis. *Engineering Applications of Artificial Intelligence*, 23(6), 950 – 960.

Maurya, M.R., Rengaswamy, R., and Venkatasubramanian, V. (2007). Fault diagnosis using dynamic trend analysis: A review and recent developments. *Engineering Applications of Artificial Intelligence*, 20(2), 133 – 146.

Mitra, P., Pal, S.K., and Siddiqi, M.A. (2003). Non-convex clustering using expectation maximization algorithm with rough set initialization. *Pattern Recognition Letters*, 24(6), 863 – 873.

Thornhill, N. (web resource). The csth web site. Accessed: 2015-02-12. http://personal-pages.ps.ic.ac.uk/~nina/CSTHSimulation/index.htm.

Thornhill, N.F., Patwardhan, S.C., and Shah, S.L. (2008). A continuous stirred tank heater simulation model with applications. *Journal of Process Control*, 18(3), 347–360.

Vachtsevanos, G., Lewis, F., Roemer, M., Hess, A., and Wu, B. (2007). *Intelligent Fault Diagnosis and Prognosis for Engineering Systems*. John Wiley & Sons, Inc.

Veenman, C.J., Reinders, M.J., and Backer, E. (2002). A maximum variance cluster algorithm. *Pattern Analysis and Machine Intelligence, IEEE Transactions on*, 24(9), 1273–1280.

Zimek, A., Schubert, E., and Kriegel, H.P. (2012). A survey on unsupervised outlier detection in high-dimensional numerical data. *Statistical Analysis and Data Mining*, 5(5), 363–387.

CHAPTER 2

AUTOMATION

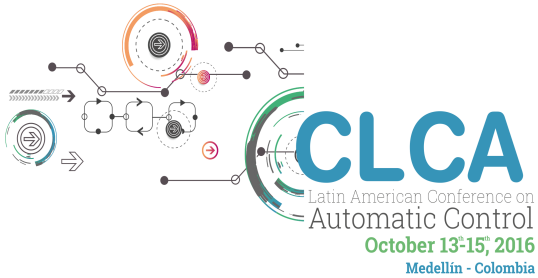

Coloured Petri Nets for Implementation of Safety Instrumented Systems in Critical Production Systems

Jeferson A L Souza*. Diolino J Santos Fo.*Paulo Eigi Miyagi*.
Jose Reinaldo Silva*. Lucas A. Moscato*.Reinaldo Squillante Jr*. José Ruben Sicchar*

***University of São Paulo, São Paulo, Brazil**
(Tel:+5511-3091-9138; e-mail: jeferson.souza@usp.br; diolinos@usp.br; pemiyagi@usp.br; reinaldo@usp.br; lamoscat@usp.br; reinaldo.squillante@usp.br; jose.sicchar@usp.br)

Abstract: The inherent complexity of critical production systems, inserted in a context of sustainability policies and environmental preservation and protection of the people, are the motivation for the design of safety control systems, which aim to reduce the risk, inherent of any production system, to a safe level. According to the experts, the concept of Safety Instrumented Systems (SIS) is a solution in that promotes the reduction of risk through hierarchical layers to prevent and / or mitigate faults. Standards such as IEC 61508/61511 refer to the performance requirements, but do not mention implementation methods. Whereas the occurrence of a fault may be associated with the occurrence of an event, Petri nets become an efficient tool for design the detection and treatment of the effects of the occurrence of faults. This paper proposes a method for implementing SIS in critical production systems from risk analysis techniques, fuzzy logic and Coloured Petri Nets, considering the integration of the prevention SIS and the mitigation SIS.

Keywords: Critical Production Systems, Faults, Safety Instrumented System, Coloured Petri Nets.

1. INTRODUCTION

In this first decade of the century XXI many studies have indicated that automation processes are undergoing transformations that have been strongly influenced by the advance of technology and computing resources, becoming increasingly complex due to their dynamic and needed to address issues such as global market competitive production and technology used, among other factors (Chen & Dai, 2004), (Santos Filho, 2000), (Wu, et al., 2008). Given this new scenario, industrial processes and their control are becoming more and more complex. Additionally, organizations have focused on policies to achieve and to demonstrate people's safety and health, environmental management system, and the capability in risk management.

In a globalized and competitive environment in which organizations are inserted, it is essential to adopt strategic plans and operational practices that ensure the ability to adapt rapidly and consequent change of the systems-productive but hitherto conceived. The expectation is that in addition to result in a process with effective cost reduction, high product quality and flexibility of production lines, and reduction of new products and delivery development times (Santos Filho, 2000) (Chen & Dai, 2004) (Wu et al., 2008), also causes the reduction of environmental impacts of the process. The results of this new scenario are Productive Systems (SPs) that perform highly complex processes (Sampaio, 2011) (Ferreira et al., 2014) that might not be achievable by conventional production methods (Mazzolini, et al., 2011). Because of this complexity inherent in any modern production system, some states, though undesirable, can be achieved, it could be mentioned: the fault states of components, design flaws, or operational errors, including intentional, and environmental events that involve the system. Such occurrences could result, depending on the complexity of the SPs, serious risks to the physical integrity of people, the environment and economic losses resulting from damage to the equipment itself (Sallak, et al., 2008). Although many studies have been presented both for diagnosis and for the treatment of a particular class of faults (Morales et al., 2007) (Ru & Hadjicostis, 2008) (Wang et al., 2008) (Zhang & Jiang, 2008) (Summers & Raney, 1999) (Sallak, et al., 2008), accidents continue to occur.

In this context, according to specialists, the use of Safety Instrumented Systems - SIS is a solution to this problem by inserting successive risk reduction layers to prevent and / or mitigate the effects of occurrence of a fault in a SP. SIS are referenced in standards such as IEC 61508 and IEC 61511, that lists the performance requirements and the life cycle for a design of a SIS. However, the standards make no mention of methods for SIS implementation.

According to the relevance of the subject, several works have been published. (Squillante JR, 2013) proposes a method for implementing the SIS prevention, in that the risk of an SP is evaluated by a HAZOP (Hazard and Operability) study. The results are refined by Bayesian networks (BN), and the control algorithm for the detection, diagnosis and treatment of a fault are modelled by classical Petri nets. (Souza, 2014) proposes a system for the mitigation of SIS, in which the critical elements of the SP are defined from risk analysis techniques, and actions of mitigation are determined by fuzzy logic. The both studies resulted in graphs of high complexity due to the interrelationship of arcs of the PN net. Another factor was the limited integration of prevention and mitigation models, revealing gaps for the actual implementation of a SIS.

This paper proposes a method for the implementation of SIS critical SPs with reference to IEC 61508 and IEC 61511, considering the integration of prevention and mitigation SIS,

from the use of high-level Petri nets - HLPN for formal modelling of control algorithms.

2. FUNDAMENTAL CONCEPTS

2.1 Safety Instrumented Systems

Safety Instrumented System (SIS) is a safety control system which aims to reduce the risks associated with SPs. In general, the role of a SIS is to monitor through security sensors, critical events in the industrial process and indicate alarms or perform preset actions through security actuators, for the prevention of accidents or mitigation of the consequences generated by these events (Goble, 1998).

According to IEC 61508, an SIS consists of independent layers and risk reduction successive, which can be implemented for safety control systems that operate independently of the Basic System Process Control - BPCS. The structure of an SIS with Reference to IEC 61508/61511 standards is illustrated in Figure 1.

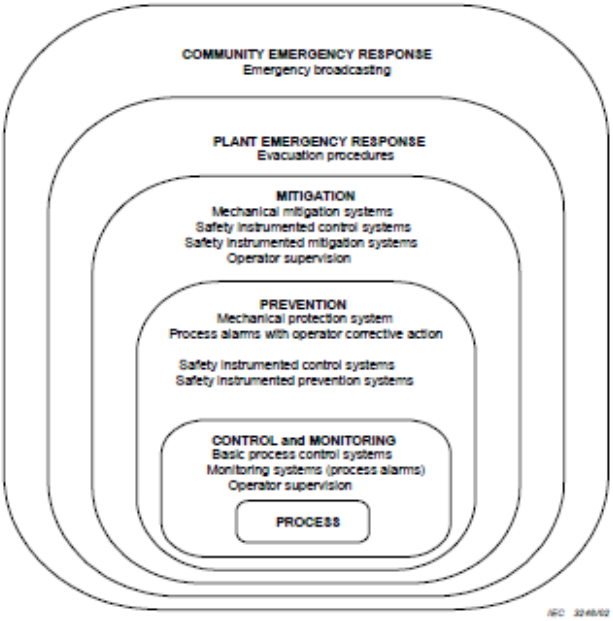

Fig. 1. Risk reduction layers (extracted from IEC 61511-1)

2.2 Risk Analysis Techniques

This section introduces the fundamental concepts of some risk analysis techniques, such as FMEA, FTA, HAZOP and What-If technique.

The FMEA technique, described in IEC 60812 (IEC 2006), consists of a detailed and systematic study of possible failures of the components of a system. The failure modes of each component are identified, and a severity level is associated with its effect, and assess the likelihood of their occurrence. The FMEA also discusses actions to eliminate, mitigate and control the causes and consequences of failures. (Lewis, 1995).

Another technique used is the Fault Tree - FTA, deductive reasoning methodology described in IEC 62025 (2008) that part of a top event, which is the occurrence of a specific fault in a system, which aims to determine the relationship fault logic components and / or operational human errors that may be associated with the occurrence of the top event. The analysis is done from the construction of a logical tree. In this way, one obtains a graph which can be used to identify all possible causes for the occurrence of a fault (Modarres, et al., 2010). The graph enables an analysis of the "top-down", which results in understanding how the event occurred. In the analysis "bottom-up" it has been "why" of the event. The advantage of FTA on the FMEA is that one can have a combination of several elements or multiple failure modes, the graph connected by logic elements such as "and" and "or".

The study of operability and risks, or HAZOP (HAZard and OPerability studies) defined in IEC 61882 (IEC, 2001) was developed for efficient and detailed examination of the variables of a process having a strong resemblance to the FMEA. Hazop identifies the ways in which the process equipment may fail or be improperly operated. It is developed by a multidisciplinary team, being guided by the application of specific words - words guide - each process variable. Thus, to generate the deviation of operational standards, which are analyzed in relation to their causes and consequences.

2.3 Petri nets

Petri net (PN) as a graphical tool and mathematics provides a uniform way for model, analysis and design of Discrete Event Systems - SEDs (Adam et al, 1998; Nassar, et al. 2008; Zurawski & Zhou, 1994), being effective as a description of technical and specification processes (Hamadi & Benatallah, 2003; Morales et al, 2007; Yoo, et al, 2010). It provides a representation that can be used both as a conceptual model and functional model of a system that can analyze and validate the operation of the system at each stage of its development cycle. The PN can also be used as a design tool, allowing for easy interpretation and identification of processes and their dynamic behavior and / or systems being modelled (Nassar et al., 2008). The models based on NP can be used for qualitative and quantitative assessment involving the analysis of the behavioral properties and performance measure, respectively. Moreover, with the development of software simulators (Zurawski & Zhou, 1994), has provided tools for editing and analysis of these models. Enables the representation of the system dynamics and structure at various levels of abstraction, according to the with-complexity system (Nassar, et al., 2008). It is able to model synchronization process, the occurrence of asynchronous events, competitors and conflict operations, or resource sharing (Adam et al, 1998; Nassar, et al, 2008).

Among the extensions of PN can mention the high-level Petri nets - HLPN (Smith, 1998) (ISO / IEC 15909, 2000) and the Coloured Petri nets - CPN (Jensen, 1997), in which the graphical representation the model is reduced, without losing the formalism of classical PN, increasing the level of abstraction and the power of process modelling, in which the network places have individual marks and separated by type, declared the identity of each variable. The arcs have markings and filters that select the type of mark that can flow through this arc and the transition that occur in different modes confined to the locality rule their pre-set and post-set. The dynamic graph composed is the result, so the whole graph, registration and declaration.

2.4 Fuzzy Logic

Fuzzy logic is becoming useful in modelling of nonlinear systems, or when the use of differential equations becomes too complex, or even in processes whose knowledge of the dynamic behaviour is not yet fully understood (Lee, 1990).

Fuzzy systems are based on the human knowledge or a set of rules that are designed to mimic human reasoning in control decisions (Zadeh, 1996). questions like "If ... (conditional) So ... (consequent)" are formulated process experts in analysis, and control actions are defined from the responses, and in its May-ria, systems multiple inputs to a single output (Zadeh, 1965), (Lee, 1990), (Stern et al., 2008). All rules are processed in parallel, with the consequent be active with its degree of membership in the system output. Unlike Boolean logic, fuzzy numbers are contained in a closed interval 0 to 1, and may take values within this range (Zadeh, 1965).

The use of fuzzy logic in CPs is referenced in the IEC61131-7 standard, which deals with the conversion of fuzzy logic in implementable language in commercial CPs.

3. PROPOSAL OF SAFETY INSTRUMENTED SYSTEM

The proposed method is outlined in the flowchart shown in Figure 2, and the steps for its implementation, described in the following items 3.2 to 3.9, are built from knowledge of independent experts and/or database obtained from field experiments, record of past operation or computer simulation of plant under study.

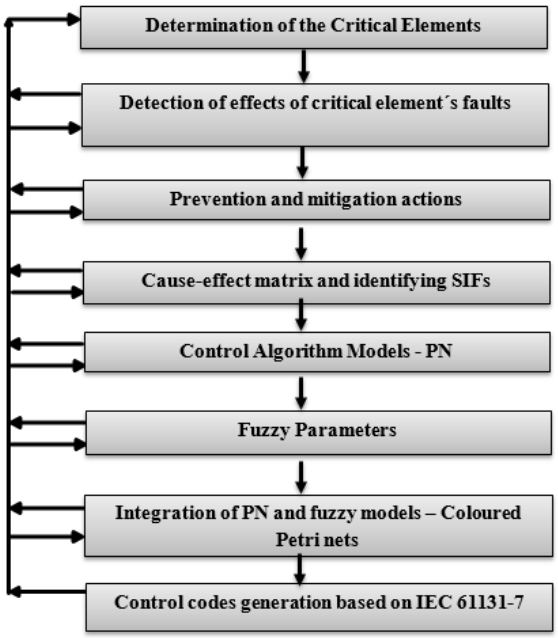

Fig. 2. Flowchart of steps of the proposed method.

To illustrate the proposed method, an application example for of a natural gas compression station is presented. Natural gas is a mixture of highly flammable hydrocarbons. To be extracted from the environment must be filtered and pressurized in compressor stations to its carriage due to consumer centres. Figure 3 illustrate an example of a gas compressor station.

3.1 Description of the proposed method

Fig. 3. Natural gas compressor station - Ecomp

3.2 Determination of the critical elements

To determine the critical elements of the process under study we utilize the risk analysis techniques FTA, FMEA and What-If. The FMEA, to associate a severity level to the occurrence of fault of a component, indicates which components monitored in the mitigation layer. Faulted components that pose risks to operators, the environment and equipment, besides violating the legislation, receives maximum severity.

Table 1. Suggested FMEA for temperature increase of the lubricating oil of shaft bearing compressor

Component	Potential Fault Mode		Potential Effects	Potential Causes	Deteccion - Control	Recommended Actions	Severity
Turbo Compressor	Lubrication		Temperature increase lubricating oil bearing	Saturated Oil	Temperature Sensors	Shut-Down (Preventive)	10
						Dioxide Carbon (Mitigate)	
	Damage	Oil Pump					
		Shaft Speed control		Bearing Wear Hardware / Software			
	Overload	Speed		Speed Control			
		Torque		Condensate Excess			

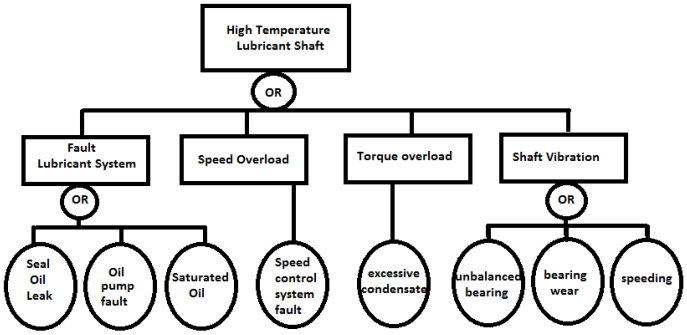

Fig. 3. Suggested FTA for the top event “High Temperature Lubricant Shaft”

3.3 Detection of effects of critical element´s faults

For each fault mode, a specific sensor links every critical component to the mitigation PLC. According to IEC 61508, such sensors must be independent of the BPCS. Redundant architectures (Squillante Jr, et al., 2011), such as the criteria voting 2oo3 (two of three), avoid spurious faults and sensor reading errors.

For the results of the FMEA and the FTA of previous step, thermocouples were inserted with the respective Tags TET-211A to TET 211D, respectively to each of the four compressor units.

3.4 Prevention and mitigation actions

For each effect of a critical fault, detected by the SIS mitigation sensors, SIS mitigation actuators implement a mitigation action, controlled by the SIS mitigation control layer, aiming to preserve people, environment and equipment.

To determine de mitigation actions will make use of *What-If* technique, based on human knowledge and records of occurrence of faults, its effects and the actions proposed to mitigate its effects.

To mitigate the effects caused by the occurrence of a fault in the compressor, beside the action of shutdown from the prevention layer, a suggested action to mitigate the effects is the forced cooling, in case of preventive layer is not sufficient or if the temporal variation of temperature proves too high.

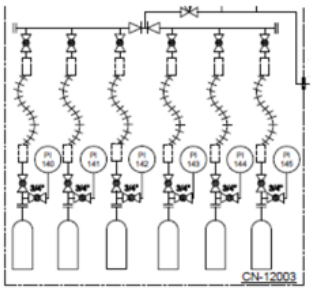

Fig. 4. P&ID of carbon dioxide cylinders of station

After this study and compilation of mitigation actions, will determine which actuators required for each mitigation action.

3.5 Cause-effect matrix and identifying SIFs

For each initiator event, represented by the sensor signals, determines their prevention and mitigation, the representation is making in an array, in which the causes are listed in columns and the effects associated with mitigation actions (actuators) in the respective lines.

Initializers common events can be grouped, representing, according to IEC 61508, the instrumented safety functions - SIFs. Mitigation actions can also be common to different SIFs. The cause-and-effect matrix for SIF 1, represented by the signals from the sensors TET211 is illustrated in Table 3.

Table 2. Cause - effect matrix for SIF 1

SIF1 / CAUSES	EFFECTS	STOP TCA	STOP TCB	STOP TCC	STOP TCD	CLOSE XV -001	CLOSE XV -017	CLOSE XV -019	CLOSE XV -020	CLOSE XV -003	CLOSE XV -018	CLOSE XV -005	CLOSE XV -022
PSHH A		X	X			X	X	X		X		X	
PSHH B			X	X		X			X	X	X	X	
PSHH C				X	X	X				X		X	X

The cause-effect matrix for mitigation of SIF 1 consists of all actions foreseen in the SIS prevention for SIF1, in addition to fast and pressurized stop with carbon dioxide from the compressor units and closing stock valves with their tags: XV-10A, XV-11A, 10B-XV, XV-11B, 10C-XV, XV-11C, 10D XV-XV-11D, 25A-XV, XV-26A, 25B-XV, XV-26B, XV-25C, XV-26C, XV-25D, XV-26D, XV-16A, XV-16B, XV-16C, XV-16D. The result is an array of 4 lines with the same initiators events SIF1 prevention, but with a total of 36 columns.

The analysis of the whole process resulted in 12 SIFs, 72 initializers events (causes), and 108 actions (effects).

3.6 Control Algorithm Models - PN

The next step is the control algorithm modelling to detect the initiator event each SIF, represented by the signs of the respective sensors, the confirmation, and treatment of fault, represented by their prevention and mitigation actions, based on the results obtained by the team of experts in the process.

Their prevention and mitigation actions are performed until all sensors indicate the safe state of their respective variables in a logical "and". After this check, the actions of prevention / mitigation are ceased, and the process should, according to IEC 61508, undergo a thorough survey process for possible fixes and maintenance for the process to be restarted.

This sequence of actions can be classified as a sequence of discrete events, so can be modelled by Petri nets. For each SIF is generated a model of prevention and mitigation, and initializers events may be common to models of prevention and mitigation, and prevention and mitigation may be common to different SIFs.

For each model generated, the properties of bounding, liveness and safety are checked, with the aid of computational tools as PIPE2 and HPSim.

The results were high extended and complex graphs, considering that the process resulted in a total of 40 PN models, 72 initializers events and 57 actuators. Figures 5 and 6 (annex) illustrates the PN model for the prevention and mitigation of SIF1, respectively.

3.7 Parameter determination – fuzzy logic

From the initiators events and their prevention and mitigation developed qualitatively in the cause-effect matrix, the next step is the analysis of these signals. From the results of What-If technical team of experts, fuzzy logic can be used to associate their actions of actuators for the ranges of process

variables, or variables associated with any failure of a component parameter.

To illustrate the algorithm, the expert reports, to a value between 10% and 30% above the set point temperature of TET211 shutdown must be performed. Longer a value above 50% would be unacceptable, which requires a mitigation action beyond the proposed shutdown. Table 7 shows this result in a fuzzy membership function implemented in the fuzzy MatLab® toolbox. Note that we have gaps in which two actions may be occurring, with different proportions.

Table 7. Membership functions for temperature

Temperature	***Action***
Set Point	BPCS
Above 30% of SP	Prevention
Above 50% of SP	Mitigate

According to the membership functions adopted in the Fig. 6 above, has three regions for temperature: Basic Control, Prevent and Mitigate. The input of time derivative of temperature was set to three values: zero, positive and negative. As for output, which is proportional to the valve opening was also set to three positions: zero or closed valve, high or 100% open and medium, open at 50%.

The Table 10 illustrate the editing of the fuzzy rules, according to the results of the *What-If* technique.

Table 10. Membership functions and percentage of valve

If	***Temperature***	***Op***	$\Delta T/\Delta t$	***Then***	***Valve***
1	BPCS				CLOSED
2	PREVENTION	AND	-		CLOSED
3	PREVENTION	AND	+		50%
4	MITIGATE	AND	+		100%
5	MITIGATE	AND	-		50%
6	MTIGATE	AND	ZERO		100%
7	PREVENTION	AND	ZERO		CLOSED

Table 11. Membership functions for temperature

Fuzzy Model	*Mamdani*
AND Method	*Min*
OR Method	*Max*
Implication	*Min*
Aggregation	*Max*
Defuzzification	*Centroid*

Applying the fuzzy logic to the whole process was obtained a total of 180 rules, resulting in a greatly compromised understanding due to the interrelationship of common actuators to different rules.

3.8 Integration of PN and fuzzy models – Coloured Petri nets

From the results obtained in fuzzy logic, the next step is the use of high-level Petri nets, in particular the Coloured Petri nets for the formal modelling of the control algorithm, considering the integration of the models in classical PN of prevention and mitigation SIFs.

Coloured Petri nets, due to its high power of representation, resulted in simplified graphs, compared with the classical PN, without losing the power of representation. Another factor that contributed to the simplification was the use of hierarchical models for all SIFs, in which the covering properties and liveliness can be checked from the use of own elements in hierarchical transitions. Figure 12 illustrates the model in CPN of the SIS with reference to IEC 61508/61511.

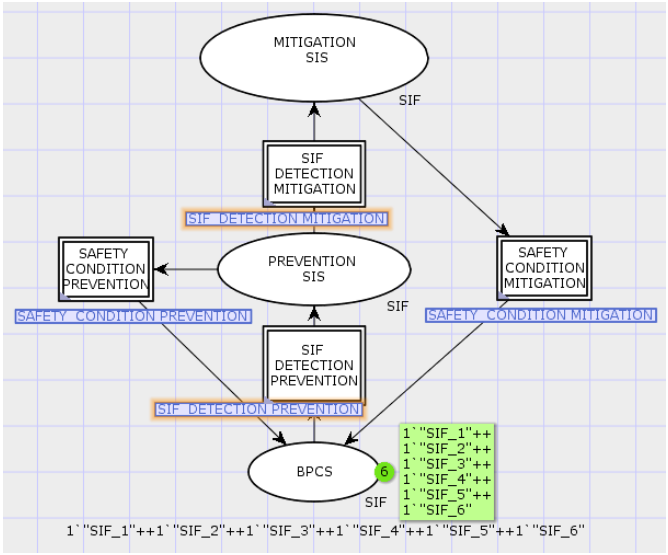

Fig. 12. CPN model for SIS, in reference to IEC 61508

The functions of fuzzy membership, obtained from the risk analysis techniques, were implemented in CPN models from the brands of distinction (multisets) in their places of the network, and use of algebraic functions to shooting of their bows. Another advantage, as already mentioned, was the fact of working with hierarchical models of prevention and mitigation, in the intervals of initializers events of their SIFs were represented synthetically in a core network, and the related actions of prevention / mitigation, associated with the lines of cause and effect matrix, they were represented in the secondary networks. The actions of prevention / mitigation are performed until the safe check condition of all sensors is satisfied, restarting the model for the level of basic control system - BPCS.

Because it is a derivative of the classic PN (folding), the properties of liveness, reversibility and safety were observed, demonstrating a proper model. Figures 13 and 14 illustrate the SIS prevention and SIS mitigation control algorithm model for

the SIF1. Other SIFs has isomorphic models.

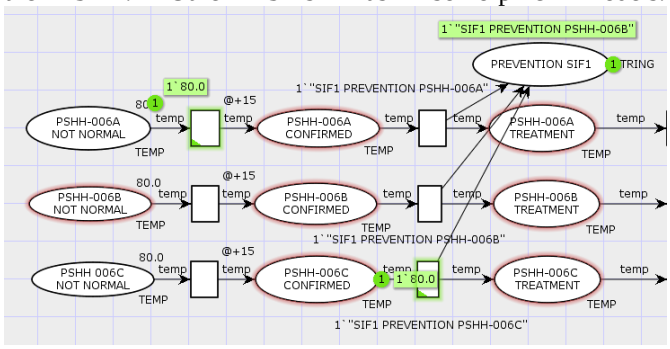

Fig. 13. CPN model for prevention – SIF1

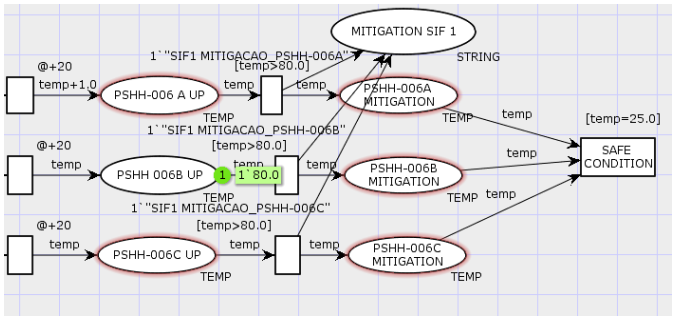

Fig. 14. CPN model for mitigation – SIF 1

3.9 *Control codes generation based on IEC 61131-7*

The control codes, implementable in commercial controllers, can be written from the results of fuzzy logic, based on the dynamical evolution of the CPN models. The IEC 61131-7 reference to conversion of fuzzy logic in structured text language. Figure 15 show an example of control code, based on fuzzy logic.

```
FUNCTION_BLOCK FUZZYCONTROL
VAR_INPUT
        temperature : REAL;
        dtemperature : REAL;
VAR_OUTPUT
        valvule : REAL; END_VAR
FUZZIFY temperature
TERM BasicControl := (0,1) (200,1) (250,0);
TERM prevent := (200,0) (250,1) (300,1) (350,0);
TERM mitigate := (300,0) (350,1) (1000,1);
END_FUZZIFY

DEFUZZIFY valvule
TERM zero := 0;
TERM medium := (0,0) (20,1) (55,1) (95,0);
TERM high := (40,0) (100,1);
ACCU : MAX;
METHOD : COG;
DEFAULT := 0; END_DEFUZZIFY
RULEBLOCK No1
        AND : MIN;
RULE 1 : IF temperature is mitigate THEN valvule IS high;
RULE 2 : IF temperature is BasicControl THEN valvule IS zero;
RULE 3 : IF (temperature is prevent) and (dtemperature is P)
        THEN valvula IS medium;
RULE 4 : IF (temperature is mitigate) and (dtemperature is N)
        THEN valvula IS medium;
```

Fig. 15. Control code, based on IEC 61131-7

4. CONCLUSIONS

The paper presents a method for the implementation of SIS to mitigate faults in critical SPs with reference to IEC 61508/61511. A team of experts in the process assist in applying risk analysis techniques to determine the critical elements. The next step consists in determine the control signals (sensors) that can be associated with the occurrence of faults of that critical elements which may or may not be associated with process variables. Fuzzy logic is used to determine the intervals of the respective sensor signals to indicate the need to promote the shutdown and enable their mitigation actions. Petri nets are used for the for the control algorithm and formal model verification. However, the use of classical PN can result in high complexity graphs, in fact verified results. The high-level Petri nets were then used, resulting in a better understanding of graphs, without losing the complexity of the classical model and the results of fuzzy logic. Another advantage is the generation of hierarchical models, the models for the prevention and mitigation can be modelled in a hierarchical manner for the different SIFS process, greatly facilitating the generation of the final control algorithm SIS.

REFERENCES

Bell, R., 2005. “Introduction to IEC 61508”. In Proceedings of ACS Workshop on Tools and Standards. Sydney, Australia.

Chen, C. and Dai, J., 2004. Design and high-level synthesis of hybrid controller. In Proc. of IEEE Conference.

IEC, I.E.C., “Programmable Controllers IEC 61131-7: Fuzzy Control programming”, 2000.

IEC, I.E.C., 2003a. “Functional safety - safety instrumented systems for the process industry sector - part 1 (IEC 61511)”

IEC, I.E.C., 2010. “Functional safety of electrical / electronic / programmable electronic safety-related systems (IEC 61508)”.

ISO/IEC 15.909, “High Level Nets: Concepts, Definitions and Graphical Notations”, Final Draft, v. 4.7.1, 2000.

Jensen, K., “Coloured Petri Nets. Basic Concepts, Analysis Methods and Paractical Use.”, Springer-Verlag, 1997.

Lee, C. C.: “Fuzzy logic in control system: fuzzy logic controller Part 1”. In IEEE Transactions n System, Man and Cybernetic, Vol 20, n^{0}2, p. 404-418, 1990.

Lewis, E.E., 1995. Introduction to Reliability Engineering. 2^0 Ed., John Wiley&Sons.

Modarres, M., Kaminskiy, M., Krivstov, V., 2010. Reliability Engineering and Risk Analysis:a practical guide.,CRC Press.

Popa, D. D., Craciunescu, A, Kreindler, L.: “A PI-Fuzzy controller designated for industrial motor control applications”. In ISIE IEEE International Symposium on Applications, Industrial Eletronics, 2008.

Sallak, M.; Simon, C.; Aubry, J., A fuzzy probabilistic approach for determining safety integrity level, IEEE Transaction on Fuzzy Systems, vol 16, n. 1, pp. 239-248, 2008.

Smith, E.; “Principles of High Level Petri Nets”, LNCS 1491, pp. 174-210.

Souza, J.A.L., “Mitigação de Falhas Críticas em Sistemas Produtivos”. Dissertação de Mestrado. Escola Politécnica da Universidade de São Paulo. 2014.

Squillante Jr, R.; Santos Fo, D.J.; Souza, J.A.L.; Junqueira, F,; Myiagi, P.E. “Safety in Supervisory Control for Critical Systems”. IFIP International Federation for Information Processing (DoCEIS 2013), vol 394, pp. 261-270,

Summers, A.; Raney, G. Common cause and common sense, designing failure out of your safety instrumented systems (SIS). In: ISA Transactions, vol 38, pp. 291-299, 1999.

Zadeh, L. A.: Fuzzy Sets. Information and Control, Vol 8, p. 338-353, 1965.

Zhang, Y; Jiang, J. Bibliographical review on reconfigurable fault-tolerant control systems, Annual Reviews in Control, vol 32, pp. 229-252, 2008.

Appendix A. PN model for SIF 1 Prevention

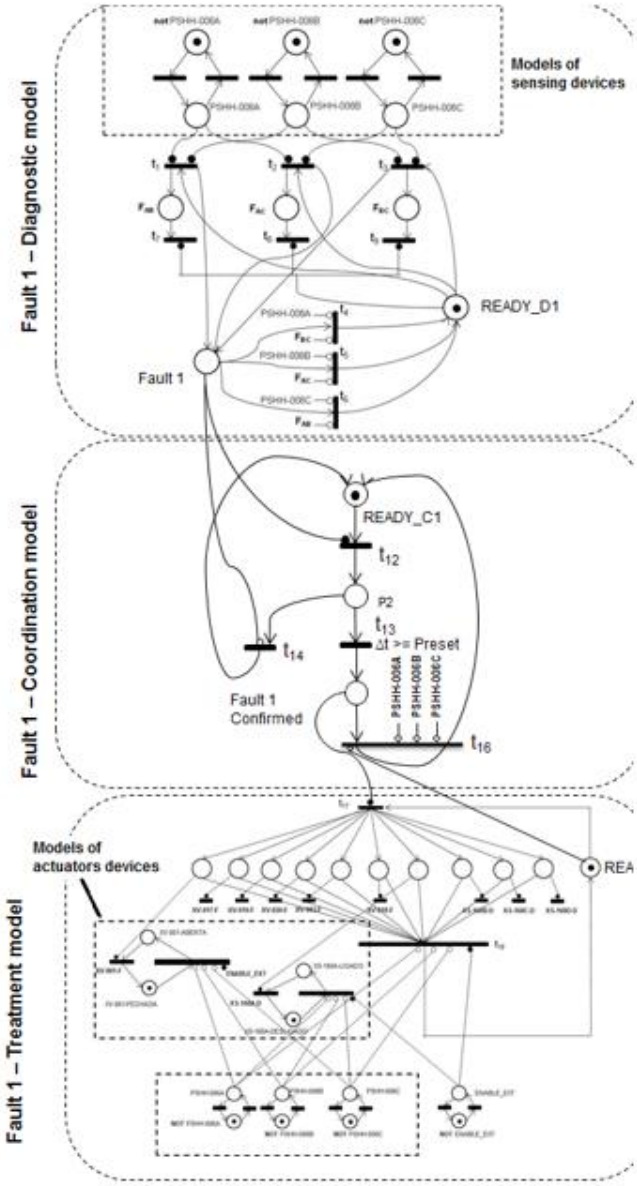

Appendix B. PN model for SIF 1 Mitigation

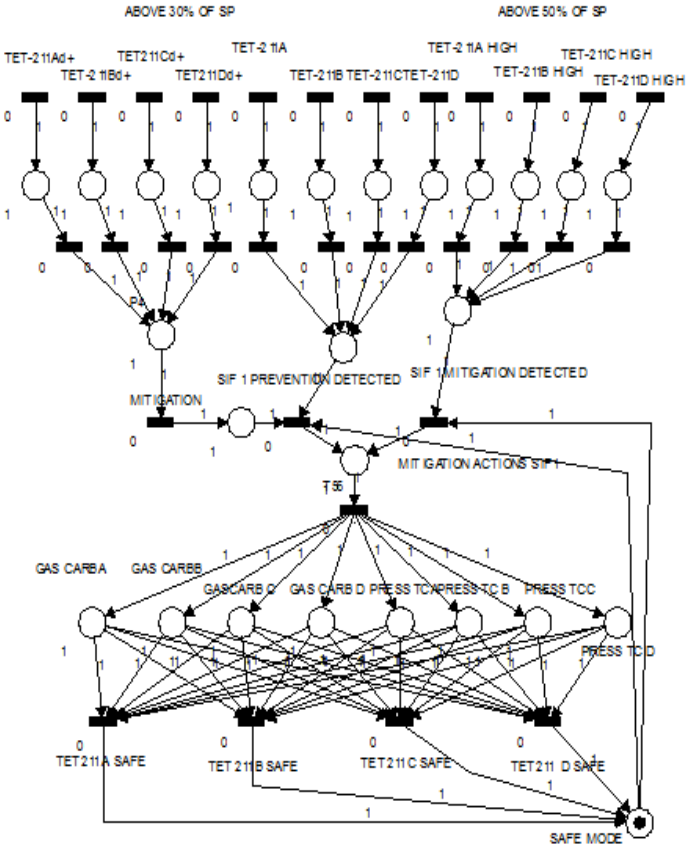

Comparación del Lenguaje VHDL-AMS con los Métodos de Simulación Orcad/Pspice y Matlab/Simulink a través de un Sistema de Distribución de Energía Eléctrica con Carga no Lineal

Frank Alberto Ibarra Hernández *. Roberto Andrés Bernal Correa.**
Carlos Alberto Canesin***

** Universidad del Sinú, Montería, Cra. 1w No. 38-153 Barrio Juan XXIII COLOMBIA (Tel: +4 781 1717; e-mail: frankibarra@unisinu.edu.co).*
**** Universidad del Sinú, Montería, Cra. 1w No. 38-153 Barrio Juan XXIII COLOMBIA (e-mail: robertobernal@unisinu.edu.co)*
**** Facultad de Ingeniería Eléctrica, Universidad Estatal de São Paulo, Ilha Solteira, Brasil, (e-mail: canesin@dee.feis.unesp.br)}*

Resumen: Este artículo presenta una plataforma de modelado y simulación de un sistema de distribución de energía eléctrica con una carga trifásica no lineal, utilizando el lenguaje VHDL-AMS (lenguaje de descripción de hardware de altísima velocidad que incluye extensiones digitales, analógicas y de señal mixta) y, además, empleando dos métodos de simulación ampliamente conocidos: Orcad/Pspice y Matlab/Simulink, con miras a establecer una comparación cuantitativa entre los dos métodos de simulación y el lenguaje VHDL-AMS. El caso de estudio usado en esta investigación consiste en un alimentador de distribución de 23 nodos, considerando un escenario real de distribución de energía eléctrica radial típico brasileño, en el cual fue aplicada una herramienta de concentración y reducción de cargas eléctricas. Los resultados de las simulaciones comparativas demuestran la eficacia y exactitud de la plataforma de simulación desarrollada en VHDL-AMS, así como también se evidencia que el método de simulación Orcad/Pspice presenta mayores similitudes con los resultados de las simulaciones en VHDL-AMS, en comparación con los resultados obtenidos en Matlab/Simulink. Los modelos en VHDL-AMS viabilizan el desarrollo de una futura arquitectura de simulación en tiempo real y control para el alimentador de distribución de energía eléctrica, utilizando los lenguajes de descripción de hardware VHDL-AMS y VHDL.

Palabras clave: Cargas Eléctricas No Lineales, Lenguajes de Descripción de Hardware, Matlab/Simulink, Orcad/Pspice, Sistemas de Distribución de Energía Eléctrica, VHDL-AMS.

1. INTRODUCCIÓN

De acuerdo a Oliveira et al. (2011), la evolución tecnológica de los dispositivos electrónicos ha ocasionado un incremento en el número de cargas no lineales, las cuales hoy por hoy aún están creciendo en todos los sectores, especialmente en el sector industrial, afectando la seguridad y la continuidad del servicio y por otra parte exigiendo un mayor esfuerzo a las tecnologías de compensación y regulación convencionales, existentes en los Sistemas de Distribución de Energía Eléctrica (SDEE).

Por otra parte, McGranaghan (2007) considera que las empresas de distribución de electricidad son responsables de las condiciones del suministro de la energía eléctrica, estas compañías necesitan herramientas de ingeniería y conocimiento científico para interpretar y aplicar la información recibida, de tal manera que puedan tomar decisiones técnicas acertadas. En este contexto, el procesamiento y análisis de los indicadores de calidad de la energía eléctrica (CEE) pasa por un proceso de investigación de los fenómenos en régimen permanente y transitorio de los sistemas de distribución.

Por lo anterior, en este trabajo, además de proponer una herramienta que utiliza el lenguaje VHDL-AMS para la simulación completa de una red de distribución de alimentación primaria con carga no lineal, considerando la existencia de elementos de compensación y regulación de tensión, compara cuantitativamente los métodos de simulación Orcad/Pspice y Matlab/Simulink con el lenguaje VHDL-AMS. Es importante mencionar que esta herramienta propuesta es fundamental para el desarrollo de un simulador en tiempo real para sistemas de distribución de energía eléctrica, en el cual, basados en los resultados comparativos de este trabajo (al ratificarse la eficacia del lenguaje VHDL-AMS vs Orcad/Pspice y Matlab/Simulink), se utilizará al lenguaje de descripción de hardware VHDL-AMS como plataforma de modelación y simulación de un sistema eléctrico y posteriormente se utilizará al lenguaje VHDL (el cual es perfectamente compatible con VHDL-AMS), para el diseño del sistema de gerenciamiento y control de la red de distribución, cumpliendo así con los objetivos de gestión de los indicadores de la CEE y el control en tiempo real de los SDEE.

2. LENGUAJE DE MODELADO VHDL-AMS

Boussetta et al. (2010) define VHDL-AMS como un súper conjunto del lenguaje VHDL, que apoya la descripción jerárquica, modelado y simulación de sistemas digitales, analógicos y de señales mixtas. En este contexto, VHDL-AMS es una extensión del lenguaje digital de descripción de hardware VHDL (VHSIC: Circuito integrado de altísima velocidad - "Very High Speed Integrated Circuit" más HDL: Lenguaje de descripción de hardware - "Hardware Description Language"). Así, Christen y Bakalar (1999) aseguran que a través del lenguaje VHDL-AMS es posible modelar y simular sistemas analógicos, digitales o mixtos, los cuales a su vez pueden ser conservativos o no conservativos y normalmente son descritos por ecuaciones diferenciales algebraicas, en las que la solución de estas ecuaciones que describen el comportamiento del sistema puede incluir discontinuidades. De otro lado, Damon y Christen (1996) publicaron que, en su naturaleza estos sistemas pueden ser eléctricos, físicos o mecánicos (térmicos). Cualquier problema que pueda ser definido por una combinación de filas de eventos (sistema digital) o ecuaciones diferenciales algebraicas simultáneas (sistema analógico) se puede modelar y simular con VHDL-AMS. Con el fin de evaluar el desempeño de un simulador desarrollado en VHDL-AMS, según Nellayappan et al. (1998), se deben tener en cuenta tres propiedades fundamentales: exactitud, eficiencia y la capacidad para ejecutar la simulación (rendimiento). La exactitud se define por la semántica del lenguaje VHDL-AMS y debe ser garantizada por los algoritmos implementados. La eficacia se mide en términos de la velocidad (rapidez) de la simulación. La capacidad para ejecutar la simulación incluye aspectos tales como necesidades de recursos y apoyo lingüístico.

3. CASO DE ESTUDIO: ALIMENTADOR DE PRUEBA UTILIZANDO EL LENGUAJE VHDL-AMS

l caso de estudio utilizado consistió en un alimentador de prueba, teniendo en cuenta un escenario real de distribución de energía eléctrica radial típico brasileño, en el cual, para el caso particular analizado, fue aplicada una herramienta de concentración y reducción de cargas eléctricas, resultando el diagrama esquemático reducido de la Fig. 1, el cual presenta:

- Una subestación eléctrica, la cual se constituye en una fuente trifásica desequilibrada con distorsiones armónicas (de 14,4 kV de tensión de línea);
- Un regulador de tensión trifásico en configuración Delta-Cerrada con un conmutador de TAP's (8 posiciones aditivas y 8 sustractivas), con una variación total de la tensión de 19,5% en las 16 posiciones;
- Once cargas pasivas inductivas trifásicas equilibradas, resultante de la porción lineal de la carga de la red;
- Un filtro capacitivo trifásico primario (carga capacitiva trifásica equilibrada);
- Una carga trifásica no lineal y desequilibrada.

Ibarra Hernandez y Canesin (2012) previamente publicaron una simulación en VHDL-AMS del alimentador de prueba de la Fig. 1, la cual fue desarrollada utilizando el software SystemVision™ (Mentor Graphics), considerando los modelos básicos de los componentes eléctricos de un sistema de distribución desarrollados en VHDL-AMS, desarrollados y publicados en este mismo trabajo de investigación.

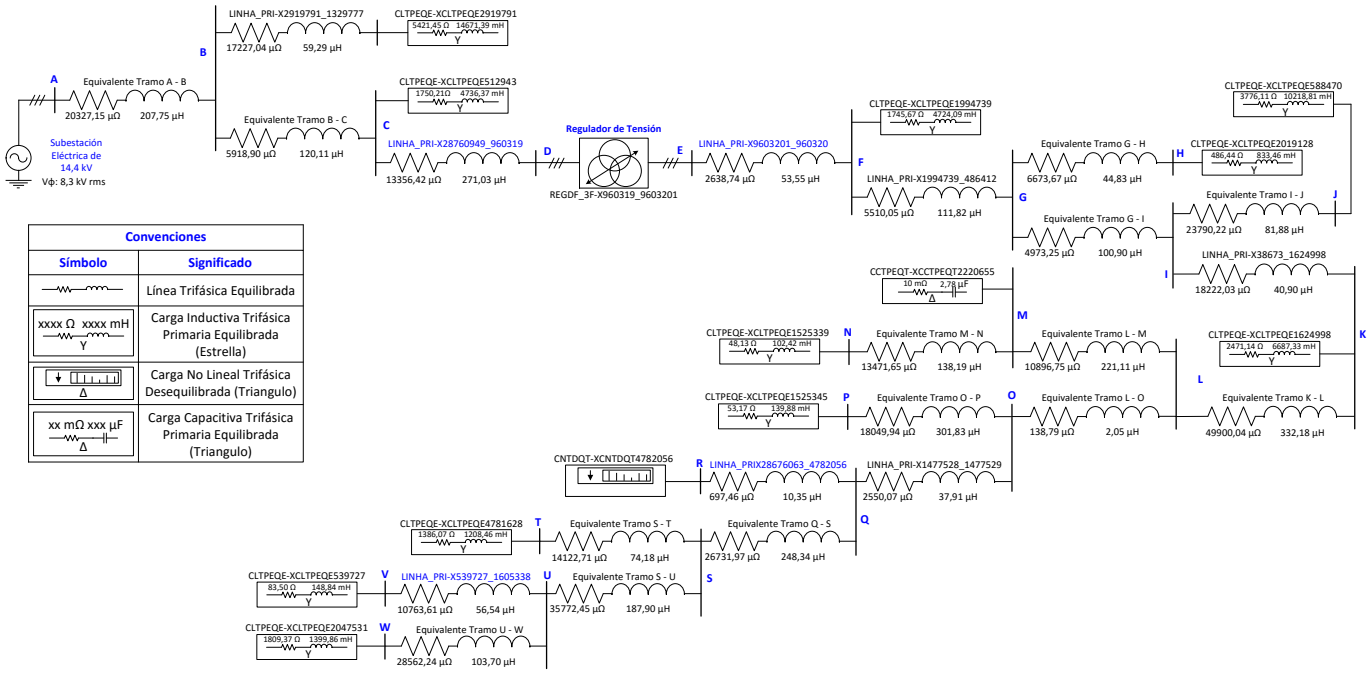

Fig. 1. Ejemplo de Alimentador de una Red de Distribución Primaria.

4. RESULTADOS DE LAS SIMULACIONES EN VHDL-AMS

El modelado se constituye en el núcleo de cualquier proceso de diseño. Esta tarea consiste esencialmente en el desarrollo de algunas descripciones abstractas de la realidad física, con el propósito principal que estas sean útiles para el proceso de diseño y operación. Los modelos pueden ser utilizados para validar las características de una parte o de la totalidad del sistema diseñado, por ejemplo, su funcionalidad o su rendimiento. Estos modelos pueden ser de simulación o ejecutables que producen una respuesta cuando se ven afectados por los estímulos. De acuerdo con Holovatyy et al. (2015), los modelos pueden describir el comportamiento y/o la estructura del sistema diseñado en varios niveles de detalle, o niveles de abstracción. Seleccionar el nivel apropiado es, por un lado, un asunto de compromiso entre la exactitud del modelo y el rendimiento (o eficiencia) de este y, por otra parte, una manera de hacer frente a la complejidad del Sistema.

En este contexto, fueron realizadas las simulaciones en VHDL-AMS del alimentador de la Fig. 1, las cuales fueron confrontadas con los métodos de simulación ampliamente conocidos Orcad/Pspice y Matlab/Simulink (utilizando la biblioteca SimPowerSystems). Las condiciones de simulación se mantuvieron idénticos en los tres ambientes de simulación, como sigue:

- Los métodos de integración para la solución numérica de las ecuaciones diferenciales son: Trapezoidal para VHDL-AMS, Newton-Raphson para Orcad/Pspice y formula de Euler mejorada para Matlab/Simulink. En este contexto, los pasos de tiempo de las simulaciones son: 71,9 µs para VHDL-AMS, 10,0 µs para Orcad/Pspice y 100,0 µs para Matlab/Simulink (automático).
- Fueron realizadas las simulaciones y almacenados los datos resultantes para el intervalo desde 500 hasta 525 milisegundos, considerándose la referencia de máximo nivel de los TAPs del regulador de tensión (TAP de la Fase A =8, TAP de la Fase B =8 y TAP de la Fase C =8).
- Se realizaron simulaciones de tensiones y corrientes para toda la red, sin embargo, en este artículo, sólo se presentan los siguientes resultados más representativos de las simulaciones (representados en las líneas de la Fig. 1 cuyos nombres están escritos en color azul):
    - La línea que alimenta la carga con la peor regulación de tensión, denominada: LINHA_PRI-X539727_1605338,
    - La línea que alimenta a la única carga no lineal trifásica desbalanceada, referenciada como: LINHA_PRIX28676063_4782056,
    - Las líneas de entrada y salida del regulador de tensión, las cuales son, respectivamente: LINHA_PRI-X28760949_960319 y LINHA_PRI-X9603201_960320.

Utilizando el lenguaje VHDL-AMS, según las simulaciones realizadas, fueron obtenidas las siguientes conclusiones para el sistema eléctrico de distribución de la Fig. 1:

- Las cinco cargas con la regulación de tensión más alta, son, respectivamente:
    - CLTPEQE-XCLTPEQE539727 (carga con la más alta regulación);
    - CLTPEQE-XCLTPEQE2047531;
    - CLTPEQE-XCLTPEQE1525339;
    - CLTPEQE-XCLTPEQE1525345 y,
    - CLTPEQE-XCLTPEQE4781628.

La nomenclatura CLTPEQE-XCLTPEQE significa: Carga inductiva trifásica equilibrada conectada en estrella, referenciada para Media Tensión.

- Basados en las simulaciones realizadas, de acuerdo al perfil de tensión del alimentador se puede concluir:
    - El escenario de regulación más favorable corresponde al TAP en la posición "-2" para las tres fases,
    - El escenario de regulación más desfavorable corresponde al TAP en la posición "8" para las tres fases. En este escenario, la carga con la peor regulación de tensión (más alta), la cual es identificada en la Fig. 1 como CLTPEQE-XCLTPEQE539727, posee una regulación igual a 11,9 % para las tres fases.

Para los tres ambientes de simulación (VHDL-AMS, Orcad/Pspice y Matlab/Simulink), los resultados de las simulaciones más representativas son presentados en las Fig. 2 hasta Fig. 17. Estos resultados son obtenidos con el TAP del regulador de tensión en la posición "8" para las tres fases.

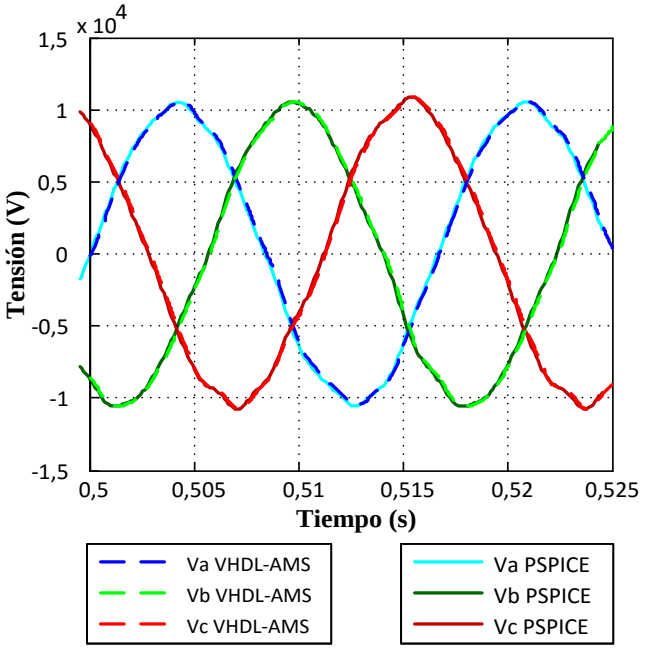

Fig. 2. Tensiones de Fase de la Línea que Alimenta a la Carga con la Peor Regulación de Tensión (LINHA_PRI-X539727_1605338). VHDL-AMS vs PSPICE.

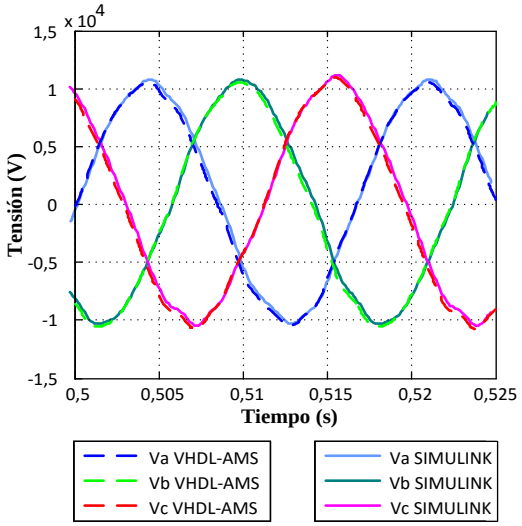

Fig. 3. Tensiones de Fase de la Línea que Alimenta a la Carga con la Peor Regulación de Tensión (LINHA_PRI-X539727_1605338). VHDL-AMS vs SIMULINK.

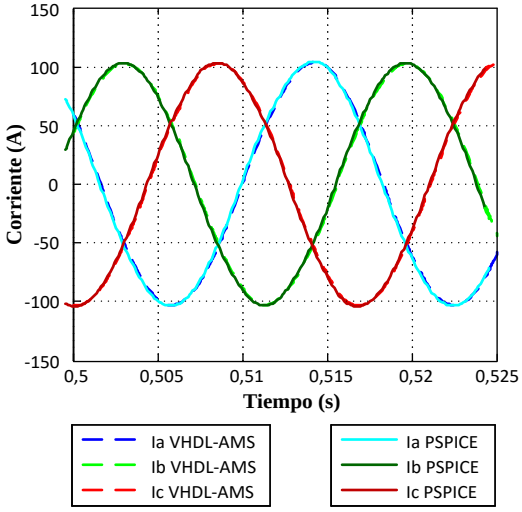

Fig. 4. Corrientes de la Línea que Alimenta a la Carga con la Peor Regulación de Tensión (LINHA_PRI-X539727_1605338). VHDL-AMS vs PSPICE.

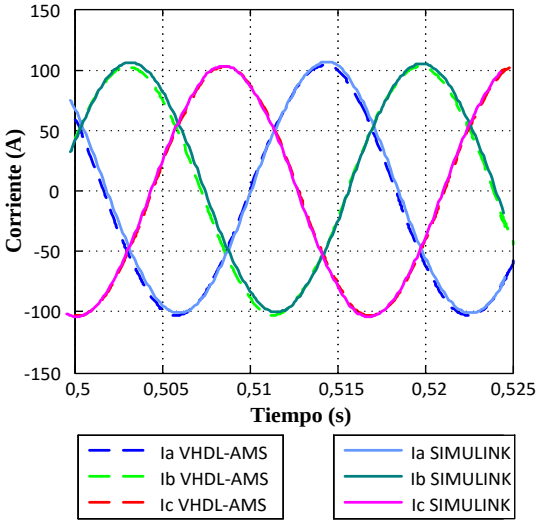

Fig. 5. Corrientes de la Línea que Alimenta a la Carga con la Peor Regulación de Tensión (LINHA_PRI-X539727_1605338). VHDL-AMS vs SIMULINK.

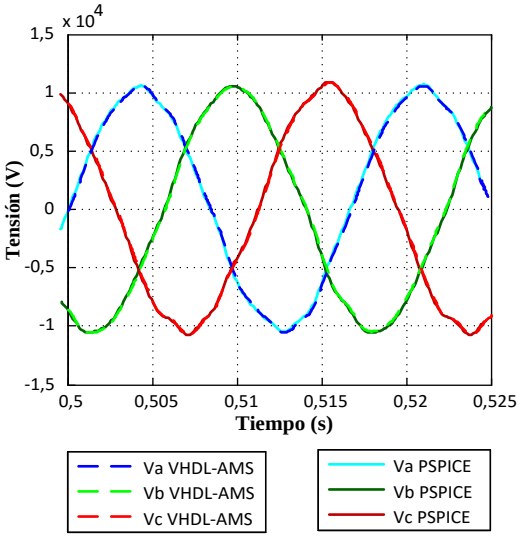

Fig. 6. Tensiones de Fase de la Línea que Alimenta a la Única Carga No Lineal Desequilibrada (LINHA_PRI-X28676063_4782056). VHDL-AMS vs PSPICE.

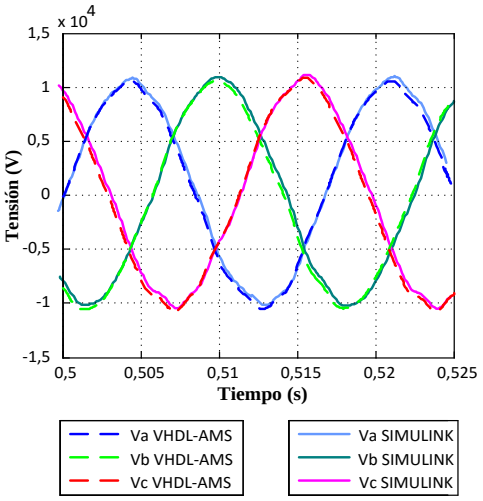

Fig. 7. Tensiones de Fase de la Línea que Alimenta a la Única Carga No Lineal Desequilibrada (LINHA_PRI-X28676063_4782056). VHDL-AMS vs SIMULINK.

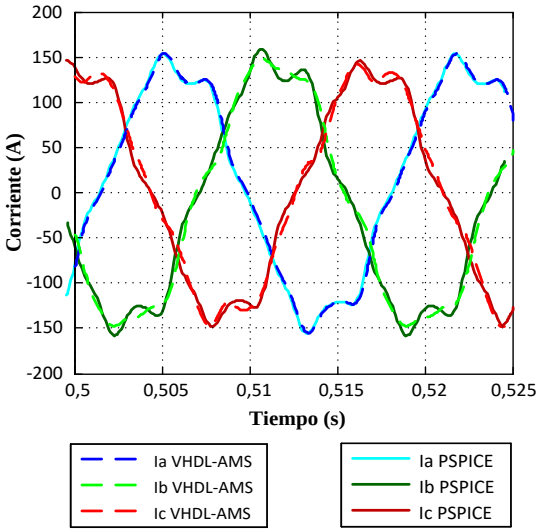

Fig. 8. Corrientes de la Línea que Alimenta a la Única Carga No Lineal Desequilibrada (LINHA_PRI-X28676063_4782056). VHDL-AMS vs PSPICE.

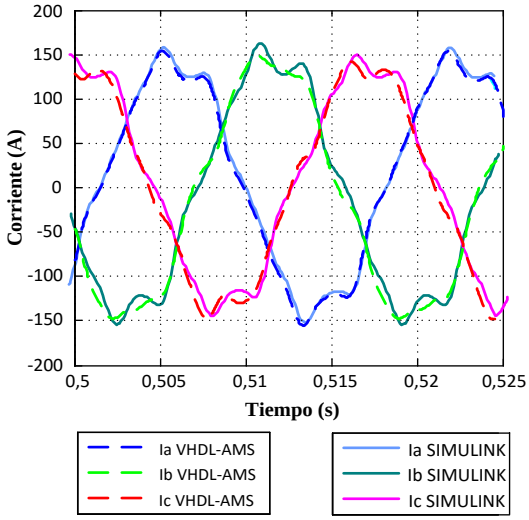

Fig. 9. Corrientes de la Línea que Alimenta a la Única Carga No Lineal Desequilibrada (LINHA_PRIX28676063_4782056). VHDL-AMS vs SIMULINK.

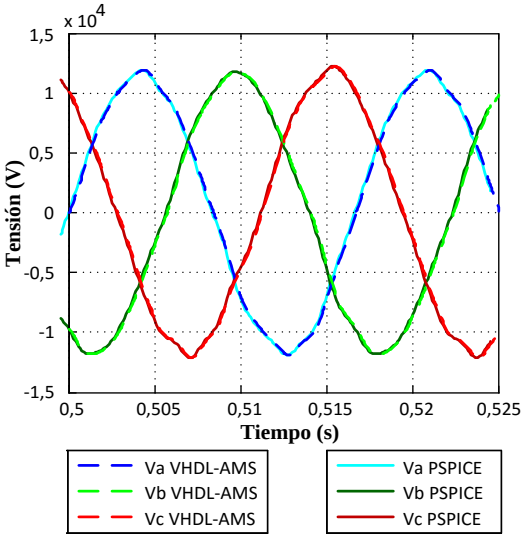

Fig. 10. Tensiones de Fase a la Entrada del Regulador de Tensión (LINHA_PRIX28760949_960319). VHDL-AMS vs PSPICE.

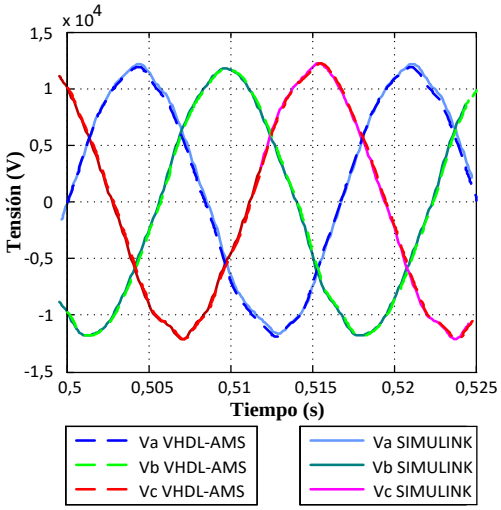

Fig. 11. Tensiones de Fase a la Entrada del Regulador de Tensión (LINHA_PRIX28760949_960319). VHDL-AMS vs SIMULINK.

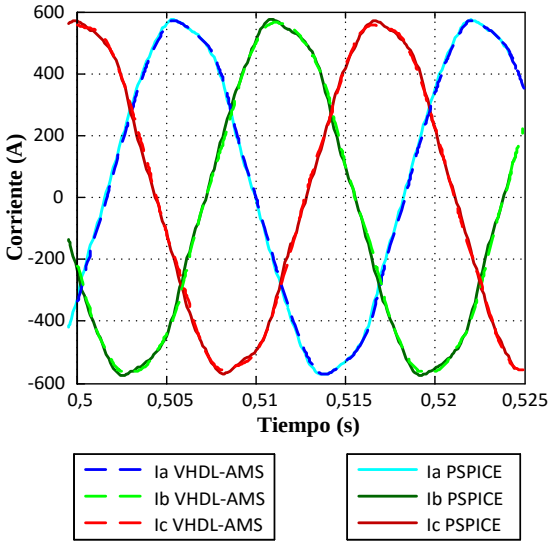

Fig. 12. Corrientes a la Entrada del Regulador de Tensión (LINHA_PRIX28760949_960319). VHDL-AMS vs PSPICE.

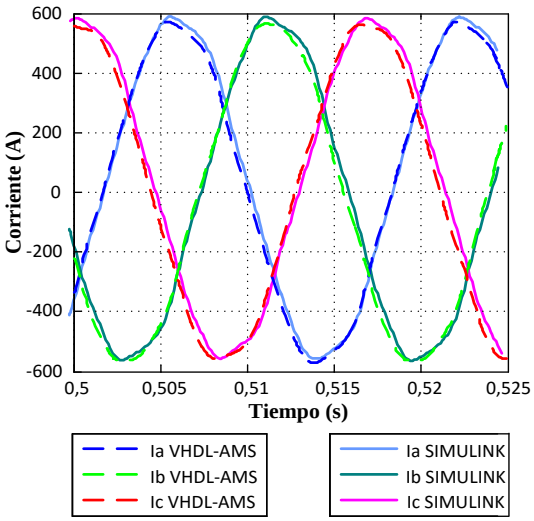

Fig. 13. Corrientes a la Entrada del Regulador de Tensión (LINHA_PRIX28760949_960319). VHDL-AMS vs SIMULINK.

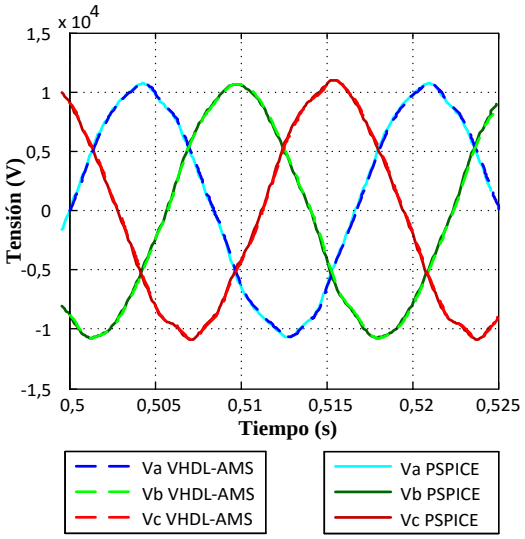

Fig. 14. Tensiones de Fase a la Salida del Regulador de Tensión (LINHA_PRIX9603201_960320). VHDL-AMS vs PSPICE.

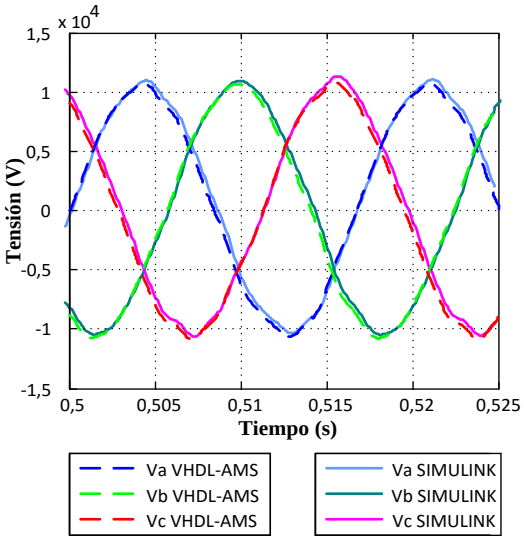

Fig. 15. Tensiones de Fase a la Salida del Regulador de Tensión (LINHA_PRIX9603201_960320). VHDL-AMS vs SIMULINK.

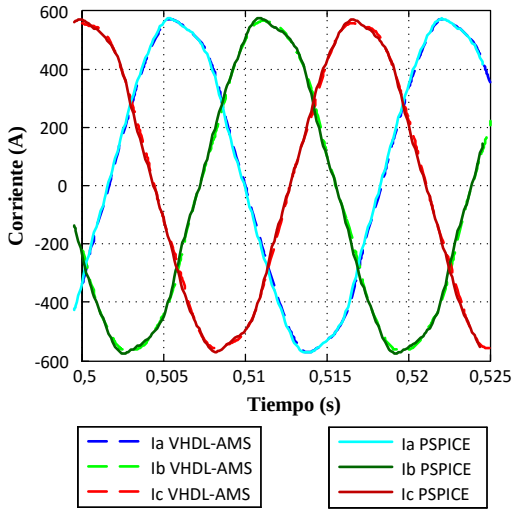

Fig. 16. Corrientes a la Salida del Regulador de Tensión (LINHA_PRIX9603201_960320). VHDL-AMS vs PSPICE.

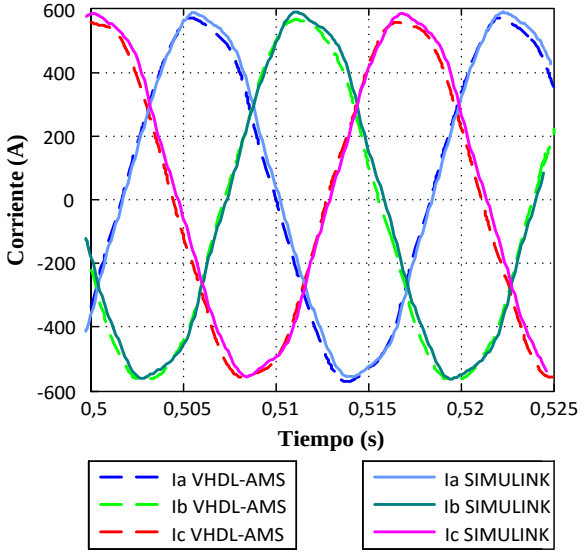

Fig. 17. Corrientes a la Salida del Regulador de Tensión (LINHA_PRIX9603201_960320). VHDL-AMS vs SIMULINK.

Las tablas 1 hasta 8 presentan una descripción cuantitativa comparativa para los resultados de las simulaciones presentados en las Fig. 2 hasta Fig. 17. En estas tablas el valor eficaz (RMS) es calculado para el estado estacionario, considerándose el periodo de 500 hasta 525 milisegundos, para los tres métodos de simulación (VHDL-AMS, Orcad/Pspice y Matlab/Simulink).

Tabla 1. Tensiones de fase y corrientes de la línea que alimenta a la carga con la peor regulación de tensión para VHDL-AMS y PSPICE

Fase	Valor RMS de estado estacionario (V) VHDL-AMS	PSPICE	%Error Métodos de Simulación
A	7.320,20	7.321,80	0,022%
B	7.364,30	7.363,40	0,012%
C	7.356,20	7.361,50	0,072%

Fase	Valor RMS de estado estacionario (A) VHDL-AMS	PSPICE	%Error Métodos de Simulación
A	72,88	73,25	0,508%
B	72,47	72,84	0,507%
C	72,63	73,04	0,563%

Tabla 2. Tensiones de fase y corrientes de la línea que alimenta a la carga con la peor regulación de tensión para VHDL-AMS Y SIMULINK

Fase	Valor RMS de estado estacionario (V) VHDL-AMS	SIMULINK	%Error Métodos de Simulación
A	7.320,20	7.312,21	0,109%
B	7.364,30	7.359,80	0,061%
C	7.356,20	7.329,81	0,360%

Fase	Valor RMS de estado estacionario (A) VHDL-AMS	SIMULINK	%Error Métodos de Simulación
A	72,88	71,78	1,524%
B	72,47	71,39	1,520%
C	72,63	71,42	1,688%

Tabla 3. Tensiones de Fase y Corrientes de la Línea que Alimenta a la Única Carga No Lineal Desequilibrada para VHDL-AMS y PSPICE

Fase	Valor RMS de estado estacionario (V) VHDL-AMS	PSPICE	%Error Métodos de Simulación
A	7.333,00	7.332,70	0,004%
B	7.377,00	7.374,10	0,039%
C	7.369,00	7.372,60	0,049%

Fase	Valor RMS de estado estacionario (A) VHDL-AMS	PSPICE	%Error Métodos de Simulación
A	101,95	101,98	0,033%
B	105,05	105,22	0,163%
C	98,78	98,86	0,085%

Tabla 4. Tensiones de Fase y Corrientes de la Línea que Alimenta a la Única Carga No Lineal Desequilibrada para VHDL-AMS y SIMULINK

Fase	Valor RMS de estado estacionario (V) VHDL-AMS	SIMULINK	%Error Métodos de Simulación
A	7.333,00	7.331,50	0,020%
B	7.377,00	7.362,52	0,197%
C	7.369,00	7.351,05	0,244%

Fase	Valor RMS de estado estacionario (A) VHDL-AMS	SIMULINK	%Error Métodos de Simulación
A	101,95	101,85	0,100%
B	105,05	104,54	0,490%
C	98,78	98,52	0,255%

Tabla 5. Tensiones de Fase y Corrientes a la Entrada del Regulador de Tensión para VHDL-AMS y PSPICE

Fase	Valor RMS de estado estacionario (V) VHDL-AMS	PSPICE	%Error Métodos de Simulación
A	8.239,90	8.238,60	0,016%
B	8.232,70	8.228,20	0,055%
C	8.280,50	8.283,40	0,035%

Fase	Valor RMS de estado estacionario (A) VHDL-AMS	PSPICE	%Error Métodos de Simulación
A	403,98	405,29	0,324%
B	405,64	406,98	0,329%
C	400,08	401,49	0,351%

Tabla 6. Tensiones de Fase y Corrientes a la Entrada del Regulador de Tensión para VHDL-AMS y SIMULINK

Fase	Valor RMS de estado estacionario (V) VHDL-AMS	PSPICE	%Error Métodos de Simulación	Fase	Valor RMS de estado estacionario (A) VHDL-AMS	PSPICE	%Error Métodos de Simulación
A	8.239,90	8.238,60	0,016%	A	403,98	405,29	0,324%
B	8.232,70	8.228,20	0,055%	B	405,64	406,98	0,329%
C	8.280,50	8.283,40	0,035%	C	400,08	401,49	0,351%

Tabla 7. Tensiones de Fase y Corrientes a la Salida del Regulador de Tensión para VHDL-AMS y PSPICE

Fase	Valor RMS de estado estacionario (V) VHDL-AMS	PSPICE	%Error Métodos de Simulación	Fase	Valor RMS de estado estacionario (A) VHDL-AMS	PSPICE	%Error Métodos de Simulación
A	7.414,50	7.414,20	0,004%	A	403,98	405,29	0,324%
B	7.459,40	7.456,50	0,039%	B	405,64	406,98	0,329%
C	7.451,00	7.454,60	0,048%	C	400,08	401,49	0,351%

Tabla 8. Tensiones de Fase y Corrientes a la Salida del Regulador de Tensión para VHDL-AMS y SIMULINK

Fase	Valor RMS de estado estacionario (V) VHDL-AMS	SIMULINK	%Error Métodos de Simulación	Fase	Valor RMS de estado estacionario (A) VHDL-AMS	SIMULINK	%Error Métodos de Simulación
A	7.414,50	7.414,50	0,000%	A	403,98	400,09	0,972%
B	7.459,40	7.457,89	0,020%	B	405,64	401,67	0,988%
C	7.451,00	7.436,54	0,194%	C	400,08	395,91	1,052%

5. CONCLUSIONES Y TRABAJO FUTURO

En este trabajo fue desarrollada una plataforma de modelado y simulación en VHDL-AMS, la cual fue comparada con dos métodos de simulación bien conocidos (Orcad/Pspice y Matlab/Simulink), utilizando un alimentador de distribución de energía eléctrica en media tensión, teniendo en cuenta un escenario real de distribución de energía eléctrica radial típico brasileño, en el cual fue aplicada una herramienta de concentración y reducción de cargas eléctricas. Los resultados de las simulaciones comparativas demostraron la eficacia y exactitud de la plataforma de simulación desarrollada en VHDL-AMS.

Con base en el análisis cuantitativo de los resultados obtenidos en las tablas I hasta VIII podemos concluir:

- Los mayores porcentajes de error en los métodos de simulación VHDL-AMS vs Orcad/Pspice fueron respectivamente: 0,072% para las tensiones y 0,563% para las corrientes.
- Los mayores porcentajes de error en los métodos de simulación VHDL-AMS vs Matlab/Simulink fueron respectivamente: 0,360% para las tensiones y 1,688% para las corrientes.

Considerando las conclusiones anteriores, se evidencia que el método de simulación Orcad/Pspice presentó mayores similitudes con los resultados de las simulaciones en el lenguaje de descripción de hardware VHDL-AMS, en comparación con los resultados obtenidos en Matlab/Simulink.

Se debe resaltar que los resultados obtenidos en este artículo servirán como base para el desarrollo de una Arquitectura de Simulación en Tiempo Real y Control (ASTR&C) para el alimentador de distribución de energía eléctrica, con el fin de analizar la calidad de la energía y mejorar las acciones de control en los sistemas de distribución, buscando de esta forma aumentar la confiabilidad y sostenibilidad del sistema eléctrico de potencia. Esta arquitectura utilizará los lenguajes de descripción de hardware VHDL-AMS, para la simulación en tiempo real, y VHDL para el desarrollo de un sistema de gerenciamiento de la distribución y control.

Ambos lenguajes VHDL y VHDL-AMS, junto con la información del sistema de distribución de energía eléctrica, permitirán la simulación en tiempo real y el control de los alimentadores de distribución de energía eléctrica.

Desde el punto de vista de la docencia e investigación, este trabajo se constituye en un enlace entre los sistemas eléctricos de potencia (redes de distribución de energía eléctrica) y los sistemas electrónicos que utilizan lenguajes de descripción de hardware (lenguaje VHDL-AMS). De esta forma, se utilizó una herramienta de modelado y simulación, diseñada originalmente para describir sistemas analógicos, digitales y de señal mixta (VHDL-AMS), para una aplicación focalizada a los sistemas eléctricos de distribución.

AGRADECIMIENTOS

Los autores agradecen a la Fundación de Apoyo a la Investigación del Estado de Sao Paulo (FAPESP) y a la Universidad del Sinú por el apoyo financiero para el desarrollo de este trabajo.

REFERENCIAS

Boussetta H., Marzencki M., Basrour S. y Soudani A. (2010). Efficient Physical Modeling of MEMS Energy Harvesting Devices With VHDL-AMS. *IEEE Sensors Journal*, 9, pp. 1427-1437.

Christen E. y Bakalar K. (1999). VHDL-AMS a hardware description language for analog and mixed-signal applications. *IEEE Transactions on Circuits and Systems II: Analog and Digital Signal Processing*, 46, pp. 1263-1272.

Damon D. y Christen E. (1996). Introduction to VHDL-AMS. 1. Structural and discrete time concepts. *IEEE International Symposium on Computer-Aided Control System Design*, 13, pp. 264-269.

Frey P., Nellayappan K., Shanmugasundaram V., Mayiladuthurai R. S., Chandrashekar C. L. y Carter H. W. (1998). SEAMS: simulation environment for VHDL-AMS. *Conference in Simulation*, 1, pp. 539-546.

Holovatyy A., Teslyuk V. y Lobur M. (2015). VHDL-AMS model of delta-sigma modulator for A/D converter in mems interface circuit. *International Conference on Perspective Technologies and Methods in MEMS Design (MEMSTECH)*, 11, pp. 55-57.

Ibarra Hernandez F. A. y Canesin C. A. (2012). Electrical Power Distribution System modeling with VHDL-AMS for the construction of a Real-Time Digital Simulator

using FPGAS devices. *IEEE/IAS International Conference on Industry Applications (INDUSCON)*, 10, pp. 1-7.

McGranaghan M. F. (2007). Quantifying Reliability and Service Quality for Distribution Systems. *IEEE Transactions on Industry Applications*, 43, pp. 188-195.

Oliveira, L. C. O., E Melo G. A., Souza J. B., Canesin C. A., Bonatto B. D., Belchior F. N. et al. (2011). Harmonic propagation analysis in electric energy distribution systems. *International Conference on Electrical Power Quality and Utilization (EPQU)*, 11, pp. 1-6.

Modeling of a Variable-BVR Rotary Valve Free Piston Expander/Compressor

Sergei Gusev * **Andres Hernandez** ** **Davide Ziviani** *
Martijn van den Broek *

* *Ghent University, Department of Flow, Heat and Combustion Mechanics, Graaf Karel de Goedelaan 5, Kortrijk, Belgium (e-mail: Sergei.Gusev@UGent.be, Davide.Ziviani@UGent.be, Martijn.vandenBroek@UGent.be).*
** *Ghent University, Department of Electrical Energy, Systems and Automation, Technologiepark 914 B-9052 Zwijnaarde, Belgium (e-mail: Andres.Hernandez@UGent.be)*

Abstract: The concept of a free-piston expansion/compression unit with a variable Built-in Volume Ratio (BVR) is proposed. This device has no crankshaft mechanism which provides a possibility to optimize the expansion process free of mechanical limitations. An additional degree of freedom is used, namely the rotation to control the in- and the outlet ports timing. Further, the operation in the expander mode will be described.
In most of the existing linear expanders/compressors, bouncing chambers or devices are used to reverse the piston movement at extreme positions. This approach is characterized by relatively high energy losses due to irreversibility of such a process. As an alternative, a fully controlled movement of the piston is proposed. This paper is focused on the control algorithm based on rules, which have been obtained and based on the insight in the system. Including the rotation timing, resulting in an optimal expansion process with an outlet pressure matching with the required one.

1. INTRODUCTION

Steady state operating volumetric compressors and expanders are widely studied machines. The challenge is to use such devices under strongly varying in- and outlet pressure and temperature conditions, especially at relatively high pressure ratios, which is frequently the case in waste heat recovery for non-stationary applications. For instance, the heat recovery from truck flue gases by means of an Organic Rankine Cycle (ORC) requires an expansion device with adjustable Built-in Volume Ratio (BVR). Fixed BVR machines cannot follow variations in the evaporating pressure caused by changes in both the flow rate and the temperature of the exhaust gases, resulting in a non-optimal operation of the system.

To overcome the lack of commercially available expanders, a novel variable-BVR expander has been proposed by the authors as an alternative to existing solutions, mainly conversion of compressors to expanders (Imran et al., 2016). Based on the results obtained during the tests performed on an ORC laboratory setup, the proposed idea intends to be a solution for challenges in expander technology established during these experiments.

The long-term objective is to develop a commercial unit meeting the requirements for a micro-scale ORC-system: inexpensive, scalable, flexible and efficient. The short-term objective, which has to be reached in the frame of the current project, is to develop a setup meant to validate the behavior of the main components and to demonstrate the feasibility to synchronize the linear and the rotational movement of a piston in order to achieve any required volume ratio. A proposal for a patent has been filed.

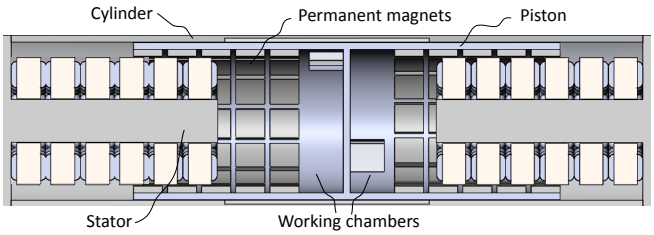

Fig. 1. Expander cutaway view

In this paper, the first approach towards the design of a control strategy for the proposed machine, is reported. The mathematical modeling and the numerical results, which led to the consideration of a controller design, are presented and discussed.

2. NOVEL VARIABLE-BVR EXPANDER

The mechanical design and the operation principle of the test prototype with an embedded linear generator (Fig. 1) is described in previous publications (Gusev et al., 2016). The piston rotates while moving, closing and opening the

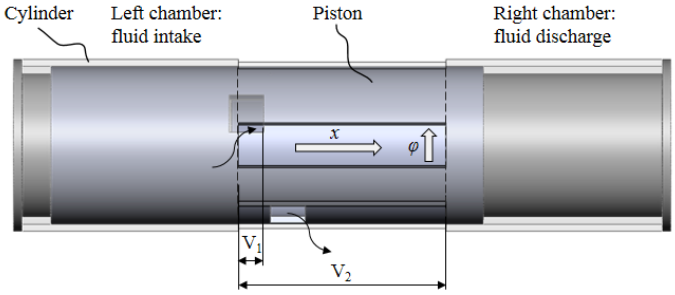

Fig. 2. Variable volume ratio

intake port at the required moment defined by the model. The built-in volumetric ratio can be expressed as:

$$BVR = \frac{V_2}{V_1} = \frac{1}{\chi}, \tag{1}$$

where V_1 is the volume at the moment of closing of the inlet port and V_2 is the volume of the working chamber after the expansion. The piston relative displacement χ corresponds with the volume V_1.

The $BVR = 10$ at $\chi = 0.1$ is shown in Fig. 2 when the leading-bottom corner of the piston skirt opening leaves the inlet opening of the cylinder. Since the rotation and translation of the piston have to be synchronized, the model is focused on the accurate definition and control of the piston position in both dimensions by means of rules, dictated by the thermodynamic model. The control coefficients, obtained from this model trigger the control sequence accelerating or decelerating the piston. The feedback signal is provided by the translation and the rotation encoders.

Since at the beginning of the prototype design, leakages are unavoidable and the discharge of expensive or toxic working fluids into the atmosphere is unacceptable, air is chosen as a working fluid.

In order to avoid complications with an embedded design, it was decided to separate translation and rotation movement and to use standard components. Several industrial linear motors operating in a brake mode are compared, its characteristics provided by the manufacturers are used as input for the model.

The chosen configuration is based on a standard linear motor consisting of a moving primary coil section and a secondary magnetic section (Fig. 2). In the adjusted design, two moving magnetic secondary sections are placed back-to-back on a linear guide system and two primary coil sections are fastened outside (Fig. 4). Such a configuration allows to equalize electromagnetic attraction forces and to reduce drastically the friction losses in the linear guiding system. Moreover, the maximal static force is twice the size, compared to a single-coil design for almost the same setup size and it is 6.2 kN in total. The inlet pressure applied to the piston can vary from 0.6 to 1.6 MPa. Other major setup parameters are summarized in Table 1.

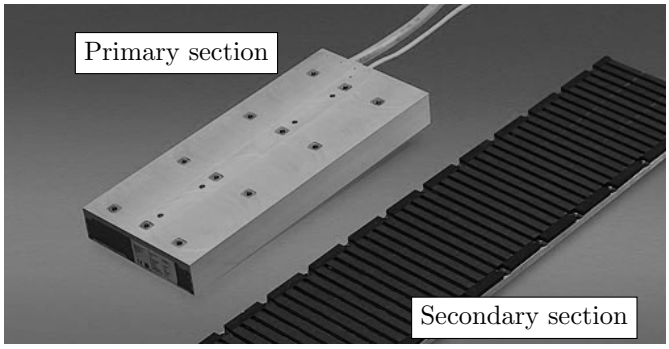

Fig. 3. Standard linear motor

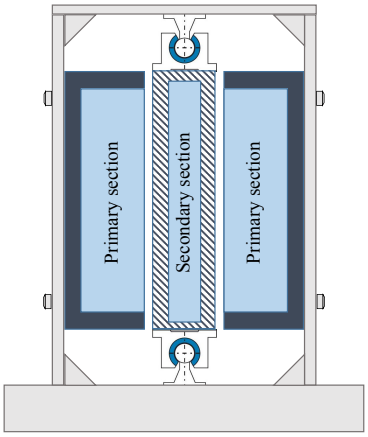

Fig. 4. Adjusted design

Table 1. Main parameters of the designed test setup

Bore (m)	Stroke (m)	Frequency (Hz)	Moving mass (kg)
0.08	0.23 - 0.31	5 - 10	30

3. THE EQUATION OF MOTION

3.1 Translation

The model of the free-piston expander is based on the same approach as (Mikalsen and Roskilly, 2008). The dynamics of the piston translation is dictated by Newton's second law:

$$F_{p,cyl} - F_{p,dis} - F_{fr} - F_{el} = m_p \frac{d^2x}{dt^2}, \tag{2}$$

where $F_{p,cyl}$ and $F_{p,dis}$ are gas forces in opposing working chambers, the friction force F_{fr}, the electromagnetic force F_{el} and the piston mass m_p.

The gas forces are applied to the same central element and defined by the pressure profile of an expansion process (Fig. 5) which is simulated using the expander hybrid gray box model designed in previous studies. The CoolProp library connected to Python is used (Bell et al., 2014) in order to calculate thermodynamical parameters.

The working fluid entering the expander is cooled down since the expander wall temperature is typically between the in- and the outlet temperature of the working medium. At the end of the expansion, the heat flux reverses. This heat transfer from or to the expander walls is taken

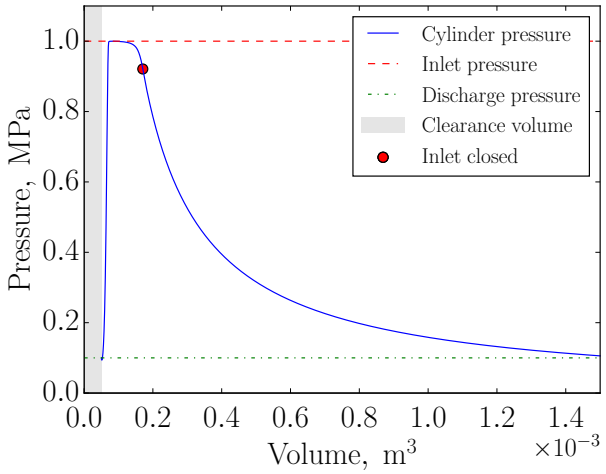

Fig. 5. pV-diagram

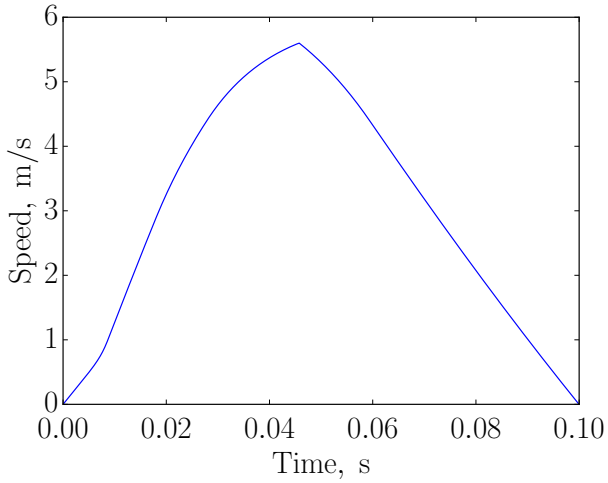

Fig. 6. Linear velocity profile

into account. The friction force F_{fr} is dependent on the speed of the piston. The correlation for dynamic friction behaviors of pneumatic cylinders obtained in (Tran and Yanada, 2013) is used. The heat produced by the friction is also incorporated into the model.

The translation speed changes under the applied electromagnetic force F_{el}, which is constant and acting alternately accelerating and decelerating the piston, in order to stop the piston at its extreme left and right positions, so all kinetic energy is absorbed and transformed into electricity. The approach is similar to (Petrichenko et al., 2015). The resulting equation can be written as follows:

$$F_{el}(t) = \frac{\pi D^2}{4}\left(p_{cyl}(t) - p_{dis}\right) - F_{fr}\left(\frac{dx}{dt}\right) - m_p\frac{d^2x}{dt^2}\,, \quad (3)$$

where D - is the piston diameter, p_{cyl} and p_{dis} are pressures in the working chamber and the discharge port respectively. The Equation 3 is used to control the drive of the linear motor, the position sensor is used for feedback of the piston position. The rotation is synchronized with the translation in order to obtain the required discharge pressure at the end of the expansion (Fig. 6).

3.2 Rotation

A servo motor attached to the expander on the opposite side of the linear generator side rotates the piston with an average frequency of 1/2 the frequency of the translation since there are two inlet and two outlet ports in each working chamber. The general equation for torque balance at the motor shaft can be written for the prototype as follows:

$$T_{el} = T_j + T_{fric}\,, \quad (4)$$

where T_{el} electromagnetic torque, T_j - inertia torque and T_{fric} - friction torque. The moment of inertia defining the inertia torque is the sum of moments of inertia of all components in the rotation train: the servo motor, the piston and shafts. These can be calculated using the sizes of the components used. These components rotate about the same axis and are have cylindric shape. The moment of inertia of a hollow cylinder is:

$$J = \frac{1}{8}m(D_{out}^2 + D_{in}^2)\,, \quad (5)$$

where m is the mass of the rotating component, D_{out} - the outer diameter, D_{in} - the inner one which is equal to zero for shafts and the servo motor rotor. The shaft mass and the diameter is relatively small and therefore can be neglected.

For the calculations of the friction torque, the same correlation as for the linear motion can be used (Tran and Yanada, 2013) with adjustments for the rotational motion by substitution of the peripheral speed of the piston instead of the linear one.

The resulting equation, used for the servo motor control can be written as follows:

$$T_{el}(t) = \frac{d^2\varphi}{dt^2}\left[\frac{1}{8}\left(m_{rot}D_{rot}^2 + m_{cyl}\left(D_{cyl,out}^2 + D_{cyl,in}^2\right)\right) + \right.$$
$$\left. + \frac{D_{cyl}}{2}F_{fric}\left(\frac{\varphi(t)}{dt}\right)\right], \quad (6)$$

where D_{rot} - is the servo motor rotor diameter, $D_{cyl,out}$ and $D_{cyl,in}$ are the outer and the inner diameter of the piston.

There is no influence op working pressures on the rotation since the in- and the outlet ports are placed axisymmetrically and therefore the pressure induced forces are compensated.

4. CONTROL STRATEGY

The control strategy here proposed corresponds to an algorithm designed based on the mechanical insight, where a set of rules are proposed to achieve the desired performance.

4.1 Intake and discharge.

The working medium enters the expander through a rectangular port formed by the openings in the housing and the skirts. The mass flow rate is dependent on the port area S, the pressure difference between the inlet pressure p_{su}

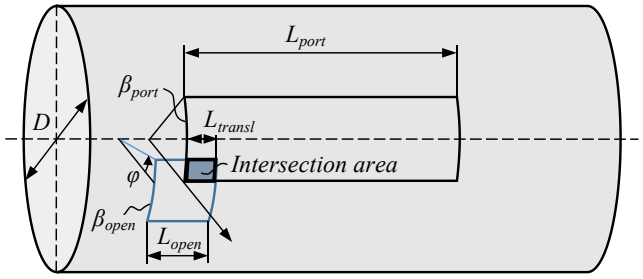

Fig. 7. Schematic of the port geometry.

Table 2. Inlet port and the skirt opening sizes

L_{open} (m)	L_{port} (m)	β_{open} (rad)	β_{port} (rad)
0.02	0.23	$\pi/12$	$\pi/12$

and the pressure in the cylinder p_{cyl}. The intersection area is changing according to the rotation and the translation of the piston (Fig. 7).

The position of the lower left corner of the cylinder wall opening is chosen as the reference point. The start of the intake process corresponds with the position of the piston when the lead-top corner of the skirt opening is at the reference point. A simplified algorithm defining the overlap of two rectangular openings is used to calculate the intersection area (Eq. 7):

$$\begin{aligned} S(t) = (&max(0, min(L_{transl}(t), L_{port}) \\ &- max(0, L_{transl}(t) - L_{open})) \times \\ &\times (max(0, min(\varphi(t), \beta_{port}) \\ &- max(0, \phi(t) - \beta_{open})) \cdot \frac{\pi D}{2} \cdot n \,, \end{aligned} \tag{7}$$

where n is the number of ports. There are two axisymmetric ports used in current configuration. The inlet port and the skirt opening sizes are shown in Table 2.

A similar model is applied to estimate the mass flow rate during the discharge process. The corresponding pressures p_{cyl} and p_{dis} are used.

4.2 Optimization criteria

Filling factor. The stroke length is defined in previous simulations and is kept constant. The piston movement profile under the applied forces defines the frequency of the machine, which must be maximized for a higher mass flow rate of the working medium. However, the higher the piston speed during the intake phase, the more difficult to maximize the inlet area for a higher filling factor. The definition of a filling factor is introduced by (Lemort et al., 2009) and means the measured flow rate divided by the displacement. Ideally, the density of the working fluid at the end of the intake is equal to the one at the inlet port. The actual density of the working fluid in the cylinder divided by the ideal one gives the indication of the intake efficiency.

$$\phi_{ff} = \frac{\rho_{cyl}}{\rho_{su}} \tag{8}$$

Table 3. Adjustable control parameters for different inlet pressures.

Pressure, MPa	$k1$	$k2$	$k3$	$k4$	$k5$	$k6$
1.0	0.41	1.05	0.426	0.242	0.15	0.006
0.6	0.75	1.09	1.0	0.242	0.15	0.007

A non-optimized velocity profile is shown on Fig. 6. As it can be seen on pV-diagram (Fig. 10), the inlet port closes relatively late causing a significant pressure drop of about 100 kPa at the end of the intake. The filling factor in this case is about 0.89.

After the optimization, the filling factor rises above the unity, which, beside the optimization, is caused by cooling down of the working fluid during the intake process due to a lower temperature of the expander. A normalized filling factor can be applied by using the actual temperature in the working chamber instead of the inlet temperature.

Intake efficiency. Another optimization criterion can be the intake efficiency expressed as a ratio of surface areas of the actual and ideal pV-diagrams from the opening of the inlet until it closes. After the rotation and translation adjustment, the values of 0.96 - 0.97 are obtained.

The linear motion and the rotation of the piston have to be synchronized in order to achieve the required BVR and a maximal inlet area during the intake. The maximal inlet area is theoretically achievable only if the motion of the piston is defined by square waves of both the rotation and the translation, which is impossible in practice due to a certain mass and the moment of inertia characterizing the piston. It is possible to approach such an ideal movement profile by reducing the piston acceleration while the inlet is open for more accurate timing control by rotation. The rotation has to be also adjusted.

Fig. 8 and Fig. 9 show the control algorithm for the piston linear movement and the rotation respectively. The adjustable parameters $k1$ - $k6$ allowing the pressure ratio of 1.0 and 0.6 MPa are shown in Table 3.

4.3 Translation control

Intake: $F_{em} = F_{nom} \cdot k1$ - the electromagnetic force is limited by the factor $k1$ during the inlet phase.

$p_{cyl} < p_{dis} \cdot k2$ - the piston is forced to move until the inlet port opens and the cylinder pressure starts to increase until a certain value defined by $k2$.

$F_{em} = -F_{del_p} + F_{fric}$ - the piston speed is kept constant as long as the inlet is open ($\varphi > \beta_{port} + \beta_{open}$). All forces are compensated by the electromagnetic one.

Acceleration: While the piston speed is lower then v_{max}, the nominal force (F_{nom}) is applied.

Brake: The electromagnetic force is adjusted so the piston reaches its extreme right position with $v = 0$ (Fig. 11). A PI-action can be applied at the end of the stroke in order to compensate a linear positioning error. It is important to avoid an overshoot since it means a mechanical impact of the piston on the stator.

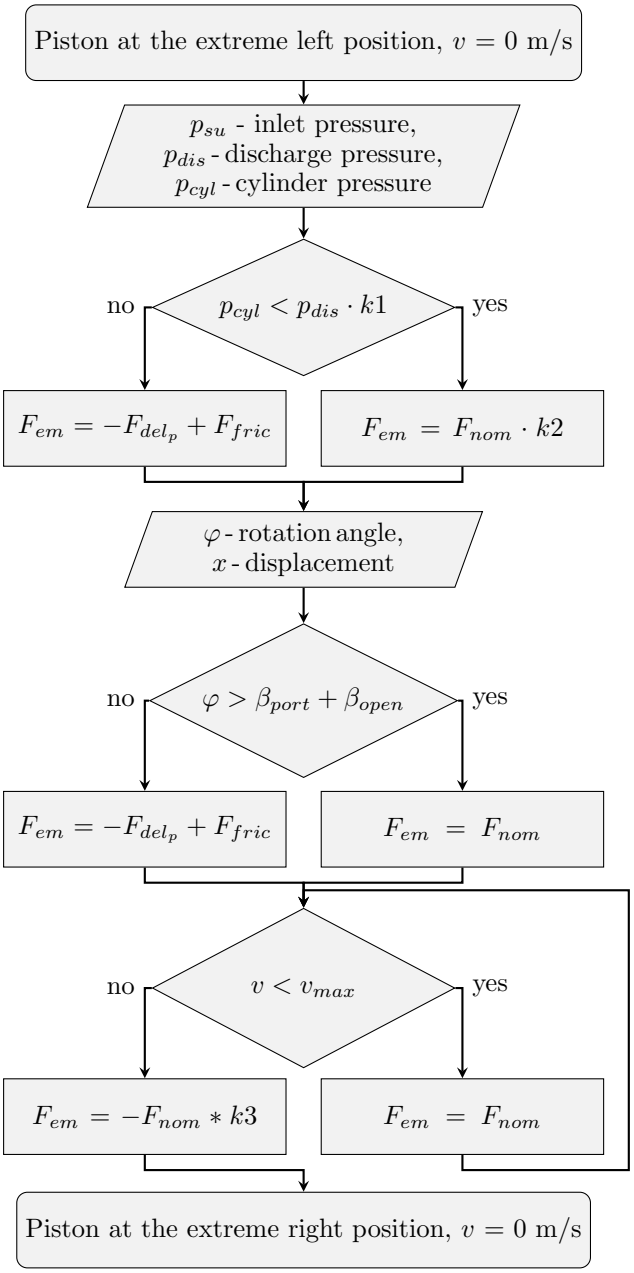

Fig. 8. Piston linear movement algorithm

4.4 Rotation control

Intake: While the piston starts to move away from its extreme left position, the rotation velocity is ω_0. By applying a decelerating torque of $-T_{nom}$ at the moment defined by $k4$, the rotation decreases, ideally down to zero ($k5 = 0$), when the skirt opening is aligned with the inlet opening. The resulting speed can be adjusted by the coefficient $k5$ if the rotation should not be completely stopped but just reduced to allow a higher piston response. This is an open loop control since a high positioning accuracy is not required.

The piston travels to the right without rotation. When the displacement reaches a certain value defined by $k6$, the rotation is accelerated with a torque of T_{nom} in order to close the inlet port when it is dictated by the thermodynamic model.

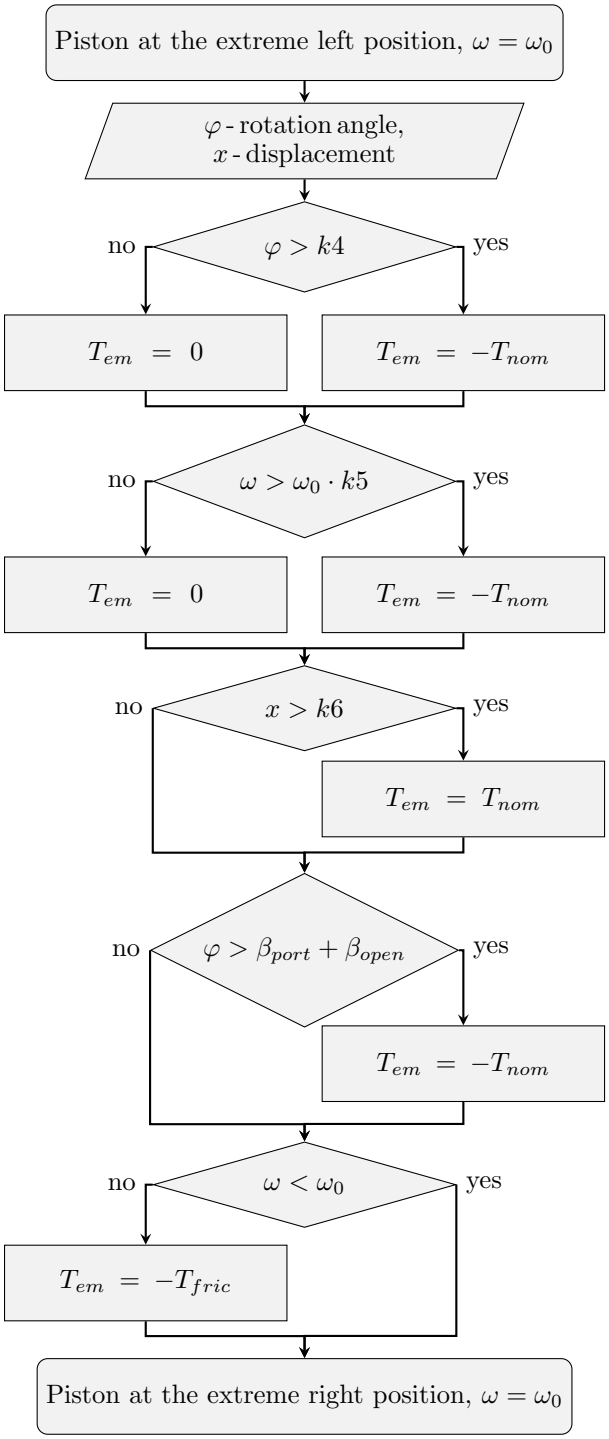

Fig. 9. Piston rotation algorithm

Deceleration After the inlet is closed ($\varphi > \beta_{port} + \beta_{open}$), the piston rotation speed needs to be reduced until it reaches ω_0, then the piston rotates with a constant speed. The torque applied from the servo motor is equal to the one caused by friction. At the end of the stroke, a PI-action can be applied for a better accuracy.

The resulting velocity profile vs. time is shown on Fig.12. It can be seen that the higher the inlet pressure, the faster the piston reaches its maximal translation speed, so a lower brake force is needed to decelerate it until the extreme right position.

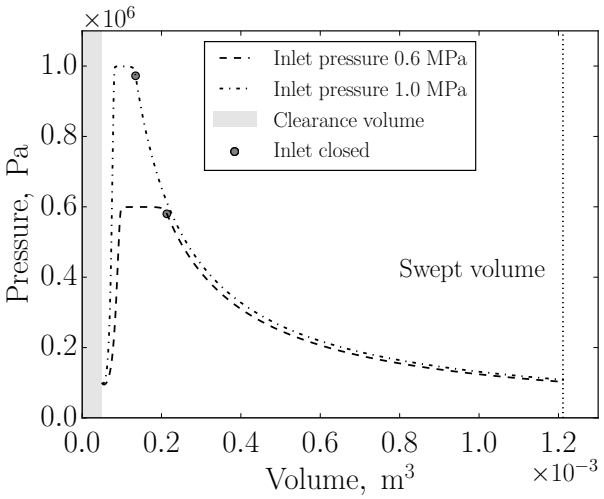

Fig. 10. Piston velocity vs. displacement

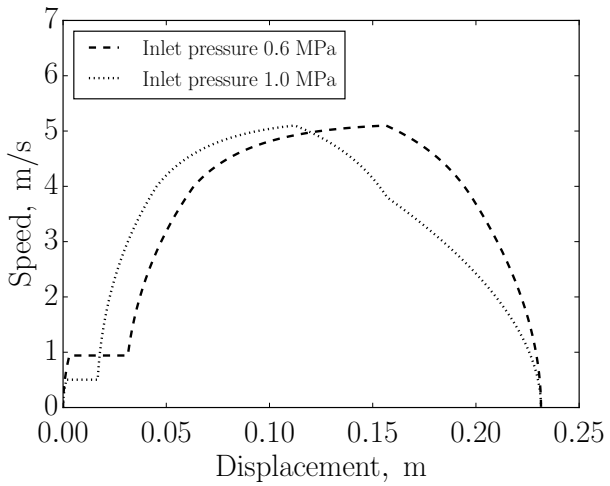

Fig. 11. Piston velocity vs. displacement

Two inlet pressures 1.0 MPa and 0.6 MPa are compared and the configuring factors are identified (Fig. 10).

By performing such simulations within the expected inlet pressure range with a certain step, a matrix of these parameters can be obtained and used in real time to adjust the piston movement under varying inlet pressure.

4.5 Parameters description

Variables: Inlet pressure

Constants: Inlet temperature, outlet pressure, expander geometry, zero piston velocity at the end of expansion phase.

Adjustable parameters: k1, k2, k3, k4, k5, k6.

Efficiency indicators: frequency, filling factor, intake efficiency, power output: to maximize.

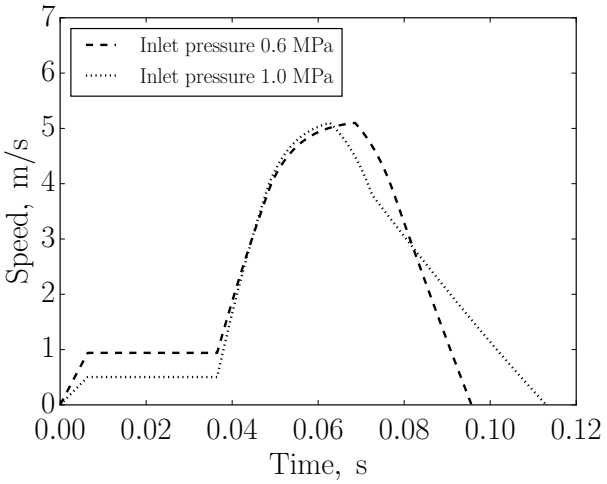

Fig. 12. Piston velocity vs. displacement

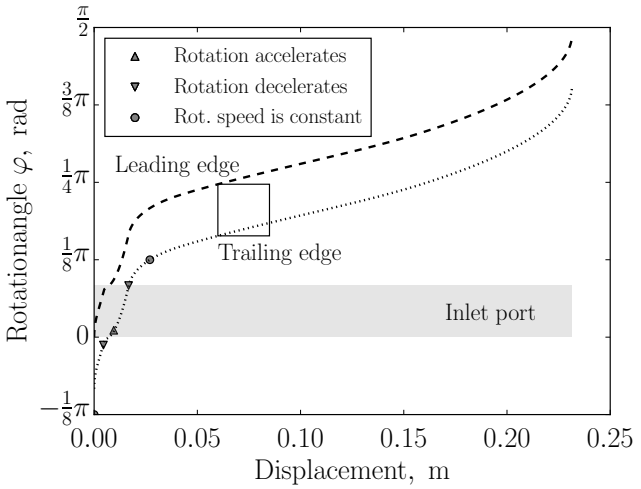

Fig. 13. Piston velocity vs. displacement

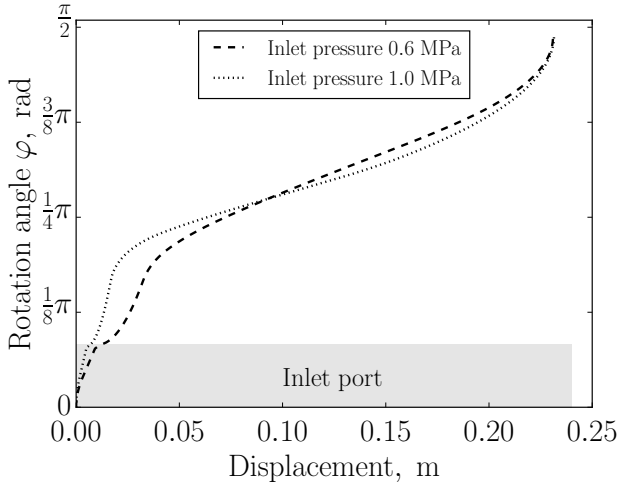

Fig. 14. Piston velocity vs. displacement

5. RESULTS AND DISCUSSIONS

The developed model is based on parameters of the selected linear motor and the servomotor and allows to synchronize the rotation with the linear movement of the expander. By decreasing the linear speed during the intake phase, the pressure loss at the inlet can be reduced. However, reduced translation speed means lower frequency and the mass flow rate through the expander, so the optimum has to be found (Fig. 12).

The rotation of the piston can be increased or decreased when necessary for a better fit of the inlet. A moderate rotating acceleration/deceleration is achievable in combination with the piston deceleration during the intake. The final deceleration must be adjusted so the leading edge of the skirt opening reaches the outlet port at the end of the stroke. In this case this angle is $\pi/2$ (Fig. 13). Two rotation/translation profiles for different inlet pressures are shown on Fig. 14

The shape of the inlet port needs to be adjusted to "follow" an optimal intake profile in order to keep the inlet intersection area around its maximum during the intake phase. Otherwise higher pressure ratios will require high dynamics from electromagnetic train or will cause relatively high intake losses.

The presented model is focused on the inlet control and therefore simplified by setting the outlet pressure as constant.

6. CONCLUSIONS

The dynamics of the system depend on the linear generator used. Industrial linear motors are characterized by large moving masses. It is possible to reduce the weight of the piston if magnets are directly attached to it. A high dynamics of the piston movement is necessary to increase the resulting frequency and the volumetric flow rate of the machine. A relatively high static force is required to keep the piston under control at its extreme positions. The use of a position encoder ensures the high accuracy of the inlet timing, which is crucial for the system efficiency.

The proposed system contains no bouncing devices such as gas- or mechanical springs, which are typically used in free piston machines. Instead, the piston movement is fully controlled, so its velocity becomes zero at both extreme positions. A higher system efficiency is expected since mechanical wear or thermodynamic irreversibilities are avoided.

REFERENCES

Bell, I.H., Wronski, J., Quoilin, S., and Lemort, V. (2014). Pure and pseudo-pure fluid thermophysical property evaluation and the open-source thermophysical property library coolprop. *Industrial & engineering chemistry research*, 53(6), 2498–2508.

Gusev, S., Ziviani, D., De Viaene, J., Derammelaere, S., and van den Broek, M. (2016). Modelling and preliminary design of a variable-bvr rotary valve expander with an integrated linear generator. In *Proceedings of the 17th International Refrigeration and Air Conditioning Conference at Purdue*.

Imran, M., Usman, M., Park, B.S., and Lee, D.H. (2016). Volumetric expanders for low-grade and waste heat recovery applications. *Renewable and Sustainable Energy Reviews*, 57, 1090–1109.

Lemort, V., Quoilin, S., Cuevas, C., and Lebrun, J. (2009). Testing and modeling a scroll expander integrated into an organic rankine cycle. *Applied Thermal Engineering.*, 29, 3094–3102.

Mikalsen, R. and Roskilly, A. (2008). The design and simulation of a two-stroke free-piston compression ignition engine for electrical power generation. *Applied Thermal Engineering*, 28(56), 589–600.

Petrichenko, D., Tatarnikov, A., and Papkin, I. (2015). Approach to electromagnetic control of the extreme positions of a piston in a free piston generator. *Modern Applied Science*, 9(1), 119–128.

Tran, X.B. and Yanada, H. (2013). Dynamic friction behaviors of pneumatic cylinders. *Intelligent Control and Automation*, 4(2).

Appendix A. NOMENCLATURE

A.1 Latin characters

D	diameter	(m)
F	force	(N)
L	length	(m)
m	mass	(kg)
n	number of ports	(-)
p	pressure	(Pa)
S	intersection area	(m^2)
t	time	(s)
V	volume	(m^3)
x	displacement	(m)

A.2 Greek characters

β	port angle	(rad)
Δ	difference	(-)
υ	speed	(m/s)
φ	angle of rotation	(rad)
ϕ	filling factor	(-)
χ	relative displacement	(-)

A.3 Subscript

cyl	cylinder
dis	discharge
el	electromagnetic
fr	friction
max	maximal
min	minimal
open	opening
port	port
rot	rotation
su	supply

Models for Planning and Supervisory Control for the feeding raw material in cement production [1]

Edgar CHACÓN R. [*,***] **Juan CARDILLO A.** [**]

[*] *Dpto. de Computación, Escuela de Ingeniería de Sistemas, Facultad de Ingeniería, Universidad de Los Andes, Mérida Venezuela, echacon@ula.ve*

[**] *Dpto. Sistemas de Control, Escuela de Ingeniería de Sistemas, Facultad de Ingeniería, Universidad de Los Andes, Mérida Venezuela, ijuan@ula.ve*

[***] *Unidad Académica de Ingeniería de Sistemas, Universidad Católica de Cuenca, Cuenca Ecuador*

Abstract:
The clinker production process is mainly affected by the quality of the raw material. The chemical composition required for the formation of clinker is giving by the mixing of different limestone sources, clay, and iron ore. The optimal combination may be determined in principle by linear programming techniques, but the variation of the quality of limestone mines is high, so it is necessary to adjust the mix online, by using transport mechanisms which are discrete and sharing other resources. The feed to the mill is divided into two processes : crushing and forming stacks (pre- homogenization) and the mixture preparation online in the mill for forming flour (homogenization).
The goal is to design mechanisms that allow the proper proportions of minerals to the furnace inlet through programming online resources for pre–homogenization : the limestone quarries, trucks, crusher and transport mechanism of the raw material to deposit. Supervisory control techniques are used, and models are constructed as discrete event systems to ensure that the mixture is as homogeneous as possible over time. A particular architecture (Holonic architecture), it is used in the solution; which allows an easy and effective implementation of an on-line supervisor. Supervisor uses the material existence and cost knowledge. A reference is made to an application that is a Discrete Event System model interpreter for the implementation of the supervisor.

Keywords: Discrete Event Systems, Integrated Automation, Cement industry, Planning, Supervisory Control.

1. INTRODUCCIÓN

The cement industry is critical in the development of contemporary society to be basic raw material in the construction industry . The central element in the manufacture of cement is the clinker production, obtained by calcining a mixture mainly of: Calcium Oxide (CaO), silicon dioxide (SiO_2), Aluminum Oxide (Al_20_3), and iron oxide (Fe_20_3) found in limestone, clay and the iron ore. The process for Portland cement production is shown in Figure 1, and it is divided into the following stages:

(1) Conveying limestone; it is transported to warehouses in the cement plant and placed in cells having the same quality.
(2) Crushing and pre-homogenizing, which reduces the size of the limestone rocks that can be used by the raw mill and at this stage a first mixture of stone from different sources is performed to obtain a limestone (CaO) pre - homogenizing. The mixture is made to comply with predetermined percentages of limestone.
(3) Homogenizing. It makes a mixture of limestone (pre-homogenizing) with iron ore and clay to achieve the ideal blend, and in some cases corrective limestone is added. A stage of homogenization process is the raw milling , where minerals are reduced to a diameter of millimeters, so that the mixture is given particle level. Then, this milled mixture is carried deposits where homogenization of the mixture is complete, and then fed to the furnace. The product obtained is the raw meal, which feeds the oven.
(4) Clinkering, consisting in transforming the mixture (raw meal) in clinker by a cooking process; and finally,
(5) Cement production. By grinding the clinker and adding other products like gypsum, limestone, pozzolan, among others, that give texture and resistance

[1] Thanks to the Senescyt of Ecuador who partially funded the project and Cementos Guapán in Azogues, Ecuador for the information provided.

to use. The product obtained is distributed in bags (50 kg), or in bulk.

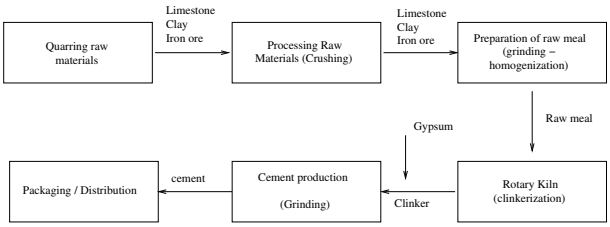

Fig. 1. General Process flow for the Production of cement. Modified from Huntzinger and Eatmon [2009]

When having the homogenized mixture, the mixture quality will determine its performance in the clinkering process. The oven has a continuous operation, so the input product must maintain a constant flow. The flow is determined by the oven capacity product quality at its input.

Input limestone comes from different quarries and has a high variability in their chemical composition and moisture levels , not only for its origin from different quarries, but also by the geological formation of the quarries. Limestone has an economic value according to their origin. The issue is to maintain an ideal choice for a flow that is determined by the furnace capacity to process raw meal mix at the lowest cost. The cost includes the cost of raw material and processing cost in the oven. The cost of processing furnace varies according to the quality of the raw meal.

An ideal mixing quality for the oven, which is feasible with available feedstock is established. It seeks to get that quality over time constantly mixing raw material from different quarries through dynamic allocation of resources and routes for forming pre-homogenizing limestone crushing corrective clay and preparation of corrective limestone, in amounts sufficient to maintain the constant flow of feeding to the furnace. The second step is feeding the mill uses a shared resource that is the transport system inputs, it goes from the tank pre-homogenized until the hoppers at the entrance to the mill.

Planning, programming, monitoring and even control production processes, can be obtained from models that reflect the behavior of the system in each of the above situations. Everything based on the basic objective is to produce, and which focuses on a request from a customer that accrues on, either in a delivery in warehouse or a production order in production or both. In most cases, when planning in a production process it is assumed for convenience a normal operation behavior; if required to do planning online, then you need to know the state of the process in order to generate an acceptable plan and, this is nothing more than take the product model (product route) and map on the set of available process equipment, incorporating physical constraints, considerations interconnection delays, which sets the schedule of when an order should start and completion date. Similarly, it requires a model for supervisory control schemes, whether coordination between units or supervision in each unit (resource). It is necessary to establish a planning mechanism for determining the amount of principal limestone, clay and limestone corrective to be produced; the online selection of the limestone quarries that is based on the quality obtained in the crushing process; supervisory control mechanism associated with the coordination of the stages.

The paper is organized as follows: the first section presents roughly the methodology to be used (This has been proven in commercial applications for companies in Merida, Venezuela and Medellin, Colombia) for the behavioral model of the process, in particular the model of the product routing. In the second section, the functional units and the associated IDEF diagrams are defined. In a third section the product route and Petri nets models associated with it and the functional units are shown, and as the model of behavior of the process is determined. A fourth unit shows how the pattern of behavior found is the model used for planning, programming, monitoring the process. Finally results and future work are presented. The results were found using a software tool developed by Janus Systems Merida.

2. PRODUCTION SYSTEMS MODELING USING DISCRETE EVENT SYSTEMS TECHNIQUES

To obtain a useful model production we require that serves to identify the model; in our case the models are used for: Planning, Programming, Supervision, Coordination, Monitoring of the production process. So far the useful descriptions thresholds used to detect conditions of the system; or the occurrence of events that can initiate, continue, enable, stop a process. This leads us naturally to the use of a description based on discrete event system, regardless of the nature or form of processing that has each of the entities making up the production process. A Dynamic Discrete Event System is a system whose dynamics is defined by changes in discrete variables, and this dynamic is driven by the occurrence of events. Within the formal techniques for the representation of Discrete Event Systems to find those based on Finite State Automata Ramadge and Wonham [1989], Wonham [2014] and Petri nets DAVID and ALLA [2001], David and Alla [2005]. Discrete Event Systems allow modeling the behavior of systems at different levels of the plant, from the plant floor allowing applications for PLC programming Uzam et al. [1996], Fabian and Hellgren [1998], Zhou and Twiss [1998]; at the supervisory level, in the description and supervisory control of batch processes Andreu et al. [1994, 1995], Viswanathan et al. [1998], Tittus and Åkesson [1999b,a], Tittus and Lennartson [1999], supervision of hybrid systems Antsaklis et al. [1998], Lemmon et al. [1999]; for levels of management, modeling and implementation of business processes van der Aalst [1998], van Der Aalst and Van Hee [2004], van Der Aalst et al. [2003a,b]; and integration between different levels Vernadat [2014], ISA-95 [2000], Chacón et al. [2008].

As we see, there are many authors who use DES as natural models to describe the production process (logical part), it is necessary to establish a production process configuration (physical part) so it can be executed. Figure 2 shows the procedure for establishing a configuration and run production activities, which is similar to the procedure proposed in Covanich and McFarlane [2009]. From the point of view of modeling, we see that is the model of behavior (route product) which is the generator of the

entire sequence shown in Figure 2, and therefore of the Planning, Programming, and Execution.

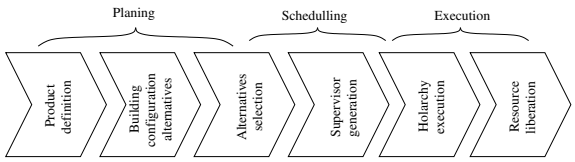

Fig. 2. Steps to establish a configuration

2.1 Product Model

A product model indicates the sequence of steps necessary to obtain a product , as shown in Figure 3. At each step, the competencies (skills) necessary for their implementation, as well as inputs (raw materials and services) and outputs for stage specified. In addition, information about the time needed to perform the step.

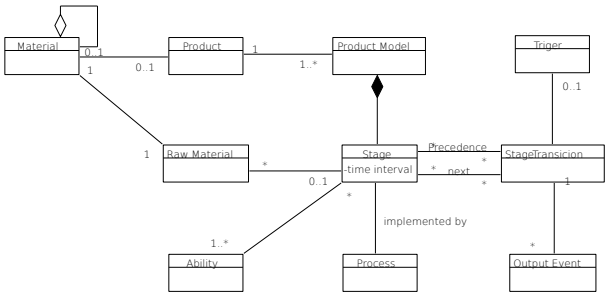

Fig. 3. Product Model, Production Model in UML

2.2 Description of the behavior of the Functional Unit

A functional unit is defined as responsible for carrying out a required skill, either in a business process or a production process. To describe the behavior of the functional unit, we rely on the deployment architecture shown in Figure 4. In our case, we only focus on the skills required in the production process. Functional Units generate services for a product. The relationship between the model and the functional units is obtained by the skills required by the product model and provided by the Functional Unit.

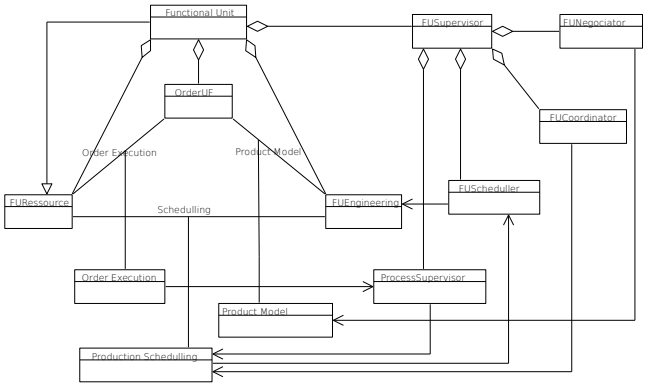

Fig. 4. Functional Unit model in UML

As shown, the Functional Unit has a core containing the holarchies management, consisting of a set of behavioral models that describes the functionality of the entities belonging to the unit. This set of structured models can be grouped to form holarchies . A holarchy shows a model in principle overall (useful) of the functional unit to accomplish a target.

This core set of universal behavior patterns in the UF depending on the purpose of production; considers aspects such as: normal condition , degradation of the operational condition and the functional abnormality between the components of the unit as well as the condition and the levels of the raw material. Models built in this way can be used *to track* the processes occurring in the entities (unit, plant and equipment).Supervisors can also be generated (coordination and supervisory functions) and drivers for regulation.

Functional Unit (**FU**), as a whole, is responsible for evaluating the feasibility of an activity and the execution of that activity (programming, implementation); as well as achieve coordination with other FU for the implementation of activities through cooperative interactions (runtime). The dynamic behavior of the FU can be described by Discrete Event Systems (DES), in our case, we use hierarchical Petri nets.

2.3 Modelling by Petri Nets

Petri Nets can describe the different processes that occur in a production system in an easy way. We use the same model for planning and programming activities and to monitor the actual process. The network locations represent us process states, or the resources used, as shown in Figure 5.

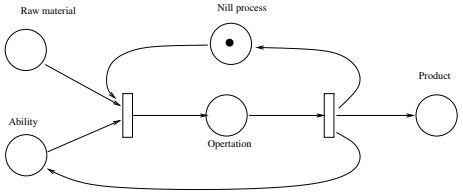

Fig. 5. Petri net for overall description of a process

In Johnsson [1997] the concept of interpreted Petri nets to assign meanings to places and transitions, so they represent the production process is used. Places, transitions, arcs and tokens have a semantics that can describe in sufficient detail the production process. In the description of the process model, a place represents: a needed input; if it is associated with resource indicates capabilities (in the case of equipment / functional units), or abilities (human resource) y and the amount of effort necessary to accomplish the task, the arcs define the amount of product consumed or generated into the process or the quantity of resource capability used. The network shown in Figure 5 corresponds to a product model and it will be used for planning. On the other hands, Timed Petri Nets allow duration or dates associated models, representing a production process. Transitions are associated with the occurrence of the events on the plant floor, and its implementation these events are captured by the installed technology. An event can be associated with the arrival of a production order, the completion of a task.

2.4 Behavior model for a production unit

The behavior of an elementary process can be expressed by a Discrete Event Systems, and the composition of elementary models based on interactions associated with transitions, allows us to obtain the overall behavior of a system. This methodology has been validated by Janus Sistemas in several applications. In Chacón et al. [2008] it is described the methodology to generate behavioral models of the production processes to planning, monitoring and supervise the process. In this paper we present only part of the methodology that allows us to model behavior of the first stage of the process of obtaining clinker (pre-homogenization) in order to the construction of the model consists of:

(1) Product description routes, such as establishing an acceptable configuration, represented in IDEF (IDEF).
(2) Description of functional units, their skills (abilities) and their interactions. Description of the states of the unit depending on regions and operation modes, and its representation in IDEF.
(3) Building product model, and its representation by Petri Nets.
(4) Construction of models of functional units and their representation using Petri Nets.
(5) Obtaining behavioral models using the model projection path product on equipment (Functional Units).
(6) Using the model of behavior in the previous step, get the model to planning, monitoring, and supervision a production order.
(7) Generate a plan and schedule for the production order and its monitoring mechanisms.

As shown, the pattern of behavior is nothing more than a holarchy models. These models are represented in Petri nets and lead to the global model of the production process, which is used to plan, schedule, monitor and follow a production order. The application used interprets these types of models efficiently. This approach to implementation of automation can be used interchangeably if the company is hierarchical, heterarchical or holonic.

3. CASE STUDY: PRE - HOMOGENIZATION STAGE IN CLINKER PRODUCTION

3.1 Modeling the whole production process

The first step in building models is to achieve global flows of information and products. The IDEF0 model in Figure 6 shows the information and products flows for the Clinker production process.

Thus, the clinker production process is described in the first 4 major stages of the 5 shown in section 1: Quarries, Crushing – Pre-homogenisation, homogenisation, and Clinker cooking (several limestone). Transportation between quarries and crushing is given by trucks. Interconnection between pre - homogenisation and mill is given by a belt (limestone, corrective limestone, clay and iron ore). Interconnections should be multiplexed to allow the transport of different products. Between the homogenizer and the furnace only the raw flour is transported.

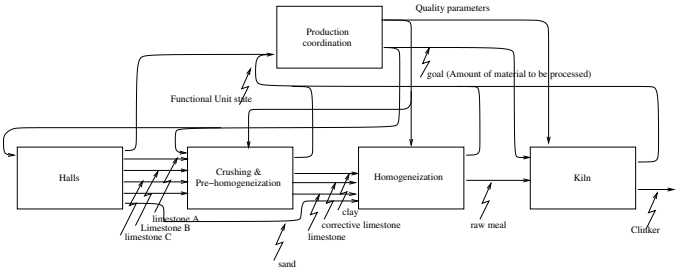

Fig. 6. General model (IDEF0) for the activities in the Clinker manufacturing process

3.2 Modeling the pre-homogenization process

The main raw material of the process comes from accumulations of limestone from different quarries and have a high variability in their chemical composition and moisture levels as it was said in introduction. The first step is the conditioning of the raw material in order to be transported and processed by the mill. Preparing raw material consists of three separate threads that are conditioning main limestone, limestone corrective preparation and conditioning of clay; these processes use the same resources: crusher and trucks. All these elements are stored in piles for subsequent transport to the raw mill, along with iron ore (ferrous sand).

The feeding process the raw mill, recovering the pre-homogenized limestone, corrective limestone, clay and sand corrective ferrous from the formed piles. The entire process eliminate variability in two stages, in the first, homogenization of the main product, and in the second phase, a completion is performed adding minerals that are not present in the limestone.

To determine the sources of raw material, the system takes into account: availability, quality and cost of raw materials stored in order to determine the optimal combination. The result gives tons of raw material from each source to use. In general, the expected quality of the raw meal is given in table 1.

Material	Min	Max
CaO	65	68
SiO_2	20	23
Al_20_3	4	6
Fe_2O_3	2	4
MgO	1	5

Table 1. Range of the main components

The properties of the raw materials are given in the table 2.

	Sou 1		Sou. 2		Sou. 3	
Material	Min	Max	Min	Max	Min	Max
SiO_2	8	25	x	x	x	x
Al_20_3	1	4,5	x	x	x	x
Fe_2O_3	1	4	x	x	x	x
CaO	40	43	45	x	x	x
MgO	0,3	1	x	x	x	x

Table 2. Range of the main components by quarry

A IDEF description associated with the physical structure of the plant, corresponding to the steps of Figure 6, is

given in Figure 7. The figure shows the information and product flows shown for the two processes analyzed. It can be realized that pre - homogenization part has a feeding system that is discret and, the the second part (homogenization) has a feeding systems that is by batch. The output of the whole process should be continuous, and this is achieved by the use of a temporary storage system between stages.

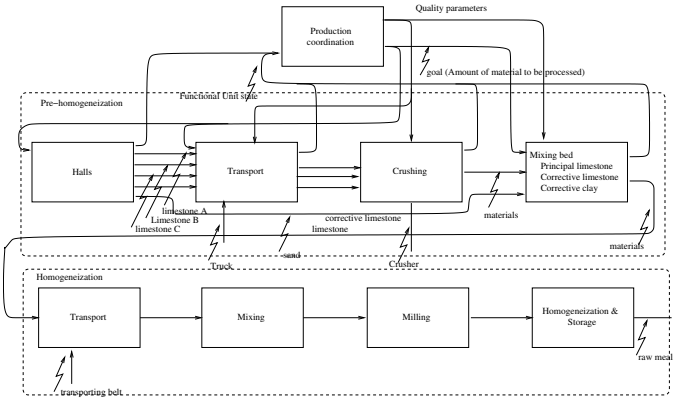

Fig. 7. Pre - homogenisation and Homogenization processes in the production of Clinker

3.3 Functional units in the first part: Crushing process and Pre-homogenization processes

The Functional Units in the pre - homogenisation are: Quarries, Transport Unit, Grinding Unit and Storage Unit. The process should produce three products: the main limestone, corrective limestone and, clay corrective. These products are three of the four inputs to the raw mill. The main resources that are used at this stage are the crusher and trucks. This stage consists of three processes: the transport of materials , mixing crushing of materials and creating layered stacks . The three processes are given separately and are the result of a plan that specifies the amount of material that has been produced and the quality expected as the IDEF shown in Figure 8.

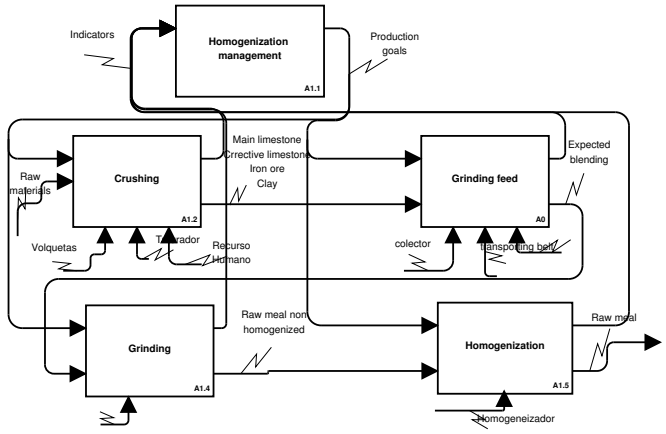

Fig. 8. Products and information flows in the process of homogenization

The crusher is the primary constraint and is used to form the stacks of main limestone, limestone and corrective corrective clay. The amount of each of the materials is determined by the optimization system by using figures in the table 3. The crusher works 8 hours/day, 5 days/week and must process at least the amount of product that will be consumed by the furnace daily taking into account the performance of the raw material in the clinkering process. The amount of production is known by a weighbridge system. The information and products flows are shown in the IDEF Figure 9

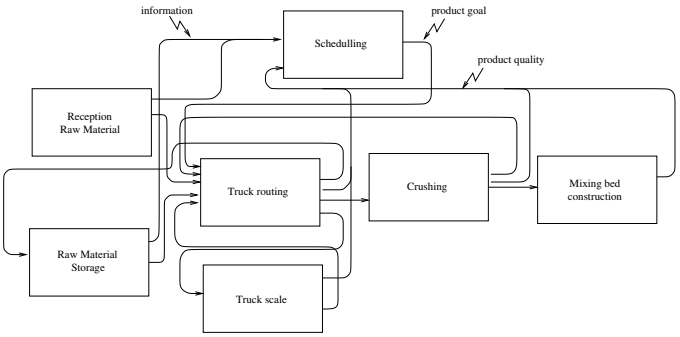

Fig. 9. IDEF0 for homogenisation process

Preparation of the main limestone The objective in the first step is to mix the various limestone quarries for a pre-homogenised limestone with a percentage of CaO over 70 % (Titration 100).

This process gets a product that, in addition to calcium oxide, has silicon, aluminum, iron and magnesium with the values given in Table 3. The product is stored in stacks of layers of material.

	SiO_2 (%)	$Al_2 0_3$ (%)	Fe_2O_3 (%)	CaO
Min	7	1	1	70
Max	10	4.5	4	75

Table 3. Expected range of chemical components of the limestone mixing bed

The properties of the materials, according to their origin, are given in the table 4.

Cantera	SiO_2 (%)	$Al_2 0_3$ (%)	Fe_2O_3 (%)	CaO (%)
A	13.1	1.7	0.8	45.2
B	6.9	0.5	0.2	50.7
C	2.5	0.7	2.8	45.5
Arcilla	43.3	27.4	11.5	0.5

Table 4. Chemical composition of limestone in each quarry

The estimated amount of $\%CaO$ in the limestone pre - homogenized is done by the following calculation:

$$\%CaO = \frac{\%CaO_1 \times M_1 + \%CaO_2 \times M_2}{M_1 + M_2} \quad (1)$$

Moisture and the presence of clay affect the grinding process, so that when selecting the sources of limestone, humidity is a new restriction on the crusher. Deficiencies of other chemicals are resolved in the process of feeding raw flour mill.

For the mixing bed in formation, the expected amount of CaO is calculated for each truck using the following equation:

$$\%CaO_{ac_k} = \frac{\%CaO_{ac_{k-1}} Mass_{ac_{k-1}} + \%CaO_k Mass_k}{Mass_{ac_{k-1}} + Mass_k} \quad (2)$$

It has an on-line analyzer for percent of CaO pre- homogenized, and similarly another analyzer for feeding to the mill.

Preparation of corrective clay Clay provides the silicon component necessary for the preparation of the clinker, but due to the amount of moisture that is, it must be mixed with limestone so it can be crushed. The result is a clay with a high percentage of limestone.

Preparation of corrective limestone Corrective limestone is limestone with a high percentage of CaO. It will be used in the raw mill to ensure the required percentages of calcium carbonate. If the pre-homogenization process was efficient, the amount of corrective limestone must tend to zero.

4. BEHAVIORAL MODELS OF FUNCTIONAL UNITS AND PRODUCT IN PETRI NETS

The flow of information and products crushing activity shown in Figure 10. Management should plan crushing activities according to the needs of pre-homogenized Limestone, corrective Limestone and corrective Clay. Then, the management system makes an vehicles assignment, to define routes according to the on-line calculation of the product quality that has being obtained.

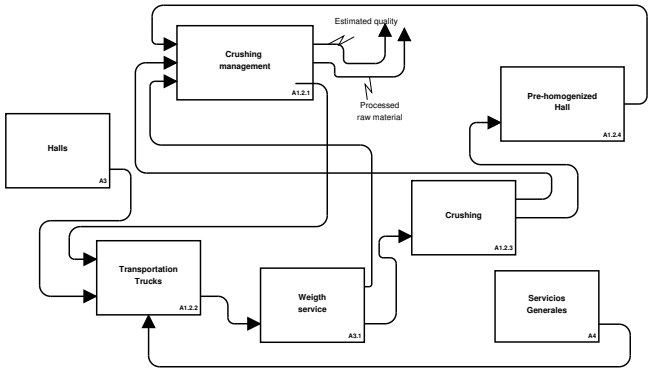

Fig. 10. Flow of information and products in the grinding process

Products and raw materials are materials and are described as defined by ISA-88. Table 5 presents this information.

Material	Material class
Limestone_A	Limestone
Limestone_B	Limestone
⋮	
Clay	Clay
Corrective limestone	Crushed limestone
Production limestone	Crushed limestone

Table 5. Materials

For a stage, which is complex, it has a tool that tracks each stage. Using a holonic structure, an interpreter models follow the patterns of behavior of the stage to monitor and supervise the process.

Figure 11 shows the behavioral model in Petri Nets for the production process of the main limestone.

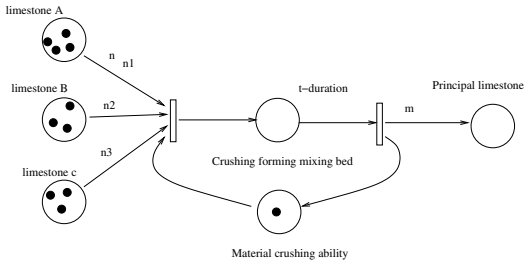

Fig. 11. Product Model (Behavior of the production process)

The behavior model production process limestone is shown in Figure 12. We can see that this is just the instantiation (in detail) of the product model on the equipment, in order to have the physical process, including capabilities, restrictions, etc.

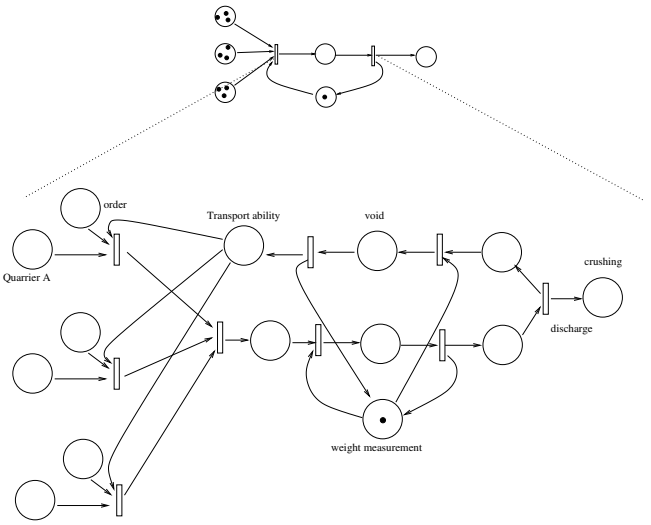

Fig. 12. Production process that implements the steps of production Product Model

Resources for Production The table 6 contains information of physical infrastructure. These elements are considered as functional units with abilities to perform the tasks of planning and monitoring. The components of the equipment hierarchy are considered as a functional units, which are able to build internal plans, track activities, monitor the implementation of activities and execute activities.

5. GENERATING A PRODUCTION PLAN, AND SUPERVISORY CONTROL SYSTEM: FENIX

For planning, a network is constructed from network behavior Figure 11. The information contained in the network allows to validate the feasibility of the implementation of a process. This requires a transformation of the initial network in a network that includes supplies and equipment using information from existing products in inventory and equipment that are available.

In case there are several production orders that use the same input and the same product, the initial network build

Equipment	Father Equipment	Ability	is a FU
Cement Plant		Cement production	yes
Quarry	Cement Plant	Limestone storage	yes
Quarry Limestone_A	Quarry	Limestone_A storage	yes
⋮	⋮	⋮	⋮
Crushing system	Cement plant	Material crushing	yes
Crusher	Crushing system	Crushing	yes
Transportation belt	Crushing system	transport crushed material	no
Mixing bed feeder	Crushing system	Mixing bed feeder	no
Quarry transport	Cement plant	Material transport	yes
Truck_1	Quarry transport	Truck material transport	yes
⋮	⋮	⋮	⋮

Table 6. Physical infrastructure

a global network validating the viability of the overall process according to steps (schedule of resources).

Thus, an implementation of the expected behavior of the system for the crusher & Pre-homogenization is shown in Figure 13. The crusher is a resource that can not be shared simultaneously , and this means that only one product can be over a period of time.

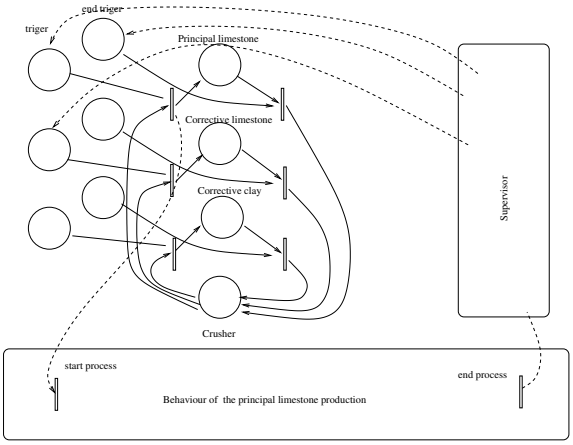

Fig. 13. Behavior of the crushing system

A scheme for tracking an order in the grinding process and the status of the order is shown in Figure 14.

This is feasible in this manner due to the availability of an application capable of interpreting these models and will run equipment assignments based on the quality of the batteries in training. The variability of the batteries minimizes ensuring product quality at the entrance of the mill.

6. CONCLUSIONS

The implementation of a monitoring scheme based online behavioral models ensures quality objectives raised, decreasing allocation tasks truck when performing this automatically. The same monitoring system allows integration with the administrative processes of the organi-

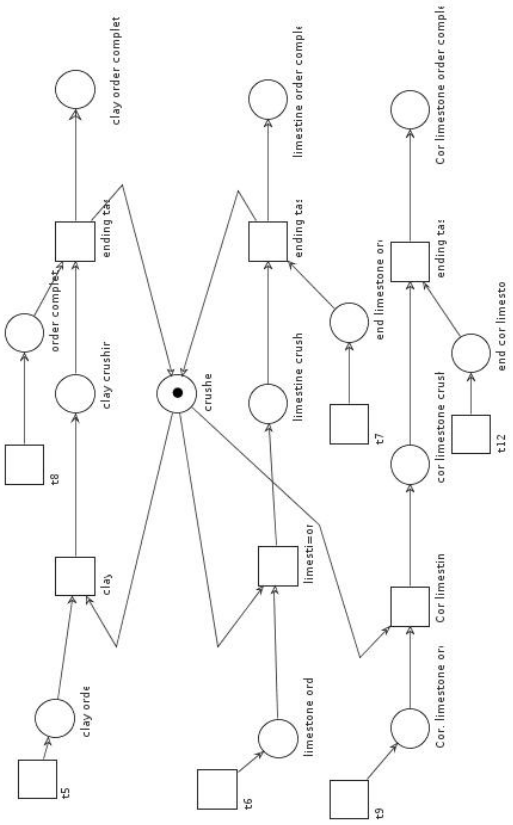

Fig. 14. Dynamic allocation of equipment according to the type of material to be produced

zation maintaining current existence of materials, use of equipment, hours worked, etc.

The modeling process is relatively easy, and the possibility of interpretation models for application reduces development time supervisors, eliminates the possibility of errors in coding, and allows you to incorporate new models of behavior when changes such as occur add a new quarry, changes in the quality of material or new specifications for the stacks of material.

The technology used for the implementation of supervisors is inexpensive and using PLC (programmable control devices) ensures the reliability of the instrumentation on the plant floor.

REFERENCES

Andreu, D., Pascal, J., Pingaud, H., and Valette, R. (1994). Batch process modelling using petri nets. In *Systems, Man, and Cybernetics, 1994. Humans, Information and Technology., 1994 IEEE International Conference on*, volume 1, 314–319. IEEE.

Andreu, D., Pascal, J., and Valette, R. (1995). Interaction of discrete and continuous parts of a batch process control system. In *ADEDOPS Workshop, Imperial College, Londo*.

Antsaklis, P., Koutsoukos, X., and Zaytoon, J. (1998). On hybrid control of complex systems: A survey. *Journal européen des systèmes automatisés*, 32(9–10), 1023–1045.

Chacón, E., Albarrán, J.C., Chacón, R., Rojas, O., and Gutiérrez, D. (2008). Metodología para la automati-

zación integrada de procesos de producción basada en el enfoque holónico. In *XIII CLCA/VI CAC*.

Chacón, E., Besembel, I., Rivero, M., and Cardillo, J. (2008). *Advances in Robotics, Automation and Control*, chapter The holonic production unit: an approach for an architecture of embedded production process, 301–314. ITech_ISA.

Covanich, W. and McFarlane, D. (2009). Assessing ease of reconfiguration of conventional and holonic manufacturing systems: Approach and case study. *Engineering Applications of Artificial Intelligence*, 22, 1015 – 1024.

DAVID, R. and ALLA, H. (2001). On hybrid petri nets. *Discrete Event Dynamic Systems: Theory and Applications*, 11, 9–40.

David, R. and Alla, H. (2005). *Discrete, Continuous, and Hybrid Petri Nets*. Springer.

Fabian, M. and Hellgren, A. (1998). Plc-based implementation of supervisory control for discrete event systems. In *Decision and Control, 1998. Proceedings of the 37th IEEE Conference on*, volume 3, 3305–3310. IEEE.

Huntzinger, D.N. and Eatmon, T.D. (2009). A life-cycle assessment of portland cement manufacturing: comparing the traditional process with alternative technologies. *Journal of Cleaner Production*, 17(7), 668–675.

IDEF (????). Integrated definition models. http://www.idef.com/.

ISA-95 (2000). Ansi/isa–s95.00.01–2000, enterprise-control system integration. part 1: Models and terminology. Technical report, ISA.

Johnsson, C. (1997). Recipe-based batch control using high-level grafchart. Technical report, Department of Automatic Control, Lund Institute of Technology.

Lemmon, M., He, K., and Markovsky, I. (1999). Supervisory hybrid systems. *Control Systems, IEEE*, 19(4), 42–55.

Ramadge, P.J. and Wonham, W.M. (1989). The control of discrete event systems. *Proceedings of the IEEE*, 77(1), 81–98.

Tittus, M. and Åkesson, K. (1999a). Deadlock avoidance in batch processes. In *Proc. of 14th IFAC World Congress, Beijing, PR China*, 397–402. Citeseer.

Tittus, M. and Åkesson, K. (1999b). Petri net models in batch control. *Mathematical and Computer Modelling of Dynamical Systems*, 5(2), 113–132.

Tittus, M. and Lennartson, B. (1999). Hierarchical supervisory control for batch processes. *Control Systems Technology, IEEE Transactions on*, 7(5), 542–554.

Uzam, M., Jones, A., and Ajlouni, N. (1996). Conversion of petri net controllers for manufacturing systems into ladder logic diagrams. In *Emerging Technologies and Factory Automation, 1996. EFTA'96. Proceedings., 1996 IEEE Conference on*, volume 2, 649–655. IEEE.

van Der Aalst, W. and Van Hee, K.M. (2004). *Workflow management: models, methods, and systems*. MIT Press.

van der Aalst, W.M. (1998). The application of petri nets to workflow management. *Journal of circuits, systems, and computers*, 8(1), 21–66.

van Der Aalst, W.M., Ter Hofstede, A.H., Kiepuszewski, B., and Barros, A.P. (2003a). Workflow patterns. *Distributed and parallel databases*, 14(1), 5–51.

van Der Aalst, W.M., Ter Hofstede, A.H., and Weske, M. (2003b). Business process management: A survey. In *Business process management*, 1–12. Springer.

Vernadat, F. (2014). Enterprise modeling in the context of enterprise engineering: State of the art and outlook. *International Journal of Production Management and Engineering*, 2(2), 57–73.

Viswanathan, S., Johnsson, C., Srinivasan, R., Venkatasubramanian, V., and Ärzen, K.E. (1998). Automating operating procedure synthesis for batch processes: Part i. knowledge representation and planning framework. *Computers & chemical engineering*, 22(11), 1673–1685.

Wonham, W. (2014). *SUPERVISORY CONTROL OF DISCRETE-EVENT SYSTEMS*. University of Toronto.

Zhou, M. and Twiss, E. (1998). Design of industrial automated systems via relay ladder logic programming and petri nets. *Systems, Man, and Cybernetics, Part C: Applications and Reviews, IEEE Transactions on*, 28(1), 137–150.

CHAPTER 3

BIOMEDICAL - BIOENGINEERING

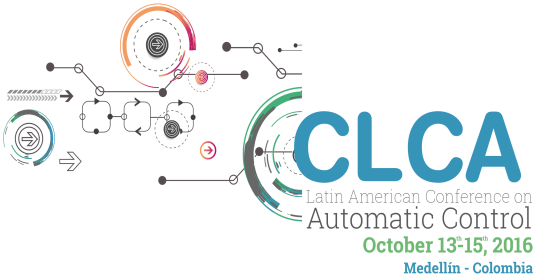

Desarrollo de la etapa tobillo-pie de un sistema de rehabilitación de marcha para niños con PCI.

Calderón-Romero F.*, Calva-Yáñez M. B.*, Niño-Suárez, Paola A.*, Portilla-Flores, Edgar A., Santiago-Valentín E. ****

** Instituto Politécnico Nacional, Escuela Superior de Ingeniería Mecánica y Eléctrica Unidad Azcapotzalco, Av. de las Granjas No. 682, Col. Santa Catarina, C.P. 02250, Delegación Azcapotzalco, Ciudad de México, (e-mail: fercalderon02@gmail.com, pninos@ipn.mx, b_calva@hotmail.com)*

*** Instituto Politécnico Nacional, Centro de Innovación y Desarrollo Tecnológico en Cómputo, Av. Juan de Dios Bátiz s/n esq. Miguel Othón de Mendizábal, Colonia Nueva Industrial Vallejo, C.P. 07700, Ciudad de México, (e-mail: aportilla@ipn.mx, e.santiag.valentin@gmail.com)*

Abstract: Se presenta en este artículo el diseño del concepto de un sistema para rehabilitación de la marcha en infantes con parálisis cerebral, PCI y la metodología para el diseño de la primera etapa: tobillo-pie. La cual involucra el análisis del miembro inferior para obtener un modelo matemático del mismo, determinando su cinemática y la trayectoria que sigue el tobillo durante el ciclo de marcha, para encontrar un mecanismo que pueda emular su movimiento, en este caso fue un mecanismo de cuatro barras. La metodología incluye el planteamiento de un problema de optimización numérica para encontrar la síntesis dimensional del mecanismo utilizando un algoritmo metaheurístico. La mejor solución obtenida se implementó en CAD, el análisis de funcionamiento mediante simulación permitió evaluar su funcionalidad como dispositivo de rehabilitación y determinar la factibilidad de construcción del sistema. Adicionalmente, el modelo en CAD se enlazo con un software de análisis matemático para realizar un control de posición para evaluar su operación y desempeño.

Keywords: mecanismo 4 barras, diseño óptimo, rehabilitación motora.

1. INTRODUCCION

El desarrollo de sistemas de rehabilitación de marcha, ha sido una temática de interés a nivel mundial desde hace varios años. Sin embargo, estos sistemas tienen como objetivo de diseño un uso general, especialmente en adultos con problemas de Accidentes Cerebro Vasculares, ACV, o con lesiones en alguna estructura muscular del sistema locomotor inferior o para rehabilitación motora como parte de un entrenamiento o acondicionamiento físico. Su uso en infantes ha quedado supeditado a la generación de dispositivos o elementos adicionales que adecuen el sistema de rehabilitación a su talle y necesidades.

Son escasos, los reportes en la literatura del desarrollo de sistemas de rehabilitación cuyo diseño se haya centrado en las necesidades de rehabilitación que tienen los niños, especialmente aquellos que padecen parálisis cerebral, PC. Aun teniendo en cuenta que las alteraciones de la marcha son frecuentes en niños con esta afectación y que se ha reportado que la prevalencia de la parálisis cerebral en países occidentales oscila entre 1,5 a 2,5 niños por cada 1000 nacidos vivos, Paneth, et al. (2006). Además, existe evidencia que indica que la terapia orientada al aparato locomotor, destinada a recuperar la capacidad de la marcha, es efectiva en los procesos de rehabilitación en pacientes con alteraciones de este tipo, Goudriaan et al., (2014). Por lo cual, la posibilidad de incrementar la eficacia de la rehabilitación utilizando los avances tecnológicos en las áreas de robótica, mecatrónica y biomecánica, es un campo de investigación que se debe considerar. Especialmente, con el fin de apoyar la rehabilitación en pacientes con edades entre 2-12 años, que por sus características, su rehabilitación utilizando los equipos existentes no siempre es adecuada. Especialmente, aquellos que padecen Parálisis Cerebral Infantil, PCI y que no identifican las posturas adecuadas durante el proceso de marcha, porque aún no han aprendido a caminar, a diferencia de un paciente que por una afectación específica deja de hacerlo y puede usar un equipo convencional.

Una relación de los resultados más relevantes reportados en la literatura a nivel de investigación, se presentan en Kubo, et al. (2011) y en Dollar and Herr, (2008). Producto del éxito de las investigaciones realizadas, en el mercado se encuentran principalmente dos sistemas avanzados para rehabilitación. El LOCOMAT que fue diseñado para rehabilitación de pacientes victimas de ACV y de lesiones en espina dorsal y de cadera; dicho sistema consiste en una órtesis de marcha robótica y un sistema de apoyo de peso corporal combinados con una caminadora, que mueve las piernas del paciente de acuerdo a una trayectoria que emula los patrones de marcha, como se observa en Jezernik, et al. (2004). El sistema GE-O también fue diseñado para cumplir la misma tarea que LOKOMAT, pero utilizando un mecanismo de doble corredera en cada pie y un sistema para soporte de peso corporal. El mecanismo permite el reentrenamiento de la marcha, así como también la capacidad de subir y bajar escaleras, según lo presentado en Hesse S., et al. (2010).

En los grandes Centros de Rehabilitación en América Latina, ya se utilizan equipos de rehabilitación automatizados como los mencionados, sin embargo se ha detectado la necesidad de desarrollar sistemas propios, especialmente para la rehabilitación en pacientes con edades entre 2-12 años, que dadas sus características, su rehabilitación no siempre es eficaz utilizando los equipos actuales y sus adecuaciones.

Tomando en cuenta esta necesidad, el grupo de investigación que presenta este artículo, lleva tres años trabajando en este proyecto. La primera parte del desarrollo, fue la investigación inicial del problema a partir de la información recopilada de diferentes fuentes; pediatras, ortopedistas, terapistas y pacientes, se realizó el diseño del concepto del sistema de rehabilitación, el cual se presenta en Figueroa et al. (2014). Inicialmente, se desarrolló la etapa que corresponde al tobillo-pie. Para ello se obtiene la cinemática directa del miembro inferior, luego la trayectoria que sigue el tobillo a partir del desplazamiento angular de las articulaciones de rodilla y cadera en el plano sagital y de los parámetros estructurales de la extremidad inferior, y con base en esta trayectoria se elige un mecanismo capaz de reproducirla. En Figueroa (2016), se presentó un primer diseño a partir de un robot manipulador del tipo PPR, la base es un robot cartesiano y el grado de libertad rotacional corresponde al efector final de tipo placa para el pie. Se realizaron varias pruebas sobre este prototipo y se optó por evaluar otras opciones para reducir el número de actuadores y suavizar la trayectoria a seguir, utilizando el diseño concurrente para lograrlo.
En este artículo se presenta el nivel de desarrollo que se ha alcanzado al considerar un nuevo mecanismo para esta etapa, se propuso el uso de un mecanismo de cuatro barras, debido a que su topología permite la generación de trayectorias que corresponden al movimiento de interés para la rehabilitación del tobillo y solo utiliza un actuador, luego se presenta la síntesis dimensional del mecanismo, que se realiza a partir de una metodología basada en el diseño óptimo. El problema de diseño se plantea como un problema de optimización numérica y se resuelve mediante el uso de técnicas heurísticas; los resultados obtenidos determinan las dimensiones del mecanismo seleccionado, se presenta el diseño en CAD del mecanismo, la evaluación de su operación y su esquema básico de control.

En la sección 2 se presentan las generalidades del diseño del concepto del sistema de rehabilitación. En la sección 3 la metodología para el diseño de la estructura de la etapa tobillo-pie. En la sección 4, se evalúa el diseño a partir de un modelo en CAD que se enlaza con un sistema de control de posición desarrollado en Simulink de MatLab. Las conclusiones del trabajo se presentan en la sección 5.

2. SISTEMA DE REHABILITACIÓN DE MARCHA

Una generalización del diseño del concepto del sistema de rehabilitación de marcha, desarrollado en Figueroa (2016), se sintetiza en la Figura 2. El sistema está compuesto por un mecanismo para cada pie, que le proporciona al paciente la capacidad de realizar el seguimiento de la trayectoria natural del tobillo; este mecanismo está unido a un sistema de sujeción de rodilla para impedir que el paciente rote de manera incorrecta la rodilla al momento de realizar la terapia y emular su movimiento real al caminar.

El sistema tiene un soporte de peso corporal, el cual además permite a la cadera del paciente realizar la trayectoria correcta en el plano transversal al caminar (movimiento arriba y bajo). También tiene un dispositivo en forma de pechera para mantener al paciente erguido, junto con un mecanismo que apoya al paciente para que realice el balanceo correcto de los brazos y así llevar a cabo el movimiento correspondiente al tronco durante el proceso de marcha. Los mecanismos de cadera, soporte de peso corporal, balanceo de brazos y pechera están unidos a una estructura de soporte común.

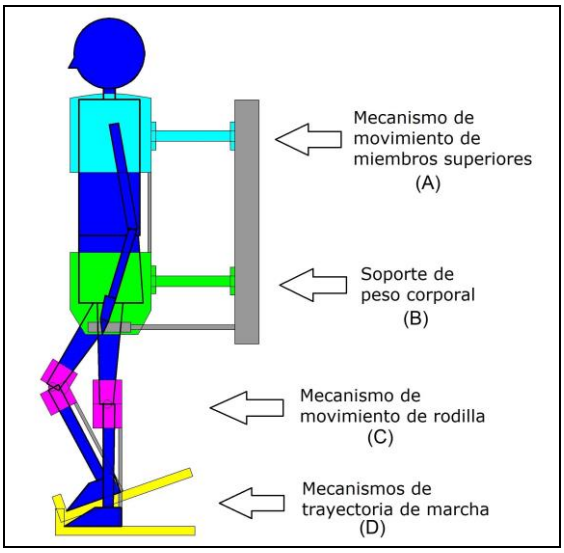

Figura 1. Diseño del Concepto, Sistema de Rehabilitación para Infantes

La metodología propuesta para el desarrollo del Sistema de Rehabilitación de Marcha se presenta en el diagrama de flujo de la Figura. 2. Se basa en el diseño concurrente, donde las etapas de diseño interactúan entre sí, de tal forma que las limitaciones del funcionamiento de un sistema son determinadas tanto por sus componentes, como por sus interconexiones, Portilla (2006). Así, una representación matemática (cinemática y dinámica) del sistema que contenga toda la información relevante, permite definir el proceso de síntesis. El enfoque concurrente integra varias estrategias de diseño, incluyendo el diseño mediante uno o varios problemas de optimización numérica, que son resueltos a partir de diversas técnicas heurísticas, dada la complejidad de su solución. Así como verificar el diseño realizado, utilizando prototipos virtuales y simulación en tiempo real, a partir de diferentes configuraciones como "software-in-the-loop", Isermann, (2008).

La etapa correspondiente a tobillo-pie, se diseñó con la metodología presentada y tiene la finalidad de reproducir el movimiento natural del miembro inferior durante la locomoción en el plano sagital, tomando como referencia el

tobillo. A partir de la cinemática del miembro inferior, se obtuvo la trayectoria que el tobillo sigue en el plano sagital y con base en esta se seleccionaron los mecanismos idóneos para seguirla. Con técnicas de optimización numérica se encontraron las dimensiones adecuadas del mecanismo que se diseñó en CAD, como se presenta a continuación.

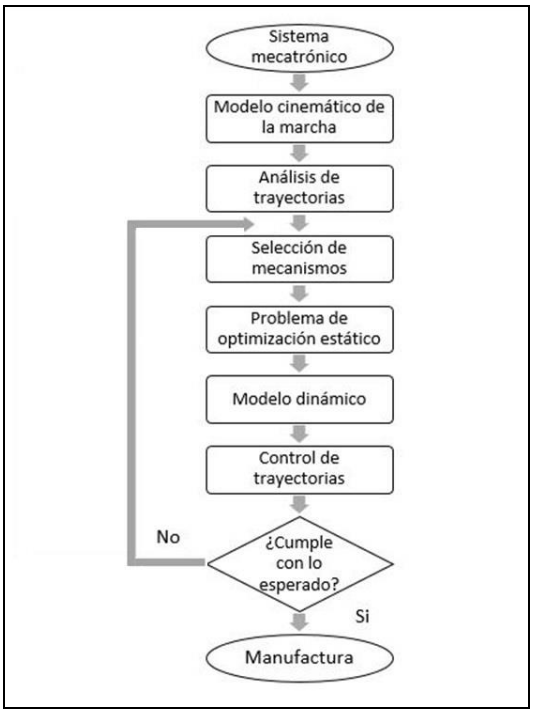

Figura 2. Metodología de diseño utilizada para el desarrollo del sistema de rehabilitación de marcha

2.1 Modelo cinemático de la extremidad inferior

El diseño del mecanismo para la etapa pie-tobillo se basó en el análisis del movimiento del tobillo, el cual está limitado por la morfología de la articulación tibioperonea-astragalina, como se describe en Whittle, (1996), que solo permite la extensión y la flexión. Se necesita del pie para actuar tanto como una estructura semi rígida (como un resorte durante la transferencia de peso y como un brazo de palanca durante el despegue) o como una estructura rígida que permite estabilidad adecuada para mantener el peso del cuerpo. Generalmente para la reproducción y análisis de este movimiento de marcha se modela el tobillo y el pie como un segmento rígido.

El modelo cinemático de interés se obtuvo a partir de considerar como un doble péndulo invertido, al miembro inferior del cuerpo humano (pierna) en el plano sagital, tomando como punto de referencia la articulación coxofemoral ubicada en la base de la cadera y como efector final la articulación tibioperonea-astragalina ubicada en el tobillo, tal como se observa en la Figura 3.
Con esta configuración, la cinemática directa de la pierna está dada en (1) y (2):

$$X = l_1 \cos(q_1) + l_2 \cos(q_1 + q_2) \quad (1)$$

$$Y = l_1 \sin(q_1) + l_1 \sin(q_1 + q_2) \quad (2)$$

dónde l_1 y l_2 son los distancias cadera-rodilla y rodilla-tobillo, respectivamente y q_1 y q_2 son los ángulos de rotación respecto al eje Z, de la cadera y la rodilla respectivamente.

2.2 Trayectoria que sigue el tobillo.

La marcha es una sucesión de movimientos que se realiza de manera repetitiva en el denominado ciclo de marcha, dicho ciclo se genera en tres fases: 1) fase de apoyo, que representa el 60% del ciclo y en la cual el pie de referencia está tocando el suelo mediante el talón; 2) fase de balanceo, que representa un 40% del ciclo y en donde el pie de referencia no toca el suelo, mientras que el pie contralateral está oscilando; y 3) fase de doble apoyo, donde los dos pies tocan el suelo, es decir; el pie de referencia está en contacto inicial del talón mientras que el pie contralateral está en fase de despeje, representando el 10% de la fase de apoyo y el 10% de la fase de balanceo, como se presenta en Benedetti, et al. (1998). Con el fin de generar una trayectoria como la que realiza el tobillo durante la locomoción humana proyectada en el plano sagital, tomando como datos de base los ángulos formados por las articulaciones de cadera y rodilla durante un ciclo de marcha estándar reportados en Benedetti, et al. (1998), y utilizando la herramienta interpolación shape- preserving Interpolat, que está incluida en el software Matlab R2013b®, se generaron los polinomios con los cuales es posible calcular los ángulos de movimiento de la articulación de la cadera (q_1) y de la rodilla (q_2) al realizar una marcha normal. Los polinomios están parametrizados a partir del porcentaje del ciclo de marcha, x, lo que permite encontrar el valor de los ángulos (q_1) y (q_2) en cualquier etapa del ciclo de marcha, como se observa en (3) y (4).

$$\begin{aligned} q_1 = {} & 2.2667\text{e-}12 * x^7 - 1.9823\text{e-}09 * x^6 + 6.649\text{e-}07 * x^5 \\ & - 0.00010766 * x^4 + 0.0085951 * x^3 - 0.29899 * x^2 \\ & + 2.7138 * x + 27.113 \end{aligned} \quad (3)$$

$$\begin{aligned} q_2 = {} & 8.3621\text{e-}12 * x^7 - 5.7855\text{e-}09 * x^6 + 1.5442\text{e-}06 * x^5 \\ & - 0.00019883 * x^4 + 0.012581 * x^3 - 0.3539 * x^2 \\ & + 3.5788 * x + 6.0304 \end{aligned} \quad (4)$$

La trayectoria de desplazamiento del tobillo en el plano sagital, se obtiene a partir de un conjunto de 12 puntos de precisión, calculados utilizando la cinemática directa dada en (1) y (2), utilizando los ángulos (q_1) y (q_2) que se generan a partir de (3) y (4), en las diferentes etapas del ciclo de marcha. La trayectoria del tobillo obtenida se observa en la Figura 3, es relevante observar que dicha trayectoria tiene forma de gota. Esta forma es una característica importante para seleccionar el tipo de mecanismo que se puede utilizar para el diseño del sistema de rehabilitación de tobillo.

2.3 Diseño del mecanismo.

Como un parámetro de diseño importante, se consideró que el mecanismo a utilizar realizará la trayectoria obtenida de forma natural, por ello se seleccionó un mecanismo de cuatro barras para el diseño de la etapa tobillo-pie, ya que su topología permite la generación de trayectorias de tipo gota.

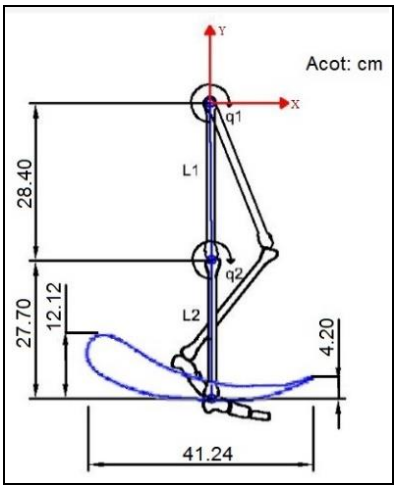

Figura 3. Diagrama esquemático del miembro inferior, con medidas para un infante promedio de 6 años.

Las dimensiones del mecanismo seleccionado se obtienen al plantear el problema de diseño como un problema de optimización estático, en el cual se consideran aspectos sobre posiciones y velocidades a partir de describir paramétricamente al sistema con su modelo cinemático; estableciendo funciones que permitan evaluar su desempeño y un conjunto de restricciones, las cuales se deben cumplir para dicha evaluación. El diseño óptimo del mecanismo tiene como finalidad obtener un error mínimo en el seguimiento de la trayectoria propuesta, para ello se tomó el conjunto de parámetros que determinan la dimensión del mecanismo de cuatro barras, así como el desempeño funcional en el seguimiento de trayectoria como elementos del problema de optimización. Una explicación detallada de la función de desempeño del sistema, las restricciones y cotas de diseño o restricciones geométricas, se puede consultar en Vega, et al. (2014).

La trayectoria que el mecanismo debe realizar se definió a partir de los 12 puntos de precisión ya obtenidos, a dichos puntos se les adicionó un error de 1 centímetro en el límite superior e inferior, como se observa en la Figura 4. De esta manera, se puede asegurar que el punto del acoplador del mecanismo de 4 barras sigue la trayectoria natural del tobillo en el plano sagital, la línea continua entre los dos puntos de frontera definidos, teniendo como error máximo los limites propuestos en el problema de optimización.

Así, el diseño óptimo del mecanismo de cuatro barras se resolvió como un problema de optimización numérica mediante el algoritmo de Evolución Diferencial, el detalle de la solución del problema de optimización se presenta en Calva-Yañez, et al. (2015).

La verificación de funcionamiento se realizó por simulación en un software de CAD, donde se pudo observar que la trayectoria que realiza el mecanismo pasa entre los puntos de precisión generados para el seguimiento de la misma y por el centro de los límites colocados. En la Figura 5 se observa un diseño básico en CAD del mecanismo simplificado, que se utilizó para verificar que con las dimensiones obtenidas, sigue la forma deseada cuando es actuado.

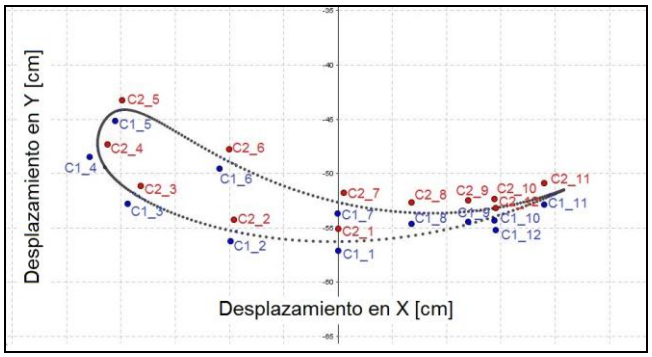

Figura 4. Trayectoria generada por el mecanismo de cuatro barras limitada.

A partir de las dimensiones obtenidas a través de la mejor solución del problema de optimización estático para la síntesis dimensional, se generó un modelo en CAD para la manufactura del mecanismo, con el fin de evaluar que las dimensiones obtenidas fueran adecuadas. El detalle del CAD se observa en el Anexo A. El detalle del prototipo virtual se presenta en el Anexo B.

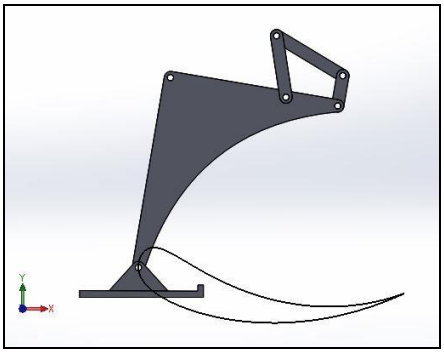

Figura 5. Modelo en CAD simplificado del mecanismo de cuatro barras.

3. SISTEMA DE CONTROL PROPUESTO

A partir de un prototipo virtual se pueden realizar pruebas de operación y desempeño del mecanismo, antes de su manufactura, esta técnica es conocida como “software-in-the-loop”. El modelo en CAD final, con todas sus propiedades, es exportado al software SimMechanics de Simulink y es enlazado con el algoritmo de control desarrollado también en Simulink de Matlab, el enlace se presenta en el Anexo B.

El esquema de control planteado se encarga de que el actuador siga la trayectoria a la velocidad deseada, la cual es establecida por el terapeuta, se probó con un algoritmo de control simple, dado que la trayectoria a seguir la realiza el mecanismo por sí mismo.

En la Figura 6 se presenta el esquema de control a implementar. El modulo encargado de la realización de trayectorias, toma el modelo cinemático y los ángulos para cadera y rodilla ya presentados y modificando los valores de longitud de las extremidad inferior de los pacientes, en este caso niños, genera la familia de trayectorias a seguir para la marcha de infantes de 2 a 12 años.

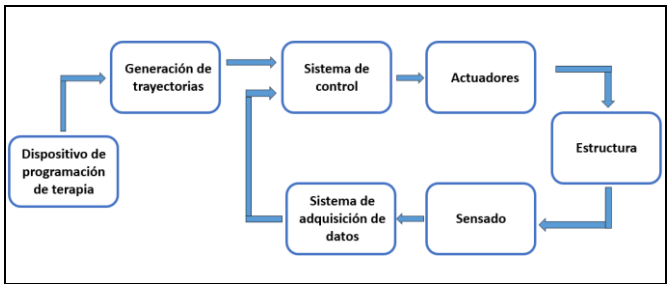

Figura 6. Esquema de control para el mecanismo de rehabilitación etapa tobillo-pie.

Para el diseño del control PD se determina primero la dinámica del mecanismo, a partir de la velocidad de centro de masa dado por:

$$v_{ix} = A_i\dot{\theta}_2 \quad (5)$$

$$v_{iy} = B_i\dot{\theta}_2 \quad (6)$$

$$\dot{\theta}_i = C_i\dot{\theta}_2 \quad (6)$$

donde

$$A_2 = -l_2\sin(\theta_2+\alpha_2) \quad (8)$$

$$A_3 = -r_2\sin(\theta_2) - l_3C_3\sin(\theta_3+\alpha_3) \quad (9)$$

$$A_4 = -l_4C_4\sin(\theta_4+\alpha_4) \quad (10)$$

$$B_2 = l_2\cos(\theta_2+\alpha_2) \quad (11)$$

$$B_3 = r_2\cos(\theta_2) + l_3C_3\cos(\theta_3+\alpha_3) \quad (12)$$

$$B_4 = l_4C_4\cos(\theta_4+\alpha_4) \quad (13)$$

$$C_3 = \frac{r_2\sin(\theta_4-\theta_2)}{r_4\sin(\theta_3-\theta_2)} \quad (14)$$

$$C_4 = \frac{r_2\sin(\theta_3-\theta_2)}{r_4\sin(\theta_3-\theta_4)} \quad (15)$$

El Lagrangiano del Sistema (L) se define como la diferencia de la energía cinética (T) y la energía potencial (U),

$$L = T - U \quad (16)$$

Donde la energía cinética se calcula como:

$$T = \sum_{n=2}^{4}\left[\frac{1}{2}m_i\left(v_{ix}^2+v_{iy}^2\right)+\frac{1}{2}J_i\dot{\theta}_i\right] \quad (17)$$

ó como,

$$T = \frac{1}{2}\sum_{n=2}^{4}\left[m_i\left(\alpha_i^2+\beta_i^2\right)+C_i^2J_i\right]\dot{\theta}_2^2 \quad (18)$$

Esta sumatoria se puede escribir como,

$$\Omega_{(\theta_2)} = \sum_{n=2}^{4}\left[m_i\left(A_i^2+B_i^2\right)+C_i^2J_i\right] \quad (19)$$

Y reescribiendo la ecuación de la energía cinética se tiene,

$$T = \frac{1}{2}\Omega_{(\theta_2)}\dot{\theta}_2^2 \quad (20)$$

La energía potencial de cada eslabón está definida por,

$$U_i = m_igD_i \quad (21)$$

donde:

$$D_2 = l_2\sin(\theta_2+\alpha_2) \quad (22)$$

$$D_3 = r_2\sin(\theta_2) + l_3\sin(\theta_3+\alpha_3) \quad (23)$$

$$D_4 = r_1\sin(\theta_1) + l_4\sin(\theta_4) \quad (24)$$

El Lagrangiano se reescribe entonces como,

$$L = \frac{1}{2}\Omega_{(\theta_2)}\dot{\theta}_2^2 - m_igD_i \quad (25)$$

La ecuación de movimiento de Euler-LaGrange se obtiene de

$$\frac{d}{dt}\left(\frac{\partial L}{\partial\dot{\theta}_2}\right)-\frac{\partial L}{\partial\theta_2} = \tau \quad 26)$$

donde τ, es el torque externo aplicado, entonces:

$$\frac{\partial L}{\partial\dot{\theta}_2} = \Omega_{(\theta_2)}\dot{\theta}_2 \quad (27)$$

$$\frac{d}{dt}\left(\frac{\partial L}{\partial\dot{\theta}_2}\right) = \Omega_{(\theta_2)}\ddot{\theta}_2 + \frac{d}{dt}\left(\Omega_{(\theta_2)}\right)\dot{\theta}_2 \quad (28)$$

$$\frac{\partial L}{\partial\theta_2} = \frac{1}{2}\frac{\partial}{\partial\theta_2}\left(\Omega_{(\theta_2)}\right)\dot{\theta}_2^2 + m_ig\frac{\partial}{\partial\theta_2}\left(D_i\right) \quad (29)$$

Así se obtiene el modelo dinámico del mecanismo de 4 barras

$$\Omega_{(\theta_2)}\ddot{\theta}_2+\frac{d}{dt}\left(\Omega_{(\theta_2)}\right)\dot{\theta}_2-\left[\frac{1}{2}\frac{\partial}{\partial\theta_2}\left(\Omega_{(\theta_2)}\right)\dot{\theta}_2^2+m_ig\frac{\partial}{\partial\theta_2}\left(D_i\right)\right]=\tau \quad (30)$$

Generalizando el modelo dinámico del mecanismo, se considera un algoritmo de control tipo PD definido así,

$$\tau = K_p\tilde{q} - K_v\dot{q} + g(q) \quad (31)$$

$$\tilde{q} = q_d - q \quad (32)$$

donde $\tilde{q}\epsilon\mathbb{R}^n$, es el vector de error de posición que se define como la diferencia entre la posición deseada q_d y la posición actual del robot q, es decir,

$$\tilde{q} = (q_d - q) \quad (33)$$

Adicionalmente, $K_p\epsilon\mathbb{R}^{nxn}$ es una matriz definida positiva, denominada la ganancia proporcional. Y $K_v\epsilon\mathbb{R}^{nxn}$ es la ganancia derivativa, la cual también es una matriz definida positiva, que tiene el efecto de amortiguamiento o freno mecánico a través de la inyección de velocidad articular q´, cuya finalidad es mejorar el desempeño del control proporcional. La ecuación en lazo cerrado del sistema, tomando como tal el modelo dinámico general es,

$$M(q)\ddot{q} + C(q,\dot{q})\dot{q} + g(q) = \tau \quad (34)$$

$$M(q)\ddot{q} + C(q,\dot{q})\dot{q} + g(q) = K_p\tilde{q} - K_v\dot{q} + g(q) \quad (35)$$

de tal forma que la variable de interés es la posición de la articulación, por lo tanto para obtenerla del sistema en lazo cerrado, se define la aceleración como como,

$$\ddot{q} = M(q)^{-1}[-K_p\tilde{q} - C(q,\dot{q})\dot{q} - K_v\dot{q}] \quad (36)$$

finalmente las variables de estado en el sistema se definen como la primera y segunda derivada del vector de error de posición,

$$\tilde{q} = q_d - q \tag{37}$$

$$\dot{\tilde{q}} = 0 - \dot{q} \tag{38}$$

$$\ddot{\tilde{q}} = -\dot{q} \tag{39}$$

$$\dddot{\tilde{q}} = -\ddot{q} \tag{40}$$

de forma tal que la ecuación que define el problema de control de posición en variables de estado esta dada por,

$$\begin{bmatrix} \dot{\tilde{q}} \\ \ddot{q} \end{bmatrix} = \begin{bmatrix} \dot{q} \\ -M(q)^{-1}[-K_p\tilde{q} - C(q,\dot{q})\dot{q} - K_v\dot{q}] \end{bmatrix} \tag{41}$$

El algoritmo de control se implementó en el software Simulink® de Matlab®, para que en conjunto con el prototipo virtual se verifique el funcionamiento del mecanismo. En el Anexo B se observa el esquema de conexión, donde se integra el modelo en CAD realizado en SOLIDWORKS, con el algoritmo de control desarrollado en Simulink de Matlab, a partir de la técnica de simulación en tiempo real, conocida como "software-in-the-loop", se verifica la operación del sistema. La pantalla de resultados se presenta en ese mismo anexo.

6. CONCLUSIONES

Con el fin de imitar el movimiento natural de las extremidades inferiores del cuerpo humano durante la marcha, en este artículo se presenta una metodología de diseño para un sistema de rehabilitación de marcha, que a partir del enfoque de diseño concurrente, permitirá llevar a cabo la manufactura del sistema completo una vez determinada la síntesis dimensional de los mecanismos que conformaran a dicho sistema, el tipo de actuadores a utilizar en cada subsistema, así como la ley de control a implementar para llevar a cabo el seguimiento de la trayectoria en cada etapa del ciclo de marcha. El problema de diseño se planteó como un problema de optimización numérica y se resuelve mediante el uso de técnicas heurísticas; los resultados obtenidos determinan las dimensiones del mecanismo seleccionado y permiten su reconfigurabilidad para que pueda ser utilizado para niños de 2 a 12 años.

Como trabajo a futuro, esta llevar a cabo el diseño de las etapas restantes del sistema de rehabilitación con base en la metodología presentada, integrando cada etapa y sincronizando toda su operación mediante el sistema de control. De igual forma, que en el caso del diseño de los mecanismos, la sintonización de las leyes de control que se generan, se realiza mediante técnicas heurísticas, para garantizar un mínimo error en el seguimiento de la velocidad de la trayectoria a partir de proponer la sintonización de la ley de control como un problema de optimización numérica.

REFERENCIAS

Benedetti M., Catani F., Leardini A., Pignotti E., Giannini S. (1998). Data Magnagement in gait analysis for clinical application. *Clinical Biomechanics*, Elsevier, 3 (3), 204-215.

Calva Y. M. B., Niño S. P. A., Villarreal C. M. G., Sepúlveda C. G., Portilla F. E. A. (2013). Differential Evolution for the Control Gain's Optimal Tuning of a Four-bar Mechanism. *POLIBITS*, 47, 67-73.

Calva-Yáñez M. B., Calderón-Romero F., Portilla-Flores E. A., Niño-Suarez P. A., Vega-Alvarado E. (2015). Diseño de mecanismo para seguimiento de trayectoria de tobillo en rehabilitación de marcha. Congreso de la Asociación Mexicana de Mecatrónica A.C., MECAMEX.

Dollar A., Herr H. (2008). Lower Extremity Exoskeletons and Active Orthoses: Challenges and State of the Art. *IEEE Transactions on Robotics*, 24(1). 144-158.

Figueroa M., Niño P, Portilla E., Medina A. (2014). A Robotic System to Gait Training for Children with Cerebral Palsy. En *VI Latin American Conference on Biomedical Engineering CLAIB 2014. 309-312.* IFMBE Proceedings Series. Springer. Paraná, Entre Ríos, Argentina

Figueroa Amador M. T. (2016). Diseño de un sistema robótico para rehabilitación de marcha enfocado a niños con parálisis cerebral. *Tesis para obtener el grado de Maestría en Ingeniería de Manufactura*, SEPI- ESIME Azcapotzalco, Instituto Politécnico Nacional, Ciudad de México, México.

Goudriaan M., Jonkers I., Van Dieen J. H., Bruijn S. M. (2014). Arm Swing in human walking: What is the drive?. *Gait and Posture*, Elsevier, 40, 321-326.

Hesse S., Waldner A., Tomelleri C. (2010). Research Innovative gait robot for the repetitive practice of floor walking and stair climbing up and down in stroke patients. *Journal Neuro Engineering and Rehabilitation*, 7 (30) 1-10.

Isermann Rolf. (2008). Mechatronic systems innovative products with embedded control. *Control Engineering Practice*, Elsevier, 16, 14-29.

Jezernik S., Colombo G., and Morari M. (2004). Automatic gait-pattern adaptation algorithms for rehabilitation with a 4- DOF robotic orthosis. *IEEE Transactions on Robotics and Automation*, 20 (3), 574–582.

Kubo K., Miyoshi T., Kanai A. and Terashima1 K. (2011). Gait Rehabilitation Device in Central Nervous System Disease: A Review. *Journal of Robotics.* Volume 2011, 2-14.

Paneth N., Hong T., Korzeniewski S. (2006). The descriptive epidemiology of cerebral palsy. *Clinical Perinatal*, 33, 251-267.

Portilla Flores Edgar Alfredo. (2006). Integración simultánea de aspectos estructurales y dinámicos para el diseño óptimo de un sistema de transmisión de variación continúa. *Tesis de Doctorado, Departamento de Ingeniería Eléctrica*, CINVESTAV, Ciudad de México, México.

Vega A. E., Santiago V. E., Portilla F. E. A., Calva Y. M. B. (2014). Diseño Óptimo de un Mecanismo de Cuatro Barras Utilizando Inteligencia de Cúmulo. *En Memorias del XVI Congreso Latinoamericano de Control Automático.* Quintana Roo, México, p. 432-437.

Apéndice A. MODELO EN CAD

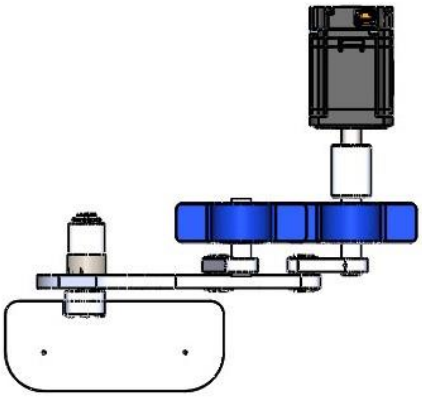

Figura A1. Vista Superior

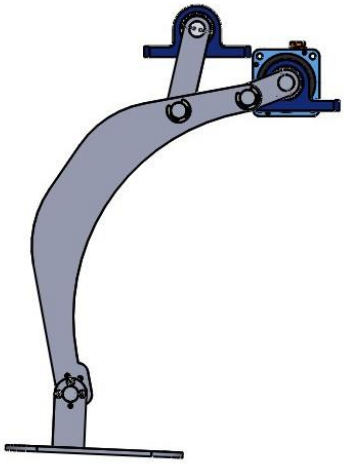

Figura A1. Vista Lateral

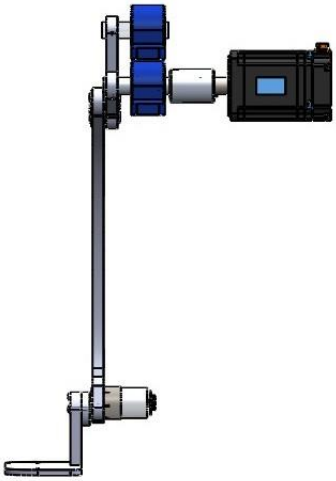

Figura A1. Frontal

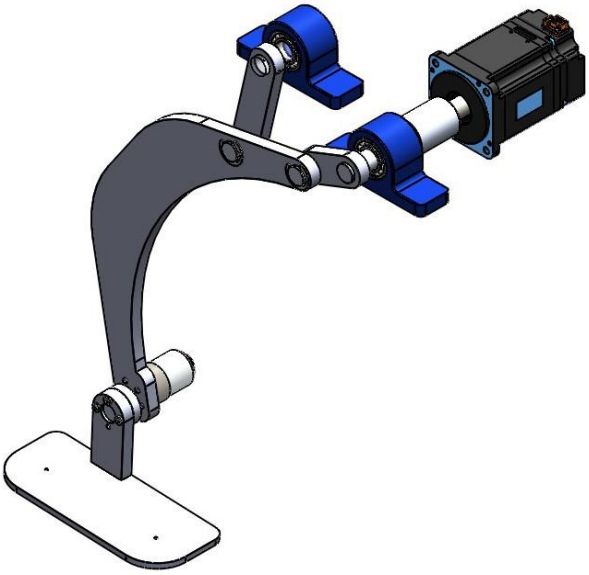

Figura A1. Vista Completa

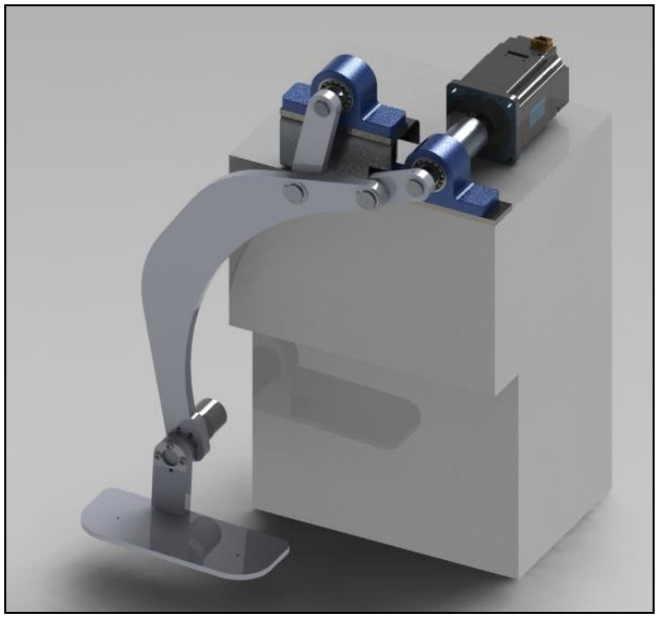

Figura A1. Modelo en CAD en 3D

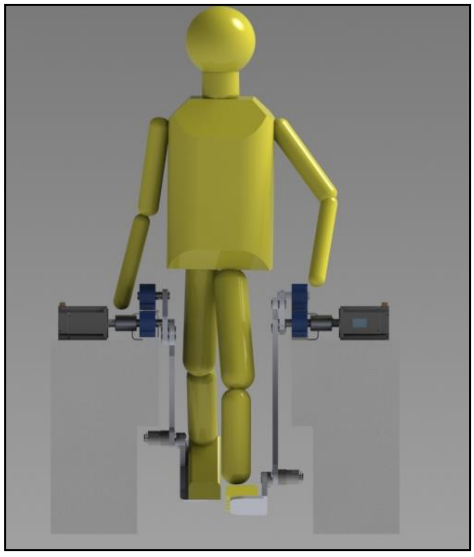

Figura A5. Modelo 3D Vista Frontal

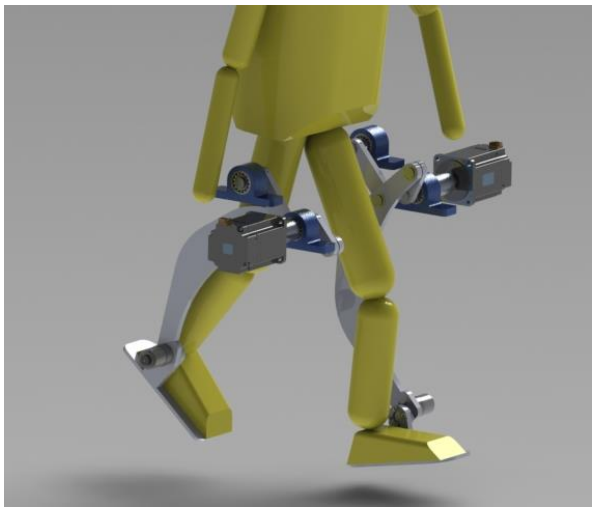

Figura A6. Modelo 3D Vista Lateral

Apéndice B. SIMULACIÓN SOFTWARE IN THE LOOP

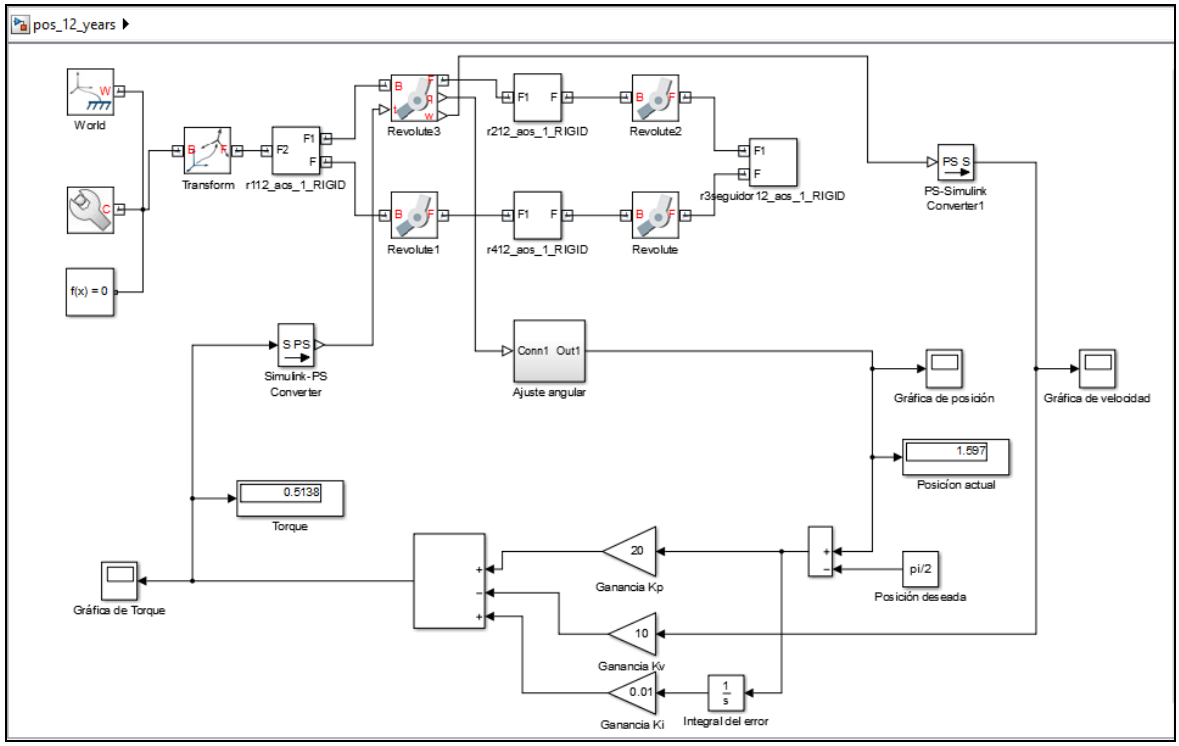

Figura B1. Acople modelo virtual en SimMechanics y el control en Simulink

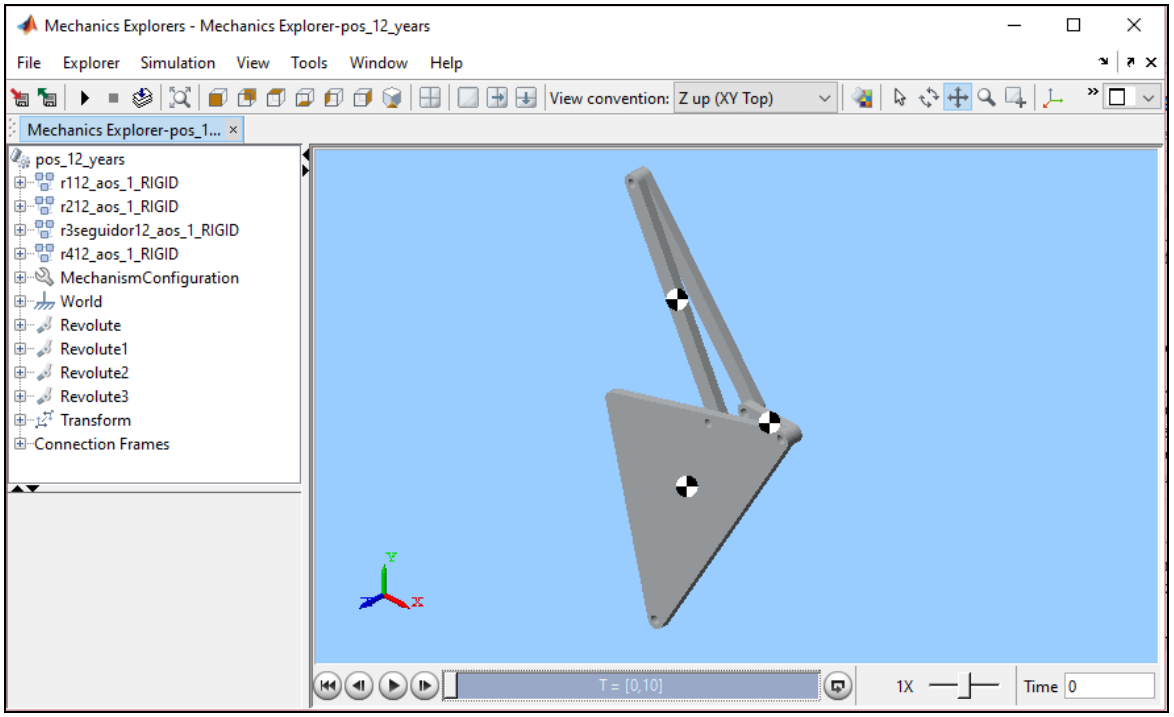

Figura B2. Modelo CAD ACTUADO en entorno de simulación SimMechanics de Simulink®.

Drive System Development for Gait Rehabilitation Exoskeleton

Sergey González-Mejía*, José Miguel Ramírez-Scarpetta**

** School of Electrical and Electronic Engineering, Universidad del Valle, Cali, Colombia (Tel: +57-2-4028239; e-mail: sergey.gonzalez@correounivalle.edu.co).*
*** School of Electrical and Electronic Engineering, Universidad del Valle, Cali, Colombia (e-mail: jose.ramirez@correounivalle.edu.co)*

Abstract: The research considers an assisted rehabilitation platform with a lower limbs exoskeleton, it has a crane to support the weight of patient and exoskeleton, and also, it includes a control system to synchronize the patient´s position on treadmill. This paper focuses on development of drive system for trajectory tracking control based on angular positions in a lower limb exoskeleton walking on a treadmill. It describes the logic states for servo-controllers algorithm and human-machine interface development to manage the drive system. It is presented experimental results under different operating conditions and performance analysis of the system.

Keywords: Assisted, drive, exoskeleton, gait, human-machine interface, joint, platform, rehabilitation, tracking, trajectory.

1. INTRODUCTION

The trajectory tracking control based on the joint angle position is important at early stage of rehabilitation, which can help the affected limb to achieve continuous and repetitive training. The main problem to address in the position control is the generation of an appropriate path that can be used for passive training (Meng et al. 2015). Robotic gait training is an emerging technique for retraining walking ability following spinal cord injury. A challenge is determining an appropriate gait trajectory and level of assistance for each patient, since patients have a wide range of sizes and impairment levels. In (Emken et al. 2008), it demonstrates how a lightweight and powerful robot can record subject-specific, trainer-induced leg trajectories during manually assisted gait, then replay those trajectories for an assisted therapy. Vallery et al. (2009) proposed a method for online trajectory generation that can be applied for hemiparetic patients; desired states for one disabled leg are generated online based on the movements of the other leg. An instantaneous mapping between legs is performed by exploiting physiological interjoint couplings. In this way, the patient generates the reference motion for the affected leg autonomously. The paper (Duschau-Wicke et al. 2010) presents a patient-cooperative strategy that allows patients to influence the timing of their leg movements along a physiologically meaningful path; the path control strategy, generates a compliant virtual that keeps the patient legs within a tunnel around the desired spatial path. In (Hussain et al. 2013), a trajectory tracking controller based on a chattering-free robust variable structure control law was implemented in joint space to guide the patient limbs on physiological gait trajectories; the performance of the robotic orthosis was evaluated during two gait training modes, namely, trajectory tracking mode with maximum compliance and trajectory tracking mode with minimum compliance.

In this research is considered a lower limbs exoskeleton (Ramírez-Scarpetta & Caicedo 2012); it is a rehabilitation orthosis for balancing and gait in patients with motor disabilities. The exoskeleton imposes torques in joints, respecting the motion ranges, in order to develop gait therapies (Ramírez-Scarpetta 2016).

This paper details the development of a tracking system based on angular positions in sagittal plane for the lower limbs exoskeleton. In second section the assisted rehabilitation platform description is presented; the third section displays the drive system development for trajectory tracking control and the last section the performance achieved by the tracking system is showed.

2. ASSISTED REHABILITATION PLATFORM DESCRIPTION

The Industrial Research Group, GICI, of Universidad del Valle developed an assisted rehabilitation platform for human gait, Fig. 1, which consists of three stages: the first stage is the user interface that it is installed on a PC and it is managed by therapist only, to manage the therapy, patient information and gait parameters; the outputs of this stage are the angular paths describing a natural gait, logic controls of the interface buttons and values of gait speed and step length; the second stage is the engineering level to manage the angular trajectories tracking; the information from the previous stage goes into a PC that has a human-machine interface installed, with a logic button panel for movements execution of gait and sends the trajectories towards a development system based on processor (National Instruments 2012); this system transmits the values of angular positions towards a drive system of exoskeleton by RS-485 communication. This orthosis is actuated by servo-motors (Harmonic Drive AG 2010c) in hips and knees joints,

driven by servo-controllers SC-610 (Harmonic Drive AG 2010a), ankles are not actuated. The position control of the joints is implemented in the servo-controllers, which is a cascade control structure for position, speed and current (González-Mejía & Ramírez-Scarpetta 2014); the weight of the exoskeleton and the patient is supported by a crane; the third stage is the control system for synchronizing position on a treadmill, which uses a kinect to know the patient position on the band.

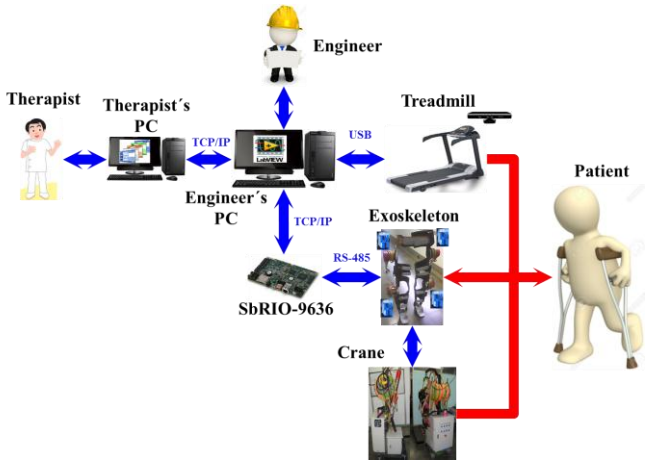

Fig. 1. Assisted rehabilitation platform for human gait.

This paper focuses on development of the drive system for trajectory tracking control based on angular positions in a lower limb exoskeleton carrying a mannequin and walking on a treadmill, Fig. 2.

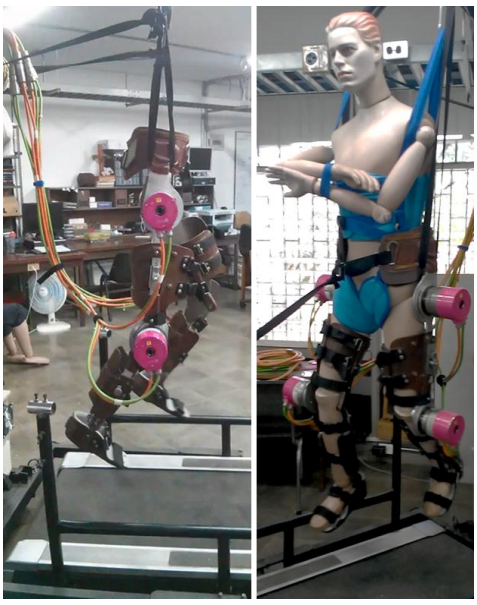

Fig. 2. Lower limbs exoskeleton on treadmill.

The Fig. 3 shows in general way, the drive system structure for rehabilitation platform; it details the interaction between the therapist PC, engineer PC, development system and the exoskeleton servo-controllers, also, the process of the data transmission.

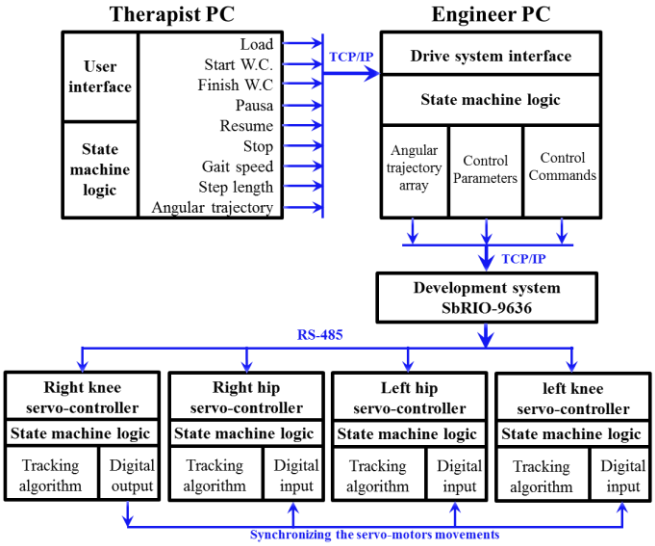

Fig. 3. Drive system structure for rehabilitation platform.

3. DRIVE SYSTEM DEVELOPMENT FOR TRAJECTORY TRACKING CONTROL

The research analyzes the results obtained in the master thesis (González-Mejía 2014), for selecting a path pattern that generates a natural gait in the sagittal plane; the selected database (Troje 2002), are displacement data (x, y, z) with an external reference frame, then the system origin is moved to the position of total mass center of system, COM, and then is applied the inverse kinematics algorithm to calculate the angles generated in lower limbs joints. In Fig. 4 it is shown that the origin of coordinate system has been positioned on the total COM of exoskeleton-patient. The purpose in the thesis (González-Mejía 2014), is the design and deployment of a control for static balance in exoskeleton of lower limbs on sagittal plane, which it is based on the concept of support area and the horizontal deflection of total COM of system. Further, a control strategy is designed to compensate the loss of balance when the system undergoes to large deviations.

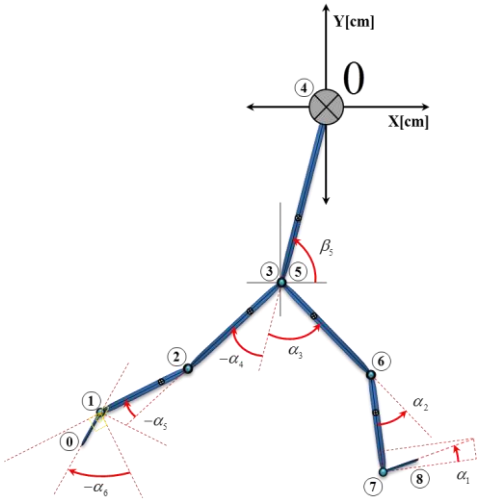

Fig. 4. Reference system in total COM .

The angular trajectories with origin on total COM are physically implementable in the tracking control system of servo-motors.

In the drive system development, a human-machine interface is created under the LabView® platform; the process of sending angular trajectories towards the drive system in the exoskeleton is managed. The angular trajectory assigned to each joint must be organized in an array of one hundred data. These arrays are decomposed and sent via RS-485 communication to the specified servo-controller, in order to rebuild the array by an algorithm programmed into the servo-controller.

In communication frame, three data are sent to the servo-controller: the angle value *Array[i]*, the position in the array to store the data, *i*, and the amount of data in the trajectory array, *length(Array)*. With this information into servo-controller, the algorithm can reconstruct and store in a new array the path that was sent. Then, the servo-controller of right knee is specified as master and the other slaves. The master role is to lead the synchronization of movement of the other servo-motors, since, the slaves servo-controllers begin to read the trajectories arrays and to apply the angles values when the master indicates.

In the routine for reading trajectories arrays, the program looks up the angle value in the array and replace it in Eq. (1), then it executes the movement, $Angulo_{motor}$, and moves to the next angle of the array. To this process, it is configured a runtime called sampling time or reading, t_m.

The movement of the servo-motor is given by Eq. (1).

$$Angulo_{motor}[i] = \left(AngularGain\left(Array[i] * \frac{100}{360} \right) \right) + Offset \quad (1)$$

The relationship between i and gait cycle time, t_{gait}, is given by Eq. (2).

$$t_{gait} = (t_m)i \quad (2)$$

AngularGain, *Offset* and sample time are control parameters that can be modified from interface and then are sent to the servo-controllers via RS-485 communication. The *AngularGain* parameter varies the step length, the Offset corrects the posture angle of the patient and sample time governs the cycle gait.

The time of cycle gait, t_{gait}, is Eq. (3).

$$t_{gait} = \frac{2L_p}{V_m} \quad (3)$$

Where, L_p is the step length and V_m is gait speed and in compliance with limits, t_m, it has Eq. (4).

$$V_m \leq L_p \leq \left(\frac{t_{gait_{max}}}{t_{gait_{min}}} \right) V_m \quad (4)$$

The output variables of the therapist interface are the inputs of human-machine interface in engineering level; the output variables are the events caused by the logic of button panel, and the parameterized angular trajectories for natural gait, the gait speed and the step length, which lead to calculate the cycle time of gait, Eq. (3).

3.1 Programming of Servomotors' Controllers

The program into servo-controllers has a structure of state machine, Fig. 5.

The states are activated by the action on the button panel of engineering interface. Following, the states are described:

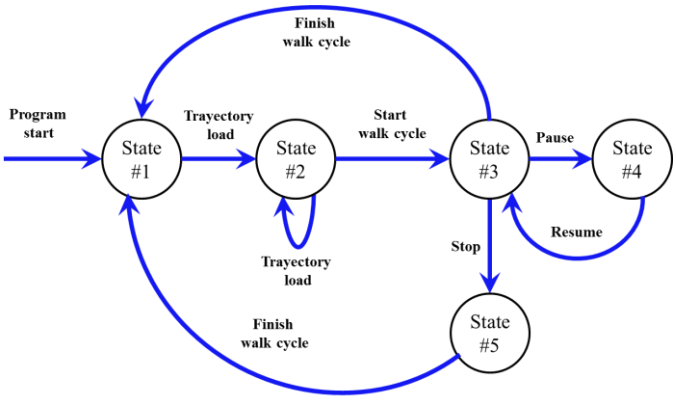

State #1: Software initialized.
State #2: Angular trajectory loaded.
State #3: Exoskeleton is walking.
State #4: Exoskeleton paused.
State #5: Exoskeleton stopped suddenly.

Fig. 5. State machine for servo-controllers program.

***Software initialized*:** The servo-controllers are turned on and the human-machine interface is running. It is loaded the operation settings of the servo-controllers, such as digital inputs and outputs, parameters velocity and acceleration, home position, etc. In this state, when servo-controllers are turned on, the angular position of joints is calibrated to zero and thus, servo-motors are positioned in an initial condition before turn. Also, it is allowed to activate the command *Trajectory load*.

Angular trajectory loaded: When the control command, *Trajectory load*, is executed, the angular trajectories are sent from the interface to the servo-controllers via RS-485. The arrays are reconstructed by servo-controller´s program and is waited the full send of trajectories. It is allowed to activate the commands *Trajectory load* and *Start walk cycle*.

Exoskeleton is walking: When executing the command, *Start walk cycle*, the exoskeleton performs walking cycles and only in this state, the user can send control parameters*: walking time*, *walk cycles*, *offsets* and *angular gains*.

To perform gait movements, the Fig. 6 shows the algorithm executed inside of servo-controllers.

The first three steps in algorithm, the servo-motors move to an initial position; this is necessary for smooth movement and ramp up without generating the *follow error* (Harmonic Drive AG 2010b) in the servo-controller, and avoid strong changes in the angular acceleration. This generates the gait initial step in the exoskeleton. It is allowed to activate the commands *Finish walk cycle*, *Pause* and *Stop*.

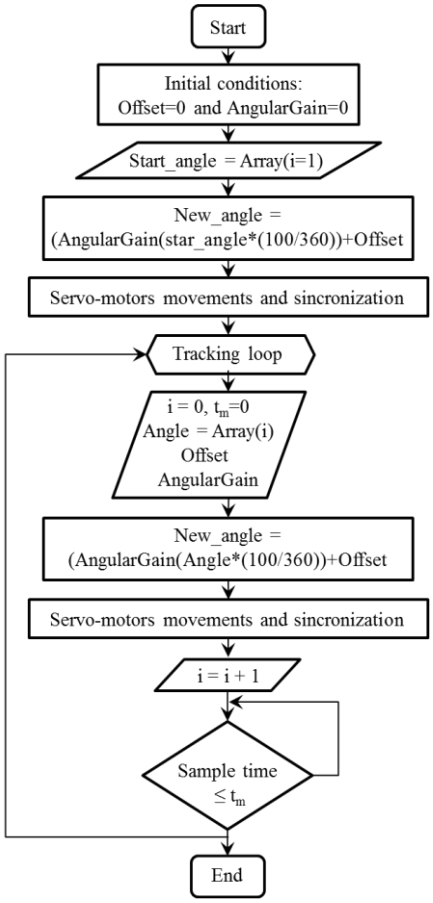

Fig. 6. Angular position tracking algorithm.

Exoskeleton paused: It is activated by a request, *Pause*, from the interface. The servo motors are positioned in the closest trajectory for double support phase Fig. 7. It is allowed to activate the command *Resume* to return to the state #3.

Exoskeleton stopped suddenly: When executing the *Stop* command, the exoskeleton is suddenly stopped by user decision due to an emergency. It is allowed to activate the command Finish walk cycle to return to the state #1, which generates a smooth ramp-down motion without generating an error in the servo-controller. This generates the gait final step in the exoskeleton.

Reading commands and data received by serial communication is performed through interruptions.

For the servo-motors synchronization a master-slave topology is used, where the master is the servo-controller of right knee and the others are slaves. The master handles a digital output and slaves handle a digital input, the connection is shown in Fig. 3.

The synchronization is done through a digital pin and its status is evaluated: the master and slave load angle value in a motion buffer (Harmonic Drive AG 2010b); then, the master generates a high state to be read by slaves and thus apply movement. In this way, it is achieved that the servo motors move synchronously due to management master.

Fig. 7. Exoskeleton in double support phase.

3.2 Human-Machine Interface Development

The human-machine interface is divided into three stages: The first stage sends the corresponding angular trajectory to each servo-motor, the second sends the control parameters to all servo-controllers and the third handles the control commands. Following, stages of the interface developed in the LabView® platform are explained, Fig. 8.

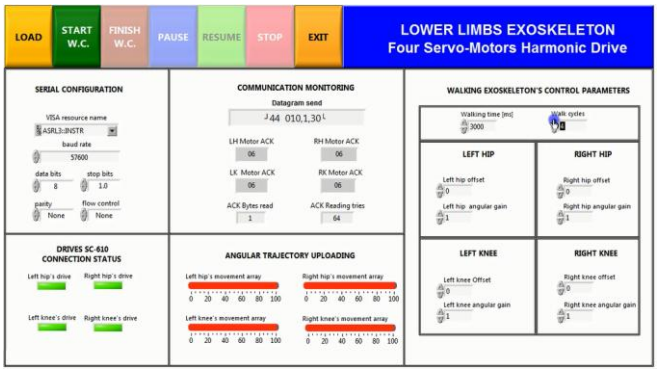

Fig. 8. Human machine interface.

The control parameters are on the right side of the interface; for each joint actuated is applied: *Offsets* and *angular gains* in angular positions, and in general way, it sets *walking time*

and *walk cycles* to generate the movements; the upper left side shows the control commands, which are under a logic button panel: *Load*, *Start walking cycle*, *walk Finish cycle*, *Pause*, *Resume*, *Stop* and *Exit*; the right side shows the settings parameters for serial communication; the lower right side and center shows the connectivity between the interface and the drive system, and indicators for transmit/receive data and evolution of loading for angular trajectories, respectively.

Sending angular trajectory array: The conception of general code implemented for sending the trajectory array for each servo-controller is shown in Fig. 3. Mainly, it takes a data in the array, the position of this data into array, the amount of array data and then those values are included into writing datagram of servo-controller; then the datagram is sent and it is expected to read an ACK character from the servo-controller. This algorithm is contained in three *While* cycles: the internal cycle re-transmits the datagram even if the algorithm cannot read the ACK; the middle one is for transmitting each array value of trajectory and the external is for perform array transmission for each servo-controller.

Sending control parameters: This stage is activated after sending all the angular trajectories and the same concept explained in the previous section is applied, with the difference that this code does not have the intermediate while loop and it sends the control parameters periodically.

Sending control commands: The management of these sending commands is given by the state machine programmed into servo-controllers.

4. TRACKING SYSTEM PERFORMANCE

The trajectory tracking system was tested by referring to the detailed database in the third section; it contains one hundred data for hip and knee joints, and with a sampling time of $15\,(ms)$. With different sampling times, the tracking trajectory of each servo-motor with the reference is compared. The Fig. 9 and Fig. 10 show that angular trajectories tracking without load by each servo-motor is successful.

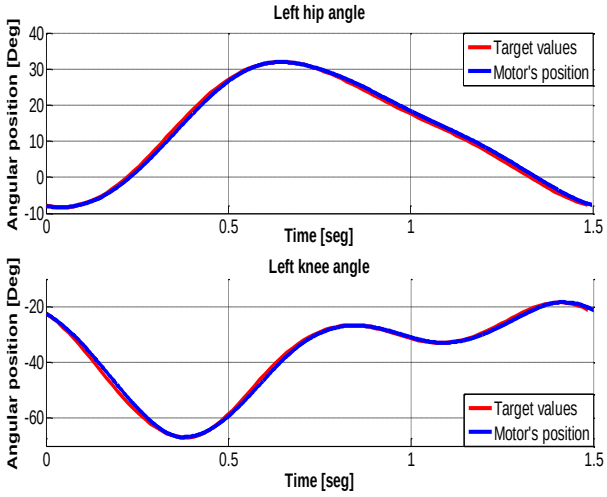

Fig. 9. Angular tracking trajectories of left side servo-motors.

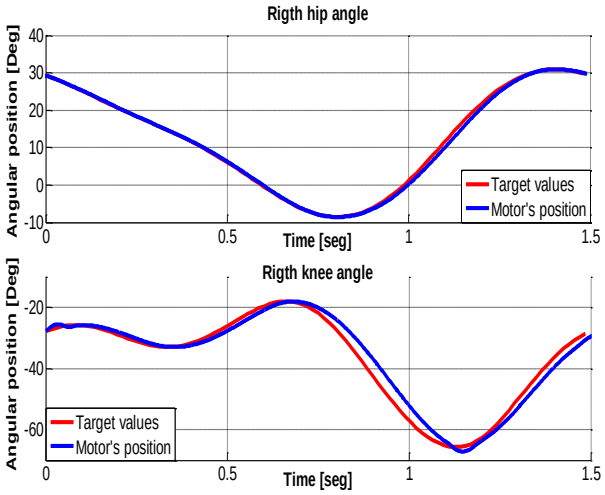

Fig. 10. Angular tracking trajectories of servo-motors right side.

Varying the sampling time, t_m, and operating the system without load, it achieved a walking time from $1(s)$ to $3.5(s)$, the results are shown in Fig. 11.

Furthermore, with the servo-motor assembly in knee joint of exoskeleton, it achieved a walking time from $2(s)$ to $5(s)$, the difference is due to the servo motor executes the last command given by the servo-controller even if it has not reached the desired position. Smooth and stepless movements are achieved, Fig. 12.

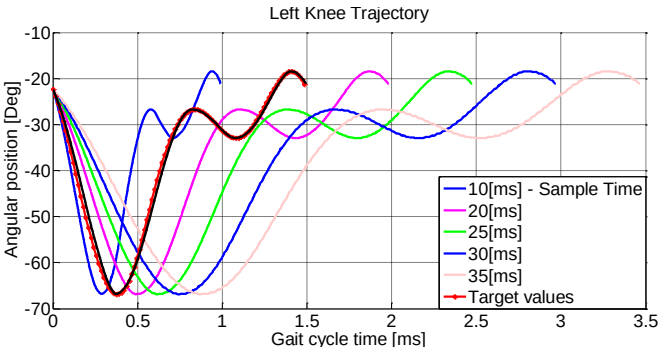

Fig. 11. Trajectory tracking of left knee servo-motor without load.

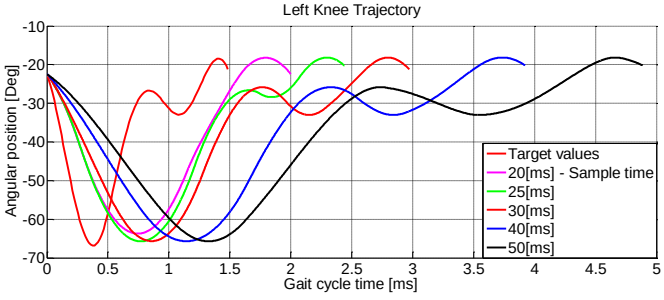

Fig. 12. Trajectory tracking of servo-motor of left knee with load.

5. CONCLUSIONS

The performance of drive system for trajectory tracking control based on angular positions in a lower limb exoskeleton was successful; the system fulfilled the required actions, timing, positioning, good tracking and a correct communication; the conception of logic states allowed to develop an appropriated human-machine interface to manage the drive system of rehabilitation platform; an algorithm for angular trajectories tracking was implemented in the servo-controllers; the master-slave topology developed generates synchronized and smooth movements in the gait of exoskeleton; the deployment of a deterministic sampling time in the platform, allowed to impose a correct cycle gait time.

For future works, an assist-as-needed control will be developed to measure the effectiveness of the patient rehabilitation.

6. ACKNOWLEDGEMENTS

This work is part of doctoral research of Sergey González, funded by Colciencias; he is on paid leave given by Universidad Santiago de Cali, and the research project: "Gait assisted with an exoskeleton", funded by Colciencias, Code 1106-521-28248, Contract 0462-2012.

7. REFERENCES

Duschau-Wicke, A. et al., 2010. Path Control: A Method for Patient-Cooperative Robot-Aided Gait Rehabilitation. *IEEE Transactions on Neural Systems and Rehabilitation Engineering*, 18(1), pp.38–48.

Emken, J.L. et al., 2008. Feasibility of Manual Teach-and-Replay and Continuous Impedance Shaping for Robotic Locomotor Training Following Spinal Cord Injury. *IEEE Transactions on Biomedical Engineering*, 55(1), pp.322–334.

González-Mejía, S., 2014. *Diseño e implementación de una estrategia de control para equilibrio en posición bípeda de un exoesqueleto de miembros inferiores*. Master thesis, Universidad del Valle.

González-Mejía, S. & Ramírez-Scarpetta, J.M., 2014. Design and Implementation of a control strategy for static balance of a lower limbs exoskeleton. *Ingeniería y Competitividad*, 16(1), pp.229 – 238.

Harmonic Drive AG, 2010a. Product Documentation SC-610 Series Servo Controllers. Available at: http://www.harmonicdrive.de/english/products/servoproducts/servo-controller/sc-610/product-documentation.html.

Harmonic Drive AG, 2010b. Set-up-Software Work Bench v5 for SC-610-Series Servo Controllers. , pp.1 – 35. Available at: http://www.treffer.com.br/produtos/harmonicdrive/PDF/setup_software_sc_610.pdf [Accessed June 1, 2016].

Harmonic Drive AG, 2010c. The CHA Series digital AC hollow-shaft servo actuator. Available at: http://www.harmonicdrive.de/english/products/servoproducts/servoactuators/cha/ [Accessed February 8, 2014].

Hussain, S., Xie, S.Q. & Jamwal, P.K., 2013. Robust Nonlinear Control of an Intrinsically Compliant Robotic Gait Training Orthosis. *IEEE Transactions on Systems, Man, and Cybernetics: Systems*, 43(3), pp.655–665.

Meng, W. et al., 2015. Recent development of mechanisms and control strategies for robot-assisted lower limb rehabilitation. *Mechatronics*.

National Instruments, 2012. sbRIO-9636 Support - National Instruments. Available at: http://sine.ni.com/psp/app/doc/p/id/psp-1029/lang/es [Accessed February 19, 2014].

Ramírez-Scarpetta, J.M., 2016. *Marcha asistida con un exoesqueleto*, Cali.

Ramírez-Scarpetta, J.M. & Caicedo, E., 2012. *Exoesqueleto para rehabilitación asistida de pacientes con pérdida parcial o completa del movimiento de los miembros inferiores. Fase 1: equilibrio*, Cali: Universidad Del Valle.

Troje, N.F., 2002. The little difference: Fourier based gender classification from biological motion. *Dynamic Perception R P Wrtz and M Lappe eds Aka Press Berlin*, pp.115–120.

Vallery, H. et al., 2009. Reference Trajectory Generation for Rehabilitation Robots: Complementary Limb Motion Estimation. *IEEE Transactions on Neural Systems and Rehabilitation Engineering*, 17(1), pp.23–30.

Output-Feedback Model Predictive Control for Tight Glycaemic Control in Patients at the Intensive Care Unit

E. Aguirre-Zapata * **and J. Garcia-Tirado** **

* *Instituto Tecnológico Metropolitano, Calle 73 No 76A - 354, 050034, Medellín - Colombia. Facultad de Ingenierías, Grupo de Automática, Electrónica y Ciencias Computacionales. (email: estefaniaaguirre97289@correo.itm.edu.co).*
** *Instituto Tecnológico Metropolitano, Calle 73 No 76A - 354, 050034, Medellín - Colombia. Facultad de Ciencias Económicas y Administrativas, Grupo de Calidad, Metrología y Producción, (email: josegarcia@itm.edu.co).*

Abstract: the glucose homoeostasis is responsible for regulating the blood glucose concentration to stay around of 5.56 *mmol/L*. However, this regulatory mechanism may be affected by Diabetes Mellitus (Type 1, Type 2, and gestational) or as a side effect of a critical condition especially in patients who are at an intensive care unit (ICU). From the control engineering point of view, there is an approach to deal with pathological conditions leading to the glucose impairment and is based on the automatic control of insulin infusion in order to avoid dangerous conditions as hyperglycaemia and hypoglycaemia. This paper describes the design and simulation of a model predictive controller combined with an Extended Kalman filter for tight glycemic control of patients at the ICU. From the simulations performed, the controller is able to deal with the enteral feeding delivered to the patient, which is an unavoidable disturbance in a realistic scenario. The paper concludes that care must be paid to perform the controller tuning, especially the matrix related to the state penalty. Finally, future would be directed to the design of nonlinear model predictive controllers in order to obtain better controller performance.

Keywords: Model predictive control, Intensive care patients, Extended Kalman filter, output-feedback, tight glycemic control, Diabetes Mellitus.

1. INTRODUCTION

In healthy subjects, the glucose homeostasis is responsible for guaranteeing the healthy levels of blood glucose. This natural regulation is performed by means of neuro-hormonal compensations, acting selectively on excess and lack of carbohydrates (Barrett, 2013). In this control loop, the pancreas acts as an actuator (releases insulin and glucagon) and some elements present in the blood are as sensors carrying information about the blood glucose concentration levels to the liver and pancreas. However, this control loop may be broken due to a deficiency in the production of the insulin hormone (Type 1 Diabetes Mellitus), resistance to the action of insulin (Type 2 Diabetes Mellitus) or as side effect of other pathologies, especially in patients who are at the ICU (Aldworth et al., 2015), (Bequette, 2007).

Patients at the ICU may present serious episodes of hyperglycemia in response to stress after severe trauma. The organism of the ill triggers a series of neuro-hormonal stimuli that in the acute phase of illness increases glucose production and decreases its uptake by the muscle, resulting in a significant increase in the blood glucose levels (Villamarín and Puentes, 2009). Studies have shown that hyperglycemia episodes increased the hospital stay, mortality rates, and the probability of patient follow up once they leave the ICU (Umpierrez et al., 2002). The above motivated the research in tight glycaemic control at the ICU by manipulating a continuous insulin infusion. This led to a decrease in the mortality rate regarding to the malfunction of the glucose homeostasis (Van den Berghe et al., 2006). Existing approaches of tight glycaemic control using controllers based on modified versions of the Bergma's minimal model use the plasma glucose as the measured variable. Although plasma glucose is the controlled variable and hence the main variable, the measurement of the plasma glucose, even at the ICU, is invasive, expensive, and in most ICU facilities not continuously available. In this sense, alternative measurement approaches as from a continuous glucose monitor (CGM) should be taken into account (Block et al., 2008).

Using a CGM at the ICU allow tighter control of glucose levels in blood given that the availability of continuous measurements of interstitial glucose every 5 min for $24h/day$ would free the patient of the invasive tests and would represent a decrease in the costs of treatment and monitoring of hyperglycemia for the health system (Block et al., 2008).

Model Predictive Control (MPC) became an appealing alternative to perform glycaemic control and mainly to avoid hypoglycemic episodes. MPC includes a process model in order to predict the future process behavior using an optimization framework, allowing a direct addressing of process constraints.

A coupled estimation-control strategy is tested in a scenario of tight glycaemic control at the ICU. To perform the design of the estimator and controller, a modified version of the Bergman's minimal model is used as it is presented in (Lin et al., 2011) together with an additional equation relating the interstitial glucose with the plasma glucose and hence allowing the use of a CGM (King et al., 2007).

The remainder of the paper is as follows. In Section 1, the problem is stated. In Section 2, the equations of the mathematical model for controlling hyperglycemia in ICU patients is presented. A new equation is added in order to allow the measurement of the interstitial glucose instead of plasma glucose. The output feedback strategy using the coupling of a MPC and an Extended Kalman Filter is presented in Section 3. Results are presented in Section 4. Conclusions and final comments are addressed in Section 5.

2. PROBLEM STATEMENT

Nowadays, the control of blood glucose levels in patients at the ICU in Colombian hospitals is performed by taking blood samples for subsequent evaluation of plasma glucose levels. The samples are analyzed using an analytical procedure in the laboratory causing delays for the decision making. Following the protocol of Colombian hospitals, blood glucose must be monitored every 2h at the ICU which leads to 12 laboratory assays every day at around US 40 (120.000 COP) (Hospital Universitario de Bucaramanga S.A, 2012).

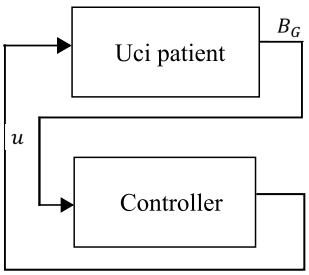

Fig. 1. Normal control of glucose levels in ICU patients

In Figure 1, the typical glycaemic control scheme, from measuring plasma glucose is presented (Magni et al., 2007) where B_G and u stand for the blood glucose and exogenous insulin input. In this paper, an output-feedback controller based on an Extended Kalman Filter (EKF) coupled to a MPC is proposed as shown in Figure 2 where I_G, the interstitial glucose, is the measured variable instead of B_G and x_{ext} is the estimated state.

The interstitial glucose monitoring using a CGM represents the possibility of performing tight glycemic control in patients at the ICU with a reduction of hypoglycemic episodes and a decrease in the cost of monitoring for the local health system.

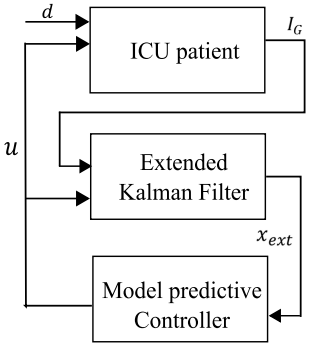

Fig. 2. Control of glucose levels in ICU patients proposed

3. MATHEMATICAL MODEL FOR TIGHT GLYCAEMIC CONTROL

A model for tight glycaemic control, based on the Bergman's minimal model is available in (Lin et al., 2011). From the equations, it is possible to identify four main compartments, i.e., blood, interstitium, stomach, and intestine, where the processes of metabolism, distribution, and use of insulin and glucose occur. An abstraction of the compartments involved in the extended mathematical model and the dynamic relationships between the various terms is presented for the sake of comprehension in Figure 3 where continuous arrows represent mass transfer among compartments and dotted arrows represent the diffusion from the blood compartments to the interstitium.

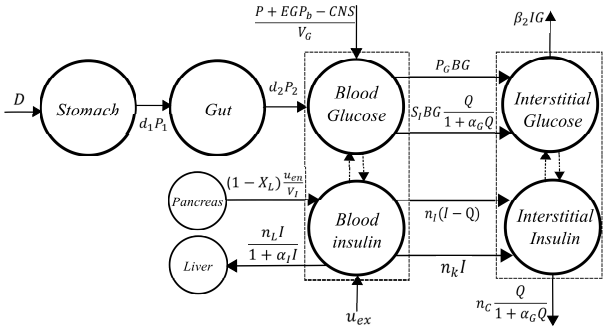

Fig. 3. Model Compartments including the Interstitium

The mathematical model under study includes five states: blood glucose (BG), insulin concentration in the interstice (Q), insulin in plasma (I), the amount of glucose in the stomach (P_1) where carbohydrates are broken down in smaller molecules, and the amount of glucose in the gut (P_2) where glucose molecules are absorbed and transported into the bloodstream. The equations of the mathematical model are summarized as follows:

$$\frac{dB_G}{dt} = -P_G B_G - S_i \frac{B_G Q}{1+\alpha_G Q} + \frac{P + EG_{P_b} - CNS}{V_G} \quad (1)$$

$$\frac{dQ}{dt} = n_I(I-Q) - n_C \frac{Q}{1+\alpha_G Q} \quad (2)$$

$$\frac{dI}{dt} = -n_K I - n_L \frac{I}{1+a_I I} - n_I(I-Q) + \frac{u_{ex}}{V_I} + (1-x_L)\frac{u_{en}}{V_I} \quad (3)$$

$$\frac{dP_1}{dt} = -d_1 P_1 + D; \quad (4)$$

$$\frac{dP_2}{dt} = -\min(d_2 P_2, P_{max}) + d_1 P_1; \quad (5)$$

where $P(t)$, as it is defined in (6), corresponds to the glucose appearance into the bloodstream from the enteral nutrition and u_{en} is the endogenous insulin production.

$$P(t) = min(d_2 P_2, P_{max}) + PN \quad (6)$$

$$u_{en} = k_1 e^{-I(t)\frac{k_2}{k_3}} \quad (7)$$

The model proposed by Lin was developed for the control of blood glucose levels by administering exogenous glucose and insulin to patients at the ICU. However, although this model allows to establish the existing relationship between glucose and insulin, it does not give a way to include the interstitial glucose to relate the measurements from a CGM to the plasma glucose. In order to include the use of a CGM at the ICU, an equation relating the interstitial glucose and plasma glucose is added as presented in (8) (King et al., 2007).

$$\frac{dI_G}{dt} = \beta_1 B_G - \beta_2 I_G \quad (8)$$

A description of the model variables and parameters together with its units and numerical values are presented in the Appendix A.

4. STATE ESTIMATION AND MODEL BASED CONTROL

4.1 ***Extended Kalman Filter design***

The Extended Kalman Filter (EKF) is a variation of the Kalman filter addressing nonlinear systems with smooth nonlinearities (Pascual, 2004). The EKF derivation is based on the linearization of the nonlinear system around a nominal trajectory state and was originally proposed by Stanley Schmidt to allow the use of the Kalman filter in a nonlinear systems setting (Simon, 2006) (Schmidt, 1966).

The discrete-time EKF is composed by four parts (Simon, 2006): the equations of the nonlinear dynamic system (9)-(12), the initialization to the *a priori* estimation error covariance and the *a priori* estimated state (13) and (14), the linearization point to point (15)-(16) and (19)-(20), and the update equations (17)-(18) and (21)-(23).

Mathematical formulation

(1) Dynamic system equations:

$$x_{k-1} = F_k(x_k, u_k, w_k) \quad (9)$$

$$y_k = h_k(x_k, v_k) \quad (10)$$

$$w_k \sim N(0, Q_{e,k}) \quad (11)$$

$$v_k \sim N(0, R_{e,k}) \quad (12)$$

(2) EKF initialization:

$$\hat{x}_0^+ = E(x_0) \quad (13)$$

$$P_{e,0}^+ = E[(x_0 - \hat{x}_0)(x_0 - \hat{x}_0)^T] \quad (14)$$

(3) for $k = 1, 2...n$

(a) Calculation of matrices of partial derivatives:

$$F_{k-1} = \frac{\partial f_{k-1}}{\partial x}|_{\hat{x}_{k-1}^+, u_k} \quad (15)$$

$$L_{k-1} = \frac{\partial f_{k-1}}{\partial w}|_{\hat{x}_{k-1}^+, u_k} \quad (16)$$

(b) A priori state estimate and estimation error covariance:

$$P_{e,k}^- = F_{k-1} P_{e,k-1}^+ F_{k-1}^T + Q_{e,k-1} \quad (17)$$

$$\hat{x}_k^- = f_{k-1}(\hat{x}_{k-1}^+, u_{k-1}) \quad (18)$$

(c) Calculation of matrices of partial derivatives:

$$H_k = \frac{\partial h_k}{\partial x}|_{\hat{x}_k^-, u_k} \quad (19)$$

$$M_k = \frac{\partial h_k}{\partial v}|_{\hat{x}_k^-, u_k} \quad (20)$$

(d) Updating the state estimation and estimation error covariance:

$$K_k = P_{e,k}^- H_k^T (H_k P_{e,k}^- H_k^T + R_{e,k})^{-1} \quad (21)$$

$$\hat{x}_k^+ = \hat{x}_k^- + K_k[y_k - h_k(\hat{x}_k^-)] \quad (22)$$

$$P_{e,k}^+ = (I - K_k H_k) P_{e,k}^- \quad (23)$$

where $x_k \in \mathbb{R}^n$ is the system state, $\hat{x}_0^+$ is the initial condition state, $P_{e,0}^+$ is the initial condition for the a *posteriori* estimation error covariance, $P_{e,k}^-$ is *a priori* estimation error covariance, K_k is the Kalman gain, $\hat{x}_k^-$ *a priori* estimated state, $\hat{x}_k^+$ *a posteriori* estimated state, $P_{e,k}^+$ is the *a posteriori* estimation error covariance. $R_{e,k}$ and $Q_{e,k}$ are the covariances of the model and measurement noises which in turn are knobs of the filter together with $\hat{x}_0^+$ and $P_{e,0}^+$.

Initial conditions and filter tuning: as pointed out before, in a real-life application the enteral feed is the unexpected disturbance entering to the process. Considering this disturbance, an enlarged state is defined as

$$x_k = [B_{G,k}\ I_{G,k}\ Q_k\ I_k\ P_{1,k}\ P_{2,k}\ D_k]^T \quad (24)$$

where the states are defined in discrete-time with a given sample time. Given the operating point of the glucose-insulin system, the EKF was initialized as follows, where variables are with proper units

$$\hat{x}_0 = [5\ 5\ 10.7655\ 20\ 22\ 111\ 0.7672]^T$$

The filter tuning was performed by a trial-and-error procedure by means of the mean quadratic error as performance

criterion. The weighting matrices allowing the most acceptable filter performance are presented below:

$$Q_{e,k} = \begin{bmatrix} 100 & 0 & 0 & 0 \\ 0 & 100 & 0 & 0 \\ 0 & 0 & 100 & 0 \\ 0 & 0 & 0 & 100 \end{bmatrix} \tag{25}$$

$$R_{e,k} = 1 \tag{26}$$

$$P^{+}_{e,0} = \begin{bmatrix} 100 & 0 & 0 & 0 \\ 0 & 100 & 0 & 0 \\ 0 & 0 & 100 & 0 \\ 0 & 0 & 0 & 100 \end{bmatrix} \tag{27}$$

4.2 ***Model Predictive Control design***

The design of the MPC was made taking into account the elements presented in (Van den Boom and Backx, 2010). The design considerations are presented as follows.

Prediction model: the mathematical model presented in Section 3 was linearized around the following operating point

$$x_{ss} = [5 \ 5 \ 10.7655 \ 20 \ 22 \ 111]^T \tag{28}$$

$$u_{ss} = [7.5933 \ 0]^T \tag{29}$$

where x_{ss} corresponds to the operating point of states and u_{ss} corresponds to the operating point of inputs. Then, the linearized model is discretized with a sample time of $T_s = 1min$. The linear discrete-time model of glucose-insulin system at the ICU is written as

$$\begin{aligned} x_{k-1} &= F_k x_k + G_k u_k + B_d d \\ y_k &= H_k x_k \end{aligned} \tag{30}$$

with F_k the state matrix, G_k is the input matrix, B_d is the matrix relating the unknown disturbance to the model, and H_k is the output matrix. The numerical values of the latter matrices are

$$F_k = \begin{bmatrix} 0.9758 & 0 & -0.007 & -0.00 & 0 & 0.0005 \\ 0.009 & 0.990 & -0.00 & -0.00 & 0 & 0 \\ 0 & 0 & 0.994 & 0.002 & 0 & 0 \\ 0 & 0 & 0.002 & 0.814 & 0 & 0 \\ 0 & 0 & 0 & 0 & 0.965 & 0 \\ 0 & 0 & 0 & 0 & 0.034 & 0.993 \end{bmatrix} \tag{31}$$

$$G_k = \begin{bmatrix} -0.0000 \\ -0.0000 \\ 0.0004 \\ 0.2870 \\ 0 \\ 0 \end{bmatrix} \tag{32}$$

$$Bd = \begin{bmatrix} 0 \\ 0 \\ 0 \\ 0 \\ 0.9828 \\ 0.0171 \end{bmatrix} \tag{33}$$

$$H_k = [0 \ 1 \ 0 \ 0 \ 0 \ 0] \tag{34}$$

The reader is advised about the notation abuse since x_k is used for both the nonlinear and linear models. In this sense, it worth to point out that the notation depends on the context. For instance, x_k in the linear model stands for the state in deviation variables.

Objective function: in the literature of MPC three cost functions appear typically, i.e., GPC (Generalized Predictive Control), LQPC (Linear Quadratic Predictive Control) and zone control (Van den Boom and Backx, 2010). In this case study the following LQPC cost function was chosen

$$J(\tilde{\Delta u}, x_0) = \hat{x}_N^T P_c \hat{x}_N + \sum_{k=0}^{N_p-1} \hat{x}_k^T Q_c \hat{x}_k + \sum_{k=0}^{N_c-1} \Delta u_k^T R_c \Delta u_k \tag{35}$$

Where N_p is the prediction horizon, N_c is the control horizon, and P_c, Q_c, and R_c are the tuning knobs of the controller weighting the state at the final horizon, the state in the time window, and the control effort, respectively. The following optimization problem is solved at each sampling time using the quadprog command from the optimization toolbox in Matlab.

$$\begin{aligned} &\underset{\tilde{\Delta u}}{min} \ J(\tilde{\Delta u}, x_0) \\ &s.t \\ &x_k \geq 0 \\ &0 \leqslant u_{ex,k} \leqslant 20 \ mU/min \end{aligned} \tag{36}$$

with J as in (35).

Constraints

State constraints: the only state constraint considered is that every state should be greater than zero.

$$x_k \geq 0$$

where $x_k = [B_{G,k} \ I_{G,k} \ Q_k \ I_k \ P_{1,k} \ P_{2,k}]^T$.

Input constraints: as it was shown before, the control input corresponds to u_{ex}, the exogenous insulin. In this sense, the smaller amount of insulin to be infused is zero and the largest amount is provided by the physical constraint of the catheter.

$$0 \leqslant u_{ex,k} \leqslant 20 mU/min$$

Initial conditions and controller tuning: the MPC was designed by setting a control horizon $N_c = 50$, and a prediction horizon $N_p = 100$. Regarding to the setting up of the weighting matrices, a greater weight was assigned for states $B_{G,k}$ and $I_{G,k}$ because the purpose of the MPC is to control glucose levels. The tuning of the matrices P_c, Q_c, and R_c was performed by a trial-and-error procedure such that an acceptable performance of the MPC is reached. The matrices are presented below

$$Q_c = \begin{bmatrix} 10000 & 0 & 0 & 0 & 0 & 0 \\ 0 & 10000 & 0 & 0 & 0 & 0 \\ 0 & 0 & 1 & 0 & 0 & 0 \\ 0 & 0 & 0 & 1 & 0 & 0 \\ 0 & 0 & 0 & 0 & 1 & 0 \\ 0 & 0 & 0 & 0 & 0 & 1 \end{bmatrix} \quad (37)$$

$$P_c = \begin{bmatrix} 10000 & 0 & 0 & 0 & 0 & 0 \\ 0 & 10000 & 0 & 0 & 0 & 0 \\ 0 & 0 & 1 & 0 & 0 & 0 \\ 0 & 0 & 0 & 1 & 0 & 0 \\ 0 & 0 & 0 & 0 & 1 & 0 \\ 0 & 0 & 0 & 0 & 0 & 1 \end{bmatrix} \quad (38)$$

$$R_c = 1 \quad (39)$$

5. THE COUPLING OF THE EKF AND THE MPC

The separation principle states that if a stable observer is combined with a stable controller, the resulting coupled system is stable and functional. In this case, an EKF is tuned to work with the MPC to perform an output feedback to control the blood glucose concentration of a patient at the ICU. The simulation of the MPC coupled with EKF was performed in the software Matlab® version 2016*a* using the *Runge Kutta* numerical method with a fixed step of 1 min during 1000 *min*. The state of the glucose-insulin system was estimated using the designed EKF from the measurement of the interstitial glucose ($I_{G,k}$). The behavior of the EKF is shown in Figure 4

Once known the complete state of the system, the MPC is coupled to the EKF so that it will control the blood glucose, by just measuring the interstitial glucose. In a first approximation, the system was perturbed changing the enteral feeding from $D_k = 0.7672$ *mmol/min* to $D_k = 1.5344$ *mmol/min* at time $k = 250$ *min*. The results are reported in Figure 5.

As seen in Figure 5, by perturbing the system at time $k = 250$ *min* with the enteral feeding $D_k = 1.5344$, the blood glucose level reaches an overshoot of $B_{G,k} \approx 5.6$ *mmol/L* to which the MPC responds by infusing of insulin $u_{ex,k} \approx 18.5$ *mU/min*. It is important to make evident the existence of a steady-state error due mostly to the use of a linear controller in a highly nonlinear system.

6. FINAL COMMENTS

First, according to the evidence from the simulations, it is concluded that the design of combined control and estimation schemes becomes a reachable technology to be used in health care applications as the presented. In this sense, the filter and controller should be carefully tuned together in order to guarantee the desired closed-loop behavior. To control hyperglycemia in patients at the ICU is important to weight the main state $B_{G,k}$ (Blood glucose). It is also important to note that the performance of the MPC is not as expected due to the nonlinearity of the real system.

In a future work, regarding to the state estimation, different nonlinear strategies such as the Unscented Kalman Filter (UKF) and Particle Filters (PF) with different configurations are desired to be tested. In this sense, better estimation strategies will be coupled with more reliable

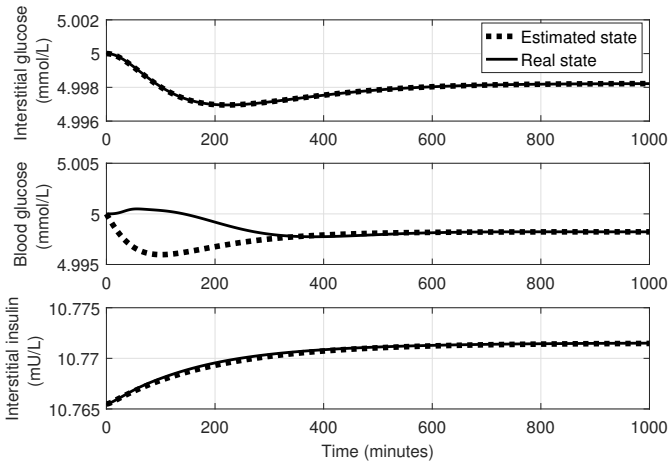

(a) Estimation of $I_{G,k}$,$B_{G,k}$ and Q_k

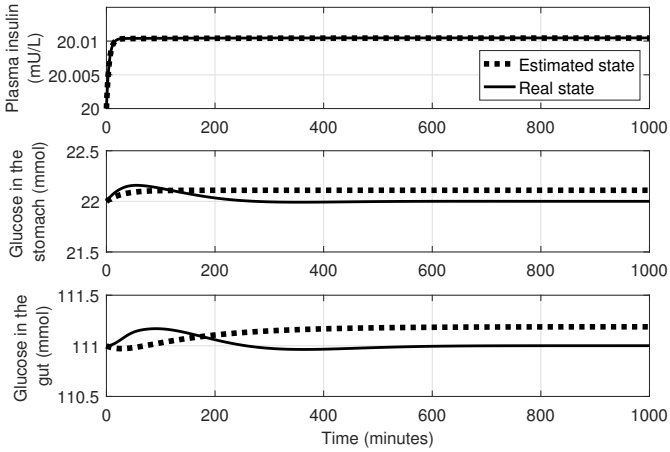

(b) Estimation of $I_{G,k}$,$P_{1,k}$ and $P_{2,k}$

Fig. 4. States estimated by using an EKF

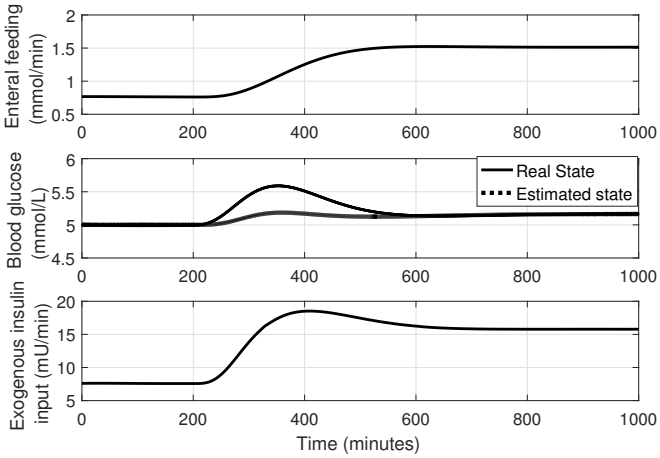

Fig. 5. Plasma glucose control when the system has been disturbed with enteral feeding $D_k = 1.5344$.

model-based controllers such as the nonlinear MPC. Since the literature about nonlinear MPC is vast, a careful review should be done in order to test the state-of-the

art of the strategy and hence to propose control schemes tailored to the specific case study.

REFERENCES

Aldworth, J., Al Bache, N., Hegelund, M.H., Linnenkamp, U., Magliano, D., Oomatia, F., Patterson, C., Peer, N., Pritulskiy, A., Saleh, M.M.A., Shelestova, E., Tamayo, T., Usher-Smith, J., Xiuying, Z., and Samrawit Yisahak (2015). *IDF Diabetes Atlas*. 7 edition.

Barrett, K.E. (2013). *Ganong's Review of Medical Physiology (24a)*. McGraw Hill Mexico.

Bequette, B.W. (2007). Analysis of algorithms for intensive care unit blood glucose control. *Journal of diabetes science and technology*, 1(6), 813–824.

Block, C.D., Vertommen, J., Manuel-y Keenoy, B., and Gaal, L.V. (2008). Minimally-invasive and non-invasive continuous glucose monitoring systems: Indications, advantages, limitations and clinical aspects. *Current diabetes reviews*, 4(3), 159–168.

Hospital Universitario de Bucaramanga S.A (2012). Insulin Administration Protocol (in Spanish).

King, C., Anderson, S.M., Breton, M., Clarke, W.L., and Kovatchev, B.P. (2007). Modeling of calibration effectiveness and blood-to-interstitial glucose dynamics as potential confounders of the accuracy of continuous glucose sensors during hyperinsulinemic clamp. *journal of diabetes science and technology*, 1(3), 317–322.

Lin, J., Razak, N.N., Pretty, C.G., Le Compte, A., Docherty, P., Parente, J.D., Shaw, G.M., Hann, C.E., and Chase, J.G. (2011). A physiological intensive control insulin-nutrition-glucose (icing) model validated in critically ill patients. *Computer methods and programs in biomedicine*, 102(2), 192–205.

Magni, L., Raimondo, D.M., Bossi, L., Dalla Man, C., De Nicolao, G., Kovatchev, B., and Cobelli, C. (2007). Model predictive control of type 1 diabetes: an in silico trial. *Journal of diabetes science and technology*, 1(6), 804–812.

Pascual, A. (2004). Ekf y ukf: two extentions of the kalman filter for nonlinear systems in an inverted pendulum (in spanish).

Schmidt, S.F. (1966). Applications of state space methods to navigation problems. *Advances in Control Systems*, 3, 293–340.

Simon, D. (2006). *Optimal state estimation: Kalman, H infinity, and nonlinear approaches*. John Wiley & Sons.

Umpierrez, G.E., Isaacs, S.D., Bazargan, N., You, X., Thaler, L.M., and Kitabchi, A.E. (2002). Hyperglycemia: an independent marker of in-hospital mortality in patients with undiagnosed diabetes. *The Journal of Clinical Endocrinology & Metabolism*, 87(3), 978–982.

Van den Berghe, G., Wilmer, A., Hermans, G., Meersseman, W., Wouters, P.J., Milants, I., Van Wijngaerden, E., Bobbaers, H., Bouillon, R., et al. (2006). Intensive insulin therapy in the medical icu. *New England Journal of Medicine*, 354(5), 449.

Van den Boom, T.J. and Backx, T. (2010). Model predictive control. *DISC Course, Lecture Notes*, 16.

Villamarín, R.I. and Puentes, F.E. (2009). Intensive insulin therapy in patients with severe sepsis and septic shock (in Spanish). *Medical files*, 9(2), 165–173.

Appendix A. MATHEMATICAL MODEL PARAMETERS

Table A.1. System parameters

P	Value	Units	Description
B_G	*State*	$mmol/L$	Blood glucose
I_G	*State*	$mmol/L$	Interstitial glucose
Q	*State*	mU/L	Interstitial insulin
I	*State*	mU/L	Plasma insulin
P_1	*State*	$mmol$	Glucose in the stomach
P_2	*State*	$mmol$	Glucose in the gut
P_G	0.006	min^{-1}	Patient endogenous glucose removal
S_I	0.002	$L/mU/min$	From former model since it is identified online
α_G	0.0154	L/mU	Saturation of insulin-stimulated glucose
$P(t)$	*Fcn*	$mmol/min$	External nutrition
EG_{P_b}	1.16	$mmol/min$	Basal endogenous glucose production
CNS	0.3	$mmol/min$	Insulin independent central nervous system glucose uptake
V_G	13.3	L	Glucose distribution volume
V_I	3.15	L	Insulin distribution volume
α_I	0.0017	L/mU	Saturation of plasma insulin disappearance
n_C	0.003	min^{-1}	Parameter
n_I	0.003	min^{-1}	Transcapillary difussion rate
n_K	0.0542	min^{-1}	Kidney clearance
n_L	0.1578	min^{-1}	Patient specific liver clearance
u_{ex}	7.5933	mU/min	Exogenous insulin input
x_L	0.67	[]	First pass endogenous insulin hepatic uptake
u_{en}	*Fcn*	mU/min	Endogenous insulin production
d_1	0.0347	min^{-1}	Transport rate
d_2	0.0069	min^{-1}	Transport rate
$D(t)$	0.7672	$mmol/min$	Disturbance-Amount of dextrose from enteral feeding
P_{max}	6.11	$mmol/min$	Saturation value of P_2
$PN(t)$	0	$mmol/min$	Parenteral dextrose (intravenous)
k_1	45.7	mU/min	Base rate for endogenous insulin production
k_2	1.5	[]	Generic constant for exponential suppression
k_3	1000	[]	Generic constant for exponential suppression
β_1	0.0099	min^{-1}	Parameter
β_2	0.0099	min^{-1}	Parameter

Sistema vestible para detección de estados fisiológicos y emocionales en entornos industriales.

S. Ponce[1], N. Lopez[1,2] , D. Piccinini[1], M. Roberti[1], M. Caggioli[1] , S. Avetta[1], N. Andino[1], A. Sparapani[1] C. Garcia[1] and O.L. Quintero[3]

[1] Universidad Tecnológica Nacional/Facultad Regional San Nicolás, GADIB, San Nicolás, Argentina
[2]Universidad Nacional de San Juan, GATEME, CONICET, San Juan, Argentina.
[3]Grupo de Investigación en Modelado Matemático, GRIMMAT, Universidad EAFIT, Medellín, Colombia

Abstract: This paper presents the design and implementation of a wearable system for monitoring physiologic variables. The system is composed by a master module, responsible for receiving the data and the Wi-Fi transmission. Also, a set of node sensors (or slaves) were developed, allowing the acquisition of multiple biological signals in a modular and versatile arrangement. The nodes are connected by Low Energy Blue-tooth to the Master. In this paper we present the nodes for pulse oximetry, temperature, electrodermal activity and voice acquisition. The results are encouraging and the entire system has an adequate performance and versatility.

Keywords: wearable sensor, wireless, low energy, electrodermal activity, pulse oximetry

1. INTRODUCCIÓN

En los últimos años las tecnologías vestibles se incorporaron al quehacer humano, para monitoreo fisiológico [1], del sueño [2], deporte de alto rendimiento [3], estudios de personalidad y salud mental [4], marketing y más. Estas tecnologías ayudan a comprender el comportamiento del ser humano en un ambiente no estructurado, en sus actividades cotidianas, lo que significa un valor agregado sobre los estándares de evaluación fisiológica conocidos.

En este trabajo se propone una nueva aplicación y el diseño de un sistema *ad hoc*, con la finalidad de monitorear el comportamiento fisiológico y emocional de operarios industriales en entornos peligrosos. En particular la siderurgia es una industria pesada, por lo cual, las consecuencias de sus trabajadores ante accidentes es potencialmente más grave que en otras actividades. La mayoría de los accidentes e incidentes se deben al incumplimiento de los procedimientos de seguridad. Distracciones, subestimación de los riesgos de la tarea, mala predisposición, estados de ánimo, uso de medicamentos, drogas y otros factores son sólo algunas causas por lo que las personas omiten el cumplimiento de los pasos de seguridad. El objetivo de este trabajo es diseñar y desarrollar un sistema vestible que registre y envíe a una central de control las variables fisiológicas y el audio durante una jornada de trabajo. Con el análisis de estas señales se establecerán patrones de conducta y comportamiento en los ambientes peligrosos y la posibilidad de accionar sistemas de alarma frente a cambios.

Un sistema vestible debe cumplir condiciones de diseño, tales como almacenamiento de datos, conexión inalámbrica, eficiencia en la alimentación, portabilidad, versatilidad y capacidad de acoplar otros sensores, entre otras. El sistema propuesto consta de un módulo maestro encargado de la recepción, sincronización, empaquetamiento y transmisión de datos inalámbrica. Este módulo se conecta a diversos nodos sensores, (Fig. 1) los que adquieren una señal biológica, los procesan y dan formato adecuado para su envío en forma inalámbrica al maestro. Se presentarán nodos sensores de oximetría de pulso para medición de saturación de oxígeno (SpO2) y frecuencia cardíaca (Hbpm); de temperatura y sudoración a través de la respuesta galvánica o actividad electrodérmica (EDA); y de adquisición de voz para monitoreo de emociones o contenido semántico del habla. Estas variables se adquieren y visualizan a través de una interfaz de usuario en una computadora personal (PC).

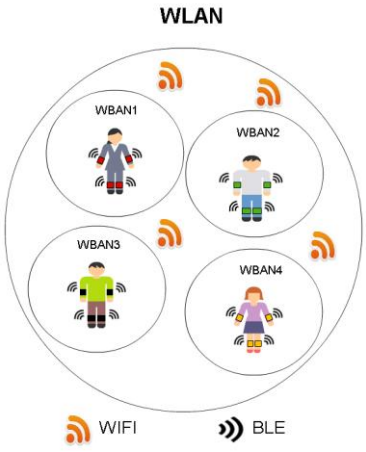

Fig 1. Esquema general del sistema

2. MATERIALES Y MÉTODOS

En esta sección se presentan los nodos sensores y el módulo maestro, como también los protocolos de comunicación entre ellos. Para realizar la comunicación entre los nodos sensores y el maestro se utilizó Bluetooth Low Energy (BLE) [5]. Dicha tecnología permite implementar una red de dispositivos de baja potencia utilizados en el cuerpo, técnicamente denominada WBAN (Wireless Body Area

Network). Se conforma una red del tipo estrella, en dónde cada nodo sensor centraliza su información en el maestro. La seguridad de las redes WBAN ha evolucionado rápidamente en los últimos años, por lo que este desarrollo ofrece enlaces encriptados punto a punto, con algoritmos avanzados como el utilizado, denominado AES-128. Para lograr un óptimo monitoreo y procesamiento de las variables medidas, los datos adquiridos son transmitidos y almacenados en un servidor, el cual permite el acceso desde cualquier estación de trabajo que se encuentre dentro de la red WLAN.

A. *Módulo Maestro*

El módulo maestro (Fig. 2) realiza la recepción por medio de BLE y la transmisión a través de WiFi. La función más importante que realiza esta etapa es comportarse como gateway: interconectando la red WBAN con la red WLAN, esta interconexión de ambas tecnologías se realiza utilizando el microcontrolador CC3200 de la firma Texas Instruments. Dicho microcontrolador es de 32 bits, su núcleo se basa en ARM Cortex-M4 a 80 MHz, y cuenta con un radio WiFi para brindar conectividad inalámbrica bajo las normas B de 11Mbps, G de 54Mbps y la tan difundida norma N de 72Mbps. El CC3200 brinda conexiones encriptadas punto a punto bajo algoritmos AES, DES, SHA2 y MD5 y cumple con estándares de emisión de radiofrecuencia internacionales. La recepción BLE en el módulo maestro, está gestionada por el circuito integrado CC2564, que no sólo es compatible con la normativa Low Energy, sino también con la Classic, entrando en la categoría de dispositivos “Smart Ready”. Permite la conexión simultánea de hasta 7 dispositivos Classic y 10 dispositivos Low Energy. Esta convivencia de múltiples protocolos otorga una mayor flexibilidad para conectarse a nodos compatibles con cualquier revisión de la norma Bluetooth, sean o no compatibles con el protocolo LE (Low Energy). Esto permite recibir variables fisiológicas tanto de nodos sensores propios, como de demás nodos existentes en el mercado, que se comuniquen vía la mencionada tecnología inalámbrica.

B. *Nodos sensores*

Los nodos sensores fueron diseñados a partir de una plataforma base con un microcontrolador CC2650 de Texas Instruments, que permite expandir la circuitería electrónica según la variable fisiológica considerada. Estos microcontroladores son del tipo ARM Cortex-M3 de 32bits, corriendo a una frecuencia de reloj de 48MHz. Esta plataforma base cumple con requerimientos específicos de consumo, entradas/salidas y de transmisión por RF. Gracias al ultra bajo consumo de 6.1mA (Tx), permite operar durante largos períodos de tiempo, aún con baterías pequeñas. En este caso, se aumentó considerablemente la autonomía gestionando correctamente las frecuencias de adquisición de variables, recurriendo al modo “sleep” cuando el mismo se encuentra en estado ocioso, lo que permitió alcanzar consumos de 1uA. Adicionalmente se diseñó electrónica específica para lograr que cuando los sensores no se utilicen por periodos prolongados, se apaguen.

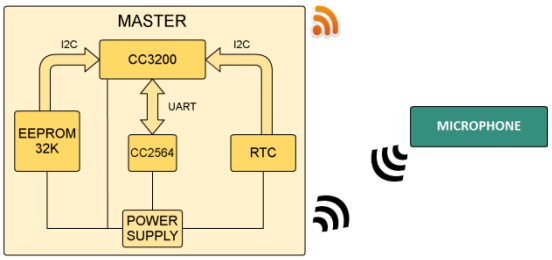

Fig. 2: Diagrama en bloques del Módulo Maestro.

El radio de acción de RF es de 2.4GHz: aportando conexiones compatibles con tecnología BLE, Zigbee y 6LowPAN. Además cumple con las normas de radiofrecuencia más importantes como la FCC de EEUU, ETSI/EN de Europa y la japonesa, ARIB. Para dar mayor versatilidad al sistema, la plataforma base se completa con expansiones específicas según la variable a sensar, en forma intercambiable según la aplicación:

1. Módulo de Frecuencia cardíaca y oximetría de pulso:
Con un solo módulo (Fig. 3) se registran ambas variables, mediante un emisor LED de frecuencia específica para absorción por los hematíes o glóbulos rojos, lo que indica el grado de oxigenación y además permite inferir la frecuencia cardíaca [6]. La colocación de estos sensores debe realizarse sobre la piel directamente. Para este módulo se utilizó el AFE4403 de Texas Instruments, el cual es un front-end analógico (AFE) totalmente integrado ideal para aplicaciones de oxímetro de pulso. El dispositivo se comunica con un microcontrolador externo o un procesador host mediante la interfaz SPI™. La señal recibida por el fotodiodo tiene tres componentes:

1. Una componente pulsátil o de corriente alterna AC que surge como resultado de los cambios en el volumen de sangre a través de las arterias.
2. Una señal de corriente constante DC que se refleja o transmite en los componentes invariantes en el tiempo en el camino de la luz, la cual se denomina señal de pletismografía.
3. La luz ambiental que entra en el fotodiodo.

El componente de AC es por lo general una pequeña fracción de la señal pletismográfica. Por lo tanto, la ganancia de señal permitida se determina por la amplitud de la componente de corriente continua. La constante ' R' relaciona las señales del LED rojo e infrarrojo y se calcula de la siguiente manera:

$$R = (ACrms\ LedRojo / DC\ LedRojo) / (ACrms\ LedIR / DC\ LedIR) \quad (1)$$

Donde *ACrms* es el valor de RMS de la señal AC. El valor preciso de SpO_2 porcentual se calcula basándose en la calibración empírica del valor R para el dispositivo específico.

$$SpO_2\ \% = 110 - 25 \times R \quad (2)$$

La señal obtenida por este método se envía al módulo maestro y luego se procesa en MatLab®, con una frecuencia de muestreo de 500Hz. En esta etapa se realiza un filtrado para separar la componente de continua del LED rojo e IR, mediante un filtro Butterworth pasabanda de segundo orden

de 0,5 a 5Hz. Posteriormente se extraen los picos correspondientes al pulso cardíaco de la señal del LED IR con un filtro Butterworth pasabajos de segundo orden con frecuencia de corte 1,25Hz. Estas curvas de SpO_2 y Hbpm se presentan para visualización por parte del supervisor y además se extraen los valores numéricos instantáneos mediante las fórmulas anteriores.

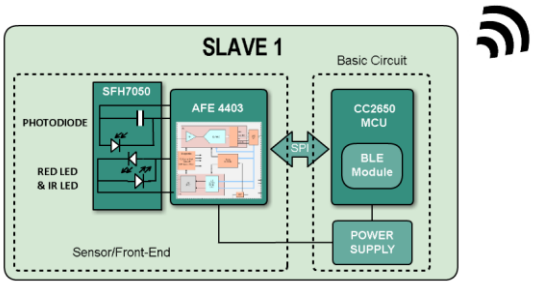

Fig. 3 Diagrama en bloques Nodo Sensor de ECG y SpO2.

2. Módulo de temperatura y EDA:

Este nodo (Fig. 4) registra la temperatura corporal a través del sensor integrado LMT70, el cual otorga una salida analógica con precisión de 0.1ºC. Este sensor, de pequeño tamaño (0.9x0.9mm) se coloca en la espalda, pecho u otra zona corporal donde se registre la temperatura corporal y sus variaciones. Debido a que la salida de este sensor es de tipo analógica, se estimó la temperatura con el bloque ADC del CC2650 que posee el nodo sensor. Dicho nivel de tensión responde a una función de primer orden como función transferencia del sensor:

$$T = -0.1921266499\ (°C)/mV * V_{TAO} + 211.2190436\ °C \qquad (3)$$

La anterior ecuación se obtuvo a través de mediciones provenientes de ensayos e interpolando linealmente, para un rango comprendido entre 30°C y 45°C, donde V_{TAO} es el nivel de tensión de salida obtenido en el LMT70. En este mismo nodo sensor se registra la actividad electrodérmica (EDA), la cual se basa en la conductancia de la piel y se modifica con la sudoración y por consiguiente, con la actividad del sistema nervioso simpático producto de la excitación psicológica o fisiológica.

3. Módulo de adquisición de voz:

La función de este módulo es adquirir la señal de voz a través de un micrófono inalámbrico comercial que cuente con conexión Bluetooth, digitalizarla, almacenarla y transmitirla para un posterior procesamiento. El mismo se comunica directamente (Fig. 2) con el circuito integrado CC2564 y este envía los datos al CC3200, contenido dentro de la misma placa maestra. La transmisión de datos hacia la PC se realiza a través de WI-FI en protocolo UDP.

Los datos transmitidos a la PC desde el módulo maestro se reciben y visualizan en una interfaz gráfica de usuario GUI, la cual es modular para adecuarse a los nodos elegidos para cada aplicación. La interfaz fue programada en Matlab®, para utilizar el potencial de cálculo matemático para el posterior análisis multimodal y correlación de los datos.

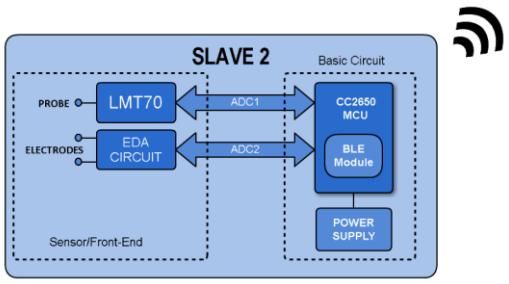

Fig. 4 Diagrama en bloques Nodo Sensor de temperatura y EDA.

Para el protocolo experimental se contó con 10 voluntarios (5 hombres y 5 mujeres, entre 20 y 40 años, sin antecedentes de enfermedad respiratoria o vascular) quienes efectuaron las pruebas en 10 sesiones, previo consentimiento informado.

3. RESULTADOS

En esta sección se presentarán los resultados obtenidos en cada nodo sensor en pruebas experimentales. En el caso de SpO_2 y Hbmp, el sensor se colocó en el dedo de los voluntarios, en un ambiente no estructurado, y se registraron las 10 sesiones de cada voluntario en condiciones normales, sin someterlo a ejercicio ni esfuerzos de ningún tipo. La Fig. 5 muestra el valor medio obtenido para cada voluntario en 10 sesiones y la desviación estándar (SD) de estas mediciones, a fin de obtener una medida de repetibilidad del instrumento.

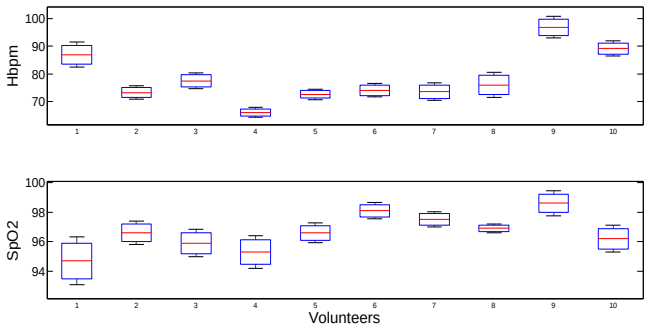

Fig. 5: Diagrama de cajas y bigotes representando el promedio y SD de la medición de Hpbm (arriba) y SpO_2(abajo) en las 10 sesiones de cada voluntario. Se aprecia la variabilidad entre voluntarios pero con escasa SD.

Se realizó una medición comparativa con un instrumento comercial (*Medix OXi-3*), al que se tomó como estándar para calcular el error absoluto de medición en los 10 voluntarios. Los valores obtenidos (1,38 para SpO_2 y 0,22 para Hbpm) muestran un desempeño adecuado para la estimación de las variables oxígeno en sangre y frecuencia cardíaca. Por otro lado debe destacarse que el objetivo de este trabajo es detectar cambios y variabilidad de estos registros, atribuibles a estados fisiológicos o emocionales y no son usados con fines de diagnóstico.

Para el nodo de temperatura y EDA se contrastaron los valores registrados con temperatura ambiente y con temperatura corporal, usando un equipo medidor de temperatura *Fluke 54II* [7]. Los valores comparados con el sensor comercial muestran una relación directa, que cumple con la precisión establecida por el fabricante de 0,1°C. Este

valor es consecuente con el objetivo de este trabajo, ya que se esperan detectar pequeñas variaciones de temperatura corporal.

La EDA [8] se testeó colocando el sensor sobre la muñeca de los voluntarios y realizando actividad física, conformando la curva de registro que se aprecia en la Figura 6 a modo de ejemplo. Se observa el cambio de conductividad a consecuencia de la sudoración, como una modificación de la tensión medida en el sensor. La señal obtenida con el micrófono conserva los contenidos frecuenciales y de calidad deseados, ya que dependen del micrófono comercial usado y no es parte del diseño específico para este proyecto.

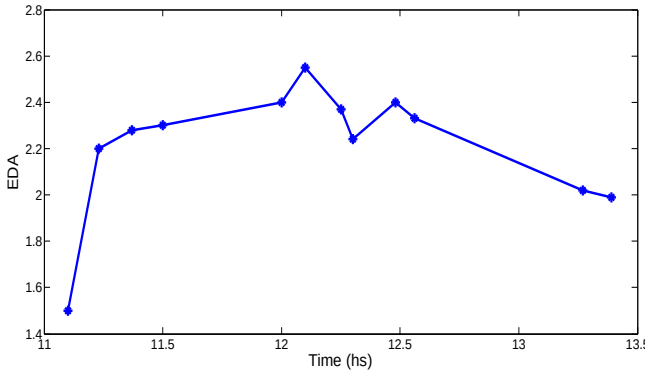

Figura 6: Respuesta del sensor de sudoración en función el tiempo, registrando la tensión proporcional a la conductividad galvánica de la piel.

La interfaz gráfica permite visualizar los módulos diseñados hasta el momento con claridad y en forma amigable.

4. CONCLUSIONES

El sistema cumple con las expectativas de desempeño, precisión, y repetibilidad de un dispositivo vestible, como también condiciones de autonomía, bajo peso y costo requeridos en estos equipos. Los valores obtenidos de SpO2, Hbpm, Temperatura y EDA se encuentran en el rango esperado y sin errores de medición en las pruebas efectuadas.

El diseño implementado con nodos sensores comunicándose en forma inalámbrica con el módulo maestro posibilitó la eliminación de conexiones cableadas en la plataforma de sensores vestibles, lo que disminuyó las fallas en el sistema debido a movimientos bruscos de los usuarios. Además la utilización de WiFi para la conexión a la red WLAN posibilitó el monitoreo tanto en aplicaciones hogareñas como industriales. De esta manera, se pueden realizar ampliaciones de la red de datos y visualizaciones a mayores distancias, y desde cualquier dispositivo con conexión WiFi (PCs, tablets, smartphones, etc). Este es un desarrollo preliminar, y en próximos trabajos se agregarán sensores inerciales y de electromiografía a fin de ampliar las variables registradas.

Son necesarias pruebas en un ambiente controlado con inducción de emociones o de alteraciones fisiológicas y ambientales a fin de validar el desarrollo y obtener los datos para un análisis multimodal de las señales. Sin embargo, la construcción de un modelo de comportamiento debe ser personalizado. Esto requiere la recolección de datos previos, y un modelo dinámico de ajuste y aprendizaje para cada operario.

REFERENCIAS

[1] Teng X-F, Zhang Y-T, Poon CCY, Bonato P (2008): Wearable medical systems for p-Health. IEEE Reviews in Biomedical Engineering, 1:62-74.

[2] Bonato P (2010): Wearable sensors and systems. From enabling technology to clinical applications. IEEE Eng Med Biol Mag, 29:25-36.

[3] Anzaldo D (2015): Wearable sport technology – Market landscape and compute SoC trends. IEEE Conference Publications: International SoC Design Conference: 217-218.

[4] Chen B, Patel S, Buckley T, Rednic R, McClure D, Shih L, Tarsy D, Welsh M and Bonato P (2011): A Web-Based system for home monitoring of patients with Parkinson´s disease using wearable sensors. IEEE Transactions on Biomedical Engineering, Vol. 58, No 3:831-836.

[5] https://www.bluetooth.com.

[6] Asada HH, Shaltis P, Reisner A, Rhee S, Hutchinson RC(2003): Mobile monitoring with wearable photoplethysmographic biosensors. IEEE Eng Med Biol Mag , 22:28-40.

[7] http://en-us.fluke.com/products/thermometers/thermometer.html.

[8] Piccinini D, Andino N, Ponce S, Roberti M, López N.(2015): Wearable system for acquisition and monitoring of biological signals. Journal of Physics: Conference Series.Bristol: IOP Publishing ,Institute of Physics.

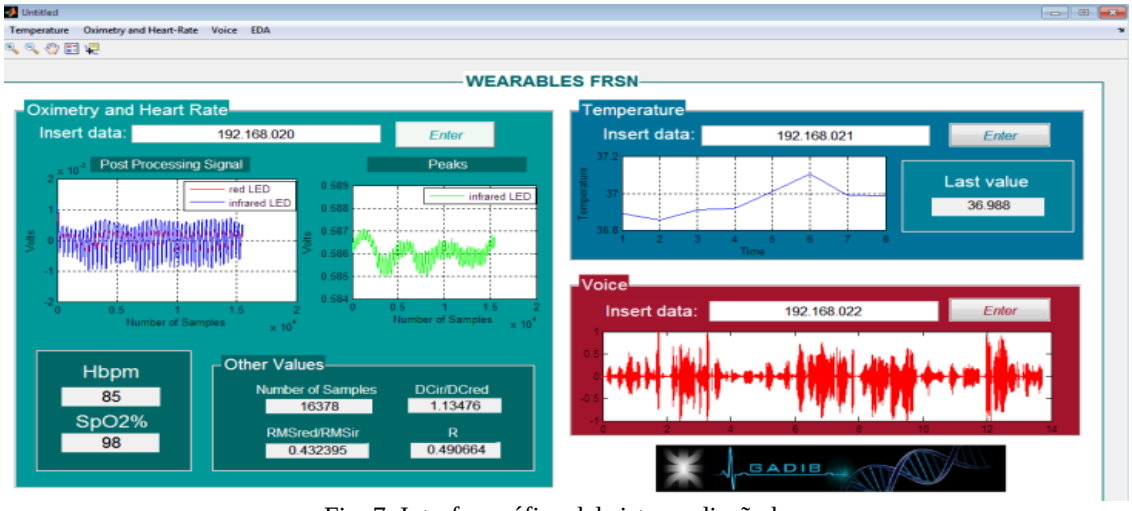

Fig. 7: Interfaz gráfica del sistema diseñado.

CHAPTER 4

BIOPROCESSES

Advanced Control of a fed-batch reaction system to increase the productivity in the polyhydroxyalkanoates production process.

Cesar García*, Alejandro Acosta** and Silvia Ochoa***

*SIDCOP Research Group, University of Antioquia-Colombia (tel: +57 2198483; cesar.garciae@udea.edu.co).
**Biotransformación Research Group, University of Antioquia-Colombia (tel: +57 2198483; alejandro.acosta@udea.edu.co).
***SIDCOP Research Group, University of Antioquia-Colombia (tel: +57 2198568; silvia.ochoa@udea.edu.co).

In this work, the optimizing control of the fed-batch process for the production of Polyhydroxyalkanoates is carried out by formulating and solving a dynamic optimization problem in order to maximize the process productivity. The optimization problem is subject to constraints on the feed flow rates, the final volume and the maximum concentrations able to be reached on the substrate and nitrogen-source in order to avoid inhibition. For solving the dynamic optimization problem, different parameterization strategies of the control vector were used in order to compare their effect on the dynamic behavior of the biological variables, and therefore, on the process productivity. Results have shown that sinusoidal parameterization of the control profiles lead to higher productivity values while avoiding abrupt changes on the microorganism environment. Furthermore, it is shown that coupling the optimizing control to a neural network soft-sensor developed for predicting the number average molecular weight of the biopolymer is a good strategy in order to fulfill the end-product specifications. In this case, the optimal solution leads to a productivity over 300 g, while keeping the number average molecular weight at common reported values for important applications (between $4x10^5$ - $2x10^6$ g/mol).

Keywords: Advanced Control, Optimization, State Estimation, Biotechnology, Simulation.

1. INTRODUCTION

Polyhydroxyalkanoates (PHAs) are polymers from biological origins, which are currently claimed to be an environmentally friendly option for replacing petroleum based plastic materials in a wide number of applications. However, production costs of these plastic materials are still higher than the petroleum based ones, which has prevented the expansion of the biopolymer industry, despite the fact of its innumerable environmental advantages. Therefore, in the last years, scientists have put many effort in improving the technical and economic feasibility of the process. Some of these works focused on using alternative low cost substrates (Lee & Na 2013), (Dietrich, Illman & Crooks 2013). Other works have focused on using tools from the Process Systems Engineering (PSE), in order to address the optimization and control of the process, towards increasing its productivity (Keshavarz & Roy 2010), (Khanna & Srivastava 2006) and (López , Bucalá & Villar 2010).

In this work, it is proposed to maximize the productivity of the PHA's production process by applying an optimizing control strategy based on a first principle model containing the most relevant dynamics for the process (substrates, biomass, polymer, dissolved Carbon Dioxide and Dissolved Oxygen). It is also expected to include characteristics of the desired product such as molecular weight distribution (MWD), the Number Average Molecular Weight (Mn), the Weight Average Molecular Weight (Mw) and/or the Polydispersity Index (PDI). Due to the importance of assuring some of these characteristics, the optimizing control strategy proposed in this work, is coupled to a soft-sensor developed for predicting the Number Average Molecular Weight (Mn).

2. MODELLING OF THE PHA's PROCESS

The developed model is based on the work by (Shahhosseini 2004), (Khanna & Srivastava 2006), (Amicarelli et al. 2008) and (Chatzidoukasa, Penlogloub & Kiparissides 2013). The model is described by equations (1-8), where the dynamic equations describing the behavior of the biomass (X), substrate (S), biopolymer (P), nitrogen-source (N), dissolved oxygen (O_2L) and dissolved carbon dioxide (CO_2) concentrations are given. The specific growth rate (μ) depends on the glucose concentration (S), nitrogen-source concentration (N) and Dissolved Oxygen concentration (O_2L), following a sigmoidal relationship. F_1, F_2 and F_3 correspond to the feed flow rates of the substrate, nitrogen-source and oxygen, respectively. S_{in}, N_{in} and O_{in} correspond to the concentrations of substrate, nitrogen-source and oxygen in the feed. Finally, V is the fermentation volume.

$$\mu = \mu_m \left(\frac{\left(\frac{N}{S}\right)}{\left(\frac{N}{S}\right)+K_{sr}} \right) * \left(1 - \left(\frac{\frac{N}{S}}{S_m} \right)^{n_k} \right) * \left(\left(\frac{O_2L}{K_{ox}*X+O_2L} \right) \right) \quad (1)$$

$$\dot{X} = \mu X - \frac{F_1+F_2}{V} X \quad (2)$$

$$\dot{S} = -\left(\left(C_{sx}\, \mu X \right) + \left(R_{csx}\, X \right) + C_{sp}\left((K_1 \mu X) + (K_2 X) \right) \right) + \frac{F_1}{V} S_{in} - \frac{F_1+F_2}{V} S \quad (3)$$

$$\dot{P} = (K_1 \mu X) + (K_2 X) - \frac{F_1+F_2}{V} P \quad (4)$$

$$\dot{N} = -\left((C_{nx}\,\mu\,X) + (R_{cnx}\,X)\right) + \frac{F_2}{V}N_{in} - \frac{F_1+F_2}{V}N \quad (5)$$

$$\dot{O_2L} = ((KL(O_{2Leq} - O_2L)) - (K_3\mu X) - ((K_4K_1\mu X) + (K_4K_2X)))) + \frac{F_3}{V}O_{in} - \frac{F_1+F_2}{V}O_2L \quad (6)$$

$$\dot{CO_2} = (\alpha_1\mu + \alpha_2)X + \alpha_3 - \frac{F_1+F_2}{V}CO_2 \quad (7)$$

$$\dot{V} = F_1 + F_2 \quad (8)$$

The model contains 19 parameters. For identifying those parameters, a hybrid strategy combining the simulated annealing and the interior point method was used. The objective function for parameter identification is given by (9).

$$\text{SSWR} = \sum_{i=1}^{n}\sum_{j=1}^{m}\frac{\Delta_{ij}}{W_j^2} \quad (9)$$

Where SSWR represents the sum of the square weighed residuals, n and 'm' are the total number of experimental data points and variables, respectively. W_j is a normalization factor for each variable. Δ_{ij} is the difference between the predicted and experimental data. Experimental data for identification and validation was taken from (Khanna & Srivastava 2005). For finding an optimal set of parameters, the methodology by (Wu et al. 2013) was applied. Results showed that only 7 parameters are identifiable. Therefore, a re-optimization strategy was performed for finding a better value for these sensitive parameters while keeping fixed the remaining 12 parameters. Figure 1 shows the model results after parameter identification. It can be observed that model predictions are in good consent with experimental data.

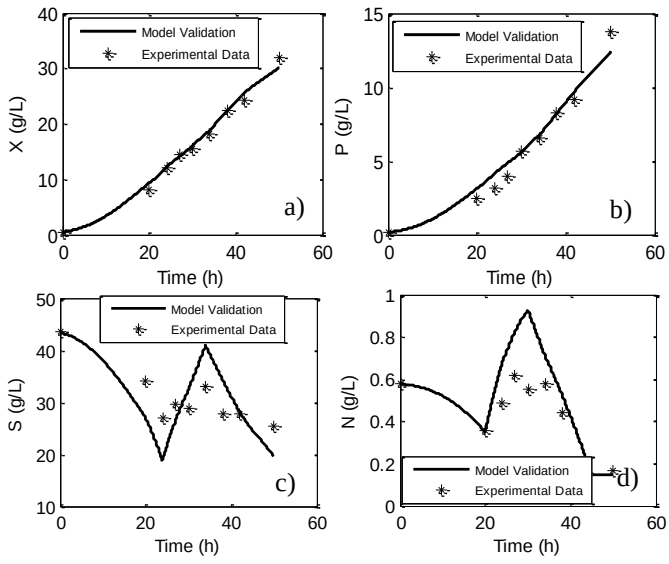

Figure 1. Model validation for fed-batch PHA production. Results for the main state variables: a) Biomass, b) Biopolymer, c) Substrate, d) Nitrogen Source.

3. SOFT–SENSOR DEVELOPMENT FOR MOLECULAR WEIGHT DISTRIBUTION

In the case of polymer production, end-product properties are highly related to the Molecular Weight Distribution (MWD) achieved during the process, (Sudesh, Abe & Doi 2000). Therefore, it is important to control the MWD during the process operation. However, it has to be considered that one of the main limitations for controlling is the difficulty of getting cheap and reliable on-line measurements of the MWD. Previous works by (Penloglou et al. 2010) and (Penloglou et al. 2012) proposed the combination of a polymerization and a macroscopic model in order to determine the MWD in the PHA production. However, the mentioned works don´t take into account any control strategy in order to achieve a desired final molecular weight distribution. Based on the mentioned works, a structured macroscopic/polymerization kinetic model was simulated in order to obtain enough "in silico data" for building an Artificial Neural Network (ANN) capable of predicting the number average molecular weight (Mn). Such ANN is used as a soft-sensor inside the optimizing control strategy, in order to monitor the Mn during the process operation and to drive the optimization towards finding the conditions for assuring maximal productivity while keeping the Mn at a pre-established range (i.e. required for the biopolymer to fulfill certain mechanical/performance properties)

For simulating the macroscopic/polymerization kinetic model reported by (Penloglou et al. 2010), (Kumar & Ramkrishna 1996) and (Saliakas et al. 2007), a mathematical technique called fixed pivot was used in order to discretize the set of ordinary differential equations that describe the model. It is important to notice that the integration between the macroscopic and the polymerization models is the most important partof the MWD-prediction.. The polymerization model allows predicting Mn as a function of the monomer production rate ($J_M(t)$). Furthermore, $J_M(t)$ is determined by the way the microorganisms use the available substrate for producing the biopolymer. A simple approach that avoids the use of complex metabolic models) for estimating $J_M(t)$ is to calculate the monomer concentration via the consumption rate of the substrate (Penloglou 2015), which is predicted by the macroscopic model presented in section 2, specifically, by using equation (3).

Figures 2a-2b compare the results obtained for the polymer and substrate concentrations by using the described simulation (Model validation), against actual experimental data reported in (Penloglou et al. 2010). Furthermore, figure 2c presents a comparison between the simulation results for the number average molecular weight (Mn), the "real" experimental data and the results presented (Penloglou et al. 2010). Differences between simulation results at this work and the ones reported in the literature are caused by different kinetic parameters in each case, due to the fact that not all kinetic parameters were reported. Therefore, those missing kinetic parameters (the so-called adjusted parameters in Table 1) were estimated in this work through optimization (i.e. performing a similar procedure than the one explained in section 2 for parameter identification).

Table 1. Parameters of the polymerization model

Parameters	Reported by (Penloglou et al. 2012)	Adjusted Parameters
k_i (h^{-1})	0.62 ±9 x 10^4	0.64x10^4
k_P(h^{-1})	0.46±5x10^5	0.44x10^5
k_t^* (h^{-1})	0.14±1x10^1	0.101x10^1
k_{m1}^*(h^{-1})	0.11±2x10^{-3}	0.114x10^{-3}
k_{m2}(l/mol/h)	0.85±15x10^7	0.75x10^7
k_d^*(h^{-1})	0.83±6x10^2	0.25x10^2
$Y_{\frac{M}{F}}$	0.35±2x10^{-2}	0.23x10^{-2}

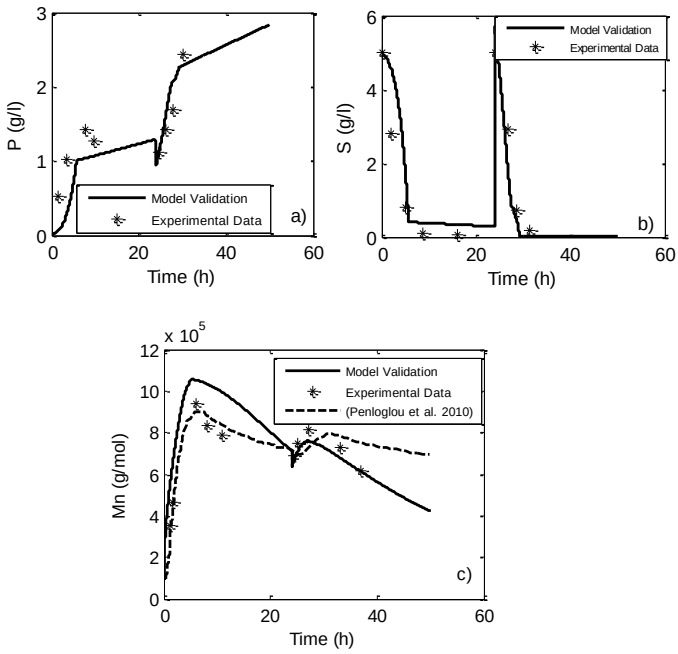

Figure 2. Simulation of the macroscopic/polymerization model: a) Polymer, b) Substrate, c) Number Average Molecular Weight (Mn).

After simulating and validating the mentioned macroscopic/polymerization kinetic model, it was possible to get the required "in silico data" for building an Artificial Neural Network for predicting the Mn. A feed-forward network was built using the following set consisting on input and "measured" variables as an regressor.(i.e. calculated by the first principles model described in section 2): [F_1(t-1); F_1(t-2); F_2(t-1); F_2(t-2); X(t-1); X(t-2); S(t-1);S(t-2); N(t-1); N(t-2); P(t-1); P(t-2); CO_2(t-1); CO_2(t-2)]. Finding such regressor was not a straightforward task. Therefore, the selection was carried out as suggested by (Amicarelli et al. 2014). The network was trained and validated by using respectively, 70% and 30% of the "in silico" data. The network training was carried out by the Levenberg-Marquardt back propagation algorithm. A trial and error approach was used to minimize the error in order to determine the optimal number of hidden layers and neurons. The ANN obtained is composed of 14 neurons at the input layer, and 12 and 1 in the first and second hidden layers, respectively. Results obtained for prediction of Mn by the ANN have shown a very good fit, with a mean absolute Error of 0.85% and R2 of 0.999. Figure 4 compares the ANN predictions against the validation data.

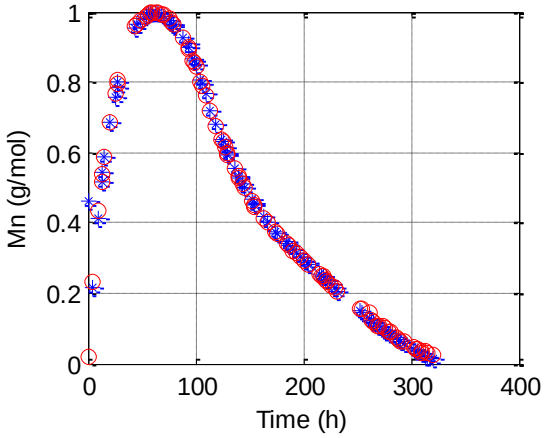

Figure 4. ANN predictions for Mn (red) vs. Validation Data (blue). Normalized data.

4. OPTIMIZING CONTROL

In this section, the development of the optimizing control strategy for maximizing the productivity in a fed-batch PHA process is explained. The objective of the optimizing control strategy is to keep the process operating at maximum productivity, while fulfilling the constraints. In order to assure the end-product specifications for the biopolymer, it is desirable to maintain the average number molecular weight inside a desired range of values. Therefore, the optimizing control is integrated with the ANN state estimator. Figure 5 shows the diagram of the control strategy, which includes the use of the developed ANN and the solution of the dynamic optimization problem through formulating the optimizing control problem. The manipulated variables in this process are the substrate and nitrogen-source feed flow rates.

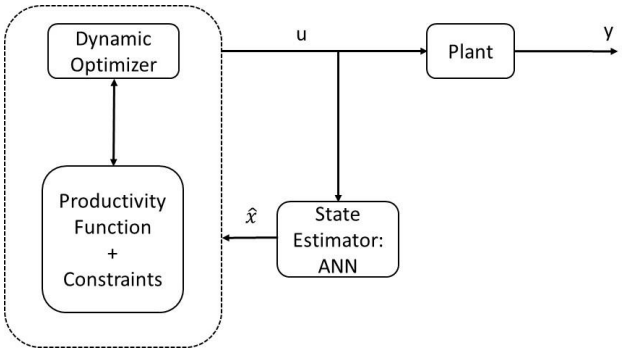

Figure 5. Advanced Control strategy: Optimizing Control + State Estimator

For solving the dynamic optimization problem, the so-called *control vector parameterization approach* was used (Banga et al. 2005). It is important to notice that different parameterizations of the control vector can be usedhaving different impact on the state variables, and therefore on the productivity. For this reason, four different feeding strategies were compared in this work: i) constant feed flow, ii) single

pulse, iii) piecewise constant, and iv) sinusoidal parameterization. .

For the piecewise constant parameterization, the feed flow rates are described by equations (10-11).

$$F_{1,2} = \sum_{j=1}^{m} a_{iok}\varphi(t_{i-1}, t_i)(u_{max} - u_{min}) + u_{min} \quad (10)$$

$$\varphi(t_{i-1}, t_i) = \begin{cases} 0, & t < t_{i-1} \\ 1, & t_{i-1} \le t < t_i \\ 0, & t \ge t_i \end{cases} \quad (11)$$

Where m=12 is the number of steps. u_{max}=0.3 and u_{min}=0 correspond to the maximum and minimum values for each step. The a_{iok} is the parameter that defines the control vector profile, and is therefore the decision variable of the dynamic optimization problem. For this specific case, this type of parameterization uses 12 parameters for each flow rate.

On the other hand, the sinusoidal parameterization of the feed flow rates was implemented as described by equation (12) (Ochoa 2016).

$$F_{1,2} = a_o + a_1 Cos\left(w_1\left(\frac{t-t_0}{t_f-t_0}\right) + \emptyset_1\right) + a_2 Cos\left(w_2\left(\frac{t-t_0}{t_f-t_0}\right) + \emptyset_2\right) \quad (12)$$

Where w_1, w_2 are the frequency, and $\emptyset_1$ and $\emptyset_2$ are the phase angle of the sinusoidal profile. For this specific case, this type of parameterization uses seven parameters for each flow rate.

The dynamic optimization problem is described in equation (15):

$$\underset{F_1(t), F_2(t), S_{in}, N_{in}}{Maximize} \; (P(t_f) * V(t_f)) \quad (15)$$

s.to. $F_1 \geq 0\left(\frac{L}{h}\right)$ (15a)

$0 \le F_2 \le 2\left(\frac{L}{h}\right)$ (15b)

$\max\left(S(t)\right) \le 90.11\left(\frac{g}{L}\right)$ (15c)

$\max\left(N(t)\right) \le 10.11\left(\frac{g}{L}\right)$ (15d)

$S_{in} \le 800\left(\frac{g}{L}\right)$ (15e)

$N_{in} \le 70\left(\frac{g}{L}\right)$ (15f)

$V \le 10L$ (15g)

Where t_f is the duration of the process. Constraints (15a-15b) take care of the maximum and minimum values allowable for F_1 and F_2, respectively. Max S and max N, are the maximum substrate and nitrogen-source concentrations allowed during the fermentation (i.e. for avoiding inhibition). S_{in} and N_{in} are the substrate and nitrogen-source concentrations in the feed flows F_1 and F_2, respectively. V is the fermentation volume.

The dynamic optimization problem expressed in (15) was solved at two different scenarios, in order to compare and to show the importance of including end-product specifications as part of the control problem during PHA production. The scenarios are, i) Optimizing control without constraints on Mn, and ii) Optimizing control with constraints on Mn.

4.1 Optimizing control without constraints on Mn

Figures 6 and 7 show the optimal F_1 and F_2 feeding profiles for each parameterization case, obtained by solving the dynamic optimization problem given by equation (15) where no constraints on Mn are used.

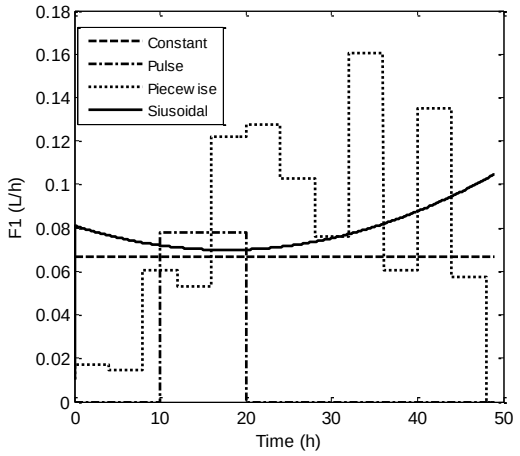

Figure 5. Optimal Feeding profiles for substrate (F_1)

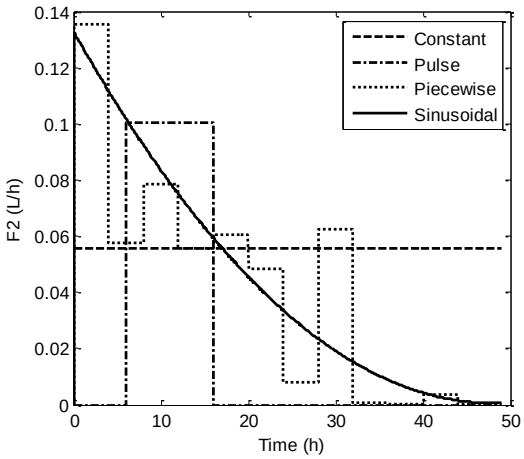

Figure 6. Optimal feeding profiles for nitrogen-source (F_2)

As it can be observed, the sinusoidal parameterization is a smooth strategy (i.e. avoids abrupt and sudden changes in the microorganisms environment), which helps reducing inhibitory effects on the microorganism. Inhibitory effects are more pronounced when the microorganism experiences a rapid increase on the substrate/ nutrient concentrations. Such rapid scenarios are more prompted to take place when step type policies (as for example, when the pulse or piecewise constant feeding policies are followed) are used.
Table 2 shows the productivity reached by applying the four kinds of profiles to the fed-batch PHA production.

Furthermore, the required nitrogen-source and substrate feed concentrations for keeping that productivity are shown. The constant and pulse feeding policies are usually used in practice due to the easiness of implementation. However, as results show in Table 2, these policies resulted in very low productivity values, when compared against the sinusoidal and piecewise constant policies. The sinusoidal feeding policy resulted in the higher productivity, followed by the piecewise constant. Furthermore, the computational time for solving the dynamic optimization by the sinusoidal parameterization was lower for the sinusoidal than for the piecewise constant (results not shown). This is due to the fact that the sinusoidal approach has a lower number of decision variables, which of course impacts the time for reaching an optimal solution. The lowest computational time was reached for the constant feeding policy, and the pulse strategy, respectively. The substrate and nitrogen-source concentrations on the feed are quite similar for all strategies, except for the single pulse.

Table 2. Feeding strategies comparison respect to productivity

Feeding Strategy	Productivity (g)	Nin (g/L) in F2	Sin(g/L) in F1
Constant	364.45	48.66	495.93
Pulse	183.61	38.44	790.59
Piecewise	402.90	43.37	448.52
Sinusoidal	405.17	42.35	463.61

As mentioned, the piecewise and sinusoidal feeding strategies reached higher productivity values by using a similar tendency in the feed rates. However, the abrupt changes on the feed flows calculated by the piecewise strategy could generate cellular stress due to the strong and rapid variations that take place on the microorganism environment, which is reflected on the substrate/nutrients concentrations on the culture media as shown Figure 7. Such stress will definitively affect the performance of the microorganism.

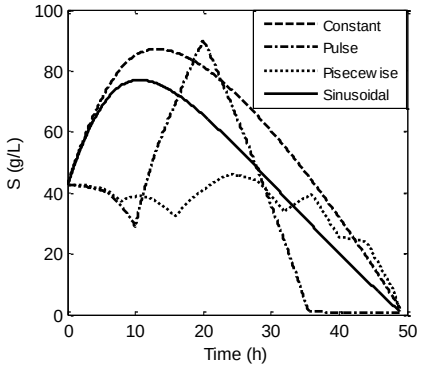

Figure 7. Substrate behavior due to the profiles F_1

Figure 8 shows the predicted number average molecular weight distribution (Mn) by the neural network (described in section 3), when the sinusoidal parameterization is used for the input flows F_1 and F_2 (profiles shown in figures 5 and 6)). As it is shown, the predicted Mn results in a finalvalue of $1x10^5$ if the optimizing control problem doesn´t consider constraints on the Mn which is a low value for industrial and commercial applications. Therefore, in the next section, implementation of the optimizing control including constraints on Mn is addressed.

4.2 Optimizing control coupled with constraints on Mn

Taking into account that the sinusoidal parameterization showed the best results in the previous case, such parameterization was used in the present scenario. The dynamic optimization problem is the same as in equation (15-15g) but including the following constraint on Mn (Gonzales García et al. 2013)

$$400000\left(\frac{g}{mol}\right) \leq Mn(t) \leq 2000000\ \left(\frac{g}{mol}\right) \qquad (16)$$

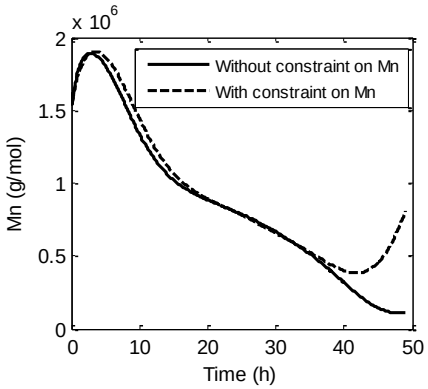

Figure 8. Optimizing control results for Mn: without and with constraint on Mn.

The objective is to keep Mn inside the desired range in order to obtain a polymer with adequate thermoplastic properties. Figure 9 show the feeding profiles that keep Mn at the desired range shown in Figure 8. It is important to notice that the final Mn is $8.07x10^5$ g/mol, which corresponds to values reported in the literature for PHA applications. Finally, the productivity reached was 369.13 g which is lower than in the previous case, but still fulfilling the required constraint on Mn.

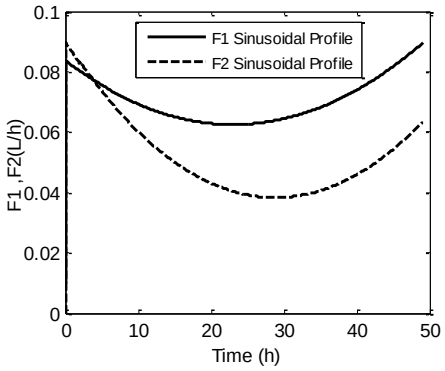

Figure 9. Carbon Source Profile F_1 and Nitrogen Source Profile F_2 with constrint in Mn

4. CONCLUSIONS

Advanced control strategies, as optimizing control, are essential tools that can be implemented in order to achieve maximal productivity and profitability in bioprocess applications. By applying the optimizing control concept coupled to a soft-sensor for the number average molecular weight it was possible to reach high profitability while keeping desired end-product specifications..

Sinusoidal parameterization has shown to provide higher productivity through the use of smooth feeding profiles that are suitable for avoiding cellular stress due to substrate shock. Furthermore, as such parameterization uses a lower number of parameters; the dynamic optimization problem was solved in a faster way.

Further work is now directed towards applying the optimizing control-ANN strategy developed here in a 500L pilot plant, for producing polyhydroxyalkanoates by using a mixture of vinasses/molasses as carbon source.

ACKNOWLEDGMENTS

Financial support from COLCIENCIAS through the project grant 669-2014 is gratefully acknowledged.

REFERENCES

Amicarelli, AN, Quintero, OL, di Sciascio, FA & Álvarez, HD 2008, 'Estudio Comparativo de técnicas para estimación de biomasa en bioproceso tipo batch', *XXIº Congreso Argentino de Control Automático*, Buenos Aires-Argentina.

Amicarelli, A, Quintero , & di Sciascio, 2014, 'Behavior comparison for biomass observers in batch processes', *ASIA-PACIFIC JOURNAL OF CHEMICAL ENGINEERING*, vol 94, pp. 81–92.

Banga, JR, Balsa-Canto, , Moles, CG & Alonso, AA 2005, 'Dynamic optimization of bioprocesses: Efficient and robust numerical strategies', *Journal of Biotechnology*, vol 117, no. 4, pp. 407–419.

Chatzidoukasa, C, Penlogloub, G & Kiparissides, 2013, 'Development of a structured dynamic model for the production of polyhydroxybutyrate (PHB) in Azohydromonas lata cultures', *Biochemical Engineering Journal*, vol 71, pp. 72– 80.

Dietrich, , Illman, & Crooks, 2013, 'Differential sensitivity of polyhydroxyalkanoate producing bacteria to fermentation inhibitors and comparison of polyhydroxybutyrate production from Burkholderia cepacia and Pseudomonas pseudoflava', *BMC Research Notes*, pp. 6-219.

Gonzales García, , MEZA CONTRERAS, JC, GONZÁLEZ REYNOSO, & CÓRDOVA LÓPEZ, JA 2013, 'Síntesis y biodegradación de Polihidroxialcanoatos: Plásticos de Origen Microbiano', *Rev. Int. Contam. Ambie*, vol 29, no. 1, pp. 77-115.

Keshavarz, T & Roy, I 2010, 'Polyhydroxyalkanoates: bioplastics with a green agenda', *Current Opinion in Microbiology*, vol 13, pp. 321-326.

Khanna , S & Srivastava, 2006, 'Optimization of nutrient feed concentration and addition time for production of poly(-hydroxybutyrate', *Enzyme and Microbial Technology 39*, vol 39, pp. 1145–1151.

Khanna, & Srivastava, AK 2005, 'A Simple Structured Mathematical Model for Biopolymer (PHB) Production', *Biotechnology Progress*, vol 21, no. 3, pp. 830-838.

Kumar, S & Ramkrishna, D 1996, 'On the solution of population balance equations by discretization--I. A Fixed Pivot Technique', *Chemical Engineering Science*, vol 51, no. 8, pp. 1311-1332.

Lee, G & Na, J 2013, 'Future of microbial polyesters', *Microbial Cell Factories*, pp. 12-54.

López , A, Bucalá , V & Villar, 2010, 'Application of Dynamic Optimization Techniques for Poly(β-hydroxybutyrate) Production in a Fed-Batch Bioreactor.', *Ind. Eng. Chem. Res.*, vol 49, pp. 1762–1769.

Ochoa, S 2016, 'A new approach for finding smooth optimal feeding profiles in fed-batch fermentations', *Biochemical Engineering Journal* , vol 105 , pp. 177–188.

Penloglou, G 2015, 'Personal Communication'.

Penloglou, , Roussos, A, Chatzidoukas, C & Kiparissides, C 2010, 'A combined metabolic/polymerization:kinetic model on the microbial production of poly(3-hydroxybutyrate)', *New Biotechnology*, vol 27, no. 4, pp. 1-10.

Penloglou, G, Chatzidoukas, C, Kiparissides, & xxx, X 2012, 'Microbial production of polyhydroxybutyrate with tailor-made properties: an integrated modelling approach and experimental validation.', *Biotechnology advances*, vol 1, no. 30, pp. 329-337.

Saliakas, , Chatzidoukas, C, Krallis, , Meimaroglou, & Kiparissides, 2007, 'Dynamic Optimization of Molecular Weight Distribution Using Orthogonal Collocation on Finite Elements and Fixed Pivot Methods: An Experimental and Theoretical Investigation', *Macromolecular Reaction Engineer*, vol 1, pp. 119–136.

Shahhosseini, 2004, 'Simulation and optimisation of PHB production in fed-batch culture of Ralstonia eutropha', *Process Biochemistry*, vol 39, pp. 963–969.

Sudesh, K, Abe, H & Doi, Y 2000, 'Synthesis, structure and properties of polyhydroxyalkanoates: Biological polyesters', *Progress in Polymer Science*, vol 25, pp. 1503-1555.

Wu, W, Lai, SY, Jang, F & Chou, 2013, 'Optimal adaptive control schemes for PHB production in fed-batch fermentation of< i> Ralstonia eutropha', *Journal of Process Control*, vol 8, no. 23, pp. 1159-1168.

Dissolved Oxygen Dynamic Model for Endospore-Forming Bacteria batch bioprocess

Adriana N. Amicarelli, Alex Alzate and Fernando A. di Sciascio

Instituto de Automática UNSJ - CONICET, Av. San Martín (Oeste) 1109 Argentina (Tel.: +54 264 4213303 / Fax: +54 264 4213672; e-mail: inaut@inaut.unsj.edu.ar).

Abstract: This paper extends and generalizes a model of Dissolved Oxygen (DO) dynamic developed for the δ - endotoxins of *Bacillus thuringiensis* (*Bt*) batch production process to a DO dynamical model that can be used for a broad class aerobic Endospore-forming Bacteria (AEFB). The most significant feature of this type of microorganism is the endospores generation in their life cycle. The generalization of the model allows to use the same parametric model structure for process control and state estimation purposes in a considerable variety of AEFB batch bioprocesses by selecting an appropriate set of parameters for each specific bioprocess.

Keywords: Bioprocess Model, Aerobic Endospore-Forming Bacteria (AEFB), Batch Process, Control Process, State Estimation.

1. INTRODUCTION

In a previous work (Amicarelli et al., 2010) the authors developed a dissolved oxygen (DO) dynamics model to complete a pre-existing model (Atehortúa et al., 2007) for the δ - endotoxins of *Bacillus thuringiensis* (*Bt*) batch production process. The inclusion of this dynamic is useful for control purposes since the dissolved oxygen in the culture medium is a key variable to maintain the aerobic microorganism population in adequate levels and conditions for the effectiveness of the fermentation process. This mentioned model was successfully considered in subsequent works to propose different DO control strategies through different approaches i) control based on **Lyapunov theory** (Amicarelli et al., 2010), ii) control based on **nonlinear dynamic inversion** (Rómoli et al., 2016), iii) **Predictive Control Based Model** (CPBM) (Alzate et al., 2016) and **classical controllers** as PID, PI. Is important also to mention that dissolved oxygen concentration can also be used for estimating the microorganisms concentration in the culture medium when the oxygen consumption for the microorganism is known (Amicarelli et al., 2015; A Amicarelli et al., 2014; di Sciascio & Amicarelli, 2008; Rómoli et al., 2016). As was mentioned early, model was initially developed for *Bt* batch fermentation but is possible to extend the use of this model for a more general class of microorganism named: Aerobic Endospore-forming Bacteria (AEFB). The Endospore-forming Bacteria (EFB) are microorganism as *Bacillus* and *Clostridium* that can survive in hostile environments by producing endospores and then rapidly germinating to vegetative cells and growth when they encounter favorable environmental conditions. *Bacillus* genus are Gram-positive, aerobic or facultative Endospore-forming Bacteria, that is, *Bacillus* are organism capable of growth in the presence of oxygen, and forms a type of resting cell called endospore. *Bacillus* is a large group, including *Bacillus cereus*, *Bacillus clausii*, *Bacillus halodenitrificans*, *Bacillus subtilis*, *Bacillus thuringiensis*, among others. *Bacillus* spores, also called endospores, are resistant to harsh chemical and physical conditions. *Clostridium*, *Sporolactobacillus* are group of anaerobic spore forming bacteria. *Clostridium* genus consists of more than a hundred known species such as *Clostridium perfringens*, *Clostridium botulinum*, *Clostridium difficile*, *Clostridium tetani* and *Clostridium sordellii*. *Clostridium thermocellum* are used commercially to produce ethanol, *Clostridium acetobutylicum* to produce acetone, and *Clostridium diolis* to convert fatty acids to yeasts and propanediol, among others. The processes that involve AEFB have two classes of cells: vegetative cells and sporulated cells. The proposed dissolved oxygen model (Amicarelli et al., 2010) allows estimating or quantifying how much oxygen is consumed for vegetative growth and for cell maintenance for *Bt* fermentations. When the EFB are in the vegetative state, their growth, as well as their substrate utilization and decay processes are almost the same as for common bacteria. When the culture medium exhibit nutritional limitation, the EFB sporulate (Atehortúa et al., 2006; Errington, 2003; Hoch, 1993; Sonenshein, 2000). In general, the bioprocess models available in literature normally include cellular dynamics: the main substrate and generation of product dynamics. However, dissolved oxygen is not considered as a part of the model. Nevertheless, it is feasible to include this dynamic since it can be easily measured online. Furthermore, this is a useful variable for the manipulation as control action of bioprocess.

In this work, the authors extend the use of the DO model for control and estimation purposes, to other batch bioprocess with similar characteristics with the aim to achieve other products. Example of bioprocess with other finalities can be

the production of biosurfactant by *Bacillus subtilis* (Davis et al., 2001; Yeh et al., 2006). The genus *bacillus* have general features that include the degradation of substrates derived from vegetal and animal sources including cellulose, starch, pectin, proteins, agar, hydrocarbons, and others; antibiotic production; nitrification; denitrification; nitrogen fixation; facultative lithotrophy; autotrophy; acidophily; alkaliphily; psychrophily; thermophily; and parasitism (Todar, 2006). Three microorganisms are currently in use for industrial riboflavin production. The *hemiascomycetes Ashbya gossypii*, a *lamentous fungus*, and *Candida famata* are naturally producers of this vitamin (Stahmann et al., 2000). Vitamins, C, B2 (riboflavin), vitamin B12, linolenic acid, and ergosterol are produced by the use of microorganisms. Gram positive bacteria, producing inhibitory substances like cyclic peptides and bacteriocins, with a broad antimicrobial spectrum and a history of safe use in food (Cleveland et al., 2001; Holzapfel et al., 1995). A relevant related paper is the work of Park, Rittmann, and Bae (Park et al., 2009) when it is developed a model called Life-Cycle Kinetic Model for Endospore – Forming Bacteria. This model includes Germination, Sporulation and dissolved oxygen dynamics. However, the expression and balances are impractical for control an estimation purposes due to their complexity and the difficulties to measure each involved variable online. Motivated in this fact, in the present work, the authors report the use of a simple parametric dynamic model for these objectives allowing better control of dissolved oxygen concentration in the culture medium of this class of bioprocesses.

This paper is organized as follows: Section 2 presents the model and it generalization for AEFB. Section 3 presents validations model through experimental data and model comparisons. Finally, in Section 4 conclusions are stated.

2. GENERALIZATION OF THE PROPOSED DISSOLVED OXYGEN DYNAMIC MODEL

The standard model for dissolved oxygen balance is:

$$\frac{dC_{DO}(t)}{dt} = K_L a\left(C_{sat} - C_{DO}(t)\right) - q_{O_2} X(t) \;= OTR(t) - OUR(t) \tag{1}$$

Where X is the total cells concentration, C_{DO} is the dissolved oxygen concentration, C_{sat} the oxygen saturation in equilibrium with the oxygen partial pressure of the gaseous phase, $K_L a$ is the volumetric oxygen mass transfer rate, and q_{O_2} is the net specific oxygen uptake rate. The first term in the second member is the rate of aeration or OTR (oxygen transfer rate from air bubble to liquid phase), and the second term is the rate of oxygen consumption by cells or OUR (oxygen uptake rate of cells per volume of broth).

The aeration term (OTR) can be written as follows (Amicarelli et al., 2010):

$$OTR(t) = K_{air} F_{air}\left(C_{sat} - C_{DO}(t)\right) \tag{2}$$

where K_{air} is an oxygen consumption parameter by growth (constant for each fermentation), and F_{air} is the inlet air flow rate that enters the bio-reactor. For a given bioreactor configuration, F_{air} is mainly a function of the impeller agitation speed. Based on experimental evidence (Atehortúa et al, 2007), it is assumed that the oxygen consumption rate (OUR) depends on the total cells X, that is, both vegetative and sporulated cells consume oxygen at different rates, therefore:

$$\mathrm{OUR}(t) = q_{O_2} X(t) \tag{3}$$

Because dissolved oxygen is considered as a second substrate q_{O_2} is:

$$q_{O_2} = \frac{\mu_X}{Y_{X/O_2}} = \frac{\mu_X}{Y^{\max}_{X/O_2}} + m_{O_2} \tag{4}$$

Where Y_{X/O_2} the observed biomass yield is based on oxygen consumed, $Y^{\max}_{X/O_2}$ is the true biomass yield based on oxygen used for growth, m_{O_2} is the oxygen consumption coefficient for respiration maintenance, and μ_X is the net specific growth rate of total cells.

$$\mathrm{OUR}(t) = q_{O_2} X(t) = \underbrace{\frac{\mu_X}{Y^{\max}_{X/O_2}} X(t)}_{\substack{O_2 \text{ consumption} \\ \text{for biomass growth}}} + \underbrace{m_{O_2} X(t)}_{\substack{O_2 \text{ consumption} \\ \text{for cell maintenance}}} \tag{5}$$

With the aim to define μ_X, from the total cells balance:

$$X(t) = X_v(t) + X_s(t) \tag{6}$$

where X_v is the vegetative cells concentration, X_s is the sporulated cells concentration and the vegetative cell balance:

$$\frac{dX_v(t)}{dt} = \underbrace{\mu X_v(t)}_{\text{Growth rate of vegetative cell}} - \underbrace{k_d X_v(t)}_{\substack{\text{death rate of} \\ \text{vegetative cell}}} - \underbrace{k_s X_v(t)}_{\substack{\text{sporulation rate of} \\ \text{vegetative cell}}} \tag{7}$$

where μ is the gross specific growth rate of vegetative cells, k_d is the relative death rate of vegetative cells, k_s is a kinetic constant representing the spore formation rate, and μ_v is the net specific growth rate of vegetative cells.

$$\mu_v = \mu - k_d - k_s \tag{8}$$

Operating with (6) and (7):

$$\begin{aligned}\frac{dX(t)}{dt} &= \frac{dX_v(t)}{dt} + \frac{dX_s(t)}{dt} = (\mu - k_d) X_v(t) \\ &= (\mu - k_d)\underbrace{\frac{X_v(t)}{X(t)}}_{f_v} X(t) = (\mu - k_d) f_v X(t) = \mu_X X(t)\end{aligned} \tag{9}$$

where f_v is a fraction of vegetative cells, then:

$$\mu_X = \frac{1}{X(t)}\frac{dX(t)}{dt} = \frac{d[\log X(t)]}{dt} = (\mu - k_d) f_v \tag{10}$$

$$k_d^{(n)} = k_{d_{\max}}\left(\frac{1}{1+e^{G_d(t_0+nT_0-P_d)}}\right) - k_{d_{\max}}\left(\frac{1}{1+e^{G_d(t_0-P_d)}}\right) \quad (11)$$

As was stated before, dissolved oxygen C_{DO} is considered a second limited growth substrate, therefore μ is modeled using a double Monod kinetic expression (Ryder & Sinclair, 1972).

$$\mu = \mu(S, C_{DO}) = \mu_{\max}\left(\frac{S(t)}{(K_S + S(t))}\frac{C_{DO}(t)}{(K_O + C_{DO}(t))}\right), \quad 0 \le \mu \le \mu_{\max} \quad (12)$$

Now, replacing (10) in (5) $\mu_X X(t) = (\mu - k_d) X_v(t)$ and taking into account that $X(t) = X_v(t) + X_s(t)$, we obtain:

$$OUR(t) = \left[\frac{\mu - k_d}{Y_{X/O_2}^{\max}} + m_{O_2}\right] X_v(t) + m_{O_2} X_s(t) = q_{O_2}^v X_v(t) + q_{O_2}^s X_s(t)$$
$$q_{O_2}^v = \frac{\mu - k_d}{Y_{X/O_2}^{\max}} + m_{O_2}, \quad q_{O_2}^s = m_{O_2} \quad (13)$$

Where $q_{O_2}^v$, and $q_{O_2}^s$ are the specific oxygen uptake rate for vegetative and sporulated cells respectively. Equation (13) shows explicitly that both vegetative and sporulated cells consume oxygen at different rates. This is a similar model to the model of oxygen uptake rate proposed by Park et al. (p. 1023, Equation (A.9)), (Park et al., 2009) for endospore-forming bacteria.

We now analyse if the net specific oxygen uptake rate q_{O_2} does become negative.

Taking into account that $0 \le \mu \le \mu_{\max}$, $k_d \ge 0$, $Y_{X/O_2}^{\max} > 0$, $f_v \ge 0$, and $m_{O_2} \ge 0$. Comparing (5) and (13) it is obvious that $q_{O_2} \ge 0$ if always $q_{O_2}^v \ge 0$ because $q_{O_2}^s = m_{O_2}$ is positive. Then, we analyze if $q_{O_2}^v$ does become negative.

$$q_{O_2}^v = \frac{\mu - k_d}{Y_{X/O_2}^{\max}} + m_{O_2} \ge 0 \;\rightarrow\; k_d - Y_{X/O_2}^{\max} m_{O_2} \le \mu$$

For *Bacillus thuringiensis* $q_{O_2}^v$ is positive because the inequality $0 \le k_d - Y_{X/O_2}^{\max} m_{O_2} \le \mu \le \mu_{\max}$ always holds, therefore q_{O_2} is also positive.

$$\begin{cases} Y_{X/O_2}^{\max} = 263.15 \\ m_{O_2} = 0.00073 \\ k_d = 0.1 \end{cases} \Rightarrow \mu \ge \underbrace{k_d}_{0.1} - \underbrace{Y_{X/O_2}^{\max} m_{O_2}}_{0.192} = -0.092$$

Alternatively, by replacing ($\mu_X X(t) = dX(t)/dt$) in (5), we obtain an equivalent model of oxygen uptake rate:

$$\text{OUR(t)} = \frac{1}{Y_{X/O_2}^{\max}}\frac{dX(t)}{dt} + m_{O_2} X(t) \quad (14)$$

This form of implementation of the oxygen consumption model has been widely reported in the literature; see the review by Garcia-Ochoa et al, 2010, p. 296, Equation (12) (Garcia-Ochoa et al., 2010), and references therein. This model form has also been specifically applied to modelling *Bacillus thuringiensis* oxygen uptake rate (Amicarelli et al., 2010; Ollis, 1983; Rowe et al., 2003).

The oxygen uptake rate models (5), (13), and (14) are mathematically equivalent. The model (13) was significantly more explanatory power than model (14), but from a computational point of view, the last one is better than the others. This is so, because the time-discretized model (15) is a linear difference equation with constant coefficients.

$$\text{OUR(t)} = \frac{1}{Y_{X/O_2}^{\max}}\frac{dX(t)}{dt} + m_{O_2} X(t) \;\xrightarrow[T_0]{}\; OUR^{(n)} = \left[\frac{1}{Y_{X/O_2}^{\max} T_0} + m_{O_2}\right] X^{(n)} - \frac{1}{Y_{X/O_2}^{\max} T_0} X^{(n-1)} \quad (15)$$

Consequently, the proposed model for Dissolved Oxygen Balance:

$$\frac{dC_{DO}(t)}{dt} = K_{air} F_{air}\left(C_{sat} - C_{DO}(t)\right) - \frac{1}{Y_{X/O_2}^{\max}}\frac{dX(t)}{dt} - m_{O_2} X(t) \quad (16)$$

3. VALIDATIONS AND EXPERIMENTATIONS

3.1 Data pre-processing

In this section, we will compare batch experiments of bacillus fermentations with the results achieved with the proposed model (16). The variables of the dissolved oxygen model are presented in Table 1 and the parameters values for *Bacillus thuringiensis* (*Bt*) are presented in Table 2. With the aim to generalize the model for others microorganism, there are tacked experimental data of batch fermentations of *Bacillus subtilles* (*Sb*) from the work of Park Park, Rittmann, and Bae (Park et al., 2009). The parameters values identified in this work for the dissolved oxygen model for *Sb* fermentations are presented in Table 3. The saturation concentration of oxygen (C_{sat}) is also a function of time, because the composition of the gas phase (in equilibrium with the liquid phase) varies with time. However, to simplify the model, the time dependency was not considered in the present formulation.

Table 1: Variables in the Dissolved Oxygen model

Symbol	Description
X	Total cell concentration $\left[g\ L^{-1}\right]$
C_{DO}	Dissolved oxygen concentration $\left[g\ L^{-1}\right]$
K_O	Oxygen saturation constant $\left[g\ oxygen\ L^{-1}\right]$
C_{sat}	Oxygen saturation concentration (DOC concentration in equilibrium with the oxygen partial pressure of the gaseous phase) $\left[g\ L^{-1}\right]$
Y_{X/O_2}	Observed biomass growth yield based on oxygen consumed $\left[g\ cells\ g\ oxygen^{-1}\right]$
$\frac{1}{Y_{X/O_2}^{\max}}$	Oxygen consumption constant by growth [dimensionless] $\left[g\ oxygen\ g\ cells^{-1}\right]$

K_{air}	Ventilation constant $\left[L^{-1}\right]$
$K_L a$	Volumetric oxygen mass transfer rate $\left[h^{-1}\right]$
q_{O_2}	Net specific oxygen uptake rate $\left[g\ oxygen\ \ g\ cells^{-1}h^{-1}\right]$
F_{air}	Inlet air flow rate that enters the bioreactor $\left[L\,h^{-1}\right]$
OTR	Oxygen transfer rate $\left[g\ oxygen\ \ L^{-1}h^{-1}\right]$
OUR	Oxygen uptake rate $\left[g\ oxygen\ \ L^{-1}h^{-1}\right]$
T_S	Sample time $\left[h\right]$
m_{O_2}	Oxygen consumption constant for maintenance [h^{-1}] $\left[g\ oxygen\ \ g\ cells^{-1}h^{-1}\right]$

Table 2: Parameters in the model for *Bt* fermentations

Symbol	Value
C_{sat}	0.00745
m_{O_2}	0.729 10^{-3}
$1/Y^{\max}_{X/O_2}$	3.795 10^{-3}
K_{air}	2.114 10^{-3}

Table 3: Parameters in the model for *Sb* fermentations

Symbol	Value
C_{sat}	0.0090
m_{O_2}	20.77 10^{-3}
$1/Y^{\max}_{X/O_2}$	6.2 10^{-3}
K_{air}	2.1

Agitation speed was set as high as possible to obtain better mass transfer between air bubbles and liquid. Obviously, a natural limit to this speed is the shear forces caused during liquid agitation; thus, the K_{air} value is obtained from DO experimental data at the nominal agitation speed (N= 400 rpm). The value of the air inlet flow was 1320 Lh^{-1}. The collected data from the B*t* fermentations is a set of measurements of biomass concentration and dissolved oxygen concentration. A sampling time Ts = 0.1 hours was selected by using Fourier frequency analysis. The biomass concentration data record must be increased to have the same experimental data record length as the dissolved oxygen concentration (approximately from 18 to 180 samples).

In this paper, Gaussian Process regression has been used as an imputation method for filling in the missing values (di Sciascio & Amicarelli, 2008), see Fig.1 and Fig.2 for *Bt* and *Sb* respectively. The collected data from the *Sb* fermentations is a set of biomass measurements and in the work of Park (Park et al., 2009) there are not reported experimental DO data in correspondence with the biomass concentration, despite of this, we compare the DO obtained by the model of Park and our model (see Figure 4).

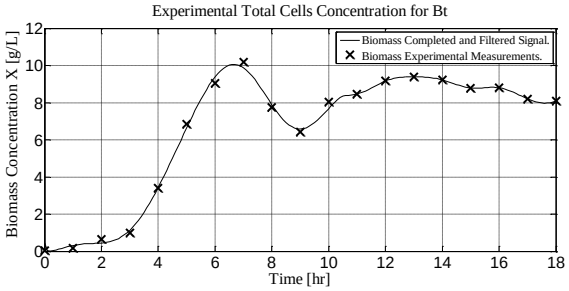

Fig 1. Experimental measurements of biomass concentration and completed filtered biomass for *Bacillus thuringiensis* fermentation.

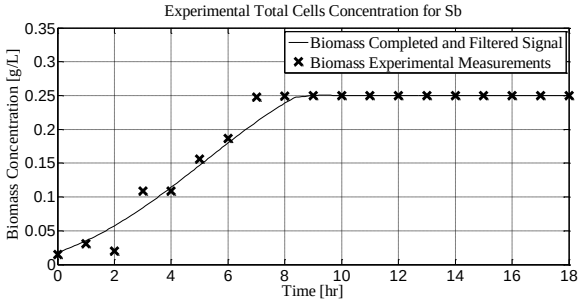

Fig 2. Experimental measurements of biomass concentration and completed filtered biomass for *Bacillus subtiles* fermentation (experimental data from (Park et al., 2009)).

3.2 Model Parameter Estimation for Sb fermentation.

The estimation of the dissolved oxygen model parameters m_{O_2}, $\frac{1}{Y^{\max}_{X/O_2}}$, and K_{air} for fermentations of *Bacillus thuringiensis* was developed in (Amicarelli et al., 2010). Now it is necessary to estimate the same parameters for *Bacillus Subtiles (Sb).* The proposed continuous DO dynamic model for a batch system is:

$$\frac{dC_{DO}(t)}{dt} = K_{air}F_{air}\left(C_{sat} - C_{DO}(t)\right) - \frac{1}{Y^{\max}_{X/O_2}}\frac{dX(t)}{dt} - m_{O_2}X(t) \tag{17}$$

The approximate discrete-time model of continuous-time dynamic model (17) is:

$$\frac{\left(C_{DO}(t_k) - C_{DO}(t_{k-1})\right)}{T_s} = -\frac{1}{Y^{\max}_{X/O_2}}\cdot\frac{\left(X(t_k) - X(t_{k-1})\right)}{T_s} - m_{O_2}\cdot X(t_k) + K_{air}\cdot F_{air\,in}\left(C_{sat} - C_{DO}(t_k)\right) \tag{18}$$

$$t_k = k\cdot T_s,\ 1\le k\le N,$$
$$C_{DO}(t_0) = C_{DO}(0),\ X(t_0) = X(0)$$

Operating algebraically with (18):

$$C_{sat}-C_{DO}(t_k)=\frac{1}{1+K_{air}\cdot F_{air\,in}\cdot T_s}\cdot\left(C_{sat}-C_{DO}(t_{k-1})\right)$$
$$+\frac{\frac{1}{Y^{\max}_{X/O_2}}}{1+K_{air}\cdot F_{air\,in}\cdot T_s}\cdot\left(X(t_k)-X(t_{k-1})\right)+\frac{m_{O_2}\cdot T_s}{1+K_3\cdot F_{air\,in}\cdot T_s}\cdot X(t_k) \qquad (19)$$
$$t_k=k\cdot T_s,\ 1\le k\le N,$$
$$C_{DO}(t_0)=C_{DO}(0),\ X(t_0)=X(0)$$

Notice that (19) can be written compactly in the following form:

$$\hat{y}(t_k|\boldsymbol{\theta})=\theta_1\varphi_1(t_k)+\theta_2\varphi_2(t_k)+\theta_3\varphi_3(t_k)=\boldsymbol{\theta}^{\mathrm{T}}\boldsymbol{\varphi}(t_k) \qquad (20)$$

This last equation (20) represents a discrete-time linearly parameterized model where:

$$\hat{y}(t_k|\boldsymbol{\theta})=C_{sat}-C_{DO}(t_k),$$
$$\boldsymbol{\varphi}(t_k)=\begin{bmatrix}\varphi_1(t_k)\\ \varphi_2(t_k)\\ \varphi_3(t_k)\end{bmatrix}=\begin{bmatrix}C_{sat}-C_{DO}(t_{k-1})\\ X(t_k)-X(t_{k-1})\\ X(t_k)\end{bmatrix},$$
$$\boldsymbol{\theta}=\begin{bmatrix}\theta_1\\ \theta_2\\ \theta_3\end{bmatrix}=\frac{1}{1+K_{air}\cdot F_{in}\cdot T_S}\cdot\begin{bmatrix}1\\ \frac{1}{Y^{\max}_{X/O_2}}\\ m_{O_2}\cdot T_S\end{bmatrix} \qquad (21)$$

A column vector $\boldsymbol{\theta}$ featuring the unknown parameters are the parameters vector, whereas $\boldsymbol{\varphi}(t_k)$ is the regression vector formed by known signals. From a set of N input-output experimental data, sampled at equally-spaced time intervals Ts, it is possible to estimate the parameters vector $\boldsymbol{\theta}$ and, there from the physical parameters estimates $\frac{1}{Y^{\max}_{X/O_2}}$, m_{O_2}, and K_{air} (see (21)). Then, the estimated parameters of the model are obtained directly from (21):

$$\boldsymbol{K}=\begin{bmatrix}\frac{1}{Y^{\max}_{X/O_2}}\\ m_{O_2}\\ K_{air}\end{bmatrix}=\begin{bmatrix}\frac{\theta_2}{\theta_1}\\ \frac{\theta_3}{\theta_1\cdot T_S}\\ \frac{1-\theta_1}{F_{air\,in}\cdot T_S\cdot\theta_1}\end{bmatrix} \qquad (22)$$

3.3 Model Results

The results obtained with the proposed model for the *Bt* and *Sb* fermentations are shown in Fig. 3 and 4 respectively. Results for *Bt* fermentations were previously reported and discussed in (Amicarelli et al., 2010). However, an example of the behavior represented by the model in (16) for *Bacillus thuringiensis* can be seen in Fig. 1. In the case of *Bacillus subtiles*, we considered the experimental results reported by (Park et al, 2009). With this information, we obtained the DO output values with our proposed model and we finally compared these results with the ones reports by Park et al. in Fig. 4.

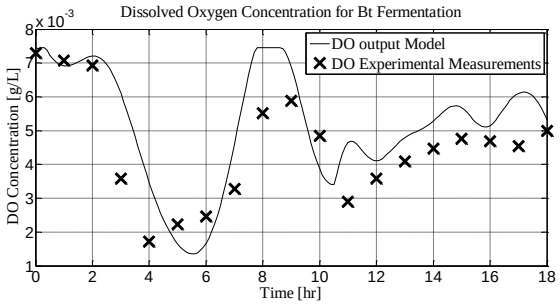

Fig. 3. DO Concentration Approximation Model for *Bacillus thuringiensis* fermentation.

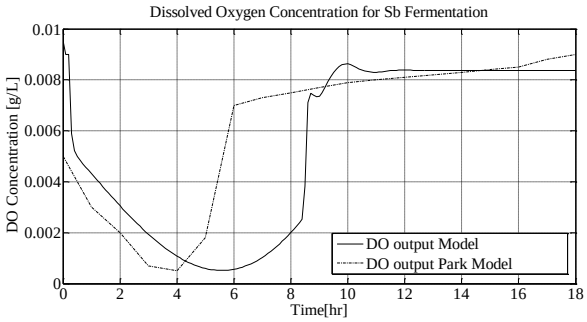

Fig. 4. DO Concentration Approximation Model for *Bacillus subtiles* fermentation.

With reference to Fig. 4, it can be observed that our DO model output adequately represent the dynamic behavior according to the considered biomass data. Oxygen consumption is evident during the first hours of fermentation (approximately 8 h) since the process is on the microorganism exponential growth stage. Next, the oxygen requirements decrease in the sporulation stage. Park's model predicts a DO level recovery two hours before (see Fig. 6). This is may be due to the affection of the others terms involved in such model. See, equation A.9 in (Park et al, 2009). It can be concluded that for practical aims and control purposes for the DO variable for this process. Our proposed model (16) satisfactory represents the behavior of *Bt* and *Sb* batch fermentations. Moreover, the model is based on the biomass values only. This is clear advantage when is compared with more complex models that require more variables, which are in many cases hard to obtain. Biomass data that can be sensed provided the specific sensors, o by a proper estimators design as proposed and validated in the previous papers: (di Sciascio & Amicarelli, 2008), (Adriana Amicarelli et al., 2014), (Amicarelli et al., 2015), (Rómoli et al., 2016).

4. CONCLUSIONS

This paper presented an extension or generalization of a dissolved oxygen dynamic model for batch fermentations. The generalization was performed from a particular previous model for *Bacillus thuringiensis* (Amicarelli et al., 2010) and was now extended for a more general class of aerobics microorganism named Aerobic Endospore-Forming Bacteria

(AEFB). This model generalization allows the scientific community to use the same model for control and state estimation purposes not only in *Bt* but also in a considerable variety of bioprocesses. The model was validated with experimental data of batch fermentations with *Bacillus Subtiles* and *Bacillus thuringiensis*. The model was also compared against more complex obtaining similar results, making easy its practical implementation for related applications.

ACKNOWLEDGMENT

The authors wish to thank the following organizations who contributed to the completion of this work: Universidad Nacional de San Juan (UNSJ, Argentina), and Consejo Nacional de Investigaciones Científicas y Técnicas (CONICET, Argentina).

REFERENCES

Alzate, A., Amicarelli, A., Gómez, L., & di Sciascio, F. (2016). Métodos de Quasi-Monte Carlo para el Cálculo de Conjuntos en Teoría de Conjuntos en Control. In Argencon 2016. Buenos Aires Argentina: IEEE Argentina.

Amicarelli, A., di Sciascio, F., Toibero, J., & Alvarez, H. (2010). Including dissolved oxygen dynamics into the Bt δ-endotoxins production process model and its application to process control. Brazilian Journal of Chemical Engineering, 27, 41-62.

Amicarelli, A., Montoya, L. Q., & di Sciascio, F. (2015). Substrate Feeding Strategy Integrated with a Biomass Bayesian Estimator for a Biotechnological Process. International Journal of Chemical Reactor Engineering, Accepted for publication.

Amicarelli, A., Quintero, O., & Sciascio, F. (2014). Behavior comparison for biomass observers in batch processes. Asia-Pacific Journal of Chemical Engineering, 9, 81-92.

Amicarelli, A., Quintero, O., & Sciascio, F. (2014). Behavior comparison for biomass observers in batch processes. Asia-Pacific Journal of Chemical Engineering, 9, 81-92.

Atehortúa, P., Álvarez, H., & Orduz, S. (2006). Comments on: "A Sporulation Kinetic Model for Batch Growth of B. thuringiensis". The Canadian Journal of Chemical Engineering, 84, 386-388.

Atehortúa, P., Álvarez, H., & Orduz, S. (2007). Modeling of growth and sporulation of Bacillus thuringiensis in an intermittent fed batch culture with total cell retention. Bioprocess and Biosystems Engineering, 30, 447-456.

Cleveland, J., Montville, T. J., Nes, I. F., & Chikindas, M. L. (2001). Bacteriocins: safe, natural antimicrobials for food preservation. International journal of food microbiology, 71, 1-20.

Davis, D., Lynch, H., & Varley, J. (2001). The application of foaming for the recovery of surfactin from B. subtilis ATCC 21332 cultures. Enzyme and microbial technology, 28, 346-354.

di Sciascio, F., & Amicarelli, A. N. (2008). Biomass estimation in batch biotechnological processes by Bayesian Gaussian process regression. Computers & Chemical Engineering, 32, 3264-3273.

Errington, J. (2003). Regulation of endospore formation in Bacillus subtilis. Nature Reviews Microbiology, 1, 117-126.

Garcia-Ochoa, F., Gomez, E., Santos, V. E., & Merchuk, J. C. (2010). Oxygen uptake rate in microbial processes: an overview. Biochemical engineering journal, 49, 289-307.

Hoch, J. A. (1993). The phosphorelay signal transduction pathway in the initiation of Bacillus subtilis sporulation. Journal of cellular biochemistry, 51, 55-61.

Holzapfel, W., Geisen, R., & Schillinger, U. (1995). Biological preservation of foods with reference to protective cultures, bacteriocins and food-grade enzymes. International journal of food microbiology, 24, 343-362.

Ollis, D. F. (1983). A Simple Batch Fermentation Model: Theme and Variations. Annals of the New York Academy of Sciences, 413, 144-156.

Park, S., Rittmann, B. E., & Bae, W. (2009). Life-cycle kinetic model for endospore-forming bacteria, including germination and sporulation. Biotechnology and Bioengineering, 104, 1012-1024.

Rómoli, S., Amicarelli, A., Ortiz, O., Scaglia, G., & di Sciascio, F. (2016). Nonlinear Control of the Dissolved Oxygen Concentration Integrated With a Biomass Estimator for Production of Bacillus Thuringiensis δ-Endotoxins. Computer & Chemical Engineering, Accepted for publication.

Rowe, G. E., Margaritis, A., & Wei, N. (2003). Specific Oxygen Uptake Rate Variations during Batch Fermentation of Bacillus thuringiensis Subspecies kurstaki HD-1. Biotechnology progress, 19, 1439-1443.

Ryder, D., & Sinclair, C. (1972). Model for the growth of aerobic microorganisms under oxygen limiting conditions. Biotechnology and Bioengineering, 14, 787-798.

Sonenshein, A. L. (2000). Control of sporulation initiation in Bacillus subtilis. Current opinion in microbiology, 3, 561-566.

Stahmann, K.-P., Revuelta, J., & Seulberger, H. (2000). Three biotechnical processes using Ashbya gossypii, Candida famata, or Bacillus subtilis compete with chemical riboflavin production. Applied Microbiology and Biotechnology, 53, 509-516.

Todar, K. (2006). Todar's online textbook of bacteriology: University of Wisconsin-Madison Department of Bacteriology.

Yeh, M.-S., Wei, Y.-H., & Chang, J.-S. (2006). Bioreactor design for enhanced carrier-assisted surfactin production with Bacillus subtilis. Process Biochemistry, 41, 1799-1805.

Nonlinear State Estimation for Batch Process with Delayed Measurements

Jhon A. Isaza * **Julián E. Rendón** ** **Juan Pablo Viana** ** **Héctor A. Botero** **

* *Faculty of Engineering and Architecture, Universidad Nacional de Colombia, Sede Manizales, Carrera 27 No 64-60, Colombia (e-mail: jaisazah@unal.edu.co)*
** *Department of Electrical Energy and Automatica, Universidad Nacional de Colombia, Sede Medellín, Carrera 80 No 65-223, Colombia (e-mail: jerendonr@unal.edu.co, jpvianav@unal.edu.co, habotero@unal.edu.co)*

Abstract: This paper presents a nonlinear state estimation subject to delayed measurement for the biomass in a batch bioprocess. The estimator scheme is based on an Extended Kalman Filter with state augmentation method to incorporate delayed measurements. A methodology to use the sample-state augmentation method is described. The proposed estimator is applied in the δ-endotoxins production of *Bacillus thuringiensis*. Simulation results show the feasibility of the proposed estimator.

Keywords: Batch Process, Extended Kalman Filter, Fixed Lag Smoothing, Delayed Measurements.

1. INTRODUCTION

The constant research and development in state estimation techniques have applications in electrical, electromechanical, navigation systems and now have been found a great potential for application in chemical and biotechnological processes (Mohd Ali et al., 2015). However, to achieve those practical applications is necessary to solve some problems from the academic field, such as the handling of nonuniform and delayed information.

For the handling of nonuniform and delayed information some authors have developed different methods in state estimation techniques (Gopalakrishnan et al., 2011; Guo and Huang, 2015; Guo et al., 2014; Patwardhan et al., 2012; Peñarrocha et al., 2012; Wang et al., 2012). The methods fall into two types: based on measurements fusion and based on augmented state. The based on measurement fusion method only applies to discrete systems and is designed for the Kalman filter and its variations. By contrast, the based on augmented state method retains the representation of the state space, making it more promising to facilitate its extension to different types of estimators. Furthermore, the conservation of the state space representation allows the subsequent analysis of features such as: convergence, observability and robustness.

However, in the mentioned papers the tools have been applied to specific problems, and therefore a few applications in batch bio-process with delayed measurement has been reported, except some cases with fed-batch bio-process without the dissolved oxygen dynamic (Zhao et al., 2015; Guo and Huang, 2015).

Therefore, this paper describes a methodology for incorporating delayed and multisampling measurements in nonlinear state estimation techniques, based in literature (Gopalakrishnan et al., 2011), to estimate the biomass in the batch production process δ-endotoxins of *Bacillus thuringiensis (Bt)* considering the dissolved oxygen concentration. As a technique of estimation a Filter Extended Kalman is used, however the methodology can be extended other to process.

The paper is organized as follows. In Section 2 the methodology for incorporate delayed measurement in estimation state techniques is described. Then in Section 3 is presented the mathematical model of δ-endotoxins production process of *Bt* followed by the estimator scheme based on a Extended Kalman Filter with sample-state augmentation method. The Section 4 presents simulation results of the estimation scheme for the δ-endotoxins production process of *Bt*. Finally, the conclusions of this paper are exposed in the Section 5.

2. METHODOLOGY FOR INCORPORATE DELAYED MEASUREMENT IN ESTIMATION STATE TECHNIQUES

2.1 Methods for incorporate delayed measurements

In a Supervisory Control And Data Acquisition (SCADA) system all information is stored discreetly, according the following assumptions:

Assumption 2.1. Sampling delays associated with online measurements are considered negligible compared to sampling delays associated with off-line measurements.

Assumption 2.2. The information obtained from the online sensors is more susceptible to problems of

noise and precision that obtained from laboratory or specialized equipment analysis. The first is subject to the characteristics of the signal conditioning system sensors. In the second, it is assumed strict adherence to high quality standards and metrology.

Assumption 2.3. The storage of offline information is subject to human error at check data to the SCADA system. Errors can be represented with spurious or missing data.

A characterization of phenomena occurring in the acquisition and storage of each source of information is presented in Figure 1.

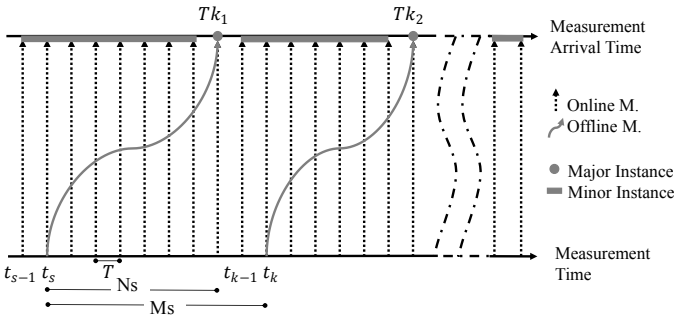

Figure 1. Characterization of phenomena occurring in the acquisition and storage of information sources. Source: modified by the author of (Guo and Huang, 2015).

In Figure 1, the lower horizontal line represents the time instants in which the measurements or sampling are performed. Moreover, the upper horizontal line represents time instant in which measurements are obtained and stored in the SCADA system. The straight, dashed and vertical lines represent the measurements online − obtained by the sensors −. It is noteworthy that these measurements are sampled with a sampling period fixed T and delay measurement is considered negligible. Offline measurements − obtained from the analysis of samples in laboratory or specialized equipment − are represented with a continuous and curve line. Note that each of the off-line measurements may have different measurement delays Tk_i, that is, the time between sample taken and measuring arrival $N_s = \delta + \tau_s$ is variant. M_s represents the time period between two successive samplings offline.

Moreover, to incorporate the different measurements on state estimation techniques two moments are presented: major instance and minor instance. Major instance refers to the moment in which both measures are available (online and offline). Minor instance refers to moment in which only available online measurement. When they used information sources with different characteristics, collateral problems such as: multi-sampling or asynchronism, missing and spurious data, redundant information, among others are presented (Guo and Huang, 2015; Guo et al., 2014).

In this sense, there are different methods to manage and incorporate nonuniform and delayed information in stochastic state estimation techniques. The methods can be classified into two types: fusing measurements and

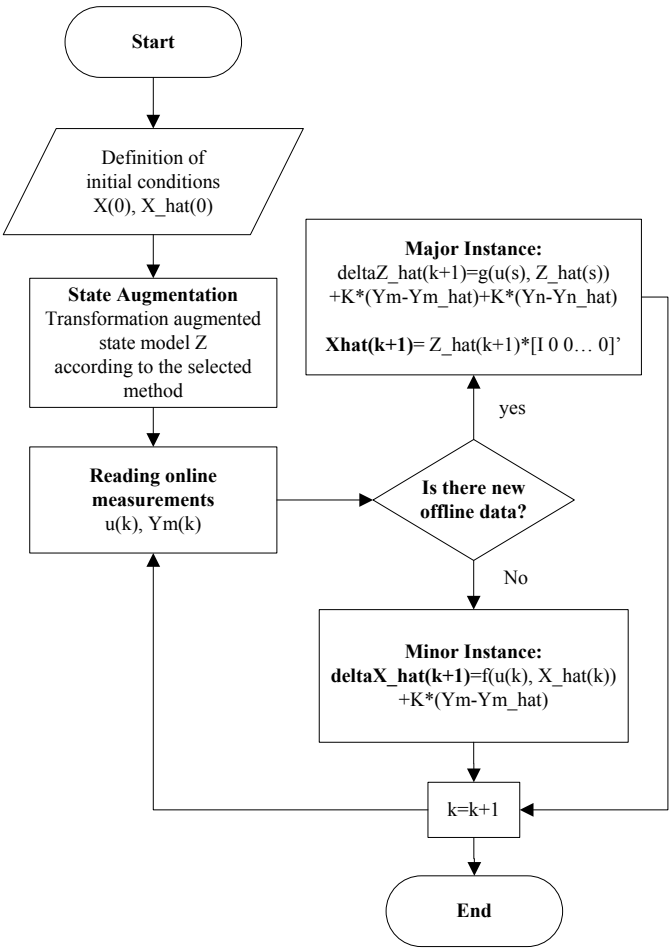

Figure 2. Flowcharts for programming algorithms by state augmentation methods. Source: Author's elaboration.

state augmentation (Gopalakrishnan et al., 2011; Guo and Huang, 2015; Guo et al., 2014; Patwardhan et al., 2012; Peñarrocha et al., 2012; Wang et al., 2012).

Fusing measurements method is based on the readjustment of the estimate in major instance. The readjustment of the present state is performed by recalculating entire trajectory of the Kalman filter (Prasad et al., 2002). The methods based on fusing measurements only applies to discrete systems and are conceived to the Kalman filter and its amendments (Alexander, 1991; Larsen et al., 1998).

On the other side, the augmented state method is based on increasing the state space with information of offline measurement and subsequently extended model is incorporated into the state estimation technique. As shown in the algorithm of Figure 2, in these methods is only modified the model and the representation of the state space is conserved. Because of this, these methods become favorable for its extension to different estimation and control techniques. In (Anderson and Moore, 2005) state augmentation is defined for fixed-lag smoothing method. In the Fixed-Lag Smoothing method, the N_s past states are smoothed based on online measurements of the minor instances. When offline and delayed measurement is obtained, both measurements (offline and online) are used to smooth out the state between s and $s + N_s$. Methods based on augmentation state, retains the state

space representation, favoring its extension to different types of estimators (Anderson and Moore, 2005; Simon, 2006) including deterministic estimation techniques.

2.2 Augmented state method

Next, a brief mathematical description of representing a linear system augmented state is presented based on (Gopalakrishnan et al., 2011).

Consider the following discrete-time linear system:

$$x(k+1) = A_k x(k) + B_k u(k) + \varepsilon(k) \tag{1}$$

for the system (1) nonuniform and delayed measurements can be represented as:

$$\begin{aligned} y^1(k) &= C_k^1 x_a(k) + v^1(k) \\ y^2(s) &= C_s^2 x_b(s) + v^2(s) \end{aligned} \tag{2}$$

where $x(k) \in \mathbb{R}^n$, $u(k) \in \mathbb{R}^l$ and $y^i(k) \in \mathbb{R}^m$ are states, inputs and outputs of the system respectively. $\varepsilon(k)$ and $v^i(k)$ correspond to uncertainty modeling and measurement noise respectively. A_k, B_k and C_k are the matrices representing the state space. Should be noted that the outputs $y^i(k)$ can be divided into online and offline measurements (time k and s, respectively).

Now, applying the concept of state augmentation, the order of the system can be increased such that contains the information of nonuniform and delayed measurements, as shown in Equation (3).

$$\begin{aligned} Z(k+1) &= \Phi_k Z(k) + \Gamma_k U(k) + \Psi_k \epsilon(k) \\ Y(k) &= \Xi_k Z(k) + v^1(k) \end{aligned} \tag{3}$$

where the matrices of the augmented state space Φ_k, Γ_k, $\Psi_k Q \Psi_k^T$ and Ξ_k are used in place of A_k, B_k, Q and C_k respectively. Using the fixed-lag smoothing method, the augmented state (4) and the augmented matrices (5) are defined as:

$$Z(k) = [x^T(k) \;\; x^T(k-1) \;\cdots\; x^T(k-Ns)]^T \tag{4}$$

$$\Phi = \begin{bmatrix} A_k & 0 & \cdots & 0 & 0 \\ I & 0 & \cdots & 0 & 0 \\ 0 & I & \cdots & 0 & 0 \\ \vdots & \ddots & \ddots & \ddots & \vdots \\ 0 & 0 & \cdots & I & 0 \end{bmatrix}; \Gamma = \begin{bmatrix} B_k \\ 0 \\ 0 \\ \vdots \end{bmatrix};$$
$$\Psi = \begin{bmatrix} I \\ 0 \\ 0 \\ \vdots \end{bmatrix}; \Xi = \begin{bmatrix} C_k^1 & 0 & \cdots & 0 & 0 \\ 0 & 0 & \cdots & 0 & C_s^2 \end{bmatrix} \tag{5}$$

This representation can be extended to nonlinear systems. Consider the following discrete-time nonlinear system with nonuniform and delayed measurements:

$$\begin{aligned} x(k+1) &= f(x(k), u(k), \varepsilon(k)) \\ y^1(k) &= h_1(x_a(k), v^1(k)) \\ y^2(s) &= h_2(x_b(s), v^2(s)) \end{aligned} \tag{6}$$

where f, h_1 and h_2 are nonlinear functions.

As in the expression (4), the concept of state augmentation can be applied, and redefine the matrix representation as follows:

$$Z(k) = [f(x(k), u(k))^T \;\; x^T(k-1) \;\cdots\; x^T(k-Ns)]^T \tag{7}$$

$$\Phi^* = \begin{bmatrix} F_k^* & 0 & \cdots & 0 & 0 \\ I & 0 & \cdots & 0 & 0 \\ 0 & I & \cdots & 0 & 0 \\ \vdots & \ddots & \ddots & \ddots & \vdots \\ 0 & 0 & \cdots & I & 0 \end{bmatrix}; \Xi = \begin{bmatrix} H_k^{1*} & 0 & \cdots & 0 & 0 \\ 0 & 0 & \cdots & 0 & H_s^{2*} \end{bmatrix} \tag{8}$$

where $F_k^* = \frac{\partial f}{\partial x}|_{(x(k),u(k))}$, $H_k^{1*} = \frac{\partial h_1}{\partial x}|_{(x(k),u(k))}$ and $H_s^{2*} = \frac{\partial h_2}{\partial x}|_{(x(s),u(s))}$, are the Jacobian matrices for the system (6).

This method results in smoothing of the past N_s states based on the online measurements at the minor time instance. When the delayed offline measurement arrives, both offline and online measurements are used to obtain smoothed estimates from s to $s + N_s$.

In this method, the representation of the state space is preserved, so the method can be applied with different state estimation techniques. Following the application of the methodology for estimating biomass in the δ-endotoxins production of *Bt* it is proposed. As state estimation technique a Kalman Filter Extended (KFE) is used.

3. STATE ESTIMATION IN A BATCH PROCESS MODEL WITH DELAYED MEASUREMENTS

The model of the δ-endotoxins production of *Bt* proposed on (Amicarelli et al., 2010, 2013; Rómoli et al., 2016) is used. In this paper the nomenclature of some parameters are modified. The model equations are:

$$\begin{aligned} \dot{s}_p &= -\left(\frac{\mu}{y_{x/s}} + m_s\right) x_v \\ \dot{o}_d &= K_3 Q_A \left(o_d^* - o_d\right) - \left[K_1 \dot{x}_T + K_2 x_T\right] \\ \dot{x}_v &= \left(\mu - k_s - k_e(t)\right) x_v \\ \dot{x}_s &= k_s x_v \end{aligned} \tag{9}$$

where s_p is the substrate concentration, o_d is the dissolved oxygen concentration, x_v is the vegetative cells concentration, x_s is the sporulated cells concentration, μ is the specific growth rate, $y_{x/s}$ is the growth yield, m_s is the maintenance constant, Q_A is the airflow that enters the bioreactor, o_d^* is the oxygen saturation concentration, K_1 is the oxygen consumption dimensionless constant by growth, K_2 is the oxygen consumption constant for maintenance, K_3 is the ventilation constant, k_s is the spore formation kinetics and $k_e(t)$ is the specific cell death rate.

Furthermore, the constitutive equations for μ (Monod-based), k_s and k_e are given by:

$$\begin{aligned} \mu &= \mu_{\max} \frac{s_p}{K_s + s_p} \frac{o_d}{K_o + o_d} \\ k_s &= k_{s,\max} \left(\frac{1}{1 + e^{G_s(s_p - P_s)}} - \frac{1}{1 + e^{G_s(s_{p,\mathrm{ini}} - P_s)}}\right) \\ k_e(t) &= k_{e,\max} \left(\frac{1}{1 + e^{-G_e(t - P_e)}} - \frac{1}{1 + e^{-G_e(t_{\mathrm{ini}} - P_e)}}\right) \\ x_T &= x_s + x_v \end{aligned} \tag{10}$$

where $\mu_{\max}$ is the maximum specific growth rate, K_s is the substrate saturation constant, K_o is the oxygen saturation

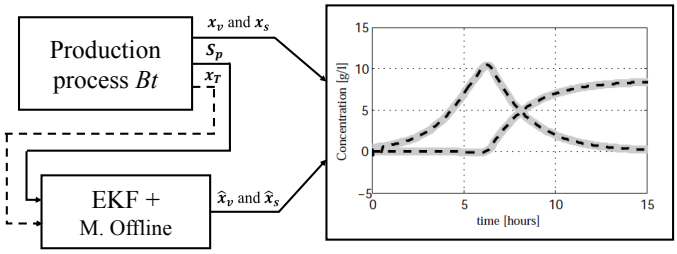

Figure 3. EKF scheme. Source: modified by the author of (Amicarelli et al., 2013).

constant,$k_{s,\max}$ is the maximum spore formation, $k_{e,\max}$ is the maximum specific cell death rate, G_s is the gain constant of the sigmoid equation for spore formation rate, G_e is the gain constant of the sigmoid equation for specific cell death rate, P_s is the position constant of the sigmoid equation for spore formation rate, P_e is the position constant of the sigmoid equation for specific cell death rate, $s_{p,\text{ini}}$ is the initial glucose concentration and t_{ini} is the initial fermentation time.

The nominal parameters for the system (9)-(10) are given in Table 1.

Table 1. Nominal Parameters of the *Bt* model.

Parameter	Values	Unit
$\mu_{\max}$	0.65	h^{-1}
$y_{x/s}$	0.37	$\text{g}\cdot\text{g}^{-1}$
K_s	3	$\text{g}\cdot\text{L}^{-1}$
K_o	1×10^{-4}	$\text{g}\cdot\text{L}^{-1}$
m_s	5×10^{-3}	$\text{g}\cdot\text{g}^{-1}\cdot\text{h}^{-1}$
$k_{s,\max}$	0.5	h^{-1}
G_s	1	$\text{g}\cdot\text{L}^{-1}$
P_s	1	$\text{g}\cdot\text{L}^{-1}$
$k_{e,\max}$	0.1	h^{-1}
G_e	5	h
P_e	4.9	h
K_1	3.795×10^{-3}	dimensionless
K_2	0.729×10^{-3}	h^{-1}
K_3	2.114×10^{-3}	L^{-1}
Q_A	1320	$\text{L}\cdot\text{h}^{-1}$
o_d^*	0.00759	$\text{g}\cdot\text{L}^{-1}$
t_{ini}	0	h
$s_{p,\text{ini}}$	32	$\text{g}\cdot\text{L}^{-1}$

Moreover for the estimation scheme proposed it is assumed that the measurement of the output s_p is online and the output x_T is offline (see in Figure 3). That is, the output s_p is sampled without delay and at the same rate of numerical solution of the EKF. Moreover, the output x_T is measured every M_s sampling times and also is obtained with a delay of N_s sampling times. In this paper it is used a common Extended Kalman Filter (EKF) of two steps. The equation (11) show the step of prediction and the equation (12) show the step of updating of the state respectively. However the methodology can be applied any extension of the Kalman filter.

$$\begin{aligned}\hat{x}\left(k|k-1\right) &= f\left(\hat{x}\left(k-1|k-1\right),k\right)\\ P\left(k|k-1\right) &= A\left(k\right)P\left(k|k-1\right)A^T\left(k\right)+Q\end{aligned} \tag{11}$$

$$\begin{aligned}\tilde{y}\left(k\right) &= y\left(k\right)-H\hat{x}\left(k|k-1\right)\\ K\left(k\right) &= P\left(k|k-1\right)H^T\left[HP\left(k|k-1\right)H^T+R\right]^{-1}\\ \hat{x}\left(k|k\right) &= \hat{x}\left(k-1|k-1\right)+K\left(k\right)\tilde{y}\left(k\right)\\ P\left(k|k\right) &= \left(I+K\left(k\right)H\right)P\left(k|k-1\right)\end{aligned} \tag{12}$$

As shown in the flowchart of Figure 2, during the minor instance, the gain of the Kalman filter K and the covariance matrix P are calculated with the linearized model without increasing state space of the system (9). Otherwise, during the major instance, are calculated with the linearized model of augmented state space (5) of the system (9). In the next section the simulation results are presented.

4. SIMULATION RESULTS

The numerical simulation results of the proposed estimation structure applied to a model of δ-endotoxins production of *Bacillus thuringiensis (Bt)* are presented in this section. All simulations presented here were conducted using the Euler integration method, with a fundamental step size of $0.1[h]$ for a total time of simulation of $15[h]$. The model parameters are shown on Table 1. The parameters shown in this table were taken according to the range to $20\,[\text{g}\cdot\text{L}^{-1}] < s_{p,\max} < 32\,[\text{g}\cdot\text{L}^{-1}]$ (Amicarelli et al., 2010). The value $s_{p,\max}$ corresponds to the initial condition of s_p since $\dot{s}_p \leq 0$. It is considered that the substrate s_p is measured online every $0.1[h]$. The total biomass x_T is measured offline with a delay interval measurement $N_s = 0.5[h]$ and successive sampling interval $M_s = 0.7[h]$. In addition, the initial time where the offline measurement is sampled is $s(0) = 0.1[h]$. In other words, in the minor instance it is only available the measurement of s_p and in the major instance the measurements of s_p and x_T is available.

The initial conditions for the model were selected to: $s_p(0) = 32\ [\text{g}\cdot\text{L}^{-1}]$, $o_d(0) = 0.74\times10^{-2}\ [\text{L}\cdot\text{h}^{-1}]$, $x_v(0) = 0.645\ [\text{g}\cdot\text{L}^{-1}]$ and $x_s(0) = 1\times10^{-5}\ [\text{g}\cdot\text{L}^{-1}]$; and for the EKF to: $\hat{s}_p(0) = s_p(0)\ [\text{g}\cdot\text{L}^{-1}]$, $\hat{o}_d(0) = o_d^*\ [\text{L}\cdot\text{h}^{-1}]$, $\hat{x}_v(0) = 10x_v(0)\ [\text{g}\cdot\text{L}^{-1}]$ and $\hat{x}_s(0) = 10x_s(0)\ [\text{g}\cdot\text{L}^{-1}]$.

Finally, initializing the elements of the matrices P, Q and R for the two filters (with and without delayed measurements) were empirically adjusted to obtain the best fit possible so that the results are comparable (see (13)-(16)).

$$P_{0|0} = diag\left(\left[10^{-1}\ 10^{-1}\ 10^{-1}\ 10^{-7}\right]\right) \tag{13}$$

$$Q = diag\left(\left[10^{-2}\ 10^{-2}\ 1\ 10^{-4}\right]\right) \tag{14}$$

$$R_1 = 1 \tag{15}$$

$$R_2 = 10^{-2} \tag{16}$$

Figures 4, 5, 6, 7 and 8 show the comparison between the actual variables x, and estimated variables $\hat{x}$ only with the on-line measurement and estimated variables with online and off-line measurements. In these figures *measured* means data simulations with noise and *real* means data simulations without noise. The figures corresponding to substrate concentration s_p, dissolved oxygen concentration o_d, vegetative cell concentration x_v and sporulated cells concentration x_s respectively.

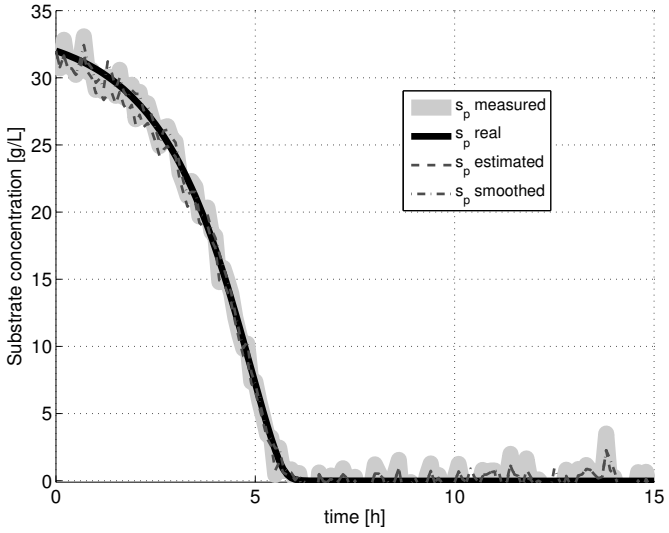

Figure 4. Substrate concentration s_p.

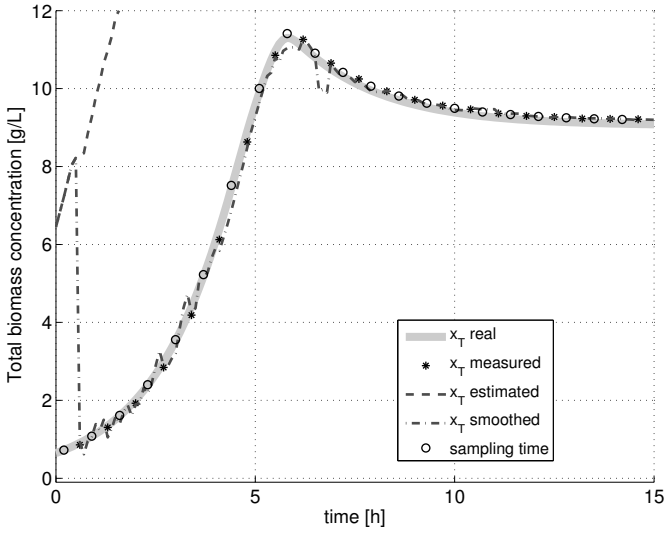

Figure 5. Total biomass concentration x_T.

In Figure 4 is possible to observe the correct estimation of the substrate concentration s_p, but this variable is not important to estimate because can be measured online. However, it is possible to notice the effect of filtering performed by the estimator in the variable s_p. In Figure 5, the EKF without off-line measurements produces an estimate that deviates from the actual value since the beginning, however, the EKF with offline measurements converges quickly when such measurement arrives. This tendency to converge continuing with each new additional off-line measurement. Additionally, Figures 6, 7 and 8 show a similar behavior is observed to the other estimated variables. In these figures, arrival times and sampling time of off-line measurement are detailed in order to visualize the effect of the off-line measurement in the EKF improved.

Finally, it was observed that it is possible to estimate the concentrations online in a batch process that includes the dynamic of dissolved oxygen concentration. The results can be used for monitoring, control or fault detection in batch processes.

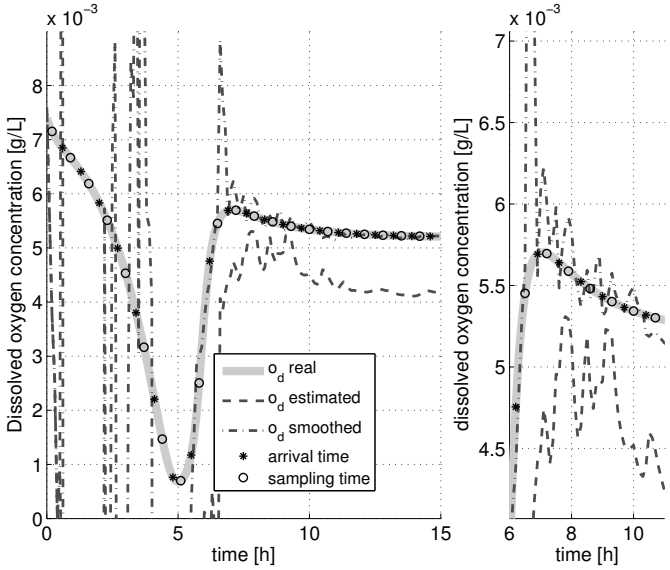

Figure 6. Dissolved oxygen concentration o_d.

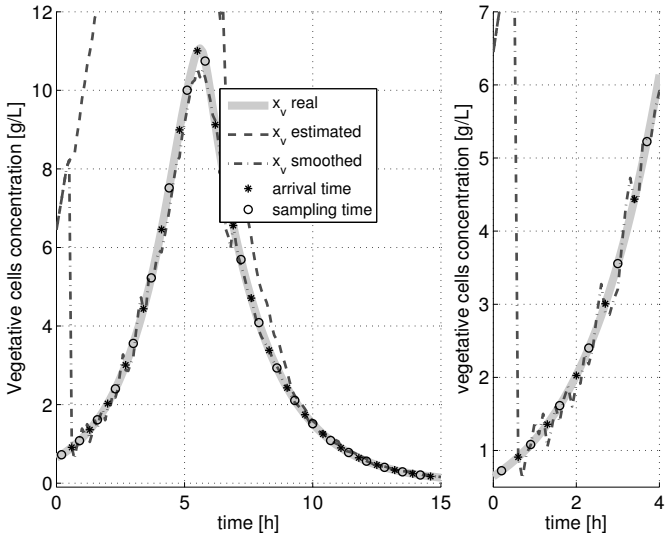

Figure 7. Vegetative cells concentration x_v.

5. CONCLUSIONS

In this paper was presented a nonlinear state estimation subject to delayed measurement for the biomass in a batch bioprocess including the dissolved oxygen dynamic. It was described the methodology for to use sample-state augmentation method. The proposed estimator was applied to the δ-endotoxins production of *Bacillus thuringiensis* and the incorporating of delayed measurements to EKF improved the performance of the estimate. Simulations show the feasibility of the proposed estimator.

REFERENCES

Alexander, H.L. (1991). State estimation for distributed systems with sensing delay. *Data Structures and Target Classification, SPIE*, 1470, 103–111. doi: 10.1117/12.44843.

Amicarelli, a., Di Sciascio, F., Toibero, J.M., and Alvarez, H. (2010). Including dissolved oxygen dynamics into

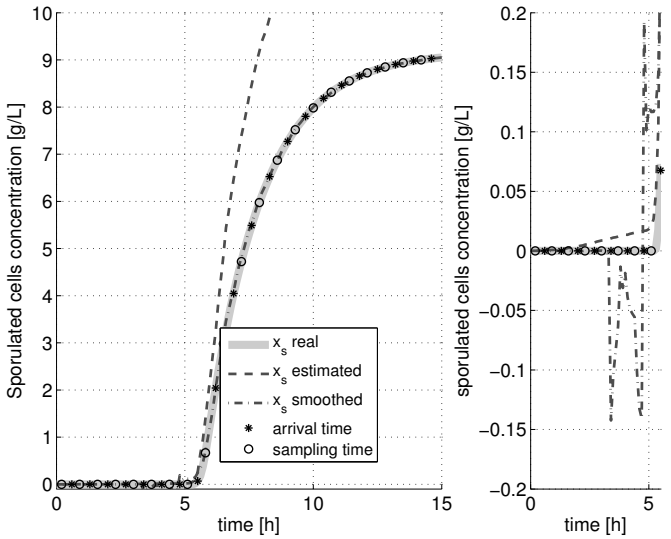

Figure 8. Sporulated cells concentration x_s.

the *bt* δ-Endotoxins Production process model and its application to process control. *Brazilian Journal of Chemical Engineering*, 27(1), 41–62.

Amicarelli, A., Quintero, O., and di Sciascio, F. (2013). Behavior comparison for biomass observers in batch processes. *Asia-Pacific Journal of Chemical Engineering*. doi:10.1002/apj.

Anderson, B.D.O. and Moore, J.B. (2005). *Optimal Filtering*. Dover Books on Electrical Engineering. Dover Publications.

Gopalakrishnan, A., Kaisare, N.S., and Narasimhan, S. (2011). Incorporating delayed and infrequent measurements in Extended Kalman Filter based nonlinear state estimation. *Journal of Process Control*, 21(1), 119–129. doi:10.1016/j.jprocont.2010.10.013.

Guo, Y. and Huang, B. (2015). State estimation incorporating infrequent, delayed and integral measurements. *Automatica*, 58, 32–38. doi:10.1016/j.automatica.2015.05.001.

Guo, Y., Zhao, Y., and Huang, B. (2014). Development of soft sensor by incorporating the delayed infrequent and irregular measurements. *Journal of Process Control*, 24(11), 1733–1739. doi:10.1016/j.jprocont.2014.09.006.

Larsen, T., Andersen, N., Ravn, O., and Poulsen, N. (1998). Incorporation of time delayed measurements in a discrete-time Kalman filter. *Proceedings of the 37th IEEE Conference on Decision and Control (Cat. No.98CH36171)*, 4(December), 3972–3977. doi:10.1109/CDC.1998.761918.

Mohd Ali, J., Ha Hoang, N., Hussain, M., and Dochain, D. (2015). Review and classification of recent observers applied in chemical process systems. *Computers & Chemical Engineering*, 76, 27–41. doi:10.1016/j.compchemeng.2015.01.019.

Patwardhan, S.C., Narasimhan, S., Jagadeesan, P., Gopaluni, B., and L. Shah, S. (2012). Nonlinear Bayesian state estimation: A review of recent developments. *Control Engineering Practice*, 20(10), 933–953. doi:10.1016/j.conengprac.2012.04.003.

Peñarrocha, I., Sanchis, R., and Romero, J. (2012). State estimator for multisensor systems with irregular sampling and time-varying delays. *International Journal of Systems Science*, 43(8), 1441–1453. doi:10.1080/00207721.2011.625482.

Prasad, V., Schley, M., Russo, L.P., and Wayne Bequette, B. (2002). Product property and production rate control of styrene polymerization. *Journal of Process Control*, 12(3), 353–372. doi:10.1016/S0959-1524(01)00044-0.

Rómoli, S., Amicarelli, A.N., Ortiz, O.A., Scaglia, G.J.E., and di Sciascio, F. (2016). Nonlinear control of the dissolved oxygen concentration integrated with a biomass estimator for production of Bacillus thuringiensis δ-endotoxins. *Computers & Chemical Engineering*, 93, 13–24. doi:10.1016/j.compchemeng.2016.05.017.

Simon, D. (2006). *Optimal State Estimation: Kalman, H, and Nonlinear Approaches*. doi:10.1002/0470045345.

Wang, W., Huang, X.h., and Wang, M. (2012). Survey of sequence measurement filtering algorithm. *Control and Decision*, 1, 2.

Zhao, L., Wang, J., Yu, T., Chen, K., and Liu, T. (2015). Nonlinear state estimation for fermentation process using cubature Kalman filter to incorporate delayed measurements. *Chinese Journal of Chemical Engineering*, 23(11), 1801–1810. doi:10.1016/j.cjche.2015.09.005.

Output-Feedback Model Predictive Control for Dissolved Oxygen Control in a Biological Wastewater Treatment Plant

Maribel Ruiz-Botero[*], **Manuel Ospina-Alarcon**[*]
Jose Garcia-Tirado[**]

[*] *Instituto Tecnológico Metropolitano, Facultad de Ingenierías, Grupo de Automática, Electrónica y Ciencias Computacionales. (e-mail: maribelruiz223350@correo.itm.edu.co, manuelospina@itm.edu.co).*
[**] *Instituto Tecnológico Metropolitano, Facultad de Ciencias Económicas y Administrativas, Grupo de Calidad, Metrología y Producción, Calle 73 No 76A - 354, 050034, Medellín - Colombia, (e-mail: josegarcia@itm.edu.co)*

Abstract: The biological wastewater treatment has become a major operation to maintain appropriate levels of organic matter in the wastewater to be discharged. This reduction of organic matter is performed by microorganisms, which require oxygen concentrations adequate to survive. Therefore, the oxygen dissolved control is a critical operation in the biological wastewater treatment plants. In this paper, the design of a coupled estimation and control strategy is presented for a biological wastewater treatment plant. The coupled estimation and control strategy is composed by a Kalman filter and a Model Predictive Controller (MPC). The results obtained showed that for disturbances nearby to the operating point, the estimated state converges to the actual state and the controller maintains the dissolved oxygen levels within a narrow range between 5.3 and 6.7$\frac{mg}{L}$ approximately.

Keywords: Dissolved oxygen, Kalman filter, model predictive control, biological wastewater treatment.

1. INTRODUCTION

Since 1960, terms such as air and water pollution started to be commonly used words. Before that date, these words went unnoticed by the average citizen Ramalho et al. (1990). Since then mankind has been continuously sensitized about the environment care, with cleaner production processes and rational use of water.

Each industrial process has special requirements regarding to the water quality. To remove such contaminants, the water is subjected to a purification treatment. The effluents of industrial wastewater must also meet minimum conditions to be discharged to the receptor stream. If water effluent does not meet the quality requirements, the stream should be recycled to the treatment plant until these requirements are fulfilled Lapeña (1989).

The secondary stage at the biological wastewater treatment refers to all biological processes either aerobics or anaerobic. This process is called activated sludge process and has been used either for the treatment of industrial or urban wastewater for about a century Ramalho et al. (1990).

Aeration is the process of mixing or dissolving air through a liquid or a substance. This operation of mass transfer is highly important in many industrial environments as well as in the biological wastewater treatment. The industrial and public services applications where aeration systems are found to range from volatile substances removal in liquid currents, subaquatic species culturing for food (industrial aquaculture), wastewater treatment and recombinant proteins design to diverse applications of biological processes where high amounts of enzymes, food, biomedical, and pharmaceutical products are produced.

The control of the dissolved oxygen (DO) concentration is a critical operation for guaranteeing the growth of a diverse group of microorganisms and multicellular organisms. This variable has a non-linear dependence of other variables such as the temperature of the culture medium, pH, biomass concentration, amount of foam among others. The most used procedure to guarantee the oxygenation of microorganisms is by means of aerators, which are basically bioreactors with an ascendant air flow (or pure oxygen flow) from the tank bottom. Main applications of aerators found in the literatures are biological wastewater treatment, general-purpose aerobic cell growth and the culturing of some multicellular organisms Åmand (2011); Amicarelli et al. (2010); Atia et al. (2011). In the case of biological treatment of wastewater, there are some aspects that difficult the DO control. First, oxygen mass transfer from gas to liquid phase is considered an activity of high energy consumption Åmand (2011). A precise tracking of operation trajectories must be taken into account, in order to avoid the cell death due to oxygen absence or cell stress inhibition by oxygen excess.

Sometimes, there is no inhibition by oxygen excess, but this operation represents cost overruns. In processes where obtaining a metabolite from cell growth, also death and inhibition phenomena are present due to absence or excess of oxygen, respectively. Moreover, production of secondary products (non-desirable products) have been reported, owing to limitations in oxygen mass transfer Åmand et al. (2013).

Due to of the importance of dissolved oxygen in the biological wastewater treatment plants and the difficulty of monitoring the main process variables a state estimator (Kalman filter) and a model-based control are presented in order to perform an output-feedback loop, as it is shown in Figure 1.

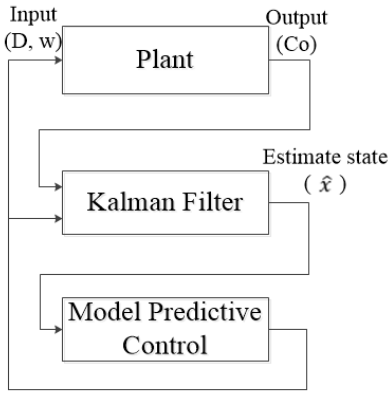

Fig. 1. Estimation and control scheme

The rest of the paper is as follows. In Section 2, materials and methods are presented in this section the mathematical model, state estimator design, and design of model predictive controller are presented. In Section 3 the results and discussion are presented. Final comments are presented in Section 4.

2. MATERIALS AND METHODS

2.1 Dynamic model of a plant for Biological Wastewater Treatment

The biological wastewater treatment is performed by a group of microorganisms called activated sludge, which is responsible for degrading organic matter. In Nejjari et al. (1999) a model for wastewater treatment plant is presented. The bioprocess is principally constituted by two sequential tanks, an aerator and a settler.

Figure 2 shows the process flow diagram of the biological wastewater treatment plant. This plant consists of an aerated treatment reactor at which the reduction of pollutants is performed from oxidation by the activated sludge. The liquid stream enters the tank, which consists of wastewater and recirculated activated sludge, and air stream, which enters the tank as bubbles through the diffusers. After the treatment with activated sludge, the water enters to a final clarifier, where the activated sludge and the treated water are separated. A part of the activated sludge stream is recycled from the clarifier to the aerated treatment reactor so that the microorganisms content in the reactor is maintained at an equilibrium, and the remainder effluent is discarded as waste sludge Moltzer (2008), Nejjari et al. (1999).

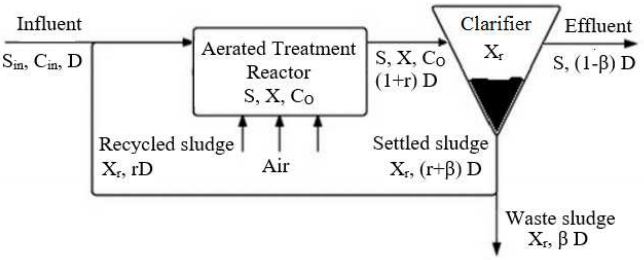

Fig. 2. Process flow diagram for a biological wastewater treatment plant. Adapted from Moltzer (2008)

The model is based on the following assumptions:

- The aerated treatment tank is considered to be perfectly mixed so that the concentration of each component is spacially homogeneous.
- Bioreaction does not take place in the clarifier.
- The sludge (biomass) is the only recycled component into the aerated treatment tank.

The model is represented for the Equations (1)-(4). These equations represent the balances of biomass (X), substrate (S), dissolved oxygen (C_o), and recycled biomass (X_r).

$$\frac{dX(t)}{dt} = \mu X(t) - D(t)(1+r)X(t) + rD(t)X_r(t) \tag{1}$$

$$\frac{dS(t)}{dt} = -\frac{\mu}{Y}X(t) - D(t)(1+r)S(t) + D(t)S_{in} \tag{2}$$

$$\frac{dC_o(t)}{dt} = -k_o\frac{\mu}{Y}X(t) - D(t)(1+r)C(t) + D(t)C_{in} + K_La(C_s - C(t)) \tag{3}$$

$$\frac{dX_r(t)}{dt} = D(t)(1+r)X_r(t) - D(t)(\beta+r)X_r(t) \tag{4}$$

$$\mu = \mu_{max}\frac{S(t)}{K_s + S(t)}\frac{C(t)}{K_c + C(t)} \tag{5}$$

In the paper presented by Nejjari et al. (1999) the dilution rate $D(t)$ and the oxygen transfer coefficient K_La are the manipulated variables. K_La is represented for $K_La = w\alpha$, where the variable parameter is the aeration rate (w) and α is the oxygen transfer rate. The parameters found in (1)-(5) and their assumed numerical values are presented in Table 1.

2.2 Linearized mathematical model

For the design of both the Kalman filter (KF) and the model predictive controller (MPC) a linearized discrete-time model is required. Therefore, in this Section the model linearization is presented. The discrete-time linearized model has the form in (6).

Table 1. Mathematical model parameters and values

Parameter	Name	Value
r	Ratio of recycled flow to influent flow	0.6
Y	Yield of cell mass	0.65
S_{in}	Substrate concentrations in the feed stream	$200\frac{mg}{L}$
K_o	Constant term	0.5
C_s	maximum dissolved oxygen concentration	$10\frac{mg}{L}$
C_{in}	Dissolved oxygen concentrations in the feed stream	$0.5\frac{mg}{L}$
β	Ratio of waste flow to influent flow	0.2
μ_{max}	Maximum specific growth rate	$0.15\frac{mg}{L}$
K_s	Affinity constant	$100\frac{mg}{L}$
K_c	Saturation constant	$2\frac{mg}{L}$
α	Oxygen transfer rate	0.018

$$\begin{aligned} x_{k+1} &= A_d x_k + B_{u_d} u_k + B_{d_d} d_k \\ y_k &= C_d x_k + D_d u_k \end{aligned} \tag{6}$$

where $x_k \in \mathbb{R}^n$ is the state, $u_k \in \mathbb{R}^m$ is the inputs, $w_d \in \mathbb{R}^l$ is the disturbances, $A_d \in \mathbb{R}^{n\times n}$ is the states matrix, $B_{u_d} \in \mathbb{R}^{n\times m}$ is the inputs matrix, $B_{d_d} \in \mathbb{R}^{n\times l}$ is the matrix showing the effect of the disturbance on the system, C_d is the output matrix, and D_d is the input incidence matrix regarding the output.

The linearization of the mathematical model was carried out in the following operating point:

Table 2. Operation point

Parameter	Value
States	
X	$177.69\frac{mg}{L}$
S	$56.66\frac{mg}{L}$
C_o	$5.61\frac{mg}{L}$
X_r	$355.38\frac{mg}{L}$
Inputs	
D	$0.1h^{-1}$
w	$80h^{-1}$
Disturbances	
S_{in}	$200\frac{mg}{L}$

The matrices A_d, B_{u_d}, B_{w_d}, C_d, and D_d of the linearized discrete model were obtained with a sampling time of $0.01h$ as

$$A_d = \begin{bmatrix} 0.9988 & 0.0008 & 0.0033 & 0.0006 \\ -0.0006 & 0.9972 & -0.0051 & -0.0000 \\ -0.0003 & -0.0006 & 0.9816 & -0.0000 \\ 0.0016 & 0.0000 & 0.0000 & 0.9992 \end{bmatrix}$$

$$B_{u_d} = \begin{bmatrix} -0.7100 & 0.0000 \\ 1.0924 & -0.0000 \\ -0.0843 & 0.0008 \\ -0.0006 & 0.0000 \end{bmatrix}$$

$$B_{w_d} = 1 \times 10^{-3} \begin{bmatrix} 0.0004 \\ 0.9986 \\ -0.0003 \\ 0.0000 \end{bmatrix}$$

$$C_d = [0\ 0\ 1\ 0]$$

$$D_d = [0\ 0]$$

The biomass and the substrate in biological wastewater treatment plants are difficult to monitor online, because the sensors available in the industry are expensive or nonexistent, so the measurements of these variables are performed offline. For this reason, the dissolved oxygen is considered as the only measurement variable online in biological wastewater treatment plants.

2.3 Kalman filter desing

The Kalman filter operates by propagating the mean and covariance of the state the over time. This filter is composed by three parts: the linear dynamic system equations, the initial condition of the *a priori* covariance of the estimation error, the Kalman filter gain, and the update equations Simon (2006).

Dynamic system equations

$$x_{k-1} = f_k(x_k, u_k, w_k) \tag{7}$$
$$x_k = h_k(x_k, v_k) \tag{8}$$
$$w_k \sim (0, Q_k) \tag{9}$$
$$v_k \sim (0, R_k) \tag{10}$$

Kalman filter initialization

$$P_k{}^- = A_{d_{k-1}} P_k{}^+ A_{d_{k-1}}^T + Q_{k-1} \tag{11}$$
$$K_k = P_k{}^+ C_{d_k}^T R_k^{-1} \tag{12}$$

Kalman filter equations

$$\hat{x}_k^- = A_{d_{k-1}} \hat{x}_{k-1}^+ B_{u_{d_{k-1}}} u_{k-1} \tag{13}$$
$$\hat{x}_k^+ = \hat{x}_k^- K_k (y_k - C_{d_k} \hat{x}_k^-) \tag{14}$$
$$P_k{}^+ = (I - K_K C_{d_k}) P_k{}^- \tag{15}$$

where x_k^- is the *a priori* estimate, P_k^- is the *a priori* covariance of the estimation error, x_k^+ is the *a posteriori* estimate, P_k^+ is the *a posteriori* covariance of the estimation error, K_k is the Kalman gain, $A_{d_{k-1}}$ is the states matrix, $B_{u_{d_{k-1}}}$ is the inputs matrix, Q_{k-1} is the model uncertainty, R_{k-1} is the measurement noise, C_{d_k} is the output matrix and y_k is the measurement.

Initial conditions and filter tuning

The Kalman filter design was performed using the linearized mathematical model presented in Subsection 2.2, adding the disturbance as a state in order to be estimated. The new mathematical model form is then Davison and Smith (1971):

$$\begin{aligned} x_{k+1} &= \begin{bmatrix} A & B_{d_d} \\ 0 & 1 \end{bmatrix} \begin{bmatrix} x_k \\ d_k \end{bmatrix} + \begin{bmatrix} B_{u_d} \\ 0 \end{bmatrix} u_k \\ y_k &= [C_d\ 0] \begin{bmatrix} x_k \\ d_k \end{bmatrix} + D_d u_k \end{aligned} \tag{16}$$

It turns out then

$$A_{d_{k-1}} = \begin{bmatrix} A_d & B_{d_d} \\ 0 & 1 \end{bmatrix}, \; C_{d_k} = [C_d \; 0], \; B_{u_{d_{k-1}}} = \begin{bmatrix} B_{u_d} \\ 0 \end{bmatrix}$$

The tuning matrices associated with the model uncertainty and the measurement noise, Q_{k-1} and R_k, respectively, were set as

$$R_k = 5 \tag{17}$$

$$Q_{k-1} = \begin{bmatrix} 5 & 0 & 0 & 0 & 0 \\ 0 & 5 & 0 & 0 & 0 \\ 0 & 0 & 5 & 0 & 0 \\ 0 & 0 & 0 & 5 & 0 \\ 0 & 0 & 0 & 0 & 5 \end{bmatrix} \tag{18}$$

The *a posteriori* covariance (P_k^+) was initialized as

$$P_0^+ = \begin{bmatrix} 60 & 0 & 0 & 0 & 0 \\ 0 & 60 & 0 & 0 & 0 \\ 0 & 0 & 60 & 0 & 0 \\ 0 & 0 & 0 & 60 & 0 \\ 0 & 0 & 0 & 0 & 60 \end{bmatrix} \tag{19}$$

In the simulation, the measurement noise is considered a white noise with zero mean and 0.01 variance.

2.4 Model predictive control design

The main elements of the model predictive control (MPC) are the prediction model, objective function, constrains, and receding horizon principle.

Prediction model

The prediction model selected for the design of the MPC is the linearized discrete model presented in the Subsection 2.2, whose structure is of the form:

$$\begin{aligned} x_{k+1} &= A_d x_k + B_{u_d} u_k + B_{w_d} d_k \\ y_k &= C_d x_k + D_d u_k \end{aligned}$$

Objective function

Cost function used for the MPC design is the used in the linear quadratic predictive control (LQPC) Garcia et al. (1989). The LQPC structure is presented in (20).

$$J(\Delta\tilde{u}, x_0) = \hat{x}_{N_p}^T P_c \hat{x}_{N_p} + \sum_{k=0}^{N_p} \hat{x}_k^T Q_c \hat{x}_k + \sum_{k=0}^{N_c} \Delta\tilde{u}_k^T R_c \Delta\tilde{u} \tag{20}$$

where J is the cost function, x_k is the state, u_k is the control signal, N_p is the prediction horizon, N_c is the control horizon, P_c is the weight matrix of the control signal, Q_c is the weight matrix of the states, and R_c is the weight matrix of the terminal state.

The optimization of the objective function was performed by using the optimization tool box MATLAB® by means of the *quadprog* command.

Constrains

The MPC design considered the following constraints on the manipulated variables:

$$\begin{aligned} 0.02h^{-1} \leq & D \leq 0.15h^{-1} \\ 0h^{-1} \leq & w \leq 300h^{-1} \end{aligned} \tag{21}$$

State constraints were not implemented since the state remained into safe and realistic values in the performed simulations. Nevertheless, state constraints may be included at any time with no major effort.

Initial conditions and controller tuning

The MPC design used a control horizon $N_c = 30$, and a prediction horizon $N_p = 60$.

Te weight matrices for the terminal state, state and inputs were set as follows.

$$P_c = \begin{bmatrix} 1 & 0 & 0 & 0 \\ 0 & 1 & 0 & 0 \\ 0 & 0 & 1000 & 0 \\ 0 & 0 & 0 & 1 \end{bmatrix} \tag{22}$$

$$Q_c = \begin{bmatrix} 1 & 0 & 0 & 0 \\ 0 & 1 & 0 & 0 \\ 0 & 0 & 1000 & 0 \\ 0 & 0 & 0 & 1 \end{bmatrix} \tag{23}$$

$$R_c = \begin{bmatrix} 1 & 0 \\ 0 & 0.1 \end{bmatrix} \tag{24}$$

The biggest weight was assigned to the dissolved oxygen state because the MPC purpose is to control the dissolved oxygen in the aerated treatment reactor.

3. RESULTS AND DISCUSSION

The results obtained by applying the controller and the estimator are presented below. The behavior of the MPC and the state estimator was evaluated under different disturbances. The considered disturbances were $250\frac{mg}{L}$, $300\frac{mg}{L}$, and $150\frac{mg}{L}$ of the substrate concentration in the feed stream. Simulations of the MPC coupled with state estimator were developed in the MATLAB® software version 2016a, using the Runge-Kutta numerical method with a fixed step of $0.01h$ during $500h$.

Figures 3 and 4 shows the system response with a disturbance of $250\frac{mg}{L}$ at the time $50h$. The former Figure present the response of the state to the disturbance and and the latter Figure presents the control actions and the disturbance estimation. In these Figures, it can be seen that the state estimator achieves the real state of the plant and the disturbance. Furthermore, it can be seen that the plant state change in the open loop regarding the status of the controlled plant. For the state X the steady state value of open loop plant is 21% superior to the state of the closed-loop plant. For the state S, the steady state value is 19% less than the state of the controlled plant. Similarly, the state X_r represents a steady state value of 14% higher with respect to the steady-state closed loop. The dissolved oxygen state presents oscillatory behavior because the rate of air intake to the treatment tank (w) presents sudden

changes between upper and lower restriction, as occurs with the dilution rate (D).

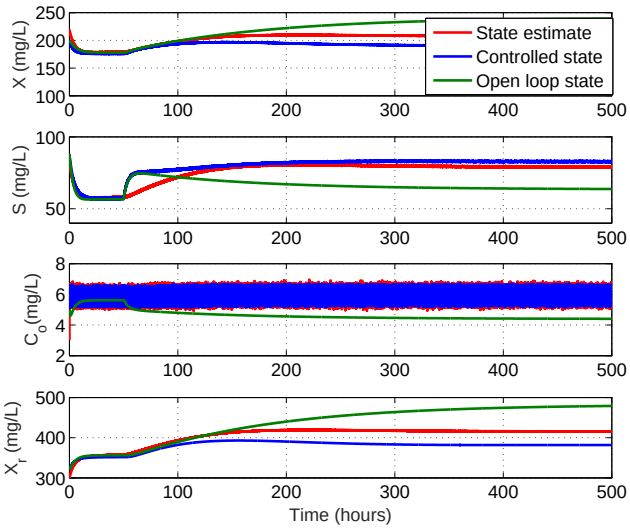

Fig. 3. State behavior with a disturbance of $250\frac{mg}{L}$ in the substrate concentration in the feed stream at the time $50h$

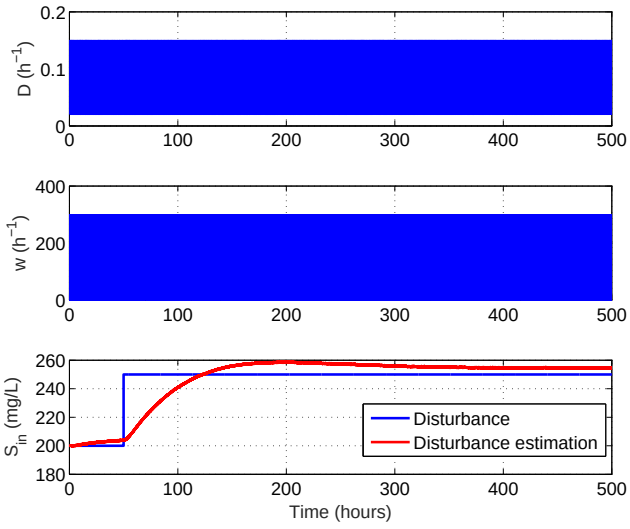

Fig. 4. Control actions and estimation disturbance ($250\frac{mg}{L}$)

The behaviors of the states with the different disturbances applied are similar (Figures 5 - 8). The biomass in the reactor and in the recycle stream in open-loop present a steady state value above than the steady state value of the closed-loop system. The substrate state presented a steady state value in open-loop below than the presented by the controlled system. The behavior of the state substrate in the closed-loop is due to that is presents lower production of biomass and recycled biomass, so that there is an insufficient concentration of microorganisms to be responsible for degrading the substrate.

Figures 5 and 7 shown the state behavior with a disturbance of $300\frac{mg}{L}$ and $150\frac{mg}{L}$, respectively. The first figure presents the biomass behavior, the second figure the substrate concentration behavior, the third figure the dissolved oxygen concentration behavior, and the final figure the recycled biomass concentration. Figures 6 and 8 present the control actions and the disturbance estimation for the plant with the aforementioned disturbances.

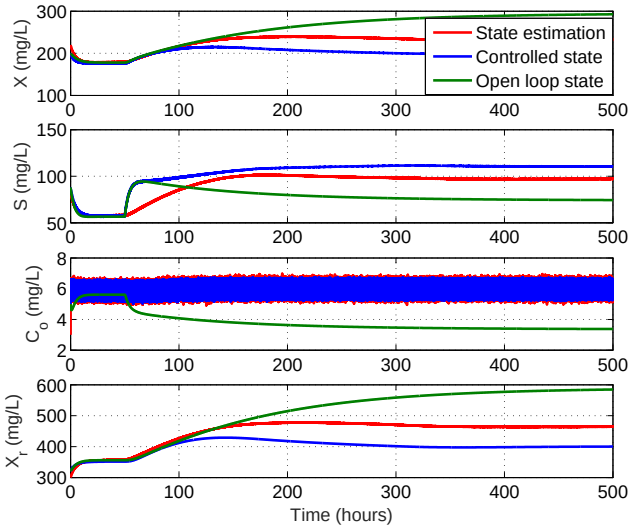

Fig. 5. State behavior with a disturbance of $300\frac{mg}{L}$ in the substrate concentration in the feed stream at the time $50h$

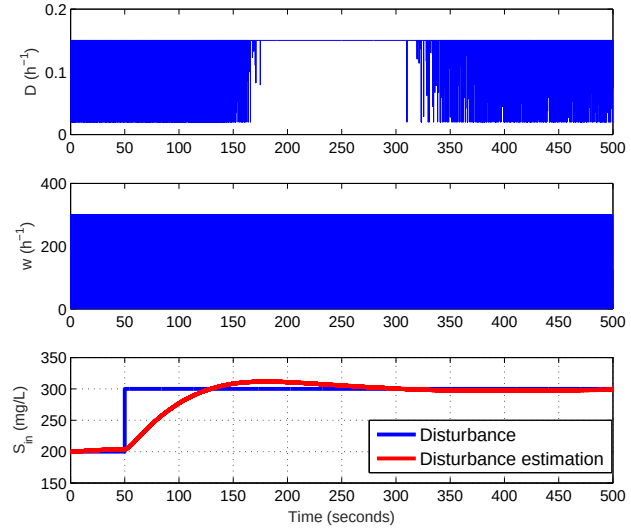

Fig. 6. Control actions and estimation disturbance ($300\frac{mg}{L}$)

In Figures 7 and 8, the estimator converges faster if compared to previous scenarios.

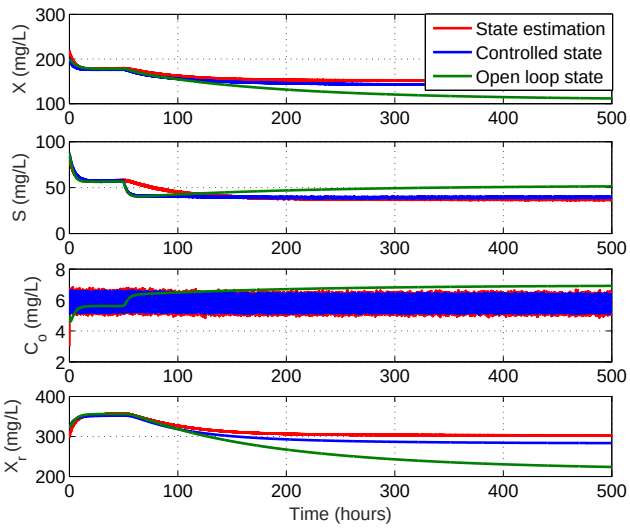

Fig. 7. State behavior with a disturbance of $150\frac{mg}{L}$ in the substrate concentration in the feed stream at the time $50h$

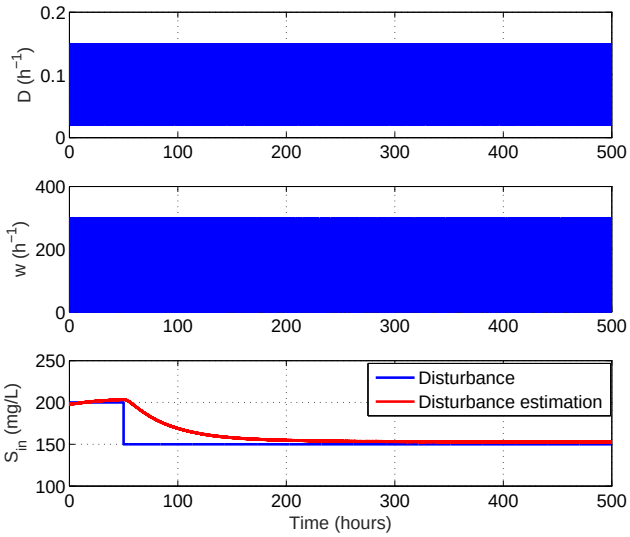

Fig. 8. Control actions and estimation disturbance $(150\frac{mg}{L})$

FINAL COMMENTS

According to the results, it can be concluded that the joint estimation strategy and control are suitable for controlling dissolved oxygen in biological treatment plants wastewater, because although oxygen has an oscillatory behavior was maintained between 5.3 and $6.7\frac{L}{mg}$ approximately. Given that the operating point for dissolved oxygen state is $5.61\frac{mg}{L}$, it can be said that the controller kept the concentration of dissolved oxygen at desired levels.

Due to the nonlinearity of the system as future work the design of a joint nonlinear strategy of estimation and control will be proposed, in order to obtain better performances both the estimator and the controller, and check the behavior of dissolved oxygen state it can be improved with this new strategy. Additionally, this new strategy could improve the oscillations in the control actions, causing these have a softer behavior.

REFERENCES

Åmand, L. (2011). Control of aeration systems in activated sludge processes–a review. *IVL Swedish Environmental Research Institute/Department of Information Technology, Uppsala University, Uppsala, Sweden.*

Åmand, L., Olsson, G., and Carlsson, B. (2013). Aeration control - A review. *Water Science and Technology*, 67, 2374–2398. doi:10.2166/wst.2013.139.

Amicarelli, A., Di Sciascio, F., Toibero, J.M., and Alvarez, H. (2010). Including dissolved oxygen dynamics into the Bt δ -Endotoxins Production process model and its application to process control. *Brazilian Journal of Chemical Engineering*, 27(01), 41–62.

Atia, D., Fahmy, F., Ahmed, N., and Dorrah, H. (2011). Design and Control Strategy of Diffused Air Aeration System. *World Academy of Science, Engineering and Technology*, (3), 666–670.

Davison, E. and Smith, H. (1971). Pole assignment in linear time-invariant multivariable systems with constant disturbances. *Automatica*, 7(4), 489–498.

Garcia, C.E., Prett, D.M., and Morari, M. (1989). Model predictive control: theory and practice—a survey. *Automatica*, 25(3), 335–348.

Lapeña, M.R. (1989). *Tratamiento de aguas industriales: aguas de proceso y residuales*, volume 27. Marcombo.

Moltzer, M. (2008). *Analysis of Robust Stability of Model Predictive Control for Biological Wastewater Treatment Plants.* Tesis de maestría, Eindhoven University of Technology, Eindhoven, Holanda.

Nejjari, F., Benhammou, a., Dahhou, B., and Roux, G. (1999). Non-linear multivariable adaptive control of an activated sludge wastewater treatment process. *International Journal of Adaptive Control and Signal Processing*, 13(May 1998), 347–365.

Ramalho, R.S., Beltrán, D.J., and de Lora, F. (1990). *Tratamiento de aguas residuales.* Reverté.

Simon, D. (2006). *Optimal state estimation: Kalman, H infinity, and nonlinear approaches.* John Wiley & Sons.

CHAPTER 5

GREEN PROCESS CONTROL

An Automated Indoor Low-Cost Greenhouse System for Research and Domestic Usage.

Adan Ruiz ** , **Mario Siller** *** , **Ofelia Begovich** ****

CINVESTAV Campus Guadalajara,
Electrical Engineering and Computer Science,
Zapopan, Jalisco, Mexico,
Av. del Bosque 1145, Col. El Bajio
** *(e-mail: aruiz@gdl.cinvestav.mx)*
*** *(e-mail: msiller@gdl.cinvestav.mx)*
**** *(e-mail: obegovi@gdl.cinvestav.mx)*

Abstract: This paper presents the design and implementation of an automated control system for a hydroponic testbed for "indoor domestic environments". This testbed is an indoor research system in which automatic control techniques, low-cost computational micro-controllers, and monitoring technologies are being explored for possible applications and deployments in low research budget and limited technology access. The goal of the system is to use automation techniques to improve crop productivity in scenarios in which even water is a scarce resource. The experimental low-cost facility at this point is focusing on control variables such as irrigation time, luminosity, temperature, and relative humidity.

Keywords: aeroponic, hydroponic, automation, control, greenhouse

1. INTRODUCTION

In the recent decades, the population is growing (UN (2004)) and have expanded the necessity to increment the food production, this has led to seek new alternatives for crop development such as indoor greenhouses. An indoor greenhouse is a small structure of glass or plastic containing plants, which can be installed into small spaces such as departments, offices, among others. Indoor farming is a new tendency around the globe, this is going to benefit communities, researchers, makers, hackers, students, any people and also the environment.

For a plant growth, it is necessary to create an environment which must have the appropriate weather conditions. For this reason, this paper presents the design and implementation of an "Automated Indoor Low-Cost Greenhouse (AILCG)" for domestic environments. This experimental low-cost facility at this point is focusing mainly in the best way to control variables such as irrigation time, luminosity, temperature and relative humidity.

There are many irrigation techniques, one of them is Hydroponics which consist in using a mineral-rich solution instead of soil (Jr. (2004)). In Hydroponics the roots obtain all nutrients necessaries for their growing. Besides, there is another irrigation technique called Aeroponic, this technique uses air and mist to provide nutrients to the plant roots, (Parker (2009)). The Hydroponics and Aeroponics irrigation techniques provide water savings, as well provides nutrients to the roots of the plants in an efficient manner, also these techniques may be used in indoor greenhouses. For the AILCG, both irrigation techniques are applied, as it will be seen later.

The research focus is control automation, and the architecture and design of the Information and Communication Technology (ICT) infrastructure. This includes system modeling, computational techniques and algorithms. Previous works for monitoring and control system for greenhouses are described in Putter and Gouws (1996), Bhutada et al. (2005), Schempf et al. (2001). A related project, for indoor farming, is the Personal Food Computer (PFC) which is an agriculture technology platform which is being used around the world (Harper and Siller (2015)).

In this work, there are several control variables considered such as the lighting for plants, temperature, humidity, with this testbed further research may be possible, by example: find better strategies to provide light to the plants.

There is a wide availability of electronic devices that can handle the AILCG sensors data such as micro-controllers, Field Programmable Gate Array (FPGA) devices, digital signal processors, PLC devices, credit card sized computers, among others. For this work, we have chosen to use a microcontroller "Arduino™ UNO based board" due the low-cost, which is near to $20 USD, this is cheaper than a PLC or an FPGA; the community support; the already developed gadgets and libraries; among other advantages cited in Badamasi (2014).

⋆ The authors would like thanks to CONACYT for the PNPC program, also thanks to Adrian Lizaray, Christian Lopez, Raul Gil and Bernardo Camacho from "Universidad Politecnica de Sinaloa" for their cooperation in this project during their scholar residence program. Finally, we give thanks to Jorge Urbina and Angel Moreno by their revision of this paper.

Micro-controllers are used to recollect data from the sensors, process information (using pre-programmed functions) and provide an output to perform an action (e.g. actuators). In this work, sensors provide information about the environment in which the crops are, this allows to collect data about the different crop phases of experimentation and provide an action through the actuators.

The proposed AILCG considers a "Light-Emitting Diode (LED)" control, the sun photo-period, different irrigation techniques control, water aeration control, and climate condition control to provide the needed tools to perform research and hence obtain a healthy plant growing.

This paper is organized as follows, Section 2 is about the AILCG as the whole, in Section 3 the control system is described, Section 4 results are shown and finally, conclusions are stated.

2. AUTOMATED INDOOR LOW-COST GREENHOUSE

The AILCG is able to cultivate plants and produce food by using 3w LED lights at 660nm (red light) and 445nm (blue light) as an alternative to sunlight (Chang and Chang (2014) and Son and Oh (2013)); a 1/4 HP water pump; several sensors and micro-controllers are used to manipulate information and actuators.

The AILCG control is based on a process of reading, sending and receiving data from the sensors using an Arduino^{TM} UNO in addition with an ethernet shield for internet access. Arduino^{TM} is an open-hardware platform designed to facilitate the use of electronics in multidisciplinary projects.

2.1 System Requirements

Some variables that influence the plant development are temperature, relative humidity, light, irrigation, and water pH.

Temperature. Is beneficial for the plants, have a temperature difference between day and night temperatures (Mohr and Schopfer (2010)), also the solution temperature is important. More information about temperature for lettuce experiments is found in Thompson et al. (1998).

pH Concentration. This value is important for plants to absorb the nutrients, pH is not the same for soil culture (organic substrate) and hydroponics (cultivation in inert substrates). The vast majority of irrigation water must be optimal pH, Domingues et al. (2012).

Ventilation. The greenhouses always should have adequate ventilation, there is a relationship between plants-space and ventilation power. Plant respiration is through their leaves, if ventilation is not adequate, the pores of the leaves will obstruct and the leaves will die. Related works to ventilation can be found in Boulard and Draoui (1995), Muñoz et al. (1999), Casas-Carrillo et al. (2015), among others.

Water aeration. The presence of oxygen in water is essential for the proper development of plant roots. The lack of oxygen is called anoxia, this causes that the root development begins a premature degradation of the roots, reaching, in extreme cases, the death of plants (Mustroph and Albrecht (2003)).

2.2 Description of the AILCG

The Figure 1 shows physical design scheme of the built AILCG as it can be seen, the structure is divided into five different tray-levels, each of them has a purpose, function and/or different works. The tray-levels are Level 0, Level 1, Level 2, Level 3 and Level 4. The AILCG is composed of a rack where there are two different types of hydroponic crops and a piping circuit for recirculating the nutrient solution through the system. At the Level 0

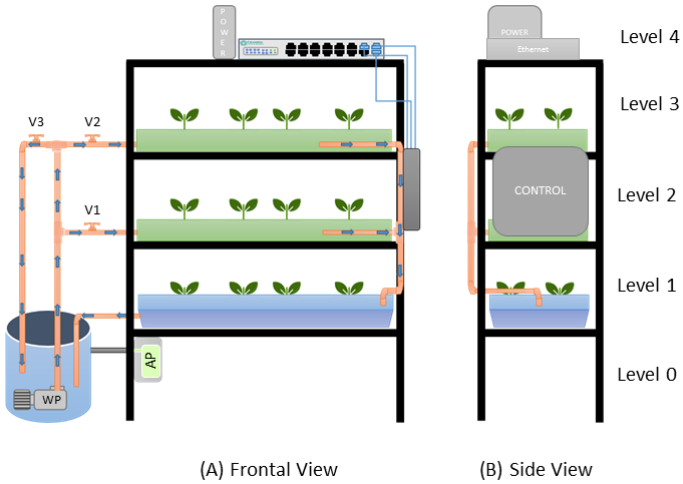

Fig. 1. AILCG Physical Design.

is located the water reservoir, which contains the nutritive solution of the plants, also the air and water pumps are found here, the last one is a submersible water pump. At Level 1 is located the first type of hydroponic technique, this is based on water culture system. At Level 2 is located another container for crop development, using an aeroponic technique, also at this tray-level is located the control box where all the sensor information is collected and is logged into a database server (MySQL database 5.6.23 running on Intel Xeon E5-2403 1.8 GHz processor, 32GB RAM) for the late information processing. At Level 3 is located the last crop, this has the same characteristics as the crop found at the second tray-level.
The power supply is located at Level 4 of the entire AILCG (control system, water and air pumps, lighting system), also there is an ethernet network switch 10/100 which is connected to the internet network, this switch allows the connection to the micro-controllers located in the control system. Those micro-controllers are able to send and receive information over the Internet using an ethernet shield.

2.3 Operation of the System

When the pump is turned on, the solution begins to flow through the pipe system to tray-levels 2 and 3, see Figure 1. The V1 and V2 valves are utilized to regulate the flow of water entering at both tray-levels, while the valve V3

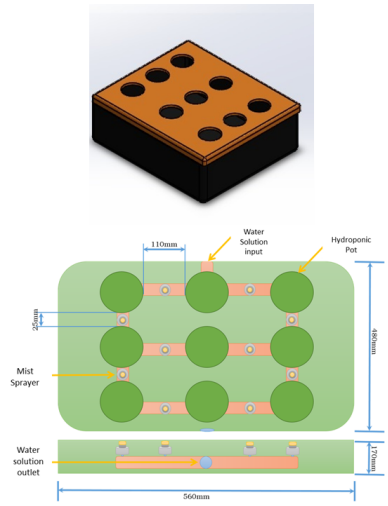

Fig. 2. Physical Design Diagram of Aeroponic Cultivation Bed.

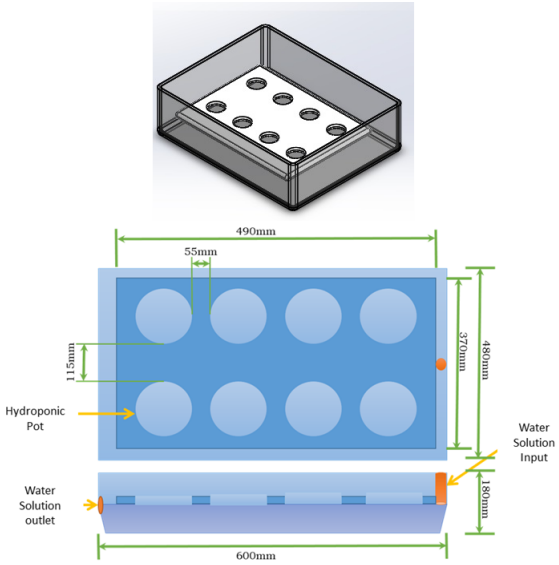

Fig. 3. Physical Design Diagram of Hydroponic Cultivation Bed.

regulates the excess flow to the container.
The nutrient solution is driven by the water pump to tray-levels 2 and 3, where nebulizers are driving out the atomized solution continuously to watering the roots of the plants. The water that is not absorbed by the crop, falls to Level 1 using drain pipes. In order to avoid the water overflow at Level 1, the amount of input water must be slightly less or equal to the amount of the output water, this allows that crops in Level 1 to receive recycled water. Also, the water overflow in Level 1 is driven to the reservoir water. The reservoir water is oxygenated using an air pump, this ensures that the entire crops will receive oxygenated water. Note that, the same cycle repeats, recirculating the water through the piping system, so the loss of solution is reduced.

Aeroponic Cultivation Bed. The cultivation beds, at tray-levels 2 and 3, have ten nebulizers each of one, which are responsible for spraying the solution to the plant roots. The solution flows through the pipes and is delivered to the crop. Also, there is an outlet to recirculate the solution. The aeroponic cultivation bed was made of styrofoam (expanded polystyrene). A sketch of aeroponic cultivation bed is shown in Figure 2.

Hydroponic Cultivation Bed. This cultivation bed, at Level 1, is designed to get the solution of the aeroponic crops (tray-levels 2 and 3) that they did not use. The nutrient solution which leaves from the cultivation bed is renovated in the reservoir where it will be oxygenated again, hence the anoxia in crops is avoided. This kind of hydroponic system is based on water culture system, so cultivation beds are floating on a base of Styrofoam allowing that plant roots are in contact with the nutrient solution every moment. Level 1 it has a transparent polypropylene container. A sketch of hydroponic cultivation bed is shown in Figure 3.

2.4 AILCG Design

The rack has four metal shelves panels and four metal beams, the metal beams forms two upright frames which are joint to the shelves using screws.

Also, recycled materials were used for the current implementation, such as an unused rack, volcanic rocks as a reusable substrate, among other materials. Each tray-levels (Levels 0-3) of the AILCG is controlled by an Arduino^{TM} microcontroller. Then there are four micro-controllers that work separately to keep the system under the required conditions. Thus, being a separate control of each of the tray-levels, if at a certain time the system fails, either by an external or internal factor, the others continue their usual functions for which they were programmed.

3. SENSORS AND CONTROL SYSTEM

The operated sensors in the control system are: "DHT11 and DHT22 (DHTXX)" which provides relative humidity and temperature in the environment, DS18B20 is a waterproof sensor to provide water solution temperature. DS18B20 and DHTXX sensors use the 1-wire protocol, which is a communication protocol designed by Dallas Semiconductor, it is based on a bus, a master and several slaves one data line (Zhang et al. (2010)).

The 1-Wire protocol specifies a master and one or more slaves which send information to a single data bus, a resistor is connected to +5V DC to "pull up" the signal.

3.1 Light Control System

LED lights are handled by a microcontroller, the input power of the LEDs is logged into a database, for this we decided to set an on/off control using a Pulse Width Modulation (PWM). The light period may be adjusted by time or by using a photo-resistance. The time-based light period might be set up from 7:00am to 7:00pm or any other time range, as shown in Figure 5.

On the other hand, given the analog value of the photo-resistance, the microcontroller decides whether to turn on or off the LEDs, this strategy allows the microcontroller perceive the sun photo-period by using a photo-resistance to receive any light beam.

It has been implemented the light control by photoresistance strategy. The photo-resistance has been placed near a window to intercept the solar light beams, due the photoresistance may perceive certain wavelength light beams, such as daylight, fluorescent light or any other lamp light.

To control the LED lights, the PWM duty cycle is influenced by an 8-bit parameter named as "LED Input Power (LIP)", it is defined by the following equation:

$$L(P) = P * 254/1023 \quad (1)$$

The equation is a cross-multiplication as described in Equation 1 where L is the function to obtain the LIP in PWM units and variable P is the measured "Analog Value of a Photoresistance(AVP)". The analog value of atmega328p microcontroller has a resolution of 4.9mV per unit, i.e. for each 5v there are 1024 units, the AVP has a value between 0 and 1023 units, and the LIP value is between 0 and 255 units. Equation 1 may be represented as an analogy: "If there is light there is a relative LED light". But in an absence of light, i.e. stormy days, we have decided to complement the Equation 1 into:

$$G(P) = \begin{cases} 255 & \text{if } L(P) > m \\ 0 & \text{otherwise} \end{cases} \quad (2)$$

Equation 2 is represented by the analogy "If there is any light there is a full power LED light", the variable m is the "photo-resistance Analog Value in the absence of Light(AVL)". The AVL is obtained by empirical observation, the experiment measured the amount of light without any kind light, and from a small sample space we determined that the expected value of m is 150, results may change due the photoresistance type, cable resistance, and other external light sources, e.g. street lamps. Finally, $G(P)$ is the LIP value.

3.2 Irrigation Control System

For an indoor plant growing there should be an automated irrigation system (Lieth and Oki (2008)). The actuators influencing directly in the irrigation are at Level 0, they are controlled by a single micro-controller. At the start of the program, the micro-controller initializes the input and output ports, then it sets up the clock and starts the process of irrigation and oxygenation (activate the water pumps and air). If is time to irrigate, the micro-controller activates the water pump using a 5v relay (compatible with 110-240v devices), until the time is up to irrigate. The same technique is used to provide the water aeration. These tasks are running continuously as shown in Figure 4.

3.3 Control System of the Levels 1,2 and 3

At the AILCG, each tray-level from 1 to 3 has a crop an independent monitoring, this means that control in the Level 1 does not interfere with the control of Level 2 and vice-versa, the same for Level 3. Temperature is an important aspect of the cultivation beds. For the temperature control, 12V DC fans are used. Each tray-level of AILCG has two low power fans that eliminate heat excess in the area of crops and lead to the required conditions for optimal plant development into AILCG.

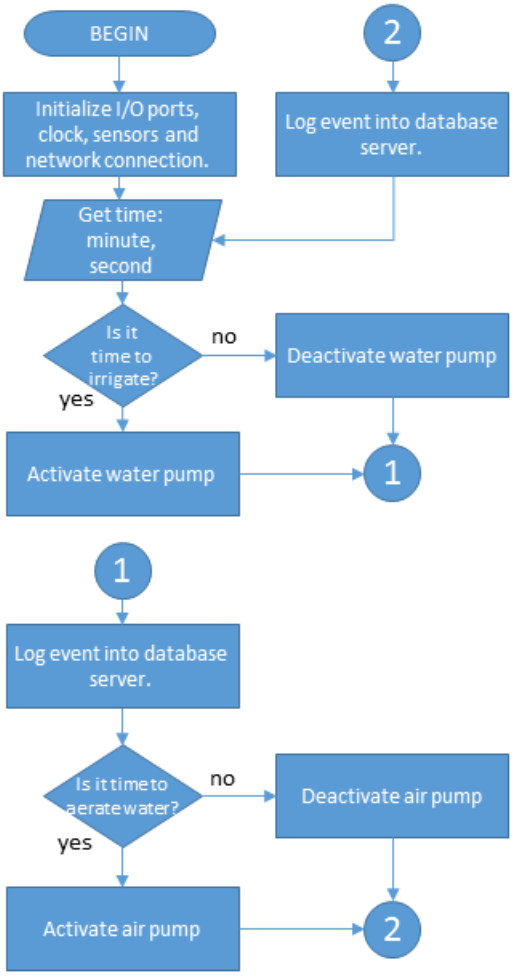

Fig. 4. Data Flow: AILCG Irrigation Control.

The first task of a micro-controller is to initialize the inputs and outputs ports, then, the clock is set up and later, it gets the information from sensors every 10 seconds to reduce the amount of data. Then based on the current time it decides to keep the LED lighting during the day (from 7hrs to 19 hrs). Also, if the air temperature is higher than 25°C or humidity is higher than 50%, multiple ventilation fans are immediately activated to regulate the temperature tray-level to a permissible one. And if the water temperature is below 20°C, a water heater is activated. At the end of this process, the collected data is sent to a database server. This process is repeated indefinitely. The Figure 5 shows a data flow chart of this process.

4. RESULTS

Figures 6 and 7 shows the physical facility of the Automated Indoor Low-Cost Greenhouse.

Figure 8 shows the data gathered from the database (MySQL Community Server 5.6.23) which is fed by the micro-controllers sensors, it is seen that the temperature starts to increase from 8:00am to 2:00pm, and then temperature decreases.

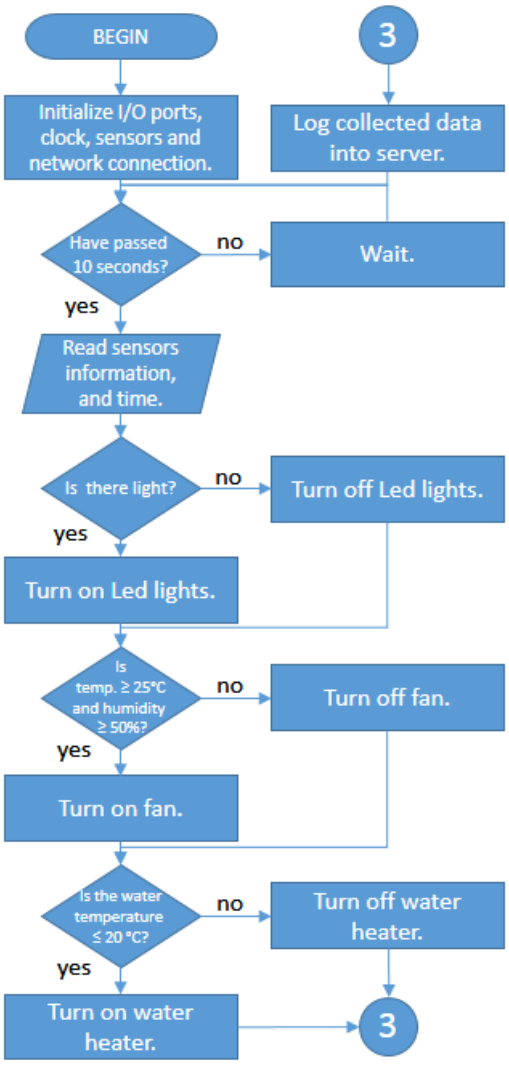

Fig. 5. Data Flow: Automated control for the crop development.

Fig. 6. Testbed setup.

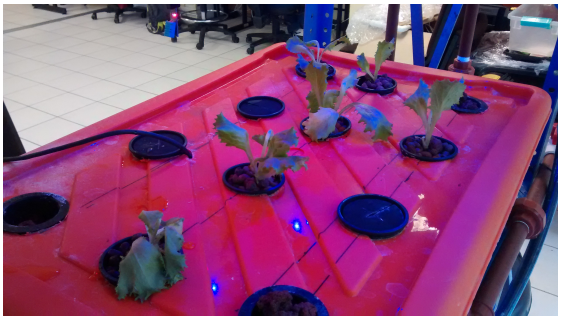

Fig. 7. LED Lights working in the testbed.

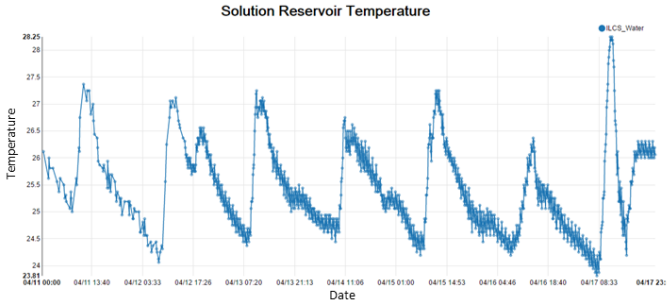

Fig. 8. Chart using data from water temperature sensor.

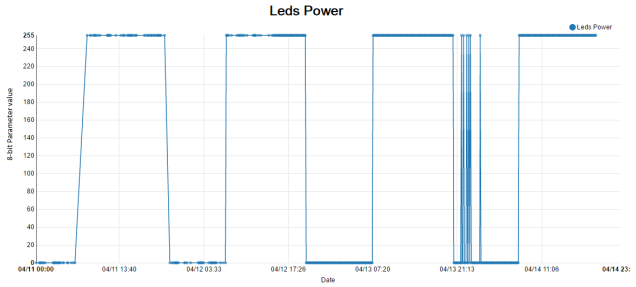

Fig. 9. Chart of LED light period.

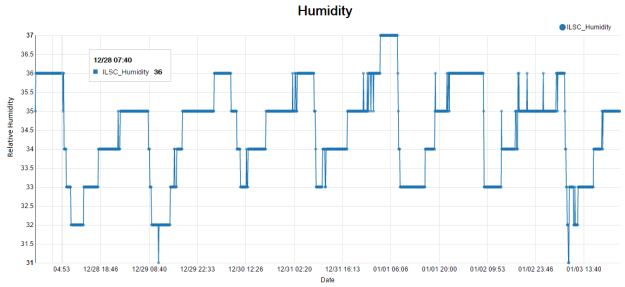

Fig. 10. Relative humidity chart.

The LED light on period is shown in Figure 9 and it is working as expected, the light period is the same period of the sunlight from 7:00hrs to 19:00hrs. Also, is shown that the date 14/04 the LIP were full at midnight due to incident light beams into the photo-resistance of external light sources, in this case, the photo-resistance was set up in front of a parking lot, by this, we deduce that the incident beams into photo-resistance were from different vehicles.

The relative humidity is increasing as the heat decreases, as shown in Figure 10, in this case, the AILCG is set up near a window in which the solar beams are heating the

equipment, reducing the humidity between 10:00am and 6:00pm.

5. CONCLUSION

A contribution of this article is the automation of a Low-Cost Indoor Greenhouse. The plants growing in the present AILCG have been more efficient by providing an adequate environment using micro-controllers, respect to a manual control. Also, we have identified and worked with four basic components that influences the plant development, which are:

- Irrigation control.
- Lighting control.
- Water condition control.
- Climate condition control.

From the experimental point of view, the data gathered from sensors and actuators allows to measure, make observations and make decisions. Finally, this AILCG provides a testbed to perform research, allowing to design new and better control strategies to indoor greenhouses.

5.1 Future Work

Today we are working with different ICT architectures, which are not part of the current article, once these architectures are validated they are going to be published on a next paper.

The next step is to implement an Internet of Plant (IoP) node consisting of a Personal Food Computer (PFC) (Harper and Siller (2015)), with the aim to contribute and share knowledge and experience to its open forum and community.

REFERENCES

Badamasi, Y.A. (2014). The working principle of an arduino. In *2014 11th International Conference on Electronics, Computer and Computation (ICECCO)*. IEEE.

Bhutada, S., Shetty, S., Malye, R., Sharma, V., Menon, S., and Ramamoorthy, R. (2005). Implementation of a fully automated greenhouse using SCADA tool like LabVIEW. In *Proceedings, 2005 IEEE/ASME International Conference on Advanced Intelligent Mechatronics.*, 741–746. IEEE.

Boulard, T. and Draoui, B. (1995). Natural ventilation of a greenhouse with continuous roof vents: Measurements and data analysis. *Journal of Agricultural Engineering Research*, 61(1), 27–35.

Casas-Carrillo, R., Begovich, O., Ruiz-Leon, J., and Siller, M. (2015). Characterizing the behavior of "greenhouse climate": a LabVIEW^{TM} application. In *2015 12th International Conference on Electrical Engineering, Computing Science and Automatic Control (CCE)*. IEEE.

Chang, C.L. and Chang, K.P. (2014). The growth response of leaf lettuce at different stages to multiplewavelength-band light-emitting diode lighting. *Scientia Horticulturae*, 179, 78–84.

Domingues, D.S., Takahashi, H.W., Camara, C.A., and Nixdorf, S.L. (2012). Automated system developed to control pH and concentration of nutrient solution evaluated in hydroponic lettuce production. *Computers and Electronics in Agriculture*, 84, 53–61.

Harper, C. and Siller, M. (2015). OpenAG: A globally distributed network of food computing. *IEEE Pervasive Comput.*, 14(4), 24–27.

Jr., J.B.J. (2004). *Hydroponics: A Practical Guide for the Soilless Grower*. CRC Press.

Lieth, J.H. and Oki, L.R. (2008). Irrigation In Soilles Production. In *Soilless Culture*, 117–156. Elsevier BV.

Mohr, H. and Schopfer, P. (2010). *Plant Physiology*. Springer.

Muñoz, P., Montero, J., Antón, A., and Giuffrida, F. (1999). Effect of insect-proof screens and roof openings on greenhouse ventilation. *Journal of Agricultural Engineering Research*, 73(2), 171–178.

Mustroph, A. and Albrecht, G. (2003). Tolerance of crop plants to oxygen deficiency stress: fermentative activity and photosynthetic capacity of entire seedlings under hypoxia and anoxia. *Physiol Plant*, 117(4), 508–520.

Parker, R. (2009). *Plant and Soil Science: Fundamentals and Applications*. DELMAR.

Putter, E. and Gouws, J. (1996). An automatic controller for a greenhouse using a supervisory expert system. In *Proceedings of 8th Mediterranean Electrotechnical Conference on Industrial Applications in Power Systems, Computer Science and Telecommunications (MELECON 96)*. IEEE.

Schempf, H., Graham, T., Fuchs, R., and Gasior, C. (2001). Automated container-handling system for container production nurseries. In *Proceedings 2001 ICRA. IEEE International Conference on Robotics and Automation (Cat. No.01CH37164)*. IEEE.

Son, K.H. and Oh, M.M. (2013). Leaf shape, growth, and antioxidant phenolic compounds of two lettuce cultivars grown under various combinations of blue and red light-emitting diodes. *HortScience*, 48.

Thompson, H., Langhans, R.W., Both, A.J., and Albright, L.D. (1998). Shoot and root temperature effects on lettuce growth in a floating hydroponic system. *Journal of the American Society for Horticultural Science*.

UN (2004). World population to 2300. Technical report, United Nations.

Zhang, C., Feng, X., and Li, L. (2010). The key technologies of a distributed temperature monitoring system based on 1-Wire bus. In *2010 8th World Congress on Intelligent Control and Automation*. IEEE.

Greenhouse Temperature Modeling and Control Based on Timed Continuous Petri Nets

J. Fraustro-Valdez *, **G. Desirena-López** *, **J. Ruiz-León** *, **O. Begovich** *

* *CINVESTAV-IPN Unidad Guadalajara, Av. del Bosque 1145, Colonia el Bajío, Zapopan, 45019, Jalisco, México.*

Abstract
This work deals with the modeling and climate control of greenhouses. In order to achieve these objectives, this paper extends previously reported greenhouse modeling methodologies and proposes a control strategy. More precisely, the model methodology is based on a modular technique using timed continuous Petri nets, and the proposed discrete control law is based on the contribution degree of controllable transitions. The model and control methodology aim to contribute by simplifying the manipulation of greenhouse variables. Thus, the possible human errors introduced during the modeling stage or operation stage are reduced. A simulation example is presented in order to illustrate the modelling methodology and the control design and its application.

Keywords: Hybrid systems, Timed Continuous Petri Net, Temperature control, Greenhouse, Modeling, Control, Product semantic, Contribution degree.

1. INTRODUCTION

Nowadays, agricultural production has managed to meet demands from a rapid growth of the world population. In particular, urban farming is getting relevant. Nevertheless, the development of crops in farms or city-farms needs specific knowledge about a greenhouse and its operation. This becomes difficult because of the complexity of the environment and the understanding of multi-variables relation involved in this kind of systems. However, with a graphical representation and an efficient modular modeling for greenhouses, it could be possible to simplify the understanding and the control of these systems.

Some advantages can be obtained when climate control is implemented in a greenhouse. Using a control methodology, it is possible to reduce risks due to randomness of weather indoor greenhouse and provide the optimal environment conditions for growing plants. In order to obtain the optimal plant environment, it is essential to automatically adjust the environment factors (temperature, humidity, light, CO_2, etc). The control of greenhouse climate is characterized by the fact that several processes, such as crop growth and greenhouse climate change, occur on different time scales. The development of the crop occurs on time scale of weeks or months, whereas most of the greenhouse climate variables change on a daily basis. Both greenhouse climate and crop growth are influenced by light, which may change on a time scale of seconds or minutes, specially on cloudy days. To obtain optimal conditions in indoor greenhouses, several mathematical models have been developed to predict the growing conditions as a function of the micro-climate variables. Most of the existing models are based on mass-energy balances. For example, in (Boulard and Baille, 1993) a greenhouse model, including natural ventilation and evaporative cooling, is presented. The authors use heat and mass balance equations to derive the model. However, this work includes a linearization stage, and the model is valid only around the operating point. In (Cunha et al., 2003), neural networks are used to deal with the linear and nonlinear identification of the behavior of a greenhouse. This method uses a large amount of data samples due to its large number of synthesis parameters, and it also requires a large computation time for training the neural network.

Greenhouse control devices are in general on-off (events) while climate variables (temperature, humidity, solar radiation, etc.) are continuous; thus, a greenhouse model represents a hybrid system. Hybrid systems, such as greenhouses, can be modeled by Discrete Event Systems (DES) using Petri Nets (PN) with a big population. Petri nets (Dessel and Esparza, 1995) are a formalism for the modeling and analysis of discrete dynamic systems. Unfortunately, the problem of modeling dynamic systems such as real systems cannot be applied in heavily marked Petri nets. However, a technique used to overcome this problem is to relax the system by *fluidification* obtaining the Timed Continuous Petri Nets ($TCPN$). $TCPN's$ are a relaxation of the Petri nets where the marking becomes continuous and the state equation is represented by a set of positive and bounded linear differential equations, which depend on the semantic of the net. Several $TCPN$ models have been proposed in the literature, for instance (Ross-León et al., 2014) for biological systems, (Tovany et al., 2013) for a greenhouse, (Desirena-Lopez et al., 2014) considers ther-

mal systems, (Júlvez and Boel, 2010) for traffic systems and (Mahulea et al., 2012) for manufacturing systems.

In this paper, in order to represent the internal environment (climate variables), the continuous part of the greenhouse is modeled by $TCPN$ using product semantics ($TCPN - PS$). This semantic has been widely used to model biological systems in (Heiner et al., 2008), (Silva and Recalde, 2002), (Baldan et al., 2011), (Tovany et al., 2013), where the nonlinear part is introduced by the join transitions (Silva and Recalde, 2004), (Garcia-Malacara et al., 2013). For these reasons, the incremental model methodology from (Tovany et al., 2013) is used to represent the temperature and humidity behaviour adding a thermal actuator to the greenhouse model. On the other hand, an On/Off local control law is presented. In (Ross-León et al., 2014) the *contribution degree* is defined as the dot product between the marking error, i.e. the difference between the required and the actual markings, and the columns of the incidence matrix. Thus, if the result is a positive scalar value, the firing of these transitions contributes to reduce the marking error for $TCPN$ models with big populations and all transitions are controllable. Based on this, the control strategy proposed by (Ross-León et al., 2014) is used and applied to $TCPN - PS$ model with controllable and uncontrollable transitions. A simulation example is presented to illustrate the modelling methodology, the control design and its application.

The paper is organized as follows. In Section 2, basic concepts related to Timed Continuous Petri Nets ($TCPN's$) systems and controllability concepts are presented. Section 3 presents a Petri net modeling procedure for greenhouses. Section 4 deals with the problem of reaching a required state and synthesizes a Lyapunov function for solving this problem. Finally, Section 5 presents an example of a greenhouse model as a case of study and the temperature control using the proposed control law.

2. FUNDAMENTALS

In this section, we provide the basic background on Petri nets (PN) and Timed Continuous Petri Nets ($TCPN$) under product server semantics (PS). Notice that $TCPN's$ under PS belong to the class of positive Nonlinear Systems (Murata, 1989), (Silva and Recalde, 2002).

2.1 Continuous and Timed continuous Petri nets

Definition 1. A Continuous Petri Net ($ContPN$) is the pair $ContPN = (N, m_0)$ where $N = (P, T, Pre, Post)$ is a Petri net (PN) and $m_0 \in \{\mathbb{R}^+ \cup 0\}^{|P|}$ is the initial marking, $P = \{p_1, \ldots, p_n\}$ and $T = \{t_1, \ldots, t_k\}$ are finite sets of elements named places and transitions, respectively. Pre, $Post \in \{\mathbb{N} \cup 0\}^{|P|\times|T|}$ are the Pre- and Post- incidence matrices, where $Pre[i, j]$ ($Post[i, j]$) represents the weight of the arc going from p_i to t_j (from t_j to p_i).

The $ContPN$ evolution rule is different from the case of discrete PN systems, since in continuous $PN's$ the firing of an enabled transition is not restricted to integer values; thus the marking $m \in \{\mathbb{R}^+ \cup 0\}^{|P|}$ is not forced to be integer. Instead, a transition t_i in a $ContPN$ is *enabled* at marking m iff for every $p_j \in {}^\bullet t_i, m[p_i] > 0$; and its *enabling degree* depends on the continuous PN semantic. The firing of the enabled transition t_i in a certain amount $\alpha_i \leq enab(t_i, m)$ leads to a new marking $m' = m + \alpha_i C[P, t_i]$, where C is the incidence matrix, defined by $C = Post - Pre$.

If m is reachable from m_0 by firing each enabled transition t_i in a certain amount $\sigma_i \leq enab(t_i, m)$, then $m = m_0 + C\vec{\sigma}$ and it is named the fundamental equation where $\vec{\sigma} \in \{\mathbb{R}^+ \cup 0\}^{|T|}$ is the firing count vector.

Definition 2. A P-invariant (P-semiflow) of a net N is a rational-valued solution Y of the equation $Y^T \cdot C = 0$.

Proposition 3. Let (N, m_0) be a system, and let I be a P-invariant of N. If $m_0 \xrightarrow{*} m'$, then $I \cdot m = I \cdot m_0$ (Dessel and Esparza, 1995).

Definition 4. A T-invariant (T-semiflow) of a net N is a rational-valued solution of the equation $C \cdot X = 0$.

Proposition 5. Let σ be a finite sequence of transitions of a net N which is enabled at marking m. Then the *Parikh* vector $\vec{\sigma}$ is a T-invariant iff $m \xrightarrow{\sigma} m$ (i.e., iff the occurrence of σ reproduces the marking m) (Dessel and Esparza, 1995).

The set of all reachable markings from m_0 is called the reachability set and it is denoted by $RS(N, m_0)$.

A $ContPN$ is bounded when every place is bounded, i.e. $\forall p \in P, \exists b_p \in \mathbb{R}$ s.t $m[p] \leq b_p$ at every reachable marking m, and it is live when every transition is live (it can ultimately be fired from every reachable marking).

Definition 6. A Timed Continuous Petri Net ($TCPN$) is a time-driven continuous-state system described by the 3-tuple (N, λ, m_0) where (N, m_0) is a continuous PN and the vector $\lambda \in \{\mathbb{R}^+ \cup 0\}^{|T|}$ represents the transition rates that determine the temporal evolution of the system. Transitions fire according to certain speed, which generally is a function of the degree rates and the instantaneous marking. Such function depends on the semantics associated to the transitions. Under infinite server semantics the flow (the transitions firing speed, denoted as $f(m)$) through a transition t_i is defined as the product of the rate, λ_i, and $enab(t_i, m)$, the instantaneous enabling of the transition, i.e., $f_i(m) = \lambda_i enab(t_i, m) = \lambda_i min_{p \in {}^\bullet t_i} \frac{m[p_j]}{Pre[p_j, t_i]}$.

The maximum transition firing rate matrix is denoted by $\Lambda = diag(\lambda_1, ..., \lambda_{|T|})$. When the flow is well defined, every continuous transition must have at least one input place, hence in the following we will assume $\forall t \in T, |{}^\bullet t| \geq 1$. The "$min$" in the above definition leads to the concept of configuration. A configuration of a $TCPN$, at marking m, is a set of (p, t) arcs describing the effective flow going through each transition. For each configuration, a configuration matrix is defined as follows:

$$\Pi(m) = \begin{cases} \frac{1}{Pre[i,j]} & \text{if } p_i \text{ is constraining } t_j \\ 0 & \text{otherwise.} \end{cases} \quad (1)$$

The flow through the transitions can be written in a vectorial form as $f_k(m) = \Lambda\Pi_k(m)m$. The dynamical behavior of a $TCPN$ system is described by its state equation:

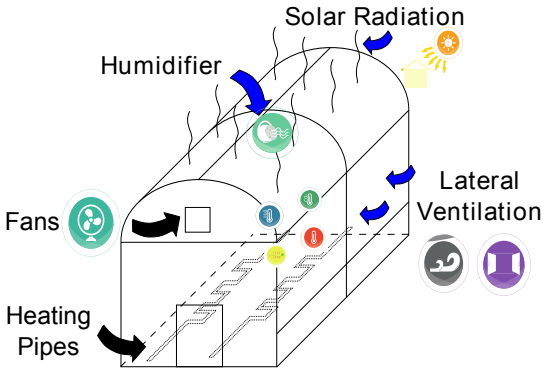

Figure 1. Greenhouse System.

$$\dot{m} = C\Lambda\Pi_k(m)m. \tag{2}$$

Under the product server semantic the flow f_i of a transition t_i is computed as

$$f_i(\tau) = \lambda_i \cdot \prod_{p \in \bullet t_i} \left\{ \frac{\mathbf{m}(p)}{\mathbf{Pre}[p, t_i]} \right\}. \tag{3}$$

Notice that $m(p)$ depends on time τ.

In product semantics, the flow through a transition t_i is the product of the marking in the input places of t_i.

The dynamical behavior of a $TCPN$ system is described by its state equation

$$\dot{m} = Cf(\tau) \tag{4}$$

where $f(\tau) = [f_1, ..., f_{|T|}]^T$.

A transition t_i in a $TCPN$ system is controllable if its flow can be reduced or stopped. In order to apply a control action in (4), a subtracting term u, such that $0 \leq u_i \leq f_i$ is added to every controllable transition t_i to indicate that its flow can be reduced. This control action is adequate because it captures the real behavior that the maximum device throughput can only be reduced. Thus, the controlled flow of transition t_i becomes $w_i = f_i - u_i$. Then, the forced state equation is given by

$$\begin{aligned} \dot{m} &= C[f - u] = Cw \\ 0 &\leq u_i \leq f_i. \end{aligned} \tag{5}$$

In order to obtain a simplified version of the state equation, the input vector u is rewritten as $u = I_u\Lambda \cdot \prod_{p \in \bullet t_i} \left\{ \frac{\mathbf{m}(p)}{\mathbf{Pre}[p,t_i]} \right\}$, where $\Lambda_{i,i} = \lambda_i$ (the firing rate of transition t_i) and $\Lambda_{i,j} = 0$, $i \neq j$ and $I_u = diag(I_{u_1}, \ldots, I_{u_{|T|}})$ with $0 \leq I_{u_i} \leq 1$ (notice that $0 \leq u_i \leq f_i$, as required in Equation (5)). Then the matrix $I_c = I - I_u$ is constructed and the state equation can be rewritten as

$$\dot{m} = CI_c f = Cw \tag{6}$$

where $I_{c_{i,i}} \in [0, 1]$ represents the control action, i.e. it represents the percentage of maximum flow allowed to go through the transitions.

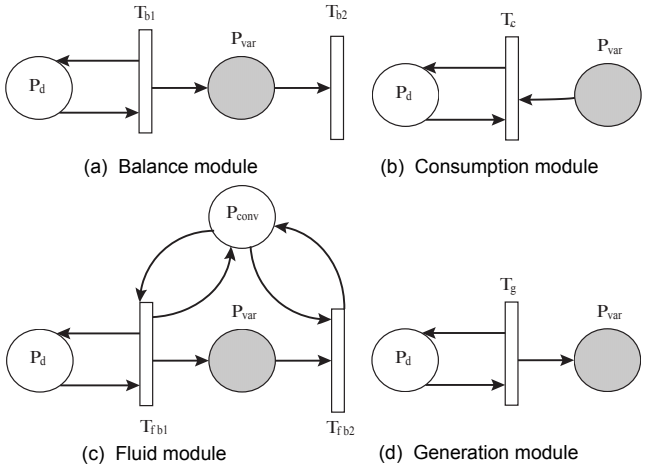

Figure 2. Elementary Modules.

3. MODELING METHODOLOGY

A greenhouse is a system composed by a building which isolates the crop from the outside environment, a set of devices such as humidifiers, coolers, fans, automatic windows, etc., allowing to adequate the indoor greenhouse climate and an irrigation system conveying water and fertilizers into the greenhouse. The inside temperature of the greenhouse is affected by external disturbances, such as solar radiation, outdoor temperature, wind speed, etc., as depicted in Fig. 1.

The indoor greenhouse temperature can be controlled by the signals turning on, or tuning off the greenhouse devices; thus, a set of events $E_g = \{a_1, \bar{a_1}, ..., \bar{a_n}\}$, which represent these signals, is defined.

The modeling methodology proposed in (Tovany et al., 2013) is incremental and uses elementary $TCPN$ modules. A Petri net elementary module is created for each device and disturbance. The elements of heat and mass balance equations can be modeled separately into: variables to be controlled, devices for control and external perturbation variables. Therefore, instead of using the $TCPN$ as a formalism to model a greenhouse, it is better to model with these elementary modules: **Generation module**, **Consumption module**, **Balance module** with infinite server semantic and **Fluid balance module** (see Fig. 2) with product semantic. The initial marking and transition firing rates are given by the parameters of plastic film and devices capacities or some of them can be measured by a meteorologic station and the rest of them can be estimated by a regression algorithm. Afterwards, these models are merged to form a single model.

Notice that the final model is a hybrid system. There is a set of differential equations to represent the indoor greenhouse temperature and a set of events to control it.

An elementary $TCPN$ module is called **balance module** as depicted in Fig. 2 (a) if it has a place p_{var} that is assigned with a marking m_{var} representing a variable x; a function p_d with a marking m_d is assigned to represent a function $d(\tau)$; and a transition t_c is created with the maximum flux λ_c=k representing a gain factor.

Module	p/Var	Transition
$q^{rad}(I_o)$	m_5	$t_1 = \eta_g$
$q^{vent}(T_o, v, T_g)$	m_6 - m_{10} - m_1	$t_2 = \rho_a c_{p,a}$ y $t_5 = \rho_a c_{p,a}$
$q^{cond}(T_o, T_g)$	m_6 - m_1	$t_3 = U_{g,o}$ y $t_6 = U_{g,o}$
$q_{p,s}(T_s, T_g)$	m_2- m_1	$t_4 = U_{g,s}$ y $t_7 = U_{g,s}$
$q(Fhum)$	m_{11} - m_1	$t_{10} = \gamma\rho_{H_2O}$ $(1-k_1)U_{hum}/A_g$
$q(\varphi^{cons}_{H_2O_{g,r}})$	m_{12} -m_1	$t_{11} = \gamma(1-k_2)$
$q(T_g, T_s)$	m_1 - m_2	$t_8 = U_{g,s}$ y $t_9 = U_{g,s}$
$q(T_{ss}, T_s)$	m_7 - m_2	$t_{12} = U_{sss}$ y $t_{13} = U_{sss}$
$q(F_{hum}, C_{H_2O})$	m_{11} - m_3	$t_{16} = \rho_{ag}(1-k_1))/A_g$
$q(C_{H_2O_{g,r}}, v, C_{H_2O})$	m_8 - m_{10} - m_3	$t_{14} = 1$ y $t_{15} = 1$
$q(\varphi^{cons}_{H_2O_{g,r}}, C_{H_2O})$	m_{12} - m_3	$t_{17} = 1$
$q(CO2_{g,r}, v, CO_2)$	m_9- m_{10} - m_4	$t_{18} = 1$ y $t_{19} = 1$
$q^{pipe}_{p,g}(T_p, T_g)$	m_1 - m_{13}	$t_{20} = t_{21} = U_{p,g}$ $t_{22} = t_{23} = U_{p,g}$ $t_{24} = \rho_{H_2O} c_{p,H_2O}$ F_p/A_g $t_{25} = \eta_p$

Table 1. Relation between variables and function places.

An elementary $TCPN$ module is called **consumption module** as depicted in Fig. 2 (b) if it has a place P_{var} that is assigned with marking m_{var} representing a variable x; a function place p_d with a marking m_d is assigned to represent a function $d(\tau)$; and a transition t_c is created with a maximum flux λ_c representing the gain factor.

An elementary $TCPN - PS$ module is called **fluid balance module** as depicted in Fig. 2 (c) if it is a representation of a balance element with proportional fluid flow relation. It is based on a balance module with an extra place p_{conv} with marking m_{conv} representing the fluid flow.

Finally, an elementary $TCPN$ is called **generation module** as depicted in Fig. 2 (d) if it has a place P_{var} that is assigned with marking m_{var} representing a variable x; a function place p_d with marking m_d is assigned to represent a function $d(\tau)$; and a transition t_g is created with maximum flux $\lambda_g = k$ representing a gain factor.

According to this procedure, first we have to associate places for the involved variables: greenhouse temperature T_g (P_1), soil temperature T_s (P_2), C_{H_2O} concentration (P_3), $C_{C_{CO_2}}$ concentration (P_4) and pipe system temperature T_p (P_{13}). Function places are associated with the variables: solar radiation I_o (P_5), outside temperature T_o (P_6), subsoil temperature T_{ss} (P_7), outside water vapor concentration $C_{H_2O_o}$ (P_8), outside carbon dioxide concentration $C_{CO_{2_o}}$ (P_9), wind speed V (P_{10}), humidifier maximum water flow F_{hum} (P_{11}), water condensation φ_{cons} (P_{12}) and the maximum water flow inside the pipes F_p (P_{14}). Secondly, for the greenhouse temperature T_g we construct a generation module for solar radiation $q^{rad(I_o)}$ and condensation φ_{cons} q^{cons}; a consumption module for the humidifier F_{hum} (q^{hum}); a balance module for soil temperature T_s (q^{T_s}); and a fluid balance module for controlled natural ventilation (q^{vent}). For the greenhouse humidity C_{H_2O} we construct: a generation module for the humidifier F_{hum} (φ^{hum}); a consumption module for condensation φ_{cons} (φ^{cond}); a balance module for outside humidity C_{H_2O}; and fluid balance module for controlled natural ventilation (φ^{vent}).

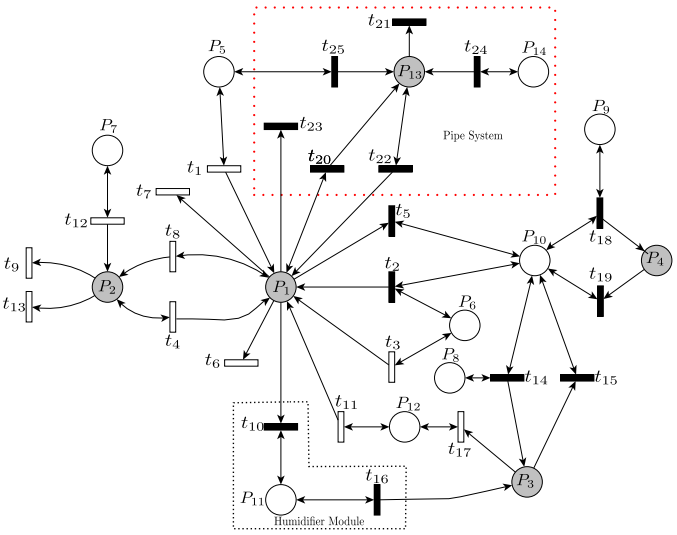

Figure 3. Greenhouse TCPN modeling.

Since soil temperature is also modeled, we construct a balance module for the greenhouse temperature T_g and soil temperature T_s. Then, we construct modules for each variable as shown in Table 1 (where parameter values are taken from (Van Straten et al., 2010)).

Then, by merging these modules we obtain the greenhouse model in $TCPN - PS$ as depicted in Fig. 3. The state equation is represented as follows:

$$\begin{aligned}
\dot{m}_1 =& (-I_{c1}\lambda_5 m_1 m_{10} - (\lambda_7 + \lambda_6 + \lambda_{23})m_1 + \lambda_4 m_2 \\
&+ (I_{c1}\lambda_2)m_6 m_{10} + \lambda_3 m_6 - I_{c2}\lambda_{10} m_{11} \\
&+ \lambda_{22} m_{13} + \lambda_{11} m_{12} + \lambda_1 m_5)/K_g \\
\dot{m}_2 =& (\lambda_8 m_1 - (\lambda_9 + \lambda_{13})m_2 + \lambda_{12} m_7)/K_s \\
\dot{m}_3 =& (-I_{c1}\lambda_{15} m_3 m_{10} + I_{c1}\lambda_{14} m_8 m_{10} \\
&+ I_{c2}\lambda_{16} m_{11} - \lambda_{17} m_3)[A_g/V_g] \\
\dot{m}_4 =& (-I_{c1}\lambda_{19} m_4 m_{10} + I_{c1}\lambda_{18} m_9 m_{10})[A_g/V_g] \\
\dot{m}_{13} =& (\lambda_{20} m_1 - \lambda_{21} m_{13} + \lambda_{24} m_{14} + \lambda_{25} m_5)/K_p.
\end{aligned} \tag{7}$$

4. CONTROL LAW

In this subsection, some controllability concepts of $TCPN$ are recalled from (Vázquez et al., 2008).

An induced equilibrium point is a marking m_a in which the system can be maintained using a specific control action u_a, i.e. $0 = C[f - u_a]$. A maximum throughput equilibrium point m_r can be computed. Thus, an important problem is that given an initial marking m_0 and a required target marking m_r (for instance, markings allowing maximum system throughput), to design a control law leading the $TCPN$ state from m_0 to m_r. This problem is formally defined as follows.

Definition 7. Let $(N; m_0; \lambda)$ be a $TCPN$ system and $(m_r; I_{cr})$ be an induced equilibrium point of the $TCPN$. Then the Regulation Control Problem (RCP) in $(m_r; I_{cr})$, denoted as $RCP(m_r; I_{cr})$, deals with the computation of

a control law $I_c(\tau)$; $0 \leq \tau \leq \tau_f$ feasible in the $TCPN$ such that $m(\tau_{ss}) = m_r$ and $I_c(\tau_{ss}) = I_{cr}$, $\forall \tau_{ss} \geq \tau_f$.

The greenhouse control problem is stated as a RCP, where the equilibrium point is given by target indoor temperature and the computed I_c. Since the set $E_g = \{a_1, \bar{a_1}, ..., \bar{a_n}\}$ is representing a set of events, then the control value of I_c in Equation (6) must be zero or one.

Notice that the modules in the modeling methodology are of type balance, generation or consumption module. Generation modules (solar radiation, condensation of moisture on walls and roof) increase the indoor temperature, while consumption modules reduce it. For fixed environmental conditions if the greenhouse heaters are turned on and coolers are turned off, then the indoor temperature will reach a maximum value, named T_{max}; otherwise if the greenhouse heaters are turned off and coolers are turned on, then the indoor temperature will reach a minimum value, named T_{min}. Thus the indoor temperature can be controlled in the range $T_R = [T_{min}, T_{max}]$.

The control law solving the RCP problem will be obtained based on the results from (Ross-León et al., 2014), which considers the control problem in live and bounded $TCPN$, with controllable transitions and infinite server semantic. In this work, the implementation of the control strategy to nonlinear hybrid systems is presented. For this reason, the product semantics is used to represent the non linearity of the system.

Definition 8. Let (N, m_0, λ) be a live and bounded $TCPN$ system and $m_r \in int(T_R)$ be the required target marking. Then the marking error is computed as

$$e(\tau) = m_r - m(\tau). \tag{8}$$

Definition 9. Let (N, m_0, λ) be a live and bounded $TCPN$ system. The **Contribution Degree** $\Psi_k(\tau)$ of a transition t_k of N is defined as

$$\Psi_k(\tau) = e^T(\tau)c_k \tag{9}$$

where c_k is the k-th column of the incidence matrix C.

Notice that the contribution degree is representing the projection (dot product) of how the transition removes/adds tokens (column c_k) over the error. Thus, it provides information about how much a transition is capable of decreasing the error marking.

Lemma 10. (Ross-León et al., 2014) Consider the definition of the marking error and let (N, m_0, λ) be a live and bounded $TCPN$ system and v a T-semiflow of N. Then $\sum_{t_k \in |v|} v_k \Psi_k(\tau) = 0$.

Proof. The result follows from

$$\sum_{t_k \in |v|} v_k \Psi_k(\tau) = e^T(\tau) C v = 0.$$

From Lemma 10 we have that the sum of every contribution degree in a given T-semifow is zero. Therefore, there must be both transitions with positive and transitions with negative contribution degrees in it.

Theorem 11. (Ross-León et al., 2014) Let (N, m_0, λ) be a live and bounded $TCPN$ system where all transitions are controllable. Then, the control law

$$I_{c_k} = \begin{cases} 1 & \text{if } \Psi_i > 0 \\ 0 & \text{otherwise} \end{cases} \tag{10}$$

leads the initial marking $m_0 = m(0)$ to the required marking $m_r \in int(T_R)$.

Proof. Let $V(\bullet)$ be the function

$$V(e) = \frac{1}{2} e^T(\tau) e(\tau). \tag{11}$$

We claim that $V(e)$ is a Lyapunov function, i.e. it is positive definite, its derivative is negative definite and it fulfils $\dot{V}(x) = 0$ only for $x = 0$, as shown below.

Clearly, (11) is positive definite. Now, the differentiate of $V(e)$ is

$$\dot{V}(e) = e^T(\tau)\dot{e} = -e^T(\tau) C I_c f(\tau). \tag{12}$$

Since $m_r \in int(T_R)$, then for every time τ there exists a transition firing vector $\sigma(\tau) > 0$ such that $e(\tau) = m_r - m(\tau) = C\sigma(\tau)$. Thus

$$e^T(\tau)e(\tau) = e^T(\tau) C \sigma(\tau) > 0 \tag{13}$$

for $e(\tau) \neq 0$. Rewriting (13) we have

$$\begin{aligned} e^T(\tau) C \sigma(\tau) &= e^T(\tau)[\sigma_1 c_1 + \sigma_2 c_2 + \cdots + \sigma_{|T|} c_{|T|}] \\ &= \sigma_1 e^T(\tau) c_1 + \sigma_2 e^T(\tau) c_2 + \cdots + \sigma_{|T|} c_{|T|} > 0. \end{aligned} \tag{14}$$

Also σ_i depends on τ. Since $\forall i, \sigma_i \geq 0$, then there exists at least one c_k such that $\sigma_k e^T(\tau) c_k > 0$ for $e(\tau) \neq 0$. Notice that $\sigma_k > 0$ is strictly positive, thus $e^T(\tau) c_k > 0$ is also strictly positive. Then from (10) we have that $I_c(k) = 1$. Substituting these values in (12), then $\dot{V}(e)$ could be zero or negative. If Equation (12) is negative, then the derivative of the Lyapunov function is negative, decreasing the system error.

However, Equation (12) could be zero when the error is different from zero iff $f(\tau) = 0$ or $I_c f(\tau) = 0$ or $I_c f(\tau) \neq 0$ is in the kernel of C or $C I_c f(\tau)$ is in the kernel of e^T. Now, we will show that these cases are not possible.

In the first case if $f(\tau) = 0$ means that the $TCPN$ system is blocked, then it is not live; a contradiction.

In the second case $I_c f(\tau) = 0$, then the flow of transitions is being blocked by I_c since its contribution degree is negative or the contribution degree is positive and I_c is not blocking, but the flow of these transitions is zero. Since the $TCPN$ is live and bounded, then by Lemma 10 there are positive and negative contribution degrees. Then there is an $I_c(k) = 1$ with its corresponding flow $f_k = 0$. Thus, at least one input place to t_k has zero tokens, meaning that the marking m is in the border, i.e. it is not in $int(T_R)$, and $\dot{V} = 0$. Then N is not evolving at all. Since the error is not zero, there exists a transition t_{j_1} such that $I_c(\tau)(j_1) = 1$, and t_{j_1} cannot be fired, thus at least one input place p_{k_1} to

Places
$I_o = 400\sin(0.00011t)\ W/m^2$
$T_o = 298 + 7\sin(0.00011t)\ K$
$T_{ss} = 293.15 + 3\sin(0.00011t)\ K$
$C_{H_2O_o} = 0.0060692 + 0.002\sin(2t)\ kg/m^3$
$v = \begin{cases} h(t) \text{ for } h(t) = 10\sin(0.001t) \geq 1 \\ 1 \qquad\qquad \text{otherwise} \end{cases}$
$\varphi_{cons} = 3 \times 10^{-10} + 2 \times 10^{-10}\sin(t)\ kg/^2s$

Table 2. Simulation parameters for **places** of the greenhouse modelled by $TCPN$.

t_{j_2} is unmarked. This procedure can be repeated until t_{j_1} is revisited. Since N is live, two cases are possible, places $p_{k_2}, \ldots, p_{k_1}$ require tokens, thus m_r is not reachable, or there exists an empty siphon (unmarked P-semiflow) and N is not live. A contradiction.

In the third case $I_c f(\tau) \neq 0$ is in the kernel of C, then a T-semiflow Υ composed by transitions $t_a, \ldots, t_n$ is being fired. It means that $\Psi_a(\tau) > 0, \ldots, \Psi_n(\tau) > 0$. However, from Lemma 10, we know that in a T-semiflow Υ there exist positive and negative $\Psi_\bullet(\tau)$. Thus not all $\Psi_\bullet(\tau)$ are positive and $I_c f(\tau)$ cannot form a T-semiflow at time τ. A contradiction.

In the fourth case $CI_c f(\tau)$ is in the kernel of e^T, but this is not possible because I_c was chosen to enforce (14) to be positive by selecting only the positive terms, thus even if f_k is not equal to σ_k, it is positive and (12) cannot be zero.

Thus $\dot{V}(e) = -e^T(\tau)CI_c f(\tau) < 0$ in all the cases, therefore (11) is a Lyapunov function. Then the error is asymptotically stable and the control (10) leads the marking from m_0 to m_r.

5. CASE OF STUDY

In this section the case of study is presented. We use greenhouse parameters values from (Van Straten et al., 2010) as in Table 2 and Table 3, but also, parameters can be estimated by a regression algorithm (Pérez-González et al., 2014). The greenhouse model is constructed with the following actuators: windows, fans, humidifier and pipe system (see Fig. 1). Using these actuators and parameters the $TCPN - PS$ greenhouse model is built according to Section 3. Notice that, the windows, fans and pipe system are represent by balance $TCPN$ modules. However, the humidifier is represented by a consumption $TCPN$ module.

This modeling methodology was implemented in a Graphical User Interface (GUI) programed in Matlab©. Each elementary Petri net module is represented by an element (icon) in the interface (for instance, actuators, perturbations) that can be added in a modular way while the $TCPN$ model is built. Therefore, the greenhouse-GUI provides facilities to operate the greenhouse system; any operator can easily manage the greenhouse, just by selecting the actuator or sensor icon in the interface and link it with another element.

The temperature T_g inside the greenhouse is depicted in Fig. 4; the system is simulated in a period of 8 hours. The figure shows that the temperature is increasing during the day and decreasing at sunset. However, the problem of

Transitions	Initial conditions
$t_1 = 0.5882$	$T_g = 288\ K$
$t_2 = t_5 = 1.3029 \times 10^3$	
$t_3 = t_6 = 7.9$	$T_s = 298\ K$
$t_4 = t_7 = 5.75$	$C_{H_2O} = 0.0026\ kg/m^3$
$t_{10} = 39470900$	
$t_{11} = 565000$	
$t_8 = t_9 = 5.75$	
$t_{12} = t_{13} = 2$	
$t_{16} = 17.4650$	
$t_{14} = t_{15} = t_{17} = t_{18} = t_{19} = 1$	
$t_{20} = t_{21} = t_{22} = t_{23} = 4.7652$	
$t_{24} = 41.7164$	
$t_{25} = 0.1120$	

Table 3. Simulation parameters for **transitions** of the greenhouse modelled by $TCPN$.

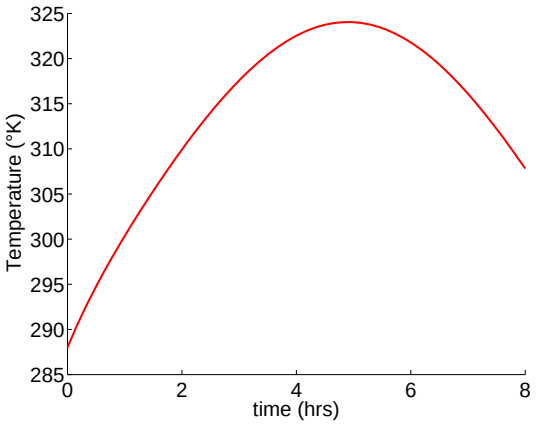

Figure 4. Temperature T_g indoor greenhouse without control.

obtaining an optimal environment for crops production in greenhouses depends on the ability to control the temperature inside; therefore, we will show that the previously proposed control law is able to control the temperature T_g.

Now, in order to apply the control law strategy, it is considered that the windows and fans are activated with the same control signal I_{c1}, in the case of the humidifier, the control signal was I_{c2}, similarly the control signal I_{c3} activate the pipe system. The system is simulated using the control strategy and establishing a set point for the temperature T_g (marking required $m_1 = 320^oK$) and it is considered that the other climate variables are not restricted.

Fig. 5 presents the temperature T_g behavior inside the greenhouse using the proposed control strategy. Notice that the simulation results show that with the control strategy the requirements are reached. Fig. 6 shows the evolution of the proposed control law for the fans and windows, humidifier and pipe system.

6. CONCLUSIONS

This work addressed the problem of modeling and reaching a required temperature environment in a greenhouse system. The modeling methodology presented provides a graphical representation of climate variables which allows an easy understanding of their interaction; moreover, the

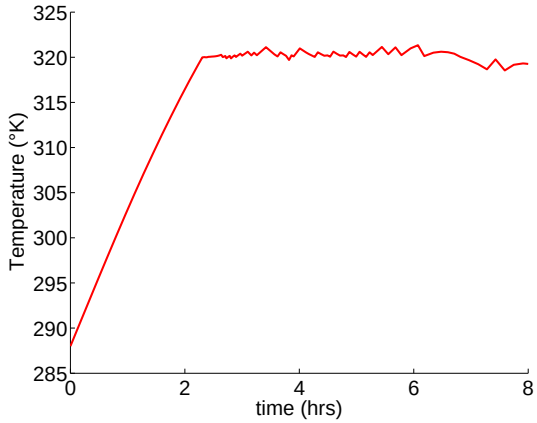

Figure 5. Temperature T_g controlled indoor greenhouse (marking required $T_g = m_1 = 320^oK$).

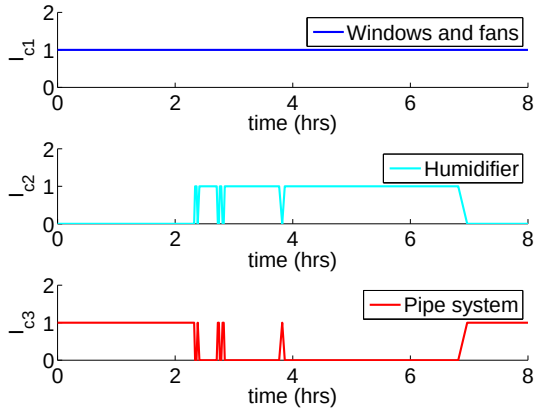

Figure 6. Control law for Pipe system, Humidifier, Windows and Fans.

proposed methodology is incremental and modular. Thus, $TCPN$ elements can be implemented in a GUI added or removed as necessary. The non-linear On-Off control law that exploits the $TCPN$ structure was presented. This control law allows to reach a required temperature when the target temperature is an interior point of the $int(T_r)$ and it is computed in polynomial time. The proposed control law uses local information of controllable transitions, using the marking error of its input and output places to determine if the firing decreases the marking error. Future work will address the problem of reaching a required temperature considering plants inside the greenhouse as a modular model in the global greenhouse $TCPN$ model.

ACKNOWLEDGMENTS

The research of J. Ruiz-León was performed during his sabbatical stay at the Institute of Information Theory and Automation, Czech Academy of Sciences, supported by CONACyT, Mexico, project 265475.

REFERENCES

Baldan, P., Cocco, N., De Nes, F., Segura, M.L., and Simeoni, M. (2011). Mpath2pn-translating metabolic pathways into petri nets. In *BioPPN2011 Int. Workshop on Biological Processes and Petri Nets, CEUR Workshop Proceedings*, volume 724, 102–116.

Boulard, T. and Baille, A. (1993). A simple greenhouse climate control model incorporating effects of ventilation and evaporative cooling. *Agricultural and Forest Meteorology*, 65(3), 145–157.

Cunha, J.B. et al. (2003). Greenhouse climate models: An overview. In *European Federation for Information Technology in Agriculture Conference, Debrecen, Hungary*.

Desirena-Lopez, G., Vazquez, L., Irevino, A.R., and Gomez-Gutierrez, D. (2014). Thermal modelling for temperature control in mpsoc's using timed continuous petri nets. In *Control Applications (CCA), 2014 IEEE Conference on*, 2135–2140. IEEE.

Dessel, J. and Esparza, j. (1995). *Free Choice Petri Nets*. Press Syndicate of the University of Cambridge.

Garcia-Malacara, J., Ramirez-Trevino, A., Vazquez, C.R., and Aguayo-Lara, E. (2013). Observer design for continuous timed petri nets with product server semantics. In *Emerging Technologies & Factory Automation (ETFA), 2013 IEEE 18th Conference on*, 1–8. IEEE.

Heiner, M., Gilbert, D., and Donaldson, R. (2008). Petri nets for systems and synthetic biology. In *Formal methods for computational systems biology*, 215–264. Springer.

Júlvez, J. and Boel, R.K. (2010). A continuous petri net approach for model predictive control of traffic systems. *Systems, Man and Cybernetics, Part A: Systems and Humans, IEEE Transactions on*, 40(4), 686–697.

Mahulea, C., Seatzu, C., Cabasino, M., and Silva, M. (2012). Fault diagnosis of discrete-event systems using continuous petri nets. *Systems, Man and Cybernetics, Part A: Systems and Humans, IEEE Transactions on*, 42(4), 970–984.

Murata, T. (1989). Petri nets: Properties, analysis and applications. *Proceedings of the IEEE*, 77(4), 541–580.

Pérez-González, A., Begovich, O., and Ruiz-Leon, J. (2014). Modeling of a greenhouse prototype using pso algorithm based on a labview tm application. In *Electrical Engineering, Computing Science and Automatic Control (CCE), 2014 11th International Conference on*, 1–6. IEEE.

Ross-León, R., Ramirez-Trevino, A., Ruiz-Leon, J., and Aguayo-Lara, E. (2014). Local control law for live and bounded continuous petri nets. In *Discrete Event Systems*, volume 12, 129–134.

Silva, M. and Recalde, L. (2002). Petri nets and integrality relaxations: A view of continuous petri net models. *Systems, Man, and Cybernetics, Part C: Applications and Reviews, IEEE Transactions on*, 32(4), 314–327.

Silva, M. and Recalde, L. (2004). On fluidification of petri nets: from discrete to hybrid and continuous models. *Annual Reviews in Control*, 28(2), 253–266.

Tovany, J.L., Ross-León, R., Ruiz-León, J., Ramírez-Treviño, A., and Begovich, O. (2013). Greenhouse modeling using continuous timed petri nets. *Mathematical Problems in Engineering*, 2013.

Van Straten, G., van Willigenburg, G., van Henten, E., and van Ooteghem, R. (2010). *Optimal control of greenhouse cultivation*. CRC press.

Vázquez, C.R., Ramírez, A., Recalde, L., and Silva, M. (2008). On controllability of timed continuous petri nets. In *Hybrid Systems: Computation and Control*, 528–541. Springer.

CHAPTER 6

INTELLIGENT CONTROL

Methods for General Motor Skills based on Neuroevolution to Stabilize a Biped Robot Simulation

Sergio Zapata*, Iván D. Mora**
Gustavo Suarez***

** Semillero de Investigación en Automática y Diseño A+D, Universidad Pontificia Bolivariana, Medellín, Colombia (e-mail: sergio.zapatave@upb.edu.co)*
*** Semillero de Investigación en Automática y Diseño A+D, Universidad Pontificia Bolivariana, Medellín, Colombia (e-mail: ivan.mora@upb.edu.co)*
**** Grupo de Investigación Matemáticas, Universidad Pontificia Bolivariana, Medellín, Colombia (e-mail: gustavo.suarez@upb.edu.co)*

Abstract: One of the main focuses of humanoid robotics is bipedal locomotion which requires a series of continuous phases, called gait cycle. Here is essential to maintain balance, compensate the dynamic of the whole multivariable and nonlinear system. Despite good bipedal gait algorithms have been achieved in various researches, performance is still not enough to be compared to biological systems. Several research projects have tried to compensate this through methods in machine learning, to autonomously generate gaits and stabilize robots. In this paper is firstly presented how a neuroevolution algorithm achieves the stability of a biped robot simulation in the sagittal plane that starts in unstable position. Then three different methods are proposed and analyzed in order to generate full body motions in any state perceived by the robot, complying with the specified task by means of the motor skills learned through neuroevolution together with the implementation of another feedforward neural network.

Keywords: Artificial Intelligence, Neuroevolution, Neural Network, Genetic Algorithm, Biped Locomotion, Stability, Nonlinear Control, Inverted Pendulum.

1. INTRODUCTION AND BACKGROUND

Humanoid robotics has made great strides in the last 30 years regarding the general control of all the robot limbs that allow them to perform complex tasks. Research has focused on human bipedal locomotion, because a machine with this capability easily works in human environments, rather than a conventional robot equipped with wheels.

However this presents great control challenges, caused by the large number of variables involved to achieve gaits without falling in a non-ideal environment. Maintaining balance is a fundamental and necessary requirement in implementing such systems (Siciliano & Khatib, 2008).

Various approaches have been studied to generate dynamically stable legged locomotion, such as the ZMP (Zero Moment Point) (Vukobratović & Borovac, 2004). Nevertheless, it is still difficult to find a robot that outperforms a biological system, leading this to research in self-teaching machines. In this way, many projects have focused on generating gaits in different kinds of robots using machine learning (Tedrake et al., 2005; Manoonpong et al., 2007; Allen & Faloutsos, 2009; Clune et al., 2009; Yosinski et al., 2011).

Though it is essential to generate whole body motions, learned by the own robot, the focus of this paper is to understand that is also important the implementation of some motor skills to achieve robot stabilization, in this case of a biped robot in a phase of the gait cycle, restricted by the sagittal plane.

While there are multiple methods in machine learning, neuroevolution algorithms are promising in this kind of problems (Gomez & Miikkulainen, 2003). Research in these algorithms has resulted in different methods in their application as it is NEAT (Stanley & Miikkulainen, 2002a), HyperNEAT (Stanley et al., 2009) or TWEANNS (Stanley & Miikkulainen, 2002b), among others. These modify the topology of the neural network as it is produced the evolution of the individuals (Back et al., 1997).

These methods have shown very good results in benchmarks such as the simultaneous stabilization of two inverted pendulums, exceeding in performance to other alternatives in unsupervised learning, e.g. reinforcement learning (Gomez & Miikkulainen, 1999).

However, the classic implementation of neuroevolution algorithms, where is evolved a neural network of fixed topology through genetic algorithms, can also have satisfactory results in several tasks related to robotics (Siciliano & Khatib, 2008).

Every individual in the genetic algorithm starts in an initial state and then when each iteration occurs it jumps to a new state, which will be the result of actions taken in the previous.

Thus the neural network acts as the agent of a reinforcement learning algorithm, in which for each state, is executed a particular action. However, while reinforcement learning

knows the actions to be made in every state, neuroevolution provides an overview of the problem and consequently the neural network is not learned for the state, but for the ultimate goal of the task.

When the optimum individual is found for the current task, a series of states and actions occurs, but the neural network is only functional for the evaluated situation and the states seen by the agent, i.e. the neural network might not be useful for other initial conditions or states (Whiteson, 2012).

In this regard, problems with large number of variables, such as humanoid robots (Benbrahim & Franklin, 1997), generate numerous states for which the neural network found, should work. Therefore if the goal is to make a robot control, capable to respond to certain situations properly, even unknown, it is required the generalization of what was learned by the trained neural network.

In this paper is presented the development of a neuroevolution algorithm to achieve the stability of a biped robot simulation in the sagittal plane that starts in an unstable position.

In this way is not taken into account the balance in the horizontal plane and also the robot foot does not slide, it is only evaluated the contact point of the foot with the surface on its front and rear boundaries that can be considered as two passive degrees of freedom, where is involved the interaction between the machine and the environment.

Furthermore three different methods of control are proposed and analyzed, based on a feedforward neural network, with the purpose to generate full body motions in any state or condition perceived by the robot, fulfilling with the specified task of balance.

Therefore, the main focus of this paper, which is the result of an ongoing research project in humanoid robotics at UPB, is to explore the generalization of what was learned from neuroevolution to achieve general motor skills for the biped robot in a controlled environment.

It should be pointed out that the learning process might be achieved with other strategies, neuroevolution was chosen because of the good results found in other tasks, as mentioned before, this means the focus of this paper is not to compare its performance with other unsupervised learning methods.

2. DESCRIPTION OF THE PROBLEM AND SIMULATION

In the context of humanoid robotics, biped locomotion is fundamental to make the robot move efficiently, emulating human behavior. In most of the gait phases implies that the robot stays on one foot, being essential a static equilibrium control, as a first step towards a subsequent locomotion algorithm. Thus it is intended that the robot stays in balance at all times, which is reduced to keep the system's center of mass within the support polygon of the foot.

To simplify the problem, the robot geometry is restricted to the sagittal plane, here is analyzed the center of mass, which position is function of seven revolute joints, i.e. flexion and extension of knee, legs, arms and the ankle of the supporting foot (see Fig. 1).

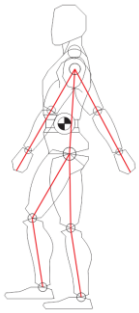

Fig. 1. Sagittal plane and joints of the robot simulation for the implementation of stability control. The red lines represent the links of the robot.

The analysis of the center of mass is based on a system of particles (Marion, 2000), according to the mass of each robot link. The weight and distances are taken from realistic data of a humanoid robot currently in development at UPB.

The center of mass position in $\hat{\imath}$ and $\hat{\jmath}$ (Landau & Lifshitz, 1988), is found as follows,

$$r_{CM}\hat{\imath} = \frac{1}{M}\sum_{i=0}^{n} \tau_i, \tag{1}$$

$$r_{CM}\hat{\jmath} = \frac{1}{M}\sum_{i=0}^{n} m_i |r_i| \sin\theta_i. \tag{2}$$

Where τ, m, θ, and r, are respectively the torque, mass, angle and distance of each particle, M is the total mass of the system. Based on this position, the corresponding to each edge of the foot is calculated, now the robot's behavior is simplified to a simple inverted pendulum.

3. NEUROEVOLUTION ALGORITHM

Every Markov state in the robot simulation is completely determined by 12 variables, including the 7 joints of the robot, the position error (e), angular position (θ), angular speed (ω), lever arm (l) and angular acceleration (α) of the inverted pendulum.

The neural network of fixed topology consists of 12 input neurons, corresponding to the variables listed above, 13 neurons in the hidden layer with hyperbolic tangent activation function and 7 neurons in the output layer with identity activation function. This output is a small increase in the angle of the 7 joints actuated, limited by the actual speed of the actuators (see Fig. 2).

A common criterion to choose the number of neurons in the hidden layer is the arithmetic mean between the inputs and outputs of the neural network. Nevertheless, a set of 90 tests with 7 to 15 neurons in this layer showed that 13 neurons presented slightly better results in the neuroevolution task.

A genetic algorithm evolves the neural network, i.e. optimizes its weights and biases to generate a stabilization move of the robot (Goldberg & Holland, 1988).

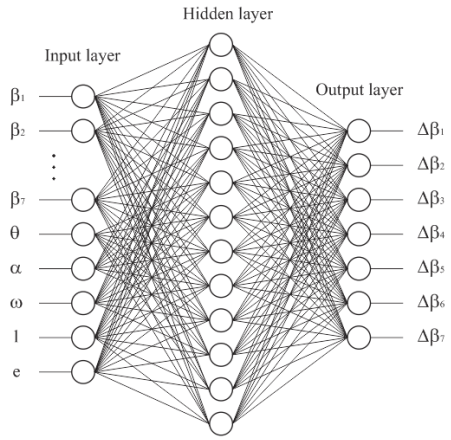

Fig. 2. Artificial neural network to be trained through genetic algorithms, it consists of 12 inputs, 13 neurons in the hidden layer and 7 neurons in the output layer.

The neural network is formed by 247 weights and 20 biases that determine the genotype of each individual of the genetic algorithm. A number of 50 individuals per generation with a crossover of 90% were configured in the genetic algorithm, to achieve good diversity and speed up the learning process. This kind of configuration converges rapidly in high dimensionality cases (Goldberg & Deb, 1991).

On the other hand, to keep the robot balanced, the inverted pendulum that represents it must remain completely vertical, i.e. in 0°, regardless if the foot lies flat on the floor or not. Thus, the fitness function is determined from the MSE (Mean Squared Error) between the reference of 0° and the pendulum angle during the simulation time.

With this, the genetic algorithm must find the individual that configures a neural network that generates a minimum MSE, and hence maintain the robot in balance.

4. RESULTS AND METHODS

Each time the neuroevolution is executed, the robot starts with a random set of angles, assumed as the initial conditions of the system, these assures a center of mass beyond the front edge of the foot, thus if no action is performed the robot will fall forwards because of gravity. Simulation is then run for 3 seconds in which is intended the robot remains stable. The control action is exemplified in Fig. 3.

To determine the effectiveness of the algorithm, were executed 150 tests, of which 89 achieved the expected balance, converging to a low MSE, in no more of 200 generations as shown in Fig. 4. The stabilization process in the simulation, for a particular condition, can be seen in Fig. 5. The corresponding progress in time of angle θ is presented in Fig. 6.

The randomness of the initial angles in some cases led to postures impossible to stabilize with a neural network, it can be said, that even a human would fall.

Thus is demonstrated that neuroevolution was effective for this task of robot stabilization, but this does not indicate that other methods in neuroevolution or in unsupervised learning achieve better or worse results for this simulation. This is not analyzed because the main focus of this paper is not to determine the performance of the various possibilities in this respect.

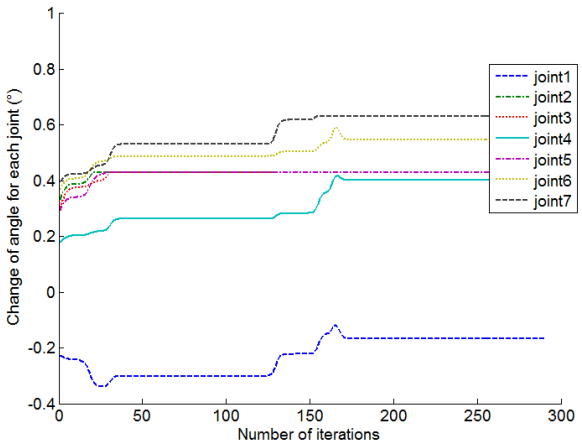

Fig. 3. Change of angles for each iteration for a particular case. The variations in the curves of each joint demonstrate the adjustments produced by the neural network to maintain the robot balanced during the simulation.

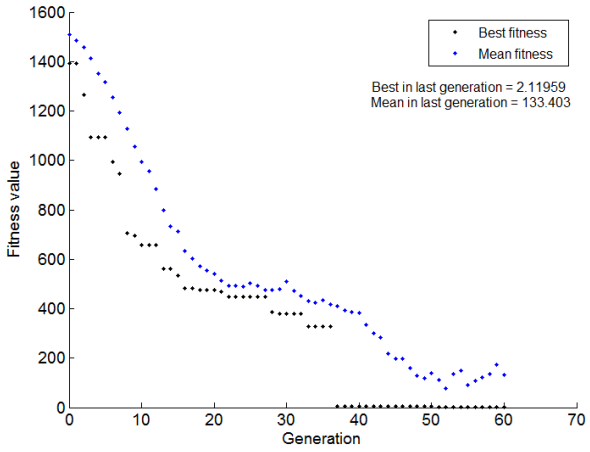

Fig. 4. Best and mean fitness for each generation of the genetic algorithm. For this particular case, the minimization of the MSE is achieved in 60 generations. The best fitness in the last generation is 2.11959, an acceptable value for the process, because with the movement of the robot to stop the falling and stay in 0°, is not possible a null MSE.

On the other hand, notorious changes were observed in the stabilization process under low variations in the states, demonstrating the high instability of the system. As pointed out previously, the algorithm is only useful while the initial conditions and the subsequent states do not change, otherwise the neural network is not robust enough to deal with other cases, and even less in systems like the evaluated.

The non-robustness of the neural network was evidenced when a slight change of 0.01° in only one angle of the initial conditions of a previous successful case, produced an entirely different result in the simulation, leading to the fall of the robot.

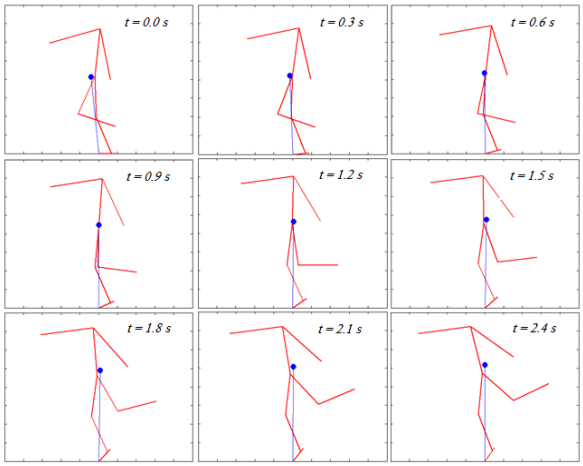

Fig. 5. Simulation of the bipedal robot in the sagittal plane, executing one stabilization process. The red lines represent the robot links and the blue line represents the inverted pendulum. As can be seen, the movement of the robot maintains it vertical.

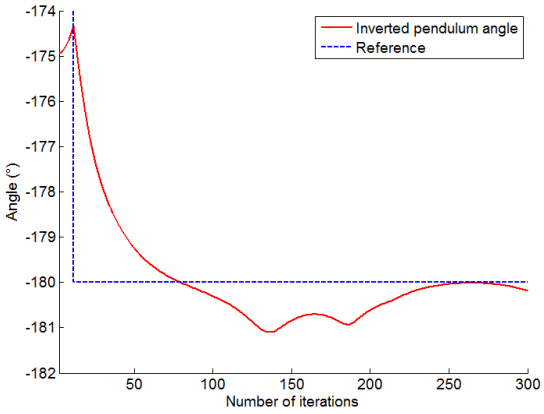

Fig. 6. Change of angle θ of the inverted pendulum representation. Here the reference is -180°, i.e. when the pendulum is vertical, moreover the actions of the neural network begin 10 iterations after the simulation is started, in this way the robot should recover from falling.

The mere implementation of neuroevolution in a real robot is unpractical, because the learning process with the genetic algorithm, for a particular case, requires a large number of tests, and the solution could be only useful for that situation.

In this sense, an offline learning of different cases in conjunction with the generalization of the motor skills and combining it with some online learning could be very useful in solving different control tasks on real robots. Therefore, to increase neural network robustness and in order to achieve an overall stability control, three approaches presented below were proposed.

4.1 Retraining of the Neural Network

One of the main causes of the low robustness is because the neural network was only trained for a particular case, therefore a possible solution is to retrain it again with the genetic algorithm, but starting with an initial population based on the individuals of the latest generation obtained in the previous case.

When evaluated this method was found that the genetic algorithm evolved again the neural network finding an optimum individual, but leaving behind the weights and biases that formed the previous neural network, being only useful again for the current case.

Although this method was not successful in the generalization of the motor skills learned previously, it provided a better overview in how to treat this problem. In this way the next two methods separate the learning process and the final motion control.

4.2 Individuals as Training Data for Neural Network

This method seeks to train a second neural network by backpropagation, its inputs are the 12 variables that define the states, and the outputs are the 267 weights and biases that determine the neural network that ultimately generates the actions for the robot. Therefore, it is intended that under a known initial condition, a specific neural network executes the right set of actions that achieve robot balance.

The neural network is made of 186 neurons in the hidden layer, chosen arbitrarily, requiring with this an updating process of 52347 weights and biases, leading to a slow learning rate and high computational cost.

Furthermore, is not guaranteed for unknown initial conditions that the neural network output defines correctly the 267 weights and biases for a neural network that achieves stability, this is because the successful solutions of the problems already executed, might be formed by very different weights, even for similar cases.

Because of the high computational cost and the other reasons exposed, this method was not tested.

4.3 Training of Neural Network with State-Action Data

When simulation is executed, the robot begins in an initial state and through the actions made inside the environment, passes to another state. In this way, although the neural network is learned according to the overview of the genetic algorithm, for each state executes an action that determines a subsequent state and its sequence will define the success rate of the process in the corresponding task.

Specifically, each simulation is executed for 3 seconds, in 300 iterations, thus having 300 different states and actions for every case evaluated. Therefore, in this method is intended to train a second neural network with sets of state-action. A diagram of this method is shown in Fig. 7.

This neural network, called neural network for robot control, is similarly formed to the executed in neuroevolution, with 12 input variables and 7 outputs, but now with 70 neurons in the hidden layer (see Fig. 8). Because the network is trained by backpropagation with the Levenberg–Marquardt algorithm, based on the state-actions sets obtained in the neuroevolution process, the possibility of losing usefulness for different cases is reduced, being with this a data fitting problem.

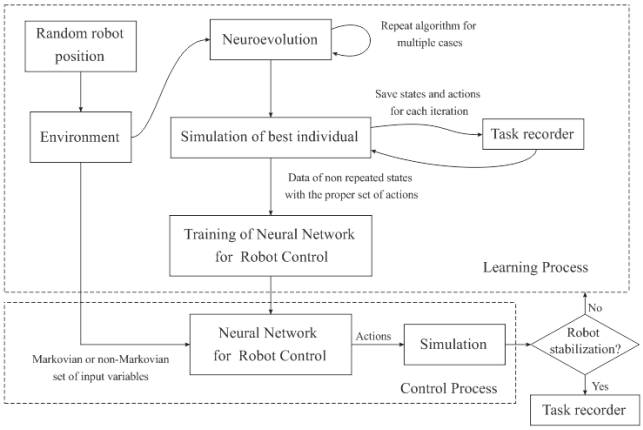

Fig. 7. Diagram of the third method proposed. Its main goal is to maintain a constant learning, initially should be prioritize the learning process, afterwards the control process, however at this stage whether stabilization is not achieved, learning must be done again.

The 89 cases that reached the stabilization produced 26700 sets of state-action, where the repeated states were deleted, according to the set of actions that achieved the least MSE.

The large number of neurons in the hidden layer was required to get a better performance in the data fitting of the neural network.

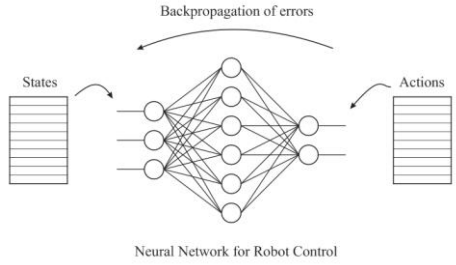

Fig. 8. Neural network for robot control, trained by backpropagation with the states-actions data.

Thereby, after being trained, tests were conducted with initial conditions already proved, obtaining actions for each state very similar to those obtained by neuroevolution, in most of the cases with an error not greater than 0.07% in the angular change of the seven joints. This similarity for a particular case can be observed in Fig. 9.

In order to have a good fitting of all the data, slight variations in the output are inevitable with the backpropagation training. Therefore, even with the low error observed, sometimes the robot simulation is no capable to maintain balance, when it should do. This demonstrates the instability of the system, where a minor change in actions, leads to a set of new states slightly different, and that together determine a different behavior than expected.

Nevertheless, this does not demonstrate the capability of the method to generate proper motor skills in other kind of tasks. With a less unstable system or unstable at all, the robot's behavior could be very close to the expected and effectuate good general motor skills (Peters, 2007), i.e. generalize a behavior through the neural network for robot control based on the experiments of the neuroevolution.

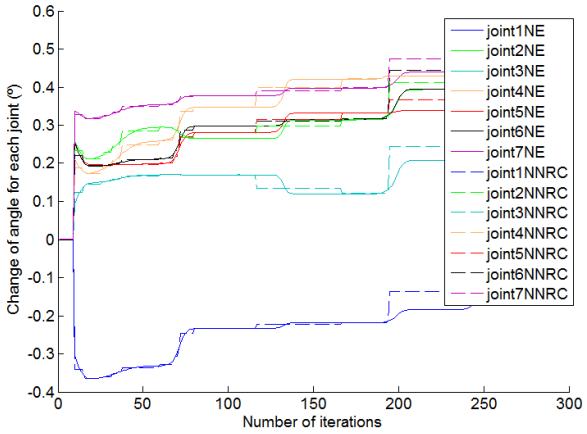

Fig. 9. Comparison between the actions commanded with neuroevolution (NE) and the actions obtained with the neural network for robot control (NNRC), denoted in dashed lines.

5. DISCUSSION

The neuroevolution process and the implementation of the third method was also applied to a simulation in which some variables of the system are unknown, specifically the angular acceleration (α) and the error (e). These cases could be considered as non-Markovian tasks.

For these cases, the neuroevolution process also achieved, in 80% of the tests, the system stabilization. The generalization of the task through the neural network for robot control was likewise effective giving the right actions for the states seen by the agent, but with the fails explained in the previous section.

Although the said failures, that are mostly caused for the system instability, as said before, a better performance could be seen in non-unstable systems, like the implementation in robots for objects manipulation (Pastor, 2009; Pastor, 2012; Lenz et al., 2015), or full body behaviors in order to create complex motor skills in locomotion tasks (Schaal, 1999), that are also of great interest for research in humanoid robotics.

6. CONCLUSIONS AND FUTURE WORK

In this paper was presented how through a neuroevolution algorithm, with a neural network of fixed topology, was achieved in 89 of 150 tests, that the simulation of a bipedal robot in the sagittal plane kept the balance over a period of 3 seconds, demonstrating the effectiveness of this class of evolutionary algorithms to provide reliable solutions in multivariable, nonlinear and unstable systems. Even in non-Markovian tasks.

Besides was demonstrated that the neuroevolution algorithm by itself is only useful for the agent with the corresponding states and initial conditions, being found that a variation of 0.01° in one joint, could lead the robot to lose the balance, this also caused by unstable nature of the system.

In order to generate a control useful for different states and then being able to produce general motor skills for the task, three approaches were proposed.

The first method, which consisted in retraining the neural network by the neuroevolution algorithm based on the previous case individuals, did not achieve good results, because the retraining process modifies the weights of the network and is not functional again for the previous case.

The second method, in which was intended to get at the output of a feedforward neural network the individuals that configured the neural network, that ultimately would give the actions, was not carried out due to the high computational cost and the limited guarantees that this method could find right individuals to perform the task.

In the third method, a neural network was trained by backpropagation with state-action datasets, obtained in the tests made through neuroevolution, had promising results being capable to output the right actions according to the state seen by the robot, even without being previously learned.

It is concluded that the third method is the most appropriate approach to generate the control of this system and other kind of tasks through full body motions.

This last approach allows the system from a simulation, learn by itself according to its surrounding environment, being able later to generalize a proper behavior to achieve a specific task, facilitating its implementation on the real robot.

In this way, research will continue around a larger number of tests to strengthen control and then assess its applicability in other types of robotic systems.

In addition the main focus of this research is to develop such controls in more complex simulations, with the system's behavior in a three dimensional environment and with the full dynamics of the robot, and thus being able to be later extrapolated to a real robot.

REFERENCES

Allen, B. F., & Faloutsos, P. (2009). Evolved controllers for simulated locomotion. In Motion in games (pp. 219-230). Springer Berlin Heidelberg.

Back, T., Fogel, D. B., & Michalewicz, Z. (1997). Handbook of evolutionary computation. IOP Publishing Ltd..

Benbrahim, H., & Franklin, J. A. (1997). Biped dynamic walking using reinforcement learning. Robotics and Autonomous Systems, 22(3), 283-302.

Clune, J., Beckmann, B. E., Ofria, C., & Pennock, R. T. (2009, May). Evolving coordinated quadruped gaits with the HyperNEAT generative encoding. In Evolutionary Computation, 2009. CEC'09. IEEE Congress on (pp. 2764-2771). IEEE.

Goldberg, D. E., & Deb, K. (1991). A comparative analysis of selection schemes used in genetic algorithms. Foundations of genetic algorithms, 1, 69-93.

Goldberg, D. E., & Holland, J. H. (1988). Genetic algorithms and machine learning. Machine learning, 3(2), 95-99.

Gomez, F. J., & Miikkulainen, R. (1999, July). Solving non-Markovian control tasks with neuroevolution. In IJCAI (Vol. 99, pp. 1356-1361).

Gomez, F. J., & Miikkulainen, R. (2003). Robust non-linear control through neuroevolution. Computer Science Department, University of Texas at Austin.

Landau, L., & Lifshitz, E. (1988). Curso de física teórica. Barcelona [etc.]: Reverté.

Lenz, I., Lee, H., & Saxena, A. (2015). Deep learning for detecting robotic grasps. The International Journal of Robotics Research, 34(4-5), 705-724.

Manoonpong, P., Geng, T., Kulvicius, T., Porr, B., & Wörgötter, F. (2007). Adaptive, fast walking in a biped robot under neuronal control and learning. PLoS Comput Biol, 3(7), e134.

Marion, J. (2000). Dinámica de las partículas y sistemas. Barcelona: Editorial Reverté.

Pastor, P., Hoffmann, H., Asfour, T., & Schaal, S. (2009, May). Learning and generalization of motor skills by learning from demonstration. In Robotics and Automation, 2009. ICRA'09. IEEE International Conference on (pp. 763-768). IEEE.

Pastor, P., Kalakrishnan, M., Righetti, L., & Schaal, S. (2012, November). Towards associative skill memories. In Humanoid Robots (Humanoids), 2012 12th IEEE-RAS International Conference on (pp. 309-315). IEEE.

Peters, J. R. (2007). Machine learning of motor skills for robotics (Doctoral dissertation, University of Southern California).

Schaal, S. (1999). Is imitation learning the route to humanoid robots?. Trends in cognitive sciences, 3(6), 233-242.

Siciliano, B., & Khatib, O. (2008). Biped Robots in the ZMP Scheme. Handbook of robotics, Springer. ISBN: 978-3-540-23957-4.

Stanley, K. O., & Miikkulainen, R. (2002a). Evolving neural networks through augmenting topologies. Evolutionary computation, 10(2), 99-127.

Stanley, K. O., & Miikkulainen, R. (2002b). Efficient evolution of neural network topologies. In Evolutionary Computation, 2002. CEC'02. Proceedings of the 2002 Congress on (Vol. 2, pp. 1757-1762). IEEE.

Stanley, K. O., D'Ambrosio, D. B., & Gauci, J. (2009). A hypercube-based encoding for evolving large-scale neural networks. Artificial life, 15(2), 185-212.

Tedrake, R., Zhang, T. W., & Seung, H. S. (2005, June). Learning to walk in 20 minutes. In Proceedings of the Fourteenth Yale Workshop on Adaptive and Learning Systems (Vol. 95585).

Vukobratović, M., & Borovac, B. (2004). Zero-moment point—thirty five years of its life. International Journal of Humanoid Robotics, 1(01), 157-173.

Whiteson, S. (2012). Evolutionary computation for reinforcement learning. In Reinforcement Learning (pp. 325-355). Springer Berlin Heidelberg.

Yosinski, J., Clune, J., Hidalgo, D., Nguyen, S., Zagal, J., & Lipson, H. (2011). Evolving robot gaits in hardware: the HyperNEAT generative encoding vs. parameter optimization. In Proceedings of the 20th European Conference on Artificial Life (pp. 890-897).

Metodología para el Control Difuso de una Planta Desalinizadora por Ósmosis Inversa

Mendoza-Montalvo J. * **Sotomayor-Moriano J.** **
Moreno-Rosario D. *** **Perez-Zuñiga G.** ****

* *Pontificia Universidad Católica del Perú, Av. Universitaria 1801 Lima, Perú (e-mail: jimmy.mendoza@pucp.pe)*
** *Pontificia Universidad Católica del Perú, Av. Universitaria 1801 Lima, Perú (e-mail: jsotom@pucp.edu.pe)*
*** *Pontificia Universidad Católica del Perú, Av. Universitaria 1801 Lima, Perú (e-mail: dennys.moreno@pucp.edu.pe)*
**** *Pontificia Universidad Católica del Perú, Av. Universitaria 1801 Lima, Perú (e-mail: gustavo.perez@pucp.pe)*

Resumen: La creciente demanda en consumo de agua desalinizada, plantea el desarrollo de sistemas de control en las plantas desalinizadoras, con los cuales se pueda lograr maximizar el rendimiento de estas en cantidad de flujo y calidad de agua permeada, así como minimizar el consumo de energía (Bartman et al., 2010). En el presente trabajo se propone una metodología para el diseño del sistema de control de una planta desalinizadora por ósmosis inversa (OI), que emplea el control difuso como una alternativa de aplicación práctica. El desempeño del sistema de control propuesto es evaluado comparándolo con otras técnicas de control. La metodología propuesta es aplicada en una planta piloto de OI experimental, empleada en investigación y enseñanza de técnicas de control para plantas multivariables.

Palabras Clave: Control Difuso, Ósmosis Inversa, Planta Multivariable, Educación en Control.

1. INTRODUCCIÓN

La escasez de agua dulce es causada e incrementada por factores como cambio climático, creciente demanda de energía, crecimiento demográfico y el uso indiscriminado de recursos hídricos (García-Rodríguez et al., 2001). Del total de agua disponible en el mundo, solo el 2.5 % es agua dulce (Gleick et al., 1993; Castillo-García et al., 2013) aprovechable para consumo humano y se encuentra concentrada en glaciares, lagos, ríos y depósitos subterráneos (Rivas-Pérez et al., 2003). Una alternativa para intentar dar solución a este problema es la desalinización de agua de mar, ya que utiliza esta vasta reserva de agua disponible en el planeta (Ramilo et al., 2003). Entre las técnicas conocidas de desalinización, la que utiliza el principio de ósmosis inversa (OI), es aquella que demanda menor cantidad de energía, por lo cual es la más eficiente y competitiva actualmente (Voutchkov, 2012).

La desalinización por OI, consiste en remover el soluto del agua, presurizando y empujando la misma a través de una membrana semipermeable. Como resultado del proceso se tiene: líquido permeado bajo en sales y, como desecho, salmuera (Dababneh and Al-Nimr, 2003). Para lograr lo anterior, la presión que se aplica a la solución con mayor concentración de soluto, debe superar la presión osmótica. Los requerimientos de presión para hacer posible este proceso alcanzan los valores de 1000 a 1200 psi para agua de mar y de 100 a 600 psi para agua salobre (Li, 2011). En el caso de los bastidores de OI para la desalinización de agua de mar, el control debe garantizar una cantidad y calidad determinada de agua sin sobrepasar los límites operativos naturales del proceso (Alatiqi et al., 1999). De manera concreta, la cantidad de producto resultante es medido por el flujo de agua permeada (F), mientras que la medida de la calidad de esta es la conductividad presente (C). Diversas estrategias han sido propuestas para el control de estas variables en bastidores de OI.

Entre las estrategias de control convencional, se propuso un controlador PI sintonizado empleando el criterio de Ziegler-Nichols para una unidad piloto de OI (Alatiqi et al., 1989). La identificación de la planta se llevó a cabo utilizando la respuesta en lazo abierto ante escalones de entrada tanto para la presión como para el pH del agua a la entrada del bastidor. Los resultados de desempeño fueron aceptables, sin embargo, un mejor control podría lograrse si se tomase en cuenta los múltiples efectos de las variables manipuladas. Otro trabajo representativo es el desarrollado por Riverol (Riverol and Pilipovik, 2005), en el cual se propone un sistema de control para una unidad de OI basado en el desacoplamiento de variables. En este caso, se controló el proceso con dos lazos de control independientes. La ventaja del sistema propuesto es su relativo fácil diseño e implementación; sin embargo, tiene la desventaja que, ante variaciones de parámetros en la planta, el controlador y desacoplador deben ser modificados.

Entre las estrategias de control avanzado, se propuso un controlador predictivo de tipo DMC basado en restricciones (Robertson et al., 1996), el cual ofrece un mejor desempeño en el control de la conductividad que el

controlador PI. Los resultados son simulaciones con uso de un software basado en DMC llamado ONLINE que actuó como caja negra, donde se variaron parámetros como los horizontes de predicción y control, así como los pesos del controlador. Otro trabajo importante propone Assef (Assef et al., 1997), quien desarrolla un controlador predictivo basado en modelo (CMPC) considerando un sistema MIMO para una planta de OI de 4 salidas (flujo, conductividad, presión en la membrana y pH de entrada) y 2 entradas (flujo de agua salobre rechazada y flujo de ácido de entrada). La identificación fue realizada a partir de un estado estacionario, aplicando escalones a cada entrada y registrando las respuestas en cada una de las salidas. Para la implementación del control también se trabajó con un sistema de tipo caja negra, el cual permitía agregar restricciones a las variables de entrada. Los resultados mostraron un incremento del rendimiento en flujo desalinizado; sin embargo, el software usado solo permite realizar cambios en los pesos y horizontes.

En la actualidad, la creciente demanda en consumo de agua desalinizada, plantea el requerimiento de sistemas de control para unidades de OI que permitan maximizar el rendimiento en términos de cantidad de flujo y calidad del agua permeada, así como minimizar el consumo de energía. En este caso, resultaría conveniente el uso de un sistema de control con el cual se logren los requerimientos mencionados y que en la práctica resulte de fácil diseño e implementación. En este trabajo se propone una metodología, la cual permite diseñar e implementar el sistema de control para una unidad de OI empleando el control difuso como una alternativa de aplicación práctica que no está basada en modelos matemáticos.

En la sección 2, se describe una unidad experimental de OI. La metodología de diseño del sistema con control difuso propuesta es desarrollada en la sección 3, donde también se describe el diseño del sistema con control predictivo GPC. En la sección 4, el desempeño del sistema de control con controladores difusos propuesto se comparará con los alcanzados por otros controladores (GPC y PI). Las conclusiones son descritas en la sección 5.

2. DESCRIPCIÓN DE UNA PLANTA PILOTO DE DESALINIZACIÓN POR OI

La planta de desalinización por OI objeto de estudio es una planta piloto que se encuentra situada en el Laboratorio de Control y Automatización de la PUCP (ver Fig. 1), en esta se pueden realizar ensayos experimentales de laboratorio aplicados a la investigación. Esta planta cuenta con componentes básicos que permiten la desmineralización y separación de sólidos disueltos del agua aplicando una presión superior y en sentido inverso a la presión osmótica. Los cuatro procesos fundamentales que se utilizan son: pre-tratamiento, presurización, separación por membrana y almacenamiento. Es decir, su construcción se basó en etapas en las cuales se eliminan los componentes orgánicos y las sales presentes en el agua de alimentación, utilizando la tecnología de OI.

El pre-tratamiento tiene como objetivo la preparación del agua de alimentación (extraída de un tanque) de tal manera que sea compatible con la membrana de OI. Esto es, la aplicación de filtros UV, filtros de carbón y filtros multimedia para eliminar sólidos en suspensión, bacterias, virus y coloides. Asimismo, se lleva a cabo el ajuste de pH, cuyo fin es la precipitación de carbonatos en el agua de alimentación y también la reducción de la conductividad del agua permeada. La etapa de presurización se lleva a cabo cuando el agua pre-tratada fluye a través de la bomba de alta presión; mediante la variación de la velocidad del motor de la bomba es posible variar la presión del agua que fluye a través de ella. La separación de iones se realiza dentro de las membranas de OI.

Estas membranas inhiben el paso de sales, pero permiten el paso de agua y como resultado se tiene un flujo de agua permeada y otro de salmuera. Dado que las membranas no ofrecen un rechazo de sales de 100 %, es usual que el agua permeada tenga algunas sales disueltas. La última etapa es la de almacenamiento y consiste en el acopio del agua producto y de la salmuera en tanques.

Fig. 1. Unidad de OI del Laboratorio de Control y Automatización de la PUCP.

Las variables controladas en este proceso son el flujo (F) y la conductividad (C) del permeado. Las variables de entrada del proceso son aquellas que mediante su manipulación se pueda alcanzar los valores deseados de las variables de salida. En este proceso las variables de entrada son la presión (P), con la que el agua salina ingresa a la membrana y que es manipulada con el variador de frecuencia de la bomba y, el potencial de hidrógeno (pH) del agua de alimentación, que es manipulada variando la cantidad de aditivo dosificado en la etapa de pre-tratamiento. La planta piloto cuenta con diversos instrumentos como sensores de P, pH, F, C e incluso sensores de temperatura. Un diagrama funcional del proceso descrito se puede observar en la Fig. 2.

Mediante ensayos experimentales en estado estacionario en esta unidad de OI, se determinaron los rangos lineales de las variables, los cuales se muestran en la Tabla 1.

Tabla 1. Rango de operación lineal de las variables del bastidor de OI.

Variable	Rango Lineal
Flujo, gpm	0.85-1.25
Presión, psi	800-1000
Conductividad, μS/cm	400-450
pH	6-7

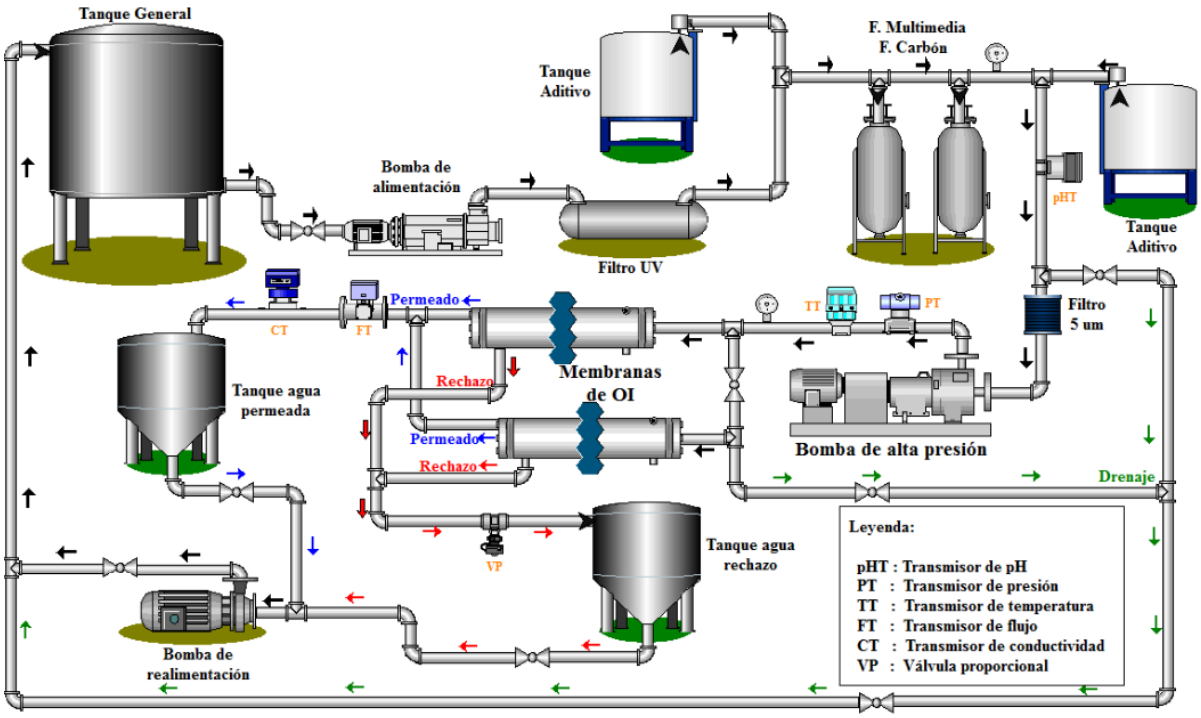

Fig. 2. Diagrama funcional de la planta piloto de OI.

Según la Tabla 1, los estados iniciales de operación del bastidor son distintos a cero, sin embargo, estos pueden ser normalizados como ceros usando la relación de las variables de entrada y salida.

3. DISEÑO DEL SISTEMA DE CONTROL PARA UNA PLANTA DESALINIZADORA POR OI

3.1 Diseño con Control Difuso

El uso del control difuso se presenta como alternativa interesante en el diseño del sistema de control de un bastidor de OI de una planta desalinizadora, debido a que este tipo de control presenta la característica principal de no utilizar un modelo del proceso durante el diseño del mismo, sino parte de conocimiento experimental previo (experiencia del operador) para desarrollar una base de reglas con la cual se pueda mantener las variables de control en las referencias deseadas. La estrategia de control propuesta usa dos bloques difusos, donde la variable elaborada por el primer controlador difuso es una de las entradas del segundo controlador difuso (ver Fig. 3). Con esta estrategia, es posible mantener la variable de conductividad eléctrica del permeado (C) en la referencia deseada tomando en consideración el efecto que tiene la manipulación de la variable presión en el agua de alimentación, durante el control de la variable flujo volumétrico del permeado (F).

Las señales de entrada del controlador son los errores en el flujo y conductividad (e_F y e_C) producidos luego de la comparación de las variables medidas con los valores de consigna. Por otro lado, las señales de salida del controlador son las variaciones en la presión (ΔP) y el pH (ΔpH) necesarios para alcanzar las referencias.

En un primer paso, se realiza el diseño del primer controlador difuso. Para ello se establece como entrada adicional la razón de cambio del flujo volumétrico del permeado con

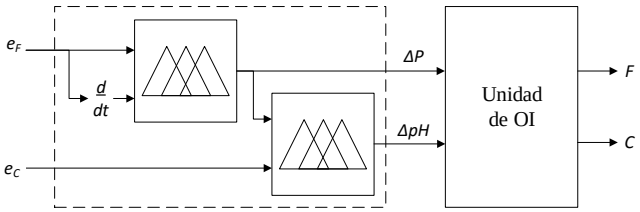

Fig. 3. Sistema de Control con Control difuso propuesto para una unidad de OI.

respecto del tiempo (de_F/dt). Posteriormente se definen 3 funciones de membresía sobre el rango de variación del flujo volumétrico del permeado, su razón de cambio y la variación de la presión del agua de alimentación. Estas funciones de membresía se refieren al grado de pertenencia con respecto a un valor lingüístico. La cantidad de las mismas fue suficiente pues la variable de flujo se caracteriza por ser una variable rápida cuando se controla mediante la presión. De acuerdo a la demanda de la planta objeto de estudio los rangos determinados fueron los siguientes: ± 0.1 gpm para el error en el flujo volumétrico del permeado, ± 0.5 gpm/s para la razón de cambio y ± 5 psi para la presión de alimentación.

El segundo controlador se diseña considerando además la influencia de la presión en el agua de alimentación, elaborada por el primer controlador, como variable de entrada adicional. Se definen, entonces, 5 funciones de pertenencia para las variables de entrada de este controlador. El rango de variación para la variable de entrada fue de ± 10 μS/cm para la conductividad, y ± 150 psi para la variable adicional. Sin embargo, debido a la fuerte interacción de esta última, se definieron 7 particiones en variable de pH con un rango de variación de ± 0.6. Seguidamente, se desarrolla la base de reglas para mantener la variación en el flujo volumétrico del permeado (ver Tabla 2).

Tabla 2. Base de reglas del primer controlador difuso.

	LF	MF	HF
DE	HP	LP	LP
Z	HP	MP	LP
IN	HP	HP	LP

donde: LF – bajo flujo, MF – medio flujo, HF – alto flujo, DE – decreciendo, Z – cero, IN – incrementándose, HP – alta presión, MP – media presión, LP – baja presión.

Con la información de la presión aplicada al agua de alimentación por parte del primer controlador difuso, se elabora la base de reglas para mantener la variación en la conductividad eléctrica del permeado (ver Tabla 3).

Tabla 3. Base de reglas del segundo controlador difuso.

	LLP	LP	MP	HP	HHP
LLC	H3	H3	H3	L1	L3
LC	H3	H3	H3	L1	L3
MC	H3	H3	M	H1	L1
HC	H3	H3	H3	H3	L3
HHC	H3	H3	H3	H3	L3

donde: LLP – muy baja presión, LP – baja presión, MP – media presión, HP – alta presión, HHP – muy alta presión, LLC – muy baja conductividad, LC – baja conductividad, MC – media conductividad, HC – alta conductividad, HHC – muy alta conductividad. L3, L2, L1, M, H1, H2, H3 corresponde la magnitud desde un bajo valor de pH hasta un valor alto de acuerdo al rango de variación establecido.

La estructura de los controladores difusos es tipo Mandani. Dado que la configuración del controlador difuso solo garantiza estabilizar las variables de control, es necesario añadir una acción integral que permita eliminar el error en estado estacionario (ver Fig. 4).

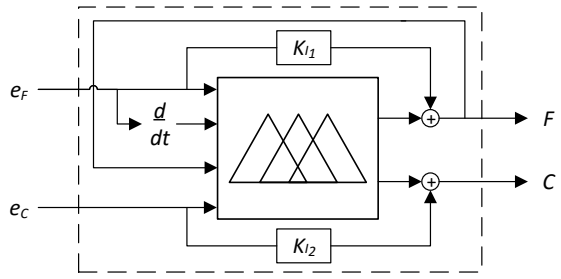

Fig. 4. Control difuso con acción integral.

Una vez determinada la estrategia del sistema de control, se procedió a la implementación del mismo considerando una ganancia de los términos integrativos nulos. Entonces, se ajusta la primera ganancia. K_{I_1}, hasta obtener una respuesta rápida para la demanda de flujo de permeado. Posteriormente, se ajusta la segunda ganancia, K_{I_2}, partiendo desde valores muy pequeños, del orden de -10^{-5}, hasta alcanzar una respuesta que garantice obtener una máxima calidad del producto.

3.2 Diseño con Control Predictivo

La Fig. 5 presenta el sistema de control basado en GPC para la planta desalinizadora por OI.

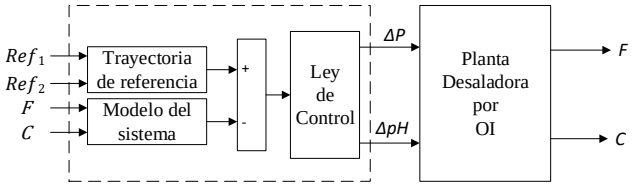

Fig. 5. Sistema de Control con Control GPC diseñado para una unidad de OI.

Para la planta piloto (2 entradas y 2 salidas) se aplicó el caso GPC multivariable, que usa un modelo CARIMA (Camacho and Alba, 2013) como se muestra en (1). Este modelo contiene las matrices polinomiales mónicas $A(z^{-1})$ y $B(z^{-1})$ de tamaño 2×2, además, la perturbación es representada por la matriz $C(z^{-1})$ que se asume constante e igual a uno.

$$A(z^{-1})y(t) = B(z^{-1})u(t-1) + C(z^{-1})\frac{e(t)}{\Delta} \qquad (1)$$

donde, $y(t)$ representa las variables de salida (F y C), siendo una matriz 2×1; $u(t)$ son las variables de control, contiene las variaciones en la presión (ΔP) y el pH (ΔpH) y es una matriz 2×1; $e(t)$ es la perturbación, ruido blanco de media cero (matriz 2×1). Para el cálculo de la ley de control, se consideró la siguiente función de costo del caso multivariable:

$$J = \sum_{N_1}^{N_2} \|\hat{y}(t+j) - w(t+j)\|_R^2 + \sum_{j=1}^{N_u} \|\Delta u(t+j-1)\|_Q^2, \quad (2)$$

donde N_1 y N_2, y N_u son los horizontes de predicción y de control respectivamente. R es una matriz diagonal positiva que pondera el seguimiento de las predicciones del modelo $\hat{y}(t+j)$ a lo largo del horizonte con la trayectoria de referencia futura $w(t+j)$, mientras que Q es una matriz diagonal positiva que pondera el esfuerzo en el control. Luego del desarrollo de las ecuaciones diofánticas, las predicciones del modelo se pueden escribir de la forma:

$$\tilde{y} = G\Delta u + f, \qquad (3)$$

donde $G\Delta u$ es la respuesta del sistema en base a acciones de control futuras y f es la respuesta libre del sistema producto del efecto de acciones pasadas. Minimizando la función objetivo (2) usando $dJ/du = 0$ y reemplazando en (3), para el caso sin restricciones, se obtiene la respuesta explícita:

$$u = (G^T RG + Q)^{-1} G^T R(w - f), \qquad (4)$$

Debido a la estrategia de control deslizante se usará solo el incremento Δu en cada instante t. Por lo tanto, solo las primeras 2 filas de $(G^T RG + Q)^{-1} G^T R$, también conocido como K, serán calculadas. Entonces la ley de control resulta:

$$\Delta u(t) = K(w - f). \qquad (5)$$

Por otro lado, en el diseño del sistema de control con PI, se empleó una estrategia convencional (Alatiqi et al., 1989):

$$C_{PI}(s) = K_p(1 + \frac{1}{t_i s}). \qquad (6)$$

4. COMPARACIÓN DEL DESEMPEÑO DEL CONTROL DIFUSO, PREDICTIVO Y PI

A continuación, se muestran las pruebas de simulación del sistema de control aplicando el controlador difuso, el controlador GPC, así como el controlador PI, con el objeto de evaluar la efectividad de los mismos frente a cambios de referencia y presencia de perturbaciones durante condiciones reales de operación. Los parámetros de los controladores fueron establecidos de tal manera que garanticen una rápida respuesta y un error en estado estacionario nulo.

Las ganancias integrativas del controlador difuso son: K_i=50 (lazo de control de flujo) y K_i=-0.0002 (lazo de control de conductividad). Para el caso del controlador GPC, los parámetros de diseño fueron: horizonte de control N_u=3, horizonte de predicción N_2=10, $R = diag(3{\cdot}10^5,2)$, $Q = diag(0.5,10^3)$. El controlador PI con ganancias del lazo de control de flujo de permeado: K_p=536 y t_i=13.8, así mismo, un K_p=-0.05 y t_i=108.6 para el lazo de control de conductividad del permeado.

La primera prueba fue llevada a cabo considerando un cambio simultáneo de la referencia en las variables de control, de 1.0 gpm a 1.2 gpm para el flujo y 450 μS/cm a 410 μS/cm para la conductividad eléctrica, emulando la operación de la planta con una producción y una calidad tales que se encuentren dentro de lo establecido por la OMS para consumo humano y además que el consumo de energía sea el necesario para lograr este objetivo. En la Fig. 6, una referencia en la variable de flujo de permeado es alcanzado en 60 s al emplear el controlador difuso, mientras que el GPC logra este objetivo en 40 s y el PI requiere 120 s. Se observa, también, que en todos los casos no existe sobreimpulso ni error en estado estacionario. Por otro lado, una referencia en la variable de conductividad del permeado se alcanza en aproximadamente 155 s, utilizando el controlador difuso, y 180 s, con el GPC, mientras que el controlador PI logra llegar a esta referencia en 295 s. Estos resultados muestran que los valores de consigna son alcanzados en menor tiempo en un caso (flujo) con uso del GPC y en otro (conductividad) con uso del controlador difuso.

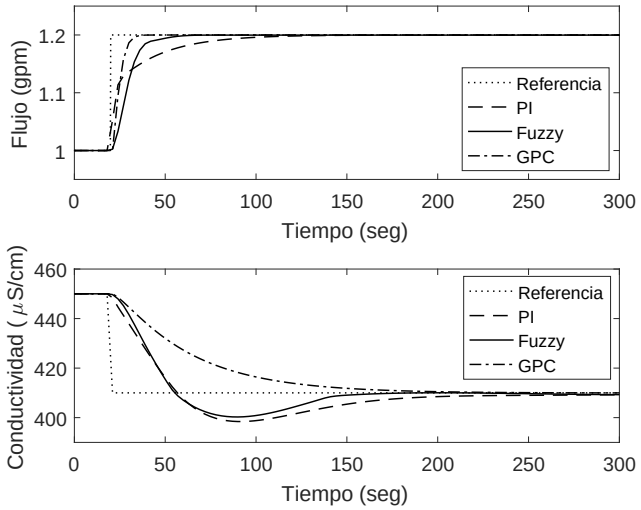

Fig. 6. Comparación de respuestas temporales para el caso de variación simultánea en ambas señales de referencia.

Para evaluar el desempeño de los controladores frente al seguimiento de una referencia, se realizó un cambio abrupto en la referencia del flujo de permeado de 1.2 gpm a 1.0 gpm, interpretándose como un instante donde la producción es mínima. Este escenario implica la disminución de la energía entregada por la bomba de alta presión, la que debe ser sopesada mediante el ajuste del valor del pH operando la bomba dosificadora. En la Fig. 7 se observa las respuestas temporales, donde el PI presenta un mayor sobreimpulso, mientras que con el controlador difuso disminuye. A su vez, el controlador GPC logra en menor tiempo alcanzar la señal de referencia, a costa de un mayor esfuerzo de control.

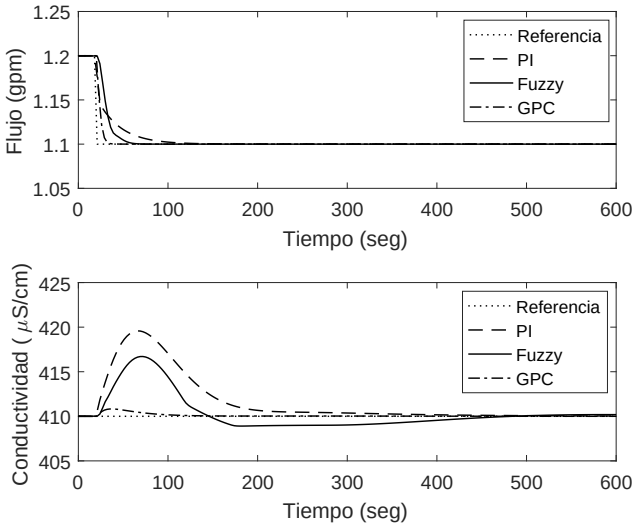

Fig. 7. Comparación de respuestas temporales para el caso de seguimiento de una referencia.

Para evaluar la respuesta ante la presencia de perturbaciones, se consideró una perturbación tipo escalón, emulando una fuga de agua producto de 0.05 gpm con el fin de evaluar el rechazo a perturbaciones en la variable de conductividad eléctrica del permeado. Esto conllevó al incremento de la presión en la bomba de alta y una disminución en el pH del agua de alimentación. En la Fig. 8 se exhiben los resultados, donde es posible observar una mayor rapidez en la atenuación de perturbaciones mediante el uso del GPC.

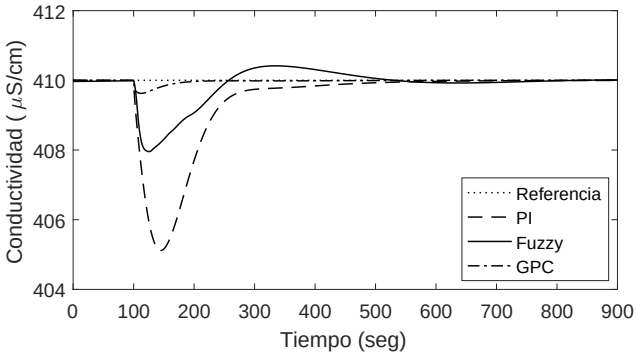

Fig. 8. Comparación de respuestas temporales en la variable de conductividad eléctrica frente a una perturbación tipo escalón en el flujo de -0.05 gpm.

Finalmente, se realizó un análisis de la robustez de los sistemas de control mediante la cuantificación de la efectividad de los controladores diseñados, utilizando los índices de desempeño: integral del error cuadrático (ISE) y el esfuerzo de la señal de control (ISU):

$$ISE = \int_{t_0}^{t_f} e^2(\sigma)d\sigma,$$
$$ISU = \int_{t_0}^{t_f} \left|\frac{\mathrm{d}u(\sigma)}{\mathrm{d}\sigma}\right| d\sigma, \quad (7)$$

donde límites de integración corresponden a los intervalos de tiempo donde las variables de control y las variables de proceso difieren en $\pm 2\,\%$ de su valor en estado estacionario.

La Tabla 4 resume los valores de los índices de desempeño para los casos de control de variable flujo volumétrico y conductividad eléctrica del permeado, además se incluye el tiempo de establecimiento aproximado para el caso del cambio en las referencias.

Tabla 4. Resultados comparativos del sistema de control.

Variable Control	Control	ISE	ISU	Ts(2 %) (seg)
F	PID	$5.37{\cdot}10^{-2}$	46.58	120
	DIFUSO	$9.15{\cdot}10^{-2}$	33.33	60
	GPC	$5.30{\cdot}10^{-2}$	33.33	40
C	PID	$8.81{\cdot}10^{3}$	0.56	295
	DIFUSO	$8.88{\cdot}10^{3}$	0.62	155
	GPC	$1.36{\cdot}10^{4}$	0.46	180

Los resultados obtenidos muestran que el GPC posee una relativa mayor eficacia para el control de las variables del proceso de desalinización por OI con respecto al controlador difuso, sin embargo, este último es una alternativa válida que no requiere del uso de un modelo matemático y de más fácil diseño. En todos los casos, el uso del controlador difuso muestra mejores resultados respecto al PI convencional.

5. CONCLUSIONES

Se propuso una metodología de fácil aplicación para el diseño del sistema de control de una planta desalinizadora por OI basada en control difuso. Las pruebas realizadas mostraron que el desempeño del sistema con el control difuso propuesto exhibe mejores resultados que el uso del PI convencional. El desempeño del sistema con un GPC, exhibe un relativo mejor desempeño que el controlador difuso propuesto, sin embargo, el diseño del GPC obliga a realizar una etapa previa de trabajos de identificación de la planta a fin de obtener su modelo matemático. La planta implementada demostró su validez para llevar a cabo tares de investigación y enseñanza de técnicas de control para plantas multivariables. Como trabajo futuro se propone aplicar la metodología propuesta en plantas reales y validar la facilidad de su implementación.

AGRADECIMIENTOS

Los autores agradecen el apoyo del Programa Nacional de Innovación para la Competitividad y Productividad (Innóvate Perú) entidad que financió el proyecto 207-FINCyT-IA-2013, en el marco del cual se desarrolló el presente artículo.

REFERENCIAS

Alatiqi, I., Ghabris, A., and Ebrahim, S. (1989). System identification and control of reverse osmosis desalination. *Desalination*, 75, 119–140.

Alatiqi, I., Ettouney, H., and El-Dessouky, H. (1999). Process control in water desalination industry: an overview. *Desalination*, 126(1), 15–32.

Assef, J.Z., Watters, J.C., Deshpande, P.B., and Alatiqi, I.M. (1997). Advanced control of a reverse osmosis desalination unit. *Journal of Process Control*, 7(4), 283–289.

Bartman, A.R., Zhu, A., Christofides, P.D., and Cohen, Y. (2010). Minimizing energy consumption in reverse osmosis membrane desalination using optimization-based control. *Journal of Process Control*, 20(10), 1261–1269.

Camacho, E.F. and Alba, C.B. (2013). *Model predictive control*. Springer Science & Business Media.

Castillo-García, F., Feliu-Batlle, V., and Rivas-Pérez, R. (2013). Time domain tuning of fractional order controllers combined with a smith predictor for automation of water distribution in irrigation main channel pools. *Asian Journal of Control*, 15(3), 819–833.

Dababneh, A.J. and Al-Nimr, M. (2003). A reverse osmosis desalination unit. *Desalination*, 153(1), 265–272.

García-Rodríguez, L., Romero-Ternero, V., and Gómez-Camacho, C. (2001). Economic analysis of wind-powered desalination. *Desalination*, 137(1), 259–265.

Gleick, P.H. et al. (1993). *Water in crisis: a guide to the world's fresh water resources*. Oxford University Press, Inc.

Li, M. (2011). Reducing specific energy consumption in reverse osmosis (ro) water desalination: An analysis from first principles. *Desalination*, 276(1), 128–135.

Ramilo, L., Gómez, S., and Coppari, N. (2003). Tecnologías de proceso para desalinización de aguas. *La Revista de la CNEA*, 3(9/10).

Rivas-Pérez, R., Peran Gonzalez, J., Pineda Reyes, B., and Perez Pereira, S. (2003). Distributed control under centralized intelligent supervision in the güira de melena irrigation system. *Ingenieria Hidraulica en Mexico*, 18(2), 53–68.

Riverol, C. and Pilipovik, V. (2005). Mathematical modeling of perfect decoupled control system and its application: A reverse osmosis desalination industrial-scale unit. *Journal of Analytical Methods in Chemistry*, 2005(2), 50–54.

Robertson, M., Watters, J., Desphande, P., Assef, J., and Alatiqi, I. (1996). Model based control for reverse osmosis desalination processes. *Desalination*, 104(1), 59–68.

Voutchkov, N. (2012). *Desalination engineering: planning and design*. McGraw Hill Professional.

Trajectory Following of Truck-Trailer Mobile Robots Integrating Linear and Fuzzy Control

Antonio Moran

Pontifical Catholic University of Peru, Lima, PERU
amoran@pucp.edu.pe

Abstract: The modeling and autonomous control of truck-trailer mobile robots for trajectory following are addressed. The robot kinematical model is analyzed and used for designing a positioning control system based on linear controllers integrated in a fuzzy-logic approach. The design takes into account both positioning performance and jack-knife avoidance. The results of robot positioning control are extended to trajectory following for which a novel strategy is proposed applicable to general shape desired trajectories. The effectiveness of the proposed methods are verified for linear, circular and sinusoidal trajectories where the mobile robot converges to the desired trajectories, avoiding jack-knife positions and with bounded values of input steering angle.

Keywords: Mobile robot, Fuzzy control, Linear-fuzzy integration, Trailer-type robot, Trajectory following

1. INTRODUCTION

Autonomous truck-trailer mobile robots are used in diverse fields in industry given their advantages in delivery and transportation applications. They can accomplish transportation tasks in a faster and cheaper way compared to multiple individual mobile robots. Their transportation capacity increases with the number of trailers pulled or pushed by a truck moving forward or backward.

However, truck-trailer mobile robots configure a complex, nonlinear, unstable, underactuated and nonholonomic system difficult to control, especially when moving backwards, which have led to an intensive research work for analyzing their motion characteristics and autonomous control. The most of work have been based on robot kinematical model valid when the robot moves at low speeds without wheels side-slipping. In this condition, the robot motion is determined only by geometrical considerations independent of masses, inertias and road friction forces.

Diverse control strategies have been proposed to make the truck-trailer robot autonomously moves describing desired trajectories in complex environments. Approximate linearization and feedback linearization of kinematic model equations were used in David et al. (2014), Altafini et al. (2001) and Laumond et al. (1998) for designing stabilizing controllers for robot positioning applicable to a limited range of operating conditions. Chained representation of robot kinematical equations have been used in Sordalen et al. (1993) and Fierro et al. (1995) for designing nonlinear controllers based on feedback linearization and backstepping techniques for positioning and path tracking control. The differentially flat structure of mobile robots has been used for designing controllers in Rouchon et al, (1993) and Michalek et al. (2012).

Fuzzy logic have been used in Cheng et al. (2009), Tanaka et al. (1994) and Kong et al. (1992) to propose diverse control strategies based on human driver experience expressed through linguistic rules. Neural networks have been applied in Nguyen et al. (1989) and Moran (2004) for training connectionist controllers based on static or dynamic learning algorithms. Other techniques based on genetic algorithms and their integration with neural networks and fuzzy systems, have been proposed in Kinjo et al. (2000). The control schemes have been applied to robot positioning, backing up, linear and nonlinear trajectory following, path planning, parallel parking, jack-knife avoidance, robots formation among other control objectives.

2. PROBLEM DEFINITION AND CONTROL STRATEGY

The problem to be solved is the designing of an autonomous control system for the positioning and trajectory following of a truck-trailer mobile robot. The positioning control problem is shown in Figure 1: the mobile robot, starting from arbitrary initial positions, should achieve the desired position without colliding with obstacles around the goal position.

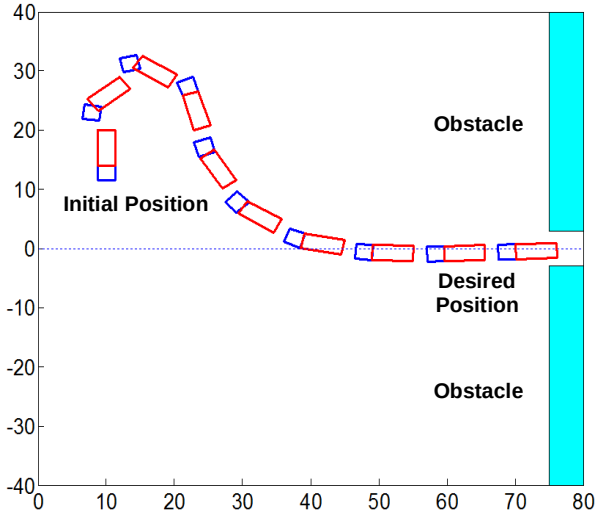

Fig. 1. Mobile robot positioning control problem.

Figure 2 shows a truck-trailer vehicle consisting of a truck with front steering wheels and traction wheels, and a passive trailer with support rear wheels. The trailer is articulated to the truck at the midpoint of the traction axis and it is pulled or pushed by the truck as it moves forward or backward.

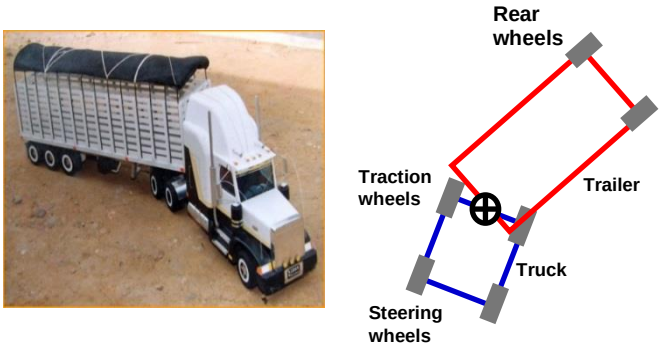

Fig. 2. Truck-trailer mobile robot.

Assuming that left and right wheels move in a similar pattern, the truck-trailer robot can be modeled as a two articulated bars as it is shown in Figure 3. Coordinates (x, y) represent the position of trailer rear wheel, θ_1 and θ_2 are the angles of truck and trailer respect to X axis, θ_{12} is the angle of truck respect to trailer, δ is the steering angle, and L_1 and L_2 are the lengths of truck and trailer, respectively. Counter clockwise angles are positive.

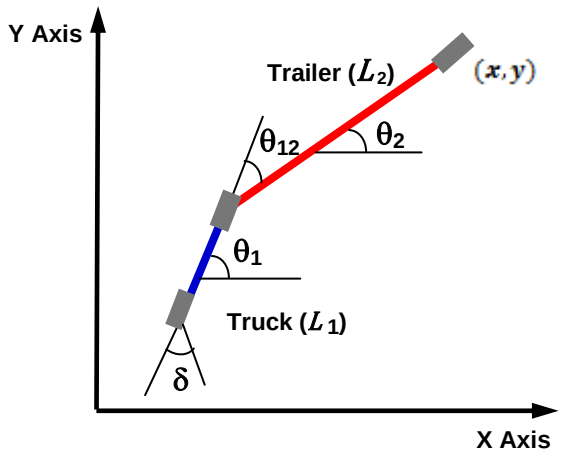

Fig. 3. Two-bars model of truck-trailer robot.

Considering the robot moves at low speeds, it can be assumed that wheels do not side-slip so that lineal velocities of traction and rear wheels are aligned to truck and trailer axis, respectively. Under this consideration, the truck-trailer mobile robot model is given by the following equations:

$$\dot{x} = v \cos\theta_{12} \cos\theta_2 \quad \ldots\ldots\ldots\ldots\ldots\ldots\ldots\ldots \quad (1)$$

$$\dot{y} = v \cos\theta_{12} \sin\theta_2 \quad \ldots\ldots\ldots\ldots\ldots\ldots\ldots\ldots \quad (2)$$

$$\dot{\theta}_1 = -\frac{v}{L_1} \tan\delta \quad \ldots\ldots\ldots\ldots\ldots\ldots\ldots\ldots \quad (3)$$

$$\dot{\theta}_2 = -\frac{v}{L_2} \sin\theta_{12} \quad \ldots\ldots\ldots\ldots\ldots\ldots\ldots\ldots \quad (4)$$

The truck-trailer angle θ_{12} is:

$$\theta_{12} = \theta_1 - \theta_2 \quad \ldots\ldots\ldots\ldots\ldots\ldots\ldots\ldots \quad (5)$$

and from equations (3), (4) and (5) the equation of $\dot{\theta}_{12}$ is obtained:

$$\dot{\theta}_{12} = \frac{v}{L_2} \sin\theta_{12} - \frac{v}{L_1} \tan\delta \quad \ldots\ldots\ldots\ldots\ldots\ldots \quad (6)$$

Considering that the traction wheels moves at constant backward speed (v=constant) and defining the state vector $\mathbf{x}$ and control vector $\mathbf{u}$ as:

$$\mathbf{x} = [y \;\; \theta_2 \;\; \theta_{12}]^T \quad \ldots\ldots\ldots\ldots\ldots\ldots\ldots\ldots \quad (7)$$

$$\mathbf{u} = \tan\delta \quad \ldots\ldots\ldots\ldots\ldots\ldots\ldots\ldots \quad (8)$$

equations (2), (4) and (6) can be represented by the following affine nonlinear state-space equation:

$$\dot{\mathbf{x}} = \boldsymbol{f}(\mathbf{x}) + \boldsymbol{g}(\mathbf{x})\mathrm{u} \qquad \ldots\ldots\ldots\ldots\ldots\ldots\ldots\ldots \quad (9)$$

The no inclusion of coordinate x in state vector $\mathbf{x}$ simplifies the controller design process without affecting the robot positioning and trajectory following capacity as far as it moves only forward or only backward.

To achieve the goal position without colliding with obstacles, it is proposed a control strategy in which the robot prioritizes the achievement of line y^*=0 with horizontal inclination θ_2^*=0°, θ_{12}^*=0° and, afterwards the robot moves straightforward to the goal position as it is shown in Figure 1. With this strategy, coordinate x is not required for control and it is applicable if there is enough space between the robot initial position and the goal position. Considering only three variables $(y, \theta_2, \theta_{12})$ the positioning control problem turns to be a stabilization problem.
Linearizing equations (2), (4) and (6) around the desired angles θ_2^*=0° and θ_{12}^*=0°, the following linear state-space equation is obtained:

$$\begin{bmatrix} \dot{y} \\ \dot{\theta}_2 \\ \dot{\theta}_{12} \end{bmatrix} = \begin{bmatrix} 0 & v & v \\ 0 & v & -v/L_2 \\ 0 & v & v/L_2 \end{bmatrix} \begin{bmatrix} y \\ \theta_2 \\ \theta_{12} \end{bmatrix} + \begin{bmatrix} 0 \\ 0 \\ -v/L_2 \end{bmatrix} \tan\delta \qquad \ldots\ldots\ldots\ldots \quad (10)$$

A full-state stabilizing control law for the linear system is given by:

$$\tan\delta = -k_1 y - k_2\theta_2 - k_3\theta_{12} \qquad \ldots\ldots\ldots\ldots\ldots \quad (11)$$

where coefficients k_1, k_2 and k_3 are properly chosen so that the closed-loop linear system is stable. This control law is only valid around θ_{12}=0 and it is not guaranteed it will stabilize the mobile robot for other angles θ_{12} in the range -90° to +90°, where the extreme values correspond to jack-knife positions. To solve this problem, a rule-based fuzzy control will be applied: the range of variation of θ_{12} will be partitioned in three parts and a simple linear controller is designed for each part. Afterwards, the three controllers are integrated in a fuzzy-logic approach as a weighted sum of their outputs (weights given by the membership values of each partition).

Figure 4 shows the partitions and membership functions of angle θ_{12} in the range -90° to +90° (*Negative Big*, *Zero*, *Positive Big*). Membership functions (MF) are described by the following equations:
Negative Big:

IF $-90^o \leq \theta_{12} \leq -60^o$ MF = 1
IF $-60^o < \theta_{12} \leq 0^o$ MF = $-\theta_{12}/60$
IF $0^o < \theta_{12} \leq 90^o$ MF = 0

Zero:

IF $-90^o \leq \theta_{12} \leq -60^o$ MF = 0
IF $-60^o < \theta_{12} \leq 0^o$ MF = $\theta_{12}/60 + 1$
IF $0^o < \theta_{12} \leq 60^o$ MF = $-\theta_{12}/60 + 1$
IF $60^o \leq \theta_{12} \leq 90^o$ MF = 0

Positive Big:

IF $-90^o \leq \theta_{12} \leq 0^o$ MF = 0
IF $0^o < \theta_{12} \leq 60^o$ MF = $\theta_{12}/60$
IF $60^o < \theta_{12} \leq 90^o$ MF = 1

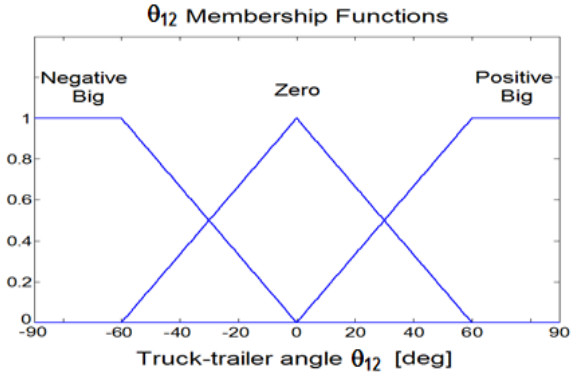

Fig. 4. Partitions and membership functions of truck-trailer angle θ_{12}.

As it was stated, control law (11) is valid when θ_{12}=*Zero*, but it does not apply for other linguistic values of θ_{12}. Then, different controllers will be designed for the other two partitions (*Negative Big* and *Positive Big*).

From equation (6), it is noted that there is an inverse relationship between $\dot{\theta}_{12}$ and $\tan(\delta)$: if $\tan(\delta)$ increases, $\dot{\theta}_{12}$ decreases and vice versa. Also, it is clear that one of the positioning control objectives is to keep truck-trailer angle θ_{12} at small values in order to avoid jack-knife positions. To do that, the following fuzzy reasoning is applied: if θ_{12} is *Positive Big*, $\dot{\theta}_{12}$ should be negative for bringing θ_{12} toward zero and, to achieve that, $\tan(\delta)$ should be positive. Similarly, when θ_{12} is *Negative Big*, $\dot{\theta}_{12}$ should be positive for bringing θ_{12} toward zero and, to achieve that, $\tan(\delta)$ should be negative. This reasoning is summarized in the following fuzzy rules:

IF θ_{12} = *Positive Big* THEN $\delta = \delta_{max}$ (positive)
IF θ_{12} = *Zero* THEN δ = Equation (11)
IF θ_{12} = *Negative Big* THEN $\delta = \delta_{min}$ (negative)
……(12)

It is important to point out that the proposed control strategy does not only focus on attainment of the desired position but also on the avoidance of jack-knife positions (angle θ_{12} close to +90° or -90°). This fuzzy control law was applied to the

mobile robot in order it attains different desired positions starting from arbitrary initial positions. Figure 1 and Figure 5 show the trajectories of the mobile robot from two different initial positions to the goal position x^*=80, y^*=0, θ_2^*=0°, θ_{12}^*=0°. In both cases, the robot is able to asymptotically achieve the goal position without colliding with obstacles around. The steering angle δ was bounded to the range from δ_{min} = -30° to δ_{max} = +30°.

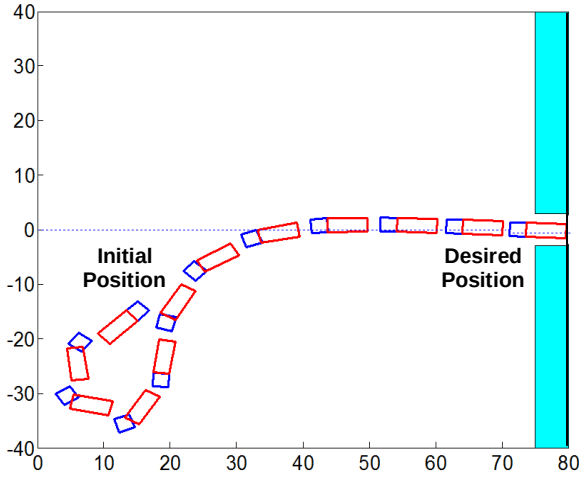

Fig. 5. Trajectory of mobile robot starting from initial position (x=10, y=-20, θ_2=-135°, θ_{12}=0°) and achieving the goal position at y^*=0.

The control law (11) can be easily modified to make the robot achieves other fixed goal positions as follows:

$$\tan\delta - \tan\delta^* = -k_1(y - y^*) - k_2(\theta_2 - \theta_2^*) - k_3(\theta_{12} - \theta_{12}^*) \quad \text{..... (13)}$$

where y^*, θ_2^* and θ_{12}^* represent the desired position of the mobile robot, and δ^* is the corresponding steering angle. It is important to coherently set the desired values of y^*, θ_2^*, θ_{12}^* and δ^* to physically realizable values to attain consistent robot responses. Figure 6 shows the trajectory of the mobile robot from an arbitrary initial position to goal position x^*=80, y^*=20, θ_2^*=0°, θ_{12}^*=0° with δ^*=0° which represents a consistent and physically attainable robot position at convergence.

It is important to note that, since velocity v is constant, when the robot converges to line y=y^* and moves along it toward the goal position, the value of $\dot{x}$ equals to v. It is equivalent to state that coordinate x is proportional to time and behaves as an independent variable.

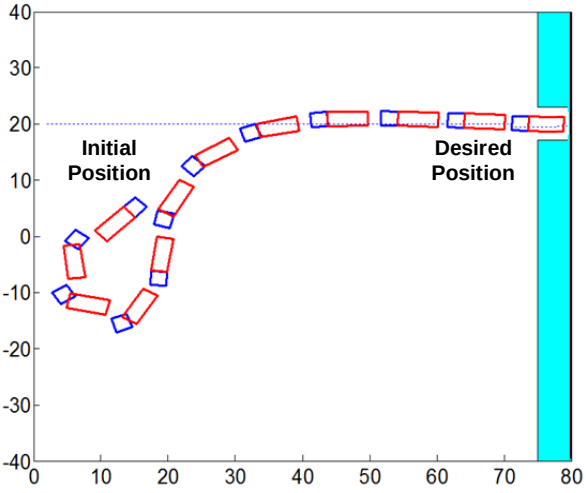

Fig. 6. Trajectory of mobile robot starting from initial position (x=10, y=0, θ_2=-135°, θ_{12}=0°) and achieving the goal position at y^*=20.

3. TRAJECTORY FOLLOWING

The controller given by equation (13) can be applied to the mobile robot for following any desired trajectory. To do that, instantaneous proper desired values of y^*, θ_2^*, θ_{12}^* and δ^* should be determined based on the robot kinematical equations and the geometry of the desired trajectory. The desired values will be found using the *perpendicular desired position methodology* explained afterwards.

3.1 Perpendicular desired position

In this approach, a perpendicular line is drawn from the present robot position coordinates (x, y) to the desired trajectory. The coordinate y of the intersection point represents the instantaneous desired coordinate y^*, and the angle of the tangent to the desired trajectory in the intersection point represents the desired trailer inclination angle θ_2^*. Using these values, the desired values θ_{12}^* and δ^* can be obtained from the robot kinematical equations and the desired trajectory equation. It is important to note that the perpendicular line between the robot present position and the desired trajectory represents the instantaneous minimum distance between them. This methodology is applicable when the computation of the intersection point is not cumbersome and it is unique. In the following, the methodology will be explained for linear and circular desired trajectories.

3.1.1 Linear desired trajectory

Figure 7 shows the linear trajectory control problem. Point P represents the robot instantaneous position given by coordinates (x, y) and line AB, with inclination angle α, represents the trajectory to be followed. The equation of line AB is:

$$y^* = ax + b \qquad \ldots\ldots\ldots\ldots\ldots\ldots \quad (14)$$

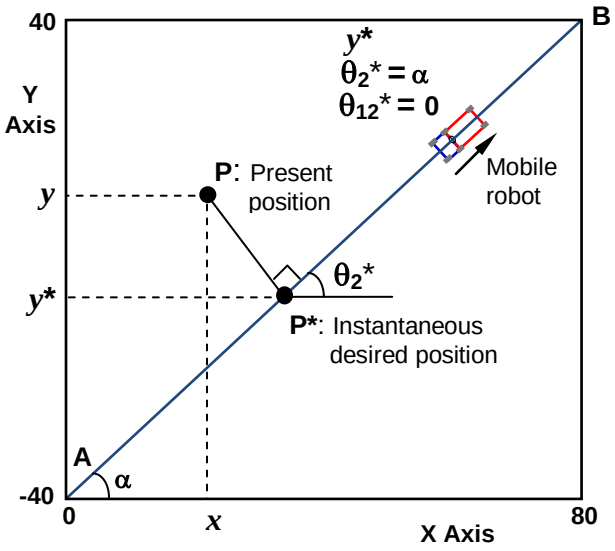

Fig. 7. Linear trajectory following. P* represents the instantaneous desired position for computing coordinate y^* and inclination angle θ_2^*.

Drawing a perpendicular line from point P to line AB, point P* is obtained whose coordinate y^* represents the instantaneous desired value of robot coordinate y. By geometrical relationships, the value of y^* is given by:

$$y^* = \frac{a\,x + a^2 y + b}{1 + a^2} \qquad \ldots\ldots\ldots\ldots\ldots\ldots\ldots\ldots \quad (15)$$

Considering that the tangent to line AB at point P* is the same line, the desired angle θ_2^* is equal to the line inclination angle α. Also, considering that truck and trailer should be aligned to line AB, it is clear that the desired value of truck-trailer angle $\theta_{12}^*=0^o$, and the desired value of steering angle $\delta^*=0^o$. Figure 8 (a) and (b) show the trajectory of the mobile robot following a linear trajectory with inclination angle $\alpha=45^o$ given by the equation:

$$y^* = x - 40 \qquad \ldots\ldots\ldots\ldots\ldots\ldots\ldots\ldots \quad (16)$$

starting from two different initial positions. In both cases, the robot asymptotically converges to the desired linear trajectory without steady-state error which verifies the effectiveness of the proposed control strategy. Similarly as the positioning control problem presented in the previous section, since velocity v is constant, when the robot converges to the desired linear trajectory and moves along it, the value of $\dot{x}$ equals to $v\cos\alpha$ which is constant. It is equivalent to state that coordinate x is proportional to time and behaves as an independent variable.

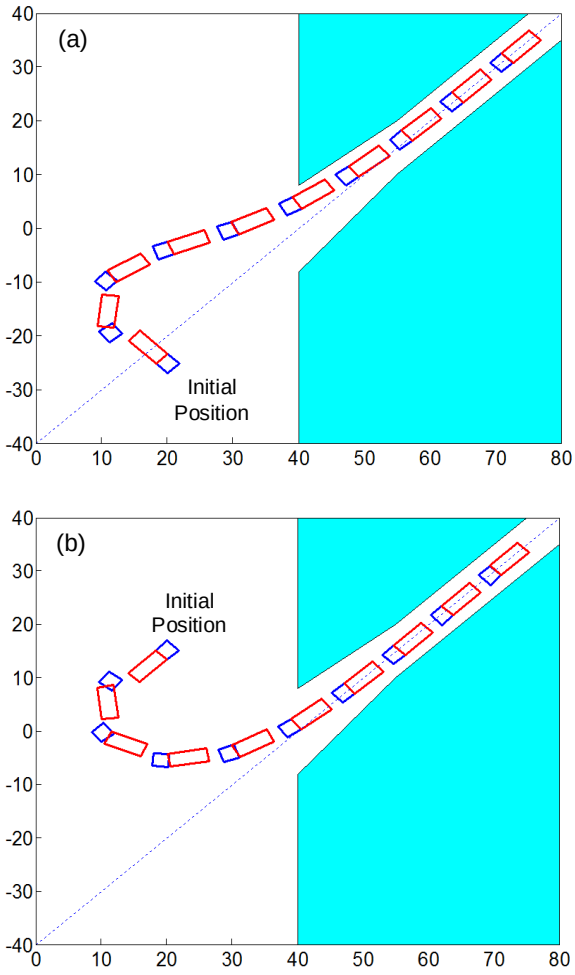

Fig. 8. Trajectories of mobile robot from two different initial positions converging into the desired linear trajectory.
Initial position (a) x=15, y=-20, θ_2=135°, θ_{12}=0°
(b) x=15, y=10, θ_2=135°, θ_{12}=0°

3.1.2. Circular Desired Trajectory

Figure 9 shows the circular trajectory control problem. Point P represents the robot instantaneous position given by coordinates (x, y) and the circular line represents the trajectory to be followed. The equation of the circular path with center C and coordinates (x_C, y_C), and radius R is:

$$y = \sqrt{R^2 - (x - x_c)^2} + y_c \qquad (x_c - R) \le x \le x_c$$

$$\ldots\ldots\ldots\ldots\ldots\ldots\ldots\ldots (17)$$

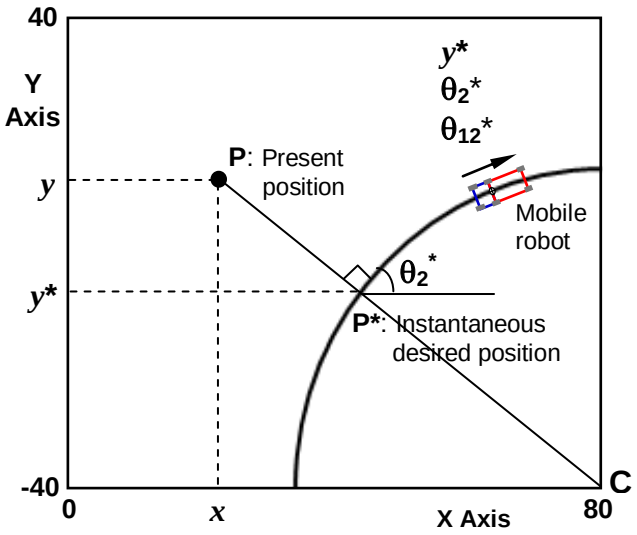

Fig. 9. Circular trajectory following. P* represents the instantaneous desired position for computing coordinate y^* and inclination angle θ_2^*.

Drawing a perpendicular line from point P to the circular path, point P* is obtained whose coordinate y^* represents the instantaneous desired value of robot coordinate y. The perpendicular line also passes by the center C of the circular path, and the distance PP* represents the minimum distance from P to the circular path. By geometrical relationships, the value of y^* is given by:

$$y^* = \frac{R(y-y_c)}{\sqrt{(x-x_c)^2+(y-y_c)^2}} - y_c \qquad \ldots\ldots\ldots\ldots \quad (18)$$

The inclination angle θ_2^* of the tangent to the circular trajectory at point P* represents the desired instantaneous inclination angle of the trailer and can be determined by geometrical relationships as:

$$\theta_2^* = \tan\left(\frac{x_c-x}{y-y_c}\right) \qquad \ldots\ldots\ldots\ldots\ldots\ldots \quad (19)$$

Differentiating equation (19) with respect to time and replacing the expressions of $\dot{x}$ and $\dot{y}$ given by equations (1) and (2) the expression of the desired truck-trailer angle θ_{12}^* is obtained as:

$$\theta_{12}^* = \operatorname{atan}\left(\frac{L_2}{R}\right) \qquad \ldots\ldots\ldots\ldots\ldots\ldots \quad (20)$$

It is noted that the value of θ_{12}^* is constant and does not depend on robot coordinates or angles. This result is expected considering the truck and trailer relative position required to describe circular trajectories, and it is the same as the result presented in Michalek et al. (2012).

Finally, considering that $\dot{\theta}_{12}^*=0$ and replacing the values of θ_{12}^* and $\dot{\theta}_{12}^*$ in equation (6), the value of δ^* is obtained which is also constant as it is expected for circular trajectories:

$$\delta^* = \operatorname{atan}\left(\frac{L_1}{\sqrt{L_2^2+R^2}}\right) \qquad \ldots\ldots\ldots\ldots\ldots\ldots \quad (21)$$

Figure 10 (a) and (b) show the trajectories of the mobile robot following a circular trajectory with center in point (80,-40) and radius R=50, starting from two different initial positions. In both cases, the robot asymptotically converges to the desired circular trajectory without steady-state error which verifies the effectiveness of the proposed control strategy.

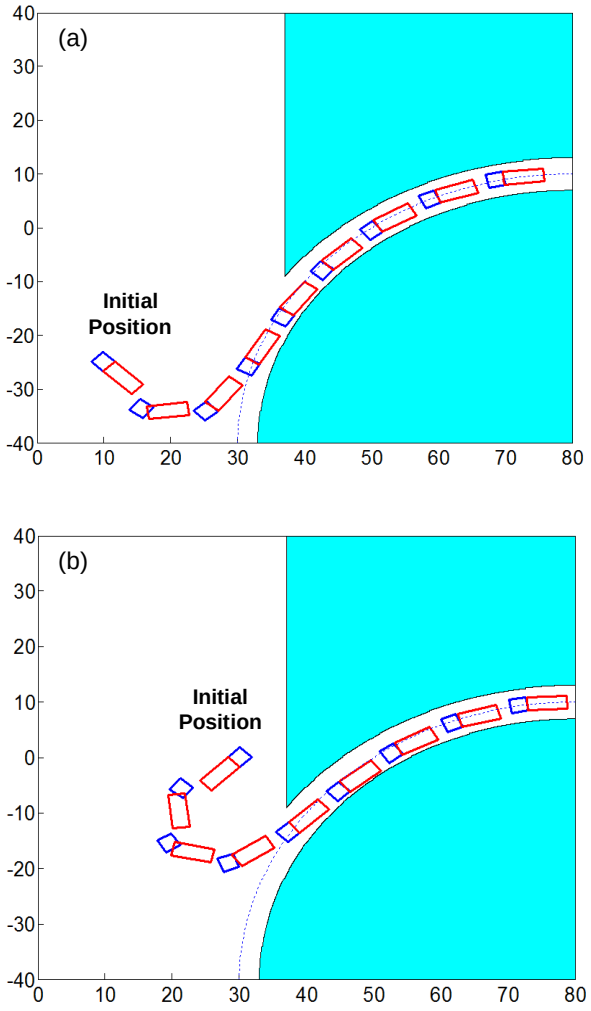

Fig. 10. Trajectories of mobile robot from two different initial positions converging into the circular desired trajectory.
Initial position (a) x=15, y=-30, θ_2=-45°, θ_{12}=0°
(b) x=25, y=-5, θ_2=-135°, θ_{12}=0°

4. EFFECT OF FUZZY PARTITIONS

As it was presented in Section 2, the proposed controller integrates three partitions of truck-trailer angle θ_{12}: *Negative Big*, *Zero* and *Positive Big*. Considering that the approximate linearized model of equation (10) is defined for partition *Zero* (small values of θ_{12}), the range of this partition plays an important role on the control performance. This effect will be analyzed through two fuzzy controllers, Fuzzy 1 and Fuzzy 2, whose partitions and membership functions are shown in Figure 11: controller Fuzzy 1 with a wider range of partition *Zero* and controller Fuzzy 2 with a narrower partition.

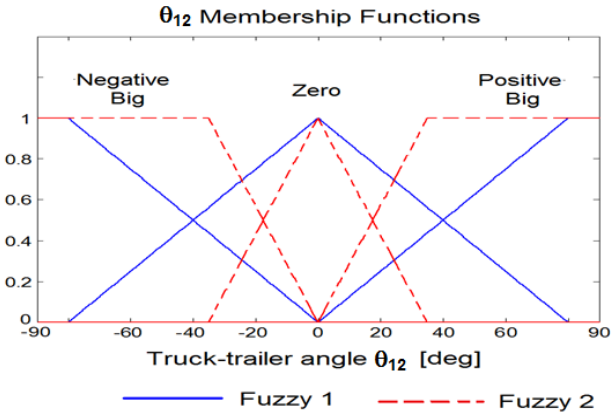

Fig. 11. Partitions and membership functions of truck-trailer angle θ_{12} for controllers Fuzzy 1 y Fuzzy 2.

Membership functions (MF) for controller Fuzzy 1 are described by the following equations:

Negative Big:

IF $-90^o \leq \theta_{12} \leq -80^o$ MF = 1
IF $-80^o < \theta_{12} \leq 0^o$ MF = $-\theta_{12}/80$
IF $0^o < \theta_{12} \leq 90^o$ MF = 0

Zero:

IF $-90^o \leq \theta_{12} \leq -80^o$ MF = 0
IF $-80^o < \theta_{12} \leq 0^o$ MF = $\theta_{12}/80 + 1$
IF $0^o < \theta_{12} \leq 80^o$ MF = $-\theta_{12}/80 + 1$
IF $80^o \leq \theta_{12} \leq 90^o$ MF = 0

Positive Big:

IF $-90^o \leq \theta_{12} \leq 0^o$ MF = 0
IF $0^o < \theta_{12} \leq 80^o$ MF = $\theta_{12}/80$
IF $80^o < \theta_{12} \leq 90^o$ MF = 1

Membership functions (MF) for controller Fuzzy 2 are described by the following equations:

Negative Big:

IF $-90^o \leq \theta_{12} \leq -35^o$ MF = 1
IF $-35^o < \theta_{12} \leq 0^o$ MF = $-\theta_{12}/35$
IF $0^o < \theta_{12} \leq 90^o$ MF = 0

Zero:

IF $-90^o \leq \theta_{12} \leq -35^o$ MF = 0
IF $-35^o < \theta_{12} \leq 0^o$ MF = $\theta_{12}/35 + 1$
IF $0^o < \theta_{12} \leq 35^o$ MF = $-\theta_{12}/35 + 1$
IF $35^o \leq \theta_{12} \leq 90^o$ MF = 0

Positive Big:

IF $-90^o \leq \theta_{12} \leq 0^o$ MF = 0
IF $0^o < \theta_{12} \leq 35^o$ MF = $\theta_{12}/35$
IF $35^o < \theta_{12} \leq 90^o$ MF = 1

Figure 12 shows the trajectory of the mobile robot for both controllers starting from the same initial position and moving toward the same fixed desired position. Although both controllers are able to conduct the mobile robot to the goal position, the robot with controller Fuzzy 1 converges faster to the desired coordinate y^*=0 and describes a trajectory with smaller turning radius. These results are explained by the fact that extreme partitions *Negative Big* and *Positive Big*, having lower membership values in controller Fuzzy 1, impose lesser restrictions on truck-trailer angle θ_{12}, which results in higher values but without reaching unwanted jack-knife positions.

Figure 13 shows the time response of truck inclination angle θ_1, trailer inclination angle θ_2, truck-trailer angle θ_{12}, and steering angle δ corresponding to the trajectories showed in Figure 12. It is noted that the response for controller Fuzzy 1 converges faster than controller Fuzzy 2 at the expense of higher values of truck-trailer angle θ_{12} and steering angle δ. In both cases jack-knife positions are avoided. From these results it is concluded that smaller ranges of the central partition *Zero* result in lower values of angle θ_{12}. These results validate the coherence of the proposed control strategy.

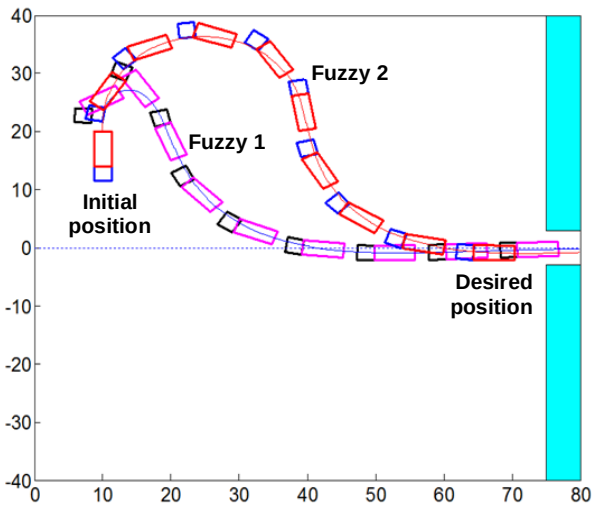

Fig. 12. Trajectories of mobile robot with controllers Fuzzy1 and Fuzzy 2 starting from the same initial position x=10, y=20, θ_2=90°, θ_{12}=0°

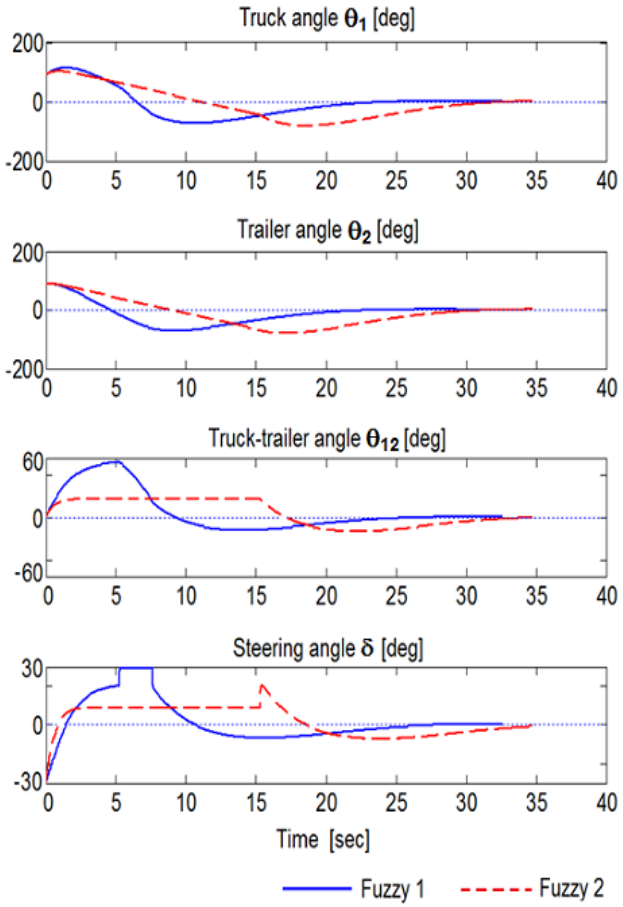

Fig. 13. Time response of truck inclination angle θ_1, trailer inclination angle θ_2, truck-trailer angle θ_{12} and steering angle δ for controllers Fuzzy 1 and Fuzzy 2.

5. CONCLUSIONS

The kinematical model and nonholonomic constraints of truck-trailer mobile robots have been derived and analyzed. A novel control strategy integrating linear controllers in a fuzzy logic approach has been proposed, assuring the robot achieve goal positions avoiding jack-knifing. The effectiveness of the trajectory following control strategies have been verified for linear and circular trajectories where the mobile robot converges to the desired trajectories with bounded values of the steering angle. The effect of the size of truck-trailer angle partitions in fuzzy control was analyzed and it was found that a wider range of the central partition results in faster convergence of the mobile robot at the expense of higher values of truck-trailer angle θ_{12} and steering angle δ. One of the main attributes of the proposed control strategy is the easy incorporation of jack-knife avoidance into the controller designing process.

6. REFERENCES

Altafini, C, Speranzon, A, and Wahlberg, B. (2001), A Feedback Control Scheme for Reversing a Truck and Trailer Vehicle. *IEEE Transactions on Robotics and Automation*, Vol.17, No.6, pp.915-922.

Cheng J., Zhang Y. and Wang Z. (2009), Backward Tracking Control of Mobile Robot with One Trailer Via Fuzzy Line-of-Sight Method, *Sixth International Conference on Fuzzy Systems and Knowledge Discovery*, Vol.6, pp.66-70.

David, J. and Manivannan, P.V. (2014). Control of Truck-Trailer Mobile Robots: A Survey. *Intelligent Service Robotics Journal*, Vol.7, pp.245-258, Springer Verlag.

Fierro, R. and Lewis, F.L. (1995). Control of Nonholonomic Mobile Robot: Backstepping Kinematics into Dynamics. *Proceedings of the 34th IEEE Control and Decision Conference*, Vol.4, pp.3805-3810.

Kinjo, H., Wang,B., and Yamamoto, T. (2000). Backward Movement Control of a Trailer Truck System Using Neuro-Controllers Evolved by Genetic Algorithm. *Proceedings of 26th Conference of IEEE Industrial Electronics Society IECON 2000*, Vol.1, pp.253-258.

Kong, S.G. and Kosko, B. (1992). Adaptive fuzzy systems for backing up a truck-and-trailer. *IEEE Transactions on Neural Networks*, Vol.3, No.2,pp.211-223.

Laumond, J.P., Sekhavat, S. and Lamiraux, F. (1998). Guidelines in Nonholonomic Motion Planning for Mobile Robots. *Lectures Notes in Control and Information Sciences* No. 229, Springer.

Michalek, M. (2012). Tracking Control Strategy for the Standard N-trailer Mobile Robot – A Geometrically Motivated Approach. *Robot Motion Control*, pp.39-51, Springer-Verlag.

Moran, A. (2004). Intelligent Car Parking Using Fuzzy-Neural Networks. *Proceedings of 2nd International Latin American and Caribbean Conference for Engineering and Technology LACCEI*, 2004, Miami, USA.

Nguyen, D. and Widrow, B. (1989). The Truck Backer-Upper: An Example of Self-Learning in Neural Networks, *Proceedings of International Joint Conference on Neural Networks IJCNN*, Vol.2, pp.357-363.

Rouchon, P., Fliess, M., Levine J. and Martin, P. (1993). Flatness, Motion Planning and Trailer Systems, *Proceedings of 32nd IEEE Conference on Decision and Control*, Vol.3, pp.2700-2705.

Sordalen, O.J. (1993). Conversion of the Kinematics of a Car with N Trailers into a Chained Form, *Proceedings of IEEE International Conference on Robotics and Automation*, pp.382-387.

Tanaka, K. and Sano, M. (1994). A Robust Stabilization Problem of Fuzzy Control Systems and its Application to Backing-up Control of a Truck Trailer, *IEEE Transactions on Fuzzy Systems*, Vol.2, No.2, pp.119-134.

CHAPTER 7

LINEAR SYSTEMS

An Integral Sliding Mode Observer for Linear Systems

Esteban Jiménez-Rodríguez * **Eliana Mejía-Estrada** **
Oscar Jaramillo * **Juan Diego Sánchez-Torres** ***

* *Department of Electrical Engineering, CINVESTAV-IPN Guadalajara, Av. del Bosque 1145 Col. El Bajío CP 45019, México (e-mail: {ejimenezr, odjaramillo}@gdl.cinvestav.mx).*
** *Department of Electrical and Control Engineering, Universidad Nacional de Colombia, Sede Medellín, Carrera 80 No 65-223, Medellín, Colombia (e-mail: elmejiaes@unal.edu.co)*
*** *Department of Mathematics and Physics, ITESO, Periférico Sur Manuel Gómez Morín 8585 C.P. 45604, Tlaquepaque, Jalisco, México (e-mail: dsanchez@iteso.mx)*

Abstract: In this paper a sliding-mode observer for linear time-invariant systems is proposed. The observer is based on integral sliding modes and the equivalent control method. In order to induce a sliding mode in the output error, a second order sliding mode algorithm is used. Convergence proofs of the proposed observer are presented. In order to expose the features of this proposal, a design example over a DC motor model is exposed, noiseless and noisy measurements cases are considered. For this case, the simulation shows the high performance of the integral observer.

Keywords: Integral Controllers, Linear Systems, Sliding-Mode Control, State Observers.

1. INTRODUCTION

A large amount of controller design methods are developed under the assumption that the state vector is available. However, the state vector can not always be completely measured, but a part of it (Luenberger, 1964). This is due to several reasons, such as there are no on-line sensors for some variables, sometimes it is impossible to install sensors due to hostile environments and some sensors are very expensive or with poor accuracy.

The state observers have taken place as a solution to this issues. The purpose of a state observer is to estimate the unmeasured state variables based on the measured inputs and outputs. Often, an observer is a replica of the original system mathematical model plus a correction signal depending on the difference between the system measured variables and the observer outputs (Luenberger, 1964; Walcott et al., 1987; Kalman, 1960; Kalman and Bucy, 1961).

Several state observers for linear systems have been proposed. A first approach is the Luenberger observer. Here, the observation problem is treated for the case when the system is completely deterministic (no statistical processes are involved) (Luenberger, 1964). When the output measurements are corrupted by zero mean, uncorrelated and white noise, the well-known Kalman Filter provides the optimal solution, once the statistical properties of noise are known (Kalman, 1960; Kalman and Bucy, 1961).

As alternative, an important class of state observers are the sliding mode observers (SMO) which have the main features of the sliding mode (SM) algorithms (Utkin, 1992). Those algorithms, are proposed with the idea to drive the dynamics of a system to an sliding manifold, that is an integral manifold with finite reaching time (Drakunov and Utkin, 1992), exhibiting very interesting features such as work with reduced observation error dynamics, the possibility of obtain a step by step design, robustness and insensitivity under parameter variations and external disturbances, and finite time stability (Utkin, 1992). In addition, some SMO have attractive properties similar to those of the Kalman filter (i.e. noise resilience) but with simpler implementation (Drakunov, 1983). Sometimes this design can be performed by applying the equivalent control method (Drakunov, 1992; Drakunov and Utkin, 1995), allowing the proposal of robust to noise observers, since the equivalent control is slightly affected by noisy measurements. On the other hand, a common and effective approach to sliding mode control is the integral SM (Matthews and DeCarlo, 1988; Utkin and Shi, 1996; Fridman et al., 2006; Galván-Guerra and Fridman, 2013). Here, it is designed an sliding manifold such that the sliding motion has the same dimension that the original system but without the influence of the matched disturbances. Those disturbances belong to the span of the control function and are rejected for the equivalent control obtained from induce the integral SM (Draženović, 1969). In order to propose that manifold, integral SM terms are designed based on the nominal system. When the system initial conditions are known, this control algorithm can be proposed with the aim to force the system trajectory starting from the sliding manifold,

eliminating the reaching phase and ensuring robustness from the initial time.

Consequently, in this paper an integral sliding mode-based observer for linear systems is proposed. The observer structure is similar to the observer presented on Drakunov (1992), but using integral SM. In addition, a step by step design of the proposed observer is provided along with a design example over a DC motor model.

The following sections are organized as follows: Section 2 presents the preliminaries for the observer. In Section 3, the integral SM observer is presented. A design example is analyzed in Section 4. In Section 5 the simulation results are shown. Finally, the conclusions of this paper are presented in Section 6.

2. MATHEMATICAL PRELIMINARIES

This section presents the previous results needed for the proposed observer.

2.1 The Super-Twisting Algorithm

Consider the first order perturbed system

$$\dot{\xi} = -u + \Delta, \tag{1}$$

where $\xi, \Delta, u \in \mathbb{R}$.

The super-twisting controller $u = \mathcal{ST}(\xi)$ (Levant, 1993), is defined as

$$\begin{aligned} \mathcal{ST}(\xi) &= \alpha_1 |\xi|^{\frac{1}{2}} \operatorname{sign}(\xi) + w \\ \dot{w} &= \alpha_2 \operatorname{sign}(\xi), \end{aligned} \tag{2}$$

with $\operatorname{sign}(x) = 1$ for $x > 0$, $\operatorname{sign}(x) = -1$ for $x < 0$ and $\operatorname{sign}(0) \in \{-1, 1\}$.

For the system (1), the controller (2) is applied, yielding the closed loop system:

$$\begin{aligned} \dot{\xi} &= -\alpha_1 |\xi|^{\frac{1}{2}} \operatorname{sign}(\xi) + q \\ \dot{q} &= -\alpha_2 \operatorname{sign}(\xi) + \dot{\Delta}, \end{aligned} \tag{3}$$

where $q = w + \Delta$.

Assuming that $\left|\dot{\Delta}\right| < \delta$, the super-twisting gains are selected as: $\alpha_1 = 1.5\delta^{\frac{1}{2}}$ and $\alpha_2 = 1.1\delta$. Therefore, a sliding mode is induced on the manifold $(\xi, q) = (0, 0)$ in a finite-time $t_q > 0$ (Moreno and Osorio, 2008). Thus, from (3), the term w in (2) becomes equal to $-\Delta$.

Now, consider the multi-variable case, with $\xi = [\xi_1 \ \dots \ \xi_p]^T, \Delta = [\Delta_1 \ \dots \ \Delta_p]^T, u = [u_1 \ \dots \ u_p]^T \in \mathbb{R}^p$. Assuming $\left\|\dot{\Delta}\right\| < \delta$, it can be shown that $\left|\dot{\Delta}_i\right| < \delta_i \ \forall i \in 1, \dots, p$. In this case, define $u = \mathcal{ST}(\xi) = [\mathcal{ST}(\xi_1) \ \dots \ \mathcal{ST}(\xi_p)]$ and note that this multi-variable case is simply the same as having p (1)-like scalar systems.

2.2 Linear Systems

Consider the following time-invariant linear system represented by the following state space equation:

$$\begin{aligned} \dot{x} &= Ax + Bu \\ y &= Cx, \end{aligned} \tag{4}$$

where $x \in \mathbb{R}^n$ is the state vector, $u \in \mathbb{R}^m$ is the input vector, $y \in \mathbb{R}^k$ is the output vector, $A \in \mathbb{R}^{n \times n}$ is the transition matrix, $B \in \mathbb{R}^{n \times m}$ is the input-state distribution matrix and $C \in \mathbb{R}^{k \times n}$ is the output matrix, which will be assumed to have full row rank so the measured outputs are independent. Additionally, it will be assumed that the pair (A, C) is observable.

This paper deals with the case when the measured output is a part of the state. In this case, the system (4) can be rewritten as:

$$\begin{aligned} \dot{x}_1 &= A_{11}x_1 + A_{12}x_2 + B_1 u \\ \dot{x}_2 &= A_{21}x_1 + A_{22}x_2 + B_2 u \\ y &= x_1, \end{aligned} \tag{5}$$

where $A_{11} \in \mathbb{R}^{k \times k}$, $A_{12} \in \mathbb{R}^{k \times (n-k)}$, $A_{21} \in \mathbb{R}^{(n-k) \times k}$, $A_{22} \in \mathbb{R}^{(n-k) \times (n-k)}$, $B_1 \in \mathbb{R}^{k \times m}$, $B_2 \in \mathbb{R}^{(n-k) \times m}$, are partitions of the matrices A and B, such that:

$$A = \begin{bmatrix} A_{11} & A_{12} \\ A_{21} & A_{22} \end{bmatrix}, \ B = \begin{bmatrix} B_1 \\ B_2 \end{bmatrix};$$

$y = x_1 \in \mathbb{R}^k$ is the measured part of the state vector and $x_2 \in \mathbb{R}^{(n-k)}$ is the unmeasured part of the state vector.

Many linear systems can be directly expressed in the form described by (5) (i.e., the measured output is a part of the state vector). If not, under the assumption that C is full rank, there is always a linear transformation which allows to express the system (4) in the form (5), as described in (Utkin, 1992). For instance, assuming the output vector y may be represented as:

$y = K_1 x_1 + K_2 x_2$, $x^T = [x_1 \ x_2]^T$, $x_1 \in \mathbb{R}^k$, $x_2 \in \mathbb{R}^{(n-k)}$, consider a coordinate transformation $x \mapsto Tx$ associated with the invertible matrix

$$T = \begin{bmatrix} K_1 & K_2 \\ I_k & 0 \end{bmatrix}$$

Applying the change of coordinates $x \mapsto Tx$, the triplet (A, B, C) has the form:

$$TAT^{-1} = \begin{bmatrix} A_{11} & A_{12} \\ A_{21} & A_{22} \end{bmatrix}, \ TB = \begin{bmatrix} B_1 \\ B_2 \end{bmatrix}, \ CT^{-1} = [I_k \ 0].$$

3. INTEGRAL SLIDING MODE OBSERVER

3.1 Observer Scheme

Based on (5), the following state observer is proposed:

$$\begin{aligned} \dot{\hat{x}}_1 &= A_{11}\hat{x}_1 + A_{12}\hat{x}_2 + B_1 u + v_0 + v_1 \\ \dot{\hat{x}}_2 &= A_{21}\hat{x}_1 + A_{22}\hat{x}_2 + B_2 u + L_2 v_1 \\ v_0 &= L_1 \tilde{x}_1 \\ v_1 &= \mathcal{ST}\{\sigma\} \\ \sigma &= \tilde{x}_1 + z, \end{aligned} \tag{6}$$

where $\hat{x}_1$ and $\hat{x}_2$ are the estimates of x_1 and x_2, respectively; $\tilde{x}_1 = x_1 - \hat{x}_1$ is the estimation error variable; $v_0 \in \mathbb{R}^k$ and $v_1 \in \mathbb{R}^k$ are the observer input injections; $\sigma \in \mathbb{R}^k$ is the sliding variable and $z \in \mathbb{R}^k$ is an integral variable to be defined thereafter. Finally, $L_1 \in \mathbb{R}^{k \times k}$ and $L_2 \in \mathbb{R}^{(n-k) \times k}$ are the observer gains.

3.2 Convergence Analysis

Define the estimation error variable $\tilde{x}_2 = x_2 - \hat{x}_2$. From (5) and (6), it follows

$$\begin{aligned} \dot{\tilde{x}}_1 &= A_{11}\tilde{x}_1 + A_{12}\tilde{x}_2 - v_0 - v_1 \\ \dot{\tilde{x}}_2 &= A_{21}\tilde{x}_1 + A_{22}\tilde{x}_2 - L_2 v_1. \end{aligned} \tag{7}$$

First, note that the σ-dynamics are given by:

$$\begin{aligned} \dot{\sigma} &= \dot{\tilde{x}}_1 + \dot{z} \\ &= A_{11}\tilde{x}_1 + A_{12}\tilde{x}_2 - v_0 - v_1 + \dot{z}. \end{aligned} \tag{8}$$

Define now $\dot{z} = -A_{11}\tilde{x}_1 + v_0$, then

$$\dot{\sigma} = A_{12}\tilde{x}_2 - v_1. \tag{9}$$

The term $A_{12}\tilde{x}_2$ is assumed to be an unknown disturbance but with bounded time derivative, with $\left|\left|\frac{d}{dt}\left[A_{12}\tilde{x}_2\right]\right|\right| < \delta$ and $\delta > 0$ is a known positive constant. Then, since $v_1 = \mathcal{ST}\{\sigma\}$, it follows that $(\sigma(t), q) = (0, 0)\ \forall t > t_q$, with $q = w - A_{12}\tilde{x}_2$.

From the above analysis and (9), it follows that the equivalent control of v_1 (Utkin, 1992) is

$$\{v_1\}_{eq} = A_{12}\tilde{x}_2,$$

which implies that the motion of the system (7) constrained to the sliding manifold $(\sigma, q) = (0, 0)$ is given by:

$$\begin{aligned} \dot{\tilde{x}}_1 &= (A_{11} - L_1 I_k)\,\tilde{x}_1 \\ \dot{\tilde{x}}_2 &= A_{21}\tilde{x}_1 + (A_{22} - L_2 A_{12})\,\tilde{x}_2. \end{aligned} \tag{10}$$

where $I_k \in \mathbb{R}^{k\times k}$ is the k-order identity matrix. Hence, the system (10) associated eigenvalues are given by

$$\det\begin{bmatrix} \lambda I_k - (A_{11} - L_1 I_k) & 0 \\ -A_{21} & \lambda I_{n-k} - (A_{22} - L_2 A_{12}) \end{bmatrix} = \det\left[\lambda I_k - (A_{11} - L_1 I_k)\right] \det\left[\lambda I_{n-k} - (A_{22} - L_2 A_{12})\right].$$

Since the pair (A_{11}, I_k) is always observable, it is possible to choose the gain L_1 so the matrix $A_{11} - L_1 I_k$ be Hurwitz. On the other hand, since the pair (A, C) was assumed to be observable, it can be shown that the pair (A_{22}, A_{12}) is also observable (Drakunov and Utkin, 1995; Shtessel et al., 2013). Then, the gain L_2 can be chosen so the matrix $A_{22} - L_2 A_{12}$ be Hurwitz. Hence, $\tilde{x}_1, \tilde{x}_2 \to 0$ as $t \to \infty$, and the convergence analysis is completed.

Remark 3.1. It is important to note that, with the proposed observer scheme (6), the dynamic behavior of the estimation blocks $\tilde{x}_1$ and $\tilde{x}_2$ can be tuned independently (see (10)).

4. DESIGN EXAMPLE

To verify the proposed observer performance, it will be applied to the following DC motor model (Utkin and Shi, 1996):

$$\begin{aligned} \dot{i} &= \frac{-R}{L} i - \frac{\lambda}{L}\omega + \frac{1}{L} V \\ \dot{\omega} &= \frac{K}{J} i - \frac{b}{J}\omega \\ y &= i \end{aligned} \tag{11}$$

where i is armature current, V is terminal voltage, ω is shaft speed, R is armature resistance, L is armature inductance, J is moment of inertia of the rotor, b is motor viscous friction constant and λ is back-EMF constant. Finally the measurable output of system is the armature current i.

Note that the DC motor model (11) has the form (5), with $i = x_1 = y$ and $\omega = x_2$; $A_{11} = -\frac{R}{L}$, $A_{12} = -\frac{\lambda}{L}$, $A_{21} = \frac{K}{J}$ and $A_{22} = -\frac{b}{J}$; $B_1 = \frac{1}{L}$ and $B_2 = 0$. Then, the integral SMO is given by (6), with $\dot{z} = -A_{11}\tilde{x}_1 + v_0$.

The simulation results for this design example are shown in the next section.

5. SIMULATION RESULTS

All simulations presented here were conducted using the Euler integration method with a fundamental step size of 1×10^{-3} [s]. The DC Motor parameters are shown in Table 1 (Utkin et al., 1999).

Table 1. Nominal Parameters of the DC motor model (11).

Parameter	Values	Unit
L	0.001	V
R	0.5	Ω
λ	0.001	$\mathrm{V \cdot s \cdot rad^{-1}}$
b	0.001	$\mathrm{N \cdot m \cdot s \cdot rad^{-1}}$
k	0.008	$\mathrm{N \cdot m \cdot A^{-1}}$
J	0.001	$\mathrm{kg \cdot m^2}$

The initial conditions for the system (11) were selected as: $i(0) = 31.5\,\mathrm{A}$ and $\omega(0) = 250\,\mathrm{rad/s}$; furthermore, for the designed observer in the form (6), the initial conditions were chosen as: $\hat{i}(0) = 25.2\,\mathrm{A}$, $\hat{\omega}(0) = 200\,\mathrm{rad/s}$, $z(0) = 0$ and $w(0) = 0$. In addition, applying super twisting algorithm (2), the parameter values for the observer were adjusted as: $L_1 = 2 \times 10^{-4}$, $L_2 = -0.01$, $\alpha_1 = 4.7434$ and $\alpha_2 = 11$.

This section is divided into two parts. In the first part, there is assumed that the current measurements are noiseless; in the second part instead, there is included a normally distributed random signal as measurement noise in the current. The applied voltage V is a DC source, with a magnitude of 16 V, which is suddenly reduced to 15 V at $t = 25$ [s].

5.1 Noiseless Measurements

In this subsection, there is assumed no noise in the current measurements. The following results were obtained:

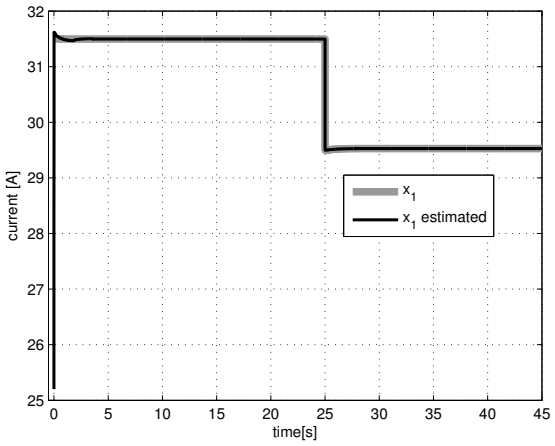

Figure 1. Armature current (i) (actual and estimated).

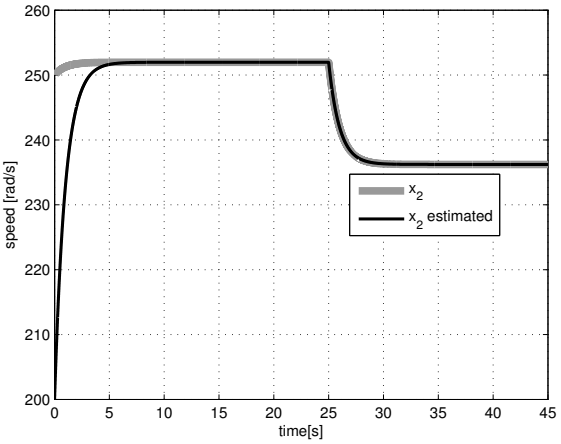

Figure 2. Shaft speed (ω) (actual and estimated).

Fig. 1 and Fig. 2 show the comparison between the actual and estimated variables corresponding to the armature current i and shaft speed ω respectively, for noiseless measurements.

5.2 Noisy Measurements

In this subsection, it is assumed that the current measurements were corrupted by a normally distributed random signal with zero mean and a variance of 10. This assumed variance corresponds to a current sensor with an accuracy of ± 9.5 A. This large variance was assumed to see significant variations in the simulation due to the noise and verify the filtering capabilities of the proposed observer. The following results were obtained:

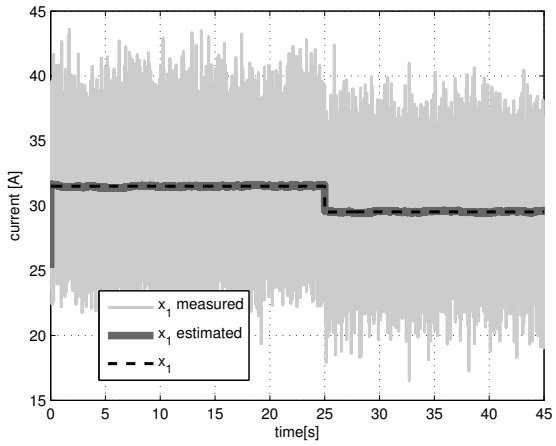

Figure 3. Armature current (i) (measured, estimated and actual).

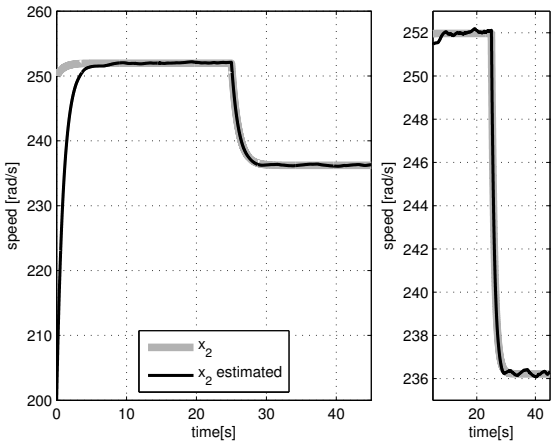

Figure 4. Shaft speed (ω) (actual and estimated).

Fig. 3 and Fig. 4 show the comparison between the actual and estimated variables corresponding to the armature current i and shaft speed ω respectively, for noisy measurements.

Based on the presented figures, it can be observed a good performance of the proposed observer. Under noisy conditions the armature current estimation $\hat{i}$ is much closer to its actual value than its measurement (Fig 3). In addition, a correct estimation of ω using the integral sliding mode observer is achieved (Figs. 2, 4) making the proposed observer suitable for observer-based control applications.

6. CONCLUSION

In this paper an integral sliding mode observer for linear time-invariant systems is proposed. The convergence of the estimation errors to zero for the proposed observer was proved. A step by step design of the proposed observer was provided along with a design example over a DC motor model. The simulation results of the example shown the filtering capabilities of the proposed observer.

ACKNOWLEDGEMENTS

The authors would like to thank the PhD Héctor A. Botero, who is currently an associate professor at the Department of Electrical and Control Engineering, Universidad Nacional de Colombia, Sede Medellín, for all his support through the realization of this paper.

Esteban Jiménez acknowledges to CONACyT, México for the MSc scholarship number 426598.

REFERENCES

Drakunov, S.V. (1983). An adaptive quasioptimal filter with discontinuous parameters. *Automation and Remote Control*, 44(9), 1167–1175.

Drakunov, S.V. (1992). Sliding-mode observers based on equivalent control method. *[1992] Proceedings of the 31st IEEE Conference on Decision and Control*. doi: 10.1109/CDC.1992.371368.

Drakunov, S.V. and Utkin, V.I. (1992). Sliding mode control in dynamic systems. *International Journal of Control*, 55, 1029–1037.

Drakunov, S.V. and Utkin, V.I. (1995). Sliding mode observers. Tutorial. *Proceedings of 1995 34th IEEE Conference on Decision and Control*, 4. doi: 10.1109/CDC.1995.479009.

Draženović, B. (1969). The invariance conditions in variable structure systems. *Automatica*, 5(3), 287 – 295.

Fridman, L., Levant, A., and Davila, J. (2006). High-order sliding-mode observer for linear systems with unknown inputs. In *2006 14th Mediterranean Conference on Control and Automation*, 1–6. doi: 10.1109/MED.2006.328736.

Galván-Guerra, R. and Fridman, L. (2013). Output integral sliding mode observer for linear time variant systems. In *Automatic Control, México 2013. CNCA 2013. National Congress of*.

Kalman, R.E. (1960). A New Approach to Linear Filtering and Prediction Problems. *Transactions of the ASME-Journal of Basic Engineering*, 82(Series D), 35–45. doi: 10.1115/1.3662552.

Kalman, R.E. and Bucy, R.S. (1961). New Results in Linear Filtering and Prediction Theory. doi: 10.1115/1.3658902.

Levant, A. (1993). Sliding order and sliding accuracy in sliding mode control. *International Journal of Control*, 58(6), 1247–1263.

Luenberger, D.G. (1964). Observing the State of a Linear System. *IEEE Transactions on Military Electronics*, 8(2). doi:10.1109/TME.1964.4323124.

Matthews, G.P. and DeCarlo, R.A. (1988). Decentralized tracking for a class of interconnected nonlinear systems using variable structure control. *Automatica*, 24(2), 187–193. doi:http://dx.doi.org/10.1016/0005-1098(88)90027-1.

Moreno, J. and Osorio, M. (2008). A lyapunov approach to second-order sliding mode controllers and observers. In *Decision and Control, 2008. CDC 2008. 47th IEEE Conference on*, 2856–2861. doi: 10.1109/CDC.2008.4739356.

Shtessel, Y., Edwards, C., Fridman, L., and Levant, A. (2013). *Sliding Mode Control and Observation*. Springer Science & Business Media.

Utkin, V.I. (1992). *Sliding Modes in Control and Optimization*. doi:10.1007/978-3-642-84379-2.

Utkin, V.I., Guldner, J., and Shi, J. (1999). *Sliding Mode Control in Electro-mechanical Systems*. Taylor and Francis.

Utkin, V.I. and Shi, J. (1996). Integral sliding mode in systems operating under uncertainty conditions. *Proceedings of 35th IEEE Conference on Decision and Control*, 4. doi:10.1109/CDC.1996.577594.

Walcott, B.L., Corless, M.J., and Zak, S.H. (1987). Comparative study of nonlinear state observation techniques. *Int. J. Control*, 45, 2109–2132.

Cálculo numérico de matrices de Lyapunov de sistemas integrales con retardo

Héctor Arismendi-Valle Daniel Melchor-Aguilar

División de Matemáticas Aplicadas, IPICYT, 78216, San Luis Potosí, SLP, México (e-mail: hector.arismendi, dmelchor@ipicyt.edu.mx)

Resumen: En este artículo se propone un algoritmo numérico para la construcción de matrices de Lyapunov de sistemas integrales con un retardo.

Palabras clave: Sistemas integrales con retardo, Funcionales de Lyapunov-Krasovskii, Matrices de Lyapunov.

1. INTRODUCCIÓN

Recientemente en Melchor-Aguilar et al. (2010), se han introducido los teoremas directo y converso de Lyapunov-Krasovskii para la estabilidad exponencial de sistemas integrales con retardo. En el mismo artículo se ha mostrado que se requiere un nuevo tipo de funcionales de Lyapunov con el fin de abordar adecuadamente la dinámica de dicha clase de sistemas. Se proporcionan expresiones generales de funcionales de Lyapunov-Krasovskii del tipo cuadrática satisfaciendo una derivada preestablecida. Estas funcionales están definidas por funciones matriciales especiales las cuales son el equivalente a las matrices de Lyapunov que aparecen en el cálculo de las funcionales de Lyapunov-Krasovskii de tipo completo para sistemas diferenciales con retardo Kharitonov and Zhabko (2003); por lo tanto, es natural llamar a dichas funciones matriciales como *Matrices de Lyapunov para sistemas integrales con retardo* y a las funcionales correspondientes *Funcionales de Lyapunov-Krasovskii de tipo completo para sistemas integrales con retardo.*

Al igual que el caso diferencial con retardos, el cálculo de la matriz de Lyapunov desempeña un rol importante en el uso de las funcionales de Lyapunov-Krasovskii de tipo completo para resolver problemas tales como el cálculo de cotas de robustez y estimados exponenciales para la solución de sistemas integrales con retardo exponencialmente estables, ver Melchor-Aguilar et al. (2010).

Sin embargo, de acuerdo a nuestro conocimiento, no se han propuesto en la literatura procedimientos computacionales para calcular las matrices de Lyapunov de los sistemas integrales con retardo a diferencia de los sistemas diferenciales con retardo para los cuales existen distintos métodos semi-analíticos y/o numéricos para el cálculo de la matriz de Lyapunov, ver el libro reciente Kharitonov (2013) para una descripción completa de dichos métodos.

La falta de algoritmos numéricos para calcular las matrices de Lyapunov de los sistemas integrales con retardo ha limitado la aplicación de las funcionales de tipo completo pero, al mismo tiempo, ha motivado la construcción de funcionales de tipo reducido para obtener condiciones de estabilidad y estabilidad robusta formuladas directamente en términos de los coeficientes de los sistemas integrales con retardo expresadas como desigualdades matriciales lineales, véase, por ejemplo, Melchor-Aguilar (2010), Mondié and Melchor-Aguilar (2012) y Melchor-Aguilar (2014).

En este artículo, se presenta un esquema numérico para calcular aproximaciones lineales a pedazos de matrices de Lyapunov de sistemas integrales con un retardo y un kernel matricial constante.

Es importante resaltar que los métodos existentes para calcular matrices de Lyapunov de sistemas diferenciales con retardo no pueden ser aplicados directamente al caso de los sistemas integrales con retardo. Más aún, resulta que las ideas principales detrás del procedimiento numérico propuesto en Garcia-Lozano and Kharitonov (2006) para sistemas diferenciales con retardo no proveen una solución al problema del cálculo de matrices de Lyapunov incluso para el caso mas sencillo de sistemas integrales escalares con retardo.

La parte restante del artículo esta organizada de la manera siguiente. En la sección 2 se presentan algunos preliminares. Se introducen las funcionales y matrices de Lyapunov para sistemas integrales con retardo. La sección 3 está dedicada a mostrar que el método numérico propuesto en Garcia-Lozano and Kharitonov (2006) para sistemas diferenciales con retardo no permite el cálculo de matrices de Lyapunov para sistemas integrales con retardo. El algoritmo numérico para calcular aproximaciones lineales a pedazos continuas de matrices de Lyapunov para sistemas integrales con retardo está dado en la sección 4. Un ejemplo ilustrando el algoritmo se proporciona en la sección 5 y el artículo finaliza con algunas conclusiones.

2. PRELIMINARES

Considerar el sistema integral con retardo

$$x(t) = F \int_{-h}^{0} x(t+\theta)d\theta, \tag{1}$$

donde $F \in \mathbb{R}^n$ y $h > 0$. Para definir una solución particular de (1) una función inicial vectorial $\varphi(\theta), \theta \in [-h, 0)$ debe ser dada. Se supone que $\varphi \in \mathcal{PC}([-h, 0), \mathbb{R}^n)$, el espacio de las funciones acotadas y continuas a pedazos que

mapean el intervalo $[-h,0)$ a $\mathbb{R}^n$, equipado con la norma de convergencia uniforme $\|\varphi\|_h = \sup_{\theta\in[-h,0)} \|\varphi(\theta)\|$.

Dada una función inicial $\varphi \in \mathcal{PC}([-h,0),\mathbb{R}^n)$, existe una solución única $x(t,\varphi)$ de (1) la cual está definida para todo $t \in [-h,\infty)$ Melchor-Aguilar et al. (2010). Está solución es continua para todo $t > 0$ y en $t = 0$ presenta una discontinuidad de tipo salto dada por

$$\begin{aligned}\Delta x(0,\varphi) &= x(0,\varphi) - x(-0,\varphi)\\ &= F\left(\int_{-h}^{0}\varphi(\theta)d\theta\right) - \varphi(-0).\end{aligned}$$

Definición 1. Melchor-Aguilar et al. (2010) El sistema (1) se dice ser exponencialmente estable si existen constantes $\mu \geq 1$ y $\alpha > 0$ tales que toda solución de (1) satisface la desigualdad

$$\|x(t,\varphi)\| \leq \mu e^{-\alpha t}\|\varphi\|_h, \quad \forall t \geq 0.$$

Para presentar las condiciones de Lyapunov-Krasovskii para la estabilidad exponencial de (1) dadas en Melchor-Aguilar et al. (2010) se introducirá un poco de terminología. Como es habitual, se define el estado natural de (1) por

$$x_t(\theta,\varphi) \triangleq x(t+\theta,\varphi), \quad \theta \in [-h,0).$$

Debido a la discontinuidad de tipo salto de la solución en $t = 0$, se sigue que $x_t(\theta,\varphi) \in \mathcal{PC}([-h,0),\mathbb{R}^n)$ para $t \in [0,h)$, mientras que $x_t(\theta,\varphi) \in \mathcal{C}([-h,0),\mathbb{R}^n)$ para $t \geq h$. Como consecuencia de ello, en el enfoque de Lyapunov-Krasovskii, las funcionales deben estar definidas en el espacio infinito dimensional $\mathcal{PC}([-h,0),\mathbb{R}^n)$.

Por simplicidad de la notación, se escribe $x_t(\varphi)$ en lugar de $x_t(\theta,\varphi)$, $\theta \in [-h,0)$. Asimismo, cuando la función inicial es irrelevante en el contexto, simplemente se escribe $x(t)$ y x_t en lugar de $x(t,\varphi)$ y $x_t(\varphi)$.

Teorema 2. Melchor-Aguilar et al. (2010) El sistema (1) es exponencialmente estable si existe una funcional continua $v : \mathcal{PC}([-h,0),\mathbb{R}^m) \to \mathbb{R}$ tal que $t \to v(x_t(\varphi))$ es diferenciable y se cumplen las condiciones siguientes:

(1) $\alpha_1\int_{-h}^{0}\|\varphi(\theta)\|^2 d\theta \leq v(\varphi) \leq \alpha_2\int_{-h}^{0}\|\varphi(\theta)\|^2 d\theta$, para constantes $0 < \alpha_1 \leq \alpha_2$,
(2) $\frac{d}{dt}v(x_t(\varphi)) \leq -\beta\int_{-h}^{0}\|x(t+\theta,\varphi)\|^2 d\theta$, para una constante $\beta > 0$.

Sea $K(t)$ la solución de la ecuación matricial

$$K(t) = \left(\int_{-h}^{0}K(t+\theta)d\theta\right)F,$$

con función inicial $K(t) = -K_0$, $t \in [-h,0)$, donde $K_0 = (I - hF)^{-1}$. La matriz $K(t)$ se conoce como la matriz fundamental del sistema (1), ver Melchor-Aguilar et al. (2010).

Suponga que (1) es exponencialmente estable. Dada $W = W^T$ se define la matriz

$$U(\tau) \triangleq \int_0^\infty K^T(t)WK(t+\tau)dt, \quad \tau \in [-h,h]. \qquad (2)$$

Note que la estabilidad exponencial del sistema (1) garantiza la existencia de la integral impropia en (2).

Definición 3. La matriz (2) es la matriz de Lyapunov del sistema (1) asociada a la matriz W.

Observación 4. La matriz fundamental $K(t)$ presenta una discontinuidad de tipo salto en $t = 0$ dada por

$$\Delta K(0) \triangleq K(0) - K(-0) = I - K_0 - (-K_0) = I.$$

Por otro lado, la matriz de Lyapunov $U(\tau)$ es continua para todo $\tau \in [-h,h]$.

También se ha demostrado un enunciado converso al Teorema 2 en Melchor-Aguilar et al. (2010). De manera más precisa, bajo la suposición de la estabilidad exponencial de (1) y definiendo en $\mathcal{PC}([-h,0),\mathbb{R}^n)$ la funcional

$$w(\varphi) = \varphi^T(-h)W_0\varphi(-h) + \int_{-h}^{0}\varphi^T(\theta)W_1\varphi(\theta)d\theta,$$

donde W_0 y W_1 son matrices definidas positivas, la funcional de tipo completo correspondiente

$$\begin{aligned}v(x_t) &= \left(F\int_{-h}^{0}x(t+\theta)d\theta\right)^T U(0)\left(F\int_{-h}^{0}x(t+\theta)d\theta\right)\\ &-2\left(F\int_{-h}^{0}x(t+\theta)d\theta\right)^T\int_{-h}^{0}U(-h-\theta)Fx(t+\theta)d\theta\\ &+\int_{-h}^{0}x^T(t+\theta_1)F^T\left(\int_{-h}^{0}U(\theta_1-\theta_2)Fx(t+\theta_2)d\theta_2\right)d\theta_1\\ &-\int_{-h}^{0}x^T(t+\theta_1)F^TK_0^TW\times\\ &\times\left[\int_{-h}^{0}\left(\int_{-h-\theta_2}^{\theta_1-\theta_2}K(\xi)d\xi\right)Fx(t+\theta_2)d\theta_2\right]d\theta_1\\ &+\int_{-h}^{0}x^T(t+\theta)\left[W_0+(\theta+h)W_1\right]x(t+\theta)d\theta, \qquad (3)\end{aligned}$$

donde $U(\cdot)$ es la matriz de Lyapunov del sistema (1) asociada con la matriz $W = W_0 + hW_1$, satisface la ecuación

$$\frac{d}{dt}v(x_t) = -w(x_t), \quad t \geq 0.$$

Se muestra en Melchor-Aguilar et al. (2010) que si el sistema (1) es exponencialmente estable entonces la funcional (3) satisface las condiciones del Teorema 2.

Se sigue de (3) que el cálculo de la matriz $U(\tau)$ es fundamental para construir la funcional $v(x_t)$. En Melchor-Aguilar et al. (2010) se demostró que $U(\tau)$ satisface las propiedades siguientes.

Lema 5. La matriz de Lyapunov $U(\tau)$ satisface la ecuación dinámica

$$U(\tau) = \left(\int_{-h}^{0}U(\tau+\theta)d\theta\right)F, \qquad \tau \geq 0. \qquad (4)$$

Lema 6. Sea $W = W^T$. Entonces la matriz de Lyapunov $U(\tau)$ satisface

$$U(\tau) = K_0^TW\int_0^\tau K(\xi)d\xi + U^T(-\tau), \quad \tau \in [0,h]. \qquad (5)$$

Lema 7. La matriz de Lyapunov $U(\tau)$ satisface

$$\begin{aligned}-K(0)WK(0) &= [U(0)F - U(-h)F]^T\\ &+ [U(0)F - U(-h)F]. \qquad (6)\end{aligned}$$

Las condiciones (4), (5) y (6) son llamadas respectivamente *la propiedad dinámica*, *la propiedad de simetría* y *la propiedad algebraica*. Claramente, estas tres propiedades

proveen una alternativa más práctica de calcular la matriz de Lyapunov que la integral impropia definida en (2).

La propiedad dinámica define $U(\tau)$ como una solución de la ecuación (4). Para calcular dicha solución se necesita conocer su correspondiente función inicial. La función inicial no esta dada explícitamente. Por otro lado, la propiedad de simetría (5) junto con la propiedad algebraica (6) proveen información implícita de la función inicial desconocida.

Como se mencionó en la introducción, existen algunos métodos para calcular matrices de Lyapunov de sistemas diferenciales con retardo Kharitonov (2013) pero, sin embargo, no pueden ser aplicados directamente al cálculo de matrices de Lyapunov de sistemas integrales con retardo. El problema principal es que para aplicar dichos métodos se necesita derivar la ecuación dinámica (1) y esto dará lugar a una ecuación matricial diferencial con retardo inestable, ver Melchor-Aguilar et al. (2010) para más detalles.

Por otro lado, parece natural analizar la posibilidad de aplicar, no los métodos para sistemas diferenciales, pero si las ideas principales detrás de ellos al caso de los sistemas integrales con retardo. Así, en la siguiente sección, se aplicarán las ideas principales en Garcia-Lozano and Kharitonov (2006) para la construcción numérica de matrices de Lyapunov para sistemas integrales con retardo.

3. APLICACIÓN DEL MÉTODO NUMÉRICO DE SISTEMAS DIFERENCIALES CON RETARDO

Siguiendo las ideas expuestas en Garcia-Lozano and Kharitonov (2006) definimos la función matricial $\Phi(\tau)$, $\tau \in [-h, 0]$, como la función inicial desconocida para la ecuación dinámica (4) y dividimos el intervalo $[-h, 0]$ en N segmentos de la misma longitud $[-(j+1)r, -jr]$,$j = 0, 1, 2, \ldots, N-1$, donde $r = \dfrac{h}{N}$.

Ahora, introducimos $N+1$ matrices desconocidas $\Phi_j = \Phi(-jr)$, $j = 0, 1, 2, \ldots, N$, y definimos la aproximación lineal a pedazos continua de la función inicial $\Phi(\tau)$ como sigue:

$$\hat{\Phi}(s) = \left(1 + \frac{s + jr}{r}\right)\Phi_j + \left(-\frac{s + jr}{r}\right)\Phi_{j+1}, \qquad (7)$$

donde $s \in [-(j+1)r, -jr]$, $j = 0, 1, 2, \ldots, N-1$.

Sea $U(\tau) = U(\tau, \Phi)$ la solución de (4) correspondiente a la función inicial Φ. Note que para la construcción de la funcional (3), $U(\tau)$ solamente se necesita conocer para los valores de $\tau \in [0, h]$. En consecuencia, también dividimos el intervalo $[0, h]$ en N segmentos de la misma longitud $[jr, (j+1)r]$, $j = 0, 1, 2, \ldots, N-1$, introducimos $N+1$ matrices desconocidas $U_j = U(jr)$, $j = 0, 1, 2, \ldots, N$, y definimos la aproximación lineal a pedazos de $U(\tau)$ como sigue:

$$\hat{U}(s) = \left(1 - \frac{s - jr}{r}\right)U_j + \left(\frac{s - jr}{r}\right)U_{j+1}, \qquad (8)$$

donde $s \in [jr, (j+1)r]$, $j = 0, 1, 2, \cdots, N-1$.

Para $\tau = jr$ se tiene

$$U(jr) = \left(\int_{-h}^{0} U(jr + \theta)\, d\theta\right) F.$$

Entonces, de acuerdo con el método en Garcia-Lozano and Kharitonov (2006), se comparan $U(jr)$ y $U((j+1)r)$ para obtener

$$\begin{aligned} U_{j+1} - U_j &= U((j+1)r) - U(jr) \\ &= \left(\int_0^r \left(U(jr + \theta) - \Phi((j-N)r + \theta)\right) d\theta\right) F. \end{aligned}$$

Sustituyendo las matrices $U(jr+\theta)$ y $\Phi((j-N)r+\theta)$ bajo la integral por sus aproximaciones lineales a pedazos (8) y (7) y usando la propiedad de simetría (5) en los puntos de la partición

$$U_j = \Phi_j^T + K_0^T W V_j, \; j = 0, 1, \ldots, N, \qquad (9)$$

donde

$$V_j = \int_0^{jr} K(\xi) d\xi, \qquad (10)$$

se llega al conjunto de N ecuaciones lineales expresadas en términos de las matrices desconocidas Φ_j, $j = 0, 1, \ldots, N-1$ siguiente:

$$\begin{aligned} &\left(\frac{r}{2}F + I\right)\Phi_j^T + \left(\frac{r}{2}F - I\right)\Phi_{j+1}^T - \frac{r}{2}\left(\Phi_{N-j} + \right. \\ &\left. + \Phi_{N-j-1}\right)F = K_0^T W \left(V_{j+1} - V_j - \frac{r}{2}\left(V_j + V_{j+1}\right)\right) \end{aligned} \qquad (11)$$

Agregando a este conjunto la ecuación algebraica (6) en los puntos de la partición

$$\left(\Phi_0 - \Phi_N\right)F + F^T\left(\Phi_0 - \Phi_N\right)^T = -K^T(0) W K(0) \qquad (12)$$

se llega a un sistema de $N+1$ ecuaciones matriciales para $N+1$ matrices desconocidas Φ_j, $j = 0, 1, \ldots, N$.

En principio, la solución del sistema de ecuaciones (11)-(12) proporciona las matrices Φ_j y la formula (7) da la aproximación deseada de la función inicial.

Considere el caso escalar y dos particiones del intervalo $[-h, 0]$, es decir. $F \in \mathbb{R}$ y $N = 2$ lo que lleva a $r = \frac{h}{2}$. En este caso, el sistema lineal de ecuaciones (11)-(12) puede ser escrito como $A\mathcal{X} = B$, donde

$$A = \begin{bmatrix} \left(\frac{r}{2}F + 1\right) & -1 & -\frac{r}{2}F \\ \frac{r}{2}F & 1 & \left(\frac{r}{2} - 1\right) \\ 2F & 0 & -2F \end{bmatrix}, \quad \mathcal{X} = \left[\Phi_0 \;\; \Phi_1 \;\; \Phi_2\right]^T,$$

$$B = \begin{bmatrix} K_0 W \left(V_1 - \frac{r}{2}V_1 F\right) \\ K_0 W \left(\left(V_1 - V_1\right) - \frac{r}{2}\left(V_1 + V_2\right)F\right) \\ 0 \end{bmatrix}.$$

Se tiene que

$$\det(A) = -rF^2 - 2F - rF^2 + 2F + rF^2 + rF^2 = 0$$

lo cual implica que la matriz A es singular para todos los valores de $F \in \mathbb{R}$ y $h > 0$.

Se sigue que el sistema de ecuaciones (11)-(12) no es consistente ya que no hay una solución única de $A\mathcal{X} = B$ y, por lo tanto, la metodología expuesta en Garcia-Lozano and Kharitonov (2006) para sistemas diferenciales con retardo no provee una solución apropiada al problema del calculo de matrices de Lyapunov para sistemas integrales con retardo.

4. APROXIMACIÓN LINEAL A PEDAZOS

El análisis en la sección 3 muestra que se requiere un nuevo método para calcular soluciones de la ecuación dinámica (4), satisfaciendo las condiciones (5) y (6) para calcular matrices de Lyapunov de sistemas integrales con retardo. En esta sección, se propone dicho método.

4.1 Función inicial aproximada

Considerar las mismas particiones de los intervalos $[-h, 0]$ y $[0, h]$ en N segmentos iguales definidos en la sección 3 y las aproximaciones lineales a pedazos continuas de la función inicial $\hat{\Phi}(s)$ y la matriz $\hat{U}(s)$ definidas respectivamente por (7) y (8).

Ahora, para $\tau = jr$ se obtiene

$$U(jr) = \left(\int_{-h}^{0} U(jr+\theta)d\theta\right) F = \left(\int_{(j-N)r}^{jr} U(\xi)d\xi\right) F.$$

Dado que $(j-N)r \leq 0$, $j = 0, 1, \ldots, N$, se puede escribir la ecuación anterior como

$$U(jr) = \left(\underbrace{\int_{(j-N)r}^{0} \Phi(\xi)d\xi}_{m_j} + \underbrace{\int_{0}^{jr} U(\xi)d\xi}_{n_j}\right) F. \quad (13)$$

Considerar el término m_j en (13). Reescribiendo la integral en suma de integrales en intervalos de longitud r y sustituyendo $\Phi(\xi)$ por su aproximación $\hat{\Phi}(\xi)$ se obtiene

$$\hat{m}_j = \sum_{k=0}^{N-j-1} \int_{-(N-j-k)r}^{-(N-j-k-1)r} \hat{\Phi}(\xi)d\xi, j = 0, 1, \cdots, N-1,$$
$$\hat{m}_N = 0,$$

donde $\hat{m}_j$ denota la aproximación del término m_j.

Sustituyendo $\hat{\Phi}(\xi)$ en la integral del lado derecho de la expresión para $\hat{m}_j$ por su aproximación lineal a pedazos (7), un término de la integral satisface

$$\int_{-(N-j-k)r}^{-(N-j-k-1)r} \hat{\Phi}(\xi)d\xi =$$
$$= \int_{-(N-j-k)r}^{-(N-j-k-1)r} \left[\left(1 + \frac{\xi + (N-j-k-1)r}{r}\right) \times \Phi_{N-j-k-1} + \left(-\frac{\xi + (N-j-k-1)r}{r}\right)\Phi_{N-j-k}\right] d\xi.$$

Cálculos directos de la ecuación anterior conducen a

$$\hat{m}_j = \frac{r}{2} \sum_{k=0}^{N-j-1} \left(\Phi_{N-j-k-1} + \Phi_{N-j-k}\right), j = 0, 1, \cdots, N-1,$$
$$\hat{m}_N = 0.$$

Considerar el término n_j en (13). De manera similar, reescribiendo la integral como suma de integrales en intervalos de longitud r y sustituyendo $U(\xi)$ por su aproximación $\hat{U}(\xi)$ se obtiene

$$\hat{n}_j = \sum_{k=0}^{j-1} \int_{(j-k-1)r}^{(j-k)r} \hat{U}(\xi)d\xi, j = 1, 2, \cdots, N, \quad (14)$$
$$\hat{n}_0 = 0$$

donde $\hat{n}_j$ denota la aproximación de n_j.

Sustituyendo $\hat{U}(\xi)$ en la integral del lado derecho de la expresión para $\hat{n}_j$ por su aproximación lineal a pedazos (7), un término de la integral satisface

$$\int_{(j-k-1)r}^{(j-k)r} \hat{U}(\xi)d\xi =$$
$$= \int_{(j-k-1)r}^{(j-k)r} \left[\left(1 - \frac{\xi - (j-k-1)r}{r}\right) U_{j-k-1} + \left(\frac{\xi - (j-k-1)r}{r}\right) U_{j-k}\right] d\xi.$$

Mediante cálculos directos se obtiene

$$\hat{n}_j = \frac{r}{2} \sum_{k=0}^{j-1} \left(U_{j-k-1} + U_{j-k}\right), \quad j = 1, \cdots, N, \quad (15)$$
$$\hat{n}_0 = 0.$$

Ahora, notar que si N es suficientemente grande entonces de (13) se sigue que

$$U_j = \left(\hat{m}_j + \hat{n}_j\right) F, \quad j = 0, 1, \ldots, N.$$

A partir de esta expresión, (14), (15) y la propiedad de simetría en los puntos de la partición (9) se llega a las ecuaciones matriciales siguientes:

- Para $j = 0$

$$\Phi_0 - \frac{r}{2} \sum_{k=0}^{N-j-1} \left(\Phi_{N-j-k-1} + \Phi_{N-j-k}\right) F = 0. \quad (16)$$

- Para $j = 1, 2, \cdots, N-1$

$$\Phi_j^T - \frac{r}{2}\left[\sum_{k=0}^{N-j-1} \left(\Phi_{N-j-k-1} + \Phi_{N-j-k}\right) + \sum_{k=0}^{j-1} \left(\Phi_{j-k-1}^T + \Phi_{j-k}^T\right)\right] F =$$
$$= K_0^T W \left(\frac{r}{2} \sum_{k=0}^{j-1} \left(V_{j-k-1} + V_{j-k}\right) F - V_j\right). \quad (17)$$

- Para $j = N$

$$\Phi_N^T - \frac{r}{2} \sum_{k=0}^{j-1} \left(\Phi_{j-k-1}^T + \Phi_{j-k}^T\right) F =$$
$$= K_0^T W \left(\frac{r}{2} \sum_{k=0}^{j-1} \left(V_{j-k-1} + V_{j-k}\right) F - V_N\right). \quad (18)$$

Notar que las ecuaciones (16)-(18) describen un sistema de $N+1$ ecuaciones matriciales para $N+1$ matrices incógnitas Φ_j, $j = 0, 1, \cdots, N$. La solución de este sistema de ecuaciones provee las matrices Φ_j, $j = 0, 1, 2, \ldots, N$ y la formula (7) permite el calculo de la aproximación deseada de la función inicial matricial.

A fin de mostrar que el sistema de ecuaciones matriciales (16)-(18) no presenta el mismo problema inconsistente

del sistema de ecuaciones matriciales (11)-(12) obtenido siguiendo las ideas del método en Garcia-Lozano and Kharitonov (2006) considerar de nuevo el caso escalar cuando $F \in \mathbb{R}$ y $N = 2$. En este caso, el sistema de ecuaciones (16)-(18) se pueden escribir como $\bar{A}\mathcal{X} = \bar{B}$, donde

$$\bar{A} = \begin{bmatrix} \left(1 - \frac{r}{2}F\right) & -rF & -\frac{r}{2}F \\ -rF & (1 - rF) & 0 \\ -\frac{r}{2}F & -rF & \left(1 - \frac{r}{2}F\right) \end{bmatrix}, \quad \mathcal{X} = [\Phi_0 \ \Phi_1 \ \Phi_2]^T,$$

$$\bar{B} = \begin{bmatrix} 0 \\ K_0 W\left(\frac{r}{2}V_1 F - V_1\right) \\ K_0 W\left(\frac{r}{2}(2V_1 + V_2)F\right) - V_2 \end{bmatrix}.$$

Se tiene que $\det(\bar{A}) = -2Fr + 1$. Luego entonces, se sigue que el único caso cuando $\bar{A}$ es singular es $F = \frac{1}{2r} = \frac{1}{h}$.

Se ha mostrado en Kharitonov and Melchor-Aguilar (2000) que el sistema integral escalar con retardo es exponencialmente estable sí y solo si $F < \frac{1}{h}$ y que $F = \frac{1}{h}$ es la frontera de la región de estabilidad. En consecuencia, para este caso, el sistema de ecuaciones (16)-(18) provee solución para todos los sistemas integrales escalares con retardo exponencialmente estables.

Observación 8. Notar que el sistema de ecuaciones matriciales (16)-(18) está bien definido sin involucrar la propiedad algebraica (6) a diferencia del método propuesto en Garcia-Lozano and Kharitonov (2006) el cual requiere la correspondiente propiedad algebraica para matrices de Lyapunov de sistemas diferenciales con retardo.

4.2 Forma vectorial

Para encontrar una solución del sistema de ecuaciones (16)-(18) es conveniente escribirlo en forma vectorial por medio de la operación vector $vec(Q) = q$, donde $q \in \mathbb{R}^{n^2}$ se obtiene apilando las columnas de $Q \in \mathbb{R}^{n \times n}$.

La vectorización de la matriz $C = AXB$ es $vec(C) = (A \otimes B)\, vec(X)$, donde

$$A \otimes B = \begin{pmatrix} b_{11}A & b_{21}A & \cdots & b_{n1}A \\ b_{12}A & b_{22}A & \cdots & b_{n2}A \\ \vdots & \vdots & \ddots & \vdots \\ b_{1n}A & b_{2n}A & \cdots & b_{nn}A \end{pmatrix}$$

es el producto de Kronecker de las matrices A y B. Por otro lado, la vectorización de la matriz $D = AX^TB$ es $vec(D) = (A \circ B)\, vec(X)$, donde $A \circ B$ está definida por

$$A \circ B = \begin{pmatrix} A_1 B_1^T & A_2 B_1^T & \cdots & A_n B_1^T \\ A_1 B_2^T & A_2 B_2^T & \cdots & A_n B_2^T \\ \vdots & \vdots & \ddots & \vdots \\ A_1 B_n^T & A_2 B_n^T & \cdots & A_n B_n^T \end{pmatrix},$$

denotando con A_j, B_j, $j = 1, 2, \ldots, N$, los vectores columna de A y B, respectivamente.

Entonces, el sistema de ecuaciones matriciales (16)-(18) puede ser escrito en forma vectorial como sigue:

- Para $j = 0$

$$(I \circ I)\,\phi_0 - \frac{r}{2}\sum_{k=0}^{N-j-1}(I \times F)\,(\phi_{N-j-k-1} + \phi_{N-j-k}) = 0.$$

- Para $j = 1, 2, \cdots, N-1$

$$(I \circ F)\,\phi_j - \frac{r}{2}\left[\sum_{k=0}^{N-j-1}(I \times F)\,(\phi_{N-j-k-1} + \phi_{N-j-k}) + \sum_{k=0}^{j-1}(I \circ F)\,(\phi_{j-k-1} + \phi_{j-k})\right]F = vec\left(K_0^T W\left(\frac{r}{2}\sum_{k=0}^{j-1}(V_{j-k-1} + V_{j-k})\,F - V_j\right)\right).$$

- Para $j = N$

$$(I \circ I)\,\phi_N - \frac{r}{2}\sum_{k=0}^{j-1}(I \circ F)\,(\phi_{j-k-1} + \phi_{j-k})\,F = vec\left(K_0^T W\left(\frac{r}{2}\sum_{k=0}^{j-1}(V_{j-k-1} + V_{j-k})\,F - V_N\right)\right),$$

donde $\phi_j = vec(\Phi_j), j = 1, 2, \ldots, N$.

4.3 Matriz de Lyapunov aproximada

Con la aproximación lineal a pedazos de la función inicial calculada, se plantea el problema de buscar la solución correspondiente de la ecuación dinámica (4). De hecho, el problema puede ser formulado como el problema de valor inicial general siguiente:

$$U(\tau) = \left(\int_{-h}^{0} U(\tau + \theta)d\theta\right)F, \quad \tau \geq 0, \tag{19}$$

$$U(\tau) = \Phi(\tau), \quad \tau \in [-h, 0]. \tag{20}$$

Notar que el problema de valor inicial (19)-(20) no se puede resolver por medio del método paso a paso conocido para construir soluciones de sistemas diferenciales con retardo Bellman and Cooke (1963).

A continuación, se propone un método para resolver el problema de valor inicial (19)-(20) el cual está inspirado en el método paso a paso para sistemas diferenciales con retardo y, en realidad, este puede ser usado para construir soluciones numéricas de sistemas integrales con retardo de la forma (1).

De (19) se tiene para $\tau \in [0, h]$

$$U(\tau) = W(\tau) + \left(\int_0^{\tau} U(\xi)d\xi\right)F, \tag{21}$$

donde

$$W(\tau) = \left(\int_{\tau-h}^{0} \Phi(\xi)d\xi\right)F.$$

Se sigue que el problema de valor inicial (19)-(20) es equivalente al problema de encontrar una solución de la ecuación integral (21).

Sean $U_0(\tau) = W(\tau)$ y $U_j(\tau)$, $j = 1, 2, 3, \ldots$, sucesiones descritas como sigue:

$$U_j(\tau) = W(\tau) + \left(\int_0^{\tau} U_{j-1}(\xi)d\xi\right)F, \quad \tau \in [0, h].$$

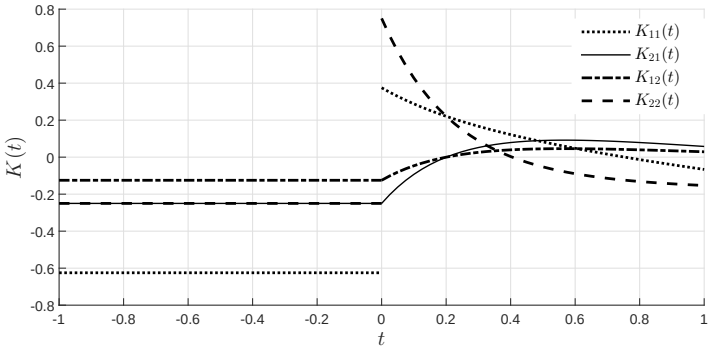

Fig. 1. Componentes de la matriz fundamenta $K(t)$.

Es posible mostrar que $U_j(\tau)$ converge (uniformemente en τ) a la matriz $U(\tau)$ cuando $j \to \infty$ y que la matriz límite $U(\tau)$ satisface la ecuación integral (21) la cual, a su vez, implica la existencia y unicidad de la solución $U(\tau)$ satisfaciendo (19) y (20). Por motivos de espacio se omiten los detalles de tal demostración.

Continuando el proceso en intervalos de longitud h se obtiene la existencia y unicidad de la solución $U(\tau)$ para $\tau \geq 0$.

La sucesión $U_j(\tau)$ proporciona un método para construir numéricamente una aproximación de $U(\tau)$ para cada $\tau \geq 0$.

Por lo tanto, usando este método, sea $\hat{U}\left(\tau, \hat{\Phi}\right)$, $\tau \in [0, h]$, la solución aproximada de la ecuación dinámica (4) correspondiente a la función inicial $\hat{\Phi}$.

5. EJEMPLO NUMÉRICO

Considerar el sistema integral con retardo (1) con $h = 1$ y

$$F = \begin{pmatrix} -1 & 1 \\ 2 & -4 \end{pmatrix}.$$

Como los valores propios de F yacen en el dominio abierto Γ cuya frontera admite la parametrización

$$\partial\Gamma = \left\{ \frac{\omega \sin(\omega)}{2\left[1 - \cos(\omega)\right]} + i\frac{\omega}{2} \middle| \, \omega \in (-2\pi, 2\pi) \right\}$$

entonces el sistema (1) es exponencialmente estable, ver Kharitonov and Melchor-Aguilar (2000).

Notar que para resolver el sistema de ecuaciones matriciales (16)-(18) se requiere calcular las matrices V_j, $j = 1, 2, \ldots, N$, definidas por (10) y, por lo tanto, calcular la matriz fundamental $K(t)$ para $t \in [0, 1]$. Debido a que la función inicial para la matriz fundamental es conocida se puede aplicar el método propuesto en la subsección 4.3 y construir $K(t)$ para $t \in [0, 1]$, ver Fig. 1.

Ahora para $W = I$ y $N = 20$ se usa el algoritmo propuesto para calcular la aproximación de la función inicial $\hat{\Phi}(\tau)$, $\tau \in [-1, 0]$, y la correspondiente matriz de Lyapunov $\hat{U}\left(\tau, \hat{\Phi}\right)$, $\tau \in [0, 1]$, ver Fig. 2.

Como se puede ver en las Figs. 1 y 2, la matriz fundamental $K(t)$ presenta una discontinuidad de tipo salto en $t = 0$ mientras que la matriz de Lyapunov es continua para todo $\tau \in [-1, 1]$ como se esperaba de la Nota 4.

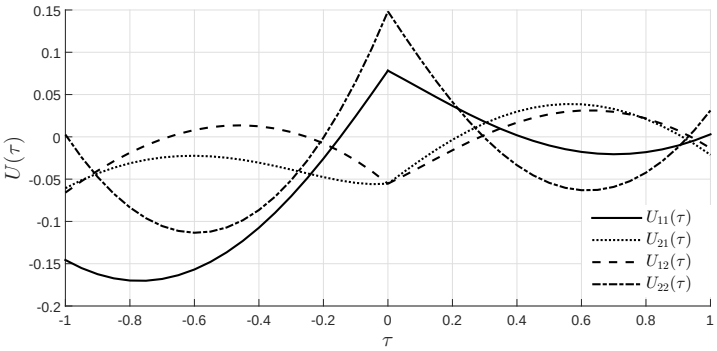

Fig. 2. Componentes de la función inicial aproximada $\hat{\Phi}(\tau)$ y la matriz de Lyapunov $\hat{U}\left(\tau, \hat{\Phi}\right)$.

6. CONCLUSIONES

En este artículo, se aborda el problema del cálculo de la matriz de Lyapunov de sistemas integrales con un retardo. Después de mostrar que los métodos numéricos existentes para calcular matrices de Lyapunov para sistemas diferenciales con retardo no pueden ser aplicados a los sistemas integrales con retardo, se propuso un algoritmo numérico para calcular aproximaciones lineales a pedazos de matrices de Lyapunov.

Es importante mencionar que el algoritmo propuesto no involucra la propiedad algebraica de la matriz de Lyapunov a diferencia del método para sistemas diferenciales con retardo el cual requiere dicha propiedad. La propiedad algebraica se puede usar para evaluar la calidad de la aproximación de la matriz de Lyapunov, un problema que se abordará en un trabajo futuro.

7. AGRADECIMIENTOS

Este trabajo fue parcialmente financiado por el proyecto CONACYT con clave 265667 : "PROGRAMA PARA UN AVANCE GLOBAL E INTEGRADO DE LA MATEMTICA MEXICANA".

REFERENCIAS

Bellman, R. and Cooke, K.L. (1963). *Differential-difference equations*. Mathematics in Science and Engineering. Academic Press, New York.

Garcia-Lozano, H. and Kharitonov, V. (2006). Numerical computation of time delay lyapunov matrices. *6th IFAC Workshop on Time-Delay Systems*, 6, 60–65.

Kharitonov, V. (2013). *Time-delay systems: Lyapunov functionals and matrices*. Birkhäuser.

Kharitonov, V. and Zhabko, A. (2003). Lyapunov-krasovskii approach to the robust stability analysis of time-delay systems. *Automatica*, 39(1), 15 – 20.

Kharitonov, V.L. and Melchor-Aguilar, D. (2000). On delay dependent stability conditions. *Syst. Control Lett.*, 40(1), 71 – 76.

Melchor-Aguilar, D. (2010). On stability of integral delay systems. *Appl. Math. Comput.*, 217(7), 3578 – 3584.

Melchor-Aguilar, D. (2014). New results on robust exponential stability of integral delay systems. *Int. J. Syst. Sci.*, 47(8), 1905–1916.

Melchor-Aguilar, D., Kharitonov, V., and Lozano, R. (2010). Stability conditions for integral delay systems. *Int. J. Robust. Nonlin.*, 20(1), 1–15.

Mondié, S. and Melchor-Aguilar, D. (2012). Exponential stability of integral delay systems with a class of analytic kernels. *IEEE T. Automat. Contr.*, 57(2), 484–489.

Condiciones de estabilidad para un tipo de sistemas inestables de alto orden con retardo que contienen ceros.

Vázquez Rosas C.D,*, del Muro Cuéllar B,*, Márquez Rubio J.F,*

**Escuela Superior de Ingeniería Mecánica y Eléctrica, Unidad Culhuacán, Instituto Politécnico Nacional, Santa Ana 1000 México D.F, 04430*
E-mail:carlos_daniel_vaz@hotmail.com, bdelmuro@yahoo.com, jfcomr23@yahoo.com.mx

Resumen: *En este trabajo se aborda el problema de estabilización de sistemas lineales invariantes en el tiempo de alto orden, que contienen un polo inestable, "n-1" polos estables y "n" ceros de fase mínima, además de contar con un retardo en su dinámica. Se presentan las condiciones suficientes de manera explícita para que el sistema pueda estabilizarse utilizando una retroalimentación estática de salida. Dichas condiciones están basadas con base en la posición de los polos y ceros del sistema, así como el tamaño máximo de retardo.*

Palabras clave: Retardo, inestable, ceros, retroalimentación

1. INTRODUCCIÓN.

Los tiempos de retardo son un fenómeno común que se presenta en diversos sistemas tales como procesos químicos (Richard et al., 2003), servomecanismos, sistemas hidráulicos etc… La presencia de un retardo en un sistema de control regularmente produce comportamientos indeseados, una de las limitantes producidas por la existencia de un retardo es que genera un decremento de la fase del sistema, lo cual se traduce en un margen de ganancia menor con respecto a un sistema libre de retardo, produciendo que algunos sistemas estables, al introducir un retardo se vuelvan inestables.

Si además del retardo, el sistema a lazo abierto es inestable, es un problema de control difícil de abordar. Diversos trabajos han afrontado la problemática de los sistemas inestables con retardo, por ejemplo, en (Huang et al., 1995), (Padma et al., 2006) se utilizan controladores tipo PID para la estabilización y control, pero las condiciones de estabilidad no se muestran de manera explícita. En (Silva et al., 2004) se utiliza una metodología basada en el teorema de Hermite-Biehler para cuasipolinomios buscando solucionar el problema de estabilización de sistemas de primer orden con retardo utilizando controladores PID, llegando a estabilizar plantas con retardos considerables de hasta dos veces la constante de tiempo inestable del sistema.

Otra manera de afrontar el problema de sistemas con retardo inestables es utilizar predicciones del efecto del retardo en el sistema, siendo el método más conocido el llamado predictor de Smith (Smith, 1957), diversos autores han realizado modificaciones a la estructura original propuesta por Smith para poder contrarrestar sus limitaciones, tal es el caso de (Liu et al., 2005) donde se propone un esquema predictor que puede utilizarse en plantas que a lazo abierto son inestables, en (Normey et al., 2008) se presenta un esquema predictor que puede utilizarse en sistemas que contienen grandes retardos. En (del Muro et al., 2009) se aborda el problema de un sistema con un polo inestable y "n" polos estables mostrando las condiciones necesarias y suficientes para estabilizar el sistema con una retroalimentación estática de salida. Otro ejemplo se presenta en (Márquez et al., 2010) que propone un esquema predictor con un controlador PI de 2 grados de libertad con el objetivo de rechazar perturbaciones y poder seguir referencias de tipo escalón. Todos los trabajos antes mencionados, no toman en cuenta el caso que existan ceros en la dinámica del sistema.

En la literatura se tienen registrados diversos trabajos para sistemas inestables con retardo que tienen ceros dentro de su dinámica. Una de las formas más usuales para afrontar el reto que representa la presencia de ceros, es diseñar el controlador tal que, exista una cancelación polo-cero en el sistema a lazo cerrado,

(Novella et al., 2012) propone una modificación a la estructura original del predictor de Smith para afrontar el caso de sistemas inestables que contienen un cero de fase mínima, pero esta estrategia se limita a tener un tiempo de retardo menor a la constante de tiempo inestable del sistema. En (Lee et al., 2010) se muestran las condiciones de estabilidad para diversos tipos de sistemas que tienen ceros, estabilizándolos con controladores tipo P, PI, PID. En (Vazquez et al., 2012) se presentan las condiciones necesarias y suficientes para sistemas de alto orden que contienen un cero de fase mínima, además de presentar una estrategia de control para afrontar grandes retardos. Cabe señalar que los trabajos anteriores solo toman en cuenta el caso que exista un solo cero de fase mínima en la dinámica del sistema.

Este trabajo presenta de manera explícita las condiciones suficientes de estabilidad para un tipo de sistemas con retardo, inestables de alto orden, con un polo inestable, "n-1" estables y "n" ceros de fase mínima utilizando como herramienta de análisis el criterio de estabilidad de Nyquist.

El trabajo se organiza de la siguiente forma: en la Sección 2 se presentan el planteamiento del problema. En la Sección 3 se muestran resultados preliminares que fueron utilizados para la obtención de los resultados de este trabajo, posteriormente en la Sección 4 se presentan los resultados principales de este trabajo. En la Sección 5 se presenta un ejemplo acompañado de una simulación numérica para verificar las condiciones de estabilidad obtenidas y finalmente en la Sección 6 se presentan las conclusiones.

2. PLANTEAMIENTO DEL PROBLEMA.

Considere un sistema lineal invariante en el tiempo con una entrada, una salida (SISO) y un retardo de tiempo a la entrada.

$$\frac{Y(s)}{U(s)} = \frac{N(s)}{D(s)} e^{-\tau s} = \mathrm{G(s)}e^{-\tau s} \quad (1)$$

Donde:

- U(s) Es la señal de entrada.
- Y(s) Es la señal de salida.
- τ>0 Es el tiempo de retardo conocido.
- N(s) Es un polinomio representado en la variable compleja s.
- D(s) Es un polinomio representado en la variable compleja s.
- G(s) Es el proceso libre de retardo.

Para el control proporcional, C(s)=k aplicado al sistema de la Ec (1) la respuesta del sistema en lazo abierto es:

$$Q(s) = C(s)G(s) = k\frac{N(s)}{D(s)} e^{-\tau s} \quad (2)$$

La ecuación a lazo cerrado del sistema de la Ec (2) es:

$$\frac{Y(s)}{R(s)} = \frac{k\mathrm{N(s)}e^{-\tau s}}{D(s) + kN(s)e^{-\tau s}} \qquad (3)$$

Donde R(s) es una entrada de referencia y el término "k" es la ganancia del control proporcional. Se puede notar que el término $e^{-\tau s}$ está localizado en la ecuación característica del sistema generando un sistema que tiene un infinito de polos lo cual dificulta su análisis de estabilidad.

3. RESULTADOS PREELIMINARES.

Se presentan los resultados preliminares que fueron utilizados para la obtención del resultado principal de este trabajo.

(Xiang et al., 2007) ***Lema 1***. Dada la función de transferencia a lazo abierto mostrada en (2) con P^+ polos inestables, el sistema a lazo cerrado es estable si la gráfica de Nyquist de (3) encierra el punto crítico (-1,0), P^+ veces en sentido anti-horario.

(Xiang et al., 2007) ***Lema 2.*** Para el sistema a lazo abierto descrito en (2)

$$\lim_{\omega\to\infty} \left|\mathrm{G(j}\omega)\right| < 1$$

Es necesario para la estabilidad a lazo cerrado.

(Xiang et al., 2007) ***Lema 3***. Dado el sistema a lazo abierto mostrado en (2) con $P^+ \geq 1$ polos inestables, una condición necesaria para la estabilidad en lazo cerrado es que $\frac{dM_G(\omega^*)}{d\omega} < 0$ para una $\omega^* > 0$

(Xiang et al., 2007) ***Lema 4.*** Para el sistema a lazo abierto descrito en (2) con $P^+ \geq 1$ polos inestables, es necesario que $\frac{d\angle G(\omega^*)}{d\omega} > 0$ para lograr la estabilidad del sistema a lazo cerrado

4. RESULTADOS PRINCIPALES.

Considere un sistema lineal con una entrada, una salida y un retardo de tiempo a la entrada con un control proporcional C(s)=k:

$$Q(s) = C(s)G(s) = k\frac{N(s)}{D(s)}e^{-\tau s} = k\frac{(s+b_1)(s+b_2)\dots(s+b_n)}{(s-a_1)(s+a_2)\dots(s+c_n)}e^{-\tau s} \quad (4)$$

Donde $b_1, b_2, \dots b_n > 0$, $a_1, a_2, \dots a_n > 0$ y $\tau > 0$.

Teorema 1. *Existe un control proporcional que estabiliza el sistema descrito en (4) si se cumplen las tres relaciones siguientes:*

i) $\tau < \frac{1}{a_1} + \sum_{i=1}^{n}\frac{1}{b_i} - \sum_{i=2}^{n}\frac{1}{a_i}$

ii) $\frac{1}{{b_1}^2} + \frac{1}{{b_2}^2} + \dots \frac{1}{{b_n}^2} < \frac{1}{{a_1}^2} + \frac{1}{{a_2}^2}\dots\frac{1}{{a_n}^2}$

iii) $b_1 b_2 \dots b_n > a_1 a_2 \dots a_n$

Demostración*: i)* Considere el sistema de la Ec (4) en el dominio de la frecuencia.

$$Q(j\omega) = \frac{(j\omega+b_1)(j\omega+b_2)\dots(j\omega+b_n)}{(j\omega-a_1)(j\omega+a_2)\dots(j\omega+a_n)}e^{-\tau j\omega} \quad (5)$$

La ecuación de magnitud es:

$$M_G(\omega) = \sqrt{\frac{(\omega^2+{b_1}^2)(\omega^2+{b_2}^2)\dots(\omega^2+{b_n}^2)}{(\omega^2+{a_1}^2)(\omega^2+{a_2}^2)(\omega^2+{a_n}^2)}} \quad (6)$$

La ecuación de fase es:

$$\angle G(\omega) = -\left(180 - tan^{-1}\frac{\omega}{a_1}\right) + tan^{-1}\frac{\omega}{b_1} + tan^{-1}\frac{\omega}{b_2} + \dots tan^{-1}\frac{\omega}{b_n} - tan^{-1}\frac{\omega}{a_2}\dots - tan^{-1}\frac{\omega}{a_n} - \omega\tau \quad (7)$$

La derivada de la ecuación (7) es:

$$\frac{d\angle G(\omega)}{d\omega} = \frac{b_1}{{b_1}^2+\omega^2} + \frac{b_2}{{b_2}^2+\omega^2} + \dots \frac{b_n}{{b_n}^2+\omega^2} + \frac{a_1}{{a_1}^2+\omega^2} - \frac{a_2}{{a_2}^2+\omega^2} - \dots \frac{a_n}{{a_n}^2+\omega^2} - \tau \quad (8)$$

La condición necesaria para la estabilidad es que, la fase tenga para alguna frecuencia positiva ω^* un valor superior a -180º.

$$\angle G(\omega^*) > -180 \quad (9)$$

Un requerimiento para obtener la trayectoria deseada en la gráfica de Nyquist, es $\frac{d\angle G(j\omega)}{d\omega}\Big|_{\omega\to 0} > 0$

$$\frac{d\angle G(\omega)}{d\omega}\Big|_{\omega\to 0} = -\tau + \frac{1}{a_1} + \frac{1}{b_1} + \frac{1}{b_2} \dots + \frac{1}{b_n} - \frac{1}{a_2} \dots - \frac{1}{a_n} < 0 \quad (10)$$

De modo que si se cumple la condición (10) existe una frecuencia $\omega^* > 0$ tal que $\angle G(\omega^*) > -180$. La fase toma un valor mayor a -180, después se requiere que la fase decrezca nuevamente a -180 efectuando la intersección con el eje real negativo con $\angle G(\omega_c) = -180$ para alguna frecuencia positiva ω_c.

Otra manera de encontrar las condiciones de retardo descritas en el Teorema 1 es con una aproximación lineal local a partir de una serie de Taylor para los términos que contengan tan^{-1} y ver cómo se comporta a valores muy pequeños del argumento (teniendo frecuencias muy bajas) con la condición:

$$f(\Theta) = tan^{-1}\Theta \cong \Theta \quad (11)$$

A partir de la condición mostrada en la Ec (9), al utilizar la aproximación lineal local de la Ec (11) en la Ec (7) se tiene:

$$-180 < -180 + \frac{\omega}{a_1} - \frac{\omega}{a_2} \dots - \frac{\omega}{b_n} + \frac{\omega}{b_1} + \frac{\omega}{b_2} \dots + \frac{\omega}{b_n} - \omega\tau \quad (12)$$

Al multiplicar por el inverso de la frecuencia, se obtiene la condición de retardo del sistema:

$$\tau < \frac{1}{a_1} + \sum_{i=1}^{n}\frac{1}{b_i} - \sum_{i=2}^{n}\frac{1}{a_i} \quad (13)$$

ii) Para el control proporcional, C(s)=k, la respuesta en frecuencia de lazo abierto es:

$$Q(j\omega) = C(j\omega)G(j\omega) = k\left(\frac{(j\omega+b_1)(j\omega+b_2)\dots(j\omega+b_n)}{(j\omega-a_1)(j\omega+a_2)\dots(j\omega+a_n)}e^{-\tau j\omega}\right) \quad (14)$$

Donde su condición de magnitud es:

$$M_Q(\omega) = k\left(\sqrt{\frac{(\omega^2+{b_1}^2)(\omega^2+{b_2}^2)\dots(\omega^2+{b_n}^2)}{(\omega^2+{a_1}^2)(\omega^2+{a_2}^2)\dots(\omega^2+{a_n}^2)}}\right) \quad (15)$$

La derivada de la ecuación (15) es

$$\frac{d}{d\omega}M_Q(\omega) = k\left(-\frac{2\omega\left(\omega^2+b_1{}^2\right)\left(\omega^2+b_2{}^2\right)\ldots\left(\omega^2+b_n{}^2\right)}{\left(\omega^2+a_1{}^2\right)^2\left(\omega^2+a_2{}^2\right)\ldots\left(\omega^2+a_n{}^2\right)} - \frac{2\omega\left(\omega^2+b_1{}^2\right)\left(\omega^2+b_2{}^2\right)\ldots\left(\omega^2+b_n{}^2\right)}{\left(\omega^2+a_1{}^2\right)\left(\omega^2+a_2{}^2\right)^2\ldots\left(\omega^2+a_n{}^2\right)} \ldots - \frac{2\omega\left(\omega^2+b_1{}^2\right)\left(\omega^2+b_2{}^2\right)\ldots\left(\omega^2+b_n{}^2\right)}{\left(\omega^2+a_1{}^2\right)\left(\omega^2+a_2{}^2\right)\ldots\left(\omega^2+a_n{}^2\right)^2} + \frac{2\omega\left(\omega^2+b_1{}^2\right)}{\left(\omega^2+a_1{}^2\right)\left(\omega^2+a_2{}^2\right)\ldots\left(\omega^2+a_n{}^2\right)} + \frac{2\omega\left(\omega^2+b_2{}^2\right)}{\left(\omega^2+a_1{}^2\right)\left(\omega^2+a_2{}^2\right)\ldots\left(\omega^2+a_n{}^2\right)} \ldots + \frac{2\omega\left(\omega^2+b_n{}^2\right)}{\left(\omega^2+a_1{}^2\right)\left(\omega^2+a_2{}^2\right)\ldots\left(\omega^2+a_n{}^2\right)}\right) \Big/ 2k\left(\sqrt{\frac{\left(\omega^2+b_1{}^2\right)\left(\omega^2+b_2{}^2\right)\ldots\left(\omega^2+b_n{}^2\right)}{\left(\omega^2+a_1{}^2\right)\left(\omega^2+a_2{}^2\right)\ldots\left(\omega^2+a_n{}^2\right)}}\right) \quad (16)$$

De la condición del Lema 3 se obtiene que es necesario que se cumpla la siguiente desigualdad:

$$\frac{2\omega\left(\omega^2+b_1{}^2\right)}{\left(\omega^2+a_1{}^2\right)\left(\omega^2+a_2{}^2\right)\ldots\left(\omega^2+a_n{}^2\right)} + \frac{2\omega\left(\omega^2+b_2{}^2\right)}{\left(\omega^2+a_1{}^2\right)\left(\omega^2+a_2{}^2\right)\ldots\left(\omega^2+a_n{}^2\right)} \ldots \frac{2\omega\left(\omega^2+b_n{}^2\right)}{\left(\omega^2+a_1{}^2\right)\left(\omega^2+a_2{}^2\right)\ldots\left(\omega^2+a_n{}^2\right)} < \frac{2\omega\left(\omega^2+b_1{}^2\right)\left(\omega^2+b_2{}^2\right)\ldots\left(\omega^2+b_n{}^2\right)}{\left(\omega^2+a_1{}^2\right)^2\left(\omega^2+a_2{}^2\right)\ldots\left(\omega^2+a_n{}^2\right)} + \frac{2\omega\left(\omega^2+b_1{}^2\right)\left(\omega^2+b_2{}^2\right)\ldots\left(\omega^2+b_n{}^2\right)}{\left(\omega^2+a_1{}^2\right)\left(\omega^2+a_2{}^2\right)^2\ldots\left(\omega^2+a_n{}^2\right)} \ldots \frac{2\omega\left(\omega^2+b_1{}^2\right)\left(\omega^2+b_2{}^2\right)\ldots\left(\omega^2+b_n{}^2\right)}{\left(\omega^2+a_1{}^2\right)+\left(\omega^2+a_2{}^2\right)\left(\omega^2+a_n{}^2\right)^2} \quad (17)$$

Despejando en la Ec (17) obtenemos:

$$\frac{1}{\left(\omega^2+b_1{}^2\right)} + \frac{1}{\left(\omega^2+b_2{}^2\right)} + \cdots \frac{1}{\left(\omega^2+b_n{}^2\right)} < \frac{1}{\left(\omega^2+a_1{}^2\right)} + \frac{1}{\left(\omega^2+a_2{}^2\right)} + \cdots \frac{1}{\left(\omega^2+a_n{}^2\right)} \quad (18)$$

A partir del Lema 1,es necesario tener $M_Q(\omega^*) > 1$ para alguna frecuencia y así encerrar el punto crítico (-1,0) obteniendo la siguiente condición:

$$k\sqrt{\frac{\left(\omega^2+b_1{}^2\right)\left(\omega^2+b_2{}^2\right)}{\left(\omega^2+a_1{}^2\right)\left(\omega^2+a_2{}^2\right)}} > 1 \quad (19)$$

Evaluando la condición (18) para frecuencias $\omega \to 0$ se obtiene:

$$\frac{1}{b_1{}^2} + \frac{1}{b_2{}^2} + \cdots \frac{1}{b_n{}^2} < \frac{1}{a_1{}^2} + \frac{1}{a_2{}^2} \ldots \frac{1}{a_n{}^2} \quad (20)$$

Podemos concluir que si se cumple (20) asegura que la magnitud del sistema decrece para frecuencias $\omega \to 0$ obteniendo $M_Q(\omega_1) > M_Q(\omega_2)$ con lo cual se logra una correcta dirección de la trayectoria de Nyquist, donde ω_1 y ω_2 son las frecuencias donde la trayectoria de Nyquist cruza el eje real negativo, al cumplirse (19) el rodeo generado encerrará al punto crítico (-1,0).

Debido a que el sistema tiene el mismo orden en el numerador y el denominador, la respuesta de la magnitud en altas frecuencias es $M_Q(\omega)\big|_{\omega\to\infty} = k$.

A partir del Lema 2, la condición de magnitud mostrada en la Ec (19) se puede escribir: $M_Q(\omega)\big|_{\omega\to\infty} = k < 1$, por lo tanto, k<1 es necesario.

Evaluando la Ecuación (19) para frecuencias $\omega \to 0$ y teniendo en cuenta que el valor de la ganancia está acotado a k<1, se obtiene la condición:

$$b_1 b_2 \ldots b_n > a_1 a_2 \ldots a_n \quad (21)$$

Si se cumplen las condiciones mostradas en el teorema 1, aseguramos que exista un rodeo al punto crítico (-1,0) en frecuencias $\omega \to 0$

Observación. El valor mínimo del controlador proporcional se puede calcular con base en la ecuación (19), obteniendo:

$$kmin > \sqrt{\frac{\left(a_1{}^2\right)\left(a_2{}^2\right)\ldots\left(a_n{}^2\right)}{\left(b_1{}^2\right)\left(b_2{}^2\right)\ldots\left(b_n{}^2\right)}} \quad (22)$$

5. EJEMPLOS.

Ejemplo 1. Considere el sistema con retardo de quinto orden con 5 ceros de fase mínima en su dinámica dado por la siguiente función de transferencia:

$$\frac{Y(s)}{U(s)} = \frac{(s+1.2)(s+1.8)(s+2.4)(s+3.3)(s+7)}{(s-1)(s+1.5)(s+2)(s+3)(s+7.3)}\, e^{-\tau s} \quad (23)$$

A partir del Teorema 1 podemos concluir que el rango de retardos bajo el cual el sistema descrito en (23) puede ser estabilizado con una retroalimentación estática de salida es: $0<\tau<1.6145$.

Para hacer el análisis de lazo cerrado se propone un tiempo de retardo τ=1.5. Utilizando la gráfica de Nyquist del sistema que se puede ver en la figura 1, podemos notar que existe un rodeo en sentido anti-horario al punto crítico (-1,0) asegurando la

estabilidad del sistema en lazo cerrado. A partir de la ecuación (22) se calcula una ganancia K=0.57 para asegurar la estabilidad a lazo cerrado del sistema.

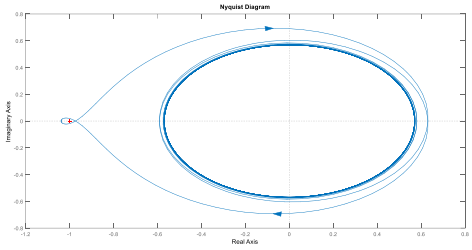

Figura1. Gráfica de Nyquist del ejemplo 1.

El comportamiento de la planta controlada en lazo cerrado se presenta en la Figura 2.

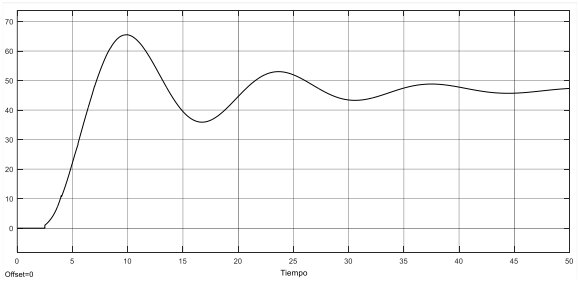

Figura 2. Comportamiento del sistema del ejemplo 1.

6. CONCLUSIONES

Los retardos son uno de los escenarios más indeseables en un sistema de control, más aún si a lazo abierto, el sistema es inestable. Pese a que la presencia de ceros se traduce en condiciones más favorables para estabilizar un sistema con retardo, pocos trabajos abordan esta situación y se limitan al caso que solo exista un cero en la dinámica del sistema. En este trabajo se hace un análisis en el dominio de la frecuencia para un tipo de sistemas de alto orden, inestables, con retardo que cuenta con "n" ceros en su dinámica en el cual se presentan las condiciones suficientes para que exista una retroalimentación estática de salida estabilizante. Se presenta un ejemplo en simulación numérica para mostrar la estabilización del sistema a lazo cerrado bajo las condiciones de estabilidad mostradas de manera explícita.

REFERENCIAS

del Muro, B., González, O. A., & Pedraza, Y. A. Stabilization of High Order Systems with Delay using a Predictor Schema. Augost 2-5. Cancun Mexico. IEEE 52nd International Midwest Symposium on Circuits and Systems. (2009)

Huang C.T.,Lin Y.S., Tuning PID controller for open-loop unstable process with time-delay, Chem. Eng. Commun. 133(1995) 11-30

Lee S.C., Wang Q.G., Stabilization conditions for a class of unstable delay processes of higher order, Journal of the Taiwan Institute of Chemical Engineers, 41 (2010) 440-445

Liu T., Cai Y. Z., Gu D. Y., Zhang W. D. New modified smith predictor scheme for integrating and unstable processes with time delay, IEEE Proceedings-Control Theory and Applications 152(2), 238-246, 2005

Márquez J.F., del Muro, B., Velasco, M., and Alvarez, J. (2010). Control based in an observer scheme for first-order systems with delay. Revista Mexicana de Ingeniería Quimica 9, 43-52.

Normey-Rico, J.E. and Camacho, E.F. Dead-time compensators: A survey. Control Engineering Practice, 16(4), 407–428. (2008)

Novella. F, del Muro, B, Control of second orden strictly-Proper Unstable System with time delay, Revista Mexicana de Ingeniería química, 2012

Padma R., Sree, M. Chidambaram, Control of Unstable Systems, Narosa Publishing House, Chennai, India, 2006.

Richard J. P. Time-Delay Systems: An Overview of Some Recent Advances and Open Problems. Automatica 39, 1667-1694. (2003)

Silva, G.J., Datta, A., and Bhattacharyya., S. PID Controllers for Time-Delay Systems. Control EngineerEngineering. Birkh¨auser. (2004)

Smith, O.J.M. Close Control of Loops with Dead Time. Chem. Eng. Prog., 53, 217–219. (1957)

Vázquez, C.D, del Muro, Basilio, Estabilización de Sistemas con Retardo de Segundo Orden que Contienen un Cero, Congreso Latinoamericano de Control Automático, Cd del Carmen, México, (2012)

Xiang C., Wang Q.-G., Lu X., Nguyen L., and T. H. Lee, Stabilization of secondorder unstable delay processes by simple controllers," J. Proc. Contr., vol. 17, pp.675-682, 2007.

Yang X.P., Wang Q. G., Hang C. C., and C. Lin, IMC-based control system design for unstable processes," Ind. Eng. Chem. Res., vol. 41, pp. 4288-4294, (2002)

Control a Distancia de un Actuador Aerodinámico Mediante Predicción de Estados

I. Estrada-Sánchez * **M. Velasco-Villa** **,[1]
H. Rodríguez-Cortés *

* *Centro de Investigación y de Estudios Avanzados del IPN Departamento de Ingeniería Eléctrica, Sección de Mecatrónica, Av. I.P.N. No. 2508, Col. San Pedro Zacatenco, 07360, Ciudad de México, (e-mails: {ivanestrada,hrodriguez}@cinvestav.mx)*
** *Instituto Politécnico Nacional, ESIME-Culhuacán, SEPI. Av. Santa Ana 1000, Col. San Francisco Culhuacán, 04453, Ciudad de México, (e-mail:velasco@cinvestav.mx).*

Resumen. En el presente trabajo se aborda el problema de control a distancia de un actuador aerodinámico con un retardo de tiempo en la señal de entrada. Se presenta una solución basada en estados estimados futuros obtenidos por medio de un predictor–observador no lineal basado en un cambio de coordenadas que produce un sistema en adelanto equivalente. La convergencia de los estados predecidos a los valores reales así como la estabilidad en lazo cerrado del sistema controlado con estados estimados se lleva a cabo mediante una funcional de Lyapunov. Se presentan resultados en simulación que muestran la eficacia del esquema de control propuesto. Finalmente, se realizan experimentos en tiempo real en una plataforma construida para tal efecto.

Keywords: Sistemas con retardos, predictor-observador, actuador aerodinámico, funcional de Lyapunov.

1. INTRODUCCIÓN

Los sistemas con retardos han sido estudiados ampliamente en los últimos años, debido a que pueden ser encontrados en varios sistemas prácticos tales como sistemas químicos, mecánicos, biológicos o sistemas en redes, etc. Estos sistemas se encuentran presentes en la mayoría de los dispositivos que utilizamos en la vida diaria (Kolmanovskii and Myshkis (1992), Niculescu (2001)). Por ejemplo en aplicaciones de teleoperación, en donde la existencia de retardos en la señal de control y en las mediciones pueden ser un factor importante en la estabilidad del sistema en lazo cerrado (Hale and Lunel (2013)). Ya sea que aparezcan en el estado, en la entrada de control o en las mediciones, éstos retardos pueden clasificarse como de transporte, de comunicación o de medición, Fridman (2014).

El problema de control de sistemas con retardo de tiempo en la entrada ha sido tratado a partir de diferentes enfoques. Empezando por ignorar su efecto, cuando el retardo es muy pequeño o mediante retroalimentaciones causales aproximadas (Münz et al. (2009)) en el caso lineal o aproximaciones de orden reducido en el caso no lineal (Maza-Casas et al. (2000), Kolmanovskii and Myshkis (1992)). Un enfoque ampliamente investigado son las técnicas de predicción de valores futuros de los estados del sistema para diseñar leyes de retroalimentación causales. En el caso lineal, el denominado Predictor de Smith (Smith (1959)) fue un parteaguas en este sentido. En el caso no lineal, la consideración de retroalimentaciones de dimensión infinita para la asignación finita del espectro del sistema (Krstic (2009)) han abierto un gran campo de oportunidad.

Para resolver el problema de control de sistemas con retardos de tiempo en la entrada, en Kim and Son (2010), se diseña un controlador robusto para compensar perturbaciones variantes en tiempo usando un observador de perturbaciones. En Li et al. (2014), se trata el problema de estabilización de una clase de sistemas lineales con múltiples retardos a la entrada por medio del diseño de una retroalimentación de dimensión infinita basada en predicción. En Roh and Oh (1999), se presenta un controlador por modos deslizantes para estabilizar sistemas con retardos en la entrada. Se propone una superficie deslizante basada en un predictor para minimizar los efectos del retardo en la entrada del sistema. En Lee and Lee (2000), se presenta un método de control robusto para sistemas lineales con retardo en la entrada y perturbaciones paramétricas. Se aborda el problema utilizando desigualdades matriciales lineales (LMI). En Chiang and Tung (2003), se presenta un controlador dinámico robusto para sistemas no lineales con incertidumbres en el modelado y en la entrada. Se analiza el problema desde la teoría de Lyapunov y el concepto de análisis funcional.

En el presente trabajo se analiza el problema de seguimiento de trayectorias para un sistema no lineal con retardo de tiempo constante a la entrada. Específicamente, se considera un actuador aerodinámico formado por una dupla barra–hélice. Para resolver el problema se diseña un predictor de los valores futuros de los estados, el cual es utilizado para diseñar una retroalimentación causal que resuelve el problema mencionado. La convergencia de los errores de predicción y seguimiento se muestra utilizando una funcional completa de Lyapunov–Krasovskii (Kharitonov (2013)).

El resto del trabajo, se organiza de la siguiente forma: en la Sección 2 se presenta el modelo dinámico del actuador

[1] M. Velasco-Villa se encuentra en estancia sabática apoyado por Conacyt (No. 260936) con adscripción en la Sección de Mecatrónica del Departamento de Ingeniería Eléctrica del CINVESTAV-IPN.

aerodinámico, justificando como su control a distancia produce un retardo de tiempo en la señal de control. En la Sección 3 se diseña un predictor–observador al utilizar un modelo en coordenadas adelantadas. En la Sección 4 se muestra una solución al problema de seguimiento de trayectorias mediante estados estimados futuros. En la Sección 5 muestra la evaluación numérica y experimental. Finalmente, en la Sección 6 se muestran las conclusiones del trabajo.

2. ACTUADOR AERODINÁMICO

Considere el sistema barra-péndulo simple actuado por una hélice, como se muestra en la Figura 1. Donde θ es el ángulo con respecto a la línea vertical, ℓ es la distancia del punto de rotación hasta el actuador aerodinámico, F es la fuerza que se genera en el actuador aerodinámico, x_i y z_i son los ejes inerciales, y u es el momento externo alrededor del eje de rotación y_i.

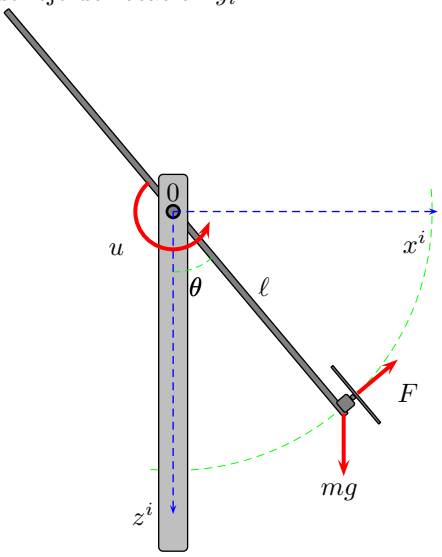

Figura 1. Actuador aerodinámico.

El modelo del actuador aerodinámico barra-hélice se obtendrá mediante la metodología de Euler-Lagrange. Para tal efecto, las energías cinética y potencial están dadas por,

$$T = \frac{1}{2}J_b\dot{\theta}^2 + \frac{1}{2}m\ell^2\dot{\theta}^2 = \frac{1}{2}\dot{\theta}^2\left(J_b + m\ell^2\right)$$
$$V = mg\ell\left(1-\cos\theta\right)$$

donde $J_b = \frac{1}{12}m_b\ell_b^2$ es el momento de inercia de la barra con respecto a su centro de gravedad. El Lagrangiano del sistema resulta entonces,

$$\begin{aligned}\mathcal{L} &= T - V \\ &= \frac{1}{2}\dot{\theta}^2\left(J_b + m\ell^2\right) - mg\ell\left(1-\cos\theta\right).\end{aligned}$$

El modelo se obtiene a partir de la ecuación de Euler-Lagrange,

$$\frac{d}{dt}\frac{\partial\mathcal{L}}{\partial\dot{\theta}} - \frac{\partial\mathcal{L}}{\partial\theta} = u.$$

Nótese que,

$$\frac{\partial\mathcal{L}}{\partial\dot{\theta}} = \left(J_b + m\ell^2\right)\dot{\theta}, \quad \frac{d}{dt}\frac{\partial\mathcal{L}}{\partial\dot{\theta}} = \left(J_b + m\ell^2\right)\ddot{\theta}$$
$$\frac{\partial\mathcal{L}}{\partial\theta} = -mg\ell\sin\theta.$$

Por lo que la ecuación que describe el movimiento del sistema resulta,

$$\left(J_b + m\ell^2\right)\ddot{\theta} + mg\ell\sin\theta = u$$

o bien,

$$\ddot{\theta} + \frac{mg\ell}{J_b + m\ell^2}\sin\theta = \frac{u}{J_b + m\ell^2}.$$

Para obtener un modelo en el espacio de estados, tome en cuenta las variables $x_1 = \theta$ y $x_2 = \dot{\theta}$. Entonces se tiene,

$$\begin{aligned}\dot{x}_1 &= x_2 \\ \dot{x}_2 &= -\frac{mg\ell}{J_b + m\ell^2}\sin\left(x_1\right) + \frac{u}{J_b + m\ell^2}.\end{aligned} \tag{1}$$

2.1 Consideración de tiempos de retardo

Asumiendo que el sistema de control se encuentra en una posición remota y que existe un canal de comunicación para el envío de la señal de control y la recepción de señales medidas como se muestra en la Figura 2. El sistema (1) puede modelarse como un sistema que incluye un retardo de tiempo τ en la señal de entrada (tiempos muertos) que puede incluir también los posibles tiempos de cómputo. Bajo estas condiciones, el sistema (1) se reescribe en la forma,

$$\begin{aligned}\dot{x}_1 &= x_2 \\ \dot{x}_2 &= a\sin\left(x_1\right) + bu\left(t-\tau\right).\end{aligned} \tag{2}$$

donde,

$$a = -\frac{mg\ell}{J_b + m\ell^2} \quad \text{y} \quad b = \frac{1}{J_b + m\ell^2}. \tag{3}$$

Nótese que en general los retardos asociados con el canal de comunicación resultan variantes en el tiempo, una estrategia comúnmente utilizada es tomar el valor máximo del retardo en el canal de comunicación y asumir el retardo τ como constante.

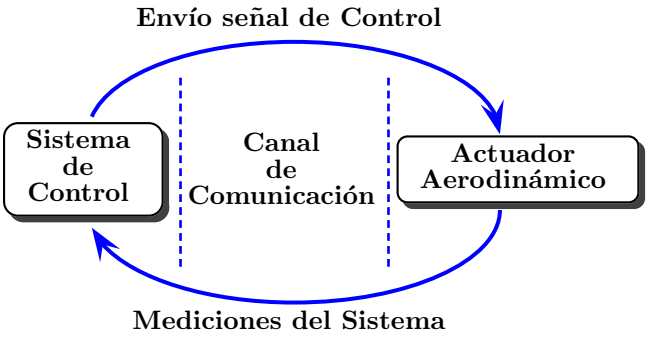

Figura 2. Sistema con retardo en el canal de comunicación.

3. PREDICTOR-OBSERVADOR PROPUESTO

El sistema (2), puede reescribirse como un sistema libre de retardos al considerar las variables adelantadas,

$$w_1\left(t\right) = x_1\left(t+\tau\right), w_2\left(t\right) = x_2\left(t+\tau\right). \tag{4}$$

Bajo estas nuevas coordenadas, se obtiene la nueva representación,

$$\begin{aligned}\dot{w}_1 &= w_2 \\ \dot{w}_2 &= a\sin\left(w_1\right) + bu\end{aligned} \tag{5}$$

en donde el retardo de tiempo ya no está presente.

Nótese que las señales w_1 y w_2 corresponden a señales futuras no medibles, por lo que es necesario diseñar un

predictor–observador para poder estimarlas. Considerando el sistema en adelanto (5), es posible proponer el siguiente predictor-observador,

$$\begin{aligned}\dot{\hat{w}}_1 &= \hat{w}_2 + \lambda_1 \left[w_1\left(t-\tau\right) - \hat{w}_1\left(t-\tau\right)\right] \\ \dot{\hat{w}}_2 &= a\sin\left(\hat{w}_1\right) + bu + \lambda_0\left[w_1\left(t-\tau\right) - \hat{w}_1\left(t-\tau\right)\right].\end{aligned} \tag{6}$$

Nótese que el predictor-observador anterior puede reescribirse tomando la señal medible $x_1\left(t\right)$ en la forma,

$$\begin{aligned}\dot{\hat{w}}_1 &= \hat{w}_2 + \lambda_1 \left[x_1\left(t\right) - \hat{w}_1\left(t-\tau\right)\right] \\ \dot{\hat{w}}_2 &= a\sin\left(\hat{w}_1\right) + bu + \lambda_0\left[x_1\left(t\right) - \hat{w}_1\left(t-\tau\right)\right].\end{aligned} \tag{7}$$

La dinámica de los errores de predicción puede analizarse al definir las señales de error,

$$e_{w_1} = w_1 - \hat{w}_1,\; e_{w_2} = w_2 - \hat{w}_2. \tag{8}$$

La dinámica del error de predicción resulta,

$$\begin{aligned}\dot{e}_{w_1} &= e_{w_2} - \lambda_1 e_{w_1}\left(t-\tau\right) \\ \dot{e}_{w_2} &= -\lambda_0 e_{w_1}\left(t-\tau\right) + a\left[\sin\left(w_1\right) - \sin\left(\hat{w}_1\right)\right].\end{aligned}$$

que puede reescribirse como,

$$\begin{aligned}\dot{e}_{w_1} &= e_{w_2} - \lambda_1 e_{w_1}\left(t-\tau\right) \\ \dot{e}_{w_2} &= -\lambda_0 e_{w_1}\left(t-\tau\right) + 2a\sin\left(\tfrac{e_{w_1}}{2}\right)\cos\left(\tfrac{w_1-\hat{w}_1}{2}\right).\end{aligned} \tag{9}$$

4. PROBLEMA DE SEGUIMIENTO DE TRAYECTORIAS

A continuación se presentará una solución al problema de seguimiento de trayectorias asociado con el sistema (2), mediante la síntesis de una retroalimentación basada en estados futuros estimados por el predictor-observador (7). Supóngase que se desea seguir una trayectoria definida por $w_{1d}\left(t\right)$ y $w_{2d}\left(t\right)$. Defínase los errores de seguimiento,

$$e_{d1}\left(t\right) = w_1\left(t\right) - w_{1d}\left(t\right),\; e_{d2}\left(t\right) = w_2\left(t\right) - w_{2d}\left(t\right). \tag{10}$$

Considere entonces la siguiente retroalimentación basada en estados futuros predecidos,

$$\begin{aligned}u\left(t\right) = \tfrac{1}{b}[&-a\sin\left(\hat{w}_1\right) - k_2\left(\hat{w}_2 - w_{2d}\right) \\ &-k_1\left(\hat{w}_1 - w_{1d}\right) + \dot{w}_{2d}]\end{aligned} \tag{11}$$

Por otra parte, de los errores de observación, (8), se tiene que, $\hat{w}_1 = w_1 - e_{w_1}$, $\hat{w}_2 = w_2 - e_{w_2}$. Entonces, la dinámica de error de seguimiento resulta,

$$\begin{aligned}\dot{e}_{d_1} &= e_{d_2} \\ \dot{e}_{d_2} &= -k_1 e_{d_1} - k_2 e_{d_2} + k_1 e_{w_1} + k_2 e_{w_2} \\ &\quad +2a\sin\left(\tfrac{e_{w_1}}{2}\right)\cos\left(\tfrac{w_1+\hat{w}_1}{2}\right).\end{aligned} \tag{12}$$

Nótese también que,

$$\begin{aligned}\tfrac{w_1+\hat{w}_1}{2} &= \tfrac{w_1+w_1-e_{w_1}}{2} = w_1 - \tfrac{e_{w_1}}{2} \\ &= e_{d_1} + w_{1d} - \tfrac{e_{w_1}}{2}.\end{aligned}$$

Finalmente, la dinámica del error en lazo cerrado (error de predicción y error de seguimiento) queda representada en la forma,

$$\begin{aligned}\dot{e}_{w_1} &= e_{w_2} - \lambda_1 e_{w_1}\left(t-\tau\right) \\ \dot{e}_{w_2} &= -\lambda_0 e_{w_1}\left(t-\tau\right) + f\left(e_w, e_d, w_d\right) \\ \dot{e}_{d_1} &= e_{d_2} \\ \dot{e}_{d_2} &= -k_1 e_{d_1} - k_2 e_{d_2} + k_1 e_{w_1} + k_2 e_{w_2} \\ &\quad +f\left(e_w, e_d, w_d\right).\end{aligned} \tag{13}$$

donde,

$$f\left(e_w, e_d, w_d\right) = 2a\sin\left(\frac{e_{w_1}}{2}\right)\cos\left(e_{d_1} - \frac{e_{w_1}}{2} + w_{1d}\right). \tag{14}$$

Observación 1. Definiendo los errores, $e_{d_{x_1}} = x_1 - x_{1d}$ y $e_{d_{x_2}} = x_2 - x_{2d}$, el error de seguimiento puede escribirse alternativamente en la forma,

$$\begin{aligned}\dot{e}_{d_{x_1}}\left(t\right) &= e_{d_{x_2}}\left(t\right) \\ \dot{e}_{d_{x_2}}\left(t\right) &= -k_1 e_{d_{x_1}}\left(t\right) - k_2 e_{d_{x_2}}\left(t\right) \\ &\quad +k_1 e_{w_1}\left(t-\tau\right) + k_2 e_{w_2}\left(t-\tau\right) + f\left(\cdot\right)\end{aligned}$$

donde, $f\left(\cdot\right) = 2a\sin\left(\frac{e_{w_1}(t-\tau)}{2}\right)\cos\left(e_{d_{x_1}} - \frac{e_{w_1}(t-\tau)}{2} + x_{1d}\right)$.

La dinámica de lazo cerrado (13) en coordenadas de los errores de predicción-observación y seguimiento, se puede expresar en forma vectorial como,

$$\begin{aligned}\begin{bmatrix}\dot{e}_{w_1}\\ \dot{e}_{w_2}\\ \dot{e}_{d_1}\\ \dot{e}_{d_2}\end{bmatrix} &= \begin{bmatrix}0 & 1 & 0 & 0\\ 0 & 0 & 0 & 0\\ 0 & 0 & 0 & 1\\ k_1 & k_2 & -k_1 & -k_2\end{bmatrix}\begin{bmatrix}e_{w_1}\\ e_{w_2}\\ e_{d_1}\\ e_{d_2}\end{bmatrix} \\ &+\begin{bmatrix}-\lambda_1 & 0 & 0 & 0\\ -\lambda_0 & 0 & 0 & 0\\ 0 & 0 & 0 & 0\\ 0 & 0 & 0 & 0\end{bmatrix}\begin{bmatrix}e_{w_1}\left(t-\tau\right)\\ e_{w_2}\left(t-\tau\right)\\ e_{d_1}\left(t-\tau\right)\\ e_{d_2}\left(t-\tau\right)\end{bmatrix} + \begin{bmatrix}0\\ f\left(e_w, e_d, w_d\right)\\ 0\\ f\left(e_w, e_d, w_d\right)\end{bmatrix}\end{aligned} \tag{15}$$

con $f\left(e_w, e_d, w_d\right)$ definida en (14).

Alternativamente, definiendo $e = \left[e_{w1}, e_{w2}, e_{d1}, e_{d2}\right]^\top$ y considerando la estructura de la ecuación anterior, el sistema (15) puede reescribirse en la forma,

$$\dot{e} = A_0 e + A_1 e\left(t-\tau\right) + \bar{f}\left(e, w_d\right). \tag{16}$$

con A_0, A_1, $\bar{f}$ definidas apropiadamente.

Nótese ahora que $f\left(e, w_d\right)$, puede acotarse por arriba como sigue,

$$\begin{aligned}\|f\left(e, w_d\right)\| &= \|2a\sin\left(\tfrac{e_{w1}}{2}\right)\cos\left(e_{d1} - \tfrac{e_{w1}}{2} + w_{1d}\right)\| \\ &\le \|2a\sin\left(\tfrac{e_{w1}}{2}\right)\|\|\cos\left(e_{d1} - \tfrac{e_{w1}}{2} + w_{1d}\right)\| \\ &\le a|e_{w1}|\end{aligned}$$

por lo tanto, es posible concluir que,

$$\|\bar{f}\left(e, w_d\right)\| \le \rho\|e\| \tag{17}$$

para una constante ρ positiva.

4.1 Estabilidad en lazo cerrado

A continuación la estabilidad del sistema en el error (16) se establecerá en dos etapas. Nótese inicialmente que $\bar{f}\left(e, w_d\right)$ corresponde a una perturbación acotada (17) para el sistema (16). Considere entonces el sistema (16) libre de perturbaciones, esto es, el sistema,

$$\begin{aligned}\dot{e} &= A_0 e + A_1 e(t-\tau) \\ e(\theta) &= \varphi(\theta),\; \theta \in [-\tau, 0]\end{aligned} \tag{18}$$

con la condición inicial $\varphi(\theta)$, $\theta \in [-\tau, 0]$ y $\varphi \in \mathcal{PC}\left([-\tau, 0], \mathbb{R}^4\right)$ al espacio de las funciones continuas a pedazos en $\mathbb{R}^4$ definidas en $[-\tau, 0]$.

Dado que los parámetros de las matrices A_0, A_1 se pueden elegir libremente (dependen del predictor (7) y la retroalimentación (11)), es siempre posible estabilizar asintóticamente el sistema (18), para un valor constante, acotado del retardo τ. Esto se puede hacer, por ejemplo, al considerar la Proposición 5.2.2, Capítulo 5 de Gu et al. (2003). Basado en lo anterior, para demostrar la estabilidad del sistema perturbado (16) se considerará, sin pérdida de generalidad, que existen constantes positivas λ_0, λ_1, k_1, k_2 que estabilizan el sistema (18) para un valor $\tau > 0$.

Suponga entonces que el sistema (18) es asintóticamente estable (es posible mostrar que para esta clase de sistemas la estabilidad resulta del tipo exponencial, Bellman and

Cooke (1963)), entonces para establecer la estabilidad del sistema (16), es posible proponer una funcional de Lyapunov de tipo completo definida en la forma,

$$v(e_t) = v_0(e_t) + \int_{-\tau}^{0} e^T(t+\theta)\left[W_1 + (\tau+\theta)W_2\right]e(t+\theta)\,d\theta \tag{19}$$

donde $e_t = e(t)$, $\theta \in [-\tau, 0]$ con,

$$v_0(e_t) = e^T(t)U(0)e(t) + 2e^T(t)\int_{-\tau}^{0} U(-\tau-\theta)A_1 e(t+\theta)\,d\theta + \int_{-\tau}^{0} e^T(t+\theta_1)A_1^T\left[\int_{-\tau}^{0} U(\theta_1-\theta_2)A_1 e(t+\theta_2)\,d\theta_2\right]d\theta_1. \tag{20}$$

La matriz de Lyapunov en (19) (Kharitonov (2013)),

$$U(\gamma) = \int_0^\infty K^T(t)WK(t+\gamma)dt$$

es definida en términos de la matriz fundamental $K(t)$ del sistema libre de perturbación (18) y

$$W = W_0 + W_1 + \tau W_2$$

con matrices W_0, W_1, W_2 definidas positivas a partir de la estabilidad exponencial del sistema (18).

Nótese que la matriz de Lyapunov $U(\gamma)$ satisface las siguientes propiedades (Kharitonov (2013)):

1. $\frac{dU(\gamma)}{d\gamma} = U(\gamma)A_0 + A(\gamma-\tau)A_1$
2. $U(-\gamma) = U^T(\gamma)$, $\gamma > 0$ y $U^T(0) = U(0)$
3. $U(0)A_0 + U(-\tau)A_1 + A_0^T U(0) + A_1^T U(\tau) = -W$

Es posible ahora mostrar el siguiente resultado.

Teorema 4.1. Suponga que existen constantes $\lambda_0, \lambda_1 > 0$ asociadas con el predictor–observador (7) y constantes $k_1, k_2 > 0$ asociadas con la retroalimentación (11) tales que el sistema (18) es exponencialmente estable. Considerando que el sistema (16) satisface (17), la solución del problema de seguimiento de trayectorias basada en estados estimados futuros tiene solución si se satisfacen las siguientes condiciones,

1. $\lambda_{min}(W_0) \geq 2\rho v + a_1\tau\rho v$
2. $\lambda_{min}(W_2) \geq a_1 v$.

Demostración. Considerando las propiedades de la matriz de Lyapunov $U(\gamma)$, después de algunos cálculos, la derivada de la funcional (19), a lo largo de la solución de (16) queda como,

$$\begin{aligned}\tfrac{d}{dt}V(e_t) = &-e^T(t)W_0e(t) - e^T(t-\tau)W_1e(t-\tau) - \int_{t-\tau}^{t} e^T(\xi)W_2e(\xi)\,d\xi \\ &+2e^T(t)U(0)\bar{f}(e,w_d) \\ &+2\bar{f}^T(e,w_d)\int_{t-\tau}^{t} U(-\tau-\xi+t)A_1e(\xi)\,d\xi\end{aligned} \tag{21}$$

Sea $v = \max_{\theta\in[0,\tau]}\|U(\theta)\|$ y $a_1 = \|A_1\|$, entonces,

$$\begin{aligned}2e^T(t)U(0)\bar{f}(e,w_d) &\leq 2\|e^T(t)U(0)\bar{f}(e,w_d)\| \\ &= 2\|e^T(t)\|\|U(0)\|\|\bar{f}(e,w_d)\| \leq 2\rho v\|e(t)\|^2 \\ 2\bar{f}^T(e,w_d)\int_{t-\tau}^{t} U(-\tau-\xi+t)A_1e(\xi)\,d\xi &\leq \tau\|\bar{f}^T(e,w_d)\|^2\|U(0)\|\|A_1\| \\ &+\|U(-\tau)\|\|A_1\|\int_{t-\tau}^{t}\|e(\xi)\|^2d\xi \\ &\leq a_1\tau\rho v\|e(t)\|^2 + a_1 v\int_{t-\tau}^{t}\|e(\xi)\|^2d\xi.\end{aligned}$$

Por lo tanto, (21) puede rescribirse en la forma,

$$\begin{aligned}\tfrac{d}{dt}v(e_t) \leq &-w(e_t) + 2\rho v\|e(t)\|^2 \\ &+a_1\tau\rho v\|e(t)\|^2 + a_1 v\int_{t-\tau}^{t}\|e(\xi)\|^2d\xi\end{aligned}$$

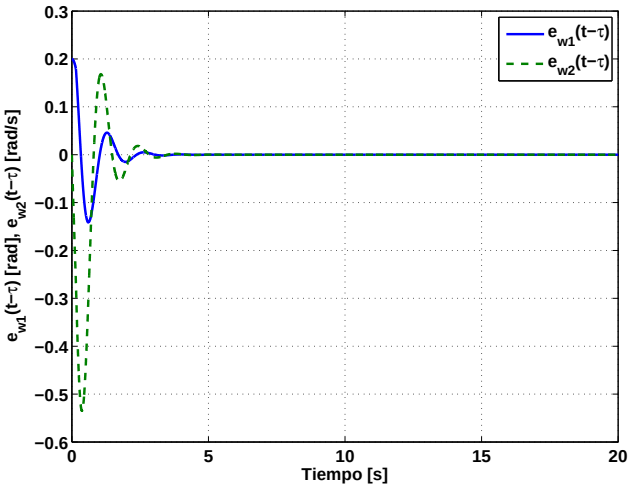

Figura 3. Errores de observación: $e_{w1}(t-\tau)$, $e_{w2}(t-\tau)$.

con

$$w(e_t) = e^T(t)W_0e(t) + e^T(t-\tau)W_1e(t-\tau) + \int_{t-\tau}^{t} e^T(\xi)W_2e(\xi)\,d\xi$$

de donde se obtiene el resultado.

5. EVALUACIÓN NUMÉRICA Y EXPERIMENTAL

Para probar el comportamiento del predictor–observador propuesto, así como la efectividad de la solución al problema de seguimiento de trayectorias basada en estados estimados futuros, se realizaron evaluaciones numéricas y experimentales. Se utilizó una trayectoria deseada descrita por las ecuaciones,

$$\begin{aligned}x_{1d} &= k_t t_b^5(r_1 - r_2t_b + r_3t_b^2 - r_4t_b^3 + r_5t_b^4 - r_6t_b^5) \\ x_{2d} &= \frac{k_t(5r_1t_b^4 - 6r_2t_b^5 + 7r_3t_b^6 - 8r_4t_b^7 + 9r_5t_b^8 - 10r_6t_b^9)}{t_f - t_i}\end{aligned}$$

donde

$$t_b = \frac{t-t_i}{t_f-t_i}$$

$r_1 = 252$, $r_2 = 1050$, $r_3 = 1800$, $r_4 = 1575$, $r_5 = 700$, $r_6 = 126$, t_i es el tiempo inicial, t_f es el tiempo final.

5.1 Resultados en simulación numérica

Los parámetros utilizados en el predictor–observador (7) y en la retroalimentación (11) se muestran en la Tabla 1.

Tabla 1. Parámetros para la simulación.

Parámetro	Valor	Parámetro	Valor
k_1	2	m	0.0816 kg
k_2	3	ℓ	0.33 m
λ_0	3	m_b	0.5367 kg
λ_1	3	J_b	0.0195 kgm^2
τ	0.15 s		

En la Figura 3 se muestran los errores de observación $e_{w_1}(t-\tau)$ y $e_{w_2}(t-\tau)$ y en la Figura 4 se presentan los errores de seguimiento $e_{d_1}(t)$, $e_{d_2}(t)$. Puede verse como los errores mostrados convergen adecuadamente al origen.

En la Figura 5 se muestra la señal de control $u(t)$ necesaria para realizar el seguimiento de la tratectoria.

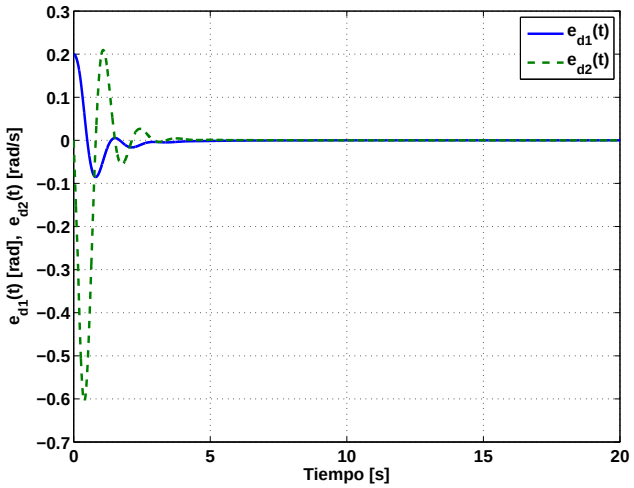

Figura 4. Errores de seguimiento: $e_{d1}(t)$, $e_{d2}(t)$.

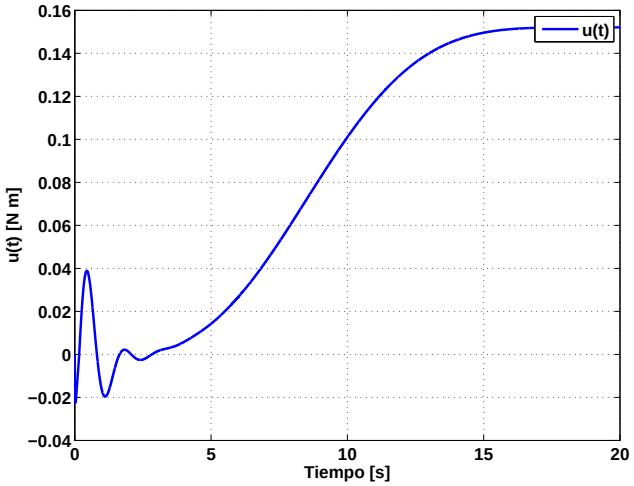

Figura 5. Señal de control: $u(t)$.

5.2 Resultados experimentales

El esquema del predictor–observador (7) y la retroalimentación propuesta (11) se implementaron en la plataforma experimental mostrada en la Figura 6. La plataforma se compone de una estructura principal que soporta una barra que actúa como péndulo, un motor tipo brushless *U2216 KV900* con una hélice, necesarios para generar la fuerza para levantar la barra. Un inclinómetro *X3Q-T* de *US Digital* para determinar el desplazamiento angular que experimenta la barra, y una tarjeta de desarrollo *eZdsp TMS320F28335* de *Spectrum Digital Inc.* para implementar el esquema propuesto.

Los parámetros utilizados en el predictor observador (7) y en la retroalimentación (11) se muestran en la Tabla 2. En

Tabla 2. Parámetros para el experimento.

Parámetro	Valor	Parámetro	Valor
k_1	0.15	λ_0	16
k_2	0.015	λ_1	10
τ	0.1 s		

la Figura 7 se muestra el error de observación $e_{w_1}(t-\tau)$, y como se puede apreciar, el error se mantiene cercano a cero. En la Figura 8 se presenta el error de seguimiento $e_{d_1}(t)$. En las Figuras 9 y 10 se muestran la señal de

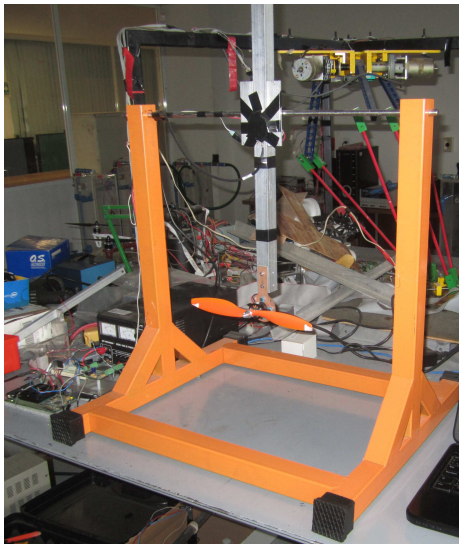

Figura 6. Sistema actuador aerodinámico.

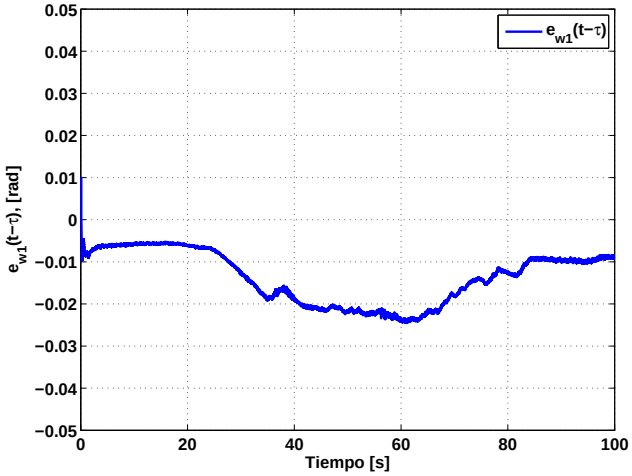

Figura 7. Error de observación: $e_{w1}(t)$.

control $u(t)$ aplicada al sistema y las trayectorias deseada y real. Es importante mencionar, que el seguimiento de la trayectoria se ve afectado debido a perturbaciones externas no modeladas, lo que hace que el sistema presente un error en estado estacionario. Para verificar esta hipótesis, se realiza una simulación sumando un término constante δ en la ecuación de la aceleración angular (2). Este término constante representa perturbaciones externas no modeladas. En la Figura 11, se muestra la trayectoria que sigue el sistema en presencia de una perturbación externa $\delta = -0.05$.

6. CONCLUSIONES

Se presenta una solución al problema de seguimiento de trayectorias asociado a un actuador aerodinámico afectado por retardos de tiempo en la señal de control. La solución propuesta se basa en estados estimados futuros obtenidos con un predictor observador que es capaz de proveer los estados futuros necesarios. Se muestra formalmente la convergencia de los errores de predicción así como la convergencia de los errores de seguimiento. El esquema de control es evaluado mediante simulaciones numéricas y con experimentos en tiempo real en una plataforma de laboratorio. Se deja como extensión a este trabajo la compensación o cancelación de perturbaciones externas.

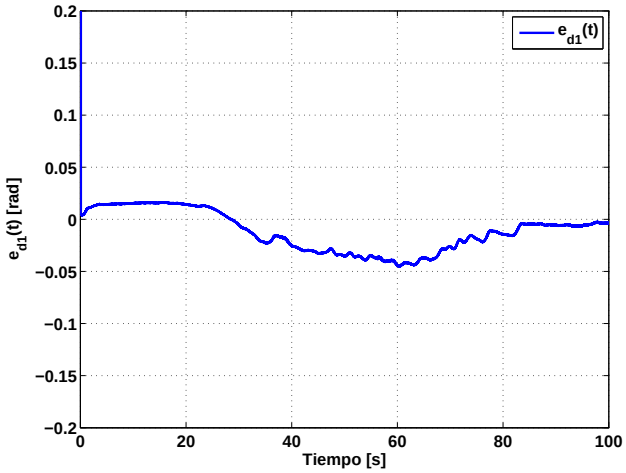

Figura 8. Error de seguimiento: $e_{d1}(t)$.

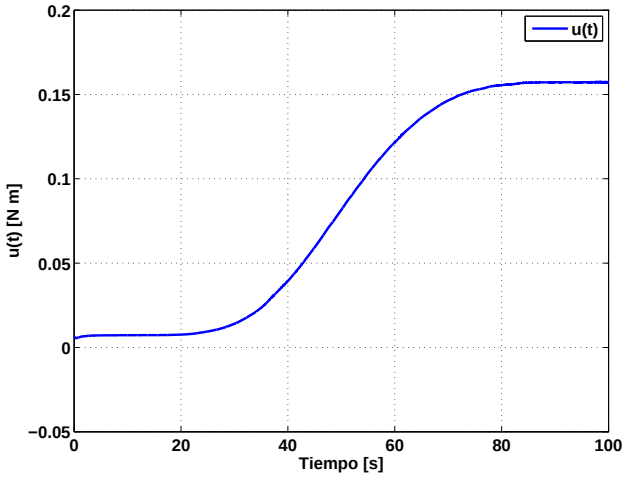

Figura 9. Señal de control: $u(t)$.

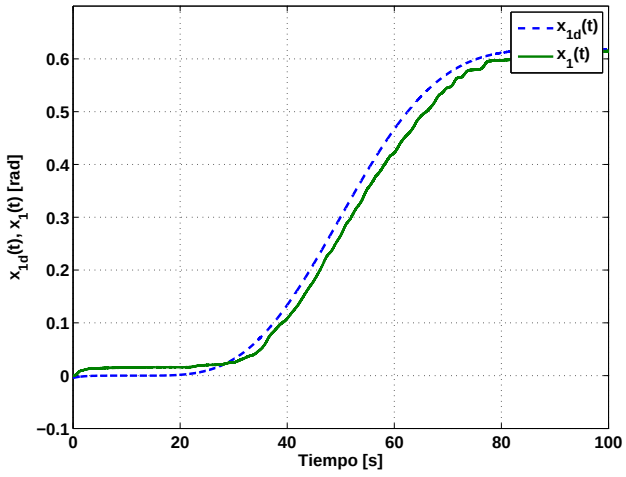

Figura 10. Trayectoria de referencia $x_{1d}(t)$ y real $x_1(t)$.

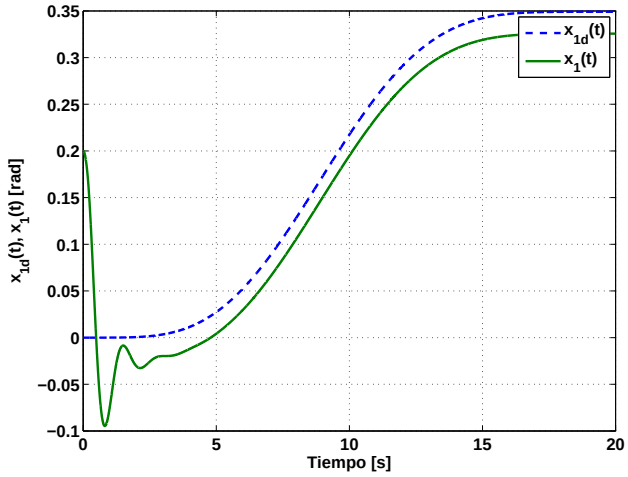

Figura 11. Trayectoria de referencia $x_{1d}(t)$ y real $x_1(t)$ con una perturbación $\delta = -0.05$.

REFERENCIAS

Bellman, R.E. and Cooke, K.L. (1963). *Differential-difference equations*. Rand Corporation.

Chiang, C.C. and Tung, T.C. (2003). Robust tracking control of uncertain nonlinear systems with an input time delay. In *Neural Networks, 2003. Proceedings of the International Joint Conference on*, volume 3, 2394–2399 vol.3. doi:10.1109/IJCNN.2003.1223787.

Fridman, E. (2014). *Introduction to Time-Delay Systems: Analysis and Control*. Birkhäuser Basel, Switzerland.

Gu, K., Chen, J., and Kharitonov, V.L. (2003). *Stability of time-delay systems*. Springer Science & Business Media.

Hale, J.K. and Lunel, S.M.V. (2013). *Introduction to functional differential equations*, volume 99. Springer Science & Business Media.

Kharitonov, V.L. (2013). *Time-Delay Systems: Lyapunov Functionals and Matrices*. Birkhäuser, Boston.

Kim, I.H. and Son, Y.I. (2010). Robust control for input time-delay systems: A disturbance observer approach. In *SICE Annual Conference 2010, Proceedings of*, 179–183.

Kolmanovskii, V. and Myshkis, A. (1992). *Applied Theory of Functional Differential Equations*. Kluwer Academic Publisher, Dordretch, The Netherlands.

Krstic, M. (2009). *Delay compensation for nonlinear, adaptive, and PDE systems*. Springer.

Lee, B. and Lee, J.G. (2000). Robust control of uncertain systems with input delay and input sector nonlinearity. In *Decision and Control, 2000. Proceedings of the 39th IEEE Conference on*, volume 5, 4430–4435 vol.5. doi: 10.1109/CDC.2001.914605.

Li, Z.Y., Zhou, B., and Lam, J. (2014). Lyapunov–krasovskii functionals for predictor feedback control of linear systems with multiple input delays. *Applied Mathematics and Computation*, 244, 303 – 311.

Maza-Casas, L., Velasco-Villa, M., and Alvarez-Gallegos, J. (2000). Compensation of input time delay for a class of nonlinear systems. In *Decision and Control, 2000. Proceedings of the 39th IEEE Conference on*, volume 5, 4428–4429. IEEE.

Münz, U., Ebenbauer, C., Haag, T., and Allgöwer, F. (2009). Stability analysis of time-delay systems with incommensurate delays using positive polynomials. *Automatic Control, IEEE Transactions on*, 54(5), 1019–1024.

Niculescu, S.I. (2001). *Delay effects on stability: a robust control approach*, volume 269. Springer Science & Business Media.

Roh, Y.H. and Oh, J.H. (1999). Sliding mode control with delay compensation for uncertain input-delay systems. In *American Control Conference, 1999. Proceedings of the 1999*, volume 1, 309–313 vol.1. doi: 10.1109/ACC.1999.782790.

Smith, O.J. (1959). A controller to overcome dead time. *iSA journal*, 6(2), 28–33.

Design of preserving order observers-based controllers for discrete-time linear systems

Jesús D. Avilés [*,⋆] **Jaime A. Moreno**[‡]
Fernanda Alvarez-Mendoza[‡]

[*] *Instituto Politécnico Nacional, Sección de Estudios de Investigación y Posgrado, ESIME-UPT, C.P. 07430, Ciudad de México, México (e-mail: jesus.david.aviles@gmail.com).*
[‡] *Instituto de Ingeniería-UNAM, Coyoacán DF, 04510, Ciudad de México, México, (e-mail: {JmorenoP,MalvarezM}@iingen.unam.mx)*

Abstract:
In this work we provide a design method of preserving order observer-based dynamic output-feedback controllers for a family of discrete-time linear systems. This design considers the absence and/or presence of disturbances/uncertainties in the discrete-time systems. The control problem is focused in two purposes: (i) the stabilization of closed-loop systems by means of upper and/or lower estimations, and (ii) the state estimation preserves the partial-order with respect to the real state trajectory at each instant time. The proposed method studies the properties of Lyapunov stability and cooperativeness. The first property determines the exponential stability of the closed loop system (with controller) in combination with exponential convergence to zero of the observation errors, when there are no uncertain terms, while the second one ensures the partial ordering between upper/lower estimations with state. The observers gain can be computed through a solution of a Bilinear Matrix Inequality (BMI) and a Linear Matrix Inequality (LMI).

Keywords: Discrete-Time Systems, Preserving Order Observers, Interval Observers, Cooperative Systems.

1. INTRODUCTION

An especial class of robust state estimators, the so-called *preserving partial-order observers* have been successfully used, for instance, in biological, electric, hydraulic systems, positive and compartmental systems and many other applications, in order to estimate uncertain/disturbed during the last fifteen years (Gouze et al., 2000; Alcaraz-Gonzalez et al., 2002; Bernard and Gouze, 2004; Avilés and Moreno, 2009, 2013; Mazenc et al., 2013; Avilés and Moreno, 2014; Mazenc et al., 2014; Raïssi et al., 2012). This observers, based in the cooperativeness theory (Angeli and Sontag, 2003; Hirsch and Smith, 2004, 2005), provided upper and/or lower estimations, which can form an interval containing the real state trajectory, instead of estimating true values of the uncertain non-measureable variables. The precursor design appeared in (Gouze et al., 2000), where the *interval observers* were proposed, which are constituted by a preserving upper and lower partial-order observer; represent a interesting technique to estimate parameters and unknown variables of biotechnological processes.

Several works have been proposed for discrete-time systems (Mazenc et al., 2013; Efimov et al., 2013a; Avilés and Moreno, 2015b); they are inspired by the growing computational interest to use sample-data systems subjected to perturbations, where show that the cooperativeness property is conserved in the interval observers for the discrete-time systems (Hirsch and Smith, 2005; Mazenc et al., 2014). Noting that the cooperativeness linear condition is expressed by means of nonnegative matrices for time-discrete systems, instead of Metzler matrices for continuous-time systems.

Recently, in (Efimov et al., 2013b) the interval observers class were implemented in the design of controllers. The output stabilization was analyzed for a class of Linear Parametric Variant (LPV) continuous-time system, implementing the estimations from the interval observers. Subsequently, in (Efimov et al., 2015) it was introduced a similar analysis for the family of LPV discrete-time systems. Additionally, in (Avilés and Moreno, 2015a) have been proposed controllers based on interval observers for stabilizing a continuous-time closed-loop scheme in absence/presence of disturbances.

In the present work, we develop a design methodology of controllers for discrete-time linear systems, using the output feedback provided by the upper and/or lower preserving partial-order observers (Avilés and Moreno, 2009, 2013, 2014). The absence and presence of uncertainties/disturbances are studied in order to guarantee both the stability of the closed-loop system and the state trajectory is bounded for the estimations of the observers. This is achieved by combination of systemic properties between

⋆ J.D. Avilés is on leave from Autonomous University of Baja California. Faculty of Engineering and Business. C.P. 21460, Tecate, B.C, México.

the stability in the sense of Lyapunov and cooperativeness. Moreover, the computational implementation is considered by means of a BMI and a LMI.

This paper is organized as follows. The notations and prelimiaries are presented in Section 2. The design method of controllers based on preserving partial-order (interval) observers, for nominal and perturbed discrete-time systems, is proposed in Section 3. Several practical aspects are mentioned in Section 4. Concluding remarks are established in Section 5.

2. PRELIMINARIES

For a better understanding, we provide the following descriptions.

2.1 Notations

$M \overset{M}{\succeq} 0$	: M is a Metzler matrix, if and only if $M_{ij} \geq 0,\ \forall i \neq j,\ \ \forall i \in 1,...,n,\ \forall j \in 1,...,n.$
$A \succeq 0$	: A is a nonnegative matrix, sii $A_{ij} \geq 0$, $\forall i,j = 1,...,n.$
$A \geq 0$	: A is a positive semi-definite matrix.
$A > 0$	: A is a positive definite matrix.
$B \leq 0$	: B represents a negative semi-definite matrix.
$B < 0$	: B represents a negative semi-definite matrix.
$x \succeq 0$	: x is a nonnegative vector, iff $x_i \geq 0, \forall i = 1,...,n.$
$x \succeq z$	: represents the partial-order between two vectors, iff $x_i - z_i \geq 0, \forall i = 1,...,n.$
$\|x\|$	: is the Euclidean norm.
$\mathbf{J}_{f(x)}$	: denotes the Jacobian matrix of the nonlinear function $f(t,x,u)$ with respect to the variable x
$\mathbf{J}_{f(u)}$	: is the Jacobian matrix of the nonlinear function $f(t,x,u)$ w.r.t the variable u.

2.2 Systems that preserver partial-order

The *cooperativeness* is a systemic property that ensures the partial order between the state trajectories and output, depending on the partial order between the initial states and inputs.

Definition 1. Consider the time-discrete nonlinear system

$$\Gamma_{\mathrm{NL}} : \begin{cases} x(k+1) = f(k, x(k), u(k)), & x(k_0) = x_{k0}, \\ y(k) = h(k, x(k), u(k)), \end{cases} \quad (1)$$

where $(x(k), u(k), y(k)) \in \mathbb{R}^n \times \mathbb{R}^m \times \mathbb{R}^p$ is the state, the input and the output vectors of Γ_{NL}, respectively, at each instant time $k \in \mathbb{N}$. We assume that $f : \mathbb{N} \times \mathbb{R}^n \times \mathbb{R}^m \to \mathbb{R}^n$ and $h : \mathbb{N} \times \mathbb{R}^n \times \mathbb{R}^m \to \mathbb{R}^p$ are continuous functions.

The system Γ_{NL} is *cooperative* if there exists an partial ordering between two initial states and two inputs (if they exist), that is; $x_0^1 \succeq x_0^2$, $u^1(k) \succeq u^2(k)$, $\forall k$. Then, the state and output trajectories will preserve the partial-order for all instant times:

$$x\left(k, k_0, x_0^1, u^1(k)\right) \succeq x\left(k, k_0, x_0^2, u^2(k)\right), \forall k \geq k_0,$$
$$y\left(k, k_0, x_0^1, u^1(k)\right) \succeq y\left(k, k_0, x_0^2, u^2(k)\right), \forall k \geq k_0,$$

where $k_0 \in \mathbb{N}$, $x_{k_0} \in \mathbb{R}^n$. □

In the following paragraphs, we present the characterization of discrete-time systems. For more details to see (Mazenc et al., 2014; Hirsch and Smith, 2005).

Proposition 2. (Hirsch and Smith (2005)). Γ_{NL} is a *discrete-time cooperative system* if and only if the following conditions are satisfied,

$$(\mathbf{a}).\ \mathbf{J}_{f(x)} \succeq 0, \quad (\mathbf{b}).\ \mathbf{J}_{f(u)} \succeq 0, \quad (\mathbf{c}).\ \mathbf{J}_{h(x)} \succeq 0. \quad \square$$

The linear cooperative systems represent a particular case of the *definition 3*; its characterization is given in the next paragraph.

Proposition 3. The Linear Time-Invariant (LTI) system described by

$$\Gamma_{\mathrm{L}} : \begin{cases} x(k+1) = Ax(k) + Bu(k), & x(k_0) = x_{k0}, \\ y(k) = Cx(k), \end{cases} \quad (2)$$

where $(x(k), u(k), y(k)) \in \mathbb{R}^n \times \mathbb{R}^m \times \mathbb{R}^p$ are the state, the input and the measurement output vectors, respectively. Γ_{L} is a *cooperative system* if and only if

$$(\mathbf{i}).\ A \succeq 0, \quad (\mathbf{ii}).\ B \succeq 0, \quad (\mathbf{iii}).\ C \succeq 0$$

For the family of discrete-time linear systems, the cooperativeness is analog to positivity property, which states that all variables: input, output and state, are nonnegative at all instant times.

2.3 Stability of discrete-time linear systems

In this subsection, the stability of the linear discrete-time systems will be analyzed.

Definition 4. (Khalil (2002)). We consider the system of the form

$$x(k+1) = Ax(k), \quad x(k_0) = x_{k0}, \quad (3)$$

where $A \in \mathbb{R}^{n \times n}$ and $k \in \mathbb{N}$, if there exist the constants $\alpha > 0$ and $\rho > 0$ such that

$$\|x(k, x_{k_0})\| \leq \alpha \|x_{k0}\| exp(-\rho k) \quad (4)$$

is satisfied for all $k \in \mathbb{N}$, $x_{k0} \in \mathbb{R}^n$, then the origin is a *globally exponentially stable equilibrium point.*

Definition 5. (Jiang and Wang (2001)). The discrete-time linear system affected by the presence of additive exogenous inputs, is given by

$$x(k+1) = Ax(k) + b(k), \quad x(k_0) = x_{k0} \quad (5)$$

is (globally) Input-State Stable (ISS) w.r.t $b(k)$, if there exist a function β of class $\mathcal{KL}$, and a function γ of class $\mathcal{K}$ such that, for each initial state $x(k_0) \in \mathbb{R}^n$ and each input $b(k)$, then the solution $x(t)$ exist for all $t \geq t_0$, it holds that

$$\|x(k, x_{k_0})\| \leq \beta(\|x_{k0}\|, k) + \gamma(\|b(k))\| \quad (6)$$

where γ is known as an *ISS-gain* for Γ_{L}.

We consider the Lyapunov function candidate

$$V(x(k)) = x^T(k) P x(k), \quad P = P^T > 0. \quad (7)$$

which satisfies

$$\alpha_1(||x(k)||) \leq V(x(k)) \leq \alpha_2(||x(k)||), \quad (8)$$
$$\Delta V = V(x(k+1)) - V(x(k)) \leq -\alpha_3(||x(k)||), \quad (9)$$

$\forall\ x(k) \in \mathbb{R}^n$, for the family of Linear time-discrete nominal systems in (3). The expression ΔV is given as the Lyapunov difference. For the disturbed system in (5), an additional condition is required:

$$\Delta V = V(x(k+1)) - V(x(k)) \leq -\alpha_3(||x(k)||) + \gamma(||b(k)||), \tag{10}$$

$\forall b(k) \in \mathbb{R}^n$.

The characterizations of both definitions *5* and *6*, can be expressed in the ambient of Linear Matrix Inequalities (LMI's).

Lema 6. Consider the nominal system in (3). If there exists a positive symmetric matrix $P = P^T > 0$ and the positive constant $\epsilon > 0$, such that

$$[A^T PA - P + \epsilon P] \leq 0 \tag{11}$$

is satisfied, then $x(k) = 0$ is an *globally exponentially stable* equilibrium point. □

Now, we present the characterization of practical stability for the system Γ_{L}, when an exogenous input $b(k)$ appears in the dynamics. In this sense, we analyze the property by means of the input-to-state stability (ISS) condition for Γ_{L} in the following Lemma.

Lema 7. Consider the perturbed system in (5). If conditions from Lemma 6 are satisfied, then the system in (5) is *ISS with respect to the input* $b(k)$.

Proof. Initially the demonstration of Lemma 6 is presented. If the Lyapunov function candidate $V(x(k)) = x^T(k)Px(k)$ is defined for the system in (3), its Lyapunov difference along the trajectory of (3) is given as

$$\Delta V = V(x(k+1)) - V(x(k)) = x^T(A^T PA - P)x \leq -\epsilon x^T Px$$

Now, the same Lyapunov function candidate is proposed for the perturbed system, then its derivative is bounded by

$$\begin{aligned}\Delta V \leq &-(1-\theta)\,\epsilon V(x(k)) - \theta\epsilon V(x(k)) + b^T(k)Pb(k) \\ &+ 2x^T(k)A^T Pb(k)\end{aligned}$$

Completing squares, the property (6) holds. ■

3. PRESERVING ORDER OBSERVER-BASED CONTROL DESIGN

In this section, we present the main results of the design of preserving order observer-based dynamic output-feedback controllers for discrete-time systems. Firstly, the controller design conditions are studied for the nominal case, then we extend the notions to deal the presence of disturbances/uncertainties in the dynamical system.

3.1 Nominal System

Consider the family of nominal systems given by

$$\Pi_{\mathrm{N}} : \begin{cases} x(k+1) = Ax(k) + B_u u(k),\ x(k_0) = x_{k0}, \\ y(k) = Cx(k), \end{cases} \tag{12}$$

where $x(k) \in \mathbb{R}^n$ is the state, $y(k) \in \mathbb{R}^p$ is the measurement output, $u \in \mathbb{R}^m$ is the control input. $A \in \mathbb{R}^{n\times n}$, $B_u \in \mathbb{R}^{n\times m}$, $C \in \mathbb{R}^{p\times n}$, are constant matrices such that are satisfied the next suppositions:

S1. The pair (A, B_u) is stabilizable, and
S2. The pair (A, C) is detectable.

3.1.1 Preserving partial-order observers

We propose an Luenberger state observer for the family of discrete-time systems Π_{N} in order to estimate the unknown state variables,

$$\Pi_{\mathrm{O}} : \begin{cases} \widehat{x}(k+1) = A\widehat{x}(k) + L(\widehat{y}(k) - y(k)) + B_u u(k), \\ \widehat{y}(k) = C\widehat{x}(k), \quad x(k_0) = x_{k0} \end{cases} \tag{13}$$

where $\widehat{x}(k)$ is the estimated state. $L \in \mathbb{R}^{n\times q}$ is the observer gain associated to the output injection.

The estimation error has been defined as $e(k) \triangleq \widehat{x}(k) - x(k)$, and the output error is $\widetilde{y}(k) \triangleq \widehat{y}(k) - y(k)$. Consistently, the dynamics of estimation error are given by

$$\Pi_{\mathrm{E}} : \begin{cases} e(k+1) = A_L e(k), \qquad e(k_0) = e_{k0}, \\ \widetilde{y}(k) = Ce(k), \end{cases} \tag{14}$$

where the matrix $A_L \triangleq A + LC$. From Π_{O}, the sufficient conditions are established to define the preserving partial-order observer for the nominal systems Π_{N}.

In the following paragraph we establish the cooperativeness conditions for the state observer Π_{O}.

Definition 8. (Avilés and Moreno (2014)). The observer Π_O is said an upper/lower preserving partial-order observer if

(i). The estimation error system Π_E is cooperative, that is, given $e_0 \succeq 0$ $(-e_0 \succeq 0)$, then $e(t) \succeq 0$ $(-e(t) \succeq 0)$, leading to, if $\widehat{x}_0 \succeq x_0$ $(x_0 \succeq \widehat{x}_0) \rightarrow \widehat{x}(t) \succeq x(t)$ $(x(t) \succeq \widehat{x}(t))$, $\forall t \geq 0$.

(ii). The estimation error converge asymptotically to zero, that is $\|\widehat{x}(k) - x(k)\| \to 0$ as $k \to \infty$. □

The first condition (i) is ensured, if

$$A_L \succeq 0 \tag{15}$$

is a nonnegative matrix, which is provide by the application of the cooperative property in the estimation error system (see *Proposition 2*). Thus, the condition guarantees the partial ordering between estimation and state trajectories for all instate times.

An upper and a lower preserving partial-order observer form an *interval observer*, whose characteristic behavior guarantees that the estimations always stay above and below the true state trajectory.

3.1.2 Control design method

Adding an output feedback control to the system Π_{O}, we provide a control based on a lower/upper preserving partial-order observer,

$$\Pi_{\mathrm{U}} : \begin{cases} \widehat{x}(k+1) = A\widehat{x}(k) + L(\widehat{y}(k) - y(k)) + B_u u(k), \\ \widehat{y}(k) = C\widehat{x}(k), \quad x(k_0) = x_{k0}, \\ u(k) = -K\widehat{x}(k), \end{cases} \tag{16}$$

where $K \in \mathbb{R}^{n\times m}$ is the controller gain. Consequently, the closed-loop system Π_{U} is combined with the estimation error system, which can be described by

$$\Pi_{\mathrm{LC}}: \left\{ \begin{bmatrix} x(k+1) \\ e(k+1) \end{bmatrix} = \begin{bmatrix} A_K & -B_u K \\ 0 & A_L \end{bmatrix} \begin{bmatrix} x(k) \\ e(k) \end{bmatrix} \right. \tag{17}$$

where the matrix $A_K = A - B_u K$. In the Theorem 9 is shown the stability condition of the augmented system (17).

Theorem 9. Consider the nominal system in (17). Suppose that the conditions (S1) and (S2) are satisfied. The system Π_{LC} is globally exponentially stable in the sense of Lyapunov, if there exist the matrices K, L, $P_1 = P_1^T > 0$, $P_2 = P_2^T > 0$ and the constants $\epsilon_1 > 0$, $\epsilon_2 > 0$, such that

$$\begin{bmatrix} A_K^T P_1 A_K - P_1 + \epsilon_1 P_1 & -A_K^T P_1 B_u K \\ -K^T B_u^T P_1 A_K & \Upsilon \end{bmatrix} \leq 0 \tag{18}$$

is fulfilled, where $\Upsilon = K^T B_u P_1 B_u K + A_L^T P_2 A_L - P_2 + \epsilon_2 P_2$.

Proof.

For the augmented system in (17), a Lyapunov function candidate is proposed as

$$V(x(k), e(k)) = x^T(k) P_1 x(k) + e^T(k) P_2 e(k), \tag{19}$$

and its Lyapunov difference along the trajectories of the system Π_{LC}, $\Delta V(x, e)$, is given by

$$\begin{bmatrix} x \\ e \end{bmatrix}^T \begin{bmatrix} A_K^T P_1 A_K - P_1 & -A_K^T P_1 B_u K \\ -K^T B_u^T P_1 A_K & \Upsilon_a \end{bmatrix} \begin{bmatrix} x \\ e \end{bmatrix}$$
$$\leq -\epsilon_1 x^T P_1 x - \epsilon_2 e^T P_2 e$$

where $\Upsilon_a = K^T B_u P_1 B_u K + A_L^T P_2 A_L - P_2$. Then, the origin, $x(k) = 0$, $e(k) = 0$, is globally exponentially equilibrium point of the augmented system Π_{LC} in (17). ■

A main result of this work is presented in the following Theorem, which considers the design of a preserving order observer-based control.

Theorem 10. Consider the nominal system Π_{N}. Suppose that conditions (S1) and (S2) are satisfied. If conditions

- Cooperativeness in (15)
- Stability in (18)

are satisfied, then the augmented closed-loop system Π_{LC} is globally exponentially stable. Moreover, Π_{U} is a preserving order observer.

Remark 11. Note that the design method presented in Theorem *10*, establishes the stabilization of Π_{N} by means of output feedback of Π_{U}. Moreover, the Theorem *10* ensures that an upper or a lower estimation bound to the real state trajectory for all times. It is possible to eject simultaneously a pair of preserving partial-order observers depending on an upper and an lower initial state, implying that the estimations form an interval, which contains the state trajectory. This is the typical notion of the interval observers.

3.2 Disturbed systems

Consider the discrete-time linear system

$$\Phi_{\mathrm{P}}: \left\{ \begin{array}{l} x(k+1) = Ax(k) + B_u u(k) + \pi(k, x(k)), \\ y(k) = Cx(k), \quad x(k_0) = x_{k0}, \end{array} \right. \tag{20}$$

where $\pi(t, x)$ represents the disturbances and/or parametric uncertainty affecting to Π_{P}. This term satisfies the inequality

$$\pi^+(k, y(k)) \succeq \pi(k, x(k)) \succeq \pi^-(k, y(k)) \tag{21}$$

which implies that the disturbance $\pi(t, x)$ is bounded by intervals, where $\pi^+(t, y)$ and $\pi^-(t, y)$ are known Lipschitz functions.

3.2.2 Preserving partial-order observers for disturbed systems

In order to estimate the unknown state of Π_{P}, two Luenberger observers are proposed, given by

$$\Phi_{O^+}: \left\{ \begin{array}{rl} \widehat{x}^+(k+1) &= A\widehat{x}^+(k) + B_u u(k) + \pi^+(t, y) \\ & \quad + L^+\left(\widehat{y}^+(k) - y(k)\right), \quad \widehat{x}^+(k_0) = \widehat{x}^+_{k0}, \\ \widehat{y}^+(k) &= C\widehat{x}^+(k), \end{array} \right. \tag{22}$$

$$\Phi_{O^-}: \left\{ \begin{array}{rl} \widehat{x}^-(k+1) &= A\widehat{x}^-(k) + B_u u(k) + \pi^-(t, y) \\ & \quad + L^-\left(\widehat{y}^-(k) - y(k)\right), \quad \widehat{x}^-(k_0) = \widehat{x}^-_{k0}, \\ \widehat{y}^-(k) &= C\widehat{x}^-(k), \end{array} \right. \tag{23}$$

where $\widehat{x}^+(k)$ and $\widehat{x}^-(k)$ are the estimate states of Π_{O^+} and Π_{O^-}, respectively. The observer gains are $L^+ \in \mathbb{R}^{n \times q}$, $L^- \in \mathbb{R}^{n \times q}$.

The estimation errors are defined as $e^+(k) \triangleq \widehat{x}^+(k) - x(k)$, $e^-(k) \triangleq x(k) - \widehat{x}^-(k)$, and the output estimate errors as $\widetilde{y}^+(k) \triangleq \widehat{y}^+(k) - y(k)$, $\widetilde{y}^-(k) \triangleq y - \widehat{y}^-(k)$. Therefore, the error dynamics are given by

$$\Phi_{E^+}: \left\{ \begin{array}{l} e^+(k+1) = A_L^+ e^+(k) + w^+(k), \quad e^+(k_0) = e^+_{k0} \\ \widetilde{y}^+(k) = Ce^+(k) \\ w^+(k) = \pi^+(k, y(k)) - \pi(k, x(k)) \end{array} \right. \tag{24}$$

$$\Phi_{E^-}: \left\{ \begin{array}{l} e^-(k+1) = A_L^- e^-(k) + w^-(k), \quad e^-(k_0) = e^-_{k0} \\ \widetilde{y}^-(k) = Ce^-(k) \\ w^-(k) = \pi(k, x(k)) - \pi^-(k, y(k)) \end{array} \right. \tag{25}$$

where $w^+(k)$ and $w^-(k)$ are errors associated to the disturbance, which represent the exogenous inputs for the systems Φ_{E^+} and Φ_{E^-}.

An extension of *definition* is presented for the family of linear disturbed systems.

Definition 12. The estimator Φ_{O^+} (Φ_{O^+}) is an upper (lower) preserving partial-order observer for the disturbed system Φ_{P}, if satisfies the following conditions:

(i). The error system estimation Φ_{E^+} (Φ_{E^-}) is cooperative: if $\widehat{x}^+_{k0} \succeq x_{k0}$ ($x_{k0} \succeq \widehat{x}^-_{k0}$), then $\widehat{x}^+(k) \succeq x(k)$ ($x(k) \succeq \widehat{x}^-(k)$), $\forall k \in \mathbb{N}$.

(ii). The estimation error converges asymptotically to a ball centered in the origin with radius β, that is, $\|\widehat{x}^+(k) - x(k)\| \to \beta$ ($\|x(k) - \widehat{x}^-(k)\| \to \beta$) as $k \to \infty$.

Note that item (i) of the definition *12*, describes the characteristics of partial ordering between the state estimations and trajectories. This is provide because the system Φ_{E^+} (Φ_{E^-}) is cooperative, implying that conditions

$$A_L^+ \succeq 0 \qquad (A_L^- \succeq 0)$$

are satisfied, if the uncertain input $w^+(k) \succeq 0$ $(w^-(k) \succeq 0)$ $\forall k \in \mathbb{N}$, and the initial state $e_{k0}^+ \succeq 0$ $(e_{k0}^- \succeq 0)$.

3.1.2 Robust control design method

The purpose is to stabilize the perturbed system Φ_{P}, and to bound dynamically the real state trajectory by means of upper/lower estimations. Thus, we propose a controller described by

$$\Phi_{\mathrm{U}} : \{\, u(k) = K\widehat{x}^+(k) + K\widehat{x}^-(k) \tag{26}$$

which is based on the upper preserving partial-order observers Φ_{O^+} and lower Φ_{O^-}, where $L^+ \in \mathbb{R}^{p\times n}$, $L^- \in \mathbb{R}^{p\times n}$ and $K \in \mathbb{R}^{n\times m}$ are design matrices.

Using the estimation errors defined in the above paragraphs, the dynamics of the augmented system, composed by the closed-loop system and the estimation errors, are described of the form

$$\Phi_{\mathrm{LC}} : \left\{ \begin{bmatrix} x(k+1) \\ e^+(k+1) \\ e^-(k+1) \end{bmatrix} = \begin{bmatrix} A_{2K}, & -B_uK, & B_uK \\ 0 & A_L^+, & 0 \\ 0 & 0 & A_L^- \end{bmatrix} \begin{bmatrix} x(k) \\ e^+(k) \\ e^-(k) \end{bmatrix} + \begin{bmatrix} \pi(k) \\ w^+(k) \\ w^-(k) \end{bmatrix} \right.$$

where $A_{2K} = A - 2B_uK$.

The following stability result and output feedback controller design from Section 2 is straightforward.

Theorem 13. Consider the perturbed system Φ_P. Suppose that conditions (S1), (S2) and the inequality in (21) are satisfied. The system Φ_{LC} is globally ISS with respect to exogenous inputs, if the matrices K, L^+, L^-, $P_i = P_i^T > 0$ and the positive constants exist $\epsilon_i > 0$, $i = 1, 2, 3$ such the next conditions

- Cooperativeness: both A_L^+, A_L^- are nonnegative matrices,
- Practical stability, given by the inequality

$$\begin{bmatrix} \Theta_1, & \bigstar, & \bigstar \\ -K^TB_u^TP_1A_{2K} & \Theta_2, & \bigstar \\ KB_u^TP_1A_{2K} & -K^TB_u^TP_1B_uK, & \Theta_3 \end{bmatrix} \leq 0 \tag{27}$$

are satisfied with
$\Theta_1 = A_{2K}^TP_1A_{2K} - P_1 + \epsilon_1P_1$,
$\Theta_2 = K^TB_u^TP_1B_uK + {A_L^+}^T P_2A_L^+ - P_2 + \epsilon_2P_2$,
$\Theta_3 = K^TB_u^TP_1B_uK + {A_L^+}^T + P_3A_L^- + \left(A_L^-\right)^T P_3 + \epsilon_3P_3$
□

Proof. The demonstration of cooperativeness condition consists on the application of *Proposition 2* in the observation systems Φ_{E^+}, Φ_{E^-}, which implies,

$$A_L^- \succeq 0, \quad A_L^+ \succeq 0$$

For the second condition, its proposed a candidate Lyapunov function for the closed-loop system Φ_{LC},

$$V\left(x, e^+, e^-\right) = x^TP_1x + {e^+}^T P_2e^+ + {e^-}^T P_3e^- \tag{28}$$

The Lyapunov difference along the trajectory of Φ_{LC}, $\Delta V\left(x, e^+, e^-\right)$ is given by the expression

$$\begin{bmatrix} x \\ e^+ \\ e^- \end{bmatrix}^T \begin{bmatrix} \Theta_1, & -P_1B_uK, & P_1B_uK \\ -KB_u^TP_1 & \Theta_2, & 0 \\ KB_u^TP_1 & 0 & \Theta_3 \end{bmatrix} \begin{bmatrix} x \\ e^+ \\ e^- \end{bmatrix} \leq \begin{bmatrix} -\epsilon_1x^TP_1x \\ -\epsilon_2\left(e^+\right)^TP_2e^+ \\ -\epsilon_3\left(e^-\right)^TP_3e^- \end{bmatrix} + \begin{bmatrix} \pi^TP_1\pi \\ \left(w^+\right)^TP_2w^+ \\ \left(w^-\right)^TP_3w^- \end{bmatrix}$$

Re-arraying terms to complete squares. the augmented system Φ_{LC} is ISS with respect to the inputs $\pi(t)$, $w^+(t)$, $w^-(t)$. ■

The Theorem 13 represents a generalization of the Theorem 9, when the estimations of an interval observer are considered in the output feedback controller. However, this design can be applied to the family of nominal discrete systems, obtaining an exponential stability in closed-loop system; Additional the upper and lower estimation errors converges to zero.

4. COMPUTATIONAL IMPLEMENTATION

The Theorems *9* and *13* state the design of output feedback controllers based on preserving order (or interval) observers for a family of discrete-time linear systems, taking into account absence/presence of disturbances.

The conditions in (18) and in (27) guarantee the stability property for the augmented systems Π_{LC} and Φ_{LC}, respectively. The matrix inequality (18) is a special case for the condition (27), when is only considered a upper/lower preserving order observer. In general, the inequality in (27) is described as nonlinear matrix inequalities in the variables $(P_i, \epsilon_i, L^+, L^-, K)$ with $i = 1, 2, 3$. There exist cases in order to convert the nonlinear matrix inequality to the ambient of LMI's. For instance, changing the bilinear term ϵ_iP_i, $i = 1, 2, 3$ by the term ϵ_iI, and if (K, L^+, L^-) are fixed, then (27) becomes a LMI in (ϵ_i, P_i), $i = 1, 2, 3$. Using the Schur's Complement, the other results are obtained. The study of this matrix inequality represents analysis for further research.

The cooperativeness conditions, given by $A_L^+ \succeq 0$, $A_L^- \succeq 0$, $A_L \succeq 0$, nonnegative matrices, represent the partial-ordering the upper/lower estimations and state trajectory. This conditions are leaded to the LMI's; They are LMI's in the variables (L^+, L^-, L).

5. CONCLUSION

In this paper, we develop a design method of preserving order observer-based dynamic output-feedback controllers for a family of discrete-time linear systems, considering the absence and/or presence of disturbances/uncertainties.

It is shown that the resulting augmented system, which combines the closed-loop systems with observer error dynamics, is globally (ISS) exponentially stable using the upper/lower estimations, depending on the (presence) absence of disturbances. Additionally, it is ensured the partial ordering between estimations and state trajectories. The observers gain can be obtained by solving a Bilinear Matrix Inequality (BMI) and a Linear Matrix Inequality (LMI).

ACKNOWLEDGEMENTS

J.D. Avilés acknowledge the support of CONACyT Mexico in the frame of National Posdoctorals Stays (CVU 208496). J. Moreno gratefully acknowledge the financial support from Fondo de Colaboración del II-FI, UNAM, project IISGBAS-122-2014, PAPIIT-UNAM under grant IN113614, and CONACyT project 241171.

REFERENCES

Alcaraz-Gonzalez, V., Harmand, J., Rapaport, A., Steyer, J., Gonzalez-Alvarez, V., and Pelayo-Ortiz, C. (2002). Software sensors for highly uncertain wwtps: a new approach based on interval observers. *Water Res*, 36(2515).

Angeli, D. and Sontag, D. (2003). Monotone control systems. *IEEE Transactions Automatic*, 48(10), 1684–1698.

Avilés, J. and Moreno, J. (2009). Cooperative observers for nonlinear systems. *Joint 48th IEEE Conference on Decision and Control and 28th Chinese Control Conference, Shanghai, China*, 6125–6130.

Avilés, J. and Moreno, J. (2013). Preserving order observers for nonlinear systems. *International Journal of Robust and Nonlinear Control*, doi: 10.1002/rnc.2975.

Avilés, J. and Moreno, J. (2014). Diseño de observadores que preservan el orden para sistemas no lineales usando transformación de coordenadas. *Congreso Latinoamericano de Control Automático*.

Avilés, J. and Moreno, J. (2015a). Método para disenar controladores basados en observadores que preservan el orden parcial para sistemas lineales. *Congreso Nacional del AMCA, Cuernavaca, Morelos*.

Avilés, J. and Moreno, J. (2015b). Observadores que preservan el orden parcial para sistemas en tiempo discreto. *Congreso Nacional del AMCA, Cuernavaca, Morelos*.

Bernard, O. and Gouze, J. (2004). Closed loop observers bundle for uncertain biotechnological models. *Journal of Process Control*, 14(3), 765–774.

Efimov, D., Perruquetti, W., Raïssi, T., and Zolghadri, A. (2013a). Interval observers for time-varying discrete-time systems. *IEEE Transactions on Automatic Control*, 58(12), 3218–3224.

Efimov, D., Raissi, T., Perruquetti, W., and Zolghadri, A. (2015). Design of interval observers for estimation and stabilization of discrete-time lpv systems. *IMA Journal of Mathematical Control and Information*, dnv023.

Efimov, D., Raissi, T., and Zolghadri, A. (2013b). Control of nonlinear and lpv systems: interval observer-based framework. *IEEE Transactions on Automatic Control*.

Gouze, J.L., Rapaport, A., and Hadj-Sadok, M.Z. (2000). Interval observers for uncertain biological systems. *Ecol Modelling*, 133(1-2), 45–56.

Hirsch, M. and Smith, H. (2005). Monotone maps: a review. *Journal of Difference Equations and Applications*, 11(4-5), 379–398.

Hirsch, M. and Smith, H. (2004). *Monotone Dynamical Systems*. Handbook of differential equations: ordinary differential equations. Vol. II, Elsevier B. V., Amsterdam 239-357.

Jiang, Z.P. and Wang, Y. (2001). Input-to-state stability for discrete-time nonlinear systems. *Automatica*, 37(6), 857–869.

Khalil, H.K. (2002). *Nonlinear Systems*. Prentice Hall, New York, USA, third edition.

Mazenc, F., Dinh, T., and Niculescu, S. (2013). Robust interval observers for discrete time systems of luenberger type. *ACC, Washington USA*, 2484–2489.

Mazenc, F., Dinh, T., and Niculescu, S. (2014). Interval observers for discrete time systems. *International Journal of Robust and Nonlinear Control*, (17), 2867–2890.

Raïssi, T., Efimov, D., and Zolghadri, A. (2012). Interval state estimation for a class of nonlinear systems. *IEEE Trans. on Aut. Control*, 57(1), 260–265.

Graph Transfer Function Representation to Measure Network Robustness

David Martínez * **Eduardo Mojica Nava** **

* *National University of Colombia, Bogotá, Colombia (e-mail: daamartinezva@unal.edu.co).*
** *National University of Colombia, Bogotá, Colombia (e-mail: eamojican@unal.edu.co)*

Abstract: In this work, we use coates determinant to obtain transfer functions from graphs and in this way analyze robustness behaviour of networks against perturbations. Furthermore, we make a comparison between obtained results and values of Sinai-Kolmogorov and Loop Entropies to observe network performance in terms of noise resilience.

Keywords: Sinai-Kolmogorov entropy, Loop entropy, robustness, Information theory.

1. INTRODUCTION

Network robustness and Entropy have been widely associated to compare network configurations and topologies aiming to define which ones are safer against perturbations. This reveals the importance of Shannon Information theory in network analysis. However, most of the Entropy network studies have been based on static network representations, i.e, graphs where Laplacian spectral analysis is not performed. In this work, we explore robustness connection between networks and a pair of measures defined through Laplacian and Adjacency matrices eigenvalues, known as Loop and Sinai-Kolmogorov (S-K) Entropies. To demonstrate how each of them behave against a noise source, we use a tool named Coates determinant and the procedure proposed in Desoer (1960) to represent five different network configurations composed by four nodes and variable spanning tree number as a Transfer function.

1.1 Preliminaries

Shannon Information Theory Information theory formulation introduced by Claude E. Shannon in 1948 through his seminal work (Shannon, 1948), which has been widely studied in many research fields beyond code optimization in Communications, such as Ecology, Microbiology and Biology, deepening specifically in two important but inversely related concepts, Entropy and Mutual Information. The former represents how much uncertainty is generated inside a communication Channel due to external factors (e.g noise), and the later measures how much information is shared between the sender and receiver in a communication process.

To understand the above description consider Fig. 1, which shows a classical representation of a communication channel according to Shannon, where the random variable $\boldsymbol{X}$ represents the delivered message by the sender **A** and

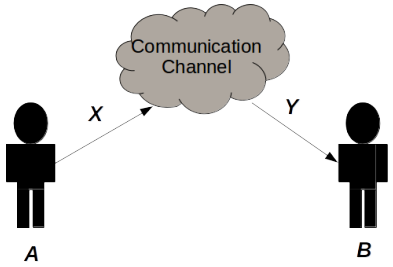

Fig. 1. Channel communications from Shannon perspective.

the the random variable $\boldsymbol{Y}$ denotes the received message in **B**. Mutual information measures how much $\boldsymbol{Y}$ seems to $\boldsymbol{X}$ and Entropy measures the difference between them (uncertainty in **B** about what $\boldsymbol{X}$ is).

To measure Entropy it is necessary to have a probability distribution which describes the likelihood $p(x)$ for every value $\boldsymbol{x}$ that $\boldsymbol{X}$ can take. Then, if we want to measure Entropy of $\boldsymbol{X}$, denoted as $H(X)$, we use the expression

$$H(X) = -\sum_{x} p(x) \log_2 p(x).$$

On the other hand, if we want to measure the Entropy of $\boldsymbol{X}$ once the value of $\boldsymbol{Y}$ is known, we need the conditional probability $p(x|y)$, through which conditional Entropy $H(X|Y)$ is given by

$$H(X|Y) = -\sum_{y} p(y) \sum_{x} p(x|y) \log_2 p(x|y).$$

Finally, to measure how much information about $\boldsymbol{X}$ is contained in $\boldsymbol{Y}$ (mutual information) we use the expression

$$I(X,Y) = H(X) - H(X|Y).$$

The above equations have been used for a long time in communications engineering, however, these have had a big application in population evolution, molecular chains, social behaviours between others, in areas such as Biol-

⋆ Sponsor and financial support acknowledgment goes here. Paper titles should be written in uppercase and lowercase letters, not all uppercase.

ogy, Microbiology, Ecology, Sociology and other fields of Engineering through graph analysis. In next sections we are going to show one of this applications, specifically in network robustness.

Complex Networks and Information Theory Graph and Complex Networks theories have had high relevance in last years in Engineering, specifically in applications such as social and sensor Networks, Internet, and smart grids, to model and design them. On the other hand, there exists a raising interest to involve Information theory definitions, specially Entropy and Mutual Information, to analyze topology, robustness and security from a static point of view, i.e, graphs whose behaviour is not described by spectral analysis but through algebraic mechanisms (Rashevsky, 1955; Solé R. V., 2004). As a result, some new perspectives have appeared to include not only Shannon Entropy but also physical and statistical definitions such as Von Neumann and Kolmogorov-Sinai entropies, to explore network behaviour by means of Laplacian spectral analysis to study dynamics and evolution. The following two sections describe the most important works which relates Entropy, Complex Networks and Graph theories, developed both in statical and dynamical environments.

1.1.2.1. A static perspective As we mentioned before, Entropy requires a probability distribution to be calculated, and in this regard, some methods have appeared. First, Rashevsky (1955) and Trucco (1956) use node dependence or automorphism concept to split the graph in vertex sets, then, dividing the number of nodes in each set by the total amount of nodes in the graph, it is possible to assign a probability for every one. In contrast, in Dehmer (2008) the probability distribution is obtained attributing a probability to each node instead of a set of them, which avoids difficult algorithms necessary to obtain graph automorphisms or vertex partitioning. Other related works have used degree distributions of network topologies such as Scale Free or Random networks to find Entropy values, meanly to describe graph heterogeneity, which is inversely correlated with network symmetry (Xiao et al., 2008).

1.1.2.2. A dynamic perspective A different research have shown ways to obtain Shannon Entropy using spectral graph analysis instead of probability distributions. Some of them have emerged to find similarities between Quantum mechanics concepts (Gibbs and Von Neumann Entropies) and Shannon theory, meanly aiming to employ MaxEnt principle in other research areas such as Ecology, Biology and Physics. First, Passerini and Severini (2008) compute Von Neumann Entropy (an extension of Gibbs Entropy) through a probability distribution taken from the normalized graph Laplacian, demonstrating that graphs with long paths (less quantity of short paths), connected components and regular shapes have higher Entropy values. Secondly, Anand and Bianconi (2009) calculate Gibbs Entropy through graph adjacency matrix and a probability distribution of having connected two nodes. This work shows a way to find a "canonical network ensemble" which satisfies structural constraints as link or node number, i.e, a set of network configurations that can accomplish the same function using the same resources.

In addition to Gibbs and Von Neumann Entropy approaches, Sinai-Kolmogorov Entropy is implemented in Demetrius and Manke (2005) to measure how much skill has a network to reject fluctuations. Its value is calculated from the largest Adjacency matrix eigenvalue (λ) through the following expression:

$$H = log(\lambda). \tag{1}$$

According to Demetrius et al. (2004), network Entropy (H) is directly correlated with the fluctuation decay rate (R), which is defined as:

$$R = \lim_{t\to\infty}\left[-\frac{1}{t}logP_\epsilon(t)\right],$$

where $P_\epsilon(t)$ is the probability that the sample mean [1] deviates more than ϵ from its unperturbed value at time $\boldsymbol{t}$. Therefore, for high values of R, network fluctuations tend to be short, whereas for low values, those tend to be longer. Consequently, since H and R are positively correlated, Entropy is a measure of network robustness [2].

On the other hand, a novel definition, named loop Entropy, has been established in De Badyn et al. (2016), which is given by the following expression:

$$S_\mathcal{G} = \sum_{i=2}^{n} log\lambda_i,$$

where $\lambda_i' s$ are the eigenvalues of the graph Laplacian $L_\mathcal{G}$ and n is the number of nodes. The sum begins from 2 because $\lambda_1 = 0$. There is a set of non negative eigenvalues associated to a sub-matrix $L_\mathcal{G}^{\{n-1\}}$ (Dirichlet Matrix) of $L_\mathcal{G}$, which is obtained by arbitrary elimination of the $\boldsymbol{i}$ row and the $\boldsymbol{i}$ column of $L_\mathcal{G}$. In this sense it is possible to obtain an Entropy expression in terms of this Dirichlet Matix as follows:

$$S_\mathcal{G} = \sum_{i=1}^{n-1} log\lambda_i(L_\mathcal{G}^{\{n-1\}}) + log(n),$$

which results in:

$$S_\mathcal{G} = log\left(n\tau(\mathcal{G})\right), \tag{2}$$

where $\tau(\mathcal{G})$ is the number of spanning trees in the graph. The above result shows a direct relation between Entropy and the number of spanning trees of a graph, which means that the network robustness increases with the number of spanning trees.

1.2 Coates Determinant

Following the procedure in Desoer (1960), it is possible to obtain a transfer function for every graph turning it into a flow graph, which is a directed graph where each node has a self-loop. This process is based in the Coates Determinant, which is given by the next expression:

$$\Delta_c = (-1)^n \sum_p (-1)^{L_\rho} C(G_o)\rho,$$

[1] Sample mean indicates that $\boldsymbol{R}$ is taken in a process where data collection is performed.

[2] Results in Demetrius and Manke (2005) shows that also in this case, Entropy and short paths are inversely proportional, therefore a Scale Free network is more robust than a Regular or Erdös-Renyi case.

where L_ρ is the number of directed loops in the $\rho_t h$ connection, Go is the flow graph G with the source node 0 deleted and $C(Go)$ is the summation of the connection gains (Desoer, 1960).

The next example explains this procedure(De Badyn et al., 2016).

Example: Initially we have the graph in Fig. 2.

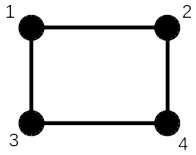

Fig. 2. 4 node graph with 4 spanning trees.

Using the procedure shown in Desoer (1960), we transform the previous graph into that shown in Fig. 3, which represents the denominator for the Transfer Function.

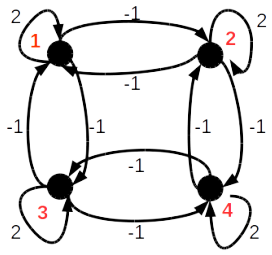

Fig. 3. Denominator graph.

In the same way, Fig. 4 represents the numerator graph for the Transfer Function. Observe that node 1 has a link from an external agent (source node), which means that it is taken as a leader and receives an input connection. In other words, the transfer function is solved for x_1.

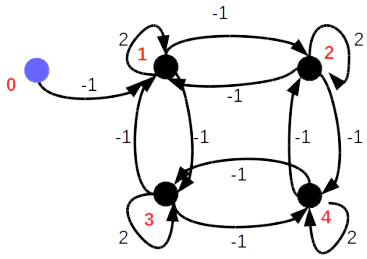

Fig. 4. Numerator graph.

According to Mesbahi and Egerstedt (2010) the ***controlled consensus dynamics*** expression is given by

$$\dot{x} = -L_{\mathcal{G}} + Bu(t) + G\omega(t), \tag{3}$$

where $\omega(t)$ represents a random disturbance to the network, x(t) the states of the nodes, and u(t) is the control input. On the other hand, in De Badyn et al. (2016) is shown an expression that represents a transfer function representation for (3), which has the form:

$$T(s) = \frac{\begin{vmatrix} sI + L_{\mathcal{G}} & -B \\ B^T & 0 \end{vmatrix}}{|\, sI + L_{\mathcal{G}} \,|},$$

where every self-loop of the flow graph has a weight of s+$L_{\mathcal{G}ii}$. Therefore, following the above procedure and using (3) to find Numerator and Denominator expressions as is exposed in Desoer (1960), we obtain the transfer function for the graph of Fig. 2, which is given by

$$T(s) = \frac{s^3 + 6s^2 + 10s + 4}{s^4 + 8s^3 + 20s^2 + 16s}.$$

2. METHODOLOGY

In this section we find Loop and Sinai-Kolmogorov entropy values for 4 different graphs whose spanning tree number varies. Then, using coates determinant and flow graphs representations for each one, we obtain a transfer function representation for each case and show the network behaviour against a disturbance emulated by means of a noise source.

2.1 Transfer Functions

In Fig. 2.1 and Fig. 6 are shown each analyzed graph. Following the procedure exposed in Desoer (1960) and in De Badyn et al. (2016) we find each transfer function, which are presented in Table 1.

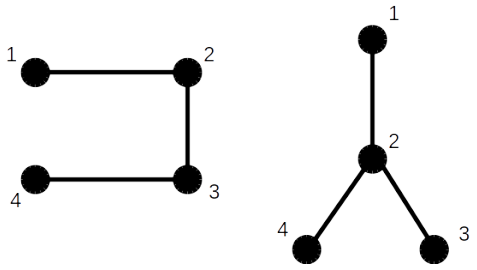

Fig. 5. **Left:** 4 nodes and 1 spanning tree graph.**Right:** The same graph including branches.

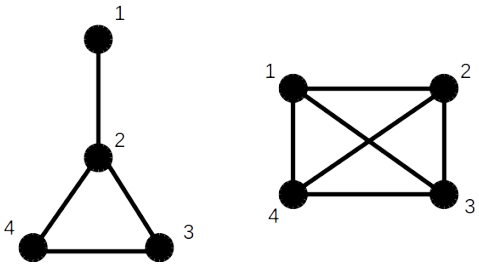

Fig. 6. **Left:** 4 nodes graph with 3 spanning trees. **Right:** complete graph with 4 nodes and 16 spanning trees.

Table 1. Transfer functions for each graph

Graph	Transfer function $T(s)$
4 nodes, 1 spanning tree	$\frac{s^3+5s^2+6s+5}{s^4+6s^3+10s^2+4s}$
4 nodes, 1 spanning tree with branches	$\frac{s^3+5s^2+5s+1}{s^4+6s^3+9s^2+4s}$
4 nodes, 3 spanning trees	$\frac{s^3+7s^2+13s+7}{s^4+8s^3+19s^2+12s}$
4 nodes, 16 spanning trees	$\frac{s^3+9s^2+24s+20}{s^4+12s^3+48s^2+64s}$

2.2 Entropy Values

Using the expressions given by (2) and (1), which corresponds to Loop and Sinai-Kolmogorov entropies respectively, we obtain the values depicted in Tables 2 and 3.

Table 2. Loop-Entropy values for each graph

Graph	Loop-Entropy
4 nodes, 1 spanning tree	1.3863
4 nodes, 1 spanning tree with branches	1.3863
4 nodes, 3 spanning trees	2.4849
4 nodes, 4 spanning trees	2.7726
4 nodes, 16 spanning trees	4.1589

Table 3. S-K Entropy values for each graph

Graph	S-K Entropy
4 nodes, 1 spanning tree	0.4812
4 nodes, 1 spanning tree with branches	0.5493
4 nodes, 4 spanning trees	0.6931
4 nodes, 3 spanning trees	0.7748
4 nodes, 16 spanning trees	1.0986

The results shown in Table 2 indicate that there is no difference in Loop entropy values for graphs with the same spanning tree numbers. It is observable in the case of one spanning tree graph. However, in Table 3 there is a distinction between those values, indicating a difference in robustness in spite of having the same quantity of spanning trees.

2.3 Relation Between Robustness and Spanning Trees Number

As we mentioned in previous sections, entropy and robustness have a direct relation. In this section we probe this assumption observing perturbation responses of each transfer function, demonstrating that almost in all cases, those networks with more spanning trees have better performances against noise. However, some cases where networks have more connections and therefore more spanning trees, do not present good performances in terms to noise response as we can observe in Figs. 7, 8, 9, 10 and 11. On the other hand, it is possible to note that the Kolmogorov-Sinai Entropy describes more precisely robustness in graphs, which is visible if we compare the data in Table 3 with results shown in the next set of figures. Besides of this, we can note that a graph with three spanning trees has better response to noise than a graph with four spanning trees and that those graphs with more connections tend to have unfavourable noise responses in spite of having high entropy values.

3. CONCLUSIONS

The results of this work have shown that Sinai-Kolmogorov Entropy is more precise than Loop entropy to elucidate

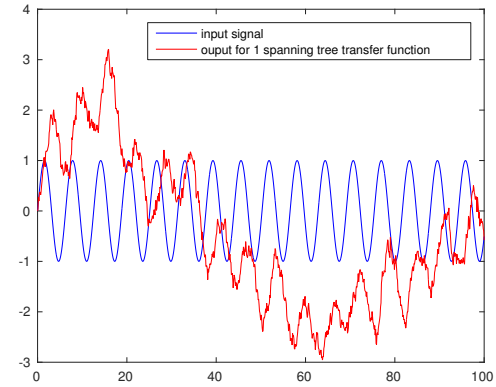

Fig. 7. Input vs. response for a 4 nodes and 1 spanning tree.

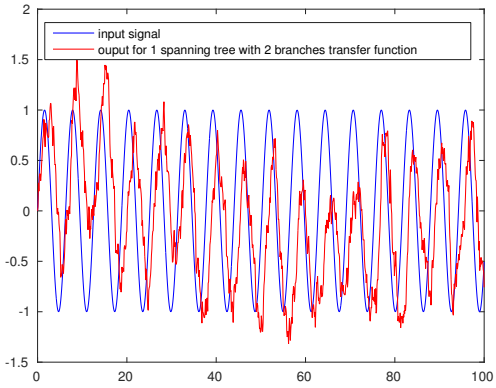

Fig. 8. Input vs. response for a 4 nodes and 1 spanning tree with 2 branches.

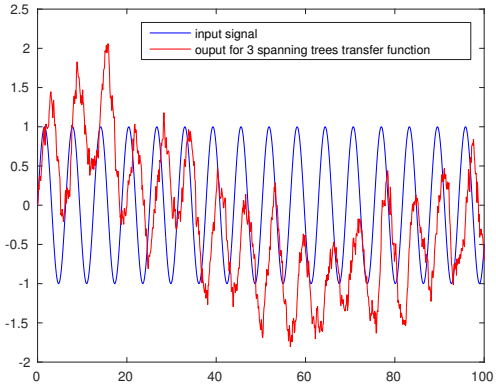

Fig. 9. Input vs. response for a 4 nodes and 3 spanning trees.

how much robustness has a network, as we can note comparing the case of a graph with two branches and the cycle graph, both with four nodes and one spanning tree.

On the other hand, it is possible to observe that in spite of having more spanning trees and therefore more node connections, some networks do not present good noise responses, which could be associated to the increase of paths for its spreading. In contrast, networks with

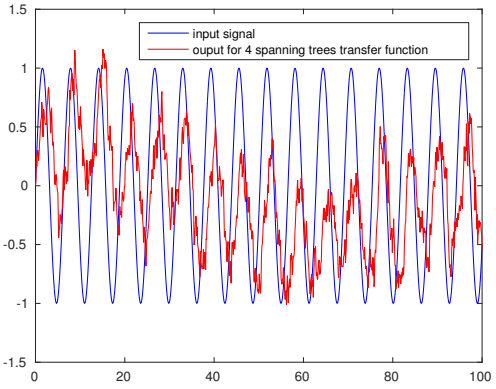

Fig. 10. Input vs. response for a 4 nodes and 4 spanning trees.

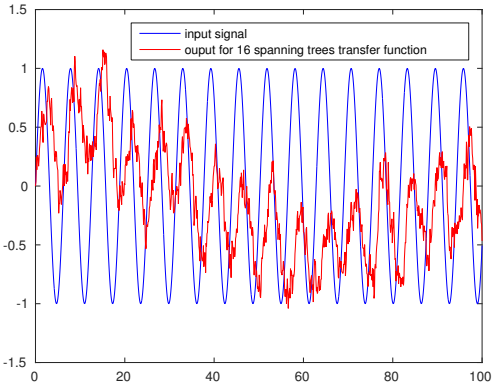

Fig. 11. Input vs. response for a 4 nodes and 16 spanning trees.

branches and low number of spanning trees can offer good possibilities to improve noise responses.

REFERENCES

Anand, K. and Bianconi, G. (2009). Entropy measures for networks: Toward an information theory of complex topologies. *Physical Review E*, 80(4), 045102. doi: 10.1103/PhysRevE.80.045102.

De Badyn, M.H., Chapman, A., and Mesbahi, M. (2016). Network entropy: A system-theoretic perspective. In *Proceedings of the IEEE Conference on Decision and Control*, volume 2016-Febru, 5512–5517. Institute of Electrical and Electronics Engineers Inc. doi: 10.1109/CDC.2015.7403083.

Dehmer, M. (2008). A NOVEL METHOD FOR MEASURING THE STRUCTURAL INFORMATION CONTENT OF NETWORKS. *Cybernetics and Systems*, 39(8), 825–842. doi:10.1080/01969720802435925.

Demetrius, L., Gundlach, V.M., and Ochs, G. (2004). Complexity and demographic stability in population models. *Theoretical population biology*, 65(3), 211–25. doi:10.1016/j.tpb.2003.12.002.

Demetrius, L. and Manke, T. (2005). Robustness and network evolution?an entropic principle. *Physica A: Statistical Mechanics and its Applications*, 346(3-4), 682–696. doi:10.1016/j.physa.2004.07.011.

Desoer, C. (1960). The Optimum Formula for the Gain of a Flow Graph or a Simple Derivation of Coates' Formula. *Proceedings of the IRE*, 48(5), 883–889. doi: 10.1109/JRPROC.1960.287625.

Mesbahi, M. and Egerstedt, M. (2010). *Graph theoretic methods in multiagent networks*.

Passerini, F. and Severini, S. (2008). The von Neumann entropy of networks. 5. doi:10.4018/978-1-60960-171-3.ch005.

Rashevsky, N. (1955). Life, information theory, and topology. *The Bulletin of Mathematical Biophysics*, 17(3), 229–235. doi:10.1007/BF02477860.

Shannon, C.E. (1948). A Mathematical Theory of Communication. *Bell System Technical Journal*, 27(3), 379–423. doi:10.1002/j.1538-7305.1948.tb01338.x.

Solé R. V., V.S. (2004). *Complex Networks*, volume 650 of *Lecture Notes in Physics*. Springer Berlin Heidelberg, Berlin, Heidelberg. doi:10.1007/b98716.

Trucco, E. (1956). A note on the information content of graphs. *The Bulletin of Mathematical Biophysics*, 18(2), 129–135. doi:10.1007/BF02477836.

Xiao, Y.H., Wu, W.T., Wang, H., Xiong, M., and Wang, W. (2008). Symmetry-based structure entropy of complex networks. *Physica A: Statistical Mechanics and its Applications*, 387(11), 2611–2619. doi: 10.1016/j.physa.2008.01.027.

Modified PI control for the Stabilization and Control of a class of High-order System with Delay

M. A. Hernández–Pérez ** **B. del Muro–Cuéllar** *
M. Velasco–Villa *,⋆ **D. F. Novella–Rodríguez** *
R. A. Garrido–Moctezuma **

* *Escuela Superior de Ingeniería Mecánica y Eléctrica, Unidad Culhuacan, Instituto Politécnico Nacional, 04430, México D.F. (e-mail: mahp_hernandez@hotmail.com, bdelmuro@yahoo.com, velasco@cinvestav.mx).*
** *CINVESTAV-IPN, Av. IPN, No. 2508, Col. San Pedro Zacatenco, 07300, México D.F. (e-mail:garrido@ctrl.cinvestav.mx)*

Abstract: In this work it is addressed the problem of the stabilization and control of a specific class of high-order unstable linear systems with time delay. The system under consideration has one unstable pole, q stable poles and a minimum phase zero. Sufficient conditions to guarantee the stability of the closed loop system by a modified PI scheme are provided. The proposed strategy consist of a modified version of the traditional PI controller, which include a first order filter and conduces to the, here called, PI_f controller. This new scheme allows the improvement of the existing results when a traditional PI is used for high-order systems with time delay. The proposed result is illustrated by its application to a numerical example: control of a Continuously Stirred Tank Reactor (CSTR) linear model.

Keywords: Unstable system, minimum phase zero, time-delay, modified PI control.

1. INTRODUCTION

Time delays often arise in control systems, either from delays in the process itself or from delays during the processing of sensed signals. Industrial processes often presents time delays introduced by the finite time that material takes to flow through pipes. In the same way time delay could be produced due to heat and mass transfer in chemical industries, heavy computations and hardware restrictions of computational systems, high inertia in systems with heavy machinery and communications delays in space craft and remote operation.

Typical examples of systems exhibiting time delays are chemical processes Richard (2003), transportation systems, communication and power systems Franklin et al. (1995); Wang et al. (1999). In some others cases, delays are introduced by sensors and actuators devices Xian et al. (2005), Liu et al. (2005). In most cases this phenomenon is one of the main causes of instability and poor performance and it produces, in general, unwanted behaviors in dynamical systems. So, it is necessary to take special attention to the stability analysis and controller design to handle systems with time delays. Thus, there exist great motivation for the study of effects causing a time delay in dynamic systems Hu and Lin (2001), Trentelman et al. (2001) and Shamsuzzoha et al. (2009). In addition, the problem becomes more complicated when the system not only has a time delay but also it is unstable. For this reason, the interest of dealing with unstable processes containing a delay term has been growing in the control community Lee et al. (2010), Sipahi et al. (2011) and Gu et al. (2003) recently.

The control problem of time delay systems has been studied by different perspectives. The simplest approach consists on the approximation of the delay operator by means of Taylor or Pade series expansions which leads to a nonminimum- phase models with rational transfer function representation Munz et al. (2009). Another approach is to compensate the effect of time delays by removing the exponential term from the characteristic equation of the process. This technique was introduced by Smith (1957) and it is well-known as Smith Predictor (SP). This technique does not have a stabilization step which restricts its application to open-loop stable plants. To deal with this disadvantage, some modifications of the original SP structure have been proposed (for instance Palmor (1996), Seshagiri et al. (2007), Kawnish and Choudhury (2012)).

Another solution to control delayed systems is to use a Proportional-Integral- Derivative (PID) controllers. PID controller is widely used in the control of industrial processes due to its simple structure in many practical processes (Silva et al. (2005)). Also, they are frequently used to stabilize unstable time-delay processes. However, stability conditions for such processes are a very challenging topic. Huang and Chen (1997), use root locus diagrams to study the stabilizability problem of unstable delay pro-

⋆ M. Velasco-Villa is on sabbatical stay supported by Conacyt (No. 260936) from Mechatronic Section of the Electrical Engineering Department.

cesses using simple controllers and show that a normalized time delay should be less than 1 for P/PI controllers, while it should be less than 2 for the case of PD controller.

Silva et al. (2005), investigated the complete set of stabilizing PID controllers based on the Hermite-Biehler theorem for quasi-polynomials. This approach requires a lot of mathematical processing, in case the system has large dimension. Moreover, this approach does not provide an explicit characterization of the stabilizing PID parameter in terms of the maximal time delay. Hwang and Hwang (2004) applied the D-partition method to characterize the stability domain in the space of system and controller parameters. Thus, the stability boundary is reduced to a transcendental equation, and the whole stability domain is drawn in a two-dimensional plane by sweeping the remaining parameters. However, this result only provides a sufficient condition regarding the size of the time delay for stabilization of first-order unstable processes.

In Xiang et al. (2007), a frequency approach for the design of P/PI controllers focused on the specific class of second order systems with an unstable pole was introduced. With a similar approach, in Lee et al. (2010), a generalization for high order systems with an unstable pole is given. In both cases, the stability results are obtained in terms of the upper bound of the time-delay, however they do not address the problem of systems with a minimum phase zero.

In this work, a modified version of the traditional PI control scheme is proposed . This new control strategy will be denoted henceforth as a PI_f controller. This new scheme, besides of keeping the basic properties of a conventional PI controller such as disturbance rejection and reference tracking of step type signals, also allows the stabilization and control of the same family of systems considered in Lee et al. (2010), but with the advantage of the delays supported by this new scheme are larger than those supported by the traditional PI. Additionally, one of the main advantages of the PI_f is that it can deal with unstable systems which include a transmission zero, which is an interesting feature from the control point of view. Sufficient conditions to stabilize high-order unstable systems with time delay and a minimum phase zero are presented in this work. The stabilization conditions are expressed in terms of the maximum allowable time–delay magnitude. Also it is provided a procedure for determining the parameter ranges of the stabilizing controller. The proposed control scheme is illustrated by a numerical example to control the temperature in an unstable linear model of a Continuously Stirred Tank Reactor (CSTR).

The rest of the work is organized as follows: Section 2 presents the problem statement. Section 3 addresses the proposed control strategy, establishing the sufficient condition for the existence of a stabilizing control structure. In Section 4, the results are applied to a numerical example. Finally in Section 5 the conclusions are presented.

2. PROBLEM STATEMENT

Consider the following class of single input single output (SISO) linear time invariant systems (LTI) with delay in the input-output path given by,

$$\frac{Y(s)}{U(s)} = G(s)e^{-\tau s} = \frac{\alpha(s+\beta)}{(s-\gamma)\prod_{m=1}^{q}(s+\delta_m)}e^{-\tau s} \qquad (1)$$

with γ, δ_m and $\beta > 0$. Note that the system has an unstable pole, q stable poles, a zero in the left half complex plane s and time delay $\tau > 0$. The objective is to provide sufficient conditions to stabilize this class of systems by a PI-modified (PI_f) illustrated in Fig. 1.

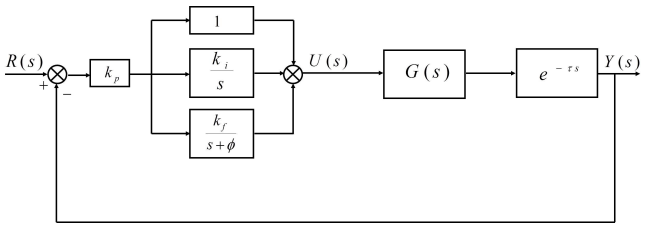

Fig. 1. Proposed control strategy PI_f

The PI_f control represented in Fig. 1 is given by,

$$H(s) = k_p\left(1 + \frac{k_i}{s} + \frac{k_f}{s+\phi}\right). \qquad (2)$$

The proposed PI_f control consists of a modification to the conventional structure of PI controller by adding a first order filter. In this approach is proven that a proposed PI_f controller not only improves the stability conditions reported in the literature using the traditional PI, but also the PI_f keeps the basic properties of a PI controller; disturbance rejection and reference tracking of step type signals.

3. PROPOSED CONTROL STRATEGY

This section present sufficient conditions to stabilize the close-loop system (1)-(2). Note that this control strategy produces an open-loop transfer function $Q(s)$ represented by,

$$Q(s) = H(s)G(s)e^{-\tau s}. \qquad (3)$$

To design a control strategy, the following theorem is stated.

Theorem 1. Consider the class of high-order time-delayed system with one unstable pole and a zero in the left half complex plane give by (1). There exists a PI_f controller given by (2) such that the corresponding closed–loop system is stable if,

$$\tau < \frac{1}{\gamma} - \sum_{m=1}^{q}\frac{1}{\delta_m} + \sqrt{\frac{1}{\gamma^2} + \sum_{m=1}^{q}\frac{1}{{\delta_m}^2}}. \qquad (4)$$

Proof. Suppose that condition (4) is satisfied. Due to the freedom selecting the parameter ϕ of the PI_f controller given by (2), it is possible to obtain a cancellation of the zero of the system (1) by $\phi = \beta$. Therefore, the open-loop response is obtained as,

$$Q(j\omega) = k_p\alpha\frac{\cancel{\left((j\omega)^2 + (k_f + k_i + \phi)j\omega + k_i\phi\right)}\ \cancel{(j\omega+\beta)}}{j\omega\,(j\omega-\gamma)\,\cancel{(j\omega+\phi)}\prod_{m=1}^{q}(j\omega+\delta_m)}e^{-j\omega\tau}. \quad (5)$$

In order to facilitate the analysis, it is possible to consider the following change of variables for k_p, k_i and k_f such that,

$$\begin{cases} \bar{k_p} = k_p(k_f + k_i + \phi) \\ \bar{k_f} = \frac{1}{k_f+k_i+\phi} \\ \bar{k_i} = \frac{k_i\phi}{k_f+k_i+\phi}. \end{cases} \quad (6)$$

From (6), the open-loop response (5) can be rewriten as,

$$Q(j\omega) = \bar{k_p}\bar{k_f}\alpha\frac{\left((j\omega)^2 + (\frac{1}{k_f})j\omega + \frac{\bar{k_i}}{k_f}\right)}{j\omega\,(j\omega-\gamma)\prod_{m=1}^{q}(j\omega+\delta_m)}e^{-j\omega\tau}. \quad (7)$$

To simplify the analysis, let us consider $k_i = 0$. Then, the phase and magnitude expression in the frequency domain of (7) are given by,

$$\angle Q(j\omega) = -\left(\pi - \arctan\left(\frac{\omega}{\gamma}\right)\right) - \omega\tau + \arctan\left(\bar{k_f}\omega\right) - \sum_{m=1}^{q}\arctan\left(\frac{\omega}{\delta_m}\right) \quad (8)$$

$$M_{Q(j\omega)} = \bar{k_p}\alpha\sqrt{\frac{1+\bar{k_f}^2\omega^2}{(\omega^2+\gamma^2)\prod_{m=1}^{q}\left(\omega^2+{\delta_m}^2\right)}}. \quad (9)$$

Taking into account the Nyquist stability criterion, system (7) will be stable if and only if $N + P = 0$, where P the number of poles in the right half complex plane and N the number of rotations to the point $(-1, 0j)$. In this case, as $P = 1$, it is required to have a counterclockwise rotation to the point $(-1; 0)$ in the Nyquist diagram.

Therefore, since the phase expression has an initial value of $-\pi$ and assuming that condition (4) is satisfied, to have a counterclockwise direction in the Nyquist diagram the magnitude expression $M_{Q(j\omega)}$ must be an strictly decreasing function of ω and the phase expression $\angle Q(j\omega)$ must be an increasing function of ω. From this fact, it is possible to prove based on (4) that,

$$\frac{d}{d\omega}\left(\frac{M_Q^2}{\bar{k_p}^2\alpha^2}\right)\Bigg|_{\omega=0} < 0. \quad (10)$$

and

$$\frac{d}{d\omega}\left(\angle Q(j\omega)\right)\Big|_{\omega=0} > 0 \quad (11)$$

Consequently, if (4) is satisfied, there exist gains $\bar{k_p}$, $\bar{k_f}$ and $\bar{k_i}$ such that the system (1) is stable in the closed-loop.

Therefore, from the decreasing and increasing properties stated in (10) and (11), and after some computations, the set of stabilizing $\bar{k_f}$ values are given by,

$$\tau - \frac{1}{\gamma} + \sum_{m=1}^{q}\frac{1}{\delta_m} < \bar{k_f} < \sqrt{\frac{1}{\gamma^2} + \sum_{m=1}^{q}\left(\frac{1}{\delta_m^2}\right)}. \quad (12)$$

When the integral part $\bar{k_i}$ is considered to be different from zero, the phase expression $\angle Q(j\omega)$ and magnitude expression $M_{Q(j\omega)}$ are represented by (13) and (14), respectively

$$\angle Q(j\omega) = -\left(\pi - \arctan\left(\frac{\omega}{a}\right)\right) - \omega\tau + \arctan\left(\bar{k_f}\omega - \frac{\bar{k_i}}{\omega}\right) - \sum_{m=1}^{q}\arctan\left(\frac{\omega}{b_m}\right) \quad (13)$$

$$M_{Q(j\omega)} = \bar{k_p}\alpha\sqrt{\frac{1+\left(\bar{k_f}\omega - \frac{\bar{k_i}}{\omega}\right)^2}{(\omega^2+a^2)\prod_{m=1}^{q}\left(\omega^2+{b_m}^2\right)}}. \quad (14)$$

Taking into account $\bar{k_i} = 0$ the magnitude expressions (14) and (9) are equivalents. In the same way, it can also be noted that (13) is equivalent to (8) when $\bar{k_i} = 0$. Considering this fact, it is possible to follow the principle of argument continuity for $\bar{k_i}$, this is, it is always possible to choose a small enough $\bar{k_i}$ gain such that conditions (10) and (11) are fulfilled. Thus, once an stabilizing $\bar{k_f}$ gain is found, it is always possible to choose a small enough $\bar{k_i}$ gain such that the Nyquist stability criterion is satisfied and the system (7) can be stabilized by a PI_f controller.

From this fact, if the phase and magnitude condition are satisfied, then there exists a adequate $k_p > 0$ such that the Nyquist diagram will start in the correct position and with a counterclockwise rotation, then the Nyquist stability criterion will be satisfied. The range of $\bar{k_p}$ values is given by,

$$\bar{k_p}(\omega_{c_1}) < \bar{k_p} < \bar{k_p}(\omega_{c_2})$$

with $\omega_{c_1} < \omega_{c_2}$ being the first two phase crossover frequencies solutions of,

$$\arctan\left(\frac{\omega_{c_i}}{\gamma}\right) - \omega_c\tau + \arctan\left(\bar{k_f}\omega_{c_i} - \frac{\bar{k_i}}{\omega_{c_i}}\right) - \sum_{m=1}^{q}\arctan\left(\frac{\omega_{c_i}}{\delta_m}\right) = 0. \quad (15)$$

where $\omega_{c_{i=1,2}}$ are crossover frequencies and $\bar{k_p}(\omega_{c_i})$ are given by

$$\bar{k_p}(\omega_{c_i}) = \frac{1}{\alpha_1}\sqrt{\frac{(\omega_{c_i}^2+\gamma^2)\prod_{m=1}^{q}\left(\omega_{c_i}^2+{\delta_m}^2\right)}{1+\left(\bar{k_f}\omega_{c_i} - \frac{\bar{k_i}}{\omega_{c_i}}\right)^2}}. \quad (16)$$

Thus, if condition (4) is is fulfilled, there always exist $\bar{k_f}$, $\bar{k_i}$ and $\bar{k_p}$ gains which are able to stabilize systems of the class (1) in close-loop by using a PI_f control structure.

Remark 2. It is worth noting that the proposed PI_f controller, in this work, not only maintains the basic properties of a convencional PI controller regarding disturbance rejection and reference tracking of step type signals. Besides, it presents two advantages over P/PI controller; as the stability condition is improved adding the term $\sqrt{\frac{1}{\gamma^2}+\sum_{m=1}^{q}\frac{1}{\delta_m{}^2}}$, i.e., the PI_f allows stabilizing systems with larger delays than the ones allowed by the conventional P/PI controller. The second advantage is that the PI_f control allows state conditions to stabilize systems with a zero which have not been addressed in the literature.

4. NUMERICAL EVALUATION

4.1 Control of CSTR by modified-PI controller

The following example has been taken from Bequette (2003). It is considered the chemical process of a unstable continuos stirred tank reactor. A general description of a CSTR is shows in Fig. 2.

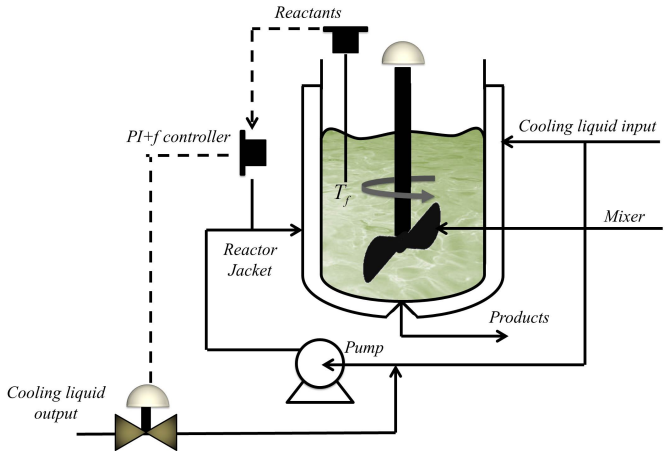

Fig. 2. Unstable continuously stirred tank reactor (CSTR).

The purpose of measuring the temperature in a reactant A is to manipulate the speed of the chemical reaction and, thus, to improve the selectivity of the reaction system. To remove the heat of the reaction, the reactor is surrounded by a jacket (coolant jacket) through which flows a coolant. Often, the heat transfer fluid is pumped through agitation nozzles that make the fluid circulate through the jacket at high velocity as you can see in Fig. 2.

From Bequette (2003) system parameters are listed in Table 1.

Differential equations of the process shown in Fig. 2 are characterized as follows:

(1) The balance of the mass on component A is,

$$V\frac{dC_A}{dt} = FC_{Af} - FC_A - V_{r_A}$$

with

$$r_A = k_0 e^{\frac{-\Delta E}{RT}} C_A$$

Table 1. CSTR parameters.

Description	Variables	Values	Unit
Volume of the reactor	V	85	ft^3
Activation energy	$-\Delta E$	32,400	$Btu/lbmol$
Heat transfer coefficient	U	75	$btu/hr^\circ F$
Heat of Reaction	$-\Delta H$	39,000	$Btu/lbmolPO$
Heat transfer area	A	88	ft^2
Frequency factor	k_0	$16.96x10^{12}$	hr^{-1}
Ideal gas constant	R	1.987	$Btu/lbmol^\circ F$
Volume cooling liquid in the chamber	V_j	21.25	ft^3
Heat capacity on reactor with density of the reagent	pc_p	53.25	$Btu/ft^3\,^\circ F$
Density of the cooling liquid with heat capacity of the cooling liquid	$p_j c_{pj}$	55.6	$Btu/ft^3\,^\circ F$

where r_A is the rate of reaction per unit volume, k_0 is the frequency factor, ΔE is the activation energy and R is the ideal gas constant, such that,

$$\frac{dC_A}{dt} = \frac{F}{V}\left(C_{Af} - C_A\right) - k_0 e^{\frac{-\Delta E}{RT}} C_A. \tag{17}$$

(2) Energy balance in the reactor,

$$\frac{dT}{dt} = \frac{F}{V}\left(T_f - T\right) + \frac{-\Delta H}{RT} k_0 e^{\left(\frac{-\Delta E}{RT}\right)} C_A - \frac{UA}{VpC_p}\left(T - T_j\right). \tag{18}$$

(3) Energy balance in the cooling liquid,

$$\frac{dT_j}{dt} = \frac{F_{jf}}{V_j}\left(T_{jf} - T_j\right) + \frac{UA}{V_j p_j C_{pj}}\left(T - T_j\right). \tag{19}$$

To get a linear representation of the CSTR model, the jacket temperature T_{jf} is considered as the manipulated (input) variable and the temperature of the CSTR T_j, as the controlled (output) variable. A tangent approximation will be obtained by considering the operating point (detailed descriptions of these parameters can be found in Bequette (2003)),

$$(C_{Af}^o, C_A^o, F^o, F_{jf}^o, T^o, T_j^o, T_f^o, T_{jf}^o) = (0.132, 0.066, 340, 28.75, 101.1, 55, 60, 50).$$

where C_A^o is the concentration of the product A, F^o is the concentration of the product A, F_{jf}^o is the flow cooling liquid (reactor jacket), T^o is the temperature in the Reactor, T_j^o is the temperature in the cooling liquid (reactor jacket), T_f^o is the Input temperature product A and T_{jf}^o is the cooling liquid temperature at the input-liquid.

The linear representation around the considered operating point it is obtained as,

$$\frac{T_j(s)}{T_{jf}(s)} = \frac{0.8714s + 6.963}{s^2 + 2.848s - 1.132}. \tag{20}$$

Notice that the linear system (20) is of the form given in equation (1) with $\tau = 0$ since it has an unstable pole, a stable pole and a zero . Using high quality sensors to determine the temperature (T_j) in CSRT reactors usually means high costs. This disadvantage in the sensor generates a dead-time in the measurement of the temperature, which creates a problem for the control strategy design, that increases its difficulty when the system is unstable. For that reason, it is possible to consider this effect by

adding an adequate time-lag to equation (20), that for this kind of reactor, the time–delay in the concentration measurement is approximately 0.3 hr. this produces,

$$\frac{T_j(s)}{T_{jf}(s)} = \frac{0.8714s + 6.963}{s^2 + 2.848s - 1.132} e^{-0.3s}. \qquad (21)$$

Taking into account equation (1), the system parameters (21) are $\gamma = 0.35$, $\delta = -3.20$, $\beta = 7.97$ and $\tau = 0.3$. From the stability condition shown in Theorem 1 and assuming that $m = 1$,

$$\tau = 0.3 < \frac{1}{\gamma} - \frac{1}{\delta} + \sqrt{\frac{1}{\gamma^2} + \frac{1}{\delta^2}} = 5.3$$

therefore, system (21) can be stabilized by a PI_f controller. To get the controller, the first step considers the free pole ϕ given by the PI_f which is located on the same position as zero β in order to cancel this dynamic. Then, $\phi = 7.97$. From equation (12), the range of values for the stabilizing gain $\bar{k_f}$ is $-2.21 < \bar{k_f} < 2.84$.

Considering $\bar{k_f} = 0.1176$, the gain $\bar{k_i}$ must be small enough to satisfy the conditions (10) and (11). For this case $\bar{k_i} = 0.022$.

From (15) and (16) the range of stabilizing gain $\bar{k_p}$ is given by $1.37 < \bar{k_p} < 14.06$. Considering $\bar{k_p} = 2$, the PI_f control is represented as:

$$PI_f = 0.23\left(1 + \frac{0.023}{s} + \frac{0.51}{s + 7.97}\right).$$

In order to illustrate that the Nyquist stability criterion has been satisfied, Fig. 3 shows the existence of counter-clockwise rotation to the point $(-1, 0j)$ in the Nyquist diagram.

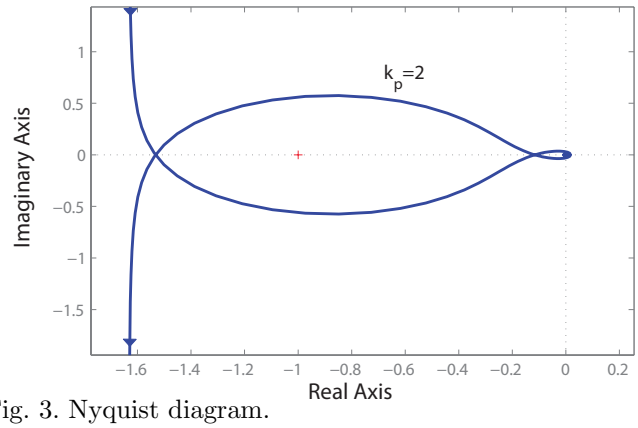

Fig. 3. Nyquist diagram.

Fig. 4 illustrates the control strategy performance regarding the reactor concentration when an unitary input reference is considered. A continues line shows the nominal system performance while a dotted line represents the system performance with a uncertainty of 28% in the time delay such that $\tau = 1.8$. In addition, the PI_f controller proves its effective disturbance rejection for step-type inputs with fast recovery when a disturbance occurs at $100hrs$. Finally, the control signal is illustrated in Fig. 5

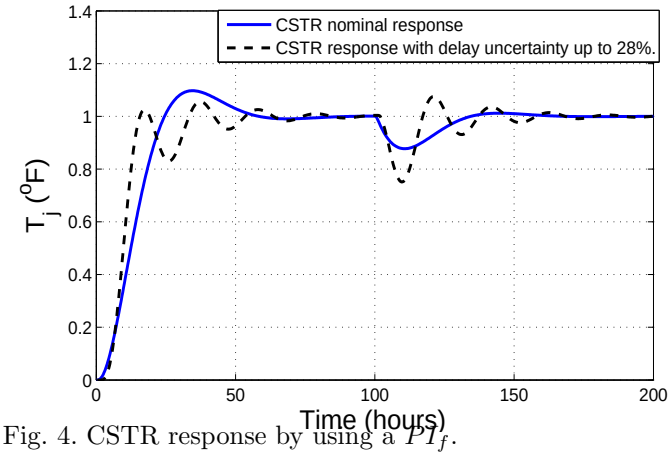

Fig. 4. CSTR response by using a PI_f.

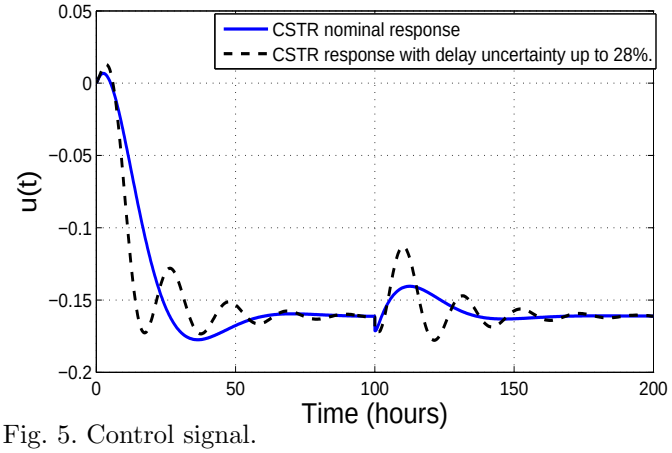

Fig. 5. Control signal.

5. CONCLUSION

This paper presents a sufficient condition for the stabilization of a high order unstable linear systme with time delay and one "stable" zero by using a modified-PI controller (PI_f). Additionally, the procedure to determine the parameters for the stabilizing gains k_p, k_i and k_f are given in order to provide an accurate PI_f controller tuning. The proposed scheme not only maintains the basic properties of a convencional PI controller, but also, the stability condition is improved allowing to stabilize systems with larger delays than the ones considered by the a conventional PI controller. Finally, an unstable continuously stirred tank reactor was used to verify the performance of the proposed strategy using a numerical simulation.

REFERENCES

Bequette, B.W. (2003). *Process Control. Modelling, Design and Simulation.* Prentice-Hall Internacional.

Franklin, G.F., Powell, .D., and Emami-Naeini, A. (1995). Feedback control of dynamic systems. *Addison Wesley Publishing Company, 3er edition.*

Gu, K., Kharitonov, V.L., and Chen, J. (2003). *Stability of Time-Delay Systems.* Birkhäuser.

Hu, T. and Lin, Z. (2001). *Control Systems with Actuator Saturation: Analysis and Design.* Birkhauser, Boston, MA.

Huang, H. and Chen, J. (1997). On stabilizing a time delayed unstable process. *Journal of the Taiwan Institute of Chemical Engineers*, 28(4), 289–299.

Hwang, C. and Hwang, J.H. (2004). Stabilisation of first-order plus dead-time unstable processes using pid controllers,. *Proceedings Control Theory and Applications*, 151(1), 89–94.

Kawnish, K. and Choudhury, M.S. (2012). A novel dead time compensator for stable processes with long dead times. *Journal of Process Control*, 22(3), 612–625.

Lee, S.C., Wang, Q.G., and Xiang, C. (2010). Stabilization of all-pole unstable delay processes by simple controllers. *Journal of Process Control*, 20(2), 235 – 239.

Liu, T., Zhang, W., and Gu, D. (2005). Analytical design of two-degree-of-freedom control scheme for open-loop unstable processes with time delay. *Journal of Process Control*, 15, 559–572.

Munz, Ebenbauer, C., Haag, T., and Allgower, F. (2009). Stability analysis of time-delay systems with incommensurate delays using positive polynomials. *IEEE Trans. Autom. Control*, 54(5), 1019 – 1024.

Palmor, Z.J. (1996). Time-delay compensation smith predictor and its modifications. *The control handbook*, 224–237.

Richard, J.P. (2003). Time-Delay Systems:An Overview of Some Recent Advances and Open Problems. *Automatica*, 39, 1667–1694.

Seshagiri, R.A., Rao, V.S.R., and Chidambaram, M. (2007). Simple analytical design of modified smith predictor with improved performance for unstable first-order plus time delay (fodtp) processes. *Ind. Eng. Chem. Res*, 46(13), 4561–4571.

Shamsuzzoha, M., Jongpal, J., and Moonyong, L. (2009). Improved analytical pid controller design for the second order unstable process with time delay. *17th European Symposium on Computer Aided Process Engineering*, 8, 1107–118.

Silva, G.J., Datta, A., and Bhattacharyya, S.P. (2005). *PID controllers for time-delay systems.* Springer, London.

Sipahi, R., Niculescu, S.I., Abdallah, C., Michiels, W., and Gu, K. (2011). Stability and stabilization of systems with time delay. *Control Systems, IEEE*, 31(1), 38–65.

Smith, O.J.M. (1957). Closer control of loops with dead-time. *Chem. Eng. Prog.*, 53(5), 217–219.

Trentelman, L., Stoorvogel, A., and Hautus, M. (2001). *Control Theory for Linear Systems.* Springer-Verlag, 1 edition.

Wang, Q.G., Lee, T.H., and Tan, K.K. (1999). Finite spectrum assignment for time- delay systems. *Lecture Notes in Control and Information Science*, (239).

Xian, L., Yong-Sheng, Y., Quing-Guo, W., and Wei-Xing, Z. (2005). A double two-degree-of-freedom control scheme for improved control of unstable delay processes. *Journal of Process Control*, 15, 605–614.

Xiang, C., Wang, Q., Lu, X., Nguyen, L., and Lee, T. (2007). Stabilization of second-order unstable delay system by simple controllers. *Journal of Process Control*, 17(8), 675–682.

Non-Singular Predefined-Time Stable Manifolds

Juan Diego Sánchez-Torres * **Esteban Jiménez-Rodríguez** **
David Gómez-Gutiérrez ** **Alexander G. Loukianov** **

* *Department of Mathematics and Physics, ITESO, Periférico Sur Manuel Gómez Morín 8585 C.P. 45604, Tlaquepaque, Jalisco, México. (e-mail: dsanchez@iteso.mx).*
** *Department of Electrical Engineering, CINVESTAV-IPN Guadalajara, Av. del Bosque 1145 Col. El Bajío CP 45019, México. (e-mail:{ejimenezr,dgomez,louk}@gdl.cinvestav.mx).*

Abstract: In this paper it is introduced a class of non-singular manifolds with predefined-time stability. That is, for a given dynamical system with its trajectories constrained to this manifold it can be shown predefined-time stability to the origin. In addition, the function that defines the manifold and its derivative along the system trajectories are continuous, therefore no singularities are presented for the system evolution once the constrained motion starts. The problem of reaching the proposed manifold is solved by means of a continuous predefined-time stable controller. The proposal is applied to the predefined-time exact tracking of fully actuated and unperturbed mechanical systems. It is assumed the availability of the state and the desired trajectory as well as its two first derivatives. As an example, the proposed solution is applied over a two-link planar manipulator and numerical simulations are conducted to show its performance.

Keywords: Predefined-Time Stability, Sliding Mode Algorithms, Second Order Systems, Mechanical Systems.

1. INTRODUCTION

Several applications are characterized for requiring hard time response constraints. In order to deal with those requirements, various developments concerning to concept of *finite-time stability* have been carried out (see for example: Roxin (1966); Weiss and Infante (1967); Michel and Porter (1972); Haimo (1986); Utkin (1992); Bhat and Bernstein (2000); Moulay and Perruquetti (2005, 2006)). Nevertheless, usually this finite time is an unbounded function of the initial conditions of the system.

With the aim to eliminate this boundlessness, the notion of fixed-time stability have been studied in Andrieu et al. (2008); Cruz-Zavala et al. (2010); Polyakov (2012); Fraguela et al. (2012); Polyakov and Fridman (2014). Fixed-time stability represents a significant advantage over finite-time stability due to its desired feature of the convergence time, as a function of the initial conditions, is bounded. That makes the fixed-time stability a valuable feature in estimation and optimization problems.

For the most of the proposed fixed-time stable system, there are problems related with the convergence time. First, the bounds of the fixed stabilization time found by Lyapunov analysis constitute usually conservative estimations, i.e. they are much larger than the true fixed stabilization time (see for example Cruz-Zavala et al. (2011), where the upper bound estimation is approximately 100 times larger than the actual true fixed stabilization time). Second, and as consequence, it is often complicated to find a direct relationship between the tuning gains and the fixed stabilization time, making this time hard to tune.

To overcome the above, a class of first-order dynamical systems with the minimum upper bound of the fixed stabilization time equal to their only tuning gain has been studied (Sánchez-Torres et al., 2014; Sánchez-Torres et al., 2015). It is said that these systems exhibit the property of *predefined-time stability*.

In this sense, this paper introduces the concept of non-singular predefined-time stable manifolds. Similarly to Jiménez-Rodríguez et al. (2016), the proposed scheme allows to define second-order predefined-time stable systems as a nested application of first-order predefined-time stabilizing functions, with the difference that such function which defines the manifold and its derivative along the system trajectories are continuous, therefore no singularities are presented for the system evolution.

Finally, this idea is used to solve the problem of predefined-time exact tracking in fully actuated mechanical systems, assuming the availability of the state and the desired trajectory and its two first derivatives measurements.

In the following, Section 2 presents the mathematical preliminaries needed to introduce the proposed results. Section 3 exposes the main result of this paper, which is the non-singular predefined-time stable manifold design. Section 4 presents a non-singular second-order predefined-time tracking controller for fully actuated mechanical systems. Section 5 describes the model of a planar two-link manipulator, where the proposed controller is applied. The

simulation results of the example are shown in Section 6. Finally, Section 7 presents the conclusions of this paper.

2. PRELIMINARIES

2.1 Mathematical Preliminaries

Consider the system

$$\dot{x} = f(x;\rho) \tag{1}$$

where $x \in \mathbb{R}^n$ is the system state, $\rho \in \mathbb{R}^b$ represents the parameters of the system and $f : \mathbb{R}^n \to \mathbb{R}^n$ is a nonlinear function. The initial conditions of this system are $x(0) = x_0$.

Definition 2.1. (Polyakov, 2012) The origin of (1) is *globally finite-time stable* if it is globally asymptotically stable and any solution $x(t, x_0)$ of (1) reaches the equilibrium point at some finite time moment, i.e., $\forall t \geq T(x_0) : x(t, x_0) = 0$, where $T : \mathbb{R}^n \to \mathbb{R}_+ \cup \{0\}$.

Definition 2.2. (Polyakov, 2012) The origin of (1) is *fixed-time stable* if it is globally finite-time stable and the settling-time function is bounded, i.e. $\exists T_{\max} > 0 : \forall x_0 \in \mathbb{R}^n : T(x_0) \leq T_{\max}$.

Remark 2.1. Note that there are several choices for $T_{\max}$. For instance, if the settling-time function is bounded by T_{m}, it is also bounded by λT_{m} for all $\lambda \geq 1$. This motivates the following definition.

Definition 2.3. (Sánchez-Torres et al., 2014; Sánchez-Torres et al., 2015) Let $\mathcal{T}$ be the set of all the bounds of the settling time function for the system (1), i.e.,

$$\mathcal{T} = \{T_{\max} > 0 : \forall x_0 \in \mathbb{R}^n : T(x_0) \leq T_{\max}\}. \tag{2}$$

The minimum bound of the settling-time function T_f, is defined as:

$$T_f = \inf \mathcal{T} = \sup_{x_0 \in \mathbb{R}^n} T(x_0). \tag{3}$$

Remark 2.2. In a strict sense, the time T_f can be considered as the true fixed-time in which the system (1) stabilizes.

Definition 2.4. (Sánchez-Torres et al., 2014; Sánchez-Torres et al., 2015) For the case of fixed time stability when the time T_f defined in (3) can be tuned by a particular selection of the parameters ρ of the system (1), it is said that the origin of the system (1) is *predefined-time stable.*

Definition 2.5. Let $h \geq 0$. For $x \in \mathbb{R}$, define the function

$$\lfloor x \rceil^h = |x|^h \operatorname{sign}(x),$$

with $\operatorname{sign}(x) = 1$ for $x > 0$, $\operatorname{sign}(x) = -1$ for $x < 0$ and $\operatorname{sign}(0) \in [-1, 1]$.

Remark 2.3. For $x \in \mathbb{R}$, some properties of the function $\lfloor \cdot \rceil^h$ are:

(i) $\lfloor x \rceil^h$ is continuous for $h > 0$.
(ii) $\lfloor x \rceil^0 = \operatorname{sign}(x)$.
(iii) $\lfloor x \rceil^1 = \lfloor x \rceil = x$,
(iv) $\lfloor 0 \rceil^h = 0$ for $h > 0$.
(v) $\frac{d|x|^h}{dx} = h \lfloor x \rceil^{h-1}$ and $\frac{d\lfloor x \rceil^h}{dx} = h |x|^{h-1}$.
(vi) For $h_1, h_2 \in \mathbb{R}$, it follows:
- $|x|^{h_1} |x|^{h_2} = |x|^{h_1+h_2}$
- $\lfloor x \rceil^{h_1} |x|^{h_2} = |x|^{h_1} \lfloor x \rceil^{h_2} = \lfloor x \rceil^{h_1+h_2}$
- $\lfloor x \rceil^{h_1} \lfloor x \rceil^{h_2} = |x|^{h_1+h_2}$

(vii) For $h_1, h_2 > 0$, then $\left\lfloor \lfloor x \rceil^{h_1} \right\rceil^{h_2} = \lfloor x \rceil^{h_1 h_2}$.

Definition 2.6. (Sánchez-Torres et al., 2014; Sánchez-Torres et al., 2015) For $x \in \mathbb{R}$, the *predefined-time stabilizing function* is defined as:

$$\Phi_p(x; T_c) = \frac{1}{T_c p} \exp\left(|x|^p\right) \lfloor x \rceil^{1-p} \tag{4}$$

where $T_c > 0$ and $0 < p \leq 1$.

Remark 2.4. It can be checked, using Remark 2.3, that the derivative of the predefined-time stabilizing function (4) is given by

$$\frac{d\Phi_p(x; T_c)}{dx} = \frac{\exp\left(|x|^p\right)}{T_c p} \left[p + (1-p) \frac{1}{|x|^p} \right], \quad \forall x \neq 0 \tag{5}$$

To handle vector systems, the above definitions are extended.

Definition 2.7. Let $h \geq 0$, $T_c > 0$, $0 < p \leq 1$ and $v = \begin{bmatrix} v_1 & \cdots & v_k \end{bmatrix}^T \in \mathbb{R}^k$. Then, the functions $\operatorname{sign}(\cdot)$, $|\cdot|^h$, $\lfloor \cdot \rceil^h$ and $\Phi_p(\cdot; T_c)$ are extended component-wise, as follows:

(i) $\operatorname{sign}(v) = \begin{bmatrix} \operatorname{sign}(v_1) & \cdots & \operatorname{sign}(v_k) \end{bmatrix}^T$
(ii) $|v|^h = \begin{bmatrix} |v_1|^h & \cdots & |v_k|^h \end{bmatrix}^T$;
(iii) $\lfloor v \rceil^h = \begin{bmatrix} \lfloor v_1 \rceil^h & \cdots & \lfloor v_k \rceil^h \end{bmatrix}^T$;
(iv) $\Phi_p(v; T_c) = \begin{bmatrix} \Phi_p(v_1; T_c) & \cdots & \Phi_p(v_k; T_c) \end{bmatrix}^T$.

Definition 2.8. Let $v = \begin{bmatrix} v_1 & \cdots & v_k \end{bmatrix}^T \in \mathbb{R}^k$. Then $\operatorname{diag}(v)$ will denote the $k \times k$ matrix defined as

$$\operatorname{diag}(v) = \begin{bmatrix} v_1 & 0 & \cdots & 0 \\ 0 & v_2 & \cdots & 0 \\ \vdots & \vdots & \ddots & \vdots \\ 0 & 0 & \cdots & v_k \end{bmatrix}.$$

Remark 2.5. The properties *(i)*, *(ii)*, *(iii)*, *(iv)* and *(vi)* of Remark 2.3 remain the same. For $v \in \mathbb{R}^k$, the derivatives of the functions $|\cdot|^h$, $\lfloor \cdot \rceil^h$ and $\Phi_p(\cdot; T_c)$ are:

$$\frac{\partial |v|^h}{\partial v} = \operatorname{diag}\begin{bmatrix} h \lfloor v_1 \rceil^{h-1} & \cdots & h \lfloor v_k \rceil^{h-1} \end{bmatrix} = h \operatorname{diag} \lfloor v \rceil^{h-1},$$

$$\frac{\partial \lfloor v \rceil^h}{\partial v} = \operatorname{diag}\begin{bmatrix} h |v_1|^{h-1} & \cdots & h |v_k|^{h-1} \end{bmatrix} = h \operatorname{diag} |v|^{h-1}$$

and

$$\frac{\partial \Phi_p(v; T_c)}{\partial v} = \operatorname{diag}\begin{bmatrix} \frac{d\Phi_p(v_1; T_c)}{dv_1} & \cdots & \frac{d\Phi_p(v_k; T_c))}{dv_k} \end{bmatrix},$$

respectively.

Remark 2.6. It is important to note that if $k = 1$, all the extensions reduce to the scalar case considered by Definition 2.5, Remark 2.3 and Definition 2.6.

From the Definition 2.6 of the stabilizing function, the following Lemma presents a dynamical system with the predefined-time stability property.

Lemma 2.1. (Sánchez-Torres et al., 2014; Sánchez-Torres et al., 2015) The origin of the system

$$\dot{x} = -\Phi_r(x; T_c) \tag{6}$$

with $T_c > 0$, and $0 < r < 1$ is predefined-time stable with $T_f = T_c$. That is, $x(t) = 0$ for $t > T_c$ in spite of the $x(0)$ value.

2.2 Motivation

Consider the following second order system:

$$\begin{aligned}\dot{x}_1 &= x_2\\ \dot{x}_2 &= -\alpha \text{sign}\left(x_2 + \beta \lfloor x \rceil^{\frac{1}{2}}\right)\end{aligned} \tag{7}$$

where $x_1, x_2, u \in \mathbb{R}$ and $\alpha, \beta > 0$. The initial conditions of this system are $x_1(0) = x_{1,0}$ and $x_2(0) = x_{2,0}$.

Let the variable $\sigma = x_2 + \lfloor x \rceil^{\frac{1}{2}}$ and its time derivative given by

$$\dot{\sigma} = -\alpha \text{sign}(\sigma) + \frac{1}{2}\beta x_2 |x_1|^{-\frac{1}{2}}. \tag{8}$$

For $\alpha > \beta/2$ a sliding motion on the manifold $\sigma = 0$ is obtained in finite time. This can verified by evaluating the dynamics of (8) when the sliding motion starts. Once the manifold $\sigma = 0$ is reached, the dynamics of (7) reduces to

$$\dot{x}_1 = -\beta \lfloor x \rceil^{\frac{1}{2}} \tag{9}$$

that is finite-time stable. Therefore, there is a time $T = T(x_{1,0}, x_{2,0})$ such that $\sigma = 0$ and $x_1 = 0$ for every time $t \geq T$, which implies that $x_2 = 0$ for $t \geq T$.

Remark 2.7. The exposed procedure is the main idea behind of the terminal sliding mode controllers (Venkataraman and Gulati, 1992) since the motion on $\sigma = 0$ is also finite time stable and, the nested high-order sliding mode controllers (Levant, 2003) since x_1 and its derivative x_2 are driven to zero in finite time and the system has a nested structure.

3. PREDEFINED-TIME STABLE NON-SINGULAR MANIFOLDS

Similarly to the nested approach presented given in (7)-(8), in order to obtain a similar second order system but with predefined-time stability, consider the double integrator system

$$\begin{aligned}\dot{x}_1 &= x_2\\ \dot{x}_2 &= u\end{aligned} \tag{10}$$

where $x_1, x_2, u \in \mathbb{R}$.

As first attempt, from (4), the variable

$$\sigma = x_2 + \frac{1}{T_{c_1} p} \exp(|x_1|^p) \lfloor x \rceil^{1-p}. \tag{11}$$

with $T_{c_1} > 0$ can be used. However, note that the dynamics of (11) is given by

$$\dot{\sigma} = u + \frac{\exp\left(|x_1|^p\right)}{T_{c_1} p}\left[p + (1-p)\frac{1}{|x_1|^p}\right] x_2 \tag{12}$$

which has a singularity at $x_1 = 0$. Therefore, the variable σ in (11) is called a singular sliding variable.

Considering that drawback, it is desirable a variable which provides the same dynamics in $\sigma = 0$ than these presented in (11), but avoiding the singularity thus (12) exposes. With this aim, let the following variables:

$$\begin{aligned}\sigma_1 &= x_1\\ \sigma_2 &= (1-p)\lfloor x_2 \rceil^{\frac{1}{1-p}} + (1-p)\lfloor \Phi_p(x_1; T_{c_1}) \rceil^{\frac{1}{1-p}},\end{aligned} \tag{13}$$

where $\lfloor \Phi_p(x_1; T_{c_1}) \rceil^{\frac{1}{1-p}} = \left[\frac{1}{T_c p}\right]^{\frac{1}{1-p}} \exp\left(\frac{1}{1-p}|x_1|^p\right) \lfloor x_1 \rceil$ with $0 < p < \frac{1}{2}$.

Hence, the system (10) can be written as

$$\begin{aligned}\dot{\sigma}_1 &= -\left[\lfloor \Phi_p(\sigma_1; T_{c_1}) \rceil^{\frac{1}{1-p}} - \frac{1}{1-p}\sigma_2\right]^{1-p}\\ \dot{\sigma}_2 &= |x_2|^{\frac{p}{1-p}} u + \psi(\sigma_1) \lfloor x_2 \rceil,\end{aligned}$$

where $\psi(\sigma_1) = \left[\frac{1}{T_{c_1} p}\right]^{\frac{1}{1-p}} \exp\left(\frac{1}{1-p}|\sigma_1|^p\right)\left[p|\sigma_1|^p + (1-p)\right]$.

Remark 3.1. The variable σ_2 in (13) is based on the approach proposed in Feng et al. (2002). However, here it is not necessary to define fractional powers in terms of odd integers.

With $u = -|x_2|^{\frac{p}{p-1}}\left[\Phi_r(\sigma_2; T_{c_2}) + \psi(x_1)\lfloor x_2 \rceil\right]$, $T_{c_2} > 0$ and $0 < r < 1$, it yields

$$\begin{aligned}\dot{\sigma}_1 &= -\left[\lfloor \Phi_p(\sigma_1; T_{c_1}) \rceil^{\frac{1}{1-p}} - \frac{1}{1-p}\sigma_2\right]^{1-p}\\ \dot{\sigma}_2 &= -\Phi_r(\sigma_2; T_{c_2}).\end{aligned} \tag{14}$$

The stability analysis of the system (14) is an direct application of Lemma 2.1. For $t > T_{c_2}$, $\sigma_2 = 0$ and the system reduces to $\dot{\sigma}_1 = -\Phi_p(\sigma_1; T_{c_1})$. Then, for $t > T_{c_1} + T_{c_2}$, $(\sigma_1, \sigma_2) = (0, 0)$. Consequently, from (13), $(x_1, x_2) = (0, 0)$ for $t > T_{c_1} + T_{c_2}$.

Remark 3.2. From (14), it can be noted x_2 cannot be zero before $\sigma_2 = 0$. Besides, once $\sigma_2 = 0$, the control signal becomes

$$u_{\sigma_2 = 0} = -|x_2|^{\frac{p}{p-1}} \psi(x_1) \lfloor x_2 \rceil = -\psi(x_1) \lfloor x_2 \rceil^{\frac{2p-1}{p-1}},$$

which is continuous since $0 < p < \frac{1}{2}$. In addition, it can be observed that the term $|x_2|^{\frac{p}{p-1}}$ in the controller vanishes in predefined time T_{c_2}, avoiding a singularity at $x_2 = 0$.

4. PREDEFINED-TIME TRACKING CONTROLLER OF A CLASS OF MECHANICAL SYSTEMS

4.1 Problem Statement

A generic model of second-order, fully actuated mechanical systems of n degrees of freedom has the form

$$M(q)\ddot{q} + C(q, \dot{q})\dot{q} + P(\dot{q}) + \gamma(q) = \tau, \tag{15}$$

where $q, \dot{q}, \ddot{q} \in \mathbb{R}^n$ are the position, velocity and acceleration vectors in joint space; $M(q) \in \mathbb{R}^{n \times n}$ is the inertia matrix, $C(q, \dot{q}) \in \mathbb{R}^{n \times n}$ is the Coriolis and centrifugal effects matrix, $P(\dot{q}) \in \mathbb{R}^n$ is the damping effects vector, usually from viscous and/or Coulomb friction and $\gamma(q) \in \mathbb{R}^n$ is the gravity effects vector.

Defining the variables $x_1 = q$, $x_2 = \dot{q}$ and $u = \tau$, the mechanical model (15) can be rewritten in the following state-space form

$$\begin{aligned}\dot{x}_1 &= x_2\\ \dot{x}_2 &= f(x_1, x_2) + B(x_1, x_2)u,\end{aligned} \tag{16}$$

where $f(x_1, x_2) = -M^{-1}(x_1)\left[C(x_1, x_2)x_2 + P(x_2) + \gamma(x_1)\right]$, $B(x_1, x_2) = M^{-1}(x_1)$ are continuous maps and the initial conditions are $x_1(0) = x_{1,0}$, $x_2(0) = x_{2,0}$.

Remark 4.1. The matrix function $M(x_1)$ is, in fact, invertible since $M(x_1) = M^T(x_1)$ is positive definite.

A common problem in mechanical systems control is to track a desired time-dependent trajectory described by the triplet $(q_d(t), \dot{q}_d(t), \ddot{q}_d(t))$ of desired position

$q_d(t) = [q_{d_1}(t) \ \cdots \ q_{d_n}(t)]^T \in \mathbb{R}^n$, velocity $\dot{q}_d(t) = [\dot{q}_{d_1}(t) \ \cdots \ \dot{q}_{d_n}(t)]^T \in \mathbb{R}^n$ and acceleration $\ddot{q}_d(t) = [\ddot{q}_{d_1}(t) \ \cdots \ \ddot{q}_{d_n}(t)]^T \in \mathbb{R}^n$, which are all assumed to be known.

To be consequent with the state space notation, the desired position and velocity vectors are redefined as $x_{1,d} = q_d$ and $x_{2,d} = \dot{q}_d = \dot{x}_{1,d}$, respectively. Then, defining the error variables as $e_1 = x_1 - x_{1,d}$ (position error) and $e_2 = x_2 - x_{2,d}$ (velocity error), the error dynamics are:

$$\begin{aligned} \dot{e}_1 &= e_2 \\ \dot{e}_2 &= f(x_1, x_2) + B(x_1, x_2)u - \ddot{x}_{1,d}, \end{aligned} \tag{17}$$

with initial conditions $e_1(0) = e_{1,0} = x_{1,0} - x_{1,d}(0)$, $e_2(0) = e_{2,0} = x_{2,0} - x_{2,d}(0)$.

The task is to design a state-feedback, second-order, predefined-time controller to track the desired trajectory. In other words, the error variables e_1 and e_2 are to be stabilized in predefined time with available measurements of x_1, x_2, $x_{1,d}$, $x_{2,d} = \dot{x}_{1,d}$ and $\ddot{x}_{1,d}$.

4.2 Controller Design

With basis on Definition 2.7, consider the non-singular transformation

$$\begin{aligned} s_1 &= e_1 \\ s_2 &= (1-p)\lfloor e_2 \rceil^{\frac{1}{1-p}} + (1-p)\lfloor \Phi_p(e_1; T_{c_1}) \rceil^{\frac{1}{1-p}}, \end{aligned} \tag{18}$$

with $0 < p < \frac{1}{2}$.

From (17), the dynamics of the system in the new coordinates (s_1, s_2) can be written as

$$\begin{aligned} \dot{s}_1 &= -\left[\lfloor \Phi_p(s_1; T_{c_1}) \rceil^{\frac{1}{1-p}} - \frac{1}{1-p} s_2 \right]^{1-p} \\ \dot{s}_2 &= \operatorname{diag} |e_2|^{\frac{p}{1-p}} \left[f(x_1, x_2) + B(x_1, x_2)u - \ddot{x}_{1,d} \right] + \Psi(s_1) e_2, \end{aligned} \tag{19}$$

where $\Psi(s_1) = \operatorname{diag} |\Phi_p(s_1; T_{c_1})|^{\frac{p}{1-p}} \frac{\partial \Phi_p(s_1; T_{c_1})}{\partial s_1}$.

Hence, for the system (19) the following controller is proposed:

$$\begin{aligned} u = -B^{-1}(x_1, x_2) \Big[& f(x_1, x_2) - \ddot{x}_{1,d} + \\ & \operatorname{diag} |e_2|^{\frac{p}{p-1}} \left[\Psi(s_1) e_2 + \Phi_r(s_2; T_{c_2}) \right] \Big], \end{aligned} \tag{20}$$

with $0 < r < 1$ and $T_{c_2} > 0$.

Thus, the system (19) closed-loop with the controller (20) has the form

$$\begin{aligned} \dot{s}_1 &= -\left[\lfloor \Phi_p(s_1; T_{c_1}) \rceil^{\frac{1}{1-p}} - \frac{1}{1-p} s_2 \right]^{1-p} \\ \dot{s}_2 &= -\Phi_r(\sigma_2; T_{c_2}). \end{aligned} \tag{21}$$

Taking into account the structure of the system (21), the following theorem states the tracking of the system (15).

Theorem 4.1. For the system (15), $q = q_d$ and $\dot{q} = \dot{q}_d$ for $t > T_{c_1} + T_{c_2}$.

Proof. The proof is similar to the stability analysis carried out in Section 3 and, hence, is omitted. ■

5. EXAMPLE: TRAJECTORY TRACKING FOR A TWO-LINK MANIPULATOR

Consider a planar, two-link manipulator with revolute joints as the one exposed in Utkin et al. (2009) (see Fig. 1). The manipulator link lengths are L_1 and L_2, the link masses (concentrated in the end of each link) are M_1 and M_2. The manipulator is operated in the plane, such that the gravity acts along the z–axis.

Examining the geometry, it can be seen that the end-effector (the end of the second link, where the mass M_2 is concentrated) position (x_w, y_w) is given by

$$\begin{aligned} x_w &= L_1 \cos(q_1) + L_2 \cos(q_1 + q_2) \\ y_w &= L_1 \sin(q_1) + L_2 \sin(q_1 + q_2), \end{aligned}$$

where q_1 and q_2 are the joint positions (angular positions).

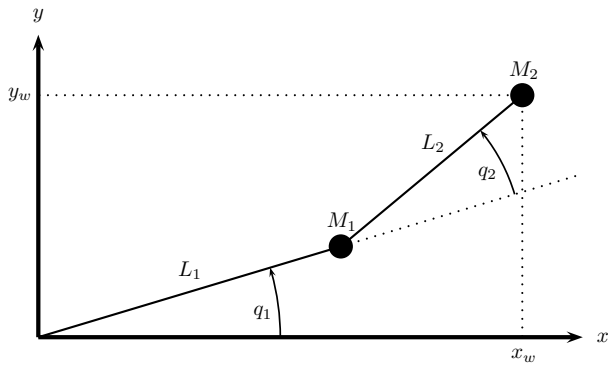

Figure 1. Two-link manipulator.

Applying the Euler-Lagrange equations, a model according to (15) is obtained, with

$$\begin{aligned} m_{11} &= L_1^2(M_1 + M_2) + 2(L_2^2 M_2 + L_1 L_1 M_2 \cos q_2) - L_2^2 M_2 \\ m_{12} &= m_{21} = L_2^2 M_2 + L_1 L_1 M_2 \cos q_2 \\ m_{22} &= L_2^2 M_2 \\ h &= L_1 L_2 M_2 \sin q_2 \\ c_{11} &= -h\dot{q}_2 \\ c_{12} &= -h(\dot{q}_1 + \dot{q}_2) \\ c_{21} &= h\dot{q}_1 \\ c_{22} &= 0, \end{aligned}$$

$$M(q) = \begin{bmatrix} m_{11} & m_{12} \\ m_{21} & m_{22} \end{bmatrix}, \quad C(q, \dot{q}) = \begin{bmatrix} c_{11} & c_{12} \\ c_{21} & c_{22} \end{bmatrix}$$

$$P(\dot{q}) = \begin{bmatrix} 0 \\ 0 \end{bmatrix}, \quad \gamma(q) = \begin{bmatrix} 0 \\ 0 \end{bmatrix}.$$

The absence of gravity term is because the manipulator is operated in the plane, perpendicular to gravity. Note also that friction terms are neglected.

For this example, the end-effector of the manipulator is required to follow a circular trajectory of radius r_d and center in the origin. To solve this problem the controller exposed in Section 4 is applied.

6. SIMULATION RESULTS

The simulation results of the example in Section 5 are presented in this section. The two-link manipulator parameters used are shown in Table 1.

The simulations were conducted using the Euler integration method, with a fundamental step size of 1×10^{-4} s. The initial conditions for the two-link manipulator were selected as: $x_1(0) = \begin{bmatrix} -\frac{3\pi}{4} & -\frac{\pi}{4} \end{bmatrix}^T$ and $x_2(0) = \begin{bmatrix} 0 & 0 \end{bmatrix}^T$. In addition, the controller gains were adjusted to: $T_{c_1} = 1$, $T_{c_2} = 0.5$, $p_1 = \frac{1}{3}$ and $p_2 = \frac{1}{2}$.

The desired circular trajectory in the joint coordinates is described by the equations $q_d(t) = x_{1,d}(t) = \begin{bmatrix} q_{d_1}(t) & q_{d_2}(t) \end{bmatrix} = \begin{bmatrix} \frac{\pi}{2}t - \pi & -\frac{\pi}{2} \end{bmatrix}$ and it corresponds to a circumference of radius 0.2828 m.

The following figures show the behavior of the proposed controller.

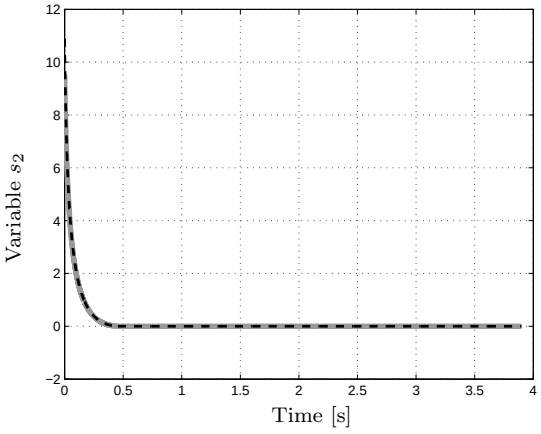

Figure 2. Variable s_2. First component (gray and solid) and second component (black and dashed). Note that $s_2(t) = 0$ for $t > T_{c_2} = 0.5$ s.

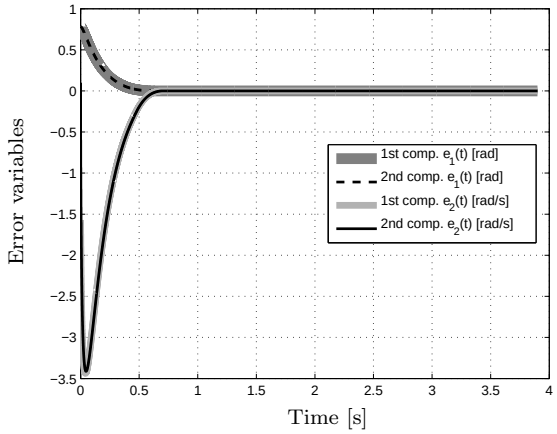

Figure 3. Error variables. First component of e_1 (dark gray and thick), second component of e_1 (black and dashed), first component of e_2 (light gray and solid) and second component of e_2 (black and solid).

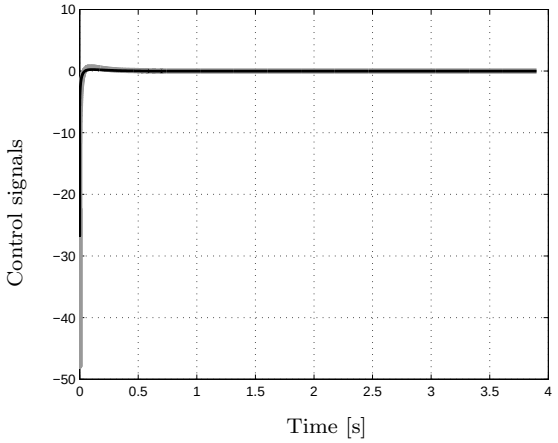

Figure 4. Control signal. First component (gray and solid) and second component (black and solid).

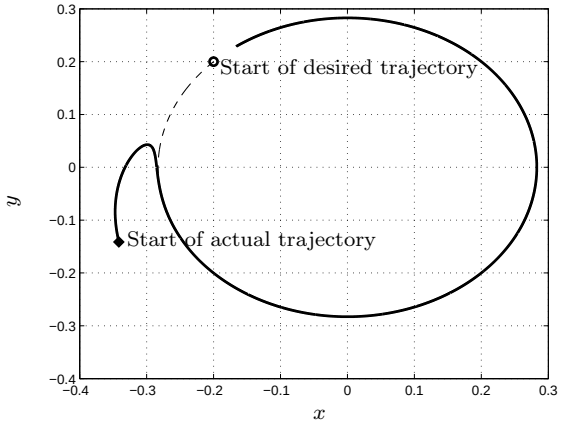

Figure 5. Actual trajectory (x_w, y_w) (black and solid) and desired trajectory $(x_{w,d}, y_{w,d})$ (black and dashed).

Note that $\sigma_2(t) = 0$ for $t \geq 0.47$ s $< T_{c_2} = 0.5$ s (Fig. 2). Once the error variables slide over the manifold $\sigma_2 = 0$, this motion is governed by the reduced order system

$$\dot{e}_1 = e_2 = -\Phi_{p_1}(e_1; T_{c_1}).$$

This imply that the error variables are exactly zero for $t > T_{c_1} + T_{c_2} = 1.5$ s. In fact, from Fig. 3, it can be seen that $e_1(t) = e_2(t) = 0$ for $t \geq 0.74$ s $< T_{c_1} + T_{c_2} = 1.5$ s. Fig. 4 shows the control signal (torque) versus time. Finally, from Fig. 5, it can be seen the reference tracking in rectangular coordinates.

Table 1. Parameters of the two-link manipulator model.

Parameter	Values	Unit
M_1	0.2	kg
M_2	0.2	kg
L_1	0.2	m
L_2	0.2	m

7. CONCLUSION

In this paper a class of non-singular manifolds with predefined-time stability was introduced. As a result, the trajectories of a given dynamical system constrained to this class of manifolds have predefined-time stability to the origin and, in addition, the function that defines the manifold and its derivative along the system trajectories are continuous, therefore no singularities are presented for the system evolution once the constrained motion starts. Besides, the problem of reaching the proposed manifold was solved by means of a continuous predefined-time stable controller.

The proposal was applied to the predefined-time exact tracking of fully actuated and unperturbed mechanical systems as an example, assuming the availability of the state and the desired trajectory as well as its two first derivatives. Furthermore, the resulting controller is applied over a two-link planar manipulator and numerical simulations are conducted to show its performance.

ACKNOWLEDGMENT

Esteban Jiménez acknowledges to CONACyT, México for the MSc scholarship number 426598.

REFERENCES

Andrieu, V., Praly, L., and Astolfi, A. (2008). Homogeneous approximation, recursive observer design, and output feedback. *SIAM Journal on Control and Optimization*, 47(4), 1814–1850.

Bhat, S. and Bernstein, D. (2000). Finite-time stability of continuous autonomous systems. *SIAM Journal on Control and Optimization*, 38(3), 751–766.

Cruz-Zavala, E., Moreno, J.A., and Fridman, L.M. (2011). Uniform robust exact differentiator. *IEEE Transactions on Automatic Control*, 56(11), 2727–2733.

Cruz-Zavala, E., Moreno, J., and Fridman, L. (2010). Uniform second-order sliding mode observer for mechanical systems. In *Variable Structure Systems (VSS), 2010 11th International Workshop on*, 14 –19.

Feng, Y., Yu, X., and Man, Z. (2002). Non-singular terminal sliding mode control of rigid manipulators. *Automatica*, 38(12), 2159 – 2167.

Fraguela, L., Angulo, M., Moreno, J., and Fridman, L. (2012). Design of a prescribed convergence time uniform robust exact observer in the presence of measurement noise. In *Decision and Control (CDC), 2012 IEEE 51st Annual Conference on*, 6615–6620.

Haimo, V. (1986). Finite time controllers. *SIAM Journal on Control and Optimization*, 24(4), 760–770.

Jiménez-Rodríguez, E., Sánchez-Torres, J.D., Gómez-Gutiérrez, D., and Loukianov, A.G. (2016). Predefined-time tracking of a class of mechanical systems. In *13th International Conference on Electrical Engineering, Computing Science and Automatic Control (CCE), 2016*.

Levant, A. (2003). Higher-order sliding modes, differentiation and output-feedback control. *International Journal of Control*, 76(9-10), 924–941.

Michel, A. and Porter, D. (1972). Practical stability and finite-time stability of discontinuous systems. *IEEE Transactions on Circuit Theory*, 19(2), 123–129.

Moulay, E. and Perruquetti, W. (2005). Lyapunov-based approach for finite time stability and stabilization. In *Proceedings of the 44th IEEE Conference on Decision and Control, and the European Control Conference, CDC-ECC '05*, 4742–4747. doi: 10.1109/CDC.2005.1582911.

Moulay, E. and Perruquetti, W. (2006). Finite-time stability and stabilization: State of the art. In C. Edwards, E. Fossas Colet, and L. Fridman (eds.), *Advances in Variable Structure and Sliding Mode Control*, volume 334 of *Lecture Notes in Control and Information Science*, 23–41. Springer Berlin Heidelberg.

Polyakov, A. (2012). Nonlinear feedback design for fixed-time stabilization of linear control systems. *IEEE Transactions on Automatic Control*, 57(8), 2106–2110.

Polyakov, A. and Fridman, L. (2014). Stability notions and Lyapunov functions for sliding mode control systems. *Journal of the Franklin Institute*, 351(4), 1831 – 1865. Special Issue on 2010-2012 Advances in Variable Structure Systems and Sliding Mode Algorithms.

Roxin, E. (1966). On finite stability in control systems. *Rendiconti del Circolo Matematico di Palermo*, 15(3), 273–282.

Sánchez-Torres, J.D., Sanchez, E.N., and Loukianov, A.G. (2015). Predefined-time stability of dynamical systems with sliding modes. In *American Control Conference (ACC), 2015*, 5842–5846.

Sánchez-Torres, J.D., Sánchez, E.N., and Loukianov, A.G. (2014). A discontinuous recurrent neural network with predefined time convergence for solution of linear programming. In *IEEE Symposium on Swarm Intelligence (SIS)*, 9–12.

Utkin, V.I. (1992). *Sliding Modes in Control and Optimization*. Springer Verlag.

Utkin, V.I., Guldner, J., and Shi, J. (2009). *Sliding Mode Control in Electro-Mechanical Systems, Second Edition (Automation and Control Engineering)*. CRC Press, 2 edition.

Venkataraman, S.T. and Gulati, S. (1992). Control of nonlinear systems using terminal sliding modes. In *American Control Conference, 1992*, 891–893.

Weiss, L. and Infante, E. (1967). Finite time stability under perturbing forces and on product spaces. *IEEE Transactions on Automatic Control*, 12(1), 54–59.

Parameter-Dependent Filter with Finite Time Boundedness Property for Continuous-Time LPV Systems ⋆

Hugo T. M. Kussaba * **Renato A. Borges** * **João Y. Ishihara** *,**

* *Department of Electrical Engineering, University of Brasília – UnB, 70910-900, Brasília, DF, Brazil (e-mail: kussaba@lara.unb.br,{raborges,ishihara}@ene.unb.br).*
** *Department of Electrical Engineering, University of California, Los Angeles (UCLA) – 90095, California, LA, United States of America*

AbstractIn this paper the problem of stable estimation for linear parameter varying (LPV) systems in finite-time setting is considered. In order to bound the states and the estimation errors, a parameter-dependent filter is proposed. Under the assumption that the parameters variation are sufficiently small, the filter existence and synthesis is characterized by linear matrix inequalities (LMI) conditions. A numerical example is provided to illustrate the proposed technique.

Keywords: Filter design, Disturbance signals, Uncertain linear systems, Linear parameter varying systems, Finite time stability, Finite time boundedness, Linear matrix inequality.

1. INTRODUCTION

Considering the challenges posed by the constant technological development, there is no doubt that the improvement of filtering techniques is of considerable importance. The use of dynamic filters to remove unwanted signal characteristics or to estimate system information from corrupted measurements is increasing within engineering. In many practical applications, this means suppressing interfering signals and reducing the effect of external noise in communication systems, electronic devices, industrial plants, among others. In fact, filter performance has been investigated under several scenarios like nonlinearities, delays, and parameter uncertainties. However, one can note that most works in the literature consider system performance only after the system had run a large amount of time, that is, filters and controllers are designed to achieve their goal only asymptotically. This is a strong theoretical limitation since for many practical applications it is important that the overall system achieves a desired state in a specified finite time. In order to fill this gap, many infinite time concepts like stability and controllability have been extended for finite time setting. In particular, a similar notion of ultimately bounded system Khalil (2002) in the finite time setting is the notion of Finite Time Stability, and in the presence of disturbances, the notion of Finite Time Boundedness (Amato et al., 2001).

The notion of Finite Time Boundedness states that the time-varying linear system

$$\dot{x}(t) = A(t)x(t) + G(t)w(t),\ \forall t \in [0,\ T] \tag{1}$$

subject to a disturbance w in a pre-specified class $\mathscr{W}$ is Finite Time Bounded (also abbreviated as FTB) with respect to $(c_1, c_2, T, R, \mathscr{W})$, with $c_2 > c_1$ and $R > 0$, if

$$x'(0)Rx(0) \leq c_1 \Rightarrow x'(t)Rx(t) \leq c_2,\ \forall t \in [0,\ T], \forall w \in \mathscr{W}.$$

In the particular case that the pre-specified class $\mathscr{W}$ is empty or $G = \mathbf{0}$, the system is said to be Finite Time Stable (FTS). Still in Amato et al. (2001), sufficient conditions for (1) being FTB are also derived in the form of a linear matrix inequality (LMI) feasibility problem. Those conditions are used for the synthesis of a state feedback controller which assures that the closed loop system is FTB. Further works in the area propose variations of the FTB definition, or of the structures of the controllers and the plant, or of the classes $\mathscr{W}$ of disturbances.

In this paper is considered a more general situation which the designer has to face an uncertain ambient—besides disturbances, the system itself has its parameters not known exactly. More specifically, it is supposed that the system is a continuous-time linear parameter varying (LPV) system. This setting is interesting because many general nonlinear systems can be converted into a LPV form (Toth, 2010). The examples range from flight and automative systems (Ganguli et al., 2002; Baslamisli et al., 2009) to anesthesia delivery (Lin et al., 2008) and diabetes control (Peña and Ghersin, 2010).

Considering the filter design problem, the goal is to guarantee that the estimation error is FTB with respect to $(c_1, c_2, T, R, \mathscr{W})$, as done in Luan et al. (2010) for stochastic systems; He and Liu (2011) for time-delay jump systems and Liu et al. (2012) for singular stochastic systems. In all these cases, the filters are designed using LMI conditions to ensure the FTB property. In principle, a very strong necessary and sufficient FTB filter design conditions could be developed based on the differential linear matrix inequality (DLMI) characterization (Amato et al., 2003, 2005, 2014) for FTB. However, this development has two drawbacks. First, it is important to salient that the DLMI approach for filtering is not trivial since the filter structure demands an analysis with an input signal, a much more challenging case than that considered by Amato et al. (2003). And second, it is noted that DLMI problems are generally computationally very expensive and in most situations even prohibitive.

⋆ Supported by the Brazilian agencies CAPES and CNPq

Therefore, it is interesting the search for solutions that uses less computational effort than the DLMIs. Thus, in this paper we aim achieving this goal by using only the LMI framework.

Under the assumption that the parameters of the plant are sufficiently slow time-varying, a new synthesis condition for a homogeneous polynomially parameter-dependent FTB filter for continuous-time LPV systems is derived in this paper. Those systems are an indexed collection of linear systems in which the indexing parameter is independent of the state (Shamma, 2012). Depending on the scenario, this indexing parameter can be seen as a parametric uncertainty of the model or a measurable parameter possibly read in real time, which can be used in the design of a controller or a filter that accounts for all possible variations of this parameter. Furthermore, the proposed approach also considers that for a particular case where the LMIs depend on a parameter α in the unit simplex, homogeneous polynomial structures can be used in the search for less conservative sets of design conditions, as done in Oliveira and Peres (2007).

This paper is organized as follows. Detailing of the problem and auxiliary lemmas are presented in Section 2. The main theorem, where LMI conditions are derived for the synthesis of a filter that solves the FTB problem for LPV systems, is proved in Section 3. A numerical example is given in Section 4 to illustrate the application of the technique. Finally, the conclusion is presented in Section 5.

In the sequel the following notation will be used: The symbol $(')$ indicates the transpose of a matrix; $P > 0$ means that P is symmetric positive definite. $\mathbb{R}$ represents the set of real numbers, $\mathbb{Z}_+ = \{0,1,2,\ldots\}$ the set of nonnegative integers. card $(\cdot)$ denotes the cardinality of a set. $\lambda_{max}(\cdot)$ and $\lambda_{min}(\cdot)$ indicate, respectively, the maximum and the minimum eigenvalue of the argument. The term $(\star)$ indicates symmetric terms in the LMIs and $\mathbf{I}$ and $\mathbf{0}$ are the identity and the zero matrices of suitable dimensions.

2. PROBLEM STATEMENT AND PRELIMINARY RESULTS

Consider a LPV system with $t \in [0,\ T]$ and

$$\begin{aligned} \dot{x}(t) &= A(\alpha(t))x(t) + B(\alpha(t))w(t), \\ y(t) &= C_y(\alpha(t))x(t) + D(\alpha(t))w(t), \\ z(t) &= C_z(\alpha(t))x(t), \end{aligned} \tag{2}$$

where $x(t) \in \mathbb{R}^n$ is the state space vector, $y(t) \in \mathbb{R}^q$ is the measured output, $z(t) \in \mathbb{R}^p$ is the signal to be estimated and $w(t) \in \mathbb{R}^r$ is the noise input with bounded L_2 norm. The parameter $\alpha(t)$ is assumed to be available online and is continuous with respect to its time dependence—which, to lighten the notation, will be omitted wherever there is no ambiguity.

All matrices are real, with appropriate dimensions and belongs to the polytope $\mathscr{P}$

$$\left[\begin{array}{c|c} A(\alpha) & B(\alpha) \\ \hline C_y(\alpha) & D(\alpha) \\ \hline C_z(\alpha) & - \end{array}\right] = \sum_{i=1}^{N} \alpha_i \left[\begin{array}{c|c} A_i & B_i \\ \hline C_{yi} & D_i \\ \hline C_{zi} & - \end{array}\right]. \tag{3}$$

For all $t \in [0,\ T]$, the system matrices are given by the convex combination of the known vertices of the polytope $\mathscr{P}$.

The vector of time-varying parameters $\alpha \in \mathbb{R}^N$ belongs for all $t \in [0,\ T]$ to the unit N-simplex Δ_N, that is:

$$\Delta_N = \left\{ \theta \in \mathbb{R}^N : \sum_{i=0}^{N} \theta_i = 1,\ \theta_i \geq 0 \right\}.$$

To account the information given by the parameter α, parameter-dependent matrices are used in the dynamics of a full order proper filter, precisely:

$$\begin{aligned} \dot{x}_f(t) &= A_f(\alpha)x_f(t) + B_f(\alpha)y(t), \\ z_f(t) &= C_f(\alpha)x_f(t), \end{aligned} \tag{4}$$

where $x_f(t) \in \mathbb{R}^n$ is the filter state and $z_f(t) \in \mathbb{R}^p$ the estimated signal. Coupling the filter to the plant, the equations that describe the augmented system dynamics are given by

$$\begin{aligned} \dot{\varsigma}(t) &= \bar{A}(\alpha)\varsigma(t) + \bar{B}(\alpha)w(t), \\ e(t) &= \bar{C}(\alpha)\varsigma(t), \end{aligned} \tag{5}$$

where $\varsigma(t) = [x(t)'\ \ x_f(t)']'$, $e(t) = z(t) - z_f(t)$, and

$$\bar{A}(\alpha) = \begin{bmatrix} A(\alpha) & \mathbf{0} \\ B_f(\alpha)C_y(\alpha) & A_f(\alpha) \end{bmatrix},\ \bar{B}(\alpha) = \begin{bmatrix} B(\alpha) \\ B_f(\alpha)D(\alpha) \end{bmatrix},$$
$$\bar{C}(\alpha) = \begin{bmatrix} C_z(\alpha) & -C_f(\alpha) \end{bmatrix}.$$

It is desirable that both the state of the plant and the error between it and the state of the filter are bounded during a finite time horizon. This motivates Definition 1.

Definition 1. Given three positive scalars c_1, c_2 and T, with $c_2 > c_1$, positive definite matrices $R_p \in \mathbb{R}^{n\times n}$ and $R_e \in \mathbb{R}^{n\times n}$ and the class of signals $\mathscr{W}_d$, the LPV system

$$\dot{\varsigma}(t) = \bar{A}(\alpha)\varsigma(t) + \bar{B}(\alpha)w(t) \tag{6}$$

is FTB with respect to $(c_1, c_2, \mathscr{W}_d, T, R_p, R_e)$, if

$$\begin{bmatrix} x(0) \\ x(0) - x_f(0) \end{bmatrix}' \begin{bmatrix} R_p & \mathbf{0} \\ \mathbf{0} & R_e \end{bmatrix} \begin{bmatrix} x(0) \\ x(0) - x_f(0) \end{bmatrix} \leq c_1$$

implies that

$$\begin{bmatrix} x(t) \\ x(t) - x_f(t) \end{bmatrix}' \begin{bmatrix} R_p & \mathbf{0} \\ \mathbf{0} & R_e \end{bmatrix} \begin{bmatrix} x(t) \\ x(t) - x_f(t) \end{bmatrix} \leq c_2$$

for all $w \in \mathscr{W}_d$ and for all $t \in [0,\ T]$.

Remark 1. It should be noted that the definition of a FTB system presented here is a specialization for LPV systems of the definition presented in Amato et al. (2001) with R chosen as:

$$R = \begin{bmatrix} R_p + R_e & -R_e \\ -R_e & R_e \end{bmatrix}. \tag{7}$$

The matrices R_p and R_e can be seen as weighting matrices that set the importance between bounding the states of the plant and the error between it and the states of the filter. In contrast to a classical scenario in which the Lyapunov stability of $x - x_f$ implies the Lyapunov stability of $z - z_f$ using a Luenberger observer as a filter, constraining the error $x - x_f$ in a region during a finite time does not necessarily imply that $z - z_f$ satisfies the same constraining. In fact, $z - z_f$ can be bounded independently of $x - x_f$, motivating the next definition.

Definition 2. Given a symmetric positive definite matrix Ω, the filter (4) is said to be Ω-bounded in finite time T if its estimation error $e(t)$ satisfies

$$e'(t)e(t) < \varsigma'(t)\Omega^{-1}\varsigma(t),\ \ \forall t \in [0,\ T]. \tag{8}$$

Taking into account the above discussion, the FTB filtering problem to be solved in this work is formally stated as follows.

Problem 1. Assuming that $\alpha \in \Delta_N$ is available online for every $t \in [0,\ T]$ and its variation is sufficiently small, find matrices $A_f(\alpha)$, $B_f(\alpha)$ and $C_f(\alpha)$ in (4), such that the augmented

system (5) is FTB with respect to $(c_1, c_2, \mathscr{W}_d, T, R_p, R_e)$ and the estimation error is Ω-bounded in finite time T.

The subsequent lemma, from Amato et al. (2001) with an extended proof in Borges et al. (2013) considering a wider class of noises, presents a sufficient condition to analyze if a LPV system is FTB and it is used in the solution of Problem 1.

Lemma 1. For a sufficiently slow varying parameter α, system (6) is FTB with respect to $(c_1, c_2, \mathscr{W}_d, T, R_p, R_e)$, if, for all $\alpha \in \Delta_N$, there exist positive definite symmetric matrices $Q_1(\alpha) \in \mathbb{R}^{2n\times 2n}$, $Q_2(\alpha) \in \mathbb{R}^{r\times r}$ and a positive scalar β such that

$$\begin{bmatrix} \bar{A}(\alpha)\tilde{Q}_1(\alpha) + \tilde{Q}_1(\alpha)\bar{A}'(\alpha) - \beta\tilde{Q}_1(\alpha) & \bar{B}(\alpha)Q_2(\alpha) \\ (\star) & -\beta Q_2(\alpha) \end{bmatrix} < \mathbf{0}, \tag{9}$$

$$\frac{c_1}{\lambda_{min}[Q_1(\alpha)]} + \frac{d}{\lambda_{min}[Q_2(\alpha)]} < \frac{c_2 e^{-\beta T}}{\lambda_{max}[Q_1(\alpha)]}, \tag{10}$$

in which $\tilde{Q}_1(\alpha) = R^{-1/2}Q_1(\alpha)R^{-1/2}$, with R given by (7).

3. MAIN RESULTS

The following theorem presents sufficient conditions, in terms of a parameter-dependent LMI, for the synthesis of matrices that solves Problem 1.

Theorem 1. Given a LPV continuous-time system (2), parameters $(c_1, c_2, d, T, R_p, R_e)$ and a fixed scalar parameter β, if, for each $\alpha \in \Delta_N$, there exist symmetric positive definite matrices $K \in \mathbb{R}^{n\times n}$, $W(\alpha) \in \mathbb{R}^{r\times r}$ and $Z(\alpha) \in \mathbb{R}^{n\times n}$; matrices $L(\alpha) \in \mathbb{R}^{n\times q}$, $M(\alpha) \in \mathbb{R}^{n\times n}$ and $F(\alpha) \in \mathbb{R}^{p\times n}$ and positive real scalars μ_1, μ_2 and μ_3, such that

$$\begin{bmatrix} \mathscr{M}_{11}(\alpha) & \mathscr{M}_{12}(\alpha) & KB(\alpha)+L(\alpha)D(\alpha) \\ (\star) & \mathscr{M}_{22}(\alpha) & Z(\alpha)B(\alpha) \\ (\star) & (\star) & -\beta W(\alpha) \end{bmatrix} < \mathbf{0}, \tag{11a}$$

$$\mathscr{M}_{11}(\alpha) = -\beta K - M(\alpha) - M'(\alpha),$$
$$\mathscr{M}_{12}(\alpha) = KA(\alpha) + L(\alpha)C_y(\alpha) + M(\alpha),$$
$$A'(\alpha)Z(\alpha) + Z(\alpha)A(\alpha) - \beta Z(\alpha),$$

$$c_1\mu_1 + d\mu_3 < c_2 e^{-\beta T}\mu_2, \tag{11b}$$
$$W(\alpha) < \mu_3 \mathbf{I}, \tag{11c}$$
$$\mu_2 R_p < Z(\alpha) < \mu_1 R_p, \tag{11d}$$
$$\mu_2 R_e < K < \mu_1 R_e, \tag{11e}$$
$$\begin{bmatrix} K & \mathbf{0} & F'(\alpha) \\ (\star) & Z(\alpha) & C_z'(\alpha) - F'(\alpha) \\ (\star) & (\star) & \mathbf{I} \end{bmatrix} > \mathbf{0}, \tag{11f}$$

then for a sufficiently slow varying parameter α there exists a filter in the form (4), such that the augmented system (5) is FTB with respect to $(c_1, c_2, \mathscr{W}_d, T, R_p, R_e)$ and the filter is also Ω-bounded in finite time T for $\Omega = \Gamma\tilde{Q}_1\Gamma'$, $\Gamma = diag(\mathbf{I}, \Gamma_{22})$, with Γ_{22} non-singular. A realization of the filter is given by the matrices:

$$\begin{aligned} A_f(\alpha) &= -K^{-1}M(\alpha), \\ B_f(\alpha) &= -K^{-1}L(\alpha), \\ C_f(\alpha) &= F(\alpha)\Gamma_{22}^{-1}. \end{aligned} \tag{12}$$

Proof. As presented in Chilali and Gahinet (1996) in the context of pole placement, consider the partitioned matrices

$$\tilde{Q}_1(\alpha) = \begin{bmatrix} X(\alpha) & U'(\alpha) \\ U(\alpha) & \hat{X}(\alpha) \end{bmatrix}, \tilde{Q}_1^{-1}(\alpha) = \begin{bmatrix} Y(\alpha) & V'(\alpha) \\ V(\alpha) & \hat{Y}(\alpha) \end{bmatrix},$$
$$H(\alpha) = \begin{bmatrix} Y(\alpha) & \mathbf{I} \\ V(\alpha) & \mathbf{0} \end{bmatrix},$$

together with the following change of variables

$$M(\alpha) = -KA_f(\alpha)U(\alpha)Z(\alpha), \tag{13a}$$
$$L(\alpha) = -KB_f(\alpha), \tag{13b}$$
$$F(\alpha) = C_f(\alpha)\Gamma_{22}U(\alpha)Z(\alpha), \tag{13c}$$
$$W(\alpha) = Q_2^{-1}(\alpha), \tag{13d}$$

where $X(\alpha)$, $Y(\alpha)$ and $Q_2^{-1}(\alpha)$ are chosen such that

$$Z(\alpha) = X^{-1}(\alpha),$$
$$W(\alpha) = Q_2^{-1}(\alpha),$$
$$K = Y(\alpha) - Z(\alpha).$$

By multiplying the LMI (11a) on the left by $\bar{H}'(\alpha)$ and on the right by $\bar{H}(\alpha)$, and multiplying the result on the left by $\tilde{H}'(\alpha)$ and on the right by $\tilde{H}(\alpha)$, with

$$\bar{H}(\alpha) = \begin{bmatrix} N(\alpha) & \mathbf{0} \\ \star & \mathbf{I} \end{bmatrix}, \tilde{H}(\alpha) = \begin{bmatrix} H^{-1}(\alpha) & \mathbf{0} \\ \star & \mathbf{I} \end{bmatrix},$$
$$N(\alpha) = \begin{bmatrix} \mathbf{I} & \mathbf{0} \\ \mathbf{0} & X(\alpha) \end{bmatrix},$$

the LMI (9) is obtained. Moreover, it is easy to see that LMI (10) is satisfied if the conditions

$$c_1\mu_1 + d\mu_3 < c_2 e^{-\beta T}\mu_2, \tag{14}$$
$$Q_2^{-1}(\alpha) < \mu_3 \mathbf{I}, \tag{15}$$
$$\mu_2 \mathbf{I} < Q_1^{-1}(\alpha) < \mu_1 \mathbf{I}, \tag{16}$$

are guaranteed.

Inequalities (14) and (15) are LMIs (11b) and (11c), respectively. By multiplying inequality (16) on the left and on the right by $R^{1/2}$, with R given by (7), one has

$$\mu_2 R < \tilde{Q}_1^{-1}(\alpha) < \mu_1 R. \tag{17}$$

Knowing that the identity $\tilde{Q}_1(\alpha)\tilde{Q}_1^{-1}(\alpha) = \mathbf{I}$ gives the equations

$$X(\alpha)Y(\alpha) + U'(\alpha)V(\alpha) = \mathbf{I},$$
$$X(\alpha)V'(\alpha) + U'(\alpha)\hat{Y}(\alpha) = \mathbf{0},$$

one has for $U(\alpha) = X(\alpha)$ that

$$V(\alpha) = -K,$$
$$\hat{Y}(\alpha) = K.$$

Consequently, inequality (17) is satisfied if, and only if

$$\mu_2 R < \begin{bmatrix} K + Z(\alpha) & -K \\ -K & K \end{bmatrix} < \mu_1 R. \tag{18}$$

Left-multiplying LMI (18) by G' and right-multiplying by G, with

$$G = \begin{bmatrix} \mathbf{I} & \mathbf{0} \\ \mathbf{I} & \mathbf{I} \end{bmatrix}$$

one can see that inequality (18) is equivalent to LMIs (11d) and (11e). At last, by multiplying LMI (11f) on the left by $\bar{H}'(\alpha)$ and on the right by $\bar{H}(\alpha)$, multiplying the result on the left by $\tilde{J}'(\alpha)$ and on the right by $\tilde{J}(\alpha)$, with

$$\tilde{J}(\alpha) = \begin{bmatrix} J^{-1}(\alpha)\Gamma_{22}^{-1} & \mathbf{0} \\ \mathbf{0} & \mathbf{I} \end{bmatrix}, J(\alpha) = \begin{bmatrix} \mathbf{I} & X(\alpha) \\ \mathbf{0} & X(\alpha) \end{bmatrix}$$

and then applying Schur complement in the resulting matrix, one has

$$e'(t)e(t) < \varsigma'(t)\Omega^{-1}\varsigma(t),$$

which guarantees the constraint in the estimation error.

By the choice of $U(\alpha)$, one has that $U(\alpha)Z(\alpha) = \mathbf{I}$ and that the filter matrices $A_f(\alpha)$, $B_f(\alpha)$ and $C_f(\alpha)$ can be recovered from the change of variables in (13).

Remark 2. It should be remarked that if β is not fixed, the proposed conditions are not longer linear for a fixed α. Actually, they are not even bilinear due to (11b). Aside from that, a binary search for a suitable β can be guided by balancing (11a) and (11b) and should not be a computational burden since β is just a scalar variable.

In the definition of Problem 1, Ω is a design parameter that must be adjusted for a suitable weighting between the size of output estimation error and the size of the filter and plant states. It should be observed that there is no loss of generality to write $\Omega = \Gamma\tilde{Q}_1\Gamma'$ and to consider the parameter Γ as invertible (Ω, Γ, $\tilde{Q}_1$ are invertible). The choice of $\Gamma = \text{diag}(\mathbf{I}, \Gamma_{22})$ allows to directly adjust the matrix C_f with a scale factor given by Γ_{22}. Consequently, the quality of the realization $\{A_f, B_f, C_f\}$ of the filter can be improved without deteriorating the estimate error.

Theorem 1 leads to a LMI feasibility problem that must be satisfied for all parameters $\alpha \in \Delta_N$. Although this is an infinite dimension problem in the parameter α, the fact that it lies in the unit N-simplex can be used to find sufficient LMI conditions written only in terms of the vertices of the polytope (Bliman et al., 2006).

In fact, using the relaxation proposed in Oliveira and Peres (2007) one can write the parameter-dependent LMIs in Theorem 1 as LMIs that are independent of the parameter α. As the level of relaxation increases, it is possible to achieve less conservative sets of conditions and tending to necessary and sufficient conditions.

For this purpose, the next Definition 3 generalizes the linear dependence on the parameter α to a homogeneous polynomial dependence.

Definition 3. A matrix $M(\alpha)$ is homogeneous polynomially parameter-dependent (HPPD) on $\alpha \in \Delta_N$ with degree g if it can be expressed as

$$M(\alpha) = \sum_{k \in \mathscr{S}_g} \alpha_1^{k_1} \alpha_2^{k_2} \cdots \alpha_N^{k_N} M_k, \tag{19}$$

with

$$\mathscr{S}_g = \left\{ k \in \left(\mathbb{Z}_+\right)^N : \sum_{i=1}^{N} k_i = g \right\}.$$

M_k are the matrices coefficients of the monomials of $M(\alpha)$, where

$$\text{card}\left(\mathscr{S}_g\right) = \frac{(N+g-1)!}{g!\,(N-1)!}.$$

The set of HPPD of $\alpha \in \Delta_N$ with degree g matrices is denoted by $\mathbb{H}_{(g)}$ and the subset corresponding to the matrices with order $m \times n$ is denoted by $\mathbb{H}_{(g)}^{m\times n}$.

The relaxation proposed in Oliveira and Peres (2007) can be used in the parameter-dependent LMIs of Theorem 1 by forcing a homogeneous polynomial structure in the LMI variables $L(\alpha)$, $M(\alpha)$ and $F(\alpha)$, turning them into HPPD matrices. The relaxed condition is given by the LMIs stemming from the matrices coefficients of the HPPD matrices, and the LMI variables are the matrix coefficients of the monomials of the HPPD matrices. Whilst this procedure is systematic, it can become very complex as the degree g of the HPPD matrices increases. Nevertheless, the specialized parser ROLMIP [1] can be used to automatically carry this relaxation (Agulhari et al., 2012).

[1] Available for download at `http://www.dt.fee.unicamp.br/~agulhari/rolmip/rolmip.htm`.

It is important to note that for the particular case that $g = 0$, the recuperation of the filter from the LMI variables using (12) is free from the parameter α, and consequently, the assumption that α can be read in real time is no longer required; the filter is robust in the sense that the parameter can be considered uncertain. The reason why is used degrees greater than zero is that a sequence of less conservative LMI relaxations may be obtained in the conditions of Theorem 1 by increasing the degree g, as will be clearer in the next theorems.

Theorem 2. For given $\bar{g}$ and $\bar{\mu}_2$, let $c_2^*(\bar{g})$ be the optimal solution of

$$\begin{aligned} &\min \quad c_2 \\ &\text{such that (11) holds with } g = \bar{g} \text{ and } \mu_2 = \bar{\mu}_2. \end{aligned}$$

Then, $c_2^*(\bar{g}+1) \leq c_2^*(\bar{g})$.

Proof. If there exist scalars μ_1,$\bar{\mu}_2$ and μ_3; matrix $K \in \mathbb{R}^{n\times n}$; and matrices W, Z, L, M, $F \in \mathbb{H}_{(g)}$ such that (11) holds, then μ_1, $\bar{\mu}_2$, μ_3, K and the following matrices

$$\left(\sum_{i=1}^{N}\alpha_i\right)W, \left(\sum_{i=1}^{N}\alpha_i\right)Z, \left(\sum_{i=1}^{N}\alpha_i\right)L, \left(\sum_{i=1}^{N}\alpha_i\right)M, \left(\sum_{i=1}^{N}\alpha_i\right)F,$$

belonging to $\mathbb{H}_{(g+1)}$, are a particular solution to (11), since $\alpha \in \Delta_N$. Hence, the minimization of c_2 subject to (11) for $\bar{g}+1$ produces at least the same optimal value obtained with $\bar{g}$, which implies that $c_2^*(\bar{g}+1) \leq c_2^*(\bar{g})$.

Theorem 3. For given $\bar{g}$, $\bar{\mu}_1$ and $\bar{\mu}_3$, let $c_1^*(\bar{g})$ and $d^*(\bar{g})$ be the optimal solution of problems

$$\begin{aligned} &\max \quad c_1 \\ &\text{such that (11) holds with } g = \bar{g} \text{ and } \mu_1 = \bar{\mu}_1, \end{aligned}$$

$$\begin{aligned} &\max \quad d \\ &\text{such that (11) holds with } g = \bar{g} \text{ and } \mu_3 = \bar{\mu}_3, \end{aligned}$$

respectively. Then $c_1^*(\bar{g}) \leq c_1^*(\bar{g}+1)$ and $d^*(\bar{g}) \leq d(\bar{g}+1)$.

Proof. Similar to Theorem 2.

The optimization problems in Theorem 2 and Theorem 3 can be seen as optimum filtering problems within FTB context. For example, to design a filter which rejects the maximum possible types of disturbances, one may try to maximize d.

The computational complexity of the LMIs is estimated by the number of scalar variables V and the number of LMI scalar rows L. For Theorem (1),

$$V = n(p+q+n)\,\text{card}\left(\mathscr{S}_g\right) + n(n+1) + \frac{q(q+1)}{2} + 3, \tag{20}$$

$$L = (2n+r)\,\text{card}\left(\mathscr{S}_{g+f+1}\right) + (4n+p+r)\,\text{card}\left(\mathscr{S}_{g+f}\right) + n + 1. \tag{21}$$

By increasing the degree g, the number of decision variables is also increased and in consequence, the complexity of the LMIs also raises. However, by using an extension of Pólya's theorem (Oliveira and Peres, 2005, 2007), and based on the fact that the time-varying parameters α belong to the unit N-simplex, the conditions of Theorem (1) may also be improved using a sufficiently large positive integer f with no increase in the number of variables for a given degree g by multiplying the LMIs (11) by the factor $\left(\sum_{i=1}^{N}\alpha_i\right)^f$.

Table 1. Minimum upper bounds of c_2 and maximum lower bounds of c_1 and d for different values of g and f.

Degree g	Index f	c_2	c_1	d
0	0	3.5381	-	0.5027
1	0	3.2441	-	0.5307
1	1	3.1724	0.0042	0.5307
1	2	3.1720	0.0042	0.5307
2	0	3.1511	0.0118	0.5308
2	1	3.0856	0.0164	0.5308
2	2	3.0856	0.0164	0.5308
3	0	3.0856	0.0164	0.5308
3	1	3.0656	0.0175	0.5309

4. NUMERICAL EXAMPLE

The numerical example was performed using the solver SeDuMi (Sturm, 1999) and the parsers YALMIP (Löfberg, 2004) and ROLMIP (Agulhari et al., 2012) within Matlab environment.

Consider the system (2) with matrices in polytope (3) with the following vertices

$$A_1 = \begin{bmatrix} -1.0 & 2.0 \\ -3.0 & -2.0 \end{bmatrix}, A_2 = \begin{bmatrix} -1.0 & 2.0 \\ -3.0 & -1.0 \end{bmatrix},$$
$$A_3 = \begin{bmatrix} -2.0 & 2.0 \\ -3.0 & -2.0 \end{bmatrix}, A_4 = \begin{bmatrix} -2.0 & 2.0 \\ -3.0 & -1.0 \end{bmatrix},$$
$$B_1 = \begin{bmatrix} -0.5 \\ 0.1 \end{bmatrix}, B_2 = \begin{bmatrix} -0.1 \\ 0.1 \end{bmatrix}, B_3 = \begin{bmatrix} -0.5 \\ 0.5 \end{bmatrix}, B_4 = \begin{bmatrix} -0.1 \\ 0.5 \end{bmatrix},$$
$$C_{y1} = [1.0 \ 0.5], C_{y2} = [1.2 \ 0.5],$$
$$C_{y3} = [1.0 \ 0.6], C_{y4} = [1.2 \ 0.6],$$
$$C_{z1} = [0.6 \ 1.0], C_{z2} = [1.0 \ 1.0],$$
$$C_{z3} = [0.6 \ 1.2], C_{z4} = [1.0 \ 1.2],$$
$$D_1 = D_2 = 0.1, D_3 = D_4 = 0.2$$

and the slowly varying parameter

$$\alpha(t) = \left(\tfrac{1}{2}\sin^2(\omega t), \tfrac{1}{2}\sin^2(\omega t), \tfrac{1}{2}\cos^2(\omega t), \tfrac{1}{2}\cos^2(\omega t)\right), \quad (22)$$

with ω sufficiently small. It is easy to check that (22) belongs to Δ_4 for all $t \geq 0$.

Theorems 2 and 3 along with Pólya's relaxation are applied with $\bar{\mu}_1 = 1$, $\bar{\mu}_2 = 1$, $\bar{\mu}_3 = 1$ and $\beta = 0.6$ in order to investigate the effect of increasing g and f in the search of minimum upper bounds of c_2 attained by the conditions of Theorem 2 and also in the search of maximum lower bounds of c_1 and d attained by the conditions of Theorem 3. The chosen FTB parameters for this example are $c_1 = 0.1$, $c_2 = 2$, $d = 1$, $T = 1.5$, $R_e = 4\mathbf{I}$ and $R_p = 4\mathbf{I}$. The results of the optimization problem are summarized in Table 1 (when the parameter is the value being optimized the corresponding value of the parameter should be ignored).

As can be seen in Table 1, the conditions of Theorem 3 are not able to provide a robust filter nor a LPV filter with a $c_1 > 0$. Also, by using degree $g = 3$ and $f = 1$ it was possible to obtain an upper bound to c_2 approximately 13.35% smaller than the robust filter corresponding to $g = 0$ and $f = 0$. Finally, as illustrated by the maximum lower bounds obtained by d, it may happen that the gain obtained increasing g and f is not appreciable. In this case, it would be better use the robust filter corresponding to $g = 0$ if existent.

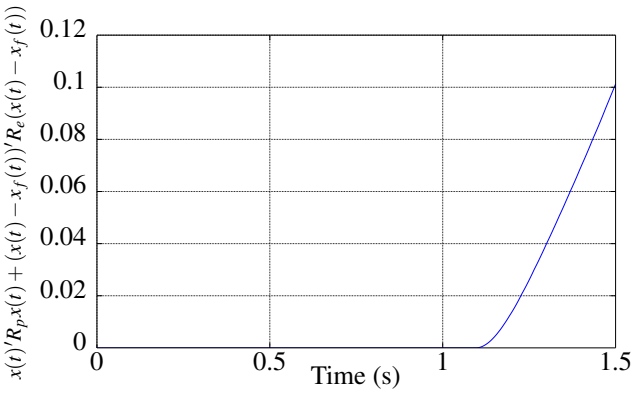

Figure 1. Sum of the weighted quadratic norm of the states of the plant and observation error.

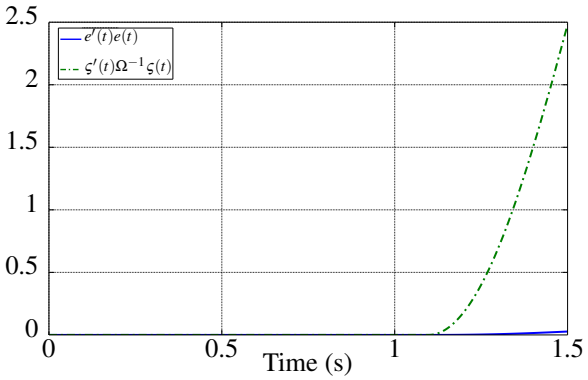

Figure 2. Time simulation comparing the norm of the error with the bound imposed by Ω.

Consider now system (2) with the varying parameter (22) with $\omega = 0.001$. We wish to check if the FTB filter obtained by Theorem 2 with $\bar{\mu}_2 = 1$, $g = 3$ and $f = 1$ satisfies the FTB condition with respect to $(0.1, 3.06, \mathscr{W}_1, 1.5, 4\mathbf{I}, 4\mathbf{I})$ and the Ω-bound condition defined in (8) considering a disturbance given by the step function

$$w(t) = \begin{cases} 0, & \text{if } t \leq 1.1s, \\ 0.9, & \text{if } t > 1.1s, \end{cases}$$

which represents the worst type of signal belonging to the class $\mathscr{W}_1$. Since this filter is obtained using the assumption that α is a slowly varying parameter, one must verify if $\dot{\alpha}$ is really sufficiently small by time-domain simulations. Considering zero initial conditions, a time-simulation was performed in the time interval $t \in [0, 1.5s]$.

As shown in Figure 1, the designed filter satisfies the FTB condition and

$$\max_{t\in[0,1.5s]} \left\{ \begin{bmatrix} x(t) \\ x(t) - x_f(t) \end{bmatrix}' \begin{bmatrix} R_p & \mathbf{0} \\ \mathbf{0} & R_e \end{bmatrix} \begin{bmatrix} x(t) \\ x(t) - x_f(t) \end{bmatrix} \right\} = 0.06,$$

which is approximately 2% of the value of $c_2 = 3.0653$. Moreover, as can be seen in Figure 2, the estimation error of the filter also satisfies the Ω-bound condition defined in (8). The tracking error is shown in Figure 3. Although the choice of Γ_{22} did not nullify the error between z and z_f, it ensured a maximum error of 0.0764. The difficulty of having a null estimation error in a finite time horizon is due to the small time that the filter has to dynamically estimate the output z.

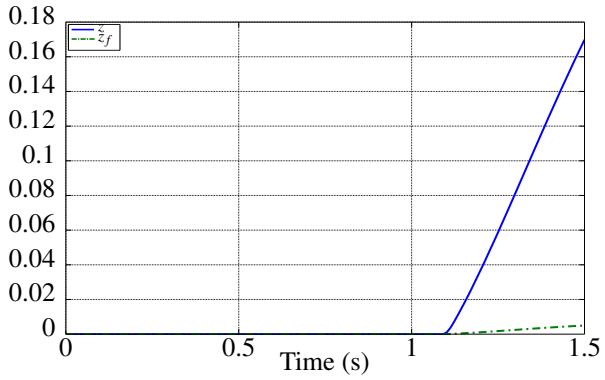

Figure 3. Time simulation of the outputs z and z_f.

5. CONCLUSION

This paper considers the problem of filter design for LPV continuous-time systems. The filter was obtained under the assumption that the parameter of the LPV system is sufficiently slow time-varying. If this assumption is satisfied the obtained filter guarantees that the augmented system is bounded during a finite time horizon under the presence of bounded disturbances. The design conditions are represented by a LMI feasibility problem, which can be relaxed via homogeneous polynomials techniques and Pólya's theorem. It was shown that a sequence of less conservative conditions may be obtained by increasing the degree g of the HPPD matrices or increasing the positive integer f based on Pólya's theorem. To handle the algebraic manipulation involved in the construction of the relaxation of the parameter-dependent LMIs, the specialized parser ROLMIP was used, easing the work.

REFERENCES

Agulhari, C.M., de Oliveira, R.C.L.F., and Peres, P.L.D. (2012). Robust LMI Parser: a computational package to construct LMI conditions for uncertain systems. In *XIX Brazilian Conference on Automation (CBA 2012)*, 2298–2305. Campina Grande, PB, Brazil.

Amato, F., Ariola, M., and Cosentino, C. (2005). Finite-time control of linear time-varying systems via output feedback. In *Proceedings of the 2005 American Control Conference*, 4722–4726. Portland, OR, USA.

Amato, F., Ariola, M., Cosentino, C., Abdallah, C.T., and Dorato, P. (2003). Necessary and sufficient conditions for finite-time stability of linear systems. In *Proceedings of the 2003 American Control Conference*, volume 5, 4452 – 4456.

Amato, F., Ariola, M., and Dorato, P. (2001). Finite-time control of linear systems subject to parametric uncertainties and disturbances. *Automatica*, 37(9), 1459–1563.

Amato, F., Ambrosino, R., Ariola, M., Cosentino, C., and De Tommasi, G. (2014). *Finite-Time Stability and Control*. Springer, London, UK.

Baslamisli, S.Ç., Köse, İ.E., and Anlaş, G. (2009). Gain-scheduled integrated active steering and differential control for vehicle handling improvement. *Vehicle System Dynamics*, 47(1), 99–119.

Bliman, P.A., Oliveira, R.C.L.F., Montagner, V.F., and Peres, P.L.D. (2006). Existence of homogeneous polynomial solutions for parameter-dependent linear matrix inequalities with parameters in the simplex. In *Proceedings of the 45th IEEE Conference on Decision and Control*, 1486–1491. San Diego, CA, USA.

Borges, R.A., Ishihara, J.Y., Rocha, I.G., Risso, L.O., and Kussaba, H.T.M. (2013). Finite time robust filtering for time-varying uncertain polytopic linear systems. In *Proceedings of the 2013 European Control Conference*, 1854–1859. Zurich, Switzerland.

Chilali, M. and Gahinet, P. (1996). $\mathscr{H}_\infty$ design with pole placement constraints: an LMI approach. *IEEE Transactions on Automatic Control*, 41(3), 358–367.

Ganguli, S., Marcos, A., and Balas, G. (2002). Reconfigurable LPV control design for Boeing 747-100/200 longitudinal axis. In *Proceedings of the 2002 American Control Conference*, volume 5, 3612–3617. IEEE.

He, S. and Liu, F. (2011). Robust L_2-L_∞ filtering of time-delay jump systems with respect to the finite-time interval. *Mathematical Problems in Engineering*. `http://www.hindawi.com/journals/mpe/2011/839648/`.

Khalil, H.K. (2002). *Nonlinear Systems*. Prentice Hall, Upper Saddle River, NJ, 3rd edition.

Lin, H.H., Beck, C., and Bloom, M. (2008). Multivariable LPV control of anesthesia delivery during surgery. In *Proceedings of the 2008 American Control Conference*, 825–831. IEEE.

Liu, C., Zhang, Y., and Sun, H. (2012). Finite-time H_∞ filtering for singular stochastic systems. *Journal of Applied Mathematics*. `http://www.hindawi.com/journals/jam/2012/615790/`.

Löfberg, J. (2004). YALMIP: A toolbox for modeling and optimization in MATLAB. In *Proceedings of the 2004 IEEE International Symposium on Computer Aided Control Systems Design*, 284–289. Taipei, Taiwan. `http://control.ee.ethz.ch/~joloef/yalmip.php`.

Luan, X., Liu, F., and Shi, P. (2010). Finite-time filtering for non-linear stochastic systems with partially known transition jump rates. *IET Control Theory & Applications*, 4(5), 735–745.

Oliveira, R.C.L.F. and Peres, P.L.D. (2005). Stability of polytopes of matrices via affine parameter-dependent Lyapunov functions: Asymptotically exact LMI conditions. *Linear Algebra and Its Applications*, 405, 209–228.

Oliveira, R.C.L.F. and Peres, P.L.D. (2007). Parameter-dependent LMIs in robust analysis: Characterization of homogeneous polynomially parameter-dependent solutions via LMI relaxations. *IEEE Transactions on Automatic Control*, 52(7), 1334–1340.

Peña, R.S.S. and Ghersin, A.S. (2010). LPV control of glucose for diabetes type I. In *Engineering in Medicine and Biology Society (EMBC), 2010 Annual International Conference of the IEEE*, 680–683. IEEE.

Shamma, J.S. (2012). An overview of LPV systems. In *Control of Linear Parameter Varying Systems with Applications*, 3–26. Springer.

Sturm, J.F. (1999). Using SeDuMi 1.02, a MATLAB toolbox for optimization over symmetric cones. *Optimization Methods and Software*, 11(1–4), 625–653. `http://sedumi.ie.lehigh.edu/`.

Toth, R. (2010). *Modeling and Identification of Linear Parameter-Varying Systems*. Lecture Notes in Control and Information Sciences. Springer.

PID Optimal Controller with Filtered Derivative Part for Unstable First Order Plus Time Delay Systems

J. A. Cárdenas-Valderrama*, J. F. Marquez-Rubio*, O. Jiménez-Ramírez*

**Instituto Politécnico Nacional, ESIME Unidad Culhuacán, Sección de Estudios de Posgrado e Investigación, Av. Santa Ana, 1000, México DF, 04430, México,*
(e-mail: cardenas.v@live.com.mx, jfcomr23@yahoo.com.mx, cuauhpitzote@hotmail.com)

Abstract: A typical problem in the derivative part of the PID controllers is its practical implementation. This work avoids to assume high values for the filter coefficient instead, a stability analysis of a proposed filtered PID controller to the case of systems with time delay, particularly the Unstable First Order plus Time Delay (UFOPTD) systems is presented. This analysis becomes interesting since analytical results have not been presented in literature. The aim of the obtained results is to illustrate how the stability conditions are modified when different values of the filter coefficient are chosen. In fact, the parametric stabilization region is obtained based in previous literature results. As a second goal of the present research is to obtain the optimal parameters of the proposed filtered PID controller such that the energy of control input and system states be minimized. An optimization methodology based on the second method of Lyapunov is obtained.

Keywords: PID controller, Stabilization, Time-delay, Unstable Processes, Optimization.

1. INTRODUCTION

Time-delay of control inputs is a common phenomenon in diverse application fields, including chemical processes, hydraulic systems and servomechanisms. Recently, some systems are remotely controlled generating a time delay between the controlled system and the control stage. The control problem of time delay systems arises mainly by the induced transcendental term in the characteristic equation, which gives as result a characteristic equation having an infinite number of poles. Due to the complexity of the problem, several researchers have devoted its efforts for designing control strategies that provide an adequate performance of the system; see for instance Seshagiri, et al., (2007). To the case of open-loop stable process, the well-known Smith Predictor Compensator (SPC) has been used as a traditional control structure Seshagiri, et al., (2007). Considering a similar approach, some works have been reported in order to deal with unstable processes, see for instance, Liu et al., (2005), Seshagiri and Chidambaram (2005). As a first attempt to analyse a generalized class of delayed systems, the case of first order delayed system has been widely studied by using the basis provided by the SPC, see for instance Seshagiri, et al., (2007), Michiels et al., (2002), Marquez et al., (2012). With a simple and different perspective, some authors have regarded to analyse the case when the system is controlled by a Proportional (P), Proportional-Integral (PI) and Proportional-Integral-Derivative (PID). Nesimioglu and Soylemez Nesimioglu and controllers. Hwang and Hwang (2004) used the D-partition technique to estimate the stabilization limits of PID compensation, showing that an UFOPTD system can be stabilized if $\theta < \theta_{un}$, where θ is the time-delay and θ_{un} is the unstable constant-time. Silva and Bhattacharyya (2005) provided a complete parametrization of the stabilizing P and PI controllers in the case $\theta < \theta_{un}$ and the stabilizing PID controllers for the case $\theta < 2\theta_{un}$. Recently, Marquez et al., (2014) consider the stabilization of UFOPTD system by using a traditional Proportional-Derivative (PD) controller, showing that the derivative term minimizes the effects of the time-delay. In Lee et al., (2010) some results about the stabilization of a delayed system with one unstable pole and several stable poles by using P, PI, PD and PID controllers are provided. An important issue in the derivative part of PID controllers is its practical implementation. The solution of using a filter to the derivative action has been widely proposed in the literature. However, just high values of the filter coefficient is suggested in order to recuperate the inherent derivative action of the controller. The task of this work is to analyze the stability properties when a filtered PID controller is considered to the case of UFOPTD system and showing how the stability conditions of the closed-loop system can be modified for different values of the filter coefficient. As we mentioned before, the control strategies previously cited only provides stability results and there are not result related to the performance of the controlled variable. It is known that when a control strategy is applied to a system it is desired to obtain optimal performance of the system with respect to specific variables. Also, in this work a simple and effective methodology to obtain the optimal gains k_p, k_i and k_d gains is proposed in order to minimize the energy at the control input and the system states. The proposed optimization methodology is based on an approximation of the delay term as well as on the second method of Lyapunov. It is important to note that the proposed optimization strategy assumes that the stabilizing region of the control parameters is known, and such stabilizing regions are obtained from previous literature results such as Lee et

al., (2010) and Marquez et al., (2014). This work is organized as follows. Section 2 presents the problem formulation. After this, in Section 3 some preliminary results are given. Then, Section 4 presents the main results of this work. In Section 5 a numerical example is given and finally in Section 6 some conclusions are provided.

2. PROBLEM FORMULATION

Consider an UFOPTD system given by,

$$\bar{G}(s) = \frac{Y(s)}{U(s)} = \frac{b}{s-a}e^{-\theta s}, \qquad (1)$$

a PID controller with filtered derivative part of the form,

$$\bar{C}(s) = \bar{k}_p + \frac{\bar{k}_i}{s} + \frac{\bar{k}_d s}{\frac{s}{N}+1} \quad or,$$

$$\bar{C}(s) = \frac{\left(N\bar{k}_d + \bar{k}_p\right)s^2 + \left(N\bar{k}_p + \bar{k}_i\right)s + N\bar{k}_i}{s(s+N)}, \qquad (2)$$

where N is known as coefficient filter, and the control scheme shown in Fig 1. If the parameters $\bar{k}_p$, $\bar{k}_i$ and $\bar{k}_d$ are known in the case of the typical form of PID controller (without filter at derivative term), a traditional and heuristic way to implement in practice the controller given in (2) is setting N as $N \gg 0$. Notice that for $N \gg 0$ in (2) the properties of the non-filtered PID controller are recovered. However there is not a guideline to set the filter coefficient N or an explanation if the closed-loop system remains stable when N decreases. This work considers this problem to the proposed filtered PID controller, it is provided the allowable value of the coefficient filter such that the closed loop is stable and it is shown how the stability properties are modified due to the values of N. Consider a system given by (1) and a PID controller given by (2). The open loop transfer function given by,

$$\bar{C}(s)\bar{G}(s) = \frac{\left(\left(N\bar{k}_d + \bar{k}_p\right)s^2 + \left(N\bar{k}_p + \bar{k}_i\right)s + N\bar{k}_i\right)be^{-\theta s}}{s(s+N)(s-a)}, \qquad (3)$$

can be separated as follows,

$$C(s)G(s) = \left(k_p + \frac{k_i}{s} + k_d s\right)\frac{b}{(s-a)(s+N)}e^{-\theta s}, \qquad (4)$$

where $k_p = N\bar{k}_p + k_i$, $k_d = N\bar{k}_d + \bar{k}_p$, $k_i = N\bar{k}_i$ and

$$C(s) = \left(k_p + \frac{k_i}{s} + k_d s\right) \qquad (5)$$

$$G(s) = \frac{b}{(s-a)(s+N)}e^{-\theta s} \qquad (6)$$

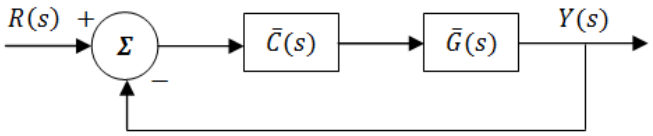

Fig 1. A control scheme UFOPTD system.

Notice that the closed-loop stability properties of the system (1) with the controller (2) can be obtained from the closed-loop stability properties of system (6) controlled by (5). In fact the stability properties of the closed-loop system (5)-(6) are presented in Lee et al., (2010).

3. PRELIMINAR RESULTS

Consider a system given by (6) and a PID controller by (5). The following result establishes the closed-loop stability conditions.

[Lee et al., (2010)] **Lemma 1.** A necessary condition for a PID controller to stabilize the system given by (6) is,

$$\theta < \sqrt{\left(\frac{1}{a}\right)^2 + \left(\frac{1}{N}\right)^2} + \frac{1}{a} - \frac{1}{N} \qquad (7)$$

If this condition is satisfied then the range of $\frac{k_d}{k_p}$ values for which a solution exists to the PID stabilization problem are given by,

$$\theta - \frac{1}{a} + \frac{1}{N} < \frac{k_d}{k_p} < \sqrt{\left(\frac{1}{a}\right)^2 + \left(\frac{1}{N}\right)^2}, \qquad (8)$$

and $\frac{k_i}{k_p}$ should be such that,

$$atg(\omega) + atg\left(\frac{k_d}{k_p}a\omega - \frac{k_i}{k_p}\frac{1}{a\omega}\right) - atg\left(\frac{a\omega}{N}\right) - \theta a\omega > 0,$$

for some $\omega > 0$, and

$$\frac{Na}{b}\sqrt{\frac{(1+\omega_{c1}^2)\left(1+\frac{a^2\omega_{c1}^2}{N^2}\right)}{1+\left(\frac{k_d}{k_p}a\omega_{c1} - \frac{k_i}{k_p}\frac{1}{a\omega_{c1}}\right)^2}} < k_p < \frac{Na}{b}\sqrt{\frac{(1+\omega_{c2}^2)\left(1+\frac{a^2\omega_{c2}^2}{N^2}\right)}{1+\left(\frac{k_d}{k_p}a\omega_{c2} - \frac{k_i}{k_p}\frac{1}{a\omega_{c2}}\right)^2}}, \qquad (9)$$

with $\omega_{c1} < \omega_{c2}$ being the first two phase crossover solved from,

$$atg(\omega) + atg\left(\frac{k_d}{k_p}a\omega - \frac{k_i}{k_p}\frac{1}{a\omega}\right) - atg\left(\frac{a\omega}{N}\right) - \theta a\omega = 0.$$

4. MAIN RESULTS

In this section the main results of this work are depicted. The following result provides the stability conditions such that the PID controller given by (2) stabilizes the system given by (1). The main aim of the following result is to illustrate how the stability conditions are modified with respect to different values of the filter coefficient N.

Theorem 2. Consider a system given by (1), a PID controller of the form (2) and the control feedback (Fig 1). A necessary condition for a filtered PID controller stabilizes the closed-loop system is:

i) $\theta < \frac{2}{a}$ with $N \gg a$ (the case of non filtered PID, [Lee et al., (2010)])

ii) $\theta < \frac{1}{a}$ with $N \ll a$

iii) $\frac{1}{a} < \theta < \frac{2}{a}$ with $N > \frac{2-2a\theta}{a\theta^2-2\theta}$

Proof. i) From the necessary condition (7) given in Lemma 1, it should be noticed that with $N \gg a$, the term $\frac{1}{N} \to 0$ which leads to the condition,

$$\theta < \sqrt{\left(\frac{1}{a}\right)^2 + \frac{1}{a}} = \frac{2}{a}$$

The condition (7) gives the necessary condition to stabilize the delayed system with one unstable pole and one stable, in our case the stable pole position is given by the value of the filter coefficient N. Therefore, high values of N ($N \gg a$), (7) is expressed as $\theta < \frac{2}{a}$.

Proof. ii) From the necessary condition (7) given by Lemma 1, if $N \ll a$ is considered i.e, $N = xa$ with $x \ll a$. Since the term $\left(\frac{1}{a}\right)^2 \ll \left(\frac{1}{xa}\right)^2$ then the term $\left(\frac{1}{a}\right)^2$ can be remove from the expression and we obtain,

$$\theta < \sqrt{\left(\frac{1}{xa}\right)^2 + \frac{1}{a} - \frac{1}{xa}} = \frac{1}{a}$$

Proof. iii) From the necessary condition (7) given in Lemma 1and the inequality for filter coefficient N we obtain,

$$N > \frac{2 - 2a\theta}{a\theta^2 - 2\theta}$$

This result only is valid for the range $\frac{1}{a} < \theta < \frac{2}{a}$.

In what follows a simple and effective methodology to obtain the optimal k_p, k_i and k_d control parameters in order to minimize the energy of the input control and states system. It is important to note that the following optimization strategy assumes that the stabilizing region of the control parameters is known and such regions can be computed following Lemma 1 (Lee et al 2010). In order to obtain a rational representation on the complex variable "s" of the delay term the first step of the proposed methodology considers a second order Pade approximation, which can be expressed as,

$$e^{-\theta s} = \frac{s^2 - \frac{6}{\theta}s + \frac{12}{\theta^2}}{s^2 + \frac{6}{\theta}s + \frac{12}{\theta^2}} \qquad (10)$$

Then, by substituting the approximation (10) into the process given by (1), a rational representation on the complex variable "s" of the plant is obtained,

$$G(s) = \frac{b\left(s^2 - \frac{6}{\theta}s + \frac{12}{\theta^2}\right)}{(s-a)(s+N)\left(s^2 - \frac{6}{\theta}s + \frac{12}{\theta^2}\right)} \qquad (11)$$

Taking into account the approximated system (11), the proposed filtered PID (2), and the closed loop system shown in Figure 1, a closed-loop state space representation of the form,

$$\dot{\boldsymbol{x}} = \boldsymbol{A}\boldsymbol{x} + \boldsymbol{B}u$$
$$y = \boldsymbol{C}\boldsymbol{x} + \boldsymbol{D}u, \qquad (12)$$

is obtained with,

$$A = \begin{bmatrix} 0 & 1 & 0 & 0 & 0 \\ -\frac{12}{\theta^2} & -\frac{6}{\theta} & b & 0 & 0 \\ 0 & -\frac{12\,k_d}{\theta^2} & a - b\,k_d & k_i & k_p - Nk_d \\ 0 & 0 & 0 & 0 & 1 \\ 0 & \frac{12}{\theta} & -b & 0 & -N \end{bmatrix}, B = \begin{bmatrix} 0 \\ 0 \\ k_d \\ 0 \\ 1 \end{bmatrix},$$

$$C = \begin{bmatrix} 0 & -\frac{6}{\theta} & b & 0 & 0 \end{bmatrix}, \quad D = [0] \qquad (13)$$

Now, based on the second method of Lyapunov an optimization process to obtain the optimal k_p, k_i and k_d control parameters is derived. The performance index defined to evaluate the behaviour of the system is given by,

$$J = \int_0^\infty \boldsymbol{x}^{\boldsymbol{T}}\boldsymbol{Q}\boldsymbol{x}dt = \boldsymbol{x}^{\boldsymbol{T}}(0)\boldsymbol{P}\boldsymbol{x}(0), \qquad (14)$$

where:

$\boldsymbol{x}$ is the states vector.

$\boldsymbol{P}$ is a Define Positive Matrix.

$\boldsymbol{Q}$ is a Define Positive Matrix.

$\boldsymbol{A}$ is a nxn Matrix.

J is the performance index.

The main objective of the optimization process is to minimize the behavior index (14) assuring closed-loop stability. In this way, the solution of the following equation is required,

$$\boldsymbol{A^T P + PA} = -\boldsymbol{Q} \qquad (15)$$

From the second method of Lyapunov it is known that if the equation (15) has a unique solution, the closed-loop system given by (12) is stable. Equation (15) should be solved by proposing $\boldsymbol{Q}$ and solving to $\boldsymbol{P}$. This step requires that one of the control gains (for instance k_p and k_d, k_p and k_i or k_i and k_d) are given from the stable region computed with Lemma 1 (Lee et al. 2010). Notice that the resultant matrix $\boldsymbol{P}$ contains the control parameters of the control. Once that $\boldsymbol{P}$ is obtained, $\boldsymbol{P}$ is replaced into the performance index (14). Then, in order to minimize the performance index (14), the derivative of the performance index (14) is computed and the optimal gain (for instance k_i, k_d *or* k_p) is solved from,

$$\frac{dJ}{dx} = 0 \qquad (16)$$

5. SIMULATION RESULTS

Example 3. Consider a UFOPTD system given by (1) with his unstable pole $a = 1$. From the results of the Theorem 2., θ values are in the range given by,

$$1 < \theta < 2$$

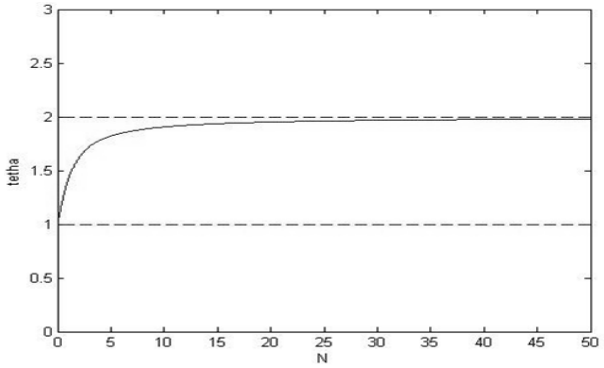

Fig. 2. Permissible region for N.

Fig 2. is a plot of θ-N that shows the maximum value that could be θ for a set of values of N. It can be seen that for small values of N, the maximum value of θ is close to 1 and for big values of N, the maximum value of θ converges to 2. Notice that for $N = 50$, the maximum value of θ.is close to 2.

Example 4. Consider a UFOPTD system given by,

$$\bar{G}(s) = \frac{1}{s-1}e^{-1.3s},$$

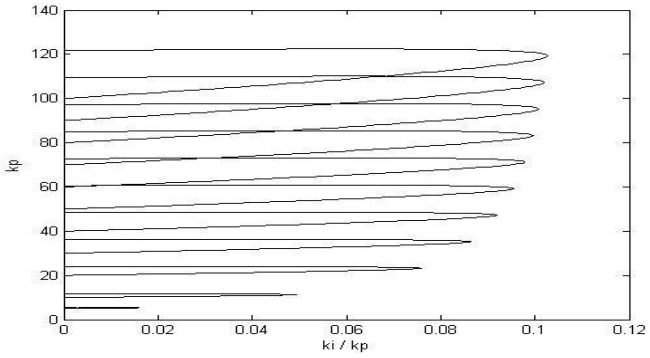

Fig 3. Stability regions for 5 < N < 100.

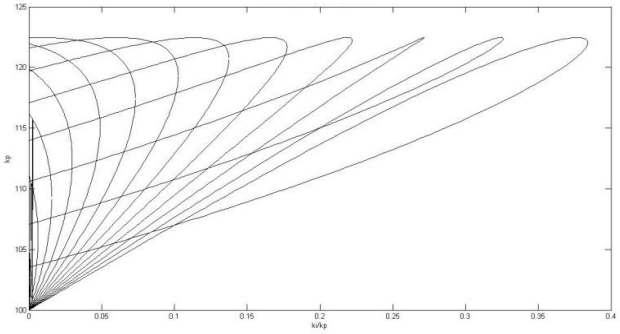

Fig 4. Stability regions for $0.35 < \frac{k_d}{k_p} < 0.95$.

and a PID controller by (2). We have rewritten the system and PID controller in the form given by (6)-(5). Following the Theorem 2, we can see the condition $\theta < \frac{2}{a}$ is satisfied due to $1.3 < 2$. From the (7), the range of N values is,

$$N > 0.65934066$$

Following the Lemma 1, the range of $\frac{k_d}{k_p}$ values is,

$$0.3 + \frac{1}{N} < \frac{k_d}{k_p} < \sqrt{1 + \left(\frac{1}{N}\right)^2},$$

$$atg(\omega) + atg\left(\frac{k_d}{k_p}\omega - \frac{k_i}{k_p}\frac{1}{\omega}\right) - atg\left(\frac{\omega}{N}\right) - 1.3\omega > 0,$$

For positive values of ω such that $\frac{k_i}{k_p} \geq 0$, and

$$1.3\sqrt{\frac{\left(1+\omega_{c1}^2\right)\left(1+\frac{\omega_{c1}^2}{N^2}\right)}{1+\left(\frac{k_d}{k_p}\omega_{c1}-\frac{k_i}{k_p}\frac{1}{\omega_{c1}}\right)^2}} < k_p < 1.3\sqrt{\frac{\left(1+\omega_{c2}^2\right)\left(1+\frac{\omega_{c2}^2}{N^2}\right)}{1+\left(\frac{k_d}{k_p}\omega_{c2}-\frac{k_i}{k_p}\frac{1}{\omega_{c2}}\right)^2}}.$$

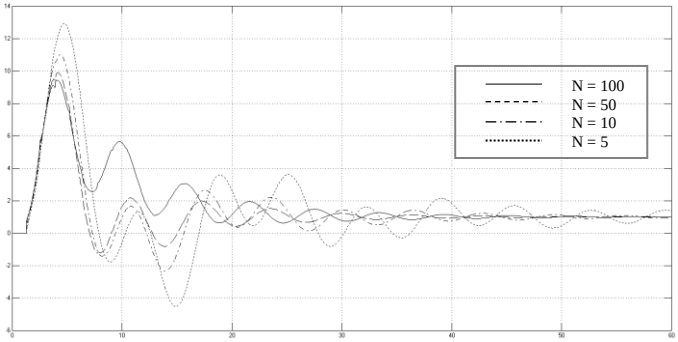

Fig 5. Output system for PID optimal parameters.

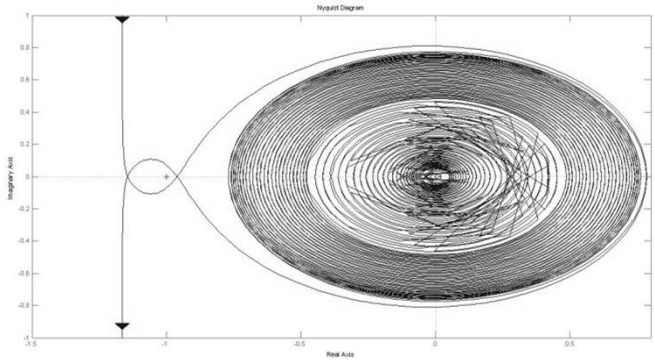

Fig 6. Nyquist plot of the closed-loop.

Table 1. comparison between approximate J and real J.

N	$\frac{k_d}{k_p}$	$J_{approximate}$	J_{real}	error rate
100	0.85	199.5011	200.9235	0.7079
	0.75	124.9385	127.1771	1.7602
	0.65	119.3475	121.4983	1.7702
	0.55	163.8896	166.2439	1.4162
	0.45	399.749	401.1684	0.3538
	0.35	7453.3	5753.6545	22.8039
50	0.85	202.3155	203.7388	0.6986
	0.75	128.8108	131.0875	1.7368
	0.65	125.9473	128.6289	2.0848
	0.55	178.3854	180.8468	1.3610
	0.45	472.3632	471.8013	0.1190
	0.35	16275	9984.886	38.6489
10	0.85	222.4695	224.292	0.8126
	0.75	170.5749	173.5998	1.7425
	0.65	205.3699	207.3216	0.9414
	0.55	433.4463	435.4711	0.4650
	0.45	4921.2	4346.442	11.6792
5	0.95	491.8966	470.7528	4.2984
	0.85	267.4086	270.0312	0.9712
	0.75	284.9237	287.5156	0.9015
	0.65	557.7871	560.7171	0.5225
1	1.35	72018	64714	10.1419

There are infinite stability regions due filter constant N and for each $\frac{k_d}{k_p}$ value of the range, there is a stability region of $k_p - \frac{k_i}{k_p}$. In this work we take some values for N and $\frac{k_d}{k_p}$ in order to show some stability regions of $k_p - \frac{k_i}{k_p}$ as well as compute some approximated performance indexes.

We compute J for some values of N and $\frac{k_d}{k_p}$ with (10), (11) and (13), and we compare it against real J obtained by simulation.

Table 1 shows approximate J, real J and the error rate for some values of N and $\frac{k_d}{k_p}$. Notice that the minimum J occurs when $N = 100$ and we conclude that a big value of N (with respect to the unstable constant a) to obtain minimum J.

Note that we use a small $\frac{k_d}{k_p}$ value, the error rate increases due to the use of a Pade approximation for time delay. We obtain the minimum J when we use $\frac{k_d}{k_p} = 0.75$. Thus, we take $N = 100$ - $\frac{k_d}{k_p}$ =0.65, $N = 50$ - $\frac{k_d}{k_p}$ =0.65, $N = 10$ - $\frac{k_d}{k_p}$ =0.75 and $N = 5$ - $\frac{k_d}{k_p}$ =0.85, and we show the output variable in Fig 5.

The satisfied closed-loop stability condition on the Nyquist plot is shown in Fig 6. for optimal values of k_i, k_p and k_d with $N = 100$. This plot shows one anticlockwise encircle to the critical point (-1,0) due to the one unstable pole.

6. CONCLUSIONS

In this paper, the stabilization of UFOPTD systems is investigated. The stability conditions by the PID controller with filtered derivative part are established to different N values.

The analysis provides exact stability region in terms of control parameters and indicates that stability can be achieved as long as $\theta < \frac{2}{a}$ and we have illustrated it through an example and its simulation. Comparison between approximate J and real J shows that Pade approximation is a good representation for time delay. To obtain the best J, it is necessarily choose a big N value and fixing an intermediate value of the $\frac{k_d}{k_p}$ range.

REFERENCES

C. Hwang, J. Hwang (2004). *Stabilization of first-order plus dead-time unstable processes using PID controllers*, IEE Proc. Control Theory Appl., Vol. 151, pp. 89-94.

Lee S. C., Wang Q. G. and Xiang C. (2010). *Stabilization of all-pole unstable delay processes by simple controllers*, Journal of Process Control, Vol. 20, pp. 235-239. 2010.

Liu T., Zhang W. and Gu D. (2005). *Analytical design of two-degree of freedom control scheme for open-loop unstable processes with time delay*, J. Process Control, Vol. 15, pp. 559-572.

Marquez-Rubio J. F., Del-Muro-Cuéllar B. Velazco-Villa M. and Novella-Rodríguez D. F. (2012). *Observer PID Stabilization Strategy for Unstable First-Order Linear Systems with Large Time Delay*, Industrial & Engineering Chemistry Research, Vol. 51, pp. 8477-8487.

Marquez-Rubio J. F., Del-Muro-Cuéllar B. and Alvarez-Ramírez j. (2014). *Stabilization Region of PD Controller for Unstable First Order Process with Time Delay*, International Journal of Control, Automation and Systems, Vol. 12(2), pp. 747-761.

Michiels W., Engelborghs K., Vansevnant P. and Roose D. (2002). *Continuous pole placement for delay equations*, Automatica, Vol. 38, pp. 747-761.

Nesimioglu B. S. and Soylemez M. T. (2010). *A simple derivation of all stabilizing proportional controller for*

first order time-delay systems, Asian J. Contrl, Vol. 14, pp. 1-7.

Normey-Rico J. E. and Camacho E. F. (2009). *Unified approach for robust dead-time compensator design*, J. Process Control, Vol. 19, pp. 38-47.

Seshagiri R. A. and Chidambaram M. (2005), *Enhanced Smith predictor for unstable processes with time delay*, Ind. Eng. Chem. Res., Vol. 44, pp. 8291-8299.

Seshagiri R. A. , Rao V. S. R. and Chidambadam M. (2007). *Simple analytical design of modified Smith Predictor with improved performance for unstable first-order plus time delay (UFOPTD) processes*, Ind. Eng. Chem. Res., Vol. 46, pp. 4561-4571.

Silva G. J. and Bhattacharyya S. P., *PID controller for time-delay systems*, Birkhuser. Boston, 2005.

SISO Pole Placement Algorithm: A Linear Transformation Approach

Nicolás E. Faedo * **Ernesto Aljinovic** ** **Virginia Mazzone** *

* *IACI - Departamento de Ciencia y Tecnología, Universidad Nacional de Quilmes, Roque Saenz Peña 352, Bernal, Buenos Aires, Argentina.*
** *Área de Matemática Superior - Departamento de Ciencia y Tecnología, Universidad Nacional de Quilmes, Roque Saenz Peña 352, Bernal, Buenos Aires, Argentina.*

Abstract: In this paper, an algorithm for SISO Pole Placement based on linear algebra concepts it's developed. This algorithm uses the knowledge of the degrees of certain polynomials associated to the *Internal Model Principle* and *Stable Zero-Pole cancellations* involved in the equation of the closed loop and it's coefficients, generating a linear system of equations for the desired closed loop poles in a systematic way.

Keywords: pole placement, SISO systems, linear algebra, diophantine equations

1. INTRODUCTION

The central problem in control is to find a way to act on a given process such that it behaves close to a desired behavior. Furthermore, this approximate behavior should be achieved in presence of uncertainty of the process and of uncontrollable external disturbances acting on the process. That means, given the closed loop of one degree of freedom shown in Figure 1, where the nominal model of the process to be controlled is $G_0(s)$, find a controller $K(s)$ that ensure that the nominal loop is stable and, if it's possible, to reach a desire behavior previously defined.

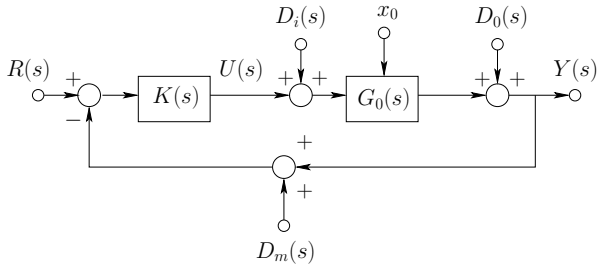

Fig. 1. Closed loop of one degree of freedom

In the loop shown in Figure 1 we use transfer functions and Laplace transforms to describe the relationships between signals in the loop, where $R(s)$ is the reference input, $U(s)$ is the control signal, $Y(s)$ is the output of the loop, $D_i(s)$ is the input disturbance, $D_0(s)$ is the output disturbance and $D_m(s)$ is the measurement noise. We also use x_0 to denote the initial conditions of the model. For linear time-invariant (LTI) systems, the nominal model and the controller can be written as

$$G_0(s) = \frac{B(s)}{A(s)} \qquad K(s) = \frac{P(s)}{L(s)}$$

The poles of the four sensitivity functions governing the closed loop belong to the same set, namely the roots of the characteristic equation $A(s)L(s) + B(s)P(s) = 0$. The poles have a deep impact on the dynamics of a transfer function; they define the stability of the loop. In this way, there exists a technique which deals with the choice of the roots of the characteristic equation, that is, given polynomials $A(s)$, $B(s)$ (defining the model) and given a polynomial $A_{cl}(s)$ (defining the desired location of closed loop poles), it is possible to find polynomials $P(s)$ and $L(s)$ such that

$$A(s)L(s) + B(s)P(s) = A_{cl}(s) \tag{1}$$

The Equation (1) is known as a Diophantine equation and the controller synthesis by solving it is known as pole placement. Polynomial Diophantine equations play a crucial role in the polynomial theory of control systems synthesis. Systems are described by input-output relations, similarly to the classical control techniques, however, the transfer functions are not regarded as functions of complex variable but as algebraic objects. Applications include closed loop pole placement (Kučera, 1993), minimum variance control (Hunt, 1993), LQ and LQG optimal compensators (Kučera, 1991) or adaptive and predictive control (Hunt, 1993). It is well known that, if the controller is biproper, the solution of the equation exists if

$$\deg\{P(s)\} = \deg\{L(s)\} \geq n - 1$$

with $n = \deg\{A(s)\}$. In this context, the minimum order controller is then of degree $n - 1$ and the condition on coprimeness between $A(s)$ y $B(s)$ is necessary to guarantee the existence and uniqueness of the solution (Sylvester theorem) (Goodwin et al., 2001). Solving this equation basically implies solving a linear system of equations, which involves a Sylvester matrix. A suitable and fast algorithm for invert this type of matrices was developed in (Li, 2011).

Many times control objective for the closed loop is to track a specific reference or reject a disturbance of a known frequency. In order to accomplish this we present a systematic way to solve the system equation obtained from using Internal Model Principle (IMP) defined for the first time in (Francis and Wonham, 1975), which establish

that the *reference or disturbance generating polynomial* (o simply *generating polynomial*) must be in the denominator of $K(s)$ (Goodwin et al., 2001). This can also be achieved by solving the Diophantine equation (1). Sometimes it is desirable to force the controller to cancel a subset of stable poles and/or zeros of the plant model, this is also taking into account by this systematization, which arises to an algorithm to solve this problem in an automatic way. This approach can be used for design adaptive controllers, or simply synthesize PID controllers.

2. LINEAR TRANSFORMATION APPROACH

2.1 Notation

Let $X(s) = x_n\, s^n + x_{n-1}\, s^{n-1} + \cdots + x_1\, s + x_0$ be a polynomial with real coefficients.

Notation 1. The set of all coefficients of $X(s)$ (in decreasing power order) is denoted by $C_X = \{x_n, x_{n-1}, \cdots, x_1, x_0\}$

Notation 2. The degree of $X(s)$ is denoted by $\deg\{X(s)\}$

Let $\mathbb{V}, \mathbb{W}$ be finite-dimensional vector spaces over a field K and choose bases $V = \{v_1, \ldots, v_m\}$ for $\mathbb{V}$ and $W = \{w_1, \ldots, w_n\}$ for $\mathbb{W}$.

Notation 3. The dimension of $\mathbb{V}$ is denoted by $\dim\{\mathbb{V}\}$.

Notation 4. Let $v^* \in \mathbb{V}$. The coordinates of v^* in the basis V are denoted by $(v^*)_V \in \mathbb{R}^m$.

Notation 5. Let $T : \mathbb{V} \longrightarrow \mathbb{W}$ be a linear transformation from $\mathbb{V}$ to $\mathbb{W}$. The matrix associated to T choosing bases V and W is denoted by T_{VW}.

Definition 1. The external direct sum of $\mathbb{V}$ and $\mathbb{W}$, denoted by $\mathbb{V}\tilde{\oplus}\mathbb{W}$ is defined as the set of all ordered pairs (v, w) with $v \in \mathbb{V}$ and $w \in \mathbb{W}$. Scalar multiplication is defined by $c(v, w) = (cv, cw)$ with $c \in K$, and addition is defined by $(v, w) + (v', w') = (v + v', w + w')$. One checks the other classical axioms for a vector space.

Note that the external direct sum of $\mathbb{V}$ and $\mathbb{W}$ can be expressed as the internal direct sum of $(\mathbb{V}, 0)$ and $(0, \mathbb{W})$. A basis for $\mathbb{V}\tilde{\oplus}\mathbb{W}$ is given by

$$\left\{\{(v_i, 0)\} \bigcup \{(0, w_j)\}\right\}$$

2.2 Pole Placement

Given the control loop of one degree of freedom as in Figure 1. Let $G_0(s)$ be the process nominal model and $K(s)$ the biproper controller defined as

$$G_0(s) = \frac{B(s)}{A(s)} \equiv \frac{B}{A} \qquad K(s) = \frac{P(s)}{L(s)} \equiv \frac{P}{L}$$

where

$$\begin{aligned} A &= a_n\, s^n + a_{n-1} s^{n-1} + \cdots + a_1\, s + a_0 \\ B &= b_m\, s^m + b_{m-1} s^{m-1} + \cdots + b_1\, s + b_0 \\ P &= p_{n-1}\, s^{n-1} + p_{n-2} s^{n-2} + \cdots + p_1\, s + p_0 \\ L &= l_{n-1}\, s^{n-1} + l_{n-2} s^{n-2} + \cdots + l_1\, s + l_0 \end{aligned}$$

The degrees of the polynomials are as it follows

$$\begin{aligned} \deg\{A\} &= n \\ \deg\{B\} &= m \qquad m \leq n \\ \deg\{P\} &= n - 1 \\ \deg\{L\} &= n - 1 \end{aligned}$$

The closed loop polynomial $A_{cl}(s) \equiv A_{cl}$ is given by the following Diophantine equation

$$A\, L + B\, P = A_{cl}$$

where

$$\deg\{A_{cl}\} = \deg\{A\} + \deg\{L\} = 2n - 1$$

and so

$$A_{cl} = c_{2n-1}\, s^{2n-1} + c_{2n-2}\, s^{2n-2} + \cdots + c_1\, s + c_0$$

Let $\mathbb{V}_l$, $\mathbb{V}_p$, $\mathbb{W}$ be finite-dimensional vector spaces over $\mathbb{R}$ such as

$$\begin{aligned} \mathbb{V}_l &= \text{span}\{s^{n-1}, s^{n-2}, \ldots, s, 1\} \\ \mathbb{V}_p &= \text{span}\{s^{n-1}, s^{n-2}, \ldots, s, 1\} \\ \mathbb{W} &= \text{span}\{s^{2n-1}, s^{2n-2}, \ldots, s, 1\} \end{aligned}$$

Notice that $L \in \mathbb{V}_l$, $P \in \mathbb{V}_p$ and $A_{cl} \in \mathbb{W}$. Although in this case $\mathbb{V}_l$ is exactly the same space as $\mathbb{V}_p$, we keep the subscripts for the sake of clarity. Let $\mathbb{V}_l\tilde{\oplus}\mathbb{V}_p$ be the external direct sum of $\mathbb{V}_l$ and $\mathbb{V}_p$. Let V and W be a basis for $\mathbb{V}_l\tilde{\oplus}\mathbb{V}_p$ and $\mathbb{W}$ respectively, such as

$$V = \left\{\{(s^{n-1}, 0), (s^{n-2}, 0), \ldots, (s, 0), (1, 0)\} \bigcup \{(0, s^{n-1}), (0, s^{n-2}), \ldots, (0, s), (0, 1)\}\right\} \tag{2}$$

$$W = \{s^{2n-1}, s^{2n-2}, \ldots, s, 1\} \tag{3}$$

Define the linear transformation Φ as it follows

$$\begin{aligned} \Phi &: \mathbb{V}_l\tilde{\oplus}\mathbb{V}_p \longrightarrow \mathbb{W} \\ \Phi\{(l, p)\} &\mapsto A\, l + B\, p \end{aligned}$$

The construction of the matrix associated to the linear transformation Φ in the bases V and W starts by computing the transformation of every vector of V

$$\begin{aligned} \Phi\{(s^{n-1}, 0)\} &\mapsto A\, s^{n-1} = a_n\, s^{2n-1} + \cdots + a_0\, s^{n-1} \\ \Phi\{(s^{n-2}, 0)\} &\mapsto A\, s^{n-2} = a_n\, s^{2n-2} + \cdots + a_0\, s^{n-2} \\ &\vdots \qquad\qquad \vdots \\ \Phi\{(s, 0)\} &\mapsto A\, s = a_n\, s^{n+1} + \cdots + a_0\, s \\ \Phi\{(1, 0)\} &\mapsto A = a_n\, s^n + \cdots + a_0 \\ \Phi\{(0, s^{n-1})\} &\mapsto B\, s^{n-1} = b_m\, s^{m+n-1} + \cdots + b_0\, s^{n-1} \\ \Phi\{(0, s^{n-2})\} &\mapsto B\, s^{n-2} = b_m\, s^{m+n-2} + \cdots + b_0\, s^{n-2} \\ &\vdots \qquad\qquad \vdots \\ \Phi\{(0, s)\} &\mapsto B\, s = b_m\, s^{m+1} + \cdots + b_0\, s \\ \Phi\{(0, 1)\} &\mapsto B = b_m\, s^m + \cdots + b_0 \end{aligned} \tag{4}$$

Getting coordinates in basis W yields

$$\begin{aligned} (A\, s^{n-1})_W &= (C_A, 0, 0, \ldots\ldots\ldots\ldots, 0, 0, 0) \\ (A\, s^{n-2})_W &= (0, C_A, 0, \ldots\ldots\ldots\ldots, 0, 0, 0) \\ &\vdots \\ (A\, s)_W &= (0, 0, 0, \ldots\ldots\ldots\ldots, 0, C_A, 0) \\ (A)_W &= (0, 0, 0, \ldots\ldots\ldots\ldots, 0, 0, C_A) \\ (B\, s^{n-1})_W &= (\overbrace{0, \ldots, 0}^{n-m}, C_B, 0, 0, \ldots, 0, 0, 0) \\ (B\, s^{n-2})_W &= (0, \ldots, 0, 0, C_B, 0, \ldots, 0, 0, 0) \\ &\vdots \\ (B\, s)_W &= (0, \ldots, 0, 0, 0, 0, \ldots, 0, C_B, 0) \\ (B)_W &= (0, \ldots, 0, 0, 0, 0, \ldots, 0, 0, C_B) \end{aligned} \tag{5}$$

Notice that every vector in $\mathbb{R}^{2n}$ defined above it's a shift of the coefficients of A and B polynomials respectively. Define

the following submatrices $\xi_A \in \mathbb{R}^{2n\times n}$ and $\xi_B \in \mathbb{R}^{2n\times n}$ (in columns)

$$\xi_A = \underbrace{\left[\,(A\,s^{n-1})^T_W \;\cdots\; (A)^T_W\,\right]}_{\dim\{\mathbb{V}_l\}=n}$$

$$\xi_B = \underbrace{\left[\,(B\,s^{n-1})^T_W \;\cdots\; (B)^T_W\,\right]}_{\dim\{\mathbb{V}_p\}=n}$$

Then, the matrix associated to the transformation in the bases V and W (in columns)

$$\Phi_{VW} = [\,\xi_A|\xi_B\,]$$

Where $\Phi_{VW} \in \mathbb{R}^{2n\times 2n}$ is a *Sylvester Matrix* associated to the polynomials A and B, and $|\Phi_{VW}| \neq 0$ because A and B are coprime. Moreover, because of the shifting property of the columns of ξ_A and ξ_B (and knowing the dimensions of $\mathbb{V}_l$, $\mathbb{V}_p$ and $\mathbb{W}$) constructing the matrix it's straightforward. With Φ_{VW} computed (which is systematic) knowing the coefficients of L and P it's reduced to solve the following linear system of equations:

$$[\,\xi_A|\xi_B\,]\begin{bmatrix}C_L\\C_P\end{bmatrix} = C_{A_{cl}} \longrightarrow \begin{bmatrix}C_L\\C_P\end{bmatrix} = [\,\xi_A|\xi_B\,]^{-1}\,C_{A_{cl}}$$

2.3 Internal Model Principle

Adding the Internal Model Principle to the loop, given by the *generating polynomial* $\Gamma(s) \equiv \Gamma$ where

$$\deg\{\Gamma\} = q$$

the pole placement problem can be reformulated: the *generating polynomial* must appear as part of the denominator of the controller. To accomplish that goal, one chooses

$$L = \Gamma\bar{L}$$

and the closed loop equation can be rewritten as

$$\bar{A}\,\bar{L} + B\,P = A_{cl} \quad \text{where} \quad \bar{A} = \Gamma\,A$$

including Γ inside the term that represents the denominator of the plant, creating an equivalent model of degree $\bar{n} = n + q$. Now, using the same criterion of design a biproper controller with one degree less than the plant:

$$\begin{aligned}\deg\{P\} &= \bar{n} - 1 = n + q - 1\\ \deg\{L\} &= \bar{n} - 1 = n + q - 1\\ \deg\{A_{cl}\} &= 2n + q - 1\end{aligned}$$

and

$$\deg\{\bar{L}\} = \deg\{L\} - \deg\{\Gamma\} = n - 1$$

Let ${}^{\mathrm{I}}\mathbb{V}_{\bar{l}}$, ${}^{\mathrm{I}}\mathbb{V}_p$, ${}^{\mathrm{I}}\mathbb{W}$ be vector spaces over $\mathbb{R}$ such as

$$\begin{aligned}{}^{\mathrm{I}}\mathbb{V}_{\bar{l}} &= \mathrm{span}\{s^{n-1}, s^{n-2}, \ldots, s, 1\}\\ {}^{\mathrm{I}}\mathbb{V}_p &= \mathrm{span}\{s^{n+q-1}, s^{n+q-2}, \ldots, s, 1\}\\ {}^{\mathrm{I}}\mathbb{W} &= \mathrm{span}\{s^{2n+q-1}, s^{2n+q-2}, \ldots, s, 1\}\end{aligned}$$

So that $\bar{L} \in {}^{\mathrm{I}}\mathbb{V}_{\bar{l}}$, $P \in {}^{\mathrm{I}}\mathbb{V}_p$ and $A_{cl} \in {}^{\mathrm{I}}\mathbb{W}$. Let ${}^{\mathrm{I}}\mathbb{V}_{\bar{l}}\tilde{\oplus}{}^{\mathrm{I}}\mathbb{V}_p$ be the external direct sum of ${}^{\mathrm{I}}\mathbb{V}_{\bar{l}}$ and ${}^{\mathrm{I}}\mathbb{V}_p$. Construct bases ${}^{\mathrm{I}}V$ and ${}^{\mathrm{I}}W$ in the same way as in (2) and (3). Define the linear transformation ${}^{\mathrm{I}}\Phi$ as it follows

$$\begin{aligned}{}^{\mathrm{I}}\Phi &: {}^{\mathrm{I}}\mathbb{V}_{\bar{l}}\tilde{\oplus}{}^{\mathrm{I}}\mathbb{V}_p \longrightarrow \mathbb{W}\\ {}^{\mathrm{I}}\Phi\{(\bar{l}, p)\} &\mapsto \bar{A}\,\bar{l} + B\,p\end{aligned} \tag{6}$$

Computing the corresponding maps to every vector in ${}^{\mathrm{I}}V$ in the same way as in (4) and getting it's coordinates in the basis ${}^{\mathrm{I}}W$ as in (5), construct the submatrices ${}^{\mathrm{I}}\xi_{\bar{A}} \in \mathbb{R}^{2n+q\,\times\, n}$ and ${}^{\mathrm{I}}\xi_B \in \mathbb{R}^{2n+q\,\times\, n+q}$ as it follows (in columns)

$${}^{\mathrm{I}}\xi_{\bar{A}} = \underbrace{\left[\,(\bar{A}\,s^{n-1})^T_{{}^{\mathrm{I}}W} \;\cdots\; (\bar{A})^T_{{}^{\mathrm{I}}W}\,\right]}_{\dim\{{}^{\mathrm{I}}\mathbb{V}_{\bar{l}}\}=n}$$

$${}^{\mathrm{I}}\xi_B = \underbrace{\left[\,(B\,s^{n+q-1})^T_{{}^{\mathrm{I}}W} \;\cdots\; (B)^T_{{}^{\mathrm{I}}W}\,\right]}_{\dim\{{}^{\mathrm{I}}\mathbb{V}_p\}=n+q}$$

Then, the matrix associated to the transformation in the bases ${}^{\mathrm{I}}V$ and ${}^{\mathrm{I}}W$ (in columns)

$${}^{\mathrm{I}}\Phi_{{}^{\mathrm{I}}V{}^{\mathrm{I}}W} = \left[\,{}^{\mathrm{I}}\xi_{\bar{A}}\middle|{}^{\mathrm{I}}\xi_B\,\right]$$

Where ${}^{\mathrm{I}}\Phi_{{}^{\mathrm{I}}V{}^{\mathrm{I}}W} \in \mathbb{R}^{2n+q\,\times\, 2n+q}$ is a *Sylvester Matrix* associated to the polynomials $\bar{A}$ and B; and $|{}^{\mathrm{I}}\Phi_{{}^{\mathrm{I}}V{}^{\mathrm{I}}W}| \neq 0$ because $\bar{A}$ and B are coprime.

Example 1. Given

$$G_0(s) = \frac{s+1}{s^2 + 4\,s + 4}$$

we aim to design a biproper controller applying the Internal Model Principle with the *generating polynomial* $\Gamma = s(s^2+1)$.

The degrees of the polynomials

$$\begin{aligned}\deg\{A\} &= n = 2\\ \deg\{B\} &= m = 1\\ \deg\{\Gamma\} &= q = 3\\ \deg\{L\} = \deg\{P\} &= n + q - 1 = 4\\ \deg\{\bar{L}\} &= n - 1 = 1\\ \deg\{A_{cl}\} &= 2n + q - 1 = 6\end{aligned}$$

The corresponding dimensions

$$\dim\{{}^{\mathrm{I}}\mathbb{V}_{\bar{l}}\} = 2, \quad \dim\{{}^{\mathrm{I}}\mathbb{V}_p\} = 5, \quad \dim\{{}^{\mathrm{I}}\mathbb{W}\} = 7 \tag{7}$$

Computing $\bar{A}$ yields

$$\begin{aligned}\bar{A} &= \Gamma\,A = s^5 + 4\,s^4 + 5\,s^3 + 4\,s^2 + 4\,s\\ C_{\bar{A}} &= \{1, 4, 5, 4, 4, 0\}\end{aligned}$$

After defining the transformation ${}^{\mathrm{I}}\Phi$ as in (6) the corresponding ${}^{\mathrm{I}}\xi_{\bar{A}} \in \mathbb{R}^{7\times 2}$ and ${}^{\mathrm{I}}\xi_B \in \mathbb{R}^{7\times 5}$ (which are shifts of the coefficients of the polynomials $\bar{A}$ and B according to the dimensions stated in (7))

$${}^{\mathrm{I}}\xi_{\bar{A}} = \underbrace{\begin{bmatrix}1&0\\4&1\\5&4\\4&5\\4&4\\0&4\\0&0\end{bmatrix}}_{\dim\{{}^{\mathrm{I}}\mathbb{V}_{\bar{l}}\}} \qquad {}^{\mathrm{I}}\xi_B = \underbrace{\begin{bmatrix}0&0&0&0&0\\1&0&0&0&0\\1&1&0&0&0\\0&1&1&0&0\\0&0&1&1&0\\0&0&0&1&1\\0&0&0&0&1\end{bmatrix}}_{\dim\{{}^{\mathrm{I}}\mathbb{V}_p\}}$$

Computing the coefficients of $\bar{L}$ and P involves the following linear system

$$\begin{bmatrix}\bar{l}_1\\\bar{l}_0\\p_4\\p_3\\p_2\\p_1\\p_0\end{bmatrix} = \underbrace{\begin{bmatrix}1&0&0&0&0&0&0\\4&1&1&0&0&0&0\\5&4&1&1&0&0&0\\4&5&0&1&1&0&0\\4&4&0&0&1&1&0\\0&4&0&0&0&1&1\\0&0&0&0&0&0&1\end{bmatrix}^{-1}}_{{}^{\mathrm{I}}\Phi^{-1}_{{}^{\mathrm{I}}V{}^{\mathrm{I}}W}} \begin{bmatrix}c_6\\c_5\\c_4\\c_3\\c_2\\c_1\\c_0\end{bmatrix}$$

Where $C_{A_{cl}} = \{c_6, c_5, c_4, c_3, c_2, c_1, c_0\}$ are the coefficients of the desired closed loop polynomial A_{cl}. If we choose $A_{cl} = (s+3)^6$, then the controller transfer function is given by

$$K(s) = \frac{45s^4 + 209s^3 + 482s^2 + 853s + 729}{s(s^2+1)(s-31)} \tag{8}$$

The steady state response of the closed loop of Figure 1 is indeed the one chosen, but the transient response is affected by the dynamics of the zeros of the controller and the nominal model. The behavior of this zeros is undesirable if they are located at the right side of the poles in the left semi-plane of the complex plane (Seron et al., 1997). This can be sometimes avoided if we propose *Stable Zero-Pole cancellations* between the controller and the plant, as we explain in the following section.

2.4 Stable Zero-Pole cancellations

In addition to the implementation of the Internal Model Principle, it's from interest to obtain a systematic way to perform *Stable Zero-Pole cancellations*. To achieve that goal, the controller denominator(numerator) must include the pole(zero) dynamics to cancel. Suppose that the stable dynamics to cancel are represented by two polynomials $\alpha(s) \equiv \alpha$ (poles) and $\beta(s) \equiv \beta$ (zeros) such that

$$A = \alpha\,\tilde{A}$$
$$B = \beta\,\tilde{B}$$

where

$$\deg\{\alpha\} = w$$
$$\deg\{\beta\} = z$$

The Diophantine equation associated to the closed loop

$$A\,L + B\,P = A_{cl} \longrightarrow \alpha\,\tilde{A}\,L + \beta\,\tilde{B}\,P = A_{cl} \tag{9}$$

Choosing $L = \beta\,\tilde{L}$ and $P = \alpha\,\tilde{P}$ the equation (9) can be expressed as

$$\tilde{A}\,\tilde{L} + \tilde{B}\tilde{P} = \tilde{A}_{cl}$$

with $A_{cl} = \alpha\,\beta\,\tilde{A}_{cl}$ so that the remaining closed loop poles after the cancellations ($\tilde{A}_{cl}$) can be chose arbitrarily. The corresponding degrees using the same design criterion (biproper controller of one degree less than the plant) remains as follows

$$\deg\{\tilde{L}\} = n - z - 1$$
$$\deg\{\tilde{P}\} = n - w - 1$$
$$\deg\{\tilde{A}_{cl}\} = 2n - z - w - 1$$

Let ${}^{\mathrm{Z}}\mathbb{V}_{\tilde{l}}$, ${}^{\mathrm{Z}}\mathbb{V}_{\tilde{p}}$, ${}^{\mathrm{Z}}\mathbb{W}$ be vector spaces over $\mathbb{R}$ such as

$${}^{\mathrm{Z}}\mathbb{V}_{\tilde{l}} = \mathrm{span}\{s^{n-z-1}, s^{n-z-2}, \ldots, s, 1\}$$
$${}^{\mathrm{Z}}\mathbb{V}_{\tilde{p}} = \mathrm{span}\{s^{n-w-1}, s^{n-w-2}, \ldots, s, 1\}$$
$${}^{\mathrm{Z}}\mathbb{W} = \mathrm{span}\{s^{2n-z-w-1}, s^{2n-z-w-2}, \ldots, s, 1\}$$

So that $\tilde{L} \in {}^{\mathrm{Z}}\mathbb{V}_{\tilde{l}}$, $\tilde{P} \in {}^{\mathrm{Z}}\mathbb{V}_{\tilde{p}}$ and $\tilde{A}_{cl} \in {}^{\mathrm{Z}}\mathbb{W}$. Let ${}^{\mathrm{Z}}\mathbb{V}_{\tilde{l}} \tilde{\oplus} {}^{\mathrm{Z}}\mathbb{V}_{\tilde{p}}$ be the external direct sum of ${}^{\mathrm{Z}}\mathbb{V}_{\tilde{l}}$ and ${}^{\mathrm{Z}}\mathbb{V}_{\tilde{p}}$. Construct bases ${}^{\mathrm{Z}}V$ and ${}^{\mathrm{Z}}W$ in the same way as in (2) and (3). Define the linear transformation ${}^{\mathrm{Z}}\Phi$ as it follows

$${}^{\mathrm{Z}}\Phi : {}^{\mathrm{Z}}\mathbb{V}_{\tilde{l}} \tilde{\oplus} {}^{\mathrm{Z}}\mathbb{V}_{\tilde{p}} \longrightarrow {}^{\mathrm{Z}}\mathbb{W}$$
$${}^{\mathrm{Z}}\Phi\{(\tilde{l}, \tilde{p})\} \mapsto \tilde{A}\,\tilde{l} + \tilde{B}\,\tilde{p}$$

Using the same criterion as in (4) and (5) with bases ${}^{\mathrm{Z}}V$ and ${}^{\mathrm{Z}}W$ respectively, the submatrices ${}^{\mathrm{Z}}\xi_{\tilde{A}} \in \mathbb{R}^{2n-z-w \times n-z}$ and ${}^{\mathrm{Z}}\xi_{\tilde{B}} \in \mathbb{R}^{2n-z-w \times n-w}$ (in columns)

$${}^{\mathrm{Z}}\xi_{\tilde{A}} = \underbrace{\left[\, (\tilde{A}\,s^{n-z-1})^T_{{}^{\mathrm{Z}}W} \;\cdots\; (\tilde{A})^T_{{}^{\mathrm{Z}}W} \,\right]}_{\dim\{{}^{\mathrm{Z}}\mathbb{V}_{\tilde{l}}\}=n-z}$$

$${}^{\mathrm{Z}}\xi_{\tilde{B}} = \underbrace{\left[\, (\tilde{B}\,s^{n-w-1})^T_{{}^{\mathrm{Z}}W} \;\cdots\; (\tilde{B})^T_{{}^{\mathrm{Z}}W} \,\right]}_{\dim\{{}^{\mathrm{Z}}\mathbb{V}_{\tilde{p}}\}=n-w}$$

Then, the matrix associated to the transformation in the bases ${}^{\mathrm{Z}}V$ and ${}^{\mathrm{Z}}W$

$${}^{\mathrm{Z}}\Phi_{{}^{\mathrm{Z}}V\,{}^{\mathrm{Z}}W} = \left[\, {}^{\mathrm{Z}}\xi_{\tilde{A}} \,|\, {}^{\mathrm{Z}}\xi_{\tilde{B}} \,\right]$$

Where ${}^{\mathrm{Z}}\Phi_{{}^{\mathrm{Z}}V\,{}^{\mathrm{Z}}W} \in \mathbb{R}^{2n-z-w \times 2n-z-w}$ is a *Sylvester Matrix* associated to the polynomials $\tilde{A}$ and $\tilde{B}$; and $|{}^{\mathrm{Z}}\Phi_{{}^{\mathrm{Z}}V\,{}^{\mathrm{Z}}W}| \neq 0$ because $\tilde{A}$ and $\tilde{B}$ are coprime.

3. DEVELOPMENT OF THE ALGORITHM

Combining the criterion developed in Section 2.3 and Section 2.4 one can construct a linear transformation that takes into account the Internal Model Principle and Stable Zero-Pole cancellations at the same time, providing a systematic way to obtain the matrix involved in the determination of the coefficients of the desired closed loop polynomial. Choosing

$$\begin{aligned} L &= \Gamma\,\beta L^* \\ P &= \alpha\,P^* \\ A_{cl} &= \alpha\,\beta A^*_{cl} \end{aligned} \tag{10}$$

The corresponding Diophantine equation remains as follows

$$A^*L^* + B^*P^* = A^*_{cl}$$

where

$$A^* = \frac{\Gamma}{\alpha}\,A \quad \text{and} \quad B^* = \frac{1}{\beta}\,B \tag{11}$$

The corresponding degrees are

$$\deg\{L^*\} = n - z - 1$$
$$\deg\{P^*\} = n + q - w - 1$$
$$\deg\{A^*_{cl}\} = 2n + q - z - w - 1$$

Let ${}^*\mathbb{V}_{l^*}$, ${}^*\mathbb{V}_{p*}$, ${}^*\mathbb{W}$ be vector spaces over $\mathbb{R}$ such as

$${}^*\mathbb{V}_{l^*} = \mathrm{span}\{s^{n-z-1}, s^{n-z-2}, \ldots, s, 1\}$$
$${}^*\mathbb{V}_{p^*} = \mathrm{span}\{s^{n+q-w-1}, s^{n+q-w-2}, \ldots, s, 1\}$$
$${}^*\mathbb{W} = \mathrm{span}\{s^{2n+q-z-w-1}, s^{2n+q-z-w-2}, \ldots, s, 1\}$$

So that $L^* \in {}^*\mathbb{V}_{l^*}$, $P^* \in {}^*\mathbb{V}_{p^*}$ and $A^*_{cl} \in {}^*\mathbb{W}$. Let ${}^*\mathbb{V}_{l^*} \tilde{\oplus} {}^*\mathbb{V}_{p^*}$ be the external direct sum of ${}^*\mathbb{V}_{l^*}$ and ${}^*\mathbb{V}_{p^*}$. Construct bases ${}^*V$ and ${}^*W$ in the same way as in (2) and (3). Define the linear transformation ${}^*\Phi$ as it follows

$${}^*\Phi : {}^*\mathbb{V}_{l^*} \tilde{\oplus} {}^*\mathbb{V}_{p^*} \longrightarrow {}^*\mathbb{W}$$
$${}^*\Phi\{(l^*, p^*)\} \mapsto A^*\,l^* + B^*\,p^*$$

Using the same criterion as in (4) and (5) with bases ${}^*V$ and ${}^*W$ respectively, the construction of the submatrices ${}^*\xi_{A^*} \in \mathbb{R}^{2n+q-z-w \times n-z}$ and ${}^*\xi_{B^*} \in \mathbb{R}^{2n+q-z-w \times n+q-w}$ (in columns)

$$\begin{aligned} {}^*\xi_{A^*} &= \underbrace{\left[\, (A^*\,s^{n-z-1})^T_{{}^*W} \;\cdots\; (A^*)^T_{{}^*W} \,\right]}_{\dim\{{}^*\mathbb{V}_{l^*}\}=n-z} \\ {}^*\xi_{B^*} &= \underbrace{\left[\, (B^*\,s^{n+q-w-1})^T_{{}^*W} \;\cdots\; (B^*)^T_{{}^*W} \,\right]}_{\dim\{{}^*\mathbb{V}_{p^*}\}=n+q-w} \end{aligned} \tag{12}$$

Then, the matrix associated to the transformation in the bases ${}^*V$ and ${}^*W$

$$ {}^*\Phi_{*V*W} = [\, {}^*\xi_{A^*} \,|\, {}^*\xi_{B^*} \,] $$

Where $\Phi^*_{VW} \in \mathbb{R}^{2n+q-z-w \times 2n+q-z-w}$ is a *Sylvester Matrix* associated to the polynomials A^* and B^*.

In synthesis, the algorithm can be summarized in the following simple steps

(i) Choose the *generating polynomial* Γ and the stable dynamics to cancel α (poles) and β (zeros).
(ii) Compute A^* and B^* as in (11) and extract their corresponding coefficients.
(iii) Using the information of the degrees of the denominator of the plant A (n), the generating polynomial Γ (q), the desired pole cancellations α (w) and the desired zero cancellations β (z) construct the submatrices ${}^*\xi_{A^*}$ and ${}^*\xi_{B^*}$ performing the corresponding shifts to the coefficients of the polynomials A^* and B^* as in (12).
(iv) Choose the desired dynamics for the closed loop polynomial A^*_{cl} of degree $(2n+q-z-1)$.
(v) Solve the corresponding linear equation system involving the matrix associated to the linear transformation $\Phi^* \in \mathbb{R}^{2n+q-z-w \times 2n+q-z-w}$ to find the coefficients of L^* and P^*.
(vi) Compute L, P and A_{cl} as in (10).

Example 2. (Example 1 revisited). We recall the Example 1, but this time we will force the Stable Zero-pole cancellations in addition of the Internal Model Principle using the algorithm stated before. In this case, we cancel all stable factors, that is $z = 1$ and $w = 2$, and

$$ A^* = s(s^2+1) \quad \text{and} \quad B^* = 1. $$

$$ \begin{aligned} \deg\{L^*\} &= n - z - 1 = 0 \\ \deg\{P^*\} &= n + q - w - 1 = 2 \\ \deg\{A^*_{cl}\} &= 2n + q - z - w - 1 = 3 \end{aligned} $$

The corresponding dimensions

$$ \dim\{{}^*\mathbb{V}_{l^*}\} = 1, \quad \dim\{{}^*\mathbb{V}_{p^*}\} = 3, \quad \dim\{{}^*\mathbb{W}\} = 4 $$

Constructing the submatrices ${}^*\xi_{A^*} \in \mathbb{R}^{4\times 1}$ and ${}^*\xi_{B^*} \in \mathbb{R}^{4\times 3}$ yields

$$ {}^*\xi_{A^*} = \underbrace{\begin{bmatrix} 1 \\ 0 \\ 1 \\ 0 \end{bmatrix}}_{\dim\{{}^*\mathbb{V}_{l^*}\}} \qquad {}^*\xi_{B^*} = \underbrace{\begin{bmatrix} 0 & 0 & 0 \\ 1 & 0 & 0 \\ 0 & 1 & 0 \\ 0 & 0 & 1 \end{bmatrix}}_{\dim\{{}^*\mathbb{V}_{p^*}\}} $$

Computing the coefficients of L^* and P^* involves the following linear system

$$ \begin{bmatrix} l_0^* \\ p_2^* \\ p_1^* \\ p_0^* \end{bmatrix} = \underbrace{\begin{bmatrix} 1 & 0 & 0 & 0 \\ 0 & 1 & 0 & 0 \\ 1 & 0 & 1 & 0 \\ 0 & 0 & 0 & 1 \end{bmatrix}^{-1}}_{{}^*\Phi^{-1}_{*V*W}} \begin{bmatrix} 1 \\ 9 \\ 27 \\ 27 \end{bmatrix} $$

Solving the system of equations using the matrix of the linear transformation ${}^*\Phi_{*V*W}$ computed before, the final controller is given by the following transfer function

$$ K(s) = \frac{\alpha P^*}{\Gamma \beta L^*} = \frac{9(s+2)^2(s^2+2.889s+3)}{s(s^2+1)(s+1)} \qquad (13) $$

In Figure 2 we show the step response from reference input to output using the controller developed in (8) and using the controller with zero-pole cancellations (13). An output disturbance $d_0(t) = sin(t)$ was injected at $t = 5[sec.]$.

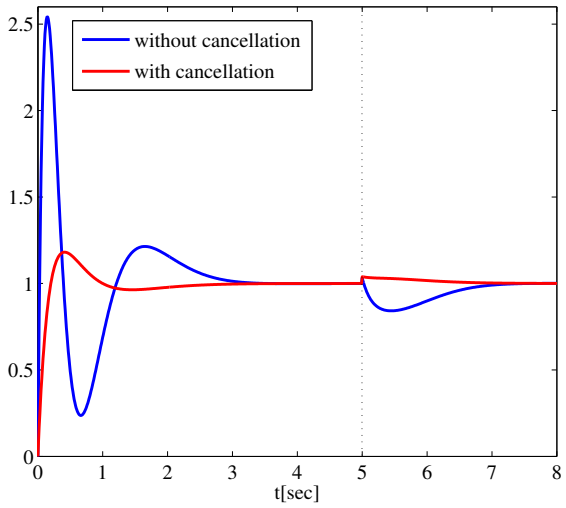

Fig. 2. Step response from reference input to output

4. CONCLUSIONS

In this work, we developed a simple and systematic algorithm to design SISO controllers based on a input-output mathematical model using linear algebra concepts. It considers the *Internal Model Principle* and allows to perform *Stable Zero-Pole cancellations* in the same linear transformation. The extrapolation of this algorithm to the discrete domain it's straightforward, which implies that it can be easily implemented in a microcontroller. In this way, it can be coupled to a model identification system turning the controller into an adaptive one, showing the versatility of the algorithm developed.

REFERENCES

Francis, B.A. and Wonham, W.M. (1975). The internal model principle for linear multivariable regulators. *Applied mathematics and optimization*, 2(2), 170–194.
Goodwin, G.C., Graebe, S.F., and Salgado, M.E. (2001). *Control system design*, volume 240. Prentice Hall New Jersey.
Hunt, K.J. (1993). *Polynomial methods in optimal control and filtering*. 49. Iet.
Kučera, V. (1991). *Analysis and design of discrete linear control systems*. Prentice-Hall, Inc.
Kučera, V. (1993). Diophantine equations in control—a survey. *Automatica*, 29(6), 1361–1375.
Li, H. (2011). A note on the inversion of sylvester matrices in control systems. *Mathematical Problems in Engineering*.
Seron, M.M., Braslavsky, J.H., and Goodwin, G.C. (1997). *Fundamental Limitations in Filtering and Control*. Springer.

CHAPTER 8

MOBILE ROBOTS

A Performance Evaluation Approach for Embedded Controllers of Mobile Robots ⋆

G.A. Acosta * **J.A. Saldarriaga,** ** **J.A. Jiménez** ***

* *Politécnico Colombiano Jaime Isaza Cadavid, Medellín, Colombia, Cr. 40 7-151 (e-mail: gaacosta@elpoli.edu.co).*
** *Politécnico Colombiano Jaime Isaza Cadavid, Medellín, Colombia, Cr. 40 7-151 (e-mail: jaime_saldarriaga91091@elpoli.edu.co)*
*** *Departamento de Ciencias de la Computación y la Decisión, Facultad de Minas, Universidad Nacional de Colombia, Medellín, Colombia, (e-mail: jajimen1@unal.edu.co)*

Abstract: The application of metrics quality of control (*QoC*) in mobile robotics could be a difficult task because not always is possible access the data of embedded control units of the robot effectors. This paper presents an heuristic geometric-based altrernative for performance evaluation of embedded controllers. Geometric characteristics of simple circular and linear paths described by the robot are considered for performance evaluation of the controllers. For experimental evaluation of our approach, two PI embedded controllers were designed and implemented in a two wheeled mobile robot (2WMR). Results of conducted experiments showed that our approach constitutes an alternative of performance evaluation of embedded controllers when it is not possible to access data of the control units.

Keywords: Mobile robots; PI controllers; Tuning methods; System identification; Performance analysis.

1. INTRODUCTION

Motion control of wheeled mobile robots (WMRs) remains an important research topic because it support motion tasks like path following and trajectory tracking [Morin and Samson (2008)]. A broad range of approaches to effectors control of WMRs have been reported. Comasolivas et al. (2015) used the quantitative feedback theory (QFT) to design a proportional-integral-derivative (PID) controller for a robot with four omnidirectional wheels. Kanjanawanishkul (2012) present a review motion control of WMRs using model predictive control (MPC), also several experiments to comparison between path following and trajectory tracking for an omnidirectional mobile robot and an unicycle-type mobile robot were conduced and results discussed. Two-wheeled mobile robots (2WMRs) were developed by Ahmad et al. (2013) and Malu et al. (2014) and low level motion control implemented trough PID controllers.

Soft computing is another alternative for motion control of WMRs. A complete discussion on the application of fuzzy logic in reactive navigation of mobile robots is presented by Hong et al. (2012). The authors also present a case study in which basic behaviours such as goal reaching, emergency situation, obstacle avoidance, wall following and an action coordination system were implemented using fuzzy logic. Xu et al. (2013) designed and implemented a Takagi-Sugeno fuzzy logic controller (FLC) for a two-wheeled inverted pendulum, and Hanafi et al. (2013) developed a 2WMR for cleaning air ducts and corridors based on a reactive navigation architecture in which a fuzzy logic controller allows the robot to follow close walls.

Other works present comparative performance studies of different strategies to control effectors of 2WMRs. A performance analysis of three controllers, including lead-lag compensator, PID controller and FLC for DC motor control of a field survey 2WMR was conduced by Shamshiri et al. (2013). A comparison of FLC, linear quadratic controller (LQR) and a PID controller to balancing the tilt angle of two wheeled inverted pendulum robot is presented by Bature et al. (2014). A comparative investigation about the performance of a PID and an FLC linear position and tilt angle controllers was developed by Nasir et al. (2011). In these works, time-domain specifications such as rise time, settling time and percent overshoot were used for performance analysis of controllers. In this paper, we propose an alternative method for motor control evaluation based on geometric characteristics of two simple trajectories described by a 2WMR.

The main contributions of this paper are: 1) an heuristic-based alternative for performance evaluation of low-level motion controllers is provided. Unlike classical time-domain methods, our approach is based on geometrical characteristics of simple and real trajectories described by a robot, 2) design and implementation of two embedded feedback controllers, one for each motor, that receive velocity references and make that motors achieve and maintain these values until new references are received, and 3) implementation of an identification process in which

⋆ The authors thank their institutions of origin, Politécnico Colombiano Jaime Isaza Cadavid and Universidad Nacional de Colombia, for the support provided in the development of this work.

the robot acts as a drive unit and a data acquisition system. For this, a C program for applying PWM signals to the motors, obtaining data from encoders and wireless transmission of these data was developed.

This article is organized as follows. In this first section, we highlight the importance of motor control in mobile robotics. In section 2 our heuristic geometric-based approach for controller performance evaluation is presented. In section 3 the modelling of robot and effectors is detailed. In section 4, the design procedure of embedded controllers is discussed. In section 5, experiments are conducted and results are presented and, finally, conclusions are drawn in section 6.

2. A GEOMETRIC-BASED APPROACH FOR PERFORMANCE CONTROLLER EVALUATION

In a control loop, the error is defined as the deviation of the controlled variable with respect to a reference value. A way to evaluate the Quality of Control (QoC) of a system is quantifying the cumulative error, for which, in the case of discrete-time controllers, is essential to know the error $e(nT)$ at each sampling instant $T = 1/f_s$. Some performance indices based on cumulative error for QoC evaluation are: Integral of Absolute Error (IAE) and Integral of Squared Error (ISE). However these metrics are difficult or impossible to apply in the field of mobile robotics when motors control is carried out by sealed units that only receive reference values, but do not send actual motor speed data.

In this paper we propose an heuristic method for performance evaluation of controllers based on geometric characteristics of two simple trajectories: linear and circular displacements. This approach can be applied in those cases where it is difficult, if not impossible, to establish the error $e(nT)$.

Metric based on the linear displacements Linear movement of differential robots is obtained when the speeds of its driving wheels (left and right) are exactly equals at all time, this is, when $v_{_L}(t) = v_{_R}(t)$. However, the uncertainty inherent to any real control system, causes, at least for finite intervals of time, that these speeds will be different. Thus, the actual robot path differs from the purely linear. This fact suggests that we could use the deviations of the actual path of the robot with respect to ideal straight-line path, to establish a metric for performance evaluation of motor control schemes on differential robots. Relative to Figure 1, we define the metric $Cumulative\ Absolute\ Distance - CAD$ such as

$$CAD = \sum_{k=k_0}^{k_f} |d_k|,\ k \in \mathbb{Z}. \tag{1}$$

where d_k is the k-th perpendicular distance between the actual trajectory and the ideal straight-line trajectory.

Metric based on the circular displacements Otherwise, when $v_{_L}(t) \neq v_{_R}(t)$ the robot describes curved paths. An special case is when $v_{_L}(t) = k_1$, $v_{_R}(t) = k_2$, and $k_1 \neq k_2$, in which the path obtained should be to a perfect circle of radius R. But as previously mentioned, due to the uncertainty associated to real control systems, is possible

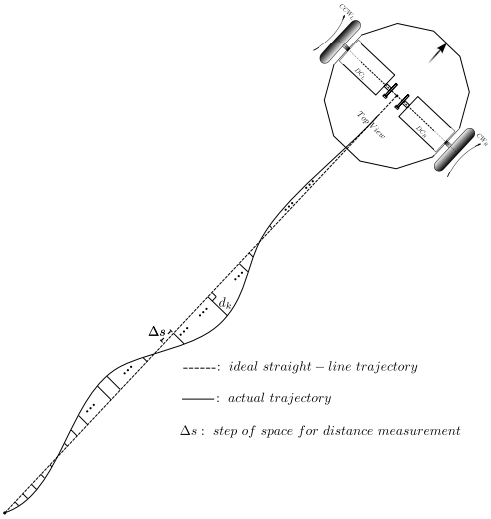

Fig. 1. Linear path and distances for CAD definition

to obtain open circular paths such as shown in 2. In this figure, ΔC corresponds to *aperture distance* or distance between initial point A and final point B of the described path. Because the actual path does not correspond to a perfect circle, then we define a *circle-base* with center in O and ϕ_r diameter passing through the midpoint P of ΔC.

The diameter of the *circle-base* is set as follows: with center in P, draw an arc that cuts the circular trajectory at C and D points to get the chord $\overline{CD}$. Once the midpoint M of $\overline{CD}$ is set, the $\overline{MP}$ line segment is drawn and extends until cuts the circular path at Q point. In this way we establish as the diameter ϕ_r, of the $circle - base$, the length of $\overline{PQ}$ segment and its midpoint O as its center.

Now we can define the metric $Circular\ Trajectory\ Error - CTE$ such as

$$CTE = |\phi_r - \phi_t|. \tag{2}$$

where the theoretical diameter ϕ_t of the ideal circular trajectory is calculated using Equation 6.

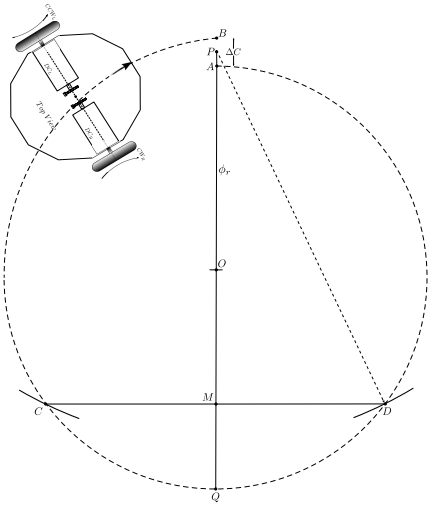

Fig. 2. Open circular path and geometry for CTE definition

3. SYSTEM MODELING

Kinematic Modeling The kinematic modeling refers to the study of motion of a mechanical system without considering the forces and torques involved. For a 2WMR the Kinematic model allows to express its velocities as functions of velocities of its wheels and its geometric parameters [Dhaouadi et al. (2013), Alves et al. (2011)].

For 2WMRs a pure rolling motion without slipping is obtained when the robot rotates around an external point located over the common axis of both driving wheels. This point is known as the instantaneous center of curvature (ICC) or instantaneous center of rotation (ICR). The ICC will move by changing velocities of the two driving wheels, allowing the robot carry out different paths. At each time instant, right and left wheels follow paths around the ICC at the same angular velocity $\omega = d\psi/dt$ as is shown in Figure 3. Table 1 shows the symbols used in this section, with $L = 22.1$ cm. The linear velocities of the driving wheels are given by

$$v_{_L} = \omega(R + \frac{L}{2}). \tag{3}$$

$$v_{_R} = \omega(R - \frac{L}{2}). \tag{4}$$

where R is the distance between the ICC and the middle point $C_{_R}$ between the two wheels. The angular velocity of the robot is obtained subtracting (4) from (3) and is expressed by

$$\omega = \frac{v_{_L} - v_{_R}}{L}. \tag{5}$$

By adding (3) and (4) and substituting (5) in the result we obtain

$$R = \frac{v_{_L} + v_{_R}}{v_{_L} - v_{_R}} \cdot \frac{L}{2}. \tag{6}$$

Equations (5) and (6) allow to establish the angular velocity of the robot and the instantaneous radius of curvature as functions of linear velocities of the wheels and their separation L. Finally, the linear velocity of the midpoint $C_{_R}$ is given by the average of the wheel velocities

$$v_{_{CR}} = \omega R = \frac{v_{_L} + v_{_R}}{2}. \tag{7}$$

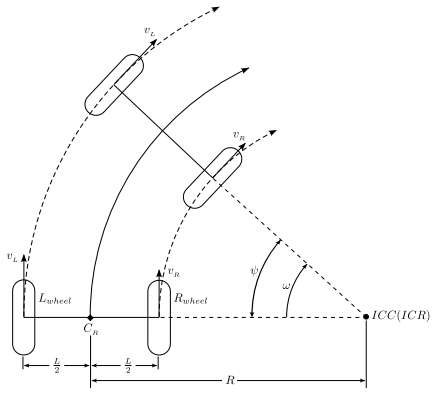

Fig. 3. Differential drive motion of a mobile robot

Effectors Modeling In a previous work [Acosta et al. (2014)] a teaching and research **Car-li**ke **Au**ton**o**mou**s** vehicle (*Carlitos*) was designed and constructed. This 2WRM is used here for experimental validation of our approach. The block diagram of *Carlitos* is shown in Fig. 4. Actuation system is composed of two DC motors with coupled gearboxes and a dual H-bridge motor driver for PWM control signals amplification. The proprioceptive sensory system integrates quadrature encoders mounted over the axes of both DC motors, and a CMPS03 digital compass for estimation of robot head orientation. Encoders provide 1125 counts per revolution.

The exteroceptive system is made up of a sonars ring with twelve SRF02 devices for distance measurement to surrounding obstacles. The top side of sonars ring has a 802.15.4 radio for wireless command reception and data transmission. Processing unit correspond to a 32-bit microcontroller capable of operate up 50 MHz. We use the Freescale MCF51QE128 microcontroller to process pulses from encoders and generate PWM control signal for each motor. Control algorithms were coded in C language and programmed in microcontroller's internal flash memory.

Carlitos robot was conceived and designed having in account modularity and scalability criteria.

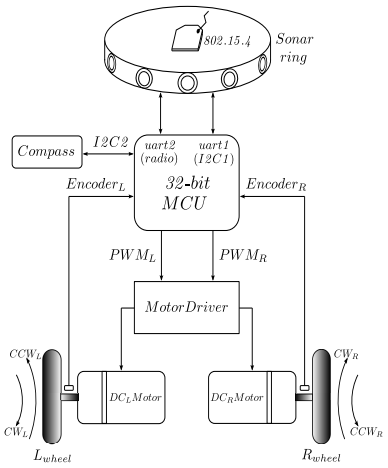

Fig. 4. Block diagram and a picture of the experimental robot

To take advantage of the robot's resources, a C language algorithm was developed to support the effectors modelling task. Initially the robot was placed in an obstacles free indoor environment awaiting the start command sent from a PC via a 802.15.4 radio link. As is shown in Figure 5, once received the *start* order, an step PWM signal with a duty cycle (DC) of 50% it is generated by the microcontroller to drive both motors. This signal was

Table 1. Kinematic model variables

Parameter	Description
L	Distance between support points of wheels (cm)
R	Instantaneous radius of curvature (cm)
$C_{_R}$	Midpoint between driver wheels (cm)
ψ	Robot orientation angle (rad)
ω	Angular velocity of 2WMR ($rad \cdot s^{-1}$)
$v_{_L}$, $v_{_R}$	Velocities of wheels along the ground ($cm \cdot s^{-1}$)
$v_{_{CR}}$	Linear velocity of $C_{_R}$ ($cm \cdot s^{-1}$)

maintained for 1.8 seconds. Subsequently, the duty cycle of the PWM signal was incremented to 60%. This step was also maintained by 1.8 seconds. During the total displacement (3.6 seconds), the number of pulses per sampling period $T = 1/f_s = 0.1\ s$ was captured from the encoders and sent to a PC via the wireless link. Anything additional resources to those available in mobile robotic platform were required for the actuators modeling.

The databases obtained from the test (Figure 5-a) were used, in combination with the system identification toolbox^{TM} of Matlab®, to get a mathematical model of the actuators. We choose an approach of lower-order as the first-order-plus dead-time (FOPDT) to model the dynamic behavior of DC motors. The form of a FOPDT model is given by

$$G(s) = \frac{Ke^{-\theta s}}{\tau s + 1}. \tag{8}$$

With the model parameters $K = 2.63$ (process gain), $\tau = 0.2222$ (time constant), and $\theta = 0.1159$ (dead-time), we obtain

$$G(s) = \frac{2.63e^{-0.1159s}}{0.2222s + 1}. \tag{9}$$

The correlation factor given by the system identification toolbox^{TM} for the models of both motors was of 94.02%.

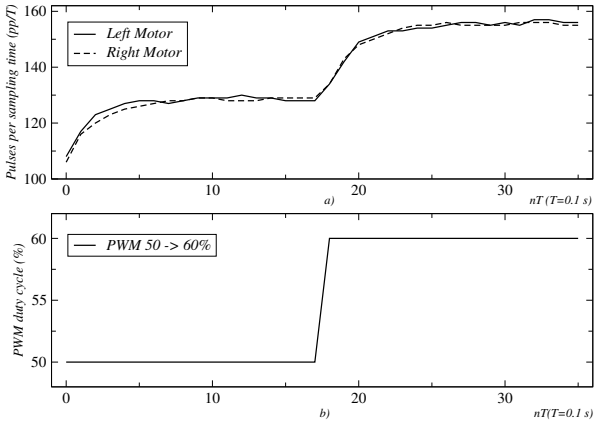

Fig. 5. Step test: a) response of actuators, and b) PWM signal of stimulus

4. EMBEDDED CONTROLLERS DESIGN

Two proportional-integral (PI) feedback controllers were implemented in the robot microcontroller, one for each motor and two model-based tuning methods were applied: Ciancone-Marlin and Cohen-Coon. For a PI discrete-time controller the transfer function is given by

$$D(z) = \frac{q_0 z + q_1}{z - 1}. \tag{10}$$

Next, we present in detail the methods used to determine the q_0 and q_1 parameters.

4.1 Ciancone-Marlin Method

To determine the controller parameters K_c (controller gain) and T_i (integral time), Ciancone and Marlin defined the parametric relationship $fractionaldeadtimeT_f$ such as

$$T_f = \frac{\theta}{\theta + \tau} = \frac{0.1159}{0.1159 + 0.2222} = 0.3428. \tag{11}$$

Additional relationships such as dimensionless gain G_x and dimensionless reset time τ_y were defined by

$$G_x = K_c K. \tag{12}$$

$$\tau_y = \frac{\tau_i}{\theta + \tau}. \tag{13}$$

both expressions correlated with T_f. According to correlation tuning data presented in Table 2 [García et al. (2014)], $G_x = 1.032$ and $\tau_y = 0.881$.

Table 2. Ciancone-Marlin tunning table for PI controllers

T_f	G_x	τ_y
0.0	1.417	0.748
0.1	1.417	0.748
0.2	1.193	0.964
0.3	1.032	0.881
0.4	0.918	0.818
0.5	0.861	0.756
0.6	0.722	0.693
0.7	0.464	0.631
0.8	0.608	0.568
0.9	0.594	0.506
1.0	0.558	0.443

For discrete-time systems θ_d is calculated as

$$\theta_d = \theta + \frac{T}{2} = 0.1159 + \frac{0.1}{2} = 0.1659. \tag{14}$$

Thus, the parameters of the PI controller are calculated by

$$\tau_i = \tau_y(\theta_d + \tau) = 0.881(0.1659 + 0.2222) = 0.3419. \tag{15}$$

$$K_c = \frac{G_x}{K} = \frac{1.032}{2.63} = 0.3924. \tag{16}$$

with these values q_0 and q_1 are calculated as

$$\begin{aligned} q_0 &= K_c(1 + \frac{T}{2\tau_i}) \\ &= 0.3924(1 + \frac{0.1}{2 \times 0.3419}) = 0.4498. \end{aligned} \tag{17}$$

$$\begin{aligned} q_1 &= -K_c(1 - \frac{T}{2\tau_i}) \\ &= -0.3924(1 - \frac{0.1}{2 \times 0.3419}) = -0.335. \end{aligned} \tag{18}$$

4.2 Cohen-Coon Method

Cohen and Coon noted that the response of many processing units to a change in input had sigmoidal form, which could be approximated to the response of a FOPDT system. The controller parameters could be determined from the parameters of the plant by the following semi-empirical relationships

$$K_c = \frac{\tau}{K\theta}(0.9 + \frac{\theta}{12\tau}) = \frac{0.2222}{2.63 \times 0.1659}(0.9 + \frac{0.1659}{12 \times 0.2222}) = 0.49. \quad (19)$$

$$\tau_i = \frac{\theta(30\tau + 3\theta)}{9\tau + 20\theta} = \frac{0.1659(30 \times 0.2222 + 3 \times 0.1659)}{9 \times 0.2222 + 20 \times 0.1659} = 0.2235. \quad (20)$$

As in the above method q_0 and q_1 are calculated by

$$q_0 = K_c(1 + \frac{T}{2\tau_i}) = 0.49(1 + \frac{0.1}{2 \times 0.2235}) = 0.5996. \quad (21)$$

$$q_1 = -K_c(1 - \frac{T}{2\tau_i}) = -0.49(1 - \frac{0.1}{2 \times 0.2235}) = -0.3804. \quad (22)$$

Figure 6 shows the response of the two controllers to a setpoint speed of 100 pp/T. Note that the wheel speeds are expressed in pulses per sampling time (pp/T). At the top, the response of Ciancone-Marlin controller and, at the bottom, the response of Cohen-Coon controller. A C language program for effectors control, data acquisition and its wireless transmission, was developed and programmed in the internal flash memory of the robot microcontroller. Figure 6 was drawn with the data received. The difference equation for PI controller implementation is given by

$$m(k) = q_0 e(k) + q_1 e(k-1) + m(k-1). \quad (23)$$

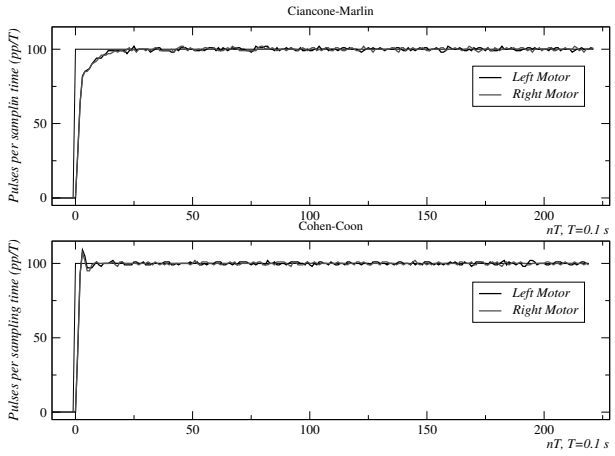

Fig. 6. Step responses of controllers, Ciancone-Marlin (top), and Cohen-Coon (bottom)

5. VALIDATION EXPERIMENTS

Two simple trajectories and its geometrical characteristics were considered for controllers performance evaluation. Equations (5) and (6) shows how to synthesize the two paths of interest for this study:

i. *Circular path.* The path is a circle of radius R with center in ICC. For locate the ICC outside the line segment that connects both wheels, must meet $|R| = L/2$ condition. The robot moves clockwise when $v_L > v_R$.
ii. *Linear path.* The robot moves straight line when $\omega = 0$, this is met for $v_L = v_R$.

Should be noted that the actual trajectories of the robot differ from the theoretical because of uncertainty in the measurements of the sensors and uncertainty in control commands.

Circular displacement. For validation of CTE metric defined by Equation 2, three circular paths C_1, C_2 and C_3 were conducted for each controller. The reference velocities for each path were established as, C_1: $v_L = 80$, $v_R = 60$, C_2: $v_L = 100, v_R = 80$, and C_3: $v_L = 120, v_R = 100$. Table 3 presents the experimental results obtained for the Ciancone-Marlin controller and table 4 for Cohen-Coon controller.

Table 3. Results of CTE metric for Ciancone-Marlin controller

Path	ϕ_r (cm)	ϕ_t (cm)	CTE (cm)
C_1	153	148.4	4.6
C_2	193.4	190.8	2.6
C_3	235	233.5	1.5
Mean			2.90

Table 4. Results of CTE metric for Cohen-Coon controller

Path	ϕ_r (cm)	ϕ_t (cm)	CTE (cm)
C_1	151.5	148.4	3.1
C_2	192.6	190.8	1.8
C_3	234.7	233.5	1.2
Mean			2.03

Linear displacement Also, experiments of linear displacement for validation of the CAD metric, defined by Equation 1, were conducted. This time the set-points of velocity were $v_L = v_R = 100pp/T$ and real trajectories were of approximately 430 centimetres. Step of space Δs (Figure 1), for distance measurement was of 30 cm. The results obtained are given in table 5.

Table 5. CAD metrics for embedded controllers

Metric	Ciancone-Marlin	Cohen-Coon
CAD	55.6	50.3

For comparative purposes, two metrics for quality of control (QoC) evaluation were considered, these are: IAE and ISE. These two metrics express QoC in terms of the error $e(t)$, which is defined as the difference between the set-point $r(t)$ and the system output $y(t)$. Continuous-time and discrete-time forms of IAE and ISE are given by

$$IAE = \int_{t_0}^{t_f} |e(t)|dt \approx \sum_{k=k_0}^{k_f} |r(kT) - y(kT)|. \quad (24)$$

$$ISE = \int_{t_0}^{t_f} e(t)^2 dt \approx \sum_{k=k_0}^{k_f} (r(kT) - y(kT))^2. \quad (25)$$

where $t_0(k_0)$ and $t_f(k_f)$ are the initial and final continuous (discrete) times of the evaluation interval and $T = 0.1\ s$. Table 6 shows the results obtained by applying both metrics to the controllers considered.

Table 6. IAE & ISE metrics for embedded controllers

	Ciancone-Marlin		Cohen-Coon	
Metrics	DC_L	DC_R	DC_L	DC_R
IAE	450	453	317	286
ISE	17584	17693	13613	13430

Results analysis Comparing results obtained from the circular path experiments (Tables 3 and 4), we can observe that the CTE metric was better for Cohen-Coon controller than for Ciancone-Marlin for the three considered trajectories. Similarly, for the linear paths, the best CAD metric (Table 5) was obtained with the Cohen-Coon controller. In this way, we can conclude that the Cohen-Coon controller offers a better performance for simple trajectories in a 2WMR than the Ciancone-Marlin controller. This result is consistent when we consider the QoC metrics calculated in table 6 for the two controllers. Both, IAE and ISE values, say us that the better performance was obtained with the Cohen-Coon controller.

Our performance evaluation approach of low level motion controllers in 2WMRs is useful in situations where is difficult or impossible to obtain the error from embedded controllers to calculate standard QoC metrics. In that sense, our approach constitute a performance evaluation alternative based on real graphics drawn for the robot during its displacement.

6. CONCLUSION

In this paper, an heuristic geometric-based alternative for performance evaluation of effectors controllers in mobile robots has been presented. Two embedded PI controllers, Ciancone-Marlin and Cohen-Coon, were designed and implemented for motion control of a 2WMR for experimental validation of our approach. Geometric characteristics of circular and linear paths were considered for performance evaluation of both controllers based on two defined metrics: CAD and CTE. Validation experiments and a comparative with IAE and ISE metrics showed that our approach constitutes a valid alternative for performance evaluation of embedded controllers of a mobile robot.

REFERENCES

K. Kanjanawanishkul. Motion control of a wheeled mobile robot using model predictive control: A survey. *KKU Research Journal*, volume 17, issue 5, pages 811–837, 2012.

P. Morin, and C. Samson. Motion control of wheeled mobile robots. In B. Siciliano, O. Khatib, editors, *Handbook of Robotics*, pages 799–826. Springer, 2008.

R. Comasolivas, J. Quevedo, T. Escobet and A. Escobet. Low level control of an omnidirectional mobile robot. *23rd Mediterranean Conference on Control and Automation (MED)*, pages 1160–1166. Torremolinos, Spain, 2015.

A.A. Mahfouz, A.A. Aly, and F.A. Salem. Mechatronics design of a mobile robot system. *I.J. Intelligent Systems and Applications*, volume 5, issue 3, pages 23–36, 2013.

S.K. Malu, and J. Majumdar. Kinematics, localization and control of differential drive mobile robot. *Global Journal of Researches in Engineering: H Robotics & Nano-Tech*, volume 14, issue 1, 2014.

T.S. Hong, B. Karasfi, and D. Nakhaeinia. Application of fuzzy logic in mobile robot navigation. In E. Dadios, editor, *Fuzzy Logic-Controls, Concepts, Theories and Applications*, pages 21–36. InTech, 2012.

J.-X. Xu, Z.-Q. Guo, and T.H. Lee. Design and implementation of a Takagi-Sugeno-type fuzzy logic controller on a two-wheeled mobile robot. *IEEE Trans. Ind. Electron.*, volume 60, issue 12, pages 5717–5728, 2013.

D. Hanafi, Y.M. Abueejela, and M.F. Zakaria. Wall follower autonomous robot development applying fuzzy incremental controller. *Intelligent Control and Automation*, volume 4, issue 1, pages 18–25, 2013.

G.A. Acosta, J.C. Herrera, and O. Zapata. Control de navegación basado en comportamientos para pequeños robots móviles. *Revista Politécnica*, volume 10, issue 18, pages 125–134, 2014.

L.E. García, and M. Arroyave. Desarrollo e implementacion de un controlador con ganancia programable para un autoclave. *Revista Politecnica*, volume 9, issue 1, pages 21–30, 2009.

R. Dhaouadi, and A. Abu Hatab. Dynamic modelling of differential-drive mobile robots using Lagrange and Newton-Euler Methodologies: a unified framework. *Advance in Robotics & Automation*, volume 2, issue 2, pages 1–7, 2013.

S.F.R. Alves, J.M. Rosario, H. Ferasoli Filho, L.K.A. Rincon, and R.A.T. Yamasaki. Conceptual bases of robot navigation modeling, control and applications. In A. Barrera, editor, *Advances in Robot Navigation*, InTech, 2011.

R. Shamshiri, and W.I.W. Ismail. Design and simulation of control systems for a field survey mobile robot platform. *Research Journal of Applied Sciences, Engineering and Technology*, volume 6, issue 23, pages 2307–2315, 2013.

A.A. Bature, S. Buyamin, M. N. Ahmad, and M. Muhammad. A comparison of controllers for balancing two wheeled inverted pendulum robot. *International Journal of Mechanical & Mechatronics Engineering*, volume 14, pages 62–68, 2014.

A.N.K. Nasir, M.A. Ahmad, R. Ghazali, and N.S. Pakheri. Performance comparison between fuzzy logic controller (FLC) and PID controller for a highly nonlinear two-wheels balancing robot. *First International Conference on Informatics and Computational Intelligence*, pages 176–181, 2011.

Delayed Observer Control for a Leader-Follower Formation with Time-gap Separation.

R. D. Cruz-Morales. A. Rodríguez-Ángeles. M. Velasco-Villa.

CINVESTAV-IPN
Departamento de Ingeniería Eléctrica , Sección de Mecatrónica
Av. I.P.N. No. 2508, Col. San Pedro Zacatenco 07360, México, D.F.
(e-mail: rdcruz,aangeles,velasco@cinvestav.mx).

Abstract: The main objective of this paper is to maintain a leader follower formation with a time gap separation between the mobile robots, with this control, the longitudinal distance variation between robots only depends on the leader velocity. The formation problem is solved using an observer that serves as a virtual reference to the follower robot that, correspond to the leader trajectory delayed τ units of time. The strategy is theoretically formally proven, and numerical simulations are presented.

Keywords: Time-gap separation, mobile robots, leader-follower formation.

1. INTRODUCTION

Mobile robots have been studied for many years, by using formation of mobile robots several problems have been solved and allowing dangerous, repetitive or security tasks, as is the case of patrolling different areas with obstacles Matveev et al. [2012]. For example, the cooperation among robots to complete tasks in which is required a formation that recreates a virtual structure to carry a heavy object, or just to maintain a geometric configuration between them Mehrjerdi et al. [2011] along a path. Some formations with mobile robots try to imitate the animal behavior with the objective of resembling a swarm or herd as in Sun and Wang [2007] where controlling and switching different formations between robots using synchronization to create the swarm movement. Another techniques use robots that move combining their sensors to improve the security by maximizing the possibilities of detecting dangerous situations, obstacles or covering areas on military search and rescue tasks or even security patrols Balch and Arkin [1998]. Sometimes, the formation can switch the leader in order to maintain the formation while the real leader avoids an obstacle and then the formation retakes the original leader or completes a specific goal with all the agents as a team Swaminathan et al. [2015]. In other cases mobile robots are used in rescue and recovery tasks in different environments as in Murphy et al. [2009], where several robots are use in mining accidents to manipulate fan doors, push aside obstacles, recolect gas, temperature reading and video.

The leader-follower formation has been studied for many years, is one of the most used formation, in some cases the formation is only studied for one follower as in Consolini et al. [2008], where only one robot is considered to prove the stability of the formation with the proposed control, In Tanner et al. [2004], Desai et al. [1998], the stability conditions are stablished for a set of followers using graph theory to prove the stability of a chained leader-follower formation, proving as well the conditions for safety and robustness. Leader-follower formation in most of the cases, is based on a longitudinal distance separation between robots Kawabe [2000], thats why the follower robot does not always track the same path that the leader robot describes, especially when the leader goes in a curved path. When the robots have to go on a predetermiated road, tracking the described path of the leader robot is very important. For that reason this paper focuses mainly in a time-gap separation between the robots that maintain the leader-follower formation, in contrast with most of the papers that the objective is to maintain a predetermined distance between the leader and the follower robot. This strategy is used in Adaptive Cruise Control (ACC) as in Bareket et al. [2003], where it has been shown that it is better to maintain a time-gap separation on the road that having a predeterminated distance. Taking into consideration the analysis made in Seppelt and Lee [2007] which shows the limitations of the ACC, it is possible to say that maintaining a security distance by taking a secure time-gap is better than only taking a secure longitudinal distance.

A time-gap separation strategy to perform the leader-follower formation is presented, the use of an observer that estimates the time delayed trajectory of the leader mobile robot serves as desired reference trajectory for the follower robot.

The document is presented as follows: first, the kinematic model of the mobile robot and the problem formulation is presented. The development of the observer and its convergence properties are presented in the next section. The work continues presenting the observer based strategy control together with its related convergence proof. Then, numerical simulations with two robots are done to show

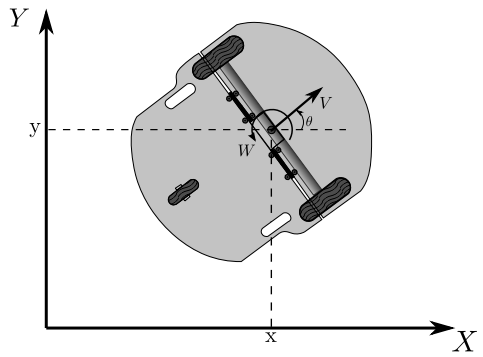

Fig. 1. Mobile robot type (2,0).

the performance of the proposed strategy. Finally, the paper closes with some conclusions.

2. KINEMATIC MODEL AND PROBLEM FORMULATION

It is considered a pair of differentially driven mobile robots (tipe(2,0)) as shown in Fig. 1. Their kinematic model are given by Canudas et al. [1996],

$$\begin{bmatrix} \dot{x}_i(t) \\ \dot{y}_i(t) \\ \dot{\theta}_i(t) \end{bmatrix} = \begin{bmatrix} \cos\theta_i & 0 \\ \sin\theta_i & 0 \\ 0 & 1 \end{bmatrix} \begin{bmatrix} v_i(t) \\ w_i(t) \end{bmatrix}, \quad i = L, F. \tag{1}$$

where (x_i, y_i) are the coordinates of the middle point of the robot axis in the plane $X - Y$, θ_i is the orientation of the vehicle with respect to X and v_i, w_i are the linear and angular input velocities respectively. It is assumed that the mobile robots are made up of rigid bodies, the wheels are non-deformable and they are moving on an horizontal plane, the contact between the wheels and the ground is in a single point of the plane and satisfy the pure rolling and non-slipping conditions along the motion, and the robot fulfills the non-holonomic constraint,

$$\dot{x}_i \sin(\theta_i) - \dot{y}_i \cos(\theta_i) = 0 \tag{2}$$

It will be set $i = L$ for the leader robot and $i = F$ for the follower one.

2.1 Problem formulation.

Consider a leader robot describing any feasible trajectory on the $X - Y$ plane. It is desired that a follower robot tracks the trajectory described by the leader robot delayed τ units of time, where τ represents the desired time gap separation between the leader and the follower robot.

The delayed leader trajectory is obtained by considering an input-delay observer based on the actual measurements of the leader robot. Under these conditions, it is intended that the follower robot tracks the delayed states provided by the observer. This time gap separation, based on a leader time delayed trajectory, is depicted in Fig. 2.

3. OBSERVER DESIGN

The development of the mentioned observer will be described taking into account the following assumptions.

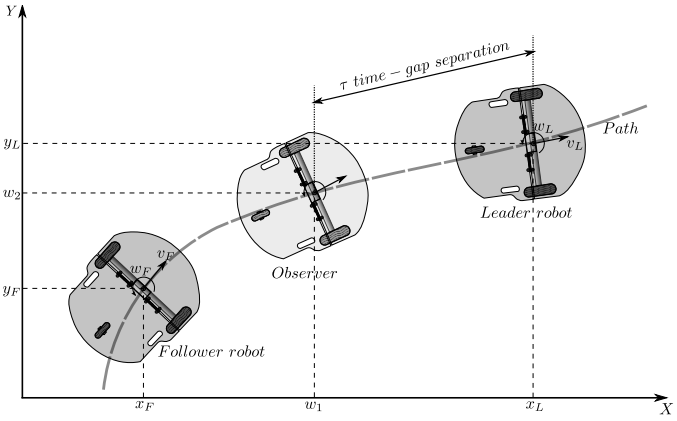

Fig. 2. Leader-follower formation with observer.

Assumption 1. The leader mobile robot variables $x_L(t)$, $y_L(t)$, $\theta_L(t)$, $v_L(t)$, $w_L(t)$ are available for measurement.

Assumption 2. The input leader robot signals $v_L(t)$, $w_L(t)$ are bounded for all t, this is

$$\sup\{v_L\} \leq \bar{v}_L, \ \sup\{w_L\} \leq \bar{w}_L \tag{3}$$

for some positive constants $\bar{v}_L$, $\bar{w}_L$.

To desing the observer for the delayed leader trajectory, consider the delayed variables,

$$w_1(t) = x_L(t-\tau), \ w_2(t) = y_L(t-\tau), \ w_3(t) = \theta_L(t-\tau) \tag{4}$$

Notice that the variables defined in (4) are available for design purposes based on Assumption 1. Hence, by taking the time derivative of (4), it is possible to obtain a virtual system that will serve as a reference for the follower robot, given by,

$$\begin{bmatrix} \dot{w}_1(t) \\ \dot{w}_2(t) \\ \dot{w}_3(t) \end{bmatrix} = \begin{bmatrix} v_L(t-\tau)\cos(w_3(t-\tau)) \\ v_L(t-\tau)\sin(w_3(t-\tau)) \\ w_L(t-\tau) \end{bmatrix}. \tag{5}$$

Based on the virtual system (5), a delayed observer can be proposed in the form,

$$\begin{bmatrix} \dot{\hat{w}}_1(t) \\ \dot{\hat{w}}_2(t) \\ \dot{\hat{w}}_3(t) \end{bmatrix} = \begin{bmatrix} v_L(t-\tau)\cos(\hat{w}_3(t)) + \lambda_1 e_{w_1}(t) \\ v_L(t-\tau)\sin(\hat{w}_3(t)) + \lambda_2 e_{w_2}(t) \\ w_L(t-\tau) + \lambda_3 e_{w_3}(t) \end{bmatrix} \tag{6}$$

where,

$$\begin{aligned} e_{w_1}(t) &= w_1(t) - \hat{w}_1(t) \\ e_{w_2}(t) &= w_2(t) - \hat{w}_2(t) \\ e_{w_3}(t) &= w_3(t) - \hat{w}_3(t) \end{aligned} \tag{7}$$

are the observation error variables, and λ_1, λ_2, λ_3 are constant positive design gains.

3.1 Observation error analysis

To analyze the observation error, a change of coordinates is done in the form,

$$\begin{bmatrix} e_1 \\ e_2 \\ e_3 \end{bmatrix} = \begin{bmatrix} \cos(w_3) & \sin(w_3) & 0 \\ -\sin(w_3) & \cos(w_3) & 0 \\ 0 & 0 & 1 \end{bmatrix} \begin{bmatrix} e_{w_1} \\ e_{w_2} \\ e_{w_3} \end{bmatrix} \tag{8}$$

this is,

$$
\begin{aligned}
e_1 &= e_{w_1}\cos(w_3) + e_{w_2}\sin(w_3)\\
e_2 &= -e_{w_1}\sin(w_3) + e_{w_2}\cos(w_3)\\
e_3 &= e_{w_3}.
\end{aligned} \tag{9}
$$

The observation error dynamics is obtained by taking the time derivative of (9). Taking the first line, and defining $\lambda_1 = \lambda_2 = \lambda$,

$$
\begin{aligned}
\dot{e}_1 &= \dot{e}_{w_1}\cos(w_3) - e_{w_1}\dot{w}_3\sin(w_3) + \dot{e}_{w_2}\sin(w_3)\\
&\quad + e_{w_2}\dot{w}_3\cos(w_3)\\
&= v_L(t-\tau)2\sin^2\left(\frac{e_3}{2}\right) - \lambda e_1 + e_2 w_L(t-\tau).
\end{aligned}
$$

Now with the second line of system (9),

$$
\begin{aligned}
\dot{e}_2 &= -\dot{e}_{w_1}\sin(w_3) - e_{w_1}\dot{w}_3\cos(w_3) + \dot{e}_{w_2}\cos(w_3)\\
&\quad - e_{w_2}\dot{w}_3\sin(w_3)\\
&= v_L(t-\tau)\sin(e_3) - \lambda e_2 - e_1 w_L(t-\tau)
\end{aligned}
$$

finally,

$$
\begin{aligned}
\dot{e}_3 &= w_L(t-\tau) - w_L(t-\tau) - \lambda_3 e_{w_3}\\
&= -\lambda_3 e_3.
\end{aligned}
$$

The observation error dynamics is,

$$
\begin{aligned}
\dot{e}_1 &= -\lambda e_1 + v_L(t-\tau)2\sin^2\left(\frac{e_3}{2}\right) + e_2 w_L(t-\tau)\\
\dot{e}_2 &= -\lambda e_2 + v_L(t-\tau)\sin(e_3) - e_1 w_L(t-\tau)\\
\dot{e}_3 &= -\lambda_3 e_3.
\end{aligned} \tag{10}
$$

The observation convergence properties can be formally stated in the next lemma.

Lemma 3. Suppose that Assumptions 1 and 2 are satisfied and that $\lambda_1, \lambda_2, \lambda_3 > 0$. Then, the states defined by the observer given in (6) exponentially converge to the leader robot trajectory delayed τ units of time.

Proof. Notice first that for $\lambda_3 > 0$,

$$
\dot{e}_3(t) = -\lambda_3 e_3(t) \tag{11}
$$

is exponentially stable, so, now the problem reduces to demonstrate that e_1 and e_2 also converge to the origin. With this aim, define,

$$
\bar{e}(t) = [\, e_1(t)\ e_2(t)\,]^T \tag{12}
$$

then, the dynamics of $e_1(t)$, $e_2(t)$ can be expressed in the form,

$$
\dot{\bar{e}}(t) = \bar{A}\bar{e}(t) + \bar{F}(e_3, \hat{w})v_L(t-\tau) \tag{13}
$$

where,

$$
\bar{A} = \begin{bmatrix} -\lambda_1 & w_L(t-\tau) \\ -w_L(t-\tau) & -\lambda_2 \end{bmatrix} \tag{14}
$$

$$
\bar{F}(e_3, \hat{w}) = \begin{bmatrix} 2\sin^2\left(\frac{e_3}{2}\right) \\ \sin(e_3) \end{bmatrix}. \tag{15}
$$

To show the convergence to the origin of $\bar{e}(t)$, notice that,

$$
\left|\left|\bar{F}(e_3, \hat{w})v_L(t-\tau)\right|\right| \leq \left|\left|\bar{F}(e_3, \hat{w})\right|\right| |v_L| \leq \beta\,|e_3|\,\bar{v}_L \tag{16}
$$

with $\beta > 0$. Therefore, $\bar{F}(e_3, \hat{w})$ tends to zero as $e_3(t)$ converges to the origin, regardless of the evolution of $e_1(t)$ and $e_2(t)$. Therefore, $\bar{F}(e_3, \hat{w})v_L(t-\tau)$ is a vanishing signal for the system given by (13), this fact implies that the exponential convergence of the observation errors $e_1(t)$, $e_2(t)$ depend on the perturbation-free system (13) this is, on the system,

$$
\dot{\bar{e}}(t) = \bar{A}\bar{e}(t) \tag{17}
$$

A candidate Lyapunov function of the form,

$$
V = \frac{1}{2}e_1^2 + \frac{1}{2}e_2^2 \tag{18}
$$

produces

$$
\begin{aligned}
\dot{V} &= e_1\dot{e}_1 + e_2\dot{e}_2\\
&= e_1(-\lambda e_1 + e_2 w_L(t-\tau)) + e_2(-\lambda e_2 - e_1 w_L(t-\tau))\\
&= -\lambda e_1^2 - \lambda e_2^2\\
&= -2\lambda(\frac{1}{2}e_1^2 + \frac{1}{2}e_2^2)\\
&= -2\lambda V
\end{aligned} \tag{19}
$$

This concludes the proof.
In what follows, the estimated state $\hat{w}(t)$ will be used as a desired trajectory for the follower robot in order to solve the leader-follower formation problem. Notice that τ represents the time gap between the vehicles.

4. TIME GAP TRACKING CONTROL STRATEGY

Consider the follower robot dynamics,

$$
\begin{bmatrix} \dot{x}_F(t) \\ \dot{y}_F(t) \\ \dot{\theta}_F(t) \end{bmatrix} = \begin{bmatrix} \cos(\theta_F)v_F(t) \\ \sin(\theta_F)v_F(t) \\ w_F(t) \end{bmatrix} \tag{20}
$$

and take into account the reference trayectory of system (6). From system (20) it is possible to initially define,

$$
\begin{aligned}
\dot{x}_F &= v_F\cos(\theta_F) = \xi_1\\
\dot{y}_F &= v_F\sin(\theta_F) = \xi_2\\
\dot{\theta}_F &= w_F \qquad\qquad = \xi_3
\end{aligned} \tag{21}
$$

for

$$
\begin{aligned}
\xi_1 &= \dot{\hat{w}}_1 - k_1\tilde{x}\\
\xi_2 &= \dot{\hat{w}}_2 - k_2\tilde{y}\\
\xi_3 &= \dot{\hat{w}}_3 - k_3\tilde{\theta}
\end{aligned} \tag{22}
$$

with

$$
\begin{aligned}
\tilde{x} &= x_F - \hat{w}_1\\
\tilde{y} &= y_F - \hat{w}_2\\
\tilde{\theta} &= \theta_F - \hat{w}_3
\end{aligned} \tag{23}
$$

From (21) it is obtained,

$$
\cos^2(\theta_F)v_F + \sin^2(\theta_F)v_F = \xi_1\cos(\theta_F) + \xi_2\sin(\theta_F) \tag{24}
$$

so the control signals are,

$$
v_F = (\dot{\hat{w}}_1 - k_1\tilde{x})\cos(\theta_F) + (\dot{\hat{w}}_2 - k_2\tilde{y})\sin(\theta_F) \tag{25}
$$

$$
w_F = \dot{\hat{w}}_3 - k_3\tilde{\theta}. \tag{26}
$$

To analyze the tracking error, consider now the new error signals,

$$\begin{bmatrix} e_{s_1} \\ e_{s_2} \\ e_{s_3} \end{bmatrix} = \begin{bmatrix} \cos(\theta_F) & \sin(\theta_F) & 0 \\ -\sin(\theta_F) & \cos(\theta_F) & 0 \\ 0 & 0 & 1 \end{bmatrix} \begin{bmatrix} \tilde{x} \\ \tilde{y} \\ \tilde{\theta} \end{bmatrix}. \quad (27)$$

The dynamic of the tracking error can be obtained by taking the time derivative of system (27). Notice that,

$$\begin{aligned} \dot{e}_{s_1} &= \dot{\tilde{x}}\cos(\theta_F) - \tilde{x}\dot{\theta}_F \sin(\theta_F) + \dot{\tilde{y}}\sin(\theta_F) + \tilde{y}\dot{\theta}_F\cos(\theta_F) \\ &= v_F - v_L(t-\tau)\cos(e_{s_3}) + w_F(e_{s_2}) - \lambda_1 e_{w_1}\cos(\theta_F) \\ &\quad -\lambda_2 e_{w_2}\sin(\theta_F), \end{aligned}$$

The second line of (27) produces,

$$\begin{aligned} \dot{e}_{s_2} &= -\dot{\tilde{x}}\sin(\theta_F) - \tilde{x}\dot{\theta}_F\cos(\theta_F) + \dot{\tilde{y}}\cos(\theta_F) - \tilde{y}\dot{\theta}_F\sin(\theta_F) \\ &= v_L(t-\tau)\sin(e_{s_3}) - w_F e_{s_1} + \lambda_1 e_{w_1}\sin(\theta_F) \\ &\quad -\lambda_2 e_{w_2}\cos(\theta_F). \end{aligned}$$

Finally,

$$\begin{aligned} \dot{e}_{s_3} &= \dot{\tilde{\theta}} \\ &= w_F - \dot{\hat{w}}_3. \end{aligned}$$

The tracking error dynamic takes the form,

$$\begin{aligned} \dot{e}_{s_1} &= v_F - v_L(t-\tau)\cos(e_{s_3}) + e_{s_2}w_F - \lambda_1 e_{w_1}\cos(\theta_F) \\ &\quad -\lambda_2 e_{w_2}\sin(\theta_F) \\ \dot{e}_{s_2} &= v_L(t-\tau)\sin(e_{s_3}) - e_{s_1}w_F + \lambda_1 e_{w_1}\sin(\theta_F) \\ &\quad -\lambda_2 e_{w_2}\cos(\theta_F) \\ \dot{e}_{s_3} &= w_F - k_3\tilde{\theta}. \end{aligned} \quad (28)$$

Notice that the control signals, in the new coordinates (27) with $k_1 = k_2 = k$, take the form,

$$\begin{aligned} w_F &= \dot{\hat{w}}_3 - k_3 e_{s_3} \\ v_F &= -k e_{s_1} v_L(t-\tau)\cos(e_{s_3}) + \lambda_2 e_{w_2}\sin(\theta_F) \\ &\quad +\lambda_1 e_{w_1}\cos(\theta_F) \end{aligned} \quad (29)$$

4.1 Controlled system with observed states

System (28) in closed loop with the control signal (29), produces the system,

$$\begin{aligned} \dot{e}_{s_1} &= -k e_{s_1} + e_{s_2}\dot{\hat{w}}_3 - k_3 e_{s_2} e_{s_3} \\ \dot{e}_{s_2} &= -e_{s_1}\dot{\hat{w}}_3 + k_3 e_{s_1} e_{s_3} + m_1 \\ \dot{e}_{s_3} &= -k_3 e_{s_3} \end{aligned} \quad (30)$$

where,

$$m_1 = v_L(t-\tau)\sin(e_{s_3}) + \lambda(e_1\sin(e_{s_3}+e_3) - e_2\cos(e_{s_3}+e_3))$$

is a time varying term that do no explicitly depend on the tracking errors e_{s_1} and e_{s_2}. Notice from (30) that e_{s_3} is exponentially stable, and remember that e_1, e_2 and e_3 are exponentially stable, so the stability of (30) can be stated by considering the subsystem,

$$\begin{aligned} \dot{e}_{s_1} &= -k e_{s_1} + e_{s_2}\dot{\hat{w}}_3 - k_3 e_{s_2} e_{s_3} \\ \dot{e}_{s_2} &= -e_{s_1}\dot{\hat{w}}_3 + k_3 e_{s_1} e_{s_3} \end{aligned} \quad (31)$$

Remark 4. Note that the variable $m_1(t)$ depend on the observation errors $e_1(t)$, $e_2(t)$ and on the tracking error $e_{s_3}(t)$, that have previously been proven that exponentially converge to the origin. Therefore $m_1(t) \to 0$ as $t \to \infty$.

Since the functions m_1 is independent of $e_{s_1}(t)$, $e_{s_2}(t)$, it can be considered as an exogenous input signal. This fact allows to establish the stability of the closed loop system given by system (30) in terms of the free-perturbation system (31).

Lemma 5. Suppose that $k, k_3 > 0$ and that the angular input velocity of the follower robot satisfies for all t that $w_F(t) \neq 0$. Then, the closed loop tracking error dynamic given by Eqn. (30) is asymptotically stable. Consequently, the observer-based feedback (29) asimptotically solves the time-gap tracking problem associated with the leader and follower robots.

Proof. The statement of the lemma is equivalent to state the stability of system (31). With this aim consider the candidate Lyapunov function,

$$V = \frac{1}{2}e_{s_1}^2(t) + \frac{1}{2}e_{s_2}^2(t) \quad (32)$$

therefore,

$$\begin{aligned} \dot{V} &= e_{s_1}(t)\dot{e}_{s_1}(t) + e_{s_2}(t)\dot{e}_{s_2}(t) \\ &= -k e_{s_1}^2(t). \end{aligned} \quad (33)$$

Under this condition, it is clear that,

$$\dot{V} \leq 0.$$

Therefore, the states of the system given by Eqn. (31) are stable. To show that the states converge to the origin, notice that $\dot{V}$ is uniformily continuous since $\ddot{V}$ is bounded. Invoquing Barbalat's lemma Slotine et al. [1991], $\dot{V} \to 0$ and consequently, from the first line of (31) it is obtained

$$0 = e_{s_2}\dot{\hat{w}}_3 - k_3 e_{s_2} e_{s_3} \quad (34)$$

this is,

$$(\dot{\hat{w}}_3 - k_3 e_{s_3})e_{s_2} = 0 \quad (35)$$

Considering the assumption that $w_F \neq 0$, thus $\dot{\hat{w}}_3 \neq 0$, and taking into account that $e_{s_3} \to 0$, it is clear that $e_{s_2} \to 0$ as $t \to \infty$.

5. NUMERICAL SIMULATIONS

To show the effectiveness of the observer-based solution proposed in this work a three petals geometric trajectory is proposed for the leader robot. This path involves orientation and velocity changes that influence the relative distance between the robots. The equations that describe the desired leader trajectory are given as,

$$\begin{aligned} x &= 0.2(a+b)\cos(npt)\cos(pt) \\ y &= 0.2(a+b)\cos(npt)\sin(pt) \end{aligned} \quad (36)$$

where $n = 3$ corresponds to the number of petals, $a = 13$, $b = 7$, $p = (2\pi/20)$. Equation (36) allows to define the input signals for the leader robot as,

$$v_L = \sqrt{\dot{x}^2 + \dot{y}^2}, \quad w_L = \frac{(\ddot{y}\dot{x} - \ddot{x}\dot{y})}{(\dot{x}^2 + \dot{y}^2)} \quad (37)$$

Table 1.

Robot	x[m]	y[m]	θ[rad]
Leader	4	0	$\pi/2$
Follower	4	0	$\pi/2$
Observer	3	-0.5	0

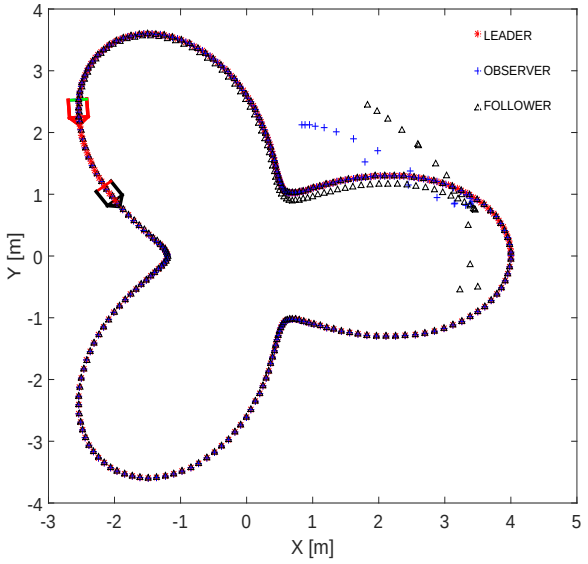

Fig. 3. Leader follower formation

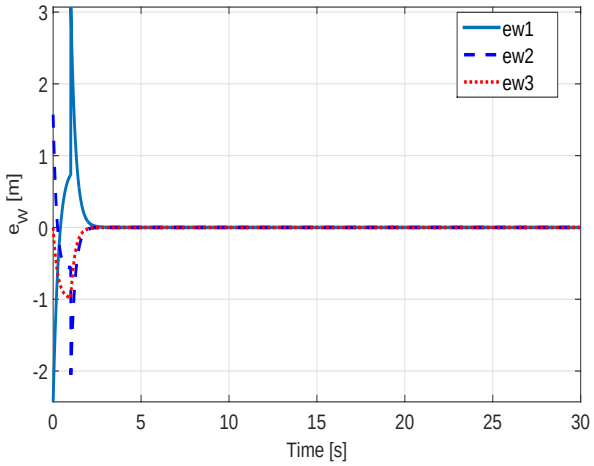

Fig. 4. Observation errors

The initial conditions for the simulation are shown in Table 1. The gain used for the observer is $\lambda = 4$, and the gains used for the control law are set as $k_1 = k_2 = 2,\ k_3 = 4$. The time-gap separation was considered as $\tau = 1sec.$ The time evolution on the plane of the leader, the follower and the estimated trajectories are shown in Fig. 3.

The observation errors $e_{w_1}(t),\ e_{w_2}(t)$ and $e_{w_3}(t)$ are depicted in Fig. 4 where it is shown their fast convergence.

The tracking position errors $e_{s_1}(t),\ e_{s_2}(t)$ and $e_{s_3}(t)$ are shown in Fig. 5 and the control signal evolution for both, the leader and the follower robots are shown in Fig. 6.

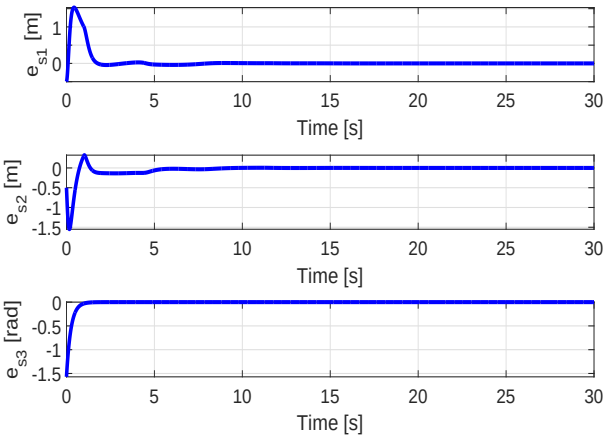

Fig. 5. Position tracking errors

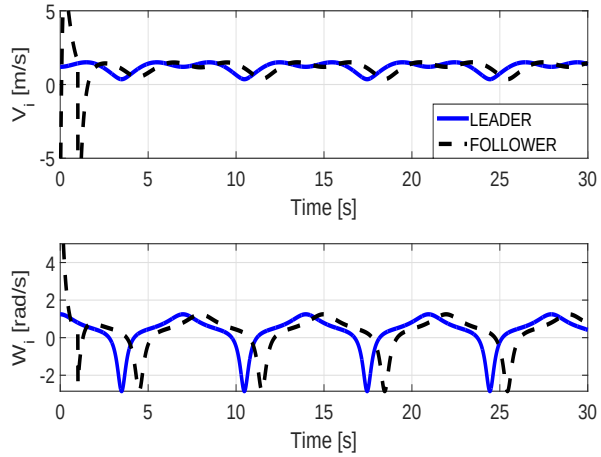

Fig. 6. Control signal evolution

Notice that despite the initial conditions errors, all the signals converge adequately as expected by the theoretical developments.

Figure 7 shows the evolution of the position in x, y of the observer, leader, and follower robot.

It is evident that the time gap separation of $\tau = 1sec.$ is kept along the simulation after the transient has passed. Meanwhile in Fig. 8, it is shown how the separation or relative distance between the robots $d(t) = \sqrt{(x_L - x_F)^2 + (y_L - y_F)^2)}$ varies accordingly to the velocity of the robots in order to satisfy the time gap separation.

6. CONCLUSIONS

Based on a delayed observer strategy, the leader-follower fomation is solved for a pair of differentially driven nonholonomic mobile robots. It is shown that under the assumption of a leader angular velocity different from zero, the observation and tracking errors exponentially converge to the origin while a desired constant time gap is maintained constant between the vehicles. Numerical simulations show the efectiveness of the proposed leader-follower

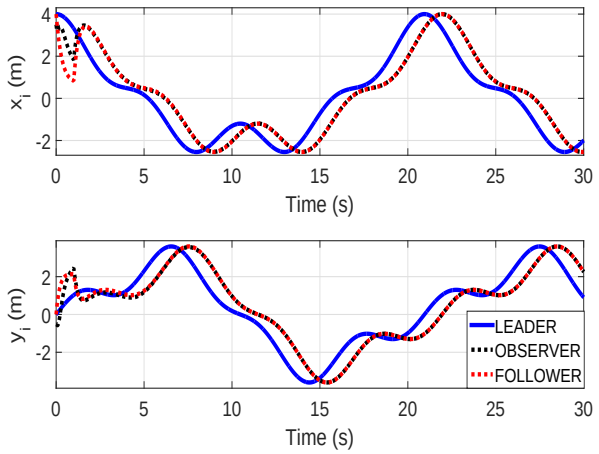

Fig. 7. x, y position evolution

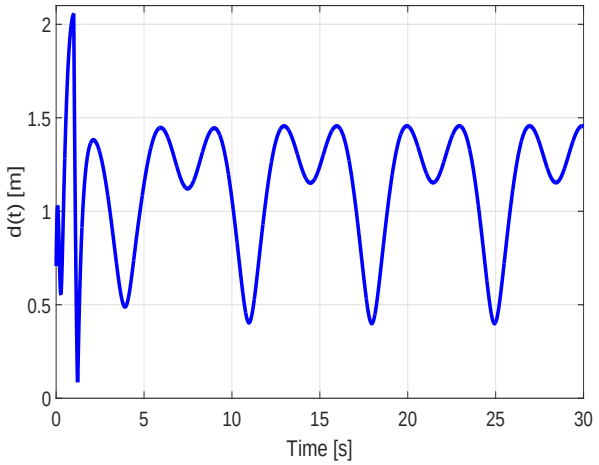

Fig. 8. Relative distance between leader and follower robots

solution. The simulations shown that the proposed control law can solve the problem of leader follower formation tracking the same path that the leader robot performed.

REFERENCES

Tucker Balch and Ronald C Arkin. Behavior-based formation control for multirobot teams. *Robotics and Automation, IEEE Transactions on*, 14(6):926–939, 1998.

Zevi Bareket, Paul S Fancher, Huei Peng, Kangwon Lee, and Charbel A Assaf. Methodology for assessing adaptive cruise control behavior. *Intelligent Transportation Systems, IEEE Transactions on*, 4(3):123–131, 2003.

DE Canudas, Bruno Siciliano, and Georges Bastin. *Theory of robot control*. GBR, 1996.

Luca Consolini, Fabio Morbidi, Domenico Prattichizzo, and Mario Tosques. Leader–follower formation control of nonholonomic mobile robots with input constraints. *Automatica*, 44(5):1343–1349, 2008.

Jaydev P Desai, Jim Ostrowski, and Vijay Kumar. Controlling formations of multiple mobile robots. In *Robotics and Automation, 1998. Proceedings. 1998 IEEE International Conference on*, volume 4, pages 2864–2869. IEEE, 1998.

Taketoshi Kawabe. Vehicle spacing control with string stability using simple communication and a spacing sensor. In *Proceedings of the 7th World Congress on Intelligent Systems*, 2000.

Alexey S Matveev, Chao Wang, and Andrey V Savkin. Real-time navigation of mobile robots in problems of border patrolling and avoiding collisions with moving and deforming obstacles. *Robotics and Autonomous systems*, 60(6):769–788, 2012.

Hasan Mehrjerdi, Jawhar Ghommam, and Maarouf Saad. Nonlinear coordination control for a group of mobile robots using a virtual structure. *Mechatronics*, 21(7): 1147–1155, 2011.

Robin R Murphy, Jeffery Kravitz, Samuel L Stover, and Rahmat Shoureshi. Mobile robots in mine rescue and recovery. *Robotics & Automation Magazine, IEEE*, 16 (2):91–103, 2009.

Bobbie D Seppelt and John D Lee. Making adaptive cruise control (acc) limits visible. *International Journal of Human-Computer Studies*, 65(3):192–205, 2007.

Jean-Jacques E Slotine, Weiping Li, et al. *Applied nonlinear control*, volume 199. Prentice-Hall Englewood Cliffs, NJ, 1991.

Dong Sun and Can Wang. Controlling swarms of mobile robots for switching between formations using synchronization concept. In *Robotics and Automation, 2007 IEEE International Conference on*, pages 2300–2305. IEEE, 2007.

Siddharth Swaminathan, Mike Phillips, and Maxim Likhachev. Planning for multi-agent teams with leader switching. In *Robotics and Automation (ICRA), 2015 IEEE International Conference on*, pages 5403–5410. IEEE, 2015.

Herbert G Tanner, George J Pappas, and Vijay Kumar. Leader-to-formation stability. *Robotics and Automation, IEEE Transactions on*, 20(3):443–455, 2004.

Kinematic control for an omnidirectional mobile manipulator ⋆

F. Mirelez-Delgado *,** **A. Morales-Díaz** * **R. Ríos-Cabrera** *

* *Centro de Investigación y de Estudios Avanzados del Instituto Politécnico Nacional Unidad Saltillo Ramos Arizpe, Coah. 25900, México*
Phone number:+52-844-4389600 Ext. 8500
** *e-mail: flabio.mirelez@cinvestav.mx*

Abstract: This paper presents a kinematic control for an omnidirectional mobile manipulator using quaternions notation for the orientation of the end-effector. We describe the Denavit-Hartenberg parameters for the robot and the sensor. The inverse kinematics for the robot is calculated by using the pseudo-inverse of the geometric Jacobian. In order to obtain a desired position for the end-effector a RGB-D camera is attached to the robot. An algorithm to extract specific object color from a white background in an image is implemented using the RGB-D sensor. The algorithm is able to find the object's contour and centroid. Experimental results shows that the kinematic control assisted by a RGB-D camera allows to reach and grasp objects of interest.

Keywords: Robot kinematics, redundant manipulator, robot vision, control.

1. INTRODUCTION

Industrial robots are mainly manipulator arms fixed on the ground to perform dumb, dangerous, dull, dirty and overall repetitive tasks. Contrary to the traditional stationary and pre-programmed production robots, Autonomous Industrial Mobile Manipulators (AIMM) can provide assistance at multiple locations (Madsen et al. (2015)). Basically, a mobile manipulator is a stationary manipulator mounted on a mobile robot so that the locomotion and manipulation tasks may be performed simultaneously. These capabilities give the mobile manipulator advantages over stationary ones, like a bigger task space and a greater autonomy.

The task performed by an AIMM includes feeding raw material to workstations, sub-assembly work, goods transportation, and status monitoring of machines. Of all these applications, transportation and loading seem to be the ones with the most potential for the short term actions, according to Hvilshj et al. (2009).

The autonomy of a mobile manipulator increases if the robot is equipped with more sensors, for example a camera. With a simple camera, the mobile manipulator can have a better understanding of its environment, but it is necessary to establish methodologies and algorithms to ensure a correct interaction between the robot and the objects of interest, or even with other systems in manufacturing plants.

The interest in vision-based robotic systems for monitoring has increased in recent years due to the tendency of reduced cameras costs and in general all the associated processing systems (Hutchinson et al. (1996)). According to Corke (1996) the visual control has matured quickly and has been applied to robot manipulators as it is based on the visual perception of the robot and the location of a piece of interest.

This paper deals with the complete kinematic model for an omnidirectional base with four mecanum wheels and a manipulator with five degrees of freedom. Both parts make an omnidirectional mobile manipulator. The principal aim is to develop a control law that allows to set the end-effector at any desired position and then to be able to reach and grasp objects of interest. Moreover a RGB-D camera is used to identify the object's centroid where the end-effector must be placed once the control law is applied. To test the control law and to obtain the object's centroid, a Kuka youBot robot and an Asus Xtion pro RGB-D camera are used.

The remaining sections of this paper are as follows; Section 2 shows the related work about Kuka youBot and the AIMM in an industrial scenario. Section 3 presents the forward kinematic model for the omnidirectional mobile manipulator and section 4 presents the method to obtain the youBot's inverse kinematic model. Section 5 explaines the image processing for the object localization. The control law is described in section 6. The validation for this proposal is presented in section 7 and finally section 8 provides conclusions and future work.

2. RELATED WORK

2.1 Previous related papers

The Kuka youBot is an omnidirectional mobile manipulator specially developed for academic and research purpuses Bischoff et al. (2011).

The arm direct kinematics can be found clearly expresed in Dwiputra et al. (2014) where Modelica software is used

⋆ The first author thanks to CONACyT for the PhD scolarship no. 395788 and to CINVESTAV for support to attend the conference.

a unified inverse kinematics for Kuka youBot is established allowing to resolve efficiently the singularities of the whole kinematic model. However the author does not use the Denavit-Hartenberg parameters for the kinematic model and can not control the pose for the youBot's end-effector.

A well documented work is presented in Keiser (2013), where the author applied a torque control at the youBot arm in order to pickup objects from the ground. The objects identification is acomplish by using an RGB-D sensor and the Point Cloud Library. The RBG-D sensor is fixed in a supporting structure located on the back of the mobile platform, allowing the objects appear inside the sensor's field of view. However the arm control was implemented as an open loop, it means that the arm's trajectory is computed offline.

In Dogar et al. (2014) a group of Kuka youBots is used to manipulate forniture parts to assembly a table. In this work the robots are supervised by an external camera array that allows the system to know the element's position at any time. Moreover some robots have a camera in hand configuration, resulting into an extremelly controlled experimental environment.

In Schoen and Rus (2013) four youBots are used, two of them are the suppliers and the rest serve as assemblers. The proposal uses adaptive planning, where even if there are missing pieces, the robots are able to adjust the planning task to assemble the final object. Another aspect of the article is that it handles subtasks times, so it can get a parameterization of all homework time and measure the efficiency of the proposed algorithm. The vision system is composed by several cameras that allows to track the robots and the assembly parts, and with that information, the authors are able to hand over parts from one robot to another without resting the pieces on the surface.

Another recent work related to assembly parts is described in Wang et al. (2013), where the Kuka youBot locates a furniture piece that is randomly placed on the floor. To achieve accurate part identification and the robot location, the authors use an array of radio frequency identifiers in the robot to compute its location.

2.2 Original contribution

From authors knowledge regarding youBot kinematics, few research has focused on this topic, furthermore, there are not works reported that deals with the whole kinematic model of this robot. Some works present the kinematic model for the arm manipulator (Zhang and Zhou (2013); Dwiputra et al. (2014)) and only one exposes their own method to obtain the youBot's whole kinematic model (Sharma et al. (2012)), but only for end-effector position leaving apart the parametrization of the pose. The novelty of this work resides on the use of quaternions to parametrize the end-effector orientation. The complete kinematic model for the robot is obtained using the Denavit-Hartenberg parameters. The proposed control law minimizes the end-effector's errors for pose and position, allowing the robot to reach and to grasp objects of interest. The desired objects are identified by a RGB-D camera and computer vision algorithms.

The Kuka youBot's mobile base has four Mecanum wheels that allow free displacement in the Cartesian plane. However in this kind of system it is necesary to consider the rollers disposition inside the Mecanum wheel in order to obtain a better kinematic model. According to Nagatani et al. (2000), the kinematic configuration of an omnidirectional mobile robot is given by the set of equations (1).

$$\begin{aligned} \dot{x} = v_l &= \frac{1}{4}(dw_{b1} + dw_{b2} + dw_{b3} + dw_{b4}) \\ \dot{y} = v_t &= \frac{1}{4}(-dw_{b1} + dw_{b2} + dw_{b3} - dw_{b4})\tan(\alpha_b) \\ \dot{\theta_b} = v_a &= \omega = \frac{1}{4}(dw_{b1} + dw_{b2} + dw_{b3} + dw_{b4})\beta \end{aligned} \quad (1)$$

where dw_{bi} (for $i = 1, \ldots, 4$) represents the linear velocity of each wheel of the platform. The variables v_t, v_l and v_a are the transversal, longitudinal and angular velocities respectively. The α_b and β parameters are computed experimentally because they depend on the roller's angle inside the Mecanum wheel.

The mobile platform movement is given by the combination of the wheel's linear velocities. For example, the lateral traslation and rotation movements are depicted in Figure 1, where the faded platform shows where the robot will be at a certain time.

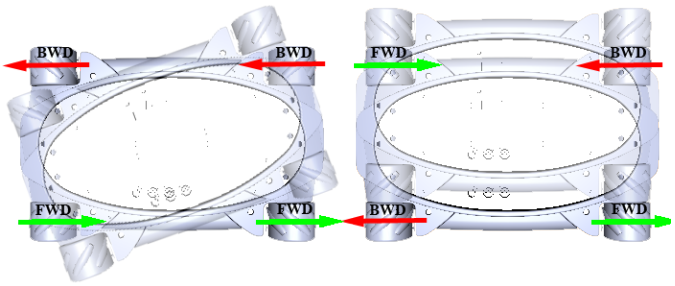

Fig. 1. Mobile platform movement according to the individual rotation combination of the four mecanum wheels.

The mobile platform can be considered as a robot with three degrees of freedom, the first two are prismatic (displacement on x-axis and y-axis) and the third is rotational around the z-axis.

On the other hand, the Kuka youBot arm is a manipulator with five degrees of freedom (all of them are rotational). The distance between the body and their respective joint limits can be seen in Figure 2. The end-effector is a two fingers gripper that allows the grasping and manipulation of small objects.

The referential frames for each joint can be appreciated in the Figure 3. The Denavit-Hartenberg parameters for the omnidirectional mobile manipulator (mobile platform and the arm) are shown in the Table 1. The parameters of Tables 1 allow the computation of the homogeneous transformation matrix as described in equation (2).

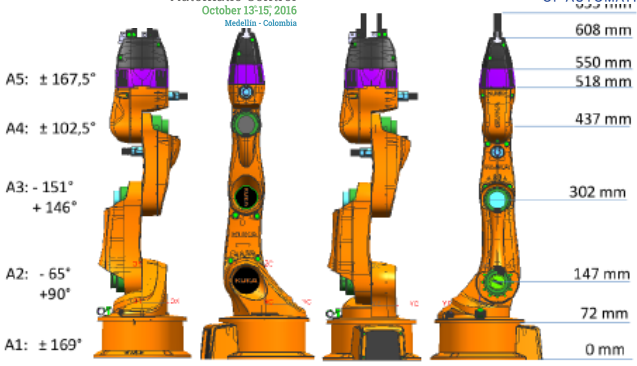

Fig. 2. Kuka youBot arm manipulator specifications.

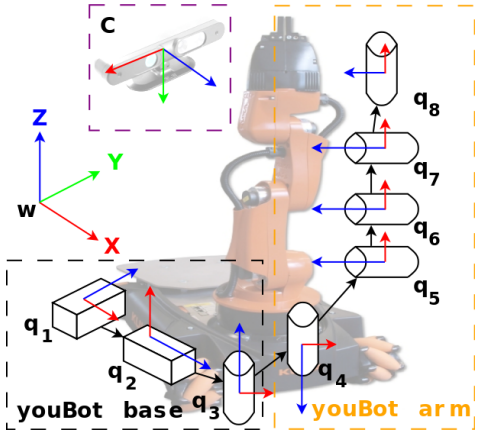

Fig. 3. Referential frame position for each joint and RGB-D sensor.

Table 1. Denavit-Hartenberg parameters for omnidirectional mobile manipulator and the fixed sensor.

Body	θ	d	a	α
1	0	q_1	0	$-\frac{\pi}{2}$
2	$\frac{\pi}{2}$	q_2	0	$\frac{\pi}{2}$
3	$q_3 - \frac{\pi}{2}$	0	0	$-\frac{\pi}{2}$
4	$-q_4$	0.2	0.15	π
5	$q_5 - \frac{\pi}{2}$	0.075	0.033	$-\frac{\pi}{2}$
6	q_6	0	0.155	0
7	q_7	0	0.135	0
8	q_8	0	0.218	0
C	0	0.8	0.2	$-\frac{3\pi}{4}$

$$T_i^{i-1} = \begin{bmatrix} C\theta_i & -S\theta_i C\alpha_i & S\theta_i S\alpha_i & a_i C\theta_i \\ S\theta_i & C\theta_i C\alpha_i & -C\theta_i S\alpha_i & a_i S\theta_i \\ 0 & -S\alpha_i & C\alpha_i & d_i \\ 0 & 0 & 0 & 1 \end{bmatrix} \quad (2)$$

Where S and C are the sine and cosine functions, respectively. T_i^{i-1} means the displacements and rotations needed to align the previous frame coordinates with the actual one. The total transformation matrix (from world frame coordinates **w** until last joint frame coordinates**8**) is given by the successive multiplication of each homogeneous transformation.

$$T_8^{\mathrm{W}} = T_1^{\mathrm{W}} T_2^1 \dots T_8^7 \quad (3)$$

The end-effector position is given by the first three terms of the last column in the homogeneous matrix T_8^{W}.

$$EE_{pos} = T_8^w(1:3,4) \quad (4)$$

Moreover the end-effector's orientation is described by the submatrix $T_8^{\mathrm{W}}(1:3,1:3)$.

3.1 Quaternions

Quaternions are used for calculations involving three-dimensional rotations and can be used as an alternative to other methods, such as Euler angles and rotation matrices. In this paper, the end-effector pose will be depicted by quaternions because this formulation has no singularities, it means that the end-effector can be placed at any desired point in 3D space with a unique solution for all its joints. The procedure to obtain the end-effector pose in a quaternion representation is as follows:

First the rotation matrix must be extracted from the total homogeneous transformation.

$$Rot = T_8^{\mathrm{W}}(1:3,1:3) \quad (5)$$

The rotation around the main axes is obtained and is put in a vector form.

$$R = Rot - Rot^T \quad (6)$$
$$r(0) = -R(2,3) \quad (7)$$
$$r(1) = R(1,3) \quad (8)$$
$$r(2) = -R(1,2) \quad (9)$$
$$r_0 = \frac{r}{|r|} \quad (10)$$

The next step is to find the principal angle that describes the quaternion.

$$angle_y = \frac{|r|}{2} \quad (11)$$
$$angle_x = \frac{\mathrm{Tr}(Rot) - 1}{2} \quad (12)$$
$$angle = \tan^{-1}\left(\frac{angle_y}{angle_x}\right) \quad (13)$$

The quaternion to described the end-effector's orientation is defined as:

$$Quat = \left[\cos\left(\frac{angle}{2}\right), r_0 \sin\left(\frac{angle}{2}\right)\right]; \quad (14)$$

Finally the end-effector's pose and position is:

$$EE = [EE_{pos}, Quat] \quad (15)$$

4. INVERSE KINEMATICS

YouBot's inverse kinematics is obtained using the geometric Jacobian, which is related to the forward kinematics

shown below. The ... can be programmed using open source codes such as OpenNI and OpenCV.

Jacobian is constructed as follows:

$$J_g = \begin{bmatrix} j_{p_i} & \cdots & j_{p_n} \\ & \cdots & \\ j_{o_i} & \cdots & j_{p_n} \end{bmatrix} \tag{16}$$

Where j_{p_i} have two values according to the robot modelling show in Figure 3:

- For the prismatic joints:
$$j_{p_i} = Z_{i-1} \tag{17}$$
Where Z_{i-1} is the third column of R^w_{i-1}.
- For the revolute joints:
$$j_{p_i} = Z_{i-1} \times (p_i - p_{i-1}) \tag{18}$$
Where p_e are the first three elements of the fourth column of T^{W}_i and p_{i-1} are the first three elements of the fourth column of T^{W}_{i-1}.

The end-effector's orientation can be described into the geometric Jacobian as:

$$J_{g_o} = \begin{bmatrix} -Quat(2) & -Quat(3) & -Quat(4) \\ Quat(1) & Quat(4) & -Quat(3) \\ -Quat(4) & Quat(1) & Quat(2) \\ Quat(3) & -Quat(2) & Quat(1) \end{bmatrix} \tag{19}$$

With equation (19) a temporal Jacobian can be constructed.

$$J_{temp} = \begin{bmatrix} I_{3x3} & \mathbf{0} \\ \mathbf{0} & J_{g_o} \end{bmatrix} \tag{20}$$

The Jacobian matriz using quaternions to describe the end-effector orientation is computed using the temporal Jacobian and the geometric Jacobian from equation (16).

$$J = J_{temp} J_g \tag{21}$$

The Jacobian can be splitted in two matrix, one for the position and the other for orientation.

$$J_{pos} = J(1:3,:) \tag{22}$$
$$J_{ori} = J(4:7,:) \tag{23}$$

The last step is to obtain the pseudo-inverse for each part of the Jacobian.

$$J_{pos_{pi}} = {J_{pos}}^T (J_{pos} {J_{pos}}^T)^{-1} \tag{24}$$
$$J_{ori_{pi}} = {J_{ori}}^T (J_{ori} {J_{ori}}^T)^{-1} \tag{25}$$

With these pseudo-inverse matrices, the joints values can be computed for a desired position and pose of the end-effector.

5. IMAGE PROCESSING

The Asus Xtion Pro (see Figure 4) is capable of obtaining a color image (RGB), a matrix (image) with depth values and a point cloud map. With the RGB image and the point cloud, the centroid of a desired object can be obtained. The main advantage of using this kind of sensors is that

Fig. 4. RGB-D sensor characteristics.

The procedure to extract an object of interest from an RGB image is to convert the image from the RGB color space to HSV color space. The conversion is because the HSV color space is more robust to illumination variations than the RGB color space. The next step is to process the image in order to find all the blue pixels in the scene, then all the pixels found are gathered into a contour, so that the centroid of this pixels group can be computed (see Figure 5). The object's centroid is paired with the pointcloud in order to obtain its 3D position with respect to the camera.

The object's position must be in world's coordinates. The homogeneous transformation between the inertial frame **w** and the camera frame allows to pass the object's position from camera to the world. The first three parameters of the Table 1 and the D-H parameters for the camera are considered to calculate the homogeneous transformation.

$$T^{\mathrm{W}}_c = T^{\mathrm{W}}_1 T^1_2 T^2_3 T^3_c \tag{26}$$

With the transformation T^{W}_c the object's centroid (P_c) can be projected into the inertial frame as follows:

$$P_{\mathrm{W}} = T^{\mathrm{W}}_c [P_c, 1]^T \tag{27}$$

Where the first three terms of P_{W} are the coordinates of the object in the inertial frame.

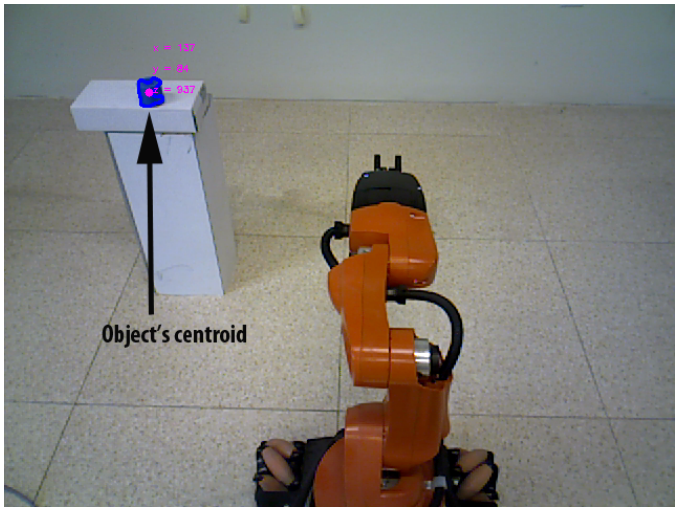

Fig. 5. Image processing with the Asus Xtion Pro to extract the blue object from the scene and compute its centroid.

The control law proposed in this paper is a PD control for the youBot's end-effector. The desired pose and position for the end-effector are the centroid of the object that are measured by the RGB-D sensor and can be rewritten as follows:

$$\begin{aligned} EE_{pos_d} =& [x_d, y_d, z_d] = P_{\mathrm{W}}(1:3) \\ Vec_q =& \frac{EE_{pos_d}}{|EE_{pos_d}|} \\ Quat_d =& \left[\cos\left(\frac{angle_d}{2}\right), Vec_q \sin\left(\frac{angle_d}{2}\right)\right] \end{aligned} \tag{28}$$

Finally, the end-effector desired position is constructed as:

$$Pos_d = [EE_{pos_d}, Quat_d]^T \tag{29}$$

The control law proposed is:

$$\dot{q} = k_1 \dot{q}_{pos} + k_2 \dot{q}_{ori} \tag{30}$$

Where:

$$\dot{q}_{pos} = J_{pos_{pi}} \begin{bmatrix} (Pos_d(1) - EE(1)) \\ (Pos_d(2) - EE(2)) \\ (Pos_d(3) - EE(3)) \end{bmatrix} \tag{31}$$

$$\dot{q}_{ori} = J_{ori_{pi}} \begin{bmatrix} (Pos_d(4) - EE(4)) \\ (Pos_d(5) - EE(5)) \\ (Pos_d(6) - EE(6)) \\ (Pos_d(7) - EE(7)) \end{bmatrix} \tag{32}$$

$$\tag{33}$$

The terms of $\dot{q}$ are the velocities for each joint of the mobile manipulator and k_1, k_2 are positive gains.

7. EXPERIMENTAL RESULTS

To validate the control law proposed in this paper an object was place in a random place inside the sensor's field of view (Figure 6). In this experiment the object is a blue cilinder that can be easily segmented with the RGB-D camera. Once the object's centroid is obtained the youbot's end-effector is moved in order to reach and grasp the desired object. Figure 7 shows the evolution of the robot joints. The values for the control gains were $k_1 = 0.15$ and $k_2 = 0.001$ and the desired angle for the end-effector orientation was -90 degrees respect to Y axis, it means, parallel to $X-Y$ plane and pointing along to X axis.

The velocities for each joint are depicted in Figure 8, where it can be seen that the velocities converge to zero.

The object's position with respect to the robot is shown in Figure 9. In this case it can be appreciated that the frontal distance decreases as long as the youBot's end-effector reachs the object.

Finally, Figure 10 describe how the position and orientation error for the end-effector asymptotically converge to zero.

8. CONCLUSIONS

In this paper a complete kinematic model for an omni-directional mobile manipulator was introduced with the end-effector orientation parameterized with quaternions as a novelty. The kinematic control is assisted by a RGB-D camera that allows to obtain the position of an object of interest in world coordinates. This position is the desired value for the robot's end-effector. The experiments demonstrate that kinematic control can be used to grasp objects of interest. Moreover this paper shows the viability to implement RBG-D cameras as a sensor to get information related to the environment and increase the performance of the robot. As future work an improvement of the object

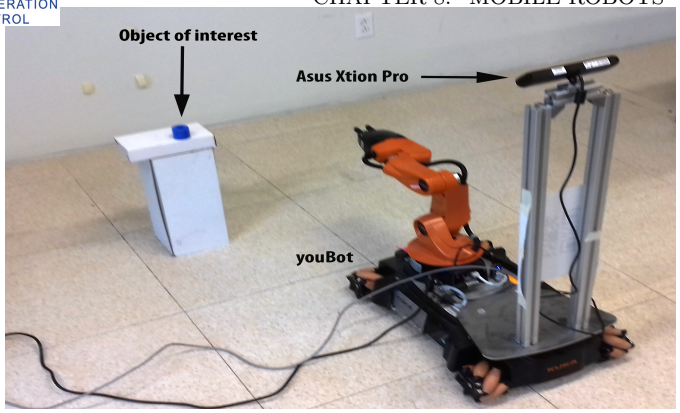

Fig. 6. Experimental set, consists of a Kuka youBot with an asus xtion pro mounted on a fixed structure and a blue object placed on a white table at a random position.

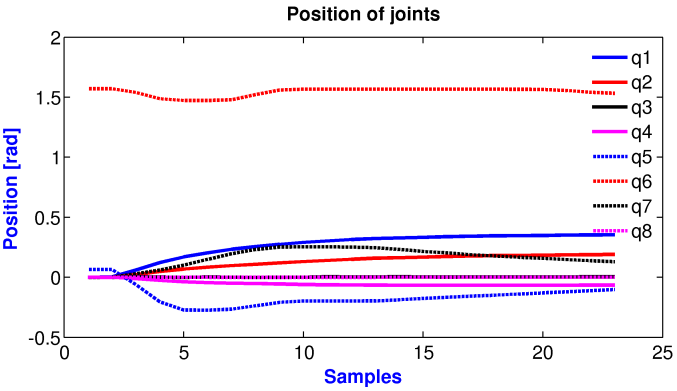

Fig. 7. Joint's positions along the experiment.

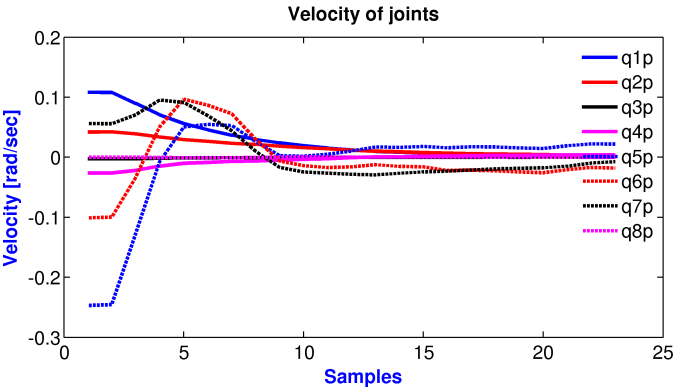

Fig. 8. Joint's velocities performance.

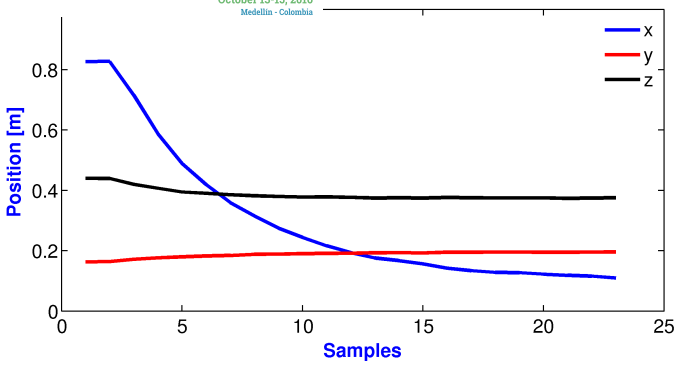

Fig. 9. Object's position for the experiment.

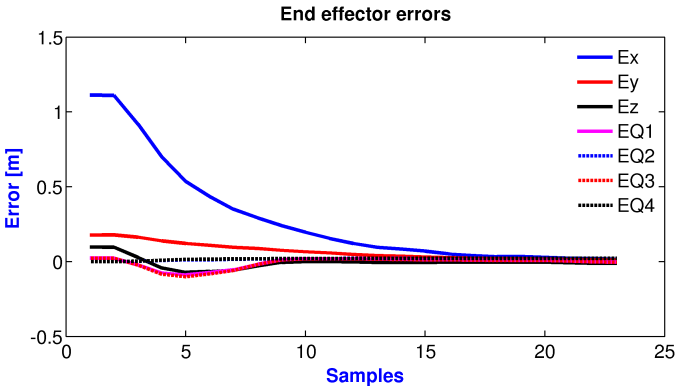

Fig. 10. End effector pose and position errors.

detection algorithm is required because the illumination variations affect the object detection rate. The stability proof must be done in order to tune the control gains and to demonstrate mathematically the convergency for this kind of control.

REFERENCES

Bischoff, R., Huggenberger, U., and Prassler, E. (2011). Kuka youbot - a mobile manipulator for research and education. In *Robotics and Automation (ICRA), 2011 IEEE International Conference on*, 1–4.

Cho, Y.C. and Jeon, J.W. (2008). Remote robot control system based on dtmf of mobile phone. In *2008 6th IEEE International Conference on Industrial Informatics*, 1441–1446. doi:10.1109/INDIN.2008.4618331.

Corke, P. (1996). *Visual control of robots: high-performance visual servoing*. Robotics and mechatronics series. Research Studies Press.

Dogar, M., Knepper, R.A., Spielberg, A., Choi, C., Christensen, H.I., and Rus, D. (2014). Towards coordinated precision assembly with robot teams. *Proceedings of the International Symposium of Experimental Robotics*.

Dwiputra, R., Zakharov, A., Chakirov, R., and Prassler, E. (2014). Modelica model for the youbot manipulator. In *Proceedings of the 10th International Modelica Conference, March 10-12, 2014, Lund, Sweden*, 1205 – 1212.

Hutchinson, S., Hager, G., and Corke, P. (1996). A tutorial on visual servo control. *Robotics and Automation, IEEE Transactions on*, 12(5), 651–670.

ıhj, M., Bgh, S., Madsen, O., and Kristiansen, M. (2009). The mobile robot "little helper": Concepts, ideas and working principles. In *Emerging Technologies Factory Automation, 2009. ETFA 2009. IEEE Conference on*, 1–4.

Keiser, B. (2013). *Torque Control of a KUKA youBot Arm*. Master's thesis, Robotics and Perception Group, University of Zurich.

Madsen, O., Bøgh, S., Schou, C., Andersen, R.S., Damgaard, J.S., Pedersen, M.R., and Krüger, V. (2015). Integration of mobile manipulators in an industrial production. *Industrial Robot: An International Journal*, 42(1), 11–18.

Nagatani, K., Tachibana, S., Sofne, M., and Tanaka, Y. (2000). Improvement of odometry for omnidirectional vehicle using optical flow information. In *Intelligent Robots and Systems, 2000. (IROS 2000). Proceedings. 2000 IEEE/RSJ International Conference on*, volume 1, 468–473 vol.1.

Schoen, T. and Rus, D. (2013). Decentralized robotic assembly with physical ordering and timing constraints. In *Intelligent Robots and Systems (IROS), 2013 IEEE/RSJ International Conference on*, 5764–5771.

Sharma, S., Kraetzschmar, G.K., Scheurer, C., and Bischoff, R. (2012). Unified closed form inverse kinematics for the kuka youbot. In *Robotics; Proceedings of ROBOTIK 2012; 7th German Conference on*, 1–6.

Wang, J., Adib, F., Knepper, R., Katabi, D., and Rus, D. (2013). Rf-compass: Robot object manipulation using rfids. In *Proceedings of the 19th Annual International Conference on Mobile Computing & Networking*, MobiCom '13, 3–14. ACM, New York, NY, USA.

Zhang, L. and Zhou, C. (2013). Kuka youbot arm shortest path planning based on geodesics. In *Robotics and Biomimetics (ROBIO), 2013 IEEE International Conference on*, 2317–2321.

Navigation Assistance System for the Visually Impaired People Using the Modified Fictitious Force Algorithm

Sánchez B. David. Ortega H. Christian.
Sotomayor O. Nelson, Chávez G. Danilo

Escuela Politécnica Nacional
Departamento de Automatización y Control Industrial, Ladrón de Guevara E11-253,
Quito, Ecuador

(e-mail: david.sanchez@epn.edu.ec, christian.ortega01@epn.edu.ec,
nelson.sotomayor@epn.edu.ec, danilo.chavez@epn.edu.ec)

Abstract: This work is focused on the implementation of a prototype that assists, complementary to the white cane, in the navigation of blind people by detecting obstacles with artificial vision. The navigation system was developed based on the Kinect sensor coupled to a helmet, which in addition to providing a color image of the environment, it is also capable of delivering a depth image of the same; this information was processed in a computer and based on the modified fictitious force algorithm by Scaglia et al. (2009), an obstacle free route was determined, which is transmitted to the user through audible messages; furthermore a complementary vibration system was implemented and mounted on a vest, which will serve as backup in order to alert the person about near obstacles. The prototype also has an identification and decoding system for QR codes that helps for a better orientation of the visually impaired person within the environment in which they manage themselves.

Keywords: Visual disability, vision, fictitious force, depth, navigation.

1. INTRODUCTION

Nowadays people deprived partial or totally of the sense of sight are limited in their mobilization for the development of several important aspects of their lives. Mobilizing involves a risk because of the obstacles that stand in their way, therefore several devices have been developed that help these people in their navigation; especially in places where there are suspended objects, as these cannot be detected by the white cane. Unfortunately, access to these devices is limited due to their high cost and lack of information about the existence of them.

INEC (2011) underline that the limited visual ability of individuals influences their lives in several important aspects such as social, academic and occupational. Navigation for these people either in work or in a domestic environment implies a big challenge because of the many obstacles that threaten their physical integrity, and the inadequacy of the cities for the blind; so, most of them should be guided by a walking stick, a guide dog, a relative or a friend.

Through this prototype and using the Microsoft Kinect tool, an assistance system for the blind was developed to complement the white cane in order to allow them to safely navigate through the detection and avoidance of obstacles, which they could collide with; especially objects that are not at floor level. In addition, more information on the environment that surrounds the visually impaired person is provided by detecting certain visual messages that could be located at specific points of importance, such as an information desk or an emergency exit.

The work is divided as stated below: Section 2 presents the main characteristics of the used sensor, section 3 describes the implemented prototype, section 4 shows the acquisition and processing of the delivered image by the Kinect sensor to set the initial navigation parameters, section 5 details how the modified fictitious force algorithm was implemented using artificial vision for obstacle avoidance, section 6 explains about the QR codes detection and their functionality within navigation, section 7 is about the generation and emission of audible instructions, while in section 8 system operation and interaction vibration button are explained. In Section 9 experimental results for people with and without visual impairment are shown.

2. MICROSOFT KINECT SENSOR

The Microsoft Kinect sensor for windows was used in the color image acquisition, which is used to find defined pattern matching within the entire image that determine the existence of a two-dimensional bar code (QR Code); as well as the depth image, which delivers depth information to digitized objects within the image and based on this, perform the necessary calculations of angles and required distances for the development of the implemented algorithm.

The Fig. 1, show the most important technical specifications about the Kinect for Windows for example, the minimum or maximum distance visible into the range the navigation or the horizontal and vertical field of view, some of the most important characteristics used into the algorithm.

Feature	Kinect for Windows 1	Kinect for Windows 2
Color Camera	640 x 480 @30 fps	1920 x 1080 @30 fps
Depth Camera	320 x 240	512 x 424
Max Depth Distance	~4.5 M	~4.5 M
Min Depth Distance	40 cm in near mode	50 cm
Horizontal Field of View	57 degrees	70 degrees
Vertical Field of View	43 degrees	60 degrees
Tilt Motor	yes	no
Skeleton Joints Defined	20 joints	26 joints
Full Skeletons Tracked	2	6
USB Standard	2.0	3.0
Supported OS	Win 7, Win 8	Win 8
Price	$299	TBD

Fig. 1. Technical Specifications.

2.1 Depth Sensor

Display a three-dimensional image and provide depth values are two of the main features of the sensor and are precisely those that differentiate it from other devices.

Kean et al. (2011) describe that the sensor has two depth ranges. The default range and near range, which is only available on the Kinect for Windows sensor, as shown in Fig. 2.

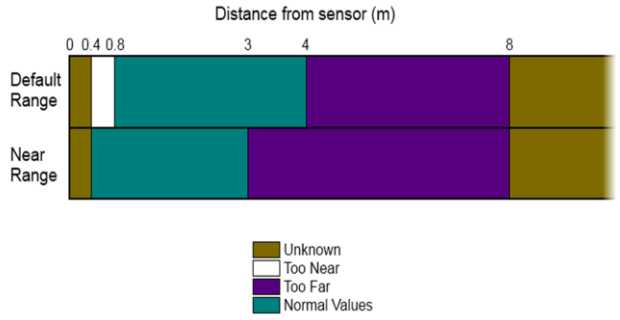

Fig. 2. Microsoft (2014) shows Kinect sensor depth ranges.

2.2 Limitations

Kinect sensor has several limitations that make that depth of certain regions of the scene cannot be estimated or if estimated, the data reliability is not acceptable by Salvatore (2014).

One of the great problems is caused by the infrared projection points because when they impact on an object, they generate a shadow in another on a greater distance, as seen in Fig. 3. The result is that depth in the affected areas by these shadows cannot be determined. This manifests as zero value pixels ("black zones") in the depth image as underlined by Córdova (2013).

Besides sensor's own internal limitations, limitations also exist by external factors, in particular because of the objects' surface properties, such objects may include translucent objects, reflective objects, black color objects, concave objects or reflective cavities. A strong brightness change (sunlight) is another limitation since sunlight, also being composed of infrared rays, prevents the sensor's infrared beam itself to be detected by the IR camera.

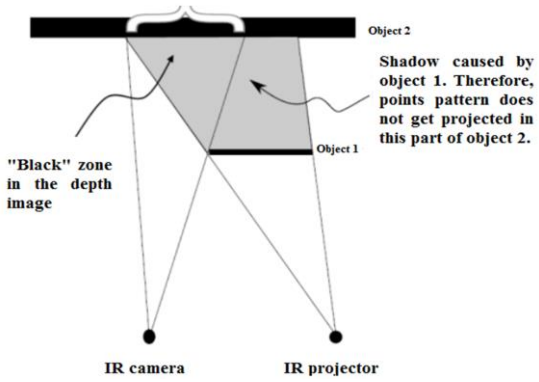

Fig. 3. Limitation due to projected shadows.

3. BLOCK DIAGRAM

The principal block diagram about the application is shown in the Fig. 4.

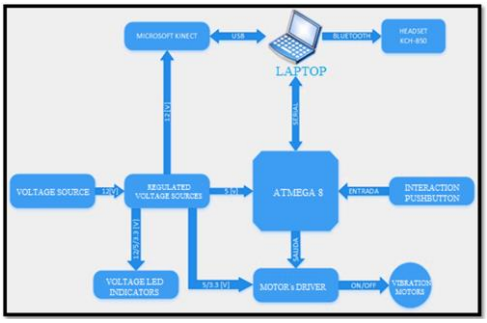

Fig. 4. Block Diagram.

The main processor in the application is the laptop , which receives depth data issued by the Kinect sensor that are necessary for the generation of repulsive forces of the obstacles and the attractive force of the user so that it can implement the algorithm modified fictitious force. All the mathematical development for the algorithm is implemented within the laptop reason why the bluetooth communication is used by a headset to communicate obstacle free route to the visually impaired person. Serial communication between the laptop and microcontroller is used to activate the vibration motors located in the vest, in addition, this communication is used to transmit user requirements through interaction button. All electronic elements are fed according to the technical specifications of the manufacturer.

4. IMAGE ACQUISITION AND PROCESSING OF THE KINECT SENSOR

The overall program structure is based on the acquisition and processing of both, color and depth image, which are delivered by the Kinect sensor. Data is processed in the LabVIEW 2013 Software, which through serial

communication transmits information to a microcontroller in order to enable or disable vibration motors; as well as receive and transmit the actions performed by the user via an interaction button. This button enables or disables the voice instructions issued by the developed system or issues the system's use instructions.

Kinect sensor initialization was performed using the toolkit 'Microsoft Kinect API v1.0' and its own LabVIEW library, where the inclination angle, that should have the sensor based on the user's height, is calculated.

In order to obtain the maximum depth value that the Kinect sensor can visualize a triangle between points ABC is formed as shown in Fig. 5, it is also used to estimate a user's height, which corresponds to a leg of the triangle in mention. Furthermore, it is established through testing and error that the proper distance as the second leg should be approximately 2 m, the calculation of an ideal depth (*D_IDEAL*) is performed using the Pythagorean Theorem.

This value of ideal depth is not applicative since it shows the ground as an obstacle to avoid when that's not the truth, thus it was decided to find a desired depth value (*D_WISHED*) that will show the obstacles to be avoided limited to a minimum height (h '). Based on several tests and because it is a complementary system to the white cane, it is determined that the minimum height of the obstacle to be avoided is 35% of the approximate user's height value, which is calculated by the system. To find the desired depth value, a similarity between the A'BC' and ABC is established achieving to eliminate the safety depth measure (D_SEC), the resulting expression is shown in (1)

$$DMÁX = D\_WISHED = D\_IDEAL\left(\frac{h - h'}{h}\right) \quad (1)$$

Based on (1) it is determined that desired depth is 65% of the ideal depth. Establishing this depth as the maximum threshold value (THR_MÁX) that the Kinect sensor can visualize in its environment.

Kean et al. (2011) underline that the minimum established threshold in the Kinect sensor is specified by its limited permissible depth acquisition, which is 45cm in near mode, therefore the value of THR_MIN is equal to this distance.

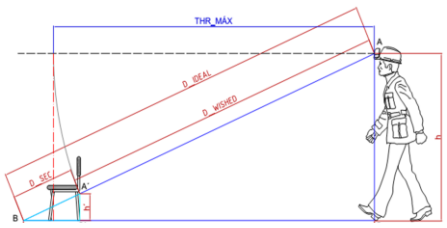

Fig. 5. Getting the maximum depth of vision.

6. ALGORITHM IMPLEMENTATION OF FICTITIOUS MODIFIED FORCE BY ARTIFICIAL VISION

The modified fictitious force algorithm will determine an obstacle free route where the visually impaired person can navigate without the possibility of getting impacted by any objects around them. To fulfill this purpose, there are required the following input data to the system: The amount of digitized objects in the sensor's image processing and the distances that these are from the person.

For the algorithm implementation it is necessary to establish a coordinate axes system that is considered for the mathematical and geometric algorithm development, as well as generate the repulsive force emitted by the objects in the environment. It is also necessary to establish an attractive force that is always attached to the visually impaired person within their navigation and finally, these forces will relate with a vector sum, generating a final vector containing the rotation direction necessary to avoid the impact of the person with the obstacles, as Ribeiro (2005) indicate.

5.1 Coordinate axes System.

The established coordinate axes system will remain invariant during the development of the algorithm throughout the mathematical processing of the navigation system and it is attached to the visually impaired person as shown in Fig. 6.

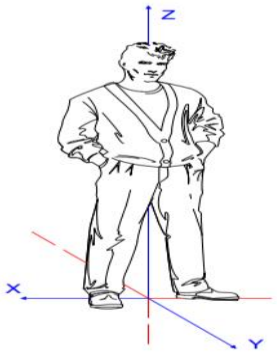

Fig. 6. Coordinate axes System.

5.2 Repulsive Force Generation.

In order to generate a repulsive force emitted by the obstacles, force shall be understood as a vector and therefore it has characteristics such as a direction (incidence angle) and a module, which is inversely proportional to the distance between the person and the obstacle's center of mass. The mathematical expression showing the magnitude calculation for the repulsive force $|\overrightarrow{Fr}|$ is (2).

$$|\overrightarrow{Fr}| = \begin{cases} 0, & si\ Pmed > Pmáx \\ \frac{Pmáx - Pmed}{Pmáx - Pmín}, & si\ Pmed < Pmáx \end{cases} \quad (2)$$

Where:

Pmáx = Maximum vision depth set in the Kinect sensor.

Pmed = Measured depth between the obstacle and the visually impaired person.

Pmín = Minimum vision depth set in the Kinect sensor.

As it can be seen in (3), the repulsive force magnitude is null when objects are outside the range of vision, as well as an increase in module is seen as the obstacle gets closer to the person. Finally, magnitude is greater than 1 when the distance to the obstacle is less than the depth of investment forces which warrants immediate evasion action.

$$|\overrightarrow{Fr}| = \begin{cases} 0, & si\ Pmed > Pmáx \\ (0,1], & si\ Pinv \leq Pmed < Pmáx \\ > 1, & si\ Pmed < Pinv \end{cases} \quad (3)$$

Where:

Pinv = Depth set for the investment of the final evasion force.

The angle theta (θ) shown in Fig. 7, is defined by (4), mathematical expression that relates the data of horizontal vision angle of the Kinect sensor, the missing value of 61° to complete the reference to the *x* positive axis and the *x* coordinate of each object's center of mass. An example of the above is shown in Fig. 8. It should be noted that the value of 0.0890625 is the relation between pixel and maximum horizontal vision angle of the Kinect sensor.

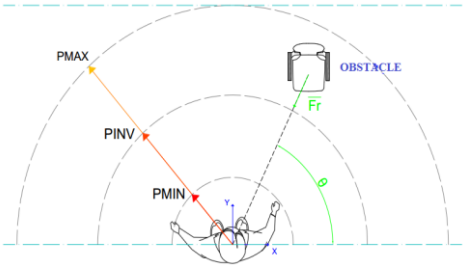

Fig. 7. Generation of a fictitious repulsive force from the obstacle to the visually impaired person.

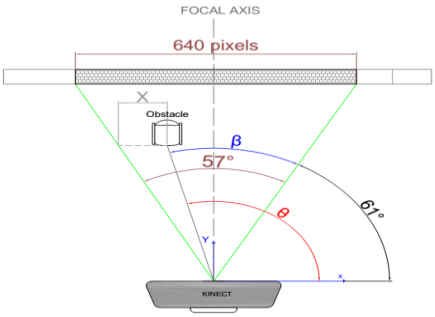

Fig. 8. Repulsion angle generated by the obstacle.

$$\theta = \left((640 - x)(0.0890625)\right) + 61 \quad (4)$$

Where:

x = Horizontal position of the digitized obstacle's center in the navigation environment.

5.3 *Attractive Force Generation.*

An attractive force from mobile robots algorithms is one that drives the robot to reach a certain point in its trajectory called 'goal', as mentioned by Ribeiro (2005).

Adapting this definition for the visually impaired person, such force is mentioned as a vector that is attached to the user, with a direction in the *y* positive axis and with a constant magnitude equal to 1. This force is responsible for generating the movement towards in the person's trajectory. Fig. 9 shows the attraction force ($\overrightarrow{Fa}$) that the user generates on their route.

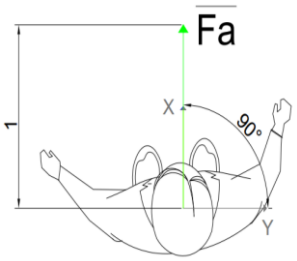

Fig. 9. Attractive force generated in the user.

5.4 *Final Rotation Force.*

The attraction and repulsion forces obtained above are related in order to calculate a specific evasion angle, which represent the direction of an obstacle free route within the digitized environment by the Kinect sensor.

For obtaining this angle, vector addition is applied by the polygon method, in this case vectors are all fictitious forces generated by both the obstacles and the user, thus a final resultant force ($\overrightarrow{Ff}$) is obtained with a module and angle value, referred to the *x* positive axis.

Based on the critical depths established as the Kinect sensor vision, the following consideration can be seen: if the obstacle is within the region between the investment depth forces ($Pinv$) and the Kinect's minimum vision depth ($Pmín$), the vector's magnitude will have a greater value than the unit. To calculate the final repulsive force magnitude when two or more objects are digitized by the Kinect sensor in the environment, (2) is used, with the difference that the measured depth ($Pmed$) is set as the average of all obstacles distances calculated from the visually impaired person, also leaving this magnitude value escaladed as shown in (3) and Fig. 10.

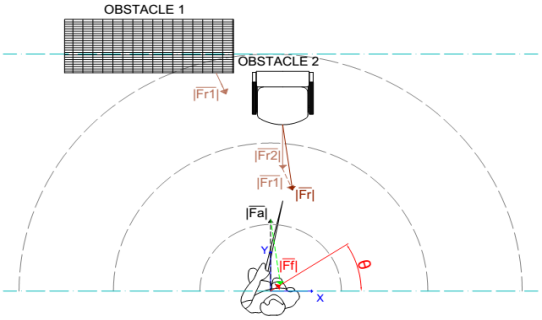

Fig. 10. Final force obtaining in an environment with the presence of two obstacles, vector sum by the polygon method for repulsive vectors and subsequent vector sum by the polygon method with the attraction force.

6. TWO-DIMENSIONAL BARCODE IDENTIFICATION

Two-dimensional barcodes identification, including the so-called QR codes, has its use in this work when it comes to suppress the Kinect sensor limitations. The designed algorithm for QR codes detection is comprised in 4 stages, which allow to optimize code reading and reproduction of the same in the user's navigation. The first stage will be responsible for Kinect's RGB image processing into a grayscale image. The second analyzes and locates search patterns (small squares in 3 of the 4 corners of a QR code) across the vision range. The third stage is responsible for decoding the hidden message within the limited area by the search patterns as in Fig. 11. Lastly, there is the stage of the audible messages play, which has a memory system that prevents repetitive playback of a same visualized code more than once within a time interval.

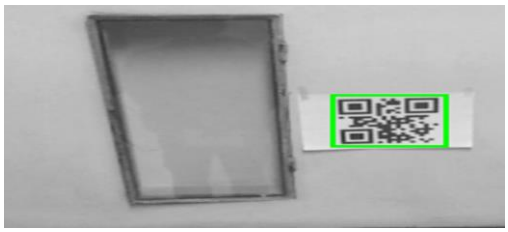

Fig. 11. QR code reading.

7. TRANSMISSION OF INSTRUCTIONS AND VEST.

7. 1 Audible messages generation as control instructions.

Audible messages are the control actions that are delivered to the visually impaired people, which will be emitted by the main processor (computer) via a bluetooth headset.

As shown in Fig. 12, control actions will be issued to the visually impaired person according to the region where the final rotational force is oriented. If the evasion angle is from 85° to 95°, an instruction to keep forward without altering their direction will be emitted. If the angle is between 260° and 280°, it means that the obstacle is in front of the user and they are forced to stop in their trajectory, then they must evaluate the obstacles existence with a head movement so they can know which route to be heading.

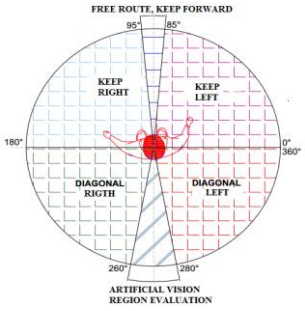

Fig. 12. Evasion angle interpretation for control instructions.

7.2. Switching and vibration interaction system

This system consists of vibration motors and a button, both placed in the user's vest. Motors' objective shown in Fig. 13 is to give an emergency notice, supported by the sense of touch against a possible collision with objects, while the purpose of the button is to transmit the system any desired requirement by the user.

A button that generates an external interrupt to the microcontroller was used, so it allows the user to have an interaction with the navigation system. Its main features are: enable or disable navigation instructions through an instantaneous pulse; as well as emitting the use or interpretation instructions of each of the audible messages that the person will hear through a long pulse (approx. 4 s).

Fig. 13. Vibration motors and interaction button location.

8. PROTOTYPE DESCRIPTION

The prototype consists of six main parts:

- A white industrial helmet with all necessary adaptations to incorporate the Kinect sensor.
- Sensor Kinect, which is responsible for depth image acquisition.
- Mini Headset KCH-850, is the device by which the user will hear all audible messages issued by the system.
- Control, communication and power supply regulation module; which is mainly the system responsible of communication between the computer and the microcontroller Atmega8.
- Power supply, which is a LiPo battery in charge of supplying power to the entire system.
- Vest with all fastenings and necessary compartments to incorporate all electronic, vibration, pulsation and power systems.

Due to the location of the Kinect sensor (helmet), the system focuses on the avoidance of obstacles that are above the waist, reaching a reliable navigation with 60cm high objects and 1.8m away, which is enough because the project is a complementary system, not a substitute to the white cane.

9. EXPERIMENTAL RESULTS

Tests on the prototype with visually impaired people were performed using the system with and without the white cane; as the prototype is a complementary system.

9.1 Obstacle detection Ranges.

These tests were performed in order to validate the calibrated distances as a range of maximum and minimum depth necessary for obstacles visualization within a given space as shown in Fig. 7. The minimum depth that the sensor can visualize is 45 [cm] due to Kinect's self-limitation, the maximum depth will be set by the algorithm that calculates the inclination and the sensor's maximum depth based on the user's approximate height. Table 1 shows a sampling for different heights and depth ranges established by the Kinect sensor.

Table 1. Maximum and minimum depth ranges

User's approximate height [m]	Minimum Depth			Maximum Depth		
	Calculated [cm]	Real [cm]	Error [%]	Calculated [m]	Real [m]	Error [%]
1.55	45	46.2	2.66	1.64	1.66	1.21
1.66	45	45.8	1.77	1.68	1.70	1.19
1.74	45	46.5	3.33	1.72	1.71	0.58
1.78	45	46.0	2.22	1.74	1.74	0
1.82	45	46.2	2.66	1.75	1.77	1.14

9.2 Obstacles detection with a minimum established height.

These tests were developed in order to validate the navigation system's ability to detect obstacles that have as minimum height the established relation between the user's height and the maximum vision depth that is set in the Kinect sensor. Table 2 shows the obtained results for this design condition verification.

Table2. Obstacle detection with minimum height

User's approximate height [m]	Obstacle's minimum height [m]	Samples	Desk table 80 [cm]		Trash can 60 [cm]	
			Detected	Error [%]	Detected	Error [%]
1.55	0.54	5	5	0	5	0
1.66	0.58	5	5	0	5	0
1.74	0.60	5	5	0	2	60
1.78	0.62	5	5	0	1	80
1.82	0.64	5	5	0	0	100

9.3 Results with visually impaired people

These tests were performed by 6 people (4 women and 2 men) of different ages in the range of 30 to 56 years old and with three different types of visual impairment:

- Low vision.
- Total blindness acquired.
- Total blindness of birth.

Tests with the white cane were performed by 3 people with total visual impairment, and these were held in different structured and unstructured environments both indoors and outdoors. Halls, a parking lot, a backyard and an auditorium were chosen.

System's operation was verified in narrow roads such as corridors, where the system tends to make the blind person moves in a oscillating way because evasion depends entirely on the interpretation of the instruction by the user and the inclination taken by them. Fig. 14 shows an example of a person with total acquired visual disability moving in an oscillating way.

The usefulness of vibration backup system was reflected, as when the system allowed the user to get too close to the walls (less than 1m), vibration alerted him to stop or lower his speed until another voice instruction is emitted by the system.

Fig. 14. Navigation of a visual impaired person in a narrow corridor.

The decrease in the user's speed significantly influenced in the results since the system could emit instructions that were more efficient, thus oscillating displacement in narrow aisles decreased.

People with a more developed sense of orientation as in the case of people with total blindness of birth, assimilated better the system's instructions and therefore their navigation was more efficient; however, like blind people with some level of acquired visual impairment, they decreased their speed when they didn't have their white cane's help, which helped to a better navigation.

10. CONCLUSIONS

- The implemented prototype is not intended to replace the white cane, but rather being a complementary system that assist the visually impaired people in their navigation, so they do not crash with obstacles that cannot be detected by the white cane and represent a potential danger, such as tall or hanging objects.
- The implementation of the modified fictitious force algorithm helps to despise supposed obstacles that the camera vision manifests in the user's trajectory, such as the ground, where any evasion action should be emitted.
- Detection and especially instruction for obstacles avoidance in the environment depend largely on the speed with which the user walks. The system has a higher efficiency when the person moves at a slower pace as it allows the system to end a voice instruction before moving on to the next.

- To cover with more accuracy and efficiency the environment that surrounds a blind person, it was determined that it is not sufficient to use a single sensor as the system's feedback since areas, where the presence of another sensor can contribute to the evasive action, are neglected.

- The vibration system incorporated into the vest has a great importance in the prototype's development, since along with the white cane, it manifests as the last safety resort to alert the user about the presence of a near obstacle.

REFERENCES

INEC. (2011). *2010 Census Results*. [Online]. Available: www.ecuadorencifras.gob.ec/resultados/.

Kean, S., Hall, J., and Perry, P. (2011). *Meet the Kinect*, New York: Apress.

Microsoft. (2014). *Coordinate Spaces*. *Microsoft*. [Online]. Available: https://msdn.microsoft.com/en-us/library/hh973078.aspx.

Córdova, F. (2013). *Theft/abandonment detection of indoors objects using depth cameras*. [Online]. Available: http://arantxa.ii.uam.es/~jms/pfcsteleco/lecturas/20121212FabricioACordovaLucero.pdf.

Scaglia, G. (2009). *Mobile robot navigation in unstructured environments using linear algebra*. Madrid: RIAI.

Ribeiro, M. Isabel (2005). *Obstacle Avoidance*. [Online]. Available:http:user.isr.ist.utl/~mir/pub/ObstacleAvoidance.pdf.

Salvatore, J., Osio, J., Morales, M (2014). *Object detection using Kinect sensor*. LACCEI.

Null-space based control for human escorting by using Mobile Robots

Daniel Herrera, Javier Gimenez, Marcos Toibero, Ricardo Carelli

Instituto de Automática-CONICET, Universidad Nacional de San Juan, Av.Libertador Oeste 1109, San Juan-Argentina (e-mail: {dherrera, jgimenez, mtoibero, rcarelli}@inaut.unsj.edu.ar).

Abstract: Sharing the workspace or interacting directly with people in a social way is currently a key challenge in the design of mobile robot applications. An interesting field of study is related with the so-called hidden dimension, which relates the sense of security that a human feels when interacting with another one. Therefore, the researchers have been interested in developing human-friendly applications by abstracting social cues for the robotic design. One of these is the social zone, which acts like a repulsive potential field, and if it is not respected, an uncomfortable situation for humans is produced. In robotics, many approaches have been proposed to define and to avoid these fields, which contributes to improve the human comfort during interactions at least from a qualitative perspective. This paper proposes a novel null-space-based (NSB) algorithm for a non-holonomic mobile robot platform, which is programmed to escort a human in a behavior-based paradigm. The emphasis is posed in the evasion of other humans in the environment by considering them as elliptical potential fields with non-holonomic motion. Finally, simulation results are presented to show the performance of the proposed control algorithm.

Keywords: Robot navigation, Human-centered design, Human factors, Non-linear control.

1. INTRODUCTION

According to the proxemic studies developed by Hall (1963), the human respects social zones during different kind of interactions, i.e. there are distances to describe intimate and social spaces depending of the task, the situation, and even of cultural or personal preferences.

When a robot navigates in a human-shared environment, it is supposed that it must also respect these social zones to improve its social acceptance. As consequence of this hypothesis, in robotics, some conventions have been established. For example, Chi-Pang et al. (2011) discuss different types of personal space for humans according to the situation, e.g., they assume an egg-shaped personal space for the human while it is moving, due to they should have a long and clear space to walk (giving the sense of safety). For this, they consider that the length of the semi-major axis of the potential field is proportional to the human velocity. Scandolo and Fraichard (2011) use personal space in their social cost map model for path simulation. Guzzi et al. (2013) incorporates a potential field that dynamically modifies its dimensions according to the relative distance with the human to avoid an occlusion event or "deadlocks". In Ratsamee et al. (2013), a human-friendly navigation is proposed, where the concept of personal space or "hidden space" is used to prevent uncomfortable feelings when humans avoid or interact with robots. This is based on the analysis of human motion and behavior (face orientation and overlapping of personal space).

In reference to the human following, in Kluge et al. (2002) it is given more relevance to the coordination between human and a mobile robot platform. It is based on the dynamic obstacle avoidance denominated "velocity obstacles" (Fiorini and Shiller, 1998). This allows the robot changing its orientation and velocity according to the locomotion of the followed person in a dynamic environment. In Loper et al. (2008) a robotic system for human following is presented, which is capable to answer verbal and non-verbal instructions under non-structured conditions. For detecting and following a human it is used a Kalman filter and a PID control respectively. Doisy et al. (2012) propose algorithms for human following by using depth images of Kinect® sensor. The first constitutes a following algorithm of the human path, and the second one is an adaptive algorithm that additionally uses a range sensor to identify and generate dynamically a path for the robot in a previously mapped scenario. Guansheng et al. (2013), developed a vision based algorithm by using a mobile robot endowed with a Kinect® sensor to follow humans, where the skeleton tracking function allows to get the human position. Consequently the control is used to maintain this skeleton in the center of the image and in a fixed distance from the robot. Similarly, in Machida et al. (2012) it is proposed a control algorithm for mobile robots based in the 3D Kinect® information to generate linear and angular velocity commands.

Regarding the behavior-based control, the problem is divided into sub-problems to be individually controlled. Generally, there are overlapping interests between these

tasks, and it should be chosen a behavior that balances the sub-objectives. The performance of the control system depends on how these controllers are fused. In Antonelli et al. (2005) an experimental comparison among three approaches are analyzed: the layered control system, the motor scheme control and null-space behavioral control (Chiaverini, 1997). The main difference between them is the way they manage the sub-task outputs. Specifically, the null-space based approach derives from an inverse kinematics solution by exploiting the kinematic redundancy, in which there are more degrees of freedom than necessary to fulfil the task. From a practical point of view, the kinematic redundancy is not strictly present in the robotic system, but the task can give redundancy to the system. In robotic manipulators, the simplest method to define the null-space is based on the inverse Jacobian (Whitney, 1969). This theory for redundant robotic manipulators has been proposed for the execution of different formation-control missions with multi-mobile-robots systems (Antonelli et al., 2009), whose collective task make the system redundant.

This paper proposes to use the null-space based (NSB) approach to establish an cooperative leader-follower control that considers multiple kinematic tasks during the interaction with humans. The first one consists in keeping out of social zones of humans, which are defined by considering an elliptical potential fields moving with a non-holonomic nature. Additionally, two secondary tasks are proposed in the NSB paradigm, which are related to keep the orientation and distance of the formation. The designed control is simulated to test its performance. It has been made emphasis in the evasion of humans with the above mentioned social zones.

In this way, in Section 2 an elliptical potential field is proposed, and, the Jacobian, that relates the potential variation with the motion of the robot is established. Later, in Section 3 the avoidance of this field is defined through the minimum norm solution, i.e. by using the pseudo-inverse of the Jacobian matrix, where additional secondary tasks to keep the formation with the human leader are included as part of a null-space based design. Finally, the performance of the algorithm is tested through simulation in Section 4. Also, the paper conclusions are presented in Section 5.

2. SOCIAL POTENTIAL FIELD

When a human walks between other humans, there are social zones which are interpreted as repulsive potential fields. In general, they are distance dependent.

In this way, given a global reference system $x-y$ and the human posture $\{x_h, y_h, \theta_h\}$ at time t, it is considered the reference system x^*-y^* rotated by θ_h. (see Fig. 1). By using these coordinates, let's define the following potential field,

$$V_h(t) = \exp\left\{-\left(\frac{x^*-x_h^*}{a}\right)^2 - \left(\frac{y^*-y_h^*}{b}\right)^2\right\},$$

where (x^*, y^*) is a point of the potential field in the rotated framework x^*-y^*; and (x_h^*, y_h^*) the human position and the center of this field, a is the major-axis length of the elliptical Gaussian form, and b is the minor-axis length (see Fig. 1).

Let's define a shape-variant potential field by considering the major-axis as time dependent. It is based on a social heuristic that considers that a human needs a long and clear space to move while walking (Chi-Pang et al., 2011).

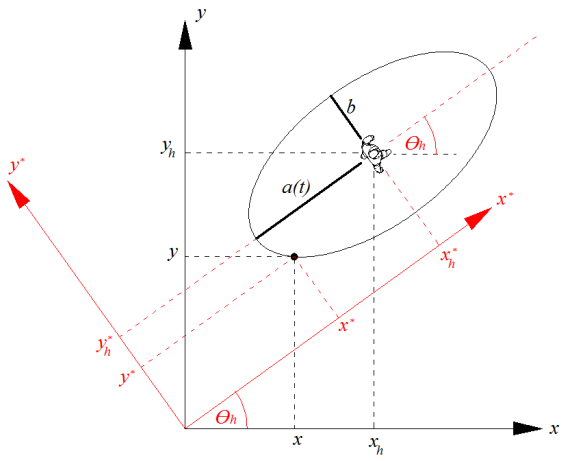

Fig. 1. Schematic description of the social zone.

In consequence, the time-derivative of this field is

$$\frac{dV_h}{dt} = \left[\frac{\partial V_h}{\partial x^*}, \frac{\partial V_h}{\partial y^*}, \frac{\partial V}{\partial x_h^*}, \frac{\partial V_h}{\partial y_h^*}, \frac{\partial V_h}{\partial a}\right] \begin{bmatrix} \dot{x}^* \\ \dot{y}^* \\ \dot{x}_h^* \\ \dot{y}_h^* \\ \dot{a} \end{bmatrix}.$$

Solving this expression through algebraic steps, it results that

$$\begin{aligned}\frac{dV_h}{dt} =& -2V_h\left[(x^*-x_h^*)/a^2, (y^*-y_h^*)/b^2\right]\dot{\mathbf{x}}^* + \cdots \\ &+ 2V_h\left[(x^*-x_h^*)/a^2, (y^*-y_h^*)/b^2\right]\dot{\mathbf{x}}_h^* + \cdots \\ &+ 2V_h\frac{(x^*-x_h^*)^2}{a^3}\dot{a}, \end{aligned} \quad (1)$$

where $\dot{\mathbf{x}}^* = [\dot{x}^*, \dot{y}^*]^T$, $\dot{\mathbf{x}}_h^* = [\dot{x}_h^*, \dot{y}_h^*]^T$. It can be compactly expressed like

$$\dot{V}_h = \mathbf{J_s}\dot{\mathbf{x}}^* - \mathbf{J_s}\dot{\mathbf{x}}_h^* + J_f\dot{a}. \quad (2)$$

By considering the rotation matrix,

$$\mathbf{R} = \begin{bmatrix} \cos\theta_h & \sin\theta_h \\ -\sin\theta_h & \cos\theta_h \end{bmatrix},$$

it is possible to express it in the $x-y$ global framework, i.e.,

$$\begin{bmatrix} x^* \\ y^* \end{bmatrix} = \mathbf{R}\begin{bmatrix} x \\ y \end{bmatrix}, \quad \begin{bmatrix} x_h^* \\ y_h^* \end{bmatrix} = \mathbf{R}\begin{bmatrix} x_h \\ y_h \end{bmatrix}.$$

By considering the time-derivative of this expressions, it is obtained

$$\begin{aligned}\dot{\mathbf{x}}^* &= \begin{bmatrix} \cos\theta_h & \sin\theta_h & -\sin\theta_h x + \cos\theta_h y \\ -\sin\theta_h & \cos\theta_h & -\cos\theta_h x - \sin\theta_h y \end{bmatrix}\begin{bmatrix} \dot{x} \\ \dot{y} \\ \dot{\theta}_h \end{bmatrix}, \\ &= \mathbf{R}\dot{\mathbf{x}} + \mathbf{p}\dot{\theta}_h, \end{aligned} \quad (3)$$

where $\mathbf{p} := \begin{bmatrix} -\sin\theta_h x + \cos\theta_h y \\ -\cos\theta_h x - \sin\theta_h y \end{bmatrix}$. Similarly for the human position,

$$\dot{\mathbf{x}}_h^* = \begin{bmatrix} \cos\theta_h & \sin\theta_h & -\sin\theta_h x_h + \cos\theta_h y_h \\ -\sin\theta_h & \cos\theta_h & -\cos\theta_h x_h - \sin\theta_h y_h \end{bmatrix} \begin{bmatrix} \dot{x}_h \\ \dot{y}_h \\ \dot{\theta}_h \end{bmatrix},$$

$$= \mathbf{J}_h^* \begin{bmatrix} \dot{x}_h \\ \dot{y}_h \\ \dot{\theta}_h \end{bmatrix}.$$

If additionally it is considered a non-holonomic motion for the human gait (Arechavaleta et al., 2006; Leica et al., 2014), i.e,

$$\begin{bmatrix} \dot{x}_h \\ \dot{y}_h \\ \dot{\theta}_h \end{bmatrix} = \begin{bmatrix} \cos\theta_h & 0 \\ \sin\theta_h & 0 \\ 0 & 1 \end{bmatrix} \begin{bmatrix} \nu_h \\ \omega_h \end{bmatrix} = \mathbf{J}_h \begin{bmatrix} \nu_h \\ \omega_h \end{bmatrix},$$

then it results,

$$\dot{\mathbf{x}}_h^* = \mathbf{J}_h^* \mathbf{J}_h \begin{bmatrix} \nu_h \\ \omega_h \end{bmatrix}, \tag{4}$$

where $\mathbf{J}_h^* \mathbf{J}_h := \begin{bmatrix} 1 & -\sin\theta_h x_h + \cos\theta_h y_h \\ 0 & -\cos\theta_h x_h - \sin\theta_h y_h \end{bmatrix}$.

In this way, by substituting (3) and (4) in (2), results that

$$\dot{V}_h = \mathbf{J_s R}\dot{\mathbf{x}} + \mathbf{J_s p}\omega_h - \mathbf{J_s} \mathbf{J}_h^* \mathbf{J}_h \begin{bmatrix} \nu_h \\ \omega_h \end{bmatrix} + J_f \dot{a},$$

$$:= \mathbf{J}_o \dot{\mathbf{x}} + g.$$

Therefore, the total repulsive effect over each agent i in a position $\mathbf{x}_i := (x_i, y_i)$ is calculated as the sum of all the repulsive effects V_{hj} generated by n human obstacles in the shared scenario, i.e.

$$V_i = \sum_{j=1}^{n} V_{hj},$$

and, in consequence

$$\dot{V}_i = \sum_{j=1}^{n} \dot{V}_{hj} = \sum_{j=1}^{n} \mathbf{J}_{oj} \dot{\mathbf{x}}_i + \sum_{j=1}^{n} g_j. \tag{5}$$

3. NULL-SPACE BASED CONTROL

Let $\mathbf{q} \in \mathbb{R}^m$ be the task variables that represent the states of the system to be controlled. Also, let $\mathbf{x} := [x_1, x_2, \cdots, x_n, y_n]^T \in \mathbb{R}^{2n}$ be the array with the positions (x_n, y_n) of the n members of the formation. Then, the relation between $\mathbf{q}$ and $\mathbf{x}$ is expressed like

$$\mathbf{q} = f(\mathbf{x}).$$

By considering its temporal derivative

$$\dot{\mathbf{q}} = \frac{df(\mathbf{x})}{d\mathbf{x}} \dot{\mathbf{x}} = \mathbf{J}(\mathbf{x}) \dot{\mathbf{x}}, \tag{6}$$

where $\mathbf{J} := \mathbf{J}(\mathbf{x}) \in \mathbb{R}^{m \times 2n}$ is the Jacobian matrix associated to the task. In this way, the redundancy of this system is given by the condition $m < 2n$, where $2n$ is interpreted as the degrees of freedom of the system. In this way, the problem is focused on defining control actions for each member to carry out the formation control objectives. A solution to this problem is typically given by considering the minimum norm solution, i.e., by using the pseudo-inverse of the Jacobian matrix $\mathbf{J}^\dagger := \mathbf{J}^\dagger(\mathbf{x}) = \mathbf{J}^T(\mathbf{J}\mathbf{J}^T)^{-1}$ as follows

$$\dot{\mathbf{x}}_d = \mathbf{J}^\dagger \dot{\mathbf{q}}. \tag{7}$$

The desired velocities $\dot{\mathbf{x}}_d$ could be applied directly to certain kind of robots, however it is usual to define the i-tasks through position errors, therefore it is used the so-called closed-loop inverse-kinematics (CLIK) version of the algorithm for each task, namely

$$\dot{\mathbf{x}}_{di} = \mathbf{J}_i^\dagger(\mathbf{x}) \left(\dot{\mathbf{q}}_{di} + \mathbf{K}_i \tilde{\mathbf{q}}_i \right). \tag{8}$$

where $\mathbf{K}_i$ is a positive defined design matrix, and, $\tilde{\mathbf{q}}_i$ is the task error defined as $\tilde{\mathbf{q}}_i := \mathbf{q}_{di} - \mathbf{q}$. i is the task number which are organized by priority. In this way, according to (Baillieul et al., 1984; Chiaverini, 1997), a non-minimun norm solution of CLIK for three tasks can be written as

$$\dot{\mathbf{x}}_d = \dot{\mathbf{x}}_{d1} + \left(\mathbf{I} - \mathbf{J}_1^\dagger \mathbf{J}_1 \right) \left[\dot{\mathbf{x}}_{d2} + \left(\mathbf{I} - \mathbf{J}_2^\dagger \mathbf{J}_2 \right) \dot{\mathbf{x}}_{d3} \right]. \tag{9}$$

Each task velocity is computed individually and the overall NSB control action always fulfills the highest priority task at non-singular configurations. However the fulfillment of the lower priority tasks should be discussed in a case-by-case basis.

3.1 Stability analysis

By multiplying each member of (9) by $\mathbf{J}_1$ under the assumption that it is a full-range matrix, and noting that $\mathbf{J}_1(\mathbf{I} - \mathbf{J}_1^\dagger \mathbf{J}_1) = 0$, then

$$\dot{\mathbf{q}}_1 = \dot{\mathbf{q}}_{d1} + \mathbf{k}\tilde{\mathbf{q}}_1. \tag{10}$$

This expression can be expressed as $\dot{\tilde{\mathbf{q}}} = -\mathbf{k}\tilde{\mathbf{q}}_1$. If it is also defined a Lyapunov candidate function with the form

$$\mathcal{V} = \frac{1}{2} \tilde{\mathbf{q}}_1^T \tilde{\mathbf{q}}_1, \tag{11}$$

then the time derivative of this function results

$$\dot{\mathcal{V}} = -\tilde{\mathbf{q}}_1 \mathbf{k} \tilde{\mathbf{q}}_1,$$

where $\mathbf{k}$ as a positive defined matrix makes the system asymptotically stable, i.e. $\tilde{\mathbf{q}}_1 \to 0$ with $t \to \infty$.

To establish the stability for secondary tasks, it is supposed that the secondary task does not affect the primary task and the two tasks are in consequence compatible.

It is expressed by the linearly independence of the subspaces $\mathcal{N}(\mathbf{J}_1)$ and $\mathcal{N}(\mathbf{J}_2)$, namely

$$\mathcal{N}^\perp(\mathbf{J}_1) \cap \mathcal{N}^\perp(\mathbf{J}_2) = \{0\},$$

when

$$\mathcal{N}^\perp(\mathbf{J}_1) \equiv \mathcal{N}(\mathbf{J}_2)$$

i.e, the subspaces $\mathcal{N}^\perp(\mathbf{J}_1)$ and $\mathcal{N}^\perp(\mathbf{J}_2)$ are orthogonal. It can be expressed as

$$\mathcal{R}(\mathbf{J}_2^\dagger) \subseteq \mathcal{N}(\mathbf{J}_1), \tag{12}$$

or well,

$$\mathbf{J}_2 \mathbf{J}_1^\dagger = 0.$$

In this way, if (9) is pre-multiplied by $\mathbf{J}_2$ then it results that

$$\dot{\mathbf{q}}_2 = \dot{\mathbf{q}}_{d2} + \mathbf{k}\tilde{\mathbf{q}}_2,$$

which analogously to (10) by considering the Lyapunov candidate function (11) results to be asymptotically stable.

Similarly for the third task,

$$\mathcal{R}(\mathbf{J}_3^\dagger) \subseteq \mathcal{N}(\mathbf{J}_1) \cap \mathcal{N}(\mathbf{J}_2). \tag{13}$$

In this way, following a similar procedure for the second task, the third task is demonstrated to be also asymptotically stable, provided that the third task does not affect the second and the first tasks.

3.2 Problem statement

Let us consider a formation of two agents of which one is a human. For this, it must be guaranteed two facts: the first one is related to the mutual coordination between formation members, and, the second one related to the presence of another humans in the environment.

To guarantee the stability of the first problem, it must be designed a control in which the human acts like a leader, i.e., he is capable to move freely, while the formation is moving accordingly to maintain a pre-established formation posture or shape. In this way, the formation is named as human-centered because it is not possible to govern the human actions.

On the other hand, for the second fact, the presence of humans and its avoidance must be established as primary goal. These two design qualities are established in the following Sections.

First, let's $\mathbf{x} := [x_1, y_1, x_2, y_2]^T$ be a vector with the Cartesian positions $(x_i, y_i), i = \{1, 2\}$ of both agents, where the first agent is a robot follower and the second agent a human leader. Later, the variables for each task are defined as follows.

3.3 Principal task: Social zone avoidance

The meddling avoidance of the robot into human social zones is defined as the principal task. Then, let's V_i be the task variable that represents the repulsive effect over each individual because of the presence of other individuals. For this, consider (5) to be expressed for both agents (human and robot) like

$$\begin{bmatrix}\dot{V}_1\\ \dot{V}_2\end{bmatrix} = \begin{bmatrix}\mathbf{J}^{(1)} & \mathbf{0}_{1\times 2}\\ \mathbf{0}_{1\times 2} & \mathbf{J}^{(2)}\end{bmatrix}\dot{\mathbf{x}} + \begin{bmatrix}g_1\\ g_2\end{bmatrix}, \\ := \mathbf{J}_1\dot{\mathbf{x}} + \mathbf{g}, \tag{14}$$

where $\mathbf{J}^{(i)} := \sum_{j=1}^{n}\mathbf{J}_{oj}, g_i := \sum_{j=1}^{n} g_j$ are the Jacobians and compensation motion factor for each individual $i = \{1, 2\}$ under the presence of n human obstacles.

In this way, the minimal norm solution for the formation in this task is expressed as,

$$\dot{\mathbf{x}}_{d1} = \mathbf{J}_1^{\dagger}\left(\dot{\mathbf{V}}_d + \mathbf{K}_1\tilde{\mathbf{V}} - \mathbf{g}\right), \tag{15}$$

where $\mathbf{V}_d := [V_{d1}, V_{d2}]^T$ and $\tilde{\mathbf{V}}_d := [V_{d1} - V_1, V_{d2} - V_2]^T$.

Note that in the expression (14) the resultant Jacobian $\mathbf{J}_1$ brings out an uncoupled condition for the agents, i.e., each individual is in charge of avoiding its obstacles. In consequence, the robot agent is controlled to avoid its human obstacles, and, as a trivial fact, the human agent avoids its obstacles by himself without affecting the system stability.

The incorporation of $\mathbf{g}$ improves the performance of the evasion of humans compared to other approaches for common dynamic obstacles. This is because it does not only take into account the linear motion of the obstacle, but also it is related to the angular motion of the human obstacle, and, its dynamic shape.

3.4 Secondary task: Formation posture

Let's $\mathbf{q}_2 := [\gamma, x_f, y_f]^T$ be the formation posture variables, where

$$\gamma = \operatorname{atan}\frac{y_1 - y_2}{x_1 - x_2}, \quad x_f = x_2, \quad y_f = y_2, \tag{16}$$

with γ the orientation of the formation and (x_f, y_f) the position of the formation. In consequence,

$$\mathbf{q}_2 = f(\mathbf{x}).$$

Note that the position of the formation is centered on the human leader. It is given to guarantee that the human is free to move in whatever direction he wants; therefore, the formation is capable to keep the formation posture by itself.

By considering its time derivative, it results

$$\dot{\mathbf{q}}_2 = \mathbf{J}_2\dot{\mathbf{x}} \tag{17}$$

where,

$$\mathbf{J}_2 := \begin{bmatrix}\frac{y_1 - y_2}{d^2} & -\frac{x_1 - x_2}{d^2} & -\frac{y_1 - y_2}{d^2} & \frac{x_1 - x_2}{d^2}\\ 0 & 0 & 1 & 0\\ 0 & 0 & 0 & 1\end{bmatrix}, \tag{18}$$

and, its pseudo-inverse is expressed like

$$\mathbf{J}_2^{\dagger} = \begin{bmatrix} y_1 - y_2 & \frac{(y_1 - y_2)^2}{d^2} & -\frac{(x_1 - x_2)(y_1 - y_2)}{d^2}\\ -(x_1 - x_2) & -\frac{(x_1 - x_2)(y_1 - y_2)}{d^2} & \frac{(x_1 - x_2)^2}{d^2}\\ 0 & 1 & 0\\ 0 & 0 & 1\end{bmatrix},$$

where $d^2 = (x_1 - x_2)^2 + (y_1 - y_2)^2$.

The minimal norm solution for this task is expressed as,

$$\dot{\mathbf{x}}_{d2} = \mathbf{J}_2^{\dagger}\left(\dot{\mathbf{q}}_{2d} + \mathbf{K}_2\tilde{\mathbf{q}}_2\right), \tag{19}$$

where $\mathbf{q}_{2d} := [\gamma_d, x_{fd}(t), y_{fd}(t)]^T$, $\tilde{\mathbf{q}}_2 := \mathbf{q}_{2d} - \mathbf{q}_2$, and, $\mathbf{K}_2 := k_2\mathbf{I}_3$. In this way, if the desired trajectory for the formation is the human trajectory, i.e., $x_{fd}(t) = x_h$, $y_{fd}(t) = y_h$, then it results in a trivial solution for the human leader and a control action for the robot, which are given by

$$\dot{\mathbf{x}}_{d2} = \mathbf{J}_2^{\dagger}\left[\begin{pmatrix}0\\ \dot{x}_h\\ \dot{y}_h\end{pmatrix} + \mathbf{k}_2\begin{pmatrix}\gamma_d - \gamma\\ 0\\ 0\end{pmatrix}\right], \\ = \begin{bmatrix}k_2(y_1 - y_2)\tilde{\gamma}\\ k_2(x_1 - x_2)\tilde{\gamma}\\ \dot{x}_h\\ \dot{y}_h\end{bmatrix}.$$

3.5 Tertiary task: Formation shape

Finally, the tertiary task is related to the formation shape, i.e., the distance between the individuals. Let's consider $q_3 := d$ as the only formation shape variable, where

$$d = \sqrt{(x_1 - x_2)^2 + (y_1 - y_2)^2}, \tag{20}$$

which is the distance between them. By considering its time derivative, it results

$$\dot{q}_3 = \mathbf{J}_3\dot{\mathbf{x}} \tag{21}$$

where,

$$\mathbf{J}_3 := \left[-\frac{x_1 - x_2}{d}, -\frac{y_1 - y_2}{d}, \frac{x_1 - x_2}{d}, \frac{y_1 - y_2}{d}\right], \quad (22)$$

and, its pseudo-inverse is expressed like

$$\mathbf{J}_3^{\dagger} := \left[-\frac{x_1 - x_2}{2d}, -\frac{y_1 - y_2}{2d}, \frac{x_1 - x_2}{2d}, \frac{y_1 - y_2}{2d}\right]^T, \quad (23)$$

The minimal norm solution for this task is expressed as,

$$\dot{\mathbf{x}}_{d3} = \mathbf{J}_3^{\dagger}\left(\dot{q}_{3d} + k_3\tilde{q}_3\right), \quad (24)$$

where $q_{3d} := d_d$, $\tilde{q}_3 := q_{3d} - q_3$ and k_3 is a positive design constant.

Note that this task does not affect the second one.

3.6 Mobile robot control

Once that each task of the formation has been defined in the Cartesian space and, it has been expressed the control actions for each agent as (9), it results

$$\dot{\mathbf{x}}_d = [\dot{x}_d^{(1)}\dot{y}_d^{(1)}\dot{x}_d^{(2)}\dot{y}_d^{(2)}]^T,$$

where $(\dot{x}_d^{(k)}, \dot{y}_d^{(k)}), k = \{1, 2\}$ are the $x-y$ velocities for each k agent. As mentioned the control actions for the human leader are trivial, i.e. $\dot{x}_2 = \dot{x}_d^{(2)}$ and $\dot{y}_2 = \dot{y}_d^{(2)}$. However the control actions generated for the robot must be expressed like robot commands of linear and angular velocity. To this aim, consider the kinematic model of a differential drive mobile robot as follows

$$\begin{bmatrix}\dot{x}_1\\ \dot{y}_1\end{bmatrix} = \begin{bmatrix}\cos\theta_r & -r\sin\theta_r\\ \sin\theta_r & r\cos\theta_r\end{bmatrix}\begin{bmatrix}\nu_r\\ \omega_r\end{bmatrix} := \mathbf{J}_r\mathbf{u}_r \quad (25)$$

where θ_r is the robot orientation, r is the distance from the middle of the wheels to a point in a perpendicular direction, and, $\{x_r, y_r\}$ is the Cartesian robot position. Note that $\dot{\theta}_r$ is not expressed in this model because the robot orientation is not controlled when the objectives are focused on the formation, i.e., it is only controlled the robot relative position to get a formation orientation. In this way by considering (25), it can be expressed the control action for the mobile robot as

$$\mathbf{u}_r := \mathbf{J}_r^{-1}\begin{bmatrix}\dot{x}_d^{(1)}\\ \dot{y}_d^{(1)}\end{bmatrix}. \quad (26)$$

3.7 Discussion

Even when the proposed solution results in a flexible formation by considering as priority the posture of the formation over its shape, it can be also selected other possible variable combination to give rigid characteristics with similar results.

Based on a leader-follower formation it must be always guaranteed that the formation trajectory is given by the leader trajectory. In this way, to get a rigid formation, the variables should be chosen as follows. For the second task, $\mathbf{q}_2 := [d, x_f, y_f]^T$ and for the third task $q_3 := \gamma$.

By following a similar procedure, the task priorities could be redefined with equal valid results, but by giving different priorities to the formation orientation γ and the formation shape d.

4. SIMULATION RESULTS

In order to test the performance of the proposed control, it is considered a simulated Pioneer 3AT robot which is programmed to follow a human. The simulations are focused on showing the performance under the presence of both static and dynamic obstacles, where the human obstacles have been defined as elliptical potential fields with non-holonomic motion as previously detailed.

Additionally, the effect of the compensation factor g, as shown in (15), has been tested by considering the two cases, the first one where the motion of the obstacle is not considered, i.e., $g = 0$ and, the second one when the motion of the human obstacle is characterized by $g \neq 0$, which relates the variation of the potential field with the motion of the robot during the meddling event. This effect is only present during the evasion of dynamic obstacles and it is related with a compensation of the human motion that allows to avoid him in a more suitable way.

In this way, the parameters were chosen as

Table 1. Parameters Simulation

Description	**Parameters**	
Leader trajectory	$x_d = 20\arctan(0.03t)$	$y_d = 0.5$
Social zone	$a = b + 1.2\nu_h$	$b = 0.5$
Formation	$\gamma_d = \pi/4[rad]$, $d_d = 2.5[m]$	
	$k_1 = 0.0001$, $k_2 = 1.2$, $k_3 = 2$	

4.1 Simulation 1: Lateral meddling

For the first simulation let's consider a dynamic human obstacle, which has both: rotation and translation motions. These effects are included as part of the g compensation by considering the human obstacle velocities ν_h and ω_h. For this case, it is considered a constant linear velocity of the human obstacle, i.e., the major-axis of the potential field is fixed while the human is moving in a sinusoidal trajectory. Additionally, it is considered a static human obstacle. The time-parametrized trajectories are presented in Fig. 2.

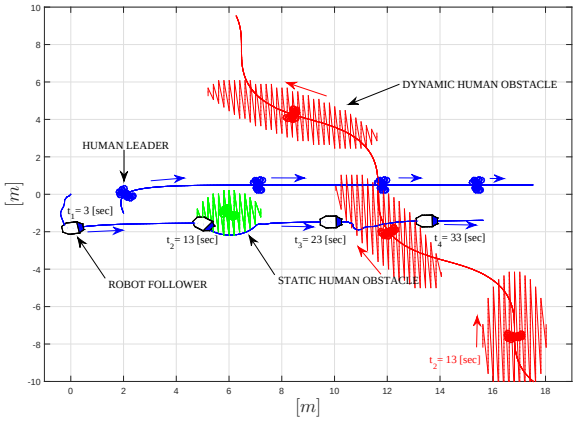

Fig. 2. Top view trajectories.

Also, the motion errors for each sub-task are presented in Fig. 3, where it is also presented an augmented view of the trajectories developed by the robot during the

evasion of the dynamic obstacle. Note that by including the motion compensation term g it is reduced the meddling in the social zone during the evasion as consequence of considering the variation of the field with the motion, which in this case generates a fastest deviation to avoid the human social zone. This effect can be also seen in a lower potential repulsion values over the robot during the simulation time (see Fig. 3c).

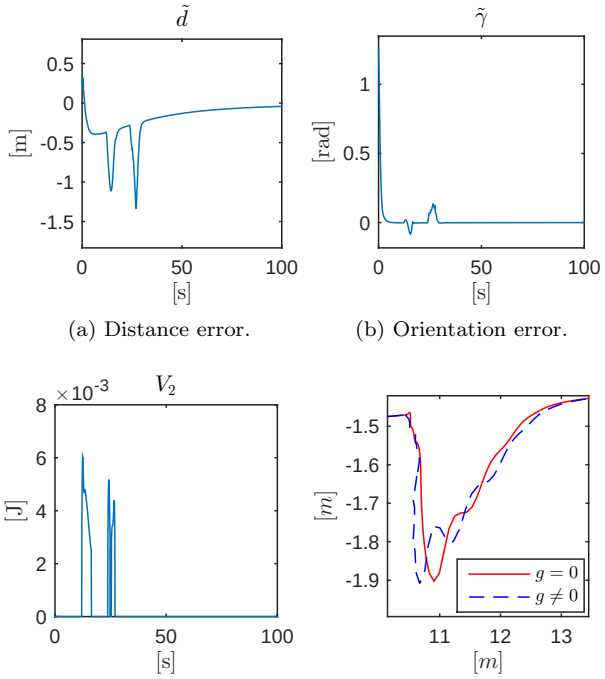

(a) Distance error. (b) Orientation error.

(c) Repulsive potential field over robot. (d) Dynamic object "g" effect.

Fig. 3. Formation motion errors during lateral meddling.

4.2 Simulation 2: Front meddling

For this simulation it is proposed to consider a frontal meddling between the robot and a human obstacle with time variant velocity. In this case, it is emphasized the improving of the performance, regarding the avoidance of the meddling in the elliptical social field when its major axis is not fixed but defined as $a := a(t) = b + k_a \nu_h$, where b is a constant that defines the minor axis of the potential field, k_a is a positive constant design, and, ν_h is the linear velocity of the human obstacle.

The time-parametrized trajectories are presented in Fig. 4.

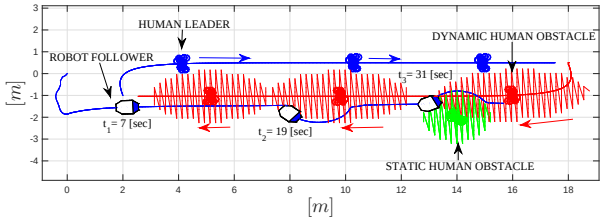

Fig. 4. Top view trajectories.

Additionally, the motion errors for each sub-task are presented in Fig. 5, where it is also presented an augmented view of the trajectories developed by the robot during the evasion of the dynamic obstacle. Note that by including the motion compensation term g, it is reduced the meddling in the social zone during the evasion by getting a longer but an early evasion.

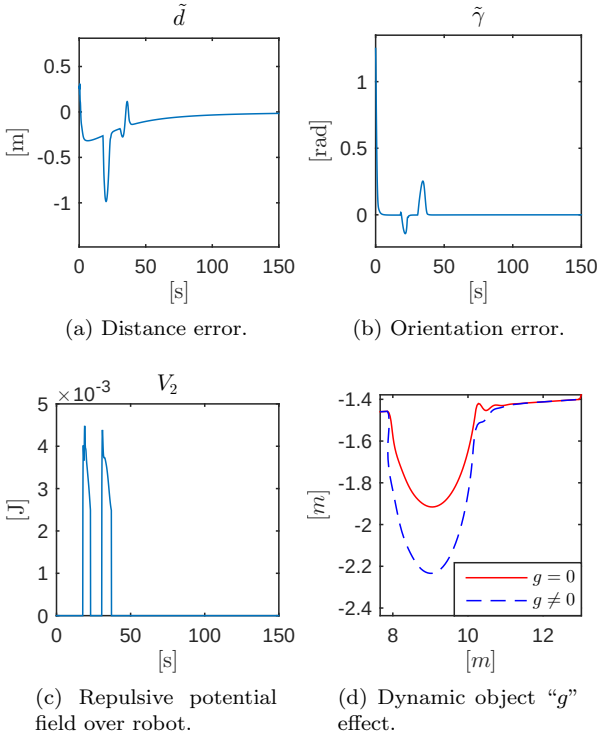

(a) Distance error. (b) Orientation error.

(c) Repulsive potential field over robot. (d) Dynamic object "g" effect.

Fig. 5. Formation motion errors during frontal meddling.

5. CONCLUSION

This paper has presented a novel null-space based (NSB) motion control to follow a human in an unstructured scenario by considering a differential drive mobile robot. For this, it has been proposed the definition of a "social" potential field, which according the researchers, improves the social acceptance of the mobile robots during human-robot interactions. Additionally, it has been supposed a non-holonomic motion of the human obstacles that allows to define a more natural behavior during human obstacle evasion. As a complementary part of the motion control, it has been proposed a flexible formation control where the human is considered as part of the formation. For this, it has been necessary to consider a leader/human-centered scheme. Finally, simulation results are presented to contrast the positive effect that has the inclusion of the potential field variation during the motion of the human obstacle, regarding lower meddling in the social zone of the human obstacles. It is believed that the proposed algorithm improves the social acceptance of mobile robots during interactions with humans.

REFERENCES

Antonelli, G., Arrichiello, F., and Chiaverini, S. (2009). Experiments of formation control with multirobot systems using the null-space-based behavioral control. *IEEE Transactions on Control Systems Technology*, 17(5), 1173–1182.

Antonelli, G., Arrichiello, F., and Chiaverini, S. (2005). Experimental kinematic comparison of behavioral approaches for mobile robots. *IFAC Proceedings Volumes*, 38(1), 295–300.

Arechavaleta, G., Laumond, J.P., Hicheur, H., and Berthoz, A. (2006). The nonholonomic nature of human locomotion: a modeling study. In *IEEE/RAS-EMBS International Conference on Biomedical Robotics and Biomechatronics*, 158–163.

Baillieul, J., Hollerbach, J., and Brockett, R. (1984). Programming and control of kinematically redundant manipulators. In *23rd IEEE Conference on Decision and Control*, 768–774.

Chi-Pang, L., Chen-Tun, C., Kuo-Hung, C., and Li-Chen, F. (2011). Human-centered robot navigation towards a harmoniously human robot coexisting environment. *IEEE Transactions on Robotics*, 27(1), 99–112.

Chiaverini, S. (1997). Singularity-robust task-priority redundancy resolution for real-time kinematic control of robot manipulators. *IEEE Transactions on Robotics and Automation*, 13(3), 398–410.

Doisy, G., Jevtić, A., Lucet, E., and Edan, Y. (2012). Adaptive person-following algorithm based on depth images and mapping. *Proc. of the IROS Workshop on Robot Motion Planning*.

Fiorini, P. and Shiller, Z. (1998). Motion planning in dynamic environments using velocity obstacles. *The International Journal of Robotics Research*, 7, pp. 760772.

Guansheng, X., Shuangna, T., Hexu, S., Weipeng, L., and Huawang, L. (2013). People-following system design for mobile robots using Kinect sensor. In *25th ChineseControl and Decision Conference (CCDC)*, 3190–3194.

Guzzi, J., Giusti, A., Gambardella, L.M., Theraulaz, G., and Di Caro, G.A. (2013). Human-friendly robot navigation in dynamic environments. In *IEEE International Conference on Robotics and Automation (ICRA)*, 423–430.

Hall, E.T. (1963). A system for the notation of proxemic behavior. *American Anthropologist*, 65(5), 1003–1026.

Kluge, E.P., Bank, D., and Boris (2002). Key technologies in robot assistants: Motion coordination between a human and a mobile robot. *Transactions on Control, Automation and Systems Engineering*, 4.

Leica, P., Toibero, J.M., Roberti, F., and Carelli, R. (2014). Switched control to robot-human bilateral interaction for guiding people. *Journal of Intelligent and Robotic Systems*, 77(1), 73–93.

Loper, M.M., Koenig, N.P., Chernova, S.H., Jones, C.V., and Jenkins, O.C. (2008). Mobile human-robot teaming with environmental tolerance. In *International Conference on Human-Robot Interaction (HRI)*, 157–163.

Machida, E., Meifen, C., Murao, T., and Hashimoto, H. (2012). Human motion tracking of mobile robot with Kinect 3D sensor. In *SICE Annual Conference (SICE)*, 2207–2211.

Ratsamee, P., Mae, Y., Ohara, K., Kojima, M., and Arai, T. (2013). Social navigation model based on human intention analysis using face orientation. In *IEEE/RSJ International Conference on Intelligent Robots and Systems (IROS)*, 1682–1687.

Scandolo, L. and Fraichard, T. (2011). An anthropomorphic navigation scheme for dynamic scenarios. In *IEEE International Conference on Robotics and Automation (ICRA)*, 809–814.

Whitney, D.E. (1969). Resolved motion rate control of manipulators and human prostheses. *IEEE Transactions on Man-Machine Systems*, 10(2), 47–53.

Stable Null-Space Path-Following Controller for Car-Like Robots

J.M. Toibero, F. Roberti, D. Herrera, A.N. Amicarelli and R. Carelli

Instituto de Automática (INAUT) – Conicet/UNSJ, Av. San Martín Oeste 1109
ARGENTINA (Tel: 54-264-421-3303; e-mail: mtoibero@inaut.unsj.edu.ar)

Abstract: This paper proposes a novel path following controller for Car-Like robots. This controller incorporates the saturation of the vehicle steering angle by considering of a Null-Space design. This way, the controller has a double objective: the primary task is to avoid the saturation of the steering angle by considering an appropriate Gaussian functional, and as a secondary task the robot asymptotically follows a specified path in the null space of the main task. This work includes the control system stability analysis according to Lyapunov theory, and reports simulation and experimental results for an outdoor Car-Like robot verifying the correct system behavior.

1. INTRODUCTION

Motion control of nonholonomic wheeled robots is one of the most frequently used applications (Matveev, 2013), (Fang, 2005), (Chen, 2011), (Hwang, 2009) and (Lenain, 2010). In particular, car-like robots are widely used in industrial and agriculture applications since they have a good load capability and are well suited to maneuver in the field.

From a control point of view, the path-following behavior allows the use of the desired velocity over the path as an extra variable and gives also an extra degree of freedom (Andaluz, 2012) when compared with trajectory tracking controllers where the velocity is given.

On the other hand, when designing a path following controller, the robot dynamic model can be used as in (Wang, 2011) or neglected as in (Akhar, 2015). In this last case, only the kinematics are considered.

Moreover, when inertial sensors are available, it can also be considered lateral motions, slipping and skidding. These undesirable motions appear in outdoor environments due to slippery surfaces, as mud or snow, and also when high speeds or uneven terrains are considered. This work considers the robot kinematics only. So, it can be applied to any robot without the need to know its dynamic model. As is well known, the dynamic information is greatly appreciated in the experimental stage since load may vary as well as the terrain conditions. Nevertheless, a dynamic compensation can be designed and be aggregated in cascade next to the kinematic controller (Martins, 2009) and (rossomando, 2012). In our particular case, low velocities are considered in order to make the dynamics influence over the controller performance less noticeable. It is also assumed that wheels roll with no skip or slippage. The selection of a path following task itself support these assumptions, since there are not velocities profiles to follow at every instant and the lineal velocity may be selected slow enough.

In any case, the controllers must deal with the non-holonomic constraint proper of this kind of robots. Due to the presence of the wheels, these robots cannot move in arbitrary directions in its configuration space. This motivates the development of highly nonlinear control techniques (Morin, 2008). Additionally, in car-like robots appears a physical limitation in the steering angle value. This saturation in the actuator is of great importance for the path following task since defines all the feasible paths to be followed by a certain robot. In (Yang, 2004) it is considered the velocity saturation of the actuators for differential drive robots by changing coordinates and by an input transformation for a path tracking problem. Simulations are provided to support the results.

One of the contributions of this paper is the inclusion of this information (the maximum steering angle) into the controller design. To do this, it is proposed the design of a null-space based strategy in order to allow the controller to be multi-task. Null-space based controllers are common in redundant robots and are widely used in order to set priorities for different behaviors in a single control command (Flacco, 2012) and (LaValle, 2006). However, the use of this technique on underactuated systems is not frequently reported. In (Arrichiello, 2010) the null space is considered along with velocity saturation by dynamically scaling different velocity task commands in such a way that the hierarchy of task priorities is preserved in spite of actuator velocity saturations.

Instead of having multiple behaviors we propose to deal with the actuator saturation as main task and to follow a path as a secondary one. In general, one of the objectives of null-space based controllers is to combine compatible tasks in order to give a robust solution. For instance, usual tasks to combine are the path following with the obstacle avoidance. In our case, considered tasks can be conflictive. Clearly, if saturation appears as a consequence of the given path to follow, then the path cannot be exactly followed by the robot because the primary task, which accomplishment is mandatory, will avoid this saturated value. In this case, the secondary task will not be fulfilled and we said that both tasks are conflictive or not compatible.

Another option to take into account this saturation is provided in (Hach, 2011) where is analyzed the relation between the

linear velocity and the turning radius. As a result, it is possible to act over the velocity in order to avoid the steering saturation under slipping.

Benefits of the inclusion of the maximum steering angle into the controller design are the possibility to set a new maximum value for the steering angles that could be different from the known maximum mechanical value; or to select different maximum values for each side. Moreover, it could also be possible to dynamically change these values according to the robot surroundings in order to avoid collisions or hazardous locations. This way, the path is indirectly changed without the need to use a path planner.

A second contribution of this paper is the path following controller design and its associated stability analysis. Finally, experimental results over an autonomous outdoor car-like robot show the feasibility and the good performance of the overall strategy.

The work is organized as follows: in Section 2 it is given a robot model description and both controllers are explained in detail, including their associated stability proof. Then, in Section 3 experimental results are reported. Finally, in the conclusion section, results are summarized.

2. MODELS AND CONTROLLERS

2.1 Robot Kinematic Model

The simplified kinematic model of a car-like robot with point of interest in (x_R, y_R) at a given fixed positive distance a from the rear axis as shown in Fig. 1, is given by

$$\begin{bmatrix}\dot{x}_R\\ \dot{y}_R\end{bmatrix} = \begin{bmatrix}cos(\theta_R) & -a\,sin(\theta_R)\\ sin(\theta_R) & +a\,cos(\theta_R)\end{bmatrix}\begin{bmatrix}v\\ \omega\end{bmatrix} \quad (1)$$

or

$$\dot{\chi} = D\,u \quad (2)$$

Being

$$\chi = \begin{bmatrix}x_R\\ y_R\end{bmatrix}$$

the point of interest in $\mathcal{R}^2$. Besides,

$$D = \begin{bmatrix}cos(\theta_R) & -a\,sin(\theta_R)\\ sin(\theta_R) & a\,cos(\theta_R)\end{bmatrix}$$

and finally, the linear and angular velocities are

$$u = \begin{bmatrix}v\\ \omega\end{bmatrix}.$$

Notice that and θ_R is the angle between the vehicle and the x Cartesian axis, and which time derivative ω is the robot angular velocity and is given by

$$\omega = \dot{\theta}_R = \frac{v}{L}tan(\delta) \quad (3)$$

where L is the distance between axes. From this last expression it can be obtained the steering angle (or the direction angle) δ as

$$\delta = atan\left(\frac{\omega L}{v}\right). \quad (4)$$

Control actions are v and δ, assumed to be constrained by:

$$v_{MIN} < v < v_{MAX} \quad (5)$$

$$|\delta| < \delta_M \quad (6)$$

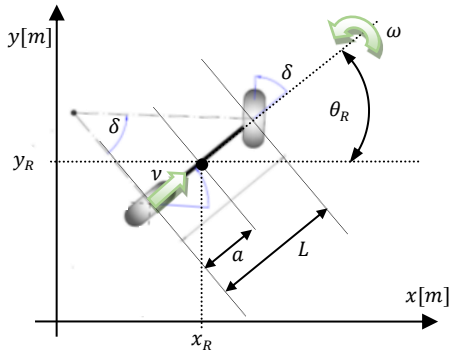

Fig. 1. Car-like robots simplified kinematic model

2.2 Path Following Controller

By time derivation of (2) it is obtained the second order system

$$\ddot{\chi} = D\dot{u} + d \quad (7)$$

with

$$d = \begin{bmatrix}-v\omega\,sin(\theta_R) - a\omega^2\,cos(\theta_R)\\ +v\omega\,cos(\theta_R) - a\omega^2\,sin(\theta_R)\end{bmatrix}.$$

In this case, commands v and δ are obtained from $\dot{u}$ by a single integration. By considering (7) only, it is possible to design a path following controller by feedback linearization.

The objective of this controller is to prove that both:

1) the Cartesian distance error over the path

$$\tilde{\chi} = \chi_d - \chi$$

followed at a given desired velocity v_d and

2) the orientation error $\tilde{\theta} = \theta_d - \theta_R$ between the robot and the path tend asymptotically to zero, or

$$\lim_{t\to\infty}\{\tilde{\chi}\} = \lim_{t\to\infty}\{\chi_d - \chi\} = 0 \quad (8)$$

$$\lim_{t\to\infty}\{\tilde{\theta}\} = \lim_{t\to\infty}\{\theta_d - \theta_R\} = 0. \quad (9)$$

In (8): $\chi_d = [x_d \quad y_d]^T$ is the closest point to the robot over the path with orientation θ_d.

The path following controller block diagram is illustrated in Fig. 2.

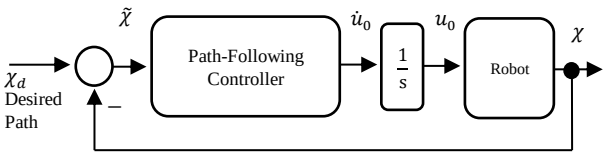

Fig. 2. Path-following controller block diagram

Theorem 1

Control action obtained by simple discretization from

$$\dot{u}_0 = D^{-1}(\gamma - d) \quad (10)$$

applied to the kinematic model (1) along with the constraints (5) and (6) satisfy control objectives (8) and (9) asymptotically. Where,

$$D^{-1} = \begin{bmatrix} cos(\theta_R) & sin(\theta_R) \\ -\frac{sin(\theta_R)}{a} & \frac{cos(\theta_R)}{a} \end{bmatrix}$$

and

$$\gamma = \ddot{\chi}_d + k_1\dot{\tilde{\chi}} + k_2\,\tilde{\chi}$$

with k_1 and k_2 are definite positive constants.

Proof 1: By replacing the expression for $\dot{u}_0$ (10) into the model (7)

$$\ddot{\chi} = D\dot{u}_0 + d$$

$$\ddot{\chi} = \gamma = \ddot{\chi}_d + k_1\dot{\tilde{\chi}} + k_2\,\tilde{\chi}$$

In such a way that

$$\ddot{\tilde{\chi}} + k_1\dot{\tilde{\chi}} + k_2\tilde{\chi} = 0.$$

Proving this way that following errors tend asymptotically (exponentially) to zero for any $k_1 > 0$ and for any $k_2 > 0$. Provided that the error time derivative is given by

$$\dot{\tilde{\chi}} = \dot{\chi}_d - \dot{\chi}.$$

Where, in this case $\dot{\chi}_d$ is the desired velocity over the path, namely:

$$\dot{x}_d = v_d\,cos(\theta_d)$$
$$\dot{y}_d = v_d\,sin(\theta_d).$$

Finally, $\ddot{\chi}_d$ can be computed as the temporal variation of $\dot{\chi}_d$ by simple discretization (Euler method).
□

2.3 Steering angle saturation avoider controller

In order to consider the saturation for the steering angle δ, it is proposed to use the following Gaussian scalar function U with the aim to penalize the increment of the direction angle module

$$U = U_1 + U_2 = k_G e^{-\frac{(\delta-\delta_M)^2}{k^2}} + k_G e^{-\frac{(\delta+\delta_M)^2}{k^2}} \quad (11)$$

being δ_M the maximum allowed value for the robot direction angle and k is the variance value (as can be appreciated in Fig.3 for some arbitrary values), Functional U has low values for any allowable steering angle whereas its value increases when δ approaches δ_M according to the variance value k. The peaks appearance can be modified this way with the variance constant.

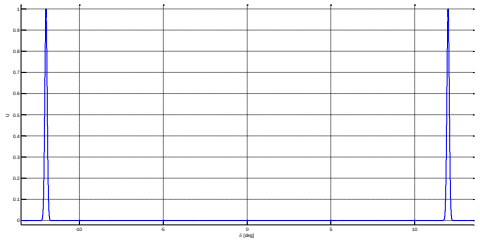

Fig. 3. U function for $\delta_M = 12º, k_G = 1$ and $k = 0.15$

Notice that in this case we selected the same maximum value for both directions sides, but different values can be assigned at each side following the same derivations.
In order to find the relation between U and the robot control commands it is next computed its temporal derivative provided its dependence on both velocities: linear and angular

$$\dot{U} = \frac{\partial U}{\partial \delta}\dot{\delta} = \frac{\partial U}{\partial \delta}\left(\frac{\partial \delta}{\partial v}\dot{v} + \frac{\partial \delta}{\partial \omega}\dot{\omega}\right)$$

From this last expression, the Jacobian that relates the derivative of both magnitudes can be obtained. Or,

$$\dot{U} = J_v\dot{u} \quad (12)$$

where

$$\gamma_v = \frac{2L}{k^2}\,\frac{(\delta-\delta_M)U_1 + (\delta+\delta_M)U_2}{(v^2 + L^2\omega^2)} \quad (13)$$

and

$$J_v = \gamma_v\,[\omega \quad -v] \quad (14)$$

are introduced only to clarify the nomenclature. The controller design requires the calculation of the Jacobian pseudo-inverse J_v^+ according to

$$J_v^+ = J_v^T(J_vJ_v^T)^{-1} \quad (15)$$

since J_v is not a squared matrix. This way

$$J_vJ_v^T = \gamma_v^2(v^2 + \omega^2) \quad (16)$$

whose inverse is the scalar

$$(J_vJ_v^T)^{-1} = \frac{1}{\gamma_v^2(v^2 + \omega^2)} \quad (17)$$

which is finally multiplied by J_v^T

$$J_v^+ = \frac{1}{\gamma_v(v^2 + \omega^2)}\begin{bmatrix}\omega \\ -v\end{bmatrix} \quad (18)$$

Note. The computation of the pseudo-inverse of can be verified by:

$$J_vJ_v^+ = \frac{\gamma_v}{\gamma_v(v^2 + \omega^2)}[\omega \quad -v]\begin{bmatrix}\omega \\ -v\end{bmatrix} = 1.$$

As can be seen, the Gaussian potential function U depends on the steering angle δ only. The proposal is now to design a controller to satisfy the following control objective:

$$\lim_{t\to\infty}\{\tilde{U}\} = \lim_{t\to\infty}\{U_d - U\} = \lim_{t\to\infty}\{-U\} = 0. \quad (19)$$

It is clear that this controller will provide infinite pairs of control efforts u_1 that keep the steering angle away from its maximum value δ_M. Hence, a second controller based on the computation of the Jacobian pseudo-inverse J_v^+ is considered in Theorem 2.
The steering saturation avoidance controller block diagram can be seen in Fig. 4.

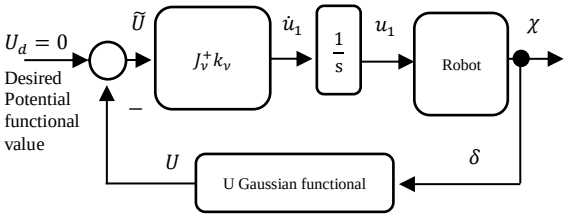

Fig. 4. Steering angle saturation angle avoidance controller block diagram

Theorem 2

Control actions obtained by simple discretization from

$$\dot{u}_1 = \begin{bmatrix} \dot{v} \\ \dot{\omega} \end{bmatrix} = -J_v^+ k_v U \tag{20}$$

satisfy control objective (19) asymptotically. Being in (20): k_v a definite positive constant and J_v^+ the Jacobian pseudo inverse of (14).

Proof 2: By replacing (20) in (12)

$$\dot{U} + k_v U = 0$$

Thus, guaranteeing that the potential function error tends asymptotically to zero or $\forall k_v > 0 \Rightarrow U \to 0$. On other words, the potential function will operate always in the steering angle saturation free zone, or, the steering angle δ obtained from (4) with the control actions obtained by simple discretization from (20) will always satisfy the constraint (6) for $U_d = 0$. Notice also that these values are obtained by minimizing the norm of $[\omega \quad -v]^T$.
□

The next step to complete the controller design is to combine both effects in this sense: from the infinite possible values given by (20), apply the ones that follow the path according to (10). This procedure is detailed in the next Section.

2.4 Null-Space Controller

Effects of the proposed controllers can be joined together by a null-space design. In effect, the saturation avoidance for the direction angle (20) with the path following controller (10) are considered in a single controller.

Theorem 3

Control action obtained by simple discretization from

$$\dot{u} = \begin{bmatrix} \dot{v} \\ \dot{\omega} \end{bmatrix} = J_v^+ k_v \tilde{U} + J_0 \dot{u}_0 \tag{21}$$

being

$$J_0 = (I_{2x2} - J_v^+ J_v)$$

the projection of $\dot{u}$ over the null space of J_v, always satisfy control objective (19) and can also satisfy control objectives (8) and (9) only when the path following controller fulfill constraint (6) for the steering angle.

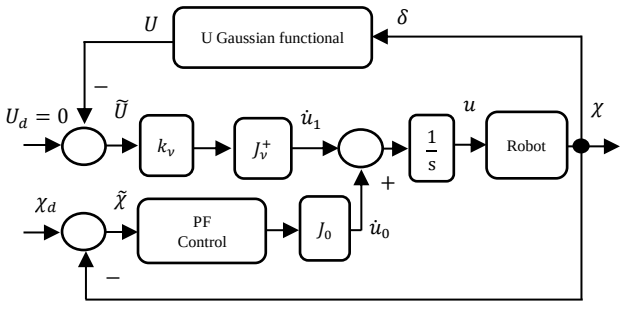

Fig. 5. Null-space based controller block diagram

Proof 3: The null-space based controller block diagram is depicted in Fig.5. The first term of (21) is the particular solution of (12) which enables to calculate the control actions needed to avoid the steering angle saturation. The second term of (21) is the homogeneous solution of the above equation, which contributes to a motion in the null space only, without affecting the task space motion.

In our particular case, the accomplishment of the secondary task is not guaranteed. If when considering the secondary task solely, the steering angle is not saturated, the robot will travel the path with errors tending asymptotically to zero and both tasks will be successfully achieved: following the path without errors.
Otherwise, if saturation appears, it will be avoided by the proper accomplishment of the primary task and position error will inevitably appear. Values of the steering angle beyond the maximum allowable δ_M are due to the impossibility to follow a given path or to a large posture error between the robot and the closest point over the path. That is, saturation avoidance is prioritized since is the primary task in (21).

Next, the proper accomplishment of primary and secondary objectives must be proved. To do this, and beginning with the primary one, the overall control action (21) is replaced in (12) to obtain the closed loop equation for the primary control objective. Thus,

$$\dot{U} = J_v \dot{u} = J_v \left(J_v^+ k_v \tilde{U} + J_0 \dot{u}_0 \right)$$

noticing that $J_v J_v^+ = 1$ and $J_v J_0 = 0$

$$\dot{U} = k_v \tilde{U} + J_v J_0 \dot{u}_0 = k_v \tilde{U}.$$

It can be concluded that the path following controller (10) does not affect the saturation avoidance task. In other words, independently of the control actions given by the path following controller u_0, the value for the steering angle will always meet constraint (6).
Nonetheless, to prove the accomplishment of the second objective, the overall control action (21) is replaced into the car-like robot kinematic model (7)

$$\ddot{\chi} = D\left(J_v^+ k_v \tilde{U} + J_0 \dot{u}_0 \right) + d. \tag{22}$$

As can be seen from (22), the secondary objective will only be satisfied if is not in conflict with the primary one. This condition is given by

$$\dot{U} = J_v \dot{u} \approx 0 \tag{23}$$

since Gaussian functions are considered in U, these values have a slope near to zero and not exactly zero when the values of δ in (11) are within the maxima for each side and hence

$$\tilde{U} = 0 \tag{24}$$

Next, by definition, the values of $\dot{u}$ belong to the null-space of J_v, and by invoking the idempotent property for the projection operator J_0

$$J_0 \dot{u} = \dot{u}. \tag{25}$$

Under considerations (23) to (25), (22) is modified to

$$\ddot{\chi} = D\dot{u}_0 + d \tag{26}$$

proving this way, the secondary task accomplishment provided that there is no conflict with the primary one. As expected, the robot will asymptotically follow the path only if the direction angle is not saturated by the path.

□

Desired Velocity. The path following is performed at a given desired velocity v_d, which is constrained to be minor than a maximum velocity v_{MAX} and to be positive, since null values for the desired velocity annul the Jacobian J_v

$$0 < v_{MIN} < v_d < v_{MAX}.$$

It was proved in the previous subsection 2.2 that distance errors tend to zero as well as the robot velocity tends to the desired velocity v_d. For this reason, to improve the controller practical results is considered the following expression for the desired velocity

$$v_d = v_{MIN} + \frac{v_{MAX}}{1 + \lambda_v |\tilde{\chi}|} \tag{27}$$

being $\lambda_v > 0$ a design constant that allows to adjust the penalization value for the path following errors.

3. SIMULATION RESULTS

Simulations were carried out using Matlab in order to show the overall controller performance. From here on, for each figure four plots appear: the trajectory travelled by the robot, the steering angle, the linear velocity and the path following error. Figures 6 and 7 show the evolution when the maximum steering angle is gradually constrained from an initial 16º value in Fig.6 to 8º value in Fig.7. The setting is a commonly found one in olive gropes: 80m of straight paths connected by 3m radius circular paths. Desired velocity is set to 1.5m/s.

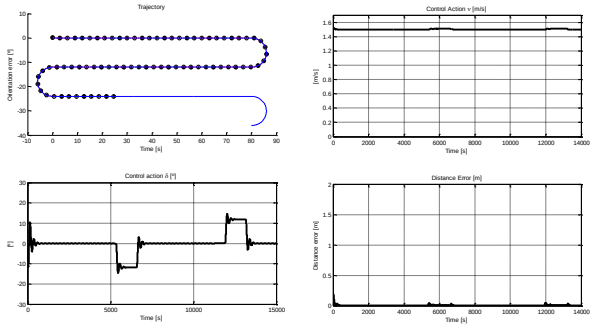

Fig. 6. Path follower simulations for $\delta_M = 16º$.

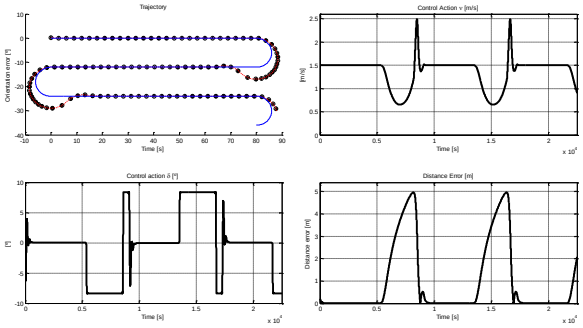

Fig. 7. Path follower simulations for $\delta_M = 8º$.

As can be seen, the appearance of saturation in the steering angle directly affects the path following controller performance. From null distance error in Fig.6 to a maximum value of 5m in Fig.8.

In the path following controller, linear velocity decreases under the appearance of errors and increases when the robot is able to properly follow the path again.

4. EXPERIMENTAL RESULTS

To verify the correct controller behavior, it was designed a path following task adjusting the path shape and the saturation values in δ_M for a typical path used in agricultural applications. As said before, the controller output is the derivative $\dot{u}$ of the control action u, and hence the command is obtained by its simple integration

$$\begin{bmatrix} v_k \\ \omega_k \end{bmatrix} = T_s \begin{bmatrix} \dot{v}_k \\ \dot{\omega}_k \end{bmatrix} + \begin{bmatrix} v_{k-1} \\ \omega_{k-1} \end{bmatrix} \tag{28}$$

where $T_s = 0.1s$ is the sample time and the k sub index denotes the variables temporal instant.
Finally, from v and ω is obtained the direction angle δ by means of (4)

$$\delta_k = \text{atan}\left(\frac{\omega_k L}{v_k}\right).$$

To perform the experimental test it was considered a 1:10 scale car-like robot fully autonomous conceived from a Tamiya RC vehicle (Soria, 2014) (Fig.8). In particular, the distance between axis is $L = 0.35cm$, the point of interest was fixed at a distance $a = 0.2cm$ from the rear axis; and the maximum direction angle physically allowed by the robot is $\delta_{ROBOT} = 18º$. This robot has an on-board PC connected to a low level microcontroller-based board which is at charge of the low-level control for the front wheels servo-motor and the DC motor. Velocity is obtained from a magnetic encoder within a rear-wheel. The values for the robot states: δ and v are sent each sample time from the onboard pc to the low-level board.

Fig. 8. Autonomous Outdoor Car-Robot

Real tests were performed over straight paths connected by circular curves (Figure 9.a). Two experiments show the controller performance with and without saturation. Saturation if forced to appear when the circle radius is changed from $2m$ in Fig.9 to $1m$ in Fig.10.
Selected parameter values were: $v_{MAX} = 1m/s$, $v_d = 0.5m/s$, $v_{MIN} = 0.1m/s$, $\lambda_v = 1$, $k_v = 25$, $\delta_M = 16º$, $\kappa_v = 3$.
It can be seen the good controller performance as in the first case when the robot is able to follow the path, and the errors appearance in the second case when the path cannot be followed by the same robot.

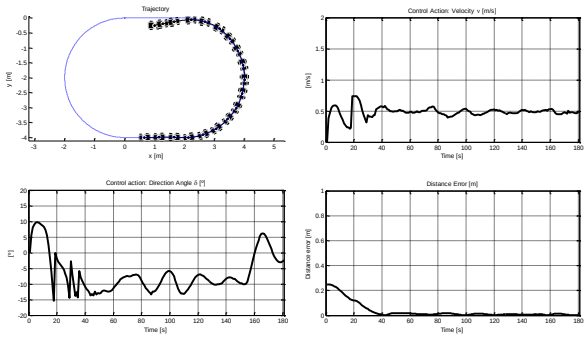

Figure 9: Trajectory without δ saturation

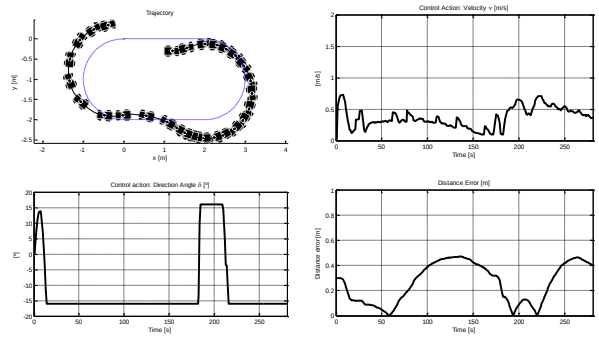

Figure 10: Trajectory with δ saturation

6. CONCLUSIONS

It has been presented a new controller to take into account the steering angle saturation in a path following task for car-like mobile robots.

It was designed a null-space strategy with two control objectives. The primary objective is to keep the direction angle between both a priori established maximum values. Next, in the null space of this objective remains the secondary: a stable path following controller based on the robot kinematic model. Simulation and experiments over a real platform expose the good performance of this strategy.

REFERENCES

Akhtar A, Nielsen C, Waslander S. (2015) Path following using dynamics transverse feedback linearization for Car-Like Robots. *IEEE Trans. On Robotics*. 31:2.

Matveev A, Hoy M, Katupitiya J et al. (2013) Nonlinear sliding mode control of an unmanned agricultural tractor in the presence of sliding and control saturation. *Robotics and Autonomous Systems*. 61:9, 973-987.

Andaluz V., Roberti F., Toibero JM et al. (2012) Adaptive Unified Motion Control of Mobile Manipulators. *Control Engineering Practice*. 20:12, 1337-1352.

Andaluz V, Roberti F, et al. (2011) Adaptive dynamic path-following control of an unicycle-like mobile robot. *Lecture Notes in Computer Science*. 563-574.

Bouton N, Lenain R, Thuilot B et al. (2010) A new device dedicated to autonomous mobile dynamic stability: application to an off-road mobile robot. *Proc. of the IEEE Int. Conf. on Robotics and Automation*.3813-3818.

Eaton R, et al. (2008) Autonomous Farming: Modeling and control of agriculture machinery in a unified framework. *Proc. Int. Conf. on Mechatronics and Machine Vision in Practice*. 499-504.

Fang H, Lenain R, et al (2005). Trajectory tracking control of farm vehicles in presence of sliding. *IEEE IROS*. 58-63.

Lenain R, et al. (2006) Mobile robot control in presence of sliding: application to agricultural vehicle path tracking. *Proc. of the IEEE Int. Conf. on Decision and Control*.

De Luca A, Oriolo G, Samson C. (1997) Planning. *Robot Motion, Chapter 4 Feedback control of a nonholonomic car-like robot*. Springer-Verlag, Ed. J.P. Laumond.

Soria CV, Paoloni W. (2014) Instrumentación de un robot industrial tipo car-like. 24º Arg. Conf. on Aut. Control.

Arrichiello F, et al. (2010) The null-space based behavioral control for mobile robots with velocity actuator saturations. *IJRR*. 29-10,1317-1337.

Flacco F, De Luca A, Khatib O. (2012) Control of Redundant Robots under hard joint constraints: saturation in the null space. *IEEE ICRA*. 2012, 285-292.

Hach O, et al. (2011) Avoiding steering actuator saturation in off-road mobile robot path tracking via predictive velocity control. *IEEE IROS*.

Morin P, Samson C. (2008) Motion control of wheeled mobile robots. Chapter 34 In: Springer Handbook of Robotics/Springer, Heidelberg. 799-826.

Chen B. and Z. Jiao (2011), "Adaptive path following control of car-like mobile robot using dynamic model," *IEEE Conf. on Ind. Electronics and App. ICIEA*, 239-244.

Wang Y, Tan R, Wang S et al. (2011) Car-like mobile robot oriented acceleration control method. *IEEE Int. Conf. on Mechatronics and Automation.*

Yang E, Gu D, Mita T et al. (2004) Nonlinear tracking control of a car-like mobile robot via dynamic feedback linearization. *Proc. Of the Control Conference.*

Raeisi Y, Shojaei K, Chatraei A. (2015) Output feedback trajectory tracking control of a car-like drive wheeled mobile robot using RBF neural network. *Proc. Int. Power electronics drive systems and technologies Conf.*

Hwang C, Shih C. (2009) A distributed active-vision network-space approach for the navigation of a car-like wheeled robot. *IEEE Trans. On Ind. electronics*.56:3, 846-855.

Lenain R, Lucet E, Grand C, et al. Accurate and stable mobile robot path tarcking: an integrated solution for off-road and high speed context. IEEE IROS. 2010.

Martins F, et al. (2009) Dynamic modeling and adaptive dynamic compensation for unicycle-like mobile robots. *IEEE Int. Conf. on Advanced Robotics.*

Rossomando F, Soria C, Carelli R. (2012) Neural network-based compensation control of mobile robots with partially known structure. Control Theory & applications IET. 6:12, 1851-1860.

LaValle S. (2006) Planning algorithms. Section13.1.2 kinematics for wheeled systems. Cambridge Univ. Press NY, USA.

CHAPTER 9

NEW ENERGIES

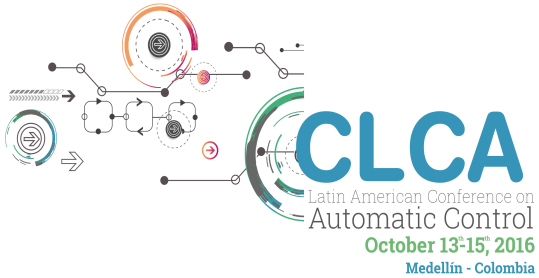

A Hamiltonian approach for stabilization of Microgrids including Power converters dynamic ⋆

Sofía Avila-Becerril * **Gerardo Espinosa-Pérez** *

* *Facultad de Ingeniería, Universidad Nacional Autónoma de México, Edificio de Posgrado, 2o. piso, Ciudad Universitaria, 04510 México D.F., MEXICO (e-mail: soavbec@comunidad.unam.mx; gerardoe@unam.mx).*

Abstract: The Microgrids are part of a special class of power systems that offer an attractive option for the use of sustainable energy. The study imposes several challenges from the point of view of control; in the literature this problem has been addressed by assuming that the dynamics of power converters has been drastically simplified. In this article, we exploit the Hamiltonian structure exhibited by the network and we develop a distributed control scheme for a mesh topology including dynamic converters.

Keywords: Power Systems, Hamiltonian, Microgrids, Passivity.

1. INTRODUCTION

The evolution of Electric Power Systems has lead to the conception of a special kind of networks called *smart grids* (Farhangi (2010); Fang et al. (2012)) which join information technology with power systems engineering and has caused a change in the paradigm of Electric Power Systems. The *Microgrids* are part of these intelligent networks and according to Fang et al. (2012) are groups that combine loads, lines and distributed generation sources (e.g. solar panels and small wind turbines) interconnected with the main network via power converters.

On the one hand, Microgrids offer an attractive solution for sustainable energy power supply since they are based on the use of renewable energy sources, leading to a semi-autonomous distributed generation network capable to satisfy the requirements of (relatively) small communities as stated in Guerrero et al. (2013). On the other hand, the aforementioned characteristics still imposes theoretical challenges (see Hill and Chen (2006)) like stability properties analysis, design of protocols for reliable energy dispatch, achievement of power quality standards, among others.

From an structural point of view, the main complication to design, analyze and control, comes from the fact that due to the heterogeneous nature of the energy sources it is necessary to include, for each of them, a power converter whose objective is to shape the generated energy to make it compatible with the rest of the system. This situation imposes a two–level control problem since the power converters must be individually controlled first, to later on approach the control problem of the complete grid. The usual way to address the problem is with the so-called *droop control* (see Lasseter (2002); Barklund et al. (2008); Pedrasa and Spooner (2006); Marwali et al. (2007) and references therein) where, in general, assumptions as constant voltage amplitudes and a simplified model of the power converters are needed. While the results are based on graph theory. Simpson-Porco et al. (2013) show that the model of the Microgrid, consisting of loads and power converters equipped with frequency droop controllers, can be equivalently represented as the model of coupled oscillators. In this case, the attention is restricted to the active power flow under the assumption that the voltage magnitudes are fixed on each bus. In another general study, Schiffer et al. (2014) assume that the Microgrid has been reduced by the Kron reduction (also see Dorfler and Bullo (2013)). These converters are modeled as a chain of integrators, so that all nodes have a power converter and a frequency and voltage droop controllers can be implemented, the last allows them to propose a stability analysis of the Microgrid in terms consensus.

It is clear that considering simplified models for the power converters limits the possibility for including important phenomena exhibited by Microgrids like the related with power quality issues and disturbances during the operation of the power electronics based devices. Thus, in this paper the control problem of Microgrids including the power converters dynamic is approached.

This contribution considers, as illustrative case study, a *meshed* network equipped with energy sources that are connected to the grid via *DC/AC converters*. The control problem is to design a control law for the converters such that the closed–loop system achieves a prescribed power flow. The desired power flow is viewed as a desired trajectory for the Microgrid and the corresponding tracking control problem is solved. For this, it is exploited the Hamiltonian structure exhibited by the power converters and the network itself. In this sense, the whole system is represented as the interconnection of port-controlled

⋆ Part of this work was supported by DGAPA-UNAM under grant IN116516.

Hamiltonian systems via another port-controlled Hamiltonian system (PCH). As a result, the controller design and the stability analysis are remarkable simplified. Relaxations of some assumptions, technical proofs and extensive numerical testing are deferred to a journal article follow.

The rest of the paper is organized in the following way: Section 2 presents the Hamiltonian model for the meshed network. Section 3 is devoted to the power converter model and the design of local controllers. In Section 4 the complete system is presented and its stability properties are stated. Finally, the desired steady–state behavior is formulated in Section 5.

2. MICROGRID STRUCTURE

A Microgrid is an electrical network connected to a distribution system, of low and medium voltage, combining (typically renewable) energy generating units and loads. In the network can be identified: Distributed Generation (DG) units, power converters, transmission lines and loads. In this section the mathematical model of each component is presented from PCH perspective, later to present a comprehensive and modular model of Microgrid. Finally, the control law for the inverters are extended to a distributed control law that stabilizes the complete Microgrid.

2.1 Network dynamical model

In this section the structure and dynamic of the network that interconnects the generation systems (i.e. power converters) with the loads are addressed. The network is viewed as an electrical circuit showing that its dynamic behavior corresponds to the exhibited by a Hamiltonian system. An approach based on Graph theory (see Bollobás (1998)) that closely follows Avila-Becerril et al. (2015) is considered.

Consider that the power network is represented by a graph composed by n nodes and b edges. Hence, there exist $n-1$ independent current constraints and $b-n+1$ independent voltages constrains, established by Kirchhoff laws. Consider now a given tree of the circuit (integrated by the n nodes and $n-1$ edges such that no loops are formed) and its corresponding co-tree (given by the set of $b-(n-1)$ edges that do not belong to the tree). Under these conditions and exploiting the concepts of basic cutsets and loopsets of the graph (also see Wellstead (1979)), the current and voltage constraints can be obtained as

$$\begin{bmatrix} I & H \end{bmatrix} \begin{bmatrix} i_t \\ i_c \end{bmatrix} = 0, \qquad \begin{bmatrix} -H^T & I \end{bmatrix} \begin{bmatrix} v_t \\ v_c \end{bmatrix} = 0 \tag{1}$$

where the matrix $H \in \mathbb{R}^{(n-1)\times b-(n-1)}$, known as the *fundamental loop matrix*, completely characterizes the topology of the circuit, while I is a generic identity matrix of proper dimensions. From (1) above, it is clear that the structure of H determines how the tree currents and the co-tree voltages can be generated as linear combinations of the co-tree currents and the tree voltages, respectively, via

$$i_t = -Hi_c, \quad v_c = H^T v_t. \tag{2}$$

The entries of H (and H^T) are 1 if a co-tree current (a tree voltage) points into a given basic ambit (decreases in the same direction than a given basic loop), -1 if points out the basic ambit (if decreases in the opposite direction than the basic loop) and 0 if does not belong to the basic cutset (basic loopset).

As usual, the lumped elements are of three kinds, namely, sources, energy stores (inductors and capacitors) and dissipators. Besides, as in Brayton and Moser (1964), it is considered that the circuit is complete, so that the sources, the capacitors and some (voltage-controlled) dissipators are considered as branches while all the inductors and some (current-controlled) dissipators are chords, leading to the partitions

$$i_t = \begin{bmatrix} i_1 \\ i_C \\ i_{Rt} \end{bmatrix}; \; v_t = \begin{bmatrix} v_1 \\ v_C \\ v_{Rt} \end{bmatrix}; \; i_c = \begin{bmatrix} i_{Rc} \\ i_L \end{bmatrix}; \; v_c = \begin{bmatrix} v_{Rc} \\ v_L \end{bmatrix} \tag{3}$$

where $v_1, i_1 \in \mathbb{R}^{n_1}$ are the port variables of the sources, $v_C, i_C \in \mathbb{R}^{n_2}$ the variables associated with the capacitors and $v_{Rt}, i_{Rt} \in \mathbb{R}^{n_3}$ the corresponding to the tree dissipators, such that $n_1 + n_2 + n_3 = n - 1$. For the co-tree variables, $v_{Rc}, i_{Rc} \in \mathbb{R}^{n_4}$ conform the co-tree dissipators, while $v_L, i_L \in \mathbb{R}^{n_5}$ the inductors, with $n_4+n_5 = b-(n-1)$.

Under the partition presented, the matrix H takes the form

$$H = \begin{bmatrix} H_{1R} & H_{1L} \\ H_{CR} & H_{CL} \\ H_{RR} & H_{RL} \end{bmatrix} \tag{4}$$

where each sub-matrix, of appropriate dimensions, represents the interconnections among the different tree and co-tree elements.

The port variables of the capacitors and inductors are related with the energy function of the network $H_a : \mathbb{R}^{n_2\times n_5} \to \mathbb{R}_{\geq 0}$ defined as

$$H_a(q_C, \lambda_L) = \sum_{i=1}^{n_2} H_{aCi}(q_{Ci}) + \sum_{i=1}^{n_5} H_{aLi}(\lambda_{Li}) \tag{5}$$

where $q_{Ci} \in \mathbb{R}$ is the i-th entry of the electrical capacitor charges vector $q_C \in \mathbb{R}^2$ and $\lambda_{Li} \in \mathbb{R}$ the i-th entry of the linkage inductor fluxes vector $\lambda_L \in \mathbb{R}^5$. Then, it holds that

$$\dot{q}_{Ci} = f_{Ci}; \;\; e_{Ci} = \frac{\partial H_a(q,\lambda)}{\partial q_{Ci}}; \;\; i = 1, \ldots, n_2 \tag{6a}$$

$$\dot{\lambda}_{Li} = e_{Li}; \;\; f_{Li} = \frac{\partial H_a(q,\lambda)}{\partial \lambda_{Li}}; \;\; i = 1, \ldots, n_5 \tag{6b}$$

While the dissipators satisfies

$$f_{Rti} = \psi_{ti}(e_{Rti}); \;\; e_{Rci} = \psi_{ci}(f_{Rci}) \tag{7}$$

where $\psi_{ti}(\cdot)$, $\psi_{ci}(\cdot)$ are assumed bijective functions and f_{Rti}, e_{Rti}, e_{Rci}, f_{Rci} are, respectively, the i-th entry of $f_{Rt} \in \mathbb{R}^{n_3}$, $e_{Rt} \in \mathbb{R}^{n_3}$, $e_{Rc} \in \mathbb{R}^{n_4}$, $f_{Rc} \in \mathbb{R}^{n_4}$.

Microgrid's Topology. Typical topologies can be found in Avila-Becerril et al. (2015), in terms of the *fundamental loop matrix*. In this paper, the analysis is focused in the so–called *Mesh* network since it states the more general and reliable topology. We assume that each transmission line is modeled by the π model Kundur et al. (1994), *i.e.*, a series circuit composed by a resistor and an inductor with a shunt capacitor. Under this structure, the lines are two–port systems giving the possibility to connect either a source or a load.

The structure of a Mesh topology satisfies:

F.1. All the sources are connected to all the loads via transmission lines.
F.2. The loads are parallel connected with one capacitor of the π model.
F.3. The sources are parallel connected with one capacitor of the π model.
F.4. There exist transmission lines that connects a source with another source.

As shown in Avila-Becerril et al. (2015), if the resistors involved in the π model are considered as tree dissipators then $n_3 = n_5$ and identifying the co–tree dissipators with the loads, $H_{RL} = I$, $H_{RR} = 0$ of proper dimension, while $H_{CR} = I$ and $H_{1R} = 0$. In addition, due to **F.1** and **F.2**, $n_1 = n_2 = n_4$ while **F.3** leads to the elimination, for analysis purposes, of each of the capacitors parallel connected to the sources.

Even that the network model can be formulated under this general scenario Avila-Becerril et al. (2015), with the aim to, first, situate the contribution with respect the related literature Schiffer et al. (2014), Simpson-Porco et al. (2013), and second, to simplify the presentation, the following assumption is considered:

A.1. The network is lossless or dominantly inductive.

Under assumption **A.1**, the tree dissipators are no longer included. The model can be obtained from equations (1) and (6), under F.1-4. An advantage of this model lies in property that it exhibits a port–controlled Hamiltonian structure (Van der Schaft (1999)). Indeed, defining the state variables $x_3 = q_C$ and $x_4 = \lambda_L$, the model can be written in matrix form as

$$\dot{x}_{34} = \mathbb{J}_{34}\nabla_{x34}H_a(x_3, x_4) - F_{34}f_{Rc} + G_{34}e_1 \qquad (8)$$

where $x_{34} = \begin{bmatrix} x_3^T & x_4^T \end{bmatrix}^T \in \mathbb{R}^{(n_1+n_3)}$, $\nabla_{x34}H_a(x_3, x_4) = \frac{\partial H_a(x_3,x_4)}{\partial x_{34}}$ and

$$\mathbb{J}_{34} = \begin{bmatrix} 0 & -H_{CL} \\ H_{CL}^T & 0 \end{bmatrix} = -\mathbb{J}_{34}^T; \quad G_{34} = \begin{bmatrix} 0 \\ H_{1L}^T \end{bmatrix}$$

$$\mathbb{F}_{34} = \begin{bmatrix} I \\ 0 \end{bmatrix}$$

subject to the constraints

$$f_1 = H_{1L}f_L, \quad e_{Rc} = e_C = \psi_c(f_{Rc}) \qquad (9)$$

This equation shows the demanded current to the sources as a linear combination of the transmission line currents connected to them. In the sequel, it is assumed ideal sources in the sense that they can provide any amount of current, so that only steady state stability issues can be approached.

3. SOURCES AND LOADS DYNAMICAL MODELS

In this section we study the inclusion of power converter models into the Microgrid description and loads modeling from an energy–based perspective.

3.1 Source model

In the sequel, sources are viewed as a one–port dynamical systems with port–variables given by the output voltage e_{1i} and the delivered current f_{1i} with $i = 1, 2, \ldots, n_1$. These systems are composed by a microsource that fed a power converter. In this paper the microsources are considered as constant voltage sources. Note that including a source dynamic in a Hamiltonian framework states only an additional step in the formulation of a single Hamiltonian system that describes the whole Microgrid.

In Figure 1 is presented the topology of the i-th electronic inverter, *i.e.* it consist of the aforementioned voltage source which delivers a voltage $V_i \in \mathbb{R} > 0$, a switching array, that modulates the input voltage via the signal $u_i \in \mathbb{R}$ and a second order LC filter.

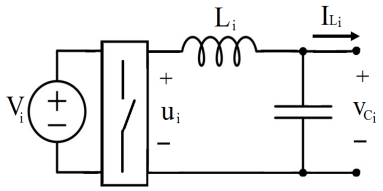

Fig. 1. Illustrative power converter DC/AC

Let $x_{1i} \in \mathbb{R}$ denote the linkage inductor flux and $x_{2i} \in \mathbb{R}$ the electrical capacitor charge of each converter. From a direct application of Kirchhoff laws, the dynamic model for the i-th device, $i = 1, 2, \ldots, n_1$, is given by

$$\dot{x}_{1i} = -C_i^{-1}x_{2i} + Vu_i \qquad (10a)$$
$$\dot{x}_{2i} = L_i^{-1}x_{1i} - f_{1i} \qquad (10b)$$

where it has been assumed a linear constitutive relationship for both the inductors and the capacitors with $L_i \in \mathbb{R} > 0$ the inductance and $C_i \in \mathbb{R} > 0$ the capacitance.

If $H_{ci} : \mathbb{R} \times \mathbb{R} \to \mathbb{R}_{\geq 0}$ is the stored energy function, given by

$$H_{ci}(x_{1i}, x_{2i}) = \frac{1}{2}L_i^{-1}x_{1i}^2 + \frac{1}{2}C_i^{-1}x_{2i}^2, \qquad (11)$$

then, model (10), can be equivalently written as a port–controlled Hamiltonian system of the form

$$\dot{x}_{12i} = \mathbb{J}_{12i}\nabla_{x12i}H_{ci}(x_{1i}, x_{2i}) + G_{12i}u_i - \begin{bmatrix} 0 \\ f_{1i} \end{bmatrix} \qquad (12)$$

where $x_{12i} = \begin{bmatrix} x_{1i} & x_{2i} \end{bmatrix}^T \in \mathbb{R}^2$ while

$$\mathbb{J}_{12i} = \begin{bmatrix} 0 & -1 \\ 1 & 0 \end{bmatrix} = -\mathbb{J}_{12i}^T; \quad G_{12i} = \begin{bmatrix} V_i \\ 0 \end{bmatrix}$$

In this context, the port-variables of each converter are the capacitor voltage $e_{1i} = C_i^{-1}x_{2i} \in \mathbb{R}$ and the output current $f_{1i} \in \mathbb{R}$.

The structure considered for the power converters is only illustrative. Actually, the switching array is just a representation of several topologies used in practice and has been over simplified for presentation purposes. However, it has been widely shown (see for example Ortega et al. (2013)) that common converter topologies can be represented under a Hamiltonian structure.

It is now convenient to illustrate how the output voltage of the converter can be controlled to achieve a prescribed value. To do this, it is necessary to introduce the concept of *admissible trajectories* which refers to the set of state trajectories that a given dynamical system can reproduce

under a specific input. For the defined Microgrid sources, this set is given by the solutions of

$$\dot{x}^{\star}_{12i} = \mathbb{J}_{12i}\nabla_{x12i\star}H^{\star}_{ci} + G_{12i}u^{\star}_i - \begin{bmatrix} 0 \\ i_{Li} \end{bmatrix}, \qquad (13)$$

that recover the behavior of (12) under the input $u^{\star}_i$.

Equation (13) allows to identify $x^{\star}_{12i}$ as the desired steady–state behavior for the sources variables. Thus, it is possible to immediately formulate a control problem by defining the error signal $\tilde{x}_{12i} = x_{12i} - x^{\star}_{12i}$ and finding the control input u_i that renders this variable to zero. In the next proposition a controller that achieves asymptotic stabilization of the prescribed behavior for each non interconnected power converters is developed, leaving to Section 4 the Microgrid stabilization.

Proposition 1. Consider a DC/AC power converter of the form (12) and assume

A.2 The state x_{12i} and the output current f_{1i} are available for measurement.
A.3 The parameters L_i and C_i are known.
A.4 The prescribed steady–state behavior $x^{\star}_{12i}$ is known.

Under these conditions, the control law

$$u_i = V_i^{-1}[\dot{x}^{\star}_{1i} + C_i^{-1}x^{\star}_{2i} - K_{1i}L_i^{-1}\tilde{x}_{1i}] \qquad (14)$$

with the desired state satisfying

$$\dot{x}^{\star}_{2i} - L_i^{-1}x^{\star}_{1i} + i_{Li} - K_{2i}C_i^{-1}\tilde{x}_{2i} = 0 \qquad (15)$$

and $K_{1i} > 0$ and $K_{2i} > 0$, guarantees that

$$\lim_{t\to\infty} \tilde{x}_{12i} = 0$$

Proof. From (12) and (13) the error dynamic is given by

$$\dot{\tilde{x}}_{12i} = \mathbb{J}_{12i}\nabla_{\tilde{x}12i}\tilde{H}_{ci}(\tilde{x}_{1i}, \tilde{x}_{2i}) + G_{12i}\tilde{u}_i \qquad (16)$$

where

$$\tilde{H}_{ci}(\tilde{x}_{1i}, \tilde{x}_{2i}) = \frac{1}{2}L_i^{-1}\tilde{x}^2_{1i} + \frac{1}{2}C_i^{-1}\tilde{x}^2_{2i} \qquad (17)$$

and $\tilde{u}_i = u_i - u^{\star}_i$.

On the other hand, (14) and (15) can be written as

$$G_{12i}\tilde{u}_i = -K_{12i}\nabla_{\tilde{x}12i}\tilde{H}_{ci}(\tilde{x}_{1i}, \tilde{x}_{2i}) \qquad (18)$$

with $K_{12i} = diag\{K_{1i}, K_{2i}\} \in \mathbb{R}^{2\times 2}$. Substitution of (18) in (16) leads to the closed–loop error dynamic

$$\dot{\tilde{x}}_{12i} = [\mathbb{J}_{12i} - K_{12i}]\nabla_{\tilde{x}12i}\tilde{H}_{ci}(\tilde{x}_{1i}, \tilde{x}_{2i}) \qquad (19)$$

If $\tilde{H}_{ci}(\tilde{x}_{1i}, \tilde{x}_{2i})$ in (17) is considered as a Lyapunov function candidate, its time derivative along the trajectories of the error dynamic (19) is given by

$$\dot{\tilde{H}}_{ci}(\tilde{x}_{1i}, \tilde{x}_{2i}) = -\left(\nabla_{\tilde{x}12i}\tilde{H}_{ci}\right)^T K_{12i}\nabla_{\tilde{x}12i}\tilde{H}_{ci} < 0$$

expression that, due to the linear structure of the Lyapunov function, implies the claimed asymptotic stability property.

□

In Section 4 it is shown that these stability properties are preserved if these devices are interconnected through the network.

3.2 Load model

Modeling of electrical loads in a Hamiltonian framework is a topic that has been widely studied since many years ago Ortega et al. (2013). It is clear that the port–variables of the loads attached to the network, the current f_{Rc} and the voltage e_{Rc}, can be related with a port–controlled Hamiltonian system. Moreover, if the interconnection between this system and the network (8) is carried out in a power preserving way, it is obtained another Hamiltonian system.

We now assume that the system operates around a prescribed admissible trajectory, as already illustrated in (13) for the power converter sub–system. Hence, the concept of *Incremental Passivity*, studied in Pavlov and Marconi (2008) and in the case of electrical circuits in Jayawardhana et al. (2007), states a way to characterize the input–output behavior of the loads via the following assumption

A.5 The port–variables of each load, related by the constitutive relationship (9), satisfies the incremental passivity condition

$$(e_{Rc} - e^{\star}_{Rc})^T\left[\psi_c^{-1}(e_{Rc}) - \psi_c^{-1}(e^{\star}_{Rc})\right] > 0$$

for a given admissible trajectory $e^{\star}_{Rc}(t) \in \mathbb{R}^{n_1}$.

4. MICROGRID STABILIZATION

In this section a complete model for the approached Microgrid is presented. Consider first the interconnection between the sources (power converters) and the network. Notice that the n_1 individual power converters of the form (12) can be pilled up as

$$\dot{x}_1 = -C^{-1}x_2 + Vu$$
$$\dot{x}_2 = L^{-1}x_1 - f_1$$

with total stored energy function

$$H_c(x_1, x_2) = \frac{1}{2}x_1^T L^{-1}x_1 + \frac{1}{2}x_2^T C^{-1}x_2 \qquad (20)$$

where $x_1 = col\{x_{1i}\} \in \mathbb{R}^{n_1}$, $x_2 = col\{x_{2i}\} \in \mathbb{R}^{n_1}$, $V = diag\{V_i\} \in \mathbb{R}^{n_1\times n_1}$, $u = col\{u_i\} \in \mathbb{R}^{n_1}$, $L^{-1} = diag\{L_i^{-1}\} \in \mathbb{R}^{n_1\times n_1}$ and $C^{-1} = diag\{C_i^{-1}\} \in \mathbb{R}^{n_1\times n_1}$.

On the one hand, the vector $f_1 \in \mathbb{R}^{n_1}$ stand for the currents injected to the network satisfying the constraint (9), which in terms of the network stored energy takes the form

$$f_1 = H_{1L}\frac{\partial H_a(x_{34})}{\partial x_4} \qquad (21)$$

with $H_a(x_{34})$ as in (5) and where it has been used the identity (6b). On the other hand, the voltage of the source ports are given by the output converter voltages

$$e_1 = C^{-1}x_2 \qquad (22)$$

While the variables $f_{Rc}, e_{Rc} \in \mathbb{R}^{n_1}$ of the network load ports, under (7) and (6a), can be represented as

$$f_{Rc} = \psi_c^{-1}\left(\frac{\partial H_a(x_{34})}{\partial x_3}\right) \qquad (23)$$

Representing the power converters model in a Hamiltonian structure, using (20), together with (8), the port variables (21), (22) and (23), leads to a dynamic description of the complete Microgrid.

Proposition 2. The dynamic behavior of the complete Microgrid conformed by the network (8) with sources (10a-10b) and loads satisfying assumption **A.2**, can be represented by the port-Hamiltonian system

$$\dot{x} = \mathbb{J}_T\nabla_x H_T(x) - g_{RT}\Psi(x_{34}) + G_T u \qquad (24)$$

with state $x = \left[\, x_1^T \;\; x_2^T \;\; x_3^T \;\; x_4^T \,\right]^T \in \mathbb{R}^{(3n_1+n_2)}$, the total stored energy function

$$H_T(x) = H_c(x_1, x_2) + H_a(x_3, x_4)$$

and matrices of appropriate dimensions

$$\mathbb{J}_T = \begin{bmatrix} 0 & -I & 0 & 0 \\ I & 0 & 0 & -H_{1L} \\ 0 & 0 & 0 & -H_{CL} \\ 0 & H_{1L}^T & H_{CL}^T & 0 \end{bmatrix} = -\mathbb{J}_T^T; \quad g_{RT} = \begin{bmatrix} 0 & 0 \\ 0 & 0 \\ 0 & I \\ I & 0 \end{bmatrix};$$

$$G_T u = \begin{bmatrix} Vu \\ 0 \\ 0 \\ 0 \end{bmatrix} \quad \Psi(x_{34}) = \begin{bmatrix} 0 \\ \psi_c^{-1}\left(\dfrac{\partial H_a(x_{34})}{\partial x_3}\right) \end{bmatrix}$$

□

We now can develop a control strategy to stabilize the complete grid following the same procedure than the followed in Section 3.1. In this sense, it is necessary to define the *admissible trajectories* which for system (24) are the solutions of

$$\dot{x}^\star = \mathbb{J}_T \nabla_{x^\star} H_T(x^\star) - g_{RT}\Psi^\star(x_{34}^\star) + G_T u^\star \tag{25}$$

where $u^\star \in \mathbb{R}^{n_1}$ is the control input that generates the admissible trajectory $x^\star \in \mathbb{R}^{3n_1+n_2}$. So that, with the definition of the desired system, the error variable is set as $\tilde{x} = x - x^\star$ and their corresponding error dynamic is

$$\dot{\tilde{x}} = \mathbb{J}_T \nabla_{\tilde{x}} H_T(\tilde{x}) - g_{RT}\tilde{\Psi}(\tilde{x}_{34}) + G_T \tilde{u}$$

where $\tilde{u} = u - u^\star$. In this case, the associated stored energy–like function takes the form

$$\tilde{H}_T(\tilde{x}) = \frac{1}{2}\tilde{x}^T P x \tag{26}$$

with the matrix $P = diag\left\{L^{-1}, C^{-1}, C_a^{-1}, L_a^{-1}\right\} > 0$. Under the foregoing scenario, it is possible to formulate the main stabilization result of the paper, i.e. the proof that the local controllers developed for the power converters are capable of stabilize the entire Microgrid. This result is included in the next

Proposition 2. Consider a Microgrid system of the form (24). Assume **A.1**–**A.3** from Proposition 1 are verified and in addition assume that

A.4 The parameters L_a and C_a are known.

Under these conditions, the control law

$$u = V^{-1}[\dot{x}_1^\star + C^{-1}x_2^\star - K_1 L^{-1}\tilde{x}_1] \tag{27}$$

with $K_1 = diag\{K_{1i}\} \in \mathbb{R}^{n_1 \times n_1}$ and the desired state satisfying the constraints

$$\begin{aligned} \dot{x}_2^\star - L^{-1}x_1^\star + H_{1L}L_a^{-1}x_4^\star - K_2 C^{-1}\tilde{x}_2 = 0, \\ \dot{x}_3^\star + H_{CL}\nabla_{x_4^\star}H_T^\star - K_3\nabla_{\tilde{x}_3}\tilde{H}_T + \varphi_c^{-1}(v_C^\star) = 0 \\ \dot{x}_4^\star - H_{1L}^T\nabla_{x_2^\star} - H_{CL}^T\nabla_{x_3^\star} - K_4\nabla_{\tilde{x}_4}\tilde{H} = 0 \end{aligned} \tag{28}$$

where K_1, K_2, K_3, K_4 are diagonal positive gains, guarantees that

$$\lim_{t\to\infty} \tilde{x} = 0$$

Proof. The control law in equations (27) and (28) can be equivalently written as

$$G_T\tilde{u} = -\mathbb{K}_T\nabla_{\tilde{x}}\tilde{H}_T$$

with $\mathbb{K}_T = diag\{K_1, K_2, K_3, K_4\} \in \mathbb{R}^{(4n_1)\times(4n_1)} > 0$. Using this expression and considering (26) as a Lyapunov function, its time derivative along the trajectories of the closed loop system, under **A.5**, yields

$$\dot{\tilde{H}}_T \leq 0,$$

so that $\tilde{H}_T$ is non-increasing and its argument $\tilde{x}$ is bounded. Moreover, since $\dot{\tilde{H}}$ is zero only in $\tilde{x} = 0$ the equilibrium is asymptotically stable.

□

Remark. The importance of the presented result lies in the fact that the controller (27-28) guarantees that, for any admissible trajectory, the error between the actual value of the capacitors parallel connected with the loads, will tend to the desired value $x_3^\star$. Therefore, by ensuring that this desired value corresponds to a sinusoidal function with a prescribed amplitude and frequency, then both voltage and frequency stability of the power network will be achieved.

5. STEADY STATE DESIRED BEHAVIOR

The proposed method for specifying the desired values is based on the following rationale: The steady state behavior of the voltage $C^{-1}x_2^\star$ establish the voltage $C_a^{-1}x_3^\star$, accordingly a natural choice is to associate to each power converter the voltage

$$C_i^{-1}x_{2i}^\star = A_i^\star \sin(\omega_s t + \delta_i^\star),$$

where $\omega_s \in \mathbb{R}$ takes the same value for all the power converters, while the magnitude $A_i : \mathbb{R}_{\geq 0} \to \mathbb{R}_{\geq 0}$ and the phase $\delta_i \in \mathbb{R}_{\geq 0} \to \mathbb{S}$ must be determined to get an adequate power flow. Let the complex admittance be denoted as $Y_{ik} := G_{ik} + jB_{ik} \in \mathbb{C}$ with conductance $G_{ik} \in \mathbb{R}$ and susceptance $B_{ik} \in \mathbb{R}$ and let $\mathcal{N}_i$ be the set of neighbors of the $i-th$ node for which $Y_{ik} \neq 0$. That said, the desired active and reactive power at the $i-th$ node for a lossless microgrid $P_i^\star : \mathbb{S}^{n_1+n_2} \times \mathbb{R}^{n_1+n_2} \to \mathbb{R}$ and $Q_i^\star : \mathbb{S}^{n_1+n_2} \times \mathbb{R}^{n_1+n_2} \to \mathbb{R}$, are obtained as

$$P_i^\star = \sum_{k\sim\mathcal{N}_i} |B_{ik}|A_i^\star A_k^\star sin(\delta_i^\star - \delta_k^\star) \tag{29a}$$

$$Q_i^\star = |B_{ii}|A_i^{\star 2} - \sum_{k\sim\mathcal{N}_i} |B_{ik}|A_i^\star A_k^\star cos(\delta_i^\star - \delta_k^\star) \tag{29b}$$

with

$$B_{ii} := \hat{B}_{ii} + \sum_{k\sim N_i} B_{ik}$$

and $\hat{B}_{ii} \in \mathbb{R}$ the shunt susceptance.

The power flow equations above (29) are static and model the network when it is balanced, that is, the net sum of power consumption, injections and dissipated power is zero, and determine the desired steady state operation of the network. The steady state can be determined by finding, for a given set of load conditions, the active and reactive power flow of the network and the magnitudes and phase angles of all nodes.

In other words, one way to generate the desired trajectories is solving the power flow equations (29). We propose to fix the active and reactive power at the loads, through the resistances, and solve equations (29a) and (29b) in order to calculate the desired magnitude $A_i^\star$ and the phases $\delta_i^\star$ of the n_1 nodes with voltage $C^{-1}x_2^\star$. Once founded the voltages $C^{-1}x_2^\star = A_i^\star \sin(\omega_s t + \delta_i^\star)$ that meets the load power demand, the restriction (28) is incorporated for

$x_1^\star \in \mathbb{R}^{n_1}$ such that the control law $u \in \mathbb{R}^{n_1}$ in (14) can be implemented.

Note that the algebraic equations (29) are non linear, both in the voltage and in the angle, therefore the solution involves the use of a numerical methods, for example Newton-Raphson. In the last years, the control community has been engaged in research from solubility conditions of the power flow equations (see for example Simpson-Porco et al. (2015); Dvijotham et al. (2015) and the references therein) to the optimization problem (Madani et al. (2015); Wei and Bandi (2015) between others). However these studies are out of the scope of this paper.

6. CONCLUSION

This paper has addressed the problem of stabilizing a Meshed Microgrid which, unlike as is usual in the literature, has been included the dynamics of the power converters. It has been shown that a distributed control law developed for each source converter preserves its stabilizing properties even when the converters are interconnected to the network through a Mesh topology. Crucial to reach the presented results has been the Hamiltonian structure exhibited by the different devices that conform the grid.

ACKNOWLEDGEMENTS

Part of this work was supported by DGAPA-UNAM under grant IN116516.

REFERENCES

Avila-Becerril, S., Espinosa-Pérez, G., and Fernández-Carrillo, P. (2015). Stability and consensus of electrical circuits via structural properties. *IFAC-PapersOnLine*, 48(13), 111–116.

Barklund, E., Pogaku, N., Prodanović, M., Hernandez-Aramburo, C., and Green, T.C. (2008). Energy management in autonomous microgrid using stability-constrained droop control of inverters. *Transactions on Power Electronics, IEEE*, 23(5), 2346–2352.

Bollobás, B. (1998). *Modern graph theory*, volume 184. Springer Science & Business Media.

Brayton, R. and Moser, J. (1964). A theory of nonlinear networks i. *Quart. Appl. Math*, 22(1), 1–33.

Dorfler, F. and Bullo, F. (2013). Kron reduction of graphs with applications to electrical networks. *Circuits and Systems I: Regular Papers, IEEE Transactions on*, 60(1), 150–163.

Dvijotham, K., Chertkov, M., and Low, S. (2015). A differential analysis of the power flow equations. *arXiv preprint arXiv:1506.08814*.

Fang, X., Misra, S., Xue, G., and Yang, D. (2012). Smart gridthe new and improved power grid: A survey. *Communications Surveys & Tutorials, IEEE*, 14(4), 944–980.

Farhangi, H. (2010). The path of the smart grid. *Power and Energy Magazine, IEEE*, 8(1), 18–28.

Guerrero, J.M., Chandorkar, M., Lee, T.L., and Loh, P.C. (2013). Advanced control architectures for intelligent microgrids, part i: decentralized and hierarchical control. *IEEE Transactions on Industrial Electronics*, 60(4), 1254–1262.

Hill, D.J. and Chen, G. (2006). Power systems as dynamic networks. In *Circuits and Systems, 2006. ISCAS 2006. Proceedings. 2006 IEEE International Symposium on*, 4–pp. IEEE.

Jayawardhana, B., Ortega, R., García-Canseco, E., and Castanos, F. (2007). Passivity of nonlinear incremental systems: Application to pi stabilization of nonlinear rlc circuits. *Systems & control letters*, 56(9), 618–622.

Kundur, P., Balu, N., and Lauby, M. (1994). *Power system stability and control*, volume 7. McGraw-hill New York.

Lasseter, R.H. (2002). Microgrids. In *Power Engineering Society Winter Meeting, 2002. IEEE*, volume 1, 305–308. IEEE.

Madani, R., Lavaei, J., and Baldick, R. (2015). Convexification of power flow problem over arbitrary networks. In *IEEE 54th Ann. Conf. Decis. Contr.(CDC)*.

Marwali, M.N., Jung, J., Keyhani, A., et al. (2007). Stability analysis of load sharing control for distributed generation systems. *IEEE Transactions on Energy Conversion*, 22(3), 737.

Ortega, R., Perez, J.A.L., Nicklasson, P.J., and Sira-Ramirez, H. (2013). *Passivity-based control of Euler-Lagrange systems: mechanical, electrical and electromechanical applications*. Springer Science & Business Media.

Pavlov, A. and Marconi, L. (2008). Incremental passivity and output regulation. *Systems & Control Letters*, 57(5), 400–409.

Pedrasa, M.A. and Spooner, T. (2006). A survey of techniques used to control microgrid generation and storage during island operation. In *Proceedings of the 2006 Australasian Universities Power Engineering Conference (AUPEC'06)*, 1–6.

Schiffer, J., Ortega, R., Astolfi, A., Raisch, J., and Sezi, T. (2014). Conditions for stability of droop-controlled inverter-based microgrids. *Automatica*, 50(10), 2457–2469.

Simpson-Porco, J.W., Bullo, F., et al. (2015). A solvability condition for reactive power flow. In *2015 54th IEEE Conference on Decision and Control (CDC)*, 2013–2017. IEEE.

Simpson-Porco, J.W., Dörfler, F., and Bullo, F. (2013). Synchronization and power sharing for droop-controlled inverters in islanded microgrids. *Automatica*, 49(9), 2603–2611.

Van der Schaft, A. (1999). *L2-gain and passivity in nonlinear control*. Springer-Verlag New York, Inc.

Wei, E. and Bandi, C. (2015). Fairness considerations in network flow problems. In *2015 54th IEEE Conference on Decision and Control (CDC)*, 6909–6914. IEEE.

Wellstead, P. (1979). *Introduction to physical system modelling*. Academic Press London.

Control Basado en Pasividad para MPPT en Sistemas Fotovoltaicos Conectados a la Red Eléctrica

I. Ortega-Velázquez * **D. R. Espinoza-Trejo** ** **G. Espinosa-Pérez** *

* *Universidad Nacional Autónoma de México (e-mail: gerardoe@unam.mx).*
** *Coordinación Académica Región Altiplano, Universidad Autónoma de San Luis Potosí, (e-mail: drespinozat@ieee.org)*

Abstract: Para operar un módulo fotovoltaico en el punto de máxima potencia, es necesario tener una carga que sea capaz de consumir dicha potencia, es por eso que en este artículo se propone una interconexión a la red eléctrica del módulo mediante dos convertidores de potencia, uno de ellos es un convertidor elevador, el cual tendrá la tarea de mantener el módulo fotovoltaico en el punto de máxima potencia, y el segundo es un inversor, el cual se encargará de transmitir la potencia extraída del modulo a la red eléctrica. Estos dos objetivos se pueden lograr con un buen diseño de dos leyes de control, las cuales se diseñarán con técnicas basadas en pasividad.

Keywords: Control basado en pasividad, interconexión de sistemas pasivos, convertidor cd/cd elevador, inversor, sistemas fotovoltaicos, MPPT conectado a la red eléctrica.

1. INTRODUCCIÓN

La tecnología para el aprovechamiento de la energía solar fotovoltaica (FV) ha presentado un crecimiento significativo en los últimos años, Romero et al. (2015). No obstante, ésta aún presenta interesantes retos que resolver, tales como mejorar: *i*) *eficiencia* y *ii*) *seguridad*. Con respecto a la eficiencia, el algoritmo de *seguimiento de punto de máxima potencia* (MPPT *por sus siglas en inglés*) juega un papel sumamente importante. Por ejemplo, es bien conocido que ante condiciones de irradiancia no-uniformes la eficiencia total del sistema FV (SFV) puede verse seriamente afectada. Esto es debido a la operación de los módulos FV (MFV) en un punto de potencia sub-óptimo (*máximo local* de la curva característica P-V). Además, debido a la naturaleza del convertidor cd/cd, empleado para ajustar el punto de máxima potencia (PMP), existen pérdidas en regimen transitorio, ocasionadas por caídas abruptas de irradiancia o cambios de referencia. Así, recientemente se ha propuesto operar el algoritmo de búsqueda (MPPT) en conjunto con una estrategia de control retroalimentada, lo cual mejora significativamente el desempeño del MPPT ante variaciones climáticas.

Básicamente, existen 2 modos de operación: el *control por modo voltaje* y el *control por modo corriente*. Este último, presenta una problemática de inestabilidad cuando el objetivo de control se plantea como un *problema de regulación*, ver Kakosimos (2013). Debido a que es una práctica común establecer la referencia como una señal *constante a tramos*, la mayoría de los enfoques propuestos, hasta ahora en la literatura, consideran el control por modo voltaje, Espinoza et al. (2015). Pocos estudios empleando el control por modo corriente aparecen reportados en la literatura, Bianconi (2013). Sin embargo, resulta natural emplear el control por modo corriente para compensar caídas de irradiancia abruptas, debido a que es la corriente del MFV la que se modifica significativamente ante cambios de irradiancia. No obstante, esto implica realizar un seguimiento de la trayectoria de corriente del MFV en el PMP, ver Fig. 1.

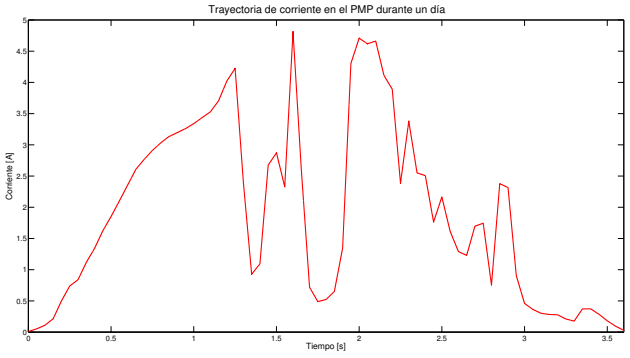

Fig. 1. Trayectoria de corriente en el PMP durante un día.

En consecuencia, en este artículo se explotan *propiedades de pasividad*, de los elementos que componen al sistema MPPT, para diseñar una ley de control que garantice el seguimiento de trayectorias, y en consecuencia, la transferencia de máxima potencia. De hecho, el modelo del convertidor cd/cd elevador está descrito por un modelo hamiltoniano, ver Schaft (2000), el cual describe un mapeo entrada-salida pasivo, al igual que el inversor. Sin embargo, la entrada de control desaparece en el balance energético, ocasionando dificultades para diseñar el control. Este artículo toma como referencia previos resultados propuestos en la literatura para el seguimiento de trayectorias, Cisneros (2014). El propósito de este estudio fue diseñar un control dinámico sobre el modelo incremental, del cual se definen la entrada y salida pasivas.

El artículo está organizado de la siguiente manera. En la Sec. 2 se presenta un análisis de la estructura del sistema. En la Sec. 3 se presentan las propiedades de pasividad del sistema en estudio. En la Sec. 4 se presenta el diseño del controlador

PI para el convertidor cd/cd elevador y para el inversor como MPPT. Una evaluación numérica en MATLAB se presenta en la Sec. 5. Finalmente, se presentan comentarios finales y trabajo futuro en la Sec. 6.

2. ANÁLISIS DEL SISTEMA

El sistema con el que se trabajará a lo largo de este estudio se presenta en la Fig. 2, el cual consta de ocho secciones: *i*) el módulo fotovoltaico (MFV), *ii*) un filtro de entrada, *iii* un convertidor cd/cd elevador, *iv*) un inductor de enlace, *v*) un capacitor que genera el bus de dc, *vi*) un inversor, *vii*) un inductor de enlace con la red eléctrica y *viii*) dos bloques que generan dos leyes de control, una para cada convertidor. Tomando en cuenta las leyes de Kirchhoff y las relaciones

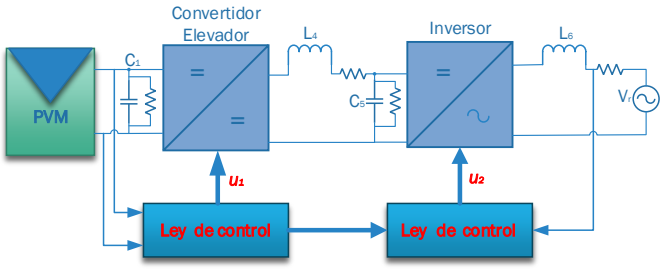

Fig. 2. Sistema conectado a la red eléctrica

constitutivas de los elementos, entonces es posible llegar a la representación matemática mostrada en (1-6):

$$C_1\dot{z}_1 + \frac{1}{R_1}z_1 + z_2 = i_p \tag{1}$$

$$L_2\dot{z}_2 + R_2z_2 - z_1 + u_1z_3 = 0 \tag{2}$$

$$C_3\dot{z}_3 + \frac{1}{R_3}z_3 + z_4 - u_1z_2 = 0 \tag{3}$$

$$L_4\dot{z}_4 + R_4z_4 - z_3 + z_5 = 0 \tag{4}$$

$$C_5\dot{z}_5 + \frac{1}{R_5}z_5 + u_2z_6 - z_4 = 0 \tag{5}$$

$$L_6\dot{z}_6 + R_6z_6 - u_2z_5 = -V_r \tag{6}$$

donde z_1 es el voltaje del MPV, z_2 es la corriente de entrada del convertidor elevador, z_3 es el voltaje de salida del convertidor elevador, z_4 es la corriente del inductor de enlace, z_5 es el voltaje de entrada del inversor, z_6 es la corriente de salida del inversor.

Sin embargo, en lugar de trabajar con voltajes y corrientes en el sistema, se realizará un cambio de variables para trabajar con flujos y cargas, recordando que $V_C = Cq$ e $i_L = L\phi$, donde q es carga del capacitor, y ϕ flujo magnético del inductor. Como resultado, el modelo matemático se puede representar en forma matricial a través de una estructura Hamiltoniana (7):

$$\dot{x} = (J(u_1, u_2) - R)\nabla_x H(x) + E \tag{7}$$

donde

$$H(x) = \frac{1}{2}x^T Dx$$

$$x = \begin{bmatrix} q_{C_1} \\ \phi_{L_2} \\ q_{C_3} \\ \phi_{L_4} \\ q_{C_5} \\ \phi_{L_6} \end{bmatrix} = \begin{bmatrix} x_1 \\ x_2 \\ x_3 \\ x_4 \\ x_5 \\ x_6 \end{bmatrix} \quad E = \begin{bmatrix} i_p \\ 0 \\ 0 \\ 0 \\ 0 \\ -V_r \end{bmatrix}$$

$$R = \begin{bmatrix} R_1 & 0 & 0 & 0 & 0 & 0 \\ 0 & R_2 & 0 & 0 & 0 & 0 \\ 0 & 0 & R_3 & 0 & 0 & 0 \\ 0 & 0 & 0 & R_4 & 0 & 0 \\ 0 & 0 & 0 & 0 & R_5 & 0 \\ 0 & 0 & 0 & 0 & 0 & R_6 \end{bmatrix}$$

$$J(u) = \begin{bmatrix} 0 & -1 & 0 & 0 & 0 & 0 \\ 1 & 0 & -u_1 & 0 & 0 & 0 \\ 0 & u_1 & 0 & -1 & 0 & 0 \\ 0 & 0 & 1 & 0 & -1 & 0 \\ 0 & 0 & 0 & 1 & 0 & -u_2 \\ 0 & 0 & 0 & 0 & u_2 & 0 \end{bmatrix}$$

$$D = \begin{bmatrix} C_1^{-1} & 0 & 0 & 0 & 0 & 0 \\ 0 & L_2^{-1} & 0 & 0 & 0 & 0 \\ 0 & 0 & C_3^{-1} & 0 & 0 & 0 \\ 0 & 0 & 0 & L_4^{-1} & 0 & 0 \\ 0 & 0 & 0 & 0 & C_5^{-1} & 0 \\ 0 & 0 & 0 & 0 & 0 & L_6^{-1} \end{bmatrix}$$

Algunas características del sistema son las siguientes:

- El sistema cuenta con dos entradas de control, una de ellas se usará para MPPT del MPV y la otra para inyectar a la red la potencia extraída del MPV.
- Ninguna de las dos señales de control son afín a la entrada, y sólo actúa en cuatro canales del sistema.
- El sistema es sub-actuado.
- La matriz $R > 0, R = R^T$; $J = -J^T$ y $D > 0, D = D^T$.

2.1 *Prueba de estabilidad del convertidor*

La función de almacenamiento de energía del sistema es

$$V(x) = \frac{1}{2}x^T Dx \tag{8}$$

cuya derivada evaluada a lo largo de las trayectorias del sistema está dada por:

$$\dot{V}(x) = x^T D[(J(u_1, u_2) - R)\nabla_x H(x) + E]. \tag{9}$$

Notar que $x^T D = \nabla_x^T H(x)$ y $J(u_1, u_2)$ es una matriz antisimétrica que se encuentra en una forma cuadrática. Por lo tanto, este termino es cero para todo tiempo, entonces:

$$\dot{V}(x) = -\nabla_x^T H(x) R \nabla_x H(x) + \nabla_x^T H(x) E. \tag{10}$$

Ahora, se define $\mu = E$ y $y = \nabla_x H(x)$ entonces

$$\dot{V}(x) = -y^T Ry + y^T \mu \tag{11}$$

por lo tanto, el sistema es estrictamente pasivo a la salida desde $\mu \longrightarrow y$. Esto quiere decir que con $\mu = 0$, $\dot{V}(x)$ es definida negativa, entonces podemos concluir estabilidad asintótica al punto de equilibrio $x = 0$.

Conjectura 1. Debido a que la ley de control se encuentra en el término antisimétrico, el cual es cero en la prueba de estabilidad, el sistema siempre es, global y asintóticamente estable, sin importar la ley de control, con entrada $\mu = 0$.

El problema que se resuelve en este documento es para cuando μ es diferente de cero.

3. ANÁLISIS DE PASIVIDAD DEL SISTEMA

Debido a que la señal de control no entra en todos los canales del sistema, se propone separar al sistema en cuatro subsistemas, dos de ellos que no dependan de ninguna de las

señales de control, los otros dos sub-sistemas deberán depender de una de las señales de control cada uno, es decir

$$\Sigma_1 : \tag{12}$$

$$\dot{x}_1 = -\frac{1}{R_1 C_1}x_1 - \frac{1}{L_2}x_2 + i_p \tag{13}$$

$$\Sigma_2 : \tag{14}$$

$$\dot{\bar{x}}_2 = [J_2 u_1 - \bar{R}_2]\nabla_{\bar{x}_2} H_2(\bar{x}_2) + E_2 \tag{15}$$

$$H_2(\bar{x}_2) = \frac{1}{2}\bar{x}_2^T D_2 \bar{x}_2 \tag{16}$$

donde

$$J_2 = \begin{bmatrix} 0 & -1 \\ 1 & 0 \end{bmatrix} \quad \bar{R}_2 = \begin{bmatrix} R_2 & 0 \\ 0 & R_3 \end{bmatrix} \quad E_2 = \begin{bmatrix} \frac{1}{C_1}x_1 \\ -\frac{1}{L_4}x_4 \end{bmatrix}$$

$$\bar{x}_2 = \begin{bmatrix} x_2 \\ x_3 \end{bmatrix} \quad D_2 = \begin{bmatrix} L_2^{-1} & 0 \\ 0 & C_3^{-1} \end{bmatrix}.$$

$$\Sigma_3 :$$

$$\dot{x}_4 = -\frac{R_4}{L_4}x_4 + \frac{1}{C_3}x_3 - \frac{1}{C_5}x_5$$

$$\Sigma_4 :$$

$$\dot{\bar{x}}_4 = [J_4 u_2 - \bar{R}_4]\nabla_{\bar{x}_4} H_4(\bar{x}_4) + E_4$$

$$H_4(\bar{x}_4) = \frac{1}{2}\bar{x}_4^T D_4 \bar{x}_4$$

donde

$$J_4 = \begin{bmatrix} 0 & -1 \\ 1 & 0 \end{bmatrix} \quad \bar{R}_4 = \begin{bmatrix} R_5 & 0 \\ 0 & R_6 \end{bmatrix} \quad E_4 = \begin{bmatrix} \frac{1}{L_4}x_4 \\ -V_r \end{bmatrix}$$

$$\bar{x}_4 = \begin{bmatrix} x_5 \\ x_6 \end{bmatrix} \quad D_4 = \begin{bmatrix} C_5^{-1} & 0 \\ 0 & L_6^{-1} \end{bmatrix}.$$

3.1 Análisis de pasividad de Σ_1

Se propone la función de almacenamiento de energía

$$V(x_1) = \frac{1}{2C_1}x_1^2 \tag{17}$$

con derivada evaluada a lo largo de las trayectorias del sistema dada por

$$\dot{V}(x_1) = \frac{1}{C_1}x_1\left(-\frac{1}{R_1 C_1}x_1 - \frac{1}{L_2}x_2 + i_p\right). \tag{18}$$

Se define $\mu_1 = -\frac{1}{L_2}x_2 + i_p$, $y_1 = \frac{1}{C_1}x_1$ entonces

$$\dot{V}(x_1) = -\frac{1}{R_1}y_1^2 + y_1^T\mu_1 \tag{19}$$

por lo tanto es estrictamente pasivo a la salida desde $\mu_1 \longrightarrow y_1$.

3.2 Análisis de pasividad de Σ_2

Se propone la función de almacenamiento de energía

$$V(\bar{x}_2) = \frac{1}{2}\bar{x}_2^T D_2 \bar{x}_2 \tag{20}$$

con derivada evaluada a lo largo de las trayectorias del sistema

$$\dot{V}(\bar{x}_2) = \nabla_{\bar{x}_2}^T H(\bar{x}_2)[(J_2 u_1 - \bar{R}_2)\nabla_{\bar{x}_2} H(\bar{x}_2) + E_2]. \tag{21}$$

Debido a que J_2 es una matriz anti-simétrica este término es cero para todo tiempo, entonces

$$\dot{V}(\bar{x}_2) = -\nabla_{\bar{x}_2}^T H(\bar{x}_2)\bar{R}_2\nabla_{\bar{x}_2} H(\bar{x}_2) + \nabla_{\bar{x}_2}^T H(\bar{x}_2)E_2. \tag{22}$$

Se define $\Upsilon_2 = E_2$ y $Y_2 = \nabla_{\bar{x}_2} H(\bar{x}_2)$ entonces

$$\dot{V}(\bar{x}_2) = -Y_2^T\bar{R}_2 Y_2 + Y_2^T\Upsilon_2 \tag{23}$$

por lo tanto el sistema es estrictamente pasivo a la salida desde $\Upsilon_2 \longrightarrow Y_2$.

3.3 Análisis de pasividad de Σ_3

Se propone la función de almacenamiento de energía

$$V(x_4) = \frac{1}{2L_4}x_4^2 \tag{24}$$

con derivada evaluada a lo largo de las trayectorias del sistema dada por

$$\dot{V}(x_4) = \frac{1}{L_4}x_4\left(-\frac{R_4}{L_4}x_4 + \frac{1}{C_3}x_3 - \frac{1}{C_5}x_5\right). \tag{25}$$

Se define $\mu_4 = \frac{1}{C_3}x_3 - \frac{1}{C_5}x_5$, $y_4 = \frac{1}{L_4}x_4$ entonces

$$\dot{V}(x_4) = -R_4 y_4^2 + y_4^T\mu_4 \tag{26}$$

por lo tanto es estrictamente pasivo a la salida desde $\mu_4 \longrightarrow y_4$.

3.4 Análisis de pasividad de Σ_4

Se propone la función de almacenamiento de energía

$$V(\bar{x}_4) = \frac{1}{2}\bar{x}_4^T D_4 \bar{x}_4 \tag{27}$$

con derivada evaluada a lo largo de las trayectorias del sistema

$$\dot{V}(\bar{x}_4) = \nabla_{\bar{x}_4}^T H(\bar{x}_4)[(J_4 u_2 - \bar{R}_4)\nabla_{\bar{x}_4} H(\bar{x}_4) + E_4]. \tag{28}$$

Debido a que J_4 es una matriz anti-simétrica este término es cero para todo tiempo, entonces

$$\dot{V}(\bar{x}_4) = -\nabla_{\bar{x}_4}^T H(\bar{x}_4)\bar{R}_4\nabla_{\bar{x}_4} H(\bar{x}_4) + \nabla_{\bar{x}_4}^T H(\bar{x}_4)E_4. \tag{29}$$

Se define $\Upsilon_4 = E_4$ y $Y_4 = \nabla_{\bar{x}_4} H(\bar{x}_4)$ entonces

$$\dot{V}(\bar{x}_4) = -Y_4^T\bar{R}_4 Y_4 + Y_4^T\Upsilon_4 \tag{30}$$

por lo tanto el sistema es estrictamente pasivo a la salida desde $\Upsilon_4 \longrightarrow Y_4$.

Una vez realizada la prueba de pasividad de los cuatro sub-sistemas, es posible ver al sistema en general como una interconexión de sistemas pasivos como el mostrado en la Fig.3, y por los teoremas de pasividad de sistemas retroalimentados, podemos concluir que el sistema es pasivo $i_p \longrightarrow y_1$ y $-V_r \longrightarrow z_6$.

Una vez realizada la descomposición y garantizando que la ley de control no afecta las propiedades de estabilidad del sistema, se trabajará con los sistemas Σ_2 y Σ_4 para el diseño de las dos leyes de control, debido a que la estructura de Σ_2 y Σ_4 son iguales, se presentará la técnica en general y después se aplicara para cada caso.

4. DISEÑO DEL CONTROLADOR

Como se mencionó anteriormente, la ley de control no aparece de forma explícita en la prueba de estabilidad, por lo tanto se propone trabajar con el sistema incremental que se obtiene al definir un error del estado y del control, como se muestra a continuación:

$$\tilde{x}_{(2,4)} = \bar{x}_{(2,4)} - x_{\star_{(2,4)}} \tag{31}$$

$$\tilde{u}_{(1,2)} = u_{(1,2)} - u_{\star_{(1,2)}} \tag{32}$$

donde $x_{\star_{(2,4)}}$ y $u_{\star_{(1,2)}}$, son los valores deseados, los subíndices (2,4) se refieren al sub-sistema Σ_2 y Σ_4 y los sub-indices (1,2)

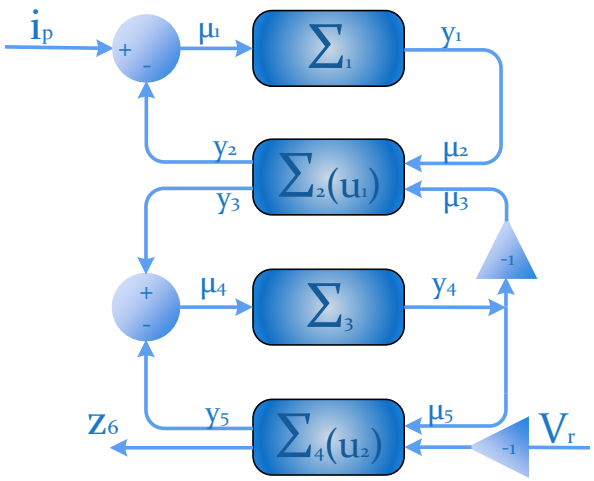

Fig. 3. Sistema completo

se refieren a las leyes de control, entonces el objetivo de control es que

$$\lim_{t\to\infty} \tilde{x}_{(1,2)} = 0$$

garantizando estabilidad interna del sistema completo.

Los valores deseados deben pertenecer a las trayectorias admisibles del sistema. Las trayectorias admisibles del sistema se obtienen partiendo del hecho de que dada una trayectoria deseada existe una señal de control deseada que la genera, esto es

$$\dot{x}_{\star_{(2,4)}} = [J_{(2,4)}u_{\star_{(1,2)}} - \bar{R}_{(2,4)}]\nabla_{x_{\star_{(2,4)}}} H_{(2,4)}(x_{\star_{(2,4)}}) + \tag{33}$$

$$+ E_{(2,4)}. \tag{34}$$

Por lo tanto, se sustituyen las ecuaciones (31-34) en la dinámica de los sistema Σ_2 y Σ_4 obteniendo

$$\dot{\tilde{x}}_{(2,4)} = \\ = [J_{(2,4)}u_{(1,2)} - \bar{R}_{(2,4)}]\nabla_{(\tilde{x}_{(2,4)}+x_{\star_{(2,4)}})} H_{(2,4)}(\tilde{x}_{(2,4)} + x_{\star_{(2,4)}}) \\ + E_{(2,4)} - \dot{x}_{\star_{(2,4)}}$$

al sustituir el valor de $\dot{x}_{\star_{(2,4)}}$ se tiene la dinámica del error de seguimiento

$$\dot{\tilde{x}}_{(2,4)} = [J_{(2,4)}u_{1,2} - \bar{R}_{(2,4)}]\nabla_{\tilde{x}_{(2,4)}} H_{(2,4)}(\tilde{x}_{(2,4)}) \\ + J_{(2,4)}\nabla_{x_{\star_{(2,4)}}} H_{(2,4)}(x_{\star_{(2,4)}})\tilde{u}_{(1,2)} + \tilde{E}_{(2,4)}$$

4.1 Dinámica del error de seguimiento

La función de almacenamiento de energía del error de seguimiento es

$$V_{(2,4)}(\tilde{x}_{(2,4)}) = \frac{1}{2}\tilde{x}^T_{(2,4)} D_{(2,4)} \tilde{x}_{(2,4)} \tag{35}$$

con derivada evaluada a lo largo de las trayectorias del error de seguimiento

$$\dot{V}_{(2,4)}(\tilde{x}_{(2,4)}) = \nabla^T_{\tilde{x}_{(2,4)}} H_{(2,4)}(\tilde{x}_{(2,4)})\dot{\tilde{x}}_{(2,4)} \tag{36}$$

$$\tag{37}$$

al sustituir la dinámica del error se tiene

$$\dot{V}_{(2,4)}(\tilde{x}_{(2,4)}) = \\ - \nabla^T_{\tilde{x}_{(2,4)}} H_{(2,4)}(\tilde{x}_{(2,4)})\bar{R}_{(2,4)}\nabla_{\tilde{x}_{(2,4)}} H_{(2,4)}(\tilde{x}_{(2,4)}) + \\ + \nabla^T_{\tilde{x}_{(2,4)}} H_{(2,4)}(\tilde{x}_{(2,4)})J_{(2,4)}\nabla_{x_{\star_{(2,4)}}} H_{(2,4)}(x_{\star_{(2,4)}})\tilde{u}_{(1,2)} + \\ + \nabla^T_{\tilde{x}_{(2,4)}} H_{(2,4)}(\tilde{x}_{(2,4)})\tilde{E}_{(2,4)}$$

entonces el sistema es pasivo desde la entrada $U_{(2,4)} \longrightarrow Y_{(2,4)}$, donde

$$U_2 = \begin{bmatrix} \upsilon_2 \\ \upsilon_3 \end{bmatrix} = \begin{bmatrix} \tilde{u}_1 \\ \tilde{E}_2 \end{bmatrix}$$

$$Y_2 = \begin{bmatrix} \gamma_2 \\ \gamma_3 \end{bmatrix} = \begin{bmatrix} -\nabla^T_{x_{\star_2}} H_2(x_{\star_2}) J_2 \nabla_{\tilde{x}_2} H_2(\tilde{x}_2) \\ \nabla_{\tilde{x}_2} H_2(\tilde{x}_2) \end{bmatrix}$$

por lo tanto

$$\dot{V}_2(\tilde{x}_2) = \gamma_2^T \upsilon_2 - \gamma_3^T \bar{R}_2 \gamma_3 + \gamma_3^T \upsilon_3. \tag{38}$$

Entonces, el sistema Σ_2 es pasivo desde $\upsilon_2 \longrightarrow \gamma_2$ y estrictamente pasivo a la salida $\upsilon_3 \longrightarrow \gamma_3$.

$$U_3 = \begin{bmatrix} \upsilon_5 \\ \upsilon_6 \end{bmatrix} = \begin{bmatrix} \tilde{u}_2 \\ \tilde{E}_4 \end{bmatrix}$$

$$Y_4 = \begin{bmatrix} \gamma_5 \\ \gamma_6 \end{bmatrix} = \begin{bmatrix} -\nabla^T_{x_{\star_4}} H_4(x_{\star_4}) J_4 \nabla_{\tilde{x}_4} H_4(\tilde{x}_4) \\ \nabla_{\tilde{x}_4} H_4(\tilde{x}_4) \end{bmatrix}$$

por lo tanto

$$\dot{V}_4(\tilde{x}_4) = \gamma_5^T \upsilon_5 - \gamma_6^T \bar{R}_4 \gamma_6 + \gamma_6^T \upsilon_6. \tag{39}$$

Entonces, el sistema Σ_4 es pasivo desde $\upsilon_5 \longrightarrow \gamma_5$ y estrictamente pasivo a la salida $\upsilon_6 \longrightarrow \gamma_6$.

Analizando 38 y 39, podemos observar que el primer término en ambas ecuaciones, no conocemos el signo, sin embargo υ_2 y υ_5 son las variables de diseño, por lo tanto podemos garantizar que éste sea negativo, con una buena elección de υ_2 y υ_5; el segundo término es una función cuadrática de γ_2 para la ecuación 38 por lo tanto siempre es positivo, ya que $\bar{R}_2 > 0$, el segundo término en la ecuación 39 también es una función cuadrática que depende de y_6 por lo tanto siempre es positivo, ya que $\bar{R}_4 > 0$ entonces podemos garantizar que el segundo término de 38 y 39 siempre son negativos; del tercer término de ambas ecuaciones no es posible definir signo.

4.2 Diseño de $\upsilon_{(2,5)}$

Se propone un control PI, con

$$\dot{\eta}_{(2,5)} = -\gamma_{(2,5)} \tag{40}$$

y señal de control $\upsilon_{(2,5)} = -k_{p_{(2,5)}}\gamma_{(2,5)} + k_{i_{(2,5)}}\eta_{(2,5)}$, con la siguiente función de almacenamiento de energía

$$V_{(2,5)}(\tilde{x}_{(2,4)}, \eta_{(2,5)}) = \frac{1}{2}\tilde{x}_2^T D_2 \tilde{x}_2 + \eta_2^T k_{i_2} \eta_2 + \\ + \frac{1}{2}\tilde{x}_4^T D_4 \tilde{x}_4 + \eta_5^T k_{i_5} \eta_5$$

y derivada

$$\dot{V}_{(2,5)} = \gamma_2^T \upsilon_2 - \gamma_3^T \bar{R}_2 \gamma_3 + \gamma_3^T \upsilon_3 - \eta_2^T k_{i_2} \gamma_2 \\ + \gamma_5^T \upsilon_5 - \gamma_6^T \bar{R}_4 \gamma_6 + \gamma_6^T \upsilon_6 - \eta_5^T k_{i_4} \gamma_5$$

al sustituir $\upsilon_{(2,5)}$

$$\dot{V}_{(2,5)} = \gamma_2^T(-k_{p_2}\gamma_2 + k_{i_2}\eta_2) - \gamma_3^T \bar{R}_2 \gamma_3 + \gamma_3^T \upsilon_3 - \eta_2^T k_{i_2} \gamma_2 \\ + \gamma_5^T(-k_{p_5}\gamma_5 + k_{i_5}\eta_5) - \gamma_6^T \bar{R}_4 \gamma_6 + \gamma_6^T \upsilon_6 - \eta_5^T k_{i_4} \gamma_5$$

se puede observar que el término que depende de $k_{i_{(2,5)}}$ se cancela, quedando

$$\dot{V}_{(2,5)} = -\gamma_2^T k_{p_2} \gamma_2 - \gamma_3^T \bar{R}_2 \gamma_3 + \gamma_3^T \upsilon_3 \tag{41}$$

$$- \gamma_5^T k_{p_5} \gamma_5 - \gamma_6^T \bar{R}_4 \gamma_6 + \gamma_6^T \upsilon_6 \tag{42}$$

Se puede ver el signo esta definido en todos los términos, excepto en $\gamma_3^T \upsilon_3$ y $\gamma_6^T \upsilon_6$, por lo tanto, como éstos dependen de $\tilde{x}_1$ y $\tilde{x}_4$, se analizará la dinámica del error de los sistemas Σ_1 y Σ_3.

Se define la señal de error $\tilde{x}_1 = x_1 - x_{1_\star}$ y sustituimos en el sistema Σ_1

$$\dot{\tilde{x}}_1 = -\frac{1}{R_1 C_1} x_1 - \frac{1}{L_2} x_2 + i_p - \dot{x}_{1_\star} \tag{43}$$

donde $x_{1_\star}$ es la dinámica deseada, que se define como

$$\dot{x}_{1_\star} = -\frac{1}{R_1 C_1} x_{1_\star} - \frac{1}{L_2} x_{2_\star} + i_p \tag{44}$$

al sustituir la dinámica deseada en la dinámica del error se tiene

$$\dot{\tilde{x}}_1 = -\frac{1}{R_1 C_1} \tilde{x}_1 - \frac{1}{L_2} \tilde{x}_2 \tag{45}$$

Se propone la función de almacenamiento de energía

$$V_1(\tilde{x}_1) = \frac{1}{2C_1} \tilde{x}_1^2 \tag{46}$$

con derivada evaluada a lo largo de las trayectorias del sistema

$$\dot{V}_1(\tilde{x}_1) = \frac{1}{C_1} \tilde{x}_1 \left(-\frac{1}{R_1 C_1} \tilde{x}_1 - \frac{1}{L_2} \tilde{x}_2 \right) \tag{47}$$

si definimos $\upsilon_1 = \frac{1}{L_2} \tilde{x}_2$, $\gamma_1 = \frac{1}{C_1} \tilde{x}_1$ entonces

$$\dot{V}_1(\tilde{x}_1) = -\frac{1}{R_1} \gamma_1^2 + \gamma_1^T \upsilon_1 \tag{48}$$

por lo tanto es estrictamente pasivo a la salida desde $\upsilon_1 \longrightarrow \gamma_1$.

Ahora se define la dinámica del error $\tilde{x}_4 = x_4 - x_{4_\star}$ y sustituimos en el sistema Σ_3

$$\dot{\tilde{x}}_4 = -\frac{R_4}{L_4} x_4 + \frac{1}{C_3} x_3 - \frac{1}{C_5} x_5 - \dot{x}_{4_\star} \tag{49}$$

donde $x_{4_\star}$ es la dinámica deseada, que se define como

$$\dot{x}_{4_\star} = -\frac{R_4}{L_4} x_{4_\star} + \frac{1}{C_3} x_{3_\star} - \frac{1}{C_5} x_{5_\star} \tag{50}$$

al sustituir la dinámica deseada en la dinámica del error se tiene

$$\dot{\tilde{x}}_1 = -\frac{R_4}{L_4} \tilde{x}_4 + \frac{1}{C_3} \tilde{x}_3 - \frac{1}{C_5} \tilde{x}_5 \tag{51}$$

Se propone la función de almacenamiento de energía

$$V_4(\tilde{x}_4) = \frac{1}{2L_4} \tilde{x}_4^2 \tag{52}$$

con derivada evaluada a lo largo de las trayectorias del sistema

$$\dot{V}_4(\tilde{x}_4) = \frac{1}{L_4} \tilde{x}_4 \left(-\frac{R_4}{L_4} \tilde{x}_4 + \frac{1}{C_3} \tilde{x}_3 - \frac{1}{C_5} \tilde{x}_5 \right) \tag{53}$$

si definimos $\upsilon_4 = \frac{1}{C_3} \tilde{x}_3 - \frac{1}{C_5} \tilde{x}_5$, $\gamma_4 = \frac{1}{L_4} \tilde{x}_4$ entonces

$$\dot{V}_1(\tilde{x}_1) = -R_4 \gamma_4^2 + \gamma_4^T \upsilon_4 \tag{54}$$

por lo tanto es estrictamente pasivo a la salida desde $\upsilon_4 \longrightarrow \gamma_4$.

El diagrama de bloques del sistema completo en coordenadas del error es el que se muestra en la Fig. 4 cuya función de almacenamiento de energía es la suma de las funciones de almacenamiento de energía de los sistemas descritos anteriormente

$$V(\tilde{x}, \eta_2, \eta_5) = \frac{1}{2} \tilde{x}^T D x + \eta_2^T k_{i_2} \eta_2 + \eta_5^T k_{i_5} \eta_5$$

con derivada

$$\begin{aligned} \dot{V}(\tilde{x}, \eta_2, \eta_5) = & -\gamma_2^T k_{p_2} \gamma_2 - \gamma_3^T \bar{R}_2 \gamma_3 + \gamma_3^T \upsilon_3 \\ & - \gamma_5^T k_{p_5} \gamma_5 - \gamma_6^T \bar{R}_4 \gamma_6 + \gamma_6^T \upsilon_6 \end{aligned}$$

Se puede observar que $\dot{V}(\tilde{x}, \eta_2, \eta_5)$ es semidefinida negativa ya que no depende de todos los estados. Sin embargo, utilizando

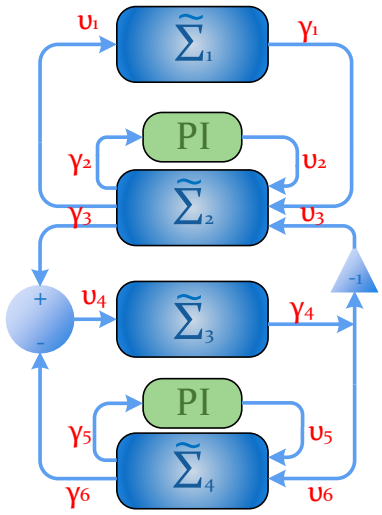

Fig. 4. Sistema completo

el lema de Barbalat, podemos concluir estabilidad asintótica, ya que $\tilde{x}, \eta_{(2,5)} \in L_\infty, \dot{\tilde{x}}\dot{\eta} \in L_\infty \, \tilde{x}, \eta \in L_2 \, V(\tilde{x}, \eta_2, \eta_5) \in L_\infty \Rightarrow \tilde{x} \to 0, t \to \infty$. Como la función de almacenamiento de energía es radialmente no acotada, se concluye estabilidad global.

5. VALIDACIÓN NUMÉRICA

Los parámetros que se utilizaron para la validación numérica del controlador son los mostrados en la Tabla 1. Divido a que

Table 1. Parámetros del sistema

Parámetro	Símbolo	Valor	Unidades
Capacitor de entrada	C_1	1	mF
Pérdidas de C_1	R_1	1	$M\Omega$
Inductor	L_2	0.4	mH
Pérdidas de L_2	R_2	0.1	Ω
Capacitor C_3	C_3	25	μF
Pérdidas de C_3	R_3	1.1	$M\Omega$
Inductor de enlace	L_4	1	mH
Pérdidas de L_4	R_4	0.13	Ω
Capacitor C_5	C_5	47	μF
Pérdidas de C_5	R_5	1.4	$M\Omega$
Inductor de salida	L_6	40	mH
Pérdidas de L_6	R_6	0.06	Ω
Voltaje de red eléctrica	V_r	$127 * \sqrt{2}$ $f = 60$	$[V]$, $[Hz]$
Ganancia integral 1	k_{i_2}	$2.5e^{-6}$	$--$
Ganancia proporcional 1	k_{p_2}	$0.15e^{-3}$	$--$
Ganancia integral 2	k_{i_5}	$25e^{-8}$	$--$
Ganancia proporcional 2	k_{p_5}	$1.5e^{-5}$	$--$

se tienen dos señales de control, es posible imponer dos de los estados del sistema las cuales serán las señales de referencia del sistema.

Una de las señal de referencia deseadas es la corriente del inductor L_2 la cual se obtuvo mediante el hecho de que la corriente de maxima potencia es el 92% de la corriente de cortocircuito. Por lo tanto, se cortocircuito el modelo de un panel que tiene las mismas condiciones de irradiancia y temperatura que el panel a controlar.

La segunda señal de referencia que se desea imponer, es la corriente de salida, pues con ésta, es posible controlar la potencia que queremos inyectar a la red eléctrica, la cual esta limitada

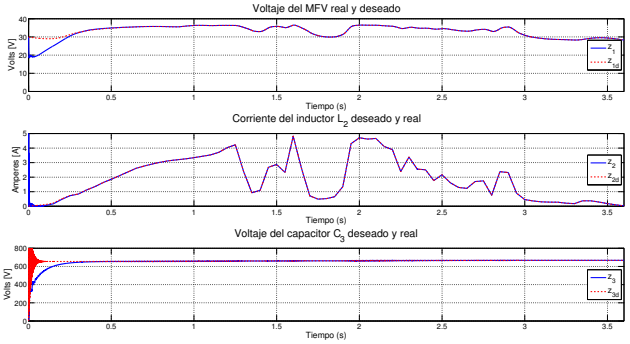

Fig. 5. Primeros tres estados y estados deseados del sistema

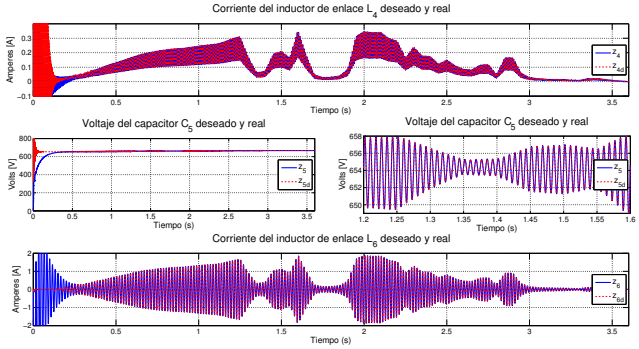

Fig. 6. Últimos tres estados y estados deseados del sistema

por la potencia del MPV. Como se quiere trabajar en el punto de máxima potencia del MPV, la potencia de salida del sistema debe ser igual al de entrada menos la potencia disipada por las resistencias de perdidas de los elementos, esto es

$$P_s = P_e - P_p$$

donde P_s es la potencia de salida, P_e es la potencia del MPV, P_p es la potencia de pérdidas. Como P_e se debe al MPV, y éste trabaja con corriente directa, la potencia se calcula de la siguiente manera

$$P_e = z_1 i_p.$$

Como solo se requiere extraer potencia activa de sistema, la potencia de salida se calcula con la siguiente ecuación

$$P_s = V_{r_{RMS}} z_{6_{RMS}}$$

y la potencia de pérdidas esta dada por

$$P_p = \frac{1}{R_1} z_1^2 + \frac{1}{R_2} z_2^2 + \frac{1}{R_3} z_3^2 + \frac{1}{R_4} z_4^2 + \frac{1}{R_5} z_5^2 + \frac{1}{R_6} z_6^2$$

por lo tanto la señal z_{6d} esta dada por

$$z_{6_{RMS}} = \frac{P_e - P_p}{V_{r_{RMS}}}$$

Los parámetros del MFV simulado, son los que se muestran en la Tabla 2

Table 2. Parámetros MPV

Parámetro	Símbolo	Valor	Unidades
Voltaje de máxima potencia	V_m	35.2	V
Voltaje de circuito abierto	V_{oc}	44.2	V
Corriente de máxima potencia	I_m	4.95	A
Corriente de corto circuito	I_{sc}	5.2	A

En la Fig. 5 se puede observar que se logra el seguimiento de la señal deseada en los primeros tres estados, donde la primer gráfica muestra el voltaje del MPV, el cual varía entre 29 y 39[V], dependiendo de las condiciones de irradiancia, en la segunda gráfica se muestra la corriente extraída del MFV, en la que se observan los cambios abruptos de irradiancia que incide en el MPV. En la última gráfica se muestra el voltaje de salida del convertidor elevador, el cual pareciera que llega a un valor constante.

En la Fig. 6 se puede observar que se logra el seguimiento de la señal deseada en los últimos tres estados, donde la primer gráfica muestra la corriente de enlace entre ambos convertidores de potencia, la cual en estado permanente siempre es positiva, esto quiere decir que la transferencia de potencia siempre es del MPV a la red eléctrica. En las gráficas del centro se muestra el voltaje del bus de corriente directa del inversor, del lado

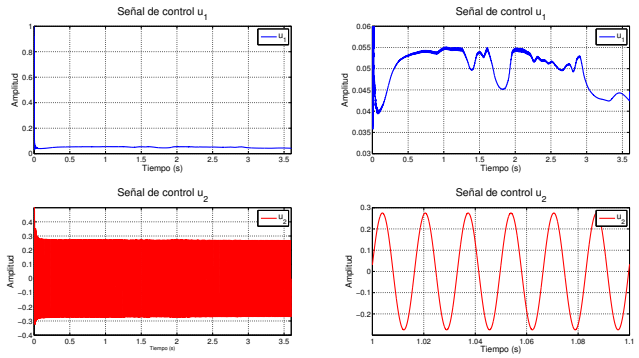

Fig. 7. Señales de control, u_1 y u_2.

izquierdo se observa el voltaje del bus en todo el tiempo de simulación y del lado izquierdo se puede observar un zoom de dicha gráfica, en el cual se aprecia la variación del voltaje del bus. En la última gráfica se muestra la corriente transmitida a la red eléctrica, la cual no es constante, ya que depende de las condiciones climáticas en las que este el MPV.

En la Fig. 7 podemos observar las dos señales de control, la primer gráfica del lado izquierdo es la señal de control en todo el tiempo de simulación, donde es posible ver que pertenece a un valor entre cero y uno. La gráfica del lado derecho, es un zoom de la señal de control u_1 donde se observa mejor la variación de ésta, para mantener al MPV en el punto de máxima potencia. La gráfica que se encuentra en la parte inferior izquierda es la señal de control u_2 la cual permanece en un intervalo entre -1 y 1 que es correcto para un inversor, sin embargo, por el tiempo de simulación no se aprecia la forma de onda de esta señal de control, por eso, en la parte inferior derecha se muestra un zoom de la señal de control u_2 la cual es una señal sinusoidal de amplitud 2.8.

Finalmente en la Fig. 8 se muestra la potencia extraída del MPV, la potencia entregada a la red eléctrica y la potencia de pérdidas del sistema.

6. CONCLUSIONES

En este artículo se muestra que es posible trabajar un MPV en el punto de máxima potencia y transferir dicha potencia a la red eléctrica, dependiendo exclusivamente de un buen diseño de las dos leyes de control. Un punto muy importante es el calculo de las valores deseados ya que debe haber un equilibrio entre la potencia extraída del MPV y la inyectada a la red eléctrica.

Como trabajo futuro queda pendiente la implementación física del sistema.

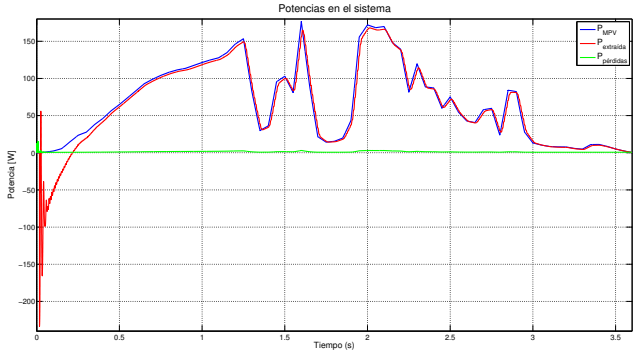

Fig. 8. Potencia extraída del MPV, potencia entregada a la red y pérdidas del sistema.

7. BIBLIOGRAFÍA

E. Romero-Cadaval, B. Francois, M. Malinowski, and Q. C. Zhong. *Grid-Connected Photovoltaic Plants: An Alternative Energy Source, Replacing Conventional Sources*. *IEEE Ind. Electron. Mag.*, vol. 9, no. 1, pp. 18-32, Mar. 2015.

P. E. Kakosimos, A. G. Kladas, and S. N. Manias. *Fast Photovoltaic-System Voltage or Current-Oriented MPPT Employing a Predictive Digital Current-Controlled Converter*. *IEEE Trans. Ind. Electron.*, vol. 60, no. 12, pp. 5673-5685. Dec. 2013.

D. R. Espinoza-Trejo, E. Bárcenas-Bárcenas, D. U. Campos-Delgado y C. De Angelo. *Voltage-Oriented Input–Output Linearization Controller as Maximum Power Point Tracking Technique for Photovoltaic Systems* IEEE Transactions on Industrial Electronics, Vol. 62, No. 6, June 2015

E. Bianconi, J. Calvente, R. Giral, E. Mamarelis, G. Petrone, C. A. Ramos-Paja, G. Spagnuolo, and M. Vitelli. *A Fast Current-Based MPPT Technique Employing Sliding Mode Control*. *IEEE Trans. Ind. Electron.*, vol. 60, no. 3, pp. 1168-1178, Mar. 2013.

Arjan van der Schaft. L2-Gain and Passivity Techniques in Nonlinear Control. pages 125–136.

Rafael Cisneros, Romeo Ortega. *Global Tracking Passivity–Based PI Control for power converters: an application to the Boost and Modular Multilevel converters*. 2014.

Hassan K. Khalil. Nonlinear Systems. *Third edition*.

Bayu Jayawardhana, Romeo Ortega. *Passivity of Nonlinear Incremental Systems: Application to PI Stabilization of Nonlinear RLC Circuits*. Conference on Decision Control 2006.

Ahmad El Khateb, Nasrudin Abd Rahim. *Maximum power point tracking of single-ended primary-inductor converter employing a novel optimisation technique for proportional-integralderivative controller*. IET Power Electronics 2013

Control of Sustainable Industrial Processes

Jesús-Antonio Hernández-Riveros[1]*; Kevin J. Berrio[1]; Gerardo J. Amador[2]*****

[1] *Facultad de Minas, Universidad Nacional de Colombia. Medellín, Colombia*

[2] *Facultad de Ingeniería, Universidad Nacional de Honduras*

*(e-mail: jahernan@unal.edu.co)

**(e-mail: kjberrio@unal.edu.co)

***(e-mail: gjamadors@unal.edu.co)

Abstract: The concept of sustainability is known more than 30 years ago, being a topical worked in the academic sphere more frequently than in industry. The pillars of sustainability (financial, environmental and social) are not commonly found in process control and industrial projects as one of its drivers. In the environmental area, reducing consumption of energy, raw materials and waste production is essential. This article describes a procedure to determine how to improve the energy efficiency of a dynamic process reducing energy consumption in the system while fulfilling its control objectives. Bond Graph method is used for modeling a complex case in its mechanical and electrical versions. The magnitude of various components of the system is manipulated so that during its transient behavior the system response reaches a steady state consuming the least possible amount of energy, without sacrificing production efficiency. To force the system to meet a given reference and reduce power consumption, a PID controller is applied to manipulate the external source. An evolutionary algorithm is used to modify the elements magnitude and to tune the PID controller. This proposal focuses on saving energy in controlled dynamic industrial processes through an optimization process that significantly improves performance.

Key Words: Sustainability, Evolutionary Computation, Dynamical Systems, Energy Efficiency, MAGO algorithm, Bond Graph, PID.

1. INTRODUCTION

1.1 Sustainable Industrial Processes

An industrial process with a focus on sustainability is defined as the set of stages through which the processing of raw products materials, products, residues and waste, taking into account the rational use of energy, optimizing utilization of materials and minimizing or eliminating the presence of residues and waste (Pérez & Meza, 2013). Globally the issue of sustainability in development since 1983, when the Brundtland Commission (CFR, 1987) the term sustainability was defined as "the ability to meet the needs of the present generation without compromising the ability of future generations to meet their own needs." In a study by the World Bank (WBG, 2011) makes evident that by including the hub of sustainability (financial, environmental and social) in every action of the organization, two positive effects arise: There is an improvement in its financial performance, resulting in more than 5% better performance with respect to those not including these criteria, and demonstrates how investors are decided by those companies that have the three pillars of sustainability as their top three priorities.

Nowadays, what matters is not only that the system performs under its designed nominal conditions but that its operation has a minimal environmental footprint. The challenge for control engineering is to achieve a more sustainable way for process operation, using less energy, less raw materials, and producing less waste, besides satisfying various behavior references.

Energy consumption is part of the environmental shaft of sustainability and represents a high impact factor in any industrial process. This work focuses on reducing the energy demand of an industrial system while meeting its goals of control.

1.2 Energy Efficiency

Energy Efficiency actions are understood as activities that are aimed at improving or maintaining production at the lowest possible energy consumption (Pareja & Parra, 2014). In others words, optimize energy use. The purpose is to obtain the expected performance in a production process, but with the least possible energy. For these characteristics can talk about optimization of industrial processes. This optimization is linked directly to maximize or minimize some indicator of performance or process efficiency.

A very common case, and an easy way to illustrate the term energy efficiency, is finding the optimum value of a given function and that is also global. This amount can be a

maximum or minimum value, as appropriate. This article presents a method to improve energy efficiency in a production process that consumes energy, by manipulating the magnitude of some components of the system. The efficiency in its natural and controlled behaviors, with different dynamical instantiations of the manipulated elements, is compared.

The remainder of this paper is divided into four sections. Section 2 presents the problem to be solved by the description of a mechanical system, its electrical equivalent and the equations of state using the Bond Graph technique. In section 3 the energy consumption of a dynamic element of the system is evaluated. Similarly, the total consumption by a comparison between energy consumption in the element and the external source without control action vs power consumption with control action, manipulating three separate system components. In section 4, the analysis is rethought modifying the system by controlling the external source via a PID controller and looking for minimal power consumption in both the element of interest and in the source. The conclusions are presented in Section 5.

2. PROBLEM TO BE SOLVED

2.1 Mechanical System

The mechanical system of Figure 1, which consists of two masses (m1 and m2), two springs (k1 and k2) and a damper (R1) is modeled.

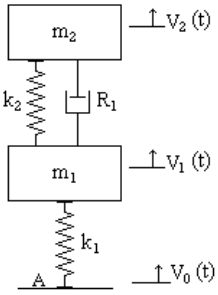

Fig.1. Mechanical System to be modeled

The system is moved from the bottom at a certain speed (Vo). The value of the speed of the mass 1 (V1) and mass 2 (V2) at the top, are unknown.

Subsequently for ease the reader's interpretation, energy analysis based on the equivalent electrical model is performed.

2.2 Bond Graph

Bond Graph is a technique that is used to model multidisciplinary dynamic systems. Proposed by H. M. Payne in 1954 to model mechanical systems (Paynter, 1992), it is based on power exchanges between the constituent elements of a circuit under study. Then it expanded to other energy domains: electrical, hydraulic, thermal, acoustic, pneumatic, structural, chemical, magnetic (Breedveld, 1985), (Karnopp, Margolis, & Rosenberg, 2006) (Borutzky, 2011), even economical systems (Mukherjee, Karmakar, & Samantaray, 2006). The great advantage of Bond Graph method is that it provides the state equations of the system in terms of energy, based on power.

The power flow between systems, subsystems and components is represented by a line or "bond" which carries associated the variables effort e(t) and flow f(t), Figure 2, the product of these variables gives the instantaneous power P(t) transmitted by the "bond".

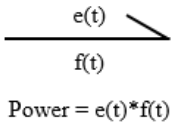

Fig. 2. Graphical representation of instantaneous power.

Other important variables in the description of dynamic systems are momentum p(t) and displacement Q(t). The moment is defined as the integral of the effort over time (Equation 1). The displacement Q(t) is the integral of flow over time (Equation 2).

$$P(t) = \int_0^t e(t)dt \tag{1}$$

$$Q(t) = \int_0^t f(t)dt \tag{2}$$

The **energy ports** are those elements in which the system stores or dissipates energy. They can be of various types, according to the energy domain: resistor, stiffness, inertia, effort source and flow source.

Resistive element: elements or situations where there is a loss of energy. It is represented by R, see Figure 3.

Example: Electrical resistance, damper, mechanical friction, pressure drop.

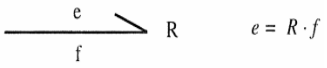

Fig. 3. Resistive Port

Compliant element: element which is capable of storing potential energy and return completely to the system without any loss. Is represented by the symbol K, see Figure 4.

Example: electrical capacitor, ideal spring, hydro pneumatic accumulator, etc.

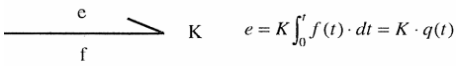

Fig. 4. Compliant Port

Inertial element: elements or phenomena in which there is a mathematical relationship between the effort and the momentum, which in mechanics is defined as the integral over time of the force. It is represented by the symbol I, see Figure 5.

Example: Moving at a speed, *v*, of an object of a frictionless mass *m*, rotation of a rigid body, inductance.

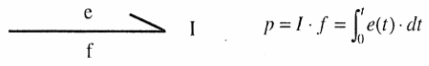

Fig. 5. Inertial port.

Sources of flow (Figure 6) are those elements that supply kinetic energy to the system. They are represented by *Sf*, and physical examples are intensity or speed sources and hydraulic pumps. The sources of effort (Figure 6) inject potential energy. They are represented by *Se*. Examples are voltage, pressure, force.

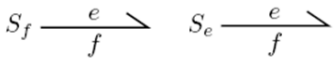

Fig. 6. Flow and Effort sources representation.

2.3 System Modeling

Bond Graph technique is used for modeling mechanical system of Figure 1. The first thing necessary is to determine the "bond" of each element and junction in which an effort or flow is applied (each bond has an associated effort and flow).

After defining all physical interactions occurring in the system proceeds to link the bond (Vera Alvarez & Caballero Ocaña, 2008) taking into consideration the following criteria:

• The O symbol is used for the junction of bonds where their effort is the same.

• The 1 symbol is used for the junction of bonds where their flow is the same.

• The bonds using a source (effort or flow) enter the junction.

• The bonds that not use a source (effort or flow) leave the junction.

Given the above criteria, the Bond Graph model equivalent to the system in its mechanical and electrical versions is presented in Figure 7.

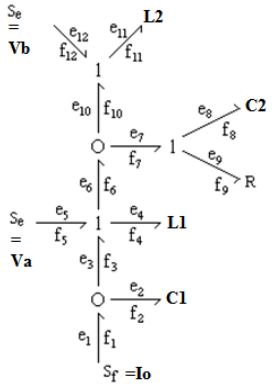

Fig.7. Bond Graph scheme

2.4 System and Equations

The analysis was done based on the electrical model (Figure 8). The system consists of an input direct current (Io), two capacitors (C1 and C2), two coils (L1 and L2), two sources of DC voltage, a resistance (R) and a switch. The current source is connected to the system through a switch on a time instant.

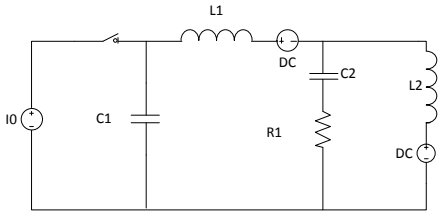

Fig.8. Equivalent electrical System

From the scheme, flow equations in capacitors and effort equations in coils can be obtained, as follows:

Flow 2 = Intensity in capacitor C1

$$f2 = Io - \frac{p1}{L1} \quad (3)$$

Flow 8 = Intensity in capacitor C2

$$f8 = \frac{p1}{L1} - \frac{p2}{L2} \quad (4)$$

Effort 4 = Voltage in coil L1

$$e4 = \frac{q1}{C1} - Va - R1\left(\frac{p1}{L1} - \frac{p2}{L2}\right) - \frac{q2}{C2} \quad (5)$$

Effort 12 = Voltage in coil L2

$$e12 = R1\left(\frac{p1}{L1} - \frac{p2}{L2}\right) - \frac{q2}{C2} - Vb \quad (6)$$

Where p1 and p2 are the momentum in coils 1 and 2 respectively, and q1 and q2 are the displacements in capacitors, all time-dependent variables.

Considering that:

$$\frac{dq(t)}{dt} = f(t) \quad (7)$$

$$\frac{dp(t)}{dt} = e(t) \quad (8)$$

It is replaced in the above equations and have:

$$f2 = \frac{dq1(t)}{dt} = Io - \frac{p1(t)}{L1} \quad (9)$$

$$f8 = \frac{dq2(t)}{dt} = \frac{p1(t)}{L1} - \frac{p2(t)}{L2} \quad (10)$$

$$e4 = \frac{dp1(t)}{dt} = \frac{q1(t)}{C1} - Va - R\left(\frac{p1(t)}{L1} - \frac{p2(t)}{L2}\right) - \frac{q2(t)}{C2} \quad (11)$$

$$e12 = \frac{dp2(t)}{dt} = R\left(\frac{p1(t)}{L1} - \frac{p2(t)}{L2}\right) - \frac{q2(t)}{C2} - Vb \quad (12)$$

In this case, we are interested in energy consumption in the coil 2. The calculation of the power consumed by this element can be expressed by Equation 13:

$$Pot12(t) = \left[R\left(\frac{p1(t)}{L1} - \frac{p2(t)}{L2}\right) + \frac{q2(t)}{C2} - Vb \right]^2 \Big/ L2 \quad (13)$$

The energy consumed by this element in a defined time is:

$$En12(t) = \int_0^{Tf} Pot12(t)dt \quad (14)$$

3. ENERGY ANALYSIS

The equations of energy consumption for a system element, the coil 2, were presented. It aims to minimize the energy consumed by this element in its transitory state until it reaches its natural value (voltage in electrical circuit, force in mechanical version). Manipulating the magnitude of another element of the system the coil 2 reaches its natural value voltage with minimal power consumption. In Section 4, the manipulation of another element of the system is performed by a PID control.

Next, energy analysis taking as a starting point the behavior in the natural state of the system is presented. The results are compared after handling other system elements, which are: the resistor R1 and capacitors C1 and C2 (Figure 9):

3.1 Natural Response

Table 1 presents results of energy consumption for this case.

Table 1. Results of Natural State

Energy	Units of Energy
Coil 2	5,9973E+03
Total	5,3093E+06

3.2 Energy Control by System Elements

3.2.1 Energy Control by Resistance Handling.

The control action is placed in the circuit resistance R1, so that its magnitude remains time dependent. Control is directly manipulating the magnitude of the resistor R1.

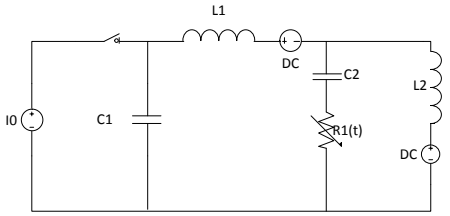

Fig. 9. Electrical System with variable resistor

The goal is to minimize the energy consumed by the coil L2 in the transient using the control action in the resistance R1 (t), until it reaches its natural voltage value.

3.2.2 Optimization Algorithm

The objective function is expressed by equation 15.

$$\min_{R(t)} \int_0^{Tf} Pot12(t)dt = \min_{R(t)} \int_0^{Tf} \left(\left[R(t)\left(\frac{p1(t)}{L1} - \frac{p2(t)}{L2} \right) + \frac{q2(t)}{C2} - Vb \right]^2 \Big/ L2 \right) dt$$

$$s.t.$$

$$R(t) > 0 \forall t \quad (15)$$

Given the nonlinearity, uncertainty in the convexity and the structure of the model in differential equations, this is a complicated problem to solve by traditional optimization algorithms. For this reason, a heuristic technique for its solution is used: The Multidynamics Algorithm for Global Optimization (MAGO, by its acronym in English); formally presented in (Hernandez & Ospina, 2010).

The Multidynamics Algorithm for Global Optimization (MAGO) is an evolutionary heuristic method that transforms groups of individuals to achieve a goal, likening their behavior to the process of evolution of species. Unlike other evolutionary algorithms, MAGO does not used genetic operators for the evolutionary process but statistical from the same population.

In this paper, MAGO is used to modify the magnitude of some system elements in the transitory in order to reduce energy consumption in the coil L2 and also to calculate the parameters of the PID controller to force behavior in the coil L2 while achieving minimum energy consumption throughout the system.

MAGO was born as a hybrid among distribution estimation algorithms and the statistical quality control. As with other evolutionary algorithms MAGO begins with a population of possible solutions distributed randomly throughout the search space, which is divided autonomously by the algorithm into three subgroups with their own evolution, called Emergent Dynamics, Crowd Dynamics and Accidental Dynamics.

The MAGO algorithm uses the covariance matrix of the population of each generation to establish an exploration distribution and creating three subgroups or dynamics that make all individuals in each generation. Emergent Dynamics (G1) creates a small group of individuals within the population around the individual with better genetic characteristics, displacing the best ones and making them compete with each other. This group is the evolutionary elite of each generation, that is, the fittest individuals contributing with their genes to the next generation. They are spread throughout the search space. The second group, the Crow Dynamics (G2), generates individuals around the current population mean and first standard deviation. This population subgroup, located in a sector of the search space, is changing its location during the evolutionary process. The crow dynamics can be close to the emergent dynamics, but never enough to be confused. Only until there is sufficiency and necessary to ensure full exploration of the search space conditions, these two dynamics could be merged within the territory, usually at the end of the evolutionary cycle. The third group, the Accidental Dynamics (G3), follows the quantum speciation, in that is established throughout the search space generation by generation in isolation from other individuals of the other dynamics. Their role is to maintain diversity and ensure the stability of the algorithm. These subgroups cannot interbreed. In every generation the union of the three subgroups formed all the current population. In Figure 10 the MAGO basic flow is shown.

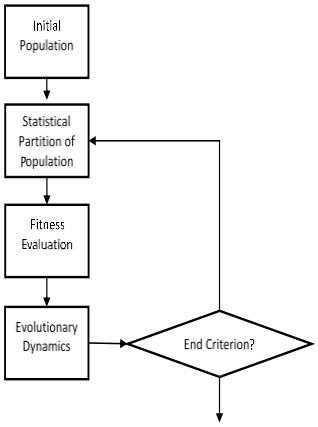

Fig.10. Flow Diagram of MAGO

Following, the pseudocode of the MAGO is presented:

1: j = 0, Generation of the initial population with a uniform random distribution in the search space.

2: Repeat.

3. Evaluate each individual through the objective function.

4: Calculate the covariance matrix of the population and the first, second and third dispersion.

5: Calculate the cardinalities N1, N2 and N3 of the groups G1, G2 and G3.

6: Select N1 of the best individuals, modify according to the objective function and make them compete. Pass the winners the next generation j + 1.

7: Conduct a sampling from the uniform distribution in the hyper-rectangle [LB (j), UB (j)] with N2 individuals, and move on to the next generation j + 1.

8: Conduct a sampling from the uniform distribution throughout the search space with N3 individuals and move on to the next generation j + 1.

9: j = j + 1.

10: Until some termination criterion is satisfied.

3.2.3 Simulation and Results

For simulation and analysis of the results the following steps were taken:

a. Define model parameters

For the model of Figure 9 the following parameters were set:

L1 = 1 L2 = 1 C1 = 1 C2 = 1

R = 1,56 (Initial Value to calculate R(t))

Va = 5 Vb = 5 I0 = 20

The simulation begins with a quasi-optimum value of R, which has an apparent minimum consumption of energy in the coil 2. Since the percentage of saved energy and the variables behavior are compared, the units of each element are ignored.

The initial conditions are zero for the state variables:

Initial displacement capacitor 1: q1(t=0) = 0;

initial displacement capacitor 2: q2(t=0) = 0;

Initial momentum coil 1: p1(t=0) = 0;

Initial momentum coil 2: p2(t=0) = 0;

The simulation time is 100 seconds.

b. Simulating natural response of the system and observe the following behaviors:

• Power in the coil 2.

• Energy consumed in the coil 2.

• Behavior of p2(t) corresponding to the momentum or time integral of voltage.

c. Run optimization to find R(t) and simulate the model including manipulation of the magnitude of R1. Observe and compare results with respect to the natural state response of the system.

In Table 2 the power consumption of both the coil 2 and the total system are compared, by control action and without it on the resistance R1.

Table 2. Comparison 1

Energy on coil 2	**Units of Energy**
Without Control (R1 Fixed)	5,997E+03
With Control (R1 Variable)	5,943E+03
Total Energy	**Units of Energy**
Without Control (R1 Fixed)	5,309E+06
With Control (R1 Variable)	5,474E+06

A slight decrease in the energy consumption for the coil 2, after the control action by varying the resistor R1 is seen.

3.3 Energy Control by Capacitor Handling C1 (variable)

The results in the implementation of control in the case of capacitor C1 are presented in Table 3.

Table 3. Comparison 2

Energy on coil 2	**Units of Energy**
Without Control (R1, C1, Fixed)	5,997E+03
With Control (C1 Variable)	5,914E+03
Total Energy	**Units of Energy**
Without Control (R1, C1, Fixed)	5,309E+06
With Control (C1 Variable)	5,595E+06

A slight decrease in the power consumption of the coil L2 after the control action from capacitor C1 in the system is seen.

3.4 Energy Control by Capacitor Handling C2 (variable)

The results in the implementation of control for the case of the capacitor C2 are presented in Table 4.

Table 4. Comparison 3

Energy on coil 2	Units of Energy
Without Control (C2 Fixed)	5,997E+03
With Control (C2 Variable)	3,303E+03
Total Energy	**Units of Energy**
Without Control (C2 Fixed)	5,309E+06
With Control (C2 Variable)	7,247E+06

The decrease in energy consumption in the coil L2 is visible when the transitory is handled from C2 to reach the natural response.

The results show that near the C2 element, a PID controller must be located to minimize energy consumption in the transitory state of the system and to force a reference behavior on element L2.

4. CONTROL BASED ON ENERGY EFFICIENCY

From the above results it is evident that it is possible to minimize energy consumption in both the system and as in a specific element (coil L2), manipulating different elements of the system.

In order to control the steady state response of the system, in this case, momentum P2 and a reference in coil L2, by the particular configuration of the system placing a resistor in parallel with the source was decided. This arrangement is equivalent to a controllable external source. See Figure 11.

Additionally, it will be noted how power consumption is changed in the coil. The magnitude of the additional resistance will be varied by adjusting the parameters of a PID controller.

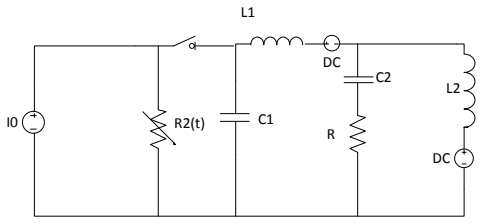

Fig.11. System with variable resistor R2 in parallel with the intensity source.

In this case the system of equations is derived with Bond Graph in the same manner as above, except for the circuit equation (9) which changes as follows (see equation 16):

$$f2 = \frac{dq1(t)}{dt} = Io - \frac{p1(t)}{L1} - \frac{q1(t)}{C1R2} \qquad (16)$$

4.1 Natural Response (Without Controller)

The results of energy consumption for the natural state case are presented in Table 5.

Table 5. Natural State Response

Energy	Units of Energy
Coil 2	1,014E+03
Total	4,466E+06

4.2 Response with Resistor R2 controlled

The reference is set to a magnitude of 10 units in the L2 element (voltage in the electrical system and force in the mechanical system). The initial value of R2 is 0.7.

In Figure 12 the proposed implementation of a PID controller varying the value of the resistor R2 as a method of controlling the intensity source is appreciated. The results of energy consumption for this case are presented in Table 6. , In Figures 13 and 14, from the results for energy optimization in L2, can be observed the control action and the energy consumption (momentum) in L2.

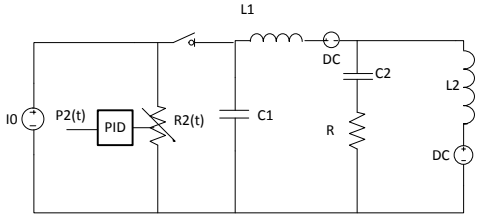

Fig. 12. System configuration with PID control.

Table 6. Results for R2 Controlling only energy consumption in L2.

Energy	Units of Energy
Coil 2	1,0105E+03
Total	4,6496E+06

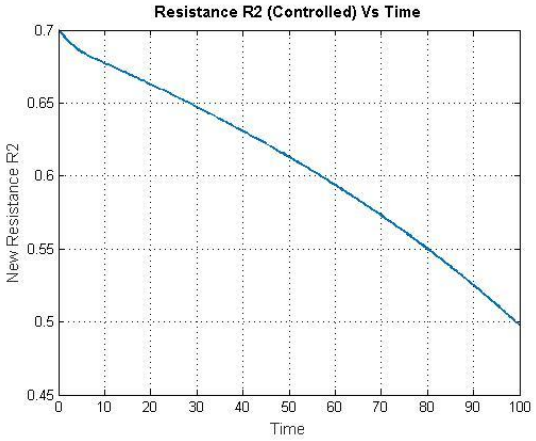

Fig. 13. Control Action (R2), energy optimization in L2

From the above results it can be concluded that when only minimizing power consumption, the response system to the

reference, whose value is 10, is severely affected. The effect is observed in the ITAE.

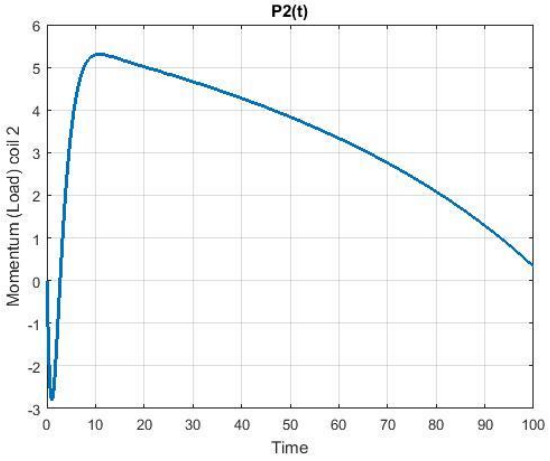

Fig. 14. Response of the momentum P2 in L2

To make the system response does not deviate from the desired reference, the problem will be considered with two goals, the first one, minimizing the energy consumed by the coil 2 and the second one, minimizing the ITAE.

Since finding a single point of Pareto Frontier is the new purpose, the problem is treated as a mono-objective problem with one restriction, specified by equation 17.

$$ITAE \leq W * ITAEREF \tag{17}$$

Where:
ITAEREF is the minimum value of ITAE found for this objective function, whose approximate value is 1.436e2, and W is a weight to moving through the Pareto frontier. With that weight, a more or less priority to the objective of minimizing the ITAE is given.

In the MAGO algorithm this restriction is handled as a penalty function in the objective function, if the restriction is violated, as in equation 18. This penalizes those furthest values from the optimum.

$$Fobj = Fobj + (ITAE - W * ITAEREF)^2 \tag{18}$$

Table 7 presents the different results on several values of W.

Table 7. Energy Optimization in L2 considering ITAE

W	Energy in Coil	Total Energy
0.5	1,102E+03	3,905E+06
1	1,101E+03	3,839E+06
1.5	1,087E+03	3,960E+06
3	1,074E+03	4,081E+06
4.5	1,068E+03	4,009E+06
4.6	1,068E+03	3,943E+06
4.7	1,067E+03	3,943E+06
4.8	1,067E+03	4,007E+06
5	1,448E+03	4,505E+06
6	1,488+03	4,580+06

Table 8 shows the total results for the best weight value, which is W = 4.7

Table 8. Energy Optimization in L2 considering ITAE, W=4.7, best case.

Energy	Units of Energy
Energy in Coil	1,067E+03
Total Energy	3,943E+06
ITAE	6,411E+02
Kp	9,993E-01
Ki	2,804E-01
Kd	0,919E-01

In Figures 15 and 16 the control action and the P2 response on the coil are shown.

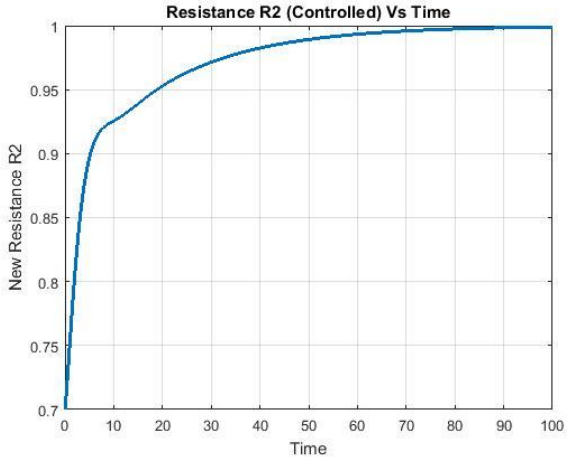

Fig. 15. Control Action (R2), energy optimization with ITAE in L2

From tables and graphs it can be concluded that a reduction in consumed energy by the element L2 is obtained with respect to the ITAE optimization. Further, the response system satisfies adequately the reference.

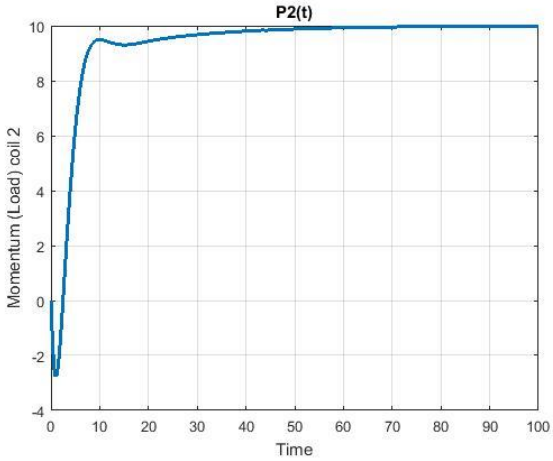

Fig. 16. Response of energy (momentum P2) in L2 and ITAE (reference = 10) in L2.

5. CONCLUSIONS

It is possible to modify the energy consumption of an engineering system applying advanced optimization algorithms and using PID controllers, so that such consumption is minimal and in turn the system meets a desired behavior.

The proposed method first was applied to achieve energy savings in the transitory state of the system. Therefore, in processes where consumption in the transitory state is greater, energy savings will also be higher.

The method was also successful when it is applied to achieve a desired behavior and in turn minimizing energy consumption. With a broader sensitivity analysis, better energy savings for the established control conditions can be found.

The proposed method is independent of the energy domain of the engineering system. Here it was applied to mechanical and electrical system engineering cases. Its extension to mechatronic or multidomain systems, by Bond Graph modeling, is elementary.

Among the experiments, it was apparent that it is possible to minimize energy consumption or increase energy efficiency of the system, including additional elements. A possible future work is to find both the optimal location and the best element that minimize energy consumption and maximize the system efficiency while simultaneously the given conditions are met.

Including sustainability as one of the criteria for tuning controllers adds more value to the organization from the financial, producing savings from planning, gaining control engineering greater recognition, generating lower risks and better environmental and social performance.

Extending the control of sustainable industrial systems throughout the lifecycle of the process or product, in addition to meeting the nominal production conditions, is an option to facilitate the assessment of the water footprint, carbon footprint and energy footprint, compliance with current regulations and becomes an excellent complement to the traditional indicators of projects.

ACKNOWLEDGEMENTS

The participation of Kevin J. Berrio Castro was partially sponsored by the Project 645 - Young Researchers 2015, from COLCIENCIAS.

REFERENCES

CFR - Council on Foreign Relations (1987) Brundtland Report. http://www.cfr.org/economic-development/report-world-commission-environment-development-our-common-future-brundtland-report/p26349 Retrieved: May 30, 2015, 13:46

Borutzky, W. (Ed.). (2011). Bond Graph Modelling of Engineering Systems. New York, NY: Springer New York. http://doi.org/10.1007/978-1-4419-9368-7.

Breedveld, P. C. (1985). Multibond graph elements in physical systems theory. Journal of the Franklin Institute, 319(1-2), 1–36. http://doi.org/10.1016/0016-0032(85)90062-6.

Hernández, J. A., & Ospina, J. D. (2010). A multi dynamics algorithm for global optimization. Mathematical and Computer Modelling, 52(7-8), 1271–1278. http://doi.org/10.1016/j.mcm.2010.03.024

Karnopp, D., Margolis, D., & Rosenberg, R. (2006). System Dynamics. (John Wiley and Songs, Ed.). New Jersey.

Mukherjee, A., Karmakar, R., & Samantaray, A. (2006). Bond Graph in Modeling, Simulation and Fault Identification. (I. K. International Publishing, Ed.). New Delhi

Pareja, R., & Parra, L. (2014). Eficiencia Energética: Herramienta para la sostenibilidad (1st ed.). Colombia.

Paynter Henry. "An epistemic prehistory of Bond Graphs". En P. Breedveldand G. Dauphin-Tanguy, Eds., Bond Graphs for Engineers. Amsterdam. North-Holland.

Pérez, J. L., & Meza, V. S. (2013). Los procesos industriales sostenibles y su contribución en la prevención de problemas ambientales. *Industrial Data*, *16*(1).

Vera Álvarez, C., & Caballero Ocaña, M. (2008). Introduccion a La Tecnica De Bond Graph En La Dinamica Ferroviaria. Ferroviaria'9R, 291–308. Retrieved from http://ruc.udc.es/bitstream/2183/10640/1/CC41 art 28.pdf.

WBG - World Bank Group. (2011). International Finance Corporation, The business case for sustainability. http://www.ifc.org/wps/wcm/connect/topics_ext_content/ifc_external_corporate_site/ifc+sustainability/learning+and+adapting/knowledge+products/publications/publications_brochure_businesscaseforsustainability Retrieved: May 30, 2015. 13:00.

Modeling and Event-Driven Simulation of a Photovoltaic System Controlled with Two Configurations of Perturb & Observe Maximum Power Point Tracking

Guillermo Gallo, Juan Ruiz, Mario Bolaños, Gustavo Osorio, Fabiola Angulo

Universidad Nacional de Colombia. Man, izales, Colombia (e-mail: ggalloh@unal.edu.co, jaruizt@unal.edu.co, mabolanosn@unal.edu.co, gaosoriol@unal.edu.co, fangulog@unal.edu.co)

AbstractIn this article, we have modeled and simulated a photovoltaic (PV) System in order to compare two different approaches of Maximum Power Point Tracking (MPPT) control structures. Firstly, we analysed the system controlled with Perturb & Observe MPPT directly applied to the duty cycle and the necessary simulations were performed and compared with the experimental results. Secondly, we coupled an average current mode control structure to the MPPT, improving the settling time and reducing the steady-state oscillations. Finally, we presented the resulting conclusions.

Keywords: Solar Energy, Piecewise Linear Analysis, Average Current Control Mode, DC/DC Power Converters, Maximum Power Point Tracking.

1. INTRODUCTION

Photovoltaic (PV) energy is a locally available renewable resource with a lower carbon footprint which becomes essential due to the environmental impacts caused by the growing use of the conventional fossil fuels. In addition, recent efforts seek to make this kind of energy more feasible through the improvement of the system components efficiency and the implementation of governmental policies to encourage its use. For instance, the solar PV global capacity has increased from 16 GW in 2008 to 177 GW in 2014, (REN21 (2015)), and its study has become more attractive to researches of different fields.

The photovoltaic system is mainly composed by the elements shown in figure 1. The PV source transforms sunlight directly into electricity and its behavior shows a nonlinear characteristic with a maximum power point (MPP) described by the current-voltage (I-V) curve and the power-voltage (P-V) curve, (Sera et al. (2007); Tian et al. (2012); Barth et al. (2016)). The MPP is constantly changing according to the connected load and the environmental conditions, hence it is necessary to adopt an intermediate stage between the PV source and the load, known as an Maximum power point tracking (MPPT) system. This guarantees constant power and the highest energy harvesting possible. The load may be represented by a resistance in the case of a non regulated DC bus. It can also be represented by a constant voltage load, in the case of a regulated DC bus or a battery, (Chiang et al. (2009); Farahat et al. (2012)).

The MPPT system is composed mainly of a DC-DC converter, (Erickson and Maksimovic (2001); Rashid (2004)), controlled by an MPPT algorithm, (Verma et al. (2016);

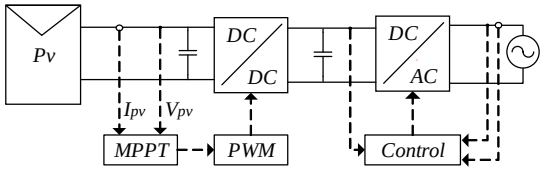

Figure 1. Photovoltaic system control

de Brito et al. (2013)), which is capable of matching the electrical characteristics of the connected load to the MPP characteristics located in the P-V curve. There are some works in the literature where the MPPT algorithm directly affects the duty cycle of the converter, (E. Koutroulis and Voulgaris (2001); N. Femia and Vitelli (2004)). This kind of systems presents an inadequate voltage or current regulation. In consequence the converter presents an increased switching stress and losses, (Villalva et al. (2010)). Other works in the literature present MPPT systems accompanied by control structures that improve the performance of its stationary and transitory responses, (Villalva et al. (2010); Kislovski (1990)). For instance, the presence of a proportional and integral controller can reduce losses and stress, and can improve the settling time of the converter and avoids oscillation and overshoot, (M. G. Villalva and Ruppert (2009)).

In this work, we present a Photovoltaic System controlled with two structures that contains the MPPT technique, Figure 2. Firstly, we analyzed the system controlled with Perturb & Observe MPPT. We performed simulations and compared them with experimental results. Secondly, the MPPT control was coupled with an average current mode control structure. We simulated and compared the results with the first control structure findings. For these tests,

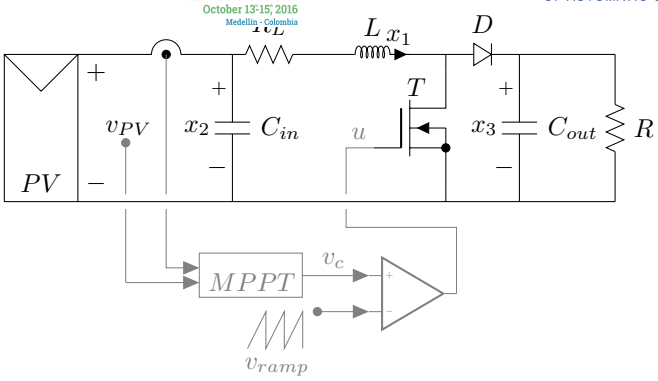

(a) First Control Configuration

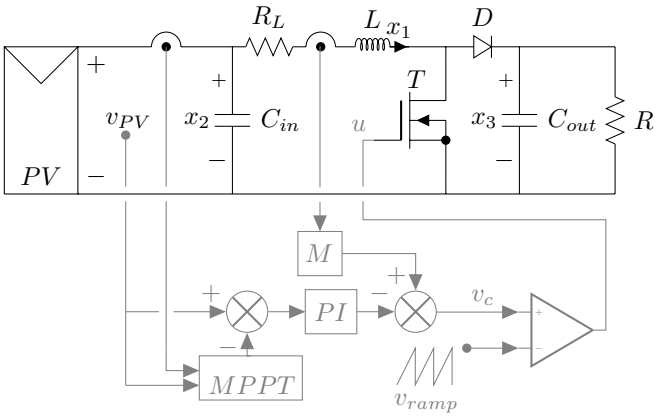

(b) Second Control Configuration

Figure 2. Photovoltaic system with two MPPT control configurations

an event driven simulation based on hybrid systems that include the complete PV source dynamics is proposed. The hybrid systems combine the structures of differential equations systems with discrete maps, (V. Acary and Brogliato (2011)). This kind of approach may present sliding dynamics, known also as Filippov systems, (Filippov (1988)), that introduce simulation issues,(Gallo et al. (2012)). In order to solve this problem, the equations that describe the sliding zones are found and considered in the modeling of the system.

This paper is organized as follows. In section II, we present a brief description of Perturb & Observe Maximum Power Point Tracking. In section III, we present the modeling and identification of the panel and the hybrid model of the whole system for each control configuration. In section IV we present numerical and experimental results and the comparison between the two control configurations. In section V, we present the corresponding conclusions.

2. PERTURB & OBSERVE MAXIMUM POWER POINT TRACKING

Solar panels are formed by arrays of solar cells, which convert radiation from the sun into useful electricity. Each cell has only one point of operation in which the power supplied is maximum, and it depends on external factors such as temperature, radiation and the load. The maximum power point tracking or MPPT is done by varying the value of the load so that the photovoltaic system can deliver the maximum possible power. Load variations are controlled by a DC-DC power converter, which has the characteristic of increasing or reducing the resistance sustained at the panel terminals, by modifying the duty cycle.

Tracking the maximum power point means a breakthrough in improving the efficiency of photovoltaic systems. Several tested methods exists in the literature, however one of the most widely used algorithms is the Perturb and Observe (P & O), thanks to its performance and simplicity. This algorithm is based on perturbing a control parameter by small steps and observing the changes of the power, forcing the system to iterate around the maximum power point.

The fundamental principle of the control strategy is to obtain the digital PWM signal through continuous iteration of the duty cycle around an operation point. The algorithm starts by taking note of voltage v_{PV} and current i_{PV} at the terminals of the PV panel in order to calculate the power delivered by the source. After perturbing the duty cycle, it is necessary to measure the power again. If the system power increases, the MPPT algorithm perturbs the duty cycle in the same direction. Otherwise the perturbation is in the opposite direction.

The systems considered in this work are shown in Figure 2. They consist of two photovoltaic MPPT systems based on a boost converter structure, that feeds a resistive load. The PV systems exhibits a high nonlinear complexity due to the characteristics of the PV source and the nonlinear elements such as the semiconductors in the DC-DC converter. Therefore, its modeling and simulation may result in a challenging problem. For instance, different approaches have been proposed in the literature such as the linearization of the PV system and the simplification of the PV module in a constant voltage or a constant current source, (Villalva et al. (2010); Urtasun et al. (2013); Espinoza-Trejo et al. (2015); Xiao et al. (2007)). However, in order to have a deeper understanding of the system, a modeling approach that includes not only the complete dynamics of the PV source, but also the high frequency components of the DC-DC converter should be taken into account.

2.1 Photovoltaic source modeling

A photovoltaic panel can be mathematically modeled by theoretical equations based on an equivalent circuit. There are different models that vary in complexity and precision. In order to describe the electrical behavior of the PV source, the five parameters model of Figure 3, was used. This model is the most widely used in the literature, (Villalva et al. (2009); Aoun et al. (2014)), where a current source is used to model the incident radiation, the diode models the polarization phenomenon and the resistances R_s and R_p represent the power losses by connections in series and in parallel.

The mathematical equation that describes the model of the 5 parameters is given by the equation 1.

$$I_{PV} = I_{ph} - I_s(e^{\frac{V_{PV}+I_{PV}R_s}{N_s a V_T}} - 1) - \frac{V_{PV} + I_{pv}R_s}{R_p}, \quad (1)$$

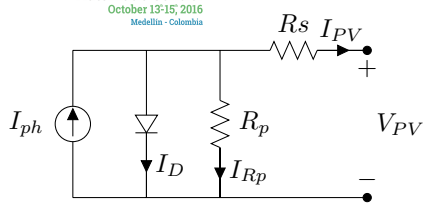

Figure 3. Five Parameters Model

where:

I_{PV}	Current at the terminals of the panel.
I_{ph}	Photogenerated current.
V_{PV}	Voltage at the terminals of the panel.
R_s	Equivalent series resistance.
R_p	Equivalent parallel resistance.
I_s	Saturation current of the diode.
a	Diode ideality factor.
N_s	Number of cells connected in series.
V_T	Thermal diode voltage (kT/q).

The equation 1 is mathematical implicit and it is usually solved using numerical methods, such as Newton Raphson. However, in simulation, this approach may lead to longer simulation times and convergence problems. Therefore, it was necessary to express the equation 1 in a explicit way, using the Lambert W approach, (Efstratios I. Batzelis and Papathanassiou (2014)).

The photovoltaic arrays do not exhibit a linear relationship $V-I$, and parameters such as parasitic resistances R_p and R_s need to be adjusted with experimental data or with special devices because most commercial panels do not provide this information. In (Villalva et al. (2009)) the parameters of the R_p and R_s are calculated from an iterative process that adjusts the $V-I$ curve with the basic data provided by the manufacturer, such as short circuit current, open voltage, current and voltage at the maximum power point and maximum power. In this way it is possible to estimate the parameters for a reliable model of the solar panel without resorting to specialized measuring devices. We used the solar panel SYK50-18M. Table 1 shows its characteristic data at standard test conditions; temperature of $25°C$ and radiation of $1000W/m^2$.

Table 1. Parameters for a solar panel SYK50-18M.

Behavior under standard conditions	STD
Power at the maximum power point (Pmax)	50 W
Open circuit voltage (Voc)	22.24 V
Voltage at maximum power point (Vmpp)	18 V
Short circuit current (Isc)	3.06 A
Current at maximum power point (Impp)	2.78 A
TC I_{sc}	$0.034\%/°K$
TC U_c	$-0.34\%/°K$
Cell number Ns	36
Diode ideality factor a	1.3
Parallel resistance R_p	454.9310 Ω
Series resistance R_s	0.2660 Ω

The graphs in Figure 4 were simulated with parameters R_p and R_s obtained as is shown in (Villalva et al. (2009)). In graphics 4(a) and 4(b) shown V-I and V-P curves respectively for a variant radiation and graphic 4(c) and 4(d) the behavior of the source under temperature variations.

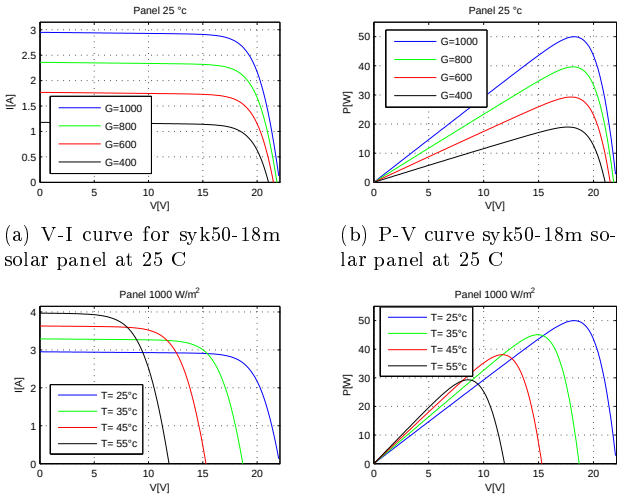

(a) V-I curve for syk50-18m solar panel at 25 C

(b) P-V curve syk50-18m solar panel at 25 C

(c) I-V curve syk50-18m solar panel at 1000 W/m^2

(d) P-V curve syk50-18m solar panel at 1000 W/m^2

Figure 4. Voltage vs. current and voltage vs. power delivered by a photovoltaic panel. Variation in $(a)(b)$ radiation and $(c)(d)$ temperature.

2.2 Hybrid system modeling

Both systems of Figure 2 present three configurations or states depending of the values (ON, OFF) of the diode and the transistor, Table 2.2.

Table 2. State Transition Table

State	T	D
S_1	ON	OFF
S_2	OFF	ON
S_3	OFF	OFF

Figure 5 depicts the three circuit configurations of both solar systems.

The whole system can be expressed as:

$$\dot{x} = A_i x + B \tag{2}$$

where $i \in \{1, 2, 3\}$. The A and B matrices are different for each control structure.

First Control Structure This systems is of third order and its A and B matrices are defined as follows:

$$A_1 = \begin{bmatrix} -\frac{R_L}{L} & \frac{1}{L} & 0 \\ -\frac{1}{C_{in}} & 0 & 0 \\ 0 & 0 & -\frac{1}{RC_{out}} \end{bmatrix} \tag{3}$$

$$A_2 = \begin{bmatrix} -\frac{R}{L} & \frac{1}{L} & -\frac{1}{L} \\ -\frac{1}{C_{in}} & 0 & 0 \\ \frac{1}{C_{out}} & 0 & -\frac{1}{RC_{out}} \end{bmatrix} \tag{4}$$

$$A_3 = \begin{bmatrix} 0 & 0 & 0 \\ 0 & 0 & 0 \\ 0 & 0 & -\frac{1}{RC_{out}} \end{bmatrix} \tag{5}$$

$$B = \begin{bmatrix} 0 \\ \frac{f(x_2)}{C_{in}} \\ 0 \end{bmatrix} \tag{6}$$

where $f(x_2)$ is the explicit solution of the equation 1 using the Lambert W approximation, (Efstratios I. Batzelis and

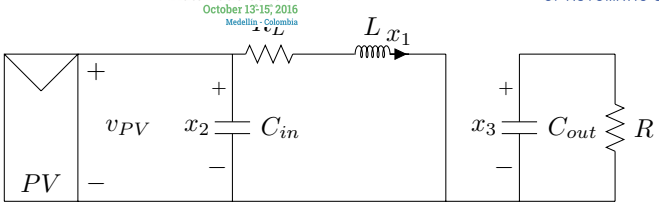

(a) State 1. $T = ON$, $D = OFF$

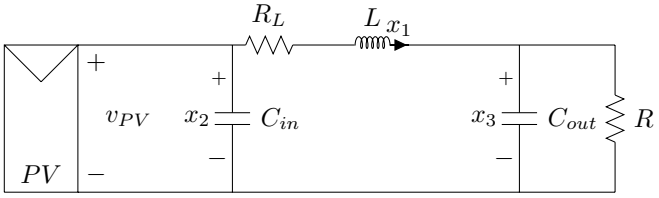

(b) State 2. $T = OFF$, $D = ON$

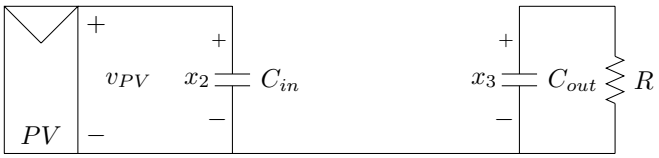

(c) State 3. $T = OFF$, $D = OFF$

Figure 5. Circuits configurations

Papathanassiou (2014)). $f(x_2)$ gives the value of the panel current (I_{PV}) for an input voltage, x_2. The whole system may be represented by the hybrid automata in Figure 6. In this automata the states s_i are associated to the matrices A_i and B_i. The conditions of transition are defined as: $c_{1,2} : u = 0$; $c_{2,1} : u = 1$; $c_{2,3} : x_1 = 0$; $c_{3,1} : u = 1$.

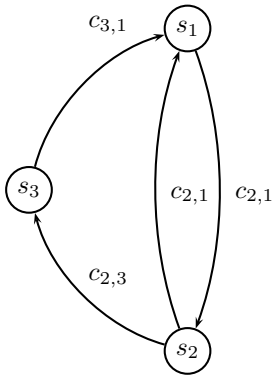

Figure 6. Hybrid Automaton

The variable u is defined as follows:

$$u = \begin{cases} 1 \ if \ v_c \geq v_{ramp} \\ 0 \ if \ v_c < v_{ramp} \end{cases} \tag{7}$$

v_c is the duty cycle and it is calculated by the MPPT algorithm.

Second Control Structure In this case, we add a new state variable (x_4) corresponding to the integral of the error. A and B are defined as follows:

$$A_1 = \begin{bmatrix} -\frac{R_L}{L} & \frac{1}{L} & 0 & 0 \\ -\frac{1}{C_{in}} & 0 & 0 & 0 \\ 0 & 0 & -\frac{1}{RC_{out}} & 0 \\ 0 & 1 & 0 & 0 \end{bmatrix} \tag{8}$$

$$A_2 = \begin{bmatrix} -\frac{R}{L} & \frac{1}{L} & -\frac{1}{L} & 0 \\ -\frac{1}{C_{in}} & 0 & 0 & 0 \\ \frac{1}{C_{out}} & 0 & -\frac{1}{RC_{out}} & 0 \\ 0 & 1 & 0 & 0 \end{bmatrix} \tag{9}$$

$$A_3 = \begin{bmatrix} 0 & 0 & 0 & 0 \\ 0 & 0 & 0 & 0 \\ 0 & 0 & -\frac{1}{RC_{out}} & 0 \\ 0 & 1 & 0 & 0 \end{bmatrix} \tag{10}$$

$$B = \begin{bmatrix} 0 \\ \frac{f(x_2)}{C_{in}} \\ 0 \\ -V_{ref} \end{bmatrix} \tag{11}$$

This system can be represented by the hybrid automata in Figure 6. The states s_i are associated with the matrices A_i and B_i. The conditions of transition are the same as the previous system. Furthermore, the variable u is defined by the equation 7. v_c is defined as:

$$v_c = k_p \left(x_2 - V_{ref}\right) + k_p k_i x_4 - M x_1 \tag{12}$$

In this system a sliding dynamic appears. This dynamic is defined by the states s_1 and s_2. The transition between this states is defined by control variable v_c and the ramp signal v_{ramp}. When the signal control is over the ramp signal, the DC-DC converter works in the state 1 (s_1). In other case, the DC-DC converter works in the state 2 (s_2). There are some parameters values that forces the v_c signal to slide on the ramp signal. This behaviour can block an event-driven simulation, (V. Acary and Brogliato (2011)). To overcome this drawback, a Filippov regularization was used to formulate a new field that flows onto the ramp, (Filippov (1988)).

3. NUMERICAL AND EXPERIMENTAL RESULTS

This section shows the simulation results compared to the ones obtained experimentally for the first control structure. It also compares the response to perturbations between the control structures. Two main tests show the validity of the operation of the method P&O. The first is a sweep by varying the duty cycle of the PWM $0\% - 100\%$, in order to observe what percentage of the cycle is at the maximum power point (MPP). The second test verifies that the algorithm finds the MPP and stays near to this point.

Table 3. Desing parameters

In Capacitor C_1	100 μ F
Out Capacitor C_2	220 μ F
Inductor H	0.020 H
Sampling frequency F_s	1 KHz
Perturbation $\triangle$ en P&O	0.1

Simulations and experimental results were obtained by using the design parameters shown in Table 3. In Figure 7 and 8 a duty cycle sweep is performed from 0 % - 100 %, the signal is represented by $\text{Reference}_{\text{PWM}}$, which moves of 0-10, 10 being the 100 % of D. A very good

mulated data and the data acquired experimentally is observed. There is a more pronounced ripple in Figure 8, because the acquisition card has an input filter that ensures the digital control and also the number of plotted points is much smaller.

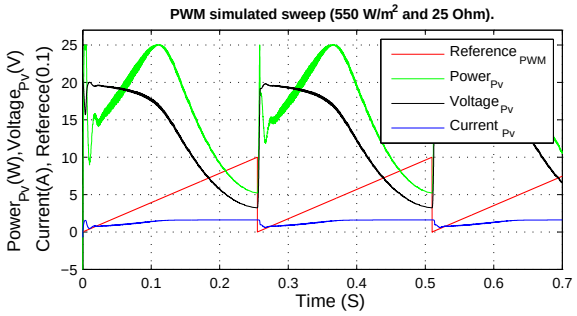

Figure 7. PWM simulated sweep.

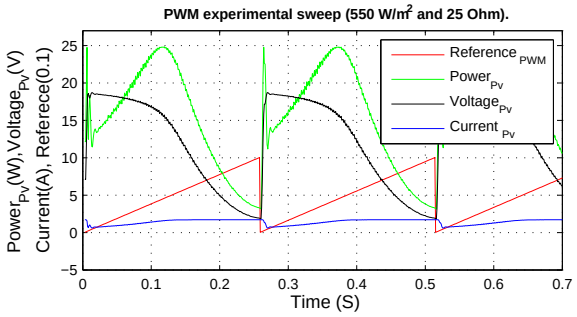

Figure 8. PWM experimental sweep.

Figures 9 and 10 show how the MPPT algorithm achieves the maximum power point in simulation and experimentally. The arrival times at MPP are very close and the differences lie in the impossibility to maintain a constant radiation and temperature, because the test took place under atmospheric conditions.

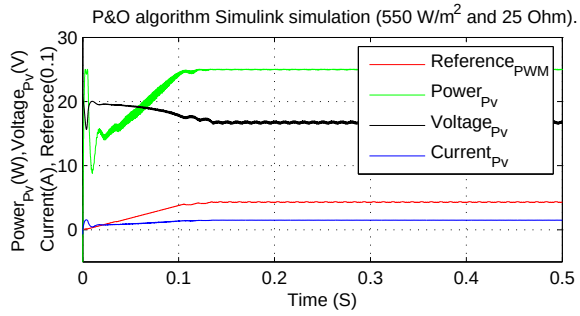

Figure 9. Perturb and observe simulated algorithm.

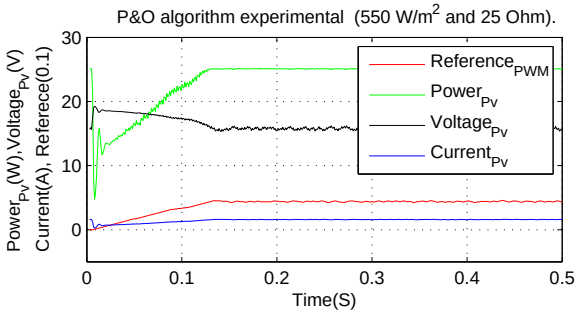

Figure 10. Perturb and observe experimental algorithm.

Figure 11 shows a zoom of the duty cycle signal. The values vary periodically around the MPP, even though the graphics vary somewhat, they show that the period has an equal number of steps.

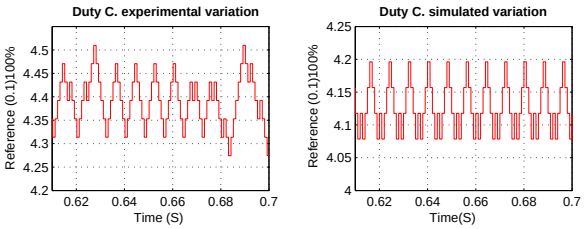

(a) a (b) b

Figure 11. Zoom in PWM signal (a) experimental and (b) simulated.

Tests with other radiation levels are also depicted, for example in Figure 12 a maximum power point tracking for a radiation of approximately $390W/m^2$ and a load 50Ω are shown.

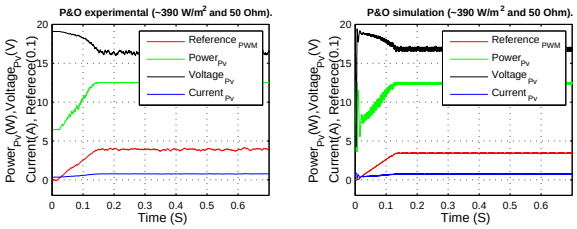

(a) (b)

Figure 12. Results (a) experimental and (b) simulation for radiation of approximately $390W/m^2$ and 50Ω

For the second control structure we used the same parameters as the first. The parameters of the PI controller are defined as: $k_p = 0.5$, $k_i = 100$, $M = 2$. Figure 13 shows the response to perturbations in the two control structures, where the second control structure presents better settling times and lower steady-state oscillations.

4. CONCLUSION

In this work, simulation and experimental results of a photovoltaic system conformed by a solar source, a boost power converter, a Perturb and Observe algorithm and a purely resistive load are presented. The system was controlled with two MPPT structures. The first structure

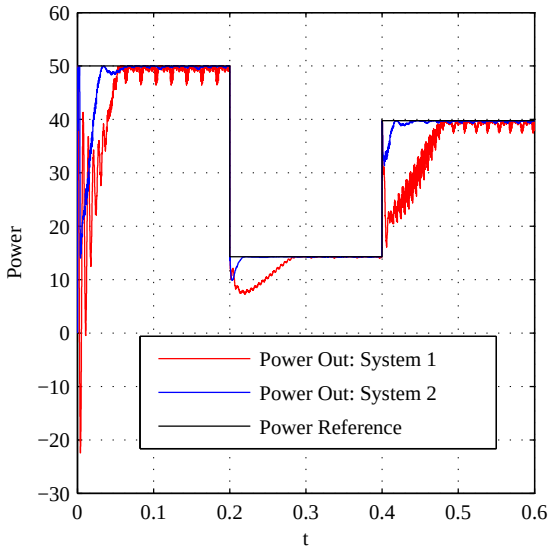

(a) Response to disturbances

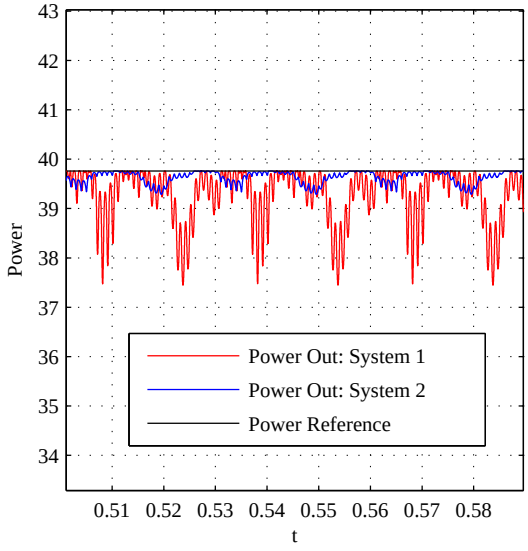

(b) Zoom

Figure 13. Comparison between the two control techniques

acts directly on the duty cycle of the converter. In the second structure, the MPPT control is coupled with an average current mode control structure. The last structure improves the settling time and the steady-state oscillations of the converter.

ACKNOWLEDGEMENTS

Research supported by COLCIENCIAS. Project: "Análisis de la eficiencia de convertidores electrónicos de potencia en aplicaciones de generación de energía eléctrica, a partir de fuentes no convencionales".

REFERENCES

Aoun, N., Chenni, R., Nahman, B., and Bouchouicha, K. (2014). Evaluation and Validation of Equivalent Five-Parameter Model Performance for Photovoltaic Panels Using Only Reference Data. (September), 235–245.

Barth, N., Jovanovic, R., Ahzi, S., and Khaleel, M.A. (2016). {PV} panel single and double diode models: Optimization of the parameters and temperature dependence. *Solar Energy Materials and Solar Cells*, 148, 87 – 98. doi:http://dx.doi.org/10.1016/j.solmat.2015.09.003. Solar Cells and Storage.

Chiang, S.J., Shieh, H.J., and Chen, M.C. (2009). Modeling and control of pv charger system with sepic converter. *IEEE Transactions on Industrial Electronics*, 56(11), 4344–4353. doi:10.1109/TIE.2008.2005144.

de Brito, M., Galotto, L., Sampaio, L., de Azevedo e Melo, G., and Canesin, C. (2013). Evaluation of the main mppt techniques for photovoltaic applications. *Industrial Electronics, IEEE Transactions on*, 60(3), 1156–1167. doi:10.1109/TIE.2012.2198036.

E. Koutroulis, K.K. and Voulgaris, N.C. (2001). Development of a microcontroller-based, photovoltaic maximum power point tracking control system. *IEEE Trans. Power Electron*, 46–54.

Efstratios I. Batzelis, I.A.R. and Papathanassiou, S.A. (2014). An explicit pv string model based on the lambert function and simplified mpp expressions for operation under partial shading. *IEEE Transactions on Suntainable Energy*, 5.

Erickson, R. and Maksimovic, D. (2001). *Fundamentals of Power Electronics*. Power electronics. Springer US.

Espinoza-Trejo, D.R., Bárcenas-Bárcenas, E., Campos-Delgado, D.U., and Angelo, C.H.D. (2015). Voltage-oriented input #x2013;output linearization controller as maximum power point tracking technique for photovoltaic systems. *IEEE Transactions on Industrial Electronics*, 62(6), 3499–3507. doi: 10.1109/TIE.2014.2369456.

Farahat, M., Metwally, H., and Mohamed, A.A.E. (2012). Optimal choice and design of different topologies of dc–dc converter used in {PV} systems, at different climatic conditions in egypt. *Renewable Energy*, 43, 393 – 402. doi: http://dx.doi.org/10.1016/j.renene.2011.10.021.

Filippov, A.F. (1988). *Differential equations with discontinuous rigth-side (1960-russian)*. Kluwer Academic Publishers.

Gallo, G., Osorio, G., and Olivar, G. (2012). Event-driven simulation of filippov systems: The case of a nonlinear wien bridge oscillator. In *Circuits and Systems (LASCAS), 2012 IEEE Third Latin American Symposium on*, 1–4. doi:10.1109/LASCAS.2012.6180299.

Kislovski, A.S. (1990). Dynamic behavior of a constant-frequency buck converter power cell in a photovoltaic battery charger with a maximum power tracker. *Tenth Brazilian Power Electronics Conf.*

M. G. Villalva, J.R.G. and Ruppert, E.F. (2009). Analysis and simulation of the p&o mppt algorithm using a linearized photovoltaic array model. *Tenth Brazilian Power Electronics Conf.*

N. Femia, G. Petrone, G.S. and Vitelli, M. (2004). Optimizing duty-cycle perturbation of P&O MPPT technique. *Electronics Specialists Conf*, 3(5), 1198–1208.

Rashid, M. (2004). *Power Electronics: Circuits, Devices, and Applications*. Pearson/Prentice Hall.

I s 2015 global status report. Technical report.

Sera, D., Teodorescu, R., and Rodriguez, P. (2007). PV panel model based on datasheet values. *IEEE International Symposium on Industrial Electronics*, (4), 2392–2396. doi:10.1109/ISIE.2007.4374981.

Tian, H., Mancilla-David, F., Ellis, K., Muljadi, E., and Jenkins, P. (2012). A cell-to-module-to-array detailed model for photovoltaic panels. *Solar Energy*, 86(9), 2695 – 2706. doi: http://dx.doi.org/10.1016/j.solener.2012.06.004.

Urtasun, A., Sanchis, P., and Marroyo, L. (2013). Adaptive voltage control of the dc/dc boost stage in pv converters with small input capacitor. *IEEE Transactions on Power Electronics*, 28(11), 5038–5048. doi: 10.1109/TPEL.2013.2240702.

V. Acary, O.B. and Brogliato, B. (2011). *Nonsmooth Modelind and Simulation for Switched Circuits*. Springer.

Verma, D., Nema, S., Shandilya, A., and Dash, S.K. (2016). Maximum power point tracking (mppt) techniques: Recapitulation in solar photovoltaic systems. *Renewable and Sustainable Energy Reviews*, 54, 1018 – 1034. doi:http://dx.doi.org/10.1016/j.rser.2015.10.068.

Villalva, M.G., Siqueira, T.G.D., and Ruppert, E. (2010). Voltage regulation of photovoltaic arrays: small-signal analysis and control design. *IET Power Electronics*, 3(6), 869–880. doi:10.1049/iet-pel.2008.0344.

Villalva, M., Gazoli, J., and Filho, E. (2009). Comprehensive Approach to Modeling and Simulation of Photovoltaic Arrays. *IEEE Transactions on Power Electronics*, 24(5), 1198–1208. doi:10.1109/TPEL.2009.2013862.

Xiao, W., Dunford, W.G., Palmer, P.R., and Capel, A. (2007). Regulation of photovoltaic voltage. *IEEE Transactions on Industrial Electronics*, 54(3), 1365–1374. doi:10.1109/TIE.2007.893059.

Neural Control for Photovoltaic Panel Maximum Power Point Tracking

Martin J. Loza-Lopez * **T.B. Lopez-Garcia** *
Riemann Ruiz-Cruz ** **Edgar N. Sanchez** *

* *Centro de Investigación y Estudios Avanzados del IPN, Zapopan, Jal 45030 México, (e-mail: {mdloza,tblopez,sanchez}@ gdl.cinvestav.mx)*
** *ITESO University, Periferico Sur Gomez Morin 8585, Tlaquepaque, Jalisco, México C.P. 45604 ,(e-mail: riemannruiz@iteso.mx)*

Abstract: With the rise in the use of renewable energies, solar panels have proven to be reliable and have a favorable cost-benefit ratio, producing energy free of noise and air pollution. Solar panels are subject to considerable variations in working conditions due to changes in solar irradiation levels and temperature, that affect its semiconductor properties. To be able to profit as much as possible from this source of energy, control of the modules and perturbation rejection is very important to obtain the highest viable amount of electrical power. This work is concerned with the on-line identification and control of a photovoltaic system using neural networks. Having on-line identification and control allow the system to be more adaptable to changes in weather and other variations than with common off-line methods.

Keywords: Photovoltaic systems, solar energy, high order neural networks, Kalman filter, maximum power point tracking.

1. INTRODUCTION

This work is concerned with the application of recurrent high order neural networks to design a robust photovoltaic panel model and to control the output voltage of the panel (V_{PV}) to obtain the maximum power available.

It is important to understand the impact that different uncertainties and parameter variations have on the mathematical model of solar panels, since their parameters are so dependent on weather conditions. In the field of neural networks there are several studies that focus on the characterization and modeling of solar panels based on artificial intelligence, as can be seen in Hadjab et al. (2012). Another popular use of artificial neural networks is that of designing maximum power point trackers for solar photovoltaic (SPV) modules, as can be observed in Zhang and Bai (2005), Ramaprabha et al. (2011) and Alabedin et al. (2011). The methods applied in these studies are fuzzy logic controllers, genetic algorithms, and radial basis functions; and they are usually off-line methods.

In order to solve the problem of time-varying parameters and uncertainties, in this paper the on-line identification and control is proposed. The maximum power point (MPPT) is obtained by means of a searching algorithm; then the system is controlled to track the MPPT using a neural network to identify the model on-line. Then a controller which regulates the switching frequency of an insulated-gate bipolar transistor (IGBT) in the DC-DC buck converter, based on the identified model, is developed.

The advantage of this method is that the model is not greatly affected by the high frequency noise created by the IGBT and other perturbations, and so it is possible to reduce the use of filters. A conventional maximum power point tracker *perturb and observe* is used to find the output voltage of the solar panel (V_{PV}) necessary to have the maximum electrical power.

This paper is organized as follows. In section 2, mathematical preliminaries are given, including a review of photovoltaic systems, neural networks and the Kalman filter. In section 3, the neural control is presented, starting with the model of the DC-DC buck converter, and continuing with the identification and control design. In section 4, the results are validated using Simulink's Simscape Power Systems Blocks [1], and a comparison of the neural controller developed with a discrete sliding modes controller is shown. Finally, in section 5, the conclusions are presented.

2. MATHEMATICAL PRELIMINARIES

2.1 MPPT algorithm applied to photovoltaic systems

Photovoltaic systems use solar cells to capture solar energy and convert it into electricity. These systems are generally made from modified silicon and other semiconductor materials, they are usually long lasting (25 to 30 years); with the advance of technology there has been a rise in variety of manufacturers and models available, for a lower price.

Solar panels can me modeled using an equivalent circuit which consists of a current source I_{cc} (whose value in amperes depends on the irradiance at the moment of measurement), a diode for discharge, and two resistors; one of them represents losses due to bad connections (R_s)

[1] Simulink/Simscape Power Systems are trademarks of The MathWorks, Inc.

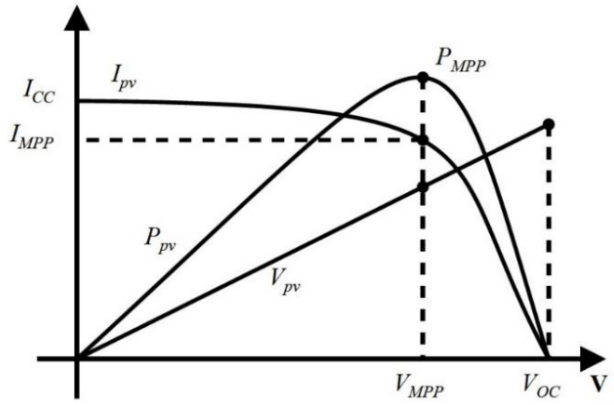

Fig. 1. VI graph of solar panel

and the other represents the leakage current from the capacitor (R_{sh}). The equation that defines the behavior of said equivalent model is (Cubas et al., 2014):

$$I_{PV} = I_{cc} - I_o(e^{\frac{q(V_{PV}+I_{PV}R_s)}{nkT}} - 1) - \frac{V_{PV}+I_{PV}R_s}{R_{sh}} \quad (1)$$

where k is the Boltzman constant, T is the absolute temperature in the photovoltaic panel, I_o is the inverse saturation current of the diode, q is the charge of the electron, n is the ideality factor of the diode.

From (1), it is clear that there exists a relationship between the voltage and the current in the photovoltaic panel. This relationship can be observed in Fig. 1, which shows the existence of a unique maximum power point, P_{MPP}, for each solar panel depending on the temperature and irradiance at the moment of measurement.

To be able to successfully follow the maximum power point of the solar panel, it is necessary to have a reference voltage which corresponds to that point, and to design a controller to track that reference voltage; this is commonly known as a maximum power point tracker (MPPT). In the literature, there are several algorithms that have been developed for this purpose, based on neural networks, incremental conductance, fuzzy logic, etc, (Esram and Chapman, 2007). In this paper, the MPPT algorithm used is known as the *perturb and observe* method which can be implemented in real-time, and it is one of the algorithms most commonly used for this purpose. This algorithm is based on the following criterion: the voltage of the solar panel is perturbed and if for this new value the power obtained has been incremented, then a change in that direction will be spurred; if on the contrary, the new power value has decreased, a new perturbation will be realized in the opposite direction.

The next step is to manipulate the voltage of the panel (V_{PV}) to track the voltage generated by the algorithm (V_{MPP}), this is accomplished by using a DC-DC Buck converter, discussed in section 3, which forces the electrical output power of the solar panel to reach the desired value.

2.2 Recurrent High Order Neural Networks (RHONN)

In the field of neural networks, usually k denotes a sampling step, where $k \in 0 \cup \mathbb{Z}^+$. Also considering the traditional definitions of $|\cdot|$ as the absolute value and $\|\cdot\|$ as an adequate norm for a vector or matrix. Considering a MIMO nonlinear system (Zhang and Bai, 2005):

$$x_{k+1} = F(x_k, u_k) \quad (2)$$
$$y_k = h(x_k) \quad (3)$$

where $x \in \mathbb{R}^n, u \in \mathbb{R}^n \times \mathbb{R}^m \to \mathbb{R}^n$ is a nonlinear map. For (2), u is the input vector, it is chosen as a state feedback function of the state:

$$u_k = h(x_k)$$

Substituting this in (2) to obtain an unforced system:

$$x_{k+1} = F(x_k, h(x_k)) = \tilde{F}(x_k). \quad (4)$$

Defining a discrete-time recurrent high order neural network (Alanis et al., 2007):

$$\hat{x}^i_{k+1} = (w^i)^T z^i(\hat{x}_k, u_k), i = 1, ..., n \quad (5)$$

where $\hat{x}^i$ is the sate of the i-th neuron, n is the state dimension, w^i is the respective on-line adapted weight vector, and $z^i(\hat{x}_k, u_k)$ is given by:

$$z^i(\hat{x}_k, u_k) = [z^{i1}...z^{iL_i}]^T = [\prod_{j\in I_1} \psi_{ij}^{dij(1)} ... \prod_{j\in I_{L1}} \psi_{ij}^{dij(L_1)}]^T \quad (6)$$

where L_i is the respective number of high order connections, $I_1, I_2, ..., I_{L_i}$ is a collection of non-ordered subsets of $1, 2, ..., n$, and ψ_i is given by:

$$\psi_i = [S(\hat{x}_1)...S(\hat{x}_n)u_1...u_m]^T \quad (7)$$

where $S(\cdot)$ is defined as a logistic function.

Assuming that the system (2) is observable, it is approximated by the discrete time RHONN parallel representation (Rovithakis and Christodoulou, 2000) :

$$x^i_{k+1} = (w^{i*})^T z^i(x_k, u_k) + \epsilon^{zi} \quad (8)$$

where x^i is the i-th plant state, ϵ^{zi} is a bounded approximation error, which can be reduced by increasing the number of adjustable weights (Rovithakis and Christodoulou, 2000) .

Assuming that there exists an ideal weight vector w^{i*} such that the norm of the approximation error can be minimized on a compact set $\Omega^{zi} \subset \mathbb{R}^{L_i}$. The ideal weight vector w^{i*} is used only for analysis, assuming that it exists and is an unknown constant (Rovithakis and Christodoulou, 2000) . Defining the estimate of the weight as w_i and the estimation error as:

$$\tilde{w}^i_k = w^{i*} - w^i_k \quad (9)$$

Since w^{i*} is assumed to be a constant, the next expression is true:

$$\tilde{w}^i_{k+1} - \tilde{w}^i_k = w^i_k - w^i_{k+1} \quad (10)$$

2.3 Kalman Filter

The Kalman filter (KF) estimates the state of a linear system with additive state and output white noises (Feldkamp, L.A., Feldkamp, T.M., Prokhorov, 2001; Brown

and Hwang, 1997; Song and Grizzle, 1992) . For KF-based neural network training, the network weights become the states to be estimated. The error between the neural network output and the measured plant output is considered to be additive white noise. Since the neural network mapping is non linear, an extended Kalman filter (EKF) is applied (Sanchez, E. N., Alanis A.Y., 2004) . The goal of the training is to find the optimal weight values that minimize the prediction errors. In this paper, a EKF-based training algorithm is used, described by:

$$\begin{aligned} w_{k+1}^i &= w_k^i + \eta_i K_k^i e_k, i = 1, ..., n \\ K_k^i &= P_k^i H_k^i M_k^i \\ P_{k+1}^i &= P_k^i - K_k^i (H^i)^T P_k^i + Q^i \end{aligned} \tag{11}$$

with:

$$\begin{aligned} M_k^i &= [R^i + (H^i)^T P_k^i H_k^i]^{-1} \\ e_k &= y_k - \hat{y}_k \end{aligned}$$

where $e_k \in \mathbb{R}^p$ is the observation error and $P_k^i \in \mathbb{R}^{L_i \times L_i}$ is the weight estimation error covariance matrix at step k, $w^i \in \mathbb{R}^{L_i}$ is the weight vector, L_i is the respective number of neural network weights, $\hat{y} \in \mathbb{R}^p$ is the neural network output, $y \in \mathbb{R}^p$ is the plant output, n is the number of states, $K^i \in \mathbb{R}^{L_i \times p}$ is the Kalman gain matrix, $Q^i \in \mathbb{R}^{L_i \times L_i}$ is the NN weight estimation noise covariance matrix, $R^i \in \mathbb{R}^{p \times p}$ is the error noise covariance, and finally, $H^i \in \mathbb{R}^{L_i \times p}$ is a matrix, in which each entry is the derivative of the i-th neural output with respect to ij-th NN weight, given as:

$$H_k^{ij} = \left[\frac{\partial \hat{y}_k}{\partial w_k^{ij}} \right]^T \tag{12}$$

where $j = 1, ..., L_i$ and $i = 1, ..., n$. Usually, P^i and Q^i are initialized as diagonal matrices.

The use of EKF algorithms allows for an accurate parameter identification performed on-line. On-line identification using recurrent neural networks using the Kalman filter has been analyzed in different works such as Straub and Schroder (1996) and in Rajesh et al. (2010) where the EKF training algorithm is compared with the maximum likelihood estimation (MLE) and the mean square error algorithms for neural network modeling of a nonlinear system and it was found that EKF is the fastest to converge and has good performance compared to the other algorithms. A similar scheme as the one presented in this paper for identifying a recurrent high order neural network can be seen in Antonio-Toledo et al. (2015), where it is used with neural inverse optimal control for trajectory tracking of a three-phase induction motor. The same strategy for identification is implemented in Ruiz et al. (2012) to control a doubly fed induction generator (DFIG) with block control technique.

3. NEURAL CONTROL DESIGN

3.1 Buck Converter model

The buck converter circuit used has a capacitor at the connection point with the solar panel, as can be seen in Fig. 2, to be able to take V_{PV} as a state.

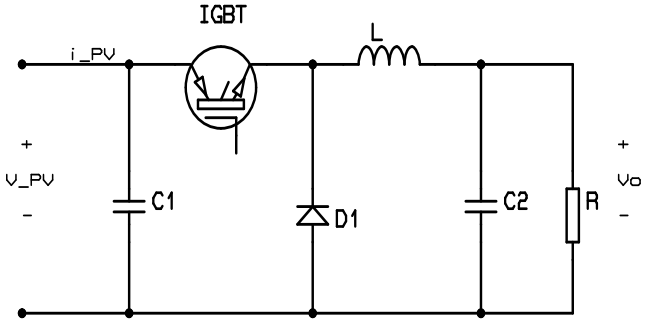

Fig. 2. Buck Model

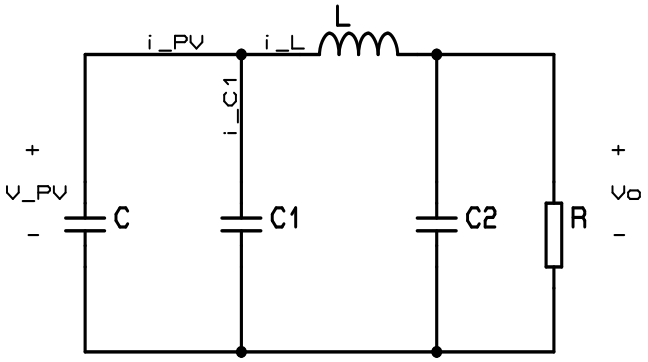

Fig. 3. Buck equivalent circuit with u=1

Three states are taken into account in the model, which are: the voltage given by the solar panel V_{PV}, the voltage at the output load resistor V_o and the current flowing through the inductor i_L.

$$\begin{aligned} x_1 &= V_{PV} \\ x_2 &= V_o \\ x_3 &= i_L \end{aligned}$$

Two models are obtained depending on the state of the IGBT control input, u; afterwards, these are combined into a single state space model, which will be used for the identification.

When the IGBT is in conduction mode ($u = 1$), the equivalent circuit can be seen in Fig. 3. The corresponding state space is defined as:

$$\begin{aligned} \dot{x}_1 &= -\frac{x_3}{C_1} + \frac{i_{PV}}{C_1} \\ \dot{x}_2 &= -\frac{x_2}{C_2 R} + \frac{x_3}{C_2} \\ \dot{x}_3 &= \frac{x_1}{L} - \frac{x_2}{L} \end{aligned} \tag{13}$$

When the IGBT is in non-conduction mode ($u = 0$), the equivalent circuit can be seen in Fig. 4. This way, the state space is defined as:

$$\begin{aligned} \dot{x}_1 &= -\frac{i_{PV}}{C_1} \\ \dot{x}_2 &= -\frac{x_2}{RC_2} + \frac{x_3}{C_2} \\ \dot{x}_3 &= -\frac{x_2}{L} \end{aligned} \tag{14}$$

From the state spaces (13) and (14), a new state space model can be obtained:

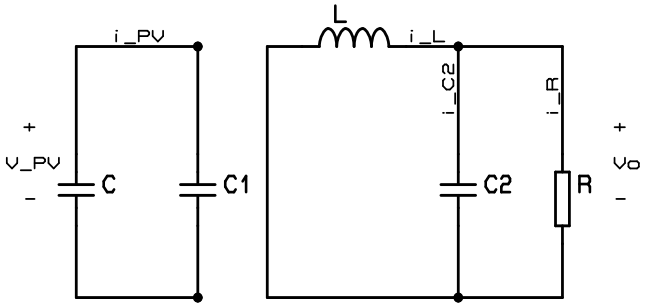

Fig. 4. Buck equivalent circuit with u=0

$$\begin{aligned}\dot{x}_1 &= \frac{i_{PV}}{C_1} + \alpha_{13}x_3u \\ \dot{x}_2 &= \alpha_{22}x_2 + \alpha_{23}x_3 \\ \dot{x}_3 &= \alpha_{32}x_2 + \alpha_{31}x_1u\end{aligned} \tag{15}$$

where,

$$\alpha_{13} = -\frac{1}{C_1},$$
$$\alpha_{22} = -\frac{1}{RC_2}, \quad \alpha_{23} = -\frac{1}{C_2}$$
$$\alpha_{32} = -\frac{1}{L}, \quad \alpha_{31} = \frac{1}{L}.$$

The model (15), can also be written as:

$$\dot{x} = f(x) + g(x)u, \tag{16}$$

where,

$$f(x) = \begin{bmatrix} \frac{i_{PV}}{C_1} \\ \alpha_{22}x_2 + \alpha_{23}x_3 \\ \alpha_{32}x_2 \end{bmatrix},$$
$$g(x) = \begin{bmatrix} \alpha_{13}x_3 \\ 0 \\ \alpha_{31}x_1 \end{bmatrix}.$$

In order to obtain a discrete-time model, the Euler discretization method is used:

$$\begin{aligned}x^1_{k+1} &= x^1_k + \alpha^1_k + \alpha^2 x^3_k u_k \\ x^2_{k+1} &= x^2_k + \alpha^3 x^2_k + \alpha^4 x^3_k \\ x^3_{k+1} &= x^3_k + \alpha^3 x^2_k + \alpha^6 x^1_k u_k \\ y(k) &= x^1_k\end{aligned} \tag{17}$$

where,

$$\alpha^1_k = \frac{t_s i_{PVk}}{C_1}, \quad \alpha^2 = -\frac{t_s}{C_1},$$
$$\alpha^3 = -\frac{t_s}{RC_2}, \quad \alpha^4 = \frac{t_s}{C_2},$$
$$\alpha^5 = -\frac{t_s}{L}, \quad \alpha^6 = \frac{t_s}{L}.$$

3.2 Identification

Based on the structure of (17), the RHONN proposed for the DC-DC Buck converter is as follows:

$$\begin{aligned}\hat{x}^1_{k+1} &= w^{11}_k \hat{x}^1_k + w^{12}_k S(\hat{x}^3_k) + w^{13}_k S(i_{PVk}) + 0.01u_k \\ \hat{x}^2_{k+1} &= w^{21}_k \hat{x}^2_k \\ \hat{x}^3_{k+1} &= w^{31}_k \hat{x}^3_k + w^{32}_k \hat{x}^2_k + w^{33}_k u_k \\ \hat{y}_k &= \hat{x}^1_k\end{aligned} \tag{18}$$

where, $S(\cdot)$ is a logistic function, as was seen in the mathematical preliminaries. The second and third equations in (18) correspond to the internal dynamics of the system. The second equation describes the dynamics of the voltage at the load resistor of the buck converter; due to the nature of the converter, this voltage will always be lower than V_{PV}. The third equation represents the dynamics of the current through the inductor. The weight vectors are updated online using the extended Kalman filter (EKF), the estimation error is defined by:

$$\tilde{x_k} = x_k - \hat{x}_k \tag{19}$$

It is worth to note that the states need to be measurable.

3.3 Control Design

The control is based on the identification described in the previous subsection, its objective is that the voltage at the output of the solar panel reaches the trajectory given by the MPPT, then the tracking error is defined as

$$e_k = \hat{x}^1_k - x^{1ref}_k. \tag{20}$$

The dynamic error is obtained as follows:

$$\begin{aligned}e_{k+1} &= \hat{x}^1_{k+1} - x^{1ref}_{k+1} \\ &= w^{11}_k \hat{x}^1_k + w^{12}_k S(\hat{x}^3_k) + w^{13}_k S(i_{PVk}) \\ &\quad +0.01u_k - x^{1ref}_{k+1}.\end{aligned} \tag{21}$$

The desired dynamic error is $e_{k+1} = -k_1 e_k$, which implies a control law as:

$$u_{eq} = \frac{-1}{0.01}\left(k_1 e_k - x^{1ref}_{k+1} + w^{11}_k \hat{x}^1_k + w^{12}_k S(\hat{x}^3_k) + w^{13}_k S(i_{PVk})\right) \tag{22}$$

where, $0 < k_1 \leq 1$ is a control design constant to minimize the error asymptotically.

4. SIMULATION RESULTS

In order to test the performance of the proposed neural controller, a simulation is developed implementing the DC-DC Buck converter and the solar panel by means of Simscape Power Systems[2] blocks, which allows to consider the components dynamics for future real-time implementation.

For the realized test, the temperature in the cell is considered constant at 25 °C. At the beginning a 0 W/m^2 irradiance is applied, then at 1.5 seconds it is increased to 500 W/m^2, finally at 3 and 4.5 seconds the irradiance is changed to 1000 and 3000 W/m^2 respectively. At the beginning of the simulation the plant is left in open-loop to identify the states, then at 0.2 seconds the loop is closed and the controller starts to operate. In Fig. 5, the theoretical power level given by (1), using the photovoltaic panel model and applying the previously described irradiance changes, is shown in the red dot line; and the power obtained by the proposed MPPT is displayed in blue line. It can be seen that the convergence time of the controller and the tracking error are within acceptable boundaries.

In Fig. 6, the identification errors are shown. It can be seen that the estimated state with the biggest error is the

[2] Simscape Power Systems is a trademark of The MathWorks, Inc.

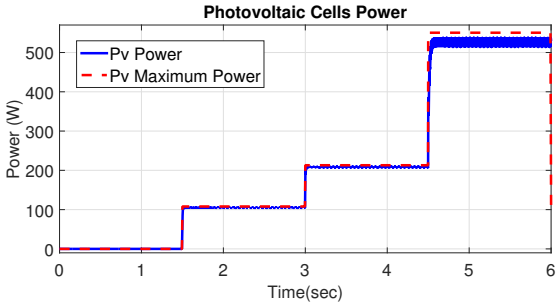

Fig. 5. Photovoltaic power at different irradiance values

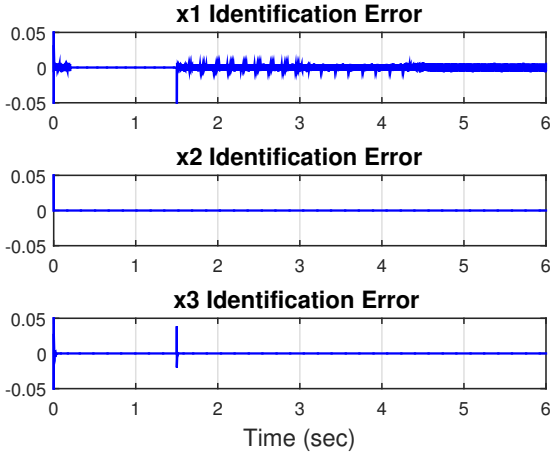

Fig. 6. Identification error

Table 1. Statistical comparison of controllers

	NN Controller		DSM Controller	
	Mean	SD	Mean	SD
0%	0.4267	**2.2182**	-0.1681	2.8135
10%	0.3131	2.2822	-0.1488	2.9877
20%	0.4472	2.3697	**-0.1284**	3.322
30%	0.4143	2.5501	-0.1388	3.5537
40%	0.4639	2.4802	-0.168	4.0019

voltage given by the solar panel, especially when irradiation levels go from $0\,\mathrm{W/m^2}$ to $500\,\mathrm{W/m^2}$, nevertheless the errors remain within adequate bounds for the entire simulation event though changes in irradiance are applied.

In order to compare the proposed neural algorithm with a same class but different controller, an additional simulation is performed using a discrete sliding mode controller (DSM) based on Khiari et al. (2004), with parametric changes in the DC-DC Buck converter components. Table 1, shows the mean and the standard deviation (SD) of the error with changes in capacitance and inductance values to different percentages. The best values for each statistical measure are emphasized in bold. It is evident that the error mean is lower when using the DSM controller but the SD increases when parametric changes exist, while the neural controller mean and SD remain mostly constant. The error in the mean of the neural controller can be attribute to the always existing identification errors.

5. CONCLUSION

This paper presents a novel application of the neural network on-line identification using the EKF as in Sanchez, E. N., Alanis A.Y. (2004), to achieve a photovoltaic panel MPP reference tracking. This method for identification provides robustness against parametric changes in the components. The results validate the performance of the proposed controller for irradiance changes compared to a DSM controller, proving its precision and high reaction velocity. The simulation was developed using Simscape Power Systems which includes the different component dynamics, establishing the basis for a real-time implementation.

REFERENCES

Alabedin, a.M.Z., El-Saadany, E.F., and Salama, M.M.a. (2011). Maximum power point tracking for Photovoltaic systems using fuzzy logic and artificial neural networks. *2011 IEEE Power and Energy Society General Meeting*, 1–9. doi:10.1109/PES.2011.6039690.

Alanis, A.Y., Sanchez, E.N., and Loukianov, A.G. (2007). Discrete-time backstepping induction motor control using a sensorless recurrent neural observer. In *Proceedings of the IEEE Conference on Decision and Control*, 6112–6117. doi:10.1109/CDC.2007.4434164.

Antonio-Toledo, M.E., Sanchez, E.N., and Loukianov, A.G. (2015). Real-time neural inverse optimal control for position trajectory tracking of an induction motor. In *System of Systems Engineering Conference (SoSE), 2015 10th*, 193–198. doi: 10.1109/SYSOSE.2015.7151923.

Brown, R.G. and Hwang, P.Y.C. (1997). *Introduction to Random Signals and Applied Kalman Filtering*. 4. doi: 10.1521/ijgp.2010.60.4.455.

Cubas, J., Pindado, S., and De Manuel, C. (2014). Explicit expressions for solar panel equivalent circuit parameters based on analytical formulation and the lambert W-function. *Energies*, 7(7), 4098–4115. doi: 10.3390/en7074098.

Esram, T. and Chapman, P.L. (2007). Comparison of Photovoltaic Array Maximum Power Point Tracking Techniques. *IEEE Transactions on Energy Conversion*, 22(2), 439–449. doi:10.1109/TEC.2006.874230.

Feldkamp, L.A., Feldkamp, T.M., Prokhorov, P. (2001). Neural Network training with the nprKF. In *International Joint Conference on Neural Networks'01*, 109–114.

Hadjab, M., Berrah, S., and Abid, H. (2012). Neural network for modeling solar panel. *INTERNATIONAL JOURNAL OF ENERGY*, 6(1), 9–16.

Khiari, B., Sellami, A., Andoulsi, R., M'Hiri, R., and Ksouri, M. (2004). Discrete control by sliding mode of a photovoltaic system. In *Control, Communications and Signal Processing, 2004. First International Symposium on*, 469–474. doi:10.1109/ISCCSP.2004.1296330.

Rajesh, M.V., Archana, R., Unnikrishnan, A., and Gopikakaumari, R. (2010). Comparative study on ekf training algorithm with em and mle for ann modeling of nonlinear systems. In *Proceedings of the 29th Chinese Control Conference*, 1407–1413.

Ramaprabha, R., Gothandaraman, V., Kanimozhi, K., Divya, R., and Mathur, B.L. (2011). Maximum power

point tracking using GA-optimized artificial neural network for Solar PV system. *2011 1st International Conference on Electrical Energy Systems*, (1), 264–268. doi: 10.1109/ICEES.2011.5725340.

Rovithakis, G.A. and Christodoulou, M.A. (2000). *Adaptive control with recurrent high order neural networks / theory and industrial applications.*

Ruiz, R., Sanchez, E.N., and Loukianov, A.G. (2012). Real-time neural block control for a doubly fed induction generator. In *World Automation Congress (WAC), 2012*, 1–6. Puerto Vallarta, Mexico.

Sanchez, E. N., Alanis A.Y., C.G. (2004). Recurrent neural networks trained with kalman filtering for discrete chaos recontruction. In *Asian-pacific workshop on chaos control and synchronization'04*. Melbourne, Australia.

Song, Y. and Grizzle, J.W. (1992). The Extended Kalman Filter as a Local Asymptotic Observer for Nonlinear Discrete-Time Systems. In *American Control Conference, 1992*, 3365–3369.

Straub, S. and Schroder, D. (1996). Identification of nonlinear dynamic systems with recurrent neural networks and kalman filter methods. In *Circuits and Systems, 1996. ISCAS '96., Connecting the World., 1996 IEEE International Symposium on*, volume 3, 341–344 vol.3. doi:10.1109/ISCAS.1996.541603.

Zhang, L. and Bai, Y.F. (2005). Genetic algorithm-trained radial basis function neural networks for modelling photovoltaic panels. *Engineering Applications of Artificial Intelligence*, 18(7), 833–844. doi: 10.1016/j.engappai.2005.02.004.

Optimal Power Dispatch in a Microgrid

Martin J. Loza-Lopez * **Riemann Ruiz-Cruz** **
T.B. Lopez-Garcia * **Edgar N. Sanchez** *
Juan Diego Sánchez-Torres **

* *Centro de Investigación y Estudios Avanzados del IPN, Zapopan, Jal 45030 México, (e-mail: {mdloza,tblopez,sanchez}@ gdl.cinvestav.mx)*
** *ITESO University, Periferico Sur Gomez Morin 8585, Tlaquepaque, Jalisco, México C.P. 45604 ,(e-mail: {riemannruiz,dsanchez}@iteso.mx)*

Abstract: This paper is concerned with the power dispatch in a microgrid. The dispatch problem is formulated as linear program. Thus, the proposed solution is the application of neural network that solves linear programming on-line. This proposal in motivated by the increasing electric energy demand and the rising need to incorporate sustainable energy sources to the power grid in a reliable scheme. A microgrid is an interconnection of distributed energy sources (DES), with the tendency to include renewable energies that offer many advantages to customers and utilities. The different DES that compose the microgrid are controlled independently to track the optimal reference provided by the proposed method in order to supply a demanded power output minimizing the consumed power from the main grid.

Keywords: Electric energy distribution, Neurodynamic optimization, Linear programming, Power management

1. INTRODUCTION

The optimization of the power dispatch within a microgrid is a big challenge for many engineering areas as control, power electronics and modeling. Different studies have been performed in this area, some examples are presented in Chowdhury and Crossley (2009). In the presented work, the optimal amount of power to be supplied by each energy source in a microgrid simulation, to produce a maximum amount of energy, is analyzed. Because of the varying output power that renewable energy sources present, large-scale, real-time optimization procedures are required, most of them in the form of linear programming. In contrast to the publications which use recurrent neural networks for microgrid optimization (Aquino et al., 2010), the proposed approach provides *fixed convergence time* to the solution and the tuning of only one network parameter.

The optimization problem is stated to maximize or minimize an objective function with the manipulation of the value of decision variables, sometimes, subject to equality and/or inequality constraints. These problems typically require large-scale real-time linear programming procedures. Most of the time, sequential algorithms as the classical simplex or the interior point methods are implemented. However, these approaches have the disadvantage that the computing time required for a solution is greatly dependent on the problem dimension and structure.

Dynamical systems which can solve real-time optimization were introduced in Pyne (1956) . Since then, other major contributions have been proposed by Korovin and Utkin (1974) , Pazos and Bhaya (2009) , Wang (1993) and Wilson (1986). Due to its inherent massive parallelism, these systems are able to solve optimization problems faster than those using more popular optimization algorithms executed on general-purpose digital computers (Cichocki and Unbehauen, 1993), with great flexibility to parametric variations (Pyne, 1956).

Although the previous studies exhibit high performance, it is necessary to tune several network parameters, that increase linearly with the optimization problem dimension, since for every decision variable there is an individual selection of each activation function. In addition, the fixed time characteristic is not presented in most of the mentioned references.

In this paper, a dynamical system for the solution of linear programming in a predefined convergence time is proposed. Its design is considered as a sliding mode control problem, where the network structure is based on the Karush-Kuhn-Tucker (KKT) optimality conditions (Karush, 1939; Kuhn and Tucker, 1951) and the KKT multipliers are regarded as control inputs. The problem is solved without the individual selection of each stabilizing input, instead, a multivariable function based on the unit control (Utkin, 1992) is used. On the other hand, the fixed time stability (Polyakov, 2012)property ensures system convergence time independent of the initial conditions. This controller is used in the KKT multiplier design, enforcing a sliding mode in which the optimization problem is solved.

The proposed approach has attractive features such as: fixed time convergence to the optimization problem solution and a fixed number of parameters (one in this case), regardless of the optimization problem dimension. Therefore, it offers the scalability characteristic, that

allows the possibility of adding other energy sources to the microgrid.

In the following, Section 2 presents the mathematical preliminaries and some useful definitions. In Section 3 the basis of the linear programming problem are established and the proposed algorithm is presented. Section 4 describes the microgrid connection and the controllers implemented along with the linear programming problem for the power dispatch and shows the simulation results. Finally, in Section 5 the conclusions are presented.

2. MATHEMATICAL PRELIMINARIES

Consider the system

$$\dot{\xi} = f(t, \xi) \tag{1}$$

where $\xi \in \mathbb{R}^n$ and $f : \mathbb{R}_+ \times \mathbb{R}^n \to \mathbb{R}^n$. For this system, its initial conditions or initial states are $\xi(t_0)$ where $t_0 \in \mathbb{R}_+$. The time variable t is defined on the interval $[t_0, \infty)$.

The idea of the sliding mode control is highly related with the finite- time stability. This time however often depends on the initial conditions of the system. The case when convergence time is uniform and independent of the initial conditions is known as fixed time stability Cruz-Zavala et al. (2010). Polyakov (2012) gives a precise statement of the fixed time stability :

Definition 2.1. (Globally fixed-time attraction). Let a non-empty set $M \subset \mathbb{R}^n$. It is said to be globally fixed-time attractive for the system (1) if any solution $\xi(t, \xi_0)$ of (1) reaches M in some finite time moment $t = T(\xi_0)$ and the settling-time function $T(\xi_0) : \mathbb{R}^n \to \mathbb{R}_+ \cup \{0\}$ is bounded by some positive number $T_{\max}$, i.e. $T(\xi_0) \leq T_{\max}$ for $\xi_0 \in \mathbb{R}^n$.

Note that there are several choices for $T_{\max}$, for example if $T(x_0) \leq T_{\mathrm{m}}$ for a positive number T_m, also $T(x_0) \leq \lambda T_{\mathrm{m}}$ with $\lambda \geq 1$. This motivates the definition of a set which contains all the bounds of the settling-time function.

Definition 2.2. (Settling-time set). Let the set of all the bounds of the settling-time function for system (1) be defined as follows:

$$\mathcal{T} = \{T_{\max} \in \mathbb{R}_+ : T(x_0) \leq T_{\max}\}. \tag{2}$$

In addition, the minimum bound for the settling-time function of (1) is defined as:

Definition 2.3. (Minimum bound for the settling-time set). Consider the set $\mathcal{T}$ defined in (2), let the time $T_f \in \mathbb{R}$ such that

$$T_f = \{T \in \mathcal{T} : T \leq T_{\max}, \forall T_{\max} \in \mathcal{T}\}. \tag{3}$$

Note that for some systems $T_{\max}$ can be tuned by a particular selection of the system parameters, this notion refers to the prescribed-time stability which is given in Fraguela et al. (2012) and the predefined-time stability Sanchez-Torres et al. (2015). The prescribed-time stability based design and the predefined-time stability based design are explained in the following definitions.

Definition 2.4. (Prescribed-time based design). Consider the set $\mathcal{T}$ defined in (2). The particular case when for the system (1), $T_{\max}$ can be tuned by a particular selection of the system parameters ρ, $T_{\max} = T_{\max}(\rho)$, is referred to the notion of the prescribed-time stability which is given in Fraguela et al. (2012). This design is performed by selecting $T_{\max}(\rho) \in \mathcal{T}$ and calculating the inverse of the settling-time function, allowing the tuning of ρ.

It is worth to note, the true fixed stabilization time for a system designed based on prescribed-time stability is unknown but bounded by $T_{\max}(\rho)$. In contrast, a designed system with predefined-time stability has a known stabilization time.

Definition 2.5. (Predefined-time based design). The particular case when for the system (1), the time T_f defined in (3) can be tuned by a particular selection of the system parameters ρ, $T_f = T_f(\rho)$, is referred to the notion of the predefined-time stability.

With the definition of a predefined-time attractive set, the following lemma provides a Lyapunov characterization of a class of these sets on the state space:

Lemma 2.1. (Lyapunov function Sanchez-Torres et al. (2015)). If there exists a continuous radially unbounded function

$$V : \mathbb{R}^n \to \mathbb{R}_+ \cup \{0\}$$

such that $V(x) = 0$ for $x \in M$ and any solution $x(t)$ satisfies

$$\dot{V} \leq -\frac{\alpha}{p} \exp(V^p) V^{1-p} \tag{4}$$

for $\alpha > 0$ and $0 < p \leq 1$, then the set M is globally predefined-time attractive for the system (1) and $T_{\max} = \frac{1}{\alpha} + t_0$.

Proof See Sanchez-Torres et al. (2015).

Definition 2.6. (Predefined-time stabilizing function). For $x \in \mathbb{R}^n$, the predefined-time stabilizing function is defined as

$$\Phi_p(x) = \frac{1}{p} \exp\left(\|x\|^p\right) \frac{x}{\|x\|^p} \tag{5}$$

where $0 < p \leq 1$.

With the definition of the stabilizing function, let the following dynamic system:

Lemma 2.2. (Predefined-time stable dynamical system). For every initial condition x_0, the system

$$\dot{x} = -\frac{1}{T_c} \Phi_p(x) \tag{6}$$

with $T_c > 0$, and $0 < p \leq 1$ is predefined-time stable with settling-time T_c. That is, $x(t) = 0$ for $t > t_0 + T_c$ in spite of the x_0 value.

Proof See Sanchez-Torres et al. (2015).

In order to apply the previous result to control design, consider the dynamic system

$$\dot{\xi} = \Delta(\xi, t) + u \tag{7}$$

with $\xi, u \in \mathbb{R}^n$ and $\Delta : \mathbb{R}_+ \times \mathbb{R}^n \to \mathbb{R}^n$. The main objective is to drive the system (7) to the point $\xi = 0$ in a predefined fixed time in spite of the unknown non-vanishing disturbance $\Delta(\xi, t)$. A solution to this problem which does not require an individual selection of each of the n control variables based on the *unit control* is presented in the following theorem:

Theorem 2.1. (Predefined-time multivariable control). Let the function $\phi(\xi, t)$ to be bounded as $\|\Delta(\xi, t)\| \leq \delta$, with $0 < \delta < \infty$ a known constant. Then, by selecting the control input

$$u = -\left(\frac{1}{T_c} + \delta\right)\frac{\xi}{\|\xi\|}\exp(\|\xi\|)$$

with T_c being a scalar, the system (7) is globally predefined-time stable with settling-time upper bounded by T_c.

Proof: See Sanchez-Torres et al. (2015).

2.1 Linear Programming Problem Statement

Let the following linear programming problem:

$$\begin{cases} \min_x & \mathbf{c}^T x \\ \text{s.t.} & \mathbf{A}x = \mathbf{b} \\ & l \le x \le h \end{cases} \tag{8}$$

where $x = [\, x_1 \ \dots \ x_n \,]^T \in \mathbb{R}^n$ are the decision variables, $\mathbf{c} \in \mathbb{R}^n$ is a cost vector, $\mathbf{A}$ is an $m \times n$ matrix such that $\text{rank}(\mathbf{A}) = m$ and $m \le n$; $\mathbf{b}$ is a vector in $\mathbb{R}^m$ and, $l = [\, l_1 \ \dots \ l_n \,]$, $h = [\, h_1 \ \dots \ h_n \,] \in \mathbb{R}^n$.

Let $y = [\, y_1 \ \dots \ y_m \,]^T \in \mathbb{R}^m$ and $z = [\, z_1 \ \dots \ z_n \,]^T \in \mathbb{R}^n$. Hence, the Lagrangian of (8) is

$$L(x, y, z) = \mathbf{c}^T x + z^T x + y^T(\mathbf{A}x - \mathbf{b}). \tag{9}$$

The KKT conditions establish that x^* is a solution for (8) if and only if x^*, y and z in (8)-(9) are such that

$$\nabla_x L(x^*, y, z) = \mathbf{c} + z + \mathbf{A}^T y = 0 \tag{10}$$
$$\mathbf{A}x^* - \mathbf{b} = 0 \tag{11}$$
$$z_i x_i^* = 0 \text{ if } l_i < x_i^* < h_i, \ \forall i = 1, \dots, n. \tag{12}$$

3. A RECURRENT NEURAL NETWORK (RNN) FOR LINEAR PROGRAMMING PROBLEM

Following the KKT approach, from Loza-Lopez et al. (2015) a recurrent neural network which solves the problem (8) in finite time is proposed. For this purpose, let $\Omega_e = \{x \in \mathbb{R}^n : \mathbf{A}x - \mathbf{b} = 0\}$ and $\Omega_d = \{x \in \mathbb{R}^n : l \le x \le h\}$. According to (8), $x^* \in \Omega$ where $\Omega = \Omega_d \cap \Omega_e$.

From (10), let

$$\dot{x} = -\mathbf{c} + \mathbf{A}^T y + z, \tag{13}$$

then, y and z must be designed such that Ω is an attractive set, fulfilling conditions (10)-(12). For this case, in addition to condition (12), z is considered such that

$$\begin{cases} z_i \ge 0 & \text{if } x_i \ge h_i \\ z_i \le 0 & \text{if } x_i \le l_i \end{cases}, \tag{14}$$

and the variable $\sigma \in \mathbb{R}^m$ is defined as

$$\sigma = \mathbf{A}x - \mathbf{b}. \tag{15}$$

In order to obtain predefined-time stability to the solution x^*, the terms y and z are proposed in (13) as

$$y = (\mathbf{A}\mathbf{A}^T)^{-1}\left[\mathbf{A}\mathbf{c} - \mathbf{A}z + \frac{1}{T_s}\phi(\sigma)\right] \tag{16}$$

and

$$z = \left(\|\mathbf{c}\| + \frac{1}{T_s}\right)\varphi(x, l, h) \tag{17}$$

respectively, where $T_s > 0$.

For this case, the multivariable activation functions are $\varphi(x, l, h) = [\, \varphi_1(x, l_1, h_1) \ \dots \ \varphi_n(x, l_n, h_n) \,]^T$, with $\varphi_i(x, l_i, h_i)$ of the form

$$\varphi_i(x, l_i, h_i) = \begin{cases} -\dfrac{x_i - l_i}{\|x - l\|}\exp(\|x - l\|) & \text{if } x_i \le l_i \\ 0 & \text{if } l_i < x_i < h_i \\ -\dfrac{x_i - h_i}{\|x - h\|}\exp(\|x - h\|) & \text{if } x_i \ge h_i \end{cases} \tag{18}$$

and

$$\phi(\sigma) = -\frac{\sigma}{\|\sigma\|}\exp(\|\sigma\|). \tag{19}$$

Therefore, with the structure given by (13) and the KKT multiplier as in (16) and (17), with activation functions (18) and (19), the following theorem presents a RNN which solves (8) in predefined-time.

Theorem 3.1. (Predefined-time RNN for linear programming). For the RNN

$$\dot{x} = -\mathbf{c}\Lambda + \left(\|\mathbf{c}\| + \frac{1}{T_s}\right)\Lambda\varphi(x, l, h) + \frac{1}{T_s}\mathbf{A}^+\phi(\sigma) \tag{20}$$

where $\Lambda = I - \mathbf{A}^T(\mathbf{A}\mathbf{A}^T)^{-1}\mathbf{A}$, $\mathbf{A}^+ = \mathbf{A}^T(\mathbf{A}\mathbf{A}^T)^{-1}$ and $T_s > 0$, the point x^* is globally predefined-time stable with settling-time T_s.

Proof: The dynamics of (15) is given by

$$\dot{\sigma} = \mathbf{A}\left(-\mathbf{c} + \mathbf{A}^T y + z\right). \tag{21}$$

Therefore, with the selection of y as in (16), the system (21) reduces to

$$\dot{\sigma} = -\frac{1}{T_s}\frac{\sigma}{\|\sigma\|}\exp(\|\sigma\|).$$

Thus, from *Theorem 2.1*, a sliding mode is induced on the manifold $\sigma = 0$. Therefore, the set Ω_e is predefined-time attractive with settling-time T_s.

On the manifold $\sigma = 0$, the equivalent value of ϕ is the solution of $\dot{\sigma} = 0$. Resulting to $\phi_{\text{eq}} = 0$ or $y_{\text{eq}} = (\mathbf{A}\mathbf{A}^T)^{-1}[\mathbf{A}\mathbf{c} - \mathbf{A}z]$. Therefore, the dynamics of (13) on that manifold is

$$\dot{x} = -\mathbf{c}\Lambda + \Lambda z. \tag{22}$$

With the selection of z as in (17), the resulting system (22) is

$$\dot{x} = -\mathbf{c}\Lambda + \Lambda\left(\|\mathbf{c}\| + \frac{1}{T_s}\right)\varphi(x, l, h).$$

Consider the Lyapunov function $V = \|x\|$. Its derivative is given by $\dot{V} = \frac{x^T}{\|x\|}\dot{x}$. Therefore

$$\begin{aligned} \dot{V} &= \frac{x^T}{\|x\|}\left[-\mathbf{c}\Lambda + \Lambda\left(\|\mathbf{c}\| + \frac{1}{T_s}\right)\varphi(x, l, h)\right] \\ &\le \frac{x^T}{\|x\|}\left[\frac{1}{T_s}\varphi(x, l, h)\right]. \end{aligned} \tag{23}$$

Replacing the Lyapunov function

$$\dot{V}\begin{cases} \le -\dfrac{1}{T_s}\exp(V) \text{ if } x < l \text{ or } x > h \\ = 0 \text{ if } l \le x \le h \end{cases} \tag{24}$$

From *Theorem 2.1*, the set Ω_d is predefined-time attractive with settling-time T_s.

In the set Ω_d the equivalent value of φ, φ_{eq}, is the solution to $\dot{x} = 0$. With the application of *Theorem 2.1*, the conditions (11) and (12) are satisfied, providing predefined-time convergence to the set Ω. Now, by using the equivalent control method, the solution of $\dot{x} = 0$ and $\dot{\sigma} = 0$ in (13) for $t > T_s$ has the form

$$\mathbf{c} + \mathbf{A}^T y_{\text{eq}} + z_{\text{eq}} = 0.$$

Therefore, the condition (10) is fulfilled, implying the point $x^* \in \Omega$ is globally predefined-time stable. ■

Remark 3.1. Note that, in contrast to the most of the RNN presented in the literature, this scheme only needs the tuning of one variable, namely T_s in spite of the problem dimensions.

4. OPTIMIZATION OF THE POWER DISPATCH IN A MICROGRID SIMULATION

The optimization algorithm previously presented is applied to the power dispatch problem within a simulated microgrid in order to minimize the consumption of power provided by the utility grid.

4.1 Microgrid Description

The simulated microgrid is connected as in Loza-Lopez et al. (2014), with a *wind power system* (WPS), a connection point with the *utility grid system* (UGS) and a DC voltage bus, which includes the output load, a *solar power system* (SPS), and a *battery bank system* (BBS).

The microgrid simulation is performed in Simulink with the Simscape Power Systems [1] libraries, which include the dynamic simulation of electronic components in order to produce a better approach to a real electrical microgrid. Discrete sliding modes controllers are applied to solar, battery bank and wind power systems.

Wind Power System. The connection and control of the WPS is as in Ruiz et al. (2011) which includes a doubly fed induction generator (DFIG) with a mechanical interconnection to a wind turbine. The DFIG stator is directly connected to the utility grid while the rotor is coupled by a back to back converter. This connection scheme requires two different controllers; one is the grid side controller (GSC), which is in charge of maintaining a fixed voltage in the capacitor, and the second one is the rotor side controller (RSC), which controls the electrical torque T_e according to the mechanical torque T_m in the connection with the wind turbine. Both of these controllers maintain a desired power factor of the energy delivered to the grid.

In Rapheal et al. (2009) the maximum mechanical power for a wind turbine is directly related to a constant value of its tip speed ratio λ :

$$\lambda = \frac{\omega_t R_t}{v}$$

where w_t is the turbine rotor angular speed in rad/s , v is the wind speed m/s and R_t is the wind turbine rotor radius (m). In order to produce the maximum power from the WPS under wind speed variations, λ needs to be transform to an electrical torque (Ruiz et al. (2011)) and be passed as the reference to track by the RSC. In Fig. 1, the performance under wind speed variations of the WPS can be observed, in this case the λ reference to track corresponds to the maximum power point given by the wind turbine block in Simulink.

[1] Simulink/Simscape Power Systems are trademarks of The MathWorks, Inc.

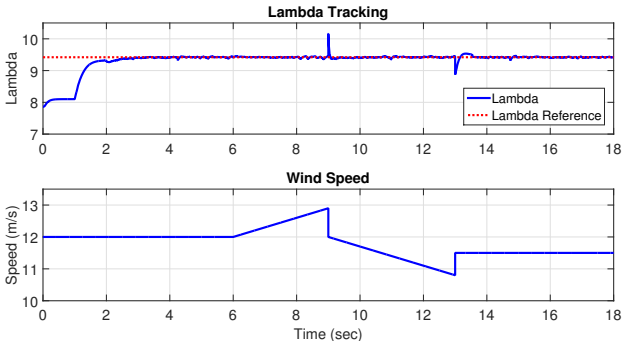

Figure 1. WPS lambda tracking under wind speed variations.

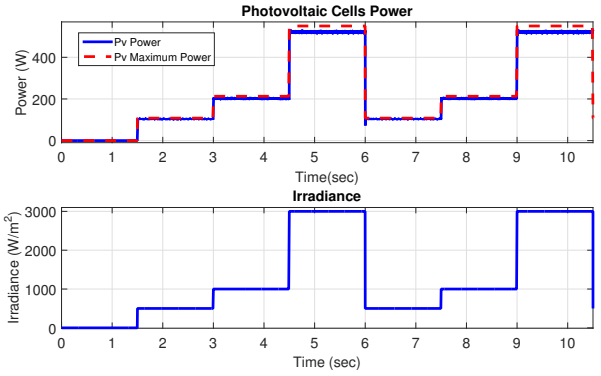

Figure 2. SPS maximum power tracking under irradiance variations.

Solar Power System. The SPS is simulated by a 213 W Simscape Power Systems block with a maximum power point tracker (MPPT) control system, which includes an *perturb and observe* algorithm (de Brito et al. (2013)) to obtain the photovoltaic panel voltage that corresponds to the maximum power $V_{pv_{max}}$, and a DC-DC buck converter in order to track this voltage.

The DC-DC buck converter is directly connected to the output of the SPS as in Koutroulis et al. (2001),this allows the $V_{pv_{max}}$ tracking without the problem of high voltage in the output of the converter. A discrete equivalent control is applied to the insulated-gate bipolar transistor (IGBT) of the DC-DC converter with a pulse width modulation (PWM) block interface. The IGBT switching produces noise in the required measurements for the control system as it would in real time application. In Fig 2, the performance of the SPS along with the MPPT control system under irradiance variations is displayed, the blue line corresponds to the maximum power obtained by the buck converter with the perturb and observe algorithm, and the red dot line is the maximum theoretical power in the photovoltaic panel.

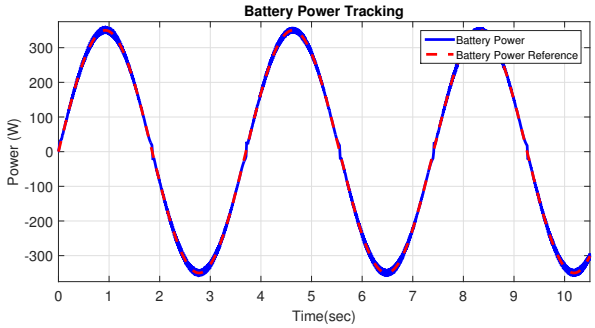

Figure 3. Battery power and reference.

Battery Bank System. The BBS is simulated by a lead-acid 24 V, 100 Ah battery Simulink block. The control system for this BBS is implemented using a parallel buck and boost DC-DC converters; the first one is used under discharge conditions and the second one under charge conditions. A discrete equivalent controller is applied to the each converter, and they switch according to the sign of the reference power to track. In Fig 3, the performance of these controllers acting together is displayed. The blue line is the power given or extracted by the BBS, and the red dot line is a sinusoidal power reference to track.

4.2 Microgrid Optimization Approach

The main goal for this test is to optimize the power dispatch of the microgrid based on the output power of the load at time k (P_{L_k}).

The optimization problem is expressed as follows:

$$\begin{cases} \text{Minimize} & 10P_{G_k} - 500P_{W_k} - 500P_{S_k} - 200P_{B_k} \\ \text{s.t.} & P_{G_k} + P_{W_k} + P_{S_k} + P_{B_k} = P_{L_k} \\ & P_{G_{min}} \leq P_{G_k} \leq P_{G_{max}} \\ & P_{W_{min}} \leq P_{W_k} \leq P_{W_{max}} \\ & P_{S_{min}} \leq P_{S_k} \leq P_{S_{max}} \\ & P_{B_{min}} \leq P_{B_k} \leq P_{B_{max}} \end{cases} \tag{25}$$

In order to match the form of the equation (8), the needed matrices are established as: $\mathbf{c}^T = [10 \ -500 \ -500 \ -200]^T$, $x = [P_{G_k} \ P_{W_k} \ P_{S_k} \ P_{B_k}]^T$, $\mathbf{A} = [1 \ 1 \ 1 \ 1]$, $\mathbf{b} = [P_{L_k}]$, $l = [P_{G_{min}} \ P_{W_{min}} \ P_{S_{min}} \ P_{B_{min}}]$ and $h = [P_{G_{max}} \ P_{W_{max}} \ P_{S_{max}} \ P_{B_{max}}]$. Where $P_{G_k}, P_{W_k}, P_{S_k}$ and P_{B_k} are the UGS, WPS, SPS and BBS powers at time k, and the matrices l and h are their corresponding minimum and maximum power values according to the wind speed in the WPS, the temperature and irradiance in the SPS and the state of charge of the BBS.

4.3 Simulation Results

The presented optimization method uses the measured load power as the vector $\mathbf{b}$ and the matrices defined in the previous section to set the references of power for the microgrid. Due to incentivize the use of the available power given by the SPS, WPS and BBS, the expectation is that the power references for these three systems are set near to their maximum power limits. For this test the settling time T_c is set to $5e^{-5}$ sec to guarantee an appropriate reference

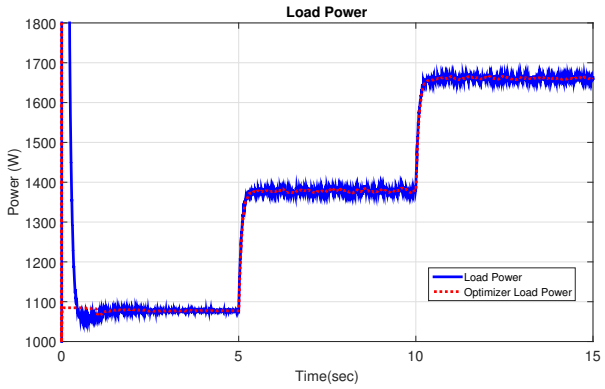

Figure 4. Load power and references sum

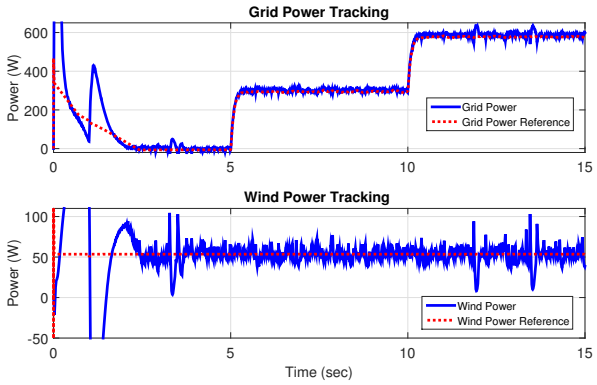

Figure 5. UGS and WPS power tracking

tracking, the wind speed is set to 12 m/s which correspond to a $P_{W_{min}}$ and $P_{W_{max}}$ of 0 and 53.5 W. The temperature and irradiance in the photovoltaic panel are set to 25 °C and 3000 W/m^2 with a $P_{S_{min}}$ and $P_{S_{max}}$ of 0 and 530 W. The state of charge of the battery is 50% which is a neutral state with a discharging and charging maximum powers of −500 and 500 W respectively. Even though the UGS is simulated by an infinite bus, in this test the $P_{G_{min}}$, and $P_{G_{max}}$ are fixed to −1000 and 1000 W . Three different loads are implemented, at the beginning a 0.13 Ω resistor is connected to the DC voltage bus, at 5 seconds a 0.5 Ω is added in parallel and at 10 seconds another 0.5 Ω is connected in the same way.

In Fig 4, the red dot line represents the sum of all the power references given by the optimization method, and the blue line is the measured load power. It can be seen that the equality restriction given in (25) is respected.

In Fig. 5, the UGS and the WPS power dynamics are shown. It can be seen that wind power reference is near to the maximum power limit as expected to the related cost fixed in (25). In the UGS power dynamics it can be seen that when the WPS, BBS and SPS powers are not enough to supply the power of the load, the remaining power is delivered through the UGS. This condition occurs particularly when the two 5Ω parallel resistors are added to the DC bus in 5 and 10 seconds.

In Fig. 6, the blue lines represent the SPS and BBS power and the red dot lines are the optimal power references. It can be seen that the limits established in (25) for these two systems and the reference tracking are fulfilled. The SPS

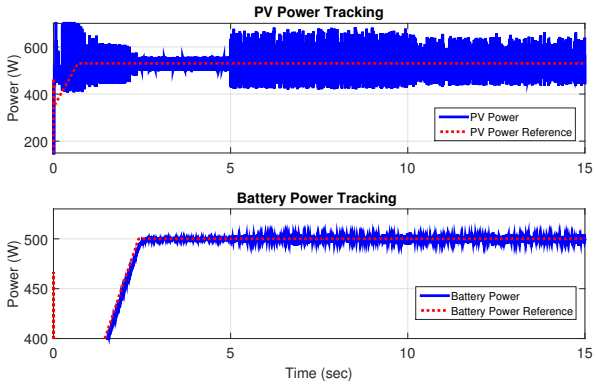

Figure 6. SPS and BBS power tracking.

power reference remains almost all the simulation in the maximum value allowed for this system, this is because of the previously fixed cost related to this system.

5. CONCLUSION

In this paper the optimal power dispatch within a microgrid is found. The microgrid consists of a connection point with the utility grid, a battery bank system, a solar panel system and a wind power system, with appropriate control systems for the last three. A novel recurrent neural network which solves linear programming problem, provides the references to be followed by each controller. The main features of the proposed neural network are predefined convergence time and the tuning of only one parameter. The simulation results validate the use of the presented optimization algorithm. In all simulations, the component dynamics with real parameters were taken into account, which provide a feasible framework for future real-time implementation.

REFERENCES

Aquino, R., Carvalho, M., Neto, O., Lira, M.M.S., de Almeida, G., and Tiburcio, S. (2010). Recurrent neural networks solving a real large scale mid-term scheduling for power plants. In *Neural Networks (IJCNN), The 2010 International Joint Conference on*, 1–6.

Chowdhury, S. and Crossley, P. (2009). *Microgrids and Active Distribution Networks*. IET renewable energy series. Institution of Engineering and Technology.

Cichocki, A. and Unbehauen, R. (1993). *Neural networks for optimization and signal processing*. J. Wiley.

Cruz-Zavala, E., Moreno, J., and Fridman, L. (2010). Uniform second-order sliding mode observer for mechanical systems. In *Variable Structure Systems (VSS), 2010 11th International Workshop on*, 14 –19.

de Brito, M.A.G., Galotto, L., Sampaio, L.P., d. A. e Melo, G., and Canesin, C.A. (2013). Evaluation of the main mppt techniques for photovoltaic applications. *IEEE Transactions on Industrial Electronics*, 60(3), 1156–1167.

Fraguela, L., Angulo, M., Moreno, J., and Fridman, L. (2012). Design of a prescribed convergence time uniform robust exact observer in the presence of measurement noise. In *Decision and Control (CDC), 2012 IEEE 51st Annual Conference on*, 6615–6620.

Karush, W. (1939). *Minima of functions of several variables with inequalities as side constraints*. Master's thesis, Dept. of Mathematics, Univ. of Chicago, Chicago, Illinois.

Korovin, S.K. and Utkin, V.I. (1974). Using sliding modes in static optimization and nonlinear programming. *Automatica*, 10(5), 525 – 532.

Koutroulis, E., Kalaitzakis, K., and Voulgaris, N.C. (2001). Development of a microcontroller-based, photovoltaic maximum power point tracking control system. *IEEE Transactions on Power Electronics*, 16(1), 46–54. doi:10.1109/63.903988.

Kuhn, H.W. and Tucker, A.W. (1951). Nonlinear programming. In *Proc. Second Berkeley Symp. on Math. Statist. and Prob. (Univ. of Calif. Press)*.

Loza-Lopez, M.J., Loukianov, A.G., Sanchez, E.N., Ruiz-Cruz, R., and Snchez-Torres, J.D. (2015). On-line optimization of the power supplied in a microgrid prototype. In *Smart Cities Conference (ISC2), 2015 IEEE First International*, 1–6.

Loza-Lopez, M.J., Sanchez, E.N., and Ruiz-Cruz, R. (2014). Microgrid laboratory prototype. In *Power Systems Conference (PSC), 2014 Clemson University*, 1–5. doi:10.1109/PSC.2014.6808120.

Pazos, F.A. and Bhaya, A. (2009). Control Liapunov function design of neural networks that solve convex optimization and variational inequality problems. *Neurocomputing*, 72(1618), 3863 – 3872.

Polyakov, A. (2012). Nonlinear feedback design for fixed-time stabilization of linear control systems. *IEEE Transactions on Automatic Control*, 57(8), 2106–2110.

Pyne, I.B. (1956). Linear programming on an electronic analogue computer. *American Institute of Electrical Engineers, Part I: Communication and Electronics, Transactions of the*, 75(2), 139–143.

Rapheal, M.S.A., Ram, V.G., Ramachandaramurthy, V.K., and Hew, W.P. (2009). Dynamic response of different wind generator topologies connected to medium size power grid. In *PowerTech, 2009 IEEE Bucharest*, 1–6.

Ruiz, R., Sanchez, E.N., Loukianov, A.G., and Harley, R.G. (2011). Discrete-time block control for a doubly fed induction generator coupled to a wind turbine. In *Proceedings of the IEEE International Conference on Control Applications (CCA)*. Denver, CO, USA.

Sanchez-Torres, J., Sanchez, E., and Loukianov, A. (2015). Predefined-time stability of dynamical systems with sliding modes. In *American Control Conference (ACC), 2015*, 5842–5846.

Utkin, V. (1992). *Sliding modes in control and optimization*. Springer Verlag.

Wang, J. (1993). Analysis and design of a recurrent neural network for linear programming. *IEEE Transactions on Circuits and Systems I: Fundamental Theory and Applications*, 40(9), 613–618.

Wilson, G. (1986). Quadratic programming analogs. *IEEE Transactions on Circuits and Systems*, 33(9), 907–911.

Performance evaluation of MPC for Waste Heat Recovery applications using organic Rankine cycle systems ⋆

Andres Hernandez [*,**] **Clara Ionescu** [*] **Sergei Gusev** [***]
Adriano Desideri [**] **Martijn van den Broek** [***] **Vincent Lemort** [**]
Robin De Keyser [*]

[*] *Department of Electrical energy, Systems and Automation, Ghent University, Belgium (e-mail: Andres.Hernandez@UGent.be).*
[**] *Thermodynamics laboratory, Energy system research unit, University of Liege, Belgium.*
[***] *Department of Flow, Heat and Combustion Mechanics, Ghent University, Belgium.*

Abstract: Organic Rankine Cycle (ORC) technology has demonstrated to be a suitable tool for recovering waste heat at low temperatures. The fluctuating nature of the waste heat source (varying temperature and mass flow) makes of waste heat recovery applications a challenging task. In this contribution Model Predictive Control (MPC) and more classical PID-like controllers are investigated, where special attention is paid to the analysis of the control performance for heat source profiles coming from different applications. A dynamic model of a real regenerative ORC unit equipped with a single screw expander developed in the Modelica language is used to test and compare the PID and MPC based control strategies. Results show that for low amplitude variations PID and MPC can perform equally good, but in case of large variations MPC is a more effective control strategy as it allows a safer and more efficient operation, operating close to the boundary conditions where production is maximized.

Keywords: Model Predictive control, Renewable energy systems, Process control, organic Rankine Cycle.

1. INTRODUCTION

Reducing the world-wide industrial energy consumption is a major concern in order to ensure guarantee a sustainable development. Despite all efforts to achieve a more efficient production, waste heat losses are still an important concern. An attractive technology able to recover heat at low temperatures is the Organic Rankine Cycle (ORC) system.

ORC power units stand out for their reliability and cost-effectiveness Verneau (1979),Angelino et al. (1984). Replacing the water by an organic compound opened new challenges, regarding the cycle design, selection of the fluid, modeling, simulation and control design Sun and Li. (2011); Colonna and Van Putten. (2007). Such thermodynamic units are designed to operate around certain steady-state conditions, however due to the highly fluctuating nature of the heat source, they are forced to operate at part-load conditions. Control design plays an essential role to enable a safe and optimal performance of the ORC unit. Safe operation is achieved by an accurate regulation of the superheating, since it is already recognized that low values for superheating maximize the cycle efficiency Hernandez et al. (2014) and avoid the formation of liquid droplets at expander inlet that can damage the expansion machine Wei et al. (2007).

Most of the current studies are restricted to guarantee safety conditions by regulating the superheating (see Grelet et al. (2015) and the references therein), but little attention has been paid to the performance of the power unit in terms of energy production. In order to maximize the output power the evaporating temperature is usually considered as the most relevant controlled variable Quoilin et al. (2011). In Feru et al. (2014), the modeling and control of a waste heat recovery system for a Euro-VI heavy-duty truck engine was achieved through the use of a switching model predictive control strategy to guarantee safe operation of the WHR system and to maximize output power. Also in the automotive field, the problem of maximizing the power produced by an ORC waste heat recovery system on board a diesel-electric railcar is tackled using dynamic real-time optimization Peralez et al. (2015). In Hernandez et al. (2015), an experimental study is conducted using an 11 kW_{el} pilot plant, showing that the constrained Model Predictive Control (MPC) outperforms PID based strategies, as it allows to accurately regulate the evaporating temperature with a lower control effort while keeping the superheating in a safer operating range.

In this study we investigate the performance of MPC and PID based strategies to optimally recover waste heat through ORC technology. Using existent components from the ThermoCycle library Quoilin et al. (2014), a dynamic model of an ORC system is built for simulation purposes. The model dynamics

⋆ The results presented in this paper have been obtained within the frame of the IWT SBO-110006 project The Next Generation Organic Rankine Cycles (www.orcnext.be), funded by the Institute for the Promotion and Innovation by Science and Technology in Flanders, Belgium. This financial support is gratefully acknowledged.

are coherent with those observed on real systems as presented in Desideri et al. (2014), where the dynamic models is experimentally validated using a low-capacity (11 kWe) waste heat recovery unit equipped with a single screw expander. Using the developed dynamic model, insight on the system dynamics and optimal operation is achieved, resulting in the development of a real-time optimizer to compute the optimal evaporating temperature which maximizes the power generation. The controller's task is to track the optimal set-point generated by the optimizer while ensuring a minimum superheating value for safely operation.

The paper is structured as follows. Section 2 introduces the architecture and main characteristics of the ORC system. Next, in section 3 the Extended Prediction Self-Adaptive (EPSAC) approach to MPC used in this study is briefly described. A low-order model suitable for prediction is then developed using parametric identification as described in section 4. The control structure, design and tuning of the proposed PID and MPC based strategies is described in section 5, followed by the simulation results in section 6. Finally a conclusion section summarizes the main outcome of this contribution.

2. PROCESS DESCRIPTION

This section describes the architecture and main characteristics of the ORC system used for evaluating the performance of the developed control strategies.

2.1 The Organic Rankine Cycle System

In order to assess the performance of the different developed control strategies, a dynamic model of the ORC system presented in Fig. 1 has been developed in the Modelica language using existent components from the Thermo Cycle library Quoilin et al. (2014). The developed model is then exported into Simulink/Matlab environment by means of the Functional Mock-Up Interface (FMI) open standard.

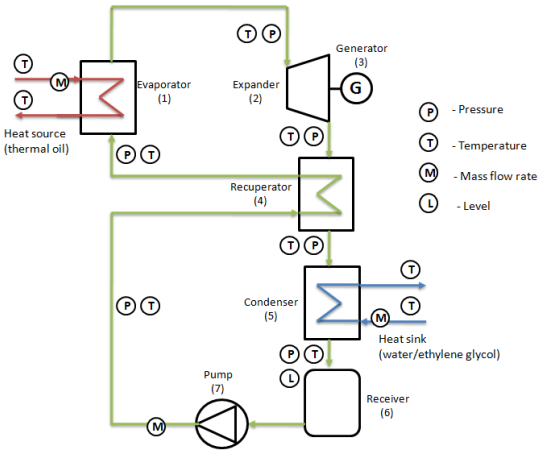

Fig. 1. Schematic layout of the pilot plant available at Ghent University, campus Kortrijk (Belgium)

The system based on a regenerative cycle and solkatherm (SES36) as working fluid, shows a nominal power of 11 kWe. The expander is originally a single screw compressor adapted to run in expander mode. It drives an asynchronous generator connected to the electric grid through a four-quadrant inverter, which allows varying the generator rotational speed (N_{exp}). During the simulations performed in this paper, the generator rotational speed is kept constant at 3000 rpm to emulate an installation directly connected to the grid. The circulating pump (N_{pp}) is a vertical variable speed 14-stage centrifugal pump with a maximum pressure of 14 bar and 2.2 kWe nominal power.

Starting from the bottom of the scheme it is possible to recognize the liquid receiver (b) installed at the outlet of the condenser (a) where the fluid is collected in saturated liquid condition. From the receiver outlet, the fluid is pumped (c) through the regenerator (d) cold side, and the evaporator (e), where it is heated up to superheated vapor, reaching its maximum temperature at the evaporator outlet. The fluid, after being expanded in the volumetric machine (f), enters the regenerator hot side, and then it flows into the condenser (a) to close the cycle.

In order to assess the performance of the different developed control strategies a dynamic model of the ORC system (Fig. 1) has been developed in the Modelica language using existent components from the ThermoCycle library Quoilin et al. (2014). The developed model is then exported into Simulink/Matlab® environment by means of the Functional Mock-Up Interface (FMI) open standard.

2.2 Conditions for optimal operation of an ORC unit

In order to optimally operate an ORC unit, two main conditions need to be satisfied: **i)** keep the cycle in a safe condition during operation and **ii)** maximize the net output power. Safe operation of the ORC unit is important as it allows a longer life expectancy in all components. In this concern, an accurate regulation of superheating (ΔT_{sh}), is the main priority since a minimum value of superheating has to be guaranteed in order to avoid a wet expansion (i.e., formation of liquid droplets at the expander inlet that can damage the expansion machine). The superheating is defined as:

$$\Delta T_{sh} = T_{exp,in} - T_{sat,ev} \tag{1}$$

where $T_{exp,in}$ is the temperature measured at the inlet of the expander and $T_{sat,ev}$ the evaporating temperature, corresponding to the temperature at which the fluid undergoes the phase transition from saturated liquid to saturated vapor at the fixed evaporating pressure $p_{sat,ev}$.

In order to maximize the output power the evaporating temperature represents the most relevant control variable Quoilin et al. (2011), which needs to be adapted depending on the heat source conditions Hernandez et al. (2015). The main terms to assess the performance of the ORC system are the net output power and the cycle efficiency, which are defined as:

$$\dot{W}_{el,net} = \dot{W}_{exp} - \dot{W}_{pump} \tag{2}$$

$$\eta_{cycle} = \frac{\dot{W}_{el,net}}{\dot{Q}_{in,ORC}} \tag{3}$$

where $\dot{W}_{exp}$ is the expander electrical power, $\dot{W}_{pump}$ is the pump electrical power and $\dot{Q}_{in,ORC}$ is the thermal power supplied to the ORC system in the evaporator.

2.3 Optimal evaporating temperature

Previous studies have demonstrated the existence of an optimal evaporating temperature which maximizes the output power for a given heat source conditions, where a real-time optimizer (RTO) can be built using a steady-state model Quoilin et al.

(2011) or by means of extremum-seeking algorithm Hernandez et al. (2016). In this paper the first approach is chosen, thus leading to the following correlation used in the RTO:

$$T_{sat,opt} = -290.915 + 183.33 * log_{10}(T_{hf}) + 10.636 * \dot{m}_{hf} \quad (4)$$

Equation (4) is valid in the range of $0.5 \leq \dot{m}_{hf} \leq 1.5\,\mathrm{kg/s}$ and $90 \leq T_{hf} \leq 125\,^{\circ}\mathrm{C}$ given a constant saturation temperature in the condenser of $p_{sat,cd} = 1.4\,\mathrm{bar}$.

3. MODEL PREDICTIVE CONTROL

A brief introduction to EPSAC algorithm is presented in this section. For a detailed description the reader is referred to De Keyser (2003); Hernandez et al. (2015).

3.1 Computing the Predictions

Using EPSAC algorithm, the measured process output can be represented as:

$$y(t) = x(t) + n(t) \quad (5)$$

where $x(t)$ is the model output which represents the effect of the control input $u(t)$ and $n(t)$ represents the effect of the disturbances and modeling errors, all at discrete-time index t. Model output $x(t)$ can be described by the generic system dynamic model:

$$x(t) = f[x(t-1), x(t-2), \ldots, u(t-1), u(t-2), \ldots] \quad (6)$$

Notice that $x(t)$ represents here the model output, not the state vector. Also important is the fact that f can be either a *linear* or a *nonlinear* function.

Furthermore, the disturbance $n(t)$ can be modeled as colored noise through a filter with the transfer function:

$$n(t) = \frac{C(q^{-1})}{D(q^{-1})} e(t) \quad (7)$$

with $e(t)$ uncorrelated (white) noise with zero-mean and C, D monic polynomials in the backward shift operator q^{-1}. The disturbance model must be designed to achieve robustness of the control loop against unmeasured disturbances and modeling errors Maciejowski. (2002).

A fundamental step in the EPSAC methodology consists of the prediction. Using the generic process model (5), the predicted values of the output are:

$$y(t+k|t) = x(t+k|t) + n(t+k|t) \quad (8)$$

$x(t+k|t)$ and $n(t+k|t)$ can be predicted by recursion of the process model (6) and by using filtering techniques on the noise model (7), respectively De Keyser (2003).

3.2 Computing the optimal control action

A key element in linear MPC is the use of base (or free) and optimizing (or forced) response concepts Maciejowski. (2002). In EPSAC, the future response can be expressed as:

$$y(t+k|t) = y_{base}(t+k|t) + y_{optimize}(t+k|t) \quad (9)$$

The two contributing factors have the following origin:

- $y_{base}(t+k|t)$ is the effect of the past inputs, the a priori defined future base control sequence $u_{base}(t+k|t)$ and the predicted disturbance $n(t+k|t)$.
- $y_{optimize}(t+k|t)$ is the effect of the additions $\delta u(t+k|t)$ that are optimized and added to $u_{base}(t+k|t)$, according to $\delta u(t+k|t) = u(t+k|t) - u_{base}(t+k|t)$. The effect of these additions is the discrete time convolution of $\Delta U = \{\delta u(t|t), \ldots, \delta u(t+N_u-1|t)\}$ with the impulse response coefficients of the system (G matrix), where N_u is the chosen control horizon.

The control ΔU is the solution to the following constrained optimization problem:

$$\begin{aligned} \Delta U = & arg \min_{\Delta U \in \mathbb{R}^{N_u}} \sum_{k=N_1}^{N_2} [r(t+k|t) - y(t+k|t)]^2 \\ & subject\ to\ |M.\Delta U \leq N \end{aligned} \quad (10)$$

where N_1 and N_2 are the minimum and maximum prediction horizons, N_u is the control horizon, $r(t+k|t)$ is a future set-point or reference sequence. The various process input and output constraints can all be expressed in terms of ΔU, resulting in matrices M, N. Since (10) is quadratic with linear constraints in decision variables ΔU, then the minimization problem can be solved by a quadratic programming (QP) algorithm Maciejowski. (2002).

4. SYSTEM IDENTIFICATION

A trade-off between complexity of the model and prediction accuracy has to be made, in order to ensure the correct performance of the MPC strategy. In this work we have chosen a pragmatic approach by performing a parametric identification based on experimental data recorded in the available setup.

The model has been identified from the manipulated variable, pump speed (N_{pp}) to the evaporating temperature ($T_{sat,ev}$) and superheating (ΔT_{sh}). The identification has been performed using a multisine excitation signal and the prediction error method (pem) Ljung (2007). The sampling time $T_s = 1\,\mathrm{s}$ has been chosen according to the fastest dynamics of the system.

It is important to notice that in practice it is also possible to measure the temperature and mass flow rate of the heat source (T_{hf}) and ($\dot{m}_{hf}$), making possible to use them as measured disturbances. Therefore, models from these variables to evaporating temperature ($T_{sat,ev}$) and superheating (ΔT_{sh}) are also built. The nominal operating conditions of the system are presented in table 1.

Table 1. Nominal operating conditions considered for the Identification Procedure

Parameter	*Description*	*Value*	*Unit*
N_{pp}	Pump rotational speed	1680	rpm
N_{exp}	Expander rotational speed	3000	rpm
$T_{sat,ev}$	Evaporating temperature	100	$^{\circ}C$
ΔT_{sh}	Superheating	20	$^{\circ}C$
T_{hf}	Temperature hot fluid	120	$^{\circ}C$
$\dot{m}_{hf}$	Mass flow rate hot fluid	1.0	kg/s
T_{cf}	Temperature cold fluid	15	$^{\circ}C$
$\dot{m}_{cf}$	Mass flow rate cold fluid	3.0	kg/s
$\dot{W}_{el,net}$	Net output power	11	kW
η_{cycle}	Cycle efficiency	6	%

The identified model is presented in (11) in the form of discrete-time transfer functions using the backwards shift operator q^{-1}.

$$\frac{\Delta T_{sh}(t)}{N_{pp}(t)} = \frac{-0.063q^{-1}+0.059q^{-2}}{1-2.44q^{-1}+1.955q^{-2}-0.51q^{-3}} \quad (11a)$$

$$\frac{\Delta T_{sh}(t)}{T_{hf}(t)} = \frac{0.47q^{-1}}{1-0.51q^{-1}} \quad (11b)$$

$$\frac{\Delta T_{sh}(t)}{m_{hf}(t)} = \frac{-2.98q^{-1}+4.29q^{-2}-1.31q^{-3}}{1-1.35q^{-1}-0.11q^{-2}+0.46q^{-3}} \quad (11c)$$

$$\frac{T_{sat}(t)}{N_{pp}(t)} = \frac{0.066q^{-1}-0.063q^{-2}}{1-2.42q^{-1}+1.91q^{-2}-0.49q^{-3}} \quad (11d)$$

$$\frac{T_{sat}(t)}{T_{hf}(t)} = \frac{0.0017q^{-11}-0.0017q^{-12}}{1-3.6q^{-1}+4.88q^{-2}-2.95q^{-3}+0.67q^{-4}} \quad (11e)$$

$$\frac{T_{sat}(t)}{m_{hf}(t)} = \frac{2.43q^{-1}-6.16q^{-2}+5.33q^{-3}-1.6q^{-4}}{1-2.93q^{-1}+3.12q^{-2}-1.42q^{-3}+0.23q^{-4}} \quad (11f)$$

5. CONTROL STRUCTURE AND TUNING

In this section the control structure and tuning procedure of the proposed strategies are discussed.

Three control strategies are developed in order to control the ORC unit, two based on PID and one based on MPC. In all strategies we make use of the real-time optimizer (RTO) to compute, as a function of the varying heat source conditions, the optimal evaporating temperature $T_{sat,opt}$ which will be used as reference to the controller, as illustrated in Fig. 2.

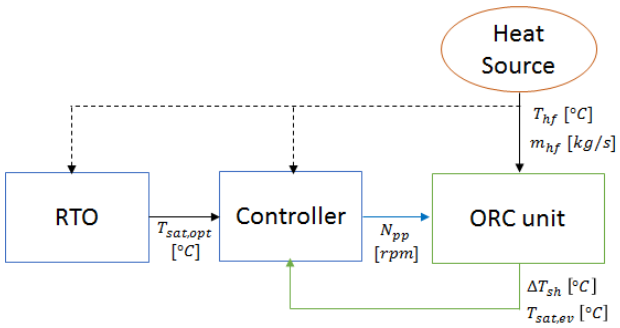

Fig. 2. Control structure of the proposed closed loop including the real-time optimizer (RTO).

An important element on the control design are the physical constraints and the safety conditions of the system. For which, the controller is required to respect the input (pump speed) and output (superheating) constraints, summarized in table 2.

Table 2. Operation constraints of the ORC unit

Variable	*max*	*min*	Δ
Pump Speed N_{pp}	1320 rpm	2100 rpm	60 rpm/s
Superheating ΔT_{sh}	–	10 °C	-

5.1 PI strategy

This strategy is based on a PI controller which is used to track the optimal evaporating temperature $T_{sat,opt}$. The PI controller is tuned using the transfer function which relates the speed in the pump to the evaporating temperature (11) for the following design specifications: settling time $T_{set} = 60$ s, overshoot percent $OS\% = 0$ and robustness $R_o = 0.7$, obtaining the PI parameters:

$$PI_{T_{sat,ev}} = K_p\left(1+\frac{1}{T_i s}\right) = 0.189\left(1+\frac{1}{1.7813 s}\right) \quad (12)$$

During the implementation phase the clamping anti-reset windup scheme is used to clip the control action into the permissible range of the pump (table 2).

5.2 Switching PIs

In order to improve the performance of the PI strategy, essentially to what refers to safety conditions, an override control (here called switching PI strategy) is implemented. In this strategy the $PI_{T_{sat,ev}}$ controller is used to follow the optimal evaporating temperature set-point unless that superheating value goes below a threshold value $\Delta T_{sh} < 10\,°C$, in which case another PI controller for superheating $PI_{DT_{sh}}$, is used with set-point at $\Delta T_{sh,ref} = 10\,°C$, in order to bring the system back to a safe stage.

While the PI controller for the evaporating temperature is the same used on the basic PI strategy (12), the PI controller for superheating is tuned using the transfer function which relates the speed of the pump to the superheating found in (11), for the following design specifications: settling time $T_{set} = 60s$, overshoot percent $OS\% = 0$ and robustness $R_o = 0.7$, the following PI parameters are obtained:

$$PI_{\Delta T_{sh}} = K_p\left(1+\frac{1}{T_i s}\right) = -1.1\left(1+\frac{1}{0.98 s}\right) \quad (13)$$

5.3 MPC-EPSAC

In this strategy a constrained MPC-EPSAC controller is implemented to track the optimal evaporating temperature $T_{sat,opt}$, while ensuring superheating will remain above 10 °C.

In MPC, a balance between acceptable control effort and acceptable control error can be obtained via many tuning parameters (e.g., the reference trajectory design parameter α; the prediction horizon N_2 and the control horizon design parameter N_u). Closed loop performance is designed using the N_2 parameter, whereas larger values provide a more conservative and robust control. The control horizon N_u is used to structure the future control scenario, reducing the degrees of freedom from N_2 to N_u. Structuring leads to simplified calculations and has generally a positive effect on robustness. The design parameter α in the reference trajectory can vary in the range of: $0 \leq \alpha \leq 1$. A value of α closer to 1 means a smoother variation of the set-point and hence a less aggressive control action.

A trade-off between closed loop speed and robustness has been obtained for $N_2 = 15$, $N_u = 1$ and $\alpha = 0.5$. The main goal is to achieve a response without overshoot $OS\% = 0$ and settling time of about 60 s. Another important element in the design of the controller is the choice of the disturbance model (7), during this study the 'default' filter $C(q^{-1}) = 1$ and $D(q^{-1}) = 1 - q^{-1}$ has been chosen leading to zero steady-state error Maciejowski. (2002). Notice that this filter choice acts like the integral action for PID controllers.

6. SIMULATION RESULTS AND DISCUSSION

The present study focuses on investigating which are the advantages of using advanced controllers such as MPC compared to PID-like strategies for the optimal operation of an ORC system in waste heat recovery applications. The control strategy task is to accurately regulate the evaporating temperature (given by the RTO), in order to maximize the energy production, while avoiding formation of liquid droplets that could damage the expander by ensuring an small amount of superheating ΔT_{sh}. Thus in this study we will focus on answering two questions:

- which are the heat source conditions which represent the main challenge for any controller? and

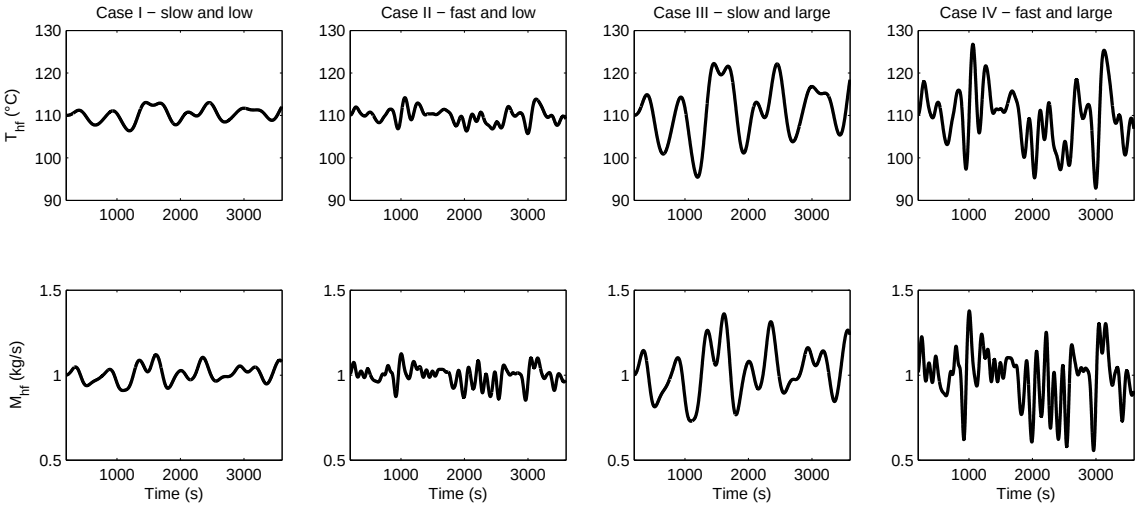

Fig. 3. Heat source profiles due to temperature T_{hf} and mass flow rate m_{hf} variations. Case I: slow and low amplitude variations. Case II: fast and low amplitude variations. Case III: slow and large amplitude variations. Case IV: fast and large amplitude variations.

- which controller produces the highest output power while keeping the safety conditions?

In order to answer those questions, we introduce four different scenarios depicted in figure 3, in which the controllers will be tested. The heat source variations are due to the combination of slow, fast, low or large transitions in temperature T_{hf} and mass-flow-rate m_{hf}:

- Case I: slow and low amplitude transitions. $T_{hf} = \pm 5\,^{\circ}\mathrm{C}$ and $\dot{m}_{hf} = \pm 0.1\,\mathrm{kg/s}$
- Case II: fast and low amplitude transitions. $T_{hf} = \pm 5\,^{\circ}\mathrm{C}$ and $\dot{m}_{hf} = \pm 0.1\,\mathrm{kg/s}$
- Case III: slow and large amplitude transitions. $T_{hf} = \pm 15\,^{\circ}\mathrm{C}$ and $\dot{m}_{hf} = \pm 0.3\,\mathrm{kg/s}$
- Case IV: fast and large amplitude transitions. $T_{hf} = \pm 18\,^{\circ}\mathrm{C}$ and $\dot{m}_{hf} = \pm 0.4\,\mathrm{kg/s}$

The three strategies tested for cases I and II (not shown here) result on good closed-loop performance, i.e., the difference in terms of tracking capabilities and control effort is negligible. During those heat source conditions the controllers are able to track correctly the quick transitions, meaning that the controllers have a high enough bandwidth and superheating remains into the desired limits.

Large amplitude variations in the heat source cause sudden drops in the superheating value, as depicted in Fig. 4 at time instant 1350 s. The switching mechanism avoids the superheating to decrease dramatically compared to the PI strategy, nevertheless, it still undergoes the threshold value of 10 °C. For the case of MPC, the most important element to highlight is the fact that this control strategy always respects the hard-output-constraint of $\Delta T_{sh} > 10\,^{\circ}\mathrm{C}$. Because it uses a model for prediction, it is able to better compensate possible sudden drops in the superheating, thus resulting in a higher net output power and higher life expectancy of the actuator, both due to the smoother control effort (i.e., lower pump speed N_{pp} variations).

Previous observations are more evident when analyzing the results for case IV, (i.e., fast and large amplitude variations), where sudden drops in the superheating value are observed

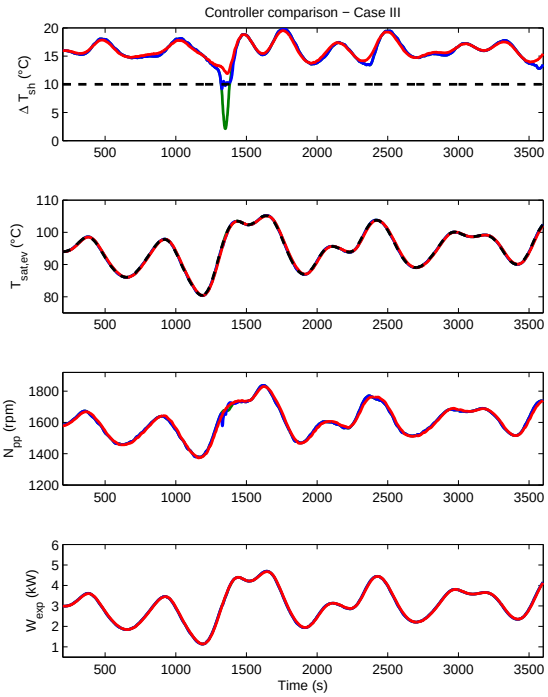

Fig. 4. Controllers comparison for Case III. Solid green- PI strategy; solid blue- Switching PI and solid red- represents MPC-EPSAC strategy.

at time instants 1038 s, 1350 s, 2080 s, 2664 s and 3080 s as depicted in Fig. 5.

The simulation results obtained suggest that MPC outperforms the PI based strategies for the case of large amplitude variations in the heat source. Hence, resulting in a desirable strategy regarding safety conditions. In a real industrial context, using a single PI would be an unsafe and therefore unusable strategy. Instead, the switching PI (in solid blue line) regulate

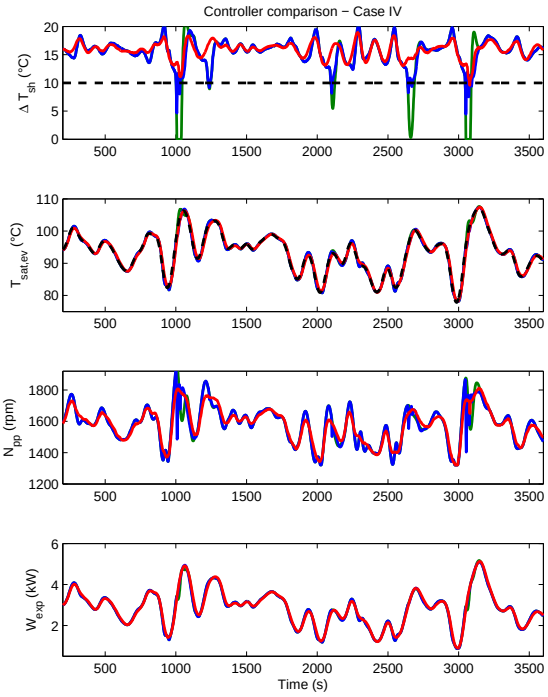

Fig. 5. Controllers comparison for Case IV. Solid green- PI strategy; solid blue- Switching PI and solid red- represents MPC-EPSAC strategy.

both evaporating temperature and superheating, thus enabling a safer operation while keeping smooth transition between the controllers. However, there is no direct control on how much can superheating decrease, as observed in for cases III and IV where superheating values close to 5 °C were observed.

7. CONCLUSION

In the present contribution three different PI and MPC based strategies have been designed and tested in simulation, with the goal of optimizing the working conditions of an ORC unit for WHR applications.

Results suggest that large amplitude variations in the waste heat source (e.g. cases III and IV), represent the most challenging situation for control design. Hence, implementation of advanced controllers such as MPC is highly recommended as it generates the same or higher net electrical output power compared to PID-based strategies while offering a safer operation. This is achieved by more accurately regulating the optimal evaporating temperature generated by the optimizer, while keeping the superheating at safe values, resulting also in a higher efficiency of the system. On the other hand, for the case of low amplitude variations (e.g. cases I and II), PID-like strategies might offer a satisfactory performance.

Future work includes adding more degrees of freedom by manipulating the expander speed, or by acting on the mass flow rate and/or temperature of the heat sink.

REFERENCES

Angelino, G., Gaia, M., and Macchi., E. (1984). A review of italian activity in the field of organic rankine cycles. In *proceedings of the International VDI-Seminar*, 465–482.

Colonna, P. and Van Putten., H. (2007). Dynamic modeling of steam power cycles.: Part i modeling paradigm and validation. *Applied Thermal Engineering*, 27(2-3), 467 – 480.

De Keyser, R. (2003). *Model based Predictive Control for Linear Systems*, chapter invited in UNESCO Encyclopaedia of Life Support Systems (EoLSS). Article contribution 6.43.16.1, Oxford, 35 pages.

Desideri, A., van den Broek, M., Gusev, S., Lemort, V., and Quoilin, S. (2014). Experimental campaign and modeling of a low-capacity waste heat recovery system based on a single screw expander. In *22nd International Compressor Engineering Conference*. Purdue, USA.

Feru, E., Willems, F., de Jager, B., and Steinbuch, M. (2014). Modeling and control of a parallelwaste heat recovery system for euro-vi heavy-duty diesel engines. *energies*, 7, 6571–6592.

Grelet, V., Dufour, P., Nadri, M., Lemort, V., and Reichel, T. (2015). Explicit multi-model predictive control of a waste heat rankine based system for heavy duty trucks. In *In IEEE Conference on Decision and Control, Osaka, Japan*.

Hernandez, A., Desideri, A., Ionescu, C., De Keyser, R., Lemort, V., and Quoilin, S. (2016). Real-time optimization of organic rankine cycle systems by extremum-seeking control. *Energies*, 9(5), 334.

Hernandez, A., Desideri, A., Ionescu, C., Quoilin, S., Lemort, V., and De Keyser, R. (2014). Increasing the efficiency of organic rankine cycle technology by means of multivariable predictive control. In *Proc. of the 19th World IFAC Congress (IFAC 2014)*.

Hernandez, A., Desideri, A., Ionescu, C., Quoilin, S., Lemort, V., and De Keyser., R. (2015). Experimental study of predictive control strategies for optimal operation of organic rankine cycle systems. In *Proceedings of the European Control Conference (ECC15)*. Linz, Austria.

Ljung, L. (2007). *System identification: theory for the user*. Prentice-Hall.

Maciejowski., J. (2002). *Predictive Control: With Constraints*. Pearson Education. Prentice Hall.

Peralez, J., Tona, P., Nadri, M., Dufour, P., and Sciarretta, A. (2015). Optimal control for an organic rankine cycle on board a diesel-electric railcar. *Journal of Process Control*, 33, 1 – 13.

Quoilin, S., Aumann, R., Grill, A., Schuster, A., and Lemort., V. (2011). Dynamic modeling and optimal control strategy for waste heat recovery organic rankine cycles. *Applied Energy*, Vol. 88, 2183–2190.

Quoilin, S., Desideri, A., Wronski, J., Bell, I., and Lemort., V. (2014). Thermocycle: A modelica library for the simulation of thermodynamic systems. In *Proceedings of the 10th International Modelica Conference*. Lund, Sweden.

Sun, J. and Li., W. (2011). Operation optimization of an organic rankine cycle (orc) heat recovery power plant. *J. Applied Thermal Engineering*, Vol. 31, 2032–2041.

Verneau, A. (1979). Waste heat recovery by organic fluid rankine cycle. In *In Proceedings from the First Industrial Energy Technology Conference*, 940–952. Houston, TX.

Wei, D., Lu, X., Lu, Z., and Gu., J. (2007). Performance analysis and optimization of organic rankine cycle (orc) for waste heat recovery. *J. Energy Conversion and Management*, Vol. 48, 1113–1119.

CHAPTER 10

NONLINEAR SYSTEMS

Control of underactuated unmanned surface vessels with linear flatness-based filters

Bardalez L.*, Sotomayor-Moriano J., Enciso L.*****
**Pontificia Universidad Católica del Perú, Av.Universitaria 1801*
Lima, Perú (e-mail: lbardalezg@pucp.pe).
***Pontificia Universidad Católica del Perú, Av.Universitaria 1801*
Lima, Perú (e-mail: jsotom@pucp.pe).
****Pontificia Universidad Católica del Perú, Av.Universitaria 1801*
Lima, Perú (e-mail: lenciso@pucp.pe).

Abstract: Proper functioning of unmanned surface vessels requires effective trajectory tracking. To achieve this, upon selecting the method for control system design, the knowledge required regarding vessel dynamics described by a model must be taken into account. In this case, it would be advantageous to design the controller requiring the least task effort in modeling for fulfilling the tracking requirements. This paper proposes an active disturbance rejection control system based on linear filters applied to tracking arbitrary trajectories of an underactuated unmanned surface vessel, as an alternative that uses a simple model. Finally, a performance comparison between the proposed control and another control technique (whose design requires a more complex model) is presented.

Keywords: Disturbance rejection, Nonlinear control, Marine systems, Flatness based control.

1. INTRODUCCIÓN

Unmanned surface vessel (USV) control is focused on path-following and trajectory-tracking problems, reducing the USV's tracking error.

Currently, there are many control techniques for fully actuated USV's (Fossen, 2000; Fossen, 2011), where the number of actuators is the same as the number of degrees of freedom; however, underactuated USV (UUSV) control is a field that still requires further investigation as the number of actuators is lesser than the degrees of freedom. The techniques used for the latter can be classified according to the required knowledge level of the mathematical model chosen for the control system design.

In non-linear control, when employing controllers such as those based on the stability method of Lyapunov and additional modifications (Do, 2010; Ding, et. al., 2011; Bao-Li, 2013), backstepping (Ding, et. al., 2011; Yang, et. al., 2014) and successive linearization (Chwa, 2011), complete knowledge of parameters of the UUSV mathematical model is required. In addition, some of these methods (Ding, et. al., 2011; Bao-Li, 2013) do not exhibit robustness to parametric variations or to non-modeled disturbances.

In learning-based control, developing a model based on neural networks requires data acquisition and performing controller optimization, which facilitates its design since it does not depend closely on UUSV modeling. An advantage of these techniques is the adaptability, which provides control under various operating conditions (Dai, et al., 2012; Pan, et al., 2013). The main disadvantage is the computational cost of the adaptation mechanism as well as the number of calculations at each time interval.

In active disturbance rejection control, ultra-local models or dynamic simplified models are used (Li, et. al., 2012; Li, et. al., 2013), avoiding the use of complex mathematical models. The main disadvantage found in these controllers is that, due to their design, the inherent UUSV kinematics is ignored and only a priori known geometrics can be tracked.

This paper presents the design of active disturbance rejection control based on linear flatness-based filters applied on an underactuated unmanned surface vessel (UUSV) to track arbitrary trajectories. This design employs the knowledge of system kinematics and only requires knowledge of dynamic parameters regarding the actuators, which in practice are easily recognizable.

Section 2 describes the system dynamic model. Section 3 includes a review of active disturbance rejection control, emphasizing the robust generalized proportional-integral controller as a linear flatness-based filter. Section 4 presents the controller design for a UUSV. Simulation testing results are analyzed and contrasted with a controller based state-feedback linearization in section 5. Conclusions are described in Section 6.

2. SYSTEM DYNAMIC MODEL

Considering a UUSV with coordinated axes and actuator arrangement as defined in Figure 1, where positions x and y, yaw angle ψ (measured from the X-axis), surge and

displacement speeds *u* and *y*, yaw speed *r*, driving force *F* and steering torque *T*.

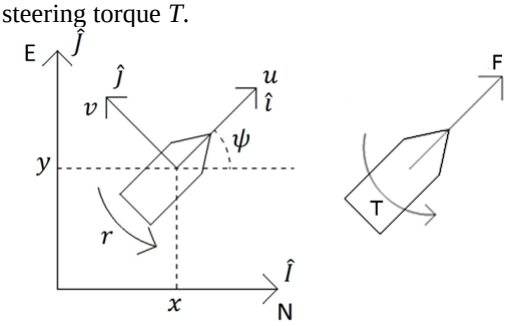

Figure1. Bottom view of coordinated system (left) and actuator arrangement (right).

The dynamic model of this UUSV (Fossen, 2011) is presented in (1)

$$\begin{aligned} \dot{\eta} &= R(\psi)\nu \\ M\dot{\nu} + C(\nu)\nu + D(\nu)\nu &= B_\tau \tau \end{aligned} \tag{1}$$

$$\eta = \begin{bmatrix} x \\ y \\ \psi \end{bmatrix}, \nu = \begin{bmatrix} u \\ v \\ r \end{bmatrix}, \tau = \begin{bmatrix} F \\ T \end{bmatrix}$$

$$R(\psi) = \begin{bmatrix} \cos\psi & -\sin\psi & 0 \\ \sin\psi & \cos\psi & 0 \\ 0 & 0 & 1 \end{bmatrix}$$

$$M = \begin{bmatrix} M_{11} & 0 & 0 \\ 0 & M_{22} & M_{23} \\ 0 & M_{23} & M_{33} \end{bmatrix}$$

$$C(\nu) = \begin{bmatrix} 0 & 0 & -M_{22}v - M_{23}r \\ 0 & 0 & M_{11}u \\ M_{22}v + M_{23}r & -M_{11}u & 0 \end{bmatrix}$$

$$D(\nu) = \begin{bmatrix} D_{11}(u) & 0 & 0 \\ 0 & D_{22}(v,r) & D_{23}(v,r) \\ 0 & D_{32}(v,r) & D_{33}(v,r) \end{bmatrix}; \quad B_\tau = \begin{bmatrix} 1 & 0 \\ 0 & 0 \\ 0 & 1 \end{bmatrix}$$

Where $R(\psi)$ is rotation matrix from the UUSV system fixed $\hat{\imath} - \hat{\jmath}$ to the inertial system $\hat{I} - \hat{J}$, M is the full mass matrix, $C(v)$ is the Coriolis matrix, $D(v)$ is the damping matrix composed of non-linear functions and B_τ is the geometric matrix of system actuators.

This mathematical model was chosen since it adequately approximates the actual UUSV dynamics and it will make possible to illustrate the effectiveness of the proposed controller exposed to a highly non-linear dynamic behavior.

In the case of fully actuated USV's, the model would also include a force *H* applied in the transversal axis (Wondergem et. al. 2011); however, in small USV's, it is common to avoid this configuration because it would reduce available space, increase USV's weight and consume more energy.

3. ACTIVE DISTURBANCE REJECTION CONTROL

3.1. Active disturbance rejection control

The dynamics of a system of order *n* can be expressed according to (2), where μ is the control action, *b* is a system constant; and *f(...)* is a function that depends on unknown and non-linear system dynamics and on its endogenous and exogenous disturbances *w*:

$$x^{(n)} = f\left(x, \dot{x}, \ldots, x^{(n-1)}, u, w\right) + b\mu \tag{2}$$

There are different alternatives to control (2) that are based on active disturbance rejection control (ADRC), where the objective is to eliminate the term *f(...)* from the dynamics in order to simplify controller design. The best known solution entails the use of extended state observers (ESO), which estimates the term *f(...)* and the derivatives of *x* (Gao, 2006; Han, 2009). Another approach is to use a model-free control through intelligent PID controllers (Fliess, 2013), in which the term *f(...)* is estimated and eliminated through integrals of variables *x* and *u*. It is also possible to perform control without the estimation of the term *f(...)* through the use of GPI controllers (Sira et. al., 2010). These controllers are robust to polynomial disturbances in time (Morales and Sira, 2010); however, they are not robust against complex disturbances. For the latter case, in (Sira, et. al., 2008), a robust GPI controller that includes an integral action in the resulting transfer function is proposed and, in (Sira, et. al, 2010), a further order reduction is proposed.

3.2. Robust GPI Controller

The general structure of a robust GPI controller can be generalized as in (3) (Luviano-Juárez, et. al., 2008), where *n* is the order of the system, *m* is the order considered in the disturbance *f(...)* and e_x is the tracking error with respect to reference x^*; thus, $e_x = x - x^*$.

$$\mu = -\frac{1}{b}\frac{\lambda_{n+m-1}s^{m+n-1} + \lambda_{n+m-2}s^{m+n-2} + \cdots + \lambda_1 s + \lambda_0}{s^m\left(s^{n-1} + \lambda_{2n+m-2}s^{n-2} + \cdots + \lambda_{n+m+1}s + \lambda_{n+m}\right)}e_x \tag{3}$$

For the particular case of a system with first order dynamics and first order (constant) disturbance, the controller in (4) is used, where closed-loop dynamics can be chosen by selecting ζ and ω_n; and the corresponding controller parameters can be obtained from (5).

$$\mu = -\frac{1}{b}\frac{\lambda_1 s + \lambda_0}{s}e_x \tag{4}$$

$$s^2 + \lambda_1 s + \lambda_0 \equiv s^2 + 2\zeta\omega_n + \omega_n^2 \tag{5}$$

Similarly, for a system with second order dynamics and first order (constant) disturbance, the controller is shown in (6) and the characteristic equation in (7).

$$\mu = -\frac{1}{b}\frac{\lambda_2 s^2 + \lambda_1 s + \lambda_0}{s(s + \lambda_3)}e_x \tag{6}$$

$$s^4 + \lambda_3 s^3 + \lambda_2 s^2 + \lambda_1 s + \lambda_0 \equiv \left(s^2 + 2\zeta\omega_n + \omega_n^2\right)^2 \tag{7}$$

3.3. Configuration of a linear flatness-based filter

A flat system is a system whose inputs and outputs can be expressed in function of a variable and its derivatives (Sira, et. al. 2004). Without loss of generality, the controller shown in (6) is used. Thus, the robust GPI controller can be seen as a flat system (Sira, et. al, 2010) since, through definition of the filtered error e_f in (8), tracking error e_x and the control action u can be expressed as a function of e_f as in (9) and (10). As a result, the controller can be expressed as an integrator chain in (11).

$$e_f = \frac{1}{s(s+\lambda_3)} e_x \tag{8}$$

$$e_x = \ddot{e}_f + \lambda_3 \dot{e}_f \tag{9}$$

$$\mu = -\frac{1}{b}\left(\lambda_2 \ddot{e}_f + \lambda_1 \dot{e}_f + \lambda_0 e_f\right) \tag{10}$$

$$\begin{aligned} \dot{z}_1 &= z_2 \\ \dot{z}_2 &= -\lambda_3 z_2 + e_x \\ \mu &= \frac{1}{b}\left((\lambda_2\lambda_3 - \lambda_1)z_2 - \lambda_0 z_1 - \lambda_2 e_x\right) \end{aligned} \tag{11}$$

4. CONTROL SYSTEM DESIGN

4.1. Problem formulation

The goal is that a UUSV can follow arbitrary trajectories defined in time without restrictions in their form and with speed of approximately 1 *m/s.*, x_d and y_d will be used to denote a point of the desired trajectory at a given time instant. The proposed control system is presented in Figure 2.

4.2. Trajectory Controller Design

In the dynamic model presented in (1) the states derivatives can be isolated (12).

$$\begin{aligned} \dot{x} &= u\cos\psi - v\sin\psi \\ \dot{y} &= u\sin\psi + v\cos\psi \\ \dot{\psi} &= r \\ \dot{u} &= U_u(u)u + U_{vr}vr + U_{rr}r^2 + U_F F \\ \dot{v} &= V_v(v,r)v + V_r(v,r)r + V_{uv}uv + V_{ur}ur + V_T T \\ \dot{r} &= R_v(v,r)v + R_r(v,r)r + R_{uv}uv + R_{ur}ur + R_T T \end{aligned} \tag{12}$$

U_i, V_j and R_k can be obtained from (1); however, in accordance with ARDC, (12) can be taken to the form (13), where its values are not considered.

$$\begin{aligned} \dot{x} &= u\cos\psi - v\sin\psi \\ \dot{y} &= u\sin\psi + v\cos\psi \\ \dot{\psi} &= r \\ \dot{u} &= \cdots + U_F F \\ \dot{v} &= \cdots \\ \dot{r} &= \cdots + R_T T \end{aligned} \tag{13}$$

Defining the reference trajectory x_r and y_r, generated from the desired trajectory and errors regarding the trajectory in reference $e_x = x - x_r$ and $e_y = y - y_r$, the dynamics of these errors can be expressed by (14). It can be observed that the kinematics of the UUSV naturally appears in these dynamics, which obliges the use of such structure in the controller design.

$$\begin{bmatrix} \ddot{e}_x \\ \ddot{e}_y \end{bmatrix} = \begin{bmatrix} U_F\cos\psi & -u\sin\psi \\ U_F\sin\psi & u\cos\psi \end{bmatrix} \begin{bmatrix} F \\ r \end{bmatrix} + \begin{bmatrix} \cdots - \dot{v}\sin\psi - vr\cos\psi - \ddot{x}_r \\ \cdots + \dot{v}\cos\psi - vr\sin\psi - \ddot{y}_r \end{bmatrix} \tag{14}$$

It is considered that r varies faster than the remaining variables and can be used as an intermediate control; also, the control of r is carried out using torque T.

Using (14) the control can be decoupled through (15). In addition, the remainder terms in (14) can be encapsulated in disturbance dynamics, resulting in decoupled dynamics (16).

$$\begin{bmatrix} \mu_x \\ \mu_y \end{bmatrix} = \begin{bmatrix} U_F\cos\psi & -u\sin\psi \\ U_F\sin\psi & u\cos\psi \end{bmatrix} \begin{bmatrix} F \\ r \end{bmatrix} \tag{15}$$

$$\begin{bmatrix} \ddot{e}_x \\ \ddot{e}_y \end{bmatrix} = \begin{bmatrix} \mu_x + f_x(\eta,\nu,\tau) \\ \mu_y + f_y(\eta,\nu,\tau) \end{bmatrix} \tag{16}$$

In this manner, the system can be controlled by two independent control laws (17) similar to (6)

$$\begin{aligned} \mu_x &= -\frac{\lambda_2 s^2 + \lambda_1 s + \lambda_0}{s(s+\lambda_3)} e_x, \\ \mu_y &= -\frac{\lambda_2 s^2 + \lambda_1 s + \lambda_0}{s(s+\lambda_3)} e_y, \end{aligned} \tag{17}$$

where parameters are selected using (7) and must be the same for both controllers since similar responses are desired in both directions.

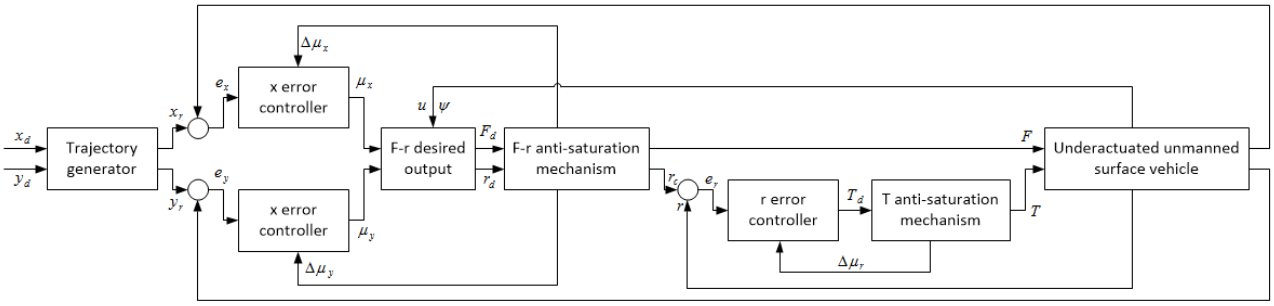

Figure 2. Proposed control system.

The desired control action is isolated from (15), obtaining (18); due to the presence of u in the denominators, its value in the controller should be set in a range between u_{min} and u_{max} using the definition of the function (19). The values $u_{min} > 0$ and u_{max} are chosen such that the desired performance of r is not greatly reduced, thus the desired control can be expressed by (20).

$$\begin{bmatrix} F_d \\ r_d \end{bmatrix} = \begin{bmatrix} \frac{\cos\psi}{U_F} & \frac{\sin\psi}{U_F} \\ -\frac{\sin\psi}{u} & \frac{\cos\psi}{u} \end{bmatrix} \begin{bmatrix} \mu_x \\ \mu_y \end{bmatrix} \quad (18)$$

$$u_p = sat(u, u_{\min}, u_{\max}) = \begin{cases} u_{\min}, u < u_{\min} \\ u, u_{\min} \le u \le u_{\max} \\ u_{\max}, u_{\max} < u \end{cases} \quad (19)$$

$$\begin{bmatrix} F_d \\ r_d \end{bmatrix} = \begin{bmatrix} \frac{\cos\psi}{U_F} & \frac{\sin\psi}{U_F} \\ -\frac{\sin\psi}{u_p} & \frac{\cos\psi}{u_p} \end{bmatrix} \begin{bmatrix} \mu_x \\ \mu_y \end{bmatrix} \quad (20)$$

In contrast, fully actuated USV's model would present F and H in (13), resulting (21). Errors could be controlled using both actuators, so r would not be considered as an actuator and ψ could be freely controlled by T. Each controller can be design using (6) and (7).

$$\begin{bmatrix} \ddot{e}_x \\ \ddot{e}_y \end{bmatrix} = \begin{bmatrix} U_F\cos\psi & -V_H\sin\psi \\ U_F\sin\psi & V_H\cos\psi \end{bmatrix} \begin{bmatrix} F \\ H \end{bmatrix} + \begin{bmatrix} \cdots - \dot{v}\sin\psi - vr\cos\psi - \ddot{x}_r \\ \cdots + \dot{v}\cos\psi - vr\sin\psi - \ddot{y}_r \end{bmatrix} \quad (21)$$
$$\ddot{\psi} = \cdots + R_T T$$

4.3. Design of angular velocity controller

Since the angular velocity r was considered to behave as a system actuator, this should be controlled on its respective subsystem. Using the torque T as an actuator in

$$\dot{e}_r = \cdots + R_T T, \quad (22)$$

where e_r is the error between the angular velocity measured in the system and the desired angular velocity (20). In a similar way to (16), the subsystem is presented based on a change of variable and a term of disturbance dynamics

$$\dot{e}_r = \mu_r + f_r(\eta, \nu, \tau). \quad (23)$$

Since the subsystem is a first order system, the control law (4) will be used as well as the selection of parameters from (5)

$$\mu_r = -\frac{\gamma_1 s + \gamma_0}{s} e_r, \quad (24)$$

$$s^2 + \gamma_1 s + \gamma_0 \equiv s^2 + 2\zeta_r \omega_r + {\omega_r}^2, \quad (25)$$

The desired torque is calculated by

$$T_d = (1/R_T)\mu_r. \quad (26)$$

4.4. Anti-saturation mechanism

Controllers using integral terms often present saturation, resulting in performance reduction. An anti-saturation mechanism is used to avoid this problem, using the projection of saturated actuator errors (27) with respect to the desired actuator values (20) on the decoupled control presented in (17). Consequently, the corrections are calculated by (28), where β_F and β_r are parameters that determine the aggressiveness of the anti-saturation mechanism and $\Delta\mu_x$ and $\Delta\mu_y$ are the required corrections to be applied in (17).

$$F = sat(F_d, F_{\min}, F_{\max}), \qquad r = sat(r_d, r_{\min}, r_{\max}) \quad (27)$$

$$\begin{bmatrix} \Delta\mu_x \\ \Delta\mu_y \end{bmatrix} = \begin{bmatrix} U_F\cos\psi & -u\sin\psi \\ U_F\sin\psi & u\cos\psi \end{bmatrix} \begin{bmatrix} \beta_F(F - F_d) \\ \beta_r(r - r_d) \end{bmatrix} \quad (28)$$

In this manner, the controllers (17) expressed in form of linear flatness-based filters (11) including the anti-saturation mechanism, will present the following form

$$\begin{aligned} \dot{p}_1 &= p_2 - \Delta\mu_x \\ \dot{p}_2 &= -\lambda_3 p_2 + e_x \\ \mu_x &= (\lambda_2\lambda_3 - \lambda_1)p_2 - \lambda_0 p_1 - \lambda_2 e_x, \\ \dot{q}_1 &= q_2 - \Delta\mu_y \\ \dot{q}_2 &= -\lambda_3 q_2 + e_y \\ \mu_y &= (\lambda_2\lambda_3 - \lambda_1)z_2 - \lambda_0 z_1 - \lambda_2 e_y. \end{aligned} \quad (29)$$

In addition, because torque T may also present saturation

$$T = sat(T_d, T_{\min}, T_{\max}), \quad (30)$$

an anti-saturation mechanism is provided based on the difference between the effective torque and the desired torque

$$\Delta\mu_r = R_T\beta_T(T - T_d), \quad (31)$$

so the resulting controller in form of a linear flatness-based filter is

$$\begin{aligned} \dot{h}_1 &= e_r - \Delta\mu_r \\ \mu_r &= -\gamma_1 e_r + \gamma_1\Delta\mu_r - \gamma_0 m_1 \end{aligned} \quad (32)$$

4.5. Trajectory generator

Since the initial values of the desired trajectory x_d, y_d may be distant from the UUSV's origin point, a trajectory reference generator x_r, y_r is provided, based on a simplified mathematical model of the UUSV in the form

$$\begin{aligned} \dot{x}_r &= u_r\cos\psi_r \\ \dot{y}_r &= u_r\sin\psi_r \\ \dot{\psi}_r &= \omega \\ \dot{u}_r &= a \end{aligned} \quad (33)$$

where the control objective is that x_r, y_r follow x_d, y_d. The controller for the simplified UUSV (33) can be developed using a procedure similar to the one used for the original UUSV.

5. SIMULATION RESULTS AND ANALYSIS

The parameters of the vehicle in (Wondergem et. al. 2011) were used to carry out simulations:

$$M = \begin{bmatrix} 25.8 & 0 & 0 \\ 0 & 33.8 & 1.0115 \\ 0 & 1.0115 & 2.76 \end{bmatrix}$$

$$C(\nu) = \begin{bmatrix} 0 & 0 & -33.8v - 1.0115r \\ 0 & 0 & 25.8u \\ 33.8v + 1.0115r & -25.8u & 0 \end{bmatrix}$$

$$D(\nu) = \begin{bmatrix} 0.72 + 1.33|u| & 0 & 0 \\ 0 & 0.86 + 36.28|v| & -0.11 \\ 0 & -0.11 - 5.04|v| & 0.5 \end{bmatrix}$$

Table 1 shows the parameters used for the UUSV controller and the trajectory generator. All parameters are expressed in IS units.

Table 1. Controller design parameters

USV		Trajectory generator	
Z	1.2	ζ	1
ω_n	1	ω_n	1
F_{min}	-10	a_{min}	-0.5
F_{max}	10	a_{max}	0.5
r_{min}	-2	ω_{min}	-1
r_{max}	2	ω_{max}	1
u_{min}	1	u_{min}	0.01
u_{max}	1	u_{max}	2
β_F	0.5	β_F	0.5
β_r	0.5	β_r	0.5
ζ_r	0.7		
ω_r	5		
T_{min}	-10		
T_{max}	10		
β_T	0.05		

The trajectory used in the simulation, using a simulation time of 100 seconds, was

$$\begin{aligned} x_d &= 20\cos(t/30)\cos(t/20), \\ y_d &= 20\cos(t/30)\sin(t/20). \end{aligned} \qquad (34)$$

In addition, a variable external force with inclination of 10° in respect to axis X was applied.

The proposed controller was compared with a controller based on state-feedback linearization (Fahimi, 2008), the latter requiring knowledge of all model (1) parameters for its design.

In the following figures, FPL is the controller based on linear flatness-based filters, LRE is the controller based on state-feedback linearization, and DT is the desired trajectory.

Figure 3 shows trajectory tracking performed by both controllers. It shows that the LRE converges faster than FPL; however, after the approach, both properly follow the trajectory. Figure 4 shows the tracking of position variables separately.

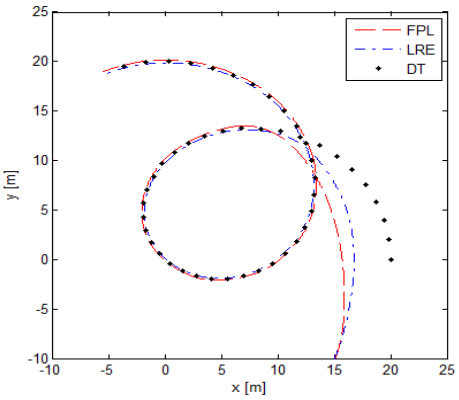

Figure 3. Trajectory tracking

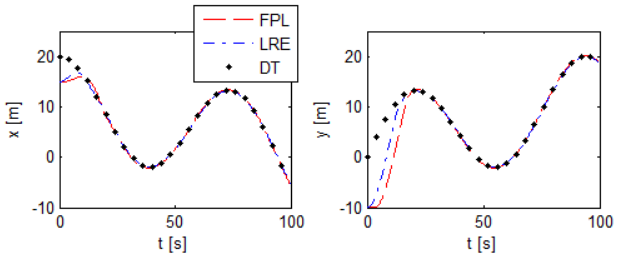

Figure 4. Position evolution

Figure 5 shows that the FPL presents greater error at the beginning; this is due to the use of the trajectory generator, which limits the distance to the reference regarding the original position of the UUSV. The zoom in Figure 5 reveals that both controllers have similar absolute errors after approaching to the trajectory. However, oscillations are found in the FPL error since the term *f(...)* is not constant (contrary to what was considered in (4) and (6)).

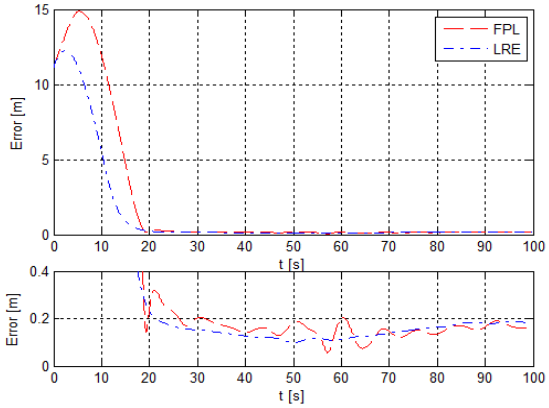

Figure 5. Absolute tracking error

Figure 6 presents the applied external disturbance and the resulting control action for times lesser than 30 seconds. A delay time in the FPL is evidenced; however, it is observed that the latter does not exhibit large oscillations in the torque applied, in comparison to the LRE. For times greater than 30 seconds, the control action in both cases follows the same tendency.

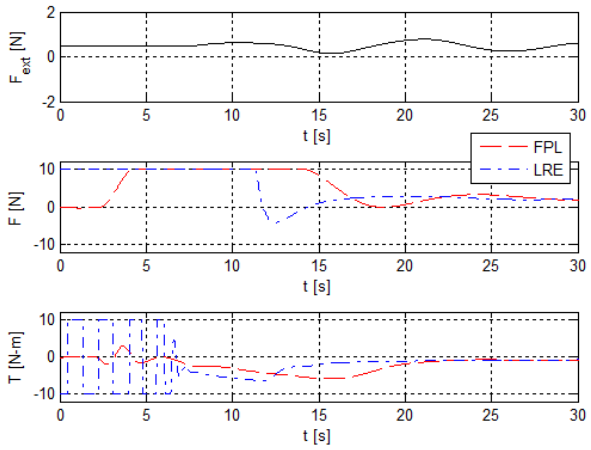

Figure 6. Control action ($t < 30$)

6. CONCLUSIONS

A control system for a UUSV was proposed, with a trajectory controller and an angular velocity controller for tracking arbitrary form trajectories. The proposed design of the system controllers was carried out using active disturbance rejection control based on linear flatness-based filters, requiring a deeper analysis compared to the fully actuated case. Comparisons were made between the trajectory tracking of the FPL control proposed and the LRE control, obtaining similar results; however, the torque applied in the FPL control shows less oscillation. The main advantage of the proposed control with respect to the LRE and other control techniques is that its design only requires knowledge of the dynamic parameters related to the actuators (in practice easily recognizable). A future paper will propose a strategy of trajectory generation and develop methodology for calculation of parameters. Given that the structure kinematics as presented is akin to a group of marine, land and air systems, it is recommended to assess the implementation of the proposed controller in these systems.

REFERENCES

Bao-Li, M.; Wen-Jing, X. (2013) Global asymptotic trajectory tracking and point stabilization of asymmetric underactuated ships with non-diagonal inertia/damping matrices. *International Journal of Advanced Robotic Systems*, vol. 10.

Chwa, D. (2011). Global tracking control of underactuated ships with input and velocity constraints using dynamic surface control method. *IEEE Transactions on Control Systems Technology*, 19(6), pp 1357-1370.

Dai, S. L.; Wang, C.; Luo, F. (2012). Identification and learning control of ocean surface ship using neural networks. *IEEE Transactions on Industrial Informatics*, 8(4), pp 801-810.

Ding, F.; Wang, Y.; Wang, Y. (2011). Trajectory-tracking controller design of underactuated surface vessels. *IEEE OCEANS 2011*, pp 1-5.

Do, K. D. (2010). Practical control of underactuated ships. *Ocean Engineering*, 37(13), pp 1111-1119.

Fahimi, F. (2008) *Autonomous robots: modeling, path planning, and control*. Springer Science & Business Media.

Fliess, M., Join, C. (2013). *Model-free control*. International Journal of Control, 86(12), pp 2228-2252.

Fossen, T. (2000). A survey on nonlinear ship control: from theory to practice. *Proceedings of the 5th IFAC Conference on Manoeuvring and Control of Marine Craft*, pp 23-25

Fossen, T. (2011). *Handbook of marine craft hydrodynamics and motion control, first edition*, John Wiley & Sons, UK.

Gao, Z. (2006). Active disturbance rejection control: a paradigm shift in feedback control system design. *American Control Conference, 2006*: pp 7.

Han, J. (2009). From PID to active disturbance rejection control. *IEEE transactions on Industrial Electronics, 56(3)*, pp 900-906.

Li, R.; Li, T.; Zheng, Q.; Li, Q. (2012). Ship tracking control based on linear active disturbance rejection control. *2012 Third International Conference on Intelligent Control and Information Processing (ICICIP)*, pp 201-205.

Li, R.; Li, T.; Bu, R. (2013). Disturbance decoupling control based trajectory tracking for underactuated ships. *2013 32nd Chinese Control Conference (CCC)*, pp 8108-8113.

Luviano-Juárez, A., Cortés-Romero, J., & Sira-Ramírez, H. (2008). *Chaotic synchronization between oscillators using robust GPI control*. 5th International Conference on Electrical Engineering, Computing Science and Automatic Control. CCE 2008. pp. 114-119. IEEE.

Morales, R., & Sira-Ramirez, H. (2010). Trajectory tracking for the magnetic ball levitation system via exact feedforward linearisation and GPI control. *International Journal of Control*, 83(6), pp 1155-1166.

Pan, C. Z.; Lai, X. Z.; Yang, S. X.; Wu, M. (2013). An efficient neural network approach to tracking control of an autonomous surface vehicle with unknown dynamics. *Expert Systems with Applications*, 40(5), pp 1629-1635.

Sira-Ramirez, H., & Agrawal, S. K. (2004). *Differentially flat systems*. CRC Press.

Sira-Ramirez, H., Beltrán-Carbajal, F., & Blanco-Ortega, A. (2008). A generalized proportional integral output feedback controller for the robust perturbation rejection in a mechanical system. *STA*, 5(4), pp 24-32.

Sira-Ramirez, H; Luviano-Juarez, A.; Cortés-Romero, J. (2010). A generalized proportional integral approach to sliding mode controller design in switched systems. In: *2010 49th IEEE Conference on Decision and Control (CDC)*. IEEE, p 5092-5097.

Yang, Y.; Du, J., Liu, H.; Guo, C.; Abraham, A. (2014). A trajectory tracking robust controller of surface vessels with disturbance uncertainties. *IEEE Transactions on Control Systems Technology*, 22(4), pp 1511-1518.

Wondergem, M., Lefeber, E., Pettersen, K. Y., & Nijmeijer, H. (2011). Output feedback tracking of ships. IEEE Transactions on Control Systems Technology, 19(2), pp 442-448.

Estabilización de una Bicicleta sin Conductor mediante el Enfoque de Control por Rechazo Activo de Perturbaciones

Mauro Baquero-Suárez*, John Cortés-Romero†, Jaime Arcos-Legarda‡ y Horacio Coral-Enriquez§

*†‡ *Electrical Engineering Department, Universidad Nacional, Bogotá D.C., Colombia,*
e-mail: [mabaqueros,jacortesr,wjarcosl]@unal.edu.co.

§ *Mechatronics Engineering Department, Universidad de San Buenaventura, Bogotá D.C., Colombia,*
e-mail: hcoral@usbbog.edu.co.

Abstract: This work proposes an ADRC (Active Disturbance Rejection Control) estrategy using GPI (Generalized Proportional Integral) observers to automatically stabilize a riderless moving bicycle with a time variant forward speed. A bicycle has an unstable and non-linear behavior when in its upright position that can be modeled as a LPV (Linear-Parameter-Varying) system, making the design of feedback controllers for stabilizing this plant a challenging problem. The ADRC scheme simplifies the bicycle model to a linear system by grouping all unmodelled linear and non-linear terms of the model together with external disturbances into an additive unified disturbance signal as equivalent input of the plant, which is estimated via the GPI observer and then rejected through the control law. The control strategy effectiveness is validated by a co-simulation between ADAMS and MATLAB, which exhibits a high performance of the proposed technique on a non-linear bicycle model closer to the real world physics than simplified mathematical models.

Keywords: Autonomous bicycle, Active disturbance rejection control, Generalized proportional integral control, Disturbance observers, Multibody systems dynamics, Co-Simulation.

1. INTRODUCCIÓN

Una bicicleta es un sistema que tiene una dinámica inestable, similar al péndulo invertido, pero con una velocidad de avance que varía las fuerzas y momentos que actúan sobre ella. Básicamente, su inclinación es afectada por la gravedad, la posición de su centro de masa, la velocidad de avance y la posición angular de la dirección [Gordon Wilson, 2004].

Varias investigaciones, muestran que puede lograrse la estabilización autónoma de una bicicleta bajo cierto rango de velocidad de avance, mediante algún sistema de control en su dirección. La mayor dificultad radica en las incertidumbres de los modelos desarrollados hasta el momento, porque solamente capturan el comportamiento esencial de la bicicleta y algunas de sus perturbaciones. En [Åström et al., 2005, Limebeer and Sharp, 2006], se presentan varios modelos matemáticos de diferente complejidad y sus condiciones de estabilidad. En [Meijaard et al., 2007, Papadopoulos, 1987], dividen teóricamente la bicicleta en cuatro partes rígidas y obtienen un modelo lineal en espacio de estado con parámetros variantes (LPV), a partir de las ecuaciones diferenciales de movimiento provenientes del balance de energías (Euler-Lagrange). La validación de este modelo, se desarrolló en [Kooijman, 2006] mediante la adquisición de datos en tiempo real de una bicicleta en movimiento adaptada con sensores y un laptop configurado para esta aplicación. En [Chen and Dao, 2010], muestran mediante simulaciones el desempeño de un controlador PI vectorial sobre un modelo obtenido a partir de un método de identificación de sistemas, que utiliza un conjunto de datos tomados de una bicicleta en movimiento. En [Iuchi et al., 2005], estabilizan una bicicleta mediante dos controladores lineales independientes, uno controla la dirección, y el otro, un brazo sujeto al marco para variar su centro de masa. En [Cerone et al., 2010], la estabilizan mediante un controlador de realimentación de estado con ganancias que se ajustan automáticamente, solucionando una LMI (Linear Matrix Inequality) dependiente de la velocidad de avance. Y en [Michini and Sean Torrez, 2007], se implementa un controlador LQR en la dirección que logra estabilizar una bicicleta que se mueve a velocidad constante por medio de un motor eléctrico acoplado en la rueda trasera.

En este trabajo, se abordó el problema de estabilización de una bicicleta en movimiento y sin conductor, proponiendo una estrategia de control basada en la metodología de Rechazo Activo de Perturbaciones, la cual, ha sido aplicada a un amplio número sistemas inciertos perturbados para el seguimiento robusto de referencias [Cortés Romero et al., 2014]. El esquema propuesto considera un modelo lineal simplificado de la dinámica de la bicicleta,

pero perturbado. Bajo esta técnica, las perturbaciones son unificadas en una señal equivalente a la entrada de control, que tiene en cuenta de manera conjunta las dinámicas no modeladas y perturbaciones externas asociadas. Esta señal de perturbación es estimada mediante un observador GPI y rechazada en línea por medio de una ley de control por realimentación de estado que es función de esta estimación [Cortés Romero et al., 2010]. La estrategia de control basada en observador GPI, logra que el sistema de lazo cerrado recupere el desempeño del modelo lineal nominal tanto como la sintonización de las ganancias del observador lo permitan. También, esta estrategia tiene una propiedad de acción integral que asegura la regulación del error de seguimiento a cero, permitiendo una estabilización robusta de la bicicleta en su posición vertical.

2. MODELAMIENTO DE LA BICICLETA

Cuando la bicicleta está en movimiento, su naturaleza inestable se forma por el desbalance de fuerzas y momentos que se originan por la reacción que ejerce el suelo en dirección contraria de su peso, su velocidad de avance y los giros producidos por la dirección del manubrio. Existen otros efectos que se producen por el movimiento giratorio de las ruedas y el contacto continuo que existe entre ellas y alguna superficie irregular del suelo, los cuales son, precesión giroscópica, deformación, deslizamiento y fricción dinámica. Todos estos factores imponen en el sistema una dinámica compleja que dificulta su estabilización.

2.1 Ecuaciones del Movimiento de la Bicicleta

Considere inicialmente el esquema simplificado que se muestra en la Fig. 1, el cual, describe a la bicicleta como un sistema que se desplaza en un plano horizontal, con su masa concentrada en el punto (b,h), y con un eje de dirección vertical, lo que implica que tiene un ángulo con respecto al eje x de $\alpha = 90°$, y una distancia horizontal con respecto al punto de contacto de la rueda frontal de $c = 0$. Este sistema tiene tres grados de libertad (δ,φ,ψ) con respecto al sistema de coordenadas (x, y, z), localizado en el punto de contacto de la rueda trasera.

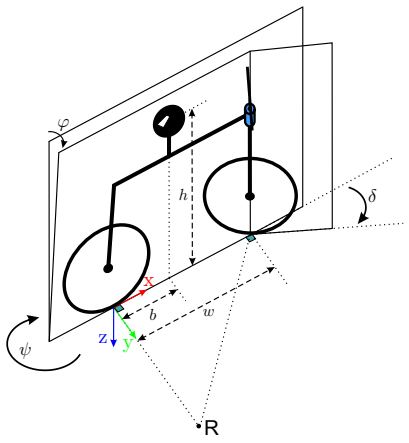

Figura 1. Esquema de la bicicleta en su forma simplificada.

Este sistema simplificado, puede modelarse mediante la siguiente ecuación diferencial linealizada que resulta de los pares actuando en el sistema debido a las fuerzas gravitacional y centrífuga y un balance de momento angular con respecto al eje x [Goldstein, 1953], cuando se mueve a cierta velocidad de avance:

$$Jw\ddot{\varphi}(t) - m_t ghw\varphi(t) = D\dot{\delta}(t)v(t) + m_t h\delta(t)v(t). \quad (1)$$

La ecuación (1) representa un sistema dinámico de orden $n = 2$, que relaciona la rotación en la dirección $\delta(t)$, con el ángulo de inclinación $\varphi(t)$. Esta ecuación tiene dos polos ubicados en

$$p_{1,2} = \pm\sqrt{\frac{m_t gh}{J}}, \quad (2)$$

y un cero en

$$z = -\frac{m_t v(t)h}{D}, \quad (3)$$

que depende de la velocidad de avance $v(t)$. En el Cuadro 1, están consignados los parámetros requeridos por la ecuación (1). Estos parámetros se obtuvieron de los valores de masa y su distribución en los cuerpos de un modelo CAD (Computer Assisted Design) de una bicicleta de montaña real, desarrollado con el software Solid Edge ST4 tal y como se muestra en la Fig. 2.

Cuadro 1. Parámetros de la bicicleta entera.

Item	Símbolo	Valor	Unidad
Masa total de la bicicleta	m_t	12.514197	Kg
Momento de inercia con respecto al eje x	J	4.095365	Kg · m^2
Producto de inercia con respecto a los ejes xz	D	3.492466	Kg · m^2
Distancia entre ejes	w	1.06016	m
Altura del centro de gravedad	h	0.502656	m
Distancia horizontal del centro de gravedad	b	0.514899	m
Gravedad	g	9.807	m/s^2
Velocidad de avance	$v(t)$	Variable	m/s

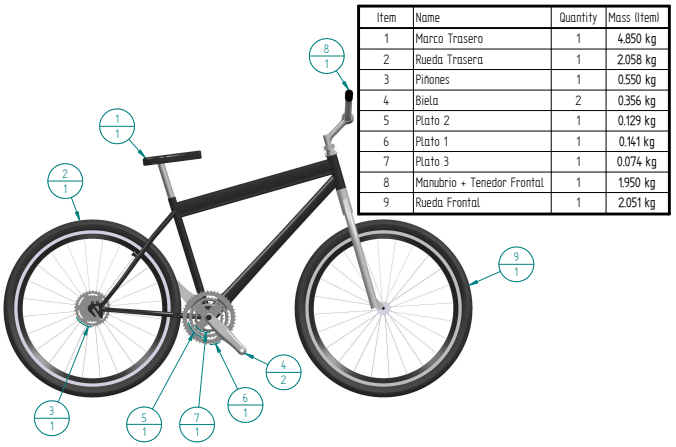

Figura 2. Modelo CAD de una bicicleta real.

Una extensión de la formulación anterior, se obtiene a partir de las ecuaciones linealizadas de movimiento presentadas en [Papadopoulos, 1987, Schwab et al., 2005], las cuales, describen la dinámica fundamental de una bicicleta conceptual que consiste de cuatro cuerpos rígidos llamados como, el marco trasero, el tenedor frontal con el manubrio (marco frontal), y las ruedas trasera y frontal. Se asume que los cuatro cuerpos están interconectados mediante articulaciones de revolución, y que son simétricos con respecto al eje longitudinal x. El contacto entre las ruedas y una superficie del suelo asumida como plana y nivelada, es modelada por restricciones holonómicas en la dirección

normal y por restricciones no-holonómicas en su dirección longitudinal y lateral. La Fig. 3 muestra el esquema de la bicicleta conceptual con sus cuatro cuerpos rígidos, su sistema de coordenadas (x,y,z), y sus tres grados de libertad, los cuales son, el ángulo de inclinación $\varphi(t)$, el ángulo de dirección $\delta(t)$ y la velocidad de avance definida como $v(t) = -R_{rw}\dot{\theta}_r(t)$. Este modelo tampoco tiene en cuenta el par de perturbación ejercido sobre el eje de la dirección, que se genera por el efecto de la precesión giroscópica en la rueda frontal.

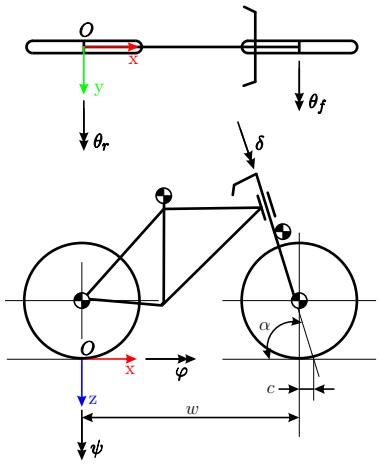

Figura 3. Esquema de la bicicleta en su forma básica.

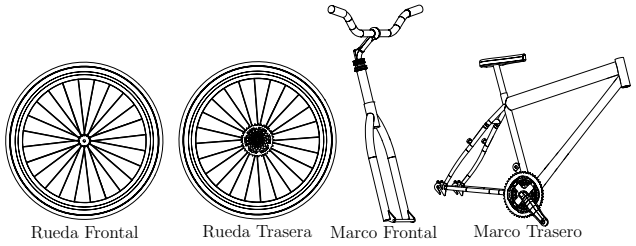

Figura 4. Modelo de la bicicleta dividida en cuatro cuerpos.

Las ecuaciones linealizadas del movimiento, son dos ecuaciones diferenciales de segundo orden acopladas dinámicamente, de la forma $\mathbf{M}\ddot{q} + \mathbf{C}\dot{q} + \mathbf{K}q = \mathbf{f}$, las cuales, pueden escribirse con mayor detalle de la siguiente manera:

$$\mathbf{M}\ddot{\mathbf{q}}(t) + v(t)\mathbf{C}_1\dot{\mathbf{q}}(t) + \left(\mathbf{K}_0 + v(t)^2\mathbf{K}_2\right)\mathbf{q}(t) = \mathbf{f}(t), \quad (4)$$

en donde,

$$\mathbf{q}(t) = \left[\ \varphi(t)\ \ \delta(t)\ \right]^{\mathrm{T}} \quad \text{y} \quad \mathbf{f}(t) = \left[\ T_\varphi(t)\ \ T_\delta(t)\ \right]^{\mathrm{T}}.$$

$T_\varphi(t)$ es el par de inclinación considerado como una perturbación exógena, $T_\delta(t)$ es el par de dirección aplicado al eje del manubrio (entrada de control) y $\varphi(t)$ y $\delta(t)$ son las variables de inclinación y dirección. Los parámetros son: 1) La matriz simétrica de masa $\mathbf{M}$, la cual entrega la energía cinética de la bicicleta a una velocidad de avance de cero. 2) La matriz de amortiguamiento dependiente de la velocidad de avance $\mathbf{C} = v(t)\mathbf{C}_1$, la cual captura los pares giroscópicos antisimétricos que se deben a las variaciones en la dirección e inclinación. 3) La matriz de rigidez $\mathbf{K}$ la cual es la suma de dos partes: una parte simétrica independiente de la velocidad y proporcional a la aceleración gravitacional $g\mathbf{K}_0$, y otra parte $v^2\mathbf{K}_2$ que se origina por los efectos centrífugos y giroscópicos. Los coeficientes de las matrices $\mathbf{M}$, $\mathbf{C}_1$, $\mathbf{K}_0$ y $\mathbf{K}_2$ fueron calculados por medio del algoritmo propuesto en [Meijaard et al., 2007], el cual utiliza los parámetros consignados en el Cuadro 2, que se derivan del modelo CAD dividido en cuatro cuerpos tal y como se muestra en la Fig. 4. Este algoritmo entrega los siguientes resultados:

$$\begin{aligned}\mathbf{M} &= \begin{bmatrix} 4.09537 & 0.31541 \\ 0.31541 & 0.16216 \end{bmatrix}, \quad \mathbf{C}_1 = \begin{bmatrix} 0 & 4.11551 \\ -0.58511 & 0.51821 \end{bmatrix}, \\ \mathbf{K}_0 &= \begin{bmatrix} -61.76730 & -4.80033 \\ -4.80033 & -1.31521 \end{bmatrix}, \quad \mathbf{K}_2 = \begin{bmatrix} 0 & 6.69605 \\ 0 & 0.57886 \end{bmatrix}.\end{aligned} \quad (5)$$

Cuadro 2. Parámetros básicos de la bicicleta.

Parámetro	Símbolo	Valor
Distancia entre ejes	w	1.06 m
Paso	c	0.06 m
Ángulo del cabezal	α	arctan(3.51) rad
Gravedad	g	9.81 m/s^2
Velocidad de avance	v	variable m/s
Rueda trasera:		
Radio	R_{rw}	0.32 m
Masa	m_{rw}	2.61 kg
Momentos de inercia de masa	(A_{xx}, A_{yy}, A_{zz})	$(0.09, 0.18, 0.09)$ kg · m^2
Marco trasero:		
Posición del centro de masa	(x_{rf}, y_{rf}, z_{rf})	$(0.42, 0.003, -0.56)$ m
Masa	m_{rf}	5.91 kg
Momentos de inercia de masa	$\begin{bmatrix} B_{xx} & 0 & B_{xz} \\ & B_{yy} & 0 \\ \text{sym.} & & B_{zz} \end{bmatrix}$	$\begin{bmatrix} 0.32 & 0 & 0.05 \\ & 0.56 & 0 \\ \text{sym.} & & 0.26 \end{bmatrix}$ kg · m^2
Marco frontal:		
Posición del centro de masa	(x_{ff}, y_{ff}, z_{ff})	$(0.94, 0, -0.75)$ m
Masa	m_{ff}	1.95 kg
Momentos de inercia de masa	$\begin{bmatrix} C_{xx} & 0 & C_{xz} \\ & C_{yy} & 0 \\ \text{sym.} & & C_{zz} \end{bmatrix}$	$\begin{bmatrix} 0.14 & 0 & -0.01 \\ & 0.13 & 0 \\ \text{sym.} & & 0.03 \end{bmatrix}$ kg · m^2
Rueda frontal:		
Radio	R_{fw}	0.32 m
Masa	m_{fw}	2.05 kg
Momentos de inercia de masa	(D_{xx}, D_{yy}, D_{zz})	$(0.09, 0.18, 0.09)$ kg · m^2

Mediante manipulaciones algebraícas, la ecuación diferencial (4) se escribe en la forma de un sistema en espacio de estado, seleccionando $\varphi(t)$, $\delta(t)$ y sus derivadas $\dot{\varphi}(t)$ y $\dot{\delta}(t)$, como las variables del estado $\mathbf{x(t)}$, $T_\delta(t)$ y $T_\varphi(t)$ como las entradas $\mathbf{u(t)}$, y el estado $\mathbf{x(t)}$, como la salida $\mathbf{y(t)}$, porque puede medirse en la realidad. Entonces, Las ecuaciones en espacio de estado resultan así:

$$\begin{aligned}\dot{\mathbf{x}}(\mathbf{t}) &= \mathbf{A(v)x(t)} + \mathbf{Bu(t)}, \\ \mathbf{y(t)} &= \mathbf{Cx(t)} + \mathbf{Du(t)},\end{aligned} \quad (6)$$

en donde,

$$\begin{aligned}\mathbf{x(t)} &= \left[\ \varphi(t)\ \ \delta(t)\ \ \dot{\varphi}(t)\ \ \dot{\delta}(t)\ \right]^{\mathrm{T}}, \quad \mathbf{y(t)} = \mathbf{x(t)}, \\ \mathbf{u(t)} &= \left[\ T_\varphi(t)\ \ T_\delta(t)\ \right]^{\mathrm{T}}.\end{aligned} \quad (7)$$

Las matrices $\mathbf{A(v)}$, $\mathbf{B}$, $\mathbf{C}$ y $\mathbf{D}$, se obtienen con las siguientes operaciones algebraícas tomadas de [Schwab et al., 2012]:

$$\begin{aligned}\mathbf{A(v)} &= \begin{bmatrix} \mathbf{0} & \mathbf{I} \\ -\mathbf{M}^{-1}\left(\mathbf{K}_0 + v(t)^2\mathbf{K}_2\right) & -\mathbf{M}^{-1}\left(v(t)\mathbf{C}_1\right) \end{bmatrix}, \\ \mathbf{B} &= \begin{bmatrix} \mathbf{0} & \mathbf{0} \\ \mathbf{M}^{-1}\begin{bmatrix} 1 \\ 0 \end{bmatrix}, & \mathbf{M}^{-1}\begin{bmatrix} 0 \\ 1 \end{bmatrix} \end{bmatrix}, \quad \mathbf{C} = \mathbf{I} \quad \text{y} \quad \mathbf{D} = \mathbf{0}.\end{aligned} \quad (8)$$

La dependencia de $\mathbf{A}$ sobre la velocidad $v(t)$, califica este modelo como un sistema LPV, debido a que (6) describe un sistema lineal invariante en el tiempo (LTI), para cada valor del parámetro variante en el tiempo $v(t)$. Tomando

como base el análisis reportado en [Cerone et al., 2010], las trayectorias de sus valores propios para varios valores de $v(t)$ y las trayectorias de la parte real de sus valores propios como función de $v(t)$, se muestran en las Figuras 5 y 6 respectivamente, ambas en un intervalo de $[0, 10]$ m/s.

Cuando $v(t)$ es cero, el sistema tiene cuatro valores propios reales, ubicados en $\lambda_1 = 3.8804$, $\lambda_2 = 2.5721$, $\lambda_3 = -3.8819$ y $\lambda_4 = -2.6598$, los cuales están marcados con círculos rojos en la Fig. 5. La ubicación de λ_1 y λ_2 en el semiplano derecho, explica la inestabilidad de la bicicleta en su posición vertical. Este sería el estado más crítico para controlar $\varphi(t)$, actuando solamente sobre $\delta(t)$. A medida que $v(t)$ aumente, λ_1 y λ_2 se convierten en complejos conjugados y sus partes reales disminuyen hasta ubicarse dentro del semiplano izquierdo y estabilizar el sistema, a partir de $v(t) = 3.15$ m/s. También, λ_4 se incrementa desplazándose hacia el semiplano derecho, retornando el sistema a su condición inestable desde $v(t) = 3.95$ m/s.

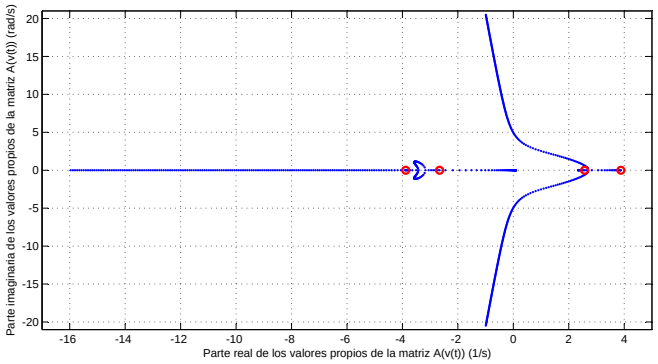

Figura 5. Trayectorias de los valores propios del modelo LPV con $v(t)$ entre 0 y 10 m/s.

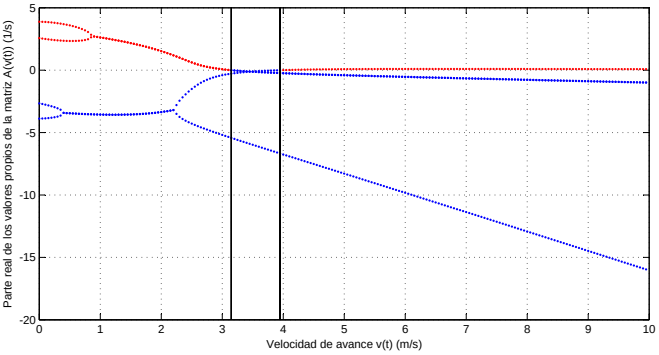

Figura 6. Parte real de los valores propios de la matriz $A(v(t))$ como una función de $v(t)$.

La Fig. 6 muestra una franja de equilibrio para valores de $v(t)$ entre 3.15 m/s y 3.95 m/s, donde la bicicleta sin control se hace auto-estable, debido a que todos los valores propios están dentro del semiplano izquierdo. Por fuera de esta franja, existen dos zonas inestables que están localizadas antes de $v_w = 3.15$ m/s, y después de $v_c = 3.95$ m/s. La zona en la cual la velocidad está por debajo de v_w, es la más difícil de estabilizar porque la acción de control debe ser fuerte y rápida para contrarrestar las oscilaciones laterales de la bicicleta originadas por la baja velocidad de avance. La otra zona, en donde la velocidad está por encima de v_c, la estabilidad podría lograrse con acciones de control tenues y lentas en comparación con la zona anterior. Con esta información podría diseñarse un sistema de control que sea capaz de estabilizar la bicicleta con una mínima velocidad de avance, asegurando su efectividad para velocidades más elevadas.

La estrategia de control propuesta, será diseñada para estabilizar la bicicleta con una velocidad $v(t) \geq 1.5$ m/s, la cual, es más baja que la mínima velocidad de estabilización conseguida en [Michini and Sean Torrez, 2007].

2.2 Modelo Dinámico Virtual Construido en ADAMS

Para construir un modelo dinámico en ADAMS, el modelo CAD desarrollado en Solid Edge, fue importado al entorno ADAMS/View y se completaron los siguientes procedimientos:

1. Se ingresa el valor de masa de cada cuerpo del modelo CAD.
2. Se interconectan todos los cuerpos mediante articulaciones de revolución.
3. Se establece para las articulaciones, el modelo de fricción de Coulomb que se muestra en la Fig. 7, con los siguientes parámetros:

$$\mu_s = 0.05, \quad \mu_d = 0.03, \quad v_s = 0.1, \quad v_d = 2v_s.$$

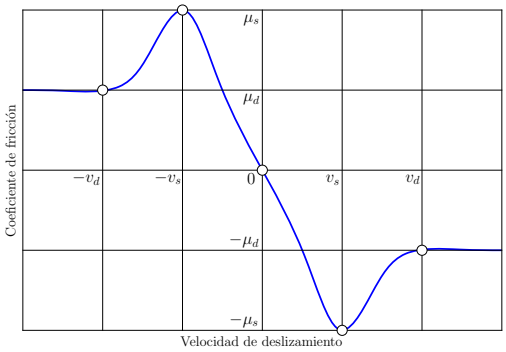

Figura 7. Modelo de fricción de Coulomb.

4. Se crea una superficie solida plana que funcionará como la pista donde se moverá la bicicleta, y se modelan las fuerzas de contacto y de fricción entre la bicicleta y la pista por medio de la herramienta *Contact Forces*, utilizando los parámetros del Cuadro 3.

Cuadro 3. Parámetros usados para modelar las fuerzas de contacto y de fricción.

Fuerza normal de impacto		
Materiales / Parámetros	**acero vs asfalto**	**caucho vs asfalto**
Rigidez	1.0E+008	1.0E+008
Exponente de fuerza	2.2	2.2
Amortiguamiento	1.0E+004	1.0E+004
Profundidad de penetración	1.0E-004	1.0E-004
Fuerza de fricción de Coulomb		
Materiales / Parámetros	**acero vs asfalto**	**caucho vs asfalto**
Coeficiente de fricción μ_s	0.6	0.72
Coeficiente de fricción μ_d	0.4	0.72
Velocidad de transición v_s	0.1	0.1
Velocidad de transición v_d	1.0	1.0

5. Se agregan los actuadores que moverán la bicicleta.
6. Se construyen acoples virtuales para simular las relaciones de transmisión de las articulaciones enlazadas.
7. Se expecifican las variables de entrada y salida que serán manipuladas de forma externa.
8. Se exporta el modelo no lineal de ADAMS/View hacia MATLAB/Simulink, por medio de la herramienta ADAMS/Controls.

La Fig. 8 muestra el modelo dinámico completado en ADAMS. El bloque naranja representa el modelo exportado a MATLAB.

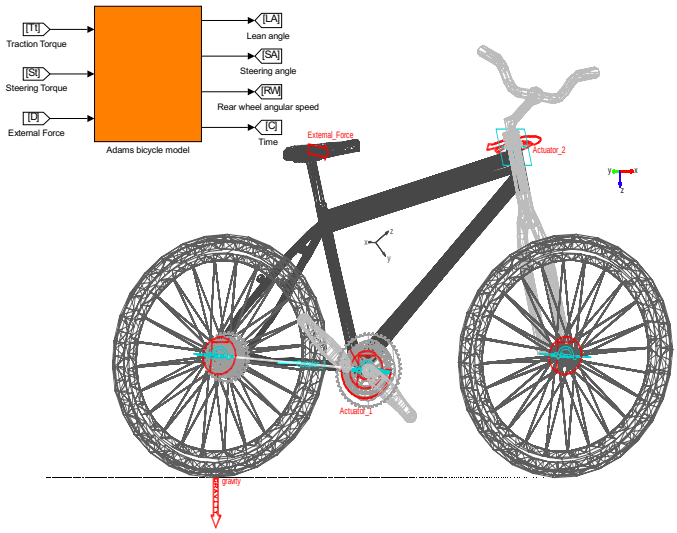

Figura 8. Modelo dinámico virtual.

3. ESTRATEGIA DE CONTROL BASADA EN OBSERVADOR GPI

Esta estrategia, es una de las metodologías relacionadas al control mediante el rechazo activo de perturbaciones (ADRC). Este enfoque busca la cancelación de diferentes tipos de perturbaciones aditivas endógenas y exógenas que afectan a la planta, para que el sistema de lazo cerrado tenga un desempeño similar a un modelo lineal simplificado, permitiendo que alguna ley de control lineal imponga un seguimiento robusto de alguna referencia fluida en la entrada. Las perturbaciones pueden ser efectivamente estimadas a través de un observador GPI que las agrupa en una señal desconocida pero uniformemente y absolutamente acotada, y rechazadas por medio del controlador, el cual, es diseñado para realimentar esta señal y regular el sistema lineal resultante [Gao, 2006].

3.1 Formulación del Problema

Considerando un modelo matemático expresado como el siguiente sistema:

$$y^{(n)}(t) = \varrho u(t) + \phi(t, y(t), \dot{y}(t), \dots y^{(n-1)}(t)) + \zeta(t), \quad (9)$$

en donde ϱ, es la constante que acompaña a la entrada del sistema; el término $\phi(t, y(t), \dot{y}(t), \dots y^{(n-1)}(t))$, es una función que reune el resto de las dinámicas internas que hacen parte del modelo, ya sean lineales o no lineales; y último término $\zeta(t)$, es la función que representa las perturbaciones externas. Este sistema sin perturbaciones, $\zeta(t) = 0$, es diferencialmente plano debido a que internamente sus variables son expresadas como funciones diferenciales de la salida $y(t)$ [Sira Ramírez and Sunil K. Agrawal, 2004]. Bajo el enfoque ADRC, las dinámicas internas y las perturbaciones externas del sistema (9), son asociadas en un término aditivo unificado, llamado $\xi(t)$. De esto, resulta un sistema simplificado que puede ser definido como:

$$y^{(n)}(t) = \varrho u(t) + \xi(t). \quad (10)$$

El objetivo de control es gobernar la salida $y(t)$ de (10) y obligarla a seguir alguna trayectoria fluida de referencia definida como $y^*(t)$, independientemente de la función de perturbación desconocida pero uniformemente acotada $\xi(t)$. Para esto se asume lo siguiente:

(a). La función de perturbación $\xi(t)$ es completamente desconocida, mientras que la ganancia ϱ, es perfectamente conocida.
(b). Siendo m un número entero positivo, la m-ésima derivada con respecto al tiempo de $\xi(t)$ es uniformemente y absolutamente acotada. Es decir, que existe un valor constante K_m tal que $\sup_t \left|\xi^{(m)}(t)\right| \leq K_m$.

La característica (a), asegura la independencia de $\xi(t)$ con respecto a $u(t)$. Esto permite proponer una ley de control sin limitaciones que sea robusta, aunque haya incertidumbre en el valor real de ϱ. La característica (b), fue definida para establecer la existencia de una solución para la ecuación diferencial (10).

3.2 Enfoque Basado en Observador GPI

Teniendo en cuenta el sistema (10), se propone un observador al estilo Luenberger para la estimación del estado relacionado al sistema y de la función de perturbación $\xi(t)$. El esquema de estimación consiste de una copia de la planta lineal simplificada, pero aumentada por un modelo aproximado de la función de perturbación y con inyecciones ponderadas del error de estimación $(y(t) - \hat{y}(t))$. Este esquema debe garantizar una dinámica estable y arbitrariamente gobernada por el error de estimación.

Asumiendo que la función $\xi(t)$, puede modelarse localmente como un polinomio en función del tiempo $z(t)$, más un término residual $r(t)$, es decir,

$$\xi(t) = z(t) + r(t) = b_0 + b_1 t + \dots + b_{m-1} t^{m-1} + r(t), \quad \forall t, \quad (11)$$

en donde $z(t)$, es un polinomio de Taylor invariante con respecto al tiempo, de orden $(m-1)$, y con coeficientes arbitrarios reales. $z(t)$ puede definirse como el modelo interno de la perturbación aditiva en la entrada del sistema e incorporarse como parte del observador, cuyo error de estimación, es forzado a converger a una pequeña vecindad de cero. A causa de esto, se asume que la función residual $r(t)$ y sus derivadas con respecto al tiempo $\dot{r}(t), \ddot{r}(t), \dots, r^{(m)}(t)$, son uniformemente y absolutamente acotadas.

Considerando la aproximación de $d^m \xi(t)/dt^m = r^{(m)}(t) \approx 0$, el modelo interno de la función de perturbación es embebido dentro del modelo aumentado del sistema, el cual, es caracterizado por el siguiente vector de estado extendido, $x(t) = [x_1(t)\ x_2(t)\ \dots\ x_{n+m}(t)]^{\mathrm{T}}$ con $x_1(t) =$

$y(t)$, $x_2(t) = \dot{y}(t)$, …, $x_n(t) = y^{n-1}(t)$, $x_{n+1}(t) = \xi(t)$, …, $x_{n+m}(t) = \xi^{(m-1)}(t)$. Entonces, el modelo aumentado del sistema en espacio de estado, resulta así [Cortés Romero et al., 2011]:

$$\dot{x}(t) = Ax(t) + B\varrho u(t) + E\xi^{(m)}(t), \quad y(t) = Cx(t), \quad (12)$$

con $A = \begin{bmatrix} 0 & 1 & 0 & \dots & 0 \\ 0 & 0 & 1 & \dots & 0 \\ \vdots & & & \ddots & \vdots \\ 0 & 0 & 0 & \dots & 1 \\ 0 & 0 & 0 & \dots & 0 \end{bmatrix} \in \mathbb{R}^{(n+m)\times(n+m)}$, $B = \begin{bmatrix} 0 \\ \vdots \\ 1_{\text{n-ésima posición}} \\ \vdots \\ 0 \end{bmatrix} \in \mathbb{R}^{(n+m)\times 1}$, $C = \begin{bmatrix} 1 & 0 & \dots & 0 \end{bmatrix} \in \mathbb{R}^{1\times(n+m)}$, y $E = \begin{bmatrix} 0 & 0 & \dots & 1 \end{bmatrix}^{\mathrm{T}} \in \mathbb{R}^{(n+m)\times 1}$.

Ahora, denotando $\hat{x}_j(t)$ como la estimación de $x_j(t)$ para $j = 1, 2, \dots, n+m$, el observador extendido GPI propuesto para la estimación del estado $x(t)$, es planteado de la siguiente manera:

$$\dot{\hat{x}}(t) = A\hat{x}(t) + B\varrho u(t) + L(y(t) - \hat{y}(t)), \quad \hat{y}(t) = C\hat{x}(t), \quad (13)$$

en donde $\hat{x}(t) = \begin{bmatrix} \hat{x}_1(t) & \hat{x}_2(t) & \dots & \hat{x}_{n+m}(t) \end{bmatrix}^{\mathrm{T}}$ es la estimación del vector de estado y $L = \begin{bmatrix} \ell_{n+m-1} & \dots & \ell_1 & \ell_0 \end{bmatrix}^{\mathrm{T}}$ es el vector de ganancias del observador.

Definiendo el error de estimación como $\tilde{e}_x(t) = x(t) - \hat{x}(t)$, el vector del error de estimación resultante $\tilde{e}_x(t) = \begin{bmatrix} \tilde{e}_{x1}(t) & \tilde{e}_{x2}(t) & \dots & \tilde{e}_{x(n+m)}(t) \end{bmatrix}^{\mathrm{T}}$, satisface

$$\dot{\tilde{e}}_x(t) = (A - LC)\tilde{e}_x(t) + E\xi^{(m)}(t) = A_e\tilde{e}_x(t) + E\xi^{(m)}(t), \quad (14)$$

con $A_e \in \mathbb{R}^{(n+m)\times(n+m)}$ y su polinomio característico en función de la variable compleja s, que está dado por:

$$P_{\tilde{e}_x}(s) = \det(sI - A_e) = s^{n+m} + \ell_{n+m-1}s^{n+m-1} + \dots + \ell_1 s + \ell_0. \quad (15)$$

Los coeficientes ℓ_{n+m-1}, …, ℓ_1 y ℓ_0 de la función polinomial $P_{\tilde{e}_x}(s)$, deben seleccionarse para que todas sus raíces estén ubicadas a la izquierda del eje imaginario del plano complejo $\mathbb{C}$. Entonces, todas las trayectorias de los errores de estimación $\tilde{e}_{x1}(t)$, $\tilde{e}_{x1}(t)$, …, $\tilde{e}_{x(n+m-1)}(t)$ y $\tilde{e}_{x(n+m)}(t)$, convergen globalmente a una pequeña vecindad de cero donde permanecerán acotadas. Esta vecindad puede ajustarse reduciéndola tan pequeña como se desee, mediante una adecuada selección de las ganancias ℓ_{n+m-1}, …, ℓ_1 y ℓ_0.

Una aproximación de bajo orden para la función de perturbación ($\dot{\xi}(t) \approx 0$), requiere un diseño de un observador de alto ancho de banda, el cual, podría entregar estimaciones ruidosas en las aplicaciones prácticas. Aumentando el orden de la aproximación, se soluciona el problema de estimaciones ruidosas y se construye una mejor aproximación de la función de perturbación, pero el problema de localización de los valores propios del observador y las ganancias de la estrategia de control, para que impongan sobre la planta un seguimiento óptimo de la referencia, se vuelve más difícil.

3.3 Controlador Basado en Observador GPI

El controlador es diseñado con el objetivo de establecer de una manera dominante, un polinomio característico del error de seguimiento de alguna trayectoria deseada. Para realizar esto, la ley de control debe estar compuesta por:

- Un término de prealimentación, para los casos cuando la trayectoria de referencia de la salida plana, puede conocerse y/o manipularse.
- La realimentación del estado $\hat{x}(t)$, estimado por el observador GPI y ponderado por las ganancias del controlador.
- Un término de rechazo activo de las perturbaciones, el cual, es básicamente la estimación aproximada de la función de perturbación $\hat{\xi}(t) = z(t)$, que también entrega el observador GPI.

Con respecto al sistema (10), la ley de control basada en observador GPI para el seguimiento de trayectorias, tiene la siguiente estructura:

$$u(t) = \frac{1}{\varrho}\left[[y^*(t)]^{(n)} - \sum_{k=0}^{n-1} \gamma_k \left(\hat{x}_{k+1}(t) - [y^*(t)]^k \right) - \hat{x}_{n+1}(t) \right], \quad (16)$$

en donde el conjunto de los coeficientes $\{\gamma_0, \dots, \gamma_{n-1}\}$, son seleccionados para que todas las raíces del polinomio $p_c(s) = s^n + \gamma_{n-1}s^{n-1} + \dots + \gamma_0$ estén ubicadas en el semiplano izquierdo de $\mathbb{C}$. El error de seguimiento de la salida de lazo cerrado, $e_y(t) = y(t) - y^*(t)$, es gobernado por el siguiente polinomio característico:

$$e_y^{(n)}(t) + \gamma_{n-1}e_y^{(n-1)}(t) + \dots + \gamma_0 e_y(t) = (\xi(t) - \hat{x}_{n+1}(t)) + \sum_{k=0}^{n-1} \gamma_k \tilde{e}_{x(k+1)}(t). \quad (17)$$

La ley de control (16), conduce la trayectoria del error de seguimiento del sistema controlado, hacia una pequeña vencindad de cero, que puede reducirse tanto como se desee, mediante una selección apropiada del conjunto de los coeficientes $\{\gamma_0, \dots, \gamma_{n-1}\}$. La única restricción para la selección de estos coeficientes, es que $p_c(s)$ sea un polinomio Hurwitz, es decir, con todas sus raíces a la izquierda del eje imaginario de $\mathbb{C}$.

4. CASO DE ESTUDIO

En la estrategia propuesta, se diseña un controlador de velocidad de avance para el sistema de tracción, que permite a la bicicleta seguir perfiles suaves de velocidad con aceleraciones controladas, y luego, se diseña un controlador de inclinación, para maniobrar el sistema de dirección, permitiendo compensar la inclinación durante su recorrido.

4.1 Controlador de Velocidad de Avance

Asumiendo que $v(t) = -R_{rw}\dot{\theta}_r(t)$, se propone controlar la velocidad angular de la rueda trasera $\dot{\theta}_r(t)$, aplicándole el par requerido a su eje de giro. La dinámica de la tracción en la bicicleta, puede simplificarse como un conjunto de fuerzas y momentos que intervienen en la rueda trasera para generar su movimiento. La Fig. 9, muestra en un diagrama de cuerpo libre, las fuerzas y momentos concentrados en la rueda trasera, en donde v es la velocidad lineal del centro de masa, F_n es la fuerza normal concentrada en el eje, la cual, es exactamente el peso de la bicicleta, asumiendo que se mueve sobre una superficie plana, F_f es la fuerza de fricción que ejerce el suelo sobre la rueda y T_{rw} es el par aplicado por el actuador.

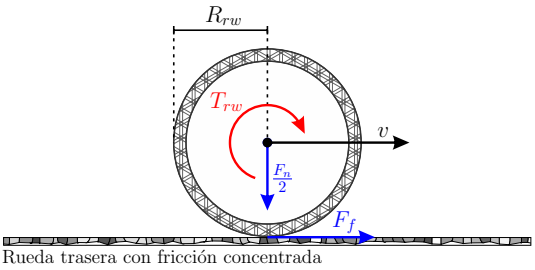

Figura 9. Diagrama de cuerpo libre de la rueda trasera.

A partir de las fuerzas y momentos definidos en la Fig. 9, se deriva el siguiente modelo lineal de parámetros concentrados:

$$\begin{aligned} m_t\dot{v}(t) &= F_f(t), \\ A_{yy}\ddot{\theta}_r(t) + \mu_d\dot{\theta}_r(t) &= T_{rw}(t) - F_f(t)R_{rw}, \end{aligned} \tag{18}$$

en donde m_t es la masa total de la bicicleta, A_{yy} es el momento de inercia de la rueda con respecto a su eje de giro (Ver Cuadro 2), y $\mu_d = 0.03$, es el coeficiente de fricción dinámico establecido para la articulación de la rueda en la sección 2.2. Combinando estas dos ecuaciones tenemos que:

$$\left(A_{yy} + m_t R_{rw}\right)\dot{v}(t) + \mu_d v(t) = T_{rw}(t)R_{rw}. \tag{19}$$

El modelo de primer orden (19), no considera deslizamiento ni deformación de la rueda trasera cuando hay tracción, es decir, que no hay fricción dinámica entre el suelo y la rueda, y el coeficiente de deslizamiento del suelo siempre es constante, independientemente del par aplicado en su eje [Canudas de Wit and Tsiotras, 1999]. La función de transferencia desde el par T_{rw}, hasta la velocidad $v(t)$, es:

$$G_{vT}(s) = \frac{R_{rw}}{\left(A_{yy} + m_t R_{rw}\right)s + \mu_d}. \tag{20}$$

Considerando la función de transferencia $G_{vT}(s)$, una acción de control PI es adecuada para gobernar su salida $v(t)$, debido a que es esencialmente un sistema estable de primer orden, con una curva de nyquist localizada dentro del primer y cuarto cuadrante del plano de $\mathbb{C}$ [Åström and Hägglund, 2006]. Definiendo $v^*(t)$ como la referencia de velocidad deseada, la acción de control PI es expresada como:

$$T_{rw}(t) = -K_p e_v(t) - K_i\int_0^t e_v(t)dt, \tag{21}$$

en donde $e_v(t) = v(t) - v^*(t)$ es el error de seguimiento. Entonces, la función de transferencia de lazo cerrado desde la referencia $v^*(t)$, hasta la salida $v(t)$ nos resulta:

$$T_o(s) = \frac{K_p s + K_i}{s^2 + \dfrac{\mu_d + K_p R_{rw}}{A_{yy} + m_t R_{rw}}s + \dfrac{K_i R_{rw}}{A_{yy} + m_t R_{rw}}}. \tag{22}$$

La sintonización de las ganancias K_p y K_i, puede realizarse mediante una localización arbitraria de los dos polos de $T_o(s)$, entregados por la ecuación característica,

$$s^2 + \frac{\mu_d + K_p R_{rw}}{A_{yy} + m_t R_{rw}}s + \frac{K_i R_{rw}}{A_{yy} + m_t R_{rw}} = 0. \tag{23}$$

Suponiendo que los polos deseados de lazo cerrado son caracterizados por un amortiguamiento relativo (ζ) y una frecuencia natural (ω_0), entonces, la ecuación característica deseada se convierte en

$$s^2 + 2\zeta\omega_0 s + \omega_0^2 = 0. \tag{24}$$

Igualando los coeficientes de las ecuaciones (23) y (24), y con una adecuada selección de ζ y ω_0, se determinan las ganancias K_p y K_i así:

$$\begin{aligned} K_p &= \frac{2\left(A_{yy} + m_t R_{rw}\right)\zeta\omega_0 - \mu_d}{R_{rw}}, \\ K_i &= \frac{\left(A_{yy} + m_t R_{rw}\right)\omega_0^2}{R_{rw}}. \end{aligned} \tag{25}$$

Las ganancias K_p y K_i, fueron calculadas a partir de los valores, $\zeta = 1$ y $\omega_0 = 2$, los cuales, ubican las raíces de la ecuación característica (24), en $s_{1,2} = -2$. Este controlador fue complementado con un esquema *Anti-Windup*, para eliminar rápidamente los grandes incrementos de la acción integral que sobrepasan los niveles mínimos y máximos preestablecidos en la salida del actuador [Åström and Hägglund, 1995]. Físicamente, esta configuración limita la aceleración en la tracción, reiniciando dinámicamente el integrador del controlador con una constante de tiempo que depende de la ganancia de la señal de realimentación del Anti-Windup, calculada como:

$$K_a = 4/\left(\sqrt{K_i/2K_p}\right). \tag{26}$$

4.2 Controlador de Inclinación

Para estabilizar la inclinación, se propone un esquema de dos lazos de control en cascada, diseñados con la misma estrategia basada en observador GPI. El primer lazo, genera la referencia de posición angular requerida en la dirección para estabilizar la bicicleta, y el segundo lazo, se encarga de seguir esta referencia. La Fig. 10 muestra un esquema general del controlador de inclinación.

Controlador Estabilizador: Este controlador, genera la referencia de posición angular $\delta^*(t)$ que debe seguir la dirección para dirijir el ángulo de inclinación $\varphi(t)$, hacia la referencia $\varphi^*(t) = 0$. El controlador estabilizador es diseñado en un punto de operación, asumiendo una velocidad de avance constante $v(t) = v_m\ \forall t$, donde $v_m \geq 1.5$ m/s, para establecer una relación lineal entre $\delta(t)$ y $\varphi(t)$, y poder formular la siguiente función de transferencia a partir del modelo de segundo orden (1):

$$\varphi(s) = \left(\frac{\dfrac{v_m D}{wJ}s + \dfrac{m_t v_m^2 h}{wJ}}{s^2 - \dfrac{m_t g h}{J}}\right)\delta^*(s), \tag{27}$$

en donde se extrae una variable intermedia $u_s(s)$ (control auxiliar), dividiendo el sistema en las siguientes dos funciones de transferencia:

$$\delta^*(s) = \overbrace{\left[\frac{wJ}{v_m^2\left(\dfrac{D}{v_m}s + m_t h\right)}\right]}^{H(s)} u_s(s), \tag{28}$$

y

$$\varphi(s) = \left(\frac{1}{s^2 - \dfrac{m_t g h}{J}} \right) u_s(s). \tag{29}$$

La ecuación (29) puede aproximarse a un sistema diferencialmente plano, referido en el dominio del tiempo como,

$$\ddot{\varphi}(t) = u_s(t) + \xi_1(t). \tag{30}$$

Este sistema, puede verse como una planta nominal compuesta de una doble derivada en el tiempo $\ddot{\varphi}(t) = u_s(t)$, perturbada por una función desconocida y variante en el tiempo $\xi_1(t)$.

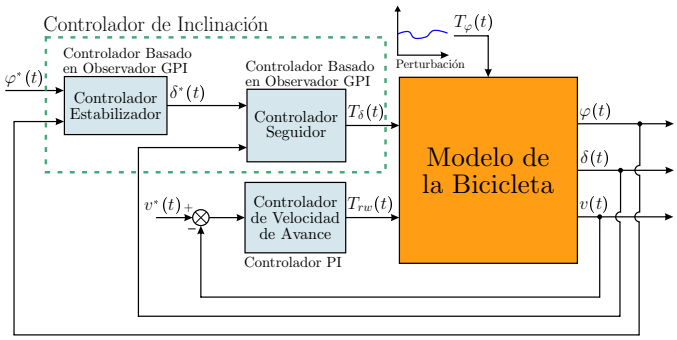

Figura 10. Esquema general del controlador de inclinación.

Debido a que las variaciones de inclinación de la bicicleta son relativamente suaves, se utiliza una aproximación lineal de primer orden como modelo interno de la función de perturbación $\xi_1(t)$. Según la metodología presentada en la sección 3, se formula el siguiente observador GPI para el sistema simplificado (30), aproximando el modelo interno de la perturbación como $\dot{\xi}_1(t) = \dot{r}_1(t) \approx 0$:

$$\dot{\hat{x}}(t) = A\hat{x}(t) + Bu_s(t) + L(y(t) - \hat{y}(t)), \quad \hat{y}(t) = C\hat{x}(t), \tag{31}$$

Con $\hat{x}(t) = [\hat{x}_1(t)\ \hat{x}_2(t)\ \hat{x}_3(t)]^{\mathrm{T}}$, la matriz $A \in \mathbb{R}^{3\times 3}$ con la misma forma de (12), $B = [0\ 1\ 0]^{\mathrm{T}}$, $C = [1\ 0\ 0]$ y $L = [l_2\ l_1\ l_0]^{\mathrm{T}}$; en donde $\hat{x}_1(t)$, $\hat{x}_2(t)$ y $\hat{x}_3(t)$, son las estimaciones de $\hat{\varphi}(t)$, $\dot{\hat{\varphi}}(t)$ y $\hat{\xi}_1(t)$ respectivamente.

La dinámica del error de estimación para este observador GPI, es dominada por los valores propios de $(A - LC)$, entonces, una apropiada selección de las ganancias del observador $L = [l_2\ l_1\ l_0]^{\mathrm{T}}$, debe ubicar las raíces del polinomio característico:

$$\det(sI - (A - LC)) = s^3 + l_2 s^2 + l_1 s + l_0, \tag{32}$$

a la izquierda del eje imaginario de $\mathbb{C}$. La selección de las raíces del polinomio característico del error de estimación, afecta el ancho de banda del observador GPI y puede contaminar con ruido sus salidas. Entonces, una sintonización apropiada del observador que adquiera un compromiso entre desempeño en la estimación y sensibilidad al ruido, puede lograrse utilizando el método *Characteristic Ratio Assignment* (CRA) propuesto en [Kim et al., 2003], para el control de respuesta transitoria de sistemas LTI. Según el método CRA, fue definida la constante de tiempo dominante generalizada como $\tau = 0.12$, para establecer sobre el observador un bajo ancho de banda (≈ 65.2 rad/s); y un parámetro inicial $\alpha_1 = 3.1$, para mantener una respuesta transitoria adecuadamente amortiguada. Estos dos parámetros ubican las raíces del polinomio característico del error de estimación en: $[-35.4\ \ -25.8\ \ -18.9]$.

Ahora, el objetivo de control es gobernar la salida $\varphi(t)$ del sistema (30), para obligarla a seguir la referencia $\varphi^*(t) = 0$ idependientemente de la función de perturbación desconocida $\xi_1(t)$. Entonces, se propone la siguiente ley de control:

$$u_s(t) = \ddot{\varphi}^*(t) - K_1\left[\dot{\hat{\varphi}}(t) - \dot{\varphi}^*(t)\right] - K_0\left[\hat{\varphi}(t) - \varphi^*(t)\right] - \hat{\xi}_1(t), \tag{33}$$

teniendo en cuenta que $\varphi^*(t) = \dot{\varphi}^*(t) = \ddot{\varphi}^*(t) = 0$. Reemplazando la ley de control en el sistema de lazo abierto (30), la dinámica del error de seguimiento de lazo cerrado $e_\varphi(t) = \varphi(t) - \varphi^*(t)$ del sistema de control, está dominantemente gobernada por $e_\varphi\left(s^2 + K_1 s + K_0\right) \approx 0$. Para este polinomio fueron seleccionadas las ganancias $K_0 = 18$ y $K_1 = 9$, cuyos valores ubican las raíces en $[-6\ \ -3]$ y establecen un tiempo de asentamiento de 1.53 segundos en la respuesta transitoria del error de seguimiento. La acción de control parcial $u_s(t)$, puede convertirse seguidamente en la referencia de posición angular $\delta^*(t)$, por medio de la ecuación (28).

Controlador Seguidor: Para iniciar con la formulación del controlador para el seguimiento de $\delta^*(t)$, es considerado el modelo de cuarto orden (8). Tomando la última fila de este sistema de ecuaciones representado en espacio de estado, se tiene lo siguiente:

$$\begin{aligned}\ddot{\delta}(t) = {} & a_{41}\varphi(t) + a_{42}\left(v^2(t)\right)\delta(t) + a_{43}\left(v(t)\right)\dot{\varphi}(t) \\ & + a_{44}\left(v(t)\right)\dot{\delta}(t) + b_{41}T_\varphi(t) + b_{42}T_\delta(t),\end{aligned} \tag{34}$$

en donde $a_{42}\left(v^2(t)\right)$, $a_{43}\left(v(t)\right)$ y $a_{44}\left(v(t)\right)$ son funciones dependientes de $v(t)$, $T_\delta(t)$ es el par aplicado a la dirección y $T_\varphi(t)$ es el par reflejado en la dirección por el efecto de fuerzas laterales aplicadas en la bicicleta, consideradas como perturbaciones externas. Aplicando la metodología ADRC, las dinámicas internas y perturbaciones externas definidas en (34), son asociadas en un término aditivo unificado definido como $\xi_2(t)$, para simplificar la ecuación tal y como se muestra seguido:

$$\ddot{\delta}(t) = \kappa u(t) + \overbrace{f\left(v(t), v^2(t), \delta(t), \dot{\delta}(t), \varphi(t), \dot{\varphi}(t), T_\varphi(t)\right)}^{\xi_2(t)}. \tag{35}$$

$u(t)$ es la entrada del sistema que está especificada como el par $T_\delta(t)$, $\kappa = b_{42}$ es la constante que acompaña a la entrada, y $\xi_2(t)$, es la función llamada como la perturbación de entrada. Entonces, se diseña un observador GPI para estimar las variables de estado y la perturbación de entrada que constituyen al sistema, para luego realimentarlas en la ley de control que logra el seguimiento robusto de $\delta^*(t)$.

Debido a todos los términos que deben asociarse en la función de perturbación $\xi_2(t)$ para lograr una representación simplificada de la planta tal y como se muestra en (35), una aproximación local de bajo orden para el modelo interno de esta compleja función de perturbación $(d\xi_2(t)/dt \approx 0)$, conlleva a la necesidad de diseñar un observador de alto ancho de banda. Es por esto, que se decide diseñar un observador GPI extendido con una aproximación del modelo interno de la perturbación, definida como $d^4\xi_2(t)/dt^4 \approx 0$.

Según la metodología de la sección 3, basándose en el sistema simplificado (35) y la aproximación del modelo interno de la función de perturbación $d^4\xi_2(t)/dt^4 = d^4r_2(t)/dt^4 \approx 0$, un observador GPI extendido es formulado de la siguiente manera:

$$\dot{\hat{x}}(t) = A\hat{x}(t) + B\kappa u(t) + F(\delta(t) - \hat{\delta}(t)), \quad \hat{\delta}(t) = C\hat{x}(t), \quad (36)$$

con $\hat{x}(t) = [\hat{x}_1(t)\ \hat{x}_2(t)\ \hat{x}_3(t)\ \hat{x}_4(t)\ \hat{x}_5(t)\ \hat{x}_6(t)]^{\mathrm{T}}$, la matriz $A \in \mathbb{R}^{6\times6}$ con la misma forma de (12), $B = [0\ 1\ 0\ 0\ 0\ 0]^{\mathrm{T}}$, $C = [1\ 0\ 0\ 0\ 0\ 0]$ y el vector de ganancias $F = [\wp_5\ \wp_4\ \wp_3\ \wp_2\ \wp_1\ \wp_0]^{\mathrm{T}}$. $\hat{x}_1(t)$, $\hat{x}_2(t)$ y $\hat{x}_3(t)$ son las versiones estimadas de $\delta(t)$, $\dot{\delta}(t)$ y $\xi_2(t)$ respectivamente.

La dinámica del vector del error de estimación que resulta del observador GPI extendido, será dominada por los valores propios de la matriz $(A - FC)$. Para este caso, el método de relaciones características (CRA) no es eficiente en la sintonización de las ganancias $\{\wp_0, \wp_1, \ldots, \wp_5\}$ del observador GPI extendido, por la estructura de sexto orden en la que se ha definido el modelo aumentado del sistema en espacio de estado. Una alternativa mejor elaborada para seleccionar una localización aceptable de los valores propios del observador GPI extendido consistiría en utilizar un método de optimización. Un regulador cuadrático lineal (LQR), es el adecuado para solucionar este problema de localización porque tiene como objetivo encontrar para un sistema en espacio de estado expresado como $\dot{x}(t) = Ax(t) + Bu(t)$, una ley de control $u(t) = -Kx(t)$ que minimiza el siguiente índice de desempeño [Naidu, 2002]:

$$V = \int_0^\infty \left[x^T(t)Qx(t) + u^T(t)Ru(t)\right]dt, \quad (37)$$

Tentativamente, las matrices Q y R fueron seleccionadas con los siguientes valores:

$$Q = \mathrm{diag}\left\{100,\ 100,\ 940\times10^6,\ 100,\ 1000,\ 1000\right\},$$
$$R = 0.1,$$

con los cuales, el método de optimización LQR entrega como resultado las siguientes cantidades para el vector de ganancias del observador GPI extendido $F = [\wp_5\ \wp_4\ \ldots\ \wp_0]^{\mathrm{T}}$:

$$F = [98.96\ \ 4396.05\ \ 97840.65\ \ 19697.99\ \ 1987.36\ \ 100]^{\mathrm{T}}.$$

Entonces, las raíces del polinomio característico del error de estimación, definido como:

$$\det(sI - (A - FC)) = s^6 + \wp_5 s^5 + \wp_4 s^4 + \wp_3 s^3 + \wp_2 s^2 + \wp_1 s + \wp_0, \quad (38)$$

son ubicadas en: $[-50\ \ -24.37+36.67\mathrm{i}\ \ -24.37-36.67\mathrm{i}\ \ -0.05+0.09\mathrm{i}\ \ -0.05-0.09\mathrm{i}\ \ -0.1]$, las cuales, establecen un ancho de banda de ≈ 90 rad/s en la dinámica del error de estimación. En [Teppa Garran and Garcia, 2014], está reportado un algoritmo para sintonizar las ganancias de un observador GPI por medio del método LQR.

Ahora, la ley propuesta para el controlador seguidor es la siguiente:

$$u(t) = \frac{1}{\kappa}\left[\ddot{\delta}^*(t) - K_3(\dot{\hat{\delta}}(t) - \dot{\delta}^*(t)) - K_2(\hat{\delta}(t) - \delta^*(t)) - \hat{\xi}_2(t)\right], \quad (39)$$

en donde $\delta^*(t)$, $\dot{\delta}^*(t)$ y $\ddot{\delta}^*(t)$ son la referencia de posición angular de la dirección y sus derivadas respectivamente.

Reemplazando esta ley de control en el sistema de lazo abierto (35), la dinámica del error de seguimiento $e_\delta(t) = \delta(t) - \delta^*(t)$ del sistema de control de lazo cerrado, quedará dominantemente gobernada por $e_\delta(t)(s^2 + K_3 s + K_2) \approx 0$. Un diseño admisible de la ley de control, se obtuvo con las ganancias $K_2 = 1760$ y $K_3 = 88$, las cuales, ubican las raíces del polinomio característico en: $[-57.3\ \ -30.7]$. Estas raíces establecen un tiempo de asentamiento de 0.15 segundos, en la respuesta transitoria del error de seguimiento.

5. SIMULACIÓN

Para verificar la estrategia de control propuesta, fue necesario desarrollar una co-simulación con ADAMS y MATLAB. La Fig. 18 muestra un diagrama de bloques con la estrategia de control completa, programada en MATLAB/Simulink. Las derivadas con respecto al tiempo de la trayectoria de referencia $\delta^*(t)$ fueron aproximadas por la siguiente función de transferencia:

$$D(s) = \frac{s\omega_n^2}{s^2 + 2\varsigma\omega_n + \omega_n^2}, \quad (40)$$

que corresponde a una derivada filtrada por un sistema de segundo orden, con una respuesta transitoria caracterizada por los parámetros ς y ω_n. Un diseño admisible para el filtro se obtuvo con $\omega_n = 50$ y $\varsigma = 0.75$, los cuales, establecen un ancho de banda de 3.5 Hz y un tiempo de asentamiento de 0.115 segundos en su respuesta transitoria.

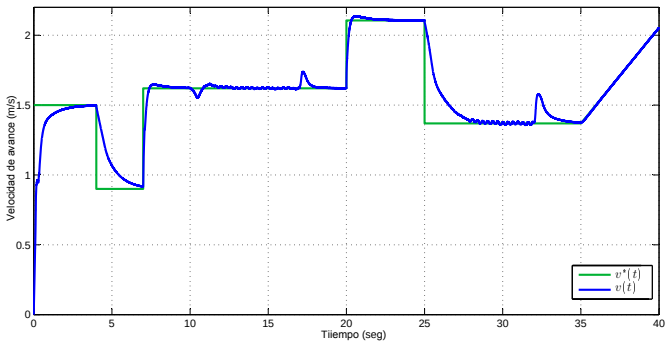

Figura 11. Salida de velocidad de avance $v(t)$.

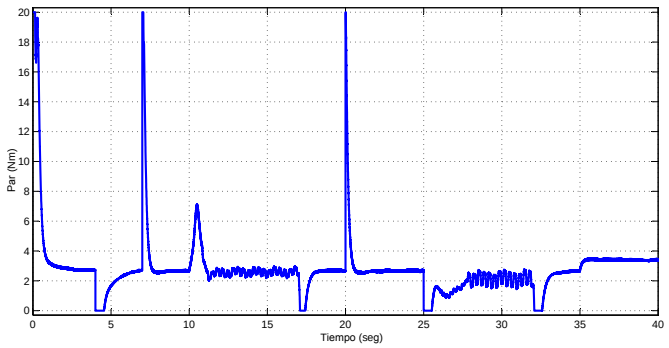

Figura 12. Par aplicado en la rueda trasera $T_{rw}(t)$.

En la co-simulación, se demuestra que las estrategias de control de velocidad e inclinación logran estabilizar la bicicleta actuando en ella desde el reposo ($v(0) = 0$ m/s), y con una inclinación inicial de 5.5° ($\varphi(0) = 0.096$ rad).

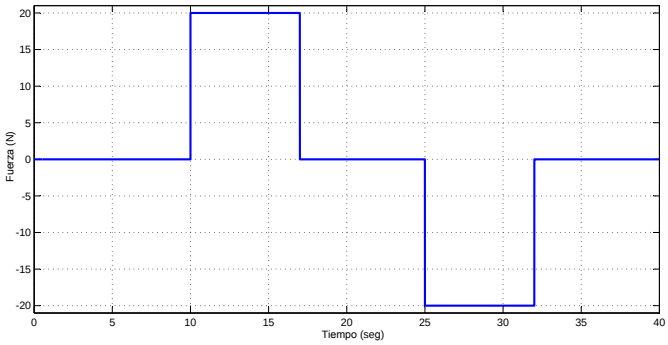

Figura 13. Fuerza externa aplicada en el marco trasero.

En la Fig. 11 se muestra la velocidad $v(t)$ alcanzada por la bicicleta y se observa el desempeño del controlador PI en el seguimiento de la referencia $v^*(t)$. El par $T_{rw}(t)$ generado por la acción PI se muestra en la Fig. 12. Algunos sobrepicos de velocidad que aparecen cuando la referencia es constante se originan por el perfil de fuerza externa de la Fig. 13 aplicado al marco trasero.

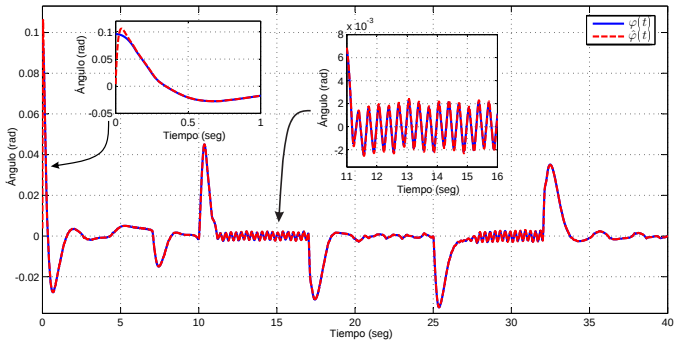

Figura 14. Salida de inclinación $\varphi(t)$ y su estimación $\hat{\varphi}(t)$.

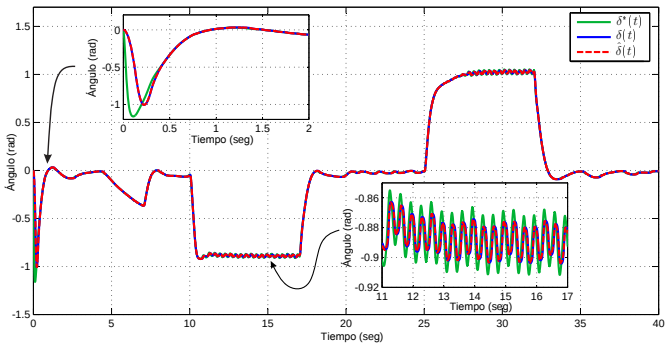

Figura 15. Salida de dirección $\delta(t)$ y su estimación $\hat{\delta}(t)$.

Ante los cambios de velocidad y la fuerza externa inyectada en el sistema, la Fig. 14 muestra claramente que el controlador de inclinación es efectivo en la estabilización de $\varphi(t)$. El controlador estabilizador hace su parte generando la referencia balanceadora $\delta^*(t)$, mientras que el controlador seguidor cumple con su tarea de imponer un seguimiento robusto de esa referencia al sistema de dirección, tal y como se muestra en la Fig. 15. La acción de control $T_\delta(t)$ generada por el controlador seguidor, muestra en la Fig. 16 que el mayor par aplicado al manubrio se produce en los primeros segundos de la simulación, en

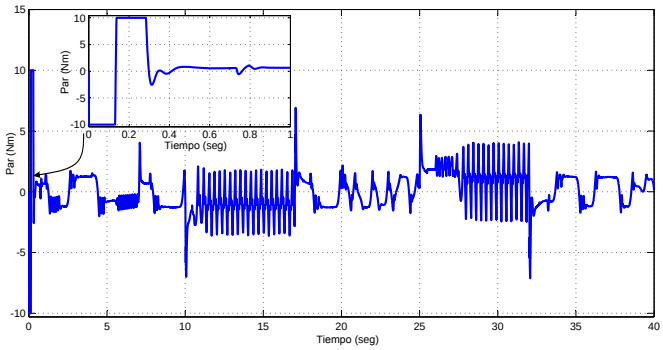

Figura 16. Par aplicado en la dirección $T_\delta(t)$.

donde excede los límites de saturación preestablecidos (-10 a 10 Nm). Esto se debe a la inclinación inicial y su arranque desde el reposo.

Figura 17. Simulación de la bicicleta en ADAMS/View.

La Fig. 17, exhibe la simulación interactiva de la bicicleta controlada en el entorno ADAMS/View.

6. CONCLUSIONES

Se demuestra en los resultados que el esquema de control ADRC propuesto, cumple satisfactoriamente con el objetivo de estabilización de la bicicleta en su posición vertical. Aunque el controlador estabilizador es capaz de generar una referencia apropiada para balancear la inclinación, tiene sus limitaciones debido a que está basado en un modelo simplificado de segundo orden. Se ha pensado para un trabajo posterior, diseñar un controlador estabilizador más efectivo con alguna otra estrategia para sistemas no lineales, basándose en el modelo LPV de cuarto orden. El controlador seguidor exhibe un desempeño destacable en el seguimiento de trayectorias y rechazo de las perturbaciones, que puede mejorarse aumentando el orden de la aproximación del modelo interno de la función de perturbación. El controlador de velocidad de avance tiene un buen desempeño para los requerimientos de este trabajo, pero debe mejorarse el seguimiento de la referencia si se considera en el futuro plantear una estrategia de control que además de estabilizar la inclinación, posibilite el desplazamiento siguiendo alguna trayectoria.

Aunque el controlador estabilizador fue diseñado sobre un punto de operación, asumiendo una velocidad de avance constante, puede observarse su contundencia estabilizando

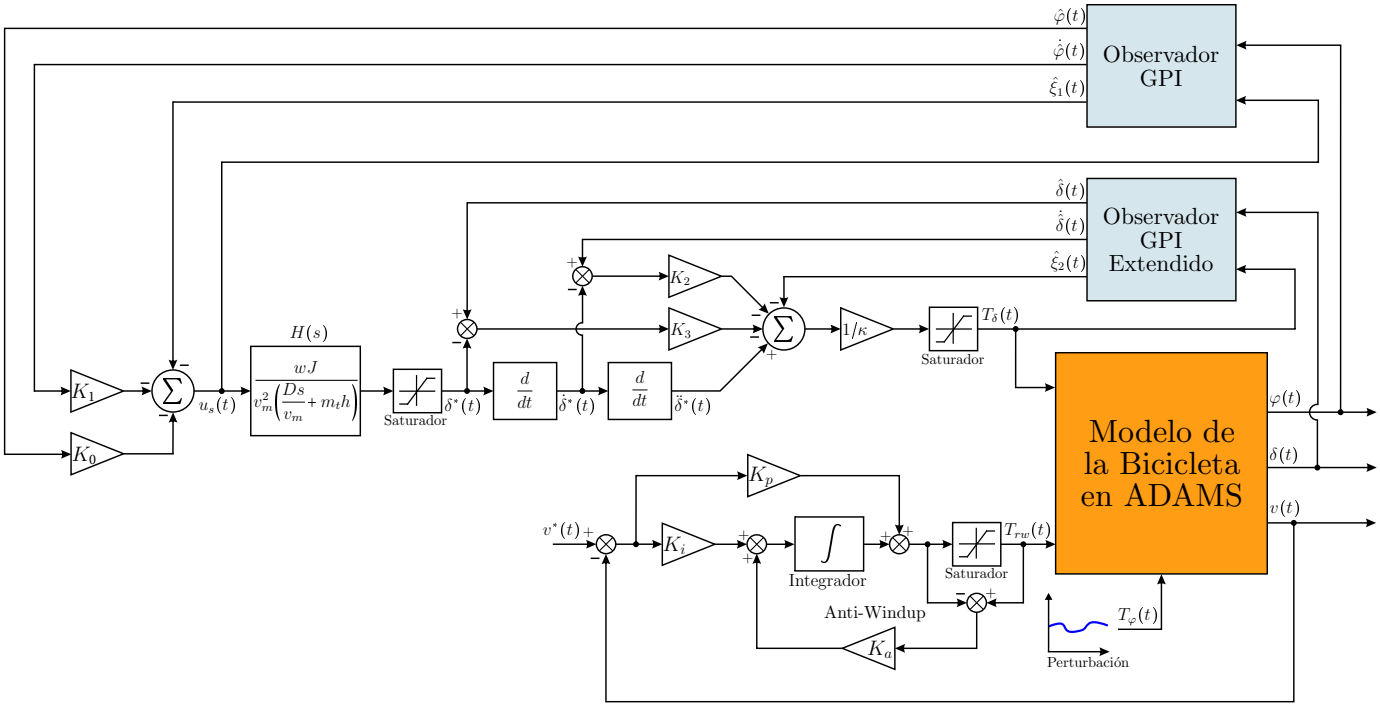

Figura 18. Esquema detallado del sistema de control de la bicicleta.

la bicicleta en un rango por encima y por debajo del valor nominal (v_m = 1.5 m/s). El desempeño y robustez del controlador estabilizador se reduce tanto como la velocidad de avance disminuya del valor nominal, hasta el punto donde el sistema de lazo cerrado se vuelve inestable (cuando $v(t) \approx 0.85$ m/s).

La efectividad de la estrategia de control propuesta, radica en la estimación activa de las posibles no-linealidades y perturbaciones que afectan al modelo virtual durante su libre movimiento, por medio de dos observadores GPI, los cuales, reestablecen el desempeño del modelo lineal simplificado de la bicicleta, permitiendo así, que la estructura lineal de la leyes de control establecidas en los lazos de estabilización y seguimiento, impongan las dinámicas de las referencias de entrada. El seguimiento de la referencia de velocidad de avance que establece el controlador PI al sistema de tracción, ayuda notablemente al controlador de inclinación porque limita la magnitud y la tasa de variación de las perturbaciones exógenas que afectan al sistema, incrementando su controlabilidad puesto que se controlan las variaciones de sus parámetros dependientes de esta variable. Un trabajo interesante para desarrollar a futuro, sería proponer alguna estrategia de control que sea igualmente dependiente de la velocidad de avance, con sus ganancias auto-sintonizables mediante algún criterio de optimización, para mejorar la robustez del sistema de lazo cerrado ante las perturbaciones e incertidumbres del modelo.

REFERENCIAS

Canudas de Wit, C. and Tsiotras, P. (1999). Dynamic tire friction models for vehicle traction control. In *Decision and Control, 1999. Proceedings of the 38th IEEE Conference on*, volume 4, 3746 – 3751. doi: 10.1109/CDC.1999.827937.

Cerone, V., Andreo, D., Larsson, M., and Regruto, D. (2010). Stabilization of a Riderless Bicycle, A Linear-Parameter-Varying Approach [applications of control]. *Control Systems, IEEE*.

Chen, C.K. and Dao, T.K. (2010). A Study of Bicycle Dynamics via System Identification. *Symposium on Computer, Communication, Control and Automation*.

Cortés Romero, J., Luviano Juárez, A., Álvarez Salas, R., and Sira Ramírez, H. (2010). Fast identification and control of an uncertain brushless dc motor using algebraic methods. In *12th International Power Electronics Congress (CIEP)*, 9 – 14.

Cortés Romero, J., Ramos, G., and Coral Henriquez, H. (2014). Generalized proportional integral control for periodic signals under active disturbance rejection approach. In *ISA Transactions - The Journal of Automation*, volume 53, 1901 – 1909.

Cortés Romero, J., Hebertt Sira Ramirez, and Alberto Luviano Juarez (2011). Control Lineal Robusto de Sistemas no Lineales Diferencialmente Planos. In *Revista Iberoamericana de Automática e Informática Industrial*, volume 8, 14 – 28.

Gao, Z. (2006). Active Disturbance Rejection Control: a Paradigm Shift in Feedback Control System Design. In *American Control Conference, 2006*, 7 pp.–. doi: 10.1109/ACC.2006.1656579.

Goldstein, H. (1953). *Classical Mechanics*, 186. Addison-Wesley, first edition.

Gordon Wilson, D. (2004). *Bicycling Science*, chapter 8, 263 – 310. The MIT Press, third edition.

Iuchi, K., Hiroshi Niki, and Toshiyuki Murakami (2005). Attitude Control of Bicycle Motion by Steering Angle and Variable COG Control. In *31st Annual Conference of IEEE Industrial Electronics Society, 2005. IECON 2005.*, 6, 6 pp.–.

Kim, Y., Keel, L., and Bhattacharyya, S. (2003). Transient Response Control via Characteristic Ratio Assignment. volume 48, 2238 – 2244.

Kooijman, J.D.G. (2006). *Experimental Validation of a Model for the Motion of an Uncontrolled Bicycle*. Master's thesis, Delft University of Technology, The Netherlands.

Limebeer, D.J. and Sharp, R.S. (2006). Single-Track Vehicle Modeling and Control. Bicycles, Motorcycles and Models. *IEEE Control Systems Magazine*.

Meijaard, J.P., Jim M. Papadopoulos, Andy Ruina, and Schwab, A.L. (2007). Linearized Dynamics Equations for the Balance and Steer of a Bicycle: a Benchmark and Review. *Proceedings Of The Royal Society A*.

Michini, B. and Sean Torrez (2007). Autonomous Stability Control of a Moving Bicycle. Technical report, Massachusetts Institute of Technology, USA, 77 Massachusetts Ave, Rm 33-336 - Cambridge MA 02139.

Naidu, D.S. (2002). *Optimal Control Systems*, chapter 3, 101 – 147. CRC Press, first edition.

Papadopoulos, J.M. (1987). Bicycle Steering Dynamics and Self-stability: a Summary Report on Work in Progress. Cornell bicycle research project, Cornell University, Ithaca, NY.

Schwab, A., Meijaard, J., and Papadopoulos, J. (2005). Benchmark Results on the Linearized Equations of Motion of an Uncontrolled Bicycle. *Int. J. Mech. Sci. Technol.*

Schwab, A.L., Meijaard, J.P., and Kooijman, J.D.G. (2012). Lateral Dynamics of a Bicycle with a Passive Rider Model: Stability and Controllability. *Vehicle System Dynamics*, 50.

Sira Ramírez, H. and Sunil K. Agrawal (2004). *Differentially Flat Systems*, chapter 2, 11 – 28. Marcel Dekker, Inc, first edition.

Åström, K.J. and Hägglund, T. (1995). *PID Controllers: Theory, Design, and Tuning*, chapter 3, 80 – 92. ISA, second edition.

Åström, K.J. and Hägglund, T. (2006). *Advanced PID Control*, chapter 3, 64 – 92. ISA, first edition.

Åström, K.J., Klein, R.E., and Lennartsson, A. (2005). Bicycle, Dynamcs and Control. *IEEE Control Systems Magazine*.

Teppa Garran, P. and Garcia, G. (2014). Adrc Tuning Employing the LQR Approach for Decoupling Uncertain MIMO Systems. In *Information Technology and Control*, volume 43, 157 – 165.

Modelado y diseño de un control predictivo para un levitador neumático

Luis Edo García Jaimes*, Maribel Arroyave Giraldo**

**Institución Universitaria de Envigado. legarcia47@gmail.com*
***Institución Universitaria de Envigado. maribel.arrgi@gmail.com*

Resumen: Este artículo presenta la modelación matemática de un levitador neumático y el cálculo de algunos de sus parámetros a partir de datos experimentales. Se diseñan para el levitador controladores predictivos con diferentes valores del parámetro de ponderación del esfuerzo de control y se compara su desempeño utilizando métricas de la integral del error y de respuesta temporal. Los resultados obtenidos muestran el cumplimiento de los objetivos en lo que se refiere al diseño y modelado del levitador y al buen desempeño de los controladores implementados.
Palabras clave: levitador neumático, modelación, control predictivo, automatización.

1. INTRODUCCIÓN

En este artículo se presentan los resultados del proyecto "Desarrollo de un levitador neumático para el laboratorio de automatización de la Institución Universitaria de Envigado", se dan a conocer detalles del modelado del levitador y del diseño de algoritmos de control para regular la posición de una esfera ubicada dentro del tubo del levitador.

En la literatura se referencian algunos trabajos sobre levitadores neumáticos, Mosquera et al (2012) presentan el diseño, modelado y control de posición de un sistema de levitación neumático. Utilizan un controlador PID para controlar la posición de una esfera a una altura deseada mediante el ajuste de la velocidad de un motor y un sensor de ultrasonido que permite al sistema en lazo cerrado obtener la información para controlar la altura, Escaño y Muñoz (2004) describen la identificación y control de posición de un sistema de levitación neumática. El sistema utiliza realimentación visual para detectar la altura del objeto, la cual se controla mediante un compresor de aire accionado por un variador de velocidad. El sistema es utilizado como banco de pruebas, donde se implementaron diferentes técnicas de control, Lajas (2005) realiza el control en tiempo real de la altura de un objeto suspendido dentro del flujo de aire, utilizando diferentes estrategias de control como control PID y Control H ∞.

El artículo es un estudio de caso en el cual se diseña y construye el levitador y se obtienen experimentalmente los parámetros específicos del mismo. Está conformado por cuatro secciones, la primera corresponde a la introducción, en la segunda se muestran los esquemas y planos producto del diseño del sistema, en la tercera se presentan los resultados y el diseño del controlador predictivo, en la cuarta se analizan los resultados del desempeño de los controladores implementados y finalmente, se resumen las principales conclusiones del proyecto.

En el proyecto se construye el levitador y se obtiene un modelo no lineal del mismo utilizando leyes físicas descritas por ecuaciones diferenciales, cuyos coeficientes se calculan experimentalmente a diferencia de otros trabajos similares, en los cuales el modelo se obtiene directamente mediante la identificación de sistemas. Luego se linealiza el modelo alrededor de un punto de equilibrio que represente matemáticamente la dinámica del sistema y, a partir del modelo linealizado, se diseñan el controlador predictivo y el controlador PI.

2. MATERIALES Y MÉTODOS

El objetivo del trabajo es presentar la forma como se obtuvo la dinámica del levitador y diseñar e implementar algoritmos de control predictivo y comparar su desempeño con respecto a métricas de la integral del error y de respuesta temporal.

2.1 Diseño del modulo

En la Fig.1 se muestra el diagrama de instrumentación del sistema, este incluye el tubo de acrílico, la esfera que es el elemento a posicionar, el sensor de posición infrarrojo GP2D12, la tarjeta de adquisición de datos, el PC con el algoritmo de control de posición y que está conectado por puerto USB a la tarjeta, el ventilador centrífugo accionado por un motor trifásico de 0.5 Hp cuya velocidad es regulada por un variador.

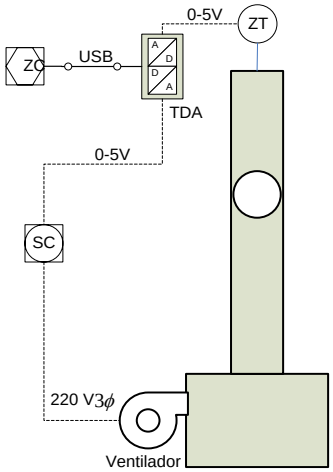

Fig.1. Diagrama de instrumentación.

2.2. Modelado matemático

El modelo matemático del levitador neumático involucra elementos mecánicos, aerodinámicos y eléctricos. La Fig.2 muestra las fuerzas que actúan sobre la esfera ubicada dentro del tubo. Buckner et al (2009).

Aplicando la segunda ley de Newton se obtiene (1) y (2):

$$\sum F_y = m_b \frac{d^2y}{d^2t} = m_b \frac{dv_b}{dt} \qquad (1)$$

$$m_b \frac{dv_b}{dt} = -F_g + F_D \qquad (2)$$

F_g es el peso de la esfera y F_D es la fuerza de arrastre que actúa sobre ella. Dichas fuerzas están dadas en (3) y (4):

$$F_g = m_b g \qquad (3)$$

$$F_D = \frac{1}{2} C_D \rho_a A (v_a - v_b)^2 \qquad (4)$$

En donde, m_b es la masa de la esfera, C_D es el coeficiente de arrastre, ρ_a es la densidad del aire, A es el área frontal de la esfera, v_a la velocidad del aire en el tubo y v_b la velocidad de la esfera.

Combinando (2), (3) y (4) resulta (5):

$$m_b \frac{dv_b}{dt} = -m_b g + \frac{1}{2} C_D \rho_a A (v_a - v_b)^2 \quad (5)$$

Para una esfera, (5) toma la forma (6):

$$\frac{dv_b}{dt} = -g + \frac{3}{8} \frac{C_D \rho_a (v_a - v_b)^2}{\rho_b R} \qquad (6)$$

R es el radio de la esfera y ρ_b su densidad.

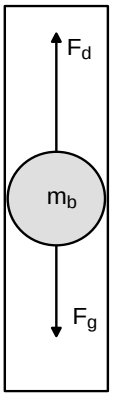

Fig.2. Fuerzas sobre la esfera

El cambio de velocidad de la columna de aire dentro del tubo se puede modelar mediante (7):

$$\frac{dv_a}{dt} = \frac{g(f,y) - v_a}{\tau_a} \qquad (7)$$

La relación $g(f,y)$ depende de la frecuencia f del voltaje aplicado al ventilador centrífugo y de la altura medida con respecto al orificio de entrada del aire al tubo y, y se obtiene experimentalmente para diferentes valores de f y de y, τ_a es la constante de tiempo del sistema del flujo de aire.

Finalmente, el sensor de distancia (GP2D12) se puede modelar como un sistema de primer orden (8):

$$\frac{dy_s}{dt} = \frac{y_b - y_s}{\tau_s} \qquad (8)$$

En donde y_b es la posición de la esfera, y_s es la posición del sensor y τ_s es su constante de tiempo que se obtiene experimentalmente.

La velocidad del aire producido por el ventilador en un punto determinado a una distancia y de la boca de insuflación está dada por (9), Escoda (2008), Ortiz (2011)

$$v = g(f,y) = \frac{C v_i \sqrt{A_0}}{y_b} \qquad [m/s] \qquad (9)$$

En donde v es la velocidad del flujo de aire en m/s en un punto dado, y_b es la altura de la esfera en metros, v_i es la velocidad de salida del aire en la boca de insuflación, A_0 es el área libre de la boca de insuflación, C es una constante que se obtiene de tablas. Para este caso $C = 5$ y $A_0 = 0.01538\ m^2$

2.3 Datos experimentales

Se obtienen con el fin de calcular la relación entre f, v_a e y_b y a partir de ella evaluar una expresión para $g(f,y)$.
En la tabla 1 se muestran los datos de la variación de la velocidad del aire en la boca del tubo en función del voltaje de control aplicado al variador y de la frecuencia del mismo.

Tabla 1. Variación de la velocidad del aire vs voltaje de control aplicado

V (Volt)	f (Hz)	(m/s)
0	0	0
0.6	6.88	1.91
1.66	19.44	5.08
2.12	24.88	6.66
2.57	30.20	7.92
2.91	34.28	9.02
3.25	38.36	9.99
3.56	41.91	10.88
3.70	43.68	11.32

Con los datos de la tabla 1 se obtiene la relación entre el voltaje de control aplicado al variador de velocidad (V), la frecuencia de la alimentación aplicada a la turbina (f) en Hz y la velocidad de salida del aire en la boca del tubo (v_i) en m/s (10), (11):

$$f = 11.874V - 0.242 \quad [Hz] \quad (10)$$
$$v_i = 3.029V + 0.097 \quad [m/s] \quad (11)$$

De las curvas de respuesta dadas por el fabricante para el sensor de distancia GP2D12 se obtiene (12) que relaciona el voltaje de salida del sensor con la distancia del cuerpo, Abarca, Loor y Robalino (2008).

$$V_s = \frac{21.78}{y_b} + 0.402 \quad [Volt] \quad (12)$$

En donde V_s es la salida del sensor en voltios y y_b la distancia de la esfera al sensor en cm. Como se trabaja con voltajes de 0 a 5V se utilizó un amplificador con ganancia 1.9 con lo cual la (12) se transforma en (13) y (14):

$$V_s = \frac{41.4}{y_b} + 0.764 \quad [Volt] \quad (13)$$
$$y_b = \frac{41.4}{V_s - 0.764} \quad [cm] \quad (14)$$

Combinando (9), (11) y (14) y organizando las unidades se obtiene (15)

$$g(f, y) = 1.498(3.029V + 0.097)(V_s - 0.764) \quad (15)$$

En donde V es el voltaje de salida hacia el variador (generado por la ley de control) y V_s es la lectura del sensor.

3. RESULTADOS Y DISCUSIÓN

En la tabla 2 se dan los parámetros del sistema real con el cual se realizaron las pruebas para obtener los parámetros del levitador.

Tabla 2. Parámetros del levitador

$m_b[Kg]$	0.0279
$R[m]$	0.07
$A[m^2]$	0.01538
$\rho_b[\frac{Kg}{m^3}]$	19.42
$\rho_a[\frac{Kg}{m^3}]$	1.196
$\tau_a[s]$	2
$\tau_s[s]$	0.04
C	0.5
C_D	0.05

Reemplazando estos valores en el modelo descrito por (6), (7), (8) y (15), resulta (16):

$$\frac{dv_b}{dt} = -9.81 + 0.1649(v_a - v_b)^2$$
$$\frac{dv_a}{dt} = \frac{1.498(3.029V + 0.097)(V_s - 0.764) - v_a}{2} \quad (16)$$
$$\frac{dy_s}{dt} = \frac{y_b - y_s}{0.04}$$

Tomando como variables de estado: $x_1 = v_b,\ x_2 = v_a,\ x_3 = y_s$ y como punto de equilibrio $y_b = 40cm$ se obtiene (17):

$$\dot{x}_1 = -9.81 + 0.1649(x_2 - x_1)^2$$
$$\dot{x}_2 = -0.5x_2 + 0.075 + 2.35V \quad (17)$$
$$\dot{x}_3 = -25x_3 + 1000$$

La ecuación (17) describe el comportamiento dinámico del levitador, representa un sistema no lineal que al linealizarlo alrededor del punto de equilibrio propuesto arroja la siguiente ecuación de estado:

$$\begin{bmatrix}\dot{x}_1\\ \dot{x}_2\\ \dot{x}_3\end{bmatrix} = \begin{bmatrix}-2.543 & 2.543 & 0\\ 0 & -0.5 & 0\\ 0 & 0 & -25\end{bmatrix}\begin{bmatrix}x_1\\ x_2\\ x_3\end{bmatrix} + \begin{bmatrix}0\\ 2.35\\ 0\end{bmatrix}V$$
$$v_b = [1 \quad 0 \quad 0]\begin{bmatrix}x_1\\ x_2\\ x_3\end{bmatrix} \quad (18)$$

La función de transferencia correspondiente a (18) que relaciona la velocidad de la esfera con el voltaje de control aplicado al variador de velocidad está dada por (19):

$$G_p(S) = \frac{V_b(S)}{V(S)} = \frac{5.9761S + 149.401}{(S + 25)(S + 2.543)(S + 0.5)} \quad (19)$$

Según (19), la función de transferencia que relaciona la posición de la esfera con el voltaje de control aplicado al variador de velocidad es (20):

$$G_p(S) = \frac{Y_b(S)}{V(S)} = \frac{5.9761S + 149.401}{S(S + 25)(S + 2.543)(S + 0.5)} \quad (20)$$

Al discretizar el modelo con T=0.5 s resulta (21):

$$G_p(z) = \frac{0.08743z^{-1} + 0.24577z^{-2} + 0.04094z^{-3}}{1 - 2.0592z^{-1} + 1.2776z^{-2} - 0.21839z^{-3}} \quad (21)$$

3.1 Controlador predictivo

El control predictivo es una estrategia de control que se basa en la utilización de forma explícita de un modelo del proceso para predecir el valor de las variables controladas a lo largo de un horizonte temporal especificado por el usuario, calculando el valor de las variables manipuladas para hacer que en ese horizonte las variables controladas estén en sus valores de referencia. Hay una serie de elementos comunes a todos los controladores predictivos: el modelo de predicción, la función objetivo y la ley de control Camacho y Bordons (2000).

Para aplicaciones industriales es conveniente el uso de un modelo CARIMA (*Controller Auto-Regressive Integrated Moving-Average*), dado en (22):

$$y(t) = \frac{z^{-d}B(z^{-1})}{A(z^{-1})}u(t-1) + \frac{C(z^{-1})}{\Delta A(z^{-1})}e(t) \quad (22)$$

Donde $u(t)$ y $y(t)$ son las variables de entrada y salida respectivamente y $e(t)$ es un ruido blanco de media cero.

El algoritmo de control consiste en aplicar la secuencia de control que minimice la función de coste (22):

$$J = \sum_{j=N_1}^{N_2} \delta(j)[y(t+j|t) - w(t+j)]^2 + \sum_{j=1}^{N_u} \lambda(j)[\Delta u(t+j-1)]^2 \quad (23)$$

Donde $y(t+j|t)$ es la predicción óptima de la salida $w(t+j)$ es la trayectoria de referencia, $\delta(j)$ y $\lambda(j)$ son factores de ponderación, N_1 y N_2 son el horizonte mínimo y máximo de predicción y N_u es el horizonte de control.
El último término de (22) y con $C(z^{-1}) = 1$, se puede escribir en la forma (24):

$$\frac{1}{\Delta A(z^{-1})} = E_j(z^{-1}) + z^{-j}\frac{F_j(z^{-1})}{\Delta A(z^{-1})} \quad (24)$$

Con $E_{j+1} = E_j + f_{j,0}z^{-j}$ y $F_j = [1 - E_j\hat{A}]z^j$

Así (22) se puede escribir matricialmente como (25):

$$y = Gu + F(z^{-1})y(t) + G'(z^{-1})\Delta u(t-1) \quad (25)$$

Donde:
$G_j = BE_j = g_o + g_1z^{-1} + g_2z^{-2} + \cdots$

$$y = \begin{bmatrix} y(t+d+1|t) \\ y(t+d+2|t) \\ \vdots \\ y(t+d+N|t) \end{bmatrix} \quad G = \begin{bmatrix} g_o & 0 & \dots & 0 \\ g_1 & g_o & \dots & 0 \\ \vdots & \vdots & \vdots & \vdots \\ g_{N-1} & g_{N-2} & \dots & g_o \end{bmatrix}$$

$$u = \begin{bmatrix} \Delta u(t) \\ \Delta u(t+1) \\ \vdots \\ \Delta u(t+N-1) \end{bmatrix} \quad F(z^{-1}) = \begin{bmatrix} F_{d+1}(z^{-1}) \\ F_{d+2}(z^{-1}) \\ \vdots \\ F_{d+N}(z^{-1}) \end{bmatrix}$$

$$G'(z^{-1}) = \begin{bmatrix} z[G_{d+1}(z^{-1}) - g_0] \\ z^2[G_{d+2}(z^{-1}) - g_0 - g_1z^{-1}] \\ \vdots \\ z^N[G_{d+N}(z^{-1}) - g_0 \dots - g_{N-1}z^{(N-1)}] \end{bmatrix}$$

$$F(z^{-1}) = \begin{bmatrix} F_{d+1}(z^{-1}) \\ F_{d+2}(z^{-1}) \\ \vdots \\ F_{d+N}(z^{-1}) \end{bmatrix} \quad (26)$$

Los dos últimos términos de (25) dependen sólo del pasado y se pueden agrupar dentro del vector f, por tanto (27):

$$y = Gu + f \quad (27)$$

Llevando (27) a (23), la función de costo a minimizar se convierte en (28):

$$J = (Gu + f - w)^T(Gu + f - w) + \lambda u^T u \quad (28)$$

La ley de control para el GPC queda (29):

$$\Delta u = K(w - f) \quad (29)$$

Siendo K, la primera fila de $(G^TG + \lambda I)^{-1}G^T$

3.2 *Prueba de los controladores diseñados*

Se estimaron diferentes controladores tomando como base la variación en el factor de ponderación del esfuerzo de control. En todos los casos se realizaron las pruebas del sistema variando el *set-Point* del 60% al 70% de la altura máxima que puede alcanzar la esfera dentro del tubo del levitador.

La fig. 3 corresponde a la respuesta del sistema con el controlador predictivo con $\lambda = 10$, horizonte mínimo de predicción $N_1 = 1$ y horizontes máximos de predicción y de control $N_1 = N_2 = 5$

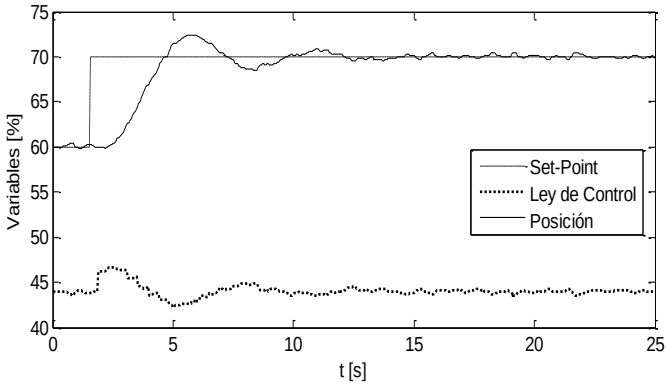

Fig. 3. Cambio de la posición de la esfera del 60% al 70% con el controlador predictivo $\lambda = 10$

La Fig.4 corresponde a la evolución de la posición de la esfera con $\lambda = 5$ conservando los otros parámetros en sus valores originales.

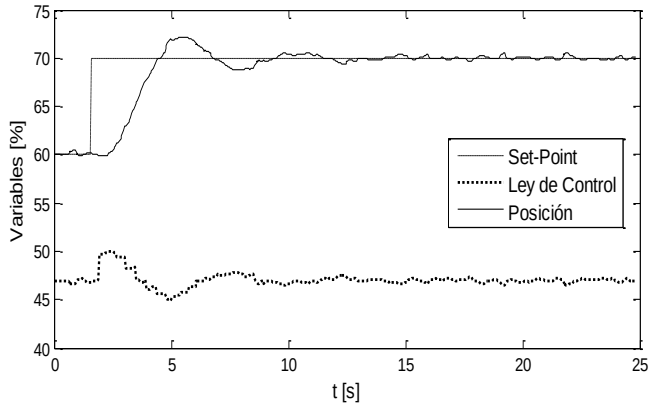

Fig. 4. Cambio de la posición de la esfera del 60% al 70% con el controlador predictivo $\lambda = 5$

La Fig.5 corresponde a la evolución de la posición de la esfera con $\lambda = 0.5$ conservando los demás parámetros en sus valores originales.

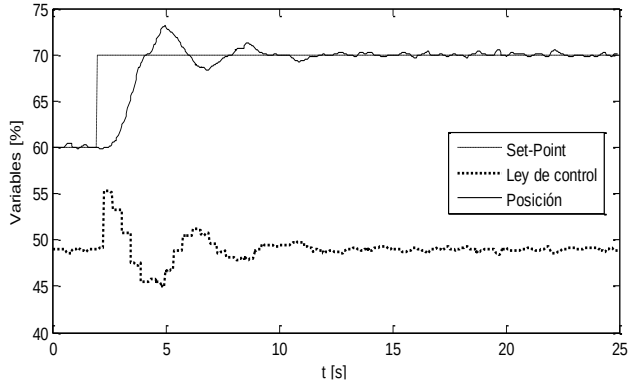

Fig. 5. Cambio de la posición de la esfera del 60% al 70% con el controlador predictivo $\lambda = 0.5$

Finalmente se trabajó con un controlador PI en el cual sus parámetros se estimaron utilizando asignación de polos Iserman (1991), García (2011). La fig. 6 muestra la respuesta del sistema con este controlador

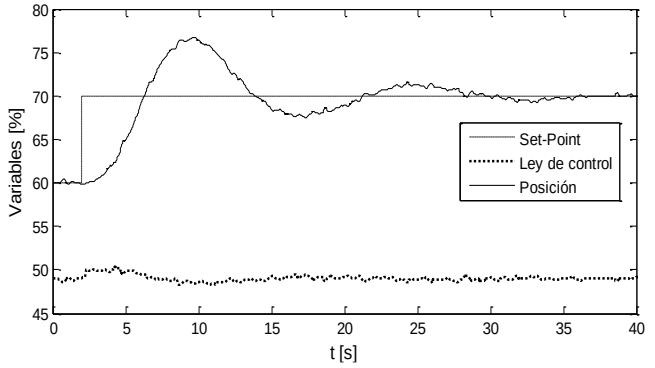

Fig. 6. Cambio de la posición de la esfera del 60% al 70% con el controlador PI

3.3 Análisis de resultados

Se obtuvo el modelo matemático del levitador utilizando las leyes de Newton y se calcularon algunos de sus parámetros a partir de datos experimentales. El modelo inicial es no lineal y para realizar el control del mismo se linealizó alrededor de un punto de equilibrio seleccionado.

En la tabla 3 se presentan los valores obtenidos al utilizar métricas de la integral del error a cada uno de los controladores evaluados.

Tabla 3. Valores de los criterios de la Integra del error

CRITERIO	IAE	ICE	IAET	IE
$\lambda = 10$	32.01	193.5	141.2	1102
$\lambda = 5$	29.41	180.5	126.0	1177
$\lambda = 0.5$	25.43	145.5	110.6	1227
PI	84.68	449.8	887.8	1962

La tabla 4 muestra los valores obtenidos al utilizar métricas de la respuesta temporal para evaluar el desempeño de los controladores.

Tabla 4. Valores de respuesta temporal

	t_s [s]	$Mp\%$	e_{ss}
$\lambda = 10$	13	22	0
$\lambda = 5$	11	24	0
$\lambda = 0.5$	10	30	0
PI	30	40	0

Al analizar los valores obtenidos para las métricas de la integral del error, se observa que, a medida que se disminuye el factor de ponderación del esfuerzo de control, dichos valores disminuyen, lo cual indica que la respuesta del sistema converge más rápido hacia el *set-point* pero a costa de un mayor esfuerzo de control, esto se ve en el criterio IE (índice de energía) que es un indicador de dicho esfuerzo. Por su parte, el controlador PI presenta los índices mayores debido a su respuesta más oscilatoria y al mayor tiempo de establecimiento.

Los controladores predictivos implementados mostraron un desempeño adecuado, las respuestas de la posición de la esfera con estos controladores se muestra en las fig. 3, 4 y 5 y en ellas se aprecia que al aplicar un cambio en el set-point del 60% al 70% el sistema presenta inicialmente un sobreimpulso significativo (22%, 24% y 30%) con tiempos de establecimiento de 13 s, 11 s y 10 s, respectivamente sin oscilaciones significativas y con error de estado estable aceptable igual a cero. Por otro lado, el controlador PI (fig. 6) presenta un sobreimpulso alto (40%) y tiempo de establecimiento de 30 s, su error de estado estable es cero.

4. CONCLUSIONES

Con los dos algoritmos de control, el sistema presentó un desempeño adecuado en cuanto a exactitud (error de estado estable aceptable), estabilidad y velocidad de respuesta se refiere, lo que indica que este tipo de controladores son

apropiados para regular sistemas no lineales y con dinámicas complejas.

Los controladores predictivos pueden considerarse como una opción posible y robusta a problemas de control de complejidad media a elevada debido a la facilidad y rapidez con que éstos pueden ser implementados en una aplicación de control determinada, su desventaja radica en que se requiere del conocimiento del modelo del sistema en forma precisa, para obtener un buen desempeño del sistema.

Los resultados obtenidos muestran el cumplimiento de los objetivos en lo que respecta al diseño y construcción del levitador y al buen desempeño de los controladores implementados.

AGRADECIMIENTOS

Los autores expresan sus agradecimientos a la institución Universitaria de Envigado, por la financiación del proyecto.

REFERENCIAS

Abarca, Loor, S. y F. Robalino, G.(2008). *Medición y Control de Nivel con Aplicación de dsPIC.* Tesis de grado. Escuela superior politécnica del litoral. Facultad de Electricidad y computación.

Application note for an infrared, triangultation-based distance sensor with an analog, non-linear output. (22 de 03 de 2001). Recuperado el 10 de Noviembre de 2013, de: http://zuff.info/SharpGP2D12_E.html

Buckner, Jernigan y Fahmy (2009) *Implementing a Remote Laboratory Experience into a Joint Engineering Degree Program: Aerodynamic Levitation of a Beach Ball*. IEEE transactions on education, pág. vol 52. N 2.

Camacho, E. Bordons, C. (2000). *Model Predictive Control*. Springer Verlag, 1999. Universidad de Sevilla.

Escoda, S.(2008) *Manual práctico de ventilación*. Rosellón Barcelona: s.n. Pág. 45.

García, L. (2011). *Control Digital. Teoría y práctica.* Politécnico Colombiano JIC. Tercera edición. ISBN 978-958-9090-25-1

GP2D12 (2015) *Data Sheet. Overview of the Sharp GP2D12 specifications.* http://zuff.info/SharpGP2D12. Consultado 12 marzo/2013

Iserman, R. Lachman,K. (1991) *Adaptive Control Systems*. Prentice Hall.

Lajas, F. B.(2005) *Diseño de estrategias de control para un sistema de levitación neumática*. Escuela superior de Ingenieros - Universidad de Sevilla. 2005

Mosquera, V. Bacca, G and Quiñones, M. (2012) *Control de posición de un sistema de levitación*. Revista Universitaria en Telecomunicaciones Informática y Control. Vol. 1. N° 2. ISSN 2227 – 3735. Popayán.

Mott, R. (1996) *Mecánica de fluidos aplicada*. 4ª Edición. Pearson Educación, 1996. México

Muñoz, D and Escaño, J (2004). *Identificación y control de posición de un sistema de levitación neumática*. XXV Jornadas de Automática Ciudad Real. Recuperado el 20 de marzo de 2014 de: http://www.ceautomatica.es/old/actividades/jornadas/XXV/documentos/39-anessiuore.pdf.

National Instrument. (2012). *User guide and specifications NI USB 6008/6009.*

Ortiz, P. Ramírez, J. Cardona, L (2011) *Modelo matemático y control de un sistema de fluidos.* Instituto Tecnológico Metropolitano. ISBN: 978-958-8743-08-0

Nonlinear state estimation using online FTIR spectroscopy in polymerization processes

C. Zuluaga-Bedoya * **and J. Garcia-Tirado** *

* *Instituto Tecnológico Metropolitano, Calle 73 No 76A - 354, 050034, Medellín - Colombia. Facultad de Ciencias Económicas y Administrativas, Grupo de Calidad, Metrología y Producción, (email: zuluagabedoya@gmail.com, josegarcia@itm.edu.co).*

Abstract: Fourier-Transform Infrared spectroscopy (FTIR) is a powerful tool for inferring chemical composition of a sample from the analysis of its infrared spectrum of absorption or emission. The industrial usage of this analyzer is typically reduced to species characterization, without taking advantage of the potential in quantitative analysis. In the case of the polymers, there are some variables related with product quality, which are strongly related to molecular properties of polymer chains, such as Molecular Weight Distribution (MWD). Using state estimation techniques and monomer concentration measurements is possible to obtain an average of molecular weight distribution. A comparison using a nonlinear state estimation technique, the Extended Kalman Filter (EKF), is presented using either the reactor temperature or the monomer concentration as measured variable under different scenarios of noise and sampling time. The EKF based on monomer concentration produced better estimates according with the used performance indexes.

Keywords: State estimation, Extended Kalman Filter, Optical spectroscopy, Polymerization, Average molecular weight distribution, Process monitoring.

1. INTRODUCTION

Polymers have some variables related with product quality (rheological properties, mechanical strength, chemical resistance, thermal stability, etc.), and they are strongly related to molecular properties of polymer chains, such as Molecular Weight Distribution (MWD), Chain Sequence distribution (CSD) and Long-Chain Branching (LCD) (Apostolos et al., 2006). Therefore, an effective control of these properties would lead to obtain the desired product specifications. In order to accomplish control tasks, measurements must be carefully selected. However, these measurements are not often available. As Santos and coworkers pointed out in (Santos et al., 2005), the lack of instruments able to measure and monitor the quality of the polymer resin has been recognized as one of the most important problems in the field of polymerization reactor control.

State estimators are used when a complete measurement of the process variables is not feasible, which occurs when instruments generate high investment costs or do no meet the process requirements, that is, when there exist corrosive environments, signal transport issues, or even, when there is no technology for account some variables.

The main purpose of this work is to make a connection between FTIR and nonlinear state estimation techniques to account for molecular chain properties that define the quality of the products. With a proper online monitoring of these variables, such the average molecular weight, more efficient control loops can be implemented in the industry. In this paper, a polymerization of MMA benchmark is used in order to test the behavior of two EKF formulations for the estimation of the product quality variables by incorporating the composition measurements from the FTIR.

The paper is organized as follows: in Section 2, an introduction about FTIR spectroscopy is presented, highlighting its principal features and potential use in online monitoring. Then, an overview of literature for online monitoring of average molecular weight in polymerization processes and an estimation scheme with FTIR measurements is shown in Section 3. Section 4 contains a MMA free-radical polymerization case study with two EKF applications using different measurements. Final comments are given in Section 5.

2. FTIR TECHNOLOGY IN STATE ESTIMATION

Strictly, FTIR is a subdivision of Near-Infrared spectroscopy (NIR). This technology was developed to overcome limitations of dispersive spectrometers. The absorptive signals are collected simultaneously for the whole wavelength spectrum through the use of an interferometer. This advantage compared to dispersive NIR spectrometers is the reason of faster scanning speed, higher detector sensibility, simpler mechanical design, internal wavelength calibration, constant resolution, and negligible stray light. Consequently FTIR allows a more wide use in the chemical process industry (Santos et al., 2005).

In Figure 1, a typical FTIR spectrum of poly methyl methacrylate (PMMA) is shown. The spectrum has some representative peaks, according to the chemical groups present in the sample. Each chemical group has an absorption band at a characteristic wavenumber. The peak area can be related to the component concentration by using the Beer-Lambert law. However, in industrial applications, multiple components are present in a sample. Therefore, multivariate statistical methods are required, which are enclosed in a discipline called chemometrics. Appropriated experiments must be conducted in order to develop a chemometric model, including: pre-calibration, calibration,

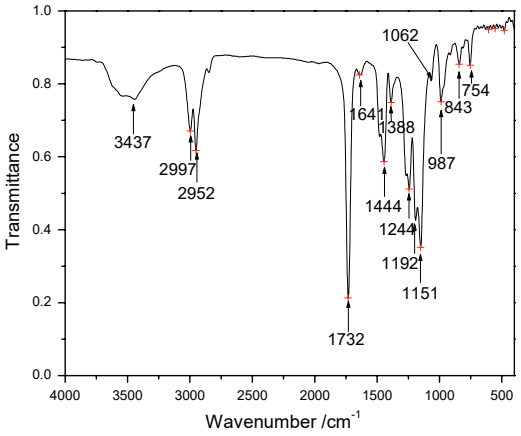

Fig. 1. FTIR spectrum of PMMA (Duan et al., 2008).

online validation, and model maintenance (Feng et al., 2015). Chemometric models are based on multivariate statistics and are usually identified using partial least-squares (PLS), principal component regression (PCR) or methods based on Petri nets. Depending on structure of the calibration models, recalibration periods should be specified.

3. PROCESS MONITORING USING ONLINE SPECTROSCOPY

It is well-known that most industries still have challenges related to measurement and control issues. For instance, the oil sand industry requires online measurements of many chemical and physical properties such as bitumen, water content, clays fraction, chloride concentration, viscosity, etc. The first challenge is to develop in-situ probes resistant to aggressive environments (erosion and corrosion) reducing replacing time. Another challenge is related to presence of multi-phase flows and process units where interface measurements are required. Also, there are some complex compositions in the streams, characterized by different particle size distributions (PSD). The last challenge is about the timing of lab data analysis, which are not suitable for online applications as real-time process control and optimization (Feng et al., 2015). Applications using FTIR including polymerization processes are presented as follows.

3.1 FTIR applications

Applications of FTIR in the chemical process industry are focused in polymerization and crystallization reactions, where some internal properties such particle size distribution (PSD), molecular weight distribution (MWD) or crystal size distribution (CSD) are fundamental to assess the quality of the products. However, there are additional industries where FTIR is successfully employed, such as the pharmaceutic industry, medicine, and atmospheric gas monitoring. In (Gallignani et al., 2014), a quality control procedure using FTIR to determine concentration of furosemide is presented. This work emphasize the advantages of FTIR compared to common pharmaceutical analysis. Other applications are found in the area of gas observations in greenhouses and FTIR imaging for histopathology in prostate cancer. Additionally to monitoring and control purposes, FTIR spectrometry can be useful for the study of kinetics in high-throughput reactive systems. In polymerization, it is a powerful technique for determination of catalyst activity, copolymer concentration, degree of homogeneity, among other properties.

3.2 FTIR in polymerization

Polymers have some variables related to the product quality (rheological properties, mechanical strength, chemical resistance, thermal stability, etc.), and these in turn are strongly related to molecular properties of polymer chains, such as Molecular Weight Distribution (MWD), Chain Sequence distribution (CSD) and Long-Chain Branching (LCD) (Apostolos et al., 2006). In this sense, process control is being redirected to the control of these properties in order to produce desired product specifications.

Due to the complexity of most polymerization processes, control algorithms require the use of reliable process models, which can provide useful insight about molecular properties of polymer chains. Molecular properties are typically studied by means of population balances at the expense of a considerable computational burden which is not feasible in monitoring and control applications. Consequently, there are some methods to approximate a model based on population balances, including the method of moments, that is the most applied, but some alternatives like orthogonal collocation method or fixed pivot methods have been used with prominent results (Apostolos et al., 2006).

Estimation techniques in polymerization are focused in the use of Kalman filtering strategies. The work of Kiparissides and coworkers presented an online optimizing control of molecular weight properties in a batch polymerization reactor (Kiparissides et al., 2002). The strategy used a state/parametric estimation step. In the first case, an Extended Kalman filter (EKF) produced an estimate of the state variables and the termination rate constant, which is a time-varying kinetic parameter. In a different contribution, a comparison among three formulations of the EKF and a nonlinear moving horizon estimator (MHE) is made to predict the concentration of impurities at the beginning of the batch using the complete nonlinear model and available measurements (Salau et al., 2014). The results showed acceptable results for the MHE at expenses of high computational burden. Similar approaches has been studied in (Shahrokhi and Fanaei, 2002), where a EKF was implemented for MWD estimation. Then, a cascade control loop was designed, with molecular weight $\overline{M}_w$ as controlled variable of the master loop and the reactor temperature T as controlled variable of the slave loop.

In (Shahrokhi and Fanaei, 2001) a discussion about the drawbacks and implementation issues of the EKF is presented. In this contribution, the importance of the observability condition, and its fulfillment for a proper estimation is remarked. However, the authors also remarked the possibility of designing a reduced-order state estimator when the observability condition is not met. The observable states are estimated by an EKF and the remaining states by an open-loop observer if the detectability property is guaranteed. This observability issues are found in most polymerization cases, because moments of dead polymer are not present in measurable properties.

The control of molecular properties of polymers are tackled using feedforward loops in (Graichen et al., 2005), where an EKF is designed in order to estimate the reaction heat and heat transfer coefficients. Again, as molecular properties moments

are not observable, they are calculated using an open loop observer, which is fed by measurements and estimated states computed by the EKF.

In the work of (Othman et al., 2004), a complete study of the dynamic evolution of styrene suspension polymerization is presented, using near infrared spectroscopy to feed a nonlinear control of molecular weight. Average molecular weight and monomer concentration are estimated by a near infrared spectrometer. The authors remark the feasibility of spectroscopy as a complement or possible substitute of gel permeation chromatography (GPC) analysis for molecular weight measurements as well as techniques to measure component concentrations (high pressure liquid chromatography- HPLC), because these methods have an appreciable lag between sampling and availability of the measurement in spite of their online feature. This work also remarked the need to estimate instantaneous molecular weight while polymerization takes place. The estimation procedure requires off-line and online calibration using PLS technique. Once near-infrared spectrometer measures are validated, a process model for styrene suspension polymerization and kinetics relations were used to obtain expressions for instantaneous molecular weight and average molecular weight. Afterwards, high gain observers were designed for some kinetic parameters as the reaction rate R_p and the ratio k_f/k_p. Also, effects of monomer, initiator, and solvent concentrations on the average molecular weight were analyzed. Finally, the authors selected monomer concentration (monomer inlet flow rate) as a manipulated variable for instantaneous molecular weight control. Feedback performance initially depended on convergence of high gain observers, but once stabilized, the strategy permitted the production with approximately constant molecular weight and polydispersity index, which is very attractive for industrial applications.

3.3 Monomer measurements

Some contributions related to polymerization monitoring and control use monomer concentration measurements instead of temperature as measured variables of the state estimator. This is because information about reaction kinetics is better transferred from the former source of information. In the work of (Eaton and Ricker, 1995) an Extended Kalman Filter is developed for tracking the particle size trajectory using online composition measurements. In (Ling and Kravaris, 2016), a state observer is designed for a series of polycondensation reactors. The authors proposed two measurements sources, with different sampling times. Also a correction for inter-sample behavior is implemented as well as Smith predictor for dead time issues.

In the present work, the Extended Kalman Filter (EKF) is used due to its predominant use in most of industrial applications regarding specially to chemical processes (Shenoy et al., 2010; Kiparissides et al., 2002). Previous works showed adequate performances of the EKF when plant-model mismatch is negligible under Gaussian uncertainties, therefore, an appropriate process model is of utmost importance for an acceptable filter performance.

4. CASE STUDY

The selected case study is the free-radical MMA polymerization studied in (Monsalve-Bravo et al., 2014) and it is considered a benchmark in polymerization modeling. This process

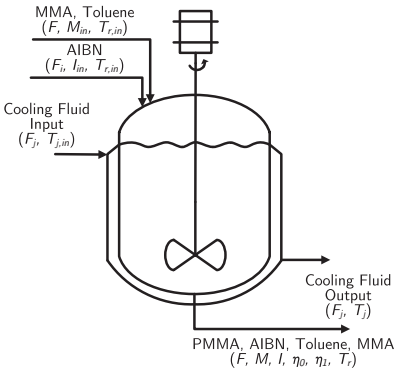

Fig. 2. Process flow diagram for MMA polymerization reactor (Monsalve-Bravo et al., 2014)

was selected due to the importance of polymer chain properties, specially, the average molecular weight. Typically, the reactor temperature is used as measured variable. In the present work, the behavior of the designed EKF will be compared using two possible sources of information, i.e., temperature and monomer composition from a FTIR.

4.1 Process description

The process is carried out in a continuous stirred tank reactor (CSTR) with azo-bis-isobutyronitrile (AIBN) as initiator and toluene as a solvent. This reaction is highly exothermic and the generated heat is removed through a cooling jacket. The process is performed in a heterogeneous phase. Figure 2 shows the process flow diagram for the reactor. This polymerization process keeps a set of reactions that take place in series when only a polymer chain is analyzed and in parallel when focus is in the whole reaction medium.

Initiation:	$I \xrightarrow{k_0} 2R^*$
	$R + M \xrightarrow{k_I} P_1$
Propagation:	$P_i + M \xrightarrow{k_0} P_{i+1}$
Monomer transfer:	$P_i + M \xrightarrow{k_{fm}} P_i + D_i$
Addition termination:	$P_i + P_j \xrightarrow{k_{tc}} D_{i+j}$
Disproportionation termination:	$P_i + P_j \xrightarrow{k_{td}} D_i + D_j$

Regarding to the energy expenditure, the propagation step is the most sensitive since the generated reaction heat is greater than the reaction heats of the remaining reactions. Moreover, monomer transfer and termination stages have higher impact in the molecular weight distribution.

4.2 Mathematical model

Following assumptions of (Daoutidis et al., 1990), conservation principles around reactor vessel and jacket are applied, giving the following material and energy balances:

$$\frac{dM}{dt} = -(k_p + k_{fm})MP_0 + \frac{F(M_{in} - M)}{V} \quad (1)$$

$$\frac{dI}{dt} = -k_I I + \frac{F_I I_{in} - FI}{V} \quad (2)$$

$$\frac{d\eta_0}{dt} = (0.5k_{tc} + k_{td})P_0^2 + k_{fm}MP_0 - \frac{F\eta_0}{V} \quad (3)$$

$$\frac{d\eta_1}{dt} = M_{w,m}(k_p + k_{fm})MP_0 - \frac{F\eta_1}{V} \quad (4)$$

$$\frac{dT}{dt} = \frac{(-\Delta H)k_p M}{\rho C_p}P_0 - \frac{UA}{\rho C_p V}(T - T_j) + \frac{F(T_{in} - T)}{V} \quad (5)$$

$$\frac{dT_j}{dt} = \frac{F_j(T_{j,in} - T_j)}{V_j} + \frac{UA}{\rho_j C_{p,j} V_j}(T - T_j) \quad (6)$$

with the additional equations for the molar concentration of the live polymer chains and reaction kinetics:

$$P_0 = \sqrt{\frac{2fIk_I}{k_{td} + k_{tc}}} \quad (7)$$

$$k_q = k_{0,q}e^{-E_q/RT}, \qquad q = p, fm, I, td, tc \quad (8)$$

where M, I, η_0, η_1, T_r and T_j are the monomer and initiator concentration, the zero-order and first-order moments of dead polymer, an the reactor and cooling jacket temperature, respectively. The input variables are the inlet volumetric flow rate F, the inlet monomer concentration M_{in}, and the volumetric flow rate in the cooling jacket F_j. All model parameters values are taken from (Daoutidis et al., 1990). The complete input variables vector is measured because each one can be used to close control loops. The output variables are either the reactor temperature or the monomer concentration given by the FTIR spectrometer. Here, the calibration model of FTIR is not shown due to space limitations. As mentioned before, the most important variables in polymerization processes are related to the chain distribution. In the MMA process, the variable showing the quality of the polymer is the average molecular weight $\overline{M}_w$ which is given by:

$$\overline{M}_w = \frac{\eta_0}{\eta_1} \quad (9)$$

4.3 Estimator design

As stated before, observability must be analyzed before any state estimation design. In this process, observability is analyzed in Table 1, showing the rank and condition number of the observability matrix $\mathcal{O}$ around the operating point. As it can be seen, $\mathcal{O}$ does not have complete rank by measuring either the reactor temperature or the monomer concentration. The system is only observable when the first order moment is measured. Since the first order moment is a fictitious state, there is no way to provide a real measurement and hence observability cannot be guaranteed. In the literature, the lack of observability in this system is attributed to the two non-observable states η_0 and η_1 (Shahrokhi and Fanaei, 2001; Ray, 1985).

If the system dynamics is reduced at only four state variables M, I, T_r and T_j, as is proposed by (Shahrokhi and Fanaei, 2001), observability is guaranteed with different combination of sensors as shown in Table 2. The practitioner might find more practical the selection of the temperature sensor for state estimation. Nonetheless, FTIR spectrometer helps out to provide a better estimates as suggested by the condition number of the observability matrix. This fact suggests that with the monomer concentration measurement, obtained from a FTIR spectrometer, observability is better conditioned with respect to the traditional temperature measurement.

Table 1. Observability condition of complete model

Measurements	Obs.	Rank	Cond. Numb
M	✗	4	6.31E+24
T_r	✗	4	1.58E+26
T_j	✗	4	3.49E+28
$[M\ T_r]$	✗	4	1.30E+25
$[\eta_0\ T_j]$	✗	5	1.28E+27
$[M\ \eta_0\ T_j]$	✗	5	6.78E+24
$[\eta_0\ \eta_1\ T_j]$	✓	6	5.26E+10

Table 2. Observability condition of reduced model

Measurements	Obs.	Rank	Cond. Numb
M	✓	4	5.64E+4
T_r	✓	4	3.27E+8
T_j	✓	4	5.75E+10
$[M\ T_r]$	✓	4	6.02E+4
$[M\ T_j]$	✓	4	3.01E+6

The next step is to design two EKF to contrast the performance using different measurements, the reactor temperature, as usually, and the monomer concentration provided by a FTIR spectrometer. Both filters are tuned equally with same initial conditions. The *a posteriori* estimation error covariance matrix is initialized as:

$$P_0^+ = 10^2 \cdot I_6 \quad (10)$$

where I_6 stands for the identity matrix with same order of the system. The initial value of the *a posteriori* estimated state is set as:

$$\hat{x}_0^+ = [7,7608\,0, 10001\,0, 00032\,20, 925\,328\,297]^T \quad (11)$$

where variables are presented with proper units. The tuning matrices Q and R are also the same for both EKF filters and are fixed as:

$$Q = \begin{bmatrix} 10^{-8} & 0 & 0 & 0 & 0 & 0 \\ 0 & 10^{-12} & 0 & 0 & 0 & 0 \\ 0 & 0 & 10^{-16} & 0 & 0 & 0 \\ 0 & 0 & 0 & 10^{-12} & 0 & 0 \\ 0 & 0 & 0 & 0 & 10^{-9} & 0 \\ 0 & 0 & 0 & 0 & 0 & 10^{-9} \end{bmatrix} \quad (12)$$

$$R = 10^{-6} \quad (13)$$

These matrices were found by trial-error methods, but taking into account some considerations around variables, units and squared measurement uncertainties. In that sense, $R = R_u R_u^T$ where R_u is the matrix that contains measurements uncertainties. The values of Q related to η_0 and η_1 are the lowest, due to this variables are based on moments approximation for the polymer chain.

4.4 Results and discussion

The nonlinear model of the process, (1) to (8), was simulated in MATLAB® using the fourth order Runge-Kutta numeric method with a time-step of 1 s. The simulation time was 10 h. The measurement noises followed a normal distribution with zero-mean and standard deviations of 0.01 $°C$ for reactor temperature measurement and 0.001 $kmol/m^3$ for monomer concentration measurement. Plant simulation was initialized in the steady state point of the system:

$$x_0 = [7,7908\,0, 1006\,0, 00031\,20, 9425\,329, 59\,296, 65]^T \quad (14)$$

$$u = [1\ 8\ 3.26]^T \quad (15)$$

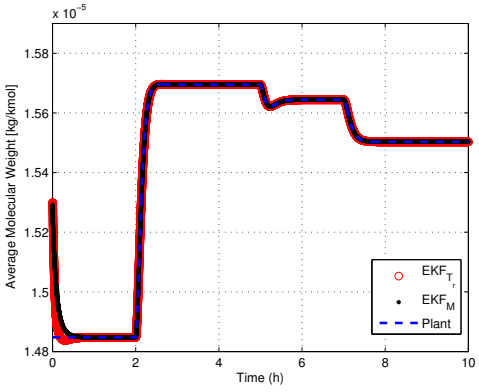

Fig. 3. State estimation without measurement noise and different initial state

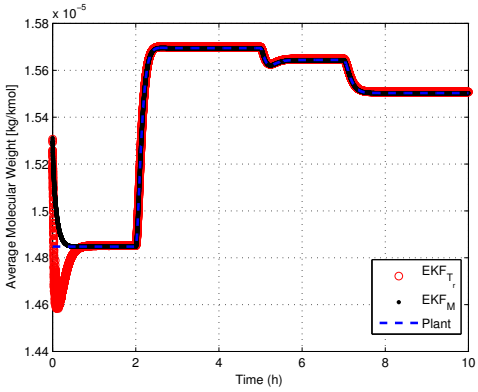

Fig. 4. State estimation with measurement noise and unknown initial state

Model uncertainties were not considered. At 2 hours, the inlet volumetric flow F changed from 1 m^3/h to 1.1 m^3/h. After 5 hours of simulation, monomer inlet concentration M_{in} was changed from 8 $kmol/m^3$ to 8.2 $kmol/m^3$. Finally, at 7 hours, the cooling jacket volumetric flow was changed from 3.2636 m^3/h to 3.5 m^3/h. Also, the sampling time of both EKF is set in 1 s, which same of time-step solution of the plant.

When the estimator is initialized in the same as plant values, it shows the fitting between both estimates and the real values is appropriate, which is reasonable because all inputs are known. The changes in input variables are followed without any mismatch.

Effects from changes in the initial state When different initial conditions are set to the plant and filters, both filters showed convergence to the real values. Normally, the real value of the initial state is unknown, so the filter is initialized at an approximated guess. Figure 3 presents the estimated state when initial values are different from plant (nominal). The simulation shows that the difference is noticed by the filters. The EKF_{T_r} has a greater overshoot than the EKF_M. In fact, this minimal difference is evidenced in Table 3, where some performance indexes are shown for the different scenarios. The changes on input variables were also followed.

Effect of measurement noise. Measurement noise is added to the reactor temperature for EKF_{T_r} and to the monomer concentration for the EKF_M filter. In this case, a zero-mean white noise with R as in (13) is considered. Although measurement noise has appreciable effects over all state variables, only the average molecular weight is of interest in this process.

The effect of noise is evidenced in Figure 4. The EKF_{T_r} converges slower than EKF_M. An appreciable difference in the time-error index, suggesting a possible steady state error is shown in Table 3. Again EKF_M is prominently better in first hours of simulation, despite that it is stated elsewhere that estimation with monomer concentration in first hours can lead a wrong estimated of average molecular weight (Othman et al., 2004).

Effect of sampling time. In real applications, monomer measurements take more time than temperature measurements. Despite the use of FTIR for online measurement of monomer concentration, this data present a larger sampling time, compared with availability of temperature data. Literature has encountered that for FTIR spectrometry, depending on calibration model, availability of the data is around 6-10 seconds, that mean, that there is a delay time between radiation measurement and final concentration value retrieving. In this sense, a change in sampling time of EKF_M was performed in order to analyze its effects on the estimation quality of the average molecular weight. The sampling time for EKF_M was switched from 1 s to 10 s, while sampling time of EKF_{T_r} was kept in 1 s, with the aim of run more realistic simulations. Figure 5 shows the better performance for EKF_M in spite of a larger sampling time. This result is very important for industrial implementations. In the Figure 6 a zoom on the first 0.45 h can be seen in order to appreciate the transient behavior of the filters.

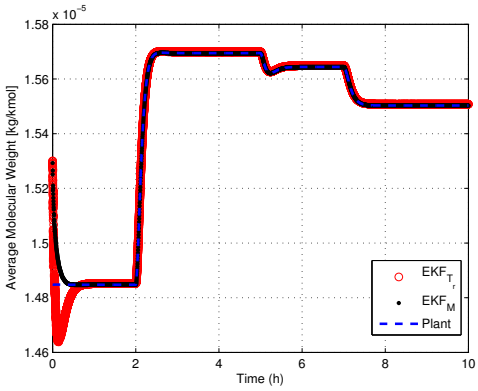

Fig. 5. State estimation for different sampling time of filters

In Table 3, the error indexes are presented for all studied cases, i.e., with same initial state, with measurement noise, and with different sampling time. MSE is the mean square error and ITAE stands for integral of time absolute error.

5. FINAL COMMENTS

Advantages of using spectroscopy for online monitoring were discussed with emphasis on FTIR spectroscopy. When complex nonlinear processes are dealt with, a reliable process model together with available measurements give an appealing alternative for process monitoring. The observability analysis showed that even if the observability property is not fulfilled, some states can be estimated if the detectability property is guaranteed. Additionally, FTIR measurements can improve the performance of the EKF estimation scheme. It is important to

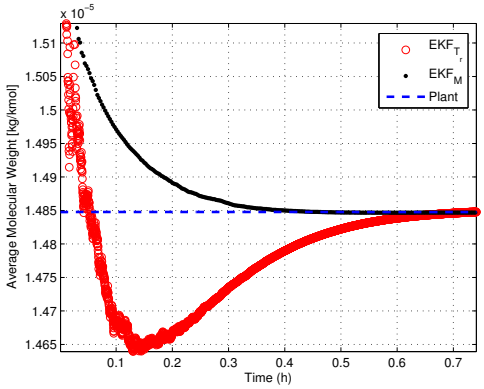

Fig. 6. State estimation for different sampling time of filters (detailed)

Error Index	$\mathbf{EKF_{T_r}}$	$\mathbf{EKF_M}$
Without noise and $\hat{x}_0 = x_0$		
MSE	1.985×10^{-20}	1.985×10^{-20}
ITAE	9.252×10^{-10}	9.253×10^{-10}
Effect of initial estimated state		
MSE	1.048×10^{-15}	8.515×10^{-16}
ITAE	5.974×10^{-9}	5.459×10^{-9}
Effect of measurement noise		
MSE	3.292×10^{-15}	1.266×10^{-15}
ITAE	2.410×10^{-7}	3.850×10^{-8}
Effect of sampling time		
MSE	7.611×10^{-16}	7.614×10^{-16}
ITAE	2.332×10^{-7}	3.531×10^{-8}

Table 3. Error index for all scenarios

take into account realistic aspects as the sampling time of the composition measurements, because EKF_M preserves the best performance compared to conventional EKF_{T_r}, even when information is available every 10 s. In that way, current process monitoring in polymerization system can be improved, combining both FTIR spectroscopy and nonlinear state estimation techniques.

Finally, it is important to emphasize that many estimation schemes and especially the EKF needs a statistical identification step to find out the real noise covariances by using appropriate methods like the autocovariance least square (ALS). Additional analysis to be performed consist to incorporate the temperature and monomer concentration measurements together to achieve a more robust estimator, and that probably may deal with time-delay and asynchronous information. Finally, more reliable nonlinear filters like the Unscented Kalman Filter (UKF), the Nonlinear Moving Horizon Estimator (NMHE), and the Particle Filters need to be tested for comparison purposes.

REFERENCES

Apostolos, K., Dimitris, M., Vassilis, S., Christos, C., and Costas, K. (2006). *Dynamic Optimization of Molecular Weight Distribution in Batch Polymerization Reactors*, volume 39. IFAC.

Daoutidis, P., Soroush, M., and Kravaris, C. (1990). Feedforward/feedback control of multivariable nonlinear processes. *AIChE Journal*, 36(10), 1471–1484.

Duan, G., Zhang, C., Li, A., Yang, X., Lu, L., and Wang, X. (2008). Preparation and characterization of mesoporous zirconia made by using a poly (methyl methacrylate) template. *Nanoscale Research Letters*, 3(3), 118–122.

Eaton, M.T. and Ricker, N.L. (1995). Extended Kalman Filtering for Particle Size Control in a Fed-batch Emulsion Polymerization Reactor. In *American Control Conference (ACC), 1995*, June, 2697–2701. Seattle, Washington.

Feng, E., Domlan, E., and Kadali, R. (2015). Spectroscopic measurements in oil sands industry-from laboratories to real-time applications. *IFAC Proceedings Volumes (IFAC-PapersOnline)*, 48(8), 199–204.

Gallignani, M., Rondón, R.a., Ovalles, J.F., and Brunetto, M.R. (2014). Transmission FTIR derivative spectroscopy for estimation of furosemide in raw material and tablet dosage form. *Acta Pharmaceutica Sinica B*, 4(5), 376–383.

Graichen, K., Hagenmeyer, V., and Zeitz, M. (2005). Adaptive Feedforward Control with Parameter Estimation for the Chylla – Haase Polymerization Reactor. 3049–3054.

Kiparissides, C., Seferlis, P., Mourikas, G., and Morris, A.J. (2002). Online Optimizing Control of Molecular Weight Properties in Batch Free-Radical Polymerization Reactors. *Industrial & Engineering Chemistry Research*, 41(24), 6120–6131.

Ling, C. and Kravaris, C. (2016). State Observer Design for Monitoring the Degree of Polymerization in a Series of Melt Polycondensation Reactors. *Processes*, 4(1), 4.

Monsalve-Bravo, G.M., Moscoso-Vasquez, H.M., and Alvarez, H. (2014). Scale-up of continuous reactors: Using phenomenological-based models. *Chimica Oggi/Chemistry Today*, 32(3), 20–26.

Othman, N.S., Fevotte, G., Peycelon, D., Egraz, J., and Suau, J. (2004). Control of polymer molecular weight using near infrared spectroscopy. *AIChE Journal*, 50(3), 654–664.

Ray, W.H. (1985). Polymerization Reactor Control. *1985 American Control Conference*, 3–8.

Salau, N.P.G., Trierweiler, J.O., and Secchi, A.R. (2014). State Estimation of Chemical Engineering Systems Tending To Multiple Solutions. *Brazilian Journal of Chemical Engineering*, 31(03), 771–785.

Santos, A.F., Silva, F.M., Lenzi, M.K., and Pinto*, J.C. (2005). Monitoring and Control of Polymerization Reactors Using NIR Spectroscopy. *Polymer-Plastics Technology and Engineering*, 44(1), 1–61.

Shahrokhi, M. and Fanaei, M.A. (2001). State Estimation in a Batch Suspension Polymerization Reactor. *Iranian Polymer Journal*, 10(3), 1026–1065.

Shahrokhi, M. and Fanaei, M.A. (2002). Molecular Weight Control of a Batch Polymerization Reactor. *Iranian Polymer Journal*, 11(6), 403–411.

Shenoy, A.V., Prasad, V., and Shah, S.L. (2010). Comparison of unconstrained nonlinear state estimation techniques on a MMA polymer reactor. *IFAC Proceedings Volumes (IFAC-PapersOnline)*, 9(PART 1), 159–164.

On Optimal Predefined-Time Stabilization

Esteban Jiménez-Rodríguez[†] **Juan Diego Sánchez-Torres**[‡]
Alexander G. Loukianov[†]

[†]*Department of Electrical Engineering, CINVESTAV-IPN, Av. del Bosque 1145 Col. El Bajío C.P. 45019, Guadalajara, Jalisco, México. E-mail: {ejimenezr,louk}@gdl.cinvestav.mx*
[‡]*Department of Mathematics and Physics, ITESO, Periférico Sur Manuel Gómez Morín 8585 C.P. 45604, Tlaquepaque, Jalisco, México. E-mail: dsanchez@iteso.mx*

Abstract: This paper addresses the problem of optimal predefined-time stability. Predefined-time stable systems are a class of fixed-time stable dynamical systems for which the minimum bound of the settling-time function can be defined a priori as a explicit parameter of the system. Sufficient conditions for a controller to solve the optimal predefined-time stabilization problem for a given system are provided. These conditions involve a Lyapunov function that satisfy both a certain differential inequality for guaranteeing predefined-time stability and the steady-state Hamilton-Jacobi-Bellman equation for guaranteeing optimality. Finally, this result is applied to the predefined-time optimization of the sliding manifold reaching phase.

Keywords: Hamilton-Jacobi-Bellman Equation, Lyapunov Functions, Optimal Control, Predefined-Time Stability.

1. INTRODUCTION

Finite-time stable dynamical systems provide solutions to applications which require hard time response constraints. Important works involving the definition and application of finite-time stability have been carried out in Roxin (1966); Haimo (1986); Utkin (1992); Bhat and Bernstein (2000); Moulay and Perruquetti (2005, 2006). Nevertheless, this finite stabilization time is often an unbounded function of the initial conditions of the system. Making this function bounded to ensure the settling time is less than a certain quantity for any initial condition may be convenient, for instance, for optimization and state estimation tasks. With this purpose, a stronger form of stability, in which the convergence time presents a class of uniformity with respect to the initial conditions, called *fixed-time stability* was introduced. The notion of fixed-time stability is presented in Andrieu et al. (2008) for homogeneous systems and it was proposed in Cruz-Zavala et al. (2010); Polyakov (2012); Polyakov and Fridman (2014) for systems with sliding modes.

When fixed-time stable dynamical systems are applied to control or observation, it may be difficult to find a direct relationship between the gains of the system and the upper bound of the convergence time; thus, tuning the system in order to achieve a desired maximum stabilization time is not a trivial task. A simulation-based approximation to select the values of the tuning parameters is proposed in Fraguela et al. (2012) under the concept of *prescribed-time stability*; this method permits to design robust sliding differentiators for noisy signals by expressing the gains as functions of the desired settling time. Therefore, prescribed-time stable systems present a way to surmount the tuning problem. However, this prescribed time usually constitutes a conservative estimation of the upper bound of the convergence time; that is, the prescribed time is commonly larger, maybe quite larger, than the *true* amount of time the system takes to converge.

To overcome the above, another class of dynamical systems which exhibit the property of *predefined-time stability*, have been studied (Sánchez-Torres et al., 2014; Sánchez-Torres et al., 2015). For this systems the prescribed-time stability coincides with the fixed-time stability when the true settling time is considered. The upper bound for the convergence time of the proposed kind of systems appears explicitly in their dynamical equations; in particular, it equals the reciprocal of the system gain. This bound is not a conservative estimation but truly the minimum value that is greater than all the possible exact settling times. All the mentioned properties of predefined-time stable systems are characterized by a suitable Lyapunov theorem.

On the other hand, the infinite-horizon, nonlinear nonquadratic optimal asymptotic stabilization problem was addressed in Bernstein (1993). The main idea of the results are based on the condition that a Lyapunov function for the nonlinear system is at the same time the solution of the steady-state Hamilton-Jacobi-Bellman equation, guaranteeing both asymptotic stability and optimality. Nevertheless, returning to the first paragraph idea, the finite-time stability is a desired property in some applications, but optimal finite-time controllers obtained using the maximum principle do not generally yield feedback controllers. In this sense, the optimal finite-time stabilization is studied in Haddad and L'Afflitto (2016), as an extension of Bernstein (1993). Since the results are based on the framework developed in Bernstein (1993), the controllers obtained are in fact feedback controllers.

Consequently, as an extension of the ideas presented in Bernstein (1993); Sánchez-Torres et al. (2015); Haddad and L'Afflitto (2016), this paper addresses the problem of *optimal predefined-time stabilization*, namely the problem of finding a state-feedback control that minimizes certain performance measure, guaranteeing at the same time predefined-time stability of the closed-loop system. In particular, sufficient conditions for a controller to solve the optimal predefined-time stabilization problem for a given system are provided. These conditions involve a Lyapunov function that satisfy both a certain differential inequality for guaranteeing predefined-time stability and the steady-state Hamilton-Jacobi-Bellman equation for guaranteeing optimality. Finally, this result is applied to the predefined-time optimization of the sliding manifold reaching phase.

In the following, Section 2 presents the mathematical preliminaries needed to introduce the proposed results. Section 3 exposes the main results of this paper, which are the sufficient conditions for a controller to solve the optimal predefined-time stabilization problem and a particularization to affine systems. Section 4 shows the application of the obtained results to the predefined-time optimization of the sliding manifold reaching phase, and the simulation results are shown in Section 5. Finally, Section 6 presents the conclusions of this paper.

2. MATHEMATICAL PRELIMINARIES

2.1 Predefined-Time Stability

Consider the system

$$\dot{x}(t) = f(x(t)), \qquad x(0) = x_0, \tag{1}$$

where $x \in \mathbb{R}^n$ is the system state and $f : \mathbb{R}^n \to \mathbb{R}^n$ is a nonlinear function such that $f(0) = 0$, i.e.the origin is an equilibrium point of (1).

First, the concepts of finite-time, fixed-time and predefined-time stability are reviewed.

Definition 2.1. (Polyakov, 2012) The origin of (1) is *globally finite-time stable* if it is globally asymptotically stable and any solution $x(t, x_0)$ of (1) reaches the equilibrium point at some finite time moment, i.e., $\forall t \geq T(x_0) : x(t, x_0) = 0$, where $T : \mathbb{R}^n \to \mathbb{R}_+ \cup \{0\}$.

Definition 2.2. (Polyakov, 2012) The origin of (1) is *fixed-time stable* if it is globally finite-time stable and the settling-time function is bounded, i.e. $\exists T_{\max} > 0 : \forall x_0 \in \mathbb{R}^n : T(x_0) \leq T_{\max}$.

Remark 2.1. Note that there are several choices for $T_{\max}$. For instance, if the settling-time function is bounded by T_{m}, it is also bounded by λT_{m} for all $\lambda \geq 1$. This motivates the following definition.

Definition 2.3. (Sánchez-Torres et al., 2014) Let $\mathcal{T}$ be the set of all the bounds of the settling time function for the system (1), i.e.,

$$\mathcal{T} = \{T_{\max} > 0 : \forall x_0 \in \mathbb{R}^n : T(x_0) \leq T_{\max}\}. \tag{2}$$

The minimum bound of the settling-time function T_f, is defined as:

$$T_f = \inf \mathcal{T} = \sup_{x_0 \in \mathbb{R}^n} T(x_0). \tag{3}$$

Definition 2.4. (Sánchez-Torres et al., 2014) For the case of fixed time stability when the time T_f defined in (3) can be tuned by a particular selection of the parameters of the system (1), it is said that the origin of the system (1) is *predefined-time stable*.

The following Lyapunov-like lemma provides a characterization of predefined-time stability.

Lemma 2.1. (Sánchez-Torres et al., 2014) Assume there exist a continuous radially unbounded function $V : \mathbb{R}^n \to \mathbb{R}_+ \cup \{0\}$, and real numbers $\alpha > 0$ and $0 < p \leq 1$, such that:

$$V(0) = 0 \tag{4}$$

$$V(x) > 0, \qquad \forall x \neq 0, \tag{5}$$

and the derivative of V along the trajectories of the system (1) satisfies

$$\dot{V} \leq -\frac{\alpha}{p}\exp(V^p)V^{1-p}. \tag{6}$$

Then, the origin is globally predefined-time stable for (1) and $T_f = \frac{1}{\alpha}$.

2.2 Optimal Control

Consider the controlled system

$$\dot{x}(t) = f(x(t), u(t)), \qquad x(0) = x_0, \tag{7}$$

where $x \in \mathbb{R}^n$ is the system state, $u \in \mathbb{R}^m$ is the system input, which is restricted to belong to a certain set $\mathcal{U} \subset \mathbb{R}^m$ of the admissible controls, and $f : \mathbb{R}^n \times \mathbb{R}^m \to \mathbb{R}^n$ is a nonlinear function with $f(0, 0) = 0$.

The system (7) is to be controlled to minimize the performance measure

$$J(x_0, u(\cdot)) = \int_0^{t_f} L(x(t), u(t))\mathrm{d}t, \tag{8}$$

where $L : \mathbb{R}^n \times \mathbb{R}^m \to \mathbb{R}$ is a continuous function, assumed to be convex in u. To this end, define the minimum cost function as

$$J^*(x(t), t) = \min_{u \in \mathcal{U}} \left\{ \int_t^{t_f} L(x(\tau), u(\tau))\mathrm{d}\tau \right\}. \tag{9}$$

Defining the *Hamiltonian*, for $p \in \mathbb{R}^n$ (usually called the costate)

$$\mathcal{H}(x, u, p) = L(x, u) + p^T f(x, u), \tag{10}$$

the *Hamilton-Jacobi-Bellman* (HJB) equation can be written as

$$0 = \min_{u \in \mathcal{U}} \left\{ \mathcal{H}\left(x, u, \frac{\partial J^*(x,t)}{\partial x}^T\right) \right\} + \frac{\partial J^*(x,t)}{\partial t}, \tag{11}$$

and it provides a sufficient condition for optimality.

For infinite-horizon problems (limit as $t_f \to \infty$), the cost does not depend on t anymore and the partial differential equation (11) reduces to the steady-state HJB equation

$$0 = \min_{u \in \mathcal{U}} \mathcal{H}\left(x, u, \frac{\partial J^*(x)}{\partial x}^T\right). \tag{12}$$

3. OPTIMAL PREDEFINED-TIME STABILIZATION

The main result of this paper is presented in this section. First, the notion of optimal predefined-time stabilization is defined.

Definition 3.1. Consider the optimal control problem for the system (7)

$$\min_{u\in\mathcal{U}(T_c)} J(x_0,u(\cdot)) = \int_0^\infty L(x(t),u(t))\mathrm{d}t \tag{13}$$

where

$$\mathcal{U}(T_c) = \{u(\cdot) : u(\cdot) \text{ stabilizes (7) in a predefined time } T_c\}.$$

This problem is called the *optimal predefined-time stabilization problem* for the system (7).

The following theorem gives sufficient conditions for a controller to solve this problem.

Theorem 3.1. Assume there exist a continuous radially unbounded function $V : \mathbb{R}^n \to \mathbb{R}_+ \cup \{0\}$, real numbers $T_c > 0$ and $0 < p \leq 1$, and a control law $\phi^* : \mathbb{R}^n \to \mathbb{R}^m$ such that:

$$V(0) = 0 \tag{14}$$
$$V(x) > 0, \quad \forall x \neq 0, \tag{15}$$
$$\phi^*(0) = 0 \tag{16}$$
$$\frac{\partial V}{\partial x} f(x,\phi^*(x)) \leq -\frac{1}{T_c p}\exp(V^p)V^{1-p} \tag{17}$$
$$\mathcal{H}\left(x,\phi^*(x),\frac{\partial V}{\partial x}^T\right) = 0 \tag{18}$$
$$\mathcal{H}\left(x,u,\frac{\partial V}{\partial x}^T\right) \geq 0, \quad \forall u \in \mathcal{U}(T_c). \tag{19}$$

Then, with the feedback control

$$u^*(\cdot) = \phi^*(x(\cdot)) = \arg\min_{u\in\mathcal{U}(T_c)} \mathcal{H}\left(x,u,\frac{\partial V}{\partial x}^T\right), \tag{20}$$

the origin of the closed-loop system

$$\dot{x}(t) = f(x(t),\phi^*(x(t))) \tag{21}$$

is predefined-time stable with $T_f = T_c$. Moreover, the feedback control law (20) minimizes $J(x_0,u(\cdot))$ in the sense that

$$J(x_0,\phi^*(x(\cdot))) = \min_{u\in\mathcal{U}(T_c)} J(x_0,u(\cdot)) \tag{22}$$
$$= V(x_0), \tag{23}$$

i.e., the feedback control law (20) solves the optimal predefined-time stabilization problem for the system (7).

Proof. Predefined-time stability with predefined time T_c follows directly from the conditions (14)-(17) and applying the Lemma 2.1 to the closed-loop system (21).

To prove (23), let $x(t)$ be the solution of system (21). Then,

$$\dot{V}(x(t)) = \frac{\partial V}{\partial x} f(x(t),\phi^*(x(t))).$$

From the above and (18) it follows

$$\begin{aligned} L(x(t),\phi^*(x(t))) &= L(x(t),\phi^*(x(t))) + \\ &\quad \frac{\partial V}{\partial x} f(x(t),\phi^*(x(t))) - \dot{V}(x(t)) \\ &= \mathcal{H}\left(x(t),\phi^*(x(t)),\frac{\partial V}{\partial x}^T\right) - \dot{V}(x(t)) \\ &= -\dot{V}(x(t)). \end{aligned}$$

Hence,

$$\begin{aligned} J(x_0,\phi^*(x(\cdot))) &= \int_0^\infty -\dot{V}(x(t))\mathrm{d}t \\ &= -\lim_{t\to\infty} V(x(t)) + V(x_0) \\ &= V(x_0). \end{aligned}$$

Now, to prove (22), let $u(\cdot) \in \mathcal{U}(T_c)$ and let $x(t)$ be the solution of (7), so that

$$\dot{V}(x(t)) = \frac{\partial V}{\partial x} f(x(t),u(t)).$$

Then

$$\begin{aligned} L(x(t),u(t)) &= L(x(t),u(t)) + \frac{\partial V}{\partial x} f(x(t),u(t)) - \dot{V}(x(t)) \\ &= \mathcal{H}\left(x(t),u(t),\frac{\partial V}{\partial x}^T\right) - \dot{V}(x(t)). \end{aligned}$$

Since $u(\cdot)$ stabilizes (7) in predefined time T_c, using (18) and (19) we have

$$\begin{aligned} J(x_0,u(\cdot)) &= \int_0^\infty \left[\mathcal{H}\left(x(t),u(t),\frac{\partial V}{\partial x}^T\right) - \dot{V}(x(t))\right]\mathrm{d}t \\ &= -\lim_{t\to\infty} V(x(t)) + V(x_0) + \\ &\quad \int_0^\infty \mathcal{H}\left(x(t),u(t),\frac{\partial V}{\partial x}^T\right)\mathrm{d}t \\ &= V(x_0) + \int_0^\infty \mathcal{H}\left(x(t),u(t),\frac{\partial V}{\partial x}^T\right)\mathrm{d}t \\ &\geq V(x_0) \\ &= J(x_0,\phi^*(x(\cdot))). \end{aligned}$$

□

Remark 3.1. The conditions (18) and (19) together are exactly the steady-state Hamilton-Jacobi-Bellman equation (12).

Remark 3.2. It is important that the optimal predefined-time stabilizing controller $u^* = \phi^*(x)$ characterized by Theorem 3.1 is a feedback controller.

Although Theorem 3.1 provides sufficient conditions for a controller to solve the optimal predefined-time stabilization problem for a given system, it does not provide a closed form expression for the feedback controller. Instead, the feedback controller is obtained by solving (20). To obtain a closed form expression for the controller, the result of Theorem 3.1 is specialized to affine systems of the form

$$\dot{x}(t) = f(x(t)) + B(x(t))u(t), \qquad x(0) = x_0, \tag{24}$$

where $x \in \mathbb{R}^n$ is the system state, $u \in \mathbb{R}^m$ is the system control input, $f : \mathbb{R}^n \to \mathbb{R}^n$ is a nonlinear function with $f(0) = 0$ and $B : \mathbb{R}^n \to \mathbb{R}^{n\times m}$.

The performance integrand is also specialized to

$$L(x,u) = L_1(x) + L_2(x)u + u^T R_2(x)u, \tag{25}$$

where $L_1 : \mathbb{R}^n \to \mathbb{R}$, $L_2 : \mathbb{R}^n \to \mathbb{R}^{1\times m}$ and $R_2 : \mathbb{R}^n \to \mathbb{R}^{m\times m}$ is a positive definite matrix function.

The following corollary of Theorem 3.1 provides an *inverse optimal controller* which solves the optimal predefined-time stabilization problem for the affine system (24) with performance integrands of the form (25).

Corollary 3.1. Assume there exist a continuous radially unbounded function $V : \mathbb{R}^n \to \mathbb{R}_+ \cup \{0\}$, and real numbers $T_c > 0$ and $0 < p \leq 1$ such that

$$V(0) = 0 \tag{26}$$

$$V(x) > 0, \quad \forall x \neq 0, \tag{27}$$

$$\frac{\partial V}{\partial x}\left[f(x) + B(x)\left[-\frac{1}{2}R_2^{-1}(x)\left[L_2(x) + \frac{\partial V}{\partial x}B(x)\right]^T\right]\right] \leq -\frac{1}{T_c p}\exp(V^p)V^{1-p} \tag{28}$$

$$L_2(0) = 0 \tag{29}$$

$$L_1(x) + \frac{\partial V}{\partial x}f(x) - \frac{1}{4}\left[L_2(x) + \frac{\partial V}{\partial x}B(x)\right]R_2^{-1}(x)\left[L_2(x) + \frac{\partial V}{\partial x}B(x)\right]^T = 0. \tag{30}$$

Then, with the feedback control

$$u^* = \phi^*(x) = -\frac{1}{2}R_2^{-1}(x)\left[L_2(x) + \frac{\partial V}{\partial x}B(x)\right]^T, \tag{31}$$

the origin of the closed loop system

$$\dot{x}(t) = f(x(t)) + B(x(t))\phi^*(x(t)) \tag{32}$$

is predefined-time stable with $T_f = T_c$. Moreover, the performance measure $J(x_0, u(\cdot))$ is minimized in the sense of (22) and

$$J(x_0, \phi^*(x(\cdot))) = V(x_0), \tag{33}$$

i.e., the feedback control law (31) solves the optimal predefined-time stabilization problem for the system (24).

Proof. We can see that the hypotheses of Theorem Theorem 3.1 are satisfied. The control law (31) follows from $\frac{\partial}{\partial u}\left[\mathcal{H}\left(x, u, \frac{\partial V}{\partial x}\right)\right] = 0$ with $L(x, u)$ specialized to (25). Then, setting $u^* = \phi^*(x)$ as in (31), the conditions (26), (27) and (28) become the hypotheses (14), (15) and (17), respectively. The hypothesis (16) follows from (29).

Since $\phi^*(x)$ satisfies $\frac{\partial}{\partial u}\left[\mathcal{H}\left(x, u, \frac{\partial V}{\partial x}\right)\right]_{u=\phi^*(x)} = 0$, and noticing that (30) can be rewritten in terms of $\phi^*(x)$ as

$$L_1(x) + \frac{\partial V}{\partial x}f(x) - {\phi^*}^T(x)R_2(x)\phi^*(x) = 0. \tag{34}$$

the hypothesis (18) is directly verified.

Finally, from (18), (31) and the positive definiteness of $R_2(x)$ it follows

$$\begin{aligned}
\mathcal{H}\left(x, u, \frac{\partial V}{\partial x}\right) &= L(x, u) + \frac{\partial V}{\partial x}\left[f(x) + B(x)u\right] \\
&= L(x, u) + \frac{\partial V}{\partial x}\left[f(x) + B(x)u\right] - \\
&\quad L(x, \phi^*(x)) - \frac{\partial V}{\partial x}\left[f(x) + B(x)\phi^*(x)\right] \\
&= \left[L_2(x) + \frac{\partial V}{\partial x}B(x)\right](u - \phi^*(x)) + \\
&\quad u^T R_2(x)u - {\phi^*}^T(x)R_2(x)\phi^*(x) \\
&= -2\,{\phi^*}^T(x)R_2(x)(u - \phi^*(x)) + \\
&\quad u^T R_2(x)u - {\phi^*}^T(x)R_2(x)\phi^*(x) \\
&= [u - \phi^*(x)]^T R_2(x)[u - \phi^*(x)] \\
&\geq 0,
\end{aligned}$$

which is the hypothesis (19). Applying Theorem 3.1, the result is obtained.

□

Remark 3.3. The feedback controller (31) provided by Corollary 3.1 is an inverse optimal controller in the following sense: instead of solving the steady-state HJB equation directly to minimize some given performance measure, it is defined a family of predefined-time stabilizing controllers that minimize a certain cost function. In this case, one can flexibly specify $L_2(x)$ and $R_2(x)$, while from (34) $L_1(x)$ is parametrized as

$$L_1(x) = {\phi^*}^T(x)R_2(x)\phi^*(x) - \frac{\partial V}{\partial x}f(x) \geq 0. \tag{35}$$

Remark 3.4. It is not always easy to satisfy the hypotheses (26)-(30) of Corollary 3.1. However, for affine systems of relative degree one the functions $L_2(x)$ and $R_2(x)$ can be easily chosen to fulfill these conditions.

This motivates the following section.

4. INVERSE OPTIMAL PREDEFINED-TIME STABLE REACHING LAW

In this section, first, some basic concepts corresponding to integral manifolds and sliding mode manifolds are reviewed. For this purpose, consider again the autonomous unforced system (1)

$$\dot{x}(t) = f(x(t)), \qquad x(0) = x_0,$$

Definition 4.1. (Drakunov and Utkin, 1992) Let $\sigma : \mathbb{R}^n \to \mathbb{R}^m$ be a smooth function, and define the manifold $\mathcal{S} = \{x \in \mathbb{R}^n : \sigma(x) = 0\}$. If for an initial condition $x_0 \in \mathcal{S}$, the solution $x(t, x_0) \in \mathcal{S}$ for all t, the manifold $\mathcal{S}$ is called an *integral manifold*.

Definition 4.2. (Drakunov and Utkin, 1992) If there is a nonempty set $\mathcal{N} \subset \mathbb{R}^n - \mathcal{S}$ such that for every initial condition $x_0 \in \mathcal{N}$, there is a finite time $t_s > 0$ in which the system state reaches the manifold $\mathcal{S}$ then the manifold $\mathcal{S}$ is called an *sliding mode manifold*.

Remark 4.1. A sliding mode on a certain sliding manifold can only appear if f is a non-smooth (possibly discontinuous) function. For this case, the solutions of (1) are understood in the Filippov sense (Filippov, 1988).

With the above definitions, the main objective of the controller is to optimally drive the trajectories of affine system (24) to the set $\mathcal{S}$ in a predefined time. The function $\sigma : \mathbb{R}^n \to \mathbb{R}^m$ is selected so that the motion of the system (24) restricted to the sliding manifold $\sigma(x) = 0$ has a desired behavior.

The dynamics of σ are described by

$$\dot{\sigma}(t) = a(x(t)) + G(x(t))u(t), \qquad \sigma(x(0)) = \sigma_0, \tag{36}$$

where $a(x) = \frac{\partial \sigma}{\partial x}f(x)$ and $G(x) = \frac{\partial \sigma}{\partial x}B(x)$.

It is assumed that $\sigma(x)$ is selected such that the matrix $G(x) \in \mathbb{R}^{m \times m}$ has inverse for all $x \in \mathbb{R}^n$. It means that the system (36) has relative degree one.

Now, consider the optimal predefined time stabilization problem (13) for the system (36). The aim is to choose the functions V, L_2 and R_2 such that the hypotheses of Corollary 3.1 are satisfied. To this end, assume that $V(\sigma)$

is a Lyapunov function candidate. Its derivative along the trajectories of the system (36) closed loop with (31)

$$\dot{\sigma} = a(x) + G(x)\phi^*(x),$$

is calculated as

$$\begin{aligned}\dot{V} &= \frac{\partial V}{\partial \sigma}\left[a(x) + G(x)\phi^*(x)\right] \\ &= \frac{\partial V}{\partial \sigma}\left[a(x) + G(x)\left(-\frac{1}{2}R_2^{-1}(x)L_2^T(x) - \right.\right. \\ &\quad \left.\left.\frac{1}{2}R_2^{-1}(x)G^T(x)\frac{\partial V}{\partial \sigma}^T\right)\right].\end{aligned}$$

Then, choosing

$$L_2(x) = 2a^T(x)\left[G^{-1}(x)\right]^T R_2(x), \tag{37}$$

$$R_2(x) = \frac{T_c p}{2}\exp(-V^p(\sigma(x)))\left[G^T(x)G(x)\right], \tag{38}$$

the derivative of V becomes

$$\dot{V} = -\frac{1}{T_c p}\exp(V^p)\left|\left|\frac{\partial V}{\partial \sigma}\right|\right|^2.$$

Finally, V must be chosen such that

$$\left|\left|\frac{\partial V}{\partial \sigma}\right|\right|^2 = V^{1-p}. \tag{39}$$

It can easily be checked that

$$V(\sigma) = c^i(\sigma^T\sigma)^i > 0, \quad \forall \sigma \neq 0 \tag{40}$$

with $i = \frac{1}{p+1}$ and $4i^2c = \frac{4c}{(p+1)^2} = 1$, satisfies (39).

Example 4.1. Consider a pendulum system with Coulomb friction

$$\begin{aligned}\dot{x}_1 &= x_2, \\ \dot{x}_2 &= -\frac{g}{L}\sin(x_1) - \frac{V_s}{J}x_2 - \frac{P_s}{J}\text{sign}(x_2) + \frac{1}{J}u,\end{aligned} \tag{41}$$

where x_1 is the angular position, x_2 is the angular velocity, u is the input torque, J is the moment of inertia, g is the gravity acceleration, L is the length of the pendulum, and P_s and V_s are friction constants.

Due to the structure of the model (41), a good candidate for σ is $\sigma(x) = x_2 + kx_1$ with $k > 0$. The dynamics of σ are described by the equation (36) with $a(x) = -\frac{g}{L}\sin(x_1) - \frac{V_s}{J}x_2 - \frac{P_s}{J}\text{sign}(x_2) + kx_2$ and $G(x) = \frac{1}{J}$. The functions V, R_2 and L_2 are selected according to (37)-(40) as

$$\begin{aligned}V(\sigma) &= c^{\frac{1}{p+1}}\sigma^{\frac{2}{p+1}}, \\ R_2(x) &= \frac{T_c p}{2J^2}\exp(-c^{\frac{p}{p+1}}\sigma^{\frac{2p}{p+1}}), \text{ and} \\ L_2(x) &= \frac{T_c p}{J}\exp(-c^{\frac{p}{p+1}}\sigma^{\frac{2p}{p+1}})\left[-\frac{g}{L}\sin(x_1) - \frac{V_s}{J}x_2 - \right. \\ &\quad \left.\frac{P_s}{J}\text{sign}(x_2) + kx_2\right],\end{aligned}$$

and $u^* = \phi^*(x)$ is implemented as in (31).

Finally, according to (35) the resulting function L_1 is

$$L_1(x) = \frac{2J^2}{4T_c p}\exp(c^{\frac{p}{p+1}}\sigma^{\frac{2p}{p+1}})\left[L_2(x) + \frac{1}{J}\frac{\partial V}{\partial \sigma}\right]^2 - \frac{\partial V}{\partial \sigma}a(x).$$

5. SIMULATION RESULTS

The simulation results of the Example 5.1 are presented in this section. The pendulum parameters are shown in Table 1.

Table 1. Parameters of the pendulum model (41).

Parameter	Values	Unit
M	1	kg
L	1	m
$J = ML^2$	1	$\text{kg}\cdot\text{m}^2$
V_s	0.2	$\text{kg}\cdot\text{m}^2\cdot\text{s}^{-1}$
P_s	0.5	$\text{kg}\cdot\text{m}^2\cdot\text{s}^{-2}$
g	9.8	$\text{m}\cdot\text{s}^{-2}2$

The simulations were conducted using the Euler integration method, with a fundamental step size of 1×10^{-3} s. The initial conditions for the system (41) were selected as: $x_1(0) = \pi/2\,\text{rad}$ and $x_2(0) = 0\,\text{rad/s}$. In addition, the controller gains were adjusted to: $T_c = 1$, $k = 2$ and $p = 1/2$.

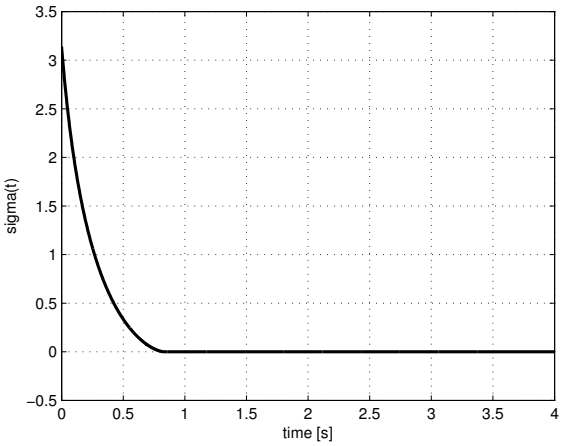

Figure 1. Function $\sigma(x(t))$.

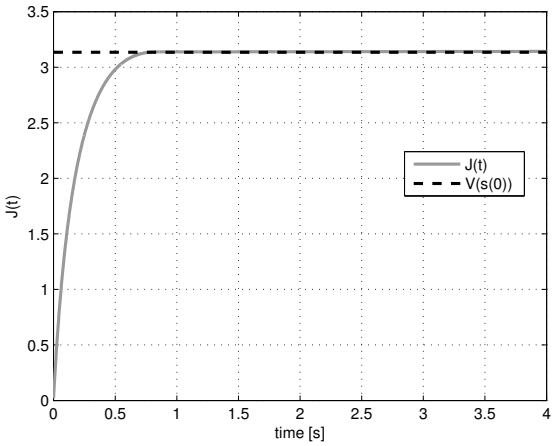

Figure 2. Function $J(t) = \int_0^t [L_1 + L_2 u + u^T R_2 u]\text{d}\tau$.

Note that $\sigma(t) = 0$ for $t \geq 0.827\ s < T_c = 1\ s$ (Fig. 1). Once the system states slide over the sliding manifold $\sigma(x) = 0$, this motion is governed by the reduced order system

$$\dot{x}_1(t) = -kx_1(t) = x_2.$$

This imply that the system state tends exponentially to zero at a rate of $\frac{1}{k}$ (Fig. 3). Fig. 4 shows the control signal (torque) versus time. Finally, from Fig. 2, it can be seen

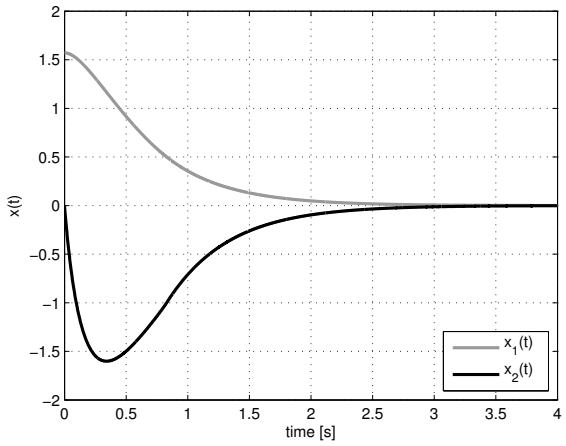

Figure 3. Evolution of the states.

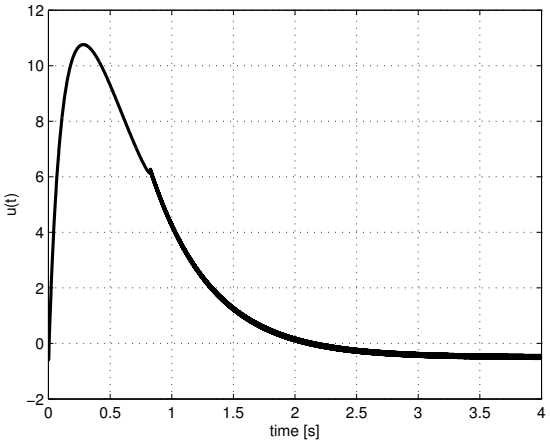

Figure 4. Control input.

that the cost as a function of time grows quickly to a steady state value, corresponding to $V(\sigma(0))$.

6. CONCLUSION

In this paper, the problem of optimal predefined-time stability was addressed. Sufficient conditions for a controller to guarantee both predefined-time stability and optimality were provided. The results were applied to the predefined-time optimization of the sliding manifold reaching phase. This application was illustrated by an example, which was simulated.

ACKNOWLEDGEMENTS

Esteban Jiménez acknowledges to CONACyT, México for the MSc scholarship number 426598.

REFERENCES

Andrieu, V., Praly, L., and Astolfi, A. (2008). Homogeneous approximation, recursive observer design, and output feedback. *SIAM Journal on Control and Optimization*, 47(4), 1814–1850.

Bernstein, D.S. (1993). Nonquadratic Cost and Nonlinear Feedback Control. *International Journal of Robust and Nonlinear Control*, 3(1), 211–229.

Bhat, S. and Bernstein, D. (2000). Finite-time stability of continuous autonomous systems. *SIAM Journal on Control and Optimization*, 38(3), 751–766.

Cruz-Zavala, E., Moreno, J., and Fridman, L. (2010). Uniform second-order sliding mode observer for mechanical systems. In *Variable Structure Systems (VSS), 2010 11th International Workshop on*, 14 –19.

Drakunov, S.V. and Utkin, V.I. (1992). Sliding mode control in dynamic systems. *International Journal of Control*, 55, 1029–1037.

Filippov, A.F. (1988). *Dierential equations with discontinuous righthand sides*. Kluwer Academic Publishers Group, Dordrecht.

Fraguela, L., Angulo, M., Moreno, J., and Fridman, L. (2012). Design of a prescribed convergence time uniform robust exact observer in the presence of measurement noise. In *Decision and Control (CDC), 2012 IEEE 51st Annual Conference on*, 6615–6620.

Haddad, W.M. and L'Afflitto, A. (2016). Finite-Time Stabilization and Optimal Feedback Control. *IEEE Transactions on Automatic Control*, 61(4), 1069–1074. doi:10.1109/TAC.2015.2454891.

Haimo, V. (1986). Finite time controllers. *SIAM Journal on Control and Optimization*, 24(4), 760–770.

Moulay, E. and Perruquetti, W. (2005). Lyapunov-based approach for finite time stability and stabilization. In *Proceedings of the 44th IEEE Conference on Decision and Control, and the European Control Conference, CDC-ECC '05*, 4742–4747. doi: 10.1109/CDC.2005.1582911.

Moulay, E. and Perruquetti, W. (2006). Finite-time stability and stabilization: State of the art. In C. Edwards, E. Fossas Colet, and L. Fridman (eds.), *Advances in Variable Structure and Sliding Mode Control*, volume 334 of *Lecture Notes in Control and Information Science*, 23–41. Springer Berlin Heidelberg.

Polyakov, A. (2012). Nonlinear feedback design for fixed-time stabilization of linear control systems. *IEEE Transactions on Automatic Control*, 57(8), 2106–2110.

Polyakov, A. and Fridman, L. (2014). Stability notions and Lyapunov functions for sliding mode control systems. *Journal of the Franklin Institute*, 351(4), 1831 – 1865. Special Issue on 2010-2012 Advances in Variable Structure Systems and Sliding Mode Algorithms.

Roxin, E. (1966). On finite stability in control systems. *Rendiconti del Circolo Matematico di Palermo*, 15(3), 273–282.

Sánchez-Torres, J.D., Sanchez, E.N., and Loukianov, A.G. (2015). Predefined-time stability of dynamical systems with sliding modes. In *American Control Conference (ACC), 2015*, 5842–5846.

Sánchez-Torres, J.D., Sánchez, E.N., and Loukianov, A.G. (2014). A discontinuous recurrent neural network with predefined time convergence for solution of linear programming. In *IEEE Symposium on Swarm Intelligence (SIS)*, 9–12.

Utkin, V.I. (1992). *Sliding Modes in Control and Optimization*. Springer Verlag.

Reducción de dimensionalidad para sistemas de ecuaciones diferenciales parciales con geométrica irregular usando el método de descomposición ortogonal propia y elementos finitos

Yulánderson Salguero-Rodríguez*, Richard Rios Patiño*, Jairo J. Espinosa Oviedo*

**Universidad Nacional de Colombia, Facultad de Minas, GAUNAL, Medellín, Colombia (ysalgueror@unal.edu.co, rriospa@unal.edu.co, jairo.espinosa@iee.org)*

Resumen: En el control de procesos se utilizan ecuaciones diferenciales parciales (EDPs) para describir procesos físicos mediante las leyes de transferencia de masa, energía o cantidad de movimiento y ecuaciones fundamentales. Sin embargo, los modelos de EDP conducen a sistemas de infinita dimensión, que son inviables para el control y simulación de procesos. Las técnicas de reducción de dimensionalidad como la descomposición ortogonal propia (DOP) son necesarias para obtener modelos de orden reducido adecuados para los sistemas de control. El método DOP ha funcionado para la reducción de dimensionalidad en los dominios espaciales cartesianos con mallado regular. No obstante, una limitación del método DOP corresponde al orden de almacenamiento de la información empírica de los sistemas en la matriz de datos para sistemas EDP con dominio no cartesiano. Por lo tanto, nuestra contribución es mostrar que las funciones DOP y sus respectivas varianzas son invariantes con respecto a la orden de almacenamiento. Usando COMSOL-Matlab/Simulink y el método DOP, se utilizó un sistema de transferencia de calor en dos dimensiones con varios órdenes de almacenamiento en la matriz de datos, con el fin de comparar los respectivos modelos de orden reducido. También proporcionamos la aplicación de la interfaz COMSOL-Matlab para obtener modelos de orden reducido usando un calentador de oficina (sistema de calor de dos dimensiones).

Palabras clave: DOP, mallado irregular, COMSOL, EDP.

1. INTRODUCCIÓN

En la actualidad, se ha logrado la simulación de sistemas complejos y de gran escala en diversas áreas. Generalmente, los modelos que representan estos sistemas se describen por ecuaciones diferenciales parciales (EDPs), las cuales resultan de aplicar leyes fundamentales (masa, energía y cantidad de movimiento). Los sistemas EDPs son aproximados generalmente por un elevado número de ecuaciones diferenciales ordinarias (EDOs), resultantes de la aplicación de métodos numéricos (diferencias finitas, volúmenes o elementos finitos) (Agudelo et al., 2006) (Astrid, 2004) (Antoulas, 2005b).

Estos sistemas EDOs pueden llegar al orden de miles o millones de ecuaciones, lo cual dificulta la realización de simulaciones, optimizaciones y control (Antoulas et al., 2001); esto teniendo en cuenta aspectos como: elevados tiempos en simulación, errores numéricos por operaciones con punto flotante, alto uso de memoria, problemas de mal condicionamiento, entre otros (Antoulas, 2005a). Por ejemplo, estos sistemas ODEs puede conllevar a problemas mal condicionados en optimizaciones en tiempo real como producto de su gran número de ecuaciones.

Debido a lo anterior, se hace necesario el uso de técnicas de reducción de dimensionalidad, para la obtención de modelos adecuados para simulación, optimización y control como es el método de descomposición ortogonal propia (DOP), también conocido como análisis de componentes principales o descomposición de Karhunen – Loeve (Chao Xu, 2011). En términos simples, este método utiliza descomposiciones espectrales y proyección Galerkin en la aproximación de un sistema EDO sobre el espacio reducido generado por las funciones base. Este método provee la aproximación óptima de bajo rango en términos del error medio cuadrático (Trefethen & Bau, 1997) (Laub, 2005).

El método DOP ha sido ampliamente utilizado en diversos modelos que provienen de sistemas dinámicos de gran escala tales como: flujo de fluidos, transferencia de calor, procesamiento de imágenes, sistemas micro electromecánicos, oceanografía y aero-elasticidad entre otros (Cai & White, 2009). Para estas aplicaciones este método tiene la ventaja de agrupar características tanto de los modelos empíricos basados en datos, como de los modelos físicos obtenidos con leyes fundamentales.

Este método de reducción de dimensionalidad ha mostrado un adecuado funcionamiento utilizando mallados regulares (Agudelo et al., 2007) (Astrid, 2004). A pesar de esto, no siempre es posible abordar las geometrías espaciales con un mallado regular, haciendo necesario el uso de mallados irregulares para aproximar el modelo EDP original. Esta situación involucra un cambio en el concepto de vecindad espacial en el mallado irregular; por lo cual es necesario establecer una manera de almacenar espacialmente los datos en la matriz de datos. De esta forma, el objetivo de este

artículo es aplicar el método de elementos finitos utilizando un mallado irregular y DOP, para obtener el modelo de orden reducido en un sistema EDP; e igualmente, estudiar el efecto del orden de almacenamiento de los datos de simulación o empíricos en la matriz de datos.

Las simulaciones presentadas en este artículo fueron realizadas utilizando la plataforma de simulación COMSOL Multiphysics y Matlab. COMSOL es una herramienta para el análisis de elementos finitos en sistemas físicos. Aunque la configuración de COMSOL es eficaz a la hora de resolver varios tipos de problemas, el tiempo de simulación puede llegar a ser grande, dependiendo de muchos factores como: número de variables, complejidad del sistema EDP y del número de nodos utilizados en el mallado. El método DOP no puede ser implementado en COMSOL, por lo cual se realiza utilizando COMSOL con Matlab. En este artículo se presenta la simulación de transferencia de calor bidimensional utilizando un mallado regular e irregular, evaluando el efecto del orden de almacenamiento en el modelo de orden reducido (MOR).

La estructura en la que se presenta este documento es la siguiente: en la sección 2 se presenta una descripción de la plataforma de simulación. En la sección 3 se presenta una breve introducción al método DOP. En la sección 4 son presentados los resultados de simulaciones para los casos de estudio, en el cual se involucra la transferencia de calor en dos dimensiones. En la sección 5 se presentan las conclusiones de este trabajo.

2. PLATAFORMA DE SIMULACIÓN

COMSOL posee algunos de los modelos más comunes de aplicación en las ciencias e ingeniería como: acústica, dinámica de fluidos computacionales, procesos químicos, corrosión, electroquímica, geomecánica, transferencia de calor entre otros (COMSOL, 2010). Una vez es definido el módulo de simulación o el grupo de EDPs a utilizar se especifica la geometría de estudio. En la interfaz del modelo se pueden introducir varios tipos de condiciones al sistema de EDPs como: valores iniciales, condiciones de frontera y condiciones iniciales. Finalmente se realiza el mallado sobre la geometría de estudio para poder realizar la simulación.

La interfaz entre COMSOL y Matlab puede ser utilizada cargando el modelo de COMSOL en Matlab, en donde el usuario puede introducir o cambiar cualquiera de los parámetros numéricos de la simulación como: propiedades del material, valores iniciales, condiciones iniciales o de frontera, por medio del uso de funciones de Matlab en COMSOL, o por medio de comandos desde la interfaz de Matlab, para mayor detalle se puede referir a la documentación que acompaña esta conexión (COMSOL, 2013).

Al utilizar COMSOL con Matlab se pueden efectuar diversas acciones como, por ejemplo: cargar un modelo de COMSOL en la ventana de Matlab, evaluar una expresión o variable, extraer la información relacionada con el mallado utilizado, modificar las condiciones iniciales y de frontera, extraer la solución numérica EDO. Para cargar un modelo en Matlab es utilizado el comando *mphload*, el cual permite crear una estructura que contiene todas las instrucciones del modelo en COMSOL. Las variables o expresiones pueden ser evaluadas en la ventana de trabajo por medio del uso del comando *mpheval*, en el cual se especifican las coordenadas espaciales y temporales a evaluar. El mallado utilizado para simular el modelo consta de diversos elementos tales como: elementos y vértices, si se requiere conocer esta información es posible utilizar el comando *mphxmeshinfo*.

Finalmente, es posible obtener el sistema EDO lineal en espacios de estado, correspondiente a la solución numérica del modelo EDP, para ello se utiliza el comando *mphstate*. Este comando importa en Matlab las matrices que representan el sistema, las cuales son utilizadas posteriormente para la obtención del modelo de orden reducido. Para mayores detalles se puede referir a la documentación de estos programas (COMSOL, 2015).

3. REDUCCIÓN DE DIMENSIONALIDAD USANDO DOP

En la descomposición ortogonal propia, se busca representar las variables del sistema como la suma de funciones base ortonormales según (1).

$$x(z,t) \approx \hat{x}(z,t) = \sum_{j=1}^{n} a_j(t)\,\varphi_j(z) \qquad (1)$$

En donde $\varphi_j(z)$ representan un conjunto de funciones base ortonormales (funciones base DOP) en el dominio espacial z y $a_j(t)$ son los coeficientes variantes con el tiempo o coeficientes DOP asociados con cada función base. La reducción de modelos a través de DOP puede realizarse a través de 5 pasos, a saber:

1. Generación de la matriz snapshot: La matriz snapshot es construida por las respuestas del sistema cuando se introduce señales ricas en frecuencias en las entradas. En la simulación son tomados k observaciones utilizando un tiempo de muestreo determinado (Δt), según (2).

$$X_{snap} = \left(x(t = \Delta t), \dots, x\,(t = k\Delta t)\right) \qquad (2)$$

2. Obtención de las funciones base DOP: estas funciones son obtenidas a través del cálculo de la descomposición en valores singulares (SVD) de la matriz X_{snap}.

$$X_{snap} = \Phi \Sigma \Psi^{T} \qquad (3)$$

en donde Φ y Ψ son matrices ortonormales, y Σ es la matriz que contiene los valores singulares de la matriz snapshoot. Las columnas de Φ son las funciones base DOP.

3. Selección de las funciones DOP más relevantes: se realiza verificando los valores singulares de la matriz X_{snap}. El grado de correlación entre una función base

(φ_j) y los datos se obtiene a través del valor singular correspondiente (σ_j). Es importante resaltar que los valores singulares se encuentran ordenados de mayor a menor, indicando que la primera función base DOP es el elemento más importante. El criterio para determinar el número de funciones base está dado en (4), donde r es el rango de la matriz de datos.

$$P_n = \frac{\sum_{j=1}^{n} \sigma_j}{\sum_{j=1}^{r} \sigma_j}, n = 1, 2, \dots, r \qquad (4)$$

Como los valores propios son positivos, esto implica que:

$$0 < P_1 \leq P_2 \leq P_3 \leq \cdots P_r = 1 \qquad (5)$$

la cantidad P_n es utilizada para determinar el orden de truncamiento de las funciones base DOP. El número de funciones DOP base es determinado por la fracción de los primeros valores singulares que sea lo suficientemente grande para representar la información de los datos. En ese orden de ideas se puede construir el modelo de orden reducido con un número de ecuaciones n.

4. Construcción del modelo de orden reducido: para obtener el modelo de los primeros n coeficientes DOP, se utiliza la proyección de Galerkin. Lo anterior consiste en definir una función residual con la diferencia entre el modelo original y el modelo aproximado, esta se muestra en (6).

$$\dot{x}(t) = Ax(t) + Bu(t) + Fd(t) \qquad (6)$$

$$R(x) = \dot{x}(t) - Ax(t) - Bu(t) - Fd(t) \qquad (7)$$

Remplazando el modelo aproximado por su aproximación $x_n(t)$ en (7) se tiene:

$$\langle R(x_n), \varphi_j(zd) \rangle = 0; j = 1, 2, \dots, n \qquad (8)$$

En donde $\langle \cdot, \cdot \rangle$ representa el producto interno. Al aplicar el producto interno se tiene:

$$\langle \Phi_n \dot{a}(t), \Phi_n \rangle = \langle A\Phi_n a(t) + Bu(t) + Fd(t), \Phi_n \rangle \qquad (9)$$

evaluando el producto interno, se obtiene un modelo para los primeros n coeficientes dependientes del tiempo y por lo tanto un modelo de orden reducido con n estados:

$$\dot{a}(t) = A_r a(t) + B_r u(t) + F_r d(t) \qquad (10)$$
$$x_n(t) = \Phi_n a(t) \qquad (11)$$

en donde $A_r = \Phi_n^T A \Phi_n$, $B_r = \Phi_n^T B$ y $F_r = \Phi_n^T F$.

5. Validación del modelo de orden reducido.

4. BENCHMARKS

En esta sección se presentan algunos *benchmarks* utilizando reducción de dimensionalidad por el método de DOP presentado previamente. El primer *benchmark* es un modelo de transferencia de calor bidimensional, utilizando varios ordenes de almacenamiento, esta simulación busca evaluar el efecto que tiene el orden de almacenamiento en la matriz de datos para el MOR. El segundo *benchmark* es un sistema de calefacción representado por un modelo de transferencia de calor bidimensional con geometría irregular, con esta simulación se muestra el uso de elementos finitos en un mallado irregular y DOP en la obtención del modelo de orden reducido de un sistema EDP.

Para verificar el desempeño de los modelos de orden reducido, se calcular un error relativo con respecto a los datos generados por el modelo original. El error es tomado como el máximo valor calculado del error, y se muestra en (12).

$$e = max_z \frac{|W(z,t) - Wr(z,t)|}{W(z,t)} \qquad (12)$$

En donde $W(z,t)$ es el valor del modelo original en la coordenada espacial z en el tiempo t y $Wr(z,t)$ es el valor del modelo de orden reducido.

4.1 Transferencia de calor con diferentes órdenes de almacenamiento.

En el primer *benchmark* se presenta la transferencia de calor bidimensional en una placa, cuya temperatura es fijada en dos de sus fronteras (ver Fig. 1), la altura y el ancho de la placa corresponden a 0,15 m. La expresión que modela este fenómeno es la mostrada en (13).

$$\rho C \frac{\partial T}{\partial t} = k \frac{\partial^2 T}{\partial x^2} + k \frac{\partial^2 T}{\partial y^2} + h \frac{Ta - T}{\Delta z} \qquad (13)$$

La densidad (ρ) de la placa es de 2700 $\frac{Kg}{m^3}$, la capacidad calorífica de la placa (C) es de 900 $\frac{J}{KgK}$, el material posee una conductividad térmica (k) de 234 $\frac{W}{mK}$ y un coeficiente convectivo de transferencia de calor hacia el ambiente (h) de 20 $\frac{W}{m^2K}$.

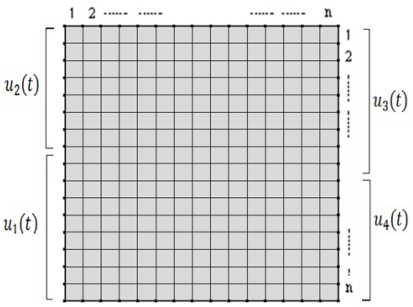

Fig. 1: Geometría de la placa con cuatro entradas

Las condiciones de frontera e iniciales de este sistema son las siguientes:

$$u_1(t) = T\left(0{,}0{:}\frac{L}{2}, t\right) = 300\ K, \qquad u_2(t) = T\left(0, \frac{L}{2}{:}L, t\right) = 350\ K$$
$$u_3(t) = T\left(L, 0{:}\frac{L}{2}, t\right) = 300\ K, \qquad u_4(t) = T\left(L, \frac{L}{2}{:}L, t\right) = 300\ K$$
$$T(x, y, 0) = 300\ K, \qquad Ta = 300\ K$$

En la simulación de este fenómeno, las derivadas parciales con respecto a las dimensiones (x e y) se remplazan por una aproximación con diferencias finitas, este sistema adquiere la forma matricial presentada en (14). Donde $T(t)$ es el vector de temperaturas de todos los puntos de la malla en el instante t y $u(t)$ es un vector con las entradas del sistema.

$$\dot{T}(t) = AT(t) + Bu(t) \qquad (14)$$

Esta simulación es realizada en Matlab – Simulink, utilizando dos órdenes de almacenamiento diferentes (ver Fig. 2). El primer orden de almacenamiento es en forma de líneas verticales, y el segundo en forma de diagonales. El objetivo de esta simulación fue evaluar el efecto del orden de almacenamiento de los datos en la descomposición ortogonal propia, mostrando que tanto los valores propios como las direcciones de variabilidad se preservan pese al orden de almacenamiento.

a)

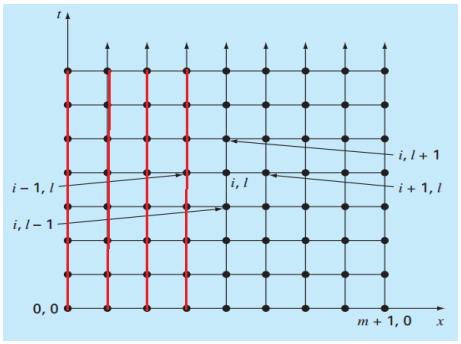

b)

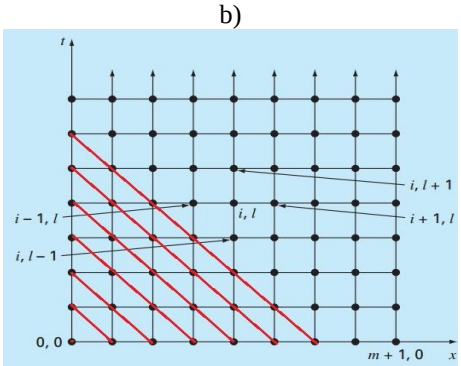

Fig. 2: Ordenes de almacenamiento utilizados a) vertical b) diagonal

Para reducir la dimensionalidad de este modelo, se generó una señal rica en frecuencias sobre cada entrada del modelo. Los dos modelos originales se corren con la misma señal y se almacenan las salidas del sistema con los dos órdenes de almacenamiento mencionados en la matriz snapshot. Posteriormente, se calcula la SVD de ambas matrices en (15) y (16), junto con el porcentaje de variabilidad acumulada por os primeros modos usando (4).

$$T_{snap1} = \Phi_1 \Sigma_1 \Psi_1^T \qquad (15)$$
$$T_{snap2} = \Phi_2 \Sigma_2 \Psi_2^T \qquad (16)$$

En la tabla 1, se presentan los primeros 10 valores singulares para los dos modelos de orden reducido en mención, mostrando igualdad para ambos órdenes de almacenamiento. Lo anterior, implica que independientemente del tipo de ordenamiento utilizado en los nodos, los valores obtenidos mediante el método DOP son iguales.

Tabla 1: Valores singulares SVD

Orden vertical	Orden diagonal
257965.94	257965.94
8802.82	8802.82
6973.34	6973.34
4332.24	4332.24
2625.61	2625.61
2052.83	2052.83
1149.80	1149.80
651.56	651.56
519.75	519.75
260.96	260.96

En la Fig. 3 se presenta el valor acumulado (P_n) para cada valor singular, del cual se puede notar que con 10 modos se captura un porcentaje superior al 99% de la variabilidad de los datos.

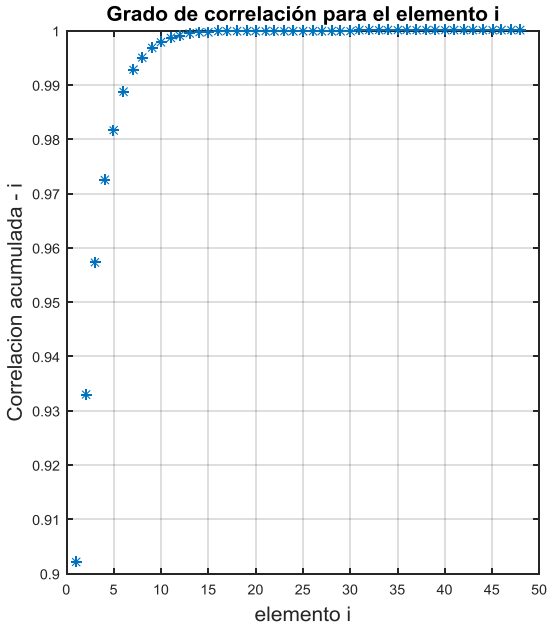

Fig. 3: Variabilidad acumulada descrita por los valores singulares

En la Fig. 4 se presentan los resultados obtenidos para el perfil de temperatura y el error relativo asociado en estado estable, para el modelo de orden reducido utilizando tanto el orden de almacenamiento vertical, como diagonal con 10 funciones base (n=10). El error máximo cometido por la aproximación es de 0.6%, por lo cual se puede afirmar que el modelo de orden reducido representa de manera adecuada el sistema original.

a)

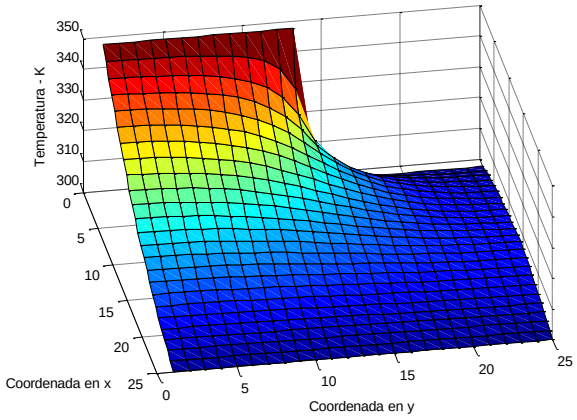

b)

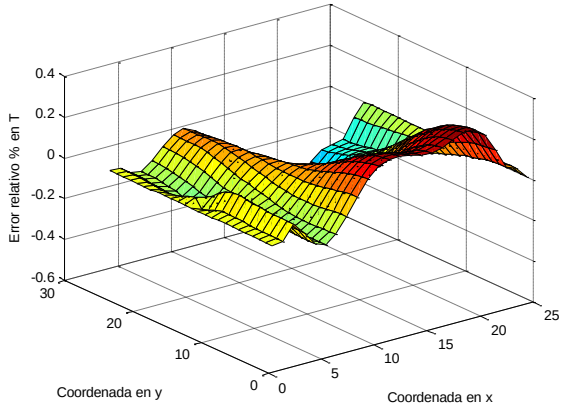

Fig. 4: MOR a) perfil de temperatura b) error asociado

En la Fig. 5 y 6, se presenta la gráfica del primer y segundo modo U_1 y U_2 en ambos modelos de orden reducido tanto en almacenamiento vertical como diagonal. De estas figuras se puede notar que ambos modos son iguales para los dos órdenes de almacenamiento propuestos. Esto indica que independientemente del tipo de ordenamiento utilizado en los nodos, los valores singulares y modos obtenidos mediante el método DOP son iguales.

a)

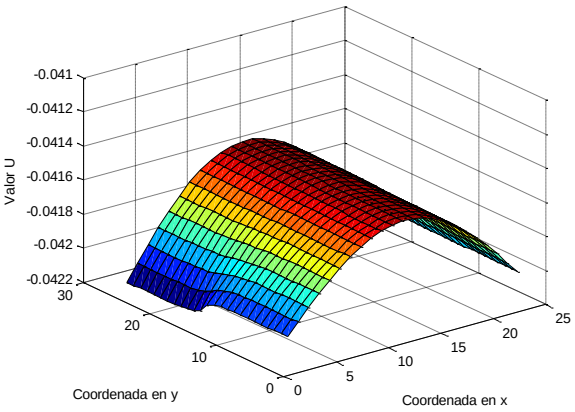

b)

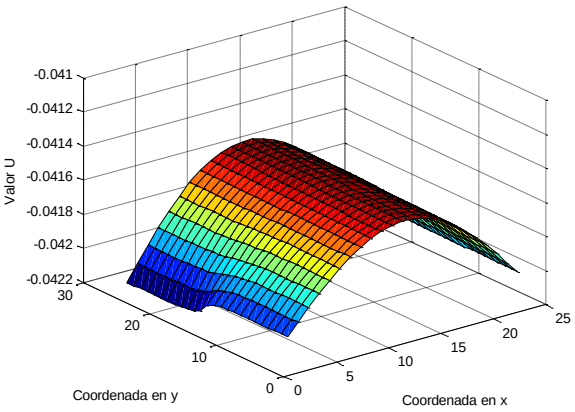

Fig. 5: Comparación primer modo U_1

a)

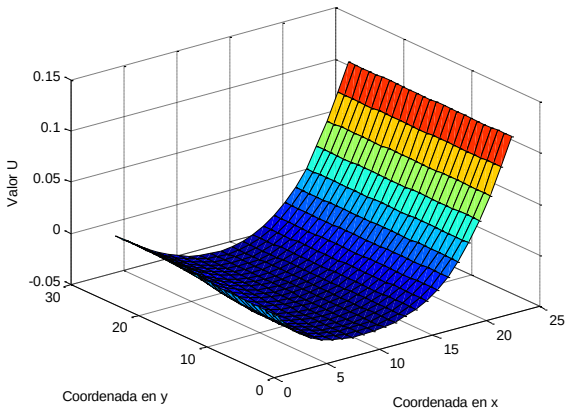

b)

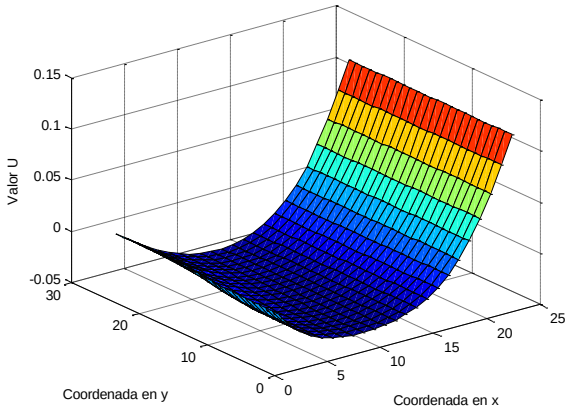

Fig. 6: Comparación segundo modo U_2 almacenamiento a) vertical b) diagonal

4.2 Transferencia de calor con geometría irregular

Considere un sistema de calentamiento compuesto por una tubería central con agua caliente a una temperatura constante (ver Fig. 7). El sistema se encuentra conformado por varias aletas bidimensionales como se muestra en la figura.

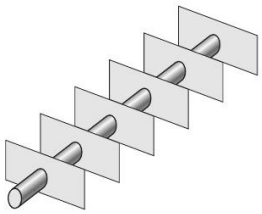

Fig. 7: calefacción. Adaptado de Hunton (Hunton, 2004)

A través de un balance de energía en las aletas considerando transferencia de calor por convección y el uso de la ecuación de Laplace se llega a la expresión que modela este fenómeno en (17):

$$\rho C\frac{\partial T}{\partial t} = k\frac{\partial^2 T}{\partial x^2} + k\frac{\partial^2 T}{\partial y^2} + h(Ta - T) + Q\Delta z \qquad (17)$$

en donde ρ es la densidad del material, C es la capacidad calorífica de la placa, k es la conductividad térmica del material, h es el coeficiente convectivo, Q es la tasa de transferencia de calor desde el interior del tubo. Las propiedades del fenómeno simulado son las siguientes:

$$\rho = 2700\frac{Kg}{m^3}, \quad C = 900\frac{J}{KgK}, \quad L = 0.1m,$$
$$\Delta z = 0.01m, \quad h = 900\frac{W}{m^2K}, \quad k = 234\frac{W}{mK},$$
$$H = 0.1m, \quad Q = 1000\frac{W}{m^3}$$

Las condiciones iniciales del sistema de transferencia de calor son las siguientes:

$$T(x, y, 0) = 295\ K, \quad Ta = 295\ K$$

En la Fig. 8 se presenta el mallado utilizado para simular el sistema. Al utilizar elementos finitos, el sistema EDP es aproximado con un sistema EDO, el cual se muestra a continuación en (18):

$$\dot{T}(t) = AT(t) + Bu(t) \qquad (18)$$

donde $T(t)$ es el vector de temperaturas de todos los puntos de la malla en el instante t y $u(t)$ es un vector con las entradas del sistema. En este caso las entradas del sistema son la fuente de calor Q y la temperatura ambiente Ta. Este sistema EDO es de orden 3648.

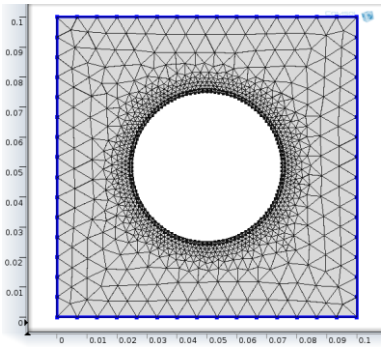

Fig. 8: mallado utilizado por COMSOL en la simulación

Para obtener el modelo de orden reducido se realizó análogamente al primer *benchmark*. Para este propósito, se utilizó la interfaz Matlab – COMSOL, en la cual se introducía como una función de Matlab los datos de las señales de entrada a la interfaz de COMSOL para generar la matriz snapshot. Posteriormente, se calcula la SVD de la matriz snapshot en Matlab y se escoge el número de funciones base (n) para aproximar el modelo, según el aporte de los valores singulares de acuerdo a (4).

$$T_{snap} = \Phi\Sigma\Psi^T \qquad (15)$$

En la Fig. 9 se presenta el valor acumulado (P_n) para cada valor singular. De esta figura se puede inferir que con un valor n=5 se capta un porcentaje superior al 99% de la información contenida en la matriz T_{snap} para este modelo. Por lo tanto, se lograda pasar de un sistema EDO de orden 3648, a un sistema EDO de dimensión 5.

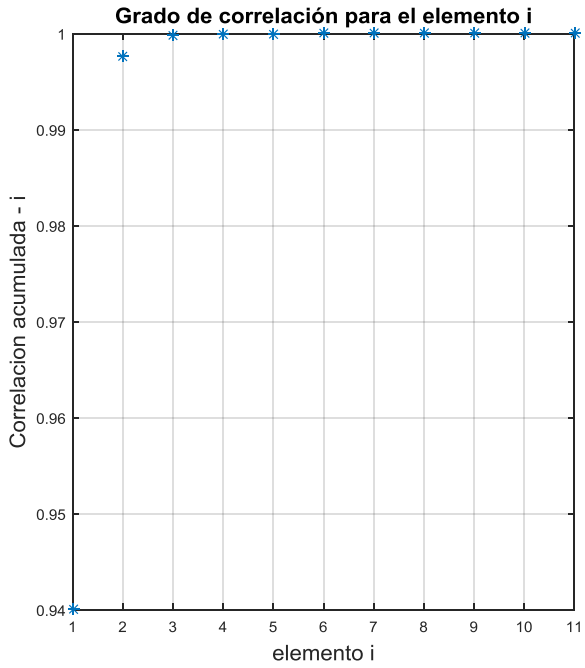

Fig. 9: variabilidad acumulada T_{snap}.

El MOR se obtuvo utilizando proyecciones de Galerkin, y está dado por (16):

$$\dot{a}(t) = A_r a(t) + B_r u(t) \quad (16)$$
$$x_n(t) = \Phi_n a(t)$$

En donde $A_r = \Phi_n^T A \Phi_n$, $B_r = \Phi_n^T B$. Para validar el modelo se realiza la simulación en COMSOL del proceso de transferencia de calor descrito previamente por (17) con sus respectivas condiciones iniciales y entradas al sistema mostradas previamente. Esta simulación es comparada con los resultados entregados por el MOR con n=5 utilizando las mismas entradas del sistema. En la Fig. 10 se presenta el perfil de temperatura del modelo original y del modelo de orden reducido. El error asociado al MOR tiene un valor máximo de $3.5x10^{-7}$%.

a)

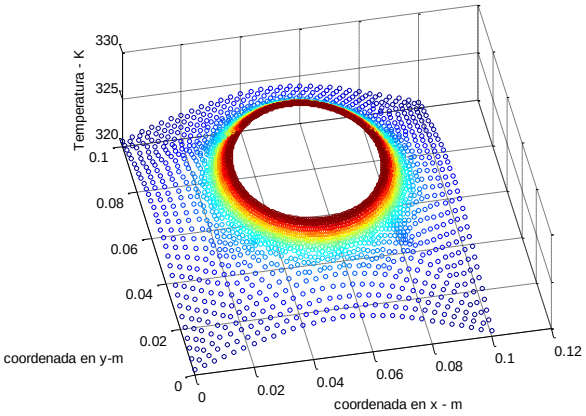

b)

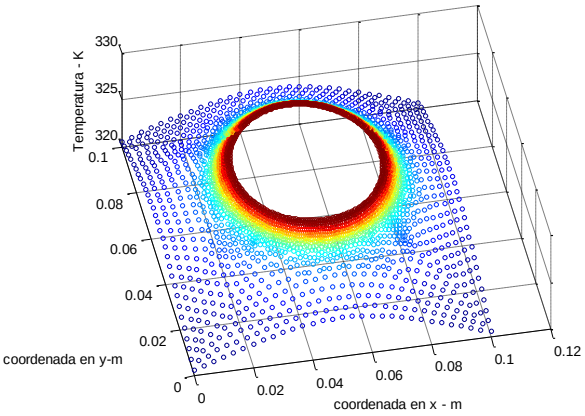

Fig. 10: validación MOR calentador de oficina. a) original b) reducido

Para validar el comportamiento dinámico del MOR, se eligió 4 puntos cercanos a la fuente de calor, estos se muestran en la Fig. 11. De esta forma, se realizó la comparación de la temperatura en estos 4 nodos con el paso del tiempo para el modelo original y el MOR, estos se presentan en la Fig. 12. El error asociado al MOR tiene un valor máximo de 0.6% el cual es bajo e indica que en el comportamiento dinámico el MOR representa de manera adecuada al sistema original.

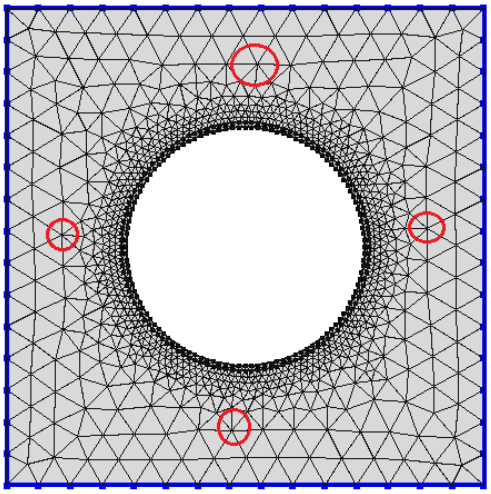

Fig. 11: puntos de validación comportamiento dinámico

a)

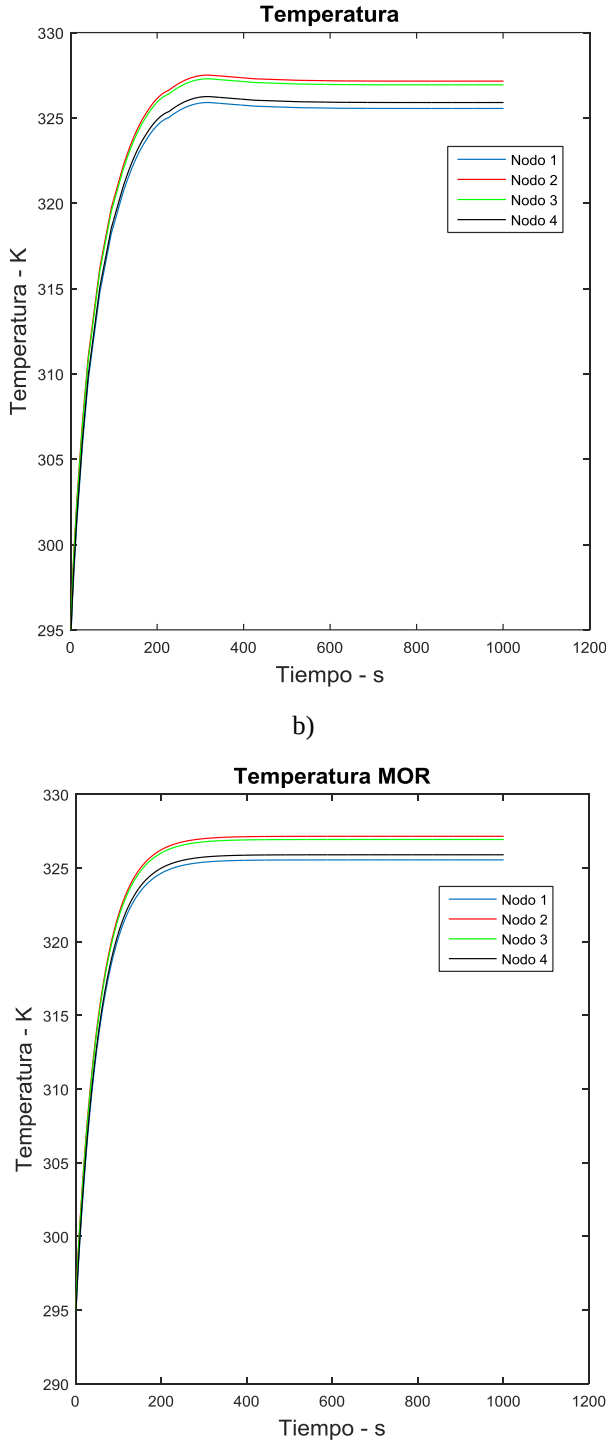

b)

Fig. 12: validación comportamiento dinámico a) modelo original b) modelo de orden reducido

En la Fig. 13 se presenta el efecto que tiene en el perfil de estado estable el primer modo U_1 en su sentido positivo y negativo. En el sentido positivo el primer modo disminuye la temperatura en toda la geometría del modelo. En el sentido negativo el primer modo aumenta la temperatura en toda la geometría.

a)

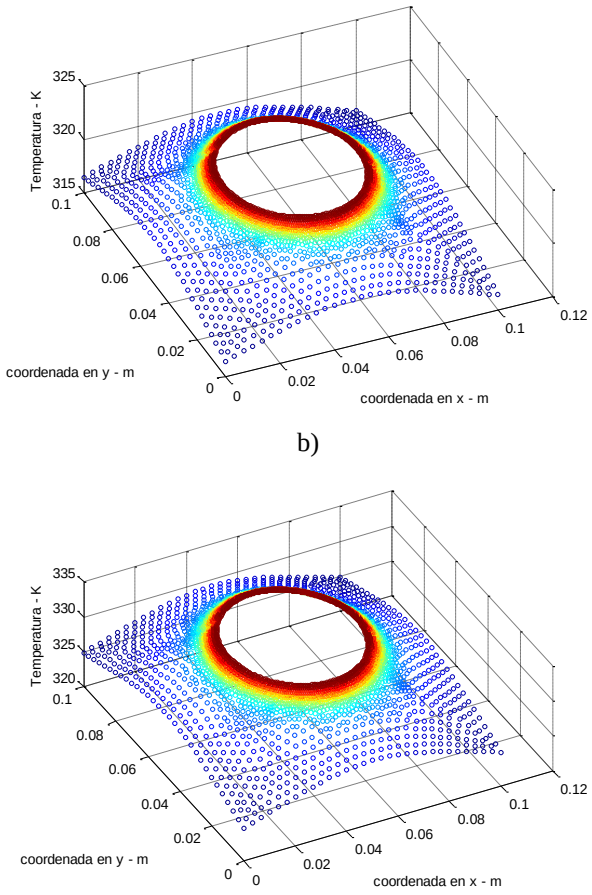

b)

Fig. 13: efecto primer modo U_1 a) positivo b) negativo

En la Fig. 14 se presenta el efecto que tiene en el perfil de estado estable el segundo modo U_2 en su sentido positivo y negativo, respectivamente. En el sentido positivo el segundo modo disminuye la temperatura en los extremos de la placa y aumenta la temperatura en las cercanías de la fuente de calor. En el sentido negativo el segundo modo aumenta la temperatura en los extremos de la placa y disminuye la temperatura en las cercanías a la fuente de calor.

a)

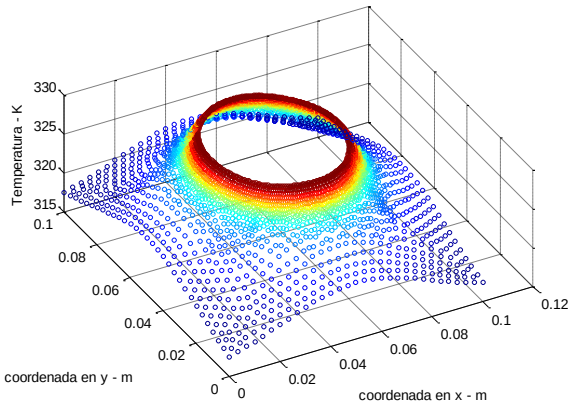

b)

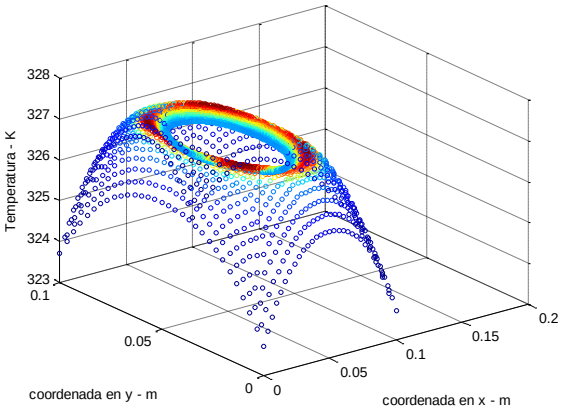

Fig. 14: efecto segundo modo U_2 a) positivo b) negativo

5. CONCLUSIONES

En este artículo se abordó el problema de reducción de dimensionalidad para sistemas EDP con geométrica irregular usando el método de DOP y elementos finitos. En este trabajo se evaluó el efecto del orden de almacenamiento de los datos de simulación en la matriz de snapshot a través de un sistema de transferencia de calor en dos dimensiones. Una contribución de este trabajo fue mostrar que los modos y sus varianzas asociadas son invariantes respecto al orden de almacenamiento de los datos en la matriz snapshot.

La integración de COMSOL y Matlab permite simular sistemas EDP con geometría irregular usando el método de elementos finitos. A través de la plataforma de simulación COMSOL se puede extraer la solución numérica del sistema EDP a Matlab, como también la información relacionada con el mallado, las condiciones de frontera, entre otros datos importantes. Posteriormente, esta información permite obtener modelos de orden reducido utilizando el método de DOP en Matlab.

Los resultados mostrados en el caso de estudio para el MOR al utilizar COMSOL y Matlab son satisfactorios, tanto en el estado estable, como en el comportamiento dinámico, por lo cual se puede considerar adecuado el uso combinado de Matlab y COMSOL en la aplicación del método DOP en sistemas de EDP como este, en el cual se utiliza un mallado irregular al aplicar el método de elementos finitos.

5. AGRADECIMIENTOS

Los autores agradecen a Colciencias y a la Universidad Nacional de Colombia a través de la convocatoria jóvenes investigadores e innovadores 645 de 2014 por el apoyo en la financiación de este proyecto.

BIBLIOGRAFÍA

Agudelo, O. M., Espinosa, J. J., & De Moor, B. (2006). *Application of POD and Predictive Control Techniques to the control of the Temperature Profile of an one-dimensional bar.* Salvador, Brazil: XII Latin-American Congress on Automatic Control (CLCA 2006).

Agudelo, O. M., Espinosa, J. J., & De Moor, B. (2007). *Control of a Tubular Chemical Reactor by means of POD and Predictive Control Techniques.* Grecia: European Control Conference 2007 (ECC'07).

Antoulas, A. C. (2005a). An overview of approximation methods for large-scale dynamical systems. *Annual Reviews in control 29*, 181 - 190.

Antoulas, A. C. (2005b). *Approximation of large scale dynamical systems.* United States: SIAM.

Antoulas, A. C., Sorensen, D. C., & Gugercin, S. (2001). A survey of model reduction methods for large-scale systems. *Contemporary Mathematics, AMS publications, vol. 280*, 193 - 219.

Astrid, P. (2004). *Reduction of Process Simulation Models: a proper orthogonal decomposition approach.* Eindhoven: Phd. tesis Technische Universiteit Eindhoven.

Cai, L., & White, R. E. (2009). Reduction of Model Order Based on Proper Orthogonal Decomposition for Lithium-Ion Battery Simulations. *Journal of The Electrochemical Society, 156*, A154 - A161.

Chao Xu, E. S. (2011). *Model Order Reduction for High Dimensional Linear Systems based on Rank-1 Incremental Proper Orthogonal Decomposition.* San Francisco: IEE.

COMSOL. (2010). *Introduction to COMSOL Multiphysics.* Estados Unidos: COMSOL A B.

COMSOL. (2013). *Livelink for MATLAB user's guide.* Estados Unidos: COMSOL AB.

COMSOL. (2015). Combining COMSOL Multiphysics® and MATLAB®. Estados Unidos: COMSOL AB.

Hunton, D. V. (2004). *Fundamentals of finite element analysis.* Estados Unidos: Mc Graw Hill.

Laub, A. J. (2005). Matrix Analysis for Scientists & Engineers. Filadelfia: Society for industrial and applied mathematics - SIAM.

Trefethen, L. N., & Bau, D. (1997). Numerical Linear algebra. Filadelfia: Society for industrial and applied mathematics - SIAM.

CHAPTER 11

OBSERVERS

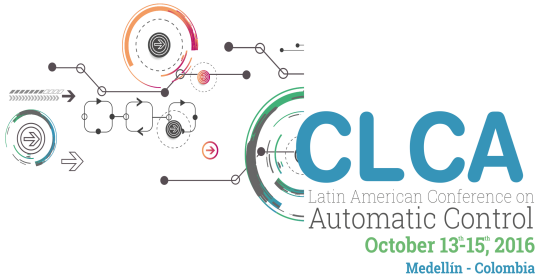

A Soft Sensor for Biomass in a Batch Process with Delayed Measurements

Jhon A. Isaza * **Juan Diego Sánchez-Torres** **
Esteban Jiménez-Rodríguez *** **Héctor A. Botero** ****

* *Faculty of Engineering and Architecture, Universidad Nacional de Colombia, Sede Manizales, Carrera 27 No 64-60, Colombia (e-mail: jaisazah@unal.edu.co).*
** *Department of Mathematics and Physics, ITESO, Periférico Sur Manuel Gómez Morín 8585 C.P. 45604, Tlaquepaque, Jalisco, México. (e-mail: dsanchez@iteso.mx).*
*** *Department of Electrical Engineering, CINVESTAV-IPN Guadalajara, Av. del Bosque 1145 Col. El Bajío CP 45019, México (e-mail:ejimenezr@gdl.cinvestav.mx).*
**** *Department of Electrical Energy and Automatica, Universidad Nacional de Colombia, Sede Medellín, Carrera 80 No 65-223, Colombia (e-mail: habotero@unal.edu.co)*

Abstract: This paper presents a soft sensor to estimate the biomass concentration in a batch bioprocess used in production of δ-endotoxins of *Bacillus thuringiensis*, subject to delayed measurements. The soft sensor proposed is based on a cascade observer-predictor algorithm. The observer stage is based on a class of second order sliding mode algorithms, allowing a fixed-time estimation of the biomass. Additionally, the prediction stage offsets the effect of the delay in measurements. Simulations show the feasibility of the proposed observer.

Keywords: cascade observer-predictor, delayed measurements, δ-endotoxins production of *Bacillus thuringiensis*, fixed-time observer, Smith predictor.

1. INTRODUCTION

Measuring variables in industrial processes, such as bioprocess, is necessary to carry out tasks of control, diagnosis and fault detection, identification and monitoring (Walcott et al., 1987; Dochain, 2003). For some variables, the work of measurement is hard, costly and difficult to perform due to the unavailability of reliable devices, time delays, errors in the measurement system, high costs of devices and hostile environments for primary measuring devices (Bequette, 2002). Therefore, in order to make estimates by measurements of other variables related directly or indirectly to the variable difficult to measure has been used the state estimators. This dynamic systems are applied to a specific process, with a combination of software and hardware, and they are commonly named as virtual sensors or soft sensors.

However, the soft sensors technology transfer to industrial bioprocesses require to solve some problems such as observer schemes that allowing the use of delayed measurements. To overcome such problem, some authors have developed different methods to incorporate nonuniform and delayed information in state estimation techniques. In (Gopalakrishnan et al., 2011; Guo and Huang, 2015; Guo et al., 2014) have incorporated asynchronous and delayed information to stochastic estimation techniques (Kalman filter and its modifications) but these only apply to discrete systems. Other authors present deterministic estimation techniques with asynchronous and delayed measurement for hybrid systems, with a continuous model for the process and a discrete model for the effects of sensor and sampling. These observers are grouped into three types: Piecewise (Wang et al., 2015), Cascade (Khosravian et al., 2015b,a) and distributed (Zeng and Liu, 2015). This deterministic techniques can to solve the problems of estimating independently or in stages. This feature allows adaptation and extension to solving future problems in state estimation. For example, a mathematical application of a high gain observer in cascade with a predictor was proposed in (Khosravian et al., 2015a). However, a few papers show applications in state estimation in bioprocess with delayed measurements (Zhao et al., 2015).

Therefore, in this paper a cascade observer-predictor for the process of δ-endotoxins production process of *Bt* with fixed time convergence and delayed measurements is considered. The cascade observer-predictor structure is based on the observer presented in (Khosravian et al., 2015b,a) and the Sliding Mode Observer (SMO) proposed in (Sánchez et al., 2015). The proposed observer allows the exact and fixed-time reconstruction of the biomass (vegetative cells and sporulated cells) in the reactor when measurements are delayed.

In the following, the Section 2 presents the mathematical model δ-endotoxins production process of *Bt* with Delayed Measurement. The cascade observer-predictor is presented in Section 3 and presents some mathematical

preliminaries in order to introduce the basics of fixed time stability and predictor stability. The Section 4 presents simulation results of the cascade observer-predictor for the δ-endotoxins production process of *Bt*. Finally, the conclusions of this paper are exposed in the Section 5.

2. BATCH PROCESS MODEL WITH DELAYED MEASUREMENT

The model of the δ-endotoxins production of *Bt* proposed on (Amicarelli et al., 2010; Rómoli et al., 2016) is used. In this paper the block-wise form of the equations is modified to allow a straightforward design of a second order sliding mode observer. The model equations are

$$\begin{aligned}\dot{s}_p &= -\left(\frac{\mu(s_p,o_d)}{y_{x/s}}+m_s\right)x_v\\ \dot{o}_d &= K_3Q_A\left(o_d^*-o_d\right)-K_1\left(\mu(s_p,o_d)-k_e(t)\right)x_v\\ &\quad -K_2\left(x_v+x_s\right)\\ \dot{x}_v &= \left(\mu-k_s(s_p)-k_e(t)\right)x_v\\ \dot{x}_s &= k_sx_v\end{aligned} \tag{1}$$

where s_p is the substrate concentration, o_d is the dissolved oxygen concentration, x_v is the vegetative cells concentration, x_s is the sporulated cells concentration, μ is the specific growth rate, $y_{x/s}$ is the growth yield, m_s is the maintenance constant, Q_A is the airflow that enters the bio-reactor, o_d^* is the oxygen saturation concentration, K_1 is the oxygen consumption dimensionless constant by growth, K_2 is the oxygen consumption constant for maintenance, K_3 is the ventilation constant, k_s is the spore formation kinetics and $k_e(t)$ is the specific cell death rate. Furthermore, the constitutive equations for $\mu(s_p,o_d)$ (Monod-based), $k_s(s_p)$ and $k_e(t)$ are given by:

$$\begin{aligned}\mu(s_p,o_d) &= \mu_{\max}\frac{s_p}{K_s+s_p}\frac{o_d}{K_o+o_d}\\ k_s(s_p) &= k_{s,\max}\left(\frac{1}{1+e^{G_s(s_p-P_s)}}-\frac{1}{1+e^{G_s(s_{p,\mathrm{ini}}-P_s)}}\right)\\ k_e(t) &= k_{e,\max}\left(\frac{1}{1+e^{-G_e(t-P_e)}}-\frac{1}{1+e^{-G_e(t_{\mathrm{ini}}-P_e)}}\right)\end{aligned} \tag{2}$$

where $\mu_{\max}$ is the maximum specific growth rate, K_s is the substrate saturation constant, K_o is the oxygen saturation constant,$k_{s,\max}$ is the maximum spore formation, $k_{e,\max}$ is the maximum specific cell death rate, G_s is the gain constant of the sigmoid equation for spore formation rate, G_e is the gain constant of the sigmoid equation for specific cell death rate, P_s is the position constant of the sigmoid equation for spore formation rate, P_e is the position constant of the sigmoid equation for specific cell death rate, $s_{p,\mathrm{ini}}$ is the initial glucose concentration and t_{ini} is the initial fermentation time.

Assumption 2.1. It is assumed that the measurements of the outputs s_p and o_d are continuously measured with a delay time $\tau>0$. The delay τ is considered to be known and constant.

Defining $x_1=s_p$, $x_2=o_d$, $x_3=x_v$, $x_4=x_s$ and considering the Assumption 2.1, the model (1) can be written as:

$$\begin{aligned}\dot{x}_1(t) &= b_1(x_1(t),x_2(t))x_3(t)\\ \dot{x}_2(t) &= b_{21}(x_1(t),x_2(t))x_3(t)\\ &\quad +f_2(x_2(t))+b_{22}x_4(t)\\ \dot{x}_3(t) &= b_3(x_1(t),x_2(t))x_3(t)\\ \dot{x}_4(t) &= b_4(x_1(t))x_3(t)\end{aligned} \tag{3}$$

where

$$\begin{aligned}b_1(x_1(t),x_2(t)) &= -\left(\frac{\mu(x_1(t),x_2(t))}{y_{x/s}}+m_s\right)\\ f_2(x_2(t)) &= K_3Q_A\left(o_d^*-x_2(t)\right)\\ b_{21}(x_1(t),x_2(t)) &= -K_1(\mu(x_1(t),x_2(t))-k_e(t))-K_2\\ b_{22} &= -K_2\\ b_3(x_1(t),x_2(t)) &= \mu(x_1(t),x_2(t))-k_s(x_1(t))-k_e(t)\\ b_4(x_1(t)) &= k_s(x_1(t))\end{aligned} \tag{4}$$

and with the measurements

$$y(t)=\left[x_1(t-\tau)\ x_2(t-\tau)\right]^T \tag{5}$$

The block-wise form (3)-(5) allows a straightforward design of a second order sliding mode observer. The nominal parameters for the system (3) are given in Table 1.

Table 1. Nominal Parameters of the BT model.

Parameter	Values	Unit
$\mu_{\max}$	0.65	h^{-1}
$y_{x/s}$	0.37	$\mathrm{g}\cdot\mathrm{g}^{-1}$
K_s	3	$\mathrm{g}\cdot\mathrm{L}^{-1}$
K_o	1×10^{-4}	$\mathrm{g}\cdot\mathrm{L}^{-1}$
m_s	5×10^{-3}	$\mathrm{g}\cdot\mathrm{g}^{-1}\cdot\mathrm{h}^{-1}$
$k_{s,\max}$	0.5	h^{-1}
G_s	1	$\mathrm{g}\cdot\mathrm{L}^{-1}$
P_s	1	$\mathrm{g}\cdot\mathrm{L}^{-1}$
$k_{e,\max}$	0.1	h^{-1}
G_e	5	h
P_e	4.9	h
K_1	3.795×10^{-3}	dimensionless
K_2	0.729×10^{-3}	h^{-1}
K_3	2.114×10^{-3}	L^{-1}
Q_A	1320	$\mathrm{L}\cdot\mathrm{h}^{-1}$
o_d^*	0.00759	$\mathrm{g}\cdot\mathrm{L}^{-1}$
t_{ini}	0	h
$s_{p,\mathrm{ini}}$	32	$\mathrm{g}\cdot\mathrm{L}^{-1}$

3. PROPOSED SOFT SENSOR SCHEME

3.1 Observability Analysis

Let the vector $\mathcal{H}$ which contains the measured outputs of the system (3), $x_1(t-\tau)$, $x_2(t-\tau)$ and their derivatives be defined as

$$\mathcal{H}=\left[\,x_1(t-\tau)\ x_2(t-\tau)\ \dot{x}_1(t-\tau)\ \dot{x}_2(t-\tau)\,\right]^T \tag{6}$$

Similarly to the analysis presented in Sánchez et al. (2015), the observability analysis for the system (3) determines the existence of a diffeomorphism between the vector $\mathcal{H}$ and the delayed state vector $x=\left[\,x_1(t-\tau)\ x_2(t-\tau)\ x_3(t-\tau)\ x_4(t-\tau)\,\right]^T$.

The existence of this diffeomorphism can be evaluated, at least locally, by checking if the observability matrix defined as $\mathcal{O}=\frac{\partial\mathcal{H}}{\partial x(t-\tau)}$ is invertible. For the system (3), the observability matrix is calculated from (6) and is given by

$$\mathcal{O} = \begin{bmatrix} 1 & 0 & 0 & 0 \\ 0 & 1 & 0 & 0 \\ * & * & b_1(x_1(t-\tau), x_2(t-\tau)) & 0 \\ * & * & b_{21}(x_1(t-\tau), x_2(t-\tau)) & b_{22} \end{bmatrix} \quad (7)$$

where it follows that the determinant of (7) is $\det(\mathcal{O}) = b_{22} b_1(x_1(t-\tau), x_2(t-\tau))$. Therefore, this system is observable for $t \geq \tau$. However, it can be shown that $|\det(\mathcal{O})|$ achieves a very small value (about 1×10^{-9}), which compromises the numerical invertibility of the observability matrix $\mathcal{O}$ (Sánchez et al., 2015).

To overcome this numerical drawback, the following scaling transformation of the state is proposed:

$$\begin{aligned} x_{1s}(t-\tau) &= \beta_1 x_1(t-\tau) \\ x_{2s}(t-\tau) &= \beta_2 x_2(t-\tau) \end{aligned} \quad (8)$$

with β_1 and β_2 real positive constants to be defined thereafter.

Thus, using the notation $x_i^\tau = x_i(t-\tau)$ for $i = 1, \ldots, 4$, the system (3) under the scaling (8) becomes:

$$\begin{aligned} \dot{x}_{1s}^\tau &= b_1^s(x_1^\tau, x_2^\tau) x_3^\tau \\ \dot{x}_{2s}^\tau &= f_2^s(x_2^\tau) + b_{21}^s(x_1^\tau, x_2^\tau) x_3 + b_{22}^s x_4^\tau \\ \dot{x}_3^\tau &= b_3(x_1^\tau, x_2^\tau) x_3^\tau \\ \dot{x}_4^\tau &= b_4(x_1^\tau) x_3^\tau \end{aligned} \quad (9)$$

where $b_1^s(x_1^\tau, x_2^\tau) = \beta_1 b_1(x_1^\tau, x_2^\tau)$, $f_2^s(x_2^\tau) = \beta_2 f_2(x_2^\tau)$, $b_{21}^s(x_1^\tau, x_2^\tau) = \beta_2 b_{21}(x_1^\tau, x_2^\tau)$ and $b_{22}^s = \beta_2 b_{22}$.

3.2 Observer-Predictor Scheme

In this section a cascade observer-predictor scheme is represented. Based in the structure presented in Khosravian et al. (2015b), the proposed scheme is composed for a SMO and Smith predictor. A block diagram of this proposal is shown in Figure 1. In this figure the sensor block separately block process is proposed to clarify, in this paper, the problem of delay occurs in the dynamics of the sensor.

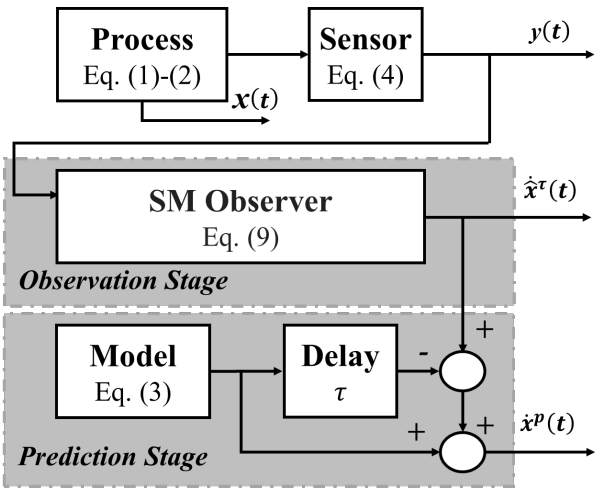

Figure 1. Observer-Predictor scheme

An explanation of the scheme of Figure 1 is as follows.

Observation Stage (SM Observer): First, from (8)-(9) the following Sliding Mode Observer is proposed in order to provide an estimation of the delayed state variables:

$$\begin{aligned} \hat{x}_1^\tau &= \beta_1^{-1} \hat{x}_{1s}^\tau \\ \hat{x}_2^\tau &= \beta_2^{-1} \hat{x}_{2s}^\tau \\ \dot{\hat{x}}_{1s}^\tau &= b_1^s(\hat{x}_1^\tau, \hat{x}_2^\tau)\hat{x}_3^\tau + k_{11}\phi_1(\tilde{x}_{1s}^\tau) \\ \dot{\hat{x}}_{2s}^\tau &= f_2^s(\hat{x}_2^\tau) + b_{21}^s(\hat{x}_1^\tau, \hat{x}_2^\tau)\hat{x}_3^\tau + b_{22}^s \hat{x}_4^\tau + k_{21}\phi_1(\tilde{x}_{2s}^\tau) \\ \dot{\hat{x}}_3^\tau &= b_3(\hat{x}_1^\tau, \hat{x}_2^\tau)\hat{x}_3^\tau + k_{12}\left[b_1^s(\hat{x}_1^\tau, \hat{x}_2^\tau)\right]^{-1}\phi_2(\tilde{x}_{1s}^\tau) \\ \dot{\hat{x}}_4^\tau &= b_4(\hat{x}_1^\tau)\hat{x}_3^\tau + k_{22}\left[b_{22}^s\right]^{-1}\phi_2(\tilde{x}_{2s}^\tau) \end{aligned} \quad (10)$$

where $\hat{x}_1^\tau$, $\hat{x}_2^\tau$, $\hat{x}_{1s}^\tau$, $\hat{x}_{2s}^\tau$, $\hat{x}_3^\tau$ and $\hat{x}_4^\tau$ are the estimates of x_1^τ, x_2^τ, x_{1s}^τ, x_{2s}^τ, x_3^τ and x_4^τ, respectively; $\tilde{x}_{1s}^\tau = x_{1s}^\tau - \hat{x}_{1s}^\tau$ and $\tilde{x}_{2s}^\tau = x_{2s}^\tau - \hat{x}_{2s}^\tau$ are the error variables; the observer input injections $\phi_1(\cdot)$ and $\phi_2(\cdot)$ are of the form $\phi_1(\cdot) = \lfloor\cdot\rceil^{\frac{1}{2}} + \theta\lfloor\cdot\rceil^{\frac{3}{2}}$ and $\phi_2(\cdot) = \frac{1}{2}\lfloor\cdot\rceil^0 + 2\theta\cdot + \frac{3}{2}\theta^2\lfloor\cdot\rceil^2$, with the parameter $\theta \geq 0$, the function $\lfloor\cdot\rceil^\alpha = |\cdot|^\alpha \text{sign}(\cdot)$ is defined for $\alpha \geq 0$, where $\text{sign}(x) = 1$ for $x > 0$, $\text{sign}(x) = -1$ for $x < 0$ and $\text{sign}(0) \in \{-1, 1\}$; and λ_1, $\lambda_2 > 0$, and k_{11}, k_{12}, k_{21}, k_{22} are the observer positive gains.

The SMO (10) was proposed in a previous paper (Sánchez et al., 2015). This observer is fixed-time convergent and also has time-invariance property, according to the definition of Khosravian et al. (2015a). A detailed stability test of observer (10) without delay in measurements has been previously published (Sánchez et al., 2015). However, the problem considered in this paper is to estimate the current state $x(t)$ when the measurements of the output are delayed such that the output measurement at time t is $y(t) = h(x(t-\tau))$ for some know constant delay $\tau \geq 0$. In this sense a prediction stage it is proposed to offset the effect of the delay in the measurement.

Prediction Stage (Model + Delay): Second, based on (Khosravian et al., 2015a) a Smith predictor compensating the delay may be considered as

$$\dot{x}^p(t) = \dot{\hat{x}}^\tau(t) + f(x^p(t)) - f(x^p(t-\tau)) \quad (11)$$

where the prediction of the current state is denoted by $x^p \in \mathbb{R}^n$ and $\hat{x}^\tau$ is the estimate x subject to delayed output measurements (5). Moreover, with the system model (3) and the known delay τ for output measurement (5), it is possible to know the dynamics of the predicted states without delay $f(x^p(t))$ and delayed $f(x^p(t-\tau))$.

The stability of the Observer-Predictor structure is such that the estimate state converge asymptotically/exponentially to the system trajectories (1)-(2), if the estimates provided by the Observer (SMO) converge asymptotically/exponentially to the delayed system state (Khosravian et al., 2015a). In this sense the definition of finite time convergent include asymptotically/exponentially convergent and fixed-time convergent of SMO (10) is a stronger form of finite time (Polyakov, 2012). In the next section the simulation results are presented.

4. SIMULATION RESULTS

This section presents the numerical simulation results of the proposed estimation structure. The simulations parameters were:

- Fundamental step size of $1 \times 10^{-5}[h]$. This time is small due to requirement of robust differentiation in the estimation scheme.
- Model parameters like shown on Table 1.

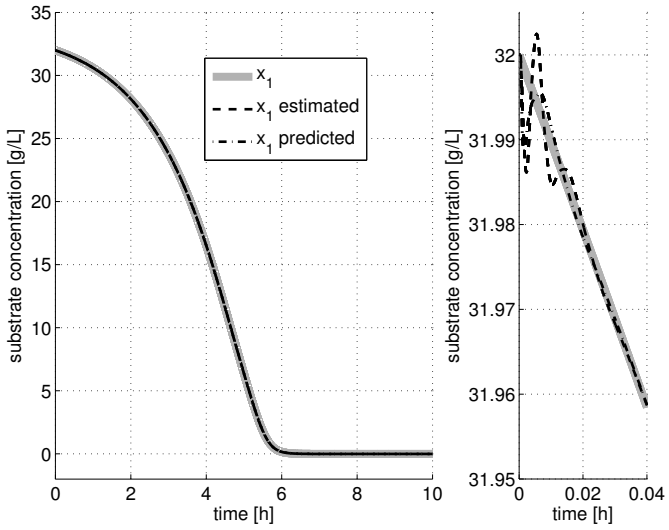

Figure 2. Substrate concentration s_p with $\tau = 5 \times 10^{-5}[h]$.

- The parameters shown in this table were taken according to the range to $20\,[\mathrm{g}\cdot\mathrm{L}^{-1}] < s_{p,\max} < 32\,[\mathrm{g}\cdot\mathrm{L}^{-1}]$.
- The value $s_{p,\max}$ corresponds to the initial condition of s_p since $\dot{s}_p \leq 0$.
- The substrate concentration $s_p = x_1$ and the dissolved oxygen concentration $o_d = x_2$ are assumed to be measured, noiseless and delayed, and the initial conditions $\hat{x}^\tau_{1s}$ and $\hat{x}^\tau_{2s}$ were taken as the scaled initial conditions of x_1 and x_2 respectively
- The delay is a known constant $\tau \geq 0$. However, since the vegetative cells concentration $x_v = x_3$ and the sporulated cells concentration $x_s = x_4$ aren't measured, the initial conditions $\hat{x}^\tau_3$ and $\hat{x}^\tau_4$ were taken different from x_3 and x_4, respectively.
- Another thing that should be noted is that with the selected values of β_1 and β_2, the minimum value of $|\det(\mathcal{O}_s)|$ is around 2.

Figures 2, 3, 4 and 5 show the comparison between the actual x, estimated $\hat{x}^\tau$ (SMO without prediction) and predicted x^p (SMO with prediction) variables corresponding to substrate concentration s_p, dissolved oxygen concentration o_d, vegetative cell concentration x_v and sporulated cells concentration x_s when the delay measurement is $\tau = 5 \times 10^{-5}[h]$. It can be noticed that, despite initial estimation error $x(0) = \left[32,\ 0.74 \times 10^{-2},\ 0.645,\ 1 \times 10{-}5\right]^T$, and $\hat{x}^\tau(0) = x^p(0) = \left[32,\ 0.74 \times 10^{-2},\ 6.45,\ 1\right]^T$ the fixed time convergence of the estimated variables is achieved.

Figures 6 and 7 show the comparison between the actual and estimated variables corresponding to x_v and x_s when measurements of s_p and o_d are delayed with $\tau = 1 \times 10^{-1}[h]$ with SMO (SMO without prediction) and predicted x^p (SMO with prediction). Based on the presented results, it can be observed a good performance of the observer-predictor scheme proposed while the only SMO does not converge. A correct and fast estimation of x_v and x_s using the cascade observer-predictor is achieved making the proposed system suitable for observer-based control applications.

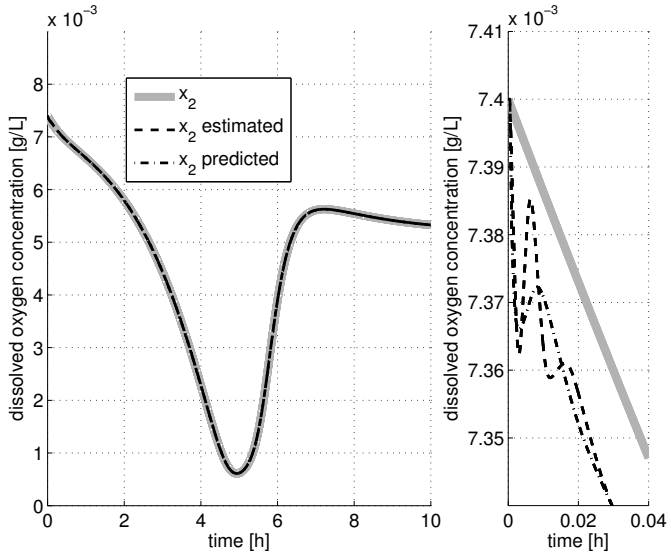

Figure 3. Dissolved oxygen concentration o_d with $\tau = 5 \times 10^{-5}[h]$.

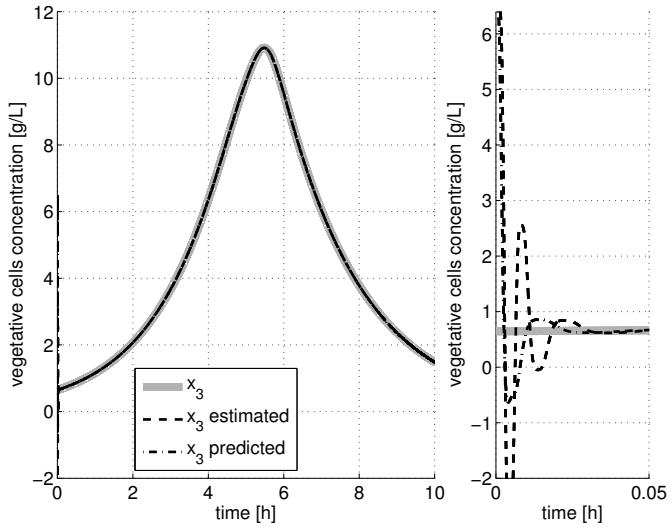

Figure 4. Vegetative cells concentration x_v with $\tau = 5 \times 10^{-5}[h]$.

Finally, Figures 8 and 9 show the effect of increased the delay measurement in s_p and o_d for estimation of x_v and x_s respectively in booth cases only SMO and SMO-predictor. The Integral Time Absolute Error (ITAE) of only SMO tends to infinity for delays in measuring higher than $\tau = 6 \times 10^{-5}[h]$, while the cascade observer-predictor scheme keep the convergence of error when the delay increase.

5. CONCLUSIONS

In this paper was presented a soft sensor to estimate the biomass in a batch bioprocess subject to delayed measurements. The soft sensor proposed is based on a cascade sliding mode observer-predictor. The observer stage is based on a class of second order sliding mode algorithms, allowing a fixed-time estimation of the biomass. The prediction stage offsets the effect of the delay in measurements. Convergence proof and numerical

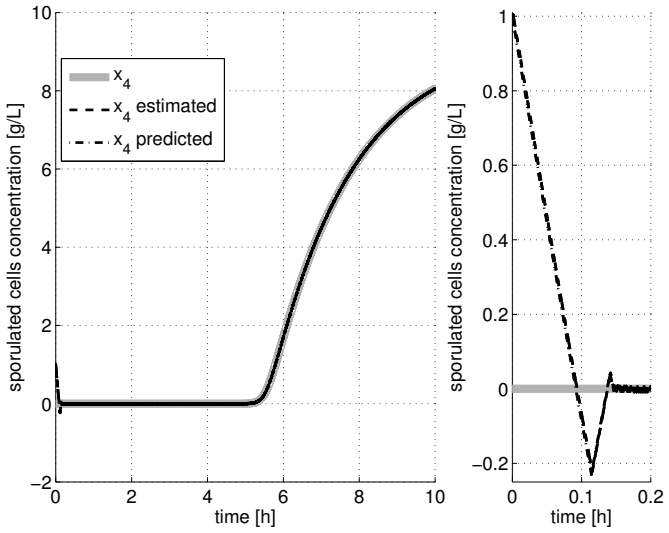

Figure 5. Sporulated cells concentration x_s with $\tau = 5 \times 10^{-5}[h]$.

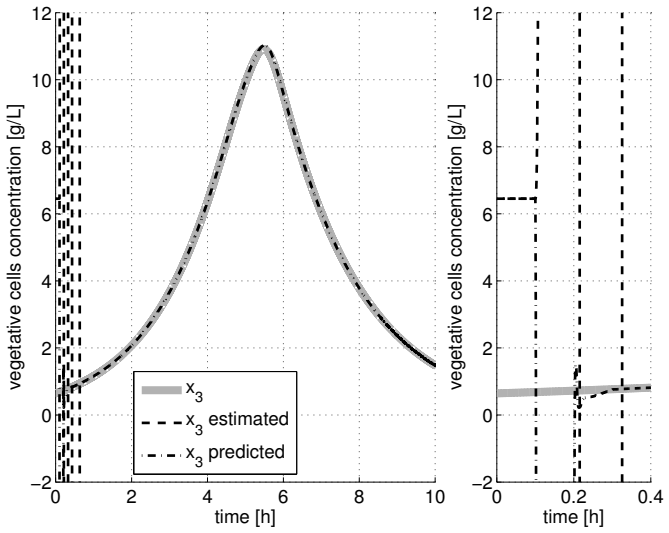

Figure 6. Vegetative cells concentration x_v with $\tau = 0.1[h]$.

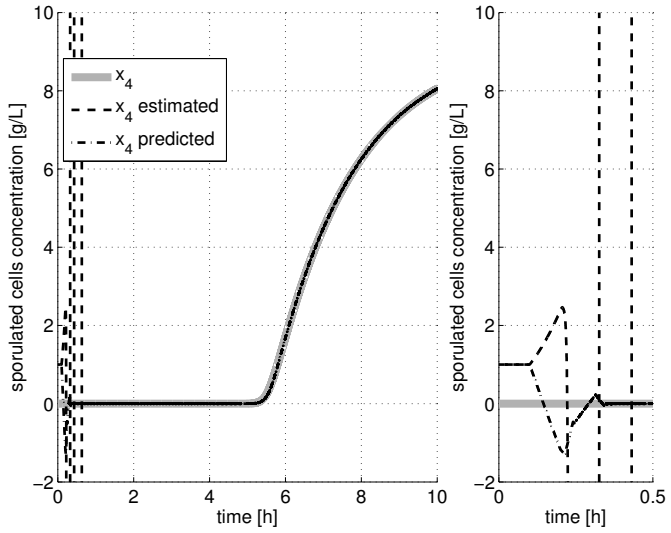

Figure 7. Sporulated cells concentration x_s with $\tau = 0.1[h]$.

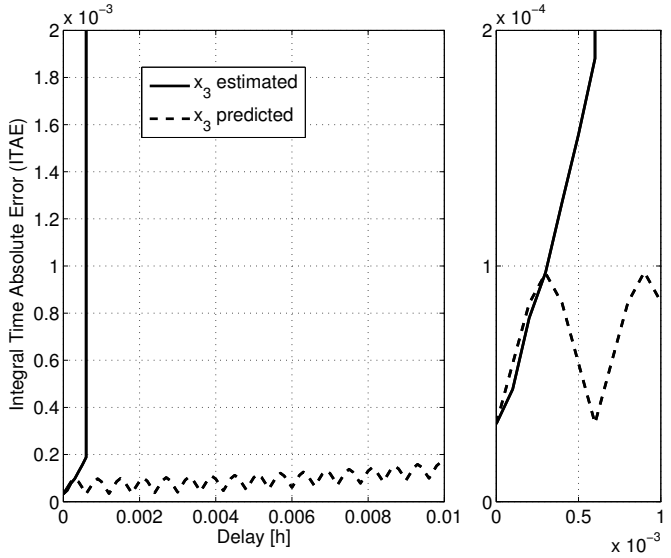

Figure 8. Delay effect to estimate x_v.

simulations shown the feasibility of the cascade observer-predictor proposed.

REFERENCES

Amicarelli, A., di Sciascio, F., Toibero, J.M., and Alvarez, H. (2010). Including Dissolved Oxygen Dynamics into the Bt delta-Endotoxins Production Process Model and its Application to Process Control. *Brazilian Journal of Chemical Engineering*, 27(1), 41–62.

Bequette, B. (2002). Behavior of a CSTR with a recirculating jacket heat transfer system. In *Proceedings of the American Control Conference.*, volume 4, 3275 – 3280.

Dochain, D. (2003). State and parameter estimation in chemical and biochemical processes: a tutorial. *Journal of Process Control*, 13(8), 801 – 818.

Gopalakrishnan, A., Kaisare, N.S., and Narasimhan, S. (2011). Incorporating delayed and infrequent measurements in Extended Kalman Filter based nonlinear state estimation. *Journal of Process Control*, 21(1), 119–129.

Guo, Y. and Huang, B. (2015). State estimation incorporating infrequent, delayed and integral measurements. *Automatica*, 58, 32–38. doi: 10.1016/j.automatica.2015.05.001.

Guo, Y., Zhao, Y., and Huang, B. (2014). Development of soft sensor by incorporating the delayed infrequent and irregular measurements. *Journal of Process Control*, 24(11), 1733–1739.

Khosravian, A., Trumpf, J., and Mahony, R. (2015a). State Estimation for Nonlinear Systems with Delayed Output Measurements. (Cdc), 6330–6335. doi: 10.1016/j.automatica.2016.01.024.

Khosravian, A., Trumpf, J., Mahony, R., and Hamel, T. (2015b). State Estimation for Invariant Systems on Lie Groups with Delayed Output. *Automatica*, 68, 254–265.

Polyakov, A. (2012). Nonlinear feedback design for fixed-time stabilization of linear control systems. *IEEE Transactions on Automatic Control*, 57(8), 2106–2110.

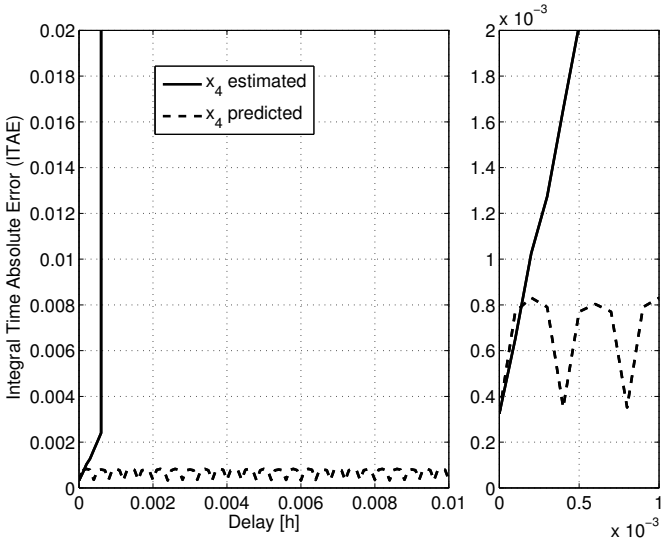

Figure 9. Delay effect to estimate x_s.

Rómoli, S., Amicarelli, A.N., Ortiz, O.A., Scaglia, G.J.E., and di Sciascio, F. (2016). Nonlinear control of the dissolved oxygen concentration integrated with a biomass estimator for production of Bacillus thuringiensis δ-endotoxins. *Computers & Chemical Engineering*, 93, 13–24. doi:10.1016/j.compchemeng.2016.05.017.

Sánchez, J.D., Isaza, J.A., Jaramillo, O., Jimenez, E., and Botero, H. (2015). A Fixed-Time Convergent Observer for Biomass in a Batch Process. In *IEEE CCAC 2015 Conference Proceedings*, volume 1, 1–4.

Walcott, B.L., Corless, M.J., and Zak, S.H. (1987). Comparative study of nonlinear state observation techniques. *Int. J. Control*, 45, 2109–2132.

Wang, H.P., Tian, Y., and Vasseur, C. (2015). Piecewise continuous hybrid systems based observer design for linear systems with variable sampling periods and delay output. *Signal Processing*, 114, 75–84. doi: 10.1016/j.sigpro.2015.01.009.

Zeng, J. and Liu, J. (2015). Distributed moving horizon state estimation: Simultaneously handling communication delays and data losses. *Systems & Control Letters*, 75, 56–68. doi:10.1016/j.sysconle.2014.11.007.

Zhao, L., Wang, J., Yu, T., Chen, K., and Liu, T. (2015). Nonlinear state estimation for fermentation process using cubature Kalman filter to incorporate delayed measurements. *Chinese Journal of Chemical Engineering*, 23(11), 1801–1810. doi:10.1016/j.cjche.2015.09.005.

Control y estimación de par en un motor Diésel con turbocompresor y recirculación de gases de escape ⋆

José Luis Mendoza-Soto * **H. Rodríguez Cortés** **
Luis Alvarez-Icaza ***

* *Universidad Nacional Autónoma de México, Av. Universidad 3000, C. P. 04510 México (e-mail: eemsj03@yahoo.com.mx).*
** *Av. Instituto Politécnico Nacional 2508, Delegación Gustavo A. Madero, San Pedro Zacatenco, 07360 Ciudad de México, D.F. (e-mail: hrodriguez@cinvestav.mx)*
*** *Instituto de Ingeniería, Universidad Nacional Autónoma de México 04510 Coyoacán D. F., México, (e-mail: alvar@pumas.iingen.unam.mx)*

Resumen: Se propone una estrategia de control para un motor diésel con turbocompresor de geometría variable basada en retroalimentación estática de los estados. La técnica utilizada permite evitar el uso de la técnica de extensión dinámica del sistema para linealización exacta. Adicionalmente se propone un estimador de par de carga. El desempeño del controlador y el estimador propuestos se verifica por medio de simulaciones en el modelo no lineal del sistema motor-turbocompresor.

Keywords: Motor Diésel, realimentación estática, inmersión e invariancia, estimación de par, turbocompresor.

1. INTRODUCCIÓN

El control de velocidad, relación aire combustible y de flujo de gases recirculados en un motor diésel incrementa la eficiencia con la que se utiliza el combustible. A diferencia de los motores a gasolina en los que se busca mantener operando al motor en una relación aire combustible (AFR) cercana a la relación estequiométrica, en los motores diésel se busca que la mezcla de combustible tenga una relación mayor a la estequiométrica. Este incremento de AFR se obtiene al incrementar la masa de aire fresco que entra a la cámara de combustión por medio de una turbina impulsada por la energía cinética de los gases de escape. La turbina de geometría variable tiene la característica de poder cambiar el ángulo de ataque de sus aspas para controlar la potencia que toma de los gases de escape. El incremento de la relación aire combustible produce un incremento en la potencia que el motor es capaz de proporcionar reduciendo la relación tamaño del motor - potencia suministrada. La desventaja de una AFR alta es que el combustible no se quema por completo, con lo que se producen emisiones contaminantes, en especial las emisiones de óxido de nitrógeno NO_x. Una forma de reducir estas emisiones es agregar filtros de emisiones a la salida del múltiple de escape. Otra forma de controlar las emisiones en un motor diésel es con la recirculación de gases de escape al utilizar una válvula entre los múltiples de admisión y de escape. Parte de los gases de escape pueden recircularse hacia el múltiple de admisión con lo que se reduce la cantidad de emisiones y se consigue precalentar el aire fresco que entra al múltiple admisión logrando una mejor combustión. La desventaja de recircular gases de escape es que se reduce la energía utilizada para mover la turbina que impulsa al compresor que alimenta de aire al múltiple de admisión, por lo tanto la relación aire combustible no es capaz de mantenerse. Adicionalmente, la potencia entregada por el motor se reduce. Por lo anterior la recirculación de gases de escape se realiza solo cuando las condiciones de potencia exigidas al motor lo requieren y por el contrario, cuando la potencia exigida al motor es baja se da prioridad a la recirculación de gases de escape.

⋆ Trabajo realizado bajo el patrocinio de CONACYT.

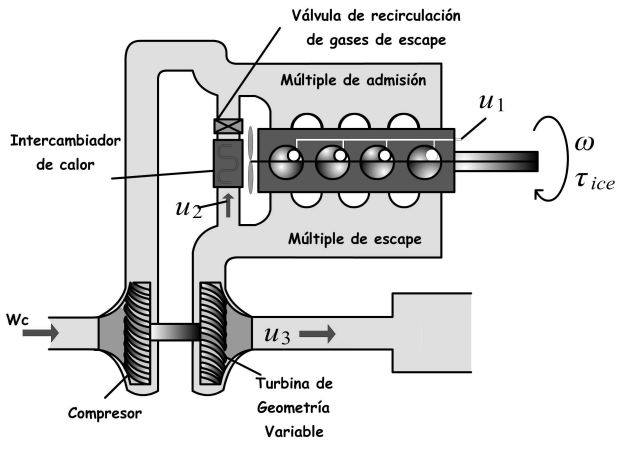

Figura 1. Esquema de un motor diesel

En la literatura aparecen estrategias para el control del sistema de alimentación de aire de motores diésel turbocargados separado del control de la velocidad.

Existen diferentes controladores para regular el aire alimentado al motor diésel por medio de un sistema turbocargador. En Jankovic et al. (2000) se emplea linealización entrada-salida y diseño de Lyapunov para la obtención de un controlador no lineal. En Nieuwstadt et al. (2000) se presentan controladores PI descentralizados con la estimación de variables como la presión. En los dos casos anteriores se presentan resultados experimentales.

En Larsen et al. (2000) se utiliza un enfoque de pasivación indirecta utilizando un par entrada-salida para estabilizar la dinámica cero del sistema y por medio de otro par entrada salida se realiza la pasivación, los autores presentan resultados en simulación. En Upadhyay et al. (2002) se diseña un controlador basado en modos deslizantes para el control de la inyección de aire, donde el desempeño del controlador se evalúa mediante simulaciones.

En Ayadi and Houcine (2004) se linealiza el modelo del turbocompresor alrededor de un punto de operación para diseñar un controlador basado en la propiedad de planitud diferencial con respecto a la salida definida por el error en la presión del múltiple de escape. Los autores presentan resultados en simulación. En Ortner and del Re (2007) se utilizó control predictivo para optimizar el sistema de aire del motor, en este artículo presentan resultados experimentales. En Plianos et al. (2007) se propone un controlador por medio del enfoque clásico de linealización por realimentación dinámica de estados.

Para realizar el control de velocidad del motor diésel en Outbib et al. (2002) se presenta un controlador no lineal por diseño de Lyapunov donde se utiliza del flujo de combustible como variable de control. En Song and Grigoriadis (2003) se controla la velocidad de un motor diesel con modelo simplificado en presencia de perturbaciones en el par de carga y con retardos de transporte. El esquema de diseño de control propuesto se basa en ganancias programadas y un enfoque de parámetros lineales variables (LPV) y desigualdades matriciales (LMI's).

En Wahlström and Nielsen (2010) se presenta una estrategia que toma en cuenta el control de la velocidad y el sistema de alimentación de aire del motor. Se utilizan controladores PID para regular directamente los valores deseados de la fracción de gases de escape recirculados (EGR) y la relación aire combustible (AFR). A diferencia de otras estrategias en donde se controlan de forma indirecta a través de la presión en los múltiples de admisión y de escape. Los autores de este trabajo proponen una función de costo para sintonizar las ganancias del controlador PID.

En Mendoza-Soto and Alvarez-Icaza (2012) se controla en conjunto la velocidad del motor diésel y el sistema de alimentación de aire utilizando una combinación de control predictivo generalizado y linealización entrada-estado. En dicho trabajo se utiliza un modelo que toma en cuenta la dinámica de velocidad y la alimentación de aire.

En Haoping et al. (2014) los autores utilizan una variación del modelo utilizado en Mendoza-Soto and Alvarez-Icaza (2012) y usan una combinación de los controladores presentados en Outbib et al. (2006) y Marcelin et al. (2009). Los autores muestran sus resultados por medio de simulaciones numéricas.

En este trabajo que se propone un controlador para regular la velocidad de un motor diésel, la relación aire combustible AFR y el flujo de gases de escape de manera simultánea con cambios en el par de carga. Además, se propone una estimador de par de carga para el motor diésel.

El controlador propuesto en este artículo se basa en el trabajo presentado en Rodriguez et al. (2006) en donde se muestra una forma alterna para linealización entrada-salida de sistemas linealizables por retroalimentación dinámica del estado.

El estimador propuesto se basa en la técnica de inmersión e invarianza, Astolfi et al. (2008). La prueba de estabilidad se realiza utilizando la aproximación lineal de la dinámica de lazo cerrado.

Este artículo se organiza como sigue. En la sección 2 se presenta una descripción del modelo de un motor diésel equipado con un turbocompresor de geometría variable. La sección 3 discute el diseño del controlador propuesto. En la sección 4 se presenta un estimador para el par de carga del motor. La sección 5 muestra los resultados obtenidos mediante simulación. Finalmente la sección 6 presenta las conclusiones de este trabajo.

2. MODELO DEL SISTEMA MOTOR-TURBOCOMPRESOR DE GEOMETRÍA VARIABLE

El modelo del sistema motor-turbocompresor que se utiliza en este artículo se obtiene de los modelos utilizados en Jankovic et al. (2000) para el control de flujo de aire y en Outbib et al. (2006) para el control de velocidad en motores de combustión interna diésel.

Al utilizar la ley de conservación de la materia en el múltiple de admisión se puede escribir

$$\frac{d}{dt}m_a = W_c - \dot{m}_{ao} \tag{1}$$

donde W_c es el flujo de aire que entra desde el compresor al múltiple de admisión y $\dot{m}_{ao}$ es el flujo de aire que se bombea dentro de la cámara de combustión. Aplicando la ley de gases ideales en el múltiple de admisión

$$m_a = \frac{p_1 V_1}{r T_1} \tag{2}$$

donde m_a es la masa de aire, r es la constante para el aire, V_1, p_1, T_1 son el volumen, la presión y la temperatura del múltiple de admisión, respectivamente. $\dot{m}_{ao}$ está dada por la expresión

$$\dot{m}_{ao} = \eta_v \left(\dot{m}_{ao}\right)_{th} \tag{3}$$

con

$$\left(\dot{m}_{ao}\right)_{th} = \frac{n V_{cy} \omega p_1}{4\pi r T_1} \tag{4}$$

donde η_v es la eficiencia volumétrica, ω es la velocidad angular del motor, V_{cy} es el volumen de cada cilindro, p_1

es la presión del múltiple de admisión y n es el número de cilindros.

La eficiencia volumétrica se considera de acuerdo a Outbib et al. (2006) de manera simplificada en forma polinomial como

$$\eta_v(\omega) = \alpha_0 + \alpha_1\omega + \alpha_2\omega^2 \tag{5}$$

con α_0, $\alpha_2 > 0$ y $\alpha_1 < 0$.

Al derivar respecto al tiempo la función (2) se obtiene la dinámica de la presión en el múltiple de admisión

$$\frac{d}{dt}p_1 = \frac{rT_1}{V_1}\left(\dot{m}_{ai} - \eta_v(\dot{m}_{ao})_{th}\right) \tag{6}$$

Por otro lado la dinámica para el eje del motor puede obtenerse a partir de la ecuación

$$\dot{\omega} = \frac{1}{J\omega}(P_i - P_L) \tag{7}$$

donde J es la inercia del motor que se asume constante, P_i es la potencia indicada que resulta de la combustión, y P_L es la potencia de carga del motor que se compone de la potencia perdida por fricción y de la potencia de freno que aparece como perturbación externa.

La potencia indicada puede calcularse como

$$P_i = \eta_i P_{th} u_1 \tag{8}$$

donde u_1 es el flujo de combustible, P_{th} es el valor calorífico neto inferior para el combustible diésel y η_i denota la eficiencia de conversión del combustible.

La eficiencia η_i puede aproximarse por una forma polinomial para fines de control como muestra Outbib et al. (2006) como

$$\eta_i = a_\lambda + b_\lambda A_{FR} + c_\lambda A_{FR}^2 \tag{9}$$

con

$$A_{FR} = \frac{\dot{m}_{ao}}{u_1} \tag{10}$$

al sustituir las ecuaciones (8) − (10) en (7) obtiene la ecuación dinámica para la velocidad. El modelo para la dinámica de velocidad presentado en Outbib et al. (2006) se puede expresar como

$$\begin{aligned}\dot{\omega} = &\frac{P_{th}a_\lambda}{J\omega}u_1 + \frac{P_{th}c_\lambda n^2 V_{cy}^2}{16JV_1^2\pi^2 u_1}\eta(\omega)_v^2\,\omega p_1^2 \\ &+ \frac{P_{th}b_\lambda}{J}\left(\frac{nV_{cy}}{4V_1\pi}\right)\eta_v(\omega)\,p_1 - \frac{1}{J}\tau_L\end{aligned} \tag{11}$$

$$\dot{p}_1 = \frac{rT_1}{V_1}W_c - \eta_v(\omega)\frac{nV_{cy}}{4V_1\pi}\omega p_1 \tag{12}$$

donde la ecuación de velocidad angular se expresa en términos del par de carga τ_L del motor.

El modelo presentado en Jankovic et al. (2000) para la alimentación de aire se obtiene aplicando la ley de gases ideales

$$p_i = \frac{rm_iT_i}{V_i},\ i = 1,2 \tag{13}$$

donde p representa la presión, T la temperatura, m la masa y el subíndice $i = 1, 2$ se refiere el múltiple de admisión y de escape, respectivamente. Se aplica la ley de conservación de la materia en los múltiples de admisión y de escape tomando en cuenta los flujos másicos que entran y salen de cada múltiple.

La dinámica de las presiones en los múltiples de admisión y de escape se obtiene al derivar las expresión (13) respecto al tiempo y aplicando la ley de conservación de la materia en cada múltiple. Se asume que la temperatura en cada múltiple cambia muy lento por lo que se considera constante.

La dinámica para el sistema turbocompresor se obtiene a partir de

$$\dot{P}_c = \frac{1}{\tau}(\eta_m P_t - P_c) \tag{14}$$

donde τ es una constante de retardo del turbcompresor, η_m es la eficiencia del turbocompresor, P_t y P_c son las potencias de la turbina y del compresor dadas por

$$P_t = W_t c_p \eta_t T_2\left(1 - \left(\frac{p_a}{p_2}\right)^\mu\right) \tag{15}$$

$$P_c = W_c c_p \frac{1}{\eta_c}T_a\left(\left(\frac{p_1}{p_a}\right)^\mu - 1\right) \tag{16}$$

con W_t el flujo a través de la turbina, η_t y η_c las eficiencias de la turbina y del compresor, respectivamente, p_a es la presión atmosférica y T_a es la temperatura ambiente. La constante $\mu = 0.285$ es la relación de calores específicos. donde u_2 y u_3 son los flujos de gases de escape recirculados y a través de la turbina, respectivamente. V_2 y p_2 son el volúmen y la presión en el múltiple de admisión, P_c es la potencia del compresor η_m es la eficiencia del turbocompresor, τ es una constante de retardo del turbocompresor, μ es la relación de calores específicos. Las constantes k_t y k_c dependen de la eficiencia de la turbina y del compresor.

El modelo de cuarto orden obtenido de las ecuaciones (11) − (16) es

$$\dot{\omega} = k_1\frac{u_1}{\omega} + k_2\eta_v^2(\omega)\frac{\omega p_1^2}{u_1} + k_3 p_1\eta_v(\omega) - k_4\tau_L \tag{17}$$

$$\dot{p}_1 = k_5\left(k_c\frac{P_c}{\left(\frac{p_1}{p_a}\right)^\mu - 1} + u_2 - k_s p_1\right) \tag{18}$$

$$\dot{p}_2 = k_6(k_s p_1 + u_1 - u_2 - u_3) \tag{19}$$

$$\dot{P}_c = -k_7 P_c + k_8\left(1 - \left(\frac{p_a}{p_2}\right)^\mu\right)u_3 \tag{20}$$

donde $k_s(\omega) = k_e\eta_v(\omega)\omega$ y las diferentes constantes se agrupan como sigue

$$k_1 = \frac{P_{th}a_\lambda}{J} \quad k_2 = \frac{P_{th}c_\lambda n^2 V_{cy}^2}{16JV_1^2\pi^2} \quad k_3 = \frac{P_{th}b_\lambda nV_{cy}}{4JV_1\pi}$$
$$k_4 = \frac{1}{J} \qquad k_5 = \frac{rT_1}{V_1} \qquad k_6 = \frac{rT_2}{V_2}$$
$$k_7 = \frac{1}{\tau} \qquad k_8 = \frac{1}{\tau}\eta_m k_t \qquad k_e = \frac{nV_{cy}}{4\pi rT_1}$$

El espacio de configuración de los estados del sistema dinámico (17) − (20) es el conjunto abierto

$$\Omega = \left\{ \omega > 0, \frac{p_1}{p_a} > 1, \frac{p_2}{p_a} > 1, P_c > 0 \right\} \quad (21)$$

El objetivo del controlador es regular la relación aire-combustible A_{FR}, la fracción de gases de escape recirculados E_{GR} y la velocidad angular del motor a valores de operación deseados. Las señales de control deseadas que producen los valores de $\overline{A_{FR}}$ y $\overline{E_{GR}}$ deseados se obtienen por medio de

$$\bar{u}_2 = \Gamma_1 \Gamma_2 \bar{u}_1 \quad (22)$$

$$\bar{u}_3 = (\Gamma_1 + 1)\, \bar{u}_1 \quad (23)$$

$$\Gamma_1 = \frac{\left(\Gamma_{1a} + \sqrt{{\Gamma_{1a}}^2 + 4(1 - \overline{E_{GR}})\overline{A_{FR}}} \right)}{2} \quad (24)$$

$$\Gamma_{1a} = \overline{A_{FR}}(1 - \overline{E_{GR}}) + 15.6\overline{E_{GR}} - 1$$

$$\Gamma_2 = \frac{\overline{E_{GR}}}{1 - \overline{E_{GR}}} \quad (25)$$

Dada una velocidad angular $\bar{\omega}$ deseada, un par de carga τ_L , los puntos de equilibrio del sistema (17) − (20) y las ecuaciones (22) − (25) se obtiene el flujo de combustible y el valor de las variables de estado que producen $\overline{A_{FR}}$ y $\overline{E_{GR}}$ como

$$\bar{u}_1 = \frac{k_e^2 k_4 \bar{\omega} \tau_L}{k_1 k_e^2 + k_2 \left(\Gamma_1 \Gamma_2 + \Gamma_1\right)^2 + k_3 k_e \left(\Gamma_1 \Gamma_2 + \Gamma_1\right)} \quad (26)$$

$$\bar{p}_1 = \frac{-\bar{u}_1 + \bar{u}_2 + \bar{u}_3}{k_e \eta_v(\bar{\omega})\, \bar{\omega}} \quad (27)$$

$$\bar{p}_2 = p_a \left(1 - \frac{k_7}{k_8 \bar{u}_3} \bar{P}_c \right)^{-\frac{1}{\mu}} \quad (28)$$

$$\bar{P}_c = \frac{(-\bar{u}_2 + k_e \eta_v(\bar{\omega})\, \bar{\omega} \bar{p}_1)}{k_c} \left(\left(\frac{\bar{p}_1}{p_a} \right)^{\mu} - 1 \right) \quad (29)$$

donde los términos con barra superior representan los valores de referencia para cada una de las variables.

3. FORMULACIÓN DEL CONTROL

El sistema dinámico dado por las ecuaciones (17) − (20) es linealizable por retroalimentación dinámica del estado Mendoza-Soto and Alvarez-Icaza (2012).

El método de control que se presenta en Rodriguez et al. (2006) es un alternativa para controlar por retroalimentación estática en sistemas que son linealizables entrada-salida utilizando retroalimentación dinámica del estado. Entonces, de acuerdo a Rodriguez et al. (2006) existe una ley de control de realimentación de estados estática linealizante entrada-salida para el sistema dinámico (17) − (20).

Para el desarrollo del controlador por retroalimentación estática se toman como salidas

$$y_1 = \omega \quad (30)$$

$$y_2 = p_1 \quad (31)$$

$$y_3 = P_c + \frac{k_8}{k_6} p_2 - \frac{k_8}{k_6} \frac{p_a}{1 - \mu} \left(\frac{p_2}{p_a} \right)^{1-\mu} \quad (32)$$

donde la salida y_3 se toma como se propone en Marcelin et al. (2009).

Proponiendo las señales de salida en términos de las señales de error

$$\tilde{y}_1 = y_1 - \bar{y}_1 \quad (33)$$

$$\tilde{y}_2 = y_2 - \bar{y}_2 \quad (34)$$

$$\tilde{y}_3 = y_3 - \bar{y}_3 \quad (35)$$

Al derivar respecto al tiempo la ecuación (33) y considerando que las señales de referencia $\bar{y}$ son constantes para el caso de regulación se obtiene

$$\dot{\tilde{y}}_1 = q_1(\omega)\, u_1 + q_2(\omega, p_1) + \frac{q_3(\omega, p_1)}{u_1} \quad (36)$$

donde

$$q_1(\omega) = \frac{k_1}{\omega} \quad (37)$$

$$q_2(\omega, p_1) = (k_3 p_1 \eta_v(\omega) - k_4 \tau_L) \quad (38)$$

$$q_3(\omega, p_1) = k_2 \eta_v^2(\omega)\, \omega p_1^2 \quad (39)$$

para el proceso de realimentación estática como se utiliza en Outbib et al. (2006) y como se propone en Rodriguez et al. (2006) el control u_1 puede proponerse de tal forma que la estructura de lazo cerrado resulta con una estructura lineal en términos de una ganancia K_1 entonces

$$\dot{\tilde{y}}_1 = q_1(\omega)\, u_1 + q_2(\omega, p_1) + \frac{q_3(\omega, p_1)}{u_1} = -K_1 \tilde{y}_1 \quad (40)$$

de donde resulta la señal de control

$$u_1 = \frac{-(q_2 + K_1 \tilde{y}_1) + \sqrt{(q_2 + K_1 \tilde{y}_1)^2 - 4 q_1 q_3}}{2 q_1} \quad (41)$$

con $K_1 > 0$.

Para el diseño de la señal de control u_2 se toma la ecuación (34) y se obtiene la primera derivada respecto al tiempo

$$\dot{\tilde{y}}_2 = k_5 \left(k_c \frac{P_c}{\left(\frac{p_1}{p_a} \right)^{\mu} - 1} + u_2 - k_s p_1 \right) \quad (42)$$

definiendo la dinámica

$$\dot{\tilde{y}}_2 = k_5 k_c \frac{P_c}{\left(\frac{p_1}{p_a} \right)^{\mu} - 1} + k_5 u_2 - k_5 k_s p_1 = -K_2 \tilde{y}_2 \quad (43)$$

entonces se puede proponer la señal u_2 como

$$u_2 = -\frac{K_2}{k_5} \tilde{y}_2 - k_c \frac{P_c}{\left(\frac{p_1}{p_a} \right)^{\mu} - 1} + k_s p_1 \quad (44)$$

con $K_2 > 0$.

La señal de control u_3 se diseña a partir de la ecuación (35). Al derivar la salida $\tilde{y}_3$ una vez respecto al tiempo resulta

$$\dot{\tilde{y}}_3 = k_8 \left(1 - \frac{1}{\left(\frac{p_2}{p_a} \right)^{\mu}} \right) (k_s p_1 + u_1 - u_2) - k_7 P_c \quad (45)$$

que no depende de la señal de control u_3 por lo que se requiere derivar nuevamente respecto al tiempo para obtener

$$\ddot{\tilde{y}}_2 = \varphi_1 + \varphi_2 + \varphi_3 - \varphi_4 u_3 \tag{46}$$

con

$$\varphi_1 = k_8 \left(1 - \frac{1}{\left(\frac{p_2}{p_a}\right)^{\mu}}\right)\left(-\dot{u}_2 + \dot{u}_1 + p_1\dot{k}_s + k_s\dot{p}_1\right) \tag{47}$$

$$\varphi_2 = \frac{\mu k_8 k_6}{p_a\left(\frac{p_2}{p_a}\right)^{\mu+1}}\left(u_1 - u_2 + k_s p_1\right)^2 \tag{48}$$

$$\varphi_3 = k_7^2 P_c \tag{49}$$

$$\varphi_4 = \frac{\mu k_8 k_6}{p_a\left(\frac{p_2}{p_a}\right)^{\mu+1}}\left(u_1 - u_2 + k_s p_1\right) + k_7 k_8\left(1 - \left(\frac{p_a}{p_2}\right)^{\mu}\right) \tag{50}$$

entonces se puede proponer la señal de control u_3 de forma que la dinámica de $\tilde{y}_3$ sea asintóticamente estable de acuerdo a

$$\ddot{\tilde{y}}_3 = \varphi_1 + \varphi_2 + \varphi_3 - \varphi_4 u_3 = -2K_3\dot{\tilde{y}}_3 - K_3^2\tilde{y}_3 \tag{51}$$

de donde resulta

$$u_3 = \frac{2K_3\dot{\tilde{y}}_3 + K_3^2\tilde{y}_3 + \varphi_1 + \varphi_2 + \varphi_3}{\varphi_4} \tag{52}$$

con $K_3 > 0$.

En este punto es posible expresar el resultado principal de este artículo.

Proposición 1: Considere el sistema dinámico (17) − (20) en lazo cerrado con las leyes de control definidas en (41), (44) y (52). Entonces existen ganancias K_1, K_2 y K_3 tales que la dinámica en lazo cerrado es asintóticamente estable en el conjunto abierto (21).

Demostración : En términos de las coordenadas de error en la salida la dinámica en lazo cerrado puede expresarse por las ecuaciones siguientes

$$\dot{\tilde{y}}_1 + K_1\tilde{y}_1 = 0 \tag{53}$$

$$\dot{\tilde{y}}_2 + K_2\tilde{y}_2 = 0 \tag{54}$$

$$\ddot{\tilde{y}}_3 + 2K_3\dot{\tilde{y}}_3 + K_3^2\tilde{y}_3 = 0 \tag{55}$$

donde es evidente que con $K_1 > 0$, $K_2 > 0$ y $K_3 > 0$ se obtiene un sistema en lazo cerrado asintóticamente estable en el conjunto abierto (21).

4. ESTIMACIÓN DEL PAR DE CARGA

Se define el error de estimación de par de carga como sigue

$$z = k_4\tau_L - k_4\hat{\tau}_L + \beta(\omega) \tag{56}$$

donde $k_4\hat{\tau}_L + \beta(\omega)$ es el valor estimado del par de carga y $\beta(\omega)$ es una función de la velocidad. De acuerdo a la técnica de inmersión e invariancia, el objetivo es ahora garantizar que el error de par converja a cero. Al obtener la derivada de z respecto al tiempo

$$\dot{z} = -k_4\dot{\hat{\tau}}_L + \frac{d\beta(\omega)}{d\omega}\dot{\omega} \tag{57}$$

sustituyendo (17) en (57)

$$\dot{z} = -k_4\dot{\hat{\tau}}_L + \frac{d\beta(\omega)}{d\omega}\left(k_1\frac{u_1}{\omega} + k_2\eta_v^2(\omega)\frac{\omega p_1^2}{u_1} + k_3 p_1\eta_v(\omega) - k_4\tau_L\right) \tag{58}$$

entonces se puede definir una dinámica para $\dot{\hat{\tau}}_L$ utilizando señales medibles como

$$\dot{\hat{\tau}}_L = \frac{1}{k_4}\frac{d\beta(\omega)}{d\omega}\left(k_1\frac{u_1}{\omega} + k_2\eta_v^2(\omega)\frac{\omega p_1^2}{u_1} + k_3 p_1\eta_v(\omega) - k_4\hat{\tau}_L + \beta(\omega)\right) \tag{59}$$

Sustituyendo (59) en (58) se obtiene

$$\dot{z} = -\frac{d\beta(\omega)}{d\omega}\left(k_4\left(\tau_L - \hat{\tau}_L\right) + \beta(\omega)\right) \tag{60}$$

al sustituir la ecuación (56) en (60) se obtiene la dinámica para z

$$\dot{z} = -\frac{d\beta(\omega)}{d\omega}z \tag{61}$$

Al definir

$$\frac{d\beta(\omega)}{d\omega} = \Gamma \tag{62}$$

con $\Gamma > 0$ se obtiene una dinámica asintóticamente estable para z

$$\dot{z} = -\Gamma z \tag{63}$$

entonces el par de carga del motor puede obtenerse a partir de

$$\tau_L = \frac{k_4\hat{\tau}_L - \beta(\omega)}{k_4} \tag{64}$$

donde $\beta(\omega) = \Gamma\omega$, y $\hat{\tau}_L$ puede calcularse al resolver la ecuación (59).

Al sustituir el par de carga en la dinámica del motor en lazo cerrado con el controlador definido por (41), (44) y (52) por el par de carga estimado se obtiene la forma siguiente

$$\dot{\mathbf{x}} = \mathbf{f}(\mathbf{x}, \beta(\mathbf{x}, z)) \tag{65}$$

con $\mathbf{x} = \begin{bmatrix}\omega & p_1 & p_2 & P_c\end{bmatrix}^T$. La aproximación lineal de (65) y (61) alrededor del punto de equilibrio $\bar{\mathbf{x}} = \begin{bmatrix}\bar{\omega} & \bar{p}_1 & \bar{p}_2 & \bar{P}_c\end{bmatrix}^T$ y $z = 0$ queda como

$$\dot{\mathbf{x}}_\delta = A\mathbf{x}_\delta + Bz_\delta \tag{66}$$

$$\dot{z}_\delta = -\Gamma z_\delta \tag{67}$$

Note que el sistema (66) − (67) es un sistema interconectado con Bz_δ como el término de interconexión. Dado que A es Hurwitz es posible utilizar la proposición 4.10 de R. Sepulchre and Kokotovic (1997) para concluir estabilidad asintótica local.

5. RESULTADOS EN SIMULACIÓN

Para la simulación de los resultados se utilizó Matlab. La simulación del controlador se realizó tomando un tiempo de muestreo de 1 ms y asignando valores de ganancia $K_1 = 1$, $K_2 = 1.5$, $K_3 = 3$ y $\Gamma = 10$.

En la figura (2) se muestra en línea continua la evolución de los estados del motor aplicando el controlador propuesto y en línea punteada el valor de la referencia para cada estado. Se dan cambios escalón cada 5 segundos en el par de carga aplicado al motor para observar el desempeño del control. El par de carga aplicado es inicialmente de 1000 Nm, después de 5 segundos se incrementa a 1400 Nm y a los 10 segundos se reduce a a 1300 Nm. En esta prueba se ajusta el valor de $E_{GR} = 0$ y la relación $A_{FR} = 21$ y se da una referencia de 1000 rpm al estado de velocidad del motor. La figura (3) muestra las señales de control

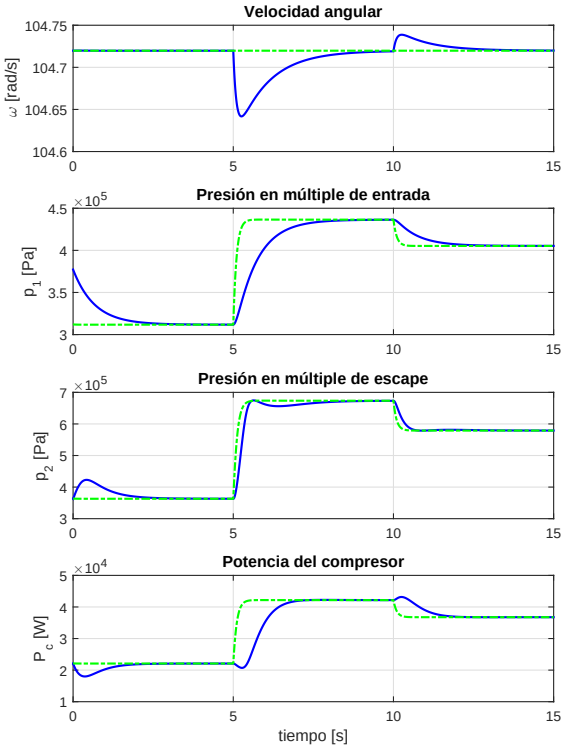

Figura 2. Estados con cambios en el par de carga

obtenidas. Se observan etapas transitorias al momento de aplicar cambios del par de carga. También se observa el comportamiento de la relación aire combustible ante los cambios en la carga del motor. En todos los casos las señales llegan a su valor de referencia. En la figura (4) se muestra el comportamiento del estimador de par de carga propuesto en la sección IV. El par de carga estimado $\hat{\tau}_m$ se presenta en línea continua y el par de carga τ_m a estimar en línea discontinua. Se observa que el valor estimado llega al valor real para diferentes cambios escalón en el par de carga.

La figura (6) se muestra el comportamiento de los estados para cambios en la fracción de gases de escape recirculados

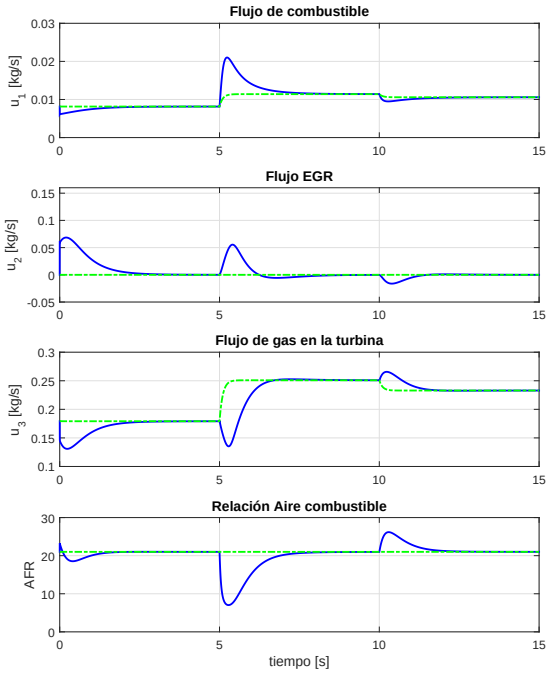

Figura 3. Señales de control con cambios de par

Figura 4. Par de carga estimado

E_{GR}. En esta prueba se ha mantenido constante el par de carga en 1000 Nm y una velocidad de referencia constante en 1000 rpm, mientras se aplican cambios en la fracción de gases de escape recirculados de 0, 0.1 y 0.2 cada 5 segundos. Se observa que al incrementar la cantidad de gases de escape recirculados la potencia en el compresor empieza a reducirse debido a la disminución de los gases que impulsan la turbina. En la figura (5) se observa el comportamiento de las señales de control al aplicar cambios en el flujo E_{GR}. También se observa que la relación aire combustible no puede mantenerse en condiciones de recirculación de gases de escape. La relación A_{FR} solo puede mantenerse constante si se incrementa el flujo de gases de escape que impulsa la turbina, lo que ocurre cuando no hay gases de escape recirculados al múltiple de admisión.

6. CONCLUSIÓN

En este trabajo se ha propuesto un controlador para un motor Diésel con sistema turbocompresor y de recirculación de gases de escape utilizando una estrategia de re-

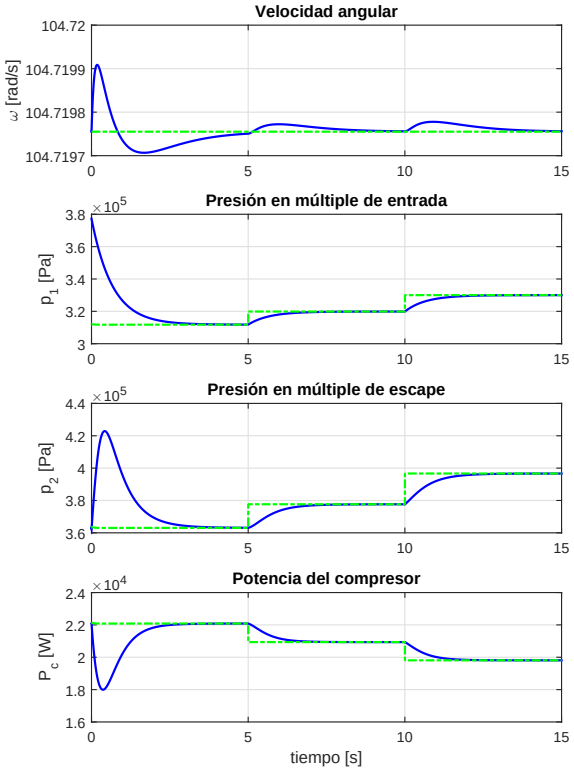

Figura 5. Estados con cambios de E_{GR}

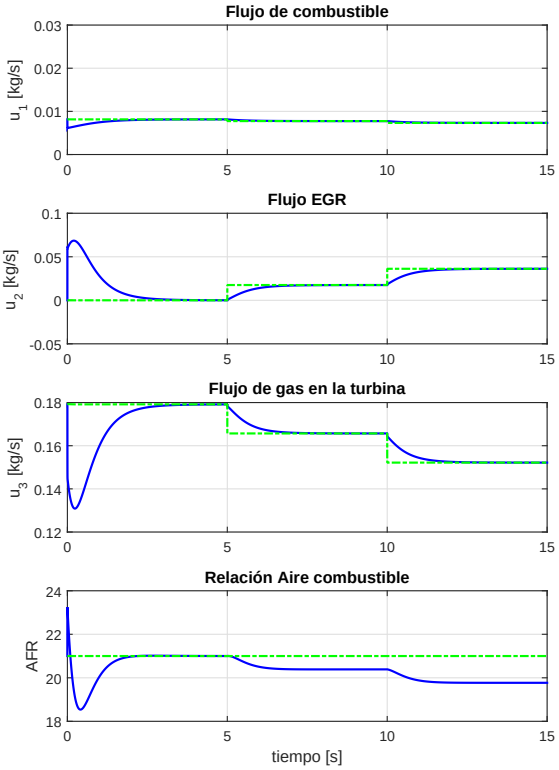

Figura 6. Señales de control y relación aire combustible

troalimentación estática de los estados. Adicionalmente se ha propuesto un estimador de par de carga por el método de inmersión e invarianza. Las simulaciones muestran el desempeño del controlador propuesto funcionando en lazo cerrado con el estimador de par. El esquema de control utilizado muestra un buen desempeño para alcanzar las referencias cuando se presentan cambios de tipo escalón en el par o cambios en las señales de referencia.

$p_{th} = 43\ MJ$	$T_2 = 550\ K$	$\tau = 0.15\ s$
$p_a = 100000\ Pa$	$V_{cy} = 0.0018\ m^3$	$n = 5$
$V_2 = 0.001\ m^3$	$V_1 = 0.005\ m^3$	$\eta_t = 0.9$
$b_\lambda = 0.01543$	$c_\lambda = -0.00014073$	$\mu = 0.285$
$a_\lambda = 0.0371$	$J = 4000\ kg \cdot m^2$	$\eta_c = 0.9$
$c_p = 1012.2 \frac{J}{kgK}$	$r = 287 \frac{J}{kgK}$	$\eta_m = 0.8$
$\alpha_0 = 7.73 \times 10^{-1}$	$\alpha_1 = -1.54 \times 10^{-3}$	
$\alpha_2 = 2.49 \times 10^{-6}$	$T_1 = T_a = 300\ K$	

Cuadro 1. Parámetros del motor diésel.

REFERENCIAS

Astolfi, A., Karagiannis, D., and Ortega, R. (2008). *Nonlinear and Adaptive Control with Applications*. Springer-Verlag., London.

Ayadi, Mounir. Langlois, N. and Houcine, C. (2004). Polynomial control of nonlinear turbocharged diesel engine model. In *Proceedings of the IEEE Conference on Industrial Technology (ICIT)*, 1384–1389. Hammamet, Tunisia.

Haoping, W., Yang, T., Jerome, B., and Ahmed, E.H. (2014). Modeling and dynamical feedback control of a vehicle diesel engine speed and air path. *Journal of Dynamic Systems, Measurement, and Control*, 136, 1–7.

Jankovic, M., Jankovic, M., and Kolmanovsky (2000). Constructive Lyapunov control design for turbocharged diesel engines. *IEEE Transactions on Control Systems Technology*, 8(2), 288–299.

Larsen, M., Jankovic, M., and Kokotovic, P.V. (2000). Indirect passivation design for a diesel engine model. In *Proceedings of the 2000 IEEE International Conference on Control Applications*, 25–27. Anchorage, Alaska USA.

Marcelin, D., Nicolas, L., and Houcine, C. (2009). Dynamic feedback linearization applied to asymptotic tracking: generalization about the turbocharged diesel engine outputs choice. In *American Control Conference*, 3458–3463. St. Louis, MO, USA.

Mendoza-Soto, J.L. and Alvarez-Icaza, L. (2012). Generalized predictive control of a turbocharged diesel engine. In *American Control Conference*, 5725–5730. Montréal, Canada.

Nieuwstadt, M., Kolmanovsky, I., Stefanopoulou, and A. Jankovic, M. (2000). EGR-VGT control schemes: experimental comparison for a high-speed diesel engine. *IEEE Control Systems Magazine*, 20(3), 63–79.

Ortner, P. and del Re, L. (2007). Predictive control of a diesel engine air path. *IEEE Transactions on Control Systems Technology*, 15(3), 449–456.

Outbib, R., Dovifaaz, X., Rachid, A., and Ouladsine, M. (2002). Speed control of a diesel engine: A nonlinear appoach. In *Proceedings of the 2002 American Control Conference*, 3293–3294. Anchorage, Alaska USA.

Outbib, R., X., D., A., R., and M., O. (2006). A theoretical control strategy for a diesel engine. *Journal of Dynamic Systems, Measurement, and Control*, 128, 453–457.

Plianos, A., Achir, A., Stobart, R., Langlois, N., and Chafouk, H. (2007). Dynamic feedback linearization based control synthesis of the turbocharged diesel engine. In *Proceedings of the 2007 American Control Conference*, 4407–4412. New York, USA.

R. Sepulchre, M.J. and Kokotovic, P.V. (1997). *Constructive Nonlinear Control*. Springer-Verlag, London.

Rodriguez, H., Astolfi, A., and Ortega, R. (2006). On the construction of static stabilizers and static output trackers for dynamically linearizable systems, related results and applications. *International Journal of Control*, 79, 1523–1537.

Song, Q. and Grigoriadis, K.M. (2003). Diesel engine speed regulation using linear parameter varying control. In *IEEE Proceedings of the American Control Conference*, 779–784. Denver, Colorado.

Upadhyay, D., Utkin, V.I., and Giorgio, R. (2002). Multivariable control design for intake flow regulation of a diesel engine using sliding mode. In *Proceedings of the 15th Triennial World Congress IFAC*, 1389–1394. Barcelona, Spain.

Wahlström, Johan. Eriksson, L. and Nielsen, L. (2010). Egr-vgt control and tuning for pumping work minimization and emission control. *IEEE Transactions on Control Systems Technology*, 18, 993–1003.

Fixed-Time Convergent Unknown Input Observer for LTI Systems

Juan G. Rueda-Escobedo * **Jaime A. Moreno** *
Pablo Oliva-Fonseca *

* *Eléctrica y Computación, Instituto de Ingeniería, Universidad Nacional Autónoma de México, 04510 México D.F., México (e-mails: JRuedaE@iingen.unam.mx; JMorenoP@ii.unam.mx; POlivaF@iingen.unam.mx).*

Abstract: In this work, a family of non linear observers for linear time invariant systems is presented. The algorithms have the capability of providing an estimate of the system internal state in finite time. The observer converges in fixed-time since it exists an upper bound for the convergence time which is independent of the initial error. This note also provides a methodology to apply the proposed algorithms when unknown inputs are present, and how to retain its properties. Simulation examples are provided to contrast the behavior of the nonlinear observer with a classic Luenberger one.

Keywords: Observers, Estimation Algorithms, Finite-Time, Fixed-Time

1. INTRODUCTION

In the field of automatic control, the problem of reconstructing unmeasured variables is almost always present. This task is handled by observers. The classical methods to design this class of algorithms only provide strategies that asymptotically reconstruct the desired variables. However, in recent years, algorithms capable of estimating the internal state of linear time invariant (LTI) systems, and some nonlinear ones, have appeared (Raff and Allgöwer, 2008; Menard et al., 2010; Pin et al., 2013). Nevertheless, these methods required to put the analyzed system in specific coordinates to handle the observer design. An upgrade with respect to finite-time convergent observers are the fixed-time convergent ones (Cruz-Zavala et al., 2011, 2012; Polyakov, 2012). Fix-time means that the convergence time can be upper bounded with independence of the initial error. These algorithms do not only give a theoretical improvement with respect to asymptotic convergence, but also help to separate the effect of the observer from the controller when the last is nonlinear (Cruz-Zavala et al., 2011; Atassi and Khalil, 2000).

Recently, the authors presented in (Rueda-Escobedo et al., 2016) a discontinuous finite-time convergent observer for LTI systems. In this note, the previous result is extended to include continuous versions of the algorithm. This new version not only keeps the finite-time convergence, but provides fixed-time convergence. In contrast to other available methods, the design of the proposed algorithms can be done in the original system's coordinates, and the gains can be chosen using the same techniques required for the design of linear observers.

In real systems it is not uncommon to have uncertainties and perturbations, which can be modeled as unknown inputs. In this situation it is desirable to have an observer capable of reconstructing the internal state of the system despite the presence of the unknown inputs. Commonly in the literature, this kind of observers are called *unknown input observers* (UIO). Sufficient and necessary conditions for the existence of an UIO for a given LTI system are already known, and can be found in (Hautus, 1983). This kind of observers have found application especially in the field of fault detection (Chen and Saif, 2006; Hwang et al., 2010; Yin et al., 2014). Given the importance of this topic, this work also provides a methodology to apply the proposed algorithm to the observation problem in the presence of unknown inputs. It has to be said that under some stronger assumptions than those needed for the existence of an UIO, the proposed observer retains the fixed-time convergence.

The paper organization is as follows; in Section 2 the observation algorithm is presented together with its convergence analysis and properties. In Section 3, a methodology for design UIO for linear systems is explained; this methodology can be used with any observer, but is intended to be used with the one proposed in this work. Finally, in Section 4, the design of the proposed algorithm is illustrated, step by step, for a perturbed linear system.

A general LTI system is considered. The system is described by

$$\begin{aligned} \dot{x} &= A\,x + B\,u(t), \\ y(t) &= C\,x, \end{aligned} \tag{1}$$

where $x \in \mathbb{R}^n$, $u(t) \in \mathbb{R}^r$, and $y(t) \in \mathbb{R}^q$. Matrices A, B, and C have appropriate dimensions an are assumed to be known. The only available signals are the input $u(t)$ and the output $y(t)$. Additionally, it is required that the pair (A, C) is observable in order to be able of design an observer with arbitrary speed of convergence.

Let $\hat{x}(t)$ be the estimate of $x(t)$. Under the previous assumptions, the following is an observer for system (1):

$$\begin{aligned} \dot{\hat{x}} =& A\,\hat{x} + B\,u(t) - L(C\hat{x} - y(t)) \\ & - P^{-1}N(t)\sum_{i=1}^{2} k_i \lceil N(t)\hat{x} - \psi(t) \rfloor^{p_i}. \end{aligned} \tag{2}$$

The symbol $\lceil\cdot\rfloor^p$ takes the signed p power of its argument in the scalar case and for vectors it is understood element-wise, that is, $\lceil\cdot\rfloor^p = |\cdot|^p \mathrm{sign}(\cdot)$. The exponents p_i have to be chosen such that $p_1 \in [0, 1)$ and $p_2 > 1$, and the gains k_i need only to be positive. Matrix L is designed to make $A - LC$ Hurwitz, and matrix P is computed from the algebraic Lyapunov equation

$$\big(A - LC\big)^\top P + P\big(A - LC\big) = -R,\ R = R^\top > 0.$$

Matrix $N(t)$ and signal $\psi(t)$ are related by the equality $\psi(t) = N(t)x(t)$, and are computed as

$$\begin{aligned} \frac{\mathrm{d}}{\mathrm{d}t}N =& -\big(A + KC\big)^\top N - N\big(A + KC\big) + C^\top C, \\ N(t_0) =& 0, \end{aligned}$$

$$\begin{aligned} \frac{\mathrm{d}}{\mathrm{d}t}\psi =& -(A + KC)^\top \psi + C^\top y(t) \\ & - N(t)\big(Ky(t) - Bu(t)\big), \\ \psi(t_0) =& 0. \end{aligned}$$

Here, the matrix K has to be proposed such that the matrix $A + KC$ is anti-Hurwitz. Taking the dynamics of $N(t)$, and the derivative of $N(t)x(t)$, the dynamics for $\psi(t)$ is gotten.

Notice that $N(t)$ is the constructibility gramian (Hespanha, 2009, Chap. 15) of system $\dot{\chi} = (A + KC)\chi$ with output $C\chi$. If the pair (A, C) is observable, so is the pair $(A + KC, C)$, since the term $KC\chi$ represents an output injection. Then $N(t)$ acquires full rank, and becomes bounded from below, i.e. $N(t) \geq \alpha(t^\star)\mathbb{I}$ for $t \geq t^\star > t_0$. Since K is chosen to make the matrix $A + KC$ anti-Hurwitz, $N(t)$ will remain bounded (Abou-Kandil et al., 2003, Chap. 1).

The property $\psi(t) = N(t)x(t)$, and the full rank of $N(t)$, makes the nonlinear terms in (2) a direct injection of the estimation error:

$$\lceil N(t)\hat{x} - \psi(t) \rfloor^{p_i} = \lceil N(t)\big(\hat{x} - x\big) \rfloor^{p_i}.$$

Also notice that this terms are only zero if the estimation error is zero, while the linear term in the algorithm becomes zero whenever the estimation error belongs to $\ker(C)$.

This algorithm has the following properties

Theorem 1. Consider system (1) and the algorithm (2). If the pair (A, C) is observable, then for any $t^\star > t_0$ $N(t) \geq \alpha(t^\star)\mathbb{I}$ for $t \geq t^\star$. Fix $t^\star$ to make α constant. Then $\hat{x}(t) \equiv x(t)$ for

$$t \geq t^\star + \frac{\lambda_M^{\frac{p_1+1}{2}}(P) n^{p_1}}{2^{\frac{p_1-1}{2}}(1-p_1)k_1\alpha^{p_1+1}} + \frac{\lambda_M^{\frac{p_2+1}{2}}(P) n^{p_2}}{2^{\frac{p_2-1}{2}}(p_2-1)k_2\alpha^{p_2+1}},$$

where $\lambda_M(\cdot)$ denotes the greatest eigenvalue of its argument. This means that (2) converges in finite time. Since the time needed for the estimate to reach the actual state does not depend on the initial error, it is said that the algorithm converges in fixed-time. △

The larger the value of α, the smaller the time needed to converge. Taking $t^\star$ bigger makes $\alpha(t^\star)$ larger; however, the function $\alpha(t^\star)$ is upper bounded, then there exists a value for $t^\star$ from which α does not increase further. The value of α can be controlled through the design of K. About this, it is recommendable to make the real part of the eigenvalues of $A + KC$ close to zero.

2.1 Convergence Analysis and Proof of Theorem 1

The convergence analysis of (2) is going to be handled through the study of the error dynamics. For this purpose, let us define the estimation error as $e(t) = \hat{x}(t) - x(t)$. Taking the time derivative of $e(t)$ yields

$$\dot{e} = \big(A - LC\big)e - P^{-1}N(t)\sum_{i=1}^{2} k_i \lceil N(t)e \rfloor^{p_i}. \tag{3}$$

If the solution $e(t) = 0$ is attractive and stable then the algorithm converges to $x(t)$. To investigate that matter, take as Lyapunov function candidate $V(e) = \frac{1}{2}e^\top Pe$, and its derivative along the trajectories of (3) satisfies

$$\dot{V}(t) \leq -\frac{1}{2}e^\top(t)R\,e(t) - \sum_{i=1}^{2}\frac{k_i}{n^{p_i}}\|N(t)e(t)\|_1^{p_i+1}, \tag{4}$$

because

$$e^\top(t)N(t)\lceil N(t)e(t)\rfloor^{p_i} \geq \frac{1}{n^{p_i}}\|N(t)e(t)\|_1^{p_i+1}.$$

From (4) it is clear that $e(t) = 0$ is asymptotically stable. Furthermore, due to the observability of system (1), matrix $N(t)$ is bounded from below by $\alpha\mathbb{I}$ for $t \geq t^\star$ for some $t^\star$, then

$$\begin{aligned} &\frac{k_i}{n^{p_i}}\|N(t)e(t)\|_1^{p_i+1} \geq \\ &\qquad \frac{k_i\alpha^{p_i+1}}{n^{p_i}}\left(\frac{2}{\lambda_M(P)}\right)^{\frac{p_i+1}{2}} V^{\frac{p_i+1}{2}}(t). \end{aligned}$$

The last inequality allows us to change (4) into two simultaneous differential inequalities

$$\dot{V}(t) \leq -\frac{p_i+1}{n^{p_i}}\left(\frac{2}{\lambda_M(P)}\right)^{\frac{p_i+1}{2}} V^{\frac{p_i+1}{2}}(t),$$

with solution

$$V(t) \leq \left(V^{\frac{1-p_i}{2}}(t^\star) - \frac{2^{\frac{p_i-1}{2}}(1-p_i)k_i\alpha^{p_i+1}}{\lambda_M^{\frac{p_i+1}{2}}(P)n^{p_i}}(t-t^\star)\right)^{\frac{2}{1-p_i}}. \tag{5}$$

Notice that $V(t)$ satisfies both inequalities for all $t \geq t^\star$. Between t_0 and $t^\star$, the Lyapunov function does not increase, this is prevented by the quadratic term in its derivative. For the convergence time calculation, it is assumed that $V(t)$ remains constant in the interval $[t_0, t^\star)$.

For $i = 2$, the appropriate inequality is going to be used to estimate the time needed to guarantee $V(t) \leq 1$, whereas the inequality for $i = 1$ will be used to calculate the necessary time for $V(t)$ to decrease from a unitary value to zero.

According to the described process, (5) is rewritten for $i = 2$:

$$t - t^\star \geq \frac{\lambda_M^{\frac{p_2+1}{2}}(P)n^{p_2}}{2^{\frac{p_2-1}{2}}(p_2-1)k_2\alpha^{p_2+1}}\left(1 - \frac{1}{V^{\frac{p_2-1}{2}}(t^\star)}\right).$$

Taking the limit when $V(t^\star) \to \infty$, it is clear that for

$$t \geq t^\star + \frac{\lambda_M^{\frac{p_2+1}{2}}(P)n^{p_2}}{2^{\frac{p_2-1}{2}}(p_2-1)k_2\alpha^{p_2+1}} = t_1$$

$V(t) \leq 1$. Now assume that $V(t_1) = 1$, using inequality (5) with $i = 1$, we proceed to estimate the time needed to reach zero. This happens when the *rhs* of (5) equals zero, then $V(t) \equiv 0$ for

$$t \geq t_1 + \frac{\lambda_M^{\frac{p_1+1}{2}}(P)n^{p_1}}{2^{\frac{p_1-1}{2}}(1-p_1)k_1\alpha^{p_1+1}}.$$

Then the time needed for $V(t)$ to decrease from its initial value to zero is at most

$$t^\star + \frac{\lambda_M^{\frac{p_1+1}{2}}(P)n^{p_1}}{2^{\frac{p_1-1}{2}}(1-p_1)k_1\alpha^{p_1+1}} + \frac{\lambda_M^{\frac{p_2+1}{2}}(P)n^{p_2}}{2^{\frac{p_2-1}{2}}(p_2-1)k_2\alpha^{p_2+1}},$$

which is independent from the initial error. This concludes the proof of Theorem 1.

3. UNKNOWN INPUT OBSERVER DESIGN

In this section, a perturbed linear system will be considered. Take again into consideration system (1), but now with an unknown input $\nu(t) \in \mathbb{R}^q$

$$\begin{aligned} \dot{x} &= A\,x + B\,u(t) + D\,\nu(t), \\ y(t) &= C\,x. \end{aligned} \tag{6}$$

It is assumed that matrix D is also known. Without loss of generality, it is assumed that $\text{rank}(C) = m$, and $\text{rank}(D) = q$.

The existence of an observer capable of estimating x without the knowledge of $\nu(t)$ is conditioned to the system to be strong* detectable (Hautus, 1983). If the system is strong* detectable, then $\lim_{t\to\infty} y(t) = 0$ implies $\lim_{t\to\infty} x(t) = 0$ with independence of the unknown input and the initial state. This property can be tested through the following criteria:

Theorem 2. (Hautus, 1983)(Moreno, 2001) The system (6) is strong* detectable if and only if

$$\text{rank}\begin{bmatrix} s\mathbb{I} & -D \\ C & 0 \end{bmatrix} = n + q, \quad \forall\, s \in \mathbb{C}_0^+$$

and

$$\text{rank}(CD) = q,$$

where $\mathbb{C}_0^+$ is the closed right half plane of the complex plane. △

The first condition means that all the transmission zeros of the system have negative real part, and that the system is detectable. The second statement requires that $m \geq q$, in other words, it is required at least the same number of outputs as the unknown inputs.

Suppose the rank condition for CD is met. Define the matrix

$$S = \begin{bmatrix} S_1 \\ S_2 \end{bmatrix},\ S \in \mathbb{R}^{m\times m} \tag{7}$$

with

$S_1 = (C\,D)^+ = (D^\top C^\top C\,D)^{-1} D^\top C^\top,\ S_1 \in \mathbb{R}^{q\times m}$,

$S_2 = Q\big(\mathbb{I}_m - C\,D\,S_1\big),\ S_2 \in \mathbb{R}^{(m-q)\times m}$,

and $Q \in \mathbb{R}^{(m-q)\times m}$ such that S_2 has full row rank. Take the $n \times n$ matrix

$$T = \begin{bmatrix} T_1 \\ T_2 \end{bmatrix} = \begin{bmatrix} S_1\,C \\ \begin{bmatrix} S_2\,C \\ M \end{bmatrix} \end{bmatrix}, \tag{8}$$

with $M \in \mathbb{R}^{(n-m)\times n}$ in such a way that makes T invertible and $MD = 0$.

Taking the linear transformation $z = T\,x$, the system is transformed into

$$\begin{aligned} \dot{z}_1 &= \bar{A}_{11}z_1 + \bar{A}_{12}z_2 + \bar{B}_1 u(t) + \nu(t), \\ \dot{z}_2 &= \bar{A}_{21}z_1 + \bar{A}_{22}z_2 + \bar{B}_2 u(t), \end{aligned} \tag{9}$$

with $\bar{A} = TAT^{-1}$, $\bar{B} = TB$, and $z_i = T_i x$, $i = \{1, 2\}$. Define as output $\bar{y}(t) = S\,y(t)$, this yields

$$\bar{y}(t) = \begin{bmatrix} \bar{y}_1(t) \\ \bar{y}_2(t) \end{bmatrix} = \begin{bmatrix} z_1 \\ \bar{C}_{22}z_2 \end{bmatrix}.$$

With this transformation, the state is partitioned into the corrupted part by the unknown input z_1, and the part free from its effect z_2. Notice that the corrupt part can be recovered directly from the output, whereas the other part has to be reconstructed from $\bar{y}_2$. This transformation is classic and can be found in many texts, see for example (Kudva et al., 1980) and (Moreno, 2001).

To be able to reconstruct the full state, at least asymptotically, it is required that the pair (A, C) is detectable. If $m = q$ only $\bar{y}_1$ would be available, and from the detectability it can be concluded that $z_2 \to 0$ as $t \to \infty$, then any estimate of z_2 that goes to zero can be used. If $m > q$, i.e. there are more

known inputs, a better estimation of z_2 can be attempted. The detectability of pair (A, C) implies the detectability of pair $(\bar{A}_{22}, \bar{C}_{22})$, and an observer for z_2 can be designed using $\bar{y}_2$ as output, and z_1 and $u(t)$ as input. The interesting case is when $(\bar{A}_{22}, \bar{C}_{22})$ is observable. In such case, the velocity of convergence for a z_2 observer can be assigned. If one uses the observer proposed in Section 2, it is possible to reconstruct z_2 in fixed-time, and also the original state using the relation $x = T^{-1}z$.

Let us summarize the previous discussion. Suppose that the pair (A, C) is observable, that $\text{rank}(CD) = q$, and that $m > q$. Under these conditions the observer proposed in Section 2 can be used to estimate, in fixed-time, the internal state of a linear system with unknown inputs. This is done through the state and output transformation $z = Tx$, $\bar{y}(t) = S\,y(t)$, with T as in (8) and S as in (7). This puts the system into the form shown in (9). Then the methodology presented in the previous section can be applied to design an observer for the subsystem

$$\begin{aligned} \dot{z}_2 &= \bar{A}_{22}z_2 + \bar{A}_{21}z_1 + \bar{B}_2u(t), \\ \bar{y}_2(t) &= \bar{C}_{22}z_2. \end{aligned}$$

This allows the fixed-time reconstruction of the original state through $\hat{x} = T^{-1}\hat{z}$ with $\hat{z} = [\bar{y}_1^\top \ \hat{z}_2^\top]^\top$.

4. NUMERICAL EXAMPLE

To exemplify the observer design proposed in previous sections, let us consider the following system:

$$\begin{aligned} \dot{x} &= \begin{bmatrix} 1 & 2 & -1 \\ -7 & -6 & 2 \\ -1 & -2 & 0 \end{bmatrix} x + \begin{bmatrix} 0 \\ 0 \\ 1 \end{bmatrix} u(t) + \begin{bmatrix} -1 \\ 2 \\ 2 \end{bmatrix} \nu(t), \\ y(t) &= \begin{bmatrix} 1 & 0 & 1 \\ 2 & 1 & 0 \end{bmatrix} x. \end{aligned} \tag{10}$$

Now, the system has to be transformed in order to decouple the corrupted and uncorrupted dynamics. For this matter, define the transformation matrix as

$$T = \begin{bmatrix} T_1 \\ T_2 \end{bmatrix} = \left[\begin{array}{ccc} 1 & 0 & 1 \\ \hline 2 & 1 & 0 \\ 0 & 1 & -1 \end{array}\right] \tag{11}$$

In this case, matrix S is $\mathbb{I}_2$, which is clear after comparing T and C. Applying the transformation to the system, it becomes

$$\begin{aligned} \dot{z}_1 &= -2\,z_1 + [1 \ -1]z_2 + u(t) + \nu(t), \\ \dot{z}_2 &= \begin{bmatrix} -3 & 1 \\ -4 & 0 \end{bmatrix} z_2 + \begin{bmatrix} 1 \\ 2 \end{bmatrix} z_1 + \begin{bmatrix} 0 \\ -1 \end{bmatrix} u(t), \\ \bar{y}_1 &= z_1, \\ \bar{y}_2 &= [1 \ 0]z_2. \end{aligned} \tag{12}$$

Since the pair $(\bar{A}_{22}, \bar{C}_{22})$ is observable, we can proceed to design an observer for z_2.

To estimate z_2 with the proposed observer, we set $L = 0$, $p_1 = 1/3$, $p_2 = 2$, $k_1 = k_2 = 5$, and $K = [3.7 \ 3.9]^\top$. For $R = \mathbb{I}_2$, this configuration yields

$$P^{-1} = \frac{1}{17}\begin{bmatrix} 42 & 36 \\ 36 & 60 \end{bmatrix}.$$

For the simulation, the input u was set in $\cos(t)$; for the unknown input, a triangle wave of amplitude and period 2 was chosen. The system was initialized in $x_0 = [10 \ \ -5 \ \ 3]^\top$. To compare the response of the proposed algorithm, a linear one was also simulated. For the linear observer, the gain $\bar{L} = [4 \ 6]^\top$ was chosen. For both observers, the initial conditions were set in zero, $\hat{z}_2(t_0) = 0$.

From Figure 1 to 3, the estimate of x provided by the proposed observer and the linear observer can be compared with the true state. In the plots, it can be observed that the estimate produced with the nonlinear algorithm got closer to the true state much faster than the linear one. This can be corroborated in Figure 4, in which the norm of the estimation error was plot. From this last graph, the finite-time convergence can be established in less than two seconds.

To exhibit the fixed-time convergence, the simulation was repeated with different initial conditions. The initial value of the estimation error was increased in one order of magnitude in each successive simulation. As can be seen in Fig 5, the convergence time stay under $2.6[s]$ although the initial error was increased above 10^6 in magnitude. Between the trajectories for $O(10^5)$ and $O(10^6)$ there is no appreciable difference, and this characteristic is maintained for orders of magnitude beyond 10^6.

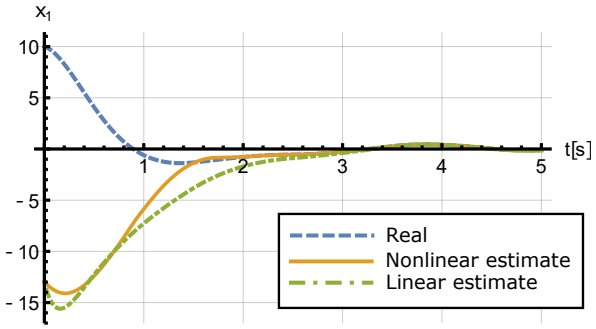

Fig. 1. Estimate of $x_1(t)$.

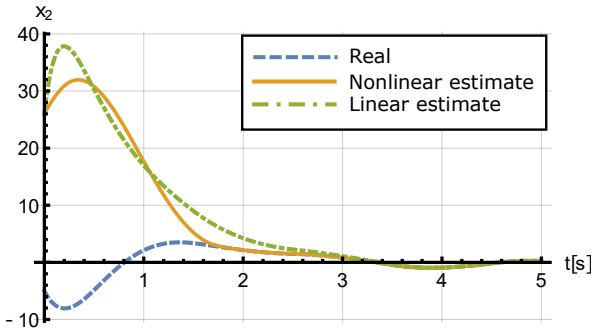

Fig. 2. Estimate of $x_2(t)$.

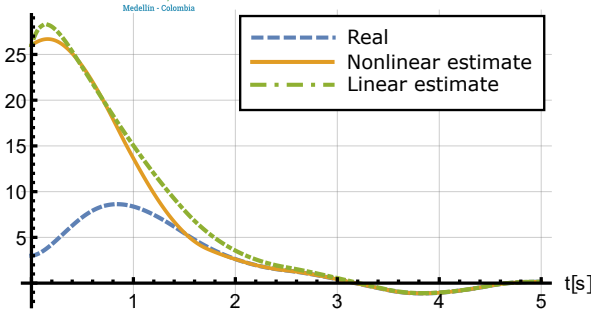

Fig. 3. Estimate of $x_3(t)$.

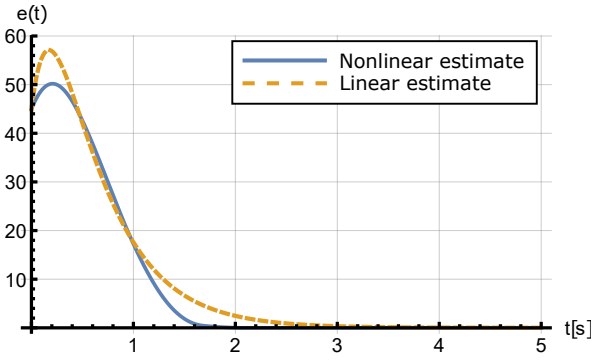

Fig. 4. Error norm.

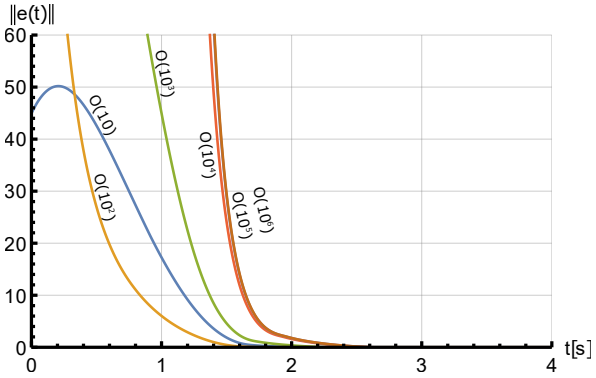

Fig. 5. Error norm for different magnitude of the initial error.

5. CONCLUSION

In this work, a novel fixed-time convergent observer for any observable linear time-invariant systems is presented. The observer is globally convergent, and its design can be done in the system original coordinates, in contrast with other finite-time convergent algorithms. It is also provided a methodology to apply this observer in the case of perturbed systems, and can be used as an unknown input observer. In such situation, if there is enough information available, the algorithm keeps its properties, that is, the algorithm can provide an estimate of the perturbed system state in fixed time.

ACKNOWLEDGEMENT

The authors thank the financial support from PAPIIT-UNAM (Programa de Apoyo a Proyectos de Investigación e Innovación Tecnológica), project IN113614; Fondo de Colaboración II-FI UNAM, Project IISGBAS-100-2015; CONACyT (Consejo Nacional de Ciencia y Tecnología), project 241171; and CONACyT CVU: 491701, and 620585.

REFERENCES

Abou-Kandil, H., Freiling, G., Ionescu, V., and Jank, G. (2003). *Matrix Riccati Equations in Control and Systems Theory*. Birkhäuser Basel.

Atassi, A. and Khalil, H. (2000). Separation results for the stabilization of nonlinear systems using different high-gain observer designs. *Systems & Control Letters*, 39(3), 183 – 191.

Chen, W. and Saif, M. (2006). Fault detection and isolation based on novel unknown input observer design. In *2006 American Control Conference*.

Cruz-Zavala, E., Moreno, J.A., and Fridman, L. (2012). Asymptotic stabilization in fixed time via sliding mode control. In *Decision and Control (CDC), 2012 IEEE 51st Annual Conference on*, 6460–6465.

Cruz-Zavala, E., Moreno, J.A., and Fridman, L.M. (2011). Uniform robust exact differentiator. *IEEE Transactions on Automatic Control*, 56(11), 2727–2733.

Hautus, M. (1983). Strong detectability and observers. *Linear Algebra and its Applications*, 50, 353 – 368.

Hespanha, J.P. (2009). *Linear Systems Theory*. Princeton Press, Princeton, New Jersey.

Hwang, I., Kim, S., Kim, Y., and Seah, C.E. (2010). A survey of fault detection, isolation, and reconfiguration methods. *IEEE Transactions on Control Systems Technology*, 18(3), 636–653.

Kudva, P., Viswanadham, N., and Ramakrishna, A. (1980). Observers for linear systems with unknown inputs. *IEEE Transactions on Automatic Control*, 25(1), 113–115.

Menard, T., Moulay, E., and Perruquetti, W. (2010). A global high-gain finite-time observer. *IEEE Transactions on Automatic Control*, 55(6), 1500–1506.

Moreno, J. (2001). Existence of unknown input observers and feedback passivity for linear systems. In *Decision and Control, 2001. Proceedings of the 40th IEEE Conference on*, volume 4, 3366–3371 vol.4.

Pin, G., Lovera, M., Assalone, A., and Parisini, T. (2013). Kernel-based non-asymptotic state estimation for linear continuous-time systems. In *American Control Conference (ACC), 2013*, 3123–3128.

Polyakov, A. (2012). Fixed-time stabilization of linear systems via sliding mode control. In *Variable Structure Systems (VSS), 2012 12th International Workshop on*, 1–6.

Raff, T. and Allgöwer, F. (2008). An observer that converges in finite time due to measurement-

pdates. In *17th IFAC World Congress*, 1051–1067.

Rueda-Escobedo, J., Moreno, J.A., and Oliva-Fonseca, P. (2016). Finite-time state estimation for lti systems with a first-order sliding mode. In *14th International Workshop on Variable Structure Systems*, to appear.

Yin, S., Wang, G., and Karimi, H.R. (2014). Data-driven design of robust fault detection system for wind turbines. *Mechatronics*, 24(4), 298 – 306.

Observer Designs for a Turbocharger System of a Diesel Engine

María Tejada Zuñiga * **Matti Noack** ** **Johann Reger** **

* *Pontificia Universidad Católica del Perú, Lima, Peru (e-mail: mctejadaz@pucp.pe)*
** *Control Engineering Group, Technische Universität Ilmenau, P.O. Box 10 05 65, D-98684, Ilmenau, Germany (e-mail: matti.noack@tu-ilmenau.de, reger@ieee.org)*

Abstract: We consider observer designs for an exhaust-gas turbocharger based on a third order nonlinear model of the air path of a diesel engine. To propose an observer, the system is analyzed in view of different observability properties for nonlinear systems. We derive explicit constraints for the system state guaranteeing observability. Based on that we design a high-gain observer and a sliding mode observer for the system. The performance of both designs has been assessed through a simulation study.

Keywords: Nonlinear Systems, Observability Analysis, High-Gain Observer, Sliding-Mode Observer, Turbocharger Diesel Engine

1. INTRODUCTION

Over the last decades, diesel engines have gained interest because they provide higher fuel efficiency than gasoline engines. However, diesel engines have the disadvantage to require a complicated exhaust gas treatment. One way to achieve a better power utilization and an improved treatment of exhaust gases is the use of turbochargers. Fig. 1 shows the structure of such turbocharger system.

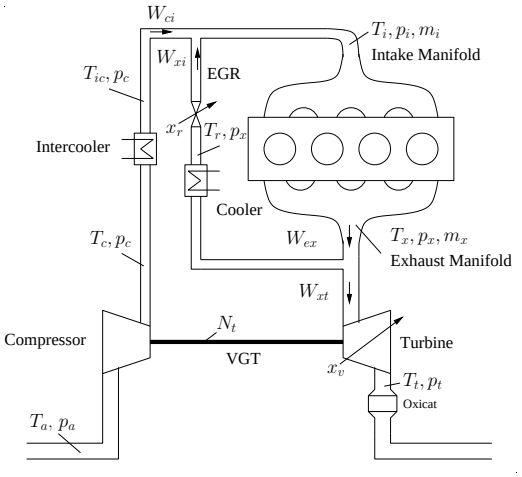

Fig. 1. Schematic diagram of a turbocharged diesel engine with EGR (Herceg et al., 2006).

The function of the turbocharger is to increase the power density of the engine by pushing additional fresh air into the cylinders of the engine in order to burn more fuel without smoke generation, allowing for the injection of more fuel without reaching the smoke bound. The turbine has a variable geometry (VGT) so as to adapt the turbine efficiency based on the operating point of the engine, driven by the energy in the exhaust gas.

The second feedback path to the intake manifold from the exhaust manifold is due to exhaust gas recirculation which is controlled by an exhaust gas recirculation (EGR) valve. The oxygen in the intake is replaced by recirculated exhaust gases, thereby reducing the temperature profile of the combustion and hence the emissions of nitrogen oxides. The interactions are relatively complex. The VGT actuator is usually used to control the intake manifold absolute pressure (MAP) while the EGR valve controls the mass air flow (MAF) into the cylinders. Both the EGR and VGT paths are driven by the exhaust gases. However, both the EGR and VGT actuator are equipped with position sensors. For a detailed description refer to Ladommatos et al. (1996) and references therein.

Vast research has been dedicated to the control of diesel engines. Many controllers were proposed in the literature, e.g., Lyapunov controller design (Janković and Kolmanovsky, 2000), controllers based on a Linear Parameter-Varying (LPV) model for turbocharged diesel engine (Jung and Glover, 2003), indirect passivation (Larsen et al., 2000), predictive control (Ferreau et al., 2007), feedback linearization (Dabo et al., 2009) and sliding mode control (Utkin et al., 2000). Other approaches for air-to-fuel ratio control of turbocharged diesel engines were also proposed in the literature (Fredriksson, 1999; Guzzella and Onder, 2013; Janković et al., 1998). The different solutions are mostly nonlinear and model-based. Usually it is assumed that the state variables be measurable or somehow computable.

However, full state information is not the case for many systems in practice, as was explained in Fredriksson and Egardt (2002). The intake manifold pressure or boost pressure is measurable. The compressor power may be

computed in principle. But the sensors used for computing the compressor power are quite expensive, and, therefore, it is often assumed to be unmeasurable. So as to relax this assumption the use of observers for estimating the unmeasurable states may be considered a solution; first designs have been proposed only in the recent past (Glenn et al., 2011; Salehi et al., 2013; Qu et al., 2015).

The focus of this contribution is on estimating the states of this turbocharger model. To this end, the model is analyzed in terms of observability first. Within the observability analysis we shall consider two concepts of observability for nonlinear systems, namely, weak observability and uniform observability. Local weak observability is an indispensable condition for the design of observers, see Hermann and Krener (1977). The uniform observability, as introduced by Gauthier and Bornard (1981), is a stronger concept and allows for the stable design of High-Gain observers. Afterwards, we investigate the application of two different observer approaches on the turbocharger system: a high-gain observer and a sliding-mode observer. The performances of both are compared in terms of design, complexity and robustness.

The paper is structured as follows: The following section recalls the nonlinear model of the turbocharger system, based on a simplification of a more complete physical model. Section 3 presents the observability analysis of the nonlinear system using the observability rank condition analytically and more extensive numerical calculations. In Sections 4 and 5 we present the high-gain observer and sliding-mode observer design, respectively. Both observers are simulated and results are presented in Section 6. Conclusions are drawn in Section 7.

2. MODELING

The modeling of the air path system of a diesel engine, which is composed of a turbocharger with variable turbine geometry, exhaust gas recirculation and intercooler, is not an easy task and consists largely of identification and map creation, as Wahlström and Eriksson (2011) had presented in detail. Moreover, complicated functional relationships arise, for example, by attaching flow functions.

Through versatile measurements describing the couplings, a comprehensive information flow exists for the system which then can be used for observation. However, this results in a very complex mathematical model to be mastered. Fortunately, simplifications and approximations have been made.

Against this background, here we use a fully parameterized nonlinear model of the turbocharger which is based on the approach from Janković and Kolmanovsky (2000). This is a simplified third-order nonlinear model derived from an eighth-order nonlinear mean-value model of the air path of a turbocharged diesel engine with EGR and VGT. The full-order air path model is of eighth order with states: intake and exhaust manifold pressure (p_i and p_x), oxygen mass fractions in the intake and exhaust manifolds, turbocharger speed and the two states describing the actuator dynamics for the two control signals.

For more simplicity the model is reduced to a third-order model subject to the following assumptions: The oxygen mass fraction variables are ignored since they are not coupled with other engine dynamics and are difficult to measure. The temperature variables are omitted because temperature dynamics are slow when compared with pressure and flow dynamics.

The detailed derivation of the eighth-order nonlinear model of the engine under investigation may be found in Jung et al. (2002). In Table 2 all variables and parameters are listed. Reducing the consideration to the third-order model, we may refer to just three states p_i, p_x, and P_c that represent the intake manifold pressure, the exhaust manifold pressure, the power transferred by the turbocharger, respectively. Then the following system description is obtained:

$$\Sigma : \begin{cases} \dot{p}_i = \dfrac{RT_i}{V_i}(W_{ci} + W_{xi} - W_{ie}) \\ \dot{p}_x = \dfrac{RT_x}{V_x}(W_{ie} + W_f - W_{xi} - W_{xt}) \\ \dot{P}_c = \dfrac{1}{\tau}(-P_c + P_t) \end{cases} \tag{1}$$

Following the analysis of the turbine mass-flow presented by Schollmeyer (2010), the flow rates as well as the compressor and turbine power are given by

$$\begin{aligned} W_{ci} &= \frac{\eta_c}{c_p T_a} \frac{P_c}{(\frac{p_i}{p_a})^{\mu} - 1}, \\ W_{xi} &= \frac{A_{egr}(x_{egr}) p_x}{\sqrt{RT_x}} \sqrt{\frac{2p_i}{p_x}(1 - \frac{p_i}{p_x})}, \\ W_{ie} &= \eta_v \frac{p_i N V_d}{120 R T_i}, \\ W_{xt} &= (a x_{vgt} + b) \left(c \left(\frac{p_a}{p_x} - 1 \right) + d \right) \frac{p_x}{p_{ref}} \\ &\quad \times \sqrt{\frac{T_{ref}}{T_x}} \sqrt{\frac{2p_i}{p_x} \left(1 - \frac{p_a}{p_x} \right)}, \\ P_t &= W_{xt} c_p T_x \eta_t \left(1 - \left(\frac{p_a}{p_x} \right)^{\mu} \right) \end{aligned}$$

with the constant parameters: compressor and turbine efficiency η_c and η_t, volumetric efficiency η_v, intake manifold temperature T_i, exhaust manifold temperature T_x, and time constant of the turbocharger power transfer τ.

The control inputs of the diesel engine model based on (1), are the EGR position x_{egr} and the VGT position x_{vgt}. For simplifying the considerations of the model, however, the effective areas of the valves, i.e. $A_{vgt} = a x_{vgt} + b$ and A_{egr}, are used as control inputs. Furthermore, the control inputs A_{egr} and A_{vgt} are constrained due to the minimal and maximal EGR and VGT positions. The intake manifold pressure or boost pressure, is measurable and forms the system output.

It should be noted that the model has a singularity when the pressure in the intake manifolds equals the ambient pressure, that is, if $p_i = p_a$ then the compressor flow becomes infinite. There exists also another singularity when the turbine stalls. The simplified model can not handle this situation and, as explained in (Fredriksson and Egardt, 2002), the system is only valid on the set $\Omega = \{(p_i, p_x, P_c) : p_i > p_a, p_x > p_a, P_c > 0\}$. Fortunately,

it may be demonstrated that Ω is invariant, thus, every trajectory starting in Ω stays in Ω (Janković et al., 1998).

Table 1. Parameters of the model (Janković and Kolmanovsky, 2000)

	Description	Value	Unit
N	Engine Speed	2000	$[rpm]$
W_f	Fuel rate	5	$[kg/h]$
R	Specific gas constant	287	$\left[\frac{J}{kg \cdot K}\right]$
p_i	Intake manifold pressure	-	$[hPa]$
p_x	Exhaust manifold pressure	-	$[hPa]$
p_{ref}	Reference pressure	101.3	$[hPa]$
p_a	Ambient pressure	101.3	$[hPa]$
P_c	Compressor Power	-	$[kW]$
T_i	Intake manifold temperature	313	$[K]$
T_x	Exhaust manifold temperature	509	$[K]$
T_{ref}	Referent Temperature	298	$[K]$
T_a	Ambient Temperature	298	$[K]$
V_i	Volume of the intake manifold	0.006	$[m^3]$
V_x	Volume of the exhaust manifold	0.001	$[m^3]$
V_d	Displacement Volume	0.002	$[m^3]$
η_m	Turbo mechanical efficiency	98	[%]
η_c	Compressor isentropic efficiency	61	[%]
η_t	Turbine isentropic efficiency	76	[%]
η_v	Volume efficiency	87	[%]
c_P	Specific heat at constant pressure	1014.4	$\left[\frac{J}{kg \cdot K}\right]$
c_v	Specific heat at constant volume	727.4	$\left[\frac{J}{kg \cdot K}\right]$
μ	constant	0.286	–
a	Parameter a	−0.136	–
b	Parameter b	0.176	–
c	Parameter c	0.4	–
d	Parameter d	0.6	–

For our analysis we may refer to system (1) in terms of system

$$\Sigma : \begin{cases} \dot{x} = F(x,u)\,, \\ y = h(x)\,, \end{cases} \tag{2}$$

where here $F : \mathbb{R}^3 \times \mathbb{R}^2 \to \mathbb{R}^3$ and $h : \mathbb{R}^3 \to \mathbb{R}$ differentiable in x sufficiently often. The function expressions of $F(x,u)$ correspond to the right side of the system (1), that is $x = (p_i, p_x, P_C)^\top$ and $h(x) = x_1$.

3. OBSERVABILITY

For nonlinear systems there exist various observability concepts. In this contribution, in particular, we consider *weak observability* and *uniform observability* which are significant for the observer approaches to be applied later, following Besançon (2007).

Consider a single-output system of class Σ from (2). In general, the observability map is

$$\mathfrak{o}_n(x) := \begin{pmatrix} h(x) \\ \mathcal{L}_F h(x) \\ \mathcal{L}_F^2 h(x) \\ \vdots \\ \mathcal{L}_F^{n-1} h(x) \end{pmatrix},$$

where $\mathcal{L}_F^k$ describes the k-th Lie derivative with respect to $F(\cdot, u)$. Observability may then be characterized by the solvability of the resulting system of nonlinear equations for the state x. In view of the implicite function theorem, the Jacobian of this map may be used for showing *local solvability*. The Jacobian of the observability map is called *observability matrix*, given by

$$\mathcal{O}_n(x) := \begin{pmatrix} \frac{\partial}{\partial x} h(x) \\ \frac{\partial}{\partial x} \mathcal{L}_F h(x) \\ \frac{\partial}{\partial x} \mathcal{L}_F^2 h(x) \\ \vdots \\ \frac{\partial}{\partial x} \mathcal{L}_F^{n-1} h(x) \end{pmatrix},$$

where $\frac{\partial}{\partial x}(\cdot)$ denotes the gradient.

Here it is important to note that the observability map and its Jacobian will actually also depend on the input. Excluding that these inputs may cause conflicts with observability, naturally, leads to the stronger concept of *uniform observability*. A system is uniformly observable if the observability map may be solved uniquely for the state, whatever the input. In this case, every input is a so-called universal input.

The analytical expression of the observability matrix for the turbocharger system is rather lengthly, and not easy to analyze. In order to get an impression of observability, the analysis is made first for the free system, i.e. with inputs indentical to zero. In this case the observability matrix is

$$\mathcal{O}_3(x) = \begin{pmatrix} 1 & 0 & 0 \\ * & \beta_1(x_1) & 0 \\ * & * & \beta_1(x_1)\dfrac{\partial \beta_3(x_2)}{\partial x_2} \end{pmatrix} \tag{3}$$

where

$$\beta_1(x_1) = \frac{RT_i}{V_i} \frac{\eta_c}{c_p T_a} \frac{1}{\left(\left(\frac{p_i}{p_a}\right)^{\mu} - 1\right)}$$

$$\beta_3(x_2) = \frac{c_p \eta_t T_x}{\tau} \left(1 - \frac{p_a}{p_x}^{\mu}\right) b \left(c\left(\frac{p_x}{p_a} - 1\right) + d\right) \frac{p_x}{p_{ref}} \times \sqrt{\frac{T_{ref}}{T_x}} \sqrt{\frac{2p_a}{p_x}(1 - \frac{p_a}{p_x})}$$

In order to probe whether the autonomous system is at least *locally weakly observable*. For showing this, we use the observability rank condition presented by Hermann and Krener (1977), i.e., we check whether $\operatorname{rank}\big(\mathcal{O}_3(x)\big) = 3$. Thus, it is only necessary to verify that its diagonal elements are different from zero.

In the region of interest Ω we have that $\beta_1(x_1) \neq 0$. Fig. 2 shows that the values of the third element of the diagonal will also never be zero. Therefore we conclude that the system is at least locally weakly observable on the set Ω.

The remaining analysis is concerned with the evaluation of the inputs to determine whether these are universal. The complete model in affine form is given by

$$F(x,u) = \begin{pmatrix} * \\ * \\ * \end{pmatrix} + \begin{pmatrix} * \\ * \\ 0 \end{pmatrix} u_1 + \begin{pmatrix} 0 \\ * \\ * \end{pmatrix} u_2,$$

in this way it is easy to see that the inputs are not coupled. Then for simplifying the analysis, we analyzed each input independent from each other. That is, analyzing u_1 we set $u_2 \equiv 0$ and vice versa. It turns out that the

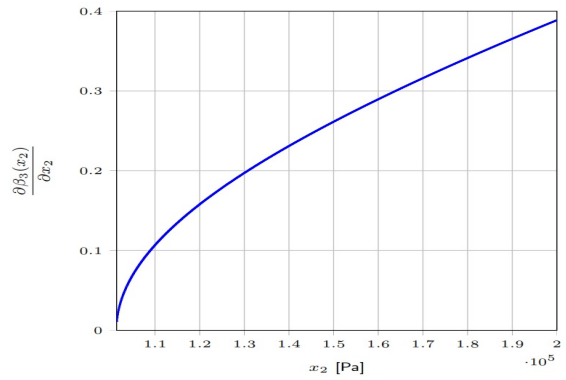

Fig. 2. Values of $\frac{\partial \beta_3(x_2)}{\partial x_2}$ in the region of interest

respective observability matrices $\mathcal{O}_3(x, u_i)$ do not show triangular structure. Therefore, the analytic calculation of its determinant results in a complex task even with the help of computational software. However, for getting an impression we may plot the determinant as a function of states, considering the dynamics of the system and the entire range of input values. Note that the range of operation was obtained fixing two states maximizing the other, Fig. 3 shows that the determinant of $\mathcal{O}_3(x, u_1)$ is never zero for the relevant range of states, analogously Fig. 4 shows the same result for the second input.

Therefrom we may assume that there is no relevant states in which the determinant becomes zero. In view of this analysis, each input turns out an universal input and we may conclude that the turbocharger system is uniformly observable in the operation area of validity Ω.

4. HIGH-GAIN OBSERVER

The rationale of the high-gain (HG) observers is to find a linear output injection which is able to dominate the nonlinear terms for stabilizing the estimation error dynamics, which is governed by a constant gain matrix. Due to their inherent simple structure, HG observers are frequently used in practical applications. This also makes the HG observer applicable to the turbocharger system. It is simple practice to choose the observer gain via eigenvalue placement (Röbenack, 2012), however, formal existence conditions are more complicated. In many cases, there is a finite bound on the maximum feasible Lipschitz constant of the nonlinear part for which the error dynamics can be stabilized. The existing results can be improved significantly if the structure of the linear part is taken into account.

Following Gauthier et al. (1992) and Moreno and Vargas (2000) assume the non-linear system in the form (2). Due to the uniform observability of system (1), $z = \mathfrak{o}_3(x)$ is a local diffeomorphism and the system may be transformed into nonlinear observer normal form (ONF). That is, we have

$$\left.\begin{aligned} \dot{x} &= F(x,u) \\ y &= x_1 \end{aligned}\right\} \quad \begin{array}{c} \mathfrak{o}_3(x) \\ \rightleftharpoons \\ \mathfrak{o}_3^{-1}(z) \end{array} \quad \left\{\begin{aligned} \dot{z} &= Az + b\,\varphi(z,u,\dot{u}) \\ y &= c^\top z \end{aligned}\right. \tag{4}$$

where

$$A = \begin{pmatrix} 0 & 1 & 0 \\ 0 & 0 & 1 \\ 0 & 0 & 0 \end{pmatrix}, \quad b = \begin{pmatrix} 0 \\ 0 \\ 1 \end{pmatrix}, \quad c^\top = (1\ 0\ 0)\,.$$

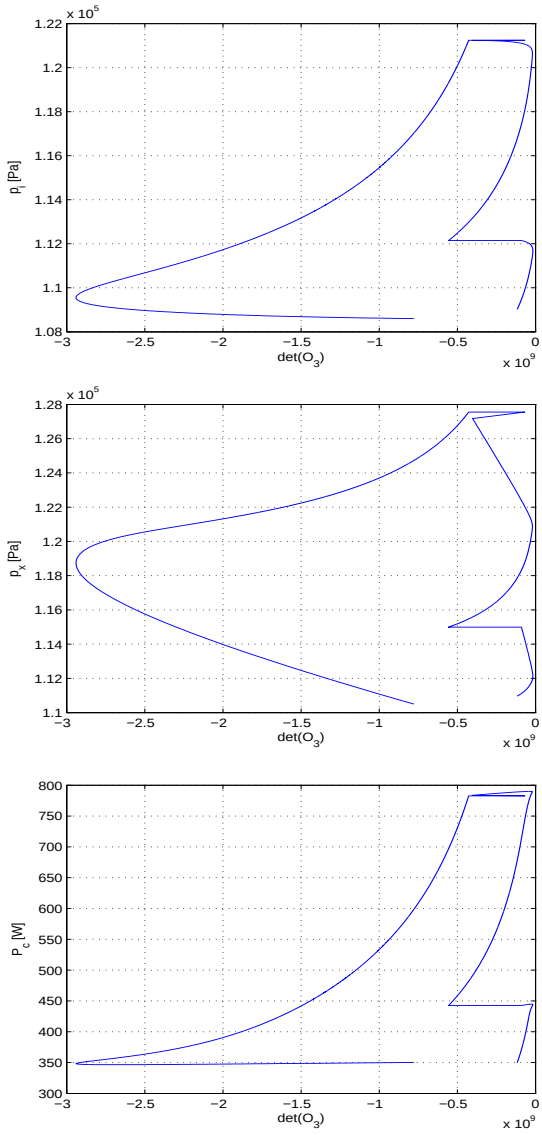

Fig. 3. Range of the determinant of $\mathcal{O}_3(x, u_1)$

In this equation, function φ describes the nonlinearities of the system. Furthermore, we will take benefit from

$$\dot{x} = \left(\frac{\partial \mathfrak{o}_3(x)}{\partial x}\right)^{-1} \dot{z} \tag{5}$$

which is very useful for the observers design in original coordinates. This way, only the observability matrix $\mathcal{O}_3(x)$ needs to be inverted which is much simpler than determining the complete inverse transformation of a nonlinear mapping.

In view of the global observability of the system in ONF (4) we design the observer

$$\begin{aligned} \dot{\hat{z}} &= A\hat{z} + b\,\varphi(\hat{z},u,\dot{u}) - l(\epsilon)(\hat{y} - y) \\ \hat{y} &= c^\top \hat{z} \end{aligned} \tag{6}$$

with

$$l(\epsilon) = \begin{pmatrix} \epsilon^{-1} & 0 & 0 \\ 0 & \epsilon^{-2} & 0 \\ 0 & 0 & \epsilon^{-3} \end{pmatrix} \begin{pmatrix} k_1 \\ k_2 \\ k_3 \end{pmatrix} = \Lambda(\epsilon) k$$

for some $\epsilon > 0$ and $k_i > 0$ such that they correspond to the coefficients of a Hurwitz polynomial. Choosing ϵ

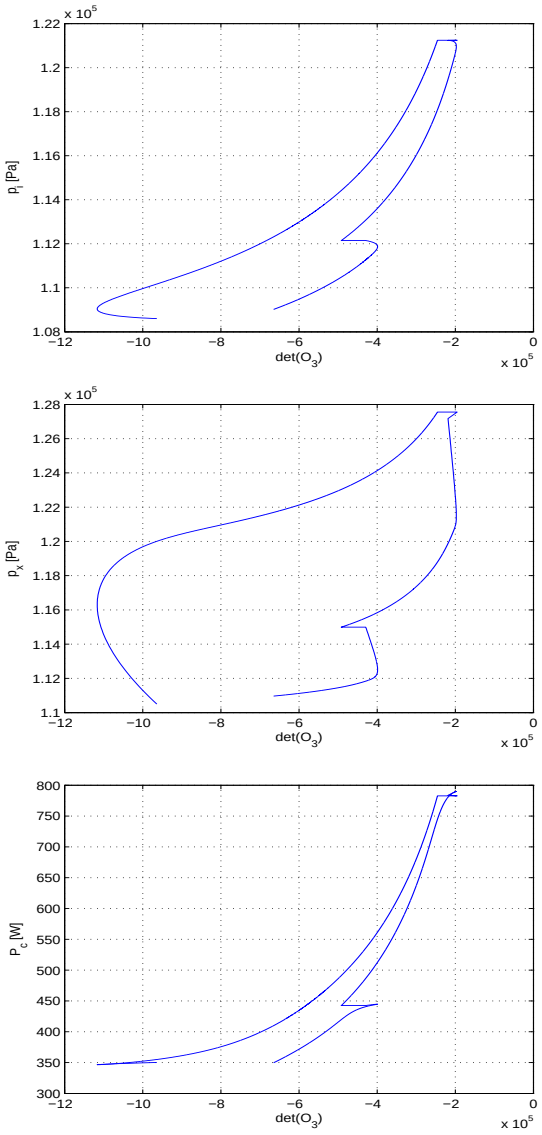

Fig. 4. Range of the determinant of $\mathcal{O}_3(x, u_2)$

sufficiently small, the observers will have a stable state estimation error dynamics. It is clear that for small ϵ the diagonal entries of $\Lambda(\epsilon)l$ will be large, thus the name *high-gain observer*.

In original coordinates this state observer takes the form

$$\begin{aligned}\dot{\hat{x}} &= F(\hat{x}, u) - \left(\frac{\partial \mathfrak{o}_3(\hat{x})}{\partial \hat{x}}\right)^{-1} l(\epsilon)(\hat{y} - y) \\ \hat{y} &= \hat{x}_1\end{aligned} \tag{7}$$

which shows just the necessity to invert the Jacobian.

5. SLIDING MODE OBSERVER

Continuous observers usually converge to the origin only in the absence of disturbances. Sliding-mode (SM) observers have been designed to resolve this issue by using discontinuous or non-Lipschitz continuous injection terms. SM observers, generally speaking, are known to show a remarkable robustness against disturbances and may further show a finite convergence time, at least theoretically. Different designs for SM observers were proposed, as for example, the generalized super-twisting observer (GSTO) and homogeneous SM observers Moreno (2013). Those approaches may guarantee different properties, but are well-studied only for second order systems. The SM observer that we adopt here for the third order system (1) was first proposed in (Moreno and Dochain, 2013). For a system in ONF this observer takes the form

$$\begin{aligned}\dot{\hat{z}}_1 &= -L\, k_1 |\hat{y} - y|^{\frac{2}{3}} \operatorname{sign}(\hat{y} - y) + \hat{z}_2 \\ \dot{\hat{z}}_2 &= -L^2\, k_2 |\hat{y} - y|^{\frac{1}{3}} \operatorname{sign}(\hat{y} - y) + \hat{z}_3 \\ \dot{\hat{z}}_3 &= -L^3\, k_3 \operatorname{sign}(\hat{y} - y) + \phi(\hat{z}, u, \dot{u}) \\ \hat{y} &= \hat{z}_1\end{aligned}$$

The gains k_1, k_2 and k_3 again are all positive, selected in order to guarantee the convergence of the observer in absence of external perturbations. The choice of gains may follow the condition $k_1 k_2 > k_3$. It may be motivated by imposing a Hurwitz polynomial for a linear error dynamics. Thus, one is left with choosing some appropriate $L > 0$.

In the original coordinates, the SM observer for system (1) again only requires the inversion of $\mathcal{O}_3(x)$. In order to have a representation similar to the HG observer let $L = \frac{1}{\epsilon}$. Then the observer in original coordinates reads

$$\begin{aligned}\dot{\hat{x}} &= F(\hat{x}, u) - \left(\frac{\partial \mathfrak{o}_3(\hat{x})}{\partial \hat{x}}\right)^{-1} l(\epsilon) \begin{pmatrix} |\hat{y} - y|^{\frac{2}{3}} \operatorname{sign}(\hat{y} - y) \\ |\hat{y} - y|^{\frac{1}{3}} \operatorname{sign}(\hat{y} - y) \\ \operatorname{sign}(\hat{y} - y) \end{pmatrix} \\ \hat{y} &= \hat{x}_1\end{aligned} \tag{8}$$

Stability and convergence of the associated state estimation error dynamics was shown by Moreno and Dochain (2013).

6. RESULTS

The performance of the observers designed for the turbocharger system was studied by simulations performed in MATLAB. The three states of the turbocharger model shall be estimated from the input manifold pressure p_i as the ouput and the inputs. The values of the normalized inputs for the scenario of simulation were the EGR position $x_{egr} = 0.7$ and the VGT position $x_{vgt} = 0.6$.

The state estimation errors obtained with the HG observer, using different ϵ values are shown in Fig. 5. Furthermore, the values of constants design k_1, k_2 and k_3 were set considering three poles placed at -10. It can be seen that the one with smallest ϵ yields a more pronounced peaking, as expected. Besides the peaking, as known from the literature, for smaller ϵ we also expect

- faster convergence of the observation error,
- amplification of the measurement noise,
- better attenuation of process disturbances.

These trade-offs always have to be taken into account in the design procedure.

The state estimation errors using the SM observer with different values of $L = \frac{1}{\epsilon}$ where $L_1 < L_2 < L_3$ are shown in Fig. 6. For simulating comparable dynamics, the remaining

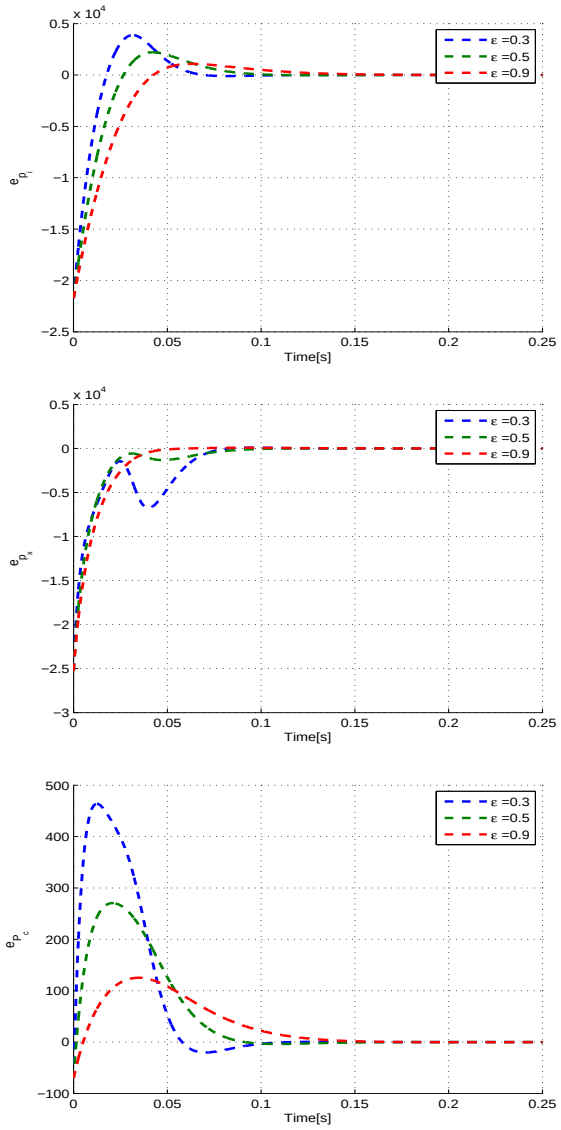

Fig. 5. Estimation errors using the high-gain observer

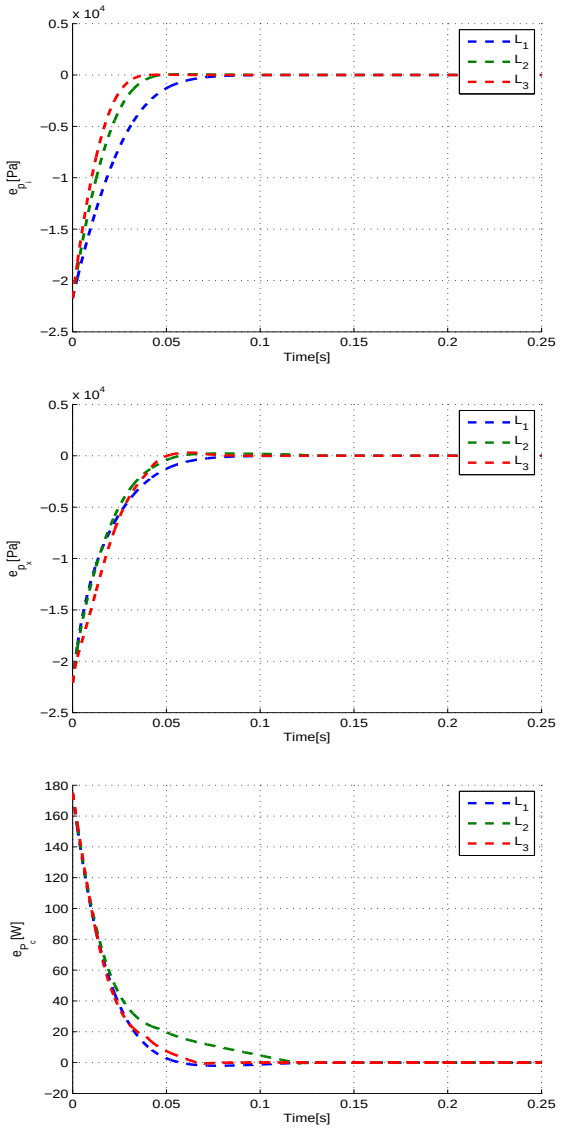

Fig. 6. Estimation errors using the sliding-mode observer

design values have been kept as in the same. No particular parameter tuning was made.

It can be seen that the one with largest L yields a faster convergence of the observation error. Furthermore, this method improves the HG observer since, remarkably, the peaking phenomenon turns out not present in the results. The performance of the designed observers has been assessed by imposing measurement noise. More precisely, in the simulations the measured output was contaminated by additive normally distributed noise with zero mean and standard deviation 3.4832×10^3. The transient performance of the estimation errors is shown in Figures 7–9.

The convergence velocity of the observation error increases while the gain of the nonlinear part increases. There exists a trade-off for the HG observer in the selection of this gain. That is, for high gains the perturbation is dominated better, but to the price that the measurement noise is amplified and the peaking phenomenon is more pronounced.

On the other hand, the Figures 8–9 show a slower convergence of the error for the Sliding Modes observer, however, in this case, the measurement noise is not present in the results.

For the two observer approaches taken in consideration the estimated intake and exhaust manifold pressure as well as the compressor power are very close to the state variables of the real system.

7. CONCLUSION

The observability analysis for a model of turbocharger in a diesel engine has been performed using weak and uniform observability concepts. Operating the system in the invariant set of the usual operation range we have shown that the system is uniformly observable. Based on this, we have designed a high-gain observer and a sliding-mode observer so as to obtain estimates for the turbocharger states. Imposing a similar estimation error dynamics, simulations with experimental testbed-data show that both observers are able to reconstruct suitably the desired states. How-

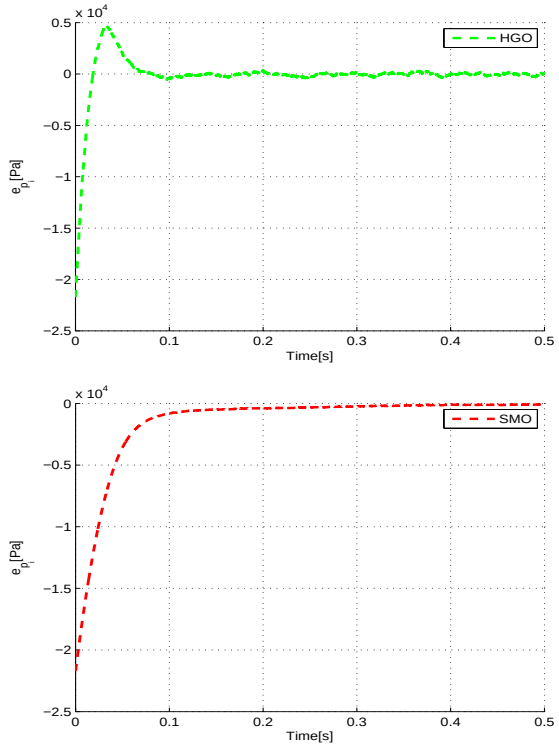

Fig. 7. Estimation error wrt. state p_i in presence of noise

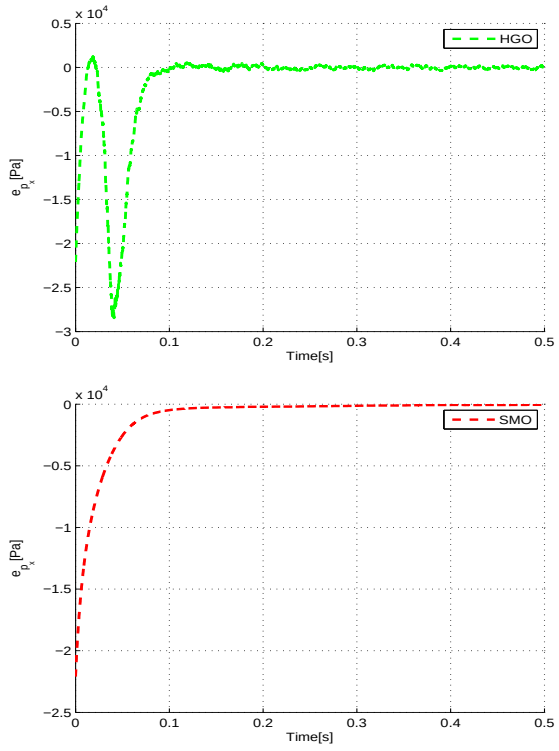

Fig. 8. Estimation error wrt. state p_x in presence of noise

ever, simulations also show that the sliding-mode observer shows no peaking and is less prone to noise.

Future work will concentrate on the design of output-feedack controllers for the turbocharger system, based on the presented observer studies.

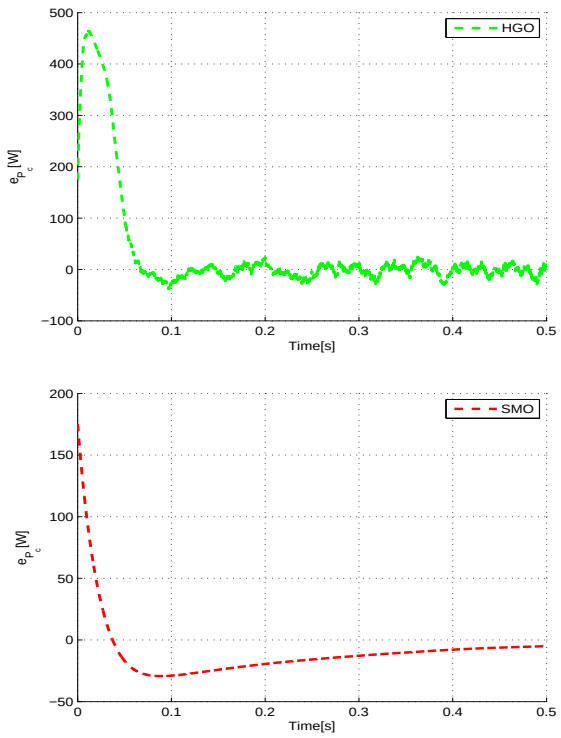

Fig. 9. Estimation error wrt. state P_C in presence of noise

ACKNOWLEDGMENT

The authors gratefully acknowledge insightful discussions with Jaime Moreno on the observability properties and observer design for nonlinear systems.

REFERENCES

Besançon, G. (2007). An overview on observer tools for nonlinear systems. In G. Besançon (ed.), *Nonlinear observers and applications*, volume 363 of *Lecture notes in control and information sciences*, 1–33. Springer, Berlin.

Dabo, M., Langlois, N., and Chafouk, H. (2009). Dynamic feedback linearization applied to asymptotic tracking: generalization about the turbocharged diesel engine outputs choice. In *American Control Conf.*, 3458–3463.

Ferreau, H.J., Ortner, P., Langthaler, P., del Re, L., and Diehl, M. (2007). Predictive control of a real-world diesel engine using an extended online active set strategy. *Annual Reviews in Control*, 31(2), 293–301.

Fredriksson, J. (1999). *Nonlinear control of turbocharged diesel engines*. Ph.D. thesis, Department of Signals and Systems, Chalmers University of Technology.

Fredriksson, J. and Egardt, B. (2002). Estimating exhaust manifold pressure in a turbocharged diesel engine. In *IEEE Conf. on Control Appl.*, 701–706.

Gauthier, J.P. and Bornard, G. (1981). Observability for any u(t) of a class of nonlinear systems. *IEEE Trans. on Autom. Control*, 26(4), 922–926.

Gauthier, J.P., Hammouri, H., and Othman, S. (1992). A simple observer for nonlinear systems applications to bioreactors. *IEEE Trans. on Autom. Control*, 37(6), 875–880.

Glenn, B.C., Upadhyay, D., Utkin, V.I., Washington, G.N., and Hopka, M.B. (2011). Observer design of critical

states for air path flow regulation in a variable geometry turbocharger exhaust gas recirculation diesel engine. *Int. Journal of Engine Research*, 12(6), 501–512.

Guzzella, L. and Onder, C. (2013). *Introduction to Modeling and Control of Internal Combustion Engine Systems*. Springer, Berlin.

Herceg, M., Raff, T., Findeisen, R., and Allgöwer, F. (2006). Nonlinear model predictive control of a turbocharged diesel engine. In *IEEE Conf. on Control Appl.*, 2766–2771.

Hermann, R. and Krener, A.J. (1977). Nonlinear controllability and observability. *IEEE Trans. on Automatic Control*, 22(5), 728–740.

Janković, M., Janković, M., and Kolmanovsky, I. (1998). Robust nonlinear controller for turbocharged diesel engines. In *American Control Conf.*, 1389–1394.

Janković, M. and Kolmanovsky, I. (2000). Constructive Lyapunov control design for turbocharged diesel engines. *IEEE Trans. on Control Systems Techn.*, 8(2), 288–299.

Jung, M. and Glover, K. (2003). Control-oriented linear parameter-varying modelling of a turbocharged diesel engine. In *IEEE Conf. on Control Appl.*, 155–160.

Jung, M., Ford, R.G., Glover, K., Collings, N., Christen, U., and Watts, M.J. (2002). Parameterization and transient validation of a variable geometry turbocharger for mean-value modeling at low and medium speed-load points. Technical report, SAE.

Ladommatos, N., Balian, R., Horrocks, R., and Cooper, L. (1996). The effect of exhaust gas recirculation on combustion and nox emissions in a high-speed direct-injection diesel engine. Technical report, SAE.

Larsen, M., Janković, M., and Kokotović, P.V. (2000). Indirect passivation design for a diesel engine model. In *IEEE Conf. on Control Appl.*, 309–314.

Moreno, J.A. (2013). On discontinuous observers for second order systems: properties, analysis and design. In *Advances in Sliding Mode Control*, 243–265. Springer.

Moreno, J.A. and Dochain, D. (2013). Finite time converging input observers for nonlinear second-order systems. In *52th IEEE Conf. on Decision and Control*, 3554–3559.

Moreno, J.A. and Vargas, A. (2000). Approximate high-gain observers for uniformly observable nonlinear systems. In *39th IEEE Conf. on Decision and Control*, 784–789.

Qu, Q., Wang, H., and Tian, Y. (2015). Nonlinear observer based sliding mode control for a turbocharged diesel engine air-path equipped with EGR and VGT. In *Chinese Automation Congress*, 121–126. Wuhan.

Röbenack, K. (2012). Structure matters – some notes on high gain observer design for nonlinear systems. *Systems, Signals and Devices*, 9, 1–7.

Salehi, R., Shahbakhti, M., Alasty, A., and Vossoughi, G. (2013). Nonlinear observer design for turbocharger in a si engine. In *American Control Conf.*, 5231–5236.

Schollmeyer, M. (2010). *Beitrag zur modellbasierten Ladedruckregelung für Pkw-Dieselmotoren*. Ph.D. thesis, Leibniz Universtät Hannover.

Utkin, V., Chang, H.C., Kolmanovsky, I., Cook, J., et al. (2000). Sliding mode control for variable geometry turbocharged diesel engines. In *American Control Conf.*, 584–588.

Wahlström, J. and Eriksson, L. (2011). Modelling diesel engines with a variable-geometry turbocharger and exhaust gas recirculation by optimization of model parameters for capturing non-linear system dynamics. *Journal of Automobile Engineering*, 225(7), 960–986.

CHAPTER 12

OPTIMIZATION

Evolutionary selection of optimal weighting matrices for LQR controllers and parameters of robust PID on benchmark plants

Jesús-Antonio Hernández-Riveros and Cindy-Vanessa Carmona-Cadavid
Universidad Nacional de Colombia – Sede Medellín, Facultad de Minas
{jahernan, cvcarmonac}@unal.edu.co

***Abstract*:** The optimal controller LQR (Linear Quadratic Regulator) is presently used for controlling complex systems when these have strict performance requirements. For its design, it is necessary to have a state space model and also the value of the Q and R matrices, which are essential components for the proper performance of the LQR algorithm on the process. The weighting matrices Q and R should be defined by the analyst to balance the regulation performance and the control effort, and to compare the results with the specified design goals. Iterative methods such as trial and proof, Bryson method or pole allocation, are commonly used for the tuning of those matrices; methods that to find a solution, take a significant time and in many cases fail to meet certain performance features in the process. The application of the LQR controller has been limited by the uncertainty in finding the right weighting factors. In this paper, the evolutionary algorithm MAGO (Multidynamics Algorithm for Global Optimization) is used for calculating the Q and R matrices. The LQR is tested on Benchmark type plants. The results are compared with PID (proportional, integral, derivative) controllers of the optimal and optimal-robust types. With the evolutionary process, uncertainty in the calculation of the matrices Q and R is eliminated. In addition, the LQR controller performs better when optimized with the MAGO algorithm.

Key Words: LQR, PID, Optimization, Robustness, Evolutionary Algorithms, Performance Criteria.

1. INTRODUCTION

Optimal control is a branch of modern control theory (Vinter, 2000) that focuses on those properties of the control strategies that provide solutions to problems by minimizing an objective function, or otherwise, a function depending on the performance of a system variable. Those indices or performance functions may include a measurement error, the control effort or some other important characteristic from the control system; performance indices most commonly used in control loops are: IAE, ITAE, IE and ISE (Åström and Hägglund, 1995). So, when minimizing some of these performance indices in conjunction with the controllers tuning, is a situation that can be formulated as an optimization case. A problem with this approach is that the controller and the plant are loosely coupled, yielding multiple kinds of uncertainty. Addressing this uncertainty, when tuning optimal controllers via an evolutionary algorithm, is the purpose of this paper.

An earlier step to the controllers tuning is the modeling of the plant; this allows us to design and select a control strategy. The model of a system or process is considered an imitation of reality where a mathematical model is a particular way of representing the dynamic effects of a system (Roffel and Betlem, 2006). Each model developed is directly related to the use stablished for it. When talking about models for control purposes, there are two main representations for the process: transfer function (Laplace domain) and state space; representations that are determined by the control strategy to be implemented.

The LQR (Linear Quadratic Regulator) is a control strategy well known in the modern theory of optimal control, for systems represented in state space. This strategy ensures certain characteristics of robustness in closed loop. LQR has been used in various fields of engineering (Lewis and Syrmos, 1995). This control strategy is based on developing a law of control, optimal and robust, that minimizes the sum of control efforts and the deviation of the output signal (state) from the desired value (Set-Point), giving a weighting to each of these through the matrices R and Q respectively. To generate or give value to these matrices are available for selection, the method of Bryson, pole allocation and the trial and proof method (Johnson, 1987), where the latter is the most used.

One of the current trends in the tuning of controllers is the use of Evolutionary Algorithms (EA) to determine the optimal parameters of the controller. AE have been used in various fields of engineering (Fleming and Purshouse, 2002), LQR tuning (Ghoreishi et al., 2011; Tijani et al,

2013; Hassani 2014) drivers in tuning PID controllers (Li et al., 2006; Hernández-Riveros, Urrea-Quintero, Carmona-Cadavid, 2014), showing successful solutions in each case applied.

AE are widely studied as a heuristic tool for solving nonlinear systems, continuous, discontinuous, convex and not convex optimization problems where traditional methods are not effective, and in many cases, to support successful solutions. AE are based on biological or natural principles for the study and design of human-made systems (Yu Xinjie and Mitsuo Gen, 2010), such as the theory of natural selection (Darwin, 1859), heredity (Ayala and Kiger, 1984) and population genetics (Fisher, 1930).

In this paper, the use of an evolutionary algorithm, MAGO, (Hernández and Ospina, 2010) as a tool to minimize a characteristic performance index in a control loop, to thereby obtaining optimal values of the controller parameters is proposed. MAGO only requires two parameters provided by the analyst: the number of generations and population size; features that facilitate its use. The results obtained for adjusting the weights of the Q and R matrices in the LQR controller are compared with LQR tuned by trial and proof (since this is one of the most used methods) and two PID strategies (optimum PID and optimum-robust PID). These last strategies are also tuned with MAGO because they have better performance when compared with traditional methods for tuning PID controllers optimizing some criterion of overall performance (Hernández-Riveros, Urrea-Quintero, Carmona-Cadavid, 2014). PID strategies as comparative method are applied because they are one of the control strategies most used in the industry.

This paper is divided into the four following topics: the problem of process representation, description of LQR and PID controllers, evolutionary tuning, result analysis and some conclusions.

2. PROCESS REPRESENTATION

A model is characterized by a structure that represents the formalization or abstraction of a given study process. At present, there are different applications for models and therefore several analytical approaches have yielded different structures or forms of models, such as those based on data (deterministic, stochastic), based on time (continuous, discrete), symbolic (mathematical, conceptual), etc.; these representations will be used upon the design criterion.

It should be remembered when achieving the objective of modeling, that the model should not be too complex, however, it should give a sufficient description of the system. That is, every model has a degree of uncertainty, either by lack of information or structural uncertainty, or by the approximation or parametric uncertainty (Roffel and Betlem, 2006).

For the design of controllers are used two typical representations of a system, they are state space and transfer function. These representations depend on the selected control structure. Currently, it is a fact that these two approaches, input-output and state space, complement each other, offering a much wider range for control systems.

2.1 State Space Models

The concept of state is proposed by Kalman in the early 1960s, and initiates what is known as modern control. Modern control refers to the control in state space. Its analysis is focused on three types of variables in the dynamic system, the input variable, the output variable and the state variables. Their general representation is given in equations (1-2):

$$\dot{x}(t) = f(x,u,t) \quad (1)$$

$$y(t) = g(x,u,t) \quad (2)$$

Where (1) is the equation of state of the system and (2) is the equation of system output. After linearizing equations (1-2) around a point of operation, the following invariants equations in time (3-4) are obtained.

$$\dot{x}(t) = Ax(t) + Bu(t) \quad (3)$$

$$y(t) = Cx(t) + Du(t) \quad (4)$$

Where A is an n_xn matrix, of the system states, B is an n_xm input matrix, C is a k_xn output matrix and D is a direct transmission k_xm matrix.

2.2 Transfer Function Model

The representation of the process in transfer function and block diagrams is widely used for the analysis and design of control systems. Although most processes are highly nonlinear, the approximation in transfer function is very useful for analysis of the system in open and closed loop operating around an operating point (Ogunnaike and Harmon, 1994). Its general form of representation is given by (5).

$$y(s) = G_P(s)u(s) \quad (5)$$

Where, *Gp(s)* represents the "transfer" of the input *u(s)* to the output *y(s)* of the process. Thus, an input-output structure of the system to be analyzed is obtainined.

2.3 Benchmark Models of the Plant

As a model of the plant, two test representations proposed by (Åström and Hägglund, 2000) are selected; the transfer function representation is used for tuning the PID controller and its state space representation for tuning the LQR.

2.4 Plant in Transfer Function

The models of the plant are present on equations (6) y (7).

$$G(s) = \frac{K_p e^{-\tau_m s}}{T_{m1}^2 s^2 + 2\xi_m T_{m1} s + 1} \quad (6)$$

$$G(s) = \frac{K_p e^{-\tau_m s}}{(1+T_{m1}s)(1+T_{m2}s)} \quad (7)$$

The values used in the plant represented by (6) are: Kp = 1, τm = 1, ξ = 1 y $Tm1$ in a range of 1, 10 and 20. For (7), the following values are used: Kp = 1, τ_m = 1, $Tm1$ = 1 and $Tm2$ = a*Tm1, where $a \leq 1$. In Tables 1 and 2, the transfer

functions according to the value of the parameters for each of the suggested plants are presented.

2.5 Plant in State Space

The systems with delay are classified in the infinite-dimensional models, because they are associated with the characteristic equation of infinite system's eigenvalues, i.e., infinite solutions to the problem; this is why for their analysis are used specific tools for finite-dimensional system (Niculescu et al., 1998). Among some of those tools are the Padé approximation, Fourier-Languerre series and the rational approach for the optimum of Hankel. Thus, a system with delay can be described in a finite-dimensional space where these changes are just alternative "forms" to analyze complex problems. In this paper, the Padé approximation is used for models (6) and (7), to obtain the 6 models presented in Tables 1 and 2, in its controllable canonical form (Levine, 1996) for its representation in state space. By the size of the matrices is presented as an example the model for the plant *G2* to *reg2* (7).

Table 1: Transfer Function for the plant (6)

Plant in the equation (6)	
$G_{p1\_servo1}(s)=\frac{e^{-s}}{s^2+2s+1}$	$G_{p1\_servo1}(s)=G_{p1\_reg1}(s)$
$G_{p1\_servo2}(s)=\frac{e^{-s}}{100s^2+20s+1}$	$G_{p1\_servo2}(s)=G_{p1\_reg2}(s)$
$G_{p1\_servo3}(s)=\frac{e^{-s}}{400s^2+40s+1}$	$G_{p1\_servo3}(s)=G_{p1\_reg3}(s)$

Table 2: Transfer Function for the plant (7)

Plant in the equation (7)	
$G_{p2\_servo1}(s)=\frac{e^{-s}}{(1+s)(1+0.1s)}$	$G_{p2\_servo1}(s)=G_{p2\_reg1}(s)$
$G_{p2\_servo2}(s)=\frac{e^{-s}}{(1+s)(1+0.5s)}$	$G_{p2\_servo2}(s)=G_{p2\_reg2}(s)$
$G_{p2\_servo3}(s)=\frac{e^{-s}}{(1+s)(1+s)}$	$G_{p2\_servo3}(s)=G_{p2\_reg3}(s)$

For the analysis in state space it is essential to ensure that the process is controllable, this is why the models obtained from (6) and (7) in the controllable canonical form, must meet the criterion of controllability, this criterion indicates the capacity of the system to reach a final status from any initial state.

$$A=\begin{bmatrix} -0.045 & -0.97 & -12.7 & -107.5 & -579.6 & -1814.4 & -2661.1 & -1330.7 \\ 1 & 0 & 0 & 0 & 0 & 0 & 0 & 0 \\ 0 & 1 & 0 & 0 & 0 & 0 & 0 & 0 \\ 0 & 0 & 1 & 0 & 0 & 0 & 0 & 0 \\ 0 & 0 & 0 & 1 & 0 & 0 & 0 & 0 \\ 0 & 0 & 0 & 0 & 1 & 0 & 0 & 0 \\ 0 & 0 & 0 & 0 & 0 & 1 & 0 & 0 \\ 0 & 0 & 0 & 0 & 0 & 0 & 1 & 0 \end{bmatrix} \quad (8)$$

$$B=\begin{bmatrix} 1 \\ 0 \\ 0 \\ 0 \\ 0 \\ 0 \\ 0 \\ 0 \end{bmatrix} \quad C=\begin{bmatrix} 0 & 2 & -84 & 1680 & -20160 & 151200 & -665280 & 1330560 \end{bmatrix} \quad D=0$$

For this case, the controllability matrix is found and calculated and therefore is verified that the range of the matrix "A" and the range of the array "ctrb" for each of the proposed cases have a value of equal rank and corresponds to (8) .

3. TUNING OF CONTROLLERS

Tuning controllers consists in determining the best values of a set of parameters to drive the selected control strategy ensuring that the process behavior meets design specifications. The tuning may be also optimal under some performance criterion. There are two forms of operation of the controller: as regulator, where the desired value *ysp* (reference value or Set-Point) remains constant so the system should be insensitive to disturbances, and as servomechanism, where the desired value *ysp* can change over time, so that a good tracking of this is desired.

3.1 Linear Quadratic Regulator –LQR

The LQR since its introduction in the early 1960s is a control strategy that has been in the focus of research. One of the most representative properties of this control strategy is that automatically ensure closed-loop stability because it has wide margins of phase and gain (Levine, 1996), features that give robustness to the control loop.

For the development of the LQR controller, the plant must be described in state space, equations (3-4). From this restriction, a quadratic objective function is defined and represented as a function of the states *x (t)* and the input *u (t)* as in equation (9).

$$J=\int_{t1}^{tf}\left(x^T(t)Qx(t)+u^T(t)Ru(t)\right)dt \quad (9)$$

Where Q is an $n\times n$ matrix and R is an $m\times m$ matrix, semi-definite and positive-definite respectively, assigning weights to each of the terms of the function, i.e. a balance in output and input "energies" of the plant is performed. The control law that governs this structure of optimal states feedback control is given in (10).

$$u(t)=-Kx(t) \quad (10)$$

$$K(t)=R^{-1}B^TP(t) \quad (11)$$

$$\dot{P}(t)=P(t)BR^{-1}B^TP(t)-Q-P(t)A-A^TP(t) \quad (12)$$

Equation (12) is the *matrix Riccati differential equation*. When the final time (*tf*) of the integral in (9) tends to infinity, the solutions of the Riccati equation will remain constant at the value of the initial time, therefore equation (12) equals zero, obtaining the *algebraic equation Riccati*. There is only one solution for P (t), when solving this equation, if it is replaced in (11) an optimal constant value K for states feedback is obtained.

3.2 Tuning methods for LQR

For tuning the Q and R parameters of LQR controller, different methods are used, (Ghoreishi, 2001), some of them are:

a. Bryson Method: Based on the normalization of variables seeking the maximum acceptable value will be one. This is because the units of the states "x" (for the Q matrix) and control action "u" (for the R matrix) are very different. See equation (13). Although in many cases this method can produce very good results, usually is applied as a starting point and then the tuning is refined by trial and proof.

$$Q = diag\{q_1,...,q_n\} \quad R = diag\{r_1,...,r_m\}$$

$$q_i = \left\{\frac{1}{x_i^2(\max)}\right\}_{i=1}^{n} \quad r_j = \left\{\frac{1}{u_j^2(\max)}\right\}_{i=1}^{m} \qquad (13)$$

b. Trial and Proof Method: (or heuristic method) is an iterative process that makes use of prior knowledge and behavior of the system to control with the purpose of adjusting the matrices Q and R such that a desired behavior is achieved. The method requires a large amount of time to obtain a satisfactory response. One commonly used option is to take as a starting matrices Q and R, those in equation (14a).

$$Q = P*(C'C)$$
$$R = dig\{r_1,...,r_m\} \qquad (14a)$$

With a positive real multiplicative factor *P* varying until obtaining the desired value and for *R* a constant value that its size will depend on the number of entries to the system *u(t)*.

Another trial and proof way for tuning the LQR controller is the manual application of the Bryson method, equation (14b).

$$Q = dig\{q_1,...,q_n\}$$
$$R = dig\{r_1,...,r_m\} \qquad (14b)$$

c. Pole Allocation Method: With this method, the poles of the closed loop system are placed in certain values defined by the analyst, all thanks to prior knowledge of the process. For using this method it is necessary to have actual measurements or otherwise apply observers to estimate the actual value of the process variables, for which there is no physical measurement.

It is evident that although there are different tuning methods for the LQR controller, all require at the end a tuning by trial and proof to achieve the desired results in the process. Some methods need bay by trial and proof a starting point for some possible values of the parameters Q and R. It can be concluded that with just this method is possible to obtain optimum tuning parameters for the LQR controller. This is the path taken in this paper.

3.3 Optimal PID Controller

The Proportional Integral Derivative Controller, PID, is one of the feedback control algorithms most widely used in industry and with an extensive background (Åström and Hägglund, 1995; O'Dwyer, 2009). The output, *u*, (control action) is a composite of three effects, *Kc* the proportional action, *Ti* the integral time and *Td* the derivative time, which are calculated on the basis of the difference between the desired value (Set-Point) of the controlled variable *ysp* and the actual controlled variable *y*. The control law in continuous time for the ideal PID controller is presented in equation (15).

$$u(t) = K_c * \left[e(t) + \frac{1}{T_i}\int_{t_{ini}}^{t} e(t)\,dt + T_d\frac{de(t)}{dt} \right] \qquad (15)$$

An optimal PID controller consists in adjusting its parameters *Kc*, *Ti* and *Td* so that an objective function (error between the actual output of the plant regarding the desired value and / or effort control) is minimized. See Equation (16).

$$J(\underbrace{K_c, \quad T_i, \quad T_d}_{x}) = \min_x \left\{ J_{ITAE} = \int_0^{\infty} t\,|e(t)|dt \right\} \qquad (16)$$

3.4 Optimal Robust PID

A robust PID controller is a control strategy that meets a measure of specific robustness that is, finding a quantitative measure of how stable is the control loop. For knowing robustness have different alternatives, highlighting the methods based on the internal model control (Rivera et al, 1986) and those considering the tuning from the values of margin of phase and closed loop gain (Lee, 2004). The latter leaded to the use of the maximum sensitivity function (called *Ms*) as a measure of system robustness (Aström & Hägglund, 2004; Alfaro et al, 2009).

The margins of phase, *Am*, and the phase, *φm*, in the frequency domain are defined in equations (17) and (18), respectively

$$A_m = \frac{1}{|G_c(j\omega_p)G(j\omega_p)|} \qquad (17)$$

$$\phi_m = \arg|G_c(j\omega_g)G_p(j\omega_g)| + \pi \qquad (18)$$

Where, ω_p and ω_g are obtained through the equations (19) and (20).

$$|G_c(j\omega_p)G(j\omega_p)| = 1 \qquad (19)$$

$$\arg\left[G_c(j\omega_g)G(j\omega_g) \right] = -\pi \qquad (20)$$

The gain margin as a measure of robustness indicates that in the event that the system model is incorrect, the static gain may increase in a factor Am before the system becomes unstable. Typical specification values for the gain margin are $2 \leq Am \leq 5$.

The phase margin as a measure of robustness indicates that if there is an error in modeling the process, this may suffer an additional phase delay of φm degrees, on the frequency ωg, before the system becomes unstable. Typical specification values for phase margin are $30° \leq \varphi m \leq 60°$.

The sensitivity function (21), is used to determine the control loop tolerance to variations in the process to be controlled, but now is applied to establish a measure of robustness (21).

$$S(s) = \frac{1}{1 + G_c(s)G_p(s)} \tag{21}$$

$$M_S = \max_{\omega} |S(j\omega)| = \frac{1}{\min_{\omega} |1 + G_c(j\omega)G_p(j\omega)|} \tag{22}$$

When thinking in the design of controllers, it is desirable to have small values of *Ms* because a high robustness is obtained. This measure of robustness (M_S) can simultaneously ensure bounds for the gain and phase margins (23), (Vilanova & Alfaro, 2011).

$$A_m \geq \frac{M_S}{M_S - 1}, \phi_m \geq 2\sin^{-1}\left(\frac{1}{M_S}\right) \tag{23}$$

Typical values of *Ms* range in the order of 1.4 to 2; involving for the case of $Ms = 2$, an $Am \geq 2$ and an $\varphi m \geq 29°$. In the case of $Ms = 1.4$, values of $Am \geq 3.5$ and $\varphi m \geq 41°$ are guaranteed.

A robust optimal PID controller is one that meets simultaneously with an index of performance and a specified measure of robustness. This measure is established as an additional constraint in the optimization problem, minimizing a target function, for example an integrated performance index

4. EVOLUTIONARY TUNING

4.1 Optimization Criteria

To ensure an optimal performance of the control loop and additionally its effect is reflected in the control objective (assuring quality, efficiency in the final product) is necessary to associate the control problem to a performance index. For our particular case, the optimum parameters Q and R of LQR controller are obtained when a criterion of overall performance of the control loop is minimized. These results will be compared with the response of the system using a PID (optimal and robust) tuned by an evolutionary algorithm.

In many cases it is easier to represent the performance of the control loop in the time domain, because it presents an overview of the whole problem without going into specifics. When thinking an optimization problem is more "easy" to design a control strategy when considering as objective function an overall performance index (Levine, 1996, chapter 10.2) such as: IAE (24) and ITAE (25).

$$IAE = \int_0^{\infty} |e(t)| dt \tag{24}$$

$$ITAE = \int_0^{\infty} t|e(t)| dt \tag{25}$$

It is not often that such performance indices are used to tuning controllers in the field, but they are commonly used in the design of automatic tuning algorithms and as a reference point for the control strategies simulation (Levine, 1996 chapter 70.3).

4.2 Evolutionary Algorithms

Evolutionary Algorithms (EA) emulate the synthetic theory of evolution or neo-Darwinian theory of natural selection, which merge the theory of natural selection (Darwin, 1859), heredity (Ayala and Kiger, 1984) and genetic population (Fisher, 1930). The evolution can be seen as the change in the genetic characteristics in a population. In every species there are variations that are inherited and inheritable and others are modified due to the environment. Hereditary variations (caused by mutations) occurring randomly in all organisms are the raw material of evolution acting the natural selection on them. Synthetic theory of evolution says that mutation and natural selection complement each other, and none of these processes, by itself, can lead to evolutionary change.

As natural evolution begins with an initial population of individuals, an evolutionary algorithm begins with the selection of an initial set of potential solutions to a particular problem; this set can be selected randomly or using prior information of the problem. AE include operators to select and create a sequence of new individuals. These operators are crossover and mutation. The crossover operator performs an exchange of genetic material between "parents" to generate new "spring" and the mutation operator makes small variations in the "parents". Once a new set of possible solutions is generated, it is evaluated using a "fitness" function. The best individuals are favored “survival of the fittest”, leaving these as new parents and the process is cyclically repeated to find the best solution in a delimited search space

4.3 Multidynamics Algorithm for Global Optimization

The Multidynamics Algorithm for Global Optimization (MAGO, by acronym) is an evolutionary heuristic method that transforms groups of individuals to achieve a goal, resembling their behavior to the process of evolution of species. Formally presented in (Hernandez and Ospina, 2010), MAGO was born of a hybrid among estimation distribution algorithms and statistical control of quality. As in EA, MAGO begins with a population of possible solutions randomly distributed throughout the search space, which is divided autonomously by the algorithm in three subgroups, with its own evolution. In every generation the actual entire population is observed as having a normal distribution, with the aim of establish according to the different levels of standard deviation how many individuals will belong to each subgroup. Thus, the exploration is done by creating new individuals that are governed by any of these subgroups or dynamics. The cardinality of these subgroups changes in each generation, according to a rule inspired by methods of statistical control. MAGO uses the

covariance matrix of the population of each generation, to establish a distribution of exploration and create three subgroups or dynamics making the whole individuals in each generation. The subgroup named Emerging Dynamics (G1) creates a small group of individuals around the individual with better genetic characteristics; this group is the evolutionary elite of each generation, i.e. fittest individuals to contribute with their genes to the next generation. The Crowd Dynamics (G2) follows a similar process, around the current population mean, applied to a largest portion of the population. This dynamics is always close to the emerging dynamics, but never close enough to be confused. Only until there are sufficient and necessary conditions to ensure full exploration of the search space, these two dynamics could be merged within a territory, usually at the end of the evolutionary. The Accidental dynamics (G3) is the quantum speciation. It is established in isolation from individuals of the other dynamics in generation by generation. This portion of the population is always formed spontaneously and contains a number of entirely new individuals. Thus the main diagonal of the covariance matrix is different from zero, ensuring numerical stability of the evolutionary process. G1, G2 and G3 cannot interbreed.

The Emerging Dynamics is created with N1 test individuals being better than their predecessors, and the original elite group of individuals who were not defeated by the individuals tested. A number of the fittest individuals move towards the best of the entire population. For each of these individuals a mutant is created using a stochastic crossover between the chosen individual and the best of all. This mutant is evaluated using the objective function, and if its value is better than that obtained in the test individual, the mutant is who goes to the next generation rather than its predecessor. For each individual, *i*, in the generation, *j*, $x_i^{(j)}$, a test individual, *t*, is created according to the rule presented in equation (26).

$$x_t^{(j)} = x_i^{(j)} + F^{(j)}\left(x_B^{(j)} - x_m^{(j)}\right) \tag{26}$$

Where $x_B^{(j)}$ is the best of all individuals in the generation *j*, and the mean of the population is $x_m^{(j)}$. To incorporate information about the present characterizations between the problem variables, the matrix $F^{(j)}$ is chosen as defined in equation (27). Where, $S^{(j)}$ is the simple covariance matrix of the individuals in generation *j*.

$$F^{(j)} = S^{(j)} \Big/ \left\| S^{(j)} \right\| \tag{27}$$

The Crowd Dynamics is created with N2 individuals through a uniform distribution in the hyper-rectangle $[LB^{(j)} \quad UB^{(j)}]$.

For its part, the Accidental Dynamics introduces in each generation N3 new individuals, created by a uniform distribution over the whole search space. Thus, the dispersion of the population and diversity are always guaranteed, even if the other two groups already have converged.

The covariance matrix of the population, $S^{(j)}$, and its diagonal $diag(S^{(j)})$ are taken into account for the cardinality of each dynamics in the generation j. If $Pob^{(j)}$ is the possible solutions set under consideration in the generation *j*, the three groups can be defined as in equation (28). If N1, N2 and N3 are the cardinalities of the sets G1, G2 and G3, then the cardinality of the Emerging Dynamics, Crowd Dynamics and Accidental Dynamics are set, respectively. This way of defining the elements of each group is dynamic in nature and autonomous in MAGO. Cardinalities depend on the dispersion of the whole population in generating *j*.

$$\begin{aligned}
G_1 &= \left\{ x \in Pob(j) \Big/ \begin{array}{l} XM(j) - \sqrt{diag(S(j))} <= x \\ <= XM(j) + \sqrt{diag(S(j))} \end{array} \right\} \\
G_2 &= \left\{ x \in Pob(j) \Big/ \begin{array}{l} XM(j) - 2\sqrt{diag(S(j))} < x \\ <= XM(j) + \sqrt{diag(S(j))}, or, \\ XM(j) + \sqrt{diag(S(j))} <= x \\ < XM(j) + 2\sqrt{diag(S(j))} \end{array} \right\} \\
G_3 &= \left\{ x \in Pob(j) \Big/ \begin{array}{l} x <= XM(j) - 2\sqrt{diag(S(j))}, or, \\ x >= XM(j) + 2\sqrt{diag(S(j))} \end{array} \right\}
\end{aligned} \tag{28}$$

Where, $XM(j)$ is the mean of the actual population and $Pob(j) = G1 \cup G2 \cup G3$.

Following, the pseudo algorithm of MAGO is presented.

Pseudocode of MAGO

1: j = 0, Generation of the initial population, with a uniform randomly distribution in the search space.
2: Repeat
3: Evaluate each individual by means of the objective function
4: Calculate the covariance matrix of the population and the first, second and third dispersion.
5: Calculate the N1, N2 and N3 cardinalities of groups G1, G2 and G3.
6: Select N1 of the best individuals, modify according to the objective function and make them compete. Winners pass to the next generation j + 1.
7: Sampling N2 individuals from the uniform distribution in the hyper rectangle [LB (j), UB (j)], and move on to the next generation j + 1.
8: Sampling N3 individuals from the uniform distribution throughout the whole search space and move to the next generation j + 1.
9: j = j + 1
10: Do until a termination criterion is satisfied.

Figure 1 shows the flowchart of the MAGO.

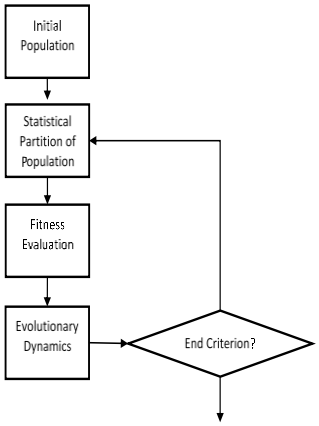

Figure 1: General scheme of MAGO.

4.4 Optimization Problem

AE have been used successfully in the tuning of the Q and R matrices from LQR controllers (Ghoreishi et al., 2011; Tijani et al, 2013) and tuning parameters of PID (Li et al controllers, 2006, Hernandez-Riveros, Urrea-Quintero, Carmona-Cadavid, 2014). MAGO as optimization tool has presented efficient outcomes when facing with problems in the continuous domain (Hernandez and Villada, 2012). Here, MAGO is used for tuning the LQR and PID controllers, minimizing the ITAE as performance criterion of the control loop.

The optimization problem for the LQR controller is defined in equations (29) and (30) respectively.

$$LQR \rightarrow J(\underbrace{Q, \quad R}_{x}) = \min_{x}\left\{J_{ITAE} = \int_0^{\infty} t\left|e(t)\right|dt\right\} \quad (29)$$

Where, Q and R, are definite positive matrices, represented in equation (31).

$$Q = dig\left[x1 \quad x2 \quad x3 \quad x4 \quad x5 \quad x6 \quad x7 \quad x8\right] \quad (30)$$

$$R = x9$$

The optimization problem for the PID controller is defined in equation (31).

$$PID \rightarrow J(\underbrace{K_c, \quad T_i, \quad T_d}_{x}) = \min_{x}\left\{J_{ITAE} = \int_0^{\infty} t\left|e(t)\right|dt\right\} \quad (31)$$

$$Sujeto\_a : 1.4 \le M_s \le 2$$

Where, Kc, Ti, Td are tuning parameters taking positive real values for the robust optimal PID controller.

5. RESULT ANALYSIS

MAGO has been used for tuning the robust LQR and PID controllers. MAGO setting parameters are 150 generations and 100 individuals. The ITAE values obtained in simulations using MAGO as an optimization tool are presented In Table 3. Column 1 shows the models described in Tables 1 and 2; column 2 shows the control loop performance index ITAE, which is divided into four columns: first, the values obtained in (Hernández-Riveros, Urrea-Quintero, Carmona-Cadavid, 2014) for the PID controller, in the second, the PID with an additional robustness criterion, third the LQR selecting optimally via MAGO the parameters Q and R and finally, LQR manually tuned by trial and proof.

For plants in the mode of regulation Gp2_Reg, see Table 2, equation (6), shown in Figure 2, all the responses obtained with the PID MAGO present oscillation. In responses obtained with the robust PID small oscillations are also appreciated. This is not observed in the results presented for the LQR tuned by trial and proof and with MAGO, where for all plants operating as regulator, smooth responses without oscillations were obtained. For comparison, the PID Robust is used, but it can be seen evidently that the LQR-MAGO performs better in all cases.

Table 3: Performance Index, ITAE, for different control strategies.

PLANT	ITAE			
	Óptimal PID	Robust Optimal PID	LQR-MAGO	LQR-Manual
Gp2_Reg1	3.1052	3.1456	0.0528	0.3665
Gp2_Reg2	3.6071	5.5162	0.0633	0.3838
Gp2_Reg3	3.6738	4.7662	0.0699	0.3908
Gp1_Servo1	2.0486	2.2160	1.0371	1.5997
Gp1_Servo2	2.8532	4.1787	0.9531	1.7051
Gp1_Servo3	2.7827	2.8601	1.5140	3.1584
Gp1_Reg1	3.6623	4.8168	0.0700	1.1311
Gp1_Reg2	3.6427	4.2466	0.1904	2.3062
Gp1_Reg3	4.4240	3.4411	0.2806	1.4324
Gp2_Servo1	72.686	1.3717	0.7030	1.0120
Gp2_Servo2	69.494	1.9321	1.0128	1.7356
Gp2_Servo3	63.241	2.0490	0.9911	1.5473

Responses tuning the Q and R parameters by MAGO are presented in Figure 3, for Gp1_Servo plants, corresponding to Table 1, equation (5). These responses are smoother than those obtained with PID-MAGO and robust-PID- MAGO. The LQR-MAGO presents a small over peak, but not affecting significantly the value of ITAE performance criteria, achieving a shorter establishment time than the other three control strategies.

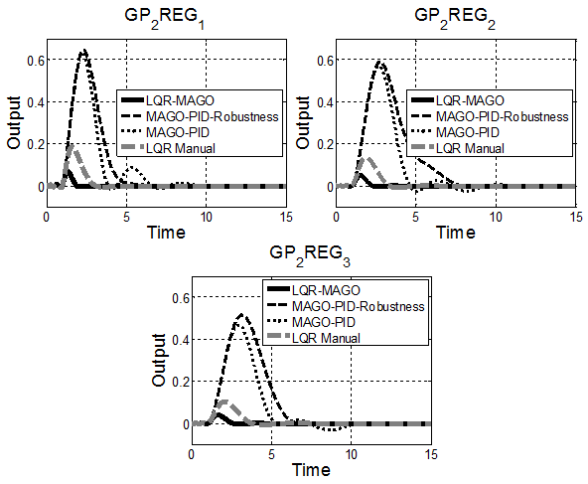

Figure 2: Response of plant 2 as regulator.

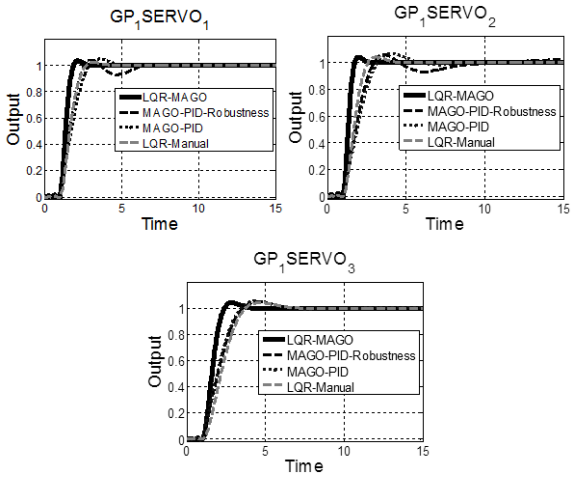

Figure 3: Response of plant 1 as servomechanism.

For Gp1_Reg plants, corresponding to Table 1, equation (5), Figure 4 shows the comparative results of the four controllers for each of the proposed cases revealing their own robust characteristics and also good performance in systems operating as regulator. For this particular case, the evolution of dynamics of the optimization algorithm MAGO is presented in Figure 5 together the evolution of the objective function (ITAE) throughout the generations.

Regarding the evolution of the objective function, around the 100th generation the ITAE remains constant, giving to think that the algorithm has already found the solution. But when the behavior of the dynamics of MAGO are checked (Emergent, Crowd and Accidental), it can see that the dynamics are not yet stable, as the Emerging Dynamics dominates too quickly, but in generation 120 a better individual is found and therefore Emerging Dynamics decreases and the Crowd Dynamics grows.

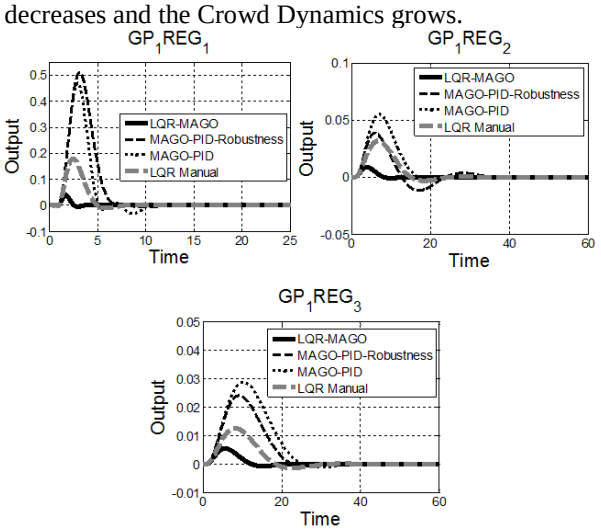

Figure 4: Response of plant 1 as regulator.

In Figure 6, a predator-prey behavior type is observed for the Emerging and Crowd Dynamics, characteristic of the behavior of the species in Nature. For this particular case the predator, that is, the individual who benefits from the quarry to preserve its species is the Emerging Dynamics and the Crowd Dynamics is the prey. When there is very little population in the Emerging Dynamics, i.e. very few predators, it is evident that the Crowd Dynamics increases; and when the Emergent Dynamics increases, decrease the Crowd Dynamics. Where there is a point when the Emerging Dynamics dominates, that is the predator, indicating that more generations are needed. Additionally, in Figure 6, the behavior of population in different generations is shown.

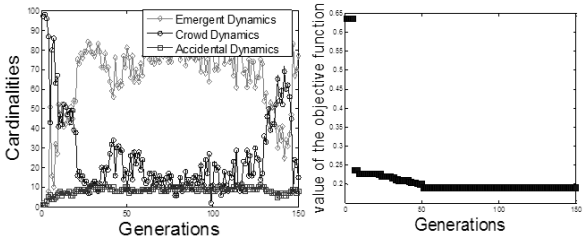

Figure 5: a) Cardinalities, b) Value of function (ITAE)

Regarding the evolution of the objective function, around 100th generation the ITAE remains constant, giving to think that the algorithm has already found the solution. But when the behavior of the dynamics of MAGO are checked (Emergent, Crowd and Accidental), it can see that the dynamics are not yet stable, as the Emerging Dynamics dominates too quickly, but in generation 120 a better individual is found and therefore Emerging Dynamics decreases and the Crowd Dynamics grows. In Figure 6, a predator-prey behavior type is observed for the Emerging and Crowd Dynamics, characteristic of the behavior of the species in Nature. For this particular case the predator, that is, the individual who benefits from the quarry to preserve its species is the Emerging Dynamics and the Crowd Dynamics is the prey. When there is very little population in the Emerging Dynamics, i.e. very few predators, it is evident that the Crowd Dynamics increases; and when the Emergent Dynamics increases, decrease the Crowd Dynamics. Where there is a point when the Emerging Dynamics dominates, that is the predator, indicating that more generations are needed. Additionally, in Figure 6, the behavior of population in different generations is shown.

The first image corresponds to the initial population matching to the variables X1 and X2, that is, 2 of the 10 variables used in MAGO for tuning the LQR. For generation 2, how the dynamics discriminate can see, in generation 8 the search space has been explore to find the best individual, this displacement is apparent in the following generations.

In Figure 7, results obtained for the four control strategies are presented.

Due to its characteristics of robustness, the LQR has very good results in processes that operate as a regulator, which is evident in soft and rapid responses in the simulation of the three plants.

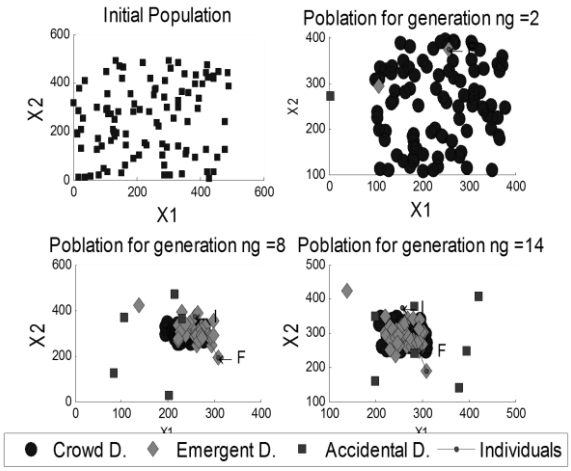

Figure 6: Population

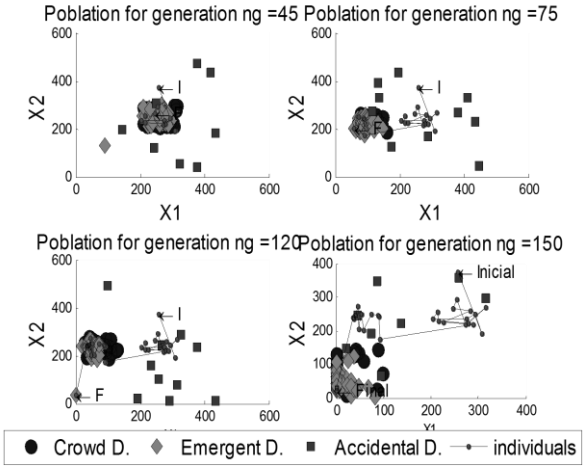

Figure 7: Dynamics Evolution (cardinalities) of MAGO.

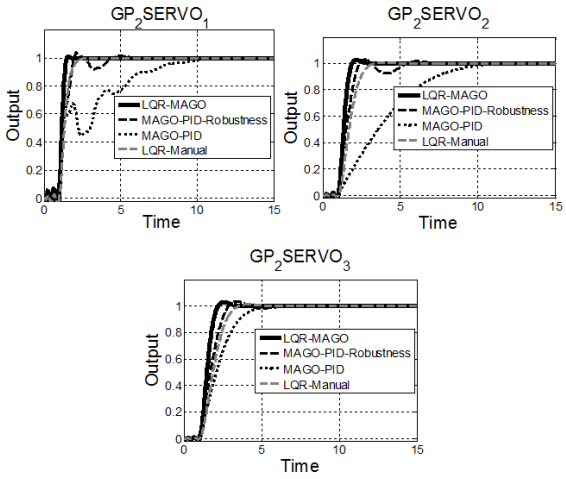

Figure 8: Response of plant 2 as servomechanism.

6. CONCLUSIONS

When talking about tuning controllers, either PID or LQR (strategies that are discussed in this paper), everything is reduced to the characterization and adjusting of the value of three or more tuning parameters, generally obtained by trial and proof, to ensure the desired performance of the control loop. This tuning procedure involves uncertainty and time to obtain the right controller parameters. This challenge has been solved applying the evolutionary algorithm MAGO as a tool of optimization; where for each of the cases studied successful results are achieved in obtaining the optimum tuning values of parameters Q and R for the LQR controller. Likewise for Kc, Ti, Td parameters of the optimal PID controller considering an additional robustness index in the optimization problem. When the performance of each one of the control strategies discussed is compared, better results for the LQR case tuned with the algorithm MAGO are noticeable; highlighting LQR characteristics controller in terms of robustness. With this evolutionary adjustment of the Q and R weight matrices and the PID parameters calculation, uncertainty is removed and best of the benefits from this type of control loops can be taking as advantage.

ACKNOWLEDGEMENTS

The participation of Cindy-Vanessa Carmona-Cadavid was partially sponsored by the Project 645 Young Researchers 2015, from COLCIENCIAS.

REFERENCES

Alfaro V. M., Vilanova R., Arrieta O. 2009. Robust tuning of Two-Degree-of-Freedom (2-DoF) PI/PID based cascade control systems. *Journal of Process Control*, 19(10), 1658-1670.

Åström K. J., Hägglund T., 1995. *PID Controllers: Theory, Design, and Tuning*, ISA, Research Triangle Park, NC.

Åström K. J., Hägglund T., 2000. Benchmark Systems for PID Control. *IFAC Workshop on Digital Control -Past, present, and future of PID Control*. Spain.

Åström K. J., Hägglund T. 2004. Revisiting the Ziegler–Nichols step response method for PID control. *Journal of process control*, 14(6), 635-650.

Ayala F. J., Kiger J. A. 1984. *Genética moderna*. Ediciones Omega, Barcelona, España.

Beker-Jr G. A., Gammel J. L. 1961. The Padé Approximant. *Journal of Mathematical Analysis and Applications*, 2, pp. 21-30.

Darwin C. 1859. *The origin of species*. London: John Murray.

Fisher R. A., (1930). *The genetical theory of natural selection.* Oxford University Press, Oxford

Fleming P. J., Purshouse R. C. 2002. Evolutionary algorithms in control systems engineering: a survey. *Control Engineering Practice*, *10*(11), 1223-1241.

Ghoreishi S. A., Mohammad, A. N., Basiri S. O. 2011. Optimal Design of LQR Weigthing Matrices based on Intelligent Optimization Methods, *International Journal of Intelligent Inofrmation Processing*, 2(1), pp.

Glacier C., Hognas G., Makita P., Toivonen H. T. 1991. Approximation of delay systems - a case study. *International Journal of Control*, 53 (2), pp. 369-390.

Hangos K., Cameron I., 2001. *Process Modelling and Model Analysis.* Elsevier Science. Vol. 4 Process Systems Engineering.

Hassani K., Lee Won-Sook. 2014. Optimal Tuning of linear Quadratic Regulators Using Quantum Particle Swarm Optimization. In *Proceedings of the Int. Conference of Control, Dynamic Systems, and Robotic*.59,1-59,8.

Hernández J. A., Ospina J. D., 2010. A multi dynamics algorithm for global optimization. *Mathematical and Computer Modelling*, *52*(7), 1271-1278.

Hernández-Riveros Jesús-Antonio, Villada-Cano Daniel., 2012. Sensitivity Analysis of an Autonomous Evolutionary Algorithm. *Lecture Notes in Computer Science. Volume 763. Advances in Artificial Intelligence.* Springer.

Hernández-Riveros Jesús-Antonio, Urrea-Quintero Jorge-Humberto, Carmona-Cadavid Cindy. 2014. Evolutionary Tuning of Optimal Controllers for Complex Systems. *In Proceedings of the International Conference on Evolutionary Computation Theory and Applications (ECTA-2014)*, pp. 11-20.

Lee C. H. 2004. A survey of PID controller design based on gain and phase margins. *International Journal of Computational Cognition*, 2(3), 63-100.

Levine W. S. 1996. *The Control Handbook*. U.S.: CRC Press.

Lewis F. L., Syrmos V. L. 1995.*Optimal Control*. New York: Wiley.

Li Y., Ang K. H., Chong G. C. 2006. PID control system analysis and design. *IEEE Control Systems Magazine 26*(1), 32-41.

Niculescu S. I., Verriest E. I., Dugard L., Dion J. D. 1998. Stability and Robust Stability of Time-Delay Systems: A Guided Tour. *Stability and Control of Time-Delay Systems*. London; Springer-Verlag, 228, pp. 1-71.

O'Dwyer A. 2009. *Handbook of PI and PID Controller Tuning Rules. (Vol. 2).* Imperial College Press. London.

Ogunnaike B. A., Harmon A. 1994. *Process Dynamics, Modeling, and Control*, Oxford University Press.

Rivera D. E., Morari M., Skogestad S. 1986. Internal model control: PID controller design. *Industrial & engineering chemistry process design and development*, 25(1), 252-265.

Roffel B., Betlem B., 2006. *Process Dynamics and Control: Modeling for Control and Prediction*, John Wiley & Sons Ltd. Chichester, England.

Tijani I. B., Akmeliawati R., Abdullateef A. I. 2013. Control of an inverted pendulum using MODE-based optimized LQR controller. *8th IEEE Conference on Industrial Electronics and Applications (ICIEA)*.

Xinjie Yu., Mitsuo Gen. 2010. *Introduction to Evolutionary Algorithms*. Springer, London.

Evolutive Extension: A biological approach to heuristic algorithms ⋆

A. Pérez-González, O. Begovich, J. Ruiz-León

CINVESTAV-IPN Unidad Guadalajara Zapopan, Jalisco, Mexico.
Email: [aperez, obegovi, jruiz]@gdl.cinvestav.mx

Abstract: In this paper, we propose an extended form of bio-inspired heuristic algorithm, called Evolutive Extension (EvE) in this work, based on the evolutive approach. EvE is an optimization algorithm which considers several nature examples to construct a list of norms and procedures in search to obtain a better performance than other heuristic algorithms. This method, as many similar ones, is focused on the task of finding an optimum solution to a minimization problem. Using as a base method the Differential Evolution algorithm (DE), EvE includes the abstraction of natural phenomena like elitism, extinction, symbiosis, parasitism, and different forms of reproduction. The study of performance is carried out by a statistical analysis of the results obtained from several executions over a list of typical test functions. The performance of the algorithm and its comparison against the performance of the original form of Differential Evolution is shown. This investigation includes the analysis of the calibration parameters for EvE, also seen from a statistical approach. The presented results show a better performance for EvE algorithm, due to its low number of iterations required to achieve the minimum for each of the test functions proved in this paper. Also, for EvE algorithm it is possible to define a region in which one lies the calibration parameters that allows to the algorithm to solve all the presented tests functions in the less number of iterations, which gives an easy reference to tune up the algorithm.

Keywords: Evolutive Extension, Differential Evolution, Optimization, Heuristic Method, Bio-inspired Algorithm.

1. INTRODUCTION

Heuristic methods take significant relevance, due to their ability to handle a great number of engineering problems that do not have an analytic solution, or the solution of the problem is too complex to obtain (Cooper (1964)), (Pearl (1984)). The heuristic methods offer a good solution if we consider that not always the optimum solution is reachable by the algorithm, but the solution found is acceptable, and the time required to compute it can be considerably low.

A common approach for heuristic methods is the bio-inspired trend: Genetic Algorithms: Houck et al. (1995), Evolutive Computing: Eiben and Schoenauer (2002), social behavior-based algorithms (like Ant Colony: Bilchev and Parmee (1995), or PSO: Pérez-González et al. (2014)), Evolutive Methods: Mühlenbein et al. (1988), etc. This investigation selects the evolutive methods as base of construction, due to the easy and universal understanding of the behavior of life as a constant mechanism of adaptation and optimization. Evolution represents the nature's way to solve a problem. This perspective motivates the attempts to replicate the behavior of evolution in a computational algorithm, where a problem represents the natural environment, and each possible solution is a member of a population in constant fight to survive.

Evolutive methods are based on populations of solutions. Thus, for each iteration of an evolutive algorithm, there is not a unique solution, but a set of them. These methods are based on generating, selecting, combining and replacing a set of solutions. Due to the maintenance of a group instead of a unique solution throughout the entire search process, evolutive methods usually present higher computing times than another heuristic methods (Cormen et al. (2001)).

In an evolutive method, the evolution process operates over the chromosomes, and not directly over the individuals. This allows a "natural selection" procedure, in which the chromosomes with better properties are most often reproduced. In this reproduction process, evolution takes place by means of the combination of the chromosomes of the parents. This process is called recombination. Besides the recombination process, mutations must be considered as a way to alter the chromosomes of any member of the population. Also, an evolutive algorithm is considered as a "no-memory" method, because in the process of formation of chromosomes, only information from the previous period is considered (Bäck (1996)).

An evolutive algorithm integrates and implements efficiently two fundamental ideas: simple representations for the solutions of the problem and simple

⋆ The research of J. Ruiz-León was performed during his sabbatical stay at the Institute of Information Theory and Automation, Czech Academy of Sciences, supported by CONACyT, Mexico, project 265475.

transformations to modify and improve these representations (Martı (2003)). To put in practice this scheme in a computational algorithm, it is necessary: to specify a chromosomic representation, where the number of chromosomes is proportional to the size of the problem; an initial population built in this representation; and a stop criterion based on a finite number of iterations or in an error bound. Also, an evaluation measure is necessary to establish a selection-elimination criterion for chromosomes, and finally it is needed to define one or more recombination rules, and one or more mutation rules (Fleetwood (2004)).

As we mentioned before, there are many optimization algorithms in the bio-inspired approach, and many of them use the evolutive structure. Evolutive algorithms commonly use a binary codification to represent the chromosomic form for each candidate solution in the search space of a problem. This binary representation simplifies the execution of tasks as recombination and mutation, because it is only necessary to replace some bits into the complete chain to perform those instructions, but it is also necessary to translate the original form of the search space to a binary representation, and backwards to the original form after all the evolutive operations (Schmitt (2001)). Only the translation cost can be expensive for some applications, where it is preferable to work directly over the original search space.

Differential Evolution (DE) is a bio-inspired algorithm that deals with that situation, when the search space is a subset of $\Re^n$. Using a set of simple arithmetic rules, DE deals with the mutation and recombination tasks, showing a great capacity to solve problems of high complexity (Storn and Price (1997)).

The aim of this work, is to propose an extension of the DE algorithm, the Evolutive Extension (EvE) algorithm. EvE is based on the inclusion of operations than can represent some natural phenomena trying to improve the searching capacity of the original algorithm. These new rules are introduced in order to modulate the capacity of greedy search, multiple initialization, premature convergence and regional search, as characteristics that define the performance of a heuristic algorithm, according to Storn and Price (1995).

The main contribution of this work is the proposal of the EvE algorithm itself. Of course, it is necessary to include not only the structure of the algorithm, but also its performance, comparing it with the original Differential Evolution algorithm, to show the superiority of EvE. Also, this work shows a statistical approximation to the problem of calibration for EvE. The structure of this paper is the following: Section 2 presents the original DE algorithm; Section 3 presents the EvE algorithm; Section 4 presents the test functions used in this paper; and Section 5 presents and discusses the results of DE and EvE solving the minimization problem of each test function. Finally, we offer some conclusions about all the implementation.

2. DIFFERENTIAL EVOLUTION ALGORITHM

Differential Evolution is a heuristic algorithm based on the survival of a population into an environment that test the superiority of each member, forcing them to compete between all of them (Price et al. (2006)). Let PRN be the number of individuals PR_p^g that conforms a population, and let VPR_p^g be the p-th mutant vector with $p = 1, ..., PRN$, from the g-th generation of vectors. Then, the recombination process is defined by:

$$U_{p,m}^g = \begin{cases} VPR_{p,m}^g & if\ rand(0,1) < C_r \\ & or\ m = I_{rand}, \\ PR_{p,m}^g & otherwise, \end{cases} \quad (1)$$

where $U_{p,m}^g$ is the m-th element of the p-th trial vector U from the g-th generation, C_r is a recombination crossover, which directly modulates how the combination between the original parent PR and the mutant VPR happens, and I_{rand} is an aleatory positive integer in the range $[1, M]$ with $m = 1, ..., M$ (where M is the dimension of the search space), and it allows to guarantee that $U_p^g \neq PR_p^g$ while there exist enough genetic diversity within the population.

In the current literature, several variations of DE algorithms are presented. Such variations are defined by the expression that allows the calculation of the mutant vectors VPR_p^g (Storn and Price (1995)). The most common and generalized form according to Das and Suganthan (2011), is the random/1 form, calculated as follows:

$$VPR_p^g = PR_{r1}^g + F(PR_{r2}^g - PR_{r3}^g), \quad (2)$$

where $r1 \neq r2 \neq r3$ are aleatory positive integers uniformly distributed in the range $[1, PRN]$. F, called mutation factor, is a constant to fix in the interval $[0, 2]$ (Fleetwood (2004)), and it regulates the capability of exploration (near to 2) and exploitation (near to 0) for the DE algorithm.

A selection process is carried out based on the performance of each recombined individual, by the expression:

$$PR_p^{g+1} = \begin{cases} U_p^g & if\ f(U_p^g) < f(PR_p^g), \\ PR_p^g & otherwise, \end{cases} \quad (3)$$

where $f(\ )$ represents an evaluation function, or cost function that maps from the search space $\Re^n$ to $\Re$. Also, for each iteration, it is convenient to include a global superiority memory with the form:

$$Gbest = \begin{cases} U_p^g & if\ f(U_p^g) < f(Gbest), \\ Gbest & otherwise, \end{cases} \quad (4)$$

such that, at the end of the execution of DE, $Gbest$ is presented as the best solution found.

3. EVOLUTIVE EXTENSION ALGORITHM

DE algorithm takes directly a set of candidate solutions from the search space, and operates them to improve the cost of each one in search of solving an optimization problem. As we mentioned before, this evolutive process uses mutation and recombination in a simple set of arithmetic rules. But is it possible to improve the searching capacity of the algorithm? There exist another natural behavior than can be expressed as a simple arithmetic rule in search of obtaining better and/or faster results? EvE algorithm tries to implement an answer to those questions, considering basic evolutive behaviors inspired in biology, such as elitism, extinction, symbiosis, parasitism and different forms of reproduction. Elitism and extinction

have been considered in another bio-inspired algorithms, but never in a scheme as complete as EvE.

Elitism: Our first approach is the elitism. In nature, elitism represents the recognition of the best members of a population, propitiating their survival and reproduction. Computationally speaking, elitism represents the addition of certain memory to an algorithm. A memory driven by attributes has an effective and subtle effect in the search, allowing the identification of an attribute than represents a set of possible solutions. Thus, an already identified attribute can prevent that a non-revised candidate solution be accessed, due that it contains the already exploited attribute, or, on the other hand, the identified attribute can redirect the search to non-revised candidate solutions which have the desired attribute. EvE takes into consideration two kinds of memory:

- A short term memory, where the attributes of recently visited solutions are stored. This memory allows to perform intense exploration over specific region of the search space.
- A long term memory, where the frequencies of the occurrence of attributes are stored, seeking to identify the regions in the search space defined by the attributes. Long term memory also allows to diversify the search orientation.

Let X be the search space and $N(x)$ the selection of each one of the PRN individuals that forms the EvE's population. Then:

$$E_n(x) = N_n^*(x) \setminus PR_i, \tag{5}$$

represents the association of each PR with a previously declared attribute, after checking its compliance. That is, the equivalence class where each PR is associated with the compliance of an attribute. Then, EvE uses two attributes to perform its elitism memory:

$$\begin{aligned} \exists PR_i^g, \varepsilon, \gamma : \|PR_i^g - PR_i^{g+1}\| < \varepsilon, \\ |f(PR_i^g) - f(PR_i^{g+1})| > \gamma, \end{aligned} \tag{6}$$

and

$$\begin{aligned} \exists PR_i^g, \delta, \sigma : \|PR_i^g - PR_i^{g+1}\| > \delta, \\ |f(PR_i^g) - f(PR_i^{g+1})| < \sigma. \end{aligned} \tag{7}$$

Expression 6 defines a significant cost change region, in which a small modification in an individual causes a high change in its evaluation cost, so, the search can be diversified allowing a great variety of evaluation costs; whereas expression 7 defines a significant step region, in which it is necessary to perform great modifications to the individuals in order to obtain a small change in its evaluation cost: in this region, the search can be intensified by the steps required by each individual to perform an improvement. For each individual, 6 and 7 represent mutually exclusive attributes.

Extinction: Our second proposed rule is extinction. In nature, extinction is the total elimination of the members of a population, due to their incapacity to adapt to the environment. For EvE algorithm, it is necessary to compensate the greedy characteristic that produces premature convergence in the population. Let $E_x = 0$ represent a counter, then:

$$E_x = \begin{cases} E_x + 1 \; if \; \|Gbest - PR_i^g\| = 0, \\ E_x \qquad\qquad\qquad otherwise. \end{cases} \tag{8}$$

E_x increases every time a member of the population replicates the best individual found at the moment. When E_x surpass an extinction bound, all the members of the population are reinitialized, and the chromosomes of the best solution found are reinserted in the population, in a random index:

$$PR_{randi(PRN)}^{0_n} = Gbest^{g_{n-1}}, \tag{9}$$

where the super index 0_n represents the generation in which the population has been reinitialized.

Reproduction: For the standard DE algorithm, reproduction only happens by the recombination of the chromosomes of a parent and a mutant generated under the same index. EvE algorithm recombines diversified individuals in search of generating a more aggressive attitude, covering faster the search space. The first reproduction model is the multipoint crossing. Let PR_i^g and PR_j^g be two members of the population, which belong to the same region (expression 6 or 7), then, they can generate two new members by:

$$\begin{aligned} PR_{(i|j),m_{mod2=0}}^{g+1_a} &= PR_{i,m}^g, \\ PR_{(i|j),m_{mod2\neq 0}}^{g+1_a} &= PR_{j,m}^g, \end{aligned} \tag{10}$$

$$\begin{aligned} PR_{(i|j),m_{mod2=0}}^{g+1_b} &= PR_{j,m}^g, \\ PR_{(i|j),m_{mod2\neq 0}}^{g+1_b} &= PR_{i,m}^g. \end{aligned} \tag{11}$$

Expression 10 represents the formation of one of two children, the (a) child, in which the odd chromosomes are taken from the parent with index j, and the even chromosomes are taken from the parent with the index i. The expression 11 represents the formation of the second child (b), whose chromosomes are taken in the contrary way. We also use the index $(i|j)$ to represent that each one of the children can take the index of any of the two parents, only if they improve their evaluation cost, that is, if child (a) or (b) surpass both parents, it takes the index of the parent with the worst performance; if one of the children surpass the performance of only one parent, it takes its index; if both children surpass both parents, child (a) takes the i index, and child (b) takes the j index.

Using the elitist memory of EvE algorithm, it is possible to establish an attraction between two members of the population. Let PR_i^g and PR_j^g be two individuals with a common attribute, but with $\|PR_i^g - PR_j^g\| > \varepsilon$, where ε is a fixed constant that represents at least $\|UB - LB\|/2$ (UB and LB are the upper and lower bounds of each dimension of the search space, respectively). Then:

$$PR_{(i|j),m}^{g+1} = \frac{1}{2} PR_{i,m}^g + \frac{1}{2} PR_{j,m}^g, \tag{12}$$

where, the individual with the worst evaluation cost is eliminated from the population, and, as in the previous reproduction model, the index $(i|j)$ represents that the child takes the index of the parent with the worst performance, if the mentioned child is not the individual with the worst performance.

Parasitism: Another natural phenomena considered in the EvE algorithm is parasitism. In nature, parasitism is the survival of an individual at the expense of a second one.

In the EvE algorithm, we represent that idea giving to a member of the population the capacity to mimic another one of better performance, in search of guaranteeing its survival. Let PR_i^g and PR_j^g be two individuals of EvE's population, and there exists recognition of PR_i^g's good performance, and PR_j^g has the parasite property. Then:

$$PR_{j,m}^{g+1} = (1-\rho)PR_{i,m}^g + (\rho)PR_{j,m}^g, \tag{13}$$

where ρ is a constant in the range $[0,1]$, and defines an "infection ratio". Parasitism helps the EvE algorithm to assign good properties to individuals with bad performance, which allows to perform a more aggressive search.

Symbiosis: The final nature example used to create EvE algorithm is the symbiosis phenomena. In nature, symbiosis establishes a relationship of mutual benefit. Let PR_i^g be an individual with symbiotic attitude, then, its mutation model takes the form:

$$\begin{aligned} VPR_i^g = PR_i^g + F(Gbest - PR_i^g) \\ + F(PR_{r1}^g - PR_{r2}^g), \end{aligned} \tag{14}$$

which simulates a mutual benefit relation between PR_i^g and $Gbest$. The first one guarantees that its children contain information of the individual of best performance, and the second one ensures its reproduction. In Equation 14, $r1 \neq r2$ are random integers uniformly distributed in the range $[1, PRN]$ (Qin and Suganthan (2005)).

4. TEST FUNCTIONS

The study of the performance of a heuristic algorithm is commonly realized through the data mining from several executions over a set of test functions. According to Price et al. (2006), it is possible to classify those test functions in three kinds:

- Unimodal functions: Only contain a global minimum, with no local minimums.
- Unconstrained multimodal functions: Present at least two local minimums, but their global minimum does not depend of the domain of the function.
- Constrained multimodal functions: There is no global minimum defined for these functions. The minimum evaluation value depends of the domain of the function.

For this paper, we use the test functions presented in Tables 1, 2 and 3.

Table 1. Unimodal Test Functions

Sphere:
$f(x) = \sum_{j=1}^{N} x_j^2,$
$-10 \leq x_j \leq 10,\ j = 1, ..., N,\ f(x^*) = 0, x^* = 0.$
Generalized Rosenbrock:
$f(x) = \sum_{j=1}^{N-1} (100(x_{j+1} - x_j^2)^2 + (x_j - 1)^2),$
$-20 \leq x_j \leq 20,\ j = 1, ..., N,\ f(x^*) = 0, x^* = 1.$
Schwefels Ridge:
$f(x) = \sum_{k=1}^{N} ((\sum_{j=1}^{k} x_j)^2),$
$-50 \leq x_j \leq 50,\ j = 1, ..., N,\ f(x^*) = 0, x^* = 0.$

For Tables 1, 2 and 3, x^* represents the value in which the test function has its minimum evaluation cost, $f(x^*)$.

5. EXECUTION AND RESULTS

In order to solve each of the test functions presented in the last section, it is necessary to specify all the execution conditions. First, for each test function, $N = 10$, that is, $x \in \Re^{10}$. Also, for all x^* values, we tolerate an error of $e = \pm 10^{-6}$. Finally, for EvE algorithm it is necessary to establish some programing factors. The extinction bound is set as $3PRN$ trying to guarantee that the extinction phenomena will not be triggered by a population with a low genomic variety, and the infection ratio is 0.25, as a fixed small step for the parasitism phenomena that allows that the parasite does not duplicate the parasited individual. In practice, those parameters show good results, avoiding excessive reinitialization or premature convergence. In order to compare the original DE algorithm against EvE, we use the same number of individuals in both of them, $PRN = 50$.

The first approach is to let the calibration parameters for DE and EvE be selected in a random way, thus $C_r \in [0,1]$ and $F \in [0,2]$, in a uniform distribution. That is, we want to know for which calibration parameters each algorithm requires the less number of iterations to solve each of the minimization problems. Then, we perform 1000 executions for each algorithm, trying to cover most of the $C_r \times F$ plane, and every time, C_r and F are randomly chosen.

Then, for DE and EvE, we can identify a "comfort zone", CZ, as the $C_r \times F$ region where a test function is minimized with the less number of iterations. Figure 1 and Figure 2 show an example of the comfort zone.

Table 2. Unconstrained Multimodal Test Functions

Ackley:
$f(x) = -20e^{-0.2\sqrt{\frac{1}{N}\sum_{j=1}^{N} x_j^2}} - e^{\frac{1}{N}\sum_{j=1}^{N} \cos(2\pi x_j)} + 20 + e,$
$-30 \leq x_j \leq 30,\ j = 1, ..., N,\ f(x^*) = 0, x^* = 0.$
Rastrigin:
$f(x) = \sum_{j=1}^{N} (x_j^2 - 10\cos(2\pi x_j) + 10),$
$-6 \leq x_j \leq 6,\ j = 1, ..., N,\ f(x^*) = 0, x^* = 0.$
Salomon:
$f(x) = -\cos(2\pi\|x\|) + 0.1\|x\| + 1,\ \|x\| = \sqrt{\sum_{j=1}^{N} x_j^2},$
$-50 \leq x_j \leq 50,\ j = 1, ..., N,\ f(x^*) = 0, x^* = 0.$

Table 3. Constrained Multimodal Test Functions

Schwefel:
$f(x) = -\frac{1}{N}\sum_{j=1}^{N} x_j \sin(\sqrt{\lvert x_j \rvert}),$
$-500 \leq x_j \leq 500,\ j = 1, ..., N,\ f(x^*) = -418.983, x^* = 420.9687.$
Rana:
$f(x) = \sum_{j=1}^{N-1} x_j \sin(\alpha)\cos(\beta) + x_{(j+1) mod N}\cos(\alpha)\sin(\beta),$
$\alpha = \sqrt{\lvert x_{j+1} + 1 - x_j \rvert},\ \beta = \sqrt{\lvert x_{j+1} + 1 + x_j \rvert},$
$-512 \leq x_j \leq 512,\ j = 1, ..., N,\ f(x^*) = -511.708, x^* = -512.$

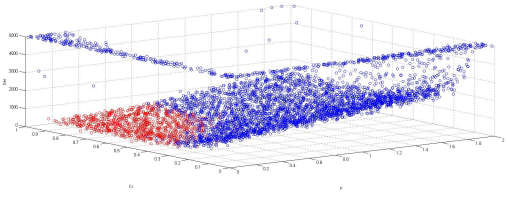

Figure 1. Comfort zone, in red, for EvE in the sphere function

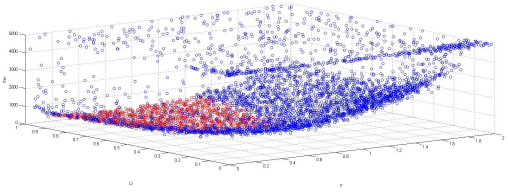

Figure 2. Comfort zone, in red, for DE in the sphere function

The z axis in Figures 1 and 2 represent the number of iterations required to solve the problem. As we can see, both algorithms can solve the sphere function of $\Re^{10}$. The red region represents the comfort zone, in which the problem is solved in less than 500 iterations. It is easy to see that, for EvE algorithm, the comfort zone is more clearly defined that for DE algorithm.

The process is as follows: after 1000 executions for each algorithm in each function, a vector that storages the number of iterations required to achieve the minimum evaluation value is read, and if the number of iterations is at most 500, the index of that stored value is used to access to the C_r and F values that allow that performance. Then, the minimum and maximum values of C_r and F that have the "at most 500 iterations" property defines the CZ of DE and EvE. To avoid to take in consideration some minimum or maximum at the extremes of the distribution, it is necessary to discard the calculated value if it is isolated, that is, if this value has no at least another point with the property of "at most 500 iterations" in a neighborhood of 0.01, in order to guarantee that there is at least two (C_r, F) coordinated pairs in the CZ bounds. Using the CZ of each algorithm, 1000 new executions are performed. The success ratio is computed by the number of success with less than 500 iterations over the number of executions.

Table 4 summarizes the results of DE and EvE algorithm for the Unimodal test functions.

Table 4. Results for Unimodal Test Functions

Function	DE CZ	EvE CZ	Success ratio
Sphere	$0.23 \leq C_r \leq 0.97$	$0.31 \leq C_r \leq 1$	$P(DE) = 0.841$
	$0.11 \leq F \leq 0.61$	$0.13 \leq F \leq 0.42$	$P(EvE) = 0.997$
Generalized	$0.55 \leq C_r \leq 0.95$	$0.53 C_r 0.95$	$P(DE) = 0.712$
Rosenbrock	$0.10 \leq F \leq 0.81$	$0.13 \leq F \leq 0.51$	$P(EvE) = 0.991$
Schwefels	$0.32 \leq C_r \leq 0.97$	$0.28 \leq C_r \leq 0.99$	$P(DE) = 0.883$
Ridge	$0.13 \leq F \leq 0.78$	$0.13 \leq F \leq 0.87$	$P(EvE) = 0.998$

As we can see in Table 4, Unimodal test functions do not represent a high challenge, neither for DE nor for EvE. Table 5 presents the results for the Unconstrained Multimodal functions, and Figure 3 and Figure 4 show an example of the CZ of each algorithm in this kind of functions.

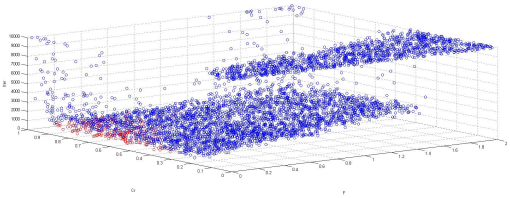

Figure 3. Comfort zone, in red, for EvE in the Rastrigin function

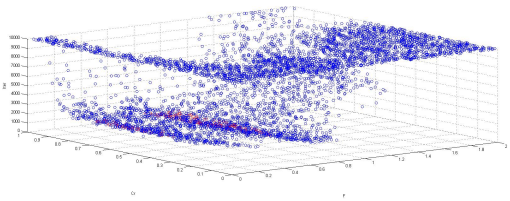

Figure 4. Comfort zone, in red, for DE in the Rastrigin function

Table 5. Results for Unconstrained Multimodal Test Functions

Function	DE CZ	EvE CZ	Success ratio
Ackley	$0.66 \leq C_r \leq 1$	$0.55 \leq C_r \leq 1$	$P(DE) = 0.641$
	$0.21 \leq F \leq 0.48$	$0.13 \leq F \leq 0.26$	$P(EvE) = 0.887$
Rastrigin	$0.36 \leq C_r \leq 0.86$	$0.50 \leq C_r \leq 0.96$	$P(DE) = 0.744$
	$0.78 \leq F \leq 0.96$	$0.11 \leq F \leq 0.28$	$P(EvE) = 0.903$
Salomon	$0.44 \leq C_r \leq 1$	$0.54 \leq C_r \leq 0.98$	$P(DE) = 0.573$
	$0.63 \leq F \leq 1.12$	$0.18 \leq F \leq 0.76$	$P(EvE) = 0.781$

Table 5 still exhibits the superiority of EvE over DE. Although the success ratio is considerably low for Unconstrained Multimodal functions in comparison with the success ratio achieved in Unimodal functions, it is important to remember that we only consider as a success the achievement of the minimum in less than 500 iterations.

Finally, Table 6 summarizes the results for the most difficult kind of test functions used in this paper, the Constrained Multimodal functions. Also, Figures 5 and 6 present an example of the CZ for these functions.

Table 6. Results for Constrained Multimodal Test Functions

Function	DE CZ	EvE CZ	Success ratio
Schwefel	$0.40 \leq C_r \leq 0.99$	$0.35 \leq C_r \leq 1$	$P(DE) = 0.693$
	$0.36 \leq F \leq 0.81$	$0.12 \leq F \leq 0.32$	$P(EvE) = 0.910$
Rana	$0.32 \leq C_r \leq 0.99$	$0.33 \leq C_r \leq 1$	$P(DE) = 0.469$
	$0.38 \leq F \leq 1.72$	$0.13 \leq F \leq 1.05$	$P(EvE) = 0.687$

For all the three kinds of test functions considered in this paper, EvE algorithm shows a superiority in the capacity to achieve the minimum evaluation value in less iterations. Also, it is important to note that no execution has success ratio of 1, and that is intrinsically a heuristic behavior, there exist random components in both algorithms that cause to mismatch some parts of the execution, like the initialization step, or the selection of the components of the mutation equations. Nevertheless, the superiority of EvE algorithm surpass with 0.218 points the performance of DE in the worst EvE case. For the better DE case, EvE has a superior performance with 0.115 points of success ratio over the DE's performance.

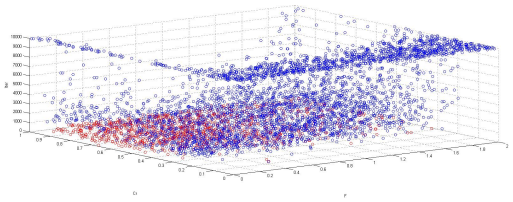

Figure 5. Comfort zone, in red, for EvE in the Rana function

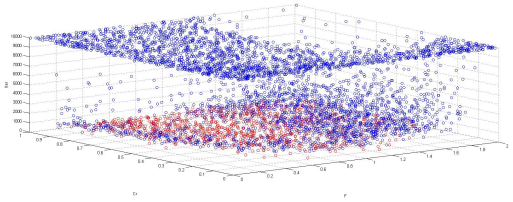

Figure 6. Comfort zone, in red, for DE in the Rana function

6. CONCLUSIONS

In this paper, a new bioinspired heuristic algorithm is presented, and its performance is discussed. Using the evolutionary approach, and the Differential Evolution algorithm as a base of construction, we take some natural processes as inspiration to construct a set of operations that improve the performance of the EvE algorithm, from the extinction process to avoid the premature convergence behavior, to the parasitism phenomena, that allows to explore the search space using a convex combination. As a competition scheme, we take several classic test functions and run over them the EvE algorithm and the original DE algorithm to make a point of comparison. In all the cases, EvE has a better performance than DE, but it is important to mention that the execution cost is higher for EvE, than for DE, this is obviously due to the set of rules adding to extend the algorithm. Nevertheless, this cost is not far above than DEs cost, thanks to the use of a programing scheme of one rule at a time, that is, if an individual is recombined, it is not candidate anymore for a multipoint crossing procedure, and so on, until the end of each generation.

Another important characteristic that arises from our results is the definition of the CZ. It is easy to see that for DE algorithm, CZ is not clearly defined for all the test function, whereas for EvE, we can conclude that a CZ of $0.55 \leq C_r \leq 0.95$ and $0.18 \leq F \leq 0.26$ covers all our test functions, providing EvE a better generalization property.

As future work, EvE will be compared against another heuristic algorithms. Also, it will be necessary to formally define its execution cost. And, at the same time, it is proposed as future work the formal explanation of every EvE rule and process (remembering that this is an introductory paper); as well as the addition of new rules that may improve its performance.

ACKNOWLEDGEMENTS

We sincerely thank to CONACyT for the economic incentives provided during this investigation and to CINVESTAV for the provided resources.

REFERENCES

Bäck, T. (1996). *Evolutionary algorithms in theory and practice: evolution strategies, evolutionary programming, genetic algorithms*. Oxford university press.

Bilchev, G. and Parmee, I.C. (1995). The ant colony metaphor for searching continuous design spaces. In *Evolutionary Computing*, 25–39. Springer.

Cooper, L. (1964). Heuristic methods for location-allocation problems. *Siam Review*, 6(1), 37–53.

Cormen, T.H., Leiserson, C.E., Rivest, R.L., and Stein, C. (2001). *Introduction to algorithms*, volume 6. MIT press Cambridge.

Das, S. and Suganthan, P.N. (2011). Differential evolution: a survey of the state-of-the-art. *IEEE Transactions on Evolutionary Computation*, 15(1), 4–31.

Eiben, A.E. and Schoenauer, M. (2002). Evolutionary computing. *Information Processing Letters*, 82(1), 1–6.

Fleetwood, K. (2004). An introduction to differential evolution. In *Proceedings of Mathematics and Statistics of Complex Systems (MASCOS) One Day Symposium, 26th November, Brisbane, Australia*.

Houck, C.R., Joines, J., and Kay, M.G. (1995). A genetic algorithm for function optimization: a matlab implementation. *NCSU-IE TR*, 95(09).

Martı, R. (2003). Procedimientos metaheurısticos en optimización combinatoria. *Matemátiques, Universidad de Valencia*, 1(1), 3–62.

Mühlenbein, H., Gorges-Schleuter, M., and Krämer, O. (1988). Evolution algorithms in combinatorial optimization. *Parallel Computing*, 7(1), 65–85.

Pearl, J. (1984). *Heuristics: intelligent search strategies for computer problem solving*. Addison-Wesley Pub. Co., Inc., Reading, MA.

Pérez-González, A., Begovich, O., and Ruiz-Leon, J. (2014). Modeling of a greenhouse prototype using PSO algorithm based on a LabView application. In *11th International Conference on Electrical Engineering, Computing Science and Automatic Control (CCE)*, 1–6. IEEE.

Price, K., Storn, R.M., and Lampinen, J.A. (2006). *Differential evolution: a practical approach to global optimization*. Springer Science & Business Media.

Qin, A.K. and Suganthan, P.N. (2005). Self-adaptive differential evolution algorithm for numerical optimization. In *IEEE Congress on Evolutionary Computation*, volume 2, 1785–1791. IEEE.

Schmitt, L.M. (2001). Theory of genetic algorithms. *Theoretical Computer Science*, 259(1), 1–61.

Storn, R. and Price, K. (1995). *Differential evolution-a simple and efficient adaptive scheme for global optimization over continuous spaces*, volume 3. ICSI Berkeley.

Storn, R. and Price, K. (1997). Differential evolution–a simple and efficient heuristic for global optimization over continuous spaces. *Journal of global optimization*, 11(4), 341–359.

Parameter Optimization of Sliding Mode Observer-based Controller for 2 DOF Stewart Platform ⋆

Sajjad Keshtkar * **Jaime Moreno** * **Alexander Poznyak** ‡

* *Instituto de ingeniería, Universidad Nacional Autónoma de México, (e-mail: diesel253m@gmail.com).*
† *Instituto de ingeniería, Universidad Nacional Autónoma de México, (e-mail: jmorenoP@iingen.unam.mx).*
‡ *Automatic Control Department, CINVESTAV - IPN, Mexico City 2508, Mexico, (e-mail: apoznyak@ctrl.cinvestav.mx)*

Abstract: This paper considers gain parameter election of a class of nonlinear controller-observer for a systems with uncertainty, using Paerto-set approach. The presented observer based on Super-twisting observer is used for velocity estimation/reconstruction signals based on the available plant input/output information and can be calculated on-line. The signal then is injected to the classical sliding mode controller to provide a feedback control in presence of unmodeled dynamics and perturbations. To guarantee the convergence of the proposed algorithm the gain parameters must be time-varying and depending on available current measurements. The optimal selection of the gains are proposed in this work. A simulation study on a 2 degrees of freedom Stewart platform is presented to show the effectiveness of the scheme.

Keywords: Sliding mode control, Super-Twisting observer, Pareto Optimization, Stewart Platform, Parallel Manipulator.

1. INTRODUCTION

1.1 Brief survey

Previous work (Keshtkar et al. (2016)) has considered the use of sliding mode controller-observer for high performance control and observation of a Stewart platform in presence of unmodeled dynamics and perturbations. The paper builds on this work and examines the parameter election of such a scheme within the broader context of optimization theory.

In the named work, the control based on sliding mode techniques is proposed for the case when not all states are measured directly but are estimated on-line by the second-order *sliding mode* (SM) observer. Such a design approach can reduce the cost of the controlled system, avoid the fragility of velocity sensors, and eliminate the difficulty of the sensors installation. Recently the design of such observers for nonlinear systems has received a great deal of attention: the standard Luenberger Nikolaos and Costas (1998); Xiaosong et al. (2010), the SM observers Edwards and Tanb (2006); Shtessel et al. (2014); Utkin et al. (2008), the extended Kalman filter Gobbo et al. (2001); Weiss and Moore (1980) and H_∞ observers Jung et al. (2006). Among them, adaptive sliding mode (SM) observers are particulary attractive technology due to their robustness against disturbances, parameter deviations and measurement noise and are widely used in different fields Shtessel et al. (2014). Some works Kima et al. (2004); Li et al. (2005); Zheng et al. (2000) propose the adaptive SM observer for sensorless induction motor drive. In Utkin et al. (2008) the adaptive SM observer - controller system was proposed for the induction machine control under unknown parameters and partial state variable information. In Fridman et al. (2008) the authors proposed a feedback linearization-based controller with a high-order SM observer running parallel and applied to a quadrotor unmanned aerial vehicle. The high-order SM observer works as an observer and estimator of the effect of the external disturbances such as wind and noise.

The problem treated in previous paper can be described as follows: estimate on-line unknown variables first and then, use these estimates to design a SM controller. However, the parameters of the controller as well as the observer are admitted to be time-varying and state-dependent. In this work the optimal selection of these gain parameters using the Pareto-set optimization method is presented. The task is to provide a simultaneous optimization two different functions by the same arguments. A standard technique for generating the Pareto set in multicriteria optimization problems is to minimize (convex) weighted sums of the different objectives for various different settings of the weights. The concept has applications in academic fields such as economics, engineering, and the life sciences (See Jornada and Leon (2016); Khoroshiltseva et al. (2016); Luo et al. (2016); Wan et al. (2016)).

1.2 Main contribution

This paper presents

⋆ The authors gratefully acknowledge the financial support from DGAPA-UNAM.

- An adaptive sliding mode controller, which uses the state estimated on-line by the adaptive Super-Twist observer;
- Optimization gain parameters of the named observer and controller by Pareto-set approach;
- Application of the studied approach to a new two DOF Stewart platform as a solar tracker

2. SYSTEM DESCRIPTION AND CONTROL DESIGN

Consider the mathematical model of 2 DOF Stewart platform

$$\begin{aligned} \dot{X}_1(t) &= X_2(t) \\ \dot{X}_2(t) &= f(X,t) + g(X_1,t)\,u + \xi(t) \\ y(t) &= X_1(t) \end{aligned} \tag{1}$$

- $X_1(t)$, $X_2(t) \in \mathbb{R}^2$ are the states of the system;

- $X(t) := \left(X_1^\top(t), X_2^\top(t)\right)^\top \in \mathbb{R}^4$;

- $u \in \mathbb{R}^2$ is a control to be designed,

- $y(t) \in \mathbb{R}^2$ is a measurable output at time $t \geq 0$,

- $\xi(t) \in \mathbb{R}^2$ is bounded unmeasurable term including external and internal perturbations/uncertainties: for all $t \geq 0$, $\|\xi(t)\| \leq \xi^+ < \infty$,

- $f(X,t) \in \mathbb{R}^2$

- $g(X_1,t) \in \mathbb{R}^{2\times 2}$

Remark 1. Notice that in the model (1) only the half of coordinates ($X_1(t)$) is available in time; $X_2(t)$ is supposed to be estimated online.

2.1 Observed sliding mode control design

To estimate the non-measurable coordinate $X_2(t)$ in (1) we apply a popular second-order sliding mode (super-twisting) observers Shtessel et al. (2014):

$$\begin{aligned} \dot{\hat{X}}_1 &= \hat{X}_2 + \lambda \left\| y - \hat{X}_1 \right\|^{1/2} \mathrm{Sign}\left(y - \hat{X}_1\right) \\ \dot{\hat{X}}_2 &= f\left(\hat{X},t\right) + g(X_1,t)\,u + \alpha \mathrm{Sign}\left(y - \hat{X}_1\right) \end{aligned} \tag{2}$$

The parameters α and λ are constant in the original publications. The vector function $\mathrm{Sign}(z)$ is defined as follows

$$\begin{aligned} \mathrm{Sign}(z) &:= (\mathrm{sign}(z_1), ..., \mathrm{sign}(z_n))^\intercal \\ \mathrm{sign}(z_i) &:= \begin{cases} 1 & \text{if } z_i > 0 \\ -1 & \text{if } z_i < 0 \\ \in [-1,1] & \text{if } z_i = 0 \end{cases} \end{aligned} \tag{3}$$

New variable $e := \left(X - \hat{X}\right)$ which characterizes the error of estimated state and is governed by the following equations:

$$\begin{aligned} \dot{e}_1 &= e_2 - \lambda \|e_1\|^{1/2} \mathrm{Sign}(e_1) \\ \dot{e}_2 &= F_e\left(t, X_1, X_2, \hat{X}_2\right) - \alpha \mathrm{Sign}(e_1) \end{aligned} \tag{4}$$

where

$$F_e\left(t, X_1, X_2, \hat{X}_2\right) = \left[f(X,t) - f\left(\hat{X},t\right)\right] + \xi(X,t) \tag{5}$$

describes unmodeled dynamics and external perturbation effects. Obviously, it is unmeasurable.

The feedback control law $u\left(\hat{X},t\right)$ must derive the states of the systems to the desired values. i.e., $\lim_{t\to\infty} \hat{X}_1 = X_1^*$, $\lim_{t\to\infty} \hat{X}_2 = 0$. By defining the *"ideal"* sliding surface (Utkin (1992)(:

$$\sigma\left(\hat{X}\right) := \dot{\hat{X}}_1 + C\left(\hat{X}_1 - X_1^*\right) = \hat{X}_2 + C\left(\hat{X}_1 - X_1^*\right) = 0 \tag{6}$$

where $C = \mathrm{diag}(c_1, c_2)$ is a diagonal matrix with positive elements, the SM controller $u\left(\hat{X},t\right)$ structure can be defined as

$$u\left(\hat{X},t\right) = -k\left(\hat{X},t\right)\left[g(X_1,t)\right]^{-1} \mathrm{Sign}\left(\sigma\left(\hat{X}\right)\right) \tag{7}$$

where the state estimates $\hat{X}$ are generated by the observer (2) with varying parameters, that is,

$$\begin{aligned} \dot{\hat{X}}_1 &= \hat{X}_2 + \lambda\left(\hat{X},t\right)\left\| y - \hat{X}_1 \right\|^{1/2} \mathrm{Sign}\left(y - \hat{X}_1\right) \\ \dot{\hat{X}}_2 &= f\left(\hat{X},t\right) + g(X_1,t)\,u + \alpha\left(\hat{X},t\right) \mathrm{Sign}\left(y - \hat{X}_1\right) \end{aligned} \tag{8}$$

2.2 Gain parameters tuning

First by the physical reasons we may accept the following assumptions.

H1 The vector-function $f(X,t)$ and $g(X_1,t)$ are Lipschitzian with respect to the first argument on $t \geq 0$, i.e.,

$$\begin{aligned} \left\| f(X,t) - f\left(\hat{X},t\right) \right\| &\leq L_f \left\| X - \hat{X} \right\| = L_f \|e\| \\ \left\| g(X_1,t) - g\left(\hat{X}_1,t\right) \right\| &\leq L_g \left\| X_1 - \hat{X}_1 \right\| = L_g \|e_1\| \end{aligned}$$

H2 The matrix $g(X_1,t)$ function is invertible everywhere, namely

$$\left\| \left[g(X_1,t)\right]^{-1} \right\| \leq g_{-1}^+ < \infty, \quad \left(\|g\|^2 := \mathrm{tr}\left\{g g^\intercal\right\}\right)$$

Notice that by (5)

$$\left\| F_e\left(t, X_1, X_2, \hat{X}_2\right) \right\|^2 \leq 2L_f \|e\|^2 + 2\left(\xi^+\right)^2 \tag{9}$$

The classical second-order scheme corresponds to the case $L_f = 0$. The situation, corresponding the inequality (9), has not been considered elsewhere. The adaptation parameters $k = k\left(\hat{X}, e_1, t\right)$ of the controller (7) and $\lambda\left(\hat{X},t\right)$, $\alpha\left(\hat{X},t\right)$ of the observer (8) are designed as

$$\left.\begin{aligned} k = k\left(\hat{X}, e_1, t\right) &:= (p_0)^{-1}\left[\rho + \varkappa\left(\hat{X}, e_1, t\right) \right. \\ &\left. + \gamma\sqrt{p_0/2}\right], \quad \rho \geq \sqrt{p_0/2} \\ \varkappa\left(\hat{X}, e_1, t\right) &:= \left\| f\left(\hat{X},t\right) + \alpha \mathrm{Sign}(e_1) + \right. \\ &\left. C\left[\hat{X}_2 + \lambda \|e_1\|^{1/2} \mathrm{Sign}(e_1)\right] \right\| \end{aligned}\right\} \tag{10}$$

and

$$\left.\begin{aligned} \lambda\left(\hat{X},t\right) &:= \begin{cases} (\eta_1(\gamma) + \sqrt{p_1/2})/p_1 \sqrt{\|e_1\|} \\ \text{if} \quad \sqrt{\|e_1\|} \geq \epsilon > 0 \\ \text{and} \\ (\eta_1(\gamma) + \sqrt{p_1/2})/p_1 \epsilon \\ \text{if} \quad \sqrt{\|e_1\|} < \epsilon \end{cases} \\ \alpha\left(\hat{X},t\right) &:= \alpha > 0 \end{aligned}\right\} \tag{11}$$

Theorem 1. Under the assumptions *H1-H2* the SM controller (7) with the adaptive gain parameters (10)-(11) guarantees the finite-time convergence of the closed-loop system trajectories to a μ-zone around the desired values, namely, for the "storage" function

$$V(t) := V\left(\sigma\left(\hat{X}(t)\right), e_1(t), e_2(t)\right) = \frac{p_0}{2}\left\|\sigma\left(\hat{X}(t)\right)\right\|^2 + \frac{p_1}{2}\|e_1(t)\|^2 + \frac{p_2}{2}\|e_2(t)\|^2 \quad (12)$$
$$p_0,\ p_1,\ p_2\ > 0$$

we guarantee that it becomes less than μ^2 for all $t \geq t_f = \gamma^{-1}\sqrt{2W(0)}$ fulfilling

$$W(t) := \left[\sqrt{V(t)} - \mu\right]_+^2 = 0 \quad (13)$$

where

$$[z]_+ := \begin{cases} z \text{ if } z \geq 0 \\ 0 \text{ if } z < 0 \end{cases}$$

$$\mu := \mu_0\left(\alpha, \gamma, e_2^+\right) + \mu_1(\epsilon)\, e_2^+$$
$$\mu_0\left(\alpha, \gamma, e_2^+\right) := \eta_0\left(\alpha, e_2^+\right) + \frac{10}{27}\gamma\epsilon\sqrt{\frac{p_1}{2}} \quad (14)$$
$$\mu_1(\epsilon) := \left[\sqrt{\frac{p_2}{2}} + \epsilon\frac{10}{27}\left(p_1 + \sqrt{2L_f}p_2\right)\right]$$

and

$$\eta_0(\alpha) := p_2 e_2^+\left(\alpha\sqrt{n} + \sqrt{2}\xi^+ + \sqrt{2L_f}e_2^+\right) + \gamma\sqrt{\frac{p_2}{2}}$$
$$\eta_1(\gamma) := \gamma\sqrt{\frac{p_1}{2}} + \left(p_1 + \sqrt{2L_f}p_2\right)e_2^+,\ \gamma > 1$$
$$e_2^+ = 2c/\sqrt{b^2 + 4ac} + b \quad (15)$$
$$a := \sqrt{2L_f}p_2,\ c := (\gamma - 1)\,\epsilon\frac{10}{27}\sqrt{\frac{p_1}{2}},\ \epsilon > 0$$
$$b := \epsilon\frac{10}{27}\left(p_1 + \sqrt{2L_f}p_2\right) + p_2\left(\alpha\sqrt{n} + \sqrt{2}\xi^+\right)$$

The initial values of the observer $\hat{X}_2(0)$ should be not so far from the real values $X_2(0)$ fulfilling $\left\|X_2(0) - \hat{X}_2(0)\right\| \leq e_2^+$ [1].

3. OPTIMIZATION OF THE CONTROLLER PARAMETERS

The control gain (10) contains three free parameters p_0, p_1, p_2 which should be selected in such a way that the resulting behavior would be as better as possible. Without loss of generality we may select the parameters p_0, p_1 and p_2 of the controller as follows

$$p_0 + p_1 + p_2 = 1$$

implying

$$p_2 = 1 - p_1 - p_0 \quad (16)$$

Indeed, since

$$\arg\min_{u \in U_{adm}} V = \arg\min_{u \in U_{adm}} \frac{1}{p_0 + p_1 + p_2} V$$

the multiplication of the function V by any positive constant does not change the optimal control parameters. If we fix the value $p_0 \in (0,1)$, then in view of (16) we have only one free parameters $p_1 \in (0,1)$ which should be selected to fulfill the following optimality requirements:

1) to make the "workability zone" $e_2^+ = \dfrac{2}{\mathcal{F}_1(p_1)}$ as much as possible which corresponds to the minimization of the function

[1] The proof is described in Keshtkar et al. (2016)

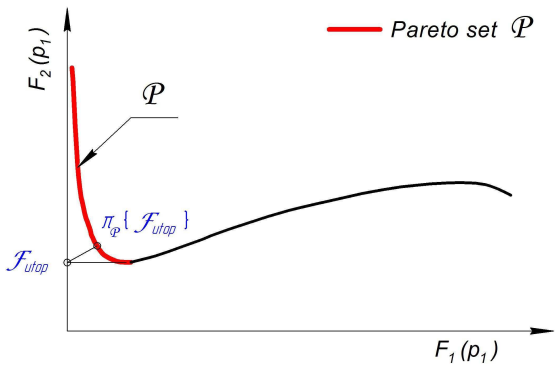

Fig. 1. The set of Pareto optimal points.

$$\mathcal{F}_1(p_1) := \sqrt{p_1}r_1 + \frac{1 - p_1 - p_0}{\sqrt{p_1}}r_2 + \sqrt{\left(\sqrt{p_1}r_1 + \frac{1 - p_1 - p_0}{\sqrt{p_1}}r_2\right)^2 + \frac{1 - p_1 - p_0}{p_1}r_3} \to \min_{p_1 \in (0,1)}$$

2) to make the convergence zone μ minimal possible one which corresponds to the minimization of the function

$$\mu = \mathcal{F}_2(p_1) := r_1 + \frac{r_2}{\mathcal{F}_1(p_1)} + \frac{r_3}{\mathcal{F}_1^2(p_1)} \to \min_{p_1 \in (0,1)}$$

One can see that we deal with the multi-functional optimization problem

$$\mathcal{F}_1(p_1) \to \min_{p_1 \in (0,1)}$$
$$\mathcal{F}_2(p_1) \to \min_{p_1 \in (0,1)}$$

and it is clear that simultaneous optimization two different functions by the same arguments p_1 is impossible. That's why we need to apply the, so-called, "*Pareto-set approach*". A standard technique for generating the Pareto set in multicriteria optimization problems is to minimize (convex) weighted sums of the different objectives for various different settings of the weights. *Pareto efficiency*, or *Pareto optimality*, is a state of allocation of resources in which it is impossible to make any one individual better off without making at least one individual worse off Ehrgott (2005).

The term is named after Vilfredo Pareto (1848–1923), an Italian engineer and economist who used the concept in his studies of economic efficiency and income distribution. Many real-world problems involve simultaneous optimization of several incommensurable and often competing objectives. Usually, there is no single optimal solution, but rather a set of alternative solutions. These solutions are optimal in the wider sense that no other solutions in the search space are superior to them when all objectives are considered. They are known as *Pareto-optimal solutions* Ehrgott (2005).

In our case the Pareto set looks as in the Fig.1.

It this figure

$\mathcal{P}$ is the Pareto set,

$\mathcal{F}_{utop} = \left(\min_{p_1 \in (0,1)} \mathcal{F}_1(p_1), \min_{p_1 \in (0,1)} \mathcal{F}_2(p_1)\right)$ is the utopia point,

$\pi_{\mathcal{P}}\{\mathcal{F}_{utop}\}$ is the projection of the utopia point $\mathcal{F}_{utop}$ to the Pareto set.

Definition. *The parameters p_1^* and p_2^*, corresponding to the point $\pi_{\mathcal{P}}\{\mathcal{F}_{utop}\}$ on the Pareto set, we will referred to as the* ***optimal parameters*** *of the control algorithm.*

4. NUMERICAL SIMULATIONS

The work described in previous sections will now be applied to a 2 DOF Stewart platform (2 rotations), which has been used as a solar tracker for photovoltaic panels. The main objective of the simulation is to control the rotations and the angular velocity of the moving platform of the parallel robot. The optimal parameters will be compared with the arbitrary tuned values obtained in previous paper.

The proposed mechanism (see Fig. 2) consists of two active linear actuators and one passive rod attached to a triangular base with spherical joints. Each actuator is made of upper and lower rods, connected by translational kinematic pair (screw mechanism). An anti-plunging strut, connected rigidly to the base and from the other end by Hooke's joint to the moving platform, inhibits the translational movements and one rotation, giving the system the desired two DOF.

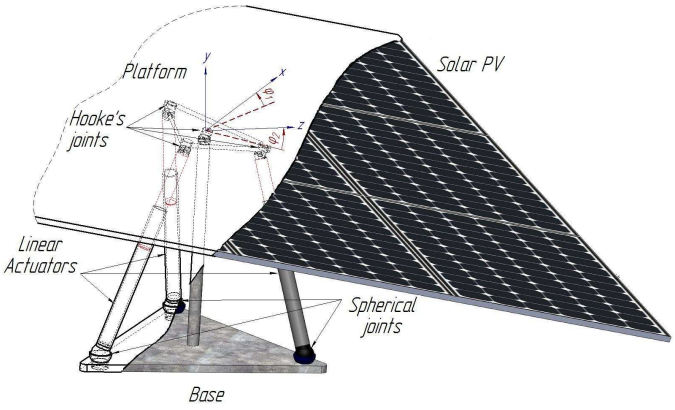

Fig. 2. Solar tracker on tripod type platform with two rotating DOF.

The orientation of the moving platform, and consequently the solar photovoltaic (PV) panel attached to it, regulates by changing the lengths of two actuators. This causes a corresponding change in the angle of the inclination of panel respect to the ground. In this case the variables $X(t) := (x_1, x_2, x_3, x_4) = (\varphi_1, \varphi_2, \dot{\varphi}_1, \dot{\varphi}_2)$ refer to the angular rotation and angular velocities of the moving platform. The trajectory of tracking is given either by the precalculated mathematical algorithms or by the measurement of light intensity in real time. This mechanism is specially important in solar tower applications to reach the permissable angle errors between the mirror and the central receiver located in the tower structure. For the model (1) we have:

$$\xi(t) = 1,5sin(x_1 + t)$$

$$f(X,t) = \begin{pmatrix} -\dfrac{x_3 x_4 \left(J_y c_{2x_2} - J_z s_{2x_2}\right)}{\left(J_y s_{x_2}^2 + J_z c_{x_2}^2\right)} \\ \dfrac{x_3^2 x_4 \left(J_y c_{2x_2} - J_z s_{2x_2}\right)}{J_x} \end{pmatrix} \tag{17}$$

$$g(X_1,t) = \begin{pmatrix} \dfrac{\sum \cos\gamma_{1,j}}{\left(J_y s_{x_2}^2 + J_z c_{x_2}^2\right)} & 0 \\ 0 & \dfrac{\sum \cos\gamma_{2,j}}{J_x} \end{pmatrix}$$

where J_i, $i = x, y, z$ are the main inertia moments of the moving platform and the angles γ_i $(0 < \gamma_i < \pi/2)$ are the inclination of the actuators respect to the fixed coordinate system for details see Keshtkar et al. (2016).

Remark 2. For all $X \in \mathbb{R}^4$

$$J_y s_{x_2}^2 + J_z c_{x_2}^2 \geq \min\{J_y, J_z\} > 0$$

The parameters of system and those that are participating in the controller realization, are given in Table 1.

Table 1. Numerical values of the parameters.

$p_0 = 0,2$	$\alpha = 2$	$\gamma = 1$	$J_z[\text{kgm}^2] = 2.5$
$p_{1opt} = 0.1040$	$e_2^+ = 4$	$h[\text{m}] = 0.4$	$x_1^*[\text{rad}] = 20$
$p_{2opt} = 0.6960$	$L_f = 2$	$R[\text{m}] = 0.4$	$x_2^*[\text{rad}] = 10$
$c_1 = 1.5$	$\xi^+ = 2$	$r[\text{m}] = 0.2$	$x_3^*[\text{rad/s}] = 0$
$c_2 = 1.6$	$n = 2$	$J_x[\text{kgm}^2] = 2$	$x_4^*[\text{rad/s}] = 0$
$\epsilon = 1$	$L_g = 1$	$J_y[\text{kgm}^2] = 2$	

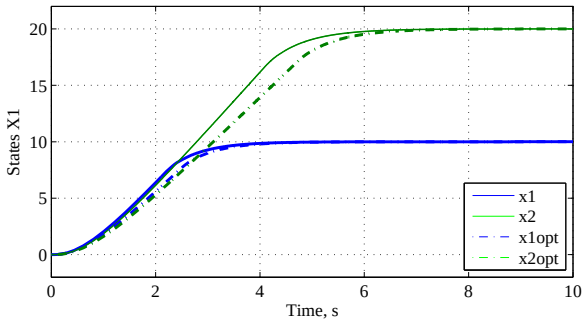

Fig. 3. Real and estimated of X_1.

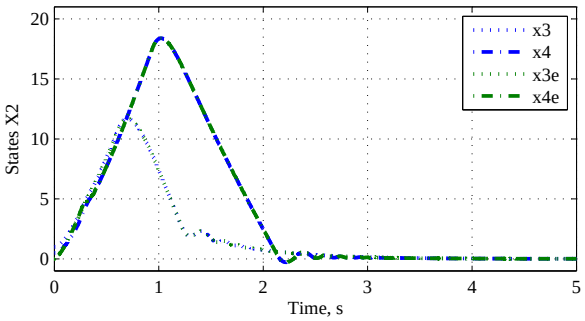

Fig. 4. Angular positions reached by conventional and optimal parameters.

From the figures 3 and 5 one can see the behavior of the real states X and the control U of the system obtained by both classical and optimal parameters of the gain. The angular position does not changes its trajectory when in

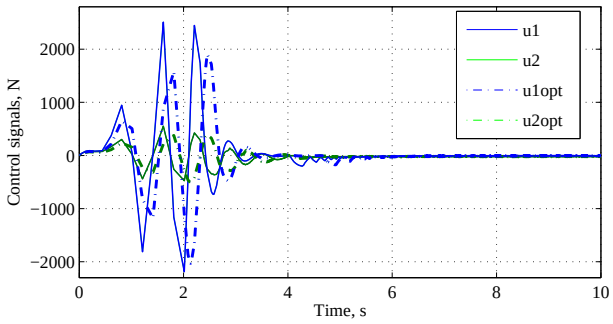

Fig. 5. Control signals representation.

the control signals we see a reduction in the control signal values.

Finally, Fig. 6 illustrates the time-variations of the adaptive control parameters $k = k(\hat{x}(t), t)$, $\lambda = \lambda(\hat{x}(t), t)$ providing the desired dynamics of the considered closed-loop system.

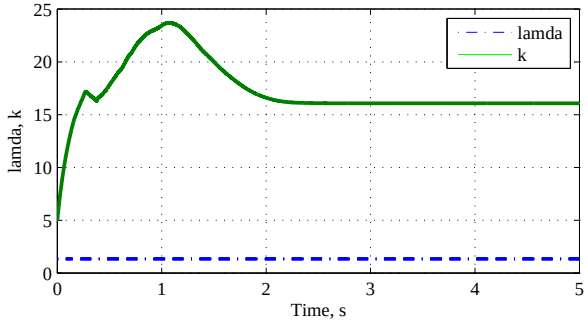

Fig. 6. Tuned parameters k and λ.

5. CONCLUSION

This paper has focused on reconstructing optimally the gain parameters in a feedback sliding mode controller-observer. Novel adaptive sliding mode observers based on Super-Twisting with the tuning gain is presented for this purpose. The proposed controller-observer robustly reconstruct the states in the presence of unknown bounded coupling strengths and a class of unknown bounded uncertainties/ nonlinearities/disturbances. The Pareto-set optimization approach is derived for exact selection of the gain parameters. A parallel manipulator with two DOF is used to demonstrate the novelty of the proposed approach via numerical simulations.

REFERENCES

Edwards, C. and Tanb, C.P. (2006). Sensor fault tolerant control using sliding mode observers. *Cont Eng Practice*, 14, 897–908.

Ehrgott, M. (2005). *Multicriteria Optimization*. Springer, Berlin, Heidelber, New York, 2 edition.

Fridman, L., Mokhtari, A., and Benallegu, A. (2008). High-order sliding-mode observer for a quadrotor uav. *Int. J. Robust Nonlinear Control*, 18, 427–440.

Gobbo, D.D., Napolitano, M., Famouri, P., and Innocenti, M. (2001). Experimental application of extended kalman filtering for sensor validation. *IEEE Trans on Control Systems Tech*, 9, 376–380.

Jornada, D. and Leon, V.J. (2016). Biobjective robust optimization over the efficient set for pareto set reduction. *European Journal of Operational Research*, 252(2), 573 – 586.

Jung, J., Huh, K., Fathy, H.K., and Stein, J.L. (2006). Optimal robust adaptive observer design for a class of nonlinear systems via an h-infinity approach. *American control conference*, In Proceedings of the 2006, 3637–3642.

Keshtkar, S., Keshtkar, J., and Poznyak, A. (2016). Adaptive sliding mode control for solar tracker orientation. *2016 American Control Conference*, (accepted).

Khoroshiltseva, M., Slanzi, D., and Poli, I. (2016). A pareto-based multi-objective optimization algorithm to design energy-efficient shading devices. *Applied Energy*.

Kima, S.M., Hanb, W.Y., and Kima, S.J. (2004). Design of a new adaptive sliding mode observer for sensorless induction motor drive. *Electric Power Systems Research*, 70, 16–22.

Li, J., Xu, L., and Zhang, Z. (2005). An adaptive sliding-mode observer for induction motor sensorless speed control. *IEEE TRANSACTIONS ON INDUSTRY APPLICATIONS*, 41(4), 1039–1047.

Luo, Q., Wu, J., Yang, Y., Qian, J., and Wu, J. (2016). Multi-objective optimization of long-term groundwater monitoring network design using a probabilistic pareto genetic algorithm under uncertainty. *Journal of Hydrology*, 534, 352 – 363.

Nikolaos, K. and Costas, K. (1998). Nonlinear observer design using lyapunov auxiliary theorem. *Sys and Cont Letters*, 34(5), 241–247.

Shtessel, Y., Edwards, C., Fridman, L., and Levant, A. (2014). *Sliding Mode Control and Observation*. Birkhauser.

Utkin, V., Buss, M., and Rao, S. (2008). An adaptive sliding mode observer for induction machines. *ACC*, 1947–1951.

Utkin, V. (1992). *Sliding Modes in Control and Optimization*. Spronger Verlag.

Wan, L., Yuan, J., and Wei, L. (2016). Pareto optimization scheduling with two competing agents to minimize the number of tardy jobs and the maximum cost. *Applied Mathematics and Computation*, 273, 912 – 923.

Weiss, H. and Moore, J. (1980). Improved extended kalman filter design for passive tracking. *IEEE Trans. Autom. Contr.*, AC-25, 897–908.

Xiaosong, H., Fengchun, S., and Yuan, Z. (2010). Estimation of state of charge of a lithium-ion battery pack for electric vehicles using an adaptive luenberger observer.

Energies, 3, 1586–1603.

Zheng, Y., Fatta2, H.A.A., and Loparo, K.A. (2000). Nonlinear adaptive sliding mode observer-controller scheme for induction motors. *Int. J. Adapt. Control Signal Process*, 14, 245–273.

Synthesis of Four-bar Mechanisms for Trajectory Control Using the Modified Brainstorm Optimization Algorithm and Linkage Normalization

Pedro Bautista-Camino * **Eduardo Vega-Alvarado** *
Edgar Alfredo Portilla-Flores * **Paola Andrea Niño-Suárez** **
Maria Bárbara Calva-Yañez *

* *Instituto Politécnico Nacional, México - CIDETEC - Laboratorio de Mecatrónica (e-mail: peterbc1@gmail.com)*
** *Instituto Politécnico Nacional, México - ESIME Azcapotzalco - SEPI*

Abstract: The Modified Brainstorm Optimization (MBSO) algorithm, explored in recent literature, is an efficient metaheuristic optimization technique inspired on the process of solving a problem by humans when they get together to interchange ideas and opinions, complementing each other in order to reach a general solution. This paper presents a novel application of MBSO for the dimensional synthesis of four-bar planar mechanisms for trajectory control, with three different case studies. The four-bar mechanisms are used in a wide variety of industrial applications because of their simplicity, but the associated design process is a very complex task, so they are a good example of hard optimization problems. MBSO was modified to handle design constraints by implementing the feasibility rules of Deb. Additionally, a normalization function was incorporated considering the aesthetics of the mechanisms, to avoid unfeasible combinations because of the lenght of their components. Simulation results show a high-precision control of the proposed trajectories for the designed mechanisms, thus suggesting that MBSO can be used successfully as a tool for solving design engineering cases.

Keywords: MBSO, optimization, dimensional synthesis, bar normalization, four-bar mechanism.

1. INTRODUCTION

In recent years, the use of metaheuristics has been a very effective tool for solving real world problems. In engineering, *synthesis* is the process for designing mechanical systems; the dimensional synthesis is the length calculus of the components of a mechanism for producing a specific movement or behavior. The application of metaheuristics in this kind of numerical problems has been treated previously in related literature as in Santiago-Valentin (2016); Jiménez et al. (2014); Portilla-Flores et al. (2014), among others.

The Brainstorm Optimization Algorithm is a relatively new algorithm proposed by Shi (2011), that has been used successfully in engineering optimization problems as in Duan et al. (2013), Jordehi (2015) and Fernández-Jiménez (2014), among others. Subsequently a modification of the original algorithm was proposed by (Zhan et al., 2012) called Modified Brainstorm Optimization Algorithm (MBSO) which computationally improves the performance of the original algorithm; this algorithm is used in this work. In this paper, a new proposal based on MBSO with the addition of the rules of Deb (2000) for handling constrains is presented, as a tool for solving real world optimization problems.

The four-bar mechanism is used in many industrial applications because of its simplicity; however, its synthesis for trajectory tracking is a complex task that can not be solved efficiently by using deterministic methods. Three case studies are presented here, in order to test the efficiency of the MBSO algorithm and the quality of its results; this cases are variations of a four-bar mechanism that are designed for controlling specific trajectories. In the modeling of the problems was included a normalization function for the links (Capistran-Gumersindo, 2015), in order to improve the aesthetic of the mechanisms; this means that the ratio between the bars should be balanced. A mechanism is more aesthetic as it is better suited for its manufacturing; it implies an enhance on stress distribution, the use of cheaper and/or less specialized materials, etc.

This paper is distributed as follows: In Section 2 the methodology is introduced, including the analysis of the four-bar mechanism, the optimization strategy and the computational implementation. In Section 3 the results of the case studies are analyzed, while the final discussion is

⋆ The authors would like to thank Instituto Politécnico Nacional (IPN) of México, for its support via Secretaría de Investigación y Posgrado (SIP) with the project SIP-20161615.

presented in Section 4. Finally, there is an appendix with the data tables resulting from the simulation carried out.

2. METHODOLOGY

This research addresses the dimensional synthesis of a four-bar mechanism with three different case studies for trajectory control; so, as a first point the general model of this mechanism is developed.

2.1 Kinematics of the mechanism

The four-bar mechanism is one of the most used devices in machinery design due to its simplicity for controlling movements with one freedom degree. These mechanisms have been well studied in the corresponding literature; a detailed description is in Sanchez-Marquez et al. (2014). Fig. 1 shows a planar mechanism whose elements are: a reference bar (r_1), a crank bar (r_2), a couple bar (r_3) and a rocker bar (r_4).The equation of the closed loop is in (1):

$$\boldsymbol{r}_1 + \boldsymbol{r}_4 = \boldsymbol{r}_2 + \boldsymbol{r}_3 \tag{1}$$

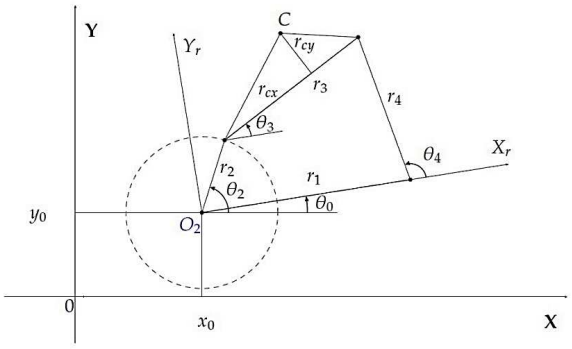

Fig. 1. Four-bar mechanism

The spinning of r_2 is determined by the angle θ_2, and this causes the oscillation of r_4, which in turn produces the movement of r_3 in a closed trajectory. Each point in this trajectory is determined by the position of the coupler C, whose spacial coordinate is established in the system OX_rY_r as indicated in (2),

$$\begin{aligned} C_{xr} &= r_2 cos\theta_2 + r_{cx} cos\theta_3 - r_{cy} sin\theta_3 \\ C_{yr} &= r_2 sin\theta_2 + r_{cx} sin\theta_3 + r_{cy} cos\theta_3 \end{aligned} \tag{2}$$

In the global coordinate system, this point can be expressed as in (3)

$$\begin{bmatrix} C_x \\ C_y \end{bmatrix} = \begin{bmatrix} cos\theta_0 & -sin\theta_0 \\ sin\theta_0 & cos\theta_0 \end{bmatrix} \begin{bmatrix} C_{xr} \\ C_{yr} \end{bmatrix} + \begin{bmatrix} x_0 \\ y_0 \end{bmatrix} \tag{3}$$

It is important to note that equations (2), (3), and the expressions of the mechanism kinetics are enough to calculate any position of point C along the trajectory of the mechanism.

2.2 Design constraints

Since the case studies presented are taken from real-world problems, in order to solve the synthesis of the required four-bar mechanisms it is necessary to consider the following constraints:

- Law of Grashof: This law establishes that for a planar four-bar linkage, *the sum of the shortest bar and the largest bar cannot be larger than the sum of the remaining bars, if a continual relative rotation between two elements is desired* (Norton, 1995). It is expressed in (4),

$$\boldsymbol{r}_1 + \boldsymbol{r}_2 \leq \boldsymbol{r}_3 + \boldsymbol{r}_4 \tag{4}$$

So, the relationships in (5) must be satisfied,

$$\boldsymbol{r}_2 < \boldsymbol{r}_3, \quad \boldsymbol{r}_3 < \boldsymbol{r}_4, \quad \boldsymbol{r}_4 < \boldsymbol{r}_1 \tag{5}$$

- Sequence of angles: The coupler of the mechanism must pass in a logical order along the points that delimited the trajectory (precision points). It can be achieved if the angular positions corresponding to each of the precision points are ordered in magnitude as shown in (6), where n is the number of precision points in the desired path.

$$\sum_{i=1}^{n-1} \theta_2^i - \theta_2^{i+1} \leq 0 \tag{6}$$

2.3 Objective function

Since an objective function is a mathematical relationship for measuring the performance of a system, for these case studies the mean square error between the calculated points and the desired points is used, so the ideal value is zero. This objective function is expressed in (7), where n is the number of points precision, C_{xd}^i and C_{yd}^i represent the components x and y of the desired points, and C_x^i and C_y^i correspond to the similar components for the calculated points of the system, that are a function of θ_2.

$$f(\theta_2^i) = \sum_{i=1}^{n} [(C_{xd}^i - C_x^i)^2 + (C_{yd}^i - C_y^i)^2] \tag{7}$$

Additionally, a second objective function is considered in order to avoid a disproportionated mechanism, in spite of this unbalanced mechanism could deliver a zero error, taking into account that the expression in (7) does not consider a balance on the final length of the bars. The extra function for normalizing the length of the bars is described in (Capistran-Gumersindo, 2015), and corresponds to the equation (8),

$$f(\boldsymbol{x}) = \frac{\sqrt{\sum_{i=1}^{6} \sum_{j=1}^{6} (x_i - x_j)^2}}{\sqrt{\sum_{i=1}^{6} x_i^2}} \tag{8}$$

where $\boldsymbol{x}$ is a vector formed by the variables that represents the magnitude of the bars, as expressed in (9),

$$\boldsymbol{x} = [r_1, r_2, r_3, r_4, r_{cx}, r_{cy}]^T = [x_1, x_2, x_3, x_4, x_5, x_6,]^T \tag{9}$$

The merge of functions (7) and (8) forms the weighted sum indicated in (10), where w_1 and w_2 are the coefficients for controlling the aesthetic of the mechanism. With a value

of w_2 bigger than w_1 the bars tend to resemble each other, but the precision of the generated trajectory decreases; by the opposite, a bigger value on w_1 will produce more precision with less aesthetic.

$$f_r = w_1 f(\theta_2^i) + w_2 f(\boldsymbol{x}) \tag{10}$$

2.4 Case studies

Three case studies for the synthesis of four-bar mechanisms are developed, with their respective numerical optimization problems:

(1) Control of a linear trajectory (*CS1*): The mechanism must follow a trajectory which describes a vertical line; the set of precision points describing this line is listed in (11), while the vector of design variables is given by (12).

$$\omega_1 = \begin{bmatrix} (20,20), & (20,25), & (20,30) \\ (20,35), & (20,40), & (20,45) \end{bmatrix} \tag{11}$$

$$\begin{aligned} \boldsymbol{p} &= [r_1, ..., r_4, r_{cx}, r_{cy}, \theta_0, x_0, y_0, \theta_2^1, ..., \theta_2^6]^T \\ &= [p_1, ..., p_{15}]^T \end{aligned} \tag{12}$$

where the variables r_1, ... , r_4 are the length of the bars, r_{cx} and r_{cy} are the components of the coupler, θ_0 is the angle of inclination of the mechanism, x_0 and y_0 are the components of the relative coordinate system, and $\theta_2^1 ... \theta_2^6$ represent the position angular for each precision point in θ_2. The upper and lower range for each variable are listed in (13):

$$\begin{aligned} r_1, r_2, r_3, r_4 &\in [0, 60] \\ r_{cx}, r_{cy}, x_0, y_0 &\in [-60, 60] \\ \theta_0, \theta_2^1, \theta_2^2, \theta_2^3, , \theta_2^4, \theta_2^5, \theta_2^6 &\in [0, 2\pi] \end{aligned} \tag{13}$$

So, the problem is defined by the expression in (14),

$$\begin{aligned} \min\ & f(\boldsymbol{p}) = w_1 f(\theta_2^i) + w_2 f(\boldsymbol{x}) \\ & \boldsymbol{p} \in \Re^{15} \end{aligned} \tag{14}$$

Subject to the conditions in (15):

$$\begin{aligned} g_1(\boldsymbol{p}) &= p_1 + p_2 - p_3 - p_4 \leq 0 \\ g_2(\boldsymbol{p}) &= p_2 - p_3 \leq 0 \\ g_3(\boldsymbol{p}) &= p_3 - p_4 \leq 0 \\ g_4(\boldsymbol{p}) &= p_4 - p_1 \leq 0 \\ g_5(\boldsymbol{p}) &= p_{10} - p_{11} \leq 0 \\ g_6(\boldsymbol{p}) &= p_{11} - p_{12} \leq 0 \\ g_7(\boldsymbol{p}) &= p_{12} - p_{13} \leq 0 \\ g_8(\boldsymbol{p}) &= p_{13} - p_{14} \leq 0 \\ g_9(\boldsymbol{p}) &= p_{14} - p_{15} \leq 0 \end{aligned} \tag{15}$$

(2) Trajectory tracking with unaligned points (*CS2*): For this case, the mechanism must follow a trajectory that passes along the points indicated by the set in (16), with a previously established sequence of angles for each precision point, as shown in (17),

$$\omega_2 = \begin{bmatrix} (3,3), & (2.759, 3.363), & (2.372, 3.663) \\ (1.890, 3.862), & & (1.355, 3.943) \end{bmatrix} \tag{16}$$

$$\theta_2^i = \{\frac{\pi}{6}, \frac{\pi}{4}, \frac{\pi}{3}, \frac{10\pi}{24}, \frac{\pi}{2}\} \tag{17}$$

Additionally θ_0, x_0 and $y_0 = 0$; so, the solution is reduced to the design vector in (18):

$$\begin{aligned} \boldsymbol{p} &= [r_1, r_2, r_3, r_4, r_{cx}, r_{cy}]^T \\ &= [p_1, p_2, p_3, p_4, p_5, p_6]^T \end{aligned} \tag{18}$$

where the upper and lower limits for each variable are given by (19):

$$\begin{aligned} r_1, r_2, r_3, r_4 &\in [0, 50] \\ r_{cx}, r_{cy} &\in [-50, 50] \end{aligned} \tag{19}$$

The optimization problem is defined in (20):

$$\begin{aligned} \min\ & f(\boldsymbol{p}) = w_1 f(\theta_2^i) + w_2 f(\boldsymbol{x}) \\ & \boldsymbol{p} \in \Re^6 \end{aligned} \tag{20}$$

Subject to the constraints in (21):

$$\begin{aligned} g_1(\boldsymbol{p}) &= p_1 + p_2 - p_3 - p_4 \leq 0 \\ g_2(\boldsymbol{p}) &= p_2 - p_3 \leq 0 \\ g_3(\boldsymbol{p}) &= p_3 - p_4 \leq 0 \\ g_4(\boldsymbol{p}) &= p_4 - p_1 \leq 0 \end{aligned} \tag{21}$$

(3) Motion generation delimited by a set with ten pairs of precision points (*CS3*): For this case, the mechanism must generate a path such that the coupler passes between every pair of the precision points included in the Table 1:

Table 1. Set of points for *CS3*

P1	(1.768 , 2.3311)	(1.9592 , 2.44973)
P2	(1.947 , 2.6271)	(2.168 , 2.675)
P3	(1.595 , 2.7951)	(1.821 , 2.804)
P4	(1.019 , 2.7241)	(1.244 , 2.720)
P5	(0.479 , 2.4281)	(0.705 , 2.437)
P6	(0.126 , 2.0521)	(0.346 , 2.104)
P7	(-0.001 , 1.720)	(0.195 , 1.833)
P8	(0.103 , 1.514)	(0.356 , 1.680)
P9	(0.442 , 1.549)	(0.558 , 1.742)
P10	(1.055 , 1.905)	(1.186 , 2.088)

The vector of design variables is defined by (22):

$$\begin{aligned} \boldsymbol{p} &= [r_1, .., r_4, r_{cx}, r_{cy}, \theta_0, x_0, y_0, \theta_2^1, ..., \theta_2^{10}]^T \\ &= [p_1, ..., p_{19}]^T \end{aligned} \tag{22}$$

The limits for each variable are expressed by (23),

$$\begin{aligned} r_1, r_2, r_3, r_4 &\in [0, 60] \\ r_{cx}, r_{cy}, x_0, y_0 &\in [-60, 60] \\ \theta_0, \theta_2^1, ..., \theta_2^{10} &\in [0, 2\pi] \end{aligned} \tag{23}$$

For this case the trajectory is defined for a set of point pairs precision; so, the modification of the objective function in (24) is used:

$$\begin{aligned} \min\ & f(\boldsymbol{p}) = w_1(Error_1 + Error_2) + w_2 f(\boldsymbol{x}) \\ & \boldsymbol{p} \in \Re^{19} \end{aligned} \tag{24}$$

and the partial errors are defined in (25):

$$Error_1 = \sum_{i=1}^{n}[(C^i_{1xd} - C^i_x)^2 + (C^i_{1yd} - C^i_y)^2]$$
$$Error_2 = \sum_{i=1}^{n}[(C^i_{2xd} - C^i_x)^2 + (C^i_{2yd} - C^i_y)^2] \quad (25)$$

This problem is subject to the constraints in (26):

$$\begin{aligned}
g_1(\boldsymbol{p}) &= p_1 + p_2 - p_3 - p_4 \leq 0 \\
g_2(\boldsymbol{p}) &= p_2 - p_3 \leq 0 \\
g_3(\boldsymbol{p}) &= p_3 - p_4 \leq 0 \\
g_4(\boldsymbol{p}) &= p_4 - p_1 \leq 0 \\
g_5(\boldsymbol{p}) &= p_{10} - p_{11} \leq 0 \\
g_6(\boldsymbol{p}) &= p_{11} - p_{12} \leq 0 \\
g_7(\boldsymbol{p}) &= p_{12} - p_{13} \leq 0 \\
g_8(\boldsymbol{p}) &= p_{13} - p_{14} \leq 0 \\
g_9(\boldsymbol{p}) &= p_{14} - p_{15} \leq 0 \\
g_{10}(\boldsymbol{p}) &= p_{15} - p_{16} \leq 0 \\
g_{11}(\boldsymbol{p}) &= p_{16} - p_{17} \leq 0 \\
g_{12}(\boldsymbol{p}) &= p_{17} - p_{18} \leq 0 \\
g_{13}(\boldsymbol{p}) &= p_{18} - p_{19} \leq 0
\end{aligned} \quad (26)$$

2.5 Optimization Strategy

The Brainstorm Optimization algorithm was proposed by Shi (2011), based in four ideas developed by Osborn (1957). Zhan et al. (2012) presented an enhanced version, MBSO, which is used in this work. It is inspired on the process of solving a problem by humans when they get together to interchange ideas and opinions, complementing each other in order to reach a general solution. In the algorithm the ideas are represented with vectors of real numbers corresponding to the design variables. The ideas are grouped accordingly to their similarity, in a process called clustering; then, it is determined whether one of these central ideas will be replaced for a completely new one. New ideas can be formed from one or two clusters, and a process of competition is produced (Zhan et al., 2013); the complete MBSO is described in the Algorithm 1.

MBSO uses the parameters listed in the Table 2. The process of creating a new idea is governed by the relationship in (27). This equation indicates that the new idea Y_1 in the *nth* dimension (d) is a random number between the limits L_d and H_d if and only if a random number is lower than a preset probability P_r. Otherwise, the new idea will be generated by adding noise; this noise is produced from the difference between two elements of the same dimension from another two ideas, picked randomly and multiplied by a random number between 0 and 1. The function *rand* generates random numbers with a uniform distribution.

$$Y^d_{1new} = \begin{cases} rand(L_d, H_d) & if(rand(0,1) < P_r) \\ p^d_i + rand(0,1)(p^d_a - p^d_b) & otherwise \end{cases} \quad (27)$$

Experiment design A set of 300 simulations was executed for each case study, with 30 executions for each combination of weights; these combinations start with $w_1 = 1$ and $w_2 = 0$, and by subtracting 0.1 and adding 0.1 respectively they finish in $w_1 = 0.1$ and $w_2 = 0.9$. The number of evaluations of the objective function was taken as a stop condition, with the values of 350,000, 150,000 and 350,000 for *CS1*, *CS2*, and *CS3*, respectively; the values of the complementary parameters are listed in the Table 3.

Algorithm 1 Modified Brain Storm Optimization

```
Randomly generate N ideas and evaluate them
while (CurrentEval ⩽ EvalMax) do
    Cluster the N ideas into M clusters, keep the best idea in each cluster as the cluster center
    if (rand(0,1) < P_R) then
        Randomly select a cluster and replace its center with a randomly generated idea
    end if
    for (i = 1 to N) do
        if (rand(0,1) < P_G) then ▷ Create an idea based on one cluster
            Randomly select a cluster j with probability P_j
            if (rand(0,1) < P_C1) then
                Add random values to the selected cluster center, to generate a new idea Y_i
            else
                Add random values to a random idea from the selected cluster, to generate a new idea Y_i
            end if
        else ▷ Create an idea based on two clusters
            Randomly select two clusters, j_1 and j_2
            if (rand(0,1) < P_C2) then
                Combine two cluster center and add a random value to generate a new idea Y_i;
            else
                Combine two random ideas from the two clusters and add a value to generate a new idea Y_i;
            end if
        end if
        Evaluate the idea Y_i and replace X_i if Y_i is better than X_i;
    end for
end while
```

The constraints are handled by implementing in MSBO the feasibility rules of Deb (2000), which dictate that:

Table 2. Parameters of the MBSO algorithm

Number of ideas	N
Number of clusters	M
Probability of replacing a full idea	P_R
Probability of replacing one component of the idea	P_r
Probability of creating a new idea based in one cluster	P_G
First probability of center cluster idea	P_{C1}
Second probability of center cluster idea	P_{C2}

Table 3. Tuned parameters for all cases

Parameter	***CS1***	***CS2***	***CS3***
N	45	100	100
M	10	20	30
P_R	0.4	0.4	0.4
P_G	0.8	0.8	0.8
P_{C1}	0.8	0.7	0.8
P_{C2}	0.8	0.7	0.7
P_r	0.01	0.01	0.01

(1) Between two feasible individuals the one with the best value in the objective function is selected.
(2) Between a feasible individual and another unfeasible, the feasible one will be chosen.
(3) Between two infeasible individuals, the individual with the lower sum of constraint violations will be accepted.

The feasibility is measured by the sum of constraint violation determined by (28), where p is the number of constraints; only inequality constraints were used in the three case studies:

$$SVR = \sum_{i=1}^{p} max(0, g_i(\boldsymbol{p})) \tag{28}$$

3. RESULTS

In all the three case studies it was found that, without the normalization function, the mechanisms tend to be quite disproportionate, specially in *CS2* and *CS3*; e.g., in the second case the value of r_2 for a combination of weights $w_1 = 1$ and $w_2 = 0$ is about ten times smaller than the rest of the bars. These results can be consulted in the appendix of this paper. On the other hand, if it is given more weight to the normalization function, the obtained mechanisms tend to present unexpected behaviors since bars are more like each other and they appear to be more a double rocker device. The best aesthetic and functional mechanisms were generated when the weight assigned to the normalization coefficient was in the range $0 < w_2 < 0.5$.

Table 4. Statistical analysis - *CS1*

Weight 0.1+0.9					
Average	0.5107	σ^2	0.3311	Best	0.0706
Median	0.1998	σ	0.5754	Worse	2.0423
Weight 0.5+0.5					
Average	1.2645	σ^2	0.4008	Best	0.15381
Median	1.2354	σ	0.633	Worse	2.43293
Weight 0.9+0.1					
Average	0.3881	σ^2	0.0862	Best	0.13537
Median	0.2995	σ	0.2936	Worse	1.30035
Weight 1+0					
Average	0.3823	σ^2	0.2603	Best	0.0019
Median	0.0454	σ	0.5102	Worse	1.6361

MBSO generated good results from the point of view of engineering as they converged to feasible solutions in the three problems, and the values of the objective function shown quality results corresponding to acceptable trajectories. Tables 4, 5, and 6 show the statistic analysis for *CS1*, *CS2*, and *CS3*, respectively, taking into account the extreme and the medium cases regarding the weights. In the first two case studies, the value $\sigma^2 < 1$ indicates that the results tend to be accurate.

For *CS1*, the best result was obtained with the combination of weights of 0.9 to the mean square error function and 0.1 to the normalization function; a simulation of the corresponding mechanism is shown in Fig. 2.

For the second problem the mechanisms generated without the normalization function are very disproportionate; in this case the best combination of weights was $w_1 = 0.7$ and $w_2 = 0.3$, whose corresponding mechanisms is presented in

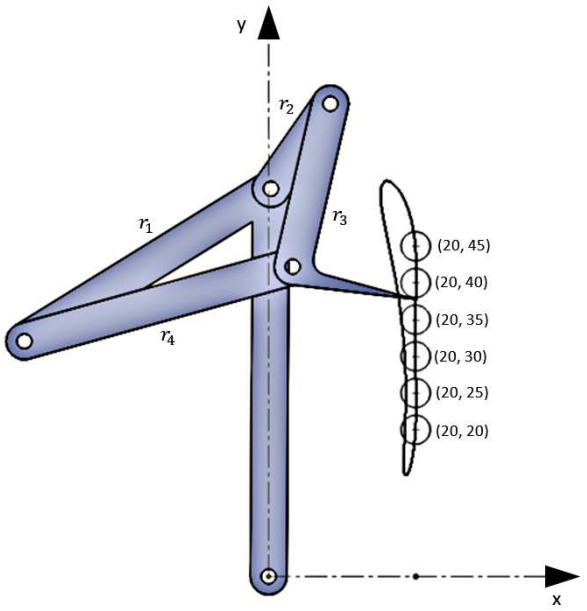

Fig. 2. Mechanism for the first case study

Fig. 3. It is noteworthy that in this case the trajectory marked by the mechanism has a error that could be questionable for the purpose of an optimal trajectory tracking, but otherwise complies with the ratio of the bars; without the normalization function the mechanism would be infeasible in the real world.

As in the second case, for *CS3* the mechanisms produced without a normalization tend to be physically irreproducible; the algorithm generated its best result with $w_1 = 0.7$ and $w_2 = 0.3$. This mechanism is shown in Fig. 4.

4. CONCLUSION

As noted in the results section, the use of an additional function for normalization allow to control the size of the bars by simply varying the proportion in a weighted sum. Depending on how much accuracy is required in the trajectory less weight should be assigned to the normalization function; on the other hand, if the weight assigned to the normalization function is greater than 0.5 the obtained mechanisms have bars that tend to be very similar among themselves, generating unexpected behaviour. This suggests that the adequate range for aesthetic mechanisms should be $w_2 \in [0, 0.5]$. This range allows to have a balance

Table 5. Statistical analysis - *CS2*

Weight 0.1+0.9					
Average	0.0924	σ^2	2.03E-17	Best	0.0924
Median	0.0924	σ	4.51E-09	Worse	0.0924
Weight 0.5+0.5					
Average	0.1247	σ^2	4.70E-13	Best	0.1247
Median	0.1247	σ	6.86E-07	Worse	0.1247
Weight 0.9+0.1					
Average	0.0379	σ^2	9.37E-10	Best	0.0379
Median	0.0379	σ	3.06E-05	Worse	0.03803
Weight 1+0					
Average	0.0031	σ^2	2.56E-08	Best	0.0028
Mediana	0.0031	σ	0.00016	Worse	0.0035

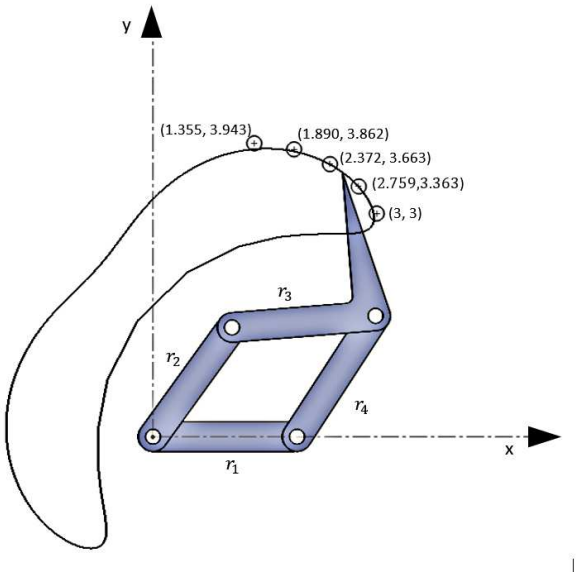

Fig. 3. Mechanism for the second case study

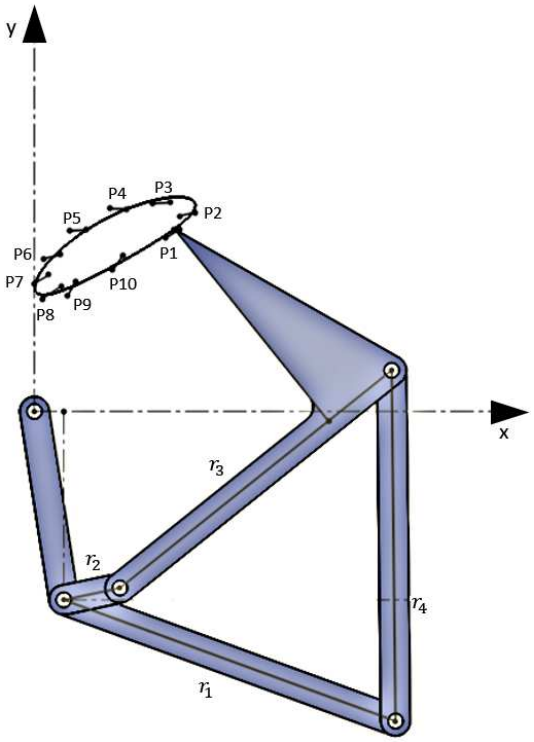

Fig. 4. Mechanism for the third case study

between the aforementioned aesthetics and the precise control of the trajectories, in order to produce solutions that are acceptable from the point of view of engineering.

Analyzing the MSBO from the point of view of computing, the algorithm meets the requirements for its use in optimization since it presents a steady behavior, obtaining competitive results that suggest that MSBO can be use as a tool for real world problems. However, the algorithm still needs new adjustments, so it is proposed as a future research work, focusing in the algorithm tuning and in the use of normalization functions for other case studies; this is in order to validate its operation as a tool in the synthesis to feasible solutions, accordingly with the constraints consider in the modeling stage.

REFERENCES

Capistran-Gumersindo, E. (2015). *Cómputo inspirado en la naturaleza para la optimizacion mono-objetivo de un efector final de tres dedos.* Master's thesis, Laboratorio Nacional de Informatica Avanzada, Mexico.

Deb, K. (2000). An efficient constraint handling method for genetic algorithms. *Computer Methods in Applied Mechanics and Engineering.*

Duan, H., Li, S., and Shi, Y. (2013). Predator–prey brain storm optimization for dc brushless motor. *IEEE Transactions on Magnetics*, 49(10), 5336–5340.

Fernández-Jiménez, M. (2014). *Optimización de un mecanismo de cuatro barras usando el algoritmo de optimización basado en tormenta de ideas.* Master's thesis, Laboratorio Nacional de Informatica Avanzada, Mexico.

Jiménez, V.P., Sánchez, O.F.A., and Mauledoux, M. (2014). Diseño de un efector final de tres dedos para agarre óptimo. *DYNA: revista de la Facultad de Minas. Universidad Nacional de Colombia. Sede Medellín*, 81(184), 93–101.

Jordehi, A.R. (2015). Brainstorm optimisation algorithm (bsoa): An efficient algorithm for finding optimal location and setting of facts devices in electric power systems. *International Journal of Electrical Power & Energy Systems*, 69, 48–57.

Norton, R.L. (1995). *Diseño de Maquinaria, una Introduccion a la Sintesis y Analisis Mecanismos y Maquinas.* McGraw Hill.

Osborn, A. (1957). *Applied Imagination-Principles and Procedures of Creative Writing.* Charles Scribner's Sons.

Portilla-Flores, E., Santiago-Valentin, E., Solano-Palma, A., Vega-Alvarado, E., and Calva-Yáñez, B. (2014). Cálculo de fuerza para agarre óptimo de un efector final de tres dedos utilizando el algoritmo de forrajeo de bacterias. *Second International Conference on Advanced Mechatronics, Design and Manufacturing Technology.*

Sanchez-Marquez, A., Vega-Alvarado, E., Portilla-Flores, E.A., and Mezura-Montes, E. (2014). Synthesis of a planar four-bar mechanism for position control using the harmony search algorithm. In *Electrical Engineering, Computing Science and Automatic Control (CCE), 2014 11th International Conference on*, 1–6. IEEE.

Santiago-Valentin, E. (2016). *Optimización de sistemas mecatronicos utilizando herramientas de inteligencia ar-*

Table 6. Statistical analysis - *CS3*

Weight 0.1+0.9					
Average	1.1679	σ^2	0.6338	Best	0.13004
Median	1.265	σ	0.7961	Worse	2.64519
Weight 0.5+0.5					
Average	2.57	σ^2	6.1875	Best	0.191
Median	1.5815	σ	2.4874	Worse	8.2547
Weight 0.9+0.1					
Average	2.4647	σ^2	15.435	Best	0.4662
Median	0.8776	σ	3.9288	Worse	12.4385
Weight 1+0					
Average	3.7664	σ^2	29.218	Best	0.3041
Median	0.633	σ	5.4054	Worse	13.508

tificial. Master's thesis, Instituto Politécnico Nacional, México.

Shi, Y. (2011). Brain storm optimization algorithm. In *Advances in Swarm Intelligence*, 303–309. Springer.

Zhan, Z.h., Chen, W.n., Lin, Y., Gong, Y.j., Li, Y.L., and Zhang, J. (2013). Parameter investigation in brain storm optimization. In *Swarm Intelligence (SIS), 2013 IEEE Symposium on*, 103–110. IEEE.

Zhan, Z.h., Zhang, J., Shi, Y.h., and Liu, H.l. (2012). A modified brain storm optimization. In *Evolutionary Computation (CEC), 2012 IEEE Congress on*, 1–8. IEEE.

Appendix A. RESULTS OF THREE STUDY CASES OF THE MAIN WEIGHTS

Table A.1. Main weights of the CS1

Weight 0.1+0.9						
	r_1	r_2	r_3	r_4	r_{cx}	r_{cy}
Best	36.084	34.994	36.084	36.084	35.799	35.894
Worse	49.701	12.906	13.411	49.663	-1.164	12.869
	θ_0	x_0	y_0	θ_2^1	θ_2^2	θ_2^3
Best	4.078	-17.102	41.158	3.095	3.266	3.427
Worse	5.703	19.934	22.020	0.548	0.714	0.892
	θ_2^4	θ_2^5	θ_2^6	**F.O**		
Best	3.578	3.725	3.868	**0.0706**		
Worse	1.087	1.335	1.681	**2.0423**		
Weight 0.5+0.5						
	r_1	r_2	r_3	r_4	r_{cx}	r_{cy}
Best	30.476	27.127	30.044	30.46	25.245	25.209
Worse	41.972	23.304	41.962	41.96	-50.923	-44.808
	θ_0	x_0	y_0	θ_2^1	θ_2^2	θ_2^3
Best	3.802	-8.144	52.152	2.61	2.7974	2.991
Worse	1.9	-60	18.436	3.484	3.5913	3.696
	θ_2^4	θ_2^5	θ_2^6	**F.O**		
Best	3.191	3.399	3.606	**0.1538**		
Worse	3.797	3.894	3.987	**2.4323**		
Weight 0.9+0.1						
	r_1	r_2	r_3	r_4	r_{cx}	r_{cy}
Best	39.452	14.133	22.785	37.883	23.342	17.332
Worse	43.732	6.0066	10.835	43.717	-28.829	59.999
	θ_0	x_0	y_0	θ_2^1	θ_2^2	θ_2^3
Best	3.696	0.309	52.83	2.267	2.636	2.985
Worse	2.862	-49.718	36.512	3.882	4.021	4.155
	θ_2^4	θ_2^5	θ_2^6	**F.O**		
Best	3.343	3.717	4.115	**0.1353**		
Worse	4.284	4.411	4.534	**1.3**		
Weight 1+0						
	r_1	r_2	r_3	r_4	r_{cx}	r_{cy}
Best	50.44	6.191	8.794	47.872	-8.510	-10.107
Worse	59.527	8.582	8.595	59.518	8.484	-40.094
	θ_0	x_0	y_0	θ_2^1	θ_2^2	θ_2^3
Best	4.513	27.018	35.655	0.508	1.022	1.385
Worse	3.253	59.999	46.489	1.153	1.277	1.406
	θ_2^4	θ_2^5	θ_2^6	**F.O**		
Best	1.716	2.049	2.417	**0.0019**		
Worse	1.531	1.650	4.641	**1.6361**		

Table A.2. Main weights of the CS2

Weight 0.1+0.9				
	r_1	r_2	r_3	r_4
Best	1.861134	1.790211	1.811698	1.861134
Worse	1.861238	1.790278	1.811783	1.861238
	r_{cx}	r_{cy}	**F.O**	
Best	1.808446	1.846364	**0.092499**	
Worse	1.808516	1.84644	**0.092499**	
Weight 0.5+0.5				
	r_1	r_2	r_3	r_4
Best	1.927416	1.785747	1.927416	1.927416
Worse	1.925981	1.784889	1.925981	1.925981
	r_{cx}	r_{cy}	**F.O**	
Best	1.69976	1.946801	**0.12476**	
Worse	1.699511	1.947457	**0.124764**	
Weight 0.7+0.3				
	r_1	r_2	r_3	r_4
Best	1.946624	1.844081	1.946624	1.946624
Worse	1.957514	1.850633	1.957514	1.957514
	r_{cx}	r_{cy}	**F.O**	
Best	1.585674	1.963814	**0.093646**	
Worse	1.587307	1.956146	**0.093749**	
Weight 0.9+0.1				
	r_1	r_2	r_3	r_4
Best	1.990289	1.921494	1.990289	1.990289
Worse	2.012848	1.934196	2.012847	2.012848
	r_{cx}	r_{cy}	**F.O**	
Best	1.477738	1.947855	**0.037909**	
Worse	1.482921	1.929627	**0.038037**	
Weight 1+0				
	r_1	r_2	r_3	r_4
Best	20.32431	2.12592	20.31793	20.3206
Worse	33.67168	2.040306	33.64924	33.65048
	r_{cx}	r_{cy}	**F.O**	
Best	2.252166	-0.04672	**0.002893**	
Worse	2.328561	-0.10588	**0.003544**	

Table A.3. Main weights of the CS3

Weight 0.1+0.9					
	r_1	r_2	r_3	r_4	r_{cx}
Best	2.700134	2.650182	2.700054	2.700064	2.682684
Worse	36.04836	5.31E-06	32.4994	35.81544	29.10311
	r_{cy}	θ_0	x_0	y_0	θ_2^1
Best	2.68294	0.12403	1.440574	-0.78327	0.004591
Worse	36.04546	3.409883	-28.3069	38.10563	0.506397
	θ_2^2	θ_2^3	θ_2^4	θ_2^5	θ_2^6
Best	0.005812	0.005814	2.853636	3.057053	3.342652
Worse	0.747988	2.205879	2.329498	2.877531	4.023138
	θ_2^7	θ_2^8	θ_2^9	θ_2^{10}	**F.O**
Best	3.419362	3.419477	3.419516	6.283183	**0.130049**
Worse	4.055401	4.955032	5.078083	5.825513	**2.645194**
Weight 0.5+0.5					
	r_1	r_2	r_3	r_4	r_{cx}
Best	1.22209	1.206991	1.213745	1.21838	1.219299
Worse	44.80746	8.87E-07	42.24817	44.78088	-40.4217
	r_{cy}	θ_0	x_0	y_0	θ_2^1
Best	1.216139	5.273249	1.36589	1.61437	3.49E-05
Worse	15.79192	2.947508	-36.8667	-19.0761	0.771197
	θ_2^2	θ_2^3	θ_2^4	θ_2^5	θ_2^6
Best	3.56587	3.876966	4.367836	4.92191	5.350395
Worse	1.153899	1.687836	2.513014	3.569076	3.617679
	θ_2^7	θ_2^8	θ_2^9	θ_2^{10}	**F.O**
Best	5.614382	5.766777	6.26176	6.275974	**0.191004**
Worse	4.006044	4.504363	4.716411	6.177327	**8.2547**
Weight 0.7+0.3					
	r_1	r_2	r_3	r_4	r_{cx}
Best	4.74585	0.77120	4.67949	4.71595	3.58997
Worse	50.55098	0.98628	41.34927	41.43773	2.519878
	r_{cy}	θ_0	x_0	y_0	θ_2^1
Best	3.307737	5.932793	0.394543	-2.53523	0.514331
Worse	-18.3359	4.160592	17.42196	10.73462	2.258997
	θ_2^2	θ_2^3	θ_2^4	θ_2^5	θ_2^6
Best	0.880699	2.16406	2.750446	3.303229	3.807311
Worse	2.479596	2.852924	3.796082	4.388886	4.768158
	θ_2^7	θ_2^8	θ_2^9	θ_2^{10}	**F.O**
Best	4.261585	5.273711	5.594033	6.14547	**0.590077**
Worse	4.992503	4.997823	4.998617	4.998661	**2.226639**
Weight 0.9+0.1					
	r_1	r_2	r_3	r_4	r_{cx}
Best	54.92273	1.007059	35.39606	45.01554	23.03694
Worse	58.62993	3.87E-07	43.21731	43.27921	5.305051
	r_{cy}	θ_0	x_0	y_0	θ_2^1
Best	13.63005	5.746743	-14.44	-19.5711	0.535914
Worse	-24.2068	2.007463	-1.31272	-22.4677	0.981415
	θ_2^2	θ_2^3	θ_2^4	θ_2^5	θ_2^6
Best	1.023879	2.019396	2.633527	3.192861	3.719558
Worse	1.499258	1.893784	2.620466	3.169049	3.557299
	θ_2^7	θ_2^8	θ_2^9	θ_2^{10}	**F.O**
Best	4.345817	4.921324	5.297749	5.998191	**0.466286**
Worse	4.020403	5.104533	5.242441	5.635895	**12.43857**
Weight 1+0					
	r_1	r_2	r_3	r_4	r_{cx}
Best	43.8394	1.114893	5.066177	43.83902	3.456882
Worse	58.77674	2.33E-15	46.45654	48.70741	6.787923
	r_{cy}	θ_0	x_0	y_0	θ_2^1
Best	-0.74177	5.357885	-2.21474	0.95963	0.565488
Worse	20.25242	1.795314	15.26328	18.06667	0.060799
	θ_2^2	θ_2^3	θ_2^4	θ_2^5	θ_2^6
Best	1.01483	2.03882	2.604173	3.137856	3.670335
Worse	0.543971	1.060257	1.391867	2.104119	2.653932
	θ_2^7	θ_2^8	θ_2^9	θ_2^{10}	**F.O**
Best	4.314163	4.900529	5.312059	6.053438	**0.304117**
Worse	3.204741	5.267743	5.746124	6.227666	**13.50808**

CHAPTER 13

POWER SYSTEMS

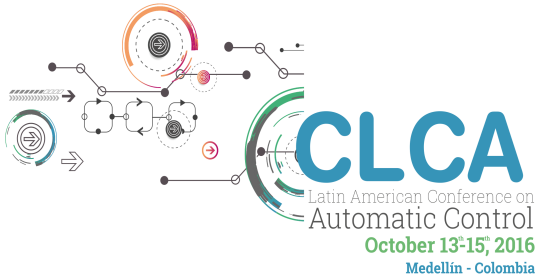

Condiciones de existencia de estado estacionario en circuitos eléctricos con CPL

Michael Rojas * **Gerardo Espinosa-Pérez** *

* *Faultad de Ingeniería, Universidad Nacional Autónoma de México (e-mail:michrojasg@comunidad.unam.mx,gerardoe@unam.mx).*

Resumen
En el presente trabajo se muestra una método para obtener condiciones de existencia de estado estacionario constante en circuitos eléctricos al emplear propiedades estructurales que presentan este tipo de sistemas. En trabajos recientes se han podido establecer condiciones de estado estacionario para circuitos de corriente directa hasta con dos cargas CPL; el objetivo principal del presente escrito es mostrar que es posible establecer este tipo de condiciones de existencia de estado estacionario de manera sistemática vía sus propiedades estructurales.

Keywords: Estado estacionario constante, CPL, árbol, co-árbol, circuitos eléctricos, matriz de transferencia.

1. Introducción

El análisis de los circuitos eléctricos es una línea de estudio que comenzó a principios del siglo XX (Higgins (1949)) pero que en la actualidad y con el avance de la tecnología los problemas alrededor de éstos aumentan, esto causa que las generalizaciones que existen de ellos en la práctica resulten inútiles ante la presencia de fenómenos que producen comportamientos caóticos,bifurcaciones, ciclos límite y generalmente inestabilidad, de ahí, que la caracterización de dichos fenómenos es de suma importancia para comprender y evitar este tipo de comportamientos.

En Roska (1978) y Fujisawa and Kuh (1971) se muestran resultados del problema de unicidad y existencia de las soluciones en sistemas de redes no lineales, desde esta perspectiva, la falta de solución o la existencia de múltiples soluciones en las redes nos indica la existencia de fenómenos físicos como la inestabilidad de voltaje que, asociados a los sistemas de potencia, este tipo de singularidades se han incrementado en las últimas décadas a causa del crecimiento casi exponencial de las cargas, [1] y por consiguiente el aumento de la potencia demandada. Los tipos de cargas se pueden reducir a tres, resistivas, capacitivas e inductivas en sus variantes lineales y no lineales, pero, con el desarrollo de la electrónica y sus ramas esta visón se ha modificado debido a la naturaleza de estos sistemas, por esta razón el re-estudio del comportamiento de los circuitos eléctricos bajo la influencia de este tipo de cargas es de suma importancia, en general es posible analizar y modelar el comportamiento de cualquier carga en función del tipo de demanda de potencia que posee, ya sea demanda variable o constante.

El estudio de la representación de cargas en sistemas eléctricos se ha desarrollado en Karlsson and Hill (1994) con la identificación y modelado de cargas no lineales, mientras en Hill (1993) y Overbye (1994) se enfocan en el modelado de cargas para el estudio de la estabilidad de voltaje. Existen dispositivos complejos en su estructura pero con características de demanda de potencia bien definida, estos dispositivos son modelados en función de la potencia que consumen, para fines generales en el presente análisis, este tipo de cargas se denominan CPL, [2] que en Belkhayat et al. (1995) son consideradas generalizaciones de convertidores de potencia con características específicas que producen inestabilidad (Jusoh (2004) y X.Liu and Cross (2007)), problemática por la cual en S.Sanchez and Molinas (2012) se propone un método para conocer las características de estabilidad de redes de circuito eléctricos en corriente directa CPL, mientras en Barvanov et al. (2015) se muestran las restricciones que debe tener la carga para mantener las condiciones de estado estacionario. En el presente escrito se aborda el problema de existencia de estado estacionario en redes eléctricas con CPL bajo ciertas configuraciones específicas.

El trabajo se estructura como sigue, en la Sección 2 se hace un compendio de la teoría básica necesaria para entender el desarrollo del presente, mientras en la Sección 3se muestran las condiciones para la existencia de estado estacionario en configuraciones de circuitos eléctricos con CPL y como es posible establecerlas a través de propiedades estructurales de los circuitos eléctricos.

2. Preliminares

2.1. *Condiciones de existencia de estado estacionario constante*

La representación entrada-salida de circuitos eléctricos excitados con fuentes de voltaje constante se muestra en la siguiente ecuación Barvanov et al. (2015)

⋆

[1] En el presente el concepto de carga se refiere al dispositivo físico al cual se quiere proveer de una cierta potencia

[2] Cargas de potencia constante por sus siglas en inglés

$$Y(s) = G(s)U(s) + k \tag{1}$$

donde $G(s) \in \mathbb{R}^{m\times m}$ es la función de transferencia, $Y(s) = \mathscr{L}\{y(t)\}$ es el vector de salidas (voltajes en las cargas), $U(s) = \mathscr{L}\{u(t)\}$ es el vector de entradas (corrientes en las cargas), donde el operador $\mathscr{L}$ indica la transformada de *Laplace* y $k \in \mathbb{R}^m$ representa la relación entre las entradas (corrientes de las cargas) y la fuente de excitación, donde m es el número de CPL dentro del sistema. Las entradas u y las salidas y son variables conjugadas de puerto, es decir, el producto entre éstas ($u^T y$) tiene unidades de potencia, además establecen la relación de las CPL con el sistema como se muestra en la siguiente ecuación

$$-y_i(t)u_i(t) = P_i > 0, \quad i \in \mathscr{M} \tag{2}$$

donde y_i y u_i son el $i-esimo$ elemento de los vectores que representan las variables de puerto, donde $i = 1,2,3,\ldots,m \in \mathscr{M}$ siendo m el número de CPL dentro del sistema. De acuerdo con esto la definición de estado estacionario se presenta a continuación.

Definición 1. {Barvanov et al. (2015),Definición 1} El sistema representado por (1) conectado a una CPL por medio de (2), posee estado estacionario constante si y sólo si existen vectores constantes $\bar{u}$ y $\bar{y} \in \mathbb{R}^m$ tal que:

$$\bar{y} = G(0)\bar{u} + k \tag{3}$$

$$\bar{y}_i\bar{u}_i = -P_i, \quad i \in \mathscr{M} \tag{4}$$

□.

Dado que la matriz de transferencia $G(0) \in \mathbb{R}^{m\times m}$ es posible establecer la siguiente suposición

Suposición 1. La parte simétrica de la matriz de transferencia $G(0)$ es de signo definido y sin pérdida de generalidad se asume que es **positiva definida**, es decir

$$G(0) + G^T(0) > 0. \tag{5}$$

▽

El análisis de existencia de estado estacionario constante se encuentra dado por la restricción dada por (2), por esta razón y para conocer el comportamiento de la potencia dentro del sistema, se multiplica por la entrada u la salida expresada en (1), obteniendo la siguiente expresión

$$\bar{u}_i(g_i\bar{u} + k_i) = -\underbrace{P_i}_{\bar{y}_i\bar{u}_i}; \quad i \in \mathscr{M} \tag{6}$$

donde $G^T(0) := [g_1 \quad g_2 \quad \cdots g_m]$, con base en la (6), es posible realizar la siguiente proposición

Proposición 1. El estado estacionario constante existe si y sólo si la solución de (6) sobre la entrada $u \in \mathbb{R}$.

◊

donde la condición para que (6) tenga solución es la siguiente

$$\frac{1}{2}k^T[G(0) + G^T(0)]^{-1}k \geq \sum_{i=1}^{m} P_i \tag{7}$$

sí lo anterior es cierto, según la definición, existe estado estacionario constante. En realidad la condición dada por (7) se presentó en Sanchez et al. (2013) como una condición necesaria y suficiente, pero sólo representa la cantidad máxima de potencia que el sistema es capaz de disipar(Barvanov et al. (2015)), es decir, es la cota superior de potencia que la CPL puede demandar a la fuente. Cabe mencionar que la condición dada por (7) es necesaria y suficiente para circuitos eléctricos en donde $m = 1$, es decir, sólo tienen dentro de su configuración una CPL, si $m > 1$ se tiene la siguiente proposición

Proposición 2. {Barvanov et al. (2015), Proposición 1} Se asume que existe una matriz $T := diag\{t_i\} \in \mathbb{R}^{m\times m}$ tal que

$$\begin{bmatrix} TG(0) + G^T(0)T & Tk \\ (Tk)^T & 2\underline{1}_m^T TP \end{bmatrix} > 0 \tag{8}$$

entonces, *no existe* estado estacionario constante para el sistema representado por(1) y (2).

◊

Aplicando el complemento de Schur a la LMI dada por (8) se tiene

$$\begin{aligned} &TG(0) + G^T(0)T > 0 \\ &\underline{1}_m^T TP > \frac{1}{2}(Tk)^T[TG(0) + G^T(0)T]^{-1}Tk. \end{aligned} \tag{9}$$

donde ambas condiciones se deben satisfacer para garantizar la existencia de estado estacionario, se puede observar que ambas condiciones representan una generalización del resultado mostrado en Sanchez et al. (2013)

2.2. *Caracterización de sistemas eléctricos vía propiedades estructurales*

En Avila-Becerril et al. (2015) se desarrolla una técnica de modelado de circuitos eléctricos con base en sus propiedades estructurales, para aprovechar dichas propiedades se hace uso de la teoría de grafos[3], donde una gráfica orientada G consiste en un conjunto finito de nodos $\mathscr{V}(G) = \{v_1, v_2, \ldots, v_n\}$ y un conjunto finito de bordes $\mathscr{E} = \{e_1, e_2, \ldots, e_b\}$, en análisis de circuitos el conjunto de nodos son el punto de interconexión de elementos del circuito, mientras que el conjunto bordes agrupa uno a uno cada puerto de dichos elementos.A cada puerto de cada elemento se asocian dos variables, el voltaje v en las terminales del elemento y la corriente i que fluye a través del elemento.

Con base en lo anterior es posible definir el espacio de bordes $C_1(G)$ como un espacio vectorial real b-dimensional de todas las funciones $\mathscr{E}(G) \in \mathbb{R}$ donde se encuentran las corrientes que fluyen a través de los bordes, de la misma forma es posible definir el espacio dual $C^1(G)$ donde se encuentran todos los voltajes v. Las variables de puerto de los elementos que se encuentran inter-conectados, al ser circuitos eléctricos, deben cumplir con las restricciones impuestas por las leyes de Kirchoff, dichas restricciones se encuentran dadas en función de *cusets* y *loopsets* básicos que se generan en gráficas especiales, **árbol** y**co-árbol**.
Un árbol es un subgráfica conectada que posee n nodos y $n-1$ bordes (ramas) de modo que en su composición no existan trayectorias cerradas, los bordes restantes (cuerdas), $b-(n-1)$ corresponden a los bordes del co-árbol. EL *cutset*

[3] Si desea conocer más de teoría de grafos consulte Gross and Yellen (1999)

básico es el conjunto de bordes conformado por una rama del árbol y al menos una cuerda del co-árbol, un *loopset* básico es un conjunto formado por una cuerda y algunas ramas en las cuales se presentan trayectorias cerradas. Con base en estos dos conjuntos es posible asociar dos matrices con el grafo, la matriz de *cutsets* básicos $C_b \in \mathbb{R}^{n-1\times b}$ y la matriz de *loopsets* básicos $B_b \in \mathbb{R}^{b-n+1\times b}$, por lo tanto, la representación de las restricciones en circuitos eléctricos se encuentran dadas por

$$i = \begin{bmatrix} i_t \\ i_c \end{bmatrix} \in C_1 : \quad \begin{bmatrix} v_t \\ v_c \end{bmatrix} \in C^1 \tag{10}$$

donde $i_t \in \mathbb{R}^{n-1}$, $v_t \in \mathbb{R}^{n-1}$ son las variables de puerto del árbol mientras que $i_c \in \mathbb{R}^{b-(n-1)}$, $v_c \in \mathbb{R}^{b-(n-1)}$ son las variables de puerto de co-árbol, de acuerdo con Wellestad (1979) es posible escribir las restricciones de corriente de la siguiente forma

$$\begin{bmatrix} I & H \end{bmatrix} \begin{bmatrix} i_t \\ i_c \end{bmatrix} = 0 \tag{11}$$

mientras que las restricciones de voltaje se expresan como

$$\begin{bmatrix} -H^T & I \end{bmatrix} \begin{bmatrix} v_t \\ v_c \end{bmatrix} = 0 \tag{12}$$

donde I es la matriz identidad y la matriz de fundamental de trayectoria cerrada $H \in \mathbb{R}^{n-1\times b-(n-1)}$. Para circuitos eléctricos la matriz H se divide como se muestra a continuación Avila-Becerril et al. (2015)

$$H = \begin{bmatrix} H_{1R} & H_{1L} \\ H_{CR} & H_{CL} \\ H_{RR} & H_{RL} \end{bmatrix} \tag{13}$$

donde H representa un mapeo lineal de los elementos de árbol a los elementos de co-árbol, en donde la corriente de árbol y el voltaje de co-árbol se encuentran representados por

$$i_t = -Hi_c \quad v_c = H^T v_t \tag{14}$$

El objetivo del presente es mostrar que para circuitos eléctricos el método descrito en Barvanov et al. (2015) se puede aplicar para circuitos con una estructura más compleja al tomar en cuenta las propiedades estructurales de los circuitos eléctricos y en una primera aproximación sin importar el número de cargas en su estructura. En la siguiente sección se muestra el análisis con un circuito con una carga para realizar el estudio de la existencia de estado estacionario para comprender y aterrizar mejor los conceptos descritos en este capítulo.

3. Circuitos con CPL

En esta sección se muestra el análisis de existencia de estado estacionario en circuitos alimentados con señales de directa con CPL en su estructura, tomando en cuenta las tres configuraciones básicas, radial, malla y anillo.

3.1. *Circuito con una carga CPL: Ejemplo introductorio*

Considere el siguiente circuito

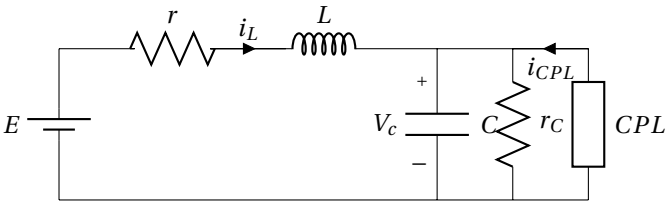

Figura 1. Cirucito con una CPL

Para poder realizar el análisis propuesto es necesario encontrar una representación entrada-estado, dicha representación esta dada por

$$G(s) = \frac{Ls + r}{LCs^2 + \left(rC + \frac{L}{r_C}\right)s + \frac{r}{r_C} + 1} \tag{15}$$

donde $k = \frac{E}{\frac{r}{r_C}+1}$ y a condición de existencia de estado estacionario constante se encuentra dado por

$$P \leq \frac{E^2}{4r\left(\frac{r}{r_C}+1\right)}. \tag{16}$$

donde el término de la izquierda de la ecuación anterior representa la máxima potencia que puede transferir la fuente al circuito, entonces surge la siguiente conjetura.

Conjecture 1. Existe estado estacionario si y sólo si la potencia que demanda la carga es menor a la máxima potencia que puede transferir la fuente al sistema.

3.2. *Circuito en configuración radial*

Las redes radiales son las configuraciones más básicas dentro de la teoría de redes, éstas constan de una sola fuente de alimentación que se encuentra conectada a todas las cargas. La configuración más básica de dicha red se encuentra representada el la Figura 2.

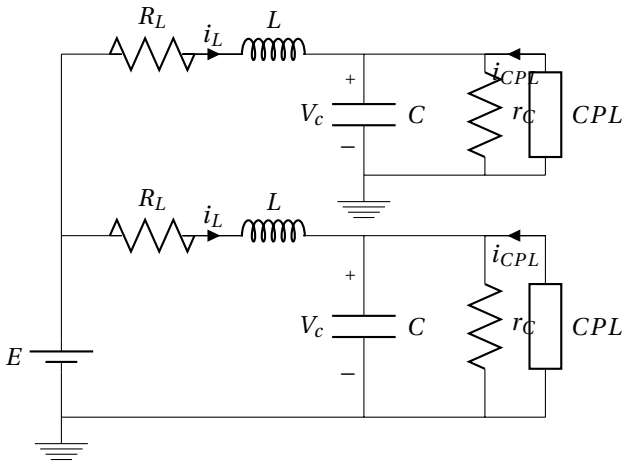

Figura 2. Red radial

El objetivo del método es obtener una representación entrada-salida de las cargas dentro del sistema, por lo tanto es necesario analizar el efecto de las CPL dentro del circuito, para realizar dicho análisis se considera a las CPL como fuentes de corriente y el efecto de la fuente de voltaje se desprecia

para obtener esta representación [4] , en la Figura 3 se muestra la simplificación del circuito ha analizar.

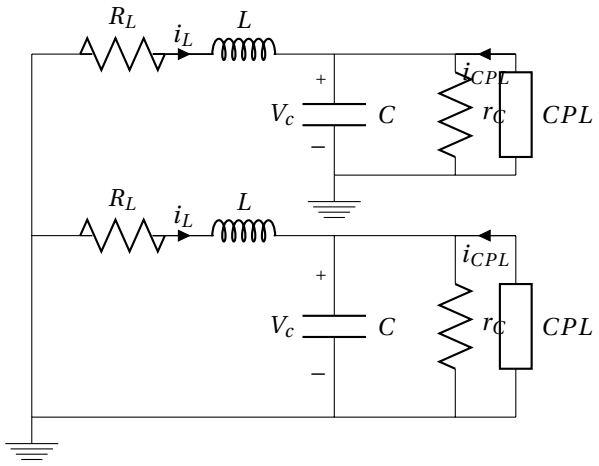

Figura 3. Red radial simplificada.

Para fines de presentar el resultado principal de este trabajo se realizan las siguientes consideraciones

$$\begin{array}{ll} n_1 & \text{Capacitores} \\ n_2 & \text{Resistencias de árbol} \\ n_3 & \text{Inductores} \\ n_4 & \text{Fuentes de corriente que representan a las CPL} \end{array} \tag{17}$$

de igual forma, el grafo asociado corresponde al mostrado en la Figura 4.

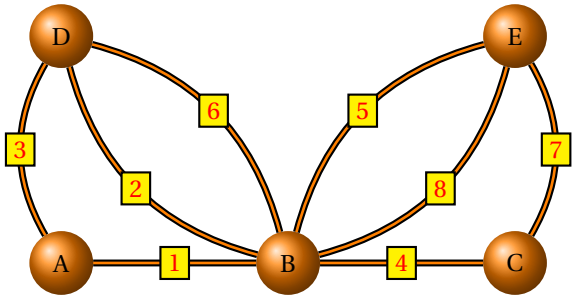

para elegir la representación en árbol y co-árbol se deben de cumplir las siguientes observaciones

Observación 1. Las variables eléctricas de los elementos controlados por voltaje pertenecen al árbol.

Observación 2. Las variables eléctricas cuyos elementos son controlados por corriente pertenecen al co-árbol

Observación 3. Para este análisis se desprecia el efecto de la fuente de voltaje.

Observación 4. El número de capacitores es igual al número de inductores, es decir $n_1 = n_3$.

Observación 5. El número de las resistencias de árbol es igual al número de inductores $n_2 = n_3$.

Observación 6. El número de fuentes de corriente (cargas de potencia constante) es igual al número de resistencias de capacitores $n_1 = n_4$.

[4] En teoría de circuitos este método se conoce como teorema de superposición

por lo tanto el árbol asociado al circuito está compuesto por todos los nodos y por el conjunto de bordes $\{6,1,5,4\}$, por consiguiente el co-árbol esta compuesto por $\{2,3,8,7\}$. Al aplicar la teoría de grafos, para un circuito con estructura radial, la matriz fundamental de trayectorias cerradas [5] se encuentra dada por

$$H = \begin{bmatrix} H_{C\uparrow} & H_{CL} \\ H_{R\uparrow} & H_{RL} \end{bmatrix}. \tag{18}$$

en donde y de acuerdo a las características estructurales de la red las sub matrices que la definen quedan representadas por

$$\begin{array}{rrl} H_{C\uparrow} = & I & \in \mathbb{R}^{n_1 \times n_1} \\ H_{CL} = & antidiag\{1\} & \in \mathbb{R}^{n_1 \times n_1} \\ H_{R\uparrow} = & 0 & \in \mathbb{R}^{n_2 \times n_2} \\ H_{RL} = & I & \in \mathbb{R}^{n3 \times n3} \end{array} \tag{19}$$

Para obtener la representación entrada-salida correspondiente a las cargas para la red radial se sigue la metodología empleada en Avila-Becerril et al. (2015), en donde las variables de puerto de los elementos eléctricos se representan como

$$\begin{array}{ll} \dot{q} = i_C, & v_C = \dfrac{\partial H_a(q,\phi)}{\partial q} = \nabla_q H_a \\ \dot{\phi} = v_L, & i_L = \dfrac{\partial H_a(q,\phi)}{\partial \phi} = \nabla_\phi H_a \\ i_{R_t} = -f_t(v_{R_t}), & v_{R_c} = -f_c(i_{R_c}) \end{array} \tag{20}$$

y las variables de estado del modelo queda representado por el siguiente conjunto de ecuaciones

$$x = \begin{bmatrix} f_a \\ e_a \end{bmatrix}; \qquad \nabla_x H_T(x) = \begin{bmatrix} \dfrac{\partial H_T(f_a,e_a)}{\partial f_a} \\ \dfrac{\partial H_T(f_a,e_a)}{\partial e_a} \end{bmatrix} = \begin{bmatrix} e_C \\ f_L \end{bmatrix} \qquad u = i_{CPL} \tag{21}$$

en donde las relaciones entre las variables de puerto están dados por las siguientes ecuaciones

$$\begin{aligned} \dot{f}_a &= -H_{C\uparrow} f_\uparrow - H_{CL} f_L \\ \dot{e}_a &= -H_{C\uparrow}^T e_c + H_{R\uparrow} e_{R_t} \end{aligned} \tag{22}$$

en donde el modelo Hamiltoniano de esta red se encuentra representado por el siguiente conjunto de ecuaciones

$$\begin{aligned} \dot{x} &= [J-R]\nabla_x H_T(x) + gu + kd \\ y &= g^T \nabla_x H_T(x) \\ z &= k^T \nabla_x H_T(x) \end{aligned} \tag{23}$$

y al emplear la matriz fundamental de trayectoria cerrada se obtiene

[5] Recordar que la matriz fundamental de trayectoria cerrada representa un mapeo lineal entre los elemento de árbol y co-árbol

$$J-R=\begin{bmatrix} 0 & -H_{CL} \\ H_{CL}^T & -H_{RL}^T(R_t^{-1})^{-1}H_{RL} \end{bmatrix}$$
$$g=\begin{bmatrix} -H_{C\uparrow} \\ -H_{RL}^T(R_t^{-1})^{-1}H_{R\uparrow} \end{bmatrix} \quad (24)$$

En donde la matriz de transferencia, desde la corriente hasta el voltaje de la carga para circuitos eléctricos con esta estructura se expresa como

$$\frac{1}{CLs^2+CH_{RL}^TR_t^{-1}H_{RL}s+H_{CL}H_{CL}^T} \quad (25)$$
$$diag\{H_{C\uparrow}(Ls+H_{RL}^TR_t^{-1}H_{RL})-H_{CL}H_{RL}^TH_{R\uparrow}R_t^{-1}\}$$

en donde la matriz de transferencia tiene como componentes en su diagonal principal las funciones de transferencia de cada carga, es posible llegar a esta simplificación gracias a las propiedades estructurales que exhibe el sitema. Para aplicar la metodología antes descrita se obtiene el valor de la matriz de transferencia cuando $s=0$

$$\frac{H_{RL}^TR_t^{-1}H_{RL}-H_{CL}H_{RL}^TH_{R\uparrow}R_t^{-1}}{H_{CL}H_{CL}^T}. \quad (26)$$

Para establecer la condición de máxima potencia que una carga puede demandar en un arreglo con n cargas es necesario analizar el comportamiento carga por carga, de esa forma es posible establecer condiciones de máxima potencia, dicha condición es la siguiente

$$P_j \leq \frac{E^2}{4\sum_{j=1}^{n} r_j} \quad (27)$$

donde P_j es la máxima potencia que puede tener la $j-ésima$ carga, n es el total de cargas presentes en el circuito.

Con base en la condición anterior y la estructura del sistema, es posible realizar la siguiente proposición

Proposición 3. Para un circuito eléctrico con la estructura mostrada en la Figura 2 existe estado estacionario, si y sólo si cada carga cumple con la condición (27)

de este modo, es posible establecer condiciones de existencia de estado estacionario con base en las propiedades estructurales de los circuitos eléctricos.

4. Conclusiones

Se establecieron condiciones de existencia de estado estacionario constante para un tipo específico de circuitos eléctricos con n CPL considerando sus propiedades estructurales, es cierto que en el presente análisis se busca establecer condiciones de existencia solamente para un tipo específico de topología, pero, a través del conocimiento de las propiedades estructurales de las topologías básicas es posible establecer condiciones de existencia vía sus propiedades estructurales, lo cual es un campo de estudio abierto para el análisis de circuitos eléctricos, así como la extensión de estas condiciones para circuitos de AC para estudiar problemas característicos de estos sistemas como el colapso de voltaje e inestabilidad en general en estos sistemas.

Para las configuraciones anillo y radial, en este momento se encuentra desarrollando las condiciones de existencia de estado estacionario bajo la misma metodología.

Agradecimientos

Parte de este trabajo se realizó con el apoyp de DGAPA-UNAM con el número $IN116516$.

Referencias

Avila-Becerril, S., Espinosa-Perez, G., and Fernanadez, P. (2015). Dynamic characterization of typilcal electrical circuits via structural properties.

Barvanov, N., Ortega, R., Griño, R., and Polyak, B. (2015). On existence and satability of equilibria of linear time-invariant systems with constant power loads. *IEEE Transactions on Circuits and Systems*, 62(12), 1–8.

Belkhayat, M., Cooley, R., and Witulski, A. (1995). Large signal stability criteria for distributed systems with constant power loads. *IEEE*.

Fujisawa, T. and Kuh, E. (1971). Some results on existence and uniqueness of solutions of nonlinear networks. *IEEE Transactions on Circuit Theory*.

Gross, J.L. and Yellen, J. (1999). *Graph theory and its applications*. Chapman and Hall.

Higgins, T.J. (1949). History of the operational calculus as used in electric ccircuit analysis. *Electrical Engineering*, 42–45.

Hill, D. (1993). Nonlinear dynamic load models with recovery for voltage stability studies. *IEEE Transactions on Power Systems*, 8(1), 166–177.

Jusoh, A.b. (2004). The instability effect of constsant power loads. *National Power and Energy Conference*.

Karlsson, D. and Hill, D. (1994). Modelling and indentification of nonlinear dynamic loads in power systems. *IEEE Transactions on Power Systems*, 9(1), 157–166.

Overbye, T. (1994). Effect of load modelling on analysis of power system voltage stability. *Electrical Power and Electrical Systems*, 16(5), 329–338.

Roska, T. (1978). On the uniqueness of solutions of nonlinear dynamic networks and systems. *IEEE Transactions on Circuit and Systems*, CAS-25(3), 161–169.

Sanchez, S., Ortega, R., Bergna, G., Molinas, M., and Griño, R. (2013). Conditions for existence of equilibrium points of systems with constant power loads. *Conferenc*.

S.Sanchez and Molinas, M. (2012). Assessment of a stability analysis tool for constant power loads in dcc-grids. In *15th International Power Electronics and Motion Control Conference*.

Wellestad, P. (1979). *Introduction to physical system modelling*. Academic Press London.

X.Liu, A.F. and Cross, A. (2007). Negative input resistence compensator for a constant power load. *IEEE Transactions on Industrial Electronics*, 54(6), 3188–3196.

Control Adaptativo por Modelo de Referencia para la Posición Angular de un Balancín Impulsado por un Motor Brushless

Carlos H. Esparza F.*, José L. Otalvarez M.*, David Calderón M.*

**Unidades Tecnológicas de Santander – UTS, Grupo de Investigación en Control Avanzado – GICAV COLOMBIA (Tel: 57-7-6917700 ext 2007; e-mail: gicav@correo.uts.edu.co). (e-mail: otalvarezjl@gmail.com)(e-mail: calderon917@gmail.com)*

Resumen: El objetivo de este trabajo fue la implementación y validación de dos técnicas de control adaptativo por modelo de referencia MRAC digital, sobre un microcontrolador de 16 bits, comparadas con un controlador PID convencional ante perturbaciones para el control de posición angular de un balancín equilibrado con el impulso de un motor sin escobillas. El sistema está conformado por una barra metálica la cual tiene acoplado a su centro de gravedad un rodamiento y en uno de sus extremos tiene el motor sin escobillas con hélice, el cual produce una fuerza de empuje que actúa sobre la barra haciendo cambiar la posición de ésta a un ángulo determinado. La velocidad del motor es controlada a través del control electrónico de velocidad ESC, empleando un microcontrolador como sistema electrónico que realimenta el ángulo de posición para generar las salidas de control al motor. Para la validación se implementó un sistema de control PID, un sistema de control MRAC con dos parámetros de adaptación y un controlador MRAC Proporcional Diferencial MRAC-PD. Los tres controladores se validaron con y sin perturbaciones, demostrando que el comportamiento de los dos controladores MRAC presenta mejores resultados ante sistemas variantes en el tiempo o sometidos a perturbaciones externas.

Palabras claves: Control Adaptativo por Modelo de referencia, Control PID, Modelo de un Balancín, Motor Brushless.

1. INTRODUCCIÓN

El control clásico PID es la técnica más común y extendida quizás por su mayor grado de implementación (Mansour 2011), debido a su madurez frente a los controles adaptativos, cuyo análisis y aplicación es más reciente. Una de las grandes limitaciones del control clásico es que la identificación del sistema real y los cálculos de los parámetros del controlador se realiza para sistemas lineales con parámetros del proceso invariantes en el tiempo (Rodríguez Rosa et al. 2012). Por el contrario, los sistemas de control avanzados, como el control Adaptativo o el predictivo (Godoy Ortega 2011; Clarke 1988), tienen la ventaja de que pueden trabajar con procesos no lineales y variantes en el tiempo.

El control adaptativo por modelo de referencia (MRAC) (Landau et al. 2011) es una técnica en la cual la respuesta deseada a una señal de entrada del proceso se especifica como un modelo de referencia. El esquema más popular de un control MRAC se puede apreciar en la fig.1; en el cual el mecanismo de adaptación mira la salida yp del proceso y la salida ym del modelo de referencia y calcula los parámetros adaptables de forma que la diferencia tienda a cero (Esparza et al. 2012). El mecanismo de adaptación puede utilizar, si están disponibles, además de señales de salida del proceso y del modelo de referencia (y_p, y_m), las señales de entrada de referencia y las variables del proceso (Rodríguez Rubio & López Sánchez 1996). La regla MIT es el enfoque original para el control adaptable basado en el modelo de referencia (Pérez Ramírez et al. 2005).

En la primera parte de este artículo se obtiene el modelo matemático de la planta, posteriormente se procede a utilizar la herramienta Matlab para realizar el control PID y los dos controles MRAC, finalmente se implementa estos tres tipos de controles obteniendo resultados que permitan concluir cuál de estos funcionan mejor ante cualquier perturbación.

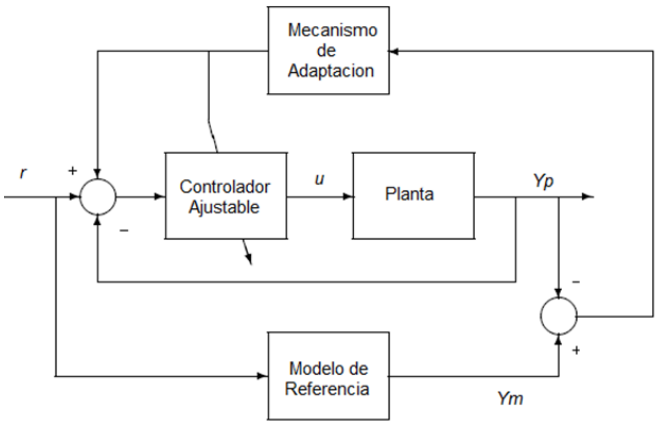

Fig. 1. Esquema general de MRAC paralelo.

2. DESARROLLO

2.1 Modelo Matemático del Balancín

En la fig.2 se puede observar el balancín con el motor *brushless* empleado en este trabajo y las fuerzas actuantes

sobre el sistema las cuales son de interés para la obtención del modelo matemático (Corvalán Aravena & Negroni Vera 2012; Martín Ballesteros & Del Río Carbajo 2013). Para obtener el modelo matemático aproximado de este sistema, se emplea la ecuación del movimiento de rotación de un sólido alrededor de su eje central de inercia, la cual es análoga a la segunda ley de Newton y se representa mediante la ecuación 1 (Viltres La Rosa 2012).

$$lF_e - lF_g sin\theta - l\beta\theta = I\alpha \tag{1}$$

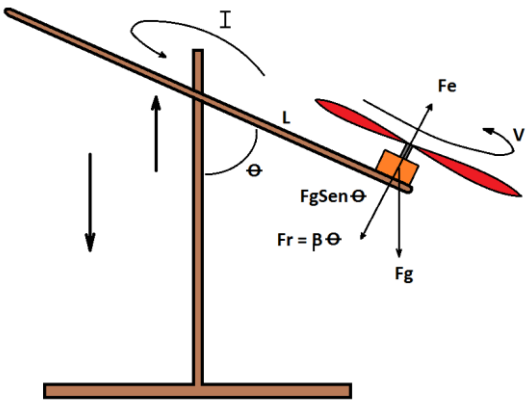

Fig. 2. Fuerzas sobre el sistema.

Donde l es la longitud desde el centro de la barra móvil a uno de sus extremos, F_g es la fuerza de gravedad que actúa sobre el motor, β es el coeficiente de rozamiento entre el motor y el aire, θ es la posición de la barra respecto al eje de giro, I es el movimiento inercial del sistema, α es la aceleración angular, F_e es la fuerza de empuje generada por el giro de la hélice, y V es la velocidad de giro de la hélice [m/s].

Para el cálculo del momento de inercia de la masa del motor se utiliza la ecuación 2, donde m es la masa del motor y l esa la longitud desde el centro de la barra móvil a uno de sus extremos.

$$\begin{aligned} I_m &= m_m l^2 \\ I_m &= 0.07kg * (0.28m)^2 \\ I_m &= 0.005488kgm^2 \end{aligned} \tag{2}$$

Para el cálculo del momento de inercia de la varilla de aluminio se utiliza la ecuación 3 donde M es la masa de la varilla y L es la longitud de la varilla.

$$\begin{aligned} I_c &= \frac{1}{12}ML^2 \\ I_c &= \frac{1}{12}0.095Kg * (0.56m)^2 \\ I_c &= 0.002482kgm^2 \end{aligned} \tag{3}$$

El momento de inercia total es la suma del momento de inercia del motor y el momento de inercia de la varilla tal como se representa en la ecuación 4.

$$\begin{aligned} I_T &= I_m + I_c \\ I_T &= 0.0079706kgm^2 \end{aligned} \tag{4}$$

Teniendo en cuenta los datos anteriores, la ecuación 1 se puede reemplazar como se presenta en la ecuación 5 y de esta manera obtener el modelo de la planta en términos de Laplace.

$$\frac{lF_e}{I} - \frac{lF_g}{I}\theta - \frac{l\beta}{I}\frac{d\theta}{dt} = \frac{d^2\theta}{dt^2} \tag{5}$$

Aplicando la transformada de Laplace a la ecuación 5 se obtiene la función de transferencia.

$$\frac{\theta(s)}{F_e(s)} = \frac{{}^{l}/_{I}}{s^2 + \frac{l\beta}{I}s + \frac{lFg}{I}} \tag{6}$$

Como se puede apreciar la ecuación 6 es de segundo orden, la cual se puede representar como aparece en la ecuación 7.

$$\frac{Y(s)}{X(s)} = \frac{K}{s^2 + 2\zeta w_n + {w_n}^2} \tag{7}$$

Haciendo la analogía entre los denominadores de la ecuación 6 y 7 se realiza la siguiente deducción:

$$2\zeta w_n = \frac{l\beta}{I} \tag{8}$$

$${w_n}^2 = \frac{lF_g}{I} \tag{9}$$

Reemplazando las variables de la ecuación 9 se obtiene que la frecuencia natural $w_n = 4.958\,{}^{rad}/_{s}$. Con el valor de la frecuencia natural, se halla el coeficiente de amortiguamiento donde zita $\zeta = 0.403$, apreciándose que este sistema es subamortiguado. Finalmente, el modelo que describe el sistema se presenta en la ecuación 10.

$$\frac{Y(s)}{X(s)} = G = \frac{20.81}{s^2 + 3.99 + 24.581} \tag{10}$$

2.2 Control Digital

Para la realización del control digital PID se utilizó la herramienta Simulink de Matlab. El diagrama de bloques de la fig.3 corresponde al control PID implementado desde Simulink. El bloque "*Serial Receive*" se encarga de leer los datos enviados desde el Arduino Mega, una vez convertidos los datos en forma de bits se muestrean para compararlo con la referencia y corregir el error.

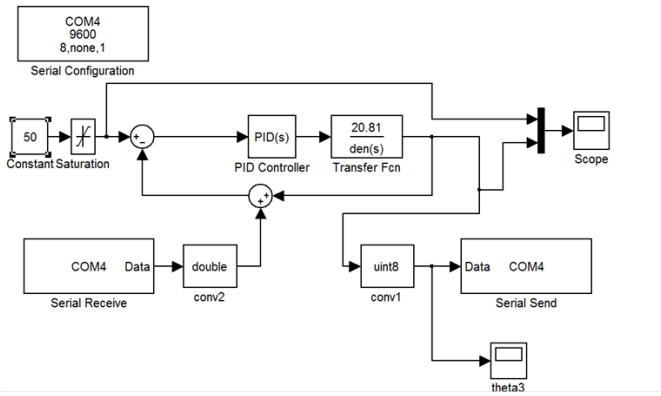

Fig. 3. Diagrama de bloques del control digital PID en Simulink.

El valor de referencia es comparado con el valor recibido del potenciómetro y el valor producido por la diferencia entre estos dos valores es enviado al bloque PID, el cual crea la señal de control correspondiente para la corrección de ese error. A la salida del PID el bloque conv1 convierte los datos a formato unit8, facilitando de esta manera que el bloque Serial Send pueda transmitir los datos a través del puerto serial.

2.3 Control Adaptativo MRAC

Para el control de posición del balancín se presentan dos sistemas MRAC: el primero con ley de control proporcional y dos parámetros de adaptación como se muestra en la ecuación 11 y el segundo con ley de control proporcional-diferencial dada por la ecuación 12 (Esparza & Núñez 2014; Jain & Nigam 2013).

$$U = \theta_1.R - \theta_2.Y \tag{11}$$

$$U = (R - Y)\left(\theta_p + \theta_d s\frac{N}{s+N}\right) \tag{12}$$

2.4 Controlador MRAC con Dos Parámetros de Adaptación Proporcional

Para la obtención de los modelos de referencia se debe plantear un modelo de referencia a partir de la respuesta en lazo cerrado del sistema. La ecuación 13 y 14 corresponde a la salida Y de la planta como el producto en términos de Laplace entre la ley de control U y la planta G (Duraisamy & Dakshinamurthy 2010).

$$Y = (\theta_1.R - \theta_2.Y)G \tag{13}$$

$$Y = (R - Y)\left(\theta_p + \theta_d s\frac{N}{s+N}\right)G \tag{14}$$

Para obtener el modelo de referencia del control proporcional de dos parámetros se despeja de la ecuación 13 la relación entre la salida Y y la entrada R del sistema, en la que G corresponde a la ecuación 10, para así obtener la ecuación 15.

$$\frac{Y}{R} = \frac{\theta_1.G}{(1+\theta_2.G)} \tag{15}$$

La salida del sistema es la multiplicación en frecuencia de la función de transferencia de la planta por la señal de control U, obteniendo:

$$Y(s) = \frac{k}{s(1+2\zeta Tws+(Tws)^2)}(\theta_1 R - \theta_2 Y) \tag{16}$$

Partiendo de la ecuación 16 la función de transferencia en lazo cerrado que relaciona la salida Y del sistema con la entrada R, se obtiene el modelo de referencia representado en la ecuación 17.

$$Mref = \frac{k\theta_1}{s(1+2\delta Tws+(Tws)^2)+k.\theta_2} \tag{17}$$

Una vez obtenido el modelo de referencia se procede a obtener las ecuaciones que describen el comportamiento de los dos parámetros de adaptación. Para obtener los dos parámetros se reemplaza la ecuación 17 en la ecuación 18 obteniendo las ecuaciones 19 y 20.

$$\frac{\partial e}{\partial \theta} = \left(\frac{\partial Y}{\partial \theta} - \frac{\partial Ym}{\partial \theta}\right) = \frac{\partial Y}{\partial x} \tag{18}$$

$$\frac{\partial e}{\partial \theta_1} = \frac{\partial\left(\frac{k\theta_1}{s(1+2\delta Tws+(Tws)^2)+k.\theta_2}.R\right)}{\partial \theta_1} \tag{19}$$

$$\frac{\partial e}{\partial \theta_2} = \frac{\partial\left(\frac{k\theta_1}{s(1+2\delta Tws+(Tws)^2)+k.\theta_2}.R\right)}{\partial \theta_2} \tag{20}$$

Aplicando la trasformada de Laplace para eliminar la derivada se obtienen las funciones de trasferencia para cada parámetro de adaptación representados en las ecuaciones 21 y 22.

$$\theta 1 = \frac{\gamma eR}{s}\left(\frac{k\theta_1}{s(1+2\delta Tws+(Tws)^2)+k.\theta_2}\right) \tag{21}$$

$$\theta 2 = \frac{\gamma eY}{s}\left(\frac{k\theta_1}{s(1+2\delta Tws+(Tws)^2)+k.\theta_2}\right) \tag{22}$$

La fig.4 corresponde al diagrama de bloques, hecho en Matlab Simulink, que describe las ecuaciones del controlador MRAC para dos parámetros.

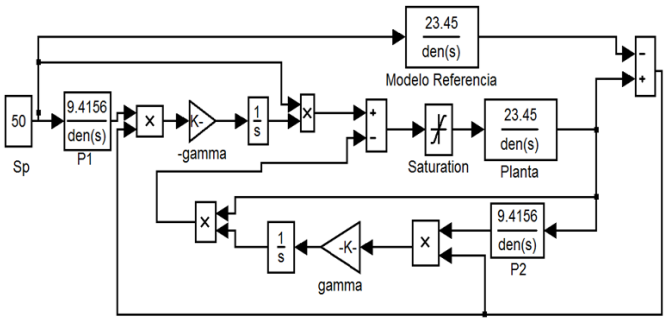

Fig. 4. Diagrama de bloques, control MRAC con dos parámetros de adaptación.

2.5 Controlador MRAC proporcional Derivativo (PD)

La ecuación 23 corresponde a un controlador MRAC con ley de control PD con filtro.

$$U = \theta_p + \theta_d \frac{Ns}{s+N} \tag{23}$$

Partiendo de la ecuación 23 y realizando el procedimiento anterior como se hizo en el control proporcional de dos parámetros se obtiene la salida del control representada en 24 y 25.

$$Y = (R-Y)\left(\frac{\theta_P(s+N)+\theta_d Ns}{s+N}\right)\left(\frac{k}{s(a_0 s+1)}\right) \tag{24}$$

$$Y = \frac{kR(\theta_P s+\theta_d Ns+\theta_p N)}{a_0 s^3+s(a_0 N+1)+s(N+k\theta_p+k\theta_d N)+k\theta_p N} \tag{25}$$

Se calculan las derivadas parciales de la salida Y para obtener las ecuaciones 26 y 27 las cuales son los parámetros del controlador adaptativo.

$$\theta_p = Z\left(\frac{k(s+N)}{(s^3+s^2(a_1+N)+s(a_2+a_1N+k\theta_p+k\theta_d N)+k\theta_p N+a_2 N)}\right) \tag{26}$$

$$\theta_d = Z\left(\frac{kNs}{(s^3+s^2(a_1+N)+s(a_2+a_1N+k\theta_p+k\theta_d N)+k\theta_p N+a_2 N)}\right) \tag{27}$$

Donde Z es el factor que se presenta en la ecuación 28.

$$Z = -\frac{\gamma e(R-Y)}{s} \tag{28}$$

La fig.5 corresponde al diagrama de bloques, hecho en Matlab Simulink, que describe las ecuaciones del controlador MRAC PD.

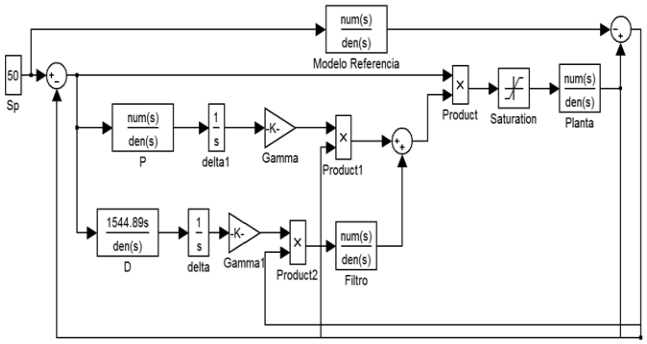

Fig. 5. Diagrama de bloques del controlador MRAC-PD.

3. RESULTADOS

Las pruebas a los diferentes tipos de controladores se realizaron en un dispositivo Arduino Mega, para lo que se discretizaron todas las ecuaciones de los sistemas de control empleando un periodo de muestreo de 50 ms. Estas pruebas consisten en analizar la respuesta del sistema de control sin y con perturbaciones, para lo que se empleó una pesa de 60 gramos que se ubica en el brazo del balancín a una distancia de 20 cm con respecto al centro del motor. Al incluir esta pesa al balancín se modifican sus parámetros y así su modelo matemático. Esta prueba con la pesa se realiza cuando el sistema ya se encuentra en estado estable ante una posición de *setpoint* dada. Las figuras 6, 7 y 8 corresponden al controlador PID, controlador MRAC dos parámetros y controlador MRAC PD respectivamente sin la pesa.

Como se puede apreciar en las figuras 6 a la 9, los tres controladores responden bien a la misma posición preestablecida, teniendo un tiempo de establecimiento menor de 5 segundos y no mostrando diferencias significativas que con lleven a la inestabilidad del sistema.

Por otra parte, las figuras 9, 10 y 11 corresponden a las pruebas realizadas con la perturbación dada por la pesa a los misms tres controladores. En los tres casos, la perturbación se realiza cuando la respuesta del sistema ya se encuentra en estado estable. Para los tres casos se realizó la perturbación pasados los 5 segundos a la respuesta al escalón.

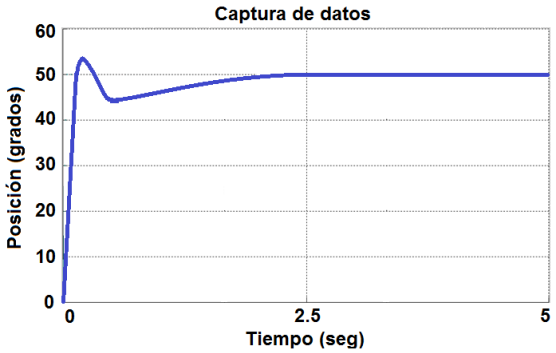

Fig. 6. Salida del controlador PID.

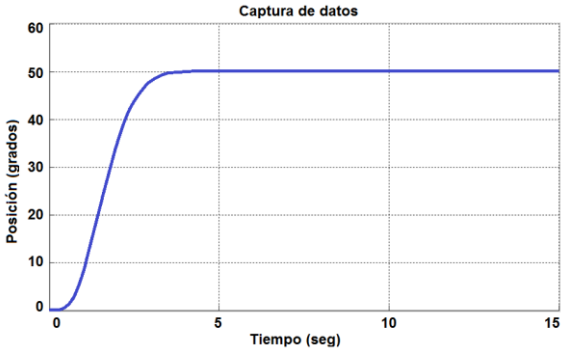

Fig. 7. Salida del controlador MRAC con dos parámetros.

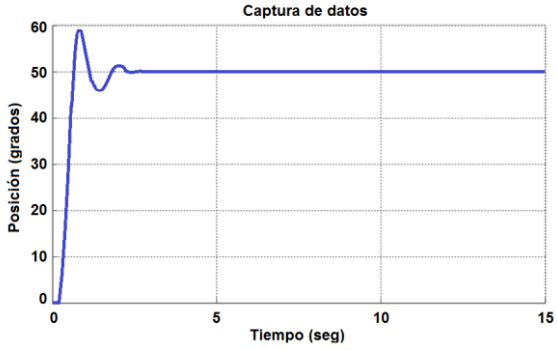

Fig. 8. Salida del controlador MRAC-PD.

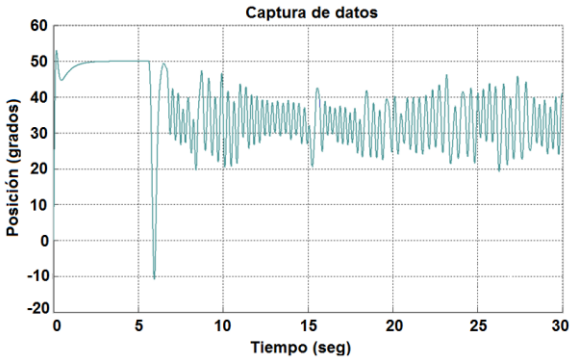

Fig. 9. Salida del controlador PID cuando se pone una pesa de 60 gramos después de su estado estable.

En la figura 9, se puede apreciar que para el caso de los sistemas de control lineales, en este caso PID, estos controladores no tienen la capacidad de responder ante perturbaciones en los parámetros del sistema.

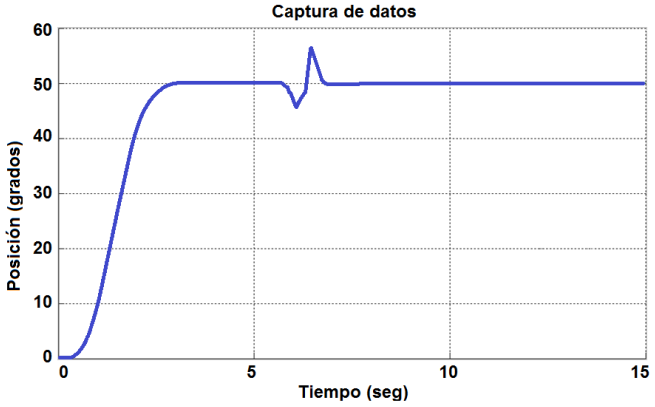

Fig. 10. Salida del controlador MRAC con dos parámetros proporcionales cuando se pone una pesa de 60 gramos después de su estado estable.

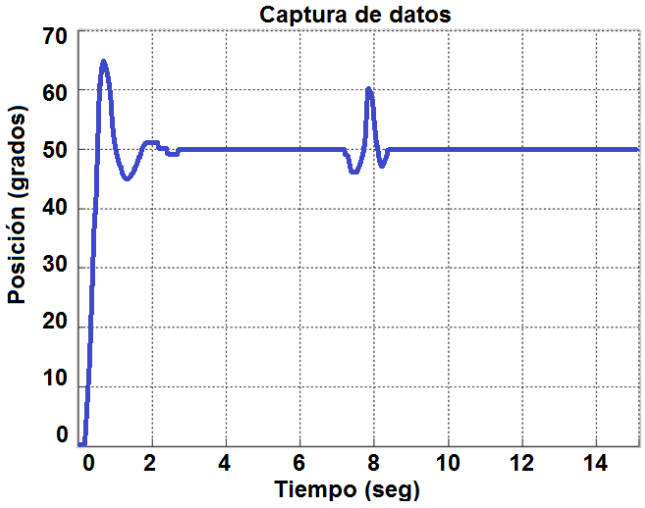

Fig. 11. Salida del controlador MRAC-PD cuando se pone una pesa de 60 gramos después de su estado estable.

Las figuras 10 y 11 muestran la respuesta de los controles MRAC de dos parámetros y el PD, cuando estos son sometidos a la misma perturbación en los parámetros físicos del modelo matemático del balancín. Esta respuesta demuestra que el sistema se estabiliza en un tiempo menor de 3 segundos, el cual es el tiempo estimado del modelo de referencia planteado para el controlador MRAC. Los resultados obtenidos muestran que los controladores de parámetros adaptativos tienen una mejor respuesta que los controladores de parámetros fijos frente a variaciones que puedan afectar las condiciones del sistema.

6. CONCLUSIONES

Uno de los objetivos de este proyecto era el de demostrar, de forma académica, como los sistemas de control avanzados, en este caso los adaptativos, se comportan de forma adecuada para sistemas no lineales o invariantes en el tiempo. Este trabajo continua con la investigación de sistemas de control adaptativos que se inició para una mesa vibratoria, planteándose como un primer acercamiento a la implementación de estos controladores para dispositivos altamente inestables como lo son los helicópteros cuadrotores. No obstante, la implementación directa del controlador diseñado no puede aplicarse para un cuadrotor ya que el modelo del balancín tiene un tiempo de respuesta lento, lo cual no es aceptable para un sistema inestable como el mencionado.

Asimismo, es importante tener en cuenta que el costo computacional de los controladores adaptativos planteados es elevado, diferente a la ecuación de diferencias de orden 2 que se implementa en el control PID digital. Lo anterior se debe a que el sistema digital debe simular el comportamiento de la planta junto con el controlador para el modelo de referencia, y a su vez ejecutar las ecuaciones de diferencias requeridas por los parámetros adaptativos de las ecuaciones 21 y 22 para el caso de control proporcional con dos parámetros de adaptación y las ecuaciones 26 y 27 para el control adaptativo proporcional diferencial.

Finalmente, una ventaja de este desarrollo fue la construcción de algoritmos para ser implementados en hardware, optimizados para el procesamiento en microcontroladores de 16 bits. Como desventaja es importante recalcar que la velocidad de procesamiento, limitada por la velocidad de procesamiento del microcontrolador, puede ser mejorada al implementarla en un sistema embebido como la Raspberry pi o una Beagleboard.

REFERENCES

Clarke, D.W., 1988. Application of generalized predictive control to industrial processes. *IEEE Control systems magazine*, 8(2), pp.49–55.

Corvalán Aravena, I. & Negroni Vera, J.J., 2012. Modelo de un Control Aproximado de un Cuadricóptero Basado en Equilibrio de un Balancín. *Trilogía Ciencia - Tecnología -Sociedad*, 24(34), pp.81–91.

Duraisamy, R. & Dakshinamurthy, S., 2010. An adaptive optimisation scheme for controlling air flow process with satisfactory transient performance. *Maejo*

International Journal of Science and Technology, 4(2), pp.221–234.

Esparza, C., Nuñez, R. & González, F., 2012. Model reference adaptive position controller with smith predictor for a shaking-table in two axes. In *Mexican International Conference on Artificial Intelligence*. Springer, pp. 271–282.

Esparza, C.H. & Núñez, R.A., 2014. Controlador Adaptativo PD por Modelo de Referencia para una Mesa Vibratoria Biaxial Basada en el Mecanismo Biela-Manivela. *Información tecnológica*, 25(2), pp.189–202.

Godoy Ortega, Y.C., 2011. *Control adaptativo en tiempo real*. Escuela Politécnica Nacional.

Jain, P. & Nigam, M.J., 2013. Design of a model reference adaptive controller using modified MIT rule for a second order system. *Advance in Electronic and Electric Engineering*, pp.2231–1297.

Landau, I.D. et al., 2011. *Adaptive control: algorithms, analysis and applications*, Springer Science \& Business Media.

Mansour, T., 2011. *PID Control, Implementation and Tuning* T. Mansour, ed., InTech.

Martín Ballesteros, Á. & Del Río Carbajo, M., 2013. *Control de posición de un balancín con Arduino*. Universidad de Valladolid.

Pérez Ramírez, J., Campoy Salguero, J.M. & Gaxiola Soto, B.A., 2005. Control adaptativo implantado en un micro-PLC. *Impulso, revista de electrónica, eléctrica y sistemas computacionales*, 1(1), pp.48–53.

Rodríguez Rosa, D., Barber Castaño, R.I. & Garrido Bullón, S., 2012. *Implementación de bloques de Simulink para control adaptativo de un motor de corriente continua*. UNIVERSIDAD CARLOS III DE MADRID.

Rodríguez Rubio, F. & López Sánchez, M.J., 1996. *Control adaptativo y robusto*, Universidad de Sevilla.

Viltres La Rosa, V., 2012. *Control de posición de un balancín con motor y hélice*. Universidad de Valladolid.

Control de Ángulo Para Sistemas Eléctricos de Potencia

Carlos M Flórez*. Juan F Villa**

*Universidad Nacional de Colombia Sede Medellín, Maestría en Ingeniería Eléctrica; e-mail: cmflorezr@unal.edu.co.
**XM E.S.P, Doctorado en Sistemas Energéticos e-mail: jfvilla@xm.com.co

Abstract: En los sistemas eléctricos de potencia al presentarse una contingencia, se produce una reacomodación natural no controlada en los ángulos de las barras que va acompañada de una redistribución de los flujos y cargas por los elementos del sistema. Por otro lado, el desarrollo de las unidades de medición fasorial en estos sistemas han posibilitado la medición del ángulo de voltaje visualizando así una forma de poder controlar esta variable. Este trabajo propone entonces un posible esquema de control fasorial para los sistemas eléctricos el cual modifique la dinámica de la evolución de los ángulos de una manera ordenada y así a pesar de las diferentes contingencias, mantener el sistema dentro de los valores tolerables por los elementos de la red. El control propuesto es implementado en un IEEE 14 obteniendo resultados satisfactorios, conservando el sistema en sus ángulos determinados y de esta forma evitando efectos adversos como sobre cargas en líneas de transmisión.

Keywords: PMU, Control de Frecuencia, WAMS, Control PI, Control en cascada, Sistemas eléctricos de potencia, Control de Ángulo.

1. INTRODUCCIÓN

Los sistemas de potencia que suministran energía a instalaciones eléctricas hoy en día están mucho más susceptibles a colapsos de lo que han estado en los últimos años debido a que estos sistemas cada vez más dependen de fuentes de generación que están localizadas remotamente de los centros de carga (Cano Esperón 2004; Kundur 1994; Ilic 2007). Dos factores fomentan que la generación esté alejada de los centros de carga:

i. Las economías de compra de energía desde fuentes remotas a más bajo costo a diferencia de generación local más costosa.

ii. El rechazo o negativa de la comunidad a permitir la construcción de nuevas plantas de generación en las zonas urbanas de alta concentración de carga, causando que se construyan plantas remotas a estos centros de carga.

Estos dos aspectos fundamentales en la operación de la red de potencia resultan en la transmisión de energía sobre largas distancias. Esto hace la red de potencia muy dependiente del sistema de transmisión para entrega de energía a los centros de carga (Ilic 2007). Por otra parte, esto también resulta en pérdidas de potencia reactiva incrementadas puesto que las impedancias de líneas de transmisión son principalmente reactivas. Entonces, cuando las líneas de transmisión se disparan, las líneas que permanecen deben tomar la carga resultando en más altas pérdidas reactivas (VArs) que resistivas (MW) lo cual resulta en una caída de voltaje en los nodos de carga que consecuentemente conllevan al sistema eléctrico en una cascada de eventualidades (Machowski et al. 2008).

Se clasifican tres tipos de estabilidades en los sistemas eléctricos de potencia: Estabilidad de Frecuencia, al cual se le asocia un sistema de estrategias de control de frecuencia. Estabilidad de Voltaje, al cual se le asocia un sistema de estrategias de control de voltaje. Y finalmente la estabilidad por el ángulo del voltaje, la cual no cuenta con una estrategia de control definida tal como los dos tipos de estabilidades anteriores (Kundur 1994).

1.1 Inestabilidad por ángulo de fase

Cuando el ángulo de fase de voltaje entre generadores remotos y generadores locales llega a ser muy grande, puede ocurrir inestabilidad en el ángulo de fase. En muchos casos, este evento ocurre en conjunto con el escenario de colapso de voltaje descrito anteriormente. Hay dos tipos de inestabilidad de ángulo de fase: Inestabilidad por Estado Estable e Inestabilidad Transitoria (Machowski et al. 2008).

La inestabilidad de estado estable sucede cuando hay una zona débilmente interconectada y ocurre un evento de transmisión que incrementa más allá de 90° el desfase entre el ángulo de generación y el ángulo de carga. Cuando dicho ángulo supera el mencionado límite, el sistema eléctrico entra en una zona de inestabilidad que lleva al sistema eléctrico al colapso (Ledesma 2008).

En cuanto a la inestabilidad transitoria, esta puede ocurrir debido al lento despeje de fallas en el sistema de transmisión. Generalmente la inestabilidad transitoria de ángulo ocurre cuando una falla en el sistema de transmisión cerca de la planta de generación no es despejada lo suficientemente rápido para evitar un desbalance prolongado entre la salida mecánica y eléctrica del generador (Cañizares et al. 2005). Una inestabilidad transitoria inducida por falla no ha sido la causa de ningún apagón en los años recientes. Sin embargo, los generadores necesitan estar protegidos de los daños que pueden resultar cuando la protección en los sistemas de transmisión es muy lenta para operar (Vaschetti et al. 2012)

2. INTRODUCCIÓN AL CONTROL ANGULAR

En la actualidad, el control de la frecuencia en los sistemas de potencia, específicamente el AGC (Automatic Generation Control) y el control de los intercambios entre países y zonas interconectadas, se apoya en los sistemas de comunicación que transmiten los valores de los intercambios medidos a través de las líneas de interconexión hasta los centros de control y a su vez hasta las centrales que, por medio de su generación, pueden controlar tanto estos intercambios como también la frecuencia del sistema (Corsi et al. 2004). El desarrollo de la tecnología de medición del fasor de tensión PMU (Phasor Measurement Unit) en los diferentes puntos del sistema eléctrico abre una nueva posibilidad, en el sentido de controlar esta variable mediante la potencia de las centrales generadoras y de esta manera controlar de una forma novedosa tanto el intercambio entre países y zonas interconectadas como la frecuencia del sistema interconectado. Así se abre la posibilidad de lo que podríamos llamar un AGC distribuido sin el uso de los canales de telecomunicación.

Los sistemas de energía eléctrica son uno de los motores principales para el desarrollo económico y social de las naciones, conformado por un conjunto de elementos como la generación, el transporte, la distribución y el consumo de la energía eléctrica (CIGRE 2007). Estos elementos constituyen un sistema complejo e integrado, el cual necesita estar coordinado y regulado para garantizar el uso racional de los recursos naturales y de infraestructura, que debe cumplir estándares de calidad en la prestación del servicio con criterios de seguridad y confiabilidad (Standards & Process 2013).

La seguridad de los sistemas de potencia requiere de la coordinación y control de las principales variables del sistema: voltaje, frecuencia y ángulo. Esto, aún en presencia de fallas del sistema, perturbaciones de la carga y salidas eventuales de unidades de generación (Corsi 2000). Si esta coordinación no se dá, el sistema se vulnera y puede llevar a una secuencia de eventos que causen colapsos de voltaje y hasta apagones generalizados, afectando el suministro de energía eléctrica (Bialek 2005).

El control actual de la frecuencia en los sistemas de potencia, específicamente el AGC y el control de intercambios de energía entre países, se apoya en los sistemas de comunicación que trasmiten los valores de las variables más importantes del sistema de energía eléctrica, como son potencia activa, voltajes, corrientes, entre otras, a través de las líneas de interconexión hasta los centros de control, y a su vez hasta las centrales eléctricas que, regulando la generación de energía, controlan tanto los intercambios como la frecuencia del sistema (Cañizares et al. 2005).

El desarrollo de la tecnología de medición fasorial de voltaje en los diferentes nodos del sistema eléctrico abrió una nueva posibilidad en el control de voltaje. Manejando la potencia activa en los grandes sistemas de generación se puede controlar tanto la frecuencia del sistema interconectado, como el intercambio de energía entre países (Fijalkowski 2009).

Actualmente, los sistemas de control utilizados para el control de frecuencia asumen condiciones de estado estacionario, donde una pequeña perturbación en la generación, por lo general, causa una disminución de velocidad, haciendo que las unidades que intervienen en el control automático de generación actúen. El sistema se reacomoda angularmente a nuevos valores. Algunas unidades permanecen en su punto de operación, esto es, no modifican su potencia eléctrica entregada, mientras que las otras están programadas para realizar el control de frecuencia y si modifican la potencia entregada al sistema. Al colapsar una unidad generadora, el sistema pierde velocidad, se producen efectos de baja frecuencia, grandes áreas del sistema se van afectadas con sobrecargas y disminución en los valores de los voltajes, debido a que por lo general los puntos de control son distantes a los puntos donde se presenta el evento, generando restricciones técnicas que encarecen el costo de operación del sistema.

Se propone el desarrollo de un esquema de control angular para aplicarlo a algunos generadores del sistema eléctrico con el objeto de mantener el ángulo en las barras dentro de unos valores deseados lo cual podría traer como beneficios una mayor seguridad del sistema eléctrico, así como la posibilidad de una mayor economía en el funcionamiento de los mismos.

3. ESTRUCTURA DEL CONTROL ANGULAR

Una posible estrategia para el control angular a un nivel primario estaría dada por el flujograma presentado en la Figura 1, en la cual se puede ver como el control de ángulo podría ser adaptado al control clásico de frecuencia. Esto trae como ventaja la aproximación de la realidad a una implementación del mismo ya que un sistema no reemplaza al otro, sino que por el contrario lo complementa.

El posible esquema angular de control se puede dividir principalmente en dos etapas. La primera etapa nos dice lo mismo que el control clásico de frecuencia, el sistema ante un evento lleva a las máquinas a un nuevo punto de operación en el cual el voltaje y la frecuencia permanecen constantes pero su distribución angular cambia. Es en este punto en el cual la

segunda etapa aparece, se hace un cálculo de error angular con el cual se procede a determinar una acción de control que se adicionará al error de velocidad de la máquina el cual será asumido por el control de frecuencia que finalmente determina la señal calculada al elemento final de control, en este caso los servomotores que dan paso al vapor o al agua. En otras palabras, la esencia del control angular se encuentra en la forma en la que se podría anidar un control, en este caso en cascada, para el lazo del control de frecuencia.

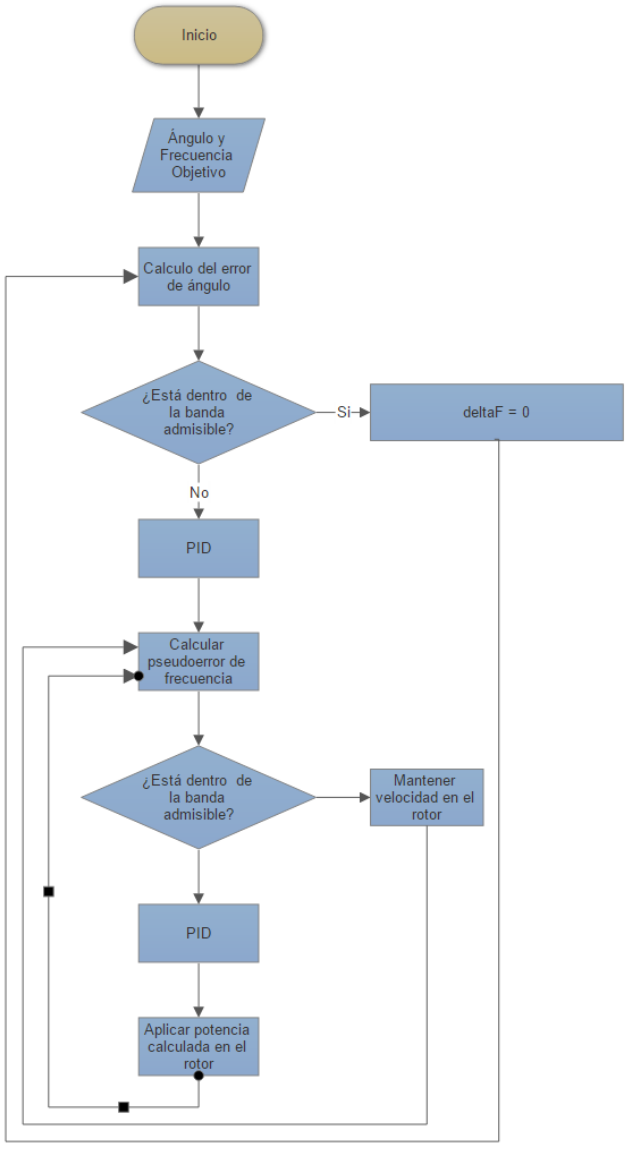

Figura 1. Esquema primario de control angular.

4. CASO DE ESTUDIO

El sistema utilizado para probar el control definido anteriormente es un IEEE de 14 barras el cual se encuentra en la Figura 2. Las respectivas simulaciones se realizaron en el software DigSilent. Para analizar las bondades del control de ángulo frente a las estrategias de control actuales, la generación y las cargas del benchmark fueron modificadas con motivo de tener un sistema al borde del colapso y de esta manera resaltar dos diferentes escenarios, uno con control angular y otro sin él.

Adicionalmente a los controles primarios se tiene un esquema de control secundario AGC, el cual se puso a prueba frente a la estrategia de control propuesta.

El esquema de control angular propuesto no necesita un reajuste de los demás esquemas de control, lo cual es una ventaja ya que el sistema de control existente no es modificado.

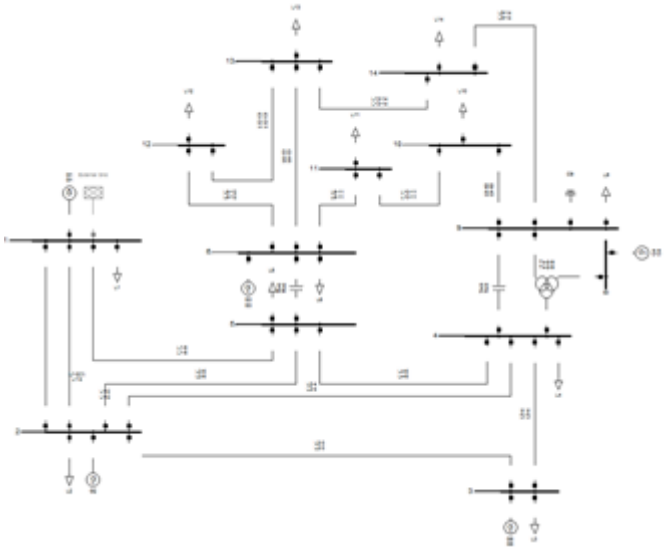

Figura 2. Sistema de prueba para el control angular. IEEE 14

4.1 Escenario de simulación

La contingencia consiste básicamente en la desconexión de una línea de transmisión que va de la barra 1 a la barra 2, obligando al sistema a redistribuir las cargas por líneas alternas. De esta manera se busca analizar cómo afecta a la red el control de generación.

En un primer escenario se presenta el control clásico de frecuencia, con el generador 1 como el Slack y un sistema de control AGC en el cual solamente participan los generadores 1 y 5. Mientras que el segundo escenario consiste en la adición del control angular del primer escenario.

4.2 Análisis estático de resultados

Como se explicó en secciones anteriores, la forma en la que se propone este control angular es de una extensión al control de frecuencia clásico, la diferencia radica principalmente en la disposición final del control la cual en el primer caso solo insta llevar el sistema a la frecuencia nominal sin tener en cuenta los factores de atraso o adelanto que en otras palabras equivalen a esfuerzos de las máquinas, mientras que el segundo caso propone llevar este control de una forma inteligente, es decir, el planteamiento adicional consiste en mantener factores de atraso y adelanto respecto a otras máquinas igualando de esta manera la forma en la que el sistema eléctrico lleva las cargas y así evitar llevar a el sistema a operar en condiciones límites de estabilidad. En la

Tabla 1 se puede ver el cambio del punto de operación antes de la falla y después de ella con el fin de hacerse a una idea del funcionamiento del control de ángulo.

Tabla 1. Valores Prefalla y Postfalla sin y con control angular

	Generador 2			Generador 3			Generador 4			Generador 5		
	PRF	PFSC	PFC	PRF	PFSC	PFC	PRF	PFSC	PFC	PRF	PFSC	PFC
Pot	150	151	160	60	60	77	40	40	52	30	32	78
An	-18	-31	-25	-39	-48	-40	-37	-48	-38	-45	-57	-48

*PRF: prefalla, PFSC: posfalla sin control de ángulo, PFC: posfalla con control de ángulo

De esta misma forma la Tabla 2 presenta el nivel porcentual con control angular y sin él, de las líneas 1-2 y 1-5 las cuales son las líneas que se distribuyen principalmente la transmisión perdida.

Tabla 2. Valores porcentuales de carga Lineas 1-2 y 1-5

	Linea 1-2			Linea 1-5		
	PRF	PFSC	PFC	PRF	PFSC	PFC
%Load	68	116	96	75	98	84

Tanto de la Tabla 1 como de la Tabla dos pueden notarse importantes cambios. En cuanto a los ángulos, estos se encuentran menos dispersos lo que favorece la estabilidad angular; mientras que la carga de las líneas se reparte de otra manera evitando una posible cadena de eventos.

4.3 Análisis dinámico de resultados

Para tener un análisis más completo de la dinámica del control angular, se presenta a continuación la dinámica del nodo Slack y el porcentaje de carga de dos de las líneas alternas que soportan la contingencia.

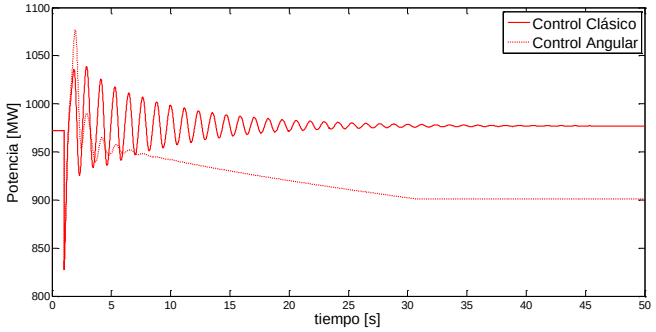

Figura 3. Potencia del Generador 1 (Slack)

Como se puede observar, la implementación de un control de frecuencia redistribuye de una manera diferente las potencias en los generadores y en este caso se disminuye en gran medida la oscilación causada por el controlador de frecuencia al intentar recuperar al sistema de la contingencia.

Debido a la naturaleza del control, es notable como se interpone una dinámica lenta pero menos oscilatoria, en otras palabras, el sistema con un lazo adicional de control tiende a volverse menos oscilatorio lo que traduce a ser más lento en llegar a la consigna. Esto es normal ya que la sintonía de los controladores no se realizó de forma determinística en la cual se garantizara que el lazo de control interno fuera más rápido que el lazo externo.

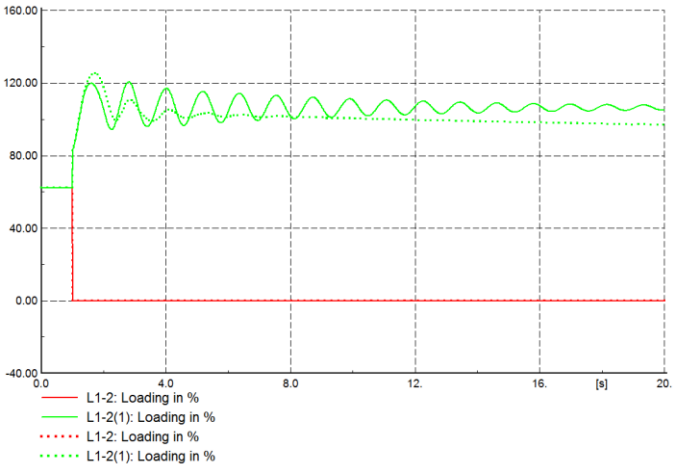

Figura 4. Porcentaje de carga de las lineas 1-2

En cuanto a las líneas de transmisión, se puede evidenciar el mismo fenómeno anterior, donde la oscilación no es prolongada y adicionalmente su nuevo punto de operación es más bajo pudiendo evitar así una cascada de eventualidades en las líneas de distribución por sobretensiones

5. CONCLUSIONES

En cuanto al control angular, se pudo observar como de forma mutua ambos controladores asumieron la carga sin entrar en algún tipo de conflicto y adicionalmente cumplen el objetivo de regular la generación de forma tal que la distribución angular del sistema no se ve mayormente afectada. Si bien no se enfatizó en la incidencia de los reguladores de voltaje en este trabajo, se espera para trabajos futuros analizar si estos juegan un papel importante en la estabilidad y robustez del control angular.

Entre las diferentes formas en las cuales se pueda desarrollar un control de ángulo, posiblemente esta es una de las mejores opciones, ya que no es necesario hacer un cambio en la tecnología existente o hacer un reajuste en las ganancias de los controladores puesto que la forma en la cual se dispone la estructura de control angular se presta para evitar estos inconvenientes, asociando el control angular como una extensión del control de frecuencia.

El control de ángulo brinda la posibilidad de operar los sistemas eléctricos de manera más económica. Al modificar la evolución dinámica de los ángulos y de los flujos por los elementos de la red ante las contingencias n-1. Dado que en la actualidad el cubrimiento por seguridad de las contingencias n-1 requiere de forma permanente de generación de seguridad en línea para el control de los flujos en la condición post falla. Con el control de ángulo la generación de seguridad actual requerida, es reemplazada por reserva rodante que solo sería usada durante la contingencia

para el control de los ángulos y de los flujos en la condición post falla a valores soportables por la red

REFERENCIAS

Bialek, J.W., 2005. Blackouts in the US/Canada and continental Europe in 2003: Is liberalisation to blame? *2005 IEEE Russia Power Tech, PowerTech*.

Cano Esperón, M., 2004. *Metodologías TCA Control Jerárquico de la Frecuencia en Sistemas de potencia interconectados Control Jerárquico de la Frecuencia en Sistemas de potencia interconectados*.

Cañizares, C.A. et al., 2005. Comparing secondary voltage regulation and shunt compensation for improving voltage stability and transfer capability in the Italian power system. *Electric Power Systems Research*, 73(1), pp.67–76.

CIGRE, 2007. COORDINATED VOLTAGE CONTROL IN TRANSMISSION NETWORKS. In *IEEE transaction on Power Systems*.

Corsi, S. et al., 2004. The coordinated automatic voltage control of the Italian transmission grid - Part II: Control apparatuses and field performance of the consolidated hierarchical system. *IEEE Transactions on Power Systems*, 19(4), pp.1733–1741.

Corsi, S., 2000. The secondary voltage regulation in Italy. *2000 Power Engineering Society Summer Meeting (Cat. No.00CH37134)*, 1(c).

Fijalkowski, J., 2009. UCTE mission and structure. , (February).

Ilic, M.D., 2007. From hierarchical to open access electric power systems. *Proceedings of the IEEE*, 95(5), pp.1060–1084.

Kundur, P., 1994. Power_System_Stability_and_Control_Kundur.pdf. , p.1197.

Ledesma, P., 2008. Regulaci ´ on de frecuencia y potencia.

Machowski, J., Bialek, J.W. & Bumby, J.R., 2008. *Power System Dynamics: Stability and Control*,

Standards, R.R. & Process, D., 2013. Glossary of Terms Used in NERC Reliability Standards.

Vaschetti, J.C., Magnago, F. & Sauchelli, V.H., 2012. Control automático de voltaje en sistemas eléctricos de potencia basado en sistemas expertos. *Informacion Tecnologica*, 23(5), pp.69–84.

Control No Lineal Basado en Pasividad para Motores de Inducción Minimizando Pérdidas de Potencia

Hoover Mujica * **Cuauhtémoc Guerrero** ** **Gerardo Espinosa-Pérez** *

* *Facultad de Ingeniería - UNAM, Edificio Posgrado 2do piso, C.U., 04510, México D.F. e-mail: hmujica@comunidad.unam.mx, gerardoe@unam.mx*
** *Universidad Autónoma de la Ciudad de México, Prolongación San Isidro No. 151, Col. San Lorenzo Tezonco, Del. Iztapalapa, México D.F. C.P. 09790, e-mail: cuauhtemoc.guerrero@uacm.edu.mx*

Resumen: Los sistemas de control para motores de inducción (MI) de alto desempeño representan un tópico de interés en la comunidad de ingeniería aplicada, debido a que las nuevas aplicaciones en las que este tipo de máquina rotatoria está involucrada, exigen la maximización del desempeño dinámico y la minimización del consumo de energía. Bajo el contexto actual, se presenta en este artículo un controlador no lineal basado en pasividad para alto desempeño que realiza el seguimiento de velocidad y norma de flujos magnéticos de rotor, en el que se propone una política de minimización de pérdidas de potencia buscando reducir el consumo de energía del motor de inducción sin degradar el desempeño dinámico. La utilidad de esta propuesta se muestra mediante simulación numérica donde se compara el consumo de energía en dos escenarios, en el primero se emplea una norma de flujos magnéticos constante equivalente al valor nominal de la máquina y en el segundo escenario se aplica una norma de flujos magnéticos *ad hoc*, la cual es variante en el tiempo y busca reducir las pérdidas de potencia. En ambos escenarios se asigna el mismo perfil de velocidad y par de carga. Los resultados muestran que implementando la política de minimización de pérdidas de potencia se mejora la eficiencia del MI en un 17.74 % para el perfil de velocidad y par de carga evaluados.

Palabras clave: Control no lineal basado en pasividad, Motor de inducción, Seguimiento de velocidad y norma de flujo magnético, Minimización de pérdidas de potencia, Diferenciador sucio compensado, Alto desempeño dinámico.

1. INTRODUCCIÓN

En distintas áreas de la industria se emplean sistema de control de movimiento de MI con un amplio rango de potencias que van desde los 100 W hasta varios MW y esto es debido principalmente a que en la actualidad se desarrollan y generan poderosos microprocesadores para realizar tareas de control a un relativo bajo costo. Sin embargo, el precio que llega a tener el *hardware* del controlador es una restricción, en particular en controladores de baja potencia y bajo desempeño. Alrededor del $80-90\,\%$ del mercado principal son controladores sencillos con requerimientos dinámicos bajos tales como bombas o ventiladores. Todos estos controladores trabajan sin sensores de velocidad y el control principal está basado en una estrategia de control escalar voltaje/frecuencia (Böcker and Mathapati, 2007).

Con la madurez que se ha alcanzado en los esquemas de control para el MI la tendencia actual que existe en las líneas de investigación es:

- Operación en regímenes de mayor eficiencia, además de realizar seguimiento de velocidad, regulación del flujo magnético de rotor, establecimiento de la mejor sintonización del controlador y garantía del óptimo consumo de energía. Asimismo, hay una tendencia a buscar esquemas de control para mejorar el desempeño dinámico como el propuesto en (Kumar et al., 2015).
- El problema de identificación es muy complejo si no se tienen disponibles las mediciones de todos los estados por lo que sigue siendo un problema teórico abierto.
- Encontrar esquemas de control *sensorless* en el cual se asegure seguimiento de la velocidad angular y se estime el flujo de rotor en lazo cerrado, ya que frecuentemente este se estima en lazo abierto como se propone en (Bensiali et al., 2015).

Esquemas de control más sofisticados son necesarios para aquellos sistemas que requieren un alto desempeño dinámico de seguimiento de velocidad, así como el rechazo de perturbaciones de origen mecánico con gran exactitud, como pueden ser en elevadores, máquinas herramientas o vehículos eléctricos. Para la mayoría de estas aplicaciones están disponibles productos estándar que utilizan el Control por Campo Orientado (FOC) o el Control Directo de Par (DTC) (Böcker and Mathapati, 2007).

En la actualidad los controladores industriales del MI han madurado a un nivel relativamente alto comparándolo con sus necesidades (Böcker and Mathapati, 2007). Aunque se han utilizado esquemas como el FOC y DTC en sistemas industriales, el control basado en pasividad (PBC por sus siglas en inglés), que básicamente se ha utilizado más en el ámbito académico tanto en el marco de referencia $\alpha\beta$

como en el marco *ab*. Esta metodología de control se ha ido afianzando ya que además de realizar seguimiento de velocidad así como de la norma del flujo magnético de rotor, al mismo tiempo respeta todas las condiciones bajo las cuales sus propiedades de estabilidad se establecen permitiendo mejorar drásticamente el desempeño (Mujica and Espinosa-Pérez, 2014). Estas cualidades han sido mostradas y evaluadas de forma experimental en (Mujica and Espinosa-Pérez, 2015), donde se determina cuál es el método para la obtención de velocidad y aceleración que permite mejorar aún mas el desempeño.

Por otro lado, es sabido que las pérdidas de potencia en el MI están dadas por la diferencia de potencia eléctrica y mecánica. Estas se producen en el cobre de los devanados tanto del estator como del rotor, por la histéresis y corrientes parásitas de estator, así como las pérdidas por fricción y rozamiento con el aire del rotor (Chapman, 2005). El diseño de los MI se han mejorado tanto que en aplicaciones a velocidad nominal constante estas pérdidas son pequeñas, pero cuando se tiene velocidades diferentes de la nominal, dichas pérdidas se incrementan significativamente. Una forma de minimizar estas pérdidas es por medio de una selección adecuada de la norma del flujo magnético de rotor.

En este sentido, existen diversos trabajos como el presentado en (Vedagarbha et al., 1997), donde se diseña un controlador no lineal que logra seguimiento exponencial sin singularidades y mejora la eficiencia de la máquina. Asimismo, en (Bodson et al., 1995) presenta un algoritmo para seleccionar la referencia de flujos de rotor del MI considerando límites máximos de voltaje y corriente a velocidad constante. Por otro lado, en (Kumar et al., 2015) se presenta un análisis de como mejorar el desempeño dinámico de los sistemas de control del MI para optimizar eficiencia utilizando un control basado en modelo. Sin embargo, en todos estos trabajos reportados anteriormente, la estrategia de control no es capaz de realizar seguimiento de velocidad y norma de flujos magnéticos de rotor con grandes tasas de variación en el perfil deseado, estas limitaciones encuentran solución en el resultado mostrado en el presente artículo.

El presente artículo está organizado de la siguiente manera: En la sección 2 se presenta el modelo matemático del MI, mientras que en la sección 3 se muestra las ecuaciones del PBC de alto desempeño para el MI. En la sección 4 se presenta el desarrollo del resultado principal, el cual es la obtención de una política de selección de la norma de flujos magnéticos que minimiza las pérdidas de potencia. Los resultados de simulación de dos experimentos se presentan en la sección 5 y por último en la sección 6 se presenta la discusión y conclusiones.

2. MOTOR DE INDUCCIÓN

En este artículo, se considera el modelo matemático del MI trifásico de múltiples pares de polos tipo jaula de ardilla, representado en un plano bifásico ortogonal equivalente por medio de la transformación de Blondel (Blondel et al., 1913). Adicionalmente, se considera también que las fases son simétricas y además distribuidas sinusoidalmente, la permeabilidad magnética en los núcleos laminados infinita, lo cual, desprecia los efectos en las ranuras, las pérdidas en el hierro y en los devanados. La principal ventaja de emplear este marco de referencia es que se evita la dependencia explícita de la posición del rotor, lo que simplifica en gran medida el análisis del sistema (Liu et al., 1989). Este modelo es conocido en la literatura como el *modelo ab* (Seely, 1962), (Meisel, 1984), modelo de Stanley (Krishnan, 2001) o modelo en el marco de referencia fijo al estator (Krause et al., 2002) y está dado por

$$\dot{I}_s = -\gamma I_s + \left(\frac{L_{sr}R_r}{\sigma L_r^2}\right)\psi_r - \left(\frac{n_p L_{sr}}{\sigma L_r}\right)\omega\mathcal{J}\psi_r + \frac{U_s}{\sigma} \quad (1a)$$

$$\dot{\psi}_r = -\left(\frac{R_r}{L_r}\right)\psi_r + (n_p\omega\mathcal{J})\,\psi_r + \left(\frac{R_r L_{sr}}{L_r}\right) I_s \quad (1b)$$

$$\dot{\omega} = \left(\frac{1}{J}\right)\underbrace{\frac{n_p L_{sr}}{L_r} I_s^T \mathcal{J}\psi_r}_{\tau_e} - \left(\frac{B}{J}\right)\omega - \frac{\tau_L}{J} \quad (1c)$$

donde $\psi_r \in \mathbb{R}^2$ es el vector de encadenamientos de flujos magnéticos de rotor, $I_s \in \mathbb{R}^2$ el vector de corrientes de estator, ω la velocidad en el eje del motor, L_s, L_r, $L_{sr} > 0$ son las inductancias en estator, rotor y mutua respectivamente, τ_e es el par electromagnético, R_s, $R_r > 0$ las resistencias en estator y rotor respectivamente, n_p el número de par de polos, $J > 0$ el momento de inercia del rotor, $B \geq 0$ el coeficiente de amortiguamiento mecánico o fricción viscosa, τ_L el par de carga externo aplicado al eje del rotor, $U_s \in \mathbb{R}^2$ los voltajes de estator, $\bar{\sigma} = 1 - \frac{L_{sr}^2}{L_s L_r}$ el coeficiente de dispersión o coeficiente de Blondel con $\sigma = L_s\bar{\sigma}$, mientras que

$$\gamma = \left(\frac{L_{sr}^2 R_r}{\sigma L_r^2} + \frac{R_s}{\sigma}\right), \qquad \mathcal{J} \triangleq \begin{bmatrix} 0 & -1 \\ 1 & 0 \end{bmatrix} = -\mathcal{J}^T.$$

Los subíndices $(\cdot)_s$ y $(\cdot)_r$ son usados la denotar variables de estator y rotor respectivamente.

3. CONTROL NO LINEAL BASADO EN PASIVIDAD DE ALTO DESEMPEÑO PARA MI

Con el objetivo de evaluar el resultado principal, se considera un esquema de control no lineal basado en pasividad de alto desempeño para el seguimiento de velocidad y norma de flujos magnéticos descrito en detalle en (Mujica et al., 2014), es decir, el $\lim_{t\to\infty}|\omega - \omega_d| = 0$ y $\lim_{t\to\infty}|\|\psi_r\| - \|\psi_{rd}\|| = 0$, donde ω_d es la velocidad de rotor deseada y $\beta \triangleq \|\psi_{rd}\|$ la norma de flujos magnéticos de rotor deseada. Dicho controlador, es generado a partir del modelo del MI descrito en (1) bajo las siguientes suposiciones:

- **S.1** Se dispone de medición de las señales de corrientes de estator I_s, velocidad ω y aceleración del rotor $\dot{\omega}$. Estas dos últimas señales se obtienen como salida de un sistema dinámico a partir de la medición de posición del rotor.
- **S.2** Todos los parámetros del modelo son conocidos.
- **S.3** El par de carga τ_L es una función desconocida, la cual es estimada en línea.
- **S.4** La velocidad deseada del rotor ω_d es una función acotada y dos veces diferenciable.
- **S.5** La norma de flujo magnético de rotor deseado β es una función estrictamente positiva, suave y acotada.

Por lo tanto, se define el error de estados y su dinámica como

$$e = \begin{bmatrix} e_{I_s} \\ e_{\psi_r} \\ e_\omega \end{bmatrix} = x - x_d \quad \Longrightarrow \quad \dot{e} = \begin{bmatrix} \dot{e}_{I_s} \\ \dot{e}_{\psi_r} \\ \dot{e}_\omega \end{bmatrix} = \dot{x} - \dot{x}_d \quad (2)$$

donde el vector de estados está dado por $x \triangleq [I_s^T, \psi_r^T, \omega]^T \in \mathbb{R}^5$ y el vector de estados deseados se establece como $x_d \triangleq [I_{sd}^T, \psi_{rd}^T, \omega_d]^T$.

En consecuencia, la ley de control impone la siguiente estructura para los voltajes de estator

$$U_s = \sigma \dot{I}_{sd} + \frac{n_p L_{sr}}{L_r} \mathcal{J} \omega_d \psi_{rd} + \left(\frac{L_{sr}^2 R_r}{L_r^2} + R_s \right) I_{sd} - \frac{L_{sr} R_r}{L_r^2} \psi_{rd} - K_{I_s} e_{I_s}, \quad (3)$$

donde se incluye un término de amortiguamiento constante K_{I_s} en el error de corrientes. Ahora, se procede a definir las expresiones necesarias para su implementación. Las corrientes deseadas de estator están dadas por

$$I_{sd} = \frac{L_r}{R_r L_{sr}} \left(\dot{\psi}_{rd} - n_p \omega_d \mathcal{J} \psi_{rd} + \frac{R_r}{L_r} \psi_{rd} \right), \quad (4)$$

mientras que los flujos de rotor deseados variantes en el tiempo se obtienen como solución del sistema dinámico

$$\dot{\psi}_{rd} = \left[n_p \omega_d + \frac{R_r}{n_p \beta^2} \tau_d \right] \mathcal{J} \psi_{rd} + \frac{\dot{\beta}}{\beta} \psi_{rd}, \qquad \psi_{rd}(0) = \begin{bmatrix} \beta \\ 0 \end{bmatrix}, \quad (5)$$

con esta última expresión se puede reescribir la ecuación (4) y se tiene que las corrientes de estator deseadas

$$I_{sd} = \frac{L_r}{L_{sr} n_p \beta^2} \tau_d \mathcal{J} \psi_{rd} + \frac{1}{L_{sr}} \psi_{rd} + \frac{L_r}{R_r L_{sr}} \frac{\dot{\beta}}{\beta} \psi_{rd} \quad (6)$$

dependen ahora de τ_d. Por lo tanto, se define el par electromagnético deseado τ_d como

$$\tau_d = J \dot{\omega}_d + B \omega_d + \hat{\tau}_L - K_\omega e_\omega, \quad (7)$$

donde

$$\hat{\tau}_L = -K_{\omega i} \int e_\omega dt, \qquad K_{\omega i} > 0, \qquad \hat{\tau}_L(0) = 0. \quad (8)$$

Ahora bien, la ley de control (3) requiere para su implementación de la derivada respecto al tiempo de I_{sd}, esta se propone como

$$\dot{I}_{sd} = \frac{L_r}{L_{sr} n_p} \left[\left(\frac{\dot{\tau}_d}{\beta^2} - \frac{2 \tau_d \dot{\beta}}{\beta^3} \right) \mathcal{J} \psi_{rd} + \left(\frac{\tau_d}{\beta^2} \right) \mathcal{J} \dot{\psi}_{rd} \right] + \frac{L_r}{R_r L_{sr}} \left[\left(\frac{\ddot{\beta} \beta - \dot{\beta}^2}{\beta^2} \right) \psi_{rd} + \left(\frac{\dot{\beta}}{\beta} \right) \dot{\psi}_{rd} \right] + \frac{\dot{\psi}_{rd}}{L_{sr}}, \quad (9)$$

así también y por consiguiente la derivada de τ_d es

$$\dot{\tau}_d = J \ddot{\omega}_d + B \dot{\omega}_d + \dot{\hat{\tau}}_L - K_\omega \dot{e}_\omega. \quad (10)$$

A partir de esta estructura, se puede demostrar que la ley de control (3) preserva propiedades de estabilidad, para detalles consultar (Mujica et al., 2014).

3.1 Perfiles Deseados de Velocidad y Aceleración

El PBC de alto desempeño para MI requiere de la medición de velocidad y aceleración, para tal propósito se emplea el siguiente método de diferenciación numérica fundamentado en un sistema dinámico lineal que es llamado *diferenciador sucio de tercer orden compensado* y está descrito por

$$\dot{z}_1 = z_2 \quad (11a)$$
$$\dot{z}_2 = z_3 \quad (11b)$$
$$\dot{z}_3 = -\lambda_1^3 z_1 - 3\lambda_1^2 z_2 - 3\lambda_1 z_3 + \lambda_1^3 \theta + 3\lambda_1^2 z_4 + 3\lambda_1 z_5 - \lambda_2^2 z_4 - 2\lambda_2 z_5 + \lambda_2^2 \bar{\omega}_d \quad (11c)$$
$$\dot{z}_4 = z_5 \quad (11d)$$
$$\dot{z}_5 = -\lambda_2^2 z_4 - 2\lambda_2 z_5 + \lambda_2^2 \bar{\omega}_d \quad (11e)$$

donde θ es la posición de rotor medida por el codificador incremental unido al eje del rotor, z_1 la posición estimada, $\omega = z_2$ la velocidad estimada de rotor, $\dot{\omega} = z_3$ la aceleración estimada, $\omega_d = z_4$ la velocidad deseada o de consigna para el PBC, $\dot{\omega}_d = z_5$ la aceleración deseada y $\bar{\omega}_d \approx \omega_d$ la señal exógena que define el perfil de velocidad que el usuario desea alcanzar, con

$$[z_1(0)\ z_2(0)\ z_3(0)\ z_4(0)\ z_5(0)]^T = [\theta(0)\ 0\ 0\ \bar{\omega}_d(0)\ 0]^T.$$

La estabilidad del sistema dinámico descrito en (11) se cumple para todo $\lambda_1 > 0$ y $\lambda_2 > 0$. Sin embargo, como primera aproximación, se recomienda asignar a $\lambda_1, \lambda_2 > 2|max(\dot{\omega}_d)|$ (dos veces el valor máximo de aceleración deseada, así se preserva el contenido frecuencial de la señal de entrada). Note, que conforme $\lambda_1 \to +\infty$, este método será una mejor aproximación al operador derivada, por lo tanto más sensible al ruido mientras que el término $\lambda_1^3 \left[\frac{3}{\lambda_1} z_4 + \frac{3}{\lambda_1^2} z_5 - \frac{1}{\lambda_1^3} \dot{z}_5 \right] \to 0$. Este último es empleado para compensar el desfase natural del sistema compuesto por (11a)-(11c). En este trabajo se consideró $\lambda_1 = 12000$ y $\lambda_2 = 800$.

4. RESULTADO PRINCIPAL

Partiendo del hecho que el PBC del MI, dado por (3)-(7), garantiza un correcto seguimiento de la velocidad deseada y de la norma del flujo de rotor deseada y considerando que ambas señales se incorporan como entradas de forma independiente a la ley de control. Entonces, se propone una política de selección de norma de flujos magnéticos que minimice las pérdidas de potencia de acuerdo a las condiciones de operación de la máquina a través del cálculo en línea de dicha norma. En la Figura 1 se muestra la estrategia de control propuesta.

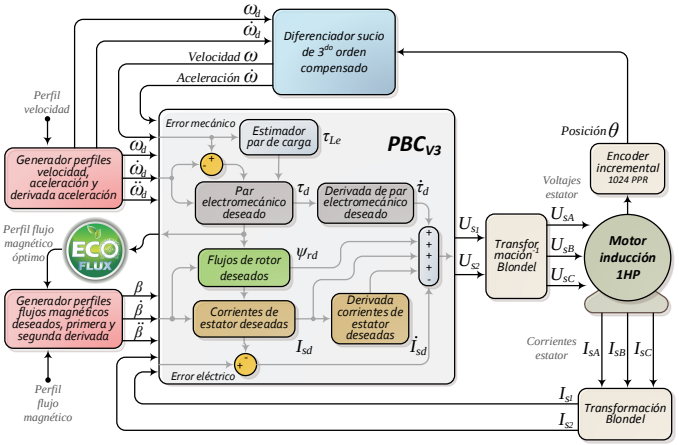

Figura 1. Esquema de control propuesto.

4.1 Pérdidas de potencia en el MI

Sean las pérdidas de conversión de potencia dadas por

$$Pot_{Per} = U_s^T I_s - \tau_e \omega, \quad (12)$$

sustituyendo (3) y (4) en (12) y considerando que la ley de control garantiza convergencia, es decir, $e_I = e_\omega \to 0$ se tiene

$$Pot_{Per} = \left(L_s - \frac{L_{sr}^2}{L_r}\right)\dot{I}_{sd}^T I_{sd} - \frac{n_p L_{sr}}{L_r}\omega_d \psi_{rd}^T \mathcal{J} I_{sd} + \left(\frac{L_{sr}^2 R_r}{L_r^2} + R_s\right) I_{sd}^T I_{sd} - \frac{L_{sr} R_r}{L_r^2}\psi_{rd}^T I_{sd} - \tau_d \omega_d \tag{13}$$

Buscando reescribir la ecuación anterior en términos de los flujos de rotor deseado, es conveniente sustituir (5) en (9) de tal forma que se obtiene

$$\dot{I}_{sd} = \frac{1}{L_{sr}}\left[\left(-\frac{L_r R_r}{n_p^2}\frac{\tau_d^2}{\beta^4} - L_r\omega_d\frac{\tau_d}{\beta^2} + \frac{\dot{\beta}}{\beta} + \frac{L_r}{R_r}\frac{\ddot{\beta}}{\beta}\right)\mathcal{I} + \left(n_p\omega_d + \frac{R_r}{n_p}\frac{\tau_d}{\beta^2} + \frac{L_r n_p \omega_d}{R_r}\frac{\dot{\beta}}{\beta} + \frac{L_r}{n_p}\frac{\dot{\tau}_d}{\beta^2}\right)\mathcal{J}\right]\psi_{rd}$$

Por lo tanto, la expresión (13) se tiene solo en términos de β y τ_d de la forma

$$\begin{aligned} Pot_{Per} = {} & \left(\frac{L_s}{L_{sr}^2} + 2\frac{L_r R_s}{R_r L_{sr}^2}\right)\dot{\beta}\beta + \left(\frac{L_r L_s}{L_{sr}^2 R_r} - \frac{1}{R_r}\right)\ddot{\beta}\beta \\ & + \left(-\frac{L_r^2 L_s}{L_{sr}^2 n_p^2} + \frac{L_r}{n_p^2}\right)\frac{\tau_d^2\dot{\beta}}{\beta^3} + \left(\frac{L_r L_s}{R_r L_{sr}^2} + \frac{L_r^2 R_s}{R_r^2 L_{sr}^2}\right)\dot{\beta}^2 \\ & + \left(\frac{L_r^2 L_s}{R_r^2 L_{sr}^2} - \frac{L_r}{R_r^2}\right)\ddot{\beta}\dot{\beta} + \left(\frac{L_r^2 L_s}{L_{sr}^2 n_p^2} - \frac{L_r}{n_p^2}\right)\frac{\dot{\tau}_d\tau_d}{\beta^2} \\ & + \left(\frac{R_r}{n_p^2} + \frac{L_r^2 R_s}{L_{sr}^2 n_p^2}\right)\frac{\tau_d^2}{\beta^2} + \frac{R_s}{L_{sr}^2}\beta^2 \end{aligned} \tag{14}$$

si se considera

$$\begin{aligned} \dot{I}_{sd}^T I_{sd} = {} & \frac{\dot{\beta}\beta}{L_{sr}^2} + \frac{L_r}{L_{sr}^2 R_r}\ddot{\beta}\beta - \frac{L_r^2}{L_{sr}^2 n_p^2}\frac{\dot{\beta}\tau_d^2}{\beta^3} \\ & + \frac{L_r}{R_r L_{sr}^2}\dot{\beta}^2 + \frac{L_r^2}{R_r^2 L_{sr}^2}\ddot{\beta}\dot{\beta} + \frac{L_r^2}{L_{sr}^2 n_p^2}\frac{\dot{\tau}_d\tau_d}{\beta^2}, \end{aligned}$$

$$\psi_{rd}^T \mathcal{J} I_{sd} = -\frac{L_r}{L_{sr} n_p}\tau_d,$$

$$I_{sd}^T I_{sd} = \left(\frac{L_r}{L_{sr} n_p}\frac{\tau_d}{\beta}\right)^2 + \left(\frac{1}{L_{sr}} + \frac{L_r}{R_r L_{sr}}\frac{\dot{\beta}}{\beta}\right)^2 \beta^2$$

y

$$\psi_{rd}^T I_{sd} = \left(\frac{1}{L_{sr}} + \frac{L_r}{R_r L_{sr}}\frac{\dot{\beta}}{\beta}\right)\beta^2$$

Para efectos del cálculo de una expresión que minimize la ecuación presentada en (14), se considera el par deseado τ_d constante y que la norma del flujo de rotor es constante, i.e., $\dot{\beta} = \ddot{\beta} = 0$ entonces las pérdidas de potencia son

$$Pot_{Per} = \left(\frac{R_r}{n_p^2} + \frac{L_r^2 R_s}{L_{sr}^2 n_p^2}\right)\frac{\tau_d^2}{\beta^2} + \frac{R_s}{L_{sr}^2}\beta^2$$

donde el extremo de dicha función es

$$\frac{\partial Pot_{Per}}{\partial \beta} = -2\left(\frac{R_r}{n_p^2} + \frac{L_r^2 R_s}{L_{sr}^2 n_p^2}\right)\frac{\tau_d^2}{\beta^3} + 2\frac{R_s}{L_{sr}^2}\beta \tag{15}$$

donde la norma de flujo de rotor que minimiza las pérdidas de potencia esta dada por

$$\beta^* = \sqrt{\sqrt{\left(\frac{L_{sr}^2 R_r}{R_s n_p^2} + \frac{L_r^2}{n_p^2}\right)}|\tau_d|}. \tag{16}$$

Se puede observar de (16) que debido a que los parámetros de la máquina son positivos esta expresión siempre será positiva. Por otro lado, evaluando la segunda derivada parcial de (15) con respecto a β, se tiene

$$\frac{\partial^2 Pot_{Per}}{\partial \beta^2} = 6\left(\frac{R_r}{n_p^2} + \frac{L_r^2 R_s}{L_{sr}^2 n_p^2}\right)\frac{\tau_d^2}{\beta^4} + 2\frac{R_s}{L_{sr}^2} > 0$$

lo cual garantiza que la β^* es un mínimo global de (13).

4.2 Política de minimización de pérdidas de potencia

Si se considera a la norma de flujo magnético de rotor que minimiza las pérdidas de potencia, dada por la ecuación (16), como entrada de referencia de la ley de control, entonces el PBC logrará los objetivos de control reduciendo el consumo de energía. Sin embargo la función (16) aplicada directamente presenta una singularidad en la ley de control, este inconveniente se muestra específicamente en la ecuación (5) cuando el motor se aproxima a velocidad cero. Dicho esto, se presenta una política de minimización de pérdidas de potencia que evita la singularidad en la ley de control y está dada por el siguiente sistema dinámico

$$\kappa = \frac{1}{2}\left[sign(\beta^* - \beta_{Min}) + |sign(\beta^* - \beta_{Min})|\right] \tag{17a}$$

$$\dot{\varsigma}_1 = \varsigma_2 \tag{17b}$$

$$\dot{\varsigma}_2 = -\lambda_3^2\varsigma_1 - 2\lambda_3\varsigma_2 + \lambda_3^2\left(\kappa\beta^* + (1-\kappa)\beta_{Min}\right) \tag{17c}$$

donde $\beta_{Min} = 2B\omega_{Nom}$ es la norma de flujos magnéticos mínima establecida para magnetizar al rotor, κ la variable que discrimina si el valor de β^* alcanza a β_{Min} y λ_3 determina la respuesta en frecuencia del sistema. Esto implica que en la ley de control descrita en (3) se deberá ahora considerar que $\beta = \varsigma_1$, $\dot{\beta} = \varsigma_2$ y $\ddot{\beta} = \dot{\varsigma}_2$, con

$$\left[\varsigma_1(0)\ \varsigma_2(0)\right]^T = \left[\bar{\beta}^*(0)\ 0\right]^T.$$

5. EVALUACIÓN NUMÉRICA

La evaluación numérica fue implementada en MATLAB-Simulink. Para el PBC de alto desempeño de MI se eligió como ganancia eléctrica $K_{I_s} = 80$, ganancias mecánicas $K_\omega = 1$ y $K_{\omega i} = 45$ y el periodo de muestreo fue de 0.1 ms. En la Tabla 1, se muestran los parámetros del MI empleados en la presente evaluación, si se considera que es un motor alimentado por 220 V_{RMS} a 60 Hz con potencia nominal de 1 HP.

Tabla 1. Parámetros motor de inducción

Par de polos	$n_p = 2$
Resistencia de estator	$R_s = 2.516\ \Omega$
Resistencia de rotor	$R_r = 1.9461\ \Omega$
Inductancia de estator	$L_s = 0.2340$ mH
Inductancia de rotor	$L_r = 0.2302$ mH
Inductancia mutua	$L_{sr} = 0.2226$ mH
Fricción viscosa	$B = 1.1 \times 10^{-4}$ N·m·s/rad
Coeficiente momento de inercia	$J = 6.04675 \times 10^{-3}$ kg·m^2

5.1 Experimento 1

En este experimento se utiliza una referencia de velocidad constante de 862.5 rpm que equivale al 50 % de la velocidad nominal, además se aplicó un par de carga de 2.06 Nm que corresponde al 50 % del valor nominal, este último fue incorporado como fricción viscosa. Con el objetivo de identificar que valor de norma de flujo magnético de

rotor induce menores pérdidas de potencia y satisface el seguimiento de velocidad, se propuso un perfil de norma de flujo de rotor (β) como se muestra en la Figura 2 (en color azul), en donde además se puede observar la norma de flujo calculada, obtenida por la ecuación (16), que minimiza las pérdidas.

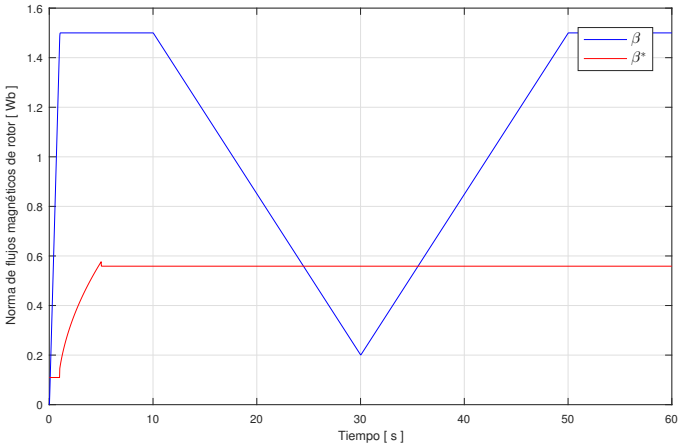

Figura 2. Referencias de normas de flujo de rotor.

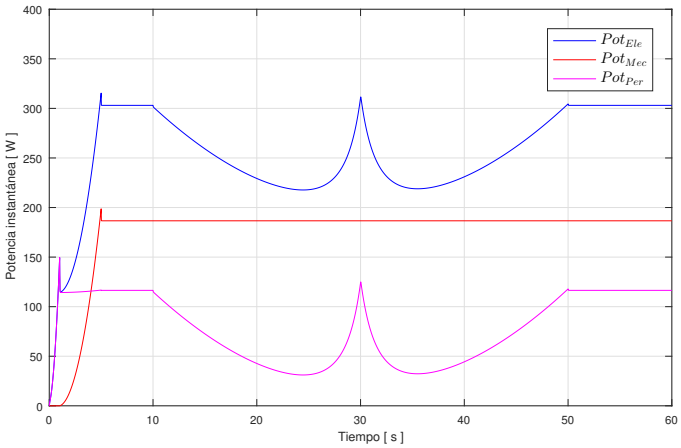

Figura 3. Potencia eléctrica, mecánica y pérdidas de potencia.

Por otro lado, en la Figura 3 se pueden observar la potencia eléctricas (azul), mecánica (rojo) y las pérdidas (magenta) existentes en la operación del MI. Es importante destacar de ambas figuras que la solución de la política de minimización de pérdidas de potencia interseca a la norma de flujos aplicada en este experimento precisamente donde ocurre la menor perdida de potencia, estas suceden en el tiempo 24 s y 36 s, lo que prueba la validez del método.

5.2 Experimento 2

En este experimento se consideran 2 escenarios para la evaluación. El primero de estos impone una norma de flujos magnéticos de rotor constante en la región de interés, equivalente al valor nominal de la máquina $\beta_{Nom} = 0.7911$ Wb. En el segundo escenario se aplica una norma de flujos magnéticos *ad hoc*, la cual es variante en el tiempo, obtenida a partir de (17) y busca reducir las pérdidas de potencia. Estos perfiles de normas de flujo se pueden observar en la Figura 4. Cabe destacar que se aplicó un perfil de par de carga del tipo fricción viscosa con un coeficiente $B' = 0.02283$ N·m·s/rad, cuando la velocidad alcanza los 862.5 rpm el par de carga equivale a 2.06 Nm.

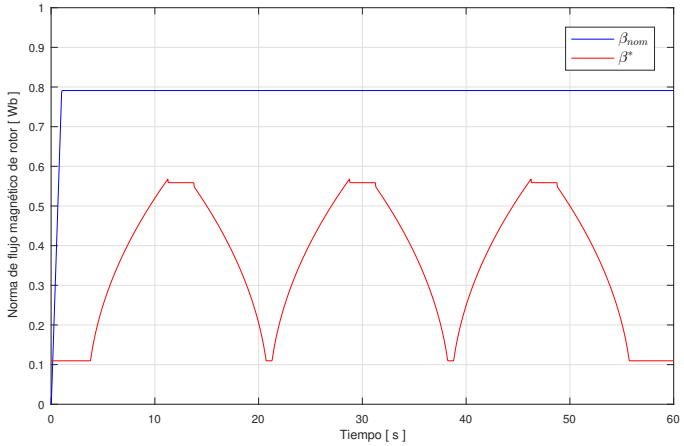

Figura 4. Perfiles de norma de flujos de rotor

El objetivo de este experimento es comparar la magnitud de pérdidas de potencia en ambos escenarios evaluados bajo las mismas condiciones, es decir, aplicando el mismo perfil de velocidad deseado, par de carga y parámetros de sintonía.

Como resultados de esta evaluación, se puede ver en la Figura 5 el correcto seguimiento del perfil de velocidad en ambos escenarios, donde ω en la velocidad obtenida con el escenario 1 y ω^* la velocidad que corresponde al escenario 2.

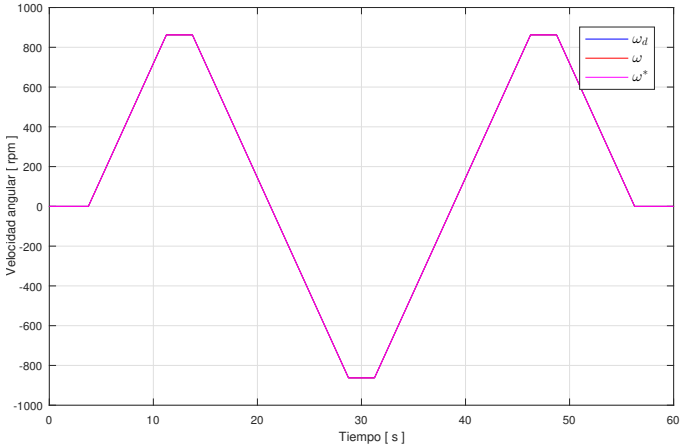

Figura 5. Seguimiento de velocidad angular de ambos escenarios

En la Figura 6 se puede observar que la norma de voltaje obtenida por el escenario 2 ($\|U_s^*\|$) es menor en amplitud comparándola con la obtenida por el escenario 1 ($\|U_s\|$).

Por otro lado, en la Figura 7 se puede observar que la norma de corrientes en el escenario 2 ($\|I_s^*\|$) tiene menor amplitud en comparación con la norma obtenida por el escenario 1 ($\|I_s\|$). Es claro que mientras el controlador realice el correcto seguimiento de velocidad y se cumplan los objetivos de control, es deseable que la norma de corrientes sea tan pequeña como sea posible, debido a que la mayor cantidad de pérdidas de potencia ocurren el los conductores por efecto Joule.

Finalmente, en la Figura 8 se puede observar como la implementación de la política de reducción de consumo energético en conjunto con el PBC del MI logra reducir las pérdidas de potencia (linea roja que corresponde al escenario 2), es decir, la línea azul (Pot_{Per}) representa las pérdidas de potencia instantánea cuando se impone una

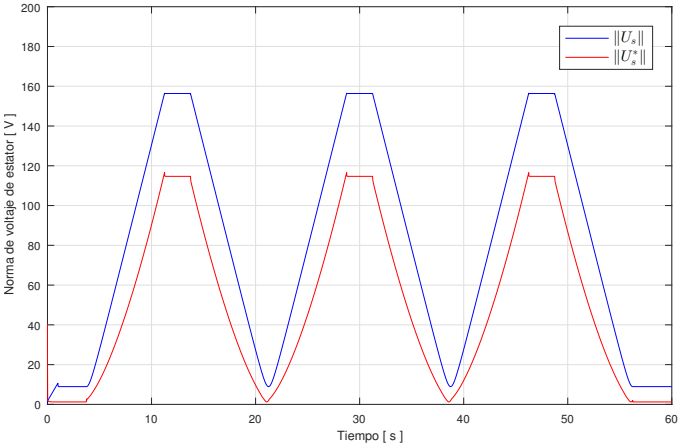

Figura 6. Comparación de norma de voltajes de estator

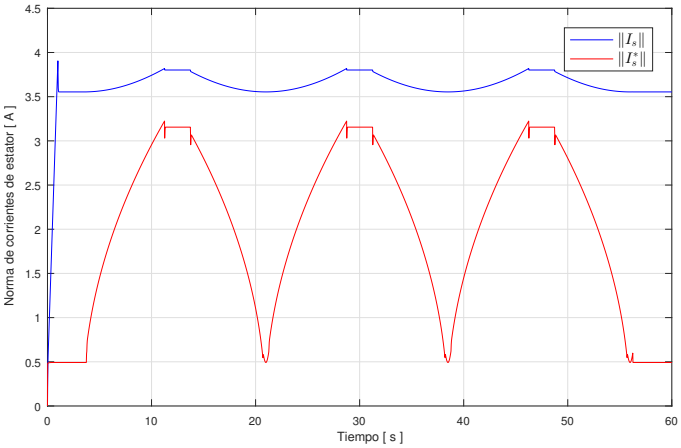

Figura 7. Comparación de norma de corrientes de estator

norma de flujos magnéticos nominal y constante (escenario 1).

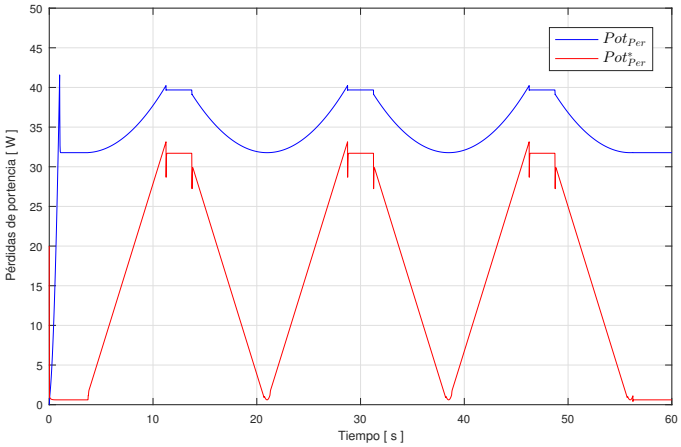

Figura 8. Comparación de pérdidas de potencia

6. CONCLUSIONES

En este artículo se presenta una política de minimización de pérdidas de potencia en conjunto con un PBC de alto desempeño del MI, i.e., además de tener una ley de control que hace un seguimiento correcto de velocidad y norma de flujo magnético de rotor permite reducir el consumo energético. Esta afirmación es corroborada por dos experimentos, los cuales muestran que un MI que opera con el mismo perfil de velocidad y par de carga puede generar menores pérdidas de potencia en los conductores si se asignada adecuadamente la norma de flujos magnéticos de rotor. Por lo tanto, si se cuantifica la energía disipada en pérdidas para el segundo experimento, se tiene que en el escenario 1 el consumo de energía es: 6267.833 J, mientras que en el escenario 2, empleando la norma calculada por (16) el consumo de energía es: 5155.869 J, lo cual representa un ahorro del 17.74 % considerando los 60 segundos que dura el experimento. Como trabajo futuro se busca implementar en forma experimental la política de reducción de consumo energético propuesta en este artículo.

REFERENCIAS

Bensiali, N., Etien, E., and Benalia, N. (2015). Convergence analysis of back-emf mras observers used in sensorless control of induction motor drives. *Mathematics and Computers in Simulation*.

Blondel, A., Mailloux, C., and Adams, C. (1913). *Synchronous motors and converters: theory and methods of calculation and testing*. McGraw-Hill Book Company.

Böcker, J. and Mathapati, S. (2007). State of the art of induction motor control. In *Electric Machines & Drives Conference, 2007. IEMDC'07. IEEE International*, volume 2, 1459–1464. IEEE.

Bodson, M., Chiasson, J.N., and Novotnak, R.T. (1995). A systematic approach to selecting flux references for torque maximization in induction motors. *Control Systems Technology, IEEE Transactions on*, 3(4), 388–397.

Chapman, S.J. (2005). *Máquinas Eléctricas*. 5a ed. edition.

Krause, P., Wasynczuk, O., and Sudhoff, S. (2002). *Analysis of electric machinery and drive systems*. IEEE Press series on power engineering. IEEE Press.

Krishnan, R. (2001). *Electric motor drives: modeling, analysis, and control*. Prentice Hall.

Kumar, N., Chelliah, T.R., and Srivastava, S. (2015). Adaptive control schemes for improving dynamic performance of efficiency-optimized induction motor drives. *ISA transactions*.

Liu, X., Verghese, G., Lang, J., and Onder, M. (1989). Generalizing the blondel-park transformation of electrical machines: necessary and sufficient conditions. *Circuits and Systems, IEEE Transactions on*, 36(8), 1058 –1067.

Meisel, J. (1984). *Principles of electromechanical-energy conversion*. R.E. Krieger.

Mujica, H. and Espinosa-Pérez (2015). Evaluación de diferenciadores numéricos para la obtención de velocidad y aceleración en control de motores eléctricos. *Congreso Nacional de Control Automático, Cuernavaca, México*.

Mujica, H. and Espinosa-Pérez, G. (2014). Control no lineal basado en pasividad de motores de inducción para alto desempeño dinámico. *Revista Iberoamericana de Automática e Informática Industrial RIAI*, 11(1), 32–43.

Mujica, H., Espinosa-Pérez, G., and Moreno, J. (2014). Seguimiento de velocidad y flujo magnético con alto desempeño en motores de inducción. *Congreso Latinoamericano de Control Automático, Cancún, México*.

Seely, S. (1962). *Electromechanical energy conversion*. Electrical and electronic engineering s. McGraw-Hill.

Vedagarbha, P., Dawson, D., and Burg, T. (1997). Rotor velocity/flux control of induction motors with improved efficiency. *Mechatronics*, 7(2), 105–127.

Dynamic Characterization of Typical Electrical Circuits via Structural Properties ⋆

Sofía Avila-Becerril * **Gerardo Espinosa-Pérez** *

* *Facultad de Ingeniería, Universidad Nacional Autónoma de México, Ciudad Universitaria, Ciudad de México (e-mail: soavbec@comunidad.unam.mx; gerardoe@unam.mx).*

Abstract: In this paper the characterization of a class of electrical circuits is carried out in terms of both stability properties and steady state behavior. The main contribution is the interpretation of the electrical topology in terms of mathematical properties derived from the structure of their models. In this sense, it is explained at what extent the topology by itself defines the dynamic behavior of the systems.

Keywords: Electrical circuits, Hamiltonian, Passivity, Graph Theory.

1. INTRODUCTION

The large number of studies on electrical circuits (Weiss and Mathis (1997), Maschke et al. (1995), Jeltsema and Scherpen (2003)) has enabled to recognize general and particular properties that in turn has allowed to generate new perspectives and methodologies for analysis and control. It is of interest to modify the dynamic behavior of the circuit so that some variables reach a desired operating point. The works that have been reported in this context, range from the characterization (see for example Van der Schaft and Maschke (2013)) to control (Ortega et al. (2003)) and applications (Jeltsema and Scherpen (2003)).

An interesting perspective on control circuits is based on the modification of its structure; this compensation means the addition of new elements like capacitors, inductors and resistors in specific locations such that the desired behavior of the electrical system is achieved. The methodology is attractive in correspondence with the study of intrinsic properties of the interconnection that can be applied for example in compensators of Electrical Power Systems. In this context, contributions have appeared where the aim is to exploit the structure of a given circuit. Van der Schaft (2010) studied the problem of shaping a resistive circuit behavior through the interconnection of another resistive circuit, viewing the second as a "controller" and leading to a methodology denoted as "partial synthesis by interconnection" which, in its turn, belong to a more general controller design called *Control by Interconnection* (CbI) (Ortega et al. (2008)). Roughly speaking, under this perspective the objective is to look at the controller as one dynamical system that interconnected with other (the plant) generates a new system with desired properties.

The situation described above, has encouraged the study of the structural properties of electrical circuits in order to recognize the dynamic behavior that can be achieved. The aim of this paper is to identify structural properties of the mathematical models of networks most used in practice, called typical circuits, and use them to characterized both their stability properties and their steady state behavior.

This approach is based on arguments of Graph theory (see Bollobás (1998)). First, the Kichhoff's laws are formulated in terms of basic cutsets and loopsets (for details see Wellstead (1979)). The stability analysis of these behaviors is developed going from simple (linear) to more complex (nonlinear) structures. The last part of the paper concerns to the characterization of the model components that influences the steady state behavior of typical topologies. These analyses are related with the operation of a Mesh network equipped with Direct Current (DC) or Alternate Current (AC) voltage sources. Some technical proofs and numerical testing are deferred to a journal article follow.

The rest of the paper is organized as follows: In Section 2 Kirchhoff's laws are stated in terms of basic cutsets and loopsets and it is presented the dynamic model of a class of electrical circuits followed by its stability analysis. The bases for the characterization of the steady state behavior of typical networks are included in Section 4 while the usefulness of the presented results is illustrated in Section 5.

2. ELECTRICAL CIRCUIT DYNAMIC

An electrical network can be defined as a oriented graph G consisting of a finite set of *nodes* $\mathcal{V}(G)$ and a finite subset $\mathcal{E}(G)$ of pairs of $\mathcal{V}$, called *edges*, where no self-loops are allowed. In electrical circuits nodes are the interconnection points of elements whereas the edges are associated to lumped one-port elements, with a voltage v *across* its terminals and a current i that flows *through* it.

Once the lumped elements are interconnected, their port variables must satisfy the Kirchhoff Current and Voltage Laws (KCL and KVL, respectively). A spanning tree (Bollobás (1998)) is a connected sub-graph containing the n nodes of the graph and $n-1$ edges such that no loops

⋆ Sponsor and financial support acknowledgment goes here.

are formed, the remaining $b-(n-1)$ edges form the corresponding co-tree. A *basic cutset* is a set of edges whose elements are one branch and some or all the chords. A *basic loopset* is a set formed by one chord and some or all branches such that a closed loop is formed. The KCL and the KVL are given in terms of the basic cutset matrix $C_b \in \mathbb{R}^{n-1\times b}$ and the basic loopset matrix $B_b \in \mathbb{R}^{b-n+1\times b}$ as

$$C_b i = 0 \ ; \ B_b v = 0 \tag{1}$$

And if $i \in \mathbb{R}^b$ and $v \in \mathbb{R}^b$ are ordered in such a way that

$$i = \begin{bmatrix} i_t \\ i_c \end{bmatrix} \in C_1; \quad v = \begin{bmatrix} v_t \\ v_c \end{bmatrix} \in C^1$$

with $i_t \in \mathbb{R}^{(n-1)}, v_t \in \mathbb{R}^{(n-1)}$ the currents and voltages of the tree and $i_c \in \mathbb{R}^{b-(n-1)}, v_c \in \mathbb{R}^{b-(n-1)}$ the currents and voltages of the co-tree, respectively, it is possible Bollobás (1998) to write down the current constraints as

$$i_t = -Hi_c, \quad v_c = H^T v_t. \tag{2}$$

where $H \in \mathbb{R}^{(n-1)\times b-(n-1)}$ is called the *fundamental loop matrix*.

In this paper it is considered a *complete* circuit (Brayton and Moser (1964)) so that it is not admitted capacitor-only loops and inductor-only cutsets. Let the circuit elements be grouped such that voltage sources, all the capacitors and some (voltage-controlled) resistors appear at the tree, while inductors and the rest (current-controlled) resistors are in the co-tree, [1] leading to

$$i_t = \begin{bmatrix} i_1 \\ i_C \\ i_{Rt} \end{bmatrix} ; \ v_c = \begin{bmatrix} v_{Rc} \\ v_L \end{bmatrix} ; \ v_t = \begin{bmatrix} v_1 \\ v_C \\ v_{Rt} \end{bmatrix} ; \ i_c = \begin{bmatrix} i_{Rc} \\ i_L \end{bmatrix}$$

where $v_1, i_1 \in \mathbb{R}^{n_1}$, $v_C, i_C \in \mathbb{R}^{n_2}$, $v_{Rt}, i_{Rt} \in \mathbb{R}^{n_3}$, such that $n_1+n_2+n_3 = n-1$, and $v_{Rc}, i_{Rc} \in \mathbb{R}^{n_4}$, $v_L, i_L \in \mathbb{R}^{n_5}$, with $n_4+n_5 = b-(n-1)$.

If the total stored energy of the circuit $H_a : \mathbb{R}^{n_2\times n_5} \to \mathbb{R}_{\geq 0}$ is defined as $H_a(q,\phi) = V_q(q) + V_\phi(\phi)$ and the port variables can be represented as

$$\dot{q} = i_C, \quad v_C = \frac{\partial H_a(q,\phi)}{\partial q} = \nabla_q H_a \tag{3a}$$

$$\dot{\phi} = v_L, \quad i_L = \frac{\partial H_a(i,\phi)}{\partial \phi} = \nabla_\phi H_a \tag{3b}$$

$$i_{Rt} = -f_t(v_{Rt}), \quad v_{Rc} = -f_c(i_{Rc}) \tag{3c}$$

where f_t and f_c are assumed to be bijective functions. With the partition introduced above the matrix H, in its turn, can be divided as

$$H = \begin{bmatrix} H_{1R} & H_{1L} \\ H_{CR} & H_{CL} \\ H_{RR} & H_{RL} \end{bmatrix} \tag{4}$$

where the subscript stand for the interconnections between tree and co–tree elements. As already reported in the literature, substitution of (3a–3c) into (2) leads to the dynamical model given by

$$\dot{x} = \mathbb{J}\nabla_x H_a(x) + \mathbb{F}(x, v_1, v_{Rt}, i_{Rc}) + \mathbb{G}E_1 \tag{5}$$

under the definitions

$$x = \begin{bmatrix} q \\ \phi \end{bmatrix} ; \ \nabla_x H_a(x) = \begin{bmatrix} \nabla_q H_a(x) \\ \nabla_\phi H_a(x) \end{bmatrix} ; \ E_1 = \begin{bmatrix} v_1 \\ 0 \end{bmatrix} \tag{6}$$

[1] For the sake of simplicity presentation current sources will be omitted of the analysis.

with matrices

$$\mathbb{J} = \begin{bmatrix} 0 & -H_{CL} \\ H_{CL}^T & 0 \end{bmatrix} ; \ \mathbb{G} = \begin{bmatrix} 0 & 0 \\ H_{1L}^T & 0 \end{bmatrix} \tag{7}$$

$$\mathbb{F}(x, v_1, v_{Rt}, i_{Rc}) = \begin{bmatrix} 0 & -H_{CR} \\ H_{RL}^T & 0 \end{bmatrix} \begin{bmatrix} v_{Rt} \\ i_{Rc} \end{bmatrix} \tag{8}$$

where

$$\begin{bmatrix} v_{Rt} \\ i_{Rc} \end{bmatrix} = \begin{bmatrix} -f_t^{-1}(-H_{RR}i_{Rc} - H_{RL}\nabla_\phi H_a(x)) \\ -f_c^{-1}(H_{1R}^T v_1 + H_{RR}^T v_{Rt} + H_{CR}^T \nabla_q H_a(x)) \end{bmatrix} \tag{9}$$

and complemented by the algebraic constraint

$$i_1 = -H_{1R}i_{Rc} - H_{1L}i_L \tag{10}$$

It is important to notice that if we concentrate on circuits with *linear* resistive elements, then

$$i_{Rt} = -R_t^{-1}v_{Rt}, \quad v_{Rc} = -R_c i_{Rc} \tag{11}$$

where $R_t = R_t^T > 0$ and $R_c = R_c^T > 0$ are diagonal matrices with the resistances of the tree and co-tree resistors, respectively.

Remark 1. The constraint (10) represents the current demanded to the voltage sources. Though, along the paper it is considered that there are ideal sources.

Remark 2. The time derivative of $H_a(x)$ along the trajectories of (5), considering $E_1 = 0$, is given by

$$\dot{H}_a(x) = \left(\nabla_x H_a(x)\right)^T \mathbb{F}(x, v_1, v_{Rt}, i_{Rc})$$

so that the stability of the network depends on the matrices H_{CR}, H_{RL}, H_{RR} and H_{1R}.

3. STRUCTURAL PROPERTIES FOR STABILITY

The steady state trajectories achievable by the system, denoted as *admissible* trajectories, are solution of

$$\dot{x}^\star = \mathbb{J}\nabla_{x^\star} H_a(x^\star) + \mathbb{F}(x^\star, v_1^\star, v_{Rt}^\star, i_{Rc}^\star) + \mathbb{G}E_1^\star \tag{12}$$

where it has been implicitly assumed the existence of an input $v_1^\star$ that generates the behavior $x^\star$. When $x^\star$ is an equilibrium point, $v_1^\star$ is constant and the steady state operation (equilibrium point) is input dependent and determined by

$$\mathbb{J}\nabla_{x^\star} H_a(x^\star) + \mathbb{F}(x^\star, v_1^\star, v_{Rt}^\star, i_{Rc}^\star) + \mathbb{G}E_1^\star = 0. \tag{13}$$

We first consider linear elements, so we identify conditions on H to guarantee *tracking* of a time-varying solution of (12) but the result applies only when the circuit is composed by linear elements, *i.e.*, when the total stored energy $H : \mathbb{R}^{n_2} \times \mathbb{R}^{n_5} \to \mathbb{R}_{>0}$ takes the form

$$H_a(x) = \frac{1}{2}x^T P x; \ \ P = diag\{C^{-1}, L^{-1}\} = P^T > 0 \tag{14}$$

with diagonal matrices $L \in \mathbb{R}^{n_5\times n_5} > 0$ and $C \in \mathbb{R}^{n_2\times n_2} > 0$ of inductances and capacitances. The resistors satisfy (11) and it is clear that

$$\nabla_x H_a(x) = Px.$$

Proposition 1. Consider a linear electrical network described by (5) and (14) with $v_1(t)$ a time-varying input such that its steady state behavior

$$\dot{x}^\star = [J-R]\,Px^\star + GE_1^\star \tag{15}$$

is well posed. Under these conditions

$$\lim_{t\to\infty} \tilde{x} = 0$$

with $\tilde{x} = x - x^\star$ if

$$ker\{H_{CR}^T\} = ker\{H_{RL}\} = 0. \tag{16}$$

Proof. The error dynamic is given by

$$\dot{\tilde{x}} = [J - R]\, P\tilde{x} + G\tilde{E}_1 \tag{17}$$

with the energy–like function

$$H_a(\tilde{x}) = \frac{1}{2}\tilde{x}^T P\tilde{x} \tag{18}$$

and the identities $\tilde{v}_C = \nabla_{\tilde{x}_1} H_a(\tilde{x}) = C^{-1}\tilde{q}$, $\tilde{i}_L = \nabla_{\tilde{x}_2} H_a(\tilde{x}) = L^{-1}\tilde{\phi}$. Take the function (18) as Lyapunov function candidate, its time derivative along (17) satisfies

$$\dot{H}_a = -zR_T^{-1}z \leq 0 \tag{19}$$

with $R_T = diag\{R_{11}, R_{22}\}$ and R_{11}, R_{22} symmetric positive definite matrices defined by

$$R_{11} = R_c + H_{RR}^T R_t H_{RR}$$
$$R_{22} = R_t^{-1} + H_{RR} R_c^{-1} H_{RR}^T$$

while

$$z = \begin{bmatrix} H_{CR}^T \tilde{v}_C \\ H_{RL}\tilde{i}_L \end{bmatrix} \tag{20}$$

The proof is completed by noting that the maximal invariant set where $\dot{\tilde{H}}_a = 0$ is $z = 0$. To guarantee that $\tilde{v}_C = \tilde{i}_L = 0$ are the only solutions, brings out $ker\{H_{CR}^T\} = ker\{H_{RL}\} = 0$ as the sufficient conditions that assure asymptotic stability of $(\tilde{x}, \tilde{v}_1) = (0, 0)$.

□

The proposition below shows that, in the case of equilibrium points, the same conditions still guarantee asymptotic stability for nonlinear capacitors and inductors.

Proposition 2. Consider an electrical network described by model (5) with $v_1^\star$ a constant input. In addition, assume that

A.1 The resistors involved in the circuit are characterized by linear constitutive relationships.

A.2 The equilibrium point $x^\star$ that correspond to $v_1^\star$ locally satisfies $x^\star = argmin\{H_a(x)\}$.

Then, the equilibrium point $(x^\star, v_1^\star)$ is locally asymptotically stable if

$$ker\{H_{CR}^T\} = ker\{H_{RL}\} = 0. \tag{21}$$

Proof. The total stored energy $H_a(x)$ is a nonlinear function. Therefore, under the assumption **A.1** the equilibria is characterized by the solutions of

$$[J - R]\, \nabla_{x^\star} H_a(x^\star) + GE_1^\star = 0$$

If assumption **A.2** holds, then, it is possible to consider the Lyapunov function candidate $H_0 : \mathbb{R}^{n_2+n_5} \to \mathbb{R}_{\geq 0}$ reported by Jayawardhana et al. (2007)

$$H_0(x) = H_a(x) - x^T \nabla_{x^\star} H_a(x^\star) - (H_a(x^\star) - x^{\star T} \nabla_{x^\star} H_a(x^\star)) \tag{22}$$

whose time derivative along the trajectories of (5), under **A.1** and $v_1 = v_1^\star$, yields

$$\dot{H}_0(x) = -z^T R_T^{-1} z.$$

□

Remark 3. The result above considers just the stability of equilibrium points. The tracking problem, up to the authors knowledge, imposes an open problem.

Motivated by Proposition 1 and Proposition 2, the final result of this section focuses in a particular class of circuits characterized by two properties.

Property 1. If the number of tree resistors is equal to the number of inductors and they are one to one series connected then

$$H_{RL} = I_2 \in \mathbb{R}^{n_3 \times n_3}; \quad H_{RR} = 0_1 \in \mathbb{R}^{n_3 \times n_4} \tag{23}$$

with I_2 as already defined and 0_1 a zero matrix.

Property 2. If the number of co–tree resistors is equal to the number of capacitors and they are one to one parallel connected then

$$H_{CR} = I_3 \in \mathbb{R}^{n_2 \times n_2}; \quad H_{1R} = 0_2 \in \mathbb{R}^{n_1 \times n_2} \tag{24}$$

with I_3 as already defined and 0_2 a zero matrix.

Remark 4. Typical networks exhibit these properties (see Avila-Becerril et al. (2015)). But is also found when modeling of inductors and capacitors losses are considered.

The dynamical behavior of the electrical network (5) under Properties 1 and 2 is described by

$$\dot{x} = \mathbb{J}\nabla_x H_a(x) + \mathbb{F}_1(x) + \mathbb{G}E_1 \tag{25}$$

where

$$\mathbb{F}_1(x) = \begin{bmatrix} -f_c^{-1}(\nabla_q H_a(x)) \\ -f_t^{-1}(\nabla_\phi H_a(x)) \end{bmatrix}$$

Under Properties 1 and 2 the dissipation terms only depend on the state; this allows to relax the assumptions about $f_c(\cdot)$ and $f_t(\cdot)$.

Proposition 3. Consider the electrical network described by (25) with $v_1^\star$ a constant input such that the steady state behavior is well posed. Assume **A.2** holds and that

A.3 The maps $f_c(\cdot)$ and $f_t(\cdot)$ define incremental output strictly passive operators in the sense that

$$(x_1 - x_2)^T \left[f_c^{-1}(x_1) - f_c^{-1}(x_2)\right] > 0$$
$$(x_1 - x_2)^T \left[f_t^{-1}(x_1) - f_t^{-1}(x_2)\right] > 0$$

hold for $x_1 \neq x_2$ and considering x_i as input.

Under these conditions the equilibrium point $(x^\star, v_1^\star)$ is locally asymptotically stable.

Proof. The equilibria of the system is characterized by

$$\mathbb{J}\nabla_{x^\star} H_a(x^\star) + \mathbb{F}_1(x^\star) + \mathbb{G}E_1^\star = 0$$

Thus, if **A.2** holds it is possible to consider the Lyapunov function candidate $H_0 : \mathbb{R}^{n_2+n_5} \to \mathbb{R}_{\geq 0}$, defined in (22), which leads, under the condition $v_1 = v_1^\star$, to

$$\dot{H}_0(x) = -(\nabla_x H_a(x) - \nabla_{x^\star} H_a(x^\star))^T \left[\mathbb{F}_1(x) - \mathbb{F}_1(x^\star)\right]$$

Using (3a) and (3b) and since **A.3** holds it is clear that $\dot{H}_0(x) < 0$ with the maximal invariance set defined as

$$\varepsilon = \{(q, \phi)\,|\,(v_C - v_C^\star) = 0, (i_L - i_L^\star) = 0\}\,. \tag{26}$$

□

4. TOPOLOGICAL STRUCTURE OF TYPICAL NETWORKS

In this section it is stated the structure of the matrix H for a generic network that captures, in an unified way, the characteristics of typical networks (For details on typical networks see the work of Fernández-Carrillo et al. (2015)). The generic network satisfies Properties 1 and 2, hence, its dynamic behavior is represented by model (25) leaving $H_{CL} \in \mathbb{R}^{n_2 \times n_5}$ and $H_{1L} \in \mathbb{R}^{n_1 \times n_5}$ to be characterized. Consider that the n_5 inductors are divided into three types, namely: n_r r-inductors, that

belong to a trajectory that connects a source with a capacitor, n_s s-inductors that belong to a trajectory that connects a source with another source and n_p p-inductors that connects a capacitor with another capacitor, such that $n_r + n_s + n_p = n_5$. Moreover, assume that the capacitors belong at least to one of the following classes

C.1 The $i-th$ capacitor, $i \in \{1, ..., n_2\}$, shares cutset with r_i r-inductors.
C.2 The $i-th$ capacitor, $i \in \{1, ..., n_2\}$, shares cutset with p_i p-inductors.

while the voltages sources satisfies that

C.3 The $i-th$ voltage source, $i \in \{1, ..., n_1\}$, shares cutset with $m_i \in \{1, ..., n_5\}$ inductors.

So that, the rows of matrix H_{CL} can be divided into: i) capacitors that hold simultaneously conditions **C.1** and **C.2** and ii) capacitors that hold only with condition **C.2**. The columns of H_{CL} are divided into three blocks each one corresponding to r, s and p inductors, respectively.

Following the stated organization, matrix H_{CL} takes the form

$$-H_{CL} = \begin{bmatrix} \mathbf{1}_{r_1}^T & 0 & \cdots & 0 & 0_s & N_1 \\ 0 & \mathbf{1}_{r_2}^T & \cdots & 0 & 0_s & N_2 \\ \vdots & \vdots & \ddots & \vdots & \vdots & \vdots \\ 0 & 0 & \cdots & \mathbf{1}_{r_z}^T & 0_s & N_z \\ 0 & 0 & \cdots & 0 & 0_s & N_{z+1} \\ \vdots & \vdots & \ddots & \vdots & \vdots & \vdots \\ 0 & 0 & \cdots & 0 & 0_s & N_{n_2} \end{bmatrix}; \qquad (27)$$

where

- $\mathbf{1}_{r_i}^T \in \mathbb{R}^{1\times r_i}$, $i = 1, \ldots, z$, are vectors filled with ones denoting the condition stated in **C.1**. In this case it has been assumed that there exist z capacitors of this kind. It holds that $r_1 + r_2 + \cdots + r_z = n_r$.
- The zero columns $0_s \in \mathbb{R}^{1\times n_s}$ reflects the fact that any capacitor can be connected to s type inductors.
- Row vectors $N_i \in \mathbb{R}^{1\times n_p}$ include the possibility that a given capacitor can be simultaneously connected to r and p type inductors. If the $i-th$ capacitor is connected to one of the p-inductors, appears a 1, otherwise is 0. If the capacitor only hold **C.1**, $N_i = 0$.
- In the rows that go from $z+1$ to n_2 only appear vectors N_i since they correspond to **C.2** class capacitors.

Property 3. *Each column of the matrix* $N = col\{N_1, \ldots, N_{n_2}\} \in \mathbb{R}^{n_2\times n_p}$ *is composed by one* 1, *one* -1 *and the rest of the entries equal to zero.*

Property 4. *The vector* $\mathbf{1}_{n_2} \in \mathbb{R}^{n_2}$, *i.e., the vector filled with ones of dimension* n_2, *is a left eigenvector of matrix* N *satisfying* $\mathbf{1}_{n_2}^T N = 0$.

Concerning the structure of matrix $H_{1L} \in \mathbb{R}^{n_1\times n_5}$, it is obtained from (10), which is given by

$$i_1 = -H_{1L} i_L$$

taking into account that $H_{1R} = 0$. Their columns are divided into three blocks corresponding to r, s and p type inductors, respectively, where the third one is zero due to the fact that sources do not belong to cutsets where p-inductors are involved. This matrix takes the form

$$H_{1L} = [\, M_r \;\; M_s \;\; 0_p \,] \qquad (28)$$

- The entries different from zero of each row of $M_r \in \mathbb{R}^{n_1\times n_r}$ shows the connection of sources with r-inductors.
- The $i-th$ row of M_r, $i = 1, 2, \ldots, n_1$ is divided into z sections leading to

$$\beta_i = [\, \beta_{ir_1} \;\; \beta_{ir_2} \;\; \cdots \;\; \beta_{ir_z} \,] \qquad (29)$$

  where each $\beta_{ir_j} \in \mathbb{R}^{1\times r_j}$, $j = 1, 2, \ldots, z$, has only one entry equal to 1 if the $i-th$ source is connected to the $j-th$ capacitor. Otherwise, the vector is zero.
- Since two sources can not be connected to the same r-inductor, each column of M_r has only one entry different from zero.
- The sum of the entries different from zero of the $i-th$ row of M_r equals ρ_i.
- The entries different from zero of each column of $M_s \in \mathbb{R}^{n_1\times n_s}$ stand for the connection of sources with other source.
- The sum of the entries different from zero of the $i-th$ row of M_s equals γ_i. Therefore, $\rho_i + \gamma_i = m_i$ of **C.3**.
- Matrix $0_p \in \mathbb{R}^{n_1\times n_p}$ is a zero matrix that exhibits the fact that sources can not be related with p-inductors.

Property 5. *The vector* $\mathbf{1}_{n_1} \in \mathbb{R}^{n_1}$ *is a right eigenvector of matrix* M_s^T *satisfying* $M_s^T \mathbf{1}_{n_1} = 0$.

This general network can be specialized to the typical circuits, for example the Mesh Network.

Mesh Network In this topology each load is connected to all sources, then $r_i = n_1$ for all $i \in \{1, 2, \ldots, r\}$. Also, the number of sources equals the number of capacitors, then $n_1 = n_2$. Finally, there are not neither p-inductors nor **C.2** class capacitors.

The matrices that topologically characterize a Mesh network are

$$H_{CL} = \begin{bmatrix} -\mathbf{1}_{n_1}^T & 0 & \cdots & 0 & 0_s \\ 0 & -\mathbf{1}_{n_1}^T & \cdots & 0 & 0_s \\ \vdots & \vdots & \ddots & \vdots & \vdots \\ 0 & 0 & \cdots & -\mathbf{1}_{n_1}^T & 0_s \end{bmatrix} \in \mathbb{R}^{n_1\times n_5}, \qquad (30)$$

where n_1 is the number of sources and $n_s < n_1$ is the number of sources connected to other source, while

$$H_{1L} = [\, M_r \;\; M_s \,] \qquad (31)$$

with the particular feature that all the partitions β_{ir_j} of the $i-th$ row of M_r include an element different from zero since all the sources are connected to all capacitors.

5. STEADY–STATE CHARACTERIZATION: TWO CASE STUDY

The aim of this section is to exploit the structure of the Fundamental Loop Matrix H under two different scenarios.

5.1 Lossless DC network

Consider a network operating under constant voltage sources, with possibly nonlinear capacitors and inductors, with linear co–tree resistances and assuming that the tree resistances $R_t = 0$. This scenario is frequently considered in practice, for example, in Electrical Power Systems under the assumption that the lines are dominantly inductive.

Properties 1 and 2 hold. Hence, model (5) reduces to

$$\dot{x} = \begin{bmatrix} R_c^{-1} & -H_{CL} \\ H_{CL}^T & 0 \end{bmatrix} \nabla_x H_a(x) + \begin{bmatrix} 0 \\ H_{1L}^T \end{bmatrix} v_1 \tag{32}$$

For stability properties of the network, Proposition 2 can be directly applied, since

$$\dot{H}_0(x) = -(v_C - v_C^\star)^T R_c^{-1}(v_C - v_C^\star) \leq 0$$

and by direct substitution of $v_C^\star$ in (32), the maximal invariant set of the system corresponds to $i_L = i_L^\star$, condition that proves that asymptotic stability is attained.

The second part is devoted to the characterization of the steady state behavior defined by the equilibria of the system, which are the solutions of

$$-R_c^{-1} v_C^\star - H_{CL} i_L^\star = 0 \tag{33a}$$
$$H_{CL}^T v_C^\star + H_{1L}^T v_1^\star = 0, \tag{33b}$$

for a given $v_1^\star$, the characterization can be carried out for the capacitor voltages or the inductor currents. If the capacitor voltages are chosen, it is possible to write that

$$v_C^\star = -\left[H_{CL} H_{CL}^T\right]^{-1} H_{CL} H_{1L}^T e_1^\star \tag{34}$$

since, from Property 3, H_{CL} is row full rank.

Departing from this last expression, in the following proposition it is illustrated how exploiting the structures for H_{CL} and H_{1L} it is straightforward to concluded the steady state operation that is achieved by a given network. The result is illustrated for the case of a Mesh circuit.

Proposition 4. Consider a Mesh electrical circuit characterized by (30) and (31). Assume that

- The network is lossless, i.e., $R_t = 0$.
- Propositions 1 and 2 hold.
- The vector of voltage sources v_1 is composed by n_1 constant values.

Under these conditions capacitor voltages achieves average consensus (Bai et al. (2011)) in the sense that

$$v_C^\star = \alpha \mathbf{1}_{n_1}. \tag{35}$$

with

$$\alpha = \frac{1}{n_1} \sum_{m=1}^{n_1} v_{1m}^\star$$

the steady state average value of v_1.

Remark 5. A direct corollary of the last proposition refers to the case when $v_1^\star = \bar{v}_1 \mathbf{1}_{n_1}$, with $\bar{v}_1 \in \mathbb{R}$. Under this condition voltage capacitor consensus (see Bai et al. (2011)) is achieved in the sense that $v_C^\star = v_1^\star$.

Remark 6. Interestingly enough, if inductive loses are included, $R_t \neq 0$, consensus is not longer preserved. Instead of, the entries of the matrix $R_c^{-1} + H_{CL} R_t^{-1} H_{CL}^T$ depends on the values of the tree resistors. However, it seems that this situation allows for designing compensation techniques, *i.e.*, adding new lumped elements to the circuit, such that the desired behavior is accomplished.

5.2 AC steady–state behavior

In this section, we study an electric network operating under sinusoidal voltage sources. In this case all the passive elements are considered linear although inductive loses are included. Hence, the circuit dynamic is described by (5) under (14) and is represented as

$$P^{-1}\dot{z} = [J - R]\, z + G e_1$$

where $z = \begin{bmatrix} v_C^T & i_L^T \end{bmatrix}^T$ and J, R and G previously defined.

Since the steady state behavior is now time–varying, the admissible trajectories are given as solution of

$$P^{-1}\dot{z}^\star = [J - R]\, z^\star + G v_1^\star \tag{36}$$

As usual (Desoer and Kuh (1969)), it is assumed that voltage and currents are of the form

$$f(t) = F cos(\omega t + \phi) = Re(\mathbb{F} e^{j\omega t})$$

with the phasor $\mathbb{F} = F e^{j\phi}$. Therefore, admissible trajectories are defined by

$$Re\left[j\omega P \mathbb{Z}^\star e^{j\omega t} - (J - R)\mathbb{Z}^\star e^{j\omega t}\right] = Re(G)(\mathbb{V}_1^\star e^{j\omega t})$$

leading to

$$\mathbb{Z}^\star = \left[j\omega P - (J - R)\right]^{-1} G \mathbb{V}_1^\star \tag{37}$$

Considering that the circuit satisfies Properties 1 and 2, *i.e.*, identities (23) and (24) hold, the model reduces to

$$sP - (J - R) = \begin{bmatrix} sC + R_c^{-1} & H_{CL} \\ -H_{CL}^T & sL + R_t \end{bmatrix}$$

where $s = j\omega$, $C \in \mathbb{R}^{n_2 \times n_2}$ is the capacitance matrix and $L \in \mathbb{R}^{n_5 \times n_5}$ is the inductance matrix. Hence, it is obtained that

$$\mathbb{Z}^\star = \begin{bmatrix} \mathbb{V}_C^\star \\ \mathbb{I}_L^\star \end{bmatrix} = \begin{bmatrix} A_1 H_{1L}^T \mathbb{V}_1^\star \\ A_2 H_{1L}^T \mathbb{V}_1^\star \end{bmatrix} \tag{38}$$

with

$$A_1 = -\left[Y_{CR} + H_{CL} Y_{LR} H_{CL}^T\right]^{-1} H_{CL} Y_{LR} \tag{39}$$
$$A_2 = Y_{LR} - Y_{LR} H_{CL}^T \left[Y_{CR} + H_{CL} Y_{LR} H_{CL}^T\right]^{-1} H_{CL} Y_{LR}$$

and diagonal admitance matrices

$$Y_{CR} = sC + R_c^{-1} \tag{40}$$
$$Y_{LR} = (sL + R_t)^{-1} = s^{-1}(L + s^{-1} R_t)^{-1} = s^{-1} D \tag{41}$$

For illustrative purposes, the steady state behavior of capacitor voltages is characterized assuming a Mesh network. In accordance with the partitions of H_{CL} and H_{1L} previously introduced, the inductance takes the form

$$L = diag\{L_r, L_s\}$$

with $L_r \in \mathbb{R}^{n_r \times n_r}$, $L_s \in \mathbb{R}^{n_s \times n_s}$. In addition, the former must be divided into z matrices as

$$L_r = diag\{L_{ri}\};\ \ i = 1, 2, \ldots, z$$

where $L_{ri} \in \mathbb{R}^{n_1 \times n_1}$ since for a Mesh network $n_r = n_1$.

From Properties 1 and 2, the dimension of R_c is $n_1 \times n_1$, due to the fact that $n_1 = n_2$, while $R_t \in \mathbb{R}^{n_5 \times n_5}$, *i.e.*, equals the dimension of L.

Under the aforementioned partitions, matrix D introduced in (41) is given by

$$D = diag\{D_r, D_s\} \tag{42}$$

where $D_r = diag\{D_{ri}\}$ with $D_{ri} = (L_{ri} + s^{-1} R_{ti})^{-1}$, $i = 1, 2, \ldots, z$, and R_{ti} submatrices of R_t of dimension corresponding to L_{ri}. Concerning matrix H_{1L}, whose structure is presented in (31), the sub–matrix $M_r \in \mathbb{R}^{n_1 \times n_r}$ is represented as

$$M_r = \begin{bmatrix} M_{r1} & M_{r2} & \cdots & M_{rz} \end{bmatrix}$$

with $M_{ri} \in \mathbb{R}^{n_1 \times r_i}$, $i = 1, 2, \ldots, z$, matrices composed by the vectors introduced in (29) exhibiting only one entry different from zero on each of their columns.

Proposition 5. Consider a Mesh electrical circuit characterized by (30) and (31). Assume that

- Propositions 1 and 2 hold.
- The vector of voltage sources v_1 is composed by n_1 sinusoidal functions.

Under these conditions the input/output relationship between the capacitor voltage phasors $\mathbb{V}_C^\star$ and the voltage source phasors $\mathbb{V}_1^\star$ is given by

$$\mathbb{V}_C^\star = -\mathbb{M}^{-1} \begin{bmatrix} \mathbf{1}_{n_1}^T D_{r1} M_{r1}^T \\ \mathbf{1}_{n_1}^T D_{r2} M_{r2}^T \\ \vdots \\ \mathbf{1}_{n_1}^T D_{rr} M_{rz}^T \end{bmatrix} \mathbb{V}_1^\star \tag{43}$$

where $\mathbb{M} = \left[s^2 C + s R_c^{-1} + diag\left\{\mathbf{1}_{n_1}^T D_{ri} \mathbf{1}_{n_1}\right\}\right]$, $i = 1, 2, \ldots, z$.

Remark 7. The idea to manipulate the capacitance, inductance and resistance values to attain a given steady state behavior is not new. In many applications this procedure is recognized as *compensation* and is related with the addition of new elements parallel or series connected with the originals. The advantage offered by the approach presented in this paper, is that the compensation analysis can be carried out in a systematic way.

6. CONCLUDING REMARKS

In this paper a dynamic characterization of a class of electrical circuits has been presented. The characterization contemplates both stability properties and steady behavior; its main feature is that it is based on the structural properties of the networks which have been obtained by using arguments from the Graph theory. It has been shown that the structure of these circuits strongly defines their dynamic behavior. The usefulness of the results reported in this paper lies in the possibility to carry out the characterization in a very systematic way. In addition, it has been shown that they offer an alternative to deal with problems like compensator location to attain a prescribed behavior.

ACKNOWLEDGEMENTS

Part of this work was supported by DGAPA-UNAM under grant IN116516.

REFERENCES

Avila-Becerril, S., Espinosa-Pérez, G., and Fernández-Carrillo, P. (2015). Stability and consensus of electrical circuits via structural properties. *IFAC-PapersOnLine*, 48(13), 111–116.

Bai, H., Arcak, M., and Wen, J. (2011). *Cooperative control design: a systematic, passivity-based approach.* Springer Science & Business Media.

Bollobás, B. (1998). *Modern graph theory*, volume 184. Springer Science & Business Media.

Brayton, R. and Moser, J. (1964). A theory of nonlinear networks i. *Quart. Appl. Math*, 22(1), 1–33.

Desoer, C. and Kuh, E. (1969). *Basic Circuit Theory.* McGraw-Hill.

Fernández-Carrillo, P., Avila-Becerril, S., and Espinosa-Pérez, G. (2015). Consenso en sistemas eléctricos de potencia mediante compensación. *Congreso Nacional de Control Automtico (AMCA) 2015*, 527 – 532.

Jayawardhana, B., Ortega, R., García-Canseco, E., and Castanos, F. (2007). Passivity of nonlinear incremental systems: Application to pi stabilization of nonlinear rlc circuits. *Systems & control letters*, 56(9), 618–622.

Jeltsema, D. and Scherpen, J. (2003). A dual relation between port-hamiltonian systems and the brayton–moser equations for nonlinear switched rlc circuits. *Automatica*, 39(6), 969–979.

Maschke, B.M., Van der Schaft, A.J., and Breedveld, P.C. (1995). An intrinsic hamiltonian formulation of the dynamics of lc-circuits. *Circuits and Systems I: Fundamental Theory and Applications, IEEE Transactions on*, 42(2), 73–82.

Ortega, R., Jeltsema, D., and Scherpen, J. (2003). Power shaping: A new paradigm for stabilization of nonlinear rlc circuits. *Automatic Control, IEEE Transactions on*, 48(10), 1762–1767.

Ortega, R., van der Schaft, A., Castanos, F., and Astolfi, A. (2008). Control by interconnection and standard passivity-based control of port-hamiltonian systems. *Automatic Control, IEEE Transactions on*, 53(11), 2527–2542.

Van der Schaft, A. (2010). Characterization and partial synthesis of the behavior of resistive circuits at their terminals. *Systems & Control Letters*, 59(7), 423–428.

Van der Schaft, A. and Maschke, B. (2013). Port-hamiltonian systems on graphs. *SIAM Journal on Control and Optimization*, 51(2), 906–937.

Weiss, L. and Mathis, W. (1997). A hamiltonian formulation for complete nonlinear rlc-networks. *Circuits and Systems I: Fundamental Theory and Applications, IEEE Transactions on*, 44(9), 843–846.

Wellstead, P. (1979). *Introduction to physical system modelling.* Academic Press London.

Energy Price and Load Estimation by Moving Horizon Estimator with Holt-Winters Model

J. Rendón * **P. Deossa** ** **A. Márquez** *** **J. Espinosa** ****

* *Universidad Nacional de Colombia, Facultad de Minas, Cr. 80 No. 65 -233, Medelln, Antioquia (e-mail: jerendonr@ unal.edu.co)*
** *Universidad Nacional de Colombia, Facultad de Minas, Cr. 80 No. 65 -233, Medelln, Antioquia (e-mail: padeossa@ unal.edu.co)*
*** *Universidad Nacional de Colombia, Facultad de Minas, Cr. 80 No. 65 -233, Medelln, Antioquia (e-mail: amarque@ unal.edu.co)*
**** *Universidad Nacional de Colombia, Facultad de Minas, Cr. 80 No. 65 -233, Medelln, Antioquia (e-mail: jespinov@ unal.edu.co)*

Abstract: With the increasing penetration of smart grid technologies, prediction and forecasting task of the power system variables such as load and spot price became a difficult task. Traditional methodologies lack performance to capture the new dynamics of the power system. The Holt Winters model is widely used to estimate seasonal series. This model requires an heuristic setting of its non-dynamic parameters. This paper proposes a comparative study between Kalman Filter and Moving Horizon Estimator as optimal dynamic identification methods for the Holt-Winters model parameters. In order to evaluate the proposed optimal setting performance, the energy price and load time series of the Colombian electrical power system were used as case study, furthermore the classical estimation methods are chosen as reference frames.

Keywords: Moving Horizon Estimator, Kalman filter, Holt-Winters, energy markets.

1. INTRODUCTION

Operation of electric power systems is focused on ensuring the safety, continuity and reliability in the generation and delivery of electricity throughout the system. A required task to meet the mentioned objectives is to plan and predict the system behavior. Predictions and forecasting of the electric power systems variable had been made since several years ago, however recently, the penetration of smart grid technologies such as: green power plants, demand response strategies, climate change and markets liberalization have increased the dynamics and uncertainties of the variables. Now prediction and forecast for dynamic problems is an increasing relevant research topic. Load and energy spot price are two important driving variables in power system planning and operation, these series have direct influence in the generation-expansion plans (long term) and the economic dispatch of the system (short term), as mentioned, the influence of the smart grid technologies are changing the dynamics of the power systems included the mentioned variables, in this sense, the seasonality properties of the mentioned time series is changing and the traditional tools used to estimate and forecast the time series are failing compromising efficiency of the power system.

The literature reports several studies about modeling. Recent publications mentions the following research topics: estimation and prediction of price and load. In (Niimura, 2006) two different kind of models are presented: statistics models and autoregressive models. Statistic models are focused in the ARMA,ARIMA and GARCH structures. Computational methods presents fuzzy models, neural networks and chaotic methods. This work concludes that model performance highly depends on the prediction horizon and the model selection depends on the expected precision and the data variance. In (Weron, 2014a) different prediction techniques are applied to energy price time series, the methodologies review includes: multiagent methods, methods of fundamental decomposition by components, regressive methods, and evolutionary computation methods are reviewed. This paper also discusses the future of predicting price and concluded that: the techniques that predict better price are combinations of the methods discussed and prediction techniques intervals, due to the high volatility presents this series. In (Suganthi and Samuel, 2012) and (Singh et al., 2012) the authors described different load prediction models such as autorregressive models, fuzzy logic, neural networks, smoothing exponential model, expert systems and ant colony algorithms. All these models and techniques are currently used for planning and forecasting power system load. In (Haghi and Tafreshi, 2007) a categorization of the methods used to predict price in all time horizons (long, medium and short term) is shown. Methods reviewed in this work are: game theory based models, fuzzy and neural networks models, statistics methods like time series and autorregressive models. The study compares the mentioned models emphasizing their advantages. Model validation is performed in short time prediction horizon with low volatility time series. In (Ramírez, 2013) time series, neural networks

and regression based methodologies are compared with exponential smoothing models including the Holt Winters in short, medium and long term horizons. Here the lowest error is achieved with the Holt-Winters model at different small time horizons compared with the other techniques. But concluded that due to the non-inclusion of external variables in the different techniques, none of them will have a goo performance in long term predictions.

Now, presented models are applied to estimation and prediction of price and load, however they have some failings as is the case autorregressive models where prediction is poor in the short term as they do not consider the effect of external variables (Ramírez, 2013), or neural networks where a high computational cost to determine the number of neurons and is considered an unstable technique (Snchez and Velsquez, 2010); similarly in fuzzy models which have a bias in the results for the same model topology (Krafft and Mantrala, 2009). Furthermore in (Goodwin, 2010), (Chatfield and Yar, 1988) and (Gardner Jr., 2006) one of the most widely used for prediction and estimation series models, is the Holt-Winter model, whose trend and seasonality are set, as prices and load time series. These papers reports a reduction in error estimation and low computational burden when the Holt Winters models is applied to short term load and price estimation but in long and medium term time windows the results do not exhibit the mentioned benefits. This lack of efficiency is attributed to the model static structure which causes a cumulative error related with the presence of exogenous variables in the data series. Facing these facts, this work evaluates the technique Moving Horizon Estimator (MHE) discussed in (Valencia et al., 2011) and (Boulkroune et al., 2010) as a method of adjustment for the Holt-Winters model. This model is rewritten in a novel way in terms of state space in order to facilitate the development and solving of proposed estimator. At the same time it also seeks to verify what are the conditions of model structure and the estimator that ensure optimal estimation error reduction. The performance is compared with other classical estimation techniques like Kalman Filter and autorregressive methods.

This paper reports these results as follows: in Section 2 the price 2013 and demand 2014 series are described, these time series will be used to compare the Holt-Winters adjustment model with optimal estimation techniques. In Section 3 the Holt-Winters model is adjusted, finally, in Section 4 the optimal estimation will be made through the proposed techniques, here the quantitative analysis of the estimation errors is made for each model. Finally the conclusions are presented.

2. TIME SERIES DESCRIPTION

This work uses the 2013 Spot Price time series (hourly resolution), shown in Fig. 1 and the 2014 first semester load for regulated users for the EPM retailer (diary resolution), shown in Fig. 2. The load and price time series are available in XM web page (XM, 2016). Series data found on this page are preprocessed and are used to formulate the Figures and the autocorrelation functions shown. These series are chosen because they have a trend and seasonality characteristics, this fact can be used to properly formulate the model and also to improve estimation techniques presented.

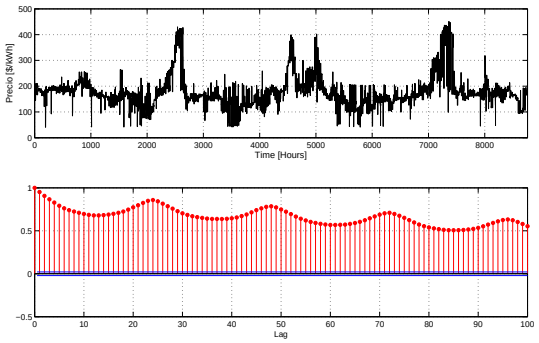

Fig. 1. Top: 2013 Price series. Bottom: 2013 Price series ACF

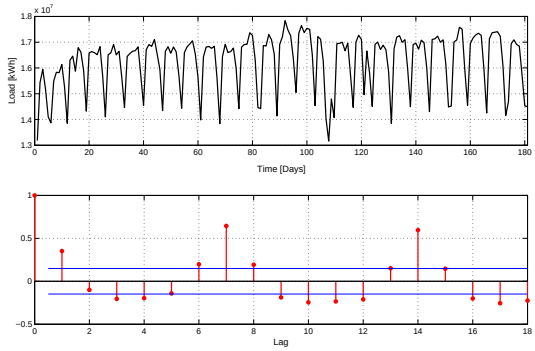

Fig. 2. Top: 2014 Load series. Bottom: 2014 Load series ACF

Figure 1 shows evidence that the time series has high random component influenced by external variables, by inspection it was thought that the series is not seasonal, but the auto correlation function (ACF) shows a seasonality component every 24 hours. Furthermore in Fig. 2 the weekly seasonality of the load series is clearly and is checked by ACF inspection. Validation of the seasonality of the series, is made through the Dickey-Fuller test (ADF Test) (Ng and Perron, 1995) and when this is not conclusive, a logarithmic transformation and adjustment of trends in the series is made to stabilize the variance and obtain a the correct conclusion, as explained in (Weron, 2014b), (Montgomery et al., 2015). Table 1 shows a summary of the results obtained for the series with and without logarithmic transformation.

Table 1. ADF test for time series

Time series	**Inspection ACF**	**ADF Test**	**Conclusion**
Price 2013	Not seasonal	0	Not seasonal
Load 2014	Seasonal	0	Not seasonal
Transformation Price 2013	Seasonal	1	Seasonal
Transformation Load 2014	Seasonal	1	Seasonal

3. THE HOLT-WINTERS MODEL

Holt-Winters (HW) models are often used in seasonal time series with disagreeable trending, seasonal or random variation, and they are grouped in additive or multiplicative. This model is the result of Holt (1957) and Peter Winston (1960) investigations, which proposed prediction methods whose principles are founded on the second-order exponential smoothing (Goodwin, 2010), (Hyndman et al., 2008). In (Gardner Jr., 2006) a complete state of the art about exponential smoothing models and the different forms of the Holt-Winters models are presented. Because the profiles of the proposed series, an additive seasonality and a linear trend will be assumed (seven days for load and 24 hours for price), based on this, an additive trend model will be used as follows:

$$\mu_k = \alpha y_k - \alpha S_{k-p} + (1-\alpha)\mu_{k-1} + (1-\alpha)T_{k-1} \quad (1)$$

$$T_k = \gamma\mu_k - \gamma\mu_{k-1} + (1-\gamma)T_{k-1} \quad (2)$$

$$S_k = \delta y_k - \delta\mu_k + (1-\delta)S_{k-p} \quad (3)$$

where μ_k is the level component, ${}_kT$ is the trend component, S_k is the seasonal component and p is the period in a seasonal cycle and α, γ and δ are parameters of the model.

Based on the presented model this work represents the Holt Winters model in a state space representation. This representation is widely used in estimation and optimization problems and control theory in general. The state space model is given as follows:

$$x_{k+1} = Ax_k + Bu_k \quad (4)$$

$$y_k = Cx_k + Du_k \quad (5)$$

$$x_k = [\,\mu_k \;\; T_k \;\; S_{k-p+1} \;\; S_{k-p+2} \;\cdots\; S_k\,]^T \quad (6)$$

$$A = \begin{bmatrix} 1-\alpha & 1-\alpha & -\alpha & 0 & \cdots & 0 \\ -\alpha\gamma & 1+\alpha\gamma & -\alpha\gamma & 0 & \cdots & 0 \\ 0 & 0 & 0 & 1 & \cdots & 0 \\ 0 & 0 & 0 & 0 & \ddots & \vdots \\ \vdots & \vdots & \vdots & \vdots & \cdots & 1 \\ -\delta(1-\alpha) & -\delta(1-\alpha) & (\delta\alpha+(1-\delta)) & 0 & \cdots & 0 \end{bmatrix} \quad (7)$$

$$B = [\,\alpha \;\; \alpha\gamma \;\; 0 \;\cdots\; 0 \;\; \delta - \delta\alpha\,]^T \quad (8)$$

$$y_k = \mu_k + T_k + S_{k-p+1} \quad (9)$$

$$C = [\,1 \;\; 1 \;\; 1 \;\; 0 \;\cdots\; 0\,] \quad (10)$$

$$D = [\,0\,] \quad (11)$$

This model does not have an input (exogenous) vector. When the model is used for prediction, it is assumed as an autonomous system. Regarding the initial values of the states there are several heuristics to estimate these values as described in (Segura and Vercher, 2001), due to the ease in calculations compared to other methods, the initial state of this model are calculated with the methodology proposed by (Makridakis et al., 1998):

- $\mu_0 = \bar{D}_1$, where $\bar{D}_1$ is the mean of all measured data for the first seasonal cycle of the series.
- $T_0 = \frac{\bar{D}_1 - \bar{D}_2}{p}$, where $\bar{D}_2$ is the mean of all measured data for the second seasonal cycle of the series.
- $So_{k-p} = \frac{D_k}{\bar{D}_1}$, for $k = 1, 2, ..., p$; where D_k is the given measure in the instant k from the first seasonal cycle.

In order to improve the identified model for the series of price and load, the optimal parameters were calculated as: $\alpha = 0.00038$, $\gamma = 0.00033$, $\delta = 0.15888$ and $\alpha = 0.0057971$, $\gamma = 0.0006222$, $\delta = 0.0046903$, respectively. The simulation results with these parameters are shown in Fig. 3 and 4.

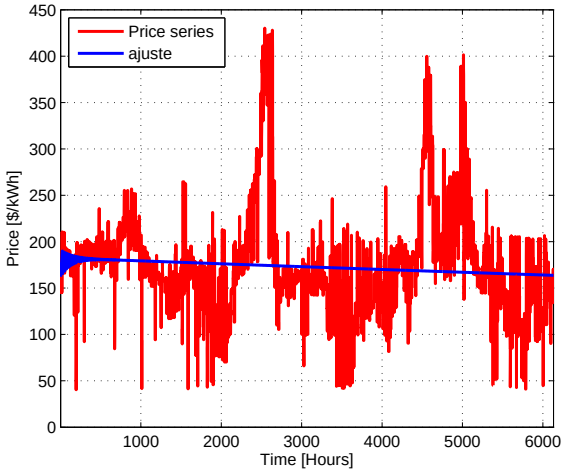

Fig. 3. Optimal adjustment HW model for price series

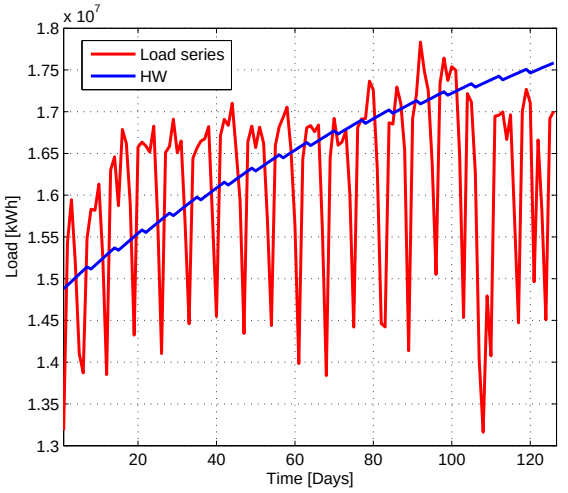

Fig. 4. Optimal adjustment HW model for load series

As can be seen in both figures, the model with $y_d = 0$, does not adjust properly to the series, and since the adjustment was not satisfactory, it was decided to make an adjustment based on parameter optimization to achieve a better result and capture the trend of the series. This model will be used for implementing the proposed estimation methods.

4. MOVING HORIZON ESTIMATOR

The Moving Horizon Estimator (MHE) is an estimation technique based on optimization. In MHE, the problem of state estimation of a given system is solved, considering all previous measurements available in a specific time window. Similarly to the Kalman filter, MHE takes into account the stochastic variables in the model, like the measurement and model noises. Therefore it acts as a complete and optimal estimator (Muske et al., 1993), (Rao

et al., 2001), (Pawlowski et al., 2010). In the literature, several applications of the MHE for dynamic systems are found. This paper explores its use with the HW model.

4.1 Mathematical structure of Moving Horizon Estimator

In order to solve the optimization problem of the MHE, it is necessary to know the matrices associating the current state x_k with the current output y_k, a previous state x_{k-N}, determined by a measurement horizon N. Those relationships are given by the expression (12) and (13) respectively, taken from (Valencia et al., 2011).

$$\tilde{x} = \Phi x_{k-N} + \gamma\tilde{u} + \alpha\tilde{w} \tag{12}$$

$$\tilde{y} = \Gamma x_{k-N} + \Lambda\tilde{u} + \Lambda_\omega\tilde{\omega} \tag{13}$$

where $\tilde{x} \in \mathbb{R}^{Nn_x}$, $\tilde{y} \in \mathbb{R}^{Nn_y}$, $\tilde{u} \in \mathbb{R}^{(N+1)n_x}$, $\tilde{\omega} \in \mathbb{R}^{(N+1)n_w}$ and they are defined in the expressions (14) to (22).

$$\tilde{x} = \left[\, x_{k-N+1} \;\; x_{k-N+2} \;\; x_{k-N+3} \;\; \cdots \; x_k \,\right]^T \tag{14}$$

$$\Phi = \left[\, A^T \;\; (A^2)^T \;\; (A^3)^T \;\; \cdots 6(A^N)^T \,\right]^T \tag{15}$$

$$\gamma = \begin{bmatrix} B & 0 & \cdots & 0 \\ AB & B & \cdots & 0 \\ A^2B & AB & \ddots & \vdots \\ \vdots & \ddots & \ddots & \vdots \\ A^{N-1}B & A^{N-2}B & \cdots & B \end{bmatrix} \tag{16}$$

$$\tilde{u} = \left[\, (u_{k-N})^T \;\; (u_{k-N+1})^T \;\; \cdots \; (u_{k-1})^T \,\right]^T \tag{17}$$

$$\tilde{\omega} = \left[\, (\omega_{k-N})^T \;\; (\omega_{k-N+1})^T \;\; \cdots \; (\omega_{k-1})^T \,\right]^T \tag{18}$$

$$\tilde{y} = \left[\, (y_{k-N+1})^T \;\; (y_{k-N+2})^T \;\; \cdots \; (y_k)^T \,\right]^T \tag{19}$$

$$\overline{C} = \begin{bmatrix} C & 0 & 0 & \cdots & 0 \\ 0 & C & \ddots & \cdots & \vdots \\ \vdots & \ddots & C & \ddots & \vdots \\ \vdots & \vdots & \cdots & \ddots & \vdots \\ 0 & 0 & \cdots & \cdots & C \end{bmatrix} \tag{20}$$

$$\Gamma = \overline{C}\Phi \tag{21}$$

$$\Lambda = \overline{C}\gamma \tag{22}$$

where $B_\omega \in \mathbb{R}^{n_w \times n_w}$ is the relationship matrix between the uncertainty modeling with states; likewise if change B with B_ω, can be found $\alpha = \gamma$, $\Lambda = \Lambda_\omega$.

In the state estimation problem, the objective is to minimize errors between the measurement and estimation at every instant of measurement, and likewise minimize modeling errors, as shown in (23).

$$\min_{\hat{x}_{k-N},\omega_{k+j}} \sum_{j=-N+1}^{0} \|(y_{k+j} - \hat{y}_{k+j})\|_Q^2 + \|\omega_{k+j}\|_R^2$$
$$\text{subject to:} \tag{23}$$
$$\hat{x}_{k+j+1} = A\hat{x}_{k+j} + Bu_{k+j} + B_\omega\omega_{k+j}$$
$$\hat{y}_{k+j} = C\hat{x}_{k+j} + v_{k+j}$$

where $y_{k+j} \in \mathbb{R}^{n_y}$ is the measurement data in the instant $k+j$, $\hat{y}_{k+j} \in \mathbb{R}^{n_y}$ is the data estimate in the instant $k+j$, $\hat{x} \in \mathbb{R}^{n_x}$ is the data estimate at a given time, $v_{k+j} \in \mathbb{R}^{n_v}$ are the measurement noises in the instant $k+j$.

In order to simplify the solution of the optimization problem, based on (13), equation (23) can be rewritten as follows:

$$\min_{\hat{x}_{k-N},\tilde{\omega}} \quad (\tilde{y} - \hat{\tilde{y}})^T\overline{Q}(\tilde{y} - \hat{\tilde{y}}) + \tilde{\omega}^T\overline{R}\tilde{\omega}$$
$$\text{subject to:} \quad \hat{\tilde{y}} = \Gamma\hat{x}_{k-N} + \Lambda_\omega\tilde{\omega} \tag{24}$$

where:

$$\overline{R} = \begin{bmatrix} R & 0 & 0 & \cdots \\ 0 & R & 0 & \cdots \\ \vdots & \ddots & \ddots & \vdots \\ 0 & \cdots & \cdots & R \end{bmatrix} \in \mathbb{R}^{Nn_v} \tag{25}$$

$$\overline{Q} = \begin{bmatrix} Q & 0 & 0 & \cdots \\ 0 & Q & 0 & \cdots \\ \vdots & \ddots & \ddots & \vdots \\ 0 & \cdots & \cdots & Q \end{bmatrix} \in \mathbb{R}^{Nn_w} \tag{26}$$

once it is replaced (13) with $\tilde{u} = 0$, in (24), the expression (27) is obtained .

$$\min_{\hat{x}_{k-N},\tilde{\omega}} \quad (\Gamma x_{k-N} + \Lambda_\omega\tilde{\omega} - \hat{\tilde{y}})^T\overline{Q}(\Gamma x_{k-N} + \Lambda_\omega\tilde{\omega} - \hat{\tilde{y}}) + \tilde{\omega}^T\overline{R}\tilde{\omega} \tag{27}$$

The expression (27) can be brought to (28).

$$\min_x \quad \frac{1}{2}x^THx + F^Tx \tag{28}$$

where H, F y x are given by:

$$H = \begin{bmatrix} \Gamma^T\overline{Q}\Gamma & \Gamma^T\overline{Q}\Lambda_\omega \\ \Lambda_\omega^T\overline{Q}\Gamma & \Lambda_\omega^T\overline{Q}\Lambda_\omega + \overline{R} \end{bmatrix} \tag{29}$$

$$F = \left[\, \tilde{y}^T\overline{Q}\Gamma \;\; \tilde{y}^T\overline{Q}\Lambda_\omega \,\right] \tag{30}$$

$$x = \begin{bmatrix} \hat{x}_{k-N} \\ \tilde{\omega} \end{bmatrix} \tag{31}$$

The solution of the optimization problem can be replaced in (12) and (13) to calculate the estimation value of x_k and y_k. In summary, the steps for performing the estimation with MHE are the follows:

(1) Define the estimation window N with N measurement data known.
(2) Define the covariance matrix R and Q.
(3) Define the matrix B_ω, this is usually choose as B Boulkroune et al. (2010).
(4) Compute Γ, Λ, $\overline{Q}$ and $\overline{R}$.
(5) Compute H and F.
(6) Compute $\hat{x}_{k-N}$ and $\tilde{\omega}$ with the optimization solve.
(7) Compute x_k y y_k.

(8) Return to fifth step, to recalculate F, with the next measurement data.

Solving the problem with the described steps generates the $\hat{y}_k$. This value should be compared with the original data series.

4.2 Simulation results

In this section a comparative study between MHE and Kalman filter (KF) with the Holt-Winters model, and the autoregressive methods is presented. The measured variable is the load and price time series described in Section 2, based on this, the objective is to estimate the states of the Holt-Winters model. The noise matrices described in equation (32) are used to stress the methodology performance.

$$\begin{aligned} w &\sim \mathrm{N}(0, Q) \\ Q &= diag(1 \times 10^5) \\ w_d &\sim \mathrm{N}(0, Q_d) \\ Q_d &= 1 \times 10^2 \\ v &\sim \mathrm{N}(0, R) \\ R &= 1 \times 10^{-3} \end{aligned} \tag{32}$$

Given that the original data is noiseless the measurement noise is considered a small value. This implies the assumption where the model noise is bigger that the measurement $R << Q$. The simulation results are shown in Fig.5 to 7.

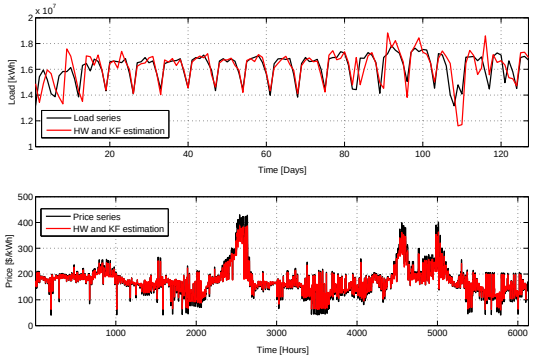

Fig. 5. Holt Winters model with Kalman Filter estimation

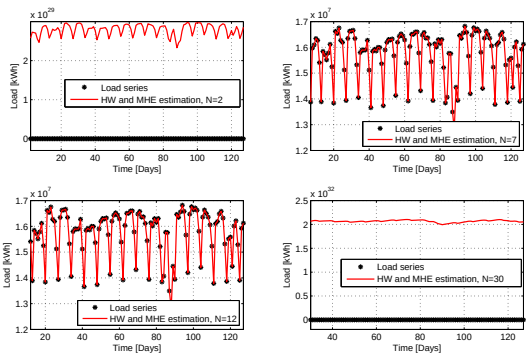

Fig. 6. Holt Winters model with MHE estimation for Load

The obtained results are compared using the mean squared error (MSE) between the estimated series and the original

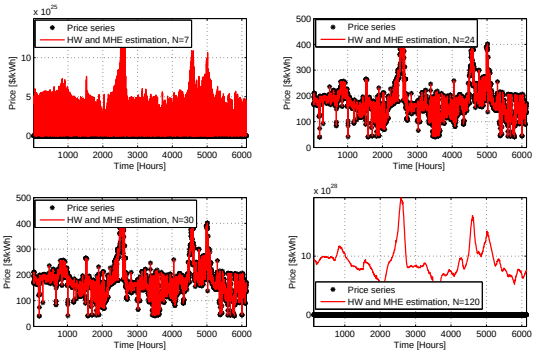

Fig. 7. Holt Winters model with MHE estimation for price

data. The results for all the estimations are shown in Table 2 and 3, in order to validate with traditional methodologies the Kalman Filter and autorregressive methods (ARMA, ARIMA, AR and MA) had been included.

Table 2. MSE for price estimation, with several methods

Estimation series error	
Estimator	**MSE for price**
MHE with $N = 7$	$4,89 \times 10^{25}$
MHE with $N = 24$	$9,15 \times 10^{-14}$
MHE with $N = 50$	$1,04 \times 10^{28}$
MHE with $N = 120$	$9,33 \times 10^{28}$
FK	$30,74$
FKI	$21,14$
MA	$10,82$
AR	$0,9543$
$ARMA$	$3,49 \times 10^4$
$ARIMA$	$0,03$

Table 3. MSE for load estimation, with several methods

Estimation series error	
Estimator	**MSE for load**
MHE with $N = 2$	$2,85 \times 10^{29}$
MHE with $N = 7$	$3,76 \times 10^{-8}$
MHE with $N = 12$	539
MHE with $N = 30$	$2,13 \times 10^{32}$
FK	9.06
FKI	5.87
$MA(q)$	$5,46 \times 10^{10}$
$AR(p)$	$31,33 \times 10^7$
$ARMA$	$2,27 \times 10^{14}$
$ARIMA$	$0,01$

Among the presented methodologies the Holt Winters with MHE presents the smallest estimation error. This happens when the lenght of the estimation window had similar value to the series seasonality. The lenght of the estimation window had a direct impact on the optimization result. This performance is explained by the model structure and the optimization method used. With the proper seasonal values the model captures all the information of the seasonal series. The MHE can replicate the identified cycle in the estimation of the remaining data series cycles. Changes in the seasonal cycles are adjusted in the next estimation, this clearly depends on the estimation window size getting the minimum error if the window size has exactly the seasonality value, if the windows size is different the correction is not optimal. When the window size is smaller than the

seasonal cycle of the series, the lack of complete seasonal data increases the error. Likewise, as the measurement window is larger than the period of the seasonality the setting error cumulates and the performance decreases. Hence it is best to select for this class of systems a horizon of measurement equal to the seasonality of the series, such that the design of the estimator is consistent with the series properties.

5. CONCLUSIONS

This work successfully presented a comparative study between an optimal estimation methodology and traditional tools in order to estimate energy load and price time series in the Colombian market. Based on a consolidated estimation model as Holt-Winters a state space model was proposed allowing to use optimal estimation methodologies to identify the Holt-Winters model states. The methodology was validated comparing the results with Kalman filter, ARMA, AR, MA and ARIMA models. The MHE methodology achieved the minimal estimation error. It is remarkable that the proposed estimation methodology highly depends of the relationship between the time series seasonality and the measurement window size. The proper selection on the estimation window brings to the estimation methodology the ability to compensated the exogenous variables effects in time series.

ACKNOWLEDGEMENTS

This project was supported by Colciencias with the scholarship given to Julián Rendón as a part of the project "Jovenes investigadores" call number 645 the doctoral scholarship of Pablo Deossa call 528.

REFERENCES

Boulkroune, B., Darouach, M., and Zasadzinski, M. (2010). Moving horizon state estimation for linear discrete-time singular systems. *IET Control Theory and Applications*, 4(3), 339–350. doi:10.1049/iet-cta.2008.0280.

Chatfield, C. and Yar, M. (1988). Holt-Winters Forecasting: Some Practical Issues. *Journal of the Royal Statistical Society. Series D (The Statistician)*, 37(2), 129–140. doi:10.2307/2348687.

Gardner Jr., E.S. (2006). Exponential smoothing: The state of the artPart II. *International Journal of Forecasting*, 22(4), 637–666. doi: 10.1016/j.ijforecast.2006.03.005.

Goodwin, P. (2010). The Holt-Winters Approach to Exponential Smoothing: 50 Years Old and Going Strong. *Foresight: The International Journal of Applied Forecasting*, (19), 30–33.

Haghi, H.V. and Tafreshi, S.M. (2007). An overview and verification of electricity price forecasting models. In *Power Engineering Conference, 2007. IPEC 2007. International*, 724–729. IEEE.

Hyndman, R., Koehler, A.B., Ord, J.K., and Snyder, R.D. (2008). *Forecasting with Exponential Smoothing: The State Space Approach*. Springer Science & Business Media.

Krafft, M. and Mantrala, M.K. (2009). *Retailing in the 21st Century: Current and Future Trends*. Springer Science & Business Media.

Montgomery, D.C., Jennings, C.L., and Kulahci, M. (2015). *Introduction to Time Series Analysis and Forecasting*. Wiley, 2nd edition.

Muske, K., Rawlings, J., and Lee, J.H. (1993). Receding Horizon Recursive State Estimation. In *American Control Conference, 1993*, 900–904.

Ng, S. and Perron, P. (1995). Unit Root Tests in ARMA Models with Data-Dependent Methods for the Selection of the Truncation Lag. *Journal of the American Statistical Association*, 90(429), 268–281. doi: 10.1080/01621459.1995.10476510.

Niimura, T. (2006). Forecasting Techniques for Deregulated Electricity Market Prices - Extended Survey. In *Power Systems Conference and Exposition, 2006. PSCE '06. 2006 IEEE PES*, 51–56. doi: 10.1109/PSCE.2006.296248.

Pawlowski, A., Guzman, J., Rodrguez, F., Berenguel, M., and Snchez, J. (2010). Application of time-series methods to disturbance estimation in predictive control problems. In *2010 IEEE International Symposium on Industrial Electronics (ISIE)*, 409–414. doi: 10.1109/ISIE.2010.5637867.

Ramírez, A. (2013). *Métodos utilizados para el pronóstico de demanda de energía eléctrica en sistemas de distribución*. Thesis, Univerdida Tecnolgica de Pereira.

Rao, C.V., Rawlings, J.B., and Lee, J.H. (2001). Constrained linear state estimationa moving horizon approach. *Automatica*, 37(10), 1619–1628. doi: 10.1016/S0005-1098(01)00115-7.

Segura, J.V. and Vercher, E. (2001). A spreadsheet modeling approach to the HoltWinters optimal forecasting. *European Journal of Operational Research*, 131(2), 375–388. doi:10.1016/S0377-2217(00)00062-X.

Singh, A., Ibraheem, I., Khatoon, S., Muazzam, M., and Chaturvedi, D. (2012). Load forecasting techniques and methodologies: A review. In *2012 2nd International Conference on Power, Control and Embedded Systems (ICPCES)*, 1–10. doi:10.1109/ICPCES.2012.6508132.

Snchez, P. and Velsquez, J.D. (2010). Problemas de investigacin en la prediccin de series de tiempo con redes neuronales artificiales.

Suganthi, L. and Samuel, A.A. (2012). Energy models for demand forecastingA review. *Renewable and Sustainable Energy Reviews*, 16(2), 1223–1240. doi: 10.1016/j.rser.2011.08.014.

Valencia, F., Lopez, J., Marquez, A., and Espinosa, J. (2011). Moving horizon estimator for measurement delay compensation in model predictive control schemes. In *2011 50th IEEE Conference on Decision and Control and European Control Conference (CDC-ECC)*, 6678–6683. doi:10.1109/CDC.2011.6161346.

Weron, R. (2014a). Electricity price forecasting: A review of the state-of-the-art with a look into the future. *International Journal of Forecasting*, 30(4), 1030–1081. doi:10.1016/j.ijforecast.2014.08.008.

Weron, R. (2014b). A review of electricity price forecasting: The past, the present and the future. HSC Research Reports HSC/14/02, Hugo Steinhaus Center, Wroclaw University of Technology.

XM (2016). Intelligent Information Management. URL `http://informacioninteligente10.xm.com.co`.

Estrategia Dinámica de Regulación de Voltaje para Convertidores Conmutados

Diego Langarica Córdoba, * **Jesús Leyva Ramos,** **
Luis H. Diaz Saldierna. **

* *CONACYT-Instituto Potosino de Investigación Científica y Tecnológica, San Luis Potosí, México (e-mail: diego.langarica@ipicyt.edu.mx).*
** *Instituto Potosino de Investigación Científica y Tecnológica, San Luis Potosí, México (e-mail: [jleyva,ldiaz]@ipicyt.edu.mx).*

Resumen: El presente trabajo propone un esquema de regulación de voltaje de salida para un convertidor elevador basado en el enfoque de control por modo corriente. La metodología de diseño considera dos lazos de control. El lazo de voltaje conformado por una acción proporcional integral (PI) y el lazo de corriente diseñado a partir del enfoque recursivo "backstepping". Así también, se diseña un estimador de la resistencia de carga considerando la teoría de inmersión e invarianza para mejorar la robustez del lazo de corriente. Como resultado se obtiene una ley de control "backstepping" dinámica adaptable que asegura estabilidad asintótica de un punto de operación con una región de atracción definida. El controlador propuesto es implementado en una plataforma *dSPACE* con el objetivo de regular la operación del convertidor en tiempo real a una potencia nominal de 150 W. Los resultados experimentales muestran una regulación y estimación precisa.

Keywords: Convertidor elevador, "backstepping", inmersión e invarianza.

1. INTRODUCCIÓN

Los sistemas electrónicos de potencia han sido estudiados ampliamente desde la era aeroespacial. Actualmente, ha resurgido un gran interés en los convertidores electrónicos conmutados debido a la adopción de nuevas tecnologías para la generación, transmisión y consumo de energía eléctrica. Como consecuencia, las técnicas tradicionales de operación, análisis y control para los convertidores electrónicos experimentan la incorporación de nuevos enfoques. Dados los requerimientos actuales de desempeño, se ha identificado la necesidad de conjuntar las áreas de electrónica de potencia y control para dar solución a problemas en diferentes aplicaciones como fuentes de alimentación ininterrumpidas, sistemas de iluminación, almacenamiento de energía, generación distribuida, entre otras, Bose (2013).

Existen diversas estrategias de control propuestas en la literatura para dar solución al problema de regulación de voltaje en convertidores de corriente directa a corriente directa (CD-CD). Entre las tradicionales se encuentran control por modo voltaje y por modo corriente (CMC), siendo esta última la que ofrece un mejor desempeño. Así también, existe CMC pico caracterizada por retroalimentar la corriente con rizo y CMC promedio, que filtra o promedia el rizo debido a la conmutación. El enfoque promedio hace uso de dos lazos de control, el externo basado en una acción proporcional integral (PI) y el interno construido mediante un filtro pasabajas y un compensador de alta ganancia, Ortiz-Lopez et al. (2007); Leyva-Ramos and Morales-Saldana (1998); Morales-Saldana et al. (2008, 2007).

Por otro lado, dentro de la literatura de control no lineal se han reportado esquemas de control basado en pasividad usando las formulaciones Euler-Lagrange y sistemas Hamiltonianos controlados por puerto, donde se explotan conceptos como interconexión, inyección de amortiguamiento y moldeado de energía, Ortega et al. (1998); Escobar et al. (1999); Konstantopoulos and Alexandridis (2013); Cisneros et al. (2014). Adicionalmente, estrategias como control adaptable, control por modos deslizantes y control "backstepping" han sido propuestas para el problema de regulación, Sira-Ramirez and Silva-Ortigoza (2006); Seleme et al. (2012); Fadil and Giri (2007).

En particular, este trabajo aborda el enfoque CMC, donde la regulación del voltaje de salida de un convertidor elevador es asegurada mediante dos lazos de control. El lazo de voltaje (externo) que considera una acción PI para generar una señal de referencia, y el lazo de corriente (interno) que utiliza las ideas recursivas de "backstepping" para asegurar la regulación de corriente. Adicionalmente se emplea un estimador de la resistencia de carga para mejorar la robustez del lazo interno. Como resultado, se obtiene una ley de control dinámica adaptable que asegura estabilidad asintótica del punto de operación con una región de atracción definida. Finalmente, el desempeño del sistema en lazo cerrado es evaluado de forma experimental considerando un convertidor operando a una potencia nominal de 150 W y sujeto a variaciones desconocidas de la resistencia de carga.

2. MODELO DEL CONVERTIDOR

La función principal de este convertidor electrónico es elevar el voltaje de salida a un nivel mayor que el voltaje de la fuente. Debido a esta característica, el uso del convertidor elevador se extiende a diversas aplicaciones como; fuentes ininterrumpidas de alimentación, tecnología vehicular, sistemas fotovoltaicos, celdas de combustible de hidrógeno y telecomunicaciones, Mohan et al. (2003), entre otros.

La configuración convencional de este convertidor se muestra en la Fig. 1, donde v_i es el voltaje de entrada, i_L es la corriente promedio del inductor, v_O es el voltaje promedio de salida, u es el ciclo de trabajo (considerado como señal de control), L, C y R denotan el valor de la inductancia, capacitancia y resistencia de carga. Finalmente M es el dispositivo activo de conmutación tipo MOSFET y D un diodo.

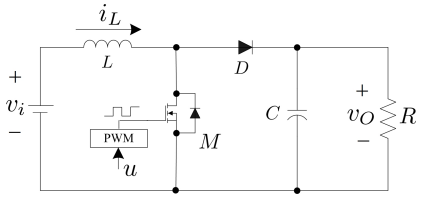

Fig. 1. Configuración convencional de un convertidor elevador.

Al aplicar las leyes de voltaje y corriente de Kirchhoff para ambos casos cuando M se encuentra apagado y encendido, se obtiene el modelo no lineal promediado (libre de rizo) para el diagrama eléctrico de la Fig. 1 como, Ortega et al. (1998); Sira-Ramirez and Silva-Ortigoza (2006)

$$\begin{aligned} \dot{i}_L &= \frac{1}{L}\Big[v_i - (1-u)v_O\Big] \\ \dot{v}_O &= \frac{1}{C}\Big[(1-u)i_L - \frac{v_O}{R}\Big], \end{aligned} \tag{1}$$

donde $[i_L, v_O]^\top \in \mathcal{I} \times \mathcal{V}$, $u \in \mathcal{U}$, con conjuntos definidos por

$$\begin{aligned} \mathcal{I} &:= \{i_L \in \mathbb{R} : 0 < i_{min} < i_L < i_{max}\}, \\ \mathcal{V} &:= \{v_O \in \mathbb{R} : 0 < v_i < v_O < v_{max}\}, \\ \mathcal{U} &:= \{u \in \mathbb{R} : 0 < u < u_{max} < 1\}. \end{aligned}$$

Nótese que las cotas máximas y mínimas se encuentran relacionadas al dimensionamiento físico del convertidor. El modelo (1) se dice que es bilineal, puesto que la señal de control u multiplica directamente a las variables de estado. Este fenómeno es después explotado en la etapa de diseño.

Observación 2.1. El modelo (1) es desarrollado asumiendo las siguientes consideraciones, Bacha et al. (2014); Sira-Ramirez and Silva-Ortigoza (2006).

- El convertidor opera en modo de continuo de conducción (MCC).
- Los dispositivos de conmutación y elementos pasivos son ideales, lo que indica que las perdidas de voltaje por conmutación y resistencias parásitas son despreciadas.
- La fuente de alimentación provee un voltaje constante.
- La carga R es considerada puramente resistiva.

Suposición 2.1. Para propósitos de control, i_L y v_O están disponibles para medición y todos los parámetros son conocidos, excepto la resistencia de carga R.

En la práctica el objetivo final de control es mantener v_O regulado a un valor constante v_{ref} a pesar de las variaciones en la resistencia de carga. Bajo este escenario de regulación, al definir una señal de control constante $u = \bar{u} \in \mathcal{U}$, los puntos de equilibrio de (1) son obtenidos como

$$\begin{aligned} \bar{v}_O &= \frac{v_i}{1-\bar{u}}, \\ \bar{i}_L &= \frac{\bar{v}_O}{R(1-\bar{u})} = \frac{\bar{v}_O^2}{Rv_i}. \end{aligned} \tag{2}$$

Observación 2.2. Para calcular el punto de equilibrio $\bar{i}_L$ es necesario conocer la resistencia de carga R con exactitud; sin embargo, en la práctica esta resistencia presenta variaciones.

Formulación del problema: considere el modelo del convertidor elevador dado por (1) considerando la observación (2.1) y la suposición (2.1). Diseñar, si es posible, una ley de control de retroalimentación de estados dinámica adaptable, tal que el equilibrio en lazo cerrado

$$\mathcal{E} := (\bar{i}_L, \bar{v}_O) \in \mathcal{I} \times \mathcal{V}$$

sea asintóticamente estable y con una región de atracción definida.

3. DISEÑO DEL CONTROLADOR

Este trabajo de investigación aborda el enfoque "backstepping" para asegurar la regulación del voltaje de salida de un convertidor elevador a un valor deseado. Este enfoque recursivo es ampliamente conocido por ofrecer simultáneamente la construcción de una ley de control y una función de Lyapunov, esto para estabilizar asintóticamente el punto de equilibrio de sistemas no lineales con una *forma estricta de retroalimentación*, Khalil (2000); Marquez (2003); Krstić et al. (1995); Sepulchre et al. (1997). Sin embargo, no es posible aplicar directamente esta técnica para estabilizar el modelo (1), ya que este no posee la forma estricta necesaria.

Considerando lo anterior, esta sección muestra como las ideas recursivas de la técnica "backstepping" estándar son consideradas para diseñar una ley de control de retroalimentación de estados con una dinámica definida, que da solución al problema formulado, aun cuando se presentan variaciones en la resistencia de carga. En este sentido, el esquema propuesto, inspirado por el control por modo corriente, hace uso de un lazo de voltaje con acción proporcional integral (PI) para generar una señal de referencia de corriente. Así también, implementa un lazo de corriente diseñado a partir del enfoque recursivo "backstepping", lo que resulta en un controlador con dinámica cero estable en el dominio de interés (vease Fig. 2). Nótese que el control indirecto del voltaje de salida mediante el control de corriente, es un enfoque robusto ante la fase no mínima impuesto por el cero (ubicado en el semiplano derecho complejo) de la función de transferencia $v_O(s)/u(s)$.

La proposición que a continuación se presenta, contiene el resultado principal del trabajo de investigación, esto es, la caracterización de una estrategia de control no lineal multilazo que resuelve el problema formulado para el convertidor elevador.

Proposición 3.1. Considere el convertidor elevador representado por (1) y la suposición 2.1. El controlador no lineal u con dinámica

$$\dot{u} = \frac{1}{\varphi}\Big[\Big(-c_1^2 + (1-u)^2\Big)e_1 - (c_1+c_2)(1-u)e_2 + \\ + (1-u)^2\frac{i_L}{LC} - (1-u)\frac{v_O}{LCR} + \ddot{i}_{ref}\Big] \tag{3}$$

con ganancias $c_1, c_2 > 0$, condición inicial $u(0) = u_0 \in \mathcal{U}$ y señales auxiliares φ, e_1, e_2 y $\ddot{i}_{ref}$ definidas posteriormente en (10), (8), (12) y (6), respectivamente, se encuentra definido y asegura que el punto de equilibrio extendido

$$\mathcal{E}_{ext} := (\bar{i}_L, \bar{v}_O, \bar{u}) \tag{4}$$

sea asintóticamente estable con una región de atracción $\mathcal{R}_a := \mathcal{I} \times \mathcal{V} \times \mathcal{U}$.

Prueba. A continuación, el enunciado anterior se prueba en tres partes, que en su conjunto, detallan completamente el diseño del controlador. Adicionalmente se muestra el diseño del estimador basado en inmersión e invarianza.

Lazo de voltaje

Para comenzar, la señal de referencia de corriente i_{ref} es generada a partir de una acción PI sobre el voltaje de salida v_O y su referencia v_{ref} como sigue (ver Fig. 2)

$$\begin{aligned} i_{ref} :=& \kappa_p\big(v_{ref} - v_O(t)\big) \\ &+ \kappa_i \int_0^t \big(v_{ref} - v_O(\tau)\big)d\tau, \end{aligned} \tag{5}$$

donde $i_{ref} \in \mathcal{I}$, κ_p y κ_i son constantes reales positivas a seleccionar.

Observación 3.1. Algunos trabajos como Ortega et al. (1998); Escobar et al. (1999); Fadil and Giri (2007), generan i_{ref} mediante el calculo en linea de (2), lo cual depende del conocimiento de la resistencia de carga R. Por el otro lado, la expresión en (5) no depende de R y además compensa error en estado estacionario debido a perdidas de conmutación y resistencias parásitas no modeladas.

Consecuentemente, la primera y segunda derivada de i_{ref}, son obtenidas como

$$\begin{aligned} \dot{i}_{ref} &= -\kappa_p\dot{v}_O + \kappa_i(v_{ref} - v_O) \\ \ddot{i}_{ref} &= -\kappa_p\ddot{v}_O - \kappa_i\dot{v}_O, \end{aligned} \tag{6}$$

las cuales son requeridas después por el lazo de corriente. Nótese que la tarea de regulación requerida, no hace uso de las derivadas de v_{ref}, ya que son consideradas iguales a cero.

Observación 3.2. La señal $\dot{v}_O$ en (6) es obtenida a través del cálculo en linea de (1), mientras que la construcción de $\ddot{v}_O$ requiere el conocimiento de $\dot{u}$, esto es,

$$\ddot{v}_O = \frac{1}{C}\Big[(1-u)\dot{i}_L - i_L\dot{u} - \frac{\dot{v}_O}{R}\Big], \tag{7}$$

lo que genera un lazo algebraico en (3), el cual es presentado mas adelante.

Lazo de corriente

Una vez detallado el lazo externo (voltaje), se define ahora el error de regulación de corriente como

$$e_1 := i_{ref} - i_L, \tag{8}$$

donde e_1 es confinado en el conjunto $\mathcal{E}_1 := \{e_1 \in \mathbb{R} : i_{min} - i_{max} < e_1 < i_{max} - i_{min}\} \subset \mathbb{R}$. La derivada en el tiempo de e_1 está dada por

$$\dot{e}_1 = \dot{i}_{ref} - \frac{v_i}{L} + (1-u)\frac{v_O}{L}, \tag{9}$$

donde el término v_O/L actúa como una entrada *virtual* mediante la cual el error de corriente puede ser forzado a cero. En este sentido, es posible definir una ley de control *virtual* con el objetivo particular de linealizar $\dot{e}_1$. Esto último se logra al seleccionar

$$\frac{v_O}{L} = \varphi := \frac{1}{(1-u)}\left(\frac{v_i}{L} - \dot{i}_{ref} - c_1e_1\right), \tag{10}$$

donde c_1 es un número real positivo a seleccionar. Consecuentemente, φ pertenece al conjunto $\Phi := \{\varphi \in \mathbb{R} : 0 < v_i/L < \varphi < v_{max}/L\}$. Por definición u es menor a la unidad; es por esto que (10) no muestra ninguna singularidad. Note que la expresión (10) transforma $\dot{e}_1$ como un sistema lineal invariante en el tiempo de la forma

$$\dot{e}_1 = -c_1e_1, \tag{11}$$

cuya solución converge asintóticamente al origen cuando $t \to \infty$.

Debido a la naturaleza *virtual* de φ, es necesario realizar un paso extra en el diseño, esto es, forzar la convergencia de v_O/L a φ cuando $t \to \infty$. Para este fin, el siguiente error es definido como

$$e_2 := \varphi - \frac{v_O}{L}, \tag{12}$$

donde consistentemente e_2 pertenece al conjunto $\mathcal{E}_2 := \{e_2 \in \mathbb{R} : v_i/L - v_{max}/L < e_2 < v_{max}/L - v_i/L\} \subset \mathbb{R}$. En consecuencia, es ahora posible relacionar el segundo error e_2 a la dinámica del error de corriente $\dot{e}_1$ incorporando v_O/L de la expresión anterior en (9), esto es

$$\dot{e}_1 = \dot{i}_{ref} - \frac{v_i}{L} + (1-u)(\varphi - e_2), \tag{13}$$

y considerando (10), (13) resulta en

$$\dot{e}_1 = -c_1e_1 - (1-u)e_2. \tag{14}$$

Entonces, el comportamiento dinámico de e_2 es calculado como

$$\begin{aligned} \dot{e}_2 &= \dot{\varphi} - \frac{\dot{v}_O}{L} \\ &= \left(\frac{\partial\varphi}{\partial u}\dot{u} + \frac{\partial\varphi}{\partial e_1}\dot{e}_1 + \frac{\partial\varphi}{\partial \dot{i}_{ref}}\ddot{i}_{ref}\right) - \\ &\quad - \frac{1}{LC}\left((1-u)i_L - \frac{v_O}{R}\right), \end{aligned} \tag{15}$$

donde las derivadas parciales quedan definidas como:

$$\frac{\partial\varphi}{\partial u} = \frac{\varphi}{(1-u)} \tag{16}$$

$$\frac{\partial\varphi}{\partial e_1} = \frac{-c_1}{(1-u)} \tag{17}$$

y

$$\frac{\partial\varphi}{\partial \dot{i}_{ref}} = \frac{-1}{(1-u)}. \tag{18}$$

Note que el sistema original (1) es ahora representado por las coordenadas de error $[e_1, e_2]^\top \in \mathcal{E}_1 \times \mathcal{E}_2$ con una dinámica especificada por (14) y (15). Con el objetivo de sintetizar una ley de control u apropiada, se requiere una función de Lyapunov tal que

$$\lim_{t\to\infty} e_1(t) = 0, \quad \lim_{t\to\infty} e_2(t) = 0, \tag{19}$$

lo que finalmente indica que

$$\lim_{t\to\infty} i_L(t) = i_{ref}, \quad \lim_{t\to\infty} v_O(t) = v_{ref}. \tag{20}$$

En este sentido, de acuerdo con (19), se propone una función candidata de Lyapunov $V : \mathcal{E}_1 \times \mathcal{E}_2 \to \mathbb{R}$

$$V := \frac{1}{2}(e_1^2 + e_2^2). \tag{21}$$

Observe que V no es una función radialmente desacotada debido a que e_1 y e_2 están físicamente acotados; en consecuencia solo estabilidad asintótica regional es asegurada. Seguidamente, la derivada en el tiempo de V a lo largo de las trayectoria del sistema (14)-(15) es calculada como

$$\dot{V} = e_1\Big(- c_1 e_1 - (1-u)e_2\Big) + e_2\dot{e}_2. \tag{22}$$

Consecuentemente, si los términos $\pm c_2 e_2^2$ con $c_2 > 0$, son agregados al segundo miembro de la expresión anterior, esta resulta en

$$\dot{V} = -c_1 e_1^2 - c_2 e_2^2 + e_2\Big(- (1-u)e_1 + c_2 e_2 + \dot{e}_2\Big), \tag{23}$$

entonces es evidente que si

$$-(1-u)e_1 + c_2 e_2 + \dot{e}_2 = 0 \tag{24}$$

se cumple en todo instante, entonces $\dot{V}$ es negativa definida y así el origen del sistema (14)-(15) es asintóticamente estable. Esto último se puede asegurar expandiendo (24) con $\dot{e}_2$ dado por (15), lo que resulta en

$$\begin{aligned} &- (1-u)e_1 + c_2 e_2 - \frac{1}{LC}\left((1-u)i_L - \frac{v_O}{R}\right) + \\ &+ \left(\frac{\partial\varphi}{\partial u}\dot{u} + \frac{\partial\varphi}{\partial e_1}\dot{e}_1 + \frac{\partial\varphi}{\partial \dot{i}_{ref}}\ddot{i}_{ref}\right) = 0; \end{aligned} \tag{25}$$

por lo tanto, al usar (16)-(18), resolver (25) para $\dot{u}$ y después manipular algebraicamente, la ecuación dinámica del controlador es obtenida como

$$\begin{aligned} \dot{u} = \frac{1}{\varphi}\Big[&\Big(- c_1^2 + (1-u)^2\Big)e_1 - (c_1 + c_2)(1-u)e_2 + \\ &+ (1-u)^2\frac{i_L}{LC} - (1-u)\frac{v_O}{LCR} + \ddot{i}_{ref}\Big]. \end{aligned} \tag{26}$$

Nótese que (26) presenta un lazo algebraico en $\ddot{i}_{ref}$, que requiere de una solución para implementar la ley de control (26) satisfactoriamente. Es por esto que, al substituir $\ddot{i}_{ref}$ de (6), $\ddot{v}_O$ de (7) en (26) y resolviendo para $\dot{u}$ resulta en la expresión explícita de la dinámica del controlador

$$\begin{aligned} \dot{u} = \frac{1}{1 - \frac{\kappa_p i_L}{C\varphi}}\Bigg(&\frac{1}{\varphi}\Big[\Big(- c_1^2 + (1-u)^2\Big)e_1 \\ &- (c_1 + c_2)(1-u)e_2 + (1-u)^2\frac{i_L}{LC} - (1-u)\frac{v_O}{LCR} \\ &- \kappa_i\dot{v}_O - \frac{\kappa_p}{C}\Big[(1-u)\dot{i}_L - \frac{\dot{v}_O}{R}\Big]\Big]\Bigg), \end{aligned} \tag{27}$$

y debido a que φ es siempre positiva, no existe singularidad alguna en (27) si

$$1 - \frac{\kappa_p i_L}{C\varphi} \neq 0, \tag{28}$$

se cumple para todo tiempo. En el punto $\mathcal{E}_{ext} := (\bar{i}_L, \bar{v}_O, \bar{u})$, φ es igual a $v_i/L(1-\bar{u})$, y la última condición (28) es satisfecha si la ganancia de control es seleccionada tal que

$$\kappa_p \neq \frac{Cv_i}{L(1-\bar{u})\bar{i}_L}, \tag{29}$$

donde al considerar (2), (29) se reescribe como

$$\kappa_p \neq \frac{RCv_i}{L\bar{v}_O}. \tag{30}$$

De este último enunciado, se concluye que si κ_P es seleccionada tal que la restriccion en (30) es satisfecha, (26) se encuentra bien definida en $\mathcal{E}_{ext}$, y por continuidad también definida en una vecindad de $\mathcal{E}_{ext}$.

Dinámica cero

Al considerar que $e_1 = e_2 = 0$, entonces implica que $i_L = i_{ref}$ y $v_O = v_{ref}$; por lo que $\dot{i}_{ref} = \ddot{i}_{ref} = 0$, y consecuentemente el controlador adquiere la forma

$$\dot{u} = \frac{(1-u)}{v_i}\left[(1-u)^2\frac{i_{ref}}{C} - (1-u)\frac{v_{ref}}{CR}\right]. \tag{31}$$

De (31), se encuentran tres puntos de equilibrio si $v_{ref} = \bar{v}_O$, $i_{ref} = \bar{i}_L$ y (2) es considerado, estos son

$$\begin{aligned} \bar{u}_{1,2} &= 1 \pm \frac{v_i}{\bar{v}_O}, \\ \bar{u}_3 &= 1. \end{aligned} \tag{32}$$

Observe que el único punto de equilibrio con significado físico es $\bar{u}_2 = 1 - v_i/\bar{v}_O$. Adicionalmente, ya que $(1-\bar{u}_2)^2 = v_i/R\bar{i}_L$ y después de una manipulación algebraica, (31) se puede representar por

$$\dot{u} = \frac{1}{RC}\left[\frac{(1-u)^3}{(1-\bar{u}_2)^2} - (1-u)\right]. \tag{33}$$

Finalmente, alrededor de $\bar{u}_2$, la expresión anterior puede ser aproximada linealmente por

$$\dot{u} = \frac{-2}{RC}(u - \bar{u}_2), \tag{34}$$

donde es demostrado que u converge asintóticamente a $\bar{u}_2$ cuando $t \to \infty$. Esto último establece que el punto de equilibrio extendido en las coordenadas del error

$$\mathcal{E}_e := (0, 0, \bar{u}) \tag{35}$$

es asintóticamente estable con una región de atracción $\mathcal{R}_e := \mathcal{E}_1 \times \mathcal{E}_2 \times \mathcal{U}$, que a su vez puede ser traducida como $\mathcal{R}_a := \mathcal{I} \times \mathcal{V} \times \mathcal{U}$.

■

Ley de adaptación

La sección anterior detalla los dos lazos de control; *i)* el lazo de voltaje basado en una acción PI, el cual por naturaleza es robusto ante variaciones de la resistencia de carga y *ii)* el lazo de corriente, el cual requiere conocer del valor de R. Con la intención de mejorar la robustez de este último lazo, se propone estimar la resistencia de carga R utilizando la teoría de inmersión e invarianza, Astolfi

et al. (2008). Este enfoque ha sido ampliamente reportado para dar solución a problemas de observación y estimación, Langarica-Córdoba et al. (2015); Langarica Córdoba and Ortega (2015), ya que estas dos tareas (según la teoría) se componen por una parte integral y otra proporcional. A continuación se muestra el desarrollo de dicho esquema de estimación.

Para comenzar, se considera $\theta = 1/R$ como un parámetro desconocido del sistema (1), por lo que la dinámica del voltaje de salida se reescribe como

$$\dot{v}_O = \frac{1}{C}(1-u)i_L - \frac{1}{C}\theta v_O. \tag{36}$$

Es ahora que se define el error de estimación de θ como

$$z = \hat{\theta} - \theta, \tag{37}$$

donde $\hat{\theta}$ es conformado por una parte integral ξ y una proporcional $\eta(V_O)$, esto es

$$\hat{\theta} = \xi + \eta(V_O). \tag{38}$$

Si se asume que θ es un parámetro desconocido pero constante, la derivada en el tiempo del error de estimación (37) queda

$$\begin{aligned} \dot{z} &= \dot{\xi} + \frac{\partial \eta}{\partial v_O}\dot{v}_O \\ &= \dot{\xi} + \frac{1}{C}\frac{\partial \eta}{\partial v_O}\Big((1-u)i_L - \theta v_O\Big). \end{aligned} \tag{39}$$

De (37), se sabe que $\theta = \hat{\theta} - z$, entonces (39) resulta en

$$\dot{z} = \dot{\xi} + \frac{1}{C}\frac{\partial \eta}{\partial v_O}\Big((1-u)i_L - (\xi + \eta(v_O) - z)v_O\Big). \tag{40}$$

Al separar (40) con respecto a la variable de error z, se halla

$$\begin{aligned} \dot{z} = \dot{\xi} &+ \frac{1}{C}\frac{\partial \eta}{\partial v_O}\Big((1-u)i_L - (\xi + \eta(v_O))v_O\Big) \\ &+ \frac{1}{C}\frac{\partial \eta}{\partial v_O} z v_O, \end{aligned} \tag{41}$$

por lo que la ley de adaptación es seleccionada como

$$\dot{\xi} = -\frac{1}{C}\frac{\partial \eta}{\partial v_O}\Big((1-u)i_L - (\xi + \eta(v_O))v_O\Big), \tag{42}$$

tal que la dinámica del error de estimación es transformada en

$$\dot{z} = \frac{1}{C}\frac{\partial \eta}{\partial V_O} V_O z. \tag{43}$$

Entonces, si $\eta(v_O) = -C\sigma v_O$, con $\sigma > 0$, resulta en

$$\frac{\partial \eta}{\partial V_O} = -C\sigma, \tag{44}$$

y la expresión (43) es simplificada como

$$\dot{z} = -\sigma v_O z. \tag{45}$$

Ya que v_O por definición es siempre positiva, entonces se puede decir que $z(t) \to 0$ cuando $t \to \infty$ y por consecuencia $\theta = \hat{\theta}$. Note que esta estimación es usada por el lazo de corriente en las expresiones (6) y (27).

Finamente, el diagrama a bloques del sistema en lazo cerrado es ilustrado en la Fig. 2, donde se identifican los dos lazos de control y el estimador con sus interconexiones.

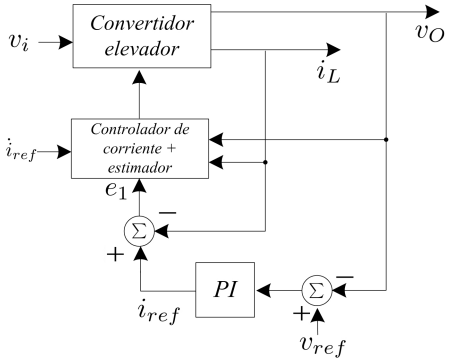

Fig. 2. Diagrama a bloques del sistema en lazo cerrado.

4. RESULTADOS EXPERIMENTALES

El desempeño de la ley de control (27) en lazo cerrado con el convertidor mostrado en la Fig. 3 es evaluado en tiempo real utilizando una plataforma de adquisición de datos DSPACE-ds1104 con un tiempo de muestreo de 25 μs. En este caso, ambas ganancias de los sensores de corriente (GSC) y voltaje (GSV) son iguales a 0.2. Así también, las frecuencias de corte de los filtros pasa bajas se escogieron de 1 kHz. La frecuencia de conmutación del circuito PWM f_s es 75 kHz con una señal diente de sierra de 10 V pico a pico. El voltaje de entrada es $v_i = 12$ V y el voltaje nominal deseado es $v_{ref} = 24$ V. La Tabla 1 conjunta todos componentes del convertidor junto con las ganancias de control utilizadas. Note que κ_p es seleccionada considerando la restricción (30).

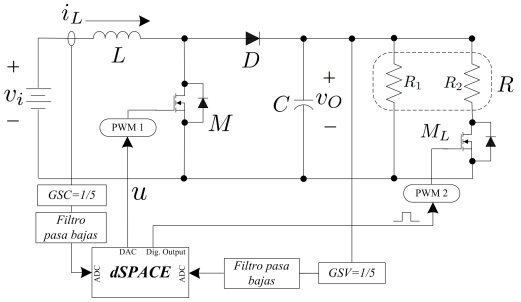

Fig. 3. Configuración experimental del sistema.

Tabla 1. Componentes del convertidor y parámetros de control.

Elemento	Valor
Capacitor C	518 μF
Inductor L	40 μH
Carga nominal R	4.1 Ω
Resistencia R_1	8.5 Ω
Resistencia R_2	8.1 Ω
MOSFET M	IRFP4468
MOSFET M_L	IRFP4232
Diodo D	SBL3045PT
Ganancia c_1	20×10^3
Ganancia c_2	35×10^3
Ganancia κ_p	6
Ganancia κ_i	1500

Para evaluar de forma experimental el desempeño del controlador bajo la tarea de regulación, variaciones en la resistencia de carga son inducidas al sistema al activar el MOSFET M_L, esto es

$$R = \begin{cases} R_1 || R_2 = 4.1\ \Omega, & \text{cuando } M_L \text{ está encendido} \\ R_1 = 8.5\ \Omega, & \text{cuando } M_L \text{ está apagado.} \end{cases} \quad (46)$$

Estas variaciones se efectúan a una razón de 2.5 Hz. Se observa que el controlador propuesto asegura la regulación de v_O a un valor fijo de 24 V, a pesar de cambios repentinos en la carga (Fig. 4a). Es notable, que en menos de 0.02 segundos después del cambio de carga, v_O regresa al valor nominal de 24 V con ligeros sobretiros. Una regulación apropiada de la corriente del inductor es observada en la Fig. 4b donde se muestra una variación de 12.5 A a 5 A, que corresponde a una potencia de salida nominal de 150 W y de 67 W, respectivamente. Simultáneamente la señal de control en Fig. 4c muestra una correcta compensación a los cambios de carga, ya que u es cercana al 50% para carga nominal y después se ajusta a 48% sin mostrar saturación alguna. En la Fig. 4d se muestra el comportamiento de las señales auxiliares v_O/L y φ, asociadas al error e_2. Finalmente se muestra una estimación apropiada de la resistencia de carga en la Fig. 4d. Esto último comprueba experimentalmente la naturaleza adaptable de la estrategia de control con respecto a variaciones desconocidas de la resistencia de carga.

5. CONCLUSIONES

Este artículo detalla explícitamente una estrategia de control para convertidores elevadores. La metodología de diseño se basa principalmente en la construcción de dos lazos de control, esto en concordancia con el enfoque de control por modo corriente. Primeramente, se diseña un lazo de voltaje basado en una acción PI para la reducción del error en estado estacionario, y después un lazo de regulación de corriente de tipo "backstepping" dinámico es propuesto. Este último lazo hace uso de una estimación de la resistencia de carga mediante el enfoque de inmersión e invarianza. Como resultado final, se propone un controlador dinámico adaptable con una región de atracción definida, lo que asegura la estabilidad asintótica del punto de operación dado. El desempeño del esquema es evaluado de forma experimental considerando cambios abruptos en la resistencia de carga. Dicho resultado exhibe una regulación del voltaje de salida y una estimación de la carga precisa. Actualmente se trabaja sobre la aplicación de este esquema a otros convertidores de CD-CD, incorporando tanto la dinámica de la fuente de entrada como incertidumbres paramétricas.

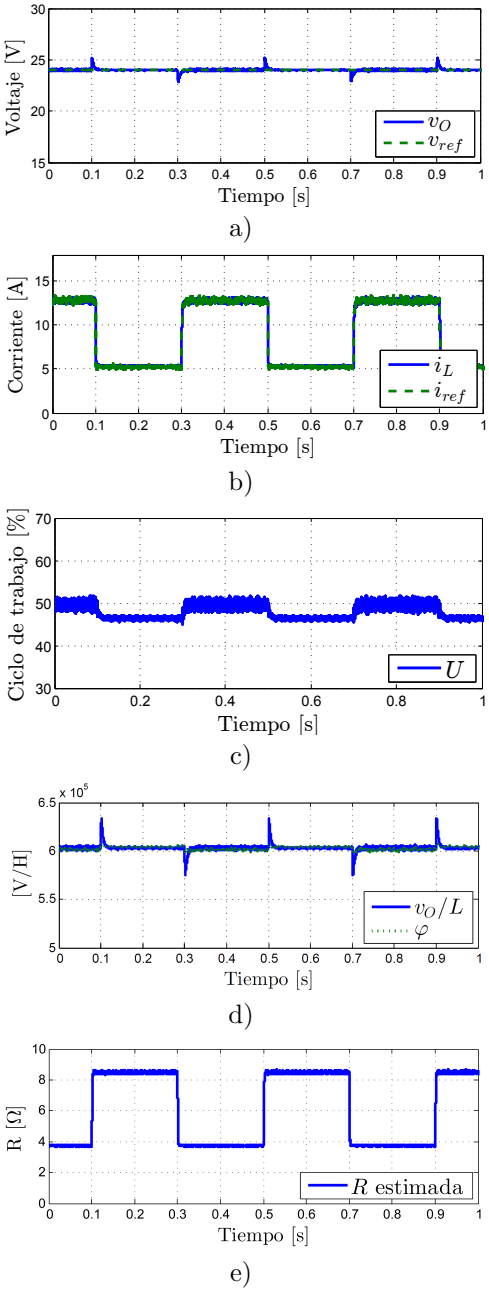

Fig. 4. Resultados experimentales. a) Regulación de voltaje, b) Regulación de corriente, c) Señal de control, d) Señal virtual φ y e) Estimación de R.

REFERENCIAS

Astolfi, A., Karagiannis, D., and Ortega, R. (2008). *Nonlinear and Adaptive Control with Applications*. Springer.

Bacha, S., Munteanu, I., and Bratcu, A.I. (2014). *Power Electronic Converters Modeling and Control: With cases Studies*. Springer.

Bose, B.K. (2013). Global energy scenario and impact of power electronics in 21st century. *IEEE Transactions on Industrial Electronics*, 60(7), 2638–2651. doi: 10.1109/TIE.2012.2203771.

Cisneros, R., Ortega, R., Pirro, M., Ippoliti, G., Bergna, G., and Cabrera, M.M. (2014). Global tracking passivity-based pi control for power converters: An application to the boost and modular multilevel converters. In *2014 IEEE 23rd International Symposium on Industrial Electronics (ISIE)*, 1359–1365. doi: 10.1109/ISIE.2014.6864812.

Escobar, G., Ortega, R., Sira-Ramirez, H., Vilain, J.P., and Zein, I. (1999). An experimental comparison of several nonlinear controllers for power converters. *IEEE Control Systems*, 19(1), 66–82. doi:10.1109/37.745771.

Fadil, H.E. and Giri, F. (2007). Backstepping based control of pwm dc-dc boost power converters. In *2007 IEEE International Symposium on Industrial Electronics*, 395–400. doi:10.1109/ISIE.2007.4374630.

Khalil, H. (2000). *Nonlinear Systems*. Prentice-Hall.

Konstantopoulos, G.C. and Alexandridis, A.T. (2013). Non-linear voltage regulator design for dc/dc boost converters used in photovoltaic applications: analysis and experimental results. *IET Renewable Power Generation*,

7(3), 296–308. doi:10.1049/iet-rpg.2012.0068.

Krstić, M., Kanellakopoulos, I., and Kokotović, P. (1995). *Nonlinear and Adaptive Control Design*. John Wiley & and Sons.

Langarica Córdoba, D. and Ortega, R. (2015). An observer–based scheme for decentralized stabilization of large-scale systems with application to power systems. *Asian Journal of Control*, 17(1), 124–132.

Langarica-Córdoba, D., Ortega, R., and Casagrande, D. (2015). Transient stabilization of multimachine power systems: Towards a global decentralized solution. *European Journal of Control*, 26, 44 – 52.

Leyva-Ramos, J. and Morales-Saldana, J.A. (1998). A design criteria for the current gain in current-programmed regulators. *IEEE Transactions on Industrial Electronics*, 45(4), 568–573. doi:10.1109/41.704883.

Marquez, H. (2003). *Nonlinear Control Systems*. Wiley.

Mohan, N., Undeland, T.M., and Robbins, W.P. (2003). *Power Electronics: Converters, Applications, and Design, 3rd Edition*. John Wiley & Sons.

Morales-Saldana, J.A., Galarza-Quirino, R., Leyva-Ramos, J., e. Carbajal-Gutierrez, E., and g. Ortiz-Lopez, M. (2007). Multiloop controller design for a quadratic boost converter. *IET Electric Power Applications*, 1(3), 362–367. doi:10.1049/iet-epa:20060426.

Morales-Saldana, J.A., Leyva-Ramos, J., Carbajal-Gutierrez, E.E., and Ortiz-Lopez, M.G. (2008). Average current-mode control scheme for a quadratic buck converter with a single switch. *IEEE Transactions on Power Electronics*, 23(1), 485–490. doi:10.1109/TPEL.2007.910907.

Ortega, R., Loría, J., Nicklasson, P., and Sira-Ramirez, H. (1998). *Passivity-based Control of Euler-Lagrange Systems:Mechanical, Electrical and Electromechanical Applications*. Springer.

Ortiz-Lopez, M.G., Leyva-Ramos, J., Diaz-Saldierna, L.H., Garcia-Ibarra, J.M., and Carbajal-Gutierrez, E.E. (2007). Current-mode control for a quadratic boost converter with a single switch. In *2007 IEEE Power Electronics Specialists Conference*, 2652–2657. doi:10.1109/PESC.2007.4342436.

Seleme, S.I., Rosa, A.H.R., Morais, L.M.F., Donoso-Garcia, P.F., and Cortizo, P.C. (2012). Evaluation of adaptive passivity-based controller for power factor correction using a boost converter. *IET Control Theory Applications*, 6(14), 2168–2178. doi:10.1049/iet-cta.2011.0218.

Sepulchre, R., Jankovic, M., and Kokotovic, P.V. (1997). *Constructive Nonlinear Control*. Springer.

Sira-Ramirez, H. and Silva-Ortigoza, R. (2006). *Control Design Techniques in Power Electronics Devices*. Springer.

Load Balancing System to Low Voltage Grid using Petri Nets ⋆

Sicchar J. R * **Silva J. R** ** **Costa C. T., Jr.** ***

* *Control Automation Depart.,Technology High College,Amazonas State University,1200 Darcy Vargas Av, CEP 69050-020, Manaus,AM,Brazil (e-mail: jvilchez@ uea.edu.br).*
** *University of São Paulo, 2231 Prof. Melo Morais Av, CEP 5508-9000, Butantã,SP,Brazil (e-mail: reinaldor@usp.br)*
*** *ITEC, Electrical Engineering Department,Federal University of Pará, Belém,PA,Brazil, (e-mail: cartav@sufpa.br)*

Abstract: Current advances of smart grids are causing a demand for new operations and services, specially to the low voltage consumers grid. Among these processes,load balancing has a prominent capability for ensuring stable states between feeders. This paper presents some results about the design of an automated process to load balancing feeders in final consumption units of a small urban smart grid using a timed sliced Hierarchical Petri net. The main objective is to analyze the proposed system and establish an efficient and reliable workflow to automate load balancing and ensure stability while minimizes intervention. As a result it improves the quality of power service to the low voltage final consumers.

Keywords: Smart Grids,Load Balancing,Timed Hierarchical Petri Nets,Final Consumption Units.

1. INTRODUCTION

The perspective of having urban smart grids became closer since new approaches were developed relying in small urban smart grid (SUSG), Shahgoshtasbi (2014) or even to mix with the legacy system centered in hydro-power in what concerns low voltage (LV) units.

In this context, load balance feeders is an important issue to the quality of energy providing service, and several direct algorithms were proposed, Shahnia et al. (2014), Sharma et al. (2014), Sicchar et al. (2015) which should now be arranged in an automated process. These "hybrid algorithms" are in fact focused on distributed energy consumption management system (EMS). Thereby forming functional flow for automated processes within SG vision, Huang et al. (2015). Its extends energy consumption management until the final consumer units in LV circuits. Where among others services, are offered the voltage stability evaluation and the load balance for for residential feeders,Sicchar et al. (2015).

In a special way, it is observed that some consumer units loads, cause imbalance between feeders in LV grid. Then, identifying a problem that affects state equilibrium feeders grid, and energy quality supplied caused by power and electrical current cause imbalances among feeders,Sharma et al. (2014).Currently, some possibles alternatives like identification and minimization of losses are being developed as Automatic Feeders Reconfiguration (AFR). It is applied in LV grid and identifies some power losses, load imbalance and switches final consumers feeders between grid feeders,Siti et al. (2011), Shahnia et al. (2014).

However, previously alternatives mentioned show a wide gap in formal modeling for load balancing system design. This does not present a formal workflow validation for the AFR process,Alt et al. (2006), Wang (2015).For this reason, we indicated as an hypothesis: Petri nets (PN) can be used into balancing process performance in LV grid.That is, by formal modeling system is possible to obtain some process that improves load balancing efficiency. At where algorithms form a system and service that supporting the final consumers.

This system also have a supervision an information systems for maintaining the LV system (but are not addressed in this work). Which managed the demand of energy consumption. Petri nets, represent in this work the structure and system architecture and workflow tasks and control in system.

This article, explains in second section background related in Petri nets definitions and the scientific review in automatic feeders reconfiguration; in third section presents a proposal to the DPMS system model; in fourth section shows proposed algorithm design in PN; in the fifth section shows design analysis and validation based on the operational flow performance followed by its respective discussion; finally, last section presents the conclusion and and points to future work lines.

2. BACKGROUND

In this section, we put background in specific review related load balancing algorithms development in LV grid.

⋆ Author José R. Sicchar, thanks to FAPEAM and Amazon State University. Author Da Costa C.T.Jr.,thanks to Federal University of Pará.

Then, we have also review about PN use in SG. It will addressed, some specific definitions of PN that will be important for the development of this proposal.

2.1 Review Stage

As load balancing method within AFR context, we first can mention the transfers overload concentrated method (losses and loads) into specific feeder, working from three-phase final consumption units. This method, is based on minimizing current consumption achieved by *Fuzzy* machine inference and *Newton-Rhampsom's* optimization algorithm, between power consumption and power variation in each feeder,Siti et al. (2011).

Another method, focused only on single-phase final consumption units, minimizing power and voltage consumption use an hybrid genetic algorithm. In this case, also taking up load transfer but reconnecting single-phase consumers in same feeder in grid, with lower load level,Shahnia et al. (2014).

We can also mention, the hybrid load consumption algorithm model for final consumption units in LV grids,based on the Unified Modeling Language (UML)-PN paradigm, Sicchar et al. (2011). Which connects data acquisition, classification, programming and consumption forecast, and sending best selection for arrangement switching feeders in load balancing.

In currently article, We will continue load balancing in final consumption units feeders model but, based on hierarchical PN paradigm, using balancing diagnostic,current and load consumption prediction, minimization consumption and optimal arrangement sequence selection flow algorithms as hierarchical sub-processes in main PN.

Thereby, contributing with efficient process in load balancing, which can be used as an alternative method and/or interface in existent LV grid, or as support process in supervision center of a small urban smart grid (SUSG).

2.2 Definitions

- *Definition 2.2.1.Petri Net.*A Petri net structure is a directed weighted bipartite graph,according " (1)",Silva (2012):

$$N = (P, T, A, w). \tag{1}$$

where: "P" is the finite set of places,$P \neq \emptyset$. "T" is the finite set of transitions, T$\neq \emptyset$."A"$\subseteq$(PxT)$\cup$(TxP) is the set of arcs from places to transitions and from transitions to places."w":A $\rightarrow$ {1,2,3,$\cdots$} is the weight function on the arcs. where: "P" is the finite set of places,$P \neq \emptyset$. "T" is the finite set of transitions, T$\neq \emptyset$."A"$\subseteq$(PxT)$\cup$(TxP) is the set of arcs from places to transitions and from transitions to places."w":A $\rightarrow$ {1,2,3,$\cdots$} is the weight function on the arcs.
- *Definition 2.2.2. Timed Petri Net.*Defined by "(2)",Silva (2012):

$$N = (P, T, A, w, M0, f). \tag{2}$$

where: (P, T, A,w,$M0$) is a marked Petri net, Silva (2012),"f": T$\rightarrow$R$^+$ is a firing time function that assigns a positive real number to each transition on the net.
- *Definition 2.2.3. Hierarchical Petri net by Place Bounded Substitution.*In a PN structure give by "(3)",Silva (2012):

$$N = (P, T, F). \tag{3}$$

There is, an Y sub-net which limited by place so the replacement of this Y sub-net, generates another net $N' = (P', T', F')$, where: i) P'= $P \setminus T \cup \{S_y\}$, S_y is the new element that replaces Y; ii) T'=$T \setminus Y$;iii)F'=$F \setminus$Int(Y),Int(Y)is the inner Y arcs set, Silva (2012).

3. PROPOSAL

According, of hypothesis and the opportunity to improvement the load balancing process in the current structure of the LV distribution grid. We propose in this article: modeling an intelligent process for load feeder balancing in final consumption units using a Timed Hierarchical Petri Net (THPN), in order to obtain reliably and efficiently workflow, formally validated.

In fact, this process is based on algorithms of artificial intelligence as fuzzy logic and optimization systems; and also forecast algorithms based on stochastic process as Markov chains,Sicchar et al. (2015).

The contribution of the validated model, could be useful in reshaping modernization of the existing LV distribution grid structure (legacy system). It can be used as the implementation of a specific service in the process of automatic feeders reconfiguration in final consumption consumer units, within the scope of small urban smart grid.

Through hierarchical PN will be performed validation system design including its inner sub-processes,that make feeders reconfiguration system, called "**DPMS**". Which is explained in following sub-section.Similarly, use of Timed transitions in proposal model are intended to represent the most realistic way possible an entire period by simulation processing system, for consumer units feeders balancing.

In this particular case, takes a granular period of 60 minutes, i.e., seeking feeder reconfiguration lasting one hour, depending on sample consumption obtained at 10 minute intervals derived from real-time measurement, in the case of a SUSG. Thus, it is not covered in this case, the load balancing flow in existing secondary grid, which is the subject of future work.

In this article, will be developed according to initial proposal of the authors,Sicchar et al. (2011) however having a contribution a broad and integrated PN with hierarchical description of its sub-process. It will be based on the system developed to consumer units energy consumption diagnose,Sicchar et al. (2015) but now considering beyond imbalance diagnostic and consumption forecasting stage, more two stages: minimizing current consumption and switching sequence selection.

3.1 DPMS Architecture

The process system, is called "**DPMS**" because of its four stages or sub-processes:"Diagnose", "Prevision", "Minimization" and "Selection", each with a specific algorithm. So, these formed the DPMS system.

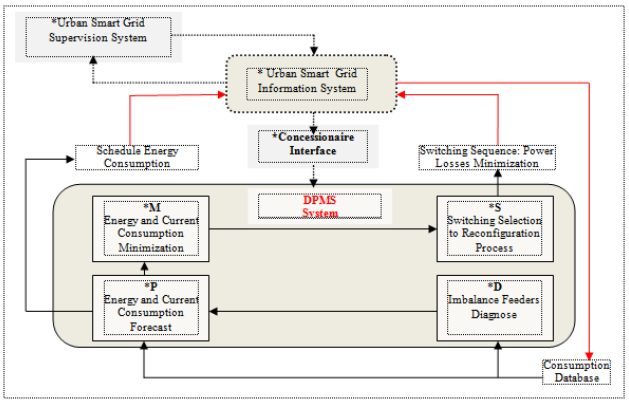

Fig. 1. DPMS Architecture

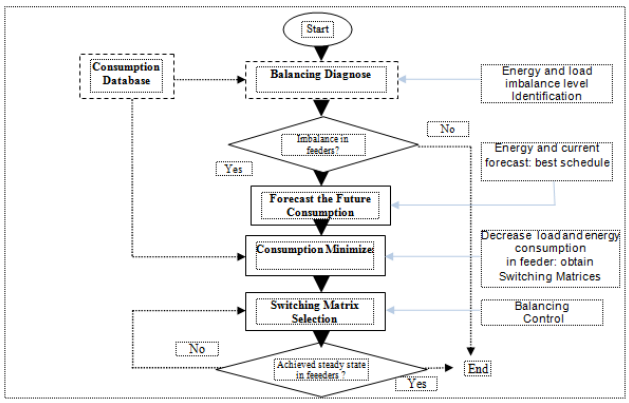

Fig. 2. DPMS Flowchart

Thus, the DPMS system has an architecture formed as mentioned above, four specific processing (whose specific algorithms are not covered in this article):

- Balancing Diagnose or only "**D**" stage, that identifies the imbalance level in each feeder, Watching two situations: "balanced feeder", thus having the algorithm operating finish; and "unbalanced feeder" that activates the remaining stages of system, in sequence, starting with the consumption forecast step.
- Prevision Consumption or simply "**P**" stage, which only is activate when an imbalance is identified (in some feeder). It forecasts the current and energy consumption in feeders and returning this processing to the SG information system, that later develops the energy future consumption matrix indicating the trend of consumption to the final consumers.
- Minimization Consumption or just "**M**" stage, which procedure some combination of switching between feeders from the current and the future consumption of the energy and electrical current obtained by "P" stage, in order to minimize power losses effects and ensuring the equilibrium state in feeders.
- Switchin Sequence or only "**S**" stage. Which chooses the best switching combination from the "M" stage.
  This, selection is based on a correlation ratio analysis between the real value of consumption and with their values from the minimization stage.The final processing is sent to the information system SG as switching sequence, to procedure in fact the AFR.

In Fig. 1 we can see the DPMS architecture system model. It can be seen as a support process for system information to supervision center in SUSG environment.It can also be inserted, as an interface in the existing secondary grid system.

Then, we have the operation flow of the DPMS system. Which is shown in more details in Fig. 2. This flow, is started from consumption data processing, and after consumption diagnosis are identified possible losses and load imbalances.

In positive case, starts energy and current consumption prediction process, in each final consumer feeder. The main objective is to obtain,the future consumption matrix of electrical current.Furthermore, the prediction results serve to minimizing consumption process.

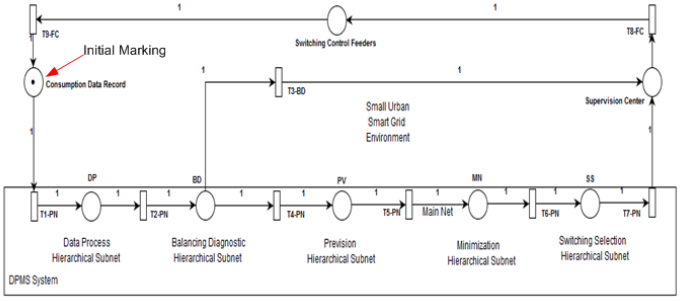

Fig. 3. DPMS THPN:Main Petri net

Followed by minimize consumption, looking for same sequences combinations of switching between feeders. Which are calculated from current and future values of electrical current consumption.

Finally, switching matrix selection chooses which through, send best combination for final consumer feeders balancing implementation. If imbalance minimizing process ends, otherwise proceeds in choosing other combinations for switching.

4. DPMS SYSTEM IN PETRI NETS

In Fig. 3 it is shown the "DPMS" system modeling in THPN. It describes the main PN of DPMS system. The hierarchical extension used is place bounded substitution (PBS) according to definition 2.2.3, being indicated with red arrow, the initial state "S0".

The inner workflow of DPMS system is formed as follows (see Fig.5):

- "**DP**".Data Process Hierarchical subnet.Which has all statistical treatmen sub-processes.It is formed by:"L_1-DP",that classifies power, current and energy consumption data."L_2-DP",which calculates average consumption."L_3-DP", that forms discrete consumption states.
- "**BD**".Balancing Diagnose Hierarchical subnet. Which has all consumption diagnose inference sub-processes. Which is represented by "L_4-BD", a PBS place that representing the inference machine design: load and energy consumption as input variables in inference system; load and energy consumption variation as

input variable; current consumption as output variable; the inference rules. And the output variable that obtain conditions to imbalance diagnose. In this work will not be covered in detail this sub-process. **BD** exit has two conditions: (final consumption unit) FCU balanced "T_9-BD"and, No balanced FCU "T_{10}-PN" that actives **PV** place.

- "**PV**".Prevision Hierarchical subnet, with electrical forecast current consumption sub-processes. It is formed by:"L_5-PV",which inserts discrete states consumption. "L_6-PV"that calculates incidences consumption. "L_7-PV", which obtain transition matrix. "L_8-PV",that obtain forecast electrical current consumption.
- "**MN**". Minimization Hierarchical subnet.It is formed by:"L_9-MN",which inserts measured electric current vector."L_{10}-MN",that inserts forecast current vector."L_{11}-MN", which forms minimization consumption vector."L_{12}-MN", that inserts minimization consumption formula."L_{13}-MN" which obtain arrangement switching matrices.
- "**SS**".Switching Selection Hierarchical subnet. Which has all switching selection inference sub-processes. Which is represented by "L_{18}-SS", a PBS place that representing the inference machine design. In this work is represented in detail the design of SS subprocess in section 5.3. After, this flow goes to supervision center (CS), and then feeder switching control (FC). The process goes through a measurement by data measurement (DM), whose flow is transferred as consumption data record (CDR).

5. RESULTS-VALIDATION ANALYSIS

In this section,we will show the validation results of DPMS system, modeled in THPN,using reachability graph, invariant analysis applied in Main DPSN THPN and also in Hierarchical DPMS THPN which shown all processes of system and also use siphon and traps analysis for validation workflow. For experimental results, was used as tool a free version of Pipe 4.3.0.

For simulation, timed transitions were used. It is distributed fixed time intervals, for each operation of subprocess,it was used T = 10 seconds,and for total integration operations add up to a full period of T = 60 seconds.

5.1 Main DPMS THPN validation

a) Reachability Graph. The Main DPMS Reachability graph is shown in Fig. 4. So, it represents the PN reachable diagram obtained from Its initial state "S0" highlighted in black, that also represents initial marking of PN.

Through Main DPMS simulation, if verifies that does not exist deadlock.However, checking a possible conflict highlighted with a black arrow on "S2" **BD** place output, between transitions "T_3-BD" and "T_4-PN", due to balancing result that evaluates two conditions: balanced FCU or unbalanced FCU. However, this "conflict", will not be controlled due to consider a random order in system simulation when it executes balancing feeders analysis.

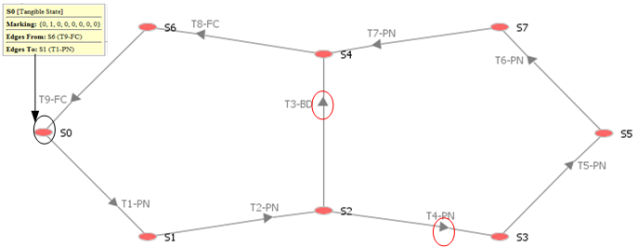

Fig. 4. Main DPMS Reachability Graph

b) Invariants Analysis. Still looking for reachability graph, we note that all processes of system are sequential.However, BD process is the most critical because to determine the end of process, if it is found that FCU feeders are balanced, or the continuation of process otherwise, activating PV process.This condition form, a specific place invariant: "PV" sub-process can not happen before "BD" sub-process.

Through, with the invariants place (P-Invariants) it can be seen that the sequence of system sub-processes will only run one at a time, up until to develop the whole workflow system.

Thus, we have the follow condition invariant: "BD", "PV","MN","SS" places cannot happen before "DP"sub-process. Thus, we have the follow condition:DP marking,BD marking,PV marking, MN marking and SS marking, should be less or equal to 1,"(4)":

$$M(DP) + M(BD) + M(PV) + M(MN) + M(SS) = 1 \quad (4)$$

We have also the follow condition: "Supervision Center"(SC),"Feeder Switching Control"(FC), "Consumption Data Record" (CDR) places cannot happen before "BD"sub-process. If any as a result of the process, FCU balanced:

$$M(BD) + M(SC) + M(FC) + M(CDR) \leq 1 \quad (5)$$

By P-Invariants result, we can verified that invariants indicates aboven, are true:

$$M(BD) + M(CDR) + M(DP) + M(FC) + M(MN) + M(PV) + M(SS) + M(SC) = 1 \quad (6)$$

The transition invariants (T-invariants) can be used to verify the order of each subprocess system. Showing the sequence of the flow system is well structured. Through, the PN Invariants is shown in $2x9$ constant"T-Invariants" matrix depending on "T_{1-PN}","T_{2-PN}","T_{3-BD}","T_{4-PN}","T_{5-PN}", "T_{6-PN}","T_{7-PN}","T_{8-FC}","T_{9-FC}" transitions:

$$T_{Inv} = \begin{bmatrix} 1 & 1 & 1 & \cdots & 1 & 1 \\ 1 & 1 & 0 & \cdots & 1 & 1 \end{bmatrix} \begin{bmatrix} T_{1-PN} \\ T_{2-PN} \\ T_{3-BD} \\ T_{4-PN} \\ T_{5-PN} \\ \vdots \\ T_{9-FC} \end{bmatrix} \quad (7)$$

We can see, also that the net is covered by positive T-Invariants, therefore it might be textbfbounded and **live**.

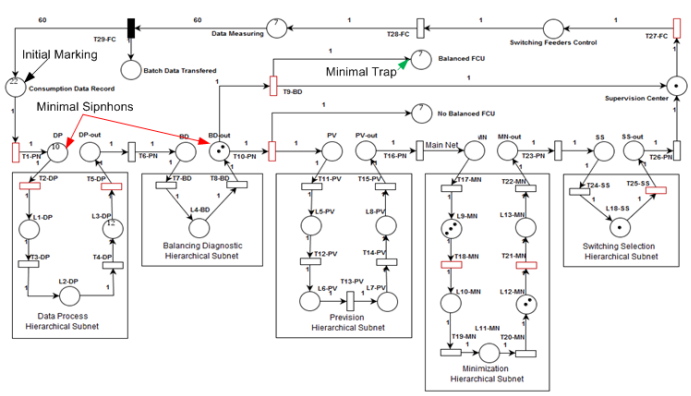

Fig. 5. DPMS THPN Simulation

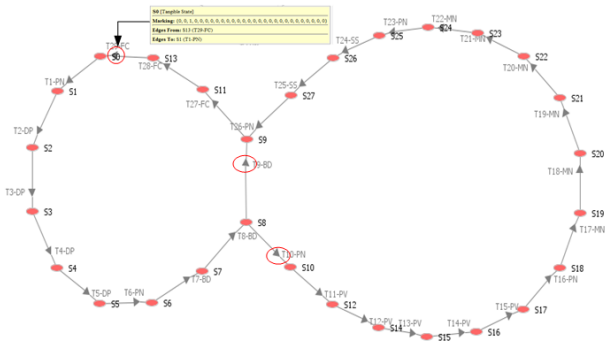

Fig. 6. DPMS THPN Reachability Graph with initial marking and conflicts

5.2 Hierarchical DPMS THPN validation

In Figure 5 it is shown the Hierarchical DPMS THPN simulation.Were performed 1500 "firings" with a period of 60 seconds between each, in order to have a complete operating in 1 minute. So, Were considered 60 FCU in SUSG, to be targets of balancing feeders analysis process. Thus, in "**CDR**" place there are electrical current and energy consumption of this 60 FCU.During DPMS system simulation is verifying efficiently workflow, and there is not deadlock or conflicts (marked in red in Figure 6) like main PN, that needs regulatory control.

However, it is found some "**siphons focus**" especially on "**DP**" and "**BDout**"(in red arrows), where are accumulated and consumed several tokens continuously, but it normalizes and adjusts over time.

It is, also found some "traps focus" in "**Balanced FCU**"(in green arrow) where which are accumulated several tokens, but this is actually equal to "**No balanced FCU**": both are only process counters, to facilitate processing system count.

The DPMS THPN Reachability graph is shown in Figure 6. It represents the diagram of reachable states of the PN. Its initial state S_0 highlighted in red. If verifies that does not exist deadlock, and that the PN it might be textbfbounded and **live**.

Looking for reachability graph, we note that all some specifics place invariant: "PV" sub-process can not happen before "BD" sub-process.But also, we have the follow

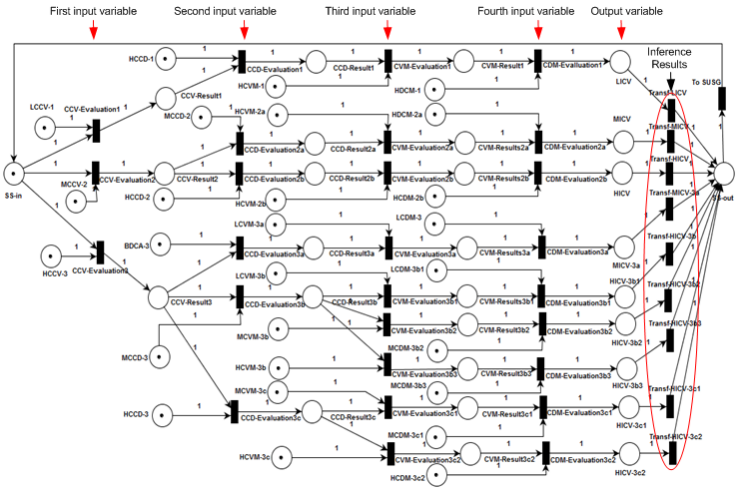

Fig. 7. Switching Selection sub-net

condition invariant: "BD", "PV","MN","SS", "SC","FC", "Data Measuring (DM)", and "CDR", places cannot happen before "DP"sub-process. Thus, we have the follow condition shown in "8":

$$\begin{aligned} &M(DP) + M(BD) + M(PV) + \\ &M(MN) + M(SS) + M(SC) + \\ &M(FC) + M(DM) + M(CDR) = 1 \end{aligned} \tag{8}$$

By P-Invariants result, we can verified that invariants indicates aboven, are true:

$$\begin{aligned} &M(BD) + M(BD - out) + M(CDR) + M(DM) + \\ &M(DP) + M(DP - out) + M(L10 - PV) + \\ &M(L11 - MN) + M(L12 - MN) + M(L13 - MN) + \\ &M(L14 - MN) + M(L15 - MN) + M(L16 - SS) + \\ &M(L1 - DP) + M(L2 - DP) + M(L3 - DP) + \\ &M(L6 - BD) + M(L7 - PV) + M(L8 - PV) \\ &M(L9 - PV) + M(MN) + M(MN - out) + M(PV) + \\ &M(PV - out) + M(SS) + M(SS - out) + \\ &M(SC) + M(FC) = 1 \end{aligned} \tag{9}$$

5.3 Switching Selection sub-net validation

For the Switching Selection sub-process was modeled an hierarchical sub-net, as illustrated in Figure 7. It is represents the model of inference selection of minimized consumption values of electric current performed by MN subprocess.

This is formed by four input variables: Current Consumption Value (CCV), Current Consumption Variation (CCD), Current Value Minimized (CVM), Current Variation Minimized (CDM)and a output variable, Current Correlation Value (ICV). All variables with three performance levels: low (L), medium (M) and high (H). With results highlighted in red, are selected the optimal switching matrix. Which can by means of this sub-net is implemented "Mamdani Fuzzy inference" model for selection of output combinations having the highest current correlation value.

In the case of the first inference rule is composed of the following stream: the first input variable "CCV" is evaluated (CCV-Evaluation1 transition), presenting as LCCV-1 result. The second input variable "CCD" is evaluated (CCD-Evaluation1 transition) presenting as HCVM-1 result. The third input variable "CVM" is evaluated

(CVM-Evaluation1 transition) and presented as HDCM-1 result. The fourth variable enters "CDM" is evaluated (CDM-Evaluation1 transition) presenting the final result of the output variable "ICV" LICV. Then transferred (transferrin-LCCV) to the output of the subnet to forward this information to the monitoring center of SUSG.

This sub-process represents "nine possible solutions" to the current variation correlation (inference rules) showed in Table 1. Which can assume low, medium and high correlation of current variation.

Table 1. Inference rules of Switching Selection sub-net

If	and	and	and	then
LCCV	HCCD	HCVM	HCDM	LICV
MCCV	MCCD	HCVM	HCDM	MICV
MCCV	HCCD	HCVM	HCDM	HICV
HCCV	LCCD	LCVM	LCDM	MICV
HCCV	MCCD	MCVM	MCDM	HICV
HCCV	MCCD	HCVM	MCDM	HICV
HCCV	MCCD	LCVM	LCDM	HICV
HCCV	HCCD	MCVM	MCDM	HICV
HCCV	HCCD	HCVM	HCDM	HICV

In this case by means of transition invariants it is possible to confirm the formation of each inference rules. Checking that they are well formed with all conditional and actions.

Rule 1 Training:

$$\begin{array}{l} CCD - Ev2b + CCV - Ev2 + CDM - Ev2b \\ CVM - Ev3a + TransfHICV + ToSUSG \end{array} \quad (10)$$

Rule 2 Training:

$$\begin{array}{l} CCD - Ev3b + CCV - Ev3 + CDM - Ev3b1 \\ CVM - Ev3b1 + TransfHICV3b + ToSUSG \end{array} \quad (11)$$

Rule 3 Training:

$$\begin{array}{l} CCD - Ev3b + CCV - Ev3 + CDM - Ev3b2 \\ CVM - Ev3b2 + TransfHICV3b2 + ToSUSG \end{array} \quad (12)$$

For the other rules can also be applied the same procedure.

6. CONCLUSION

A model Petri net, of load balancing process, called DPMS system to final consumption units in low voltage secondary grid, has been presented from which it is shown workflow formal validation. Having been used a timed hierarchical Petri net, to represent a dynamic abstraction of the operation flow of main and internal processes that form the DPMS system.Through the net synthesis,the reachability graph,invariant analysis and, workflow simulation, among others the vividness and limited network properties were checked.Verifying in summary efficiently operation of system without deadlocks and conflicts, that requested implementation of any regulatory control.

It was also presented in detail the inference procedure for switching selection sub-process. Noting that from the transition invariants is possible to verify the formation of the inference system rules.

Suggested future steps develop model DPMS system using timed hierarchical colored Petri nets,to further improve computational efficiency.

ACKNOWLEDGEMENTS

The authors thank UEPA, UFPA, USP and FAPEAM, for allowing scientific achievement of this proposal.

REFERENCES

Alt, M., Gorlatch, S., Hoheisel, A., and Pohl, H.W. (2006). Using high level petri nets for hierarchical grid workflows. In A. Round (ed.), *Advances in Enzymology*, volume 2, 1–87. Academic Press, New York, 3rd edition.

Huang, Y., Mao, S., and Nelms, R. (2015). Smooth scheduling for electricity distribution in the smart grid. volume 9, 966–977. IEEE System Journal, New York, 3rd edition.

Shahgoshtasbi, D. (2014). A new intelligent neuro–fuzzy paradigm for energy-efficient homes. In A. Round (ed.), *Advances in Enzymology*, volume 8, 664–673. Systems Journal, IEEE Transactions, New York, 3rd edition.

Shahnia, F., Wolfs, P., and Ghosh, A. (2014). Voltage unbalance improvement in low voltage residential with rooftop pvs using custom power devices. In E. Power and E. Systems (eds.), *Advances in Enzymology*, volume 55, 362–377. Elsevier, New York, 3rd edition.

Sharma, I., Cañizares, C., and Bhattacharya, K. (2014). Smart charging of pevs penetrating into residential distribution systems. In A. Round (ed.), *Advances in Enzymology*, volume 5, 1196–1209. IEEE Transactions on Smart Grid, New York, 3rd edition.

Sicchar, J., Jr., C.D.C., Salmon, A., Silva, J., Pina, I., and Gomes, R. (2011). Sistema inteligente para análise de consumo de energia elétrica em smart grid de baixa tensão. In P. in X SBAI 2011 (ed.), *Advances in Enzymology*, volume 1, 1–6. SBAI 2011, New York, 3rd edition.

Sicchar, J., Jr., C.D.C., Silva, J., and Freitas, R.D. (2015). Gerenciamento de consumo de energia em residências com frame gcr. In P. in XII SBAI 2015 (ed.), *Advances in Enzymology*, volume 1, 1–6. SBAI 2015, New York, 3rd edition.

Silva, J. (2012). Timed petri nets. chapter 16. petri nets manufacturing and computing science. In INTECH (ed.), *Advances in Enzymology*, volume 1, 359–378. Intech, New York, 3rd edition.

Siti, W., Jimoh, A., and Nicolae, D. (2011). Distribution network phase load balancing as a combinatorial optimization problem using fuzzy logic and newton-raphson. In E. Electric Power Systems (ed.), *Advances in Enzymology*, volume 22, 1079–1087. Elsevier, New York, 3rd edition.

Wang, L. (2015). Knowledge representation and general petri net models for power grid fault diagnosis. In I.J.. Magazines (ed.), *Advances in Enzymology*, volume 9, 866–1087. IET, New York, 3rd edition.

Load Frequency Control of a Multi-area Power System Incorporating Variable-speed Wind Turbines ⋆

Semaria Ruiz Alvarez * **Julián Patiño** ** **Jairo Espinosa** ***

* *Universidad Nacional de Colombia, Medellín, Colombia (e-mail: seruizal@unal.edu.co).*
** *Universidad Nacional de Colombia, Manizales, Colombia (e-mail: juapatinomu@unal.edu.co)*
*** *Facultad de Minas, Universidad Nacional de Colombia, Medellín, Colombia (e-mail: jjespino@unal.edu.co)*

Abstract: The increasing use of renewable technologies in power generation may require its participation on ancillary services like frequency regulation. For the specific case of wind sources, this may lead to participation in frequency control loops. This paper focuses on the simulation of the performance of the LFC scheme for a multi-area power system, with participation of DFIG turbines in the frequency control loops, through the *synthetic inertia method*.

Keywords: Power systems, load frequency control, wind turbine, pitch angle, multi-area system.

1. INTRODUCTION

The behavior of generation systems based on unconventional energy sources like wind and solar energies may impact several aspects related with the operation and control of power systems; one of the ongoing research topics is related with understanding the impact of these new sources on the system frequency ((Bevrani, 2009; Valencia et al., 2012; Rahmann and Castillo, 2014; Horta et al., 2015)). As wind constitutes the most extensively used renewable energy source in the world, there are many studies about control strategies for the inclusion of wind turbines in the load frequency control loops of power systems (a complete rewiew of grid requirements and control methodologies can be seen in (Daz-Gonzlez et al., 2014)). In (de Almeida et al., 2006), an optimization is proposed in order to schedule the active and reactive power that wind turbines must deliver to meet the grid requirements. Additionally, a controller for the pitch angle in the turbine was also presented, forcing the turbine to operate over a de-load curve.

In (Ramtharan et al., 2007b) and (Moore and Ekanayake, 2009), the synthetic inertia method is used, where an additional control loop is proposed to emulate the behavior of conventional units in the frequency response of wind-turbines. Also, in (Camblong et al., 2014), the dynamic model of a DFIG (Doubly-fed Induction Generator) wind turbine is proposed in order to design an LQR controller to provide frequency support using reference torque and reference pitch angle as inputs. In (Bernard et al., 2013), a MPC (Model Predictive Controller) is developed through a simplified model of the DFIG, having the quadrature-axis rotor voltage of the wind-turbine dynamic system as an input.

In spite of the considerable efforts of the previously mentioned studies, those works did not consider the application over multi-area power systems, which are increasingly common representations as power grids continue to grow in size and complexity. Additionally, it is necessary to perform a comparison between the conventional control methods used for the load frequency control as PI (Proportional-Integral) and other more complex control strategies such as as the LQR controllers or MPCs in multi-area power systems.

Based on these requirements, this paper presents the simulation of the performance of the LFC (Load Frequency Control) scheme for a multi-area power system, having into account the participation of DFIG turbines in the frequency control loops, through the *synthetic inertia method*, with PI controllers for the AGC (Automatic Generation Control), the quadrature rotor voltage and the pitch angle and employing the simplified wind turbine model proposed in (Moore and Ekanayake, 2009) and (Bernard et al., 2013). The performance of these models and its contribution are illustrated by simulation using the IEEE nine bus system benchmark.

The paper is organized as follows: in section 2, a short description about the load frequency control is presented, and next the models and control loops required for wind modeling contribution are described in section 3. Section 4.1 shows the selected benchmark. The results of including wind-turbines in the LFC control loop are presented in section 4.2. At the end, some concluding remarks can be found.

⋆ This work was supported by Colciencias through the programs "Jóvenes investigadores - Convocatoria N.645 of 2014" and "Convocatoria 528 - Convocatoria Nacional para Estudios de Doctorados en Colombia 2011".

2. LOAD FREQUENCY CONTROL

In an electric power system, the frequency of the voltage wave must rely between rigorous limit values in order to keep the quality of the electric service inside an acceptable operational margin. This is a difficult task since the frequency is related to the load-generation balance and both variables are changing during the daily operation. This difficulty increases even more if the penetration of renewable energy sources is considered. Therefore, generating units require a control system able to respond to the generation or load changes, which is known as the load frequency control (LFC), (Saadat, 1999). This control system is organized in three levels: primary, secondary an tertiary frequency control. These levels are explained in (Bevrani, 2009), as follows:

- **Primary control (LFC).** Primary control is the fastest. It operates in a time band between 2-20 seconds and acts at the local level over each generation unit.
- **Secondary control (AGC).** Secondary control operates in a time band between 2 secondsand 2 minutes. It allows the correction of the steady-state errors in system frequency. For multi-area systems, it also regulates the power exchanged between areas.
- **Tertiary control.** Tertiary control is used in large power systems. It operates in a time margin above 10 minutes and specifies the set-points to the generation units by optimizing some cost function. Because the time and the tasks involved, this control stage is often considered as part of dispatch operations, and not fully mentioned as a frequency control loop.

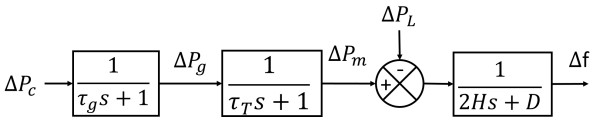

Fig. 1. Model of the set: speed-governor, turbine, generator and load (based on (Saadat, 1999)).

With the aim of designing these control systems, power system elements are modeled. For this, an equivalent model of an isolated power system is presented, where the response of all loads and generators are represented by a single damping and an equivalent inertia (see (Saadat, 1999) for a deeper description of these models). Also the dynamics of the speed-governor and the turbine are represented by first order transfer functions as illustrated in Figure 1, where:

- ΔP_m is the change in mechanical power of the generator.
- ΔP_g is the change in the governor output.
- ΔP_l is the load perturbation.
- Δf is the frequency change.
- D is the damping coefficient, due to the frequency sensitive loads.
- H is the equivalent inertia, the sum of the inertia of all generators in the system.
- ΔP_c is the control action of the LFC.

In an isolated power system, the function of the LFC is to restore frequency to its nominal value after a perturbation,

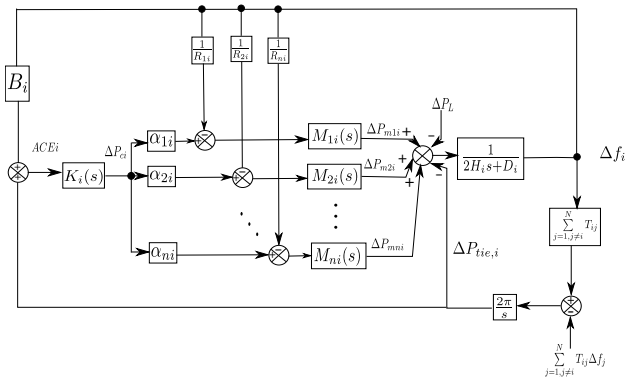

Fig. 2. Load frequency control scheme for a multi-area power system (based on Bevrani (2009)).

without taking into account power exchange. On the other hand, for interconnected systems, the control area concept has to be used, which is a group of generators and loads where the generators respond to load changes uniformly.

2.1 Load frequency control in multi-area power systems

A multi-area power system is composed by single area power systems that are interconnected by transmission lines or tie-lines. There is a LFC system on each of these single-area systems, which have the function of regulating, not only the frequency in the local area, but the power exchange with other areas (Saadat, 1999). Therefore, in the LFC dynamics, the tie-line power signal must be added in order to guarantee that the frequency deviation produced by load fluctuations in one area is controlled locally and does not propagate to other areas. Thus, each local area must be able to control its own load-generation perturbations.

Figure 2 depicts the load frequency control scheme for an N-area system, where (based on (Bevrani, 2009)):

- $M_{ni}(s)$ is the transfer function corresponding to the set of speed-governor, turbine, generator and load in area i.
- T_{ij} is the initial power exchange factor between area i and area j.
- ΔP_{tiei} is the change in the power exchange between the area i with other areas.
- Δf_j is the change in the frequency of the areas connected to area i.
- B_i is known as the *bias factor*, which allows minimize the power exchange with other areas through the input error signal in the AGC controller.
- $K_i(s)$ is the transfer function of the AGC controller.
- α_i is the participation factor of each generator in the AGC (these values are assumed equal to one for each generator if not established otherwise).

3. INCLUDING VARIABLE SPEED WIND-TURBINES IN LOAD FREQUENCY CONTROL

In order to include variable speed wind-turbines in the LFC, it is required to represent the power production of these generation units. For this, the model proposed in (Ramtharan et al., 2007a) is taken into account. There, the authors propose that the wind-turbine performs at an

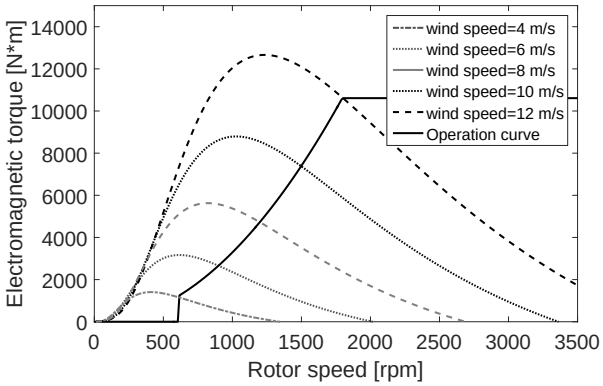

Fig. 3. Wind-turbine operation curve for different wind speeds (Thomsen, 2006)

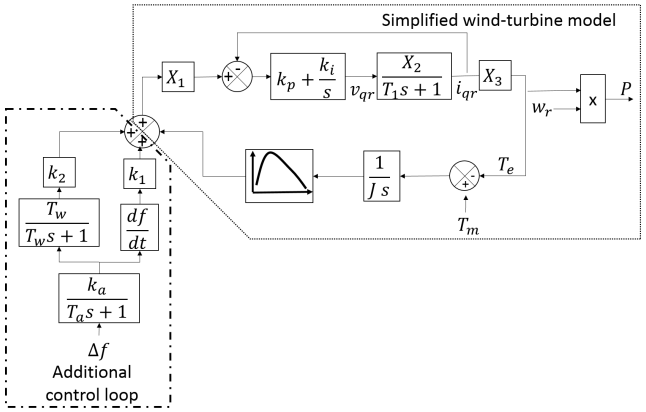

Fig. 4. Wind-turbine simplified model with additional control loop for LFC contribution (based on (Ramtharan et al., 2007a)).

operating point below its maximum power. As seen from figure 3, this results in the operating point of the wind-turbine being moved to the right regarding to its point of maximum power extraction.

The mechanical torque in each of the curves shown in Figure 3 is given by the equation (Thomsen, 2006):

$$T_m = \frac{Pm}{w_{shaft} G_b p}. \tag{1}$$

In equation (1), ω_{shaft} is the rotational speed of the wind-turbine shaft, G_b is the gearbox ratio, p denotes the number of pole pairs in the generator and P_m is the mechanical power, which is defined as:

$$P_m = \frac{1}{2}\rho\pi R^2 v^3 C_p. \tag{2}$$

There, $\rho = 1.225\ kg/m^3$ is the air density, $R = 45\ m$ is the blade's length, v is the wind speed and C_p is the efficiency coefficient described below:

$$C_p = 0.22((\frac{116}{\lambda_t}) - 0.4\beta - 5)e^{\frac{-12.5}{\lambda_t}}, \tag{3}$$

with λ_t a parameter given by Thomsen (2006):

$$\lambda_t = \frac{1}{\frac{1}{\frac{R\omega_{shaft}}{v}+0.08\beta} - \frac{0.035}{1+\beta^3}} \tag{4}$$

In this way, the value of the coefficient C_p will be depending on the pitch angle β, the wind speed v and the rotational speed ω_{shaft}. Thus, for each wind speed value an operating point slightly moved to the right is taken. At this operating point, the torque is given by equation (5), where the value of $K_{op} = 0.3$ is a constant.

$$T_{op} = K_{op} v^2 \tag{5}$$

Besides the simplified model previously described, is is also necessary to use a fraction of the power generated by the wind turbine in order to contribute to the LFC. Using the so-called *synthetic inertia model* (see (Ramtharan et al., 2007a) and Moore and Ekanayake (2009), a couple of additional loops are aggregated to the LFC: one containing a transfer function offering an output proportional (multiplying by K_1) to the frequency change rate (corresponding to the primary response of the wind turbine); and the other loop having the task of restoring the power delivered by the wind turbine after its participation in the load frequency control. The deviation frequency signal is pre-filtered, previously, by a filter with gain K_a.

Both the simplified model and the synthetic inertia model are depicted in figure 4, where:

and

- ω_r is the rotor angular speed,
- n is the number of wind-turbines,
- iq_r is the quadrature rotor current,
- vq_r is the quadrature rotor voltage, and
- X_1, X_2, X_3 and T_1 are constant values representing relationships between the internal wind generator parameters (see (Ramtharan et al., 2007a) for a detailed description of them).

A $2MW$ wind-turbine, is selected to perform the simulations, the parameters of this turbine are presented in table A.2 in section 5.

Moreover, for wind speeds equal or over the rated wind speed of the wind-turbine, a pitch angle control should be performed to maintain the angular speed of the wind-turbine at its nominal value. Additionally, when a frequency event occurs, and the turbine is operating under the action of pitch control, it is proposed to add a loop of additional control where the pitch angle is increased by a value proportional to the frequency deviation (this value is denoted by the constant R_β). This pitch control scheme is illustrated in Figure 5 with a PI controller.

The whole wind turbine model with the inclusion of control loops described above is presented in figure 6, where the variable n indicates the number of generating units, and the variable v_w indicates the wind speed. This model has an additional element compared with the models of (Ramtharan et al., 2007a) and (Moore and Ekanayake, 2009), the variable P_{ref}, which constitutes the power that the wind-turbine would deliver if it would not be contributing to system frequency control.

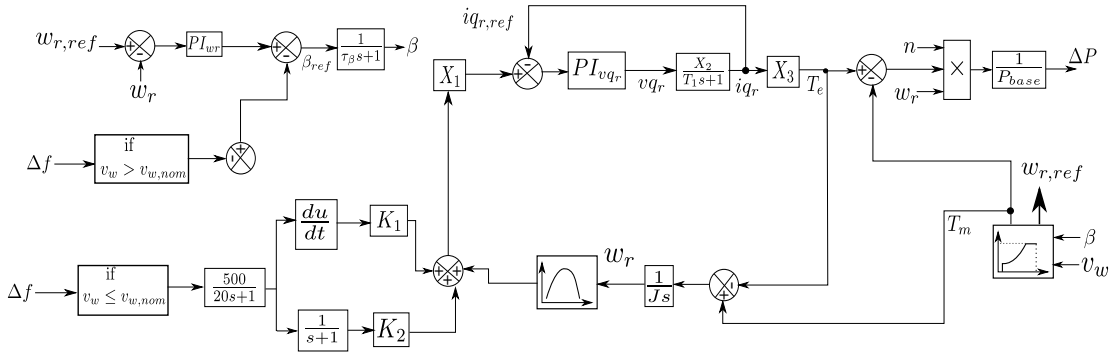

Fig. 6. Schematic diagram for wind-turbine integration in the LFC for a single area system (Moore and Ekanayake, 2009).

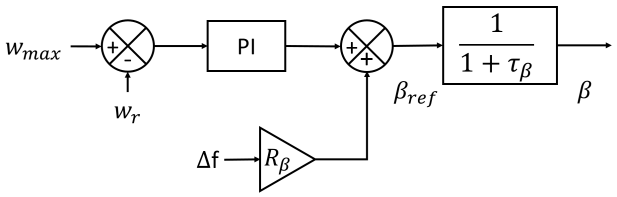

Fig. 5. Pitch control scheme for participation of wind-turbines in the LFC (based on (Ramtharan et al., 2007a)).

4. SIMULATION RESULTS

4.1 Benchmark Description

To perform the simulation of the LFC in a multi-area power system, the IEEE nine bus system is used (see (Anderson and Fouad, 2002)). This system is arbitrarily divided into in three areas, as illustrated figure 7. Each area has a generation unit and an associated load. Saturation blocks represent the operational limits of the units.

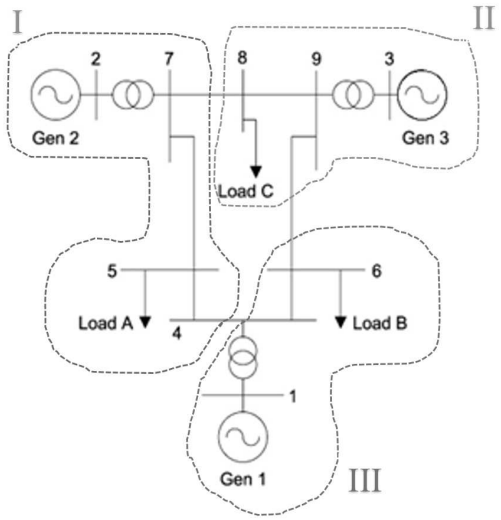

Fig. 7. IEEE 9 bus system with an arbitrary multi-area partition.

Simulations were performed using the parameters presented in table A.1 (see Appendix), taken from (Anderson and Fouad, 2002) and using 100 MVA as base power. The work is performed under the assumption of area 1 having a hydraulic turbine and generators 2 and 3 being gas turbines. Thus, each area could be represented by the scheme shown in Figure 2. Saturation blocks represent the generation units operational margins.

However, in area 3 the 50% of the conventional generation is replaced by wind-turbines with an equivalent power. A wind farm composed of 32 total turbines with a power of 2 MW for each unit. Figure 8 shows the modification of the LFC scheme to include wind turbines in the frequency regulation system.

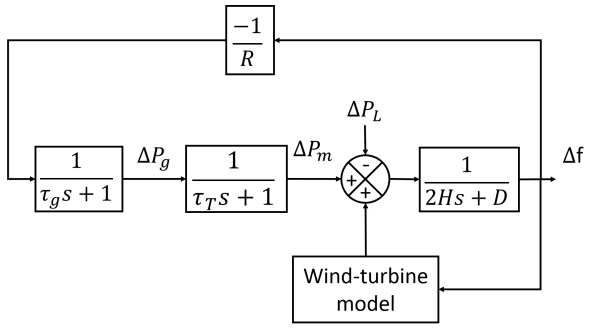

Fig. 8. LFC scheme including wind turbines for primary frequency regulation.

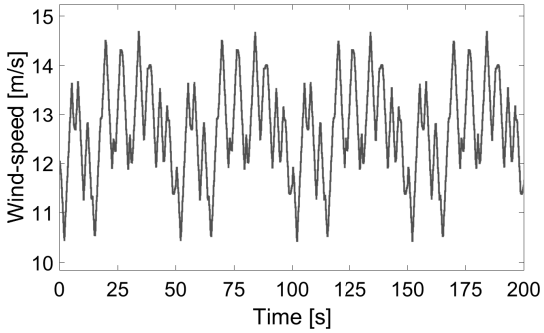

Fig. 9. Wind speed profile (from (Bernard et al., 2013)).

For simulation purposes, load disturbances are applied in each area as follows: In area 1 a perturbation of 0.01 p.u. is made at 90 seconds, in area 2 a perturbation of 0.08 p.u. is performed at 60 seconds, and in area 3 a load disturbance of 0.06 p.u. is applied at 30 seconds. Also, the wind speed profile employed to feed the wind units is shown in figure 9 as considered in in (Bernard et al., 2013).

4.2 Results

PI controllers are used in in the secondary control (AGC) of each area , and also for the regulation of the quadrature rotor current iq_r, and the pitch angle β in wind turbines. The parameters for these controllers were calculated with the Gradient Descent method, in Matlab Design Optimization-Based PID Controller toolbox (see table 1).

Table 1. Parameters for different PI controllers

Parameter	Area 1	Area 2	Area 3	iq_r	Pitch
P	0	0	0	0	7.19
I	-0.05	-0.05	-0.028	2.70	0.53

Figures 10 - 12 present the frequency deviations for each area with and without contribution of wind turbines in the LFC system of area 3. As the AGC, by design, leads to the local control of disturbances minimizing the effects in the other areas, the expected consequence is no sensible operational difference between the frequency deviations of each area. However, for each area, the inclusion of the wind farm in LFC of area 3 actually helps to compensate frequency deviations in the LFC, but only when there is enough wind to produce the required power. During the periods of low wind, disturbance effects are harder to compensate than the conventional case, due to the lack of renewable power in the system. Besides this, it is important to highlight that the presence of hydro generation in area 1 implies a greater inertia, diminishing even more the effects of frequency disturbances. The effects over areas 2 and 3 are pretty similar, because these areas have similar conditions.

The power exchanged between area 3 and the other areas is shown in figure 12. As it was said before, both frequency and power deviations are low when there is enough wind speed to sustain the power contribution of the wind farm. Once wind speed is low, area 3 needs to increase the power absorbed from the order areas in order to reduce the effects of local disturbances in the local area frequency.

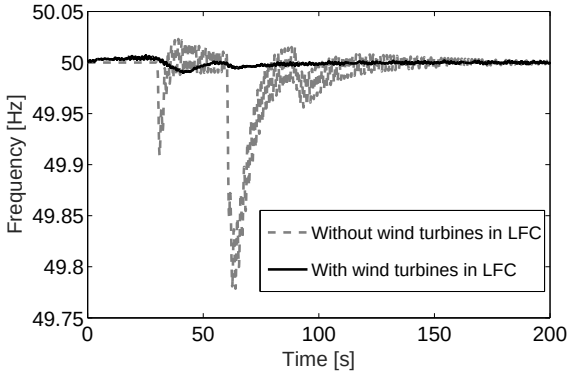

Fig. 10. Frequency deviation in area 1.

The responses of the rotor voltage vq_r and the pitch angle β_{ref} are depicted in figures 14 and 15, respectively. These figures show how the participation of wind turbines in LFC can be more stressful for them. However, a less aggressive performance could be obtained with a better tuning of the involved PI controller, or by the implementation of another kind of controllers.

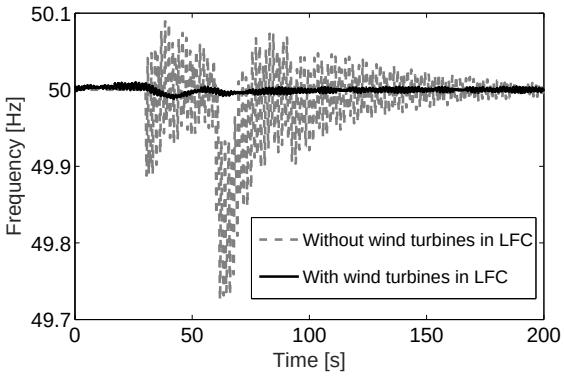

Fig. 11. Frequency deviation in area 2.

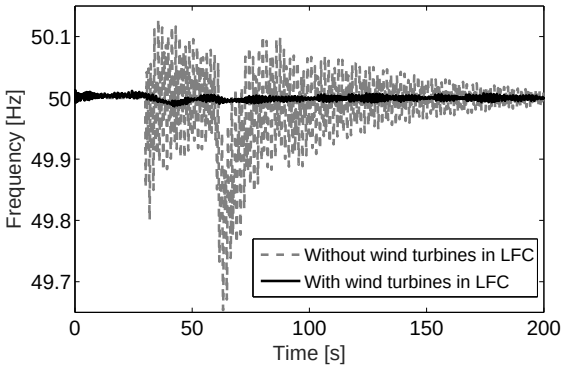

Fig. 12. Frequency deviation in area 3.

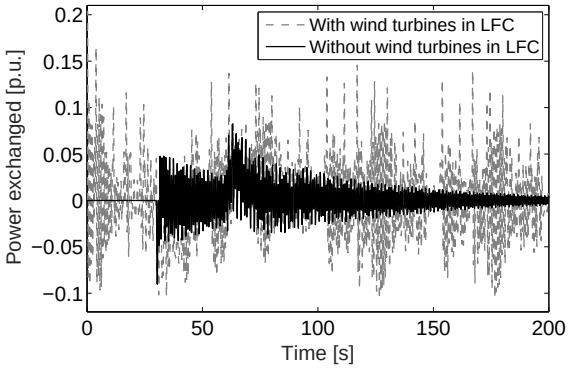

Fig. 13. Power exchange for area 3.

5. CONCLUSION

The simulation of the performance of the LFC scheme for a multi-area power system, with participation of DFIG turbines in the frequency control loops, through the *synthetic inertia method*, with PI controllers for the AGC control was presented. The results show that wind turbines are useful for frequency regulations tasks in primary control. However, the variability of wind and the effects of the decreasing inertia from conventional units can be dangerous for frequency performance. Additionally, it is also shown that the participation of wind turbines in LFC introduces more stress in the operation of these units, requiring the exploration of control techniques that help to reduce these efforts for the wind units.

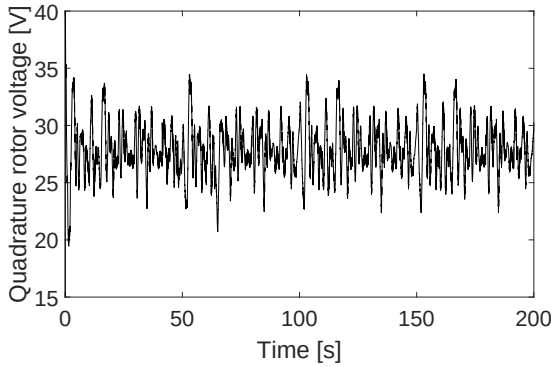

Fig. 14. Control action for the variable vq_r.

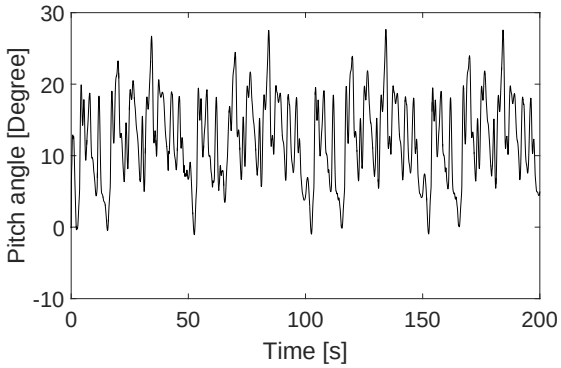

Fig. 15. Control action for the variable β_{ref}.

REFERENCES

Anderson, P.M. and Fouad, A.A. (2002). *Power System Control and Stability*. second edition.

Bernard, M.Z., Mohamed, T.H., Ali, R., Mitani, Y., and Qudaih, Y.S. (2013). PI-MPC Frequency Control of Power System in the Presence of DFIG Wind Turbines. 2013(September), 43–50.

Bevrani, H. (2009). *Robust Power System Frequency Control*. Lc. doi:10.1007/978-3-319-07278-4.

Camblong, H., Vechiu, I., Guillaud, X., Etxeberria, A., and Kreckelbergh, S. (2014). Wind turbine controller comparison on an island grid in terms of frequency control and mechanical stress. *Renewable Energy*, 63, 37–45. doi:10.1016/j.renene.2013.08.045.

Daz-Gonzlez, F., Hau, M., Sumper, A., and Gomis-Bellmunt, O. (2014). Participation of wind power plants in system frequency control: Review of grid code requirements and control methods. *Renewable and Sustainable Energy Reviews*, 34(0), 551 – 564. doi: http://dx.doi.org/10.1016/j.rser.2014.03.040.

de Almeida, R.G., Castronuovo, E.D., and Peças Lopes, J.A. (2006). Optimum generation control in wind parks when carrying out system operator requests. *IEEE Transactions on Power Systems*, 21(2), 718–725. doi: 10.1109/TPWRS.2005.861996.

Horta, R., Espinosa, J., and Patino, J. (2015). Frequency and voltage control of a power system with information about grid topology. In *Automatic Control (CCAC), 2015 IEEE 2nd Colombian Conference on*, 1–6. IEEE.

Moore, I. and Ekanayake, J. (2009). Frequency response from wind turbines. *Universities Power Engineering Conference (UPEC), 2009 Proceedings of the 44th International*, 1–5.

Rahmann, C. and Castillo, A. (2014). Fast Frequency Response Capability of Photovoltaic Power Plants: The Necessity of New Grid Requirements and Definitions. *Energies*, 7(10), 6306. doi:10.3390/en7106306.

Ramtharan, G., Ekanayake, J., and Jenkins, N. (2007a). Frequency support from doubly fed induction generator wind turbines. *IET Renewable Power Generation*, 1(1), 3–9. doi:10.1049/iet-rpg:20060019.

Ramtharan, G., Jenkins, N., and Anaya-Lara, O. (2007b). Modelling and control of synchronous generators for wide-range variable-speed wind turbines. *Wind Energy*, 10(3), 231–246. doi:10.1002/we.219.

Saadat, H. (1999). Power System Analysis Hadi Saadat.pdf.

Thomsen, S.C. (2006). *Nonlinear control of a wind turbine, ME Thesis*. Ph.D. thesis, Technical University of Denmark.

Valencia, F., Patino, J., and Espinosa, J. (2012). A performance comparison for wind power integration into the grid system. In *Alternative Energies and Energy Quality (SIFAE), 2012 IEEE International Symposium on*, 1–5. Barranquilla, Colombia. doi: 10.1109/SIFAE.2012.6478879.

Appendix A. SIMULATION PARAMETERS

Table A.1. IEEE nine bus system parameters (from Anderson and Fouad (2002))

Parameter	Value
H_1	23.64 s
H_2	6.4 s
H_3	1.505 s
MVA_{nom1}	247.5
MVA_{nom2}	192
MVA_{nom3}	128
$D1, D2, D3$	0.8
$Tg1, Tg2, Tg3$	0.2
$T_{\tau}1, T\tau 2, T\tau 3$	0.3
T_{12}	2.064 p.u.
T_{13}	6.1191 p.u.
T_{23}	14.4353 p.u.
R_1	2 p.u.
R_2	10 p.u.
R_3	7.5019 p.u.
B_1	2.8 s
B_2	10.8 s
B_3	8.3 s

Table A.2. Wind-turbine model parameters (Ramtharan et al. (2007a) and Moore and Ekanayake (2009)).

Parameter	Value
P_{nom}	2 MW
V_{nom}	966 V
K_1	5000 Nm
K_2	2000 Nm
T_w	1
K_a	500
T_a	20
R_s(Stator resistance)	0.00491 p.u.
X_{ls}(Stator reactance)	0.09273 p.u..
X_m(Magnetization reactance)	3.96545 p.u.
R_r(Rotor resistance)	0.00552 p.u
X_{lr}(Rotor reactance)	0.1 p.u.
$H = \frac{1}{2} J \frac{w_{nom}^2}{VA_{nom}}$	4.5 s
J (Inertia moment)	506.6059 Kgm^2.
P_{base} (Power base)	128 Mw.

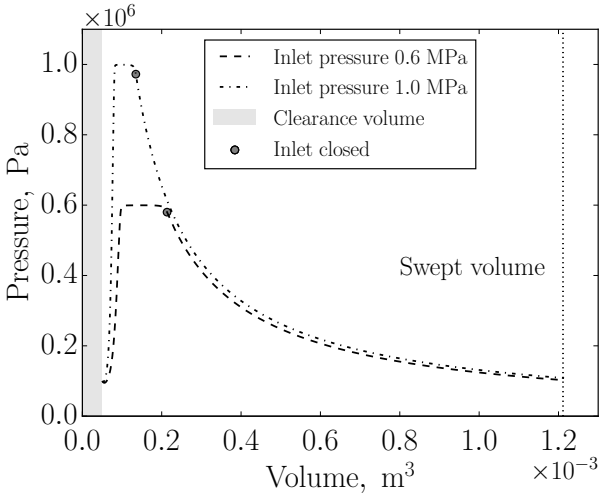

Fig. 10. Piston velocity vs. displacement

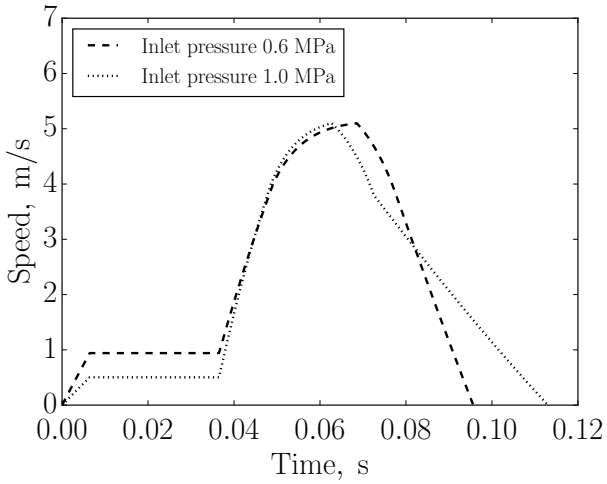

Fig. 12. Piston velocity vs. displacement

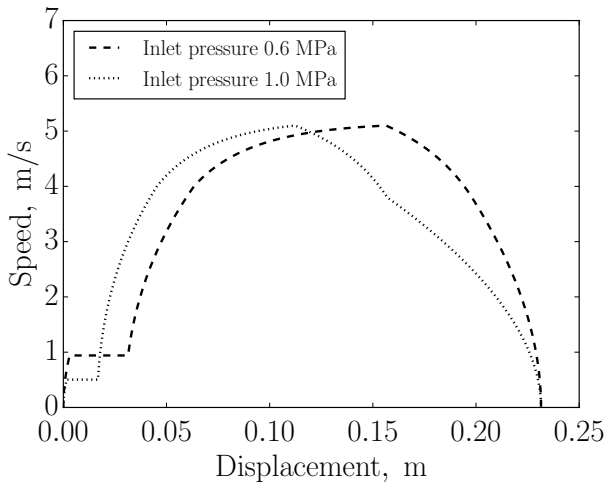

Fig. 11. Piston velocity vs. displacement

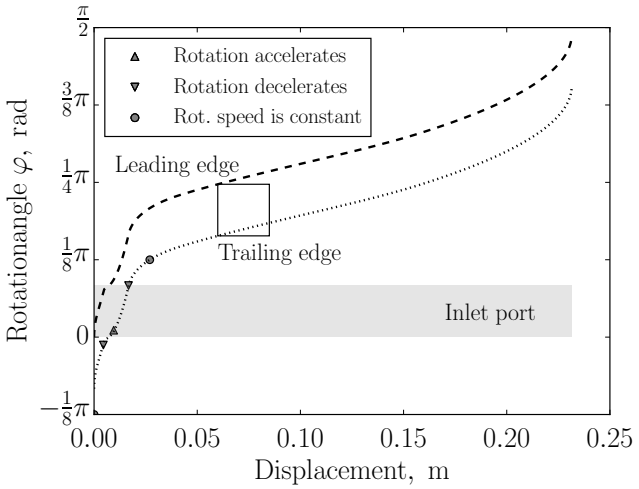

Fig. 13. Piston velocity vs. displacement

Two inlet pressures 1.0 MPa and 0.6 MPa are compared and the configuring factors are identified (Fig. 10).

By performing such simulations within the expected inlet pressure range with a certain step, a matrix of these parameters can be obtained and used in real time to adjust the piston movement under varying inlet pressure.

4.5 Parameters description

Variables: Inlet pressure

Constants: Inlet temperature, outlet pressure, expander geometry, zero piston velocity at the end of expansion phase.

Adjustable parameters: k1, k2, k3, k4, k5, k6.

Efficiency indicators: frequency, filling factor, intake efficiency, power output: to maximize.

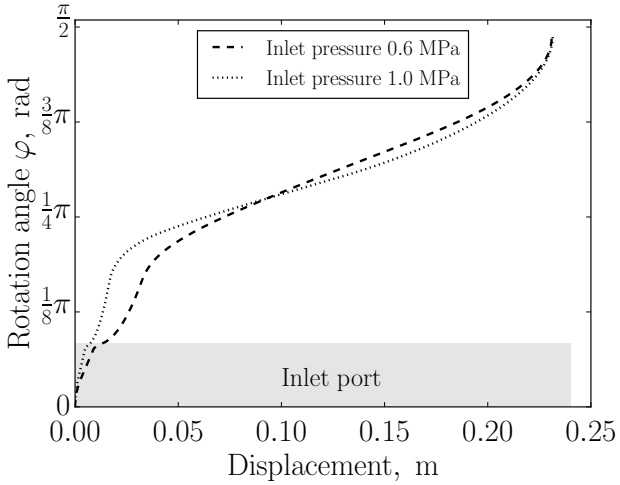

Fig. 14. Piston velocity vs. displacement

5. RESULTS AND DISCUSSIONS

The developed model is based on parameters of the selected linear motor and the servomotor and allows to synchronize the rotation with the linear movement of the expander. By decreasing the linear speed during the intake phase, the pressure loss at the inlet can be reduced. However, reduced translation speed means lower frequency and the mass flow rate through the expander, so the optimum has to be found (Fig. 12).

The rotation of the piston can be increased or decreased when necessary for a better fit of the inlet. A moderate rotating acceleration/deceleration is achievable in combination with the piston deceleration during the intake. The final deceleration must be adjusted so the leading edge of the skirt opening reaches the outlet port at the end of the stroke. In this case this angle is $\pi/2$ (Fig. 13). Two rotation/translation profiles for different inlet pressures are shown on Fig. 14

The shape of the inlet port needs to be adjusted to "follow" an optimal intake profile in order to keep the inlet intersection area around its maximum during the intake phase. Otherwise higher pressure ratios will require high dynamics from electromagnetic train or will cause relatively high intake losses.

The presented model is focused on the inlet control and therefore simplified by setting the outlet pressure as constant.

6. CONCLUSIONS

The dynamics of the system depend on the linear generator used. Industrial linear motors are characterized by large moving masses. It is possible to reduce the weight of the piston if magnets are directly attached to it. A high dynamics of the piston movement is necessary to increase the resulting frequency and the volumetric flow rate of the machine. A relatively high static force is required to keep the piston under control at its extreme positions. The use of a position encoder ensures the high accuracy of the inlet timing, which is crucial for the system efficiency.

The proposed system contains no bouncing devices such as gas- or mechanical springs, which are typically used in free piston machines. Instead, the piston movement is fully controlled, so its velocity becomes zero at both extreme positions. A higher system efficiency is expected since mechanical wear or thermodynamic irreversibilities are avoided.

REFERENCES

Bell, I.H., Wronski, J., Quoilin, S., and Lemort, V. (2014). Pure and pseudo-pure fluid thermophysical property evaluation and the open-source thermophysical property library coolprop. *Industrial & engineering chemistry research*, 53(6), 2498–2508.

Gusev, S., Ziviani, D., De Viaene, J., Derammelaere, S., and van den Broek, M. (2016). Modelling and preliminary design of a variable-bvr rotary valve expander with an integrated linear generator. In *Proceedings of the 17th International Refrigeration and Air Conditioning Conference at Purdue*.

Imran, M., Usman, M., Park, B.S., and Lee, D.H. (2016). Volumetric expanders for low-grade and waste heat recovery applications. *Renewable and Sustainable Energy Reviews*, 57, 1090–1109.

Lemort, V., Quoilin, S., Cuevas, C., and Lebrun, J. (2009). Testing and modeling a scroll expander integrated into an organic rankine cycle. *Applied Thermal Engineering.*, 29, 3094–3102.

Mikalsen, R. and Roskilly, A. (2008). The design and simulation of a two-stroke free-piston compression ignition engine for electrical power generation. *Applied Thermal Engineering*, 28(56), 589–600.

Petrichenko, D., Tatarnikov, A., and Papkin, I. (2015). Approach to electromagnetic control of the extreme positions of a piston in a free piston generator. *Modern Applied Science*, 9(1), 119–128.

Tran, X.B. and Yanada, H. (2013). Dynamic friction behaviors of pneumatic cylinders. *Intelligent Control and Automation*, 4(2).

Appendix A. NOMENCLATURE

A.1 Latin characters

D	diameter	(m)
F	force	(N)
L	length	(m)
m	mass	(kg)
n	number of ports	(-)
p	pressure	(Pa)
S	intersection area	(m^2)
t	time	(s)
V	volume	(m^3)
x	displacement	(m)

A.2 Greek characters

β	port angle	(rad)
Δ	difference	(-)
υ	speed	(m/s)
φ	angle of rotation	(rad)
ϕ	filling factor	(-)
χ	relative displacement	(-)

A.3 Subscript

cyl	cylinder
dis	discharge
el	electromagnetic
fr	friction
max	maximal
min	minimal
open	opening
port	port
rot	rotation
su	supply

Modelado y Propiedades de Pasividad de Sistemas Fotovoltaicos con MPPT Distribuido ⋆

D. R. Espinoza-Trejo * **G. Espinosa-Pérez** ** **L. M. Castro** **

* *Coordinación Académica Región Altiplano, Universidad Autónoma de San Luis Potosí (e-mail: drespinozat@ieee.org).*
** *Universidad Nacional Autónoma de México (e-mail: gerardoe@unam.mx, luismcastro@fi-b.unam.mx)*

Resumen: En este artículo se demuestra formalmente que un sistema fotovoltaico (FV), con arquitectura basada en MPPT-distribuido, está constituido por una interconexión pasiva de sistemas pasivos. El resultado se presenta, primero, para un inversor FV tipo string y posteriormente, se plantea la extensión de los resultados a inversores FV con MPPT-distribuido. Como consecuencia, este estudio establece las bases para el diseño de controladores de *seguimiento de punto de máxima potencia* y de *inyección de potencia activa/reactiva en el punto de conexión común*, para sistemas FV con MPPT-distribuido, desde una perspectiva basada en la interconexión de sistemas.

Keywords: Pasividad, Modelos Hamiltonianos, Sistemas Fotovoltaicos, MPPT-Distribuido, Generación Distribuida.

1. INTRODUCCIÓN

La energía solar fotovoltaica (FV) ha sido una de las fuentes de energía renovable con mayor crecimiento en la última década. No obstante, la tecnología solar FV aún enfrenta interesantes retos, entre los que se destacan: *i*) mejorar la eficiencia, *ii*) incrementar la seguridad, y *iii*) añadir controlabilidad a los sistemas FV (SFV) para ofrecer servicios auxiliares al sistema eléctrico tales como la regulación de las potencias activa y reactiva en el punto de interconexión, facilitando así la integración masiva de plantas FV a los sistemas eléctricos de potencia. Con respecto a la eficiencia de los SFV, el sistema de *seguimiento de punto de máxima potencia* (MPPT *por sus siglas en inglés*) juega un papel importante. Es bien conocido, que ante condiciones de irradiancia no-uniformes, éste se puede ubicar en un punto de máxima potencia *local*, subutilizando a los módulos FV (MFV), Podgurski (2013). Por otra parte, ante un evento de falla en el SFV, ver Chan (2011), la eficiencia también se puede ver deteriorada, y además, generar problemas de calidad de la energía relacionados con la inyección de harmónicas a la redes eléctricas.

Como consecuencia, en los útlimos años se han propuesto nuevas topologías de SFV, ver Kouro (2015), como solución a los retos ya mencionados. Entre éstas, se resaltan topologías de SFV con MPPT-distribuido, ver Fig. 1. Este tipo de tecnologías ofrecen varias ventajas, por ejemplo:

- El MPPT se realiza a nivel MFV;
- Tienen una estructura modular, tal que el sistema se puede reconfigurar ante un evento de falla;
- Se puede añadir controlabilidad al SFV para ofrecer servicios auxiliares al sistema eléctrico;

Debido a estas ventajas, esta topología ha sido objeto de estudio en los últimos años. En el artículo Alonso (2012), se realizó un análisis, en estado estable, con el propósito de conocer los límites sobre sombreado parcial que aún pueden ser compensados por esta topología. También se estudió la influencia del voltaje del bus de CD del inversor sobre el desempeño global del SFV. En Renaudineau (2015), se propuso un algoritmo de optimización para la asignación de referencias en cada sistema MPPT. En Kasper (2014), se realizó un estudio para determinar el tipo de convertidor cd/cd que mejor se adapta a una configuración FV con MPPT distribuido.

Así, pese a los previos estudios realizados sobre este tipo de configuraciones de SFV, un análisis de estabilidad, del SFV con MPPT-distribuido, no ha sido reportado en la literatura. En consecuencia, este artículo presenta un estudio sobre SFV con MPPT-Distribuido, basándose en las propiedades de pasividad que poseen estos sistemas, Arjan Van der Schaft (2000). De esta manera, éste establece las bases para diseño de controladores MPPT y de inyección de potencia activa/reactiva, con una perspectiva basada en la interconexión de sistemas.

El artículo está organizado de la siguiente manera. En la Sec. 2, se presenta una breve descripción de un SFV con MPPT-distribuido. En la Sec. 3, se presenta el modelo, y sus propiedades, de las diferentes etapas que conforman un SFV con interconexión a la red eléctrica. En la Sec.

⋆ Se agradece a la Secretaría de Educación Pública (SEP), a través del Programa para el Desarrollo Profesional Docente (PRODEP), por el apoyo otorgado al proyecto titulado: *Estrategias para el Diseño de Sistemas de Generación Fotovoltaica Tolerantes a Fallas.*

4, se presenta el resultado de pasividad para un SFV con inversor tipo string. En la Sec. 5, se presenta el principal resultado de este artículo, es decir, la demostración de estabilidad del SFV con MPPT-distribuido. Finalmente, el artículo concluye con una sección de comentarios finales y trabajo futuro.

2. SFV CON MPPT-DISTRIBUIDO

En esta sección se describe el sistema en estudio. La Fig. 1 muestra un diagrama eléctrico del SFV con MPPT distribuido, el cual está formado por un conjunto de N convertidores cd/cd, *en conexión cascada*, denominados como microconvertidores (MC). Notar que, cada MC maneja únicamente la potencia disponible de uno de los N-MFV. De esta manera, el voltaje en cd del convertidor cd/ca (*inversor*) es generado por la suma de voltajes de salida v_{ok} ($\forall\ k \in \{1, 2, \ldots, N\}$) de los N-MC. A través del inversor, se realiza la interconexión a la red, la cual se representa por las tensiones de fase e_{abc}. En este estudio se considera, como filtro de enlace entre el inversor y la red eléctrica, un filtro inductivo L. En estudios futuros, el análisis incorporará la dinámica de filtros LC y LCL.

3. MODELADO DEL SFV

En esta sección se presentan los modelos, y sus propiedades de pasividad, de cada una de las etapas que forman al SFV con MPPT-distribuido. Primero, se presentan las propiedades de los módulos fotovoltaicos (MFV). Después, se presenta el modelo, y propiedades, de los MC. Finalmente, se presenta el análisis para el modelo del inversor trifásico.

3.1 Modelado de los MFV

Es una práctica común describir la curva característica de un MFV a través de un mapeo no-lineal *sin memoria*, ver Mahmoud (2012), dado por:

$$i_{fv}(t) = f(v_{fv}(t), t);\ \forall\ t \tag{1}$$

tal que, la corriente del MFV i_{fv} es dependiente del voltaje v_{fv} en terminales del MFV y de la condición climatológica (*variante en el tiempo*). En la Fig. 2 se presenta la curva característica (v_{pv} - i_{pv}) para un MFV bajo condiciones de irradiancia uniforme. Como se puede observar del gráfico, la curva vive en el primer cuadrante para todas las posibles condiciones de operación del MFV.

Resultado 1. Un MFV se puede representar matemáticamente por un mapeo estático:

$$f\colon L_{2e}(U) \to L_{2e}(U)$$
$$v_{fv} \mapsto i_{fv} = f(v_{fv}),$$

el cual es un mapeo [1] entrada-salida *pasivo*, tal que, se satisface la siguiente desigualdad:

$$v_{fv} f(v_{fv}) \geq 0.$$

▼

Comentario 1. Es importante resaltar que esta propiedad de pasividad se cumple incluso bajo condiciones de irradiancia no-uniformes (*por ejemplo, sombreados parciales*).

[1] U representa un espacio lineal de dimensión finita (*adecuada en cada modelo*) con producto interno $\langle \cdot, \cdot \rangle$ y norma $\| \cdot \|$. Además, L_{2e} representa el espacio extendido del espacio Hilbert L_2.

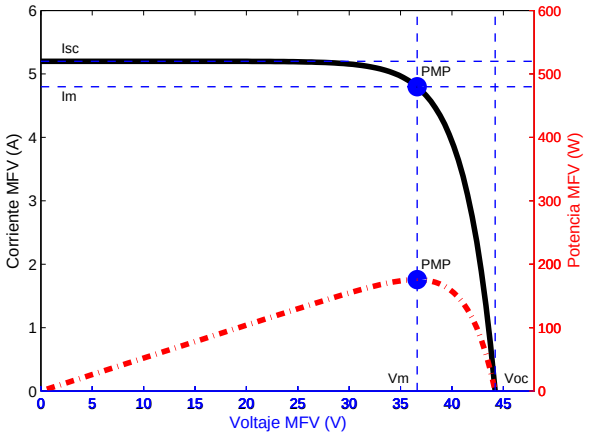

Figura 2. Curvas características de un MFV.

Bajo esta condición, la curva característica presenta puntos de máxima potencia *locales*, sin embargo, ésta aún vive en el primer cuadrante.

3.2 Modelado Dinámico del k-ésimo MC

En esta sección se presenta el modelo dinámico del MC. La Fig. 3 muestra el diagrama eléctrico del k-ésimo MC de la arquitectura fotovoltaica con MPPT-distribuido. En este estudio, cada MC está constituido por un filtro capacitivo C_1 y un convertidor cd/cd tipo elevador. El modelo se realiza a través de las variables de carga eléctrica (q_{C_1}, q_{C_2}) de los capacitores C_1, C_2, y del flujo magnético (ϕ_L) del inductor L. Las resistencias R_{C_1}, R_L y R_{C_2} representan las pérdidas en el capacitor de entrada C_1, el inductor L y el capacitor de salida C_2, respectivamente.

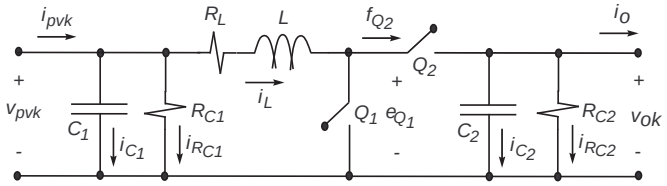

Figura 3. k-ésimo microconvertidor.

De esta manera, el modelo del k-ésimo MC se puede escribir en forma compacta por:

$$\dot{z}_{1k} = -R_{C_1}^{-1} C_1^{-1} z_{1k} + \left(i_{pvk} - L^{-1} z_{2k}\right) \tag{2}$$
$$\dot{z}_k = \left[\bar{u}_k \mathcal{J} - \mathcal{R}\right] \frac{\partial \mathcal{H}(z_k)}{\partial z_k} + \mathcal{E}_k$$

donde $z_{1k} = q_{C_{1k}}$, $z_k = [z_{2k}, z_{3k}]^T = [\phi_{Lk}, q_{C_{2k}}]^T$, $\bar{u}_k = 1 - u_k$, con $k \in \{1, 2, \ldots, N\}$ y

$$\mathcal{J} = \begin{bmatrix} 0 & -1 \\ 1 & 0 \end{bmatrix};\quad \mathcal{R} = \begin{bmatrix} R_L & 0 \\ 0 & R_{C_2}^{-1} \end{bmatrix};\quad \mathcal{E}_k = \begin{bmatrix} C_1^{-1} z_{1k} \\ -i_o \end{bmatrix}.$$

La señal u_k en (2) representa el ciclo de trabajo de cada MC. En este caso, el Hamiltoniano está dado por:

$$\mathcal{H}(z_k) = \frac{1}{2}\frac{q_{C_{1k}}^2}{C_1} + \frac{1}{2}\frac{\phi_{Lk}^2}{L} + \frac{1}{2}\frac{q_{C_{2k}}^2}{C_2}.$$

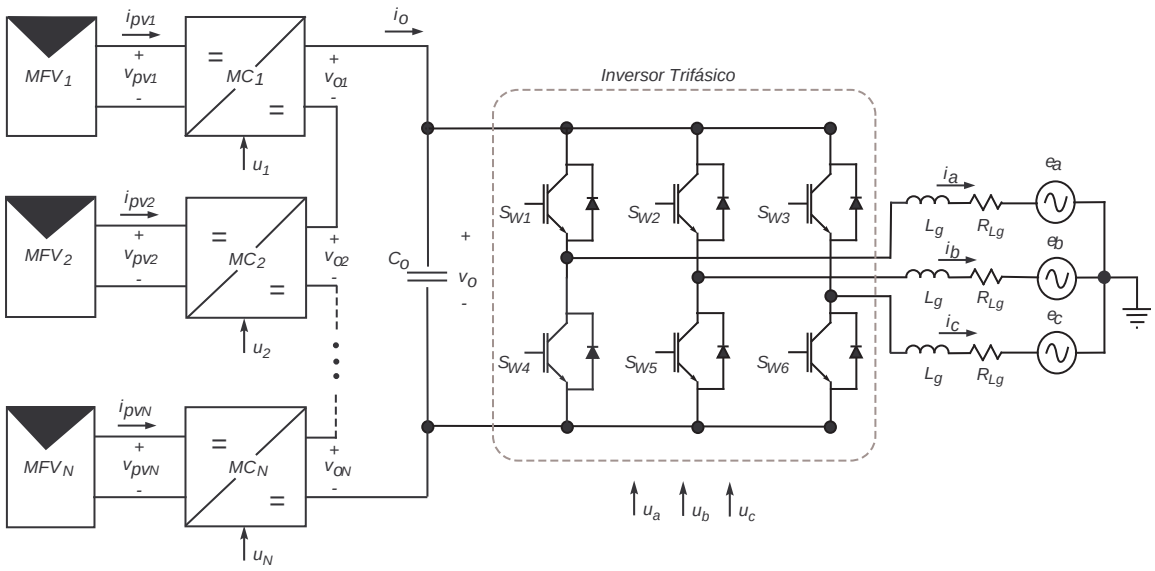

Figura 1. Sistema FV conectado a Red con MPPT Distribuido.

Notar que, $\mathcal{J}$ es una matriz anti-simétrica de 2×2, la cual se conoce como matriz de interconexión. Además, $\mathcal{R}$ es una matriz diagonal definida positiva, tal que las siguientes propiedades se satisfacen $\mathcal{J}=-\mathcal{J}^T$ y $\mathcal{R}=\mathcal{R}^T>0$. Por último, observar que el modelo en (2) se puede representar a través de una estructura interconectada como se ilustra en la Fig. 4.

En las siguientes subsecciones, se presenta el análisis para cada uno de subsistemas señalados en la Fig. 4, es decir, Σ_{1k}, Σ_k y $\Psi(\cdot)$.

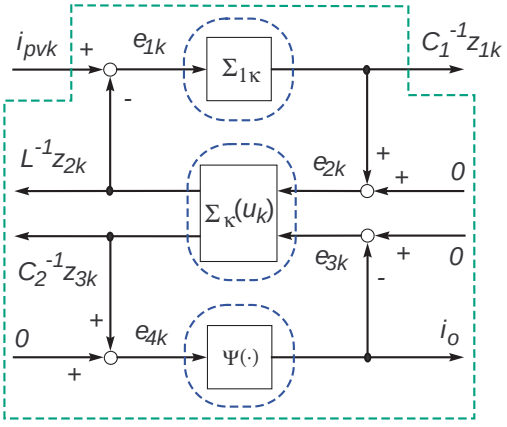

Figura 4. Estructura retroalimentada de un MC.

Subsistema Σ_{1k}**:** A partir de (2) y Fig. 4, el subsistema Σ_{1k} está dado por:

$$\dot{z}_{1k}=-R_{C_1}^{-1}C_1^{-1}z_{1k}+e_{1k}$$
$$y_k=C_1^{-1}z_{1k}.$$

donde $e_{1k}\equiv\left(i_{pvk}-L^{-1}z_{2k}\right)$. Ahora, si se define a

$$\mathcal{H}(z_{1k})=\frac{1}{2}z_{1k}^2$$

como la función de almacenamiento de energía del subsistema Σ_{1k}, entonces la derivada de $\mathcal{H}(z_{1k})$ a lo largo de las trayectorias del subsistema está dada por:

$$\begin{aligned}\dot{\mathcal{H}}(z_{1k})&=z_{1k}\dot{z}_{1k}\\&=-R_{C_1}^{-1}C_1^{-1}z_{1k}^2+z_{1k}e_{1k}.\end{aligned}$$

Puesto que $z_{1k}=C_1y_k$, *ver* (3), entonces se obtiene la derivada de $\mathcal{H}(z_{1k})$ como:

$$\dot{\mathcal{H}}(C_1y_k)=-R_{C_1}^{-1}C_1y_k^2+C_1y_ke_{1k}.$$

Por lo tanto, se obtiene que el subsistema Σ_{1k}, con entrada e_{1k} y salida y_k es *estrictamente pasivo a la salida*, Arjan Van der Schaft (2000), lo cual implica que el subsistema Σ_{1k} es $\mathcal{L}_2$ *ganancia-finita*. Además, con $e_{1k}=0$ y considerando (3), se obtiene que:

$$y(t)_k\equiv 0\ \Leftrightarrow\ z_{1k}=0,$$

lo cual demuestra que Σ_{1k} es, además, *estado-cero observable*, Arjan Van der Schaft (2000). En consecuencia, el origen de Σ_{1k} es *asintóticamente estable*.

Resultado 2. El sistema Σ_{1k} representado matemáticamente por:

$$\begin{aligned}\Sigma_{1k}\colon L_{2e}(U)&\to L_{2e}(U)\\e_{1k}&\mapsto C_1^{-1}z_{1k}=\Sigma_{1k}(e_{1k}),\end{aligned}$$

es un mapeo entrada-salida *estrictamente pasivo a la salida*, tal que, se satisface la siguiente desigualdad para algún $\epsilon_{1k}>0$, $\beta_{1k}>0$ y $\forall\, e_{1k}\in L_{2e}(U)$, $\forall\, T\geq 0$:

$$\langle\Sigma_{1k}(e_{1k}),e_{1k}\rangle_T\geq\epsilon_{1k}\parallel(\Sigma_{1k}(e_{1k}))_T\parallel_2^2-\beta_{1k}.\qquad(3)$$

▼

Subsistema Σ_k**:** A partir de (2), y considerando el Hamiltoniano $\mathcal{H}(z_k)$, se obtiene la derivada del Hamiltoniano a lo largo de las trayectorias del sistema, la cual está dada por:

$$\dot{\mathcal{H}}(z_k)=-\left(\frac{\partial\mathcal{H}(z_k)}{\partial z_k}\right)^T\mathcal{R}\left(\frac{\partial\mathcal{H}(z_k)}{\partial z_k}\right)+\left(\frac{\partial\mathcal{H}(z_k)}{\partial z_k}\right)^T\mathcal{E}_k.$$

Ahora, si se define como salida pasiva a

$$\mathcal{Y} = \left(\frac{\partial \mathcal{H}(z_k)}{\partial z_k} \right),$$

entonces, se satisface la siguiente desigualdad:

$$\dot{\mathcal{H}}(z_k) < \mathcal{Y}^T \mathcal{E}_k. \tag{4}$$

Resultado 3. El sistema Σ_k representado matemáticamente por:

$$\Sigma_k : L_{2e}(U) \rightarrow L_{2e}(U)$$
$$\mathcal{E}_k \mapsto \mathcal{Y} = \Sigma_k(\mathcal{E}_k)$$

donde $\mathcal{E}_k = [e_{2k}, e_{3k}]^T$ y $\mathcal{Y} = [L^{-1} z_{2k}, C_2^{-1} z_{3k}]^T$, es un mapeo *estrictamente pasivo* con entrada $\mathcal{E}_k$ y salida $\mathcal{Y}$, tal que se satisface la siguiente condición:

$$\langle \Sigma_k(\mathcal{E}_k), \mathcal{E}_k \rangle_T = \underbrace{e_{2k} L^{-1} z_{2k}}_{P_{pv}} + \underbrace{e_{3k} C_2^{-1} z_{3k}}_{P_o} > -\beta_{2k} - \beta_{3k}.$$

▼

Comentario 2. Es importante observar que la entrada de control $\bar{u}_k$ aparece en el subsistema Σ_k. Por lo tanto, el controlador deberá ser diseñado tal que se preserven las propiedades de pasividad, Cisneros (2015). El diseño de un controlador para este subsistema con capacidad de *seguimiento de punto de máxima potencia* se presentará en futuros trabajos.

Subsistema Ψ (Elemento de carga): En el caso de un único convertidor cd/cd elevador, es decir ($k = 1$), se requiere que el elemento de carga, representado por el mapeo $\Psi(\cdot)$, sea un sistema pasivo para garantizar propiedades de estabilidad del sistema interconectado, es decir, se asume la siguiente condición:

$$e_4 \Psi(e_4) \geq 0. \tag{5}$$

Comentario 3. En la Sec. 3.3, se demostrará que un convertidor cd/ca (*inversor*) es un elemento pasivo de la entrada v_o a la salida i_o, tal que, éste se puede conectar en terminales de un MC sin destruir las propiedades de pasividad del sistema interconectado.

3.3 Modelado del Inversor

El modelo del convertidor cd/ca trifásico (*inversor*) se presenta en esta sección en coordenadas del marco de referencia dq. Este modelo también puede ser escrito, en forma compacta, a través de una estructura hamiltoniana dada por:

$$\dot{x} = [\mathcal{J}_i - \mathcal{R}_i] \frac{\partial \mathcal{H}_i(x)}{\partial x} + g(x)m + \vartheta \tag{6}$$

donde $x = [x_1, x_2, x_3]^T = [L_g i_d, L_g i_q, C_o v_o]^T$ representa el vector de variables del sistema, $m = [m_d, m_q]^T$ representa el vector de entradas de control, y $\vartheta = [-e_d, -e_q, i_o]^T$ representa el vector de entradas externas. El Hamiltoniano, en este caso, está dado por

$$\mathcal{H}_i(x) = \frac{1}{2} L_g^{-1} x_1^2 + \frac{1}{2} L_g^{-1} x_2^2 + \frac{1}{2} C_o^{-1} x_3^2$$

y

$$\mathcal{J}_i = \begin{bmatrix} 0 & -\omega_{dq} L_g & 0 \\ \omega_{dq} L_g & 0 & 0 \\ 0 & 0 & 0 \end{bmatrix}; \quad \mathcal{R}_i = \begin{bmatrix} R_{L_g} & 0 & 0 \\ 0 & R_{L_g} & 0 \\ 0 & 0 & 0 \end{bmatrix},$$

$$g(x) = \begin{bmatrix} v_o & 0 \\ 0 & v_o \\ -i_d & -i_q \end{bmatrix}.$$

Notar que, nuevamente $\mathcal{J}_i$ es una matriz anti-simétrica, en este caso de 3×3, y $\mathcal{R}_i$ es una matriz diagonal semi-definida positiva, tal que las siguientes propiedades se satisfacen $\mathcal{J}_i = -\mathcal{J}_i^T$ y $\mathcal{R}_i = \mathcal{R}_i^T \geq 0$.

Ahora, tomando la derivada del Hamiltoniano a lo largo de las trayectorias del sistema (6) se obtiene:

$$\dot{\mathcal{H}}_i(x) = -\left(\frac{\partial \mathcal{H}_i(x)}{\partial x} \right)^T \mathcal{R} \left(\frac{\partial \mathcal{H}_i(x)}{\partial x} \right) + \cdots$$
$$\cdots + \left(\frac{\partial \mathcal{H}_i(x)}{\partial x} \right)^T g(x)m + \left(\frac{\partial \mathcal{H}_i(x)}{\partial x} \right)^T \vartheta.$$

Ahora, si se definen como salidas pasivas a

$$\mathcal{Y}_1 = g(x)^T \frac{\partial \mathcal{H}_i(x)}{\partial x},$$

y

$$\mathcal{Y}_2 = \vartheta,$$

entonces, se satisface la siguiente desigualdad:

$$\dot{\mathcal{H}}_i(x) \leq \mathcal{Y}_i^T \mathcal{E}_i, \tag{7}$$

donde $\mathcal{Y}_i = [\mathcal{Y}_1, \mathcal{Y}_2]^T$ y $\mathcal{E}_i = \left[m, \frac{\partial \mathcal{H}_i(x)}{\partial x} \right]^T$.

Resultado 4. El sistema Σ_i, descrito por (6) y representado matemáticamente por:

$$\Sigma_i : L_{2e}(U) \rightarrow L_{2e}(U)$$
$$\mathcal{E}_i \mapsto \mathcal{Y}_i = \Sigma_i(\mathcal{E}_i),$$

es un mapeo *pasivo* con entrada $\mathcal{E}_i$ y salida $\mathcal{Y}_i$, tal que se satisface la siguiente condición:

$$\langle \Sigma_i(\mathcal{E}_i), \mathcal{E}_i \rangle_T \geq -\beta_i.$$

▼

Comentario 4. A partir de este resultado, se concluye que el inversor representa un sistema pasivo de la entrada v_o a la salida i_o, tal que, éste elemento se puede interconectar a un MC preservando propiedades de pasividad. La prueba de esta afirmación se presenta en las secciones 4 y 5.

Comentario 5. Nuevamente, observar que el control de potencia activa/reactiva en el punto de interconexión a la red eléctrica, deberá ser diseñado tal que, se preserven las propiedades de pasividad del sistema Σ_i.

4. INVERSOR TIPO STRING

En esta sección se presenta el análisis de estabilidad para un inversor tipo string. Como se ilustra en la Fig. 5, esta topología FV consiste de una cadena de MFV, un único MC y un inversor. A partir de los resultados obtenidos en las secciones anteriores se demostrará, en las siguientes subsecciones, que un SFV, con inversor tipo string, está constituido por la interconexión pasiva de sistemas pasivos.

4.1 Propiedades de Pasividad SFV String

El análisis toma como referencia el sistema ilustrado en la Fig. 4, el cual satisface las siguientes restricciones de interconexión (con $k = 1$):

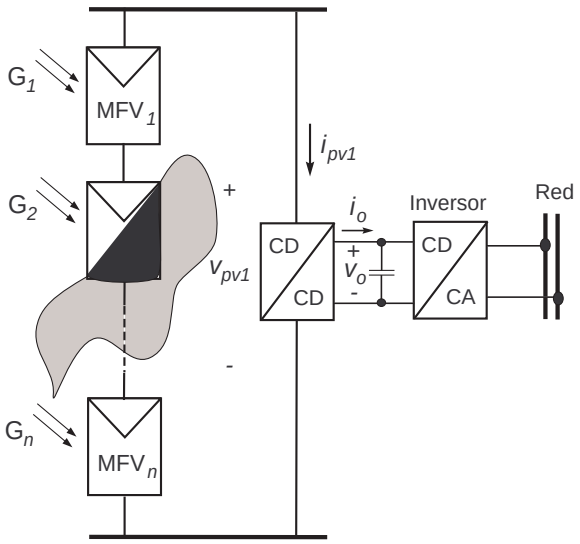

Figura 5. SFV con inversor string.

$$e_{11} = i_{pv1} - L^{-1} z_{21}$$
$$e_{21} = C_1^{-1} z_{11}$$
$$e_{31} = -i_o$$
$$e_{41} = C_2^{-1} z_{31}.$$

A partir de estas ecuaciones y usando los resultados 2-4, para cualquier $i_{pv1} \in L_{2e}(U)$, y cualquier $T \geq 0$ se cumple que

$$\begin{aligned} \langle C_1^{-1} z_{11}, e_{11} \rangle_T + \langle L^{-1} z_{21}, e_{21} \rangle_T + \\ + \langle C_2^{-1} z_{31}, e_{31} \rangle_T + \langle i_o, e_{41} \rangle_T = \\ \langle C_1^{-1} z_{11}, i_{pv1} \rangle_T \geq \\ \epsilon_{11} \parallel (C_1^{-1} z_{11})_T \parallel_2^2 - \beta_{11} - \beta_{21} - \beta_{31} = \\ \epsilon_{11} \parallel (C_1^{-1} z_{11})_T \parallel_2^2 - \beta \end{aligned}$$

con $\beta = \beta_{11} + \beta_{21} + \beta_{31}$. Como resultado, el sistema interconectado de la Fig. 4 con entrada i_{pv1} y salida $C_1^{-1} z_{11}$ es *estrictamente pasivo a la salida*, lo cual implica que un SFV con inversor string es $\mathcal{L}_2$ *ganancia-finita*.

Comentario 6. La nomenclatura empleada en este análisis es consistente con la referencia Arjan Van der Schaft (2000), es decir,

$$\langle y, u \rangle_T \equiv \int_0^T \langle y, u \rangle dt,$$

donde $\langle y, u \rangle$ denota el producto interno entre y y u.

Comentario 7. Este resultado, además, muestra un principio de conservación de energía, es decir, notar que la energía solar capturada por el MFV, es igual a la energía disipada en el convertidor cd/cd y en el elemento de carga.

5. EXTENSIÓN A MPPT DISTRIBUIDO

En esta sección se presenta el análisis para el SFV con MPPT-distribuido. De hecho, éste es una extensión del resultado que se presentó en la sección 4. El análisis se realizó únicamente para la conexión en cascada de 2 MC ($k = 2$). Se considera, como trabajo futuro, generalizar el resultado para N-microconvertidores. Por lo tanto, en este caso, el sistema interconectado se ilustra en la Fig. 6. De ésta, se puede observar que los voltajes de salida de cada MC se suman para generar el voltaje del bus de cd $e_4 = v_o$, mientras que la corriente de salida $i_o = -e_{31} = -e_{32}$ es la misma para cada MC.

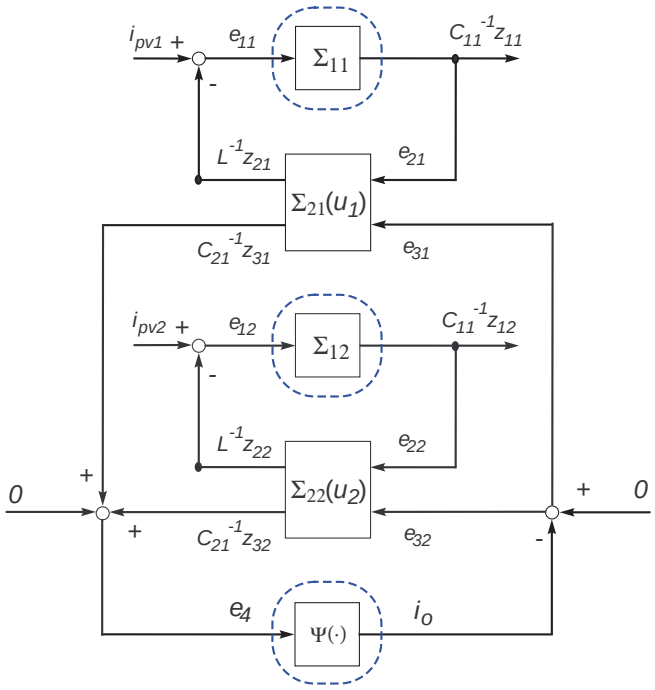

Figura 6. Conexión retroalimentada de 2 MC.

A partir del resultado 2, se puede garantizar que los subsistemas Σ_{11} y Σ_{12}, ilustrados en la Fig. 6, son *estrictamente pasivos a la salida*, y por lo tanto, se satisfacen las siguientes desigualdades $\forall\ j\ \in \{1, 2\}$:

$$\langle \Sigma_{1j}(e_{1j}), e_{1j} \rangle_T \geq \epsilon_{1j} \parallel (\Sigma_{1j}(e_{1j}))_T \parallel_2^2 - \beta_{1j}. \quad (8)$$

Además, a partir del resultado 3 se garantiza que los subsistemas $\Sigma_{21}(u_1)$ y $\Sigma_{22}(u_2)$ son estrictamente pasivos. Por lo tanto, $\forall\ j\ \in \{1, 2\}$:

$$\begin{aligned} \langle \Sigma_{2j}(\mathcal{E}_j), \mathcal{E}_j \rangle_T = \\ \underbrace{e_{2j} L^{-1} z_{2j}}_{P_{pvj}} + \underbrace{e_{3j} C_2^{-1} z_{3j}}_{P_{oj}} > \\ -\beta_{2j} - \beta_{3j}. \end{aligned} \quad (9)$$

Finalmente, la carga (*en este caso el inversor*) se modela a través del mapeo $\Psi(\cdot)$. De acuerdo con el resultado 4, este mapeo es *pasivo* de la entrada e_4 a la salida i_o. Notar que, el voltaje de entrada al inversor satisface la siguiente relación

$$v_o = e_4 = C_2^{-1}(z_{31} + z_{32}).$$

5.1 Propiedades de Pasividad SFV con MPPT Distribuido

El sistema interconectado, ilustrado en la Fig. 6, satisface las siguientes restricciones de interconexión $\forall\ j\ \in \{1, 2\}$:

$$e_{1j} = i_{pvj} - L^{-1} z_{2j}$$
$$e_{2j} = C_1^{-1} z_{1j}$$
$$e_{3j} = \Delta i_o - i_o$$
$$e_4 = C_2^{-1} \sum_{j=1}^{2} z_{3j}$$

A partir de estas ecuaciones, para cualquier $i_{pvj} \in L_{2e}(U)$ $\forall\ j\ \in \{1, 2\}$, y cualquier $T \geq 0$ se cumple que

$$\langle C_1^{-1} z_{11}, e_{11} \rangle_T + \langle L^{-1} z_{21}, e_{21} \rangle_T + \langle C_2^{-1} z_{31}, e_{31} \rangle_T +$$
$$+ \langle C_1^{-1} z_{12}, e_{12} \rangle_T + \langle L^{-1} z_{22}, e_{22} \rangle_T + \langle C_2^{-1} z_{32}, e_{32} \rangle_T +$$
$$+ \langle i_o, e_4 \rangle_T =$$
$$\langle C_1^{-1} z_{11}, i_{pv1} \rangle_T + \langle C_1^{-1} z_{12}, i_{pv2} \rangle_T \geq$$
$$\epsilon_{11} \parallel (\Sigma_{11}(e_{11}))_T \parallel_2^2 - \beta_{11} + \epsilon_{12} \parallel (\Sigma_{12}(e_{12}))_T \parallel_2^2 - \beta_{12}$$
$$- \beta_{21} - \beta_{31} - \beta_{21} - \beta_{32} \geq$$

En consecuencia, el sistema interconectado de la Fig. 6, con entrada

$$(i_{pv1}, i_{pv2})^T,$$

y salida

$$\left(C_1^{-1} z_{11}, C_1^{-1} z_{12}\right)^T$$

es *estrictamente pasivo a la salida*, lo cual implica que un SFV con MPPT-distribuido, con $k = 2$, es $\mathcal{L}_2$ *ganancia-finita*, Arjan Van der Schaft (2000).

6. CONCLUSIÓN

En este artículo se demostró formalmente, en primer lugar, que un SFV con inversor tipo string, es un sistema $\mathcal{L}_2$ *ganancia-finita*. Posteriormente, se demostró que un SFV con MPPT distribuido, para $k = 2$, es también un sistema $\mathcal{L}_2$ *ganancia-finita*. Estos resultados establecen las bases para el diseño de controladores con una perspectiva basada en la interconexión de sistemas. Se resalta que los controladores para *seguimiento del punto de máxima potencia* e *inyección de potencia activa/reactiva a la red*, deberán ser diseñados, tal que no se destruyan las propiedades de pasividad de los subsistemas que conforman al SFV con MPPT-Distribuido. Como trabajo futuro, se realizará la prueba para una conexión de N-microconvertidores en conexión cascada. Además, se considerarán, en el análisis, convertidores cd/cd tipo elevador-reductor, así como filtros de enlace, entre el inversor y la red, del tipo LC y LCL.

REFERENCIAS

R. C. N. P. Podgurski y D. J. Perreault. Submodule Integrated Distributed Maximum Power Point Tracking for Solar Photovoltaic Applications. *IEEE Trans. Power Electron.*, vol. 28, no. 6, pp. 2957-2967, Jun. 2013.

Freddy Chan y Hugo Calleja. Reliability Estimation of Three Single-Phase Topologies in Grid-Connected PV Systems. *IEEE Trans. Ind. Electron.*, vol. 58, no. 7, pp. 2683-2689, Jul. 2011.

Samir Kouro, Jose I. Leon, Dmitri Vinnikov, y Leopoldo G. Franquelo. Grid-Connected Photovoltaic Systems: An Overview of Recent Research and Emerging PV Converter Technology. *IEEE Industrial Electronics Magazine*, vol. 9, no. 1, pp. 47-61, Mar. 2015.

Ricardo Alonso, Eduardo Román, Asier Sanz, Víctor E. Martínez Santos, and Pedro Ibáñez. Analysis of Inverter-Voltage Influence on Distributed MPPT Architecture Performance. *IEEE Transactions on Industrial Electronics*, Vol. 59, No. 10, October 2012.

Hugues Renaudineau, Fabrizio Donatantonio, Julien Fontchastagner, Giovanni Petrone, Giovanni Spagnuolo, Jean-Philippe Martin, and Serge Pierfederici. A PSO-Based Global MPPT Technique for Distributed PV Power Generation. *IEEE Transactions on Industrial Electronics*, Vol. 62, No. 2, February 2015.

Matthias Kasper, Dominik Bortis, and Johann W. Kolar. Classification and Comparative Evaluation of PV Panel-Integrated DC/DC Converter Concepts. *IEEE Transactions on Power Electronics*, Vol. 29, No. 5, May 2014.

Arjan Van der Schaft. L2-Gain and Passivity Techniques in Nonlinear Control. *Springer*, 2000.

Y. Mahmoud, W. Xiao y H. H. Zeineldin. A Simple Approach to Modeling and Simulation of Photovoltaic Modules. *IEEE Trans. Sustain. Energy*, vol. 3, no. 1, pp. 185-186, Jan. 2012.

R. Cisneros, M. Pirro, G. Bergna, R. Ortega, G. Ippoliti, M. Molinas. Global Tracking Passivity-Based PI Control of Bilinear Systems: Application to the Boost and Modular Multilevel Converters. *Control Engineering Practice*,43, October 2015, 109-119.

Percolation Theory Approach to Transient Stability Analysis of Power Systems

Alejandra Machuca-Moreno * **Eduardo Mojica-Nava** **

* *Universidad Nacional de Colombia, Bogota, Colombia. (e-mail:lamachucam@unal.edu.co)*
** *Universidad Nacional de Colombia, Bogota, Colombia. (e-mail: eamojican@unal.edu.co)*

Abstract: This paper proposes a methodology for the stability assessment of a power grid based on percolation theory. Once it is proved that the rotor angle stability depends on the initial condition and the topological properties of the network, tools provided by complex network and percolation theory are used to identify the most vulnerable buses from a transient stability perspective in order to locate the best places to install control to prevent the spread of lack of synchronism through the grid. Finally, the proposed approach is tested on the transmission network system of IEEE 14.

Keywords: Smart Power Grid, Transient Stability, Complex Networks, Percolation Theory.

1. INTRODUCTION

Power system is the set of elements that generate, transmit and distribute electrical energy to consuming agents such as residential buildings, factories, street lighting, and so on. Most of power generators are electromechanical systems, they use the energy of water or fossil fuels to generate mechanical energy, which is then converted into electrical energy (A.R. Bergen (1999)). Normal operating conditions or *steady state* satisfy the following conditions:

- All machines rotate at the same velocity and they are never accelerated.
- The voltage and currents generated have the same frequency.

The first condition is called *frequency stability* while the second is known as *voltage stability*. When all generators rotate at the same velocity, the relative difference between their rotor angles remains constant. *Rotor angle stability* is the ability of the power system to maintain this synchronism.
Transient Stability is the name given to the maintenance of rotor angle stability when the system is subjected to large disturbances (Kundur et al. (2004)).

There are several methods for transient stability analysis of power systems such as:

- Automatic Learning: Based on machine learning techniques.(Wehenkel (1998))
- Direct methods: Based on obtaining Lyapunov functions for simple models of the systems. (Varaiya et al. (1985))
- Simulations in time domain: Solving differential equations using numerical methods. (M.Pavella (1994))

In practical situations, the most common way to check transient stability is running vast time-domain simulations for those that are considered the important fault scenarios. However, power systems are large scale systems, and power engineers need to predict those scenarios based on guesses; sometimes, criteria like bigger capacity are used. However, they are still guesswork made by humans, and are prone to mistakes. (M.Pavella (1994))

Currently, the power grid is continuously growing thanks to new uses of electrical energy and demand vegetative growth. Also, the envisioned future power generation will rely on renewable energy sources and they are highly stochastic, there will be an increasing number of transient disturbances acting on the power system. Considering these future conditions, it is going to be more difficult to guess the important fault scenarios.

This paper proposes an approach of transient stability analysis in the power grid based on topological information by identifying the most vulnerable generators of the grid using percolation theory. The main objective of identifying the vulnerable nodes is to place controls on them in order to prevent the loss of synchronism in the other generators of the grid.

2. REVIEW OF TRANSIENT STABILITY ANALYSIS

The equation that governs rotor motion of a synchronous machine is known as the swing equation, and is based on the elementary principle in dynamics which states that accelerating torque is the product of the moment of inertia of the rotor times its angular acceleration. It can be written for the synchronous generator in the form

$$\frac{H}{180f}\frac{d^2\delta}{dt^2} = P_a = P_m - P_e - D\frac{d\delta}{dt}, \tag{1}$$

where H is the inertia constant of the machine, f is the frequency of the system, δ is the rotor angle, P_a is the accelerating power, P_m is the mechanical power, P_e is the

electrical power and D is the damping coefficent of the machine (J.Machoswki (2008)).

Constants coefficients H and D depend on the size and capability of the machine, f is a constraint of the system, and P_m depends on the external mechanical power (water, oil, etc.), and for this analysis it is taken as a constant.

This equation shows that every time the mechanical and the electrical power are unequal the second derivative of the rotor angle is proportional to that difference; meaning that there is an acceleration in the machine.

Considering P_m as a constant, the main variable to analyze is the electric power; for simplified models this power is described as

$$P_e = P_{max} \cdot sin\delta = \frac{|E_1'||E_2'|}{X} \cdot sin\delta \tag{2}$$

For (2) the generator is supplying power through a transmission system. Voltage $|E_1'|$ is the transient internal voltage of the generator and $|E_2'|$ is the voltage at the receiving end and X is the transfer reactance between $|E_1'|$ and $|E_2'|$ (J.Grainger (1994)).

Most systems have more than one synchronous machine; for a system with n generators, the active output of the i^{th} generator is given by

$$\begin{aligned} P_e &= Re\{E_i I_i^*\} \\ &= Re\left\{E_i \sum_{j=1}^{n} Y_{ij}^* E_j^*\right\} \\ &= E_i^2 G_{ii} + \sum_{j=1}^{n} E_i E_j \left[B_{ij} sin(\delta_i - \delta_j) + G_{ij} cos(\delta_i - \delta_j)\right] \end{aligned} \tag{3}$$

$|E_i|$ and $|E_j|$ are the internal transient voltages, and B_{ij} and G_{ij} are the susceptance and conductance between generators i and j (P.Kundur (1994)).

Equation (3) demonstrates that rotor angle stability depends highly on the initial conditions of the system and its transfer admittance, which is heavily reliant on the topological structure of the power network.

3. PERCOLATION THEORY AND NETWORK RESILIENCE

Percolation theory describes the behavior of connected clusters in a graph, in order to understand this concept assume that some liquid is poured on top of a porous material, and wonder if the liquid will be able to reach the bottom of it (Broadbent and Hammersley (1957)). Percolation is a pervasive concept that arises not only from atomic and molecular solids in physics, it also comes from social, technological, and natural systems (Strogatz (2001); ben Avraham and Glasser (2007); S et al. (2000)), information diffusion in online social networks (Barrat et al. (2008)), resistor networks (Kirkpatrick (1973)), forest fires (Drossel and Schwabl (1992)), among others.

Consider a network whose edges are present with probability p; percolation studies the emergence of paths that percolate through the grid. For great values of p a lot edges are present, then big clusters of nodes connected by edges can form. The creation of a giant component during the percolation process is known as a percolation transition (Albert and lszl Barabsi (2002)).

Imagine taking a network and removing some fraction of its vertices or edges, what effect this will have on the performance of the network?, this is a practical interest that Percolation Theory can help us to analyze. It can help us to understand the macroscopic behavior of networks in relation to the microscopic states of its components (Newman (2010)).

4. TRANSIENT STABILITY APPROACH FROM A PERCOLATION THEORY PERSPECTIVE

First, the power grid must by modelled as a complex network. The regional transmission system was simulated but the local distribution system will be excluded from the analysis. The vertices of a complex network represent the generation centrals, and load or switching substations; meanwhile, the edges are modelled as the high voltage transmission lines. The topology is not hard to determine, a power network has a spatial and geographic interpretation, and its the same given to its graph model.

The admittance matrix of a power network has the same formulation of the Laplacian of a graph: the diagonal elements of the admittance matrix are equal to the degree matrix and the non-diagonal elements are the same to the adjacency matrix.

For a graph $\mathcal{G}$ formally defined as $\mathcal{G} = (V, E, \omega)$, where V is a finite set of vertices, E is a set of edges, and ω is the weight between vertices (Mesbahi and Egerstedt (2010)). The Laplacian $L(\mathcal{G}_w)$ is defined as

$$[\Delta(\mathcal{G}_w)]_{ii} = \sum_{\{j|(v_j,v_i)\ \epsilon\ E(\mathcal{G})\}} w_{ij} \tag{4}$$

$$[A(\mathcal{G}_w)]_{ij} = \begin{cases} w_{ij} & \text{if } v_i v_j \ \epsilon\ E(\mathcal{G}) \\ 0 & \text{otherwise} \end{cases} \tag{5}$$

$$L(\mathcal{G}_w) = \Delta(\mathcal{G}_w) - A(\mathcal{G}_w) \tag{6}$$

This paper considers the following considerations for the modelling of the power grid.

- It only considers the high voltage system and it is assumed balanced.
- The impedances between bus and neutral are neglected.
- All transmission line and transformers are modelled as weighted edges, the weight is equal to the impedance between nodes.
- All parallel lines are modelled as an equivalent single line.
- Shunt impedances of lines are considered.
- Loads are modelled as constant admittances.
- All generator have the same constant of inertia (13,08 s) and damping constant (2 s).

This last consideration might seem mistaken, but, to analyse the effect of topological properties of the network on its transient stability, this two variables must be uniform in the grid.

Figures 1 shows the physical topology graph of IEEE 14 and test case.

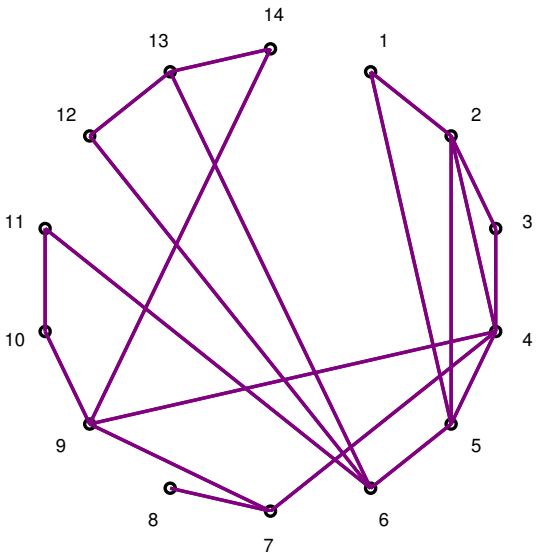

Fig. 1. Modeled graph of IEEE-14 bus test case

For the transient stability simulations it is used the Power System Analysis Toolbox - PSAT. For this specific case, all faults are balanced three phase faults on the buses, not on the high voltage lines; which means there are not changes of topology before or after the fault. In addition, all faults had a duration of 2 seconds.

For each system, a fault is simulated on every bus associated to a generator, as expected the generator suffered some kind of perturbation not only in its rotor angle but also in its frequency. Because of the duration of the fault, other synchronous machines begin to suffer this disturbances. It means every time a generator losses synchronism this perturbation percolates through the grid to reach other machines; creating a cluster of unsynchronised units. This process might be stopped or retarded by placing a control in the most vulnerable generator. Figures 2 and 3 show the frequency variation of each generator of the system for a Fault in machines 1 and 6 respectively.

Acording to the Colombian Network Code (re Regulacion de Energia y Gas CREG (1995)), all generator units must have a setting of relay tripping for low or high frequency every time that variable gets out of the range between 57.5 - 63 Hz. Then, when the frequency of the generator is 10% to the way on this limits (59.75 Hz - 60.3 Hz), the generator counts as a part of the cluster.

Figure 4 shows the size of the cluster formed by the machines whose frequency is not on the speciied limits.

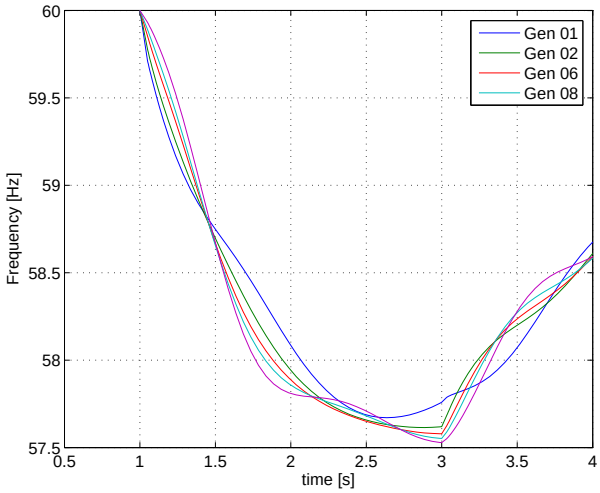

Fig. 2. Frequency variation due to fault on bus 1

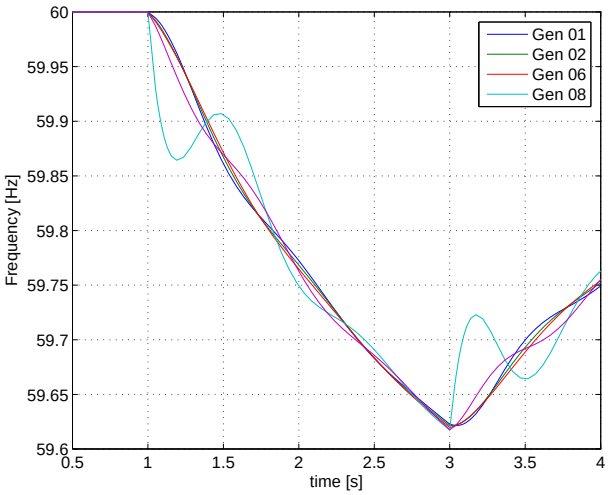

Fig. 3. Frequency variation due to fault on bus 6

When a fault is made in the bus associated to bus 1 or 2, it occurs a discrete percolation, all other generators seem to lost synchronism very fast. But, for machine 8 even when it lost synchronism right after the fault, there are several cycles before the others machines start to get out its state of synchronism. Finally, Generator 6 it starts to accelerate long afterwards the fault, but when it does all other generators begin to lost synchronism in which seems to be a delayed discrete percolation. For this test case, the bus 2 has been selected as the vulnerable node; Then, the same simulation is performed a second time with a overdamped generator 2; the damping coefficient for this machine is no longer 2, its 30 in order to emulate the controllers placed.

In Figure 5 Generator 1 and 2 dynamics does not seem to change, however, generator 6 never loss synchronism and machine 8 acceleration is some cycles delayed. The main objective of delay the percolation transition is been achieved. This gives some cycles to the smart grid to

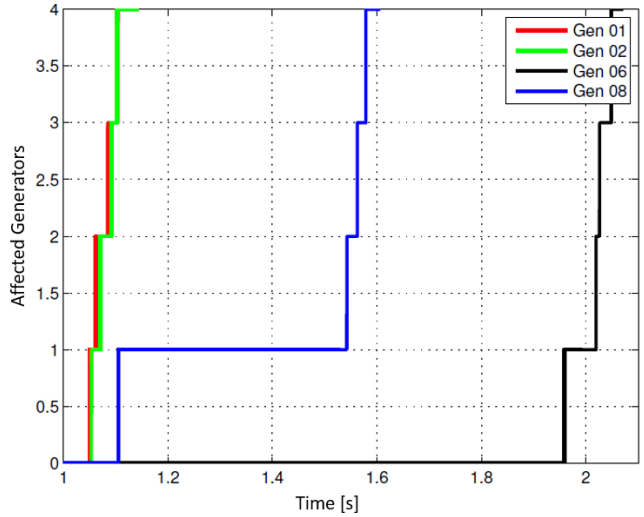

Fig. 4. Unsynchronized generators in IEEE-14 bus test case

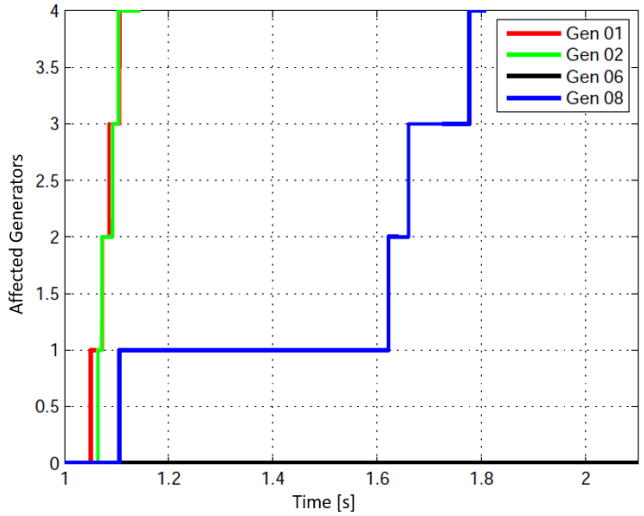

Fig. 5. Unsynchronized generators in IEEE-14 bus test case using an overdamping in machine 2

operate and prevent or decrease the potential damage of a blackout.

5. CONCLUSIONS

This paper provides an approach of network transient stability analysis using percolation and complex networks theory.

Dynamic equations demonstrates that transient stability relies heavily on the networks topological properties. In addition, the power grid characteristics show that it can be easily modelled as a complex network allowing us to use percolation theory analysis tools on it.

For a selected system, a balanced three phase fault was simulated in the generator and it was observed the frequency variation of all the generators in the network.

IEEE 14 bus system was tested and the results show how the lost of synchronism spreads through the grid; by identifying the bus associated to a generator which fault causes the most accelerated spreading and placing a control device on it can help the grid to delay and sometimes delete the percolation process improving the resilience of the grid.

REFERENCES

Albert, R. and lszl Barabsi, A. (2002). Statistical mechanics of complex networks. *Rev. Mod. Phys.*

A.R. Bergen, V. (1999). *Power Systems Analysis.* Tom Robbins, USA.

Barrat, A., Barthlemy, M., and Vespignani, A. (2008). *Dynamical Processes on Complex Networks.* Cambridge University Press, New York, NY, USA, 1st edition.

ben Avraham, D. and Glasser, M.L. (2007). Diffusion-limited one-species reactions in the bethe lattice. *Journal of Physics: Condensed Matter*, 19(6), 065107.

Broadbent, S.R. and Hammersley, J.M. (1957). Percolation processes. I. Crystals and Mazes. *Proceedings of the Cambridge Philosophical Society*, 53, 629–641.

Drossel, B. and Schwabl, F. (1992). Self-organized critical forest-fire model. *Phys. Rev. Lett.*, 69, 1629–1632.

J.Grainger, W. (1994). *Power System Analysis. United States of America.* McGraw-Hill Education, USA.

J.Machoswki, J.W.Bialek, J. (2008). *Power System Dynamics: Stability and Control.* John Wiley y Sons, United Kingdom.

Kirkpatrick, S. (1973). Percolation and conduction. *Rev. Mod. Phys.*, 45, 574–588.

Kundur, P., Paserba, J., Ajjarapu, V., Andersson, G., Bose, A., Canizares, C., Hatziargyriou, N., Hill, D., Stankovic, A., Taylor, C., Cutsem, T.V., and Vittal, V. (2004). Definition and classification of power system stability ieee/cigre joint task force on stability terms and definitions. *IEEE Transactions on Power Systems*, 19(3), 1387–1401.

Mesbahi, M. and Egerstedt, M. (2010). *Graph theoretic methods in multiagent networks.* Princeton series in applied mathematics. Princeton University Press, Princeton (N.J.).

M.Pavella, P. (1994). *Transient Stability of Power Systems: Theory and Practice.* John Wiley y Sons, United Kingdom.

Newman, M. (2010). *Networks: An Introduction.* Oxford University Press, Inc., New York, NY, USA.

P.Kundur (1994). *Power System Analysis. United States of America.* McGraw-Hill Education, USA.

re Regulacion de Energia y Gas CREG, C. (1995). *Res. 025 de 1995 - Codigo de Redes.* Ministerio de Minas y Energia - Republica de Colombia.

S, S., G, W., L., D.A., N, J., and D, S. (2000). Social percolation models. *PHYSICA. A*, 277, 239–247.

Strogatz, S.H. (2001). Exploring complex networks. *Nature*, 410(6825), 268–276.

Varaiya, P., Wu, F.F., and Chen, R.L. (1985). Direct methods for transient stability analysis of power systems: Recent results. *Proceedings of the IEEE*, 73(12), 1703–1715.

Wehenkel, L. (1998). *Automatic Learning Techniques in Power Systems.* Kluwer Academic Publishers Norwell, USA.

CHAPTER 14

PROCESS CONTROL

Adaptive Trajectory Tracking Control of a Boiler-Turbine Adopting an Algebra Approach

Sebastián Godoy Bordes, Mario E. Serrano, Santiago Rómoli, Gustavo Scaglia.

Instituto de Ingeniería Química, Universidad Nacional de San Juan, CONICET, Argentina.
(e-mail: sgodoy@unsj.edu.ar, serranoemanuel84@gmail.com, sromoli@unsj.edu.ar, gscaglia@unsj.edu.ar).

Abstract: This paper presents the development of a novel control law with parameter updating for trajectory tracking in a boiler-turbine system, which is a MIMO system where all state variables are strongly coupled. The proposed controller is simple and based on comprehensible concepts. Its design consists in representing the mathematical model using numerical methods, and then the control actions are computed through a linear algebra technique to accomplish the target of trajectory tracking control, by last, the parameter updating is based in the Lyapunov theory. The advantages of this method are the condition for the tracking error tends to zero, and the calculation of control actions, are obtained simply by solving a system of linear equations. Besides, the control technique has the ability to follow trajectories for two outputs simultaneously.

Keywords: Control System Design, Linear Algebra, Adaptive Control, Nonlinear Model, Tracking Trajectory Control.

1. INTRODUCTION

A boiler-turbine system is an energy conversion device that consists of a steam boiler and a turbine. The steam boiler part generates the thermal energy that is transferred into the turbine part. The boiler-turbine systems are able to supply electricity faster than other traditional systems, due to this systems can remain in operation, despite being disconnected of the electric grid. Then the system can be connected immediately when the grid requires it. The main control requirement of a boiler-turbine is about meeting the load demand quickly maintaining internal variables such as temperature and drum water level within the desired range to prevent the overheating or flooding in the system. In addition, the drum pressure must be controlled in order to remain bounded over a range of values according to variable operating conditions and the load demand. Also, the inputs and outputs constraints are imposed by physical limits such as the magnitude and saturation of the internal control valves. When these restrictions are added, the preliminary system becomes a multi-input multi-output (MIMO) nonlinear system (Bell et al., 1987), with state variables strongly coupled. Tracking control becomes a bigger challenge when the parametric model uncertainties that affect substantially the performance of the control system are considered. In this paper a simple control solution that addresses all the aspects mentioned above is proposed.

In general, the control structure used in the boiler-turbine must achieve the following challenges in order to be successfully applied.

1) The design method must be applied to a family of boiler turbine units. In general for each unit must be found the identification of the model and then the design of the controller. Each boiler-turbine unit has a specific model but in general, all of them show similar dynamics. For this reason, a generic control structure can be used for a general class of boiler-turbine units.

2) The control algorithms must be easy to implement and maintain. The application of advanced control methods generates, commonly, controllers that are complex, therefore it is necessary find techniques that guarantees a good performance with a simple control structure. First and second items are satisfied through techniques such as tuning method (Tan et al., 2004).

3) The performance for a wide-range load variation should be guaranteed for a single controller. In general, a variation in the load demand generates different operation points with different linearized models. Therefore, a single controller that ensure the performance in all operation points is a challenging task. Techniques such as gain schooled (Chen et al., 2004) and multi-model control (Tan et al., 2004) are used to achieve this objective.

The control process becomes even more interesting due to the severe nonlinearity in many variables over a wide operation range, tight operating constraints and the fact that the boiler-turbine plant take part, more frequently, in the grid power regulation. Furthermore the impossibility of having a accurate model without uncertainty difficult the process control (Toodeshki et al., 2008). Considering all the reasons mentioned above, the task of designing an advanced

controller for the boiler-turbine, that should be simple and easy to implement, is a challenging assignment.

The control of boiler-turbine has attracted the attention of many researches in the last years. Different control strategies have been proposed in the literature, where some of them use linearization techniques (Chen et al., 2004; Tan et al., 2005; Zheng et al., 2006; Tan et al., 2008; Sarailoo et al., 2012). Also in (Dimeo et al., 1995; Fang et al., 2004; Wu et al., 2009; Wu et al., 2010) different control methods based on Hinf are applied. In (Fang et al., 2004) the loop-shaping H\inf method is used to design the feedback controller and the final controller is reduced to a multivariable PI form. In (Wu et al., 2009; Wu et al., 2010), the nonlinear boiler-turbine dynamics were represented by the Takagi and Sugeno fuzzy model. Then, a fuzzy Hinf state feedback control law was synthesized in terms of linear matrix inequalities (LMIs). In (Thangavelusamy et al., 2013) the authors propose a Fuzzy logic based Sliding Mode Control (FSMC) to a drum-type boiler–turbine system with a proportional integral controller. The drawback of these methods lies in the need of linearizing the model for a certain range of operation.

Several authors suggest the combined application of different control techniques such as genetic algorithm (GA), fuzzy control, gain scheduling, sliding mode, for the control of boiler-turbine. In (Wu et al., 2012) the authors uses several techniques jointly, first, a nonlinear predictive control based on an online Recording Horizon Control (RHC) algorithm with genetic algorithm is designed. Second, an Hinf fuzzy controller is implemented. Finally a switching control strategy is applied to choose between the two described controllers. In (Wu et al., 2013) is presented a data-driven fuzzy modelling strategy and predictive controller for boiler-turbine. In this work the behavoir of the boiler-turbine is dived into a number of local regions taking into account the measurement data, then a multimodel-based model predictive control (MMPC) is developed. Finally a Data-driven Direct Predictive Controller (DDPC) is designed with an online update of the predictor. In (Ghabraei et al, 2015) a robust adaptive sliding mode controller (RASMC) for a multivariable nonlinear model of boiler– turbine is presented. First the authors develop an input–output feedback linearization with the purpose of overcome the coupled nonlinearities. Then a new decoupled inputs model is generated. Finally suitable sliding surface for the RASMC is considered. In these works, the complexity of the controller is incremented by the number of stages included in the control structure. Furthermore, in general, an approximation or transformation of the nonlinear system is required. In addition, most of the mentioned works focused on boiler–turbine dynamics without modeling imprecisions.

This work provides a simple solution to the above challenging problem. A new control approach originally developed for robotic systems (Scaglia et al., 2009) is applied successfully in trajectory tracking of a boiler-turbine in presence of parametric uncertainties. The technique uses numerical methods and linear algebra to solve the problem. This structure has been used successfully in different nonlinear multivariable models, (Rómoli et al., 2014, Serrano et al., 2014, Cheein et al.,2016). This simple approach suggests that knowing the value of the desired state, a value for the control action which forces the system to move from its current state to the desired one may be found. The theoretical fundamentals are based on easily understandable concepts and there is no need of complex calculations to attain the control signal. The adaptive scheme is obtained analyzing the system stability and the asymptotic stability of the complete controllers is proven through Lyapunov theory.

The paper is organized as follows: in Section 2, the dynamic model of a boiler-turbine is presented. The methodology of the controller design is shown in Section 3. The development of the parameter updating is detailed in Section 4. In Section 5, the theoretical results are validated with simulation results of the control algorithm. Finally, Section 6 presents the conclusions.

2. DYNAMIC MODEL OF THE MOBILE ROBOT

A 160MW oil-fired electrical power plant model is used in this paper constituted with a drum type boiler and a turbine. The model is based on the P16/G16 at the Sydvenska Kraft AB plant in Malmö, Sweden (Bell et al., 1987),. This model is widely used in the specialized literature (Tan et al., 2008), (Tan et al., 2005), (Fang et al., 2004; Sarailoo et al., 2012), . The boiler dynamic model is provided by both physical and empirical methods based on data acquired from a series of experiments and identifications which capture all the relevant characteristics of the process. The nonlinear boiler-turbine dynamic model is given by the following equations:

$$\begin{cases} \dot{x}_1 = -0.0018u_2x_1^{9/8} + 0.9u_1 - 0.15u_3 \\ \dot{x}_2 = (0.073u_2 - 0.016)x_1^{9/8} - 0.1x_2 \\ \dot{x}_3 = (141u_3 - (1.1u_2 - 0.19)x_1)/85 \end{cases} \quad (1)$$

$$\begin{cases} y_1 = x_1 \\ y_2 = x_2 \\ y_3 = 0.05(0.13073x_3 + 100\alpha + q_e/9 - 67.975) \end{cases} \quad (2)$$

In (1) and (2), the state variables x_1, x_2, and x_3 denote drum pressure (kg/cm^2), electric output (MW), and fluid density (kg/m^3), respectively. The inputs u_1, u_2, and u_3 are the valve positions for fuel flow, steam control, and feedwater flow, respectively. The output y_3 is the drum water level (m), and α and q_e are steam quality and evaporation rate (kg/s), respectively and are given by:

$$\alpha = \frac{(1 - 0.001538x_3)(0.8x_1 - 25.6)}{x_3(1.0394 - 0.0012304x_1)}$$

$$q_e = (0.854u_2 - 0.147)x_1 + 45.59u_1 - 2.514u_3 - 2.096 \quad (3)$$

The system presents the following physical restrictions in the control actions:

$$
\begin{aligned}
&-0.007/sec \le \frac{du_1}{dt} \le 0.007/sec \\
&-1/sec \le \frac{du_2}{dt} \le 0.1/sec \\
&-0.05/sec \le \frac{du_3}{dt} \le 0.05/sec \\
&0 \le u_i \le 1 \qquad \forall i \in (1,2,3)
\end{aligned} \tag{4}
$$

The Figure 1 shows a simplified scheme of the plant used. The boiler part has as inputs the control action u_1, u_3 and the output y_1, y_3, them the steam generated is directed to the Turbine part by means of u_2 generating the required electricity output y_2

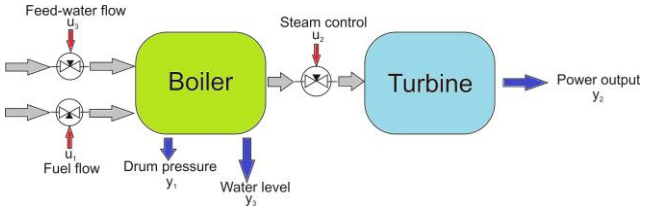

Fig.1: Simplified scheme of the plant used

Some typical operating points of the boiler-turbine model (1), are tabulated in Table I. The literature, in works such as (Bell et al., 1987; Fang et al., 2004; Tan et al., 2004) usually takes the operating point #4 as the nominal point. For more details about the points of operation see (Bell et al., 1987; Fang et al., 2004) .

TABLE I
Typical operating points of Bell and Astrom model

	#1	#2	#3	#4	#5	#6	#7
x_1^0	75.60	86.40	97.20	108	118.8	129.6	140.4
x_2^0	15.27	36.65	50.52	66.65	85.06	105.8	128.9
x_3^0	299.60	342.40	385.20	428	470.8	513.6	556.4
u_1^0	0.156	0.209	0.271	0.34	0.418	0.505	0.6
u_2^0	0.483	0.552	0.621	0.69	0.759	0.828	0.897
u_3^0	0.183	0.256	0.340	0.433	0.543	0.663	0.793
y_3^0	-0.97	-0.65	-0.32	0	0.32	0.64	0.98

3. CONTROL DESIGN

The basic objective of any design for boiler-turbine control system is to make the electrical output y_2 follows the load demand rapidly while the water level y_3 and drum steam pressure y_1 within the allowed limits are maintained. Besides fulfilling the previous objective, the proposed controller is capable of following the allowable trajectory for the outputs y_1 and y_2, holding y_3 constant within certain limits/bounds.

Remark 1: Allowable path is that one which may be physically realizable, considering the dynamics and constraints of the plant.

Remark 2: It is considered that the values of the state variable are available in every time

In this section, the control law capable of generating the signals $u_1(t)$, $u_2(t)$, $u_3(t)$, with the objective that the outputs $y_1(t)$, $y_2(t)$, $y_3(t)$, follow the desired trajectories, previously determined, $y_{1d}(t)$, $y_{2d}(t)$, $y_{3d}(t)$, is designed. Where $y_{1d}(t)$ and $y_{2d}(t)$ will be variable trajectories while $y_{3d}(t)$ will be a maintained constant. These requirements result in order to get a stipulated output power, varying as desired the pressure generated in the boiler and maintaining the water level in the boiler within a safe level, avoiding in this way that overheating occurs (Wu et al., 2010; Chen, 2013).

According to (2) the output $y_1(t)$, $y_2(t)$ are manipulated by x_1, x_2 respectively, therefore modifying the states x_1, x_2, the desired output $y_{1d}(t)$, $y_{2d}(t)$ are achieved. Then, the state variable x_3 is formulated to attain the desired value of the $y_{3d}(t)$. Once all the state variables are available, in order to achieve the tracking control objective, it is necessary calculate the control actions which lead the system to the desired trajectories, by solving a system of linear equations.

The first step of the proposed methodology is to write (1) in a matrix form:

$$
\begin{bmatrix} \theta_1 & -\theta_2 x_1^{9/8} & -\theta_3 \\ 0 & \theta_4 x_1^{9/8} & 0 \\ 0 & -\theta_5 x_1 & \theta_6 \end{bmatrix} \begin{bmatrix} u_1 \\ u_2 \\ u_3 \end{bmatrix} = \begin{bmatrix} \dot{x}_1 \\ \dot{x}_2 \\ \dot{x}_3 \end{bmatrix} \ldots \tag{5}
$$

$$
\ldots + \begin{bmatrix} 0 & 0 & 0 \\ \theta_7 x_1^{1/8} & \theta_8 & 0 \\ -\theta_9 & 0 & 0 \end{bmatrix} \begin{bmatrix} x_1 \\ x_2 \\ x_3 \end{bmatrix}
$$

Where the parameters θ are the same ones that (1)

$$
\theta_1 = 0.9 \quad \theta_2 = 0.0018 \quad \theta_3 = 0.15 \quad \theta_4 = 0.073 \quad \theta_5 = 0.012
$$
$$
\theta_6 = 1.658 \quad \theta_7 = 0.016 \quad \theta_8 = 0.1 \quad \theta_9 = 0.0022
$$

Writing (5) in symbolic form, we have:

$$
\mathbf{Au} = \dot{\mathbf{x}} + \mathbf{Bx} \tag{6}
$$

Where (6) represent the real dynamic model of the boiler-turbine. It will use to find the expressions of control actions for tracking trajectories.

*Remark 3:*The real parameters of the system boiler-turbine are $\boldsymbol{\theta} = [\theta_1, \ldots, \theta_9]^T$, while the estimated parameters used by

the proposed controller will be $\hat{\boldsymbol{\theta}} = \left[\hat{\theta}_1, \ldots, \hat{\theta}_9\right]^T$. Finally the error in the parameters election will be $\tilde{\boldsymbol{\theta}} = (\hat{\boldsymbol{\theta}} - \boldsymbol{\theta}) = \left[\tilde{\theta}_1, \ldots, \tilde{\theta}_9\right]^T$.

Remark 4: When accurate knowledge of the model is mentioned, this means that the plant parameters are known exactly $(\boldsymbol{\theta} = \hat{\boldsymbol{\theta}})$, otherwise, parametric uncertainty is considered $\tilde{\boldsymbol{\theta}} = (\hat{\boldsymbol{\theta}} - \boldsymbol{\theta})$.

Considering exact knowledge of the model and based on the inverse dynamic, it is proposed the following control law which considers (6) as a purely mathematical system

$$\mathbf{A}\mathbf{u} = \mathbf{b} \tag{7}$$

Where

$$\mathbf{b} = \boldsymbol{\sigma} + \mathbf{B}\mathbf{x}$$

$$\boldsymbol{\sigma} = \begin{bmatrix} \sigma_1 \\ \sigma_2 \\ \sigma_3 \end{bmatrix} = \begin{bmatrix} \dot{x}_{1d} + k_1 e_{x_1} \\ \dot{x}_{2d} + k_2 e_{x_2} \\ \dot{x}_{3ez} + k_3 e_{x_3} \end{bmatrix}$$

The variables x_{1d} y x_{2d} represent the desired values of the states to be achieved, x_{3ez} represents the required value that must have x_3 to attain the desired value of the y_3. The expression of the x_{3ez} will be found in the next paragraph. The constants (k_1,k_2,k_3 > 0) represent the parameter of the controller. Finally e_{x1}, e_{x2}, e_{x3} represent the individual tracking errors.

Remark 5: The value of the difference between the desired and real trajectory will be called tracking error. It is given by $e_{x_1} = x_{1d} - x_1, e_{x_2} = x_{2d} - x_2, e_{x_3} = x_{3ez} - x_3$. The tracking error is represented by $\|e_n\| = \sqrt{\left(e_{x_1}^{\ 2} + e_{x_2}^{\ 2} + e_{x_3}^{\ 2}\right)}$.

The value of x_{3ez} is found using the latest expression of (2). It aims to force y_3 for achieving the desired output value y_{3d} by varying x_{3ez}

$$y_3 = 0.05(0.13073x_3 + 100\alpha_{(x_1, x_3)} + q_{e(x_1, u)} / 9 - 67.975)$$

$$y_{3d} = 0.05\left(0.13073x_{3ez}\right) + \left(\frac{(1 - 0.001538x_{3ez})(0.8x_1 - 25.6)}{x_{3ez}(1.0394 - 0.0012304x_1)}\right) + \cdots$$

$$\cdots + 0.05\left(\frac{(0.854u_2 - 0.147)x_1}{9} + \frac{45.59u_1}{9} - \frac{2.514u_3}{9} - \frac{2.096}{9} - 67.975\right)$$

$$y_3 \to y_{3d} \quad when \quad x_3 \to x_{3ez} \tag{8}$$

.

Where the values y_{3d}, x_1, u_1, u_2, u_3 are known. The value of x_{3ez} is obtained using algorithms that find minimum of unconstrained multivariable function using derivative-free method (Brent, 2013).

Remark 6: When the algorithm is implemented in t=0 the values $u_1(0)$, $u_2(0)$, $u_3(0)$ and $x_{3ez}(0)=x_3(0)$ are obtained depending on the chosen operating point according to Table 1.

The system (7) can be considered as a system of linear equations, where $\mathbf{u}$ represents the unknown matrix, $\mathbf{A}$ the coefficient matrix, and $\mathbf{b} = \boldsymbol{\sigma} + \mathbf{B}\mathbf{x}$ the matrix of independent term. The solution of the system (7) is resolved through least square theory (Strang, 2006). Analyzing $\mathbf{A}$ is noted that it is always linearly independent, because x_1 is never zero in normal operation, therefore, the inverse of the matrix $\mathbf{A}$ exist.

$$\mathbf{u} = \mathbf{A}^{-1}\boldsymbol{\sigma} + \mathbf{A}^{-1}\mathbf{B}\mathbf{x} \tag{9}$$

Using the process of Gaussian elimination (Strang, 2006) the analytic expressions of the control actions are found

$$u_1 = \frac{1}{\theta_1}\sigma_1 + \frac{\theta_3}{\theta_1\theta_6}\left(\sigma_3 - \theta_9 x_1\right) + \ldots$$
$$\ldots\left(\frac{\theta_2}{\theta_1\theta_4} + \frac{\theta_3\theta_5}{\theta_1\theta_4\theta_6}x_1^{-1/8}\right)\left(\sigma_2 + \theta_7 x_1^{9/8} + \theta_8 x_2\right)$$

$$u_2 = \frac{1}{\theta_4}\left(\sigma_2 + \theta_7 x_1^{9/8} + \theta_8 x_2\right)x_1^{-9/8} \tag{10}$$

$$u_3 = \frac{1}{\theta_6}\left(\sigma_3 - \theta_9 x_1\right) + \frac{\theta_5}{\theta_4\theta_6}x_1^{-1/8}\left(\sigma_2 + \theta_7 x_1^{9/8} + \theta_8 x_2\right)$$

The proposed controller design is completely finished by using the relationships given in (8), which will be used to generate the control actions in (10).

Theorem 1: If the system behaviour is ruled by (6) and the controller is designed by (10), then $e_n \to 0$ with $t \to \infty$ when trajectory tracking problems are considered. The proof of Theorem 1 and the convergence to zero of tracking errors can be seen in Appendix A.

4. ADAPTIVE LAW

In this section the existence of parametric uncertainty is considered, where the estimated parameters used by the controller are far from the real values of the plant. This uncertainty, when is not taken into consideration, affects the performance of the developed controller. To compensate this effect a methodology is proposed to adapt the internal

parameters of the controller and compensate the influence of the parametric uncertainly in the trajectory tracking.

When parametric uncertainty is considered, the control action designed in (9) is modified using the estimated parameters of the model instead of real parameters

$$\mathbf{u} = \hat{\mathbf{A}}^{-1}\boldsymbol{\sigma} + \hat{\mathbf{A}}^{-1}\hat{\mathbf{B}}\mathbf{x} \tag{11}$$

Where

$$\hat{\mathbf{A}}^{-1} = \begin{bmatrix} \frac{1}{\hat{\theta}_1} & \left(\frac{\hat{\theta}_2}{\hat{\theta}_1\hat{\theta}_4} + \frac{\hat{\theta}_3\hat{\theta}_5}{\hat{\theta}_1\hat{\theta}_4\hat{\theta}_6} x_1^{-1/8}\right) & \frac{\hat{\theta}_3}{\hat{\theta}_1\hat{\theta}_6} \\ 0 & \frac{1}{\hat{\theta}_4} x_1^{-9/8} & 0 \\ 0 & \frac{\hat{\theta}_5}{\hat{\theta}_4\hat{\theta}_6} x_1^{-1/8} & \frac{1}{\hat{\theta}_6} \end{bmatrix}$$

$$\hat{\mathbf{B}} = \begin{bmatrix} 0 & 0 & 0 \\ \hat{\theta}_7 x_1^{1/8} & \hat{\theta}_8 & 0 \\ -\hat{\theta}_9 & 0 & 0 \end{bmatrix}$$

Besides, the real boiler-turbine model (6), can be descomposed considering the *Remark 3* as follows:

$$\left(\hat{\mathbf{A}} - \tilde{\mathbf{A}}\right)\mathbf{u} = \dot{\mathbf{x}} + \left(\hat{\mathbf{B}} - \tilde{\mathbf{B}}\right)\mathbf{x} \tag{12}$$

Where

$$\tilde{\mathbf{A}} = \begin{bmatrix} \tilde{\theta}_1 & -\tilde{\theta}_2 x_1^{9/8} & -\tilde{\theta}_3 \\ 0 & \tilde{\theta}_4 x_1^{9/8} & 0 \\ 0 & -\tilde{\theta}_5 x_1 & \tilde{\theta}_6 \end{bmatrix}$$

$$\tilde{\mathbf{B}} = \begin{bmatrix} 0 & 0 & 0 \\ \tilde{\theta}_7 x_1^{1/8} & \tilde{\theta}_8 & 0 \\ -\tilde{\theta}_9 & 0 & 0 \end{bmatrix}$$

The error equation of the control system when there is parametric uncertainty is obtained replacing (11) in (12).

$$\left(\hat{\mathbf{A}} - \tilde{\mathbf{A}}\right)\left(\hat{\mathbf{A}}^{-1}\boldsymbol{\sigma} + \hat{\mathbf{A}}^{-1}\hat{\mathbf{B}}\mathbf{x}\right) = \dot{\mathbf{x}} + \left(\hat{\mathbf{B}} - \tilde{\mathbf{B}}\right)\mathbf{x}$$

which is equivalent to

$$\boldsymbol{\sigma} - \dot{\mathbf{x}} = \tilde{\mathbf{A}}\hat{\mathbf{A}}^{-1}\boldsymbol{\sigma} + \tilde{\mathbf{A}}\hat{\mathbf{A}}^{-1}\hat{\mathbf{B}}\mathbf{x} - \tilde{\mathbf{B}}\mathbf{x}$$

Analyzing the left side of the equation and considering (20) and (21) in the proof of Theorem 1 we have:

$$\dot{\mathbf{e}}_x + \mathbf{K}\mathbf{e}_x = \tilde{\mathbf{A}}\hat{\mathbf{A}}^{-1}\boldsymbol{\sigma} + \tilde{\mathbf{A}}\hat{\mathbf{A}}^{-1}\hat{\mathbf{B}}\mathbf{x} - \tilde{\mathbf{B}}\mathbf{x} \tag{13}$$

Analyzing the right side of the equation, we see that all terms are pre-multiplied by matrices that contain terms which depend on the errors in the parameters. Therefore each term can be written as a function of $\tilde{\boldsymbol{\theta}}$ as follows:

$$\tilde{\mathbf{B}}\mathbf{x} = \begin{bmatrix} 0 & 0 & 0 & 0 & 0 & 0 & 0 & 0 & 0 \\ 0 & 0 & 0 & 0 & 0 & 0 & x_1^{9/8} & x_2 & 0 \\ 0 & 0 & 0 & 0 & 0 & 0 & 0 & 0 & -x_1 \end{bmatrix} \tilde{\boldsymbol{\theta}}$$

$$\tilde{\mathbf{B}}\mathbf{x} = \mathbf{G}_1\tilde{\boldsymbol{\theta}}$$

Where $\mathbf{G_1}$ is a 3x9 matrix. In the same way the remaining terms are rewritten

$$\tilde{\mathbf{A}}\hat{\mathbf{A}}^{-1}\boldsymbol{\sigma} = \mathbf{G}_2\tilde{\boldsymbol{\theta}}$$
$$\tilde{\mathbf{A}}\hat{\mathbf{A}}^{-1}\hat{\mathbf{B}}\mathbf{x} = \mathbf{G}_3\tilde{\boldsymbol{\theta}}$$

Where $\mathbf{G_2}$ and $\mathbf{G_3}$ are a 3x9 matrix. Then (13) can be replaced by

$$\dot{\mathbf{e}}_x + \mathbf{K}\mathbf{e}_x = \mathbf{G}_2\tilde{\boldsymbol{\theta}} + \mathbf{G}_3\tilde{\boldsymbol{\theta}} - \mathbf{G}_1\tilde{\boldsymbol{\theta}}$$

$$\dot{\mathbf{e}}_x = -\mathbf{K}\mathbf{e}_x + \mathbf{G}\tilde{\boldsymbol{\theta}} \tag{14}$$

Where $\mathbf{G}=\mathbf{G_2}+\mathbf{G_3}-\mathbf{G_1}$. The expression (14) represents the error equation of the control system when exist parametric uncertainties, where the term $\mathbf{G}\tilde{\boldsymbol{\theta}}$ represents the influence of the parametric uncertainties in the tracking errors. The full development of the matrices $\mathbf{G_1}$, $\mathbf{G_2}$, $\mathbf{G_3}$ and $\mathbf{G}$ are detailed in Appendix B.

Analyzing (14) and considering the following Lyapunov candidate function (Khalil et al., 1996)

$$V = \mathbf{e}_x^{\mathrm{T}}\mathbf{e}_x + \tilde{\boldsymbol{\theta}}^{\mathrm{T}}\boldsymbol{\theta} \tag{15}$$

Such that $\tilde{\boldsymbol{\theta}} = \hat{\boldsymbol{\theta}} - \boldsymbol{\theta}$ his time derivate can be considered as $\dot{\tilde{\boldsymbol{\theta}}} = \dot{\hat{\boldsymbol{\theta}}}$ due to the vector of real parameters $\boldsymbol{\theta}$ is considered constant. Then the time derivate of (15) can be written as:

$$\dot{V} = -\mathbf{e}_x^{\mathrm{T}}\mathbf{K}\,\mathbf{e}_x + \mathbf{e}_x^{\mathrm{T}}\mathbf{G}\,\tilde{\boldsymbol{\theta}} + \tilde{\boldsymbol{\theta}}^{\mathrm{T}}\dot{\hat{\boldsymbol{\theta}}} \tag{16}$$

Analyzing (16) is defined the following parameter-updating laws for the proposed adaptive controller.

$$\dot{\hat{\boldsymbol{\theta}}} = -\mathbf{G}^{T}\,\mathbf{e}_x \tag{17}$$

Substituting this expression in (16) we have

$$\dot{V} = -\mathbf{e}_x^{\,T}\mathbf{K}\,\mathbf{e}_x < 0 \tag{18}$$

Where $\mathbf{K} = diag\left(k_1, k_2, k_3\right) > 0$ and $\mathbf{e}_x$ equals to $\left[x_{1d} - x_1, x_{2d} - x_2, x_{3ez} - x_3\right]^T$, therefore, (18) is negative definite and consequently the system with the proposed adaptive controller is asymptotically stable, which means that $\mathbf{e}_x(t) \to 0$ when $t \to \infty$.

An illustrative scheme shown in Fig. 2, where it is observed that the adaptation block is continuously sensing the state variables of the boiler-turbine and the desired states to be followed of the controller. The adaptation block updating the values of the $\hat{\boldsymbol{\theta}}$ according (17) make that the tracking error $\mathbf{e}_x(t)$ tends to zero (18).

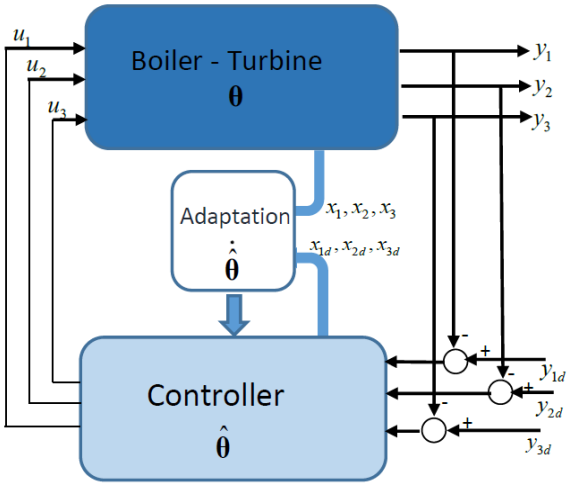

Fig. 2. Scheme. Adaptive Control Law.

5. SIMULATION RESULTS

To demonstrate the theoretical result obtained in the previous section, the proposed control system was tested in three different simulations. In the first one, the Monte Carlo method is applied to select an optimal set of controller parameters (Tempo et al., 2007); secondly, the controller developed is compared to different controllers proposed in the literature, for demanding tracking requirements; in third place, the controller is tested considering parametric uncertainty in the model. The added uncertainty is a 20% of the nominal value in all parameters of the model (Bell et al., 1987). In this simulation, the performance of the developed adaptation law is shown.

The goal of the simulations is to confirm the good performance of the controller obtained in the previous section. The simulations are performed using a simulator developed in the Matlab© platform, which considers an accurate model of the boiler-turbine. The control approach is applied on the original time-continuous system. The outputs $y_{1d}(t)$ and $y_{2d}(t)$ will be variable trajectories while $y_{3d}(t)$ will be maintained constant and equal to zero (Wu et al., 2010; Chen, 2013), .

5.1 Monte Carlo Experiment (MCE)

In this section the developed controller for boiler-turbine plant is subjected to an Monte Carlo Experimentation. The MCE aims to find the optimal parameters controller (k_1, k_2, k_3) optimizing a defined cost function. An idea widely used in the literature is to consider the cost incurred by the tracking error (Cheein et al., 2013). Let Φ be a desired trajectory, $C_{y_i}^{\Phi} = \frac{1}{2}\int_0^{t_f}\left(y_{d_i}(t) - y_i(t)\right)^2 dt$ the quadratic error of the output y_i with $i \in \{1,2,3\}$. Thus, the cost function can be represented by the combination of all quadratic errors,

$$C^{\Phi} = \frac{1}{2}\left(C_{y_1}^{\Phi} + C_{y_2}^{\Phi} + C_{y_3}^{\Phi}\right) \tag{19}$$

In this work the MCE is carried out considering N=1000 simulations. This number was calculated according to (Tempo et al., 2007) in order to have a high accuracy in the solution found. The MC experiment allows to find empirically the parameter values minimizing the cost function (19).

The system begins balanced in the operating point #4 shown in Table 1. In *t=100s* is requested a change of operating point suddenly, from #4 at #2 (see Table 1). Then it is asked to follow these desired trajectories for y_{1d} and y_{2d}:

$$\underbrace{\begin{aligned} y_{1d} &= 9\sin(0.02(t-100)) + 0.02(t-100) + 86.4 \\ y_{2d} &= 9\sin(0.03(t-100)) + 0.05(t-100) + 36.65 \end{aligned}}_{100 \le t < 800}$$

The desired value of y_{3d} equals to zero for all the experimentation. This prevents any overheating of the boiler. The desired trajectory for the electrical output and drum pressure are out of a real operating requirement. However, the goal of proposing such paths is, to show the good performance of the proposed controller to follow any demanding and difficult requirement.

Experimental considerations of MCE:

- The simulations are performed using MatLab software platform.
- All simulations are implemented with the same desired trajectory Φ .

- For each simulation, the controller parameters are chosen in a random way, as specified in (Tempo et al., 2007).

The Fig. 3 shows the temporal response obtained for the specified desired path to N=1000 simulations. As it can be seen, the controller presents a good performance, despite the demanding requirement. The Fig. 4 shows the tracking errors outputs for each simulation. The convergence time of the errors is a function of the selected value of the controller´s parameters. The Fig. 5 shows the values taken by the cost function for each simulation. The minimum cost occurs in the simulation number 593, corresponding to the values of the controller´s parameters [k_1 k_2 k_3]=[1.2, 1.12, 1.05]. This values will be used in the next simulations as the optimal parameters of the controller.

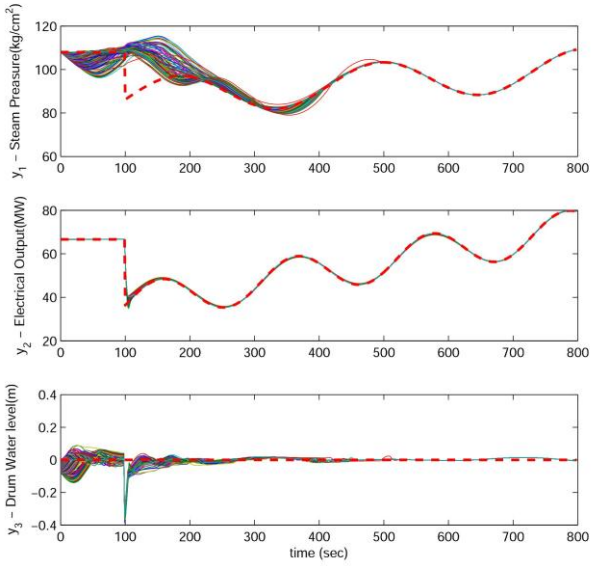

Fig. 3. Monte Carlo experimentation.

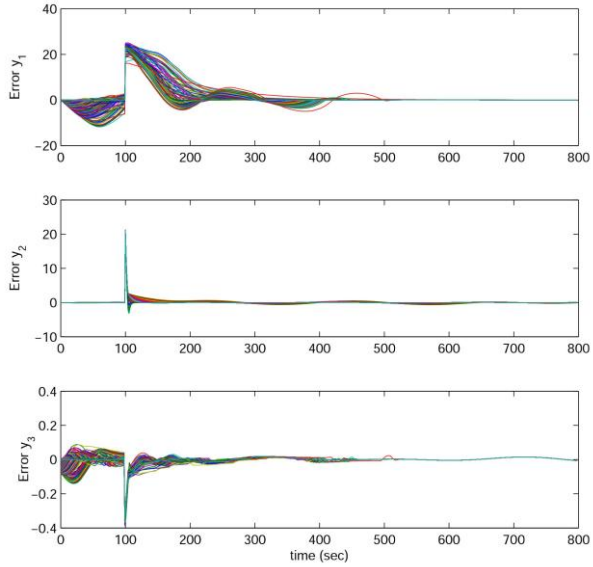

Fig. 4. Monte Carlo experiment. Outputs Errors.

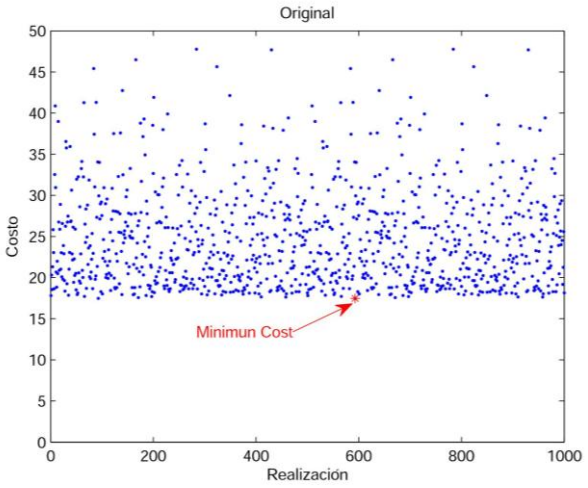

Fig. 5. Cost of Monte Carlo Experiment.

5.2 Controllers' Comparison

The performance to the proposed controller, when it does not considere uncertainties, is compared with two controllers developed in (Wu et al., 2010). The specification of the desired trajectory are (Wu et al., 2010):

- The desired path y_{1d} starts to be stabilized in 75,6 Kg/cm^2, then in *t=500s* an instant change is requested, taking a value equals to 135,4 Kg/cm^2, finally in *t=1500s* the output y_1 returns to the original value.

- The request y_{2d} suffers a set-point change from 15,27 MW to 127 MW in *t=500s*, then it returns to the original value in *t=1500s*.

- The desired trajectory y_{3d} remains constant and equals zero for the whole experiment.

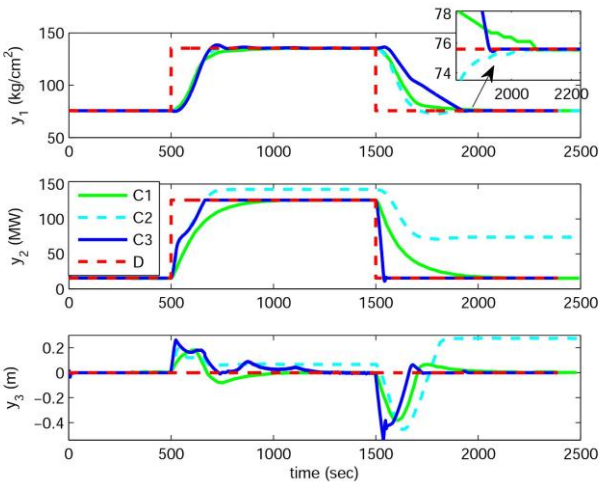

Fig. 6. Tracking trajectory. Comparison Controllers.

In this simulation the compared controller are C1= TS Control, C2= Linear Control and C3 = our proposal controller, where C1 and C2 are developed in(Wu et al., 2010). Fig. 6 shows the outputs, where in *D* represents the desired values for each output, while the Fig. 7 shows the control action. As it can be seen the response of the controller C3 have a better performance for the stipulated trajectory specially for y_2 that is the main variable to follow. In this one it can be observed that the C3 follows more quickly the desired requirements.

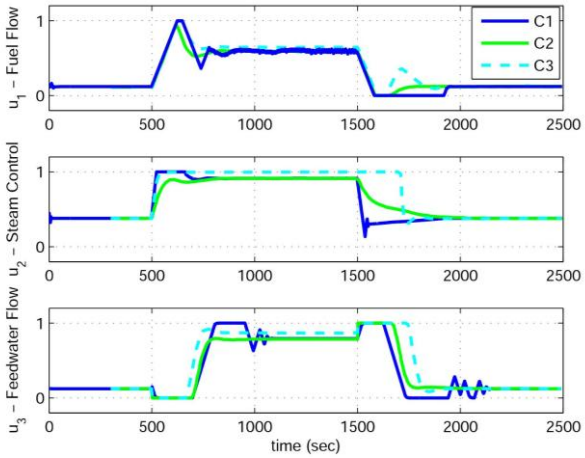

Fig. 7. Control Actions. Comparison Controllers.

5.3 Parametric Uncertain

In this section the performance of the controller incorporating the proposed adaptation law is tested. For this purpose, a comparison is performed between the controller with and without parameter updating development. The desired trajectories are formed by simultaneous set-points changes for the outputs y_1 and y_2. In this simulation it is considered a 20% of the parametric uncertainties in all parameters of the system.

The Fig. 8 shows the response of the proposed controller with and without parametric updating when the tracking trajectory is performed. In the Fig. 9 shows the tracking errors for the outputs using the proposed controller. As it can be seen the tracking error decreases, especially for the main output y_2 when the parametric updating is commissioning.

The Fig. 10 shows the cost function defined in (19) for both cases, where the cost is reduced in a 59,89% due to the adaptation law proposed.

The evolution of the estimated parameters along the time is shown in Fig. 11, where it is explained how the parameters are adapted to each change of operating point.

Despite that, the parameters tend to a fixed value.

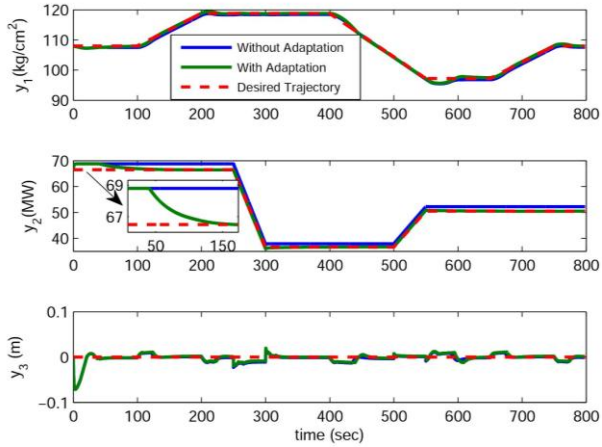

Fig. 8. Experiments with and without parameter updating.

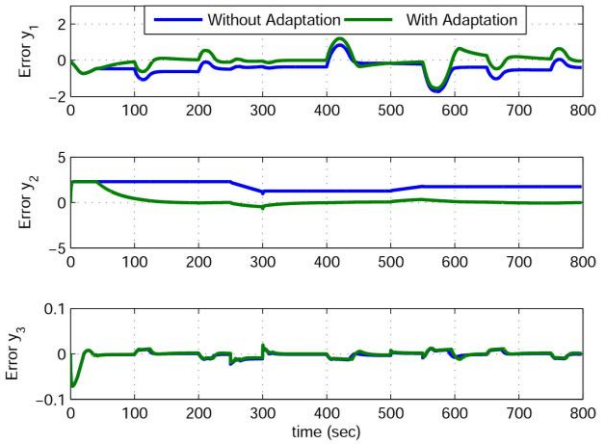

Fig. 9. Tracking errors with and without parameter updating.

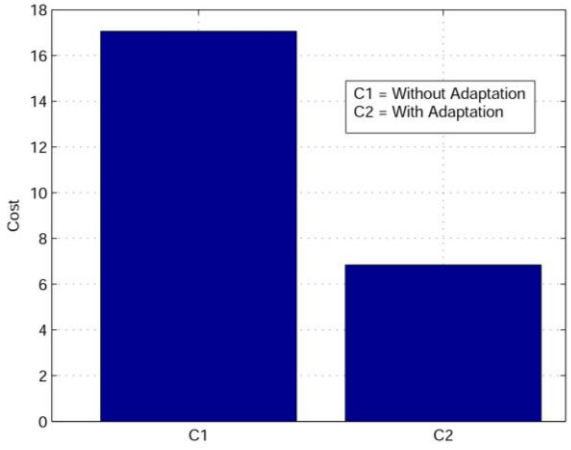

Fig. 10. Cost Function. Comparison.

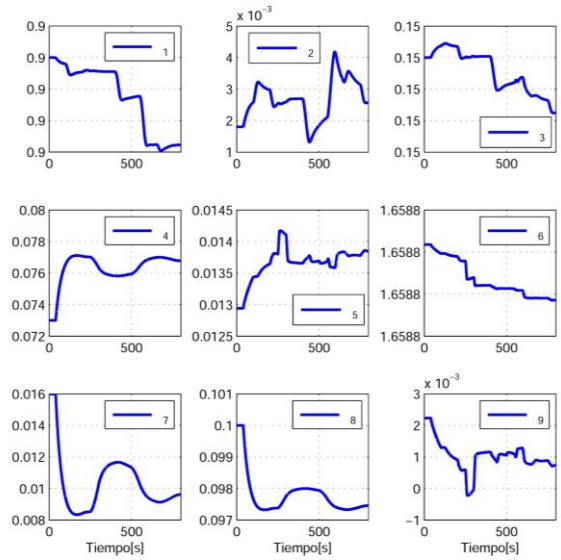

Fig. 11. Evolution of parameters estimates using parameter updating

6. ACKNOWLEDGEMENTS

This work was partially funded by the Consejo Nacional de Investigaciones Científicas y Técnicas (CONICET – National Council for Scientific Research), Argentina and the Universidad Nacional de San Juan (UNSJ), San Juan, Argentina.

7. CONCLUSION

In this paper, a new control law with parameter updating for trajectory tracking in a boiler-turbine was proposed. The control actions for a zero-error trend, are obtained through linear algebra techniques by means of the resolution of a linear system. These techniques are based on simple methods and do not require the use of coordinate transformation, and complicated adaptive scheme; the process model and the values of y_{1d} and y_{2d} are the only variables needed to be known.

The main advantages of the proposed controller are the simplicity of the design procedure and the ability to follow any path allowable for y_1 and y_2 since, in normal operating conditions. The different tests carried out in this work prove the good performance of the proposed controller design procedure, even when they are compared with a controller of the literature. In fact, the system behavior was tested, reaching better performance than those ones obtained by (Wu et al., 2010). The parameter updating is obtained through the study of the stability analysis based on Lyapunov theory. The convergence to zero of the tracking errors for the controller and for the adaptation law were demonstrated by the Lyapunov theory. The results proved that the proposed controller is capable of tracking a desired trajectory with a small error when the dynamic parameters are adapted.

REFERENCES

Bell, R. and K. J. Åström (1987). Dynamic models for boiler-turbine-alternator units: data logs and parameter estimation for a 160 MW unit, Lund Institute of Technology, Department of Automatic Control.

Brent, R. P. (2013). Algorithms for minimization without derivatives, Courier Corporation.

Cheein, F. A. A., Scaglia, G., Torres-Torriti, M., Guivant, J., Prado, A. J., Arnò, J., ... & Rosell-Polo, J. R. (2016). Algebraic path tracking to aid the manual harvesting of olives using an automated service unit. Biosystems Engineering, 142, 117-132.

Cheein, F. A. and G. Scaglia (2013). "Trajectory Tracking Controller Design for Unmanned Vehicles: A New Methodology." Journal of Field Robotics: n/a-n/a.

Chen, P.-C. and J. S. Shamma (2004). "Gain-scheduled ℓ 1-optimal control for boiler-turbine dynamics with actuator saturation." Journal of Process Control 14(3): 263-277.

Fang, F., L. Jizhen, et al. (2004). Output tracking control of a nonlinear boiler-turbine unit. Decision and Control, 2004. CDC. 43rd IEEE Conference on.

Ghabraei, S., Moradi, H., & Vossoughi, G. (2015). Multivariable robust adaptive sliding mode control of an industrial boiler–turbine in the presence of modeling imprecisions and external disturbances: A comparison with type-I servo controller. ISA transactions, 58, 398-408.

Khalil, H. K. and J. Grizzle (1996). Nonlinear systems, Prentice hall New Jersey.

Romoli, S., Scaglia, G. J. E., Serrano, M. E., Godoy, S. A., Ortiz, O. A., & Vega, J. R. (2014). Control of a Fed-Batch Fermenter Based on a Linear Algebra Strategy. IEEE Latin America Transactions, 12(7), 1206-1213.

Sarailoo, M., B. Rezaie, et al. (2012). "MLD model of boiler-turbine system based on PWA linearization approach." International Journal of Control Science and Engineering 2(4): 88-92.

Scaglia, G., L. Q. Montoya, et al. (2009). "Numerical methods based controller design for mobile robots." Robotica 27(02): 269-279.

Serrano, M. E., Scaglia, G. J., Godoy, S. A., Mut, V., & Ortiz, O. A. (2014). Trajectory tracking of underactuated surface vessels: A linear algebra approach. IEEE Transactions on Control Systems Technology, 22(3), 1103-1111.

Strang, G. (2006). Linear Algebra and Its applications. USA.

Tan, W., F. Fang, et al. (2008). "Linear control of a boiler–turbine unit: Analysis and design." ISA transactions 47(2): 189-197.

Tan, W., H. J. Marquez, et al. (2004). "Multimodel analysis and controller design for nonlinear processes." Computers & chemical engineering 28(12): 2667-2675.

Tan, W., H. J. Marquez, et al. (2005). "Analysis and control of a nonlinear boiler-turbine unit." Journal of Process Control 15(8): 883-891.

Tan, W., J. Liu, et al. (2004). "Tuning of PID controllers for boiler-turbine units." ISA transactions 43(4): 571-583.

Tempo, R. and H. Ishii (2007). "Monte Carlo and Las Vegas Randomized Algorithms for Systems and Control*:

An Introduction." European journal of control 13(2): 189-203.

Thangavelusamy, D. and L. Ponnusamy (2013). "Elimination of chattering using fuzzy sliding mode controller for drum boiler turbine system." Journal of Control Engineering and Applied Informatics 15(2): 78-85.

Wu, J., J. Shen, et al. (2012). "GA-based nonlinear predictive switching control for a boiler-turbine system." Journal of control theory and applications 10(1): 100-106.

Wu, J., M. Krug, et al. (2009). H∞ fuzzy tracking control for boiler-turbine systems. Control and Automation, 2009. ICCA 2009. IEEE International Conference on, IEEE.

Wu, J., S. K. Nguang, et al. (2010). "Robust tracking control of boiler–turbine systems." ISA Transactions 49(3): 369-375.

Wu, X., J. Shen, et al. (2013). "Data-driven modeling and predictive control for boiler–turbine unit." Energy Conversion, IEEE Transactions on 28(3): 470-481.

Zheng, K., A.-H. Lee, et al. (2006). "Steady-state bumpless transfer under controller uncertainty using the state/output feedback topology." Control Systems Technology, IEEE Transactions on 14(1): 3-17.

Appendix A

Theorem 1: Considering accurate knowledge of the model according *Remark 4* and replacing the expression of the control actions (9) in the system (6) are obtained the error equation of the control system.

$$\begin{aligned}&\mathbf{A}\left(\mathbf{A}^{-1}\boldsymbol{\sigma}+\mathbf{A}^{-1}\mathbf{B}\mathbf{x}\right)=\dot{\mathbf{x}}+\mathbf{B}\mathbf{x}\\&\boldsymbol{\sigma}+\mathbf{B}\mathbf{x}=\dot{\mathbf{x}}+\mathbf{B}\mathbf{x}\\&\left(\boldsymbol{\sigma}-\dot{\mathbf{x}}\right)=0\end{aligned}\tag{20}$$

According to (7) we have $\boldsymbol{\sigma}-\dot{\mathbf{x}}=\dot{\mathbf{e}}_{\mathbf{x}}+\mathbf{K}\mathbf{e}_{\mathbf{x}}$, where $\mathbf{K}=diag\left(k_1,k_2,k_3\right)>0$ and $\mathbf{e}_{\mathbf{x}}=\left[x_{1d}-x_1,x_{2d}-x_2,x_{3ez}-x_3\right]^T$, thus (20) can be written as follows

$$\dot{\mathbf{e}}_{\mathbf{x}}=-\mathbf{K}\mathbf{e}_{\mathbf{x}}\tag{21}$$

The expression (21) represent the error equation of the control system when there is no presence of parameter uncertainty.

It is now considered the Lyapunov candidate function

$$V=\frac{1}{2}\mathbf{e}_{\mathbf{x}}{}^{T}\mathbf{e}_{\mathbf{x}}>0\tag{22}$$

The time derivative of the Lyapunov candidate function can be written as

$$\dot{V}=\mathbf{e}_{\mathbf{x}}{}^{T}\dot{\mathbf{e}}_{\mathbf{x}}=-\mathbf{e}_{\mathbf{x}}{}^{T}\mathbf{K}\,\mathbf{e}_{\mathbf{x}}<0\tag{23}$$

is negative definite.

Hence, one can straightforwardly conclude that the system controlled by proposed controller (10), when there is no presence of parameter uncertainty, has an asymptotically stable equilibrium at the origin, which means that $\mathbf{e}_{\mathbf{x}}(t)\to 0$ when $t\to\infty$. ■

Appendix B

Equation (13) represent the error equation of the control system in function of the system matrix, when there is parametric uncertainty

$$\dot{\mathbf{e}}_{\mathbf{x}}+\mathbf{K}\mathbf{e}_{\mathbf{x}}=\tilde{\mathbf{A}}\hat{\mathbf{A}}^{-1}\boldsymbol{\sigma}+\tilde{\mathbf{A}}\hat{\mathbf{A}}^{-1}\hat{\mathbf{B}}\mathbf{x}-\tilde{\mathbf{B}}\mathbf{x}\tag{24}$$

The objective is replace the right side of the equation (24) by expressions that depend on $\tilde{\boldsymbol{\theta}}=\left[\tilde{\theta}_1,\ldots,\tilde{\theta}_9\right]^T$. Tacking the last term of the right side of (24):

$$\tilde{\mathbf{B}}\mathbf{x}=\begin{bmatrix}0\\ \tilde{\theta}_7x_1^{9/8}+\tilde{\theta}_8x_2\\ \tilde{\theta}_9x_1\end{bmatrix}$$

Therefore

$$\tilde{\mathbf{B}}\mathbf{x}=\begin{bmatrix}0&0&0&0&0&0&0&0&0\\0&0&0&0&0&0&x_1^{9/8}&x_2&0\\0&0&0&0&0&0&0&0&-x_1\end{bmatrix}\tilde{\boldsymbol{\theta}}\tag{25}$$

$$\tilde{\mathbf{B}}\mathbf{x}=\mathbf{G}_1\tilde{\boldsymbol{\theta}}$$

Proceeding in the same way and using the Symbolic Math Toolbox of MatLab, the expression of the two remaining terms of (24) were obtained. The expression of the term $\tilde{\mathbf{A}}\hat{\mathbf{A}}^{-1}\boldsymbol{\sigma}$ is equivalent to:

$$\tilde{\mathbf{A}}\hat{\mathbf{A}}^{-1}\boldsymbol{\sigma}=\begin{bmatrix}a_{11}&\cdots&a_{19}\\ \vdots&\ddots&\vdots\\ a_{91}&\cdots&a_{99}\end{bmatrix}\tilde{\boldsymbol{\theta}}=\mathbf{G}_2\tilde{\boldsymbol{\theta}}\tag{26}$$

Where the elements a_{ij} are equal to zero excepting the positions $\left\{a_{11},a_{12},a_{13},a_{24},a_{35},a_{36}\right\}$, whose expression are

$$a_{11} = \left(\frac{\sigma_1}{\hat{\theta}_1} + \frac{\sigma_3 \hat{\theta}_3}{\hat{\theta}_1 \hat{\theta}_6} + \sigma_2 \left(\frac{\hat{\theta}_2}{\hat{\theta}_1 \hat{\theta}_4} + \frac{\hat{\theta}_3 \hat{\theta}_5 \, x_1^{-1/8}}{\hat{\theta}_1 \hat{\theta}_4 \hat{\theta}_6} \right) \right)$$

$$a_{12} = -\frac{\sigma_2}{\hat{\theta}_4}$$

$$a_{13} = \left(-\frac{\sigma_3}{\hat{\theta}_6} - \frac{\sigma_2 \hat{\theta}_3 \, x_1^{-1/8}}{\hat{\theta}_4 \hat{\theta}_6} \right)$$

$$a_{24} = \frac{\sigma_2}{\hat{\theta}_4}$$

$$a_{35} = -\frac{\sigma_2 \, x_1^{-1/8}}{\hat{\theta}_4}$$

$$a_{36} = \left(\frac{\sigma_3}{\hat{\theta}_6} + \frac{\sigma_2 \hat{\theta}_5 \, x_1^{-1/8}}{\hat{\theta}_4 \hat{\theta}_6} \right)$$

The expression of the $\tilde{\mathbf{A}}\hat{\mathbf{A}}^{-1}\hat{\mathbf{B}}\mathbf{x}$ is equivalent to:

$$\tilde{\mathbf{A}}\hat{\mathbf{A}}^{-1}\hat{\mathbf{B}}\mathbf{x} = \begin{bmatrix} b_{11} & \cdots & b_{19} \\ \vdots & \ddots & \vdots \\ b_{91} & \cdots & b_{99} \end{bmatrix} \tilde{\boldsymbol{\theta}} = \mathbf{G}_3 \tilde{\boldsymbol{\theta}} \qquad (27)$$

Whose nonzero elements are:

$$b_{11} = x_1 \left(\hat{\theta}_3 \hat{\theta}_5 \hat{\theta}_7 - \hat{\theta}_3 \hat{\theta}_4 \hat{\theta}_9 \right) + \hat{\theta}_2 \hat{\theta}_6 \hat{\theta}_8 x_2 + \ldots$$

$$\ldots + \hat{\theta}_2 \hat{\theta}_6 \hat{\theta}_7 x_1^{9/8} + \frac{\hat{\theta}_3 \hat{\theta}_5 \hat{\theta}_8 \, x_2 x_1^{-1/8}}{\hat{\theta}_1 \hat{\theta}_4 \hat{\theta}_6}$$

$$b_{12} = \frac{\hat{\theta}_8 \, x_2}{\hat{\theta}_4} - \frac{\hat{\theta}_7 \, x_1^{9/8}}{\hat{\theta}_4}$$

$$b_{13} = -\frac{\hat{\theta}_5 \hat{\theta}_7 \, x_1}{\hat{\theta}_4 \hat{\theta}_6} + \frac{\hat{\theta}_9 \, x_1}{\hat{\theta}_6} - \frac{\hat{\theta}_5 \hat{\theta}_8 \, x_2 x_1^{-1/8}}{\hat{\theta}_4 \hat{\theta}_6}$$

$$b_{24} = \frac{\hat{\theta}_8 \, x_2 + \hat{\theta}_7 x_1^{9/8}}{\hat{\theta}_4}$$

$$b_{35} = -\frac{x_1^{-9/8}}{\hat{\theta}_4} \left(\hat{\theta}_8 x_2 + \hat{\theta}_7 x_1^{9/8} \right)$$

$$b_{36} = -\frac{\hat{\theta}_9 \, x_2}{\hat{\theta}_6} + \frac{\hat{\theta}_5 x_1^{-9/8}}{\hat{\theta}_4 \hat{\theta}_6} \left(\hat{\theta}_8 x_2 + \hat{\theta}_7 x_1^{9/8} \right)$$

The matrices $\mathbf{G}_1, \mathbf{G}_2, \mathbf{G}_3$ are completely constituted by know values. The matrix $\mathbf{G}$ is equal to $\mathbf{G} = \mathbf{G}_2 + \mathbf{G}_3 - \mathbf{G}_1$ and your expression is

$$\mathbf{G}\tilde{\boldsymbol{\theta}} = \begin{bmatrix} a_{11}+b_{11} & 0 & 0 \\ a_{12}+b_{12} & 0 & 0 \\ a_{13}+b_{13} & 0 & 0 \\ 0 & a_{24}+b_{24} & 0 \\ 0 & 0 & a_{35}+b_{35} \\ 0 & 0 & a_{36}+b_{36} \\ 0 & -x_1^{9/8} & 0 \\ 0 & -x_2 & 0 \\ 0 & 0 & x_1 \end{bmatrix}^T \tilde{\boldsymbol{\theta}}$$

An Approach of a Numerical Methods Controller for Nonlinear Chemical Processes

Javier Guevara*, Leonardo Guevara*, Oscar Camacho*, Gustavo Scaglia, Andrés Rosales***

** Departamento de Automatización y Control Industrial, Escuela Politécnica Nacional Quito, Ecuador (e-mail: dario.guevara, cesar.guevara01, oscar.camacho, andres.rosales}@epn.edu.ec)*
*** Instituto de Ingeniería Química, CONICET, Universidad Nacional de San Juan San Juan, Argentina (e-mail: gscaglia@unsj.edu.ar)*

Abstract: In this paper is presented an approach of Numerical Methods Controller (NMCr) based on an empirical linear model of the processes. The controller is developed for self-regulating processes with an open loop response similar as a first order plus dead time (FOPDT) model, and can be tuned using the characteristic parameters taken from the reaction curve. The performance of the proposed controller is tested in two nonlinear chemical processes and the results are compared, by simulations, against a PID controller using the ISE performance index to measure it.

Keywords: numerical methods, chemical processes, nonlinear processes, model approximation, FOPDT, characteristic parameters.

1. INTRODUCTION

The methodology based on linear algebra and numerical methods concepts to design control algorithms is a simple and relatively new method that allows the control of highly nonlinear systems. It have been applied to the design of different class of control systems such as trajectory tracking of mobile robots and UAV's (Scaglia, G. et al. (2006, 2009), Rosales, A. et al. (2010), Guerrero, F. et al. (2013)), chemical plants and bioprocesses (Quintero, O. L. et al. (2008), Scaglia, G. et al. (2014), Suvire, R. et al. (2013), Godoy, S. et al. (2013)) just to name some applications. Its main advantage is that the conditions for the tracking error tends to zero and control actions are obtained with low computational cost which makes it easy to implement in a microcontroller. These conditions are found by solving a system of linear equations and finding the conditions for the system to have exact solution.

For all the previous applications, the controllers were designed based on the complete process model. Therefore, for each different process a different control law is produced and its application is just for the process under analysis. Besides, the development of a complete model for industrial processes is difficult mainly due to the complexity of the process, the lack of knowledge of some process parameters and the possible higher order of the manipulated variables. Therefore, the methodology of numerical controller method using complete models can produce more complex controllers. An efficient alternative modelling method for process control is the use of empirical models, most times FOPDT models can work satisfactory for analysis and design of process control (Camacho O. and Smith C, 2000).

In a previous work, Guevara, L. et al. (2016) presented an approach of numerical methods controller (NMCr) based on a FOPDT model, also tuning equations are presented based on the characteristic parameters of the process, which are obtained from the reaction curve method. The results obtained, using the proposed approach, in several higher order linear systems showed a good performance.

This work shows the application of the proposed Numerical Method Controller (NMCr), based on a FOPDT model of the actual process, to nonlinear chemical processes. The performance and robustness of the proposed controller are tested through simulations in two nonlinear chemical processes. The first process is a mixing tank with variable dead time, and the second process is a continuous stirred tank reactor. In both cases the results are compared against a PID controller.

This paper is organized as follows: Section II presents the basic concepts required to controller design, section III presents the development of the proposed controller. Then in section IV the simulation results are presented divided in two cases of study and finally conclusions and future works are presented in section V.

2. BASIC CONCEPTS

2.1 First Order Plus Dead Time System (FOPDT)

Introducing a step change at the process input and then recording the transmitter output, produces a reaction curve that represent the dynamic behaviour of actual process (Seborg, D. E. et al. (2011)). The typical open loop response is overdamped as is shown in Fig. 1, and it is called a FOPDT system. The transfer function of a First Order Plus Dead Time system is:

$$G(s) = \frac{y(s)}{u(s)} = \frac{k\, e^{-t_0 s}}{\tau s + 1} \qquad (1)$$

Where, k is the gain of the process, τ is the time constant of the process and t_0 is the dead time or delay.

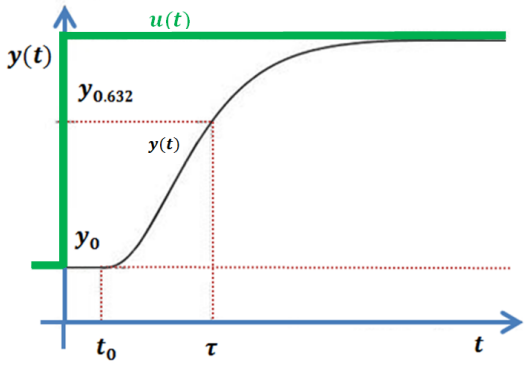

Fig. 1. Typical Response FOPDT.

2.2 Taylor Approximation for Dead Time

Dead time is not specified in the methodology based on linear algebra or numerical methods, therefore, an approximation to replace the dead time must be considered. For instance, in this article the Taylor approximation is used, similar to Camacho, O. et al. (1997). Hence, the dead time expression is substituted as follows:

$$e^{-t_0 s} \approx \frac{1}{1+t_0 s} \tag{2}$$

Replacing (2) in (1), it is obtained:

$$G(s) = \frac{k}{(\tau s+1)(t_0 s+1)} \tag{3}$$

2.3 Euler Approximation

This approximation is used for discretization of an integral term, replacing it by a finite difference. Thus, if the slope value is known in a time period T, an estimate value of the next state y_{n+1} could be obtained using a linear approximation (Chaves, E. (2010)).

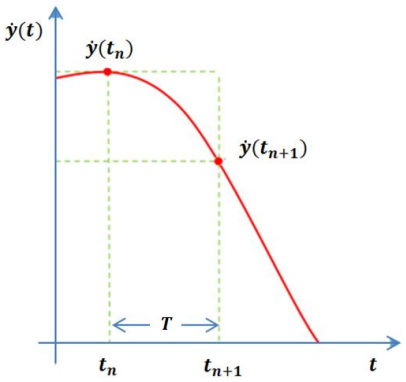

Fig. 2. Euler Approximation.

The derivate approximation is represented by:

$$\dot{y}_n \approx \frac{y_{n+1}-y_n}{T} \tag{4}$$

3. CONTROLLER DESIGN

In this section, it is shown the development of the proposed numerical methods controller based on a FOPDT model. The transfer function with the Taylor approximation is considered for design purposes. Simplifying some terms in (3) and reorganizing for ease of calculation, two parameters (K_A and K_B) are included, they contain the characteristic parameters of the system (t_0 and τ). Consecuently, The transfer function can be represented as follows:

$$G(s) = \frac{y(s)}{u(s)} = \frac{k\,K_B}{s^2+K_A s+K_B} \tag{5}$$

Where:

$$K_A = \frac{t_0+\tau}{t_0\,\tau}[=][\text{time}]^{-1} \tag{6}$$

$$K_B = \frac{1}{t_0\tau}[=][\text{time}]^{-2} \tag{7}$$

Then, solving (5) a second order differential equation is obtained:

$$\ddot{y} + K_A\,\dot{y} + K_B y = k K_B\,u \tag{8}$$

Representing (8) in matrix form, it is found:

$$\begin{bmatrix}\dot{y}_1\\ \dot{y}_2\end{bmatrix} = \begin{bmatrix}0 & 1\\ -K_B & -K_A\end{bmatrix}\begin{bmatrix}y_1\\ y_2\end{bmatrix} + \begin{bmatrix}0\\ k\,K_B\end{bmatrix}[u] \tag{9}$$

Where, y_1 and y_2 are the state variables of the system and u the controller output. Then, the system can be described by the following differential equations:

$$\dot{y}_1 = y_2 \tag{10}$$

$$K\,K_B\,u = \dot{y}_2 + K_A\,y_2 + K_B\,y_1 \tag{11}$$

Using the Euler approximation in the previous equations, the following equations are obtained:

$$y_{2\,n} = \frac{y_{1\,n+1}-y_{1\,n}}{T} \tag{12}$$

$$K\,K_B\,u_n = \frac{y_{2\,n+1}-y_{2\,n}}{T} + K_A\,y_{2\,n} + K_B\,y_{1\,n} \tag{13}$$

To make the variation of the error decrease slowly, a first tuning parameter to calibrate the response of the controller is added, it is named K_x and takes values from 0 to 1. If a faster response is required, the value of K_x should be close to 0 and if a slower response is required, the value should be close to 1. This tuning parameter is introduced in (12), and it affects the difference between reference value and output value, the error. It can be considered as a proportional tuning parameter. The resulting expression is:

$$y_{2\,n} = \frac{y_{1\,ref\,n+1}-y_{1\,n}-K_x(y_{1\,ref\,n}-y_{1\,n})}{T} \tag{14}$$

Where, $y_{1\,ref\,n}$ is the reference and $y_{1\,n}$ is the measured output. To reduce the resulting expressions, the difference between the reference $y_{1\,ref\,n}$ and the actual $y_{1\,n}$ can be represented by e_n.

To ensure that the controller compensates disturbances, an integral term is added, therefore it eliminates the steady state error, it is called (NMCr+I). This integral term is formed by

the integral of error multiplied by the second tuning parameter K_i. For implement it, the integral term is represent by:

$$Integral\ term = K_i\ T\ e_{T\ n} \tag{15}$$

Where, $e_{T\ n}$ is the total error accumulated represented by (16) and T is the sampling period:

$$e_{T\ n} = e_{\ n} + e_{T\ n-1} \tag{16}$$

Adding this integral term into (14), the following equation is obtained:

$$y_{2\ n} = \frac{y_{1\ ref\ n+1} - y_{1\ n} - K_x e_{\ n}}{T} + K_i\ T\ e_{T\ n} \tag{17}$$

Assuming that the current value of variable $y_{2\ n}$ is the same required for a next state $y_{2\ n+1}$. Then, replacing (16) in (13) and solving the output controller $u_{\ n}$, the control law is obtained:

$$u_{\ n} = \frac{1}{k\ K_B\ T^2}[y_{1\ ref\ n+1} - y_{1\ n} + K_x e_{\ n} - T\ y_{2\ n} + T^2 K_i e_{T\ n}] + \frac{y_{1\ n}}{k} + \frac{K_A y_{2\ n}}{k K_B} \tag{18}$$

Where:

$$y_{2\ n} = \frac{y_{1\ n} - y_{1\ n-1}}{T} \tag{19}$$

Equation (19) represents the derivative term of the controlled variable. The sampling time value (T) is recommended to be in the range τ /10 < T < τ /4.

The discrete approximation of the derivative, works well if the process does not present noise, but if noise is present, it is necessary to add a low-pass filter, as is done in a PID controller when the derivative term is present.

The integral term eliminates the steady state error, but a higher value of K_i produces a more oscillatory response. Therefore, it should be found a relationship between the two tuning parameters. Therefore, several tests in systems with different characteristics parameters were done, and minimizing the Integral Squared Error (ISE), a criterion for getting an initial value of K_i was obtained. K_x close to 1 is a good starting value, and substituting it into (20), the integral tuning parameter can be obtained.

$$K_i = \frac{0.2\ K_x}{\tau}\ [=][\text{time}]^{-1} \tag{20}$$

4. STUDY CASES

The proposed controller was tested in two very common chemical processes whose models have already been used in previous works.

4.1 Mixing Tank

The mixing tank is a nonlinear chemical process. The tank receives two streams, a hot stream $W_1(t)$, and a cold stream $W_2(t)$. The outlet temperature is measured at a point 125 ft downstream from the tank. The complete model (Camacho, O. and Smith C., 2000), it is described by the following equations.

Energy balance around tank:

$$W_1(t)Cp_1(t)T_1(t) + W_2(t)Cp_2(t)T_2(t) - (W_1(t) + W_2(t))Cp_3(t)T_3(t) = V\rho Cv_3\frac{dT_3(t)}{dt} \tag{21}$$

Pipe delay between the tank and the sensor location:

$$T_4(t) = T_3(t - t_0) \tag{22}$$

Transportation lag (Variable delay time):

$$t_0 = \frac{L\ A\rho}{W_1(t)+W_2(t)} \tag{23}$$

Temperature transmitter:

$$\frac{dTO(t)}{dt} = \frac{1}{\tau_T}\left[\frac{T_4(t)-100}{100} - TO(t)\right] \tag{24}$$

Valve position:

$$\frac{dV_p(t)}{dt} = \frac{1}{\tau_{V_p}}[m(t) - V_p(t)] \tag{25}$$

Valve equation:

$$W_2(t) = \frac{500}{60}C_{VL}V_p(t)\sqrt{G_f \Delta P_V} \tag{26}$$

Where:

$W_1(t)$ = mass flow of hot stream, lb/min

$W_2(t)$ = mass flow of cold stream, lb/min

Cp = liquid heat capacity at constant pressure, Btu/lb-°F

Cv = liquid heat capacity at constant volume, Btu/lb-°F

$T_1(t)$ = hot flow temperature, °F

$T_2(t)$ = cold flow temperature, °F

$T_3(t)$ = liquid temperature in the mixing tank, °F

$T_4(t)$ = equal to $T_3(t)$ delayed by t_0, °F

t_0 = dead time or transportation lag, min

ρ = density of the mixing tank contents, lbm/ft^3

V = liquid volume, ft^3

$TO(t)$ = transmitter output signal on a scale from 0 to 1

$Vp(t)$ = valve position, from 0 (closed) to 1 (open)

$m(t)$ = fraction of controller output, from 0 to 1

C_{VL} = valve flow coefficient, gpm/psi$^{1/2}$

G_f = specific gravity, dimensionless

ΔP_V = pressure drop across the valve, psi

τ_T = time constant of the temperature sensor, min

τ_{V_p} = time constant of the actuator, min

A = pipe cross section, ft^2

L = pipe length, ft

The steady-state values and parameters used in this example are presented in Camacho, O. and Smith C., (2000), except L and A which has new values: 80 ft and 0.08 ft^2 respectively.

4.2 Continuous Stirred Tank Reactor (CSTR)

In the reactor, an exothermic reaction takes place ($A \rightarrow B$). The reactor is surrounded by a jacked where a cooling liquid flows to remove the heat of reaction. The process information and steady-state values used in this example were taken from Rojas, R. et al. (2014). The complete model is described by the following equations.

Component balance on reactant A:

$$\frac{dC_A(t)}{dt} = \frac{f}{V}[C_{Ai}(t) - C_A(t)] - r_A(t) \quad (27)$$

Energy balances on the reactor:

$$\frac{dT(t)}{dt} = \frac{f}{V}[T_i(t) - T(t)] - \frac{\Delta H_R}{\rho C_p} r_A(t) - \frac{UA}{V\rho C_p}[T(t) - T_j(t)] \quad (28)$$

Energy balances on the jacket:

$$\frac{dT_j(t)}{dt} = \frac{UA}{V_j \rho_j C_{pj}}[T(t) - T_j(t)] - \frac{F_j(t)}{V_j}[T_j(t) - T_{ji}(t)] \quad (29)$$

The reaction rate for this CSTR:

$$r_A(t) = k_0 e^{-E/RT(t)} C_A(t) \quad (30)$$

The valve equation:

$$F_j(t) = f_{max} \propto^{[u(t)-1]} \quad (31)$$

Where:

$C_A(t)$ = concentration of reactant in the reactor, lbmol/ft^3

$T(t)$ = temperature in the reactor, °R

T_j = temperature of boiling liquid in cooling jacket, °R

$r_A(t)$ = rate of reaction, lbmol/ft^3-min

f = process feed rate, ft^3/min

V = volume of reactor, ft^3

ΔH_R = heat of reaction, Btu/lbmol

ρ = density of reactor contents, lb_m/ft^3

C_p = heat capacity of reactants and products, Btu/lb_m°R

A = heat transfer area, ft^2

U = overall heat-transfer coefficient, Btu/min ft^2 °R

ρ_j = density of the coolant, lb_m/ft^3

C_{pj} = specific heat of the coolant, Btu/lb_m°R

F_j = coolant rate, ft^3/min

f_{max} = maximum flow through the valve, ft^3/min

$\propto$ = valve rangeability parameter, dimensionless

k_0 = Arrhenius frequency parameter, 1/min

E = activation energy of the reaction, Btu/lbmol

R = ideal gas law constant, Btu/lbmol°R

$u(t)$ = valve position, from 0 (closed) to 1 (open)

5. SIMULATION RESULTS

To test the proposed controller, set point changes were made to test tracking references and also disturbances were introduced to prove regulation tasks. The controller performance is measured using the Integral of Squared Error (ISE). The results are compared with a PI controller, tuned using the equations proposed by Dahlin (Smith, C. et al. (1997)), since this control is the most popular alternative in process control.

5.1 Characteristic and tuning parameters

Introducing a step change at the input (valve position) and then recording the transmitter output, the characteristic parameters of the FOPDT models are taken from the result reaction curves and are presented in Table 1.

Table 1. Characteristic Parameters

Process	Parameter			
	k	τ	t_0	t_0/τ
Mixing Tank	0.89	2.29	1.33	0.58
CSTR	1.03	5.55	2.45	0.44

Using these values and formulas for Dahlin synthesis, the tuning parameters for PI controller are obtained. The integral parameter used in NMCr+I is obtained using (20). The tuning parameters of both controllers are presented in Table 2.

Table 2. Controller Tuning Parameters

Process	PI		NMCr+I	
	K_p	K_i	K_x	K_i
Mixing Tank	0.978	0.436	0.8	0.069
CSTR	2.18	0.18	0.8	0.028

5.2 Performance Test

The Fig. 3 shows the $T_4(t)$ response in the mixing tank, when a set point changes from 150 °F to 160 °F is produced, and a disturbance at time 100 min occurs, the hot water flow, $W_1(t)$, changes from 250 lb/min to 260 lb/min. Figure 3 shows that the NMCr+I has a faster response, generating a little more overshoot than PI, and it returns smoothly to the set point value at same time that the PI.

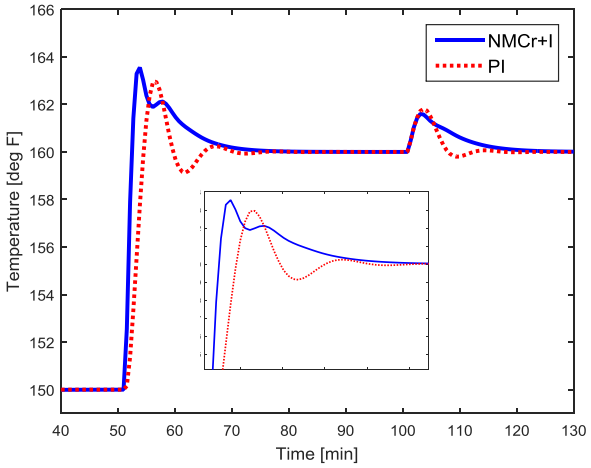

Fig.3 Response for set point and disturbance changes in mixing tank.

The Fig. 4 shows the temperature response $T(t)$ in reactor, when changes from 690 °R to 700 °R occurs and also a disturbance at time 160 min happens when the inlet feed temperature, $T_i(t)$, changes from 578 °R to 583 °R. According with this, the NMCr+I has a faster response with a small overshoot, besides it is less affected by the disturbance.

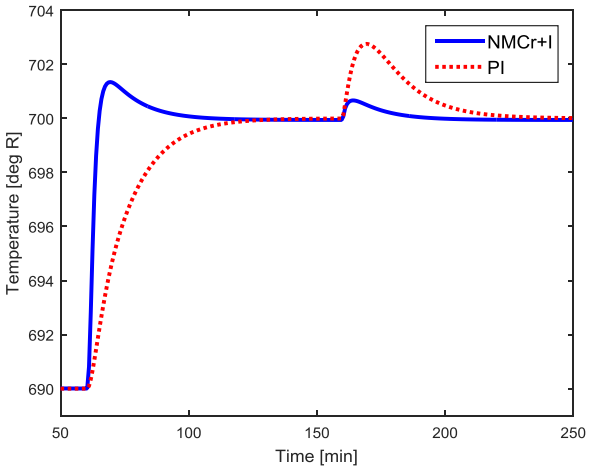

Fig.4 Response for set point and disturbance changes in CSTR.

The results obtained using the performance index ISE are shown in Table 3. In both cases, NMCr+I presented better performance than the PI controller.

Table 3. Results of Performance Index

Index	Controller	Process	
		Mixing Tank	CSTR
ISE	PI	0.0297	0.00188
	NMCr+I	0.0282	0.00036

5.3 Robustness Test

In order to test the robustness of the proposed controller, modelling errors are introduced. The errors used are the same for each one of the characteristic parameters (k, τ and t_0). Figures 5 and 6 depict the resulting ISE curves as a function of time and modelling errors.

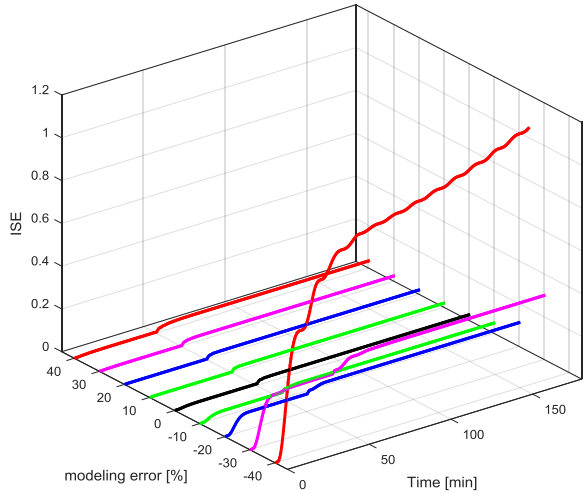

Fig.5 Model error vs ISE for NMCr+I in Mixig Tank.

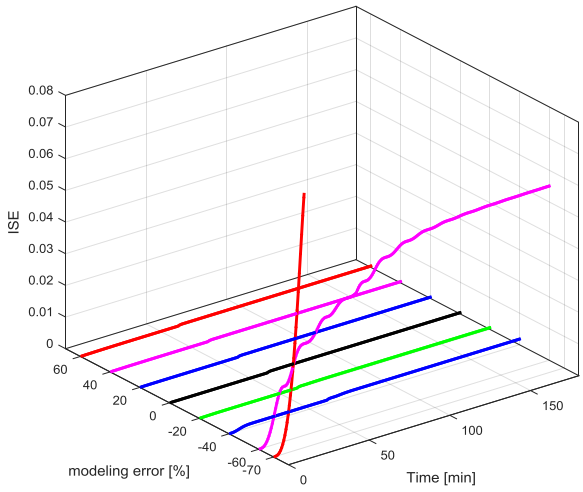

Fig.6 Model error vs ISE for NMCr+I in CSTR.

The errors were increased until the process begins to oscillate and not return to set point value.

Fig. 7 shows the temperature response, using PI and NMCr+I, in the mixing tank when modelling errors are introduced. The first change was introduced at 100 [min] with a -5% model error. The second change was introduced at 150 min with a -20% model error and the last change was introduced at 220 min with a -50% model error.

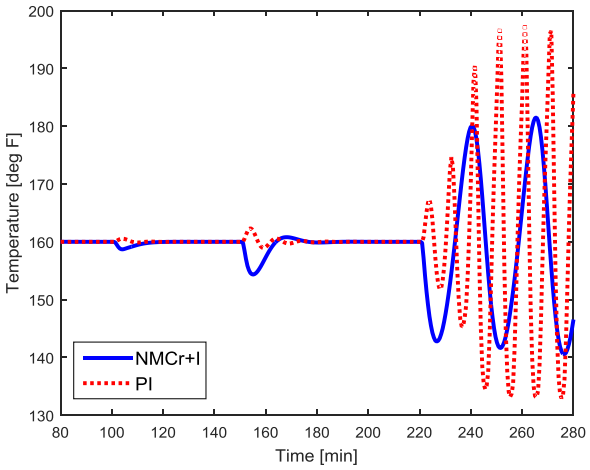

Fig.7 Response for model error changes in mixing tank.

Fig. 8 shows the response of temperature in CSTR similar to the previous case. The first change was introduced at 150 min. with a -8% model error. The second change was introduced at 200 min with a -32% model error and the last change was introduced at 270 min with an excessive -80% model error.

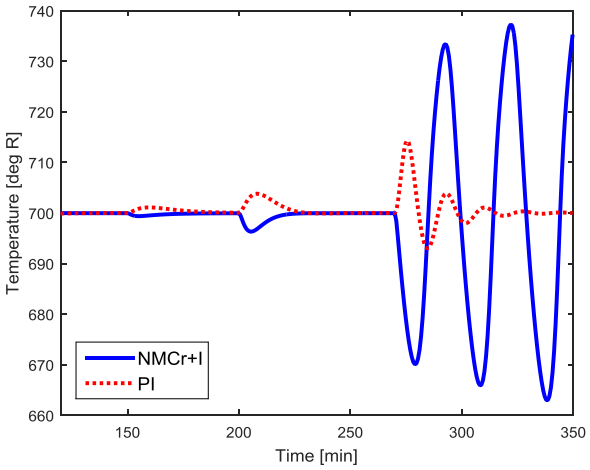

Fig.8 Response for model error changes in CSTR.

The previous results have shown that if modelling errors close to 30% are considered, the proposed control approach is still stable. Therefore, the NMCr+I is robust for reasonable errors.

6. CONCLUSIONS

This work presented the application for nonlinear processes of a Numerical Methods Controller based on a FOPDT model.

The results showed that proposed controller works well for the two different cases of study.

The performance and robustness tests proved that the proposed approach can be considered as a control alternative for nonlinear self-regulating processes.

An optimal tuning procedures, such as computational and intelligent optimization techniques, could be used to get better tunings parameters for the proposed approach.

In future works the proposed approach will be implemented in a real self-regulating open loop processes.

ACKNOWLEDGMENTS

Oscar Camacho thanks PROMETEO project of SENESCYT, Republic of Ecuador, for its sponsorship for the realization of this work.

This work was partially funded by the Consejo Nacional de Investigaciones Científicas y Técnicas (CONICET – National Council for Scientific Research), Argentina.

REFERENCES

Camacho, O., Smith, C. and Chacón, E. (1997). Toward an Implementation of Sliding Mode Control to Chemical Processes. IEEE International Symposium on Industrial Electronics, pp. 1101–1105.

Camacho, O., Smith, C. (2000). Sliding mode control: an approach to regulate nonlinear chemical processes. ISA Transactions, vol. 39, pp. 205-218.

Chaves E. (2010). Integración numérica en el tiempo, 1st ed., España: Universidad de Castilla.

Godoy, S., Serrano, E., Scaglia, G., Ortiz, O. and Secchi, H. (2013). Control de trayectoria basado en Métodos Numéricos aplicado a un birreactor fed-batch. Proceedings of XV Reunión de Trabajo en Procesamiento de la Información y Control.

Guerrero, F. and Menéndez, O. (2013). Modelación, simulación y Control de Sistemas Aéreos no Tripulados utilizando Inteligencia Artificial. Eng. Thesis, Escuela Politécnica Nacional, Quito, Ecuador.

Guevara, L., Guevara, J., Scaglia, G., Camacho, O. and Rosales, A. (2016). A New Approach of a Numerical Methods Controller for Self-Regulating Processes. Proceedings of IEEE Argencon.

Quintero, O. L., Scaglia, G., Amicarelli, A. and Di Sciascio, F. (2008). Bio process control strategy based on numerical methods and linear algebra: second approach. Proceedings of 27th IASTED International Conference on Modelling, Identification and Control, pp. 292-297.

Rojas, R., Camacho, O. and González, L. (2004). A sliding mode control proposal for open-loop unstable processes. ISA Transactions, vol. 43, pp. 243-255.

Rosales, A., Scaglia, G. , Mut V., and Di Sciascio, F. (2010) .Formation control and trajectory tracking of mobile robotic systems – a linear algebra approach. Robotica, vol. 29, No. 3, pp. 335–349.

Scaglia G., Mut, V. and Di Sciascio, F. (2006). Trajectory Control Of Mobile Robots Based On Numerical Methods. Proceedings of XII Congreso Latinoamericano de Control Automátic.

Scaglia, G., Quintero, O. L. , Mut, V.,di Sciascio, F. (2009). Numerical Methods Based Controller Design for Mobile Robots. Robotica, vol. 27, pp. 269-279.

Scaglia G., Aballay, P., Serrano, E., Ortiz, O., Jordan, M and Vallejo, M. (2014). Linear algebra based controller design applied to a bench-scale oenological alcoholic

fermentation. Control Engineering Practice, vol. 25, pp. 66-74.

Seborg, D. E., Edgar, T. F., Mellichamp, D. A., Doyle III, F. J. (2011). Process dynamics and control, 3rd ed. John Wiley & Sons, Inc.

Smith, C. and Corripio, A. (1997). Principles and practice of automatic process control, New York: John Wiley & Sons, Inc.

Suvire, R., Scaglia, G., Serrano, E., Vega, J. and Ortiz, O. (2013). Trajectory Tracking Controller Design Based on Linear Algebra with Integral Accion: Application to CSTR Systems. VII Congreso Argentino de Ingeniería Química (CAIQ.

Bioprocesses Control Based on Linear Algebra

M. C. Fernández*, M. N. Pantano*, D. Patiño, O. Ortiz*, G. Scaglia*.**

** Instituto de Ingeniería Química, Universidad Nacional de San Juan (UNSJ), CONICET, Av. Lib. San Martín Oeste 1109, San Juan J5400ARL, Argentina. (e-mail: mcfernandez@unsj.edu.ar; npantano@unsj.edu.ar; rortiz@unsj.edu.ar; gscaglia@unsj.edu.ar)*

*** Instituto de Automática, Universidad Nacional de San Juan (UNSJ), CONICET, Av. Lib. San Martín Oeste 1109, San Juan, Argentina. (e-mail: dpatino@inaut.unsj.edu.ar)*

Abstract: Fed-batch fermenters have gained particular attention due to its wide range of high valued products production possibilities. Nowadays, the optimization and control of these systems is an important task given its significant economic impact and particular characteristics. The paper proposes a linear algebra based controller for nonlinear and multivariable bioprocesses. It involves finding the control actions to make the system follow predefined optimal concentration profiles. The controller parameters are selected with a Monte Carlo experiment. Finally, the good performance of the controller is proved under normal conditions and adding perturbations in the control action.

Keywords: nonlinear dynamics control, fed-batch fermentation, penicillin production, profiles tracking control.

1. INTRODUCTION

On the one side, the increasingly demand of high added value products, with specific characteristics for the market, has made essential the dispose of reliable tools in the production area. Due to this fact, in the last few years the optimization and control techniques development has become a fundamental topic for scientific investigations. On the other side, the bioprocesses industry has demonstrated to be an excellent option for the obtaining of a long variety of products in a natural and ecological way. Although, this kind of processes have many complications, and that is what make them to be the biggest challenge from control engineer's viewpoint (Ashoori et al., 2009).

The biological processes have been characterized for using microscopic organisms to obtain valuable substances. For example: recombinant proteins, vaccines and antibiotics in the pharmaceutical industry, or beer, wine, yeast in the manufacturing of agro-food goods, biogas and compost in the treatment of urban and industrial solid organic wastes and wastewater (Mangesh and Jana, 2008), or biopolymers in the chemical industry (Chung et al., 2015), between others.

A bioreactor can be operated in one of the following forms: batch, fed-batch or continuous. The continuous operation mood is characterized to work in a stationary way, while in batch and fed-batch procedures, the states vary in the time. This particularity of batch and fed-batch processes added to the many difficulties that any bioprocess present, make the control of them to be an arduous task to achieve. Some of the mentioned complications are: the nonlinear and unstable dynamic behavior of microorganisms which means strong modeling approximations; the presence of numerous external disturbances; troubles for most of the representative variables on-line measurement; both the initial states of the process and the parameters of the model may vary randomly from batch to batch (Liang and Chen, 2003). All this avoid the possibility of using classic industrial controllers, like PI and PID controllers, being necessary to implement control algorithms specifically developed for bioprocesses (De Battista et al., 2012).

The objective of this work is to develop a control technique for a fed-batch penicillin production process. It consists in tracking predefined state variables profiles (preferably optimized ones) with minimal error. The methodology was originally designed for robotics systems by Scaglia et al (Scaglia et al., 2009, Scaglia et al., 2010) and lately extended to other systems like unmanned vehicles (Cheein and Scaglia, 2014), chemical processes (Serrano et al., 2014a), underactuated surface vessels (Serrano et al., 2013, Serrano et al., 2014b), between others, all of them with excellent results in the path tracking.

The main advantage of this procedure is the application of linear algebra for the controller design. Here the control action (substrate feed rate) is obtained solving a linear equations system, although the controller structure rises from a nonlinear mathematical model. This means that the controller performance is independent from the operation point, obtaining good result even when the initial conditions and the parameters change.

The paper is organized as follows: The description of the system and the process is presented in Section 2. The controller design and the selection of its parameters are exposed in Section 3. While in Section 4, the simulation results are shown, this include: the performance under normal conditions and with perturbation in the control action. Finally, in Section 5, the conclusions are exposed.

2. SYSTEM AND PROCESS DESCRIPTION

The system under study is a fed-batch bioreactor for penicillin production. The substrate and the microorganism used are glucose and Penicillum crysogenum, respectively. The equations that model the process were originally proposed in (Cuthrell and Biegler, 1989), from which many optimization and control papers have been written (Lim et al., 1986, Luus, 1993, Riascos and Pinto, 2004, Ronen et al., 2002). It is a single input multi output system (SIMO), where the input is the substrate feed rate, and the outputs are the cells, product (penicillin) and substrate concentrations inside the reactor. The mathematical model of the process is:

$$\begin{cases} \dot{X}(t) = \mu(X,S)X - \left(\frac{X}{S_F V}\right)U \\ \dot{P}(t) = \rho(S)X - K_{deg}P - \left(\frac{P}{S_F V}\right)U \\ \dot{S}(t) = -\mu(X,S)\left(\frac{X}{Y_{X/S}}\right) - \rho(S)\left(\frac{P}{Y_{P/S}}\right) - \left(\frac{m_s S}{K_m + S}\right)X + \left(1 - \frac{S}{S_F}\right)\frac{U}{V} \end{cases} \quad (1)$$

$$\mu(X,S) = \mu_{max}\left(\frac{S}{K_{XG}X + S}\right)$$
$$\rho(S) = \rho_{max}\left(\frac{S}{K_{PP} + S(1 + S/K_{in})}\right) \quad (2)$$
$$\dot{V}(t) = \frac{U}{S_F}$$

In these equations, the state variables are: biomass (X), product (P) and glucose (S) concentrations. The control action is the substrate feed rate (U). S_F is the substrate feed concentration. The auxiliary equation defined are: the specific biomass growth rate ($\mu(X, S)$), the specific penicillin production rate ($\rho(S)$) and the culture volume (V).

In Table 1 are shown the initial variable values, whereas in Table 2 the parameter definitions and its values.

Table 1. Initial variable values for penicillin biosynthesis

Variable	Initial value
X (g/L)	1.5
P (g/L)	0.0
S (g/L)	0.0
V (L)	7.0

Table 2. Parameters of penicillin biosynthesis model

Parameter	Definition	Value
μ_{max}	Maximum specific biomass growth rate (h^{-1})	0.11
ρ_{max}	Maximum specific production rate (gP/gX h)	0.0055
K_{XG}	Saturation parameter for biomass growth (gS/gX)	0.006
K_{PP}	Saturation parameter for production (gS/L)	0.0001
K_{in}	Inhibition parameter for production (gS/L)	0.1
K_{deg}	Product degradation rate (h^{-1})	0.001
K_m	Saturation parameter for maintenance consumption (gS/L)	0.0001
m_s	Maintenance consumption rate (gS/gX h)	0.029
$Y_{X/S}$	Yield factor for substrate to biomass (gX/g S)	0.47
$Y_{P/S}$	Yield factor for substrate to product (gP/g S)	1.2
S_F	Feed concentration (gS/L)	500

3. CONTROLLER DESIGN

3.1 Controller Structure

For the application of this technique, it is necessary to know the mathematical model that represents the process, and the reference profiles that are expected to be followed by the system.

The most important variables within de bioreactor are the cells and product concentration, so their reference profiles are expected to be tracked by the controller.

The optimal substrate feed rate presented by Riascos & Pinto (Riascos and Pinto, 2004) is taken as the reference profile for substrate feed rate. The reference concentrations of cells and penicillin are determined in an open-loop simulation of the system (see Fig. 1). For this, the feed rate mentioned, the mathematical model, and the information from Table 1 and 2, are used.

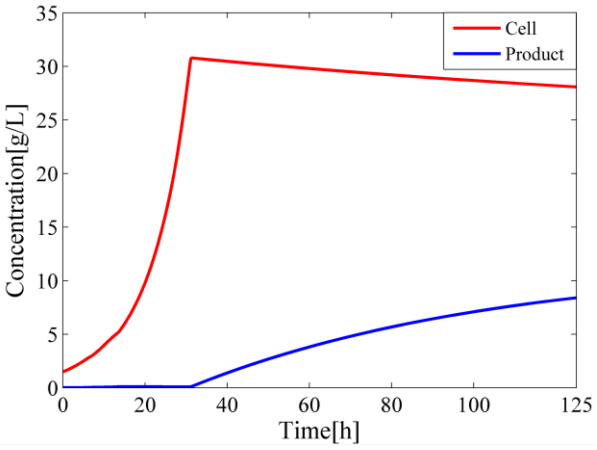

Fig. 1. Reference profiles of cells and penicillin concentration, obtained by an open-loop simulation.

In order to achieve the objective presented above, numerical methods are used to determine the evolution of the system. The method developed by Euler is used in order to integrate numerically an ordinary differential equation given an initial value.

$$\left(\frac{d\sigma}{dt}\right) = \frac{\sigma_{n+1} - \sigma_n}{T_0} \quad (3)$$

Where σ represents each state variable, σ_n is the present value of σ measured from the reactor (on-line), while σ_{n+1} is the value of σ in the next measurement instant. T_0 is the sampling time; for this study is adopted a value of 0.1 h. The process lasts 125 h.

The error in a given sampling moment is defined as the difference between the actual and reference values. As the error in $n+1$ is proportional to the error in n, σ_{n+1} can be expressed as follows:

$$\sigma_{n+1} = \sigma_{ref\,n+1} - k_\sigma \underbrace{(\sigma_{ref\,n} - \sigma_n)}_{error} \tag{4}$$

where k_σ is a proportionality factor and represents the parameter of the controller for the generic variable σ. There are three different k_σ for this model of penicillin production, k_X, k_P and k_S.

Replacing Eq. (4) in (3) is obtained the following expression. It allows the approximation of the derivatives.

$$\left(\frac{d\sigma}{dt}\right) = \frac{\overbrace{\left[\sigma_{ref\,n+1} - k_\sigma(\sigma_{ref\,n} - \sigma_n)\right]}^{\sigma_{n+1}} - \sigma_n}{T_0} \tag{5}$$

Substituting Eq. (5) in the mathematical model:

$$\begin{cases} \dot{X}(t) = \dfrac{\left(X_{ref\,n+1} - k_X\left(X_{ref\,n} - X_n\right) - X_n\right)}{T_0} = \mu(X_n, S_n)X_n - \left(\dfrac{X_n}{S_F V_n}\right)U_n \\ \dot{P}(t) = \dfrac{\left(P_{ref\,n+1} - k_P\left(P_{ref\,n} - P_n\right) - P_n\right)}{T_0} = \rho(S_n)X_n - K_{deg}P_n - \left(\dfrac{P_n}{S_F V_n}\right)U_n \\ \dot{S}(t) = \dfrac{\left(S_{ref\,n+1} - k_S\left(S_{ref\,n} - S_n\right) - S_n\right)}{T_0} = \\ \quad -\mu(X_n, S_n)\left(\dfrac{X_n}{Y_{X/S}}\right) - \rho(S_n)\left(\dfrac{P_n}{Y_{P/S}}\right) - \left(\dfrac{m_s S_n}{K_m + S_n}\right)X_n + \left(1 - \dfrac{S_n}{S_F}\right)\dfrac{U_n}{V_n} \end{cases} \tag{6}$$

With this new appreciation of the Eq. (1) as a system of linear equations, a simple possibility for calculating the control action is available. Besides, it could be expressed in a matrix form through placing the state variables as a function of U. In this way, is more straightforward to clear the control action:

$$\overbrace{\begin{pmatrix} -X_n \\ -P_n \\ S_f - S_n \end{pmatrix}}^{A} \overbrace{\frac{U_n}{S_f V_n}}^{u} = \underbrace{\begin{pmatrix} \dfrac{\left(X_{ref\,n+1} - k_X\left(X_{ref\,n} - X_n\right) - X_n\right)}{T_0} - \mu(X_n, S_n)X_n \\ \dfrac{\left(P_{ref\,n+1} - k_P\left(P_{ref\,n} - P_n\right) - P_n\right)}{T_0} - \rho(S_n)X_n + K_{deg}P_n \\ \dfrac{\left(S_{ref\,n+1} - k_S\left(S_{ref\,n} - S_n\right) - S_n\right)}{T_0} + \mu(X_n, S_n)\left(\dfrac{X_n}{Y_{X/S}}\right) + \rho(S_n)\left(\dfrac{X_n}{Y_{P/S}}\right) + \left(\dfrac{m_s S_n}{K_m + S_n}\right)X_n \end{pmatrix}}_{b} \tag{7}$$

To simplify the mathematical expression of the problem, Eq. (7) is expressed generically as follows:

$$A\,u = b$$

$$\begin{bmatrix} a_1 \\ a_2 \\ a_3 \end{bmatrix} \frac{U}{S_f V} = \begin{bmatrix} b_1 \\ b_2 \\ b_3 \end{bmatrix} \tag{8}$$

So as to find U is necessary to ask the system to have exact and unique solution. To accomplish this, **b** have to be a linear combination of **A** columns (Strang, 2006), that is to say, **A** and **b** must be parallel. This condition can be satisfied in different ways; one of them is:

$$\begin{cases} \dfrac{a_3}{a_1} = \dfrac{b_3}{b_1} \rightarrow a_3 b_1 = b_3 a_1 \\ \dfrac{a_3}{a_2} = \dfrac{b_3}{b_2} \rightarrow a_3 b_2 = b_3 a_2 \end{cases} \tag{9}$$

It is important to highlight that there are many ways to express a parallelism condition, and the results will be the same with any of them. Replacing in Eq. (9) with each corresponding matrices component values:

$$\begin{cases} \left(S_f - S_n\right)\left(\left(\dfrac{X_{ref\,n+1} - k_X\left(X_{ref\,n} - X_n\right) - X_n}{T_0}\right) - \mu(X_n, S_n)X_n\right) = \\ \left(\left(\dfrac{S_{ref\,n+1} - k_S\left(S_{ref\,n} - S_n\right) - S_n}{T_0}\right) + \mu(X_n, S_n)\left(\dfrac{X_n}{Y_{X/S}}\right) + \rho(S_n)\left(\dfrac{X_n}{Y_{P/S}}\right) + \left(\dfrac{m_s S_n}{K_m + S_n}\right)X_n\right)(-X_n) \\ \left(S_f - S_n\right)\left(\left(\dfrac{P_{ref\,n+1} - k_P\left(P_{ref\,n} - P_n\right) - P_n}{T_0}\right) - \rho(S_n)X_n + K_{deg}P_n\right) = \\ \left(\left(\dfrac{S_{ref\,n+1} - k_S\left(S_{ref\,n} - S_n\right) - S_n}{T_0}\right) + \mu(X_n, S_n)\left(\dfrac{X_n}{Y_{X/S}}\right) + \rho(S_n)\left(\dfrac{X_n}{Y_{P/S}}\right) + \left(\dfrac{m_s S_n}{K_m + S_n}\right)X_n\right)(-P_n) \end{cases} \tag{10}$$

For (10) to have solution, it is defined the "sacrificed variable", which is denoted by the subscript "ez". To select the it is necessary to analyze and interpret the role of each variable in the process. In a bioprocess, the substrate concentration directly affects cells and product concentrations, and can be regulated by varying the feed flow rate. Considering this, we chose S as sacrificed variable. Replacing S_{ref} by S_{ez} in Eq. (10):

$$\begin{cases} \left(S_f - S_n\right)\left(\left(\dfrac{X_{ref\,n+1} - k_X\left(X_{ref\,n} - X_n\right) - X_n}{T_0}\right) - \mu(X_n, S_{ez\,n})X_n\right) = \\ \left(\left(\dfrac{S_{ez\,n+1} - k_S\left(S_{ez\,n} - S_n\right) - S_n}{T_0}\right) + \mu(X_n, S_n)\left(\dfrac{X_n}{Y_{X/S}}\right) + \rho(S_n)\left(\dfrac{X_n}{Y_{P/S}}\right) + \left(\dfrac{m_s S_n}{K_m + S_n}\right)X_n\right)(-X_n) \\ \left(S_f - S_n\right)\left(\left(\dfrac{P_{ref\,n+1} - k_P\left(P_{ref\,n} - P_n\right) - P_n}{T_0}\right) - \rho(S_{ez\,n})X_n + K_{deg}P_n\right) = \\ \left(\left(\dfrac{S_{ez\,n+1} - k_S\left(S_{ez\,n} - S_n\right) - S_n}{T_0}\right) + \mu(X_n, S_n)\left(\dfrac{X_n}{Y_{X/S}}\right) + \rho(S_n)\left(\dfrac{X_n}{Y_{P/S}}\right) + \left(\dfrac{m_s S_n}{K_m + S_n}\right)X_n\right)(-P_n) \end{cases} \tag{11}$$

This system is solved using the fminsearch function in MATLAB. Note that the only unknown is $S_{ez,n+1}$, as $S_{ez,n}$ is obtained in the previous sampling time.

Once $S_{ez,n+1}$ value is calculated, it is replaced in the original matrix system (7). Then, the control action ($U_n/S_f V_n$) can be determined at any sampling time using least squares (Strang, 2006).

$$\frac{U}{S_f V} = \left(A^T A\right)^{-1} A^T b = \frac{a_1 b_1 + a_2 b_2 + a_3 b_3}{a_1^2 + a_2^2 + a_3^2} \tag{12}$$

3.2 Controller Parameters Selection

As it was introduced in subsection *3.1*, the performance of the bioreactor is directly affected by the controller parameters (k_σ). Those parameters take values among zero and one ($0 < k_\sigma < 1$), which makes the tracking error tends to zero when n tends to infinity (for space reasons, the demonstration is not shown, however, a similar example could be appreciated in (Scaglia et al., 2010)). The "*tracking error*" is defined as follows:

$$\|e_n\| = \sqrt{(X_{refn} - X_n)^2 + (P_{refn} - P_n)^2 + (S_{ezn} - S_n)^2} \tag{13}$$

The following procedure aims to find the best values for k_σ, such that the tracking error is minimized. In this test, the Monte Carlo algorithm is applied. The experiment consist in simulate the process a number of times using random values of k_σ. Then, the total error is calculated for each iteration. The k_σ that make a minimum total error are selected.

To determine the number of simulations (N) is used Eq. (14) (Tempo and Ishii, 2007). Note that in order to limit the chance of a wrong answer, an appropriate confidence (δ) and accuracy (ε) must be indicated.

$$N \geq \left[\frac{\log \frac{1}{\delta}}{\log \frac{1}{1-\varepsilon}} \right] \tag{14}$$

Depending on the precision to be obtained, δ and ε values are selected. For this study, $\delta=0.01$ and $\varepsilon=0.005$ Consequently, $N=1000$.

The tracking error $||e_n||$ was defined in Eq. (13) and the total error is found with the following expression:

$$E=\sum_{n=1}^{1250} \|e_n\| \tag{15}$$

The simulation results show that de best values for the parameters are:

Table 3. Controller Parameters

Parameter	Value
k_X	0.9798
k_P	0.976
k_S	0.8979

4. SIMULATION RESULTS

4.1 Controller operation under normal conditions

To simulate under normal conditions, the initial state variables values shown in Table I, the parameters of Table II, and the controller parameters determined in *3.2* subsection are used. Here, it is considered that there are no disturbances in the external environment that could affect the process.

Figure 2 present how the real cells and product concentration follow perfectly the references. Finally, Fig. 3 shows the tracking error. As it can be seen, this error tends to zero as the process moves forward.

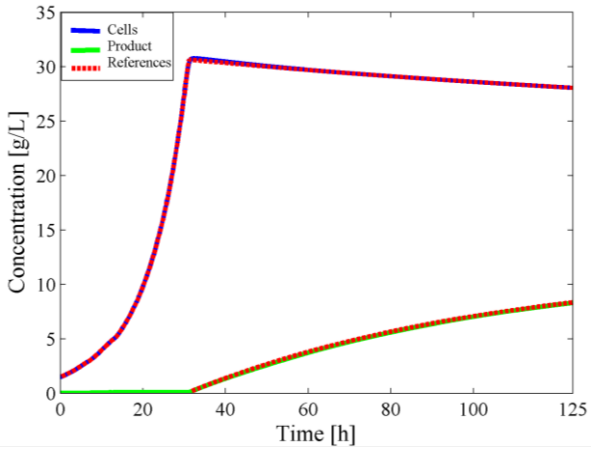

Fig. 2. Reference and real profiles of cells and penicillin concentration, obtained under normal operation conditions.

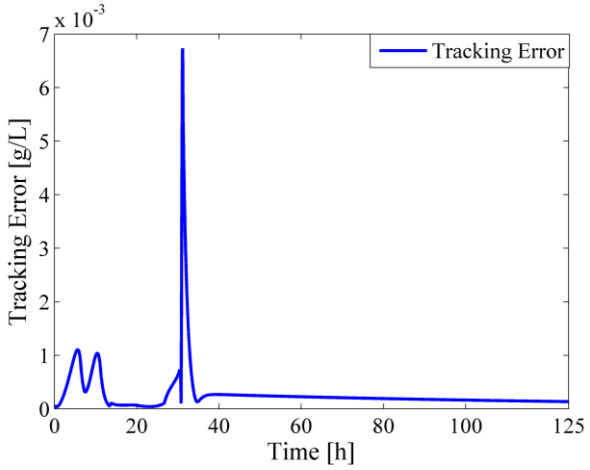

Fig. 3. Tracking error for the simulation under normal operation conditions.

4.2 Test with perturbations in the control action

In order to prove the performance of the controller, it is added a disturbance in the control action. To achieve this, the control action is affected in a 20% of its original value with a random perturbation. This can be explained as a random noise that results in non-zero-mean Gaussian disturbances (George, 2014).

Figure 4 shows the perturbed control actions. Figures 5 and 6 show the tracking of cells and product profiles in the perturbed system. Finally, Fig. 7 shows the tracking error. The disturbances in the control action cause an increasing of the tracking error, however, it remains at acceptable levels.

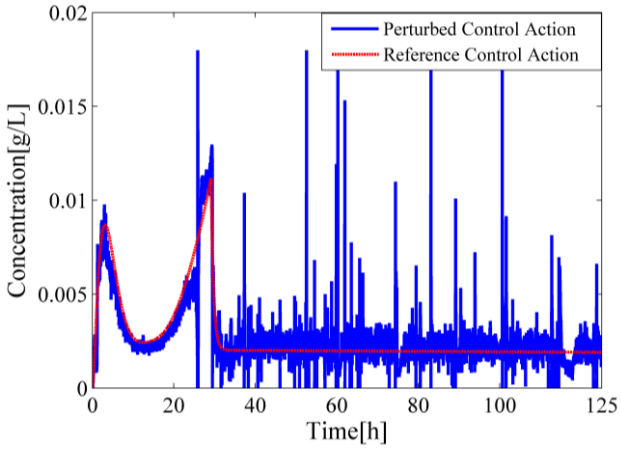

Fig. 4. Perturbed Control Action.

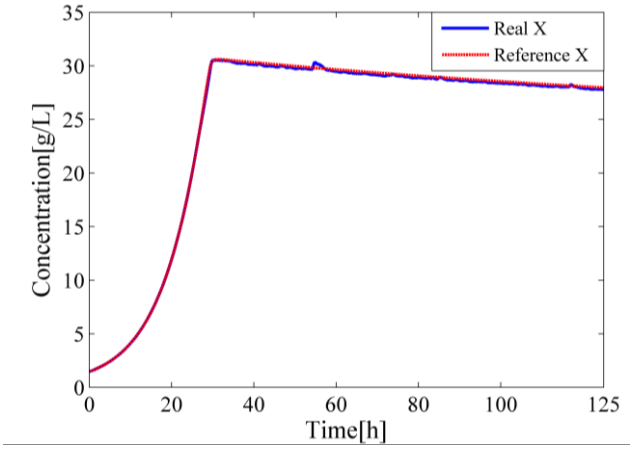

Fig. 5. Reference and real cells concentration profiles applying perturbations in the control action.

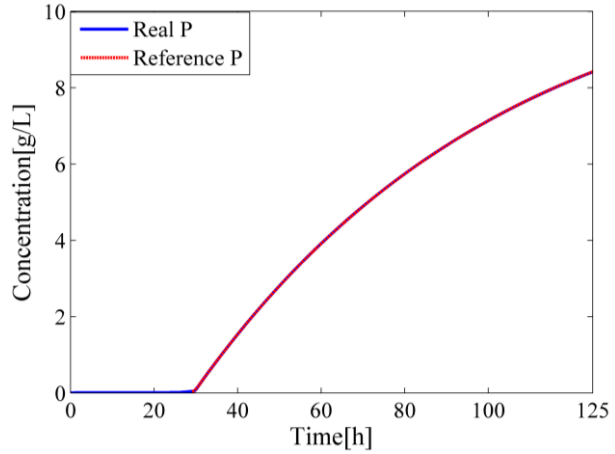

Fig. 6. Reference and real penicillin concentration profiles applying perturbations in the control action.

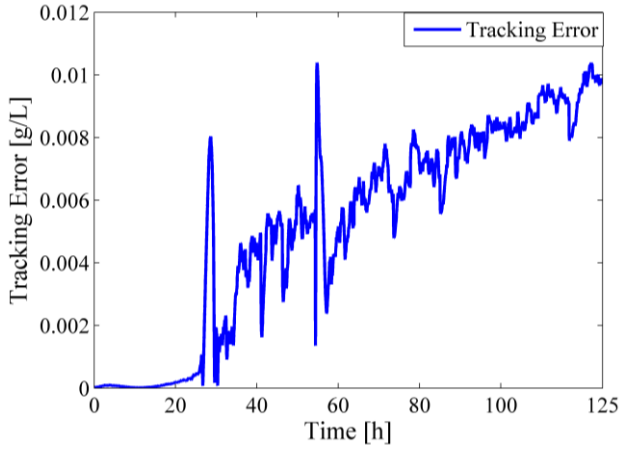

Fig. 7. Tracking error for the simulation with perturbations in the control action.

6. CONCLUSIONS

This controller has several advantages over others: it can be easily applied, there is no need to have advanced knowledge about automatic control to do it; the methodology has less mathematical complexity because it allows obtaining the control action as a solution of linear equations system, although the controller structure arises from a nonlinear mathematical model. As a result, this technique can be used in a long variety of systems. Furthermore, this controller is versatile against different disturbances; this was supported by the tests made, which results show that the controller manages to achieve the reference profile successfully at any time, and prove its good performance.

ACKNOWLEDGMENT

Grateful to the National Council of Scientific and Technological Research (CONICET) and the Chemical Engineering Institute (IIQ) from the National University of San Juan for making possible this research.

REFERENCES

ASHOORI, A., MOSHIRI, B., KHAKI-SEDIGH, A. & BAKHTIARI, M. R. 2009. Optimal control of a nonlinear fed-batch fermentation process using model predictive approach. *Journal of Process Control*, 19**,** 1162-1173.

CUTHRELL, J. E. & BIEGLER, L. T. 1989. Simultaneous optimization and solution methods for batch reactor control profiles. *Computers & Chemical Engineering*, 13**,** 49-62.

CHEEIN, F. A. & SCAGLIA, G. 2014. Trajectory tracking controller design for unmanned vehicles: A new methodology. *Journal of Field Robotics*, 31**,** 861-887.

CHUNG, H., YANG, J. E., HA, J. Y., CHAE, T. U., SHIN, J. H., GUSTAVSSON, M. & LEE, S. Y. 2015. Bio-based production of monomers and polymers by metabolically engineered microorganisms. *Current opinion in biotechnology*, 36**,** 73-84.

DE BATTISTA, H., PICÓ, J. & PICÓ-MARCO, E. 2012. Nonlinear PI control of fed-batch processes for growth rate regulation. *Journal of Process Control,* 22**,** 789-797.

GEORGE, J. 2014. On adaptive loop transfer recovery using Kalman filter-based disturbance accommodating control. *Control Theory & Applications, IET,* 8**,** 267-276.

LIANG, J. & CHEN, Y. 2003. Optimization of a fed-batch fermentation process control competition problem using the NEOS server. *Proceedings of the Institution of Mechanical Engineers, Part I: Journal of Systems and Control Engineering,* 217**,** 427-432.

LIM, H., TAYEB, Y., MODAK, J. & BONTE, P. 1986. Computational algorithms for optimal feed rates for a class of fed-batch fermentation: Numerical results for penicillin and cell mass production. *Biotechnology and Bioengineering,* 28**,** 1408-1420.

LUUS, R. 1993. Optimization of fed-batch fermentors by iterative dynamic programming. *Biotechnology and Bioengineering,* 41**,** 599-602.

MANGESH, M. G. & JANA, A. K. 2008. A comparison of three sets of DSP algorithms for monitoring the production of ethanol in a fed-batch baker's yeast fermenter. *Measurement,* 41**,** 970-985.

RIASCOS, C. A. & PINTO, J. M. 2004. Optimal control of bioreactors: a simultaneous approach for complex systems. *Chemical Engineering Journal,* 99**,** 23-34.

RONEN, M., SHABTAI, Y. & GUTERMAN, H. 2002. Optimization of feeding profile for a fed-batch bioreactor by an evolutionary algorithm. *Journal of biotechnology,* 97**,** 253-263.

SCAGLIA, G., MONTOYA, L. Q., MUT, V. & DI SCIASCIO, F. 2009. Numerical methods based controller design for mobile robots. *Robotica,* 27**,** 269-279.

SCAGLIA, G., ROSALES, A., QUINTERO, L., MUT, V. & AGARWAL, R. 2010. A linear-interpolation-based controller design for trajectory tracking of mobile robots. *Control Engineering Practice,* 18**,** 318-329.

SERRANO, M., SCAGLIA, G., ABALLAY, P., ORTIZ, O. & MUT, V. 2014a. LINEAR ALGEBRA AND OPTIMIZATION BASED CONTROLLER DESIGN FOR TRAJECTORY TRACKING OF TYPICAL CHEMICAL PROCESS. *Latin American Applied Research,* 44**,** 313-318.

SERRANO, M. E., SCAGLIA, G., MUT, V., ORTIZ, O. & JORDAN, M. 2013. Trajectory Tracking Controller Based on Linear Algebra: a case study in underactuated surface vessels. *Journal of Control Engineering and Applied Informatics,* 15**,** 15-25.

SERRANO, M. E., SCAGLIA, G. J., GODOY, S. A., MUT, V. & ORTIZ, O. A. 2014b. Trajectory tracking of underactuated surface vessels: A linear algebra approach. *Control Systems Technology, IEEE Transactions on,* 22**,** 1103-1111.

STRANG, G. 2006. Linear algebra and its applications, Thomson, Brooks/Cole, Belmont, CA. ISBN 0-030-10567-6.

TEMPO, R. & ISHII, H. 2007. Monte Carlo and Las Vegas Randomized Algorithms for Systems and Control*: An Introduction. *European journal of control,* 13**,** 189-203.

Diseño y construcción de dispositivo portátil y de bajo costo para análisis de calidad en granos de café tostado

Rubén Darío Vásquez Salazar *. Ahmed Alejandro Cardona Mesa **
Leidy Yohana Ocampo Osorio ***

**Politécnico Colombiano Jaime Isaza Cadavid, Medellín, Colombia (Tel: 3197900; e-mail: rdvasquez@elpoli.edu.co).*
***Politécnico Colombiano Jaime Isaza Cadavid, Medellín, Colombia (Tel: 3197900; e-mail: ahmed_cardona04072@elpoli.edu.co)*
****Politécnico Colombiano Jaime Isaza Cadavid, Medellín, Colombia (Tel: 3197900; e-mail: leidy_ocampo91091@elpoli.edu.co)*

Abstract: En este artículo se parte de un estudio que indica la necesidad de la comunidad caficultora del departamento de Antioquia de contar con un equipo que permita determinar la calidad de granos de café tostados de manera objetiva y automática. Se analiza el proceso de beneficio del café, sus componentes y principales parámetros para determinar la calidad posterior al proceso de tostión (o torrefacción). Se plantea la determinación de 3 atributos principales: densidad, color y humedad, este último de gran complejidad de estimación, debido a la dificultad para adquirir sensores que permitan hacerlo directamente en grano. Se propone una metodología basada en inteligencia artificial con redes neuronales para hacer dicha estimación y se diseña la mejor alternativa de un dispositivo portátil para lograr los resultados antes descritos.

Keywords: Análisis de calidad, granos de café tostados, visión por computador, software libre, bajo costo.

1. INTRODUCCIÓN

Colombia ha sido por tradición un país exportador de café de alta calidad. Según (Federación Nacional de Cafeteros de Colombia, 2016) mientras que en el mes de octubre de 1956 se producían 279.000 sacos de café de 60kg cada uno, en la actualidad en el mes de mayo de 2016 se producen 1'163.000. De forma similar, el precio en el mismo mes en 1956 era de 74.5 centavos de dólar por libra de 453.6gr excelso, y en 2016 es de 144.66 (Federación Nacional de Cafeteros de Colombia, 2016). Las exportaciones de Café para el mes de abril de 2016 fueron de 92.283 toneladas métricas por valor de US277.374.000 (Departamento Administrativo Nacional de Estadística, 2016).

Estas cifras dan cuenta del crecimiento del sector, la valorización del Café en el mercado internacional, y la importancia del producto para la economía Colombiana. Sin embargo ha sido un sector golpeado por altibajos en los precios, la tendencia ha sido al alza en consumo a nivel global, aunque un poco más baja en mercados como la Unión Europea, EEUU y Japón, que juntos representan más del 50% del consumo global, presenta más dinamismo en mercados como África y Asia (Organización Internacional del Café, 2015).

Como una estrategia para brindar valor agregado al café de la región Antioqueña, la Gobernación de Antioquia y la Cooperativa de Caficultores de Antioquia han buscado posicionar el café de esta región como un café de altísima calidad, con atributos consistentes, verificables y sostenibles y por los cuales están dispuestos a pagar precios superiores, que redunden en un mayor bienestar de los productores, con el concepto de "Cafés Especiales" (Cooperativa de Caficultores de Antioquia).

En el año 2014, en la Gobernación de Antioquia se lanzó el concurso "¿Quién se le mide?", mediante el cual se identifican problemas de la región en diferentes áreas, una de ellas la de Cafés Especiales, en la cual la Secretaría de Productividad y Competitividad indicó, a partir de un estudio y como conocedor del sector caficultor del departamento, la sentida necesidad de un equipo que permita evaluar la calidad en los granos de café tostados.

Dicho equipo debe evaluar algunos atributos que permiten determinar la calidad del café, en grano, posterior al proceso de tostión. Además, para adaptarse a las necesidades del sector, debe ser un equipo no invasivo, de modo que no se destruya la muestra, que requiera poca cantidad de la misma, posibilidad de medición in situ, material de fabricación no contaminante del alimento, peso bruto inferior a 10Kg, equipo resistente a la temperatura y humedad, entre otras características (Gobernación de Antioquia, 2014).

La metodología desarrollada y estructura del artículo es la siguiente: primero se determinan cuáles son los atributos de calidad más relevantes, particularmente para los cafés especiales del departamento de Antioquia (capítulo 2). Posteriormente se hace un análisis sobre la viabilidad de implementar un dispositivo que pueda determinarlos de forma objetiva, se selecciona la tecnología más adecuada para tal fin (capítulo 3) y se implementa buscando viabilidad económica (capítulo 4). Finalmente se realiza la validación a partir de muestras de diferentes niveles de tostión y se obtienen resultados y se analizan (capítulo 5).

2. ATRIBUTOS PARA DETERMINACIÓN DE CALIDAD EN CAFÉ TOSTADO

Antes de analizar la calidad de un grano de café tostado, es necesario conocer el proceso que éste surte para poder convertirse en un grano de la calidad exacta para producir el resultado esperado en una taza de café. La primera parte es el beneficio, mediante el cual el café pasa del árbol a la taza.

2.1 Beneficio del café

El proceso de beneficio del café, aunque no es la finalidad de este artículo describirlo detalladamente, consiste en las siguientes etapas:

- Cosecha: se recolecta del cultivo

- Despulpado: se retira la pulpa por medios mecánicos.

- Retiro del mucílago: se retira por medio de tanques de fermentación o vía mecánica

- Lavado: se elimina totalmente el mucílago.

- Secado: se elimina humedad vía exposición al sol o en equipos mecánicos.

- Trilla: se obtiene el café almendra o café verde, retirando el pergamino. El resultado es el café excelso.

- Tostión: se tuesta el café en hornos, lo que cambia sus propiedades físicas y químicas. También conocido como torrefacción. El proceso varía dependiendo de la forma cómo se aplica el calor, intensidad y tiempo del mismo.

- Molido: reducción del tamaño para facilidad de extracción de aromas y compuestos solubles

2.2 Composición

El café tostado está compuesto por diferentes elementos, los cuales, si bien no son indicadores directos de calidad, de forma indirecta afectan o benefician la calidad de los granos (Café de Colombia, 2010):

- Agua: un grano verde contiene del 10 al 13%, mientras que uno tostado no debe superar el 5%.

- Materias grasas: un grano contiene del 15 al 20% de materia grasa

- Proteínas: un grano de café verde contiene un 11%.

- Alcaloides: La cafeína es el principal alcaloide. El café Arábigo contiene de 1 a 1.5%, lo cual lo hace más suave que el Robusta con un 1.6 al 2.7%.

- Materias minerales: pequeñas cantidades de potasio, calcio, magnesio y fósforo.

- Ácidos clorogénicos: expertos atribuyen a estos ácidos las propiedades antioxidantes y antivirales.

2.3 Propiedades organolépticas

Son aquellas que pueden ser detectadas a través de los sentidos y, para las cuales, los catadores expertos en café pueden hacer una apreciación subjetiva de la calidad del grano tostado. Estas son (Café de Colombia, 2010):

- Aroma: es un olor bien conocido.

- Sabor: se puede calificar como suave, dulce, ácido, afrutado, pronunciado, alto y propio del café.

- Cuerpo: corresponde a la persistencia que tiene la bebida en la boca y a la manera como se desplaza por la lengua hacia la garganta. Una buena bebida de café presenta cuerpo completo, moderado o balanceado

- Acidez: se refiere a esa chispa ligeramente picante que se siente en la lengua y que hace que el bebedor se estremezca por un instante. Puede llegar a ser indeseable cuando se califica como agria, vinosa, picante, acre, astringente o ausente

- Impresión Global: se refiere a la calificación general de la bebida de café.

A nivel de ingeniería, algunas de estas características son difíciles de obtener, puesto que dependen de la percepción de un experto. Esta dependencia del ser humano es a su vez una desventaja, debido a que esta persona está sujeta a una gran cantidad de factores externos que afectan la medición, como enfermedades, estado anímico, nutricional, etc. Es por ello que la ingeniería debe ayudar a la determinación de ciertas características que indiquen calidad en los granos de café y de allí la necesidad que indica el estudio de la Gobernación de Antioquia.

2.4 Atributos de calidad

En general, cualquier característica física o química que se pueda medir de forma exacta en el café tostado, generará un indicador más para poder determinar su calidad. Sin embargo, no hay instrumentación disponible para hacer cualquier medición que se desee. El primer paso es entonces determinar cuáles son estos atributos requeridos para las necesidades particulares, y posteriormente determinar, desde la ingeniería, cuál es la forma más adecuada de hacer estas mediciones, e incluirlas en un equipo con las características antes descritas.

Según el informe del estudio realizado por la Secretaría de Productividad y Competitividad de la Gobernación de Antioquia (Gobernación de Antioquia, 2014), las características más importantes que se deben medir en el café para las necesidades de Antioquia son:

- Color: mundialmente medida en escala Agtron (o número Agtron), el cual va de 0 a 100, siendo 0 el más oscuro y 100 el más claro.

- Densidad: expresada en g/l.

- Peso: no se tuvo en cuenta, por ser irrelevante a nivel de ingeniería, ya que depende del tamaño de la muestra. Se considera que ya está incluida en la densidad. Se exige mínimo precisión de 0.01g.

- Humedad: en rangos del 1 al 70%.

- Dureza: medida en kgf, se plantea como variable opcional para el equipo.

Con la especialización que se tiene en cafés especiales en el departamento de Antioquia y aledaños, es imposible determinar cuáles características son las ideales para un buen café, ya que éstas dependen del mercado en el cual se va a

comercializar y el gusto y conocimiento de los consumidores. La dependencia de un experto, que exija los atributos que debe tener un café tostado sigue siendo prioritaria, y de él dependen los valores de color (Agtron), densidad, humedad y dureza que debe tener *para* obtener la taza de café deseada. Sin embargo, la ingeniería puede ayudar en este proceso, principalmente reduciendo la subjetividad humana inherente a la medición de estos atributos.

3. LA INGENIERÍA REQUERIDA PARA EL CÁLCULO DE LOS ATRIBUTOS DE CALIDAD

Teniendo claras las exigencias del mercado cafetero para el diseño de un equipo que permita analizar de forma automática y objetiva los atributos de calidad del café, se procede a analizar uno por uno, para buscar la solución más eficiente, económica y precisa.

3.1 Color

La apariencia superficial y color de la comida son los primeros parámetros de calidad que evalúan los consumidores, lo que lo convierte en un factor crítico para la aceptación de la comida por parte ellos. En (León, Mery, Pedreschi, & León, 2006) se propone la implementación de cámaras de video digitales y redes neuronales para la determinación de este atributo. En (Everard, O'Callaghan, Fagan, O'Donnell, Castillo, & Payne, 2007) se utilizan también técnicas de visión por computador para determinar características visibles en alimentos, en este caso en queso. El libro (Sun, 2016) se concentra netamente en todas las técnicas de visión computacional para la evaluación de calidad en alimentos.

Los colores son la sensación percibida por el ojo como el resultado de un estímulo. Existen diferentes técnicas para medir color en ingeniería. Un colorímetro utiliza filtros para detectar la cantidad de luz reflejada por el objeto en tres longitudes de onda del espectro visible: rojo, verde y azul, en inglés muy frecuente conocido como RGB por sus siglas. Para poder obtener una descripción numérica del color se requieren: luz, objeto y observador.

No es extraño entonces que en los artículos mencionados anteriormente, se utilicen técnicas de visión artificial con cámaras que capturan la imagen en formato RGB (espectro visible), y luego de aplicar los algoritmos de visión se pueda extraer información útil de ellos.

A nivel alimenticio, otra técnica muy utilizada es la espectrofotometría, la cual mide la reflectancia espectral (o transmitancia) de un objeto en todo el espectro de la luz visible para humanos, desde los 400 hasta los 700nm, con lo cual es posible obtener una especificación precisa del color deseado. La empresa Kónica Minolta se ha desempeñado tradicionalmente en el campo de las cámaras fotográficas y tiene gran experiencia en el tratamiento y medición del color, inclusive ofrece tanto colorímetros como espectrofotómetros, especialmente diseñados para la industria alimenticia (Konica Minolta).

Así entonces, aunque también existen métodos para determinar características de color en alimentos a nivel microscópico o en espectros no visibles al ojo humano, un análisis de color por colorimetría es altamente utilizado y suficiente para esta industria, además de ser de bajo costo de implementación a través de cámaras digitales convencionales. De poderse implementar y funcionar adecuadamente, sería la mejor opción para un equipo portátil con tecnología local de bajo costo.

La visión por computador consiste en adquirir, pre-procesar, procesar y finalmente obtener información relevante de la imagen. El análisis que requieren los granos de café tostados está relacionada principalmente con la comparación desde la almendra, que tiene un color verde o gris, hasta un tostado medio con color café de diferentes tonalidades, o un tostado excesivo que equivaldría a un café muy oscuro o negro. Es claro entonces que un grano de café va adquiriendo tonalidades más oscuras a medida que el proceso de tostión es más prolongado e intenso.

Una herramienta de visión que permite conocer la distribución de color en es espectro RGB es el histograma, el cual consiste en un eje horizontal con valores de 0 (negro) a 255 (blanco), y un eje vertical que indica la cantidad de pixeles que tienen dicha composición de color. Así, un histograma representa los niveles de cuantización de la imagen. En la curva, si se le determina el valor máximo (eje vertical), indica que su correspondiente valor horizontal es el color más presente en la imagen.

El café tostado captado a través de una cámara convencional digital RGB (Fig. 1) presenta un color principalmente café, sin embargo también presenta muchas zonas negras debido a las sombras dentro de los granos, y blancas debido al reflejo de la iluminación.

Fig. 1. Café con 3 niveles de tostión

Por lo tanto es de esperarse que el histograma (Fig. 2) tenga unos picos altos en el negro (0 en el eje horizontal) y blanco (255 en el mismo eje).

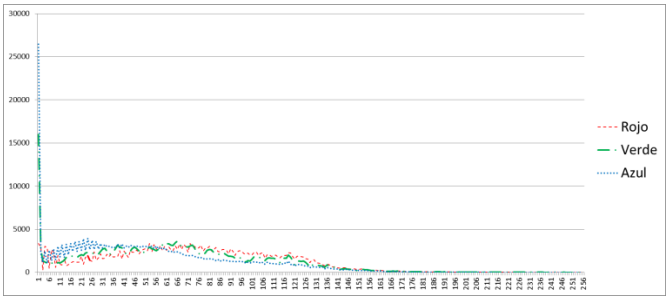

Fig. 2. Histograma aplicado a imagen de granos de café

Un algoritmo que identifique los picos en cada una de las 3 curvas R, G y B a través de una cámara digital, permitirá determinar qué tan oscuro o claro están los granos. Sin embargo, nótese que n los niveles más negros hay una gran cantidad de pixeles, debido a sombras; dichos pixeles no deben ingresar al algoritmo de detección de valores máximos. Para el caso de la figura, se podría determinar que el máximo de rojo verde y azul están en valores en el eje horizontal de 52, 65 y 23 respectivamente, el promedio de estos 3 valores es 46,67, el cual es un claro indicador de la oscuridad o claridad de los granos presentes.

Posteriormente este valor se puede convertir a escala Agrton a través de una relación lineal y, por medio de un instrumento calibrado en dicha escala, se puede obtener el valor de color de forma precisa.

3.2 Densidad

Este atributo es de fácil medición, debido a que en el mercado se encuentran fácilmente básculas digitales con precisión de 0.01g. Se requiere posibilidad de comunicación con una unidad central de procesamiento, puesto que la indicación es típicamente visual, por lo tanto con algún protocolo de comunicación serial sería posible enviar el dato de peso a la unidad central. La báscula seleccionada es marca BBG.

Se debe garantizar una muestra de café de volumen constante, en un recipiente idóneo para manipulación de alimentos, preferiblemente fabricado en vidrio o acero inoxidable. Se selecciona una placa de Petri de cristal de gran utilización a nivel de laboratorios. Su peso es de 32g y volumen interno una vez ubicada la tapa es de 80ml.

Conocido el peso (m) y volumen (v), se calcula la densidad utilizando la ecuación:

$$\rho = m/v \qquad (1)$$

3.3 Humedad

Este atributo es de difícil medición a nivel de ingeniería, especialmente por la forma del café, debido a que los granos dejan espacios en medio de ellos que afectan la medición del sensor.

El sensor más adecuado sería un termohigrómetro, el cual mide la humedad relativa del aire. Sin embargo no se podría determinar que el sensor está midiendo la humedad interna del grano, sino que estaría midiendo la del aire alrededor de los mismos; se podría suponer que, transcurrido un tiempo en condiciones cerradas y controladas, sería la misma, pero se requeriría hacer un estudio para probar dicha suposición.

Un termohigrómetro funcionaría de forma adecuada en café molido, utilizando uno similar a los que se utilizan para medir la humedad en el suelo en cultivos, lo cual ya está suficientemente probado. Sin embargo el objetivo principal de este trabajo y la necesidad de la región indican que la medición es en granos, por lo tanto se descarta.

Existen formas de medir de forma indirecta una variable, a partir de otra u otras cuyo valor ya se conozca. Para esto se requiere de una gran cantidad de datos obtenidos con equipos calibrados para dichas variables, de modo que se pueda estimar las características o parámetros en diversas áreas de estudio, que son de gran interés para los investigadores, que trabajan en lograr que sus modelos predigan estos parámetros con un alto grado de certeza y confiabilidad. Según la literatura, la técnica más utilizada para obtener estimaciones de parámetros es el clásico análisis de regresión; sin embargo, la calidad de las estimaciones por medio de esta técnica se ven limitadas cuando se presenta un problema no lineal (Baykasolu, Dereli, & Tani, 2004). Las redes neuronales artificiales establecen un método distinto que se basa en el aprendizaje y determinación de las relaciones presentes entre las variables de entrada y salida de un conjunto determinado de datos.

En (Muharrem, Sema, Serap, & Yurtsever, 2013) se utiliza el color para estimar nivel de humedad y niveles nutricionales de hojas de maní, y en (Behroozi Khazaei, Tavakoli Hashjin, Ghassemian, Khoshtaghaza, & Banakar, 2013) se utiliza la visión para estimar el nivel de humedad a partir del encogimiento de la uva al secarse y las características del cambio de color, utilizando regresiones lineales.

Las redes neuronales artificiales son un modelo simplificado del cerebro y tienen la capacidad de emular algunas características propias de los humanos, como la capacidad de memorizar y de asociar acciones, su forma de obtener conocimiento es a partir de ejemplos, es decir, no se establecen reglas predefinidas para llegar a una solución, sino que la red neuronal define sus propias reglas durante el proceso de aprendizaje, redefiniendo su comportamiento para adaptarse a una serie de datos diferentes y lograr obtener una solución confiable.

El tipo de Red Neuronal Artificial utilizada para el análisis y estimación de características de café tostado, es una Red Neuronal Backpropagation (Propagación del error hacia atrás), que se caracteriza por tener una arquitectura en capas y conexiones entre neuronas exclusivamente hacia adelante. En una red neuronal Backpropagation existe una capa de entrada con n neuronas, una capa de salida con m neuronas y mínimo una capa oculta de neuronas. Cada neurona de las capas ocultas y de salida recibe entradas de todas las neuronas de la capa anterior y envía su salida a todas las neuronas de la capa siguiente (Fig. 3).

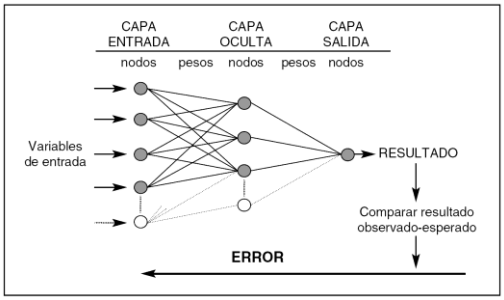

Fig. 3. Estructura básica de una RNA.

El entrenamiento de la red neuronal backpropagation consta de dos etapas, en la primera etapa el patrón de entrada es asociado a la red y propagado a través de las capas hasta llegar a la capa de salida. Obtenidos los valores de salida de la red neuronal, se comienza la segunda etapa, comparando dichos valores con la salida deseada para determinar el error. Se ajustan los pesos de la última capa proporcionalmente al error generado. Se pasa a la capa anterior con una retropopagación del error, ajustando los pesos y repitiendo este procedimiento hasta llegar a la capa de entrada. De esta forma se reajustan los pesos de las conexiones de la red neuronal, conocidos los valores de entradas y salidas deseadas del problema que se busca solucionar.

Para iniciar el proceso de aprendizaje de las redes neuronales, se utiliza un patrón de entradas y salidas de características de café tostado, a partir de 10 muestras de café en diferentes puntos de tostión, a las cuales se les mide densidad y color con el procedimiento antes descrito y, a través de otro equipo calibrado, se obtiene su humedad. Este procedimiento se repite 10 veces para cada muestra, obteniendo un total de 100 valores que se ingresan al algoritmo de entrenamiento para la red Backpropagation, una muestra de esta base de datos se presenta en la Tabla 1.

Tabla 1. Patrón de entradas y salidas de variables de café.

MUESTRA	R	G	B	GRAY	PESO	HUMEDAD	QUANTIK
1	94	92	86	92	24,63	0,5	115
2	93	89	82	90	24,63	0,5	115
3	93	92	87	92	24,63	0,5	115
4	89	86	79	86	24,63	0,5	115
5	91	87	80	87	24,63	0,5	115
6	94	93	89	93	24,63	0,5	115
7	94	90	85	91	24,63	0,5	115
8	94	93	87	93	24,63	0,5	115
9	94	93	89	93	24,63	0,5	115
10	91	87	81	88	24,63	0,5	115

Para aplicar el algoritmo de entrenamiento se procede de la siguiente forma; se inicializan los pesos de la red en valores aleatorios y menores que 1 (w_{ij}); se ingresan los valores de entradas (x_1, x_2, … x_n) correspondientes a las variables peso, RGB y GRAY, y se especifica la salida deseada que debe obtener la red (y), correspondiente a las variables humedad y Quantik respectivamente; se calculan los valores de salida de cada neurona (y_n) a partir de la sumatoria de productos entre los pesos y los valores de entrada a la red, y se aplica una función de activación sigmoidal (f):

$$y_n = f(\sum x_n * w_{ij}) \qquad (2)$$

Se aplica el mismo procedimiento para obtener todos los valores de salida en las neuronas de la capa intermedia hasta llegar a la capa de salida; se calculan los términos de error (e_n) para todas las neuronas y se propagan hacia atrás de forma proporcional para cada neurona, en la capa de salida el valor del error es equivalente a la diferencia entre el valor deseado para la variable asignada y el valor real obtenido en la salida de la red, en las capas ocultas y de entrada el error corresponde a la suma de productos entre los pesos asociados a cada neurona y el error proporcional de la neurona anterior:

$$e_n = \sum w_{ij} * e_{n-1} \qquad (3)$$

Este procedimiento se repite hasta llegar a las neuronas de la capa de entrada; obtenido el valor de error para todas las neuronas de la red, se procede a la actualización de los pesos (w'), para ello se toma el valor actual del peso y se adiciona el producto entre el error de la neurona, la derivada de la función de activación de la suma de productos calculados anteriormente (h), el valor de entrada de la neurona y un parámetro momento (n) que determina la capacidad de convergencia del algoritmo de entrenamiento:

$$w'_{ij} = w_{ij} + n * e_n * \frac{df(h)}{dh} * x_n \qquad (4)$$

Este algoritmo de entrenamiento debe iterar de manera continua hasta converger en un mínimo valor de error permisible en la salida de la red, en este caso, un valor aproximado de las variables humedad y Quantik. Finalmente, después de aplicar el algoritmo de entrenamiento se obtienen dos redes neuronales artificiales diferentes con la siguiente configuración: una primera red neuronal artificial que consta de una capa de entrada con 10 neuronas, una capa oculta con 2 neuronas y una capa de salida con 1 neurona (10:2:1), y tiene como estímulos de entradas los valores de peso, RGB y GRAY obtenidos con la balanza y el procesamiento de la imagen de la muestra de café analizada, para generar en la salida un valor estimado de humedad; la segunda red consta de una capa de entrada con 30 neuronas, una capa oculta con 5 neuronas y una capa de salida con 1 neurona (30:5:1), y cuenta con los valores de RGB y GRAY obtenidos de la imagen como estímulos de entrada, para determinar en la salida su valor estimado de nivel de tostión en escala Agtron.

Haciendo una breve descripción del algoritmo implementado y su secuencia de funcionamiento, se presentan las siguientes etapas básicas: obtener el valor del peso de una muestra de grano de café tostado por medio de la balanza digital; adquirir una imagen de la muestra de grano a partir de la cámara; aplicar técnicas de visión artificial para obtener información relevante de la imagen adquirida, comenzando con un filtro de tamaño para eliminar regiones que no aportan información, aplicar una función de histograma a la imagen para obtener el valor de los componentes RGB, cambiar el formato de imagen a escala de grises y nuevamente aplicar una función de histograma para obtener el valor del componente GRAY; ingresar estos valores obtenidos como patrones de entrada a las dos redes neuronales entrenadas previamente, para obtener los valores de humedad y nivel de tostión en escala Agtron (Fig. 4).

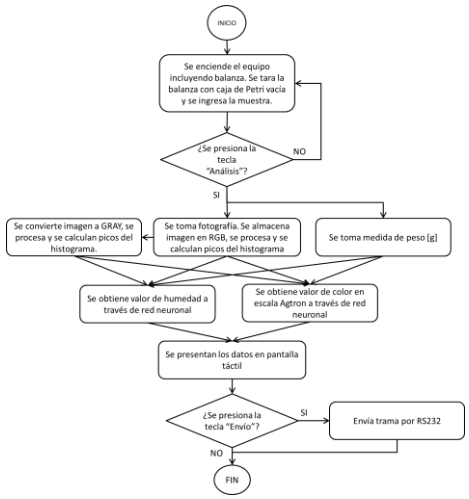

Fig. 4. Diagrama de flujo

3.4 Dureza

La medición de este atributo se descarta, debido a que es opcional dentro de los requerimientos del equipo. Además su medición requiere de medios mecánicos para su destrucción, yendo en contravía de los requerimientos del equipo. Posiblemente, a partir de los datos de color, humedad y densidad sea posible estimar la dureza, sin embargo se aleja de los alcances de este artículo, el cual se concentró principalmente en hacer medición de la humedad, buscando validar dicha estrategia. La medición de dureza queda como trabajo futuro a desarrollar y, de lograrse incluir en el equipo, añadiría características de valor agregado al mismo, en beneficio de las comunidades cafeteras de la región.

4. DISEÑO DEL PROTOTIPO

4.1 Herramientas de hardware y software

Este equipo debe entonces ser capaz de alojar los elementos descritos en el capítulo anterior, además de contar con una unidad de procesamiento capaz de recopilar toda la información y mostrarla en una interfaz hombre máquina.

En el mercado existen diferentes alternativas para desarrollar algoritmos de visión por computador. Uno de ellos, tal vez el más potente, es LabVIEW con su toolkit "Vision Development" (National Instruments, 2016), el cual permite adquirir imágenes de cámaras convencionales de bajo costo, propias o especializadas, para hacer todo el desarrollo de estos algoritmos a través de una gran cantidad de librerías. Posibilita el trabajo paralelo en procesadores, haciendo los algoritmos altamente eficientes. Sin embargo, su principal debilidad es la dependencia de un computador (personal o de escritorio) para la ejecución de dichos algoritmos, y la única alternativa son las SmartCameras capaces de ejecutarlos y que el mismo fabricante ofrece, pero a un costo superior a los U$2.000 y hasta los U$10.000 y más (National Instruments, 2016). De forma similar está Matlab, el cual también tiene una alta dependencia de computador. Ambos, LabVIEW y Matlab, tienen adicionalmente costo de licencia, el cual debe adquirirse para poder utilizar el desarrollo.

Una herramienta de gran utilización a nivel mundial es OpenCV, el cual es libre tanto para uso académico como para uso comercial, soporta tiene interfaz C, C++, Python y Java y soporta Windows, Linux, Mac OS, iOS y Android (OpenCV, 2016). OpenCV puede ejecutarse desde equipos Raspberry (Fig. 5).

Fig. 5. Raspberry Pi 2 (Raspberry, 2016)

La Raspberry puede reemplazar un computador, al alojar un sistema operativo Linux. Admite conexión de periféricos como teclado, ratón y pantalla (Fig. 6), de modo que su operación es completamente similar, aunque para tareas de automatización y análisis de imagen, puede trabajar sin éstos, y utilizar su puerto USB para adquisición e imágenes de la cámara y sus entradas y salidas GPIO para conexión de sensores y actuadores, además de posibilidades de conexión de pantallas o displays que permitan manipular de forma táctil su funcionamiento.

Fig. 6. Pantalla táctil 3.2" ref uLCD-32PTU

La capacidad de procesamiento de la Raspberry obviamente no puede compararse con un computador industrial o uno de línea corporativa de última generación, por lo tanto las tareas que se le programen deben evaluarse desde el punto de vista del desempeño. Por ejemplo en aplicaciones de visión, debe evaluarse muy de cerca si el procesamiento es en línea de un video, o simplemente desde una fotografía. El grupo de investigación ICARO ya ha realizado aplicaciones en este tipo de plataformas con procesamiento en video y funciona moderadamente bien. Para el caso particular, se requiere únicamente una fotografía del café para hacer todo el análisis, por lo tanto la capacidad de procesamiento de la Raspberry es adecuada.

4.2 Diseño de la estructura principal

La estructura principal debe ser en un material apto para la industria alimenticia. El acero inoxidable es, indiscutiblemente, este material por excelencia. Debe contener las siguientes características:

Puerta para fácil acceso de las muestras, además como aislamiento para iluminación externa (Fig. 7).

Fig. 7. Prototipo final en acero inoxidable (puerta)

Ubicación de sistema de iluminación en la parte superior, necesariamente de corriente directa, con campana difusora y ubicación de la cámara digital en la parte trasera, en un ángulo de 45° aproximadamente con la línea de visión de la cámara (Fig. 8).

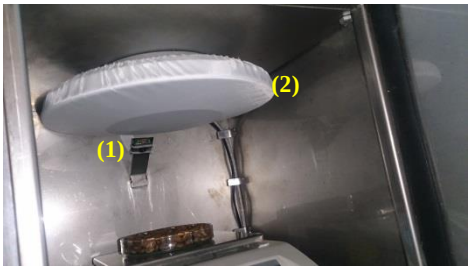

Fig. 8. Prototipo final en acero inoxidable. (1) cámara, (2) campana difusora

Ubicación de báscula en la parte inferior (Fig. 9)

Fig. 9. Prototipo final en acero inoxidable – báscula. (1) Muestra. (2) Lectura de peso.

Apertura superior para instalación de la pantalla táctil, con puerta para protección (Fig. 10).

Y espacio oculto (en la parte superior entre pantalla y lámpara) para ubicación de la unidad central de procesamiento y adaptadores de voltaje.

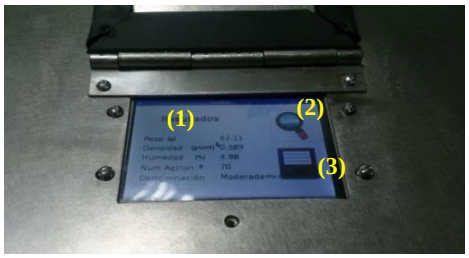

Fig. 10. Prototipo final en acero inoxidable – pantalla. (1) Resultados. (2) Análisis. (3) Envío de datos.

5. RESULTADOS

5.1 Análisis de las especificaciones técnicas del equipo

Según lo descrito en los capítulos 1 y 2, las especificaciones técnicas del equipo deben ser:

- No invasivo: cumple, al realizarse bajo técnicas de visión artificial y otros elementos que no destruyen ni invaden la muestra.

- Poca cantidad de muestra: se utilizan alrededor de 47g de muestra, la cual puede ser reutilizada.

- Posibilidad de medición in situ: es un equipo que no requiere de un computador, es autónomo, su única dependencia es energía eléctrica de 100VAC, la cual es de alta disponibilidad a nivel residencial e industrial.

- Material de fabricación no contaminante del alimento: fabricación en acero inoxidable, de aceptación en industria alimenticia.

- Peso bruto inferior a 10Kg: cumple, peso final sin muestra ni caja de Petri 6.5Kg.

- Equipo resistente a la temperatura y humedad: no se definían valores para estas variables, resiste temperaturas hasta 50°C. No tiene aberturas superiores a 2.5mm y soporta gotas de agua que caigan de forma vertical, análogo a protección IP31, certificación que no se ha solicitado.

- Medición de densidad: cumple.

- Medición de color: cumple.

- Medición de humedad: cumple

- Medición de dureza (opcional): no cumple.

5.2 Análisis de muestras de café

Para realizar las pruebas y validación del prototipo, se toman 5 muestras de café y, a cada una, se le realizan 10 pruebas en similares condiciones, retirándola, cambiando de posición los granos, y volviéndola a ingresar, esto con el fin de evaluar el desempeño del mismo. A continuación el análisis de los resultados de 3 de las muestras, en las otras no incluidas en este artículo los resultados fueron similares.

Como se puede ver en la Tabla 2, los valores de densidad y humedad son muy estables. En el caso de la densidad el valor mínimo fue de 0.47 y el máximo de 0.471g/ml, error que es despreciable. En el caso de la humedad el valor mínimo fue de 3.52 mientras que el máximo fue de 3.82, con una variación de 0.30%. Para el número Agtron, se tuvieron valores inferiores de 45 (equivalencia a medio) y máximos de 60 (equivalencia a medio claro), es decir, se tuvo un error considerable en números y un cambio de un nivel en la equivalencia; esto se puede generar debido a la reubicación y posición de los granos, lo cual es de esperarse debido a que la imagen cambia de condiciones como sombras o irregularidades en la tostión en los granos, aunque también se debe a un error típico en todos los instrumentos de medición.

Tabla 2. Muestra #1: Café con nivel de tostión medio

ANÁLISIS	DENSIDAD	HUMEDAD	AGTRON REAL	AGTRON OBTENIDO
1	0,47	3,6	50	55
2	0,47	3,74		50
3	0,471	3,81		45
4	0,47	3,82		50
5	0,47	3,63		55
6	0,47	3,52		60
7	0,47	3,63		55
8	0,47	3,68		55
9	0,47	3,63		55
10	0,47	3,73		50

Tabla 4. Muestra #3: Café con nivel de tostión alto

ANÁLISIS	DENSIDAD	HUMEDAD	AGTRON REAL	AGTRON OBTENIDO
21	0,407	1,02	40	40
22	0,407	1,01		40
23	0,407	1,02		40
24	0,407	0,99		40
25	0,407	1,03		40
26	0,407	1,01		40
27	0,407	0,99		40
28	0,407	1,01		40
29	0,407	1,02		40
30	0,407	1,01		40

En la Tabla 3 se observa la muestra #3, cuyo análisis arrojó valores estables de densidad, valores de humedad con variación 0.30% y un número Agtron igualmente estable, sin ninguna variación.

En la Tabla 4 se observa nuevamente una densidad estable con error despreciable, una humedad con variación de 0.6% en la medición y un número Agtron con una variación más grande, en 3 casos en valor 90, 1 vez en 90 y en 6 ocasiones en 100. En esta muestra aplica también el análisis realizado para la muestra #1.

Tabla 4. Muestra #5: Café sin tostión (crudo)

ANÁLISIS	DENSIDAD	HUMEDAD	AGTRON REAL	AGTRON OBTENIDO
41	0,85	9,7	100	100
42	0,85	9,7		100
43	0,849	9,65		90
44	0,849	9,7		100
45	0,85	9,7		100
46	0,849	9,71		100
47	0,849	9,66		90
48	0,849	9,68		95
49	0,849	9,66		100
50	0,849	9,65		90

5.3 Tiempo de ejecución

El equipo, una vez presionado el botón de análisis en la pantalla, toma entre 40 y 45s para entregar el resultado. En un equipo electrónico de medición esto puede parecer un tiempo significativamente alto. Sin embargo, teniendo en cuenta la aplicación para la cual fue diseñado, es un tiempo razonable por las siguientes razones:

- En el proceso de tostión, bastan unos cuantos segundos para que el café pase de un nivel de tostión bajo a alto, lo que obliga al operario a retirar el producto y posteriormente hacer su análisis. Con el producto fuera del horno, un análisis que tarde menos de un minuto es adecuado.

- El algoritmo de redes neuronales es un algoritmo iterativo, el cual tiene un gran costo computacional al requerir procesamiento hasta converger al mínimo error.

6. CONCLUSIONES

La calidad del café depende de un sinnúmero de características y atributos que frecuentemente son medidas por un experto humano, cuya percepción se puede ver afectada por diferentes factores personales, laborales, climáticos, etc. Existe la necesidad de contar con una forma exacta y repetitiva de hacer mediciones que permitan determinar de forma objetiva la calidad en los granos de café tostado.

Los desarrollos que actualmente existen en inteligencia computacional, incluyendo la visión artificial, permiten hacer mediciones a alimentos y ayudar con la identificación de características físicas de forma directa e indirecta, con el fin de garantizar la adecuada calidad final de los productos.

El uso de un algoritmo basado en redes neuronales para eliminar la necesidad de un sensor de temperatura, ayudó a

bajar el costo del equipo pero aumentando el costo computacional del mismo y generando mayor tiempo para efectuar el análisis. Aunque dicho tiempo resulta ser adecuado para la aplicación particular, se podría reducir con equipos de mejores especificaciones, aunque aclarando que esto aumentaría también el costo del mismo.

Se diseña, construye y valida un equipo que cumple con las especificaciones exigidas, que servirá de apoyo a las cooperativas, laboratorios, microempresas y, en general, tostadores de café, con tecnología de bajo costo importada, pero integración y desarrollo local.

6. AGRADECIMIENTOS

A la Gobernación de Antioquia y Secretaría de Productividad y Competitividad por haber lanzado el concurso "¿Quién se le mide?" y haber realizado el estudio de necesidades de caficultores en el departamento de Antioquia respectivamente, recursos con los que se pudo ejecutar este proyecto y financiar la patente en trámite (solicitud ante SIC # 15 280069 0000 0000 del 2015-11-24).

REFERENCIAS

Baykasolu, A., Dereli, T., & Tani, S. (Noviembre de 2004). Prediction of cement strength using soft computing techniques. Cement and Concrete Research, 2083-2090.

Behroozi Khazaei, N., Tavakoli Hashjin, T., Ghassemian, H., Khoshtaghaza, M., & Banakar, A. (2013). Application of Machine Vision in Modeling of Grape Drying Process. Journal of Agricultural Science and Technology, 1095-1106.

Café de Colombia. (2010). Clasificaciones de calidad. Recuperado el 20 de Junio de 2016, de Clasificaciones de calidad: http://www.cafedecolombia.com/particulares/es/sobre_el_cafe/el_cafe/clasificaciones_de_calidad/

Cooperativa de Caficultores de Antioquia. (s.f.). Cafés Especiales. Recuperado el 20 de Junio de 2016, de Cafés Especiales: http://www.cafedeantioquia.com/index.php/gestion-comercial/cafes-especiales

Departamento Administrativo Nacional de Estadística. (2016). Colombia, exportaciones de café, carbón, petróleo y sus derivados, ferroníquel y no tradicionales, según valores y kilos netos 1992 - 2016. Bogotá: DANE.

Everard, C., O'Callaghan, D., Fagan, C., O'Donnell, C., Castillo, M., & Payne, F. (2007). Computer Vision and Color Measurement Techniques for Inline Monitoring of Cheese Curd Syneresis. Journal of Dairy Science. Volume 90, Issue 7, 3162–3170.

Federación Nacional de Cafeteros de Colombia. (2016). Precio externo del café colombiano - promedio mensual. Bogotá: Federación Nacional de Cafeteros de Colombia.

Federación Nacional de Cafeteros de Colombia. (2016). Producción registrada - mensual. Bogotá: Federación Nacional de Cafeteros de Colombia.

Gobernación de Antioquia. (2014). Reto #6 Cafés Especiales. Medellín: Gobernación de Antioquia.

Konica Minolta. (s.f.). Food Industry Apps. Recuperado el 21 de Junio de 2016, de Food Industry Apps: http://sensing.konicaminolta.asia/wp-content/uploads/2011/05/FoodIndustryApps.pdf

León, K., Mery, D., Pedreschi, F., & León, J. (2006). Color measurement in L∗ a∗ b∗ units from RGB digital images. Food Research International Volume 39, Issue 10, 1084–1091.

Muharrem, K., Sema, K., Serap, G., & Yurtsever, S. (2013). Utilization of color parameters to estimate moisture content and nutrient levels of peanut leaves. Turkish Journal of Agriculture and Forestry, 604-612.

National Instruments. (2016). Módulo Vision Development. Recuperado el 21 de Junio de 2016, de Módulo Vision Development: http://sine.ni.com/np/app/main/p/ap/vision/lang/es/pg/1/sn/n17:vision/fmid/8519/

National Instruments. (2016). NI Smart Cameras. Recuperado el 21 de Junio de 2016, de NI Smart Cameras: http://sine.ni.com/np/app/main/p/bot/no/ap/vision/lang/es/pg/1/sn/n25:device,n17:vision,n21:11601/

OpenCV. (2016). OpenCV. Recuperado el 21 de Junio de 2016, de OpenCV: http://opencv.org/

Organización Internacional del Café. (2015). Informe del mercado de café Marzo de 2015. Londres: OIC.

Raspberry. (2016). Raspberry Pi 2. Recuperado el 21 de Junio de 2016, de Raspberry Pi 2: https://www.raspberrypi.org/wp-content/uploads/2015/01/Pi2ModB1GB_-comp.jpeg

Sun, D.-W. (2016). Computer vision technology for food quality evaluation. Londres: Elsevier.

Experimental Error in Control Sets Calculation: Implementation of low-discrepancy deterministic and stochastic sequences

Alex Alzate*, Adriana Amicarelli*, Lina Gómez†, Fernando di Sciascio*

**Instituto de Automática (INAUT) – Universidad Nacional de San Juan, Argentina*
Consejo Nacional de Investigaciones Científicas y Técnicas (CONICET), Argentina
e-mail:aalzate@inaut.unsj.edu.ar)

† Universidad Nacional de Colombia, sede Medellín, Colombia

Abstract: Set Theoretic Methods in Control using random sequences have been widely used previously as a tool for process design. In this paper, we present experimental results of determining control sets by using low-discrepancy deterministic sequences as an alternative to random sequences. We show that in certain situations this approach allows to reduce both significantly, the experimental error and the computational time.

1. INTRODUCTION

At present, almost all nonlinear control strategies are based on state-space models of the system to be controlled. These models are usually obtained by first principles modeling or by system identification techniques. Then, these models are used to emulate the real system during design stage or as part of the controller itself. Once the model is available in a state-space representation including system restrictions and system uncertainties, there are countless methods and design techniques that use different mathematical tools.

In particular, Set Methods in Control have been reported as an alternative tool to evaluate the controllability of chemical processes. This is because the Reachable, Controllable and Reversible sets are useful for the process controllability analysis, and the subsequent control system design [Alzate *et al* 2015, Gómez-Pérez *et al* 2015, Zuluaga-Bedoya *et al* 2015].

Initial approximation to calculate Reachable and Controllable Sets are based on concepts of the theory of Optimal Control [Grantham *et al* 1975]. Afterwards, and until now several articles have been published based on a wide variety of approximation methods, some of the most relevant are listed below:

i) Methods based on the solution of partial differential equations of the Hamilton-Jacobi-Bellman-Isaacs (HJBI) type [Kurzhanskiy *et al* 2002, Kurzhanskiy *et al* 2011, Oishi *et al* 2006].

ii) Level Set Methods [Mitchell 2004, Cross *et al* 2008].

iii) Ellipsoidal approximation methods [Kurzhanskiy *et al* 1997, Kurzhanskiy *et al* 2002]. On this technique, a toolbox is available for Matlab® (Ellipsoidat Toolbox) [Kvasnica *et al* 2004].

iv) Methods based on Polytopes [Bravo *et al* 2005].

v) Methods based on selecting random sequence, i.e., Monte Carlo methods [Gómez 2009].

Various papers reported the use of stochastic sequences [Calderon *et al* 2012, Alzate *et al* 2013, Alzate *et al* 2015, Zuluaga-Bedoya *et al* 2015], and, for these papers, the number of samples is based on Hoeffding's bound.

This paper proposes the implementation of low-discrepancy deterministic sequences instead of random sequences. These type of deterministic sequences are the core of the so called Quasi Monte Carlo integration methods. For several applications, it has been reported that their use instead of random sequences reduce the experimental error [Acebrón *et al* 2005, Dick *et al* 2013, Atanassov *et al* 2008, Boyle *et al* 1997, Hokayem *et al* 2003, Jank 2005].

This paper is structured as follows. Section 2 describes Set Theoretic Methods in Control and low-discrepancy deterministic sequences. Section 3 describes the phenomenological based semi-physical model and the algorithm to calculate the different sets. Section 4 presents the results obtained and their analysis and, finally, Section 5 presents the conclusions and future works.

2. BASIC CONCEPTS

2.1 Set Theoretic Methods in Control

In this section, we present the basic definitions of Set Theoretic Methods in Control used in this paper. The sets used are Reachable, Controllable and Reversible.

Consider the nonlinear dynamic continuous system

$$\dot{\boldsymbol{x}} = f(\boldsymbol{x}(t), \boldsymbol{u}(t), \theta) \tag{1}$$

Where $\boldsymbol{x} \in X \subseteq \mathbb{R}^n$ is state vector, $\boldsymbol{u} \in U \subseteq \mathbb{R}^m$ is input vector of admissible control actions, $\theta \in \Theta \subseteq \mathbb{R}^q$ is system parameters, and $f(\cdot,\cdot): X \times U \to X$. For each $\tau \in [0, t_f]$, the transition function is represented by $\phi(0, \tau, \boldsymbol{x}, \boldsymbol{u})$.

1) **Reachable Set**: Given a set Ω_τ, the Reachable Set $R_t(\Omega_\tau)$ from Ω_τ in a time $t > \tau$ is the set of all state vectors $\boldsymbol{x}$, for which exist a $\boldsymbol{x}(\tau) \in \Omega_\tau$ and $\boldsymbol{u}(\cdot) \in U$ such that $\boldsymbol{x}(t) = \boldsymbol{x}$, where U is the set of admissible control actions, and X is the set of admissible state.

$$R_t(\Omega_\tau) = \{z \in X | \exists x \in \Omega_\tau \wedge u \in U : z = \phi(\tau, t, x, u)\} \quad (2)$$

2) **Controllable Set**: Given a set Ω_τ, the Controllable Set $C_t(\Omega_\tau)$ to Ω_τ in a time $t < \tau$ is the set of all state vectors $\boldsymbol{x}$, for which exist a $\boldsymbol{u}(\cdot) \in U$ such that if $\boldsymbol{x}(t) = \boldsymbol{x}$ then $x(\tau) \in \Omega_\tau$.

$$C_t(\Omega_\tau) = \{z \in X | u \in U : \phi(\tau, t, x, u) \in \Omega_\tau\} \quad (3)$$

3) **Reversible Set**: Given a set Ω and a time t, the Reversible Set is the set of all state vectors that belong to Reachable Set of Ω in a time t and the Controllable Set of Ω in a time t.

$$\tau_t(\Omega) = \{x \in X | x \in R_t(\Omega) \wedge x \in C_t(\Omega)\} \quad (4)$$

2.2 Low-Discrepancy Deterministic Sequences

Low-discrepancy deterministic sequences are an alternative to stochastic sequences. To define these sequences, it begins with the objective to find an approximation for the integral:

$$I_s(f) = \int_{[0,1]^s} f(\boldsymbol{x}) d\boldsymbol{x} \quad (5)$$

Where s is greater than 1, for some integrable function f, by an n-point integration rule of the form:

$$Q_{n,s}(f) = \frac{1}{n} \sum_{i=0}^{n-1} f(\boldsymbol{t}_i) \quad (6)$$

where the sample points $\boldsymbol{t}_0, \ldots, \boldsymbol{t}_{n-1} \in [0,1]^s$.

A usual method to approximate the integral is the Monte Carlo (MC) method, where the sample points are an independent and identically distributed random sample from the uniform distribution over $[0,1)^s$. Applying the Strong Law of Large Numbers, (6) converge to (5) as the number of function evaluations n tends to infinity.

As an alternative to MC methods, the Quasi-Monte Carlo (QMC) method is proposed. The QMC method is an equal-weight cubature rule of the form (6), where the sample points $\boldsymbol{t}_0, \ldots, \boldsymbol{t}_{n-1} \in [0,1]^s$ are chosen from a low-discrepancy deterministic sequence. This sequences used in QMC method are classified on two types [Dick 2013]:

The 'Open' type: this uses the first n points of an infinite sequence. Thus to increase n, one only needs to evaluate the integrand at the additional cubature points.

The 'Close' type: this uses a finite point set which depends on n. Thus, a new value of n means a completely new set of cubature points.

In this paper, a sequence of type 'open' is used, and is called Halton sequence. The Halton sequence is defined by the radical inverse function.

Radical Inverse Function: For integers $i \geq 0$ and $b \geq 2$, it defines the radical inverse function $\phi_b(i)$ as follows:

If $i = \sum_{a=1}^{\infty} i_a b^{a-1}$, where $i_a \in \{0,1, \ldots, b-1\}$, then

$$\phi_b(i) := \sum_{a=1}^{\infty} \frac{i_a}{b^a} \quad (7)$$

Halton Sequence: Let $p_1, p_2, \ldots, p_s$ be the first s prime number. The Halton sequence $\boldsymbol{t}_0, \boldsymbol{t}_1, \ldots$ in dimensions s is given by

$$t_i = \left(\phi_{p1}(i), \phi_{p2}(i), \ldots, \phi_{ps}(i)\right), i = 0,1, \ldots \quad (8)$$

Expanding this sequence

$$\begin{gathered} \boldsymbol{t}_0 = (0,0,0, \ldots,0) \\ \boldsymbol{t}_1 = \left(0.1_2, 0.1_3, 0.1_5, \ldots, 0.1_{ps}\right) \\ \boldsymbol{t}_2 = \left(0.01_2, 0.2_3, 0.2_5, \ldots, 0.2_{ps}\right) \\ \boldsymbol{t}_3 = \left(0.11_2, 0.01_3, 0.3_5, \ldots, 0.3_{ps}\right) \\ \vdots \end{gathered}$$

3. MODEL AND ALGORITHM DESCRIPTION

3.1 Phenomenological Based Semi-physical Model

The Phenomenological Based Semi-physical Model used in this paper is the benchmark proposed by Bequette [Bequette 1998]. This benchmark is the mathematical model of a CSTR process, and (9) and (10) describe it. The process states are reactive concentration (x_1) and reactor temperature (x_2). The process control actions are reactive feed flow rate (u_1) and cooling liquid temperature (u_2). The meaning of each parameter and its values are reported on Table 1, and were taken from [Bequette 2002].

$$\frac{dx_1}{dt} = \frac{u_1(C_{in} - x_1)}{V} - k_0 x_1 \exp\left(-\frac{Ea}{Rx_2}\right) \quad (9)$$

$$\frac{dx_2}{dt} = \frac{u_1(T_{in}-x_2)}{V} - \frac{\Delta H k_0 x_1 \exp\left(-\frac{Ea}{Rx_2}\right)}{\rho C_p} + \frac{UA(u_2-x_2)}{V\rho C_p} \quad (10)$$

Table 1. CSTR Parameters

Variable	Value	Unit	Meaning
k_0	2.8267 10^{11}	[L/min]	Reaction kinetic constant
Ea	75361.0	[J/mol]	Activation Energy
R	8.31	[J/mol K]	Gas constant
$C_{a\,in}$	2114.5	[mol/m^3]	Input concentration
V	2.41	[m^3]	Volume Reactor
ΔH	-9.0721 10^4	[J/mol]	Enthalpy of reaction
ρ	1000.0	[Kg/m^3]	Density of solution
C_p	3571.3	[J/Kg]	Specific heat of solution
$C_{p\,j}$	3728.87	[J/Kg K]	Specific heat of cooling liquid
U	2.45 10^4	[J/min m^2 K]	Heat transfer coefficient
A	8.18	[m^2]	Heat transfer area
F_j	0.3376	[m^3/min]	Flow of cooling liquid
V_j	0.24069	[m^3]	Jacket volume
T_{in}	295.0	[K]	Input temperature

3.2 Algorithm for set calculation

The algorithm used for set calculation is the proposed for Gómez [Gómez 2009]. The algorithm is described below:

Algorithm. Algorithm for Sets calculation

Input: $\boldsymbol{x}_0, f, t, \boldsymbol{x}_{min}, \boldsymbol{x}_{max}, \boldsymbol{u}_{min}, \boldsymbol{u}_{max}$

Output: $R_t(\Omega_t), C_t(\Omega_t), \tau_t(\Omega_t)$

1: For the stochastic sequence case, the set U is generated by sampling uniformly between $\boldsymbol{u}_{min}$ and $\boldsymbol{u}_{max}$ with N sample points. For the low-discrepancy sequence case u_i is taken from the Halton sequence.

2: The differential equations are solved for each $\boldsymbol{u}_i$, with $i = 1,2,\dots,N$, the initial conditions are $\boldsymbol{x}_0$ until time t. The Reachable Set $\left(R_t(\Omega_t)\right)$ is the solution to the system $\dot{\boldsymbol{x}} = f(x,u_i)$ and the Controllable Set $\left(C_t(\Omega_t)\right)$ is the solution to the system $\dot{\boldsymbol{x}} = -f(x,u_i)$.

3: The edges of the cloud of points are determined by a convex polytope.

4: The Reversible set $\left(\tau_t(\Omega_t)\right)$ is calculate as the intersection of Reachable set and Controllable set. The dimension of Reversible set is checked. If this dimension is equal to dimension of state space, then the system is locally controllable around $\boldsymbol{x}_0$.

4. RESULTS AND ANALYSIS

The time chosen for sets calculation is 20 minutes. This time is because it is the reactor time constant, and this mean, it is the maximum time available for the controller to reach the setpoint.

It is analyzed the behavior of hipervolume for the three sets to 20 minutes, when these sets are obtained with low-discrepancy deterministic and stochastic sequences, and the number N of sample points is increased. The results are shown in Tables 2 and 3, and its graphic representation in Fig. 1, 2, and 3.

From Fig. 1, 2, and 3, it can be seen that, as it increasing the sample size increases the hypervolume of the three sets, in either sequence low-discrepancy deterministic or stochastic. In addition, it is noted that the values indicated by the low-discrepancy deterministic sequence are greater than those obtained by the stochastic one.

In order to have an error behavior for each sequence, the value to which each hypervolume tend it is used as reference. For the Controllable set would be $1.98 \cdot 10^7$, for the Reachable set would be $1.12 \cdot 10^7$, and for the Reversible set would be $5.7 \cdot 10^6$. Thus, the percentage errors for each case are shown in Tables 4 and 5, and its graphic representation in Fig. 4, 5 and 6.

From Fig. 4, 5 and 6, it can be seen that, converge rate is better to the low-discrepancy deterministic sequence that for the stochastic one. For the Reachable set is notorious the biggest difference, and because the Reversible set depends on both Reachable and Controllable sets, its value is in the middle.

The reason why the low-discrepancy deterministic sequence behaves better than the stochastic one is how they are build. Although when the sample size is increased and get closer to the real case, as it is established by the law of large numbers, in the case of the low-discrepancy deterministic sequence they are being included values than before had not been evaluated, while in the stochastic one is still possible that new values are not included.

Table 2. Values to Deterministic sequence.

N	Reachable	Controllable	Reversible
500	1.0930 10^7	1.8534 10^7	3.7394 10^6
1000	1.1010 10^7	1.8997 10^7	4.2777 10^6
5000	1.1129 10^7	1.9442 10^7	5.2134 10^6
10000	1.1145 10^7	1.9494 10^7	5.3326 10^6
50000	1.1171 10^7	1.9778 10^7	5.6450 10^6
100000	1.1175 10^7	1.9784 10^7	5.6555 10^6
500000	1.1186 10^7	1.9799 10^7	5.6771 10^6

Table 3. Values to stochastic sequence.

N	Reachable	Controllable	Reversible
500	1.0200 10^7	1.8096 10^7	2.8007 10^6
1000	1.0671 10^7	1.8760 10^7	3.3694 10^6
5000	1.0981 10^7	1.9366 10^7	5.1551 10^6
10000	1.0985 10^7	1.9565 10^7	5.1741 10^6
50000	1.1103 10^7	1.9673 10^7	5.4803 10^6
100000	1.1149 10^7	1.9751 10^7	5.6007 10^6
500000	1.1162 10^7	1.9784 10^7	5.6476 10^6

Table 4. Percentage error to deterministic sequence.

N	Reachable	Controllable	Reversible
500	2.4107	6.3939	34.3965
1000	1.6964	4.0556	24.9526
5000	0.6339	1.8081	8.5368
10000	0.4911	1.5455	6.4456
50000	0.2589	0.1111	0.9649
100000	0.2232	0.0808	0.7807
500000	0.1250	0.0051	0.4018

Table 5. Percentage error to stochastic sequence.

N	Reachable	Controllable	Reversible
500	8.9286	8.6061	50.8649
1000	4.7232	5.2525	40.8877
5000	1.9554	2.1919	9.5596
10000	1.9196	1.1869	9.2263
50000	0.8661	0.6414	3.8544
100000	0.4554	0.2475	1.7421
500000	0.3393	0.0808	0.9193

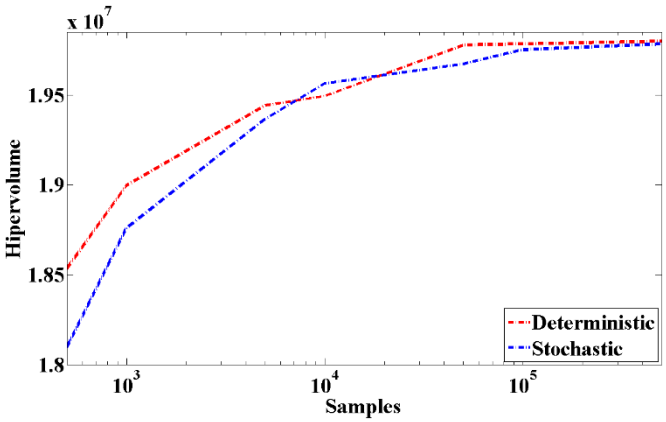

Fig. 1. Hipervolume Controllable Set.

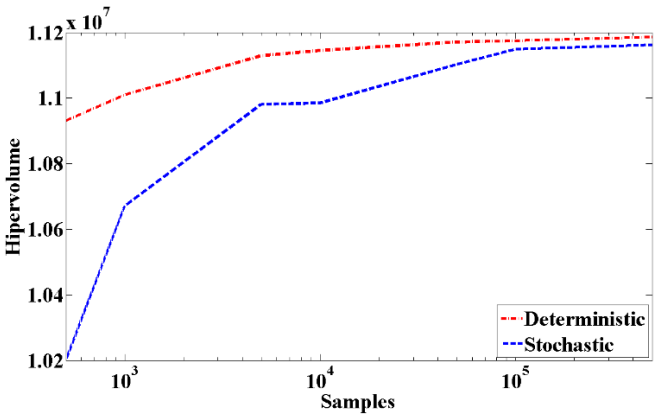

Fig. 2. Hipervolume Reachable Set.

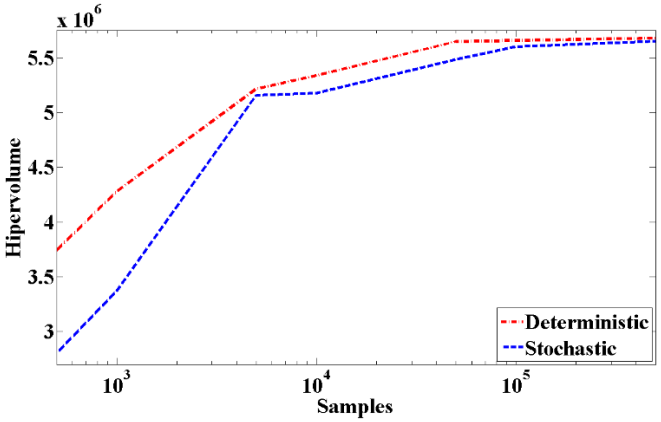

Fig. 3. Hipervolume Reversible Set.

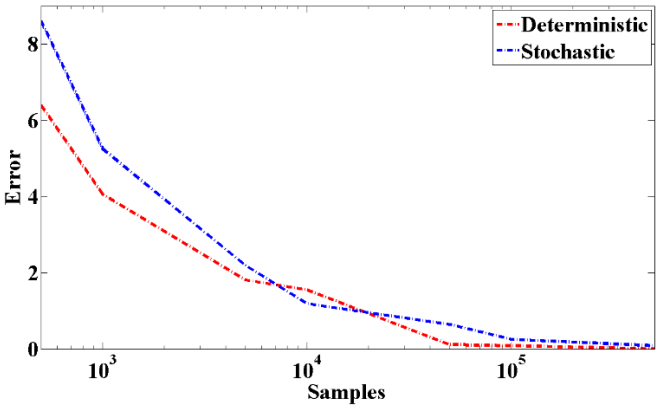

Fig. 4. Percentage error Controllable Set.

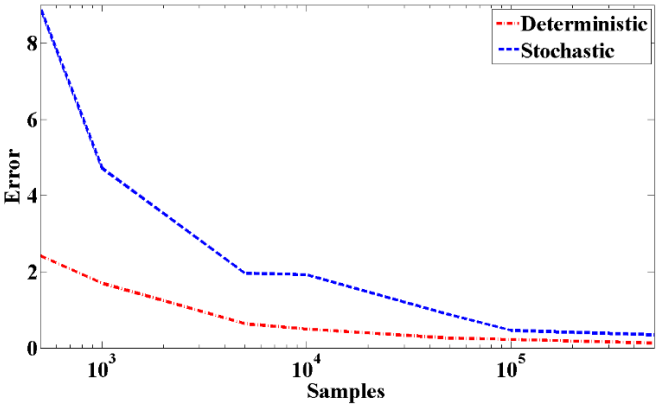

Fig. 5. Percentage error Reachable Set.

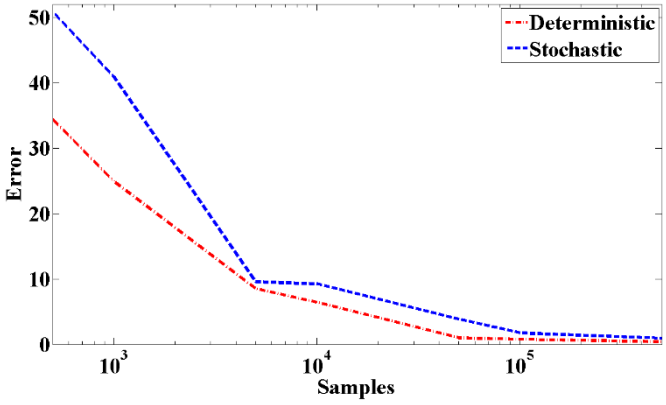

Fig. 6. Percentage error Reversible Set.

5. CONCLUSION

This paper show that low-discrepancy deterministic sequences can be used to approximately calculate the Reachable, Controllable and Reversible sets. From the analysis of results, it can be seen that the approximations obtained with low-discrepancy deterministic sequences have better convergence rate, and low percentage error than results obtained with random sequences. This situation can be explained by how each sequence is build. In the stochastic case, the fact of increasing the size of samples does not guarantee that a new value is used, instead in the low-discrepancy deterministic case it does happen.

Increasing the dimension of the system could better show the advantages of the implementation of low-discrepancy deterministic sequences over stochastic one, as is reported in literature.

ACKNOWLEDGMENT

The authors wish to thank the following organizations who contributed to the completion of this work: Universidad Nacional de San Juan (UNSJ, Argentina), and Consejo Nacional de Investigaciones Científicas y Técnicas (CONICET, Argentina).

REFERENCES

Acebrón, J. A. and Spigler, R. (2005) Fast simulations of stochastic dynamical systems, *Journal of Computational Physics*, **vol. 208**, no. 1, pp. 106–115.

Alzate, A., Gómez, L. M. and Alvarez, H. (2013) Metodología para el Diseño Simultáneo de Procesos usando Teoría de Conjuntos en Control, *XV Reunión de Trabajo en Procesamiento de la Información y Control*.

Alzate, A., Gómez, L. M. and Alvarez, H. (2015) Diseño Simultáneo de Procesos y su control usando Teoría de Conjuntos, *Prospectiva*, **vol. 13**, pp. 12–23.

Atanassov, E. and Dimov, I. T. (2008) What Monte Carlo models can do and cannot do efficiently? *Applied Mathematical Modelling*, **vol. 32**, no. 8, pp. 1477–1500.

Bequette, W. (1998) *Process Dynamics: Modeling, Analysis and Simulation*, P. Hall, Ed. Pretince Hall, New Jersey, USA.

Bequette, W. (2002) Behavior of a CSTR with a recirculating jacket heat transfer system. *Proceedings of the American Control Conference*. Anchorage, AK.

Boyle, P., Broadie, M. and Glasserman, P. (1997) Monte Carlo methods for security pricing, *Journal of Economic Dynamics and Control*, **vol. 21**, no. 8-9, pp. 1267–1321.

Bravo, J., Limon, D., Alamo, T. and Camacho, E. (2005) On the computation of invariant sets for constrained nonlinear systems: An interval arithmetic approach, *Automatica*, **vol. 41**, no. 9, pp. 1583–1589, Sep.

Calderon, C., Alzate, A., Gómez, L. M. and Alvarez, H. (2012) State Controllabillity Analysis and Re-design for a Wastewater Treatment Plant, *20th Mediterranean Conference on Control & Automation*.

Cross, E. A. and Mitchell, I. M. (2008) Level set methods for computing reachable sets of systems with differential algebraic equation dynamics, *American Control Conference*, **vol. 1**, pp. 2260–2265.

Dick, J., Kuo, F. Y. and Sloan, I. H. (2013) High-dimensional integration: The quasi-Monte Carlo way, *Acta Numerica*, **vol. 22**, no. April 2013, pp. 133–288.

Gómez, L. M. (2009) *Una Aproximación al Control de los Procesos por Lotes*, Tesis Doctoral, Universidad de San Juan, Argentina.

Gómez-Pérez, C. A., Gómez, L. M. and Alvarez, H. (2015) Reference Trajectory Design Using State Controllability for Batch Processes, *Industrial & Engineering Chemistry Research*, **vol. 54**, no. 15, pp. 3893-3903.

Grantham, W. J. and. Vincent, T. L. (1975) A controllability minimum principle, *J Optim Theory Appl*, **vol. 17**, pp. 93–114.

Hokayem, P. F., Abdallah, C. T. and Dorato, P. (2003) Quasi-Monte Carlo Methods in Robust Control Design, in *42nd IEEE Conference on Decision and Control*, December, pp. 2435–2440.

Jank, W. (2005) Quasi-Monte Carlo sampling to improve the efficiency of Monte Carlo EM, *Computational Statistics & Data Analysis*, **vol. 48**, no. 4, pp. 685–701.

Kurzhanskiy, A. B. and Varaiya, P. (2002) On Reachability Under Uncertainty, *SIAM Journal on Control and Optimization*, **vol. 41**, pp. 181–216.

Kurzhanskiy, A. B. and Varaiya, P. (2011) Reach set computation and control synthesis for discrete-time dynamical systems with disturbances, *Automatica*, **vol. 47**, pp. 1414–1426.

Kurzhanskiy, A. B. and Vályi, A. (1997) Ellipsoidal Calculus for Estimation and Control, *IIASA*.

Kurzhanskiy, A. B. and Varaiya, P. (2002) On Ellipsoidal Techniques for Reachability Analysis. Part I: External Approximations, *Optimization Methods and Software*, **vol. 17**, pp. 177–206.

Kvasnica, M., Grieder, P., Baotic, M., and Morari, M. (2004) *Hybrid Systems: Computation and Control: 7th International Workshop, HSCC 2004, Philadelphia, PA, USA, March 25-27, 2004. Proceedings*, R. Alur and G. J. Pappas, Eds. Berlin, Heidelberg: Springer Berlin Heidelberg.

Mitchell, I. M. (2004) *A toolbox of level set methods*, 1st ed., D. C. S. U. B. Columbia, Ed.

Oishi, M., Mitchell, I. M., Tomlin, C. and Saint-Pierre, P. (2006) Computing Viable Sets and Reachable Sets to Design Feedback Linearizing Control Laws Under Saturation, *Proceedings of the 45th IEEE Conference on 2006*, pp. 3801–3807

Zuluaga-Bedoya, C. C., Amicarelli, A., Gómez, L. M. and F. di Sciascio (2015) Bacillus thuringiensis process design using state controllability index, *XVI Reunión de Trabajo en Procesamiento de la Información y Control*.

Model Based Fault Detection and Isolation of a Reverse Osmosis Desalination Plant

Soto Angles Mario *. Pérez Zúñiga Gustavo*. Sotomayor Moriano Javier*

** Pontifical Catholic University of Peru, Av. Universitaria 1801, Lima, Perú Email: {mario.soto, gustavo.perez, jsotom} @pucp.pe*

Abstract: In this paper, a model based diagnosis system for a reverse osmosis desalination module with spiral wound configuration is developed. At first, a mathematical model based on differential and algebraic equations of the reverse osmosis system is obtained. From this model, a structural analysis technique is performed which allows us to obtain a structural model of the plant defined by a set of constraints. After the structural model a set of analytical redundancy relations (ARR) is obtained by applying the ranking algorithm of constraints. The comparison between the system in nominal operation with the system under different faults shows that all faults of interest were detectable and isolable.

Keywords: Fault Diagnosis, Reverse Osmosis, Analytical Redundancy Relations.

1. INTRODUCTION

According to the United Nations, close to 1.2 billion people already live in areas where freshwater is scarce. Another 1.6 billion people face chronic economic water shortage. While freshwater accounts for only 2.5%, seawater and brackish water found in oceans, seas and underground cover 97.5% of the total water in the world. Nowadays, obtaining this resource through reverse osmosis (RO) desalination method is an economically viable energy alternative (Dessouky, 2002).

Currently, installing RO desalination plants is the trending, however these systems are subject to different types of faults: in actuators such as high pressure pump, acid dosing pump, valves, and measures as flow, conductivity and temperature sensors; likewise common typical internal parameters faults of the membrane are weathering, fouling and scaling. (Gambier, 2009)

A Fault Tolerant Control (FTC) for a RO system based was developed by McFall (2007); this control was based on physical switching logic reconfiguration by installing redundant control valves, which is a disadvantage due to the high implementation costs. Gambier (2009) presents a mathematical model of a laboratory reverse osmosis plant for a FDI system design considering faults in sensors, actuators and faults in RO module such as block of a pipeline, scaling/fouling and leaks; a FTC based on control loops reconfiguration were developed in this work, but not clear isolability analysis between considered faults was considered.

Garcia (2011) performed a monitoring fault detection system based on principal component analysis (PCA) technique for a simulated RO desalination plant, this technique allows us to detect faults like offsets in pressure, temperature and concentration sensor, also blockages in filters and breakages in the membranes; but does not present faults in actuators like high pressure pump and acid dosing pump, and neither a fault isolation system is presented. Palacin (2011) presented an enhanced dynamic library of reverse osmosis plants (ROSIM) used for simulation, optimization, fault detection and a simple fault tolerant control; however faults in actuators and sensors were not considered in the work.

There are several methods for diagnosis and detection of faults with different characteristics and application fields; these include methods based on identification, in which the failures are reflected in changes of certain model parameters; knowledge-based methods using artificial intelligence techniques (Isermann, 2005).

Another approach is that concerning to the model based methods; one of them consists on the analytical redundancy method that is based on the knowledge of the set of algebraic and differential equations that conforms the process model. This method allows us to understand internal parameters that can be considered to simulate typical faults in the RO membrane; likewise this method also allows us to improve the isolability analysis of faults by adding additional redundant equations (Blanke, 2006).

This paper is structured as follows: in section 2 a detailed mathematical model is obtained where the main variables in the process are explained. In section 3 a model based fault diagnosis (MBFD) system for a RO desalination module with spiral wound configuration is developed. Section 4 consists on the simulation of the system under different faults and analysis of detectability and isolability. Section 5 presents conclusions of this

work.

2. MATHEMATICAL MODELLING OF THE REVERSE OSMOSIS SYSTEM

In Figure 1 the MBFD structure is presented and it consists in the continuous monitoring of the consistency between the output signals of the RO module with the mathematical model under the same input signals, the differences between these outputs are disclosed through a set of equations called *residuals*, from these residuals a set of analytical redundancy relations (RRA) are obtained, which depend only in terms of known variables. This set of RRA is those that allow us to detect changes when comparing the plant in normal mode of behavior and under faults. In general, the number of RRA must always exceed the number of faults considered. In this work, we consider the inclusion of an additional set of equations (redundancy) in the model for obtain a greater amount of RRA and improve isolability task.

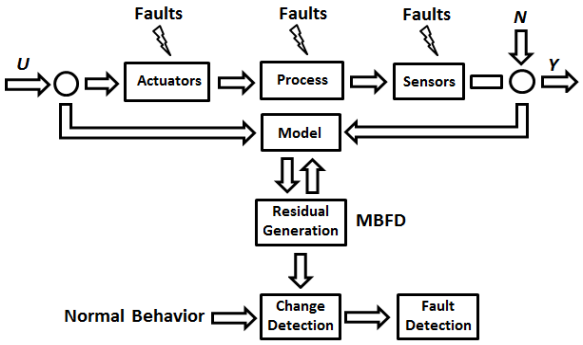

Figure 1. MBFD Structure Designed.

The MBFD method requires the thorough knowledge of the mathematical model of the plant or process under study; this is the reason for the development and complete understanding of the equations and parameters involved in the reverse osmosis desalination process. The mathematical model developed here is based on the spiral wound reverse osmosis membrane configuration because it allows us to seize the largest possible filter area compared with other configurations.

2.1. System Decomposition

System decomposition is necessary for obtaining a mathematical model of the RO module (Gambier, 2009); for the correct material balance, the system was divided into three subsystems: membrane subsystem, rejection subsystem and permeate subsystem. The considered variables are flows, pressures and concentrations.

No energy balances were made because RO works at room temperature and there is not any phase change. Subsystem decomposition is shown in Figure 2.

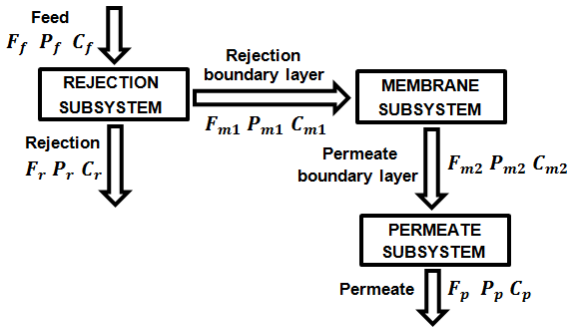

Figure 2. RO module decomposition.

2.2. Rejection subsystem

For Rejection Subsystem in Figure 2 is performed:
Global material balance:

$$dm_r/dt = F_f - F_{m2} - F_r \quad (1)$$

Where: m_r is the rejection holdup (kg), F_f is the feed flow water (kg/s), F_{m2} is the permeate boundary layer flow (kg/s), F_r is the rejection flow water (kg/s).
Partial material balance:

$$dC_r/dt = (1/m_r)\left[F_f(C_f - C_r) - F_p(C_p - C_r)\right] \quad (2)$$

Where: C_r is the rejection concentration (kg/m^3), C_f is the feed water concentration (kg/m^3), C_p is the permeate water concentration (kg/m^3), F_p is the permeate flow (kg/s).

2.3. Permeate Subsystem

For Permeate Subsystem in Figure 2 is performed:
Global material balance:

$$dm_p/dt = F_{m2} - F_p \quad (3)$$

Where m_p is the permeate holdup (kg)
Partial material balance:

$$dC_p/dt = (1/m_p)\left[F_p(C_{m2} - C_p)\right] \quad (4)$$

Where C_{m2} is the permeate boundary layer concentration (kg/m^3)

2.4. Membrane subsystem

The pressure balances are given by:

$$P_f = P_r + P_p \quad (5)$$

Where P_f is the feed pressure, P_r is the rejection pressure and P_p is the permeate pressure, all of them in Pascal (Pa).
The set of equations that define the membrane subsystem are given by:

2.4.1. Water transport equations

Permeate water flow is defined by (6) (Senthilmurugan, 2010)

$$F_p = AK_w(\Delta P - \sigma\Delta\pi) \quad (6)$$

Where A is the transfer area of the membrane (m^2), K_w is the water permeability coefficient (kg/m^2sPa), σ is osmotic pressure reflection coefficient.
The hydraulic pressure drop ΔP is given by (7)

$$\Delta P = 0.5(P_f + P_r) - P_p \quad (7)$$

The osmotic pressure drop $\Delta\pi$ is given by (8)

$$\Delta\pi = R_g T(C_{m1} - C_p)/M_m \quad (8)$$

Where R_g is the universal ideal gas constant ($m^3Pa/molK$), T is the feed solution temperature ($°K$), C_{m1} is the rejection boundary layer concentration (kg/m^3), M_m is the solute molar mass (kg/mol).

2.4.2. Salt transport equations

Permeate salt flow is defined by (9) (Dessouky, 2002)

$$F_s = K_s A(C_{m1} - C_p) \quad (9)$$

Where F_s is permeate salt flow (kg/s), K_s is the salt permeability coefficient (m/s).

Another expression for F_s is defined by (10)

$$F_s = F_p C_p \quad (10)$$

Expression for rejection boundary layer concentration of the membrane is given by equation (11) (Dessouky, 2002).

$$C_{m1} = \frac{F_f C_f + (F_f - F_p)C_r}{2F_f - F_p} \quad (11)$$

Another expression for concentration C_{m1} is also given by:

$$C_{m1} = C_{m2}\left[1 + \frac{K_w}{K_s}(\Delta P - \sigma\Delta\pi)\right] \quad (12)$$

Where the expression for permeate boundary layer concentration of the membrane can be deduced as the expression given in (13)

$$C_{m2} = \frac{C_f}{\left[1 + \frac{K_w}{K_s}(\Delta P - \sigma\Delta\pi)\left(1 - \frac{F_p}{2F_f}\right)\right]} \quad (13)$$

The model can be simplified by a assuming $C_{m2} = C_p$ and $F_{m2} = F_p$.This assumption will be considered in this work.

2.5. Additional equations for RO module

There is another way to get an expression for permeate concentration (C_p) and is given by equation in function of rejection factor (14)

$$C_p = C_{m1}(1 - R) \quad (14)$$

Expression for rejection factor is defined by (15)

$$R = \frac{(1 - F)\sigma}{1 - \sigma F} \quad (15)$$

Where the flow parameter F is given by the exponential relation in (16) (Senthilmurugan, 2010)

$$F = e^{\left[\frac{-J_v(1-\sigma)}{K_s}\right]} \quad (16)$$

Similarly another expression for obtaining permeate flow (F_p) in terms of rejection factor is given by (17)

$$F_p = \frac{K_s A R}{(1 - R)} \quad (17)$$

During filtration, accumulation of solutes occurs on the surface of the membrane (Rejection boundary layer) this accumulation produces a layer of concentration which can be determined by the model of concentration polarization (Figure 3) (Ahmed, 2010)

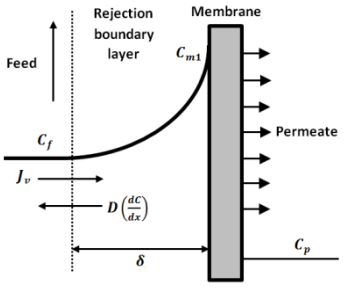

Figure 3. Concentration polarization model.

Fick's law is used to make the flow balance around the rejection boundary layer and is defined by (18)

$$J_v C_p = J_v C - D\,(dC/dx) \quad (18)$$

Expression for concentration polarization is obtained from (18) and is given by (19) (Khalaf, 2008)

$$\phi = \frac{C_{m1} - C_p}{C_f - C_p} = e^{\left(\frac{J_v}{D}\right)(\delta)} \quad (19)$$

Where ϕ is the concentration polarization factor, δ is the boundary layer thickness (m), J_v is the permeate flow velocity (m/s), D is the solution diffusion coefficient and is defined by the expression (20) (Jiang, 2014)

$$D = 6.725(10^{-6})e^{0.1546(10^{-3})C_f - \frac{2513}{273.15+T}} \quad (20)$$

Where C_f is the feed concentration, T is the feed solution temperature.

2.6. Relation between pH and conductivity

Expression that relates pH influence in permeate conductivity was taken from the experimental analysis made by Alatiqi (1989) and is given by equation 21.

$$Cd_{pH} = -0.03626(pH_f - pH_i) \quad (21)$$

Where Cd_{pH} is conductivity due to pH change, pH_f is the final value of pH, pH_i is the initial value of pH. Expression 21 shows that a positive change in pH produces a reduction of the final permeate concentration and conversely.

The final permeate concentration C_{ps} consists in the addition of concentration due to the feed pressure and the concentration due pH changes (Eq. 22).

$$C_{ps} = C_p + C_{pH} \quad (22)$$

In practice, salt content is obtained by measuring conductivity ($\mu S/cm$) instead of concentration (kg/m^3). Kohlrausch equation relates conductivity (Cd) and concentration (C) and is given by Eq. 23

$$Cd = \left[126.45 - 0.3692523\sqrt{0.001C}\right](C/58440) \quad (23)$$

2.7. Plant simulation Results

Figure 4 shows the dynamic of flows and concentrations. The simulation consider a constant value of feed pressure, where we note that flows have faster dynamic than concentrations. We can also see that brine concentration is greater than feed concentration and much higher than permeate concentration as it was expected. Boundary layer concentration is greater than feed concentration as we saw in Figure 3.

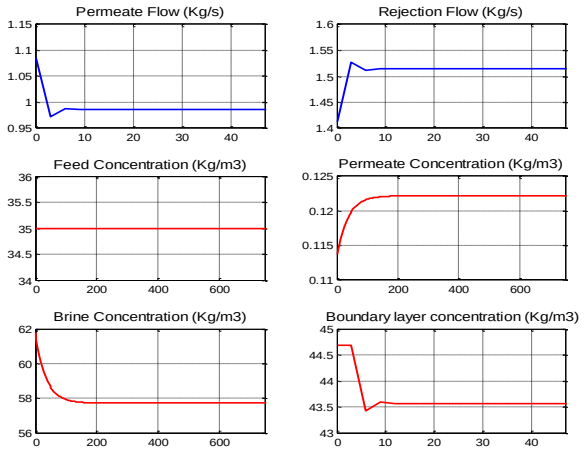

Figure 4. Plant Simulation Results.

3. FAULT DETECTION AND DIAGNOSIS SYSTEM DESIGN

3.1. Set of constraints

A set of 15 constraints that composes the structural model was obtained from the mathematical model and is shown in Table 1.

Table 1. Set of Constraints

R	EXPRESSION	R	EXPRESSION
r_1	$\frac{dC_r}{dt} = \frac{1}{m_r}[F_f(C_f - C_r) - F_p(C_p - C_r)]$	r_9	$F_p = \frac{F_s}{C_p}$
r_2	$\Delta P = 0.5(P_f + P_r) - P_p$	r_{10}	$F = e^{\left[\frac{-J_v(1-\sigma)}{K_s}\right]}$
r_3	$\Delta\pi = \frac{R_g T_f (C_{m1} - C_p)}{M_m}$	r_{11}	$R = \frac{(1-F)\sigma}{1-\sigma F}$
r_4	$J_v = K_w(\Delta P - \sigma\Delta\pi)$	r_{12}	$C_p = C_{m1}(1-R)$
r_5	$F_p = AJ_v$	r_{13}	$C_{ps} = C_p + C_{pH}$
r_6	$C_p = \frac{C_f}{\left[1 + \frac{K_w}{K_s}(\Delta P - \sigma\Delta\pi)\left(1 - \frac{F_p}{2F_f}\right)\right]}$	r_{14}	$C_{pH} = -0.03626(pH_f - pH_i)$
r_7	$C_{m1} = C_p\left[1 + \frac{K_w}{K_s}(\Delta P - \sigma\Delta\pi)\right]$	r_{15}	$C_{m1} = \frac{F_f C_f + (F_f - F_p)C_r}{2F_f - F_p}$
r_8	$F_s = K_s A(C_{m1} - C_p)$		

3.2. Set of faults

A suitable set of faults f to describe the state of the most important faults in main elements of the reverse osmosis module is defined. Fault signature vector (FSV) is given by the following expression:

$$f = (f_1, f_2, f_3, f_4, f_5, f_6, f_7)$$

Where: f_1 is the conductivity sensor fault, f_2 is the flow sensor fault , f_3 is high pressure pump fault , f_4 is the temperature sensor fault, f_5 is the membrane scaling fault, f_6 is the membrane weathering fault , f_7 is the acid pump fault (pH pump).

3.3. Incidence matrix

An incidence matrix is an arrangement that establish a relation between the known, unknown variables, and constraints. In Table 3 the incidence matrix arrangement is shown (Pérez, 2014).

3.4. Ranking Algorithm

The Ranking Algorithm is a matching algorithm that allow us to calculate the rank of each constraint, that is to say, the order in which the restrictions should be solved to find all unknown variables from the known ones. Table 2 shows the Ranking Algorithm (Blanke, 2006)

Table 2. Ranking Algorithm

Ranking Algorithm
1. Mark all known variables. Make $i = 0$
2. Find all constraints in the current table with exactly one unmarked variable. Associate rank i with these constraints and mark these constraints as well as the corresponding variable.
3. Set $i = i + 1$
4. If there are unmarked constraints whose variables are all marked, associate them with rank i, mark them and connect them with the pseudo-variable ZERO
5. If there are unmarked variables or constraints, continue with Step 2

3.5. Analytical Redundancy Relations

Constraints with the highest ranks represent the set of residual equations. As a result of application of the Ranking algorithm to the structural model we find a set of 4 residual equations that is shown highlighted in Table 3, we note that these residuals are according with the highest ranks (column R in Table 3).

Table 3. Incidence matrix

	KNOWN VARIABLES					UNKNOWN VARIABLES										
	P_f	pH	F_p	C_{ps}	T_f	C_p	C_r	ΔP	$\Delta\pi$	J_v	C_{m1}	F_s	F	R	C_{pH}	R	Z
r_1			x			x	x									2	
r_2	x							x								0	
r_3					x	x			x		x					2	
r_4								x	x	x						1	
r_5			x							x						0	
r_6			x			x		x	x							2	z
r_7						x		x	x		x					2	
r_8						x					x	x				3	z
r_9			x			x						x				2	
r_{10}										x						1	
r_{11}													x	x		2	
r_{12}						x					x			x		3	z
r_{13}				x		x									x	1	
r_{14}		x													x	0	
r_{15}			x				x				x					3	z

To get the set of analytical redundancy relations (ARRs), the set of residuals must be matched to zero (Eq. 24)

$$\begin{aligned}
&\text{ARR1: } C_p - \frac{C_f}{\left[1 + \frac{K_w}{K_s}(\Delta P - \sigma\Delta\pi)\left(1 - \frac{F_p}{2F_f}\right)\right]} = 0 \\
&\text{ARR2: } F_s - K_s A(C_{m1} - C_p) = 0 \\
&\text{ARR3: } R - \left(1 - \frac{C_p}{C_{m1}}\right) = 0 \\
&\text{ARR4: } C_{m1} - \frac{F_f C_f + (F_f - F_p)C_r}{2F_f - F_p} = 0
\end{aligned} \tag{24}$$

It was also obtained a set of 6 residuals from expressions for concentration polarization and rejection (Eq. 25). All the ARRs must be based on the reconstructed signals from the known variables.

$$
\begin{aligned}
&\text{ARR5:} = R_{r2} - \frac{C_{m1}r3 - C_{pi}}{C_{m1}r3} = 0\\
&\text{ARR6:} = C_{ps1} - C_{ps} = 0\\
&\text{ARR7:} = J_{vr3} - J_{vr1} = 0\\
&\text{ARR8:} = \frac{C_{m1}r4}{\left(1 + \left(\frac{K_w}{K_s}\right)D_{pres}r1\right)} - \frac{C_f}{\left[1 + \frac{K_w}{K_s}(D_{pres}r1)\left(1 - \frac{F_{ps}}{2F_f}\right)\right]} = 0\\
&\text{ARR9:} = \frac{C_{m1}r5}{\left(1 + \left(\frac{K_w}{K_s}\right)D_{pres}r1\right)} - \frac{C_f}{\left[1 + \frac{K_w}{K_s}(D_{pres}r1)\left(1 - \frac{F_{ps}}{2F_f}\right)\right]} = 0\\
&\text{ARR10:} = \phi_1 - \phi_{r1} = 0
\end{aligned}
\tag{25}
$$

The set of reconstructed signals from known variables is shown in Table 4; in this set we can see that all known variables are bolded.

Table 4. Reconstructed variables

$C_{m1}r3 = C_{pi} * \left(1 + \frac{K_w}{K_s}D_{pres}r1\right)$	$\Delta\pi_{r1} = \frac{(R_g \boldsymbol{T_s} C_{pi} K_w (\Delta P_r))}{M_m K_s + R_g \boldsymbol{T_s} C_{pi} K_w \sigma}$
$C_{pi} = \boldsymbol{C_{ps}} + 0.03626(\boldsymbol{pH_f} - \boldsymbol{pH_i})$	$C_{ps1} = C_{pr} + C_{pH}$
$D_{pres}r1 = \frac{J_{vr1}}{K_w}$	$C_{pH} = -0.03626(\boldsymbol{pH_f} - \boldsymbol{pH_i})$
$J_{vr1} = \frac{\boldsymbol{F_{ps}}}{A}$	$C_{pr} = \frac{\phi_{r1}(1 - R_{r1})C_f}{\phi_{r1} + R_{r1}(1 - \phi_{r1})}$
$C_{m1}r4 = C_{pi} + \phi_{r1}(C_f - C_{pi})$	$R_{r1} = \frac{(1 - F_{r1})\sigma}{1 - \sigma F_{r1}}$
$C_{m1}r5 = \phi_{r1}C_f$	$F_{r1} = e^{\left(\frac{-J_{vr1}(1-\sigma)}{K_s}\right)}$
$\phi_{r1} = e^{J_{vr1}/k}$	$C_{m_1}r1 = \frac{(F_f C_f + (F_f - \boldsymbol{F_{ps}}) * C_{ri})}{(2F_f - \boldsymbol{F_{ps}})}$
$R_{r2} = \frac{(1 - F_{r2})\sigma}{1 - \sigma F_{r2}}$	$C_{ri} = (F_f C_f - \boldsymbol{F_{ps}} C_{pi})/(F_f - \boldsymbol{F_{ps}})$
$F_{r2} = e^{\left(\frac{-J_{vr2}(1-\sigma)}{K_s}\right)}$	$J_{vr3=} k * \ln\left(\frac{C_{m1}r1}{C_f}\right)$
$J_{vr2} = K_w * (D_{pres}\, r2)$	$\phi_1 = (C_{m1}r1 - C_{pi})/(C_f - C_{pi})$
$D_{pres}\, r2 = \Delta P_r - \sigma\Delta\pi_{r1}$	
$\Delta P_r = 0.5(\boldsymbol{P_f} + P_r) - P_p$	

Two PID control loops were designed for permeate flow and permeate concentration output signals, because these are the variables of interest for quantity and quality of permeate water respectively (Alatiqi, 1989), in this way the 2 error signals of PID controllers were used to improve the isolability task. We must note that variables that make the error signals are also known.

$$
\begin{aligned}
ERR1 &= \boldsymbol{F_p ref} - \boldsymbol{F_{ps}}\\
ERR2 &= \boldsymbol{C_p ref} - \boldsymbol{C_{ps}}
\end{aligned}
\tag{26}
$$

Thus a total of 12 signals were used for fault detection and isolation analysis.

4. SIMULATION RESULTS

Results of detectability and isolability analysis are shown in the following Figures.

4.1. Normal Mode Behavior

Figure 5 shows that 12 signals designed remain at zero or very close to zero in case of normal mode behavior of the plant, which indicates no presence of faults affecting the system.

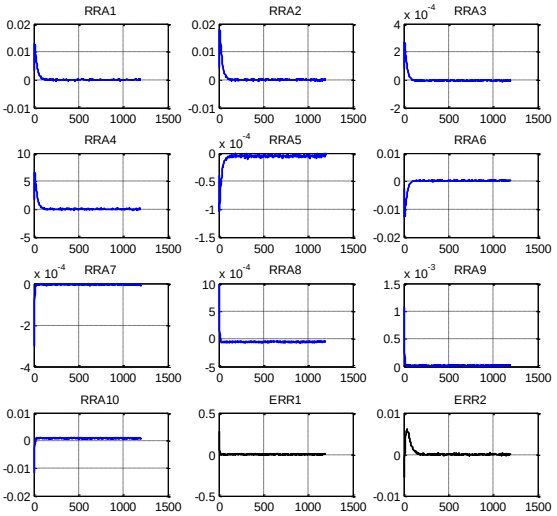

Figure 5. Normal mode behavior

For simulation, in all cases faults will be pulse type, that is to say those that occur only for a specified time interval.

4.2. Conductivity sensor fault

Figure 6 shows that this fault was detected by the RRA1, RRA2, RRA3, RRA4, RRA5, RRA6, RRA7, RRA8 and ERR2. In this fault, an additive offset of 50% of the variable occurred during the time interval of 600 to 650 seconds.

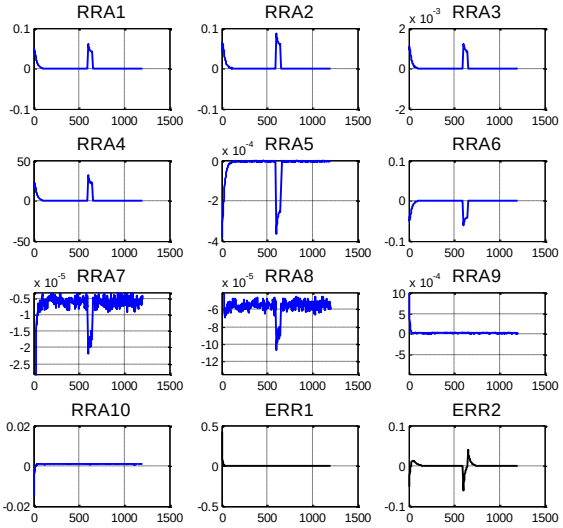

Figure 6. Conductivity sensor fault

4.3. Scaling/fouling membrane Fault

Scaling means the deposition of particles on a membrane, causing it to plug, it depends on numerous factors like pH, temperature and the presence of other ions. Scaling fault can be simulated by reducing the cross-flow velocity J_v; this fault was simulated during the time interval of 400 to 450 seconds. Figure 7 shows that scaling membrane fault was detected by RRA3, RRA4, RRA5, RRA6, RRA7, RRA8, RRA9 and RRA10.

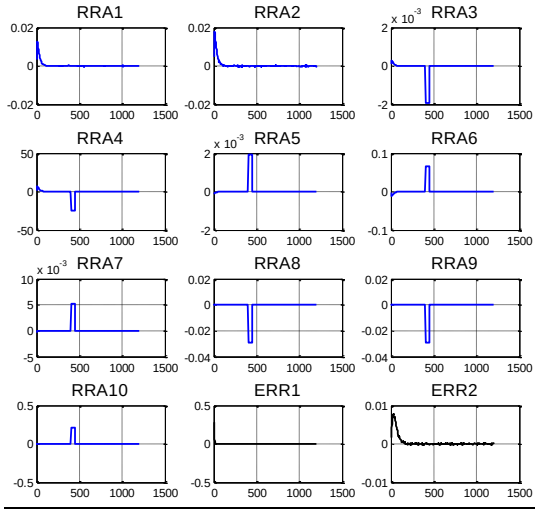

Figure 7. Scaling Fault

4.9. Summary Results

Another five faults were simulated during different time intervals. From figures 6 and 7 we see that each simulated fault corresponds to a pattern of RRAs for which is detected. A summary table of results is necessary to evaluate detectability and isolability of faults. Table 5 presents the summary results.

Table 5. Summary results

FAULT	RRA1	RRA2	RRA3	RRA4	RRA5	RRA6	RRA7	RRA8	RRA9	RRA10	ERR1	ERR2
High pressure pump	x	x	x	x	x	x	x	x	x	x	x	x
pH pump	x	x	x	x	x		x	x				x
Flow sensor	x	x	x	x	x	x	x	x	x	x	x	
Conductivity sensor	x	x	x	x	x	x	x	x				x
Temperature sensor	x				x							
Membrane weathering			x			x						
Membrane scaling/fouling			x	x	x	x	x	x	x	x		

From Table 5 we can see that all faults considered in the design corresponds to different patterns of RRAs, the patterns found not repeat each other, thus we can conclude that all elements of FSV are detectable and isolable.

5. CONCLUSIONS

A model based on analytical equations of the RO desalination plant was proposed, the model validation gave consistent and similar results to those obtained in the literature. Following this model was presented as a structural model and then common faults that may occur during the actual operation of a reverse osmosis were defined. A set of seven faults; three in sensors, two in actuators and two in internal parameters that can lead to malfunctioning of the RO membrane were considered.

Detectability analysis of seven faults in the design resulted in that all faults were detectable by the set of RRA designed. Furthermore, by analyzing isolability it was determined that all faults were isolable.

As a future work we propose the use of nonlinear observers of certain variables of interest, which will allow for obtaining additional redundancy relations to detect and isolate other faults of interest.

ACKNOWLEDGMENT

The authors acknowledge the support of the National Innovation Program for Competitiveness and Productivity (Innovate Peru) entity that financed the-FINCyT-IA-2013 207 project, under which this article was developed.

REFERENCES

Ahmed, F. (2013) *Modified Spiegler-Kedem Model to Predict the Rejection and Flux of Nanofiltration Processes at High NaCl Concentrations***.** University of Ottawa. 3,59-66.

Alatiqi, I.M., Ghabris, A.H., Ebrahim, S. (1989). System identification and control of reverse osmosis desalination. *Desalination Journal*, 75 (1989) 119-140.

Blanke, M., Kinnaert, M., Lunze, J., Staroswiecki, M. (2006) *Diagnosis and Fault-Tolerant Control*. Springer. 109-175.

Garcia D. (2011) Monitoring and Fault Detection in a Reverse Osmosis Plant using Principal Component Analysis. *IEEE Conference on Decision and Control and European Control Conference*.1-6.

Gambier A.; Miksch T.; Badreddin E. (2009). A reverse osmosis Laboratory Plant for Experimenting with Fault-Tolerant Control. *American Control Conference Hyatt Regency Riverfront, St. Louis, MO, USA. Automatica*, 27, 1039-1042

Dessouky and Ettouney (2002) *Fundamentals of Water Desalination***.** Department of Chemical Engineering College of Engineering and Petroleum Kuwait University. Elsevier, 410-435.

Isermann R. (2005) *Fault-Diagnosis Systems. An introduction from Fault Detection to Fault Tolerance***.** Springer. 61-82.

Jiang A; Ding Q, Wang J. (2014) Mathematical modeling and simulation of SWRO Process based on simultaneous method. *Hindawi Publishing Corporation, Journal of Applied Mathematics* Volume 2014, Article ID 908569, 11 pages.

Khalaf T. (2008). Estimation of concentration polarization using the Combined Film Theory/Spiegler Kedem Model and Empirical Correlation. *The 1st Regional Conference of Eng. Sci. NUCEJ Spatial ISSUE* vol 11, No2, pp 322-328.

McFall Ch, Panagiotis D. (2007) Fault-Tolerant Control of a reverse osmosis desalination process *8th International IFAC Symposium on Dynamics and Control of Process Systems, México.*, 161 -166.

Palacin L.G. (2011) *New dynamic of reverse osmosis plants with fault simulation.*. Department of Systems Engineering and Automatic Control University of Valladolid, Spain.,127-132.

Pérez G.; Sotomayor J. (2014). Análisis de Redundancia para diagnóstico de fallas de una planta desalinizadora de agua de mar**.** *Congreso Latinoamericano de Control Automático, México.*, 1-6.

Senthilmurugan, S., Ahluwalia A., Gupta S. (2005) Modeling of a spiral wound module and estimation of model parameters using numerical techniques. *Desalination*. 269-286.

Monitoramento e Avaliação de Desempenho de Sistemas MPC Utilizando Métodos Estatísticos Multivariados

Nayanne M. G. Rego Fontes* Oscar A. Z. Sotomayor*

**Programa de Pós-Graduação em Engenharia Elétrica, Universidade Federal de Sergipe, São Cristóvão, SE, Brasil (E-mails: nayannegarcia@gmail.com; oscars@ufs.br)*

Resumo: Este trabalho avalia a aplicação de métodos estatísticos multivariados, no monitoramento do desempenho de controladores preditivos. Os métodos aqui apresentados são: o PCA (Análise por componentes principais) e o ICA (Análise por componentes independentes). Ambos os métodos utilizam dados coletados diretamente do processo. O primeiro é largamente utilizado na avaliação de desempenho de MPC, enquanto o segundo, é um método mais recente que surgiu, principalmente, com o objetivo de ser utilizado em sistemas de detecção de falhas. As análises serão feitas de forma comparativa, quando aplicadas em um processo simulado característico da indústria petroquímica, operando sob controle MPC.

Palavras Chaves: Monitoramento, MPC, PCA, ICA.

1 INTRODUÇÃO

A indústria vem investindo fortemente na aplicação de controle avançado, como os controladores preditivos. Estes controladores atendem o desempenho especificado na fase inicial de operação da planta, mantendo-a operando dentro de suas restrições de forma lucrativa. Porém, o desempenho desejado do controlador deteriora-se após um dado período de operação, devido a diversos fatores. Assim, faz-se necessário o monitoramento do controlador para que o sistema de controle mantenha o desempenho desejado. Neste trabalho, abordam-se métodos de monitoramento e avaliação de desempenho de controladores preditivos (*Model Predictive Control*, MPC) usando um modelo de referência (*benchmark*) e estatísticas multivariadas. O mau desempenho do MPC advém de vários fatores, quais sejam: variação das características da matéria prima; incompatibilidade do modelo do processo com a planta; distúrbios; mau funcionamento de atuadores e sensores e manutenção inadequada. Tian *et al* (2011a) classifica as causas de deterioração do MPC em dois grupos, denominados de fatores internos e externos.

Os primeiros trabalhos sobre avaliação de desempenho e monitoramento de controladores foram propostos por Harris (1989) com o *benchmark* do controlador de variância mínima (*Minimum Variance Controller*, MVC) para sistemas de uma entrada e uma saída (SISO). Posteriormente, a técnica foi adaptada e desenvolvida para abordagem de sistemas MISO por Desborough *et al* (1993) e MIMO por Harris *et al* (1996), embora não seja adequado o uso do *benchmark* MVC, pois as restrições e as não-linearidades do algoritmo MPC fazem da teoria MVC irrealizável. Harris *et al* (1999) ainda fizeram uma revisão sobre técnicas de monitoramento e avaliação de desempenho para sistemas de controle mono e multivariáveis. Huang (1997) propõe o uso do controlador linear quadrático gaussiano (LQG) como *benchmark*, entretanto, o LQG não leva em consideração as restrições. Jelali (2006) também faz uma revisão geral sobre técnicas de avaliação de desempenho de controle e as aplicações na indústria.

Técnicas inovadoras baseadas em métodos estatísticos multivariados, tal como a análise de componentes principais (PCA), foram introduzidas para monitorar desempenho de controladores MPC por Loquast III and Seborg (2003). Zhang e Li (2006) abordam um *benchmark* simples e realizável utilizando o PCA e um filtro auto-regressivo de média móvel para monitorar o desempenho. Esse mesmo filtro é proposto por Qiang e Shaoyuan (2006), que também utilizam o PCA para a construção de um modelo de componentes principais. AlGhazzawi e Lennox (2009) apresentam uma ferramenta, para monitorar MPC, baseada em técnicas MSPC (*Multivariate statistical process control*). Com estas, desenvolveu-se um modelo objetivando compará-lo com o desempenho atual do controlador, usando PCA e Análise de Projeções em Estruturas Latentes (PLS). Tian *et al* (2011b) sugerem um *framework* unificado baseado na dinâmica do PCA.

Neste trabalho, a avaliação do controle MPC foi realizada a partir de métodos baseados em dados, utilizando-se métodos de análise estatística multivariada PCA e ICA. A partir de um processo escolhido como estudo de caso, dados foram coletados, considerando-se o processo em condições normais, para aplicação dos métodos PCA e ICA. Assim, ferramentas capazes de monitorar o MPC foram desenvolvidas. As próximas seções deste artigo são organizadas como segue. Depois de uma breve revisão dos métodos estatísticos multivariados, incluindo o PCA e o ICA, na seção 2, as estatísticas de monitoramento são introduzidas na seção 3 e, finalizando a fundamentação teórica deste trabalho, a seção 4 define o método de diagnóstico utilizado. Em seguida, para ilustrar a efetividade das técnicas, a seção 5 nos traz um estudo de

caso, seguido dos resultados experimentais. Por fim, a seção 6 finaliza o trabalho com a conclusão.

2 MÉTODOS ESTATÍSTICOS MULTIVARIADOS

Os métodos estatísticos multivariados são capazes de extrair informações de grandes conjuntos de dados multivariados e, apesar de vários métodos diferentes, todos compartilham da semelhança de identificar variáveis "artificiais", que são combinações lineares ou não-lineares das variáveis originais. Neste trabalho, utilizaram-se duas técnicas: análise de componentes principais (PCA) e análise de componentes independentes (ICA). Esses métodos são brevemente descritos a seguir. Para maiores detalhes, consultar Jackson (1991) para o PCA e Hyvärinen *et al* (2001) para o ICA.

2.1 Análise de Componentes Principais (PCA)

A ideia central do PCA é reduzir a dimensionalidade de um conjunto de dados, que consiste de um grande número de variáveis correlacionadas, com a perda mínima de informação. Isto é possível por meio da transformação dos dados em um novo conjunto de variáveis, ditas componentes principais (PCs), que são não correlacionadas e ordenadas de modo que as primeiras componentes contenham a maior parte da variação presente em todas as variáveis originais.

Para aplicação do método, quando a matriz de dados originais é coletada, esta deve ser centralizada e normalizada. Assim, dada uma matriz X_{mxp} de dados coletados, onde m é o número de medições (observações) e p o número de variáveis, a normalização da matriz de dados nos dá uma matriz Z_{mxp} de média zero e covariância igual a sua matriz de correlação. De acordo com Jackson (1991), o PCA é realizado efetuando-se a diagonalização da matriz de covariância dos dados normalizados, isto é:

$$S = E\Lambda E^T \qquad (01)$$

Em que: E é uma matriz pxp ortogonal chamada de matriz de autovetores e Λ é uma matriz diagonal pxp chamada matriz de autovalores.

Os autovalores estão dispostos em ordem decrescente, sendo que cada autovalor expressa uma porcentagem da variância total dos dados. Por meio dos autovetores, pode-se transformar as p variáveis, que são correlacionadas, em outras p variáveis, não-correlacionadas, como segue:

$$P_c = ZE \qquad (02)$$

As α primeiras componentes principais tem a maior variância e podem representar todas as p variáveis originais sem muita perda de informações. Estas, podem ser calculadas apenas com os autovetores associados aos α primeiros autovalores, ou seja:

$$T = ZP \qquad (03)$$

A matriz $P_{px\alpha}$ também é chamada de *loading vectors*. Em consequência, a matriz estimada dos dados, obtida do PCA, é dada por:

$$\hat{Z} = TP^T \qquad (04)$$

E a matriz residual, que assimila as variações no espaço observação gerado pelos autovetores associados aos $m - \alpha$ menores autovalores, é dada por:

$$E = Z - \hat{Z} \qquad (05)$$

2.2 Análise de Componentes Independentes (ICA)

A grande diferença entre PCA e ICA está no princípio utilizado para o tratamento dos dados. Enquanto as componentes principais são baseadas na descorrelação, obtendo sinais ou dados não correlacionados, gaussianos ou não, as componentes independentes são baseadas no princípio de independência estatística, obtendo sinais ou dados de variáveis não gaussianas independentes.

Para se definir um modelo para ICA, considera-se um conjunto de n variáveis aleatórias $x_1, \dots, x_n$, que foram observadas e medidas. De acordo com Hyvärinen *et al* (2001), estas variáveis podem ser escritas como uma combinação linear de n variáveis estatisticamente independentes $s_1, \dots, s_n$, como segue:

$$x_i = a_{i1}s_1 + a_{i2}s_2 + \cdots + a_{in}s_n \qquad (06)$$

Em que: $i = 1, \dots, n$, e a_{ij} são coeficientes escalares reais com $i, j = 1, \dots, n$.

Este é considerado o modelo básico do ICA e descreve como os dados observados são gerados a partir de um processo de mistura dos componentes independentes s_j. Sendo que, os coeficientes da mistura a_{ij} são desconhecidos. Tanto as componentes da mistura como os componentes independentes são estimados a partir de x_i. Essas estimações são realizadas assumindo-se algumas hipóteses, de modo que as componentes tornem-se o mais independente possível umas das outras.

Usando notação matricial, em que **x** é o vetor de variáveis aleatórias cujos elementos são as misturas, **s** é o vetor de componentes independentes e A é a matriz de mistura, de acordo com tem-se:

$$\mathbf{x} = \mathrm{A}\mathbf{s} \qquad (07)$$

Assim, como por hipótese, as componentes de **s** são estatisticamente independentes e pode-se achar um sistema de "desmistura" ou separação W, em que os componentes reconstruídos $\hat{\mathbf{s}}$ sejam o mais independente possível. Neste caso, tem-se que:

$$\hat{\mathbf{s}} = \mathrm{W}\mathbf{x} \qquad (08)$$

Nas condições normais de operação dos dados **x**, W e $\hat{\mathbf{s}}$ são obtidos utilizando-se o algoritmo FastICA proposto por Hyvärinen *et al* (2001). Como acontece no PCA, pode-se reduzir a dimensão dos dados selecionando-se as d linhas de W dominantes que tem o maior efeito na variação dos elementos do vetor de componentes principais, usando-se a norma euclidiana. Assim, tem-se duas matrizes reduzidas, W_d correspondente a parte dominante e W_e correspondente a parte excluída. Da mesma forma, pode-se selecionar as d colunas da matriz de mistura A, resultando nas matrizes A_d e A_e. Em consequência disto, tem-se os seguintes vetores de componentes independentes:

$$\hat{\boldsymbol{s}}_{\boldsymbol{d}} = \mathrm{W}_d\mathbf{x} \quad (09)$$

$$\hat{\boldsymbol{s}}_{\boldsymbol{e}} = \mathrm{W}_e\mathbf{x} \quad (10)$$

3 MONITORAMENTO DE MPC USANDO ESTATÍSTICAS MULTIVARIADAS

Para se desenvolver o modelo de referência (*benchmark*) baseado em dados para avaliação de desempenho do MPC, um período de dados de referência foi escolhido. Este deve ser um período considerado bom para os dados de operação, a partir do processo funcionando com o desempenho satisfatório do controlador. Assim, um conjunto de dados das variáveis manipuladas e controladas, juntamente com o erro de predição do modelo, são adquiridos, considerando-se o processo operando em condições normais. Tem-se então o conjunto de dados das variáveis monitoradas dado por:

$$X = [\boldsymbol{u}_1 \dots \boldsymbol{u}_j \boldsymbol{ep}_1 \dots \boldsymbol{ep}_n \boldsymbol{y}_1 \dots \boldsymbol{y}_n] \quad (11)$$

Muitos trabalhos, como Tian *et al* (2011b), Lee *et al* (2004) e Stefatos *et al* (2010), utilizam os métodos PCA e ICA estendidos para modelagem e monitoramento de sistemas dinâmicos. Estes são chamados DPCA (PCA dinâmico) e DICA (ICA dinâmico), respectivamente, cuja diferença, na sua aplicação, está no aumento da matriz de dados originais, os quais usa l observações prévias de cada variável. Assim, a matriz de dados passa a ser da seguinte forma:

$$X(l) = \begin{bmatrix} \boldsymbol{x}_k & \boldsymbol{x}_{k-1} & \cdots & \boldsymbol{x}_{k-l} \\ \boldsymbol{x}_{k+1} & \boldsymbol{x}_k & \cdots & \boldsymbol{x}_{k-l+1} \\ \vdots & \vdots & \vdots & \vdots \\ \boldsymbol{x}_{k+m} & \boldsymbol{x}_{k+m-1} & \cdots & \boldsymbol{x}_{k+m-l} \end{bmatrix} \quad (12)$$

Em que: $\boldsymbol{x}_k$ é o vetor observação das variáveis no instante k, $m+1$ é o número de amostras e l é o número de medições defasadas. O valor de $l = 1$ ou 2 é apropriado para monitoramento, segundo Chiang *et al* (2001). O fato de se introduzir na matriz de dados os valores de auto-regressão das variáveis do processo a ser monitorado, com atrasos que variam de 1 até 2, permite estabelecer correlação entre estas, que são definidas pela física do processo.

A partir desse conjunto de dados, e após centralizar e normalizar esta matriz, aplica-se os métodos já conhecidos PCA e ICA. Para detectar anormalidades no desempenho do MPC por meio do modelo PCA, usam-se duas estatísticas de monitoramento: T² de Hotelling e SPE (*Squared Prediction Error*). Estas condições anormais são identificadas nos novos dados que são coletados e analisados em tempo real. As duas estatísticas são definidas como:

$$T^2 = \boldsymbol{t}(k)^T {\Lambda_\alpha}^{-1} \boldsymbol{t}(k) \quad (13)$$

$$SPE = {||E||_2}^2 \quad (14)$$

Em que: $\boldsymbol{t}(k) = \boldsymbol{z}(k)P$ no instante k e Λ_α é a matriz diagonal dos autovalores associadas aos α componentes principais.

Os valores das estatísticas devem permanecer baixos e abaixo de um limite estatístico. Caso contrário, valores acima destes limites, indicam condições anormais. A estatística T² mede a variação dentro dos limites do modelo PCA e, de acordo com Chiang (2001), seu limite é dado pela distribuição-F:

$${T_a}^2 = \frac{\alpha(m-1)(m+1)}{m(m-\alpha)} F_a(\alpha, m-\alpha) \quad (15)$$

Em que: m é o número de amostras dos dados usada no modelo PCA; α é o número de componentes principais e a é a porcentagem da distribuição-F.

Já a estatística SPE monitora a parte do espaço de medição correspondente aos $p-\alpha$ menores valores singulares. Segundo Chiang (2001), os limites podem ser calculados por meio da seguinte aproximação:

$$Q_a = \theta_1 \left[\frac{h_0 c_a \sqrt{2\theta_2}}{\theta_1} + 1 + \frac{\theta_2 h_0 (h_0 - 1)}{{\theta_1}^2} \right]^{1/h_0} \quad (16)$$

Em que: $\theta_i = \sum_{j=\alpha+1}^{m} {\lambda_j}^i$, λ_j é o autovalor associado ao j-ésimo autovetor; $h_0 = 1 - \frac{2\theta_1\theta_3}{3{\theta_2}^2}$ e c_a é o desvio normal correspondente ao percentual $(1-a)$.

Para detectar anormalidades no desempenho do MPC por meio do modelo ICA, Lee *et al* (2004) propõem três estatísticas de monitoramento: ${I^2}_d$, ${I^2}_e$ e SPE. A estatística ${I^2}_d$ é usada para monitorar a parte sistemática que corresponde a dinâmica do sistema e é definida como:

$${I^2}_d(k) = \hat{\boldsymbol{s}}_{newd}(k)^T \hat{\boldsymbol{s}}_{newd}(k) \quad (17)$$

A estatística ${I^2}_e$ monitora a parte não sistemática das medidas do processo e é definida como segue:

$${I^2}_e(k) = \hat{\boldsymbol{s}}_{newe}(k)^T \hat{\boldsymbol{s}}_{newe}(k) \quad (18)$$

Em que: $\hat{\boldsymbol{s}}_{newd}(k) = W_d \boldsymbol{x}_{new}(k)$ e $\hat{\boldsymbol{s}}_{newe}(k) = W_e \boldsymbol{x}_{new}(k)$.

Por fim, a estatística que é usada para monitorar a parte residual da variação do processo é o SPE e é calculada como segue:

$$SPE(k) = \boldsymbol{e}(k)^T \boldsymbol{e}(k) \quad (19)$$

Em que: $\boldsymbol{e}(k) = \boldsymbol{x}_{new}(k) - \hat{\boldsymbol{x}}_{new}(k)$ e $\hat{\boldsymbol{x}}_{new}(k) = A_d \hat{\boldsymbol{s}}_{newd}(k)$.

Similar ao PCA, os valores destas estatísticas também devem permanecer baixos e abaixo de um limite estatístico. De acordo com Stefatos (2010), os limites podem ser estabelecidos, para cada estatística, usando-se o estimador de densidade kernel:

$$\hat{f}(x) = \frac{1}{m\eta} \sum_{i=1}^{m} K\left(\frac{x - x_i}{\eta}\right) \quad (20)$$

Em que: $K(u) = \frac{1}{\sqrt{2\pi}} e^{-\frac{1}{2}u^2}$ é a kernel gaussiana; $\eta = \frac{1.06}{m^{1/5}}\sigma$ é a largura de banda; m é o número de observações e σ é o desvio padrão de cada estatística. Após estimar a função densidade de cada estatística, o limite de controle é o ponto que ocupa 99% da área da função densidade.

4 DIAGNÓSTICO

Após a detecção de um mau desempenho do controlador, é importante diagnosticar a causa desse desempenho inadequado. Para localizar a causa raiz, as informações inerentes a esta causa, devem estar nos dados do modelo. Assim, um método baseado em dados para monitoramento

deve ter em seus dados de treinamento esse tipo de informação. O método utilizado neste trabalho e proposto por Tian *et al* (2011a) baseia-se no ângulo formado entre o principal autovetor dos dados detectados com mau desempenho e os principais autovetores dos dados previamente treinados no modelo. Assumindo-se que se tem g causas $(C_1, C_2, \dots, C_g)$ de deterioração de desempenho do controlador MPC, previamente conhecidas, um conjunto de dados X_i é coletado para cada causa C_i e treinado para adquirir um modelo de referência. Esse modelo é composto pelo principal autovetor e_i, que corresponde ao maior autovalor da matriz de covariância da amostra dos dados, já que o autovetor correspondente ao maior autovalor explica a maior parte das informações do subespaço. Assim, cada causa C_i define um subespaço V_i que é representado pelas características do seu autovetor e_i.

Quando um baixo desempenho é detectado pelo procedimento de avaliação de desempenho, examina-se qual subespaço $\{V_i\}^g{}_{i=1}$ está mais próximo do subespaço dos dados monitorados. Para isto, define-se o ângulo entre os dois subespaços, considerando-se V_i o subespaço dos dados do modelo, sendo $1 \leq i \leq g$ e V_m o subespaço dos dados monitorados:

$$\theta_{i,m} = cos^{-1}\left(\frac{e_i{}^T e_m}{\|e_i\|\|e_m\|}\right) \qquad (21)$$

Assim, o subespaço V_i que tiver o menor ângulo $\theta_{i,m}$ é o mais similar ao subespaço V_m e o atual mau desempenho é provavelmente causado pela causa C_i.

5 ESTUDO DE CASO

Para demonstrar a efetividade das técnicas, estas foram aplicadas em um sistema de destilação Wood- Berry. Este processo tem sido usado em muitos trabalhos como Tian (2011a) e é ilustrado pela Fig. 1.

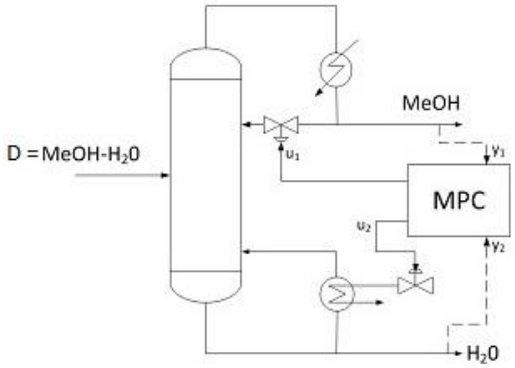

Fig. 1. Coluna de destilação Wood-Berry

5.1 Modelo de coluna de destilação Wood-Berry

A coluna de destilação Wood-Berry é um sistema de duas entradas e duas saídas para mistura de metanol e água. O diagrama apresentado na Fig. *1* indica as variáveis envolvidas na simulação. Esta foi realizada em malha fechada, usando-se a estratégia de controle MPC com restrições impostas nas entradas de ± 0.2, nas saídas de ± 1.5 e no incremento das entradas de ± 0.05, seguindo a mesma estratégia usada por Tian (2011a). Os parâmetros do controlador para o modelo *benchmark* são: o horizonte de modelo foi ajustado para 80, as matrizes de supressão foram escolhidas como matrizes identidades, o horizonte de predição e o horizonte de controle como sendo 10 e 1, respectivamente, e o tempo de amostragem foi estabelecido em 1 minuto. Além disso, o "*set point*" das variáveis controladas foram ajustadas para 1 e 0.8, respectivamente, e a variância do distúrbio *D* de 0.01. O conjunto de variáveis monitoradas foi estabelecido como sendo:

$$X = [\boldsymbol{U_1}\ \boldsymbol{U_2}\ \boldsymbol{ep_1}\ \boldsymbol{ep_2}\ \boldsymbol{Y_1}\ \boldsymbol{Y_2}] \qquad (22)$$

5.2 Treinamento dos Dados de Referência

Para criar o modelo de referência usando-se o DPCA e o DICA, simulou-se o sistema em malha fechada com uma janela de 1000 minutos, considerando-se as condições de ajustes descritas na seção 5.1, que são as condições normais do sistema. A partir destes dados, o *benchmark* foi criado, utilizando-se as técnicas estatísticas multivariadas já descritas nesse trabalho, para ser aplicado no monitoramento do sistema de controle MPC.

Para o diagnóstico das causas de deterioração do controle, estas causas devem ser previamente conhecidas e um treinamento dos dados com ocorrência destas causas deve ser realizado. Para a coluna de destilação Wood-Berry, quatro causas foram estabelecidas por Tian (2011a) e seguidas por esse trabalho, conforme segue na Tabela 1. Estas quatro causas foram: mudança da variância da distúrbio (C_1), alteração nas restrições das variáveis controladas (C_2), aumento do primeiro ganho estático de 100% (C_3), e mudança no horizonte de controle do controlador (C_4).

Tabela 1. Causas e parâmetros dos dados treinados

Causa	Condição de Operação	Parâmetro/Variável	Valor
C1	Perturbação no distúrbio	Variância	0.015
C2	Saturação nas restrições	Restrições das saídas	± 0.7
C3	Incompatibilidade de modelo do processo	Primeiro ganho estático	25.6
C4	Controlador mau sintonizado	Horizonte de controle	3

Similar a criação do modelo DPCA e DICA, os dados com as quatro causas foram simulados em uma janela de 1000 minutos. Com estes dados, o *benchmark* para diagnóstico pode ser feito, seguindo os passos da seção 4. A simulação em malha fechada do conjunto das variáveis monitoradas sob sistema de controle MPC referente ao período de referência e os quatro períodos de treinamento são mostrados em Fig. 2, Fig. 3 e Fig. 4.

5.3 Resultados Experimentais

Após definir o *benchmark*, um protótipo para o monitoramento do MPC foi desenvolvido usando-se o DPCA e o DICA, para então avaliar a capacidade destes métodos em identificar anomalias no controle do sistema. Os limites de controle das estatísticas T², SPE, $I^2{}_d$ e $I^2{}_e$ são definidos seguindo a seção 3. A cada nova medição, as estatísticas são recalculadas para um monitoramento on-line e, para avaliar o desempenho deste, quatro falhas foram inseridas no sistema, de acordo com a Tabela 2.

Tabela 2. Falhas e parâmetros

Falha	Condição de Operação	Parâmetro/Variável	Valor
F1	Perturbação no distúrbio	Variância	0.018
F2	Saturação nas restrições	Restrições das saídas	±0.5
F3	Incompatibilidade de modelo do processo	Primeiro ganho estático	28.16
F4	Controlador mau sintonizado	Horizonte de controle	2

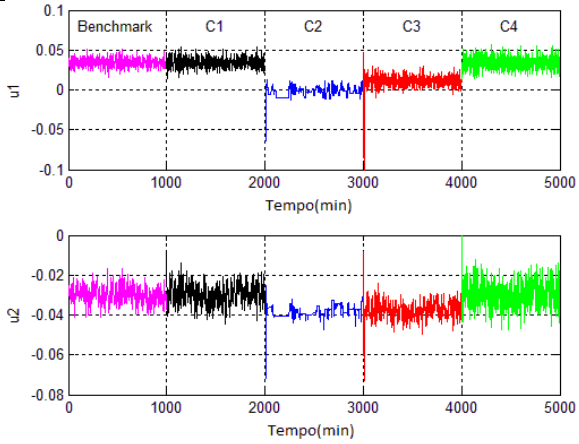

Fig. 2. Treinamento das entradas em malha fechada

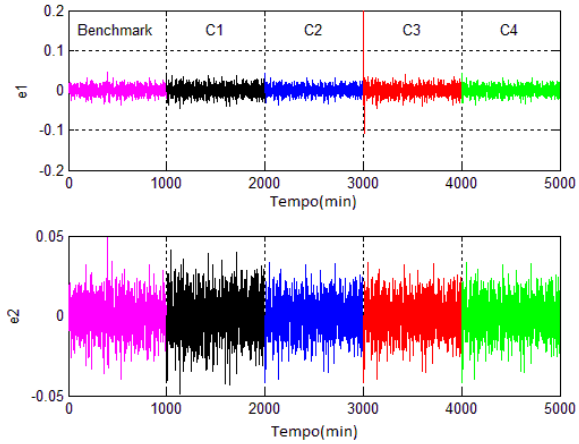

Fig. 3. Treinamento dos erros de predição em malha fechada

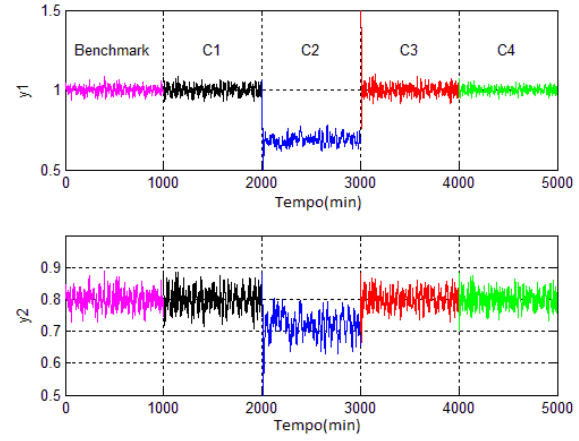

Fig. 4. Treinamento das saídas em malha fechada

O método de avaliação de desempenho, utilizando-se o DPCA e DICA, foi aplicado para todas as falhas e graficados na Fig. 5 e Fig. 6 para o DPCA e Fig. 7 e Fig. 8 para o DICA. Todas as falhas foram inseridas no instante 500 minutos. Na análise dos resultados da avaliação de desempenho tem-se que, no caso da Falha 1 e Falha 4, o DPCA mostra-se lento e menos efetivo que o DICA. Além disso, é evidente que os gráficos do DPCA, para essas falhas, não detectam anormalidades e capturam apenas aleatoriedades dominantes.

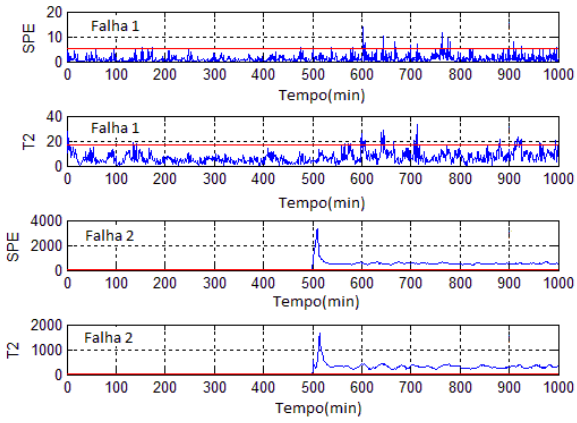

Fig. 5. Monitoramento DPCA para F1 e F2

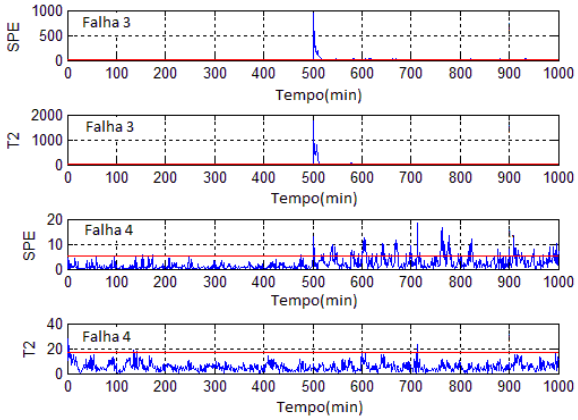

Fig. 6. Monitoramento DPCA para F3 e F4

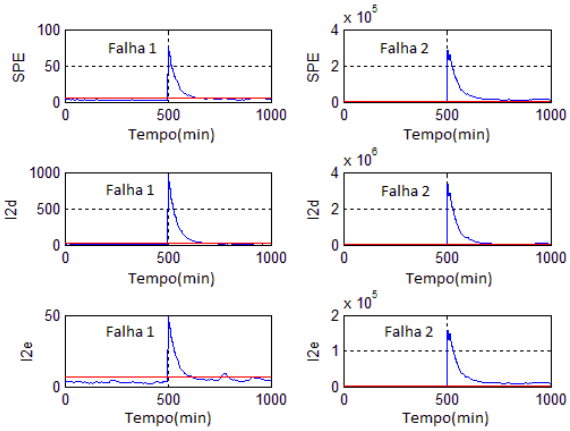

Fig. 7. Monitoramento DICA para F1 e F2

Em contrapartida, o DICA mostra-se eficiente em todos os casos. Como mostrado na Fig. 7 e Fig. 8, as estatísticas de monitoramento excedem os limites de confiança. Estes resultados já eram esperados, já que o PCA utiliza apenas as informações contidas na matriz de covariância dos dados. Em contrapartida, o ICA usa informações da distribuição dos dados, que não se encontram na matriz de covariância.

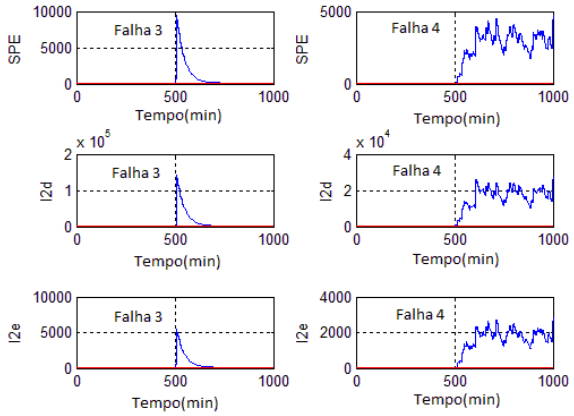

Fig. 8. Monitoramento DICA para F3 e F4

O método proposto nesse trabalho, descrito na seção 4, retrata o ângulo entre o autovetor de cada período monitorado e o autovetor de cada período treinado. O menor ângulo indicará a causa atual do mau desempenho. Os resultados são mostrados na Fig. 9 e estes demonstram que o método proposto para diagnóstico encontra com sucesso a causa raiz da degradação do desempenho para todas as falhas inseridas.

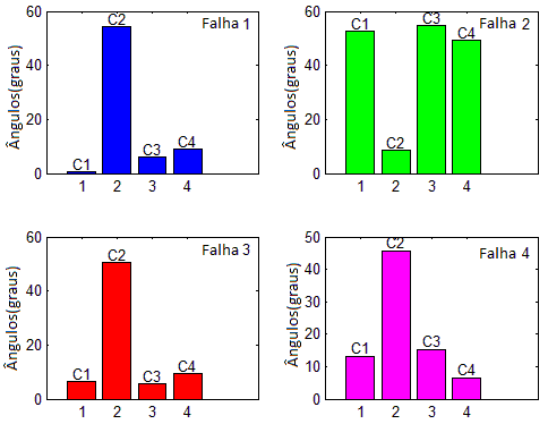

Fig. 9. Resultados do diagnóstico

6 CONCLUSÃO

Este trabalho propôs uma abordagem para avaliação de desempenho de controladores MPC, utilizando métodos estatísticos multivariados. Os métodos utilizados foram o PCA e o ICA. Estatísticas de monitoramento foram utilizadas para o monitoramento on-line e seus limites de confiança foram calculados, conforme descritos no trabalho, com o intuito de detectar as anormalidades no desempenho do controlador. A estratégia proposta para monitoramento mostrou-se capaz de detectar tais anormalidades, embora mais eficiente no uso do ICA, pois, os cálculos das estatísticas de monitoramento usadas para o PCA assumem que os dados têm uma distribuição gaussiana, o que pode levar a um pobre desempenho de monitoramento. O método proposto para diagnóstico da causa raiz das anormalidades também se mostrou eficiente em seu diagnóstico. Os resultados apresentados neste trabalho demonstram a eficácia destes métodos no monitoramento do MPC, visto a grande importância deste na indústria.

REFERÊNCIAS

AlGhazzawi, A. and Lennox, B. (2009). Model predictive control monitoring using multivariate statistics. *J. Process Control*, 19(2), 314–327.

Chiang, L. H., Russell, E. L., and Braatz, R. D. (2001). *Fault detection and diagnosis in industrial systems*. Springer, London.

Desborough, L. and Harris, T. (1993). Performance assessment measures for univariate feedforward/feedback control. *Canadian J. of Chemical Eng.*, 71, 605–616.

Harris, T.J. (1989). Assessment of closed-loop performance. *Canadian J. Chemical Eng.*, 67(10), 856–861.

Harris, T.J., Boudreau, F., and Macgregor, J.F. (1996). Performance assessment of multivariable feedback controllers. *Automatica*, 32(11), 1505–1518.

Harris, T.J., Seppala, C.T., and Desborough, D. (1999). A review of performance monitoring and assessment techniques for univariate and multivariate control systems. *J. Process Control*, 9(1), 1–17.

Huang, B. (1997). *Multivariate Statistical Methods for Control Loop Performance Assessment*. Ph.D. thesis, Dept. Chemical Eng., University of Alberta, Canada.

Hyvärinen, A., Karhunen, J. and Oja, E. (2001). *Independent Component Analysis*. John Wiley & Sons, Inc, New York.

Jackson, J. (1991). *A user's Guide to Principal Components*. Wiley, New York.

Jelali, M. (2006). An overview of control performance assessment technology and industrial applications. *Control Engineering Practice*, 14(5), 441–466.

Lee, J. M., Yoo, C. and Lee, I. B. (2004). Statistical process monitoring with independent component anlaysis. *J. of Process Control*, 14(5), 467–485.

Loquasto, F. and Seborg, D.E. (2003a). Model predictive controller monitoring based on pattern classification and pca. In *Proc. 2003 American Control Conference*, volume 3, 1968–1973. Denver, Colorado.

Qiang, Z. and Shaoyuan, L. (2006). Performance Monitoring and Diagnosis of Multivariable Model Predictive Control Using Statistical Analysis. *Chinese J. Chem Eng*, 14(2), 207-215.

Stefatos, G. and Ben Hamza, A. (2010). Dynamic independent component analysis approach for fault detection and diagnosis. *Expert Systems with Applications*, 37, 8606–8617.

Tian, X., Chen, G. and Chen, S. (2011a). A data-based approach for multivariate model predictive control performance monitoring. *Neurocomputing*, 74, 588–597.

Tian, X., Chen, G., Cao, Y. and Chen, S. (2011b). Performance monitoring of MPC based on dynamic principal component analysis. *In Proc. 18th IFAC World Congress*, 13139–13144, Italy.

Zhang, Q. and Li, S.Y. (2006). Performance monitoring and diagnosis of multivariable model predictive control using statistical analysis. Chinese J. Chem. Eng., 14(2), 207–215.

Reducción de orden del modelo de un gasificador ante incertidumbre paramétrica

Luis Santamaríia-Padilla * **Luis Alvarez-Icaza** *
Jesús Alvarez **

* *Universidad Nacional Autónoma de México, Instituto de Ingeniería, Cuidad de México, C.P.04510, México (e-mail: lsantamariap@iingen.unam.mx, alvar@pumas.iingen.unam.mx)*
** *Universidad Autónoma Metropolitana-Iztapalapa, Departamento de Ingeniería de Procesos e Hidráulica, Ciudad de México, C.P.09340, México (e-mail: jac@xanum.uam.mx)*

Resumen: Se presenta la reducción de orden del modelo de un gasificador de biomasa en configuración Imbert, el cual se representa mediante un tren de N reactores continuos de tanque agitado con retromezclado. A partir de la generación de bandas de incertidumbre debidas al desconocimiento de algunos parámetros de la cinética química y de las características de la biomasa, se reduce el número de tanques de 30 a 13 utilizando una distribución no uniforme de los nodos que discretizan al reactor, dicha representación captura el comportamiento estático del gasificador.

Palabras clave: Reducción de orden, Incertidumbre paramétrica, Reactor de gasificación, Configuración Imbert.

1. INTRODUCCIÓN

Un gasificador es un reactor tubular continuo, en el cual se tiene una fuente de carbono en estado sólido o líquido que reacciona con un agente oxidante (O_2 puro o aire) así como con agentes gasificantes (CO_2, H_2O, H_2), dando como resultado un combustible gaseoso compuesto principalmente de CH_4, H_2O, H_2, CO y CO_2, llamado gas de síntesis, el cual es fácil de manejar y posee un poder calórico utilizable (Badillo, 2014).

Dependiendo de la aplicación que demande la utilización del gas de síntesis y del tipo de biomasa que se utilice, las condiciones de operación del reactor de gasificación, temperatura, composición del gas de síntesis y consumo de biomasa, se pueden ver afectadas y repercutir en la eficiencia y seguridad del sistema. Debido a esto, es necesario contar con un esquema de control que mantenga la operación en las condiciones necesarias para que la producción del gas de síntesis sea adecuada y se realice de forma segura. Para este fin, se requiere contar con un modelo que describa el comportamiento del reactor. En la literatura existe una gran cantidad de trabajos enfocados a esta tarea, Patra y Sheth (2015) presenta el estado del arte en el modelado de gasificadores de biomasa y muestran que los principales son: modelos de equilibrio, de combinación de cinética y transporte, por dinámica de fluidos computacional, redes neuronales artificiales y mediante el uso del software de optimización de procesos químicos.

Debido a la naturaleza distribuida de esta clase de sistemas, la descripción se realiza mediante ecuaciones diferenciales parciales (EDP), se emplean métodos de diferencias finitas, elemento finito o algún paquete computacional para su discretización y simulación numérica, obteniendo sistemas de ecuaciones de alto orden (1,000-10,000 ecuaciones). Aunado a ésto, los parámetros son inciertos o su determinación resulta complicada, por lo que se han realizado estudios de sensibilidad paramétrica en los modelos para analizar si es posible mejorar la eficiencia energética del proceso, optimizar algoritmos matemáticos y para entender de mejor forma el proceso de transformación termoquímica (Pérez et al., 2015). La utilización de esta clase de modelos para fines de control resulta muy compleja, por lo que la obtención de modelos de bajo orden para su uso en diseño de controladores u observadores ha sido objeto de estudio en Badillo (2014), quien demuestra que es posible representar la dinámica de un gasificador estratificado realizando una analogía con un tren de 3 Reactores Continuos de Tanque Agitado (RCTA) en serie, ésto lo consigue discretizando al reactor colocando una malla no uniforme a prueba y error. En el trabajo de Canales (2013) se presenta una metodología para distribuir de manera sistemática los nodos mediante un factor de ponderación.

Este trabajo toma el modelo de un gasificador en configuración Imbert visto como un tren de N RCTAs (Santamaría, 2016), para generar bandas de incertidumbre debidas a los parámetros que resultan más inciertos para esta clase de sistemas (Canales, 2013; Hernández-Torres, 2016), con dichas bandas se determina una región que sirve como referencia para decidir si se tiene una representación aceptable del reactor, bajo el criterio de que los perfiles espaciales obtenidos mediante algún modelo deben permanecer dentro de dicha banda. Con base en esta idea se obtiene la representación del gasificador Imbert reali-

zando una discretización no uniforme en 13 etapas, dando un sistema de orden muy bajo comparado con trabajos similares donde discretizan uniformemente un gasificador estratificado con entrada de aire secundaria en 250 etapas (Di Blasi y Branca, 2013).

La estructura del trabajo es la siguiente, en la sección 2 se presenta el modelado del reactor de gasificación, describiendo las configuraciones que puede haber así como los procesos que se llevan a cabo dentro del reactor; de igual forma se presenta el modelo general que describe el comportamiento del sistema mediante un tren de N-RCTA con retromezclado. En la sección 3 se presenta el sistema de estudio, describiendo a detalle las zonas en las que ocurren los procesos, dimensiones, condiciones de alimentación, etc. En la sección 4 se muestran las consideraciones hechas para realizar la variación algunos parámetros de la cinética química, así como de la composición del carbonizado. En la sección 5 se presentan los resultados obtenidos cuando se eligen 13 RCTAs para representar al gasificador, en particular se muestran las gráficas correspondientes a los perfiles en estado estacionario de la composición del gas de síntesis, densidad de biomasa y carbonizado, así como de temperatura. Finalmente en la sección 6 se tienen las conclusiones obtenidas a partir del desarrollo presentado.

2. MODELADO DEL GASIFICADOR EN CONFIGURACIÓN IMBERT

2.1 Clasificación de gasificadores y procesos involucrados

Existen dos tipos principales de reactores de gasificación que se diferencían dependiendo de la dirección de los flujos dentro de ellos (Reed y Das, 1988):

- Contracorriente. La biomasa se alimenta por la parte superior, mientras que el aire entra desde el fondo. El gas de síntesis obtenido en el proceso sale por la parte superior, acompañado de una gran cantidad de alquitranes y humedad.
- Concurrentes. La biomasa y el aire fluyen hacia el fondo del reactor. El gas de síntesis que se obtiene posee un bajo contenido de alquitranes, debido a que se consumen al avanzar por el reactor. Dentro de esta clase de reactores existen dos configuraciones principales: la estratificada e Imbert (Bhavanam y Sastry, 2011); la diferencia entre estas radica en que para la primera la alimentación de biomasa y aire se da por la parte superior del reactor, además de que posee una sección transversal constante; mientras que para la segunda configuración el aire se introduce en una zona donde existe un cambio en la geometría interna del reactor, en la Fig. 1 se muestran esquemáticamente ambas configuraciones.

Dentro del reactor de gasificación, independientemente de la clasificación o configuración, el proceso se lleva a cabo en 4 etapas principales: secado, pirólisis, combustión y reducción (Reed y Das, 1988), en la Tabla 1 se presentan los rangos de temperatura a las cuales se llevan a cabo normalmente (Basu, 2006).

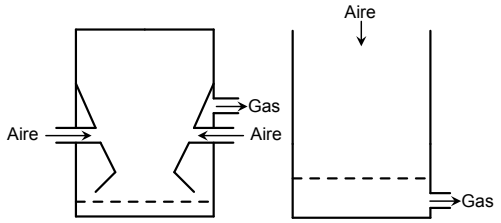

(a) Imbert (b) Estratificado

Figura 1. Gasificadores de flujos concurrentes

Tabla 1. Temperatura de las etapas del proceso de gasificación

1. Secado	(>150°C)
2. Pirólisis (devolatilización)	(150-700°C)
3. Combustión (oxidación)	(700-1500°C)
4. Reducción (gasificación)	(800-1100°C)

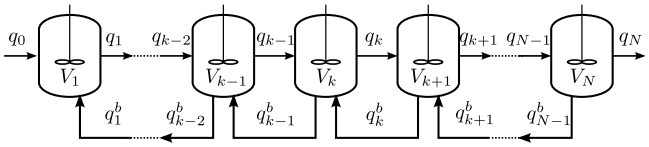

Figura 2. Tren de N RCTAs

2.2 Modelo del gasificador

Para la obtención del modelo de un gasificador en configuración Imbert se toma como referencia el trabajo de Badillo (2014), el cual parte de la ecuación de transporte generalizada (Bird et al., 1960), desarrollándola para obtener un modelo unidimensional axial de dos fases que de manera general se puede escribir como (1), obteniendo un sistema de EDPs que representan la naturaleza distribuida del reactor de gasificación.

$$\partial_t \varphi_\pi = -(\partial_Z \cdot u_\pi \varphi_\pi) + (\partial_Z \cdot D_\pi \partial_Z \varphi_\pi) + S_\pi(\varphi_\pi, \mathbf{r}), \pi = s, g \quad (1)$$

Donde: φ es la propiedad que se conserva por unidad de volumen, u_π es la velocidad del flujo convectivo en el estado π, D es el coeficiente de transporte por dispersión, S es el término fuente generalizado y $\mathbf{r}$ es el vector tridimensional del sistema de coordenadas espaciales, para el caso de reactores tubulares se tiene que $\mathbf{r} = (Z, r, \theta)$.

Para reducir el orden del modelo, Badillo (2014) identificó que la dinámica de los gases es mucho más rápida que la de los sólidos (estado cuasi-estacionario para los gases) y que es posible asumir equilibrio térmico entre fases (sólido y gas). Con base en las consideraciones anteriores, se obtiene un modelo reducido del reactor, el cual discretiza y realiza una analogía con un tren de N-RCTA con retromezclado como se muestra en la Fig. 2.

Para este trabajo se retomaron las ideas de Badillo (2014), aplicándolas para un gasificador en configuración Imbert. En la representación del sistema como un tren de N-RCTAs, se incluyó el término correspondiente a la entrada de aire en algún tanque interior y se omitió en el primero, dejando en éste sólo la entrada de biomasa. De forma general, el gasificador se representa como un sistema algebraico diferencial definido por

$$
\begin{aligned}
\dot{\mathbf{x}}_1 &= f_1(\mathbf{x}_1, \mathbf{x}_2, \mathbf{z}_1, \mathbf{z}_2, \mathbf{u}_s, \delta) \\
\mathbf{z}_1 &= g_1(\mathbf{x}_1, \mathbf{x}_2, \mathbf{u}_s, \delta) \\
&\vdots \\
\dot{\mathbf{x}}_k &= f_k(\mathbf{x}_1, \ldots, \mathbf{x}_k, \mathbf{x}_{k+1}, \mathbf{z}_{k-1}, \mathbf{z}_k, \mathbf{z}_{k+1}, \delta) \\
\mathbf{z}_k &= g_k(\mathbf{x}_1, \ldots, \mathbf{x}_k, \mathbf{x}_{k+1}, \delta) \\
&\vdots \\
\dot{\mathbf{x}}_\xi &= f_\xi(\mathbf{x}_1, \ldots, \mathbf{x}_\xi, \mathbf{x}_{\xi+1}, \mathbf{z}_{\xi-1}, \mathbf{z}_\xi, \mathbf{z}_{\xi+1}, \mathbf{u}_g, \delta) \\
\mathbf{z}_\xi &= g_\xi(\mathbf{x}_1, \ldots, \mathbf{x}_\xi, \mathbf{x}_{\xi+1}, \mathbf{u}_g, \delta) \\
&\vdots \\
\dot{\mathbf{x}}_N &= f_N(\mathbf{x}_1, \ldots, \mathbf{x}_N, \mathbf{z}_{N-1}, \mathbf{z}_N, \delta) \\
\mathbf{z}_N &= g_N(\mathbf{x}_1, \ldots, \mathbf{x}_N, \delta)
\end{aligned} \tag{2}
$$

$$
\begin{aligned}
\mathbf{x}_i &= [\rho_{B,i}\ \rho_{C,i}\ T_i]^T, \quad i = 1, \ldots, k, \ldots, \xi, \ldots, N \\
\mathbf{z}_i &= [\mathsf{C}_{O_2,i}\ \mathsf{C}_{H_2,i}\ \mathsf{C}_{CO,i}\ \mathsf{C}_{CO_2,i}\ \mathsf{C}_{CH_4,i}\ \mathsf{C}_{T,i}]^T \\
\mathbf{u}_s &= [T_0\ \dot{m}_B]^T \\
\mathbf{u}_g &= [T_{aire}\ \dot{m}_{aire}]^T
\end{aligned}
$$

donde: $\mathbf{x}_i$ son los estados lentos (densidad de sólidos ρ_B, ρ_C y temperatura del lecho T); $\mathbf{z}_i$ son los estados rápidos (concentración de los gases C, velocidad de sólidos y del gas v_s, v_g); ξ es el tanque en el cual entra el aire; $\mathbf{u}_s$ es la alimentación de biomasa (temperatura de la biomasa a la entrada T_0 y gasto másico $\dot{m}_B$); $\mathbf{u}_g$ es la alimentación de aire (temperatura del aire entrante T_{aire} y gasto másico $\dot{m}_{aire}$); f_i, g_i son funciones no lineales para estados lentos y rápidos, respectivamente; N es el número de tanques; δ la incertidumbre paramétrica, debida al desconocimiento de algunos de los parámetros de la cinética química, así como de algunas propiedades de la biomasa.

El orden M del sistema algebraico diferencial (2) se obtiene calculando la dimensión de las variables de estado, obteniendo

$$
\begin{aligned}
M &= M_d + M_a = N \times (n_s + n_g + 3) \\
M_d &= dim(\mathbf{x}) = N \times (n_s + 1) \\
M_a &= dim(\mathbf{z}) = N \times (n_g + 2)
\end{aligned} \tag{3}
$$

donde M_d es el número de ecuaciones diferenciales, M_a el número de ecuaciones algebraicas, n_s el número de especies sólidas, n_g el número de especies gaseosas. Para este estudio se considera que $n_s = 2$, $n_g = 6$, por lo que el orden del sistema es $M = 11 \times N$.

Hay diferentes criterios para seleccionar el número de tanques N con que se discretizará el sistema, de acuerdo al estudio de Kramers y Alberda (1953) en sistemas de baja dispersión es posible elegir N como

$$
N = \frac{Pe}{2} \tag{4}
$$

donde: Pe es el número de Peclet.

Hlavacek et al. (1999) propone que un reactor de lecho empacado se puede ver como un tren de N RCTAs con

$$
N = \frac{L}{d_p} \tag{5}
$$

donde: L es la longitud del reactor y d_p el diámetro de partícula.

Estos criterios no determinan la ubicación de los nodos que definen a los tanques, que usualmente se distribuyen de forma uniforme con volúmenes de control iguales. En el trabajo de Badillo (2014) se demuestra que con una malla uniforme es posible reproducir el comportamiento de un gasificador estratificado y de igual forma explora la posibilidad de distribuir los nodos de una manera no uniforme observando que se obtienen buenos resultados. En el trabajo de Canales (2013) se presenta una metodología para formar una malla no uniforme mediante un factor de ponderación, el cual determina la mejor ubicación de una cantidad dada de nodos para reproducir cuantitativa y cualitativamente el comportamiento estático del reactor.

3. DESCRIPCIÓN DEL SISTEMA DE ESTUDIO

El sistema de gasificación con que se cuenta es el GEK TOTTI de la empresa ALL Power Labs, el cual es de flujos concurrentes en configuración Imbert. En la Fig. 3 se muestran las zonas donde se llevan a cabo los procesos de secado, pirólisis, combustión y reducción, éstos se desarrollan de la siguiente manera (All-Power-Labs, 2016):

- La biomasa se almacena en una tolva, por acción de la gravedad llega al cubo de secado, el cual es un intercambiador de calor que toma energía del gas de síntesis, precalentando la biomasa a temperaturas de $100 - 200°C$, gracias a esto se reduce su contenido de humedad, dejándolo por debajo del 30 %.
- Posteriormente la biomasa seca llega a la zona de pirólisis, donde se transforma en carbonizado y en una gran cantidad de alquitranes gaseosos inflamables; ésto se lleva a cabo tomando energía proveniente de zonas más bajas del reactor y del gas de síntesis, alcanzando temperaturas entre $400 - 600°C$.
- Después de la zona de pirólisis los alquitranes gaseosos descienden a la zona de combustión, donde una porción de estos y del carbonizado se quema, liberando energía que se utiliza en el resto de los procesos, mientras los alquitranes restantes se descomponen en CO y H_2.
- La zona de combustión se encuentra en la región comprendida entre la entrada del aire y el final de un estrangulamiento que existe dentro del reactor, se tienen 5 boquillas que suministran el aire precalentado a alrededor de $600°C$, gracias a esto se incrementa la eficiencia de la combustión permitiendo alcanzar temperaturas entre $1000 - 1300°C$, facilitando que los alquitranes que fluyen hacia abajo se quemen y se obtenga un gas de síntesis más limpio.
- El vapor de agua y dióxido de cabono producidos en la zona de combustión, reaccionan con el carbonizado caliente en la zona de reducción obteniéndose H_2, CO y CH_4. Esta zona comienza debajo del estrangulamiento y se extiende hasta la rejilla donde se deposita el carbonizado que ya no reaccionó, alcanzando temperaturas mayores a $600°C$. El gas de síntesis resultante alcanza temperaturas entre $700 - 800°C$.

El gasificador piloto del Institudo de Ingeniería, es un modelo que ofrece una potencia máxima de 10kW, en la Tabla 2 se listan las características principales que proporciona el fabricante (All-Power-Labs, 2016), así como recomendaciones de la biomasa a utilizar y en la Fig. 4 se presentan sus dimensiones así como la ubicación de los

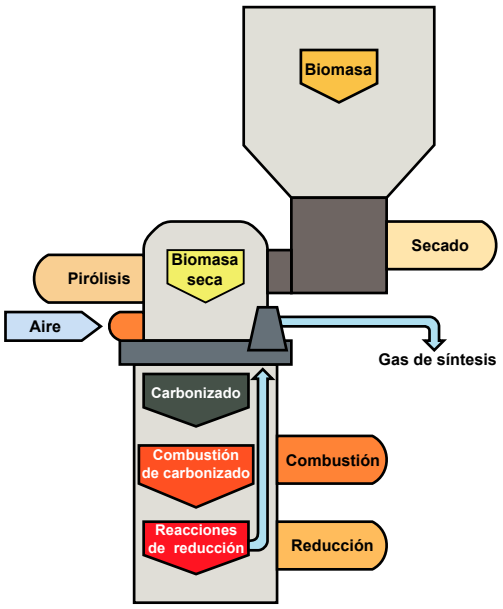

Figura 3. Esquema del gasificador GEK

Tabla 2. Características del gasificador de $10kW$ y requerimientos de la biomasa

Rango de potencia de salida	$2 - 10kW$
Consumo de biomasa	$160 - 320\ kg/dia$
Rango de flujo de gas	$5 - 27\ m^3/hr$
Tamaño de partícula	$1.27 - 3.81\ cm$
Porcentaje de humedad máxima de la biomasa	30 %
Proporción de carbono fijo y volátiles	> 0.25
Contenido de cenizas	$> 5\,\%$

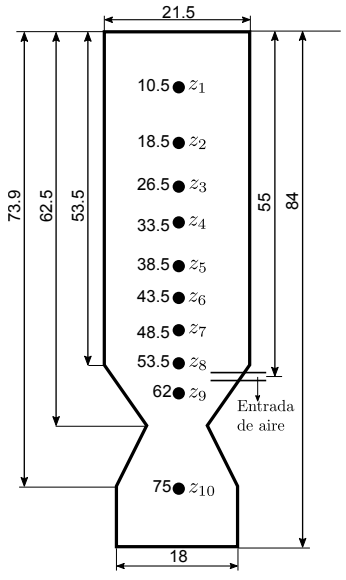

Figura 4. Dimensiones del gasificador en cm

termopares z con que está instrumentado.

Con las recomendaciones dadas por el fabricante se puso en marcha el reactor utilizando astillas de madera y se llevó a una condición de operación estable de encendido, en la Fig. 5 se muestra el perfil de temperatura con una banda de incertidumbre debida a la variación de las

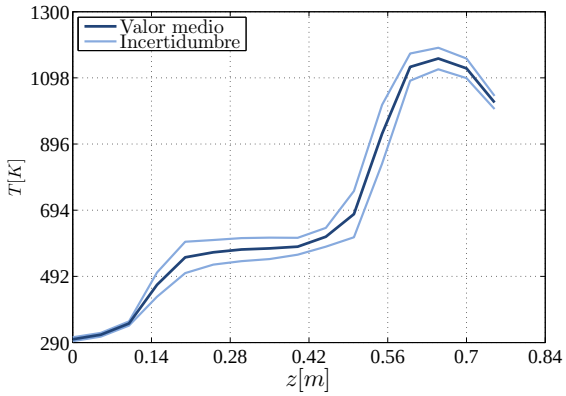

Figura 5. Perfil de temperatura experimental

Tabla 3. Composición del gas de síntesis, μ - valor medio, σ - desviación estándar

	μ	σ
$\%H_2$	18.94	1.39
$\%CO$	20.72	1.15
$\%CO_2$	8.77	1.06
$\%CH_4$	2.18	0.29

mediciones en los termopares. De igual forma, en la Tabla 3 se presenta la composicón del gas de síntesis registrada en el analizador de gases, donde el valor de la media se considera una composición nominal, mientras que con la desviación estándar se define una banda de incertidumbre en las mediciones.

4. CONSIDERACIONES PARA LA SIMULACIÓN

El punto de partida es el modelo obtenido en Santamaría (2016), en el cual se muestra que se reproduce el comportamiento estático del gasificador con un tren de 30 RCTAs y donde se desprecian los primeros 10 cm del reactor debido a que en dicha zona no se lleva a cabo ninguna reacción. De igual forma se determina que el mejor ajuste a los datos experimentales se obtiene con un $Pe = 6$; de este trabajo también se toman las condiciones de alimentación, las características de la biomasa y los parámetros de la cinética química.

Como se mencionó anteriormente, un problema que se presenta en esta clase de sistemas, es que algunos parámetros son inciertos o difíciles de determinar, además que pueden cambiar durante el proceso, principalmente los relacionados con las propiedades de la biomasa. Por lo tanto estos factores afectarán la predicción hecha por el modelo al compararla contra datos experimentales. Debido a esto es razonable asumir que una buena representación del sistema será aquella que permanezca dentro de una banda de incertidumbre inducida por la variación de algunos parámetros de un modelo nominal. A partir de ésta premisa se retoman los trabajos de Canales (2013) y Hernández-Torres (2016), donde consideran que los parámetros que en general son inciertos son la energía de activación de la pirólisis E_{p1}, el diámetro inicial de la partícula d_{p0} y la entalpía de reacción del carbonizado ΔH_{c5}. Para este trabajo se considera adicionalmente la composición del carbonizado, debido a que Santamaría (2016) identificó que este parámetro es clave para la determinación de la composición del gas de síntesis. En la Tabla 4 se presen-

Tabla 4. Porcentaje de variación de los parámetros

Parámetro	Nominal	Perturbación
Ep_1 $[kJ/mol]$	68.25	$\pm 5\,\%$
ΔH_{c5} $[kJ/kg]$	-2.5×10^4	$\pm 5\,\%$
d_{p0} $[cm]$	2.54	$\pm 20\,\%$
Composición del carbonizado	$95\,\%$ C $2.5\,\%$ H $2.5\,\%$ O	$95\,\%$ C $2-4\,\%$ H $1-3\,\%$ O

tan los valores nominales de los parámetros mencionados anteriormente, así como el porcentaje de perturbación que se considera para cada uno.

5. RESULTADOS

Se realizaron simulaciones considerando una discretización uniforme del reactor con 30 RCTAs, variando de manera aleatoria los parámetros de la Tabla 4 dentro del rango permitido; a partir de estos resultados se generó una banda de incertidumbre debida a la perturbación de dichos parámetros. El paso siguiente es obtener una discretización del gasificador de menor orden cuya solución se encuentre dentro de dicha banda; debido a que el trabajo de Canales (2013) no abarca la configuración Imbert, como una primera aproximación se realizó la distribución no uniforme de los nodos a prueba y error hasta obtener perfiles que cumplieran con la condición de estar dentro de la banda de incertidumbre. El número de tanques considerado para este trabajo es de $N = 13$, en las Figs. 6 a 8 se muestran los perfiles obtenidos cuando el gasificador se representa con 13 RCTAs, la banda de incertidumbre para cada caso y el modelo cuando $N = 30$.

De las Figs. 6 a 8 es posible observar que las zonas donde la banda de incertidumbre se incrementa son en la parte superior e inferior del reactor, mientras que en la zona central, que es por donde se tiene la entrada de aire, dicha banda es pequeña. Al realizar la distribución de los tanques, se observó que la zona que se puede tener menos cubierta es la superior, ya que utilizando sólo 2 tanques, ubicados a 0.2 y 0.33 m medidos desde la cima, se pudo capturar el comportamiento de dicha zona. Para el caso de la parte inferior del reactor hubo que utilizar 4 tanques, localizados a 0.68, 0.73, 0.78, y 0.82 m, con ellos se obtiene una buena aproximación y además se captura el comportamiento del reactor al momento de efectuar las reacciones de gasificación. Estos tanques son clave para que la composición del gas de síntesis obtenida con el modelo de orden reducido se aproxime a los datos experimentales. En la Tabla 5 se presenta la comparación de la composición del gas de síntesis cuando se considera $N = 13$, $N = 30$ y el rango de valores que puede tomar debido a la incertidumbre en la medición del analizador de gases. Finalmente la zona central fue donde se distribuyeron el resto de los tanques, se ubicaron en 0.43, 0.47, 0.5, 0.52, 0.55, 0.58 y 0.6 m, pues esta zona es donde el cambio de temperatura es más abrupto, teniendo como consecuencia que las velocidades de reacción cambien drásticamente y por lo tanto se debe prestar mayor atención para capturar el comportamiento del gasificador.

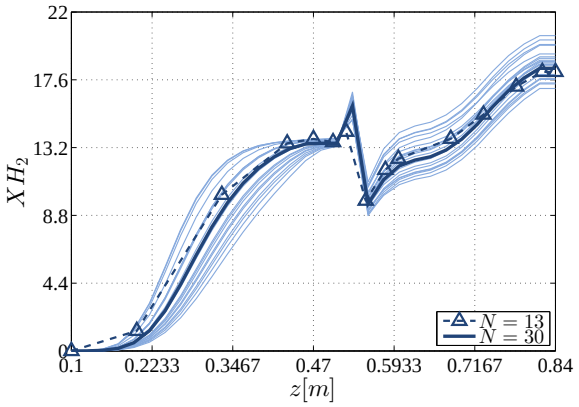

(a) Concentración H_2

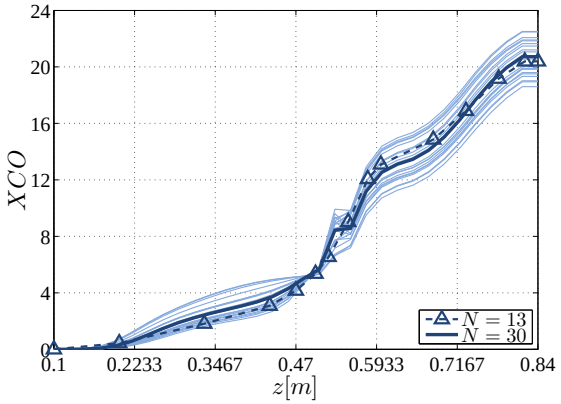

(b) Concentración CO

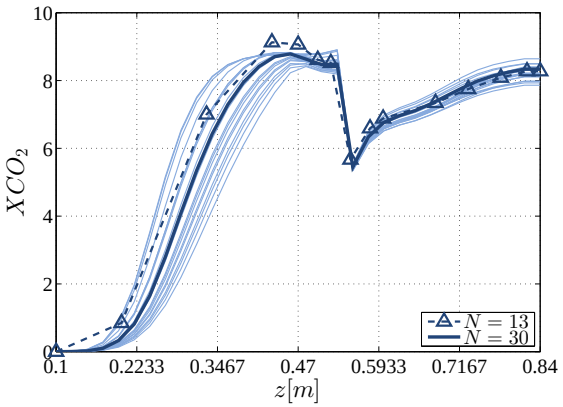

(c) Concentración CO_2

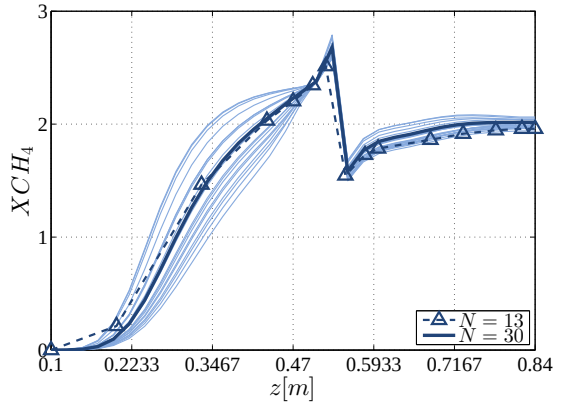

(d) Concentración CH_4

Figura 6. Perfiles espaciales de concentración de los gases

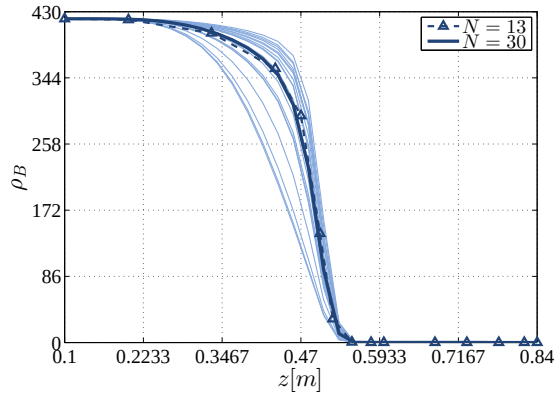

(a) Densidad de la biomasa

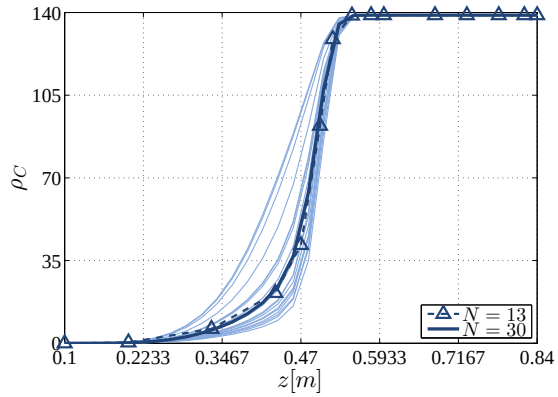

(b) Densidad del carbonizado

Figura 7. Perfiles espaciales de densidades de sólidos

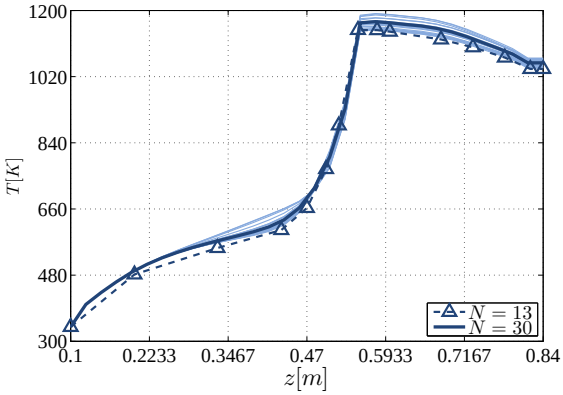

Figura 8. Perfil espacial de la temperatura

Tabla 5. Concentración de los gases en la salida

	$N = 13$	$N = 30$	Exp.
H_2	18.12	18.35	17.55-20.33
CO	20.39	20.7	19.57-21.87
CO_2	8.28	8.34	7.71-9.83
CH_4	1.959	2.02	1.89-2.47

6. CONCLUSIÓN

Se demostró que es posible reducir el orden del modelo del gasificador representado mediante un tren de N-RCTA, considerando una banda de incertidumbre definida por el desconocimiento de algunos de los parámetros de la cinética química, así como de algunas propiedades de la biomasa. Utilizando como primera aproximación un número de 13 tanques, se muestra que es posible representar el comportamiento estático del reactor distribuyendo de manera no uniforme la ubicación de los nodos, obteniendo un perfil de temperatura y una composición del gas de síntesis muy parecida al caso cuando se consideran 30 tanques, permaneciendo dentro de la banda de incertidumbre mencionada anteriormente. Este es un primer paso para utilizar un algoritmo como el propuesto por Canales (2013) y puede servir de guía para realizar los ajustes necesarios a dicho algoritmo para poder usarlo con esta clase de reactores; de esta forma será posible contar con una metodología para obtener modelos de bajo orden que sean manejables y permitan aplicar técnicas de control y monitoreo avanzadas para reactores de gasificación en configuración Imbert.

REFERENCIAS

All-Power-Labs (2016). Power pallet support. URL `http://www.allpowerlabs.com/support/support-power-pallet`.

Badillo, U. (2014). *Modelado, Observación y Control de Reactores de Gasificación*. Tesis de doctorado, Programa de Maestría y Doctorado en Ingeniería UNAM.

Basu, P. (2006). *Combustion and gasification in fluidized beds*. CRC press.

Bhavanam, A. y Sastry, R. (2011). Biomass gasification processes in downdraft fixed bed reactors: a review. *International Journal of Chemical Engineering and Applications*, 2(6), 425–433.

Bird, R.B., Stewart, W.E., y Lightfoot, E.N. (1960). Transport phenomena. *Madison, USA*.

Canales, L. (2013). *Reducción de orden en modelos para reactores de gasificación*. Tesis de maestría, Programa de Maestría y Doctorado en Ingeniería UNAM.

Di Blasi, C. y Branca, C. (2013). Modeling a stratified downdraft wood gasifier with primary and secondary air entry. *Fuel*, 104, 847–860.

Hernández-Torres, O. (2016). *Análisis dinámico y caracterización de reactores de gasificación*. Tesis de maestría, Programa de Maestría y Doctorado en Ingeniería UNAM.

Hlavacek, V., Puszynski, J.A., Viljoen, H.J., y Gatica, J.E. (1999). Model reactors and their design equations. *Ullmann's encyclopedia of industrial chemistry*.

Kramers, H. y Alberda, G. (1953). Frequency response analysis of continuous flow systems. *Chemical Engineering Science*, 2(4), 173–181.

Patra, T.K. y Sheth, P.N. (2015). Biomass gasification models for downdraft gasifier: A state-of-the-art review. *Renewable and Sustainable Energy Reviews*, 50, 583–593.

Pérez, J.F., Benjumea, P.N., y Melgar, A. (2015). Sensitivity analysis of a biomass gasification model in fixed bed downdraft reactors: Effect of model and process parameters on reaction front. *Biomass and Bioenergy*, 83, 403–421.

Reed, T. y Das, A. (1988). *Handbook of biomass downdraft gasifier engine systems*. Biomass Energy Foundation.

Santamaría, L.A. (2016). *Modelado y caracterización experimental de un gasificador en configuración Imbert*. Tesis de maestría no publicada, Programa de Maestría y Doctorado en Ingeniería UNAM.

Stencil computation for the approach to the numerical solution heat transfer problems on SoC FPGA

Luis F. Castaño * **Gustavo A. Osorio** **

* *Instituto Tecnológico Metropolitano, Medellín, Colombia (e-mail: luiscastano@itm.edu.co).*
Universidad Nacional de Colombia, Manizales, Colombia (e-mail: lfcastanol@unal.edu.co)
** *Universidad Nacional de Colombia, Manizales, Colombia (e-mail: gaosoriol@unal.edu.co).*

Abstract: A common kernel used in scientific computing is the stencil computation. FPGA based heterogeneous systems has been used to overcome stencil algorithm performance limitations due to the memory bandwidth on CPU and GPU based systems. Performance improvement is achieved through the combination of several data flow optimization techniques, taking advantage of the FPGA inherent parallelism. However 2D array architectures used in most cases, involves the need of considerable amount of FPGAs to simulate problems with sizes that can be treated by a CPU or GPU based system at a lower cost. In this document is presented a FPGA based system that use a one-dimensional array of processing elements for a stencil computation. The data-path is designed to reuse the processing elements and reduce the number of memory transfers using registers arrays to store data temporarily. The proposed architectures are implemented in a *ZedBoard Zynq Evaluation and Development Kit* using *Vivado® Design Suite* and *Xilinx SDK*. System performance is evaluated for the approach to numerical solution of heat transfer problems modelled with the heat equation for the one-dimensional case using stencil algorithm. An architecture for the Laplace equation for the two-dimensional case derived from the heat equation approach is proposed.

Keywords: FPGA, stencil computation, heat equation, Laplace equation

1. INTRODUCTION

A common kernel used in scientific computing is the stencil computation, particularly for linear algebra algorithms, partial differential equations (PDE) and image processing. It is quite efficient for the approach to the numerical solution of PDE using the explicit finite difference scheme (10). However, performance of algorithms based on stencil is limited by the remarkable difference between the maximum throughput and maximum bandwidth memory on multi-core CPU and GPU based systems (3). For this reason the study of optimization methods for stencil algorithms implementation has been of interest.

Cache blocking techniques have been developed to overcome the bandwidth limitations by exploiting the temporal and spatial locality. Studies on optimization of stencil computation over CPU or GPU can be found in (5; 6; 9; 11).

In (3) Sano *et al.* assert that with optimization methods for CPU or GPU based systems performance limitations could remain even though optimization methods due to memory bandwidth. FPGA-based accelerators are used as an alternative given that this devices has shown better performance with lower power consumption (1; 2). The performance improvement of the stencil computing scheme using FPGAs is study in (1; 3; 4; 7; 8).

FPGA based systems take advantage of the inherent parallelism for performance improvement through the combination of several data flow optimization techniques. For instance, grid array architectures as proposed in (3; 7) use streaming and pipelining to accelerate stencil computation. However, the use of such architectures involves the need of considerable amount of FPGAs to simulate problems for mesh sizes that can be treated by a CPU or GPU with suitable performance at a lower cost.

The use of FPGA based system has always represented multiple challenge from the number representations to the design flow complexity. The recent development of design tools has allowed overcoming many of these challenges. In (1) Schmitt *et al.* demonstrate the feasibility to deal with a grid of 4096×4096 on a single FPGA using a High-Level Synthesis (HLS) tool for system design.

With the aim to explore the optimization of stencil computation on an single FPGA in this work we present the algorithm implementation over a SoC FPGA, with a methodology that allows high level and traditional Register Transfer Level (RTL) methods for system description. A custom IP created using VHDL for the programmable logic (PL) section interacts with an ARM core that acts as

⋆ This work was supported by the AE&CC research group of the Instituto Tecnológico Metropolitano through the project P14208.

the host processor. A baseline architecture use a specific kernel as the processing element (PE) and a control unit for a sequential implementation of the stencil algorithm. For system parallelization is developed a data-path with a one-dimensional array of processing elements with feedback through a registers bank, with the aim to reduce the resources utilization and memory transfer operations.

System performance is evaluated for the approach to numerical solution of the one-dimensional heat equation with a maximum of 32 PE for a single FPGA. Performance analysis shows the improvement achieved in terms of elapsed time for the execution of stencil algorithm with two proposed parallel architectures in comparison with the execution time of the sequential algorithm written in C running on Linux over a Intel Xeon E5-2667 at 2.90GHz with 32 GB of RAM. The speed-up factor led to determine that implemented architectures offer different performance optimization due to the memory structure. Problem and system description are detailed in sections 2 and 3 respectively. Performance analysis and numerical results are presented in section 4. Finally conclusions and future work are drawn in section 5.

2. PROBLEM DESCRIPTION

2.1 Heat equation

Consider the PDE shown in (1).

$$\frac{\partial u}{\partial t} = \alpha \frac{\partial^2 u}{\partial x^2}, \qquad 0 < x < L \tag{1}$$

This expression represents a 1D parabolic PDE which is used to model the heat distribution over time in a bar with length L. Given an initial value and boundary conditions problem as shown in (2), equation solution shows the temperature variation in the space-time domain.

$$\begin{cases} u(x,0) = f(x) \\ u(0,t) = 0 \\ u(L,t) = 0 \end{cases} \tag{2}$$

An approach to the numerical solution of this equation is obtained using the explicit finite difference method. Defining J and N as the number of points for discretization in the space and time domain respectively, the approximate solution is obtained using (3).

$$u_j^{n+1} = u_j^n + \alpha(u_{j+1}^n - 2u_j^n + u_{j-1}^n) \tag{3}$$

From this expression a stencil kernel circuit is obtained as shown in Fig. 1.

This kernel is used to calculate each one of the mesh points as shown in Algorithm 1.

2.2 Laplace equation

Consider the elliptic PDE shown in (4) for $0 \leq x \leq l$ and $0 \leq y \leq h$.

$$\frac{\partial^2 u}{\partial x^2} + \frac{\partial^2 u}{\partial y^2} = 0 \ in \ (0,l) \times (0,h) \tag{4}$$

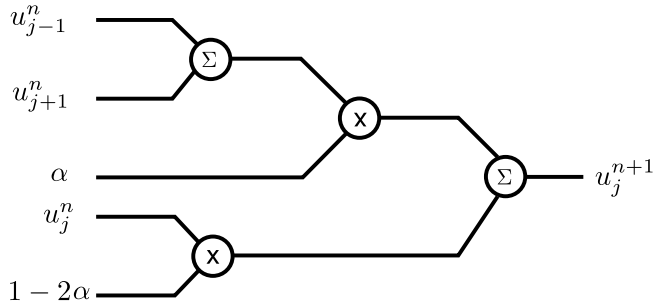

Fig. 1. Block diagram of the circuit for implementing the stencil operation for the heat equation with the explicit scheme.

Algorithm 1 Pseudocode for the stencil computation to obtain the approach to the numerical solution of heat equation with the explicit scheme

```
for n from 0 to N-1 do
    for j from 1 to J-2 do
        u_j^{n+1} ← (1 − 2α)u_j^n + α(u_{j+1}^n + u_{j−1}^n)
    end for
end for
```

Given the boundary conditions as shown in (5), equation solution shows the steady state temperature distribution in a two-dimensional rectangular plate.

$$\begin{cases} u(x,0) = u(x,h) = f(x) \\ u(0,y) = u(l,y) = g(x) \end{cases} \tag{5}$$

An approach to the numerical solution of this equation could be obtained using the explicit finite difference method as shown in (6).

$$u_{i,j}^{k+1} = \frac{u_{i-1,j}^k + u_{i+1,j}^k + \beta^2(u_{i,j-1}^k + u_{i,j+1}^k)}{2(1+\beta^2)} \tag{6}$$

where $\beta = \frac{\Delta x}{\Delta y}$

If there is a homogeneous distribution along x and y then the expression is as shown in (7).

$$u_{i,j}^{k+1} = \frac{u_{i-1,j}^k + u_{i+1,j}^k + u_{i,j-1}^k + u_{i,j+1}^k}{4} \tag{7}$$

The stencil kernel circuit is obtained from (7) as shown in Fig. 2.

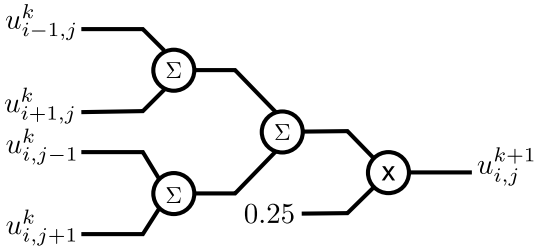

Fig. 2. Block diagram of the circuit for implementing the stencil operation for the Laplace equation with the explicit scheme.

This kernel is used to calculate each one of the mesh points as shown in Algorithm 2.

Algorithm 2 Pseudocode for the stencil computation to obtain the approach to the numerical solution of Laplace equation with the explicit scheme

```
for n from 0 to N − 1 do
    for j from 1 to h − 1 do
        for i from 1 to l − 1 do
            u^{n+1}_{i,j} ← 0.25(u^n_{i+1,j} + u^n_{i−1,j} + u^n_{i,j+1} + u^n_{i,j−1})
        end for
    end for
end for
```

3. SYSTEM DESCRIPTION

The system is implemented in a *ZedBoard Zynq Evaluation and Development Kit* using *Vivado® Design Suite*. The design takes advantage of the XC7Z020CLG484-1 *Xilinx* SoC FPGA architecture. The *ZYNQ-7* processing system (PS) for the *ARM® Cortex®-A9 MPCore™* interacts with a custom IP created for the programmable logic (PL) section. The ARM core acts as the host processor where the main application runs. The custom IP is used to calculate the approach to the numerical solution of the PDE using the stencil scheme. The system block diagram is shown in Figure 3.

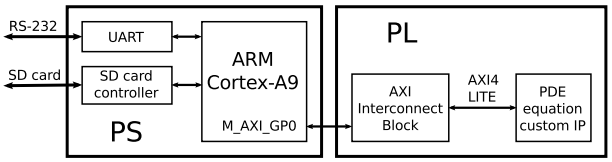

Fig. 3. Block diagram of the system implemented in *Vivado®*. Communication between PS and PL is made through AXI4-Lite interface with a fixed 32 data bits.

The source code for the PS is written in C over *Xilinx Software Development Kit (SDK)*. The application works as a host program to serve as user interface through serial terminal console. From this application, data such as mesh size, initial values, boundary conditions and control commands are send to the custom IP. Likewise, the status signals, performance counters and numerical results are reading from the PL. The last are written to a SD memory card.

The custom IP is fully described in VHDL. It is connected to the *ZYNQ-7* PS in a block design over *Vivado® IP integrator* tool. Communication between PS and PL sections is made through *AXI4-Lite* interface with fixed 32 data bits.

For number representation is used a customized 32-bit floating-point format with rounding to the nearest. The floating-point adders and multipliers used in the stencil kernel are described as combinational circuits, therefore there is no output latency in terms of the system clock cycles.

3.1 Architecture for the approach to the numerical solution of the one dimensional heat equation

A baseline architecture is designed for a sequential implementation of the stencil algorithm. The block diagram is shown in Figure 4.

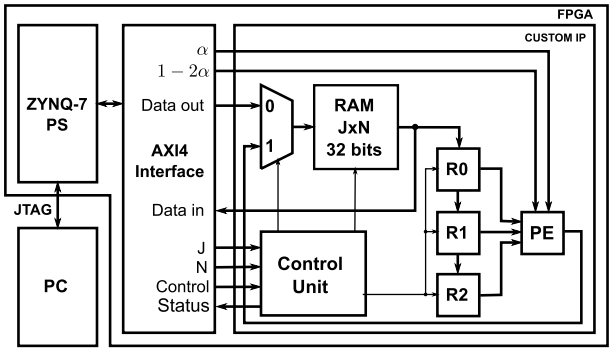

Fig. 4. Block diagram of the sequential baseline architecture. The stencil kernel is used as the processing element (PE) of the datapath.

Through serial console the mesh size ($J \times N$) is defined. The initial values and boundary conditions are setting and written to the RAM from host application. A control signal is sent to the control unit of the custom IP to start processing the memory data. The control unit is a finite state machine that coordinates the sequence of the stencil algorithm.

The registers R_0, R_1 and R_2 are connected in cascade to allow data streaming from memory. The term u_j^{n+1} calculated by the stencil kernel is saved to the RAM via multiplexer. A status signal from control unit tells the host application that has finished processing. Finally, memory data is read from the PL and stored in a file on SD card through PS. The flow chart for the stencil algorithm implemented in the heterogeneous system is shown in Fig. 5. Operations outside the dashed line are executed in PS and those found within the dashed line are executed in PL.

A performance counter is used to determine the number of clock cycles used to calculate all mesh points. This amount also can be calculated from the state machine sequence as shown in (8).

$$n_{CLK} = (N-1)(8J-8)+2 \tag{8}$$

To optimize the system performance for the implemented stencil algorithm and exploit the FPGA features, a variation of the baseline architecture described in section **??** is proposed. In order to increase the amount of space domain points that can be processed in one clock cycle more registers and PE are used. In Fig. 6 is shown the implementation for a $8 \times N$ mesh, with six PE and a register bank for eight data.

The control unit of this architecture has less states due to the J terms for the time step $n+1$ are obtained concurrently. To keep results available to calculate the values for the next time step without RAM access, the PE outputs are also stored concurrently in the register bank

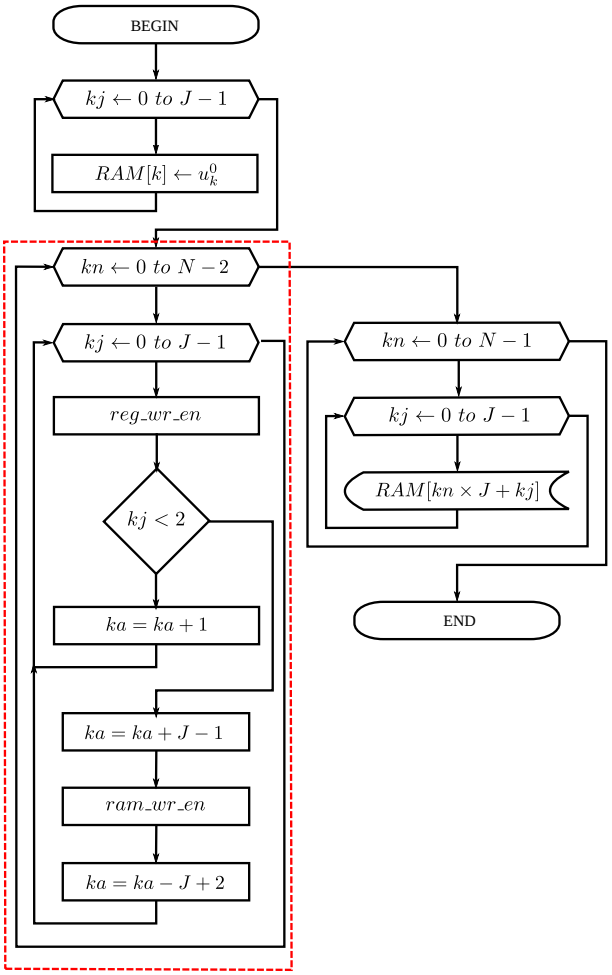

Fig. 5. Flow chart for the stencil algorithm implemented. Operations outside the dashed line are executed in PS and those found within the dashed line are executed in PL. The sequence for the execution of the stencil algorithm is coordinated by the control unit which is described in VHDL as a finite state machine. The counters k_j and k_n are used to control the loops. The counter k_a is used to address the RAM.

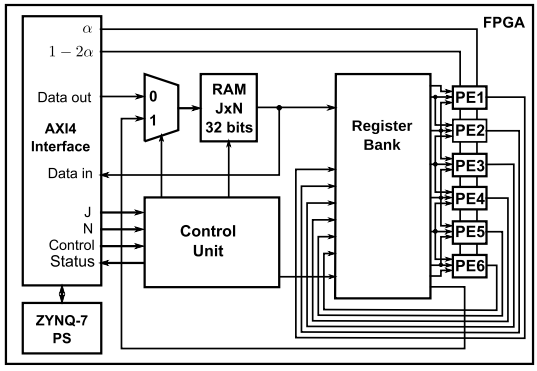

Fig. 6. Block diagram of the implementation for a $8 \times N$ mesh with concurrent processing.

trough internal multiplexers. With this configuration the algorithm inner loop is simplified.

The concurrent processing improves the algorithm performance, but data storage is still sequential given that the system has only one RAM. Therefore a memory structure that allows concurrent storage is proposed as shown in Fig. 7. In this architecture the inner loop is suppressed from the control unit sequence.

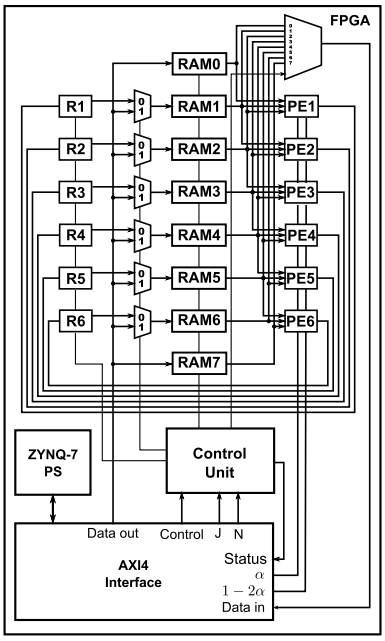

Fig. 7. Block diagram of the implementation for a $8 \times N$ mesh with concurrent processing and storage.

3.2 Architecture for the approach to the numerical solution of the two dimensional Laplace equation

From the architecture with concurrent processing and storage is developed a data-path with a two-dimensional register array to obtain the approach to the numerical solution of the 2D Laplace equation. The block diagram of the implemented circuit for a $8 \times N$ mesh is shown in Fig. 8.

4. EVALUATION

4.1 System performance

The system performance in terms of the time required for the algorithm execution is measured using an internal counter enabled from control unit. In Table 1 is shown the elapsed time in microseconds for 8, 16 and 32 points in the space domain and 512 iterations. The speed-up achieved with the parallel architectures (A_2 and A_3) is calculated in relation to the baseline architecture (A_1). The processing time for A_3 does not vary with respect to number of PE given that it just depends on the number of iterations.

Table 1. Algorithm execution time in microseconds obtained with the performance counter for J space points and N iterations.

$(J \times N)$	t_{A1} $[\mu s]$	t_{A2} $[\mu s]$	t_{A3} $[\mu s]$	Speedup t_{A1}/t_{A2}	Speedup t_{A1}/t_{A3}
8x512	286.18	138.52	30.68	1.215	2.066
16x512	613.22	261.64	30.68	2.344	19.987
32x512	1267.30	671.72	30.68	1.887	41.307

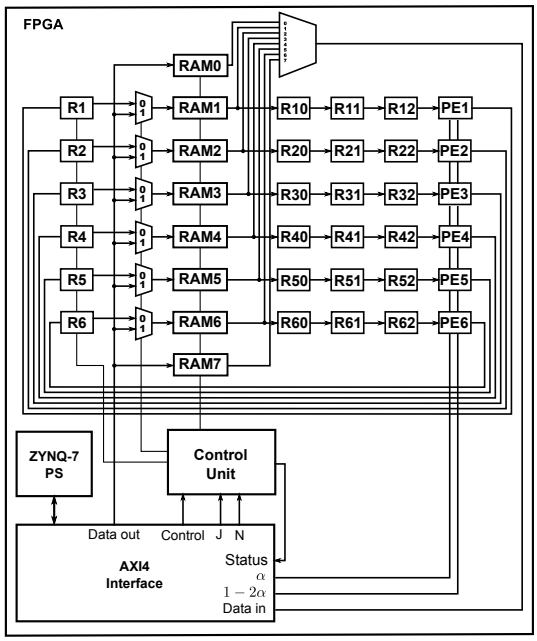

Fig. 8. Block diagram of the implementation for a $8 \times N$ mesh with concurrent processing and storage.

The speed-up achieved in comparison with the execution time of the algorithm written in C running on linux over a Intel Xeon E5-2667 at 2.90GHz with 32 GB of RAM is shown in Table 2. The values of t_{CPU} are the elapsed times used by the CPU processor to performs the nested loop.

Table 2. Speedup achieved in comparison with the execution time of the algorithm written in C running on linux over a Intel Xeon E5-2667 at 2.90GHz with 32 GB of RAM

$(J \times N)$	t_{CPU} $[\mu s]$	Speed-up t_{CPU}/t_{A1}	Speed-up t_{CPU}/t_{A2}	Speed-up t_{CPU}/t_{A3}
8x512	17.0	0.059	0.122	0.554
16x512	37.5	0.061	0.143	1.222
32x512	78.5	0.062	0.117	2.558

Performance can be improved for A2 if are stored only the results of the iteration N. Algorithm execution time in microseconds and speed-up obtained without storing all mesh for J space points and N iterations are shown in Table 3.

Table 3. Algorithm execution time in microseconds and speed-up obtained without storing all mesh points for J space points and N iterations.

$(J \times N)$	t_{A2} $[\mu s]$	Speed-up t_{A1}/t_{A2}	Speed-up t_{CPU}/t_{A2}
8x512	11.02	27.82	1.54
16x512	11.74	57.46	3.19
32x512	13.82	91.70	5.68

The stencil scheme used has four floating-point operations. Therefore with a 100 MHz clock the system has a peak performance of 400 MFLOPS in A_1 and 12 GFLOPS in A_2 and A_3. However, considering the number of mesh points, the stencil floating-point operations and the algorithm execution time, the system performance in GFLOPS corresponds to the values shown in Table 4.

Table 4. System performance in GFLOPS considering the number of mesh points, the stencil operations and the execution time

	$GFLOPS_{A1}$	$GFLOPS_{A2}$	$GFLOPS_{A3}$
8x512	0.053	0.118	0.534
16x512	0.048	0.125	1.068
32x512	0.046	0.097	2.136

The FPGA resources utilization respect to the PE is summarized in Table 5 for A_1, A_2 and A_3. This reports corresponds to implementation using 65536x32 RAM for A_1 and A_2 and 512x32 RAM for A_3. The parallel implementations for 62 PE could not be performed because the circuit exceed the number of available FPGA slices.

4.2 Numerical results

For initial values a triangular function is generated and send from PS section. Results of the approach to the numerical solution of the 1D heat equation are stored in the SD card. Data values are printed in a text file using 15 decimal digits precision format. In Fig. 9a is shown a mesh for the approximated solution for 32 points and 2048 iterations plotted with MATLAB®. The percent error with respect to Matlab® results for the same mesh size, initial values and boundary conditions is shown in Fig. 9b. Although the error obtained until iteration 2048 does not exceed 0.007%, it is observed that is accumulative with the increase of time steps. This happen mainly because of rounding of the floating-point operations.

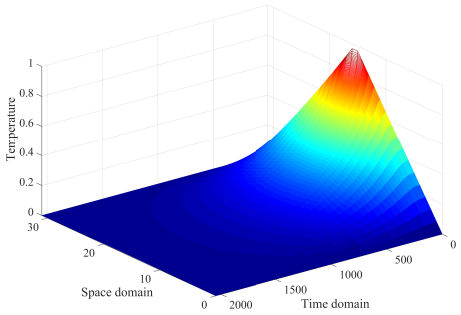

(a)

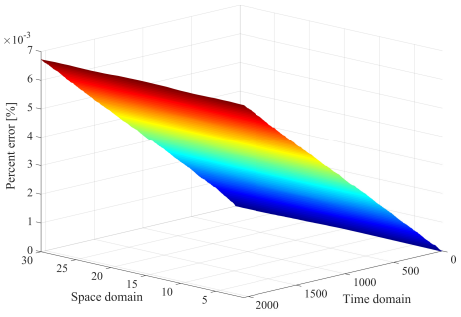

(b)

Fig. 9. (a) Approach to the numerical solution of the 1D heat equation obtained with the baseline architecture. (b) Percent error in comparison with Matlab® simulation. The plots are made using the Matlab® mesh function.

Table 5. FPGA resources utilization for the approximation to the numerical solution of heat equation.

	A1	A2			A3		
		6 PE	14 PE	30 PE	6 PE	14 PE	30 PE
Slice LUTs/ 53200	2461 (4.63%)	9381 (17.63%)	20131 (37.84%)	41953 (78.86%)	9212 (17.32%)	23244 (43.69%)	42600 (80.08%)
Slice Registers/ 106400	1692 (1.59%)	1404 (1.32%)	1792 (1.68%)	2581 (2.43%)	1641 (1.54%)	2068 (1.94%)	3136 (2.95%)
F7 Muxes/ 26600	182 (0.68%)	142 (0.53%)	246 (0.92%)	374 (1.41%)	160 (0.6%)	2240 (8.42%)	256 (0.96%)
F8 Muxes/ 13300	27 (0.2%)	59 (0.44%)	59 (0.44%)	187 (1.41%)	0 (0%)	1056 (7.94%)	128 (0.96%)
Block RAM Tile/ 140	58 (41.43%)	58 (41.43%)	58 (41.43%)	58 (41.43%)	4 (2.86%)	0 (0%)	16 (11.43%)
DSPs/ 220	4 (1.82%)	24 (10.91%)	56 (25.45%)	120 (54.55%)	24 (10.91%)	56 (25.45%)	120 (54.55%)

5. CONCLUSIONS AND FUTURE WORK

In this paper is presented a FPGA based heterogeneous system for stencil computation. The system is designed for the approach to the numerical solution of parabolic PDE for a one dimensional heat transfer problem with initial value and boundary conditions. The implementation is made using the SoC architecture of a XC7Z020CLG484-1 *Xilinx* FPGA of the ZedBoard.

Three different architectures based in the explicit finite difference method are described. Performance analysis shows the improvement achieved in terms of execution time for the stencil algorithm with two proposed parallel architectures. The speedup factor led to determine that implemented architectures offer different performance optimization due to the memory structure. However in both cases the use of the registers array allows to take advantage of spatial and temporal locality reducing the need of memory transfer operations.

For future work more deep performance analysis in terms of accuracy, precision, data transfer, scalability and power consumption could be performed. This evaluation should allow performance comparison with CPU and GPU based systems. Otherwise the study of variation for the implemented architectures to address bigger heat transfer problems in 2D using parabolic and elliptic PDEs could be developed.

ACKNOWLEDGEMENTS

This work was supported by the *AE&CC* research group of the Instituto Tecnológico Metropolitano through the project P14208. Luis Castaño acknowledges the financial support by the scholarship *Estudiantes Sobresalientes de Posgrado* Universidad Nacional de Colombia.

REFERENCES

[1] Schmitt, C., Schmid, M., Hannig, F., Teich, J., Kuckuk, S. and Harald Köstler, *A Challenge of Portable and High-Speed FPGA Accelerator*, in Proceedings of the Second International Workshop on High-Performance Stencil Computations, HiStencils 2015, pp. , 2015

[2] T. Usui, R. Kobayashi and K. Kise, *A Challenge of Portable and High-Speed FPGA Accelerator*, in Proceedings of the 11th International Symposium on Applied Reconfigurable Computing, ARC 2015, Springer International Publishing pp. 383-392, 2015

[3] K. Sano, Y. Hatsuda and S. Yamamoto, *Multi-FPGA Accelerator for Scalable Stencil Computation with Constant Memory-Bandwidth*, IEEE Transactions on Parallel and Distributed Systems, vol. PP, 2014

[4] R. Kobayashi and K. Kise, *Scalable stencil-computation accelerator by employing multiple FPGA*, IPSJ Transactions on Advanced Computing Systems, pp. 1-13, 2013

[5] V. Bandishti, I. Pananilath and U. Bondhugula, *Tiling Stencil Computations to Maximize Parallelism*, en Proceedings of the International Conference for High Performance Computing, Networking, Storage and Analysis, IEEE, pp. 1-11, 2012

[6] J. M. Cecilia, J. L. Abellán, J. Fernández, M. E. Acacio, J. M. García, M. Ujaldón, *Stencil computations on heterogeneous platforms for the Jacobi method: GPUs versus Cell BE*, The Journal of Supercomputing, Springer Science+Business Media, vol. 62, No. 2, pp. 787-803, 2012

[7] R. Kobayashi, S. Takamaeda-Yamazaki and K. Kise, *Towards a Low-Power Accelerator of Many FPGAs for Stencil Computations*, en Proceedings of the Third International Conference on Networking and Computing, IEEE, pp. 343-349, 2012

[8] K. Sano, Y. Hatsuda and S. Yamamoto, *Scalable Streaming-Array of Simple Soft-Processors for Stencil Computations with onstant Memory-Bandwidth*, en Proceeding of the 19th Annual International Symposium on Field-Programmable Custom Computing Machines, IEEE, pp. 234-241, 2011

[9] R. Strzodka, M. Shaheen, D. Pajak and H. Seidel, *Cache Accurate Time Skewing in Iterative Stencil Computations*, en Proceedings of the International Conference on Parallel Processing, IEEE, pp. 571-581, 2011

[10] A. R. Brodtkorb, C. Dyken, T. R. Hagen, J. M. Hjelmervik and O. O. Storaasli, *State-of-the-art in heterogeneous computing*, Scientific Programming, IOS Press Amsterdam, vol 18, pp. 1-33, 2010

[11] K. Datta, S. Kamil, S. Williams, L. Oliker, J. Shalf and K. Yelick, *Optimization and Performance Modeling of Stencil Computations on Modern Microprocessors*, SIAM Review, vol. 51, no. 1, pp. 129-159, 2009

Trajectory tracking controller for a nonlinear bioprocess

María N. Pantano*, María C. Fernández*, Mario E. Serrano*, Oscar A. Ortiz*, Gustavo J. Scaglia*.

** Instituto de Ingeniería Química, Universidad Nacional de San Juan (UNSJ), CONICET, Av. Lib. San Martín Oeste 1109, San Juan J5400ARL, Argentina (e-mail: npantano@unsj.edu.ar)*

Abstract: This paper aims to develop a simple but efficient control technique based on a linear algebra approach for tracking optimal profiles of a nonlinear multivariable fed-batch bioprocess. The methodology proposed allows, knowing the desired states, to find the values for the control actions by solving a system of linear equations. Its main advantage is that the condition for the tracking error tends to zero. The efficiency of the proposed controller is tested through several simulations. The optimal controller parameters are selected through Montecarlo Randomized Algorithm in order to minimize a cost index.

Keywords: Multivariable control, trajectory tracking, nonlinear systems, algebraic approaches, optimal trajectories.

1. INTRODUCTION

Fed-batch processes are widely used in the biotechnological industry, which is demanding for more efficient, reliable and safer processes to optimize production and improve power quality (De Battista et al., 2012). In a fed-batch operation, one or more nutrients are gradually supplied to the bioreactor, but no product is withdrawn until the process is finished. Its main advantages are the avoidance of substrate overfeeding which can inhibit the growth of microorganisms and catabolite repression. On the other hand, from the control engineer's viewpoint, the fed-batch fermentation is characterized for a large number of obstacles: complex dynamic behavior of microorganisms, the process model usually contains strongly time-varying parameters, changes in initial conditions, input saturation, external disturbances and the stiffness and nonlinearity of the model equations (Rani and Rao, 1999, Bayen and Mairet, 2013, Renard et al., 2006, Lee et al., 1999, Johnson, 1987).

Several control techniques are studied today associated with optimization and control of bioprocess, such as: bio-inspired algorithms (Rocha et al., 2014), genetic algorithms (Sarkar and Modak, 2003, Sarkar and Modak, 2004), robust control (Renard et al., 2006, Renard and Wouwer, 2008), nonlinear fuzzy control (Cosenza and Galluzzo, 2012),evolutionary algorithms (Ronen et al., 2002), model predictive control (MPC) (Ashoori et al., 2009) and nonlinear MPC (Craven et al., 2014, Santos et al., 2012), adaptive stochastic algorithms (Carrasco and Banga, 1997), neural network model (Saint-Donat et al., 1991, Tholudur and Ramirez, 1996), etc. Most of the control literature for fed-batch cultures focuses on open-loop operation owing to the highly nonlinear and inherently difficult dynamic behavior (Berber, 1996). These methods have good results in biological processes; however, they have limitations regarding the need for advanced specific knowledge, the difficulty of mathematical processing (especially in nonlinear systems), trouble with real-time implementation and the need for a complicated database of the processes (Alford, 2006). Besides that, in the open-loop control strategies, the main disadvantage is that no compensation is made for modeling mismatch or random disturbances during the process operation (Lee et al., 1999, Chang, 2003, Chung et al., 2006, Soni and Parker, 2004). It is therefore important to design a controller to track the optimal policy considering disturbance compensation for the closed-loop control problem.

The aim of this work is to solve the problem of tracking optimal profiles of an important biological system, which has a complex dynamics and a strong nonlinearity. The proposed methodology to achieve the stated objective is based on solving a system of linear equations. One of the key features of this technique is its simple approach, which suggests that knowing the value of the desired state, analyzing the conditions for a system to have an exact solution and then solving the system of linear equations; it can find the values for the control actions, which forces the system to move from its current state to the desired one.

The main advantages of this method are its simplicity, versatility and accuracy even under parametric uncertainty. The methodology for the controller design is very simple, nonlinear model is used; thus, its performance is independent of the operating point, and has an excellent performance against the set point changes. The optimal controller parameters are selected through Montecarlo Experiments in order to minimize a proposed cost index. The computing power required to perform the mathematical operations is low. Furthermore, the developed algorithm is easier to implement in a real system because the use of discrete equations allows direct adaptation to any computer system or programmable device. Moreover, because its simplicity and the mathematical tools that it use, this methodology is applicable to many systems, not only to bioprocesses.

The case study proposed for control is the Lee-Ramirez fed-batch bioreactor (Lee and Ramirez, 1992), developing a mathematical model for the induced foreign protein production by recombinant bacteria in a fed-batch bioreactor.

The advantage of using this system is that it has been already used by a number of researchers using different techniques, so the available data can be used to assess other methods.
The controller efficiency is tested through simulations using Matlab® software. The assays include a simulation in normal operation conditions and then, the control system under parametric uncertainty is analyzed through a Montecarlo randomized algorithm.

The paper is organized as follows. In Section 2, the mathematical model of the proposed system is presented and the optimal profiles are defined. Then, the controller design is considered in Section 3. The results of the simulation tests to demonstrate the efficiency of the controller are shown in Section 4. Finally, Section 5 outlines the conclusions of the work.

2. MATHEMATICAL MODEL

The mathematical model used here is taken of Balsa Canto et al. (Balsa-Canto et al., 2000). Although simple, it can effectively describe the dynamics of the bioprocess.
The original model was developed by Lee and Ramirez (Lee and Ramirez, 1992), who described the dynamics of the process of induced foreign protein production by recombinant bacteria and then used it to obtain an optimal control policy to maximize the foreign protein production with a nutrient and inducer feeding strategy (Lee and Ramirez, 1994). The same problem was studied by Tholudur and Ramirez (Tholudur and Ramirez, 1996) using neural network parameter function models. Carrazco and Banga (Carrasco and Banga, 1997) used adaptive stochastic algorithms to obtain better results. Since the performance index exhibits a very low sensitivity with respect to the controls, Tholudur and Ramirez (Tholudur and Ramirez, 1997) constructed a modified parameter function set to increase the sensitivity to the controls. Balsa-Canto also used the same parameter function set (Balsa-Canto et al., 2000). A genetic algorithm to optimize the same system considering multiple control variables was presented in (Sarkar and Modak, 2004).
The operation of the fed-batch bioreactor considering two control variables (u_1 and u_2, nutrient and inducer feed rates) is described by seven differential equations (1).
The state variables are the reactor volume x_1 *(L)*, the cell density x_2 *(g/L)*, the nutrient concentration x_3 *(g/L)*, the foreign protein concentration x_4 *(g/L)*, the inducer concentration x_5 *(g/L)*, the inducer shock factor on the cell growth rate x_6, and the inducer recovery factor on the cell growth rate x_7 (both dimensionless).
The model parameters were described by Lee and Ramirez (Lee and Ramirez, 1992). The concentration of nutrient feed stream is N, I is the concentration of inducer in the inducer feed stream, and Y is the growth yield coefficient. In addition, g is the specific growth rate, R is the foreign protein production rate, p is a Monod-type constant and K_1, K_2 are the shock and recovery parameters respectively.

$$\left.\begin{aligned}
\dot{x}_1 &= u_1 + u_2 \\
\dot{x}_2 &= x_2 g - \frac{u_1+u_2}{x_1} x_2 \\
\dot{x}_3 &= \frac{u_1 N}{x_1} - \frac{u_1+u_2}{x_1} x_3 - \frac{g}{Y} x_2 \\
\dot{x}_4 &= x_2 R - \frac{u_1+u_2}{x_1} x_4 \\
\dot{x}_5 &= \frac{u_2 I}{x_1} - \frac{u_1+u_2}{x_1} x_5 \\
\dot{x}_6 &= -K_1 x_6 \\
\dot{x}_7 &= K_2 (1 - x_7)
\end{aligned}\right\} \quad (1)$$

Where,

$$g = \left(\frac{x_3}{14.35 + x_3 \left(1 + \frac{x_3}{111.5}\right)} \right) \left(x_6 + \frac{x_7 0.22}{0.22 + x_5} \right) \quad (2)$$

$$R = \left(\frac{0.233 x_3}{14.35 + x_3 \left(1 + \frac{x_3}{111.5}\right)} \right) \left(\frac{0.0005 + x_5}{0.022 + x_5} \right) \quad (3)$$

$$K_1 = K_2 = \frac{x_5 p}{0.034 + x_5} \quad (4)$$

The two control variables are the glucose feeding rate, u_1 *(L/h)*, and inducer feeding rate u_2 *(L/h)* to the fed-batch bioreactor. The desired variables to follow are the reactor volume x_1, the cell density x_2, and the foreign protein concentration x_4.
It may be noted that the desired trajectories to track are directly the optimal profiles of controlled variables (x_1, x_2, and x_4). These trajectories were obtained by an open-loop simulation of the bioprocess using the optimal feeding policies achieved by Balsa Canto et al. (Balsa-Canto et al., 2000).

3. METHODOLOGY FOR CONTROLLER DESIGN

The proposed controller methodology is based on approximating the differential equations of the mathematical model (1) through the Euler method. Hence, the control problem for tracking optimum profiles of volume (x_1), cell density (x_2), and protein concentration (x_4) is reduced to the resolution of a system of linear equations.
To achieve the control goal, the feed flow rate of nutrient (u_1) and inducer (u_2) are available to be used as control actions. Therefore, the goal is to find the values of u_1 and u_2 such that the variables x_1, x_2 and x_4 follow paths desired with minimal tracking error.

3.1. Controller methodology

The first step for this technique, is rearrange the system of equations (1) in matrix form as $A\boldsymbol{u}=b$. The matrix $\boldsymbol{u}$ is composed of the control variables, for this model, u_1 and u_2:

$$\overbrace{\begin{pmatrix} 1 & 1 \\ -1 & -1 \\ (N-x_3) & -x_3 \\ -1 & -1 \\ -1 & (I-x_5) \end{pmatrix}}^{A} \overbrace{\begin{pmatrix} u_1 \\ u_2 \end{pmatrix}}^{u} = \overbrace{\begin{pmatrix} \dot{x}_1 \\ \dot{x}_2 \frac{x_1}{x_2} - x_1 g \\ \dot{x}_3 x_1 + \frac{g}{Y} x_2 x_1 \\ \frac{\dot{x}_4 x_1}{x_4} - \frac{R x_2 x_1}{x_4} \\ \dot{x}_5 x_1 \end{pmatrix}}^{b} \quad (5)$$

Remark 1. The variables x_6 and x_7 are not directly related with the control variables, therefore, are not considered in the controller design.

According to the rule of numerical integration of Euler, the differential equations can be approximated as follow:

$$\dot{x}_i = \frac{x_{i,n+1} - x_{i,n}}{T_0} \quad (6)$$

Where T_0 is the sample time, $x_{i,n}$ represents the state variable i in n instant and $x_{i,n+1}$ the state variable i in $(n+1)$ instant.

Defining the following expression:

$$\overbrace{x_{i,ref,n+1} - x_{i,n+1}}^{error_{i,n+1}} = k_i \overbrace{(x_{i,ref,n} - x_{i,n})}^{error_{i,n}} \quad (7)$$

Where, $x_{i,ref,n}$ and $x_{i,ref,n+1}$ are the reference values in the n instant and the next sample time respectively, the constant k_i is the controller parameter for the variable i.

Then, the immediately reachable value of each state variable is:

$$x_{i,n+1} = x_{i,ref,n+1} - k_i \overbrace{(x_{i,ref,n} - x_{i,n})}^{error_{i,n}} \quad (8)$$

Therefore, the values of the real state variables in the next sample time ($x_{i,n+1}$) are function of the reference profiles, the actual state variable and the controller parameters. So, all values are known.

Consequently, substituting (8) in (6):

$$\dot{x}_i = \frac{\overbrace{\left[x_{i,ref,n+1} - k_i (x_{i,ref,n} - x_{i,n})\right]}^{x_{i,n+1}} - x_{i,n}}{T_0} \quad (9)$$

Now, replacing (9) in each differential expression appearing in (5), the process model can be rewritten, see (10).

The values of x_1, x_2, and x_4 are the references to follow, therefore are known (the reference values as well as the real system values). Note that, the Eq. (10) is a system of five equations and two unknowns, which normally has no solution. Therefore, the unknown variables of this system are defined as "*sacrificed variables*" and are written as $x_{i,ez}$ corresponding, in this case, to $x_{3,ez}$ and $x_{5,ez}$. The key of this technique is that the values adopted by such variables forces the equation system (10) to have exact solution, which implies error not only be minimal, but equal zero.

$$\begin{pmatrix} 1 & 1 \\ -1 & -1 \\ (N-x_{3,n}) & -x_{3,n} \\ -1 & -1 \\ -1 & (I-x_{5,n}) \end{pmatrix} \begin{pmatrix} u_{1,n} \\ u_{2,n} \end{pmatrix} = \begin{pmatrix} \left(\frac{x_{1,ref,n+1} - k_1 (x_{1,ref,n} - x_{1,n}) - x_{1,n}}{T_0}\right) \\ \left(\frac{x_{2,ref,n+1} - k_2 (x_{2,ref,n} - x_{2,n}) - x_{2,n}}{T_0}\right) \frac{x_{1,n}}{x_{2,n}} - x_{1,n} g \\ \left(\frac{x_{3,ez,n+1} - k_3 (x_{3,ez,n} - x_{3,n}) - x_{3,n}}{T_0}\right) x_{1,n} + \frac{g}{Y} x_{2,n} x_{1,n} \\ \left(\frac{x_{4,ref,n+1} - k_4 (x_{4,ref,n} - x_{4,n}) - x_{4,n}}{T_0}\right) \frac{x_{1,n}}{x_{4,n}} - R x_{2,n} \frac{x_{1,n}}{x_{4,n}} \\ \left(\frac{x_{5,ez,n+1} - k_5 (x_{5,ez,n} - x_{5,n}) - x_{5,n}}{T_0}\right) x_{1,n} \end{pmatrix} \quad (10)$$

To simplify the mathematical treatment, the equations system is expressed as follows:

$$\begin{pmatrix} a_{31} & a_{32} \\ a_{51} & a_{52} \\ a_{11} & a_{12} \\ a_{21} & a_{22} \\ a_{41} & a_{42} \end{pmatrix} \begin{pmatrix} u_1 \\ u_2 \end{pmatrix} = \begin{pmatrix} b_3 \\ b_5 \\ b_1 \\ b_2 \\ b_4 \end{pmatrix} \Rightarrow Au = b \quad (11)$$

Remark 2: the order of the rows are altered to the Gaussian elimination because the system presents three linearly dependents rows.

To accomplish the target, the system (10) must have exact solution. Then, the vector ***b*** must be contained in the space formed by the columns of ***A***, ie, the vector ***b*** must be a linear combination of the column vectors of matrix ***A***.

In order to find the values of the $x_{i,ez}$ so that the system to have exact solution, the Gauss elimination process is carried out.

Then, the *necessary* and *sufficient condition* for the system to have exact solution is:

$$\begin{aligned} 0 &= (a_{31}a_{52} - a_{32}a_{51})(a_{31}b_1 - b_3a_{11}) - (a_{31}b_5 - b_3a_{51})(a_{31}a_{12} - a_{32}a_{11}) \\ 0 &= (a_{31}a_{52} - a_{32}a_{51})(a_{31}b_2 - b_3a_{21}) - (a_{31}b_5 - b_3a_{51})(a_{31}a_{22} - a_{32}a_{21}) \\ 0 &= (a_{31}a_{52} - a_{32}a_{51})(a_{31}b_4 - b_3a_{41}) - (a_{31}b_5 - b_3a_{51})(a_{31}a_{42} - a_{32}a_{41}) \end{aligned} \quad (12)$$

This equations system is solved for each sampling period by iteration methods, where the unknown variables $x_{3,ez,n+1}$ and $x_{5,ez,n+1}$ (*sacrificed variables*) are calculated.

Once the values of $x_{3,ez,n+1}$, $x_{5,ez,n+1}$ are found, the matrix ***A*** and ***b*** are completely known at (n) time. Therefore, the control variables $u_{1,n}$ and $u_{2,n}$ (***u*** vector) can be calculated solving the system (10) by the least squares method:

$$(A^T A)u = A^T b \Rightarrow u = (A^T A)^{-1} A^T b \quad (13)$$

The solution allows finding the control actions ($u_{1,n}$ and $u_{2,n}$) to be applied at time n to follow the desired trajectories with a minimal error.

Remark 3. The following constraints on the control variables are considered (Balsa-Canto et al., 2000): $0.0 \leq u_1 \leq 1.0$ and $0.0 \leq u_2 \leq 1.0$.

Remark 4. In Eq. (8) note that:

- If $k_i = 0$, the reference trajectory is reached in only one step.

Remark 5. The parameters k_i, $i = \{1,2,3,4,5\}$, satisfied $0 < k_i < 1$, which allows the tracking error tends to zero.

Remark 6. The tracking error is the value of the difference between the reference and real trajectory, and is calculated as:

$$\|e_n\| = \sqrt{e_{1,n}{}^2 + e_{2,n}{}^2 + e_{4,n}{}^2} \; ; \; E = T_0 \sum_n \|e_n\| \qquad (14)$$

$$e_{1,n} = \frac{x_{1,ref,n} - x_{1,n}}{x_{1,\max}} \qquad (15)$$

$$e_{2,n} = \frac{x_{2,ref,n} - x_{2,n}}{x_{2,\max}} \qquad (16)$$

$$e_{4,n} = \frac{x_{4,ref,n} - x_{4,n}}{x_{4,\max}} \qquad (17)$$

Where: $x_{1,max} = 1{,}9\ L$, $x_{2,max} = 13{,}92\ g/L$, and $x_{4,max} = 3{,}1\ g/L$

Note that the tracking error is dimensionless.

Theorem 1. If the system behavior is ruled by (10) and the controller is designed by (13), then, $e_{i,n} \to 0$, $n \to \infty$, when profile tracking problems are considered. The proof of this theorem is not shown because space reasons.

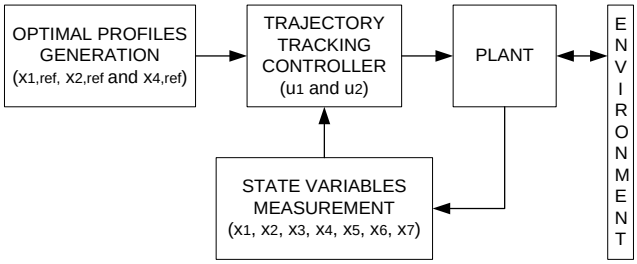

Figure 1. Architecture of the trajectory tracking controller.

Figure 1 shows the architecture of the control system proposed herein. In this work, the optimal profiles are taken from literature (Balsa-Canto et al., 2000), the focus is in the trajectory tracking of such profiles.

4. RESULTS AND DISCUSSION

In order to evaluate the performance of the controller, various simulation tests employing Matlab® were carried out:

- A randomized algorithm to synthetize the optimal controller parameters (k_i).
- Simulation under normal operating conditions using the optimal values of the controller parameters found in previous section.
- Simulation considering parametric uncertainty.

4.1. Optimal controller parameters.

The aim in this subsection is to find the values of the controller parameters, for which the tracking error is minimal (the bioreactor behavior directly depends on the adjustment of parameters k_i). To achieve the target, a Montecarlo experiment is performed.

In the field of systems and control, Montecarlo methods have been found useful especially for problems related to robustness of uncertain systems (Tempo and Ishii, 2007).

In this work, the Montecarlo experiment consisted on randomize the controller parameters and then simulate the process, this is repeated a large number of trials (N) and the tracking error is calculated in every one.

Now, considering by definition that Montecarlo randomized algorithm (MCRA) is a randomized algorithm that may produce an incorrect result, but the probability of such an incorrect result is bounded (Motwani and Raghavan, 1995), the number of simulations necessary to ensure a certain degree of confidence and accuracy (confidence boundaries) is achieved using the following expression (Tempo and Ishii, 2007):

$$N \geq \left\lceil \frac{\log \frac{1}{\delta}}{\log \frac{1}{1-\varepsilon}} \right\rceil \qquad (18)$$

Where δ= confidence and ε= accuracy.

It is fixed $\delta = 0.01$ and $\varepsilon = 0.005$. Therefore, $N \geq 920$.

The initial conditions used to simulate the system are shown in Table 1.

Feeding concentrations and parameters values can be seen in Table 2.

Table 1 Initial conditions for the state variables [g/L].

$x_{1,0}$	$x_{2,0}$	$x_{3,0}$	$x_{4,0}$	$x_{5,0}$	$x_{6,n}$	$x_{7,0}$
1.0	*0.1*	*40.0*	*0.01*	*0.01*	*1.0*	*0.01*

Table 2 Feeding concentrations and parameters (Tholudur and Ramirez, 1997).

N (g/L)	***I(g/L)***	***Y***	***p (h^{-1})***
40	*100*	*0.51*	*0.09*

The final time for the process is $T_f = 10\ h$ and the sample time for simulations is $T_0 = 0.1\ h$

The k_i values found for the minimum tracking error after 1000 simulations (total simulation time: 75 min) are presented in Table 3.

Table 3 Optimal k values after Montecarlo experiment.

k_1	k_2	k_3	k_4	k_5
0.9501	*0.5463*	*0.1459*	*0.1563*	*0.2624*
E=0.0014 – Iteration Nº 202				

4.2. Normal conditions operation.

This section shows the results of the simulation of the closed loop control using the controller proposed in this work without environmental disturbances. The optimal controller parameters achieved in the previous subsection and the state variables initial values are used. The evolution of the controlled system can be seen in the following figures.

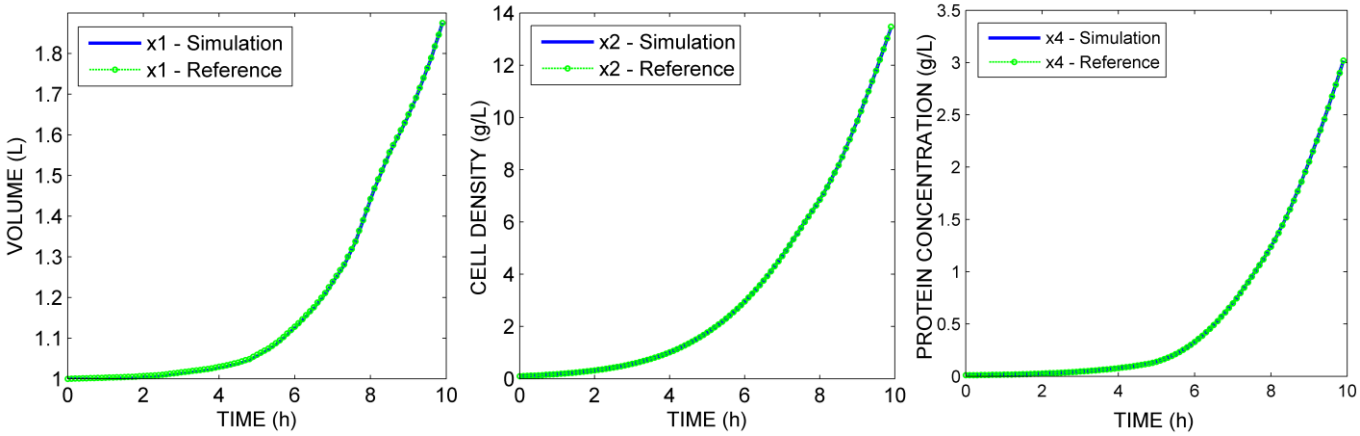

Figure 2. Tracking optimal profiles of desired variables (x_1, x_2, and x_4) in normal operation conditions.

A very good controller performance can be observed, the optimal desired profiles are successfully tracking as can be seen in Fig. 2.

Note that the tracking error defined by (14), remains low and acceptably bounded as shows Fig. 3.

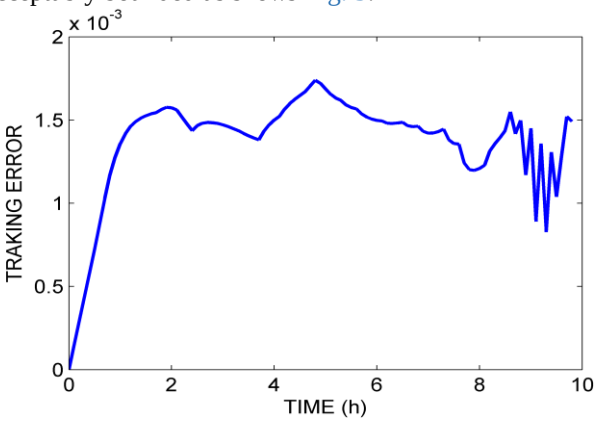

Figure 3. Tracking error *(e)* in normal operation conditions.

It is noteworthy that not only the desired variables follow the optimal profiles, but also the other variables track their respective reference profiles (it is not show here for space reasons).

4.3. *Parametric uncertainty.*

In this subsection, the MC Method is applied to make an analysis of the system in case of appearing modeling errors. For this, a determined error is introduced in the model parameters (15% above and below their nominal values) and perform 500 simulations (N = 500). In each simulation the parameters are chosen in a random way by MC sampling experiment (Auat Cheein et al., 2013). The parameters under disturbance are the concentration of nutrient feed stream ***N***, the concentration of inducer in the inducer feed stream ***I***, the Monod-type constant ***p*** and the growth yield coefficient ***Y***. The initial conditions and the sampling time are the same used in the previous subsection.

The number of simulations taken to carry out this test is considering the confidence $\delta = 0.01$ and accuracy $\varepsilon = 0.01$. Therefore, replacing in (18), $N \geq 500$.

Figures 4 shows the behavior of the system with the controller proposed in this work, which presents a good response against parametric uncertainty.

It is noteworthy that the controller design is focused in the tracking optimal profile of the desired variables, not of control variables. This is one of the advantages, since it allows control of the system even under disturbances.

The simulation tests carried out along this work show a very good performance of the control law developed.

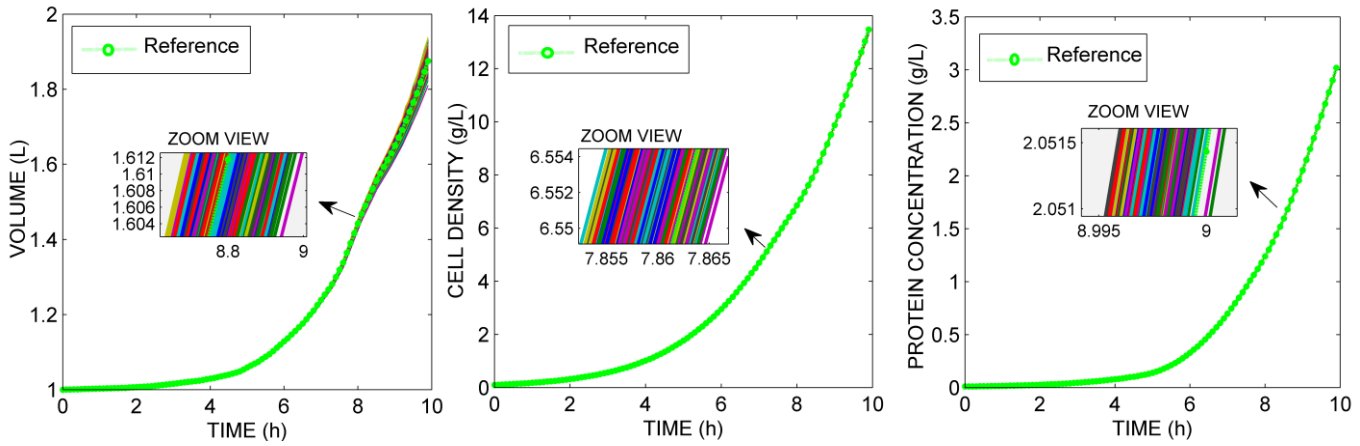

Figure 4. Tracking optimal profiles (desired variables x_1, x_2, and x_4) under parametric uncertainty (±15%, 500 simulations).

5. CONCLUSIONS

The controller design of an important biological system consisting on seven differential equations with three desired variables and two control actions was presented in this work. The advantages of the methodology employed is its simplicity and accuracy since reduces the controller design to a resolution of a linear equations system for the calculation of the control actions, which achieve the tracking optimal trajectories of desired variables with a minimal tracking error, even under parametric uncertainties. This methodology can be implemented only with basic knowledge of linear algebra. The optimal controller parameters were successfully found through a Montecarlo experiment. Moreover, through closed-loop simulation tests, this proposed control structure was shown to be simple and efficient, even considering the mismatches in the model parameters.

ACKNOWLEDGMENT

This work was funded by the *Consejo Nacional de Investigaciones Científicas y Técnicas* (CONICET- *National Council for Scientific Research*) and *Instituto de Ingeniería Química, Facultad de Ingeniería - Universidad Nacional de San Juan*, Argentina.

REFERENCES

ALFORD, J. S. 2006. Bioprocess control: Advances and challenges. *Computers & Chemical Engineering,* 30**,** 1464-1475.

ASHOORI, A., MOSHIRI, B., KHAKI-SEDIGH, A. & BAKHTIARI, M. R. 2009. Optimal control of a nonlinear fed-batch fermentation process using model predictive approach. *Journal of Process Control,* 19**,** 1162-1173.

AUAT CHEEIN, F. A., PEREIRA, F. M. L., DI SCIASCIO, F. & CARELLI, R. 2013. Autonomous Simultaneous Localization and Mapping driven by Monte Carlo uncertainty maps-based navigation. *The Knowledge Engineering Review,* 28**,** 35-57.

BALSA-CANTO, E., BANGA, J. R., ALONSO, A. A. & VASSILIADIS, V. S. 2000. Efficient optimal control of bioprocesses using second-order information. *Industrial and Engineering Chemistry Research,* 39**,** 4287-4295.

BAYEN, T. & MAIRET, F. 2013. Minimal time control of fed-batch bioreactor with product inhibition. *Bioprocess and Biosystems Engineering,* 36**,** 1485-1496.

BERBER, R. 1996. Control of Batch Reactors-A Review (Reprinted from Methods of Model Based Process Control, 1995). *Chemical engineering research & design,* 74**,** 3-20.

CARRASCO, E. F. & BANGA, J. R. 1997. Dynamic optimization of batch reactors using adaptive stochastic algorithms. *Industrial & engineering chemistry research,* 36**,** 2252-2261.

COSENZA, B. & GALLUZZO, M. 2012. Nonlinear fuzzy control of a fed-batch reactor for penicillin production. *Computers & Chemical Engineering,* 36**,** 273-281.

CRAVEN, S., WHELAN, J. & GLENNON, B. 2014. Glucose concentration control of a fed-batch mammalian cell bioprocess using a nonlinear model predictive controller. *Journal of Process Control,* 24**,** 344-357.

CHANG, D. M. 2003. The Snowball Effect in Fed-Batch Bioreactions. *Biotechnology progress,* 19**,** 1064-1070.

CHUNG, Y.-C., CHIEN, I.-L. & CHANG, D.-M. 2006. Multiple-model control strategy for a fed-batch high cell-density culture processing. *Journal of Process Control,* 16**,** 9-26.

DE BATTISTA, H., PICÓ, J. & PICÓ-MARCO, E. 2012. Nonlinear PI control of fed-batch processes for growth rate regulation. *Journal of Process Control,* 22**,** 789-797.

JOHNSON, A. 1987. The control of fed-batch fermentation processes—a survey. *Automatica,* 23**,** 691-705.

LEE, J., LEE, S. Y., PARK, S. & MIDDELBERG, A. P. J. 1999. Control of fed-batch fermentations. *Biotechnology Advances,* 17**,** 29-48.

LEE, J. & RAMIREZ, W. F. 1992. Mathematical modeling of induced foreign protein production by recombinant bacteria. *Biotechnology and bioengineering,* 39**,** 635-646.

LEE, J. & RAMIREZ, W. F. 1994. Optimal fed-batch control of induced foreign protein production by recombinant bacteria. *AIChE Journal,* 40**,** 899-907.

MOTWANI, R. & RAGHAVAN, P. 1995. Randomized algorithms (cambridge international series on parallel computation). Cambridge University Press.

RANI, K. Y. & RAO, V. R. 1999. Control of fermenters–a review. *Bioprocess Engineering,* 21**,** 77-88.

RENARD, F. & WOUWER, A. V. 2008. Robust adaptive control of yeast fed-batch cultures. *Computers & Chemical Engineering,* 32**,** 1238-1248.

RENARD, F., WOUWER, A. V., VALENTINOTTI, S. & DUMUR, D. 2006. A practical robust control scheme for yeast fed-batch cultures–an experimental validation. *Journal of Process Control,* 16**,** 855-864.

ROCHA, M., MENDES, R., ROCHA, O., ROCHA, I. & FERREIRA, E. C. 2014. Optimization of fed-batch fermentation processes with bio-inspired algorithms. *Expert Systems with Applications,* 41**,** 2186-2195.

RONEN, M., SHABTAI, Y. & GUTERMAN, H. 2002. Optimization of feeding profile for a fed-batch bioreactor by an evolutionary algorithm. *Journal of biotechnology,* 97**,** 253-263.

SAINT-DONAT, J., BHAT, N. & MCAVOY, T. J. 1991. Neural net based model predictive control. *International Journal of Control,* 54**,** 1453-1468.

SANTOS, L. O., DEWASME, L., COUTINHO, D. & WOUWER, A. V. 2012. Nonlinear model predictive control of fed-batch cultures of micro-organisms exhibiting overflow metabolism: assessment and robustness. *Computers & Chemical Engineering,* 39**,** 143-151.

SARKAR, D. & MODAK, J. M. 2003. Optimisation of fed-batch bioreactors using genetic algorithms. *Chemical Engineering Science,* 58**,** 2283-2296.

SARKAR, D. & MODAK, J. M. 2004. Optimization of fed-batch bioreactors using genetic algorithm: multiple control variables. *Computers & Chemical Engineering,* 28**,** 789-798.

SONI, A. S. & PARKER, R. S. 2004. Closed-loop control of fed-batch bioreactors: A shrinking-horizon approach. *Industrial & engineering chemistry research,* 43**,** 3381-3393.

TEMPO, R. & ISHII, H. 2007. Monte Carlo and Las Vegas Randomized Algorithms for Systems and Control: An Introduction. *European Journal of Control,* 13**,** 189-203.

THOLUDUR, A. & RAMIREZ, W. F. 1996. Optimization of Fed-Batch Bioreactors Using Neural Network Parameter Function Models. *Biotechnology Progress,* 12**,** 302-309.

THOLUDUR, A. & RAMIREZ, W. F. 1997. Obtaining smoother singular arc policies using a modified iterative dynamic programming algorithm. *International Journal of Control,* 68**,** 1115-1128.

CHAPTER 15

ROBOTICS

Consenso en la dinámica de los estados de robots móviles tipo (3,0) ⋆

J. P. Sánchez-Santana [*,**,***] **M. G. Villarreal-Cervantes** [**]
J. F. Guerrero-Castellanos [***] **S. Ramírez-Martínez** [***]

[*] *Universidad Politécnica de Puebla, Tercer Carril del Ejido "Serrano" s/n, San Mateo Cuanalá, Juan C. Bonilla, C. P. 72640 Puebla, México, jose.sanchez@uppuebla.edu.mx*
[**] *Instituto Politécnico Nacional - CIDETEC, Av. Juan de Dios Bátiz s/n, Col. Nueva Industrial Vallejo, Deleg. Gustavo A. Madero, México D.F. C.P. 07700, mvillarrealc@ipn.mx*
[***] *Benemérita Universidad Autónoma de Puebla - FCE, Av. San Claudio y 18 Sur, Col. San Manuel, Puebla, Pue. México.C.P. 72570, fguerrero@ece.buap.mx*

Resumen En este trabajo se presenta la importancia de los sistemas ciberfísicos desde la perspectiva de comunicación y consumo energético, para el caso particular, de los sistemas multiagentes que ejecutan el problema de consenso promedio, con la variante de aplicar control disparado por eventos. Para lo cual se desarrolla una estrategia de control formal para lograr el consenso en la dinámica de los estados de robots móviles tipo (3,0) aplicando control disparado por eventos, a través de la consideración de $n-$agentes representados por un integrador de orden uno, que definen la posición y orientación de los robots. La estrategia de control se válida a través de simulación para mostrar la convergencia al consenso promedio, dado por las distintas condiciones iniciales en la dinámica de los estados en los robots, es decir, cada estado converge a un punto, el cual corresponde al promedio de sus condiciones iniciales. Aunado a ello, se da evidencia de los resultados para visualizar la estabilidad y buen comportamiento del control disparado por eventos aplicado a sistemas multiagentes, para el caso de arquitectura centralizada.

Keywords: Consenso promedio, robot móvil (3,0), sistemas multiagentes, control disparado por eventos.

1. INTRODUCCIÓN

Actualmente, identificar la interacción en los sistemas elementales y que son miembros de un sistema de mayor relevancia trae consigo desarrollos científicos y tecnológicos que determinan una verdadera prueba en su funcionamiento en un entorno, por mínimo o complejo que éste sea. Con relación a ello, se define un sistema ciberfísico (CPS: Cyber-Physical Systems) como aquel que tiene una capacidad de integración de funciones, elementos y procesos de cómputo para la comunicación en seguimiento y control de las entidades del mundo físico, Shi et al. (2011) y Rajkumar (2012). Dichos sistemas se caracterizan por estar conformados por sistemas embebidos, redes de comunicación y algoritmos de control, en los que los lazos de retroalimentación son afectados, tanto por la naturaleza de los procesos físicos como por los inherentes a la implementación de los procesos computacionales. Debido a la heterogeneidad del hardware, un CPS puede abarcar múltiples dispositivos, con diferentes arquitecturas, protocolos e interfaces, por lo que tienden a ser híbridos y distribuidos.

Ante el evidente procesamiento de datos, para el monitoreo, análisis y control de las señales presentes en los CPS, asimismo como en los canales de comunicación, es importante distinguir la existencia de tiempo discreto, a través de las plataformas y redes digitales, donde se vislumbra un particular interés por lograr consumo energético de alto aprovechamiento, definiendo la tecnología vanguardista bajo el concepto de los sistemas mecatrónicos embedidos, Al-Ali and Al-Jarrah (2009).

De la gran diversidad de sistemas ciberfísicos, es posible disdinguir a los sistemas multiagentes (SMA) para lograr actividad colaborativa. Donde es importante comprender la combinación sinérgica lograda por los sistemas mecatrónicos embebidos, dada la relación estrecha del sotfware y hardware, sumados a interacción de piezas mecánicas con su entorno. Particularmente, en dichos sistemas se ha identificado un desarrollo exponencial para resolver problemas relacionados con calidad y velocidad de procesamiento, precisión, memoria, arquitecturas de datos, sistemas

⋆ El primer autor agradece a la Universidad Politécnica de Puebla, al CIDETEC-IPN y la FCE-BUAP por amparar los estudios de posgrado, asimismo, al PRODEP por la beca para estudios de posgrado de alta calidad. El segundo autor agradece el apoyo brindado por el COFAA del Instituto Politécnico Nacional y de SEP-CONACYT a través de los proyectos 20140926 y 182298. El tercer autor agradece el apoyo brindado por la Vicerrectoría de Investigación y Estudios de Posgrado de la BUAP a través del proyecto GUCJING13-I.

operativos, redes, comunicación efectiva, autonomía e inteligencia artificial, logrando posicionar a un CPS como el ente tecnológio para la cuarta revolución industrial, como es comentado en Shiyong Wang and Zhang (2016).

Ahora bien, la actividad colaborativa requiere de algoritmos de control basados en red (NCS: Networked Control Systems) que determinan un correcto funcionamiento de los elementos que interactuán en un CPS, de acuerdo a Gao et al. (2008). Es evidente considerar que el consumo energético es prioritario, debido al alto procesamiento de señales, por consiguiente es necesario evaluar la posibilidad de optimizar y extender los recursos energéticos bajo el paradigma de control de sistemas disparado por eventos.

La ingeniería de control establece la formalidad en analizar un sistema, a partir de su modelo matemático, para lograr estabilidad del sistema ante perturbaciones, donde las dinámicas que predominan su estudio son determinantes para elegir un análisis adecuado, y sean evaluadas en tiempo continuo o tiempo discreto. Para ello se requiere de la implementación adecuada de las estrategias de control en las unidades de procesamiento, que indudablemente trabajan en tiempo discreto, de ahí la importancia de distinguir que los sistemas se pueden emular de forma síncrona y asíncrona, es decir, para determinar las activaciones de las acciones de control en cada cierto intervalo de tiempo o bajo la restricción de la dinámica del sistema, respectivamente, y actualmente basado en eventos, como en Durand and Marchand (2009).

En un sistema de control síncrono es la progresión autónoma del tiempo, contínuo o discreto, lo que dispara la ejecución de las acciones, mientras que en los sistemas de control asíncrono, y en específico basados en eventos, es la *propia evolución dinámica* del sistema la que decide cuándo se ejecutará la próxima acción de control. Esta circunstancia, al ser implementada en una unidad de procesamiento, para una aplicación de alta demanda de cálculo, se traduce en una reducción en la comunicación del bus de datos y el uso del procesador, generando ahorro de energía. En la Fig. 1 se muestra la diferencia entre el muestreo basado en tiempo continuo t, síncrono T, y asíncrono t_k (en eventos), distinguir que las señales conservan el comportamiento de $f(t)$, de ahí la iniciativa de utilizar señales discretas y recientemente señales asíncronas, las cuales contienen la información necesaria.

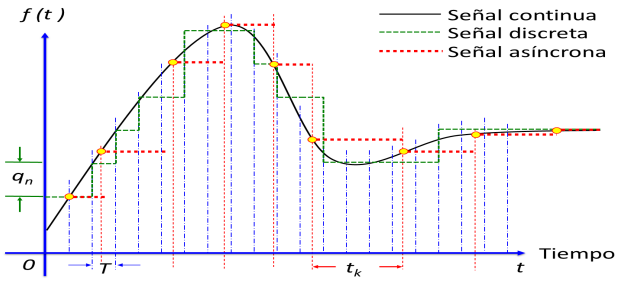

Figura 1. Señal muestreada en el tiempo.

El estado del arte para el consenso promedio en grafos fuertemente conectados y no direccionados es emergente, en Cai and Ishii (2012) se presenta un formalismo para el estudio de SMA con redes de topología general para grafos no direccionados, donde la comunicación de los agentes se da de forma síncrona o asíncrona, demostrando el desarrollo de algoritmos que garantizan el consenso. En particular, en Olfati-Saber and Murray (2004a); Olfati-Saber et al. (2007) estudia algoritmos para lograr consenso, considerando tiempo invariante en el sistema, el cual consta de una red de agentes que determinan una topología de comunicación fija o variante, representada por grafos con topología de tipo balanceados y fuertemente conectados, como elementos necesarios y suficientes para garantizar convergencia.

La motivación por el uso de microprocesadores embebidos de recursos limitados para reunir información y realizar las actualizaciones del controlador en los agentes, hace posible la generación de estrategias de control que sean activadas de forma asíncrona o por eventos. Particularmente, en Dimarogonas and Frazzoli (2009); Dimarogonas and Johansson (2009); Seyboth et al. (2011) se presentan estrategias de control distribuido activado por eventos para el SMA, sólo requiriendo información de los agentes vecinos para la implementación del controlador, con la consideración del formalismo en tiempo discreto. En consecuencia, se requiere el análisis de los sistemas involucrados en tiempo discreto, o en la ocurrencia de un evento, es decir, de forma asíncrona, y con control centralizado o descentralizado, resultados en este sentido son presentados en Seyboth et al. (2013); Fax and Murray (2004); Yan et al. (2014); Olfati-Saber and Murray (2004b).

La variedad de SMA donde se ha aplicado el consenso trae consigo un discernimiento en la diversidad de sistemas mecatrónicos, por lo que el interés particular se encuentra en robots móviles, como lo planteado en Yamaguchi (2003), para coordinar desplazamiento de los agentes y realizar tareas de colaboración.

En este trabajo se analiza el problema de consenso promedio desde la perspectiva de tiempo asíncrono, primordialmente en la ocurrencia de un evento, para probar que la propuesta del algoritmo garantice estabilidad al promedio de los estados de forma arbitraria para esquemas de comunicación de grafos fuertemente conectados y no direccionados.

En la sección 2 se presenta los recursos matemáticos involucrados en el desarrollo del presente trabajo, en la sección 3 se define la estrategía de control y se demuestra la estabilidad de la ley de control, aunado al caso particular del SMA integrado por cuatro robots móviles tipo (3,0), en la sección 4 se analiza los resultados de simulación, y finalmente, establecer las conclusiones y perspectivas en la sección 5.

2. RECURSOS MATEMÁTICOS

2.1 Teoría de grafos

Las topologías de comunicación de los SMA pueden ser representadas mediante grafos, donde los nodos corresponden a los agentes y las aristas a la comunicación entre ellos.

Definición 1. Un grafo G se define como un par de conjuntos (V, E), donde V es un conjunto finito de puntos $v_1, v_2, v_3, ..., v_n$ llamados vértices o nodos y E es un conjunto finito de aristas, bordes o enlaces e_{ij}, cada uno de los cuales une pares ordenados de vértices.

Se denomina un grafo dirigido si las aristas tienen dirección del vértice i (punto inicial) al vértice j (punto final). Así, el grado del vértice i es el número de aristas que tienen punto inicial en el mismo. Caso contrario en un grafo no dirigido, en el cual las aristas no tienen dirección y por lo tanto el grado del vértice es el número de aristas incidentes en sí mismo.

Definición 2. La matriz de adyacencia de un grafo G es la matriz $A(G)$ de tamaño $n \times n$ y cuyas entradas están dadas por $a_{ij} = 1$ si $(i,j)\ \epsilon\ E$ y $a_{ij} = 0$ en otros casos.

Definición 3. La matriz de grado asociada al grafo G es una matriz diagonal $D(G)$ cuyos elementos $d_{i,j}$ corresponden al grado de salida del nodo i.

Definición 4. La matriz Laplaciana se denota por $L(G)$ de tamaño $n \times n$ cuyas entradas están dadas por el valor de d_{ij} si $i = j$ o $-a_{ij}$ si $i \neq j$. También puede determinarse por:

$$L = D - A. \tag{1}$$

Para grafos no dirigidos, la matriz Laplaciana es simétrica y semi-definida positiva, *i.e*, $L = L^T \geq 0$.

2.2 El problema de consenso para un SMA

Consenso significa buscar un acuerdo respecto al valor de una variable de interés, la cual depende de los estados de todos los agentes que sean miembros del sistema. Un *algoritmo de consenso* es una regla de interacción que especifica el intercambio de información entre un agente y todos sus vecinos en la red multiagente. En estos algoritmos la variable de interés es el estado de información de cada agente, por lo que se asume que existe una interacción vecino a vecino entre los integrantes del equipo. En consecuencia, cada agente actualiza su valor de información de acuerdo a los estados de sus vecinos.

La representación de un grafo considera que existe un SMA, donde cada agente se denota por x_i y a su vez cada uno presenta la dinámica de un integrador simple:

$$\dot{x}_i(t) = u_i(t),\ i \in N \tag{2}$$

donde: $u_i(t)$ es la entrada de control y N el número de agentes. Por lo tanto, la forma matricial de la dinámica de los agentes $x_i = [x_1, ..., x_N]^T$, las entradas de control $u = [u_1, ..., u_N]^T$ y las condiciones iniciales $x(0)$ permiten representar al SMA (2).

De acuerdo a Seyboth et al. (2013) el protocolo estándar de consenso para un SMA se define:

$$u_i(t) = -\Sigma_{j\epsilon N_i}(x_i(t) - x_j(t)), \tag{3}$$

con N_i que representa a los agentes vecinos j con respecto al elemento i.

Asumiendo que el grafo es conectado y no dirigido la ley de control (3) resuelve global y asintóticamente el problema de consenso promedio. El valor promedio de los estados de los agentes se define como:

$$x_i(t) \xrightarrow{t\to\infty} \frac{1}{N}\sum_{i\epsilon N} x_i(0). \tag{4}$$

Finalmente, el sistema en lazo cerrado puede ser escrito en forma vectorial como:

$$\dot{x}(t) = -Lx(t), \tag{5}$$

2.3 Control disparado por eventos

En este trabajo, el estudio se enfoca a la clase de sistemas dinámicos de la forma:

$$\dot{x} = f(x) + g(x)u \tag{6}$$

donde: $x \in \mathcal{X} \subset \mathbb{R}^n$, $u \in \mathcal{U} \subset \mathbb{R}^p$, f y g son funciones Lipschitz que se desvanecen al origen. Si el sistema admite un control por retroalimentación $k : \mathcal{X} \to \mathcal{U}$ que estabiliza al sistema asintóticamente, entonces existe una Función de Lyapunov de Control (CLF) $V : \mathcal{X} \to \mathbb{R}$, la cual es una función suave, definida positiva tal que:

$$\dot{V} = \frac{\partial V}{\partial x} f(x) + \frac{\partial V}{\partial x} g(x)k(x) \tag{7}$$

Es necesario notar que si se asume que k es suave, entonces V existe y es suave. En el presente trabajo solo se requerirá que V sea suave, lo cual es menos restrictivo.

En el marco de trabajo de *control disparado por eventos* generalmente se trabaja con dos funciones:

- *Función evento* $\bar{e} : \mathcal{X} \times \mathcal{X} \to \mathbb{R}$ indica si es necesario $(\bar{e} \leq 0)$ o no recalcular y aplicar la señal de control al proceso. La función de evento $\bar{e}$ toma el valor del estado actual x como una entrada y una memoria m del valor que tomo el estado la última vez en la que $\bar{e}$ fue negativa.
- *Función de retroalimentación* $k : \mathcal{X} \to \mathcal{U}$, la cual se usa como en el caso clásico.

Definición 5. Un control por retroalimentación disparado por eventos $(k, \bar{e})$ se dice ser semi-uniformemente MSI (Minimal Sampling Interval) si para todo $\delta > 0$ y todo x_0 en la esfera de radio δ con centro en el origen $\mathcal{B}(\delta)$, la duración de tiempo entre dos eventos consecutivos, puede ser acotado por debajo por algún $\underline{\tau} > 0$.

Se sabe que para un sistema no lineal de la forma (6) con un control disparado por eventos semi-uniformemente MSI $(\bar{e}, k)$, la solución con condiciones iniciales $x_0 \in \mathcal{X}$ en el instante $t = 0$, se define como la solución del sistema:

$$\dot{x} = f(x) + g(x)k(m) \tag{8}$$

$$\begin{cases} m = x & \text{si } \bar{e}(x,m) \leq 0,\ x \neq 0 \\ \dot{m} = 0 & \text{en otros casos} \end{cases} \tag{9}$$

$$\text{con } x(0) := x_0 \text{ and } m(0) = x(0)$$

Teorema 2.1. (Fórmula universal de disparo por evento). Si existe una CLF para el sistema (6), entonces el control disparado por eventos $(\bar{e}, k)$, es MSI, suave en $\mathcal{X}\backslash\{0\}$ y es tal que:

$$\frac{\partial V}{\partial x} f(x) + \frac{\partial V}{\partial x} g(x)k(m) < 0, \quad x \in \mathcal{X}\backslash\{0\} \tag{10}$$

$$k_i(x) := -b_i(x)\delta_i(x)\gamma(x) \tag{11}$$

$$\bar{e}(x,m) := -a(x) - b(x)k(m) \tag{12}$$

$$-\sigma\sqrt{a(x)^2 + \bar{\theta}(x)b(x)\Delta(x)b(x)^T} \tag{13}$$

con las consideraciones planteadas en Marchand et al. (2013).

2.4 Modelo cinemático del robot (3,0)

De acuerdo a la clasificación establecida por Campion and Bastin (1996) el robot móvil (3,0) es un robot holónomo

con tres ruedas omnidireccionales que tiene tres grados de movilidad y no contempla grado de direccionabilidad, para moverse en cualquier dirección con cualquier orientación. Una vista isométrica del robot móvil se muestra en la Fig. 2, donde puede identificarse un sistema de coordenada inercial {w} y un sistema de coordenadas $\{m\}$ se fijan en el plano de movimiento y en el robot móvil, respectivamente. Sea $\dot{\eta}_w = [\dot{x}_w\ \dot{y}_w\ \dot{\phi}_w]^T$ y $\dot{\eta}_m = [\dot{x}_m\ \dot{y}_m\ \dot{\phi}_m]^T$ la velocidad linear y angular del robot móvil con respecto al sistema de coordenadas inercial $\{w\}$ y al sistema de coordenadas del móvil $\{m\}$, respectivamente. Se asume que el robot móvil tiene una estructura rígida, con ruedas que no se deforman, no deslizan y su movimiento es en un plano horizontal (suelo) con un punto de contacto entre la rueda y el suelo; considerando los ángulos descritos por el eje Y_m y el eje axial de la rueda como $\delta_1 = \frac{\pi}{6}$ y $\delta_3 = \frac{\pi}{3}$, el modelo cinemático se puede representar en (14). Cabe mencionar que los valores de los ángulos δ_1 y δ_2 forman parte del diseño del robot móvil ya que maximizan su destreza (Villarreal-Cervantes et al., 2013).

$$\begin{aligned} \dot{x}_w &= \dot{x}_m \cos\phi_w - \dot{y}_m \sin\phi_w \\ \dot{y}_w &= \dot{x}_m \sin\phi_w + \dot{y}_m \cos\phi_w \\ \dot{\phi}_w &= \dot{\phi}_m \end{aligned} \tag{14}$$

El mapeo entre la velocidad lineal de las ruedas y la velocidad angular y lineal del sistema de coordenadas del robot móvil se representa en (15) donde $\dot{\theta} = [\dot{\theta}_1\ \dot{\theta}_2\ \dot{\theta}_3]^T$ es la velocidad angular de las ruedas, $r_r = 0{,}0625m$ es el radio de las ruedas y la distancia entre el centro geométrico del móvil y la rueda se representa como $L = 0{,}287m$.

$$\begin{aligned} \dot{\theta}_1 r_r &= \frac{1}{2}\sqrt{3}\dot{x}_m + \frac{1}{2}\dot{y}_m + L\dot{\phi}_m \\ \dot{\theta}_2 r_r &= -\dot{y}_m + L\dot{\phi}_m \\ \dot{\theta}_3 r_r &= -\frac{1}{2}\sqrt{3}\dot{x}_m + \frac{1}{2}\dot{y}_m + L\dot{\phi}_m \end{aligned} \tag{15}$$

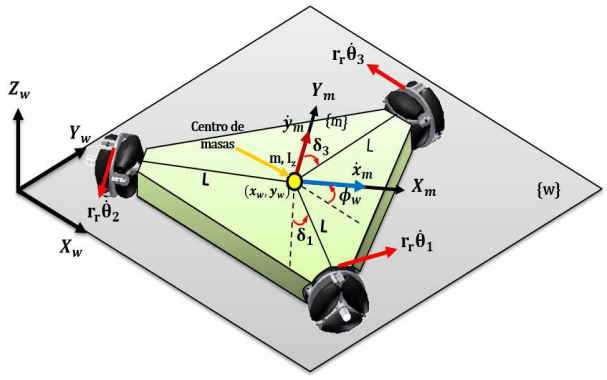

Figura 2. Diagrama esquemático del robot móvil (3,0).

3. DISEÑO DE LA ESTRATEGIA DE CONTROL

Se describe el diseño de una ley de control basado en eventos para un SMA basándose en el esquema centralizado, para este propósito, es necesario determinar una función de control de Lyapunov y posteriormente desarrollar el control disparado por eventos, aplicado a robots móviles tipo (3,0).

Considere la dinámica del modelo como un integrador simple y además los teoremas de estabilidad de Lyapunov permiten dar condiciones suficientes para la estabilidad en los puntos de equilibrio. Por lo tanto se toma en cuenta lo siguiente:

- Si una función $V(x)$ satisface la condición (16) se dice que es definida positiva. En cambio, si satisface la condición más débil de $V(x) \geq 0$ para $x \neq 0$ se dice ser semidefinida positiva.

$$V(0) = 0, \qquad V(x) > 0 \text{ en } u. \tag{16}$$

- Una función se dice definida negativa o semidefinida negativa si $-V(x)$ es definida positiva o semidefinida positiva, respectivamente. Si $V(x)$ no tiene signo definido con respecto a alguno de estos casos se dice indefinida.

Teorema 3.1. (Estabilidad Lyapunov). *El origen es estable si existe una función definida positiva y continuamente diferenciable, tal que $\dot{V}(x)$ es semidefinida negativa, y es asimétricamente estable si $\dot{V}(x)$ es definida negativa.* (Khalil, 1996).

Considerese entonces el siguiente vector de estado asociado al sistema multiagente, $x = [x_1, x_2, ..., x_N]^T$, para el sistema definido por (6) una función (17), la cual es aplicada al sistema en lazo cerrado (5), debe elegirse los elementos de L tal que $V(x)$ sea una función candidata de Lyapunov válida.

$$V(x) = \frac{1}{2}x^T L x \tag{17}$$

donde: L representa la matriz Laplaciana asociada al grafo fuertemente conectado y no direccionado.

Note que esta función de Lyapunov, es cero en el subespacio nulo de L y es mayor que cero fuera de él, debido a la topología del grafo, *i.e.* $L \geq 0$. Si se introduce el complemento ortogonal del espacio nulo de L, se tiene que $\frac{1}{2}x^T Lx \geq \frac{1}{2}\lambda_2(L)\|y\|^2$, donde $x = x_0 + y$, $y \in \ker L^\perp$ y λ_2 representa el segundo valor propio de la matriz L, que es el mínimo valor propio diferente de cero. Puesto que $\|y\|$ representa una medida de la distancia $d(x, \ker L)$ la función de Lyapunov cumple con todas las condiciones para ser considerada una candidata de Lyapunov. Ahora analizaremos si $V(x)$ es una CLF. Para ello, se evalúa la derivada temporal de $V(x)$ a lo largo de las trayectorias del sistema con control dado por (3):

$$\begin{aligned} \dot{V}(x) &= \frac{1}{2}\dot{x}^T Lx + \frac{1}{2}x^T L\dot{x} \\ &= -(Lx)^T(Lx) = \|Lx\|^2 \\ &\leq -\lambda_2(L^T L)\|y\|^2 \end{aligned} \tag{18}$$

Por lo tanto, la Función Candidata de Lyapunov es una Función de Lyapunov y el sistema es estable.

Por otro lado, se puede observar que el sistema representado en (2), puede tomar la forma de un sistema lineal y como consecuencia ser representado mediante la siguiente ecuación:

$$\dot{x} = Ax + Bu. \tag{19}$$

Así, el sistema (19) puede ser escrito en la forma $\dot{x} = f(x) + g(x)u$ considerando $f(x) = Ax$ y $g(x) = B$. Por lo tanto, la técnica de control basada en eventos descrita en

la sección 1.5 se puede aplicar de forma sistemática. En consecuencia, el siguiente paso es determinar las funciones necesarias $a(x)$ y $b(x)$ para obtener la retroalimentación $k_i(x)$ y la función de evento e. Así, igualando (18) con (8) resulta:

$$a(x) := \frac{\partial V}{\partial x} f(x) = 0, \qquad b(x) := \frac{\partial V}{\partial x} g(x) = x^T LI,$$
$$\Delta(x) := I, \quad \bar{\theta}(x) = b(x)b^T(x) - 2a(x), \quad \sigma = 0{,}9,$$

donde: I es la matriz identidad. Cabe mencionar que debido a la representación del sistema, para este caso del integrador simple, el valor de la matriz A es nulo. Por lo tanto, el valor de $a(x)$ que depende de A y la derivada de la función de Lyapunov es cero. Así, las ecuaciones que describen la acción de control y la función de evento son:

$$k_i(x) := -b_i(x)\delta_i(x)\gamma(x), \tag{20}$$

$$\bar{e}(x,m) := -b(x)k(m) - \sigma\sqrt{\bar{\theta}(x)b(x)\Delta(x)b(x)^T}, \tag{21}$$

$$\gamma(x) := \begin{cases} \dfrac{\sqrt{\bar{\theta}(x)b(x)\Delta(x)b(x)^T}}{b(x)\Delta(x)b(x)^T} & \text{si } x \in \mathcal{S} \\ 0 & \text{si } x \notin \mathcal{S} \end{cases} \tag{22}$$

El interés es verificar que el sistema en lazo cerrado definido por (3), en su ejecución, tiene como salida el consenso de los estados que conforman al SMA, los cuales han sido definidos como en (6). A través del Laplaciano se define la topología de comunicación y con ello se tiene de forma implícita la comunicación centralizada. En este sentido y de forma particular, se considera el grafo balanciado y no direccionado mostrado en la Fig. 3, para un caso específico del SMA, integrado por 4 agentes.

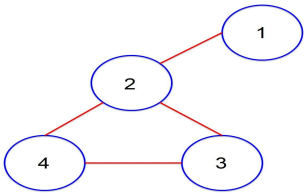

Figura 3. Grafo no dirigido con cuatro agentes.

Por lo tanto, se obtiene lo siguiente:

$$\begin{aligned} \dot{x}_1 = u_1 &= -\sum_{j\epsilon N_i}(x_1 - x_j) \\ \dot{x}_2 = u_2 &= -\sum_{j\epsilon N_i}(x_2 - x_j) \\ \dot{x}_3 = u_3 &= -\sum_{j\epsilon N_i}(x_3 - x_j) \\ \dot{x}_4 = u_4 &= -\sum_{j\epsilon N_i}(x_4 - x_j) \end{aligned} \tag{23}$$

Esta topología será la considerada para realizar consenso y la cual define la matriz Laplaciana. Por consiguiente, en relación al grafo de la Fig. 3, las matrices de Adyacencia **A**, de Grado **D** y Laplaciana **L** son:

$$D = \begin{bmatrix} 1&0&0&0 \\ 0&3&0&0 \\ 0&0&2&0 \\ 0&0&0&2 \end{bmatrix}, \; A = \begin{bmatrix} 0&1&0&0 \\ 1&0&1&1 \\ 0&1&0&1 \\ 0&1&1&0 \end{bmatrix}, \; L = \begin{bmatrix} 1&-1&0&0 \\ -1&3&-1&-1 \\ 0&-1&2&-1 \\ 0&-1&-1&2 \end{bmatrix} \tag{24}$$

La estrategia de control consiste en realizar el desplazamiento de sistemas puntuales, los cuales serán miembros del SMA, en particular, dichos agentes serán las variables de estado que definen la dinámica de cuatro robots móviles tipo (3,0), con condiciones iniciales diversas, para lograr el consenso en la posición y la orientación, a través de la topología de comunicación centralizada, definida por el grafo y ejecutando la técnica de control disparado por eventos, representada en el esquema de la Figura 4.

De acuerdo a la descripción del robot móvil tipo $(3,0)$, es posible obtener el modelo matemático que defina el desplazamiento en el sistema coordenado (X_1, X_2), considerando su estructura física y los tres grados de libertad de movilidad. Por consiguiente, el modelo cinemático del robot móvil $(3,0)$ es posible redefinir:

$$\begin{aligned} \dot{x}_{wi} &= \dot{x}_{mi}\cos\phi_{wi} - \dot{y}_{mi}\sin\phi_{wi} \\ \dot{y}_{wi} &= \dot{x}_{mi}\sin\phi_{wi} + \dot{y}_{mi}\cos\phi_{wi} \\ \dot{\phi}_{wi} &= \dot{\phi}_{mi} \end{aligned} \tag{25}$$

donde: i identifica al agente $i\epsilon N$, $\dot{x}_{mi}$ define la velocidad lineal sobre el eje de referencia X_1, $\dot{y}_{mi}$ define la velocidad lineal sobre el eje de referencia X_2, y Φ_i define la orientación del robot, en un sistema coordenado descrito por (X_1, X_2) en el sistema de referencia $\{w\}$.

Sea el vector de estado $x = [x_{11}\ x_{12}\ x_{21}\ x_{22}\ x_{31}\ x_{32}]^T = \left[\int x_w\ x_w\ \int y_w\ y_w\ \int \phi_w\ \phi_w\right]^T$ y el vector de señal de control $u = [u_1\ u_2\ u_3]^T = \left[\dot{x}_m\ \dot{y}_m\ \dot{\phi}_m\right]^T$, la representación en el vector de variables de estado x del sistema (25) se define en (26), y considere el compensador no lineal (27).

$$\begin{aligned} \dot{x}_{11} &= x_{12} \\ \dot{x}_{12} &= u_1 cos(x_{32}) - u_2 sin(x_{32}) \\ \dot{x}_{21} &= x_{22} \\ \dot{x}_{22} &= u_1 sin(x_{32}) + u_2 cos(x_{32}) \\ \dot{x}_{31} &= x_{32} \\ \dot{x}_{32} &= u_3 \end{aligned} \tag{26}$$

$$\begin{aligned} u_1 &= cos(x_{32})r_1 + sin(x_{32})r_2 \\ u_2 &= -sin(x_{32})r_1 + cos(x_{32})r_2 \\ u_3 &= r_3 \end{aligned} \tag{27}$$

Las señales r_i con $i \in \{1,2,3\}$ son señales de control. Aplicando el compensador no lineal (27) a la cinemática de un robot móvil $(3,0)$ denotada por (26) resulta en las ecuaciones (28)-(30), donde se observa que el modelo cinemático se desacopla y resulta en tres subsistemas, los cuales, Σ_1 y Σ_2 representan las ecuaciones del movimiento de traslación, mientras que el subsistema Σ_3 representa la ecuación del movimiento de rotación.

$$\Sigma_1 := \begin{cases} \dot{x}_{11} = x_{12} \\ \dot{x}_{12} = r_1 \end{cases} \tag{28}$$

$$\Sigma_2 := \begin{cases} \dot{x}_{21} = x_{22} \\ \dot{x}_{22} = r_2 \end{cases} \tag{29}$$

$$\Sigma_3 := \begin{cases} \dot{x}_{31} = x_{32} \\ \dot{x}_{32} = r_3 \end{cases} \tag{30}$$

Por lo cual, se realizará consenso en la dinámica de $\dot{x}_{12} = r_1$, $\dot{x}_{22} = r_2$ y $\dot{x}_{32} = r_3$ considerando el SMA.

4. RESULTADOS

Con la finalidad de validar los resultados teóricos obtenidos, se realizan pruebas a través de simulaciones en

Cuadro 1. Condiciones iniciales de los robots móviles tipo $(3,0)$.

CI	Agente 1	Agente 2	Agente 3	Agente 4
x_{1i} (m)	3	2	1	2
x_{2i} (m)	1	2	3	4
θ_i (rad)	$-(1/2)\pi$	0	$(5/6)\pi$	$(2/3)\pi$

MATLAB/Simulink. Se utiliza un tiempo $t = 10$s y las condiciones iniciales para cada agente son definidas en la Cuadro 1. Por tanto, se ha realizado consenso en la dinámica de los estados que determinan la traslación y orientación del SMA integrado por robot móviles tipo $(3,0)$, a partir de los sistema definidos en (28) para el desplazamiento en X_1, (29) para el desplazamiento en X_2 y (30) para la orientación de los robots, con la misma topología de comunicación, definida por el grafo de la Fig. 3, partiendo de condiciones iniciales diversas de los agentes, para lograr el desplazamiento en un punto de encuentro, particularmente, el promedio de sus condiciones iniciales de cada estado.

La estrategia de control disparado por eventos para el consenso de los tres estados que definen la locomoción de los miembros que integran al SMA, se representa en el esquema de la Fig. 4.

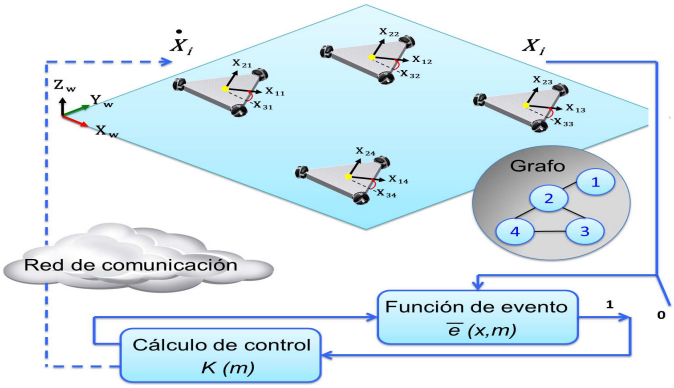

Figura 4. Estrategia de control disparado por eventos para el consenso en la dinámica de los estados del SMA que determinan la traslación y orientación.

Los resultados de simulación muestran la estabilidad del sistema para lograr el consenso del SMA, en la Fig. 5 se observa como se realiza el consenso del SMA, para lograr el desplazamiento de los robots móviles (3,0) en el sistema cordenado $X_1 - X_2$ y consensar en un punto común, cada vez que existe una señal de activación de control disparado por eventos. Las banderas de activación de evento se muestran en la Fig. 6, notar que la reducción de cálculo computacional es reducido al sólo verificar que existe activación de evento de forma asíncrona y logrando una buena estabilidad del SMA, para que en consecuencia, se aplique el control definido por la función de retroalimentación k, la cual es posible ver el comportamiento en la Fig. 7 denotando una rápida y estable ley de control. A través de la Fig. 8 se verifica el consenso del estado X_1 de forma estable al promedio de sus condiciones iniciales, de manera similar en la Fig. 9 se logra el consenso del estado X_2, y finalmente, la Fig. 10 demuestra el consenso del estado X_3, que representa la orientación de los robots.

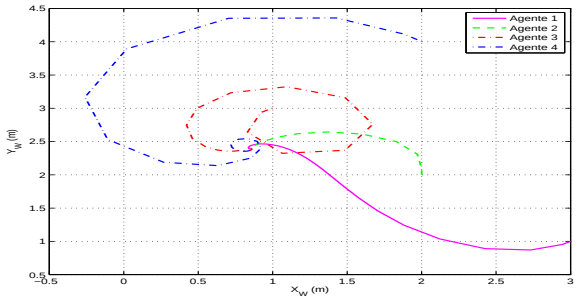

Figura 5. Consenso en la dinámica de los estados que determinan la traslación y orientación del SMA en $X_w - Y_w$.

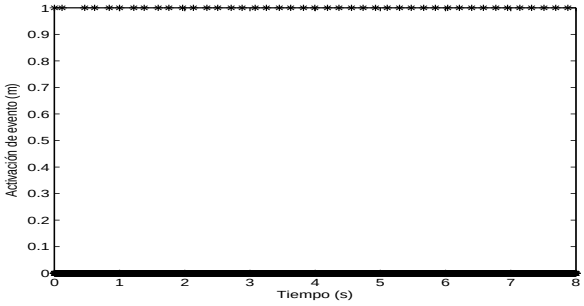

Figura 6. Respuesta de la función de evento.

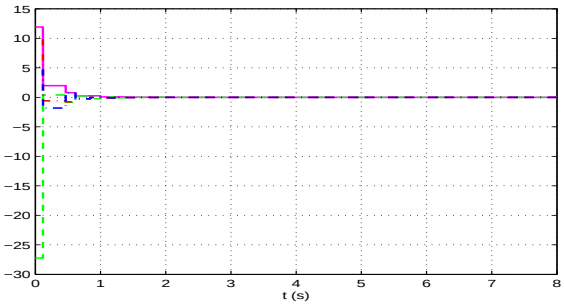

Figura 7. Respuesta de la función de retroalimentación.

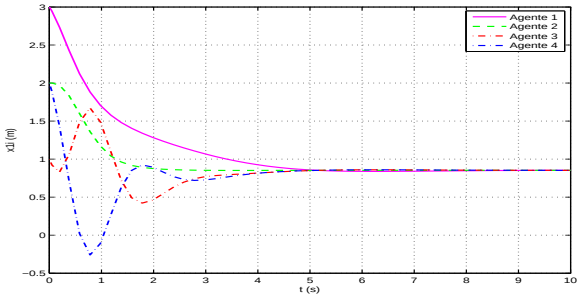

Figura 8. Conseso en posición de X_1 en el SMA.

5. CONCLUSIONES

Se presentó una estrategia de control disparado por eventos para un SMA formado por robots móviles (3,0). En este caso, la variable de estado a controlar es la posición y la orientación bajo una transformación del modelo cinemáti-

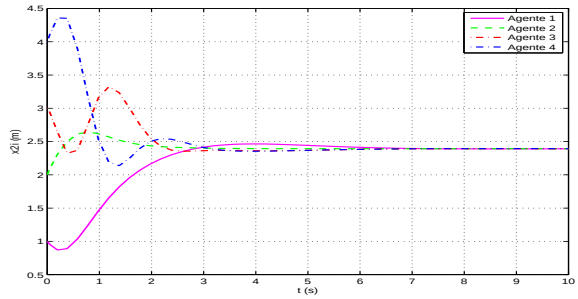

Figura 9. Conseso en posición de X_2 en el SMA.

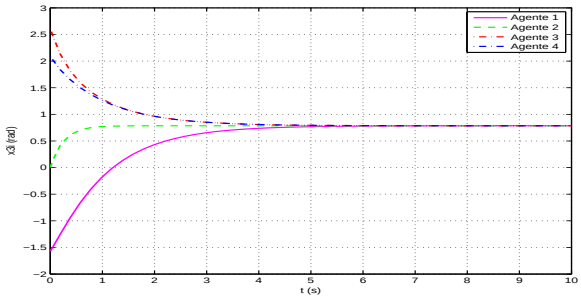

Figura 10. Conseso en orientación X_3 den el SMA.

co del robot móvil $(3, 0)$, ya que se puede considerar como un integrador simple. El caso de estudio es garantizar la estabilidad asintótica del agente en el sentido de Lyapunov, lo cual se ha demostrado en las secciones anteriores. Por otro lado, las pruebas realizadas mediante simulación han constatado que el control basado en eventos tiene un buen desempeño, sin sacrificar la dinámica del sistema. Como resultado se obtuvo la estabilización asintótica al valor del consenso promedio de las condiciones iniciales del SMA. Se corroboró que el control se actualiza únicamente cuando la función de evento se cumple y se aplica en el mismo instante de tiempo a cada uno de los agentes que forman el sistema, esto se debe a que el control es de forma centralizada.

REFERENCIAS

Al-Ali, A. and Al-Jarrah, M. (2009). Embedded systems for mechatronics. In *GCC Conference & Exhibition, 2009 5th IEEE*, 1–5. IEEE.

Cai, K. and Ishii, H. (2012). Average consensus on general strongly connected digraphs. *Automatica*, 48(11), 2750 – 2761.

Campion, G., d.N.B. and Bastin, G. (1996). Structural properties and clasification on kinematic and dynamic models of wheeled mobile robots. *IEEE Transactions on Robotics and Automation*.

Dimarogonas, D.V. and Frazzoli, E. (2009). Distributed event-triggered control strategies for multi-agent systems. In *Communication, Control, and Computing, 2009. Allerton 2009. 47th Annual Allerton Conference on*, 906–910. doi:10.1109/ALLERTON.2009.5394897.

Dimarogonas, D.V. and Johansson, K.H. (2009). Event-triggered cooperative control. In *Control Conference (ECC), 2009 European*, 3015–3020.

Durand, S. and Marchand, N. (2009). Further Results on Event-Based PID Controller. In *Proceedings of the European Control Conference 2009*, 1979–1984. Budapest, Hongrie. URL `http://hal.archives-ouvertes.fr/hal-00368535`. Département Automatique.

Fax, J.A. and Murray, R.M. (2004). Information flow and cooperative control of vehicle formations. *Automatic Control, IEEE Transactions on*, 49(9), 1465–1476.

Gao, H., Chen, T., and Lam, J. (2008). A new delay system approach to network-based control. *Automatica*, 44(1), 39 – 52. doi: http://dx.doi.org/10.1016/j.automatica.2007.04.020.

Khalil, H.K. (1996). *Nonlinear Systems*. Prentice-Hall, Englewood Cliffs, NJ, 2nd edition.

Marchand, N., Durand, S., and Castellanos, J.F.G. (2013). A general formula for event-based stabilization of nonlinear systems. *Automatic Control, IEEE Transactions on*, 58(5), 1332–1337.

Olfati-Saber, R. and Murray, R.M. (2004a). Consensus problems in networks of agents with switching topology and time-delays. *IEEE Transactions on Automatic Control*, 49(9), 1520–1533. doi:10.1109/TAC.2004.834113.

Olfati-Saber, R., Fax, J.A., and Murray, R.M. (2007). Consensus and cooperation in networked multi-agent systems. *Proceedings of the IEEE*, 95(1), 215–233.

Olfati-Saber, R. and Murray, R.M. (2004b). Consensus problems in networks of agents with switching topology and time-delays. *Automatic Control, IEEE Transactions on*, 49(9), 1520–1533.

Rajkumar, R. (2012). A cyber-physical future. *Proceedings of the IEEE*, 100(Special Centennial Issue), 1309–1312. doi:10.1109/JPROC.2012.2189915.

Seyboth, G.S., Dimarogonas, D.V., and Johansson, K.H. (2011). Control of multi-agent systems via event-based communication. *Proceedings of the 18th IFAC World Congress, 2011*.

Seyboth, G.S., Dimarogonas, D.V., and Johansson, K.H. (2013). Event-based broadcasting for multi-agent average consensus. *Automatica*, 49(1), 245–252.

Shi, J., Wan, J., Yan, H., and Suo, H. (2011). A survey of cyberphysical systems. In *International Conference on Wireless Communications and Signal Processing*, 1–6.

Shiyong Wang, Jiafu Wan, D.L. and Zhang, C. (2016). Implementing smart factory of industrie 4.0: An outlook. *International Journal of Distributed Sensor Networks*, 10.

Villarreal-Cervantes, M.G., Cruz-Villar, C.A., Alvarez-Gallegos, J., and Portilla-Flores, E.A. (2013). Robust structure-control design approach for mechatronic systems. *IEEE/ASME Transactions on Mechatronics*, 18(5), 1592–1601.

Yamaguchi, H. (2003). A distributed motion coordination strategy for multiple nonholonomic mobile robots in cooperative hunting operations. *Robotics and Autonomous Systems*, 43(4), 257–282.

Yan, H., Shen, Y., Zhang, H., and Shi, H. (2014). Decentralized event-triggered consensus control for second-order multi-agent systems. *Neurocomputing*, 133, 18–24.

Control de Seguimiento de Trayectorias para un AR.Drone 2.0 Utilizando Observadores de Estados. ⋆

J. Santiaguillo-Salinas, M.A. Rosaldo-Serrano y E. Aranda-Bricaire *

* *Departamento de Ingeniería Eléctrica, Sección Mecatrónica, CINVESTAV AP 14-740, 07000 Ciudad de México, México. (e-mail: jsantiaguillo@cinvestav.mx, marcosarosaldos@gmail.com, earanda@cinvestav.mx).*

Resumen: En este trabajo se estudia el seguimiento de trayectorias para el prototipo comercial de helicóptero de 4 rotores AR.Drone 2.0, de la empresa francesa Parrot. La estrategia de control propuesta para el seguimiento de trayectorias está diseñada utilizando la técnica de Backstepping. Para la implementación de la ley de control, se supone que sólo se conoce la posición y orientación del AR.Drone 2.0; sus velocidades longitudinales y rotacionales son estimadas mediante observadores de Luenberger y se sustituyen en la ley de control. Con la estrategia de control diseñada, se logra que un AR.Drone 2.0 converja asintóticamente a una trayectoria de vuelo preestablecida. Los resultados teóricos presentados son validados experimentalmente.

Keywords: Backstepping, Observador de Estados, Seguimiento de Trayectorias, Helicópteros de 4 Rotores, AR.Drone 2.0.

1. INTRODUCCIÓN

El AR.Drone es un tipo de vehículo aéreo no tripulado (UAV) cuya configuración consta de 4 rotores colocados en las puntas de una estructura en forma de cruz. Las principales ventajas de este tipo de UAVs son el despegue y aterrizaje en forma vertical y la capacidad de realizar vuelo estacionario (hover), la gran desventaja es que no pueden realizar vuelos de gran duración.

El AR.Drone ha sido elegido como plataforma experimental por muchos investigadores debido a su bajo costo y al gran número de sensores con los que cuenta, pero dado a que tiene un controlador interno para estabilizarlo, no es posible utilizar el modelo dinámico genérico de un helicóptero de 4 rotores. En la literatura se pueden encontrar algunos trabajos referentes al modelado y control del AR.Drone. En Falcón et al. (2013), se identifica el modelo del AR.Drone de forma experimental y posteriormente se hace pasivo mediante una ganancia no lineal. En Hernandez et al. (2013), se presenta un proceso para la identificación del modelo del AR.Drone, además, se propone un control de tipo path following para controlar su posición. Aunque el AR.Drone es de arquitectura cerrada, en Bristeau et al. (2011) se habla sobre la arquitectura interna del AR.Drone 2.0. Sin embargo, el valor de los parámetros utilizados está restringido sólo para los desarrolladores.

En la literatura para helicópteros de 4 rotores, es común el uso de filtros y observadores, debido al ruido presente en las mediciones a partir de sensores y que en algunos casos no es posible medir algún estado del sistema. En Mokhtari et al. (2012), se presenta una linealización por retroalimentación y un observador lineal para el control de un helicóptero de 4 rotores. En Wang and Shirinzadeh (2015), se utilizan observadores no lineales para estimar las velocidades e incertidumbres de un helicóptero de 4 rotores cuando se conoce su posición. Para el caso de un AR.Drone, en Vago-Santana et al. (2014) se emplea un filtro de Kalman para estimar los estados, a partir de la combinación de datos inerciales y visuales.

Este trabajo aborda el diseño y validación experimental de una estrategia de control junto con un observador de estados tipo Luenberger para lograr el seguimiento de trayectorias de un AR.Drone. Se utiliza un modelo dinámico completo, el cual es obtenido a partir del modelo dinámico de un helicóptero de 4 rotores convencional y del modelado de la dinámica interna del AR.Drone. Debido a la estructura del modelo del AR.Drone, para el diseño de la estrategia de control se utiliza la técnica de Backstepping. Aunque el AR.Drone cuenta con una gran variedad de sensores, estos pueden presentar mediciones ruidosas e incluso erróneas en algunas ocasiones. Debido a lo anterior, se emplean observadores de Luenberger para estimar las velocidades longitudinales y angulares del AR.Drone.

Este trabajo está organizado de la siguiente manera. La Sección 2 presenta el modelo dinámico completo del AR.Drone. El diseño de la estrategia de control para el seguimiento de trayectorias se muestra en la Sección 3. La Sección 4 presenta el diseño de observadores de estados para el AR.Drone. La Sección 5 presenta la plataforma experimental utilizada en este trabajo y los resultados ex-

⋆ Este trabajo está financiado parcialmente por el CONACyT, México, a través de los No. de Becario 243226 y 280703.

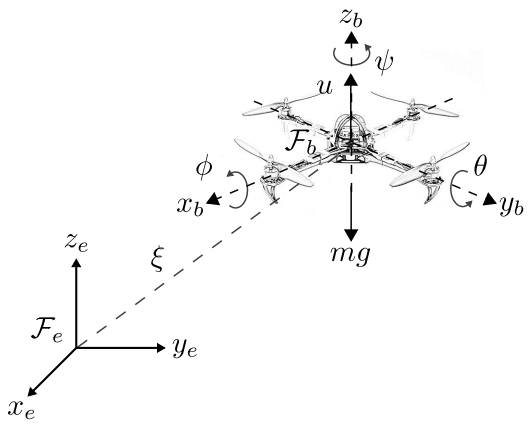

Figura 1. Diagrama XYZ de un helicóptero de 4 rotores.

perimentales obtenidos. Finalmente, algunas conclusiones y trabajo futuro se presentan en la sección 6.

2. MODELO DINÁMICO DEL AR.DRONE 2.0

A partir de la Figura 1, $\xi = [x, y, z]^T$ representa la posición del centro de masa con respecto al sistema inercial $\mathcal{F}_e$ y $\eta = [\psi, \theta, \phi]^T$ los ángulos de Euler que representan la orientación del helicóptero de 4 rotores. Utilizando el enfoque de Euler-Lagrange y basándonos en García-Carrillo et al. (2013), la dinámica no lineal completa de un helicóptero de 4 rotores puede ser expresada como

$$\ddot{x} = \frac{u}{m}\left(\cos\psi \sin\theta \cos\phi + \sin\psi \sin\phi\right) \tag{1a}$$
$$\ddot{y} = \frac{u}{m}\left(\sin\psi \sin\theta \cos\phi - \cos\psi \sin\phi\right) \tag{1b}$$
$$\ddot{z} = \frac{u}{m}\left(\cos(\theta)\cos(\phi)\right) - g \tag{1c}$$
$$\ddot{\psi} = \tilde{\tau}_\psi \tag{1d}$$
$$\ddot{\theta} = \tilde{\tau}_\theta \tag{1e}$$
$$\ddot{\phi} = \tilde{\tau}_\phi \tag{1f}$$

con m la masa del helicóptero y g la constante de gravedad. Las entradas de control u y $\tilde{\tau} = [\tilde{\tau}_\psi, \tilde{\tau}_\theta, \tilde{\tau}_\phi]^T$ son el empuje principal y los momentos angulares, respectivamente. Estos últimos se relacionan con los torques generalizados $\tau = [\tau_\psi, \tau_\theta, \tau_\phi]^T$ mediante

$$\tilde{\tau} = \mathbb{J}^{-1}(\tau - C(\eta, \dot{\eta})\dot{\eta}) \tag{2}$$

donde $\mathbb{J}$ es la matriz de inercia y $C(\eta, \dot{\eta})$ es el término de Coriolis.

Para modelar la dinámica interna del AR.Drone, se proponen las siguientes ecuaciones diferenciales

$$\ddot{z} = -a_1\dot{z} + a_3 u_z \tag{3a}$$
$$\ddot{\phi} = -b_1\dot{\phi} - b_2\phi + b_3 u_\phi \tag{3b}$$
$$\ddot{\theta} = -c_1\dot{\theta} - c_2\theta + c_3 u_\theta \tag{3c}$$
$$\ddot{\psi} = -d_1\dot{\psi} + d_3 u_\psi \tag{3d}$$

donde los parámetros a_1, a_3, b_1, b_2, b_3, c_1, c_2, c_3, d_1 y d_3 se calculan a partir de un análisis experimental mediante mínimos cuadrados utilizando el software matemático MATLAB, por el cuál se obtuvieron 4 funciones de transferencia, las cuales relacionan las entradas de control del AR.Drone con las variables de estado z,ϕ,θ, y ψ, dadas por

$$\frac{Z(s)}{U_z(s)} = \frac{a_3}{s^2 + a_1 s} = \frac{3{,}384}{s^2 + 3{,}613s} \tag{4a}$$
$$\frac{\Phi(s)}{U_\phi(s)} = \frac{b_3}{s^2 + b_1 s + b_2} = \frac{-67{,}3}{s^2 + 6{,}542s + 25{,}5} \tag{4b}$$
$$\frac{\Theta(s)}{U_\theta(s)} = \frac{c_3}{s^2 + c_1 s + c_2} = \frac{60{,}4}{s^2 + 4{,}302s + 28{,}24} \tag{4c}$$
$$\frac{\Psi(s)}{U_\psi(s)} = \frac{d_3}{s^2 + d_1 s} = \frac{3{,}828}{s^2 + 4{,}225s} \tag{4d}$$

Habiendo modelado el controlador interno del AR.Drone, podemos tener un modelo completo a partir de las ecuaciones (1a)-(1c) y (3a)-(3d) dado por

$$\ddot{x} = (g - a_1\dot{z} + a_3 u_z)\left(\tan\theta\cos\psi + \frac{\tan\phi}{\cos\theta}\sin\psi\right) \tag{5a}$$
$$\ddot{y} = (g - a_1\dot{z} + a_3 u_z)\left(\tan\theta\sin\psi - \frac{\tan\phi}{\cos\theta}\cos\psi\right) \tag{5b}$$
$$\ddot{z} = -a_1\dot{z} + a_3 u_z \tag{5c}$$
$$\ddot{\phi} = -b_1\dot{\phi} - b_2\phi + b_3 u_\phi \tag{5d}$$
$$\ddot{\theta} = -c_1\dot{\theta} - c_2\theta + c_3 u_\theta \tag{5e}$$
$$\ddot{\psi} = -d_1\dot{\psi} + d_3 u_\psi \tag{5f}$$

donde u_z, u_ϕ, u_θ y u_ϕ son las entradas de control del AR.Drone.

3. ESTRATEGIA DE CONTROL

Para el diseño de la estrategia de control para el seguimiento de trayectorias, suponemos una altura y un ángulo de guiñada constantes, por lo cuál, para mantener dicha altura y ángulo proponemos las siguientes leyes de control

$$u_z = \frac{1}{a_3}\left[a_1\dot{z} - k_{pz}\left(z - z^d\right) - k_{dz}\dot{z}\right] \tag{6}$$
$$u_\psi = \frac{1}{d_3}\left[d_1\dot{\psi} - k_{p\psi}\left(\psi - \psi^d\right) - k_{d\psi}\dot{\psi}\right] \tag{7}$$

donde a_1, a_3 y d_1, d_3 son las constantes de las funciones de transferencia para la dinámica en Z y en ψ, respectivamente, k_{pz}, k_{dz}, $k_{p\psi}$ y $k_{d\psi}$ son las ganancias de control y z^d y ψ^d son la posición deseada sobre el eje Z y el ángulo deseado de guiñada, respectivamente.

Para el diseño de la ley de control de movimiento en el plano horizontal utilizaremos la técnica de *Backstepping* Khalil (2002); Kokotovic (1992); Krstic et al. (1995). Para ello, reescribiremos la dinámica del sistema de la siguiente manera. Definimos los estados para la dinámica en X, Y, θ y ϕ como

$$\xi_1 = [\,x\ ,\ y\,]^T \tag{8a}$$
$$\xi_2 = [\,\dot{x}\ ,\ \dot{y}\,]^T \tag{8b}$$
$$\eta_1 = [\,\theta\ ,\ \phi\,]^T \tag{8c}$$
$$\eta_2 = [\,\dot{\theta}\ ,\ \dot{\phi}\,]^T \tag{8d}$$

Tomando la aproximación de primer orden de (5a)-(5b) la dinámica de los estados resulta

$$\dot{\xi}_1 = \xi_2 \tag{9a}$$
$$\dot{\xi}_2 = gA(\psi)\eta_1 \tag{9b}$$
$$\dot{\eta}_1 = \eta_2 \tag{9c}$$
$$\dot{\eta}_2 = -\beta_1\eta_2 - \beta_2\eta_1 + \beta_3 u_\eta \tag{9d}$$

donde $u_\eta = [u_\theta, u_\phi]^T = \beta_3^{-1}\left[\beta_1\eta_2 + \beta_2\eta_1 + v_\eta\right]$,

$$A(\psi) = \begin{bmatrix} \cos(\psi) & \sin(\psi) \\ \sin(\psi) & -\cos(\psi) \end{bmatrix}$$

y

$$\beta_1 = \begin{bmatrix} c_1 & 0 \\ 0 & b_1 \end{bmatrix}, \quad \beta_2 = \begin{bmatrix} c_2 & 0 \\ 0 & b_2 \end{bmatrix} \quad \text{y} \quad \beta_3 = \begin{bmatrix} c_3 & 0 \\ 0 & b_3 \end{bmatrix}$$

son matrices constantes que contienen los términos obtenidos en el modelado por funciones de transferencia del AR.Drone. Definimos los errores del sistema como

$$e_{\xi 1} = \xi_1 - \xi_1^d \tag{10a}$$
$$e_{\xi 2} = \xi_2 - \dot{\xi}_1^d \tag{10b}$$
$$e_{\eta 1} = \eta_1 - \eta_1^d \tag{10c}$$
$$e_{\eta 2} = \eta_2 - \dot{\eta}_1^d \tag{10d}$$

donde ξ_1^d son las posiciones deseadas para el AR.Drone en el plano XY y η_1^d las orientaciones deseadas, es decir, los ángulos deseados en alabeo y cabeceo. La dinámica del error en X, Y, θ y ψ resulta

$$\dot{e}_{\xi 1} = e_{\xi 2} \tag{11a}$$
$$\dot{e}_{\xi 2} = gA(\psi)e_{\eta 1} \tag{11b}$$
$$\dot{e}_{\eta 1} = e_{\eta 2} \tag{11c}$$
$$\dot{e}_{\eta 2} = v_\eta - \ddot{\eta}_1^d \tag{11d}$$

Reescribiendo la dinámica del error y tomando $v_\eta = \ddot{\eta}_1^d + w_\eta$ tenemos

$$\dot{e}_\xi = A_\xi e_\xi + B_\xi e_{\eta 1} \tag{12a}$$
$$\dot{e}_{\eta 1} = e_{\eta 2} \tag{12b}$$
$$\dot{e}_{\eta 2} = w_\eta \tag{12c}$$

donde $e_\xi = [e_{\xi 1}, e_{\xi 2}]^T$,

$$A_\xi = \begin{bmatrix} 0 & I_2 \\ 0 & 0 \end{bmatrix} \quad \text{y} \quad B_\xi = \begin{bmatrix} 0 \\ gA(\psi) \end{bmatrix}$$

con $I_2 \in \mathbb{R}^{2\times 2}$ la matriz identidad. A partir de este punto, aplicamos dos pasos del algoritmo de backstepping llegando a la siguiente ley de control

$$u_\eta = \beta_3^{-1}\left[\beta_1\eta_2 + \beta_2\eta_1 + \ddot{\eta}_1^d - \frac{1}{g}A^{-1}(\psi)\left[K_1(\xi_1 - \xi_1^d) + K_2(\xi_2 - \dot{\xi}_1^d)\right] - K_3(\eta_1 - \eta_1^d) - K_4(\eta_2 - \dot{\eta}_1^d)\right] \tag{13}$$

donde

$$K_1 = k_p + k_2 b g^2 + k_2 k_1 k_p$$
$$K_2 = bg^2 + k_1 k_p + k_d + k_2 k_p + k_2 c g^2 + k_2 k_1 k_d$$
$$K_3 = k_p + k_1 k_d + cg^2 + I + k_2 k_d + k_2 k_1$$
$$K_4 = k_2 + k_1 + k_d$$

Proposición 1. Considere el subsistema (5a)-(5b)-(5d)-(5e) y la ley de control (13). Entonces en el sistema en lazo cerrado (5a)-(5b)-(5d)-(5e)-(13) el AR.Drone converge asintóticamente de forma local a la trayectoria deseada en el plano XY, i.e. $\lim_{t\to\infty}\left(\xi_1(t) - \xi_1^d(t)\right) = 0$, y a los ángulos deseados de orientación de alabeo y cabeceo, i.e. $\lim_{t\to\infty}\left(\eta_1(t) - \eta_1^d(t)\right) = 0$.

Demostración. El procedimiento de diseño con la técnica de backstepping asegura convergencia asintótica del sistema en lazo cerrado (9a)-(9d)-(13), donde (9a)-(9d) es una aproximación de primer orden de (5a)-(5b)-(5d)-(5e). Por lo tanto, se garantiza convergencia asintótica local para el sistema en lazo cerrado (5a)-(5b)-(5d)-(5e)-(13). ■

4. DISEÑO DEL OBSERVADOR DE ESTADOS

Generalmente, es necesario conocer el estado del sistema para resolver la mayoría de los problemas de la teoría de control. Sin embargo, en muchos casos prácticos el estado del sistema no puede ser medido directamente por lo que se utilizan observadores. El observador de Luenberger es un algoritmo que permite reconstruir el estado de un sistema dinámico a partir de las mediciones de la entrada y la salida del mismo. Si un sistema es observable, es posible reconstruir completamente el estado del sistema con mediciones de su salida mediante el uso de un observador. En muchos casos prácticos el vector de estados observado es utilizado en la retroalimentación del estado para generar el control deseado. El procedimiento de diseño de observadores presentado en esta sección está basado en Ogata (2010).

Para diseñar el observador para la dinámica en X, Y, θ y ϕ, reescribimos el subsistema (9a)-(9d) de la forma

$$\dot{x}_{\xi\eta} = A_{\xi\eta}x_{\xi\eta} + B_{\xi\eta}u_\eta \tag{14a}$$
$$y_{\xi\eta} = C_{\xi\eta}x_{\xi\eta} \tag{14b}$$

donde la salida es la posición ξ_1 y la orientación η_1, que son estados medibles, $x_{\xi\eta} = [\xi_1, \xi_2, \eta_1, \eta_2]^T$,

$$A_{\xi\eta} = \begin{bmatrix} 0 & I_2 & 0 & 0 \\ 0 & 0 & gA(\psi) & 0 \\ 0 & 0 & 0 & I_2 \\ 0 & 0 & \beta_2 & \beta_1 \end{bmatrix}, \quad B_{\xi\eta} = \begin{bmatrix} 0 \\ 0 \\ 0 \\ \beta_3 \end{bmatrix}$$

y

$$C_{\xi\eta} = \begin{bmatrix} I_2 & 0 & 0 & 0 \\ 0 & 0 & I_2 & 0 \end{bmatrix}$$

Verificamos que el subsistema para la dinámica en X, Y, θ y ϕ sea observable. La matriz de observabilidad está dada por

$$\mathcal{O}_{\xi\eta} = \begin{bmatrix} C_{\xi\eta} \\ C_{\xi\eta}A_{\xi\eta} \\ C_{\xi\eta}A_{\xi\eta}^2 \\ \vdots \\ C_{\xi\eta}A_{\xi\eta}^7 \end{bmatrix} \tag{15}$$

haciendo el desarrollo y obteniendo el rango de la matriz a través del software matemático MATLAB, obtenemos que el rango de la matriz de observabilidad es $\text{rank}\,(\mathcal{O}_{\xi\eta}) = 8$, es decir, es de rango completo por columnas y por lo tanto el subsistema para la dinámica en X, Y, θ y ϕ es observable. Entonces, proponemos el siguiente observador de Luenberger

$$\dot{\hat{x}}_{\xi\eta} = A_{\xi\eta}\hat{x}_{\xi\eta} + B_{\xi\eta}u_\eta + L_{\xi\eta}(y_{\xi\eta} - \hat{y}_{\xi\eta}) \tag{16a}$$
$$\hat{y}_{\xi\eta} = C_{\xi\eta}\hat{x}_{\xi\eta} \tag{16b}$$

donde $\hat{x}_{\xi\eta} = \begin{bmatrix} \hat{\xi}_1 & \hat{\xi}_2 & \hat{\eta}_1 & \hat{\eta}_2 \end{bmatrix}^T$ son los estados observados y $L_{\xi\eta}$ es una matriz de ganancias del observador.

Proposición 2. Considere el subsistema (14a)-(14b) y el observador (16a)-(16b). Entonces existe $L_{\xi\eta}$ tal que el

sistema (16a)-(16b) es un observador para el subsistema (14a)-(14b), i.e. $\lim_{t\to\infty}\left(x_{\xi\eta}(t)-\hat{x}_{\xi\eta}(t)\right)=0$.

Demostración. Definimos el error de observación como

$$\tilde{x}_{\xi\eta}=x_{\xi\eta}-\hat{x}_{\xi\eta} \tag{17}$$

La dinámica del error de observación resulta

$$\dot{\tilde{x}}_{\xi\eta}=\left(A_{\xi\eta}-L_{\xi\eta}C_{\xi\eta}\right)\tilde{x}_{\xi\eta} \tag{18}$$

y ya que el par $(C_{\xi\eta},A_{\xi\eta})$ es observable, se puede escoger $L_{\xi\eta}$ tal que $A_{\xi\eta}-L_{\xi\eta}C_{\xi\eta}$ es Hurwitz y los errores de observación converjan asintóticamente a cero. ■

Nota 1. Cabe mencionar que se tiene un observador local para la dinámica en X, Y, θ y ϕ, ya que esta basado en la aproximación de primer orden y considerando altura y ángulo de guiñada constantes.

Ahora, modificamos la ley de control (13) utilizando las velocidades longitudinales y rotacionales estimadas $\hat{\xi}_2$ y $\hat{\eta}_2$, respectivamente, obtenidas a partir del observador (16a) con lo que obtenemos

$$\begin{aligned}u_\eta=&\beta_3^{-1}\Big[\beta_1\hat{\eta}_2+\beta_2\eta_1+\ddot{\eta}_1^d-\frac{1}{g}A^{-1}(\psi)\left[K_1(\xi_1-\xi_1^d)\right.\\&\left.+K_2(\hat{\xi}_2-\dot{\xi}_1^d)\right]-K_3(\eta_1-\eta_1^d)-K_4(\hat{\eta}_2-\dot{\eta}_1^d)\Big]\end{aligned} \tag{19}$$

Proposición 3. Considere el subsistema (14a), el observador (16a) y la ley de control (19). Las matrices $H_{\xi\eta}$ y $A_{\xi\eta}-L_{\xi\eta}C_{\xi\eta}$ son Hurwitz. Entonces en el sistema en lazo cerrado (14a)-(16a)-(19), los errores de seguimiento y de observación para la dinámica en X, Y, θ y ϕ convergen asintóticamente a cero, i.e. $\lim_{t\to\infty}\left(x_{\xi\eta}(t)-x_{\xi\eta}^d(t)\right)=0$ y $\lim_{t\to\infty}\left(x_{\xi\eta}(t)-\hat{x}_{\xi\eta}(t)\right)=0$.

Demostración. Primeramente, identificamos a la matriz $H_{\xi\eta}$, a partir de los errores de seguimiento (10a)-(10d). Para ello, tenemos que la dinámica del error para X, Y, θ y ϕ en lazo cerrado con la ley de control diseñada por backstepping (13) resulta

$$\dot{e}_{\xi\eta}=H_{\xi\eta}e_{\xi\eta} \tag{20}$$

donde $e_{\xi\eta}=[e_{\xi1},e_{\xi2},e_{\eta1},e_{\eta2}]^T$ y

$$H_{\xi\eta}=\begin{bmatrix}0&I_2&0&0\\0&0&gA(\psi)&0\\0&0&0&I_2\\-\frac{K_1}{g}A^{-1}(\psi)&-\frac{K_2}{g}A^{-1}(\psi)&-K_3I_2&-K_4I_2\end{bmatrix}$$

y a partir del procedimiento de diseño de backstepping, se sabe que la matriz $H_{\xi\eta}$ es Hurwitz. Definimos los errores de seguimiento para el observador como

$$\hat{e}_{\xi1}=\hat{\xi}_1-\xi_1^d \tag{21a}$$
$$\hat{e}_{\xi2}=\hat{\xi}_2-\dot{\xi}_1^d \tag{21b}$$
$$\hat{e}_{\eta1}=\hat{\eta}_1-\eta_1^d \tag{21c}$$
$$\hat{e}_{\eta2}=\hat{\eta}_2-\dot{\eta}_1^d \tag{21d}$$

La dinámica del error de seguimiento considerando ahora (19) resulta

$$\dot{e}_{\xi\eta}=H_{\xi\eta1}e_{\xi\eta}+H_{\xi\eta2}\hat{e}_{\xi\eta} \tag{22}$$

donde

$$H_{\xi\eta1}=\begin{bmatrix}0&I_2&0&0\\0&0&gA(\psi)&0\\0&0&0&I_2\\-\frac{K_1}{g}A^{-1}(\psi)&0&-K_3I_2&-\beta_1\end{bmatrix}$$

y

$$H_{\xi\eta2}=\begin{bmatrix}0&0&0&0\\0&0&0&0\\0&0&0&0\\0&-\frac{K_2}{g}A^{-1}(\psi)&0&\beta_1-K_4I_2\end{bmatrix}$$

y la dinámica del error de seguimiento para el observador

$$\dot{\hat{e}}_{\xi\eta}=G_{\xi\eta1}e_{\xi\eta}+G_{\xi\eta2}\hat{e}_{\xi\eta}+L_{\xi\eta}C_{\xi\eta}(e_{\xi\eta}-\hat{e}_{\xi\eta}) \tag{23}$$

donde

$$G_{\xi\eta1}=\begin{bmatrix}0&0&0&0\\0&0&0&0\\0&0&0&0\\-\frac{K_1}{g}A^{-1}(\psi)&0&\beta_2-K_3I_2&0\end{bmatrix}$$

y

$$G_{\xi\eta2}=\begin{bmatrix}0&I_2&0&0\\0&0&gA(\psi)&0\\0&0&0&I_2\\0&-\frac{K_2}{g}A^{-1}(\psi)&-\beta_2&-K_4I_2\end{bmatrix}$$

Para estudiar el sistema completo, organizamos las ecuaciones para $\dot{e}_{\xi\eta}$ y $\dot{\hat{e}}_{\xi\eta}$ en forma matricial como

$$\begin{bmatrix}\dot{e}_{\xi\eta}\\\dot{\hat{e}}_{\xi\eta}\end{bmatrix}=\begin{bmatrix}H_{\xi\eta1}&H_{\xi\eta2}\\G_{\xi\eta1}+L_{\xi\eta}C_{\xi\eta}&G_{\xi\eta2}-L_{\xi\eta}C_{\xi\eta}\end{bmatrix}\begin{bmatrix}e_{\xi\eta}\\\hat{e}_{\xi\eta}\end{bmatrix} \tag{24}$$

Definimos el siguiente cambio de variables

$$\begin{bmatrix}e_{\xi\eta}\\\tilde{e}_{\xi\eta}\end{bmatrix}=\begin{bmatrix}I_8&0\\I_8&-I_8\end{bmatrix}\begin{bmatrix}e_{\xi\eta}\\\hat{e}_{\xi\eta}\end{bmatrix} \tag{25}$$

con $I_8\in\mathbb{R}^{8\times8}$ la matriz identidad y donde es posible notar que $\tilde{e}_{\xi\eta}=e_{\xi\eta}-\hat{e}_{\xi\eta}=\tilde{x}_{\xi\eta}$,con lo que obtenemos

$$\begin{bmatrix}\dot{e}_{\xi\eta}\\\dot{\tilde{e}}_{\xi\eta}\end{bmatrix}=\begin{bmatrix}H_{\xi\eta1}+H_{\xi\eta2}&-H_{\xi\eta2}\\0&(H_{\xi\eta1}-G_{\xi\eta1})-L_{\xi\eta}C_{\xi\eta}\end{bmatrix}\begin{bmatrix}e_{\xi\eta}\\\tilde{e}_{\xi\eta}\end{bmatrix} \tag{26}$$

y ya que $H_{\xi\eta1}+H_{\xi\eta2}=H_{\xi\eta}$ y $H_{\xi\eta1}-G_{\xi\eta1}=A_{\xi\eta}$ finalmente tenemos

$$\begin{bmatrix}\dot{e}_{\xi\eta}\\\dot{\tilde{e}}_{\xi\eta}\end{bmatrix}=\begin{bmatrix}H_{\xi\eta}&-H_{\xi\eta2}\\0&A_{\xi\eta}-L_{\xi\eta}C_{\xi\eta}\end{bmatrix}\begin{bmatrix}e_{\xi\eta}\\\tilde{e}_{\xi\eta}\end{bmatrix} \tag{27}$$

La matriz del sistema (27) es triangular superior por bloques, por lo que sus eigenvalores coinciden con los eigenvalores de los bloques que se encuentran en la diagonal principal, en este caso $H_{\xi\eta}$ y $A_{\xi\eta}-L_{\xi\eta}C_{\xi\eta}$. Ya que las matrices $H_{\xi\eta}$ y $A_{\xi\eta}-L_{\xi\eta}C_{\xi\eta}$ son Hurwitz, entonces tanto el sistema controlado como el observador son estables, por lo que el sistema completo también es asintóticamente estable, y tanto los errores de seguimiento como los errores de observación convergen a cero. ■

Nota 2. Para el caso de la dinámica en Z y ψ, se realiza un procedimiento similar al ya presentado, tanto para el diseño de los observadores como para el análisis del control con observador.

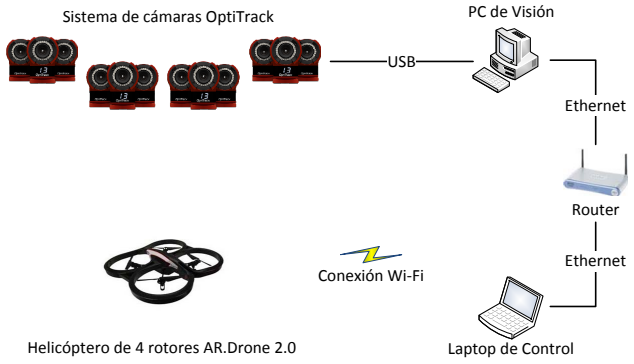

Figura 2. Plataforma experimental.

5. EXPERIMENTACIÓN

5.1 Plataforma experimental

Para validar los resultados teóricos obtenidos, la estrategia de control con observador diseñada se implementa en una plataforma experimental. La plataforma se muestra en la Figura 2 y está formada por un AR.Drone 2.0, un sistema de visión y un sistema de control y comunicación.

AR.Drone 2.0. Es un helicóptero de 4 rotores comercial, fabricado por la empresa francesa Parrot. El AR.Drone 2.0 se puede controlar a través de aplicaciones para equipos con arquitectura de PC con sistemas operativos basados en Linux, utilizando una conexión Wi-Fi. El AR.Drone 2.0 cuenta con una estructura con tubos de fibra de carbono, con piezas de plástico nylon con 30 % de fibra de vidrio, 2 cascos de protección de polipropileno expandido, un casco para exteriores y otro para interiores, nanorevestimiento que repele líquidos, así como espuma para aislar el centro inercial de las vibraciones producidas por los motores. En la parte electrónica, el AR.Drone 2.0 cuenta con un procesador ARM Cortex A8 de 1 GHz de 32 bits con Linux 2.6.32, una memoria RAM DDR2 de 1 GHz, un puerto USB 2.0 que se puede utilizar para grabar video en una memoria USB o conectar un GPS, 2 cámaras de video, una vertical QVGA de 60 FPS y una horizontal HD 720p de 30 FPS.

Los sensores con los que cuenta el AR.Drone 2.0 son:

- Giroscopio de 3 ejes con precisión de 2000°/seg
- Acelerómetro de 3 ejes con precisión de ± 50 mg
- Magnetómetro de 3 ejes con precisión de 6°
- Sensor de presión con una precisión de ± 10 Pa
- Sensor de ultrasonido para medir la posición vertical

El AR.Drone 2.0 tiene 4 motores inrunner sin escobillas de 28,500 RPM y 14.5 W con controladores con CPU AVR de 8 MIPS.

Sistema de visión. La localización del AR.Drone 2.0 (posición y orientación) se realiza a través de un sistema de visión que consta de 12 cámaras marca OptiTrack modelo Flex 13 y una PC Core i3 con Windows 7 que tiene el software Motive:Tracker. Dicho software está diseñado para el rastreo de objetos en 6 DOF con alta precisión y con soporte para el procesamiento en tiempo real. Las cámaras Flex 13 tienen una resolución de 1.3 MP a 120 FPS y cuentan con una tarjeta interna de procesamiento de imágenes, lo cual libera parcialmente al sistema operativo de realizar dicha tarea. Por medio del puerto USB las cámaras reciben alimentación y realizan el envío de datos.

Cabe mencionar, que del sistema de visión sólo se obtienen la posición en el espacio XYZ y el ángulo de guiñada ψ; los ángulos de alabeo y cabeceo, ϕ y θ, respectivamente, se obtienen a partir de los sensores con los que cuenta el AR.Drone 2.0.

Sistema de control y comunicación. Se cuenta con una Laptop Core i5 con un sistema operativo Ubuntu 12.04 con ROS en su versión Fuerte Turtle, que realiza los cálculos del control y los envía al AR.Drone 2.0 vía Wi-Fi. ROS es un framework flexible de código abierto, que permite la escritura de software para el control de robots. Se trata de una colección de herramientas, librerías y convenciones que simplifican la creación de comportamientos complejos y robustos en robots. ROS permite el diseño de manera individual de procesos que se pueden acoplar de manera flexible en tiempo de ejecución. Estos procesos se pueden agrupar en paquetes que pueden ser fácilmente compartidos y distribuidos, con lo que se logra la reutilización de código.

La comunicación entre la PC de visión y la Laptop de control se hace a través de una transmisión basada en una arquitectura cliente/servidor (NatNet SDK) a través de una red local mediante una conexión Ethernet.

5.2 Experimentos

A continuación se presenta un experimento utilizando las velocidades longitudinales y rotacionales en los ejes X, Y y Z obtenidas a partir de los observadores diseñados en este trabajo. En los experimentos, primero se procedió a despegar al AR.Drone, de ahí ponerlo en modo hover y entonces comenzar con el seguimiento de trayectoria. Una vez terminado el seguimiento de trayectoria, se vuelve a poner en modo hover y posteriormente se aterriza.

La trayectoria deseada en el plano XY es una Lemniscata de Gerono dada por

$$\xi_1^d(t) = \left[1.0\cos\left(\frac{2\pi t}{T}\right), 0.5\sin\left(\frac{4\pi t}{T}\right)\right]^T \qquad (28)$$

con un periodo de $T = 60$ s. Se tienen una altura y un ángulo de guiñada constantes, donde la altura deseada es de $z^d = 1$ m y el ángulo de guiñada deseado es de $\psi^d = 0^o$. La Fig. 3 muestra el movimiento del AR.Drone 2.0 en el espacio.

Las figuras 4 y 5 presentan los errores de posición y orientación del AR.Drone, respectivamente.

6. CONCLUSIONES Y TRABAJO FUTURO

Este trabajo presenta una estrategia de control para lograr el seguimiento de trayectorias de un helicóptero de 4 rotores AR.Drone 2.0 de Parrot. Dicha estrategia de control esta diseñada utilizando el método de backstepping y está basada en el uso de observadores para reconstruir las velocidades longitudinales y rotacionales del AR.Drone. Como se puede observar en los resultados experimentales

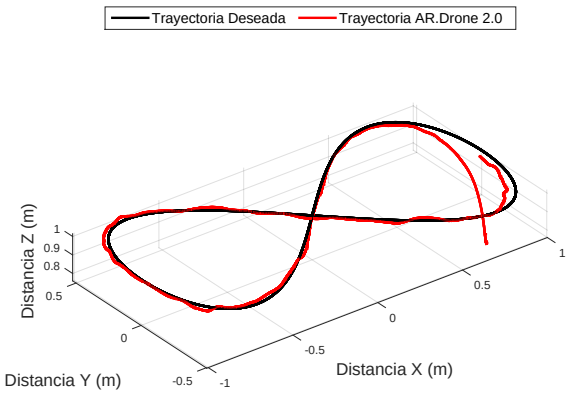

Figura 3. Movimiento en el espacio del AR.Drone.

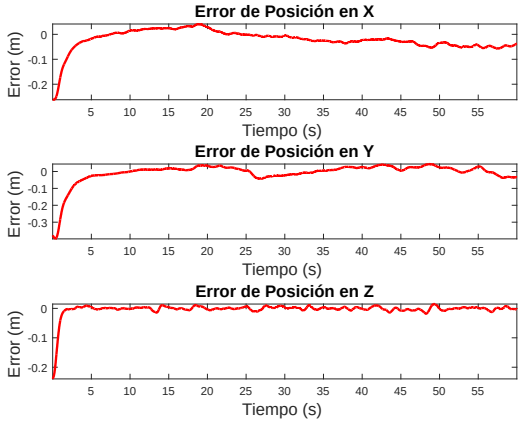

Figura 4. Errores de posición del AR.Drone.

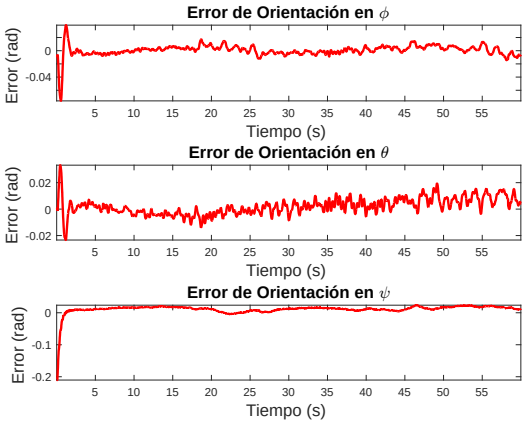

Figura 5. Errores de orientación del AR.Drone.

obtenidos, los errores de observación convergen a cero y el AR.Drone logra el seguimiento de trayectorias.

Para este tipo de vehículo, el error que se tiene en el seguimiento de trayectorias puede considerarse aceptable debido a que se despreciaron los efectos no lineales que se presentan debido al desbalanceo y deformaciones en las hélices, ejes y engranes del AR.Drone. Así mismo, se despreciaron las turbulencias generadas por las hélices y otros efectos aerodinámicos, e.g. el efecto suelo. Cabe recordar que los resultados obtenidos en este trabajo son locales, ya que para el diseño de la estrategia de control y de los observadores, se utilizó una aproximación de primer orden del modelo completo del AR.Drone.

Como trabajo futuro, se plantea la utilización del modelo completo del AR.Drone, para el cual se diseñará una estrategia de control no lineal y se emplearán observadores no lineales para estimar las velocidades longitudinales y rotacionales, con lo que se pretende mejorar el desempeño y obtener resultados más generales. También, se plantea el uso de varios helicópteros de 4 rotores AR.Drone 2.0 para formar un sistema multi-agente y diseñar estrategias de control para la coordinación de movimiento de este tipo de sistemas, en particular, para lograr vuelo en formación.

REFERENCIAS

Bristeau, P. J., Callou, F., Vissiére, D., Petit, N., 2011. The navigation and control technology inside the ar.drone micro uav. 18th IFAC World Congress.

Falcón, P., Barreiro, A., Cacho, M. D., 2013. Modeling of parrot ardrone and passivity-based reset control. 2013 9th Asian Control Conference (ASCC), 1–6.

García-Carrillo, L. R., Dzul-López, A. E., Lozano, R., Pégard, C., 2013. Modeling the quad-rotor mini-rotorcraft. In: Quad Rotorcraft Control. Advances in Industrial Control. Springer London, Ch. 2, pp. 23–34.

Hernandez, A., Copot, C., De keyser, R., Vlas, T., Nascu, I., 2013. Identification and path following control of an ar.drone quadrotor. 2013 17th International Conference on System Theory, Control and Computing (ICSTCC), 583–588.

Khalil, H. K., 2002. Nonlinear Systems. Prentice Hall.

Kokotovic, P. V., 1992. The joy of feedback: nonlinear and adaptive. IEEE Control Systems Magazine 12 (3), 7–17.

Krstic, M., Kokotovic, P. V., kanellakopoulos, I., 1995. Nonlinear and Adaptive Control Design. John Wiley & Sons, Inc.

Mokhtari, A., M'Sirdi, N. K., Meghriche, K., Belaidi, K., 2012. Feedback linearization and linear observer for a quadrotor unmanned aerial vehicle. Advanced Robotics 20 (1), 71–91.

Ogata, K., 2010. Modern Control Engineering. Prentice Hall.

Vago-Santana, L., Santos-Brandão, A., Sarcinelli-Filho, M., Carelli, R., 2014. A trajectory tracking and 3d positioning concontrol for the ar.drone quadrotor. 2014 International Conference on Unmanned Aircraft Systems (ICUAS), 756–767.

Wang, X., Shirinzadeh, B., 2015. Nonlinear augmented observer design and application to quadrotor aircraft. Nonlinear Dynamics 80 (3), 1463–1481.

Control Robusto QFT Sobre un Robot Móvil de Autobalance Basado en Péndulo Invertido Empleando un Sistema Embebido

Rafael A. Núñez* Oscar M. Gómez* Néstor A. León

**Unidades Tecnológicas de Santander,*
Grupo de Investigación en Control Avanzado – GICAV, Bucaramanga, 6800005
Colombia (e-mail:{rrodriguez, ogomez, nleon} @ correo.uts.edu.co).

Resumen: En este artículo se presenta un control robusto QFT diseñado bajo la herramienta 'QFT Control Toolbox for Matlab (QFTCT)', con el objetivo de mantener en autobalance un robot móvil basado en péndulo invertido que emplea un sistema de procesamiento embebido Beaglebone Black, sistema en el cual se implementa el controlador mediante ecuaciones en diferencias. Los resultados obtenidos demuestran que en el modelo péndulo invertido se debe asegurar un centro de masa bajo, mediante el anexo de un contrapeso en la parte inferior del cuerpo del prototipo, aumentando de tal forma las prestaciones del control QFT en aspectos de estabilidad robusta y rechazo de perturbaciones sobre el autobalance del robot. Además se determina que la dificultad de garantizar una distribución de peso sobre el cuerpo del péndulo genera una inclinación constante que lleva al sistema a ser inestable en espacios de funcionamiento reducidos, causa que es solucionada mediante un control PID u otro tipo de control, capaz delimitar el desplazamiento del móvil del prototipo. Estableciendo finalmente que el control de un sistema péndulo invertido requiere de dos controladores autobalance y posición.

Palabras claves: Control robusto, Quantitative feedback theory (QFT), Péndulo Invertido, Robot de autobalance.

1. INTRODUCTION

La mayoría de métodos de análisis y diseño de sistemas realimentados para mecanismo tipo péndulo invertido consideran que se dispone de una planta suficientemente exacta. No obstante, en aplicaciones reales no se cuenta con un modelo estricto ya que existe un error considerable de modelo así como también de un alto grado de incertidumbre dentro del modelo estimado (Sánchez 1996). Para diseñar controladores con buenas prestaciones de desempeño ante procesos con alto grado de incertidumbre, en los últimos treinta años se han desarrollado un conjunto de teorías de control avanzado que permiten mitigar los efectos de la incertidumbre del sistema, en las que se encuentran el método H∞ (Francis 1983), método LTF (Loop Tranfer Recovery) (Stein 1981), método de diseño IMC (Internal Model Control) (Zafiriou 1989), método de Kharatinov (Barmish 1993), Método de Sintesís-μ (Packard 1993), método GPC (Generalized Predictive Control) (Clarke 1988) y el método QFT (Quantitavive Feedback Theory) (Horowitz 1982), teorías que a través de los años han realizado aportes importantes en el desarrollo de técnicas de control avanzado, aplicados principalmente en las áreas de procesos químicos, robótica, estructuras flexibles y control de aeronaves (Dorato 1993). Para el control de sistemas subactuados tipo péndulo invertido se han aplicado ampliamente estas técnicas de control avanzado, tal como se propone en (Pérez Polo 2012), donde se desarrolló un control de posición por asignación de polos más integrador, de un péndulo invertido por medio de movimientos caóticos, cuyo objetivo es incrementar la fuerza de la acción de control para conseguir movimientos caóticos para hacer pivotar el péndulo sobre el carro con ruedas. El modelo matemático del sistema se obtuvo por medio de ecuaciones de Euler-LaGrange, determinando las condiciones necesarias para el movimiento caótico de la varilla por medio de la función de Melnikov. Se ha tomado un enfoque no lineal del sistema del péndulo invertido, lo que ha permitido implementar un controlador no lineal para estabilizar el sistema tal como se propone en (Frías 2013), donde se determino una funcion candidata de Lyapunov en combinación con el principio de invariancia de La Salle para diseñar el controlador de estabilización del sistema en lazo cerrado. Se pudo demostrar que el sistema es asintóticamente estable localmente, alrededor del punto de equilibrio es inestable, con un dominio de atracción calculable.

En este trabajo se presenta el desarrollo de un control robusto a partir de la teoría QFT para la estabilidad un sistema basado en la estructura de un péndulo invertido, la cual se caracteriza por ser un sistema no lineal, de fase no mínima, inestable con considerables incertidumbres paramétricas, ya que se consideran variaciones del peso, fricción de las ruedas, largo del robot, cambios del centro de masa e inercia del móvil (Jun 2011); lo que hace necesario implementar técnicas de control robusto, en espacial aplicando la teoría de realimentación cuantitativa QFT. En la sección 2. se describen las generalidades de la metodología de control robusto QFT. En la sección 3. se plantea el prototipo basado en péndulo invertido implementado, el modelo matemático de la planta mediante el uso de ecuaciones Euler-Lagrange y

la linealización en ecuaciones de estado. En la sección 4. se muestra el proceso de diseño del controlador robusto QFT y finalizando con la sección 5. donde se exponen los resultados obtenido de la implementación del controlador propuesto para el autobalance de un prototipo robot móvil basado en el péndulo invertido.

2. TEORÍA DE REALIMENTACIÓN CUANTITATIVA

La teoría de realimentación cuantitativa QFT propone explícitamente el uso controladores realimentados para reducir simultáneamente los efectos de la incertidumbre de la planta y las especificaciones de desempeño deseadas a partir del diseño en el domino de la frecuencia (Rasmussen 1999). El diseño de controladores QFT requiere como punto de partida, un modelo de la planta con incertidumbres que seguidamente es evaluado bajo un conjunto de frecuencias de interés de acuerdo al ancho de banda de sistema, con esto se establece para cada frecuencia una representación fase [°]-magnitud [dB] de la planta con incertidumbre sobre el plano de Nichols, denominando tal proceso como plantillas o *templates* del sistema, las cuales conceptualmente permiten evaluar la naturaleza del sistema y el grado de inestabilidad del mismo utilizando el criterio de estabilidad de Nyquist en el diagrama de Nichols (Houpis 2005). A partir de las plantillas y las especificaciones de desempeño robusto que se muestran el tabla 1. se construyen una serie de inecuaciones cuadráticas, una por cada especificación, cuya solución se representa en forma gráfica en el diagrama de Nichols por medio de contornos o *bounds* para cada frecuencia de interés. El objetivo de la técnica QFT es conseguir un controlador $G(j\omega)$ que modifique la respuesta del lazo nominal L_o de tal forma que se ubique por encima de los contornos o bordee las zonas restringidas para satisfacer las restricciones y al mismo tiempo minimizar el esfuerzo de control.

Tabla 1. Especificaciones de Desempeño

Especificación	Definición
Estabilidad Robusta	$\left\|\frac{y}{r}\right\| = \left\|\frac{L(j\omega)}{1+L(j\omega)}\right\| < \delta_u(\omega)$
Rechazo de Perturbación a la Salida	$\left\|\frac{y}{d}\right\| = \left\|\frac{1}{1+L(j\omega)}\right\| < \delta_S(\omega)$
Rechazo de Perturbación a la Entrada	$\left\|\frac{y}{u_d}\right\| = \left\|\frac{P(j\omega)}{1+L(j\omega)}\right\| < \delta_p(\omega)$
Seguimiento de Referencia	$\alpha_L(\omega) \leq \left\|\frac{PGF(j\omega)}{1+L(j\omega)}\right\| \leq \alpha_U(\omega)$
Rechazo a Ruido	$\left\|\frac{y}{n}\right\| = \left\|\frac{PG(j\omega)}{1+L(j\omega)}\right\| < \delta_n(\omega)$
Esfuerzo de Control	$\left\|\frac{u}{n}\right\| = \left\|\frac{G(j\omega)}{1+L(j\omega)}\right\| < \delta_c(\omega)$

La estabilidad robusta es una especificación que es garantizada mediante el margen de fase y margen de ganancia mínimo que el sistema debe contener, tomando como criterio teórico lo recomendado por Bode para un margen de ganancia entre 3dB y 5dB (Ogata 2010), y lo establecido por Biernson para un margen de fase entre 30 ° y 60° (Biernson 1988). Con base en la especificación de desempeño de la Tabla 1. y los criterios de Bode y Biernson, se establece que para conseguir un $MG = 5dB$ y un $MF = 45°$, δ_U debe ser igual a $\delta_U = 1.3$. De manera que el δ_U queda dado por las ecuaciones 1 y 2.

$$MF \geq 180° - \arccos\left(\frac{0.5}{\delta_U} - 1\right) \quad (1)$$

$$MG \geq 1 + \frac{1}{\delta_U} \quad (2)$$

El rechazo de perturbación a la salida del sistema, está caracterizada a partir de la función de sensibilidad S dada por la ecuación 3, la cual permite estudiar el rango de frecuencias en la cual el sistema atenúa las perturbaciones de carga del sistema al ser realimentado, siendo ésta directamente proporcional al grado de sobrepaso de la respuesta transitoria con respecto el nivel de referencia (Dorf 2011).

$$S = \frac{1}{1+L} \quad (3)$$

Con base en la función de sensibilidad S, la especificación de desempeño de rechazo de perturbación a la salida, y la planta nominal $P_0(s)$, se obtiene la inecuación cuadrática dada por la ecuación 5, a partir de la inecuación 4.

$$\left|\frac{1}{1+gp\,e^{j(\emptyset+\theta)}}\right| < \delta_S(\omega) \quad (4)$$

$$g^2p^2 + 2gp\cos(\emptyset+\theta) + 1 - \frac{1}{\delta_S^2(\omega)} \leq 0 \quad (5)$$

Donde p representa la magnitud de la planta nominal, g es la incógnita de la inecuación, en este caso es la magnitud del controlador necesaria para alcanzar la especificación, $\delta_S(\omega)$ equivale a la cuantificación del rechazo de perturbaciones, esta puede ser una constante o una función de transferencia (Houpis 2005), y θ y $\emptyset$ son los argumentos de la planta nominal y el controlador respectivamente. Para resolver la inecuación cuadrática dada por la ecuación 5, se utilizan técnicas de análisis numérico a través de métodos iterativos de acuerdo a la metodología planteada en (Chait 1993). Cada solución real de la ecuación 5, equivale a un punto en el diagrama de Nichols, y el conjunto de N puntos conforman la línea de un contorno para la especificación de rechazo de perturbaciones de salida.

Existen otras especificaciones de desempeño como limitación del esfuerzo de control y seguimiento de referencias que al igual que la estabilidad y el rechazo de perturbaciones son

directamente proporcionales a una función de sensibilidad dada con respecto a la función del transferencia de lazo abierto del sistema (Houpis 2005), de manera que el diseño de compensadores utilizando la metodología QFT se debe hacer directamente sobre L_0 y no sobre las funciones de sensibilidad de cada especificación, para cuantificar de forma directa el grado de cumplimiento según lo requerido por el diseñador y las prestaciones del proceso, técnica denominada *loop-shaping* del controlador (I. Horowitz 1959), el cual consiste en agregar ceros polos y ganancias sobre la función $L_0 = GP_0$ específicamente sobre G quien es el compensador (Gera 1980).

3. MODELO MATEMÁTICO Y PARÁMETROS

Se construyó el robot móvil basado en péndulo invertido como se muestra en la Fig. 5, el cual es diseñó con base a un modelo de la compañía *Strawson Design*® denominado *beagleMIP* (beagleboard 2014). El robot está construido en acrílico de 3mm con ayuda de una cortadora de láser, seguido se crea una tarjeta integrada externa que se implementa de manera fácil sobre el sistema embebido *Beaglebone Black*, el cual contiene un procesador ARM de 1 Ghz, 512 MB de RAM, puerto Ethernet, puerto USB, entrada microSD, S.O Debian, 46 puertos digitales y analógicos.

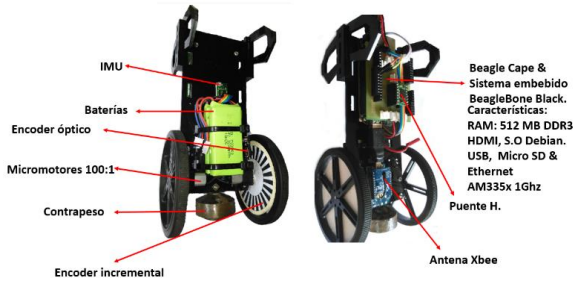

Fig. 1. Robot móvil de autobalance basado en péndulo invertido.

El robot móvil está integrado con un sistema de comunicación inalámbrica que permite visualizar el ángulo de balance y la posición del robot sobre el área de trabajo incorporando un antena de transmisión *Xbee* que está conectada a un software de comunicación serial llamado *realterm*® y un sistema de visualización *kst2*®, conectada directamente al puerto USB del sistema embebido.

Para la obtención del modelo matemático del robot móvil basado en péndulo invertido se utilizaron las ecuaciones de Euler-Lagrange (Acosta 2004), partiendo del estudio de la fuerza conservativa dada por la ecuación 6, fuerzas no conservativas dada por la ecuación 7 y el *lagrangiano* dado por la ecuación 8.

$$\frac{d}{dt}\left(\frac{\partial \mathrm{L}}{\partial \dot{\mathrm{q}}_\mathrm{i}}\right) - \frac{\partial \mathrm{L}}{\partial \mathrm{q}_\mathrm{i}} = 0 \tag{6}$$

$$\frac{d}{dt}\left(\frac{\partial \mathrm{L}}{\partial \dot{\mathrm{q}}_\mathrm{i}}\right) - \frac{\partial \mathrm{L}}{\partial \mathrm{q}_\mathrm{i}} = \mathrm{Q}_\mathrm{i} \tag{7}$$

$$\mathrm{L} = \mathrm{T} - \mathrm{U} \tag{8}$$

Donde:

$qi \;=\; Grado\ de\ libertad$
$Qi \;=\; Fuerzas\ no\ conservativas\ en\ el\ modelo$
$L \;=\; Lagrangiano$
$T \;=\; Energía\ cinética\ total$
$U \;=\; Energía\ potencial\ total$

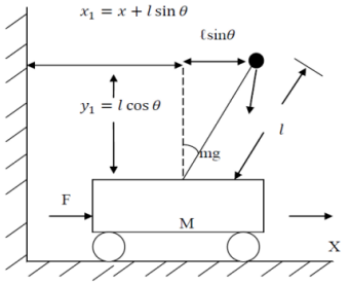

Fig. 2. Diagrama de cuerpo libre péndulo invertido.

A partir del diagrama de cuerpo libre mostrado en la Fig. 2. se obtiene el modelo no lineal de balance dado por la ecuación 9, y el modelo no lineal de posición del carro dado por la ecuación 10 (M. G. Houpis 2012).

$$(M+m)\ddot{x} + ml\ddot{\theta}\cos\theta - ml\dot{\theta}^2\sin\theta + b\dot{x} = F \tag{9}$$

$$(I+ml^2)\ddot{\theta} + ml\ddot{x}\cos\theta - mgl\sin\theta = 0 \tag{10}$$

Si el robot operara cerca de un punto de equilibrio vertical de 0° con oscilaciones no mayores a ±5°, se realiza una aproximación lineal del comportamiento dinámico del sistema, descrito por las ecuaciones 11 y 12 (M. G. Houpis 2012).

$$(M+m)\ddot{x} + ml\ddot{\theta} + b\dot{x} - F = 0 \tag{11}$$

$$(I+ml^2)\ddot{\theta} + ml\ddot{x} - mgl\theta = 0 \tag{12}$$

La representación del sistema en variables de estados está dada por la ecuación 13.

$$\dot{x} = \begin{bmatrix} 0 & 1 & 0 & 0 \\ 0 & -\dfrac{b(I+ml^2)}{(M+m)I+ml^2M} & -\dfrac{m^2l^2g}{(M+m)I+ml^2M} & 0 \\ 0 & 0 & 0 & 1 \\ 0 & \dfrac{mlb}{(M+m)I+ml^2M} & \dfrac{mlg(M+m)}{(M+m)I+ml^2M} & 0 \end{bmatrix} + \begin{bmatrix} 0 \\ \dfrac{I+ml^2}{(M+m)I+ml^2M} \\ 0 \\ -\dfrac{ml}{(M+m)I+ml^2M} \end{bmatrix} F \tag{13}$$

$$Y = [0 \quad 0 \quad 1 \quad 0]$$

En la Tabla 2. se muestra los parámetros físicos del robot móvil de autobalance basado en péndulo invertido y la variación de los parámetros del sistema. La masa del carro se determinó mediante la suma del peso de los motores y ruedas, con una incertidumbre de 20%, por posible variación en el tipo de ruedas o motores con diferente peso. La Masa del péndulo se definió a partir del peso del cuerpo del robot con todos los componentes que están sobre él, sin tomar los motores y ruedas, con incertidumbre del 20% por incremento de peso o disminución del mismo al agregar o quitar componentes. La fricción de la ruedas está condicionada al tipo de rueda, para el robot las ruedas son de caucho, y la superficie de trabajo concreto, por tanto se estableció un coeficiente de fricción de 0.5, con un rango de incertidumbre entre 0.1 a 1. Coeficiente que abarca la fricción dada por este tipo de polímero ante diversos tipos de superficies (Callister 2007). La inercia del péndulo es calculada mediante la relación (ml^2)⁄3, siendo proporcional a peso del cuerpo del péndulo y la variación del centro de masa (Patete 2011). El centro de masa, se determinó balanceando el robot horizontalmente, tomando diferentes puntos de apoyo hasta conseguir una posición de equilibrio, estableciendo una incertidumbre de 2% de error por la forma en que se calcula, y la posible redistribución de masas sobre el cuerpo del robot.

Tabla 2. Especificaciones de Desempeño

Parámetro	Valor
Masa del carro (M)	$0.04\ Kg$
Masa del péndulo (m)	$0.3\ Kg$
Inercia del péndulo (l)	$0.00005\ Kg.m^2$
Fricción ruedas (b)	$0.5\ kg * mts^2$
Centro de masa (Ls)	$0.03\ m$
Largo del péndulo (L)	$0.15\ m$
Gravedad (g)	$9.8\ m/s^2$

4. DISEÑO DEL CONTROLADOR

Para el diseño del controlador se utilizó la herramienta 'The QFT Control Toolbox (QFTCT) for Matlab' (M. G. Houpis 2012), gracias a su capacidad de representar de forma exacta el espacio de incertidumbre, la representación de especificaciones de desempeño, el cálculo y construcción de contornos y el diseño y análisis de controladores y pre-filtros utilizando la técnica *loop-shaping*.

Se definió el modelo del robot móvil basado en péndulo invertido con incertidumbres, generando una familia de plantas evaluada ante un conjunto de frecuencias de interés entre 0.001 a 100Khz obtenidas a partir del diagrama de Bode del sistema. Con base en la variación de los parámetros y del conjunto de frecuencias de interés, calculan las plantillas mostradas en la Fig. 2.

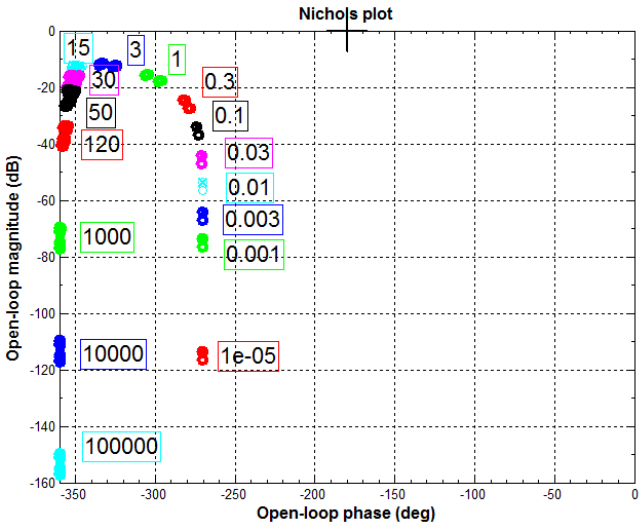

Fig. 2. Plantillas o *Templates* del sistema

La especificación de rechazo de perturbación a la salida de la Tabla 1. se definió $\delta_S(\omega)$ como una función de transferencia cuya respuesta temporal representa el comportamiento deseado ante un perturbación de carga tipo escalón unitario, que en la vida real representa un cambio de pendiente en la superficie de contacto del robot. El controlador debe ser capaz de mitigar los efectos de la perturbación en menos 1s, y lograra que el sistema de estabilice en su punto de equilibrio, 0°. La función de transferencia se calculó con base en lo propuesto en (d'Azzo 2003), y está dada por la ecuación 14.

$$\delta_S(\omega) = \frac{s^2 + 3.99\ s}{s^2 + 7.979s + 16.92} \tag{14}$$

La respuesta en frecencia de la función de transferencia de la ecuación 14, se muestra en la Fig. 3.

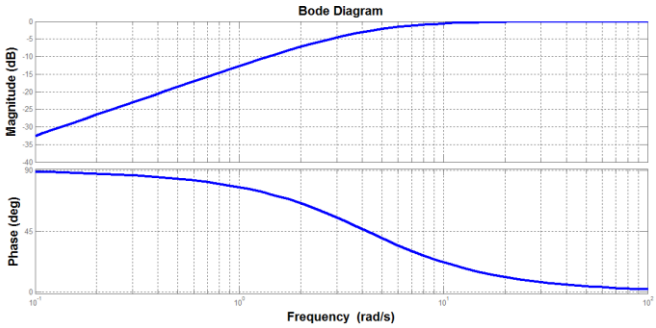

Fig. 3. Respuesta en frecuencia del modelo de rechazo de perturbación a la salida.

La respuesta temporal de la especificación $\delta_S(\omega)$ se muestra en la Fig. 4, y se comprueba que la función de transferencia definida cumple con los criterios de diseño.

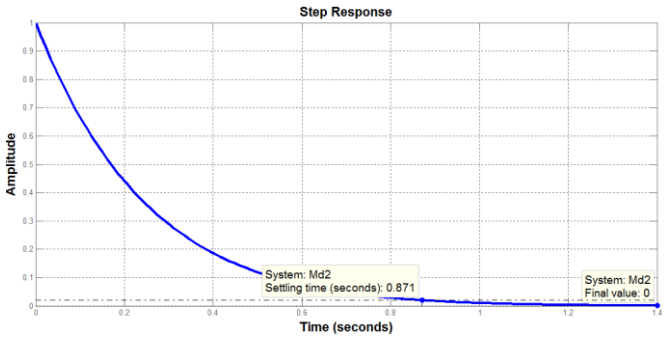

Fig. 4. Respuesta en el tiempo del modelo de rechazo de perturbación a la salida.

Los intercepto de las N soluciones de las inecuaciones cuadráticas de las especificaciones de estabilidad robusta, y rechazo de perturbaciones de entrada se muestran en la figura 5.

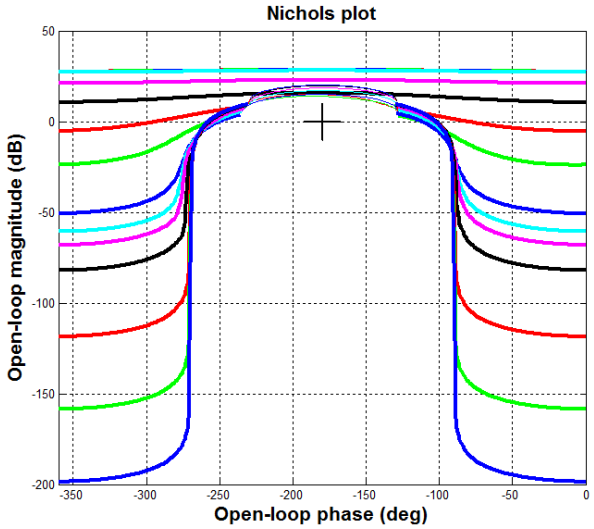

Fig. 5. Intercepto de contornos para cada frecuencia de interés.

A partir de los contornos, se diseña el controlador utilizando la técnica *loop-shapping*, la cual permite agregar polos y ceros de manera que la función del lazo L_0 cumpla unas restricciones determinadas. En este caso, se logró cumplir los requisitos establecidos por las especificaciones de diseño con un margen de fase y ganancia mínimo de 45° y $5dB$ respectivamente, y rechazo de perturbación en las frecuencias de interés, ya que el controlador aportó la fase y ganancia suficiente a la función del lazo nominal L_0 para que la respuesta en el diagrama Nichols quedara por encima de la intersección de cada contorno. El controlador está constituido por un integrador, el cual hace que el sistema mantenga un error de estado estable cercano acero, y un polo y dos ceros reales, quienes movieron horizontalmente la función de lazo L_0 hasta alcanzar la zona de las especificaciones deseadas. En la Fig. 6. Se observa la respuesta de la función de lazo nominal L_0 con el controlador diseñado de la ecuación 15.

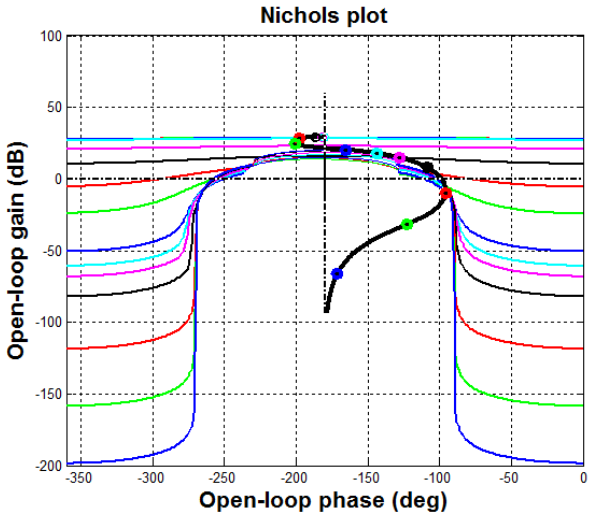

Fig. 6. Función de lazo abierto sintonizada ante las especificaciones de control establecidas.

$$G(s) = \frac{-0.9605s^2 - 42.07s - 146}{6.323x10^{-5}s^2 + s} \qquad (15)$$

Dado que el controlador es inestable, es necesario analizar la estabilidad interna del sistema. Un sistema es internamente estable si para entradas acotadas, el sistema genera señales acotadas en cualquier punto del sistema de control. De igual forma si los polos y ceros de las funciones de transferencia en cualquier punto del sistema de control se encuentran en el semiplano derecho del plano S, entonces el sistema de control es internamente estable (Morari 1989). Para analizar la estabilidad interna del controlador propuesto, se determina la estabilidad a partir de la ecuación 16.

$$\begin{pmatrix} y \\ u \end{pmatrix} = \begin{pmatrix} \frac{pc}{1+pc} & \frac{p}{1+pc} \\ \frac{c}{1+pc} & \frac{-pc}{1+pc} \end{pmatrix} \begin{pmatrix} r \\ d_i \end{pmatrix} \qquad (16)$$

Donde c representa el controlador diseñado, p representa la planta nominal, y es la salida del sistema, u es la salida del controlador, r es la señal de referencia y d_i es la perturbación de entrada a la planta. A partir de la ecuación 16 y el algoritmo que se propone en (Xue 2007), se determinó que el sistema de control diseñado, aunque es estable externamente, no cumple la condición de estabilidad interna ya que existe cancelación de polos inestables en la función del lazo $H(s)P(s)C(s)$. No obstante se alcanzaron las especificaciones de desempeño planteadas desde el enfoque QFT.

Para validar el controlador se realiza un análisis de las respuesta del sistema en lazo cerrado ante señales de prueba, para determinar tanto en el dominio del tiempo como en el domino de la frecuencia las especificaciones de desempeño del controlador. Los límites de las especificaciones aparecen como líneas punteadas, y la respuesta del sistema en lazo cerrado debe estar por debajo de estos límites.

En la Fig. 7 representa el análisis de la estabilidad robusta, en donde se observa que el controlador diseñado para todas las frecuencias de interés cumple con los criterios de estabilidad robusta del sistema.

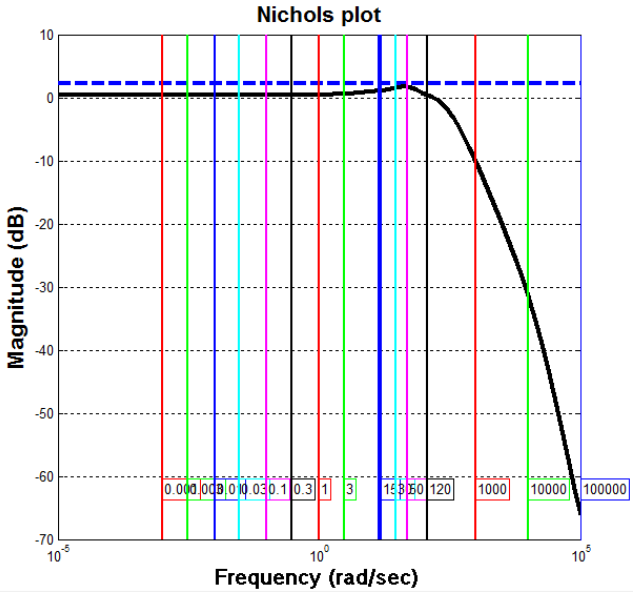

Fig. 7. Análisis de estabilidad.

La Fig. 8. muestra la respuesta del sistema ante rechazo de perturbaciones, donde el controlador tiene un comportamiento aceptable ante las perturbaciones de salida del sistema en todo el rango de frecuencias de interés, no obstante, es importante anotar que señales de alta frecuencia pueden afectar la respuesta del sistema, dado que en la figura 8 se observa que para frecuencias mayores a $1krad/s$ la respuesta del sistema en lazo cerrado supera el límite de estabilidad robusta.

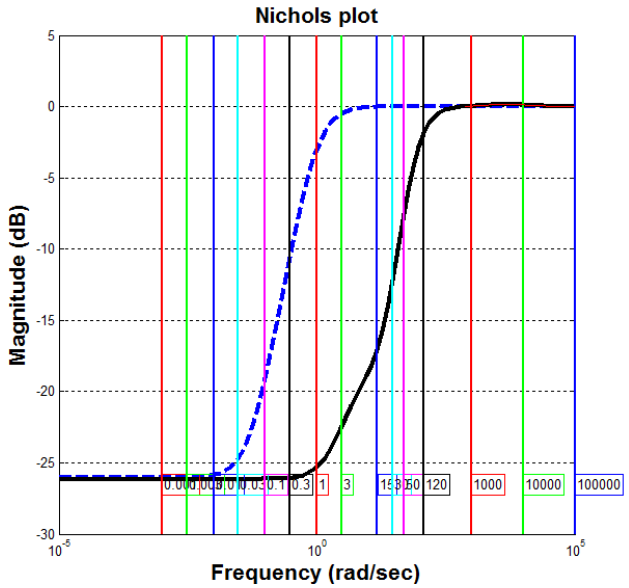

Fig. 8. Análisis de rechazo de perturbaciones en el dominio de la frecuancia.

La Fig. 9 muestra la respuesta en el dominio del tiempo de todas las plantas del espacio de incertidumbre cuando el sistema tiene una señal de referencia igual a cero y es sometido a una señal de perturbación de carga tipo escalón unitario. Para todas las posibles respuestas, se observa que cumplen con un tiempo de establecimiento inferior a 1s, y la salida en estado estable es cercana a cero. Eso es coherente con el análisis que se realizó en el domino de la frecuencia de la figura 8.

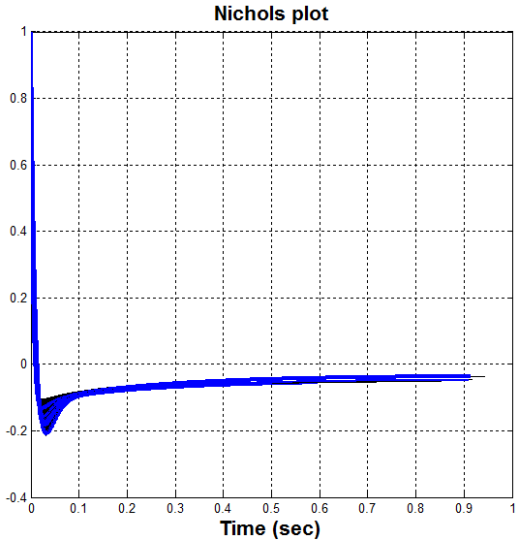

Fig. 8. Análisis de rechazo de perturbaciones en el dominio del tiempo.

Con el análisis del controlador tanto en el domino del tiempo como en el dominio de la frecuencia, este se implementa en el sistema embebido Beaglebone Black®. Para ello, se verificó que la función de transferencia del controlador fuera propia, es decir, que el numerador sea menor o igual al grado del denominador, ya que en caso de no cumplir no sería un controlador realizable físicamente. Se discretizó el controlador con un periodo de muestreo de 10ms y un retenedor de orden cero, el cual se seleccionó de acuerdo a la dinámica del robot y al desempeño del sistema embebido, para su posterior programación utilizando ecuaciones en diferencia en el lenguaje de programación Python.

5. RESULTADOS

Se validó el comportamiento del sistema real frente a la planta simulada, con el fin de asegurar que el controlador implementado tenga un comportamiento similar al controlador diseñado, y cumpla con las especificaciones de desempeño. En la Fig. 10 se aprecia un seguimiento cercano al 85% del sistema real ante el modelo de simulación. Esto indica que el uso de ecuaciones de *euler-lagrange* para identificar el modelo matemático del robot de autobalance basado en péndulo invertido, es adecuado y se pueden conseguir resultados aceptables.

Se realizaron pruebas en las cuales se observó el comportamiento del sistema ante la variación de la referencia de equilibrio, perturbaciones sobre el cuerpo del péndulo y

bloqueo de ruedas. La respuesta del sistema con controlador QFT ante una referencia de equilibrio de 0° fue inestable, saturando los actuadores del sistema. Se pudo verificar que la causa de la inestabilidad estaba en la distribución de peso sobre el cuerpo del robot móvil de autobalance y una posible necesidad de implementación extra de un control de posición, con la capacidad de limitar el área de desplazamiento horizontal del robot.

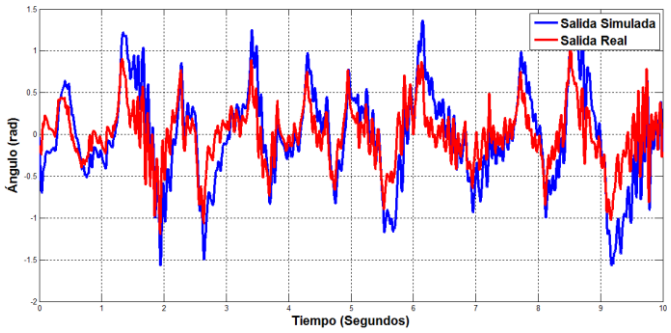

Fig. 10. Respuesta modelo simulado ante el modelo real.

Para mitigar el problema de inestabilidad, se varió la referencia del ángulo de balance, con el fin de mantener una distribución de peso sobre el cuerpo del robot, encontrándola en 14.49°, referencia en la cual se mantuvo una estabilidad constante generando los resultados deseados, con una variación de $+/-5°$ grados respecto a la referencia. Este análisis demostró que el controlador QFT es capaz de mantener el robot en equilibrio siempre y cuando la referencia de balance establecida mantenga una distribución de peso sobre el cuerpo del prototipo, aspecto importante que demostró la desventaja de la arquitectura implementada, caso que no debería suceder si el sistema fuera de masa puntual.

La inestabilidad interna conlleva a que el sistema sea estable solo ante superficies sin obstáculos con perturbaciones de no más de 5 grados ante la referencia. También es importante observar que el desplazamiento de la posición del carro del robot móvil basado en péndulo invertido ante cualquier perturbación genero un movimiento de casi 6 metros desde el punto partida, efecto que se compenso agregando un lazo de control de posición horizontal sobre el carro del robot móvil basado en péndulo invertido, mediante un controlador PID, sintonizado directamente desde el algoritmo QFT alojado sobre el sistema embebido, variando las constantes Ki, Kp, Kd, sumando la acción de control con la del controlador QFT, obteniendo finalmente las constantes definidas por $Ki = 0.0686, Kp = 0.238$ y $Kd = 0.08$. Con este controlador en conjunto con la estrategia QFT, se mejoró la respuesta del sistema, tal como se muestra en la Fig. 11.

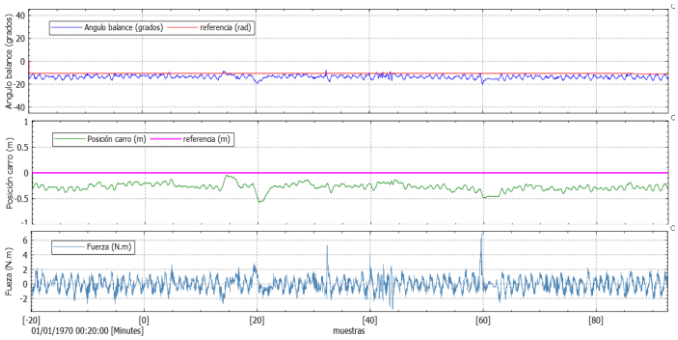

Fig. 11. Respuesta control QFT más PID ante referencia de peso distribuido.

En los resultados obtenidos se observó, que el sistema es capaz de aceptar cambios de referencia sin importar el efecto de distribución de peso ante la inclinación, generando un desplazamiento del móvil hasta lograr mantener su estabilidad sin cambios relevantes, a la vez dentro de cada rango de referencia variado se ingresó un conjunto de perturbaciones sobre el cuerpo del robot y en las ruedas, generando siempre el rechazo de aproximadamente el 90% de atenuación ante las mismas de manera adecuada sin perder la estabilidad. Un aspecto importante de este resultado es que el sistema no sigue la referencia de balance directamente, si no contrariamente aumenta su oscilación cada vez más a medida que se aleja de la referencia nominal donde el peso estaba distribuido (sistema gana más inclinación), validando la importancia de que todo sistema basado en péndulo invertido debe contener un control tanto en su balance como en su desplazamiento.

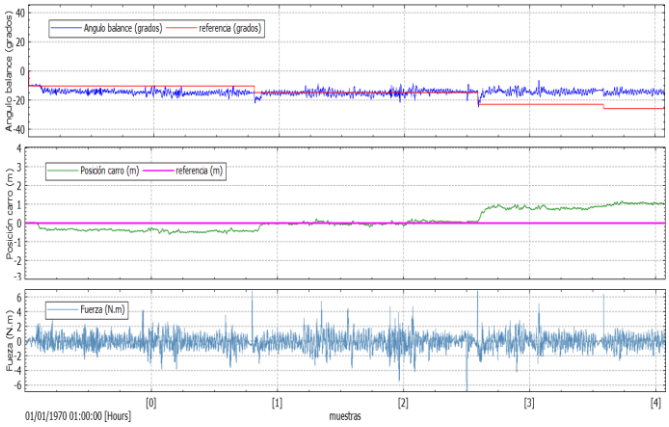

Fig. 12. Respuesta del robot móvil basado en péndulo invertido con controlador de autobalance QFT y posición del carro PID ante cambios de referencia, perturbación y bloqueo de ruedas.

6. CONCLUSIONES

Respecto a la etapa de adquisición de datos la IMU, siendo el elemento principal de medición, resulto ser muy sensible a ruidos de baja y alta frecuencia, por tanto la solución fue el diseño del filtro complementario, que está integrado por un filtro pasa bajos y un filtro pasa altos, los cuales están inmersos dentro de las características propias de cada sensor como lo son el acelerómetro y el giroscopio, con esto se

obtuvo un mejor rendimiento de la evaluación del ángulo vertical de inclinación del robot móvil.

Con relación al dispositivo procesador de datos Beagle Bone Black®, se encontró que es un sistema rápido, versátil y con una cantidad aceptable de entradas y salidas analógicas y digitales, dichas características fueron convenientes para el desarrollo del sistema, aunque presento sensibilidad al ruido producido por lo micromotores, por ende se hizo necesario aislar la etapa de potencia de la de control atreves, de un puente H, de tecnología Mosfet que requiere bajo consumo de energía, esto puso fin al problema descrito.

La identificación matemática del sistema fue en un 90% acertada, esto se vio reflejado en el comportamiento óptimo del controlador sobre el modelo real, ocasionando que al cambiar valores en las incertidumbres físicas del robot; como lo son la masa y la altura, mantuviera su equilibrio vertical y estuviera limitado en su posición horizontal. Al realizar las pruebas físicas de los motores, en cuanto a fuerza utilizando un dinamómetro, se pudo establecer que el torque máximo generado por cada uno de ellos era aproximadamente de 6.9 N.m, esto con el fin de efectuar el respectivo escalamiento de la señal de control y limitar la energía transmitida desde los actuadores al robot móvil.

Ya que toda técnica no robusta de control estima el análisis de una sola planta de un sistema cualquiera, no tiene en cuenta factores que pueden variar las condiciones de la misma, como lo son la masa, centro de masa y altura, en el caso del prototipo móvil de autobalance, con la técnica de realimentación cuantitativa QFT, fue posible alterar todos estos factores y tenerlos por incertidumbres, lo cual genera no solo una sino un conjunto de plantas para las cuales el controlador que se obtiene, sigue siendo eficiente y mantiene estable el sistema.

El controlador QFT diseñado para el modelo del prototipo de robot móvil basado en péndulo invertido que obtuvo un excelente rechazo de perturbación, rapidez de respuesta y estabilidad robusta, fue en última instancia el controlador que se implementó, sin embargo fue necesario un control PID de posición, para limitar el área de acción del prototipo, por tanto, se realiza una fusión de los dos controladores lo cual genero una robustez de un 95% aproximadamente, hasta el punto de poder variar la referencia de equilibrio sin tener problemas con presencia de perturbaciones en la ruedas y cuerpo, además de que elimina la importancia de que la arquitectura implementada debe tener el peso distribuido sobre el cuerpo.

El control robusto QFT, es eficaz y mantiene el robot móvil de autobalance en equilibrio, cumpliendo la especificaciones de desempeño a pesar de no cumplir las condiciones de estabilidad interna a cause de cancelación de polos inestables. Estas condiciones de funcionamiento están sujetas a la arquitectura implementada sobre el cuerpo del robot, ya que debe tener el peso distribuido sobre la referencia de balance, generando desplazamiento horizontal críticamente en el carro del robot desde el punto de partida, siendo este un gran problema al momento de evaluar el sistema en áreas con poco espacio y obstáculos sobre la misma, efecto que es eliminado con un controlador extra, encargado del desplazamiento horizontal del carro del robot móvil de autobalance basado en péndulo invertido.

REFERENCIAS

Acosta, R. «Obtención de la ecuación de Euler-Lagrange utilizando los vectores base y vectores recíprocos.» *Artículo de investigaciòn Acosta Ingenierìa* , 2004: pp. 17 - 2.

Barmish, B. R., & Kang, H. I. « A survey of extreme point results for robustness of control systems.» *Automatica vol. 29, no 1*, 1993: pp. 13-35.

beagleboard. *https://beagleboard.org.* 03 de 20 de 2014. https://beagleboard.org/blog/2014-02-03-project-spotlight-robotics-cape/ (último acceso: 30 de 06 de 2015).

Biernson, G. *Principles of Feedback Control.* New York: John Wiley & Sons, 1988.

Callister, W. D., & Rethwisch, D. G. *Materials science and engineering: an introduction* . New York: Wiley., 2007.

Chait, Y., & Yaniv, O. «Multi-input/single-output computer-aided control design using the quantitative feedback theory.» *International Journal of Robust and Nonlinear Control*, 1993: pp. 47-54.

Clarke, D. W. «Applications of Generalized Predictive Control to Industrial Processes.» *IEEE Control Systems Society*, 1988: pp. 49 - 55.

d'Azzo, J. J., Sheldon, S. N., & Houpis, C. H. *Linear control system analysis and design with MATLAB.* New York: Marceld Dekk, 2003.

Dorato, P., Tempo, R., & Muscato, G. «Bibliography on robust control.» *Automatica, vol. 29, no 1*, 1993: p. 201-213.

Dorf, R. C., & Bishop, R. H. *Modern control systems.* New Jersey: Prentice Hall, 2011.

Francis, G. Zames y B. A. «Feedback, Minimax Sensitivity, and Optimal Robustness.» *IEEE transactions on automatic control vol. 28, nº 5*, 1983: pp. 585 - 601.

Frías, O. O. G. «Estabilización del Péndulo Invertido Sobre Dos Ruedas mediante el método de Lyapunov.» *Revista Iberoamericana de Automática e Informática Industrial RIAI*, 2013: 30-36.

Gera, A., & Horowitz, I. «Optimization of the loop transfer function†.» *International Journal of Control*, 1980: pp. 389-398.

Horowitz, I. «Fundamental theory of automatic linear feedback control systems.» *IRE Transactions on Automatic Control*, 1959: pp. 5-19.

Horowitz, I. «Quantitative feedback theory.» *In IEE Proceedings D-Control Theory and Applications* , 1982: pp. 215-226.

Horowitz, Isaac. «Fundamental theory of automatic linear feedback control systems.» *IRE Transactions on Automatic Control*, 1959: pp. 5-19.

Houpis, C. H., Rasmussen, S. J., & Garcia-Sanz, M. *Quantitative feedback theory: fundamentals and applications.* Boca Raton: CRC Press, 2005.

Houpis, M. García Sanz y C. H. *Wind Energy Systems: Control Engineering Design.* Boca raton: CRC Press, 2012.

Jun, W. Jia. «Simulation studies of inverted pendulum based on PID controllers.» *Simulation Modelling Practice and Theory*, 2011: pp. 440 - 449.

Morari, M., & Zafiriou, E. *Robust process control* . Englewood Cliffs: Prentice hall, 1989.

Ogata, K. *Ingeniería de control moderna.* Madrid: PEARSON EDUCATION, 2010.

Packard, A., J. Doyle, and G. Balas. «Linear, multivariable robust control with a µ perspective.» *ASME Journal of Dynamic Systems, Measurement and Control*, 1993: p. 310-319.

Patete, A., Aguirre, I., & Sánchez, H. «Control de un péndulo invertido basado en un modelo reducido.» *Revista INGENIERÍA UC*, 2011: pp. 12-22.

Pérez Polo, Pérez Molina, & Gil Chica. «Swing-up and positioning control of an inverted wheeled cart pendulum system with chaotic balancing motions.» *International Journal of Non-Linear Mechanics*, 2012: 655–665.

Rasmussen, C. H. Houpis y S. J. *Quantitative feedback theory.* New York: Marcel Dekker, 1999.

Sánchez, F. Rodríguez Rubio y M. J. López. *Control Adaptativo y robusto.* Sevilla - España: Secretariado de publicaciones de la universidad de Sevilla, 1996.

Stein, J. C.Doyle y G. «Multivariable Feedback Design: Concepts for a Classical/Modern Synthesis.» *IEEE Transactions on Automatic Control, vol. 26, nº 1*, 1981: pp. 4 - 16.

Xue, D., Chen, Y., & Atherton, D. P. *Linear feedback control: analysis and design with MATLAB.* Philadelphia: Siam, 2007.

Zafiriou, M. Morari y E. *Robust Process Control,» Englewood Cliff, vol. 37, nº 12.* Englewood Cliffs: Prentice hall, 1989.

Control Servovisual No Calibrado De Robots Planares Sin Modelo Dinámico

Alejandro Gutiérrez–Giles * **Maximiliano Bueno–López** **

* *Departamento de Control y Robótica. División de Ingeniería Eléctrica de la Facultad de Ingeniería. Universidad Nacional Autónoma de México. Apdo. Postal 70–256, México, D. F., 04510, México.*
alejandrogilesg@comunidad.unam.mx
** *Facultad de Ingeniería, Programa de Ingeniería en Automatización. Universidad de La Salle*
Cra. 2 No. 10-70 Piso 7 Bloque C, Bogotá D.C., Colombia.
mbueno@lasalle.edu.co

Resumen
El control servovisual de robots manipuladores representa una opción natural en ambientes no estructurados y es especialmente atractivo cuando la labor a realizar puede expresarse directamente en coordenadas de imagen. En el presente artículo se muestra una propuesta de control servovisual no calibrado para robots planares en el cual no se requiere el modelo dinámico del sistema. El método se valida mediante simulaciones numéricas y se compara con otra metodología reportada en la literatura, obteniendo un buen desempeño por parte del esquema propuesto.

Keywords:
Robotic manipulators, Visual control, GPI Observers, Robust control, Kinematics

1. INTRODUCCIÓN

La utilización de cámaras para controlar el movimiento y posición del efector final de un robot manipulador viene creciendo en los últimos años (Hutchinson et al., 1996). Uno de los principales retos de esta estrategía es reducir los errores que se obtienen al utilizar únicamente encoders y poder extraer la mayor información posible de la imagen obtenida (parámetros de imagen) la cual será utilizada por el controlador (Chaumette y Hutchinson, 2007). Cuando la información visual procedente de una o varias cámaras, ya sean fijas o móviles, se utiliza para cerrar el lazo de control se puede hablar de *control servovisual* (Bueno-López, 2012). El control servovisual ofrece ventajas con relación al control visual en lazo abierto, principalmente ser independiente de la precisión de los sensores de visión así como la precisión del robot (Sciavicco y Siciliano, 1996). La utilización de diferentes estrategias de control aplicadas al control servovisual ha incrementado en las últimas decadas, desde los clásicos PID combinados con algunas otras estrategias hasta lógica difusa han sido combinados con visión para lograr un mejor desempeño de los robots manipuladores.
La principal aplicación del control servovisual se encuentra en entornos no estructurados, ya que la cámara puede proporcionar no solo información del robot sino también de su espacio de trabajo. Al emplear sistemas de visión la calibración de estos y el tiempo computacional toman alta relevancia ya que el desempeño del contralador depende en gran medida de estos parámetros. Con base en lo anterior se puede afirmar que tener un algoritmo de control servovisual que no requiere calibración es un gran aporte.

En (Arteaga-Pérez y Bueno-López, 2015) y (Bueno-López y Arteaga-Pérez, 2012) se presentan algoritmos de control servovisual en 2D y 3D sin calibración del sistema de visión, en estos casos los autores emplean un clásico PID y lógica difusa para controlar la posición del efector final de un robot manipulador.
Además de los problemas descritos anteriormente, otro factor de importancia en los controladores servovisuales es la necesidad de tener el modelo dinámico del sistema calculado con la mayor precisión posible. Son pocos los controladores de este tipo que no requieren dicho modelo, lo que es una contribución de este artículo.

Para lidiar con el problema de estimación de perturbaciones y robustez ante dinámicas no modeladas se utilizarán los observadores Proporcionales Integrales Generalizados (GPI, por sus siglas en inglés). Sin embargo, una aplicación directa de esta metodología no es del todo adecuada para realizar el control servovisual debido a que, aunque no se requiere el conocimiento de todo el modelo, se requiere conocer tanto la matriz de inercia del manipulador como la matriz de rotación de la cámara con respecto a un sistema fijo en la base del manipulador. Además, la metodología GPI estándar se basa en la estimación y perturbación en línea de todas las perturbaciones tanto externas como internas, aunque éstas sean beneficiosas para estabilizar al sistema. En contraste, en este trabajo se plantea aprovechar las propiedades de pasividad de los robots manipuladores seriales para obtener un algoritmo más robusto y con un desempeño mejorado.

La contribución de principal de este trabajo es la adaptación del esquema reportado en Arteaga-Pérez y Gu-

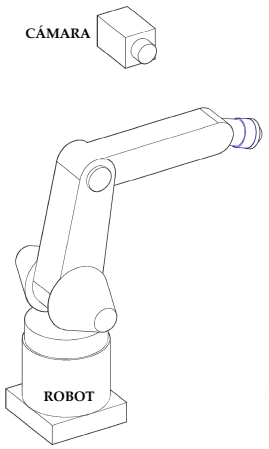

Figura 1. Robot manipulador y cámara fija

tiérrez-Giles (2014) al control servovisual en coordenadas de imagen de robots rígidos completamente actuados. El controlador citado fue modificado añadiendo amortiguamiento para compensar los diferentes tiempos de muestreo entre el lazo de visión y el lazo de control articular. Para validar la mejora del algoritmo, se realizó una comparación con el método GPI estándar, donde se muestra el mejor desempeño del esquema propuesto en este trabajo.

El artículo está organizado como sigue: en la Sección 2 se introduce el modelo matemático del sistema consistente en un robot manipulador y una cámara. El resultado principal se muestra en la Sección 3. En la Sección 4 se presentan algunas simulaciones numéricas para ilustrar las ventajas del esquema propuesto. Finalmente en la Sección 5 se dan algunas conclusiones y posibles directrices para trabajo futuro.

2. MODELADO

2.1 Modelo dinámico del manipulador

Considérese un robot manipulador rígido de n grados de libertad.

Su dinámica está dada por (Sciavicco y Siciliano, 1996)

$$\boldsymbol{H}(\boldsymbol{q})\ddot{\boldsymbol{q}} + \boldsymbol{C}(\boldsymbol{q},\dot{\boldsymbol{q}})\dot{\boldsymbol{q}} + \boldsymbol{D}\dot{\boldsymbol{q}} + \boldsymbol{g}(\boldsymbol{q}) = \boldsymbol{\tau}\,, \tag{1}$$

donde $\boldsymbol{q} \in \Re^n$ es el vector de coordenadas generalizadas, $\boldsymbol{H}(\boldsymbol{q}) \in \Re^{n\times n}$ es la matriz de inercia, positiva definida, $\boldsymbol{C}(\boldsymbol{q},\dot{\boldsymbol{q}})\dot{\boldsymbol{q}} \in \Re^n$ es el vector de fuerzas centrífugas y de Coriolis, $\boldsymbol{D} \in \Re^{n\times n}$ es la matriz diagonal positiva semidefinida que contiene los coeficientes de fricción viscosa, $\boldsymbol{g}(\boldsymbol{q}) \in \Re^n$ es el vector de torques debidos a la gravedad y $\boldsymbol{\tau} \in \Re^n$ es el vector de los torques que actúan en las articulaciones. Por simplicidad, en este trabajo se asume que todas las articulaciones del robot manipulador son de revolución, en cuyo caso se cumplen las siguientes propiedades (Arteaga-Pérez, 1998).

Propiedad 2.1. $\forall \boldsymbol{z}, \boldsymbol{q} \in \Re^n$, se satisface

$$\lambda_{\rm h}\|\boldsymbol{z}\|^2 \leq \boldsymbol{z}^{\rm T}\boldsymbol{H}(\boldsymbol{q})\boldsymbol{z} \leq \lambda_{\rm H}\|\boldsymbol{z}\|^2\,, \tag{2}$$

donde $0 < \lambda_{\rm h} \leq \lambda_{\rm H} < \infty$, $\lambda_{\rm h} \triangleq \min_{\forall \boldsymbol{q}\in\Re^n} \lambda_{\min}\left(\boldsymbol{H}(\boldsymbol{q})\right)$ y $\lambda_{\rm H} \triangleq \max_{\forall \boldsymbol{q}\in\Re^n} \lambda_{\max}\left(\boldsymbol{H}(\boldsymbol{q})\right)$. Las funciones $\lambda_{\min}(\cdot)$ y $\lambda_{\max}(\cdot)$ denotan el valor propio mínimo y el valor propio máximo de la matriz en el argumento, respectivamente. △

Propiedad 2.2. Si se calcula $\boldsymbol{C}(\boldsymbol{q},\dot{\boldsymbol{q}})$ utilizando los símbolos de Christoffel del primer tipo, se cumple que la matriz $\dot{\boldsymbol{H}}(\boldsymbol{q}) - 2\boldsymbol{C}(\boldsymbol{q},\dot{\boldsymbol{q}})$ es antisimétrica, *i.e.*, $\forall \boldsymbol{z} \in \Re^n$

$$\boldsymbol{z}^{\rm T}\left(\dot{\boldsymbol{H}}(\boldsymbol{q}) - 2\boldsymbol{C}(\boldsymbol{q},\dot{\boldsymbol{q}})\right)\boldsymbol{z} = 0\,. \tag{3}$$

△

Las coordenadas del efector final en el espacio Cartesiano están dadas por

$$\boldsymbol{x} \triangleq \begin{bmatrix}\boldsymbol{p}\\ \boldsymbol{\phi}\end{bmatrix}\,, \tag{4}$$

donde $\boldsymbol{x} \in \Re^n$, $\boldsymbol{p} \in \Re^{n-m}$ es la posición del efector final y $\boldsymbol{\phi} \in \Re^m$ es alguna parametrización de la orientación (*e.g.*, ángulos de Euler). La relación entre las velocidades en el espacio Cartesiano y el espacio articular está dada por la cinemática diferencial, *i.e.*,

$$\dot{\boldsymbol{x}} = \boldsymbol{J}(\boldsymbol{q})\dot{\boldsymbol{q}}\,, \tag{5}$$

donde $\boldsymbol{J}(\boldsymbol{q}) \in \Re^{n\times n}$ es el Jacobiano analítico del manipulador. Para que esta cinemática diferencial esté bien definida en el espacio de destreza del robot, se debe de tomar en cuenta la siguiente suposición.

Suposición 2.1. El robot no pasa por ninguna singularidad, por lo que $\boldsymbol{J}^{-1}(\boldsymbol{q})$ siempre existe.

△

2.2 Modelo de la cámara

Considérese un robot manipulador en movimiento planar en conjunto con una cámara fija como se representa en la Figura 1. Mediante el sistema de visión se obtienen las coordenadas del efector final en el espacio de imagen, definidas como $\boldsymbol{y} \in \mathcal{R}^2$. En este escenario, la relación entre las coordenadas Cartesianas y las coordenadas de imagen está dada por la Proyección de Perspectiva (Kelly, 1996)

$$\boldsymbol{y} = \alpha_\lambda \boldsymbol{R}_\phi \left(\boldsymbol{x} - \begin{bmatrix}{}^cO_{\rm R1}\\ {}^cO_{\rm R2}\end{bmatrix}\right) + \begin{bmatrix}u_0\\ v_0\end{bmatrix}\,, \tag{6}$$

donde $\boldsymbol{y} \in \mathcal{R}^2$ es el vector de coordenadas de imagen, $\alpha_\lambda \triangleq (\alpha_{\rm c}\lambda_v)\,/\,({}^cO_{\rm R3} - \lambda_v)$, $\alpha_{\rm c}$ es el número de pixeles por unidad de distancia en el plano de imagen, ${}^cO_{\rm R3}$ el desplazamiento del origen del sistema coordenado asignado a la cámara con respecto a la base del robot, sobre el eje z,

$$\boldsymbol{R}_\phi \triangleq \begin{bmatrix}\cos(\phi_{\rm c}) & \sin(\phi_{\rm c})\\ \sin(\phi_{\rm c}) & -\cos(\phi_{\rm c})\end{bmatrix} \tag{7}$$

es la matriz de rotación del sistema coordenado de la cámara con respecto a la base, $\phi_{\rm c}$ es el ángulo de rotación sobre un eje perpendicular a los planos (paralelos) de la cámara y del plano de movimiento del robot, ${}^cO_{\rm R1}$ y ${}^cO_{\rm R2}$ son los desplazamientos del origen del sistema coordenado asignado a la cámara con respecto a la base, sobre los ejes x e y, respectivamente y u_0, v_0 son los desplazamientos del pixel coincidente con el eje principal de la cámara y el origen del sistema coordenado asociado al plano de imagen.

Propiedad 2.3. La matriz $\boldsymbol{R}_\phi \in \boldsymbol{o}(2)$ definida en (7) es simétrica. △

2.3 Modelo dinámico en coordenadas de imagen

Si se considera que la cámara permanece fija con respecto al sistema coordenado de la base del robot, se puede obtener la cinemática visual diferencial, que relaciona las velocidades articulares y en coordenadas de imagen. Derivando (6) con respecto al tiempo se obtiene

$$\dot{\boldsymbol{y}} = \alpha_\lambda \boldsymbol{R}_\phi \dot{\boldsymbol{x}} = \alpha_\lambda \boldsymbol{R}_\phi \boldsymbol{J} \dot{\boldsymbol{q}} \,. \tag{8}$$

Tomando en cuenta la Suposición 2.1 y la Propiedad 2.3 se puede obtener

$$\dot{\boldsymbol{q}} = \frac{1}{\alpha_\lambda} \boldsymbol{J}^{-1} \boldsymbol{R}_\phi \dot{\boldsymbol{y}} \tag{9}$$

$$\ddot{\boldsymbol{q}} = \frac{1}{\alpha_\lambda} \left(\dot{\boldsymbol{J}}^{-1} \boldsymbol{R}_\phi \dot{\boldsymbol{y}} + \boldsymbol{J}^{-1} \boldsymbol{R}_\phi \ddot{\boldsymbol{y}} \right) . \tag{10}$$

De acuerdo con lo anterior, el modelo dinámico del manipulador en términos de las coordenadas de imagen está dado por

$$\boldsymbol{H}_{\mathrm{v}}(\boldsymbol{q})\ddot{\boldsymbol{y}} + \boldsymbol{C}_{\mathrm{v}}(\boldsymbol{q}, \dot{\boldsymbol{q}})\dot{\boldsymbol{y}} + \boldsymbol{D}_{\mathrm{v}}(\boldsymbol{q})\dot{\boldsymbol{y}} + \boldsymbol{g}_{\mathrm{v}}(\boldsymbol{q}) = \boldsymbol{f}_{\mathrm{v}} \,, \tag{11}$$

donde

$$\boldsymbol{H}_{\mathrm{v}}(\boldsymbol{q}) \triangleq \frac{1}{\alpha_\lambda} \boldsymbol{R}_\phi \boldsymbol{J}^{-\mathrm{T}} \boldsymbol{H}(\boldsymbol{q}) \boldsymbol{J}^{-1} \boldsymbol{R}_\phi \tag{12}$$

$$\boldsymbol{C}_{\mathrm{v}}(\boldsymbol{q}, \dot{\boldsymbol{q}}) \triangleq \frac{1}{\alpha_\lambda} \boldsymbol{R}_\phi \boldsymbol{J}^{-\mathrm{T}} \boldsymbol{C}(\boldsymbol{q}, \dot{\boldsymbol{q}}) \boldsymbol{J}^{-1} \boldsymbol{R}_\phi \tag{13}$$

$$+ \frac{1}{\alpha_\lambda} \boldsymbol{R}_\phi \boldsymbol{J}^{-\mathrm{T}} \boldsymbol{H}(\boldsymbol{q}) \dot{\boldsymbol{J}}^{-1} \boldsymbol{R}_\phi \tag{14}$$

$$\boldsymbol{D}_{\mathrm{v}}(\boldsymbol{q}) \triangleq \frac{1}{\alpha_\lambda} \boldsymbol{R}_\phi \boldsymbol{J}^{-\mathrm{T}} \boldsymbol{D} \boldsymbol{J}^{-1} \boldsymbol{R}_\phi \tag{15}$$

$$\boldsymbol{g}_{\mathrm{v}}(\boldsymbol{q}) \triangleq \boldsymbol{R}_\phi \boldsymbol{J}^{-\mathrm{T}} \boldsymbol{g}(\boldsymbol{q}) \tag{16}$$

Por otra parte, el vector de fuerzas generalizadas $\boldsymbol{f}_{\mathrm{v}} \in \Re^2$ y el vector de pares de entrada $\boldsymbol{\tau}$ están relacionados por

$$\boldsymbol{\tau} = \boldsymbol{J}^{\mathrm{T}} \boldsymbol{R}_\phi \boldsymbol{f}_{\mathrm{v}} \,. \tag{17}$$

Las matrices que definen el modelo en coordenadas de imagen satisfacen las siguientes propiedades en forma de lemas, análogas a las Propiedades 2.1 y 2.2

Propiedad 2.4. La matriz $\boldsymbol{H}_{\mathrm{v}}(\boldsymbol{q}) \in \Re^{2\times 2}$ es simétrica y positiva definida.

△

Demostración. Nótese que (12) es simétrica por la Propiedad 2.3. Debido a que $\alpha_\lambda > 0$ y tomando en cuenta la Propiedad 2.1 sigue la afirmación.

□

Propiedad 2.5. La matriz $\dot{\boldsymbol{H}}_{\mathrm{v}}(\boldsymbol{q}) - 2\boldsymbol{C}_{\mathrm{v}}(\boldsymbol{q}, \dot{\boldsymbol{q}})$ es antisimétrica.

△

Demostración. Mediante cálculo directo, omitiendo los argumentos para mayor claridad, se tiene

$$\begin{aligned} \dot{\boldsymbol{H}}_{\mathrm{v}} - 2\boldsymbol{C}_{\mathrm{v}} = & \frac{1}{\alpha_\lambda} \boldsymbol{R}_\phi \Big(\dot{\boldsymbol{J}}^{-\mathrm{T}} \boldsymbol{H} \boldsymbol{J}^{-1} + \boldsymbol{J}^{-\mathrm{T}} \dot{\boldsymbol{H}} \boldsymbol{J}^{-1} \\ & + \boldsymbol{J}^{-\mathrm{T}} \boldsymbol{H} \dot{\boldsymbol{J}}^{-1} - 2\boldsymbol{J}^{-\mathrm{T}} \boldsymbol{C} \boldsymbol{J}^{-1} \\ & - 2\boldsymbol{J}^{-\mathrm{T}} \boldsymbol{H} \dot{\boldsymbol{J}}^{-1} \Big) \boldsymbol{R}_\phi \,. \end{aligned} \tag{18}$$

Utilizando las Propiedades 2.2 y 2.3 se obtiene

$$\dot{\boldsymbol{H}}_{\mathrm{v}} - 2\boldsymbol{C}_{\mathrm{v}} = \frac{1}{\alpha_\lambda} \boldsymbol{R}_\phi \left(\dot{\boldsymbol{J}}^{-\mathrm{T}} \boldsymbol{H} \boldsymbol{J}^{-1} - \boldsymbol{J}^{-\mathrm{T}} \boldsymbol{H} \dot{\boldsymbol{J}}^{-1} \right) \boldsymbol{R}_\phi \,. \tag{19}$$

Debido a que el lado derecho de (19) equivale al negativo de su transpuesta, se demuestra la afirmación.

□

Lema 2.1. El mapeo $(\boldsymbol{f}_{\mathrm{v}} - \boldsymbol{g}_{\mathrm{v}}) \to \dot{\boldsymbol{y}}$ es pasivo, con función de almacenamiento $V = \frac{1}{2} \dot{\boldsymbol{y}}^{\mathrm{T}} \boldsymbol{H}_{\mathrm{v}} \dot{\boldsymbol{y}}$.

△

Demostración. Derivando V a lo largo de las trayectorias de (11), sustituyendo (8) y utilizando la Propiedad 2.5 se obtiene

$$\dot{V} = -\dot{\boldsymbol{y}}^{\mathrm{T}} \boldsymbol{D}_{\mathrm{v}}(\boldsymbol{q}) \dot{\boldsymbol{y}} \leq 0 \,, \tag{20}$$

dado que $\boldsymbol{D}$ en (1) y por lo tanto $\boldsymbol{D}_{\mathrm{v}}$ en (11) son matrices positivas semidefinidas.

3. RESULTADO PRINCIPAL

Tomando como base la pasividad del mapeo $(\boldsymbol{f}_{\mathrm{v}} - \boldsymbol{g}_{\mathrm{v}}) \to \dot{\boldsymbol{y}}$ se puede utilizar el algoritmo de Slotine-Li (Slotine y Li, 1987) para obtener un controlador basado en pasividad. Para lograr esto, se definen

$$\dot{\boldsymbol{y}}_{\mathrm{r}} = \dot{\boldsymbol{y}}_{\mathrm{d}} - \boldsymbol{\Lambda}(\boldsymbol{y} - \boldsymbol{y}_{\mathrm{d}}) \tag{21}$$

$$\boldsymbol{s} = \dot{\boldsymbol{y}} - \boldsymbol{y}_{\mathrm{r}} \,, \tag{22}$$

donde $\boldsymbol{y}_{\mathrm{d}} \in \Re^2$ es la posición visual deseada y $\Lambda \in \Re^2$ es una matriz de ganancias positiva definida. Realizando el cambio de variables y sustituyendo en (11) resulta

$$\boldsymbol{H}_{\mathrm{v}} \dot{\boldsymbol{s}} + \boldsymbol{C}_{\mathrm{v}} \boldsymbol{s} + \boldsymbol{D}_{\mathrm{v}} \boldsymbol{s} = \boldsymbol{f}_{\mathrm{v}} - \boldsymbol{H}_{\mathrm{v}} \ddot{\boldsymbol{y}}_{\mathrm{r}} - \boldsymbol{C}_{\mathrm{v}} \dot{\boldsymbol{y}}_{\mathrm{r}} - \boldsymbol{D}_{\mathrm{v}} \dot{\boldsymbol{y}}_{\mathrm{r}} - \boldsymbol{g}_{\mathrm{v}} \,. \tag{23}$$

Es conocido que la ley de control $\boldsymbol{f}_{\mathrm{v}} = \boldsymbol{H}_{\mathrm{v}} \ddot{\boldsymbol{y}}_{\mathrm{r}} + \boldsymbol{C}_{\mathrm{v}} \dot{\boldsymbol{y}}_{\mathrm{r}} + \boldsymbol{D}_{\mathrm{v}} \dot{\boldsymbol{y}}_{\mathrm{r}} + \boldsymbol{g}_{\mathrm{v}} - \boldsymbol{K}_{\mathrm{v}} \boldsymbol{s}$ estabiliza el sistema de forma asintótica con margen de ganancia infinito. Sin embargo, esta ley de control tiene básicamente dos inconvenientes para su implementación:

- Requiere conocer el modelo dinámico del manipulador.
- Se necesita medir la velocidad en coordenadas de imagen $\dot{\boldsymbol{y}}$, lo que es muy complicado, debido a que la información obtenida por las cámaras comúnmente es discreta al estar definida en píxeles y además el tiempo de adquisición y procesamiento es considerablemente alto.

Para solventar estos dos problemas se emplearán los Observadores Proporcionales Integrales Generalizados (GPI, por sus siglas en inglés) introducidos en Sira-Ramírez et al. (2010). Sin embargo, para eliminar la necesidad de conocer la matriz de inercia del sistema, se utilizará la modificación presentada en Arteaga-Pérez y Gutiérrez-Giles (2014). Primero, se define el error de seguimiento $\boldsymbol{e} \triangleq \boldsymbol{y} - \boldsymbol{y}_{\mathrm{d}}$. Entonces, la dinámica del error está dada por

$$\dot{\boldsymbol{e}}_1 = \boldsymbol{e}_2 \tag{24}$$
$$\dot{\boldsymbol{e}}_2 = \boldsymbol{H}_{\mathrm{v}}^{-1}\left(\boldsymbol{f}_{\mathrm{v}} - \boldsymbol{C}_{\mathrm{v}}\boldsymbol{s}\right) + \boldsymbol{H}_{\mathrm{v}}^{-1}\boldsymbol{w}_1 - \boldsymbol{\Lambda}\dot{\boldsymbol{e}}\,, \tag{25}$$

donde $\boldsymbol{e}_1 \triangleq \boldsymbol{e}$ y

$$\boldsymbol{w}_1 \triangleq -\left(\boldsymbol{H}_{\mathrm{v}}\ddot{\boldsymbol{y}}_{\mathrm{r}} + \boldsymbol{C}_{\mathrm{v}}\dot{\boldsymbol{y}}_{\mathrm{r}} + \boldsymbol{D}_{\mathrm{v}}\dot{\boldsymbol{y}} + \boldsymbol{g}_{\mathrm{v}}\right). \tag{26}$$

Para emplear los observadores GPI se hacen las siguientes suposiciones Arteaga-Pérez y Gutiérrez-Giles (2014).

Suposición 3.1. El vector $\boldsymbol{w}_1$ puede ser localmente modelado como un vector de polinomios de Taylor dependientes del tiempo, de grado $p-1$, más un término residual, *i.e.*,

$$\boldsymbol{w}_1 = \sum_{i=0}^{p-1} \boldsymbol{a}_i t^i + \boldsymbol{r}_{\mathrm{a}}(t)\,, \tag{27}$$

donde $\boldsymbol{a}_i$ es un vector de coeficientes constantes y $\boldsymbol{r}_{\mathrm{a}}(t)$ es un vector de términos residuales.

△

Suposición 3.2. El vector $\boldsymbol{r}_{\mathrm{a}}(t)$ y por lo menos sus primeras p derivadas con respecto al tiempo, existen.

△

Dadas las suposiciones anteriores, se puede escribir el modelo interno para la señal desconocida $\boldsymbol{w}_1(t)$ como

$$\dot{\boldsymbol{w}}_1 = \boldsymbol{w}_2 \tag{28}$$
$$\dot{\boldsymbol{w}}_2 = \boldsymbol{w}_3 \tag{29}$$
$$\vdots$$
$$\dot{\boldsymbol{w}}_{p-1} = \boldsymbol{w}_p \tag{30}$$
$$\dot{\boldsymbol{w}}_p = \boldsymbol{r}_{\mathrm{a}}^{(p)}(t) \tag{31}$$

Con base en este modelo interno, se propone el observador de estados

$$\dot{\hat{\boldsymbol{e}}}_1 = \hat{\boldsymbol{e}}_2 - \boldsymbol{\Lambda}\boldsymbol{e} + \boldsymbol{\lambda}_{p+1}\tilde{\boldsymbol{e}} \tag{32}$$
$$\dot{\hat{\boldsymbol{e}}}_2 = \boldsymbol{\lambda}_p\tilde{\boldsymbol{e}} \tag{33}$$
$$\dot{\hat{\boldsymbol{w}}}_1 = \hat{\boldsymbol{w}}_2 + \boldsymbol{\lambda}_{p-1}\tilde{\boldsymbol{e}} \tag{34}$$
$$\dot{\hat{\boldsymbol{w}}}_2 = \hat{\boldsymbol{w}}_3 + \boldsymbol{\lambda}_{p-2}\tilde{\boldsymbol{e}} \tag{35}$$
$$\vdots$$
$$\dot{\hat{\boldsymbol{w}}}_{p-1} = \hat{\boldsymbol{w}}_p + \boldsymbol{\lambda}_1\tilde{\boldsymbol{e}} \tag{36}$$
$$\dot{\hat{\boldsymbol{w}}}_p = \boldsymbol{\lambda}_0\tilde{\boldsymbol{e}}\,, \tag{37}$$

donde $\tilde{\boldsymbol{e}} \triangleq \boldsymbol{e}_1 - \hat{\boldsymbol{e}}_1$ y $\boldsymbol{\lambda}_0, \ldots, \boldsymbol{\lambda}_{p+1} \in \Re^{n\times n}$ son las matrices diagonales de coeficientes del vector de polinomios

$$\boldsymbol{\rho}(\boldsymbol{\sigma}) = \boldsymbol{\sigma}^{p+2} + \boldsymbol{\lambda}_{p+1}\boldsymbol{\sigma}^{p+1} + \cdots + \boldsymbol{\lambda}_1\boldsymbol{\sigma} + \boldsymbol{\lambda}_0\,, \tag{38}$$

con $\boldsymbol{\sigma} \in \Re^n$. A continuación se propone la ley de control basada en las señales obtenidas por el observador

$$\boldsymbol{f}_{\mathrm{v}} = -k_{\mathrm{d}}\hat{\boldsymbol{R}}_\phi\boldsymbol{J}^{-\mathrm{T}}\dot{\boldsymbol{q}} - \boldsymbol{K}_{\mathrm{v}}\left(\hat{\boldsymbol{e}}_2 + \boldsymbol{\Lambda}\boldsymbol{e}\right) - \hat{\boldsymbol{w}}_1\,, \tag{39}$$

donde $k_{\mathrm{d}} > 0$, $\boldsymbol{K}_{\mathrm{v}} \in \Re^{n\times n}$ es una matriz de ganancias, positiva definida y $\hat{\boldsymbol{R}}_\phi$ es el estimado de la matriz de rotación de la cámara.

Comentario 3.1. El primer término del lado derecho de (39) fue incluido en este trabajo a diferencia del algoritmo presentado en Arteaga-Pérez y Gutiérrez-Giles (2014). Lo anterior se debe a que el amortiguamiento añadido por el término $\hat{\boldsymbol{e}}_2$ depende del ancho de banda del sistema de visión, que usualmente suele ser muy pobre con respecto a la dinámica del manipulador. El inconveniente de añadir este término disipativo es la necesidad de medición de la velocidad articular $\dot{\boldsymbol{q}}$.

△

Comentario 3.2. Como se supone que no se conoce exactamente la matriz de rotación de la cámara $\boldsymbol{R}_\phi$, para implementar la ley de control no se debe de emplear (17) sino

$$\boldsymbol{\tau} = \boldsymbol{J}^{\mathrm{T}}\hat{\boldsymbol{R}}_\phi\boldsymbol{f}_{\mathrm{v}}\,. \tag{40}$$

Utilizando (24), (25), (28)–(31) y (32)–(37) se puede obtener la dinámica del error de observación

$$\begin{aligned}\ddot{\tilde{\boldsymbol{e}}}_1 + \boldsymbol{\lambda}_{p+1}\dot{\tilde{\boldsymbol{e}}}_1 + \boldsymbol{\lambda}_p\tilde{\boldsymbol{e}}_1 &= \boldsymbol{H}_{\mathrm{c}}^{-1}\left(-\boldsymbol{K}_{\mathrm{v}}\boldsymbol{s} + \boldsymbol{K}_{\mathrm{v}}\tilde{\boldsymbol{e}}_2\right.\\ &\qquad \left.-k_{\mathrm{d}}\hat{\boldsymbol{R}}_\phi\boldsymbol{J}^{-\mathrm{T}}\dot{\boldsymbol{q}} - \boldsymbol{C}_{\mathrm{c}}\boldsymbol{s} + \tilde{\boldsymbol{w}}_1\right)\\ &= \boldsymbol{r}_{\mathrm{b}}(t) + \tilde{\boldsymbol{w}}_1\,,\end{aligned} \tag{41}$$

donde

$$\begin{aligned}\boldsymbol{r}_{\mathrm{b}}(t) \triangleq\ & \boldsymbol{H}_{\mathrm{c}}^{-1}\left(-\boldsymbol{K}_{\mathrm{v}}\boldsymbol{s} + \boldsymbol{K}_{\mathrm{v}}\tilde{\boldsymbol{e}}_1 - \boldsymbol{C}_{\mathrm{c}}\boldsymbol{s}\right)\\ &+ \left(\boldsymbol{H}_{\mathrm{c}}^{-1} - \boldsymbol{I}\right)\tilde{\boldsymbol{w}}_1\,.\end{aligned} \tag{42}$$

Derivando p–veces (41) con respecto al tiempo, se obtiene

$$\begin{aligned}\tilde{\boldsymbol{e}}_1^{(p+2)} &+ \boldsymbol{\lambda}_{p+1}\tilde{\boldsymbol{e}}_1^{(p+1)} + \ldots\\ &\ldots + \boldsymbol{\lambda}_1\dot{\tilde{\boldsymbol{e}}}_1 + \boldsymbol{\lambda}_0\tilde{\boldsymbol{e}}_1 = \boldsymbol{r}_{\mathrm{a}}^{(p)}(t) + \boldsymbol{r}_{\mathrm{b}}^{(p)}(t)\,.\end{aligned} \tag{43}$$

Si se define

$$\boldsymbol{z} \triangleq \begin{bmatrix} \tilde{\boldsymbol{e}}_1 \\ \vdots \\ \tilde{\boldsymbol{e}}_1^{(p+1)} \end{bmatrix}, \tag{44}$$

se puede reescribir la dinámica (43) como un sistema lineal invariante en el tiempo definido por

$$\dot{\boldsymbol{z}} = \boldsymbol{A}\boldsymbol{z} + \boldsymbol{B}\bar{\boldsymbol{r}}_{\mathrm{ab}}\,. \tag{45}$$

A continuación se enuncia el resultado principal de este trabajo.

Proposición 3.1. Sea una trayectoria deseada en coordenadas de imagen $\boldsymbol{y}_{\mathrm{d}}$ acotada con al menos sus primeras $p+2$ derivadas con respecto al tiempo acotadas y la ley de control (39) en conjunto con el observador (32)–(37) en lazo cerrado con (11). Defínase una región $\mathcal{D} \in \Re^{n(p+1)}$ como

$$\mathcal{D} \triangleq \left\{\boldsymbol{z} \in \Re^{n(p+1)} \middle| \|\boldsymbol{z}\| \leq y_{\max}\right\}, \tag{46}$$

donde $y_{\max}$ es una constante arbitrariamente grande. Entonces, es posible encontrar una combinación en las raíces del polinomio (38) para hacer que las variables deslizantes $(\boldsymbol{s},\ \dot{\boldsymbol{s}})$, los errores de seguimiento $(\boldsymbol{e},\ \dot{\boldsymbol{e}},\ \ddot{\boldsymbol{e}})$ y los errores de observación $\boldsymbol{z}$ definidos en (44) tiendan a una vecindad arbitrariamente pequeña alrededor del origen.

△

Por razones de espacio no se incluye la demostración de esta Proposición, aunque el procedimiento es muy similar al seguido en Arteaga-Pérez y Gutiérrez-Giles (2014).

4. SIMULACIONES

Para poner a prueba la validez del método propuesto se realizó una comparación con el algoritmo GPI estándar como el presentado en Gutierrez-Giles et al. (2016) con la correspondiente modificación para el control servovisual, dado por (c.f. (32)–(37))

$$\dot{\hat{e}}_1 = \hat{e}_2 + \boldsymbol{\lambda}_{p+1}\tilde{\boldsymbol{e}} \tag{47}$$
$$\dot{\hat{e}}_2 = \boldsymbol{H}_{\mathrm{v}}^{-1}\boldsymbol{f}_{\mathrm{v}} + \hat{\boldsymbol{w}}_1 + \boldsymbol{\lambda}_p\tilde{\boldsymbol{e}} \tag{48}$$
$$\dot{\hat{\boldsymbol{w}}}_1 = \hat{\boldsymbol{w}}_2 + \boldsymbol{\lambda}_{p-1}\tilde{\boldsymbol{e}} \tag{49}$$
$$\dot{\hat{\boldsymbol{w}}}_2 = \hat{\boldsymbol{w}}_3 + \boldsymbol{\lambda}_{p-2}\tilde{\boldsymbol{e}} \tag{50}$$
$$\vdots$$
$$\dot{\hat{\boldsymbol{w}}}_{p-1} = \hat{\boldsymbol{w}}_p + \boldsymbol{\lambda}_1\tilde{\boldsymbol{e}} \tag{51}$$
$$\dot{\hat{\boldsymbol{w}}}_p = \boldsymbol{\lambda}_0\tilde{\boldsymbol{e}}\,, \tag{52}$$

en conjunto con la ley de control (c.f. (39))

$$\boldsymbol{f}_{\mathrm{v}} = \hat{\boldsymbol{H}}_{\mathrm{v}}\left(-2\xi\omega_{\mathrm{n}}\hat{\boldsymbol{e}}_2 - \omega_{\mathrm{n}}^2\boldsymbol{e} - \hat{\boldsymbol{w}}_1\right)\,, \tag{53}$$

donde $\xi, \omega_{\mathrm{n}} > 0$ son ganancias de control y $\hat{\boldsymbol{H}}_{\mathrm{v}}$ es un estimado de la matriz $\boldsymbol{H}_{\mathrm{v}}$ definida en (12). Nótese que a diferencia del algoritmo propuesto en este trabajo el GPI estándar no requiere medición de velocidad aunque sí se necesita conocer la matriz de inercia $\boldsymbol{H}_{\mathrm{v}}$

Se utilizó el modelo de un robot de dos grados de libertad, dado en forma paramétrica por (Spong et al., 2006)

$$\begin{bmatrix} \theta_1 + 2\theta_2 c_2 & \theta_3 + \theta_2 c_2 \\ \theta_3 + \theta_2 c_2 & \theta_3 \end{bmatrix}\ddot{\boldsymbol{q}} + \begin{bmatrix} -\theta_2 s_2 \dot{q}_2 & -\theta_2 s_2(\dot{q}_1 + \dot{q}_2) \\ \theta_2 s_2 \dot{q}_1 & 0 \end{bmatrix}\dot{\boldsymbol{q}} + \begin{bmatrix} \theta_4 c_1 + \theta_5 c_{12} \\ \theta_5 c_{12} \end{bmatrix} + \begin{bmatrix} \theta_6\dot{q}_1 + \theta_8 \mathrm{sign}(\dot{q}_1) \\ \theta_7\dot{q}_2 + \theta_9 \mathrm{sign}(\dot{q}_2) \end{bmatrix} = \boldsymbol{\tau}\,. \tag{54}$$

Con el objeto de llevar a cabo una simulación lo más realista posible, se utilizaron los valores reportados en Reyes y Kelly (2001).

Se analizaron tres casos de simulación: (i) la cámara está perfectamente calibrada, lo que implica $\hat{\boldsymbol{R}}_\phi = \boldsymbol{R}_\phi$ y $\hat{\boldsymbol{H}}_{\mathrm{v}} = \boldsymbol{H}_{\mathrm{v}}$, (ii) la cámara está girada 5[°] sobre el eje perpendicular al plano de imagen y (iii) la cámara está girada 45[°] sobre el eje perpendicular al plano de imagen. La trayectoria deseada para todos los casos fue un círculo en el plano de imagen, de 300[pixeles] y un periodo de 30[seg]. Después de dos vueltas al círculo la posición deseada se mantiene constante. Las ganancias para el controlador–observador propuesto dado por (32)–(37) y (39) fueron $\boldsymbol{\lambda}_0 = 1.6384\boldsymbol{I}$, $\boldsymbol{\lambda}_1 = 6.656\boldsymbol{I}$, $\boldsymbol{\lambda}_2 = 9.6\boldsymbol{I}$ y $\boldsymbol{\lambda}_3 = 5.6\boldsymbol{I}$, *i.e.,* los polos del observador fueron colocados en $p_1 = p_2 = p_3 = -0.8$ y $p_4 = -3.2$. Para la ley de control se eligieron $k_{\mathrm{d}} = 200$, $K_{\mathrm{v}} = \mathrm{diag}(0.5, 0.5)$ y $\Lambda = \mathrm{diag}(10, 10)$. Para el controlador GPI estándar se eligieron $\boldsymbol{\lambda}_0 = 50625\boldsymbol{I}$, $\boldsymbol{\lambda}_1 = 13500\boldsymbol{I}$, $\boldsymbol{\lambda}_2 = 1350\boldsymbol{I}$ y $\boldsymbol{\lambda}_3 = 60\boldsymbol{I}$, *i.e.,* los polos del observador fueron colocados en $p_1 = p_2 = p_3 = p_4 = -15$. Las ganancias de control en este caso fueron $\boldsymbol{\xi} = \mathrm{diag}(18, 18)$ y $\boldsymbol{\omega}_{\mathrm{n}} = \mathrm{diag}(12.5, 12.5)$.

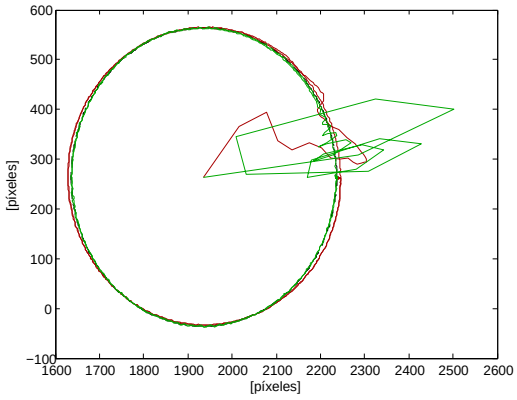

Figura 2. Cámara calibrada, seguimiento de trayectoria: deseada (- - -), GPI estándar (—) y PBC-GPI (—).

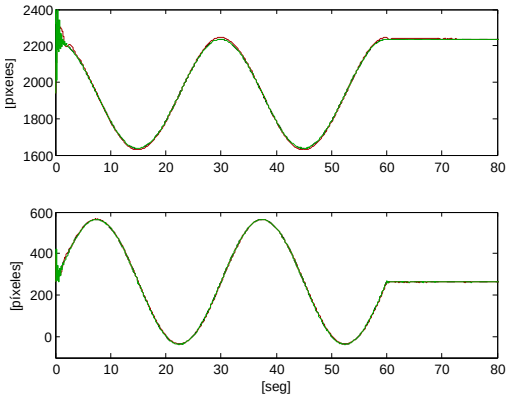

Figura 3. Cámara calibrada, seguimiento de trayectoria: deseada (- - -), GPI estándar (—) y PBC-GPI (—).

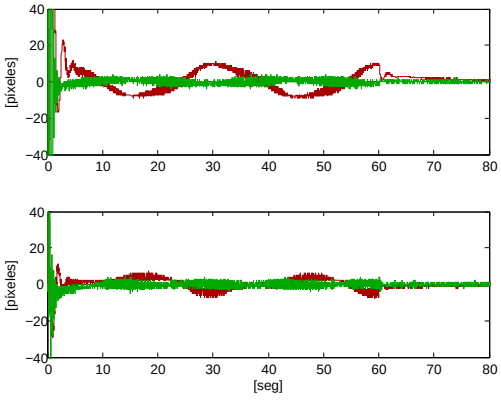

Figura 4. Cámara calibrada, errores de seguimiento: GPI estándar (—) y PBC-GPI (—).

En la Figura 3 se muestra la evolución de las trayectorias en el plano de imagen para el caso en el que la cámara está calibrada. En la Figura 4 se muestra la evolución de cada coordenada de imagen contra el tiempo y en la Figura 4 los errores correspondientes para cada coordenada visual. Se puede observar que en este caso el desempeño del controlador GPI estándar es mejor que el GPI Basado en Pasividad (PBC–GPI, por sus siglas en inglés) propuesto en este trabajo. No obstante, para el caso (ii), *i.e.,* cuando existe

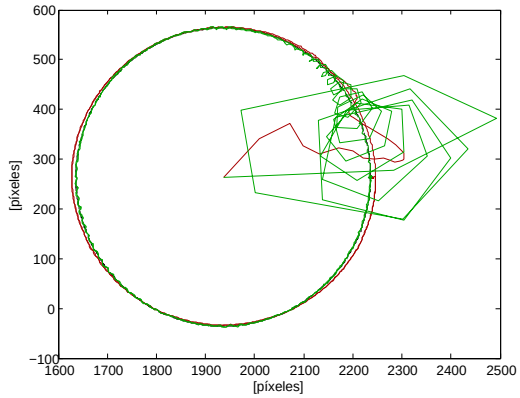

Figura 5. Cámara rotada 5[°], seguimiento de trayectoria: deseada (- - -), GPI estándar (—) y PBC-GPI (—).

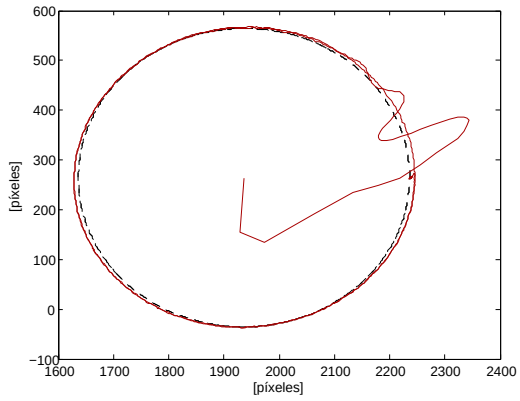

Figura 6. Cámara rotada 45[°], seguimiento de trayectoria: deseada (- - -) y PBC-GPI (—).

una pequeña rotación de la cámara, el desempeño del GPI estándar se degrada bastante como puede apreciarse en la Figura 5. Como puede verse en esta misma figura, el desempeño del PBC–GPI siguió siendo parecido al caso de perfecta calibración de la cámara.

Por último, si la cámara está rotada un ángulo considerable como en el caso (iii), el sistema con controlador GPI estándar se vuelve inestable. En contraste el controlador PBC–GPI servovisual propuesto en este trabajo sigue manteniendo un buen desempeño, como se muestra en la Figura 6.

5. CONCLUSIONES

El esquema de controlador–observador propuesto en este trabajo tiene algunas ventajas sobre los existentes en la literatura. Primero, no requiere conocer el modelo dinámico del manipulador, lo que resulta en una implementación más sencilla. Además es fácil de sintonizar, lo que también puede representar una ventaja en la práctica. Debido a que el diseño está inspirado en el control basado en pasividad, a diferencia de los esquemas basados en el principio de equivalencia cierta, el controlador no cancela dinámicas beneficiosas para la estabilización del sistema, *e.g.,* términos disipativos, por lo que se logra un mejor desempeño comparativamente. La robustez del algoritmo se puso a prueba mediante simulaciones numéricas, en el que se mostró que incluso con rotaciones considerables de la cámara el desempeño continuaba siendo bueno.

Como trabajo futuro se plantea la validación experimental del esquema propuesto. En otra dirección, se estudiará la posibilidad de no utilizar medición de las velocidades articulares. Por último, se analizará la posibilidad de extender el algoritmo presentado para control servovisual en el espacio de tres dimensiones (3D).

6. AGRADECIMIENTOS

Alejandro Gutiérrez-Giles agradece al **CONACYT** bajo la beca doctoral con CVU No. **334785**.

REFERENCIAS

Arteaga-Pérez, M.A. (1998). On the properties of a dynamic model of flexible robot manipulators. *ASME Journal of Dynamic Systems, Measurement, and Control*, 120, 8–14.

Arteaga-Pérez, M.A. y Bueno-López, M. (2015). 3D visual servoing control for robot manipulators without parametric identification. *IEEE Latin America Transactions*, 13(3), 569–577.

Arteaga-Pérez, M.A. y Gutiérrez-Giles, A. (2014). On the GPI approach with unknown inertia matrix in robot manipulators. *International Journal of Control*, 87(4), 844–860.

Bueno-López, M. y Arteaga-Pérez, M.A. (2012). Fuzzy vs nonfuzzy in 2D visual servoing for robot manipulators. *International Journal of Advanced Robotic Systems*, 10(1), 1–11.

Bueno-López, M. (2012). *Control servovisual de robots manipuladores en 3D*. Dr. eng., Universidad Nacional Autónoma de México, Avenida Universidad 3000, Coyoacán, México, D.F.

Chaumette, F. y Hutchinson, S. (2007). Visual servo control part ii: Advanced approaches. *IEEE Robotics and Automation Magazine*, 109–118.

Gutierrez-Giles, A., Arteaga-Perez, M.A. y Sira-Ramirez, H. (2016). Generalized proportional integral observer-based force control in robot manipulators. *REVISTA IBEROAMERICANA DE AUTOMATICA E INFORMATICA INDUSTRIAL*, 13(2), 238–246.

Hutchinson, S., Hager, G.D. y Corke, P.I. (1996). A tutorial on visual servo control. *IEEE Transactions on Robotics and Automation*, 12 (5), 651–670.

Kelly, R. (1996). Robust asymptotically stable visual servoing of planar robots. *Robotics and Automation, IEEE Transactions on*, 12(5), 759–766.

Reyes, F. y Kelly, R. (2001). Experimental evaluation of model–based controllers on a direct−drive robot arm. *Mechatronics*, 11, 267–282.

Sciavicco, L. y Siciliano, B. (1996). *Modeling and Control of Robot Manipulators*. McGraw-Hill.

Sira-Ramírez, H., Ramírez-Neria, M. y Rodríguez-Ángeles, A. (2010). On the linear control of nonlinear mechanical systems. 49th IEEE Conference on Decision and Control, Atlanta, GA, USA.

Slotine, J.J.E. y Li, W. (1987). On the adaptive control of robot manipulators. *The International Journal of Robotics Research*, 6(3), 49–59.

Spong, M.W., Hutchinson, S. y Vidyasagar, M. (2006). *Robot Modeling and Control*. John Wiley and Sons.

Diseño de trayectorias caóticas en robots móviles

J. J. Cetina-Denis*, A. Arellano-Delgado*,
A. López-Parra*, R. M. López-Gutiérrez, C. Cruz-Hernández***

** Departamento de Electrónica y Telecomunicaciones. Centro de Investigación Científica y de Educación Superior de Ensenada, B. C. (CICESE), México. 22860;*
e-mail: jcetina@cicese.edu.mx, aarellan@cicese.mx, lopezpa@cicese.edu.mx, ccruz@cicese.mx.
*** Facultad de Ingeniería, Arquitectura y Diseño, Universidad Autónoma de Baja California, B.C. México 22860.*
(e-mail: roslopez@uabc.edu.mx)

Resumen: En este trabajo se aborda el problema de diseño de trayectorias caóticas en robots móviles. En particular, con base en el mapa de Hénon se inducen comportamientos caóticos en las velocidades lineales y angulares de un robot móvil diferencial tipo Khepera III, con propósitos de patrullaje aprovechando las propiedades del caos. Se reportan tanto resultados numéricos como experimentales. Por último, se muestra que las trayectorias del robot Khepera III son impredecibles.

Palabras clave: Robot móvil diferencial, caos, diseño de trayectorias, mapa de Hénon, aplicaciones de robots caóticos.

1. INTRODUCCION

Los estudios de comportamientos de búsqueda de alimentos en grupos de animales (especialmente de las hormigas), son de gran ayuda en la solución de muchos problemas, sobre todo de optimización. Recientemente, los biólogos han descubierto que las hormigas realizan actividades de búsqueda de manera caótica (Li, et al., 2014).

Tratando de imitar este comportamiento, se han realizado diversos trabajos en el diseño de trayectorias caóticas para robots móviles. Algunos utilizan sistemas caóticos junto con las ecuaciones de comportamiento de un robot diferencial para obtener un modelo matemático que le brinda a este un movimiento caótico (Nakamura & Sekiguchi, 2001); otros (Martins-Filho & Macau, 2006) utilizan el conocido mapa estándar, el cual es un sistema caótico simple discreto de dos dimensiones, para generar una serie de puntos localizados caóticamente en un plano para ser seguidos por el robot; mientras que otros (Volos, et al., 2012) emplean un generador aleatorio de bits caótico. También ha habido trabajos, (Curiac & Volosencu, 2014) que estudian la generación de comportamientos caóticos de robots móviles durante el recorrido de una trayectoria fronteriza.

Entre las aplicaciones que se dan a los robots con trayectorias caóticas se encuentran el patrullaje de áreas o fronteras, búsqueda de elementos peligrosos (por ejemplo explosivos), rescate, exploración de terrenos inhóspitos, etc.

En este trabajo se diseñan trayectorias caóticas en robots móviles. A continuación mencionamos las principales diferencias a los anteriores trabajos al emplear el mapa de Hénon para proporcionar velocidades a las ruedas de un robot móvil diferencial (Khepera III), de manera que se genere una trayectoria caótica que permita al robot patrullar un área de trabajo de manera eficiente e impredecible para observadores externos (intrusos, etc). La principal ventaja del método utilizado en este trabajo radica en el hecho de que la trayectoria caótica seguida por el robot emerge del comportamiento caótico en las velocidades de sus ruedas y no es resultado directo de la manipulación de su posición.

El trabajo se organiza de la siguiente manera: En la sección 2 se discute acerca de los sistemas caóticos y sus propiedades, describiendo con detalle el mapa de Hénon. En la sección 3 se describe el modelo matemático del robot diferencial, hablando de las características del robot Khepera III, el cual será utilizado en la etapa numérica y experimental de este trabajo. En la sección 4 se describen los experimentos realizados y se muestran los resultados numéricos y experimentales obtenidos. Finalmente, en la sección 5 se mencionan las conclusiones y el trabajo futuro.

2. SISTEMAS CAOTICOS

La teoría de caos puede definirse como el estudio cualitativo del comportamiento dinámico aperiódico mostrado por sistemas deterministas no lineales. Puede ser observado en gran cantidad de sistemas naturales e ingenieriles.

Entre las principales propiedades de los sistemas caóticos se encuentran las siguientes:

- Alta sensibilidad a condiciones iniciales.
- Deterministas con comportamiento aparentemente aleatorio.
- Oscilatorios, pero no periódicos.

Sensibilidad a condiciones iniciales indica que el sistema caótico tendrá evoluciones temporales drásticamente diferentes, a pesar que éstas se generen a partir de condiciones iniciales ligeramente diferentes. Esta característica es deseable en robots de patrullaje, ya que ocasionaría que la trayectoria generada caóticamente del mismo sea altamente impredecible. Sin embargo, las trayectorias son deterministas debido a que, conociendo las ecuaciones y las condiciones iniciales del sistema, es posible predecir su comportamiento. Tomando en cuenta estas propiedades podemos decir que un robot, cuya trayectoria sea caótica será altamente impredecible para el observador

externo, pero transparente para el diseñador y para cualquier observador que tenga conocimiento de las ecuaciones y los valores de las condiciones iniciales utilizadas para su diseño.

2.1 Mapa de Hénon

El mapa de Hénon es un sistema dinámico discreto en el tiempo de dos dimensiones, representado por las siguientes ecuaciones (Hénon, 1976):

$$x_h(n+1) = 1 - a\,x_h^2(n) + y_h(n+1), \qquad (1)$$
$$y_h(n+1) = b\,x_h(n)$$

El mapa depende de los parámetros a y b, los cuales para el mapa clásico de Hénon tienen valores de $a = 1.4$ y $b = 0.3$ para la generación de caos. Para otros valores de a y b el mapa puede ser intermitente, converger a una órbita periódica o presentar un punto fijo. La figura 1 muestra el atractor caótico generado por el mapa de Hénon representado en (1).

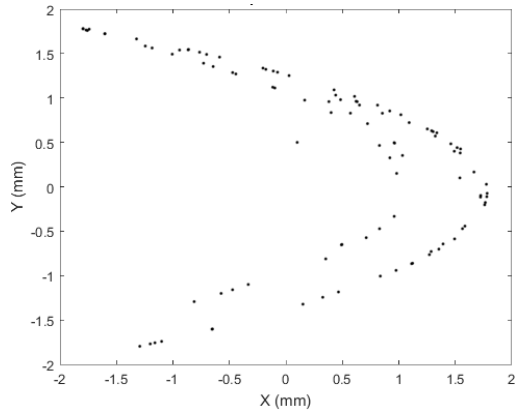

Fig. 1. Atractor caótico de Hénon.

3. MODELO MATEMATICO DE UN ROBOT DIFERENCIAL

Un robot móvil diferencial es aquel cuyo movimiento está basado en dos ruedas de tracción independiente, colocadas en ambos lados del cuerpo del robot (figura 2). El movimiento se consigue aplicando diferentes velocidades a cada una de las ruedas motrices. De esta forma, se puede hacer que el robot avance en línea recta fijando ambos motores a la misma velocidad, o que gire en una u otra dirección aplicando diferentes velocidades. En este trabajo se usará el modelo aproximado del robot Khepera III.

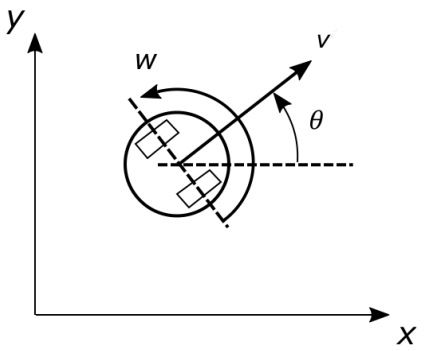

Fig. 2. Robot móvil diferencial.

En el trabajo realizado por Suster-Jadlosvska (2010) se reporta el siguiente modelo para un robot diferencial tomando en cuenta las siguientes consideraciones:

- El robot se mueve en una superficie perfectamente plana sin deslizamiento, despreciando la resistencia de las llantas.
- La posición del robot está dada por las coordenadas x, y y un ángulo θ, el cual representa la rotación del robot en relación al sistema de coordenadas.

La posición y la rotación del robot en el plano están basadas en las siguientes ecuaciones, formando el modelo cinemático del robot (Suster & Jadlovská, 2010):

$$\dot{x} = v\cos\theta, \qquad (2)$$
$$\dot{y} = v\,\mathrm{sen}\,\theta,$$
$$\dot{\theta} = w.$$

con v y ω definidas como:

$$v = \frac{V_l + V_r}{2} \qquad (3)$$
$$w = \frac{V_r - V_l}{l} \qquad (4)$$

donde:

v : Velocidad lineal,
w : Velocidad angular,
θ : Angulo de orientación del robot,
l : Distancia entre las ruedas, $l = 8.841\ cm$.

4. EXPERIMENTACION Y RESULTADOS

El objetivo que se persigue en este trabajo es emplear el mapa caótico de Hénon (1) para propiciar un comportamiento caótico a las velocidades lineal (v) y angular (w) del robot móvil diferencial descritos por (2).

Despejando las velocidades de las ruedas izquierda y derecha de las ecuaciones (3) y (4), obtenemos los histogramas mostrados en la figura 3. Se puede observar que los valores de v_l son mayormente negativos y los de v_r positivos, lo cual es indicio de que las trayectorias del robot se basarán principalmente en giros cerrados hacia la izquierda. Debido a esto, a los valores de v_l y v_r se les realiza una dispersión de manera que el histograma de las velocidades de las ruedas sea uniforme, como se muestra en la figura 4. De esta manera, la dispersión permite realizar un re-escalamiento de los valores a un rango utilizable por el robot, limitando sus velocidades mínimas y máximas que puede alcanzar.

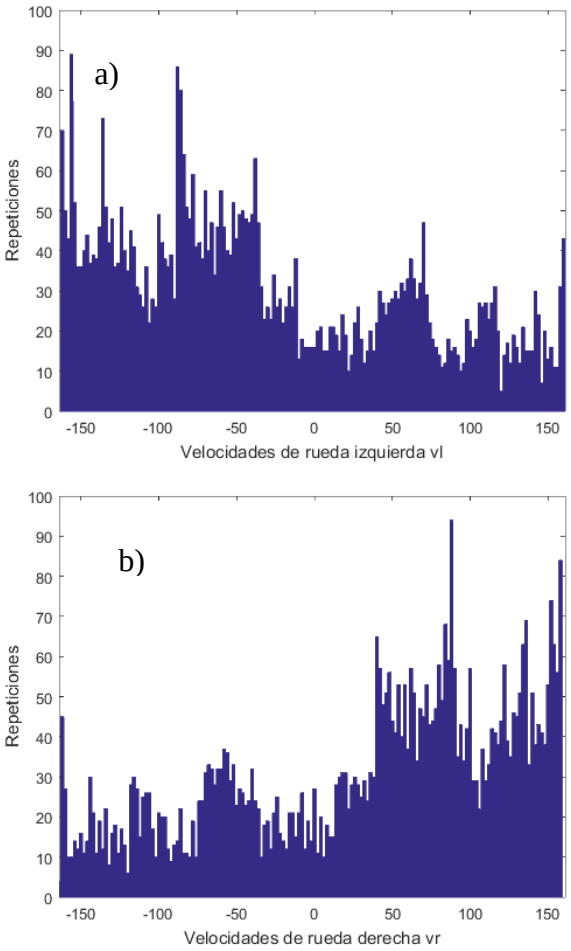

Fig. 3. Histogramas de velocidades de las ruedas: a) izquierda y b) derecha.

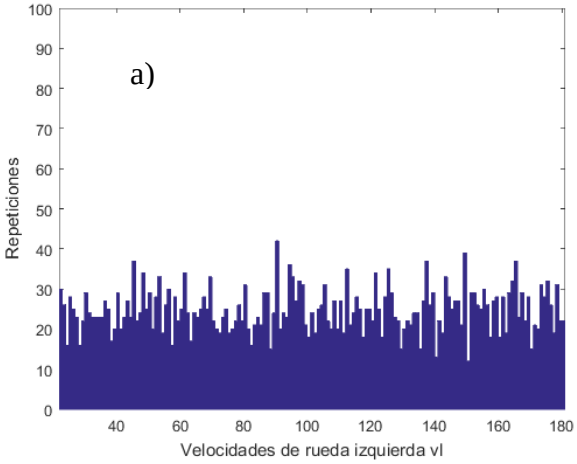

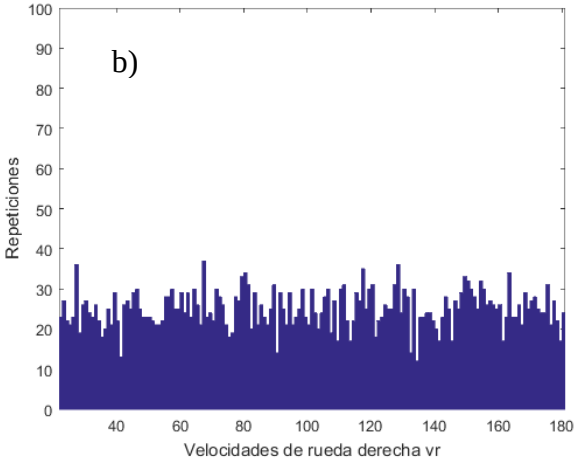

Fig. 4. Histogramas después de la dispersión de las velocidades de las ruedas: a) izquierda y b) derecha.

Este rango de velocidades no incluye velocidades negativas, de manera que el robot no se mueva en reversa, de modo que la trayectoria generada abarque mayor área de cobertura en menor tiempo.

4.1 Algoritmo para generar caos en el robot móbil

Se emplea el siguiente algoritmo (ver figura 5) tanto para las simulaciones numéricas como para el proceso experimental para generar trayectorias caóticas en el robot diferencial, el cual se describe como:

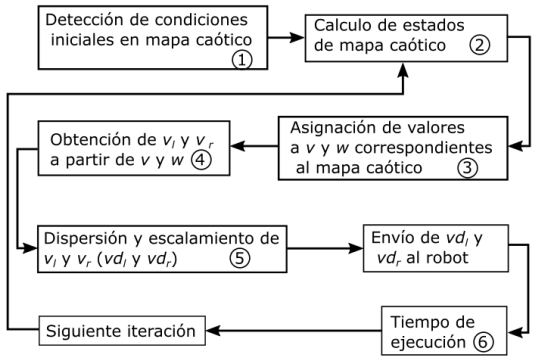

Fig. 5. Diagrama de bloques del algoritmo implementado para generar caos en el robot.

Las ecuaciones correspondientes a las etapas del diagrama de bloques de la figura 5 son las siguientes:

Paso 1:
$$x_0: Posicion\ inicial\ x\ del\ robot.$$
$$y_0: Posicion\ inicial\ y\ del\ robot.$$
$$x_h(0) = x(0),$$
$$y_h(0) = y(0),$$
$$n = 0.$$

Paso 2:
$$x_h(n+1) = 1 - a\,{x_h}^2(n) + y_h(n),$$
$$y_h(n+1) = b\,x_h(n)$$

Paso 3:
$$v = x_h(n+1),$$
$$w = y_h(n+1)$$

Paso 4: $v_l = v - (l\,w)$, $v_r = v + (l\,w)$

Paso 5: $vd_l = floor\big(((1000\,v_l) - floor(1000\,v_l)\big) * 180) + 20$, $vd_r = floor\big(((1000\,v_r) - floor(1000\,v_r)\big) * 180) + 20$

Paso 6: $t = 2$ segundos.

El tiempo de ejecución de dos segundos en el paso 6, es para permitir que el robot tenga la oportunidad de desplazarse pertinentemente y pueda tener mayor cobertura del área de trabajo.

Se trabajó con una laptop HP que cuenta con un procesador A10 de 1.9 GHz, 12 GB de memoria RAM y Windows 10 de 64 bits. Las simulaciones numéricas y el trabajo experimental se programaron utilizando Matlab R2015a. Se emplearon cámaras Flex 13 con el software Motive de la compañía Optitrack para la verificación de los resultados experimentales.

4.2 Límites del área de trabajo del robot

El área de patrullaje es una mesa de 900 x 1500 mm que cuenta con bordes de 35 mm de altura. El objetivo de control es que el robot diferencial cubra la mayor área posible de esta mesa de manera caótica. El robot debe cambiar su trayectoria cuando llega a alguno de los límites del área de trabajo para evitar colisionar con ellos. En este caso, se adopta un movimiento reflexivo. Cuando el robot sensa una aproximación a uno de estos límites, el robot cambia su dirección de movimiento siguiendo la estrategia mostrada en la figura 6. El robot adquiere una trayectoria de salida en un ángulo que refleja el de entrada.

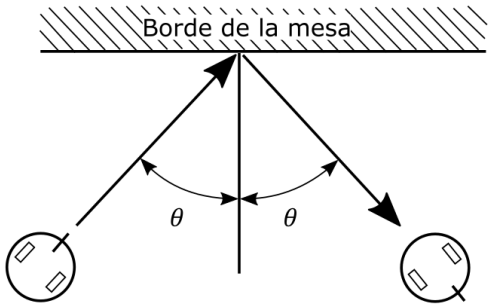

Fig. 6. Estrategia reflexiva de evasión de bordes.

4.3 Resultados numéricos

En esta parte se reportan los resultados obtenidos de las simulaciones numéricas en las figuras 7, 8, 9 y 10. Iniciando la trayectoria del robot en el origen $(x, y, \theta) = (0{,}0{,}0°)$, se realizan simulaciones numéricas con base en el algoritmo de generación caótica con 10, 100, 300 y 500 iteraciones. El cuadro negro representa los límites del área de trabajo (mesa) descrita anteriormente. Cada color representa un lapso de tiempo de dos segundos durante el cual el robot utiliza las velocidades obtenidas por cada iteración antes de pasar a las siguientes.

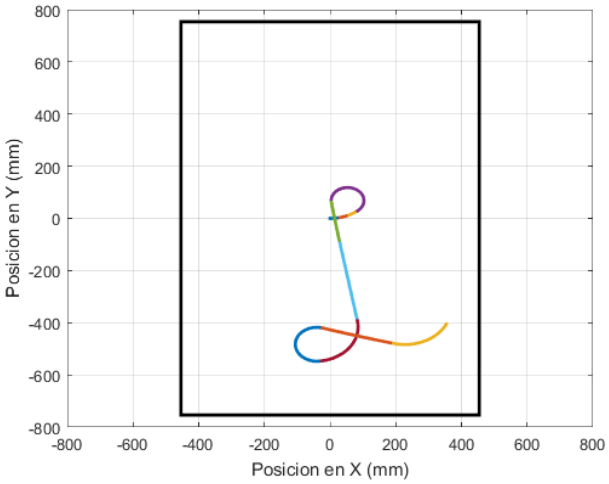

Fig. 7. Trayectoria del robot para 10 iteraciones del algoritmo.

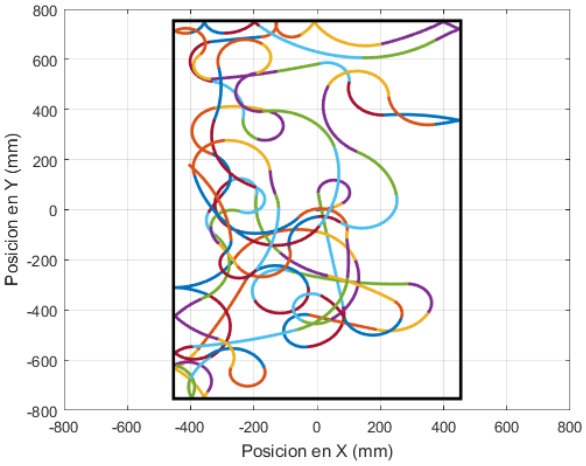

Fig. 8. Trayectoria del robot para 100 iteraciones del algoritmo

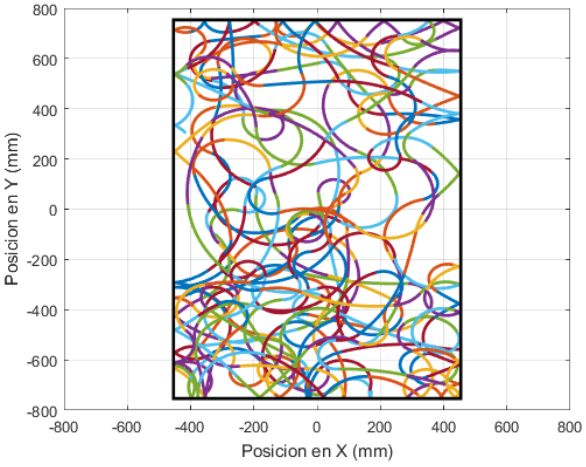

Fig. 9. Trayectoria del robot para 300 iteraciones del algoritmo

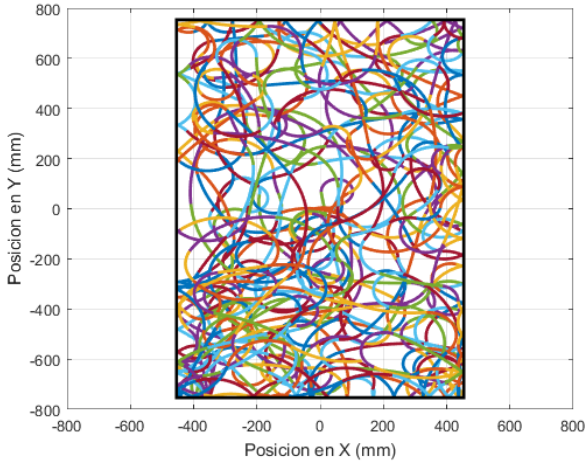

Fig.10. Trayectoria del robot para 500 iteraciones del algoritmo

De las figuras 7, 8, 9 y 10 se aprecia que las trayectorias del robot son impredecibles y que con 300 iteraciones cubre (patrulla) gran parte del área de trabajo. Es importante mencionar, que en la simulación numérica no se consideran las dimensiones reales del robot, por lo que el área cubierta en realidad por éste es mucho mayor que la mostrada en las gráficas.

Se puede observar también de estos resultados (figuras 7, 8, 9 y 10), que la trayectoria seguida en todos los casos bajo las mismas condiciones iniciales es la misma, confirmando la naturaleza determinista del caos.

Por otra parte, se realizan simulaciones utilizando tres diferentes posiciones iniciales (en milímetros) con la misma orientación ($\theta_0 = 90°$) en los casos: a) $x_0 = 0,\ y_0 = 0;$ b) $x_0 = 0.1,\ y_0 = 0;$ c) $x_0 = 200,\ y_0 = 400.$

Para cada caso, se realizan 100 iteraciones del algoritmo para comparar las trayectorias generadas. Los resultados se muestran en la figuras 11, 12 y 13.

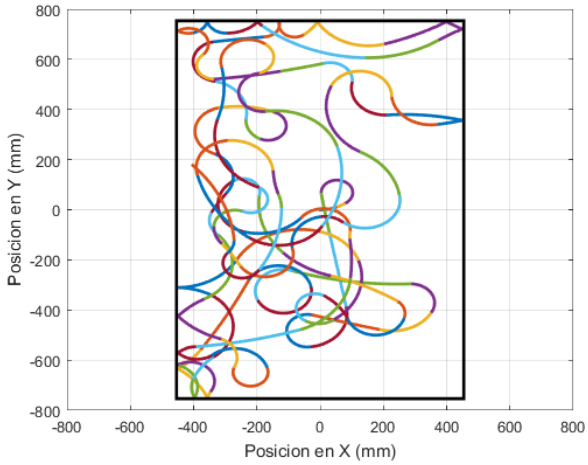

Fig. 11. Trayectoria del robot generada por las condiciones iniciales del inciso a).

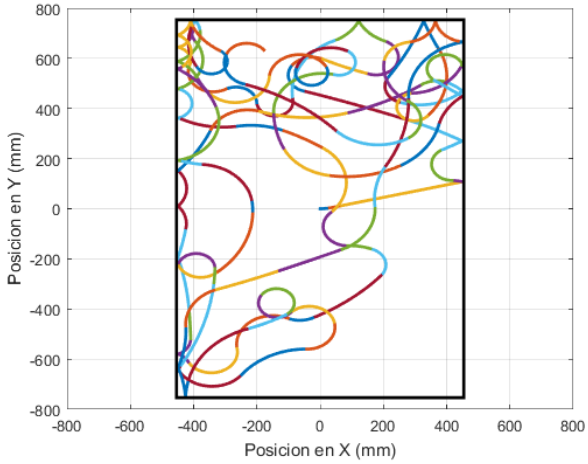

Fig. 12. Trayectoria del robot generada por las condiciones iniciales del inciso b).

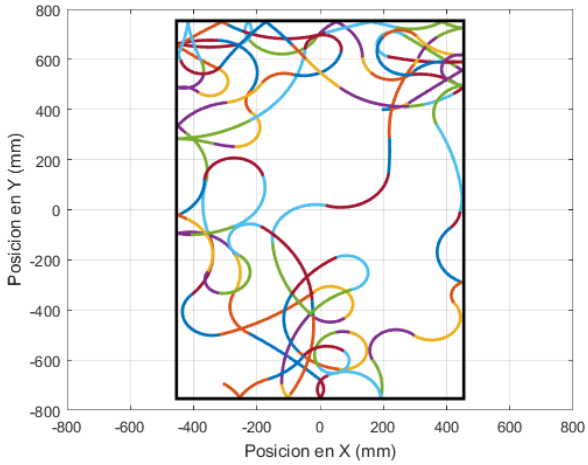

Fig. 13. Trayectoria del robot generada por las condiciones iniciales del inciso c).

Como se puede observar, las trayectorias cambian drásticamente a pesar de tener un cambio de únicamente 0.1 milímetros en el eje x, demostrando la sensibilidad a condiciones iniciales propias de un sistema caótico.

4.4 Resultados experimentales

Se realizaron tres experimentos con el robot diferencial Khepera III, utilizando diferentes condiciones iniciales con 100 iteraciones para cada uno de los siguientes casos: a) $x_0 = 207.4,\ y_0 = 0.2,\ \theta_0 = 218.4$; b) $x_0 = -1.3,\ y_0 = -0.7,\ \theta_0 = 359.3$; c) $x_0 = -0.7, y_0 = -0.4, \theta_3 = 359.9.$

Los resultados experimentales obtenidos se muestran en las figuras 14, 15 y 16.

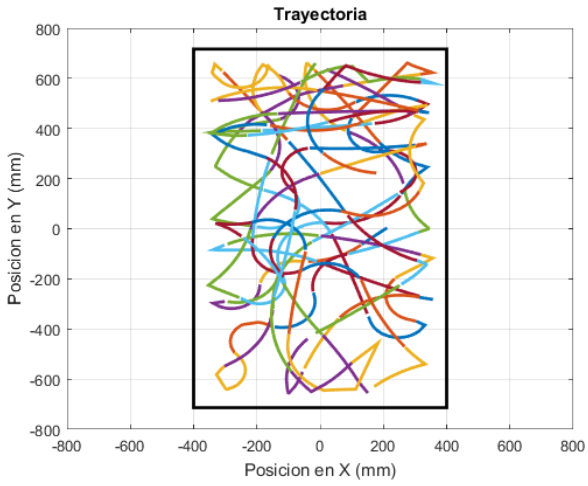

Fig. 14. Resultado experimental con las condiciones iniciales del inciso a).

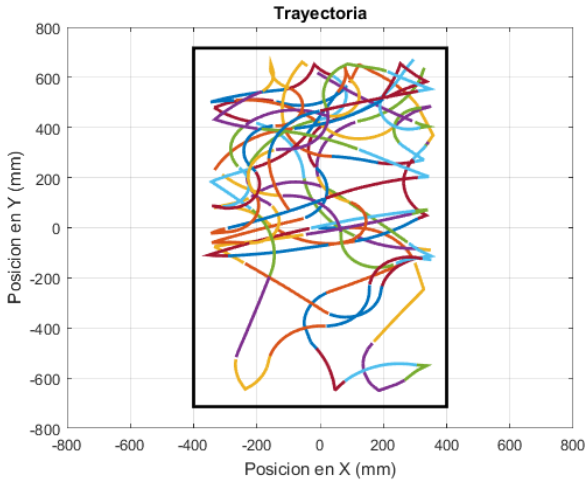

Fig. 15. Resultado experimental con las condiciones iniciales del inciso b).

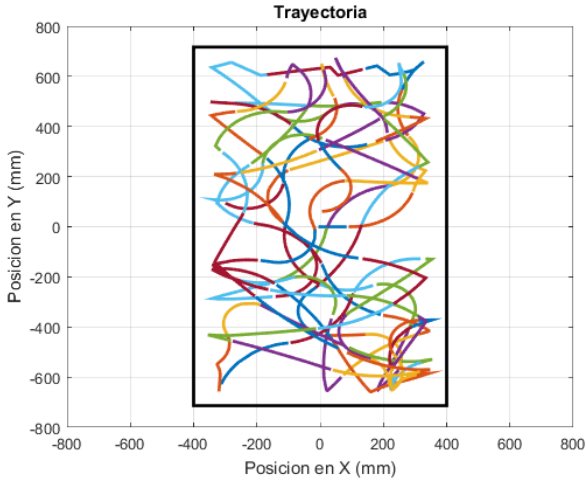

Fig. 16. Resultado experimental con las condiciones iniciales del inciso c).

Se puede observar de las figuras 15 y 16 que un pequeño cambio en milímetros en las condiciones iniciales, produce en el robot trayectorias completamente diferentes e impredecibles, demostrando experimentalmente que la propiedad caótica de sensibilidad a las condiciones iniciales se cumple. Se puede ver también, que con 100 iteraciones queda cubierta – por el patrullaje - la mayor parte del área de trabajo.

Cabe mencionar que estos resultados experimentales son preliminares, es necesario mejorar el algoritmo de evasión de bordes para que el ángulo de reflexión sea más preciso y utilizar otros sistemas caóticos para comparar su desempeño. De igual manera es necesario ajustar algunos detalles del área de trabajo y del programa generador de trayectorias.

Entre las condiciones que afectan los resultados experimentales se encuentran las limitaciones físicas intrínsecas del robot Khepera III, así como algunas características del área de prueba.

5. CONCLUSIONES

En este trabajo se empleó el mapa de Hénon para inducir comportamientos caóticos en las velocidades lineales y angulares de un robot móvil diferencial tipo Khepera III, con propósitos de patrullaje aprovechando las propiedades del caos. Los resultados numéricos y experimentales obtenidos, confirman que estas trayectorias son impredecibles. Como trabajo futuro se plantea la mejora de la programación de la estrategia de evasión de bordes, de manera que la etapa experimental refleje con mayor precisión los resultados obtenidos en las simulaciones numéricas. Además, se implementaran otros sistemas caóticos para comparar el comportamiento y las trayectorias generadas por el robot. Se trabajará en la verificación de la presencia de caos en las trayectorias generadas del robot móvil diferencial, empleando otros indicadores de caos.

AGRADECIMIENTOS

Este trabajo fue financiado por el CONACYT, México. A través del proyecto de investigación entre instituciones, Ref. 166654.

REFERENCIAS

Curiac, D. & Volosencu, C., 2014. A 2D chaotic path planning for mobile robots accomplishing boundary surveillance missions in adversarial conditions. *Communications in Nonlinear Science and Numerical* Simulation, 19(10), p. 3617–3627.

Hénon, M., 1976. A Two-Dimensional Mapping with a Strange Atractor. *Comm. Math. Phys*., 50(1), pp. 69-77.

Li, L.; Peng, H.; Kurths, J.; Yang, Y.; Schellnhuber, H., 2014. Chaos–order transition in foraging behavior of ants. *Proceedings of the National Academy of Sciences of the United States of North America*, 11(23), p. 8392–8397.

Martins-Filho, L. & Macau, E., 2006. Kinematic control of mobile robots. *ABCM Symposium Series in Mechatronics*, Volumen 2, p. 258–264.

Nakamura, Y. & Sekiguchi, A., 2001. The Chaotic Mobile Robot. *IEEE Transactions on Robotics and Automation*, p. 898–904.

Suster, P. & Jadlovská, A., 2010. Neural tracking trajectory of the mobile robot Khepera II internal model control structure. *International Conference Process*, Czech Republic, Kouty nad Desnou.

Volos, Kyprianidis & Stouboulos, 2012. A chaotic path planning generator for autonomous mobile robots. *Robotics and Autonomous Systems*, 60(4), p. 651–656.

Formación en grupos de robots móviles

A. López-Parra * **A. Arellano-Delgado.** **
C. Cruz-Hernández *** **R. Martínez-Clark** ****
J.J. Cetina-Denis *****

* *Departamento de Electrónica y Telecomunicaciones, Centro de Investigación Científica y de Educación Superior de Ensenada (CICESE).(e-mail: lopezpa@cicese.edu.mx).*
** *(e-mail: aarellan@cicese.mx).*
*** *(e-mail: ccruz@cicese.mx).*
**** *(e-mail: rigomar@cicese.edu.mx).*
***** *(e-mail: jcetina@cicese.edu.mx).*

Resumen: Este trabajo aborda el problema de formación de redes de robots móviles sin colisiones con base en la teoría de sistemas complejos. En particular, la formación de 5 robots móviles conectados en estrella, utilizando el modelo linealizado y controlable obtenido por retroalimentación dinámica del modelo de un robot diferencial tipo Khepera III. Se diseña una trayectoria para el robot maestro en forma de "8", lográndose el seguimiento en formación por un grupo de robots evitando colisiones. Los resultados se proporcionan en simulaciones numéricas.

Palabras clave: Formación de robots, robot diferencial Khepera III, sistemas complejos.

1. INTRODUCCIÓN

En años recientes, el control de sistemas multiagente ha atraído la atención de las ciencias computacionales y de la comunidad de control. Con ayuda de las investigaciones en los campos de sistemas complejos y comportamientos colectivos se han propuesto algunos protocolos de control para lograr el desempeño y beneficios de agentes coordinados tal como la formación. Entre las ventajas que presentan los sistemas multiagente se encuentran: un grupo aumenta la eficiencia y efectividad de la tarea asignada, el uso de grupos de robots permite enfrentar fallas de mejor forma, son capaces de realizar tareas que son imposibles para un solo robot, etc.

En Adel Abbaspour (2015) se logra formación óptima con la ayuda de varias técnicas de optimización numéricas. Se utilizan como base robots con ruedas con el propósito de manipular un objeto en común. Finalmente, se utiliza una aproximación virtual para demostrar cómo se logra la formación óptima. En Shanying Zhu (2015) utilizan el modelo de una partícula propulsada para describir los comportamientos colectivos emergentes en un grupo de agentes móviles. En Yanyan Dai (2015) se plantea una estrategia de formación para múltiples robots con evasión de obstáculos y restricciones de velocidad.

Este trabajo propone la formación de un grupo de robots móviles con evasión de colisiones utilizando la teoría de sistemas complejos. Primeramente se presenta el modelo matemático de un robot diferencial y como llevarlo a un sistema equivalente lineal donde es posible aplicar el controlador. Posteriormente se propone el uso de la teoría de grafos y sistemas complejos para formar una red de 5 robots. Estos robots pueden obtener información de los vecinos con los que esten conectados con propósitos del objetivo de control.

2. SISTEMAS COMPLEJOS

En esta sección, se proporciona breve descripción sobre redes dinámicas complejas y las condiciones de sincronización. En este trabajo se consideran redes dinámicas complejas de nodos idénticos, linealmente acoplados mediante la primer variable de estado de cada nodo, siendo cada nodo un subsistema dinámico *n-dimensional* descrito como sigue

$$\dot{\mathbf{x}}_i = f(\mathbf{x}_i) + \mathbf{u}_i, \qquad i = 1, 2, \ldots, N, \tag{1}$$

donde $\mathbf{x}_i = (x_{i1},\ x_{i2},\ ...,\ x_{in})^T \in \mathbb{R}^n$ son las variables de *estado* del nodo i, $\mathbf{u}_i = (u_{i1}, 0, ..., 0)^T \in \mathbb{R}^n$ es la señal de *control* del nodo i y es definida por

$$u_{i1} = c\sum_{j=1}^{N} a_{ij}\Gamma\mathbf{x}_j, \qquad i = 1, 2, \ldots, N, \tag{2}$$

la constante $c > 0$ representa la *fuerza de acoplamiento* de la red compleja y $\Gamma \in \mathbb{R}^{n\times n}$ es una matriz constante de conexiones que indica que variables de estado están acopladas. Mientras que, $\mathbf{A} = (a_{ij}) \in \mathbb{R}^{N\times N}$ es la *matriz de acoplamiento*, la cual representa la topología de acoplamiento de la red compleja. Si existe una conexión entre el nodo i y el nodo j, entonces $a_{ij} = 1$; de otra forma $a_{ij} = 0$ para $i \neq j$. Los elementos de la diagonal de la matriz de acoplamiento $\mathbf{A}$ se definen como sigue

$$a_{ii} = -\sum_{j=1,\ j\neq i}^{N} a_{ij} = -\sum_{j=1,\ j\neq i}^{N} a_{ji}, \tag{3}$$

sí el grado del nodo i es d_i, entonces $a_{ii} = -d_i$, $i = 1, 2, \ldots, N$. Sí asumimos que la red compleja está conecta-

da sin nodos aislados. Entonces, $\mathbf{A}$ es una matriz de acoplamiento simétrica e irreducible. En este caso, se puede ver que un valor propio de la matriz de acoplamiento $\mathbf{A}$ es cero con multiplicidad 1 y todos los demás valores propios son estrictamente negativos, ver Wang y Chen (2002) y Wang (2002).

El estado de sincronización de los nodos en sistemas complejos, puede caracterizarse por los valores propios diferentes de cero de la matriz de acoplamiento $\mathbf{A}$. En la red dinámica compleja definida por (1)-(2) habrá sincronización (asintótica) sí (Wang (2002)):

$$\mathbf{x}_1(t) = \mathbf{x}_2(t) = \ \ldots \ = \mathbf{x}_N(t), \ \text{cuando}\, t \to \infty. \tag{4}$$

La condición de acoplamiento difusivo (3) garantiza que el estado de sincronización es una solución $\mathbf{s}(t) \in \mathbb{R}^n$, de un nodo aislado, es decir, satisface

$$\dot{\mathbf{s}}(t) = f\left(\mathbf{s}(t)\right), \tag{5}$$

donde $\mathbf{s}(t)$ puede ser un *punto de equilibrio*, una *órbita periódica* ó un *atractor caótico*. En consecuencia el estado de sincronización,

$$\mathbf{x}_1(t) = \mathbf{x}_2(t) = \ \ldots \ = \mathbf{x}_N(t) = \mathbf{s}(t), \tag{6}$$

de la red dinámica compleja (1)-(2) se determina por las dinámicas de un nodo aislado, la fuerza de acoplamiento c, la matriz de conexión Γ y la matriz de acoplamiento $\mathbf{A}$, ver Wang y Chen (2002) y Wang (2002).

3. MODELO MATEMÁTICO DE UN ROBOT DIFERENCIAL

En ésta sección, se describe el modelo matemático de un robot móvil diferencial basado en 2 ruedas independientes con un mismo eje de rotación. El movimiento se produce a partir de los cambios que se dan en los actuadores de locomoción. En este trabajo, se usará el modelo matemático aproximado del robot Khepera III. La figura 1 muestra una vista general del robot.

Figura 1. Vista general del robot diferencial tipo Khepera III.

En Suster y Jadlosvska (2010) se plantea el siguiente modelo para un robot diferencial tomando en cuenta las siguientes consideraciones:

- El robot se mueve en una superficie perfectamente plana sin deslizamiento, además no contempla la resistencia de las llantas.
- La posición del robot está dada por las coordenadas x, y y un ángulo θ, el cual representa la rotación del robot en relación al sistema de coordenadas.
- El robot se controla por las velocidades angulares ω_L y ω_R. La relación entre las velocidades angulares ω_L, ω_R y las velocidades lineales V_L, V_R es la siguiente:

$$V_L = rw_L, \tag{7}$$

$$V_R = rw_R, \tag{8}$$

donde r es el radio de la llanta del robot $r = 2.05\ cm$.

La posición y la rotación del robot en el espacio están basadas en las ecuaciones siguientes, formando el modelo cinemático del robot

$$\dot{x} = vcos(\theta), \tag{9}$$

$$\dot{y} = vsen(\theta), \tag{10}$$

$$\dot{\theta} = \omega, \tag{11}$$

con v y ω definidas como

$$v = \frac{V_L + V_R}{2}, \tag{12}$$

$$\omega = \frac{V_R - V_L}{b}, \tag{13}$$

donde b es la distancia entre las ruedas $b = 8.841\ cm$.

Las entradas al robot son las velocidades V_L y V_R y las salidas corresponden a x, y y θ. Estas ecuaciones permiten conocer la posición y rotación del robot sabiendo las condiciones iniciales y las velocidades independientes de cada una de las ruedas. De las ecuaciones del robot se observa que es un sistema no lineal de la forma,

$$\dot{\mathbf{q}} = f(\mathbf{q})\mathbf{u}, \ \mathbf{u} \in \mathbb{R}^m, \tag{14}$$

donde $\mathbf{q}$ y $\mathbf{u}$ representan los estados del sistema y entradas respectivamente del robot diferencial (9)-(13).

3.1 Linealización por retroalimentación dinámica

Debido a que las entradas se encuentran acopladas en (12) y (13), es necesario utilizar alguna técnica que nos permita desacoplarlas para aplicar el controlador de formación de grupo de robots. Una de éstas técnicas como se plantea en Deluca (2002) es la linealización por retroalimentación dinámica.
La retroalimentación dinámica consiste en encontrar, si es posible, un compensador dinámico de la forma

$$\begin{aligned} \dot{\xi} &= a(q,\xi) + b(q,\xi)u, \\ \omega &= c(q,\xi) + d(q,\xi)u. \end{aligned} \tag{15}$$

Con i estados ξ y m entradas externas u, para que el sistema (14) y (15) sean equivalentes a través de una trasformación de estados $\mathbf{z} = T(\mathbf{q}, \xi)$ a un sistema lineal controlable.

Para lograr este propósito, se define apropiadamente un sistema con m salidas de la forma,

$$\eta = h(\mathbf{q}). \tag{16}$$

Después se deriva la salida hasta que las entradas aparezcan en forma explícita. Este algoritmo forma el estado ξ del compensador dinámico (15). El algoritmo termina después de un número finito de diferenciaciones, cuando el sistema es invertible en las salidas elegidas. Definiendo el vector de salidas como $\eta = (x, y)$ y obteniendo el compensador se tiene:

$$\dot{\xi} = a = u_1 cos(\theta) + u_2 sen(\theta), \tag{17}$$

$$\omega = \frac{u_2 cos(\theta) - u_1 sen(\theta)}{\xi}. \tag{18}$$

En las nuevas coordenadas se tiene

$$\begin{aligned} z_1 &= x, \\ z_2 &= y, \\ \dot{z_1} &= \dot{x} = vcos(\theta) = \xi cos(\theta), \\ \dot{z_2} &= \dot{y} = vsen(\theta) = \xi sen(\theta), \\ \ddot{z_1} &= \ddot{x} = u_1, \\ \ddot{z_2} &= \ddot{y} = u_2. \end{aligned} \tag{19}$$

Nótese que el sistema en las nuevas coordenadas (19) es lineal con entradas desacopladas u_1 y u_2 como era el propósito. Asumiendo que el robot debe seguir una trayectoria deseada $(X_d(t), Y_d(t))$, en el modelo lineal equivalente (19) es sencillo diseñar una ley de control para la trayectoria (con coordenadas cartesianas) como sigue

$$u_1 = c_1(\dot{X}_d(t) - \dot{x}) + c_2(X_d(t) - x), \tag{20}$$

$$u_2 = c_3(\dot{Y}_d(t) - \dot{y}) + c_4(Y_d(t) - y), \tag{21}$$

con $c_i > 0$, $i = 1, 2, 3, 4$.

4. FORMACIÓN DE ROBOTS

En esta sección, se aborda el problema de formación de una red de robots, el cual consiste en establecer el movimiento de un grupo de robots para que, de una manera coordinada o colaborativa, lleven a cabo una tarea común específica: vigilancia, búsqueda de objetos peligrosos en lugares inhóspitos, exploración, rescate, recolección de información y transporte de objetos; las cuales pueden realizarse en ambientes diversos utilizando redes de robots móviles terrestres, aéreos, espaciales, marinos o submarinos Couzin (2002). Con fines de consistencia de notación, se realiza el siguiente cambio de variables

$$\begin{aligned} \dot{x} &= \dot{x_1}, \\ \dot{y} &= \dot{x_2}, \\ \dot{\theta} &= \dot{x_3}. \end{aligned} \tag{22}$$

Cada nodo i toma la forma,

$$\dot{x_i} = f(x_{i1}, x_{i2}, x_{i3}, u_{i1}, u_{i2}). \tag{23}$$

En donde $x_{i1} \in \mathbb{R}^n$ es el vector de estados que se desenvuelve sobre el eje x del robot i-ésimo y $\mathbf{u}_i = (u_{i1}, u_{i2}, 0, ..., 0)^T$ es el vector de entradas de control. En este caso, el controlador para la entrada u_{i1} tendría la siguiente forma,

$$u_{i1} = \sum_{j=1}^{N} c_{ij} a_{ij} x_{i1} + \delta_{ij}(a_{ij} x_{i1} + \Delta_{ij}) + \sum_{j=1}^{N} c_{ij} a_{ij} \dot{x}_{i1}, \tag{24}$$

donde c_{ij} es la fuerza de acoplamiento entre los robots i y j, a_{ij} es un elemento de la matriz de acoplamiento $A = [a_{ij}]$, Δ_{ij} es la *distancia esperada* entre los robots i y j y δ_{ij} es el *coeficiente de repulsión* entre los robots i y j, el cual puede tomar los siguientes valores,

$$\delta_{ij} = \begin{cases} 0, & \text{si } |x_{i1} - x_{j1}| > \Delta_{ij}, \\ \delta, & \text{si } |x_{i1} - x_{j1}| \leq \Delta_{ij}. \end{cases} \tag{25}$$

4.1 Evasión de colisiones

El controlador propuesto en (24) es suficiente para lograr el objetivo de control de formación de robots, sin embargo debido a que los robots obtienen información sólo de los vecinos con los que están conectados y no con los demás robots de la red, es necesario modificar el controlador para evitar colisiones entre los robots que conforman la red. En Martínez Clark (2014) se propone la siguiente modificación a los controladores, aplicándolo a las dos entradas disponibles se tiene:

$$u_{i1} = \sum_{j=1}^{N} c_{ij} a_{ij} x_{i1} + \delta_{ij}(a_{ij} x_{i1} + \Delta_{ij}) - r_{ij} sign(x_{i1} - x_{j1}) + \sum_{j=1}^{N} c_{ij} a_{ij} \dot{x}_{i1}, \tag{26}$$

$$u_{i2} = \sum_{j=1}^{N} c_{ij} a_{ij} x_{i2} + \delta_{ij}(a_{ij} x_{i2} + \Delta_{ij}) - r_{ij} sign(x_{i2} - x_{j2}) + \sum_{j=1}^{N} c_{ij} a_{ij} \dot{x}_{i2}, \tag{27}$$

donde r_{ij} es el *coeficiente anticolisiones* entre el robot i y j y puede tomar los siguientes valores,

$$r_{ij} = \begin{cases} 0, & \text{si } \| \boldsymbol{l_{ij}} \| > m, \\ r, & \text{si } \| \boldsymbol{l_{ij}} \| < m, \end{cases} \tag{28}$$

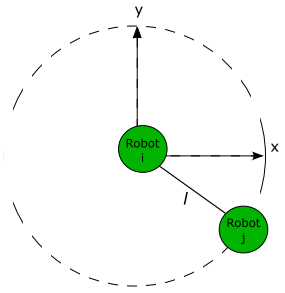

Figura 2. Vector $\boldsymbol{l}$ formado entre los robots i, j.

donde m es el *umbral de colisión* en metros, el cual se ajusta a las dimesiones de los robots y/o la distancia que se desee mantener entre ellos en la formación, $\| \boldsymbol{l_{ij}} \|$ es la *norma euclidiana* formada por las posiciones en cada eje como se observa en la figura 2, esto es,

$$\| \boldsymbol{l_{ij}} \| = \sqrt{(x_j - x_i)^2 + (y_j - y_i)^2}, \tag{29}$$

y $sign(k)$ es la *función signo* que para efectos en este trabajo se utiliza la defición dada en Kwakernaak et al. (1991),

$$sign(k) = \begin{cases} 1, & \text{si } k > 0, \\ 0, & \text{si } k = 0, \\ -1, & \text{si } k < 0. \end{cases} \quad (30)$$

4.2 Formación de una red de robots en topología estrella

Para la formación de una red de robots, se conectarán 5 nodos utilizando el modelo lineal descrito en la sección 3.1. En la red se usarán conexiones dirigidas en estrella para tener un mejor funcionamiento del controlador como se plantea en Martínez Clark (2014). La figura 3 muestra el grafo utilizado, se tiene un robot maestro N1 y 4 robots esclavos N2, N3, N4 y N5.

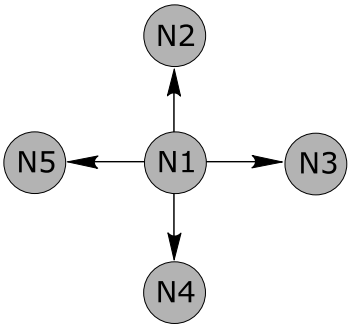

Figura 3. Grafo con conexiones dirigidas utilizado para la formación de 5 robots móviles.

La matriz de acoplamiento correspondiente al grafo en estrella de la figura 3 es

$$A(G)_{estrella} = \begin{bmatrix} 0 & 0 & 0 & 0 & 0 \\ 1 & -1 & 0 & 0 & 0 \\ 1 & 0 & -1 & 0 & 0 \\ 1 & 0 & 0 & -1 & 0 \\ 1 & 0 & 0 & 0 & -1 \end{bmatrix}. \quad (31)$$

Las ecuaciones que describen el movimiento del robot i (con $i = 1, 2, ..., 5$) estan descritas por

$$\begin{aligned} \dot{x_i} &= v_i cos(\theta_i), \\ \dot{y_i} &= v_i sen(\theta_i), \\ \dot{\theta_i} &= \omega_i, \\ \dot{\xi_i} &= a_i = u_{i1} cos(\theta_i) + u_{i2} sen(\theta_i), \end{aligned} \quad (32)$$

con entradas u_{i1} y u_{i2} definidas por (26) y (27).

5. RESULTADOS NUMÉRICOS

En esta sección, se reportan los resultados obtenidos de simulaciones numéricas realizadas en Matlab. Se plantea una ruta deseada en forma de "8" para el robot maestro N1, mientras los robots esclavos tienen la función de seguir al robot maestro en formación simulando un cuadrado. Las condiciones iniciales y valores de parámetros utilizados en la simulación numérica son los siguientes:
$(x_1(0), y_1(0), \theta_1(0), \xi_1(0)) = (3, -1.5, 0, 0.01)$,
$(x_2(0), y_2(0), \theta_2(0), \xi_2(0)) = (-2, 0, \frac{\pi}{4}, 0.01)$,
$(x_3(0), y_3(0), \theta_3(0), \xi_3(0)) = (4, 2, \pi, 0.01)$,
$(x_4(0), y_4(0), \theta_4(0), \xi_4(0)) = (2, -2, \pi, 0.01)$,
$(x_5(0), y_5(0), \theta_5(0), \xi_5(0)) = (3, 0, \frac{\pi}{3}, 0.01)$,
$c_{11} = c_{21} = 0.3$, $c_{12} = c_{22} = 3$, $\delta_{12x} = \delta_{13x} = \delta_{14x} = \delta_{15x} = 50$, $\delta_{12y} = \delta_{13y} = \delta_{14y} = \delta_{15y} = 50$, $r_{21} = r_{31} = r_{41} = r_{51} = r_{12} = r_{32} = r_{42} = r_{52} = r_{13} = r_{23} = r_{43} = r_{53} = r_{14} = r_{24} = r_{34} = r_{54} = r_{15} = r_{25} = r_{35} = r_{45} = 10$, $m = 0.5$.
Con $(X_d, Y_d) = (4sen(\frac{t}{10}), 4sen(\frac{t}{20}))$ y distancias propuestas entre los robots para la formación:
$\Delta_{12x} = -1, \Delta_{13x} = 1, \Delta_{14x} = -1, \Delta_{15x} = 1, \Delta_{12y} = 1, \Delta_{13y} = 1, \Delta_{14y} = -1, \Delta_{15y} = -1$.

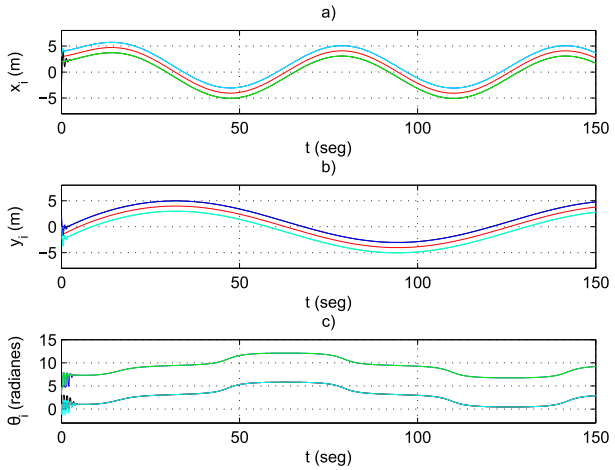

Figura 4. Trayectorias temporales de los robots: a) x_i, b) y_i y c) θ_i, con i = 1,2,...,5.

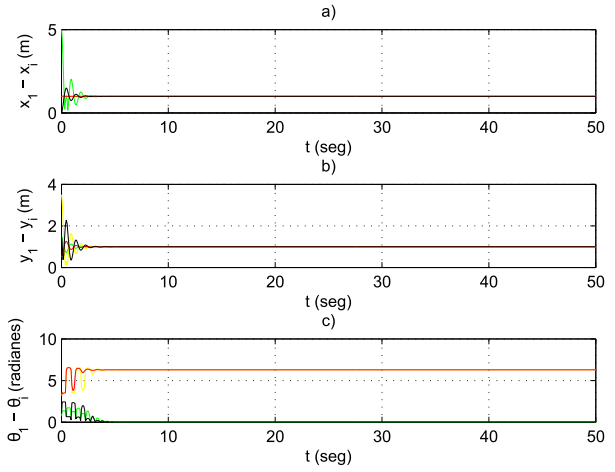

Figura 5. Dinámicas de los errores: a) x_1–x_i, b) y_1–y_i, c) θ_1–θ_i, con i = 2,3,...,5.

En la figura 4 se observa como los robots tienden a las distancias propuestas, por lo que existirá un error entre los robots en las posiciones x y y como se aprecia en la figura 5. En la figura 6 se ilustran las entradas para cada una de las llantas w_L y w_R. Mientras que en la figura 7 se muestran las posiciones iniciales arbitrarias de la red de 5 robots conectados en estrella. En la figura 8 se observa como los robots esclavos N2, N3, N4 y N5 siguen al robot maestro N1 (el rojo) en su trayectoria en forma de "8", respetando el umbral de distancia propuesto. En la evolución de la simulación es posible observar como los robots tienden a las

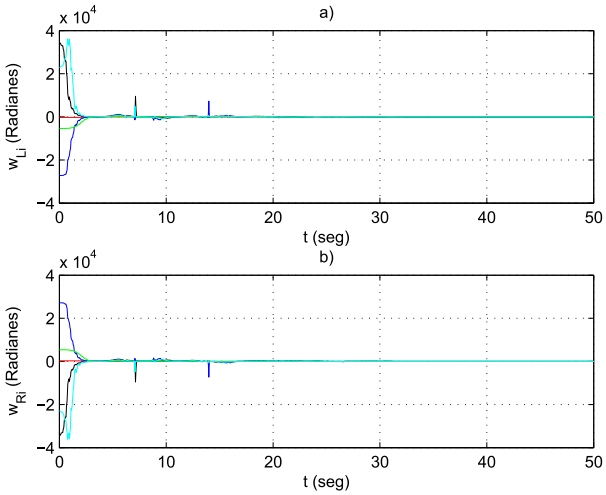

Figura 6. Entradas para las llantas: a) w_{Li} y b) w_{Ri}, con $i = 1,2,\ldots,5$.

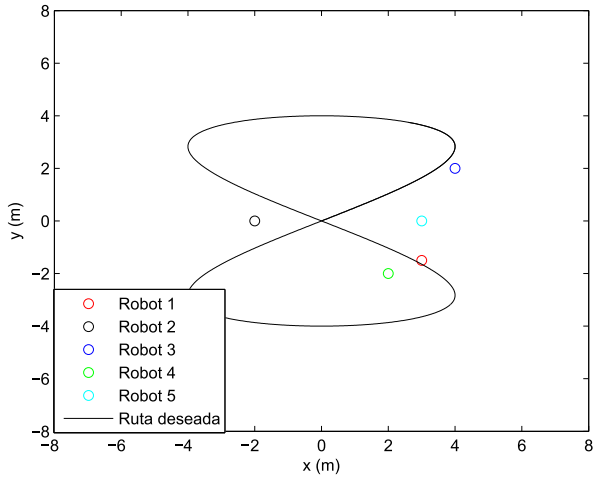

Figura 7. Posición inicial de la red de 5 robots conectados en estrella en el plano (x, y), el circulo rojo representa el robot maestro.

distancias esperadas llegando a una formación cuadrada y evitando las posibles colisiones entre ellos que pudiesen presentarse. En 9 se tienen las trayectorias que sigue cada robot en la formación propuesta siguiendo al maestro. En implementaciones experimentales debe tomarse en cuenta que el umbral de distancia anticolisiones siempre debe ser menor a las distancias esperadas, ya que, si este caso se da, la constante anticolisiones nunca dejará llegar a los robots a las distancias propuestas en la formación. Además, es necesario considerar la velocidad mínima y máxima que un robot real permite para acotar los valores que pueden tomar las entradas. Para esto puede usarse una función saturación que limite los valores tomando en cuenta las siguientes consideraciones

- Si el valor de la entrada es mayor al valor máximo de velocidad angular, este se acotará al valor máximo.
- Si el valor de la entrada está en el rango entre el valor mínimo y el valor máximo, quedara igual.

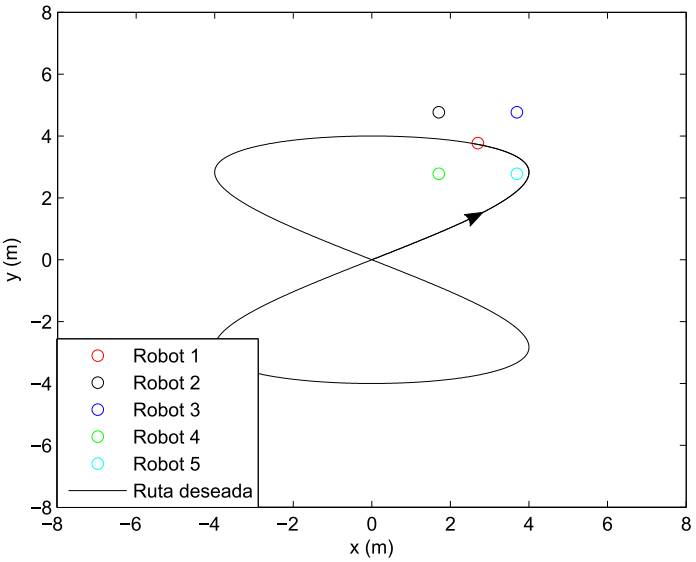

Figura 8. Trayectoria final de la red de robots siguiendo la ruta del maestro con la formación propuesta en el plano (x, y), el circulo rojo representa al robot maestro.

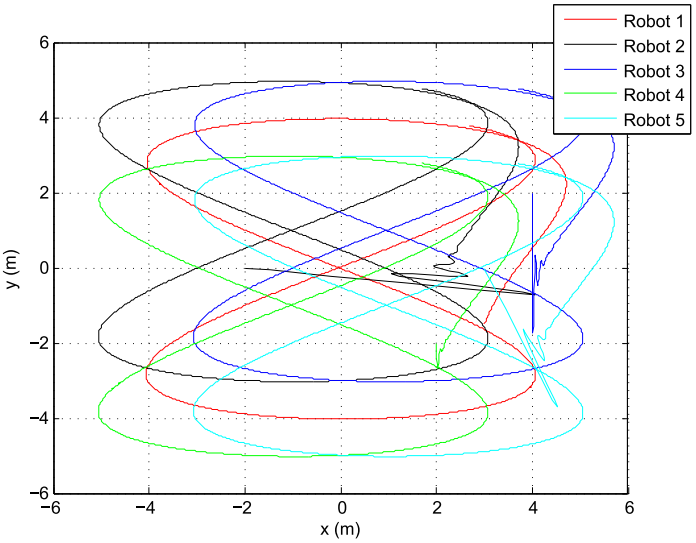

Figura 9. Trayectoria de cada robot en el plano (x, y), el trazo de color rojo representa la ruta del robot maestro.

- Si es valor se encuentra entre 0 y el valor mínimo se acotará al valor mínimo.

Esto puede ser expresado matemáticamente como,

$$w_{l,rreal} = sign(w_{l,r}) sat_{lim}(w_{l,r}) \tag{33}$$

Utilizando la función saturación que se observa en la figura 10, los valores reales de W_{real} se limitan a,

$$w_{real} = \begin{cases} w_{max}, & \text{si } w_{l,r} >= lim_{sup}, \\ w_{l,r}, & \text{si } lim_{inf} < w < lim_{sup}, \\ lim_{min}, & \text{si } 0 <= w <= lim_{inf}. \end{cases} \tag{34}$$

Donde lim_{inf}, lim_{sup} representan el límite superior e inferior de velocidad. Para las simulaciones aquí presentadas se utilizaron 5 nodos, sin embargo pueden agregarse n

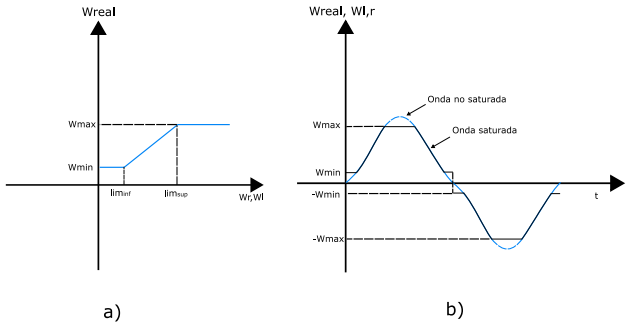

Figura 10. a) Función saturación para limitar los valores de W, b) Ejemplo del recorte de onda de la función saturación.

cantidad de agentes. En la parte experimental los límites estarán dados por las capacidades de procesamiento del equipo y/o cámaras.

6. CONCLUSIONES

En este trabajo se realizó la formación de una red de 5 robots móviles homogéneos utilizando la teoría de sistemas complejos y aplicando linealización por retroalimentación dinámica al modelo aproximado de un robot diferencial tipo Khepera III. Se logró el seguimiento por un grupo de robots de una trayectoria deseada en forma de "8", evitando colisiones y manteniendo una formación constituyendo un cuadrado. Con los resultados numéricos obtenidos queda mostrado que es posible implementar formación en grupos de robots móviles tipo diferencial, permitiendo aplicaciones como reconocimiento, búsqueda, exploración, patrullaje, vigilancia, etc. Las cuáles serán objeto de trabajo futuro de forma experimental con una red de robots móviles tipo Khepera III.

AGRADECIMIENTOS

Trabajo financiado por el CONACYT México, a través del Proyecto de Investigación entre Instituciones Ref. 166654.

REFERENCIAS

Adel Abbaspour, Khalil Alipour, Hadi Zare Jafari y S. Ali A. Moosavian. Optimal formation and control of cooperative wheeled mobile robots. *Center of Excellence in Robotics and Control, Advanced Robotics and Automated Systems Lab, Department of Mechanical Engineering, K.N.Toosi University of Technology, 19991 43344, Tehran, Iran, C. R.Mecanique,* 343 (2015) 307–321.

Couzin, I. D., Krause, J., James, R., Ruxton, G. D. y Franks, N. R. Collective memory and spatial sorting in animal groups. *J. Theor. Biol. 218, 1–11*, 2002.

De Luca Alessandro, Oriolo Giuseppe y Marilena Vendittelli. Control of wheeled mobile robots: an experimental overview. *Dipartimento di Informatica e Sistemistica, Università degli Studi di Roma La Sapienza, Italy* (2002).

Kwakernaak, H., Sivan, R. y Strijbos. Modern signals and systems. *Prenice-Hall International* (1991).

Martínez Clark Rigoberto. Control de comportamientos colectivos en grupos de robots móviles. Tesis de maestría. *Centro de Investigación Científica y de Educación Superior de Ensenada CICESE, Ensenada Baja California.* Agosto del 2014.

Martínez-Clark R. , Cruz-Hernández C. , Reyes-De la Cruz D., Arellano-Delgado A. , Pinedo-Lomelí L.F. Formación de agentes: una aplicación al patrullaje. *Congreso Nacional de Control Automático, Cuernavaca, Morelos, AMCA, México.* 2015.

Martínez-Clark R. , Cruz-Hernández C. , Reyes-De la Cruz D., Arellano-Delgado A. , Pinedo-Lomelí L.F. Diseño de un controlador para la formación de grupos de robots móviles. *XVI Congreso Latinoamericano de Control Automático, CLCA, Cancún, Quintana Roo, México.* 2014, 6-11.

Shanying Zhu, Lihua Xie, Cailian Chen y Xinping Guan. Collective behavior of mobile agents with state-dependent interactions. *Centre for E-City, School of Electrical and Electronic Engineering, Nanyang Technological University, Singapore 639798, Singapore*, Automatica 51 (2015) 394–401.

Šuster Peter y Jadlosvská Anna. Neural tracking trajectory of the mobile robot Khepera II internal model control structure. *International Conference Process Control, Kouty nad Desnou, Czech Republic* 2010.

X.F. Wang. Complex networks: topology, dynamics and synchronization. *International Journal of Bifurcation and Chaos*, 12(5), 885-916, (2002).

X.F. Wang y Chen. Synchronization in small-world dynamical networks. *Int. J. Bifurc. Chaos,* 12(1), 187-192, (2002).

Yanyan Dai , YoonGu Kim, SungGil Wee, DongHa Lee y SukGyu Lee. A switching formation strategy for obstacle avoidance of amulti-robot system based on robot priority model. *Department of Electrical Engineering, Yeungnam University, Gyeongsan, Gyeongsangbuk, South Korea,* ISA Transactions 56(2015)123–134.

Generalized Proportional Integral Control for Aperiodic Gait Stabilization of a Bipedal Robot with Seven Degrees of Freedom ⋆

Arcos-Legarda Jaime * **Cortes-Romero John** ** **Tovar A.** ***

* *Department of Mechanic and Mechatronic Engineering, Universidad Nacional de Colombia, Bogotá, Colombia, (wjarcosl@unal.edu.co).*
** *Department of Electric and Electronics Engineering, Universidad Nacional de Colombia, Bogotá, Colombia, (jacortesr@unal.edu.co)*
*** *Mechanical Engineering, Indiana University-Purdue University Indianapolis, Indianapolis, Indiana, USA, (tovara@iupui.edu)*

Abstract: The main goal of this paper is to achieve asymptotically stable walking for a bipedal robot over an Aperiodic Gait pattern. The five-link planar bipedal robot has one degree of under-actuation, four actuators and point feet. Trajectory tracking and multi-orbital stability were performed using Generalized Proportional Integral (GPI) controller. The stability of the multi-periodical walking was tested through the computation of Poincaré return maps. This analysis was performed by numerical simulation with a gait pattern reconfiguration. The results of the simulation show that the GPI control achieved a performance robust enough to overcome the gait pattern reconfiguration without changes in the control law with an event-based action. The robot analyzed corresponds to a prototype under development at the Control Laboratory of the *Universidad Nacional de Colombia, Bogotá*.

Keywords: Bipedal Robots, Aperiodic Gait, GPI Control, Hybrid Systems.

1. INTRODUCTION

Although the study of bipedal walking robots has been a highly active research area, bringing outstanding achievements in the last three decades, important problems are still unsolved regarding the design and control of bipedal robots. One of the open issues in which research needs to focus is in ensuring the stability of aperiodic gaits, Grizzle et al. (2014). Even if we can assume that the nature of the walking is a periodic repetition of movements, there are some factors like uneven ground or external disturbances, that may produce the needs to interrupt the periodicity of the gait. This paper proposes a control system and a trajectory generation strategy that ensure the stability of the walking in the changes of periodic gait patterns.

The control strategies to achieve a stable gait in the presence of uneven ground or external disturbances have been based on the use of event-based feedback controllers, as it was proposed by Grizzle et al. (2003) and Hamed and Grizzle (2013). In the present work a GPI robust controller was developed, which can be used with different walking patterns. A GPI robust control had been previously used in the simulation of the control of a gait exoskeleton in Arcos-Legarda et al. (2013), but without the analysis of underactuted walking phase and with a fix periodic trajectory. Whereas, the research presented here takes into a count the underactuated phase and the dynamic walking though the use of a bipedal robot with point feet.

The approach used by the GPI control is based on the assumption that the unmodeled dynamics and the external disturbances can be lumped in a total disturbance which can be approximately reconstructed by a m-order polynomial. Similar methods have been used by the authors in Arcos-Legarda et al. (2016), where a periodic gait stability in bipedal robots was achieved. Other works for active disturbance rejection for bipedal robots were developed with time-based trajectories, as Martínez-Fonseca et al. (2016) or based in Zero Moment Point (ZMP) control, like in Hill and Fahimi (2015).

This paper is organized as follows: In the section 2 are described the features of the robot and its mathematical model is developed. Section 3 presents the GPI control strategy proposed. Then a trajectory generation strategy based on the state of the robot is depicted in section 4. The simulation of the strategies proposed in the previous sections is evaluated in the section 5, and additionally a stability test is done. Finally in section 6 conclusions are drawn.

2. ROBOT MODEL

The robot's model was obtained from the study of the bipedal robot prototype shown in Fig. 1. This robot is under development at the Control Laboratory of the *Universidad Nacional de Colombia, Bogotá*. The model is described as a multibody system formed by the five-link mechanism shown in the Fig.2. The bipedal robot has a torso connected to one leg at each sides of the hip. The legs are composed of a thigh serially with a shin connected by a revolute joint, working as a knee. The leg ending has a point-foot, without ankle. The robot's movements are restricted to the saggital plane by a radial bar with central pivot located 1m away from the robot. The description of the robot shows seven degrees of freedom: the angle of the torso respect to a fix frame, two angles at the hip, two in the knees and the cartesian plane position of the hip.

⋆ This paper is a result of the research project number 28340, supported by the Engineering Research Division of the National University of Colombia.

The bipedal walking is a sequence of changes between single and double support. Here, it is assumed that the double support phase is instantaneous and that the end of the support leg has unilateral constraints. In this way it does not have rebound nor slip and its vertical reaction force is repulsive and the lateral force is inside of the friction cone. This constraint converts the end of the support leg into a pivot, which transforms the system into a five degrees of freedom mechanism. The robot has four actuators: two between the torso and the thighs and two more in the knees. Although the actuators have flexible joints to the links, here the stiffness of the union is configured to its maximum value, it in order to avoid the additional dynamic of the strings. As in Tzafestas et al. (1996), Westervelt et al. (2007) and Arcos-Legarda et al. (2016) the Lagrange's differential equation was used to find the model of the robot in the single support phase to get the Euler-Lagrange expressed as:

$$D_s(q_s)\ddot{q}_s + C(q_s,\dot{q}_s)\dot{q}_s + G_s(q_s) = B_s(q_s)u + \delta(q_s,\dot{q}_s) + \zeta, \quad (1)$$

where $q_s := [q_1 \quad q_2 \quad \dots \quad q_5]^T$ is the generalized coordinates vector, $D_s(q_s)$ is the inertial matrix, $C_s(q_s,\dot{q}_s)\dot{q}_s$ is a vector of Centripetal and Coriolis forces, $G_s(q_s)$ is a vector of forces associated to the gravity, $B_s(q_s)u$ is a vector of generalized forces, $\delta(q_s,\dot{q}_s)$ takes into account the uncertainties of the model and ζ is an unknown vector of the external disturbances.

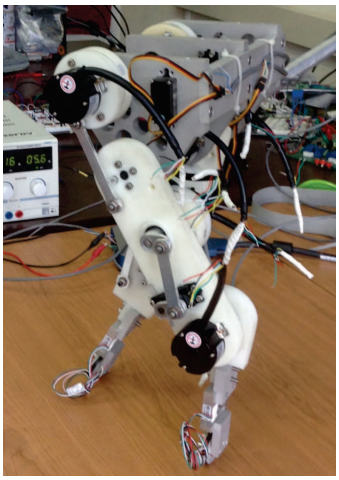

Fig. 1. Robot Prototype, under development at the Control Laboratory of the *Universidad Nacional de Colombia, Bogotá*

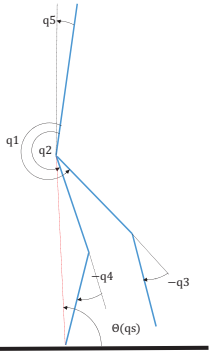

Fig. 2. Multibody Model of the Bipedal Robot

As was exposed by Hurmuzlu and Marghitu (1994), the event of exchange of the support leg produces an impact that is often studied as the collision of rigid bodies. This impact phase together with the continuous dynamic of the single support phase form a hybrid model. As proposed by Grizzle et al. (2001) and Westervelt et al. (2003), it is mandatory to take in consideration external forces affecting the system at the impact time. For this reason the exchange of support leg phase of the walking was studied with the robot as an unpinned system with an augmented model that takes into account a fix point over the robot's body, corresponding to $p_e := [p_e^h \quad p_e^v]^T$, where p_e is the position of the end of the support leg, p_e^h refers to the horizontal coordinate of that point and p_e^v to the vertical one. Hence, the generalized coordinates vector for impact phase is $q_e := [q_s^T \quad p_e^T]^T$. With the new generalized coordinate vector the dynamic model is described as:

$$D_e(q_e)\ddot{q}_e + C_e(q_e,\dot{q}_e)\dot{q}_e + G_e(q_e) = B_e(q_e)u + \delta F_{ext}, \quad (2)$$

where δF_{ext} represents impulsive forces caused by the ground reaction in the swing leg at the impact time. Based on the concept of momentum conservation, the angular momentum before and after the impact must be the same and even when the angular position remains constant in that instantaneous period of time, the velocity undergoes a sudden change. It is shown in the following equation:

$$D_e(q_e^+)\dot{q}_e^+ - D_e(q_e^-)\dot{q}_e^- = F_{ext}, \quad (3)$$

where $(q_e^-,\dot{q}_e^-)$ and $(q_e^+,\dot{q}_e^+)$ represent the position and the velocity just before and after the impact, respectively; F_{ext} is a forces vector which represents the effect of the ground reaction on each joint. Let us define $F_2 := [F_2^v \quad F_2^h]^T$ as the reaction force in the swing leg, where F_2^vrefers to the tangential reaction and F_2^h to the normal one. Following the the procedure of Westervelt et al. (2007), the principle of virtual work could be used, which yields:

$$F_{ext} = E_2(q_e^-)^T F_2, \quad (4)$$

where $E_2 := \frac{\partial p_2}{\partial q_e}$ and p_2 is the position of the swing leg end. Replacing the Eq. (4) into (3) it produces:

$$D_e(q_e^-)\dot{q}_e^- = D_e(q_e^+)\dot{q}_e^+ + E_2(q_e^-)^T F_2. \quad (5)$$

According to the assumption of the impact of rigid bodies the following are true:

- $q_e^- \equiv q_e^+$
- The velocity of the end swing leg would be equal to zero

Then the following equation can be extracted:

$$\frac{dp_2}{dt} = \frac{\partial p_2(q_e^-)}{\partial q_e}\dot{q}_e^+,$$
$$E_2(q_e^-)\dot{q}_e^+ = 0. \quad (6)$$

The Eq. (5) and (6) are collected in a matrix form to obtain

$$\begin{bmatrix}\dot{q}_e^+ \\ F_2\end{bmatrix} = \begin{bmatrix}D_e(q_e^+) & -E_2(q_e^-)^T \\ E_2(q_e^-) & 0_{2\times 2}\end{bmatrix}^{-1}\begin{bmatrix}D_e(q_e^-)\dot{q}_e^- \\ 0_{2\times 1}\end{bmatrix}, \quad (7)$$

which can be summarized in

$$\dot{q}_e^+ = \Delta(q_e^-, \dot{q}_e^-), \tag{8}$$
$$F_2 = \Sigma(q_e^-, \dot{q}_e^-). \tag{9}$$

Finally, the hybrid system is described in the Eq. (1) and (8) as:

$$\Sigma : \begin{cases} \ddot{q}_s = f(q_s,\dot{q}_s) + D_s(q_s)^{-1}B_s(q_s)u & p_2^v \neq 0 \\ \dot{q}_e^+ = \Delta(q_e^-,\dot{q}_e^-) & p_2^v = 0 \end{cases} \tag{10}$$

where

$$f(q_s,\dot{q}_s) = D_s(q_s)^{-1}\left[-C(q_s,\dot{q}_s)\dot{q}_s - G_s(q_s) + \delta(q_s,\dot{q}_s) + \zeta\right].$$

3. CONTROL DESIGN

The control of bipedal robots has several challenges. For instance, it has to deal with the fact that this system is nonlinear and Multi-Input Multi-Output (MIMO). One of the biggest challenges in the control of bipedal robots is that they are hybrid systems, because of their continuous and discrete dynamic. Finally, the point-feet structure of our prototype makes it an underactuated mechanism with its nominal state as an unstable system. Bellow a feedback control design is provided to tackle all the difficulties that bipedal robots with dynamic walking, like the one studied in this paper faces. First, the Eq. (1) is simplified as follow:

$$D_s(q_s)\ddot{q}_s + \Omega(q_s,\dot{q}_s) = B_s(q_s)u + \tilde{\xi}(q_s,\dot{q}_s), \tag{11}$$

where:

$$\Omega(q_s,\dot{q}_s) := C(q_s,\dot{q}_s)\dot{q}_s + G_s(q_s),$$
$$\tilde{\xi}(q_s,\dot{q}_s) := \delta(q_s,\dot{q}_s) + \zeta.$$

The Eq. (11) is fragmented to separate the actuated part of the system from the underactuated part. Now, let us fragment the position vector and the output matrix as

$$q_s := \begin{bmatrix} q_{b_{(N-1\times 1)}} \\ q_{(N_{1\times 1})} \end{bmatrix}, \qquad B_s(q_s) := \begin{bmatrix} B_1(q_s)_{(N-1\times p)} \\ 0_{(1\times p)} \end{bmatrix},$$

where p is the number of actuators. Once the new structure of the variables was established, the model was fragmented as:

$$\begin{bmatrix} D_{11}(q_s) & D_{12}(q_s) \\ D_{21}(q_s) & D_{22}(q_s) \end{bmatrix}\begin{bmatrix} \ddot{q}_b \\ \ddot{q}_N \end{bmatrix} + \begin{bmatrix} \Omega_1(q_s,\dot{q}_s) \\ \Omega_2(q_s,\dot{q}_s) \end{bmatrix} = \dots$$
$$\dots = \begin{bmatrix} B_1(q_s) \\ 0 \end{bmatrix} u + \begin{bmatrix} \tilde{\xi}_1(q_s,\dot{q}_s) \\ \tilde{\xi}_2(q_s,\dot{q}_s) \end{bmatrix}. \tag{12}$$

The fragmented model representation is used to express the model as a function of the actuated variables, which is

$$\left[D_{11}(q_s) - D_{12}(q_s)D_{22}^{-1}(q_s)D_{21}(q_s)\right]\ddot{q}_b + \Omega_1(q_s,\dot{q}_s) + \dots$$
$$\dots + D_{12}(q_s)D_{22}^{-1}(q_s)\left[\tilde{\xi}_2(q_s,\dot{q}_s) - \Omega_2(q_s,\dot{q}_s)\right] = \dots$$
$$\dots = B_1(q_s)u + \tilde{\xi}_1(q_s,\dot{q}_s),$$

then, it is simplified to obtain

$$\ddot{q}_b = \kappa(q_s)u + \xi, \tag{13}$$

where

$$\xi = \left[D_{11}(q_s) - D_{12}(q_s)D_{22}^{-1}(q_s)D_{21}(q_s)\right]^{-1} * \dots$$
$$\dots * \left\{-D_{12}(q_s)D_{22}(q_s)^{-1}\left[\tilde{\xi}_2(q_s,\dot{q}_s) - \Omega_2(q_s,\dot{q}_s)\right] + \dots\right.$$
$$\left.\dots + \tilde{\xi}_1(q_s,\dot{q}_s) - \Omega_1(q_s,\dot{q}_s)\right\} \tag{14}$$

and

$$\kappa(q_s) = \left[D_{11}(q_s) - D_{12}(q_s)D_{22}^{-1}(q_s)D_{21}(q_s)\right]^{-1}B_1(q_s). \tag{15}$$

Based on the simplified model described in the Eq. (13) the following assumptions are proposed.

- First, here and now ξ will be considered as a total disturbances vector, in which the endogenous and exogenous disturbances are lumped.
- Second, the total disturbances ξ and their m derivatives are considered bounded.
- Finally, it is assumed that each component of the vector ξ can be approximated by a time polynomial with order m, so that the $\frac{d^{(m+1)}}{dt^{(m+1)}}\xi_i \approx 0, \forall i = 1,2,3,4$.

With the above assumptions, the following control law is proposed:

$$u = \kappa^{-1}(q_s(s))\left(s^2 q_d(s) - K_{GPI}(q_b(s) - q_d(s))\right), \tag{16}$$

where q_d is the references vector for the controlled joints and K_{GPI} is a diagonal transfer function matrix with the following structure:

$$K_{GPI} = \begin{bmatrix} K_{GPI_{11}} & 0 & 0 & 0 \\ 0 & K_{GPI_{22}} & 0 & 0 \\ 0 & 0 & K_{GPI_{33}} & 0 \\ 0 & 0 & 0 & K_{GPI_{44}} \end{bmatrix}, \tag{17}$$

and

$$K_{GPI_{ii}} = \frac{\alpha_{i,n+m}s^{n+m} + \dots + \alpha_{i,1}s + \alpha_{i,0}}{s^{m+1}\left(s^{n-1} + \alpha_{i,2n+m-1}s^{n-2} + \alpha_{i,2n+m+1}\right)}, \forall i = 1,\cdots,4. \tag{18}$$

If the control law in the Eq. (16) is inserted into the Laplace transformation of the simplified model Eq. (13) the close loop system takes the following form:

$$s^2 q_b(s) = \kappa(q_s(s))\left[\kappa^{-1}(q_s(s))\left(s^2 q_d(s)\cdots\right.\right.$$
$$\left.\left.\cdots - K_{GPI}(q_b(s) - q_d(s))\right)\right] + \xi(s), \tag{19}$$

by simplifying this equation we get

$$s^2 q_b(s) = s^2 q_d(s) - K_{GPI}(q_b(s) - q_d(s)) + \xi(s). \tag{20}$$

The Eq. (20) describes the close loop behavior and has a special feature that corresponds to transforming of the system into a decoupled one. This feature is important because, based on that transformation the tracking control problem can be studied as a bunch of Single-Input and Single-Output (SISO) problems, instead of a more complex MIMO system. The fragmentation of the dynamic produces the following system of equations:

$$s^2 q_{b,1}(s) = s^2 q_{d,1}(s) - K_{GPI_{11}}(q_{b,1}(s) - q_{d,1}(s)) + \xi_1(s),$$
$$\vdots$$
$$s^2 q_{b,4}(s) = s^2 q_{d,4}(s) - K_{GPI_{44}}(q_{b,4}(s) - q_{d,4}(s)) + \xi_4(s).$$

Let us define the tracking error as:

$$e_i(s) = q_{b,i}(s) - q_{d,i}(s), \quad \forall i = 1, \cdots, 4,$$

thus, the close loop dynamic takes the following form:

$$s^2 e_i(s) + K_{GPI_{ii}} e_i(s) = \xi_i(s), \quad \forall i = 1, \cdots, 4, \tag{21}$$

and the error's dynamics can be described by:

$$\begin{gathered}\left(s^{2n+m} + \alpha_{i,2n+m-1} s^{2n+m-1} + \cdots + \alpha_{i,1} s + \alpha_{i,0}\right) e_i(s) = \cdots \\ \cdots = s^{m+1} \xi_i(s) \left(s^{n-1} + \alpha_{i,2n+m-1} s^{n-2} + \cdots + \alpha_{n+m+1}\right), \cdots \\ \cdots \forall i = 1, \cdots, 4,\end{gathered} \tag{22}$$

At the right side of the Eq. (22) the product $s^{m+1}\xi_i(s)$ is close to zero, for which the error's dynamics take the following form:

$$\begin{gathered}\left(s^{2n+m} + \alpha_{i,2n+m-1} s^{2n+m-1} + \cdots + \alpha_{i,1} s + \alpha_{i,0}\right) e_i(s) \approx 0 \cdots \\ \cdots \forall i = 1, \cdots, 4,\end{gathered} \tag{23}$$

Finally, the constants α can be arbitrarily chosen in order to impose a dominant dynamic in the error behavior and carry it out asymptotically to zero, which produces a stable close loop dynamic.

4. VIRTUAL HOLONOMIC CONSTRAINT FOR TRAJECTORY GENERATION

Given the control strategy developed in the previous section, it is necessary to propose a trajectory for the tracking control. Between the possibilities to solve this task is the time-based trajectory, which is an unappropriated technique for underactuated robots. And this is so because this strategy does not take into account the possible external disturbances which could cause the instability of the walking. Instead of time-based trajectories, here it is used a state-based trajectory, which has the aim of synchronizing the controlled joints with the underactuated ones. This strategy is called a virtual holonomic constraint because the restrictions are imposed via feedback control in lieu of physical or mechanical constraints, Chevallereau et al. (2009).

The trajectory generation proposed here bases its strategies in producing q_{d_i} as a function of the evolution of $\theta(q)$ and the step length, sl. Here a set of gait patterns were developed for samples of step length between 5 and 24cm. Those gait patterns were used to compute four polynomial regressions which produces 5×5 order polynomials, $q_{d_i}(\theta, sl)$. The relation in the polynomials $q_{d_i}(\theta, sl)$, which describe the references functions are given by the surfaces shown in the Fig. 3.

Few conditions to generate the gait patterns were taken into account to fulfill the unilateral constraint in the support foot reaction forces, bellow they are listed:

- The hip has a sinusoidal movement and the maximum hip high is the 98% of the high of the extended leg
- The minimum high of the hip is a function of the step length, and is chosen adequately to avoid the knee overextension
- The end of the swing leg has a movement starting and ending with a smooth trajectory with a maximum gap over 2.6 cm

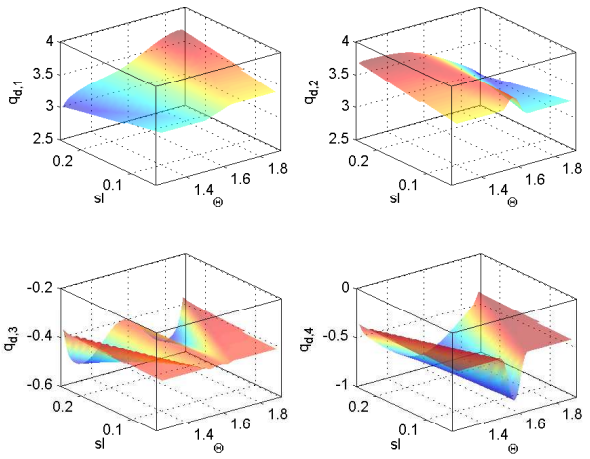

Fig. 3. Trajectory reference surfaces based on $\Theta(q)$ and step length, sl

- To prevent the robot's body take-off from the ground, the vertical reaction in the support leg must be bigger than zero, $F_1^v > 0$
- To avoid sliding of the support leg, its horizontal reaction force must be less than the friction force, $F_1^h < \mu F_1^v$,

5. SIMULATION TEST

A numerical simulation is performed to test the control law proposed, as well as the trajectory planning strategy. The controller tuning was based on the assumption that the lumped disturbances ξ_i can be approximated by five order polynomials, so that $m = 5$. Additional to the approximation of the disturbances, the coefficients α are chosen to achieve a stable and dominant behavior of the error dynamic. This in order to get an asymptotic movement of the controlled joints to the trajectory references. The root to select the α values are listed in the Table 1.

Table 1. Alpha values

	i			
	1	2	3	4
roots	-17.01	-13.09	-16.36	-13.09
	-28.92	-22.25	-27.81	-22.25
	-49.17	-37.83	-47.28	-37.83
	-83.60	-64.31	-80.38	-64.31
	-142.12	-109.32	-136.66	-109.32
	-241.61	-185.85	-232.32	-185.85
	-410.74	-315.96	-394.95	-315.96
	-698.27	-537.13	-671.41	-537.13

The robot walk was tested through the simulation of 50 steps (100 switching feet). The test started with the robot in the following convenient initial conditions.

$$q_s = [\,3.6200 \;\; 3.1284 \;\; -0.4686 \;\; -0.4593 \;\; -0.0029\,]^T,$$
$$\dot{q}_s = [\,0.6985 \;\; -4.6678 \;\; -6.9445 \;\; 3.6576 \;\; 0.1669\,]^T.$$

The first 22 steps are given with a constant step length of 20 cm. After that, the robot starts to reduce the length of the step until 10 cm, in which it stabilize its gait pattern for the rest of the simulation. Fig. 4 shows the behavior of the controlled joints,

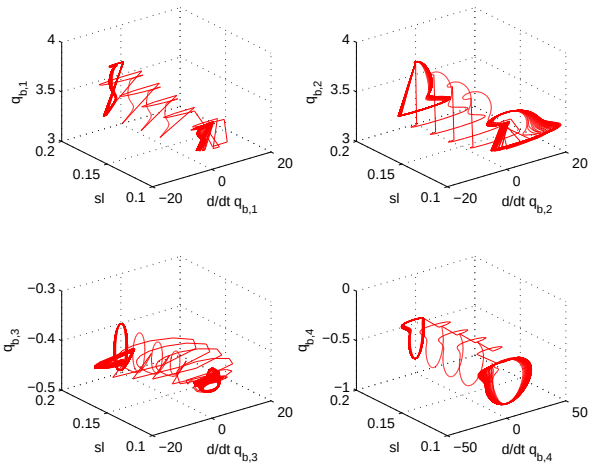

Fig. 4. States' convergence to stable cycles in the changes of step length

there, it is possible to see the evolution from one step length to another, and additionally it is shown the cycles or stable orbits at each step length.

The evolution of the walk is shown in a stick diagram in the Fig. 5. The behavior of the robot's gait with the longest step length is presented in the left side of the Fig. 5, while in the right side it is shown the gait pattern for the step length corresponding to 10 cm.

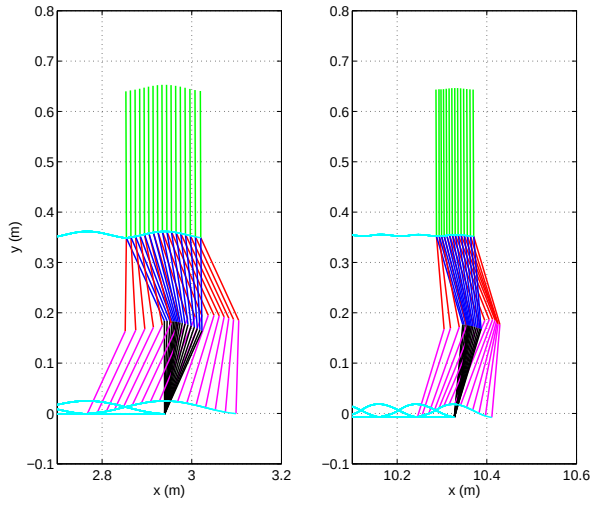

Fig. 5. Evolution of the walk in different gait patterns

5.1 Evaluation of the gait stability

Although the stability of the tracking control can be ensure with the selection of the right roots for the error's dynamics, the gait stability depends too of the walking pattern. Several approaches to deal with the global stability of the walking have been proposed, two of the more accepted are: the Zero Moment Point (ZMP) proposed by Vukobratović and Borovac (2004), which has been successful testes with robots with flat feet like ASIMO Sakagami et al. (2002); in the other hand it is the global stability of the dynamic walking of robot with point feet, which has been checked by the search of the existence of a periodic behavior in the robot's states, this methodology was effectively proved by first time in McGeer (1990), which uses the Poincaré's method to search for the presence of a periodic orbit in the evolution of the states of a passive bipedal robot.

Based in the fact that our prototype is a point feet robot, the more convenient approach to analyze the global stability of the robot is the Poincaré's method. But, with the aperiodic walk performed in the simulation test in this section, the Poincaré's method can not be applied without several conditions. Therefore, the method of Poincaré's section is used to identify periodic behavior in the dynamic of the biped at each gait pattern.

The computation of the return map for the each step length is done with the procedure presented in Chen et al. (2007), it is done through the sampling of the states in a time when a condition called the Poincaré's section is satisfied. Poincaré's section could either be a function of the robot states or can be determined by external events. Here the Poincaré's section is determined by the switching foot event, which depends of the ground level.

First, let us define the state vector as $x := [q_s^T \quad \dot{q}_s^T]^T$, then a sampling done in the Poincaré's section is divided in two sets, one for each step length in the simulations, after that, they are used to build a couple of functions that take values just before the impact time and are defined as

$$x_{sl}^-(k+1) = P_{sl}(x_{sl}^-(k)) \qquad \forall sl = 10cm, 20cm, \tag{24}$$

where $x_{sl}^-(k)$ are the k^{th} samples of the state vector just before the impact, $x_{sl}^-(k+1)$ are the state vector just before the next impact and $P_{sl}(x^-(k))$ are functions called the Poincaré return map. The stability test is summarized in the tasks of evaluating the existence of two fix points $x_{sl}^{-^*}$ such that

$$x_{sl}^-(k+1) = P(x_{sl}^{-^*}(k)) = x_{sl}^{-^*} \tag{25}$$

as well as in tasks of demonstrating the discrete systems stability of (24) in the classical sense of Lyapunov for the equilibrium points $x_{sl}^{-^*}$.

The sets of states of the robot in each switching foot are saved in vectors as bellow

$$\chi_{sl}(k) = \begin{bmatrix} x_{sl}^-(k-(\rho-1)) - x_{sl}^{-^*} \\ x_{sl}^-(k-(\rho-2)) - x_{sl}^{-^*} \\ \vdots \\ x_{sl}^-(k) - x_{sl}^{-^*} \end{bmatrix}, \tag{26}$$

where ρ represents the number of switching feet executed in the simulation. Linear regressions are performed between the $\chi_{sl}(k)$ and $\chi_{sl}(k-1)$ values. The result of the regressions give linear approximations of (24) with the following form

$$(x_{sl}^-(k+1) - x_{sl}^{-^*}) = \Phi_{sl} * (x_{sl}^-(k) - x_{sl}^{-^*}) \tag{27}$$

where the eigenvalues of Φ_{sl} must have a magnitude lower than one to guarantee the asymptotic stability of the walking. It was

evaluated and the stability of each gait pattern was proved, so it is possible conclude that the robot has stable walk for both step lengths.

6. CONCLUSION

A time-invariant GPI controller was developed to control a planar bipedal robot with point feet structure. The robot keeps stable walking even with gait pattern changes during the robot is in operation. The controller designed achieves stable walking in the reconfiguration of trajectories and it was confirmed by the Poincaré test at each walking pattern.

The trajectory generation strategy allows switching from one step length to another in a short period of time. The use of the planning trajectories strategy permits the changes between short to long steps and in the opposite way, without the design of a controller for each step length wanted. Thus, the risk to fall in an instability state caused by aperiodic gait, produced by the step length changes, were successfully tackled to ensure the dynamic walking stability.

REFERENCES

Arcos-Legarda, J., Cortes-Romero, J., and Tovar, A. (2016). Active disturbance rejection control based on generalized proportional integral observer to control a bipedal robot with five degrees of freedom. In *American Control Conference (ACC), 2016*. IEEE.

Arcos-Legarda, J., Tovar, A., Cortés, J., Díaz, H., and Sarmiento, L. (2013). Multivariable gpi control of a gait exoskeleton for people with walking disabilities. In *II International Congress of Engineering Mechatronics and Automation (CIIMA)*.

Chen, H. et al. (2007). *Passive dynamic walking with knees: A point foot model*. Ph.D. thesis, Massachusetts Institute of Technology.

Chevallereau, C., Grizzle, J.W., and Shih, C.L. (2009). Asymptotically stable walking of a five-link underactuated 3-d bipedal robot. *Robotics, IEEE Transactions on*, 25(1), 37–50.

Grizzle, J.W., Abba, G., and Plestan, F. (2001). Asymptotically stable walking for biped robots: Analysis via systems with impulse effects. *Automatic Control, IEEE Transactions on*, 46(1), 51–64.

Grizzle, J.W., Chevallereau, C., Sinnet, R.W., and Ames, A.D. (2014). Models, feedback control, and open problems of 3d bipedal robotic walking. *Automatica*, 50(8), 1955–1988.

Grizzle, J., Westervelt, E., and Canudas-de Wit, C. (2003). Event-based pi control of an underactuated biped walker. In *Decision and Control, 2003. Proceedings. 42nd IEEE Conference on*, volume 3, 3091–3096. IEEE.

Hamed, K.A. and Grizzle, J.W. (2013). Robust event-based stabilization of periodic orbits for hybrid systems: Application to an underactuated 3d bipedal robot. In *American Control Conference (ACC), 2013*, 6206–6212. IEEE.

Hill, J. and Fahimi, F. (2015). Active disturbance rejection for walking bipedal robots using the acceleration of the upper limbs. *Robotica*, 33(02), 264–281.

Hurmuzlu, Y. and Marghitu, D.B. (1994). Rigid body collisions of planar kinematic chains with multiple contact points. *The international journal of robotics research*, 13(1), 82–92.

Martínez-Fonseca, N., Castañeda, L.Á., Uranga, A., Luviano-Juárez, A., and Chairez, I. (2016). Robust disturbance rejection control of a biped robotic system using high-order extended state observer. *ISA transactions*, 62, 276–286.

McGeer, T. (1990). Passive walking with knees. In *Robotics and Automation, 1990. Proceedings., 1990 IEEE International Conference on*, 1640–1645. IEEE.

Sakagami, Y., Watanabe, R., Aoyama, C., Matsunaga, S., Higaki, N., and Fujimura, K. (2002). The intelligent asimo: System overview and integration. In *Intelligent Robots and Systems, 2002. IEEE/RSJ International Conference on*, volume 3, 2478–2483. IEEE.

Tzafestas, S., Raibert, M., and Tzafestas, C. (1996). Robust sliding-mode control applied to a 5-link biped robot. *Journal of Intelligent and Robotic Systems*, 15(1), 67–133.

Vukobratović, M. and Borovac, B. (2004). Zero-moment point-thirty five years of its life. *International Journal of Humanoid Robotics*, 1(01), 157–173.

Westervelt, E.R., Grizzle, J.W., Chevallereau, C., Choi, J.H., and Morris, B. (2007). *Feedback control of dynamic bipedal robot locomotion*, volume 28. CRC press.

Westervelt, E.R., Grizzle, J.W., and Koditschek, D.E. (2003). Hybrid zero dynamics of planar biped walkers. *Automatic Control, IEEE Transactions on*, 48(1), 42–56.

Método de optimización para la sintonización del control PD de un robot móvil ⋆

Omar Serrano-Pérez[1] * **Miguel G. Villarreal-Cervantes** *
Juan Carlos González-Robles *

* *Departamento de Posgrado, Instituto Politécnico Nacional, CIDETEC, Av.Juan de Dios Bátiz s/n, 07700, Ciudad de México, México. (Correo electrónico: {oserranop1500,mvillarrealc,jgrobles}@ipn.mx)*

.

Resumen:
Dos de los problemas de control en ingeniería, es el diseño y la sintonización para satisfacer cierto desempeño en una planta o sistema. El uso eficiente del controlador radica principalmente en la correcta sintonización. En este artículo se está interesado en el problema de sintonización del control PD en el espacio de operación para un robot móvil omnidireccional con base en el método de optimización y su solución se proporciona a través del algoritmo de evolución diferencial. Se analizan, comparan y discuten los resultados obtenidos en simulación y experimental dando como resultado un comportamiento adecuado en simulación pero un pobre desempeño en los resultados experimentales. Con el propósito de mejorar el comportamiento en forma experimental se mencionará algunas direcciones de investigación.

Keywords: Sintonización óptima, control PID, evolución diferencial, robot móvil (3,0).

1. INTRODUCCIÓN

Los robots móviles omnidireccional son ampliamente usados en una gran variedad de aplicaciones en donde principalmente los espacios son estrechos, ya que presentan la ventaja de realizar un movimiento simultáneo e independiente de traslación y rotación. El problema de control en los robot móviles se basa principalmente en el diseño y sintonización de su sistema de control para realizar una tarea en específico (Albertos, 2007). En el diseño del controlador, el diseñador debe garantizar que el origen del sistema de control en lazo cerrado sea, en al menos una región de interés, estable o asintóticamente/exponiencialmente estable. Una vez que se obtiene el controlador que cumple con las especificaciones antes mencionadas, el diseñador debe sintonizar las ganancias del sistema de control con el fin de garantizar un cierto comportamiento en la planta. Por lo tanto, para realizar una tarea con mayor precisión se requiere de una buena sintonización.

Se han estado proponiendo y usando diversas metodologías de sintonización a través del tiempo, de la1s cuales se pueden clasificar en cuatro grandes grupos (Villarreal-Cervantes, 2014): Método analítico, método heurístico, método de optimización y método adaptable. Debido a la necesidad de realizar sistemas más precisos con varios compromisos específicos a cumplir, los métodos de optimización en la sintonización de controladores son una opción viable, en donde se formula el problema de sintonización como uno de programación matemática y se utilizan técnicas de optimización numérica para resolverlo. En las últimas décadas se han estado utilizando algoritmos bio-inspirados en donde toma la abstracción de conceptos de la teoría de evolución natural, la supervivencia del más apto y la naturaleza para la sintonización de controladores con base en métodos de optimización (Fleming and Purshouse, 2002; Reynoso-Meza et al., 2014; Ruano et al., 2014). La principal motivación de utilizar este tipo de algoritmos se debe al manejo eficientemente de múltiples compromisos de lazo cerrado, los cuales en su mayoría de las veces entran en conflicto debido a su naturaleza no lineal.

Trabajos recientes se han estado enfocando en la sintonización de controladores lineales con base en métodos de optimización cuya solución se realiza con algoritmos bio-inspirados (Reynoso-Meza et al., 2016a), (Reynoso-Meza et al., 2016b), (Karer and Skrjanc, 2016), (dos Santos Coelho and Pessoa, 2011). Estos trabajos se desarrollan a través de plantas "benchmark" en donde se muestra la importancia de utilizar este tipo de estrategias de sintonización principalmente cuando se tienen varios compromisos a satisfacer. Algunos de los beneficios de este tipo de sintonización se puede observar en la estimación del estado de un operador (Zhang and Yang, 2014), en el seguimiento del sol para paneles solares (Sabir and Ali, 2016), en la dosificación del medicamento en el tratamiento de cáncer (Algoul et al., 2011), en el diseño integrado

⋆ Proyecto financiado por la COFAA y la SIP del Instituto Politécnico Nacional bajo el proyecto 20160826 y al CONACYT bajo el apoyo 182298. El primer autor reconoce el apoyo de CONACYT y BEIFI a través de una beca para realizar estudios de posgrado en el Instituto Politécnico Nacional.

estructura-control de sistemas mecatrónicos (Villarreal-Cervantes et al., 2010, 2014), entre otros.

Por tal motivo, en este trabajo se propone un método de optimización a través del planteamiento formal de un problema de optimización para la sintonización del sistema de control de un robot móvil omnidireccional. La idea principal del trabajo es proporcionar una visión general de la problemática que emerge al sintonizar las ganancias del sistema de control fuera de línea y a través de un método de optimización.

La estructura de este artículo se organiza de la siguiente manera: En la sección 2 se formula y plantea el método de sintonización para el robot móvil omnidireccional. El algoritmo que soluciona el problema de optimización se describe en la Sección 3. Los resultados numéricos y experimentales se discuten en la Sección 4 y finalmente en la Sección 5 se proporcionan las conclusiones y trabajo a futuro.

2. MÉTODO DE OPTIMIZACIÓN PARA LA SINTONIZACIÓN DEL SISTEMA DE CONTROL DEL ROBOT MÓVIL OMNIDIRECCIONAL

Para sintonización óptima del controlador se plantea un problema de optimización dinámica (POD) con el propósito de encontrar los parámetros del control PD en el espacio de operación de un robot movil omnidireccional (RMO) considerando una trayectoria predefinida, a su vez garantizar el mínimo error de posición, orientación y consumo de energía. Formalmente el problema de optimización se establece en las ecuaciones (1)-(3), donde $\bar{J} \in R$ es la función objetivo a minimizar, p^* es el vector de las variables de diseño, en $g_i \in R$ se encuentran las restricciones de desigualdad y $h_i \in R$ las restricciones de igualdad, del problema de optimización.

$$\underset{p^*}{Min} \int_0^{tf} \bar{J} dt \tag{1}$$

Sujeto a:

$$g_i(t) < 0 \ \forall \ i = 1, 2, ..., o \tag{2}$$

$$h_i(t) = 0 \ \forall \ i = 1, 2, ..., p \tag{3}$$

2.1 Variables de diseño

En esta investigación, se propone el controlador PD en el espacio de operación para un RMO, el cual se observa en la ecuación (4), donde $k_p = diag[k_{p1}, k_{p2}, k_{p3}] \in R^{3\times3}$ y $k_d = diag[k_{d1}, k_{d2}, k_{d3}] \in R^{3\times3}$ son las matrices con ganancias de dicho controlador, $J = R^{3\times3}$ dada por la ecuación (5) es la matriz Jacobiana que relaciona las fuerzas y pares ejercidos en el robot móvil con las fuerzas ejercidas por las ruedas del robot móvil, $e \in R^3$ es error de posición (lineal y angular) y $\dot{e} \in R^3$ es la velocidad del error.

$$u = J^T(k_p e + k_d \dot{e}) \tag{4}$$

$$J = \begin{bmatrix} \frac{\bar{\beta}_1}{3} & \frac{2}{3}\sin x_3 & -\frac{\bar{\beta}2}{3} \\ \frac{\bar{\beta}_3}{3} & -\frac{2}{3}\cos x_3 & \frac{\bar{\beta}_4}{3} \\ \frac{1}{3L} & \frac{1}{3L} & \frac{1}{3L} \end{bmatrix} \tag{5}$$

donde:

$$\bar{\beta}_1 = -\sin x_3 + \sqrt{3}\cos x_3 \qquad \bar{\beta}_2 = \sin x_3 + \sqrt{3}\cos x_3$$
$$\bar{\beta}_3 = \cos x_3 + \sqrt{3}\sin x_3 \qquad \bar{\beta}_4 = \cos x_3 - \sqrt{3}\sin x_3$$

En el problema de optimización se desea encontrar la mejor solución en los parámetros del sistema de control. Por tal motivo, el vector p de la ecuación (6) se considera como el vector de variables de diseño en donde se involucran a los parámetros del control PD del RMO.

$$p = [k_{p1}, k_{p2}, k_{p3}, k_{d1}, k_{d2}, k_{d3}]^T \tag{6}$$

2.2 Función objetivo

Con el propósito de garantizar una precisión en el seguimiento de la trayectoria y un consumo de energía relativamente bajo, se propone como función objetivo optimizar error de posición, error de orientación (e) y el par de entrada (u) para cada rueda del RMO en el espacio de coordenadas cartesianas, dado por la ecuación (7). Así mismo se incluye el factor de ponderación μ para resolver el POD. Por último, para normalizar las unidades en los términos (e_1, e_2, e_3), se realiza la conversión del error angular a un error lineal en e_3 obteniendo el factor L^2, donde L es la distancia del centro del robot móvil a la llanta.

$$\bar{J} = \mu_1 \bar{J}_1 + \mu_2 \bar{J}_2 \tag{7}$$

donde:

$$\bar{J}_1 = \left(\int_0^{tf} e_1^2 + \int_0^{tf} e_2^2 + L^2 \int_0^{tf} e_3^2 \right) dt$$

$$\bar{J}_2 = \left(\int_0^{tf} u_1^2 + \int_0^{tf} u_2^2 + \int_0^{tf} u_3^2 \right) dt$$

2.3 Restricciones de diseño

Para un POD, es necesario contemplar el modelo dinámico en el espacio de estados del RMO (Villarreal-Cervantes et al., 2015) como una restricción activa en el problema de optimización dada por $\dot{x} = f(x) + g(x)u$.

Por otro lado, la función de epicicloide se establece como la trayectoria a seguir altamente no lineal incluido en el problema de optimización como una restricción de igualdad. Su parametrización se observa en la ecuación (8).

$$\begin{gathered} \bar{x}_d = 0{,}8181\cos(2\pi ft) + 0{,}1818\cos(9\pi ft) \\ \bar{y}_d = 0{,}8181\sin(2\pi ft) - 0{,}1818\sin(9\pi ft) \\ \bar{\phi}_d = 0{,}4363\sin(3{,}33\pi ft) \end{gathered} \tag{8}$$

Para que el problema de optimización obtenga mejores resultados, se propone utilizar el polinomio de Bézier de 5^{to} orden con el propósito de generar una trayectoria suave del punto de inicio del RMO al punto inicial de la trayectoria parametrizada de la función epicicloide. La ecuación que describe el polinomio de Bézier está dada por la ecuación (9) tal que $\Delta_i = \frac{t_i - t_1}{t_2 - t_1}$ donde: t_i es el tiempo, $t_1 = 0$ es el tiempo inicial de la trayectoria Bézier y $t_2 = 3$ es su respectivo tiempo final.

$$\varphi_i = \Delta_i^5(126 - 420\Delta_i + 540\Delta_i^2 - 315\Delta_i^3 + 70\Delta_i^4) \tag{9}$$

3. EVOLUCIÓN DIFERENCIAL

En el presente trabajo se implementa una técnica bio-inspirada llamada evolución diferencial $ED/Rand/1/Bin$ para dar solución al POD. Los algoritmos bio-inspirados son algoritmos de optimización que permiten iterativamente mejorar una solución a través de una medida de desempeño con base en criterios en conceptos de la teoría de evolución natural, la supervivencia del más apto y la naturaleza. La selección de este algoritmo se basa en una ventaja muy importante al no requerir información adicional durante la búsqueda de las soluciones, tales como, el gradiente, la matriz hessiana, condiciones iniciales de búsqueda, etc.

El algoritmo de evolución diferencial es un método de optimización presentado a fines de la década de los noventa por (Storn and Price, 1997), donde el pseudo-código del algoritmo de ED se expone en el algoritmo 1.

Algoritmo 1 Algoritmo de evolución diferencial

Begin
  $G \leftarrow 0$
  Crear una población aleatoria $\mathbf{x}_{i,G}\ \forall_i = 1, \ldots, NP$
  Evaluar$J\left(\boldsymbol{x}_{i,G}\right), g\left(\boldsymbol{x}_{i,G}\right), \forall_i = 1, \ldots, NP$
  while G $\leqslant$ Gmax **do**
    for i$\leftarrow$1 to NP **do**
      Seleccionar aleatoriamente $\left\{i \neq r_0 \neq r_1 \neq r_2\right\} \in \boldsymbol{x}_G$.
      $j_{rand} \leftarrow randint\,(1, D)$
      for j$\leftarrow$1 to D **do**
        Proceso de mutación y cruza
      end for
      Evaluar $J\left(\boldsymbol{u}_{i,G+1}\right), g\left(\boldsymbol{u}_{i,G+1}\right)$
      if $\boldsymbol{u}_{i,G+1}$es mejor que $\boldsymbol{x}_{i,G}$ **then**
        $\boldsymbol{x}_{i,G+1} \leftarrow \boldsymbol{u}_{i,G+1}$
      else
        $\boldsymbol{x}_{i,G+1} \leftarrow x_{i,G}$
      end if
    end for
    $G \leftarrow G + 1$
  end while
End

El algoritmo comienza con una población de NP individuos. La población inicial distribuye a los individuos aleatoriamente por el espacio de búsqueda. Las generaciones siguientes se denotan como: $G = 0, 1, 2, ..., G_{max}$. Cada individuo está representado con un vector D-parámetros (variables de diseño p de la ecuación (6)), resultando: $x_{i,G} = x^1_{i,G}, ...x^D_{i,G}$.

Después de obtener la población inicial se inicia un proceso iterativo en el que se aplica a cada individuo los operadores básicos de mutación, cruza y selección.

3.1 Mutación

El operador de mutación conocido como $ED/Rand/1/Bin$ es uno de los más utilizados en la literatura, donde la mutación se da generando un individuo nuevo para cada individuo de la generación anterior, tal como se observa en la ecuación (10).

$$u_{i,G+1} = x_{r_1,G} + F(x_{r_2,G} - x_{r_3,G}) \tag{10}$$

Donde los subíndices r_1, r_2, r_3 son tres individuos de la generación G aleatoriamente elegidos y diferentes entre ellos. El factor de escala F es un parámetro de control positivo donde controla la magnitud de la variación diferencial en $(x_{r_2,G} - x_{r_3,G})$.

3.2 Cruza

La cruza es el proceso mediante el cual nuevos individuos posteriores a la primera generación son creados. La cruza se realiza mediante la combinación de los componentes del vector $x_{i,G}$ y $v_{i,G}$. Para el caso particular se utiliza la cruza uniforme tal como se observa en la ecuación (11), donde $CR \in [0, 1]$.

$$u^j_{i,G} = \begin{cases} u^j_{i,G} \text{ if } (rand_j(0,1) \leqslant CR \text{ or } j = j_{rand}) \\ x^j_{i,G} \text{ if } (rand_j(0,1) > CR \text{ and } j \neq j_{rand}) \end{cases} \quad j = 1, 2, ..., D \tag{11}$$

3.3 Selección

Finalmente, para generar la población de la generación $G + 1$ se selecciona entre el vector $u_{i,G}$ y el vector $x_{i,G}$ usando el criterio de (Deb, 2000), el cual se considera lo siguiente:

- Cualquier solución factible tiene preferencia sobre una no factible.
- Si dos soluciones son factibles, se da preferencia a la solución con la mejor función objetivo.
- Si dos soluciones son no factibles, se da preferencia a aquella que viola en menor medida las restricciones.

Los parámetros que se escogen para el algoritmo de $ED/Rand/1/Bin$ son: El tamaño de la población NP de 50 individuos, número máximo de generaciones $G_{max} = 100$, el factor de escala F se genera aleatoriamente en el intervalo de $0.3 \leq F \leq 0.9$ para cada generación y el factor de cruza $CR = 0.6$ para cada proceso de optimización.

4. RESULTADOS

Para llevar acabo las pruebas en simulación se utilizaron los parámetros cinemáticos y dinámicos del prototipo real del robot móvil omnidireccional que se encuentra en el laboratorio de Mecatrónica del "CIDETEC-IPN" en la Ciudad de México, donde los parámetros de dicho robot se observan en la Tabla 1. Estos parámetros son necesarios para la simulación en MATLAB del modelo dinámico del robot móvil. Se utiliza el método de integración de Euler con la condición inicial $x^0 = \mathbf{0} \in R^6$, el tiempo de integración $\Delta t = 0{,}005s$ y el tiempo final de sesenta y tres segundos.

Tabla 1. Parámetros del robot móvil omnidireccional (Peñaloza-Mejía et al., 2015).

Parámetro	*Descripción*	*Valor*	*Unidades*
r	*Radio de la llanta*	0.0625	m
L	*Dist del centro a la llanta*	0.287	m
m	*Masa del robot móvil*	16.31	kg
J	*Inercia de la llanta*	$5.82E^{-4}$	$\frac{kg}{m^2}$
Iz	*Inercia del robot móvil*	0.51	$\frac{kg}{m^2}$

Con el propósito de visualizar el desempeño del robot móvil omnidireccional para el seguimiento de una trayectoria altamente no lineal, se implementa para su solución el algoritmo presentado en la Sección 4. Para el algoritmo es necesario definir los parámetros siguientes: los límites del vector de variable de diseño p, los cuales se establecen como $p_{min} \in [0, 0, 0, 0, 0, 0]$ y $p_{max} \in [1000, 1000, 1000, 1000, 1000, 100]$, la condición de paro representado por el número de iteraciones $e_1 = 100$. En este trabajo se utilizó la siguiente propuesta para los valores de las ponderaciones de la función objetivo de la ecuación (7): donde $\mu_1 = 0{,}999$ y $\mu_2 = 0{,}001$. En el caso de estudio de diseño de sistemas mecatrónicos a través de un proceso de optimización, en (Portilla-Flores et al., 2011) se resuelve dicho problema mediante un algoritmo evolutivo considerando cinco corridas para validar el desempeño del algoritmo, por tal motivo en este trabajo se propone la misma métrica de cinco corridas del algoritmo, con el objetivo de encontrar la mejor solución.

Los resultados obtenidos se muestran en la Tabla 2. En la primer columna se muestra el caso de estudio y los valores propuestos en las ponderaciones, en la columna dos se muestran las corridas para cada uno de los casos de estudio, en las columnas 3,...,8, se observan los resultados óptimos de las ganancias del controlador dados por el algoritmo de ED, en la columna 9 se observa el valor de la función objetivo ($\bar{J}$) propuesta para este trabajo, en la columna 10 se muestra el valor del error producido por el RMO ($\bar{J}_1$), en la columna 11 se muestra el par de entrada en las ruedas ($\bar{J}_2$) y por último en la columna 12 se muestra el tiempo de ejecución del algoritmo para cada corrida de los casos de estudio.

Al examinar a detalle los resultados obtenidos por las corridas, se visualiza que la quinta corrida es la que mejor desempeño presenta y se resalta en color negro. Para las corridas de uno a tres sus valores óptimos están muy cercanos a su límite superior p_{max}, llegando a la conclusión que su área de búsqueda está limitada y el algoritmo no pudo encontrar mejores soluciones. En las corridas cuatro y cinco se visualiza que sus valores óptimos se encuentran distribuidos dentro de p_{min} y p_{max} concluyendo que en el intervalo propuesto se pueden encontrar mejores soluciones.

Una vez que se encuentra una buena solución de las ganancias del controlador, se procede a realizar los resultados experimentales. Haciendo una comparación entre la simulación y lo experimental, se observa primero la simulación en la Fig. 1a donde se realiza el seguimiento de trayectoria muy similar a la propuesta. Para el caso experimental de la Fig. 1b se observa que el prototipo del robot móvil bajo circunstancias reales no realiza la trayectoria adecuadamente con las ganancias óptimas encontradas por el algoritmo. También se muestra el comportamiento de la orientación del RMO en las Figs. 1c y 1d, donde se observa que en simulación la orientación del robot móvil sigue la trayectoria propuesta con una gran similitud, para el caso experimental existen errores muy notables en la orientación del robot móvil. La no correspondencia de los resultados experimentales con la simulación, se le atribuye principalmente a las dinámicas no modeladas en la simulación como el ruido en la estimación de la señal derivativa de los estados y posiblemente a la imprecisión de los parámetros del robot.

El error producido entre la posición y orientación durante el seguimiento de trayectoria se observa en las Figs. 1d y 1e, donde para el caso de simulación prevalece un error menor en comparación con el experimental, esto conlleva a que aún existe problemáticas para pasar las soluciones en simulación a la práctica real. También se observa que existe una relación importante en la asignación de μ_1 y μ_2, donde entre más ponderación tenga el error mejores serán los resultados proporcionados por el algoritmo.

En las Figs. 2a y 2b se muestra el comportamiento que tiene el par de entrada con respecto a cada rueda del RMO en simulación y caso experimental, así mismo, se observa en la Fig. 2b que la señal de control se satura, esto se le atribuye a que en el problema de optimización no se considera el ruido generado por la estimación de la velocidad angular de las ruedas. De igual forma, se observa que la saturación produce sobre impulsos que pasan a 5 $N \cdot m$, donde para el prototipo experimental que se utiliza el par de entrada máximo es de 5 $N \cdot m$ para cada motor del RMO. En simulación no sucede dicho comportamiento, se observa que existe un buen seguimiento de trayectoria y un par de entrada en el rango de 1 $N \cdot m$.

5. CONCLUSIÓN

En este trabajo se presenta un método de sintonización para el robot móvil omnidireccional con base en la formulación de un problema de optimización dinámico no lineal.

Los resultados en simulación indican que es posible obtener las ganancias del control PD en el espacio de operación con base en un método de optimización, con el propósito de proporcionar un comportamiento aceptable en el seguimiento de una trayectoria altamente no lineal. Sin embargo, los resultados experimentales indican que se requiere de una formulación diferente para poder realizar una similitud de al menos un 90 % con los resultados en simulación.

Es importante hacer notar que para una trayectoria lenta y sencilla, como por ejemplo un círculo, este método de sintonización es viable, sin embargo, para trayectorias altamente no lineales como las presentadas en este trabajo, la correspondencia de la simulación con la realidad dista mucho.

El trabajo futuro de esta investigación es incorporar en el problema de optimización, la robustez de los resultados obtenidos ante incertidumbres del sistema no lineal modelado en forma de ecuación diferencial con el propósito de tener una correspondencia de al menos un 90 %.

REFERENCIAS

Albertos, P. (2007). Lights and shadows of the intelligent control. In *European Control Conference*, 4440–4441.

Algoul, S., Alam, M., Hossain, M., and Majumder, M. (2011). Multi-objective optimal chemotherapy control model for cancer treatment. *Medical and Biological Engineering and Computing*, 49, 51–65.

Deb, K. (2000). An efficient constraint handling method for genetic algorithms. *Computer methods in applied mechanics and engineering*, 186(2), 311 – 338.

Tabla 2. Ganancias óptimas del controlador PD

$[\mu_1, \mu_2]$	*Corrida*	kp_1^*	kp_2^*	kp_3^*	kd_1^*	kd_2^*	kd_3^*	$\bar{J}$	$\bar{J}_1$	$\bar{J}_2$	*Tiempo* $[h]$
$[0{,}999, 0{,}001]$	1	638,862	424,546	966,153	39,610	322,867	6,071	0,011	0,009	0,002	0,94
	2	903,879	542,041	804,838	154,291	298,662	6,394	0,070	0,066	0,003	0,94
	3	906,479	734,172	466,998	44,889	143,653	5,887	0,008	0,005	0,002	0,95
	4	480,954	637,488	272,761	48,838	258,023	3,624	0,027	0,024	0,002	0,94
	5	**514.785**	**25.640**	**582.770**	**3.637**	**172.636**	**5.726**	**0.002**	**0.0002**	**0.002**	**0.95**
Promedio		688,991	472,777	618,704	58,253	239,168	5,540	0,023	0,020	0,002	0,94

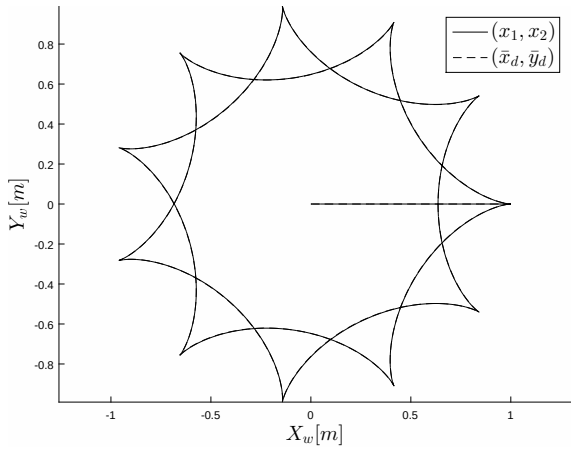

a) Trayectoria en Simulación.

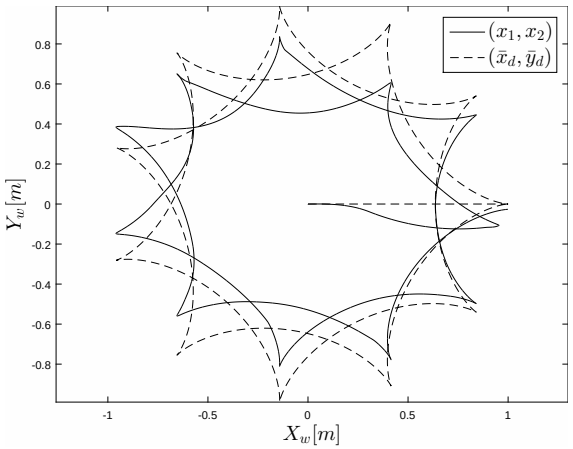

b) Trayectoria Experimental.

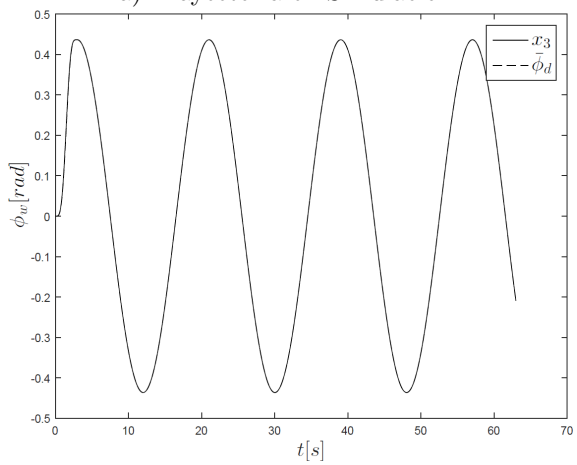

c) Orientación del RMO en Simulación.

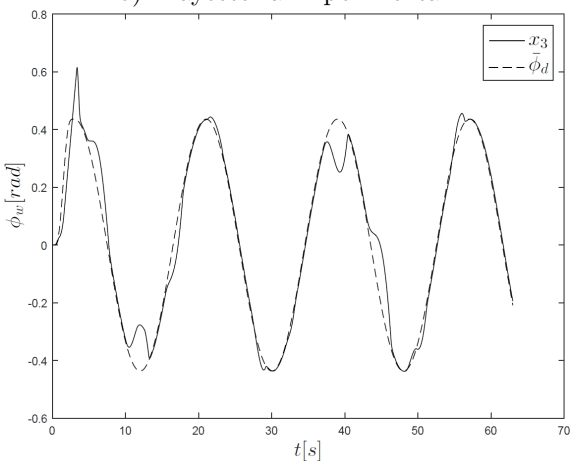

d) Orientación del RMO Experimental.

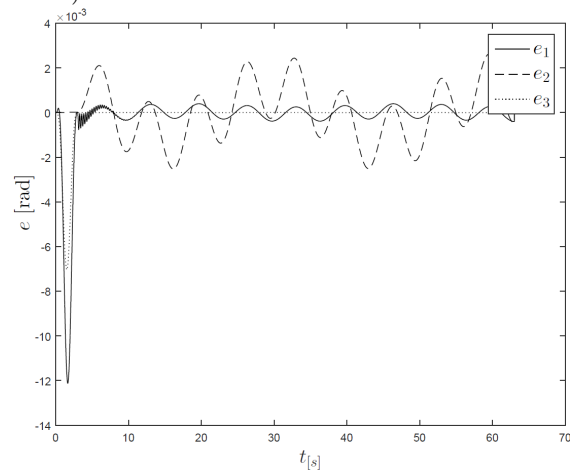

d) Error de posición y orientación en Simulación.

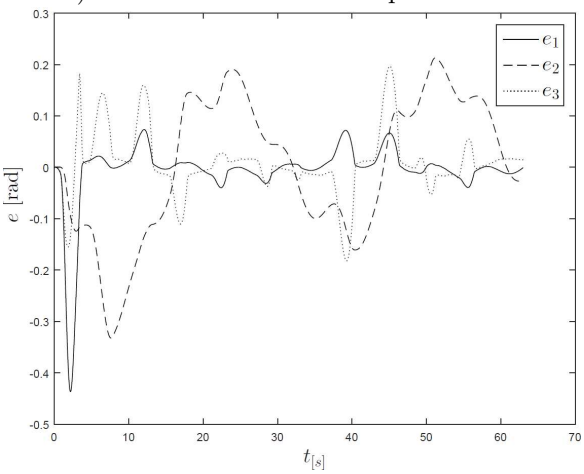

e) Error de posición y orientación Experimental.

Figura 1. Resultado de la simulación y experimental con las ganancias óptimas en posición, orientación y el error.

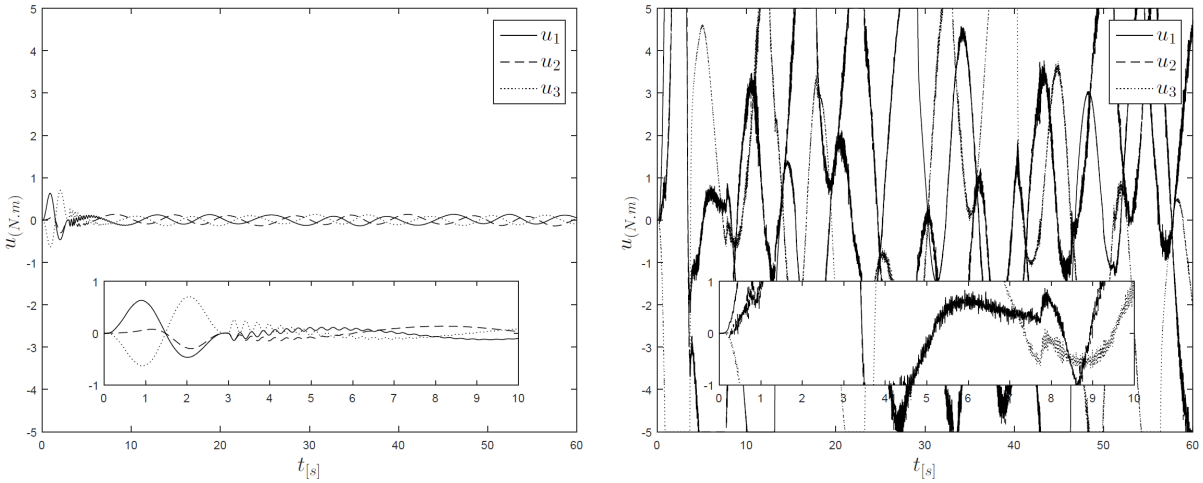

a) Par de entrada en las ruedas en Simulación.

b) Par de entrada en las ruedas Experimental.

Figura 2. Resultado de la simulación y experimentación con las ganancias óptimas en el par de entrada.

dos Santos Coelho, L. and Pessoa, M.W. (2011). A tuning strategy for multivariable {PI} and {PID} controllers using differential evolution combined with chaotic zaslavskii map. *Expert Systems with Applications*, 38(11), 13694 – 13701.

Fleming, P. and Purshouse, R. (2002). Evolutionary algorithms in control systems engineering: a survey. *Control Engineering Practice*, 10(11), 1223 – 1241.

Karer, G. and Skrjanc, I. (2016). Interval-model-based global optimization framework for robust stability and performance of {PID} controllers. *Applied Soft Computing*, 40, 526 – 543.

Peñaloza-Mejía, O., Márquez-Martínez, L.A., Alvarez, J., Villarreal-Cervantes, M.G., and García-Hernández, R. (2015). Motion control design for an omnidirectional mobile robot subject to velocity constraints. *Mathematical Problems in Engineering*, 2015, 1.

Portilla-Flores, E.A., Mezura-Montes, E., Alvarez-Gallegos, J., Coello-Coello, C.A., Cruz-Villar, C.A., and Villarreal-Cervantes, M.G. (2011). Parametric reconfiguration improvement in non-iterative concurrent mechatronic design using an evolutionary-based approach. *Engineering Applications of Artificial Intelligence*, 24(5), 757–771.

Reynoso-Meza, G., Blasco, X., Sanchis, J., and Martínez, M. (2014). Controller tuning using evolutionary multi-objective optimisation: Current trends and applications. *Control Engineering Practice*, 28, 58 – 73.

Reynoso-Meza, G., Sanchis, J., Blasco, X., and Freire, R.Z. (2016a). Evolutionary multi-objective optimisation with preferences for multivariable {PI} controller tuning. *Expert Systems with Applications*, 51, 120 – 133.

Reynoso-Meza, G., Sanchis, J., Blasco, X., and Martínez, M. (2016b). Preference driven multi-objective optimization design procedure for industrial controller tuning. *Information Sciences*, 339, 108 – 131.

Ruano, A.E., Ge, S.S., Guerra, T.M., Lewis, F.L., Principe, J.C., and Colnaric, M. (2014). Computational intelligence in control. *Annual Reviews in Control*, 38(2), 233 – 242.

Sabir, M.M. and Ali, T. (2016). Optimal {PID} controller design through swarm intelligence algorithms for sun tracking system. *Applied Mathematics and Computation*, 274, 690 – 699.

Storn, R. and Price, K. (1997). Differential evolution– a simple and efficient heuristic for global optimization over continuous spaces. *Journal of global optimization*, 11(4), 341–359.

Villarreal-Cervantes, M.G. (2014). Control pid robusto de un robot manipulador con base en un problema de optimización dinámica. *Congreso Latinoamericano de Control Automático*, 1428–1434.

Villarreal-Cervantes, M.G., Cruz-Villar, C.A., Alvarez-Gallegos, J., and Portilla-Flores, E.A. (2010). Differential evolution techniques for the structure-control design of a five-bar parallel robot. *Engineering Optimization*, 42(6), 535–565.

Villarreal-Cervantes, M.G., Cruz-Villar, C.A., and Alvarez-Gallegos, J. (2014). Synergetic structure-control design via a hybrid gradient-evolutionary algorithm. *Optimization and Engineering*, 16(3), 511–539.

Villarreal-Cervantes, M.G., Guerrero-Castellanos, J.F., Ramírez-Martínez, S., and Sánchez-Santana, J.P. (2015). Stabilization of a (3,0) mobile robot by means of an event-triggered control. {*ISA*} *Transactions*, 58, 605 – 613.

Zhang, J. and Yang, S. (2014). An incremental-pid-controlled particle swarm optimization algorithm for eeg-data-based estimation of operator functional state. *Biomedical Signal Processing and Control*, 14, 272 – 284.

Sistema para el control de trayectoria de un robot diferencial

Oscar Quiroz *. Juan Sereno **. Carlos Osorno*.**
Mónica Vallejo[4]*. Freddy Bolaños[5]*.

--***Estudiantes ingeniería de control – Universidad Nacional de Colombia, Sede Medellín.*
Semillero de Instrumentación, Control y Robótica (SInCRo)
(e-mail: oiquirozo@unal.edu.co)
*[4]*Ph.D en Informática – Departamento de Energía Eléctrica y Automática.*
Universidad Nacional de Colombia, Sede Medellín.
(e-mail: mavallejov@unal.edu.co)
[5] Ph.D en Ingeniería Electrónica-Departamento de Energía Eléctrica y automática.*
Universidad Nacional de Colombia, Sede Medellín.
(e-mail: fbolanosm@unal.edu.co)

Resumen: **Este artículo describe un sistema basado en visión artificial para el control de trayectoria de un robot diferencial en un espacio de dos dimensiones. Dicho sistema puede descomponerse en tres elementos clave: El sistema de visión artificial, las comunicaciones inalámbricas y el control de la trayectoria. En primer lugar se describe el sistema completo en forma breve, para posteriormente mostrar el diseño del control y los resultados obtenidos. Se espera que el sistema sirva como plataforma experimental para el desarrollo futuro de proyectos en los temas de visión artificial, sistemas multi-robóticos (MRS) y robótica colaborativa.**

Palabras clave: Visión artificial, Comunicación Inalámbrica, Control de Trayectoria.

1. INTRODUCCIÓN

Los sistemas robóticos están inspirados en la naturaleza y copian el comportamiento de animales como aves, peces, mamíferos e insectos, además de los seres humanos. La idea central de estos sistemas es que tengan la capacidad de ejecutar tareas que simplifiquen nuestra vida o que nos reemplacen en aquellas que son demasiado peligrosas o difíciles de hacer (Kazuo T, 1999).

Para lograrlo, los sistemas robóticos deben poseer instrumentos que les permitan interactuar con su entorno, ya sea para medir el estado de cierta variable, o para actuar sobre la misma y cambiar su estado. Una de las variables más importantes que debe medir y/o manipular un robot es su posición. Antes de realizar una tarea en la que requiera desplazarse por el entorno, este debe ser capaz de identificar su posición para luego establecer cómo llegar a un determinado lugar. Por lo tanto, establecer el estado de la posición inicial y la trayectoria que este robot debe realizar, es una de las áreas más estudiada por los sistemas robóticos autónomos, ya sean aéreos, acuáticos o terrestres (Kazuhiro K, 2007)

En este trabajo se presenta un sistema constituido por un robot diferencial capaz de recorrer una trayectoria punto a punto, rechazando perturbaciones en su posición o desviación. Se presenta la plataforma de control de posición y generación de trayectorias, integrando las áreas de Visión Artificial, Procesamiento de Señales, Telecomunicaciones y Teoría de Control.

Este documento se encuentra organizado de la siguiente forma: En la sección 2 se describe la plataforma para el control de trayectoria; en las secciones 3, 4 y 5, se explica el sistema de visión artificial (SVA), el protocolo de comunicación inalámbrica y los algoritmos de generación de trayectorias y control de posición respectivamente. Finalmente en las secciones 6 y 7 se presentan los resultados obtenidos, conclusiones y trabajo futuro en este tema.

2. PLATAFORMA

La plataforma de control de trayectoria está constituida por el robot diferencial (dos o más robots en futuros trabajos), una cámara, un sistema de comunicación inalámbrica y una unidad de procesamiento (computador), Figura 1.

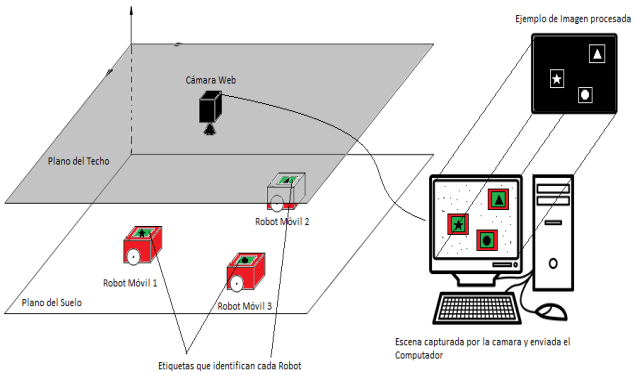

Figura 1. Plataforma para el control de trayectoria.

Acontinuacion se da una descripcion de cada subsistema.

2.1 Robot

El robot usado en la plataforma propuesta, dispone de un formato de *shield* para el estándar de Arduino. Esta característica lo hace compatible con cualquier plataforma de hardware que cumpla dicho estándar. El control de posición y trayectorias será descentralizado, es decir que el robot calculará las acciones de control, en lugar de que lo realice la unidad de procesamiento central.

Figura 2. Robot utilizado

2.2 Cámara

Para la captura en tiempo real de la posición del robot, se usa una cámara de referencia C920 del fabricante Logitech. Dicha cámara cuenta con la capacidad para grabar videos en 1080p y capturar imágenes de hasta 15 megapíxeles. En este proyecto se tomarán imágenes con una resolución de 1280x720.

2.3 Comunicación

La comunicación entre los diferentes elementos activos del sistema (procesador central, robot) se hace por medio de dispositivos inalámbricos compatibles con el protocolo 802.15.4/Zigbee. Esto permite versatilidad y flexibilidad en el control de la trayectoria del robot.

2.4 Unidad de procesamiento

La unidad de procesamiento se encarga de la captura de las imágenes del robot moviéndose en su entorno. Es la encargada de identificar la ubicación del mismo, además de contar con una interfaz de usuario que permita realizar el control de posición y trayectoria. Dicha unidad de procesamiento reside en un computador portátil Dell Latitude 15 serie 3000.

En resumen, el espacio bidimensional es censado por medio de una cámara, la cual envía los datos a una unidad de procesamiento para que ésta se encargue de realizar el reconocimiento y ubicación del robot y además de ello, servir de interfaz de usuario para permitir el control de posición y generación de trayectoria. La herramienta usada para realizar todo el procesamiento es MATLAB, y la comunicación se hace a través del protocolo Zigbee.

3. SISTEMA DE VISIÓN ARTIFICIAL (SVA)

Para ubicar al robot en el espacio bidimensional se propone un método de localización mediante visión artificial, el cual permite adquirir y procesar los datos de la cámara de tal forma que un algoritmo pueda generar la posición del robot.

3.1 Adquisición

Para el proceso de localización del robot, se diseñó una etiqueta visual, Figura 3, las cuales tienen un fondo verde, dentro del cual se ubica una figura completamente negra que identifica al robot con respecto al espacio de forma única. Las características de color usadas para construir la etiqueta se deben a que las cámaras disponen de sensores que son más sensibles al verde, y también, porque el verde es uno de los colores base para el formato RGB. Por otro lado, el uso del color negro en la etiqueta, se debe a que los píxeles en las figuras tendrán en los canales RGB niveles de gris cercanos a cero.

Figura 3. Etiqueta del robot

3.2 Pre-procesamiento

Se efectuó un análisis de diversos espacios de colores para identificar en cuál de ellos se encuentra la información relevante de la imagen (la etiqueta). Luego de dicho análisis se logró identificar que aunque la etiqueta es negra y el fondo es verde, el canal G del espacio de colores RGB funciona bien solo en los casos donde no se encuentran perturbaciones en la imagen, por lo cual no es el más adecuado para el SVA. En el espacio de colores YIQ, el canal Q cuenta con la ventaja de representar en un rango de colores del púrpura al verde y se puede evidenciar que al extraer este canal al negativo de la imagen, se extrae la información de la etiqueta y a su vez se logra omitir una cantidad considerable de perturbaciones.

3.3 Segmentación

El canal Q no extrae la información de la etiqueta en su totalidad, por lo cual es necesaria la aplicación de un umbral, el cual debe ser adaptable a las características de iluminación de la imagen. De esta forma el sistema en tiempo real será robusto ante condiciones cambiantes en el entorno. Para lograr que la umbralización del SVA se adapte a los cambios de iluminación de las imágenes, el umbral se determina en primer lugar calculando el valor máximo de nivel de gris de cada fila de la imagen. Luego de esto, se eliminan aquellos máximos con valor cero que corresponden a filas donde no hay pixeles pertenecientes a la etiqueta, a partir de estos máximos se determina su valor promedio y la desviación estándar. Para determinar el valor umbral de la imagen se tienen en cuenta las siguientes condiciones:

- Si el valor de la desviación estándar es superior a la mitad de la media (esto implica que los máximos se encuentran dispersos, debido a la presencia de verdes que no son exclusivos de la etiqueta), entonces el valor de umbral será la media, esto con el fin de tratar de eliminar todo el verde que realmente no pertenece a la etiqueta.
- Si el valor de la desviación es igual o inferior a la mitad de la media (esto implica que los máximos están menos dispersos, debido a que los verdes son únicamente de la etiqueta), entonces, para considerar la mayor cantidad de verde se define como umbral la diferencia entre la media y la desviación estándar.

Después de aplicar el proceso de umbralización automático anteriormente mencionado las imágenes de la muestra conservan total o parcialmente el ruido introducido. Para eliminarlo se clasifican como zonas de menor área que la etiqueta y el resultado es el mostrado en la Figura 4.

Figura 4. Eliminación de ruido. (a) Etiqueta pre-procesada. (b) Etiqueta umbralizada. (c) Etiqueta final, luego de eliminar ruido.

3.4 Ubicación del robot

Para la ubicación del robot se halló el centroide de la etiqueta y para la generar la trayectoria del robot se despliega una ventana en la cual se puede seleccionar la trayectoria punto a punto que debe seguir el robot, Figura 5.

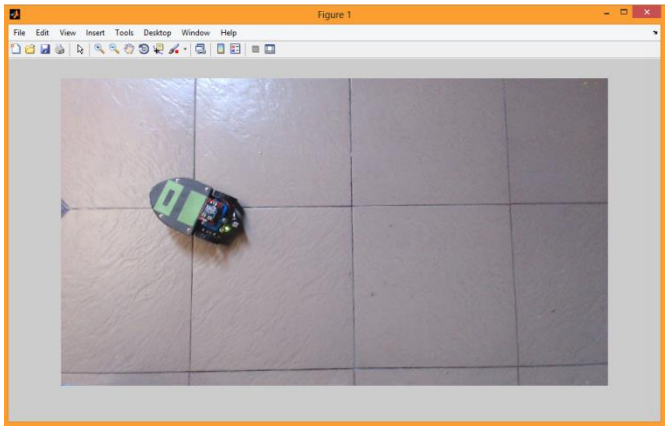

Figura 5. Interfaz gráfica para la selección de destino por parte del usuario

4. COMUNICACIÓN INALAMBRICA

En el proyecto se usaron dos tipos de módulos de comunicación que operan bajo el estándar 802.15.4/Zigbee, uno de ellos el XBee-PRO ZB S2B con conector RPSMA, el cual al ser conectado al computador actúa como coordinador, lo que posibilita usar el máximo nivel de potencia de transmisión al disponer de una fuente de alimentación ilimitada permitiendo garantizar un mayor rango de cobertura. El otro tipo de dispositivo, es el XBee-PRO ZB S2B, el cual fue configurado como dispositivo final en el robot. Por otro lado, para la configuración y pruebas de estos módulos se hizo uso de XCTU que tiene las herramientas para un rápido prototipado y puesta a punto de los módulos.

La trama API para el envío de la información debió ser creada de forma dinámica. Dado que la aplicación de visión artificial y la interfaz de control de trayectoria fueron desarrolladas en el software Matlab, se usó la misma plataforma para la creación de las tramas de los módulos XBee.

Para la creación de la trama se tuvo en cuenta solo los datos de posición y la suma de chequeo. Los datos son definidos por la aplicación de visión artificial, y el valor del *checksum* debe ser calculado para cada nueva trama.

Para la recepción de datos, el reto era almacenar toda la trama de llegada y obtener de ella los campos de interés. Es decir, de toda la trama recibida solo tomar los valores del comando enviado (posición). Para esto inicialmente se almacena toda la trama en un vector, con el fin de evitar pérdidas de bytes. Posteriormente se obtienen con punteros los valores de coordenadas de destino, y se efectúa su conversión a enteros para facilitar hacer uso de los mismos.

5. CONTROL DE TRAYECTORIA

El propósito final del trabajo es que el robot diferencial siga una trayectoria punto a punto establecida por medio de una interfaz gráfica en el ordenador. Esta trayectoria está constituida por una serie de puntos elegidos por el usuario, se desea que cada robot siga una trayectoria rectilínea entre esos puntos, Figura 6. El ordenador transmite vía inalámbrica y de manera sucesiva los datos de ubicación y orientación. El robot calcula su desviación con cada nuevo dato de posición actual que recibe y lo compara con el dato de posición deseada correspondiente, para ejercer acciones de control sobre los motores y corregir así su dirección.

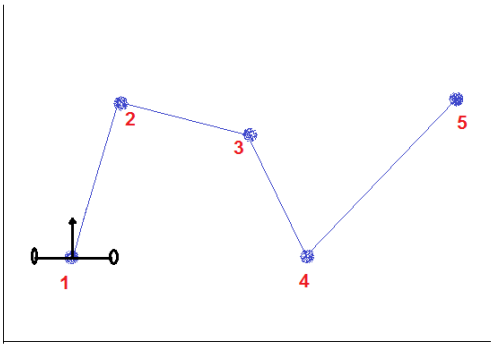

Figura 6. Geometría de la trayectoria deseada.

Se desea que la desviación del robot con respecto a la recta que une cada par de puntos (actual y deseado), sea mínima y

que la distancia entre ellos también lo sea; estos son los dos requerimientos principales para diseñar el controlador de trayectoria. Como se muestra en la Figura 7, (Xa, Ya) corresponden a la posición actual, (Xd, Yd) es la posición deseada correspondiente, VA y VB son la velocidad de los motores del robot, "alfa" y "d" son la desviación y la distancia respectivamente.

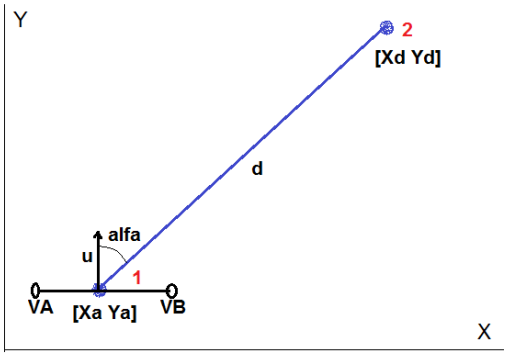

Figura 7. Geometría para el posicionamiento del robot, los números indican el par de puntos estudiados.

La velocidad del robot se controla por medio del ciclo de trabajo de la señal PWM que reciben los motores. Este ciclo de trabajo es la acción de control que se genera al comparar los dos requerimientos (desviación y distancia) con sus valores actuales. El robot es un sistema MISO con dos entradas - una salida y con el fin de simplificarlo se hace la suposición de que los motores siempre tendrán una velocidad distinta de cero en toda la dinámica de la trayectoria. Lo anterior tiene varias implicaciones. En primer lugar, el robot no se detendrá en toda la trayectoria sino que tendrá movimiento continuo (más adelante se estudia como detenerlos al final de la trayectoria), y en segundo lugar los dos requerimientos (desviación y distancia) se simplifican a uno solo. Esto se debe a que cuando se desea controlar el ángulo y los motores no se detienen, se corrige al mismo tiempo la distancia "d" entre los puntos. Por lo tanto, no se hace necesario realimentar la distancia y compararla, por lo que el diagrama de bloques del sistema de control es más simple. Para determinar cómo se comporta la señal de error que ingresa al controlador se debe dividir el ángulo de desviación en dos casos, ver Figura 8.

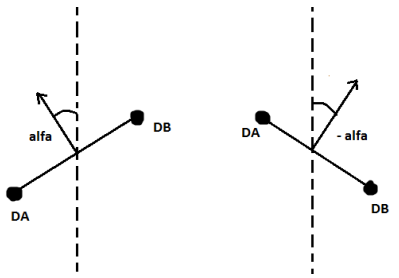

Figura 8. Posibles casos de la desviación del robot

Debido a que el requerimiento es que la desviación sea mínima, el error es la referencia menos el ángulo de orientación actual del robot. Así, en cada caso de la Figura 8, el error es el negativo del ángulo alfa. Cada caso representa el esfuerzo de control que debe hacer cada motor para minimizar la desviación. Por lo anterior, cada acción de control (ciclo de trabajo) es el error asociado a cada caso (a cada motor) multiplicado por el controlador así:

$$DA = C1 * alfa$$
$$DB = -C2 * alfa \quad (1)$$

Donde DA y DB son las acciones de control de cada motor, y C1 y C2 son la función de transferencia de los controladores que deben hallarse. Si suponemos que ambos controladores son iguales se llega a la conclusión de que una acción de control es la negativa de la otra, y se obtiene el diagrama de bloques que se muestra en la Figura 9.

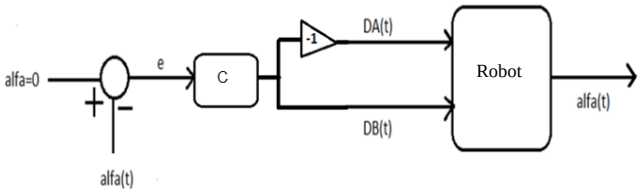

Figura 9. Diagrama de bloques del sistema de control de trayectoria simplificado.

5.1 Modelo matemático del robot

Para encontrar el controlador C, primero se debe modelar el robot conociendo como cambia su ángulo de giro en función de las velocidades de cada rueda, y por consiguiente del ciclo de trabajo de cada motor. La Figura 10 muestra la dinámica del movimiento del robot.

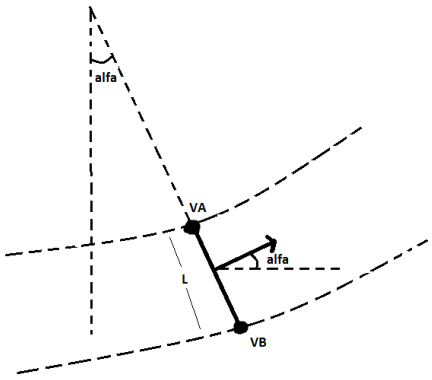

Figura 10. Análisis del movimiento del robot

Partiendo de las ecuaciones básicas del movimiento circular (Cádiz, Hevia, Reyes, 2013) y del análisis del movimiento del robot, Figura 10, se encuentra que la variación del ángulo que forma el robot es proporcional a la diferencia de las velocidades lineales de cada rueda e inversamente proporcional a la longitud del eje entre ellas.

$$\frac{d\alpha}{dt} = \frac{V_B - V_A}{L} \quad (2)$$

Ahora debe identificarse la relación que existe entre la velocidad lineal y el ciclo de trabajo. La función de transferencia entre la velocidad de un motor y su voltaje de entrada es dominantemente de primer orden, luego solo debe hallarse la constante de tiempo del sistema y su valor final, para lograrlo se hace el siguiente experimento: Al asignarle un ciclo de trabajo máximo a uno de los motores y al otro cero, se hace rodar al robot en círculos durante 5 vueltas, efectuando varias pruebas se mide el tiempo que tarda en darlas y se encuentra el promedio de la velocidad lineal máxima V_{MAX}.

Una vez se conoce la velocidad lineal máxima, sabiendo que la constante de tiempo se mide cuando la función de transferencia ha alcanzado el 63% de su valor final y teniendo en cuenta que una acción de control es la negativa de la otra, se puede entonces transformar (2) al dominio de Laplace y encontrar así la función de transferencia del robot.

$$Gp(s) = \frac{\alpha(s)}{D(s)} = \frac{2V_{MAX}}{s(L\tau s + L)} \tag{3}$$

5.2 Diseño del controlador

La cámara toma una fotografía y el algoritmo de visión artificial genera y envía las coordenadas al robot, este las recibe y calcula su desviación. Este proceso ocurre a intervalos irregulares de T = 300ms, debido a esto, el sistema a controlar esta en tiempo discreto, ver Figura 11.

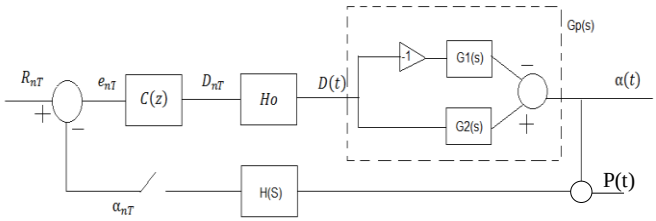

Figura 11. Sistema de control digital y análogo

Gp(s) es la función de transferencia del robot (3), C(z) es el controlador digital, H(s) es un retraso que representa a la cámara y la comunicación inalámbrica, Ho es un reconstructor de la señal muestreada de orden cero y P(t) es la perturbación en el ángulo. Debido a que $R_{nT} = 0$, nos interesa conocer cómo responde el sistema a la perturbación $P_{(t)}$ (sensibilidad). Para encontrar la función de transferencia discreta entre $P_{(t)}$ y $\alpha_{(t)}$ se utiliza (4)

$$M(z) = \frac{\alpha(z)}{P(z)}$$
$$M(z) = -\frac{C(z)G(z)H(z)}{1 + C(z)G(z)H(z)} \tag{4}$$

Dónde:

$$G(z) = (1 - z^{-1})\mathbb{Z}\left\{\frac{Gp(s)}{s}\right\} \tag{5}$$

$$H(z) = z^{-1} \tag{6}$$

Al sustituir (3) en (5) se obtiene:

$$G(z) = A\left(\frac{(z+1)^3}{z(z^2 + bz + c)}\right) \tag{7}$$

Dónde:

$$A = \frac{T^3 V_{max}}{4L\tau + 2T}$$
$$b = -\frac{8L\tau}{4L\tau + LT}$$
$$c = -\frac{2T - 4LT}{4L\tau + 2T}$$

En (7) puede notarse que el robot tiene un polo en z=0 por lo que tendrá una respuesta relativamente lenta al ciclo de trabajo, se propone entonces un control digital proporcional de la forma:

$$C(z) = K_p \tag{8}$$

La sensibilidad nominal del sistema se obtiene al reemplazar (6), (7) y (8) en (4):

$$M(z) = -\frac{AK_p(z+1)^3}{AK_p(z+1)^3 + z^2(z^2 + bz + c)} \tag{9}$$

El denominador de (9) contiene los polos de la sensibilidad nominal, por lo que si las raíces de estos polos están dentro del circulo unitario se garantiza la estabilidad del sistema (Ogata, 1996) se desea entonces encontrar un intervalo para la ganancia K_p que preserve este requerimiento, para esto, se utiliza el lugar geométrico de las raíces las cuales dependen del valor de K_p, mediante un programa iterativo se aumenta progresivamente este valor y cuando al menos una raíz se encuentre fuera del circulo unitario se detiene la iteración y se encuentra el intervalo. El resultado es:

$$0 < K_p < 0.014 \tag{10}$$

Por fuera de este intervalo el sistema será en teoría, inestable.

5.3 Simulaciones

Para comprobar el funcionamiento del sistema de control en tiempo discreto, se implementa el diagrama mostrado en la Figura 12, con la herramienta Simulink de Matlab.

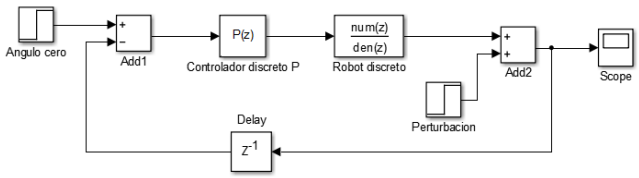

Figura 12. Diagrama de bloques en Simulink.

En un tiempo t = 0 se produce una perturbación en el ángulo alfa de 90°, escogiendo un valor $K_p = 0.008$ cercano a cero para evitar oscilaciones debido a la ganancia, la respuesta obtenida es:

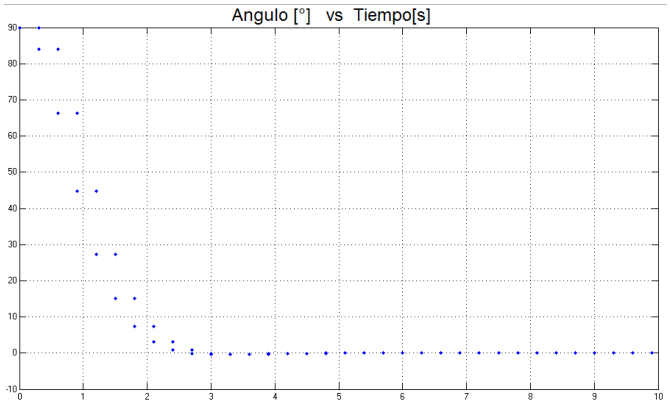

Figura 13. Desviación del robot, estable.

La respuesta mostrada en la Figura 13, corresponde a la dinámica de rotación del robot que se da en forma sobre-amortiguada, efectivamente se consigue el objetivo de control (Desviación cero), se espera ver este comportamiento en el experimento. Si usamos un controlador con valor $K_p = 0.02$ el sistema se vuelve inestable, Figura 14.

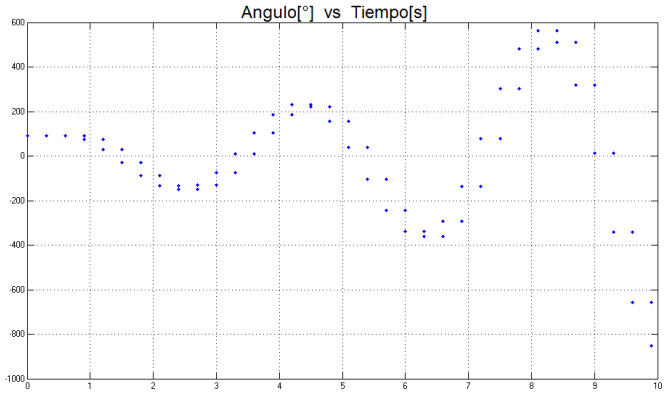

Figura 14. Desviación del robot, inestable.

Al aumentar el tiempo de retardo en la realimentación (mayor tiempo de procesamiento y envío de datos) se observa un aumento en las oscilaciones y en el tiempo muerto, Figura 15. Esto se debe a que los sistemas con retardo en su respuesta presentan raíces de fase no mínima, que dan lugar a inestabilidad si no se realiza un control apropiado. (Ogata, 2010)

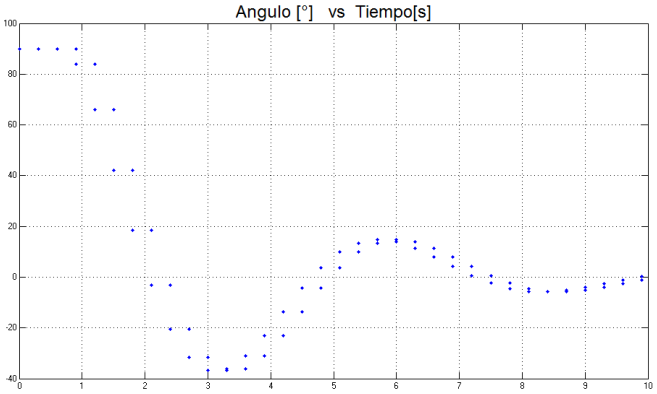

Figura 15. Desviación del robot, oscilaciones.

Se hace importante entonces la disminución del retardo entre la medición, el procesamiento y la comunicación de las coordenadas para evitar movimientos indeseados en el robot.

5.3 Algoritmo implementado en el robot

El trabajo realizado en el sistema de visión artificial genera 3 datos importantes, la posición actual, la orientación del robot y la posición deseada correspondiente. Estos datos deben utilizarse como señales de entrada que ingresan al controlador. El ángulo α es la desviación relativa que tiene cada robot con respecto a la recta que une los puntos de posición actual y deseada, el punto de orientación y el punto actual definen un vector unitario $\vec{u}$, Figura 7. Luego para generar α se deben utilizar relaciones geométricas utilizando los puntos como vectores en el espacio. Para empezar, es claro que α es el ángulo entre los vectores $\vec{u}$ y $\vec{d}$, luego mediante la ley del coseno se establece que:

$$\alpha = \cos^{-1}\left(\frac{\vec{d}\cdot\vec{u}}{\|\vec{d}\|}\right) \tag{11}$$

Dónde:

$$\|\vec{d}\| = \sqrt{(x_d - x_a)^2 + (y_d - y_a)^2} \tag{12}$$

Con lo que se llega a:

$$\alpha = \cos^{-1}\left(\frac{(x_d - x_a)\,u_1 + (y_d - y_a)u_2}{\sqrt{(x_d - x_a)^2 + (y_d - y_a)^2}}\right) \tag{13}$$

En esta ecuación:

x_d Representa la coordenada en x de la posición deseada

x_a Representa la coordenada en x de la posición actual

y_d Representa la coordenada en y de la posición deseada

y_a Representa la coordenada en y de la posición actual

u_1 Representa la coordenada en x de la posición de orientación

u_2 Representa la coordenada en y de la posición de orientación

α Es el ángulo alfa a controlar

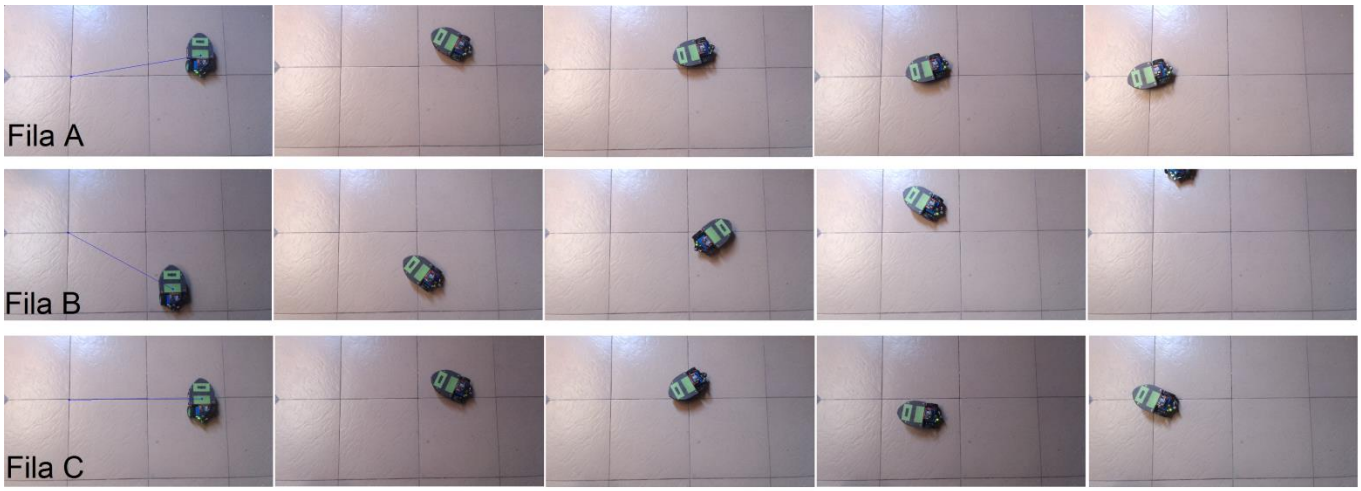

Figura 16. Fila A, robot con trayectoria estable. Fila B, trayectoria inestable. Fila C, trayectoria estable con oscilación.

Debido a que por medio de la ley de cosenos se obtiene el ángulo más pequeño entre dos vectores (Fuller, Tarwater), se desconoce el signo de esté, Figura 8. Para determinarlo, se usa el siguiente producto vectorial:

$$\|\vec{u}\ x\ \vec{d}\| = (\overrightarrow{y_d} - \overrightarrow{y_a})u_1 - (\overrightarrow{x_d} - \overrightarrow{x_a})u_2 \quad (14)$$

Luego si $\|\vec{u}\ x\ \vec{d}\| > 0$ entonces α es negativo, y será positivo en caso contrario. Este resultado es de suma importancia para la orientación del robot, pues las acciones de control de cada motor dependen del signo del ángulo α, como puede verificarse en (1) y en la Figura 8. Al reemplazar (10) y (13) en (1) el algoritmo implementado en la tarjeta será entonces:

$$DA_{nT} = 0.008\cos^{-1}\left(\frac{(x_d-x_a)\,u_1+(y_d-y_a)u_2}{\sqrt{(x_d-x_a)^2+(y_d-y_a)^2}}\right)+K5$$
$$DB_{nT} = -0.008\cos^{-1}\left(\frac{(x_d-x_a)\,u_1+(y_d-y_a)u_2}{\sqrt{(x_d-x_a)^2+(y_d-y_a)^2}}\right)+K5 \quad (15)$$

Donde $K5 = 0.01$ es adicionada para garantizar el requerimiento de que la velocidad de los motores siempre será distinta de cero para cuando $\alpha_{nT} = 0$.
En la sección experimental se entra en detalle sobre el mecanismo de parada del robot.

6. EXPERIMENTO

Se realizó el montaje mostrado previamente en la Figura 1 ubicando la cámara a un metro por encima del suelo con el brazo de una lámpara, asegurando condiciones adecuadas de luz y ubicando al robot en una superficie sin componentes importantes de verde. Al iniciar el código en MATLAB se abre una ventana que muestra la posición actual del robot y un puntero para que el usuario pueda crear la trayectoria punto a punto, escogiendo todas las posiciones deseadas de manera sucesiva, ver Figura 5. El algoritmo de visión artificial es capaz de eliminar todo el ruido y componentes de verde que no hacen parte de las etiquetas para diferentes condiciones de iluminación.

El robot comienza su movimiento en la posición 1, Figura 6. El sistema de visión genera las coordenadas y las envía al robot, este calcula su desviación α_{nT} mediante (13) y (14), determinando la potencia (ciclo de trabajo) para cada motor mediante (15). El robot se dirige en línea recta hacia la posición 2 y cuando el valor de la ecuación (12) alcanza un umbral mínimo, el sistema de visión le envía la nueva posición deseada 3, y el robot continúa su desplazamiento. Para detenerse al final de la trayectoria, el código reconoce la última posición deseada (en este caso la posición 5. Figura 6) y usa (12) para determinar cuándo apagar los motores.

Para validar el modelo del sistema de control se implementa el algoritmo de la sección 5.3 para diferentes valores de K_p y de tiempo de retardo. En la Figura 16, se muestra el resultado de las pruebas. La rotación estable proporciona la trayectoria más rápida aunque no la más óptima, se espera trabajar en trayectorias optimizadas en el futuro.

En el experimento se aplicaron perturbaciones al robot, como cambiar su dirección o su posición y pudo notarse que esté recuperó su trayectoria para redirigirse nuevamente al punto deseado, mostrando así un resultado satisfactorio del control de trayectoria.

Se realizaron numerosas pruebas en el control para puntos de llegada preestablecidos, registrando el número de veces que el robot llego a la posición deseada sin desviarse en direcciones aleatorias, los resultados son mostrados en la Tabla 1.

	Número	**Tiempo promedio de recorrido [s]**
Éxitos	25	36
Fallos	5	54
Total	30	

Tabla 1. Cuantificación de la efectividad del sistema diseñado.

7. CONCLUSIONES

El sistema de control diseñado ejerce una acción de control cada que se actualizan los datos de posición actual, deseada y orientación, si no se actualizan, el robot se mueve con la última acción ejecutada describiendo trayectorias por fuera de la deseada (inestabilidad, Figura 16). Se hizo entonces de vital importancia la sincronización y la rapidez con que se adquieren y transmiten los datos para así efectuar un control apropiado sobre la trayectoria del robot. Es por esto que el sistema en su totalidad tiene una efectividad del 83% con respecto a la precisión del movimiento y orientación del robot (ver la Tabla 1).

Como trabajo futuro, se requiere desarrollar controladores más complejos para corregir el tiempo de retardo y/o crear trayectorias óptimas. Además, se espera trabajar con un entorno de usuario diferente a Matlab, para lograr reducir el tiempo de captura de las imágenes y por lo tanto agregar mayor estabilidad al sistema.

Se encuentra en proceso la puesta a punto de un sistema de múltiples robots, el cual tiene fines académicos e investigativos.

AGRADECIMIENTOS

Este trabajo ha sido financiado por la Universidad Nacional de Colombia a través del Programa Nacional de Semilleros de Investigación, Creación e Innovación en la Modalidad de Proyectos para la introducción en la investigación, creación o innovación 2013-2015.

REFERENCIAS

Ailon, A., "Control strategies for groups of autonomous wheeled mobile robots with restricted inputs," in *Electrical & Electronics Engineers in Israel (IEEEI), 2012 IEEE 27th Convention of* , vol., no., pp.1-4, 14-17 Nov. 2012

F. Cádiz, S. A. Hevia, S. A. Reyes, “Mecánica clásica”, Departamento de física, Pontificia Universidad Católica de chile, 2013, pp. 27-34.

G. Fuller, D. Tarwater. "Vectores, Planos y Rectas" En: Geometría analítica. Pearson education. P.314-349.

Jing Zhou; Dejun Mu; Feisheng Yang; Guanzhong Dai, "A novel approach for analyzing collective dynamics of large-scale multi-robot system in task allocation," in Information and Automation (ICIA), 2014 IEEE International Conference on , vol., no., pp.1137-1142, 28-30 July 2014 doi: 10.1109/ICInfA.2014.6932820

Karl J. Aström, T. Hägglund, “Control PID avanzado”, Lund Institute of Technology, Suecia, Pearson education S.A. 2009, pp. 184-188.

Kazuhiro K, “Robotics as Systems Integration”. Integration Technology. IEEE International Conference on. 2007.

Kazuo T. “Human Friendly Robotics, a Challenge to New Robot Applications”. International Conference on Intelligent Robots and Systems. IEEE. 1999, Volume: 2, Pages: 609 – 609.

Ogata. K. “Discrete Time Control Systems” Second edition, Chapter 6, Location Poles. 1996.

Ogata. K. “Modern Control Engineering” Fifth edition, Chapter 7, Stability Analysis. 2010.

Yan; Tang Zhenmin, "Control Architecture for Autonomous Multi-Robot System: Survey and Analysis," in Intelligent Computation Technology and Automation, 2009. ICICTA '09. Second International Conference on, vol.4, no., pp.376-379, 10-11 Oct. 2009 doi: 10.1109/ICICTA.2009.805

Utilización de un sistema embebido para la teleoperación de un manipulador movil, utilizando un control discreto.

Hernández-Oliva, Noemi*, Niño-Suárez, Paola A., Portilla-Flores, Edgar A.*****

**Instituto Politécnico Nacional, C.E.C.y T. 2 Miguel Bernard, Av. Nueva Casa de la Moneda No. 133, Colonia Lomas de Sotelo, C.P. 11200, Delegación Miguel Hidalgo, Ciudad de México, (e-mail: nhernandezo@ipn.mx).*
*** Instituto Politécnico Nacional, Escuela Superior de Ingeniería Mecánica y Eléctrica Unidad Azcapotzalco, Av. de las Granjas No. 682, Colonia Santa Catarina, C.P. 02250, Delegación Azcapotzalco, Ciudad de México, (e-mail: pninos@ipn.mx)*
**** Instituto Politécnico Nacional, Centro de Innovación y Desarrollo Tecnológico en Cómputo, Av. Juan de Dios Bátiz s/n esq. Miguel Othón de Mendizábal, Colonia Nueva Industrial Vallejo, C.P. 07700, Delegación Gustavo A. Madero, Ciudad de México, (e-mail: aportilla@ipn.mx)*

Abstract: En este artículo se expone el trabajo realizado para desarrollar un sistema de control de movimiento para un manipulador móvil, el cual fue implementado por medio de un servidor ejecutado en la terminal del sistema operativo Linux Mint instalado en un sistema embebido modelo Fit-PC3i embarcado en el robot, el cual adicionalmente realiza las funciones de comunicación entre la estación base y la estación de control. Se desarrollaron leyes de control de tipo discreto para resolver el problema de regulación y seguimiento de trayectorias, con el fin de facilitar su implementación y simplificar el desarrollo de los programas, sin embargo el énfasis radica en la programación de los mismos en un sistema de este tipo.

Keywords: sistema embebido, control discreto, manipulador móvil.

1. INTRODUCCION

Un aspecto de gran interés en el desarrollo de sistemas de control es el empleo de sistemas embebidos con suficiente capacidad de cómputo para el cálculo de las diferentes operaciones a realizar. En el caso de Bruzzonea, G., et. al. (2009), se analizó la posibilidad y validación de emplear sistemas embebidos en aplicaciones practicas de robótica mediante el uso de programas desarrollados en distribuciones de Linux con las cuales se reportan una gran compatibilidad en aplicaciones de automatización. En Suppiah, et. al. (2014), se presentan técnicas que relacionan el uso de sistemas embebidos en el sector académico con el uso de plataformas experimentales, si bien el trabajo está enfocado en el área educativa se evidencia el amplio potencial del uso y aplicación de los sistemas embebidos en sistemas robóticos.

Además que en la literatura, también se encuentran varios trabajos donde el control del robot se realiza de manera inalámbrica con el fin de ser implementado en un sistema embarcado para resolver el problema de regulación o de seguimiento de trayectorias, como es el caso de Wang Z., et. al. (2012), en el cual se describe el desarrollo de un controlador para la estimación de movimiento y su posterior prueba de estabilidad empleando el método de Lyapunov, los resultados se muestran por medio de imágenes obtenidas en tiempo real y con simulaciones que demuestran la convergencia de la regulación visual propuesta; por otro lado en Chen J., et. al. (2005), únicamente se describen tres enfoques a través de los cuales se propone el uso de un controlador a partir de una función que garantice la convergencia asintótica del mismo, centrando su estudio en los diferentes métodos de control empleados.

En Hendzel Z., et. al. (2011), proponen un algoritmo de control discreto implementado en un robot móvil de dos ruedas, el cual se prueba para mostrar el desempeño a través de varios experimentos. En Horowitz, B., et. al. (2003) se describe detalladamente una metodología de diseño de controladores para vehículos autónomos mediante la implementación de sistemas embebidos, a través del cual se pueden validar su efectividad basado en el tiempo de computo que proporciona la combinación del control con la aplicación. Por esta razón, es posible hablar extensamente de las ventajas que en años recientes ha aportado el uso de software libre para aplicaciones en robótica, puesto que permiten mediante el uso de algortimos implementados en C/C++ obtener aplicaciones que no dependan de otros, al realizarse desde cero estos programas pueden ser modificado o reestructurado cada vez que sea necesario, sin necesidad de desechar la aplicación que se tenia funcionando; otra característica muy importante se obtiene del tiempo de ejecución ya que puede decirse que es en tiempo real para cada una de las tareas programadas, siendo los eventos, una de las técnicas de programación más empleadas. Sin embargo, en ninguno de estos trabajos se presenta a detalle la arquitectura de hardware o el software desarrollado para la implementación de los controles reportados.

Por lo que resulto atractivo plantear una propio con el fin de validar su efectividad en el manipulador móvil que se tiene, para aprovechar de forma adecuada las características físicas

del sistema embebido con que se cuenta y la implementación directa de controladores en tiempo discreto que se puede realizar en este tipo de dispositivos, lo que conlleva también a una reducción considerable en la cantidad de recursos computacionales que se requieren al ejecutarse cada uno de los programas desarrollados. En este artículo se presenta el desarrollo e implementación de una arquitectura de control que opera desde un sistema embebido, embarcado en un manipulador móvil teleoperado por medio de un Gamepad. Los algoritmos de control se desarrollaron en tiempo discreto, debido a que su implementación se realiza en un dispositivo digital.

La principal ventaja de este esquema de control es que el cálculo del algoritmo no está limitado por una frecuencia de muestreo, y por lo tanto se puede implementar en una gran variedad de sistemas digitales que utilicen diferentes sistemas operativos. Es por esta razón que el uso de sistemas embebidos resulta cada vez más atractivo, por la facilidad y simplicidad en la programación y por las características de hardware. Para desarrollar el sistema de control en lazo cerrado para la teleoperación del robot, se revisó el modelo cinemático continuo para una plataforma del tipo (2,0), y su modelo cinemático discreto exacto, reportados en la literatura. Al igual, se desarrolló un modelo cinemático inverso discreto para el brazo manipulador. A partir de estos modelos se diseñaron los algoritmos de control discretos.

En la sección 2 de este artículo se presenta la plataforma desarrollada y sus modelos cinemáticos en tiempo continuo y discreto, las leyes de control propuestas para el problema de regulación y seguimiento de trayectorias obtenidos se presentan en la sección 3, el desarrollo e implementación de los programas de control en el sistema embebido se encuentran en la sección 4. La sección 5 corresponde a los resultados obtenidos al implementar los programas en el sistema embebido; finalmente en la sección 6 se presentan las conclusiones del presente trabajo.

2. PLATAFORMA ROBOT MANIPULADOR

En el Laboratorio de Mecatrónica del IPN-CIDETEC, se ha diseñado y puesto en operación un manipulador móvil, conformado por un brazo de tres grados de libertad y una plataforma móvil de tipo (2,0) con locomoción diferencial, el desarrollo inicial del manipulador se presentó en Sánchez-Cristo, et al. (2013). A partir de este prototipo, se realizó una nueva propuesta para el control de operación del robot, reemplazando la teleoperación que se realizaba por medio de una computadora y un joystick, por un control directo desde un control para juego, tipo Gamepad.

El sistema de teleoperación se conforma por una estación base, desde la cual se realiza la teleoperación y otra de control, que esta embebida en el manipulador móvil, Fig. 1.

La estación base está compuesta por un control para juego Gamepad, el cual se encarga de enviar la posición final del brazo o la posición final a la que debe llegar la plataforma móvil, enlazando mediante una red WiFi el Gamepad a un sistema embebido embarcado en el robot móvil. El embebido en la estación móvil se encarga de calcular la ley de control en lazo cerrado que dirige los movimientos de los diferentes actuadores, tanto del brazo como de la plataforma, para que el manipulador móvil alcance la posición solicitada empleando un sistema operativo Linux Mint 13 Maya.

Fig. 1. Sistema de teleoperación del manipulador móvil.

2.1 *Arquitectura del Hardware*

La arquitectura de hardware diseñada para la operación remota del manipulador móvil se presenta en la Fig. 2, se observa como toda la operación de control y se calcula en el sistema embebido. Dada la cantidad de operaciones que se deben realizar y los recursos que se requieren, se seleccionó el sistema embebido modelo FitPC-3i, ya que permite realizar la conexión con otros dispositivos externos a través de sus diferentes puertos y la simplificación de los mismos, esto aunado con la capacidad de procesamiento con la que cuenta el sistema embebido.

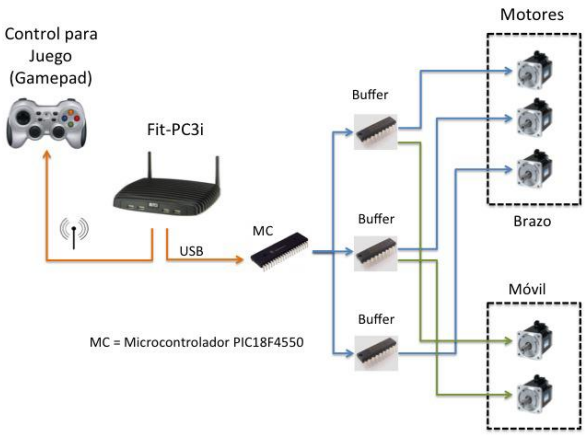

Fig. 2. Arquitectura de Hardware.

2.2 *Cinemática del manipulador móvil.*

La cinemática del manipulador móvil fue obtenida inicialmente considerándolo como un sistema acoplado, como se encuentra reportada en Niño-Suarez, et. al (2012). Para su implementación física en el sistema embebido embarcado en el robot, por simplicidad para la primera etapa

del desarrollo se consideró la cinemática desacoplada, que se presenta a continuación.

El brazo manipulador es de tipo antropomórfico, con tres grados de libertad y tres articulaciones de tipo revoluta, RRR. Es de nuestro interés el cálculo de la cinemática inversa, ya que será utilizada para el control de posición que se realizará sobre el brazo,

$$q_1 = a\tan 2\left(p_x, p_y\right) \tag{1}$$

$$q_3 = a\tan 2\left(D, \pm\sqrt{1 - D^2}\right) \tag{2}$$

con

$$D = \frac{p_x^2 + p_y^2 + p_z^2 - a_2^2 - a_3^2}{2a_2a_3}$$

$$q_2 = a\tan 2\left(\sqrt{p_x^2 + p_y^2}, p_z\right) - 2a\tan 2\left(\left(a_2 + a_3\cos q_3\right), \left(a_3\sin q_3\right)\right) \tag{3}$$

De igual forma, a partir del modelo cinemático continúo del robot móvil, dado por,

$$\begin{aligned} \dot{x}(t) &= u_1(t)\cos x_3(t) \\ \dot{y}(t) &= u_1(t)\sin x_3(t) \\ \dot{\theta}(t) &= u_2(t) \end{aligned} \tag{4}$$

Orosco (2003), obtuvo el modelo discreto exacto, que se presenta en (5):

$$\begin{aligned} \dot{x}(kT) &= u_1(kT) + 2u_1(kT)\psi\cos\left(x_3(kT) + \frac{T}{2}u_2(kT)\right) \\ \dot{y}(kT) &= u_1(kT) + 2u_1(kT)\psi\sin\left(x_3(kT) + \frac{T}{2}u_2(kT)\right) \\ \dot{\theta}(kT) &= x_3(kT) + u_2(kT) \end{aligned} \tag{5}$$

definiendo la función ψ como:

$$y\left[u_2(kT)\right] = \begin{cases} \dfrac{\sin\left(\frac{T}{2}u_2(kT)\right)}{u_2(kT)} & si\ u_2(kT) \neq 0 \\ \dfrac{T}{2} & si\ u_2(kT) = 0 \end{cases}$$

3. ALGORITMOS DE CONTROL DESARROLLADOS

Debido a que los algoritmos de control deben ser implementados en el sistema embebido, se desarrollaron controladores discretos a partir del modelo discreto exacto del brazo antropomórfico y de la plataforma móvil, considerado como un modelo desacoplado al manipulador móvil, Fig. 3.

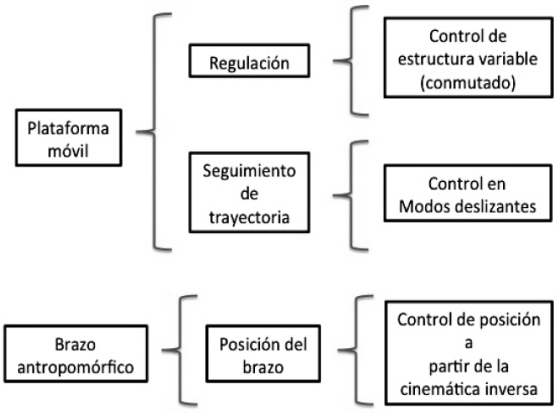

Fig. 3. Leyes de control desarrolladas.

3.1 Control para regulación del móvil

A partir del modelo presentado en (5), se propone una ley de control de estructura variable que permite resolver el problema de regulación del robot de acuerdo a su orientación inicial. Los detalles de esta propuesta de control se presentan en Hernández-Oliva, et al., (2014).

Para el primer caso, se busca que el robot se acerque a la posición deseada sobre el eje X_1, buscando una orientación final dada por x_3=0, cuando esto se logra se conmuta la ley de control para U_1 y el móvil se aproxima al origen, las leyes obtenidas son,

$$u_2 = \frac{\left(k_3 - 1\right)x_3}{T} \tag{6}$$

$$u_1 = \frac{x_2\left(k_2 - 1\right)}{2y\sin\left(x_3 + \left[\frac{k_3 - 1}{2}\right]\right)} \tag{7}$$

$$u_1' = \frac{x_1\left(k_1 - 1\right)}{2y\cos\left(x_3 + \left[\frac{k_3 - 1}{2}\right]\right)} \tag{8}$$

Para la segunda estructura de control, se busca que el robot se acerque a la posición deseada aproximándose primero al eje X_2, de manera que tenga una orientación final dada por x_3=π/2 y se conmuta de nuevo la ley de control para U_1 y el móvil se aproxima al origen.

$$u_2 = \frac{\frac{p}{2} + k_3x_3 - k_3\frac{p}{2} - x_3}{T} \tag{9}$$

$$u_1 = \frac{\frac{p}{2} + k_2\left(x_2 - \frac{p}{2}\right) - x_2}{2y\sin\left(\frac{1}{2}x_3\left(1 + k_3\right) + \frac{p}{2}\left(1 - k_3\right)\right)} \tag{10}$$

$$u_1' = \frac{\frac{p}{2} + k_2\left(x_2 - \frac{p}{2}\right) - x_2}{2y\cos\left(\frac{1}{2}x_3(1+k_3) + \frac{p}{2}(1-k_3)\right)} \quad (11)$$

Estas leyes de control discretas fueron programadas en el embebido, desarrolladas en el programa ***mover móvil*** que se presentará en la sección 4.

3.2 *Control para seguimiento de trayectoria para el móvil.*

El control por modos deslizantes en tiempo discreto es muy útil en aplicaciones prácticas debido a la simplicidad de su implementación, ya que los problemas que se presentan en tiempo continuo, como el castañeo, pueden ser reducidos y hasta eliminados si se garantiza una adecuada selección de los parámetros de control. A partir del modelo presentado en (5), se propone una ley de control por modos deslizantes en tiempo discreto para el seguimiento de trayectorias del móvil, la definición de esta ley de control se detalla en Niño-Suarez, et. al. (2012).

A partir del modelo del error dado en (12) y de las superficies deslizantes definidas en (13),

$$\begin{aligned} e_{x_1}^+ &= e_{x_1} + 2u_1 y(u_2)\cos\left(e_{x_3} + x_{3d} + \frac{T}{2}u_2\right) \\ &\quad - \Delta x_{1d} \\ e_{x_2}^+ &= e_{x_2} + 2u_1 y(u_2)\sin\left(e_{x_3} + x_{3d} + \frac{T}{2}u_2\right) \\ &\quad - \Delta x_{2d} \\ e_{x_3}^+ &= e_{x_3} + Tu_2 - \Delta x_{3d} \end{aligned} \quad (12)$$

$$\begin{aligned} s_x &= e_{x_1}^+ - e_{x_1} + g_x e_{x_1}^- \\ s_y &= e_{x_2}^+ - e_{x_2} + g_y e_{x_2}^- \\ s_t &= e_{x_3}^+ - e_{x_3} + g_t e_{x_3}^- \end{aligned} \quad (13)$$

Se proponen dos controles virtuales dados en (14) y (15),

$$w_{1x} = \frac{1}{2}\left[\Delta x_{1d} - g_x e_{x_1}^- + a s_x^-\right] \quad (14)$$

$$w_{1x} = \frac{1}{2}\left[\Delta x_{2d} - g_y e_{x_2}^- + b s_y^-\right] \quad (15)$$

A partir de los cuales cual se calcula la ley de control para u_1, dada en (16),

$$u_1 = \frac{\sqrt[2]{w_{1x}^2 + w_{1y}^2}}{y(u_2)} \quad (16)$$

Y a partir de la superficie deslizante, dada por σ_t , se obtiene la ley de control para u_2 dada en (17),

$$u_2 = \frac{1}{T}\left[\Delta x_{3d} - g_t e_{x_3}^- + d s_t^-\right] \quad (17)$$

3.3 *Control de posición para el brazo antropomórfico.*

El control de posición para el brazo manipulador se realizó utilizando un PID con compensación de gravedad en tiempo discreto. Las ecuaciones fueron implementadas en el sistema embebido mediante el programa mover brazo que se presentará en la sección 4. El detalle de cómo fue calculado este control se observa en Hernández-Oliva (2015).

4. DESARROLLO E IMPLEMENTACIÓN DEL SOFTWARE EN EL SISTEMA EMBEBIDO

Hoy en día existe un gran interés en el uso de controladores precisos, en este sentido el uso de sistemas embebidos aplicados a robótica ha tenido gran aceptación, puesto que un solo dispositivo puede sustituir componentes de hardware que requieren mayor implementación proporcionando en algunos casos peso extra al robot.

En este trabajo, las leyes de control en tiempo discreto fueron implementadas mediante programas que son ejecutados en el Fit-PC3i.

El primero, tiene como finalidad configurar la red inalámbrica y la instalación de drivers propios requeridos por el sistema operativo Linux Mint 13 Maya con el que cuenta el sistema embebido, el diagrama de flujo del programa de configuración de la red se presenta en la Fig. 4, de forma general.

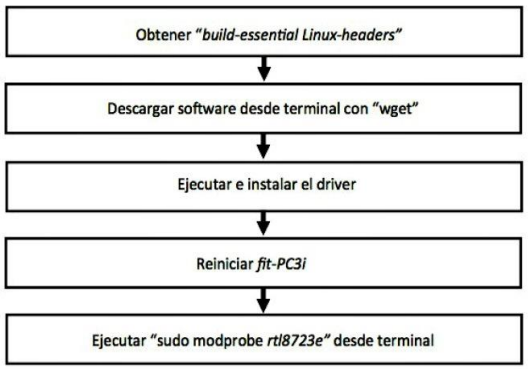

Fig. 4. Configuración de la red inalámbrica.

Una vez configurados todos los requerimientos para que el sistema embebido reconozca a los diferentes dispositivos que pueden ser integrados con él, se desarrollaron los programas que se ejecutan para realizar las diversas tareas, que fueron divididos en tres bloques, como se observa en la Fig. 5.

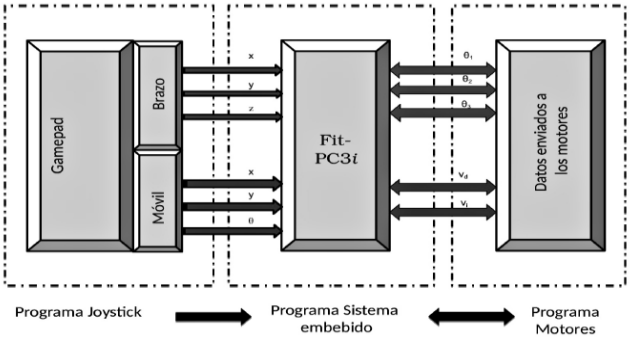

Fig. 5. Programas desarrollados en el sistema embebido.

Estos programas son ejecutados en un *servidor-cliente* instalado dentro del mismo sistema embebido. En el servidor se hace el reconocimiento de la estación base (Gamepad), con la estación de control (Fit-PC3i embebido en el manipulador móvil).

Se desarrolló el programa para el servidor y para el cliente, los cuales emplean el uso de sockets para establecer la comunicación entre estaciones. Los sockets ya han sido desarrollados para versiones de Linux y pueden ser retomados y adaptados a las necesidades de quien los emplea, puesto que son distribuidos por medio de la licencia para software libre.

Este es un programa de servidor-cliente común, que tiene como característica diferencial que su ejecución se lleva a cabo en el mismo dispositivo, esto se logra empleando una función de dominio local utilizada en sistemas operativos Linux, la cual es reportada en la literatura como AF_UNIX.

En la Fig. 5, se observa los diagramas de flujo de los programas desarrollados para el servidor y el cliente.

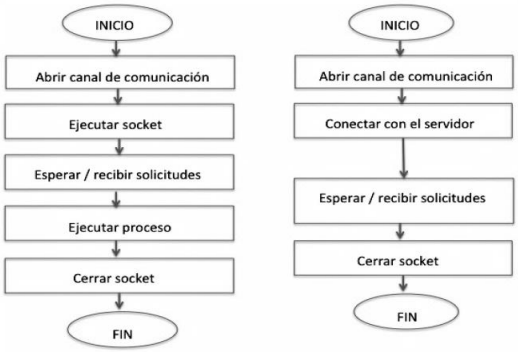

Fig. 5. Diagrama de flujo servidor (izquierdo) y cliente (derecho).

Esta función permite la instalación del servidor y la creación de la red de comunicación para el envío y recepción de los datos. El siguiente programa desarrollado es *joystick*, se encuentran disponibles versiones de Linux para enlazarse un dispositivo de juego, son programas de código abierto. Su utilizó como base un programa por eventos, cada evento es empleado para leer información de los diferentes botones del control para juego, también de esta forma es posible deshabilitar o habilitar botones. En el caso del prototipo desarrollado se utiliza el *Gamepad* modelo F710 de la marca Logitech, la configuración específica empleada, es presentada a continuación en la Tabla 1.

Tabla 1. Configuración de botones del F710

Botón	Función
B4	Mover brazo robot
B5	Mover móvil
A7	Eje Z/Angulo Θ
A3 y A4	Eje X-Y/posición x, y.
Y	Movimiento para el brazo B3

Los otros botones no fueron habilitados, por lo que aun cuando sean presionados no tendrán efecto alguno. De esta forma se evita que estos botones envíen datos a través del servidor de forma incorrecta. En este programa la opción que seleccione el operador moverá o la plataforma móvil o el brazo antropomórfico, pero no puede mover ambos a la vez por seguridad.

En la Fig. 6, se presenta el diagrama de flujo del programa, que también es ejecutado en el servidor local.

Posteriormente, se desarrolló el programa *motores*, que se encarga de la lectura de las posiciones de los actuadores y el cálculo en el sistema embebido de las leyes de control y su posterior envió a los actuadores. Este programa se realiza a través del servidor, en el cual se procesan y calculan los datos que son enviados a los diferentes actuadores que integran al manipulador móvil.

En la (Fig. 7), se observa el diagrama de flujo general de este programa.

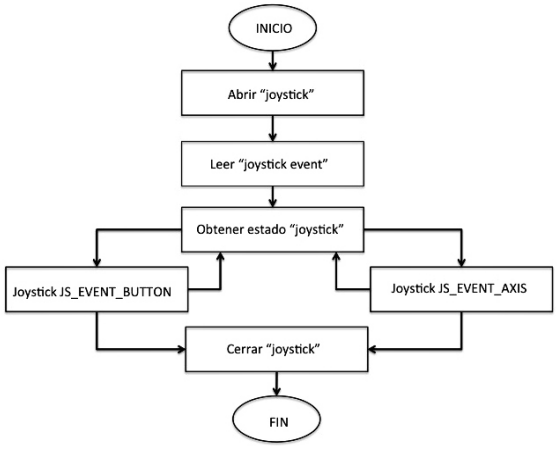

Fig. 6. Diagrama de flujo programa Joystick.

De acuerdo a la información que ingresa del programa *Joystick*, el programa *motores* determina que acción realizar, si calcular la ley de control para el desplazamiento del móvil o para el posicionamiento del brazo. Por lo cual, la operación del programa *motores* tiene dos etapas donde cada una se encarga de calcular la operación respectiva, de acuerdo al tipo de tarea que se desea que el robot realice, desplazarse o posicionar el brazo. Las dos operaciones no se pueden

realizar al tiempo dado que los modelos cinemáticos del brazo y del móvil están desacoplados.

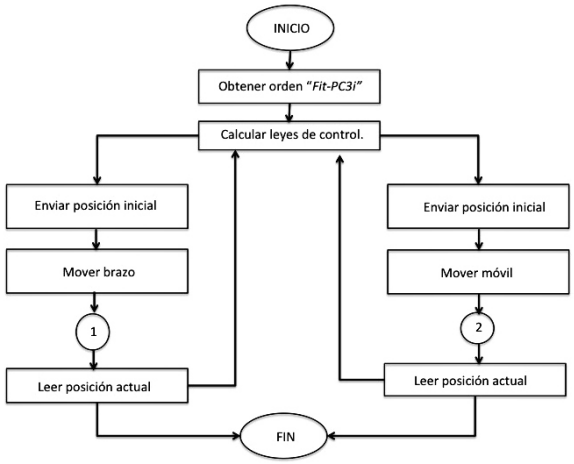

Fig. 7. Diagrama de flujo programa Motores.

La primera etapa se encarga del evaluar qué ley de control se debe calcular, es decir una vez que el control para juego envía la acción a realizar, es posible realizar la tarea de posición o seguimiento del móvil, o por otro lado enviar los valores de posición del brazo.

En la (Fig. 8) se muestra el diagrama de flujo detallado de estas opciones.

Para la opción del móvil, los algoritmos fueron desarrollados con la finalidad de convertir los valores de las leyes de control en velocidades lineal y angular para el robot, con las que se obtienen posteriormente las velocidades para la rueda derecha e izquierda que serán enviadas a los correspondientes actuadores.

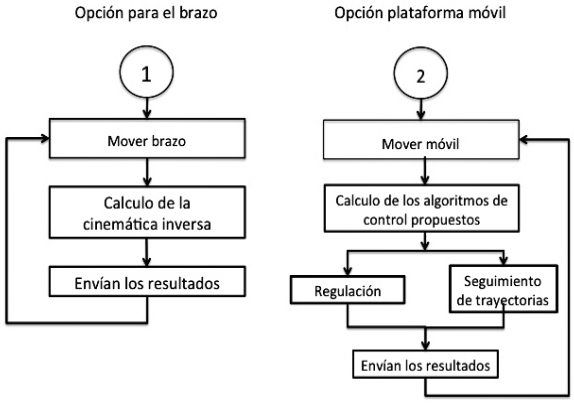

Fig. 8. Diagrama de flujo subprograma Motores.

En el caso del brazo, a partir del control de posición se le indica la posición *x*, *y*, *z* deseada y se obtienen los datos para cada actuador para lograr que el brazo realice un movimiento dentro de su espacio de trabajo.

5. RESULTADOS

Para validar los programas desarrollados y la arquitectura de hardware implementada, se realizaron diferentes pruebas al sistema por etapas, cuando se verificó su adecuado funcionamiento se integraron todos los programas y se realizó la teleoperación del manipulador móvil.

- **Comunicación Cliente-Servidor.** Se verificó que los programas para configurar el sistema como servidor-cliente operaran de manera adecuada, sobre el mismo sistema embebido.
- **Comunicación Joystick-FitPC3i.** Una vez ejecutado el servidor, se verificó que el sistema embebido reconociera el control para juego, esto por medio de la instalación previa del driver en el sistema embebido y de la conexión del nano receptor en uno de los puertos USB del Fit-PC3i.
- **Calculo de las leyes de control**. Cada uno de las leyes de control desarrolladas fueron validadas por medio de simulaciones numéricas, utilizando el software Simulink de Matlab®. Posteriormente fueron programadas una por una en el sistema embebido para verificar su efectividad.
- **Envió de datos a los actuadores.** Una vez verificado el servidor, se probaron cada uno de los programas individualmente y en conjunto en el servidor, mediante el empleo de la terminal de Linux Mint, esto a través de pruebas de comunicación. De esta manera se garantiza que los datos de movimiento de los actuadores son enviados correctamente y que la información de los encoders de los actuadores son leídos correctamente.

Con esta nueva arquitectura de hardware implementada y con el software desarrollado, fue posible operar de forma remota por medio de un Gamepad un manipulador móvil utilizando algoritmos de control en tiempo discreto, embebidos en un dispositivo de procesamiento digital en el mismo robot. Un aspecto importante en el desarrollo de este proyecto es el enfoque utilizado, donde se le da mayor énfasis al desarrollo del software, con el fin de utilizar un sistema de procesamiento digital eficaz y así eliminar tarjetas adicionales para comunicaciones y control.

Sin embargo el presente trabajo representa una opción más de diseño de control en tiempo discreto aplicado a manipuladores móviles, resaltando el uso de software libre y su implementación en un prototipo que cuenta con un sistema embebido. En trabajos como el de Vaishak, N. (2012), también se enfatiza en el usos de sistemas embebidos bajo plataformas de desarrollo en Linux, con la diferencia de que se resalta su importancia en aplicaciones de tipo industrial pero empleando un protocolo de comunicación Ethernet, dejando abierta la posibilidad de implementarse en algunas otras aplicaciones.

6. CONCLUSIONES

El control discreto debido a que ofrece mayores facilidades al momento de ser programado en un dispositivo digital, tiene como principal ventaja que el cálculo del algoritmo no está

limitado por una frecuencia de muestreo, y por lo tanto se puede implementar en una gran variedad de sistemas embebidos, lo que resulta cada vez más atractivo por la facilidad y simplicidad en la programación y por las características de hardware con que cuentan.

Los programas de control y comunicaciones se desarrollaron en C y C++, para que fueran ejecutados en el sistema embebido embarcado en el móvil; esto se logró gracias a que el sistema embebido puede ser conectado directamente a una terminal y a un monitor, razón por la cual es factible verificar la operatividad del software desarrollado. Un aspecto de gran importancia fue lograr una reducción de las tarjetas electrónicas con que contaba el prototipo previo, ya que fue factible programar funciones, que requerían un dispositivo adicional, para que el sistema embebido las realizará, obteniendo una reducción en el peso de la plataforma móvil.

Como trabajo a futuro, se prevé la implementación de cámaras en el robot, que permitan resolver el problema de regulación visual y cuya información también sea procesada en el sistema embebido por medio de la adecuación de módulos adicionales de programación, puesto que el servidor instalado permite esa conectividad.

REFERENCIAS

Bruzzonea, G., Caccia, M., Raverab, G. and Bertone, A. (2009). "Standard Linux for embedded real-time robotics and manufacturing control systems". Robotics and Computer-Integrated Manufacturing. No. 25: 178–190.

Suppiah, R. and Fauzi, M. B. A. (2014). "Introducing Embedded Systems Development on a Robotics-Based Platform". 2014 International Conference of Teaching, Assessment and Learning (TALE), pp. 103 – 108, Wellington, New Zealand, Diciembre 8-10.

Wang Z., Liu Y., Cail B., and Zhao J. (2012). "Planar Region Alignment based Visual Regulation for Mobile Robot". Proceedings of IEEE International Conference on Mechatronics and Automation, pp. 1978 – 1983, Chengdu, China, Agosto 5-8.

Chen J., Dixon W., Dawson D., and Galluzo T. (2005). "Navigation and control of a wheeled mobile robot". Proceedings of the IEEE/ASME International Conference on Advanced Intelligent Mechatronics, pp. 1145 – 1150, Monterrey, California, USA, Julio 24-28.

Hendzel Z. and Szuster M. (2011). "Discrete neural dynamic programming in wheeled mobile robot control". Commun Nonlinear Sci Numer Simulat, 16:2355 – 2362.

Horowitz, B., Liebman, J., Ma, C., Koo, T., Sangiovanni-Vincentelli, A., & Sastry, S. (2003). "Platform-based embedded software design and system integration for autonomous vehicles". Proceedings Of The IEEE, 91(1), pp. 198-211.

Sánchez-Cristo A. F., Niño-Suarez P., Portilla E., Avilés O., Villegas G., (2013). "Manipulador móvil teleoperado por un sistema de control discreto". XI Congreso Iberoamericano de Ingeniería Mecánica, CIBIM 2013. La Plata-Argentina, Noviembre 11-14.

Niño-Suárez P. A., Portilla-Flores E. A., Sánchez-Cristo A. F., Villegas-Medina G. (2012). "Manipulador móvil para rescate y exploración". XV Congreso Latinoamericano de Control Automático, CLCA 2012. Lima, Perú, Octubre 23-26.

Orosco, G. R. (2003). "Modelado, análisis y control de vehículos articulados y robots móviles. Teoría y experimentos", Tesis de doctorado. CINVESTAV.

Hernández-Oliva, Noemi, Niño-Suarez, Paola A., Portilla-Flores, Edgar A., (2014). "Esquema discreto de control de posición para teleoperación de un manipulador móvil". Second International Conference on Advanced Mechatronics, Design, and Manufacturing Technology - AMDM 2014, pp. 223-228, Bogotá Colombia, Octubre 22-24.

Hernández-Oliva, Noemi (2015). "Sistema de control de movimiento para un manipulador móvil". Tesis de Maestría en Tecnología de Cómputo. Instituto Politécnico Nacional CIDETEC.

Vaishak, N. & Ram Chandra, C. (2012). "Embedded Robot Control System Based On an Embedded Operating System, the Combination of Advanced RISC Microprocessor (ARM), DSP and ARM Linux". International Journal Of Engineering And Innovative Technology (IJEIT), 2(6), pp. 143-147.

CHAPTER 16

SIGNAL PROCESSING

Análisis de la Respuesta en Frecuencia de La Señal de Caída de Presión en el Proceso de Transporte de Fluidos.

Jenny L. Diaz C. * **Freddy Bolaños M.** **

* *Universidad Nacional de Colombia - Sede Medellín, Departamento de Procesos y Energía (e-mail: jldiazc@unal.edu.co).*
** *Universidad Nacional de Colombia - Sede Medellín, Departamento de Energía Eléctrica y Automática (e-mail: fbolanosm@unal.edu.co).*

Resumen: Durante los procesos de transporte de fluidos multifásicos con comportamientos de tipo Newtoniano y no Newtoniano, en los cuales no se dispone de sistemas de control para las entradas del proceso, son frecuentes las perturbaciones en las propiedades del fluido. Lo anterior se debe a que en este tipo de fluidos (mezcla de sólidos con agua, como las pulpas naturales por ejemplo) las propiedades dependen de la concentración, tamaño y forma de los sólidos. Así, cada vez que se presenten cambios en dichas variables, las propiedades y condiciones de flujo se ven alteradas, y por tanto, las lecturas en los sensores de presión y caudal registran valores fuera de los rangos de operación normales. Acorde con lo anterior, con este estudio se pretende desde el análisis de las señales de presión y caudal, determinar los tiempos en que ocurren perturbaciones en el sistema y se alteran las propiedades del fluido, así como identificar patrones en el espectro de frecuencias de las señales, que permitan separar los efectos de la densidad y viscosidad sobre los cambios en la caída de presión. Para tal fin, se realiza el análisis a partir de las herramientas de procesamiento digital de señales en tiempo real como la transformada de ondículas (o *Discrete Wavelet Transform* (DWT)).

Palabras claves: Flujo de fluidos, respuesta en frecuencia, espectro de frecuencias, transformada *Wavelet*.

1. INTRODUCCIÓN

Para el control del transporte de pulpas minerales a través de las diferentes unidades de procesamiento en una planta, se suelen emplear sensores de presión y caudal que permitan obtener una medición en línea de la caída de presión y el flujo volumétrico en cualquier instante de tiempo. Sin embargo, para los fluidos como las pulpas (mezcla de sólidos con agua) las variables de presión y caudal no son suficientes para implementar sistemas de control. Lo anterior se debe a que los comportamientos de tipo Newtoniano y no Newtoniano que estos fluidos presentan al fluir, limitan la precisión de la medida de las propiedades de la pulpa como densidad y viscosidad, que a su vez están directamente relacionados con la calidad del producto.

Los flujos multifásicos suelen presentar comportamientos no Newtonianos, y la caracterización de sus propiedades se encuentra restringida a la de las propiedades de cada una de las fases presentes. Hasta el momento no se le ha dado mucha importancia a la estimación en línea de las propiedades características de los fluidos multifásicos. Sin embargo, con el fin de lograr estas mediciones en línea se ha venido implementando el uso de estimadores de estado basados en modelos empíricos, que aunque logran una estimación de las propiedades, no permiten diferenciar los efectos de cada propiedad sobre la caída de presión en los procesos de flujo de fluidos a través de una tubería. Por tanto, con este trabajo se pretende identificar patrones que permitan diferenciar los efectos de densidad y viscosidad en los cambios de la caída de presión en una línea de conducción. Lo anterior a partir de modelos semifísicos de base fenomenológica para la simulación del proceso, y técnicas de procesamiento digital de señales para una señal continua, tales como transformada de ondículas (o *Wavelet*).

Para tal fin, se presenta el contexto y planteamiento del problema en la Sección 2, así cómo una breve descripción de las herramientas de procesamiento de señales empleadas en el análisis. El modelo semifísico de base fenomenológica propuesto para la simulación del proceso es presentado en detalle en la Sección 3, mientras que la metodología propuesta para el análisis de la respuesta obtenida mediante simulación es presentada en la Sección 4. Finalmente, los resultados y conclusiones obtenidos a partir de las herramientas empleadas, con base en la metodología ya mencionada, son introducidos en las secciónes 5 y 6, respectivamente.

2. TRANSPORTE DE PULPAS MINERALES EN TUBERÍAS.

En la gran mayoría de procesos industriales es común encontrar tramos de línea de conducción o tuberías, por

los cuales están circulando fluidos de dos o más fases. A este tipo de flujos, en el que coexisten dos o más fases, se les conoce como fluidos multifásicos. Un ejemplo típico de este tipo de fluidos se puede evidenciar en las plantas de procesamiento de minerales y alimentos. En estas industrias, es común procesar el material de interés con agua (generalmente) para formar una pulpa o lechada, la cual es transportada a las diferentes unidades de procesamiento donde se realiza el tratamiento correspondiente. Así, en las plantas de procesamiento de minerales se suele denominar como pulpa a la mezcla de partículas sólidas (materia prima de interés) suspendidas en un líquido.

El carácter multifásico de los fluidos puede deberse al origen mismo del fluido, o a una condición operativa de la línea de conducción. El primer caso hace referencia a la fuente, es decir, cuando en un tanque previo a la línea las materias primas son adicionadas para formar una mezcla, o existen cambios de fase. La condición operativa por su parte, hace referencia a los cambios de fase que se producen al variar alguna de las condiciones de transporte en la línea, como por ejemplo temperatura o presión, que pueden causar cambios de fase parciales durante el transporte del fluido. Con base en lo anterior, y dada la importancia de las líneas de conducción como parte fundamental de las plantas de procesamiento, resulta necesario identificar y estudiar los aspectos relevantes del fenómeno que interesan desde la ingeniera de procesos. Dichos aspectos, se refieren a comprender cómo están viajando los fluidos y cuanta energía se requiere para hacerlos mover (ΔP) entre las diferentes unidades de operación (Benretem et al., 2010).

Las propiedades de los fluidos multifásicos afectan directamente el comportamiento reológico de estos y el cálculo de la caída de presión (ΔP) cuando fluyen. Así, la importancia de la reología en el estudio del comportamiento de fluidos al interior de una tubería, radica principalmente en que dependiendo de la cantidad y forma de los sólidos, los efectos inerciales de las partículas pueden o no dominar las propiedades de la mezcla. En el caso en que se tiene partículas muy grandes, los efectos inerciales dominan y la viscosidad aparente de la mezcla será muy similar a la del líquido. Por lo tanto, se puede presentar asentamiento de las partículas al interior de la tubería formando un flujo heterogéneo. Caso contrario se tiene cuando las partículas son muy finas, puesto que la presencia de estos sólidos usualmente produce un incremento significativo en la viscosidad de la mezcla comparado con la del líquido transportador. Al interior de la tubería, en este tipo de fluidos no se depositan las partículas y resultan en flujo homogéneo, pero pasan de un comportamiento de tipo Newtoniano a no Newtoniano (He et al., 2004).

Todos los factores mencionados anteriormente, relacionados al cálculo de las propiedades de las pulpas o fluidos multifásicos condicionan los procesos de transporte, y por tanto cualquier variación en dichas propiedades se puede ver reflejada como cambios bruscos en las variables de operación, tales como la caída de presión en la línea y caudal o flujo volumétrico. Estas últimas son consideradas normalmente en las plantas de procesamiento, dado que no se dispone de dispositivos confiables y de costo moderado para la medición directa de las propiedades de interés de las pulpas, como su densidad y viscosidad. De aquí, se tiene que para modelar y representar adecuadamente el comportamiento de estos fluidos al interior de una tubería, se deben identificar las propiedades de mezcla correctamente y conocer los factores que limitan el transporte de estas al interior de una tubería.

Diferentes estudios se han desarrollado para la estimación de las propiedades de densidad y viscosidad de fluidos usando técnicas de procesamiento digital de señales. Algunos de estos estudios se han enfocado en la estimación de estas propiedades a través de montajes a nivel de laboratorio, pero no se han encontrado trabajos en que se lleve este análisis desde el dominio de la frecuencia, en tiempo real y para estimaciones en línea. Los resultados obtenidos en los trabajos de Abdallah et al. (2013), Heinisch et al. (2015), Manzaneque et al. (2014) y Eris et al. (2015), se basan en la aproximación a sistemas resonantes para la determinación de las propiedades del fluido mediante la identificación de la frecuencia de corte (w_c) y el factor de calidad (Q) para la respuesta en frecuencia. Sin embargo, y con un análisis previo de la señal disponible en el proceso de transporte de fluidos a lo largo de una línea, no fue posible identificar o reconocer un comportamiento resonante.

Para el caso de procesamiento de señales continuas, existen diferentes técnicas factibles de implementar en tiempo real, las cuales suministran información suficiente para ser analizada en línea. Algunas de estas, cómo *Wavelet* y la transformada de Fourier en tiempo corto *STFT*, permiten obtener la información espectral de señales no estacionarias (Shensa, 1992). Esta última técnica se basa en la división de la señal original en porciones finitas, sobre las cuales se aplica la transformada de Fourier para obtener la información de los componentes espectrales en el momento en que ocurren (Flórez et al., 2009). Sin embargo, y dado el principio de incertidumbre de Heisenberg, la STFT presenta problemas de resolución tiempo-frecuencia para los cuales se han desarrollado técnicas basadas en análisis de multiresolución (Martínez and Castto, 2002).

De otro lado, la transformada *Wavelet* (TW) se fundamenta en el análisis multiresolución, en el cual la señal es analizada para diferentes frecuencias con diferentes resoluciones (resolución variable), y así dar respuesta a los problemas en resolución de la transformada STFT. Con la transformada *Wavelet* es posible obtener representaciones adecuadas de las señales tanto en el dominio temporal como en el de la frecuencia de manera simultánea, permitiendo identificar los momentos de ocurrencia para determinadas componentes espectrales, como por ejemplo los cambios en estado estacionario o transitorios. Así, el principio de operación de la transformada *Wavelet* consiste en una serie de etapas de filtrado y decimación de la señal de interés. De lo anterior, al aplicar la TW a una señal, se está realizando un proceso de filtrado en el dominio temporal usando filtros paso-bajo y paso-alto que se encargan de eliminar bajas o altas frecuencias de la señal según corresponda. Este proceso se repite para las señales resultantes del proceso anterior, y se conoce

como etapa de descomposición. El número de veces que se repite el proceso de filtrado para la señal original, corresponde al número de niveles de descomposición de la señal, obteniendo como resultado un grupo de señales a diferentes bandas de frecuencia que representan la misma señal.

Computacionalmente la TW se evalúa de forma discreta, mediante la transformada *Wavelet* discreta (DWT). Esta última se basa en el análisis multiresolución o algoritmo piramidal, para la descomposición de las señales en tiempo discreto, y obtener una representación tiempo-escala de esta (Shensa, 1992). Es decir, la representación tiempo-escala se obtiene mediante procesos sucesivos de filtrado de la señal. Para esto, la secuencia discretizada de la señal es pasada por un filtro paso-bajo (de media banda), eliminando las componentes de frecuencia superiores a la mitad del ancho de banda de la señal original. En este tipo de análisis se emplean filtros de diferentes frecuencias de corte, los cuales permiten el análisis de la señal en diferentes escalas (Shensa, 1992), (Mallat, 1989) . En la Figura 1 se muestra una representación gráfica del proceso de descomposición de una señal usando un banco de filtros con diferentes frecuencias de corte.

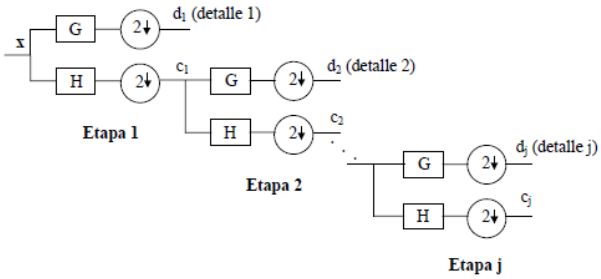

Fig. 1. Banco de filtros para la etapa de descomposición y analisis de la señal. H corresponde al filtro paso-bajo y G al filtro paso-alto. (Martínez and Castto, 2002).

De acuerdo con lo anterior, se define la transformada *Wavelet* discreta como,

$$C[j,k] = \sum_{n \in Z} f[n] \Psi_{j,k}[n] \tag{1}$$

con $C[j,k]$ los coeficientes de la transformada, $f[n]$ la señal discreta y $\Psi_{j,k}[n]$ la función de transformada Wavelet madre. Existen diferentes versiones en la literatura de esta última función que pueden ser consultadas en trabajos como los de Meyer (1993), Mallat (1989) y Shensa (1992). Los subíndices j,k se refieren a la localización en tiempo y frecuencia o escala. De acuerdo con lo anterior, la *Wavelet* se expresa acorde con la siguiente ecuación:

$$\Psi_{j,k}[n] = 2^{-\frac{j}{2}} \Psi[2^{-j} n - k] \tag{2}$$

Finalmente, y posterior al proceso de descomposición y análisis, la señal es sintetizada de acuerdo con la ecuación 2, conocida como transformada inversa.

$$f[n] = \sum_{j \in Z} \sum_{k \in Z} C[j,k] \Psi_{j,k}[n] \tag{3}$$

En los trabajos de Meyer (1993), Mallat (1989) y Shensa (1992) se explica con detalle la deducción de la transformada *Wavelet*, así como el procedimiento de cálculo, características y formas de representación, diferentes al banco de filtros.

3. MODELO DEL PROCESO PARA EL FLUJO DE FLUIDOS EN TUBERÍAS.

Para la simulación del proceso de transporte de pulpas minerales a través de una línea de conducción, se desarrolló un modelo semifísico de base fenomenológica para el proceso presentado en la Figura 2. En dicho proceso se considera un fluido de dos fases correspondiente a una mezcla de sólidos con agua. La fase solida corresponde a partículas de un material arcilloso de diferentes diámetros, mientras que para la fase líquida o medio transportador se considera agua, dada su disponibilidad a nivel industrial. En el diagrama de proceso el fluido es transportado de una unidad de procesos U-1, que para este casa de estudio corresponden a una bomba o máquina impulsora, hasta otra unidad de proceso cualquiera. La consideración anterior es debida a que los sensores de presión se encuentran localizados a la salida de la bomba (presión de descarga) y la salida de la tubería, justo antes de la siguiente unidad de proceso (U-2).

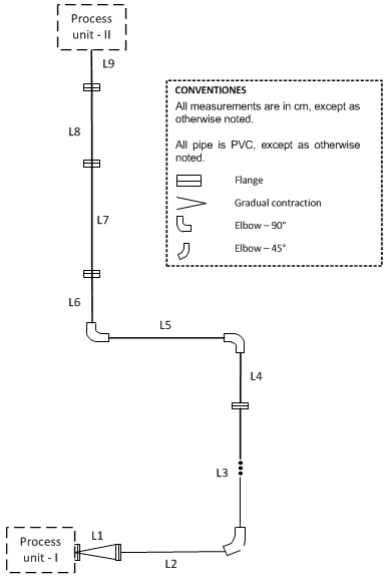

Fig. 2. Diagrama de flujo de proceso para el flujo de una pulpa mineral.

Adicional a los sensores de presión se dispone de un medidor de caudal que permite conocer el flujo volumétrico en la línea en cualquier momento. Así, este valor se considera como una entrada al modelo de flujo. Este último se constituye por un balance de energía mecánica (BEM) entre los puntos de entrada y salida del fluido en la tubería, además de ecuaciones constitutivas para el cálculo de las pérdidas de energía que experimenta el fluido debidas al rozamiento con las paredes y entre las diferentes capas de fluido. Dichas ecuaciones se presentan a continuación:

- **Balance de energía mecánica:**

$$P_2 = P_1 + \rho_{Pulp} * g * (z_1 - z_2) + \rho_{Pulp} * h_{f_{1-2}} \quad (4)$$

- **Número de Reynolds:**

$$Re = \frac{v * D_T * \rho_{Pulp}}{\mu} \quad (5)$$

- **Pérdidas de energía por fricción:**

$$h_{f_{1-2}} = (K_{Line} + \Sigma K_F) \frac{Q^2}{2 * A_T} \quad (6)$$

- **Factor k de pérdidas:** A partir del método de las 2K (Hooper, 1981) :

Para tramos de tubería,

$$K_{Line} = f_D * \frac{D_T}{L_T} \quad (7)$$

Mientas que para accesorios en la línea se tiene:

$$K_F = \frac{K_1}{Re} - K_\infty \left(1 + \frac{1}{ID_T(in)}\right) \quad (8)$$

Con K_1 and K_∞ Tomados del trabajo de Hooper (1981).

- **Factor de Fricción:**

$$f_D = \left\{-2 * log\left[\frac{\epsilon/D_T}{3.1} - \frac{5.02}{Re} log\left(\frac{\epsilon/D_T}{3.71} + \frac{14.5}{Re}\right)\right]\right\}^{-2} \quad (9)$$

Con base en las ecuaciones presentadas anteriormente y los valores de densidad, viscosidad y flujo volumétrico, obtenidos directamente en planta, se determinó la presión de salida del sistema (P2) teniendo en cuenta que la presión de descarga de la bomba se mantuvo constante en un valor de $P1 = 326328Pa$, con lo cual es posible obtener la caída de presión en la línea. Para la simulación del proceso se consideró ruido en la medición de caudal, y se realizaron diferentes perturbaciones en las propiedades de densidad y viscosidad del fluido. Lo anterior con el fin de observar cambios en la caída de presión.

A continuación se presentan los resultados obtenidos para la caída de presión en la línea, a partir de valor de presión de salida obtenido del balance de energía mecánica para el proceso de transporte de la pulpa, en el arreglo de tuberías accesorios presentado en la Figura 2. Para el desarrollo de la simulación se consideró un tiempo de simulación total de 200 segundos y un tamaño de paso igual a $h = 0.1s$. Cabe resaltar que el tamaño de paso fue seleccionado con base en el tiempo de muestreo de los sensores disponibles para la operación real. Durante la simulación se introdujeron cuatro perturbaciones al sistema, en diferentes tiempos para los valores de densidad y viscosidad de la pulpa. En la Tabla 1 se presentan el resumen de los parámetros considerados en la simulación.

Tabla 1. Parámetros de simulación

Parámetro	Símbolo	Valor de la perturbación
Tiempo de simulación	t_s	200 s
Periodo de muestreo	h	$0.1s$
Número iteraciones	Num_{Ite}	2000
Perturbación 1 (ρ)	$P_{1,\rho}$	$\rho = 0.5\%\rho_0$ en $t = 20s$
Perturbación 2 (ρ)	$t_{2,\rho}$	$\rho = 0.8\%\rho_0$ en $t = 100s$
Perturbación 3 (μ)	$t_{1,\mu}$	$\mu = 0.025Pa - s$ en $t = 140s$
Perturbación 4 (μ)	$t_{2,\mu}$	$\mu = 0.045Pa - s$ en $t = 140s$

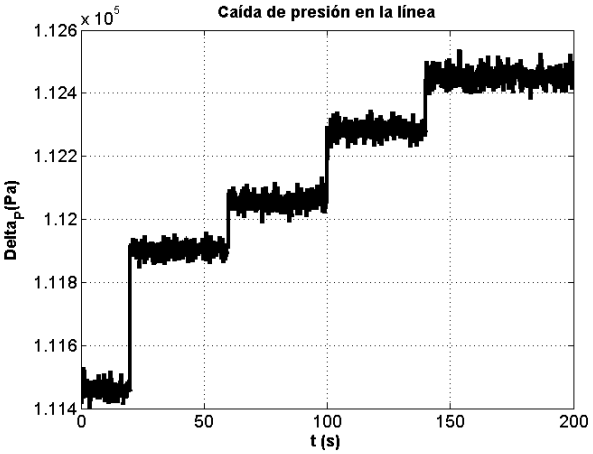

Fig. 3. Caída de presión para el fluido en la línea.

A partir del resultado de la figura 3 es posible observar la variación temporal de la caída de presión, y por tanto de la presión de salida que experimenta el fluido ante perturbaciones en las propiedades de la pulpa mineral (fluido de proceso), tales como densidad y viscosidad. De aquí se tiene que, aumentos en los valores de densidad y viscosidad conllevan a una caída de presión mayor debido a que se requiere más energía para movilizar o transportar el fluido a través de la línea o tubería. Para el caso del flujo volumétrico de pulpa mineral en la línea, esta variable que se mantuvo constante durante el ensayo.

4. METODOLOGÍA PARA EL ANÁLISIS DE LA RESPUESTA EN FRECUENCIA.

A partir de los resultados obtenidos mediante simulación para la caída de presión en la línea de conducción, y teniendo en cuenta que los valores de caudal, densidad y viscosidad de fluido son entradas al modelo, se elaboró una metodología para analizar la respuesta del sistema, en el dominio de la frecuencia, ante variaciones en las propiedades de densidad y viscosidad del fluido.

Con base en el objetivo principal de este trabajo, relacionado con la identificación en el dominio de la frecuencia de patrones que permitan distinguir la procedencia de los cambios en la caída de presión, se introdujeron perturbaciones al sistema como cambios en la densidad y viscosidad de la pulpa. Lo anterior, debido a que se quiere conocer cuándo los cambios de la caída de presión son debidos a variaciones en la densidad o cuándo se deben a cambios en la viscosidad, es decir, separar dichos efectos en la señal de presión. En la Figura 4 se presenta la metodología empleada en el análisis.

Acorde con la descripción presentada de la transformada *Wavelet*, para el cálculo de esta a una señal continua se propone implementar una estimación por tramos de la señal. Para tal fin, se define previamente un intervalo de tiempo sobre el cual se realizará el análisis, y con base en este y el periodo de muestreo (predefinido o del equipo de medición) se determina el número de itera-

ciones (Num_{Ite}). Posteriormente se determina la presión de salida conociendo ρ_P, μ_P y Q_P en cada iteración i, lo anterior con el fin de determinar la caída de presión del fluido en la línea. Adicional, y previo a la implementación se selecciona el tipo de *Wavelet* y el número de niveles en los que se desea descomponer la señal para el cálculo de la DWT. La selección del tipo de *Wavelet* y número de niveles se realiza con base el objetivo del análisis, dado que dependiendo del tipo que se seleccione se fijará la resolución temporal, y con base en los niveles se determinará las bandas de frecuencia, y por tanto la resolución en este dominio. Para el caso desarrollado en este trabajo, se evaluó el comportamiento de diferentes tipos de transformada *Wavelet* con el fin de identificar cual de estas permitía tener una buena resolución temporal, teniendo en cuenta que los tiempos de perturbación al sistema son conocidos. Para el caso de los niveles, se probaron diferentes valores entre 2 - 6, y se seleccionó aquel que permitiera establecer diferencias entre los dos tipos de perturbaciones aplicadas al sistema. De lo anterior, para la implementación de la DWT se seleccionó la función madre *Daubechies 2*, la cual además de sus propiedades de ortogonalidad y asimetría, permitió cumplir con el objetivo del presente trabajo. Para más detalle acerca de la función *Wavelet* seleccionada y sus propiedades se recomienda consultar los trabajos de (Mallat, 1989), (Meyer, 1993) .

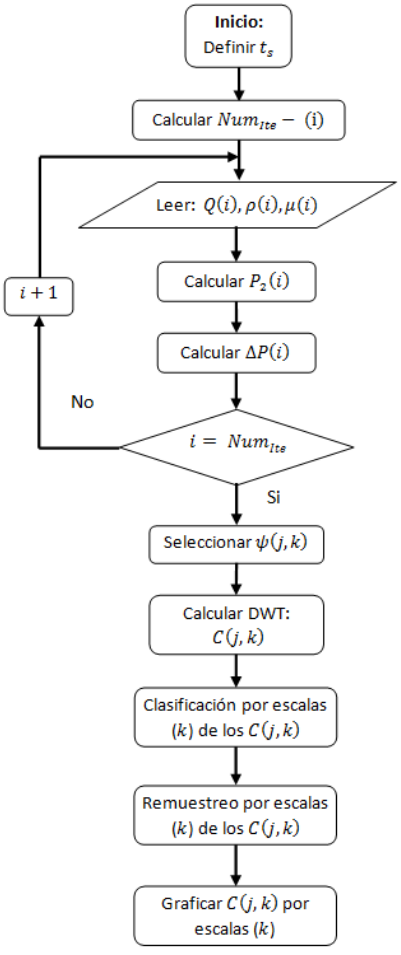

Fig. 4. Metodología para la obtención de la respuesta en frecuencia mediante la DWT.

Después de seleccionar los parámetros para el cáluclo de la DWT, se verifica que la longitud de la señal sea igual al tiempo de simulación seleccionado para el análisis ($i = Num_{Ite}$), y se procede a calcular la transformada *Wavelet* discreta, con lo cual se obtienen los coeficientes de la transformada acorde al tipo de *Wavelet* y niveles seleccionados. Luego, se realiza un tratamiento de los resultados previo a obtener el resultado gráfico de la DWT. Teniendo en cuenta que la descomposición de la señal se realiza a diferentes frecuencias de corte, y en cada nivel la longitud de las señales corresponde con la mitad de la señal en el nivel anterior, se deben separar los coeficientes por escala (k) y posteriormente realizar un proceso de remuestreo para llevar cada señal al tamaño de la señal original. Finalmente se gráfican los resultados de los coeficientes para su correspondiente escala.

5. RESULTADOS.

Con el fin de ilustrar el análisis de la respuesta en frecuencia para la señal de caída de presión de un fluido ante perturbaciones en sus propiedades (densidad y viscosidad), se presenta en las Figura 5 la respuesta del sistema ante una perturbación tipo impulso en la densidad y en la viscosidad. Para este caso, se consideró como entrada únicamente una de las propiedades dejando la otra constante.

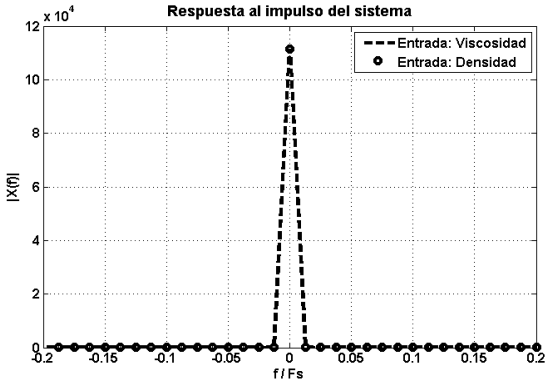

Fig. 5. Respuesta al impulso del sistema (modelo) ante diferentes pertubaciones.

De la figura anterior se puede observar que la respuesta del sistema ante perturbaciones de origen diferente, responde de la misma forma concentrada la información relevante a frecuencias muy bajas. De lo anterior se justifica el uso de la transformada *Wavelet* discreta (DWT) para lograr identificar el origen de las perturbaciones en el sistema, que se traducen en cambios en la caída de presión para fluido transportado. Es decir, dado el carácter de las perturbaciones y su relación directa para la predicción de la caída de presión, se sabe que cambios en esta última se encuentra asociados a cambios en las propiedades del sistema, pero dada la naturaleza de los fluidos analizados en este caso en que las propiedades dependen de diversos factores, como las propiedades individuales de las fases, no resulta fácil identificar cual de las propiedades es la que esta cambiando, pues como se mencionó en la sección 2, cada propiedad es afectada de forma diferente por las propiedades de las fases individuales.

En la Figura 6 se presenta el cálculo de la transformada de Fourier para la señal de caída de presión, y el espectro después de un proceso de filtrado para eliminar la frecuencia $f = 0Hz$ asociada al estado estacionario o DC del sistema utilizando un filtro *Notch*. De aquí es posible observar que toda la información no está concentrada sólo en $f = 0Hz$, y hay otras frecuencias con magnitud significativa. A partir de los resultados presentados previamente, la metodología expuesta y el modelo de proceso planteado, se presentan los resultados obtenidos mediante simulación del flujo de la pulpa mineral en la línea, teniendo en cuenta los parámetros de la Tabla 1. Los resultados presentados fueron obtenidos usando el *software Matlab*.

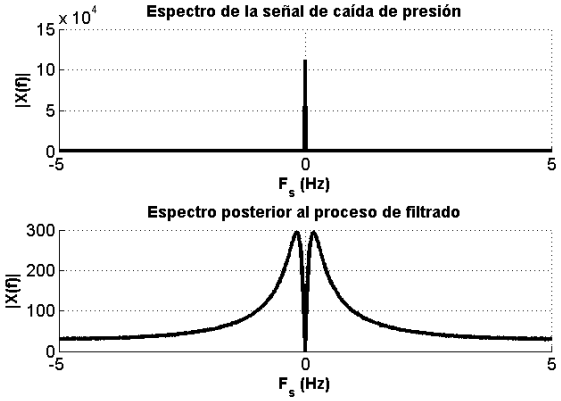

Fig. 6. Espectro para la señal de caída de presión, y la señal filtrada, para el tiempo total de simulación.

En la Figura 7 se presentan los niveles de detalle (4) y la aproximación o residuo para la señal de caída de presión, obtenidos usando la transformada *Wavelet* ($a_1(n)$). En esta, la figura superior (DP_1) corresponde a valores de altas frecuencias o primer nivel de detalle, mientras que las siguientes gráficas representan los tres niveles de detalles restantes, organizadas en orden decreciente respecto a las bandas de frecuencia. De aquí es posible apreciar que para el caso de las frecuencias más bajas ($a_1(n)$) no se dispone de información significativa, este mismo caso se presentan en el cuarto nivel de detalle (DP_4), donde a pesar de registrarse pequeñas oscilaciones no se logra reconocer ningún patrón. Para el caso del segundo y tercer nivel de detalle (DP_2, DP_3) se distinguen oscilaciones de magnitud mayor respecto a los anteriores, por tanto se presenta en la Figura 8 una ampliación del tercer nivel con el fin de identificar patrones que permitan diferenciar las perturbaciones. Finalmente, en el segundo nivel de detalle es posible identificar unos pequeños picos en los mismos tiempos en que fueron introducidas las perturbaciones al sistema. Para un mejor análisis de estos resultados se presenta en la Figura 9 una ampliación del resultado para el segundo nivel de detalle.

De la Figura 8 se logran identificar picos de magnitud significativa en los tiempos en que se realizaron las perturbaciones al sistema ($t_1 = 20s, t_2 = 60s, t_3 = 100s$ y $t_4 = 140s$), lo cual permite identificar los momentos de aparición de las perturbaciones con buena resolución temporal. Aunque para el caso de la primera perturbación en $t_1 = 20s$ para la densidad, la magnitud es considerablemente mayor que para el resto de las perturbaciones, no es posible diferenciar cuando una perturbación es debida a densidad y cuando se debe a variaciones en la viscosidad desde este nivel detalle. Lo anterior se puede justificar analizando la segunda perturbación tanto en densidad y viscosidad, $t_3 = 100s$ y $t_4 = 140s$ respectivamente, los cuales presentan magnitudes muy similares posterior al cálculo de la transformada *Wavelet*.

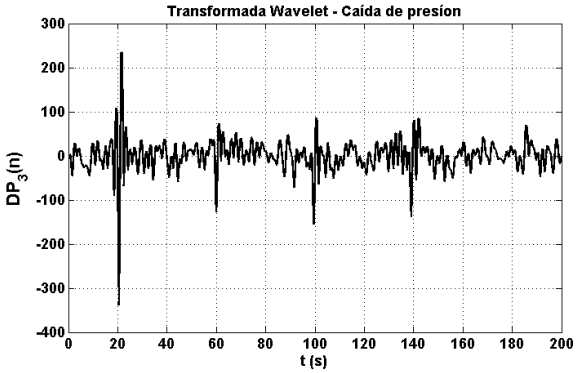

Fig. 8. Tercer nivel de detalle para la transformada *Wavelet* de la caída de presión.

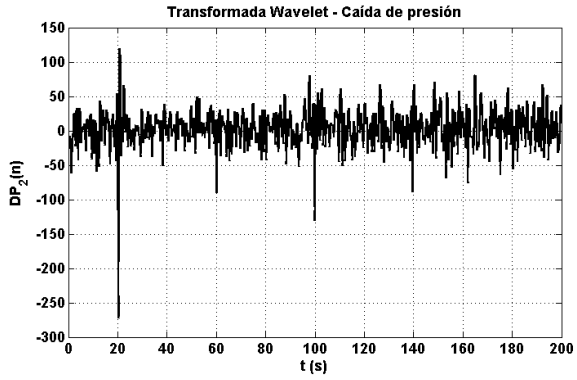

Fig. 9. Segundo nivel de detalle para la transformada *Wavelet* de la caída de presión.

Desde un análisis individual para el segundo nivel de detalle se puede reconocer que sólo las perturbaciones en la densidad del fluido alcanzan valores por encima de -100 en el eje de ordenadas, mientras que las perturbaciones en viscosidad no alcanzan a diferenciarse del resto de las oscilaciones presentes. De aquí, se tiene que un análisis para el segundo y tercer nivel de detalle, podría ser una herramienta útil para la identificación de los momentos de ocurrencia de perturbaciones en el sistema, que además permita caracterizar el origen de las perturbaciones. Así, de acuerdo con lo anterior se podría establecer como criterio que las perturbaciones que se logren reconocer a las frecuencias que corresponden a la banda del segundo nivel de detalle, están directamente asociadas a cambios en la densidad del fluido. Es decir, mediante un criterio basado en umbrales, en el que se pueda hacer la distinción entre las perturbaciones, cuando la señal de detalle sobrepase determinado valor. En el trabajo de Michel Misiti et al.

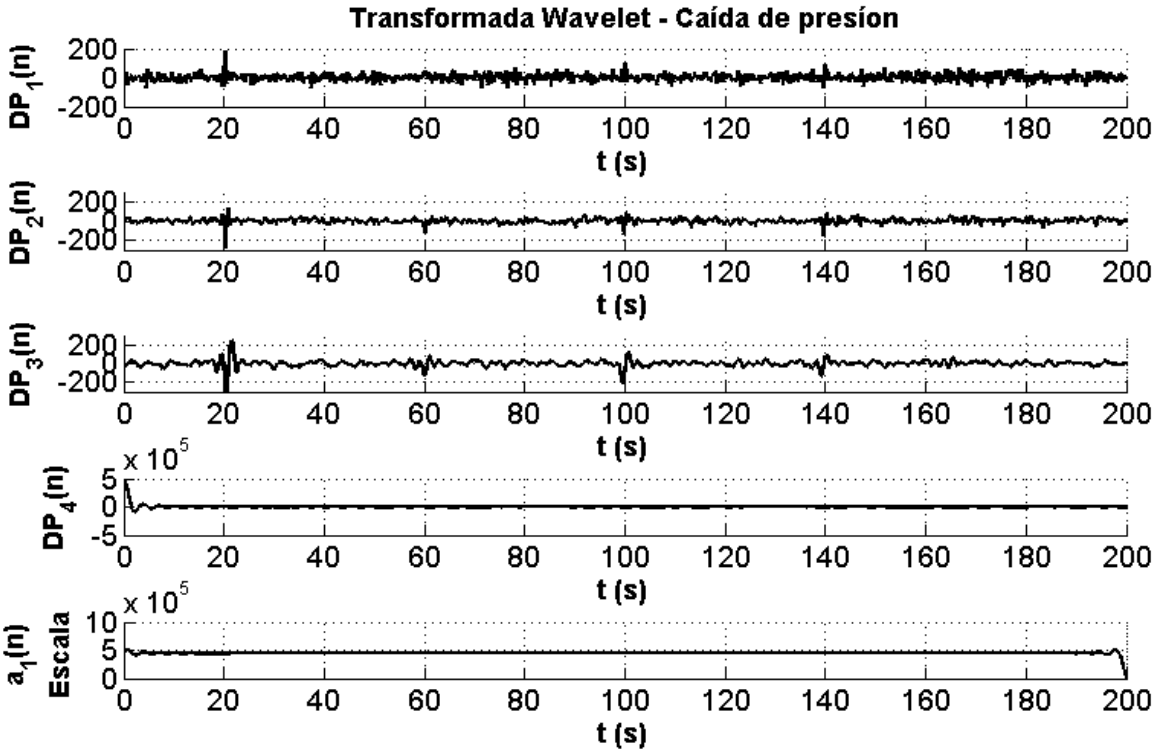

Fig. 7. Descomposición por niveles usando la transformada *Wavelet* para la señal de caída de presión.

(2003) se presenta un ejemplo de lo mencionado, en el que se usa el criterio de umbrales para el filtrado de ruido en diversas aplicaciones.

6. CONCLUSIONES.

Con base en los resultados obtenidos y partiendo del conocimiento de la dificultad que se tiene para separar los efectos de la densidad y la viscosidad sobre la caída de presión de un fluido fluyendo, el análisis en frecuencia resulta ser una herramienta de gran ayuda para la identificación de patrones que permita diferenciar dichos efectos, que desde el dominio temporal no son posibles de reconocer, cuando no se dispone de equipos de medición o estimadores para todas las variables de interés de un proceso. Este caso resulta muy frecuente en los procesos de transporte de fluidos multifásicos, para los cuales no se dispone de dispositivos confiables, o para el caso de que se cuente con ellos, implican altos costos dado los ambientes fuertemente erosivos de los fluidos como las pulpas minerales.

Dentro de las herramientas útiles para el análisis en frecuencia de una señal continua, la transformada *Wavelet* discreta resulta ventajosa frente a otras herramientas, debido a sus propiedades de multiresolución y fácil implementación, que permiten no sólo reconocer los momentos en que hay cambios en la señal de interés, sino que con una selección adecuada de los parámetros de cálculo para la transformada (tales como el número de niveles y la función *Wavelet* madre), permiten obtener una primera aproximación para diferenciar el origen de dichos cambios.

Lo anterior es posible, si se conoce cuales son las variables susceptibles a perturbaciones, que además pueden generar cambios en el proceso.

Basados en lo anterior, y a partir de los resultados obtenidos para los coeficientes de la transformada *Wavelet*, en los cuales es posible distinguir patrones referentes a cada una de las perturbaciones realizadas, es posible proponer dentro de trabajos futuros una implementación en línea. Esta última utilizando la metodología propuesta, pero cambiando en cada instante de tiempo el vector de tiempo a analizar. Es decir, tomando como entrada los valores registrados por los sensores de presión y flujo en el proceso real, y desplazando el vector conforme transcurre el tiempo. Así, a partir de esto también es posible desarrollar un protocolo de detección de perturbaciones, con base en el perfilado de las componentes *Wavelet* de la señal de caída de presión. Dicho protocolo puede estar basado en un método de umbrales o cualquier otro que permita separar el ruido de la señal de los cambios debidos a las perturbaciones.

7. AGRADECIMIENTOS

Los autores agradecen a la Universidad Nacional de Colombia Sede Medellín, por su apoyo en la realización de este trabajo.

REFERENCIAS

Abdallah, A., Heinisch, M., and Jakoby, B. (2013). Measurement error estimation and quality factor improvement of an electrodynamic-acoustic resonator

sensor for viscosity measurement. *Sensors and Actuators A: Physical*, 199, 318 – 324. doi: http://dx.doi.org/10.1016/j.sna.2013.05.033.

Benretem, A., Benidir, M., and Chaib, R. (2010). Factors influencing slurry rheology. *World Pumps*, 2010(7), 30 – 32. doi:http://dx.doi.org/10.1016/S0262-1762(10)70199-1.

Eris, G., Bozkurt, A.A., Sunol, A., Jon, A., Kiraz, A., Alaca, B.E., and Erkey, C. (2015). Determination of viscosity and density of fluids using frequency response of microcantilevers. *The Journal of Supercritical Fluids*, 105, 179 – 185. doi: http://dx.doi.org/10.1016/j.supflu.2015.04.012. Special Issue of the 14th European Meeting on Supercritical Fluids.

Flórez, E., Cardona, S., and Jordi, L. (2009). Selección de la ventana temporal en la transformada de fourier en tiempos cortos utilizada en el análisis de señales de vibración para determinar planos en las ruedas de un tren. *Revista Facultad de Ingeniería Universidad de Antioquia*, 145 – 158.

He, M., Wang, Y., and Forssberg, E. (2004). Slurry rheology in wet ultrafine grinding of industrial minerals: a review. *Powder Technology*, 147(13), 94 – 112. doi: http://dx.doi.org/10.1016/j.powtec.2004.09.032.

Heinisch, M., Voglhuber-Brunnmaier, T., Reichel, E., Dufour, I., and Jakoby, B. (2015). Application of resonant steel tuning forks with circular and rectangular cross sections for precise mass density and viscosity measurements. *Sensors and Actuators A: Physical*, 226, 163 – 174. doi:http://dx.doi.org/10.1016/j.sna.2015.02.007.

Hooper, W.B. (1981). The two-k method predicts head losses in pipe fittings. *Chemical Engineering*, 17, 96–100.

Mallat, S.G. (1989). A theory for multiresolution signal decomposition: the wavelet representation. *IEEE Transactions on Pattern Analysis and Machine Intelligence*, 11(7), 674–693. doi:10.1109/34.192463.

Manzaneque, T., Ruiz-Dez, V., Hernando-Garca, J., Wistrela, E., Kucera, M., Schmid, U., and Snchez-Rojas, J.L. (2014). Piezoelectric resonator-based oscillator for density and viscosity sensing. *Sensors and Actuators A: Physical*, 220, 305 – 315. doi: http://dx.doi.org/10.1016/j.sna.2014.10.002.

Martínez, J. and Castto, R.D. (2002). *Anlisis de la teoría de ondículas orientada a las aplicaciones en ingeniería eléctrica: Fundamentos*. E.T.S.I Industriales, Dpt. de Ingeniería Eléctrica.

Meyer, Y. (1993). *Wavelets and Operators*, volume 1. Cambridge University Press. Cambridge Books Online.

Michel Misiti, Y.M., Oppenheim, G., and Poggi, J.M. (2003). *Wavelets and their Applications*. Hermes Science/Lavoisier.

Shensa, M.J. (1992). The discrete wavelet transform: wedding the a trous and mallat algorithms. *IEEE Transactions on Signal Processing*, 40(10), 2464–2482. doi:10.1109/78.157290.

Cifrado caótico simétrico de ECG y EEG para aplicaciones en telemedicina

Murillo-Escobar M.A. * **Cardoza-Avendaño L.** **
López-Gutiérrez R.M. ** **Cruz-Hernández C.** *

* *Centro de Investigación Científica y de Educación Superior de Ensenada (CICESE), Ensenada, BC, México.*
** *Facultad de Ingeniería, Arquitectura y Diseño, Universidad Autónoma de Baja California (UABC), Ensenada, BC, México.*

Resumen: Recientemente, la telemedicina establece una conexión entre pacientes en casa y médicos en un centro clínico con el uso de sistemas de telecomunicación y dispositivos de monitoreo fisiológico. Sin embargo, la transmisión de información a través de un canal inseguro como internet o almacenamiento de datos privados, genera un problema de seguridad. La confidencialidad de la información es uno de los retos más importantes en telemedicina, donde sólo pacientes y doctores autorizados, deben tener acceso a los archivos médicos o clínicos. Por otra parte, los sistemas caóticos han sido implementados eficientemente en sistemas criptográficos para brindar alta confidencialidad a información en imágenes, texto, datos biométricos, entre otros. En este trabajo, se propone un novedoso esquema de cifrado caótico simétrico basado en dos mapas logísticos y una ronda de permutación-difusión para la protección de información clínica de electrocardiogramas ECG y electroencefalogramas EEG, tanto para su transmisión y almacenamiento de forma segura en aplicaciones de telemedicina. Las señales electrofisiológicas utilizadas en el cifrado son adquiridas de la base de datos PhysioBank. En contraste con esquemas recientes presentados en la literatura, se propone un algoritmo criptográfico novedoso validado con un análisis de seguridad, en base en simulaciones en MatLab para mostrar su eficiencia, seguridad criptográfica y su potencial uso en aplicaciones de telemedicina.

Palabras clave: cifrado, telemedicina, caos, mapa logístico, análisis de seguridad, señales electrofisiológicas.

1. INTRODUCCIÓN

El término telemedicina significa medicina a distancia y consiste en proveer servicios de atención sanitaria a distancia con el uso de tecnologías de la información y de la comunicación, con el objetivo de intercambiar datos para diagnósticos, tratamientos y prevenir enfermedades, así como para actividades de investigación y evaluación, con el fin de mejorar la salud de las personas y de las comunidades donde viven, WHO (1998).

Debido al crecimiento tecnológico en las últimas décadas, la telemedicina ofrece servicios médicos de forma remota a través de sistemas de telecomunicaciones y dispositivos de monitoreo fisiológico. Este esquema brinda servicios de salud de forma conveniente para aquellos pacientes que están discapacitados o no pueden asistir al hospital debido a cualquier razón. Sin embargo, la telemedicina presenta peligros potenciales en el intercambio de la información. Información personal y datos clínicos de pacientes son transmitidos a través de canales inseguros como internet, por lo que se genera un problema de seguridad de autentificación y confidencialidad. En la tabla 1, se presentan algunas de las ventajas y desventajas de la telemedicina presentadas por Vergeles-Blanca (2011).

Tabla 1. Algunas ventajas y desventajas de telemedicina.

Ventajas	
	Mejor accesibilidad de los pacientes.
	Mejora la gestión de la demanda.
	Reducción de las estancias hospitalarias.
	Disminución de los desplazamientos.
	Mejor comunicación entre profesionales.
Desventajas	
	Intercambio de información sensible.
	Compromiso de la confidencialidad.
	Compromiso de la seguridad
	Gran volumen de información almacenada.

Las señales electrofisiológicas humanas son utilizados comúnmente en telemedicina para determinar el estado o anomalías en pacientes, como déficit en frecuencia cardíaca, arritmias o taquicardias en electrocardiogramas ECG (señal eléctrica del corazón en el orden de los milivolts), o por otra parte, para detectar epilepsia o funciones cognitivas como perdida de memoria o concentración mediante electroencefalogramas EEG (señales eléctricas

* Agradecemos al CONACYT, por el apoyo económico brindado a través del proyecto de Grupos de Investigación en Ciencia Básica, Ref. 166654.
**Autor de correspondencia: Cruz-Hernández C. Tel.: +52.646.1750500, Fax:+52.646.1750554, CICESE, Ensenada, B.C., México. (correo electrónico: *ccruz@cicese.mx*)

generadas por el cerebro en el orden de los microvolts), Torres-García *et al.* (2013).

Uno de los objetivos de la criptografía es brindar confidencialidad, donde básicamente un algoritmo criptográfico convierte texto claro a texto cifrado, con el uso de una clave secreta que sólo personas autorizadas conocen. Por otra parte, los sistemas caóticos presentan propiedades estrechamente relacionadas con buenos procesos en criptografía, como en difusión (cambiar el valor de texto claro), permutación (cambiar la posición del texto claro), amplio espacio de claves, complejidad del sistema fuente y pseudoaleatoriedad, Alvarez y Li (2006). Es por ello, que en los últimos años se han propuesto varios esquemas de cifrado caótico para biometría, imágenes y texto, ver Cui (2010), Murillo-Escobar *et al.* (2015a), Murillo-Escobar *et al.* (2015b), Patidar *et al.* (2009), Zhou *et al.* (2014), Khan *et al.* (2007) y Murillo-Escobar *et al.* (2014a).

En la literatura, se han presentado varios esquemas de autentificación paciente-médico para telemedicina basados en dos factores de seguridad (cifrado caótico y tarjetas inteligentes) o tres factores de seguridad (cifrado caótico, tarjetas inteligentes y biometría), por ejemplo en Jiang *et al.* (2014), Xie *et al.* (2013), Lu *et al.* (2015), Yan *et al.* (2013) y Chaudhry *et al.* (2015). Sin embargo, los esquemas de autentificación propuestos y el respectivo análisis de seguridad se presentan de forma descriptiva a nivel global de autentificación, sin detalles criptográficos del algoritmo de cifrado, ni un análisis de seguridad criptográfico basado en resultados numéricos. Debido a que se omiten detalles del cifrado caótico y consecuentemente el análisis de seguridad correspondiente, la seguridad del cifrado no es verificado ni validado.

Algunos avances de cifrado caótico de datos clínicos se han presentado en la literatura. Recientemente, se han propuesto esquemas de cifrado de señales clínicas como EEG y ECG, basado en mapas caóticos como logístico y Henon, sin embargo todos ellos carecen de un análisis de seguridad básico como espacio de claves, sensibilidad a la clave, sensibilidad a la señal clara, histogramas, correlación, análisis diferencial con NPCR y UACI, tiempo de cifrado, entre otros, para demostrar y validar el sistema criptográfico propuesto, ver por ejemplo Lin (2016), Lin *et al.* (2014), Chen *et al.* (2012), Sufi *et al.* (2011), Lin y Wang (2011) y Parveen *et. al* (2011).

En este trabajo, se presenta un novedoso algoritmo criptográfico simétrico basado en dos mapas logísticos con distribución mejorada, una ronda de permutación-difusión, y una clave secreta de 128 bits representada por 32 caracteres hexadecimales para brindar confidencialidad a información clínica en aplicaciones de telemedicina, particularmente para la transmisión segura de ECG y EEG. El proceso general del algoritmo se basa en trabajos recientes presentados en Murillo-Escobar *et al.* (2015a) y Murillo-Escobar *et al.* (2015b), en donde se cifra imagen a color RGB y plantilla de huella dactilar, respectivamente. La principal diferencia radica en el pre-procesamiento propuesto (transformación) sobre la señal clara para que el algoritmo realice el adecuado cifrado de cualquier tipo de señal electrofisiológica sin importar su naturaleza o su amplitud. Se presenta un análisis de seguridad básico basado en simulaciones en MatLab y se muestra que el esquema propuesto es seguro y eficiente para su uso en telemedicina.

La organización del trabajo es de la siguiente forma: en la Sección 2 se muestran los detalles del algoritmo de cifrado caótico propuesto. Los resultados experimentales y análisis de seguridad se presentan en la Sección 3, con base a simulaciones en MatLab. Finalmente, las conclusiones son mencionadas en la Sección 4.

2. ALGORITMO DE CIFRADO PROPUESTO

La arquitectura implementada en el algoritmo de cifrado propuesto utiliza dos procesos llamados permutación y difusión. Estos procesos consisten en cambiar tanto la posición como el valor de cada uno de los elementos de la señal clara, con base a secuencias caóticas generadas por el mapa logístico.

El mapa logístico es un mapa uni-dimensional ampliamente utilizado en crecimiento de poblaciones biológicas, comportamiento complejo, generadores de números pseudoaleatorios y criptografía caótica, May (1976). En este trabajo, el mapa logístico es implementado como fuente de secuencias caóticas, el cual esta descrito matemáticamente como sigue

$$x_{i+1} = a x_i (1 - x_i), \tag{1}$$

donde $i = 1, 2, ..., j$ representa el número de iteraciones, $x_i \in (0, 1)$ es el estado del sistema, con la condición inicial $x_0 \in (0, 1)$, parámetro de control $a \in (3.999, 4)$ para garantizar secuencias caóticas y evitar ventanas periódicas, Pareek *et al.* (2006).

Se conoce que los sistemas caóticos uni-dimensionales presentan desventajas criptográficas como poco espacio de claves secretas, distribución no uniforme de datos caóticos, rangos caóticos discontinuos, entre otros, Arroyo *et al.* (2008). Sin embargo, estos mapas de baja dimension también son sumamente atractivos por su simple estructura que requiere poca memoria y operaciones aritméticas para generar datos de forma eficiente, Cristian-Iulian y Vasile-Gabriel (2007). Por lo tanto, en el algoritmo propuesto, se implementan operaciones para eliminar dichas desventajas con base a trabajo reciente en Murillo-Escobar *et al.* (2015a) y Murillo-Escobar *et al.* (2015b).

Las señales electrofisiológicas tales como el ECG y EEG son adquiridas de una base de datos de PhysioBank ATM, Physionet.org (2016). Las muestras corresponden a señales reales tanto en amplitudes como en tiempo. La duración de las señales obtenidas son de 10 segundos con distinta frecuencia de muestreo F_s (de 100 Hz para ECG y 160 Hz para EEG, ver fig. 1). La señal de ECG es obtenida de la base de datos "Apnea-ECG database (apnea-ecg)" y señal "a01" con duración de 10 segundos. En el caso del EEG, se obtiene de la base de datos "EEG Motor Movement/Imagery Dataset (eegmmidb)", grabación "S001/S001R01" y senal "Fc5" con duracion de 10 segundos. A diferencia del trabajo presentado en Cardoza *et al.* (2016), donde se capta la señal clínica de pulsos cardíacos directamente del paciente a través de un fotopletismógrafo y posteriormente es cifrada, el presente trabajo se enfoca únicamente en el cifrado de señales electrofisiológicas humanas y no en la medición directa del paciente.

Se considera como señal clara a toda aquella señal filtrada, amplificada y digitalizada, la cual puede ser de distintos tipos como electrocardiograma ECG, electroencefalograma EEG, electromiograma EMG, electroretinograma ERG, electrofonograma EPG, electrooculograma EOG, entre otros, cuyas frecuencias de muestreo puede variar. Por otra parte, el algoritmo tienen la capacidad para cifrar cualquier tipo de señal electrofisiológica de cualquier amplitud con poco o mucho ruido, esto por la transformación que lleva la señal antes de ser cifrada. Sin embargo, señales electrofisiológicas con mucho ruido no son útiles para la toma de decisiones, por lo que es de vital importancia que las señales estén bien filtradas antes del cifrado. Se define como señal clara a $P \in \mathbb{R}$ compuesta por dos vectores que corresponden a la amplitud A y al tiempo t en segundos, ambos con una longitud de datos $\ell = F_s t$. El algoritmo de cifrado se aplica únicamente al vector A y consiste en los pasos descritos a continuación.

Paso 1 (definir la clave secreta): Se utiliza una clave secreta de 128 bits definida por 32 caracteres hexadecimales de la misma forma presentada en Murillo-Escobar *et al.* (2015a), ver tabla 2. Esta se divide en cuatro secciones para la inicialización de secuencias caóticas de dos mapas logísticos. Además, con este procedimiento, se elimina el espacio de claves pequeño que presentan los mapas uni-dimensionales.

Paso 2 (transformación): El sistema criptográfico (digital) obtiene la señal clara y determina máximos-mínimos para transformar las amplitudes de la misma en amplitudes con valores entre (0,1). Para obtener esta nueva señal clara transformada, se determina el valor mínimo de A con $P_{min} = min\ (A)$, donde $P_{min} \in \mathbb{R}$ es un escalar que representa el valor mínimo en A y min representa la función para determinar el valor mínimo en A. También, se encuentra el valor máximo en A con $P_{max} = max\ (A)$, donde $P_{max} \in \mathbb{R}$ es un escalar que representa el valor máximo en A y max representa la función para determinar el valor máximo en A. Después, se determina la siguiente transformación

$$AT = \frac{A - (P_{min} - 0.01)}{P_{max} + 0.01}, \tag{2}$$

donde AT representa la señal clara transformada en valores entre (0,1) de longitud ℓ.

Paso 3 (valor Z): Todos los valores de la señal clara transformada AT se suman con datos caóticos del mapa logístico 2 iterado $I = \ell + 100$, con a_2 y x_{2_0} de la tabla 2. Los elementos de AT y datos caóticos se suman como sigue

$$Z = Z + \left(AT_i + x^{L2}_{I+1-i}\right)\ \ mod\ 1, \tag{3}$$

donde $i = 1, 2, 3, \ldots, \ell$, $Z \in (0, 1)$ es una variable inicializada en cero para incrementar la seguridad y tiene una precisión decimal de 10^{-15}, AT_i son los elementos de la señal clara transformada, x^{L2} es la secuencia caótica del mapa logístico 2 (se toman los últimos ℓ valores) y mod es la operación de módulo.

Paso 4 (cifrado): El mapa logístico 1 es iterado $T = \ell + 1000$ con a_1 y x_{1_0} como se muestra en tabla 2. Se determina una secuencia para permutación y otra para difusión con (4) y (5), respectivamente.

$$P_i = \ round\left(x^{L1}_{T-\ell+i} * (\ell - 1)\right) + 1, \tag{4}$$

donde $i = 1, 2, 3, \ldots, \ell$, $P \in [1, \ell]$ es el vector pseudoaleatorio de permutación y $round$ es la operación de redondeo al valor más cercano. Sin embargo, P contiene valores repetidos que son determinados por software y reemplazados por los faltantes de forma automática para incrementar la seguridad. El vector para el proceso de difusión se determina de la siguiente forma

$$D_i = \left\{\left(x^{L1}_{T-\ell+i} * 1000\right) + Z\right\}\ \ mod\ 1 \tag{5}$$

donde $i = 1, 2, 3, \ldots, \ell$; $D_i \in (0, 1)$. La multiplicación por 1000 se utiliza para obtener una distribución de datos del mapa logístico más uniforme, lo que ayuda a incrementar la seguridad, Murillo-Escobar *et al.* (2015a). Finalmente, el proceso de cifrado se realiza con la siguiente operación

$$C_i = (AT(P_i) + D_i)\ \ mod\ 1, \tag{6}$$

donde $i = 1, 2, 3, \ldots, \ell$ y $C \in (0, 1)$ es la señal cifrada (criptograma) con precisión decimal de 10^{-15}.

Paso 5 (Agregar datos): El valor de P_{min}, P_{max} y Z son agregados al final del criptograma en la siguiente forma
$C_{\ell+1} = Z$,
$C_{\ell+2} = 1$ si $P_{min} < 0$ o $C_{\ell+2} = 0$ si $P_{min} \geq 0$,
$C_{\ell+3} = abs(P_{min})/100000$,
$C_{\ell+4} = 1$ si $P_{max} < 0$ o $C_{\ell+4} = 0$ si $P_{min} \geq 0$,
$C_{\ell+5} = abs(P_{max})/100000$,
donde abs representa el valor absoluto.

Descifrado: El proceso de descifrado consiste en invertir todos los pasos del cifrado. Para ello, se debe obtener del criptograma los valores Z, P_{min} y P_{max}. Con el uso de exactamente la misma clave secreta (a nivel de bits), calcular los vectores pseudoaleatorios P y D de la misma forma en que en el paso 4. El proceso de descifrado se determina como sigue

$$D(P_i) = (C_i - D_i)\ \ mod\ 1, \tag{7}$$

donde $i = 1, 2, 3, \ldots, \ell$, y $D \in (0, 1)$ es la señal clara transformada descifrada. Para obtener la señal clara con amplitudes originales, se escala D con el uso de P_{min} y P_{max}.

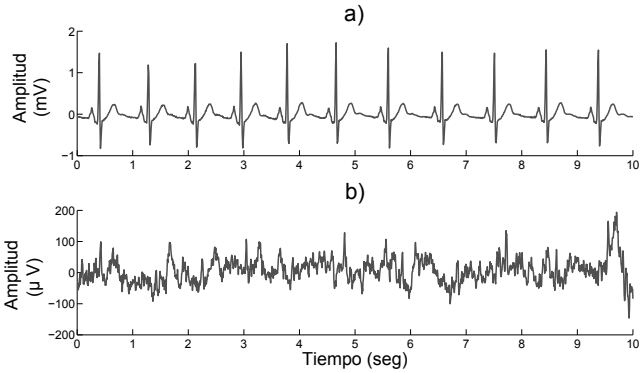

Figura 1. Señales electrofisilógicas adquiridas de PhysioBank. a) ECG de persona saludable y b) EEG canal Fc5.

Tabla 2. Llave secreta y su distribución en dos mapas logísticos, Murillo-Escobar *et al.* (2015a).

3. RESULTADOS EXPERIMENTALES

Un algoritmo de cifrado caótico debe presentar excelentes propiedades de pseudoaleatoriedad en la información

Llave secreta	Parámetro de control	Condición inicial
32 dígitos hexadecimal	$H_1, H_2, \ldots, H_{32}$ donde $H \in [0-9, A-F]$	
cálculos	$A = \frac{(H_1, H_2, \ldots, H_8)_{10}}{2^{32}+1}$ $B = \frac{(H_9, H_{10}, \ldots, H_{16})_{10}}{2^{32}+1}$	$C = \frac{(H_{17}, H_{18}, \ldots, H_{24})_{10}}{2^{32}+1}$ $D = \frac{(H_{25}, H_{26}, \ldots, H_{32})_{10}}{2^{32}+1}$
logístico 1	$a_1 = 3.999 + (\alpha_1 * 0.001)$ $\alpha_1 = (A + B + Z)\ mod\ 1$	$x1_0 = \beta_1\ mod\ 1$ $\beta_1 = C + D + Z$
logístico 2	$a_2 = 3.999 + (\alpha_2 * 0.001)$ $\alpha_2 = (A + B)\ mod\ 1$	$x2_0 = \beta_2\ mod\ 1$ $\beta_2 = C + D$

cifrada y además, poseer características intrínsecas para resistir los ataques criptoanalíticos como búsqueda exhaustiva, análisis estadístico, análisis diferencial, entre otros que pueden quebrantar un sistema criptográfico basado en caos, Alvarez y Li (2006).

En esta sección, se muestran algunos análisis de seguridad sobre el esquema de cifrado propuesto como espacio de claves, sensibilidad a la clave secreta secreta, sensibilidad a la señal clara, histogramas, correlación y tiempo de cifrado. Se utiliza programación en MatLab v7.6(R2008a) en una laptop con AMD Turion 2.0 GHz, 3.18 GB RAM y Windows XP 32 bits. Además, se implementa aritmética tipo *double* punto flotante para obtener una presición de 10^{-15} decimales.

En la fig. 2, se muestra la señal cifrada de ECG y EEG mostrados en la fig. 1, respectivamente. Se utiliza como clave secreta "1122334455667788990AABBCCDDEEFF" en ambos casos. Es importante observar que ambos criptogramas a transmitir tiene valores entre (0,1).

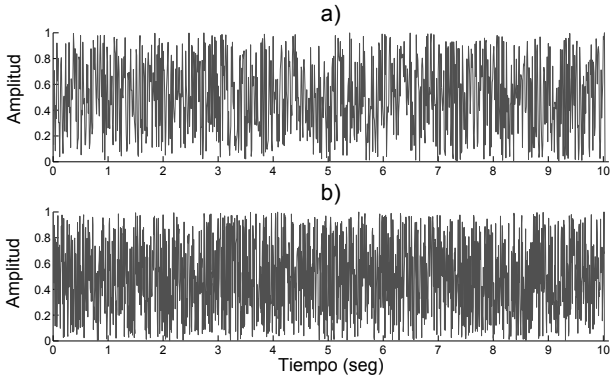

Figura 2. Señales cifradas con el algoritmo propuesto. a) ECG y b) EEG.

3.1 Ataque exhaustivo

El ataque exhaustivo consiste en probar cada una de las posibles claves secretas hasta encontrar la señal clara. Para que el sistema criptográfico pueda resistir a este tipo de ataque, en la actualidad se requiere de al menos 2^{100} posibles combinaciones, Alvarez y Li (2006). En el cifrado propuesto, se tienen 2^{128} posibles combinaciones por lo que se considera que el esquema propuesto puede resistir este tipo de ataque.

3.2 Sensibilidad a la clave secreta

Un sistema criptográfico debe presentar alta sensibilidad a mínimos cambios en la clave secreta para que genere criptogramas muy distintos si dos claves secretas muy parecidas son utilizadas. Esto aporta seguridad contra ataques diferenciales, donde se busca alguna relación entre dos o más criptogramas cifrados con claves secretas muy parecidas. En la tabla 3, se muestra el coeficiente de correlación (determinado con Eq. (8)) entre tres criptogramas de electrocardiogramas ECG1, ECG2 y ECG3, y la correlación entre tres criptogramas de electroencefalogramas EEG1, EEG2 y EEG3, generados por tres claves secretas "1122334455667788990AABBCCDDEEFF", "1122334**5**556677889900AABBCCDDEEFF" y "1122334455667788990AAB**C**CCDDEEFF". Con base a los resultados, la correlación entre criptogramas es muy cercano a cero, lo que indica prácticamente nula correlación entre criptogramas y alta sensibilidad a la clave secreta.

$$Corr = \frac{N \times \sum_{i=0}^{N}(x_i \times y_i) - \sum_{i=0}^{N} x_i \times \sum_{i=0}^{N} y_i}{\sqrt{\left(N \times \sum_{i=0}^{N}(x_i)^2 - \left(\sum_{i=0}^{n} x_i\right)^2\right) \times \left(N \times \sum_{i=0}^{N}(y_i)^2 - \left(\sum_{i=0}^{n} y_i\right)^2\right)}} \quad (8)$$

donde x y y corresponden a los valores del criptograma 1 y criptograma 2, respectivamente, y N representa la longitud. El valor de $Corr \in (-1, 1)$, donde "0" indica nula correlación.

Tabla 3. Sensibilidad a la clave secreta.

Criptograma	Correlación
ECG1 vs ECG2	0.0084
ECG2 vs ECG3	-0.0047
ECG2 vs ECG3	-0.0222
EEG1 vs EEG2	0.0068
EEG2 vs EEG3	-0.0040
EEG2 vs EEG3	0.0008

3.3 Sensibilidad a la señal clara

Además de la alta sensibilidad a la clave secreta, un sistema criptográfico también debe poseer alta sensibilidad a pequeños cambios en la señal clara. Para mostrar este efecto, se generan dos criptogramas C_1 y C_2 de dos señales claras muy parecidas con el uso de la misma clave secreta. En la fig. 3 se muestran dos señales claras para el caso de ECG, donde únicamente el elemento 100 (en 1 segundo) es modificado por una milésima. Para determinar que tan distintos son ambos criptogramas, se utilizan dos cálculos llamados NPCR (tasa de cambio de pixel neto) y UACI (intensidad de cambio promedio unificado), con la ecuación (9) y (11), respectivamente.

$$NPCR = \frac{\sum_{i=1}^{i=\ell} W(i)}{\ell} \times 100 \quad (9)$$

donde

$$W(i) = \begin{cases} 0 & \text{si } C_1(i) = C_2(i) \\ 1 & \text{si } C_1(i) \neq C_2(i) \end{cases} \quad (10)$$

y

$$UACI = \frac{100}{\ell} \sum_{i=1}^{i=\ell} |E_1(i) - E_2(i)| \quad (11)$$

En la tabla 4, se muestra el resultado de este análisis. Se determina que la diferencia entre ambos criptogramas son de más del 99 % y tienen una diferencia en magnitud del 33 % en promedio aproximadamente, para ECG y EEG.

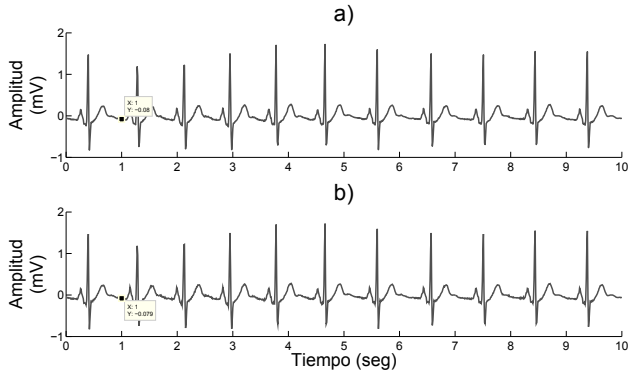

Figura 3. Señales muy parecidas para análisis diferencial. a) ECG y b) Mismo ECG con cambio en 1 seg.

Tabla 4. Sensibilidad a la señal clara.

Señal	NPCR	UACI
ECG	99.6019	33.3286
EEG	99.7507	32.9186

3.4 Histogramas

Un criptograma con distribución uniforme ayuda a resistir ataques estadísticos. Un proceso de difusión eficiente puede aportar robustez ante este tipos de ataques. Una forma visual de observar esta característica es a través de histogramas, donde se puede observar gráficamente la forma estadística de una señal. En la fig. 4 se muestran los histogramas de las señales claras de ECG y EEG, respectivamente. Mientras que en la fig. 5 se presentan los histogramas de las señales cifradas. Debido a que el algoritmo criptográfico propuesto posee un proceso de difusión eficiente, el histograma de las señales cifradas son uniformes, lo que aporta robustez ante ataques estadísticos.

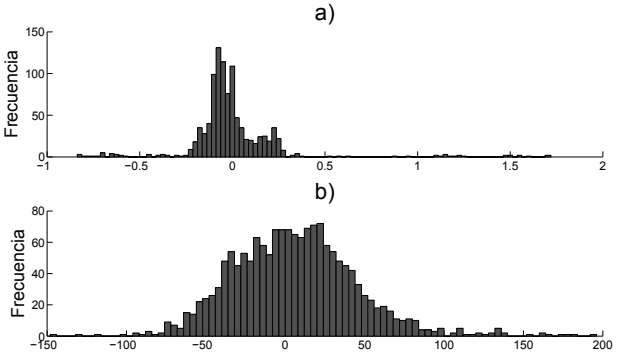

Figura 4. Histogramas de señal clara. a) ECG y b) EEG.

3.5 Tiempo de cifrado

Las aplicaciones de telemedicina requieren interacción entre paciente-médico en tiempo real. Por este motivo, el tiempo de cifrado y descifrado debe ser mínimo para disminuir el retraso en la transmisión de datos. Con base en simulaciones en MatLab y la función Tic-Toc, se determina el tiempo para cifrar y descifrar señales electrofisiológicas con el algoritmo propuesto en este trabajo. La señales utilizadas tienen 1000 datos en ECG y 1600 datos en EEG, con duración de 10 segundos. En la tabla 5 se presenta

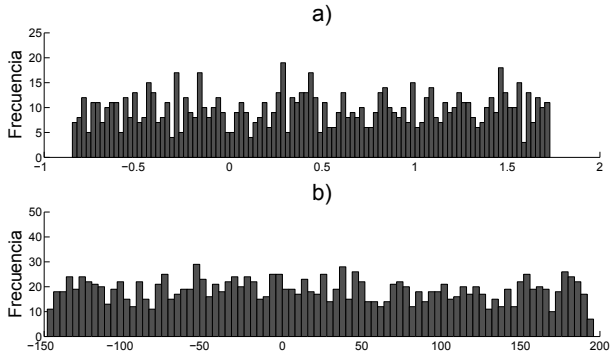

Figura 5. Histogramas de señal cifrada. a) ECG y b) EEG.

el tiempo que requiere cifrar y descifrar señales con las características mencionadas.

Tabla 5. Tiempo de cifrado y descifrado.

Señal	Cifrado (seg)	Descifrado (seg)
ECG	0.0960	0.1086
EEG	0.1587	0.1648

3.6 Análisis de comparación

En contraste con esquemas similares en la literatura, en este trabajo se presenta algunos análisis de seguridad que validan el algoritmo criptográfico propuesto para su uso en telemedicina. En la tabla 6 se presenta una comparación a nivel descriptivo, donde se muestran las ventajas y desventajas de la implementación propuesta.

Tabla 6. Comparación con esquemas similares en literatura.

	Esquema propuesto	Lin (2016)	Lin *et al.* (2014)	Chen *et al.* (2012)
Tipo de señal	ECG y EEG	EEG	EEG	ECG
Adquisición	PhysioBank	UCI KDD	NTOU	Sensado
Sistema caótico	Logístico	Logístico	Logístico	Logístico y Hénon
Espacio de claves	√	-	-	√
Histogramas	√	-	-	√
Correlación	√	√	-	-
Sensibilidad a clave secreta	√	-	√	-
Sensibilidad a señal clara	√	-	-	-
Error cuadrado medio MSE	-	√	-	-
Tiempo de cifrado	√	-	√	-
Desviación de porcentaje residual	-	-	√	-

4. CONCLUSIONES

Se presento un algoritmo criptográfico basado en mapa logístico para aplicaciones en telemedicina y se motró la eficiencia y seguridad criptográfica en ECG y EEG, mediante un análisis de seguridad básico como espacio de claves secretas, sensibilidad a la clave secreta, sensibilidad a la señal clara, histogramas y tiempo de cifrado. Los resultados indican que el algoritmo propuesto puede ser aplicado en telemedicina para el monitoreo remoto de señales electrofisiológicas de forma segura.

Otros análisis de seguridad, análisis estadísticos y mediciones métricas sobre la calidad de cifrado, deben ser aplicados en el esquema propuesto en este trabajo para incrementar la confiabilidad en aspectos de seguridad, como análisis de autocorrelación, frecuencia flotante, análisis estadístico de pseudoaleatoriedad con NIST, error medio cuadrado MSE, ataque de sólo texto claro

elegido/conocido, ataque de ruido, entre otros. Además, implementar otras señales clínicas electrofisiológicas como electromiogramas EMG, eletrooculogramas EOG o electroretinogramas ERG. También, mostrar la confidencialidad de información generada por esfignomanómetros digital (presión sanguínea), estetoscopio digital (aoscultación en arterias y órganos), oximetro de pulso (saturacion de oxigeno en la sangre), desmatoscopio digital (observación de la piel), sistemas de ultrasonido, entre otros.

REFERENCIAS

Alvarez G. y Li S. (2006). Some Basic Cryptographic Requirements for Chaos-Based Cryptosystems. *International Journal of Bifurcation and Chaos*, 16(8), 2129-2151.

Arroyo D., Alvarez G., and Fernandez V. (2008). On the inadequacy of the logistic map for cryptographic applications. *X Reunión Espanola sobre Criptología y Seguridad de la Información*, 77-82.

Cardoza L., López R.M., Murillo M.A., Mendez R. and Cruz C. (2016). Secure Transmission of Biomedical Information. *IEEE Latin America Transactions*, sometido.

Chaudhry S.A., Mahmood K., Naqvi H. y Khan M.K. (2015). An improved and secure biometric authentication scheme for telecare medicine information systems based on elliptic curve cryptography. *Journal of Medical Systems*, 39(175), 1-12.

Chen C.-K., Lin C.-L., Chiang C.-T. y Lin S.-L. (2012). Personalized information encryption using ECG signals with chaotic functions. *Information Sciences*, 193, 125–140.

Cristian-Iulian R. y Vasile-Gabriel I. (2007). Aspects regarding chaotic maps hardware implementations. *Revue Roumaine Des Sciences Techniques*, 52, 219-227.

Cui D. (2010). A Novel Fingerprint Encryption Algorithm Based on Chaotic System and Fractional Fourier Transform. *International Conference on Machine Vision and Human-machine Interface*, 168-171.

Inzunza-González E. y Cruz-Hernández C. (2013). Double Hyperchaotic Encryption for Security in Biometric Systems. *Nonlinear Dynamics and Systems Theory*, 13(1), 55-68.

Jiang Q., Ma J., Lu X. y Tian Y. (2014). Robust chaotic map-based authentication and key agreement scheme with strong anonymity for telecare medicine information systems. *Journal of Medical Systems*, 38(12), 1-8.

Khan M.K., Zhang J. y Tian L. (2007). Chaotic secure content-based hidden transmission of biometric templates. *Chaos, Solitons & Fractals*, 32, 1749-1759.

Lin C.-F. (2016). Chaotic visual cryptosystem using empirical mode decomposition algorithm for clinical EEG signals. *Journal of Medical Systems*, 40(52), 1-10.

Lin C.-F., Shih S.-H. y Zhu J.-D. (2014). Chaos based encryption system for encrypting electroencephalogram signals. *Journal of Medical Systems*, 38(49), 1-10.

Lin C.F. y Wang, B.S.H. (2011). A 2D chaos-based visual encryption scheme for clinical EEG signals. *Journal of Marine Science and Technology*, 19(6), 666-672.

Lu Y., Li L., Peng H., Xie D. y Yang Y. (2015). Robust and efficient biometrics based password authentication scheme for telecare medicine information systems using extended chaotic maps. *Journal of Medical Systems*, 39(65), 1-10.

May R.M. (1976). Simple mathematical models with very complicated dynamics. *Nature*, 261, 459-467.

Murillo-Escobar M.A., Abundiz-Pérez F., Cruz-Hernández C. y López-Gutiérrez R.M. (2014a). A novel symmetric text encryption algorithm based on logistic map. *Proceedings of the International Conference on Communications, Signal Processing and Computers*, 49-53.

Murillo-Escobar M.A., Cruz-Hernández C., Abundiz-Pérez F., y López-Gutiérrez R.M. (2014b). Cifrado caótico de plantilla de huella dactilar en sistemas biométricos. *Congreso Latinoamericano de Control Automático 2014*, 18-23.

Murillo-Escobar M.A., Cruz-Hernández C., Abundiz-Pérez F., López-Gutiérrez R.M., y Acosta Del Campo O.R. (2015a). A RGB image encryption algorithm based on total plain image characteristics and chaos. *Signal Processing*, 109, 119-131.

Murillo-Escobar M.A., Cruz-Hernández C., Abundiz-Pérez F., y López-Gutiérrez R.M. (2015b). A robust embedded biometric authentication system based on fingerprint and chaotic encryption. *Expert Systems with Applications*, 42, 8198-8211.

Pareek N.K., Patidar V. y Sud K.K. (2006). Image encryption using chaotic logistic map. *Image and Vision Computing*, 24, 926-934.

Patidar V., Pareek N.K. y Sud K.K. (2009). A new substitution-diffusion based image cipher using chaotic standard and logistic maps. *Communications in Nonlinear Science and Numerical Simulation*, 14, 3056-3075.

Parveen S., Parashar S. y Izharuddin (2011). Technique for providing security in medical signals. *International Conference on Multimedia, Signal Processing and Communication Technologies*, 68-71.

Physionet.org (2016). PhysioBank ATM. *Online*, disponible en: https://physionet.org/cgi-bin/atm/ATM [citado 20 Mayo 2016].

Sufi F., Han F., Khalil I. y Hu J. (2011). A chaos-based encryption technique to protect ECG packets for time critical telecardiology applications. *Security and Communication Network*, 4, 515–524.

Torres-García A.A., Reyes-García C.A., Villaseñor-Pineda L. Y Ramírez-Cortés J.M. (2013). Análisis de señales electroencefalográficas para la clasificación de habla imaginada. *Revista Mexicana de Ingeniería Biomédica*, 34(1), 23-39.

Vergeles-Blanca J.M. (2011). La telemedicina. Desarrollo, ventajas y dudas. *Búsqueda Bibliográfica. Internet y las Nuevas Tecnologías*, 59-61.

WHO (1998). A health telematics policy in support of WHO's Health-For-All strategy for global health development: report of the WHO group consultation on health telematics. *World Health Organization, 11–16 December, Geneva, Switzerland.*

Xie Q., Zhang J. y Dong N. (2013). Robust anonymous authentication scheme for telecare medical information systems. *Journal of Medical Systems*, 37(9911), 1-8.

Yan X., Li W., Li P., Wang J., Hao X. y Gong P. (2013). A Secure biometrics-based authentication scheme for telecare medicine information systems. *Journal of Medical Systems*, 37(9972), 1-6.

Zhou Y., Bao L. y PhilipChen C. (2014). A new 1d chaotic system for image encryption. *Signal Processing*, 97, 172-182.

Observador adaptable en tiempo real de edificios mediante propagación de ondas

Jesús Morales-Valdez * **Luis Alvarez-Icaza** *

* *Instituto de Ingeniería, Universidad Nacional Autónoma de México 04510 Coyoacán DF, México*
(e-mail: jmoralesv@iingen.unam.mx, alvar@pumas.iingen.unam.mx)

Resumen: Se presenta un novedoso observador adaptable para edificios bajo el enfoque de propagación de ondas, asumiendo que los parámetros estructurales son desconocidos y que las mediciones de desplazamiento y velocidad no pueden ser obtenidas durante la actividad sísmica. Adicionalmente, se introduce un modelo para edificios de cortante, mediante el cual estos pueden ser tratados como una barra a cortante, elástica y discretizada. Además, se hace uso de un esquema de identificación basado en el algoritmo de mínimos cuadrados normalizado con factor de olvido, junto con un observador de estados tipo Luenberguer. La meta final es identificar los parámetros de velocidad de propagación de las ondas y su factor de amortiguamiento, al mismo tiempo que las señales de desplazamiento y velocidad son recuperadas, haciendo uso únicamente de los retardos generados en la llegada del movimiento sísmico entre un piso y otro. Los resultados de simulación muestran la versatilidad del método propuesto.

Palabras clave: Propagación de ondas, identificación de parámetros, observador de estados, control de vibraciones.

1. INTRODUCCIÓN

Los edificios son un tipo particular de estructuras civiles que acumulan daños gradualmente durante su vida útil. Además, el consecuente impacto en la seguridad y fiabilidad de los mismos después de un evento sísmico, crea la necesidad de contar con métodos de evaluación temprana para determinar las condiciones actuales de los inmuebles, determinar la presencia de daño o para saber si el edificio puede colapsar. La mayoría de los métodos de monitoreo de salud estructural en ingeniería civil están basados en el análisis modal, que estudia cambios en las frecuencias naturales y en las formas modales, características que no son sensibles a daño local, especialmente cuando éste es moderado ó pequeño, (Hwang y Kim, 2004; Rahai et al., 2006; Jeong-Tae et al., 2003; Huang et al., 2012; Makarios, 2012; Michel y Gueguen, 2010). Adicionalmente, cambios en las frecuencias de vibración no son siempre un indicador confiable de la presencia de daño, pues aquellas son sensibles a condiciones ambientales, por ejemplo la temperatura, (Todorovska y Trifunac, 2008; Chang et al., 2003).

Por otra parte, las propiedades estructurales de los edificios que son investigadas tradicionalmente usando métodos de vibración, también pueden ser analizadas usando métodos de propagación de ondas, pues ambos enfoques son matemáticamente equivalentes y uno puede ser preferible al otro dependiendo de la aplicación. Los métodos de propagación de onda son un enfoque alternativo que permite identificar características locales de los edificios, analizando cambios en las características de propagación de las ondas sísmicas a través del edificio. Este tipo de métodos son potencialmente más sensibles a información local que aquellos basados en análisis vibracional y formas modales. Esta idea es seguida en (Todorovska y Rahmani, 2012; Rahmani et al., 2014), donde un algoritmo identifica cambios en las velocidades de propagación del movimiento sísmico a través de un edificio. De manera similar en (Rahmani y Todorovska, 2014), se presenta un esquema de identificación para un modelo continuo y en capas, al cual también se le estudian los efectos de torsión. Para ello se usan técnicas como la interferometría e inversión de onda, para identificar las velocidades de propagación de las ondas de cortante. Sin embargo, este tipo de métodos están desarrollados en el dominio de la frecuencia y por lo tanto no pueden operar en tiempo real. Además, para señales complejas que generan múltiples efectos de reflexión y transmisión, el algoritmo tradicional es poco preciso en la identificación de los parámetros, pues está desarrollado en lazo abierto.

En este artículo, se extienden los trabajos de (Todorovska y Rahmani, 2012; Rahmani et al., 2014) que proponen un sistema de identificación en el dominio de la frecuencia. Se propone ahora mantener el enfoque de propagación de ondas, pero se transforma la forma de procesar la información para pasar de un proceso fuera de línea a uno de identificación de parámetros y estimación de estados en tiempo real. Este método mantiene las ventajas de poder generar información local para tener mayor certeza de la ubicación del daño. Además, el algoritmo de identificación propuesto supera al enfoque de propagación tradicional y esquemas basados en las frecuencias de vibración y formas modales

en la precisión para identificar parámetros y el tiempo requerido para la estimación. Para señales complejas, se ha superado el problema de múltiples efectos de reflexión y transmisión, evitando usar técnicas de procesamiento de señales. Por otra parte, se estiman los desplazamientos y velocidades en cada uno de los pisos.
Este artículo está organizado de la siguiente manera: la sección 2 describe el modelo de edificio y el proceso de discretización usados, evitando emplear transformaciones de coordenadas para resolver el modelo original. La sección 3 describe el diseño del observador adaptable, que combina un estimador de estados con un esquema de identificación de parámetros. Los resultados de simulación se presentan en la sección 4, y finalmente, las conclusiones de este trabajo se presentan en la sección 5.

2. MODELO MATEMÁTICO

Considere el edificio de cortante de múltiples pisos mostrado en la Fig. 1, el cual es excitado por una acción sísmica $\ddot{u}_g$. Generalmente la dinámica de este sistema es gobernada por una ecuación diferencial de segundo orden, (Chopra, 1995). Sin embargo, ésta no permite estudiar los efectos de propagación de las ondas. En consecuencia, un modelo novedoso basado en el principio de movimiento inducido por ondas sísmicas es propuesto en (Morales-Valdez y Alvarez-Icaza, 2015), dando como resultado la ecuación de onda con amortiguamiento de Kelvin,

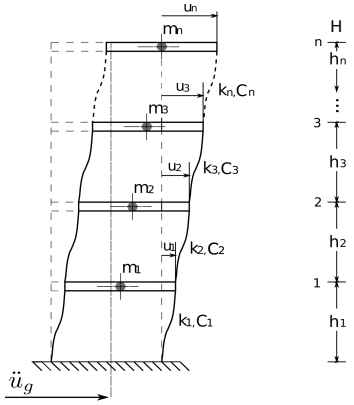

Figura 1. Edificio de cortante clásico

$$\beta_i^2 \frac{\partial^2 u_i}{\partial y^2} + \eta_i^2 \frac{\partial^2 \dot{u}_i}{\partial y^2} = \frac{\partial^2 u_i}{\partial t^2} \tag{1}$$

donde, β_i es la velocidad de cortante, η_i es una constante proporcional a la fuerza de amortiguamiento de la estructura y u_i, $i = 0, 1, 2, \ldots, n$ es el desplazamiento de cada masa m_i para cualquier instante de tiempo t. Las condiciones iniciales y de frontera para este modelo (1) son las siguientes:

$$u(y,0) = 0 \qquad 0 \le y \le H \tag{2a}$$
$$\dot{u}(y,0) = 0 \qquad 0 \le y \le H \tag{2b}$$
$$u(0,t) = u_g \qquad 0 < t \tag{2c}$$
$$\mu \dot{u}(H,t) = 0 \qquad 0 < t \tag{2d}$$

donde μ es el módulo de cortante. Además se supone lo siguiente:

A1 El edificio está inicialmente en reposo de acuerdo a (2a) y (2b), y por lo tanto $u(0)$, $\dot{u}(0)$ y $\ddot{u}(0)$ son cero.
A2 Únicamente la base de la estructura es excitada durante una actividad sísmica mediante el movimiento del terreno u_g, ver (2c).
A3 El edificio está libre de esfuerzo en el techo de acuerdo con (2d).
A4 El modelo en (1), permite tratar el modelo de edificio de cortante como una barra de cortante elástica y por lo tanto los efectos de propagación de onda pueden ser estudiados.

2.1 Semidiscretización espacial

En la práctica los edificios están construidos por diferentes materiales, geometrías, diferente número de columnas en cada piso, etc, de manera que la respuesta estructural de cada uno de ellos es diferente. En consecuencia, el modelo (1) es discretizado en la variable espacial en puntos donde se desea el comportamiento estructural, por ejemplo en los pisos. Usando una semidiscretización basada en el método de diferencias finitas, se producen diferentes velocidades de cortante y coeficientes de amortiguamiento. Para los puntos 1 hasta el $n-1$ se usa una aproximación centrada de segundo orden y un *backward* de primer orden en el punto n, dando como resultado una representación matricial acompañada de un vector de estados más un vector de condiciones de frontera. Además, se realiza una expansión en la matriz de estados para poner el vector de condiciones de frontera en función de señales de aceleración medibles. De manera que el modelo (1) puede ser aproximado por

$$\ddot{u} = \beta_M^2 \Lambda u + \eta_M^2 \Lambda \dot{u} + b\ddot{u}_g \tag{3}$$

donde β_M^2 y η_M^2 son matrices $\in \mathcal{R}^{p\times p}$, con $p = (n+1)$, y se definen de la siguiente manera

$$\beta_M^2 = \begin{bmatrix} 0 & 0 & 0 & \cdots & 0 \\ 0 & \beta_1^2 & 0 & \cdots & 0 \\ 0 & 0 & \beta_2^2 & \cdots & 0 \\ \vdots & \vdots & \vdots & \ddots & \vdots \\ 0 & 0 & \cdots & 0 & \beta_n^2 \end{bmatrix}, \qquad \eta_M^2 = \begin{bmatrix} 0 & 0 & 0 & \cdots & 0 \\ 0 & \eta_1^2 & 0 & \cdots & 0 \\ 0 & 0 & \eta_2^2 & \cdots & 0 \\ \vdots & \vdots & \vdots & \ddots & \vdots \\ 0 & 0 & \cdots & 0 & \eta_n^2 \end{bmatrix} \tag{4}$$

Note que los elementos de las matrices en (4) están relacionados con las propiedades de cada piso. Una ventaja importante de (3) es que no necesita transformación de coordenadas para encontrar la solución del sistema. Además,

$$\Lambda = \frac{1}{\Delta h^2} \begin{bmatrix} 0 & 0 & 0 & 0 & \cdots & 0 \\ 1 & -2 & 1 & 0 & \cdots & 0 \\ 0 & 1 & -2 & 1 & \cdots & 0 \\ \vdots & \vdots & \vdots & \ddots & \ddots & \vdots \\ 0 & 0 & \cdots & 1 & -2 & 1 \\ 0 & 0 & \cdots & 0 & 1 & -1 \end{bmatrix}, \qquad b = \begin{bmatrix} 1 \\ 0 \\ 0 \\ \vdots \\ 0 \\ 0 \end{bmatrix} \tag{5}$$

$$u = [u_0, u_1, u_2, \ldots, u_n]^T,\ \dot{u} = [\dot{u}_0, \dot{u}_1, \dot{u}_2, \ldots, \dot{u}_n]^T, \quad \ddot{u} = [\ddot{u}_0, \ddot{u}_1, \ddot{u}_2, \ldots, \ddot{u}_n]^T \tag{6}$$

donde $\Delta h = H/(n+1)$ para pisos uniformemente espaciados. Note que la condición de frontera se localiza en el basamento, $H = 0$, y que la aceleración en este punto se supone medible y equivalente a la actividad sísmica, es decir, $\ddot{u}_0 = \ddot{u}_g$. Las entradas u_0 y $\dot{u}_0 \in \mathcal{R}^+$ dentro de los vectores u y $\dot{u} \in \mathcal{R}^{p\times 1}$ en (6) describen el desplazamiento y la velocidad del terreno, respectivamente. Mientras los pisos restantes u_i y $\dot{u}_i$ con $i = 1, 2, \ldots, n$ representan las mediciones absolutas respectivas en cada piso. Finalmente $\ddot{u} \in \mathcal{R}^{p\times 1}$ es el vector de aceleración absoluta. Por otra parte, (3) puede ser expresada en espacio de estados como

$$\begin{bmatrix} \dot{u} \\ \dot{v} \end{bmatrix} = \begin{bmatrix} 0_{p\times p} & I_{p\times p} \\ \beta_M^2\Lambda & \eta_M^2\Lambda \end{bmatrix} \begin{bmatrix} u \\ v \end{bmatrix} + \begin{bmatrix} 0 \\ b \end{bmatrix} \ddot{u}_g \tag{7}$$

cuya salida es dada por

$$z = (\ddot{u} - b\ddot{u}_g) = \begin{bmatrix} \beta_M^2\Lambda & \eta_M^2\Lambda \end{bmatrix} \begin{bmatrix} u & v \end{bmatrix}^T \tag{8}$$

donde, $0_{p\times p}$ e $I_{p\times p}$ denotan las matrices nula e identidad de tamaño $(p \times p)$, respectivamente.

3. OBSERVADOR ADAPTABLE

En esta sección se diseña un observador adaptable, que combina un observador de estados con un esquema de identificación con el objetivo de reconstruir las señales no medibles y recuperar los parámetros desconocidos en el mismo instante de tiempo, respectivamente. Se asume que en un edificio real las matrices de parámetros β_M^2 y η_M^2 son desconocidas y que los desplazamientos y velocidades no pueden ser medidos durante la actividad sísmica.

3.1 Identificación paramétrica

Sea la ecuación de onda con amortiguamiento de Kelvin discretizada (3), la cual puede ser reescrita como

$$z = \beta_M^2\Lambda u + \eta_M^2\Lambda\dot{u}, \qquad \text{con} \qquad z = (\ddot{u} - b\ddot{u}_g) \tag{9}$$

replanteando (9) como

$$\beta_M^2\Lambda u = \psi\beta_V^2 = \psi\Theta_\beta \tag{10}$$
$$\eta_M^2\Lambda\dot{u} = \dot{\psi}\eta_V^2 = \dot{\psi}\Theta_\eta \tag{11}$$

donde, las matrices diagonales β_M^2 y η_M^2 son cambiadas por vectores β_V^2 y η_V^2 de dimensiones $\mathcal{R}^{p\times 1}$. De manera similar, los vectores u y $\dot{u}$ junto con la matriz Λ están ahora en la forma matricial ψ y $\dot{\psi}$, respectivamente con dimensión $\mathcal{R}^{p\times p}$, lo cual es conveniente para la identificación, resultando en:

$$\Theta_\beta = \begin{bmatrix} 0 & \beta_1^2 & \beta_2^2 & \beta_3^2 & \ldots & \beta_{n-1}^2 & \beta_n^2 \end{bmatrix}^T \tag{12}$$

$$\psi = \frac{1}{\Delta h^2} \begin{bmatrix} 0 & 0 & 0 & 0 & 0 & \cdots & 0 \\ u_0 & -2u_1 & u_2 & 0 & 0 & \cdots & 0 \\ 0 & u_1 & -2u_2 & u_3 & 0 & \cdots & 0 \\ 0 & 0 & u_2 & -2u_3 & u_4 & \cdots & 0 \\ \vdots & \vdots & \vdots & \vdots & \ddots & \ddots & \vdots \\ 0 & 0 & 0 & \cdots & u_{n-2} & -2u_{n-1} & u_n \\ 0 & 0 & 0 & \cdots & 0 & u_{n-1} & -u_n \end{bmatrix} \tag{13}$$

$$\Theta_\eta = \begin{bmatrix} 0 & \eta_1^2 & \eta_2^2 & \eta_3^2 & \ldots & \eta_{n-1}^2 & \eta_n^2 \end{bmatrix}^T \tag{14}$$

$$\dot{\psi} = \frac{1}{\Delta h^2} \begin{bmatrix} 0 & 0 & 0 & 0 & 0 & \cdots & 0 \\ \dot{u}_0 & -2\dot{u}_1 & \dot{u}_2 & 0 & 0 & \cdots & 0 \\ 0 & \dot{u}_1 & -2\dot{u}_2 & \dot{u}_3 & 0 & \cdots & 0 \\ 0 & 0 & \dot{u}_2 & -2\dot{u}_3 & \dot{u}_4 & \cdots & 0 \\ \vdots & \vdots & \vdots & \vdots & \ddots & \ddots & \vdots \\ 0 & 0 & 0 & \cdots & \dot{u}_{n-2} & -2\dot{u}_{n-1} & \dot{u}_n \\ 0 & 0 & 0 & \cdots & 0 & \dot{u}_{n-1} & -\dot{u}_n \end{bmatrix} \tag{15}$$

donde, Θ_β, $\Theta_\eta \in \mathcal{R}^{p\times 1}$. Por lo tanto, (9) es ahora de la forma

$$z = \psi\Theta_\beta + \dot{\psi}\Theta_\eta \tag{16}$$

donde los elementos de los vectores Θ_β y Θ_η son los parámetros a identificar del modelo. Una forma de parametrizar (16) se muestra a continuación

$$z = \Upsilon\Theta \tag{17}$$

donde $\Theta = [\Theta_\beta^T, \Theta_\eta^T]^T \in \mathcal{R}^{2p\times 1}$ y $\Upsilon = [\psi, \dot{\psi}] \in \mathcal{R}^{p\times 2p}$ es el regresor, formado por las señales no medibles de desplazamiento y velocidad, sin embargo estas serán estimadas por el observador de estados.

Mínimos cuadrados Sea $\hat{\Theta} = [\hat{\Theta}_\beta^T, \hat{\Theta}_\eta^T]^T$ el vector de parámetros estimados en (17), tal que la salida estimada está dada por

$$\hat{z} = \Upsilon\hat{\Theta} \tag{18}$$

entonces, los parámetros $\hat{\Theta}$ son identificados empleando el algoritmo de mínimos cuadrados normalizado con factor de olvido, dado por las siguientes ecuaciones, (Ioannou y Sun, 1989)

$$\dot{P} = \alpha P - \frac{P\Upsilon^T\Upsilon P}{m^2} \tag{19}$$
$$\dot{\hat{\Theta}} = P\Upsilon^T\varepsilon \tag{20}$$

donde α es el factor de olvido, P es la matriz de covarianza, la cual cumple que $P = P^T > 0 \in \mathcal{R}^{2p\times 2p}$, $P(0) > 0$, $1 > \alpha \geq 0 \in \mathcal{R}^+$, $m^2 = 1 + \left\|\Upsilon\Upsilon^T\right\|$, satisface que $\Upsilon/m \in \mathcal{L}_\infty$, asegurando que el error de estimación normalizado tiende a cero.

$$\varepsilon = \frac{z - \hat{z}}{m^2} \longrightarrow 0 \qquad \text{cuando} \qquad t \longrightarrow \infty \tag{21}$$

3.2 Observador de estados

Considerando que el par (A, D) del modelo propuesto en (7) y (8) no es completamente observable, se diseña un estimador de orden reducido considerando que las

mediciones en las condiciones de frontera son conocidas. El modelo reducido empleado es el siguiente

$$\begin{bmatrix}\dot{u}_r\\ \dot{v}_r\end{bmatrix} = \begin{bmatrix}0_{n\times n} & I_{n\times n}\\ \beta_{Mr}^2\Lambda_r & \eta_{Mr}^2\Lambda_r\end{bmatrix}\begin{bmatrix}u_r\\ v_r\end{bmatrix} - \begin{bmatrix}0_{n\times 1}\\ l_{n\times 1}\end{bmatrix}\ddot{u}_g \tag{22}$$

$$z_r(t) = (\ddot{u}_r + l\ddot{u}_g) = \begin{bmatrix}\beta_{Mr}^2\Lambda_r & \eta_{Mr}^2\Lambda_r\end{bmatrix}\begin{bmatrix}u_r & v_r\end{bmatrix}^T \tag{23}$$

$$\begin{aligned} u_r &= [u_1 - u_0,\ u_2 - u_0,\ u_3 - u_0,\ \ldots,\ u_n - u_0]^T,\\ v_r &= [v_1 - v_0,\ v_2 - v_0,\ v_3 - v_0,\ \ldots,\ v_n - v_0]^T,\\ \ddot{u}_r &= [\ddot{u}_1 - \ddot{u}_0,\ \ddot{u}_2 - \ddot{u}_0,\ \ddot{u}_3 - \ddot{u}_0,\ \ldots,\ \ddot{u}_n - \ddot{u}_0]^T,\\ l &= [1, 1, \ldots, 1]^T \end{aligned} \tag{24}$$

donde $u_r,\ v_r,\ \dot{v}_r \in \mathcal{R}^{n\times 1}$ son los vectores de desplazamiento, velocidad y aceleración relativos, respectivamente; $l \in \mathcal{R}^{n\times 1}$; $\beta_{Mr}^2 = diag[\beta_1^2, \beta_2^2, \ldots, \beta_n^2]$ y $\eta_{Mr}^2 = diag[\eta_1^2, \eta_2^2, \ldots, \eta_n^2]$ ambos $\in \mathcal{R}^{n\times n}$. Además,

$$\Lambda_r = \frac{1}{\Delta h^2}\begin{bmatrix}-2 & 1 & 0 & \cdots & 0\\ 1 & -2 & 1 & \cdots & 0\\ \vdots & \vdots & \vdots & \ddots & \vdots\\ 0 & \cdots & 1 & -2 & 1\\ 0 & \cdots & 0 & 1 & -1\end{bmatrix} \tag{25}$$

de manera que el observador adaptable propuesto usa el siguiente estimador de estados para estimar $x_r = [u_r^T,\ v_r^T]^T \in \mathcal{R}^{2n\times 1}$,

$$\dot{\hat{x}}_r(t) = \hat{A}_r(t)\hat{x}_r(t) + B_r\ddot{u}_g(t) + L\tilde{z}_r(t) \tag{26}$$

$$\hat{z}_r(t) = \hat{D}_r(t)\hat{x}_r(t), \quad \tilde{z}_r(t) = z_r - \hat{z}_r(t) \tag{27}$$

Note que el estimador de estados (26) es implementable, debido a que el par (A_r, D_r) en (22)-(23) es completamente observable con rango $2n$, (Jiménez-Fabián y Alvarez-Icaza, 2010) y por lo tanto todas las mediciones no disponibles pueden ser estimadas. Además, éste tiene la estructura de un observador Luenberger (Luenberger, 1971), donde $\hat{x}_r$, $\hat{z}_r \in \mathcal{R}^{2n\times 1}$, $\hat{A}_r$ and $\hat{D}_r$ son los estimados de x_r, z_r, A_r y D_r, respectivamente. Las matrices estimadas son definidas como

$$\hat{A}_r(t) = \begin{bmatrix}0_{n\times n} & I_{n\times n}\\ \widehat{\beta_{Mr}^2}(t)\Lambda_r & \widehat{\eta_{Mr}^2}(t)\Lambda_r\end{bmatrix} \tag{28}$$

$$\hat{D}_r(t) = \begin{bmatrix}\widehat{\beta_{Mr}^2}(t)\Lambda_r & \widehat{\eta_{Mr}^2}(t)\Lambda_r\end{bmatrix} \tag{29}$$

donde, $\widehat{\beta_{Mr}^2}(t)$ y $\widehat{\eta_{Mr}^2}(t)$ están conformadas por los estimados de β_{Mr}^2 y η_{Mr}^2, producidos por el algoritmo de mínimos cuadrados en (19) y (20), respectivamente

además, sea el error de estimación

$$\tilde{x}_r(t) = x_r(t) - \hat{x}_r(t) \tag{30}$$

cuya dinámica satisface la ecuación diferencial

$$\dot{\tilde{x}}_r(t) = \dot{x}_r(t) - \dot{\hat{x}}_r(t) \tag{31a}$$

$$= [\hat{A}_r(t) - L\hat{D}_r(t)]\tilde{x}_r(t) + \zeta(t) \tag{31b}$$

donde $\zeta(t) = [\tilde{A}_r(t) - L\tilde{D}_r(t)]x_r(t)$; Si la ganancia del observador L satisface

$$L = [0_{n\times n}\ \gamma I_{n\times n}]^T, \quad \gamma > 0 \tag{32}$$

entonces, el error de estimación $\tilde{x}_r$ es acotado. Además si el vector de parámetros estimados $\hat{\Theta}$ satisface la condición de excitación persistente, entonces la dinámica de $\dot{\tilde{x}}_r$ se reduce a

$$\dot{\tilde{x}}_r(t) = A_{r*}\tilde{x}_r(t) \tag{33}$$

$$A_{r*} = \begin{bmatrix}0_{n\times n} & I_{n\times n}\\ (1+\gamma)\beta_{Mr}^2\Lambda_r & (1+\gamma)\eta_{Mr}^2\Lambda_r\end{bmatrix} \tag{34}$$

y por lo tanto, el error de observación converge exponencialmente a cero, pues la matriz resultante A_{r*} es Hurwitz.

4. RESULTADOS DE SIMULACIÓN

A continuación se presentan los resultados de simulación para un edificio de 6 pisos, de 18 m altura y con pisos uniformemente espaciados, con separación de entre pisos de 3 m cada uno. La discretización espacial fue llevada a cabo en cada uno de los 6 niveles, donde las mediciones son registradas. El tiempo de muestreo empleado para la simulación es de 0,001 s. Con el objetivo de probar la robustez del algoritmo, se proponen propiedades heterogéneas para cada piso, de manera que las velocidades de cortante y los coeficientes de amortiguamiento a identificar son todos diferentes, es decir, $\beta_M = diag[405, 300, 250, 600, 430, 150]\ m/s$ y $\eta_M = diag[30, 42, 40, 25, 20, 10]\ Ns/m$. Para el caso de la excitación sísmica, se usó un registro sísmico recolectado en el edificio instrumentado Jalapa, ubicado en la ciudad de México en el evento ocurrido el 21 de enero de 2003, con epicentro en Colima, cuyo acelerograma se muestra en la Fig. 2. Además, suponiendo que el algorítmo propuesto es robusto a ruido de medición, el acelerograma de la Fig. 2 fue contaminado con ruido Gaussiano de media cero y varianza 1, como se ilustra en la Fig. 3

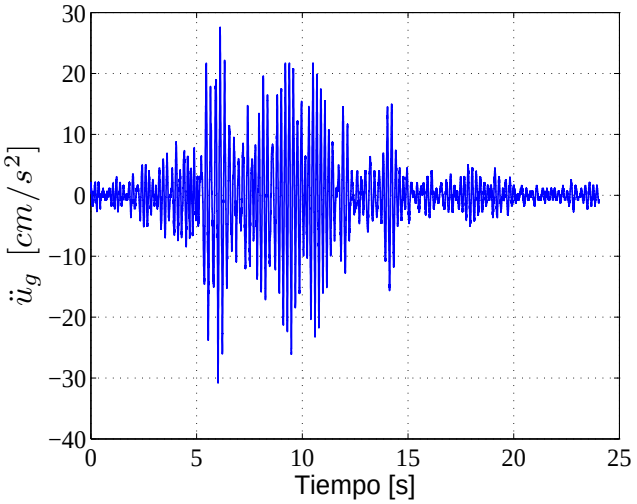

Figura 2. Excitación sísmica

Aplicando la excitación sísmica únicamente en la base del edificio, y usando mediciones de aceleración de los pisos, el observador adaptable propuesto logra recuperar la respuesta estructural del edificio identificando los parámetros estructurales de referencia. La Fig. 4 muestra la evolución de las velocidades de cortante identificadas, mientras los coeficientes de amortiguamiento identificados son presentados en la Fig. 5. En ambos casos es posible observar que

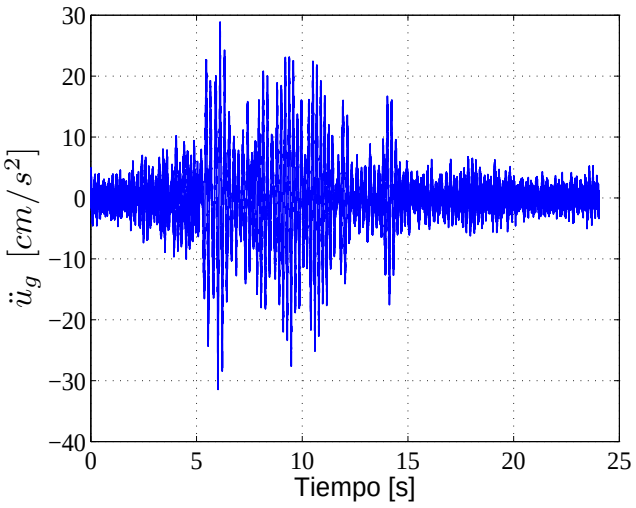

Figura 3. Excitación sísmica con ruido Gaussiano

la convergencia de los parámetros se logra en un tiempo menor a los 2 s, lo que confirma la eficacia del algoritmo. Para tiempos posteriores al señalado, la convergencia paramétrica se mantiene. Otra manera de mostrar que el esquema de identificación propuesto funciona satisfactoriamente es observando la norma del error de estimación $\|\varepsilon\|_2 = \|z - \hat{z}\|_2$, la cual efectivamente disminuye a medida transcurre el tiempo, con convergencia a cero antes de los 2 s. Una ventaja importante es que a partir de los parámetros identificados se pueden calcular los valores de rigidez de los entrepisos del edificio, empleando el modelo propuestos en (Morales-Valdez y Alvarez-Icaza, 2014). Por otra parte, la Fig. 7 muestra una comparación entre la medición de desplazamiento en el sexto piso con su respectivo estimado. De manera similar, la Fig. 8 ilustra la comparación entre la velocidad real y su estimada en el mismo piso. Note que los estimados siempre convergen a la señal de referencia, evidenciando que el observador adaptable opera satisfactoriamente. La elección del sexto piso se hizo considerando que sufre mayores efectos que el resto de los pisos durante una actividad sísmica.

Note que los resultados presentados en este artículo fueron obtenidos empleando condiciones iniciales nulas para los parámetros β_i y η_i, $\alpha = 0{,}004$ y $P(0) = 10^{10} I_{14\times 14}$ como valor inicial de la matriz de covarianza; finalmente $L = 10^3 I_{7\times 7}$.

5. CONCLUSIÓN

Se ha presentado un observador adaptable para edificios modelados bajo el enfoque de propagación de ondas, capaz de recuperar los parámetros estructurales desconocidos, como son las velocidades de propagación de onda y el amortiguamiento de Kelvin. A diferencia del enfoque tradicional, en este artículo se ha replanteado el esquema de identificación fuera de línea como uno de identificación de parámetros y estimación de estados en tiempo real. Adicionalmente, se han estimado los desplazamientos y velocidades en cada uno de los pisos. Este nuevo algoritmo mejora los métodos tradicionales de monitoreo de salud estructural. Además, los parámetros identificados pueden ser usados como indicadores de daño al compararlos con

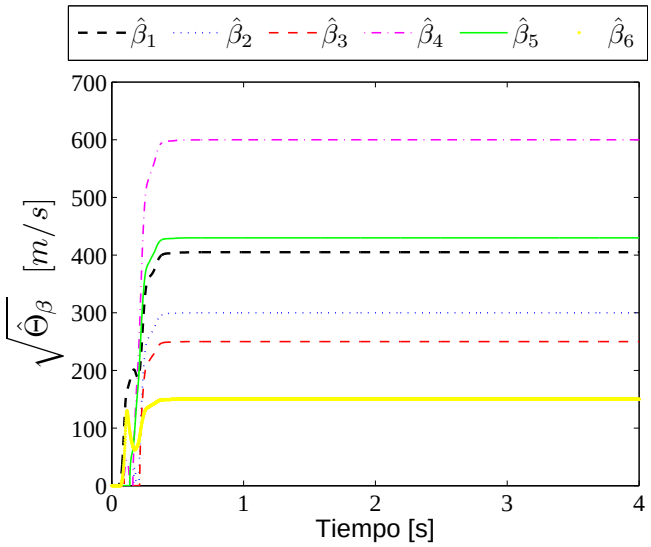

Figura 4. Evolución de las velocidades de cortante identificadas

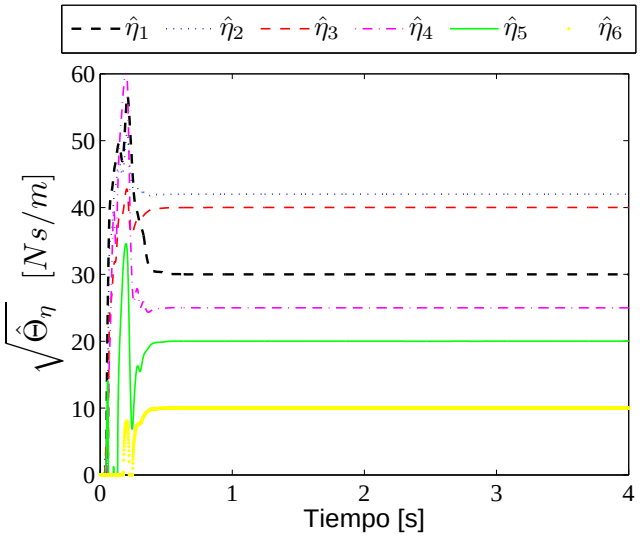

Figura 5. Evolución de los coeficientes de amortiguamiento identificados

otros de referencia, como los obtenidos directamente de las propiedades de los materiales.

AGRADECIMIENTOS

Los autores agradecen el apoyo de CONACYT. El primero también agradece el apoyo de la Coordinación de Estudios de Posgrado de la Universidad Nacional Autónoma de México. Esta investigación fue realizada con apoyo de los proyectos UNAM-PAPIIT IN109414 y IN109316.

REFERENCIAS

Chang, P.C., Flatau, A., y Liu, S. (2003). Review paper: Health monitoring of civil infrastructure. *Structural Health Monitoring*, 2(3), 257–267.

Chopra, A. (1995). *Dynamics of Structures: Theory and Applications to Earthquake Engineering*. Upper Saddle River, NJ, Prentice Hall.

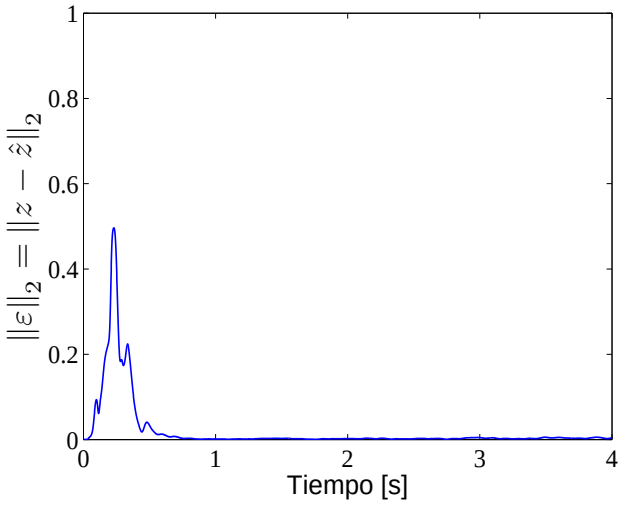

Figura 6. Norma del error paramétrico

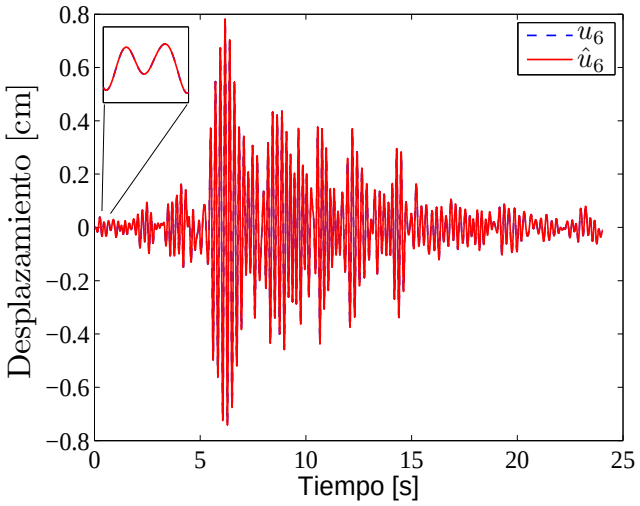

Figura 7. Comparación entre el desplazamiento real y su estimado

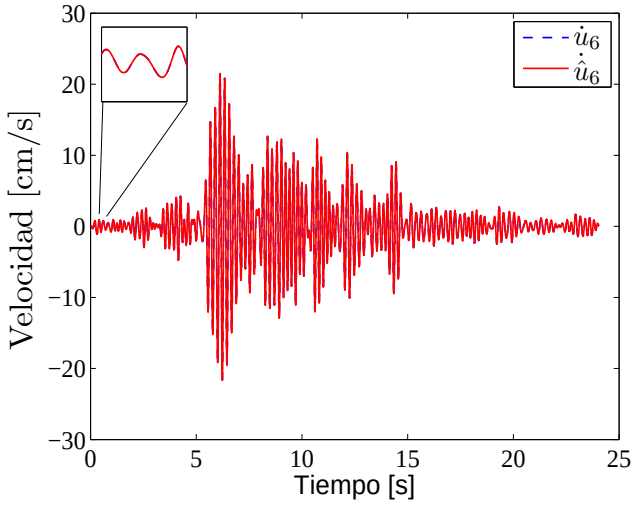

Figura 8. Comparación entre la velocidad real y su estimada

the new modal time-histories method. *The structural design of tall and special building*, 21(9), 621–641.

Michel, C. y Gueguen, P. (2010). Time-frequency analysis of small frequency variations in civil engineering structures under weak and strong motions using a reassignment method. *Structural Health Monitoring*, 9(2), 159–171.

Morales-Valdez, J. y Alvarez-Icaza, L. (2014). Building stiffness estimation by wave traveling times. In *ASME 2014 Dynamic system and control conference*, 1–8. San Antonio, TX, USA.

Morales-Valdez, J. y Alvarez-Icaza, L. (2015). Identificación paramétrica en línea de edificios con tiempos de viaje de onda. In *AMCA 2015, Memorias del Congreso Nacional de Control Automático*, 563–568. Cuernavaca, Morelos, México.

Rahai, A., Bakhtiari-Nejad, F., y Esfandiari, A. (2006). Damage assessment of structure using incomplete measure mode shape. *Structural Control and Health Monitoring*, 14, 808–829.

Rahmani, M., Ebrahimian, M., y Todorovska, M.I. (2014). Time-wave velocity analysis for early earthquake damage detection in building: application to a damaged full-scale RC building. *Earthquake Engineering and Structural Dynamics*, 44(4), 619–636.

Rahmani, M. y Todorovska, M.I. (2014). 1D System identification of a 54-story steel frame building by seismic interferometry. *Earthquake Engineering and Structural Dynamics*, 43(4), 627–640.

Todorovska, M.I. y Rahmani, M.T. (2012). System identification of building by wave travel time analysis and leyered shear beam models-spatial resolution and accuracy. *Structural Control and Health Monitoring*, 20(5), 686–702.

Todorovska, M.I. y Trifunac, M.D. (2008). Earthquake damage detection in the Imperial County Services Building III: Analysis of wave travel time via impulse response functions. *Soil Dynamics and Earthquake Engineering*, 28(5), 387–404.

Huang, Q., Xu, Y., Li, J., Su, Z., y Liu, H. (2012). Structural damage detection of controlled building structures using frequency response function. *Journal of Sound and Vibration*, 331(15), 3476–3492.

Hwang, H. y Kim, C. (2004). Damage detection in structures using a few frequency response measurements. *Journal of Sound and Vibration*, 270(1-2), 1–14.

Ioannou, P. y Sun, J. (1989). *Robust Adaptive Control*. Upper Saddle River, NJ, Prentice Hall.

Jeong-Tae, K., Yeon-Sun, R., Hyun-Man, C., y Norris, S. (2003). Damage identification in beam-type structures: Frequency-based method vs mode-shape-based method. *Engineering Structures*, 25, 57–67.

Jiménez-Fabián, R. y Alvarez-Icaza, L. (2010). An adaptive observer for shear building with an energy-dissipation device. *Control Engineering Practice*, 18, 331–338.

Luenberger, D. (1971). An introduction to observers. *IEEE Transaction on Automatic Control*, 16(6), 596–602.

Makarios, T.K. (2012). Identification on the mode shapes of spatial tall multi-storey buldings due to earthquake:

CHAPTER 17

SYSTEM IDENTIFICATION

Determinación del coeficiente de dispersión en reactores de gasificación.

Oscar Hernández-Torres * **Luis Ángel Santamaría** *
Luis Álvarez-Icaza * **Jesús Álvarez Calderón** **

* *Universidad Nacional Autónoma de México, Instituto de Ingeniería Ciudad de México C.P. 04510 Coyoacán, México (e-mails: oscaraht@gmail.com, lsantamariap@iingen.unam.mx, alvar@pumas.iingen.unam.mx)*
** *Universidad Autónoma Metropolitana-Iztapalapa, Departamento de Ingeniería de Procesos e Hidráulica, Ciudad de México, C.P.09340, México (e-mail: jac@xanum.uam.mx)*

Resumen: Se presenta una metodología no destructiva para determinar el coeficiente de dispersión en reactores de gasificación. El método desarrollado está inspirado en distribuciones de tiempo de residencia, de las cuales se obtienen métricas de forma. Con estas variables estadísticas es posible realizar una estimación del número de Peclet considerando casos de incertidumbre paramétrica. Para ilustrar el funcionamiento y alcance del método, dicha metodología se aplica a gasificadores de flujos descendentes, uno estratificado y otro en configuración Imbert; ambos modelados mediante un tren de N reactores continuos de tanque agitado con un cierto grado de retromezclado. Los resultados obtenidos mediante simulación, muestran que el número de Peclet es robustamente identificable con un error medio cuadrático plausible.

Palabras clave: Reactores de gasificación; Incertidumbre paramétrica; Coeficiente de dispersión; Número de Peclet.

1. INTRODUCCIÓN

En la actualidad las tecnologías de gasificación son de gran interés en la industria energética, ya que permiten aprovechar residuos de bajo poder calórico para obtener como productos de salida gas de síntesis y carbones vegetales. El gas de síntesis, se utiliza para la generación de energía eléctrica a partir de motores de combustión interna o turbinas de gas; mientras que el carbón vegetal se usa como sustrato para el mejoramiento de suelos debido a su capacidad para retener agua y nutrientes.

Los procesos de gasificación de biomasa son estudiados mediante modelos eulerianos unidimensionales y bidimensionales de dos fases termodinámicas constituidos por ecuaciones diferenciales parciales (EDPs) de conservación de masa y energía. Los modelos derivados son sistemas dinámicos en parámetros concentrados de alto orden con rigidez numérica considerable y alta sensibilidad paramétrica lo cual limita su aplicación en el diseño de esquemas de control y observación (Baldea y Daoutidis, 2007).

Desde el punto de vista de modelado clásico de ingeniería de reactores (Deans y Lapidus, 1960; Levenspiel, 1962), es posible reconstruir el comportamiento de un reactor tubular vacío o de lecho empacado con dispersión mediante la conexión en serie de N reactores continuos de tanque agitado (RCTAs) con un cierto grado de retromezclado, haciendo posible el análisis de estabilidad y multiplicidad de estados estacionarios de una forma más sencilla (Deckwer, 1974). La utilidad de este método de modelado para reproducir el comportamiento no lineal de reactores tubulares exotérmicos con un número pequeño de RCTAs ha sido demostrada en Sinkule et al. (1974) y Deckwer (1974), así como en estudios recientes de modelado y control de reactores tubular exotérmicos con dispersión axial (Nájera, 2012).

Badillo-Hernandez et al. (2013) presenta un método de diseño de modelos dinámicos en parámetros concentrados de orden reducido con sentido físico, estructura simple y ajustable, capaz de ilustrar características fuertemente no lineales como la bifurcación y multiplicidad de estados estacionarios. Bajo esta idea, Canales (2013) desarrolla una metodología para la elección de una malla espacial de bajo orden que logra reproducir cualitativa y cuantitativamente la dinámica espacial del modelo de un gasificador de biomasa de lecho fijo.

Sin embargo, en sistemas dinámicos termoquímicos, como es el caso de gasificadores de lecho empacado y fijo, los fenómenos de transporte como convección y dispersión están acoplados con reacciones químicas y fenómenos de transferencia de calor que dan lugar a modelos con una alta incertidumbre y sensibilidad paramétrica. Resulta entonces de gran importancia contar con los coeficientes certeros de convección y dispersión térmica, ya que de estos depende en gran parte el aprovechar al máximo las cualidades que tiene un modelo dinámico en parámetros concentrados

de orden reducido, en nuestro caso de estudio, el modelo desarrollado por Badillo-Hernandez et al. (2013) y Canales (2013).

La importancia de conocer la dispersión que existe dentro de un reactor de gasificación lleva a buscar distintas metodologías no destructivas para determinar de forma experimental el coeficiente de dispersión y así poder ajustar los modelos de parámetros concentrados.

Un método comúnmente utilizado en la Ingeniería Química para determinar el grado de dispersión presente en reactores de tanque agitado y flujo pistón es la técnica de trazadores expuesta en Levenspiel (2011). Ésta es aplicada para reacciones donde el estado de agregación de la materia es líquido. Por otra parte, los casos de estudio presentados en este trabajo están referidos a reacciones donde el estado de agregación de la materia es principalmente gas, por lo cual el propósito es desarrollar una metodología de trazadores basados en Levenspiel (2011) aplicable a los reactores de gasificación de biomasa.

En consecuencia, basados en un modelo dinámico en parámetros concentrados de orden reducido para gasificadores se propone encontrar una metodología no destructiva que permita identificar el grado de dispersión (inverso del número de Peclet) presente para una clase de reactores de gasificación tomando como punto de partida la técnica de trazadores presentada en Levenspiel (2011).

La estructura del trabajo es la siguiente, en la sección 2 se presenta el modelo que describe el comportamiento del reactor de gasificación mediante un tren de N reactores continuos de tanque agitado. En la sección 3 se presentan algunos conceptos necesarios para aplicar la técnica de trazadores. Durante la sección 4 se extiende la técnica mostrada utilizando métricas de forma, para así, en la sección 5, aplicarla a dos reactores de gasificación de flujos descendientes, uno estratificado y el otro en configuración Imbert. Finalmente, en la sección 6 se presentan las conclusiones obtenidas después de analizar los resultados obtenidos.

2. MODELO DINÁMICO DE UN REACTOR DE GASIFICACIÓN

2.1 Preliminares

Con base en el enfoque de ingeniería de reactores químicos, es posible formular esquemas de control si se parte de la ecuación de transporte generalizada (1), que surge de fenómenos de transporte y unifica las leyes de conservación de momento, energía y masa (Bird, Stewart, y Lightfoot 1960).

$$\overbrace{\partial_t \varphi}^{Almacenamiento} = \overbrace{-(\nabla \cdot \varphi \mathbf{U})}^{Convección} + \overbrace{\nabla \cdot D \nabla \varphi}^{Dispersión} + \overbrace{S(\varphi, \mathbf{r})}^{Generación}, \quad (1)$$

donde

- $\varphi \equiv$ variable que se conserva por unidad de volumen
- $\mathbf{U} \equiv$ vector de las velocidades de flujo convectivo
- $D \equiv$ *coeficiente de transporte de dispersión*
- $S \equiv$ término fuente generalizado
- $\mathbf{r} \equiv$ vector de coordenadas espaciales

La dispersión longitudinal axial modela fenómenos de flujo de naturaleza estadística, es decir, fluctuaciones elementales de la velocidad, concentración y temperatura que se repiten muchas veces a lo largo del reactor. Bajo esta visión el coeficiente de dispersión D constituye un parámetro a determinar de acuerdo al tipo de lecho empacado del equipo y régimen de flujo, entre otras propiedades físicas del fluido. En otras palabras, el grado de mezclado en el patrón de flujo de una corriente en un reactor es modelado mediante el coeficiente de dispersión D.

2.2 Modelo NRCTAs (Badillo-Hernandez et al., 2013)

Partiendo de la ecuación (1), se han desarrollado métodos de alta complejidad que logran aproximar el comportamiento de sistemas dinámicos de dimensión infinita a sistemas de dimensión finita. De acuerdo al esquema de modelado clásico de ingeniería de reactores (Coste et al., 1961; Levenspiel, 1962), se puede proponer una configuración de un conjunto de N tanques interconectados en serie y/o cascada-retro-flujo, que pueda representar el carácter distribuido de los sistemas de procesos, como se muestra en la Fig. 1.

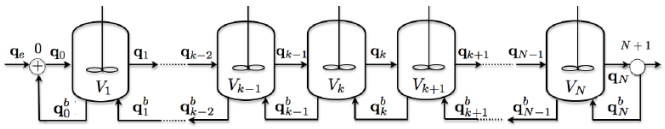

Figura 1. Representación de un tren con N tanques interconectados en cascada con flujos de retromezclado

Bajo esta idea, Badillo-Hernandez et al. (2013) presenta un modelo que logra capturar la dinámica global del sistema, el cual se puede visualizar de forma compacta por medio del sistema algebraico diferencial:

$$\mathcal{V}_k \dot{\mathbf{c}}_{s,k} = q_{k-1}^{Ms} \mathbf{c}_{s,k-1} - q_k^{Ms} \mathbf{c}_{s,k} + K_M \mathcal{M}\mathbf{Da}\, r_k \mathcal{V}_k, \quad (2a)$$

$$\mathcal{V}_k \dot{\eta}_k = \alpha \left(q_{k-1}^{H} \eta_{k-1} - q_{out,k}^{H} \eta_k \right) - Q_{\eta,k}(c,\eta) + q_k^{b,H} \eta_{k+1}, \quad (2b)$$

$$0 = q_{k-1}^{Mg} \mathbf{c}_{g,k-1} - q_1^{Mg} \mathbf{c}_{g,k} + q_k^{b,Mg} \mathbf{c}_{g,k+1} + \mathcal{M}\mathbf{Da}\, r_k \mathcal{V}_k, \quad (2c)$$

donde

$$q_k^H = v_{H,k} \mathcal{A}_k + \frac{D_{H,k} \mathcal{A}_k}{P_{eH} \Delta z_{k+1}}, \qquad q_k^{b,H} = \frac{D_{H,k} \mathcal{A}_k}{P_{eH} \Delta z_{k+1}}$$

La ecuación (2) es utilizada para representar la dinámica de un tanque interno k, se extiende de forma analóga para el primero y el último. El desarrollo y detalle del modelo completo se extiende en Badillo-Hernandez et al. (2013) y Hernández-Torres (2016).

3. TÉCNICA DE TRAZADORES

La técnica de trazadores es un experimento estímulo-respuesta, esto es, a través de una excitación se pretende conocer la cantidad de tiempo que le toma a una determinada concentración pasar a lo largo de un reactor desde un punto inicial (entrada) a un punto final (salida), Fig. 2. Como resultado, la curva generada a la salida del reactor se conoce como *distribución de tiempos de residencia* (RTD por sus siglas en inglés).

Para estimular al sistema se considera solamente el flujo en estado estacionario del fluido a través de un recipiente,

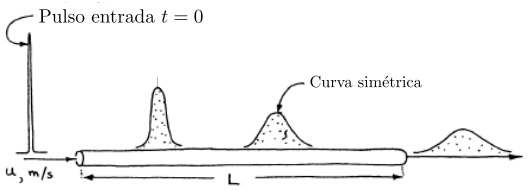

Figura 2. Experimento estimulo-respuesta.

sin reacción y sin cambios de densidad. La RTD se define a partir de la función $E(t)$ que satisface

$$\int_0^\infty E(t)dt = 1 \tag{3}$$

donde la integral es denominada como la normalización de la distribución (Levenspiel, 2011).

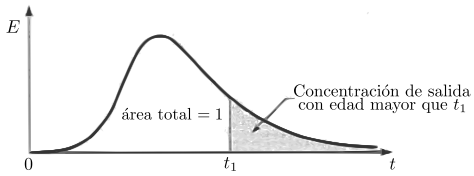

Figura 3. Distribución de tiempos de residencia E.

La curva E, que se ejemplifica en la Fig. 3, es la distribución que se necesita para tener en cuenta el flujo no ideal. Para excitar al sistema en estado estacionario sobresalen dos formas de hacerlo: a) aplicar un impulso o en su defecto, un pulso de concentración de duración muy pequeña y b) suministrar una entrada constante; posteriormente se toman lecturas a la salida del reactor para obtener las curvas de RTD (Hernández-Torres, 2016).

3.1 Modelo de dispersión (Levenspiel, 2011)

Existen distintos tipos de modelos para representar el flujo en reactores, esto depende a qué tipo de flujo se acerque más el reactor, flujo pistón o tanque agitado, e incluso un intermedio entre estos. Si se analiza el patrón de flujo pistón con pequeñas desviaciones se tienen dos modelos para analizar las curvas RTD: el de dispersión y de tanques en serie. Ambos se aplican para flujo laminar en tubos muy largos, chimeneas de hornos, flujo en lechos empacados, flujo turbulento en tuberías, etc.

Considerar un fluido en flujo pistón, el cual puede tener un cierto grado de retromezclado cuya magnitud es independiente de la posición dentro del recipiente, implica que no existen zonas muertas, ni grandes desviaciones de fluido dentro del recipiente. A este modelo se le conoce como flujo disperso en pistón o simplemente *modelo de dispersión*. Si las condiciones de intermezclado varían, la predicción de este modelo oscilará entre el flujo pistón ideal y el de tanque agitado. Este proceso de mezcla implica una redistribución de materia ya sea por deslizamiento o formación de remolinos dentro del contenedor; al repetirse un número considerable de veces este proceso durante el flujo del fluido, se considera que estas perturbaciones son de naturaleza estadística, lo cual es un fenómeno similar al que ocurre en la difusión molecular.

En consecuencia, apoyados de la ecuación diferencial que rige la difusión molecular (Ley de Fick):

$$\frac{\partial C}{\partial t} = D\nabla^2 C, \tag{4}$$

se puede obtener una ecuación que caracterice el grado de retromezclado del fluido que circula en dirección x

$$\frac{\partial C}{\partial t} = D\frac{\partial^2 C}{\partial x^2}, \tag{5}$$

donde D se denomina *coeficiente de dispersión longitudinal* o *axial*.

Realizando una transformación (Levenspiel, 1999) de la ecuación (5) se llega a la expresión

$$\frac{\partial C}{\partial \theta} = \left(\frac{D}{uL}\right)\frac{\partial^2 C}{\partial z^2} - \frac{\partial C}{\partial z}, \tag{6}$$

donde u es la velocidad de flujo, L es la longitud del reactor, $z = (ut + x)/L$ y $\theta = t/\bar{t} = tu/L$. A el grupo adimensional $\frac{D}{uL}$ se le conoce como número de dispersión del recipiente y mide el grado de dispersión axial que existe a lo largo del reactor. Por otro lado, $Pe = \frac{uL}{D}$ es conocido como el número de Peclet .

3.2 Dispersión longitudinal

Un impulso ideal introducido en un reactor se esparcirá conforme pasa a través del recipiente; a esta acción se le denomina dispersión o dispersión longitudinal. El coeficiente de dispersión D representa la difusión general del proceso:

- Un valor grande de D indica una rápida dispersión de la curva del rastreador.
- Un valor pequeño de D indica una dispersión lenta.
- $D = 0$ nos dice que no hay dispersión, por lo cual se estaría hablando de un flujo pistón ideal.

Mediante el registro de distintas curvas de trazador obtenidas a la salida del reactor se busca evaluar D o D/uL; en particular para cada curva de salida obtenida se mide:

- $\bar{t}$: tiempo medio de la curva de salida.
- σ^2 : varianza o el cuadrado de la desviación estándar.

Tomando como referencia el reactor de flujo pistón, la RTD nos lleva a dos casos distintos: (1) pequeñas desviaciones con respecto al modelo de flujo pistón, esto es cuando $D/uL < 0.01$ y (2) grandes desviaciones, es decir $D/uL > 0.01$. El primer caso va a arrojar RTD que tendrán formas gaussianas, mientras que para el segundo las curvas se vuelven asimétricas (Levenspiel, 2011; Hernández-Torres, 2016). Para cualquiera de ellos, el problema se centra en calcular las métricas estadísticas de las RTD y elegir la condición de frontera correspondiente para el modelo dinámico de estudio y así estimar el número de Peclet del reactor (Hernández-Torres, 2016).

3.3 Aplicación de la técnica de trazadores

Teniendo definidos los conceptos necesarios para identificar el grado de dispersión existente dentro de un reactor de gasificación, se toma el modelo de estudio (2) para un análisis mediante simulación. El primer paso es determinar las condiciones de frontera (recipiente abierto) para un reactor de gasificación de lecho empacado y con esto elegir las ecuaciones que se adaptan al mismo. El procedimiento para realizar el experimento es el siguiente:

1. Llevar al reactor de gasificación a un estado estacionario (punto de encendido).
2. Suministrar un pulso de aire caliente en un tiempo t_0, con flujo constante, a distintas temperaturas ΔT y duraciones Δt.
3. Observar y tomar lectura a la salida del reactor de la curva generada por el pulso.
4. Calcular el tiempo medio y la varianza $(\bar{t}, \sigma^2)$.
5. Calcular los tiempos de residencia del rastreador.
6. De acuerdo a la condición de frontera que se posea, se elige la ecuación correspondiente y se calcula el coeficiente de dispersión.
7. Se compara el D/uL obtenido mediante simulación con el valor nominal correspondiente a dicha simulación.

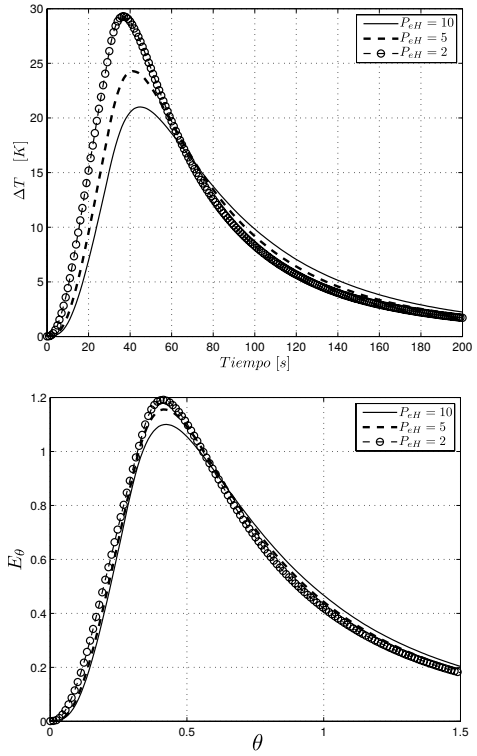

Figura 4. Curvas de los tiempos de residencia para tres distintos números de Peclet con un pulso de entrada $\Delta T_e = 700\ [K]$ y una duración de $\Delta t = 30\ [seg]$.

La Fig. 4 presenta la curva RTD obtenida utilizando el modelo (2). Sin embargo, al realizar varias pruebas y modificar parámetros tanto del modelo (2), como del pulso de entrada del rastreador, los resultados obtenidos no logran ser plausibles para garantizar una buena estimación del número de Peclet, ya que estos varían dependiendo de la cantidad de datos utilizados para calcular $\bar{t}$ y σ^2, afectando la solución de la ecuación de recipiente abierto (Hernández-Torres, 2016).

4. TÉCNICA DE TRAZADORES MEDIANTE ANÁLISIS DE MÉTRICAS DE FORMA

Con los resultados obtenidos al aplicar el método anterior e indentificando las limitaciones que éste tiene para los reactores de gasificación, surge el interés de mejorar la estimación del número de dispersión (número de Peclet) y además poder hacerlo ante la presencia de incertidumbre paramétrica. Debido a que las curvas de trazador, Fig. 4, poseen una estructura asimétrica, se propone explotar esta propiedad con base en un análisis mediante métricas de forma, las métricas utilizadas son: oblicuidad, curtosidad y coeficiente de variación.

Oblicuidad. Es el tercer momento (μ_3) respecto a la media, también llamado medida de asimetría o deformación. Su objetivo es estudiar la deformación horizontal de los valores de la variable respecto al valor central de la media. Dependiendo del valor de la oblicuidad se sabe que:

- Si $obl < 0$, la mayoría de los datos se encuentran a la izquierda de la media.
- Si $obl > 0$, entonces la mayoría de los datos se encuentran a la derecha de la media.
- Si $obl = 0$, la muestra corresponde a una distribución normal con una simetría perfecta.

$$obl = \frac{1}{N}\sum_{i=1}^{N}\left(\frac{x_i - \mu}{\sigma}\right)^3 = \frac{\mu_3}{\sigma^3}, \tag{7}$$

donde σ, es la desviación estándar y μ, es la media aritmética.

Curtosidad. El concepto de curtosis o apuntamiento de Fischer pretende comparar la curva de una distribución con la curva de la variable normal en función de la cantidad de valores extremos de la distribucion. Basándose en el dato de que una distribución normal cumple con

$$\frac{\mu_4}{\sigma^4} = 3, \tag{8}$$

la curtosidad se puede definir como

$$k = \frac{1}{N}\sum_{i=1}^{N}\left(\frac{x_i - \overline{x}}{\sigma}\right)^4 = \frac{\mu_4}{\sigma^4} - 3, \tag{9}$$

donde se ha sustraído la curtosis de la distribución normal para que el coeficiente tenga un valor de cero para una distribución normal y sirva como referencia de apuntamiento.

Coeficiente de variación. Es la relación entre la desviación estándar y su media

$$coefv = \frac{\sigma}{\mu}. \tag{10}$$

Con el uso de estas nuevas métricas, complementándolas con el método de RTD, se pretende estimar la dispersión ante incertidumbre paramétrica, ya que al realizar las pruebas experimentales no se conocen con certeza los valores de algunos parámetros. Por esta razón es necesario realizar la estimación del coeficiente de dispersión ante la presencia de perturbaciones en los parámetros que en general son más inciertos. Con base en los parámetros elegidos en el estudio de Canales (2013), se toman tres de ellos ya que son los que principalmente pueden provocar una estimación errónea del número de Peclet: la energía de activación de la pirólisis E_{p1}, el diámetro inicial de la partícula d_{p0}, y la entalpía de reacción del carbonizado ΔH_{c5}. En consecuencia, se decide perturbar dichos coeficientes dentro de un rango considerable y observar como esto afecta los resultados obtenidos.

5. APLICACIÓN DE LA METODOLOGÍA

5.1 Gasificador estratificado

En la Fig. 5 se presenta el número de Peclet nominal *vs* la métrica del coeficiente de variación ante la presencia de perturbaciones en los parámetros antes mencionados. El pulso de excitación para el sistema es de $T_e = 700\ [K]$ con una duración de $\Delta t = 30\ [seg]$.

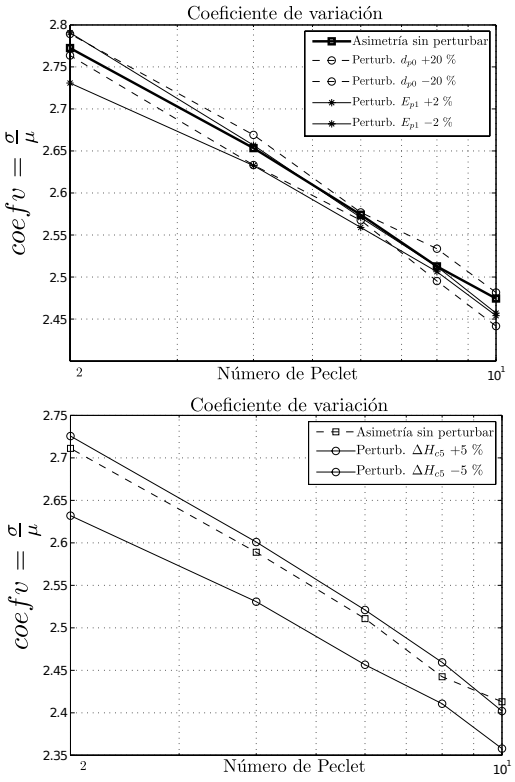

Figura 5. Métricas de forma ante la presencia de perturbaciones con un pulso de entrada de $T_e = 700\ [K]$.

Una manera de visualizar con mayor claridad la estimación del número de Peclet en relación con el Peclet nominal se puede ver en la Fig. 6; en esta gráfica se esclarece la banda de incertidumbre que se puede llegar a tener al no conocer al 100 % algunos parámetros. Así mismo también se observa el error medio cuadrático (EMC) resultante que se logró al estimar el grado de dispersión, en dicha gráfica se percibe un error por debajo del 5 % para dos parámetros (E_{p1} y d_{p0}).

5.2 Gasificador tipo Imbert

Al igual que en el reactor anterior, se aplicó el método diseñado para determinar mediante simulación el número de Peclet presente en un gasificador tipo Imbert. El modelo y los parámetros utilizados son tomados de Santamaría (2016), la principal diferencia entre el modelo presentado anteriormente y el Imbert radica en que para el último la alimentación de biomasa y aire se da en zonas distintas, pero se preserva la dirección a la cual fluyen. Los parámetros que se variaron fueron los mismos que en el gasificador estratificado, añadiendo el cambio en la composición del carbonizado, pasando de ser 100 %C a 95 %C con $2-3$ %H y $2-3$ %O, esto es debido a que para este reactor en particular la composición del carbonizado influye en la predicción correcta del gas de síntesis que se obtiene comparada contra datos experimentales (Santamaría, 2016). El modelo del gasificador Imbert corresponde a una planta piloto propiedad del Instituto de Ingeniería, en el cual el aire se alimenta a una temperatura de $600°C$, por lo que para no dañar al reactor en una situación real, se considera un incremento máximo de $T_e = 200\ [K]$, dejando como grado de libertad la duración del pulso Δt, para este trabajo se presentan los resultados obtenidos cuando $\Delta t = 10\ [s]$. Aplicando la métodología descrita anteriormente se obtuvieron las Figs. 7 a 9.

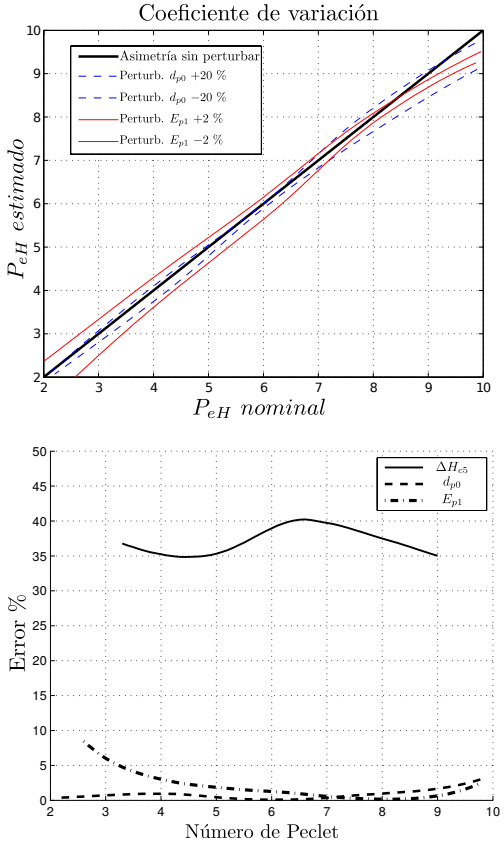

Figura 6. Número de Peclet estimado contra el nominal (arriba) y ECM para un pulso de $T_e = 700\ [K]$ (abajo).

6. CONCLUSIONES

Se diseñó una metodología basada en métricas estadísticas que fue probada ante incertidumbre paramétrica en dos modelos de reactores de gasificación. Se demostró mediante simulación que el número de P_{eH} es robustamente identificable con un EMC del 3 %. Para el gasificador estratificado se observó que el parámetro ΔH_{c5}, es el que influye más en la buena estimación de la dispersión, mientras que con los demás parámetros se crea una banda de incertidumbre muy pequeña.

Para el caso de la configuración Imbert se observa que el parámetro E_{p1} es el que más influye en la estimación del número de Peclet dentro del reactor, esto es debido a que dicho parámetro corresponde al 65 % del valor considerado

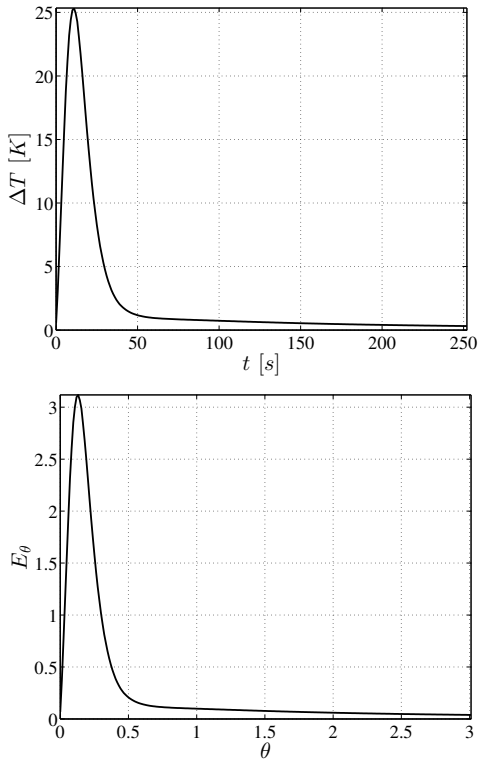

Figura 7. Curva de tiempo de residencia para $Pe = 6$ con un pulso de entrada $T_e = 200$ $[K]$ y duración $\Delta t = 10$ $[s]$

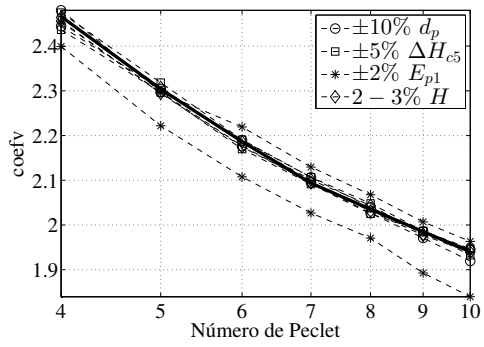

Figura 8. Métricas para un pulso de amplitud $T_e = 200[K]$ y duración $\Delta t = 10$

en el estratificado, por lo cual ante variaciones pequeñas de temperatura se afecta mas al sistema.

REFERENCIAS

Badillo-Hernandez, U., Alvarez-Icaza, L., y Alvarez, J. (2013). Model design of a class of moving-bed tubular gasification reactors. *Chemical Engineering Science*, 101, 674–685.

Baldea, M. y Daoutidis, P. (2007). Dynamics and control of autothermal reactors for the production of hydrogen. *Chemical engineering science*, 62(12), 3218–3230.

Canales, L. (2013). *Reducción de orden en modelos para reactores de gasificación.* Master's thesis, Programa de Maestría y Doctorado en Ingeniería UNAM.

Coste, J., Rudd, D., y Amundson, N.R. (1961). Taylor diffusion in tubular reactors. *The Canadian Journal of Chemical Engineering*, 39(4), 149–151.

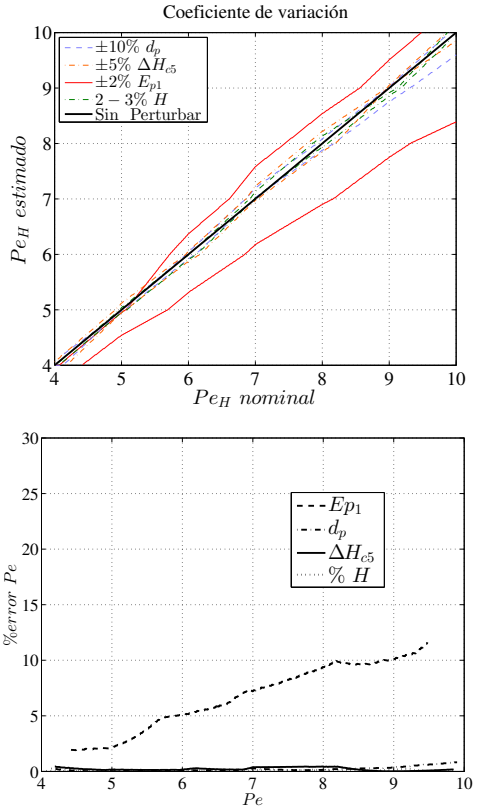

Figura 9. Comparación del Peclet estimado contra el nominal con un puslo de amplitud $T_e = 200$ y duración $\Delta t = 10$

Deans, H. y Lapidus, L. (1960). A computational model for predicting and correlating the behavior of fixed-bed reactors: I. derivation of model for nonreactive systems. *AIChE Journal*, 6(4), 656–663.

Deckwer, W.D. (1974). The backflow cell model—applied to non-isothermal reactors. *The Chemical Engineering Journal*, 8(2), 135–144.

Hernández-Torres, O. (2016). *Análisis dinámico y caracterización de reactores de gasificación.* Master's thesis, Programa de Maestría y Doctorado en Ingeniería UNAM.

Levenspiel, O. (1962). *Chemical reaction engineering: an introduction to the design of chemical reactors.* John Wiley and Sons.

Levenspiel, O. (1999). *Chemical Reaction Engineering.* John Wiley and Sons.

Levenspiel, O. (2011). *Tracer Technology: Modeling the Flow of Fluids*, volume 96. Springer Science and Business Media.

Nájera, I. (2012). *Modelado y control de una clase de reactores tubulares exotérmicos.* Master's thesis, Universidad Autónoma Metropolitana.

Santamaría, L.A. (2016). *Modelado y caracterización experimental de un gasificador en configuración Imbert.* Tesis de maestría, Programa de Maestría y Doctorado en Ingeniería UNAM.

Sinkule, J., Hlavacek, V., Votruba, J., y Tvrdik, I. (1974). Modeling of chemical reactors—xxix mixing-cell model for packed bed reactors. steady state considerations. problems of multiplicity. *Chemical Engineering Science*, 29(3), 689–696.

Methodology and proposal of control applied to a distillation column binary

H. Paz-Arias*, J. L. Benavides M, H. L. Castillo G***, C. E. Anchundia Valencia***

**Facultad de Ingeniería en Sistemas, Departamento de Informática y Ciencias de la Computación Escuela Politécnica Nacional Quito, Ecuador*
E-mail: {henry.paz; carlos.anchundia}@epn.edu.ec
***Departament of Electromechanics, University National of Loja, Loja, Ecuador,*
E-Mail: jose.benavides@unl.edu.ec
****Departament of Geology and Mines, University National of Loja, Loja-Ecuador,*
E-Mail: hernancastil@yahoo.es

Abstract: This article describes a methodology that enables students and people associated with this process know the operation and controls the most significant parameters of a binary distillation column. To do this data is used of an event IFAC. Which start from a linearized model of the plant, that is, at a given time. In which the composition in the bottom, top and pressure are controlled. To this end, a comparison of two control strategies performed as PID (Proportional-Integrator-Derivative) and LQR (Linear Quadratic Regulator), which control a MIMO process of three input variables and three output variables. To achieve this, it has developed a program in MATLAB® / Simulink

Keywords: Chemical Industry, Distillation Columns, L.Q.R (Lineal Quadratic Regulator), PID Control (Proportional-Integrator-Derivative).

1. INTRODUCTION

Distillation is, so far, a widely used separation technique in the process industry around the world. In United, Estates exist around 40.000 distillation columns, which represent approximately 3% of total energy consumption in the country. As a result, improving this process and its control could positively affect decrease energy consumption, increase product quality and enhance protection of environmental resources.

Column distillation's monitoring and modelling, under traditional methods, constitute complex tasks due to the variety of characteristics within the process. Besides these features, the process itself is nonlinear and susceptible to operative restrictions, which reduce the efficacy of linear controllers (Werdan, 2016).

A column is physically composed three major components: (i) a condenser and an accumulator on the top; (ii) a column where the contact with liquid/vapour takes place; and (iii) a re-heater at the bottom. On the other hand, a distillation column includes a complex dynamic because of variables with six degrees of freedom, which include pressure, *flux and temperature and composition*. These last two at both the top as well as the button (Borroto, 2015).

Previous works have achieved significant results. For example, shows a response of a column with a controlled variable (CV) before a manipulated variable (MVs), represented on the X and Y-axis respectively. This reaction is a MIMO process with three inputs variables (heat, reflux, supply) and four output variables (compositions at the top, pressure, the temperature at the button and structure at the button) (Fig. 1) (Seborg, Edgar, & Duncan, 2004).

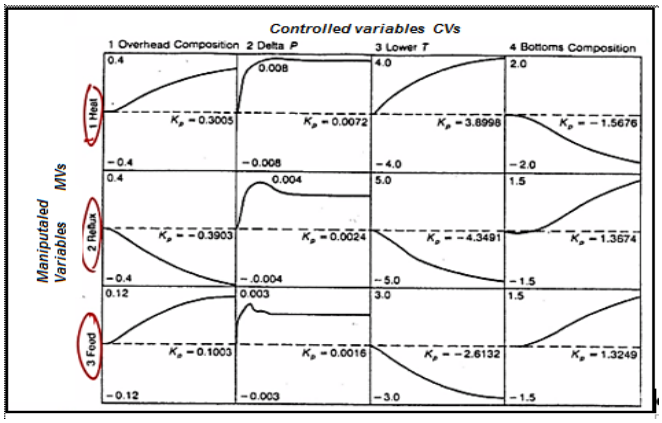

Fig .1 Individual step-response models for distillation column with three inputs and four outputs. Each model represents the step response for 120 minutes (Hokanson, 1992).

As a starting point, in (1) will be considered able to balance the function of a binary column of distillation. This equation involves an input feed (*F*), a distilled composition on the lid (*D*), and structure at the button (*B*).

$$F = D + B \tag{1}$$

In (2) is the result of applying components as in (1). In these equations, it could observe that the input feed is the sum of (i) a distillate flow times its composition; and (ii) sediment

discharge times its balance. It is important to point out that this equation is valid for both light and heavy components as well.

$$F\ ZF1 = D\ XD1 + B\ XB1 \tag{2}$$

From above two concepts raise. One of the concepts is *the reflux ratio*. This represented as the returning flow to the dome (*L*), or as the quantity of condensation that returns to the column, divided by the produced in the distillery (*D*); as shown in (3).

$$R = \frac{L}{D} \tag{3}$$

Similarly, ass in (4) represent the boiling or evaporation that returns to the column as vapour (*V*) and the resulting product (*B*).

$$S = \frac{V}{B} \tag{4}$$

The other concept to take into considerations is *the recovery fraction*. It could calculate as a division between moles leaving the dome by moles entering the dome. This represents how much of the most volatile component that goes into the column, is going to come out the dome. Ass in (5) shows this relationship. In addition, a higher value means a better purification process.

$$f_1 = \frac{DXD1}{FZF1} \tag{5}$$

To know how much could retrieve from the heavier mixture, the lighter mixture subtracts the value of one. This could do on the bottom and the feeder. As in the previous process, a lower value is preferable ass in (6) explains this (Findley, 1983).

$$f_h = \frac{B(1 - X\ B1)}{F(1 - ZF1)} \tag{6}$$

Another value to be calculated is the vapour pressure. To do so, a database with several components and their constants should enter on the Antoine equation, which describes the relationship between temperature and pure substances saturation pressure of the steam as shown in (7). Here, P_V is the vapour pressure of the pure component, while A, B and C constants are the characteristics of every single compound. *T* is the temperature in Celsius degrees.

$$P_v = 10^{A - \left(\frac{B}{T + C}\right)} \tag{7}$$

To apply the above equation should be selected components more and less volatile mix (Distilled and Sediment, themselves will be separated in a distillation column) and may try to load automatically. Elsewhere in the database generated, corresponding to the characteristics of each component, i.e., the values A, B, C of (7).

Considering that, are a mixture ideal of solutions, the Law of Raolut used. This law determines that the ratio of the steam pressure in each component of a perfect solution depends on both, only stem pressure of every component, as well as the molar fraction of each component in the solution, represented by (8). Here, P_A is the A's component partial pressure in the steam; P_A is the pressure of pure *A*'s steam and X_A is the molar fraction of *A* in the liquid state. For the calculation of the vapour in equilibrium, the bubble point procedure is used, with a pressure of 1 atm on (9, 10 and 11).

$$P_A = P_A\ X_A \tag{8}$$

$$P_A = P_A\ + P_B \tag{9}$$

$$P_A = P_A\ X_A + P_B(1 - X_A) \tag{10}$$

$$y_A = \frac{P_A\ X_A}{P} \tag{11}$$

On these equations, P is the system's total pressure, P_B is the partial pressure of pure component *B* in the vapour and X_A is the molar fraction of *A* on the steam state.

Once steam and liquid in equilibrium are calculated, the data of steam (x) and liquid (y) will be graphed to obtain a trend line of y = f(x) and x= f (y). From these, the coefficients will be extracted and entered into the database, mentioned previously (Otiniano, 2004).

1.1 Controller Design based on (PID)

The PID controller is the most common control algorithm today. Process control, more than 95% of the control loops are of PID type, although most of them are PI control (O'Dwyer, 2012).

Generally, in a control system requirements are different. The key factors are to present good performance against disturbances and noise load measuring conditions robustness to process changes and adjusted response as possible to the point. The compromise between these requirements is fundamental. For a system with only feedback error, the attempt to meet all demands with PID control is tough (Tanda, 2016).

1.2 Linear Quadratic Regulators (L.Q.R)

Assuming that the equation of states could measure the whole system's state showed on (15 and 16), then, it is possible to design a state feedback control, which allows calculating u. By doing this, it will be possible to minimise the value of the quadratic objective function, the infinite horizon defined by (12) (Guzmán, 2012) where ´ *Q* ´ and ´ *R* ´ are symmetric real definite matrices.

$$J = \int_0^{\infty} (x^T Qx + \in^{-1} u^T ru)dt \tag{12}$$

It intended that the output of this function tend to zero, with an optimal controller, to minimise control efforts. An optimal you will result in a state feedback as in (13).

$$u\_opt = -r^{-1} B^T\ P\ x \tag{13}$$

On (13), P is a positive matrix defined as a solution of the algebraic equation of Riccati as in (14) (Lewis, 1986).

$$A^T P + PA - PB\ r^{-1} B^T P + Q = 0 \qquad (14)$$

It could prove that, as A and B are a solid pair, first and second terms correspond to the controlled output energy and the control signal, respectively, minimising L.Q.R strategy. However, this correlation is inversely proportional which means that the lower is one; the greater should be the other. The role of the regulator is to establish a minimum error between behaviours in conflict, as lower as possible, as the greater the control, the lower the output (Guzmán, 2012). Sckoaert and Rawlings show how to design an M.P.C controller, with a finite horizon as a counterpart of an L.Q.R. (Moriano & Freddy, 2012) (Rawlings S. P., 1998) (Rawlings J. a., 2010).

2. METHODOLOGY AND METHODS.

2.1 Process description

The data about the distillation column considered in this article contains eight trays, one input feed, one condenser, and one boiler. These data could use on space estate matrix. A very practical problem could include a binary distillation column characterized by a pressure variation as described, which depicts a distillation column to control (Fig. 2).

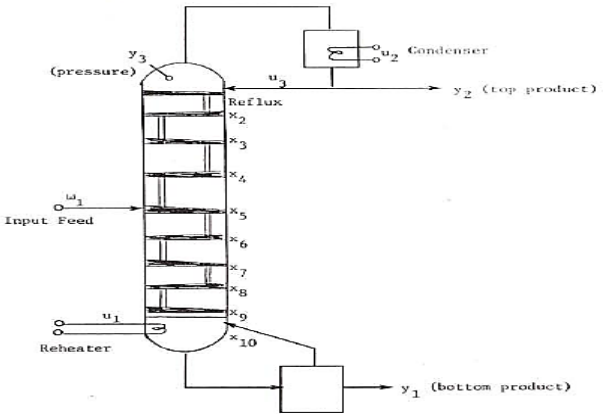

Fig. 2 Binary distillation column pressure variation (Ying Y, 1992).

To be able to execute control of an n-trays distillation column, it is necessary to take into consideration (15, 16 and 17). From these references, a linearization of the model for an 8-trays column obtained.

$$\dot{x} = Ax + Bu + Ew \qquad (15)$$

$$y = Cx \qquad (16)$$

$$y\ m = x \qquad (17)$$

On these equations, vector u is the input $u = \begin{pmatrix} u_1 \\ u_2 \\ u_3 \end{pmatrix}$ as follows:

u_1 = Temperature value on the boiler, at the button of the tower

u_2 = Refrigerant temperature at the condenser

u_3 = Reflux controller on the top

Y is the output vector $y = \begin{pmatrix} y_1 \\ y_2 \\ y_3 \end{pmatrix}$ that includes three outputs:

y_1 = The most volatile component´s composition at the button of the tower

y_2 = The most volatile component´s composition on the top of the tower

y_3 = Pressure on the top of the tower

There is also intermediate transition states:

x_1 = The most volatile component´s structure in the condenser

x_{10} = The most unstable component´s composition in the cauldron

x_{11} = Pressure

x_2 = The most volatile component´s composition in the 1st plate

x_9 = The most volatile component´s composition in the 8th plate

w_1 = Feed changing concentration on the entrance

y_m = Outputs of the systems, which could be measured.

This design is subject to control or regulate three outputs y_1, y_2, y_3, against non-measurable disturbs w_1, . For a faster and desirable response, the following limitations should consider:

$|u_1| \leq 2.5$, $|u_2| \leq 2.5$. For all three cases $t \geq 0$, $|u_3| \leq 0.30$

For $|w_1| \leq 1 y t \geq 0$. In this problem, measured outputs are chosen, and for this reason, the criteria for selection should consider the statement of the problem. In general, a controller that uses the fewer number of measured outputs is desirable (E.J.Davison, 1967).

2.2 Variables involved in the process

The object under study is a distillation tower that includes some variables such as Temperature, Pressure, Level, and Flow. Every single output has a variable. The variables involved during the analysis are u1, u2, u3 and y1, y2, y3 which will substitute with the acronyms *Tf, Tr, Re (inputs)* and *Cf, Ct, Pt (outputs)* for comprehension purposes as shown in Table 1.

Table 1 Variables involved in the analysis of binary distillation tower

PLANT MODEL	
Inputs	**Outputs**
Temperature on the button of the boiler (*Tf*) [˚C]	Product or composition at the button (*Cf*) [g/ml x100 =%, or in molar fraction which is dimensionless]

Temperature at the refrigerant or condenser which means temperature on the top exit (*Tr*) [˚C]	Product or composition on the top(*Cto*) [g/ml x100 =%, o en or in molar fraction which is dimensionless]
Reflux (*Re*) [*g/min*]	Pressure on the top (*Pt)* [N/ m^2 or Pa or Pascal]
Disturbances	
Input feed, flow or mixture (*Fv*) [*g/min*]	

2.3 Controller design based on PID

The design part of a plant model in state space previously defined matrices A, B, C and D, which can establish the behaviour of the three inputs combined with the three outputs.

Thus, through a program in MATLAB® constant signals and open loop input (Te-Re) were applied (Te-Co) and (Ebb), to analyse the behaviour of the outputs (Co-Bottom), (Co-Top) and (Pt). Thus all three functions are chosen coupled transfer (18, 19 and 20 respectively), which were most affected by these changes at its input and, that verifying that both affect the change in the outputs.

Output 1 (Composition at the bottom):

$$\frac{0.0025S^{10}+0.0007S^{9}+0.0001S^{8}}{S^{11}+0.3102S^{10}+0.0389S^{9}+0.0026S^{8}+0.0001S^{7}} \quad (18)$$

Output 2 (Composition in Tope):

$$\frac{0.}{S^{11}+0.3102S^{10}+0.0389S^{9}+0.0026S^{8}+0.0001S^{7}} \quad (19)$$

Output 3 (Pressure in the Tope):

$$\frac{0.0001S^{9}}{S^{11}+0.3102S^{10}+0.0389S^{9}+0.0026S^{8}+0.0001S^{7}} \quad (20)$$

The open-loop system coupled and uncoupled and three respectively (Fig, 3).

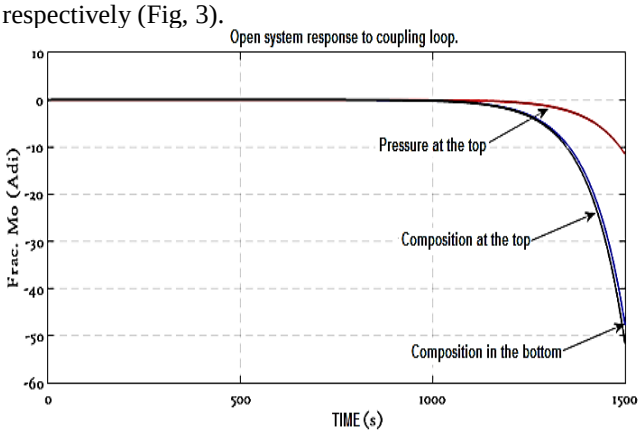

Fig. 3 Answer open-loop process, when excited with a step signal coupling

Then, to stabilise the system, a PID controller is implemented, establishing the conditions setpoint variables normalised considering the composition on the bottom (sediment) is as close to zero, the structure at the top (distilled) is as close to one, and pressure on top is as close to one.

The aforementioned means that the vapour pressure ($\bar{X}v$) more fluid pressure ($\bar{X}_l$) equals one atm, as shown in the following equation (21). Stressing that the pressure variation in the model description assumed a value constant 1 atm.

$$\bar{X}v + \bar{X}_l = 1atm \quad (21)$$

Related at a given time, using linearized data at a given time, to reflect this behaviour the response of the input variables and process output uncoupled, i.e., nine transfer functions (three output variables that combine analysed three output variables).

For the self-tuning of the PID control algorithm is first performed a study of controllability of the output variables, that is to say, know the final state and the initial situation of the matrix, as shown in (22) and (23).

$$X(n) - X(0) = matrix\ \ arrays \quad (22)$$

$$[D*CB*CAB*CA*2B...C*A*n-1*B] = n \quad (23)$$

Such matrix Controllability, shows that the process is not controllable. Then Observability analysis of the output variables is the final state, and the initial condition of the array is known, X (n) -X (0) = matrix arrays such as in (24).

$$[D*CB*CAB*CA*2B...C*A*m-1*B] = m \quad (24)$$

The PID control applied to coupled and uncoupled the system and five respectively (Fig. 4, 5, 6).

2.4 Controller design based on L.Q.R

L.Q.R provides a great freedom for designing and delivers a low computational cost for control law. This makes it possible to implement a digital control system. However, although L.Q.R control is proportional, it is necessary to include an integral action for removing possible stationary errors over those variables deemed necessaries (Ying Y, 1992).

To apply L.Q.R, it develops a program that allows obtaining a step-like response with an optimal value. After that, calculate Q's structure for every single element, where the diagonal of the matrix are the restrictions of the elements or the value of the states. In (25) indicates that maximum and minimum values of the outputs should take for every intermediate space

$$Q = \frac{1}{(Maximum\ Value\ -\ (Minimum\ Value\ ))^2} \quad (25)$$

Namely, R should calculate. But, in this case, the values are every intermediate space inputs. Then, they replaced in (26). This could achieve simulating the system as in (Fig. 5). by this, maximum and minimum of process.

$$R = \frac{1}{(Maximum\ \ Value\ -\ (Minimum\ \ Value\ ))^2} \quad (26)$$

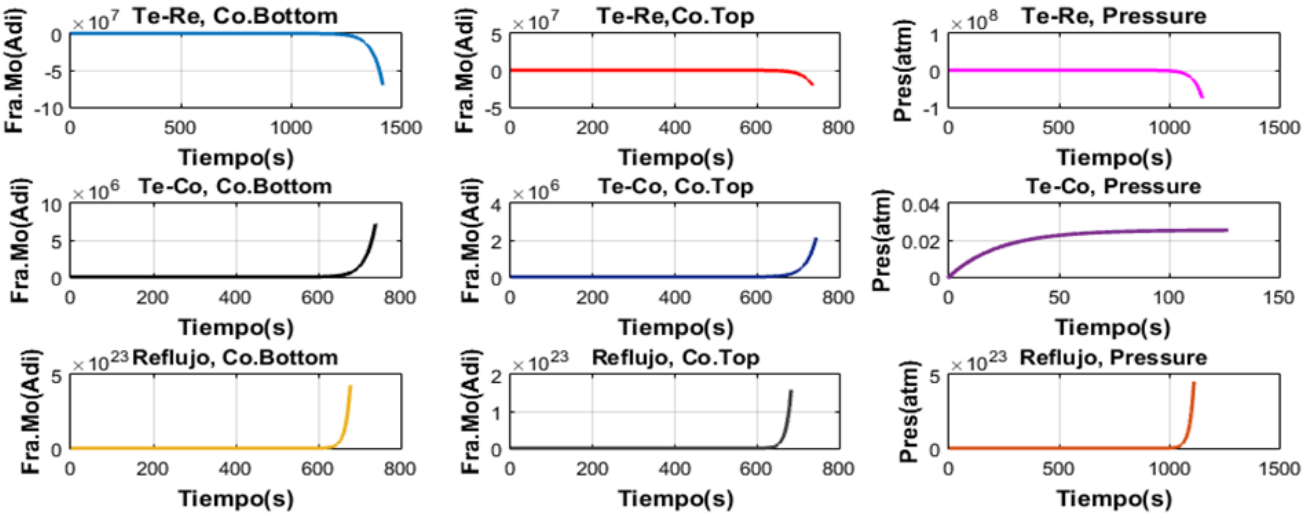

Fig. 3 Response process when excited with a step signal to open loop and decoupling.

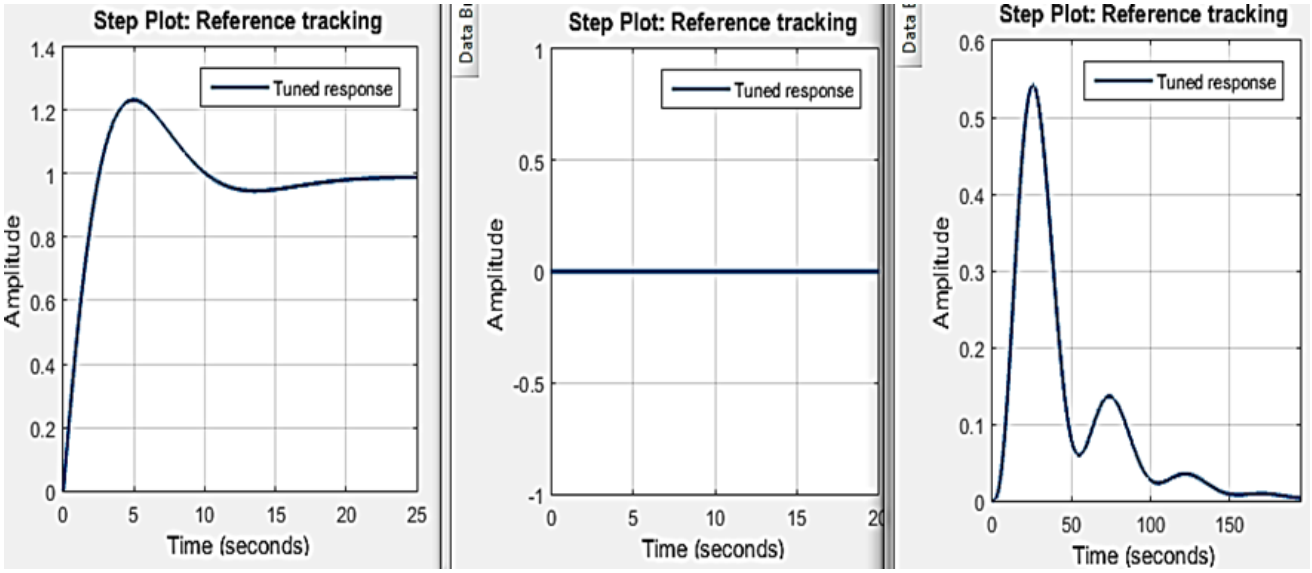

Fig. 4 Response PID controller coupling.

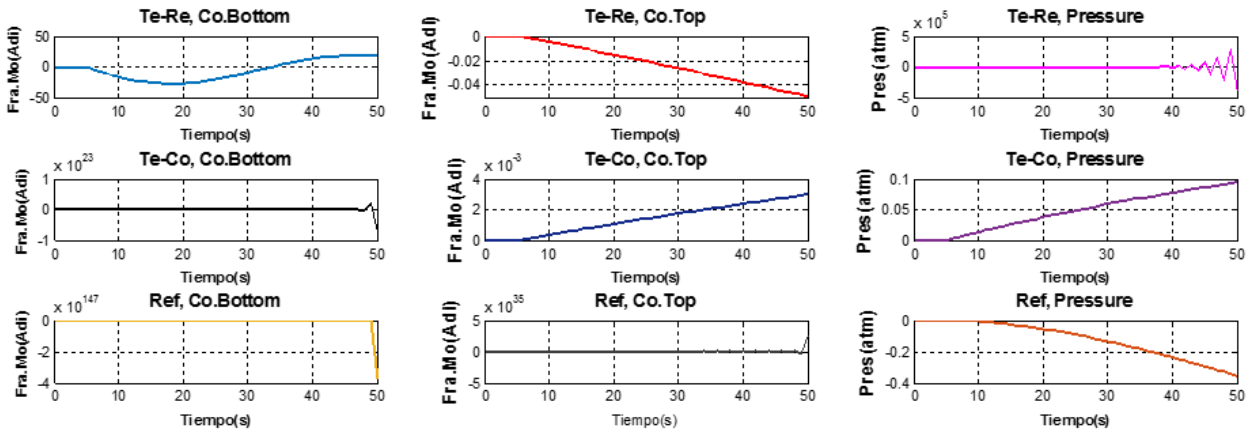

Fig.5 Answer the PID controller, with decoupling.

Table 2 shows all values in the quadratic performance matrix Q, which obtained by replacing the outputs on every intermediate space.

Table 2 Values Hall adds Matrix Quadratic performance Q.

44.44	0	0	0	0	0	0	0	0	0	0
0	44.44	0	0	0	0	0	0	0	0	0
0	0	44.44	0	0	0	0	0	0	0	0
0	0	0	44.44	0	0	0	0	0	0	0
0	0	0	0	44.44	0	0	0	0	0	0
0	0	0	0	0	44.44	0	0	0	0	0
0	0	0	0	0	0	44.44	0	0	0	0
0	0	0	0	0	0	0	44.44	0	0	0
0	0	0	0	0	0	0	0	44.44	0	0
0	0	0	0	0	0	0	0	0	44.44	0
0	0	0	0	0	0	0	0	0	0	12.5

Next, the values of the quadratic performance values R showed in Table 3.

Table 3 Found quadratic matrix R, production values

44.44	0	0
0	44.44	0
0	0	12.5

The values found previously replaced on (27) to obtain feedback gains for controller optimization, as shown in Table 4.

$$K = lqr\ (A, B, Q, R) \tag{27}$$

Table.4 feedback values for each state

Name	*Value*	*Name*	*Value*
K1	0.0041	K7	0.0017
K2	7.16X10-4	K8	-0.0036
K3	-0.2491	K9	0.3980
K4	0.0024	K10	8.619x10-4
K5	-0.0037	K11	-0.0024
K6	-0.0965		

Show the model for distillation column system in a space state, where *x1* to *x11* were calculated as intermediate states (Fig. 7).

Following the program developed, a step-like input of amplitude one applied to the data found previously as shown in (Fig. 6). The behaviour of the three outputs (composition at the button, composition on the top, pressure on the top) can see. They do not follow any reference, but they do minimise the error of the reference. By applying L.Q.R strategy, the behaviour could determine.

Following the execution of the program, eleven intermediate stated calculated (Fig. 8). Their values identified which fulfill the purpose of this kind of control (Fig. 9).

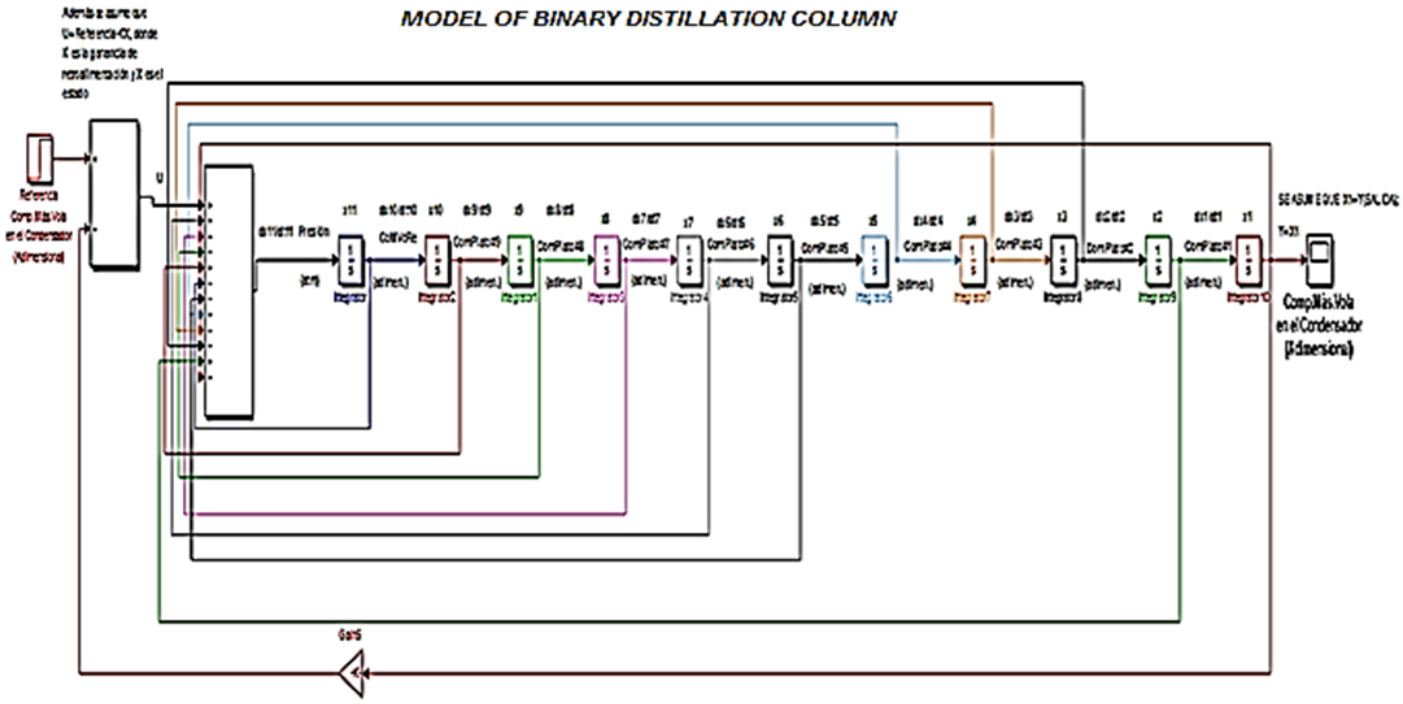

Fig. 7 State area scheme carried Simulink / MATLAB ®, Source: Author

.

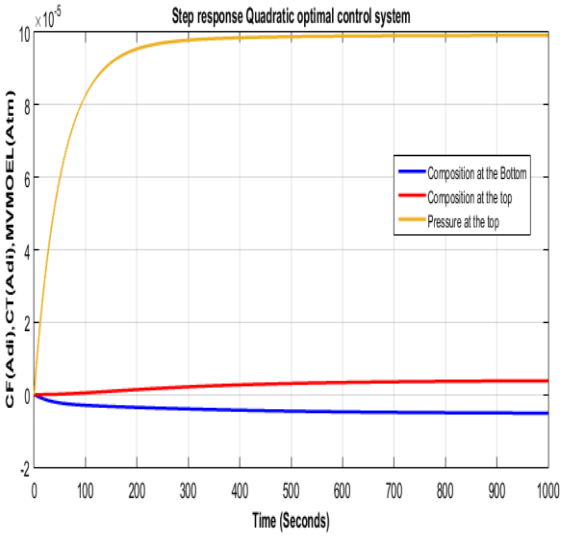

Fig. 8 Step system response quadratic optimal control

3 DISCUSSION

Then shown in Table 5 the result obtained when applied to the distillation column a PID controller, coupled with transfer functions coupled and uncoupled.

Table.5 Results with the PID for features transfer coupled and uncoupled, the meaning of F-M is (Molar Fraction)

	Controller (PID) Coupled			*Controller (PID) Uncoupled*		
	Co.Bo	*Co.To.*	*Pre.To*	*Co.Bo*	*Co.To.*	*Pre.To*
Overshoot	20%	n/m	n/m	n/m	n/m	n/m
Stabilization time	20 s	n/m	n/m	n/m	n/m	n/m
Rise time	3 s	n/m	n/m	n/m	n/m	n/m
Error on stable state	0.2 F-M	n/m	n/m	n/m	n/m	n/m

In Table 6 shown the result obtained when applied to the distillation column a L.Q.R controller, coupled with transfer functions coupled and uncoupled.

Table. 6 Feedback values for each state

	Controller (L.Q.R)
Overshoot	Too small to be considered
Stabilization time	Exceeds 1.000 seconds, except for pressure, which got stable on 290
Rise time	Too low for 11 seconds
Error on stable state	Too small to be considered

4 CONCLUSIONS

It has developed a theory-based methodology to be used by students and people, in general, related to the sector of refinement of a mixture, starting to find some values that allow the simulation of processes, soon to verify them.

Data used were a combination of water vapour and alcohol, which inflow is constant; assuming that this fluid is entering the column is laminar or turbulent, as it is considered a gas, although it could obtain future data from a mixture of ethanol-water.

Assuming that the composition behaves like an ideal solution in this work using the Type, I for control of the most significant parameters of the distillation column made.

It is important to analyse these advanced control methods because currently most of the systems that apply to columns of binary distillation bring these built techniques, all to stabilise and increase productivity, by controlling key variables involved in the process.

These control methods based on neural networks and fuzzy logic to minimise the time of stabilisation process significantly, the advanced control using L.Q.R method allows control of all intermediate states.

REFERENCES

Borroto, M. A. (2015). Identificación y Control Predictivo de una columna de destilación Etanol-Agua. CIE2015 (p. 1). Villa Clara: UCLV. Retrieved Julio 2, 2015

E.J.Davison. (1967). Control of a distillation column with pressure variation (Vol. 45). Toronto, Ontario, Cánada: Trans Institute of Chemical Engineers. Retrieved Julio 05, 2014

Findley, M. (1983). Selection of Control Measurements. In AIChEMI Modular Instruction. T.F. Edgar, Ed, Series A, Vol.4, New York.

Guzmán, T. (2012). Event-Based LQR Control for Attitude Stabilization of a Quadrotor. XV Congreso Latinoamericano de Control Automático, 23-26.

Hokanson, G. (1992). Dynamic Matrix Control Multivariable Controllers.

Lewis, F. W. (1986). Optimal Estimation.

Moriano, P., & Freddy, N. (2012, Julio/Septiembre). Modelado y control de un nuevo sistema bola viga con levitación magnética. RIAI (Revista Iberoamericana de Automática e Informártica Industrial), 9(3), 258. Retrieved Marzo 08, 2015

O'Dwyer, A. (2012). An Overview of Tuning Rules for the PI and PID Continuous-Time Control of Time-Delayed Single-Input, Single-Output. PID Control in the Third Millennium - Lessons, 3-44.

Otiniano, M. (2004). Cálculos en Destilación continua para sistemas binarios ideales utilizando hoja de cálculo. Revista Soc. Química, 70(4), 220.

Rawlings, J. a. (2010). ´´ Model Predictive Control Theory and Design´´. Nob Hill Publising .

Rawlings, S. P. (1998). ¨Constrained Linear Quadratic Regulations¨ (Vol. 43). EEE Transactions on Automatic Control.

Seborg, D., Edgar, T., & Duncan, M. (2004). Process Dynamics and Control. NJ-EEUU: John Wiley&Sons, Inc.

Tanda, M. a. (2016). Herramienta para la sintonía robusta decontroladores PI/PID de dos grados de libertad. Revista Iberoamericana de Automática e Informática Industrial RIAI, Vol 13, 22-31.

Werdan, J. P. (2016, Abril 08). Modelagem Empirica de Colunas de Destilação Utilizando Redes Neurais de Wavelets para Otimização E Controle de Processos. BEQ. Retrieved Abril 10, 2016.

Ying Y, M. a. (1992). Bilinear Control Strategy for paper making process (Vol. 111).

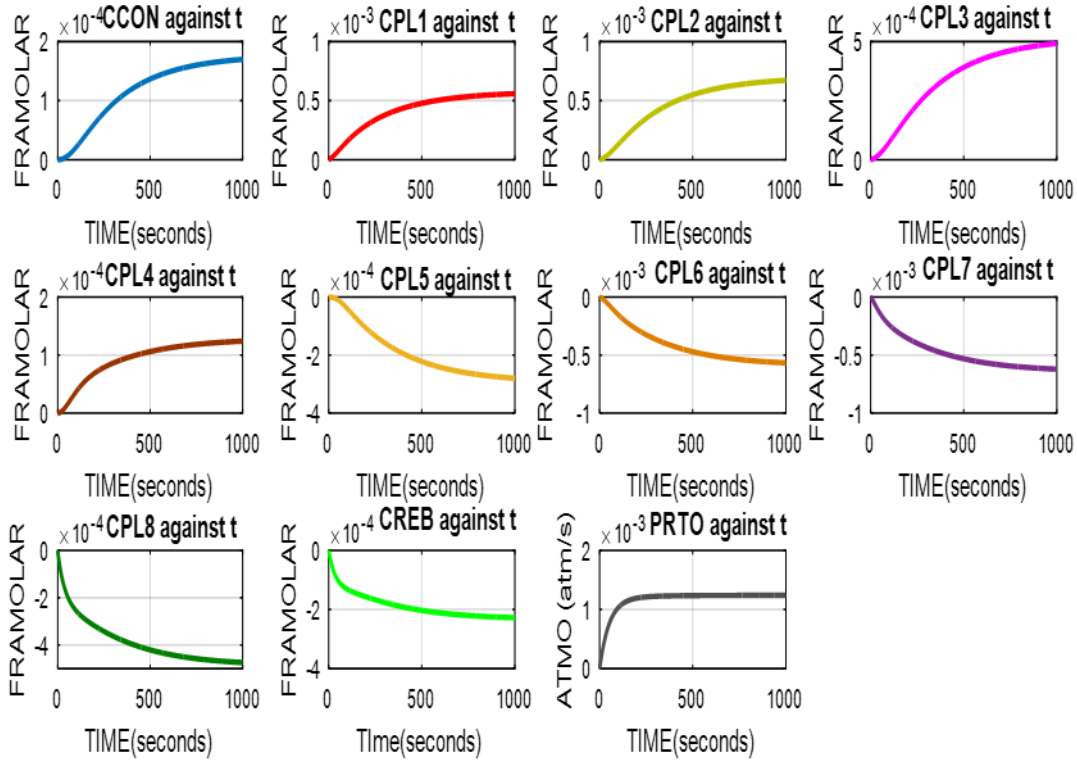

Fig. 9 L.Q.R regulator response

Modeling and parameter estimation of a 4-wheel Mobile Robot ⋆

Oscar Barrero, * **Harold F. Murcia** * **and Juan D. Valenciano** *

* *Facultad de Ingeniería, Grupo de Investigación D+TEC, Programa de Electrónica, Universidad de Ibagué, Carrera 22 calle 67, Ibagué 730001, Colombia. (e-mail: oscar.barrero@Unibague.edu.co).*

Abstract: In this paper we present a new model for skid-steering mobile robots, taking into account the relation between the friction and angular velocity of the vehicle. Then, by using the parameter estimation toolbox of Simulink-Matlab, we calculate the model parameters with a good fitting to real data. Finally, we design a state space feedback controller with integral action, to make the controller robust against the friction phenomena that present the vehicle when turning. The simulation results show good performance of the controller in reference tracking as well as control actions.

Keywords: Unmanned Ground Vehicle, Skid-Steering Mobile Robot, Parameter Identification, Linear Quadratic Regulator.

1. INTRODUCTION

Mobile robots have generated a significant interest from companies and universities in recent years, specially for the navigation system and automatic tasks. The unmanned ground vehicles (UGV) are one of the most popular platform among mobile robots due to its wide range of applications e.g: Planetary exploration, military operations, mining, inspection and surveillance, rescue, clean up of hazardous substances, health care, among others, etc., where a high degree of autonomy is required, hence, motion control systems become a fundamental part on its development (Siegwart et al. (2011)).

In mobile robots, motion planning for nonholonomic systems has been an active area of research in the last years, as consequence, much effort has been oriented to solve trajectory tracking problem using kinematic models, but not much research has be done on the low level control, the problem of the angle and speeds control and the dynamics of the UGV's. (Ortigoza et al. (2012)).

Wheeled skid-steering is a kind of UGV with two degrees of freedom (DOF) based on controlling of relative velocities of left and right wheels, similarly to differential drive vehicles. Skid steering mobile robots are widely used as outdoor mobile robots due to some advantages as: simple and robust mechanical structure, faster response, strong traction, and high maneuverability, including zero-radius turning, over alternative wheel configurations such as Ackermann or axle-articulated (Velázquez and Lay-Ekuakille (2011)).

However, this locomotion scheme present special difficulties when addressing the motion control. Skid-steering kinematics is not straightforward, since it is not possible to predict the exact motion of the vehicle only from its control inputs due to skid phenomena. Some authors have used models based nonlinear control techniques by explicitly considering dynamics and drive models (Alhelou et al. (2015)), in some works the kinematics have been addressed as the relation of linear and angular velocities with the position of the vehicle (Mandow et al. (2007)). But, major skid effects have not been considered (Morales et al. (2010)), which arise at a lower level, in the relation between drive velocities and vehicle velocities (Elshazly et al. (2014)).

Most of the previous works stated above do a design of a control system for dynamic and drive independently without considering the combination between dynamic and drive model. Therefore, the goal of this paper is to design and implement a robot control which will be used as inner loop control in trajectory tracking.

In this paper, a state space model of the dynamic drive parts of the Rover based on (Kozłowski and Pazderski (2004)) is developed in section II. Section III, focuses in the design of a LQR controller with integral action. Section IV is dedicated for extensive simulation results and Section V is devoted to conclusions and ideas for future work. Finally, acknowledgments and references complete the paper.

2. PROBLEM FORMULATION

Consider the following master slave system for trajectory tracking (See Figure 1). A high level controller generates the angle and linear speed references according to the desired trajectory and the low level controller ensures the achieving those values and rejecting disturbances in the robot movements. This paper is focused on the inner loop in order to control the angle of the robot and its linear speed manipulating the voltages applied on the motors.

The mechanical platform consist in two gear motors coupling with two wheels each one using chain transmission. A car battery energizes the motor drivers which are

⋆ Financial support by the Research Project 15-343-INT of Universidad de Ibague, is gratefully acknowledged.

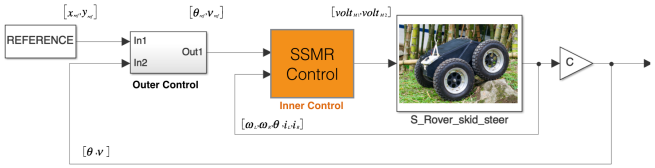

Fig. 1. Angular and speed control of Skid-Steer Mobile Robot (SSMR) in path following applications.

manipulated by the Controller Unit through pulse width modulation (PWM). Each motor has a gear transmission with a reduction 16:1, an encoder autonics E50s and a current sensor Allegro ACS709. Additionally the system need an angle sensor for the rotation control, whereby a magnetometer on a NAVIO board was added to the instrumentation of the robot. The Figure 2 illustrates the main components in the control system and the interaction between them.

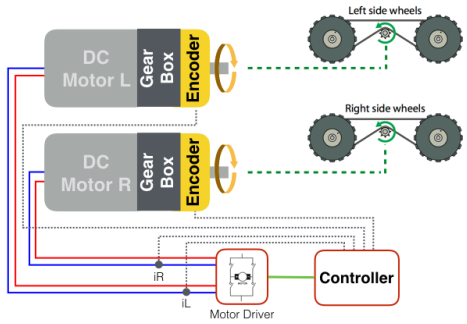

Fig. 2. Drive system scheme of SSMR. A magnetometer sensor is also required for angle control of the Robot.

2.1 Skid-Steer Mobile Robot Model

The mathematical model of the vehicle can be divided in three parts: kinematics, dynamics and drive models. This paper focuses especially on the dynamic part. The main equation that describes the dynamics of the robot is given by (C.Linares and A Gallegos (2015); Jeon et al. (2014); Elshazly et al. (2014))

$$\bar{M}(q)\dot{\eta} + \bar{C}(\dot{q})\eta + \bar{R}(\dot{q}) = \bar{B}(q)\tau; \tag{1}$$

where $\eta = [v_x, \omega]^T$, v_x is the relative front velocity, ω is the rotational velocity of the robot, τ is the torque input and $q = [X, Y, \theta]^T$ represents the generalized coordinates of the center of mass of the robot. The matrices $\bar{M}, \bar{B}, \bar{C} and \bar{R}$ are given respectively:

$$\bar{M} = \begin{bmatrix} m & 0 \\ 0 & mX_G\dot{\theta} \end{bmatrix} \tag{2}$$

$$\bar{C} = \begin{bmatrix} 0 & mX_G\dot{\theta} \\ -mX_G\dot{\theta} & 0 \end{bmatrix} \tag{3}$$

$$\bar{R} = p_w|\omega| \begin{bmatrix} F_{rx}(\dot{q}) \\ X_G F_{ry}(\dot{q}) + M_r \end{bmatrix} \tag{4}$$

$$\bar{B} = \frac{1}{r} \begin{bmatrix} 1 & 1 \\ -c & c \end{bmatrix} \tag{5}$$

$$\begin{bmatrix} vx \\ \omega \end{bmatrix} = 0.5 \begin{bmatrix} r & r \\ -\frac{r}{Y_G} & \frac{r}{Y_G} \end{bmatrix} \begin{bmatrix} \omega_L \\ \omega_R \end{bmatrix} \tag{6}$$

It is noteworthy to mention that we found very important to multiply the term $p_w|\omega|$ to the original matrix $\bar{R}$, because we realized that the friction in x and y direction is proportional to the angular speed of the car. Now, using equation (6) we can rewrite the model equation (1) in function of the new state space vector $[\omega_L, \omega_R]^T$ as shown in (7),

$$\bar{M}p \begin{bmatrix} \dot{\omega_L} \\ \dot{\omega_R} \end{bmatrix} + \bar{C}p \begin{bmatrix} \omega_L \\ \omega_R \end{bmatrix} + \bar{R}(\dot{q}) = \bar{B}\tau, \tag{7}$$

where,

$$\bar{B}\tau = \bar{B}N \begin{bmatrix} Km_L & 0 \\ 0 & Km_R \end{bmatrix} \begin{bmatrix} ia_L \\ ia_R \end{bmatrix} = \bar{B}Km \begin{bmatrix} ia_L \\ ia_R \end{bmatrix} \tag{8}$$

$$\bar{M}p = \frac{1}{2} \begin{bmatrix} m & m \\ -(\frac{mx_G^2 + I}{Y_G}) & (\frac{mx_G^2 + I}{Y_G}) \end{bmatrix} \tag{9}$$

$$\bar{C}p = \frac{rmX_G\omega}{2} \begin{bmatrix} -Y_G & Y_G \\ -1 & -1 \end{bmatrix} \tag{10}$$

$$\begin{bmatrix} \dot{\omega_L} \\ \dot{\omega_R} \end{bmatrix} = (\bar{M}p)^{-1}(\bar{B}Km \begin{bmatrix} ia_L \\ ia_R \end{bmatrix} = -\bar{C}p \begin{bmatrix} \omega_L \\ \omega_R \end{bmatrix} - \bar{R}). \tag{11}$$

Finally, we can rewrite (7) defining and augmented state space vector $x(t) = [\omega_L, \omega_R, \theta, ia_L, ia_R]^T$, as result the model can be written as

$$\begin{bmatrix} \dot{\omega_L} \\ \dot{\omega_R} \\ \dot{\theta} \\ \dot{ia_L} \\ \dot{ia_R} \end{bmatrix} = \begin{bmatrix} -\bar{M}p^{-1}\bar{C}p & 0 & \bar{M}p^{-1}\bar{B}Km \\ -0.5Y_G & 0.5Y_G & 0 & 0 & 0 \\ -NKb_L/La & 0 & 0 & -Ra/La & 0 \\ 0 & -NKb_R & 0 & 0 & -Ra/La \end{bmatrix} + \cdots \tag{12}$$

$$+ \begin{bmatrix} 0 & 0 \\ 0 & 0 \\ \frac{K_{pwm}}{La} & 0 \\ 0 & \frac{K_{pwm}}{La} \end{bmatrix} \begin{bmatrix} V_L \\ V_R \end{bmatrix} - \begin{bmatrix} \bar{M}p^{-1}\bar{R} \\ 0 \\ 0 \\ 0 \end{bmatrix} \tag{13}$$

2.2 Parameter Estimation and Validation

Once the model was determined, we performed a parameter estimation (grey box) using MATLAB Simulink. The Table 1 shows some parameters which were measured from the robot directly and the Table 2 shows the estimated parameters. A series of experiments around the operation region was carried out to acquire the real signals used in estimation and validation of the model parameters.

The data obtained in the test was divided in two part, 70% for training and 30% for validation. Then, the data was standardize to a standard deviation of one for being used in the parameter estimation toolbox of Simulink-Matlab, as shown in Figure 3.

Table 1. System parameters

Parameter	Rep.	Value	Unit
Robot mass without wheels	m	58	kg
Wheel radius	r	0.4	Meters
Wheel wide	w	0.06	Meters
Robot wide	a	0.4	Meters
Robot long	L	0.6	Meters
Motor resistance	Ra	0.33	Ω
Motor gear ratio	N	16	

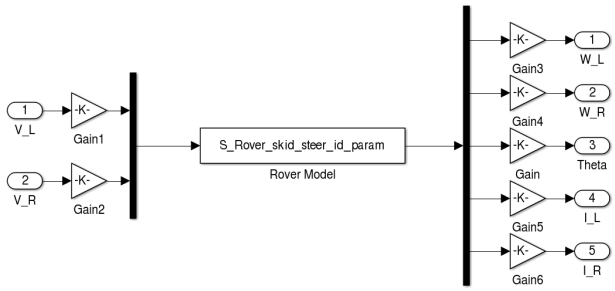

Fig. 3. Block diagram for parameter estimation in Simulink-Matlab

Then, we define the parameters to be estimated (see Table 2) and set as estimation algorithm the least squares with LevenbergMarquardt. It is important to note that the sampling time and the quantizer were Ts=60 milliseconds and 10 bits respectively. The experiments used the Rover platform from the University of Ibagué in a 30 x 15 meters asphalt space (See Figure 4).

Fig. 4. The picture shows the Rover: A four wheel skid-steering mobile Robot.

Table 2. Estimated parameters

Parameter	Rep.	Value	Unit
y coordinate rotation center	Y_G	0.38	m
x coordinate rotation center	X_G	0.059	m
Electromotive force constant RM	Kb_R	0.0525	$V/rad/sec$
Electromotive force constant LM	Kb_L	0.0692	$V/rad/sec$
Motor torque constant RM	Km_R	0.0320	$N.m/Amp$
Motor torque constant LM	Km_L	0.0379	$N.m/Amp$
Motor inductance	La	0.0688	H
Moment of inertia of the robot	I	15	$kg.m^2$
Friction coefficient in x direction	u_x	0.01	
Friction coefficient in y direction	u_y	1.2	
Proportional constant of friction	p_w	0.184	

Model Validation The input data for the experiments were generated from the pilot with a remote control "Spektrum Dx8i" and using the MATLAB function "idinput" around the operation point. The Figure 5 illustrates the results of the estimation for each state variable: Angular velocity of the left wheel ω_L, Angular velocity of the right wheel ω_R, rotation angle of the robot θ, Left motor current ia_L and Right motor current ia_R. As is depicted in Figure 5, the model parameters found fit pretty good to the real data.

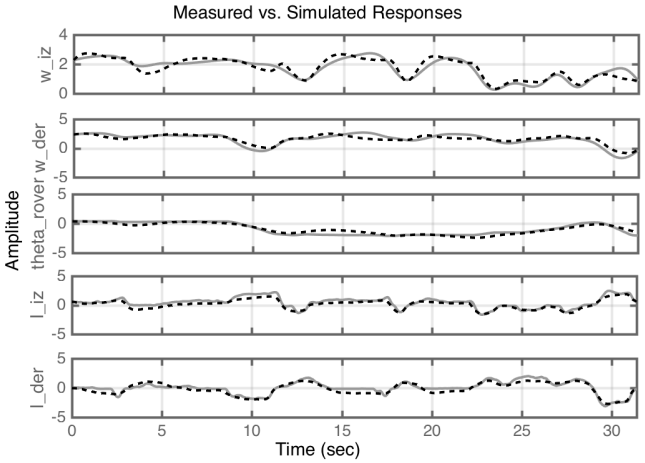

Fig. 5. Parameter Estimation validation: Dashed line: Experimental data and continuous line: Model response.

Linear Model In order to design a Linear Quadratic Regulator (LQR) controller, we need to linearized the model described in (12), as result we have equation (14), note that we are not taken into account the friction effect represented by $\bar{R}$,

$$\begin{bmatrix} \dot{\omega_L} \\ \dot{\omega_R} \\ \dot{\theta} \\ \dot{i_L} \\ \dot{i_R} \end{bmatrix} = A \begin{bmatrix} \omega_L \\ \omega_R \\ \theta \\ i_L \\ i_R \end{bmatrix} + B \begin{bmatrix} V_L \\ V_R \end{bmatrix} \tag{14}$$

$$A = \begin{bmatrix} -\bar{M}p^{-1}\widehat{\bar{C}p} & 0 & \bar{M}p^{-1}\bar{B}Km \\ -\dfrac{1}{Y_R+Y_L} & \dfrac{1}{Y_R+Y_L} & 0 \quad 0 \quad 0 \\ -\dfrac{NKb_L}{La} & 0 & 0 \quad -\dfrac{Ra}{La} \quad 0 \end{bmatrix} \tag{15}$$

$$B = \begin{bmatrix} 0 & 0 \\ 0 & 0 \\ 0 & 0 \\ \dfrac{K_{pwm}}{La} & 0 \\ 0 & \dfrac{K_{pwm}}{La} \quad 0 \end{bmatrix} \tag{16}$$

Where K_{pwm} is the conversion a duty cycle given by: $Volt_{Batt}/100$.

$$\widehat{\bar{C}p} = \frac{rmX_G}{(Y_R+Y_L)^2} \begin{bmatrix} C1 & C2 \\ C3 & C4 \end{bmatrix} \tag{17}$$

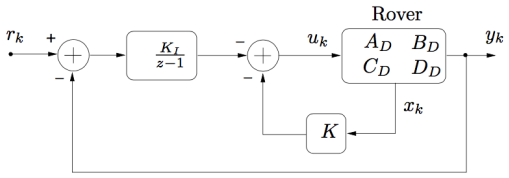

Fig. 6. Block diagram of state space feedback control strategy with integral action.

Where $C1 = 2(\bar{\omega_L} - \bar{\omega_R})$, $C2 = 2(\bar{\omega_R} - \bar{\omega_L})$, $C3 = Y_R(2\bar{\omega_L} - \bar{\omega_R}) + Y_L\bar{\omega_R}$ and $C4 = Y_L(\bar{\omega_L} - 2\bar{\omega_R}) + Y_R\bar{\omega_L}$.

3. CONTROL DESIGN

Using the same sample time used in the parameter identification, the continuous time system given by (14) was discretized using zero-order hold method, as result we have the discrete time model given in (18),

$$x_{k+1} = A_D x_k + B_D u_k \tag{18}$$

Where A_D and B_D are the discrete-time counterparts of the continuous time state matrix A and input matrix B. For the sake of simplicity we use the same notation to represent the continuous and discrete time versions of the state x and input u.

3.1 LQR Control

Using the above discrete time model, a Linear Quadratic Regulator (LQR) feedback controller with integral action is designed, see Figure 6. Due to the fact that in the linear model the friction was neglected, the integral action is needed to make the controller more robust against this.

In Figure 6 r_k are the references inputs for ω_k and v_{xk}, y_k are the model outputs ω_k and v_{xk} and u_k the control actions V_L and V_R which correspond to the motor voltages. Besides, the controller design consist of finding K and K_I such that we minimize the cost function given in (19),

$$J(u) := \sum_{k=1}^{\infty} x_k^T Q x_k + u_k^T R u_k, Q \geq 0, R > 0. \tag{19}$$

Before solving the LQR problem we have to introduce the dynamic effect of the integral loop into the model, hence, an augmented state space representation is used, as it can be seen in (20), where we have two additional state variable, namely, xi the integral error of ω and v_x.

$$\begin{bmatrix} x_{k+1} \\ xi_{k+1} \end{bmatrix} = \begin{bmatrix} A_D & 0_{n\times 2} \\ -C_D & I_2 \end{bmatrix} \begin{bmatrix} x_k \\ xi_k \end{bmatrix} + \begin{bmatrix} B_D \\ 0 \end{bmatrix} u_k \tag{20}$$

As result, the control action is defined as shown in (21)

$$u_k = -K_I xi_k - K x_k. \tag{21}$$

The LQR solution is calculated using the control toolbox of Matlab, using the following Q and R matrices,

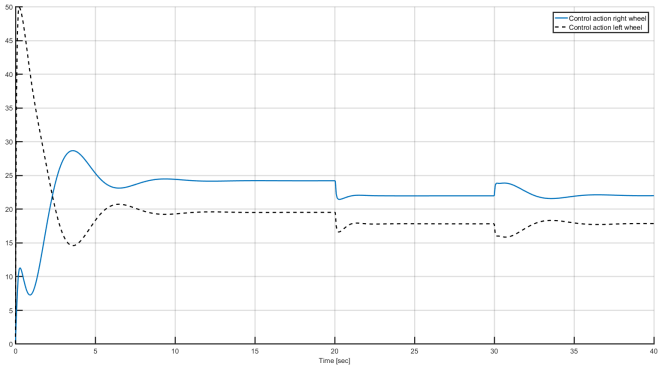

Fig. 7. Rover control actions. Dashed line control action for left wheel, solid line for the right wheel. x axis is time in seconds, and y axis is magnitude in percentage.

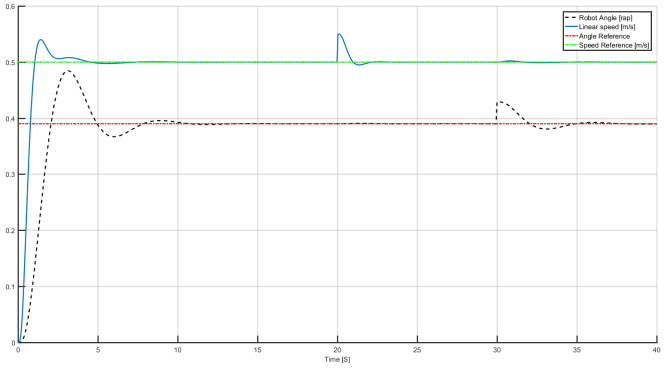

Fig. 8. Rover outputs response. Solid line v_x response in m/s, dashed line θ response in radians and references: 0.5 m/s for v_x and 0.39 $rads$ for θ. x axis is time in seconds with step disturbances at 20 seconds for v_x and 30 seconds for θ.

Q = diag([0.1 0.1 1 1 1 100 100]), R = diag([0.01 0.01]),

we have as result,

$$K = \begin{bmatrix} 109.3160 & -56.4872 & -590.0479 & 6.8042 & -0.3231 \\ -59.1257 & 122.2041 & 586.5384 & -0.3307 & 6.7130 \end{bmatrix} \tag{22}$$

$$K_I = \begin{bmatrix} 39.3801 & -39.4175 \\ -37.6415 & -41.7103 \end{bmatrix}. \tag{23}$$

Next, we test in simulation the design linear controller but using the nonlinear model, the responses are shown in Figures 7 and 8. As can be seen, the close-loop system response quite well, it follows the references in a short time, and the control action are into the rank of values.

4. CONCLUSION

A new model for skid-steering mobile robot is presented, taking into account the relation of the friction and the angular velocity of the robot. Grey box modeling was carried out using the parameter estimation toolbox of Simulink-Matlab with good fitting results. Then, an feedback state space control strategy with integral action was presented and solved using LQR optimal solution (See Figures 7 and 8). The simulation showed very interesting and promising

results in control actions and tracking references. Rewriting the model, such that the state space vector were variables which can be easily measured, it makes possible the implementation of the controller in future. Therefore, as future work, we will implement the controller in the real vehicle, and also explore the design of a nonlinear controller like sliding mode control.

REFERENCES

Alhelou, M., Dib, A., and Albitar, C. (2015). Trajectory tracking for skid-steering mobile robots using sliding-mode control. In *Control Conference (ASCC), 2015 10th Asian*, 1–6. IEEE.

C.Linares, A.A.E.R. and A Gallegos, J. (2015). Seguimiento robusto de trayectorias en la transportación de objetos por un robot móvil. In AMCA (ed.), *Congreso Nacional de Control Automático*, pp. 417 –422.

Elshazly, O., Abo-Ismail, A., Abbas, H.S., and Zyada, Z. (2014). Skid steering mobile robot modeling and control. In *Control (CONTROL), 2014 UKACC International Conference on*, 62–67. IEEE.

Jeon, S., Jeong, W., and Park, D. (2014). A stable tracking control of skid steered mobile platform. In *Informatics in Control, Automation and Robotics (ICINCO), 2014 11th International Conference on*, volume 2, 556–561. IEEE.

Kozłowski, K. and Pazderski, D. (2004). Modeling and control of a 4-wheel skid-steering mobile robot. *Int. J. Appl. Math. Comput. Sci*, 14(4), 477–496.

Mandow, A., Martinez, J.L., Morales, J., Blanco, J.L., Garcia-Cerezo, A., and Gonzalez, J. (2007). Experimental kinematics for wheeled skid-steer mobile robots. In *Intelligent Robots and Systems, 2007. IROS 2007. IEEE/RSJ International Conference on*, 1222–1227. IEEE.

Morales, J., Martínez, J.L., Mandow, A., Pequeno-Boter, A., and García-Cerezo, A. (2010). Simplified power consumption modeling and identification for wheeled skid-steer robotic vehicles on hard horizontal ground. In *Intelligent Robots and Systems (IROS), 2010 IEEE/RSJ International Conference on*, 4769–4774. IEEE.

Ortigoza, R., Aranda, M., Ortigoza, G., Guzmán, V., Vilchis, M., González, G., Lozada, J., and Carbajal, M. (2012). Wheeled mobile robots: a review. *Latin America Transactions, IEEE (Revista IEEE America Latina)*, 10(6), 2209–2217.

Siegwart, R., Nourbakhsh, I.R., and Scaramuzza, D. (2011). *Introduction to autonomous mobile robots*. MIT press.

Velázquez, R. and Lay-Ekuakille, A. (2011). A review of models and structures for wheeled mobile robots: Four case studies. In *Advanced Robotics (ICAR), 2011 15th International Conference on*, 524–529. IEEE.

Modelo ARMAX para un mezclador oxígeno-aire para pediatría e incubadoras neonatales

José Dávalos-Pinto(*), Roberto Tantaleán-Carrasco(**), Bruno Castillón-Lévano(***)

(*)Pontificia Universidad Católica del Perú jdavalo@pucp.edu.pe
(**)Pontificia Universidad Católica del Perú rtantalean@pucp.edu.pe
(***)Pontificia Universidad Católica del Perú bruno.castillon@pucp.edu.pe
Sección de Electricidad y Electrónica. Av. Universitaria 1801, Lima 32, Perú.

Abstract: The work presented aimed to find an ARMAX model for a gas mixer describing its dynamics. The method considered conducting an identification nonparametric which was to excite the mixer input signals by a computer to determine basic but valuable information generated. Then a parametric identification which consisted excite the mixer input with a pseudo random binary signal to obtain the data with which the model coefficients were obtained was performed. Before it was necessary to define the model structure and the method of least squares model errors minimized. The cross-validation tests and correlation performed showed the effectiveness of the method. Based on the results of the mixer, it is concluded that the Valve-oxigen duct-transmisor and Compressor-air duct-transmisor subsystems are fourth-order delay.

Keywords: Mixer, Model ARMAX, experimental modeling, least squares method, cross validation.

1. INTRODUCCIÓN

La necesidad de apoyar satisfactoriamente a un sector poco atendido de la población como son los neonatos prematuros justifica el desarrollo de alternativas tecnológicas como el mezclador de gases para las incubadoras. Se busca suministrar un porcentaje adecuado de oxígeno al neonato y resolver problemas de extrema gravedad como el nacimiento prematuro. Esta deficiencia coadyuva a la alta tasa de mortalidad infantil de cerca de 35 de cada 1000 nacidos (Díaz L. et al., 2003), en la cual los neonatos constituyen un alto porcentaje.

La carencia de incubadoras impide ampliar la cobertura de atención y las deficiencias técnicas en el diseño de las incubadoras convencionales dejan algunas veces secuelas irreversibles en los recién nacidos, tal como la fibroplasia retrolental o ceguera causada por la administración inadecuada de oxígeno (AENOR, 1997).

El control de la cantidad de oxígeno administrado es importante porque demasiado oxígeno puede ocasionar daño a la retina. A pesar de las consecuencias de no administrar cuidadosamente la dosis de oxígeno a los niños prematuros, este se suministra inadecuadamente debido a la falta de mezcladores de aire-oxígeno adecuados (Sola A. et al., 2005).

El alto uso de oxígeno, el filtrado excesivo del flujo de aire y el tiempo muerto para la desinfección que usualmente es de una semana a un mes ocasiona la elevación del costo operativo de la incubadora.

El habitáculo que aloja al neonato no es completamente estéril, aumentando la posibilidad de contagio del neonato de alguna enfermedad, por otro lado, las incubadoras no pueden brindar tratamientos de oxigenación por si mismas teniendo que emplearse equipos adicionales, elevando los costos de atención y finalmente, el ruido en el habitáculo puede ser muy elevado pudiéndole provocar estrés y problemas en su desarrollo.

La baja cobertura de atención neonatal en el Perú se puede paliar con una mayor inversión por parte del Estado; pero las deficiencias técnicas del diseño convencional sólo podrán ser subsanadas por mejores conceptos.

La incubadora CPAP es un equipo para el soporte respiratorio en pacientes neonatales y pediátricos, usado para la administración de presión positiva nasal continua de las vías respiratorias en recién nacidos prematuros con insuficiencia respiratoria SDR. El sistema opera con flujo continuo de presión limitada en modo CPAP permitiendo la máxima estabilidad y control de presión, flujo de aire y oxigeno, humedad y temperatura, a través de una cánula

NCPAP convencional. La manipulación del flujo de aire y oxigeno para obtener la concentración de la mezcla resultante es importante(ver figura 1).

1.1 Identificación

Cuando se analiza un sistema del que se tiene poco conocimiento, lo razonable es realizar una *implementación experimental* para obtener una respuesta transitoria o una respuesta en frecuencia que posibilite conseguir una información básica pero importante de la dinámica y de las perturbaciones.
Basándose en los resultados, como constante de tiempo, puntos de inflexión, orden del sistema, intervalo de muestreo apropiado se puede mejorar la estructura del modelo y pueden ser necesarios nuevos experimentos.

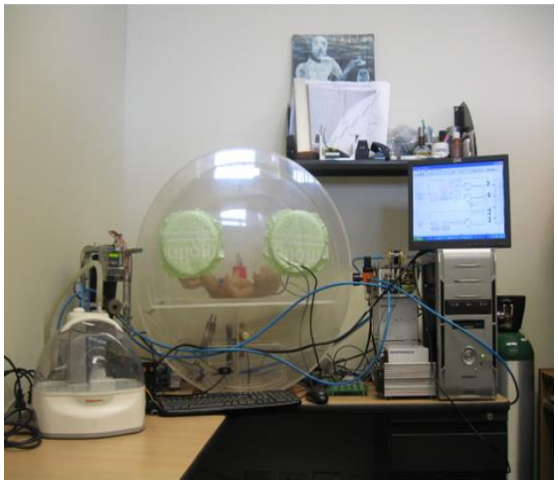

Figura 1. Incubadora neonatal con la instrumentación para los subsistemas del Mezclador.

Las *estructuras de modelo* se obtienen del conocimiento previo del proceso y de las perturbaciones. En algunos casos, el único conocimiento previo que se tiene es que el proceso se puede describir como un sistema lineal en un rango de operación concreto, siendo natural utilizar representaciones de sistemas lineales de tipo general como los modelos de caja negra.

El modelo ARMAX será considerado por su flexibilidad para expresar el error como ruido blanco gaussiano de media móvil. Los polinomios están definidos por la ecuación 1:

(1)

$$A(q^{-1})y(t) = B(q^{-1})q^{-nk}u(t) + C(q^{-1})e(t)$$

donde $u(t), y(t)$ y $e(t)$ son la entrada, salida y ruido del sistema respectivamente, $A(q^{-1})$, $B(q^{-1})$ y $C(q^{-1})$ los polinomios en función del operador desplazamiento q^{-1} y nk el retardo del sistema.

Cuando se formula un problema de identificación se introduce un *criterio* para tener una medida de hasta qué punto un modelo se ajusta a los datos experimentales. El principio de los mínimos cuadrados, es un método basado en la minimización de la suma de los cuadrados del error.

La *estimación de parámetros* se puede formular como un problema de optimización, en el que el mejor modelo es aquel que mejor se ajusta a los datos de acuerdo con un criterio. El vector de regresión $\varphi(t)$ y el vector de parámetros θ están definidos por la ecuación 2 y 3 respectivamente:

(2)

$$\varphi(t) = [-y(t-1)..-y(t-na),,,u(t-1)..u(t-nb),,,e(t-1)..e(t-nc)]^T$$

(3)

$$\theta = [a1..a_{na},,,b1..b_{nb},,,c1..c_{nc}]^t$$

La identificación paramétrica implica conocer la respuesta a la *señal seudo binaria aleatoria* (SBPA) que permite obtener la matriz de *datos de trabajo*. Generalmente, se requiere un tratamiento previo de los datos para hacerlos más adecuados al proceso de identificación, como por ejemplo: aplicar filtrado, eliminar valores medio, eliminar transitorios indeseables, etc.

Todo proceso de identificación parte de un conjunto de datos obtenidos de forma experimental del sistema que se modela con una parte de los datos para la estimación y los datos restantes para la *validación* del modelo.

2. MATERIALES Y MÉTODOS

El diseño experimental considera dos subsistemas: un subsistema FO flujo oxígeno formado por una válvula, un ducto de plástico corrugado y un transmisor de flujo; el subsistema FA flujo aire consta de un compresor, un ducto de plástico corrugado y un transmisor de flujo; ambos transmisores son Honeywell AWM5104N.

Con relación al software se utilizaron programas de aplicación en MATLAB y SIMULINK desde una PC la cual tuvo una tarjeta de adquisición de datos de National Instruments NI6024.

2.1 Identificación No paramétrica

La identificación no paramétrica empezó con un experimento para conocer la característica estática con la finalidad de evaluar una zona de trabajo lineal para ambos subsistemas, se escogió el pto. de operación en (Xop=12LPM, Uop=6LPM).

Luego se realizó un experimento de respuesta a la señal escalón (y pulso) consistente en variar tanto el voltaje del compresor como el voltaje de la válvula dentro de la zona de trabajo y observar la variación del flujo de aire y oxígeno. El tiempo de muestreo escogido fue de 0.8s.

2.2 Identificación paramétrica

Para la identificación paramétrica se realizó un experimento que consistió en generar una SBPA (señal binaria pseudo aleatoria) capaz de excitar todos los modos de ambos subsistemas para obtener la matriz de datos de trabajo de entrada-salida. Los parámetros de la señal SBPA fueron: tiempo de conmutación de 3.2s., tiempo mínimo y máximo 3 y 25s. respectivamente y la duración del ensayo 250s.

Los valores observados son previamente tratados antes de inicializar la estimación con la finalidad de alcanzar un mejor ajuste.
Para la fase de estimación del modelo ARMAX se utilizaron 2000 datos y para la fase de validación 500 datos (que no fueron usados para la estimación), la validación cruzada permitió mostrar el grado de ajuste entre el modelo estimado y los datos observados.

3. RESULTADOS Y DISCUSION

Se presenta los resultados de los experimentos conducentes a la obtención del modelo ARMAX del mezclador oxígeno-aire de la incubadora neonatal. El resultado del ensayo

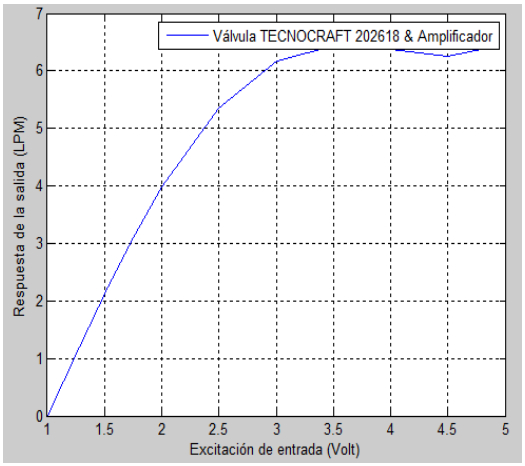

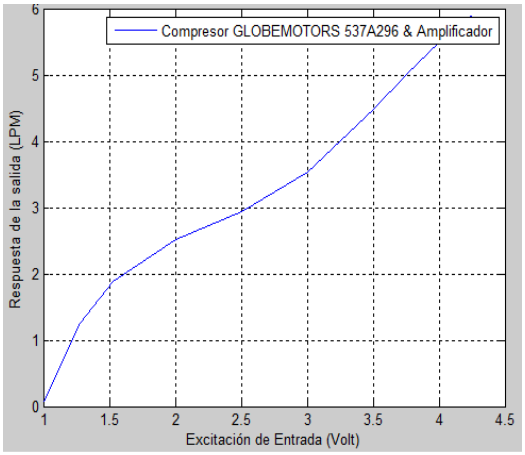

Figura 2. Curvas de característica estática para los subsistemas del mezclador.

La respuesta al escalón para los subsistemas permitieron medir el retardo en el Ducto de Oxigeno que es 0.05 s. y en el Ducto de Aire 0.03 s.

Los resultados del experimento de respuesta a la señal SBPA para ambos subsistemas se muestran en la figura 3.

de la curva característica estática de los subsistemas se muestra en la figura 2.

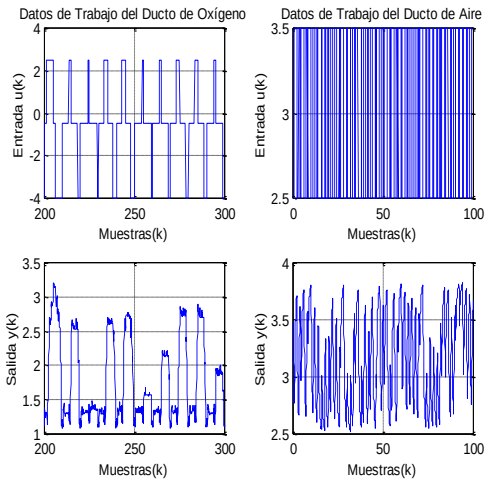

Figura 3. Respuesta a la señal SBPA de los subsistemas del mezclador.

La estructura de modelo considerada según la respuesta de correlación cruzada de residuos se muestra un tramo que sale del rango de confidencia, luego los parámetros del modelo tienen error. Los resultados de correlación se muestran en la figura 4.

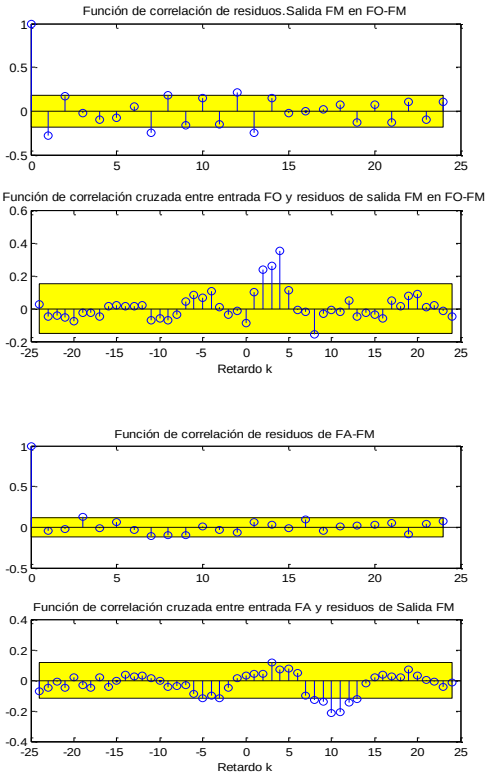

Figura 4. Autocorrelación y correlación cruzada de los subsistemas del mezclador.

Para el modelo estimado del ducto de aire el MSE es 0.0165 y el MSE para el modelo estimado del ducto de oxígeno es 0.0610.

La estructura de modelo implementada en Simulink para los subsistemas Ducto de aire y Ducto de oxígeno del mezclador se muestra en la figura 5.

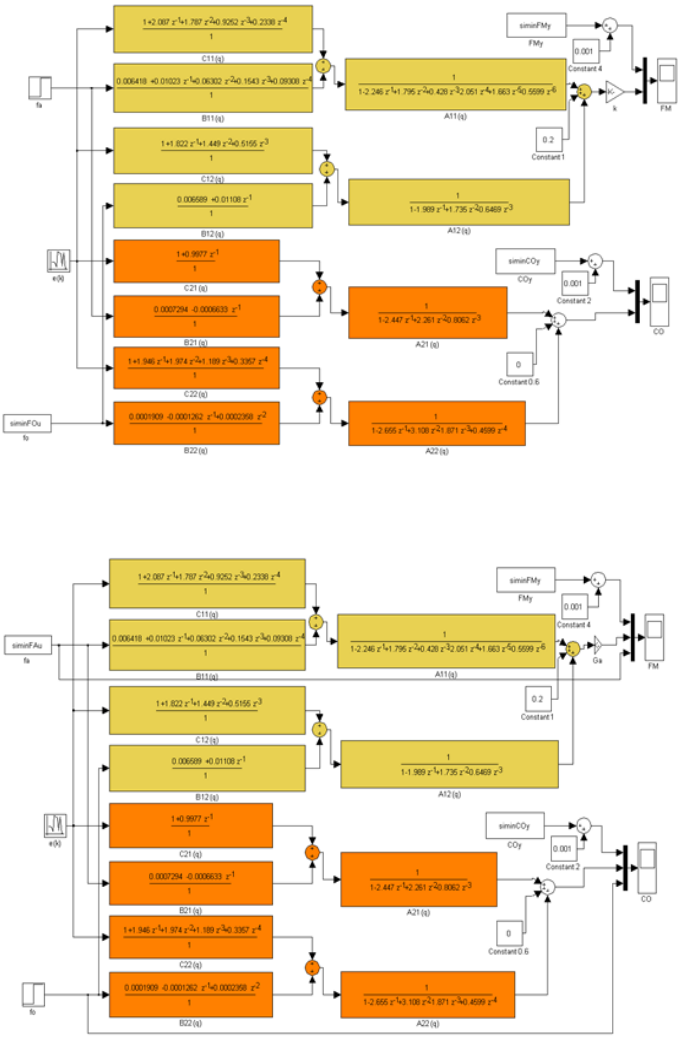

Figura 5. Diagrama Simulink para la respuesta del mezclador ante los subsistemas del mezclador.

Los resultados de la prueba de validación cruzada tanto del subsistema Ducto de Oxígeno como del Ducto de Aire muestran el buen ajuste entre los datos observados y los datos estimados con modelo ARMAX.

Los resultados de la validación por simulación para los subsistemas se muestran en la figura 6.

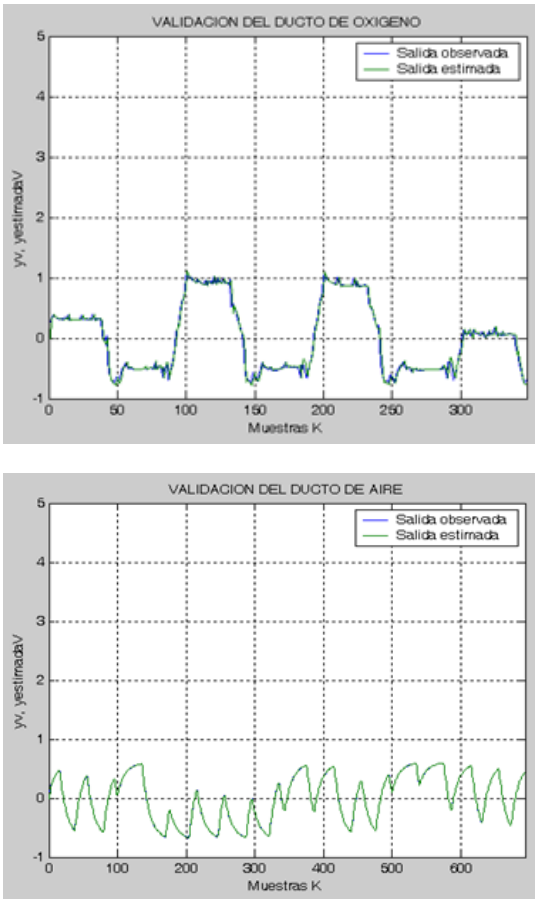

Figura 6. Validación cruzada de los subsistemas del mezclador.

Para el ducto de aire la estructura de modelo ARMAX [3 2 1 4] es:
FM(z) =

(0.0006418+0.001023z^-1+0.0063z^-2+0.01543z^-3+ 0.009308z^-4) z^-2*FA(z)/
(1- 2.246z^-1+1.795z^-2+0.428z^-3-2.051z^-4+1.663z^-5 - 0.5599z^-6) +…
(1+ 2.087z^-1+1.787z^-2+0.925z^-3+ 0.234z^-4)*E(z)/
(1-2.246z^-1+1.795z^-2+0.428z^-3 - 2.051z^-4+1.663z^-5 - 0.5599z^-6)

Para el ducto de oxígeno la estructura de modelo ARMAX [4 3 4 5] es:
FM(z) =

(0.006589 + 0.01108z^-1)*z^-3*FO(z)/
(1 - 1.989z^-1 +1.735z^-2 - 0.6469z^-3) +...
(1+1.822z^-1 +1.449z^-2 +0.5155z^-3)*E(z)/
(1 -1.989z^-1 +1.735z^-2 - 0.6469z^-3)

La respuesta en régimen permanente del mezclador oxígeno-aire tiene un ajuste aceptable y se muestra en las figura 7.

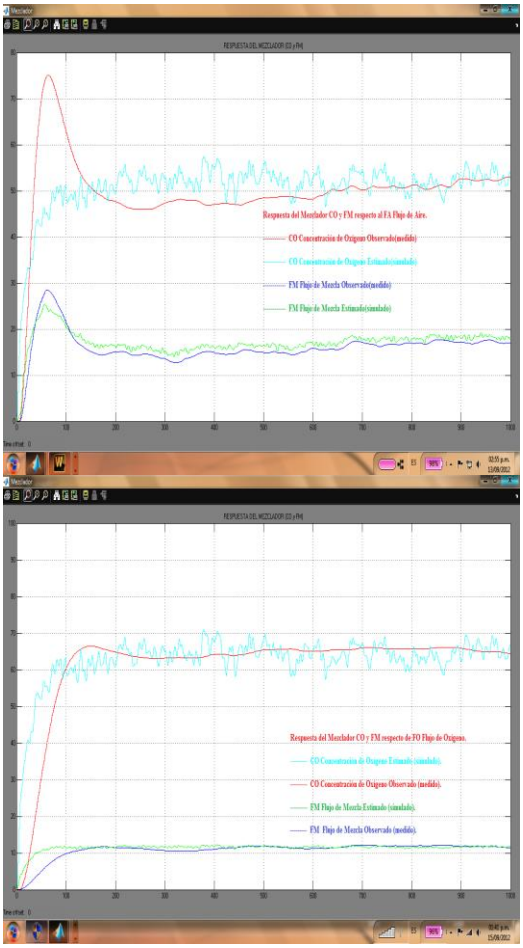

Figura 7. Respuesta en régimen permanente de los subsistemas del Mezclador.

4. CONCLUSIONES

Las estructuras de modelo ARMAX[3 2 1 4] y ARMAX[4 3 4 5] explican la dinámica del mezclador de la incubadora neonatal mediante ecuaciones en diferencias.

Los coeficientes se estimaron usando el criterio de mínimos cuadrados alcanzándose para el modelo estimado del ducto de aire el MSE es 0.0165 y para el modelo estimado del ducto de oxígeno el MSE es 0.0610.

Los modelos propuestos son simplificaciones de la realidad que posibilitaran el diseño de un controlador.

5. REFERENCIAS

Astrom K.J. and Wittenmark. B. (1997). Computer-Controlled Systems. Theory and Design, Third Edition, Prentice Hall.

Ljung L. (1996). Development of System Identification, 13 th Triennial World Congress, San Francisco, USA., pp. 141-146.

Ljung L. and Guo L (1996). Estimating the Total Error from Standard Model Validation Tests, 13 th Triennial World Congress, San Francisco, USA., pp. 133-138.

Mendel J. M. (1973). Discrete Techniques of Parameter Estimation. The Equation Error Formulation, Marcel Dekker, N.Y.

Poolla K., Khargonekar P. P., Tikku A., Krause J. and Nagpal K. (1994). A Time-Domain Approach to Model Validation, IEEE Transaction Automatic Control, AC- 39, pp. 951-959.

Soderstrom T. and Stoica P. (1989). System Identification, Prentice Hall.

Sola A., Chow L., Rogido M. *Retinopatía de la prematuridad y oxigenoterapia: una relación cambiante*, Anales de Pediatría (Asociación Española de Pediatría), 62(1), pp 463(2005)

CHAPTER 18

TRAFFIC CONTROL

A Comparison Between Macroscopic and Microscopic Urban Traffic Simulation Including Motorcycle Dynamics. ⋆

C. Portilla * **A. Acosta** * **A. Marquez** * **J. Espinosa** *

* *Universidad Nacional de Colombia, Medellín, Colombia, (e-mail: crportil, afacosta, amarque, jjespino}@unal.edu.co*

Abstract: This paper presents the comparative analysis of two types of road traffic models including motorcycle dynamics: A macroscopic model corresponding to an extension of the S-model, and the microscopic model found in the Simulation of Urban MObility (SUMO) simulator, namely the Kraußmodel. Furthermore, both models are tested in a case study and validated by means of the app Traffic Sensors which has been developed for acquiring multimodal traffic volumes. simulation results show that the accuracy of the modified S-model is improved by including an optimal motorcycle factor.

Keywords: Traffic modelling, dynamic modelling, parameter estimation, traffic simulation, motorcycle influence.

Currently, large cities have an increasing number of vehicles and externalities such as congestion, pollution and increased fuel consumption, among others. However, not only cars are contributing to the problem, but also other vehicles such as public transportation buses, trucks, bicycles, pedestrians and motorcycles (Bellemans et al., 2002). Hence, the proposed traffic models should represent every dynamic of urban traffic composition and their relationships, regardless of its macroscopic or microscopic modelling. The main goal of these models is to manage traffic networks efficiently, in order to monitor, control and take decisions in real time. The microscopic traffic models describe dynamics for each vehicle as a particle, involving characteristics such as speed, acceleration, position and manoeuvres of single vehicles, while macroscopic models consider the traffic as a fluid with properties such as density, average speed and flow. However, each model is used for different purposes (He et al., 2014). Microscopic models generally have a high computational cost in large-scale networks hindering real-time applications and they are not easy to validate with real data. On the other hand, macroscopic models are often inaccurate, but have few variables allowing an easy validation and a lower computational cost. Actually, the inclusion of other kinds of vehicles (different to cars) in macroscopic or microscopic simulation is not easy because they consider vehicles with similar characteristics to cars. In this sense, if motorcycles or other vehicles are taken into account in an urban network, they could lead to an inaccurate simulation.

The aim of this work is to compare the incorporation of motorcycle dynamics in microscopic and macroscopic simulation including motorcycle dynamics in a simplified case study. Microscopic simulation is achieved thanks to the Simulation of Urban MObility (SUMO) open-source package. SUMO has been actively developed from 2002 by the *Institute of Transportation Systems* at the German Aerospace Center (DLR), featuring a validated car-following model and several tools for network and demand modelling. Furthermore, the Traffic Control Interface (TraCI) allows to interact with the simulation in real-time. Specifically, in this work the implementation of TraCI for the Matlab® environment, namely TraCI4Matlab has been used (Acosta et al., 2014). The macroscopic simulation was performed in Matlab® considering the S model proposed in (Lin et al., 2012), which is a well-known macroscopic model used mainly in control applications. These simulations were carried out in a case study located in the city of Medellin (Colombia) and validated with data obtained through Traffic Sensors, which is an Android application that allows to collect traffic data for different vehicle types.

This paper is organized as follows: Sections 1 and 2 present a review of microscopic and macroscopic models and simulation. Section 3 presents a case study in the city of the Medellín. Section 4 briefly describes the software tools developed for simulation and data acquisition. In Section 5 experimental results are showed. Finally, in section 6, conclusions are presented.

1. MICROSCOPIC TRAFFIC MODELS

Microscopic traffic models consider the behaviour of each vehicle using first-order differential equations "in a framework close to Newtonian mechanics" (Bellomo and Dogbe, 2011). Thus, these models consider the dynamics of each vehicle in relation to the vehicles that surround it. For this reason, microscopic models are known as models based on stimulus and response. The importance of microscopic models lies in the difficulty of macroscopic models to

⋆ Research supported by: COLCIENCIAS under the doctoral scholarship, convocation number 647 and a special acknowledgement to COLCIENCIAS project: Modelamiento y control de tráfico urbano en la ciudad de Medellín etapa 2, código 1118-669-45309, CT 202-2015. Universidad Nacional de Colombia Proyecto HERMES 25374.

represent different phenomena such as the type of vehicles and drivers and the effect of lane changes (Kesting et al., 2008).

Microscopic models have allowed to describe the heterogeneous behaviour of drivers (Ossen and Hoogendoorn, 2011) and lane change manoeuvres and their impacts, which validates several features found empirically in macroscopic models (Kesting et al., 2007; Laval and Daganzo, 2006). These models consist of two main types: longitudinal models, where the most remarkable are car following models, which describe the movement of vehicles along a lane; and lateral models, which describe lane change and overtaking manoeuvres.

The general form of a car following model is described by the differential equations (4) and (5) (Wilson and Ward, 2011).

$$\dot{x}_n = v_n \tag{1}$$
$$\dot{v}_n = f(s_n, \Delta v_n, v_n) \tag{2}$$

Where the relative velocity is defied as:

$$\Delta v_n = \dot{s}_n := v_{n-1} - v_n \tag{3}$$

Additionally, s_n is the distance between vehicle bumpers and v_{n-1}, v_n denote the velocity of the leader and the follower vehicles. Thus, equations (4) and (5) describe how the movement of a single vehicle is influenced by its velocity and the relative position and velocity to its leader. In general, the function f given in equation (4) can be considered as nonlinear and many times includes a delay that accounts for the reaction time of the driver.

1.1 Microscopic traffic simulation

Microscopic traffic simulation constitutes an important research area with applications such as the characterization of driving behaviour and the development of Advanced Driving Assistance Systems (ADAS) (Bifulco et al., 2013).

There are currently many commercial and open-source microscopic traffic simulators. Among them, Simulation of Urban MObility (SUMO) has proven to be a robust and reliable open-source tool for traffic researchers, featuring tools for network and demand modelling, and a high capacity of integration. Furthermore, SUMO has the Traffic Control Interface (TraCI), which allow to interact with the simulator in real-time from different programming languages. SUMO and TraCI can be used in a high variety of applications, including on-line traffic lights control, dynamic routing and vehicular communications. SUMO has been used in this work for microscopic simulation.

The car-following model used by SUMO corresponds to a modified version of model by Stefan Krauß (Krauß, 1998), whose main equation is given by (Nagel et al., 2003):

$$v_{safe} = \tilde{v}(t) + \frac{g(t) - \tilde{v}(t)\tau}{\bar{v}/b + \tau} \tag{4}$$
$$v_{des} = \min\{v(t) + ah, v_{safe}, v_{max}\} \tag{5}$$
$$v(t+h) = \max\{0, v_{des} - \epsilon a \eta\} \tag{6}$$

Where $\tilde{v}(t)$ is the velocity of the leader, $g(t)$ is the gap between the two vehicles, τ is the follower braking reaction time, $\bar{v}$, a and b are the average speed of the two cars, their maximum acceleration and deceleration, respectively. Finally ϵ and η are the noise amplitude and a random number between 0 and 1. The Krauß model is a collision free model whose main assumption is that the braking distance of the follower plus the distance given by his/her reaction time is lower than the braking distance of the leader plus the space between the leader and the follower.

Although microscopic traffic simulators have been successfully validated in many scenarios around the world, there are still some aspects that need further improvements, including the refinement of lane change models and the incorporation of mixed traffic conditions, specially in scenarios from countries like India and Colombia, where there is a lower lane-dependency in the driving behaviour.

2. MACROSCOPIC TRAFFIC MODEL

From a macroscopic approach, the S model has been chosen in this work (Lin et al., 2011). This model was developed for control purposes based on BLX (Lin et al., 2012) and van den Berg urban traffic models (van den Berg et al., 2004). Consider two intersections (u and d) as showed in Figure 1, where the road between them is known as a link (u, d). At every time step k, the S model has into account two states: the total number of vehicles in the link $n_{u,d}(k)$, and the number of queued vehicles that are expected to turn in direction o $q_{u,d,o}(k)$. These vehicles can be modelled as:

$$n_{u,d}(k+1) = n_{u,d}(k) + \left(\alpha^{\text{enter}}_{u,d}(k) - \alpha^{\text{leave}}_{u,d}(k)\right) c_{\text{d}}, \tag{7}$$

$$q_{u,d,o}(k+1) = q_{u,d,o}(k) + \left(\alpha^{\text{arriv}}_{u,d,o}(k) - \alpha^{\text{leave}}_{u,d,o}(k)\right) c_{\text{d}}, \tag{8}$$

Where $\alpha^{\text{enter}}_{u,d}(k)$ is the vehicular flow entering to link (u, d) at time step k, $\alpha^{\text{leave}}_{u,d}(k)$ is the outflow from link (u, d) in direction o and $\alpha^{\text{arriv}}_{u,d,o}(k)$ is the arrival flow to the queue after a time delay $\tau(k)c_{\text{d}} + \gamma(k)$. These flows can be described by the following equations:

$$\alpha^{\text{enter}}_{u,d}(k) = \sum_{i \in I_{u,d}} \alpha^{\text{leave}}_{i,u,d}(k), \tag{9}$$

$$\alpha^{\text{leave}}_{u,d}(k) = \sum_{o \in O_{u,d}} \alpha^{\text{leave}}_{u,d,o}(k), \tag{10}$$

$$\alpha^{\text{arriv}}_{u,d,o}(k) = \beta_{u,d,o}(k)\, \alpha^{\text{arriv}}_{u,d}(k), \tag{11}$$

Where $O_{u,d}$ and $I_{u,d}$ are the output and input nodes from link (u, d), and

$$\alpha^{\text{leave}}_{u,d,o}(k) = \min\left\{ \frac{\mu_{u,d,o}\, g_{u,d,o}(k)}{c_{\text{d}}}, \right.$$
$$\left. \frac{q_{u,d,o}(k)}{c_{\text{d}}} + \alpha^{\text{arriv}}_{u,d}(k), \frac{\beta_{u,d,o}(k)(C_{d,o} - n_{d,o}(k))}{c_{\text{d}}} \right\}, \tag{12}$$

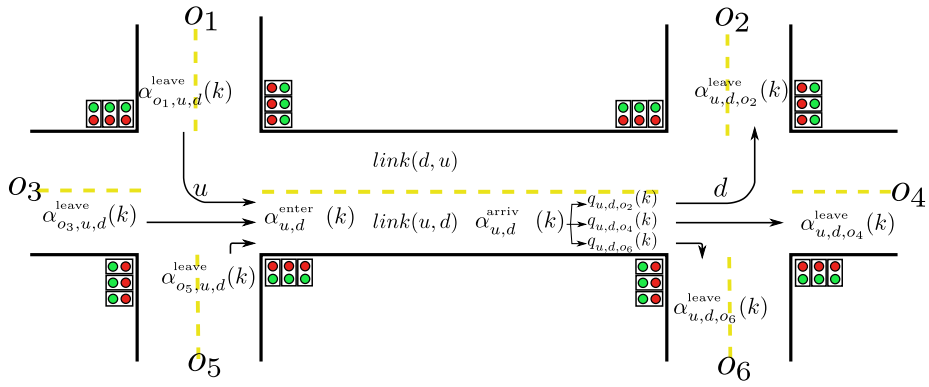

Fig. 1. Two intersections interconnected in an urban traffic network.

$$\alpha^{\text{arriv}}_{u,d}(k) = \frac{c_{\text{d}} - \gamma(k)}{k}\alpha^{\text{enter}}_{u,d}(k - \tau(k)) + \frac{\gamma(k)}{c_{\text{d}}}\alpha^{\text{enter}}_{u,d}(k - \tau(k) - 1), \quad (13)$$

Where c_{d}, $\mu_{u,d,o}$, $g_{u,d,o}(k)$, $\beta_{u,d,o}(k)$, $n_{d,o}(k)$ and $C_{d,o}$ represent the cycle time of the traffic light, saturation flow, green time of the traffic light, the split ratio of vehicles, the number of vehicles in link (d,o), and the link capacity (d,o), respectively. Additionally,

$$\tau(k) = \text{floor}\left\{\frac{(C_{u,d} - q_{u,d}(k)\ l)}{N^{\text{lane}}_{u,d} v^{\text{free}}_{u,d} c_{\text{d}}}\right\}, \quad (14)$$

$$\gamma(k) = \text{rem}\left\{\frac{C_{u,d} - q_{u,d}(k)\ l}{N^{\text{lane}}_{u,d} v^{\text{free}}_{u,d} c_{\text{d}}}\right\}, \quad (15)$$

$$q_{u,d}(k) = \sum_{o \in O_{u,d}} q_{u,d,o}(k), \quad (16)$$

Where l, $N^{\text{lane}}_{u,d}$ and $v^{\text{free}}_{u,d}$ are the average length of the vehicles, the number of lanes in link (u,d) and the free flow speed. Hence, the S model is described by equations (16)–(7)

2.1 S Model extension

In order to include the effect of motorcycles in the S model, the Passenger Car Equivalent (PCE) concept is added, where one possible representation of motorcycles is through a factor between vehicles (cars) and motorcycles. This concept is clearly defined in (Yperman, 2011), and can be included explicitly in the inflow as:

$$\alpha^{\text{enter}}_{u,d}(k) = \alpha^{v_{\text{enter}}}_{u,d}(k) + \text{M}_{\text{F}}\ \alpha^{m_{\text{enter}}}_{u,d}(k) \quad (17)$$

Where $\alpha^{v_{\text{enter}}}_{u,d}(k)$ is the measured vehicle inflow, $\alpha^{m_{\text{enter}}}_{u,d}(k)$ is the measured motorcycle inflow and M_{F} is the motorcycle factor which can take values between 0 and 1.

3. CASE STUDY

In order to validate the macroscopic and microscopic models, a traffic experiment was proposed in the city of Medellin, specifically in the 30th Street towards the 70th Avenue, which corresponds to the link (o_1,u), as showed in Figure 2

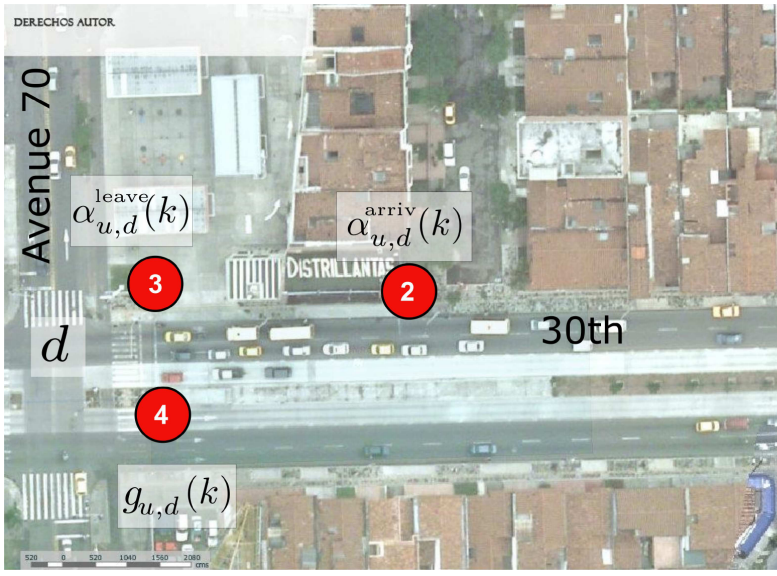

Fig. 2. Map of case study and distribution of tasks.

The experimental data were obtained on August 20th 2015 at 9:00 am (-5 GMT) with the help of four participants labelled in Figure 2 with numbers from 1 to 4. The data collected was classified into cars and motorcycles for all cases. Each participant had a variable to be measured, that is: Participant 1 measures the inflow to link (u,d) $\alpha^{\text{enter}}_{u,d}(k)$, participant 2 measures the arrival flow at the end of the queue $\alpha^{\text{arrive}}_{u,d}(k)$, participant 3 measures the outflow from link (u,d) $\alpha^{\text{leave}}_{u,d}(k)$ and participant 4 measures the green and red time of traffic light $g_{u,d}(k)$. The information of each measurement point was recorded in plain text through the android mobile application, namely *Traffic Sensors*, developed in the project (MOYCOT, 2016) specifically for this purpose. Traffic Sensors is briefly described in section 4.

This case study was modelled in the Simulation of Urban MObility (SUMO) microsimulator (including motorcycles), to compare the results with the experimental data and with the results obtained with the S model.

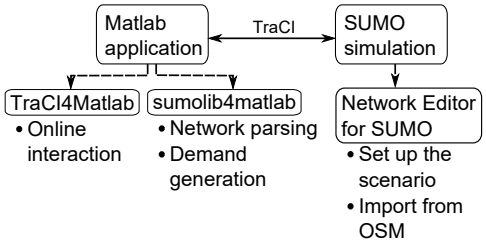

Fig. 3. Online simulation scheme integrating SUMO and Matlab through TraCI4Matlab. Tools for demand generation in Matlab (sumolib4Matlab) and graphical network editing (Network Editor for SUMO) are also showed. This figure has been taken from the work (Noreña et al., 2015)

4. SOFTWARE TOOLS

4.1 TraCI4Matlab

As mentioned earlier, the software package used in this work for microscopic simulation is SUMO, which can output a wide variety of aggregated and disaggregated data including vehicle trajectories, densities, emissions and traffic lights states. These data can be obtained at the end of the simulation in form of XML files, or in execution time through the TraCI API. On the other hand, the macroscopic models were developed and analysed in Matlab®. Furthermore, traffic lights control strategies are also developed in this environment in the MOYCOT project (Noreña et al., 2015). These reasons motivated the development of an implementation of TraCI for the Matlab language, which was called TraCI4Matlab. Thanks to the commands provided by TraCI4Matlab, it is possible to retrieve and change the properties of the objects in the SUMO simulation in real time, as showed in figure 3. Additionally, TraCI4Matlab was developed using agile methodologies including the re-engineering of the available Python implementation, which shortened the development time considerably. Furthermore, tools for traffic demand generation in Matlab and graphical network editing have been developed under the same methodologies (Acosta et al., 2015).

4.2 Traffic Sensors

Traffic Sensors is a lightweight Android application aimed to the collection of multi-modal traffic data and traffic lights states, which allowed the validation of the microscopic and macroscopic simulations described in this work. The data obtained with traffic sensors is time-stamped using the clock of the device, enabling synchronized collaborative experiments. Furthermore, Traffic Sensors synchronizes these data with a remote server, simplifying the collection and analysis tasks.

5. EXPERIMENTAL RESULTS

Taking into account the mean square error in the number of vehicles between the experimental data and theoretical data (S model), the optimal Passenger Car Equivalent (PCE), M_F, was found as showed in Figure 4(b), where several simulations were performed varying the PCE between 0 and 1 with an increment of 0.1. It was found that the value yielding the minimum mean square error is $M_F = 0.6$. Additionally, Figure 4(a) shows the traffic light signal with G and R representing, respectively, the green and red traffic light states.

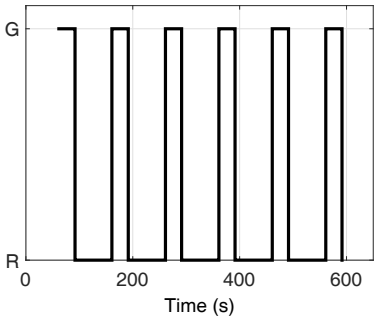

(a) Traffic light signal for green and red times

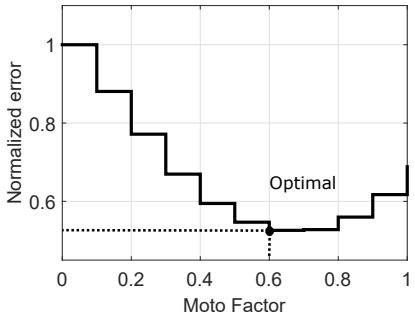

(b) Moto factor against normalized mean square error

Fig. 4. Traffic light signal and Moto Factor calculation.

Furthermore, the same scenario was implemented in the SUMO microsimulator and compared with the macroscopic simulation, through the modified S model (2.1) with typical parameters (theoretical data), and with the real data (experimental data). The main states of the link, total number of vehicles and total queued vehicles are showed in Figure 5. In addition, Figure 5 shows some accuracy differences between the theoretical and simulation data. The first ones are apparently closer to the real data, with an error of 2.39 veh and 2.7 veh for the number of vehicles and vehicles in queue, respectively. On the other hand, the errors for simulation data are 4.02 veh and 1.89 veh. In this way, theoretical results show an improvement of 13.89% over the results obtained in microsimulation. This improvement was achieved thanks to the inclusion of the optimal motorcycle factor for this specific link.

6. CONCLUSION AND FURTHER RESEARCH

This paper compared a microscopic and macroscopic model in an experimental scenario including motorcycles. Both simulations were performed using traditional methods, however, in the macroscopic modelling an equivalence factor between cars and motorcycle (M_F) was included using the S model, making a substantial difference. Further research will include a dynamic motorcycle factor or other representation, where there will be an explicit interaction between motorcycles and cars considering the particularities of each vehicle.

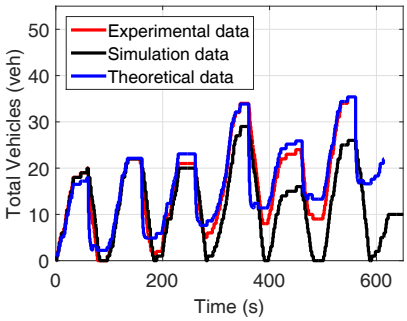

(a) Total number of vehicles in link

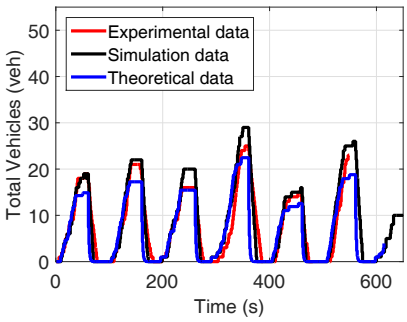

(b) Total queue of vehicles

Fig. 5. Comparison between microscopic model, macroscopic model and real data.

7. ACKNOWLEDGMENTS

Research supported by: COLCIENCIAS under the doctoral scholarship, convocation number 647 and a special acknowledgement to COLCIENCIAS project: Modelamiento y control de tráfico urbano en la ciudad de Medellín etapa 2, código 1118-669-45309, CT 202-2015. Universidad Nacional de Colombia Proyecto HERMES 25374.

REFERENCES

Acosta, A., Espinosa, J., and Espinosa, J.E. (2014). TraCI4matlab: Re-engineering the Python implementation of the TraCI interface. In *Proceedings of the 2nd SUMO User Conference SUMO2014*, 145–156. Deutsches Zentrum für Luft - und Raumfahrt e.V., Deutsches Zentrum für Luft - und Raumfahrt e.V.

Acosta, A., Espinosa, J.E., and Espinosa, J. (2015). Developing Tools for Building Simulation Scenarios for SUMO Based on the SCRUM Methodology. In *Proceedings of the 3rd SUMO User Conference SUMO2015*, 23–35. Deutsches Zentrum für Luft - und Raumfahrt e.V., Deutsches Zentrum für Luft - und Raumfahrt e.V.

Bellemans, T., De Schutter, B., and De Moor, B. (2002). Models for traffic control. *JOURNAL A*, 43(3/4), 13–22.

Bellomo, N. and Dogbe, C. (2011). On the modeling of traffic and crowds: A survey of models, speculations, and perspectives. *SIAM review*, 53(3), 409–463.

Bifulco, G.N., Pariota, L., Simonelli, F., and Di Pace, R. (2013). Development and testing of a fully Adaptive Cruise Control system. *Transportation Research Part C: Emerging Technologies*, 29, 156–170. doi: 10.1016/j.trc.2011.07.001.

He, Q., Head, K.L., and Ding, J. (2014). Multi-modal traffic signal control with priority, signal actuation and coordination. *Transportation Research Part C: Emerging Technologies*, 46, 65–82.

Kesting, A., Treiber, M., and Helbing, D. (2007). General lane-changing model MOBIL for car-following models. *Transportation Research Record: Journal of the Transportation Research Board*.

Kesting, A., Treiber, M., and Helbing, D. (2008). Agents for traffic simulation. *arXiv preprint arXiv:0805.0300*.

Krauß, S. (1998). *Microscopic modeling of traffic flow: Investigation of collision free vehicle dynamics*. Ph.D. thesis, Universitat zu Koln.

Laval, J.A. and Daganzo, C.F. (2006). Lane-changing in traffic streams. *Transportation Research Part B: Methodological*, 40(3), 251–264.

Lin, S., De Schutter, B., Xi, Y., and Hellendoorn, H. (2011). Fast model predictive control for urban road networks via MILP. *Intelligent Transportation Systems, IEEE Transactions on*, 12(3), 846–856.

Lin, S., De Schutter, B., Xi, Y., and Hellendoorn, H. (2012). Efficient network-wide model-based predictive control for urban traffic networks. *Transportation Research Part C: Emerging Technologies*, 24, 122–140.

MOYCOT (2016). MOYCOT. URL `http://gaunal.unalmed.edu.co/moycot`.

Nagel, K., Wagner, P., and Woesler, R. (2003). Still flowing: Approaches to traffic flow and traffic jam modeling. *Operations research*, 51(5), 681–710.

Noreña, L., Sarrazola, A., Acosta, A., Marquez, A., Espinosa, J., and Espinosa, J. (2015). Urban traffic control in the city of medellín: A PID control approach. In *2015 Workshop on Engineering Applications - International Congress on Engineering (WEA)*, 1–6. doi: 10.1109/WEA.2015.7370145.

Ossen, S. and Hoogendoorn, S.P. (2011). Heterogeneity in car-following behavior: Theory and empirics. *Transportation research part C: emerging technologies*, 19(2), 182–195.

van den Berg, M., De Schutter, B., Hegyi, A., and Hellendoorn, J. (2004). Model predictive control for mixed urban and freeway networks. In *Proceedings of the 83rd Annual Meeting of the Transportation Research Board*, volume 19. Citeseer.

Wilson, R.E. and Ward, J.A. (2011). Car-following models: fifty years of linear stability analysis–a mathematical perspective. *Transportation Planning and Technology*, 34(1), 3–18.

Yperman, I. (2011). Commuting by motorcycle: impact analysis. *Transport and Mobility Leuven, Belgium*.

Generalized Predictive Traffic Control for Isolated Intersections

Anna Sarrazola, Laura Noreña, Alejandro Marquez, Jairo Espinosa

Departamento de Energía Eléctrica y Automática, Universidad Nacional de Colombia, Colombia, (e-mail: amsarrazolaa@unal.edu.co, lmnorenam@unal.edu.co, amarque@unal.edu.co, jespinov@unal.edu.co)

Abstract: This paper contains the results of simulation in the implementation of a Generalized Predcitive Control (GPC) Model for a traffic light system of an isolated intersection of network traffic, using the SUMO microsimulator as simulated plant and the linear prediction model called Modified Multi-class Queueing Networks (MMQM) for the GPC.

Keywords: GPC controller,MMQM, traffic light control, microsimulation, SUMO.

1. INTRODUCTION

The steady growth of big cities as focus of economic activity has generated an increased demand of transportation and traffic. Therefore, the mobility is negatively affected by phenomena such as congestion delaying the total journey time of the users. Furthermore the pollution and toxic emissions increase due to these phenomena affecting the quality of living of the citizens (Papageorgiou et al., 2003).

Due to the inherent dynamic nature of the traffic network, its evolution in time can be represented by mathematical dynamic models, which are used in simulation environments for analyzing the behavior of variables of interest that describe the network. These models are key elements for the design of traffic control strategies for achieving a sustainable mobility for the users. Dynamic modeling of vehicular traffic is an important factor in the monitoring and control of traffic (Yang et al., 2010) (Lighthill and Whitham, 1955) (Daganzo, 1995).

In order to simplify the implementation of controllers in large traffic networks, some linear traffic models have been developed. Multi-Class Queueing Networks (MQN)(Le et al., 2013) are a simple and important linear representation due to different class relations allowing to describe any traffic. Howevwer, this model assumes a certain quantity of vehicles leaving each class at every time step (regardless of whether there are available vehicles or not). Therefore, a modification of this model was proposed in a previous work (Norena et al., 2015). We have called Modified Multiclass Queueing Networks (MMQN). The MMQN model assumes that what goes out of a class is a proportion of the current number of vehicles in that case. It is worth to notice that the MMQN model is still linear, which is suitable for Generalized Predictive Controller (GPC) implementation.

The whole proposal, apart from the MMQN, consist on estimate the parameters of the proposed model assuming a SUMO as the real system. SUMO is a high performance microscopic traffic simulator featuring tools to generate traffic demand and to import road networks from several sources (Krajzewicz et al., 2012). In addition, a Kalman filter-based (Kalman, 1960) GPC scheme using the MMQN as the prediction model is implemented through simulation.

This paper is organized as follows: Section 2 presents the mathematical formulation of the Modified Multi-class Queueing Network Based Model; Section 3 describe the case study, including its modeling via MMQN, design of experiment, parameter identification, state estimation structure and GPC scheme; Section 4 presents a numerical simulation of the proposed case study.

2. MODIFIED MULTI-CLASS QUEUEING NETWORK BASED MODEL

The Multi-class Queueing Networks Based Model (MQN) is a representation of urban traffic networks proposed in (Le et al., 2013). The modified Multi-class Queueing Network Based Model (MMQN) modeling methodology is motivated by the MQN methodology in an attempt to address some issues.

2.1 Definition of the network elements

It is assumed that time evolves in discrete steps (n = 0,1,2...) corresponding to traffic light cycles (Le et al., 2013). The network state maintains counts of the quantity of vehicles at different abstractions of locations based on the following 3 types of classes:

- Delay (D): this class represents a portion of a (multilane) street where vehicles are in free flow regime. This class can only evolve to another delay (D) class or a route (R) class (Le et al., 2013).
- Roure (R): this class represents a portion of a (multiline) street where drivers decide where to go among all options of turning. This class typically evolves into queue (Q) classes (Le et al., 2013).

⋆ Research supported by project: Modelamiento y control de tráfico urbano en la ciudad de Medellín etapa 2, código 1118-669-45309

- Queue (Q): this class represents a turning direction before an intersection (Le et al., 2013).

Let K_D, K_R and K_Q be the number of classes of each type. Classes are indexed by $k = 1, ..., k$ with $K = K_D + K_R + K_Q$. Classes of type $j \in D, R, Q$ are denoted by H_j and they are numbered as follows: $H_D = 1, ..., K_D$, $H_R = K_D + 1, ..., K_D + K_R$ and $H_Q = K_D + K_R + 1, ..., K_D + K_R + K_Q$ (i.e the delay (D) classes are the first to be numbered, followed by the route (R) classes an finally the queue (Q) classes) (Le et al., 2013).

The network state for a class k, denoted by $x_k(n)$, is an instantaneous count of vehicles in the class $k \in H_{D,R,Q}$. The state vector $(X(n) \in \mathbb{R}^{\urcorner}$ is the vector formed by all state related to each class (i.e $X(n) = [x_1(n)...x_k(n)]^T$) (Le et al., 2013).

Vehicles leaving any class, except classes of type Q, move to other classes through predefined links. A link l is a connection between its source class, denoted by $s_l \in H_{D,R}$, and its destination class, denoted by $d_l \in H_{D,R,Q}$. Links are indexed by $l = 1, ..., L$. Each link l connecting two classes, say $s_l = x_k$; $k \in H_{D,R}$ and $d_l = x_k^{'}$; $k^{'} \in H_{D,R,Q}$, has an associated number $\alpha_{k,k'} \in [0, 1]$, which is a dimensionless number that defines the proportion of the current number of vehicles that will go from the states k to the state $k^{'}$ over a whole traffic light cycle. Furthermore, if it is not a link, for example from class i to the class j, define $\alpha_{i,j} = 0$. Additionally, Q-type classes (recall Q-type classes are just before intersections) have an associated maximum flow rate of vehicles leaving these kind of classes in an unitary time step (a traffic light cycle). These flow rates are labeled as $f_{i,max}$; $i \in F$, where i indexes the phases and $F = \{1, ..., f\}$ is the set of all phases of the intersection. A phase is an arrangement of the different turning options in an intersection given a configuration of the traffic light. Consequently, every phase has a duration $g_{ui}(n)$, which corresponds to the amount of time the phase i is active in a whole traffic light cycle.

The last element considered by this model is the arrival of vehicles to an intersection. Vehicles arrive exogenously according to the demand that arrives to a class k, denoted by $a_k(n)$; $k \in H_{D,R,Q}$. Each class k has associated a demand $a_k(n)$, which is positive if exogenous vehicles can arrive to class k and zero if they cannot.

2.2 Network Equations

According to the previous subsection, the proposed MMQN equations are:

Si $k \in H_{D,R}$:

$$x_k(n+1) = x_k(n) + a_k(n) + \sum_{j \in H_{D,R}} \alpha_{j,k} x_j(n) - \sum_{j \in H_{D,R}} \alpha_{k,j} x_k(n)$$

Si $k \in H_Q$:

$$x_k(n+1) = x_k(n) + a_k(n) + \sum_{j \in H_{D,R}} \alpha_{j,k} x_j(n) - \sum_{i \in F} g_{ui}(n) f_{i,max}$$

3. CASE STUDY

An isolated urban intersection, is taken as example for applying the GPC. The prediction model used in the GPC strategy will be the MMQN.

3.1 Case study definition

It is a scenario of an isolated intersection composed by four links $O1a, O2a, O3a$ and $Oa4$ that intersect at the point as shown in Figure 1. In each link, the vehicles have two intentions of rotation: right turn and circulation in a straight line trajectory.

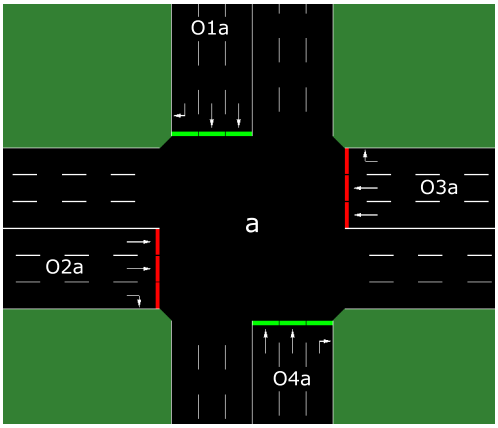

Fig. 1. Isolated intersection view from SUMO

In this intersection, vehicles can arrive from any street and they can also turn in the direction according to the phases configuration show on Figure 2.

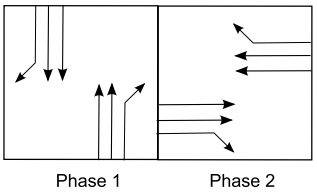

Fig. 2. Phases for an isolated intersection

As shown in equation 1, the duration of phase 2, $g_{u2}(n)$ is the complement of the duration of phase 1, $g_{u1}(n)$ to complete the total cycle time cd.

$$g_{u2}(n) = cd - g_{u1}(n) \tag{1}$$

The equations representing the model of the intersection using MMQM are presented below:

$$x_1(n+1) = x_1(n) + a_1(n) - \alpha_{1,5} x_1(n) \tag{2}$$

$$x_5(n+1) = x_5(n) + \alpha_{1,5} x_1(n) - \alpha_{5,9} x_5(n) - ... - \alpha_{5,10} x_5(n) - \alpha_{5,11} x_5(n) \tag{3}$$

$$x_9(n+1) = x_9(n) + \alpha_{5,9} x_5(n) - g_{u_1}(n) f_1$$

$$x_{10}(n+1) = x_{10}(n) + \alpha_{5,10} x_5(n) - g_{u_1}(n) f_1$$

$$x_{11}(n+1) = x_{11}(n) + \alpha_{5,11} x_5(n) - g_{u_1}(n) f_1$$

$$x_2(n+1) = x_2(n) + a_2(n) - \alpha_{2,6}x_2(n) \quad (4)$$

$$x_6(n+1) = x_6(n) + \alpha_{2,6}x_2(n) - \alpha_{6,12}x_6(n) - ... - \alpha_{6,13}x_6(n) - \alpha_{6,14}x_6(n) \quad (5)$$

$$x_{12}(n+1) = x_{12}(n) + \alpha_{6,12}x_6(n) - g_{u_2}(n)f_2$$
$$x_{13}(n+1) = x_{13}(n) + \alpha_{6,13}x_6(n) - g_{u_2}(n)f_2$$
$$x_{14}(n+1) = x_{14}(n) + \alpha_{6,14}x_6(n) - g_{u_2}(n)f_2$$

$$x_3(n+1) = x_3(n) + a_3(n) - \alpha_{3,7}x_3(n) \quad (6)$$

$$x_7(n+1) = x_7(n) + \alpha_{3,7}x_3(n) - \alpha_{7,15}x_7(n) - ... - \alpha_{7,16}x_7(n) - \alpha_{7,17}x_7(n) \quad (7)$$

$$x_{15}(n+1) = x_{15}(n) + \alpha_{7,15}x_7(n) - g_{u_2}(n)f_3$$
$$x_{16}(n+1) = x_{16}(n) + \alpha_{7,16}x_7(n) - g_{u_2}(n)f_3$$
$$x_{17}(n+1) = x_{17}(n) + \alpha_{7,17}x_7(n) - g_{u_2}(n)f_3$$

$$x_4(n+1) = x_4(n) + a_4(n) - \alpha_{4,8}x_4(n) \quad (8)$$

$$x_8(n+1) = x_8(n) + \alpha_{4,8}x_4(n) - \alpha_{8,18}x_8(n) - ... - \alpha_{8,19}x_8(n) - \alpha_{8,20}x_8(n) \quad (9)$$

$$x_{18}(n+1) = x_{18}(n) + \alpha_{8,18}x_8(n) - g_{u_1}(n)f_4$$
$$x_{19}(n+1) = x_{19}(n) + \alpha_{8,19}x_8(n) - g_{u_1}(n)f_4$$
$$x_{20}(n+1) = x_{20}(n) + \alpha_{8,20}x_8(n) - g_{u_1}(n)f_4$$

3.2 Experimental set up

The controlled signal for the MMQM model and SUMO was $g_1(n)$ and the total light cycle was set to a constant value $cd = 60[s]$. The input vehicle demand was considered as a disturbance (in this case known) for estimating the parameters. The inputs were chosen in order to avoid saturating the intersection. Additionally, the cumulative sum of the vehicles entering each link, for one hour (3600 seconds) is as follows.

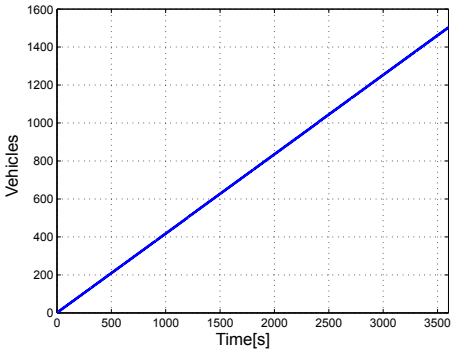

Fig. 3. Input demand

Table 1 shows a constant flow of vehicles entering each lane of each link.

Table 1. Input demand vehicles

Link	Input flow [veh/h]
o1a	500
o2a	300
o3a	400
o4a	400

3.3 Parameter estimation

The parameter identification was done using the Parameter Estimation Toolbox from Simulink, which performs the estimation through optimization procedures based on input/output data. The identified parameters were $f_{i,max}$ in this case $f1, f2, f3, f4$ related with the maximum output flow of vehicles that can cross from one link to another through the intersection. They depend directly on the input demand of vehicles $a_i(n)$ of each link and must take nonnegative values. The parameters $\alpha_{1,5}, \alpha_{2,6}, \alpha_{3,7}, \alpha_{4,8}, \alpha_{5,9}, \alpha_{5,10}, \alpha_{5,11}, \alpha_{6,12}, \alpha_{6,13}, \alpha_{6,14}, \alpha_{7,15}, \alpha_{7,16}$ $\alpha_{7,17}, \alpha_{8,18}, \alpha_{8,19}, \alpha_{8,20}$ are not estimated, they are assumed to be a constant and balanced for a distribution of vehicles on each turning direction.

An input signal was designed in such a way that the green light time changes in an interval between 10 and 50 seconds to ensure that a cycle time (60 seconds) contains both phases. The identified parameters are shown in Table 2

Table 2. Parameter estimation

Parameter	Value
f_1	0.0072
f_2	0.0046
f_3	0.0053
f_4	0.0067

Figure 4 shows the comparison between the MMCM model and the SUMO data when the input signal is applied. Both respond to the control signal, decreasing the vehicles accumulation when the green light time increases and vice-versa. It can also be noticed that the model trend fits the SUMO data.

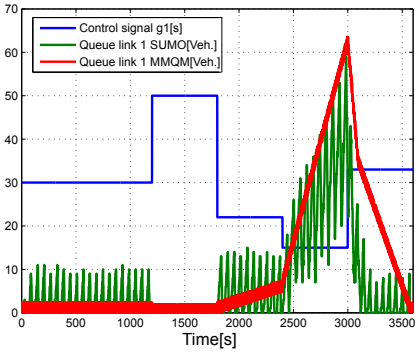

(a) Phase 1 comparison

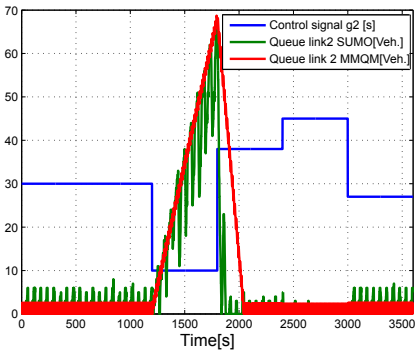

(b) Phase 2 comparison

Fig. 4. Comparison: estimated parameters - SUMO - control action

3.4 State estimator

A Kalman filter based estimator was designed using the extended model described in equations (Kalman, 1960). This model includes an integral action for representing the uncertainties in the system.

$$\begin{aligned} x(n+1) &= Ax(n) + Bu(n) + Gw(n) + B_d d(n) \\ y(n) &= Cx(n) + v(n) \\ d(n+1) &= d(n) + B_{w_d} w_d(n) \end{aligned} \tag{10}$$

The terms G_w and V_n corresponds to the process and measurement noise, respectively, d_n is included for tracking purposes. For the filter design the system is written as follows:

$$\begin{bmatrix} x(n+1) \\ d(n+1) \end{bmatrix} = \begin{bmatrix} A & B_d \\ 0 & I \end{bmatrix} \begin{bmatrix} x(n) \\ d(n) \end{bmatrix} + \begin{bmatrix} B \\ 0 \end{bmatrix} u(n) + \begin{bmatrix} G & 0 \\ 0 & B_{w_d} \end{bmatrix} \begin{bmatrix} w(n) \\ w_d(n) \end{bmatrix} \tag{11}$$

$$y(n) = [C \;\; 0] \begin{bmatrix} x(n) \\ d(n) \end{bmatrix} + v(n)$$

Covariance matrices tuned to design the filter were $Qn = 10^5 I$ y $Rn = 10I$, $Bd = B$. Finally, the state observer is:

$$\begin{bmatrix} \hat{x}(n+1) \\ \hat{d}(n+1) \end{bmatrix} = \begin{bmatrix} A & B_d \\ 0 & I \end{bmatrix} \begin{bmatrix} \hat{x}(n) \\ \hat{d}(n) \end{bmatrix} + \begin{bmatrix} B \\ 0 \end{bmatrix} u(n) + L\left(y - [C \;\; 0] \begin{bmatrix} \hat{x}(n) \\ \hat{d}(n) \end{bmatrix} \right) \tag{12}$$

3.5 Generalized Predictive Control (GPC)

This section provides a Generalized Predictive Control with prediction horizon $N_p = 10$ for tracking references. The objective function is described as follows (explained in *section 3.3*):

$$\min_U \sum_{j=1}^{N} ||y(n+j) - y_{ref}||_Q^2 + \sum_{j=0}^{N} ||u(n+j)||_R^2 \tag{13}$$

Subject to:

$$\begin{aligned} & x(n+j+1) = Ax(n+j) + Bu(n+j) \\ & y(n+j) = Cx(n+j) \\ & 10 \leq u_i(n+j) \leq 50 \;\; \forall j = 1, ..., N \\ & 0 \leq y_i(n+j) \leq 44 \;\; \forall j = 1, ..., N \\ & u_1(n+j) + u_2(n+j) = 60 \;\; \forall j = 1, ..., N \end{aligned}$$

The aim is to have the minimum queue length, thus the reference signal is set to zero (no queue). The constraints denote minimum and maximum values for the phase duration u_i. The sum of phase durations is the total cycle time (60s), the maximum and minimum values of queue length y_i based on link the capacity and the variables are subject to the MMQN model.

4. SIMULATION RESULTS

The obtained queue length of each link with $y_{ref} = 0$ and constant input demands are shown in following figures:

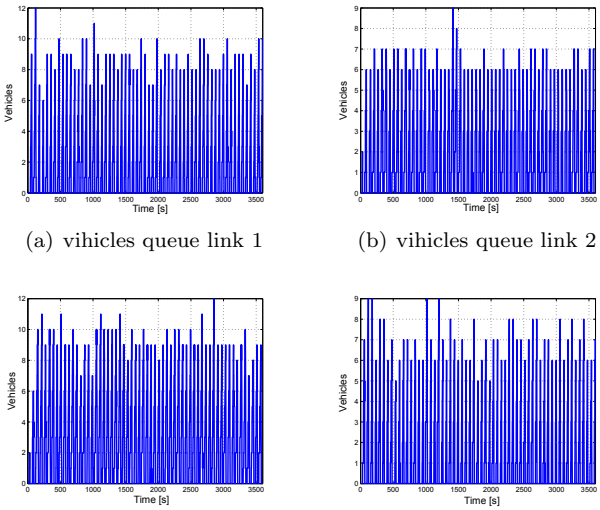

(a) vihicles queue link 1 (b) vihicles queue link 2

(c) vihicles queue link 3 (d) vihicles queue link 4

Fig. 5. Queue length with constant demand

It is noted how vehicles leaves the links every traffic light cycle, and they are not accumulated to form congestion. Also, the controller gives priority to higher demand phase, in this case Phase 1, and varies the control signal (green timing)to maintain the network balance, as shows 6.

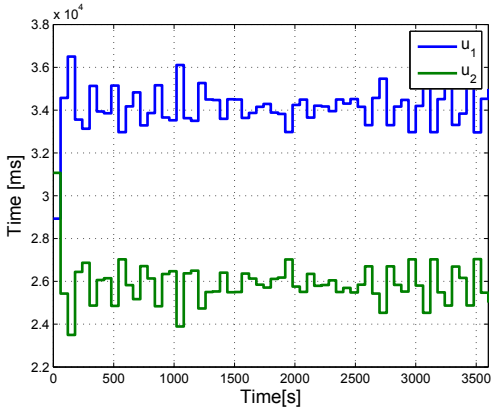

Fig. 6. GPC control signal with constant demand

In order to test the response of the GPC controller in another situation, a change on the input demand was tested. The constant input changes to variable demand in the middle of the simulation time, $t = 1800s$. Thus, figure 7 shows how the controller is looking for keeping the network balance by reducing the green time of Phase 1.

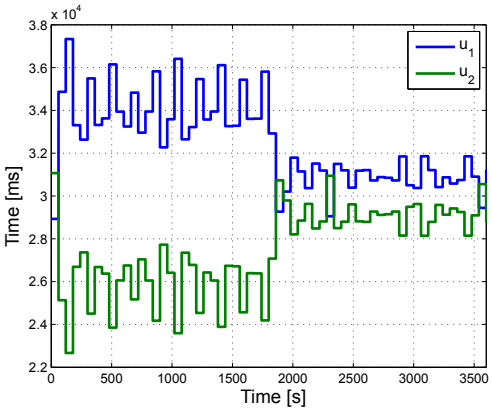

Fig. 7. GPS control signal with variable demand

4.1 Reference change

In this subsection a change of variable reference for the link 2 of phase 2 was applied, the rest of links have zero reference throughout simulation time.

According to Figure 8, it is observed how the length of the queues follows the reference, changing the value from 0 to 18 vehicles in the link 2. However, the queues do not reach the reference value due to the nature of the system, since the simulated demand is not sufficient to accumulate the desired value.

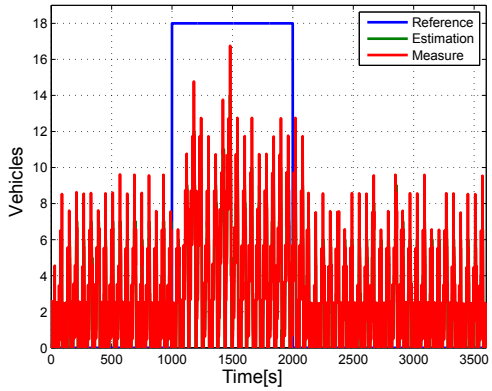

Fig. 8. Vehicles in the queue link 2 reference exchange

In Figure 9, it is observed that the time interval in Green of Phase 2 decreases in order to achieve the reference.

5. CONCLUSION

Optimal controllers are subject to covariance matrices that define the weights to give importance to some control objectives over others. Therefore the tuning of these matrices is a critical part in the design of these controllers. If the value of the R matrix is very big the controller does not respond to significant changes in demand, because the control variable is strongly penalized.

The total number of vehicles waiting at the interaction during simulation, compared between strategies fixed time and GPC, as shown in the Table 3

The GPC controller has cumulated 695 vehicles less at the intersection compared with to the fix time control strategy.

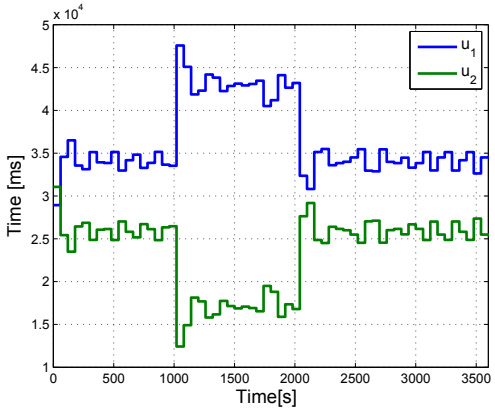

Fig. 9. GPC control signal reference exchange

Table 3. Comparison of strategies

Controller	Value
Fixed Time	29103
GPC	28408

The level of service at the intersection improved by about 3%, also the GPC controller responded satisfactorily to changes in the demand.

ACKNOWLEDGEMENTS

Research supported by COLCIENCIAS project: Modelamiento y control de tráfico urbano en la ciudad de Medellín etapa 2, código 1118-669-45309, CT 202-2015. Universidad Nacional de Colombia Proyecto HERMES 25374

REFERENCES

Daganzo, C.F. (1995). Requiem for second-order fluid approximations of traffic flow. *Transportation Research Part B*, 29(4), 277–286.

Kalman, R. (1960). A new approach to linear filtering and prediction problems. *Journal of basic Engineering*, 82(1), 35–45.

Krajzewicz, D., Erdmann, J., Behrisch, M., and Bieker, L. (2012). Recent Development and Applications of {SUMO - Simulation of Urban MObility}. *International Journal On Advances in Systems and Measurements*, 5(3), 128–138.

Le, T., Vu, H.L., Nazarathy, Y., Vo, Q.B., and Hoogendoorn, S. (2013). Linear-quadratic model predictive control for urban traffic networks. *Transportation Research Part C: Emerging Technologies*, 36, 498–512.

Lighthill, M.J. and Whitham, G.B. (1955). On Kinematic Waves. II. A Theory of Traffic Flow on Long Crowded Roads. *Proceedings of the Royal Society A: Mathematical, Physical and Engineering Sciences*, 229(1178), 317–345.

Norena, L., Sarrazola, A., Jim, E., Jaramillo, O., Portilla, C., Alejandro, M., and Espinosa, J. (2015). Model Predictive Control of an Urban Traffic Intersection Based on the Modified Multi-class Queuing Networks Models. 1–4.

Papageorgiou, M., Kiakaki, C., Dinopoulou, V., and Kotsialos, a. (2003). Review of road traffic control strategies. *Proceedings of the IEEE*, 91(12), 2043–2067.

Yang, J., Zhang, L., and Chen, Y. (2010). Modeling and control of signaling split in urban traffic network based on hybrid systems. *2010 Sixth International Conference on Natural Computation*, (Icnc), 3497–3502.

Nonlinear Model Predictive Control of a Passenger Vehicle for Lane Changes Considering Vehicles in the Target Lane

Andrés F. Acosta * **Alejandro Márquez** ** **Jairo Espinosa** ***

* *Universidad Nacional de Colombia, Medellín, Colombia (e-mail: afacostag@unal.edu.co).*
** *Universidad Nacional de Colombia, Medellín, Colombia (e-mail: amarque@unal.edu.co)*
*** *Universidad Nacional de Colombia, Medellín, Colombia (e-mail: jespinov@unal.edu.co)*

Abstract: This article presents a Nonlinear Model Predictive Control (MPC) for controlling the lateral dynamics of a passenger vehicle, based on a planar Single Track Model. This MPC controller is aimed at tracking suitable reference values on its states in order to achieve a lane change manoeuvre. Simulation results are showed for an scenario with a single vehicle and another scenario with two vehicles in the target lane, for different initial conditions that validate the proposed nonlinear MPC.

Keywords: Model-based control, Nonlinear control, Optimal control, Predictive control, Automated guided vehicles, Automotive control, Vehicle dynamics.

1. INTRODUCTION

Road traffic modelling and control play an important role for improving safety. Particularly, it has been found that lane changes are an important cause of accidents (Sen et al., 2003). In the last decades, some advancements in technologies such as computer vision and instrumented vehicles allowed applications known as Advanced Driving Assistance Systems (ADAS), including Adaptive Cruise Control (ACC) (Bifulco et al., 2013), lane keeping systems and parking assistance systems. Moreover, modelling and control of vehicle dynamics can help to improve microscopic traffic models. For example, it has been found that existing lane-change models focus on the decision making and gap acceptance models, but little attention has been paid to modelling the execution of the manoeuvre and the heterogeneity of drivers and vehicles (Toledo, 2007; Zheng, 2014).

Models that describe the dynamic behaviour of vehicles based in their physical characteristics such as dimensions, power-to-weight ratio and inertial parameters, among others, and input variables including the steering angle, the position of the accelerator and the braking pedal, sometimes also known as submicroscopic models (Maerivoet and De Moor, 2005), are models that, in general, comprise a phenomenological and an empirical component. The former is derived from the fundamental laws of moment conservation while the later is mainly focused in the modelling of the interaction forces between the tires and the road surface, due to the complexity of the structure of the tires. Among the vehicle dynamic models, one of the most common because of its simplicity and representativeness of lateral dynamics is the Single Track Model (STM), which has been successful used in vehicle control systems, including steering and acceleration control, in applications such as reference trajectory generation and tracking (Gerdts et al., 2009; Falcone et al., 2007), obstacle avoidance (Park et al., 2009) and stabilization (Guvenc et al., 2009).

This article presents a Nonlinear Model Predictive Control (MPC) of a passenger vehicle, based on a planar Single Track Model (STM), aimed at tracking suitable reference values on one of its states in order to achieve a lane change maneuver. Furthermore, two simulation cases are presented: one without the influence of vehicles in the target lane, and another that includes two vehicles in the target lane. Additionally, different initial conditions are tested in order to demonstrate the effectiveness of the proposed MPC.

This article is organized, as follows: Section 2 describes the nonlinear Single Track Model that serves as a basis for the MPC controller design. Section 3 presents the nonlinear MPC problem with reference tracking for lane changes. Section 4 shows simulation results obtained for a single vehicle. In section 5, the presence of vehicles in the target lane is considered. Section 6 shows simulation results obtained with the inclusion of vehicles in the target lane. Finally, section 7 presents the conclusions.

2. NONLINEAR SINGLE TRACK MODEL

The nonlinear vehicle model considered in this work is obtained from the linear Single Track Model (STM) found in (Rajamani, 2011) by incorporating two additional states that correspond to the position of the vehicle in global coordinates (Falcone et al., 2007). An schematic of the single track model is showed in figure 1. The STM describes the dynamics of the vehicle under the lateral forces acting on

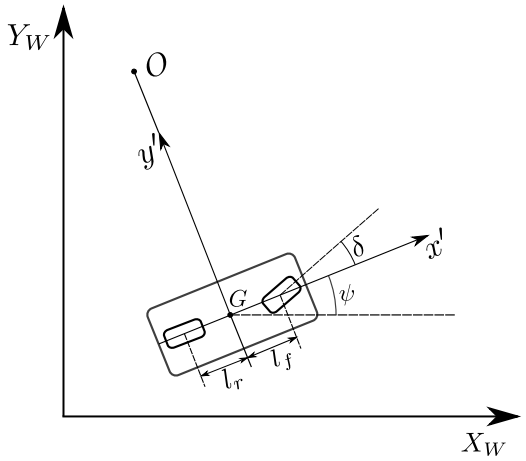

Fig. 1. The Single Track Model

it, considering a local reference frame whose coordinates are given by $[x', y']$.

This STM assumes that the longitudinal velocity of the vehicle is constant. Hence, the unidimensional input of the STM is the front wheel steering angle δ, and the states are given by $x = [y', \psi, \dot{y'}, \dot{\psi}, Y_W, X_W]^T$, being y' the lateral position of the vehicle to the instantaneous turning center O, ψ, its orientation angle and Y_W, X_W the position of the vehicle in global coordinates. The STM is described by the following dynamic equations:

$$\begin{aligned}
\ddot{y'} =& -\frac{2C_{\alpha f} + 2C_{\alpha r}}{m\dot{x'}}\dot{y'} \\
& - \left(\dot{x'} + \frac{2C_{\alpha f}l_f - 2C_{\alpha r}l_r}{m\dot{x'}}\right)\dot{\psi} + \frac{2C_{\alpha f}}{m}\delta \\
\ddot{\psi} =& -\frac{2l_fC_{\alpha f} - 2l_rC_{\alpha r}}{I_z\dot{x'}}\dot{y'} - \frac{2l_f^2C_{\alpha f} + 2l_r^2C_{\alpha r}}{I_z\dot{x'}}\dot{\psi} \\
& + \frac{2l_fC_{\alpha r}}{I_z}\delta \\
\dot{Y}_W =& \dot{x'}\sin(\psi) + \dot{y'}\cos(\psi) \\
\dot{X}_W =& \dot{x'}\cos(\psi) - \dot{y'}\sin(\psi)
\end{aligned} \quad (1)$$

where:

- m is the vehicle's mass.
- $\dot{x'}$ is the vehicle's velocity in direction of its longitudinal axis, assumed constant.
- I_z is the vehicle's yaw moment of inertia.
- l_f, l_r are the distances from the vehicle's center of mass G to its front and rear wheels, respectively.
- $C_{\alpha f}, C_{\alpha r}$ are the cornering stiffness for the front and rear wheels, respectively.

The set of equations (1) defines the nonlinear model $\dot{x} = f(x, u)$ to be used in the MPC controller. It is worth to note that small tire slip angles are assumed. Hence, the wheel's lateral forces acting on the vehicle can be considered as linear functions of the corresponding slip angles, with the cornering stiffness acting as the relating proportionality constant. The slip angle is defined as the angle between the velocity vector acting on the tire and its orientation. Moreover, small angle approximations are made in regard to the vehicle's slip angle, defined as the angle between the longitudinal axis of the vehicle and its velocity vector.

3. NONLINEAR MPC PROBLEM FORMULATION FOR LANE CHANGES

For controlling the lateral dynamics of the vehicle while tracking a reference for changing a lane with nonlinear MPC can be formulated, as follows:

$$\min_{u(k+1),\ldots,u(k+N)} \sum_{j=1}^{N} ||y_{ref} - y(k+j)||_Q^2 + ||u(k+j)||_R^2 \quad (2)$$

Subject to:

$$x(k+j+1) = f(x(k+j), u(k+j)) \quad (3)$$
$$y(k+j) = Y_W(k+j) \quad (4)$$
$$|u(k+j)| \leq u_{max} \ \ \forall j = 1, ..., N \quad (5)$$
$$|\Delta u(k+j)| \leq \Delta u_{max} \ \ \forall j = 1, ..., N \quad (6)$$

From the objective function (2), N is the prediction horizon given in number of samples and Q and R are the tuning matrices of the MPC controller. The model constraint (3) is obtained by discretizing the STM, given by the set of equations (1). It is assumed that the global coordinate Y_W of the vehicle can be measured, as stated in constraint (4). Finally, the operative constraints (5) and (6) give the maximum and minimum values for the front wheel steering angle and its maximum rate of change.

Parameter	Value	Units
m	1573	Kg
I_z	2873	Kg · m^2
l_f	1.10	m
l_r	1.58	m
C_{af}	80000	N · m/rad
C_{ar}	80000	N · m/rad
$\dot{x'}$	5.56	m/s
T_s	0.05	s
N	100	-
δ_{min}	-0.17	rad
δ_{max}	0.17	rad
$\Delta\delta_{max}$	1.5	rad/s

Table 1. Simulation parameters

4. SIMULATION RESULTS FOR A SINGLE VEHICLE

The MPC controller presented in section 3 has been tested in simulation using Matlab® and Simulink, based on the parameters found in Table 1. The parameters related to the vehicle are the same used by (Rajamani, 2011), and correspond to a passenger sedan. Satisfactory results were obtained with a sample time $T_s = 0.5$, though $T_s = 0.05$ could have been used, as in (Anderson et al., 2010), where real experiments have been made. The prediction horizon was chosen as $N = 10$, since the interest is on modelling lane changes. This value corresponds to 5s, and can be regarded as the approximate maximum duration of a lane change, according to (Toledo and Zohar, 2015). Finally, the, δ_{min}, δ_{max} and $\Delta\delta_{max}$ restrictions values have been taken from (Anderson et al., 2010) and (Falcone et al., 2007).

Figure 2 shows the trajectory obtained with the proposed MPC. A reference value of 3.3m in the Y_W state was set,

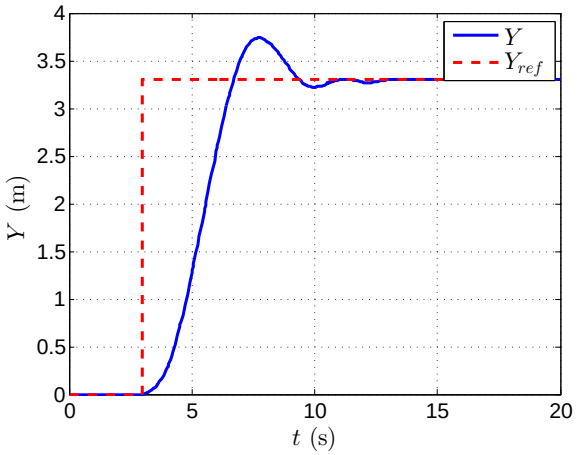

Fig. 2. Simulation results for the single vehicle scenario, showing the obtained trajectory

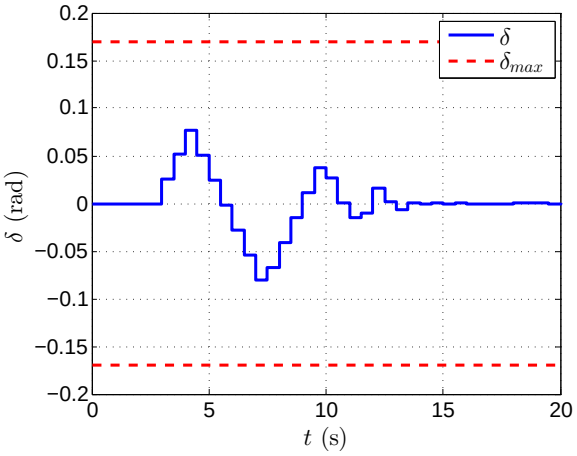

Fig. 3. Simulation results for the single vehicle scenario, showing the front wheel steering angle

which can be taken as the approximate distance between the center of two lanes. Figures 3 and 4 show the control action calculated by the MPC, its rate of change and the corresponding constraints.

5. INCLUDING VEHICLES IN THE TARGET LANE

Consider a scenario with one vehicle that wants to execute a lane change (called "subject vehicle", from now), identified with the superscript p, and vehicles in the target lane identified with the superscripts $p-1$ and $p+1$ as showed in figure 5. An additional constraint is required to prevent the subject vehicle to collision with the vehicles in the target lane, which can be defined, as follows. Let:

$$\mathbf{r_W^p}(k+j) = [X_W^p(k+j), Y_W^p(k+j)]^T \quad (7)$$

$$\mathbf{r_W^q}(k+j) = [X_W^q(k+j), Y_W^q(k+j)]^T \quad (8)$$

With $p \neq q$. Then:

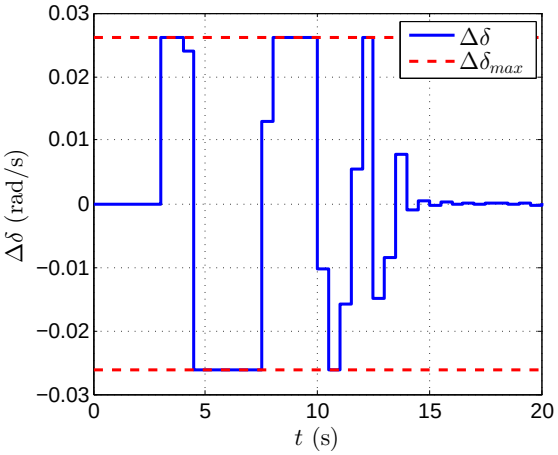

Fig. 4. Simulation results for the single vehicle scenario, showing the rate of change of the front wheel steering angle

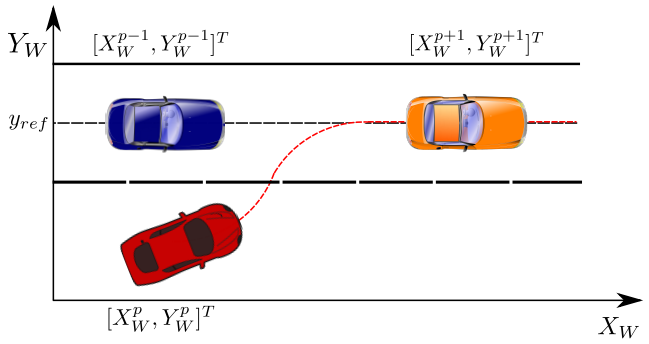

Fig. 5. Notation for the position of vehicles involved in a lane change

$$d_{p,q}(k+j) \geq d_{safe}, \forall j = 1, ..., N \quad (9)$$

With:

$$d_{p,q}(k+j) = \|\mathbf{r_W^p}(k+j) - \mathbf{r_W^q}(k+j)\| \quad (10)$$

Equations (9) and (10) state that the euclidean distance between the subject vehicle and the vehicles in the target lane must be greater than a given safety distance d_{safe}. Note that this approach assumes that the subject vehicle knows the position of those in the target lane, which could be achieved with technologies such as vehicular communications, DGPS and computer vision. Another interesting aspect is that the subject vehicle should accurately predict the position of vehicles in the target lane within the prediction horizon, which could be achieved through one of the many well-known car-following models (Li and Sun, 2012).

6. SIMULATION RESULTS CONSIDERING VEHICLES IN THE TARGET LANE

The strategy for incorporating vehicles in the target lane was tested in Matlab® and Simulink taking into account the same parameters of Table 1. The prediction of the position of vehicles in the target lane was simplified by assuming that they move at a constant speed of 5.56 m/s (20 km/h) in free flow conditions, i.e. they do not interact with each other. Additionally, the safe distance was chosen

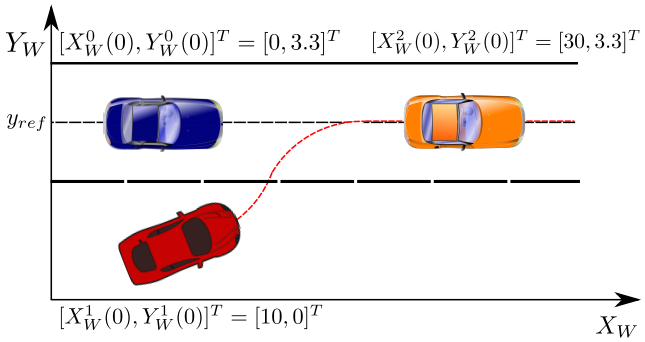

Fig. 6. Initial conditions for the simulation scenario that incorporates vehicles in the target lane

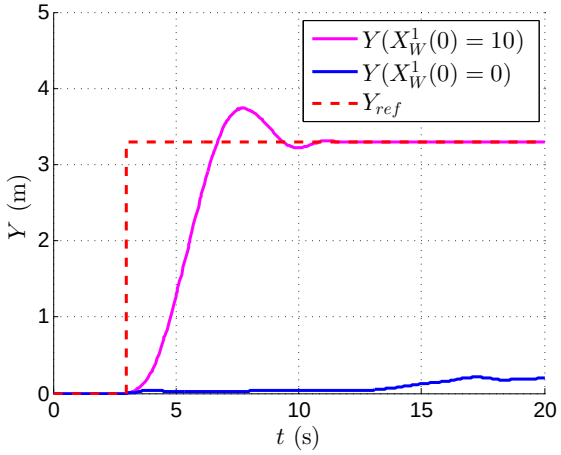

Fig. 7. Simulation results for the scenario that includes vehicles in the target lane, showing the obtained trajectory of the subject vehicle

as $d_{safe} = 2.5\,\text{m}$. Finally, the initial conditions for the simulation are showed in figure 6.

Figure 7 shows trajectories obtained for two cases: one with the initial conditions showed in figure 6, and another changing the initial condition of the subject vehicle to $[X_W^1(0), Y_W^1(0)]^T = [0, 0]^T$. In the second case note that, because the vehicle is moving at a constant speed, the initial condition does not allow it to execute the lane change, despite the MPC outputs some tries, as showed in Figure 8. Furthermore, a simulation of the second case disabling the distance constraint given in equation (9) was performed to show that this constraint is not met with one of the vehicles in the target lane, as showed in figure 9.

7. CONCLUSIONS

In this article, a nonlinear Model Predictive Control (MPC) of a passenger vehicle aimed for lane changes was presented. This MPC is based on a simplified Single Track Model (STM), including two states that describe the position of the vehicle in a global coordinate system, so that proper reference values can be tracked in order to execute the lane change maneuver. The effectiveness of the proposed MPC could be validated in simulation. Furthermore, an additional constraint was included in order to consider the influence of vehicles in the target

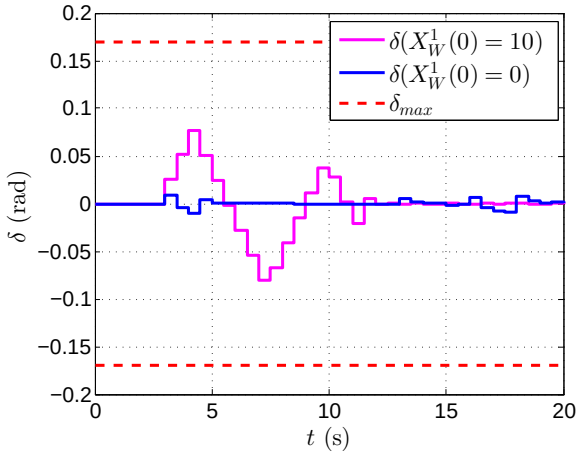

Fig. 8. Simulation results for the scenario that includes vehicles in the target lane, showing the obtained front wheel steering angle of the subject vehicle

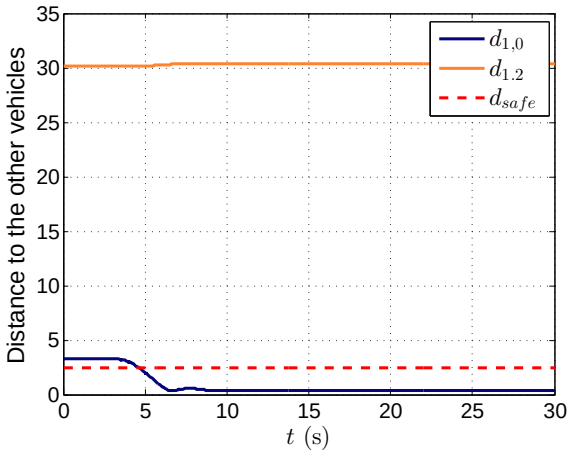

Fig. 9. Distance with vehicles in the target lane disabling the safe distance constraint

lane. Several simulations were performed to validate this strategy.

ACKNOWLEDGEMENTS

Authors would like to thank Proyecto Colciencias 111856 934640 contrato - FP44842-202-2015: Modelamiento y Control de tráfico urbano en la ciudad de Medellín Fase 2. Convocatoria 669.

REFERENCES

Anderson, S.J., Peters, S.C., Pilutti, T.E., and Iagnemma, K. (2010). An optimal-control-based framework for trajectory planning, threat assessment, and semi-autonomous control of passenger vehicles in hazard avoidance scenarios. *International Journal of Vehicle Autonomous Systems*, 8(2), 190–216.

Bifulco, G.N., Pariota, L., Simonelli, F., and Di Pace, R. (2013). Development and testing of a fully Adaptive Cruise Control system. *Transportation Research Part C: Emerging Technologies*, 29, 156–170. doi: 10.1016/j.trc.2011.07.001.

Falcone, P., Borrelli, F., Asgari, J., Tseng, H., and Hrovat, D. (2007). Predictive Active Steering Control for Autonomous Vehicle Systems. *IEEE Transactions on Control Systems Technology*, 15(3), 566–580. doi: 10.1109/TCST.2007.894653.

Gerdts, M., Karrenberg, S., Müller-Beßler, B., and Stock, G. (2009). Generating locally optimal trajectories for an automatically driven car. *Optimization and Engineering*, 10(4), 439–463.

Guvenc, B.A., Güvenç, B.A., and Karaman, S. (2009). Robust yaw stability controller design and hardware-in-the-loop testing for a road vehicle. *Vehicular Technology, IEEE Transactions on*, 58(2), 555–571.

Li, Y. and Sun, D. (2012). Microscopic car-following model for the traffic flow: the state of the art. *Journal of Control Theory and Applications*, 10(2), 133–143.

Maerivoet, S. and De Moor, B. (2005). Transportation planning and traffic flow models. *arXiv preprint physics/0507127*. URL `http://arxiv.org/abs/physics/0507127`.

Park, J.M., Kim, D.W., Yoon, Y.S., Kim, H.J., and Yi, K.S. (2009). Obstacle avoidance of autonomous vehicles based on model predictive control. *Proceedings of the Institution of Mechanical Engineers, Part D: Journal of Automobile Engineering*, 223(12), 1499–1516.

Rajamani, R. (2011). *Vehicle dynamics and control*. Springer Science & Business Media.

Sen, B., Smith, J.D., and Najm, W.G. (2003). Analysis of lane change crashes. Technical report.

Toledo, T. (2007). Driving behaviour: models and challenges. *Transport Reviews*, 27(1), 65–84.

Toledo, T. and Zohar, D. (2015). Modeling duration of lane changes. *Transportation Research Record: Journal of the Transportation Research Board*.

Zheng, Z. (2014). Recent developments and research needs in modeling lane changing. *Transportation research part B: methodological*, 60, 16–32.

Para la Escuela de Ciencias y el Departamento de Ciencias Matemáticas de la Universidad EAFIT es un orgullo ser los organizadores del XVII Congreso Latinoamericano de Control Automático, consolidando nuestro propósito de permanecer abiertos al mundo y cumplir con nuestra premisa de Inspirar, Crear y Transformar.

El área del Control Automático ha sido un prominente campo de estudio desde hace varios años que logra, mediante el desarrollo de métodos formales matemáticamente, impactar la sociedad mediante sus aplicaciones.

Durante la conferencia, se tuvieron cinco (5) cursos teóricos y prácticos: “Control Basado en Algebra Lineal”, “Control of Microgrid Power Networks”, “Asimilación de Datos, Predictive control and population games with engineering applications” y “Training of Dynamic Neural and Fuzzy-Neural Networks for Modeling and Control of Nonlinear Dynamic Systems”.

Igualmente, se tuvo tres Conferencias Magistrales con la presencia de investigadores como Arnold Heemink (Países Bajos), Carlos Canudas de Wit (Francia) y Oscar Camacho (Venezuela-Ecuador), en temas como Asimilacion de Datos, Control de tráfico y Control por modos deslizantes, respectivamente.

Este libro es el resultado de trabajos teóricos y aplicados que responden a las necesidades de Latinoamérica y que representan áreas se siguen estudiando en otros lugares del mundo. Esperamos que su contenido, presentado en tres idiomas y con contribuciones de Argentina, Brasil, Bélgica, Colombia, Ecuador, España, Francia, México, Perú y Venezuela, sean de utilidad para su proceso académico e investigativo.

Estos trabajos representan los resultados de las contribuciones, en algunos casos preliminares, de nuestro campo del conocimiento.

UNIVERSIDAD EAFIT®